

THE INTERNATIONAL ARCHIVES OF THE PHOTOGRAMMETRY, REMOTE SENSING AND SPATIAL INFORMATION SCIENCES
ARCHIVES INTERNATIONALES DES SCIENCES DE LA PHOTOGRAMMÉTRIE, DE LA TÉLÉDÉTECTION ET DE L'INFORMATION SPATIALE
INTERNATIONALES ARCHIV FÜR PHOTOGRAMMETRIE, FERNERKUNDUNG UND RAUMBEZOGENE INFORMATIONSWISSENSCHAFTEN

VOLUME
VOLUME
BAND

XXXVIII

PART
TOME
TEIL

7B

ISPRS Technical Commission VII Symposium
100 Years ISPRS
Advancing Remote Sensing Science



1910 - 2010
CENTENARY CELEBRATION VIENNA



Vienna, Austria
July 5 – 7, 2010

Papers accepted on the basis of peer-reviewed abstracts

Editors

W. Wagner, B. Székely

Organised by

ISPRS Technical Commission VII

Thematic Processing, Modeling and Analysis of Remotely Sensed Data

Supported by

Leica Geosystems, Vexcel Imaging, Stadt Wien, ESRI, RIEGL LMS, TU Wien

This compilation © 2010 by the International Society for Photogrammetry and Remote Sensing. Reproduction of this volume or any parts thereof (excluding short quotations for the use in the preparation of reviews and technical and scientific papers) may be made only after obtaining the specific approval of the publisher. The papers appearing in this volume reflect the authors' opinions. Their inclusion in this publication does not necessarily constitute endorsement by the editors or by the publisher. Authors retain all rights to individual papers.

Credits

Technical Editing: Alexandra von Beringe, Peter Doringner, Sebastian Flöry, Josef Jansa, Clemens Nothegger, Norbert Pfeifer, Andreas Roncat

using L^AT_EX's confproc class (by V. Verfaillie)

Cover Illustration: Gregor Franzen

Printed by: Buchdruckerei Ernst Becvar Ges.mbH, Vienna, Austria

Published by

Institute of Photogrammetry and Remote Sensing, Vienna University of Technology

on behalf of

ISPRS Technical Commission VII *Thematic Processing, Modeling and Analysis of Remotely Sensed Data*

Cooperating ISPRS Working Groups

- WG VII/1 *Physical Modelling and Signatures in Remote Sensing*
- WG VII/2 *SAR Interferometry*
- WG VII/3 *Information Extraction from Hyperspectral Data*
- WG VII/4 *Methods for Land Cover Classification*
- WG VII/5 *Methods for Change Detection and Process Modelling*
- WG VII/6 *Remote Sensing Data Fusion*
- WG VII/7 *Theory and Experiments in Radar and Lidar*
- ICWG III/VII *Pattern Recognition in Remote Sensing*

ISPRS Headquarters 2008-2012

c/o CHEN JUN, ISPRS Secretary General

National Geomatics Centre of China

No. 1 Baishengcun, Zizhuyuan

Beijing 100048, PR CHINA

Tel: +86 10 6842 4072

Fax: +86 10 6842 4101

Email: chenjun@nsdi.gov.cn; chenjun_isprs@263.net

ISPRS WEB Homepage: <http://www.isprs.org>

Available from

GITC bv

P.O.Box 112

8530 AC Lemmer

The Netherlands

Tel: +31 (0) 514 56 18 54

Fax: +31 (0) 514 56 38 98

E-mail: mailbox@gitc.nl

Website: www.gitc.nl

Table of Contents

Preface	xii
Symposium Committee	xiv
Reviewers	xv
 Papers	
Spectral reflectance of rice canopy and red edge position (REP) as indicator of high-yielding variety <i>Mozhgan Abbasi, Ali A. Darvishsefat, and Michael E. Schaepman</i>	1
Simulated rain rate effects on SAR Interferograms <i>Riadh Abdelfattah, A. Elmezoughi, and Z. Belhadj</i>	6
CANASAT project: monitoring the sugarcane harvest type in the state of São Paulo, Brazil <i>Daniel Alves de Aguiar, Wagner Fernando da Silva, Bernardo Friedrich Theodor Rudorff, and Marcos Adami</i>	10
Remote Sensing for physical Protection of the pipeline network - Online Monitoring of Corridor-Based Infrastructure <i>Mansour Ahmadi Ferooshani, and S. Damadi</i>	16
WinGIS - GIS software for ICT developers <i>Bernhard Aigner, and Walter Mayer</i>	23
Assessment of biophysical structure of riparian zones based on segmentation method, spatial knowledge and texture analysis <i>Thiago Alencar-Silva, and Philippe Maillard</i>	26
The role of remote sensing in fighting against terrorism- A case of Pakistan <i>Ali Asmat</i>	32
Vertical roughness mapping - ALS based classification of the vertical vegetation structure in forested areas <i>Christoph Aubrecht, Bernhard Höfle, Markus Hollaus, Mario Köstl, Klaus Steinmocher, and Wolfgang Wagner</i>	35
Observing stress of artificial night lighting on marine ecosystems - A remote sensing application study <i>Christoph Aubrecht, Chris Elvidge, Daniel Ziskin, Pedro Rodrigues, and Artur Gil</i>	41
Classification of clouds with object oriented technique <i>Hamid Azari, A.A. Matkan, Alireza Shakiba, and H. Pourali</i>	47
PLEIADES-HR imaging system: ground processing and products performances, few months before launch <i>Simon Baillarin, Chantal Panem, Laurent Lebegue, and François Bignalet-Cazalet</i>	51
Small Scale Roughness Effects on Thermal IR Spectra <i>Lee Balick, Iryna Danilina, Alan Gillespie, John Jolin, and A. Mushkin</i>	56
Mapping wetland environments in the Brazilian savannah from high resolution Ikonos image data <i>Ivan Barbosa</i>	62

Land use classification with high resolution satellite radar for estimating the impacts of land use change on the quality of ecosystem services <i>Damian Bargiel, Sylvia Herrmann, Uwe Sörgel, and P. Lohmann</i>	68
The Multi-sensor Land Classification System LCS: Automatic multitemporal land use classification system for multi-resolution data <i>Alan Beccati, Marco Folegani, Sergio D'Elia, Roberto Fabrizi, Stefano Natali, and Luca Vittuari</i>	74
Validation of the reflectance calibration of the ADS40 airborne sensor using ground reflectance measurements <i>Ulrich Beisl, and Muzaffer Adiguzel</i>	80
Accuracy of 3D face recognition frameworks <i>Vitantonio Bevilacqua, Mauro Caprioli, Marco Cortellino, Marco Giannini, Giuseppe Mastronardi, and Vito Santarcangelo</i>	86
Evaluation of a laser Mobile Mapping System for monitoring sandy coasts <i>Maja Bitenc, Roderik Lindenbergh, Kourosh Khoshelham, and Pieter van Waarden</i>	92
Automatic Registration of Air-Borne and Space-Borne Images by Topology Map-Matching with SURF Processor Algorithm <i>Anna Brook, and Eyal Ben-Dor</i>	98
The advantages of boresight effects on the hyperspectral data analysis <i>Anna Brook, and Eyal Ben-Dor</i>	103
Comparing information derived from Global land cover datasets with Landsat imagery for the Huambo province and Guinea-Bissau <i>Ana Cabral, Maria Vasconcelos, and Duarte Oom</i>	107
Application of KOMPSAT II imagery for carbon emission inventory map <i>Eunmi Chang, JR Kim, I.H. Lee, Y.S. Choi, and G.S. Kim</i>	113
Collocation-aided adjustment of heterogeneous models for satellite images <i>Wen-Chi Chang, Liang-Chien Chen, and Tee-Ann Teo</i>	117
Change detection of building models from aerial images and LIDAR data <i>Liang-Chien Chen, Li-Jer Lin, Hong-Kuei Cheng, and Shin-Hui Lee</i>	121
A New Rigorous Sensor Model for Radar Imagery Based on Exterior Orientation Elements <i>Chunquan Cheng, Jixian Zhang, Kazhong Deng, and Li Zhang</i>	127
Passive microwave soil moisture evaluations by ground based measurements in Korea <i>Minha Choi, Hyun Woo Kim, Tae Woong Kim, Jae Hyun Ahn, and Y-M. Hur</i>	132
Disaster Monitoring and Management by the Unmanned Aerial Vehicle Technology <i>Tien-Yin Chou, Mei-Ling Yeh, Ying Chih Chen, and Yen Hung Chen</i>	137
Use spectral derivatives for estimating canopy water content <i>Jan Clevers</i>	143
Multitemporal fuzzy Markov chain-based classification of very high resolution images of an urban site <i>Gilson A O P Costa, Raul Q Feitosa, Tessio Novack, and Luiz F G Rego</i>	148
Persistent Scatterer Interferometry based on TerraSAR-X imagery: the Barcelona test area <i>Michele Crosetto, Oriol Monserrat, Maria Cuevas, and Bruho Crippa</i>	154

The Light Fantastic: Using airborne lidar, in archaeological survey <i>Simon Crutchley</i>	160
Hydrological Simulation of Mahanadi River Basin and Impact of land use / land cover change on surface runoff using a macro scale hydrological model <i>VK Dadhwal, SP Aggarwal, and Nidhi Mishra</i>	165
Retrieval of Vegetation Biochemicals Using a Radiative Transfer Model and Hyperspectral data <i>Roshanak Darvishzadeh, Clement Atzberger, Andrew Skidmore, and Martin Schlerf</i>	171
Assessment of the impact of uncertainty on modelled soil surface roughness on SAR-retrieved soil moisture uncertainty <i>Eva De Keyser, Hans Lievens, Hilde Vernieuwe, J. Alvarez-Mozos, Bernard De Baets, and Niko Verhoest</i>	176
Sub-pixel precision image matching for displacement measurement of mass movement using normalised cross-correlation <i>Misganu Debella-Gilo, and Andreas Käib</i>	181
Wireless sensor networks for in-situ image validation for water and nutrient management <i>Rakesh Devadas, Simon Jones, Glenn Fitzgerald, Ian McCauley, Eileen Perry, Brett Matthews, Michelle Watt, Jelle Ferwerda, and Abbas Kouzani</i>	187
Analysis of full-waveform ALS data by simultaneously acquired TLS data: Towards an advanced DTM generation in wooded areas <i>Michael Doneus, Christian Briese, and Nikolaus Studnicka</i>	193
Remote Sensing for Drought Assessment in Arid Regions (A Case Study of Central Part of Iran, "Shirkooh-Yazd") <i>Mohsen Ebrahimi, Ali Akbar Matkan, and Roshanak Darvishzadeh</i>	199
Quality Assessment Of Image fusion Techniques For Multisensor High Resolution Satellite Images (case study: IRS-P5 and IRS-P6 satellite images) <i>Mohammad Fallah Yakhdani, and Ali Azizi</i>	204
Study on user requirements for remote sensing applications in forestry <i>Bernhard Felbermeier, Andreas Hahn, and Tomi Schneider</i>	210
Targeted Change Detection: A Novel Sensor-Independent Partially-Supervised Approach <i>Diego Fernández-Prieto, and Mattia Marconcini</i>	213
NDVI (MODIS sensor) response to interannual variability of rainfall and evapotranspiration in a soybean producing region, southern Brazil <i>Angelica Giarolla, Walter E. Baethgen, and Pietro Ceccato</i>	219
The use of aerospace photographs and remote sensing data in cartography <i>Magsad Gojamanov</i>	225
Monitoring of beaches and sand dunes using digital aerial photography with direct georeferencing <i>Jose Gonçalves, Luisa Bastos, B. Perez, and A. Magalhaes</i>	228
The use of similarity images on multi-sensor automatic image registration <i>Hernâni Gonçalves, José A. Gonçalves, and Luís Corte-Real</i>	233
A method for robust extraction of control points on high-resolution satellite images <i>J. González, Vicente Arévalo, and C. Galindo</i>	239

Airborne Hyperspectral Image Georeferencing aided by High-Resolution Satellite Images <i>Dorota Grejner-Brzezinska, Charles Toth, and Jaehong Oh</i>	243
Tree Species Detection using full waveform LIDAR data in a complex forest <i>Sandeep Gupta, Barbara Koch, and Holger Weinacker</i>	249
Super resolved remote sensing by fusion of multi spectral and spatial data <i>Eran Gur, Zeev Zalevsky, and Bahram Javidi</i>	255
Extracting olivine-rich portions of ultramafic rocks using ASTER TIR data <i>O. Bora Gürçay</i>	259
Active and passive microwave remote sensing of springtime near-surface soil thaw events at middle latitudes <i>Lijian Han, Atsushi Tsunekawa, and Mitsuru Tsubo</i>	265
Stereo radargrammetry in South-East Asia using TerraSAR-X stripmap data <i>Xueyan He, Timo Balz, Lu Zhang, and Mingsheng Liao</i>	270
Automatic Quality Control of Cropland and grasland GIS objects using IKONOS Satellite Imagery <i>Petra Helmholz, Franz Rottensteiner, and Christian Heipke</i>	275
Urban vegetation detection using high density full-waveform airborne LiDAR data - Combination of object-based image and point cloud analysis <i>Bernhard Höfle, and Markus Hollaus</i>	281
Terrain roughness parameters from full-waveform airborne LIDAR data <i>Markus Hollaus, and Bernhard Höfle</i>	287
Recognition of winding displacements for steel coils via laser light section technique <i>Patrick Hölzl, Daniel C. H. Schleicher, and Bernhard G. Zagar</i>	293
An invented approach in image registration “new era in photogrammetry” <i>Amir Saeed Homainejad</i>	299
Farmland parcels extraction based on high resolution remote sensing images <i>Tangao Hu, Wenquan Zhu, and Jinshui Zhang</i>	304
Detection of forest management operations using bi-temporal aerial photographs <i>Pekka Hyvönen, Jaakko Heinonen, and Arto Haara</i>	309
Fusion of Pan and Multispectral Images based on Contourlet Transform <i>Yonghong Jia, and Moyan Xiao</i>	314
The sensitivity of multifrequency (X, C and L-band) radar backscatter signatures to biological variables over corn and soybean fields <i>Xianfeng Jiao, Heather McNairn, Jiali Shang, and Elizabeth Pattey</i>	317
A DBMS-based 3D Topology Model for Laser Radar Simulation <i>Chulmin Jun, and G. Kim</i>	322
Data driven alignment of 3D building models and digital aerial images <i>Jaewook Jung, Costas Armenakis, and Gunho Sohn</i>	327
TerraSAR-X Stereo Digital elevation models for complex terrain conditions in alpine regions and its suitability for orthorectification purposes of optical and SAR imagery <i>Nadine Kiefl, Wolfgang Koppe, and Simon D. Hennig</i>	333

Application of multi-spectral remotely sensed imagery in agriculture <i>Svitlana Kokhan</i>	337
Variation and anisotropy of Reflectance of forest trees in radiometrically calibrated images of an airborne line sensor images – implications to species classification <i>Ilkka Korpela, and Felix Rohrbach</i>	342
High Resolution Imagery Retrieval on the Basis of Sketch-Modelling <i>Nelley M. Kovalevskaya, and K.A. Boenko</i>	348
Geoland2 - Towards an operational GMES Land Monitoring Core Service; First Results of the Biogeophysical Parameter Core Mapping Service <i>Roselyne Lacaze, Gianpaolo Balsamo, Frédéric Baret, Bradley Andrew, Jean-Christophe Calvet, Fernando Camacho, Raphaël D'Andrimont, Pacholczyk Philippe, Bruno Smets, Hervé Poilvé, Kevin Tansey, Isabel Trigo, Wolfgang Wagner, Sandra Freitas, Hassan Makhmara, Vahid Naeimi, and Weiss Marie</i>	354
Radiometric calibration of Full-Waveform Airborne Laser Scanning Data based on natural surfaces <i>Hubert Lehner, and Christian Briese</i>	360
Urban impervious surface extraction from very high resolution imagery by One-Class Support Vector Machine <i>Peijun Li, Haiqing Xu, and Shukun Li</i>	366
Building model reconstruction with LiDAR data and topographic map by registration of building outlines <i>Bo-Cheng Lin, Rey-Jer You, and Man-Chia Hsu</i>	371
Advances on Repeated Space-borne SAR Interferometry and its application to ground deformation monitoring - a review <i>Zhenguo Liu</i>	376
Multiresolution image fusion: Phase congruency for spatial consistency assessment <i>Aliaksei Makarau, Gintautas Palubinskas, and Peter Reinartz</i>	383
Detecting Human-induced Scene Changes Using Coherent Change Detection in SAR Images <i>Nada Milisavljevic, Damien Closson, and Isabelle Bloch</i>	389
Self calibration of small and medium format digital cameras <i>Donald Moe, Aparajithan Sampath, Jon Christopherson, and Mike Benson</i>	395
The aerial photos to detect changes in the landscape affected by black coal deep mining <i>Monika Mulkova, and Renata Popelkova</i>	401
Efficiency of texture measurement from two optical sensors for improved biomass estimation <i>Janet Nichol, and Muhammad Latifur Rahman Sarker</i>	407
Land cover classification in Albania <i>Pal Nikolli</i>	412
Land Cover Remote Sensing Imagery Web Retrieval in Chinese Second Round of National Land Use Inventory Program <i>Xiaogang Ning, and Yonghong Zhang</i>	417
Production of true orthophotos in practice and various application possibilities <i>Herman Novak, Martin Ulz, Ludwig Dorfstetter, and Jens Schickor</i>	420
Spatio-Temporal Characterization of Aerosols through Active Use of Data from Multiple Sensors <i>Zoran Obradovic, Debashish Das, Vladan Radosavljevic, Kosta Ristovski, and Slobodan Vucetic</i>	424

An assessment of the efficiency of LANDSAT, NIGERIASAT-1 and SPOT images for landuse/landcover analyses in Ekiti west area of Nigeria <i>Adebayo Gbenga Ojo, and Francis Abiodun Adesina</i>	430
Studying Bio-Environmental Potentials of Kusalan Area, Based on IUCN criterions, using RS and GIS technologies <i>Djafar Oladi, and Nabi Ahsani</i>	436
PROVIDING processing lines and test data for the GMES Land Monitoring Core Service <i>Philippe Pacholczyk, Roselyne Lacaze, and Hassan Makhmara</i>	441
A comparison of total shortwave surface albedo retrievals from MODIS and TM data <i>Marlon Pape, and Michael Vohland</i>	447
The capabilities of TerraSAR-X imagery for retrieval of forest parameters <i>Roland Perko, Hannes Raggam, Karlheinz Gutjahr, and Mathias Schardt</i>	452
Road extraction from ALOS images using mathematical morphology <i>Fabiana Silva Pires de Castro, and Jorge Antonio Silva Centeno</i>	457
Inferring fluctuations of the aquifer by monitoring the area of small lakes in a brazilian savanna region using a temporal sequence of 50 landsat images <i>Carlos Henrique Pires-Luiz, and Philippe Maillard</i>	463
Real-Time Image Processing for Road Traffic Data Extraction from Aerial Images <i>Dominik Rosenbaum, Jens Leitloff, Franz Kurz, Oliver Meynberg, and Tanja Reize</i>	469
Change detection of building footprints from airborne laser scanning acquired in short time intervals <i>Martin Rutzinger, Benno Rüf, Michael Vetter, and Bernhard Höfle</i>	475
Land Cover and Land Use classification assessment for a creation of a National Mapping Agency framework <i>Carolina Sanchez Hernandez, and Glen Hart</i>	481
Object-oriented methods for landslides detection using high resolution imagery, morphometric properties and meteorological data <i>Ionut Sandric, Bogdan Mihai, Zenaïda Chitu, Andreea Gutu, and Ionut Savulescu</i>	486
Assessment of very high resolution satellite data fusion techniques for landslide recognition <i>Leonardo Santurri, Roberto Carlà, Federica Fiorucci, Bruno Aiazzi, Stefano Baronti, Alessandro Mondini, and Mauro Cardinali</i>	492
Simulation assisted high-resolution PS-InSAR analysis <i>Alexander Schunert, Timo Balz, Kang Liu, Mingsheng Liao, Uwe Sörgel, and Jan Dirk Wegner</i>	498
Topographic estimation by TERRASAR-X <i>Umut Gunes Sefercik, and Uwe Sörgel</i>	504
Characterisation of long-term Vegetation Dynamics for a semi-arid wetland using NDVI time series from NOAA-AVHRR <i>Ralf Seiler</i>	511
Semi-automatic assessment of Norway spruce (<i>Picea abies</i>) in modern digital aerial photographs <i>Rudolf Seitz, Armin Troycke, Peter Rebhan, and Bernd Grubert</i>	517
Using remote sensing products for environmental analysis in South America <i>Yosio Edemir Shimabukuro, G. Pereira, G.B.S. Silva, F.B. Silva, F.S. Cardozo, and E.C. Moraes</i>	523

Detection of highways in high resolution images using Mathematical Morphology techniques <i>Erivaldo Silva</i>	530
Canasat project: monitoring of the sugarcane cultivation area in south central Brazil <i>Wagner Fernando da Silva, Daniel Alves de Aguiar, Bernardo Friedrich Theodor Rudorff, and Luciana Miura Sugawara</i> 535	
Enhancing urban digital elevation models using automated computer vision techniques <i>Beril Sirmacek, Pablo d'Angelo, Thomas Krauss, and Peter Reinartz</i>	541
An adaboost-based iterated MRF model with linear target prior for synthetic aperture radar image classification <i>Xin Su, Chu He, Xinping Deng, Wen Yang, and Hong Sun</i>	547
Deriving water fraction and flood map with the EOS/MODIS data using regression tree approach <i>Donglian Lillian Sun, and Yunyue Yu</i>	552
Environmental impact assessment using Neural Network Model: A case study of the Jahani ,konarsiah and Kohe Gach salt plugs, SE Shiraz, Iran <i>Mohammad Hasan Tayebi, Majid Hashemi Tangestani, and Hasan Roosta</i>	557
Hyperspectral evaluation of the pear trees on the basis of the genetic collection of the different species <i>Janos Tamas, and Zoltán Szabó</i>	563
Analysis of RapidEye imagery for annual landcover mapping as an aid to European Union (EU) Common Agricultural Policy <i>Brooke Tapsall, Pavel Milenov, and Kadim Tasdemir</i>	568
Identification of beach features/patterns through artificial neural networks techniques using IKONOS data <i>Ana Teodoro, Hernâni Gonçalves, Joaquim Pais-Barbosa, Fernando Veloso-Gomes, and Francisco Taveira-Pinto</i> ..	574
Remotely sensed data and GIS in land resources management for regional planning over semi-arid parts of NE Brazil <i>Harendra S. Teotia, Klaus A. Ulbricht, and Guttemberg da Silva Silvino</i>	580
Automatic 3D Change Detection based on optical satellite stereo imagery <i>Jiaojiao Tian, Houda Chaabouni-Chouayakh, Peter Reinartz, Thomas Krauß, and Pablo d'Angelo</i>	586
Prospective Space Missions with L-Band Microwave Radiometric Systems <i>Yuriy Tishchenko, Victor Savorskiy, Mikhail Smirnov, Vladimir Ablyazov, and Alexander Khaldin</i>	592
Validation of a semi-automatic classification approach for urban green structure <i>Øivind Due Trier, and Einar Lieng</i>	596
Comparison of grid-based and segment-based estimation of forest attributes using airborne laser scanning and digital aerial imagery <i>Sakari Tuominen, and Reija Haapanen</i>	602
ALTM ORION: Bridging conventional LIDAR and full waveform digitizer technology <i>Valerie Ussyshkin, and Livia Theriault</i>	606
Surface temperature estimation using artificial neural network <i>Maurício Roberto Veronez, G. Wittmann, A. O. Reinhardt, and R.M. Da Silva</i>	612
Analysing the facial morphology with a three-dimensional geometrical features approach <i>Enrico Vezzetti, Flaviana Calignano, and Sandro Moos</i>	618

Quantitative Prognosis of Oil and Natural Gas Fields <i>Anatoliy Vostokov, Vadim Lyalko, Arthur Hodorovsky, and Aleksander Apostolov</i>	622
DEM generation from airborne LiDAR data by an adaptive dual-directional slope filter <i>Cheng-Kai Wang, and Yi-Hsing Tseng</i>	628
Semiautomatic classification of tree species by means of multi-temporal airborne digital sensor data ADS40 <i>Lars Waser, Christian Ginzler, Meinrad Kuchler, and Emmanuel Baltsavias</i>	633
Fusion of ALS Point Cloud Data with High Precision Surveying Data <i>Aloysius Wehr, Hamid Duzelovic, and Christian Punz</i>	639
Change analysis with TerraSAR-X data <i>Diana Weihsing, Felicitas von Poncét, Oliver Lang, and Michael Schlund</i>	644
An overview of two decades of systematic evaluations of canopy radiative transfer models <i>Jean-Luc Widlowski</i>	648
Tropical Biodiversity Mapping from Hyperion Image in Bogor Indonesia <i>Antonius Wijanarto, and Fahmi Amhar</i>	654
A New Strategy for DSM Generation from High Resolution Stereo Satellite Images Based on Control Network Interest Matching <i>Zhen Xiong, and Yun Zhang</i>	658
SAR stereo-mapping based on DEM <i>Shucheng Yang, Guoman Huang, and Zheng Zhao</i>	664
Weakly Supervised Polarimetric SAR Image Classification with Multi-modal Markov Aspect Model <i>Wen Yang, Dengxin Dai, Jun Wu, and Chu He</i>	669
Lunar Geomorphy 3D Visualization Method <i>Zhou Yang, Xu Qing, Zhang BaoMing, Li JianSheng, and Lan ChaoZhen</i>	674
Pixel level fusion methods for remote sensing images: A current review <i>Jinghui Yang, Jixian Zhang, Haitao Li, Yushan Sun, and Pengxian Pu</i>	680
Identification of historical land use by the help of aerial photography <i>Vaclav Zdimal</i>	687
Development of a supervised software tool for automated determination of optimal segmentation parameters for eCognition <i>Yun Zhang, Travis Maxwell, Hengjian Tong, and Vivek Dey</i>	690
Research on Change Detection in Remote Sensing Images by using 2D-Fisher Criterion Function Method <i>Baoming Zhang, Ke Chen, Yang Zhou, Mingxia Xie, and Hongwei Zhang</i>	697
Evaluation of time series of MODIS data for transitional land mapping in support of bioenergy policy development <i>Fuqun Zhou, Aining Zhang, Huili Wang, and Gang Hong</i>	703
Author Index	708
Keyword Index	711

Preface

These are the proceedings of the ISPRS Technical Commission VII Symposium that was held on July 5–7, 2010, at the Vienna University of Technology, Austria. The proceedings consist of two parts: Part A collects all papers that were accepted on the basis of peer-reviewed full manuscripts; Part B contains papers which have been selected based on a review of the submitted abstracts.

The topic of the symposium was “100 Years ISPRS – Advancing Remote Sensing Science” to celebrate the foundation of the International Society for Photogrammetry (ISP) on July 4, 1910, on the initiative by Prof. Eduard Doležal. The Society changed its name to the International Society for Photogrammetry and Remote Sensing (ISPRS) in 1980, reflecting the increasing integration of the two disciplines. In our modern digital age, photogrammetry and remote sensing have virtually grown together, having as their common scope the extraction of reliable information from non-contact imaging and other sensor systems about the Earth and its environment through recording, measuring, analysing and representation.

Given the particular occasion the themes of the symposium extended beyond the traditional realms of Commission VII (“Thematic Processing, Modelling and Analysis of Remotely Sensed Data”) by inviting contributions from the other ISPRS Commissions as well. Contributions that provided a comprehensive overview of the major research areas in remote sensing, highlighting past achievements and identifying challenges for the future, were particularly welcome. The conference topics were

- Multi-spectral and hyperspectral remote sensing
- Microwave remote sensing
- Lidar and laser scanning
- Geometric modelling
- Physical modelling and signatures
- Change detection and process modelling
- Land cover classification
- Image processing and pattern recognition
- Data fusion and data assimilation
- Earth observation programmes
- Remote sensing applications
- Operational remote sensing applications

We would like to take this opportunity here to sincerely thank the reviewers of both the full-papers and the abstracts for their valuable time and expertise! Each paper within Part A was reviewed by at least two reviewers and revised according to their comments. Only 60% of the submitted full papers finally made it through this review process. Also each abstract was reviewed by two peers, most of them by even three or more peers. Without question, the reviewer’s effort was not in vain as it has helped to raise the quality of the papers and has allowed us to put together a high-quality technical programme.

Nevertheless, we also would like to add some self-criticism here. Within ISPRS the importance of a proper review process is broadly recognised. Also, more and more ISPRS colleagues rightfully request that all papers published in the *International Archives of the Photogrammetry, Remote Sensing and Spatial Information Sciences* (such as those contained in the current volume) shall be covered by prominent indexing and abstracting databases. Yet, there is no standard ISPRS reviewing system, nor is there a professional editorial support and indexing service. Consequently, every organiser of an ISPRS workshop, symposium or congress needs to reinvent the wheel by building up his/her own system for reviewing and handling the scientific contributions and for producing the proceedings. Having never organised an event with more

than hundred people, the learning curve has been particularly steep for us. As a result, mistakes were unavoidable and we would like to apologise with the authors and reviewers for any inconvenience that they may have experienced. We are confident that together we will be able to solve this challenge for future scientific meetings to the benefit of our discipline.

Finally, we want to highlight the very positive fact that we have received many excellent papers from scientists from developing regions. This suggests to us that ISPRS has been quite successful in stimulating the exchange of scientists from around the world and diverse cultural background. This will become the ever more important as climate change, continued population growth and shrinking natural resources have all become truly global problems that require, as one small part of the solution, global observation capabilities to better understand of how we have to act locally.

Vienna, June 2010

Wolfgang Wagner

Balázs Székely

Symposium Committee

Organising Committee

Wolfgang Wagner, Vienna University of Technology, Austria (Chairman)
Balázs Székely, Vienna University of Technology, Austria (Scientific Coordinator)

Wouter Dorigo, Vienna University of Technology, Austria
Michael Franzen, Bundesamt für Eich- und Vermessungswesen, Austria
Juha Hyypä, Finnish Geodetic Institute, Finland
Josef Jansa, Vienna University of Technology, Austria
Norbert Pfeifer, Vienna University of Technology, Austria
Werner Schneider, University of Natural Resources and Applied Life Sciences, Austria
Klaus Steinnocher, Austrian Institute of Technology, Austria

Scientific Committee

Richard Bamler, DLR, Germany
Arnold Dekker, CSIRO, Australia
Diego Fernandez, ESA
Wolfgang Förstner, Bonn University, Germany
Garik Gutman, NASA, USA
Michael Schaepman, Universität Zürich, Switzerland
Johannes Schmetz, EUMETSAT
Uwe Sörgel, Leibniz Universität Hannover, Germany
Niko Verhoest, Ghent University, Belgium
Jixian Zhang, Chinese Academy of Surveying and Mapping, China
Yun Zhang, University of New Brunswick, Canada
Qiming Zhou, Hong Kong Baptist University, China

Reviewers

We gratefully acknowledge the support of the following colleagues who generously helped us in the review of the full-papers and abstracts:

Luis Carlos Alatorre
Paul Aplin
Roman Arbiol
Costas Armenakis
Clement Atzberger
Christoph Aubrecht
Manos Baltasvias
Richard Bamler
Georg Bareth
Zoltan Bartalis
Annett Bartsch
Enton Bedini
Eyal Ben-Dor
Santosh P. Bhandari
Horst Bischof
Christian Briese
Manfred Buchroithner
Ana Cabral
Liang-Chien Chen
Jan Clevers
Rene Colditz
Jackson Cothren
Jean-Francois Crétaux
Michele Crosetto
Wouter Dorigo
Peter Dorninger
Ian Dowman
Diego Fernandez
Michael Franzen
Steffen Fritz
Garik Gutman
Stefan Hasenauer
Christian Heipke
Manuela Hirschmugl
Thorsten Hoberg
Bernhard Höfle
Markus Hollaus
Pai-Hui Hsu
Tangao Hu
Juha Hyypä
Arnold Irschara

Josef Jansa
Sanna Kaasalainen
Helmut Kager
Wilfried Karel
Akira Kato
Viktor Kaufmann
Akila Kemmouche
Richard Kidd
Géza Király
Mathias Kneubühler
Ilkka Korpela
Tatjana Koukal
Nelley Kovalevskaya
Olaf Kranz
Claudia Künzer
Peijun Li
Bo-Cheng Lin
Roderik Lindenbergh
Zhengjun Liu
Zhong Lu
Aliaksei Makarau
Clément Mallet
Gottfried Mandlbürger
Lauri Markelin
Helmut Mayer
Ian McCallum
Thomas Melzer
Gábor Molnár
Werner Mücke
Sonoyo Mukai
Vahid Naeimi
Alexey Nekrasov
Wenige Ni-Meister
Johannes Otepka
Gintautas Palubinskas
Nicolas Paparoditis
Charles Paradzayi
Sang-Eun Park
Carsten Pathe
Norbert Pfeifer
Camillo Ressler

Victor F. Rodríguez-Galiano
Petri N. Rönholm
Dominik Rosenbaum
Franz Rottensteiner
Nilda Sánchez
Michael Schaeppman
Johannes Schmetz
Thomas Schneider
Alexander Schunert
Gabriela Seiz
Jie Shan
George Sithole
Julian Smit
Ben Somers
Uwe Sörgel
Klaus Steinnocher
Uwe Stilla
Haigang Sui
Anna Nora Tasseti
Tee-Ann Teo
Thi Nhat Thanh Nguyen
Gábor Timár
John Trinder
Jaan-Rong Tsay
Niko Verhoest
Loureal Camille Verzosa
Karsten Vogt
Francesco Vuolo
Wolfgang Wagner
Peter Waldhäusl
Miao Wang
Björn Waske
Aloysius Wehr
Uwe Weidner
Gui-Song Xia
Mitsunori Yoshimura
Yu Zeng
Jixian Zhang
Li Zhang
Yun Zhang
Qiming Zhou

SPECTRAL REFLECTANCE OF RICE CANOPY AND RED EDGE POSITION (REP) AS INDICATOR OF HIGH-YIELDING VARIETY

M. Abbasi¹, A.A. Darvishsefat², M. E. Schaepman³

¹Department of Forestry, Faculty of Earth Science and Natural Resource, Shahrekord University, Shahrekord, Iran

²Department of Forestry, Faculty of Natural Resource, University of Tehran, Karaj, Iran

³University of Zurich, Winterthurerstrasse 190, CH – 8057 Zurich, p +41 44 635 51 60

Michael.Schaepman@geo.uzh.ch, adarvish@ut.ac.ir, mozhgan.abasi@gmail.com

KEY WORDS: Spectral reflectance, rice, red edge position, first derivative, high-yielding variety

ABSTRACT:

Rice is the staple food in Iran. More than 80 percent of rice area is distributed in the two northern provinces of Mazandaran and Gilan, so that investment in increasing the quantity and quality can impact an effective role in economic independence and sustainable agriculture. Increased efficiency in rice production is possible through varietal technology, advances in yield enhancement, and the successful development of hybrid technology. Nondestructive methods such as study the spectral reflectance of rice fields is a reliable way in remote sensing study. In this study we tested the possibility to predict high-yielding rice varieties based on the spectral reflectance data in the red edge position (REP). Spectral reflectance of rice canopies from 350 to 2500 nm were acquired under clear sky in rice field. The obtained results indicate that REP of Hybrid, Tarom, Neda and Khazar varieties are at longer wavelength, so they are predicted as more productive rice varieties.

1. INTRODUCTION

Remotely sensed data provide considerable potential for estimating agricultural area and yield forecasting at local, regional, and global scales (Kamthongkiat, et al., 2005; Xiao et al., 2006; Serra et al., 2007, Khajeddin & Pourmanafi, 2007; Ansari Amoli & Alimohmmadi, 2007). Estimation these information by remote sensing mainly depended on the spectral characteristics of field crops. Many studies using rice spectral reflectance data has been done to estimate its product and health condition at red edge region (Yang and Cheng, 2001; Xue, et al., 2004; Shen et al., 2007; Wang et al., 2008).

Some parameters such as chlorophyll content, nitrogen, LAI, biomass and relative water content were studied in the first derivative reflectance curve in the red edge region (Jago et al., 1999; Yoder and Pettigrew-Crosby, 1995; Skidmore and Mutanga 2007). This position is the point of maximum slope on the reflectance spectrum of vegetation between red and near-infrared wavelengths. Technically, the red edge is a spectral reflectance feature characterized by darkness in the red portion of the visible spectrum, due to absorption by chlorophyll, contrasting strongly with high reflectance in the NIR, due to light scattering from refraction along interfaces between leaf cells and air spaces inside the leaf (Bonham-Carter, 1988; Dawson and Curran, 1998, Tinetti et al., 2006). Field crop

reflectance actually was a kind of mixed reflectance, influenced not only by rice canopy but also by soil. Extraction REP which is based on derivative analysis minimizes interpolation errors and soil background effects and computationally, it is one of the simpler curve fitting techniques (Shafri et al., 2006).

Hybrid varieties have the potential to raise the yield of rice and thus overall rice productivity and profitability in the north of Iran. So this has led the public and private sectors to develop the use of hybrid rice technology in recent years. Successful deployment of using hybrid rice in sustainable management, however, requires information about the area and productivity of different rice cultivars. Spectral field reflectance could use in remote sensing data for accessing this information. The increase reflectance in the near infrared range and caused a shift in the position of the red edge toward longer wavelengths depend upon the productivity element in vegetation; have shown the most productivity of some cultivar rather than the other ones. The objectives of this study were to prepare the spectral fingerprint of most important rice cultivars of northern of Iran and study the red edge position related to high-yielding of different rice varieties.

2. MATERIAL AND METHODS

This research was conducted in the rice research institute in Amol in the north of Iran. Spectral field measurements of seven different cultivars were acquired on different plots (Figure 1). A total of 76 spectrums from rice cultivars named Hybrid, Tarom, Neda, Nemat, Shiroudi, Khazar and Fajr (10–12 sample for each cultivars was measured) were analyzed. Figure 2 shows the crown canopy of each cultivar to be measured. A full range (350–2500 nm) portable spectroradiometer (ASD FieldSpec Pro FR) was used for spectral measurements. The field of view of optical sensor was 25 which positioned 30–40cm above the samples at nadir position. The measurements were conducted under clear sky between 10:00 and 14:00 local time in 27 August 2007. The noise spectra in water

absorption feature wavelength was removed based on standard deviation calculated of all reflectance values in each wavelength. The first derivative spectral curves calculated in Matlab software and the red edge position in this spectral range extracted based on the specified maximum slope.

$$FSD_{\lambda} = \frac{R_{\lambda+1} - R_{\lambda}}{\Delta\lambda}$$

FSD: First Derivative at λ wavelength

R: Reflectance



Figure 1: Spectral filed measurements of rice varieties



Khazar



Hybrid



Fajr



Shiroudi



Nemat



Neda



Tarom

Figure 2: The canopy of seven rice variety to be measured

3. RESULT AND DISCUSSION

After spectral measurements, the result of performed processes on data was spectral curves at 2500-350 nm wavelengths. All the curves were quality reviewed and the noise spectra in water absorption feature were removed based on the standard deviation of all reflectance values in each wavelength. Figure 3 shows spectral characteristics of studied rice cultivars after necessary preprocessing. The first derivative Curve in the range of red edge wavelengths calculated (Figure 4) and the highest value obtained in this range as the maximum possible slope is determined as the red edge position for each of the seven

cultivars (Fig. 6). Based on these results, the red edge position of the hybrid cultivar was the highest wavelength (724 nm) than the rest of rice cultivars. REP of Tarom, Khazar, Neda was at 716 nm while for Nemat, Shiroudi and Fajr were determined at 700, 694 and 694 nm, respectively (Figure 5). The results showed that Hybrid variety was the most likely variety than the others and has the highest chlorophyll and nitrogen concentrations inverse Shiroudi and Fajr variety based on spectral characteristics.

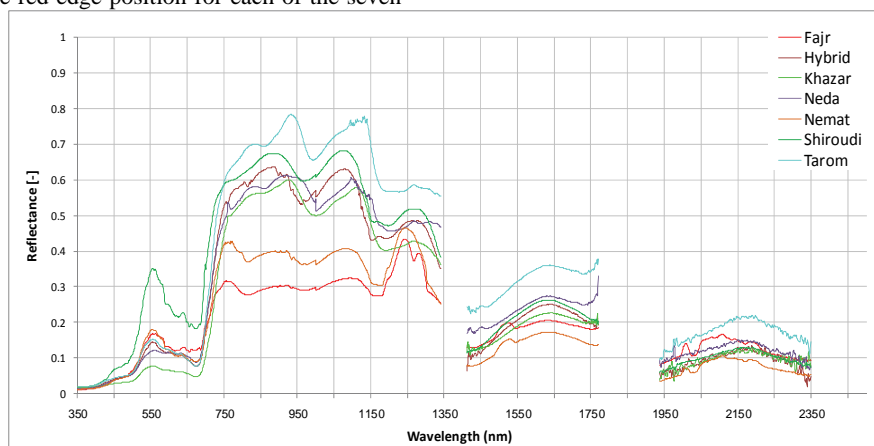


Figure 3: Spectral reflectance curves of seven rice variety of north of Iran

Red edge region are relatively insensitive to changes of biophysical factors such as soil cover percentage, optical properties, canopy structure, atmospheric effects, irradiance and solar zenith angle (Shafri et al., 2006; Clevers, 1999 and 2000), therefore this region is a reliable range to investigate the biochemical variables from canopy reflectance. The obtained Results from literatures proved the Relationship between chlorophyll and red edge position so that with increasing chlorophyll and nitrogen concentration the REP moves towards the longer wavelengths (Boochs et al, 1990 ;Curran et al., 1990 ; Fillella and Penuelas 1994; Shafri et al., 2006). The

obtained results by Nemat Zade and Sattari (2003) also Allah Gholipour (2007) show that Hybrid variety is a high-yielding variety equal to 25-20% times than the other variety in this study. REP of Hybrid rice that positioned at longer wavelength could indicate more chlorophyll/nitrogen concentration and leaf area index, rather than the other varieties. Mutanga and Skidmore (2007) studied the relationship between REP and nitrogen content of grass vegetation. They indicated that nitrogen content correlated well with wavelength at 713nm and 725 nm as determined REP.

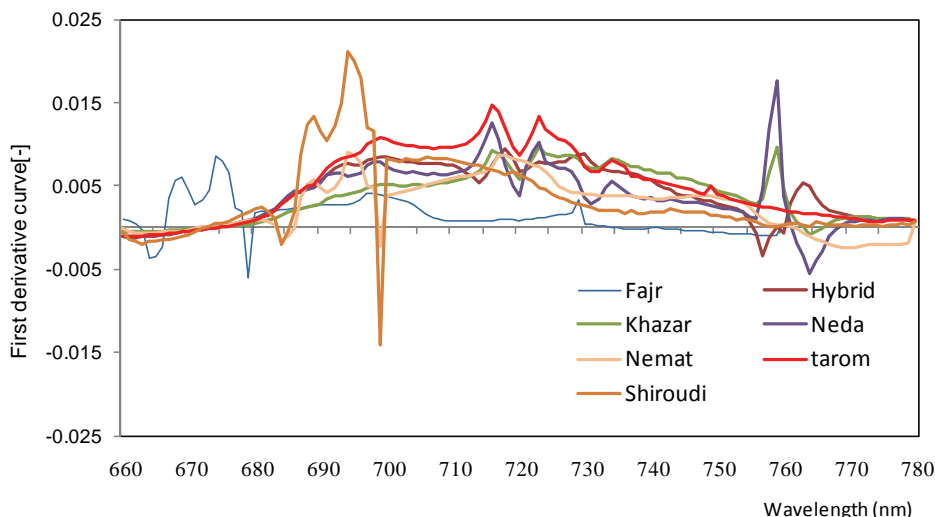


Figure 4: The first derivative spectral reflectance curves of seven rice varieties at red edge region (660-780 nm)

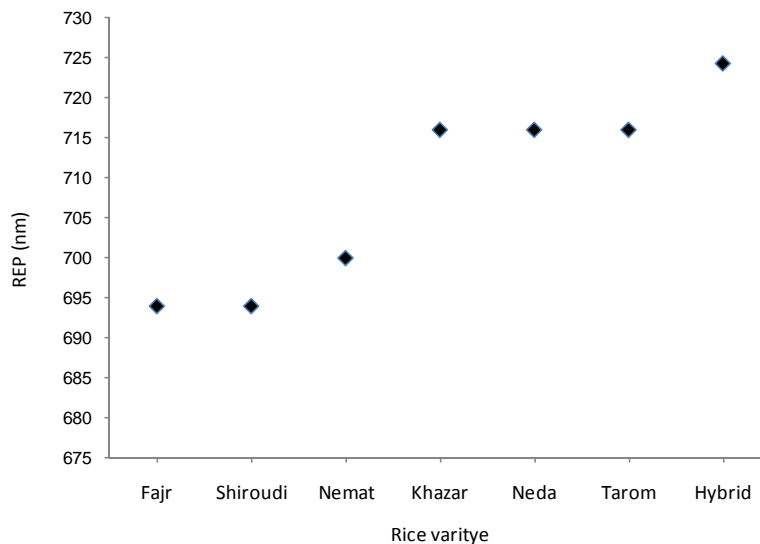


Figure 5: Red edge position (REP) obtained for each rice variety

4. CONCLUTIONS

Compared to traditional methods for indicating high-yielding rice variety and monitoring their filed area using remote sensing is quicker, exact, and more comfortable, especially on a large scale. Field spectroscopy can provide reliable information for applications of airborne or spaceborne remote sensing with data support and pertinent correction reference on the basis of spectral analysis, shifting distance of red edge position.

ACKNOWLEDGEMENTS

We acknowledge the contribution of the participating Rice Research Institute of Iran located in Amol. We also wish to acknowledge the field work support we received from

the staff of Geo-information department of Wageningen University.

REFERENCES

- Ansari Amoli,A., Alimohammadi,A., 2007. A new multitemporal classification approach for land cover mapping in Iran by using hyperspectral MODIS data. 10th International Symposium on Physical Measurements and Signatures in Remote Sensing (ISPMSRS07), Davos, Switzerland, March 12 – 14.
- Bonham-Carter, G.F., 1988. Numerical procedures and computer program for fitting an inverted Gaussian model to vegetation reflectance data. *Computers & Geosciences*, 14(3), 339-356.
- Boochs, F., Kupfer, G., Dockter, K., & Kubauch, W., 1990. Shape of the red as vitality indicator for

- plants. *International Journal of Remote Sensing*, 11 (10), 1741–1753.
- Clevers, J.G.P.W., 1999. The use of imaging spectrometry for agricultural applications, *ISPRS Journal of Photogrammetry and Remote Sensing*, 54 (5), 299–304.
- Clevers, J.G.P.W., De Jong, S.M., Epema, G.F., van der Meer, F., Bakker, W., & Skidmore, A.K., 2002. Derivation of the red edge index using MERIS standard band setting. *International Journal of Remote Sensing*, 23, 3169–3184.
- Curran, P.J. Dungan, J.L., & Gholz, H.L., 1990. Exploring the relationship between reflectance red edge and chlorophyll content in slash pine, *Tree Physiology* 7, 33–48.
- Dawson, T.P., & Curran, P.J., 1998. A new technique for interpolating the reflectance red edge position. *International Journal of Remote Sensing*, 19, 2133–2139.
- Fillella, I. & Penuelas, J., 1994. The red edge position and shape as indicators of plant chlorophyll content, biomass and hydric status. *International Journal of Remote Sensing*, 15,(7), 1459–1470.
- Jago, R.A., Cutler, M.E., & Curran, P.J., 1999. Estimating canopy chlorophyll concentration from field and airborne spectra. *Remote Sensing of Environment*, 68, 217–224.
- Allah Gholipour, 2007. (Report in Persian). <http://www.agristore.ir/class.aspx?tid=8&sid=41&la=fa>
- Kamthonkiat, D., Honda, K., Turrall, H., Tripathi, N. K., Wuwongse, V., 2005. Discrimination of irrigated and rainfed rice in a tropical agricultural system using SPOT vegetation NDVI and rainfall data. *International Journal of Remote Sensing*, 26(12), 2527–2547.
- Khajedin, S.J., & Pourmanafi, S., 2007. Determination of Rice Paddies Areas Using Digital Data IRS Sensors Around Zayandeh Rud in Isfahan Region, *Journal of Science and Technology of Agriculture and Natural Resources*, 11(40), 449–464.
- Mutanga, O., & Skidmore, A.K., 2007. Red edge shift and biochemical content in grass canopies. *ISPRS Journal of Photogrammetry & Remote Sensing*, 62, 34–42.
- Nemat Zadeh, & G., Sattari, M., 2003. Study some of the nuclear genome of rice cultivars on different fertility control, (*Oryza sativa* L.) for Hybrid rice seed production. *Journal of Agricultural Science (In Persian)*, Volume 34 (1), 213–219.
- Serra, P., More, G., & Pons, X., 2007. Monitoring winter flooding of rice fields on the coastal wetland of Ebre delta with multitemporal remote sensing images. *Geoscience and Remote Sensing Symposium, 2007. IGARSS 2007. IEEE International*, 2495–2498.
- Shafri, H.Z.M., Salleh, M.A.M., & Ghiyamat, A., 2006. Hyperspectral remote sensing of vegetation using red edge position techniques. *American Journal of Applied Science*, 3(6), 1864–1871.
- Shen, Y., Lo, J.C. & Cheng, S.P., 2000. Development of remote sensing techniques to identify nitrogen status of paddy rice. (in Chinese with English abstract). *Chin. J. Agromet.* 7, 23–32.
- Tinetti, G., Rashby, S., & Yung, Y.L., 2006. Detectability of red-edge-shifted vegetation on terrestrial planets orbiting m stars. *The Astrophysical Journal*, 644, 129–132.
- Wang, F. M., Huang, J. F. & Wang, X. Z., 2008. Identification of Optimal Hyperspectral Bands for Estimation of Rice Biophysical Parameters. *Journal of Integrative Plant Biology*, 50 (3), 291–299.
- Xiao, X., Boles, S., Froelking, S., Li, C., Babu, J.Y., Salas, W., & Moore, B., 2006. Mapping paddy rice agriculture in South and Southeast Asia using multi-temporal MODIS images. *Remote Sensing of Environment*. 100, 95–113.
- Xue, L., Cao, W., Luo, W., Dai, T., & Zhu, Y., 2004. Monitoring leaf nitrogen status in rice with canopy spectral reflectance. *American Society of Agronomy*, 96, 135–142.
- Yang, C.M., & Cheng, C.H., 2001. Spectral characteristics of rice plants infested by brown planthoppers. *Proceedings of Natural Science*, 25(3), 180–186.
- Yoder, B.J., & Pettigrew-Crosby, R.E., 1995. Predicting nitrogen and chlorophyll content and concentrations from reflectance spectra (400–2500 nm) at leaf and canopy scales, *Remote Sensing of Environment*, 53(3), 199–211.

SIMULATED RAIN RATE EFFECTS ON SAR INTERFEROGRAMS

A. Elmzoughi¹, R. Abdelfattah^{1,2} and Z. Belhadj¹

¹ URISA, École Supérieure des Communications, Tunis, Route de Raouède Km 3.5, 2083, Tunisia .

² Département ITI, Telecom Bretagne, Institut TELECOM, CS 83818 - 29238 Brest Cedex 3 - France

Email: riadh.abdelfattah@supcom.rnu.tn and ziad.belhadj@supcom.rnu.tn

Commission TC VII

KEY WORDS: InSAR, Atmospheric effects, Interferograms, Signal delay.

ABSTRACT:

In this paper we discuss influence of the rain rate on SAR interferograms. Calculations of the path delay for different rain rate intensities was made by considering a physical model for the rain drops and applying the Rayleigh approximation. The calculations do not include estimations of the delay due to the melting layer of precipitations and due to the precipitating cloud above the melting layer since they could be neglected. On simulated examples of interferograms considering perfectly flat areas, we show that there is a strong increase in a propagation delay associated with rain rate and that, the rain can induce a considerable propagation delay of several centimeters.

1 INTRODUCTION: INTERFEROMETRY AND ATMOSPHERIC EFFECTS

ERS1 and ERS2 provide 2D measurements of the earth surface with a high resolution of 4×20 m. The phase value of every resolution cell is defined as a superposition of the term which corresponds to the geometric distance, a term which corresponds to propagation effects, ψ_{prop} , and the term which represents the scattering within the resolution cell. By creating an interferogram, effectively the phases corresponding to two measurements are subtracted from each other and if objects within resolution cells did not move and did not change from one acquisition to the other, the differential phase is mainly defined by the propagation effects and the difference in observation geometries. Furthermore, if a reference elevation model is available one can remove the topographic phase component. The remaining phase would fully be determined by the propagation through the ionosphere, $\Delta\psi_{iono}$, and atmosphere, $\Delta\psi_{atm}$ (Zebker et al., 1994):

$$\begin{aligned} \Delta\psi_{prop} &= \Delta\psi_{iono} + \Delta\psi_{atm} \\ &= \Delta\psi_{iono} + (\Delta\psi_{hydr} + \Delta\psi_{wet} + \Delta\psi_{liquid}) \end{aligned} \quad (1)$$

Indeed, the atmospheric component in its turn depends on hydrostatic part, propagation through the dry atmosphere, wet delay, propagation through water vapor and liquid part, caused by propagation through volume filled with liquid droplets.

The hydrostatic and ionospheric parts are dominating the delay signal, but they hardly vary over the interferogram and may easily be removed from the rest of the signal. The wet part, caused by propagation through a volume filled with liquid particles, have a stochastic spatial behavior and therefore it is more difficult to compensate for them (Moissev et al., 2002).

In this paper we will discuss influence of rain on the atmospheric phase delay. Calculations of the path delay for different rain rate intensities was made by considering a physical model for the rain drops and applying the Rayleigh approximation. Then in order to illustrate our study, some interferograms were generated and discussed.

2 SIMULATED SIGNAL DELAY INDUCED BY THE RAIN DROPS

2.1 The physical model

For radar applications there is a great agreement that raindrops can be well approximated by oblate spheroids (Nelson and Gokhale, 1972) characterized by their axis ratio e . In the literature, a great number of theoretically derived relations between the axis ratio and the equivolume sphere diameter D were derived (Imai, 1950) (Spilhaus, 1948). Most of these relations are describing the equilibrium shape (shape of the rain drop in absence of perturbation). However, the derived axis ratio from a linear fit to the wind-tunnel data of Pruppacher and Beard (Pruppacher and Beard, 1970) represents a very useful one:

$$e = 1.03 - 0.062 \times D. \quad (2)$$

The Drop Size Distribution (DSD) represents the number of particles that have the same equivalent diameter and noted $N(D)$ located in a volume of $1m^3$. Based on extensive measurements, Marshall and Palmer proposed a single-parameter negative exponential relation in (Marshall and Palmer, 1948):

$$N(D) = 8000 \times \exp(-\wedge D), \quad (3)$$

where the spherical equivalent diameter D is in mm and \wedge is the parameter of the exponential distribution function which can be related to the rain rate through the following equation:

$$\wedge = 4.1/R^{0.21}, \quad (4)$$

where R is given in mm/hr.

An other important physical parameter for the rain drops is their complex dielectric constant since it is related to transmission, absorption and backscattering phenomena. It depends principally on the exiting wavelength (water activity) and the temperature. Evaluated for a wavelength of 5.6 cm (which corresponds to the ERS1/2 wavelength) and at 10°C the dielectrical constant can be approximated by (Marshall and Palmer, 1948):

$$\epsilon \simeq 70 + 30i \quad (5)$$

where $i = \sqrt{-1}$.

2.2 Phase delay computing

It was shown in (Oguchi, 1983) that for the case of coherent propagation in rain the propagation phase delay, δ in mm/km, can be calculated as:

$$\delta = 10^{-3} \frac{2\pi}{k^2} \int \text{Re}(f(D))N(D)dD, \quad (6)$$

where k is the wave number (corresponding to a wavelength of 56 mm for the case of ERS1/2) and $f(D)$ is the forward scattering amplitude in mm and $N(D)$ is in $\text{mm}^{-1}\text{m}^{-3}$.

In this case $f(D)$ can be evaluated using Rayleigh approximation (Brangi and Chandrasekar, 2001). The scattered amplitude for h-polarized incidence wave can be then calculated as:

$$f(D) = \frac{k^2}{24} D^3 (\epsilon - 1) \Lambda, \quad (7)$$

where ϵ is the relative permittivity of water and Λ is given by:

$$\Lambda = \frac{1}{1 + \lambda_1(\epsilon - 1)}, \quad (8)$$

where

$$\lambda = \frac{1 - \lambda_2}{2} \quad \text{and} \quad \lambda_2 = \frac{1 + f^2}{f^2} \left(1 - \frac{1}{f} \tan^{-1}(f)\right), \quad (9)$$

where

$$f = e^{-2} - 1. \quad (10)$$

As we can conclude the expression of $\text{Re}(f(D))$ is very complicated and cannot be used directly for deriving an analytical expression for the phase delay related to the rain. Thus more suitable expressions are needed.

In order to overcome this problem, we have simulated the forward scattering amplitude for D ranges between 1 and 8 mm. we have fixed the temperature at 10°C and the wavelength at 5.6 cm. In these conditions, the value of ϵ can be approximated by $70 + 30j$. Then, for a given value of D , the corresponding axis ratio e is computed using equation 2. Then, $f(D)$ is computed using equations 3 and 5-11. From the resulting curve of the real part we can derive a powerless relation between $\text{Re}(f(D))$ and D that have the forme αD^β . Coefficients α and β are estimated by the non linear regression algorithm. For our simulation $\alpha = 3.7 \times 10^{-4}$ and $\beta = 3.02$. Figure 1 shows the good agreement between the Rayleigh approximation and the powerless one.

After replacing $\text{Re}(f(D))$ by its powerless expression and performing some simple mathematical manipulations equation 6 becomes:

$$\begin{aligned} \delta &= \frac{8\lambda^2 \alpha \Lambda^{-\beta}}{2\pi} \int D^\beta \exp(-D) dD \\ &= \frac{8\lambda^2 \alpha \Lambda^{-\beta}}{2\pi} \Gamma(\beta) \end{aligned}, \quad (11)$$

where $\Gamma(\cdot)$ is the gamma function.

Finally a simple expression relating the phase delay to the rain rate can be derived using equation 4 as:

$$\delta = \frac{8\lambda^2 \alpha 4.1^{-\beta} R^{0.21\beta}}{2\pi} \Gamma(\beta). \quad (12)$$

The path delay for different rain intensities were calculated. It should be noted that raindrop diameter is usually truncated at 8

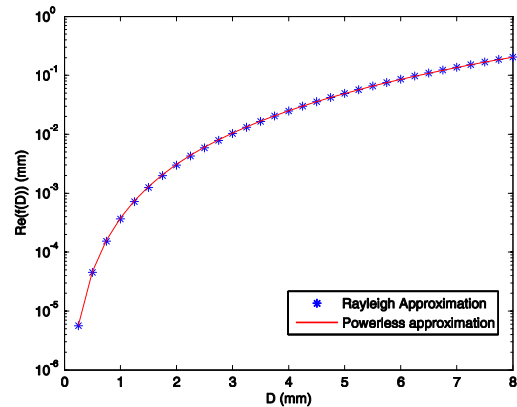


Figure 1: Fitting Rayleigh approximation to a powerless one.

mm, since particles with a larger diameter are unstable. In Figure 2 the result of these calculations is given. It can be seen that for high rain intensities the path delay can be as high as several centimeters.

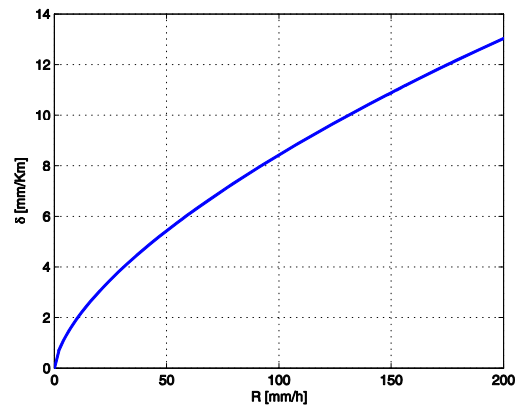


Figure 2: Path delay as a function of the rain rate.

3 SIMULATED INTERFEROGRAMS

Our simulation for this work consists in generating two interferograms for a perfectly flat area. The first one was generated without taking into consideration any rain effects and the second one takes into a consideration a layer of rain that covers the imaged area. Figure 3 and 4 show the considered computation geometry.

3.1 Computing geometry

In figure 3, \vec{B} designates the baseline vector, θ the incidence angle, T the radar swath and r_1 and r_2 are ranges between a fixed point in the imaged area and the position of the radar for the first and the second acquisition respectively. In the absence of rain $\Delta\psi_{prop}$ depends only in r_1 and r_2 (Abdelfattah and Nicolas, 2002):

$$\Delta\psi_{prop} = \frac{4\pi}{\lambda} (r_2 - r_1). \quad (13)$$

Thus, rain free interferogram can be directly generated using r_1 and r_2 . If we consider the configuration of figure 3 and after performing some geometrical manipulations we can deduce that:

$$\begin{aligned} r_1 &= \sqrt{x^2 + y^2 + H^2} \\ r_2 &= \sqrt{(x - B_x)^2 + (y - B_y)^2 + (H + B_z)^2} \end{aligned} \quad (14)$$

for

$$\begin{aligned} x &\in [H \tan(\theta) - \frac{T}{2}, H \tan(\theta) + \frac{T}{2}] \\ y &\in [-\frac{T}{2}, \frac{T}{2}] \end{aligned}$$

Now, let consider the configuration with the presence of a rain layer of figure 4. h designates the height of the rain layer and r_{1r} and r_{2r} are ranges between a fixed point in the imaged area and the intersection points of r_1 and r_2 with the top of the rain layer respectively. r_{1r} and r_{2r} corresponds exactly to the path crossed by the radar signal through the rain medium. Also, r_{1r} and r_{2r} can be computed using some simple geometrical manipulations. Here we avoided to give expressions of r_{1r} and r_{2r} for reasons of clarity. Let R_1 and R_2 the rain rates corresponding to the first and the second acquisition respectively. The phase difference due to propagation through the rain is then :

$$\Delta\psi_{prop-r} = r_{2r} \times \delta(R_2) - r_{1r} \times \delta(R_1). \quad (15)$$

and the total phase difference, from which the rain contaminated interferogram is computed, is:

$$\Delta\psi = \Delta\psi_{prop} + \Delta\psi_{prop-r}. \quad (16)$$

It should be noted that these calculations do not include estimations of the delay due to the melting layer of precipitations and due to the precipitating cloud above the melting layer. However, we expect that contribution of the melting layer is rather limited since it occupies the limited height range (usually in the order of few hundred meters). The precipitating cloud on the other hand can have a rather large height range, but due to the fact that the relative permittivity of ice is much smaller than the one of water the contribution of the precipitating cloud to the signal delay would be negligible.

3.2 Interferograms generation and discussion

In order to simulate interferograms we have fixed the configuration parameters to be equal to the ERS 1/2 radar ones. Table 1 shows their values.

Parameter	Simulation value
H	785 Km
θ	23°
λ	56 mm
T	10 Km
\vec{B}	[10 10 100]m
Pixel Resolution	50×50m
h	10 Km

Table 1: simulation parameters

Note that the rain was considered to be uniform, with the same rain rate, for the hole area. Figure 5 shows resulting phase delay (in cm) for different rain rates. From these results, we can conclude that there is a strong increase in a propagation delay associated with rain rate and that, the rain can induce a considerable propagation delay of several centimeters. Also we can verify by these results that the rain induced phase delay presents very small variation between the nearest and the most far point in the imaged area. Therefore, in these conditions, the rain induced phase delay can be considered as constant all over the imaged zone. Thus its effect on the interferogram will be a simple translation of the fringes. This fact is clear in figure 6 which shows the rain-free and some rain-contaminated interferograms. As expected, interferograms for the area, considered to be perfectly flat, consists in a succession of parallel fringes. The amount of the fringes

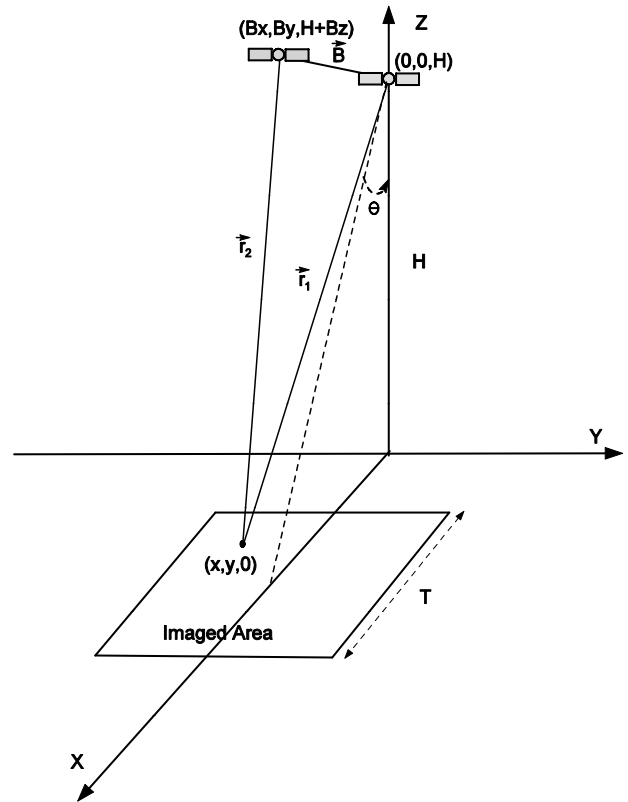


Figure 3: Geometry used for InSAR computations for a flat area in the absence of rain.

transition can be deduced by dividing the rain induced delay by $\lambda/2$. For example, light rain with 5mm/hr induce a transition of approximately half a fringe. We can easily verify this result by comparing the rain-free and the rain-contaminated interferograms.

4 CONCLUSION

In this paper we discussed the influence of the rain rate on SAR interferograms. Calculations of the path delay for different rain rate intensities was made by considering a physical model for the rain drops and applying the Rayleigh approximation. The calculations do not include estimations of the delay due to the melting layer of precipitations and due to the precipitating cloud above the melting layer since they could be neglected. Simulated examples of interferograms considering perfectly flat areas were generated and showed that there is a strong increase in a propagation delay associated with rain rate and that, the rain can induce a considerable propagation delay of several centimeters causing translation of interferogram's fringes.

REFERENCES

- Abdelfattah, R. and Nicolas, J.M., 2002. Topographic SAR interferometry formulation for high-precision DEM generation, *IEEE Transaction on Geoscience and Remote Sensing*, vol. 40, NO. 11, pp. 2415-2426.
- Bringi, V.N. and Chandrasekar, V., 2001. Polarimetric Doppler Weather Radar. Principles and Applications, 1st ed. Cambridge, U.K.: Cambridge Univ. Press.

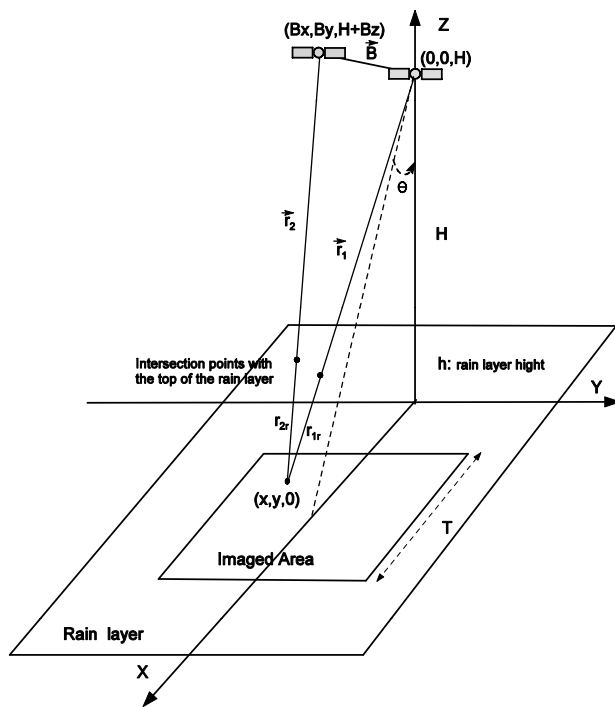


Figure 4: Geometry used for InSAR computations for a flat area in the presence of rain.

Imai, I., 1950. On the velocity of falling drops, *Geophys. Mag.*, vol. 21, pp. 244-249.

Marshall, J.S. and Palmer, W.M., 1948. The distribution of rain-drops with size, *J. Meteorol.*, vol. 5, pp. 165-166.

Moisseev, D.N., Hanssen, R.F. and van Leijen, F.J., 2002. Water vapor observations with SAR, microwave radiometer and GPS: comparison of scaling characteristics, *Proc. of the 6nd European Conference on Radar Meteorology*, Delft, The Netherlands.

Nelson, A.R. and Gokhale, N.R., 1972. Oscillation frequencies of freely suspended water drops, *J. Geophys. Res.*, vol. 77, pp. 2724-2727.

Oguchi, T., 1983. Electromagnetic wave propagation and scattering in rain and other hydrometeors, *Proc. IEEE*, vol. 71, pp.1029-1077.

Pruppacher, H.R. and Beard, K.V., 1970. A wind tunned investigation of the internal circulation and shape of water drops falling at terminal velocity in air, *Quart. J. R. Met. Soc.*, vol. 96, pp. 247-256.

Spilhaus, A.F., 1948. Rain drop size, shape and falling speed, *J. Meteorol.*, vol. 5, pp. 108-110.

Zebker, H.A., Werner, C.L., Rosen, P.A. and Hensley, R.S., 1994. Accuracy of topographic maps derived from ERS-1 interferometric radar, *IEEE Transaction on Geoscience and Remote Sensing*, vol. 32, pp. 823-836.

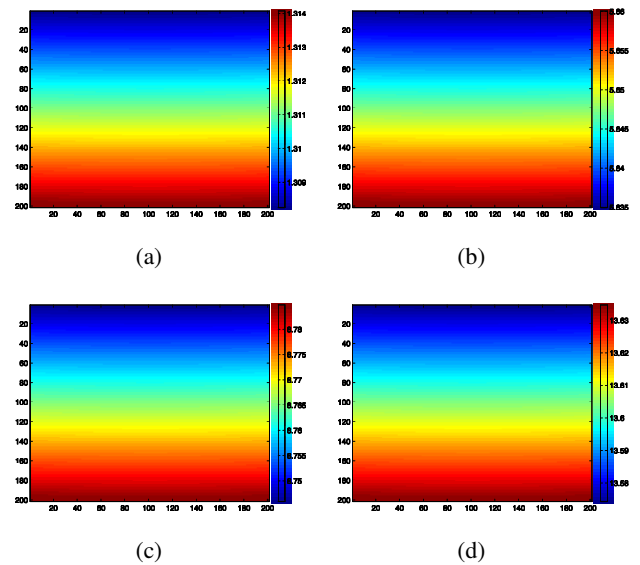


Figure 5: Rain induced signal delay (in cm) for a rain rate of (a) 5 mm/h (b) 50 mm/h (c) 100 mm/h (d) 200 mm/h.

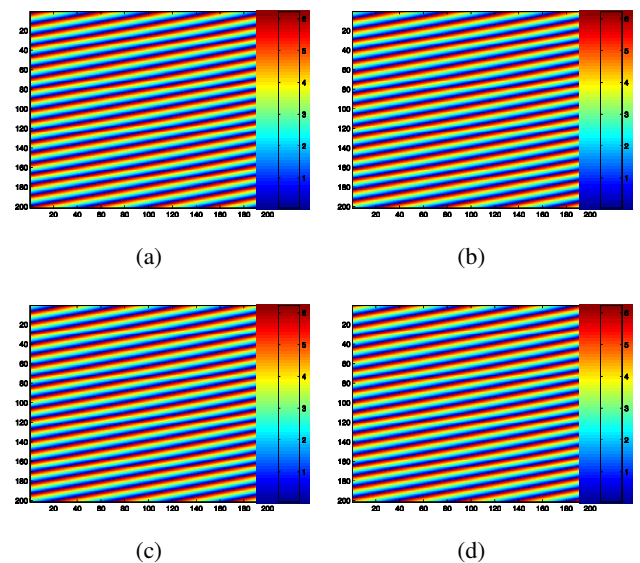


Figure 6: Resulting interferograms (a) rain free (b) 5 mm/h (c) 50 mm/h (d) 100 mm/h.

CANASAT PROJECT: MONITORING THE SUGARCANE HARVEST TYPE IN THE STATE OF SÃO PAULO, BRAZIL

Daniel Alves de Aguiar¹, Wagner Fernando da Silva¹, Bernardo Friedrich Theodor Rudorff¹, Marcos Adami¹

¹National Institute for Space Research (INPE), Remote Sensing Division (DSR),
São José dos Campos, 12227-010, São Paulo State, Brazil.
{daniel; wagner; bernardo, adami}@dsr.inpe.br

KEYWORDS: burnt sugarcane; unburnt sugarcane; satellite monitoring; multitemporal analysis; environmental.

ABSTRACT

In order to increase the sustainability the ethanol production process from sugarcane, it is necessary to reduce actions that harm the environment. One of these actions is the burning of sugarcane straw prior to harvest. In Brazil, agro-environmental protocols between the government and the sugar-ethanol sector have been signed. The agro-environmental protocol in the state of São Paulo requires the total termination of burning by 2017. To meet the objectives of the protocol, remote sensing satellite images are used to monitor and inspect the burning reduction each season. Using satellite images, the Canasat project has mapped the harvesting method (with or without burning) in the state of São Paulo since the 2006/07 season. The objective of this study is to present the methodology utilized and to evaluate the evolution of the harvesting method between the 2006/07 and 2008/09 seasons. The harvest type was also evaluated for each declivity class. Results demonstrated that the unburnt harvest increased from 50.9% in the 2006/07 season to 65.8% in the 2008/09 season. In the three seasons analyzed, approximately 97% of the total area available for harvest in the state is located in areas with a favorable declivity for harvesting without burning, i.e., mechanically. The western region of the state had the greatest expansion in sugarcane cultivated area and also the largest increases in areas of unburnt harvest.

1. INTRODUCTION

Brazil is the world's largest producer of sugarcane FAO (2009). Industrial-scale production occurs primarily in the states located in the Northeast and South-Central regions of the country. The state of São Paulo, in the South-Central region, is the largest producer in the country and was responsible for 61% of Brazil's sugarcane production in the 2008/09 season (UNICA, 2009).

The country is attempting to achieve sustainable ethanol production and to obtain its socio-environmental certification (Goldemberg, 2007; Goldemberg et al., 2008). One of the principle goals in this endeavor is to terminate the burning of sugarcane straw prior to harvest. Therefore, in 2007, São Paulo's State Secretary for the Environment (SMA) and representative in the sugar-energy sector signed the agro-environmental protocol for the sugar-ethanol sector. This protocol decrees, among other measures, ending the burning of sugarcane straw by 2014 in areas that are mechanically harvested (declivity less than or equal to 12%) and by 2017 in areas that are harvested non-mechanically (declivity greater than 12%; <http://homologa.ambiente.sp.gov.br/etanolverde/english.asp>). It is worth to mention that manual harvest of sugarcane can only be performed by burning the straw.

The implementation of this protocol has contributed to increasing the monitoring and inspection capacity of the sugar-energy sector. Using remote sensing satellite images, information can be obtained at multiple time-points, and therefore providing a monitoring system for the sugarcane production process. Furthermore, this crop is generally grown in large areas and possesses a long phenological cycle and a long harvest period, averaging 12 months and 8 months, respectively. These characteristics facilitate crop identification in the images (Abdel-Rahman and Ahmed, 2008).

In Brazil, since 2003, the National Institute for Space Research (*Instituto Nacional de Pesquisas Espaciais* - INPE), the Industry Sugarcane Association (UNICA), the Center for Advanced Studies on Applied Economics (CEPEA) of the Luiz de Queiroz Agricultural School (Esalq/USP) and the Center for Sugarcane Technology (CTC) have maintained the Canasat project (www.dsr.inpe.br/canasat/eng/). Using remote sensing imagery and geoprocessing techniques, the Canasat project monitors areas planted with sugarcane. Initially, mapping was performed only in the state of São Paulo (Rudorff et al., 2005), however since 2005, mapping has been extended to the other five states in the South-Central region of Brazil (Rudorff and Sugawara, 2007). These six states are responsible for 72.7% of Brazil's sugarcane production.

One of the project activities, in the state of São Paulo, is to monitor the type of harvest (with or without burning the sugarcane straw) performed since the 2006/07 crop season. Information provided by the project has been utilized by both the government and private groups. Beginning with the 2009/2010 crop season, maps depicting the type of harvest are generated monthly and sent to the SMA of São Paulo State. The SMA inspects these maps to determine if the straw burning has been authorized.

The objective of this study is to present the methodology of the Canasat project, including the monitoring of the harvesting method, and to analyze the evolution of the harvest areas with and without straw burning from the 2006/07 to the 2008/09 crop season. The maps generated by the project may serve as a basis for greenhouse gas emission models (Lara et al., 2005), carbon storage in silos (Galdos et al., 2009), public health studies (Ribeiro, 2008) and as an aid to public policy in the agricultural sector (Moraes, 2007). These maps also allow evaluating the area of harvestable sugarcane that was not harvested due to weather or industry constrains which is essential information for accurate yield estimation.

2. METHODS

Identification of the harvesting method, either burning or not burning the sugarcane straw, is currently performed in the state of São Paulo, the largest producer of sugarcane in Brazil. São Paulo is located in Southeastern Brazil and has an area of 248,209 km². Figure 1 shows the location of São Paulo State and the area of sugarcane available for harvest in 2008/09.

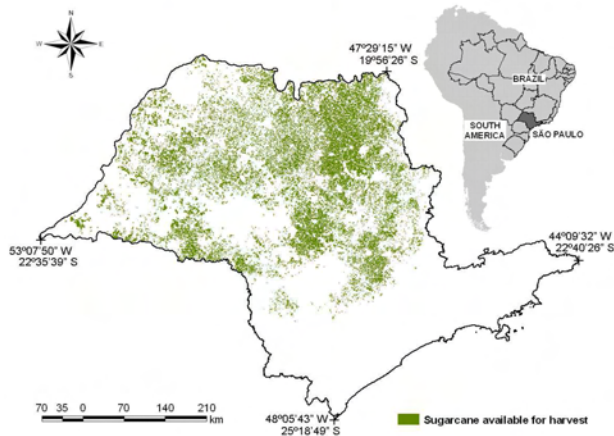


Figure 1. Location of the state of São Paulo within Brazil as well as the area containing harvestable sugarcane in the 2008/09 crop year.

The identification of the harvesting method was performed by a visual interpretation of TM (Thematic Mapper) sensor images taken from the Landsat-5 satellite. In the case of cloud cover on the TM images, CCD (Charge-Coupled Device) sensor images taken from the CBERS-2 and CBERS-2B satellites were used as an alternative (Epiphany et al., 2007). For each orbit point of the TM and CCD sensors, a database was created with the data of interest from the images obtained by the two sensors. All images were registered based on the orthorectified mosaics from TM/Landsat-7 images obtained by NASA (NASA, 2007) utilizing a first degree polynomial and nearest neighbor interpolation.

Monitoring of the harvest type is only possible after producing a map of available sugarcane for harvest. This is then utilized as a mask for the remote sensing images and allows monitoring only the sugarcane areas that available for harvested in the current crop year. This map is prepared by the Canasat project at the beginning of each crop season.

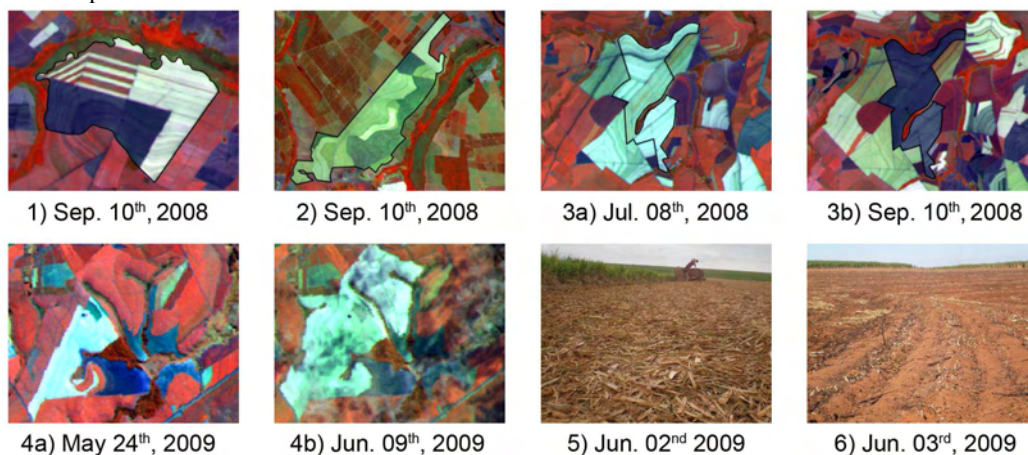


Figure 2. Temporal sequence of TM/Landsat-5 images, color composition 4(R)5(G)3(B), illustrating different harvest types (2.1 and 2.2), the change in harvest characteristics caused by post-harvest agricultural practices (2.3a and 2.3b), different harvest types due to declivity (2.4a and 2.4b), and field photos of recently harvested areas without straw burning and with straw burning (2.5 and 2.6).

In contrast with other agricultural crops, sugarcane has a long harvest season, lasting from April to December. The remote sensing images allow to identify the harvesting method, either burning or not burning the sugarcane straw, because the areas where sugarcane is harvested after burning present dark tones in response to soil exposure (Stoner and Baumgardner, 1981). Areas harvested without burning present bright tones because the ground is covered by dry leaves (Figure 2.1) (Aguir et al., 2009). In Figures 2.5 and 2.6, field photos of recently harvested areas without straw burning and with straw burning, respectively, can be seen. Both the accumulation of straw after harvest and soil exposure from burnt straw may be observed in these figures.

Over time, the correct identification of the harvest method becomes less clear. Both weather and post-harvest agricultural practices such as the burning of straw in the field after harvest are the major factors that affect this identification (El-Hajj et al., 2009). Figure 2.2 illustrates an area with plots harvested on different dates. The difference in time and the use of different post-harvest agricultural practices create changes in the color and characterization of these plots, (which are differentiated in the image). However, all plots were harvested without burning.

Figure 2.3a shows an image acquired in July of 2008 in which it is possible to observe an area harvested without burning. This same area, in September of 2008, possesses dark tones due to either the straw being burnt following the harvest or due to the soil being exposed (Figure 2.3b). Therefore, the less time that has elapsed between the harvest time and the image acquisition, the more likely it is to correctly identify the harvesting method.

Declivity is a limiting factor for mechanical harvest. For this reason, in many crop fields, harvesting is performed using both methods. In the part of the field where the declivity is over 12%, burning is still used; however, in the part of the field with lower declivity the mechanical harvest is performed. Figures 2.4a and 2.4b illustrate this situation in a sequence of two dates; in the dark plots, with a high declivity, a manual harvest was performed (after burning), and in the light areas, with a declivity of less than 12%, the sugarcane was harvested mechanically (without burning). It should be noted that Figure 2.4b shows the presence of some clouds.

A visual interpretation of the images was performed by trained interpreters in two stages: (i) the images were evaluated in chronological order, and at the moment in which an area was identified as harvested, it was assigned to the pertinent thematic class; (ii) after the visual interpretation was performed by the several interpreters, all the resultant maps were revised by a single interpreter (the reviser) to guarantee homogeneity of the interpretations.

Next, a mosaic (thematic map) was generated for the entire harvested sugarcane area in the state of São Paulo for the 2008/09 season. A declivity map, generated from the SRTM images, using the methodology described by Valeriano et al. (2006), was utilized to identify areas for mechanical harvest ($\leq 12\%$ declivity) and areas of non-mechanical harvest ($>12\%$ declivity). The intersection between the two maps permitted the evaluation of the different harvest modes by declivity.

3. RESULTS AND DISCUSSION

The total harvested area increased 20.9% (680 thousand ha) from crop year 2006/07 to 2008/09. This increase is a consequence of the expansion occurring in the state of São Paulo during this time period. Table 1 summarizes the total area harvested with and without burning, the unharvested areas for the three harvest years, and the harvest type for each declivity class. During the 2007/08 season, 5.6% of the total available area for harvest (220.871 ha) could not be evaluated due to cloud cover obscuring the images.

In the 2006/07 season, the area harvested by burning was 1.02 million hectares greater than the area harvested without burning. In the 2008/09 season this difference was 73.6 thousand hectares, which represents an increase of 73.1% in the harvested area without burning between these two seasons (Table 1a). Therefore, the percentage of the total area harvested with burning decreased each season, from 65.8% in 2006/07 to 50.9% in 2008/09. Despite the fact that the overall harvested area without burning increased considerably, the area harvested with burning did not show a considerable reduction. This indicates that, the majority of newly cultivated areas are harvested without burning. The limiting factor for the conversion of the harvest method is that the plots must be prepared for the harvesting machines. This requires adequate planting lines, and in addition, many areas have a declivity greater than 12%. Also, the vegetative cycle of sugarcane is approximately 6 to 7 years, and farmers do not reform the plots until the end of this period. Therefore, the plots currently harvested with the burning method should be gradually converted to non-burning plots or eliminated for sugarcane production if declivity is $>12\%$.

The total unharvested area increased each season, reaching 11.6% of the total available area for harvest in the 2008/09 season (Table 1a). The principle reason for this fact is that the ethanol plants under construction presented significant delays to enter in operational activity. Also, unfavorable weather conditions during the harvest season reduced the harvesting capacity (Aguiar et al., 2007).

When considering the declivity classes, in the entire state, approximately 97% of the available area for harvest during the three seasons was located at a declivity of $\leq 12\%$ (which allows for mechanical harvesting) (Table 1b). However, harvesting

with burning was predominant, especially in the areas with a declivity $>12\%$. In this declivity class, harvesting is performed manually; therefore, the straw has to be burned to easy the harvest.

Table 1. Total area of sugarcane harvested (a) per declivity class (b and c) without and with burning and the unharvested area, for the seasons of 2006/07 to 2008/09. The percentages in relation to without and with burning refer to the total harvested area while the percentage of unharvested sugarcane refers to the total available area for harvest at the beginning of each season.

(a)

Year Season	Harvest type					
	Without burning		With burning		Unharvested	
	(ha)	%	(ha)	%	(ha)	%
2008/09	1,928,561	49.1	2,002,215	50.9	514,502	11.6
2007/08*	1,667,502	46.6	1,909,235	53.4	164,321	4.1
2006/07	1,113,855	34.2	2,138,408	65.8	102,208	3.0

(b)

Year Season	Declivity $\leq 12\%$					
	Without burning		With burning		Unharvested	
	(ha)	%	(ha)	%	(ha)	%
2008/09	1,891,845	49.7	1,917,719	50.3	494,307	11.5
2007/08*	1,630,825	47.0	1,835,907	53.0	158,960	4.1
2006/07	1,089,812	34.7	2,055,017	65.3	98,877	3.0

(c)

Year Season	Declivity $>12\%$					
	Without burning		With burning		Unharvested	
	(ha)	%	(ha)	%	(ha)	%
2008/09	36,715	30.3	84,496	69.7	20,195	14.3
2007/08*	37,132	33.8	72,763	66.2	5,367	4.2
2006/07	24,043	22.4	83,392	77.6	3,331	3.0

* For the season 2007/08, a total of 220,871 ha, 5.6% of the total area available for harvest could not be evaluated because of cloud cover obscuring the images.

On the other hand, an analysis of the three seasons indicates that the percentage of the area harvested without burning increased each season. The areas harvested without burning reached 49.7% in the 2008/09 season in areas with a declivity $\leq 12\%$. The same was not true in sugarcane areas with a declivity $>12\%$. In these areas, the harvest without burning was greater in the 2007/08 season than in 2008/09 and harvesting with burning increased in the last analyzed season (Table 1c). A total of 11,993 ha could not be evaluated in areas with a declivity $>12\%$ in the 2007/08 season. If we postulate that this area was harvested with burning, the percentages of the harvesting method for the 2007/08 season at a declivity of $>12\%$ would be modified to 69.5% with burning and 30.5% without. Therefore, even in this situation, the percentage of the area harvested with burning increased slightly in the 2008/09 season in relation to the 2007/08 season, and the percentage of the area harvested without burning decreased.

Despite the fact that the percentage of sugarcane cultivated in declivities $>12\%$ is low (3%), the percentage of unharvested sugarcane in this class for the 2008/09 season was greater than in declivities $\leq 12\%$.

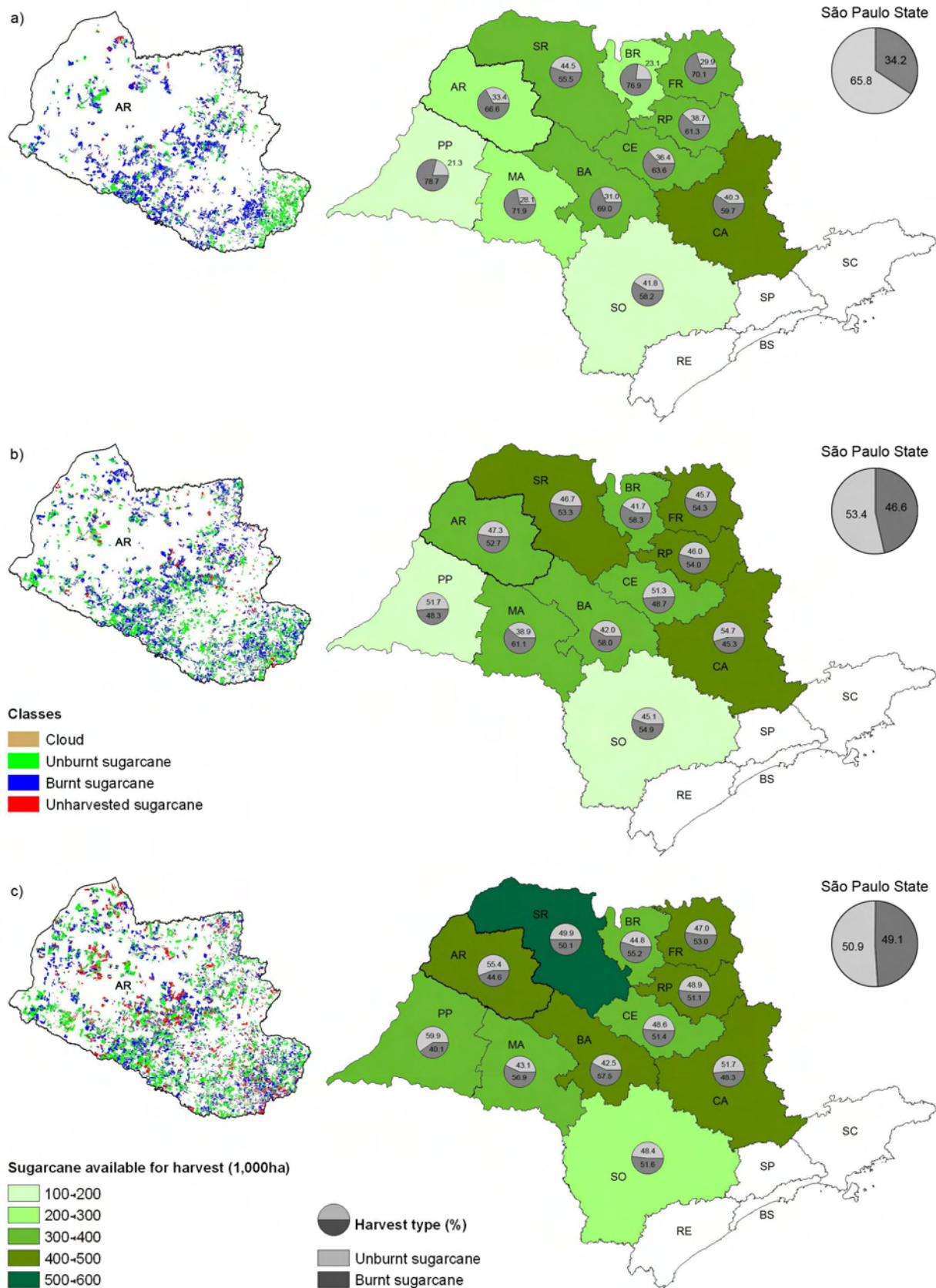


Figure 3. Area available for sugarcane harvest, the percentage of each harvest type (with or without burning) for the Administrative Regions (RA) of the state of São Paulo for the seasons of (a) 2006/07, (b) 2007/08 and (c) 2008/09 and localization of the harvest areas (with and without burning) and the unharvested areas for the RA of Araçatuba (AR). RAs: Araçatuba (AR), Baixada Santista (BS), Barretos (BR), Bauru (BA), Campinas (CA), Central (CE), Franca (FR), Marília (MA), Presidente Prudente (PP), Registro (RE), Ribeirão Preto (RP), São José do Rio Preto (SR), São José dos Campos (SC), São Paulo (SP) and Sorocaba (SO).

According to Lara et al. (2005), approximately 20 tons of dry sugarcane material is burnt per hectare, contributing to approximately 0.48 Tg of carbon per year in global emissions. Soares et al. (2009) stated that sugarcane harvested without burning eliminates methane (CH₄) and nitrous oxide (N₂O) emissions totaling 1.72 tons in carbon dioxide equivalent per hectare. This diminishes the total greenhouse gas emissions produced during sugarcane harvest by approximately 80%. Therefore, a reduction of 136,193 ha harvested with burning reduced carbon dioxide equivalent emissions by 234.2 thousand tons. Postulating that by 2014 all areas that are mechanically harvested will have attained the goals stipulated by the agro-environmental protocol, the harvests will be performed without burning and the newly planted areas will also be harvested without burning, a minimum of 3.29 million tons of carbon dioxide equivalent per year will not be released into the atmosphere. By 2017, when no sugarcane areas will be burnt for harvest this figure will be even greater (3.44 million tons of carbon dioxide equivalent per year).

Figure 3 shows the area available for sugarcane harvest and the percentage of each harvest type for the Administrative Regions (AR) of the state of São Paulo for the 2006/07 to 2008/09 seasons. It also illustrates the location of the areas of each harvest type for the AR of Araçatuba. The ARs were created by the Geographic and Cartographic Institute of São Paulo (IGC) for governmental planning. Each AR is composed of several municipalities within a specific geographic area with economic and social similarities (<http://www.igc.sp.gov.br/mapasRas.htm>).

The four ARs located in the southeast region of the state (São José dos Campos, São Paulo, Baixada Santista and Registro) possess less extensive cultivated areas and therefore do not produce sugarcane for the agroindustrial sector. This is because they possess less favorable environmental conditions for the cultivation of sugarcane, such as greater rates of rainfall or unfavorable for mechanization (Alfonsi et al., 1987). Therefore, these ARs are not monitored by the Canasat Project.

All of the ARs showed an increase in area available for sugarcane between the 2006/07 and 2008/09 seasons. This can be verified by the change in class in Figures 3a, 3b and 3c, with the exception of the Central AR in which there was an increase in area without a change in class. The ARs of São José do Rio Preto and Araçatuba were the only ARs that changed class each season, demonstrating a large expansion in cultivated sugarcane area between the analyzed seasons. São José do Rio Preto had the greatest area available for harvest in the 2008/09 season, representing 12.8% of the total area available in the state.

All ARs had increases in the percentage of unburnt harvested area between the seasons of 2006/07 and 2008/09 except for Campinas and Central. These two ARs significantly increased their percentages in the 2008/09 season in relation to that of 2007/08 (Figure 3). The largest change in harvest type occurred in the AR of Presidente Prudent where 21.3% of the harvested areas in the 2006/07 season were harvested without burning and this percentage increased to 59.9% in the 2008/09 season. This AR had the greatest percentage of burnt harvest in the 2006/07 season (78.8%) and in the 2008/09 season it was the AR with the lowest percentage of burnt harvest (40.1%). In contrast, Bauru was the AR with the greatest percentage of burnt harvest (57.5%)

Araçatuba also showed a large change in the percentage of unburnt harvest, increasing from 33.4% in the 2006/07 season

to 55.4% in the 2008/09 season (and was the AR with the second largest percentage of unburnt harvest in the last season). This change can be seen in Figure 3, in which this AR is highlighted with the localization of burnt and unburnt harvests. In the 2006/07 season the high percentage of burnt harvest (blue) can be seen, while in the 2008/09 season the majority of harvested areas are unburnt (green; there is also an increase in unharvested sugarcane).

4. FINAL CONSIDERATIONS

The use of remote sensing satellite images allowed evaluate the sugarcane harvest type, burnt and unburnt, in the state of São Paulo over the course of three seasons. Data generated by the Canasat Project demonstrated that the harvest type in the state has changed over the seasons due to governmental pressure to increase sugarcane harvest mechanization. In the 2006/07 season, 50.9% of the state's sugarcane harvest was unburnt, and this percentage increased to 65.8% in the 2008/09 season. All of the Administrative Regions in the state, except for two, showed reductions in the percentage of burnt areas. The two exceptions showed a small increase in the 2008/09 season compared to that of 2007/08. Western São Paulo is confirmed as the region with greatest expansion and also the region with the greatest increases in unburnt harvest.

For the three analyzed seasons, approximately 97% of the total area available for harvest in the state of São Paulo was located in declivities <12%; therefore, allowing mechanical harvest. The spatial analysis of the harvest type allows to establish local and regional monitoring and inspection to evaluate the effectiveness of the agro-environmental protocol to reduce and ultimately cease the pre-harvest burnt practice of sugarcane fields.

5. REFERENCES

- Abdel-Rahman, E. M. and Ahmed, F. B. 2008. The application of remote sensing techniques to sugarcane (*Saccharum spp. hybrid*) production: a review of the literature. *International Journal of Remote Sensing*, 29, pp. 3753–3767.
- Aguiar, D. A.; Silva, W. F.; Feitosa, F. F.; Gonçalves, G. G.; Rizzi, R.; Rudorff, B. F. T., 2007. Análise espacial da colheita da cana-de-açúcar no Estado de São Paulo: a influência da precipitação. In: *Simpósio Brasileiro de Sensoriamento Remoto*, Florianópolis, Brasil, vol. XIII, pp. 2231-2238.
- Aguiar, D. A.; Rudorff, B. F. T.; Adami, M.; Shimabukuro, Y. E. 2009. Imagens de sensoriamento remoto no monitoramento da colheita da cana-de-açúcar. *Revista de Engenharia Agrícola*, 29, PP. 440-451.
- Alfonsi, R. R.; Pedro Júnior, M. J.; Brunini, O.; Barbieri, V. Condições climáticas para a cana-de-açúcar. In: Paranhos, S. B. (coord.), 1987. *Cana-de-açúcar: cultivo e utilização*. Campinas: Fundação Cargill, pp. 42-55.
- Baghdadi, N.; Boyer, N.; Todoroff, P.; El Hajj, M.; Bégué, A., 2009. Integrating SPOT-5 time series, crop growth modeling and expert knowledge for monitoring agricultural practices — The case of sugarcane harvest on Reunion Island. *Remote Sensing of Environment*, 113, pp. 1724-1738.

- El Hajj, M.; Bégué, A.; Guillaume, S.; Martiné, J. F., 2009. Integrating SPOT-5 time series, crop growth modeling and expert knowledge for monitoring agricultural practices - The case of sugarcane harvest on Reunion Island. *Remote Sensing of Environment*, 113, pp. 2052-2061.
- Epiphânio, J. C. N.; Soares, J. V.; Ferreira, H. S.; Câmara, G. CBERS: the Chinese-Brazilian Earth Resources Satellite programme. In: *The Full Picture*. GEO - Group on Earth Observations, 2007. Geneva, Switzerland: Tudor Rose, v. 1, pp. 116-117. http://www.earthobservations.org/documents/the_full_picture.pdf. Access on: nov. 13rd, 2009.
- FAO (Food and Agriculture Organization of the United Nations). *FAOSTAT*. <http://faostat.fao.org/site/567/DesktopDefault.aspx?PageID=567#ancor>. Access on: nov. 10th, 2009.
- Galdos, M. V., Cerri, C. C.; Cerri, C. E. P., 2009. Soil carbon stocks under burned and unburned sugarcane in Brazil. *Geoderma*, 153, pp. 347-352.
- Goldemberg, J., 2007. Ethanol for a sustainable energy future. *Science*, 315, pp. 808-810.
- Goldemberg, J.; Coelho, S. T.; Guardabassi, P., 2008. The sustainability of ethanol production from sugarcane. *Energy Policy*, 36, pp. 2086-2097.
- Lara, L. L.; Artaxo, P.; Martinelli, L. A.; Camargo, P. B.; Victoria, R. L.; Ferraz, E. S. B., 2005. Properties of aerosols from sugar-cane burning emissions in Southeastern Brazil. *Atmospheric Environment*, 39, pp. 4627-4637.
- Moraes, M. A. F. D., 2007. Indicadores do mercado de trabalho do sistema agroindustrial da cana-de-açúcar do Brasil no período 1992-2005. *Estudos Econômicos*, 37, pp. 875-902.
- NASA. Orthorectified Landsat Enhanced Thematic Mapper (ETM+) Compressed Mosaics. Washington, DC, 2004. Available at: <https://zulu.ssc.nasa.gov/mrsid/>. Access on: mar 13rd, 2007.
- Ribeiro, H., 2008. Queimadas de cana-de-açúcar no Brasil: efeitos à saúde respiratória. *Rev. Saúde Pública*, 42, PP 70-76.
- Rudorff, B. F. T.; Sugawara, L. M., 2007. Mapeamento da cana-de-açúcar na região Centro-Sul via imagens de satélites. *Informe Agropecuário*, 28 (241), pp.79-86.
- Rudorff, B. F. T.; Berka, L. M. S.; Moreira, M. A.; Duarte, V.; Xavier, A. C.; Rosa, V. G. C.; Shimabukuro, Y. E., 2005. Imagens de satélite no mapeamento e estimativa de área de cana-de-açúcar em São Paulo: ano-safra 2003/04. *Agricultura em São Paulo*, 52 (1), pp. 21-39.
- Soares, L. H. B.; Alves, B. J. R.; Urquiaga, S.; Boddey, R. M., 2009. Mitigação das emissões de gases do efeito estufa pelo uso de etanol da cana-de-açúcar produzido no Brasil. *Agroanalysis*, especial EMBRAPA, 29, pp. http://www.agroanalysis.com.br/index.php?area=especial&esp_id=51&page=1 Access on: nov. 10th, 2009.
- Stoner, E.R.; Baumgardner, M.F. 1981. Characteristic variations in reflectance of surface soils. *Soil Science Society America Journal*, 45, pp.1161-1165.
- Valeriano, M. M.; Kuplich, T M.; Storino, M.; Amaral, B. D.; Mendes JR., J. N.; Lima, D. J. 2006. Modeling small watersheds in Brazilian Amazônia with shuttle radar topographic mission-90 m data. *Computers & Geosciences*, 32, pp. 1169 – 1181.
- UNICA (Sugarcane Industry Association). *Dados e Cotações – Estatísticas*. <http://www.unica.com.br/dadosCotacao/estatistica/>. Access on: nov. 25th, 2009.

6. ACKNOWLEDGEMENTS

We thank team of Laboratory of remote sensing in Agriculture and Forest (LAF) for mapping work and contributions.

REMOTE SENSING FOR PHYSICAL PROTECTION OF THE PIPELINE NETWORK ONLINE MONITORING OF CORRIDOR BASED INFRASTRUCTURE

M. A. Foroushani^{a,1}, S. Damadi^b

^a Planning Dept. of Oil Pipeline and Telecommunication Co. Tehran, Iran

^b Dept. Of Electrical Engineering, AmirKabir University of Technology, Tehran, Iran- sms_damadi@yahoo.com

KEY WORDS: Grand based Remote sensing, Corridor Based Data, online monitoring, invasion of the pipelines corridor, Detecting Moving object

ABSTRACT

The existing service that locates invasions along a petroleum pipeline, informs an intrusion or warns about a disaster on the Petroleum Pipeline and Telecommunication corridors by using data from the Rights of Way (ROW), which is a buffer zone on each side of a petroleum pipeline. This data is called Corridor Based Data (CBD). For many years, the ROW has been traced and monitored by using vehicles. Recently, remote sensing and sensors technology has helped key-persons to monitor the large boundaries and long corridor of the ROW, by using spatial information and sensors principle respectively. The truth is that scalability and performance of this method has not yet been widely practiced. A large interval of the data acquisition is the main weakness of space borne remote sensing methods. This is due to our need for continuous monitoring and also to make the existing service more useful. Using a concept for automotive assistance and just-in-time decision making helps overcome the limitations of existing methods. The conceptual result proposes an efficient approach to the algorithm of intrusion detection. This algorithm could be divided into two parts of object detection and motion field geo-coded methods. Ground based remote sensing on the other hand, considers unmanned monitoring of oil pipeline corridor based on the literature of the relevant domains including Context Aware Systems, remote sensing, general interaction and GIS. This paper organized as following conceptual statement. In section 1, it gives definition of monitoring pipeline corridor. Potential monitoring through remote sensing is described in section 2 and talks briefly about the pitfalls of implementations, theoretical framework, result and conclusion, are discussed in section 3, and 4 respectively.

¹No 188 Gharani St. Postal code 1598995913 IOPTC Tehran–Iran, mforoushani@gmail.com ; mobile: +98 9363482314 Tel +98 66155329 Fax +98 21 66155438

1. MONITORING PIPELINE CORRIDOR

According to (Ranking 2006; Re-published from the CIA World Factbook By Photius Coutsoukis 2009) the properties of the pipeline corridor context are reporting as follows. Briefly, pipeline facilities show that two million and twenty thousand kilometer (2,020,000 km) pipelines are distributing petroleum to consumers around the world. In Europe, Germany has 33,000 km, Ukraine 29,000 km, France 23,000 km and Italy 19,000 km of pipeline. These countries have the largest pipeline length after Russia with 243,000 km. European countries account for 1/10 of the total length of the world’s pipeline network, while the United States of America has 800,000 km of pipelines, which is equivalent to 2/5 of the total length of the world’s pipelines. It is an arguable that the pipeline infrastructure is influenced by the environmental, social and technical objectives and accordingly, some residual impact and risks are inevitable.

According to the ASME (American Society of Mechanical Engineers), (American Petroleum Institute’s Pipeline Committee 2003) the annual report of third party damage that is caused by excavation, farming or other diggings activities is responsible for 41% of the damage from 1996 to 2000 as it shows in figure 1. The importance of the damage can be graded as follows: first, damaged by third party second, corrosion and third is equipment malfunction. The pattern of the ROW in a Geo-information map is a "buffer line".

A World Petroleum Pipeline Length

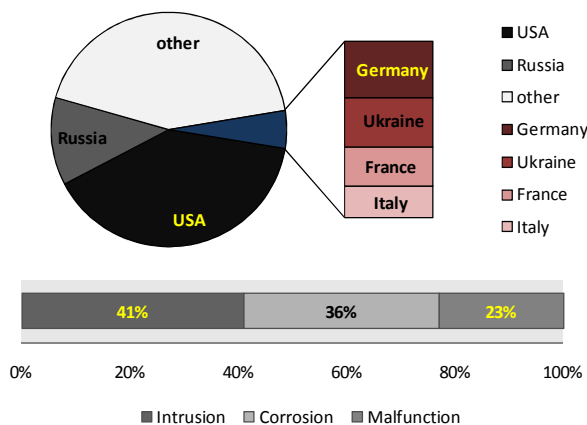


Figure 1. Damage is graded from 1996 to 2000

Figure 2 depicts the space which is allocated to operational activity, and includes a safe zone for a pipeline corridor. It aims to protect ROW from any intrusion(Enbridge Pipeline 2005). But knowing how to identify the threat and determining what action ought to take in order to prevent it happening again is a key component of ensuring on-going safety.

In the case of protecting approaches, The Oil Pipeline Transportation and beneficiary companies are interested to protect the transportation networks effectively by warn about intrusion. Usually, the damage is caused by other sectors. It is quite obvious, a safe operation and supervision of petroleum pipeline transportation follows a different policy from country to country or even a different Pipeline’s Profile (geo-location)².

² - Pipeline network like river not place in certain area, thus geographical function assign to each point of ROW. It means ROW has nature of interest from point to point.

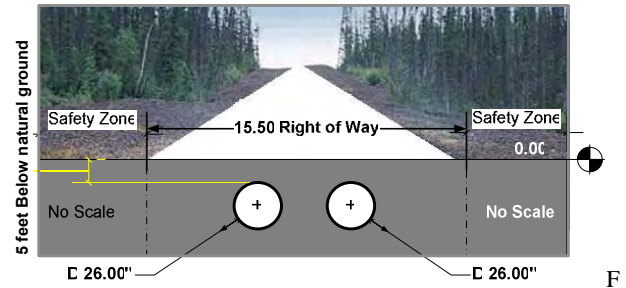


Figure 2. Right of Way Includes Area of Safety

Although the most widely used method for monitoring a pipeline network is Patrol, the other advanced application of remote sensing is also concerned. With reference to the need an application for real time monitoring of the moving object over pipeline network, space-borne and earth observation is not feasible with existing satellite. For that reason, there is no online warning about disturbance against ROW.

1.1 Established methods for monitoring

Figure 3 illustrates two widespread monitoring methods. Type A shows patrol, a legacy monitoring method uses small airplane, helicopter or car in order to trace disturbance along the ROW. Each geographical direction has its own schedule to pursue from place to place. Difficulties to access mountainous locations, involving in a costly interval of data acquisition to find out what happens along the pipeline are turned into its disadvantage.

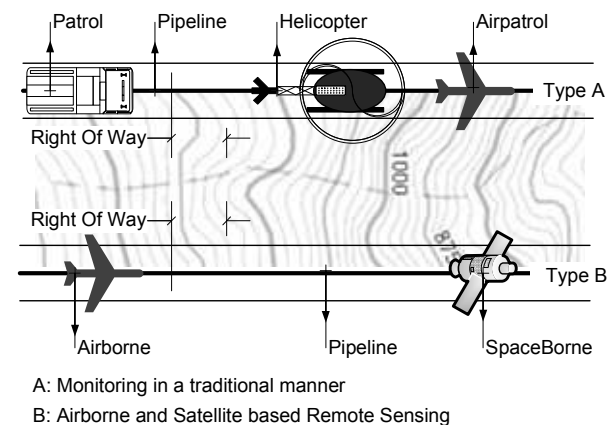


Figure 3. The Apprehensive Monitoring Techniques

Type B depicts the monitoring of pipeline corridor by new technology. Data and images have been provided by the installed scanners on the space and airborne platforms. The gathered images and data pass through the process of *Automated Classification, Noise Removal, Layer Extraction, Automated Filtering* followed by *Georeferences and Calibration of Geocoordinate System*. Final processing steps are *Data Reprocessing* and *Quality Control*. Therefore outcome help decision makers to warn about intrusions. Obviously, processing the immense number of continuous images and data makes operation too costly for the value. For this reason, high performance computer stations and GIS professional staff, enlisting the highly experienced people, special software and hardware would be involved to operate under Type B. Furthermore, a discussion of inadequacies in the current monitoring methods and present appropriate technique results from reply to impediment. Does ROW really need to

have online monitoring and why? What is the possible objective/s? Can remote sensing present the varied solution? And what is the proposed algorithm in order to improve responding to the high temporal monitoring?

In response to primary question, although observation from Patrol technique and airborne vision are appropriate steps toward the intrusion discontinued, an illegal activities may happen when patrol are moved away according to the schedule. In other words, monitoring operation is figured during a workday in below. An illegal activity is begun at 8:00 and at the same time Patrols are placed at 13:00. Patrols are far from that point thus, an unfortunate defect would be turning to disaster for company in a few hours; besides, they don't have acceptable performance in bad weather condition. Those factors proof our need to meet an online application for monitoring. Consequently, this technique could not be the best choice in order to prevent intrusion from occurring.

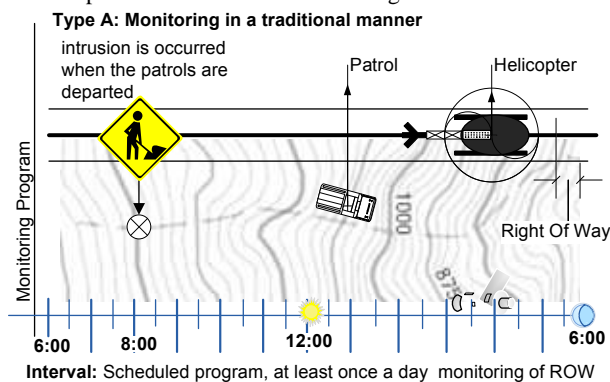


Figure 4: An intrusion is occurred after, at 8:30

In response to warning about intrusion from high temporal monitoring technique aim to fulfil the unscheduled time and enforcement action, online applications have to investigate. decision maker's choice about methods of remote sensing and its platform would be as varied as the type of pipeline construction, economics of pipeline operation, and environment in which they operate. Moreover, environmental issues and operational condition can fluctuate over the time and affect the performance of monitoring application. A few techniques relevant to the objective function are fingered by using the power of remote sensing technology.

2. POTENTIAL MONITORING THROUGH REMOTE SENSING

In the following aspects, potential monitoring through remote sensing and the proposed method with the objective of preventing the intrusion from occurring is discussed. Therefore candidate techniques followed by comparative table are introduced based on given importance weight.

2.1 Sensor platforms

In short, *Remote* as an adjective is located far away spatially, and *Sensing* as a noun is becoming aware of something via sense. Sensors are usually mounted on two platforms of Space-borne and Ground based platform. Obviously, the type of orbits and platforms determine the design of the sensors. Candidate techniques therefore are articulated based on space borne and ground based platform. Airborne scanner is omitted because of low temporal, Long Interval, inadequate number of data and limitation in flight over the pipeline's corridor.

2.1.1 Space-borne platforms: Satellites are placed at three types of orbits around the earth. In order to find which one suits our need, the principles of each type are briefed(UCAR 2009). The first type is geostationary. Its orbital period is equal to the period of earth rotation. So it must be placed in high attitude of 36000 km. Any sensor on this platform is viewing the same position at all time. In contrast resolution of imagery and mapping data are very coarse. For this reason, imaging and mapping satellites are not geosynchronous. Thus communication and weather purposes are the most common use of geosynchronous orbit.

The next type is polar orbiting satellite. This satellite passes above and over the earth's pole and the equator at the different longitudes respectively. Eventually, a polar orbiting satellite can see every part of earth surface within certain time period, which is highly desirable for remote sensing applications. It completes global coverage of the Earth during one day.

The third type of sensor is sun-synchronous. The satellite will pass over every location on the earth at the same solar local time. It must be placed in 700 km above earth surface. Resolution of imagery and mapping data is about 65 m as compared to a meter or less for an airborne scanner. Any sensor on this platform is viewing the same position every other weeks and months. Since active sensor rely on solar energy as a source of power. Sun-synchronous is a good choice for a space borne laser profile. Regarding to figure 5, sun-synchronized is removed from candidate method because its duration process of recurrent period. Although Geostationary can provide data and image at all time, the mention above reason makes its profile impractical and it wouldn't be feasible technique. Finally, polar orbiting satellite has been taken into consideration despite the limitation in discontinuous of recurrent period.

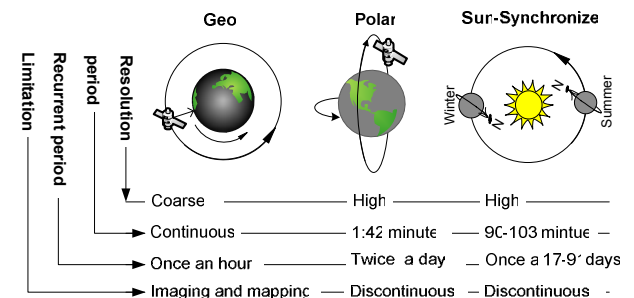


Figure 5 : A glance at space-borne scanner

2.1.2 Ground based platform :Terrestrial remote sensing is usually used for close-range and high accuracy applications. This system works at short, medium and long range of 50-100, up to 250 and 1000 meter respectively. Principle of short rang application is mapping building and small objects. Medium range sensor, with millimetres accuracy is using for 3D modelling application. Long range sensor frequently use for topographic application.

Three type of grand based scanning system, which are pleasing for this application are introduced. Panoramic scanner rotates 360 degree around its axis. It can also scan 180 degrees vertically. Single axis on the other hand can rotate 360 degree around its axis but scan only 50-60 degrees vertical swath. The addition of grand based scanner points on a fixed direction with limited angular range both horizontally and vertically.

2.2 Candidate techniques

In response to a warning from intrusion, illegalized activities over ROW will have stopped by the time the team who guards the ROW arrived over at given point. Whereas, this program is respected to scheduled program of the patrol and space- borne monitoring, there is no guarantee that a pipeline corridor equipped with a state of the art method of monitoring is protected against intrusion. Therefore, in response to the need of a continuous application, *Grand Based Platform* along with the state of the art techniques is considered. In the following section comparative technique are discussed and ranked based on the weight of the value.

2.2.1 Comparative methods and techniques: Table 1 highlights a number of advantages and disadvantages of candidate techniques. The column for A and B show certain similarities. There is the same rank of disadvantage for the *Recurrent Period*, *Cost to Process* and *Lack of Sufficient Staff*, in comparing with only two minor disadvantages of *Cost to Capacity* for ground based remote sensing technology and given *Time to Stop an Intrusion* from “technique C”.

Techniques of monitoring	Customizable platform	User Interface and	Lack of Sufficient Staff	Data Analysis & Final Report	Cost to Capacity	High Resolution	Detecting Moving object	Warn about Natural Hazard	Cost to Process	Period and recurrent Period	Concealment of Confidential area	Time to Stop an intrusion	Time to response (Push-Pull)
C- Ground based	Mobile based	Sensor	No	GSM	High	Text	Remote Sensing	Yes	Low	Real time	High	High	High-Push and Pull
B- Space Borne	Satellite&Airborne & UAV	Camera & Sensor	Yes	Powerfull waives	Medium	Image and Data	Remote sensing	Yes	High	Scheduled	Low	High	Medium-Pull Service
A- Patrol, Helicopter	Patrol, Helicopter	Human eyes	Yes	paper based Report	Low	Real world	Observation	No	High	Scheduled	Medium	low	High

Table 1. Comparative Methods and Techniques

Frequency or *Recurrent Period* defines length of time that is marked off by two observations. It is the act of observing comes back to the same area at almost same time. That is to say, a scheduled program is not provided continuous service for the company. For that reason, *Cost to Process* would make increase the expense of this process. *Cost to Process* means the money that company usually pay for a period of scheduled program. However, minimum interval would not be less than 6 to 12 hours for those candidate techniques. That is to say, “technique B” pays out a bit higher for building capacity as well as running scheduled program. On the other hand, “technique C” shows that the *Cost to Process* for real time program is arguable although the *Cost to Capacity* itself would be expensive. Regarding *The Lack of Sufficient Staff*, another weakness remarks that for both “A” and “B”. To put it another way, “technique A” always need to have on-call security and maintenance staff, as far as the requirement of professional analysts is concerned for “technique B”. Then again for “technique C” and B *Time to Stop Intrusion* is added to those

disadvantages. For a case in point of warning about intrusion over given place, how long does it take till security and maintenance staff would be there? So multiple processing must be in place with trained staff and advanced application to achieve optimum system performance and safety.

Conversely, the advantages of “technique B” over “A” are several items such as; *User Interface*, *Report Generator*, *Detecting Moving Objects*, and *Warn about Natural Hazards*, whereas with the reference to the need of notable items for the best candidate technique, some advantage are indicated. They are remarked as *Time to Response*, *Continuous Monitoring*, *Less Cost to Process Online*, *Detecting Moving Object and Needing Few Trained Staff* followed by *Customizable Platform*. In addition, *Concealment of Confidential Area* means to operate on limited area through the pipeline corridor from the level of official classification next above restricted and protected area such as; nature of interest, public awareness, historical and protected area, national park, dessert, forest, a secure place and mountainous corridor. Finally, in order to decrease the time of processing, *Push Service* would make it easy. Obviously, text processing needs as less as possible times to process. It would be an advantage to warn about intrusion at given time. To sum up, discussed parameter of the candidate technique are ranked as it shows in table2.

Low importance = -2		High importance = 2		Importance Rate	Patrol	Space Borne	Ground based
Parameter Ranked		A	B				
Cost	Lack of sufficient Staff	1	1	3	5		
	Data Analysis & Final Report	1	3	3	5		
	Cost to Process	2	1	3	5		
	Cost to Capacity	1	5	1	3		
	Customizable platform	-2	3	1	3		
Quality	User Interface	-1	5	3	3		
	Period and recurrent Period	2	1	3	5		
	High Resolution	1	5	3	3		
	Concealment of Confidential data	2	3	1	3		
Time	Time to stop an intrusion	2	5	3	3		
	Time to response (Push-Pull)	2	1	3	5		
Detection	Detecting Moving object	1	1	1	5		
	Warn about Natural Hazard	1	1	3	5		

Table 2. Specification of candidate techniques

Those parameters are classified in *cost*, *quality of data*, *frequency* and *detection*. With reference to three techniques, technique A is weighed against both B and C which are space and ground based techniques respectively. Then again each parameter are assigned own factor between -2 and 2. Low importance is of course -2 whereas 2 present high importance parameter. Therefore important rate itself is multiplied by the given rank make score. Additionally, classified parameters are ascended from -2 to 2 as is depicted in Figure 6. The graph provides the ranking information of candidate technique. From top-down point of view, the first line (light green) plots specification of “technique C” while the second and third line (Red and Blue) show a detail description of “technique B” and A respectively. From the line graphs it can be seen that there are minimum and maximum score belonged to *Customizable Platform* in the extreme left, and *Time to stop Intrusion* in the extreme right. Maximum score reach over 10 is belong to the first line in *Time to Response an Intrusion*, *Period and*

Recurrent Period and *Cost to Process*. In contrast, Red and Blue (B and A) have hardly 6 in both essential parameter of *Recurrent Period* and *Cost to Process*. Then again, Green line (C) is scored slightly less than 6 in *Detecting Moving Object* and *Warning about Natural Hazard*. Whereas Red and Blue (B and A) are scored below 2 in detecting moving object in given time. All in all, “technique C” is of course much better than “technique B” and “technique A” outside the *Malfunction*, *Time to Stop an Intrusion*, *Data Resolution* and *Cost of Capacity*.

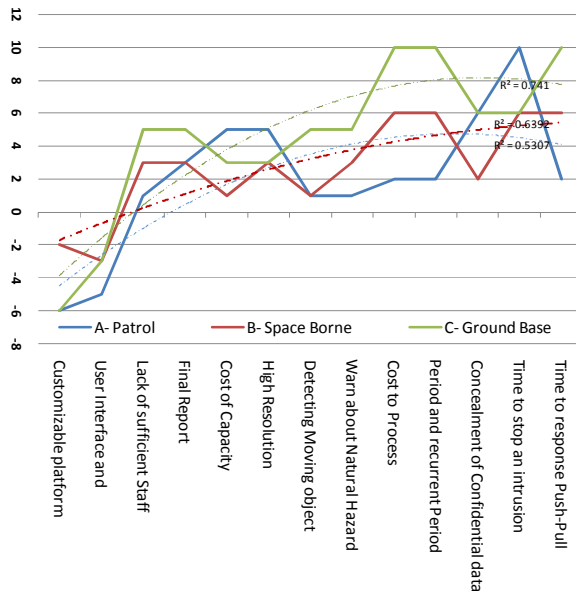


Figure 6. A quick view of candidate technique

From technical point of view, a decision to choose appropriate technique will make based on access time to the area of operation(site) in order to prevent damage from occurring, standard and a perilous of petroleum transportation, the pipeline network topology, investment and applied technologies such as SCADA, optical fibre and national infrastructure. That is to say, type C is proposed as a Ground Based Remote Sensing method (GBRS). What is more about implementation, remote sensing sensors are installed along the pipeline (ROW). These detectors are electronic devices that can sense activities against corridors in real time. Intrusion will be recognized and analyzed by utilized techniques. As an obvious benefit of push service, decision maker will received an alarm message from the point that has been threatened.

3. IMPLEMENTATION

The proposed model needs to support by information and data from the pipeline corridor samples per second. So, the service should respond to context dynamically. Systems can dynamically change their response because the context is categorized as various, reactive, context-sensitive and environmentally directed(Gregory, Anind et al. 1999). These models are mostly introduced in the boarder context of interaction systems. It can include the user and applications(Anind 2001). From *System Component* point of view, proposed models is to capture important system components such as *User*, *Location*, *Context* and *Data*. (Anind 2001) and (Schilit, Adams et al. 1994) introduce different contexts that are relevant to a user when accessing an information service. Localization and service are the main key-

points in *Context Processing* application. It is an information service, accessible with mobile devices through the mobile network and utilizing the ability to make use of the geographical position of the mobile device (Shu Wang 2008). According to (Nivala, A-M et al. 2003) there are nine types of context with sequential access of *Physical surroundings*, *Navigation history*, *Purpose of use*, *System properties*, *Time and Map user*, including *Social Culture* and *Orientation* followed by *Location Context*. The result of the defined context shows that *Context Processing* service targets many users and is available in a mobile-network communication environment. Eventually, the service of context is provided for both pull and push services. Since Push-Services do not rely on previous user interaction with the services. If the corridor be threatened by external factors or disasters the information messages will be received. As is illustrated in figure 7, technical based components from Type C are: *Detectors* (those could be any kind of Sensor/Scanner depending on the corridor situation, Geographical location and the application purpose), *Communication network*, *positioning technology*, and *data provider*.

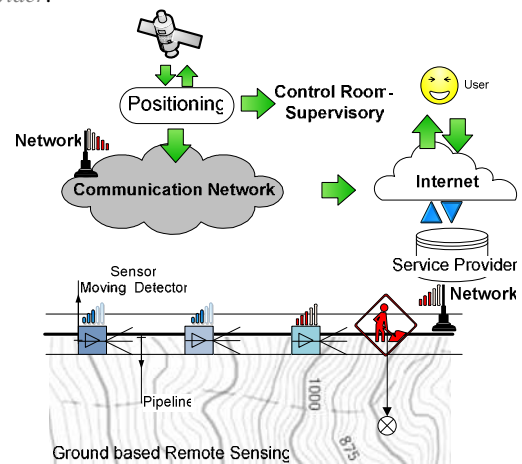


Figure 7. localization and service

Detectors, periodically report positioning information and send it all to the service providers. Obviously, the provision of the push services by such a database approach would involve a huge amount of signalling information, since the positions of all mobile devices have to be continuously transmitted to the database server and information has to be send to the devices (S. D. Hermann and A. Wolisz 2006). Supervisory and user beneficiaries can receive information through the internet with following sequential process.

If an intrusion or a disaster happens over the ROW, the actual position of the sensor/ scanner is obtained from the positioning service. Afterwards, an exact position of occurrence is sent via communication network to a so called gateway. Consequently, the gateway has the task to exchange messages among a communication network and the internet. At the same time it will store information about all the sensors. A server reads the messages and sends them to a program analyzer. Moreover, the service analyses the message and pushes it to the receiver. Then, the service will find information on whether the corridor should be under extra control. In the end, results are sent to the consumer / supervisor via an internet gateway or mobile system. Finally, proper action is taken.

3.1 Theoretical framework

Regardless of the sensor technologies and scanner, a pipeline corridor can be scanned online by the ground based remote

sensing technique. Figure 8 shows top level schema of three simple steps from *receiving signal* and *extracting process* aim to detect *moving object* over corridor and to make warning about intrusion.

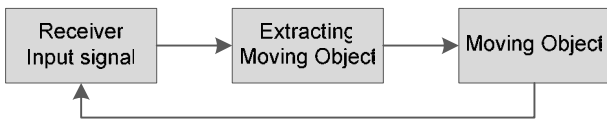


Figure 8. Top Level Framework

As it's mentioned on earlier paragraph and depicted in figure 9, receiver input signal consist of data from sensor, reference data which calls pattern data and feedback from the previous records. The next step, of the extracting moving object has three functions of revealing, de-noising and detection. This step is usually programmed based on different remote sensing application. The last step consists in the function of making warn about intrusion to decision maker, estimation and event history. Finally event history makes feed back to first step.

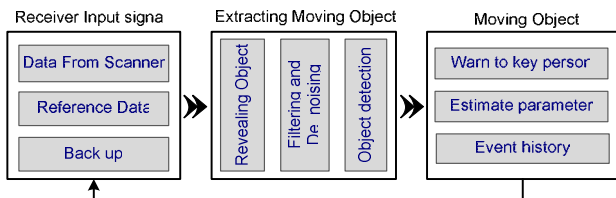


Figure 9. Classification Schema

Image and data that are gathered recently will be compared to the reference. For instance, if hardware processes just a few points (no more than 5), because there is high flow rate of data, we need a lot of time and expensive hardware. For this reason and according to the Figure 10 the problem with scanners especially LADAR is considered in three components.

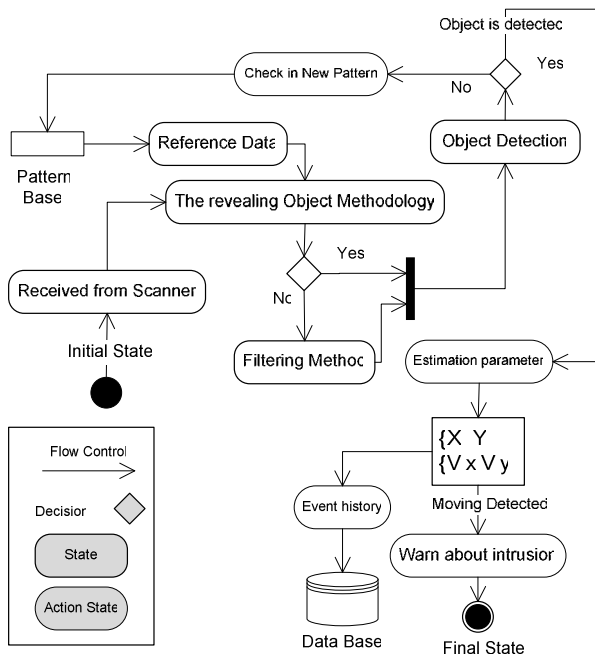


Figure 10: Process of Object Detection schema

The first component is *Classification and Filtering Process*. As far as this technique is supposed to helps us to concern certain

point instead of all the point in the corridor. Figure 10 shows how *Classification and Filtering* can reduce the time to producing report and the size of its. To put it another way, system is looking for the similarities between recent data and reference. For this reason the elimination of the frequent data interaction will take into consideration. Secondly, to reduce the process time *Defining Reference* process is introduced. Additionally, *Discrimination technique* is of assistance software to match recent data with typical shape and suitable format for moving and static objects. For instance, red colour and green can assign to moving and static objects respectively. On the other hand, it is possible to identify whether it is human or device? What it looks like. Regarding to the power of code, it is also possible to recognize the dimension of objects. For the computation of optical flow of 2D image motion the following (Yokoyama and Poggio 2000) function is presented:

$$I(x, t) \cdot I(x + dx, t + dt) \tag{1}$$

Where $I(x, t)$ = the spatiotemporal function of image intensity

t = intensity of the time

$t + dt$ = **object is assumed to remain the same**

For instance; no illumination change are supposed to occur.

Equation 1 can be expanded using Taylor order as follows:

$$\nabla^T I \cdot V + I_t = 0 \tag{2}$$

Where $\nabla I = (I_x, I_y)^T$ = the gradient

I_t = temporal derivative of $I(x, t)$

$V = (u, v)^T$ = image velocity

According to the (Barron, Fleet et al. 1994) one linear equation is insufficient to determine 2D velocity that is known as aperture problem. However it seems good enough to detect moving objects. For instance, moving object on geometric shape, (such as line circle, rectangular and....), indicates intrusion activities.

3.2 Detecting Object

It is defined the similarity between an object of previous frame $R_{prev}(m)$ and an object of current frame $R_{cur}(m')$, using estimated position of lines by optical flow.

$$\{P_1, P_2, \dots, P_n\} \in S$$

Equation (Bernhard Gruber SW. Location Based Services using a Database Federation. Institute for Geoinformation) is Detected and stored line of the current frame.

$$\{S_1, S_2, \dots, S_n\} \in R_{prev}(m) \tag{4}$$

Whereas equation (4) is defined all background line as a previous frame, then similarity is defined as follows:

$$\rho(m, m') = \frac{\sum_{j=1}^{N_m} \sum_{i=1}^{N_{j'}} l_{ij}}{\sum_{j=1}^{N_m} |S_j|} \tag{5}$$

Where $|S_j|$ is the number of element in S , and l_{ij} then these two objects $R_{prev}(m)$ and $R_{cur}(m')$ are considered as the same object if the similarity of $\rho(m, m')$ is non-zero value.

$$t_{ij} \begin{cases} 1 & \text{if } P_i \in R_{cur}(m') \text{ where } P_i \in S_j \\ 0 & \text{otherwise} \end{cases} \tag{6}$$

$$R_{prev}(m) \equiv R_{cur}(m'), \text{ if } \rho(m, m') \neq 0.$$

4. CONCLUSION

Due to the fact that if an intrusive process over the ROW causes unfortunate defects, the company mission will be under threat of inconsistency operation and the oil transportation through pipeline will stop. An occurrence into pipeline also expense company too costly for the value of rehabilitation to fix damaged parts, soil remediation and keeping a safe and clean corridor from splash with oil.

From the general point of view, physical protection plays a significant role in order to having reliable operation and makes it safer. Apparently, traditional methods of monitoring program are less successful with continuous gathering data process from pipeline corridor. Consequently, it gives company low rank in quality services. For these reason, the overall performance of existing techniques are not acceptable.

From technical point of view, a decision to choose appropriate technique has been argued based on *Time to Response an Intrusion, Period and Recurrent Period and Cost to Process* including *access time to the area of operation (site)* in order to prevent damage from occurring, *standard and a perilous* of petroleum transportation, the *pipeline network topology, investment and existing technologies* such as SCADA, optical fibre and so on. With the reference to former reason, type C as a Ground Based Remote Sensing method (GBRS) has been proposed. Regarding to the cost of operation, proposed technique might be able to recognize high risk activities as well as disaster over pipeline corridor. The next obvious benefit is stopping to spend a lot for the neighbouring corridor in order to fix pollution and pay the penalties. For this reason, the cost of the injured parties adjacent to the pipeline corridor, by using GBRS will reduce. All in all the following result from this proposal is expecting if it turns to a practical profile through the ROW. Spatial Data Infrastructure (SDI) plays role as a service provider for LBS but in this concept it is Vice versa, and SDI will be getting up-to-date from Corridor Based Data.

All intrusion over pipeline corridor would be detected according to GBRS technology and its principle. Outcome of GBRS as a high spatiotemporal information can be placed in GIS layers for Geo- Corridor Based Map. So implications of the context will give consumers and users the advantages of Geo-ICT.

REFERENCES

American Petroleum Institute's Pipeline Committee (2003). "The U.S. Oil Pipeline Industry's Safety Performance." [A report to \(Association of Oil Pipe Lines and the American Petroleum Institute's Pipeline Committee\):](#) pages 5-6.

Anind, K. D. (2001). "Understanding and Using Context." [Personal Ubiquitous Comput.](#) **5**(1): 4-7.

Barron, J. L., D. J. Fleet, et al. (1994). "Performance of optical flow techniques." [Int'l J. Computer Vision](#) **12**(1): 43-77.

Bernhard Gruber SW. Location Based Services using a Database Federation. Institute for Geoinformation, T. U. V. I. P. o. t. A. C. R., M, Gould, M, & Ramon, J, eds), in Palma, Spain, 2000:pp: 243-52.

Enbridge Pipeline (2005). "Right of Way Profile." **Canadian Crude oil Company Retrieves from Enbridge Inc. website** <http://www.enbridge.ca/pipelines/rightOfWay/>.

Gregory, D. A., K. D. Anind, et al. (1999). Towards a Better Understanding of Context and Context-Awareness. [Proceedings](#)

[of the 1st international symposium on Handheld and Ubiquitous Computing.](#) Karlsruhe, Germany, Springer-Verlag.

Kiran Yedavalli BK. Sequence-Based Localization in Wireless Sensor Networks, I. T. o. M. C., 2007;vol. 7, no. 1(Digital Object Identifier 10.1109/TMC):pp. 81-94..

Nivala, A-M, et al. (2003). [An Approach to Intelligent Maps: Context Awareness.](#) 5th International Conference on Human Computer Interaction with Mobile Devices and Services, Udine, Italy.

Ove Johnson (2004). "Some Theory behind Obstacle Detection,." [Copyright © 2004, SwedeTrack System.](#)

Ranking, Non-CIA Future Projection and Time Series. (2006). ["http://www.photius.com/rankings/index.html"](http://www.photius.com/rankings/index.html).

Re-published from the CIA World Factbook By Photius Coutsoukis (2009). Pipelines(km) Country Ranks Information Technology Associates .Photius Coutsoukis http://www.photius.com/rankings/transportation/pipelines_2009_0.html.

S. D. Hermann and A. Wolisz (2006). "Investigation of Geographical Routing Enhancements for Location Based Push Services." (In Proc. of 12th Open European Summer School (EUNICE), Stuttgart, Germany, September 2006).

Schilit, B., N. Adams, et al. (1994). Context-Aware Computing Applications. [Proceedings of the 1994 First Workshop on Mobile Computing Systems and Applications - Volume 00,](#) IEEE Computer Society.

Shu Wang, J. M. a. B. K. Y. (2008). "Location Based Services for Mobiles: Technologies and Standards." [IEEE International Conference on Communication \(ICC\) Beijing, China](#)

UCAR (2009). "Facilities Assessment Database." (Last accessed).

Yokoyama, M. and T. Poggio (2000). A contour-based Moving Object Detection and Tracking. C. s. a. A. I. Lab. Tokyo, Japan, Sony Corporation.

ACKNOWLEDGEMENT

The authors would like to thank Prof Mag. Dr.Georg Gartner* for the valuable comments. Additionally, the authors would like to appreciate the painstaking editing task done by Bas Retsios** and Babak Etemadi***.

* Univ.Prof.Mag.Dr.Georg Gartner, Cartography and Geo-Mediatechniques Department of Geoinformation and Cartography, Vienna University of Technology , Erzherzog-Johannplatz 1, A-1040 Vienna, Austria, email: georg.gartner@tuwien.ac.at Tel (+43)58801 12611, URL; <http://cartography.tuwien.ac.at>

** Ir. V. (Bas) Retsios, Software developer from department of Geo-information processing in ITC - Geo-International Institute for Geo-Information Science and Earth Observation-the Netherlands , Enschede. email : retsios@itc.nl

*** ILI Senior lecturer Mr. Babak Etemadi, Electronic engineering, babak_etemadi35@yahoo.com

WINGIS - GIS SOFTWARE FOR ICT DEVELOPERS

W. Mayer, B. Aigner

PROGIS Software GmbH, GIS Development, Postgasse 6, 9500, Villach, Austria

KEY WORDS: Agriculture, Cartography, GIS, Geography, Development, GPS/INS, Orthoimage

ABSTRACT:

PROGIS enables ICT developers to link the GIS software WinGIS, in combination with the embedded Bing Maps module to any database application based on the ActiveX developer component AXWinGIS. WinGIS provides a wide range of GIS functionalities, modules (thematic maps, ISO module, GPS modules, geocoding module) and interfaces (import / export / GPS). This is a worldwide unique solution, bringing together the advantages of an easy to use, cost efficient and versatile GIS software - WinGIS - and the outstanding potential of Microsoft (database) products and online services like Bing Maps.

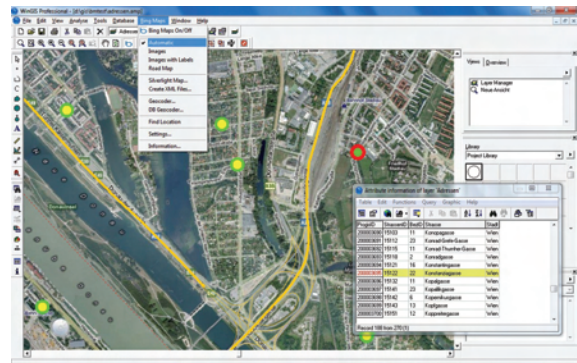
1. WINGIS – GEOGRAPHIC INFORMATION SYSTEM

WinGIS is an easy to use, easy to learn, powerful and cost efficient GIS software with extensive geographic application possibilities and facilities. Due to the integration of the online map data of Microsoft Bing Maps as „embedded Module“, the access to worldwide available geographic data like satellite and aerial images, road maps and address databases is already part of the software package. By using the ActiveX developer component, application developers have the possibility to link their application very easy with WinGIS in order to visualize, edit and administrate any data with a geographic relation.

2. MICROSOFT BING MAPS

Microsoft Bing Maps provides worldwide in high quality and continuous expanding online map data such as satellite and aerial images, road maps and extensive address databses (geocoding). The access to these geo data is integrated in WinGIS as a module and works transaction based. The access to the map data of Microsoft Bing Maps occurs online and transaction based (1 transaction = 8 image tiles with 256x256 pixels). To activate the access to Bing Maps you order a number of transactions to get your personal Bing Maps account (login data). Image tiles which are were already loaded keeps stored for 24 hours on the harddisk (cache). Therefor the online access and the transaction counting is limited to new image tiles only. Bing Maps provides continuous expanding and worldwide available map data like satellite images, im wide areas available aerial images with a resolution up to 30cm (e.g. in Europe, North America and also most of the urban regions worldwide), road maps and hybrid maps (aerial images with labels and overlaid road map).

The extensive Bing Maps online address database enables the WinGIS integrated Geocoder module to convert an address information (e.g. city, street, street number) to the corresponding coordinate (address search). The Bing Maps DB-Geocoder module converts addresses of entire database tables to the corresponding coordinates. After selection of the database (e.g. MS Access mdb file), the table and the query fields (e.g. street, city, country), for every record an online transaction converts the address to a coordinate and adds X and Y fields to the table. Therefore you get an easy and efficient possibility to locate and visualize your personal database content (e.g. customer databses).

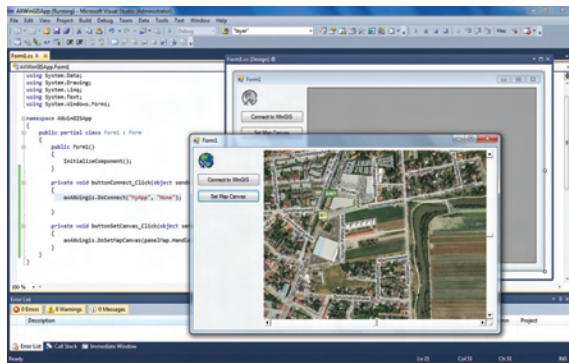


3. AXWINGIS – DEVELOPER COMPONENT

The ActiveX component AXWinGIS enables the communication between an application and WinGIS. The whole function set and every menu entry can be called directly from the application. The communication works bidirectional. Events in WinGIS (e.g. the selection of an area) are sent to the application and can be related to the corresponding database entries (attribute information).

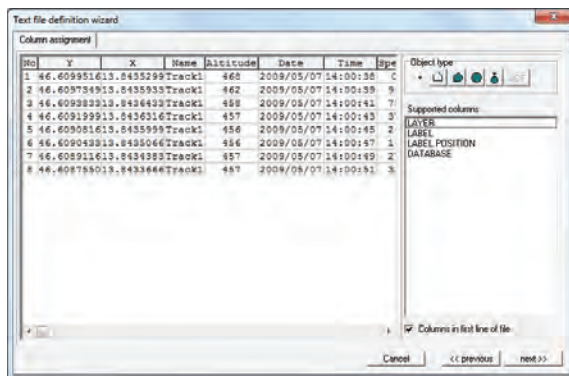
4. WINGIS CANVAS – DIRECT INTEGRATION OF A WINGIS MAP IN THE USER INTERFACE OF AN APPLICATION

WinGIS can run as an independent program with the full available user interface (menus, toolbars) beside the application, but also as an embedded map control („Canvas“). In the user interface of the application a region or window control (e.g. panel) is reserved for the map. By calling the according AXWinGIS function, the visualization of the map takes place on the defined region of the application window.



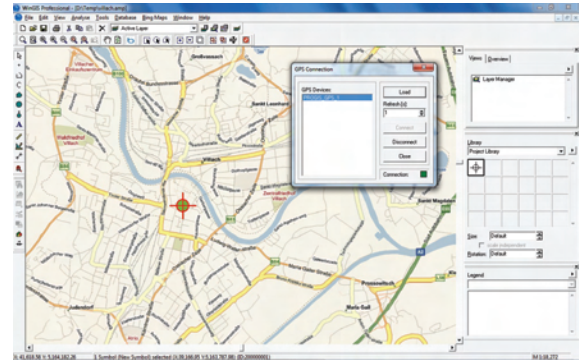
5. WORKING WITH GPS DATA

WinGIS Professional a wide range of functionalities to visualize and process GPS data. GPS recordings and the corresponding attribute data can be loaded from table structured data sources (e.g. text / GPX / CSV files, database tables) to WinGIS by a free definable import interface. GPS data can also be read directly from GPS devices over USB cable or Bluetooth connection.



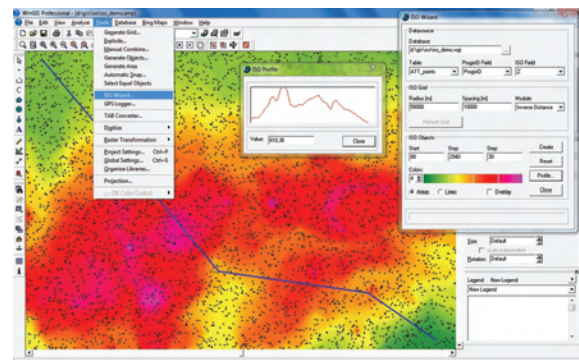
6. LIVE-GPS – TRACKING OF GPS POSITIONS IN REAL TIME

A GPS server interface receives position data and status information (e.g. current activity) from mobile devices (PDA, GPS supporting mobile phones, ...). WinGIS enables you to connect objects (symbols) with the current position data from the server in order to track these positions in real time.



7. ISO WIZZARD

This module is used for creating ISO lines and areas. The data source is a table in the internal database (IDB) but also any external database which contains geographical information (X,Y coordinates). Each ISO level is stored on a separate layer in the WinGIS project.



8. PRODUCTS AND PROJECTS

AGROffice, Dokuplant, LoGIStik, PipeGIS, FOMUMIIS, BAU-MATIC, TREE-MATIC, Z-GIS (NOE ABB), OIS – object information system for fire brigades, PROGIS MapServer for the ORF Reality Show „Taxi Orange“, several GeoINFotainment und geo marketing projects.

ASSESSMENT OF BIOPHYSICAL STRUCTURE OF RIPARIAN ZONES BASED ON SEGMENTATION METHOD, SPATIAL KNOWLEDGE AND TEXTURE ANALYSIS

Thiago Alencar-Silva ^{a,*}, Philippe Maillard ^a

^a IGC, Geography Department, University of Minas Gerais, 31270-901, Belo Horizonte, Brazil
thiago-alencar@ufmg.br; philippe@ufmg.br

KEY WORDS: Segmentation, Knowledge Base, Spatial, Texture, Analysis, Vegetation, High resolution

ABSTRACT:

Riparian forests play an important role in the ecological balance of river ecosystems. Given the narrow nature of these environments, medium resolution sensors such as Landsat have limited use. Conversely, products obtained from high-resolution images, such as Ikonos-2, have wide applications in riparian forest studies. The objective of this article is to describe a methodology for delineating riparian areas and extracting their biophysical parameters from an Ikonos scene. The methodology is divided into two stages. Firstly, the image is segmented into a riparian forest class and non-riparian classes using a segmentation algorithm and a river-based buffer. The segmentation package MAGIC (Map Guide Image Classification) was used to separate the riparian forest zones from the rest. In the second phase, texture features derived the co-occurrence matrix were used to estimate the biophysical parameters of the riparian forest. Allometric measurements were made in 70 plots of riparian area from both sides of the Pandeiros River, located in Northern Minas Gerais, Brazil. These plots were used to calibrate and validate our models based on texture parameters. The forest structure variables included height, diameter at breast height, basal area, stem density, volume, canopy openness and leaf area index which were acquired by direct measurements in the field. The results show that MAGIC segmented the riparian environment with an accuracy of more than 85% when compared with the map obtained by visual image interpretation. The best results for modeling riparian structure were obtained respectively for volume and basal area ($R^2=0.66$ and $R^2=0.61$) using Angular Second Moment, Entropy, Infrared band, distance analysis of four pixels and a window of 11×11 pixels.

RÉSUMÉ:

Les forêts riveraines jouent un rôle important dans l'équilibre écologique des écosystèmes fluviaux. Compte tenu de l'étroitesse de ces milieux, les capteurs à résolution moyenne comme LANDSAT ont un usage limité. Par compte, les produits obtenus à partir d'images haute résolution, comme Ikonos-2, ont d'amples applications pour l'études des forêts riveraines. L'objectif de cet article consiste à décrire une méthodologie pour la délimitation des zones riveraines et l'extraction de leurs paramètres biophysiques à partir d'une image Ikonos. La méthodologie est divisée en deux étapes. Tout d'abord l'image est segmentée en classe de forêt riveraine et le reste des classe non-riveraines en utilisant un algorithme de segmentation et une zone tamponnée basée sur la rivière. Le programme de segmentation MAGIC (*Map Guide Image Classification*) a été utilisé pour séparer les zones de forêt riveraines du reste. Dans la deuxième phase, des images de texture dérivées de la matrice de cooccurrence ont été utilisés pour estimer les paramètres biophysiques de la forêt riveraine. Des mesures allométriques ont été effectuées dans 70 parcelles de la zone riveraine sur les deux rives de la rivière Pandeiros, situé dans le nord de Minas Gerais, au Brésil. Ces parcelles ont été utilisées pour créer et valider les modèles en fonction des paramètres de texture. Les variables structurelles de la forêt inclus la hauteur, le diamètre à hauteur de poitrine, la surface basale, le volume, la densité des troncs, l'indice de surface foliaire et l'ouverture de la canopée, qui ont été acquis par des mesures directes sur le terrain. Les résultats montrent que MAGIC a segmenté le milieu riverain avec une précision de plus de 85% par rapport à la carte obtenue par interprétation visuelle. Les meilleurs résultats pour la modélisation de la structure de la forêt riveraine ont été obtenus respectivement pour le volume et la surface basale ($R^2 = 0,66$ et $R^2 = 0,61$) en utilisant le Second Moment Angulaire, l'Entropie, l'infra-rouge, une distance d'analyse de quatre pixels et une fenêtre de 11×11 pixels.

1. INTRODUCTION

Riparian zones can be defined as the interface between aquatic and terrestrial ecosystems that occurs along rivers and creeks (Johansen and Phinn, 2006a). Riparian zones can extend to the limit of river margin when flooded, and its vegetation plays an important role in the ecological balance of river ecosystems (Muller, 1997).

The ecological functions of riparian forest include: nutrients supply from litter fall, river bank stability, shade to stabilize water temperature, natural filtering of water pollutants, and large woody debris for stream channel development (LWRRDC, 1999a; Congalton *et al.*, 2002). In addition to these functions, riparian

vegetation acts as ecological corridors allowing the flow of fauna communities, especially in fragmented landscapes (Congalton *et al.*, 2002).

In Brazil, most of riparian zones are impacted by logging to make charcoal, agriculture at the margins, livestock and others predatory human activities. The effective inventory of these ecosystems stands as an important tool for making public policy. In this context, remote sensing and image processing techniques allow the rapid and low-cost production of maps (Jensen, 2007).

However, making riparian zones inventories using remote sensing are not an easy task given its narrow extends (Muller,

* Corresponding author.

1997). Mapping these areas and their biophysical parameters is a challenge that has motivated many authors in remote sensing (Nagler *et al.*, 2001; CSIRO, 2003; Johansen and Phinn, 2006b). Previous studies have showed that images with medium spatial resolution (Landsat-TM and ETM) suffer shortcomings for mapping narrow environments (< 30m), such as riparian zones (Congalton *et al.*, 2002; Johansen and Phinn, 2006a). Moreover, the alternative to use high-resolution image (Ikonos, Quickbird), has become affordable in recent years. The most commonly applied approach to map riparian areas using high spatial resolution is image classification. Studies by Davis *et al.* (2002) and Johansen and Phinn (2006a) showed a significant gain of accuracy in classification of riparian zones when using texture parameters in the process.

Taking advantage of the spatial knowledge that the riparian vegetation accompanies the river, buffer zones can be used as a way of optimizing the image processing. This procedure was carried out successfully to map palm swamps (Maillard *et al.*, 2008). Even though high resolution image data proved valuable for delineating riparian zones, traditional information extraction methods like threshold and classification (e.g. maximum likelihood, minimum distance) offer low accuracy. Conversely, image segmentation using Markov random fields (MRF) has produced promising results in a variety of applications, such as image segmentation and restoration (Tso and Mather, 2001). But to assess the ecological values of riparian forests, the mere classification is insufficient and biophysical parameters are often needed.

The objective of this article is to describe a methodology for delineating riparian areas and extract their biophysical parameters from an Ikonos scene. The proposed methodology includes the following stages: (i) classification of the image in two classes: riparian zone and non-riparian zone using 50 meters buffer, (ii) acquisition of texture features from riparian zones segments, and (iii) auto-correlation of visible, near-infrared and texture bands with allometric measurements data from 70 field plots. The correlation aims at elaborating explanatory models of vegetation structure.

1.1 Mapping Riparian Forest from Remote Sensing Data

A study using Landsat-5 and photo interpretation, for mapping riparian forest in the Yaquina River - Oregon/USA, showed a success ratio of only 30% between satellite images and photo interpretations (Congalton *et al.*, 2002). In another study, Johansen and Phinn (2006a) showed that the width of riparian zones is a limiting factor for their identification through products of medium spatial resolution, such as Landsat series. They pointed out that only riparian area upper than 50m could be accurately identified by Landsat-7 ETM+. Muller (1997) emphasizes the importance to develop new remote sensing methods for mapping riparian vegetation along rivers.

In a study by Davis *et al.* (2002), the analysis of high-resolution aerial photographs (resolution between 11 and 100 cm) obtained overall accuracy of 75% to classify riparian areas using maximum likelihood classification and image texture. Texture features increased the accuracy by 20-30% in almost every case. Johansen and Phinn (2006b) used an Ikonos image to classify not only the riparian zone, but also the biophysical parameters and species of a riparian savannah forest in Australia. The authors highlighted the need to use high-resolution imagery and texture parameters for mapping riparian vegetation structures. They used the following forest parameters: canopy percentage foliage cover, leaf area

index, tree crown size, tree height, stem diameter at breast height, tree species, and riparian zone width. In addition to the four bands of the Ikonos image (blue, green, red and near-infrared), eight vegetation index and measurements of texture (contrast, dissimilarity, entropy, homogeneity and variance) were used. Results showed an overall accuracy of 55% for species classification and a determination of 86% for the canopy percentage foliage using 19x19 pixels texture analysis window in the NDVI band.

Alencar-Silva and Maillard (2009) compared two different methods of classification for palm swamps in an Ikonos image: traditional per-pixel classification and region-based segmentation and classification using MAGIC (a program based on Markov Random Fields). Results have shown that MAGIC obtained better results when compared with tradition classification. MAGIC was especially good in removing the salt and pepper effect on the classified image.

1.2 Study Area

The study area is situated in the margins of the Pandeiros River in Northern Minas Gerais, Brazil, an environmental protection area (Figure 2).

The Pandeiros River is an affluent of São Francisco River, the third largest watershed of Brazil. The total area of the Pandeiros' watershed is 3921.00 km² and its elevation varies from 450 m to 850 m. The study site is 1.2 km² along a slightly meandering stretch of river (Figure 3). The marginally climate is semiarid with about 900 mm of precipitation and an average temperature of over 25°C. Precipitation varies from 124 mm per month between October and April to less than 2 mm between May and September. A land use map of the region was produce from a single Landsat-7 scene acquired in August 2009. The classes and their respective area are presented in Table 1.

Class	% of catchment
Open Water	0.33
Dry Forest	1.08
Savannah	48.85
Wetland	3.09
Plantation / Savannah Regeneration	43.61
Rock	0.12
Bare Soil	2.92

Table 1: Land-use table area of Pandeiros River

With about 44% of plantation or degraded areas, the Pandeiros watershed has been strongly impacted by human activities. The Pandeiros also hosts the largest wetland complex of the State of Minas Gerais where several species of fish bird species reproduce, some of which are rare, endemic and threatened (Biodiversitas, 2005).

Figure 3 shows the Ikonos scene of the entire study site in true-colour composition. The green areas located along the river and on the bottom right of the figure correspond to riparian forest and savannah formations, respectively. The zones in brown represent herbaceous areas. Palm swamps, characterised by a specific texture, can be seen on the left hand side of the image. The others light tone areas are bare soil. On the Ikonos scene riparian forest often appears similar to wooded savannah formation. To avoid confusion, a river buffer of 50 m was applied to the image to eliminate savannah

from the segmentation process. Figure 4 shows details of the riparian formations.

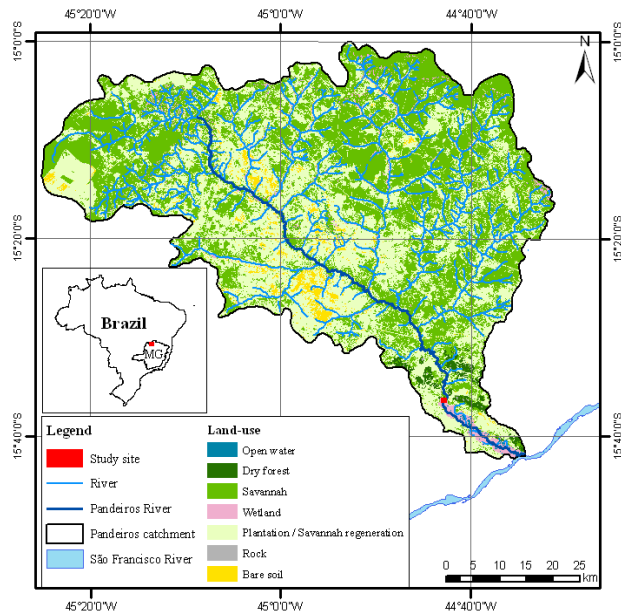


Figure 2: Land-use map and location of study area.

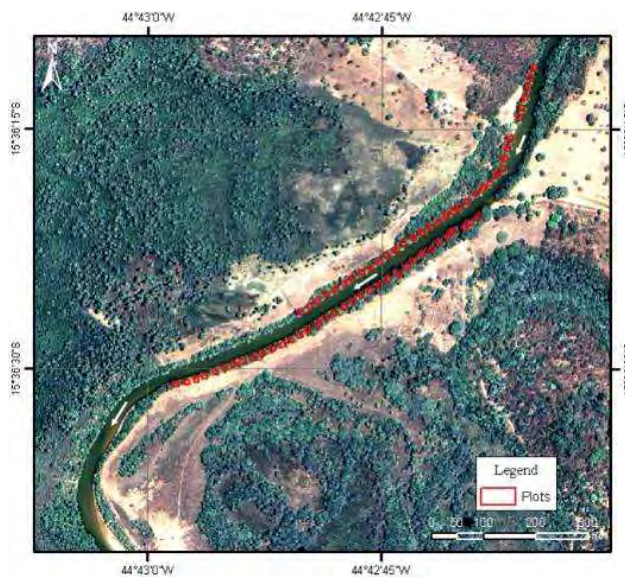


Figure 3: Location of entire study site with the 70 plots, 35 on each side.



Figure 4: Riparian forest of study site: (a) aerial view and (b) ground view (photos by Thais Amaral and Ivan Seixas – 04/2010).

2. MATERIAL AND METHODS

2.1 Fieldwork

The first field campaign (February 2008) was carried out to locate and collect allometric data. The group from the “Ecology and Plant Propagation Laboratory” (UNIMONTES University) demarcated 70 ten by ten meter plots, along both banks of the Pandeiros River. The plots were at a distance of 3 meters from the Pandeiros River and are always oriented parallel to the Pandeiros River. A 10 m gap is always left between each plot except when the area was too degraded to be considered as riparian forest. Plots 1-35 are located on the left bank while plots 36-70 on the right bank. A total of 7000 m² was surveyed.

The allometric measurements of tree height and stem circumference at breast height (CBH) were taken for all trees within each plot. Shrubs and grasses were not considered. Hemispherical photographs were taken in each plot for later computation of canopy openness and leaf area index. Altogether seven allometric measurements were produced: (i) tree height, (ii) stem diameter at breast height (DBH), (iii) basal area, (iv) volume, (v) plot density, (vi) canopy openness and (vii) leaf area index (LAI).

The second and third fieldworks were conducted in January 2009 and April 2010, respectively, to obtain ground control points (GCPs). A L1 geodetic GPS was employed to acquire GCPs, which were used for rectifying the Ikonos scene and precisely locating each plot.

2.2 Image Acquisition and Pre-processing

The Ikonos image used in this study was provided by the Forestry Institute of Minas Gerais. It was obtained with their multispectral bands (red, green and blue = 4m) and panchromatic (1m) already fused to a spatial resolution of 1 m. The data, acquired in September 2007 during the dry season showed a good visibility with no cloud cover (Figure 3). The image was registered to a UTM grid coordinate by bilinear interpolation with a root mean square error (RMSE) less than 1 meter. No atmospheric correction was applied to the image.

2.3 Data Processing

Data processing involved four steps: 1) cartographic modelling, 2) image segmentation, 3) texture feature calculation and 4) statistical modelling.

2.3.1 Cartographic Modelling

The cartographic modelling consisted in using spatial knowledge to “limit” the search to areas having a strong probability of belonging to riparian vegetation (Maillard *et al.*, 2008). This method avoids confusion between vegetation classes present in the study area, such as: palm swamps and savannah. To do so, the hydrographic network was digitized, overlaid on the image and used to build a buffer of 50 m (knowing the riparian vegetation width in the study site is well below that value). The buffer was used to mask parts of the image that fell outside of it. The Ikonos image and the mask are then fed to the segmentation algorithm which is instructed to find two classes: riparian vegetation e non-riparian vegetation.

2.3.2 Image Segmentation

The riparian vegetation was first visually interpreted in order to validate the results of the segmentation. The MAGIC program (Clausi *et al.*, 2009) was chosen to segment the image due to its excellent results reported in several studies (Maillard *et al.*, 2008; Barbosa *et al.*, 2009; Alencar-Silva and Maillard, 2009). MAGIC is an acronym that means “Map Guided Ice Classification” because it was originally developed as a tool for classification of ice sea types. The segmentation of MAGIC is unique in its implementation and the principles it embodies. It is an hybrid segmentation approaches that uses two different approaches to segmentation: “watershed” and Markov Random Field (MRF). The segmentation is started by applying a “watershed” algorithm that produces a preliminary segmentation and generates segments (areas) of 10-30 pixels depending on the noise level in the image. The smaller segments are then arranged topologically, so all contiguous segments can be determined through an adjacency graph or RAG (Region Adjacency Graph). The second step is based on the MRFs that will join or not contiguous segments if the union produces a decrease in the total energy of the neighbourhood defined by Equation 1.

$$E = E_f + \alpha E_r \quad (1)$$

where: E_f is the global spectral energy, E_r is the local spatial energy, α is normally a floating constant.

The advantage of the MRF model is its inherent ability to describe both the spatial context location (the local spatial interaction between neighboring segments) and the overall distribution in each segment (based on parameters of distribution of spectral values for example). That new approach was entitled “Iterative Region Growing Using Semantics” or IRGS and is described in Yu and Clausi (2008).

MAGIC is able to segment each band image individually or as a multivariate data. In this study, the spectral bands were used both as a multivariate dataset and individually. Three parameters have to be specified for the segmentations to take place: (i) the number of classes, (ii) β_1 , and (iii) β_2 . The number of classes varies depending on how the user wants to segment the image.

For our study two categories were desired: riparian and non-riparian. However, because there are several different elements in the non-riparian group (*i.e.* water, herbaceous, bare soil, grass, etc), tests were performed with 3, 4, 5, 6, 7 and 8 classes. The best result obtained by the MAGIC was to be used as a mask in the texture calculations.

2.3.3 Image Texture Calculations

The texture of an image can be defined as changes in spatial patterns of gray levels in a set distance (Tso and Mather, 2001). An approach widely used in texture parameters calculation is the Gray Level Co-occurrence Matrix (GLCM) (Lillesand and Kiefer, 2000). This method proposes that each element of the matrix is a probability measure of occurrence between two gray levels separated by a certain distance and direction (Haralick, 1979). In this paper five features were considered: contrast (CON), angular second moment (ASM), entropy (ENT), inverse difference moment (IDM) and correlation (COR). The Ikono’s red and infrared bands were chosen in order to calculate the five texture features. The blue and green bands were not used because they have strong correlation with the red band. Analysis window sizes

of 11x11, 15x15, 20x20, 25x25 and 30x30 pixels were used. The distances between analysis pixels vary between 3 and 7 and the four directions: 0°, 45°, 90° and 315°.

A special program was created to compute the texture feature to account for the use of a mask. MACOOC (Philippe Maillard ©2010) takes an image and a binary mask as input to compute all five texture measurements in all four directions. Because the mask can adopt just about any shape, regular texture extraction programs would have to discard the texture computation for many riparian pixel when the analysis window overlaps the zeros areas of the mask. MACOOC compensates the “incomplete” windows by adjusting the number of co-occurrences in order to compute comparable probabilities. The probabilities values are then rescaled between 0 and 10000.

Finally, the 70 plots were overlaid in the image. The average values of the four spectral channels (blue, green, red and infrared) and 20 texture bands were computed for each plot and organized in a matrix along with the allometric data. *Multiple Regression* using *Stepwise* feature selection was used to analyze the data.

3. RESULTS AND DISCUSSIONS

The results of this study are presented in two blocks: image segmentation and biophysical riparian forest modelling.

3.1 Image Segmentation Results

The best MAGIC segmentation was obtained using the image as a multivariate dataset with all four Ikonos’ bands (Table 5).

Spectral Band	Riparian %	Non-Riparian %	Total %
1 (blue)	89.19	80.71	84.16
2 (green)	-	-	-
3 (red)	88.82	75.14	80.71
4 (infrared)	-	-	-
1, 2 and 3	91.28	85.01	87.56
1, 2, 3 and 4	88.31	90.61	89.68

Table 5: MAGIC overall segmentation success (average user’s and producer’s) result for riparian and non-riparian vegetation.

The best results were obtained with five classes and an overall accuracy of 89.68% when compared with the visual interpretation. This result takes into account both omission and commission errors (Figure 4). Results obtained with the green and infrared bands had very low correlation with the interpreted image.

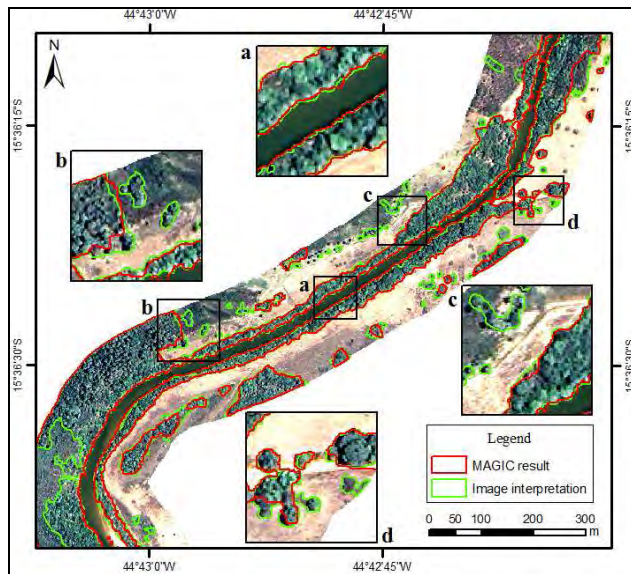


Figure 6: Segmentation result. The best finding was acquired using all Ikonos' bands.

Figure 6 shows the 50m buffered Ikonos scene. The riparian forest consists of all trees within this buffer. The polygons in green are validation data and those in red were obtained with MAGIC.

The MAGIC segmentation result points to a high visual correspondence with the validation data like in zoom window (a). The MAGIC was able to segment some features like individual trees (zoom window (d)). However, some individual features or narrow areas were not segmented properly (zoom windows (c) and (b)).

3.2 Biophysical Riparian Forest Modelling Results

From the initial 70 plots, only 62 were used to obtain the average spectral and texture values. The remaining eight plots were partially located outside the riparian mask and had to be withdrawn.

The statistical correlations results (adjusted R^2) between spectral data, textural data and the allometric and structural measurements of the plots are presented in Table 7: band 3 indicates that the texture features were computed from the red spectral band and band 4 the infrared band. The red band is much more related with allometric parameters than the infrared band for which only the LAI had some success. Basal area and volume obtained the best overall results with $R^2=0.61$ and $R^2=0.66$, respectively. The results show better correlations when using an 11x11 pixel window for the parameters DBH, Basal Area and Volume. The most successful distance between pixels is $d=4$, which showed better results with Basal Area, Volume, DBH and LAI. The best mathematical model for each allometric parameter is presented in Equation 2 to 8.

Band 3							
Parameters	Height	DBH	Basal Area	Volume	Density	Canopy Openness	LAI
w11/d3	0.34	0.52	0.50	0.64	0.07	0.32	0.45
w11/d4	0.44	0.24	0.61	0.66	0.13	0.33	0.41
w15/d3	0.39	0.30	0.36	0.42	0.20	0.44	0.46
w15/d7	0.52	0.29	0.49	0.63	0.04*	0.34	0.40
w20/d4	0.49	0.34	0.52	0.48	0.16	0.20	0.40
w30/d3	0.25	0.19	0.21	0.27	0.45	0.39	0.45
Band 4							
w30/d4	0.16	0.20	0.19	0.09	0.05	0.41	0.54

Table 7: The correlations results for band 3 and 4 (adjusted R^2 with p test value < 0.05). The left column shows the window size (w) and the lag distance between pixels (d). Boxed values are significant at $p > 0.05$.

$$\text{Height} = 64.6 - 0.001 \text{ con}_{90} - 0.00574 \text{ ent}_{135} - 0.0055 \text{ asm}_0 - 0.0065 \text{ ent}_{90} + 0.00128 \text{ idm}_{135} + 0.00064 \text{ con}_{135} \quad (2)$$

$$\text{DBH} = 184 - 0.0397 \text{ ent}_{90} + 0.0584 \text{ B} - 0.0662 \text{ R} + 0.126 \text{ cor}_0 - 0.0786 \text{ cor}_{135} - 0.0103 \text{ asm}_{90} + 0.0037 \text{ idm}_{135} - 0.005 \text{ idm}_0 - 0.00246 \text{ con}_{45} \quad (3)$$

$$\text{Basal Area} = 0.0569 + 0.000002 \text{ asm}_{135} + 0.000001 \text{ IR} - 0.000004 \text{ asm}_{45} - 0.000013 \text{ ent}_{45} \quad (4)$$

$$\text{Volume} = 80.7 + 0.00304 \text{ asm}_{135} - 0.00555 \text{ asm}_{45} - 0.0187 \text{ ent}_{45} \quad (5)$$

$$\text{Density} = 0.018 - 0.000287 \text{ con}_{90} + 0.000137 \text{ con}_{45} - 0.000190 \text{ cor}_{135} + 0.000081 \text{ idm}_0 - 0.000531 \text{ ent}_{135} + 0.000094 \text{ con}_{135} + 0.000547 \text{ ent}_{45} \quad (6)$$

$$\text{Canopy Openness} = -1129 + 0.214 \text{ ent}_{90} + 0.136 \text{ R} - 0.0865 \text{ cor}_{135} + 0.0137 \text{ con}_{135} + 0.143 \text{ asm}_{90} - 0.101 \text{ G} \quad (7)$$

$$\text{LAI} = 0.556 - 0.00203 \text{ R} + 0.000573 \text{ con}_0 - 0.00337 \text{ cor}_0 + 0.000695 \text{ idm}_0 - 0.000119 \text{ asm}_{90} + 0.00354 \text{ cor}_{45} \quad (8)$$

The direction is not a determining factor in the models and none appear to occur predominantly. It is also difficult to pinpoint a single co-occurrence measurement that stands out. In models with few parameters, the ASM seem to be reoccurring (Eq. 4 and 5). Entropy seems to come in second place. It is likely that the diversity of measurements is the best asset of these models and accounts for their strength. When all texture features are analyzed together, it can be verified that Second Angular Moment and Entropy are predominant for the best results (basal area and volume). These models are but indicative of the condition of the riparian forest and are probably not directly applicable in another region. However, but they can be used regionally to orientate the riparian restoration efforts that are currently being undertaken in various watersheds of Northern Minas Gerais by the Forest Institute of MG.

4. CONCLUSIONS AND FUTURE WORKS

In this article two methodological approaches were used to map and model the structure of riparian vegetation in a Brazilian savanna region. For this, combining a high resolution image, the MAGIC segmentation/classification software and the use of texture measurements was evaluated. The results demonstrate a great capacity of the MAGIC program to identify regions of riparian forest without the need of field data. For this step, the best results were obtained by using all four spectral bands of the Ikonos image and a sufficient number of classes to account for the wide variety of land cover within the non-riparian class.

Statistical analysis between the parameters obtained in the field and image processing results permitted the creation of explanatory vegetation structure models applicable regionally. The best models were obtained for the allometric variables basal area and volume (0.61 and 0.66), using window size of 11x11 pixels and distance analysis of four pixels. The direction did not appear to be critical but some texture parameters (ASM and Entropy) are more frequently chosen by the stepwise feature selection. Moreover, it is the diversity of measurements that appear to be most effective.

Future work will include a much broader range of plots in different segments of the river in the hope of creating a more robust set of models. Texture feature will also be made direction-invariant. The approach taken here is comparable to an object-oriented approach that is much more appropriate for high resolution images. It will eventually be integrated into a single package.

REFERENCES

- Alencar-Silva, T. and P. Maillard. 2009. Segmentação de imagem de alta resolução utilizando o programa SMAGIC. *Proceeding of XIV SBSR*, Natal, Brazil, pp. 6743-6750.
- Barbosa, I., P. Maillard and T. Alencar-Silva. 2009. Mapping wetlands variation using high resolution image in the Pandeiros wildlife sanctuary, Brazil. *Proceeding of 30th Canadian Symp. on Remote Sensing*, Lethbridge, Canada.
- Biodiversitas, 2005. Biodiversidade em Minas Gerais: um atlas para sua conservação [Biodiversity in Minas Gerais: na atlas for its conservation] (Second Edition). *Fundação Biodiversitas*, Belo Horizonte, Brazil, 242p.
- Clausi, D.A., K. Qin, M.S. Chowdhury, P. Yu, P. Maillard. Accepted April 2009. MAGIC: MAp-Guided Ice Classification, *Canadian Journal of Remote Sensing*.
- Congalton, R.G., K. Birch, R. Jones, and J. Schriever, 2002. Evaluating remotely sensed techniques for mapping riparian vegetation. *Computers and Electronics in Agriculture*, 37(1-3), pp. 113-126.
- CSIRO, 2003. Determination of sustainable river audit (SRA) habitat indicators by remote sensing, Technical Scoping Document, Technical Report 28/03, *CSIRO Land and Water*, Canberra, 105 p.
- Davis, P.A., M.I. Staid, J.B. Plescia and J.R. Johnson, 2002. Evaluation of airborne image data for mapping riparian vegetation within the grand canyon, Report 02-470, *U. S. Geological Survey*, Flagstaff, Arizona, 65p.
- Haralick, R., 1979. Stistical and structural approaches to texture. *The Institute of Electrical and Electronics Engineers, Inc.*, 67 (5), pp 786-804.
- Jensen, J. R., 2007. Remote sensing of the environment: an earth resource perspective. *Pearson Education, Inc.* Prentice Hall, London, 598p.
- Johansen, K. and S. Phinn, 2006a. Linking riparian vegetation spatial structure in Australian tropical savannas to ecosystem health indicators: semi-variogram analysis of high spatial resolution satellite imagery. *Canadian J. of Remote Sensing*, 32(3), pp. 228-243.
- Johansen, K. and S. Phinn. 2006b. Mapping structural parameters and species composition of riparian vegetation using IKONOS and Landsat ETM+ data in Australian tropical savannahs. *Photogrammetric Engineering & Remote Sensing*, 72(1), pp. 71-80.
- Lillesand, T.M., and R.W. Kiefer, 2000. *Remote Sensing and Image Interpretation*, 4th edition, John Wiley and Sons, Inc., New York, 724 p.
- LWRRDC, 1999a. Riparian land management technical guidelines: volume 1, Land and water resources research and development corporation, *Canberra*, 194p.
- Maillard, P., Alencar-Silva, T., and Clausi, D. A. 2008. An evaluation of Radarsat-1 and ASTER data for mapping veredas. *Sensors (Basel)*, v. 8, p. 6055-6076.
- Muller, E., 1997. Mapping riparian vegetation along rivers: old concepts and new methods. *Aquatic Botany*, 58, pp. 411-437
- Nagler, P.L., E.P. Glenn, and A.R. Huete, 2001. Assessment of spectral vegetation indices for riparian vegetation in the Colorado River delta, Mexico. *Journal of Arid Environments*, 49(1), pp. 91-110.
- Tso, B. and P. Mather. 2001. Classification Methods for Remotely Sensed Data (First Edition). *Taylor and Francis*, London. 242 p.
- Yu, Q. and D.A. Clausi 2008. IRGS: image segmentation using edge penalties and region growing. *IEEE Trans. Pattern Analysis and Machine Intelligence*, 30(12), pp. 2126-2139.

ACKNOWLEDGEMENTS

The authors are thankful to the Forestry Institute of Minas Gerais for providing the Ikonos data and field support. For the MAGIC package we thank Dr. David Clausi. The authors are most grateful to the Laboratory of Ecology and Plant Propagation / UNIMONTES University for providing the field data.

THE ROLE OF REMOTE SENSING IN FIGHTING AGAINST TERRORISM- A CASE OF PAKISTAN

A. Asmat^a

^a Survey of Pakistan, Murree Road, Rawalpindi, Pakistan

Technical Commission VII Symposium 2010

KEY WORDS: Remote Sensing, Surveying and Mapping, Data Acquisition, Terrorism, Pakistan

ABSTRACT:

The use of Remote Sensing (hereafter called RS) in the exploration and monitoring of natural resources inherited by land as well as planning and development domains is not innovative and new to the geospatial community. However, benefiting from RS to fight against terrorism can be an innovative and a new approach for many countries such as Pakistan and geospatial community working on this most significant issue in the current global scenario. The growing number of terrorist attacks in recent years in Pakistan has added a new dimension and value to the use of RS data and its analytical capabilities such as pattern recognition in the country. As reliable and timely supply of geospatial data is not only needed by security agencies but also by the rescue workers and teams to save loss of human lives. But the dilemma is that such data sets are mostly outdated and it is not possible to update these data sets through ground survey operations due to law and order situation of the country that started about five years ago and has not ended yet. A possible solution to the situation could be to have an intersection of traditional military warfare tactics and making maximum use of geospatial knowledge and technologies such as remote sensing for a symmetric warfare. Therefore, this paper takes a closer look at the potential supporting role of RS to help antiterrorism and rescue efforts in geospatial domain of Pakistan.

1. INTRODUCTION

Geospatial technologies such as GIS and Remote Sensing (RS) are being used for identification, monitoring, tracking, exploration and extraction as well as planning analysis of natural resources in addition to environmental protection and sustainable development. Sustainable development which aims at improving the quality of life is one of the main goals of many countries around the world. Therefore, many national planning and development processes in different countries are based on such achievement. However, terrorism would present a major threat to sustainable development or a sign of its failure. Having said that, appropriate security measures, can contribute to reduction of impacts of terrorism and consequently facilitating the achievement of development goals in the countries like Pakistan. In this respect, considering the crucial nature of geospatial data for security measures as well as rescue efforts, and considering current problems on availability, accessibility and usage of updated geospatial data for security measures, RS can be an appropriate instrument for facilitating anti-terrorism and rescue activities with provision of updated geoinformation. The conceptual, practical and instrumental aspects of RS were and are still the areas of interest for scientific and researcher communities. However, benefiting from RS to fight against terrorism, the focal point of this research, is an innovative approach for many countries like Pakistan as well as geospatial scientific and researcher communities working the world over.

The growing number of terrorist attacks in recent years in Pakistan as displays figure 1, has necessitated the use of geospatial technologies such as RS and GIS. The fact is, terrorist activities are hard to forecast and very difficult to counter especially suicidal attacks. However, the real challenge is to quickly adopt methodologies that facilitate the development of prompt as well as

operational strategies for saving life and property in real time. This is the point where RS and geospatial data play a critical role in effective response and recovery efforts as argues Hiatt, 2002; Huyck and Adams, 2002; Logan, 2002; Williamson and Baker, 2002.



Figure 1. Growing terror-related incidents in Pakistan since 2001 (Source of Numeric Data: <http://ejang.jang.com.pk/3-18-2010/>)

The timely provision of geospatial data and information of the targeted area is needed by the rescue workers and teams to save loss of human lives. A solution to the situation could be the use of geospatial knowledge and technologies such as remote sensing (RS) for provision of updated geospatial information to the needy teams. Therefore, this paper takes a closer look at the potential supporting role of RS to help antiterrorism and rescue efforts in geospatial domain of Pakistan.

2. WHY REMOTE SENSING

2.1 Ground Realities in Pakistan

Decisions, strategies and action plans are outcome of analysis that is based upon data. Therefore, to make sound decisions, objective, reliable, accessible and usable (Asmat, 2009) data is needed and data that is outdated can not be treated as reliable. As such updated data is inevitable for sound and efficient decision making. Remote sensing has emerged as one of the top shelf data collection technologies to acquire updated data in real time phenomenon. Survey of Pakistan, being the national mapping organization is responsible for collection, maintenance and delivery of geospatial data and services. Land survey through obsolete methods like Plane Tabling was and still is in use to collect geodata. Such data is then converted into digital vector format that takes months. And truth is, topographic and social landscape of the country is changing so rapidly that when map from the collected data is prepared and disposed off, it is already outdated. A comparison of existing data collection methodologies and remote sensing is listed in Table 1.

Plane Tabling Method	Remote Sensing Method
Collected data is in analogue format	Collected data is in digital format
Time taking data collection method	Quick data collection method
Fair weather is essential for data collection operation	No such condition apply due to availability of RADAR & LIDAR
Satisfactory law and order situation is prerequisite	No such condition apply
Data of features existing on ground, is collected only	Data of features existing on and beneath ground is collected
Updation process is cumbersome	Quick updation is possible as satellites revisit the same location weekly or daily in some cases.

Table 1. Comparison of Plane Tabling and Remote Sensing Data Collection Methods

From Table 1, it is obvious that RS is the right technology to be used for data collection or update data in the current scenario of Pakistan. It is recommended, that Survey of Pakistan should make use of its resources such as human, satellite imagery of entire country at 1 meter resolution and technologies for geoinformation extraction and its updation through RS technologies that fortunately exist in the department.

3. THE SUPPORTING ROLE OF REMOTE SENSING

3.1 For Counter Terrorism

From figure 1, it can be interpreted that out of 322 terrorist incidents, 202 incidents that make up more than 62% of the total number of terrorist incidents took place in areas of Quetta, FATA/Lower & Upper Dir, Peshawar as well as Swat. Some of the common factors in all these locations are:

- These areas are relatively less developed
- The areas are dominated by mountain ranges
- The law and order situation in the areas is poor
- Maps available in Survey of Pakistan of the areas are mostly outdated
- Communication infrastructure in these areas is poor
- The areas are located near Afghanistan border



Figure 2. Areas mostly hit by terrorists in Pakistan since 2001

From Figure 2, it is evident that due to mountainous areas, the administrative bodies, security agencies and rescue teams may have faced great difficulties to access the effected area, as no updated information of the area is available since 2001. In this scenario, the use of RS to generate and extract information from satellite images is the only viable solution. Moreover, trenches and under ground bunkers are also reported in media (<http://pakobserver.net/detailnews.asp?id=21126>) that were and are still being used by terrorists as hideouts. To identify such underground locations is only possible with the help of RS technologies as described in Table 1. Therefore, the arguments and real life example presented so far, proves and underscores the supportive role of RS for antiterrorism and rescue efforts. Brief summary of importance of RS for antiterrorism and rescue efforts is tabulated as Table 2.

Characteristics of Remote Sensing	Value for Antiterrorism and Rescue Efforts
Provision of updated geoinformation	The use of updated information by counter terrorism and rescue teams is fundamental to save loss of human lives and the property.
Identification of under ground objects	It is essential to track enemies hidden in caves and identify explosives buried in ground for safe movement of antiterrorism and rescue teams.
Pattern recognition	Usually video messages of terrorists recorded in open and hilly areas are broadcasted by media. RS can be used to easily

	identify such areas.
Quick information generation	Digital classification can be applied to generate information of the effected areas.
Image Maps	Satellite images can be converted into image maps by overlaying image and vector data of existing maps.

Table 2. Supportive Role of Remote Sensing for Counter Terrorism Activities

4. CONCLUSION AND RECOMMENDATIONS

The use of remote sensing(RS) technologies, knowledge and data for exploration, understanding, determination, and monitoring of factors and their linkage that affect environment, sustainable development and natural resources is not innovative and new to the scientific and researcher communities. There is nothing new about it. However, research should be geared towards benefiting from RS to fight against terrorism that effects the environment, economy and sustainable development activities of a country most. One of the important aspect and after myth of terror related incident is availability and provision of updated geoinformation of the effected area. Remote sensing technology, knowledge and data can be benefited substantially to identify terrorist hideouts over ground, underground as well as for rescue efforts to save precious loss of human lives and property. RS has played a magnificent role in symmetric warfares, which are comparatively difficult warfares. Therefore, RS technology has become a backbone of not only current warfare scenario, but countering terrorism which is dire and emergent need of the day.

REFERENCES

- Asmat Ali (2009), "What does Spatial Data Infrastructure mean to Pakistan?" Proceedings of the GSDI 11 World Conference: Spatial data infrastructure convergence: building SDI bridges to address global challenges, June 15-19, 2009, Rotterdam, The Netherlands. 20 p.
- Hiatt M (2002), "Keeping Our Homelands Safe," Imaging Notes, May/June : 20-23.
- Huyck CK and Adams BJ (2002) , "Emergency Response in the Wake of the World Trade Center Attack: The Remote Sensing Perspective," MCEER Special Report Series Engineering and Organizational Issues Relating to the World Trade Center Terrorist Attack Volume 3, MCEER-02-SP05, Buffalo, New York.
- Logan B (2002) , "The Lessons of 9/11 , "Geospatial Solutions, September: 26-30.
- Williamson R and Baker J (2002) , " Lending a Helping Hand: Using Remote Sensing to Support the Response and Recovery Operations at the World Trade Center," Photogrammetric Engineering and Remote Sensing, 68 (9) : 870-875.
- Huyck CK and Adams BJ (2003), An evaluation of the role played by remote sensing technology following the World Trade Center attack, :159-160.

VERTICAL ROUGHNESS MAPPING - ALS BASED CLASSIFICATION OF THE VERTICAL VEGETATION STRUCTURE IN FORESTED AREAS

C. Aubrecht^{a,*}, B. Höfle^b, M. Hollaus^c, M. Köstl^a, K. Steinnocher^a, W. Wagner^c

^a AIT Austrian Institute of Technology GmbH, Donau-City-Str. 1, A-1220 Vienna, Austria -
(christoph.aubrecht, mario.koestl, klaus.steinnocher)@ait.ac.at

^b Department of Geography, University of Heidelberg, Berliner Straße 48, D-69120 Heidelberg, Germany -
hoefle@uni-heidelberg.de

^c Inst. of Photogrammetry & Remote Sensing, Vienna U. of Technology, Gußhausstr. 27-29, A-1040 Vienna, Austria -
(mh, ww)@ipf.tuwien.ac.at

KEY WORDS: Forestry, Hazards, Mapping, Vegetation, Classification, Laser scanning

ABSTRACT:

In this paper we describe an approach to classify forested areas based on their vertical vegetation structure using Airborne Laser Scanning (ALS) data. Surface and terrain roughness are essential input parameters for modeling of natural hazards such as avalanches and floods whereas it is basically assumed that flow velocities decrease with increasing roughness. Seeing roughness as a multi-scale level concept (i.e. ranging from fine-scale soil characteristics to description of understory and lower tree level) various roughness raster products were derived from the original ALS point cloud considering specified point-distance neighborhood operators and plane fitting residuals. Aiming at simplifying the data structure for use in a standard GIS environment and providing new options for ALS data classification these raster layers describe different vertical ranges of the understory and ground vegetation (up to 3 m from ground level) in terms of overall roughness or smoothness. In a predefined 3D neighborhood the standard deviation of the detrended z-coordinates of all ALS echoes in the corresponding vertical range was computed. Output grid cell size is 1 m in order to provide consistency for further integration of high-resolution optical imagery. The roughness layers were then jointly analyzed together with a likewise ALS-based normalized Digital Surface Model (nDSM) showing the height of objects (i.e. trees) above ground. This approach, in the following described as 'vertical roughness mapping', enables classification of forested areas in patches of different vegetation structure (e.g. varying soil roughness, understory, density of natural cover). For validation purposes in situ reference data were collected and cross-checked with the classification results, positively confirming the general feasibility of the proposed vertical roughness mapping concept. Results can be valuable input for forest mapping and monitoring in particular with regard to natural hazard modeling (e.g. floods, avalanches).

1. INTRODUCTION

Surface and terrain roughness is an essential parameter for assessment and modeling of natural hazards such as avalanches and floods (Margreth & Funk 1999, Werner et al. 2005, Schumann et al. 2007). Basically it can be assumed that flow velocities decrease with increasing roughness (Gómez & Nearing 2005). Roughness can be seen in various scale levels, ranging from fine-scale soil characteristics to terrain features. On the micro-level soil roughness is described in a range of millimeters to centimeters. Relevant parameters in that context are land cover types such as herbaceous and grass vegetation. Relevant meso-level roughness features include objects and vegetation in a range of decimeters to meters, such as shrubs and boulders. The macro-level is determined by topography and terrain features, whereas the scale ranges from one to hundred meters (Jutzi & Stilla 2005).

In state-of-the-art avalanche modeling approaches empirically developed roughness schemes based on a set of varying land cover types are implemented (McClung 2001, Ghinoi & Chung 2005). Such land cover classification can e.g. consist of (1)

screens and boulders, (2) shrubs or mountain pines, (3) herbaceous and grass vegetation including low bushes, and (4) compact grassland or solid rock. Depending on the exposition various skid factors are derived from these surface types (see Table 1). Surface roughness is relevant for glide avalanches on micro-level as well as for snow slabs on meso- and macro-level. The estimated skid factors are introduced in snow gliding and snow pressure modeling (Höller et al. 2009). In the field of hydrology surface roughness is introduced in runoff models for detecting superficial flow velocities (Lavee et al. 1995, Rai et al. 2010). Assessment of roughness is thereby based on a coarse surface and vegetation classification. Markart et al. (2004) identified six classes ranging from very flat to very rough. Different types of vegetation can span several roughness classes. In particular this applies to forest locations, where surface roughness is depending on specific low-vegetation cover. Accordingly further parameters are needed for classification. E.g. for virgin soils the dominance of migrating plants is relevant. For grassland land use strongly affects roughness characteristics (pasturing, ski slopes, hay meadows). In moist locations the moss rate is crucial, while for areas with bushes particularly the type of plant cover is relevant.

* Corresponding author.

Land cover class		Range	Skid factor
1	Screes and boulders	>30 cm	1.2 - 1.3
2	Shrubs or mountain pines	>1 m	1.6 - 1.8
	Mounds w. veg. cover	> 50 cm	
	Cattle treading		
	Screes	10 - 30 cm	
3	Grass veg. incl. low bushes	< 1 m	2.0 - 2.4
	Fine debris mixed with veg.	< 10 cm	
	Small mounds w. veg. cover	< 50 cm	
	Grass veg. incl. superficial cattle treading		
4	Compact grassland		2.6 - 3.2
	Solid rock		
	Fine debris mixed with soil		
	Moist sinks		

Table 1. Skid factors assigned to land cover types featuring varying roughness (Margreth, 2007).

The current standard way of assessing surface and/or terrain roughness is using empirical methods in the field. Taking the macro-level as example, terrain features are described approximately via wavelength and amplitude of sinusoids. Roughness assessment on meso- and micro-level can be carried out by fitting ductile slats to the surface. All these methods require on-site inspections which gets extremely time-consuming and costly for large-area assessments. Remote sensing offers the advantage of an area-wide standardized survey and is expected to deliver roughness assessments in comparable accuracy.

In this paper we describe an approach to classify forested areas based on their vertical vegetation structure using ALS data. We see roughness as a multi-scale level concept, i.e. ranging from fine-scale soil characteristics to description of understory and lower tree level. Results of our ‘vertical roughness mapping’ concept can be valuable input for forest monitoring in particular with regard to natural hazard modeling.

2. STUDY AREA AND DATA

The study area covering approximately 10 square kilometers is located in the ‘Bucklige Welt’, a hilly region in the south-eastern part of Lower Austria (about 70 km south of the Vienna basin) also known as ‘land of the 1,000 hills’ (see figure 1). Widely dominated by forest of varying characteristics (i.e. deciduous, coniferous, and mixed forest) this is a typical rural area interrupted by a few small settlements (e.g. Haßbach, Kirchau, Kulm) and patches of agricultural land. In line with the overall characteristics of the ‘Bucklige Welt’ region the study site which belongs to the municipal area of Warth features hilly terrain conditions with maximal 300 meters elevation difference.

Employing a full waveform Airborne Laser Scanning (FWF-ALS) system ALS data were acquired in the framework of a commercial terrain mapping project covering the entire Federal State of Lower Austria (acquisition period: spring 2007). In spring favorable leaf-off conditions without snow cover could be guaranteed. For the presented research project 3D point clouds organized in tiles and consisting of XYZ coordinate triples (ASCII XYZ format) were delivered. Originally ALS-inherent information about scan geometry and radiometric information was not available for further analysis.

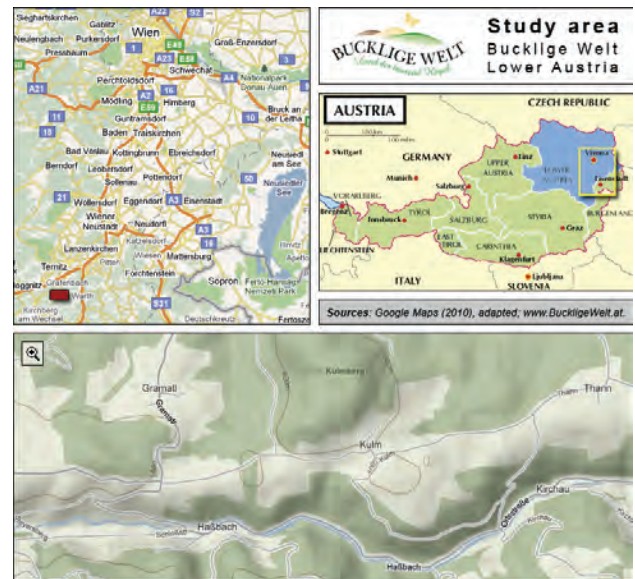


Figure 1. Study area ‘Bucklige Welt’, Lower Austria.

3. ALS BASED ROUGHNESS DESCRIPTION

This paper concentrates on products based on parameters that can be derived directly from the ALS point cloud. Only by using the 3D point cloud maximum information content is guaranteed, while preserving the highest data density and not introducing any biasing decisions on suitable target raster resolution, filter or aggregation strategies (Höfle, 2007). On the end-user side however, it is much more convenient and applicable to deal with pre-processed ‘roughness images’, i.e. featuring substantially reduced amount of data and simple raster data structure, which can be dealt with easily in standard GIS and remote sensing software packages. Computation of additional point cloud attributes and subsequent generalized raster layers requires a sophisticated software implementation, including both the mathematical definitions and intelligent management of the large amount of data which arises when working with high density laser point data.

In the following paragraphs different roughness parameters calculated on the basis of the initial ALS point cloud are described and resulting raster layer products are illustrated. In the definition of surface roughness in this context all ALS terrain points within a 0.2 m range to the ground are considered. The terrain roughness concept on the other hand just comprises objects (i.e. point clusters) close but explicitly above the terrain (>0.2 m), whereas two different vegetation story layers were analyzed for this paper: (1) very low brushwood or undergrowth from 0.2 m to 1.0 m such as bushes and shrubs, and (2) understory vegetation from 0.2 m to 3.0 m, e.g. being indicative for different tree types.

As the objective of the presented approach was to ‘look through the forest canopy’ and map the entire vertical vegetation structure (i.e. ‘roughness’ on various levels inside the woods) non-forested regions were masked out using a previously derived forest mask. This mask had been produced implementing an integrated analysis approach considering aerial imagery and ALS data (i.e. Object-based Image Analysis, OBIA).

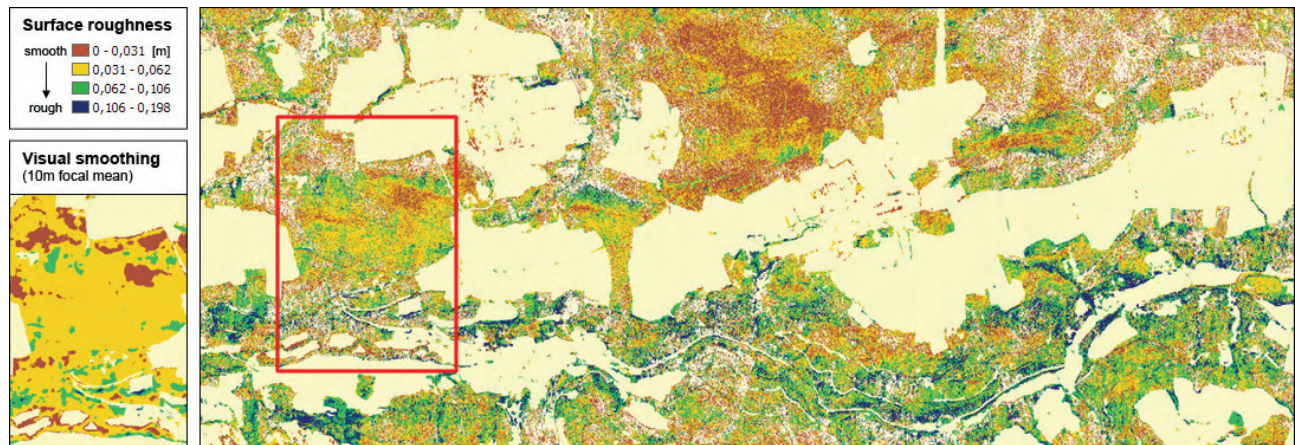


Figure 2. Surface roughness raster layer (1.0 m resolution), classified in 4 roughness categories from smooth (red) to rough (blue). Non-wooded areas are masked out (in light yellow). Detail: Smoothed visual impression through applying a focal mean operator.

3.1 Surface roughness (SR)

Surface roughness was defined as small scale height variations up to a few decimeters above ground. In mathematical terms the standard deviation of the detrended z-coordinates of all ALS terrain echoes is computed. The detrending of the ALS heights is important for slanted surfaces, where else the computed standard deviation would increase with increasing slope (i.e. height variation), even with the surface being plane. The unit of the subsequently derived SR parameter is in meters and can be compared between different flight epochs and ALS systems. Further algorithmic details can be found in Hollaus & Höfle (2010).

Figure 2 shows a derived SR raster layer featuring a terrain related variation of ± 0.2 m ($-0.2 < dz < 0.2$). All laser echoes within a 1.0 m neighborhood were considered in the plane fitting and standard deviation calculation process. The finally derived SR raster layer has a spatial resolution of 1.0 m, i.e. with the mean standard deviation value of all points falling in one predefined 1.0 m grid cell attached as attribute. Using four classes for visualization gives a good first indication on regional surface roughness variations in the study area. More than 50% of the total forested area is thus classified as having a very smooth surface (red, yellow) and around 25% show slightly higher deviations (green, blue). White pixels display ‘no data’ areas, i.e. areas where no information about the immediate surface is available. These can be data errors, but primarily it is due to the forest canopy being too dense thus preventing the laser beam from reaching the ground.

The detail image displayed in Figure 2 is the result of applying a focal neighborhood function to the original raster. The mean value of all cells of the input raster within a specified neighborhood is calculated and assigned to the corresponding cell location of the output raster. For the described raster a circular neighborhood (10 m radius) was chosen, i.e. all grid cells having its centers encompassed by this circle are included in the calculation. Using focal operations is a form of generalization smoothing the visual impression of the input data. It is particularly valuable for identifying hot spot regions and spatial patterns in heterogeneous raster data. It is very important to decide first how to deal with existing ‘no data’ values in the input data. For the displayed SR raster the option of ignoring ‘no data’ values in the calculation was chosen.

Another possibility would be to assign ‘no data’ to the output grid cell in case any of the considered neighboring cells has a ‘no data’ value. With just around 15% of the pixels in forested areas featuring ‘no data’ values it was decided to accept uncertainties entailed with ignoring those pixels and rather look at resulting generalized regional spatial patterns. It becomes clear that in the northern woods of the study area very smooth surfaces prevail while in the more heterogeneous southern parts surface in general tends to be rougher.

3.2 Terrain roughness (TR)

Terrain roughness is described as the unevenness of the terrain surface (including rocks and low vegetation) at scales of several meters. In mathematical terms this implies calculation of the standard deviation of height of non-terrain ALS echoes above terrain (normalized height) within boxes of predefined size. In contrast to the SR computation, only echoes close but above terrain (>0.2 m) are considered for the TR derivation. Two different vegetation story layers are analyzed in this context, one considering very low brushwood or undergrowth between 0.2 m and 1.0 m (e.g. bushes and shrubs; TR I; Figure 3) and the other considering understory vegetation between 0.2 m and 3.0 m (TR II; Figure 4). The second layer is particularly valuable for identifying different types of trees (e.g. large coniferous trees with few - mostly cut - branches in the lower levels or broadleaf trees with just stem and crown compared to smaller trees with branches hanging down to the ground).

Figures 3 and 4 show that these two TR parameters yield much more ‘no data’ values than the previously described SR parameter ($>70\%$ for TR I, $>60\%$ for TR II compared to $\sim 15\%$ for SR). Besides the same potential causes mentioned above being (1) data errors or (2) very dense tree crowns preventing the laser beam reaching the analyzed height level, no information in the ALS data can also signify empty space in reality. So, in fact even ‘no data’ values can provide valuable information in that context. Looking at the study site overview it is apparent that there is more TR data recorded in the southern parts of the study site. Anyhow, at this level of detail also in those areas just very little variation is detected in TR I. Values in TR II show a slightly different picture, with (1) featuring a somewhat higher information density (i.e. 37% vs. 27% for TR I) and (2) featuring more variation (i.e. mean value of 0.22 vs. 0.05 in TR I). The latter is also related to the larger vertical focus of this specific parameter ($0.2 < dz < 3.0$).

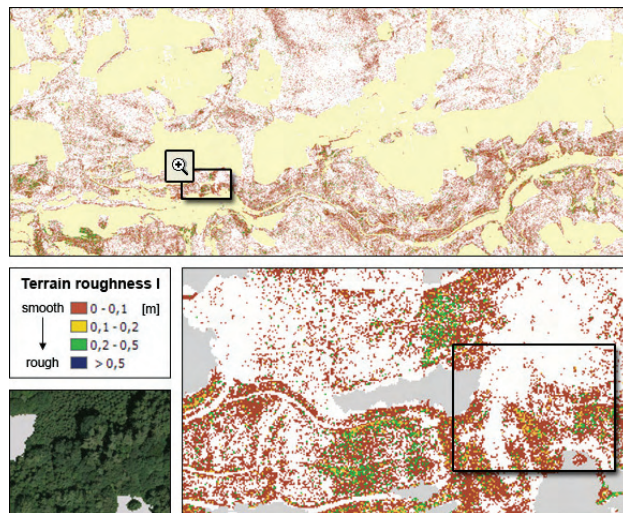


Figure 3. Terrain roughness - TR I.

Looking at the TR raster layers in more detail (details in Figures 3 and 4) local fine-scale roughness variations become visible. The spatial distribution of available information is very similar. The slightly higher data density in TR II can be an indicator of (1) vegetation being very dense in this story thus again preventing the laser beam to reach lower levels or (2) higher vegetation with branches starting somewhere around eye level, but not having any undergrowth beneath.

4. VERTICAL ROUGHNESS MAPPING – INTEGRATION OF MULTI STORY BACKSCATTER INFORMATION

After computing the ALS point cloud based roughness raster layers as described above they were jointly analyzed and combined, whereas a novel roughness classification scheme was developed, further referred to as ‘*vertical roughness*’. This novel roughness mapping concept incorporates information from various vegetation height layers using the capability of full waveform ALS, i.e. recording the entire backscatter spectrum from treetop to ground. It thus not only gives an indication of surface roughness patterns (limited to a very small height threshold above ground), but also includes information on the variance of brushwood (such as bushes and shrubs) and understory vegetation (up to 3.0 m). Results of the roughness classification were finally validated with in situ data from a field survey conducted in April 2009. The following paragraphs are dedicated to advanced classification and analysis of the ALS-derived roughness raster products. First, SR and TR layers were jointly analyzed with regard to identification of significant spatial patterns in terms of intensity and accumulation of roughness echoes. Adding yet another dimension to this integrated classification process – absolute vegetation height as illustrated by a nDSM – rounds off a novel approach of mapping roughness in wooded areas on multiple vertical levels, from now on called ‘*vertical roughness mapping (VRM)*’.

According to the basic objective of distinguishing smooth and rough surfaces, the SR raster was binary recoded with the threshold defined at $SR = 0.05$ m plus one additional ‘no data’ category. Grid cells featuring SR values larger than 0.05 were thus considered rough, while all values below that threshold were considered smooth.

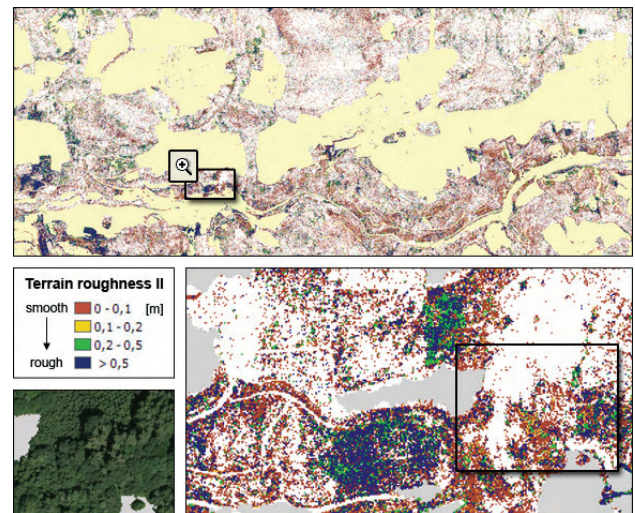


Figure 4. Terrain roughness - TR II.

Regarding the structural undergrowth information inherent in the two TR raster layers a slightly different, but yet binary classification approach was chosen. One class of pixels depicts areas where echoes are recorded in both the lower vegetation level TR I (very low brushwood or undergrowth up to 1.0 m) and the level of understory vegetation up to 3.0 m TR II. The second category includes regions where echoes were just recorded at the level of TR II, but no data exist on the lower level of TR I. Again an additional class for ‘no data’ cells was appended.

The combination of these reclassified SR and TR products ‘ $x-y$ ’ ($x \dots TR_{recl}$, $y \dots SR_{recl}$) with each layer featuring three value facets (1, 2, no data) resulted in a set of nine possible new classes (3×3 categories) describing different multi-level roughness characteristics. Most frequent classes are the categories with $x=0$ (0-0, 0-1, 0-2), i.e. having no TR data records, whereas 0-1 particularly stands out. This class covering about one third of the study area (33.4%) delineates areas with smooth surface and no recorded echoes in both levels of understory vegetation (TR I 0.2 m to 1.0 m, and TR II 0.2 m to 3.0 m).

In the previous steps information on the vertical distribution of recorded echoes within a range of 0.2 m to 3.0 m above ground was considered for VRM. In order to get an overall picture of the vertical vegetation structure another dimension was added by integrating the nDSM as third input variable, i.e. absolute height information classified in 4 story layers. The first category (‘0-x-y’) is defined as ‘vegetation up to 3.0 m’ covering about 9% of the total area. As this class boundary coincides with the upper boundary of TR II, the nDSM integration does not expand the vertical roughness information content in these areas. The biggest part of the test site’s wooded area (65.8%) is covered by trees which are between 10 m and 25 m high (category ‘2-x-y’). Integrating an additional information layer with 4 possible values to the concept results in 36 ($3 \times 3 \times 4$) classes eventually describing the full vertical vegetation structure. Figure 5 shows the new extended classification scheme – ‘*vertical roughness mapping extended (VRM^e)*’ – applied to a detail of the study area. The aerial image is given for comparison in order to provide an impression of the heterogeneous forest structure, which is already visible without even knowing how it looks like beneath the tree crown.

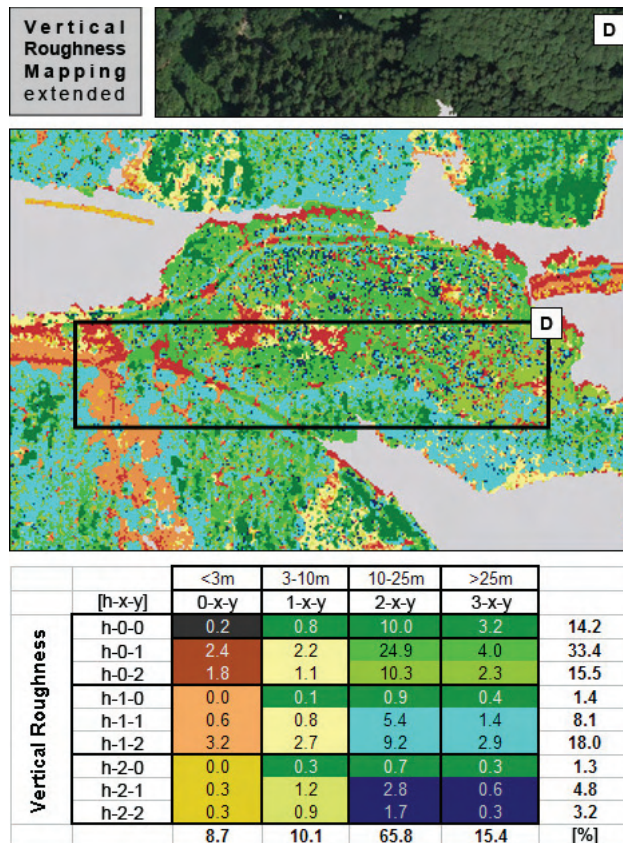


Figure 5. Vertical roughness map and classification scheme for a detail of the test site, and aerial image for comparison (D).

In fact five classes out of the 36 categories stand out each featuring more than 5% and in total covering about 60% of the test site. 22 of the remaining classes just account for less than 2% each. The by far most dominant class (25%) is ‘2-0-1’ (light green in Figure 5) featuring an overall height between 10 m and 25 m, smooth surface and no echo records regarding undergrowth. In general nearly 65% of the total forest area shows no backscatter records in the mid-vegetation level (i.e. the ‘h-0-y’ category group). In case some kind of undergrowth is present, most of the times it spans the whole vertical range between 0.2 m and 3.0 m above ground, i.e. echoes recorded in both TR I and TR II as well as ‘rough’ surface conditions (‘h-1-2’: 18%). When looking at the ‘h-1-y’ type, thus ignoring surface variation, these regions even cover 27.5% of the total study area. Classes with TR information exclusively recorded in the higher level of understory vegetation between 1.0 m and 3.0 m (i.e. the ‘h-2-y’ category) occur just very sparsely covering a total of less than 10% of the study area. Pixels assigned to these classes can mainly be attributed to large trees with branches reaching down to the 3.0 m range but not all the way down to the ground.

5. VALIDATION

For validating the results of the ALS based vertical roughness mapping in situ reference data was collected. The field survey was done on April 16, 2009 taking Haßbach (village in the southwest of the test site, see Figure 1) as starting point. Locations of reference points were stored using a Garmin eTrex GPS handheld model.

Extensive photo documentation was an essential part of the data collection allowing capturing a certain neighborhood around fixed reference point locations. A total of 24 points was collected in the course of the field survey whereas the focus was on getting a representative point set featuring different types of vegetation including scrubs and brushwood.

For this paper two selected reference points of varying characteristics will be presented in detail serving as examples for cross-validating ALS derived roughness and reality conditions. Figure 6 shows the vertical roughness map (VRM^c) for the examined area with the aerial image included for comparison and orientation reasons. For each of the two reference points (no. 463 and 464) a vertical-bar graph is presented illustrating the VRM^c pattern (class ratios) within a 10 m neighborhood (marked with red circles in the map). To illustrate reality conditions pictures from the field survey are shown in the bottom part of the figure (463: P1, 464: P2).

First, spatial roughness patterns as illustrated in the raster map and class ratio numbers are analyzed. For reference point 463 a good portion of its immediate neighborhood (63%) is classified as ‘1-1-2’ (light yellow in Figure 6), i.e. overall rather low vegetation height <10 m, recorded echoes in both terrain layers (TR I and TR II), along with ‘rough surface’. With respect to the entire study area this is a very untypical picture with ‘1-1-2’ just covering less than 3% in total. These ALS-based ratio values shown in the vertical-bar graph are confirmed by looking at the collected reference data, with photo P1 showing dense low-level deciduous vegetation with branches and leaves throughout the vertical range. Also in an additionally available reference data set (provided by the Research and Training Centre for Forests, Natural Hazards and Landscape, BFW) this region is qualitatively described as ‘young and very dense deciduous forest including undergrowth’. 21% are classified as ‘1-2-y’ (light green) while the remaining 16% are assigned to ‘0-2-y’ (orange), i.e. no recorded echoes in TR I at slightly varying overall tree height. As surface information is available anyhow (either smooth or rough) it is unlikely that too dense top-level vegetation prevented the laser beam from ‘seeing’ the lower level. As during the field campaign indeed some parts of this specific forest patch were observed not featuring any low-level brushwood the classified VRM^c information can be expected to be correct and significant.

Reference point 464 shows a completely different picture. Photo P2 in Figure 6 displays mixed and rather loose vegetation including e.g. large coniferous trees, small broadleaf bushes and leaf-covered surface. This is confirmed and even emphasized by the ALS based VRM^c. Looking at the class ratio values shown in the vertical-bar graph and at the raster layer no predominant category can be detected, but rather a heterogeneous mix of various roughness classes in the immediate neighborhood of the reference point. From bare soil (‘0-0-1’) to the largest trees (3-x-y) the entire range of roughness categories is present.

Photo documentation not necessarily delivers representative results, also because of directivity. However, during data collection attention was paid to that issue. As the field survey was carried out about two years after the ALS data had been recorded, data mismatches can be due to that temporal variation. Summing it up results are very encouraging and it seems that advanced vertical roughness mapping is possible at a certain spatial level of detail based on ALS information.

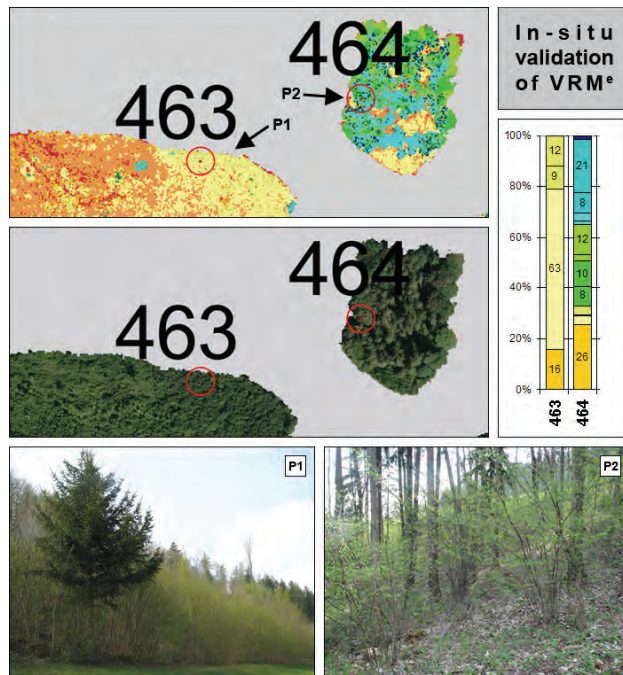


Figure 6. In situ validation of VRM^c.

6. CONCLUSION AND OUTLOOK

In this paper a novel approach of data classification and revaluation was presented with the focus on identifying 'roughness' on various vertical levels in wooded areas. Roughness parameters and corresponding raster layers were calculated and jointly analyzed in order to develop a novel roughness classification scheme considering the entire vertical structure of vegetation from surface to treetop. This classification procedure can be outlined as *vertical roughness mapping (VRM)*.

Results of the roughness classification were cross-validated against collected in situ reference data indicating a high level of thematic accuracy. As follow-on analysis several ways of smoothing the VRM^c raster files (i.e. information-preserving 'intelligent' generalization) will be tested in order to derive areal roughness hot spots useful for terrain related hazard assessments (e.g. water hazards, mass movements).

REFERENCES

- Ghinoi, A., Chung, C.-J., 2005. STARTER: a statistical GIS-based model for the prediction of snow avalanche susceptibility using terrain features – application to Alta Val Badia, Italian Dolomites. *Geomorphology*, 66, pp. 305-325.
- Gómez, J. A., Nearing, M. A., 2005. Runoff and sediment losses from rough and smooth soil surfaces in a laboratory experiment. *Catena*, 59, pp. 253-266.
- Hollaus, M., Höfle, B., 2010. Terrain roughness parameters from full-waveform airborne LiDAR data. ISPRS International Archives of the Photogrammetry, Remote Sensing and Spatial Information Sciences, in press.
- Höfle, B., 2007. Detection and Utilization of the Information Potential of Airborne Laser Scanning Point Cloud and Intensity Data by Developing a Management and Analysis System. *Dissertation*, Faculty of Geo- and Atmospheric Sciences, University of Innsbruck, Austria.
- Höller, P., Fromm, R., Leitinger, G., 2009. Snow forces on forest plants due to creep and glide. *Forest Ecol Manag*, 257, pp. 546-552.
- Jutzi, B., Stilla, U., 2005. Waveform processing of laser pulses for reconstruction of surfaces in urban areas. *International Archives of Photogrammetry and Remote Sensing*, Vol. 36, Part 8 W27 (on CD).
- Lavee, H., Kutiel, P., Segev, M., Benyamini, Y., 1995. Effect of surface roughness on runoff and erosion in a Mediterranean ecosystem: the role of fire. *Geomorphology*, 11, pp. 227-234.
- Margreth, S., 2007. Lawinenverbau im Anbruchgebiet. Technische Richtlinie als Vollzugshilfe. Umwelt-Vollzug Nr. 0704. Bundesamt für Umwelt, Bern, WSL Eidgenössisches Institut für Schnee- und Lawinenforschung SLF, Davos. 136 S.
- Margreth, S., Funk, M., 1999. Hazard mapping for ice and combined snow/ice avalanches – two case studies from the Swiss and Italian Alps. *Cold Reg Sci Technol*, 30, pp. 159-173.
- Markart, G., Kohl, B., Sotier, B., Schauer, T., Bunza, G., Stern, R., 2004. Provisorische Geländeanleitung zur Abschätzung des Oberflächenabflussbeiwertes auf alpinen Boden-/Vegetationseinheiten bei konvektiven Starkregen. BFW-Dokumentation; Schriftenreihe des Bundesamtes und Forschungszentrums für Wald, No. 3, Vienna, Austria, 88 p.
- McClung, D. M., 2001. Characteristics of terrain, snow supply and forest cover for avalanche initiation caused by logging. *Ann Glaciol*, 32, pp. 223-229.
- Rai, R. K., Upadhyay, A., Singh, V. P., 2010. Effect of variable roughness on runoff. *J Hydrol*, 382, pp. 115-127.
- Rutzinger, M., Höfle, B., Pfeifer, N., 2007. Detection of high urban vegetation with airborne laser scanning data. *Proceedings Forestsat 2007*, Montpellier, France.
- Schumann, G., Matgen, P., Hoffmann, L., Hostache, R., Pappenberger, F., Pfister, L., 2007. Deriving distributed roughness values from satellite radar data for flood inundation modeling. *J Hydrol*, 344, pp. 96-111.
- Werner, M. G. F., Hunter, N. M., Bates, P. D., 2005. Identifiability of distributed floodplain roughness values in flood extent estimation. *J Hydrol*, 314, pp. 139-157.

ACKNOWLEDGMENTS

The presented research was funded by the Austrian Research Promotion Agency (FFG) in the frame of the Austrian Space Applications Programme (ASAP). The ALS data was kindly provided by the "Amt der Niederösterreichischen Landesregierung, Gruppe Baudirektion, Abteilung Vermessung und Geoinformation".

OBSERVING STRESS OF ARTIFICIAL NIGHT LIGHTING ON MARINE ECOSYSTEMS – A REMOTE SENSING APPLICATION STUDY

C. Aubrecht^{a,*}, C.D. Elvidge^b, D. Ziskin^{b,c}, P. Rodrigues^d, A. Gil^d

^a AIT Austrian Institute of Technology,

Donau-City-Str. 1, A-1220 Vienna, Austria - christoph.aubrecht@ait.ac.at

^b National Oceanic & Atmospheric Administration, National Geophysical Data Center,
E/GC 325 Broadway, Boulder, Colorado USA 80305-3328 - chris.elvidge@noaa.gov

^c Cooperative Institute for Research in Environmental Sciences (CIRES), University of Colorado at Boulder,
216 UCB, Boulder, Colorado USA 80309-0216 - daniel.ziskin@noaa.gov

^d University of the Azores, Department of Biology,

Apartado 1422, 9501-801 Ponta Delgada, São Miguel, Azores, Portugal - (pedrorodrigues, arturgil)@uac.pt

KEY WORDS: Ecosystem, Marine, Impact Analysis, Monitoring, Satellite

ABSTRACT:

Satellite based observation of nocturnal lighting opens up a variety of research and application fields dealing with impacts of light on the environment. The National Oceanic and Atmospheric Administration's National Geophysical Data Center (NOAA-NGDC) processes and archives nighttime lights data acquired by the U.S. Air Force Defense Meteorological Satellite Program (DMSP) Operational Linescan System (OLS). Initially designed to detect moonlit clouds this sensor is equipped with a photomultiplier tube intensifying the visible band signal at night and enabling the detection of lights present at the surface of the earth. It thus provides up-to-date information on the location and impact zone of oil and gas producing facilities, heavily lit fishing boats and the artificial night sky brightness that can extend many kilometers out from urban settlements. Artificial night lighting represents a direct threat to marine ecosystems and is an excellent proxy measure for indirect impacts such as human associated chronic water pollution. A growing body of evidence indicates that artificial sky brightness is an important stressor for many marine organisms, including birds and fish. In this paper we present selected 'eco-applications' of nighttime Earth Observation including assessment of light pollution impact on coral reefs and sea turtles. Coral reefs are highly photosensitive, i.e. many species synchronize their spawning through detection of low light intensity from moonlight and reef structure is strongly influenced by illumination. Settlements and other artificial sources of lighting provide illumination brighter than the full moon, especially at shorter wavelengths. Seabirds are intimately linked with the light features of their environments since they are nocturnally active. On the Azores Islands a campaign was initiated reporting light-induced falls of marine birds. Results will be presented of taking these available in situ data as reference for analyzing spatial correlations of altered environmental conditions and actual impact cases.

1. INTRODUCTION

A consequence of the explosive expansion of human civilization has been the global loss of biodiversity and changes to life-sustaining geophysical processes on Earth. The footprint of human occupation is uniquely visible from space in the form of artificial night lighting, ranging from the burning of the rainforest to massive offshore fisheries to omnipresent lights of settlements and connecting road networks. The systematic global mapping of nighttime lights from space opens up a variety of research and application fields dealing with human impacts on the environment. Artificial night lighting represents a direct threat to marine ecosystems and is an excellent proxy measure for indirect impacts such as human associated chronic water pollution. A growing body of evidence indicates that artificial sky brightness is an important stressor for many marine organisms, including birds and fish. Increasing research activities on assessing ecological consequences of artificial night lighting ('*ecological light pollution*') in recent years have attracted the attention of both scientists and journalists (Longcore & Rich, 2004; Rich & Longcore, 2006; Hotz, 2008).

2. NIGHTTIME EARTH OBSERVATION

Satellite based observation of nocturnal lighting opens up a variety of research and application fields dealing with impacts of light on the environment. The National Oceanic and Atmospheric Administration's National Geophysical Data Center (NOAA-NGDC) processes and archives nighttime lights data acquired by the U.S. Air Force *Defense Meteorological Satellite Program* (DMSP) Operational Linescan System (OLS). This sensor was initially designed for cloud monitoring using a pair of visible and thermal spectral bands. With the DMSP satellites flying in sun-synchronous, low altitude polar orbits and with a swath width of 3,000 km each OLS collects a complete set of imagery of the earth twice a day. At night a photomultiplier tube (PMT) intensifies the visible band signal in order to enable the detection of moonlit clouds, whereas the boost in gain allows the observation of lights present at the surface of the Earth. Most lights can be linked to human settlements (Elvidge et al., 1997) and ephemeral fires (Elvidge et al., 2001a), but also gas flares and offshore platforms as well as heavily lit fishing boats can be identified.

* Corresponding author.

1992	1993	1994	1995	1996	1997	1998	1999	2000	2001	2002	2003	2004	2005	2006	2007	2008	2009	
F-10																		
	F-12																	
		F-14																
			F-15															
				F-16														

Figure 1. DMSP satellites and their respective covered time span used for time series analyses.

Nighttime image data from individual orbits meeting pre-defined quality criteria (i.e. referring to geolocation, sunlight, moonlight, cloudiness conditions) form the basis for the annual global latitude-longitude grids with 30 arc second resolution cells corresponding to approximately 1 km² at the equator (see Aubrecht et al., 2008 for more detailed explanations on data selection criteria and data composition).

NOAA's NGDC stores and maintains the long-term DMSP archive (figure 1), and has built up comprehensive experience in nighttime image processing and algorithm development related to feature identification (e.g. lights and clouds) and data quality assessment (cp. Elvidge et al., 1997; Elvidge et al., 2001b). Dating back to 1992 the data archive enables the production of a time series of inter-comparable single-year data sets for assessing temporal trends in human activity. Considering the entire available digitally preprocessed time series, temporally overlapping data from five DMSP satellites are used for inter-calibration: (1) F-10: 1992-1994, (2) F-12: 1994-1999, (3) F-14: 1997-2002, (4) F-15: 2001-2009, (5) F-16: 2004-2009.

3. SELECTED APPLICATIONS OF MARINE ECOSYSTEM MONITORING USING NIGHTTIME EARTH OBSERVATION

In the following sections we present selected applications of observing exposure of marine ecosystems to artificial night lighting. First, *coral reefs* are examined on a global scale, building up an inventory of stressors (derived from nighttime lights data) in close proximity to reef locations. Second, light pollution was observed on a more regional scale, comparing temporal patterns in *sea turtle* nesting activity with anthropogenic beach lighting development in Florida. Finally, this applications selection is concluded with a new study on mapping light pollution impact on *marine birds* on the Azores Islands where a ground data collection of light-induced bird fall locations serves as actual impact reference information.

3.1 Coral reefs

A growing body of evidence indicates that *artificial sky brightness is an important stressor for coral and other marine organisms* (Jokiel et al., 1985). In addition, satellite observations of lighting can be used as a *proxy for other stressors*, such as water pollution from urban areas, fishing and recreational use of reefs.

Coral reef ecosystems are generally found in shallow waters, between the Tropic of Capricorn and the Tropic of Cancer. Data indicating the spatial distribution of coral reef ecosystems are available on a global scale covering a total area of 255,000 km².

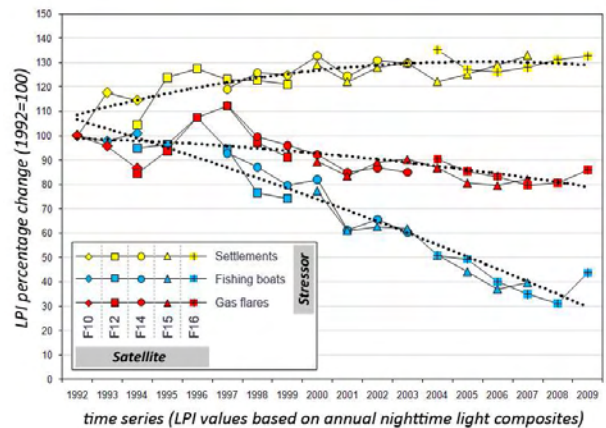


Figure 2. Lights Proximity Index relative change since 1992: (1) settlements, (2) fishing boats, (3) gas flares.

The data was obtained from 'Reefs at Risk' (Bryant et al., 1998) and originates from the United Nations Environment Programme - World Conservation Monitoring Centre (UNEP-WCMC). The initial base data had been converted into raster format at a spatial resolution of 1 km. For further spatial analyses this grid was (re-)converted into a point dataset. In the presented project a list of 330,490 coral reef point locations is used where each record is linked with a region classification table assigning the reef points to around 150 distinct geographic regions worldwide (primarily country-/archipelago-based).

For a globally consistent assessment of coral reef exposure to anthropogenic activities, reef stressors have to be derived from a spatially and temporally inter-comparable data source available on a global scale. Based on DMSP nighttime lights data, we developed an indicator (Lights Proximity Index, LPI), which integrates the brightness and distance of lights near known coral reef sites. Separate LPI values are calculated for the three stressors observable in nighttime lights: (1) human settlements, (2) gas flares, and (3) heavily lit fishing boats. The contribution of lights to the LPI declines as their distance away from the reef site increases. The initial LPI calculation is described in Aubrecht et al. (2008).

Based on the digital nighttime lights data archive a time series has been created which enables monitoring of temporal trends and detecting areas of improvement and degradation on a regional scale. First results of this temporal trend analysis were presented by Aubrecht et al. (2009). The current version of the LPI time series includes annual composites of nighttime lights from DMSP satellites F10 to F16 covering the years 1992 through 2009.

As illustrated by figure 2, results indicate that since 1992 lighting from human settlements in proximity to coral reefs has grown (yellow graph), an indication of the expansion in population and infrastructure in coastal areas in many parts of the world. In contrast, lit fishing boats activity (blue graph) has declined. This may be the result of improved regulation and management of reef areas, changes in fishing practices, or the depletion of fish stocks that are amenable to capture using bright lights. The LPI time series from gas flares (red graph) shows a more complex pattern, with dips in 1994 and 2001, a peak in 1997, and a largely steady pattern from 2002 through 2009.



Figure 3. (1) DMSP nighttime lights and superimposed Core Florida Index Beach locations; (2) warning sign indicating the legal protection status of loggerhead turtle nesting areas (photo, www.maxrharris.com/caretta); (3) baby loggerhead properly oriented towards the ocean (photo, www.dep.state.fl.us).

3.2 Sea turtles

Turtles are reptiles that are tied to the land for oviposition (egg-laying). There are seven species of marine turtles today, six of which are listed as endangered and one as threatened. The reasons for their listings are diverse, but all are human-caused: loss of habitat, habitat alteration, illegal and legal fishing, boat hits, pollution, etc. (Nicholas, 2001). One particularly adverse effect is light pollution, i.e. the presence of detrimental artificial light in the environment. *Anthropogenic beach lighting significantly impacts critical nocturnal behaviors of marine turtles* such as (1) the choosing of nesting sites for laying, incubating, and hatching eggs, (2) the returning to the sea after nesting, and (3) hatchlings finding their way to the sea after emerging from their nests (Witherington & Martin, 2000). The cues for orienting in the proper direction appear to be based upon natural light. Because of their tendency to move in the brightest direction, hatchlings show an immediate and well-directed orientation towards the water in natural conditions. Before anthropogenic lighting, dune silhouettes were typically darker than the surf. Now the reverse is often true. On artificially lighted beaches, hatchlings become misdirected by lighting sources, which leaves them unable to find the water and likely to die from dehydration and predation (Salmon, 2003; Lorne & Salmon, 2007). Furthermore, light pollution literally destroys the natural habitat, as beaches become unsuitable for nesting. Adult females favor dark beaches for their nest sites when emerging from the sea at night, with artificial lighting basically deterring them from doing so (Witherington, 1992).

In the presented study nesting activities of Loggerhead sea turtles (*Caretta caretta*) along the coast of Florida are examined and set in relation to the development of artificial night lighting as observed by DMSP-OLS (Ziskin et al., 2008). Loggerheads live in tropical and temperate oceans and have a generation time of approximately 45 years. Mature females (approximately 30 years old) tend to return to their natal beach to lay their eggs (Heppel et al., 1997). Since 1989, the Fish & Wildlife Research Institute of the Florida Fish & Wildlife Conservation Commission has coordinated the Index Nesting Beach Survey (INBS), a detailed sea turtle nesting-trend monitoring program, in conjunction with the Statewide Nesting Beach Survey (SNBS) program. The INBS program was established with a set of standardized data-collection criteria to measure seasonal nesting, and to allow accurate comparisons between beaches and between years. The INBS program is suited to these trend assessments because of its uniformity in beach-survey effort, spatial and temporal detail, as well as the specialized annual training of beach surveyors.



Figure 4. Temporal trends in loggerhead nesting counts and anthropogenic beach lighting.

To measure the temporal trend in artificial beach lighting DMSP-OLS data is used, i.e. the annual mean of persistent lights (1992-2007 time series). Imagery was inter-calibrated to account for changes in platforms and instrument fluctuations. Observations from multiple platforms were averaged. Nighttime lights data is superimposed on the locations of Core Florida Index Beaches, where surveys of Loggerhead nesting occurred (see figure 3). The brightness intensity values are then summed up for each index beach pixel. Referring to the natural nocturnal marine turtle behavior our hypothesis was that an increase in night lights along Florida's coast would result in a decrease in loggerhead sea turtle nesting. Comparing the two time series results, we find that Florida has decreased its night lighting near nesting beaches, yet total loggerhead sea turtle nesting continues to decline (see figure 4).

The observed 25% decrease in beach lighting since 1996 is most likely due to newly introduced legal restrictions. In 1986 Florida passed a law requiring localities to regulate beachfront lighting for the protection of sea turtles (*Florida Law 161.163*). This law was followed by the promulgation of a Model Lighting Ordinance in 1993.

Excerpt from Florida Law 161.163:

“Coastal areas used by sea turtles; rules.

--The [Department of Environmental Protection] shall adopt by rule a designation of coastal areas which are utilized, or are likely to be utilized, by sea turtles for nesting. The department shall also adopt by rule guidelines for local government regulations that control beachfront lighting to protect hatching sea turtles.”

Looking at the continuous decline in nesting activities along Florida's coast and taking into account the loggerhead life cycle, we come to the following conclusions. Total loggerhead nesting has declined for reasons other than contemporary levels of anthropogenic beachfront lighting. There would be approximately a 30-year lag between hatchling mortality and lowered nest counts (female maturity at the age of 30 years). With the digital DMSP data archive dating back to 1992, more than 10 years of data records would still have to be collected, before we might be able to observe direct relations. Anthropogenic lighting is furthermore expected to affect nest site choice on a scale finer than the entire state of Florida. Nesting loggerheads are predicted to favor individual beach segments with the lowest levels of anthropogenic lighting.

3.3 Seabirds

Petrels and shearwaters (Family *Procellariidae*) are known to be very sensitive to artificial lights (Imber, 1975) because they commonly attend breeding colonies at night. *Artificial lights can attract and disorientate birds* (Verheijen, 1981; Longcore & Rich, 2004), particularly fledglings during their first flight to the sea, and many of them thus fall to the ground with fatal injuries, are killed by predators or die to starvation (Le Corre et al., 2002). Oro et al. (2005) reported the increase of predation rates by yellow-legged gulls. There are two main reasons to explain this attraction: (1) The artificial lights can lead to incorrect visual orientation since the first-time navigation to the sea at night depends on visual cues given from moon and star light (Telfer et al., 1987), (2) petrels and shearwaters feed on bioluminescent squids, and inexperienced birds tend to search for lights (i.e. including artificial lights) to improve their chance of getting a meal (Imber, 1975; Klomp & Furness, 1992; Montevecchi, 2006).

Many petrels and shearwaters have undergone a substantial decline in recent times. In accordance to BirdLife International (2000), more than 50% of these species are threatened, mostly due to the presence of introduced predators and the impact of commercial fisheries. Although many of these species breed on islands inhabited by humans, very few studies focus on the impacts of artificial lights on their ecology. In Hawaii, urban lights were responsible for a large mortality of petrels (Telfer et al., 1987; Anley et al., 1997). On Réunion Island, light pollution induced mortality to all breeding species of petrels (Jouanin & Gill, 1967; Jouanin, 1987; Le Corre et al., 1996, 1999). On Canary Island of Tenerife, light-induced mortality rates are reportedly of concern for petrels and small shearwaters (Rodríguez & Rodríguez, 2009).

In the Azores, the attraction of Cory's shearwater to artificial lights has been known for a long time and since 1995 the regional government arranges rescue and awareness campaigns. This protected species is the most abundant seabird species of the Azores and is not in threat. Anyhow, populations are restricted to the Atlantic and Mediterranean Sea and their breeding population suffered a huge effective decrease in recent years (Bolton, 2001). During the last 10 years the Regional Government has carried out an awareness campaign called 'SOS Cagarro', which involves local media asking people to collect fallen birds and follow provided guidelines to release the animals safely (i.e. at the coast during daylight to avoid repeated distraction by artificial lights). Every night during the months of October and November, which is the period coinciding with the departure of juveniles from their nests for the first flight to the sea, the NGO 'Amigos dos Açores' ('Friends of Azores') formed several groups of volunteers that roam the streets and roads of São Miguel island in search of fallen birds, collecting all the Cory's shearwater they found. For each bird (dead or alive) exact place and date were recorded. We finally brought the data into GIS format in order to be able to use it for subsequent spatial analyses.

The aim of the presented study is to report light-induced falls of Cory's Shearwater on São Miguel Island, the biggest island in the Azores archipelago, and relate this data with satellite-observed nighttime lights (Rodrigues et al., 2010). Results will serve as a basis for recommendations and proposed actions to minimize light pollution stress on Cory's Shearwater and marine birds in general.

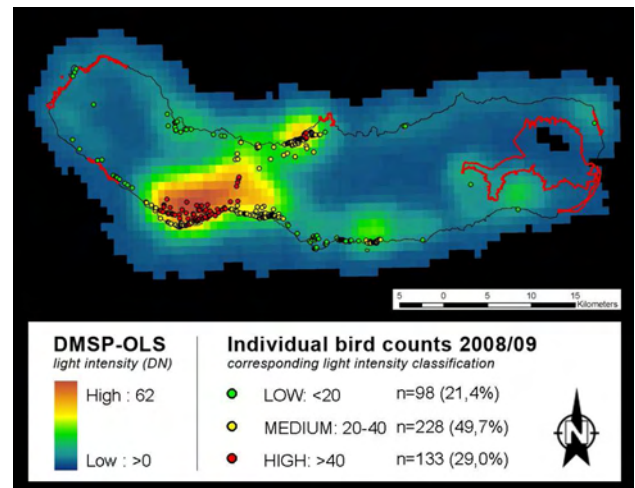


Figure 4. Spatial correlation between fallen bird records and light intensity. Important bird areas are delineated in red.

Figure 4 shows the spatial correlation of Cory's shearwater records from the 'SOS Cagarro' campaign and nighttime light intensity patterns. The bird counts are classified according to the lighting intensity at that corresponding location as derived from DMSP-OLS. Results underline the general light pollution problem in the context of adverse alteration of the natural environmental conditions for marine birds. Nearly 80% of all collected birds were found in areas with medium to high lighting intensity, while just about 20% were recorded in low light intensity regions. It can be assumed that all the fallen birds would have died without the intervention of rescue campaigns (Imber, 1975; Le Corre et al., 2002). Fallen birds, even if not injured, do not fly, but rather try to seek a dark hiding place where they would probably die of hypothermia, starvation, predation or anthropogenic causes (i.e. traffic accidents).

4. CONCLUSION AND OUTLOOK

The DMSP results indicate that it is possible to track the brightness and type of nocturnal lighting using satellite data. Calculated index values (e.g. LPI) can be used as a proxy measure for human stressors that would be difficult to observe in a consistent manner on a global scale. This includes anthropogenic stressors such as polluted urban runoff, sedimentation, and the recreational uses of marine ecosystems, which all tend to be higher in proximity to population centers. Regarding the direct impacts of artificial lighting, further research would be required to quantify the effects of artificial lighting on reef organisms. On the other hand, terrestrial studies have already confirmed direct light pollution impact on both sea turtles and marine birds (e.g. Salmon, 2003). Because of the 30 years time span female sea turtles need to return for nesting there is however no DMSP data available (i.e. archive dating back to 1992), which makes it impossible to explain temporal trends in nesting activity using nighttime earth observation.

It is known that lighting types vary spectrally (Elvidge et al. 2010) and as a result we recommend that the analysis of biological effects take into account the spectral differences in lighting types. While the DMSP nighttime lights are panchromatic, future satellite sensors may provide multispectral observations of nighttime lights (Elvidge et al. 2007), enabling more specific analysis of lighting impacts.

REFERENCES

- Ainley, D., Podolsky, R., Deforest, L., Spencer, G., 1997. New insights into the status of the Hawaiian petrel on Kauai. *Colonial Waterbirds*, 20, pp. 24-30.
- Aubrecht, C., Elvidge, C.D., Longcore, T., Rich, C., Safran, J., Strong, A., Eakin, M., Baugh, K.E., Tuttle, B.T., Howard, A.T., Erwin, E.H., 2008. A global inventory of coral reef stressors based on satellite observed nighttime lights. *Geocarto International*, 23(6), pp. 467-479.
- Aubrecht, C., Elvidge, C.D., Eakin, C.M., Ziskin, D., Baugh, K.E., 2009. Coral reef risk assessment using DMSP nighttime lights - Temporal trends and global perspectives. *ISRSE: 33rd International Symposium on Remote Sensing of Environment*. Proceedings. Stresa, Lago Maggiore, Italy, May 4-8, 2009.
- BirdLife International, 2000. *Threatened Birds of the World*. Lynx Edicions & BirdLife International, Barcelona, Cambridge.
- Bolton, M., 2001. *Censo de Cagarro Calonectris diomedea no Arquipélago dos Açores, 2001*. Unpublished Final Report, Department of Oceanography and Fisheries, University of Azores.
- Bryant, D., Burke, L., McManus, J., Spalding, M., 1998. *Reefs at risk - A map-based indicator of threats to the world's coral reefs*. World Resources Institute, Washington DC, USA.
- Elvidge, C.D., Baugh, K.E., Kihn, E.A., Kroehl, H.W., Davis, E.R., 1997. Mapping of city lights using DMSP Operational Linescan System data. *Photogrammetric Engineering and Remote Sensing*, 63, pp. 727-734.
- Elvidge, C.D., Nelson, I., Hobson, V.R., Safran, J., Baugh, K.E., 2001a. Detection of fires at night using DMSP-OLS data. In Ahern, F.J., Goldammer, J.G., Justice, C.O. (Eds.), *Global and Regional Vegetation Fire Monitoring from Space: Planning a Coordinated International Effort*. SPB Academic Publishing bv, The Hague, The Netherlands, pp. 125-144.
- Elvidge, C.D., Imhoff, M.L., Baugh, K.E., Hobson, V.R., Nelson, I., Safran, J., Dietz, J.B., Tuttle, B.T., 2001b. Nighttime lights of the world: 1994-95. *ISPRS Journal of Photogrammetry and Remote Sensing*, 56, pp. 81-99.
- Elvidge, C.D., Cinzano, P., Pettit, D.R., Arvesen, J., Sutton, P., Small, C., Nemani, R., Longcore, T., Rich, C., Safran, J., Weeks, J., Ebener, S., 2007. The Nightsat mission concept. *International Journal of Remote Sensing*, 28(12), pp. 2645-2670.
- Elvidge, C.D., Keith, D.M., Tuttle, B.T., Baugh, K.E., 2010. Spectral Identification of Lighting Type and Character. *Sensors*, 10(4), pp. 3961-3988.
- Heppell, S.S., Snover, M.L., Crowder, L.B., 1997. Sea Turtle Population Ecology. In Lutz, P.L., Musick, J.A., Wyneken, J. (Eds.), *The Biology of Sea Turtles, Volume II*. CRC Press, Boca Raton, pp. 275-299.
- Hotz, R.L., 2008. It's All About the Lighting. City Lights Are Obscuring Our Starry Nights. *The Wall Street Journal*, A10, July 25, 2008. Available at <http://online.wsj.com/article/SB121692767218982013.html>
- Imber, M. J., 1975. Behaviour of petrels in relation to the moon and artificial lights. *Notornis*, 22, pp. 302-306.
- Jokiel, P.L., Ito, R.Y., Liu, P.M., 1985. Night irradiance and synchronization of lunar release of planula larvae in the reef coral *Pocillopora damicornis*. *Marine Biology*, 88, pp. 167-174.
- Jouanin, C., 1987. Notes on the nesting of Procellariiformes in Réunion. In Diamond, A.W. (Ed.), *Studies of Mascarene Island Birds*. Cambridge University Press, Cambridge, UK.
- Jouanin, C., Gill, F., 1967. Recherche du Pétrel de Barau *Pterodroma baraui*. *L'O.R.F.O.*, 37, pp. 1-19-
- Klomp, N.I., Furness, R.W., 1992. Patterns of chick feeding in Cory's Shearwaters and the associations with ambient light. *Colonial Waterbirds*, 15, pp. 95-102.
- Le Corre, M., Probst, J.-M., de Vivies, Y.-M., Ribes, S., 1996. Opération de sauvetage réussie pour les jeunes pétrels de Barau à l'envol. *Courrier de la Nature*, 160, pp. 12-13.
- Le Corre, M., de Vivies, Y.-M., Ribes, S., 1999. Les pétrels de La Réunion en danger. *Oiseau Magazine*, 54, pp. 26-27.
- Le Corre, M., Ollivier, A., Ribes, S., Jouventin, P., 2002. Light-induced mortality of petrels: a 4-year study from Réunion Island (Indian Ocean). *Biological Conservation*, 105, pp. 93-102.
- Longcore, T., Rich, C., 2004. Ecological light pollution. *Frontiers in Ecology and the Environment*, 2(4), pp. 191-198.
- Lorne, J.K., Salmon, M., 2007. Effects of exposure to artificial lighting on orientation of hatchling sea turtles on the beach and in the ocean. *Endangered Species Research*, 3, pp. 23-30.
- Montevecchi, W.A., 2006. Influences of artificial light on marine birds. In Rich, C., Longcore, T. (Eds.), *Ecological Consequences of Artificial Night Lighting*. Island Press, Washington, D.C., pp. 94-113.
- Nicholas, M., 2001. Light Pollution and Marine Turtle Hatchlings: The Straw that Breaks the Camel's Back? *The George Wright FORUM - Protecting Dark Skies*, 18(4), pp. 77-82.
- Oro, D., de León, A., Minguez, E., Furness, R.W., 2005. Estimating predation on breeding European Storm-petrels (*Hydrobates pelagicus*) by Yellow-legged Gulls (*Larus michahellis*). *Journal of Zoology, London*, 265, pp. 421-429.
- Rich, C., Longcore, T., 2006. *Ecological Consequences of Artificial Night Lighting*. Island Press, Washington DC, USA.
- Rodrigues, P., Aubrecht, C., Gil, A., 2010. Light pollution impact on Cory's Shearwater populations on São Miguel Island, Azores archipelago - Comparing ground collection data with satellite observations of artificial night lighting. *1st World Seabird Conference*. Victoria, Canada, September 7-11, 2010. In press.
- Rodríguez, A., Rodríguez, B., 2009. Attraction of petrels to artificial lights in the Canary Islands: effects of the moon phase and age class. *Ibis*, 151, pp. 299-310.

Salmon, M., 2003. Artificial night lighting and sea turtles. *Biologist*, 50(4), pp. 163-168.

Telfer, T.C., Sincock, J.L., Byrd, G.V., Reed, J.R., 1987. Attraction of Hawaiian seabirds to lights: conservation efforts and effects of moon phase. *Wildlife Society Bulletin*, 15, pp. 406-413.

Verheijen, F.J., 1981. Bird kills at tall lighted structures in the USA in the period 1935–1973 and kills at a Dutch light-house in the period 1924–1928 show similar lunar periodicity. *Ardea*, 69, pp. 199-203.

Witherington, B.E., 1992. Behavioral Responses of Nesting Sea Turtles to Artificial Lighting. *Herpetologica*, 48, pp. 31-39.

Witherington, B.E., Martin, R.E., 2000. *Understanding, Assessing, and Resolving Light-Pollution Problems on Sea Turtle Nesting Beaches*. 2nd ed. rev. Florida Marine Research Institute Technical Report TR-2, 73 pp.

Ziskin, D., Aubrecht, C., Elvidge, C., Tuttle, B., Baugh, K., Ghosh, T., Witherington, B., Yamamoto, K., 2008. Temporal patterns in Loggerhead sea turtle nesting activity and anthropogenic beach lighting in Florida. *Eos Trans. AGU (American Geophysical Union)*, 89(53), Fall Meeting Suppl. B41A-0361. San Francisco, CA, USA.

ACKNOWLEDGMENTS

The nighttime lights data used for the presented research result from the DMSP archive run and maintained by NOAA's NGDC (Boulder, CO). The coral reef data were obtained from Reefs at Risk, WRI (Washington, DC) and originate from the UNEP-WCMC (Cambridge, UK). Turtle nesting data come from the Index Nesting Beach Survey Program (Fish and Wildlife Research Institute, FL). The 'SOS Cagarro' data were kindly provided by the NGO 'Amigos dos Açores'.

The authors thank NOAA, including the Coral Reef Watch and the Coral Reef Conservation Program, for funding work that contributed to this article. The article contents are solely the opinions of the authors and do not constitute a statement of policy, decision, or position on behalf of NOAA or the US Government.

CLASSIFICATION OF CLOUDS WITH OBJECT ORIENTED TECHNIQUE

Hamid Azari^{a,*}, AliAkbar Matkan^a, Alireza Shakiba^{ab}, seyed hossein Pourali^a

^a Remote sensing & GIS Dept., Earth Science Faculty, Shahid Beheshti University,

Tehran, Iran (azari.hamid@gmail.com, a-matkan@sbu.ac.ir, mypauk@yahoo.com, hossainpourali@yahoo.com)

KEY WORDS: Cloud Classification, Segmentation, Object Orient, Texture, Pattern, Bi-spectral, Brightness Temperature

ABSTRACT:

Rainy clouds having high densities are considered as one of the main causes of flood events, therefore detection and classification of clouds can be very valuable for flood forecasting. In this study NOAA/AVHRR satellite images were used for object oriented classification. Sixteen bands were produced and utilized for cloud classification. This included the main five bands of NOAA/AVHRR and other important information such as albedo of band 1 and 2, brightness temperature of band 3,4 and 5, solar zenith and azimuth angles, land surface temperature, sea surface temperature, normalized difference vegetation index, deviation of nadir and cloud height. Multi-resolution segmentation followed by bi-spectral technique and hierarchical classification were performed using the sixteen produced layers. The obtained kappa coefficient and the overall accuracy were relatively high (kappa= 0.887, overall Acc.= 0.905). The results of the study demonstrated that the object oriented classification can be considered as a proper method for cloud detection and classification.

1. INTRODUCTION

The detection and classification of clouds in meteorological satellite data with known pixel based approaches is principally based on spectral analyses and every so often simple spatial analyses are used additionally. When classifying structures performed with hundreds of pixels and relationships between them, these approaches are called conceptual methods. Object orient classification is a conceptual method that operates on groups of pixels (image objects) and defines the relationship between them. There are two advantages for Cloud classification with object oriented techniques. First, this approach reduces within-class spectral variation and generally removes the so-called salt-and-pepper effects that are typical in pixel-based classification. Second, a large set of features characterizing objects' spatial, textural, and contextual properties can be derived as complementary information to the direct spectral observations to potentially improve cloud classification accuracy (Liu, D and Xia,F, 2010).

While a number of studies have shown the object-based classification over land cover and land use mapping (Lewinski and Zaremski, 2004.; Shattri, et al. 2003; Oruc et al., 2005; Mathieu and Aryal, 2005; Lara et al 2006; Volker, 2003) less attention has been paid to its ability to cloud classification.(Göttsche and Olesen, 2005; haji mir rahimi and bai, 2008 in persian)

The purpose of this letter is to provide a more complete evaluation of object-based cloud classification.

2. DATA AND METHODS

2.1. Data

In this study the classification of clouds was performed using low resolution satellite image, NOAA/AVHRR data, that is taken from northeast of Iran in august of 2005 (NOAA14; 11-08-2001, 14:16 UTC). It has a spatial resolution about 1.1 km in nadir and 5 spectral channels with the following wavelength ranges have shown in table 1.

spectral channels	Range of electromagnetic
Ch1: 0.58 – 0.68 7m	VIS (visible)
Ch2: 0.725 – 1 7m	NIR (near infrared)
Ch3: 3.55 – 3.93 7m	MIR (meddle infrared)
Ch4: 10.5 – 11.5 7m	TIR (thermal infrared)
Ch5: 11.5 – 12.57m	TIR (thermal infrared)

Table1. Channel of NOAA/AVHRR

2.2. Methods

In this study, we performed the image processing (corrections and calibrations) and clipping the study area from images, primarily. Then the cloud classification was applied. Figure 1 is a schematic diagram that illustrates the steps and type of need data in this study. And Figure 2a and 2b show the visible and infrared bands respectively.

* Corresponding author: hamid azari. M.S. of remote sensing and GIS

address: Remote sensing & GIS Dept., Earth Science Faculty, Shahid Beheshti University, Velenjak St. Tehran, Iran
tel: +982122431787; fax: +982122431788

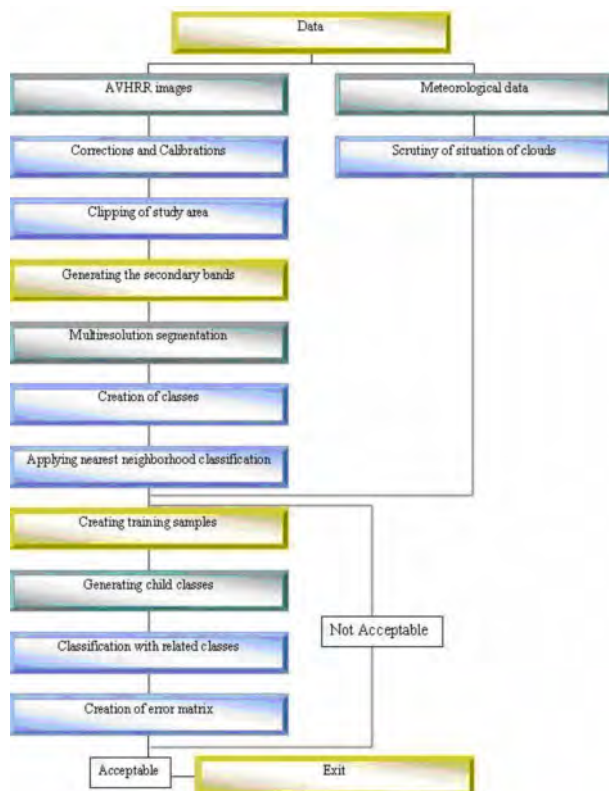


Figure 1. Schematic diagram illustrates the steps and type of data in this study

In general, the most effective method for identifying individual cloud types is to obtain a Visible and an IR image of the same scene. The Visible (VIS) channels 1 and 2 of the data were processed for albedo. The VIS image used to identify cloud shapes, textures, organizational patterns, and thicknesses. In general, the thicker a cloud is, the higher its albedo and the brighter it will appear in visible imagery. Thin clouds are often very dark or transparent in visible imagery. Cloud texture refers to its appearance in visible imagery.

Visible satellite data then was compared to an IR image in order to determine the height of the clouds. The IR channels 3, 4 and 5 of the data were processed for brightness temperature. In general, the higher a cloud is, the colder it is. In IR imagery, therefore, lower, warmer clouds will appear darker while high, cold clouds will appear brighter. We put together all this information and performed object oriented method with ecognition software and maked reliable assessments of what types of clouds are present in the image. Additional information such as from criteria, textual or contextual information of the segments then are used in an appropriate way to derive improved classification results.

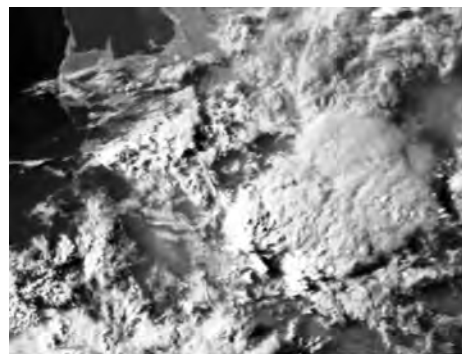


Figure 2a. Band 1 of AVHRR data

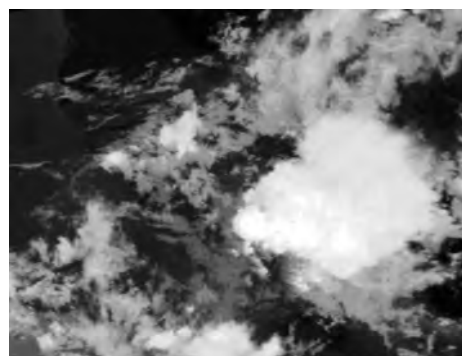


Figure 2b. Band 4 of AVHRR data

The important first step in object orient classification is segmentation. The segmentation algorithm does not only depend on the single pixel value, but also on pixel spatial continuity (texture, topology, shape, channel means, standard deviation, etc) (shattri et al, 2003). The Sixteen components are produced with PCI Geomatica in this study. The five main bands that there are in satellite images (primary components) and the other eleven components such as albedo and brightness temperature of main bands, solar zenith and azimuth angles, Land Surface Temperature (LST) & Sea Surface Temperature (SST), Normalized Difference Vegetation Index (NDVI) and deviation of nadir and cloud height are secondary components.

Form sixteen components, the ten components use directly and others have the same effects on classification. The multiresolution segmentation is selected in this study. This results to a condensing of information and a knowledge-free extraction of image objects. For this method the used AVHRR channels, brightness temperatures of band 4 and 5 and cloud height are weighted by 1, whereas the Digital Elevation Model (DEM), LST & SST and NDVI that show the free cloud areas, are weighted by 0.2 (Göttsche and Olesen, 2005). Since the clouds with medium area and more are important for this study, a fairly medium scale of 50 is chosen for the finest segmentation (level 1 that called analysis level).

Segmenting clouds were produced using infrared or albedo images followed by bi-spectral cloud classification technique. Bi-spectral techniques based on the relationship between cold and brightness temperature of clouds were also used to evaluate classification. Figure 3 shows the multiresolution segmentation that applied on image.

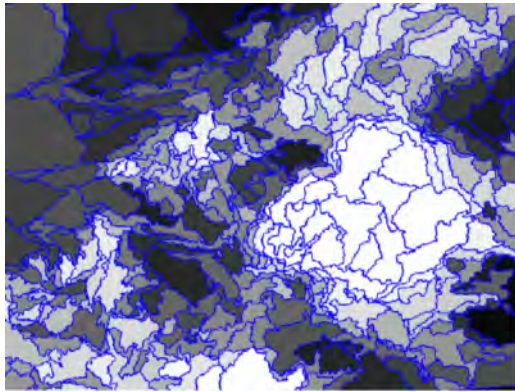


Figure3. Multiresolution segmentation in analysis level

In remote sensing studies we cannot detect a specific cloud in a range of Digital number in visible or infrared images exactly. For example, the cumulonimbus clouds (Cb) in each region and time can be detected with various range of digital number. But studies show that this type of cloud is brighter than others in VIS and IR images or stratus clouds (St) are darker than others in IR images. The other types of clouds can be detected similarly that is shown in figure 4 but texture, shape and thickness of clouds are useful option for decision. Figure 4 is the principle of bi-spectral technique in this study.

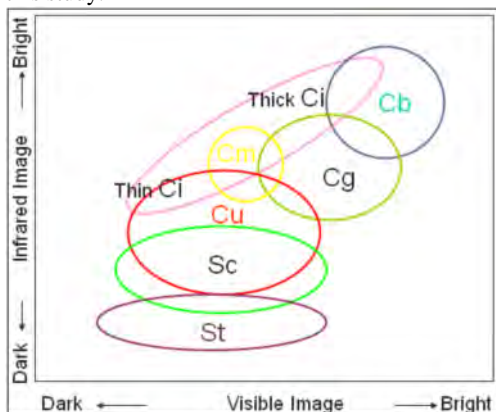


Figure4. Brightness of each type of clouds in VIS and IR images.(Ito ,2000)

3. RESULTS AND DISCUSSIONS

In this study 8 classes were identified that were included a non-cloud class (sea and terrain) and 7 cloud classes (Ns, Ci, Cb, Cu, Cg, Sc, St). After detecting of classes and scrutiny of features (mean, standard deviation, to super object, shape (area and density) and texture (homogeneity, contrast and entropy), classification was carried out. The nearest neighbor classification of level 1 object was performed for mean and standard deviation of AVHRR channels of 1, 2 and 4. The relationships between objects were included in the hierarchical classification for getting the better results. The classifications of clouds were performed in level 2 called cloud level. The result of classification illustrated in figure 5.

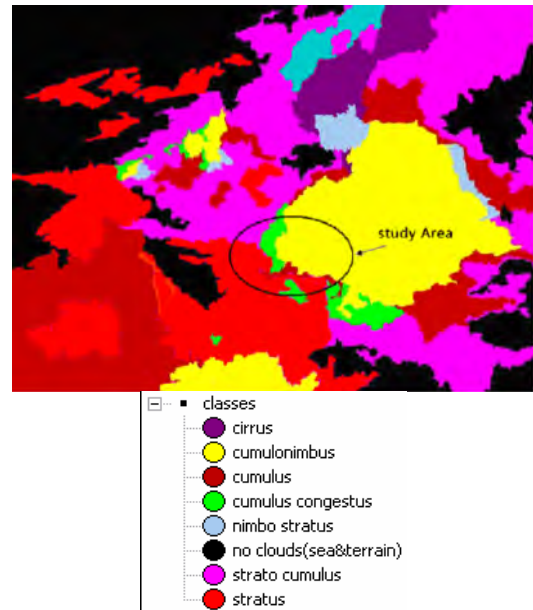


Figure 5. Classified clouds with eCognition

Since the detected cloud in sky of each area is the dominant cloud on that hour and the other type of clouds may be existed during the day, so collecting of control points for accurate assessment is not possible. So, the regions that have the most adaptation with bi-spectral cloud classification theories were used as training samples optically. The NIR and IR channels 3, 4, and 5 of the data were processed for temperature and brightness. In IR image cold clouds are high clouds, so the colors typically highlight the colder regions Mid height clouds with TB below 230k were identified as cumulonimbus cloud. Darker clouds in IR images were associated to warm stratus, Strato cumulus, cumulus clouds and thin cirrus cloud that were colder than others. Using this knowledge and bi-spectral technique, the sampling areas were selected and error matrix and kappa coefficient performed using TTA MASK in eCognition software. The obtained kappa coefficient was equal of 0.887 and the overall accuracy is 0.905 that illustrate the accurate of classification is high. The window of error matrix based on TTA Mask is showed in figure 6.

User \ Reference Class:	cirrus	cumulonimbus	cumulus	cumulus congestus	nimbo stratus	strato cumulus	stratus	no clouds (sea&terrain)	Sum
Confusion Matrix									
cirrus	2730	179	58	0	0	93	0	3060	
cumulonimbus	197	5093	0	11	0	0	0	5301	
cumulus	143	0	1981	0	23	190	0	2337	
cumulus congestus	0	0	0	1510	0	0	0	1510	
nimbo stratus	0	0	0	0	830	0	83	713	
strato cumulus	0	0	130	0	0	2926	175	3231	
stratus	0	0	176	0	94	169	2301	2644	
no clouds (sea&terrain)	0	0	0	0	0	0	348	5617	
unclassified	0	0	0	0	0	0	0	0	
Sum	3070	5272	2345	1521	724	3211	3597	6001	
Accuracy									
Producer	0.889	0.966	0.845	0.993	0.97	0.911	0.779	0.936	
User	0.892	0.961	0.848	1	0.883	0.906	0.773	0.942	
Totals									
Overall Accuracy	0.905								
KIA	0.887								

Figure 6. Error matrix based on TTA Mask

4. References

Billa, L, Mansor,Sh, Mahmud ,A.R, Ghazali ,A,H, 2004. Integration of RS, GIS and MIKE 11 Hydrodynamic Modeling for Flood Early Warning: A case study of the

Langat river basin Malaysia , *Map Asia Conference 2004*.

Göttsche Frank-M. and Olesen Folke -S., 2005, Classification of clouds and weather situations in meteorological satellite data using Definiens eCognition

haji mir rahimi M. and bai N, 2008, classification types of clouds using AVHRR images, *Geomatics 87 Conferences ,Iranian National Cartographic Centre* (in Persian language).

Ito M.,2000, *Analysis and Use of Meteorological Satellite Images*, First Edition, Chapter2, Meteorological Satellite Center, Japan Meteorological Agency,

Lara A. Arroyo, Sean P. healey, Warren B.Cohen, David Cocero and Jose A. manzanera, 2006, Using object-oriented classification and high-resolution imagery to map fuel types in a Mediterranean region. *journal of geophysical research*, VOL. 1 11, G04S04, doi: 10.1029/2005JG000120.

Lewinski S., and zaremski K., 2004, examples of object-oriented classification performed on high-resolution satellite images, *miscellanea geographica, Warszawa*. Vol.11.

Liu, D., and Xia, F., 2010. object-based classification: advantages and limitations', *Remote Sensing Letters*, 1:4, pp.187 – 194.

Mathieu, R., and Aryal j., 2005. Object-oriented classification and Ikonos multispectral imagery for mapping vegetation communities in urban areas, *SIRC 2005 – The 17th Annual Colloquium of the Spatial Information Research Centre University of Otago, Dunedin, New Zealand*

Mishra J. k., Sharma O. P., Cloud top temperature based precipitation intensity estimation using INSAT-1D data, *International journal of Remote Sensing*, 2001, vol.22, No. 6, pp.969-985.

Oruc, M., Marangoz, A. and Buyuksalih, G., 2005. comparison of pixel-based and object-oriented classification approaches using landsat-7 ETM spectral bands.

Richard L., Bankert., and David, W., Aha.,1994. Automated identification of cloud patterns in satellite imagery.14WAF-FA4.4.

Shattri, M., Wong, T.H., and Abdul R. M. Sh.,2003. object oriented classification for land cover mapping. GISdevelopment.net (accessed 29 march 2008)

Volker, W., 2003. Object-based classification of remote sensing data for change detection, *ISPRS Journal of Photogrammetry & Remote Sensing* ,58 ,pp. 225– 238.

PLEIADES-HR IMAGING SYSTEM: GROUND PROCESSING AND PRODUCTS PERFORMANCES, FEW MONTHS BEFORE LAUNCH

S. Baillarin^a, C. Panem^a, L. Lebegue^a, F. Bignalet-Cazalet^a

^a CNES (Centre National d'Etudes Spatiales), 18 avenue Edouard Belin - Toulouse Cedex4 – France -
simon.baillarin@cnes.fr

Commission VI, WG VI/4

KEY WORDS: High resolution, Sensor, Optical, Orthoimage, Mosaic

ABSTRACT:

Pleiades-HR is the highest resolution civilian earth observing system ever developed in Europe. This optical imaging project is conducted by the French National Space Agency, CNES. It will operate two satellites designed to provide optical images to civilian and military users. The first satellite is ready for launch, the second 18 months later. It will allow, in Nadir acquisition conditions, to deliver image products 20 km wide, false or natural coloured scenes with a 50 cm ground sampling distance.

Imaging capabilities have been highly optimized in order to acquire, in the same pass, along-track mosaics, stereo pairs and triplets, and multi-targets. To fulfil the operational requirements and ensure quick access to information, ground processing has to automatically perform the radiometric and geometric corrections. Since ground processing capabilities have been taken into account very early in the mission development, it has been possible to relax some costly on-board components requirements, in order to achieve a cost effective on-board/ground compromise.

Starting from a Pleiades-HR system overview, this paper gives a quick description of the ground segment functional breakdown and focuses more precisely on the image processing and associated products. The geometric accuracy is evaluated and the excellent results obtained are presented.

Finally the paper presents the ground segment architecture that will handle this “heavy” processing in the different operational Centres.

1. 1. INTRODUCTION

Pleiades-HR, the high resolution optical earth observing mission developed for both civilian and military users, is under qualification tests in CNES and ASTRIUM premises. This project consists of two agile satellites that will provide high resolution images in Panchromatic (PA) and Multi-Spectral (XS) modes with a 50 cm ground sampling distance. This system, build up in a European context (partnerships with Spain, Sweden, Belgium, Austria and Italy), will be operated in a dual context with civilian and defence users.

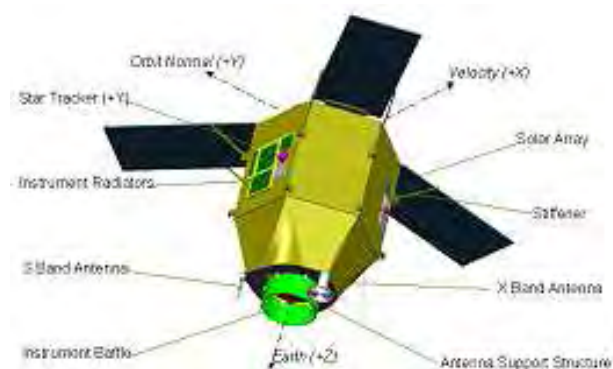


Figure 1: Pleiades-HR satellite

Imaging capabilities have been highly optimized in order to acquire several targets, in the same pass, allowing along-track image-mosaics, stereo pairs and triplets. To fulfil the operational requirements and ensure quick access to

information, ground processing has to perform automatically radiometric and geometric corrections.

First, this paper offers an overview of the image processing system and the products definition. Then the main system products are detailed and their quality assessed. Finally, the image processing architecture is briefly presented.

2. FROM SYSTEM TO PRODUCTS DEFINITION

2.1 Overview

From a ground segment point of view, Pleiades-HR architecture is defined as a classical “image-mission” loop: the User Ground Centres (also called UGCs; there are 3 different UGCs: French and Spanish Defence UGCs and French Civilian UGC) gather the different users acquisition requests, optimizing the satellite resource, and prepare the dual work plan which is finally sent by the Control Centre to the satellite, 3 times per day. After sensing, the acquired data-strips are downlinked over the receiving stations (with respect to the work plans) and the image telemetry is automatically inventoried and archived in each UGC.

Then, each UGC manages the image production requests coming from authorized users and process accordingly the archived telemetry to generate the requested product. The delay between the end of the reception and the product delivery is less than one hour.

The ground processing has also been designed to be highly interoperable; to allow federations with other earth observation systems in the GMES context. Hence, data format (catalogued

data, final image product) and data access services (online catalogued data browsing, product ordering) definitions have been major issues (Baillarin 2006).

The UGCs, including the image processing algorithms, have successfully passed system tests and are now fully integrated and ready for operations.

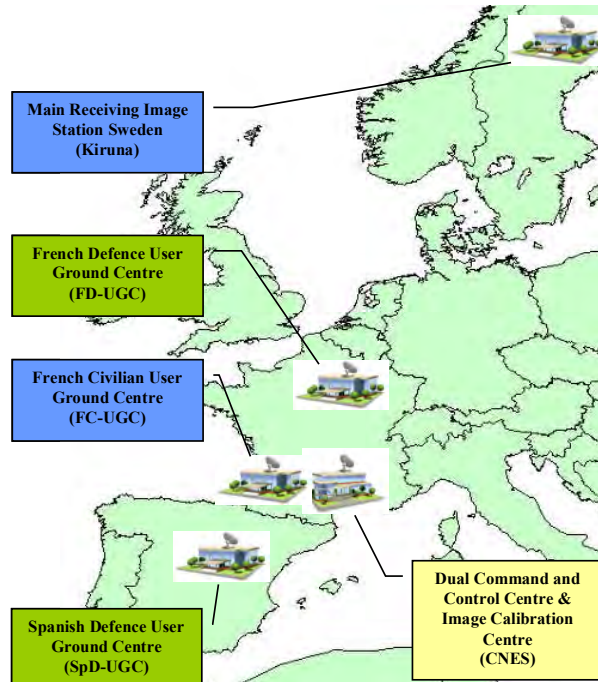


Figure 2: Pleiades-HR Ground Segment

A light version of the UGC, with image reception and production capabilities, is also available for any foreign users willing to receive and produce Pleiades-HR images (e.g. Kiruna Station).

2.2 Image products

Several types of products have been defined in order to fulfil the user needs considering that the remote sensing community is generally divided in two groups:

Users needing data for mapping purposes or using Geographic Information Systems (GIS), whatever the sensors characteristics. They usually use ortho-image products, which are resampled into cartographic projections and corrected from sensor and terrain distortions.

Users wanting to process “raw data” in order to deliver value-added products (such as 3D, geophysics data, ...) using their own methods. They need comprehensive ancillary data to compute the geometric model. Because of the specific geometry of Pleiades-HR focal plane (Kubik 2005), a “Sensor Level” product has been defined making the geometric model simpler while preserving its accuracy.

Hence, two processing levels have been defined in addition to the classical raw levels. They are presented and assessed here after.

2.3 Sensor Level

The Sensor Level product corresponds to the image that would have been delivered by a perfect standard push-broom sensor. The product is only corrected from on-board radiometric and

geometric distortions (viewing directions and high frequency attitude variations), but no ground projection is operated. All multispectral (XS) and panchromatic (PA) pixels are registered.

XS can be PAN-sharpened in the same processing flow to obtain a 0.50 m GSD 4-band colour image (blue, green, red, near infrared).

This product can be accurately located by rational functions: in addition to Pleiades-HR physical model, metadata contains direct and inverse location models that can be used by commercial software.

2.4 Ortho-image and Mosaic Level

The Pleiades-HR ortho-image is resampled into a cartographic projection and corrected from sensor and terrain distortions.

This product must be very precisely located to be used into geographic information systems (GIS). Product location is checked on an accurate DEM (Reference3D™, if available) with automatic GCPs (algorithm based on (Baillarin 2004)). Users can also give their own DEM for ortho-rectification. The final product contains associated quality metadata.

Pleiades-HR ortho-images can also be PAN-sharpened to obtain a 0.50 m GSD 4-band colour image.

Mosaics products are larger size ortho-images, automatically processed as a seamless patchwork of individual strips. This is made possible thanks to the high agility and the precise pointing capability of the platform. The strips are all converted in same geometry, using automatically computed tie points and ground control points, then radiometrically homogenised, then joined together using computed stitching-line.

3. SIMPLIFYING THE FOCAL PLANE: THE “SENSOR” PRODUCT

The complexity of the Pleiades-HR focal plane makes the classical level 1 product difficult to use. A new product level called “Sensor Level” is proposed (De Lussy 2006).

This Sensor Level product consists in a basic product specially designed for the photogrammetric community and delivered with a physical model and a rational function model.

The purpose is to generate the image which would have been acquired by a simpler push-broom sensor (SPOT-like) in the same imaging conditions in order to be able to exploit the geometric characteristics of the image (such as DEM or 3D extraction) without having to take into account the complex geometry of the real sensor.

3.1 Perfect Sensor Geometry

Due to the complexity of the focal plane (mainly because of the detector layout composed of five slightly tilted TDI arrays for the PA and five CCD arrays for each XS band), the raw products should be considered as 25 different products with their own geometrical models.

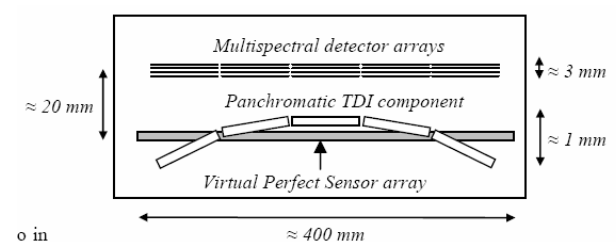


Figure 3: Focal plane layout and location of ideal array

In order to greatly simplify the use of sensor model, the Sensor Level product simulates the imaging geometry of a simple push-broom linear array, located very close to the PA TDI arrays. Besides, this ideal array is supposed to belong to a perfect instrument with no optical distortion and carried by a platform with no high attitude perturbations. This attitude jitter correction (made with a polynomial fitting) allows both for simple attitude modelling and more accurate representation of the imaging geometry by the rational functions sensor model (see further).

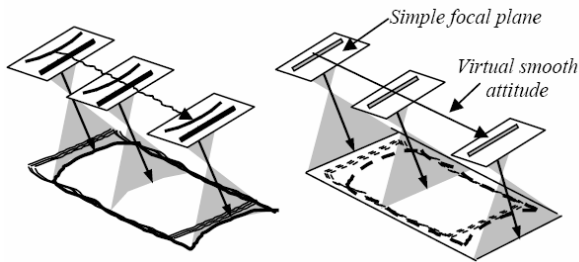


Figure 4: Perfect Sensor Geometry

3.2 Processing and image quality

The production of this ideal linear array imagery is made from the raw image and its rigorous sensor model.

The raw image is resampled into the Sensor Level geometry taking into account a DEM. The direct geolocation is made with an accurate Sensor Level geometric model. Thus, Sensor Level image and its geometric model are consistent. The impacts of the above processing on the geometric accuracy of the resulting products have to be significantly small (errors less than centimetres). These errors are due to:

- The quality of the resampling process,
- The accuracy of the DEM used (generally SRTM DTED1).

To obtain the best results:

- Resampling process is made with a highly accurate method (using spline interpolators (Unser 1999)),
- The DEM is pre-processed in order to minimize the relief artefacts due to errors and/or blunders.
- The geometric model differences between raw image and Sensor Level (especially attitude and detector model) are minimized to decrease the parallax and the altitude error effects.

Hence, the quality of a Sensor Level image is mainly linked with the quality of the corresponding raw image (the geometric budgets are detailed in (De Lussy, 2006)). The only remaining difference is due to the little parallax between Sensor Level model and Real sensor (less than $80\mu\text{rad}$) combined to a uncertainty of the DEM. In term of location accuracy, the difference between Sensor Level images and real sensor images is less than 3.10^{-3} according to the SRTM 30m accuracy at 99.7%.

3.3 Accuracy of Sensor Level geometric model

The geometric modelling refers to the relationship between raw pixels in the image and geographic coordinates on ground.

The Sensor Level product is delivered with two geometric models:

- a “rigorous sensor” model
- a rational function model

Users can choose either the rigorous sensor model, or the rational function sensor model: results are very comparable.

On one hand, the rigorous sensor model is defined from a complete set of parameters of the image acquisition:

- alignment and focal plane characteristics (linear array)
- image time stamp
- smoothed attitude and ephemeris time tagged

Such rigorous models are conventionally applied in photogrammetric processing because of the clear separation between various physical parameters and so, easier to use in block adjustments (refinement using GCP).

On the other hand, the Rational Function Model, RFM, is an approximation of the rigorous sensor model. It allows full three-dimensional sensor geolocation using a ratio of polynomials (Tao 2001), using a standardized and very simple relationship between raw pixels and geographic coordinates.

The RFM is able to achieve a very high accuracy with respect to the original rigorous sensor model. Accuracy assessment shows that RFMs yield a worst-case error below **0.02 pixel** compared with its rigorous sensor model under all possible acquisition conditions.

Therefore, when the RFM is used for imagery exploitation, the achievable accuracy is virtually equivalent to the accuracy of the original physical sensor model: the 0.02 pixel (1.4 cm) difference between the two models is an order of magnitude smaller than the planimetric accuracy and is therefore a negligible error. The RFM fully benefits from the pre-processing applied to generate the Sensor Level product (removing high frequency distortions) allowing rational functions to precisely represent this smooth geometric model. RFM can be used as a replacement sensor model for photogrammetric processing.

4. ORTHO-RECTIFIED PRODUCTS PERFORMANCES

The other set of products made available by the Pleiades-HR system are the ortho-images (and ortho-mosaic) products.

These products are ortho-rectified thanks to an accurate DEM (Reference3D™ if available, or a DTED1 System DEM by default). They are then easily usable with GIS as map products. The ortho-rectification processing takes advantage of the high location accuracy of Pleiades-HR: 14 m probable (90% of the images) and up to 25 m maximum (99.7% of the images) of circular error.

For multi-temporal registration, it will also be possible to register the ortho-image to a reference image (Reference3D™ database). Even if this processing won't increase the location accuracy, it shall guarantee a perfect multi temporal registration between images.

The method is detailed in (Baillarin 2004). It is composed of three independent steps:

- 1) Image and reference setup in the same geometry using a raw location model,
- 2) Image mis-registration measurements, using an automatic and generic process,

3) Location models improvement using a space-triangulation process and model parameters correction, including a possible DEM refining.

Moreover, thanks to the high agility and the precise pointing capability of the Pleiades-HR platform, it will be possible to acquire several successive adjacent strips within a unique pass over a targeted area.

Thus, the Pleiades-HR ortho-mosaic product will provide end-users with an image of larger size, as being the result of a seamless patchwork of individual strips. The output coverage may reach up to 10 000 km² and even more, according to the length of the neighbouring strips and the tolerated B/H ratio between acquisitions.

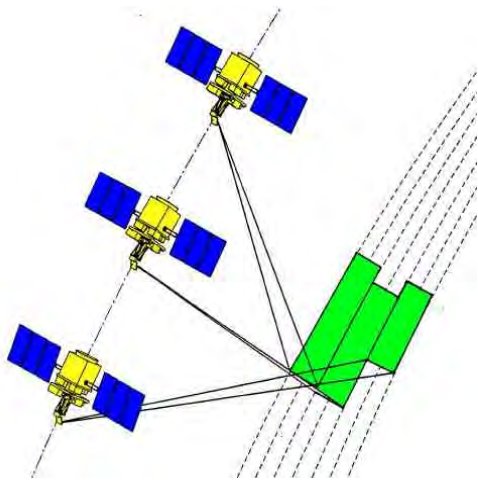


Figure 5: Pleiades-HR agility and mosaicking capability

The automatic mosaicking process relies on two geometric refining phases (as described above). The same method is used for:

Phase 1: Absolute refining of each data strip location model using Reference3D™ data.

Phase 2: Relative and finer improvement of location models using overlapping areas of adjacent strips (350m to 3.5km) and Reference3D™ DEM. The evaluation has been done using aerial images simulating Pleiades-HR acquisitions and the results were excellent. Thanks to the first phase, the absolute accuracy is less than 2.5m (0.5 Reference3D™ pixels). The second phase refines the relative model with respect to the very high resolution of the acquisition (<0.5 pixels HR).

This product represents the successful realization of the Pleiades-HR mission since it takes advantage of the main characteristics of the system: agility and high location precision. The automatic mosaicking process relies on automatic tie point selection (Baillarin 2004) and geometric models refining phases followed by local radiometric homogenisation and stitching phases (seam-less line computation).



Figure 6: Pleiades-HR mosaic (and stitching line)

5. CONCLUSION AND OUTLOOK

The Pleiades-HR image processing is very complex (about 50 times more complex than SPOT5) and therefore time consuming, especially for geometric corrections. Nevertheless, a ground processing unit has been successfully developed to handle up to an average of 200 products a day for the main civilian UGC in Spot Image premises. Based on a multi-clusters architecture (IBM Blade Center™) linked by high speed Fibre Channel to a Storage Area Network, the Pleiades-HR infrastructure is highly scalable for the different centres needs (including local receiving stations). In particular, for emergency needs, pan-sharpened ortho-rectified products (20x20km²) are processed in less than 45mn and mosaic products (60x60km²) in less than 140mn.

The realization of the Pleiades-HR ground segment is once more the opportunity to demonstrate that a global optimization of the system from board to ground design must be considered in order to relax requirements of on-board architecture and lower the overall cost of the mission.

REFERENCES

- Baillarin S, 2006, Remote Sensing Image Ground Segment Interoperability: PLEIADES-HR case study, Proceedings IGARSS, Denver, 2006
- Kubik P, 2005, PLEIADES image quality from users' needs to products definition, SPIE Europe International Symposium on Remote Sensing, Bruges, Belgium, September 19 - 22, 2005
- Unser M, 1999, Splines: A perfect fit for signal and image processing, IEEE Signal Processing Magazine, November 1999.
- De Lussy F, 2006, Pleiades-HR image system products and geometric accuracy, ISPRS, Hanover, 2006
- Tao C., Hu Y., 2001, The Rational Function Model: a tool for processing high resolution imagery. Earth Observation Magazine, 2001

Baillarin S. 2004, Validation of an automatic image ortho-rectification processing, Proceedings IGARSS, Anchorage, 2004

SMALL-SCALE ROUGHNESS EFFECTS ON THERMAL IR SPECTRA

L. K. Balick^{a,*}, I. Danilina^b, A. Gillespie^b, J. Jolin^c, A. Mushkin^d

^a Space and Remote Sensing Sciences, Los Alamos National Laboratory, Los Alamos, NM, USA – lbalick@lanl.gov

^b Earth and Space Sciences, University of Washington, Seattle, WA, USA – (arg3, Danilina)@uw.edu

^c Physical Chemistry and Applied Spectroscopy, Los Alamos National Laboratory, Los Alamos, NM, USA – jolin@lanl.gov

^d Geological Survey of Israel, Jerusalem IS, Mushkin@gsi.gov.il

Commission VII Symposium

KEY WORDS: Hyper spectral, Multispectral, Thermal, Infrared, Surface, Radiometry, Measurement

ABSTRACT:

Thermal infrared (IR) spectra of materials are affected by subpixel surface roughness that increases interactions between surface facets, thereby shifting the spectra toward a blackbody. Roughness also creates directional effects due to differential solar heating and view geometry. Three types of ground-based experiments were conducted to quantify roughness effects at scales of about 10 cm or less. First, a radiosity model was implemented and validated for natural and artificial surfaces using an imaging spectrometer. Area and resolution create practical computational limits so most simulations were performed at a resolution near 1 cm over a 1 m area. Surfaces were specified using laser profilometer data but can be simulated. Second, a well-calibrated radiometer was used to measure radiance for emissivity retrievals of different sized gravels and at different solar and view geometries. Finally, a reflectance spectrometer measured spectra for soft rocks sanded to different roughnesses.

Measurements of soft rocks with single mineral features (alabaster, soapstone, and chlorite) sanded to different roughnesses show a decrease of spectral peak height with roughness when the roughness scale is significantly larger than the wavelength. Precise measurements of two types of gravel, in three size classes of gravels, with a non-imaging spectrometer show an apparent saturation of roughness effects and a probable increase of directional effects with roughness. The modelling results show that a simple radiosity model can broadly simulate the effects of roughness. The shape of the roughness elements has a significant impact. Imaging spectrometers permit observation of small-scale spatial variations, which are not observed at pixel scales of a meter or more. Spectra go to blackbody spectra in small cracks and crevices.

1. INTRODUCTION

1.1 Background and Objectives

The radiance observed by remote sensing platforms varies significantly with subpixel surface roughness. Subpixel surface roughness occurs at spatial scales at which facets of the surface interact with each other resulting in multiple reflection or absorption/emission of photons but are not resolved in an image. The concept is quite simple but the spatial limits are not abrupt and hard to quantify. They vary with wavelength at the lower limit and pixel size at the upper limit. At the small end of the scale, facets or characteristic dimensions are large enough—on the order of 100 times the wavelength—that non-linear scattering processes are unimportant. At the upper limit, the dimensions need to be small enough so that a pixel contains a representative sample of the geometric variation of the surface: perhaps a tenth of the pixel area. The key concept is that subpixel roughness effects occur between surface facets that are not resolved in a remotely sensed image pixel. The net effects include darkening pixels in the reflectance domain, brightening pixels in the emissive domain (increasing both temperature and emissivity), reducing the depth of spectral features, and producing directional variations of observed radiance. Surfaces composed of different materials (stones in a soil matrix, for instance) will undergo non-linear spectral mixing when facets of different materials interact with each other. At thermal

infrared wavelengths, the effect is that emissivity spectra are moved closer to a blackbody spectrum in which extremely rough surfaces or cavities have an emissivity approaching 1.0 at all wavelengths. (The effects are broadly similar with surface roughness and volume scattering, such as occurs with vegetation or loosely packed particles, but volume scattering is more complex.) This paper presents studies of subpixel roughness effects across a variety of spatial scales in the long-wave infrared (LWIR, 8–14 μm) spectral range.

Because pixels can be quite large, they can contain subpixel surface roughness effects across a range of spatial scales and phenomena. Typically, one spatial scale dominates observations or, at least, one spatial scale is of primary interest. Therefore, studies of roughness effects often concentrate on a single scale or phenomenon.

1.2 Objectives

This paper presents summaries of four studies of subpixel roughness effects that range from the upper limits to the lower limits of spatial scales relevant to remote sensing. First, at the finest scale, spectral measurements of rock surfaces roughened with different grits of sandpaper are examined and related to micro-profilometer measurements of the surfaces.

* Corresponding author

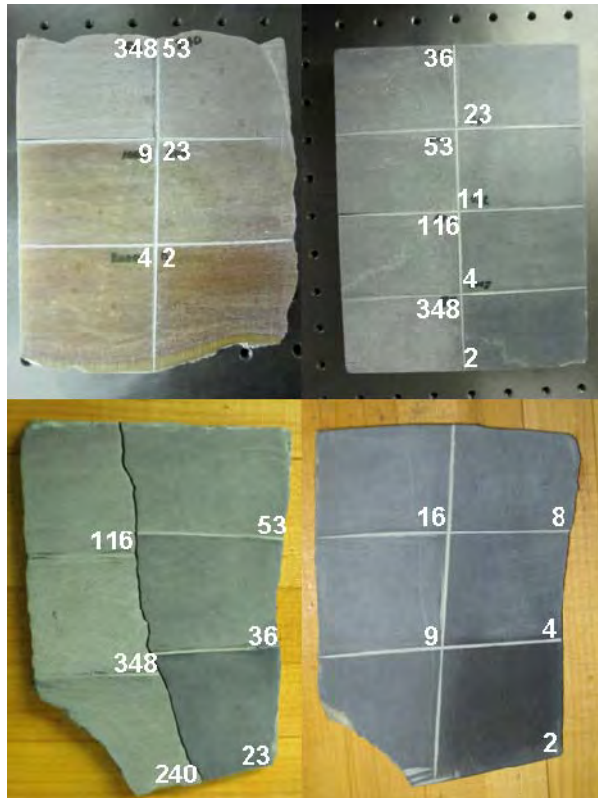


Figure 1. Flat rock surfaces sanded to U.S. grit sizes shown. Alabaster is at the upper left, soapstone at the upper right, and the two chlorite slabs are at the bottom.

Secondly, retrievals of emissivity of gravels of different sizes are made using data from a well-calibrated, highly stabilized FTIR spectrometer in the field, Balick & al., (2009). Third, a radiosity model of the impacts of roughness at centimetre scales was developed and verified. Simulations and data from special cases are presented. Finally, multi-directional satellite images are used to retrieve roughness information about the surface.

2. SURFACE ROUGHNESS STUDIES

2.1 Roughened Surfaces

Three types of fairly soft rocks were first smoothed and flattened, then hand-sanded with different grits, ranging from very smooth to very coarse and using diamond micromesh; about $2\ \mu\text{m}$ to $350\ \mu\text{m}$ average grit size. The rock types are commonly used in sculpture and are alabaster (gypsum, a sulfate), soapstone (talc, a phyllosilicate), and chlorite (another phyllosilicate closely related to soapstone). The rock surfaces and grit sizes are shown in Figure 1. Note that the different roughnesses vary in appearance in the visible wavelengths with the rougher surfaces appearing as a flat grey and becoming darker or more colourful with smoothness. Diffuse reflectance thermal IR spectra were measured with an A2 Technology Exoscan FTIR spectrometer (A2 Technology, 2010). Only the measurements in the LWIR ($8\text{--}14\ \mu\text{m}$) were used. Like most diffuse reflectance spectrometers, a small spot on the surface was illuminated with a broad-band source, and the energy reflected was measured at some range of off-nadir angles.

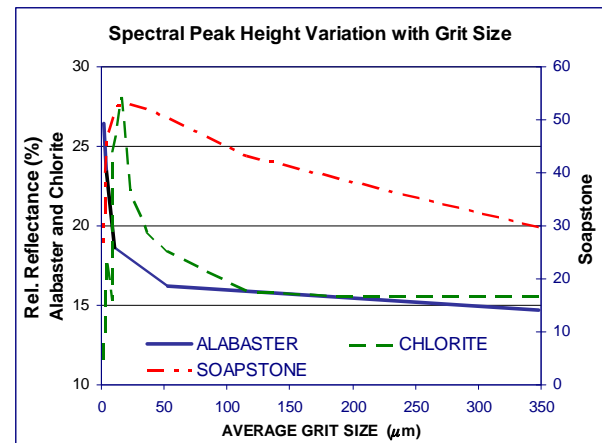


Figure 2. Plots of the spectral peak heights with mean grit size of the sandpaper used to roughen the rock. This is not the same as the actual roughness of the surface, but it is proportional to it.

The measurement is only truly diffuse reflectance if the surface is a diffuse reflector, and then Kirchhoff's Law holds: reflectance, ρ , is related to emissivity, ε , by $\rho = 1 - \varepsilon$ at any wavelength. The measure of roughness effects used here is the height of the reflectance peak.

Figure 2 shows the height variation of the spectral features with grit size for all three rock types. At values of sandpaper grits greater than about $25\ \mu\text{m}$, diffuse reflectance decreases with roughness, albeit slowly, for all three rock types. Below $25\ \mu\text{m}$, the curves are very steep. Soapstone and chlorite, which are closely related (both are steatites) increase to a peak around $25\ \mu\text{m}$, while the alabaster diffuse reflectance decreases in this range. At roughness sizes near the size of the wavelength, non-linear scattering processes occur and reflectance is no longer dominated by interactions between facets. This might be seen in these measurements between $2\ \mu\text{m}$ and $25\ \mu\text{m}$, with a possible transition out to $50\ \mu\text{m}$. Of course, sandpaper grit sizes do not actually represent the actual surface roughness. The surfaces were scanned with a Nanovea PS-50 (Nanovea, 2010) optical microprofilometer at a nominal resolution of $10\ \mu\text{m}$ in x, y, and z. The sizes of the finest grits (1,000 US grit scale and higher) are below the resolution of the profilometer. Also, the measured root mean square RMS values of the rock surfaces are well below the average grit size of the sandpaper so the values of grit size cannot be interpreted as the same as the surface roughness, just proportional to it. The actual roughness for the very fine grits must be viewed with caution. Nevertheless, spectral peak heights do decrease with roughness down to spatial scales that approach the wavelength.

2.2 Gravel: Spectral Emissivity Retrieval

Highly accurate and precise measurements of spectral emissivity in the field are notably difficult to make for a variety of reasons, including characterization of "downwelling" radiance from the surroundings and sensor calibration and stability. In this work, careful measurements were made with an extremely well-calibrated and stabilized FTIR for different roughness, nadir angle, material type, and time of day. The retrieval of emissivity generally follows that described by Salvaggio & Miller (2001) and is conceptually simple. The

method as implemented in this work requires spectral radiance measurements of the target and a reference panel and the temperature and reflectance of the panel surface. The panel is assumed to be perfectly diffuse (or, more precisely, the directional properties of the panel and target are assumed to be the same), its reflectance is the same as measured in the laboratory, and atmospheric transmission between the target and the sensor is assumed to be neglectable. It also assumes that there is no temporal variation of atmospheric transmission.

The spectral radiance at the sensor can be written as

$$L_s(\lambda, T) = \varepsilon(\lambda)L_{BB}(\lambda, T) + (1 - \varepsilon(\lambda))L^\downarrow(\lambda) \quad (1)$$

where L_s is the spectral radiance at the sensor, λ is wavelength, T is the material surface temperature, ε is the emissivity of the surface, L_{BB} is the blackbody spectral radiance at the surface (described by Planck's function) and L^\downarrow is the downwelling radiance. Solving for $\varepsilon(\lambda)$ gives

$$\varepsilon(\lambda) = (L_s(\lambda, T) - L^\downarrow(\lambda)) / (L_{BB}(\lambda, T) - L^\downarrow(\lambda)). \quad (2)$$

$L^\downarrow(\lambda)$ is comprised of all the radiance on the surface from the surroundings. Surroundings include the atmosphere and any clouds, buildings, sensors, and people in the vicinity. Variable in space and time, downwelling radiance can be complex quantity, and it is often the largest error in this approach to emissivity retrieval. Assuming the panel is a diffuse reflector, we can estimate $L^\downarrow(\lambda)$ with

$$L^\downarrow(\lambda) = (L_p(\lambda) - \varepsilon_p L_{BB}(\lambda, T_p)) / (1 - \varepsilon_p) \quad (3)$$

where the subscript p refers to the panel, T_p is invariant with wavelength and, for the panel and spectral range used, ε_p is constant with a value of 0.040. Neither T nor T_p could be measured well so they must be estimated from the data. For T , Planck's functions were draped on $L_s(\lambda, T)$ to define the T that best fit the spectrum, assuming the emissivity was 1.0 somewhere in the spectrum. To determine the temperature of the panel, we draped the Planck's function over the observed panel spectrum where the atmosphere is opaque.

Two gravel materials at three size classes were measured at three view angles, and on three different days. One gravel was a calcite with a sharp spectral feature and the other was a silicate with broad features. The three size classes had mean sizes of 0.8 cm, 1.5 cm, and 5 cm, and view nadir angles were 7°, 30°, and 60°. Figure 3 shows that the expected patterns were not clearly observed for a 30° nadir angle. At any angle, the weakest features occurred for the largest size class, as expected, but the medium size class had the strongest features. This seems partly due to the sensor view to the south, with a large portion of gravel surfaces being shaded and cool and the small gravel could not maintain as large a temperature gradient across a smaller distance. The large gravel did have the biggest changes with view nadir angle. In any case, the expectation that spectral feature depths are inversely proportional to roughness seems to be an over-simplification: it can be modulated by other factors. It is useful to note that the repeatability of the retrievals was generally in the 1–2% range, with exceptions occurring when the downwelling radiance was large.

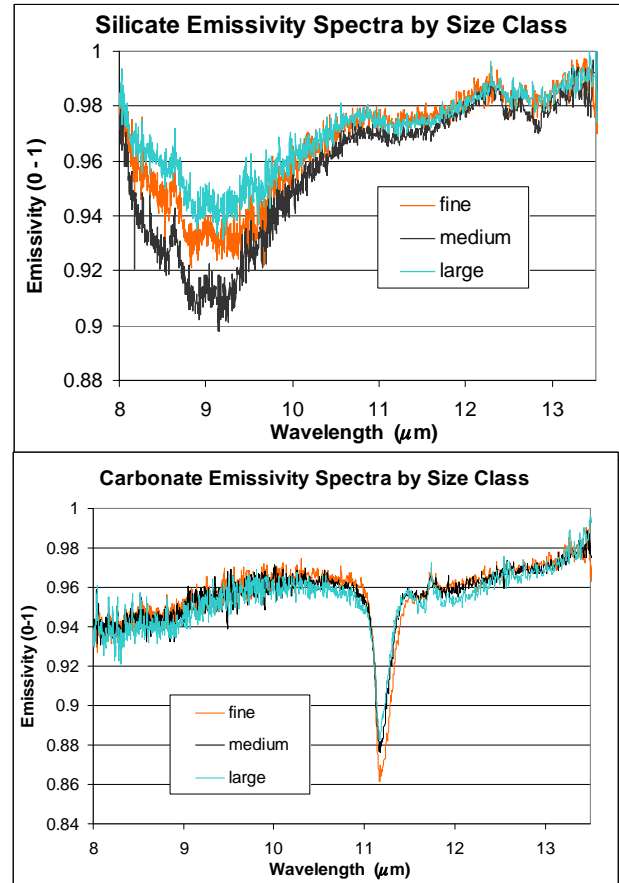


Figure 3. Retrieved emissivity spectra for gravels of different size classes for two rock types viewed at 30° from nadir.

2.3 Roughness Modelling and Validation

Radiosity models explicitly describe the radiant interactions between surface facets or points. Radiosity describes the radiative interactions between surface elements, and in the thermal IR domain includes both emitted and reflected energy. While these models can be scaled to any dimension, as a practical matter, areas of 1 m² are appropriate for high-resolution remote sensing simulations. Input digital elevation surfaces at 1 cm resolution can be easily measured with laser profilometers. Eq. 4 defines the radiosity for a number of facets or points:

$$B_i = R_i + \rho \cdot \sum_{j=1}^n B_j \cdot F_{ij}, \quad i, j = 1, 2, \dots, n \quad (4)$$

where B_i is the radiosity of a surface element i , R_i is thermal energy released from a surface element, ρ is reflectivity of the surface, F_{ij} is form factor from surface element j to surface element i , and n is the number of surface elements. The second term in equation (4) describes multiple scattering components—energy bounced one or more times among surface elements. The key step of the radiosity model is determining the form-factor matrix F . The basic form of a form factor is given by

$$F_{ji} = \frac{\cos \theta_i \cdot \cos \theta_j}{d^2 \cdot \pi} \cdot A_i, \quad (5)$$

where F_{ji} is the form factor from surface element j to surface element i , θ is the projection angle between the normal of a surface element and the line, linking the pair of elements together, A_i is the area of element i , and d is the distance between two elements (Figure 4).

The model simulates temperature and radiance variations due to roughness around some mean temperature over the course of a day. It is illumination and view angle-dependent, and while not explicitly spectral, it is wavelength-dependent and can be run for a series of spectra to simulate spectral changes. In this model, the mean temperature over time is determined by a simple heat diffusion model driven by environmental data. Mixed materials result in mixed spectra, and this can be simulated by assigning different properties to facets but assuming there is no difference of temperature..

Figure 5 shows a measured digital elevation model (DEM) of a rock surface in part a., shown graphically in part c. The DEM covers an area of 0.5 m by 0.85 m at sample spacing of 1 cm. Part b shows the change of simulated emissivity averaged over the area throughout the day. The roughness effect is largest when the sun is at moderate elevations. The DEM can then be multiplied by constants to rescale the roughness of the data. Part c shows the resulting calculation of broad-band emissivity over a range of RMS values.

The concept radiatively interacting surface elements can be extended to shapes and larger surfaces such as cracks, holes, and corners of surfaces. In these cases, terminology such as “cavity effects” and “adjacency effects” are used. In fact, imaging spectrometer instruments show that even small cracks and holes become aspectral regardless of the spectra of the materials large when view factors exist.

Figure 6 shows observations and a simulation of the effects of two depressions (cavities) about 2 cm deep in a norite rock (plagioclase and hypersthene ± olivine). The norite has overlapping reststrahlen bands from 8.5 to 10.0 μm. Parts a and b show a photograph and a thermal IR spectral image of the rock. The thermal image was made with a Telops Inc. Hyper-Cam imaging FTIR spectrometer (Telops, 2010). Part c shows a micro-DEM of the rock smoothed to a 2 mm grid. Part d shows spectra taken from the image inside and outside the depressions. Finally, part e shows the simulated emissivity of the rock. In the depressions, the spectrum is shallower and higher than on the surface, becoming significantly more like a blackbody than the outer surface.

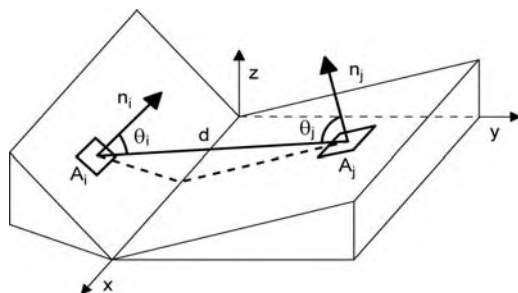


Figure 4. Schematic plot of the terms used in the form factor equation (Eq. 5).

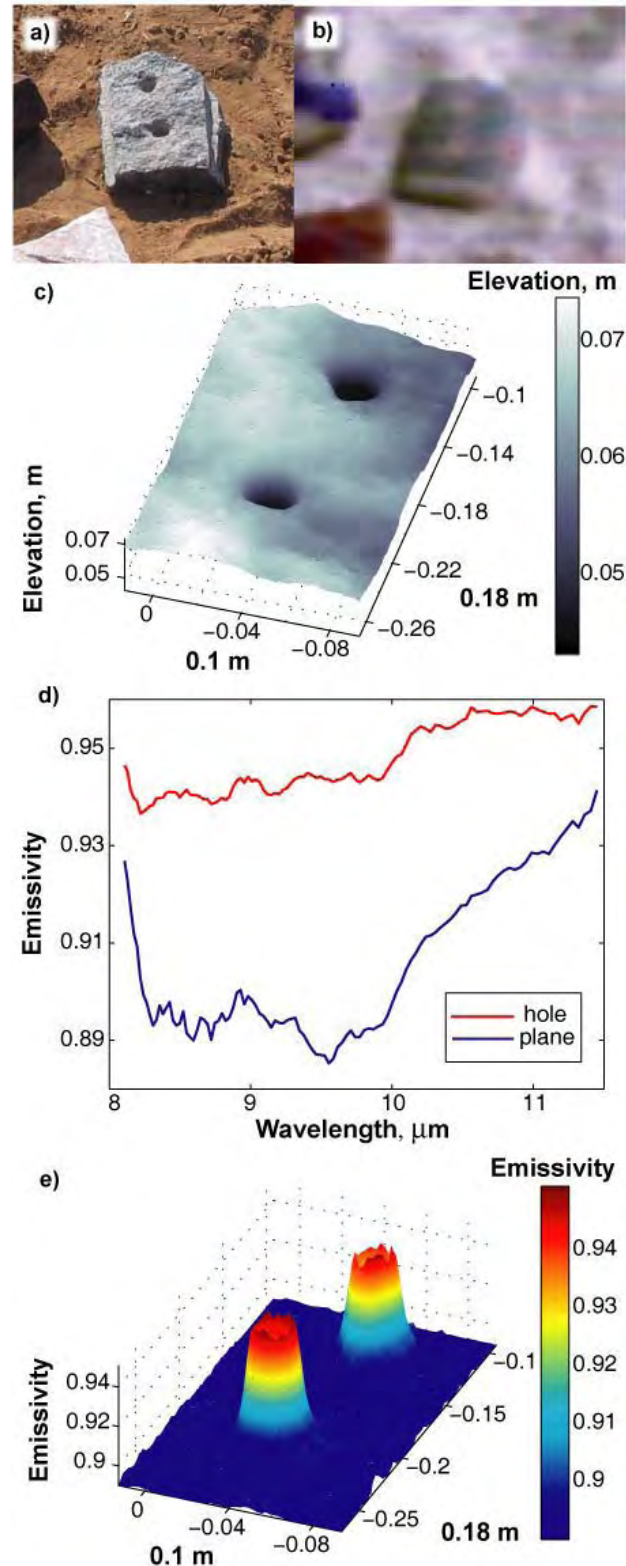


Figure 5. Simulated change of broad-band emissivity for a measured surface; the cavities in the rock become more like a blackbody than the outer surface; see text more explanation of the individual parts.

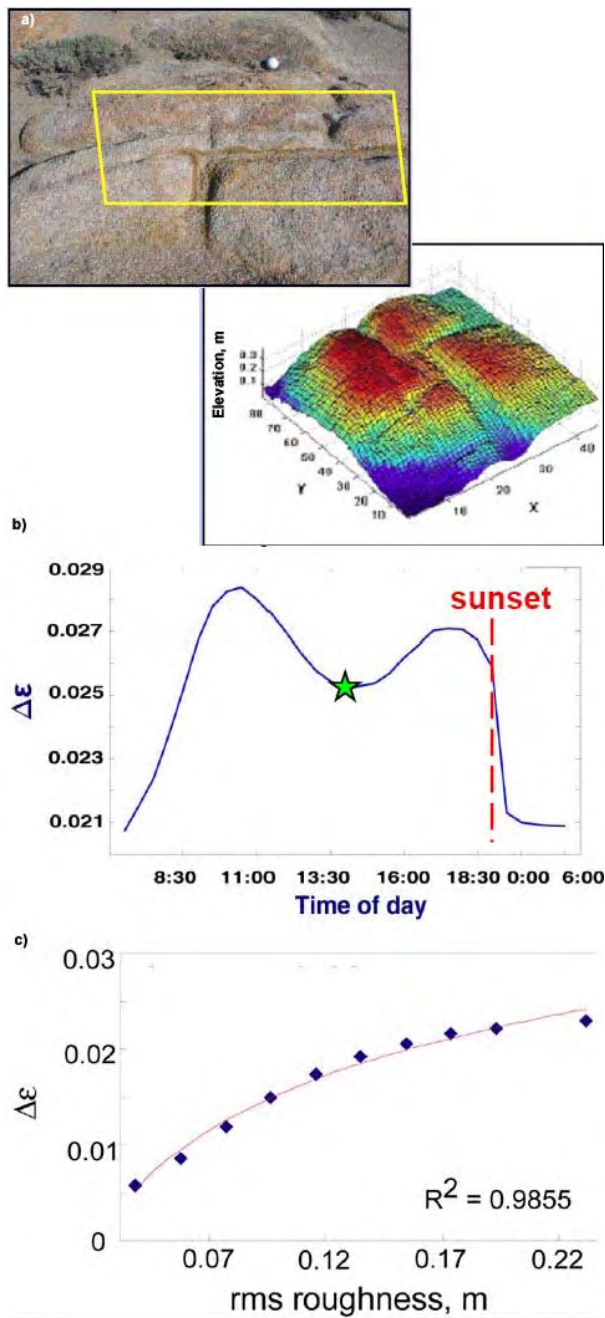


Figure 6. Simulated and observed effects of cavities on thermal IR spectra. See text for details.

Figure 7 shows another case where a form was created using plaster of Paris ($\text{CaSO}_4 \cdot 2\text{H}_2\text{O} \pm \text{CaCO}_3$) to facilitate model validation. The plaster has a single reststrahlen band centred near $8.6 \mu\text{m}$. The form has two flat surfaces with different texture (roughness) shifted 7 cm and with a wall between them. The upper surface has hole that is 3 cm in diameter and 8 cm deep. In Figure 7, part a is a photograph of the Telops Inc. Hyper-Cam and the target; part b shows a hyperspectral image of the hole (and a crack that formed during transport); and part c is a Hyper-Cam image of the wall, and the upper and lower planes. Part d shows spectra taken from a Hyper-Cam image, and Part e shows the simulations at four spectral locations. The difference between the planes is the effect of roughness with the lower, rougher plane having a somewhat higher spectrum and a

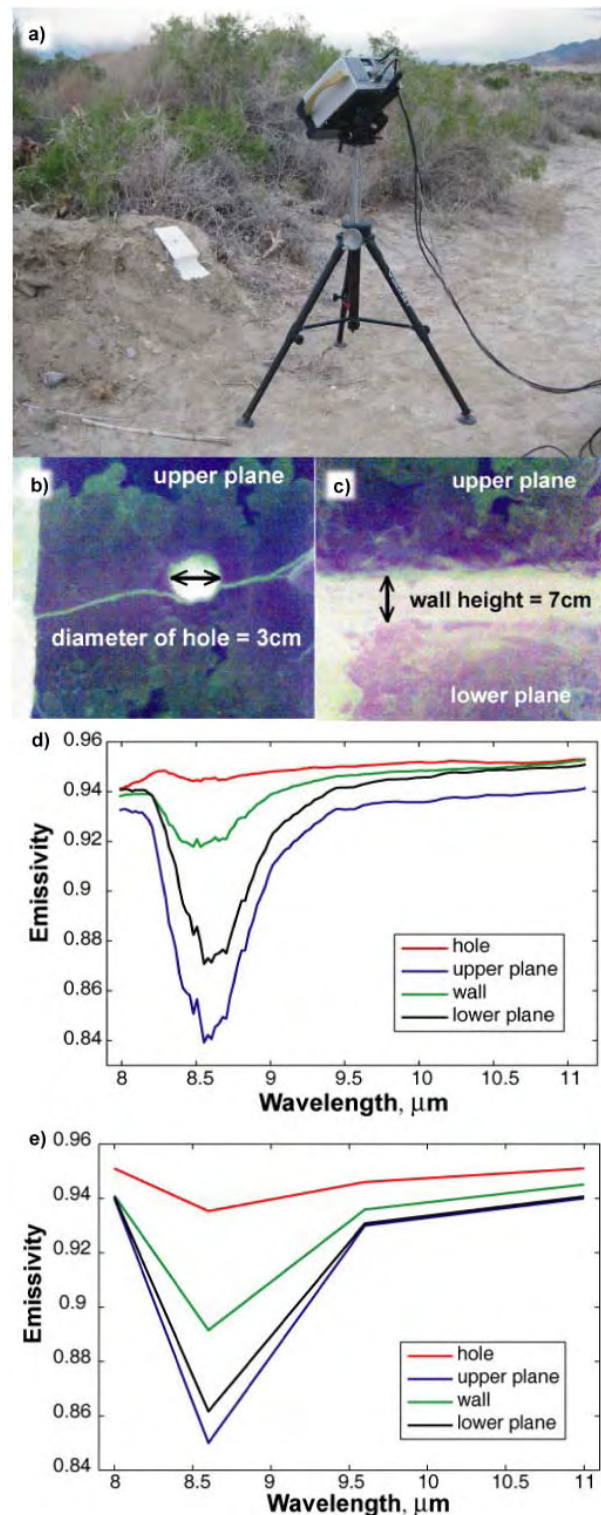


Figure 7. Simulated and observed spectra for a constructed plaster-of-Paris form. See text for details.

shallower spectral feature. The simulation did a good job on the spectral feature depth change, but not as good for the offset. The hole, both in the measurement and the simulation, had the highest emissivity spectrum, and very little of the spectral feature is present. The wall had a spectrum lower than the hole and with a clear but reduced spectral feature depth. The broad effects of radiosity were generally well simulated, impact of radiosity being proportional to view factors.

2.4 Roughness Retrieval from Directional Views

For practical applications, correcting for roughness effects on retrieved temperatures and emissivities requires remotely estimating surface roughness at sub-pixel scales. One approach that has been tested (Mushkin & Gillespie, 2005) uses bi-directional VNIR imaging, such as is available from ASTER, to estimate sub-pixel roughness at scales up to 15 m, the resolution of the acquired images. The approach makes use of differential sub-pixel shadowing in the 'down' and 'up' sun images as a relative proxy for roughness. The relative measure of roughness is the DN ratio between the two images, corrected for path radiance using "dark-object subtraction", with ratio values diverging from unity with increasing surface roughness. This ratio proxy roughness for roughness is largely insensitive to atmospheric effects, but must be calibrated to a quantitative measure of roughness, such as rms elevation. Calibration of the ratios to absolute values has been done from field measurement of micro-topography and modelling of shadows. The calibration is sensitive to regional topographic slope (within 5–10°), and sun elevation angle, and therefore requires re-calibration for each new application. A result of the calibration is shown in Figure 8. Older, smoother fans are darker (less shadowed); parts of the dry lake are smooth salt flats, and others are rough pinnacles of salt ~40 cm high.

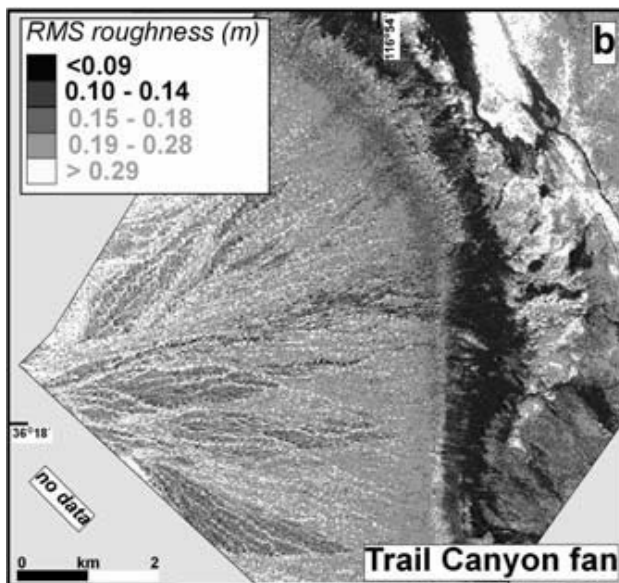


Figure 8. This is a sub-pixel roughness image calculated from two ASTER images of the Trail Canyon alluvial fan in Death Valley National Park. Image ratios were calibrated to roughness using field data.

3. SUMMARY AND CONCLUSION

Four studies look at the effects of surface roughness on the energy emitted by that surface. These studies cover spatial scales from sub-millimetre to tens of meters, and the effect of roughness across these scales is due to radiative interactions between surface elements. (There can also be a temperature effect, not discussed here.) The four studies represent different approaches to understanding the effects of surface roughness on thermal IR emittance. At sub-millimetre scales, roughness changes from sanding rocks alter diffuse reflectance by nearly a factor of two across the spectrum for the surfaces studied. Precise field measurements of radiance of gravel at centimetre

scales did not clearly show expected trends of retrieved emissivity spectra as a function of roughness (size), and part of the reason seems to be the ability of individual gravel pieces to maintain a temperature gradient resulting from differential solar heating. Modelling and model validation measurements at the 1 to 10 cm scales show predictable changes of emissivity spectra with surface roughness: emissivity goes toward a black body for rough surfaces and in corners and shapes with a strong three dimensional form. The model is an abstraction, and its heat diffusion model is simplified. For many surfaces, this has not been a problem, but for surfaces with complex geometry (more than one value of z for an x, y location) or where three-dimensional heat diffusion is important, simulations of mean temperatures break down. Radiosity-produced variations can still be simulated. Although not discussed here in detail, compensation for roughness effects is possible given two or more images of the same area from different positions (with about the same resolution) and given knowledge of the roughness or valid simulations.

Multiple radiative interactions between surface elements do tend to drive observed spectra toward a blackbody spectrum even though the material properties are constant. The impacts are significant but variable and usually don't overwhelm the signal. The effects need to be quantitatively understood in order to understand thermal spectral measurements of most surfaces in the environment. However, surface roughness, while important, is one factor among many that modulate both the magnitude and spectra of ground-leaving thermal radiance and needs to be considered in context.

REFERENCES

- Balick, L. K., M. E. Howard, H. M. Gledhill, A. Klawitter, and A. R. Gillespie, 2009. "Variation and sensitivity in spectral thermal IR emissivity measurements," IEEE WHISPERS, Grenoble, France. August 26-28, 2009.
- A2-Technology, 2010, http://www.a2technologies.com/exoscan_handheld.html
- Nanovea, 2010, <http://www.nanovea.com/Profilometers.html>
- Mushkin, A. & Gillespie A. R. (2005). Estimating sub-pixel surface roughness using remotely sensed stereoscopic data. *Remote Sensing of Environment*, 99 (1-2), p.75-83
- Salvaggio, C., and C. J. Miller, 2001, "Methodologies and protocols for the collection of midwave and longwave infrared emissivity spectra using a portable field spectrometer," SPIE, Image Exploitation and Target Recognition, Algorithms for Multispectral, Hyperspectral, and Ultraspectral Imagery VII, Volume 4381, April 2001.
- Telops, 2010. http://www.telops.com/index.php?option=com_content&view=article&id=60&Itemid=59&lang=en

ACKNOWLEDGEMENT

This work was funded by the U. S. National Nuclear Security Administration, Office of Nonproliferation Technology Development and Treaty Verification, under contract DE-AC52-06NA25396 with Los Alamos National Security, LLC. LA-UR 10-01283

MAPPING WETLAND ENVIRONMENTS IN THE BRAZILIAN SAVANNAH FROM HIGH RESOLUTION IKONOS IMAGE DATA

I. Barbosa^{ab}

^a Federal University of Minas Gerais, Geo science Institute, 31270-901, Belo Horizonte, Brazil.

^b State Forest Institute of Minas Gerais – Biodiversity Management, Belo Horizonte, Brazil

Commission VI, WG VI/4

KEY WORDS: Classification, High resolution, IKONOS, Land Cover, Texture, Vegetation, Wetlands

ABSTRACT:

Wetlands are complex ecosystems hosting a high diversity of landscape associated with water, soil and vegetation variations. It provides several essential resources for wildlife and human populations and supports a miscellany of aquatic plant species. The *Pandeiros* Wildlife Sanctuary is a unique wetland ecosystem surrounded by semi-arid savannas. It supports large communities of macrophytes and terrestrial plants and stores large quantities of organic matter. In this article we propose a methodology for classifying these wetlands using their spectral and textural signature extracted from Ikonos image data. The main plant communities were identified from low altitude photographs acquired with a microlight aircraft. Ground data also complemented these photographic records. Classification trials were made using both spectral and spatial feature (texture) to assess the most appropriate approach. As a result five classes of macrophytes (as dominant specie) and four terrestrial classes were identified with an accuracy of over 80%. Texture data brought a significant improvement to the classification.

RÉSUMÉ:

Les zones humides sont des écosystèmes complexes accueillant une grande diversité de paysages associée à l'eau, aux sols et aux variations de la végétation. Il offre plusieurs ressources essentielles pour la faune et les populations humaines et soutient une grande variété d'espèces de plantes aquatiques. Le Refuge Faunique du *Pandeiros* est un écosystème humide unique entouré par la savane semi-aride. Il supporte de grandes communautés de macrophytes et les plantes terrestres et une quantité importante de matière organique. Dans cet article, nous proposons une méthodologie de classification de ces zones humides basée sur leur signature spectrale et texturale extraite à partir des données d'image Ikonos. Les principales communautés végétales ont été identifiées à partir de photographies à faible altitude acquise avec un ULM. Des données au sol ont également complété ces documents photographiques. Des essais de classification ont été faits en utilisant les caractéristiques spatiales et spectrales (texture) pour évaluer l'approche la plus appropriée. En conséquence cinq classes de macrophytes (comme espèce dominante) et quatre classes terrestres ont été identifiés avec une précision de plus de 85%. Les données de texture ont apporté une amélioration significative à la classification.

1. INTRODUCTION

Wetlands were previously seen as dirty, dangerous and unimportant areas by most Western communities (Gooselink, 2003). Since the Ramsar Convention, a new perception of those environments spread through occident. Several governments agreed in built a framework for the conservation and wise use of these areas (Ramsar 2006). Brazil is one of the signatory parties of the convention and holds numerous wetlands in its territory.

Although Brazil recognize the importance of Wetlands, a lack of definition and specific protecting laws threat this environments. Due to this absence, we adopted the Canada's National Wetlands Working Group (1997) concept which considers wetlands areas saturated by water long enough to support aquatic process as indicated by aquatic vegetation, poorly drained soils and biological activity adapted to this particular conditions.

The Pandeiros River Flood Plain presents all this characteristics and is considered an important wetland site in Brazil. It is even more special since it is located in a region of water scarcity surrounded by savanna vegetation. It provides several ecosystem services such as recycling nutrients, fixing carbon and recharging the aquifer. Due to its relevance the State Government acknowledged this site as a Wildlife Sanctuary. However, the recognition as a protected area does not ensure the preservation of this region. Large areas still been used to raise cattle and several small ones are drained and used by communities for family farming (Barbosa, 2009).

Since it is a unique site in Brazil, identifying types of wetlands found in this environment will subsidized its proper management and conservation. Nevertheless, this task is a challenge since Pandeiros host a complex ecosystem with a high diversity of landscapes.

The inventory of wetlands demand field surveys, aerial photo interpretation and satellite imagery. Melack (2004) points out that the use of satellite images is considered the most efficient, since it allows a fast data acquisition and cartographic mapping. A large range of tools are available to classify this sort of data. However, high resolution images require more sophisticated approaches. Texture has achieved expressive results in the classification of those images. For example, Davis et al (2002) obtained an overall accuracy classification of 75% using image texture for riparian zones. Thus, as a starting point, we decide to evaluate the texture potential of classifying different groups of aquatic plants based on Ikonos images.

1.1 Gray Level Co-occurrence Matrix

Several methods can be applied to texture analysis. Among these, the Gray Level Co-occurrence Matrix (GLCM) seems to be the most commonly used (Franklin, 2001) and has been recognized as one of the best tools for specific situations of classification (Clausi, 2000; Maillard, 2003). GLCM is a second order histogram in which each entry reports the joint probability of finding a set of two grey levels at a certain distance and direction from each other over some pre-defined window (Maillard, 1999). Haralick et al (1973) was the first to extract texture features in order to classify images. 14 texture measures were originally described by Haralick. However many features are highly correlated which made five of them more popular: Contrast, Angular Second Moment, Entropy, Inverse Difference Moment and Correlation.

In this study, we aimed to evaluate the use of GLCM in the classification and segmentation of high resolution image of a wetland environment. As well as determining the optimal parameters of textures, window size and distance to be used in the study of IKONOS images for this sort of environment.

2. METHODOLOGY

2.1 Study Area

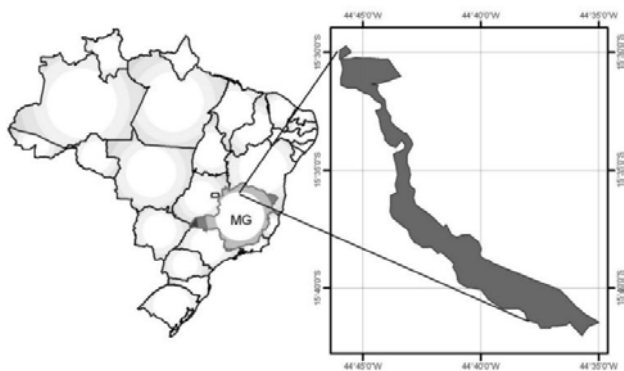


Figure 1. Location of Pandeiros Wildlife Sanctuary in Minas Gerais (MG) – Brazil.

The Pandeiros Wildlife Sanctuary (PWS) is located near the Pandeiros' River mouth, in the Northern part of the State of Minas Gerais (Figure 1). This river is an important affluent of São Francisco River and is the breeding grounds of several species of fish. It is also a refuge for numerous rare endemic and threatened bird species (Biodiversitas, 2005). The region is protected by the State government authorities and is managed by the Forest Institute of Minas Gerais (IEF-MG).

It occupies a total area of 6103 ha. and preserves a unique wetland with riparian forests, palm swamps, wet meadows, lakes and ponds (Figure 2). Climate presents two distinct periods: wet season from October to March, and dry from April to September. This variation is characteristic of the Cerrado biome where water deficit spans for about half the year.

2.2 Field Work

The first of Four field campaigns was conducted in September 2008 using a boat and an all-terrain vehicle to access difficult areas for a general reconnaissance approach. During the second one in February 2009 geodetic ground control points were collected for the geometric correction and registration of the image. A specific work area was also defined and data was acquired on the different vegetation physiognomies that could be identified on the Ikonos image. The third campaign in May 2009 was mainly dedicated to acquire low altitude photographs using a micro-light aircraft to serve as complementary validation data. The Fourth and last one in April 2010 allowed acquiring new low altitude photographs and visit a few spots where some botanical inventory was still necessary. During the last three campaigns, printed copies of the Ikonos image (scale 1:5000) were used to identify complexes both in the field and on the image. This data allowed us to divide vegetation of the study area in 9 different classes (Figure 2): *Pontederiaceae*, *Nymphaeaceae*, *Riparian forest*, *Open Water*, *Alismataceae*, *Cyperaceae*, *G – Pasture*, *H – Flooded Pasture*, *I – Bare Soil*.

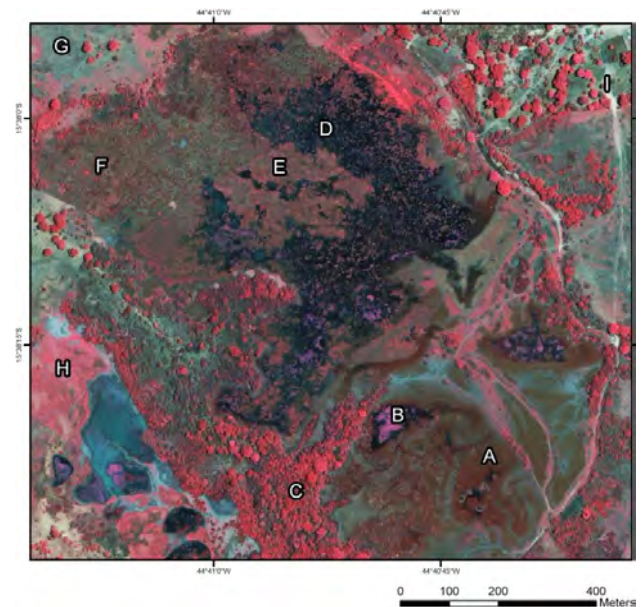


Figure 2. (a) Fusionned, false color Ikonos image of the Pandeiros. The image represents an area of 1200×1200 pixels or 144 ha. Legend: A – *Pontederiaceae*; B – *Nymphaeaceae*; C – *Riparian forest*; D – *Open Water*; E – *Alismataceae*; F – *Cyperaceae*; G – *Pasture*; H – *Flooded Pasture*; I – *Bare Soil*.

Photographic records of different vegetation typology were acquired to constitute a visual inventory of the Pandeiros. The dominant plant groups present on the photographs were identified by two botanists at the Botanic Taxonomy Laboratory of the Universidade Federal de Minas Gerais (UFMG). The aerial photographs proved to be useful for the inventory and as validation data. Since only a navigation GPS was used in the last two campaigns, care was taken to note and

draw the landscape context for all the ground control points that were mainly acquired for thematic purposes (as opposed to geodetic). These points were essential for understanding the different environments and their respective context. It is during the February campaign that the test area presented here was selected for having the largest possible number of different natural environments within the smallest area. The selected area covers 1.44 km² and is illustrated in Figure 2.

2.3 Image Acquisition and Pre-processing

One fusionned Ikonos image¹ registered to a UTM projection of the central part of the PWS was provided by the Forest Institute of Minas Gerais (Figure 2). This image was acquired in September 2006 corresponding to the end of the dry season when the water level is at its lowest. Given the flatness of the relief and geodetic ground control points, registration errors were kept below 5 meters.

2.4 Texture Pre – processing

The Ikonos's red band was selected to create the texture features due to the high reflectance response of vegetation in this channel. This band was used as input data in the program MACOOC (Philippe Maillard ©2010) which is able to produce all five texture measures in four directions: 0°, 45°, 90° and 315°. Although data was produced in four directions, we analysed this information grouped.

2.5 Gray Level Co-occurrence Matrix (GLCM) Tests

Initially, we selected a few parameters (pixel pair lag distance, window size and texture features) to conduct the first tests in order to stipulate the best value of distance.

The following values were chosen for lag distance: 3, 4, 5, 6 and 7. We did not use values 1 and 2 because of the high correlation between neighbouring pixels (especially considering the image resolution results from a fusion). A value of 7 was fixed as the maximum given that aquatic plants present homogeneous groups with little or no projection of shadows and the average object size is rarely larger than 7 meters.

Window sizes of 15, 21, 25, 31, 35 and 41 were selected. A maximum window size of 41 was selected once most of the features present in the study do not exhibit homogeneous areas larger than 1.600 m². We opted for the most commonly parameters used: Angular Second Moment (ASM), Entropy (Ent.), Contrast (Cont.), Inverse Difference Moment (IDM), and Correlation (Corr.).

Supervised classification method, which demands ground truth data, were performed using the maximum likelihood decision rule (Biehl and Landgrebe, 2002). Areas selected as training and validation samples were chosen based on field data and image interpretation. A few tests were performed to evaluate the effect of window size on the variance of the class. We chose use windows of about 11 × 11 pixels or 121 m² in the classification process. The class of bare ground was the only exception and windows of 9 × 9 pixels were chosen to maintain the integrity of the samples considering the difficulty of having "pure" samples of bare soil.

¹ Fusionning involves resampling the 4 m multispectral to 1 m using the panchromatic channel.

After apply the Supervised method to images compound by texture and spectral bands, a five steps Knock-out process (table 01) was performed in order to reduce the features types and frequencies that play the most important role in the classification process. All the combinations that achieved equal or higher values than 80% of overall accuracy were ranked and analyzed.

In a second step, tests combining the five variables of texture with 18 different sizes of window (11, 13, 15 45) were conducted using only the value 3 for distance. We submit data to classification and Knock-out process as previously mentioned.

The third step had consisted in apply the classification to each parameter of texture separately and combined with the spectral bands. All the results higher than 80% were used to find the best window size.

wind + dist	15 + 04				
Tex+S	78,1				
Cont	ASM	IDM	Ent	Corr	Spectra
79,4	78,4	79,9	76,1	77,3	59
81,3	79,8		78,4	77,8	60,3
	78,9		77,8	79,8	65
	82,5		80,5		40,1

Table 1. Knock – out example. Legend: wind+dist (window + lag distance), Tex+Spec (Texture + Spectral bands), Contrast (Cont.), Angular Second Moment (ASM), Inverse Difference Moment (IDM), Entropy (Ent.), and Correlation (Corr.).

2.6 Validation

Access in wetland areas can be very difficult and a fully systematic or random sampling scheme was impossible. Additionally, although the PWS is a protected area, most of it is still privately owned and we were not always able to have permission of access from landowners. Still, we were able to visit a total of 72 sampling sites chosen from the interpretation of image data to serve as training and validation data. To overcome the access limitations, we also used a micro-light aircraft flown at low altitudes (< 500 m) to acquire over 700 oblique photographs of the area using a digital camera (Nikon D40X) equipped with a zoom (Nikkor 18-200 mm 1:3.5-5.6). Data from the tracking log of a navigation GPS (Global Positioning System) set at a 50 m distance interval was coupled with the acquisition time of the photographs to account for the aircraft position at each shot (the camera and the GPS were previously synchronized). The level of detail on these photographs was such that the dominant plant families could easily be interpreted with the help of two botanists and the ground samples.

3. RESULTS AND DISCUSSION

This paper results are presented in three blocks: Distance definition, window definition and behaviour of textures features.

3.1 Distance definition

A supervised classification based solely on spectral bands of the Ikonos image has reached an overall accuracy of 72,5%. This is a control value to verify the efficiency of add texture features in the classification process.

After perform 150 classification according to the knock-out process, 68 results achieved values higher than 80% of overall accuracy (Combinations of lag distances 3 to 7 and windows size 15 to 41). The distance 3 was present in most of the results (34%) and there was no prevalence of a given window size. The texture features compound the results in the following percentages: ASM (72%), IDM (54%), Ent (50%), Corr (26%) and Cont (18%). However, when we consider the results with one single feature of texture, Ent. represents 40% of the results and Cont 40%. as well. The best result reached was 86,5% with a lag distance of 3, a window size of 41 and using IDM and Ent. (Table 1)

Bands	Distance	Window	Overall Accuracy
IDM+Ent+S	3	41	86,5
ASM+IDM+Ent+S	3	35	85
Ent+S	3	41	84,9
Ent+S	6	31	84,1
Ent+Vis	5	21	83,9
Cont+ASM+IDM+Ent+Cor+S	3	35	83,9
ASM+IDM+Ent+S	3	21	83,8
Cont+S	4	41	83,2
IDM+Ent+S	5	21	83
ASM+IDM+Ent+S	3	25	83

Table 2. Ten best classification results of Knock – out using all 5 texture features combined with spectral bands, lag distances between 3 and 7 and the following window sizes: 15, 21, 25, 31, 35 and 41.

3.2 Window definition

With a fixed distance of tree, 90 new classifications were performed following the knock-out approach and 67 results showed an overall accuracy exceeding 80%. Again, there was no prevalence of a given window size. We expected this result since the Knock-out technique aimed to find the best result for each size of window. In this case, 76% of the results were related with texture feature ASM, 60% with Ent, 50% with IDM, 30% with Cont and 20% with Corr. The results compound by one Texture band were analysed and the same result order was achieved. (ASM - 47%, Ent. – 29%, IDM – 18%, Cont. 12% and Corr. 0%). The best result reached was 86,7% with a window size of 41 using only contrast. (Table 2)

Bands and features	Distance	Window	Overall Accuracy
Cont+S	3	37	86,7
IDM+Ent+S	3	41	86,5
IDM+Ent+S	3	43	86,4
Ent+S	3	45	86,4
IDM+Ent+S	3	45	86,2
Ent+S	3	43	85,7
ASM+IDM+Ent+S	3	35	85
Ent+S	3	41	84,9
Ent+S	3	39	84,8
IDM+Ent+S	3	39	84,6

Table 3. Ten best classification results of Knock – out using all 5 texture features combined with spectral bands. a fixed lag distances of 3 and odd values of window sizes between 11 and 45.

This result was unexpected and led us to evaluate separately the performance of each texture features, alone and combined with spectral Ikonos's bands. During this process we have conducted 180 processes, 90 of each combining texture with the spectral bands and 90 only with each texture feature. 56 results obtained values superior to 80%. Entropy responded by 32% of cases. The contrast was surprisingly the second best feature of texture with 34% followed by IDM (23%) and ASM (18%). The top 3 results for image classification using a combination of a unique texture with the spectral bands were obtained with the contrast and the following window sizes: 37, 41 and 43.

Window	Contrast	Window	Entropy
37	86,7	45	86,4
41	86,5	43	85,7
43	86,5	41	84,9
39	86,4	39	84,8
45	85,6	27	84,2

Table 4. Ten best results of image classifications using each texture feature separately combined with spectral bands, a fixed lag distances of 3 and odd values of window sizes between 11 and 45.

When we evaluate the dispersion of the overall accuracy of classification by size of the window, we notice a general trend in

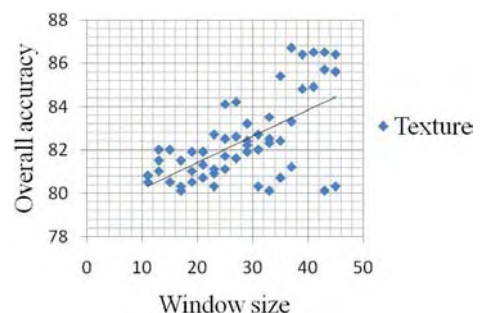


Figure 3. Graph of general dispersion of classification results of texture features according to window size.

3.3 Texture features Behaviour

Entropy is negatively correlated with window size when tested separately. However, when combined with the spectral bands tends to increase as the window size raises. The contrast is correlated positively with window size in both, when tested separately and when combined with spectral bands. In turn, the ASM presents negative correlation in both situations.

This indicates that the second angular momentum may play an important role when the window size varies between the values 11 and 30. Unlike the contrast that reaches the best results with windows between 30 and 45. Entropy presents a peculiar behaviour because it presents very significant results in all sizes of windows, but these tend to improve as the window size increases. In the Entropy plus Spectral graph, we can observe two peaks: one for windows of size 27 and one for windows of size higher than the 39.

	Window	Cont +S	ASM +S	IDM +S	Ent +S	Corr +S
Window	1,00					
Cont+S	0,89	1,00				
ASM+S	-0,83	-0,87	1,00			
IDM+S	0,38	0,08	0,13	1,00		
Ent+S	0,86	0,79	-0,66	0,27	1,00	
Corr+S	-0,60	-0,58	0,75	0,29	-0,46	1,00

Table 5. Correlation Matrix of all classification results using each texture feature separately combined with spectral band, a fixed lag distances of 3 and odd values of window sizes between 11 and 45.

	Window	Cont	ASM	IDM	Ent	Corr
Window	1,00					
Cont	0,86	1,00				
ASM	-0,69	-0,61	1,00			
IDM	-0,71	-0,74	0,84	1,00		
Ent	-0,63	-0,69	0,44	0,65	1,00	
Corr	-0,94	-0,69	0,67	0,63	0,44	1,00

Table 6. Correlation Matrix of all classification results using each texture feature separately, a fixed lag distances of 3 and odd values of window sizes between 11 and 45.

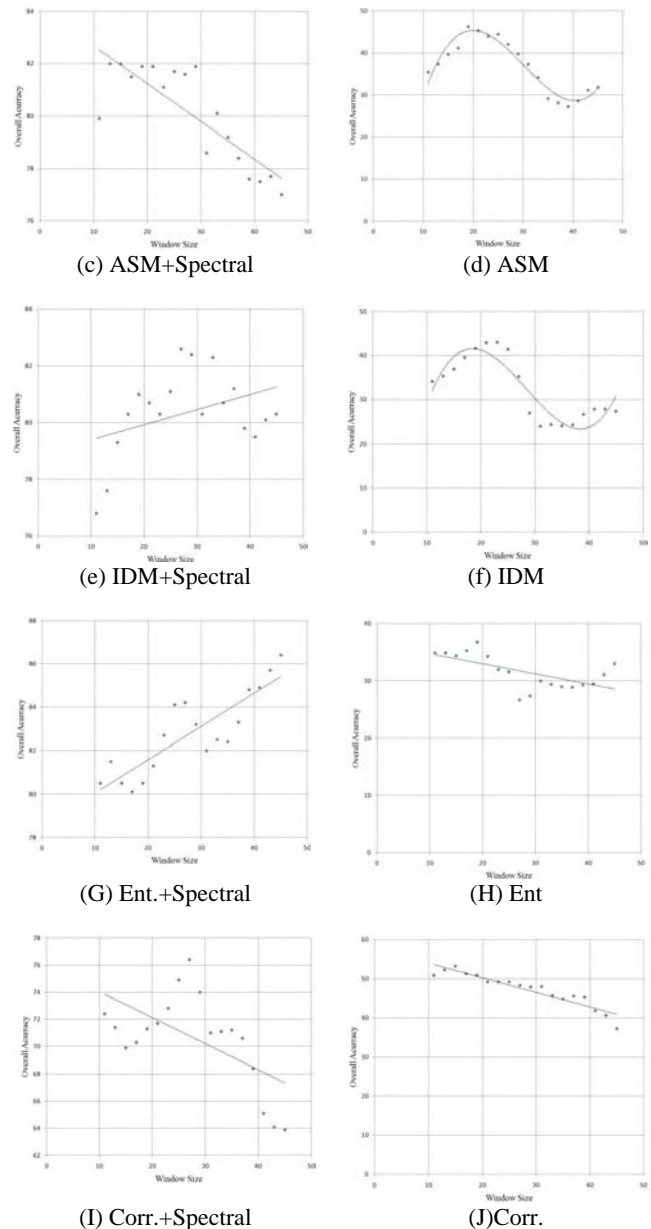
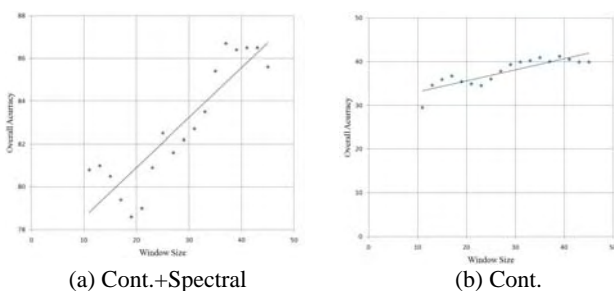


Figure 4. Dispersion Graphs of classification results of texture features according to window size for each feature processed combined and not combined with spectral bands.

4. CONCLUSION

The red band of the IKONOS image proved to be suitable for extraction of texture information to be used in the classification of aquatic vegetation in high-resolution images. Smaller distances were more efficient for image classification, as well as window sizes larger fared better. The use of a single texture feature combined with the spectral bands was very efficient. Among the parameters of texture Entropy combined with spectral bands produced good results for classification in all window sizes. While the contrast obtained the best results in windows of larger sizes and Second Angular Momentum showed good results in the windows of smaller sizes.

ACKNOWLEDGEMENTS

The authors are thankful to Forest Institute of Minas Gerais (<http://www.meioambiente.mg.gov.br>) for providing the Ikonos image and field work support, particularly José Medina da Fonseca and Célio Murilo de Carvalho Valle. The authors are also thankful to the Botanical Taxonomy Laboratory of the Universidade Federal de Minas Gerais, especially to researchers Marco Otávio Pivari and Pedro Lage Viana.

Iran, 1971), (4th Edition), Ramsar Convention Secretariat, Gland, Switzerland.

REFERENCES

- Biodiversitas, 2005. Biodiversidade em Minas Gerais: um atlas para sua conservação [Biodiversity in Minas Gerais: an atlas for its conservation] (Second Edition). *Fundação Biodiversitas*, Belo Horizonte, Brazil, 242p.
- Barbosa, I., P. Maillard and T. Alencar-Silva. 2009. Mapping wetlands variation using high resolution image in the pandeiros wildlife Sanctuary, Brazil. Proceeding of 30th Canadian Symp. On Remote Sensing, Lethbridge, Canada.
- Clausi, D. A. (2000). Comparison and fusion of co-occurrence, Gabor and MRF texture features for classification of SAR sea-ice imagery. *Atmosphere-Ocean* 39(3), 183–194.
- Davis, P.A., M.I. Staid, J.B. Plescia and J.R. Johnson, 2002. Evaluation of airborne image data for mapping riparian vegetation within the grand canyon, Report 02-470, U.S. *Geological Survey*, Flagstaff, Arizona, 65p.
- Dechka J.A., Franklin S., Watmough M., Bennett R., and W. Ingstrup D., 2002. Classification of wetland habitat and vegetation communities using multi-temporal ikonos imagery in southern saskatchewan. *Canadian Journal of Remote Sensing* 28(5) pp. 679-685.
- Franklin, S. E., 2001. *Remote Sensing for Sustainable Forest Management*. Boca Raton, FLA: Lewis Publishers.
- Haralick, R, 1979. Statistical and structural approaches to texture. *The Institute of Electrical and Electronics Engineers, Inc.*, 67 (5), pp 786-804.
- Maillard, P. (2003). Comparing texture analysis methods through classification. *Photogrammetric Engineering and Remote Sensing* 69(4), 357–367.
- Maillard P., 1999. Texture in High Resolution Digital Images of The Earth. Department of Geographical Sciences and planning, University of Queensland, Australia. PP. 328.
- Melack, J. M., 2004. *Tropical freshwater wetlands. Manual of Remote Sensing for Natural Management and Environmental Monitoring* (4th Edition), John Wiley and Sons, Hoboken, New Jersey, pp. 319-343.
- Mitsch, W. J. and Gosselind J. G., 2007. *Wetlands* (4th Edition). John Wiley and Sons Inc., Hoboken, New Jersey. pp 582
- National Wetlands Working Group, 1997. *The Canadian Wetland Classification System* (2nd Edition), University of Waterloo, Waterloo, Ontario, Canada pp. 68.
- Ramsar Convention Secretariat, 2006. *The Ramsar convention Manual: a guide to the Convention on Wetlands (Ramsar,*

LAND USE CLASSIFICATION WITH HIGH-RESOLUTION SATELLITE RADAR FOR ESTIMATING THE IMPACTS OF LAND USE CHANGE ON THE QUALITY OF ECOSYSTEM SERVICES

D. Bargiel^{ab,*}, S. Herrmann^a, P. Lohmann^b, U. Sörgel^b

^a Gottfried Wilhelm Leibniz Universität Hannover, Institute of Environmental Planning, Herrenhäuserstr. 2, D-30419, Hannover, Germany- (bargiel, herrmann)@umwelt.uni-hannover.de

^b Gottfried Wilhelm Leibniz Universität Hannover, Institute of Photogrammetry and GeoInformation, Nienburger Str.1, D-30167, Hannover, Germany – (lohm, soergel)@ipi.uni-hannover.de

KEY WORDS: Ecosystem, Land Use, Classification, Radar, Multi-temporal

ABSTRACT:

Ecosystems provide several services for human well-being. The quality of these ecosystem services is among others affected by agriculture, the main land user in Europe. Thus, it is essential to provide information about land use in agricultural areas.

In this research, land use classification of agricultural areas is carried out based on high-resolution Spotlight TerraSAR-X images (TSX-images) of two different polarisations (HH and VV). A stack of several radar images taken during the vegetation season is used for multi-temporal classification of land cover. The typical phenology of agricultural vegetation types and their individual phenological development during the year cause differences in the backscatter of the radar signal over time.

Two different study areas are investigated, one in the North East of the city of Hannover, Germany called “Fuhrberger Feld” and one in the “Gorajec area” in the very South East of Poland. These two areas represent extremely diverse European regions with regard to agro-technological level, population density, cultivation form as well as geological and geomorphological conditions. Thereby, the radar signal backscatter for different regions is tested.

Preliminary results show significant differences in the backscatter of crop types in SAR data of about 3 m, especially for grasslands, grain and broad-leaved crops. Furthermore the VV polarised radar signal has clearly lower backscattering for grains during summertime and for grasslands in general than for broad-leaved crops.

1. INTRODUCTION

Ecosystems have an important function for the quality of human life. They provide material goods and intangible values as “ecosystem services” for human well-being. They comprise all basic requirements for human well-being, e.g. food, water, air, climate, or recreation. Ecosystem services base on a complex system of ecosystems and their interactions. They enable security, health, basic material goods, and good social relationships (Millennium Ecosystem Assessment, 2005; Myers & Reichert, 1997).

Ecosystem services are affected by different direct and indirect drivers of change. Beside natural drivers, also human impacts influence the ecosystem services; one important impact is land use (Millennium Ecosystem Assessment, 2005). Although land use and ecosystem services interacted since the beginning of land cultivation, there has been an unprecedented increase of intensity in land use in the twentieth century (Poh Sze Choo et al., 2005; Ramankutty et al., 2006). This leads to numerous negative impacts on ecosystems services (Poh Sze Choo et al., 2005; Ramankutty et al., 2006; DeFries, 2004). To assess the impacts of land-use changes on ecosystem services, it is indispensable to provide precise and up-to-date information about land use and land-use change. Remote sensing affords the opportunity to derive this information. New high-resolution sensor types are particularly suitable to improve land use classification results (Poh Sze Choo et al., 2005;

Ramankutty et al., 2006). One of the new sensors is the TerraSAR-X satellite based radar sensor.

TerraSAR-X allows acquisition of multiple polarized radar images (products) with a high ground resolution of up to one meter (DLR, 2007; Fritz & Eineder, 2009). As a satellite-based radar system it is able to provide reliable and regular information about earth surface. Hence, it is especially suitable for multi-temporal land-use classification. The basic idea of the multi-temporal land-use classification is to use a stack of several products during the vegetation period. Different phenological conditions of the vegetation cause an individual backscatter of radar signal in time. In this way, a higher content of information for the classification method is available. Studies with elder systems like ERS 2 or ENVISAT-ASAR showed already the general feasibility of this approach (Schieche et al., 1999; Foody et al., 1988; Borgeaud et al., 1995; Tavakkoli Sabour et al., 2008).

The objective of this study is to conduct a multi-temporal land-use classification of TerraSAR-X images and to examine the suitability of the classification results for assessing impacts of land-use change on ecosystem services. Individual temporal backscatter patterns are identified for different crop types. Observations concentrate on European agricultural areas and on two selected ecosystem services, namely biodiversity and soil.

* Corresponding author.

2. METHODOLOGY

2.1 Study areas

Two study areas have been chosen to test the robustness and transferability of the approach. The test sites vary strongly in their sociological, ecological, economic, and geomorphological conditions. The Fuhrberg area (“Fuhrberger Feld”) is situated in Germany, in the North East of the city of Hannover (52.56 N, 9.84 E), while the second area (“Gorajec”) is located in the very South East of Poland (50.68 N, 22.85 E). The German study area is characterised by intensive agriculture, modern production methods, and large fields. The terrain is flat and the share of field margin strips, hedgerows and other habitat structures is low. The area is a water protection area and its ground water is provided as drinking water for the region of Hannover.

In contrast, in the Polish study area traditional production methods are applied and technical and agrochemical equipment standard is low. The region belongs to the least developed regions in Europe concerning its agricultural production methods (Palang et al., 2006). According to this, landscape structure is dominated by a mosaic of habitat structures, and the size of fields is exceptionally small. The characteristic land relief and loess soils of the Gorajec region cause strong soil erosion processes (Jadczyzyn 1997).

2.2 Data sets

For both study areas TerraSAR-X images were acquired in High Resolution Spotlight Mode (HS) during the growing season of the year 2009 (Table 1). The images were taken in dual polarisation VV and HH and delivered as ground range products with equidistant pixel spacing in azimuth and ground range direction (Fritz & Eineder 2009). Seven images are available for the Gorajec area and only five for the Fuhrberg region because no images could be ordered for the Fuhrberg region in August and September 2009. For the Polish Gorajec area all acquisitions are taken at an incidence angle of 31.72 °, those for the Fuhrberg area at an incidence angle of 34.75 °. Ground range resolution is 2.1 meters for Fuhrberg and 2.3 meters for Gorajec. Resolution in azimuth direction is 2.4 meters for both areas. The extent auf the scenes is 5 kilometers in azimuth and 10 kilometers in ground range according to the HS-Mode.

study area	month	day
Gorajec	March	14
Fuhrberg	March	11
Fuhrberg	April	13
Gorajec	Apri	27
Fuhrberg	June	18
Gorajec	June	10
Gorajec	July	13
Fuhrberg	July	10
Gorajec	August	4
Gorajec	September	6
Gorajec	October	9
Fuhrberg	October	17

Table 1: Availability of TerraSAR-X images

2.3 Ground truth

Ground-truth data were collected in both areas during the year 2009. Vegetation mapping was conducted to generate ground-truth information. In the Fuhrberg region, vegetation mapping was conducted on the exact acquisition dates. Therefore 152 fields have been visited regularly. Additional 46 fields were mapped in July. This results in a total number of 198 test fields for the Fuhrberg region.

In the Gorajec area, ground truth information was collected on three dates during the vegetation period of the year 2009. They covered the acquisition dates for Gorajec in April, August and October. 135 fields were mapped in the Polish study area.

The size of the investigated fields differs considerably between both study areas (Table 2). The mean size of the fields in the Fuhrberg region is 5.27 ha whereas the fields in the Gorajec area have a mean size of only 0.70 ha.

	Fuhrberg (GER)	Gorajec (PL)
sum	1048.34	94.34
max	24.36	3.12
min	0.37	0.03
mean	5.27	0.70

Table 2: Size of ground truth areas [ha]

During the field campaigns several parameters were recorded for each investigated field in a check list:

- Local situation of crop type and its phenological stage, according to the BBCH - scale for the description of growth stages of mono - and dicotyledonous plants (Meier & Bleiholder, 2006)
- Cultivation practices
- Other relevant observations (e.g. weed content, crop residues)

GPS-referenced pictures of all fields were taken. For each acquisition date the local weather conditions and moisture of surface area were recorded.

2.4 Data processing

After co-registration and georeferencing of the datasets, the multi-temporal DeGrandi filter was applied on both sets. The described procedures were performed with ENVI SARSCAPE Software.

Radiometric calibration was done according to INFOTERRA (2008):

$$\sigma_{[dB]}^0 = 10 * \log_{10} (CalFact * DN^2) + 10 \log_{10} (SIN \theta_{loc})$$

Where: σ_{dB}^0 = the calibrated pixel value in decibel
 CalFact = the calibration and processor scaling factor
 DN = the pixel intensity value
 θ_{loc} = the local incident angle which is the angle between the radar beam and the normal to reflecting surface.

3. RESULTS

3.1 Results of ground truthing

The described differences of the study areas lead to different characteristics of crops with regard to the type of cultivated plants and their appearance. This is reflected by the results of taken ground truth on-site.

15 (Fuhrberg) and 16 types of crops (Gorajec) have been recorded (Table 3). In the Fuhrberg area the presence of weeds is low on most fields. Nevertheless a gradient in the amount of weeds between different potato-fields has been detected. Some of them are completely free of weeds while others contain a certain amount of various species of weeds. The differences cannot be attributed to plant diseases. In Gorajec the amount of weeds is explicitly higher than in the Fuhrberg area. Most fields contain different kinds of weeds. Most potatoes in the Polish study area suffer from a disease.

Fuhrberg (GER)		Gorajec (PL)	
crop type	count	crop type	count
grasslands and meadows	43	grasslands and meadows	4
oat	4	oat	7
rye	33	rye	12
barley	20	barley	24
maize	13	maize	2
spelt	1	grain mixture: barley, wheat, oat	18
wheat	9	wheat	25
winter rape	8	turnip rape	2
sugar beets	18	sugar beets	3
potatoes	24	potatoes	6
fallow land	5	fallow land	3
strawberries	3	black currant	5
asparagus	12	tobacco	13
beans	1	beans	4
Lolium perenne	4	trefoil	4
		grain mixture: wheat, rye	3

Table 3: Type and quantity of crops

3.2 Measurement of signal backscatter

Measured backscatter of radar signal differs for different crops and different acquisition times. Thus an individual pattern of backscatter can be derived for every single crop type. In the following, first results of backscatter patterns (means per field) for selected crops are presented.

3.2.1 Fuhrberger Field area

Broad-leaved crops and asparagus: The comparison of HH polarised mean backscatter values per field exhibits high backscatter values for broad-leaved crops (Fig.1). Sugar beets have high backscatter values (-6 dB) during full development of leaves in June (BBCH-codes 31-39). In July, during full phenological development, values exceed -6 dB yet. Images with sugar beets have been available in June, July and October. Values of maize and potatoes rise up to -8 dB when leaves cover the ground. Potatoes reached this value in June when flowering started (BBCH-codes 60-65). In April, after sowing, backscatter values are dispersed over the whole range between -7.5 and -14 dB. Maize also reached the development state of closed canopy in June (BBCH-codes 30-32) and HH-polarised backscatter is equal to the one of potatoes. Backscatter distri-

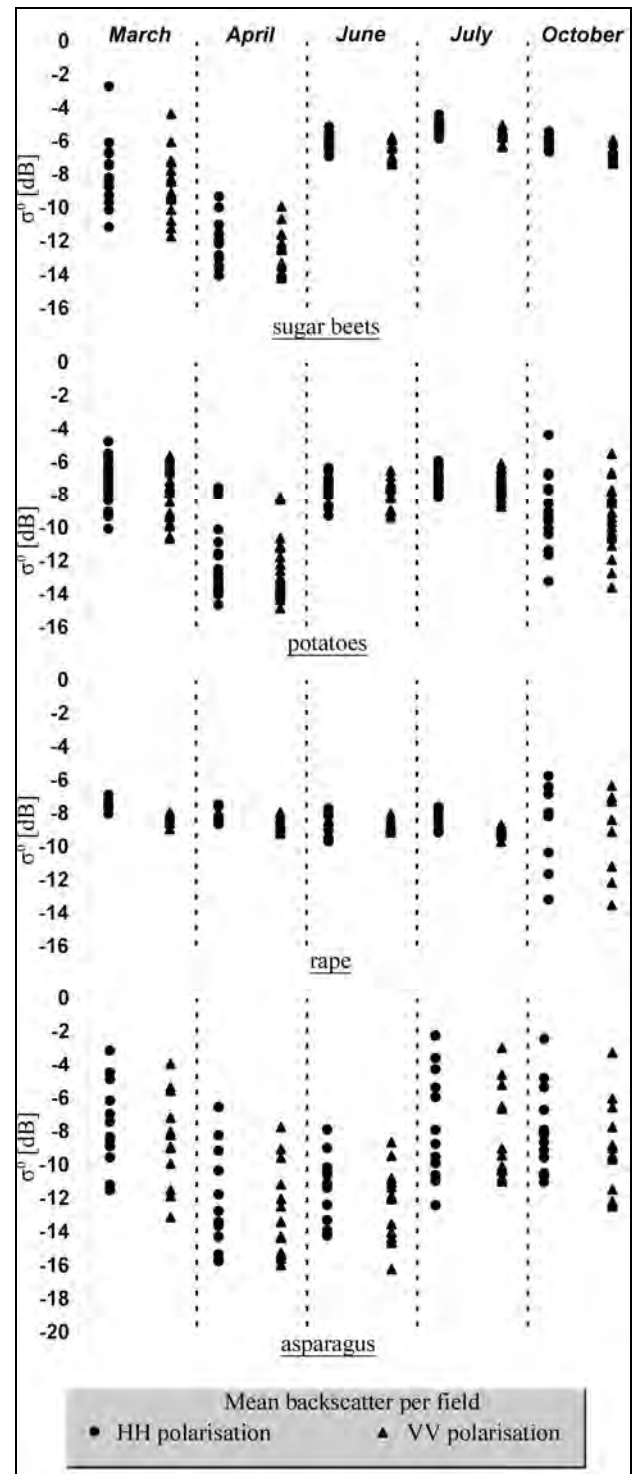


Figure 1: Backscatter distribution for broad-leaved crops and asparagus in the Fuhrberg area

bution for potatoes and maize has a wide range in October after harvesting due to differences in surface conditions. On winter rape fields, the ground was already covered in March when seven to nine leaves occurred (BBCH-codes 17-19). Accordingly, backscatter values average >-8 dB and remain on a high level of -10 dB or more up to July before harvesting started. The values for the different crops show that discrimination of broad leaved crops from those with narrow leaves is possible due to the clear difference in backscatter values. Furthermore, one can even differentiate within the

broad-leaved crops due to the time difference in development of ground covering leaves. For asparagus there is a widespread backscatter distribution recognizable for all acquisition months. The maximum backscatter values (up to -2 dB) are reached in March, July and October. Lowest values (below -14 dB) were noticed in April and June. The structure of the asparagus plant and the plantation in rows seems to influence the reflection strongly.

The analysis of the VV polarised signal shows a very similar backscatter for broad-leaved crops when compared to the HH polarised signal. Just a minor decline of values occurs at all dates.

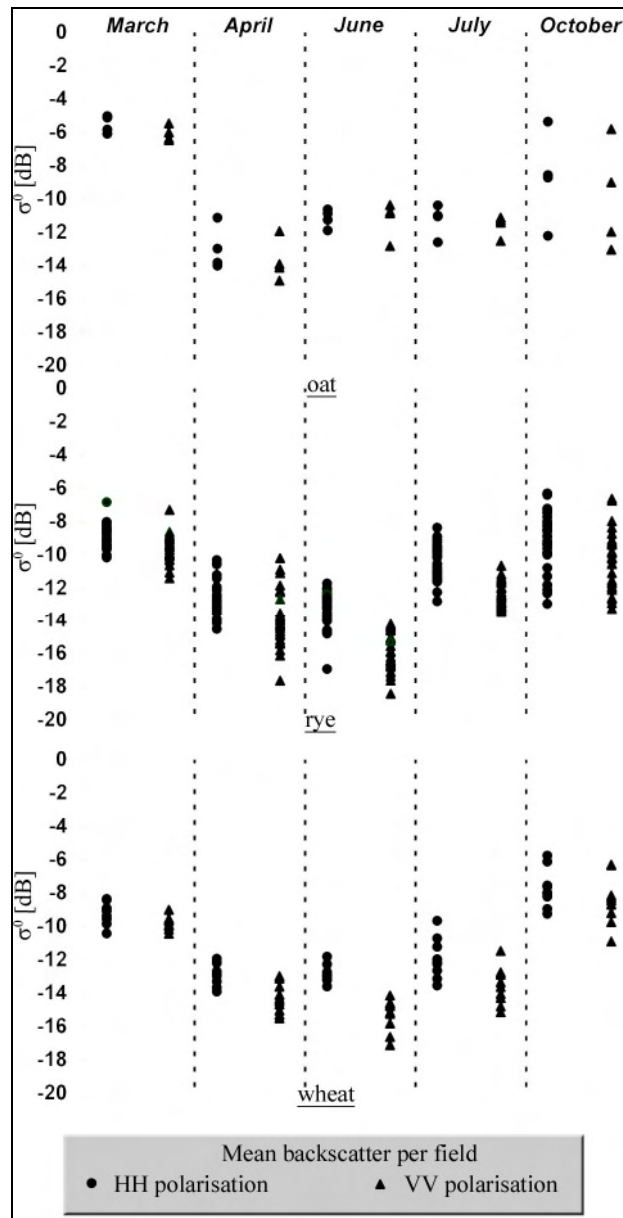


Figure 2: Backscatter distribution for grains in Fuhrberg area

Grains: Backscatter values for grains (Fig 2) differ decisively from broad-leaved crops. In April, the values exhibit a decline to <-10 dB despite of the different phenological stages for spring and winter grains. In April 2009, spring grain started the development of first leaves (BBCH-codes 11-14), while winter grain finished the development of tillers and started elongation (BBCH-codes 29-31). But, these strong differences in the

canopy structure and ground cover between winter and summer grains are not mirrored in the backscatter. After development of closed canopy in June, backscatter values remain on low level (<-11 dB) except from most oat fields where values remained above -12 dB. The backscatter of some barley and rye fields declined to -15 dB, while wheat and oat never cross the line of -14 dB. During June acquisition, all grains began flowering or fruit development (BBCH-codes 61-75). The values for barley and rye in July rose to >-12 dB. Most barley fields have a mean backscatter distribution of -9.5 to -12 dB. Rye fields have a mean backscatter from -8 dB to -12 dB. The backscatter values for wheat and oat remain on the level of June. Nearly all grains finished flowering and fruit development and were at stage of ripening (BBCH-codes 83-89) in July. Distribution of mean backscatter during October acquisition differs on wide range due to different dates of harvest.

Except for oat, backscatter of VV polarised measurement show a strong decline of approx. -2 dB in June and July compared to HH polarised data. For other months and for oat this effect cannot be recognized or the decline is not as strong.

Within the group of grains, oat is clearly discriminable because the backscatter values in June do not decrease.

Grasslands and meadows: For grasslands and meadows there is a characteristic low backscattering of the radar signal in March (Fig. 3). Its distribution ranges from -10.6 to -14.3 dB. The values are lower than for most other crops at this time. Thus, grassland could be easily discriminated from grains, bare soil in preparation and intertillage crops which existed on other fields during March acquisition. Backscattering during acquisitions in April, June and July is similar to the one of grains. In April and June, the mean backscatter is <-12 dB. It is equally distributed up to -16 dB. In July, backscatter values reach >-12 dB; the phenology varied because of previous swathe. October values then reach the level of March again.

In VV polarised mode measured backscatter signal is lower than HH polarised signal for all acquisition month. This effect is strongest in July: VV values differ from HH values by approx. 2 dB. Due to the low backscatter values in March differentiation of grasslands/ meadows and grains is possible.

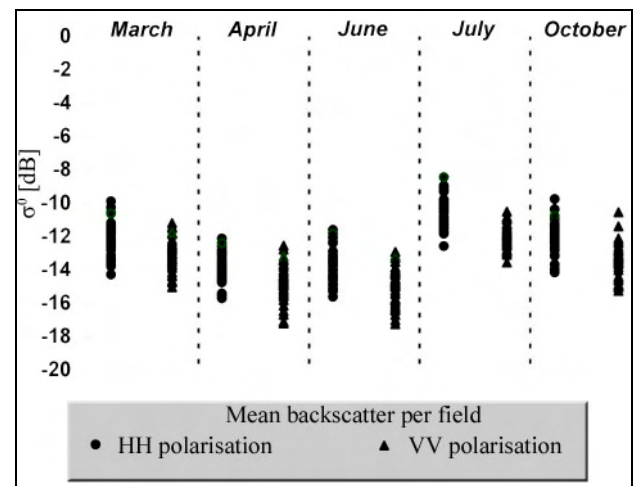


Figure 3: Backscatter distribution for grassland and meadows in the Fuhrberg area

3.2.2 Gorajec area:

Broad-leaved crops: Sugar beets show backscatter values between -8 and -10dB in June. From July to September sugar beet fields remain on a high value (>-8 dB). Compared to sugar beets in Fuhrberg area, backscatter rises during summer month

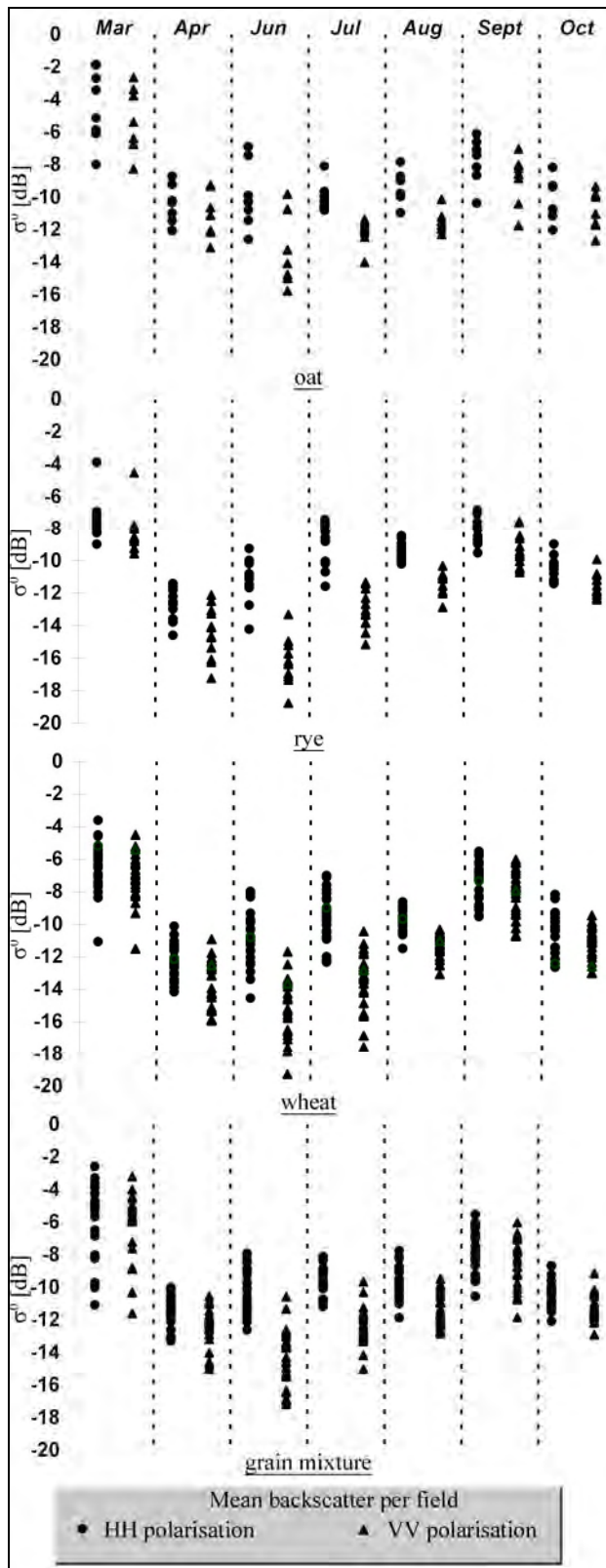


Figure 4: Backscatter distribution for grains in the Gorajec area

but does not likewise cross the line of -6 dB. Potatoes have highest backscatter during the July and August acquisitions (>-9.2 dB and >-8.2 dB). In June and September they differ within huge ranges. This is very similar to potato fields in Fuhrberg with exception of June where the values of Gorajec seem randomly distributed. Backscatter values for both maize fields

increase constantly from April to July. They remain on a level of >-10 dB until a significant decrease in October. In comparison, Fuhrberg backscatter values for maize fields increase to a higher level in June and July. Tobacco, which is also a broad-leaved crop, increases from April to July to a high level of above -7.3 dB. After reaching this peak, it turns to lower level but remains above -10 dB until harvest in October. The VV polarised backscatter value for broad-leaved crops decreases with a lower rate compared to the one of HH polarised signal. This is very similar to the results for Fuhrberg. The backscatter of broad-leaved crops is comparable to the one of Fuhrberg site, although they do not reach such high values.

Grains: Grain crops mainly exhibit high backscatter values in March (Fig. 4). In April values are significantly lower. HH polarised backscatter increase within a wide range from April to July. In August, before harvest started, most values decrease to <-10dB. This is especially recognizable for wheat and rye. After the harvest the values increase in September and then decrease in October to <-8 dB. Compared to the grain crops in Fuhrberg area, grain fields in Gorajec vary within a wider range. An increment for grain crops in July can be observed likewise, but not as clearly as in Fuhrberg. Furthermore, there is an explicit difference between both June acquisitions with wide distributed values in Gorajec and low backscattering in Fuhrberg. There is a clear difference between VV and HH backscatter during the summer month. VV values are significantly lower. In June and July a strong decrease of backscatter values can be found. In June the mean decline is between 5.1 dB for rye and 3.2 dB for barley. In July the mean decrease ranges from 4.1 dB for rye and 2.2 dB for oat. In August decrease is less with mean declines from 1.2 dB (barley) to 2.1 dB (oat). VV backscatter during the summer month decreases stronger than for grains in Fuhrberg area.

Grasslands and meadows: Measured backscatter for grasslands and meadows shows a constant value of <-10 dB. The only exceptions are two fields in March with clearly higher backscatter of >-10 dB and one measurement in June with -9.5 dB. Although grasslands do not reach values as low as the ones in Fuhrberg, they remain on a relatively low value compared to other crop types in the Gorajec region. An increment of values in July, similar to the one in Fuhrberg, cannot be found. The same effect as in Fuhrberg is observable in March, when most values are lower than grain crops or bare soils. The VV polarisation backscatter is lower during all month (average 1 dB). But during the summer month the decrease is stronger with about 2 dB. This is comparable to the Fuhrberg results for VV backscatter in grasslands and meadows.

4. CONCLUSIONS

The results of backscatter measurements for the different crops are very promising because individual backscattering patterns for the different crops can be found by using time series of images. As the images are available all over the year independent from the weather conditions, the phenological development of the plants during the year can be detected. This allows not only for a clear separation of broad-leaved crops from small leaved crops, but also for discrimination within the group of broad leaved crops (e.g. sugar beets and maize). The separation between the different grains still has some problems, with the exception of oats. But, due to its very specific reflection, especially in April, grasslands can be differentiated from all grains very clearly. This is not given for applications with optical data, when differentiation is often not available (Gonzalez-Sanpedro et al., 2008).

The high resolution of the radar images allow for a fine grained description of the inhomogeneities of the soil and/or plant structure. This is clearly visible from the different results of the German and Polish fields. These differences can be explained with the highly diverse conditions in both study areas (higher weed content, lower agricultural production standard, undulating terrain with resulting differences in local incidence angles for the radar signal, and smaller fields in Poland). This can be a disadvantage because it results in additional scatterers distorting the crop reflection. On the other hand, it might be used to derive e.g. the weed content if fields with the same crop are compared. Further investigations are necessary to come to conclusions.

These first results about the characteristic backscatter properties for different crop types which are comparable for both research areas already show the high potential for multi-temporal land-use classification with high resolution, satellite based synthetic aperture radar. Especially, the possibilities for detecting the different crop types provide a first important precondition for the derivation of soil erosion risk: crops with a high risk for erosion can be separated from those with a lower risk. This information can be mapped for the respective regions and provides input data for the C factor, an important parameter for the calculation of soil erosion with the Universal Soil Loss Equation (USLE). The provision of exact information about crops and their phenological development during the year is a central issue for the quality of erosion risk calculation (Meusburger et al., 2010).

The high resolution of the radar data allows also for the detection of smaller structures like hedgerows and field margins. It will be the next step to collect respective ground truth to compare the backscatter values of these biotope structures.

Further on, enhanced classification approaches have to be tested which make use of the information from the time series and the polarisations to derive the best classification results. An extent of the developed classification method on more subtle habitat structures within agricultural areas, e.g. woody landscape elements or field margin strips, will follow. Afterwards the suitability of the classification results for the assessment of biodiversity and soil erosion changes will be evaluated. Thus effects of land use and its changes on the selected ecosystem services will be elaborated.

5. REFERENCES

- Borgeaud, M., Noll, J., Bellini, A., 1995. On the use of ERS-1 multi-temporal SAR data for agricultural applications. IGARSS '95, *International Geoscience and Remote Sensing Symposium*, Vol. II: 904-906.
- DeFries, R.S., Foley, J.A., Asner G.P., 2004. Land-use choices: balancing human needs and ecosystem function. *Frontiers in Ecology and the Environment* 2 (5), pp. 249-257.
- DLR (Deutsches Zentrum für Luft- und Raumfahrt e.V.), 2007. TerraSAR-X: Das deutsche Radar-Auge im All. Missions-Broschüre, Raumfahrt-Agentur, Bonn.
- Foody, G.M., Curran, P.J., Groom, G.B., Munro, D.C., 1988. Crop Classification with multi-temporal X-band SAR data. IGARSS '88, *International Geoscience and Remote Sensing Symposium*, Vol. I, pp.217-220.
- Fritz, T. & Eineder, M., 2009., TerraSar-X Ground Segment Basic Product Specification Dokument., Manuscript, DLR – Deutsches Zentrum für Luft und Raumfahrt.
- Gonzales-Sanpedro, M.C., Le Toan, T., Moreno, J., Kergoat, L., Rubio, E., 2008 Seasonal variations of leaf area index of agricultural fields retrieved from Landsat data. *Remote Sensing of Environment*. 112, pp.810-824.
- INFOTERRA. 2008., Radiometric Calibration of TerraSAR-X Data., Manuscript, Infoterra Friedrichshafen.
- Jadzyszyn, J. 1997., Evaluation of soil losses influenced by different option of landscape management., *Fragmenta Agronomica. Proceedings 14th ISTRO Conference July 27 – August 1, 1997*, pp. 287-289.
- Millennium Ecosystem Assessment, 2005. Ecosystems and Human Well-being: Current State and Trends, Volume 1, Island Press, World Resources Institute, Washington D.C. , pp. 25-36.
- Meier, U. & Bleiholder, H. 2006., Growth stages of mono- and dicotyledonous plants, Agrimedia GmbH, Clenze.
- Meusburger, K., Konz, N., Schaub, M., Alewell, C., 2010. Soil erosion modelled with USLE and PESERA using QuickBird derived vegetation parameters in an alpine catchment. *International Journal of Applied Earth Observation and Geoinformation*. 12, pp.208-215.
- Myers, J.P., & Reichert, J.S., 1997., Perspective on Nature's Services. In: *Daily, G.C.: Nature's Services. Societal Dependence on Ecosystem Services...* XVII-XX. Island Press, Washington D.C.
- Palang, H., Printsman, A., Gyuro, E.K., Urbanc, M., Skowronek, E., Woloszyn, W., 2006. The forgotten rural landscapes of Central and Eastern Europe. *Landscape Ecology* 21, pp.347-357.
- Poh Sze Choo, H, D, Cooper, C. Devendra, J, Dixon, J, Gaskell, S, Khan, R, Lal, L, Lipper, J, Pretty, J, Primavera, N, Ramankutty, E, Viglizzo, Wiebe, K., 2005. Cultivated Systems. In: *Millennium Ecosystem Assessment Board: Ecosystems and Human Well-being: Current State and Trends*, , Island Press, Volume 1. pp. 747-794.
- Ramankutty, N., Graumlich, L., Achard, F., Alves, D., Chhabra, A., DeFries, R. S., Foley, J. A., Geist, H., Houghton, R. A., Goldewijk, K. K., Lambin, E. F., Millington, A., Rasmussen, K., Reid, R. S., Turner, II B. L., 2006, Global Land-Cover Change: Recent Progress, Remaining Challenges. . In: *Land-use and Land-cover Change. Local Processes and Global Impacts*. pp. 9-39, Springer-Verlag, Berlin, Heidelberg.
- Schieche, B., Erasmi, S., Schrage, T., Hurlmann, P., 1999. Monitoring and Registering of Grassland and Fallow Fields with multitemporal ERS Data within a district of Lower Saxony, Germany. IGARSS '99, *International Geoscience and Remote Sensing Symposium*, Vol. II: pp.759-761.
- Tavakkoli Sabour, S.M., Lohman, P., Soergel, U., 2008. Monitoring agricultural activities using multi-temporal ASAR ENVISAT data. *International Archives of Photogrammetry and Remote Sensing*, Band XXXVII, Teil B7-2, pp. 735-742.

THE MULTI-SENSOR LAND CLASSIFICATION SYSTEM LCS: AUTOMATIC MULTITEMPORAL LAND USE CLASSIFICATION SYSTEM FOR MULTI-RESOLUTION DATA

A. Beccati^{*a,b}, M. Folegani^a, S. D'Elia^c, R. Fabrizi^a, S. Natali^a, L. Vittuari^d

^a MEE0 srl, Research and Development, Via Saragat, 9, I-44122, Ferrara, Italy - (beccati, folegani, natali)@meeo.it

^b University Of Ferrara, Department of Mathematics, Via Saragat, 1, I-44122, Ferrara, Italy - alan.beccati@unife.it

^c ESA - ESRIN, Ground Segment Department, via Galilei 1, I-00044, Frascati, Rome, Italy

^d University of Bologna, DISTART, Viale Risorgimento 2, I-40136, Bologna, Italy

Technical Commission VII Symposium 2010

KEY WORDS: Land Cover, Land Use, Modelling, Web based, Global, Multiresolution, Multitemporal, System

ABSTRACT:

Providing land use/land cover change maps through the use of satellite imagery is very challenging and demanding in terms of human interaction, mainly because of limited process automation. One main cause is that most of land use/land cover change applications require multi-temporal acquisitions over the same area, that introduces the need for accurate pre-processing of the dataset, in both geo-referencing and radiometry. Moreover, single multi-spectral images can be hundred of megabytes in size and therefore image time series are even more difficult to be handled and processed in real time. The approach here proposed foresees the use of a robust land cover classification system named SOIL MAPPER® to reduce input data size by assigning a semantic meaning (in the land cover domain) to each pixel of a single image. Land cover transitions and land use maps can be expressed as evolutions of land cover classes (features) on temporal domain. This permits to define 'trajectories' in the features – time space, that define specific transition or periodic behaviour. The target system, named Land Classification System, provides fully automatic and real time land use/land cover change analysis and includes fundamental sub-systems for accurate radiometric calibration, accurate geo-referencing (with geolocation within the pixel size) and accurate remapping onto an Earth fixed grid. The characteristics of the selected pre-classification system and Earth fixed grid allow general application across different sensors. Land Classification System has been prototyped over 15 years of global (A)ATSR data and foresees integration of over 3 years of regional ALOS-AVNIR-2 data.

1. INTRODUCTION

Land use and land cover change (LULCC) topics are going to become more and more critical subjects for the impact they have on the global climate. They are in fact linked to climate and weather in complex ways and are fundamental inputs for modelling greenhouse gas emissions, carbon balance, natural ecosystems and human environment evolution. Both human activity and natural phenomena can affect many of these processes, that are strictly correlated, influence each other and have strong impact and consequences on environmental, social and economic aspects as well as on human health. Land cover refers to everything that covers the land surface, including vegetation, bare soil, buildings and infrastructure, inland bodies of water, and wetlands. Land use refers, instead, to societal arrangements and activities that affect land cover (Mahoney et al., 2003).

Local-to-global scale LULCC studies and application has got great benefits from the use of remotely-sensed data, mainly due to the preferred point of view of satellite platforms for the periodic monitoring of the territory. Besides existing long time series of satellite data archives, there is an ever increasing availability of satellite images with global coverage from different sources and at different resolutions. As a drawback, single multi-spectral image can be hundred of megabytes in size and the real time utilization of these datasets for online analysis is a technological challenge by itself; that, paired with the high amount of time required for semi-automated image analysis

suggests that fully automated pre-processing systems shall be used to improve satellite data exploitation and reduce the data volume at the same time.

In order to improve multitemporal satellite data usability for time series analysis, accurate image pre-processing operations shall be performed to make time series datasets homogeneous: the most important pre-processing steps are accurate geolocation and accurate radiometric calibration; digital numbers to radiance or surface reflectance conversion must be performed for quantitative analyses of multi-temporal images (Lu et al., 2004). Precise geolocation and image registration are to be addressed on a per-sensor basis, since each one has its geometric properties and correction factors.

The proposed generalised approach, named Land Classification System (LCS), aims at exploiting advanced applications for single image feature extraction, providing easy-to-use tools for land use and land cover change detection analysis over time series of data; such approach, to be readily usable by the scientific community and also by end users of land cover and land use maps, is also aimed at providing a computer aided modelling and land cover evolution analysis tool for definition of evolution models by domain experts and an high degree of automation for evolution models application in an effort to ease and speed-up the analysis of land use and land cover change phenomena, possibly in conjunction with other tools to find correlations among different factors influencing life on Earth like global climate.

In the following sections the methodological generic approach implemented on LCS is described, with specific emphasis on the critical subsystems. Moreover, a prototype application of LCS being implemented in the framework of the European Space Agency (ESA) Support by Pre-classification to specific Applications (SPA) is described; finally the preliminary results obtained during the SPA Project are discussed, with the clear aim of demonstrating the validity of the approach.

1.1 Related work

Many approaches and methodologies exist for land cover change analysis: an extensive survey is provided in (Lu et al., 2004). Similar work for multi temporal analysis systems has been performed to provide targeted land cover change studies or develop databases of land cover (Homer et al., 2004). An interesting bi-temporal approach to land cover change analysis is provided by the Land and Ecosystem Accounting (LEAC) methodology whose main goal is to provide an easy and comprehensive access to land cover data, showing the ‘stock’ available for each land cover class in the different land cover data, and providing also the changes occurred in the periods between different land cover works, as land cover flows matrix (Haines-Young and Weber, 2006). The LCS approach however is not focused on a particular change pattern, land use typology or phenomena, it is instead proposed a generalized approach to land cover change analysis that, building on top of land cover maps stock, might serve as an interactive framework and tool for scientists to help quickly verify hypothesis and improve their research activities. Lastly, the system targets also decision makers to provide a practical surveying tool to systematically provide fast response in detection of features of interests.

2. METHODOLOGY

The LCS system is a generic tool for long-term time series of satellite data management for application in the LULCC field. The term “generic” refers to the wide applicability of the system to different type of satellite-borne sensor data, permitting also multi-sensor applications, and to different time frames; moreover it refers to its ability to fully exploit the multitemporal database for different LULCC phenomena analysis.

LCS creates time series of homogeneous satellite data making use of a robust land cover classification system named SOIL MAPPER®: this system process satellite data coming from different sensors in the same way, generating land cover classification maps with the same semantic meaning, thus permitting multi-temporal and multi-sensor applications.

The stock of classification maps, are then mapped on a common reference grid to allow worldwide pixel based multi temporal analysis of land cover to be performed in relatively small amounts of time since data compression, obtained through semantic feature extraction, delivers a map stock within 6 Terabytes, that is an amount of data readily manageable by modern computer systems.

The core change detection feature of LCS are the land cover evolution models and its model matching engine: in LCS, an evolution model is defined as a sequence of expected land cover classes along the temporal line; each land cover class – temporal reference pair constitutes an evolution model element.

Land cover transitions can be represented by pairing elements which define expected land cover configuration in given points of the time line. A series of evolution model elements defines a land cover evolution pattern that can be matched with actual land cover time series data to determine if that data matches the modelled evolution pattern.

There is almost no automation in model definition and the model itself is designed to let the user precisely define each model element, also starting by a derived model from observer data, with tolerance margins in both feature and time domains. All the knowledge for multi temporal analysis is provided by domain experts in the form of evolution models.

The LCS methodology, explained hereafter in its critical subsystems, foresees three main elements that, chained together, aim at providing a consistent system for multi-temporal land cover data analysis: original data classification, Earth fixed reference system and land cover evolution modelling and matching. Moreover the layout of user interfaces suitable to ease analysis, define evolution models and perform automated model matching are described. Following subsections detail each main aspect of this methodology.

2.1 Common land cover classification system

SOIL MAPPER® is a fully automatic software that permits to generate land cover classification maps through the analysis of multispectral satellite data in the optical domain.

As input it requires multispectral remotely sensed (RS) images calibrated on Top of Atmosphere (TOA) physical values: TOA Reflectance values for Visible (VIS), Near Infrared (NIR), Short Wave Infrared (SWIR), Mid-Wave Infrared (MIR) bands and brightness temperature (BT) for Thermal Infrared (TIR) bands (Mantovani et al. 2009).

As output, it generates a preliminary classification map where each pixel is associated with one label belonging to a discrete set of spectral categories. Spectral classes detected by SOIL MAPPER® have a semantic meaning belonging to the following main categories: Vegetation, Bare soil / Built-up, Snow / Ice, Clouds / Smoke plumes, Water / Shadows, Outliers.

SOIL MAPPER® actually supports most common satellite optical sensors (from medium to very high resolution), like: MODIS, AVHRR, AATSR, MERIS, Landsat 5 TM/7 ETM+, ASTER, SPOT-4 HRVIR, SPOT-5 HRG, IRS 1-C/-D, IRS-P6, IKONOS, ALOS/AVNIR-2, QuickBird.

Recent developments to the system (MEEO, 2010) introduced an uniform classification output with similar number of semantic classes across sensors and standardised classification output that makes is suitable for LCS.

2.2 Earth Fixed Grid reference

LCS defines a multi level global Earth fixed reference on which all satellite data has to be remapped to perform multi-temporal sample-by-sample analysis. The multi-level mesh-grid has been set with a variable uniform angle sampling rate over the geographic coordinates system (Lat. Lon.) with level 0 set at 1/256th degree. Samples (grid elements) are grouped together in fixed size tiles of 64 by 64 samples called Tiles. At level 0 each Tile covers ¼ of degree in both Latitude and Longitude; each further level doubles the sampling rate in both dimensions (i.e. 1/512th degree at level 1 and so on). According to (Sahr et al.,

2003), the LCS grid system is a congruent, unaligned discrete global grid system; cell data is provided by remapping of pre-classified images, that are then stored as raster format in the Tiles archive; the target grid level for each sensor depends on the Ground Sampling Distance (GSD) of the bands used for its classification.

Since each Tile contains the same amount of pixels, the surface covered by the Tile varies with the sampling rate; depending on the sensor, precisely on its spatial resolution, that pixel size shall be under a threshold value, smaller than half of the original image pixel size in order to allow the pixel-based analysis and mitigate the displacement among the overlaid images due to systematic error into the original geo-referencing, hence defining the best fit level for that sensor. Reference grid resolution (Tile pixel resolution), across longitude, is computed at equator, taking into account that, for computational and archiving optimization reasons, the sampling rate is kept at a power of 2.

Grid Level	Ref. GSD	Pixel res.	Samples per deg.	Supported sensors
0	m	m	#	
1	1000	434,84	256	(A)ATSR, MODIS
2	500	217,42	512	MODIS HKM
3	250	108,71	1024	MODIS QKM, MERIS
4	125	54,36	2048	LANDSAT TM TIR
5	60	27,18	4096	LANDSAT ETM+ TIR
6	30	13,59	8192	LANDSAT TM/ETM+ MS
7	15	6,79	16384	LANDSAT ETM+ PAN SPOT5, AVNIR-2
8	7	3,40	32768	-
9	3,5	1,70	65536	VHR MS
10	1,75	0,84	131072	VHR MS
	0,8	0,42	262144	VHR PAN

Table 1. Grid parameters and supported sensor for levels 0-10

Table 1 lists grid parameters for levels zero to ten with reference GSD and name for a selected series of sensors. To avoid data loss during sampling, pixel threshold has been set at about half the original pixel size for medium resolution sensors at level zero, while for higher resolution the most suitable grid level is selected considering the power of 2, nearest to half of the original image resolution.

Tile mapping is the process dedicated to ingest the pre-classified scenes and remap them onto Earth Fixed Grid Tiles. The ingested scene has its original geo-reference system, thus, before applying any remapping process, a geo-referencing pre-process is required in order to avoid co-registration problems among images. It is then assumed that each input image to the ALCS system is accurately geo-referenced with accuracy below half of pixel size.

In the Tile mapping process, the original data is filtered taking into account the scope of LCS: tiles over sea are filtered out on the basis of a 4 valid pixels threshold (minimum amount of pixels detectable at supported sensor resolution) using the U. S. Geological Survey 1Km Land Sea Mask dataset (Eidenshink et al., 1994) for a per pixel coordinates test to assign each tile

pixel to either the land or sea classes. Moreover all cloud and outlier pixels classes are also removed. Tile mapping is performed using the Nearest Neighbour remapping methodology.

2.3 Land Cover Evolution Models

LCS evolution model matching is a form of change analysis that, according to (Lu et al., 2004), falls in the “classification” category and especially it is a form, or extension, of the commonly used Post-Classification Comparison. The system lays on the basis that the evolution of land cover classification over time can lead to identification of land use typologies, and also effective identification of areas of rapid land-use and land-cover variation may allow contextual detection of major disturbances such as fires, insects and flooding. The key to the identification of relevant evolution patterns is the definition of a corresponding evolution model that can be systematically used to determine if an observed data series conforms to the model pattern.

2.3.1 LCS evolution model: is defined as a sequence of expected sets of land cover classes along the temporal line, each land cover set – temporal reference pair constitutes an evolution model element (see Figure 1 for a schematic representation). Transitions can be represented by pairing elements which define expected land cover configuration in given points of the time line comprising the transition. A series of evolution model elements defines a land cover evolution pattern that, stored in computer readable form, can be automatically matched with actual land cover time series to search for the modelled feature evolution pattern (evolution model matching). Relevant metadata associated to evolution models is: model name, model type (feature category), area of applicability, applicability to grid levels (accounts for typical size / resolution requirements of the modelled feature).

Definition	Characteristics	Graphic Evolution
Non-permanent crop fields (with annual cycle)	<ul style="list-style-type: none"> Winter: Bare soil or low Veg. Spring and early summer: Increase in vegetation From mid-summer to winter: Bare soil 	
PERIODIC		
Candidate Burned areas	<ul style="list-style-type: none"> Mid-to-high vegetation at T0 Low vegetation/bare soil at T1 T1 = T0 + few days 	
TRANSITION		

Figure 1 - Description of evolution models in the land cover / time domain for a periodic phenomenon and for a transition (non-periodic) phenomenon

The land cover class value defines the expected land cover type in a given model element. Multiple land cover class values can be defined, this is obtained by setting the class tolerance parameter in an evolution model element. An element can also have the “Not” flag enabled to invert the expected land cover class values.

Each element has a temporal reference that defines a point along the timeline, either fixed or related to the previous element, where its land cover class is expected (the data sampling point of the model matching); in particular, three temporal parameters are provided: Date, Time Since Previous element (TSP) and time tolerance. All parameters are specified in unit of days, and thus the entire system is designed to work at day resolution.

The Date parameter references a date in the timeline where the element lies; this parameter can be set only on the first element of an evolution model, thus indicating the starting point of the model. Different specification for the first element Date defines different kinds of models as follows: a blank Date (no date specified) defines a non periodic model, that can be matched at any point along the timeline as a sliding temporal window; a complete date specification defines a fixed model that can be matched only at its fixed temporal reference; a partial date (i.e. without the year) defines a seasonal model that can be matched at any subset of points in the temporal line identifiable by setting the unspecified parts of the date as matching input.

TSP defines the sampling point of an element as the number of days after the previous element along the evolution model sequence, hence it is not applicable to the first element for which it is fixed to zero; Using TSP to locate elements along the timeline lets the user easily define non periodic models and apply them at any point in the timeline.

Time Tolerance (TT): defines the radius in days of a temporal interval, centred on the element's sampling point along the timeline in which the actual data can be validly sampled. That allows coping with the possibility of missing data at the element's sampling point, such as cloudy acquisitions or data gaps due to satellite revisit time. Moreover, any element of the evolution model can be set to be "Persistent", that means the expected land cover type must persist in actual data for the entire Time Tolerance of the element.

2.3.2 Model matching algorithm: key feature of LCS is automated model matching that takes as its input a single area of interest and a variable amount of details, depending on the Date specification of the actual model, for one or more time periods over which matching is to be performed. For this description we assume a single time period, in case of multiple periods, the process herein described is simply iterated over each one to deliver one result set for each period.

Taking into account the definition of an evolution model and the various options for its parameters, the simplest form of model matching is the match of a fixed model, that is tested only at a fixed point along the temporal line. This matching is performed by testing, over each grid element (here called also simply pixel) covering the area of interest, the value of relevant pixels in the stock maps archive, according to every element that composes the evolution model, verifying each pixel with the expected value in the model.

In particular, for each element, pixel data is first searched at the exact day of sampling specified by the element and, in case that data is missing the search interval is recursively extended one day in both directions to search for data within the TT. This search interval does not influence the marching outcome, unless the element is defined as persistent, that is any available data closest to the sampling point, within the TT, is used for matching with the expected set of classes for the element.

Model matching can bring four different results for each pixel, mapped on a result map with different colors for immediate visual analysis, as follows:

- No data (Black): for any element there is no data available within the classified tiles stock.

- Match (Green): for all model elements data is available and, actual pixel value fits with the main land cover class expected value of the model.
- Match within Tolerance (Yellow): for all model elements data is available and, for all observations not providing a Match result, the observed class is among the set of classes listed in the class tolerance set.
- Not match (Red): for all model elements data is available and, for at least one element, actual data does not match neither the main class, nor any of the classes in the tolerance set.

Seasonal models are matched in the same way as fixed models but any time range input detail for the model starting date can be freely specified to a full date, hence fixing the model. Each set of different values of the details specifying a full date (multi period matching), delivers its related result map.

The most general form of evolution model matching, called Non Periodic Model Matching, is designed for automated detection of the broadest evolution patterns typologies, including unpredicted events like sudden deforestation / fires, flooding and other single or multi transition phenomena whose position in the temporal line cannot be pre determined by nature. These models are characterised by an empty Date specification on their first element, hence matching these models require as input the full specification of start and end dates of each temporal range. The non periodic matching is then performed as a repetition of the fixed model matching above for each day in the time period, the model can thus be seen as sliding along the temporal line. The date of application (start of the sliding window) slides from the time period start date, to its end date minus the model duration.

The match is tested for any day in the temporal range until a match is found; when a match is found, to avoid duplication of the same match that will be reported multiple, the next test is moved forward of an entire sliding window. This non periodic matching can detect more than one match occurrence of the model in the given period if it reoccurs; to provide an immediate visual feedback over this reoccurrence, the first three occurrences of Match are marked with different tones of the result colour. Match result options have the same labels as the fixed matching but slightly different meaning as follows:

- Match: is reported when at least one matching test returns a Match at any given date within the temporal period. Depending on the number of occurrences, this is marked with different tones of green.
- Match within tolerance (Yellow): is reported when no Match is returned and at least one fixed match produces a Match with tolerance.
- Not Match (Red): is reported when no matching produced a Match or a Match with Tolerance and at least one test produced a Not Match.
- No Data (Black): is reported when all tests along the temporal interval return No Data.

Coloured result maps are displayed by the system over a dynamic reference map for immediate visual analysis of the results but also a GeoTIFF version of the map is produced and a comma separated values file format has been designed for further results analysis with other software tools.

2.4 User Interface

The LCS methodology defines key concepts of a framework for land cover change analysis and, to be effectively useable by end users, requires also a graphic user interface (GUI) to provide online analysis of its data archive, aid in definition of Evolution Models and ease of access to its automated matching engine. These functionalities are achieved through the use of Rich Web Technologies, that make the GUI a dynamic data manipulation tool to interactively access and analyse the multitemporal data. LCS foresees three different web-based interfaces, each one dedicated to serve a different typology of users: Administrators, Domain Experts and Standard users.

Domain Expert is the role of users that have the ability to perform land cover change analysis and to derive land cover evolution models from observed data; to these users LCS provides the Expert user Visual Analysis Tool (EVAT) interface including graphical tools for visual analysis of time series data (Figure 2) and graphical design evolution models (Figure 3).

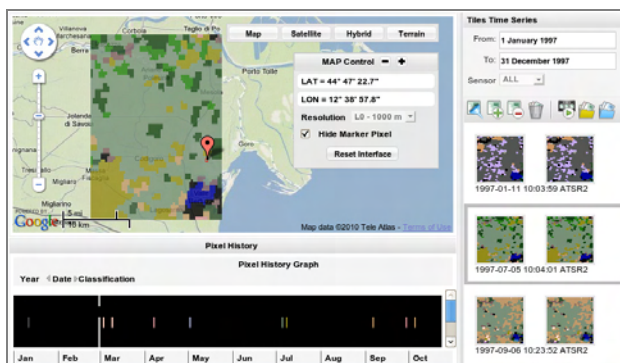


Figure 2 – Time series analysis tools (EVAT)

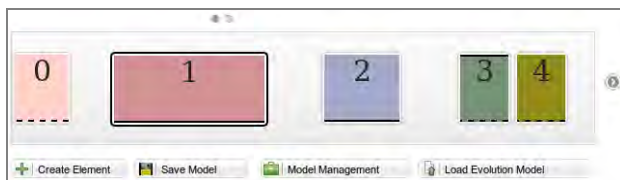


Figure 3 – Evolution Model editing tool (EVAT)

Standard user role is assigned to all users that are not interested in the evolution model edit or stock classification map analysis, hence the Visual Analysis Client (VAC) interface for these users provides ready access to LCS model matching engine by allowing selection of matching inputs: evolution model, area of interest and temporal intervals. It allows immediate visual analysis of the results map, overlaid on a scalable geographic map and also exporting these results for offline analysis or integration with other analysis tools.

Finally, administrators are a fundamental typology of users for any software system that includes access control features, different user roles and system control features like LCS data ingestion processing. The Operator Panel Interface (OPI) is the web interface for that user category and provides control over several system aspects like: user management, system status and data ingestion policies. Data ingestion in LCS is managed on a per sensor basis and the minimum control unit is one month. Overall ingestion status and input control is thus provided in tabular form with one cell per month.

3. RESULTS

For the entire ATSR-2 and AATSR data archive a prototype of LCS (named ALCS) has been implemented and a preliminary validation performed on bi temporal models over a study area with well documented large scale flooding phenomena and consequent influence on vegetation.

3.1 LCS Application to ATSR2-AATSR data: ALCS

An LCS application prototype over fifteen years (A)ATSR data (June 1995 - June 2010 a continuously updated from ESA rolling archive) has recently been implemented including all parts of the described methodology, data from the (A)ATSR Multimission Archive at NERC Earth Observation Data Centre (NEODC) at Rutherford Appleton Laboratory have been mapped, at grid level 0, into Tiles stored in the system that are accessible through the Web-based LCS interfaces.

The ALCS Prototype has been designed as a modular system that has been deployed on a computer system of five machines for computation and a storage array for hosting the Tiles. The system provides 38 cores dedicated to model matching that deliver a fast response for regional area analysis. Like its web interfaces, ALCS distributes computation leveraging the Apache web server that is installed on each of the four processing servers to receive HTTP requests from the core model matching system.

3.2 ALCS Application Case Study

The case study selected as first complete test from the end user point of view has been the flooding phenomenon occurred on the Iraq Marshlands (Lolli, 2010). This area has seen important changes during the period from 2000 to 2009. The reasons for this choice are mainly based on having an available area whose history shows in the last ten years significant changes in several environmental restoration areas. These marked changes are visible on a large scale and well monitored continuously by satellite. Furthermore, given the limited accessibility and vastness of the Iraqi marshlands, satellite data has proven to be a key source of valuable information on prevailing environmental conditions in the region.

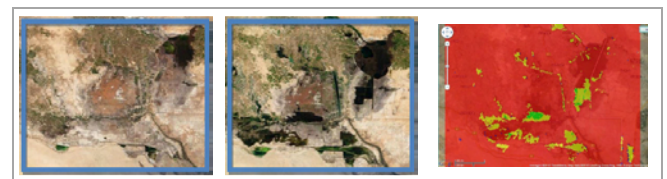


Figure 4 – True color MODIS images of study area in 2003 (left), 2004 (center) and the resulting not-water to water map for the 2003-2004 period.

Among the models created and tested for this study, the models not-to-vegetation and not-to-water, representing the bi-temporal change from not vegetation land cover classes to vegetation and from not water land cover classes to water (see Figure 4) have demonstrated their capability to identify both qualitatively and quantitatively the dimension of the flooding phenomenon over yearly periods. The confirmation about that this change has been well detected comes from the comparison between the results of this case study and the results carried out by the United Nation Environment Programme on the same area (Patrow et al. 2006).

4. CONCLUSIONS AND FUTURE WORK

The here proposed methodology, represents a step forward with respect to current approaches to LULCC analysis that are generally focused on bi-temporal analyses, with a strong limitation in the capability of extracting information and forecasting trends. The possibility to perform a real multi or hyper-temporal study of a phenomenon, with obvious consequences on its understanding, is still not exploited at all. The classification process for many of the current approaches is very labor intensive, frequently being a supervised or semi-automated classification requiring visual interpretation. This implies that most LULCC data products are released several years after the satellite images were taken, and thus, out of date to a certain extent when they are released. Nonetheless, LULCC provides a very valuable method for determining the extents of various land uses and cover types, such as urban, forested, shrubland and agriculture.

LCS is designed to perform a real multi or hyper-temporal study of a phenomenon, with obvious consequences on its understanding and to solve several limitations of similar bi/multi temporal analysis methods like:

- temporal limitations, most of applications are bi-temporal or restricted to few temporal frames while LCS efficiently provides online analysis of the entire 15 years (A)ATSR time series;
- spatial limitations: LCS is worldwide applicable;
- rapid updating limitations, many applications release their products with significant delays with respect to the date of data acquisition and/or elaboration while LCS can deliver very fast results over targeted areas of regional extent.

Moreover, since the proposed system avoids direct use of multispectral images, being based on the application of land cover evolution models directly to its stock of classified maps, there is no need for huge data transfers or processing on demand since LCS leverages the high data compression ratio delivered with association of a discrete valued semantic meaning in place of the original multi spectral data. LCS allows end users to easily apply evolution models to any area of interest over multiple periods and also provides computer aided evolution modeling with interactive series analysis tools to assist in detecting relevant patterns of land cover change to identify related phenomena.

4.1 Future work

The ALCS prototype implementation shows the potential of this methodology application to long time series that can be extended to many different sensors at different resolutions: the next data source foreseen for integration in the prototype systems is a selection AVNIR-2 datasets hosted by the European Space Agency to fully discover the potential of the LCS multi resolution grid system

Future activities foresee the involvement of selected users from several institutions with interest in LULCC to test the effectiveness of the system and its user interfaces in a short term validation campaign.

During the ALCS prototype implementation, several subjects of further study have been identified, such as: the possibility to use

area of applicability information and an evolution model ranking system to automatically chose and apply the best version of semantically equivalent (same feature label extracted) models; even for data with image geo-location and registration issues, LCS could still detects the core of a modelled feature, provided it is large enough and not completely dispatched (no overlapping region) at the analyzed resolution.

ACKNOWLEDGEMENTS

This research was supported by the European Space Agency (SPA project) and a PhD funding by Università Degli Studi di Ferrara.

REFERENCES

- Homer C, Huang C, Yang L, Wylie, B. and Coan M., 2004. Development of a 2001 National Land-cover Database for the United States. *Photogrammetric Engineering and Remote Sensing*; 70, pp. 829-840
- Eidenshinka; J. L, Faundeen J. C., 1994. The 1 km AVHRR global land data set: first stages in implementation. *International Journal of Remote Sensing*; 15(17), pp. 3443-3462
- Haines-Young R., Weber J.L., 2006. Land accounts for Europe 1990–2000. A report by the European Environment Agency, Copenhagen, Denmark.
- Lolli, A., 2010. Multitemporal analysis of satellite imagery: implementation of a land evolution model in ALCS, Master of Science Thesis, University of Bologna, Italy.
- Lu, D., P. Mausel, E. Brondízio, and E. Moran, 2004. Change detection techniques, *International Journal of Remote Sensing*, 25(12), pp. 2365–2407.
- Mahoney, J. R., Asrar G., Keinen M.S., Andrews J., Glackin M., Groat C., Hohestein W., Lawson L., 2003. The U.S. Strategic Plan for the Climate Change Science Program. A Report by the Climate Change Science Program and the Subcommittee on Global Change Research, Climate Change Science Program Office, Washington, DC, USA.
- Mantovani S., Baraldi A, Natali S., 2009. SOIL MAPPER® multi-sensor and multitemporal Applications for semantic-based image Information mining. *GeoSpatial Visual Analytics*. Springer, Netherlands, pp. 167-176.
- MEE0, 2010. SOIL MAPPER® Report description document, Issue 8.1, Ferrara, Italy. http://www.meeo.it/_RISORSE/_docs/meeo_soilmapper_Report_v8.1.pdf (accessed 03 May. 2010)
- Patrow H., Jaquet J.M., Allenbach K., Schwarzer S., Nordbacek O., 2006. Iraqi Marshlands Observation System, UNEP Technical report.
- Sahr K., White D., Kimerling A. J., 2003. Geodesic Discrete Global Grid Systems. *Cartography and Geographic Information Science*, 30(2), pp. 121-134

VALIDATION OF THE REFLECTANCE CALIBRATION OF THE ADS40 AIRBORNE SENSOR USING GROUND REFLECTANCE MEASUREMENTS

U. Beisl^{a,*}, M. Adiguezel^a

^a Leica Geosystems AG, Heerbrugg, Switzerland (Ulrich.Beisl, Muzaffer.Adiguezel)@leica-geosystems.com

Commission VII, WG VII/1

KEY WORDS: Multispectral, Camera, Radiometric, Calibration, Correction, Atmosphere

ABSTRACT:

In the past years digital airborne imaging data have become an appropriate tool to perform remote sensing tasks. With Leica XPro, a processing software for the ADS 40/80 sensor is now available that allows calculating ground reflectance data during rectification. Furthermore, a BRDF correction of the individual flight lines is possible. Since the two processing options are without additional user input, they are also used regularly for mapping purposes to speed up the mosaicking process. In this paper, a validation of the atmospheric correction and reflectance calibration is shown, using data from an image block in southern Germany, which was used in the project "Evaluation of Digital Camera Systems" by the German Society for Photogrammetry, Remote Sensing and Geoinformation (DGPF). Compressed and uncompressed image data was available in 8 and 20 cm ground pixel size together with in-situ ground reflectance measurements of different tarps and natural targets at the time of overflight. Since in the compressed data set the targets were observed several times at different view and illumination angles, also results from the BRDF correction could be compared. The results show a reasonably good agreement between reflectances measured on the ground and those calculated from image data in the atmospheric correction process. Furthermore it could be shown that the BRDF correction option considerably reduces the reflectance difference between different flight lines within selected targets of the test area. The discussion shows the limitations of the method. Finally, improvements are proposed to further increase the accuracy.

1. INTRODUCTION

During the last years there has been a growing interest in the radiometric properties of high-resolution aerial images. An assessment of the radiometric properties of large format digital cameras has been done by Markelin et al. (2008). However, up to now, no operational processes for the handling of absolute radiometric image data are yet implemented in European National Mapping Agencies (Honkavaara et al., 2009).

Attempts to perform an absolute radiometric calibration of frame images have been started for the DMC (Ryan and Pagnutti, 2009, González-Piqueras et al., 2010) and the UltraCam sensors (Alvarez et al., 2010). Molina et al. (2010) are using an empirical polynomial approach to balance the different image brightness in a DMC image mosaic.

The ADS40/80 system features an absolute radiometric calibration since 2006 (Beisl, 2006) and provides a workflow in the Leica XPro software for calculating ground reflectances (Beisl et al., 2008). A validation of the reflectance product is also shown in this symposium (Markelin et al., 2010).

ADS40 data has been used in various remote sensing applications like avalanche prediction (Bühler et al., 2009), classification of benthic habitats (Green and Lopez, 2007), canopy cover and tree species classification (Waser et al., 2008, Waser et al., 2010), urban classification (Emmolo et al., 2008), and archaeological prospection (Kellenberger and Nagy, 2008).

In this article, a validation of the radiometry of the ADS40/80 reflectance and BRDF correction products is done using an

image block from a rural area in southern Germany in order to assess the usability of the ADS40/80 system in remote sensing projects. This image block was also used in the project "Evaluation of Digital Camera Systems" by the German Society for Photogrammetry, Remote Sensing and Geoinformation (DGPF). (Cramer, 2010a).

2. MATERIALS AND METHODS

2.1 Leica ADS40/80 sensor

The Leica ADS40/80 sensor uses a line scanner principle, which is particularly suited for absolute radiometric calibration, since the focal plane is temperature stabilized, the lens aperture is fixed, and the CCD lines have a considerably higher dynamic range than any area-CCD. This way a single integration time setting can be used for a whole flight line with heavily varying surface reflectance without the need of changing the aperture.

2.2 Radiometric processing with Leica XPro

Since the dark signal non-uniformity and the photo response non-uniformity (lens falloff) are already corrected on the sensor head, the relation between raw digital numbers (DN) and calibrated digital numbers (CDN) is just a linear function with a single calibration factor c_1 (camera constant) for each of the 12 CCD lines in a sensor and the actually used integration time (IT [s]). This CDN product is the default output of the XPro rectifier ("no correction").

$$CDN = DN * 50 * c_1 / IT \quad (1)$$

* Corresponding author.

The relation between CDN and at-sensor radiances L [$W/m^2/sr/\mu m$] is simply

$$L = CDN / 50 \quad (2)$$

Since at-sensor radiances include all atmospheric effects like the path radiance and the adjacency effect, the images will suffer from a blue hue, which increases towards the borders across the flight direction. Therefore the XPro workflow provides several options for atmospheric correction. The empirical “Dark Pixel Subtraction” and “Modified Chavez Method” will produce approximate ground radiances, which are no surface property because they will still depend on the actual solar illumination.

In order to obtain an image product which is a surface property, in 2008 the “Atmospheric” option has been included in the workflow, which simulates the solar illumination and path radiance, and then calculates reflectance calibrated digital numbers ($RCDN$) (Beisl, 2008). The relation between $RCDN$ and reflectance R is

$$R = RCDN / 10000 \quad (3)$$

An additional option is the “BRDF” correction which removes the cross track gradient caused by the reflectance anisotropy of ground surfaces. This correction produces homogeneous image strips calibrated to $RCDN$.

2.3 Airborne data set

In 2008 the DGPF started a project for the “Evaluation of Digital Camera Systems”, which included assessments of the geometric and radiometric accuracy performance as well as the performance in generating digital surface models (DSM) and in manual stereo plotting. The project was carried out in the context of the EUROSDR initiative (Cramer, 2010b). A test site at Vaihingen/Enz near Stuttgart (48°56’N, 8°58’E) was chosen and medium format, large format, and hyperspectral cameras were flown by the manufacturers on several days (Cramer, 2010a). The ADS40 S/N 30120 (SH52 type) was flown on August 6, 2010 on two flight altitudes and two configurations (compressed and uncompressed image capture), as given by the DGPF directions (Table 1).

Line	GSD [cm]	Start Time [UTC]	Flight Heading [°]	Sun Azimuth [°]	Sun Zenith [°]	IT RG [ms]	IT BNIR [ms]	Tilt	config
L6	8	0957	90	141.9	37.3	1.448	1.448	N+Bw	comp
L5	8	1002	270	143.7	36.8	1.452	1.452	N+Bw	comp
L4	8	1007	90	145.7	36.3	1.474	1.474	N+Bw	comp
L3	8	1012	270	147.7	35.8	1.476	1.476	N+Bw	comp
L1	8	1028	270	153.8	34.6	1.408	1.408	N+Bw	comp
L7	8	1035	180	156.6	34.1	1.800	1.800	N	raw
L2	8	1039	270	158.6	33.8	1.432	1.432	N+Bw	comp
L8	8	1046	0	161.3	33.4	1.800	1.800	N	raw
H5	20	1054	180	164.9	33.0	4.158	2.908	N	raw
H6	20	1100	0	167.2	32.8	4.482	2.900	N	raw
H4	20	1202	90	195.1	33.0	4.040	2.790	N+Bw	comp
H3	20	1213	90	200.0	33.6	3.866	3.866	N+Bw	comp
H2	20	1228	90	206.1	34.5	3.590	2.340	N+Bw	comp
H1	20	1240	90	210.8	35.5	3.908	2.658	N+Bw	comp

Table 1. Flight lines (L#, H#), solar angles, integration times (IT) for the colour bands, viewing directions (N=nadir, Bw=backward) and compression setting (comp=compressed, raw=uncompressed) for the Vaihingen/Enz data set.

The flight project contained two different data sets: The first data set consisted of E–W flight lines at a lower level (800 m above ground, L#) and a higher level (2000 m, H#), corresponding to a ground sampling distance (GSD) of 8 and 20 cm, respectively. The data was registered in compressed mode and was used for geometric calibration. The second data set with N–S flight lines having 8 and 20 cm GSDs was registered in uncompressed mode, which increased the radiometric resolution, to be most suitable for radiometric validation.

The images, which viewed the radiometric test site (L3, L4, L7, L8, H2, H3, H5, H6) were processed with XPro 4.3 using standard settings to produce three standard products, namely at-sensor radiance (ASR), atmospherically corrected reflectances (ATM), and atmospherically and BRDF corrected reflectances (ATMBRDF).

2.4 Ground measurements

The radiometric calibration accuracy of airborne sensors is difficult to validate with absolute ground radiance measurements since cheap fiber spectrometers tend to drift in the NIR and so a stable absolute calibration for those spectrometers is difficult to obtain. Furthermore, due to changes in atmospheric transmittance the solar irradiance changes rapidly. This means that the measurements have to be taken at the very time of overflight, so measurements at different targets cannot be taken with a single spectrometer. Therefore, reflectance measurements relative to a white calibration standard (e.g. Spectralon®) are performed, instead. This requires modelling the solar irradiance either for calculating the ground radiances from the measured reflectance data or calculating a reflectance product from the image data.

Since the Leica XPro software provides a reflectance product when using the correction with “atmospheric” setting, the validation was done by comparing the XPro image reflectances with measured ground reflectances. This means testing two calibrations of the ADS sensor simultaneously (absolute radiance calibration and reflectance calibration) against the Spectralon calibration and spectrometer stability, i.e. possible deviations cannot be attributed to a single source. However, it makes sense to test the reflectance product that is finally used.

The radiometric test site contained tarps in four colours (white, blue, green, red, provided by RAG Deutsche Steinkohle), 3 Siemens stars for resolution measurements, and a grey wedge tarp, all provided by the University of Stuttgart. The University of Stuttgart made ground measurements with a nadir looking field spectrometer, a camera-based goniometer, and two Sun photometers (Schönermark, 2010).

The day was not optimal for radiometric tests, since high cirrus clouds (altitude > 3 km) passed by frequently. Thanks to an experienced flight crew, the radiometric test site could be imaged without direct cloud shadows except in line H6. However, the aerosol optical thickness (AOT) at 534.3 nm calculated from the Sun photometer data (Figure 1) shows strong haze effects during the time of ground measurements and flights. The AOT was varying between 0.4 and 1 for the different flights resulting in a change of direct solar irradiance by a factor of 1.8. Although this is partially compensated by an increase of the diffuse irradiance, without atmospheric correction, the overall image brightness will vary in this order of magnitude. Since ground reflectance measurements consist of two consecutive measurements of a target and a reference plate, even a small

irradiance change in between those measurements could cause an error.

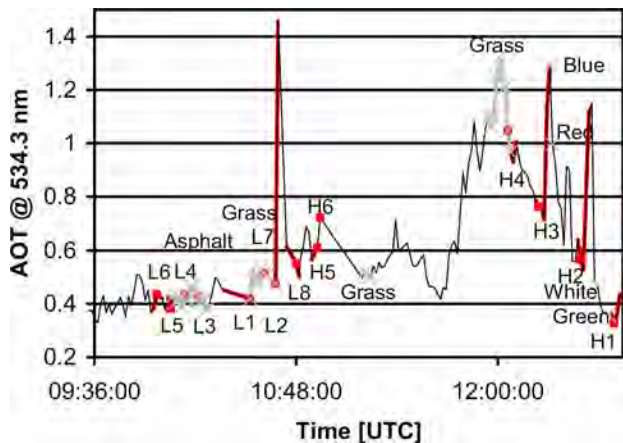


Figure 1. Aerosol optical thickness (AOT) at 534.3 nm at the radiometric test site. Red lines with labels L# and H# indicate the AOT values during the whole overflight. The red square indicates the AOT at the time of overpass. The grey lines with crosses depict the AOT during the ground measurements.

The ground reflectance measurements presented in this study were made by the first author on the day of overflight on six targets (Table 2) at the radiometric test site, which was situated at the crossing of the “geometric” E–W and “radiometric” N–S strips (Figure 2). A StellarNet EPP2000 fiber spectrometer with a spectral range of 350–1150 nm and a field of view (FOV) of 8° was used. The measurement distance to the target was 80 cm giving a circle diameter of approximately 11 cm. A 31-cm square Spectralon® plate was used as a reference before each series of target measurements. The solar illuminance was monitored with a luxmeter and whenever it changed by more than 1% a new reference measurement was done.

2.5 Validation method

The relative differences (*RD*) between the reflectances were calculated from the image products ASR, ATM, and ATMBRDF averaged over the ROIs listed in Table 2 and the ground measurements were averaged per target. By theory the atmospheric correction should result in a reduction of the *RD* between ground and image reflectances and between image reflectances of different flight lines:

$$RD = (\text{image} - \text{reference}) / \text{reference} * 100 \quad (4)$$

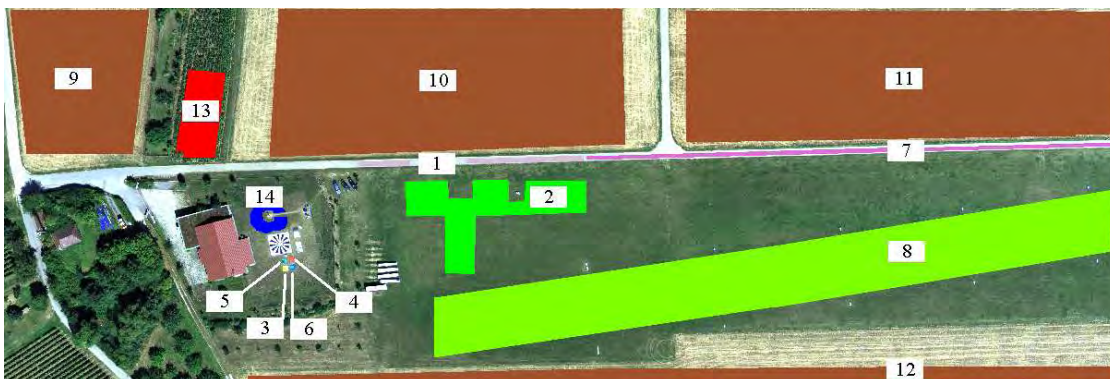


Figure 2. Radiometric test site. Numbers refer to targets and ROIs.

	Target	# of pixels in H# ROI	Total # of reference measurements	Total # of target measurements	Time [UTC]	Sun Azimuth [°]	Sun Zenith [°]
1	Asphalt_1	3124	4	30	10:14	147.7	35.8
2	Grass_1	28445	9	41	11:17	174.1	32.4
3	White tarp	22	3	6	12:35	208.1	34.9
4	Red tarp	26	1	4	12:23	203.0	34.0
5	Green tarp	23	3	7	12:29	205.5	34.4
6	Blue tarp	26	1	3	12:17	200.7	33.7
7	Asphalt_2	6841	No ground measurements				
8	Grass_2	169899					
9	Stubble_1	68215					
10	Stubble_2	186101					
11	Stubble_3	211972					
12	Stubble_4	47546					
13	Corn	10642					
14	Grass_3	2539					

Table 2. Measured ground reference targets (with measurement time and solar angles) and regions of interest (ROI) in the image data (with number of pixels in the upper altitude H#. The number in the lower altitude L# is higher by a factor of 6.25). The target locations are shown in Figure 2.

3. RESULTS AND DISCUSSION

3.1 Validation of accuracy

The reflectance calibration accuracy was first checked in the spectra of the Asphalt_1 and the Grass_1 target (Figure 3) for all flight lines that contained the target (L3, L4, L7, L8, H2, H3, H5, H8). The agreement is good for the W–E/E–W as well as the N–S/S–N lines in both flying heights. However, there are two exceptions:

First, L4 in nadir view shows a 20% relative increase, and L4 in backward view even a 40% relative increase compared to the ground measurements. The reason is that the nadir sensors view the targets at a scan angle of 20° towards the hot spot, and the backward sensors even at an angle of 25° by geometric addition of the tilt angle. The proximity to the invisible hot spot causes the brightening (In this project, the hot spot cannot be observed in neither flight direction since the maximum ADS scan angle of 32° is always smaller than the Sun zenith angle.).

This brightening is caused by BRDF effects on the ground and is always present in images with changing view angles. For a line scanner like the ADS it can be minimized by selecting targets from the center columns of the image where the view angle is small.

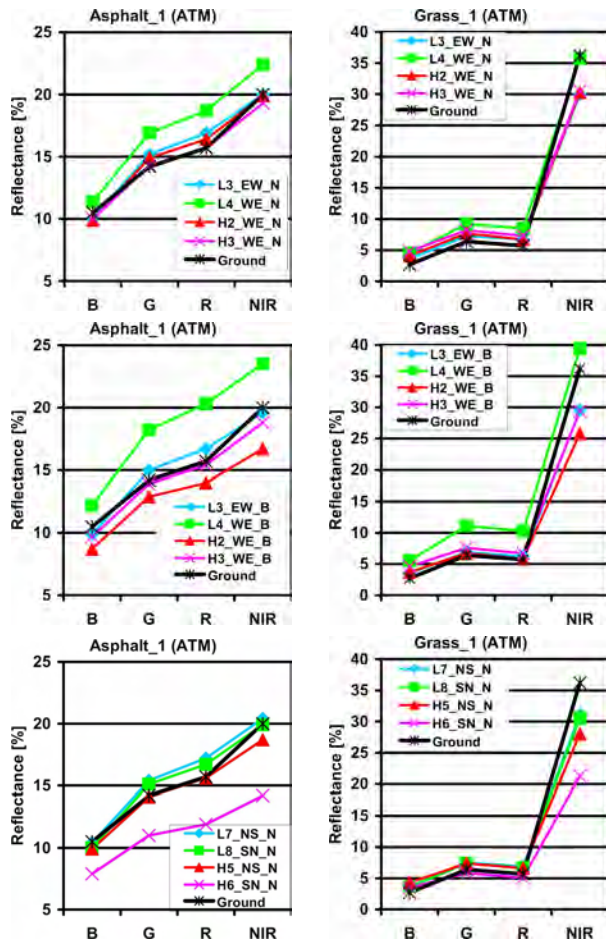


Figure 3. Reflectance spectra calculated from atmospherically corrected images of the Asphalt_1 and Grass_1 target from the nadir (top) and backward (middle) view of the E-W/W-E lines and from the nadir (bottom) view of the N-S/S-N lines compared to ground measurements.

An even better method is to align the flight and sun directions to move the hot spot far away from the observation angles. In our case this would result in selecting the N-S/S-N rather than the E-W/W-E flight lines. Figure 3 shows that flight lines perpendicular to the Sun direction (L3, L4, H2, H3) had strong BRDF effects, while flight lines in the Sun direction (L7, L8, H5, H6) had small BRDF effects, i.e. the reflectances are closer to the ground measurements, which were taken from nadir.

Second, although line H6 was flown in N-S direction and the targets are positioned in the center columns of the image, there is a strong relative discrepancy of 40% especially for the asphalt target. This can be explained by the presence of clouds and an increase of AOT, which can be seen from Figure 1. This causes a decrease in apparent reflectance. To compensate the effects of local AOT variations in the images, simultaneous irradiance measurements on the aircraft would be needed.

For a more quantitative analysis of the accuracy, two flight lines (L7, H5) were selected, since they had no apparent BRDF effects and were both flown in the N-S direction. The RD between the averaged image reflectances and the ground measurements depends very much on the type of target used (Figure 4). Target Asphalt_1 shows deviations of below 10%, while Grass_1 and the colour tarps show deviations of up to 50% in both the upper and lower flight lines. A possible cause could be

the small number of pixels that were available for the colour tarp ROIs in the upper level and the small number of target measurements (Table 2). However, the deviations are comparable also for the lower level, so this can be ruled out most likely.

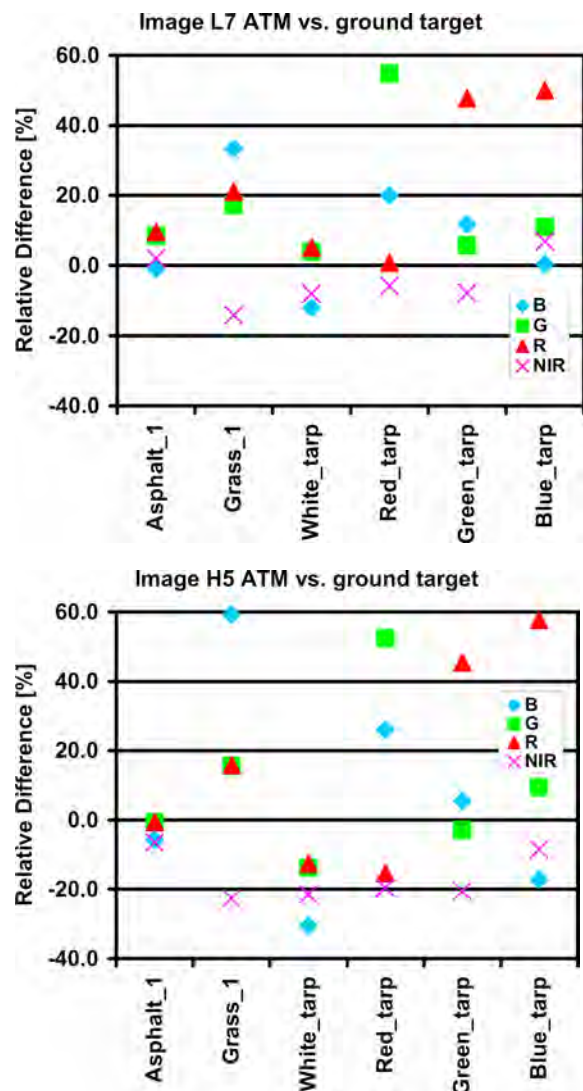


Figure 4. Relative differences of averaged image reflectances and ground reflectance measurements for two flight altitudes L7 (top) and H5 (bottom).

So the effect has to be explained in both cases by combined BRDF and atmospheric effects (Figure 1). For the colour tarps, strong reflectance anisotropy was apparent already by visual inspection (Schönermark, 2010), although they appear uniform when viewed from one direction. The view angle is the same for L7, H5, and ground measurements, but the sun position has changed between the overflight and the ground measurements, which also affects BRDF. The main reason for the discrepancies may be the unstable atmospheric conditions at the time of the ground measurements of the tarps. For the Grass_1 target we have to assume strong reflectance anisotropy, also changing with daytime. In addition, due to the current measurement setup (laboratory table with wheels and a 1m boom holding the spectrometer) a good portion of the hemisphere, which would illuminate the object diffusely, was covered by the measurement apparatus. So the diffuse illumination was different for images and ground measurements.

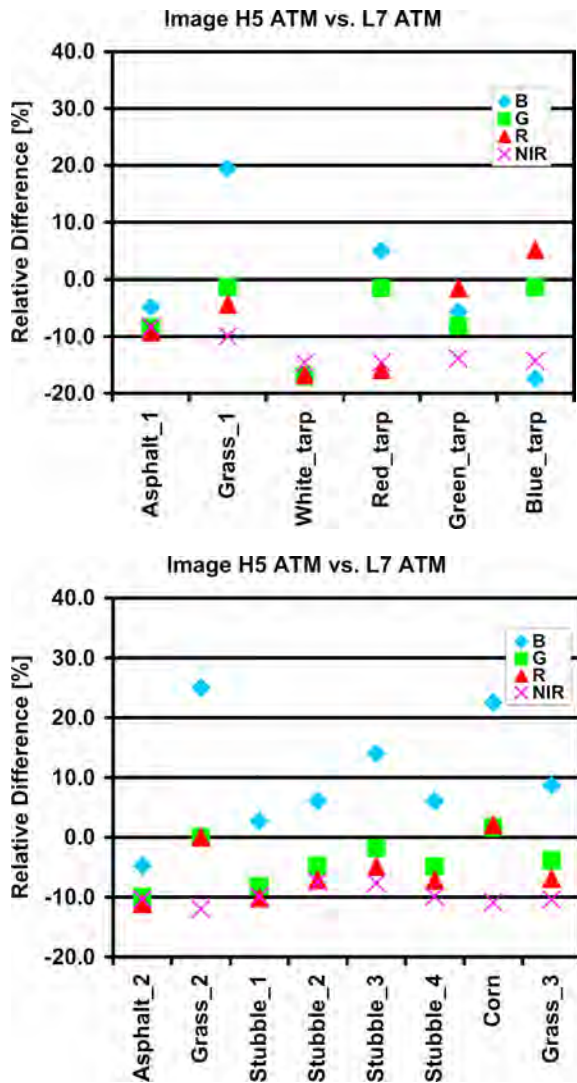


Figure 5. Relative differences of averaged image reflectances for different targets viewed from two flight lines from different altitudes, but with the same flight heading (N-S).

For a comparison of the atmospheric correction results of two different flight levels, again lines L7 and H5 were used (Figure 5). The relative difference of both was below 10% for Asphalt_1 and below 20% for Grass_1, and the colour tarps (Figure 5). For the additional vegetation targets in Figure 5 (e.g. Stubble_#), it can be seen that by averaging a large number of pixels (Table 2) the difference reduced to below 10% for R, G, and NIR. Only for the blue channel a larger discrepancy was found. This is attributed to atmospheric effects.

3.2 Validation of BRDF correction quality

To see the effect of the BRDF correction, the relative differences of the lines L4 (Backward) and L7 (Nadir) before and after the BRDF correction were evaluated using several large vegetation targets. As expected from the discussion in sec. 3.1, Figure 6 shows differences of up to 70% for the ATM corrected reflectances between the W–E and N–S flight lines L4 and L7.

After the BRDF correction, the differences for vegetation targets were generally below 10% for R, G, and B, and 20% for the NIR. Only the asphalt target showed a larger discrepancy.

This is due to the fact that the applied BRDF correction uses a correction function derived from an average statistics of the whole image. So some rare targets with a BRDF different from the average will not be corrected adequately.

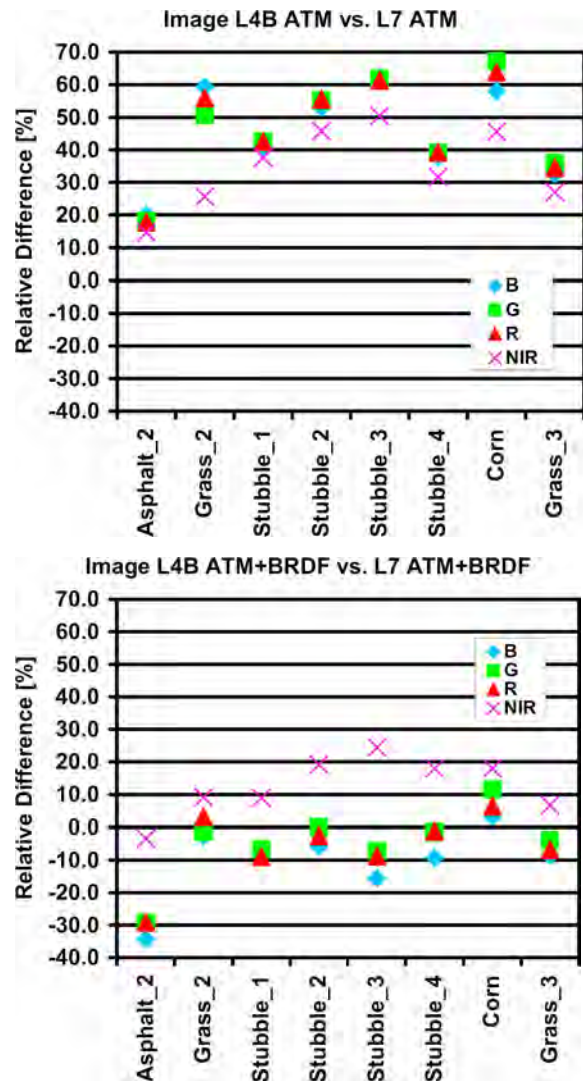


Figure 6. Relative differences of averaged image reflectances for different targets from a WE and a NS flight line of the same flight level before (top) and after (bottom) BRDF correction.

4. CONCLUSIONS

The project showed that ground reference targets used for validation (and also for in-flight calibration) have to be prepared carefully of non-specularly reflecting material and measured at the exact time of overflight. This is a tedious procedure and may be prohibitively expensive in most cases for routine remote sensing campaigns.

The ADS40/80 sensor together with the XPro “atmospheric” correction option enables the production of images with relative reflectance differences of less than 10% even for dark objects. The relative pixel-to-pixel accuracy is much higher, since the calibration and correction functions are smooth functions of the view angle.

To achieve this absolute accuracy, the following precautions have to be made. First, in the flight planning the flight line

headings have to be aligned to within $\pm 25^\circ$ with the sun azimuth of the expected flight time and day in order to avoid strong BRDF effects in the nadir line data. Second, a day with a cloudless sky is required in order to have a stable solar irradiation. A solar zenith angle of 30° – 40° results in optimal illumination.

For standard photogrammetric projects those conditions cannot always be fulfilled, but also the radiometric requirements are lower. So, since the relative accuracy is much better and since the BRDF effects can be corrected to a visually pleasing result, the “atmospheric” or “atmospheric + BRDF” options are recommended as standard settings for data processing in ADS40-photogrammetry.

Integrating the use of measured ground spectra in the reflectance calibration process in XPro (inflight calibration) could enhance the absolute accuracy by calibration of the atmospheric correction parameters to the actual weather conditions. Also the integration of a class-specific BRDF-correction would improve the absolute accuracy in case the BRDF effects cannot be avoided.

ACKNOWLEDGEMENTS

I would like to thank Lauri Markelin and Eija Honkavaara from the Finnish Geodetic Institute and Ilkka Korpela from the University of Helsinki for methodological discussions. Thanks to Ursula Kirchgäßner, Uwe Putze, and Marc Schwarzbach from the University of Stuttgart for cooperation with the ground measurements and for providing Sun-photometer data.

REFERENCES

- Alvarez, F., Catanzarite, T., Rodríguez-Pérez, J.R., and Nafria, D., 2010a. Radiometric calibration and evaluation of UltraCam X and Xp using portable reflectance targets and spectrometer data. Application to extract thematic data from the imagery gathered by the National Plan of Aerial Orthophotography (PNOA). *Proc. EuroCOW2010*, 10.2.-12.2., Castelldefels, Spain.
- Beisl, U., 2006. Absolute spectroradiometric calibration of the ADS40 Sensor. In: *Int. Arch. Photogramm. Remote Sens.*, Paris, France, Vol. XXXVI, part 1, 5 pp.
- Beisl, U., Telaar, J., and Schönermark, M.v., 2008. Atmospheric correction, reflectance calibration and BRDF correction for ADS40 image data. In: *Int. Arch. Photogramm. Remote Sens.*, Beijing, China, Vol. XXXVII, part B7, pp. 7-12.
- Bühler, Y. A., Hüni, A., Kellenberger, T. W., Itten, K. I., 2009. Towards an automated detection of avalanche deposits using their directional properties. *Proc. 6th EARSeL Workshop on Imaging Spectroscopy*, Tel Aviv.
- Cramer, M., 2010a. The DGPF-test on digital airborne camera evaluation – overview and test design. In: *PFG 02-2010*, <http://www.ifp.uni-stuttgart.de/dgpf/PDF/01-PFG02-2010-Ueberblick-FinalVersion-20100112.pdf> (acc. 18 May 2010).
- Cramer, M., 2010b. <http://www.ifp.uni-stuttgart.de/eurosd/> (accessed 18 May 2010).
- Emmolo, D., Orlando, P., Villa, B., 2008. Evaluation of capabilities of fuzzy logic classification of different kind of data. In: *Int. Arch. Photogramm. Remote Sens.*, Beijing, China, Vol. XXXVII, part B7, pp 685-689.
- Fraser, R. S., Ferrare, R. A., Kaufman, Y. J., Markham, B. L., and Mattoo, S., 1992. Algorithm for atmospheric corrections of aircraft and satellite imagery. *Int. J. Rem. Sens.*, 13(3), pp. 541-557.
- González-Piqueras, J., Hernández, D., Felipe, B., Odi, M., Belmar, S., Villa, G., and Domenech, E., 2010. Radiometric aerial triangulation approach. A case study for the Z/I DMC. *Proc. EuroCOW2010*, 10.2.-12.2., Castelldefels, Spain.
- Green, K., and Lopez, C., 2007. Using Object-Oriented Classification of ADS40 Data to Map the Benthic Habitats of the State of Texas. *Photogramm. Eng. Remote Sens.* 73(8), 861-865.
- Honkavaara, E., Arbiol, R., Markelin, L., Martinez, L., Cramer, M., Bovet, S., Chandelier, L., Ilves, R., Klonus, S., Marshal, P., Schläpfer, D., Tabor, M., Thom, C., and Veje, N., 2009. Digital airborne photogrammetry — A new tool for quantitative remote sensing?—A state-of-the-Art review on radiometric aspects of digital photogrammetric images. *Remote Sensing* 1(3), pp. 577-605.
- Kellenberger, T.W., and Nagy, P., 2008. Potential of the ADS40 aerial scanner for archaeological prospection in Rheinau, Switzerland. In: *Int. Arch. Photogramm. Remote Sens.*, Beijing, China, Vol. XXXVII, part B4, pp 1871-1877.
- Markelin, L., Honkavaara, E., Peltoniemi, J., Ahokas, E., Kuittinen, R., Hyypä, J., Suomalainen, J., and Kukko, A., 2008. Radiometric calibration and characterization of large-format digital photogrammetric sensors in a test field. *Photogramm. Eng. Remote Sens.* 74 (12), pp. 1487-1500.
- Markelin, L., Honkavaara, E., Beisl, U., Korpela, I., 2010. Validation of the radiometric processing chain of the Leica ADS40 airborne photogrammetric sensor. *ISPRS TC VII Symposium: 100 Years ISPRS - Advancing Remote Sensing Science*, July 5-7, Vienna, Austria.
- Molina, S., Villa, G., Serrano, C., Valdeperez, M., and Domenech, E., 2010. A polynomial approach for radiometric aerial triangulation. *Proc. EuroCOW2010*, 10.2.-12.2., Castelldefels, Spain.
- Ryan, R. E., and Pagnutti, M., 2009. Enhanced absolute and relative radiometric calibration for digital aerial cameras. *Proc. Photogrammetric Week 2009*, Stuttgart, Germany.
- Schönermark, M., 2010. Status report about the evaluation of the radiometric properties of digital photogrammetric airborne cameras, 2010. In: PFG 02-2010, <http://www.ifp.uni-stuttgart.de/dgpf/PDF/05-PFG-02-2010-RadiometrieKalibrierung-FinalVersion-20100108.pdf> (accessed 18 May 2010)
- Waser, L.T., Eisenbeiss, H., Kuechler, M., and Baltsavias, E., 2008. Potential and limits of airborne remote sensing data for extraction of fractional canopy cover and forest stands and detection of tree species. In: *Int. Arch. Photogramm. Remote Sens.*, Beijing, China, Vol. XXXVII, part B8, pp 1405-1411.
- Waser, L.T., Klonus, S., Ehlers, M., Kuechler, M., and Jung, Andras, 2010. Potential of digital sensors for land cover and tree species classifications - a case study in the framework of the DGPF-project. In: *PFG 02-2010*, <http://www.ifp.uni-stuttgart.de/dgpf/PDF/06-PFG-02-2010-RadiometrieKlassifizierung-FinalVersion-20100112.pdf> (accessed 18 May 2010).

ACCURACY OF 3D FACE RECOGNITION FRAMEWORKS

V. Bevilacqua ^{a,b}, M. Caprioli ^c, M. Cortellino ^b, M. Giannini ^{a,b}, G. Mastronardi ^{a,b}, V. Santarcangelo ^b

^a DEE (Dipartimento di Elettrotecnica ed Elettronica) Polytechnic of Bari
Via Orabona, 4 – 70125 Bari, Italy

^b e.B.I.S. s.r.l. (electronic Business In Security) Spin-Off of Polytechnic of Bari
Via Pavoncelli, 139 – 70125 Bari, Italy

^c DVT (Dipartimento di Vie e Trasporti) Polytechnic of Bari
Via Orabona, 4 – 70125 Bari, Italy
m.caprioli@poliba.it

KEY WORDS: CAD, 3D Geometric Modelling, Image processing.

ABSTRACT

This paper represents a survey of the state of art reached in 3D Face Recognition frameworks and show some different approaches developed and tested by its authors. We have designed a strong algorithm that is based on genetic algorithms, Principal Component Analysis (PCA) and face geometry assumptions, for head pose normalization of 3D scanned face models. Experiments conducted on the GavaDB database show a 100% success rate in correctly those models that “stare” at the camera (with a perfect alignment in 83% of the cases). A previously developed algorithm for nose-tip detection based on an adapted Khoshelham GHT has been used to create an automatic repere’s points detection system with the purpose of obtaining a biometric system for AFR (Automatic Face Recognition) using 3D Face templates. Subsequently two different methodologies, based respectively on an unsupervised self-organizing neural network (SOM) and upon a graph matching, have been implemented to validate the performance of the new 3D facial feature identification and localization algorithm. Experiments have been performed on a dataset of 23 3D faces acquired by a 3D laser camera at eBIS lab with pose and expression variations. Then an optimization of the search of the points ALS and ALD of the nose and a new graph approach for the recognition base on several new points has been implemented. Experiments have been performed on a dataset of 44 faces, acquired by a 3D laser camera at eBIS lab with pose and expression variations, scoring a result of 100% of recognition.

1. INTRODUCTION

In Computer Vision object or shape detection in 2D/3D images is very hard to solve because shapes can be subject to translations, can change by color, can be subject to scale and orientation, can endure occlusions and moreover data acquisition can introduce high levels of noise. Always more and more researchers work on 3D face processing including modelling and recognition. Usually, a 3D face is a group of high dimensional vectors of the x, y and z positions of the vertexes of a face surface. Face recognition based on 3D has the potential to overcome the challenging problems caused by the expression, illumination variations. However, many 3D face recognition approaches, especially the feature based ones require a robust and accurate facial feature localization. To the best of our knowledge, most of the methods do not use benchmark datasets to evaluate their results. Romero et al. presented the first work on benchmark datasets based on FRGC database. They manually marked landmarks of eleven facial features including nose tip and eye corners. With those marked feature locations, the results of automatic feature identification can be measured and evaluated. This paper focuses on a different task and proposes two different steps where the former concerns the automatic identification and localization of a 3D Nose facial features, and the latter is the validation of the correct data obtained by means two independent 3D face recognition tasks. Experiments was performed by using an ASE format dataset of 23 images acquired in by a 3D laser scanner based on structured light with a resolution of 640 by 480. The applied 3D reconstruction method is based on analysis of two images, obtained illuminating sequentially the target surface,

with two sinusoidal fringe patterns shifted in phase by 180° and the obtained data are a 3D clouds of point in ASE format. Due to the short integration time, images may be acquired without room darkening (normal ambient illumination). Optical methods used for measurement of 3D geometry are based on two general principles, one related to the almost direct measurement/analysis of the light flight time (lidars, interferometers and holography) and the second related to geometrical triangulation. In the last group the viewing angles of a point of the object can be calculated from its position in the registered image/images or from the applied system settings (scanning devices). Single image acquisition with a projected fringe pattern of high spatial frequency is another kind of compromise towards one-shot entire scene 3D photography. This type of acquisition is usually related to the Fourier analysis of the image. As the main drawback of this approach is its sensitivity to the quality of the registered image (fringe pattern), which directly influences the precision of the phase unwrapping procedures as well as the final accuracy. Another weak point of this method is its intrinsic low resolution and artefacts caused by the extensive filtering applied in the spatial frequency domain, and in particular, in zones close to the analyzed lobe borders. As nose tip is the most prominent feature of the face, most of the previous work perform nose tip detection and uses the nose tip as the foundation to detect other features. However, many previous facial feature identification algorithms use an assumption that the nose is the closest point to the camera or device which acquires the 3D data. Although this supposition is true in most cases, there is no 100% guarantee due to the noise. Various pose rotations and the complex situation of hair and clothes could make some places closer than the nose. Some algorithms make use of the corresponding 2D texture

information to detect the face area first then localize the nose tip within the selected 3D face crop. This technique requires 2D texture and 3D shape to correspond correctly. However, for example, in some face datasets such as the Spring2003 subset of FRGC, the 2D texture channel is not always perfectly matched with the 3D shape channel. In (Bevilacqua, V., Casorio, P., Mastronardi, G., 2008) the authors addressed automatic nose tip localisation adapting Khoshelham GHT and describe an automatic repere point detection system with the purpose of obtaining a biometric system for AFR (Automatic Face Recognition) using 3DFace templates. That research was lead on a database of 3D-faces in ASE format, the GavaDB, given by the GAVAB research group of computer science department at the University of King Juan Carlos in Madrid and the authors show their results and claim successful localization rate of nose tip by means several correspondences in terms of very close results obtained by different algorithms but using a limited dataset without benchmark evaluation. Then starting from the 3D nose tip co-ordinates, obtained running the same previous code developed to automatically localize nose tip in ASE format cloud of points, in (Bevilacqua, V., Mastronardi, G., Santarcangelo, V., Scaramuzzi, R., 2010) (Bevilacqua, V., Mastronardi, G., Piarulli, R., Santarcangelo, V., Scaramuzzi, R., Zaccaglino, P., 2009) the authors, propose firstly a new algorithm to localize other four 3D nose features, and two other different approaches to perform a 3D face recognition by using all the five nose points. In (Fazl-Ersi, E., Zelek, J. S., Tsotsos, J. K., 2007) a novel 2D face recognition method is proposed, in which face images are represented by a set of local labelled graphs, each containing information about the appearance and geometry of a 3-tuple of face feature points, extracted using Local Feature Analysis (LFA) technique. That method automatically learns a model set and builds a graph space for each individual, then proposes a two-stage method for optimal matching between the graphs extracted from a probe image and the trained model graphs is proposed and achieves perfect result on the ORL face set and an accuracy rate of 98.4% on the FERET face set.

2. PREVIOUS WORKS AND BACKGROUND

2.1 Stereo Matching

In the first work (Bevilacqua, V., Mastronardi, G., Melonascina, F., Nitti, D., 2006) has been proposed a passive intensity based stereo-matching algorithm using a constraint handling GA to search matched points. Approach used search correspondences on corresponding epipolar lines (not on the whole image), then, selected N points on the epipolar line of the first image, N points on the corresponding epipolar line in the second image are researched, the research is carried out for each couple of epipolar lines. Two stereo-matching algorithms have been proposed: for generic scenes using images from parallel cameras (or rectified images), for 3D face reconstruction using images from parallel or non-parallel cameras (camera calibration is required to compute epipolar lines). In the last case 3D reconstruction process has been implemented using these steps: Stereo-matching, calculation of 3D coordinates from matched points using triangulation, generation and visualization of a 3D mesh.



Figure 1. 3D Reconstruction through Stereo Matching.

2.2 Hough Transform

In previous work (Bevilacqua, V., Casorio, P., Mastronardi, G., 2008) we adapted Khoshelham GHT in an attempt to apply it on 3D-Face shaded model for nose-tip detection. In that way it was possible to create an automatic repere's points detection system with the purpose of obtaining a biometric system for AFR (Automatic Face Recognition) using 3DFace templates. The research was lead on a database of 3D-faces in ASE format, the GavaDB, given by the GAVAB research group of computer science department at the University of King Juan Carlos in Madrid. One of the more effective solutions for shape detection is the Hough Transform. Formulated for the first time in early '60s, it originally was able to recognize shapes that had analytical description such as straight lines, circles and ellipses in 2D intensity images. In 1981 Ballard (Ballard, D. H., 1981) proposed an extension defined Generalized Hough Transform (GHT) for generic shape detection by using the R-Table, a table that describes the shape to search respect to a reference point that could represent the center of the . Many efforts have been done in order to try to extend the GHT in three- pattern dimensional images. Khoshelham (Khoshelham, K., 2007) proposed an extension of Ballard GHT for three-dimensional images constituted by point clouds obtained by means of laser- scanner acquisitions, for generic applications.

2.3 3D Head Pose Normalization

In (Bevilacqua, V., Andriani, F., Mastronardi, G., 2009) we have first proposed a model reconstruction scheme for human head's point cloud, as it's directly returned from scanning hardware, consisting of a simple pipelining of existing, fairly renowned algorithms. Then we have designed a two-step process for model alignment, based on two different error measures and their corresponding minimization techniques. In particular we presented a software system for fully automatic alignment of the 3D model of a human face. Starting with the point cloud of a human head, previously segmented from the background, pose normalization is attended with a novel, purely geometric approach. In order to solve the 6 degrees of freedom of this problem, we exploit natural mirror symmetry of human faces, then analyse frontal profile shape and finally align model's bounding box with nose tip position.

Normalizing the position of a human face implies achievement of a perfect (or quasi-perfect) alignment of the head 3D model

wrt some kind of reference, so that subject's transformed model appears to be staring at the camera. This problem exposes the following six degrees of freedom: three angles of rotation (referred to as pitch, yaw and roll) and three measures of bounding box translation (x_c , y_c , z_c), respectively relative to the three main axes (X, Y and Z), as shown in Figure 2:

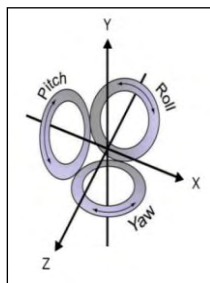


Figure 2. Main axes and corresponding rotation angles representation.

The whole algorithm is conceived as a two-step optimization process. In the first phase we exploit natural vertical symmetry of human face, acquiring knowledge about the yaw and roll angles, along with the x_c translation parameter. We designed a simple measure of the asymmetry between the two halves of a human head defined by intersection of its 3D model with a hypothetical symmetry plane, and called it Mean Symmetry Distance (MSD). It is obtained by projecting a bundle of parallel lines, perpendicular to the given plane, and intersecting it with the triangle mesh of the head. Then, for each line in the bundle, intersecting points closest to the plane are selected by each side (two total points) and the absolute difference between the distances of these points from the plane itself is computed, if applicable (that is, if the projected line actually intersects each part of the head at least once). Finally, the mean of these absolute differences will be assumed as a symmetry error value (MSD) for the considered plane. The density of the line bundle may vary according to desired accuracy. In the second phase we lean on natural vertical development of the central profile shape of human faces, gaining clues about the pitch angle. First, a sampling of the profile is extracted, resulting in a quasi-continuous vector of points, then the parameters of a first order equation are adapted for the best possible approximation of this vector. In other words, we try to find the line that best fits the shape of the profile, describing it by its explicit slope-intercept parameters. The error measure between the profile and its estimate, named Mean Profile Distance (MPD), is straightforwardly computed as the mean of point-line distances between the given linear equation and the sampling vector.

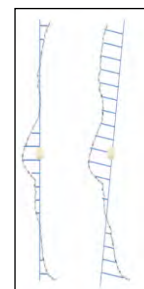


Figure 3. Extracted frontal profile shape and possible approximating lines, with the right one intuitively having a heavily lower mpd value.

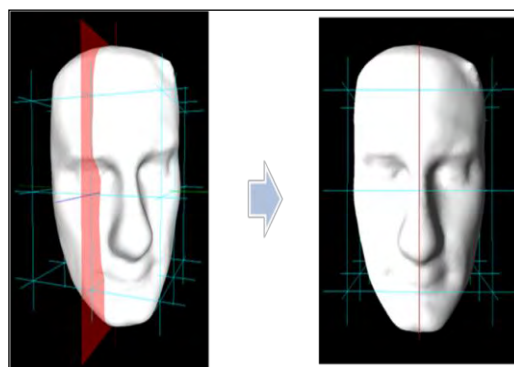


Figure 4. Head 3D model before (left) and after (right) MSD minimization process.

3. 3D FACE ENROLLMENT AND RECOGNITION

For the acquisitions of “.ase” files has been used the MainAxis's “3D CAM SURFACER”, a 3D laser scanner based on structured light with a resolution of 640 by 480, which is a good resolution for 3D processing. 3D acquisitions can be affected by random noise that consists of spikes and holes (Bowyer, K., Chang, K., Flynn, P., 2006), so has been necessary a pre-processing phase. The presented technique of 3D vectorial photography is a potentially low cost and has solid-state robustness. It can be used as an alternative for other scanning or multi-image techniques. For distances ranging from 1 to 10 meters the same order precision with the high acquisition rate. Furthermore, it has no moving parts (excluding light source cool fan), and uses white light illumination. In spite of two-acquisition based principles it permits registration, with a normal speed camera, of 3D images of objects moving with the velocity up to 1 m/sec. in darkened laboratory and up to 20 mm/sec. in normal ambient illumination conditions.

3.1 Individuation of nasal pyramid points

We have implemented the algorithms to individuate the point of the nasal pyramid.

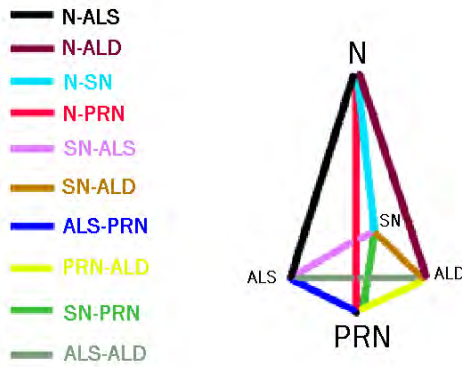


Figure 5. Nasal Pyramid



Figure 6. Map of points of repere detected

Connecting those five points we have been able to determine nose graph characterized by ten lengths. We have used a graph matching method (Fazl-Ersi, E., Zelek, J. S., Tsotsos, J. K., 2007) for the recognition. This is a geometric identification method and starts with the consideration of nose graph (G), full graph K_5 , that has as vertexes $V(G) = \{P, PRN, SN, ALS, ALD\}$ and as edges $E(G) = \{a, b, c, d, e, f, g, h, i, l\}$. This graph has been considered as weighed graph where weighs associated are the distances. Then, we have considered the dissimilarity between the geometry of the graphs as (Bevilacqua, V., Andriani, F., Mastronardi, G., 2009):

$$Z(G_i, G_j) = \frac{1}{n} \sum_{k=1}^n \frac{(e_{ik} - e_{jk})^2}{(e_{jk})^2}$$

where $G_i = \{(e_{i1}, e_{i2}, \dots, e_{in})\}$ (MODEL GRAPH) and

$G_j = \{(e_{j1}, e_{j2}, \dots, e_{jn})\}$ (TEST GRAPH).

This method works considering G_j as the graph to identify, so Z-coefficients are calculated for all the graphs of the database. At the end the graph G_i that minimizes better Z is associated to G_j .

3.2 PRN Matching

Differently from previous approach we have implemented other algorithms for the search of points of repere, considering also the points of the eyebrow arched. An unstructured organization of points as that obtained from ASE file is complicated to manage, because it is impossible to move easily in the cloud. In this context has been useful to have the points organized in a YY matrix where each position has the relative Y value. This matrix has been obtained through the creation of a polygonal mesh that interpolates the terms of the point cloud. This approach permits a more easier scansion of the surface of the face using the easy management of the data in the matrix structure. The search of points of repere has been done by the scansion of the face made by the use of a “sliding vector” on the polygonal mesh, in order to determine the geometric-statistic features typical of the face. The “sliding vector” is an observation window that contains some elements of the YY matrix that at every step “scrolls” along the particular direction of movement.

This methodology allows the individuation of the following points:

For the recognition has been implemented PRN Graph Matching. This approach is based on the matching of the distances calculated regarding a point of reference (PRN point). In this technique are considered 9 points of reference and PRN for a total of 9 distances to match.

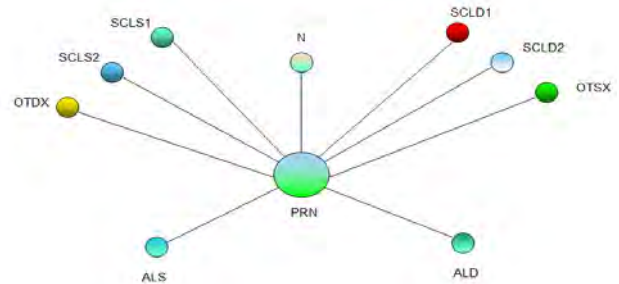


Figure 7. PRN Graph

The technique as that of K5 Graph Matching (Bevilacqua, V., Mastronardi, G., Piarulli, R., Santarcangelo, V., Scaramuzzi, R., Zaccaglino, P., 2009) is based on the use of the dissimilarity coefficient:

$$Z(G_i, G_j) = \frac{1}{n} \sum_{k=1}^n \frac{(e_{ik} - e_{jk})^2}{(e_{jk})^2}$$

where $G_i = \{(e_{i1}, e_{i2}, \dots, e_{in})\}$ (MODEL GRAPH)

and $G_j = \{(e_{j1}, e_{j2}, \dots, e_{jn})\}$ (TEST GRAPH),

where e_{ij} are the edges.

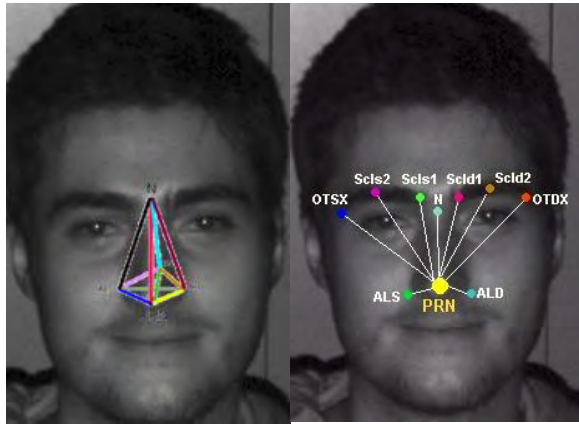


Figure 8. K5 Graph Matching and PRN Graph Matching



Figure 9. 2D images of the two twin brothers

Besides to consider only the distances between points and PRN, another difference regarding K5 Graph Matching is not considering the SN point because, being the SN-PRN distance little important, the performance get worse considering it.

3.3 Twins benchmark

During the acquisition phase has been possible acquire the faces of two twin brothers. It's very difficult for a person that doesn't know them to distinguish these two boys (in Fig.9) , but acquiring their 3D faces and obtaining the nose distances with our algorithms has been possible to notice that the two twins are different for a nose distance (Fig. 10).

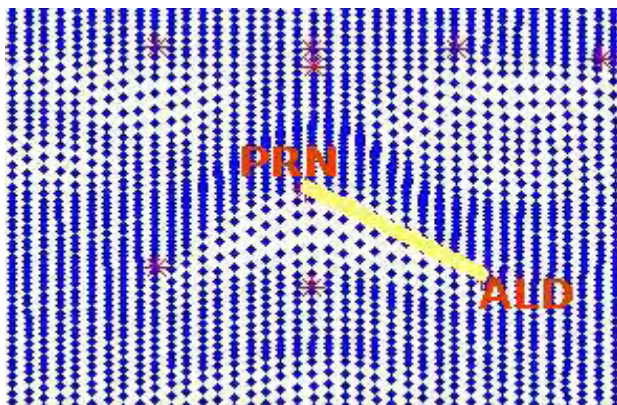


Figure 10. The PRN-ALD distance

Considering a dataset characterized by 11 acquisitions for each brother the number of misclassified acquisition has been of only two items.

4. CONCLUSIONS AND EXPERIMENTAL RESULTS

We have considered a dataset of 5 people A, B, C, D, E, and precisely 11 acquisitions of A, 6 acquisitions of B, 10 acquisitions of C, 9 acquisitions of D and then 8 acquisitions of E for a total of 44 acquisitions. Using K5 Graph Matching the performances are of 77,2%, while considering PRN Graph Matching the performances of correct recognition are of 100% showing interesting results that anyway need some further investigations.

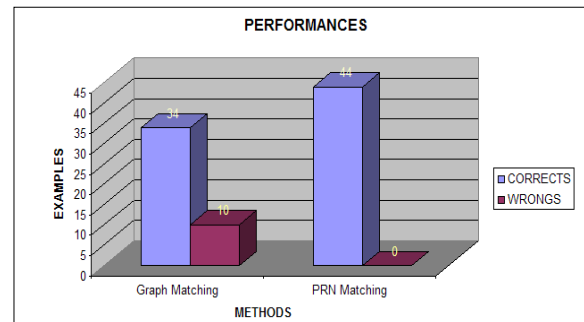


Figure 11. Performances

5. REFERENCES

- Ballard, D. H., 1981: Generalizing the Hough Transform to Detect Arbitrary Shapes, *Pattern Recognition*, Vol. 13, No. 2, 1981, pp. 111-122
- Bevilacqua, V., Mastronardi, G., Melonascina, F., Nitti, D., 2006: Stereo-Matching Techniques Optimisation Using Evolutionary Algorithms, D.-S. Huang, K. Li, and G.W. Irwin (Eds.): *ICIC 2006, LNCS 4113* © Springer-Verlag Berlin Heidelberg 2006, pp. 612-621
- Bevilacqua, V., Andriani, F., Mastronardi, G., 2009: 3D Head Pose Normalization with Face Geometry Analysis, Genetic Algorithms and PCA, *Journal of Circuits, Systems and Computers*, December 2009, Vol. 18, No. 8, pp. 1425-1439
- Bevilacqua, V., Casorio, P., Mastronardi, G., 2008: Extending Hough Transform to a Points' Cloud for 3D-Face Nose-Tip Detection, D.-S. Huang et al. (Eds.): *ICIC 2008, LNAI 5227* - © Springer-Verlag Berlin Heidelberg 2008, pp. 1200-1209
- Bevilacqua, V., Mastronardi, G., Santarcangelo, V., Scaramuzzi, R., 2010: 3D Nose Feature Identification and Localisation Through Self-Organizing Map and Graph Matching, *Journal of Circuits, Systems and Computers*, 2010, Vol. 19, N. 1, pp. 1-12
- Bevilacqua, V., Mastronardi, G., Piarulli, R., Santarcangelo, V., Scaramuzzi, R., Zaccaglino, P., 2009: Experimental Comparison among 3D innovative face recognition frameworks D.-S. Huang et al. (Eds.): *ICIC 2009, LNAI 5755* - © Springer-Verlag Berlin Heidelberg 2009, pp. 1096-1105

Bowyer, K., Chang, K., Flynn, P., 2006: A Survey of Approaches and Challenges in 3D and Multi-Model 3D+2D Face Recognition, *Computer Vision and Image Understanding*, January 2006, Vol. 101, No. 1, pp. 1-15

Fazl-Ersi, E., Zelek, J. S., Tsotsos, J. K., 2007: Robust Face Recognition through local graph matching. *Journal of Multimedia*, Vol. 2, No. 5, September 2007, pp. 31-33

Khoshelham, K., 2007: Extending Generalized Hough Transform to Detect 3D Objects in Laser Range Data. *Optical and Laser Remote Sensing Research Group, Delft University of Technology, Kluyverweg 1, 2629 HS Delft, The Netherlands; ISPRS Workshop on Laser Scanning 2007 and SilviLaser 2007, Espoo, September 12-14, Finland (2007)*

EVALUATION OF A LASER LAND-BASED MOBILE MAPPING SYSTEM FOR MONITORING SANDY COASTS

M. Bitenc^a, R. Lindenbergh^b, K. Khoshelham^b and A.P. van Waarden^c

^a Geodetic Institute of Slovenia, Jamova 2, 1000 Ljubljana, Slovenia - Maja.Bitenc@gis.s

^b Delft University of Technology, Dept. of Remote Sensing, Kluyverweg 1, 2629 HS, Delft, Netherlands
- (r.c.lindenbergh, K.KhoshElham)@tudelft.nl

^c Dutch Ministry of Public Works and Water Management, Data ICT Dienst, Derde Werelddreef 1, 2622 HA, Delft, Netherlands
- pieter.van.waarden@rws.nl

Commission VII Symposium 2010

KEY WORDS: Coast, Hazards, Mapping, DEM/DTM, Laser scanning, Mobile, Quality

ABSTRACT:

The Dutch coast is characterized by sandy beaches flanked by dunes. Its morphology is essential for the defense against flooding of the hinterland. Therefore it is monitored on a yearly basis by Airborne Laser Scanning (ALS). However, it is recognized that most erosion of the beach and first dune row takes place during storms. To assess the state of the coast immediately after a storm with ALS is expensive and difficult to organize. Here, the performance of a Land-based Mobile Mapping System (LMMS) is evaluated. A test data set was obtained by Geomaat using the StreetMapper LMMS system, employing three individual line scanners. Both the relative quality of laser point heights and of a derived Digital Terrain model (DTM) are assessed. In the first analysis height differences between close-by points are considered. Except for arbitrary close-by points, also close-by points obtained from different scanners and from different drive-lines are analyzed. It is shown that on a flat beach a precision of 3 mm is achieved and that almost no internal biases exist. In the second analysis a DTM with a grid size of 1 m is obtained using least squares. Each grid point height includes a quality description, which incorporates both measurement precision and terrain roughness. Although some problems remain with the low scanning height of 2 m, which causes shadow-effect behind low dunes, it is concluded that a laser LMMS enables the acquisition of a high quality DTM product, which is available within two days.

1 INTRODUCTION

The Dutch coast typically consists of a relatively flat sandy beach lined on a side by the dunes, which are partly covered by marram grass. This coastal area is important for the Netherlands for many reasons, e.g. as recreational and nature area, and as protection against a sea flood and storms. The last usage is especially crucial, because the most densely populated areas in the Netherlands are located just behind the coastal defense and are partly below the mean sea level. Therefore, it is essential to continuously monitor and maintain the coast in order to protect the Dutch hinterland from the sea. In 1990 a national coastal policy was adopted, with the aim of maintaining the seaward position of the coastline, as it was on January 1, 1990. To successfully maintain this so-called Basal Coast Line a suitable acquisition technique to measure beach morphology and its changes needs to be employed. Because high energy events like storms may cause large changes, as for example shown in Fig. 1, the main interest is to monitor coastal topography on the temporal and spatial scale of storm impacts. Therefore, a flexible system is needed that can access a damaged area immediately after the storm and provide the results of morphologic changes as quickly as possible (in one day). Besides, to estimate in detail the beach erosion caused by heavy storm events, high spatial resolution measurements are needed.

Since 1996 the Dutch Ministry of Transport, Public Works and Water Management (RWS, Rijkswaterstaat) annually measures the beach topography by means of Airborne Laser Scanning (ALS). The ALS technique has limitations in case of projects that include cost effective capturing of 3D data or when dense point coverage of the vertical features is required (e.g. steep dune slopes). Besides, the ALS data in general can not be provided on demand. First, because flying permissions are needed and secondly



Figure 1: A real example of a dune erosion on the Dutch coast and the possible consequence [GoogleEarth].

after-storm weather conditions may hinder or prevent the acquisition. To summarize, the ALS method offers good results in terms of quality and reliability, but is not flexible. One of the potential alternative techniques is a Land-based Mobile Mapping System (LMMS). LMMS is a complex real-time, multi-tasking and multi-sensor system, which integrates (i) a number of line scanners and/or digital cameras for surface mapping, (ii) GNSS for positioning and (iii) additional sensors like for example INS to monitor the vehicle motion. Those sensors are usually mounted on a rigid platform, placed on the roof of a vehicle. The LMMS mapping sensors can be of different type and orientation, which makes every LMMS system unique in terms of performance and thus quality. For an overview of the early LMMS see (Ellum and El-Sheimy, 2002). More recent LMMS and system providers are described in (Shan and Toth, 2008, Vosselman and Maas, 2010, Petrie, 2010). In this research the LMMS, employing a laser scanner as a mapping sensor and integrated GPS/INS system as a main

navigation sensor is discussed.

Using laser LMMS it is in principle possible to quickly obtain 3D geo-referenced data of a large extended area, such as a beach. High frequency laser pulse measurements enable high spatial resolution. Besides, higher point density is expected, because the measured ranges are smaller than in case of ALS. On the other hand, more data voids might occur behind elevated features when measuring from the ground. Besides, attention must be paid to the intersection geometry of the laser beam with the relatively horizontal beach. If scanning a horizontal surface, the geometry gets poorer further away from the trajectory. This decreases the laser point positioning quality. In order to test the laser LMMS performance on the Dutch coast RWS initiated a pilot-project. Particular interest of the RWS is the level of obtainable accuracy and processing time of a final topographic product, which is a Digital Terrain Model (DTM). The RWS requirements are twofold. First a vertical DTM accuracy of at least 10 cm at a grid spacing of 1×1 m is required, and, second, it is required that the results are available close to real-time. In this research the quality of derived LMMS laser point cloud and DTM is analyzed.

In general it is important to know the laser point quality, prior to using points in further processing, like computing a DTM. In quite some researches the theoretical or overall expected (a-priori) quality of the derived 3D laser point cloud is estimated by linearizing the geo-referencing equation. For equations of the first order error model see e.g. (Ellum and El-Sheimy, 2002, Glennie, 2007, Barber et al., 2008). The random errors of the LMMS measurements (i.e. range, scan angle, IMU angles and GPS position) and calibration parameters (i.e. lever-arms and boresight angles) are propagated to obtain a-priori 3D laser point precision. To verify those theoretical models and estimate an empirical (a-posteriori) quality of a laser point positioning, a proper Quality Control (QC) is needed. In (Habib et al., 2008) the existing QC procedures are explained in detail. However, standard and efficient procedures for validating the quality of derived laser points and further on the DTM are still missing.

In the following a procedure to evaluate the laser LMMS measurements of sandy Dutch beach morphology is described. In Section 2 the methodology to estimate both the relative quality of the LMMS laser point heights and the derived DTM is described. In Section 3 the methodology is applied on the real data and results of both quality evaluation procedures are presented. In Section 4 conclusions, which include recommendations for further work, are given.

2 METHODOLOGY

In this section first the scanning geometry at the time of each laser point acquisition is reconstructed by applying simple geometrical rules. The intersection geometry in general influences the laser point positioning quality. Thus, this influence is considered further on to compute the theoretical height precision. Here, also the random errors of LMMS measurements and calibration parameters specified for a LMMS are included.

Next, the methodology to evaluate the relative quality of LMMS laser point heights is described. The relative quality describes the relation between two points acquired in the same region in a short time period (point-to-point quality) (Kremer and Hunter, 2007). As stated already in the introduction, the quality of the whole LMMS data depends on the quality of the system measurements and calibration. The latter one varies depending on the experience of the data processor. It is therefore impossible to give a-priori relative quality quotes (Cox, 2009). For this reason here a real

laser LMMS data set is used and the empirical quality of point heights is estimated employing a QC procedure.

Terrain laser points, which were extracted from the raw data by provider Geomaat, are used to interpolate the DTM. The importance of DTM applications makes it inevitable to provide DTMs with adequate quality measures at a high level of detail, as it is for example described in (Kraus et al., 2006). The idea is to inform the user about the DTM quality and warn them of weakly determined areas. Thus, in the following an approach to evaluate the quality of each grid point height is described.

2.1 Reconstructing the scanning geometry

The instantaneous scanning geometry of a laser point can be described by the range and the incidence angle, which besides influence the footprint size. Those geometric attributes are computed for each measured laser point using point position and the trajectory position. Both data sets include the X, Y and Z coordinates and the acquisition time.

The range R is the length of the vector \vec{p} from the laser scanner position at time t to the laser point. It can be computed for each laser point once the sensor position at the time t of the laser point acquisition is known. The laser scanner position is linearly interpolated using the consecutive trajectory positions. Here it is assumed that the trajectory position directly represents the laser scanner position.

The incidence angle α is the angle between the laser beam \vec{p} and the upward normal (\vec{n}) of the surface at the laser point position. When a beam hits a surface perpendicular to it, the incidence angle is 0° and when a beam is parallel to a surface the incidence angle is 90° . The normal vector \vec{n} is computed as follows. For each laser point the closest 4 points are determined using a k Nearest Neighbor algorithm (Giaccari, 2010). A plane is fitted to all 5 points using Least Squares. The result is the normal \vec{n} of a plane at a laser point. The number $k = 4$ of neighboring laser points participating in plane fitting is chosen such that the computed normals reflect just a local surface.

The laser footprint is the area of an illuminated surface and is approximated by a circle. Thus, its diameter D_{fp} is computed in terms of the laser beam-width β and changing incidence angle α and range R , as written in Eq. 1:

$$D_{fp} = \frac{R \cdot \beta}{\cos \alpha} \quad (1)$$

2.2 Theoretical quality of laser points

The theoretical models of error propagation through the geo-referencing equation are used to estimate an expected precision of each laser point height σ_{zi} . First the specified random errors of LMMS measurements and calibration parameters are inserted in the first order model of error propagation. Besides, the real measurements as range, scan angle and the IMU angles are considered in the computation. The result is the height precision of laser point i due to L-MMS measurement errors $\sigma_{zi,m}$ (measuring precision). The value for the random range error used here is valid when the laser beam falls perpendicular to the target (Schwarz, 2009). In practice the incidence angle is changing over the acquisition area and is usually non-perpendicular as shown in Fig. 2. High incidence angles result in poor intersection geometry and affect the range measurements, (Soudarissanane et al., 2009, Lichti and Gordon, 2004, Schaer et al., 2007, Alharthy et al., 2004). For pulse laser scanners, which are used in this research, the approach in (Lichti et al., 2005) is used. At a given

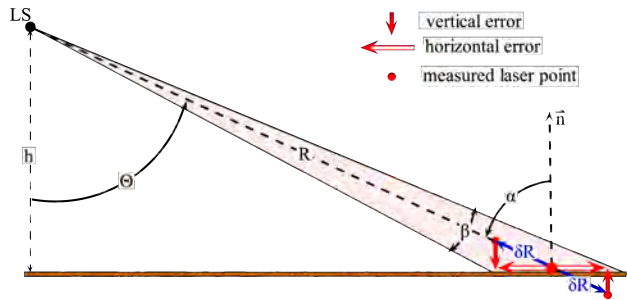


Figure 2: The range error δR due to the non-perpendicular scanning geometry and the influence of δR on vertical and horizontal laser point positioning error.

range R and knowing the beam width β from the laser scanner specifications, the range error δR is parameterized in terms of incidence angle α as given in Eq. 2 (Lichti et al., 2005):

$$\delta R = \frac{R \cdot \beta \cdot \tan \alpha}{2} \quad (2)$$

This range error δR is then propagated through the geo-referencing equation and the height precision of laser point i due to the (non-perpendicular) scanning geometry $\sigma_{Zi, \delta R}$ (geometrical precision) is computed.

Finally, the all-over theoretical height precision of point i is written as Eq. 3:

$$\sigma_{Zi} = \sqrt{\sigma_{Zi,m}^2 + \sigma_{Zi, \delta R}^2} \quad (3)$$

2.3 Empirical relative quality of laser points

In general the idea of validating the relative quality of laser data is based on checking the compatibility of laser points in areas, where data overlap (Kremer and Hunter, 2007). In (Habib et al., 2008) some QC procedures are explained. However, the acquisition area discussed in this research, i.e. the sandy beach, does not include (many) steady points or lines, that are sufficiently well defined in the laser LMMS point cloud. In other words, the beach area lacks artificial sharp edges or planes, which could be extracted from the laser points and used in a relative QC procedure. Besides, the terrain on the beach is changing smoothly. Thus finding and aligning breaklines of beach morphology is not a promising method either. Instead, the advantage of high LMMS laser point density is used and a point-to-point comparison is made. Namely, the height differences between laser points that lie so close together that their footprints partly overlap, i.e. the height differences between so-called identical points, are analyzed. Not all measured laser points are considered in the process of finding those identical points. The next two conditions are set for laser points:

- The footprint diameter might be unreasonably big in case the incidence angle is close to 90° . Therefore, just laser points that have an incidence angle less than 89.9° are considered: $\alpha_P < 89.9^\circ$.
- Because just the vertical component Z of the two points is compared, points should lie on an almost horizontal plane in order to avoid the influence of surface slope on the height difference. This requirement is considered to be fulfilled, if the z -component of the normal N_z , computed at each laser point as explained in Section 2), is: $N_{Pz} \approx 1$.

Now pairs of closest points in 3D are found using the kNN algorithm (Giaccari, 2010), where $k = 1$. The closest point pair enters the set of identical point pairs, if the 3D distance $d_{i,j}$ between laser point P_i and its nearest neighbor P_j is smaller than the minimal size of their footprint radii. At the same time the 3D distance $d_{i,j}$ should be smaller than 5 cm, thus:

$$d_{i,j} \leq \text{Min}(\min(r_i, r_j), 5 \text{ cm}), \quad (4)$$

where $i, j = 1 \dots n$ & $i \neq j$ and n the number of laser points. The height differences ΔZ between identical points are considered as an empirical quality measure. It is expected that the mean of signed height differences ΔZ equals approximately zero.

LMMS is characterized by a high laser point density, compared to ALS. This high point density has several reasons. First, from an operational viewpoint, the drive paths can be arbitrary close together, resulting in overlapping drive-lines, while the vehicle can also scan at low driving speeds. Besides, usually more laser scanners are mounted on a vehicle and measure at the same time. It is not clear a-priori that points from different drive-lines can have the same quality. That is because the acquisition time is different and the configuration of GPS satellites may have changed. Also different scanners may result in points of different quality. Therefore the height differences ΔZ of identical points are investigated for three different cases:

1. Identical points (IP) from the complete data set.
2. Identical points (IP) belonging to different scanners (scanner overlap).
3. Identical points (IP) belonging to overlapping drive-lines (drive-line overlap).

For each case the height differences of identical points are analyzed in order to estimate noise levels and possibly identify systematic errors. Besides, the correlation with geometric attributes, i.e. the range and incidence angle, of laser points is investigated.

2.4 DTM interpolation and quality

There are many different algorithms to interpolate a DTM. The more common are Nearest Neighbor, Inverse Distance Weighting, Moving Least Squares and Kriging (Shan and Toth, 2008). Many researches and books exist on those topics, however they are not discussed further in this research. The main emphasis is on the DTM quality estimation.

In general the quality of a DTM depends on a number of individual influencing factors, see (Li et al., 2005, Huaxing, 2008). The ones investigated here are: the number of terrain points (FD1), height precision of individual terrain point (FD2), terrain point distribution (FD3), the terrain roughness (FR) and interpolation method (FI). When the DTM is constructed from the existing laser data, the first three influencing factors (FD1, FD2, FD3) are usually known or can be estimated. The fourth influencing factor, the terrain roughness (FR), is related to the interpolation method (FI).

Following the research in (Kraus et al., 2006), a grid point elevation and its precision are estimated by linear interpolation (FI). Rules of error propagation based on variances and co-variances of the original terrain laser points are applied, to estimate the quality of the grid points. The output is then strictly speaking the precision of a grid point, which is denoted by a standard deviation σ_{DTM} . In other words, the systematic errors are assumed to be

zero (Kraus et al., 2006). First a grid of 1×1 m size is laid over the terrain laser points. For grid cells, which include 4 or more terrain laser points, a tilted plane is modeled in a Least Square sense by a first order polynomial as given in Eq. 5:

$$Z = a_0 + a_1X + a_2Y. \quad (5)$$

Here X, Y, Z are the coordinates of the terrain laser points (observations) that are included into the plane computation and a_0, a_1 and a_2 are the unknown plane coefficients. The graphical representation of each term in Eq. 5 is shown in Fig. 3. To make the

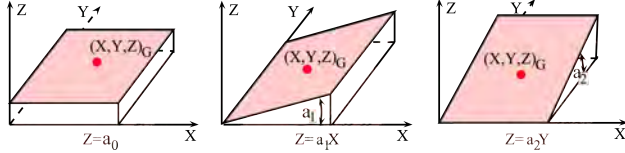


Figure 3: A graphic representation of terms given in Eq. 5; after (Li et al., 2005)

least squares computation more efficient, a new coordinate system is used with the interpolation grid point (X_G, Y_G) as the origin; therefore the method is called Moving Least Squares (MLS) adjustment (Karel and Kraus, 2006). The equation of a plane (Eq. 5) simplifies, so the plane coefficient a_0 becomes the elevation of the grid point itself, as written in Eq. 6:

$$Z_G = a_0 \quad (6)$$

The mathematical model of Moving Least Squares for linear surface fitting is then given in matrix vector notation as in Eq. 7b:

$$y \approx A \cdot x \quad (7a)$$

$$\begin{bmatrix} Z_1 \\ Z_2 \\ \vdots \\ Z_n \end{bmatrix} = \begin{bmatrix} 1 & X_1 - X_G & Y_1 - Y_G \\ 1 & X_2 - X_G & Y_2 - Y_G \\ \vdots & \vdots & \vdots \\ 1 & X_n - X_G & Y_n - Y_G \end{bmatrix} \begin{bmatrix} a_0 \\ a_1 \\ a_2 \end{bmatrix} \quad (7b)$$

Where X_i, Y_i, Z_i for $i = 1 \dots n$ are the coordinates of the n original laser terrain points included in the plane computation. Then the unknowns in vector \hat{x} and their variance-covariance matrix $\Sigma_{\hat{x}\hat{x}}$ are computed in a least squares adjustment as written in Eq. 8 and Eq. 9 respectively:

$$\hat{x} = \left(A^T \Sigma_{yy}^{-1} A \right)^{-1} A^T \Sigma_{yy}^{-1} y \quad (8)$$

$$\Sigma_{\hat{x}\hat{x}} = \left(A^T \Sigma_{yy}^{-1} A \right)^{-1} \quad (9)$$

Where Σ_{yy} is the variance matrix of observations. Here, the theoretical height precision of the laser points σ_{Z_i} computed in Section 2.2 is used. Besides, the vertical distances between the original terrain points and the modeled plane, are computed. Those residuals e are applied to calculate the Root Mean Square Error (RMSE) as written in Eq. 10 for each plane:

$$RMSE = \sqrt{\frac{e^T e}{n}} \quad (10)$$

To finally predict the DTM quality σ_{DTM} , a mathematical model after (Li et al., 2005) as written in Eq. 11 is used.

$$\sigma_{DTM}^2 = \sigma_{a_0}^2 + \sigma_e^2 \quad (11)$$

Here the standard deviation of the constant plane coefficient σ_{a_0} represents the quality of the original data and accounts for the

precision of the original laser points (FD2), their density (FD1) and distribution (FD3). The second term σ_e^2 represents the quality loss due to the representation of the terrain surface. In this research the RMSE is considered as a measure of the terrain surface roughness (FR) with respect to the plane modeled by the chosen random-to-grid MLS interpolation (FI). Therefore σ_e simply equals the RMSE as computed in Eq. 10.

3 RESULTS AND DISCUSSION

In this section the results of the quality evaluation of both LMMS laser point heights and a derived DTM are discussed for a LMMS data set representing a stretch of Dutch coast. Before these results are given, first this data set is described in more detail.

3.1 Data description

The LMMS data set was acquired on the Dutch coast near Egmond aan Zee using the StreetMapper system owned by provider Geomaat (StreetMapper, 2010, Geomaat, 2010). The acquisition took place on November 27, 2008 at the time of low tide. Within 2 hours a stretch of beach of 6 km long and 180 m wide was covered. The point cloud consists of about 56 million laser points. As experienced by Geomaat, the 3D laser point coordinates and the classification into terrain and non-terrain points can be done within 2 days. In this research a smaller representative test area of 213×101 m was chosen, which is covered by 8 drive-lines, see Fig. 4. The data set consists of 1 220 825 laser points. Each record of a laser point has 15 attributes, which are: 3D laser point position X, Y, Z , intensity I , class number C , scanning angle Θ , time of point acquisition T , drive-line number DL and scanner number SC , range R , incidence angle α , footprint diameter D_{fp} , range error due to scanning geometry δR , measuring precision $\sigma_{Z,m}$ and geometrical precision $\sigma_{Z,\delta R}$. The second data set used in this research composes of eight trajectories positions within the test area (black lines in Fig. 4).

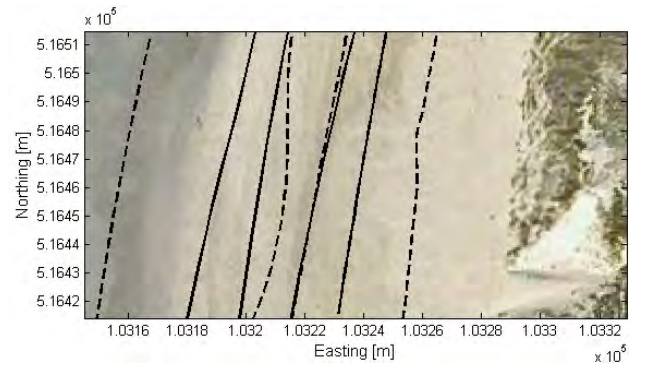


Figure 4: The digital photo of the test area [GoogleMaps]. The black dashed lines mark the trajectories driven downward i.e. from the north to the south and the solid lines mark the trajectories driven in the opposite direction.

3.2 Results of height differences of identical points

By analyzing the attributes of the identical point pairs, i.e. the scanner and drive-line number, it is concluded that the majority of identical point pairs belongs to the same scanner and the same drive-line. Fewer identical point are found in the scanner overlap and drive-line overlap (see Table 1). In Table 1 the results of height differences for the three cases are presented. The mean (avg) of height differences ΔZ is very close to zero for the

case ALL- N_z and scanner overlap. In the latter case the offset of 0,2 mm from the expected zero mean could indicate the scanners calibration error, which is in any case very small. In case of drive-line overlap the average of height differences ΔZ as expected equals to zero, thus it can be assumed there is no offset between drive-lines. In other words there is no systematic error in GPS/INS positioning. The standard deviations (std) are equal or smaller than 3.5 mm, which denotes the relative precision of LMMS laser points. Analyses of the correlation between height

		ALL- N_z	Scanner overlap	Drive-line overlap
No. of ident. point pairs		17 754	608	5 473
Height difference	min	-47	-20	-47
	max	46	36	46
ΔZ [mm]	avg	0.1	0.2	0.0
	std	3.1	2.5	3.5

Table 1: Statistics of the height differences of identical points.

differences of identical points lying on a horizontal surface and the geometric attributes, i.e. range and incidence angle, do not show a clear trend.

3.3 Results of DTM interpolation and precision estimation

Within the test area the terrain laser points, as classified by GeoMaat, are used in the following DTM analysis. In Fig. 5 a 3D surface of the interpolated DTM is shown. In this raster image each pixel represents an 1×1 m grid cell and the pixel color shows the corresponding grid point height. The grid point elevation is changing from -0.19 m at the coastline to up to 22 m in the dunes. The white holes in the DTM are results of the shadow-effect (white holes in green area) and most probably of the presence of water-bodies on the beach (white holes in blue area).

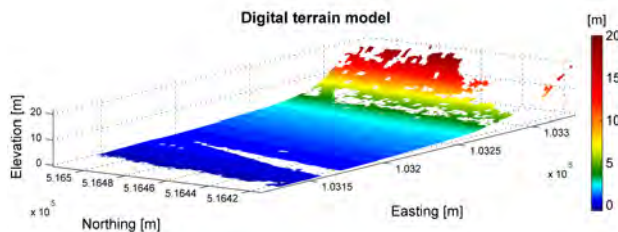


Figure 5: Raster image of interpolated DTM grid points visualized in 3D.

The height precision σ_{DTM} of the grid points, as computed by Eq. 11, varies between 0.0018 and 2.9 m. The average precision of grid points σ_{DTM} equals to 4.7 mm. For comparison, the precision of the observations σ_{Z_i} is on average 2.4 cm.

In Fig. 6 the relation between the height precision of grid points σ_{DTM} (y-axis), the number of points n (x-axis) and data quality component σ_{a0} (colorbar), is presented. Comparison of the colorbar and the y-axis scale shows, that the size of the grid point height precision σ_{DTM} depends mainly on the data quality component σ_{a0} . Besides, one can observe that, if approximately 50 or more points are included in the grid point computation, the standard deviation of grid point heights σ_{DTM} drops below 1 cm.

In Fig. 7 the spatial variation of standard deviation σ_{DTM} over the test area is shown. Green color shows grid points having a

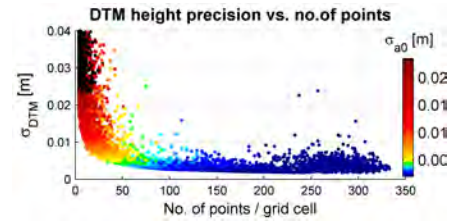


Figure 6: Correlation between the grid point height precision σ_{DTM} and the number n of terrain laser points; color-coded by the data quality component σ_{a0} .

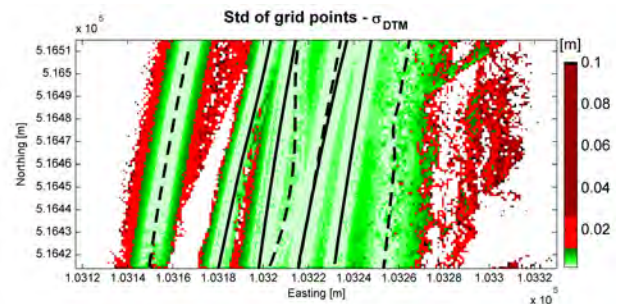


Figure 7: Grid point height precision σ_{DTM} .

height precision σ_{DTM} smaller than 1 cm. Most of the beach area has good DTM quality, which decreases with the distance from a trajectory. For example, the precision at the edges of the drive line DL11 (most left one) decreases and is at some point worse than 2.56 cm, mostly due to the lower point density. The DTM quality gets worse also in the dune area, due to the low point density, low theoretical precision of terrain laser point heights and high terrain roughness.

4 CONCLUSIONS AND FUTURE WORK

In this article most important results are the empirical laser point height precision assessed by the QC of identical points and the precision of the grid point heights estimated by a mathematical model employing results of MLS adjustment. Both values are surprisingly small.

Firstly, the empirical relative precision of laser points is around 3 mm. Besides, it was concluded there is almost no bias in the StreetMapper system. However, it is recommended to analyze bigger number of identical points. Within the QC of identical points an attempt was made to show the influence of the scanning geometry on the laser point quality. Results show that height differences between identical points do not depend neither on the range neither on the incidence angle. To verify the influence of the scanning geometry on the laser point quality it is recommended to additionally measure control points across the drive-line and compare them with the point cloud.

Secondly, the average precision of grid point height equaled to 4.7 mm. The computation was performed within the weighted MLS adjustment, using the theoretical height precision of terrain laser point as weights. It was found that the main influencing factor on the grid point height precision is the density of terrain laser points. That is, because a higher number of observations (i.e. terrain laser points) enabled partly elimination of the observation noise. The consequence is, that the precision of grid point height improved with an increasing number of terrain laser points and

exceeded the theoretical height precision of the individual terrain laser points. Rijkswaterstaat required a 1×1 m DTM having a precision better than 10 cm. Thus, it was concluded that those requirements can be easily met employing laser LMMS.

The adjustment method for the DTM quality estimation includes just the grid cells with more than 3 terrain laser points and gives strictly speaking the precision of the grid points. Using another method would allow to compute the precision for all grid cells and would result in a slightly higher coverage. To optimally profit from the available data it is recommended that this method is adaptive to both point density and surface relief. Besides, areas without any terrain laser points, resulting from the shadow-effect or surfaces covered with a water, must be separately analyzed, e.g. see (Kraus et al., 2004). On the other hand, to assess the absolute positional and height accuracy of the DTM product, external reference data of higher accuracy should be used.

A last recommendation for further projects, assessing sandy beach morphology, is to place laser scanners on a higher platform. The StreetMapper platform of 2 m above the ground resulted in quite some data gaps due to occlusions behind the pre-dunes. Based on the DTM visibility analysis, as given in (Li et al., 2005), for a particular area of interest the optimal height of the laser scanner(s) above the ground could be calculated.

ACKNOWLEDGEMENTS

The authors would like to thank the Dutch Ministry of Transport, Public Works and Water Management, for kindly giving us the StreetMapper data set. Besides authors would like to thank Geodetic Institute of Slovenia for supporting this research.

REFERENCES

- Alharthy, A., Bethel, J. and Mikhail, E., 2004. Analysis and accuracy assessment of airborne laser scanning system. In: IASPRS, Vol. XXXV-B2, Istanbul, Turkey, pp. 144–149.
- Barber, D. M., Mills, J. P. and Smith-Voysey, S., 2008. Geometric validation of a ground-based mobile laser scanning system. *ISPRS Journal of Photogrammetry and Remote Sensing* 63(1), pp. 128–141.
- Cox, C., 2009. Subject: Questions regarding the streetmapper system. Personal communication. 3D Laser Mapping Ltd.
- Ellum, C. and El-Sheimy, N., 2002. Land-based mobile mapping systems. *Photogrammetric Engineering and Remote Sensing* 68(1), pp. 13–17; 28.
- Geomaat, 2010. URL <http://cms.geomaat.pageflow.nl>. Accessed June 2010.
- Giaccari, L., 2010. Fast k-nearest neighbors search. URL <http://www.advancedmcode.org/gltree.html>. Accessed February 2010.
- Glennie, C. L., 2007. Rigorous 3d error analysis of kinematic scanning lidar systems. *Journal of Applied Geodesy* 1, pp. 147–15.
- Habib, A. F., Al-Durgham, M., Kersting, A. P. and Quackenbush, P., 2008. Error budget of lidar systems and quality control of the derived point cloud. In: IASPRS, Vol. XXXVII-B1, Beijing, pp. 203 – 209.
- Huaxing, L., 2008. *Advances in Digital Terrain Analysis. Lecture Notes in Geoinformation and Cartography*, Springer Berlin Heidelberg, chapter Modelling Terrain Complexity (Section 2), pp. 159–176.
- Karel, W. and Kraus, K., 2006. Quality parameters of digital terrain models. In: J. Hhle (ed.), *EuroSDR seminar on Automated Quality Control of Digital Terrain Models*. Aalborg, Denmark.
- Kraus, K., Briese, C., Attwenger, M. and Pfeifer, N., 2004. Quality measures for digital terrain models. In: IASPRS, Vol. XXXV-B2, Istanbul, Turkey.
- Kraus, K., Karel, W., Briese, C. and Mandlbürger, G., 2006. Local accuracy measures for digital terrain models. *The Photogrammetric Record* 21(116), pp. 342–354.
- Kremer, J. and Hunter, G., 2007. Performance of the streetmapper mobile lidar mapping system in real world projects. In: Fritsch (ed.), *Photogrammetric Week'07*, Wichmann Verlag, Heidelberg, pp. 215–225.
- Li, Z., Zhu, Q. and Gold, C., 2005. *Digital terrain modeling: principles and methodology*. New York: CRC Press.
- Lichti, D. D. and Gordon, S. J., 2004. Error propagation in directly georeferenced terrestrial laser scanner point clouds for cultural heritage recording. In: *FIG Working Week 2004*. Athens, Greece, May 22–27, 2004.
- Lichti, D. D., Gordon, S. J. and Tipdecho, T., 2005. Error models and propagation in directly georeferenced terrestrial laser scanner networks. *Journal of Surveying Engineering* 131 (4), pp. 135 - 142.
- Petrie, G., 2010. An introduction to the technology mobile mapping systems. *GEOInformatics Magazine* 13, pp. 32–43.
- Schaer, P., Skaloud, J., Landtwing, S. and Legat, K., 2007. Accuracy estimation for laser point-cloud including scanning geometry 2007. In: *5th International Symposium on Mobile Mapping Technology (MMT2007)*, Padua, Italy.
- Schwarz, R., 2009. Subject: Questions about the accuracy and precision. Personal communication. RIEGL Laser Measurement Systems GmbH.
- Shan, J. and Toth, C. K. (eds), 2008. *Topographic laser ranging and scanning: principles and processing*. Taylor & Francis Group.
- Soudarissanane, S., Lindenbergh, R., Menenti, M. and Teunissen, P., 2009. Incidence angle influence on the quality of terrestrial laser scanning points. In: *ISPRS Workshop Laserscanning'09*. Paris, France; September 1–2, 2009.
- StreetMapper, 2010. Mobile mapping system streetmapper. URL <http://www.streetmapper.net>. Accessed June 2010.
- Vosselman, G. and Maas, H.-G. (eds), 2010. *Airborne and Terrestrial Laser Scanning*. Whittles Publishing.

AUTOMATIC REGISTRATION OF AIR-BORNE AND SPACE-BORNE IMAGES BY TOPOLOGY MAP-MATCHING WITH SURF PROCESSOR ALGORITHM

Anna Brook, Eyal Ben-Dor

Remote Sensing Laboratory, Tel-Aviv University, Israel

anna.brook@gmail.com

Commission VI, WG VI/4

KEY WORDS: Automatic registration, Multi-sensors airborne and space-borne fusion, Change detection, Weight-based topological map-matching algorithm (tMM), Scaling and image rotation

ABSTRACT:

Image registration is widely used in many Remote Sensing applications. The existing automatic image registration techniques fall into two categories: the intensity-based and the feature-based methods, while the feature-based technique (which extracts structures from both images) is more suitable for multi-sensors fusion, temporal change detection and image mosaicking. Conventional image registration algorithms have greatly suffered from quantity and spatial distribution of extracted control points. In this study, we propose a novel method for automatic image registration based on topology rules (AIRTop) for temporal change detection and multi-sensors (airborne and space-borne) fusion. In this algorithm, we first apply the SURF (Speeded Up Robust Features) method to extract the landmarks structures (roads and buildings) of the given images, and then they are expressed by a topology rules, which define the permissible spatial relationships between features. The defined rules for a weight-based topological map-matching algorithm (tMM) manage the relationships between features in different feature classes (roads and buildings) and present a robust method to find a control points in both reference and sensed images. The main focus in this study is on scale and image rotation invariant the quality of the scanning system. These seem to offer a good compromise between feature complexity and robustness to commonly occurring deformations. The skew and the anisotropic scaling are assumed to be second-order effects that are covered to some degree by the overall robustness of the sensor. Experimental results show that our method can provide better accuracy than the conventional registration process.

1. INTRODUCTION

Image registration is a critical preprocessing procedure in all remote sensing applications that utilize multiple image inputs, including multi-sensor image fusion, temporal change detection, and image mosaicking. The recent interest in temporal change detection and modeling transform make the automatic image registration to important stage of preprocessing the data (Moigne et al., 2002). The automatic registration of images has generated extensive research interests in the fields of computer vision, medical imaging and remote sensing. Comprehensive reviews include Brown (1992) and Zitova and Flusser (2003).

The existing automatic image registration techniques fall into two categories: the intensity-based and the feature-based methods (Zitova and Flusser, 2003). The feature-based technique extracts salient structures from sensed and reference images by invariance and accuracy of the feature detector and by the overlap criterion. As the significant regions (e.g. roofs) and lines (e.g. roads) are expected to be stable in time at fixed position, the feature-based method is more suitable for multi-sensors fusion, temporal change detection and image mosaicking. The method generally consists of four steps (Jensen et al., 2004): 1) control points (CPs) extraction, 2) transformation model determination, 3) image transformation and re-sampling, and 4) registration accuracy assessment. Among the four steps, the first is the most complex, and its success essentially determines the registration accuracy. Thus, the detection method should be able to detect the same features in all projection and different radiometrical sensitivities regardless of the particular image / sensor deformation.

The search for discrete CPs can be divided into three main steps: 1. selection of "interesting points", 2. Description of nearest points or features, 3. matching between images. The most valued property of CPs detection is its repeatability. The description of nearest points has to be distinctive but robust to noise, potential displacements as geometric and radiometric deformations. In order to succeed, the matching technique has to be accurate and sufficient while detection scheme has to simplify the above requirements.

This paper presents a novel method for automatic image registration based on topology rules (AIRTop) for temporal change detection and multi-sensors (airborne and space-borne) fusion.

2. AUTOMATIC IMAGE REGISTRATION

The AIRTop algorithm (Figure 1) consist four stages as any conventional registration method. First, the significant features extracted by applying SURF (Speeded Up Robust Features) method on both sensed and reference images and converted to vector format. The spatial distribution and relationship of these features expressed by topology rules and converts them to potential CPs by determine transformation model between sensed and reference images. The defined rules for a weight-based topological map-matching algorithm (tMM) manage, transform and re-sampling features of sensed image according to reference. Since AIRTop has a sufficient number of CPs the registration accuracy can be estimated with test point error (TPE) technique.

* Anna Brook, the Remote and GIS Sensing Laboratory, Tel-Aviv University. Ramat Aviv P.O. Box 39040 Tel Aviv 69978, Israel, Tel: 972-3-6407049 Fax: 972-3-6406243 Email: anna.brook@gmail.com.

2.1 Significant Features

The extraction of significant features performed by SURF based on sum of Haar wavelet responses in two directions (Brown, and Lowe, 2002). The Harris corner detection is the most widely used detector up to day due to its excellent results (Lindeberg, 2004). Fast-Hessian Detector is based on integral image and approximation. Integral image represents the sum of all pixels in the input image within a rectangular region formed by origin. Approximated Hessian detector uses box filter. While, scale variations are detected by different sizes of box filter. The next stage is to make descriptor of local gray level geometry feature. The local feature representing vector is made by combination of Haar wavelet response. The values of dominant directions are defined in relation to the selected region orientation.

The final stage of features extraction based on Canny edge detector (Canny, 1986), which is popular edge operator that widely used in digital image processing including remote sensing, and lines are extracted using Hough Transform (Duda, and Hart, 1975). Since SURF image of magnitude and direction is the base layer for feature detection, we propose to adjust several stages of Canny operator. In our work the four stages of Canny operator modified into three stages. Firstly, the image is smoothed by Gaussian convolution. We could skip the first derivative operator as it provides in the SURF image. Secondly, the process of non-maximal suppression (NMS) is imposed on the smoothed SURF image. Finally, the edge tracking process exhibits hysteresis controlled by two predefined thresholds. Traditional Canny operator carries on the edge tracking controlled by two thresholds, namely a high threshold and a low threshold. The tracking of one edge begin at a pixel whose gradient is larger than the high threshold, and tracking continues in both directions out from that pixel until no more pixel whose gradient is larger than the low threshold. The process is called hysteresis. It is usually difficult to set the two thresholds properly, especially for remote sensing image. The illumination and contrast of different portions of remote sensing image are often non-uniform.

The suggested process extracts long edges related to roads features with Hough Transform prior Canny operator. Thus roof detection could be implemented without predefined thresholds. As now the long edges related to roofs features and the edge tracking is carried out by inside edges. AS, it is difficult to detect continuous and stable edges solely from the images the morphological closing operation is employed. It's produced by the combination of dilation and erosion operations. During the process, the edges detected areas are integrated into the individual roof features. Finally, all the extracted features (roads and roofs) were converted from raster to vector format and saved as GIS project. While roofs converted to polygons, roads have been converted to polylines that cross-along the central line of detected (long edged) features.

2.2 Topological Method

Topological matching is usually used to reduce the search range or check the results of geometric matching, since it is seldom used alone. Topological methods can spread the matching into the whole network, but this requires high topological similarity of two data sets. Topological transfer method (Tomaselli, 1994) is representative of this type. If the polygons are matched, then according to the relationship of polygons and polylines, polylines to polylines matching can be deduced.

Data preprocessing stage standardizes the input data sets, ensures the conflation data sets have a same data format, the same north direction, and have overlapped spatial coverage. It also ensures the data sets have maximum similarity which is the basis of common objects matching.

A Reeb graph is a topological and skeletal structure for an object of arbitrary dimensions (Berg and Kreveld, 1997). In Topology Matching, the Reeb graph is used as a search key that represents shapes of the features. A node of the Reeb graph represents a connected component in a particular region, and adjacent nodes are linked by an edge if the corresponding connected components of the object contact each other. The Reeb graph is constructed by re-partitioning each region. The Multiresolutional Reeb Graph (MRG) begins with the construction of a Reeb graph having the finest resolution desired. Second, position of an inserted vertex is calculated by interpolating the positions of the relevant two vertices in the same proportion. Thirdly, the T-sets (connected components of triangles) are calculated. Fourthly, if two T-sets between adjacent ranges are connected, corresponding R-nodes are connected by an R-edge. The complete notification as follows: 1. R-node: A node in an MRG, 2. R-edge: An edge connecting R-nodes in an MRG, 3. T-set: A connected component in a region, 4. μ -range: A range of the function μ n concerning an R-node or a T-set.

2.3 Weight-based Topological Map-matching

This subsection gives an overview of how similarity is calculated using MRGs. A weighting approach in selecting the correct feature from the candidates improves the accuracy of correct pair identification (Greenfeld, 2002). The suggested algorithm assigns weights for all candidates using similarity in linear network and transfer matching and selects the pair with highest weight score as the potentially corrected CPs. The mathematic representation of Root Mean Square (RMS) error value of map-matching process estimates accuracy of algorithm by predefined threshold. If the algorithm fails to identify the correct CPs pair among the candidate pairs and RMS error oversize threshold then the algorithm regenerates another pair with lower weight by an optional loop stage.

2.4 Test Point Error (TPE)

The cubic B-Spline convolution supports image transformation and resampling, as it is computed raw-by-raw and column-by-column (Unser et al., 1993). The results of proposed convolution tested with Test Point Error (TPE). The test points are CPs that were deliberately excluded from the calculation of the mapping parameters. The concept of this method can be extended such that the distance between corresponding 'test' lines or surfaces is measured (Nelson et al., 1997). TPE cannot be set to zero by overfitting. This method can be used only if a sufficient number of the CP's is available. Otherwise, the exclusion of several CP's may result in inaccurate estimation of mapping parameters. In our algorithm 10% of all CPs are excluded for TPE evaluation. Once again, if the algorithm fails to transform and resample sensed image and TPE error oversize threshold then the algorithm regenerates another pair with lower weight in stage 2 (Weight-based Topological Map-matching) by an optional loop stage.

3. RESULTS

The following section presents both simulated and real-world results. First, we evaluate the effect of multi-temporal

parameters settings and show the overall performance of the suggested AIRTop algorithm based on a standard evaluation set. Then, we evaluate the effect of multi-temporal and multi-sensor parameters. AIRTop has already been tested in a few real-world applications. Taking this application a bit further, we focus in this article on the more difficult problem of cameras calibration and temporal changes. AIRTop manages to calibrate the cameras even in challenging cases reliably and accurately.

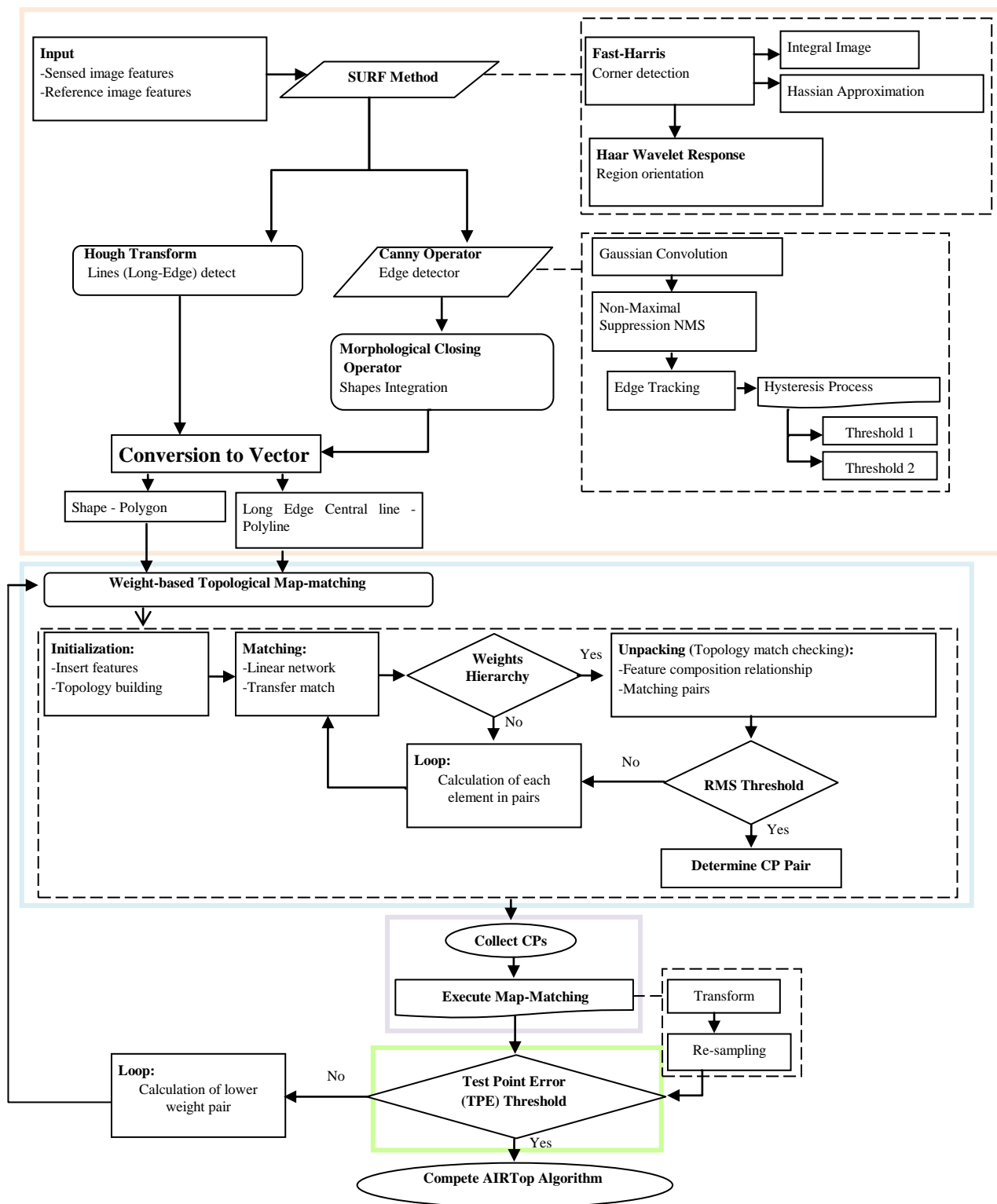


Figure 1. A flow-chart representing the AIRTop Algorithm, orange region is stage 1 (feature extraction), blue region is stage 2 (topology map-matching), purple region is stage 3 (matching process), green region is stage 4 (validation and accuracy)

3.1 Experimental evaluation

We tested our algorithm using the simulated images emphasizing the following: 1. Temporal changes simulated by adding and removing structures and lines, 2. Multi-sensor data simulated by different spatial resolution (rotation and scaling). The evaluation criterion is the repeatability score. Thus, the test sequences comprise images of real textured and structured scenes. Figure 2 shows that TPE with reasonable accuracy rate of >0.9 maintained for temporal change rate of $< 40\%$ of 26 simulated scenario of spatial variances including feature erasure and displacement. For cardinal changes ($> 40\%$) the RMS threshold in stage 2 (topological map-matching) fails to identify the correct CPs pair.

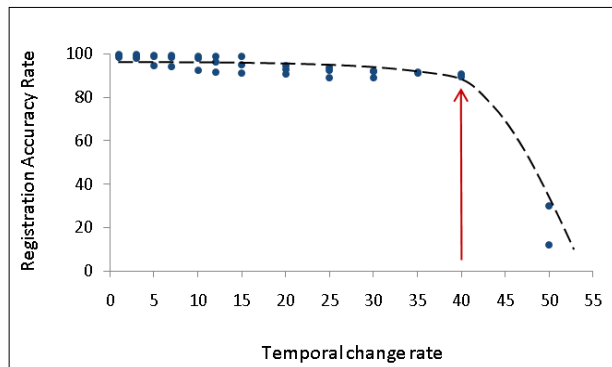


Figure 2. Temporal change versus registration accuracy, blue points are different simulation of temporal changes, black hatched line is trend line, and red cursor is RMS threshold of topological map-matching stage

An artificial scaling and rotation of simulated image evaluates matching accuracy for multi-sensor dataset. Table 1 summarizes the error in displacement, where TPE error represents Test Point error for 10% of all CPs pairs. The "Original" corresponds to original spatial resolution (0.1m) and orientation (0°) of simulated image, "Sim1" corresponds to rotation of 100° , "Sim1_1" corresponds to rotation of 100° and scaling of X2, "Sim2" corresponds to rotation of 290° , "Sim2_2" corresponds to rotation of 290° and scaling of X2.5.

Simulated dataset	Original	Sim1	Sim1_1	Sim2	Sim2_2
TPE	0.00001	0.00032	0.0056	0.00038	0.0063

Table 1. Error (in m) for simulated multi-sensor dataset when original image resolution is 0.1 m and orientation is 0°

3.2 Case Study

In this study we operated three sensors emphasizing multi-sensor registration in two selected time domains where multi-temporal changes were occurred. The selected sensors documented in table 2. Images of three sensors (table 2) was an area of 1.5×1.1 km in mid ($33^\circ 30' / 34^\circ 42'$) Israel.

Sensor	Type	Detector	Spatial Resolution	Radiometric resolution	Date
Ikonos	Spaceborne	Pushbroom	1 m	11 bit	06.2008
Panchromatic scanner 1	Airborne	Pushbroom	0.25 m	12 bit	02.2009
Panchromatic scanner 2	Airborne	Whiskbroom	0.12m	8 bit	06.2009
Panchromatic scanner 2	Airborne	Whiskbroom	0.12m	8 bit	07.2009

Table 2. Selected sensors for case study

Table 3 summarizes the error in displacement of three images (Panchromatic scanner 1, and two Panchromatic scanner 2 images) to Ikonos image from 2008 where TPE error represents Test Point error for 10% of all CPs pairs.

Simulated dataset	TPE
Panchromatic scanner 1	0.001
Panchromatic scanner 2	0.0029
Panchromatic scanner 2	0.0035

Table 3. Error (in m) for simulated multi-sensor dataset when original images resolution is 1, 0.25, 0.12 m

4. CONCLUSION

We propose an AIRTop algorithm as method for the solution of the core problem of multi-sensor and multi-temporal images registration, based on combination between SURF (Speeded Up Robust Features) method and weight-based topological map-matching algorithm (tMM). The main focus of our algorithm is on scale and image rotation invariant the quality of the scanning system. Both simulated experimental and real-world case study results shows high accuracy of registration process.

5. REFERENCES

- Berg, M., Kreveld, M., 1997. Trekking in the Alps without Freezing or Getting Tired. *Algorithmica*, 18, 306-323.
- Brown, L. G., 1992. A survey of image registration techniques, *ACM Computing Surveys*. 24(4), 325-376.
- Brown, H., Lowe, D., Invariant features from interest point groups, in *BMVC*, 2002.
- Canny, J., 1986. A computational approach to edge detection. *IEEE Transactions on Pattern Analysis and Machine Intelligence*, 8(6), 679-698.
- Duda, R.O., Hart, P.E., 1975. Use of the Hough transform to detect lines and curves in pictures, *Association for Computing Machinery*, 15, 11-15.
- Greenfeld, J.S., 2002. Matching GPS observation to location on a digital map. In: *Proceedings of 81st Annual Meeting of the Transportation Research Board*, Washington, DC.
- Jensen, J. R., 2004. *Introductory digital image processing*, 3rd Ed., Upper Saddle River, NJ: Prentice Hall.
- Lindeberg, T. 2004. Feature detection with automatic scale selection. "International Journal of Computer Vision", 30(2), 79-116.
- Moigne, J. L., W. J. Campbell, and R. F. Cromp, 2002. "An automated parallel image registration technique based on the correlation of wavelet features". *IEEE Transaction on Geoscience and Remote Sensing*, 40(8), 1849-1864.
- Nelson, S.J., Day, M.R., Buffone, P., Wald, L.L., Budinger, T.F., Hawkins, R., Dillon, W., Huhn, S., Prados, M., Chang, S., Vigneron, D.B., 1997. Alignment of volume mri and high resolution f-18 flurodeoxyglu-cose pet images for evaluation of

patients with brain tumors. *Journal of Computed Assisted Tomography*, 21, 183–191.

11.Tomaselli, L., 1994. Topological transfer: evolving linear GIS accuracy. URISA 1994 conference proceeding, 245-259.

12.Unser, M., Aldroubi, A., Eden, M., 1993. B-Spline Signal Processing: Part I Theory. *IEEE Transactions on Signal Processing*, 41, 821–832

13.Zitova, B. and J. Flusser, 2003, Image registration methods: a survey, *Image and Vision Computing*, 21(11), 977-1000.

THE ADVANTAGES OF BORESIGHT EFFECTS IN THE HYPERSPECTRAL DATA ANALYSIS

Anna Brook, Eyal Ben-Dor

Remote Sensing Laboratory, Tel-Aviv University, Israel
anna.brook@gmail.com

Commission VI, WG VI/4

KEY WORDS: Bore Sight, Dual pushbroom line-based hyperspectral sensors, Shadow Map, Stereo 3-D Map, Anomaly Detection

ABSTRACT:

The Dual push-broom line-based hyperspectral sensors combine two different instruments that are usually mount on the same optical bench. This configuration leads to problems such as co-registration of pixels and squint of the field of view known as boresight effect. Image orientation parameters and sensor boresight of any sensor during data acquisition became possible by a combination of an inertial measurement system (IMU) and GPS. The different position of the IMU, the GPS antenna and the imaging sensors, causes an orientation and boresight effect. Any small change in the correction of internal orientation affects the co-registration between VNIR and SWIR region of hyperspectral images. Correcting the boresight effect is an almost automatically key mission taken by all Dual system users. This is because the boresight effect is considered as a noise in the system and a problem that needs to be corrected prior to any data analysis. We propose to use the boresight effect as a vehicle to monitor and detect some spectral phenomena in the image that can't be obtained in corrected images. The advantage of the sensors orientation and boresight effect was investigated based on the AISA-Dual sensor that combines EAGLE for the VIS-NIR (400-970nm) and HAWK for the SWIR (980-2450nm). An experience of more than six years with this sensor, we have found that the boresight effect have some positive outcomes on the analysis results of the hyperspectral remote sensing (HRS) data. This led us to generate an HRS processing protocol where this effect is examined for gaining the most from the data. Three applications were investigated as follow: 1) enhancing shadowing effect, 2) generating a 3-D view, and 3) performing a better detection of boarder anomaly. We will demonstrate these three options and suggest a possible use of this idea from orbit.

1. INTRODUCTION

Hyperspectral imaging spectrometers produce data with high spectral resolution (in the range of 5 to 15 nm) and continues band configuration, giving processors the ability to detect subtle spectra features and defined chemical and physical properties of the sensed objects. This powerful capability is important for remote sensing applications e.g. geologic typing and surveying, agricultural monitoring and optimization, environmental damage assessment, forestry surveys, detection of man-made materials, etc.

The determination of image orientation parameters of any sensor during data acquisition became possible by combined use of an inertial measurement unit (IMU) and GPS. In this integrated system, GPS antenna, IMU and imaging sensor are located different position in airborne carrier. Because of this reason, the displacement vectors between sensors have to be determined. Similarly, axes of the IMU and imaging sensor are not same and a miss-orientation matrix exists between them. System calibration is including both calibration of individual sensor and calibration between sensors. The IMU calibration for drifts and biases and the calibration of imaging sensor for interior orientation parameter are components of sensor calibration. Calibration between sensors contains the determination of a constant displacement vector between sensors and a constant miss-orientation matrix between IMU body frame and imaging sensor frame. The boresight misalignment, the relation between the IMU and the imaging sensor is determined by bundle block adjustment using a calibration flight. The small change of correction of interior orientation affects co-registration between sensors and thus hyperspectral images of VNIR and SWIR region. The processing step that can be applied to the data is

georectification that collects generated (VNIR and SWIR) imagery and navigation data and automatically geo-locate and rectify pixel-by-pixel the image data.

AISA-Dual is an airborne imaging spectrometer designed by Specim LTD, as a research sensor that capable of producing medial to high fidelity hyperspectral remote sensing (HRS) data in the 400 to 2400 nm wavelength range. The system consists of a sensor head, containing a pair of co-boresighted grating spectrometers (VIS-NIR sensor EAGLE and SWIR sensor HAWK), two electronics racks, and a digital data recorder. It simultaneously acquires images in 198 contiguous spectral bands with spectral resolution in the range of 12nm in VNIR region, and 6nm in SWIR region. Each spectrometer consists of a set of refractive foreoptics that image the scene onto a slit. Light passing through the slit is dispersed perpendicular to the slit by a flat rating and then imaged onto a 2-D focal plane array. One dimension of the array along the slit provides spatial scene information. The second dimension of the array, along which the light from any given point in the slit has been dispersed, provides spectral information. An image is generated by moving the instrument across a scene in a push-broom fashion, perpendicularly to the instrument's slits, and recording frames of spectral and spatial information detected by the VNIR and SWIR. The system is usually operated on aircraft at altitude of 10,000 ft that together with instant field of view (IFOV) of 1 mrad provides a spatial resolution of 1.5 m. A standard AISA-Dual data set is a 3-D data cube in non-earth coordinate system. It has 286 pixels in the cross-track and hundreds of pixels in the along-track direction. The top-level performance requirements were for an instrument with fair signal to noise ratio (SNR), co-registered spectral bands taken simultaneously by different detectors, accurate location for each pixel, and accurate radiometric calibration.

* Anna Brook, the Remote and GIS Sensing Laboratory, Tel-Aviv University. Ramat Aviv P.O. Box 39040 Tel Aviv 69978, Israel, Tel: 972-3-6407049 Fax: 972-3-6406243 Email: anna.brook@gmail.com.

Since AISA-Dual instrument operated in Israel, has no GPS/INS system available, it is incapable to perform the pixel-by-pixel geo-location and rectification of the images, generated in an extensive HRS dataset. In this study, the advantage of the sensors orientation and boresight effects were investigated based on AISA-Dual HRS data. Our study shows that those "negative" effects are suitable to spectral/spatial analysis and processing of HRS images. Thus, we are suggesting three efficient and practical applications: 1) enhancing shadowing effect, 2) generating a 3-D view, and 3) performing a better detection of boarder anomaly.

2. METHODOLOGY

Apart from the image sensors, an airborne mobile-mapping system has to equip for direct geo-referencing involves one or several GPS receivers and antennas as well as an IMU. In the most ideal case, all sensors are attached to a common rigid mounting structure, preventing variations of their relative positions and orientations. In practice, AISA-Dual system is operated with no GPS/INS data available. Consequently, it is impossible to geo-locate or rectify the VNIR and SWIR images. The spatial/spectral boresight effect of AISA-Dual sensor is illustrated in Figure 1.

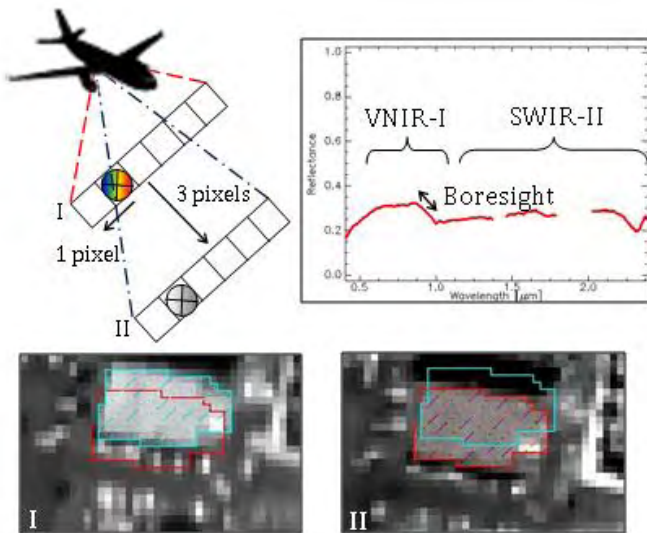


Figure 1. Boresight effect schematic demonstration, image I and II illustrating boresight then I is the target in VNIR wavelengths and II is the target in SWIR region, and the spectrum of the target then region I is concrete (target in VNIR) and II is asphalt (background in SWIR)

We suggest to converting the boresight shift into additional spectral/spatial information by calculating a simple band ratio between VNIR and SWIR images. The boresight "band ratio" presented in Figure 2.

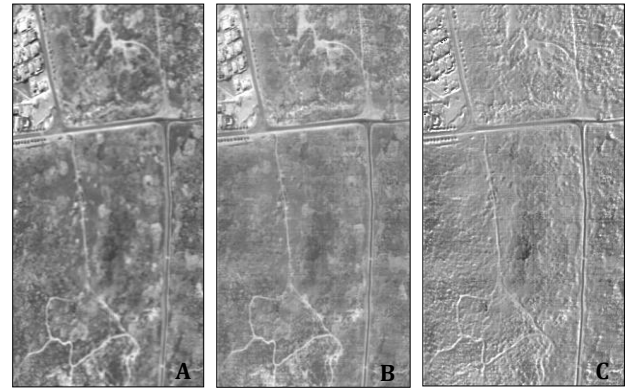


Figure 2. Additional Boresight "band" (October 31, 2009; 10:00 GMT; midlatitude summer model; 28.2 ° solar zenith, 137.6 ° azimuth angle), A is the 948nm band, B is the 1010nm band, C is the calculated band ratio (948nm/1010nm) interpreted as Boresight band

3. RESULTS

We have found that the boresight effect have applicable outcomes on the spectral/spatial analysis and processing that is based on an extensive dataset of AISA-Dual images, acquired during more than six years of operated campaigns. Three applications were investigated as follow: 1) enhancing shadowing effect, 2) generating a 3-D view, and 3) performing a better detection of boarder anomaly.

3.1 Enhancing shadowing effect

Current implementations of the de-shadowing process within the ATCOR-4 model uses image's statistics to gain knowledge about the darken area in order to correct the shadow effect. This routine is not suitable for data sets acquired on clouds shadow as the inter-comparison process is missing in the diffuse light conditions. This de-shadowing algorithm consists of a sequence of eight processing steps: an atmospheric correction, clouds and water bodies masking, five additional statistic manipulations including covariance matrixes and matched filters to define a core shadow mask, and final step is a de-shadowing that exclusively applied to the pixels in the shadow mask (Schläpfer et al., 2009).

The method suggested here is mapping shadow areas in HRS images of AISA-Dual sensor. An interpretation of boresight band is identifying core shadow areas with highly negative values and evaluating 'darkening' for each pixel in the classification shadow map. This technique provides an external shadow map for de-shadowing algorithm of ATCOR-4, allows it to skip six steps of shadow mask identification. The proposed a fully automatic method was successfully tested on six scenes covering different landscapes. The advantage of the presented method is that it does not need a human operator, and it is fast processing algorithm exclusively relying on the boresight ratio calculated band.

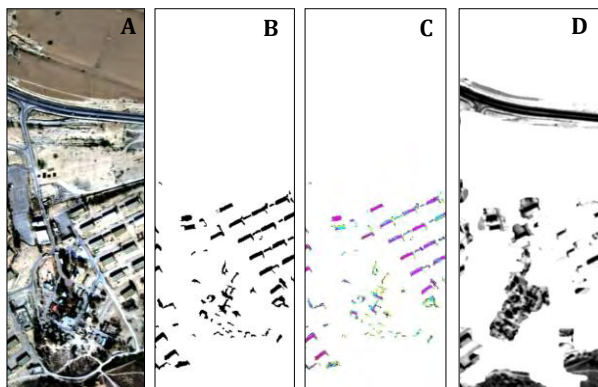


Figure 3. Shadow masks of – A is an AISA-Dual image (December 18, 2009; 11:30 GMT; 15km visibility; midlatitude winter model; 60 ° solar zenith; 205.8 ° azimuth angle), B is a boresight shadow mask, C is a boresight shadow estimation (yellow 0.1-20%, cyan 20-50%, magenta 50-80% and maroon 80-100%), D is an ATCOR-4 shadow mask

3.2 Stereo 3-D map

The simultaneous across-track stereo-data acquisition gives a strong advantage in terms of radiometric variations. Since an error of ± 3 pixel along-track and ± 1 pixels across-track for the parallax measurements in the automated matching process has been achieved with these different datasets (along-track and across-track), the potential accuracy for the across-track stereo-derived local DEM from AISA-Dual could be on the order of 3 m (1.5x1.5 pixels). The main objectives of this application are to generate and evaluate pixel based local DEMs from the boresight VNIR and SWIR images. The 3-D stereo intersection is performed using a computed geometric model to convert the pixel coordinates in both images determined in the image matching of the stereo pair to 3-D data. The non earth coordinates are determined for the measured point with a least square intersection process based on the geometric model equations and parameters (Toutin, 1995). The result is an irregular grid in the map projection system, which is transformed to a raw regular DEM.

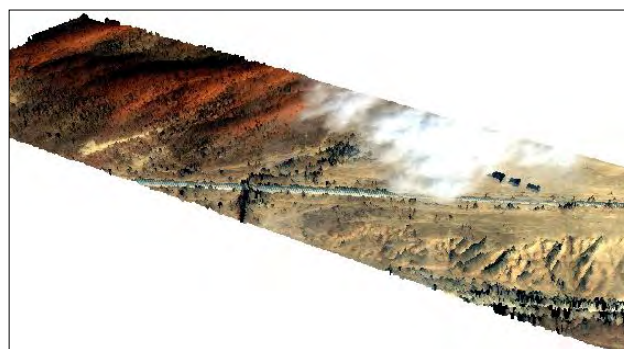
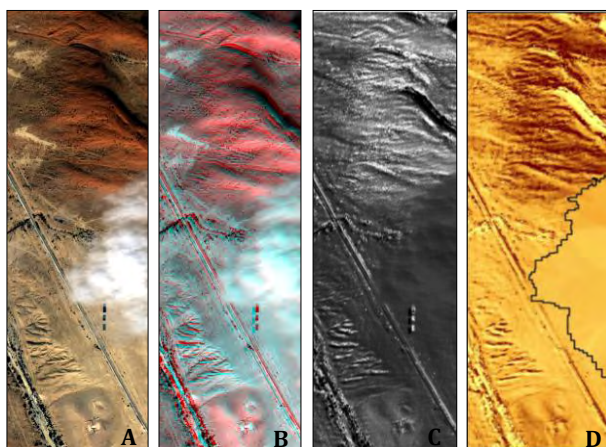



Figure 4. DEM, A is the AISA-Dual image (October 122, 2006; 08:55 GMT; midlatitude summer model; 46.4 ° solar zenith; 164.6 ° azimuth angle), B is the 3-D stereo model, C is the boresight calculated band, D is the raw DEM (cloud masked-black border) modeled with Inverse Distance Weighting (IDW) algorithm (0m  30m), E is the AISA-Dual in 3-D view (x axis 1500m, y axis 500m, z axis 30m)

3.3 Unmixing and anomaly detection

Most of the pixels collected by HRS airborne sensors contain mixed spectra from the reflected surface radiation of various materials in the sub-pixels. As a result, mixed pixels may exist when the spatial resolution of the sensor is not sufficient to separate different pure signature classes. The resulting spectral measurement is a composite of the individual pure spectra weighted by a set of scalar endmember-abundance fractions (Adams et al., 1986). Under such circumstances, target detection must be carried out at sub-pixel level. An anomaly detector enables to detect targets whose signatures are spectrally distinct from their surroundings with no a priori knowledge. In general, such anomalous targets are relatively small compared to the image background and only occur in the image with low probabilities. Two approaches are of particular interest. One was developed by Reed and Yu (Reed and Yu, 1990; Yu et al., 1993; Yu et al., 1997) and is referred to as the RX detector (RXD). The RX detects spatial/spectral anomalies using the sample covariance matrix to detect "interesting target" pixels which occur with low probabilities in the data (i.e., the size of target samples is small) compared to Gaussian distribution of the background. Second is a SVDD, (support vector approach) that is a non-parametric method with several benefits, including non-Gaussian modeling basis that can model arbitrarily shaped and multi-model distributions, scarcity and high generalization ability (Banerjee et al., 2006).

We suggest using boresight calculated band as spectral/spatial anomaly detector. Since an anomaly defined as a small target with distinct spectrum, an accurate pixel-by-pixel classification of boresight values may accentuate the targets in question.

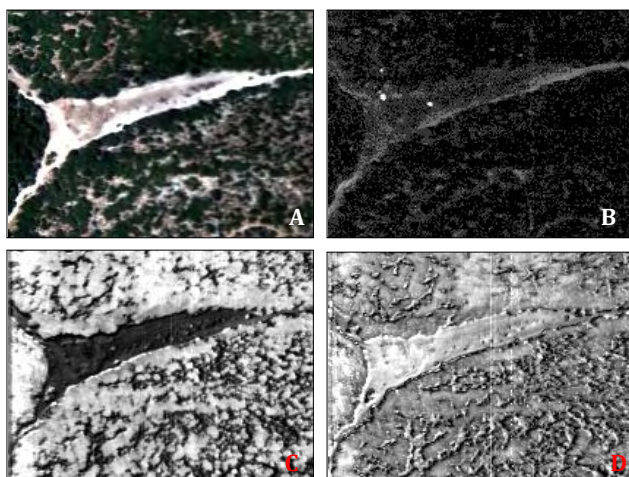


Figure 5. Anomaly detection on a bare soil field, A is the AISADual image (October 31, 2009; 10:10 GMT;; midlatitude summer model; 30.2 ° solar zenith, 141.2 ° azimuth angle), B is the RXD product, C is the SVDD product, D is the boresight band detection

4. SUMMARY AND CONCLUSIONS

Correcting the boresight effect is an almost automatically key mission taken by all Dual system users. The consideration of boresight effect as a noise in the system leads to the assumption that it needs to be corrected prior to data analysis. This work showed that boresight effect may operate as a vehicle to monitor and detect some spectral phenomena in the image. Three applications were investigated and demonstrated as follow: 1) enhancing shadowing effect, 2) generating a 3-D view, and 3) performing a better detection of boarder anomaly. First application provides an external shadow map for any de-shadowing algorithm, allows it to skips prior steps of shadow areas masking that occasionally misidentifying these areas with highly contrast dark targets. The second application deals with an extraction of 3-D information. The automated matching process has been achieved with different datasets (along-track and across-track) and potential accuracy for the across-track stereo-derived local DEM. The final application detects spectral/spatial anomaly of boresight calculated band. In this study, the advantage of the sensors orientation and boresight effects were used to generate "hidden" information within the data that other techniques could not yield.

5. REFERENCES

1. Adams, J. B., Smith, M. O. and Johnson, P. E.,1986. "Spectral mixture modeling: A new analysis of rock and soil types at the Viking Lander 1 site," *Journal of Geophysical Research*, 91, 8098-8112
2. Banerjee, A., Burlina, P., Diehl, C., 2006. "Support vector methods for anomaly detection in hyperspectral imagery", in *IEEE Transactions on Geoscience and Remote sensing*
3. Reed, I. S., and Yu, X.,1990. "Adaptivemultiple-band CFAR detection of an optical pattern with unknown spectral distribution," *IEEE Trans. Acoust., Signal Processing*, 38, 1760–1770

4. Schläpfer, D., Richter, R., Hueni, A., 2009. "Recent development in Operational Atmospheric and Radiometric Correction of Hyperspectral Imagery", in *EARSel 6* proceeding, Tel-Aviv, Israel

5. Toutin, Th., 1995. "Generating DEM from stereo-images with a photogrammetric approach: Examples with VIR and SAR data," *EARSel Advances in Remote Sensing*, vol. 4 (, no. 2), 110–117

6. Yu, X., Reed, I.S., and Stocker, A.D., 1993. "Comparative performance analysis of adaptivemultispectral detectors," *IEEE Trans. Signal Processing*,41, 2639–2656

7. Yu, X., Hoff, L. E., Reed, I. S., Chen, A.M., and Stotts, L.B. 1997. "Automatic target detection and recognition in multispectral imagery: A unified ML detection and estimation approach," *IEEE Trans. Image Processing*, 6, 143–156

COMPARING INFORMATION DERIVED FROM GLOBAL LAND COVER DATASETS WITH LANDSAT IMAGERY FOR THE HUAMBO PROVINCE AND GUINEA-BISSAU

A. Cabral*, M. Vasconcelos, D. Oom

Tropical Research Institute, GeoDes, Travessa Conde da Ribeira, nº9, 1300 Lisboa, Portugal –
(anaicabral70, maria.perestrelo, duarte.oom)@gmail.com

KEY WORDS: Classification, High resolution, Land cover, Multitemporal, Huambo, Guinea-Bissau

ABSTRACT:

Land cover maps, derived from satellite data, are a valuable tool for various global research studies and are often used in multi-temporal approaches to document the dynamics of processes such as agricultural expansion or deforestation. In this study we show how the observed land cover change tendencies diverge widely depending on the scale of observation and on the characteristics of the data sources used. For the analysis we compared land cover changes using two different scale map time-series in the period 1990 - 2009. Two regions were selected, for which there are high resolution imagery and/or ground data available for validation and verification purposes: the entire country of Guinea-Bissau and the Huambo province in Angola. The first map time series consists of data available in international projects (IGBP, GLC2000, and MODIS) obtained from classification of 1 Km resolution imagery for three dates in the study period. The second map-set results from classification and validation of 30 meter resolution images (Landsat TM and ETM+), covering the same area in approximately the same dates. For the comparisons, the different map legends had to be aggregated into a common nomenclature to define five common classes: Forests, Savannas/Shrublands, Grasslands, Croplands/Bare soil and Wetland. The results show large discrepancies in the observed trends in agricultural areas. For example for both regions, the increase in agricultural land during the analyzed period, which is observed in high resolution maps and confirmed by validation and field knowledge, is lost in the coarse resolution maps. The deforestation rates reported by the coarse resolution maps are not verified when high resolution is employed. The consequences of these observations are discussed and future work proposed.

1. INTRODUCTION

In the last years, land cover mapping has become one of the most important sources of information for environmental studies. This type of information becomes even more relevant with the establishment of international agreements such as the Kyoto Protocol, the International Convention on Biological Diversity, and the framework Convention on Climate Change, all of which call for accurate reporting of environmental variables (McCallum et al., 2006). Having information about land cover status is essential, as a baseline, in order to evaluate future changes. Remote sensing data from several satellites allowed obtaining sufficiently accurate land cover mapping in a global scale, evenly in remote areas, and has been used to derive several global land cover maps, that are freely available for a variety of applications, and which are deemed sufficiently accurate for different project types. The use of these land cover maps has been very useful in modelling studies and corresponds to a great advance in earth system science. Since these maps are developed by different and independent national and international initiatives, they were prepared using different data sources, classification systems and methodologies, which are a reflection of the different mapping standards adopted and varied interests. As a consequence, each dataset has some advantages and limitations and it is important to fully understand their applicability bounds. One way to do it is by comparison among different data sets and scales of analysis. This approach helps to better grasp what data sets should be used for monitoring, compliance assessment, and trend analysis. Several efforts have been made in recent years to improve the comparability and compatibility between land cover datasets. GOCF-GOLD

(Global Observation of Forest and Land Cover Dynamics) in conjunction with FAO (Food and Agricultural Organization) and GTOS (Global Terrestrial Observation System) developed a new Land Cover Classification System (LCCS) in order to obtain a land cover harmonization methodology (Herold et al., 2008; Jung et al., 2006). The LCCS allows that land cover features be defined at any scale or level of detail, with an absolute level of standardization of class definitions between different users (Di Gregorio and Jensen, 2000). Several studies comparing two or more global land cover products were done at regional (Kalacska et al., 2008) to global scale, which show significant disagreements and reveal uncertainties (Giri et al., 2005; Herold et al., 2008; McCallum et al., 2006). Therefore, a validation and a comparison of these global datasets are necessary before using them in global and regional studies. Different approaches are used to quantitatively estimate the accuracies of the global land cover classifications: confidence values of the classifier, comparison with other maps, cross-validation with training datasets and statistically robust spatial sampling and acquisition of ground reference information (Jung et al., 2006). The purpose of this study is two-fold: (1) to characterize land cover change, with a special focus on deforestation, in two approximately same size regions of Africa; (2) to assess the effect of using coarser resolution global land cover maps for producing the same information in the period of 1990 - 2009. To achieve these goals two different map time series are used. The first map time-series results from classification and validation of 30 meter resolution images (Landsat TM and ETM+). The second consists of data available in international initiatives (IGBP, GLC2000 and MODIS). The analysis is performed for the entire country of Guinea-Bissau

* Corresponding author.

and for the Huambo province in Angola, from where there are high resolution imagery and/or ground data available.

2. STUDY AREA AND DATA PREPARATION

2.1 Study area

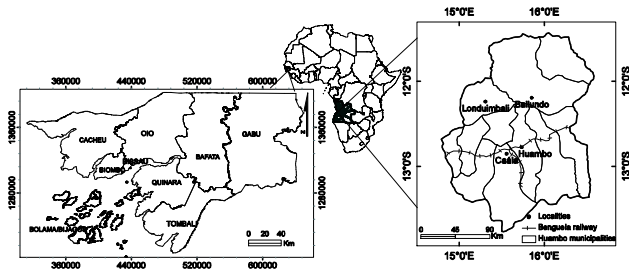


Figure 1 – Study areas

Guinea-Bissau (GB) is a country located in the west coast of Africa with approximately 36125 km². It has a continental mainland and a group of islands, the Bijagós Archipelago (Figure 1). This country is characterized mainly by a flat land surface with altitudes below 100 meters. Two large regions are found, namely, the coastal low land area, consisting largely of mangroves and swamps stretching from north to south and the inland, where open forests, as well as, closed forests dominate (especially in the southwest). Savanna woodland is present in the northern and eastern regions of the country (White, 1983). This distribution is dependent on different soils characteristics and mainly on differences in rainfall regimes between north and south, and east and west (Catarino, 2004). Two marked seasons can be observed in this region, characterized by a tropical climate: a dry season between November and April and a wet season between May and October.

The Huambo Province is located on the central plateau of Angola (Figure 1) and has an area of about 34270 km² (USAID, 2008). The region includes the higher mountains and the highest peak in Angola, the Môco Mountain with an elevation of 2620 meters, and has a wet season from October and April and a dry season between May and September. The dominant vegetation is mainly composed of *miombo* and savanna woodlands, with grasslands covering large areas of lower drainages. The *miombo* floristic formation is dominated by three species, *Brachystegia* spp., *Combretum* spp. and *Julbernardia* spp, whereas in savannas there is a dominant grass layer with *Hyparrhenia* spp and *Andropogon* spp.

2.2 Landsat data and Field data

For GB, a dataset of five scenes per date of Landsat Thematic Mapper (TM) and Enhanced Thematic Mapper (ETM+) was used for 1990, 2002 and 2007, in a total of fifteen images. The images were from the late dry season, except for 1990. A geometric correction was performed with ground control points, resulting in a RMS error less than 1 pixel. The data were resampled into Universal Transverse Mercator projection Zone 28 north, datum WGS84 with a spatial resolution of 25 meters.

Field data were collected in GB for Mangrove, Closed forest, Open forest and Savanna-woodland, in 293 geo-referenced sample plots selected from a stratified random origin regular net, surveyed in three campaigns conducted in 2007, 2008 and 2009. These data were used for classification accuracy assessment.

For Huambo, a dataset of four images per date of Landsat TM was available, free of charge, for the period 1990/1991/1992 and 2000/2001/2002 from the University of Maryland's Global Land Cover Facility (<http://glcfapp.umiacs.umd.edu/>) and Landsat ETM+ data was available for 2008/2009 from the U.S. Geological Survey (USGS) Earth Resources Observation Systems (EROS) Data Center (EDC) (<http://glovis.usgs.gov/>). The Landsat images were, already, geometrically corrected to the Universal Transverse Mercator projection Zone 33 South and with a spatial resolution of 30 meters.

A few forest inventory plots in areas of forest and savanna were collected within the Huambo province and were later used in the classification verification.

2.3 Global land cover maps

Land cover data, produced by three international initiatives (IGBP, GLC2000 and MODIS) were freely available for this study. The International Geosphere Biosphere Project (IGBP¹) (Loveland et al., 2000) distinguishes 17 land cover classes according the science requirements of IGBP's core projects and was produced based on NOAA-AVHRR imagery from 1992-1993, at a spatial resolution of 1 km.

The Global Land Cover 2000 (GLC2000²) (Fritz et al., 2003) distinguishes 22 land cover classes, developed based on the Land Cover Classification System (LCCS) and was derived from 1 km SPOT4-VEGETATION daily data from November 1999 to December 2000.

The maps produced using the Moderate Resolution Imaging Spectroradiometer (MODIS³), (Strahler et al., 1999) adopt the IGBP legend, and have two types of products, one based on Terra (T) satellite data and one based on Aqua and Terra combination (AT) satellite data, with a spatial resolution of 1 kilometre and 500 meters, respectively. The last one was converted into a 1 Km grid database to have the same cell size of the other global land cover products. These datasets were produced annually since 2001 until 2007, and in this study two maps were used for GB in 2002, one from Terra (MODIST2002) and one from Aqua/Terra combination (MODISAT2002). Another one was used for 2007 (MODISAT2007). For Huambo, also, two maps were used from 2001 (MODIST2001 and MODISAT2001) and one from 2007 (MODISAT2007).

3. METHODS

3.1 Landsat land cover maps (LAND maps)

A legend with ten land cover classes was established for the Landsat image classification in GB: Closed-forest, Open-forest, Savanna-woodland, Mangrove, Grassland, Croplands/Bare soil, Wet-vegetation, Burnt, Water, and Sand. This legend was defined according to expert knowledge and pre-existing maps at different scales. This information was used to train a supervised classification tree algorithm. Three Land cover maps were obtained for 1990 (LAND90), 2002 (LAND2000) and 2007 (LAND2007). Classification accuracy was assessed using data collected in the field between 2007 and 2009 for four vegetation classes: Mangrove, Closed Forest, Open Forest and Savanna-woodland.

¹ http://edc2.usgs.gov/glcc/tabgeo_globe.php

² <http://bioval.jrc.ec.europa.eu/products/glc2000/products.php>

³ <https://wist.echo.nasa.gov/>

A legend with height land covers classes was defined for Huambo, according to expert knowledge, descriptions of vegetation in available literature and pre-existing maps: Closed-miombo, Open-miombo, Savanna-woodland, Grassland, Croplands/Bare-Soil, Wet-vegetation, Burnt and Water. A supervised classification algorithm, based on a maximum likelihood classifier was used to produce land cover maps for 1990 (LAND90), 2000 (LAND2000) and 2009 (LAND2009). The classification accuracy was assessed based on collected data from a random origin systematic grid overlaid on high resolution photographs with dates between 2002 and 2007 and data collected on a few field plots.

Table 1 – Legend translation between the SIMP legend and the IGBP-DISCover (MODIS), LCCS (GLC2000) and LAND maps

SIMP	IGBP-DISCover	LCCS (GLC2000)	LAND (GB/Huambo)
Forest (>30% tree cover)	Evergreen Needleleaf Forest (>60%)	Montane Forest (>60%)	Closed-forest/Dense miombo (>60% tree cover)
	Evergreen Broadleaf Forest (>60%)	Closed deciduous forest (>60%)	Open-forest/Open miombo (40-60%)
	Deciduous Broadleaf Forest (>60%)	Deciduous woodland (30-60%)	Mangrove (GB) (>30%)
	Mixed Woody Savanna (30-60%)	Mosaic forest/Savanna (30-60%)	
Savannas/ Shrublands (10-30% tree cover)	Savanna	Deciduous Shrub with Sparse Trees	Savanna-woodland (10-40%)
	Closed Shrub	Open Deciduous Shrub	burnt
	Open Shrub	Open Grassland with sparse shrubs	
Grassland Croplands/ Barren	Grassland Cropland	Closed Grassland Cropland	Grassland Cropland/Bare soil
	Urban/Built-up Cropland/Natural vegetation Barren		Sand (GB)
Wetland	Permanent Wetland		Wet Vegetation

3.2 Legend harmonization

A simplified legend (SIMP) with five classes was defined. This legend accommodates all land cover categories of each land cover map legend from each data set, on an aggregated level. Legend correspondence is shown in table 1.

Combining all different forest or savanna types is a complex task due to the different classification schemes adopted by the global land cover maps. Forest definition adopted by IGBP and GLC2000 is different. GLC2000 considers a tree cover greater than 15%, while, in this range, IGBP distinguishes three classes, savannas with tree cover between 10-30%, Woody savannas between 30-60% and Forest with tree cover greater than 60%. For LAND maps, the definition of Forest adopts a tree cover greater than 30%.

Given these differences and considering the pre-existent information about study areas; maps, descriptions of vegetation, expert opinion and in situ studies (Diniz, 2006; Catarino, 2004) we decided to consider as forest all vegetation types with a tree cover greater than 40%.

Savannas and Shrublands were included in the same class in the SIMP legend, as well as, Burnt class. This option was based on the existing available information for these areas. Field knowledge shows that Burnt class occurred essentially in savannas areas for both regions. The class cropland, due to its spectral similarity with bare and urban classes, was aggregated into the same class. The class Wetland includes Permanent Wetland and Wet Vegetation. Each land cover dataset was reclassified according SIMP legend in order to make all datasets comparable, excluding the class Water.

Due to their higher resolution and accuracy levels obtained (see below), we consider LAND maps from 1990, 2000 and 2007 or 2009 (depending on study area) as reference maps in this study. There are two types of comparisons to be made between the reference maps and the coarser resolution maps (IGBP, GLC200 and MODIS). One concerns the quantity of each category and the other the location of each category (Lambin and Geist, 2006). The first compares the similarity of the proportion of each class in the classification map to the proportion of the corresponding class in the reference map. The second analyzes the location of each category in the two maps (the classification map and the reference map) in terms of similarity. Comparisons are made between the reference map and the closest date of the coarse resolution maps, i.e., LAND90 with IGBP, LAND2000 with GLC2000, and LAND 2007 or LAND 2009 with MODISAT2007.

In this study, a vector boundary was overlaid on each reclassified dataset in order to obtain data only for the study areas. The total areas of each class derived from IGBP, GLC2000 and MODIS products were calculated and compared against the LAND maps in order to quantitatively assess the agreement level of the various datasets. As the quantitative comparison could hide the real quality of the maps, since it provides the proportions of each class but not the locations, a spatial comparison was also made. This allows identifying where agreements and disagreements occur, pixel by pixel. Overlaying the global land cover datasets with LAND maps (resampled to 1Km pixel size using a nearest neighbour algorithm), pixels with the same class in both datasets retained their value and pixels with a different class are labelled with a different value, as disagreement. This allows obtaining a map that includes the classes where the two maps showed equal representation for the same land cover classes.

The Index of agreement between the two maps (the classification and the reference map) was calculated using a measure of association called Kappa (Rosenfield, 1986). Kappa index of agreement is widely used to measure the variability between two or more classified maps, i.e., how often two or more maps agree in their interpretations. The values of Kappa range from 0 indicating no correlation to 1 indicating perfect correlation.

4. RESULTS

4.1 LAND maps accuracy

Percent agreement calculated between image classification and validation data sets built for GB and Huambo (based on field and high resolution photography respectively) resulted in values above 90% for all dates. Even though the validation data

corresponds to the more recent dates, the same sample set was also used to estimate percent agreement for previous dates after removing those pixels falling in patches that, by visual inspection, showed a change in spectral response between dates. Nevertheless, since the methodologies defined in REDD⁴ assume that a validation procedure conducted for the most recent images is enough to support the validity of the classification approach to apply to an historical data set and to guarantee that the most recent LAND maps are valid. Consequently, the level of accuracy obtained (above 90% for both study areas) provides high confidence in the classifications obtained.

4.2 Areal land cover estimations

The total area of the five aggregated classes derived from the comparison of each land cover product with LAND maps are shown in Tables 2 e 3, for Guinea-Bissau and Huambo, as well as, their percentage deviations.

Table 2 – Land cover area totals in km² and their percent deviations (in parentheses) from LAND maps for IGBP, MODIST2002, MODISAT2002, GLC2000, and MODISAT2007 in Guinea-Bissau

Land cover	LAND 90	IGBP
Forest	2820	19754 (600.4)
Savannas/ Grasslands	23129	6049 (-73.8)
Grasslands	638	416 (-34.8)
Croplands/Bare soil	2881	2992 (3.8)
Wetland	553	814 (47.1)

	LAND 2000	GLC2000	MODIS T2002	MODISAT 2002
Forest	2611	6954 (166.3)	20235 (674.9)	24958 (855.8)
Savannas/ Grasslands	24480	21958 (-10.3)	7534 (-68.22)	1535 (-93.7)
Grasslands	345	0 (0)	616 (78.5)	122 (-64.6)
Croplands/Bare soil	2420	870 (-64.0)	972 (-59.8)	1638 (-32.3)
Wetland	165	3 (-98.1)	738 (347.2)	1841 (1015.7)

	LAND 2007	MODISAT 2007
Forest	2459	25900 (953.2)
Savannas /Grasslands	23648	316 (-98.6)
Grasslands	608	39 (-93.5)
Croplands/Bare soil	2914	2015 (-30.8)
Wetland	64	1822 (2746.8)

In Guinea-Bissau, for Forest class the higher percentage variation is founded in MODISAT2007 with a value of 953.2% follow by IGBP (600.4%). For Savannas/Shrubland, all maps show a negative percentage variation. Relatively to Grassland class, all maps show negative values, when comparing with the respective reference map, except MODIST2001 with a value of 78.5%. Also, the class Cropland/Bare soil show negative trend

⁴http://www.netinform.de/KE/Wegweiser/Guide2.aspx?ID=6141&Ebene1_ID=49&Ebene2_ID=1978&mode=4

for all maps except the IGBP with a n increase of 3.8%. The class Wetland show very higher values for MODISAT2007 (2746.8%) and MODISAT2002 (1015.7%) and lower for MODIST (347.2%) and IGBP (47.1%). Only the GLC2000 (-98.1) show a negative trend for this class.

In Huambo, the map with higher percentage variation, for forest class, is MODISAT2007 with 400.1% follow by MODISAT2001 (340.8%).

For Savannas/Shrubland, all maps show a negative percentage variation, except the IGBP with an increase of 3.52%. For Grassland class, all maps show a decrease of this area. Also, the class Cropland/Bare soil show a negative trend except the IGBP with an increase of 6.2%. Only the map MODISAT2007 has an increase for Wetland class. The class Wetland show very higher values for MODISAT2007.

Table 3 – Land cover area totals in km² and their percentage from LAND maps for IGBP, MODIST2001, MODISAT2001, GLC2000, and MODISAT2007 in Huambo

Land cover	LAND 90	IGBP
Forest	5920	9720 (64.1)
Savannas/ Grasslands	18539	19193 (3.52)
Grasslands	5436	4 (-99.9)
Croplands/Bare soil	3295	3500 (6.2)
Wetland	62	0 (0)

	LAND 2000	GLC2000	MODIST 2001	MODISA T2001
Forest	6107	26682 (336.9)	15168 (148.3)	26922 (340.8)
Savannas/ Grasslands	17818	3647 (-79.5)	16299 (-8.5)	4242 (-76.2)
Grasslands	4599	64 (-98.6)	502 (-89.1)	535 (-88.3)
Croplands/Bare soil	4424	1986 (-55.1)	437 (-90.1)	684 (-84.5)
Wetland	261	0 (0)	15 (-94.2)	38 (-85.4)

	LAND 2009	MODISAT 2007
Forest	5305	26535 (400.1)
Savannas/ Grasslands	19700	4560 (-76.8)
Grasslands	2759	867 (-68.5)
Croplands/Bare soil	5480	367 (-93.3)
Wetland	64	91 (42.1)

4.3 Spatial comparison

The kappa index of agreement between each map and its reference map, for Guinea-Bissau, is shown in table 4.

Table 4 – Kappa Index of Agreement for Guinea-Bissau

Land cover comparison	Kappa (%)
IGBP/LAND90	51.7
GLC2000/LAND2000	77.9
MODIST2002/LAND2000	61.4
MODISAT2002/LAND2000	52.6
MODISAT2007	51.9

The GLC2000 is the map with the best index of agreement for Guinea-Bissau. This map shows the best agreement for Savanna/Shrublands (84.1%). However, the Forest class

agreement is only 42.8% and Croplands/Bare soil is 15.1%. The MODIST2002 shows the best agreement for Forest (65.1%), followed by MODISAT2007 with 61.6% and MODISAT2002 with 58.6% and IGBP with 48.9%. For Savannas/Shrublands, the values of agreement for MODIST2002 and IGBP are respectively, 21.5% and 14.9%. The remaining maps have values lower than 10 % for this class, grassland and Croplands/Bare soil. Only class Wetland shows values of 12.7%, 11.8%, 26.7% and 32.6% for IGBP, MODIST2002, MODISAT2002, and MODISAT2007. The maps that best represent the Croplands/Bare soil class are GLC2000 and MODIST2001.

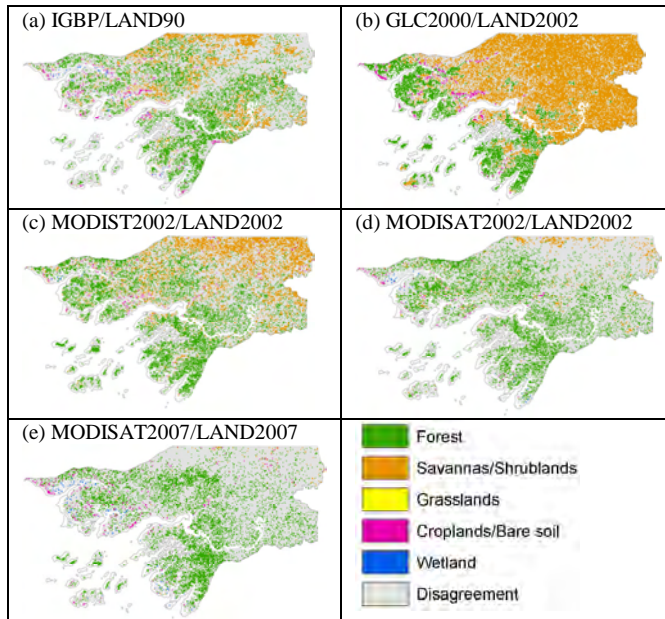


Figure 2 – Maps of agreement and disagreement, for Guinea-Bissau, between land cover products. (a) IGBP-DISCover/1990 LAND map, (b) GLC2000/2000 LAND map, (c) MODISTERRA2001/2000 LAND map, (d) MODISAQUA2001/2000 LAND map, (e) MODISAQUA2007/2007 LAND map

The kappa index of agreement between of each map and its reference map, for Huambo, is shown in table 5.

Land cover comparison	Kappa (%)
IGBP/LAND90	53.5
GLC2000/LAND2000	42.3
MODIST2001/LAND2000	46.5
MODISAT2001/LAND2000	39.5
MODISAT2009	39.6

The classes with higher agreement are the Forest class (39.1%) and Savannas/Shrublands (45.3%) for IGBP, Forest (88.1%) and Croplands/Bare soil (14.2%) for GLC2000, Forest (36.5%) and Savannas/Shrublands (26.9%) for MODIST2001, and Forest (77.4%, 81.7%, respectively) for MODISAT2001 and MODISAT2007. maps In contrast, the classes with the lower values of agreement (<10%) are Grassland, Croplands/Baresoil and Wetland for all datasets except GLC2000 with Savannas/Shrublands, Grassland and Wetland.

5. DISCUSSION

The accuracy assessment done in this study is based on the comparison of global land cover products (IGBP, GLC2000,

MODIS data) derived from coarse spatial resolution with three medium to high resolution maps. As many authors claim that is not possible to reliably identify land cover changes by comparing different datasets from different years (Giri et al., 2005; Jung et al., 2006), we try to minimize this effect by comparing each map with the reference map of the closest date.

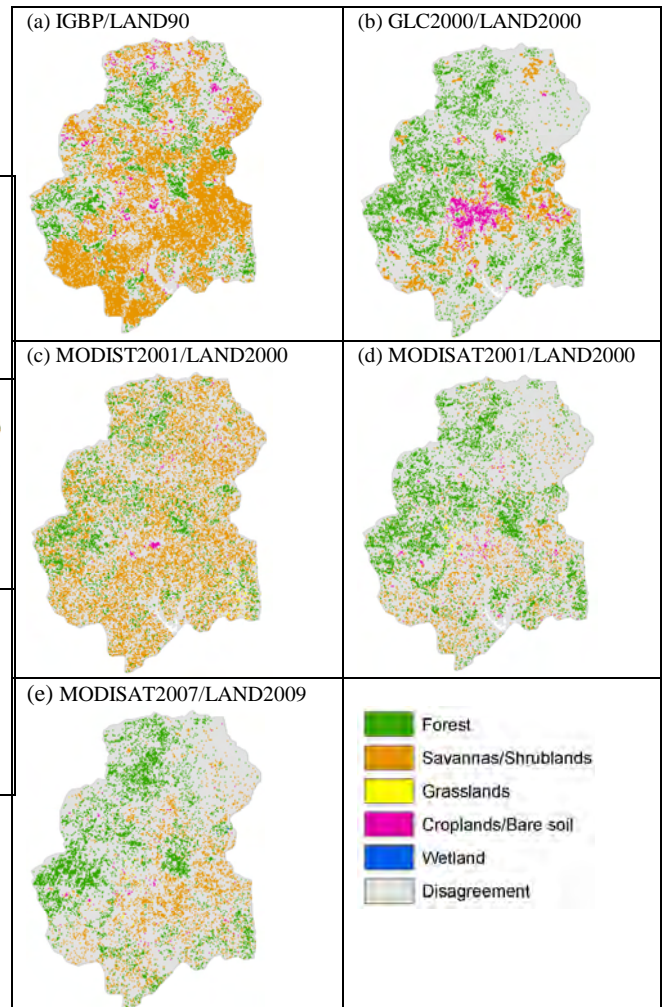


Figure 3 – Maps of agreement and disagreement, for Huambo province, between land cover products. (a) IGBP-DISCover/1990 LAND map, (b) GLC2000/2000 LAND map, (c) MODISTERRA2001/2000 LAND map, (d) MODISAQUA2001/2000 LAND map, (e)MODISAQUA2007/2009 LAND map

This analysis reveals that there are varying levels of discrepancy between the global land cover datasets and that both area totals and spatial agreement or disagreement vary from region to region. This is reflected in three main classes: Forest, Savannas/shrublands and Croplands/Bare soil. Results show that Forest and Savannas/Shrublands classes diverge largely from the reference maps. In general, Forest has high values in global maps and low values in LAND maps. This may be related to the difficulty of harmonizing the different map legends and also, with the options adopted in class aggregation. Although, the limits of tree cover chosen for Forest definition and Savannas/Shrublands for comparison were greater than 40% and between 10 and 40%, respectively, the aggregation of each legend turns difficult because the IGBP legend considers Forest above 30% and Savannas between 10 and 30%. The 10 % difference can have some influence in the Forest and Savannas/shrublands results. The visual inspection over the

Landsat images from the three years analyzed, for each study area, shows that there is an increase in Savanna-woodland which seems to be related with the conversion of forest areas. The main changes occurred in the two decades seems to be directly related to the expansion and dynamics of Cropland/bare soil. This is relevant mainly in Huambo, where the values increase substantially. This trend is not observed in global maps where this class decreases in area. The best index of agreement is obtained by the GLC2000 land cover product for Guinea-Bissau and IGBP for Huambo in assessing the aggregated area and spatial extent of the land cover classes. However, in general Guinea-Bissau shows higher values of spatial accuracy (between 51.9% and 77.9%) than Huambo (between 39.6% and 53.5%) which can be related with the landscape structure. The degrees of accuracy seem to be strongly dependent on the landscape type: structured with large contiguous patches in Guinea-Bissau and less unstructured and scattered small patches in Huambo. In more heterogeneous and fragmented regions, the coarse spatial resolution maps present more errors and uncertainties. In the case of the Huambo province located in a very mountainous region, with steep slopes, it is more difficult to produce high quality classifications than in Guinea-Bissau with a mostly flat land surface. Mapping land cover using coarse spatial resolution data can be a challenge due to landscape structure, because it can be more detailed than the resolution of the sensor (Jung et al., 2006). It is important to note that there are sharp differences between MODIST and MODISAT maps, maybe due to the combination of data sources.

6. CONCLUSIONS

This study has attempted to validate five global land cover datasets using three land cover maps derived from Landsat data as reference data and comparatively assess the agreement and mapping uncertainties between them. For that, a legend harmonization was done in order to minimize differences due to thematic class definitions. Nevertheless, the comparative analysis reveals that there are varying levels of discrepancies between the maps which suggests caution to the users when using one particular dataset, especially if several dates from different sources are employed in land cover change analysis. This is not a surprise, since global maps use diverse approaches and data from different satellite sensors with varying degrees of raw data corrections and manual manipulation during the classification process (Jung et al., 2006). Also, errors can be introduced due to the variable definition of classes.

This work aims to highlight the similarities and differences between datasets, and consequently their strengths and weaknesses, for two specific regions in Africa in order to help users to select the most appropriate dataset for their applications. Users can use areas where data have higher accuracy values and look for complementary information in disagreement areas. It intends, also, to highlight the need of producing land cover datasets using high resolution or medium to high resolution data, together with auxiliary data in order to improve the confidence on land cover information.

REFERENCES

Giri, C., Zhu, Z. and Reed, B., 2005. A comparative analysis of the Global Land Cover 2000 and MODIS land cover data sets. *Remote Sensing of Environment*, 94, pp. 123-132.

Herold, M., Mayaux, P., Woodcock, C.E., Baccini, A. and Schumullius, C., 2008. *Remote Sensing of Environment*, 112, pp. 2538-2556.

Jung, M., Henkel, K., Herold, M. and Churkina, G., 2006. Exploiting synergies of global cover products for carbon cycle modelling. *Remote Sensing of Environment*, 101, pp. 534-553.

Kalacska, M., Sanchez-Azofeifa, G.A., Rivard, B., Calvo-Alvarado, J.C. and Quesada, M., 2008. Baseline assessment for environmental services payments from satellite imagery: A case study from Costa Rica and Mexico. *Journal of Environmental Management*, 88, pp. 348-359.

Loveland, T.R., Reed, B.C., Brown, J.F., Ohlen, D.O., Zhu, Z., Yang, L. and Merchant, J.W., 2000. Development of a global land cover characteristics database and IGBP DISCover from 1 km AVHRR data. *International Journal of Remote Sensing*, 21 (6/7), pp.1303-1330

McCallum, I., Obersteiner, M., Milsson, S. and Shvidenko, A., 2006. A spatial comparison of four satellite derived 1km global land cover datasets. *International Journal of Applied Earth Observation and Geoinformation*, 8, pp. 246-255.

Rosenfield, G.H., 1986. A coefficient of agreement as a measure of thematic classification accuracy. *Photogrammetric Engineering and Remote Sensing*, 52(2), pp. 223-227.

Wu, W., Shibasaki, R., Yang, P., Ongaro, L., Zhou, Q. and Tang, H., 2008. Validation and comparison of 1 km global land cover products in China. *International Journal of Remote Sensing*, 29(13), pp. 3769-3785.

Diniz, C., 2006. *Características Mesológicas de Angola*. Instituto Português de Apoio ao desenvolvimento, Lisboa, pp.546.

Di Gregorio, A. and Jensen, L.J.M. (2000). *Land Cover Classification System (LCCS)*. FAO, Rome, pp. 180.

Lambin, E.F. and Geist, H., 2006. *Land use and land cover change: Local processes and global impacts*. Springer, Germany, pp. 130-131.

Catarino, L.M.F., 2004. *Fitogeografia da Guiné-Bissau*. Provas de doutoramento em Engenharia Agronómica, Instituto Superior de Agronomia, Universidade Técnica de Lisboa, pp. 440.

Fritz, S., Bartholomé, E., Belward, A., Hartley, A., Stibig, H.J., Eva, H., Mayaux, P., Baratlev, S., Latifovic, R., Kolmert, S., Roy, P.S., Agrwal, S., Bingfang, W., Wenting, X., Ledwith, M., Pekel, J.F., Giri, C., Mucher, S., de Badts, E., Tateishi, R., Champeaux, J.L. and Defournay, P., 2003. Harmonization, mosaicing and production of the Global Land cover 2000 database (Beta version). European commission, Joint research center, Ispra, Italy, pp.41.

Strahler, A., Muchoney, D., Borak, J., Friedl, M., Gopal, S., Lambin, E. and Moody, A., 1999. *MODIS land cover product: algorithm theoretical basis document, version 5.0*. Boston University, pp.72.

USAID, 2008. 118/119 Biodiversity and tropical forest assessment for Angola. United States agency for International Development, pp. 55.

APPLICATION OF KOMPSAT II IMAGERY FOR CARBON EMISSION INVENTORY MAP

E. M. Chang^{a,*}, J. R. Kim, Y. S. Choi, I. H. Lee, G.S. Kim

^a Ziin Consulting, 514 Yongbieachunga, 75 Naesu, Jongno, Seoul, emchang21@gmail.com

^b Ziin Consulting, 514 Yongbieachunga, 75 Naesu, Jongno, Seoul, kjrr01@gmail.com
 Chungnam Development Institution, Keunryong, Gongju, inhee@cdi.re.kr
 University of Seoul, Department of Geoinformatics, Seoul, choiys@uso.ac.kr
 Ministry of Land, Transportation and Marine Affairs, gswww@korea.kr

Commission VII,

KEY WORDS: KOMPSAT II images, classification, carbon emission

ABSTRACT:

Various approaches have been tried to estimate carbon emission model from leaf to globe. Satellite imagery is one of the sources to make land cover and land use data, usually in national or continental levels. Efforts to reduce carbon dioxide have started to be made in local governments. We tried to get LULC data for City of Boryong, Chungnam Province, using KOREAN Multi-Purpose Satellite II, 1 meter resolution data and other GIS data. Training vectors are selected from data of Korean Land Information System, supervised and unsupervised classifications were mixed to get the 5 classes and 18 classes. The more classes we get, the more error were turned out. To convert to carbon inventory, greenhouses and other point source data were digitized and weighted to make carbon emission maps. Natural ambient carbon sink can be added into policy for carbon emission inventory map, on the base of satellite images.

1. INTRODUCTION

1.1 Background of Study

Climate change is one of the critical issues in 21 century. IPCC have made a lot of effort to measure, analyze and forecast greenhouse gases. Fossil fuels have been a main target to decrease to solve the problem, but rapid industrialization has accelerated the increase in greenhouse gases. In 2009, Republic of Korea published <Comprehensive countermeasure for climate change adaptation> for planning for continuous sustainable development. Carbon emission inventory showed less than 2.5percent contribute agricultural activity to total emission in Korea, but the effect of forest and grassland have not been focused as a sink tank for carbon inventory. Parameterization of CO₂ flux over the ecosystem has been investigated in Japan (Kondo, *et als.* 2001), so the similar latitude situation can be applied into Korean peninsula. Carbon emission inventory for local administration levels are needed for the feasible action items development, so gridded data from satellite imagery can be used for generalization and localization of carbon emission inventory based on CO₂ flux over the ecosystem by Condo.

1.2 Study Purposes

It is necessary for Chungnam Province to prepare carbon emission inventory to prepare adaptation strategies before carbon trading between the provinces. It is also necessary to estimate natural emission from vegetation and crops and livestock. We aim to try a method to use KOMPSAT II imagery to estimate carbon inventory with various geographic information.

Gridded data calculated from Kondo's model can be tested at the local level of carbon emission inventory. Classification Procedure with KOMPSAT II data with other GIS data for the land cover map is an addition objective, as KOMPSAT II data are affordable for the local government- Province or County.

Data set	Year	format
<u>Imagery</u>		
Quickbird	2008	GeoTIFF
KOMPSAT II	2009	GeoTIFF
<u>GIS data</u>		
Forest Class data	2006	Shape
Digital Map(1:5000)	2007	NGII
Digital Maps etc	2007	Shape
KLIS data (cadastral data with land use)	2007	Shape
DEM	2004	txt

Table 1. Data for the Boryong City

This paper covers only results from one year study, further elaboration and verification of the result from field test will be needed. Here different approaches are tested with various GIS data to show the emission and net flux and carbon emission inventory at the level of different units of administration.

1.3 Methods

1.3.1 image processing

* Corresponding author. This is useful to know for communication with the appropriate person in cases with more than one author.

Images are obtained and pre-processed with ENVI and Erdas Imagine software. Detailed processes are shown in the figure 1 and figure 2.

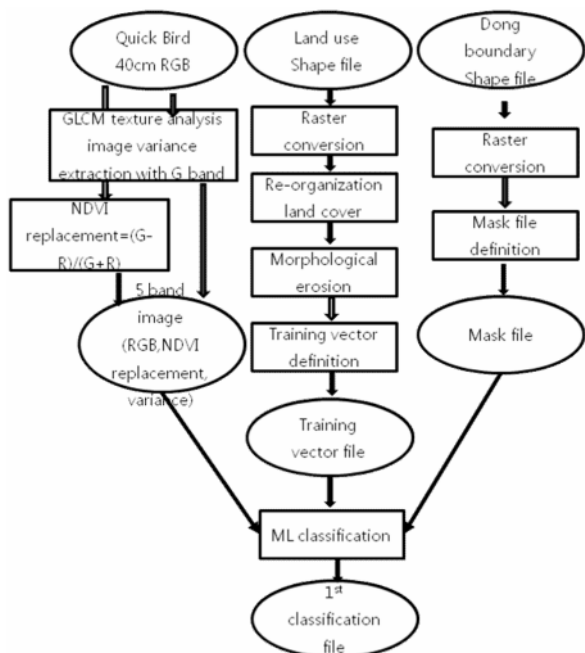


Figure 1. The first stage of image processing

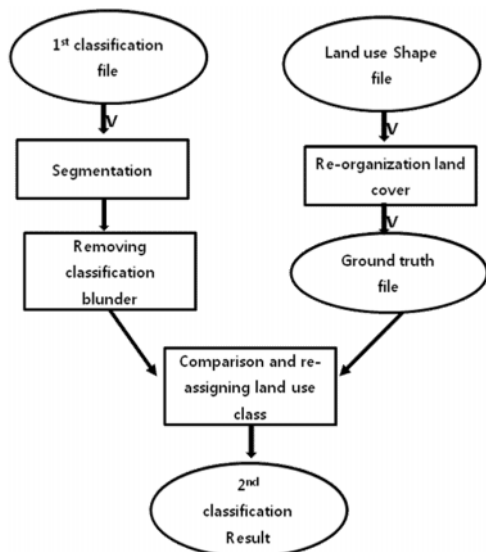


Figure 2. The Second Processes for image classification

1.3.2 Flux data conversion

Classified images are converted to net flux data using the following model based on the Kondo Model.

$$F_{CO_2} = -[bL(1+aI)] + R \quad (1)$$

$$R = R_{10} \exp [309 [(1/(283.15 - T_0)) - (1/(T - T_0))]] \quad (2)$$

F_{CO₂}: CO₂ flux(mgCO₂m⁻²s⁻¹)

I: surface radiation (observed)

R: canopy carbon CO₂ flux

R₁₀: R value at the 10 °C (0.12364 mgCO₂m⁻²s⁻¹)

T: temperature °K}

T₀: 234.13 °K

a, b: net flux parameters

2. RESULTS

2.1 Image Classification Result

The output of the first stage of classification is shown in the figure 3.

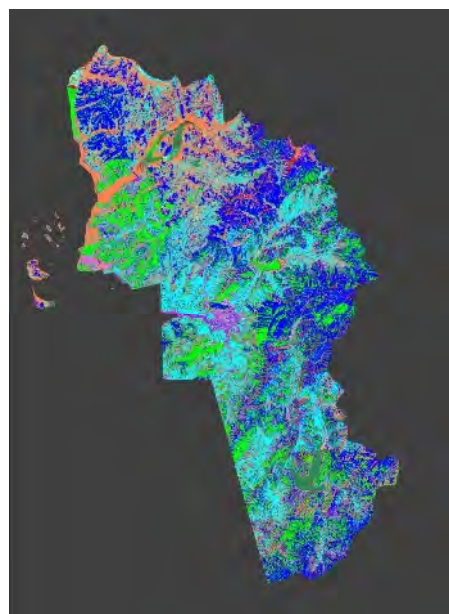


Figure 3. The output of the first classification

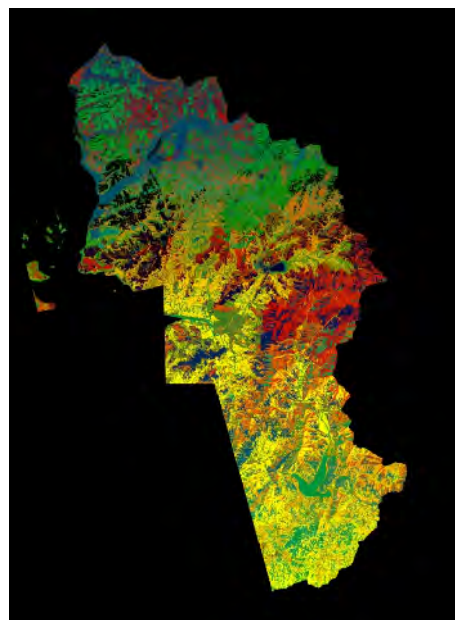


Figure 4. Segmented classification Results

Segmentation results are shown in Figure 4 for the Boryong County in Chungnam Province.

Final Classification image are shown in figure 5.

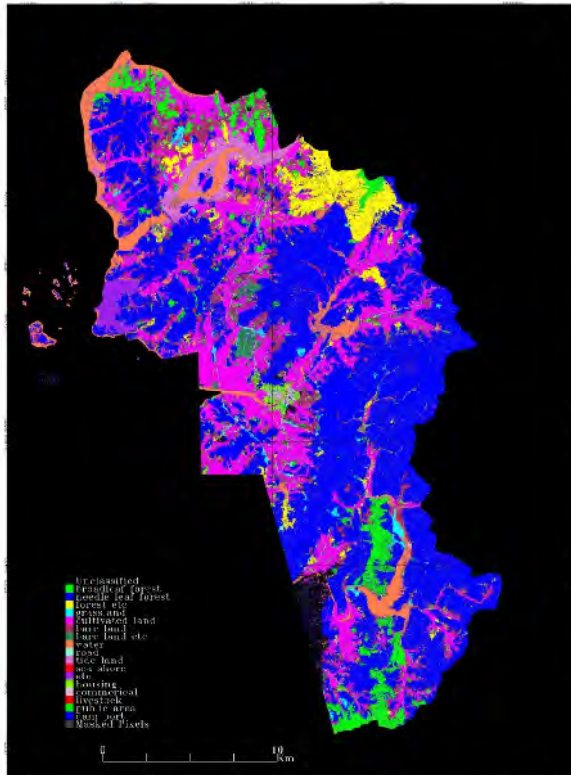


Figure 5. Final Output of Classification with Quick bird imagery

2.2 Map Algebra result

Classified images are converted into 6 classes to apply Kondo’s a, b coefficients.

Type of land cover	a ($J^{-1} \text{ m}^2 \times 10^{-4}$)	b ($\text{mgCO}_2 \text{ J}^{-1} \times 10^{-3}$)
Agriculture	5.96	3.68
Dry land	5.96	4.76
Coniferous forest	5.96	3.02
Deciduous broadleaf forest	5.96	3.04
Mixed forest	5.96	2.02
Grassland	5.96	3.37

Data: Kondo *et al.* (2001).

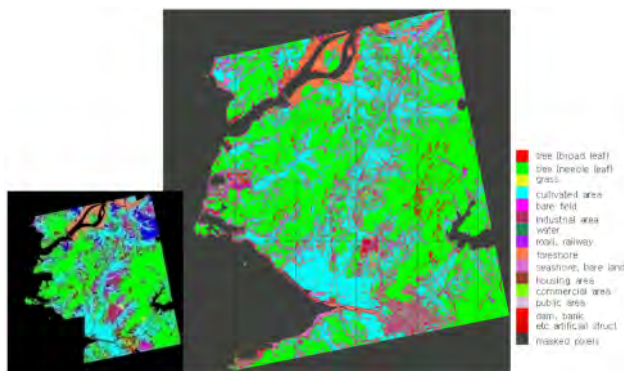


Figure 6. Classification of KOMPSAT II

2.3 KOMPSAT II data processing

The similar process are done for the KOMPSAT II image, of which the results are shown in

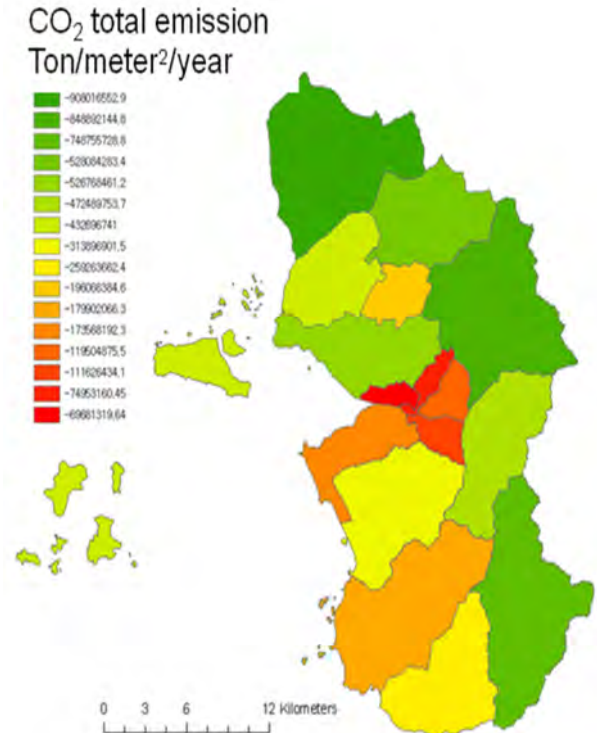


Figure 7. Map algebra data regrouped into lower level of administration unit (myun)

Figure 7 shown aggregated data for the CO2 emission for the city of Boryong, which can be compared statistics from the government document. The original gridded map with 3X3 meter also gives information on the distribution of the carbon absorption areas and carbon emission areas.

3. DISCUSSIONS AND CONCLUSIONS

Various emission inventory guidelines are being used for artificial emission focused on the fossil fuel consumption. The forest effect of absorption of carbon dioxide is estimated into earth tree saving with less powerful evidence in average. Species level experiment can give us rigid bio-atmospheric interface model, but it is difficult for policy makers. Satellite imagery with other GIS data can be used for the CO2 emission maps. The logical leap between the map algebra model and final aggregation are a limiting aspect of this study. Verification from the field study and comparisons between the images are not analyzed yet. But the output of several image classification and map algebra gives us additional and detailed information on CO2 flux. Rigid model verification will be added too.

References

Chang, E., Kim, M.H, Heo, M. and Lee, B. H. 2003, Monitoring of Graveyards in Mountainous Areas with Simulated KOMPSAT-II imagery, Proceedings of ACRS 2003 ISRS, Busan, 918-920

Garcia, I. and Zorraquino, J.V.M. 2002, Energy and environmental optimization in thermo electrical generating processes-application of a carbon dioxide capture system. *Energy* 27, 607-623.

Koerner, B. and Klopatek, J. 2002. Anthropogenic and natural CO₂ emission sources in an arid urban environment. *Environmental Pollution* Vol. 116, s45-s51.

Kondo H. Sigusa N, Murayama, S, Yamamoto, S, 2001, A Numerical Simulation of the Daily Variation of CO₂ in the central part of Japan. *Journal of the Meteorological Society of Japan*, VOL. 79, No.1 pp.11~21.

Moon Y.S and Koo, Y.S, 2006, Application of land use and land cover map for the atmospheric environments- temperature and wind field model of MM5 to vegetation distribution, *Korean Journal of Atmospheric Environment*, Vol. 22. pp 661-678

COLLOCATION-AIDED ADJUSTMENT OF HETEROGENEOUS MODELS FOR SATELLITE IMAGES

W. C. Chang^a, L. C. Chen^a, T. A. Teo^b

^a Center for Space and Remote Sensing Research, National Central University, Taiwan –
(wenchi, lcchen)@csrnr.ncu.edu.tw

^b Department of Civil Engineering, National Chiao Tung University, Taiwan - tateo@mail.nctu.edu.tw

Commission VII

KEY WORDS: Satellite, Modelling, Adjustment, Correction, Georeferencing

ABSTRACT:

The geometric correction for satellite images is an important task in remote sensor applications. The geometric correction methods for satellite images include rigorous sensor model (RSM) and rational function model (RFM). RSM describes the relationship between object points and image coordinates through exterior orientation parameters (EOPs). RFM uses the Rational Polynomial Coefficients (RPCs) to transform object coordinates into image space. Thus, treated parameters in the block adjustment for those two models are heterogeneous. In fact, the availability of those parameters is satellite dependent. Thus, the heterogeneous models between RSM and RFM should be combined in the block adjustment when those two types of images are integrated.

Considering the global geometry, the block adjustment for all images is to keep the geometrical registration consistent. There might still remain local systematic errors. Thus, this paper proposes a collocation-aided block adjustment for multi-sensor images. The Direct Georeferencing, which is one of RSM, and the RFM are combined a mathematical model for block adjustment. Then the least squares collocation is included to compensate the systematic errors for those heterogeneous models. Besides, to adapt for the weakly convergent geometry, which happens frequently, a digital elevation model is employed as the elevation control in the block adjustment.

The test data set includes GeoEye, QuickBird, WorldView-1, Kompsat-2, and Formosat-2 satellite images. The validation includes the checks for absolute accuracy and relative discrepancy among those images. Experimental results indicate that the proposed block adjustment significantly improved both the absolute accuracy and relative discrepancy.

1. INTRODUCTION

It usually contains multi-temporal or multi-sensor images in GIS applications, thus, geometric correction for satellite images is an important task. The geometric correction may be divided into two categories, namely, rigorous sensor model (RSM) and rational function model (RFM) (Fraser et al., 2006; Mayumi, et al., 2004). The treated parameters in the block adjustment for those two models are different. RSM is built up with exterior orientation parameters (EOPs). RFM uses the Rational Polynomial Coefficients (RPCs). Some of satellites companies provide EOPs instead of RPCs. Some others are on the contrary. A number of investigations have been reported regarding the comparison of RSM and RFM (Chen et al., 2006; Habib et al., 2007). However, there are few discussions about integrating the two heterogeneous models. Since the block adjustment with difference satellite sensors becomes an important work, those two types of heterogeneous models are needed to integrate.

There are two methods for RSM, namely, Bundle Adjustment (Toutin et al., 2003; Robertson, 2003) and Direct Georeferencing (DG) (Chen and Chang, 1998; Yastikli and Jacobsen, 2005). The treated orientation parameters are obtained from GPS, IMU, and star trackers. The Bundle Adjustment takes the advantages of favorable convergence geometry. Thus, the goodness of initial values for the orientation parameters might not be highly requested. DG employs the orientation parameters as a foundation to compensate systematic errors for EOPs. The approach needs good initial values as transformed from EOPs. Taking the advantages of good EOPs, DG approach derives favorable

results for those satellite images without goof convergence with less ground control points (GCPs) than Bundle Adjustment. We, thus, select DG of RSM to combine with RFM.

It is needed to combine all images in the block adjustment to keep the geometrical registration consistent. The simultaneous approach for combined adjustment is to build a mathematical model that contains those two heterogeneous geometry models. In addition, to compensate for local systematic errors, which might exist after the block adjustment, least squares collocation (LSC) is a good choice (Mikhail and Bethel, 2001; Hu and Tao, 2002). Since the least squares collocation is as an aid to compensate the local systematic error for simultaneous adjustment, we call it collocation-aided block adjustment (CABA). Besides, to adapt for the weakly convergent geometry, which happens frequently, a digital elevation model (DEM) is employed as the elevation control in the CABA.

2. METEODOLOGY

The CABA comprises two major parts. The first part is to build a combined adjustment model. It contains DG and RFM mathematics. And then it compensates the object coordinates by least squares collocation. The details of each part are given below.

2.1 Block Adjustment

It's contains three type of observation equations in block adjustment. The first one is DG observation equation. The next

one is about RFM. Ground Coordinates observation equation is the latest.

2.1.1 Direct Georeferencing: There are orbital parameters correction and object coordinates correction, which is shown in equation (1). It is employed for compensating the systematic errors of the exterior orientation.

$$\begin{aligned} v_{xi} &= (x_0 + a_0 + a_1 \cdot t - X_i) / (z_0 + c_0 + c_1 \cdot t - Z_i) - u_{xi} / u_{zi} \\ v_{yi} &= (y_0 + b_0 + b_1 \cdot t - Y_i) / (z_0 + c_0 + c_1 \cdot t - Z_i) - u_{yi} / u_{zi} \end{aligned} \quad (1)$$

where v_{xi}, v_{yi} are the residual values
 X_i, Y_i, Z_i are the ground coordinates
 x_0, y_0, z_0 are the satellite positions
 u_{xi}, u_{yi}, u_{zi} are the satellite light-of-sight vectors
 t is the time
 $a_0 \sim c_1$ are the orbital correction parameters

2.1.2 Rational Function Model: We use an affine transformation to compensate the systematic bias of RPCs. For this reason, affine transformation and object coordinates correction are included in the RFM observation equation, formulated as equation (2).

$$\begin{aligned} S &= A_0 + A_1 \cdot S_{RFM} + A_2 \cdot L_{RFM} \\ L &= B_0 + B_1 \cdot S_{RFM} + B_2 \cdot L_{RFM} \end{aligned} \quad (2)$$

where S, L are the image coordinates
 S_{RFM}, L_{RFM} are the image coordinates decided by RFM
 $A_0 \sim B_2$ are the affine coefficients

2.1.3 Ground Coordinates observation equations: It is used to distinguish GCPs ground coordinates and tie points (TPs) ground coordinates. The equation is shown in (3).

$$\begin{aligned} v_{Xi} - dX_i &= X_i^0 - X_i^{00} \\ v_{Yi} - dY_i &= Y_i^0 - Y_i^{00} \\ v_{Zi} - dZ_i &= Z_i^0 - Z_i^{00} \end{aligned} \quad (3)$$

where v_{Xi}, v_{Yi}, v_{Zi} are the residual values
 X_i^0, Y_i^0, Z_i^0 are the approximation values
 $X_i^{00}, Y_i^{00}, Z_i^{00}$ are the measured values

2.2 Least Squares Collocation

After block adjustment, the all object coordinates can be computed. In order to improve the geometric consistency between the image strips, least squares collocation is employed for compensating the local systematic errors of object coordinates. We assume that the X, Y, Z-axis are independent. Thus, we use three one-dimensional least squares collocation functions, which is shown in equation (4), to adjust the object coordinates.

$$\rho_k = \sigma_k \cdot [\Sigma_k]^{-1} \cdot v_k \quad (4)$$

where k is the x, y, z axis

ρ_k is the correct value of the interpolated point

σ_k is the row covariance matrix for the interpolated point with respect to the reference points

Σ_k is the covariance matrix for the reference points

v_k indicates the residual vectors

3. EXPERIMENTS

The test data set includes GeoEye-1, QuickBird, WorldView-1, Kompsat-2, and two Formosat-2 satellite images. Figure 1 shows the six images. The GSDs are sub-meter for GeoEye-1, QuickBird, and WorldView-1 images. Kompsat-2 image's GSD is about 1 m. And the GSDs for Formosat-2 images are more than 2m. The GCPs and independent check points (ICPs) were obtained from the ground control point database of the Ministry of the Interior, Taiwan, by manual measurements. The measurement accuracy is estimated to be better than 0.5 m. The TPs and independent check tie points (ICTPs) are acquired by manual measurements. The resolution of DEM is 5 m. The other related information is shown in Table 1 and Table 2.

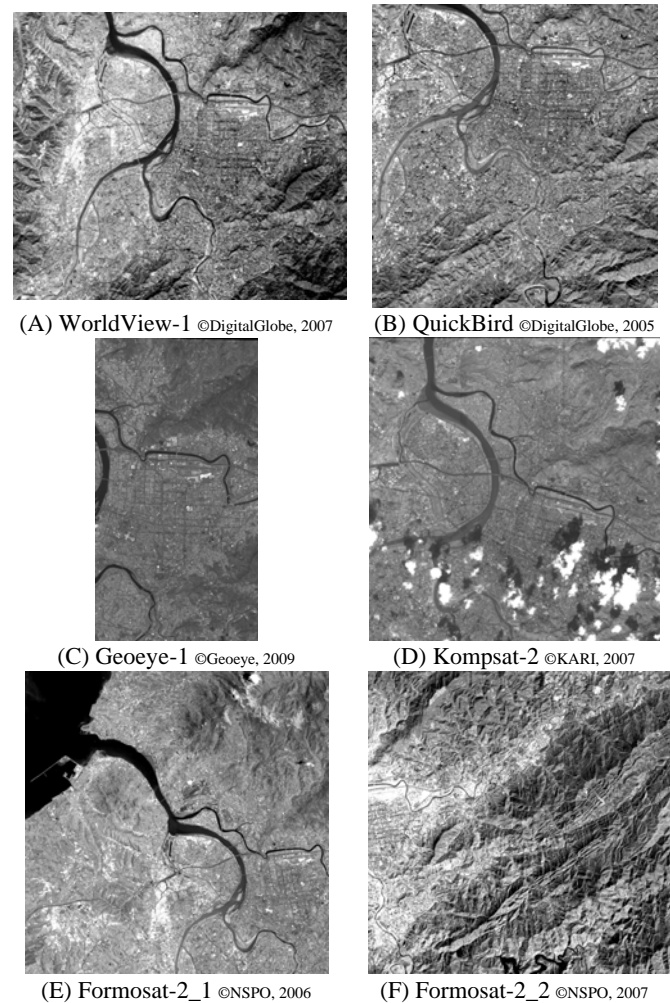


Figure 1. Test Images

Descriptions	WorldView-1	QuickBird	Geoeye-1
Geometric Model	RFM	RSM	RFM
Level	Basic	Basic	Standard
Date	2007/11/25	2005/12/23	2009/9/20
GSD (m)	0.67	0.63	0.5
Image Size	35170 x 23708	27552 x 29320	19872 x 16000
No. of GCPs/ICPs	9/31	9/20	5/6
No. of TPs/ICTPs	16/24	16/24	16/21

Table 1. Information Related to Test Data

Descriptions	Kompsat-2	Formosat-2_1	Formosat-2_2
Geometric Model	RFM	RSM	RSM
Level	1A	1A	1A
Date	2007/10/21	2006/8/19	2007/1/30
GSD (m)	1.03	2.01	2.45
Image Size	15000 x 15500	12000 x 12000	12000 x 12000
No. of GCPs/ICPs	5/12	9/18	9/22
No. of TPs/ICTPs	11/20	6/17	6/14

Table 2. Information Related to Test Data

The validation include the absolute accuracy and the geometrical consistency between images. We use ICPs and ICTPs with the proposed model to evaluate the absolute accuracy and the geometrical consistency between images, respectively. The bias between the determined object coordinates and the true coordinates is calculated to find the root mean squared error (RMSE) for the ICPs. The ICTPs' RMSE is obtained from the relative discrepancy for each image. To reveal the contributions of CABA, the results of the single image adjustment without collocation, herein named **single**, are also given. The Formosat-2, WorldView-1, Quickbird, Geoeye-1 and Kompsat-2 satellites images are labelled **FS**, **WV**, **QB**, **GE** and **KP**, respectively, in those results.

3.1 Absolute Accuracy

The results of absolute accuracy are shown as Table 3. According to Table 3, the absolute accuracy for WV is about 0.9 m and better than 0.5 m for the QB and GE images. The absolute accuracy of KP is approximately 2 m. There is a small difference between the two methods for the higher resolution images. For the two FS images, the accuracy can improve to about 3.5 m when CABA is employed.

	single	CABA	Improvement
WV-E	0.87	0.87	0.00
WV-N	0.64	0.55	0.09
QB-E	0.50	0.47	0.04
QB-N	0.62	0.50	0.11
GE-E	0.56	0.51	0.04
GE-N	0.43	0.45	-0.03
KP-E	0.94	1.01	-0.07
KP-N	1.83	2.03	-0.20
FS_1-E	6.15	2.65	3.50
FS_1-N	2.36	1.28	1.07
FS_2-E	6.92	3.67	3.25
FS_2-N	2.65	2.15	0.49

Unit: m

Table 3. Absolute Accuracy Evaluation

3.2 Geometrical Consistency

The results for geometrical consistency between images are shown as Table 4. The CABA results for the WV, QB and GE images are approximately 0.5 m. The relative discrepancy can be improved from about 3 m to less than 2 m for the KP image. The improvement is significant for those two FS images. The relative discrepancy for the former is about 9 m, with single image adjustment. This decreases to approximately 3 m using CABA. The second one is the same. The errors obtained are from 7 m to about 3 m.

	single	CABA	Improvement
WV-E	0.56	0.57	-0.01
WV-N	0.80	0.47	0.33
QB-E	0.42	0.41	0.01
QB-N	0.62	0.57	0.05
GE-E	0.49	0.38	0.12
GE-N	0.64	0.51	0.13
KP-E	1.14	1.17	-0.02
KP-N	2.82	1.83	1.00
FS_1-E	9.21	2.65	6.56
FS_1-N	6.52	3.15	3.37
FS_2-E	6.84	3.22	3.62
FS_2-N	2.34	2.53	-0.19

Unit: m

Table 4. Geometrical Consistency between Images

4. CONCLUSIONS

This paper combines DG and RFM for multi-sensor block adjustment. Two heterogeneous models with DEM as elevation control are integrated. The experimental results indicate that the proposed method can significantly improve the geometric accuracy as well as reduce discrepancies when multi-resolution images are used. Tests indicate that the proposed method should be feasible for real applications.

ACKNOWLEDGMENTS

This investigation is partially supported by the National Land Surveying and Mapping Center, Ministry of the Interior, Taiwan.

REFERENCES

- Chen, L.C., and L.Y. Chang, 1998. Three Dimensional Positioning Using SPOT Stereostrips with Sparse Control, *Journal of Surveying Engineering*, 124(2):63-72.
- Chen, L. C., Teo, T. A., and Liu, J. L., 2006. The geometrical comparisons of RSM and RFM for FORMOSAT-2 Satellite Images. *Photogrammetric Engineering and Remote Sensing*, 72(5), pp.573-579.
- Fraser, C.S., G. Dial, and J. Grodecki, 2006. Sensor Orientation via RPCs, *ISPRS Journal of Photogrammetry & Remote Sensing*, 60(3), pp.182-194.
- Habib, A., Shin, S.W., Kim, K., Kim, C., Bang, K.I., Kim, E.M., and Lee, D.C., 2007, Comprehensive Analysis of Sensor Modeling Alternatives for High Resolution Imaging Satellites. *Photogrammetric Engineering & Remote Sensing*, 73(11), pp.1241-1251.
- Hu, Y. and C.V. Tao, 2002. Updating solution of the rational function model using additional control information. *Photogrammetric Engineering and Remote Sensing*, 68(7), pp.715-723.
- Mayumi, N., C.S. Fraser, N. Takayuki, S. Takahiro, and O. Shoichi, 2004. Accuracy assessment of QuickBird stereo imagery, *The Photogrammetric Record*, 19(106), pp.128-137.
- Mikhail, E.M. and J.S. Bethel, 2001. *Introduction to modern photogrammetry*. John Wiley and Sons, New York, pp.446-454.
- Robertson, B.C., 2003. Rigorous geometric modeling and correction of QuickBird imagery. *International Geoscience and Remote Sensing Symposium*, 21-25 July, Toulouse, France, on CD-ROM.
- Toutin, T., 2003. Block Bundle Adjustment of IKONOS In-Track Image, *International Journal of Remote Sensing*, 24(4), pp.851-857.
- Yastikli, N., and K. Jacobsen, 2005. Influence of system calibration on direct sensor orientation. *Photogrammetric Engineering and Remote Sensing*, 71(5), pp.629-633.

CHANGE DETECTION OF BUILDING MODELS FROM AERIAL IMAGES AND LIDAR DATA

Liang-Chien Chen ^{a,*}, Li-Jer Lin ^b, Hong-Kuei Cheng, ^c Shin-Hui Lee, ^c

^a Center for Space and Remote Sensing Research, National Central University, No.300, Zhongda Rd., Zhongli City, Taoyuan County 320, Taiwan - lcchen@csrsr.ncu.edu.tw

^b Department of Civil Engineering, National Central University, No.300, Zhongda Rd., Zhongli City, Taoyuan County 320, Taiwan - 973202088@cc.ncu.edu.tw

^c CECI Engineering Consultants, Inc., 28th Floor, No. 185, Sec. 2, Sinhai Rd., Taipei City 10637, Taiwan - (tc561, shl)@ceci.com.tw

KEY WORDS: Change detection, Building, LIDAR, Image, Aerial

ABSTRACT:

Building models are built to provide three dimensional (3D) spatial information, which is needed for varieties of applications, such as city planning, construction of location-based services, and the like. However, three dimensional building models need to be updated from time to time. Rather than reconstructing building models for the entire area, it would be more effective to only revise the parts that have changed. In this study, we aim at finding changes with 3D building models. The proposed scheme comprises three steps, namely, (1) data registration, (2) change detection of three dimensional building models, and (3) detection of new building models. The first step performs data registration for multi-source data. The second step performs the rule-based change detection, it include examination of spectrum from aerial images, examination of height difference between building models and LIDAR points, and examination of linear features from aerial images. A double-threshold strategy is applied to cope with the highly sensitive thresholding often encountered when using the rule-based approach. In the third step, we detect the LIDAR point clouds in the new building areas by removing vegetation, ground and old building areas. We then use region growing to separate the LIDAR point clouds into different groups. Finally, we use boundary tracing to get the new building areas. Ground truth data are used for validation. The experimental results indicate that the double-threshold strategy improves the overall accuracy from 93.1% to 95.9%. To provide comprehensive observations, the different cases are scrutinized.

1. INTRODUCTION

A cyber city can be constructed which contains more spatial information than traditional two-dimensional topographic maps. This also provides the possibility to comprehensively integrate various types of 3D information. Three dimensional building models are one important part of a cyber city. Considering the rapidity of urban growth, a 3D geographic system is in need for updating the building models in the 3D information system. The effective revision of spatial data becomes important. Currently, change detection is usually done through spectral analysis of multi-temporal images. Nevertheless, building models also have three-dimensional information. So, we try to fuse the LIDAR data and aerial images for building model change detection. LIDAR data and aerial images have their own particular advantages and disadvantages in terms of horizontal and vertical accuracy. Compared with aerial images, LIDAR data provide more accurate height information but less accurate boundaries. Aerial images provide more extensive 2D information such as high resolution texture and color information. Although 3D height information can be estimated from one or several images by the use of several methods (such as stereo, shape from shading, comparison to LIDAR) the height information extracted from aerial images is still relatively less accurate. (Lee *et al.*, 2008).

Several studies of change detection using spectral imagery have been reported (Metternicht, 1999). Recently, a number of change detection methods using LIDAR data have been proposed. Murakami *et al.* (1999) used multi-temporal LIDAR data to produce Digital Surface Models (DSMs) for the detection of changes. Walter (2004) used LIDAR data for object-based classification and observation of land phenomena to determine the land-use category. There has been many studies using the vector maps (Knudsen and Olsen, 2003; Matikainen *et al.*, 2004), LIDAR data (Girardeau-Montau *et al.*, 2005; Murakami *et al.*, 1999), and aerial imagery (Jung, 2004) as the old data set. Some have used 3D building models as the old data set for this purpose (Huang, 2008).

2. METHODOLOGY

Since Lidar data and aerial images have unique advantages and disadvantages, it is natural to integrate those two data sets. In this paper, we aim to find the changed 3D building models using old building models with new LIDAR data and aerial imagery. It includes two parts in change detection. One is change detection of old buildings; the other is detection of new buildings. The workflow is shown in Fig 1.

* Corresponding author.

2.1 Data registration

First, we register the LIDAR data, aerial images and building models. The control points are measured and the mapping functions selected for registration of the three data sets to the same coordinate systems. There are two parts in this step, namely, planimetric registration and elevation registration. The image coordinate system is used as reference for planimetric registration, because the images provide high planimetric accuracy. The LIDAR coordinate system is used as reference for elevation registration, because the LIDAR data provide more accurate elevation. Planimetric registration note X and Y shifts on the plane. The elevation registration adjusts the shifts in the Z direction.

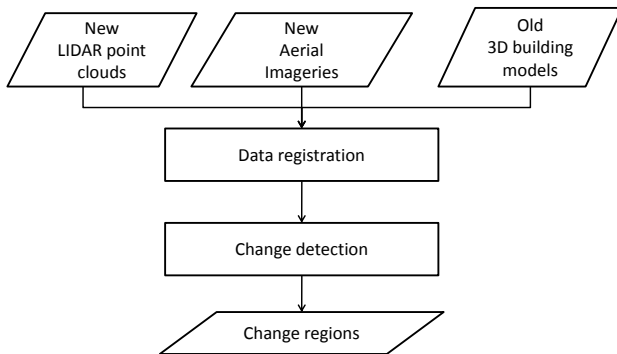


Figure 1. Workflow of the propose scheme

2.2 Change detection of 3D building models

In this part, we examine spectrum information from aerial images, height difference between the LIDAR points and the building models and linear features of the aerial images for detection of different types of change. First, we use the spectral information from the images. Here, NDVI is calculated to detect the area of vegetation for the exclusion of non-building areas. Second, we detect the LIDAR points which represent building roof planes, excluding the points on the wall and the convex points. Here, only points within the building boundaries are selected to be used for Delaunay triangulation. Third, facet orientation analysis is carried out for each triangle to detect those that might include wall points. Fourth, we calculate the center of the circumference for the triangle. The mean value and standard deviation of the elevation of the points in the circle are then calculated. Any point in a triangle with an elevation larger than two standard deviations is excluded. Fifth, we use equation 1 and the building model corner coordinates to calculate coplanarity parameters A, B, C. After this, the difference in height between the LIDAR points and the building models is calculated.

$$Z = AX + BY + C \tag{1}$$

The height differences (Δh) between the LIDAR points and building models comprise our major information about change. The workflow for calculation of height difference is shown in Fig 2. This detection process is done model by model. Since the height difference is, among others, the most important factor considered in this study, a double-threshold strategy on that is proposed to cope with the high sensitivity to thresholding often

encountered with the rule-based approach. The double-threshold strategy distinguishes the obvious types of change first, so as to have more information and different thresholds to facilitate detection of the areas subject to further examination.

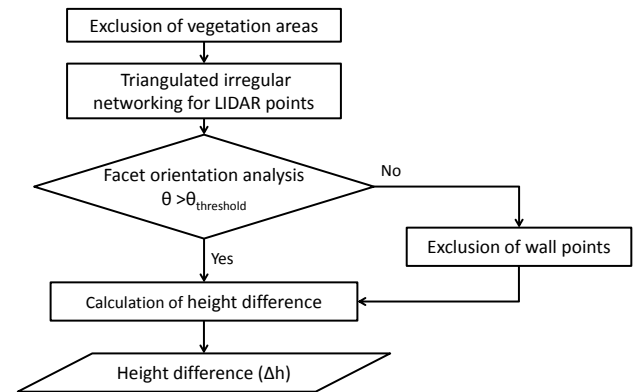


Fig 2. Calculation of height difference

Here, the line features in the aerial image give information that is used to refine the results. After this, we detect each building model to show the appropriate type of change. First, we set a double-threshold for height difference to discriminate between changed and unchanged points. The upper threshold is 3m and the low threshold is 1m. The 80% (δ_1) points in the building with height difference larger than upper threshold and the 80% (δ_2) points in the building with height difference smaller than low threshold are used to detect obvious changes and obvious unchanged in buildings. The data set between the double-threshold contain the areas subject to further examination. For the areas subject to further examination, additional information, line features from aerial images are added. The workflow for change detection is shown in Fig 3.

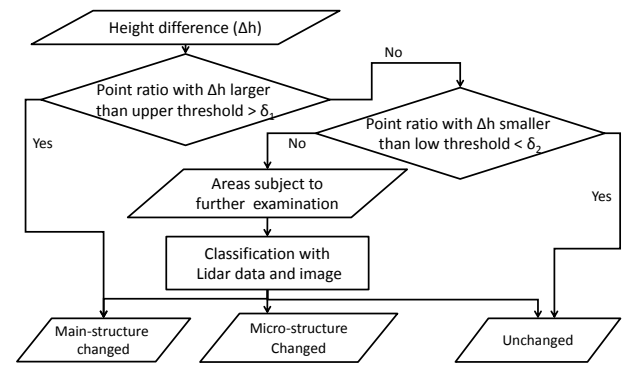


Fig 3. Change detection with double-thresholding

Line feature comparisons facilitate detection of the areas subject to further examination. The process for detection on areas subject to further examination is shown in Fig 4. Some parameters are to be set. The 50% (δ_3) points in the building with height difference larger than low threshold is used to detect the main-structure changed in buildings when the line feature comparisons are confirmed that there is no match. The 50% (δ_4) points in the building with height difference smaller than upper threshold is used to detect the unchanged in buildings when the line feature comparisons are confirmed that there is a match.

The $25m^2$ (δ_5) of change area is used to detect the micro-structure changed in buildings.

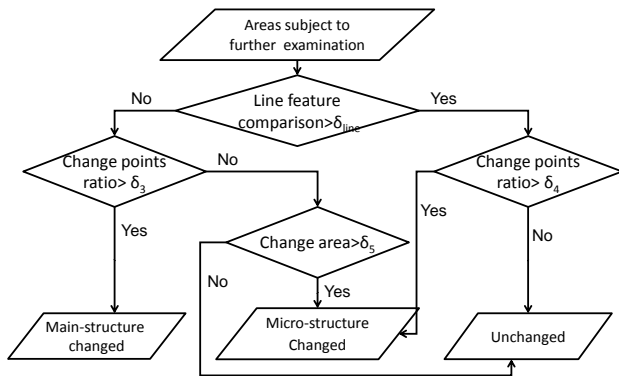


Fig 4. Change detection of areas subject to further examination

In the line feature comparisons, the aim is to compare building boundaries as they are shown in the building models and the aerial images. The idea is to extract the appropriate line features from the aerial images (i.e., the building boundaries) and compare them to the building boundaries in the models. The boundaries of the building models are first projected onto the aerial images to create the working area. Second, the line features are extracted from the aerial images by Canny edge detection and Hough transformation. Finally, the length ratio, angle and distance between model boundaries and line features are combined for line comparison (Lee *et al.*, 2008). By taking out the existing building boundaries, we can find whether there have been changes in the building models or not. The workflow for line feature comparisons procedures is shown in Fig 5.

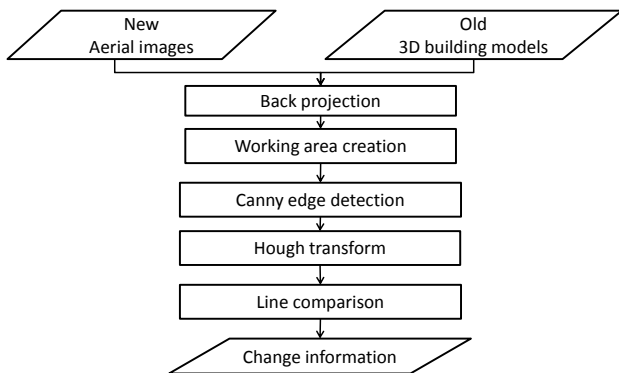


Fig 5. Workflow of line feature comparisons

2.3 Detection of new buildings

In this part, we detect the LIDAR point clouds in the new building areas by removing vegetation, ground and old building areas. First, we use NDVI to detect the area of vegetation. Second, we use the nDSM made from the LIDAR data to detect the area of ground. Finally, we use the old building models to detect the area of old buildings. After that, region growing is used to separate the LIDAR point clouds into different groups. The new building areas are detected after removing wall points and point groups with small area of the LIDAR point groups. Finally, we use the boundary tracing to get the boundaries of

new building area. The work flow for detection of new buildings is shown in Fig 6.

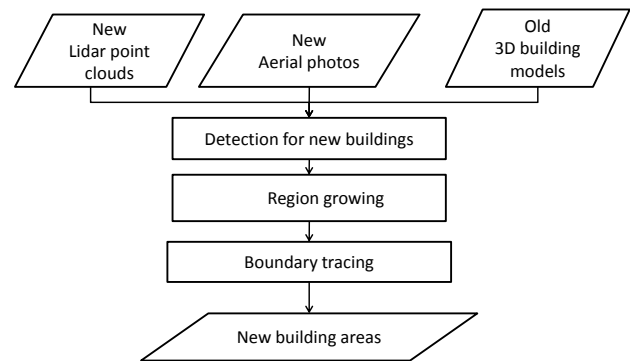


Fig 6. Workflow of detection of new buildings

3. EXPERIMENT AND RESULTS

The test site is located in Hsin-Chu City in Northern Taiwan. The old building models are polyhedral, built from a 2002 data set. It includes 492 building models. The aerial images were acquired using an UltraCam-D aerial digital camera with a 12cm resolution in June 2005. The LIDAR point clouds were acquired using a Leica ALS50 with a density of $1.7pts/m^2$ also in June 2005. The test data information is shown in Table 7. Regarding the parameters set, the NDVI threshold for detection the area of vegetation is 0.3. The threshold of facet orientation analysis between triangle's normal vector and building model's normal vector is 20° . The upper and low thresholds of height difference are 3m and 1m, respectively. Table 8 lists the four point's ratio and one change area threshold with height difference in change detection. Table 9 lists the threshold for line comparisons.

Test data information	
Lidar data	
Density	$1.7pts/m^2$
Acquisition time	June 2005
Aerial images	
Resolution	12cm
Acquisition time	June 2005
Building models	
Form	polyhedral
reconstruction time	2002

Table 7. Data information

Threshold	value
Point ratio with Δh larger than upper threshold (δ_1)	80%
Point ratio with Δh smaller than low threshold (δ_2)	80%
Point ratio with Δh larger than low threshold (δ_3)	50%
Point ratio with Δh smaller than upper threshold (δ_4)	50%
Change area (δ_5)	$25m^2$

Table 8. Threshold with height difference in change detection

As shown in Fig 10, the detection results show the main-structure changes. The blue models show the correct detection results, the red models show the omission results. As shown in Fig 11, the detection results indicate micro-structure changes. The blue models show the correct detection results, the red models show the omission result. The detection results with no change are shown in Fig 12. The blue models show the correct detection results, the red models show the omission results.

Threshold	value
Length ratio	0.7
Angle	15°
Distance between lines	10 pixels

Table 9. Threshold for line comparison

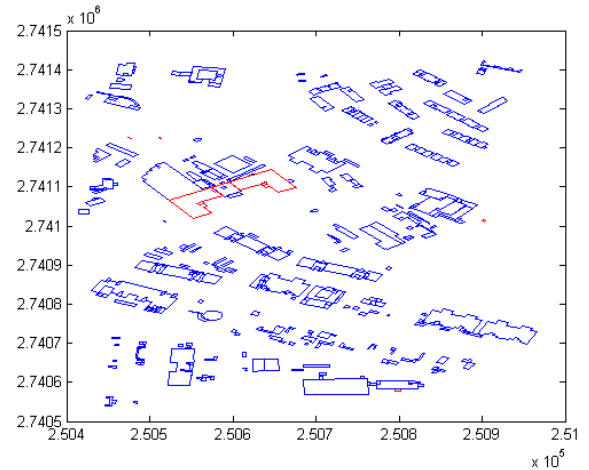


Fig 12. Detection result of no changed

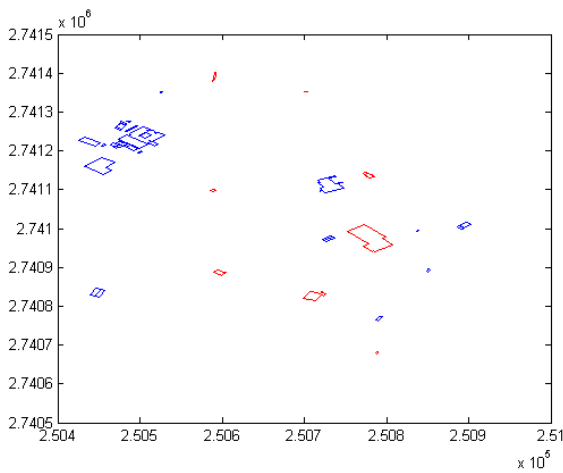


Fig 10. Detection result showing main-structure changes

Ground Truth \ TEST	TEST			
	Main-structure changed	Micro-structure changed	Unchanged	Total
Main-structure changed	25	0	10	35
Micro-structure changed	0	24	1	25
Unchanged	13	10	409	432
Total	38	34	420	492
			Diagonal total	458
Overall				0.931
Producer's		0.714	0.960	0.947
User's		0.658	0.706	0.779
Kappa				0.714

Table 13. Error matrix of detection with single-threshold strategy

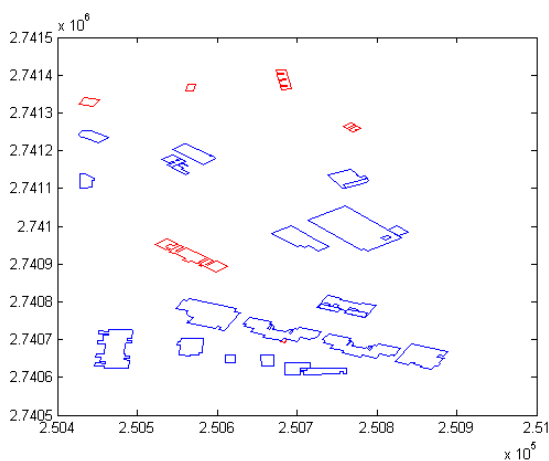


Fig 11. Detection results of micro-structure changes

Ground Truth \ TEST	TEST			
	Main-structure changed	Micro-structure changed	Unchanged	Total
Main-structure changed	31	0	4	35
Micro-structure changed	0	24	1	25
Unchanged	8	7	417	432
Total	39	31	422	492
			Diagonal total	472
Overall				0.959
Producer's		0.886	0.960	0.965
User's		0.795	0.774	0.852
Kappa				0.829

Table 14. Error matrix for detection with double-threshold strategy

After this, we used ground truth data for validation of the whole test site. The validation strategy for verification of the performance of double-threshold strategy includes two parts, i.e., double-threshold vs. single-threshold. The error matrix for the single threshold is shown in Table 13. The overall accuracy of the detection is 0.931. The producer's accuracy is 0.874, and the user's accuracy is 0.779. The error matrix for the double-threshold strategy is shown in Table 14. The overall accuracy of the detection is 0.959. The producer's accuracy is 0.937 and the user's accuracy is 0.852. The accuracy shows improvement with the double-threshold strategy.

To scrutinize the performance of the proposed method, two representative cases are discussed. These two cases explain why the detection failed. For the second part of the discussion, we look at two incorrect detections. The aerial images, LIDAR data and building models for case (a) and (b) are illustrated in Fig 15.

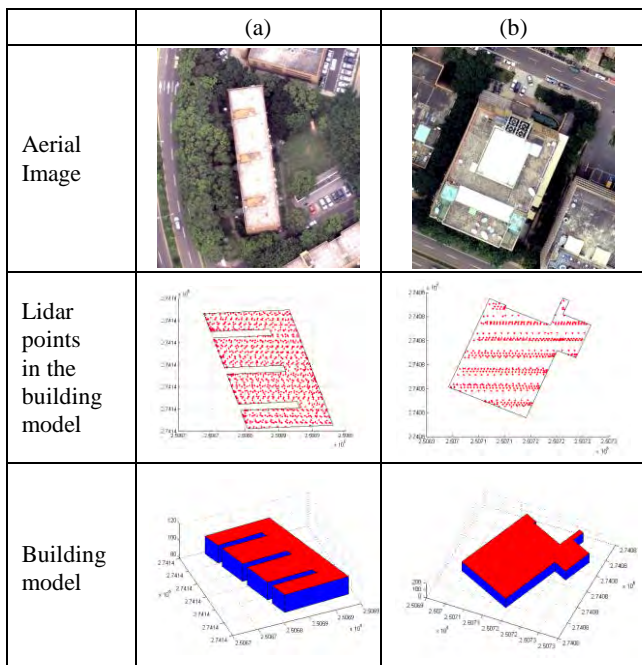


Fig 15. Incorrect detections case (a) and (b)

We observe that the ground truth data show no change for the two buildings in case (a) and (b). However, they have been classified as “changed”. Explanations are given as follows. In case (a), it is an unchanged building that has been classified to micro-structure changes. The reason is that some of the LIDAR points on the wall were not excluded. Those points cause the incorrect detection. As shown in Fig 16, the blue points are the LIDAR points within the building polygons, the green points are the points removed after Delaunay triangulation. The red points are the changed points. Notice that the detection changed points are almost the points on the wall that should be excluded.

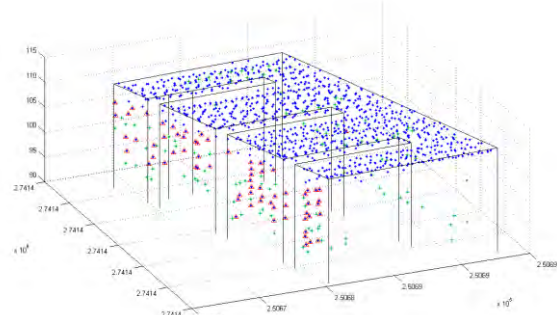


Fig 16. Changed points in case (a)

In case (b), it is an unchanged building that has been classified to main-structure changes. The reason is that the building roof has tiny roof variations. The variations cause some of the points detected as change points. Those points affect the detection. As shown in Fig 17, the blue points are the LIDAR points within the building polygons, the green points are the points removed after Delaunay triangulation. The red points are the changed points. Fig 17 shows the building roof has tiny variations.

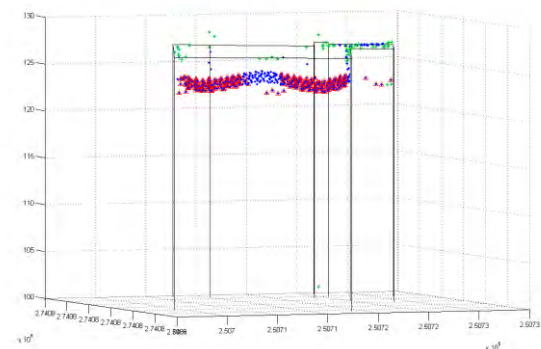


Fig 17. Changed points in case (b)

As shown in Fig 18, the detection results show the LIDAR point clouds in the new building areas by removing vegetation, ground and old building areas. As shown in Fig 18, these LIDAR points are discrete points, not regions. So, we use the region growing to separate the LIDAR point clouds into different groups. After that, we removed the wall points and point groups with small area of the LIDAR point groups. The result is shown in Fig 19. Finally, we use the boundary tracing to get the boundaries of new building area. The result is shown in Fig 20. The accuracy of new building detections is 100%. Nine new buildings in this test dataset are all detected by the proposed method. However, more test cases would be needed for comprehensive understanding.

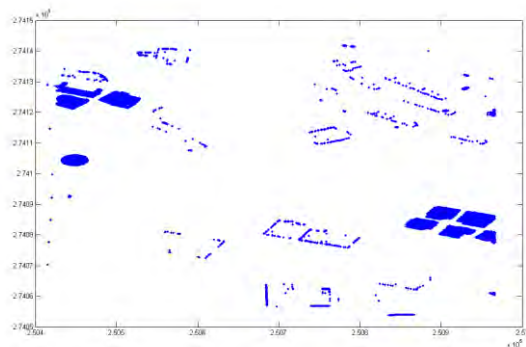


Fig 18. LIDAR point clouds detection result of new buildings

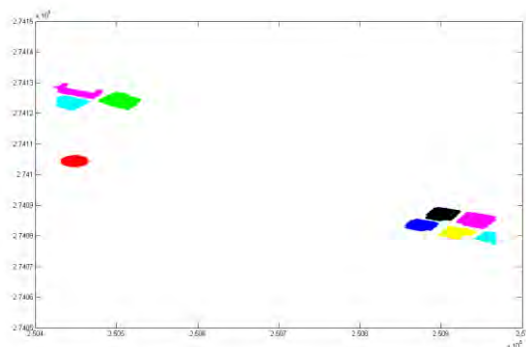


Fig 19. Detection result of new building areas

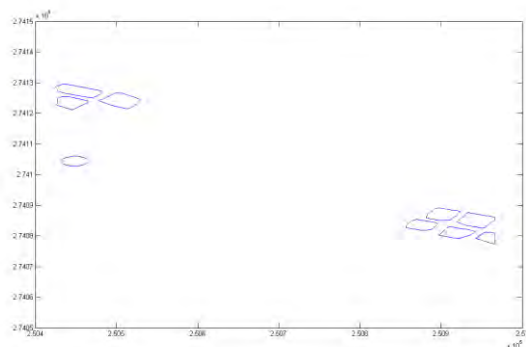


Fig 20. Result of boundary tracing

4. CONCLUSIONS

In this study, we have proposed a scheme for detection change by comparing old building models with new LIDAR and aerial imagery. The results include two parts. One is the change detection result of old buildings; the other is detection result of new building. Some change detection errors can be caused by the registration errors and tiny roof variations. If the building models of the roof are accurate and the registrations are accurate, the proposed method may achieve higher accuracy. The double-threshold strategy can also improve the accuracy. Although we only used line feature from the aerial images, texture information could also be used to refine the results. The

accuracy of new building areas detection is 100%. However, there is only few new buildings in the test site, it should increase more test cases for comprehensive understanding.

REFERENCES

- Girardeau-Montaut, D., Roux, M., Marc, R., and Thibault, G., 2005. Change Detection on Points Cloud Data Acquired with a Ground Laser Scanner, *International Archives of Photogrammetry, Remote Sensing and Spatial Information Sciences*, XXXVI (Pt. 3/W19):30-35.
- Huang, C.Y., 2008. The Integration of Shape and Spectral Information for Change Detection of Building Models, Master. National Central University, Taiwan.
- Jung, F., 2004. Detecting Building Changes from Multitemporal Aerial Stereopairs, *ISPRS Journal of Photogrammetry and Remote Sensing*, 58:187-201.
- Knudsen, T. and Olsen, B.P., 2003. Automated Change Detection for Updates of Digital Map Databases, *Photogrammetric Engineering and Remote Sensing*, 69(11):1289-1296.
- Lee, D.H., Lee, K.M. and Lee, S.U., 2008, Fusion of Lidar and Imagery for Reliable Building Extraction, *Photogrammetric Engineering and Remote Sensing*, 74(2):215-225.
- Matikainen, L., Hyypä, J., and Hyypä, H., 2004. Automatic Detection of Changes from Laser Scanner and Aerial Image Data for Updating Building Maps, *International Archives of Photogrammetry, Remote sensing and Spatial Information Sciences*, XXXV (B2):434-439.
- Metternicht, G., 1999. Change detection assessment using fuzzy sets and remotely sensed data: an application of topographic map revision, *ISPRS Journal of Photogrammetry & Remote Sensing*, 54:221-233.
- Murakami, H., Nakagawa, K., Hasegawa, H., and Shibata, T., 1999. Change Detection of Buildings Using an Airborne Laser Scanner, *ISPRS Journal of Photogrammetry and Remote Sensing*, 54:148-152.
- Walter, V., 2004. Object-based classification of remote sensing data for change detection, *ISPRS Journal of Photogrammetry & Remote Sensing*, 58:225-238.

ACKNOWLEDGMENTS

This investigation was partially supported by the National Science Council of Taiwan under Project No. NSC98-2622-E-008-003-CC2 and the CECI Engineering Consultants, Inc. under Project No.98923.

A NEW RIGOROUS SENSOR MODEL FOR RADAR IMAGERY BASED ON EXTERIOR ORIENTATION ELEMENTS

Chunquan CHENG^{a,b,*}, Jixian ZHANG^a, Kazhong DENG^b, Li ZHANG^a

^a Chinese Academy of Surveying and Mapping, Beijing, BeiJing, China. - (cspring, Zhangjx, Zhangl)@casm.ac.cn

^b China University of Mining and Technology, Xuzhou, China - kzdeng@cumt.edu.cn

Commission VII, WG VII/1

KEY WORDS: Imaging Equation, SAR, Side-Looking Radar, Sensor Model, Image Positioning, Geocoding, photogrammetry.

ABSTRACT:

Imaging equations are always considered as the most essential and basic part in photogrammetry and image mapping with remote sensing images. Rigourism and conciseness should be held as their basic characteristics. In this paper, using sensor exterior orientation including three lines and two attitude elements as the orientation parameters, new imaging equations for side-looking radar or SAR image positioning were derived. The model was based on the distance condition between sensor and object point and the azimuth condition of sensor scanning plane including antenna and radar beam center. Three forms of range-coplanarity equation were derived, the first form was in the tangent plane rectangular coordinate system, the second was in the geocentric rectangular coordinate system, and the third was the range-coplanarity equation with coordinates of image point as explicit function. The model could be easily used for side-looking radar and SAR image processing in photogrammetry field.

1. INTRODUCTION

1.1 The existing radar imaging equations

(1) Based on Range-Doppler condition model

R-D model is built with distance conditions and Doppler conditions, It is F. Leberl model when Doppler frequency value is set to zero.^[1,2]

(2) Collinearity equation model:

The imaging equation based on collinearity equation is similar with that based on optical images. This equation uses exterior orientation elements as its orientation parameters. Generally, Radar images are processed as optical linear array sensor images. Some scholars have made a modification on the collinearity equation, e.g. G. Konecny et al.^[3] put forward an improved collinearity equation in which the effect of terrain on image point location was taken into account.

(3) Polynomial model:

The application of general polynomial model in radar images is similar to that in optical images. The imaging mechanism was not considered in this model, while the polynomial model was used in it to convert all images by the same translation type.

1.2 The deficiency of R-D and collinearity equation model in Image Positioning

Doppler frequency is directly correlated with the speed of the sensor related to the object surveyed. Though it is difficult

to provide Doppler frequency of every object point, they can be acquired by assuming that it is a fixed value, or acquired by linear or polynomial model in side-looking radar images. While the discrepancy of doppler frequency may rapid increased by polynomial model in front or squint side-looking radar images, it may influence the precision of image positioning.

Researchers in the field of optical photogrammetry expected that the same orientation parameters as those in optical image orientation could be used in radar image positioning, thus collinearity equation could be introduced into radar images accordingly. Because of the differences in imaging mechanisms between optical and radar sensor, the precision of radar image positioning is often low with collinearity equation. Many scholars had made modifications on the model^[3], but the image equations are more complicated. By now, the major application of collinearity equation in radar images is geocoding, and complex photogrammetric processing such as in stereo positioning, especially in block adjustment is still uncommon.

2. COPLANARITY EQUATION

2.1 The principle of orientation with range-coplanarity equation

The model is established with the range-coplanarity equation by satisfying the range condition and coplanarity condition.

The range between the sensor and ground object point is equal to the calculation values by image column coordinate which is same as range condition in R-D model.

* Corresponding author.

All ground points related to one row images and sensor antenna are in same radar beam planarity which is determined by the sensor state vector and attitudes related to shoot time or the image row coordinate.

2.2 Analysis on the influence of attitude orientation

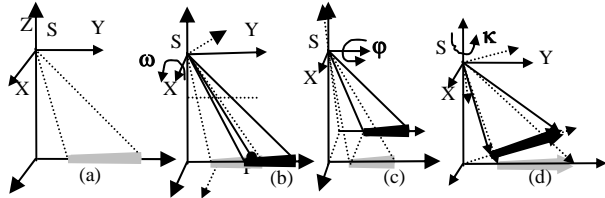


Figure 1. The influence of attitude on image positioning.

The effect of independently changing attitude angle on image positioning was analyzed as follows.

(1) Rolling angle: The existence of rolling angles resulted in changes of the aiming range. But for the same ground point, neither the distance between antenna and ground point nor the photographing time changed. Therefore, rolling angles barely influenced coordinates of the image point (fig.1b).

(2) Pitch angle: The existence of pitch angles made the aimed object shift to pre or post direction of airline, the time moment when photos were taken on the same ground point changed, and the distance between sensor antenna and ground point increased. Therefore, the row and line of the ground point in image were also changed (Fig.1c).

(3) Yaw angle: The existence of yaw angles made the aiming range of antenna rotate, the moment when photos were taken on the same ground point changed and the distance between sensor antenna and ground point increased. Therefore, the row and line of the ground point in image were also changed (Fig.1d).

2.3 Choice of rotation angle system and coplanarity equation

Three Euler angles are not independent parameters because the latter rotation angle is formed on the basis of the former one. Whether the roll(ω) angle will affect radar imaging positioning or not is determined by the adopted rotation angle system. There are 6 rotation angle orders. The ω - ϕ - κ system is generally employed in the field of optical imaging positioning, however, it is not the best rotation angle system to build the equation of radar beam scanning plane. The following discussion will provide a proof of this conclusion.

(1) Coplanarity equation derived by ω - ϕ - κ system

The rotation matrix which can transform the sensor vector coordinate system of ω - ϕ - κ rotation angle system to attitude reference frame is shown as follows:

$$R_b^A = R_x(\omega)R_y(\phi)R_z(\kappa) = \begin{bmatrix} 1 & 0 & 0 \\ 0 & \cos\omega & -\sin\omega \\ 0 & \sin\omega & \cos\omega \end{bmatrix} \begin{bmatrix} \cos\phi & 0 & \sin\phi \\ 0 & 1 & 0 \\ -\sin\phi & 0 & \cos\phi \end{bmatrix} \begin{bmatrix} \cos\kappa & -\sin\kappa & 0 \\ \sin\kappa & \cos\kappa & 0 \\ 0 & 0 & 1 \end{bmatrix}$$

$$= \begin{bmatrix} \cos\phi\cos\kappa & -\cos\phi\sin\kappa & \sin\phi \\ \cos\omega\sin\kappa + \sin\omega\sin\phi\cos\kappa & \cos\omega\cos\kappa - \sin\omega\sin\phi\cos\kappa & -\sin\omega\cos\phi \\ \sin\omega\sin\kappa - \cos\omega\sin\phi\cos\kappa & \sin\omega\cos\kappa + \cos\omega\sin\phi\sin\kappa & \cos\omega\cos\phi \end{bmatrix} \quad (1)$$

The normal line of the scanning plane is consistent with the X axis of sensor coordinate system after the attitude is rotated. Thus its unit vector is:

$$\vec{i} = R_b^A \begin{bmatrix} 1 \\ 0 \\ 0 \end{bmatrix} = \begin{bmatrix} \cos\phi\cos\kappa \\ \cos\omega\sin\kappa + \sin\omega\sin\phi\cos\kappa \\ \sin\omega\sin\kappa - \cos\omega\sin\phi\cos\kappa \end{bmatrix}$$

And the coplanarity condition equation is:

$$\vec{i}(\vec{P} - \vec{S}) = 0$$

Namely,

$$i_x(X - X_s) + i_y(Y - Y_s) + i_z(Z - Z_s) = 0 \quad (2)$$

or:

$$(X - X_s)\cos\phi\cos\kappa + (Y - Y_s)(\cos\omega\sin\kappa + \sin\omega\sin\phi\cos\kappa) + (Z - Z_s)(\sin\omega\sin\kappa - \cos\omega\sin\phi\cos\kappa) = 0 \quad (3)$$

It is seen that, ω - ϕ - κ system requires three attitude angles to constitute an expression if the scanning plane is to be obtained.

(2) Coplanarity equation derived by ϕ - κ - ω system:

The rotation matrix which can transform the sensor vector coordinate system of ϕ - κ - ω rotation angle system to attitude reference frame is shown as follows:

$$R_b^A = R_y(\phi)R_z(\kappa)R_x(\omega)$$

$$= \begin{bmatrix} \cos\phi\cos\kappa & -\cos\omega\cos\phi\sin\kappa + \sin\omega\sin\phi & \sin\omega\cos\phi\sin\kappa + \cos\omega\sin\phi \\ \sin\kappa & \cos\omega\cos\kappa & -\sin\omega\cos\kappa \\ -\sin\phi\cos\kappa & \cos\omega\sin\phi\sin\kappa + \sin\omega\cos\phi & -\sin\omega\sin\phi\sin\kappa + \cos\omega\cos\phi \end{bmatrix} \quad (4)$$

The unit vector of normal direction of radar scanning beam plane is:

$$\vec{i} = R_b^A \begin{bmatrix} 1 \\ 0 \\ 0 \end{bmatrix} = \begin{bmatrix} \cos\phi\cos\kappa \\ \sin\kappa \\ -\sin\phi\cos\kappa \end{bmatrix} \quad (5)$$

And the coplanarity condition equation can be easily obtained:

$$(X - X_s)(\cos\phi\cos\kappa) + (Y - Y_s)\sin\kappa - (Z - Z_s)(\sin\phi\cos\kappa) = 0 \quad (6)$$

(3) Coplanarity equation derived by κ - φ - ω system

In the same way, the expansion of the coplanarity condition equation is derived as:

$$(X - X_s)(\cos \kappa \cos \varphi) + (Y - Y_s)(\sin \kappa \cos \varphi) + (Z - Z_s)(-\sin \varphi) = 0 \quad (7)$$

It can be concluded that the coplanarity condition is independent of ω angle when the κ - φ - ω or φ - κ - ω rotation angle system is used.

3. RANGE-COPLANARITY EQUATIONS IN DIFFERENT COORDINATE SYSTEMS**3.1 The imaging equation in tangent orthogonal coordinate system**

It is suitable for airborne or small area spaceborne radar images to orient in tangent orthogonal coordinate system. Thereinafter, imaging equations and image processing model will be derived based on the scanning plane confirmed by φ - κ - ω system.

The distance equation based on range-coplanarity equation is the same as the one based on range-Doppler model. For slant range images, the equation is as follows:

$$(X - X_s)^2 + (Y - Y_s)^2 + (Z - Z_s)^2 = (y_s M_y + D_s)^2 \quad (8)$$

Thus, the range-coplanarity equations are obtained:

$$\begin{cases} (X - X_s)(\cos \varphi \cos \kappa) + (Y - Y_s) \sin \kappa - (Z - Z_s)(\sin \varphi \cos \kappa) = 0 \\ (X - X_s)^2 + (Y - Y_s)^2 + (Z - Z_s)^2 = (y_s M_y + R_0)^2 \end{cases} \quad (9)$$

3.2 Imaging Equation in Geocentric Orthogonal Coordinate System (GOCS)

The origin O of orbit coordinate system is the exposure station in the sensor orbit. The mathematic definitions of three axes in the coordinate system are as follows:

$$\begin{cases} \vec{Z}_o = [(Z_o)_x, (Z_o)_y, (Z_o)_z] = \vec{P}(t) / \|\vec{P}(t)\| \\ \vec{Y}_o = [(Y_o)_x, (Y_o)_y, (Y_o)_z] = (\vec{Z}_o \times \vec{V}) / \|(\vec{Z}_o \times \vec{V})\| \\ \vec{X}_o = [(X_o)_x, (X_o)_y, (X_o)_z] = \vec{Y}_o \times \vec{Z}_o \end{cases} \quad (10)$$

The normal vector of the scanning plane is:

$$\vec{i} = R_o^E R_b^o \begin{bmatrix} 1 \\ 0 \\ 0 \end{bmatrix} = \begin{bmatrix} i_x \\ i_y \\ i_z \end{bmatrix}$$

And the coplanarity condition equation is:

$$i_x(X - X_s) + i_y(Y - Y_s) + i_z(Z - Z_s) = 0$$

namely:

$$\begin{pmatrix} (X_o)_x & (Y_o)_x & (Z_o)_x \\ (X_o)_y & (Y_o)_y & (Z_o)_y \\ (X_o)_z & (Y_o)_z & (Z_o)_z \end{pmatrix} \begin{bmatrix} \cos \varphi \cos \kappa \\ \sin \kappa \\ -\sin \varphi \cos \kappa \end{bmatrix} \bullet \begin{bmatrix} X - X_s \\ Y - Y_s \\ Z - Z_s \end{bmatrix} = 0 \quad (11)$$

where

$$\begin{cases} i_x = \cos \varphi \cos \kappa (X_o)_x + \sin \kappa (Y_o)_x - \sin \varphi \cos \kappa (Z_o)_x \\ i_y = \cos \varphi \cos \kappa (X_o)_y + \sin \kappa (Y_o)_y - \sin \varphi \cos \kappa (Z_o)_y \\ i_z = \cos \varphi \cos \kappa (X_o)_z + \sin \kappa (Y_o)_z - \sin \varphi \cos \kappa (Z_o)_z \end{cases} \quad (12)$$

Thus, the range- coplanarity equation in GOCS is:

$$\begin{cases} i_x(X - X_s) + i_y(Y - Y_s) + i_z(Z - Z_s) = 0 \\ (X - X_s)^2 + (Y - Y_s)^2 + (Z - Z_s)^2 - (y_s M_y + R_0)^2 = 0 \end{cases} \quad (13)$$

3.3 The Range-coplanarity Equation with Coordinates of Image Point as Explicit Function

In order to express the above equation as a function of coordinates of the image point, the left-side of the coplanarity equation of the formula (9) is multiplied by a function F , with the value of coplanarity equation still being 0. Let F be:

$$F = \frac{-f}{\sin \varphi (X - X_s) + (Z - Z_s) \cos \varphi} \quad (14)$$

Where f is called equivalent focal length whose value does not affect the tenability of the equation, but affects the number of iterations while the equation is solved as well as the fixed weight of the observed values. f can be obtained by the following formula according to the geometric relation among pixel size, ground resolution and focal length:

$$f = \frac{H_s \cdot \mu_0}{GSD_x} \quad (15)$$

where μ_0 is the value of equivalent pixel, H_s is the height of the sensor, and GSD_x is ground resolution of corresponding azimuth of the pixel.

Meanwhile, the range equation of the formula (9) is also transformed into a function of y , that is, the range-coplanarity equation of SAR image positioning with coordinates of image point (x, y) as the explicit function can be obtained:

$$\begin{cases} x = -f \frac{\cos \varphi \cos \kappa (X - X_s) + \sin \kappa (Y - Y_s) - \sin \varphi \cos \kappa (Z - Z_s)}{\sin \varphi (X - X_s) + (Z - Z_s) \cos \varphi} = 0 \\ y = [\sqrt{(X - X_s)^2 + (Y - Y_s)^2 + (Z - Z_s)^2} - R_0] \mu_0 / M_y \end{cases} \quad (16)$$

Similarly, the range-coplanarity equation of explicit function of coordinates of image point in the geocentric coordinate system can also be obtained.

It is concluded from the above equation that the mature method based on the collinearity equation model of optical images can be easily applied in the processing of photogrammetric data of SAR images.

4. THE CORRECTION AND GEOCODING OF RADAR IMAGERY

4.1 The preprocessing of attitude angles

The φ - κ - ω system is adopted in the R-Cp model this paper, while generally ω - φ - κ system is adopted in the original attitude measurements. Before three values of attitude angles in ω - φ - κ system are used, they should be converted into the values in φ - κ - ω system.

Since different attitude systems have the same translation matrix, that is:

$$R(\omega, \varphi, \kappa) = R(\varphi, \kappa, \omega) \quad (17)$$

Set $R(\omega, \varphi, \kappa) = [a_{ij}]$, ($i, j = 0, 1, 2$), and a_{ij} is matrix element which is obtained from formula(1).

Thus, φ, κ, ω value of φ - κ - ω system can be calculated by a_{ij} .

$$\begin{cases} \varphi = -\arctan(a_{30} / a_{00}) \\ \kappa = -\arcsin(a_{10}) \\ \omega = \arctan(a_{12} / a_{11}) \end{cases} \quad (18)$$

4.2 Calculation of coordinates of ground point using image point

The coordinates of ground point can be obtained using the corresponding coordinates of the image point in combination with distance condition, coplanarity condition and earth ellipsoid equation. The coordinate (X Y Z) can be acquired by the following three equations:

$$\begin{cases} F_1 = \frac{(X - X_s)^2 + (Y - Y_s)^2 + (Z - Z_s)^2}{R_j^2} - 1 = 0 \\ F_2 = i_x (X - X_s) + i_y (Y - Y_s) + i_z (Z - Z_s) = 0 \\ F_3 = \frac{X^2 + Y^2}{(a + H)^2} + \frac{Z^2}{(b + H)^2} - 1 = 0 \end{cases} \quad (19)$$

(Where $R_j = j \cdot M_y + R_0$, R_j is the slant range of the object point, j is the column coordinate, H is geodetic altitude)

According to the least squares method, the coordinate (X, Y, Z) of the ground point can be solved iteratively.

4.3 Refinement of Orientation parameters [4]

The range-coplanarity equation of formula (16) is linearized, therefore the error equation can be obtained:

$$\begin{cases} v_x = f_{1X_s} d_{X_s} + f_{1Y_s} d_{Y_s} + f_{1Z_s} d_{Z_s} + f_{1\kappa} d_{\kappa} + f_{1\varphi} d_{\varphi} - l_1 \\ v_y = f_{2X_s} d_{X_s} + f_{2Y_s} d_{Y_s} + f_{2Z_s} d_{Z_s} + f_{2\kappa} d_{\kappa} + f_{2\varphi} d_{\varphi} - l_2 \end{cases} \quad (20)$$

Where $f.$ represents linear coefficient and l represents constant.

Correction model of observation data of exterior orientation elements expressed by low order polynomial of time parameter t :

$$\begin{cases} dp_i = b_{i0} + b_{i1}t + b_{i2}t^2 & (dp_i = dX_s, dY_s, dZ_s) \\ da_i = c_{i0} + c_{i1}t + c_{i2}t^2 & (da_i = d\varphi, dk) \end{cases} \quad (21)$$

In order to overcome the singularity of normal equation and satisfy adjustment with sparse control points, combined adjustment error equations can be formed using EO observing data along with virtual observing values of R-Cp:

$$\begin{cases} V_y = B_{Rb}b & -L_R \dots \dots P_y \\ V_x = B_{Cb}b + B_{Cc}c - L_C \dots \dots P_x \\ V_b = E_b b & -L_b \dots \dots P_b \\ V_c = & E_c c - L_c \dots \dots P_c \end{cases} \quad (22)$$

Where V_y, V_x, V_b, V_c are corrections of range equation, coplanarity equation, polynomial model parameters of EO lines and attitudes, respectively; b, c are polynomial coefficients for exterior orientation model.

The above formula can be incorporated as:

$$V = BX - L \dots \dots P \quad (23)$$

The solutions of orientations are:

$$X = (B^T P B)^T (B^T P L) \quad (24)$$

5. EXPERIMENT

The experimental material was an ALOS/PALSAR image (70Km×60Km, with pixel resolution of 3.189m in velocity direction and 9.368m in range direction), covering the mountainous areas in Shanxi province in the west of China.

There were 21 image points with ground points coordinates surveyed from 1:10,000 scale relief map.

5.1 Experiment 1: Direct Geocoding to the Earth Ellipsoid

The ephemeris and attitude data acquired from supplementary file of the image were used, and Gauss projection was also adopted.

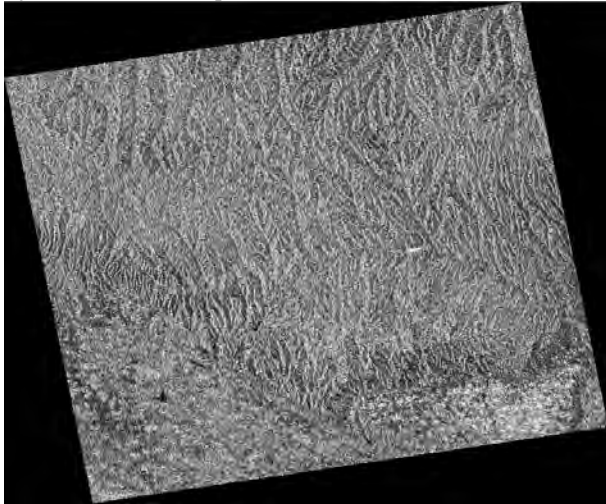


Figure2.Direct geocoding to the earth ellipsoid

Since the misaligned angle of sensor axis relative to satellite body axis was not available to the public, the three attitude angles were all set to 0; meanwhile the DEM data were used due to significant change of the terrain. The precision of direct geocoding was acquired by comparing coordinates of 21 homonymy points from geocoding image and the relief map points, and the results were listed in the “direct geocoding” column of table 1.

The results also indicated that all the check points had obvious systemic errors both in azimuth and range directions.

5.2 Experiment 2: Orthophoto correction with sparse GCPs and DEM data.

In this experiment, two surveying points were selected as control points (distributed on the top right and bottom left corners of the image) and 19 as check points so as to refine the image orientation elements, and the images were corrected with refined orientation elements and DEM data.

Through comparing calculation results and the known data of surveying object, errors of ground control points (GCPs) and check points (CPs) were listed in the “Orthophoto correction” column of table 1.

Exp content	Direct Geocoding	Orthophoto Correction	
Unit: (pixel)	21CPs	2GCPs	19CPs
RMS_x(azimuth)	3.53	0.44	1.26
RMS_y(range)	4.71	0.40	1.27
RMS_xy	5.88	0.59	1.79
MAX_error(x)	7.07	0.11	3.72
MAX_error(y)	5.77	-0.12	2.97

Table 1 The statistics of precision of check points

6. CONCLUSIONS

The collinearity equation model of radar images has such shortcomings as poor rigorousness and practicality; Range-Doppler model does not apply to the existing processing algorithms of photogrammetric data. With elements of exterior orientation as the orientation parameters, in this study a new imaging equation of radar image was constructed ---Range-Coplanarity equation. The imaging equation reflected the imaging mechanism of the radar images in the direction of range and the direction of orientation, and manifested the attribute of the image point coordinate as independent observed value of photogrammetry so that the positioning of radar image are able to easily adopt the mature algorithms of photogrammetric data processing of optical image. It also has simple form and requires less orientation parameters than R-D model and collinearity equation.

In the years past, techniques of sensor positioning and attitude determination technique had been greatly developed. With the utilization of them, the image mapping without GCPs will become a trend in future. Therefore, this image equation will bring convenience for radar image rectification, stereo positioning, block adjustment, and InSAR baseline calculation in photogrammetry. At present, related studies are still being kept on by us.

7. ACKNOWLEDGEMENT

This study is fully supported by National Natural Science Foundation of China (Project No. 40871167) and State 863 projects(Project No.200*AA12****).

8. REFERENCES

- [1] Leberl F. Radar grammetry for Image Interpretation, ITC Technical Report, 1978
- [2] F. Leberl. Radar grammetric processing[M]. Artech House, 1990
- [3] G.Konecny, W.Schuh. Reliability of Radar Image Data[J]. ISPRS Comm. I Symposium, 1988
- [4] Chunquan Cheng, Kazhong Deng, Jixian Zhang , Li Zhang. Block Adjustment of Airborne Imagery in Geocentric Orthogonal Coordinate System. ICIECS2009.

Passive microwave soil moisture evaluations by ground based measurements in Korea

M. Choi^{a,*}, Y-M. Hur^a, H. Kim^a T.-W. Kim^b, J-H. Ahn^c

^aDept. of Civil and Environmental Engineering, Hanyang University, Seoul, 133-791, Korea - (mchoi, youm1030, k4ecohydro)@hanyang.ac.kr

^bDept. of Civil and Environmental Engineering, Hanyang University, Ansan, 426-791, Korea - twkim72@hanyang.ac.kr

^cDept. of Civil Engineering, Seokyeong University, Seoul, 136-704, Korea - wrr@skuniv.ac.kr

Technical Commission VII Symposium 2010

KEY WORDS: Passive Microwave Sensors, AMSR-E, Soil Moisture, MODIS, NDVI, Korea

ABSTRACT:

Passive microwave sensors have many advantages including the ability to directly measured soil moisture at large spatial scales regardless of weather conditions or time of day. However, microwave-sensed soil moisture's inevitable limitation is that it cannot describe hydrology at the watershed because its retrieved soil moisture scale is too large. Thus, microwave-sensed soil moisture requires validation. Even if there have been great developments for microwave-sensed soil moisture with validation efforts using ground based measurements and land surface models, the validations of the remotely sensed soil moisture in Korea are very limited. This study validated Advanced Microwave Scanning Radiometer E (AMSR-E) soil moisture productions with ground based measurements at eight sites from rural development administration in Korea. The relationship between AMSR-E soil moisture and Normalized Difference Vegetation Index (NDVI) retrieved from Moderate Resolution Imaging Spectroradiometer (MODIS) for estimating soil moisture is also investigated. Overall there was a reasonable agreement between the AMSR-E and ground data, but unreliable replication was found in winter season. More intensive validation efforts should be conducted with other AMSR-E soil moisture products with vegetation information. This type of estimation provides the utility of the AMSR-E soil moisture products and MODIS NDVI as an alternative of the ground based measurements and improves soil moisture retrieval algorithms.

1. INTRODUCTION

Fresh water recognized as abundant on our planet is now drastically becoming a scarce natural resource (Falkenmark and Rockstrom, 2004). The fresh water resources stress may be more deteriorated by increasing climate change and population growth scenarios in the world including East Asia (Milly et al., 2005). To better understanding of fresh water availability linked between the land surface and the atmosphere, accurate estimation of the soil moisture is required even if its amount in water resources systems is relatively small. Soil moisture determines the partitioning of precipitation into runoff, infiltration, and surface storage, as well as the partitioning of incoming solar radiation and long wave radiation into outgoing long wave radiation, latent heat flux, ground heat flux, and sensible heat flux (Pachepsky et al., 2003).

Recently, larger spatial scaled mean surface soil moisture is available from aircraft and satellite instruments comprised of various active and passive microwave sensors (Schmugge et al., 2002). The brightness temperature (T_B) as intensity of natural thermal emission on the land surface was measured by these passive microwave sensors and surface soil moisture is successfully retrieved from the T_B observations (Jackson et al., 1995). Even if there are many advantages of monitoring soil moisture at larger scales including the ability to directly measurement soil moisture regardless of weather conditions or time of day (Jackson, 1993; Jackson and Schmugge, 1995), its inevitable limitations are existing. One of the major limitations is that it cannot describe hydrology at the watershed or field scale because its retrieved soil moisture scale is too large

(Mohanty and Skaggs, 2001; Jacobs et al., 2004). Thus, retrieved soil moisture estimates require validation.

Validation studies for the AMSR-E soil moisture products have been conducted over different continents, Europe (Wagner et al., 2007), the United States (McCabe et al., 2005; Crow and Zhan, 2007; Owe et al., 2008; Choi et al., 2008), and Australia (Drape et al., 2009). Even if AMSR-E evaluation efforts in many regions around the world to estimate the potential of the AMSR-E surface soil moisture, there have not been any evaluation efforts in Korea. This study was conducted for the initial evaluation of the AMSR-E soil moisture products in Korea. We used land parameter retrieval model products by NASA and Vrije Universiteit Amsterdam (VUA), the Netherlands following Owe et al. (2001) using ground based measurements at Korean monitoring network sites.

2. MATERIALS AND METHODS

2.1 Study Region and Ground Data

In order to validate AMSR-E retrieved soil moisture, ground measured data were obtained from 60 sites with Time Domain Reflectometry (TDR) in 10 cm depth from rural development administration in Korea (<http://weather.rda.go.kr>). Data from eight sites among the sixty sites were selected (Figure 1).

* Dept. of Civil and Environmental Engineering, Hanyang University, Seoul, 133-791, Korea – mchoi@hanyang.ac.kr



Figure 1. Study region

2.2 AMSR-E

The AMSR-E instrument provides global microwave measurements using different bands (56 km for the C band, 38 km for the X band, and 12 km for the Ka band) over two passes: ascending (1:30 pm) and descending (1:30 am). The Vrije Universiteit Amsterdam (VUA) AMSR-E soil moisture products are retrieved from the Land Surface Parameter Model (LPRM) (Owe et al., 2008). The model is based on a three-parameter forward retrieval procedure which uses one dual polarized channel (e.g., C or X band) to optimize soil moisture and Vegetation Water Content (VWC) (Owe et al., 2008). Land surface temperature is derived from the vertical polarized Ka band (e.g., 36.5 GHz). The LPRM parameterizes vegetation optical depth using Polarization ratios, Microwave Polarization Difference Index (MPDI) described as

$$MPDI = (T_{bV} - T_{bH}) / (T_{bV} + T_{bH}) \quad (1)$$

where T_{bV} and T_{bH} are the brightness temperature at vertical and horizontal polarizations, respectively.

2.3 MODIS-NDVI

Terrestrial vegetation greatly influences on the energy balance, hydrologic and biogeochemical cycle on earth. Vegetation can also serve as an indicator of anthropogenic influences on the environment (Huete et al., 1999). Vegetation Index (VI) was developed to understand the roles of vegetation as a contributor to maintain biophysical systems and as an indicator of global environmental change (Huete et al., 1999). Many VIs have been developed, and most of them are expressed as the relationship between light reflection in the red and near infrared (NIR) section of the spectrum to separate the landscape into water, soil, and vegetation (Glenn et al., 2008). Normalized Difference Vegetation Index (NDVI), one of the most common among those VIs, was developed by Rouse et al. (1974). There is a global record of NDVI data since 1981 from Advance Very High Resolution Radiometer (AVHRR) mounted on the National Oceanic and Atmospheric Administration (NOAA) satellites. This AVHRR-NDVI is currently inter-calibrated with

NDVI data from the Moderate Resolution Imaging Spectroradiometer (MODIS) on the terra and aqua satellites (Glenn et al., 2008). NDVI can be described as (Glenn et al., 2008):

$$NDVI = (\rho_{NIR} - \rho_{Red}) / (\rho_{NIR} + \rho_{Red})$$

where ρ_{NIR} and ρ_{Red} are reflectance values of Near Infrared and Red light received at the sensors. Recently, Several researchers investigated the potential use of MODIS-driven NDVI to estimate soil moisture with some success (i.e., Schnur et al., 2010). Based on their suggestions, we tested this possibility of MODIS-NDVI for estimating soil moisture at the eight selected sites in Korea. MYD13A2 product from Aqua satellite with 1km-16 day of spatio-temporal scale was used in this study.

3. EVALUATION

In this study, we validated the AMSR-E products from land parameter retrieval model products by National Aeronautics and Space Administration (NASA) and Vrije Universiteit Amsterdam (VUA), the Netherlands for ground measurements from selected Korean monitoring network sites during 2004 study period. The relationship between AMSR-E and MODIS NDVI was also tested. The ground based measurements were extracted at Aqua overpass time: 1:30 pm EST to match the time of the AMSR-E soil moisture products. Figure 2 shows that there were reasonable temporal patterns respond with precipitation events (not shown here).

Overall, VUA AMSR-E soil moisture and MODIS NDVI showed the reasonable agreement with ground based measurements (RMSE = 8-26% and BIAS = 0-24%) (Table 1). However, we found that AMSR-E soil moisture products showed relatively higher temporal variability. These patterns may likely due to vegetation transmissivity as a function of the vegetation optical depth. The vegetation transmissivity was very uncertain in densely vegetated areas because microwave polarization difference indices became very small (Owe et al., 2001).

y: AMSR-E soil moisture, x: ground based soil moisture

	Equation	R ²	BIAS	RMSE
Chuncheon	y = 1.1523x + 10.092	0.2031	-22	26
Pyeongchang	y = 0.4145x + 37.016	0.0436	-24	26
Bonghwa	y = -0.1505x + 42.148	0.0032	-16	20
Sangju	y = 0.1059x + 31.446	0.0215	12	17
Andong	y = 0.5569x + 22.383	0.0869	-8	11
Cheongsong	y = 0.7131x + 19.841	0.1195	-14	16
Nonsan	y = 0.0473x + 36.457	0.0019	0	8
Cheongju	y = 0.326x + 25.816	0.0996	2	10

Table 1. A comparison of the ground based soil moisture with AMSR-E soil moisture

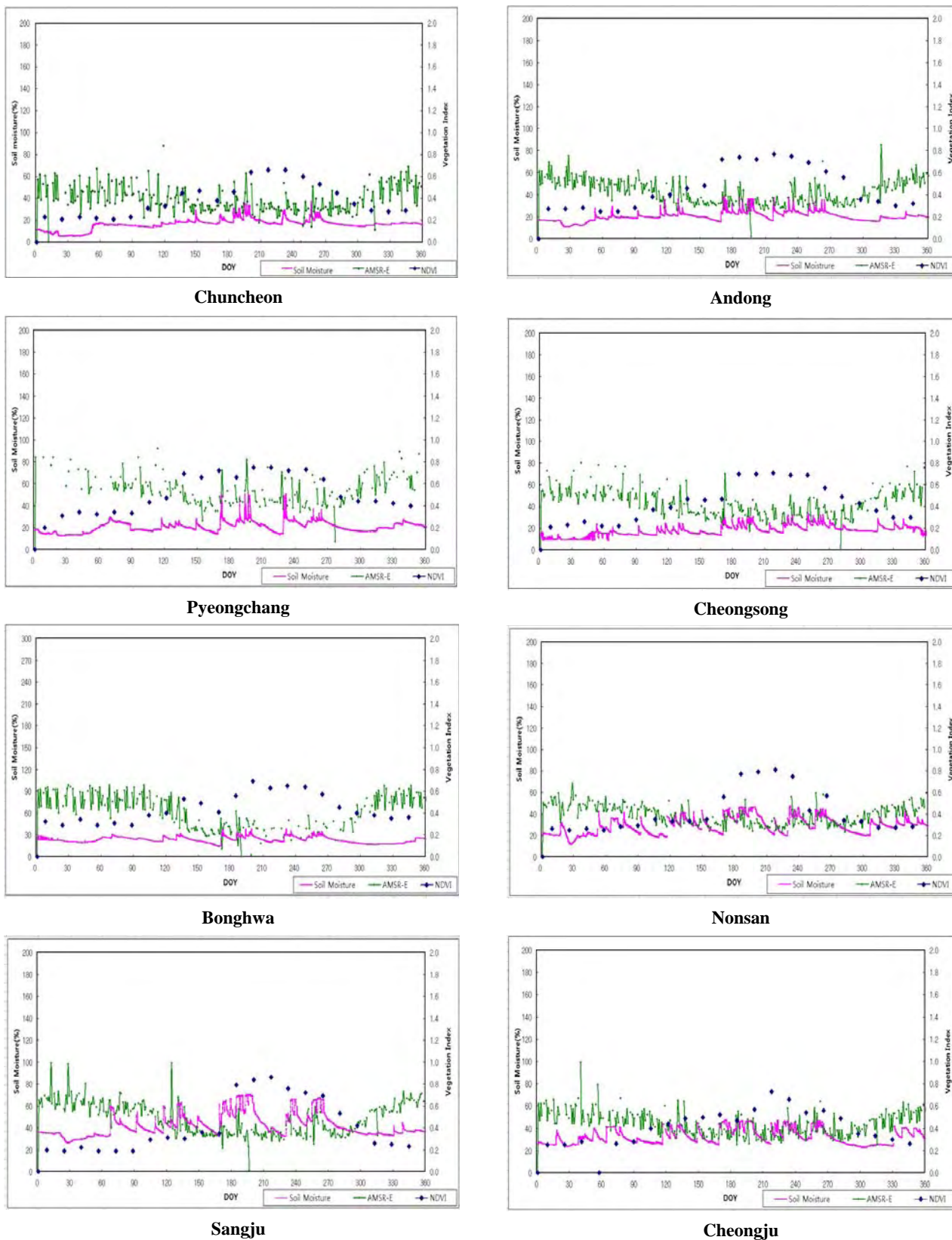


Figure 2. A comparison of the ground based and AMSR-E soil moisture with Normalized Difference Vegetation Index (NDVI)

Even if ground measuring sites are grass, highly vegetated area like forest may be included within the AMSR-E pixel (~25 km by 25 km). In addition, there were relatively larger soil moisture differences between two different systems during the winter season likely due to frozen soils.

y: MODIS NDVI, x: ground based soil moisture

	Equation	R ²
Chuncheon	$y=0.026x-0.0444$	0.5664
Pyeongchang	$y=0.0211x+0.071$	0.2463
Bonghwa	$y=0.0169x+0.0482$	0.1825
Sangju	$y=0.0199x-0.4214$	0.5475
Andong	$y= 0.0362x-0.2708$	0.4849
Cheongsong	$y=0.0281x-0.0638$	0.4665
Nonsan	$y= 0.0165x-0.0658$	0.2858
Cheongju	$y=0.0112x+0.0383$	0.1467

Table 2. Relationship between meanground based soil moisture and MODIS NDVI

We investigated the temporal variation of the AMSR-E soil moisture with MODIS NDVI. Based on the Figure 2, the VUA AMSR-E soil moisture showed better correlations with the ground data when the NDVI is higher than 0.4. These patterns were contrast with the previous finding of Choi and Jacobs (2008) that National Snow and Ice Data Centre (NSIDC) AMSR-E showed very uncertain temporal variation for dense canopies due to increased attenuation with increasing vegetation.

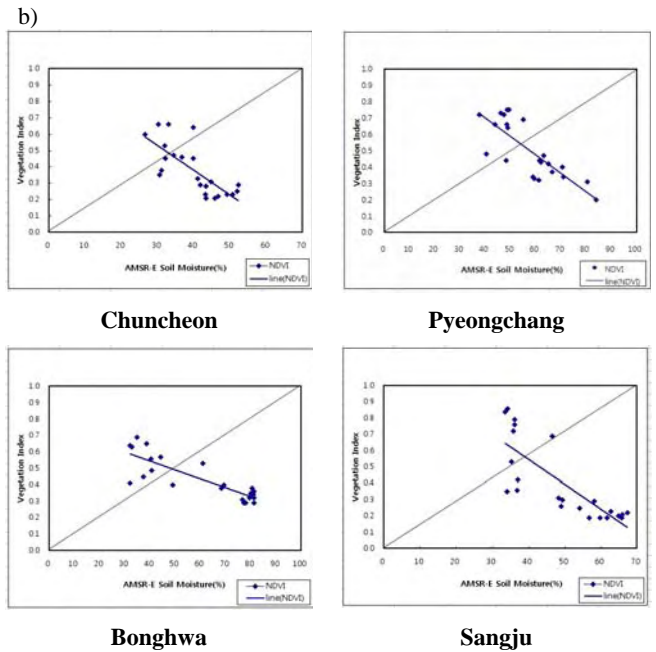
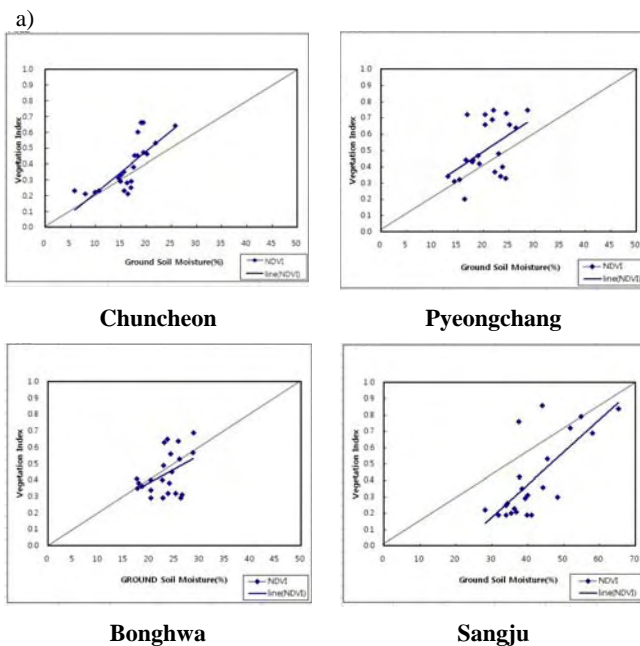


Figure 3. Relationship between mean soil moisture and NDVI a) ground based soil moisture and MODIS NDVI b) AMSR-E soil moisture and MODIS NDVI

Figure 3 showed ground soil moisture data had positive patterns with NDVI. However, there were negative relationships between the VUA AMSR-E soil moisture and MODIS NDVI. Those patterns were clear mirror even if both soil moisture data had reasonable correlations with vegetation indices (Tables 2 and 3).

y: MODIS NDVI, x: AMSR-E soil moisture

	Equation	R ²
Chuncheon	$y= -0.0151x+0.9833$	0.5676
Pyeongchang	$y=-0.0113x+1.1554$	0.6327
Bonghwa	$y=-0.0054x+0.76$	0.7087
Sangju	$y=-0.0153.x+1.156$	0.6314
Andong	$y=-0.0177x+1.2146$	0.6598
Cheongsong	$y=-0.0145x+1.0664$	0.674
Nonsan	$y=-0.017x+1.0731$	0.4001
Cheongju	$y=-0.0166x+1.1357$	0.5957

Table 3. Relationship between meanAMSR-E soil moisture and MODIS NDVI

Current results suggest that validation efforts need to be further conducted in light of various geophysical conditions such as land cover and climate types. Especially, comparison using the NSIDC AMSR-E and VUA AMSR-E soil moisture product should be conducted with vegetation indices to find reasonable validation period to replicate ground data. If we can find the appropriate relationship between MODIS NDVI and soil

moisture through extensive validation efforts, NDVI can be another alternative to estimate soil moisture at various spatial scale.

4. CONCLUSION

The soil moisture products from the VUA AMSR-E were validated using ground based measurements at eight sights from rural development administration in Korea. While there were reasonable agreements between the AMSR-E and ground soil moisture, unreliable relationships were found in winter season. More intensive validation efforts should be conducted with other AMSR-E soil moisture products with vegetation information.

References

- Choi, M., Jacobs, J.M., and Bosch, D.D., 2008. Remote sensing observatory validation of surface soil moisture using Advanced Microwave Scanning Radiometer E, Common Land Model, and ground based data: Case study in SMEX03 little river region, Georgia, U.S. *Water Resources Research*, 44, W08421, doi:10.1029/2006WR005578.
- Choi, M., and Jacobs, J.M., 2008. Temporal variability corrections for Advanced Microwave Scanning Radiometer E (AMSR-E) surface soil moisture: case study in Little River Region, Georgia, U.S. *Sensors*, 8, pp. 2617-2627.
- Crow, W.T., and Zhan, X., 2007. Continental-Scale evaluation of remotely sensed soil moisture products. *IEEE Geoscience and Remote Sensing Letters*, 4, pp. 451-455.
- Drape, C.S., Walker, J.P., Steinle, P.J., De Jeu, R.A.M., and Holmes, T.R.M., 2009. An evaluation of AMSR-E derived soil moisture over Australia. *Remote Sensing of Environment*, 113, pp. 703-710.
- Falkenmark, M., and Rockstrom, J., 2004. Balancing water for humans and nature; the new approach in ecohydrology. EARTHSCAN, London, VA.
- Glenn, E.P., Huete, A.R., Nagler, P.L., and Nelson, S.G., 2008. Relationship between remotely-sensed vegetation indices, canopy attributes and plant physiological processes: what vegetation indices can and cannot tell us about the landscape. *Sensors*, 8, pp. 2136-2160.
- Huete A.R., Justice, C., and van Leeuwen, W., 1999. MODIS vegetation index (MOD 13) algorithm theoretical basis document. Version 3. *Technical report*. http://modis.gsfc.nasa.gov/data/atbd/atbd_mod13.pdf
- Jackson, T.J., 1993, Measuring surface soil moisture using passive microwave remote sensing. *Hydrological processes*, 7, pp. 139-152.
- Jackson, T.J., Le Vine, D.M., Swift, C.T., Schmugge, T.J., and Schiebe, F.R., 1995. Large area mapping of soil moisture using the ESTAR passive microwave radiometer in Washita'92. *Remote Sensing of Environment*, 53, pp. 27-37.
- Jackson, T.J., and Schmugge, T.J., 1995. Surface soil moisture measurement with microwave radiometry. *Acta Astronautica*, 35 (7), pp. 477-482.
- Jacobs J.M., Mohanty, B.P., Hsu E.C., and Miller D., 2004. SMEX02: Field scale variability, time stability and similarity of soil moisture. *Remote Sensing of Environment*, 92(4), pp. 436-446.
- McCabe, M.F., Kalma, J.D., and Franks, S.W., 2005. Spatial and temporal patterns of land surface fluxes from remotely sensed surface temperatures within an uncertainty modeling framework. *Hydrology and Earth System Sciences*, 9, pp. 467-480.
- Milly, P.C.D., Dunne, K.A., and Vecchia, A.V., 2005. Global pattern of trends in streamflow and water availability in a changing climate. *Nature*, 438(7066), pp. 347-350.
- Mohanty, B.P., and Skaggs, T.H., 2001. Spatio – temporal evolution and time-stable characteristics of soil moisture within remote sensing footprints with varying soil, slope, and vegetation. *Advances in Water Resources*, 24, pp. 1051-1067.
- Owe, M., De Jeu, R.A.M., and Holmes, T., 2008. Multisensor historical climatology of satellite-derived global land surface moisture. *Journal of Geophysical Research*, 113:F01002, doi:10.1029/2007JF000769
- Owe, M., De Jeu, R.A.M., and Walker, J., 2001. A Methodology for surface soil moisture and vegetation optical depth retrieval using the microwave polarization difference index. *IEEE Trans Geoscience and Remote Sensing*, 39, pp. 1643-1654.
- Pachepsky, Y., Radcliffe, D., and Selim, H. 2003. Scaling methods in Soil Physics. 119, pp. CRC press.
- Rouse, J.W., Haas, R.H., Schell, J.A., and Deering, D.W., 1974. Monitoring vegetation systems in the Great Plains with ERTS, Proceedings, Third Earth Resources Technology Satellite-1 Symposium, Greenbelt: NASA SP-351, pp. 3010-3017.
- Schmugge, T.J., Kustas, W.P., Ritchie, J.C., Jackson, T.J., and Rango, A., 2002. Remote sensing in hydrology. *Advances in Water Resources* 25, pp. 1367-1385.
- Schnur, M.T., Xie, H., Wang, X., 2010. Estimating root zone soil moisture at distance sites using MODIS NDVI and EVI in a semi-arid region of Southwestern USA. *Ecological Informatics*, *In press, corrected proof*.
- Wagner, W., Naeimi, V., Scipal, K., Martinez-Fernandez, J., and De Jeu, R.A.M., 2007. Soil moisture from operational meteorological satellites. *Hydrogeology Journal*, 15, pp. 121-131.

ACKNOWLEDGEMENTS

This research was supported by Basic Science Research Program through the National Research Foundation of Korea (NRF) funded by the Ministry of Education, Science and Technology (2010-0009742 and 2010-0016717)

DISASTER MONITORING AND MANAGEMENT BY THE UNMANNED AERIAL VEHICLE TECHNOLOGY

Tien-Yin Chou^a, Mei-Ling Yeh^a, Ying-Chih Chen^a, Yen-Hung Chen^a

^a Feng Chia University, Geographic Information System Research Center, No. 100 Wenhwa Rd., Seatwen, Taichung, Taiwan 40724 - (Jimmy, Milly, Joyce, Jasonchen)@gis.tw

Technical Commission VII Symposium 2010

KEY WORDS: Hazards, Landslides, Photogrammetry, Change Detection, Monitoring, Visualization

ABSTRACT:

In the local small densely populated Taiwan, the recent spates of serious natural disasters have caused loss of lives and property. In view of above, there is important to how to depend on a high flexibility remote sensing technology for disaster monitoring and management operations. According to the Unmanned Aerial Vehicle (UAV) technology advantages such as great mobility, real-time rapid and more flexible weather conditions, and this study used the UAV technology to get the real-time aerial photos. These photos can record and analyze the overall environmental change caused by the MORAKOT typhoon. And also after the process of Image Rectification, we could get the estimated data of new collapsed lands to become the useful references of emergency rescue.

On the other hand, digital photogrammetry can apply on the camera inside and outside position parameters to produce the Digital Elevation Model (DEM) data of 5m resolution. The DEM data can simulate the latest terrain environment and provide reference for disaster recovery in the future.

1. INTRODUCTION

The Unmanned Aerial Vehicle technology has developed over several years, and there is including fixed wing vehicle and rotary wing vehicle. The characteristic of the UAV to the task of providing a good platform to replace the man was detected to ensure the security and the ability with visual images, allowing users to understand the actual situation. With advances in technology development, the functions of UAV are widely used for different purposes in recent years. These have included surveying the development of city infrastructure, researching agriculture, fishery and farming, monitoring environmental protection, highway driving, forestry management, and disaster prevention like floods or debris flow.

Since the earthquake 921 in 1999, there was have frequent natural disasters in Taiwan in recent years due to geology loose and huge changes of the global environment, it impacts people's livelihoods and security heavily. All government units in the pre-disaster preparedness, disaster response and post-disaster reconstruction in the emergency response to take various measures and contingency plans, the development of various policy really need to diversify information channels to provide assistance, in order to reduce people's lives property damage and to prevent the occurrence of secondary disasters.

The disaster areas are often located in difficult terrain with inconvenient and dangerous traffic; the officers are unable to get into there after the typhoon and earthquake. In emergency situations, the remote sensing technology can be used as real-time information gathering pipelines in order to provide real-time disaster information efficiently.

Therefore, in recent years for the land-use change and disaster detection, mostly aerial photographs or satellite images, and acquired by the interpretation of the information required; but satellite images because of the scope is too large, images of the small scale, in a small area or in the changing differences between small and require more detailed information on the occasion, often limitations and often can obviously see that al-

though the overall changes in the region, but it can not be more precise differences between local area change. Although the aerial photographs of a large scale, but because each line of surveillance photographs, none fixed, doing image comparison, and overlap, the inevitably left beads of regret. UAV can work in dangerous and unreachable areas. While its small size, easy loading, with the better of the mobility, they can be used anytime, anywhere and in a relatively harsh climate of the mission.

So in this paper, there is introducing the technology and fly procedure of UAV and used the UAV technology to get the real-time aerial photos. These photos can record and analyze the overall environmental change caused by the MORAKOT typhoon. And also after the process of Image Rectification, we could get the estimated data of new collapsed lands to become the useful references of emergency rescue. On the other hand, digital photogrammetry can apply on the camera inside and outside position parameters to produce the Digital Elevation Model (DEM) data of 5m resolution. The DEM data can simulate the latest terrain environment and calculate the debris variation which can provide reference for disaster recovery in the future.

2. UAV PAYLOADS OF EQUIPMENT

UAV payloads of equipment, due to the different mission requirements to carry the applicable equipment with high flexibility in use; it can be used in various fields to carry out a variety of different tasks. Hereby will be used in this study the instruments and equipment, their characteristics and functions is set out in Table1.

Table 1 The Specification for UAV system



Weight	8.5kg	
Payload	5.5kg	
Engine	15 c.c. oil engine	
Main Airfoil	680mm non-symmetry	
Empennage	Standard Empennage	
Operation Range	3000m / 10000ft	
Operation Time	20 minutes	
Operation Altitude	3000m / 10000ft	

Table 2 The Specification for UAV Photographing System

Instrument	Model	specifications
Digital Camera	Canon EOS 5D Mark II	Effective Pixels: 21 million pixels Focal Distance: 1.8mm, Weight: 1.2kg Shutter Speed: 3.9fps
Digital Video Camera	Canon EOS 5D Mark II	Size: 1920 X 1080 pixels Focal Distance: 1.8 mm, Weight: 1.2kg Shutter Speed: 30fps
GPS System	SiRFStarIII Chip	Position Accuracy: ±3-5m Velocity Accuracy: 0.1 m/s RMS steady state Weight: 90g

3. OPERATION PROCEDURE

In order to improve the accuracy of UAV operation effectively, we collect the basic information of mission area, such as environmental information, flying plan (Figure 1) and weather factors. Then we choose the suitable weather to do the UAV operation procedure.



Figure1 The example of flying planning (pre-operation)

After the UAV operation procedure, we can get the different kind of images. These images are included nir-ortho images and oblique shot images (Figure 2) which were are color correction and images mosaic. And in order to get the images with spatial coordinate system, we use the rubber sheeting method to collect these images. Finally, we can use these images to produce other application such like quantification of landslides or terrain simulation. Figure 3 is all the UAV operation procedure.



Figure2 The types of UAV images

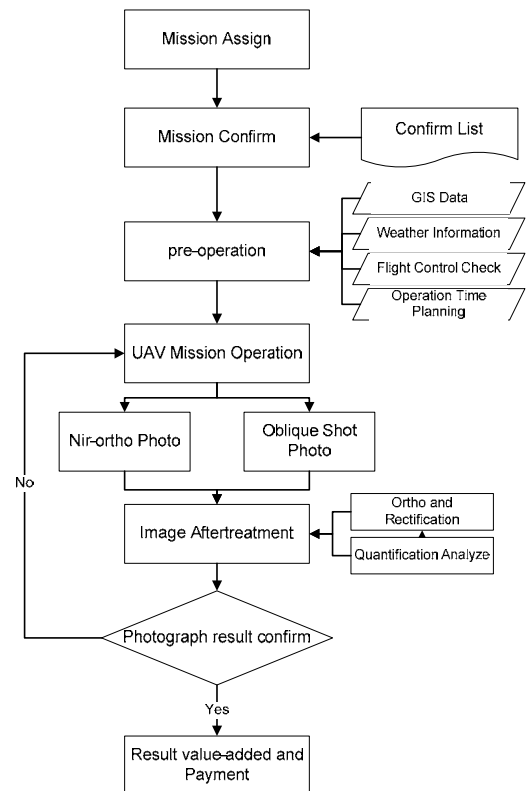


Figure 3 Operation procedure of UAV

4. EMERGENCY PHOTOGRAPHED RESULT AFTER TYPHOON MORAKOT

MORAKOT typhoon is the biggest natural disaster in Taiwan for fifty years. It brought different kinds of disasters, such like flood, dam failure, the broken of road and bridge, landslide, quake lakes, turbid water and driftwood. According to the data from Central Weather Bureau, there were total 673 people were killed and 26 were missing, more than NT 19.5 billion agricultural loss during the MORAKOT typhoon period. Because of many of these disasters were occurring simultaneously in the same place, the rescue were getting more difficult.

The obvious characteristic of MORAKOT typhoon is the huge rainfall. Even though the strength is medium, the rainfall is exceeded everyone's expectations. As Figure 4 is the cumulative rainfall of MORAKOT typhoon, it shows the rainfall center was located in the south area of Taiwan. And table 1(Shieh, etal. 2009) is the historic rainfall record; we can see the accumulation of rainfall depth of MORAKOT typhoon is reach 2583mm that gathering in 91 hours.



Figure 4 Isohyets of the cumulative rainfall of MORAKOT typhoon

Table 3 The largest rainfall records of different typhoons

Typhoons	Year	Rainfall station	Accumulation of rainfall depth (mm)
MORAKOT	2009	Yu You Shan	2583
KALMAEGI	2008	Xin Fa	1043
AERE	2004	Guan Wu	1223
TORAJI	2001	Da Nong	433.5
WINNIE	1997	Wu Du	354
HERB	1996	A Li Shan	1986.5

Because of the heavy rainfall, the Typhoon MORAKOT backdrop of heavy rain hit southern Taiwan. Particularly the debris flow disasters were happened in Jiasian Township, Liouguei Township and Namasia Township, Kaohsiung County, Alishan Township, Meishan, Chiayi County, and Laiyi Township, Pingtung County, and Sandiman Township the most serious. Figure 5 is showed the most serious disaster locations.

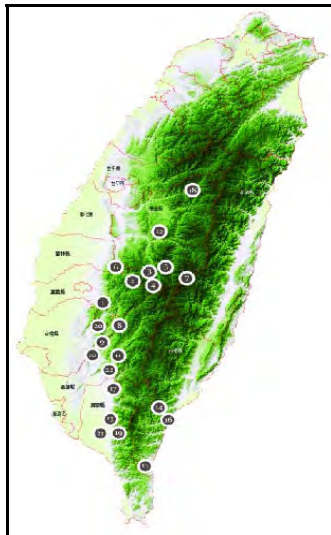
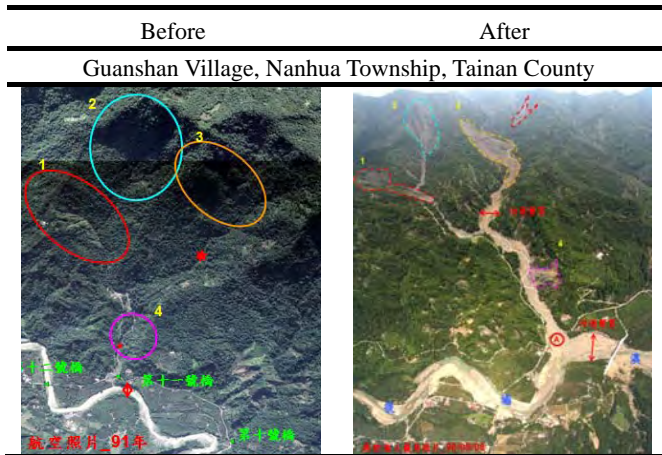


Figure 5. Disaster Areas After Typhoon MORAKOT

Soil and Water Conservation Bureau to assist this study, the use of UAV technologies to overcome transport barriers to quickly acquire all the major affected areas of the real-time disaster information, disaster follow-up analysis, disaster restoration and reconstruction work and the importance of reference information.

Table 3 The Achievement Images of Emergency Photographed After Typhoon MORAKOT

Before	After
Zhonglun Village, Zhongpu Township, Chiayi County	
Siaolin Village, Jiaxian Township, Kaohsiung County	
Taiho Village, Meishan Township, Chiayi County	
Shenmu Village, Xinyi Township, Nantou County	
Singlong Village, Liugui Township, Kaohsiung County	



5. USING UAV TECHNOLOGY TO PRODUCE THE DIGITAL TERRAIN MODEL DATA

UAV is also a part of aerial remote sensing, over the years the collection of information on the environment plays a very successful role. Because of their high mobility and high revisit rate, therefore, the use of remote unmanned vehicles in a similar way the traditional aerial surveys produced digital elevation data can be master of environmental information and analysis, providing important analysis is available. Digital Terrain Model (DEM) data is the important basic environmental information, and the data is usually used for spatial analysis research. In this study, we would use the UAV technology to produce the 5m resolution DEM data. The study area is located in HuaShan River of YunLin County. The produce was included camera calibrating, terrestrial photogrammetry, aerial photograph, and simple aerial triangulation and finally gets the DEM data.

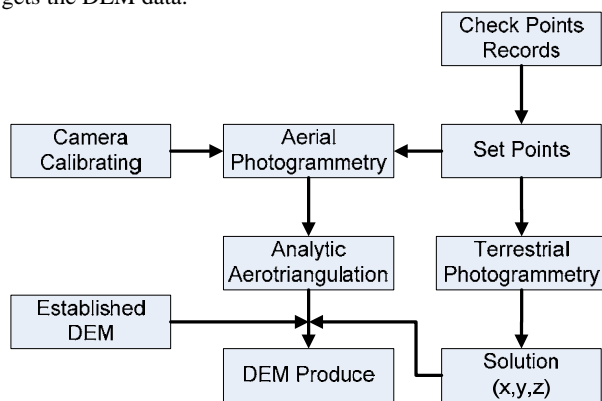


Figure 6 The Procedure of DEM Data Product

5.1 Camera Calibrating

Before using the UAV technology to execute the aerial photogrammetry, we must do the camera calibrating. The camera type is the Canon 500D. First we did the pattern sheet in the calibrated place, and then we used the camera to take positive direction, about 45 degrees up and down the images. Finally we took all the angles of images into the operational programs to get the calibrated parameters to be the reference of producing DEM data. Figure 7 is showed the images of camera calibrating procedure.

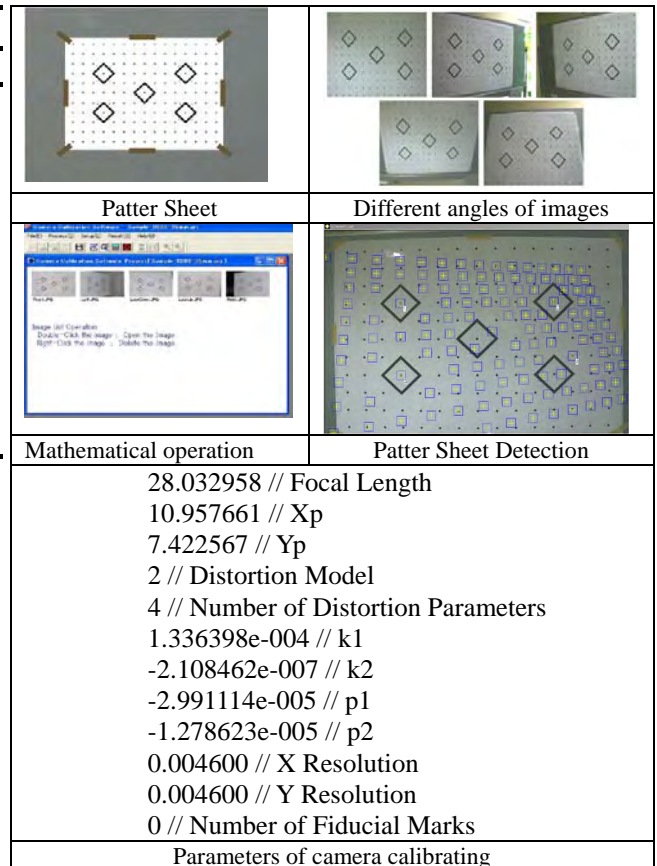


Figure 7. The images of camera calibrating procedure

5.2 Terrestrial Photogrammetry

In order to confirm the location of control points, the study area must set some aerophotography survey marks. These marks record important information about control points, such like sizes, shapes, colors, materials and positions.



Figure8 aerophotography survey marks

Besides, we executed terrestrial photogrammetry to get the control points which from aerophotography survey marks. The survey information would be the useful reference of image rectification.

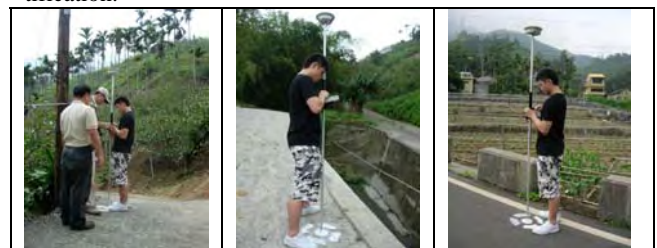


Figure 9 Terrestrial Photogrammetry

5.3 Aerial Photogrammetry

In this procedure, we use the UAV to get the aerial photos and take the aerial photogrammetry rules for example. The photogrammetry must do the vertical continuous photography. Photo-axis tilt required less than 4 degrees, Air angle less than 10 degrees, the route should be more proactive at both ends of two relative images. Figure 10 is showed the photogrammetric images and these images overlapping rate is 80%.

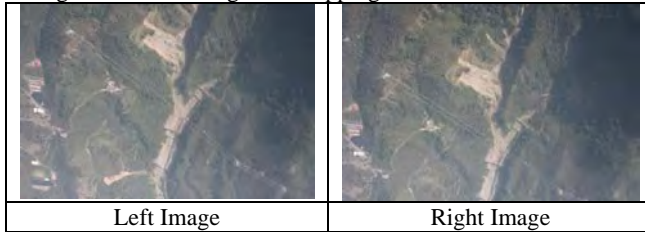


Figure 10 The photogrammetric images

5.4 Analytic Aerotriangulation and Orthorectification

In order to eliminate errors associated with the process of aerial photogrammetry, we used the Pixel by Pixel Rectification Method to do the images orthorectification. The results are showed as Figure 11. Figure 12 are showed the images after interior orientation and exterior orientation procedure operation. The triangles are control points and the square are the connected points.

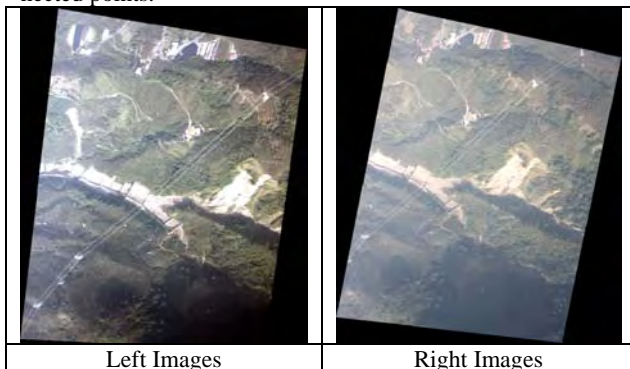


Figure 11 Orthorectified Images

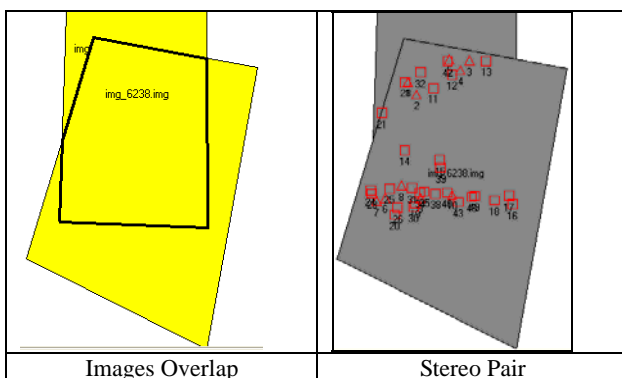


Figure 12 Images Overlap and Stereo Pair

5.5 DEM calculation results and accuracy check

After the above procedures and measured solution, we produced the 5m resolution DEM data. And the data accuracy was checked by 10 points, there is showed as Figure 13. And Figure 14 is the DEM result.

The residuals of the check points			
Point ID	rX	rY	rZ
6	-6.0546	2.2757	0.2877
27	0.1115	-0.0374	0.3052
34	-0.0072	0.0094	-0.1572
38	0.0054	0.0299	-0.1849
51	0.0000	-0.0013	-0.1788
66	-0.0052	0.0048	-0.1507
83	0.0167	-0.0263	0.0978
115	-0.0190	-0.0014	-0.0633
122	0.0938	-0.0660	0.2953
133	-0.0980	-0.0560	-0.2192
aX	aY	aZ	
-0.5956	0.2131	0.0032	
mX	mY	mZ	
1.9155	0.7204	0.2094	

Figure 13 The accuracy of DEM data

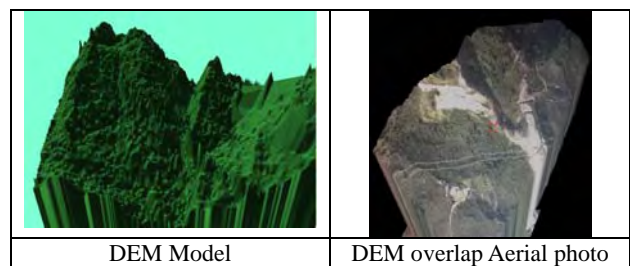


Figure 14 DEM result

6. ADD-VALUE APPLICATION OF DEM RESULT

The use of UAV produced DEM data, remote sensing information can be carried out with related sets of overlapping, and the use of value-added multimedia technology to carry out target areas show environmental change. So we can build the 3D simulation that can display the surface details and reserving time, thus reducing the overall cost. So, this study integrated updated high resolution of aerial photos and high precision DEM data to simulate the 3D environment. The simulation result shows as Figure 15.

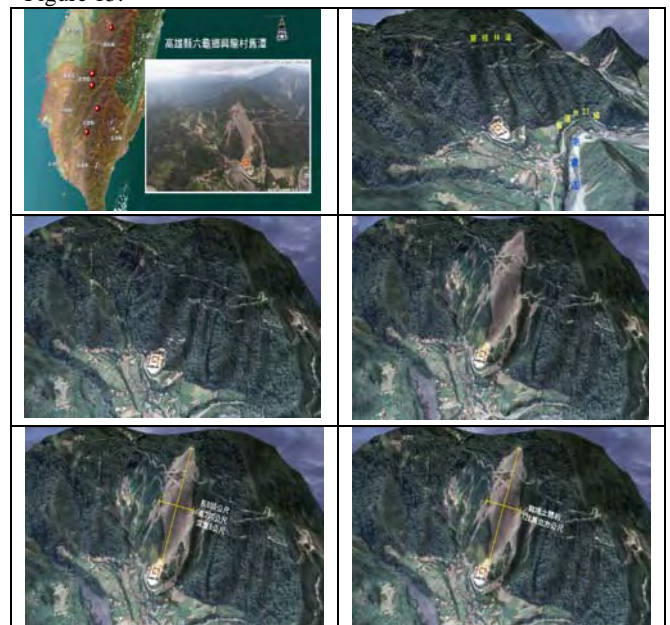


Figure 15 The Achievement Images of Photographed Image Add-value Application

7. CONCLUSIONS

The rain of typhoon is a large area, high-intensity, long the pattern, resulting in increase landslides and debris flow, and the type of disaster is no longer a local area of the flood or sediment disaster hurricane events in the MORAKOT presented for large-scale floods, landslides, debris flow, avalanches, and other barrier lake complex disasters. And a large number of earth and rock entrainment flooding upstream migration, the downstream simultaneously super-heavy rain again, so to make the amount of surge flooding downstream areas, and thus downstream river-crossing bridges, coastal highway facilities, water facilities, causing a major impact, but also in turn affect the resumption of the follow-up disaster relief construction work limitation.

So using the UAV technology is providing applicable information and assistance, therefore we need to build a procedure of disaster information collection and build. Base on this we can get effective information at appropriate time and provide the reference for the phases of disaster-preparedness, response and return. This study used the high mobility, high time-resolution and high image resolution and other features of unmanned vehicles to provide government important reference information in planning for disaster response and return.

References from Journals:

Long-Ming Huang, Wen-Fu Chen, Sheng-Jie Wu, Chang-Hang Wu, 2006, Application of Geometric Correction Method to Remotely Piloted Vehicle (RPV) Airspace Image for Surveying and Analysis of Disaster Areas, *Journal of Chinese Soil and Water Conservation*, 37(2):111-124.

Afzal Ahmed, Dr. Masahiko Nagai, Dr. Chen Tianen, Prof. Ryosuke SHIBASAKI, 2008, UAV Based Monitoring System and Object Detection Technique Development for a Disaster Area, *The International Archives of the Photogrametry, Remote Sensing and Spatial Information Sciences*. Vol. XXXVII. Part B8. Beijing.

U. Coppa, A. Guarnieri, F. Pirotti, A. Vettore, 2008, Accuracy Enhancement of Unmanned Helicopter Positioning With Low Cost System, *The International Archives of the Photogrametry, Remote Sensing and Spatial Information Sciences*. Vol. XXXVII. Part B5. Beijing.

C.L. Shieh, C.M. Wang, W.C. Lai, Y.C. Tsang, S.P. Lee, 2009, "The composite hazard resulted from Typhoon Morakot in Taiwan," *Journal of the Japan Society of Erosion Control Engineering*, Vol. 62, No.4, pp. 61-65.

Chun-Ming Wang, Shin-Ping Lee, Chen-Chian Li, Yun-Chung Tsang, Chjeng-Lun Shieh, 2010, Disaster caused by typhoon Morakot, *Journal of the Taiwan Disaster Prevention Society*, vol.2, NO.1.

ACKNOWLEDGEMENTS

Thanks for the Soil and Water Conservation Bureau to provide the funds to assist the project.

USE SPECTRAL DERIVATIVES FOR ESTIMATING CANOPY WATER CONTENT

J.G.P.W. Clevers

Wageningen University, Centre for Geo-Information, P.O. Box 47, 6700 AA Wageningen, The Netherlands –
jan.clevers@wur.nl

Commission VII

KEY WORDS: Hyper spectral, Modelling, Algorithms, Vegetation, Ecology

ABSTRACT:

Hyperspectral remote sensing has demonstrated great potential for accurate retrieval of canopy water content (CWC). This CWC is defined by the product of the leaf equivalent water thickness (EWT) and the leaf area index (LAI). In this paper the spectral information provided by the canopy water absorption feature at 970 nm for estimating and predicting CWC was studied using a modelling approach and in situ spectroradiometric measurements. The relationship of the first derivative at the right slope of the 970 nm water absorption feature with CWC was investigated with the PROSAIL radiative transfer model at a 1 nm sampling interval and tested for field spectroradiometer measurements obtained at an extensively grazed fen meadow as test site.

PROSAIL simulations (using coupled SAIL/PROSPECT-5 models) showed a linear relationship between the first derivative over the 1015 – 1050 nm spectral interval and CWC ($R^2 = 0.97$), which was not sensitive for leaf and canopy structure, soil brightness and illumination and observation geometry. For 40 plots at the fen meadow ASD FieldSpec spectral measurements yielded an R^2 of 0.68 for the derivative over the 1015 – 1050 nm interval with CWC. This relationship appeared to match the simulated relationship obtained from the PROSAIL model. It showed that one may transfer simulated results to real measurements obtained in the field, thus giving them a physical basis and more general applicability. Consistency of the results confirmed the potential of using simulation results for calibrating the relationship between this first derivative and CWC.

Another advantage of using the derivative at the right slope of the 970 nm absorption feature is its distance from the atmospheric water vapour absorption feature at 940 nm. If one cannot correct well for the effects of atmospheric water vapour, the derivative at the right slope is preferred over the one at the left slope.

1. INTRODUCTION

Biogeochemical processes, such as photosynthesis, evaporation and net primary production, are directly related to foliar water (Running and Gower, 1991; Running and Nemani, 1991). Thus, canopy water content is an important variable for mapping and monitoring the condition of the terrestrial ecosystem.

In this paper, we focus on retrieving canopy water content from optical remote sensing data, in particular hyperspectral data. Remote sensing techniques provide an integrated signal over the spatial resolution element of the detector. As a result, the canopy water content, being the amount of water per unit ground area, is a variable of interest. However, in radiative transfer (RT) models often the amount of water per unit leaf area, the so-called equivalent water thickness (EWT), is used (Hunt Jr. and Rock, 1989; Jacquemoud and Baret, 1990). By multiplying the EWT with the leaf area per unit ground area (called the leaf area index, LAI) we get the canopy water content (CWC in $\text{kg}\cdot\text{m}^{-2}$):

$$CWC = LAI \times EWT \quad (1)$$

Another way of calculating CWC is by taking the difference between fresh weight (FW in $\text{kg}\cdot\text{m}^{-2}$) and dry weight (DW in $\text{kg}\cdot\text{m}^{-2}$):

$$CWC = FW - DW \quad (2)$$

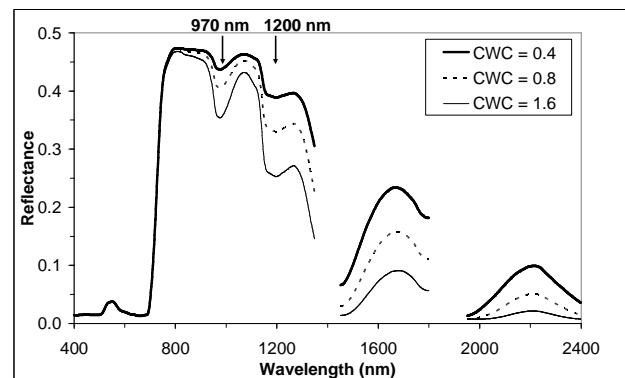


Figure 1. Example of three canopy spectral signatures as simulated with PROSAIL for different CWC values (in $\text{kg}\cdot\text{m}^{-2}$), showing the position of the 970 nm and 1200 nm absorption features.

Figure 1 shows an example of RT simulation results (using PROSAIL, see section 2.1) for a vegetation spectrum with three different CWC values. No simulation results are shown for the major atmospheric water absorption features around 1400 nm and 1900 nm, because these absorptions are such that hardly any solar radiation reaches the Earth's surface at these wavelengths. As a result, these are not used in remote sensing of land surfaces. Figure 1 shows that CWC in particular has an effect in the near-infrared (NIR) and the shortwave-infrared

(SWIR) part of the spectrum. Figure 1 also shows two water absorption features at approximately 970 nm and 1200 nm that are caused by the absorption by O–H bonds in liquid canopy water (Curran, 1989). Accurate measurements at these absorption features in the NIR are feasible with the increasing availability of hyperspectral images (Schaeppman et al., 2009).

Danson et al. (1992) showed that the first derivative of the reflectance spectrum corresponding to the slopes of the absorption features provides better correlations with leaf water content than those obtained from the direct correlation with reflectance. Rollin and Milton (1998) found moderate correlations between the first derivative at the left slope of both absorption features and CWC for a grassland site in the UK. Clevers et al. (2008) applied derivatives in a preliminary study at the field and airborne level. These studies showed that spectral derivatives at the slopes of the 970 nm and (to a lesser extent) 1200 nm absorption feature have good potential as predictors of CWC.

Recently, Clevers et al. (2010) showed that the first derivative of the reflectance spectrum at wavelengths corresponding to the left slope of the minor water absorption band at 970 nm was highly correlated with CWC. PROSAIL model simulations showed that it was insensitive to differences in leaf and canopy structure, soil background and illumination and observation geometry. However, these wavelengths are located close to a water vapour absorption band at about 940 nm (Gao and Goetz, 1990). In order to avoid interference with absorption by atmospheric water vapour, the potential of estimating CWC using the first derivative at the right slope of the 970 nm absorption feature is studied in this paper for a dataset acquired in 2008. Results are compared with PROSAIL simulations, using a new version of the PROSPECT model (Ferret et al., 2008).

2. MATERIAL AND METHODS

2.1 PROSAIL Radiative Transfer Model

PROSAIL is a combination of the PROSPECT leaf RT model (Jacquemoud and Baret, 1990) and the SAIL canopy RT model (Verhoef, 1984), which has been used extensively over the past few years for a variety of applications (Jacquemoud et al., 2009). At the leaf level, PROSAIL is using leaf chlorophyll content (C_{ab}), equivalent leaf water thickness (EWT), leaf structure parameter (N) and leaf dry matter (C_m) as inputs. At the canopy level, input parameters are LAI, leaf inclination angle distribution, soil brightness, ratio diffuse/direct irradiation, solar zenith angle, view zenith angle and sun-view azimuth angle. It also includes a parameter describing the hot-spot effect (Kuusk, 1991). In a previous study, we used an older version of PROSPECT (version 3) simulating leaf reflectance and transmittance at a 5 nm spectral sampling interval. Recently, version 5 of PROSPECT has been released, performing simulations at a 1 nm spectral sampling interval and using updated values for the specific absorption coefficients of leaf constituents (Ferret et al., 2008).

To study the relationship between derivatives and CWC (calculated from LAI and EWT), the effects of the main leaf and plant inputs on this relationship were studied. C_{ab} could be kept constant since it does not exhibit any effect beyond 800 nm. Since the specific absorption coefficient for dry matter is quite low and constant below 1300 nm (Fourty et al., 1996), a

constant value for C_m was used according to the findings of Jung et al. (2009) for a floodplain meadow. At the canopy level, the actual observation and solar angles of the experimental measurements (section 2.3) were used. Also spectral soil brightness values were obtained from the actual experiments. The other inputs for the PROSAIL simulations were varied according to the values given in Table 1.

Since the absorption features of leaf constituents are implemented in the PROSAIL model by means of look-up tables and not as continuous functions, simulated spectra have to be smoothed for calculating derivatives. The simulated spectra were smoothed using an 8 nm wide moving Savitsky-Golay filter applying a fourth-degree polynomial fit within the window according to the results of Le Maire et al. (2004).

Table 1. Nominal values and range of parameters used for the canopy simulations with the PROSAIL model.

PROSAIL parameters	Nominal values and range
Equivalent water thickness (EWT)	0.01 – 0.10 g.cm ⁻² (step of 0.01)
Leaf dry matter (C_m)	0.002 g.cm ⁻² †
Leaf structure parameter (N)	1.0 / 1.8 / 2.5
Chlorophyll concentration (C_{ab})	40 µg.cm ⁻²
Leaf area index	0.5 / 1.0 / 1.5 / 2 / 3 / 4 / 5 / 6
Leaf angle distribution	Spherical / Planophile / Erectophile
Hot-spot parameter	0.0 / 0.1
Soil reflectance	Actual values
Diffuse/direct radiation	0
Solar zenith angle	35°
View zenith angle	0°
Sun-view azimuth angle	0°

†Source: (Jung et al., 2009)

2.2 Study Site

The study site is an extensively grazed fen meadow acting as a buffer zone around a protected bog ecosystem, located in the Achterhoek area in the Netherlands and forming part of Europe's Natura-2000 ecological network. Ground sampling took place from June 9th – 11th, 2008. 40 Plots of 3 by 3 m were randomly distributed over the site. In three corners of each plot subplots of 0.5 x 0.5 m were harvested by cutting all above-ground vegetation. Vegetation fresh weight for every subplot was determined after harvesting. After drying for 24 hours at 70°C, vegetation dry weight and CWC were determined. Subsequently, the average CWC per plot was calculated.

2.3 Field Spectroradiometry

The study site was measured with an ASD FieldSpec Pro FR spectroradiometer on June 9th and 10th, 2008. Nadir measurements were performed between 11h and 15h local time, resulting in a solar zenith angle varying between 30° and 40°. All subplots of all 40 plots were measured before harvesting the biomass. Measurement height above the plot was about 1.5 m and the instrument field of view was 25°. As a result, at the plot level a circular area of about 0.35 m² was measured and each measurement represents the average of 50 readings at the same spot. The sampling interval was 1 nm. Calibration was done by using a Spectralon white reference panel.

After calculating average spectra per plot, the resulting spectra were smoothed using a 15 nm wide moving Savitsky-Golay filter (applying a second order polynomial fit within the window) to reduce instrument noise.

3. RESULTS AND DISCUSSION

3.1 PROSAIL Simulations

The simulation results obtained with the improved PROSAIL model (using PROSPECT-5) using a 1 nm spectral sampling interval showed that for many spectral positions beyond 900 nm the relationship between the first derivative and CWC is statistically significant at $p < 0.001$. In addition to the left slope of the 970 nm water absorption feature, also relationships at the right slope of this feature and at the left slope of the 1200 nm feature are highly significant (Figure 2). In this paper, focus is on the right slope of the 970 nm absorption feature, because there no influence of absorption by atmospheric water vapour is expected. Figure 2 shows that the reflectance at this right slope is increasing gradually and that the coefficient of determination (R^2) for the relationship between the first derivative of adjacent wavelengths and CWC is rather constant. Therefore, we may calculate the first derivative over a wider interval, making the choice of wavelengths for derivative calculation less critical and making the derivative calculation more robust. Experimental results later in this paper suggest that an interval between 1015 and 1050 nm is a good choice. Figure 3 provides the relationship between the first derivative over the 1015 – 1050 nm interval and CWC for variations in model input parameters as given in Table 1. There is an offset for the linear regression line because soil reflectance was not constant over the spectral interval. Field measurements at the test site yielded a reflectance of 0.39 at 1015 nm and a reflectance of 0.40 at 1050 nm. Largest scatter around the linear regression line visible in Figure 3 is caused by the variation in leaf inclination angle distribution. In the next section it will be tested whether this simulated relationship matches the one found with experimental data.

3.2 Achterhoek Study Site

For the Achterhoek site in total 40 plots were studied. Figure 4 shows the R^2 -values for the relationship between spectral derivatives and CWC. The R^2 for the 1015 – 1050 nm interval again is constant for this test site. It is lower than the best value at the left slope, but the observed R^2 -values above 0.65 are statistically significant at $p < 0.001$. The R^2 at the right slope over the 1015 – 1050 nm interval is 0.68 (Figure 5). The predictive power of the first derivative as index for estimating CWC was assessed by estimating the root mean square error of prediction (RMSEP) using the leave-one-out cross-validation approach. The calculated RMSEP is 0.21 $\text{kg}\cdot\text{m}^{-2}$ (as relative to an average CWC of 0.53 $\text{kg}\cdot\text{m}^{-2}$). The relationship is in agreement with the one found for the simulated data from PROSAIL in Figure 3, which are plotted at the background of the Achterhoek results in Figure 5.

The agreement between the experimental data and PROSAIL is good when using reflectance derivatives over the 1015 – 1050 nm interval. Therefore, the relationship between first derivative and CWC was trained with PROSAIL and then this relationship was applied on the experimental data. The calibrated relationship is given in Figure 3. When applying this relationship to the experimental data of the Achterhoek site,

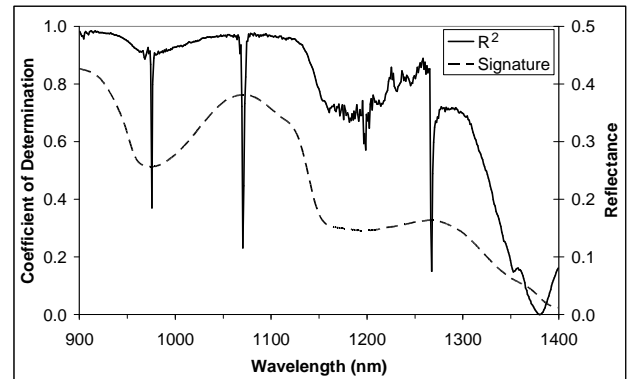


Figure 2. Coefficients of determination between CWC and first derivative of canopy reflectance as simulated by PROSAIL. The dotted line provides an example of a simulated canopy reflectance signature.

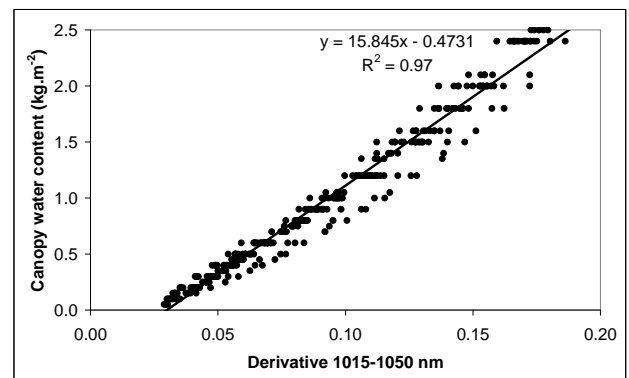


Figure 3. Relationship between first derivative of canopy reflectance over the interval 1015 – 1050 nm and CWC (PROSAIL simulations with varying input parameters according to Table 1).

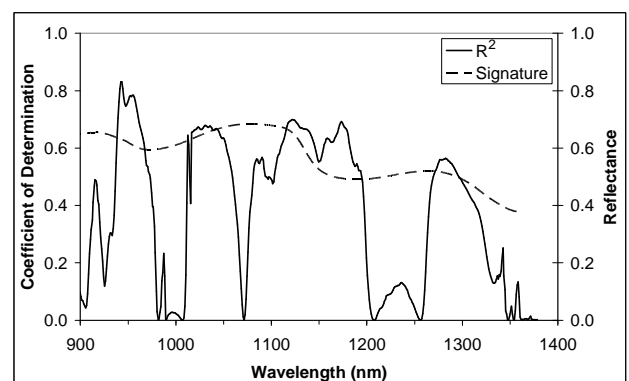


Figure 4. Coefficients of determination between CWC and first derivative of canopy reflectance as measured with the ASD FieldSpec at the Achterhoek site in 2008. The dotted line provides an example of a measured canopy reflectance signature.

Figure 6 illustrates the comparison of the estimated values with those obtained from the ASD FieldSpec measurements. The RMSEP derived from this Figure 6 is 0.25 $\text{kg}\cdot\text{m}^{-2}$. This value is about equal to the RMSEP value of 0.21 $\text{kg}\cdot\text{m}^{-2}$ obtained for the

experimental data themselves using the leave-one-out method (Figure 5). Figure 6 shows that we get a slight overestimation of CWC in this way.

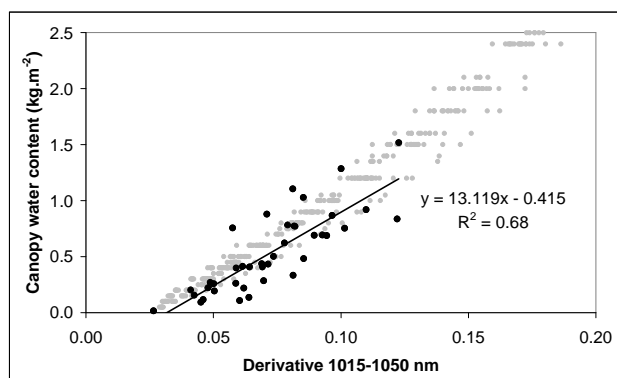


Figure 5. Relationship between first derivative of canopy reflectance over the interval 1015 – 1050 nm and CWC at the Achterhoek site in 2008. At the background the simulated relationship of Figure 3 is shown.

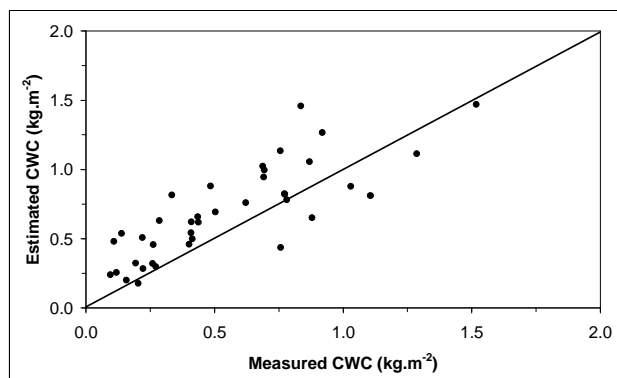


Figure 6. Comparison between CWC measurements from field samples and CWC estimations using PROSAIL simulations of the relationship between CWC and the spectral derivative over the 1015 – 1050 nm interval.

4. CONCLUSIONS

Results presented in this paper show that the spectral derivatives for wavelengths on the right slope of the water absorption feature at 970 nm can be used for estimating canopy water content (CWC). PROSAIL model simulations were performed using the improved PROSPECT-5 model as described by Feret et al. (2008). A linear relationship between first derivative over the 1015 – 1050 nm spectral interval and CWC was found, which was not very sensitive for leaf and canopy structure. Field spectroscopic measurements at a fen meadow confirmed the simulation results. The relationship between the first derivative over the 1015 – 1050 nm interval and CWC based on in-situ spectral measurements obtained in the field appeared to match the simulated relationship obtained from the PROSAIL model. This showed that one may transfer simulated results to real measurements obtained in the field,

thus giving them a physical basis and more general applicability.

Both simulated spectra and experimental FieldSpec spectra showed that the right slope of the 970 nm absorption feature is linear (constant) in the range from about 1015 nm up to about 1050 nm. Due to this broad interval, the first derivative over this 1015 – 1050 nm interval can be measured more accurately than the derivative at a certain spectral position (or narrow interval). As a result, this derivative also is more robust and less susceptible to noise. Smoothing the spectral measurements did not give better results than non-smoothed measurements. Smoothing was necessary when using narrow intervals (Clevers et al., 2008).

The PROSAIL simulations performed in this study do not include an atmospheric model. When using remote sensing observations from an airborne or spaceborne platform, one should also consider the water vapour absorption by the atmosphere. This occurs, for instance, at 940 nm and 1140 nm (Gao and Goetz, 1990; Iqbal, 1983), thus being shifted to shorter wavelengths as compared to the corresponding liquid water absorption features. This means that the effect of water vapour absorptions in the atmosphere occurs at the left slopes of the water absorption features used for estimating CWC. So, if one cannot correct well for the effects of atmospheric water vapour, it is recommended to use the first derivative, e.g., in the 1015 – 1050 nm interval.

Future work will continue focusing on higher spectral resolution instruments, in particular in the water absorption regions at 970 and 1200 nm. Instruments with a significantly higher spectral resolution would be able to assess separately water molecules in atmosphere and vegetation, allowing correct estimations for both atmospheric water vapour and liquid water in vegetation.

ACKNOWLEDGEMENTS

This work has been supported by the European Community's Marie Curie Research Training Networks Programme under contract MRTN-CT-2006-035927, Hyperspectral Imaging Network (HYPER-I-NET).

REFERENCES

- Clevers, J.G.P.W., Kooistra, L. and Schaepman, M.E., 2008. Using spectral information from the NIR water absorption features for the retrieval of canopy water content. *International Journal of Applied Earth Observation and Geoinformation*, 10(3), pp. 388-397.
- Clevers, J.G.P.W., Kooistra, L. and Schaepman, M.E., 2010. Estimating canopy water content using hyperspectral remote sensing data. *International Journal of Applied Earth Observation and Geoinformation*, 12(2), pp. 119-125.
- Curran, P.J., 1989. Remote sensing of foliar chemistry. *Remote Sensing of Environment*, 30(3), pp. 271-278.
- Danson, F.M., Steven, M.D., Malthus, T.J. and Clark, J.A., 1992. High-spectral resolution data for determining leaf water content. *International Journal of Remote Sensing*, 13(3), pp. 461-470.

Feret, J.B., François, C., Asner, G.P., Gitelson, A.A., Martin, R.E., Bidol, L.P.R., Ustin, S.L., le Maire, G. and Jacquemoud, S., 2008. PROSPECT-4 and 5: Advances in the leaf optical properties model separating photosynthetic pigments. *Remote Sensing of Environment*, 112(6), pp. 3030-3043.

Fourty, T., Baret, F., Jacquemoud, S., Schmuck, G. and Verdebout, J., 1996. Leaf optical properties with explicit description of its biochemical composition: Direct and inverse problems. *Remote Sensing of Environment*, 56(2), pp. 104-117.

Gao, B.C. and Goetz, A.F.H., 1990. Column atmospheric water vapor and vegetation liquid water retrievals from airborne imaging spectrometer data. *Journal of Geophysical Research*, 95(D4), pp. 3549-3564.

Hunt Jr., E.R. and Rock, B.N., 1989. Detection of changes in leaf water content using near- and middle-infrared reflectances. *Remote Sensing of Environment*, 30(1), pp. 43-54.

Iqbal, M., 1983. *An introduction to solar radiation*. Academic Press, Ontario, 390 pp.

Jacquemoud, S. and Baret, F., 1990. Prospect - a model of leaf optical properties spectra. *Remote Sensing of Environment*, 34(2), pp. 75-91.

Jacquemoud, S., Verhoef, W., Baret, F., Bacour, C., Zarco-Tejada, P.J., Asner, G.P., François, C. and Ustin, S.L., 2009. PROSPECT + SAIL models: A review of use for vegetation characterization. *Remote Sensing of Environment*, 113(SUPPL. 1), pp. S56-S66.

Jung, V., Hoffmann, L. and Muller, S., 2009. Ecophysiological responses of nine floodplain meadow species to changing hydrological conditions. *Plant Ecology*, 201(2), pp. 589-598.

Kuusik, A., 1991. The angular-distribution of reflectance and vegetation indexes in barley and clover canopies. *Remote Sensing of Environment*, 37(2), pp. 143-151.

Le Maire, G., François, C. and Dufrêne, E., 2004. Towards universal broad leaf chlorophyll indices using PROSPECT simulated database and hyperspectral reflectance measurements. *Remote Sensing of Environment*, 89(1), pp. 1-28.

Rollin, E.M. and Milton, E.J., 1998. Processing of high spectral resolution reflectance data for the retrieval of canopy water content information. *Remote Sensing of Environment*, 65(1), pp. 86-92.

Running, S.W. and Gower, S.T., 1991. Forest-Bgc, a general model of forest ecosystem processes for regional applications. 2. Dynamic carbon allocation and nitrogen budgets. *Tree Physiology*, 9(1-2), pp. 147-160.

Running, S.W. and Nemani, R.R., 1991. Regional hydrologic and carbon balance responses of forests resulting from potential climate change. *Climatic Change*, 19(4), pp. 349-368.

Schaepman, M.E., Ustin, S.L., Plaza, A.J., Painter, T.H., Verrelst, J. and Liang, S., 2009. Earth system science related imaging spectroscopy-An assessment. *Remote Sensing of Environment*, 113(SUPPL. 1), pp. S123-S137.

Verhoef, W., 1984. Light scattering by leaf layers with application to canopy reflectance modeling: the SAIL model. *Remote Sensing of Environment*, 16(2), pp. 125-141.

MULTITEMPORAL FUZZY MARKOV CHAIN-BASED CLASSIFICATION OF VERY HIGH RESOLUTION IMAGES OF AN URBAN SITE

G. A. O. P. Costa ^a*, R. Q. Feitosa ^a, L. F. G. Rego ^b

^a Department of Electrical Engineering

^b Department of Geography

Pontifícia Universidade Católica do Rio de Janeiro Rua Marquês de São Vicente 225, Gávea, Rio de Janeiro, CEP: 22453-900, RJ, Brasil – (gilson, raul)@ele.puc-rio.br, regoluiz@puc-rio.br

KEY WORDS: Multitemporal, Interpretation, Fuzzy Logic, High Resolution, Urban, Land Use, Land Cover

ABSTRACT:

This work discusses the application of the cascade, multitemporal classification method based on fuzzy Markov chains originally introduced in (Feitosa et al. 2009), over a set of IKONOS images of urban areas within the city of Rio de Janeiro, Brazil. The method combines the fuzzy, monotemporal, classification of a geographical region in two points in time to provide a single unified result. The method does not require knowledge of the true class at the earlier date, but uses instead the attributes of the image object being classified at both the later and the earlier date. A transformation law based on class transition possibilities projects the earlier classification to the later date before combining both results. While in (Feitosa et al. 2009) the fuzzy Markov chain-based method was evaluated over a series of medium resolution, LANDSAT images, in this work very high resolution images were processed. Additionally, while the target area of the previous work was characterized predominantly by agricultural use, in this work an urban area was the subject of classification. The results showed that the performance of the multitemporal method was consistently superior to that of the monotemporal classification of the study area, and confirmed the robustness of the fuzzy Markov chain-based method with respect to sensor characteristics and target sites.

1. INTRODUCTION

Sequences of Remote Sensing images of the same geographical area acquired at different points represent a valuable source of information that can be used to improve the accuracy and reliability of classification-based image analysis.

Most traditional multirate image classification methods can be regarded as “post-classification” approaches (Weismiller et al., 1977), which are decisively dependent on the accuracy of the initial classifications. More powerful alternatives, called “cascade-classification” approaches (Swain, 1978) use all the information contained in the image sequence, trying to explore the correlation contained in the temporal data sets.

Feitosa et al. (2009) presented a detailed overview of the most relevant efforts towards automatic cascade multitemporal schemes found in the literature. These attempts include probabilistic methods, methods based on neural networks and multi-classifier approaches.

A first attempt towards a fuzzy cascade classification technique can be found in (Mota et al., 2007). That method is restricted to applications where the true class of the object being classified at an earlier time is known. Feitosa et al. (2009) described a new fuzzy cascade multitemporal classification model, explicitly based on fuzzy Markov chains, in which object features other than the true classification are used as the information from the earlier date. In the later method, before the classifications of two images at two dates are combined, the fuzzy classification at the earlier date undergoes a temporal transformation that projects it onto the later date.

This work discusses the application of the cascade, multitemporal classification method introduced in (Feitosa et al. 2009), originally applied over an agricultural over a set of IKONOS II images of urban areas within the city of Rio de Janeiro, Brazil.

2. FUZZY MARKOV CHAINS

This section describes briefly the concept of Fuzzy Markov Chain (FMC). A complete and more general presentation about this technique and the related concepts may be found in (Avrachenkov and Sanchez, 2002).

In this work we consider images acquired at dates $t_0+t\Delta t$, where t_0 is some stipulated initial time, Δt is a given time interval, and t is any integer number. For simplicity the date $t_0+t\Delta t$ will be denoted from this point on as time t , and $t_0+(t+1)\Delta t$ as time $t+1$, for $t \in \mathbb{Z}$.

Let $\Omega = \{\omega_1, \omega_2, \dots, \omega_n\}$ be a set of n distinguishable land-use/land-cover (LULC). A binary fuzzy relation can be defined on the Cartesian product $\Omega \times \Omega$ represented by a $n \times n$ transition matrix $\mathbf{T} = \{\tau_{ij}\}$. The symbol τ_{ij} stands for the possibility that an image object belongs to the class $\omega_i \in \Omega$ at time t and to the class $\omega_j \in \Omega$ at time $t+1$, with $0 \leq \tau_{ij} \leq 1$, for $i, j = 1, \dots, n$.

This can be pictorially described by a class transition diagram (Figure 1), a weighted directed graph whose nodes correspond to classes and links to plausible class transitions between t and $t+1$. Each link is labeled with the class transition possibility τ_{ij} . For simplicity links with $\tau_{ij} = 0$ are not drawn.

* Corresponding author.

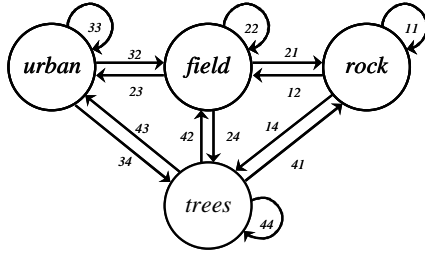


Figure 1. Class transition diagram with four classes.

The vector $'\alpha = [\alpha_1, \dots, \alpha_n]$ with $0 \leq \alpha_i \leq 1$ represents, for a particular image object, the fuzzy classification defined over Ω at time t , where α_i denotes the membership value of the object to class ω_i (for all $\omega_i \in \Omega$) at time t . It is further assumed that α_i is a function of attribute values of the image object at time t .

Based on the fuzzy label vector $'\alpha$ and on the transition matrix \mathbf{T} , the Fuzzy Markov Chain Model estimates the class membership values, represented by the vector ${}^{t+1}\beta = [{}^{t+1}\beta_1, \dots, {}^{t+1}\beta_n]$ for the same object one time unit later by applying the following formula:

$${}^{t+1}\beta_j = \perp_{i=1, \dots, n} \{ \top(\alpha_i, \tau_{ij}) \} \quad (1)$$

for $i, j = 1, \dots, n$. The symbols \top and \perp represent respectively a t -norm and a s -norm.

The transition law introduced in Equation (1) can be expressed in a more compact form by the equation below.

$${}^{t+1}\beta = '\alpha \circ \mathbf{T} \quad (2)$$

In the expression “ $\mathbf{A} \circ \mathbf{B}$ ”, the symbol “ \circ ” denotes a special type of matrix multiplication, analogous to conventional matrix multiplication, where the product is replaced by a t -norm and the summation is replaced by a s -norm operator.

The symbols ${}^{t+1}\beta$ and ${}^{t+1}\alpha$ denote different distributions although both refer to the same object at the date $t+1$. While ${}^{t+1}\alpha$ has been computed based on feature values at time $t+1$ without any temporal transition transformation, ${}^{t+1}\beta$ is the result of applying the FMC transition law, Equation (2), upon the membership grades in $'\alpha$ computed on the feature values of the image object corresponding to the same geographical object at time t .

3. MULTITEMPORAL CLASSIFICATION MODEL

3.1 Problem statement

Let $'\mathbf{I}$ and ${}^{t+1}\mathbf{I}$ denote two co-registered images of the same geographical area acquired respectively at dates t and $t+1$. Accordingly, $'\mathbf{x}$ and ${}^{t+1}\mathbf{x}$ stand for the feature vectors composed of spectral and spatial feature values describing the same geographical object respectively in $'\mathbf{I}$ and ${}^{t+1}\mathbf{I}$. We further denote with $'\mathbf{w}$ and ${}^{t+1}\mathbf{w}$ the *crisp* label vectors for the object being analyzed at times t and $t+1$. Both $'\mathbf{w}$ and ${}^{t+1}\mathbf{w}$ are n -dimensional unitary vectors of the form $[0 \dots 1 \dots 0]$ having “1” in its i -th component and “0” otherwise, indicating that the object belongs to the class ω_i at a particular time. Formally, $'\mathbf{w}$ and ${}^{t+1}\mathbf{w}$ belong to a n dimensional space Ω^n , where:

$$\Omega^n = \{ \mathbf{w} = [w_1, \dots, w_n] \mid w_i \in \{0, 1\} \text{ for all } i = 1, \dots, n \text{ and } \|\mathbf{w}\| = 1 \} \quad (3)$$

The multitemporal classification problem treated in the present work consists of identifying the vector ${}^{t+1}\mathbf{w}$ for each image object, based on the feature vectors $'\mathbf{x}$ and ${}^{t+1}\mathbf{x}$, in other words, it is about finding a function \mathbf{M} of the form:

$${}^{t+1}\mathbf{w} = \mathbf{M}({}^{t+1}\mathbf{x}, '\mathbf{x}) \quad (4)$$

3.2 General classification model

The terms monotemporal and multitemporal will be used hereafter to designate classifiers whose inputs refer respectively to a single date or to multiple dates.

The outcome of the multitemporal classifier can be viewed as the fusion of the outcome of two monotemporal classifiers. Let the first monotemporal classifier be represented by a function ${}^L\mathbf{C}$ that computes membership values for the object being classified at the later time $t+1$ based exclusively on the feature values at time $t+1$, extracted from image ${}^{t+1}\mathbf{I}$. The monotemporal classifier ${}^L\mathbf{C}$ produces a n -dimensional *fuzzy* label vector denoted by ${}^{t+1}\alpha = [{}^{t+1}\alpha_1, {}^{t+1}\alpha_2, \dots, {}^{t+1}\alpha_n]$, where ${}^{t+1}\alpha_i$ stands for the membership of the image object assigned by ${}^L\mathbf{C}$ to the class ω_i , for all $\omega_i \in \Omega$ and for at least one i , ${}^{t+1}\alpha_i \neq 0$. So, ${}^L\mathbf{C}$ can be viewed as a function of the form:

$${}^{t+1}\alpha = {}^L\mathbf{C}({}^{t+1}\mathbf{x}) \quad (5)$$

A second *monotemporal* ${}^E\mathbf{C}$ is applied to the object feature vector $'\mathbf{x}$ at time t . Analogously to the first monotemporal classifier, it generates a fuzzy label vector $'\alpha$, formally:

$$'\alpha = {}^E\mathbf{C}('\mathbf{x}) \quad (6)$$

Since $'\alpha$ refers to the membership distribution at the earlier time t and our interest is in the classification at the later time $t+1$, the FCM transition law is applied to infer the membership values at time $t+1$ based on the membership values at t . Thus, if \mathbf{T} is the class transitions matrix representing the class transitions in two consecutive instants, we may estimate the classification at time $t+1$ by combining equations (2) and (6), yielding:

$${}^{t+1}\beta = {}^E\mathbf{C}('\mathbf{x}) \circ \mathbf{T} \quad (7)$$

The two fuzzy label vectors ${}^{t+1}\alpha$ and ${}^{t+1}\beta$ are then combined in the next step by an *aggregation* function \mathbf{F} to form a *multitemporal* fuzzy label vector ${}^{t+1}\mu = [{}^{t+1}\mu_1, \dots, {}^{t+1}\mu_n]$ given by:

$${}^{t+1}\mu = \mathbf{F}({}^{t+1}\alpha, {}^{t+1}\beta) = \mathbf{F}[{}^L\mathbf{C}({}^{t+1}\mathbf{x}), {}^E\mathbf{C}('\mathbf{x}) \circ \mathbf{T}] \quad (8)$$

The final step is the defuzzification, performed by a function of the form:

$$\mathbf{H}: [0, 1]^n \rightarrow \Omega^n \quad (9)$$

that transforms the *fuzzy* label vector ${}^{t+1}\mu$ into a *crisp* one. Putting it all together, the multitemporal classifier \mathbf{M} is given by Equation (10).

$${}^{t+1}\mathbf{w} = \mathbf{M}({}^{t+1}\mathbf{x}, '\mathbf{x}) = \mathbf{H}\{ \mathbf{F}[{}^L\mathbf{C}({}^{t+1}\mathbf{x}), {}^E\mathbf{C}('\mathbf{x}) \circ \mathbf{T}] \} \quad (10)$$

3.3 Particularization of the classification model

FMC models may be built using any t -norm and s -norm composition. We favor the *max-product* composition, since it leads to a simple multitemporal classification model with an intuitive interpretation. Thus Equation (1) takes the form:

$${}^{t+1}\beta_j = \max_{i=1,\dots,n} \{ \alpha_i \tau_{ij} \} \quad (11)$$

for $i, j = 1, \dots, n$.

The defuzzification step is carried out by a hardening function \mathbf{H} that selects the fuzzy set with the highest membership grade, formally:

$$[w_1, \dots, w_n] = \mathbf{w} = \mathbf{H}(\boldsymbol{\mu}) = \mathbf{H}([\mu_1, \dots, \mu_n]), \text{ where} \quad (12)$$

$$w_j = \begin{cases} 1 & \text{for } \mu_j = \max\{\mu_1, \dots, \mu_n\} \\ 0 & \text{otherwise} \end{cases}$$

The aggregation function \mathbf{F} is the product of corresponding elements of the input fuzzy vectors. Thus,

$${}^{t+1}\boldsymbol{\mu} = \mathbf{F}({}^{t+1}\boldsymbol{\alpha}, {}^{t+1}\boldsymbol{\beta}) = [{}^{t+1}\alpha_1 {}^{t+1}\beta_1, \dots, {}^{t+1}\alpha_n {}^{t+1}\beta_n] \quad (13)$$

Putting it all together, the multitemporal classifier assigns the image object to the class $\omega_i \in \Omega$ at time $t+1$, for which

$${}^{t+1}\mu_i = \max_k \left\{ \alpha_k \max_l \left\{ \alpha_{l ik} \right\} \right\} = \max_{k,l} \left\{ \alpha_{l ik} \alpha_k \right\} \quad (14)$$

holds.

3.4 Estimating transition possibilities

The estimation of transition possibilities basically selects the set of possibility values that maximizes the classification accuracy computed upon a given training set.

The estimation procedure consists of finding the set of transition possibility values $\mathbf{T} = \{\tau_{ij}\}$ that maximizes the selected accuracy function G , for the selected image objects S of image objects at the later date (the training set) and for the selected monotemporal classifiers. This is formally expressed by:

$$\mathbf{T} = \arg \max_{\mathbf{T}} \{ G(S, {}^E\mathbf{C}, {}^L\mathbf{C}, \tilde{\mathbf{T}}) \} \quad (15)$$

The computation of transition possibilities defined in Equation (17) involves an optimization procedure. The classification model introduced in the previous sections is actually not bound to any particular parameter optimization technique. In this work, the average class accuracy was used as accuracy function, and a Genetic Algorithm was the optimization technique used to estimate transition possibilities (Schmiedle et al., 2002).

4. EXPERIMENTS

The experiments described in the following sections were designed to evaluate the proposed method over a set of high resolution IKONOS II images. The experiments aimed at comparing the outcome of the multitemporal classification with that of the monotemporal classification of the later image. We also investigated the performance of the method tuning the

performance of the earlier monotemporal classifier, as described in Section 4.4. The idea was to investigate how the method behaves with different (increasing) performances of the earlier monotemporal classifier.

The data set used in all experiments is described in the next section. Afterward, the design of the particular monotemporal classifier that composes the multitemporal scheme in the experiments is presented. The following two sections describe respectively the monotemporal classifier design and the optimization technique used to estimate transition possibilities.

4.1 Description of the data set

The test site corresponds to a 14.4 km² area, situated on the north face of the Tijuca National Park, within the city of Rio de Janeiro, an important Atlantic Forest remnant. The test-site is a subset of the area of interest of the PIMAR Project (Remote Environmental Monitoring Program), which aims at monitoring the suppression of rainforest on conservation units inside the municipality of Rio de Janeiro through high resolution optical remote sensing images (PIMAR, 2010).

This area was selected as test-site because of the noticeable sprawl of informal dwellings over legally protected natural areas. Moreover, the area contains various instances of all land cover classes considered by the PIMAR Project.

Two pan-shaped, orthorectified IKONOS II images were used in the experiments. The images actually take part of two stereo pairs, each pair acquired on the same orbit, with different elevation angles. The orthorectification was performed using digital elevation models derived from each stereo pair. For each year the image with the highest elevation angle was chosen and submitted to orthorectification.

It is important to note that because of the time of the year the images were acquired – March 2008 (late summer) and June 2009 (late autumn) respectively –, they present quite different illumination conditions, with an important presence of clouds in the 2009 image. No radiometric correction or equalization was performed over the orthorectified images.

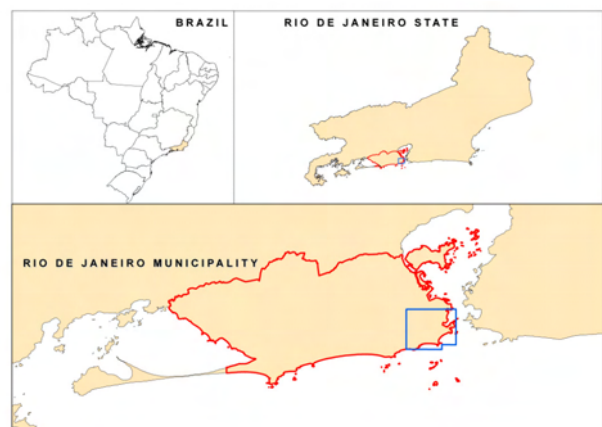


Figure 2. Area of the test-site in Rio de Janeiro municipality.

The orthorectified IKONOS II images were segmented using the multiresolution segmentation algorithm proposed by Baaz and Shäpe (2000), through the Definiens Developer 7 software. The parameters chosen for the segmentation procedure were

such that the resulting segments were small in size, as defined by the low scale parameter value, giving priority to color homogeneity instead of coherently shaped segments. The idea was to absolutely avoid that the segments disrespect the border between two different land cover objects.

Parameter	Value
Scale	30
Color	0.9
Shape	0.1
Compactness	0.5
Smoothness	0.5
Layer weights (bands 1, 2, 3 and 4)	1,1,1,1

Table 1. Segmentation parameters used in the experiments.

All segments generated from the two images were duly, visually classified by specialists. Table 2 describes the land-use classes considered. Actually, shadow segments were also classified as such, but they were not considered in the experiments.

After classification, all segments from each class in 2008 were merged to the adjacent segments of the same class, generating larger area segments. Then, only the segments from 2009 that fell completely inside the large 2008 segments (generated from the merging procedure) were selected.

For those selected segments (generated through the segmentation of the 2009 image), feature attributes were calculated from each of the two images. The feature extraction procedure was also implemented on the Definiens Developer software. The features extracted for each segment were: mean values of the four spectral bands and the textural entropy feature (for all bands in all directions).

The basic idea of the procedure described above was to produce a set of segments with class labels for 2008 and 2009, and with two sets of attributes, extracted respectively from the 2008 and 2009 images. Table 3 shows the number of segments assigned to each class, in each year and the class transitions observed from 2008 to 2009.

Label	Class	Description
Rock (ω_1)	Rock	Exposed rock (granite) formations.
Field (ω_2)	Grass field	Grass fields naturally formed over thin soil or created by anthropogenic activities.
Urban (ω_3)	Urban Area	Constructed area (buildings, roads, etc.) including bare soil areas
Trees (ω_4)	Arboreous Vegetation	Individual or clusters of trees (inside urban areas or not).

Table 2. LULC classes considered in the experiments.

2008	2009				
	Rock	Field	Urban	Trees	Total
Rock	188	10	0	1	199
Field	11	421	66	153	651
Urban	0	9	5594	220	5823
Trees	1	194	390	33947	34532
Total	200	634	6050	34321	41205

Table 3. Class transitions from 2008 to 2009.

4.2 Monotemporal classifier design

A simple design is adopted in our experiments for the earlier (\mathbf{C}) and later (${}^{t+k}\mathbf{C}$) monotemporal image classifiers. Feature vectors \mathbf{x} are built for each segment by stacking the attribute value of the segments (recorded at a specific date). It is assumed that all classes ω_i can be appropriately modelled by a Gaussian-shaped membership function $\mathbf{MF}_{\omega_i}(\mathbf{x})$ given by the formula below:

$$\mathbf{MF}_{\omega_i}(\mathbf{x}) = \exp\left[-\frac{(\mathbf{x} - \bar{\mathbf{x}}_i)^T \Sigma_i^{-1} (\mathbf{x} - \bar{\mathbf{x}}_i)}{2}\right] \quad (16)$$

for $\omega_i \in \{\text{rock, field, urban, trees}\}$, where $\bar{\mathbf{x}}_i$ and Σ_i correspond respectively to the mean and to the covariance matrix of the class ω_i .

4.3 Optimization procedure

The transition possibility values were estimated, as mentioned in Section 3.4, by a Genetic Algorithm (GA) using as objective function the average class accuracy. The genes were the transition possibility values. The GA design used in the experiments was the same as in (Feitosa et al., 2009).

4.4 Simulating monotemporal classifiers with tunable performance

The multitemporal classification based on fuzzy Markov chains is evaluated for for monotemporal classifiers with varying performances. Such evaluation scheme can be done by defining a simulated monotemporal classifier ${}^{t+k}\mathbf{C}^*$ with tuneable performance, that is, for all image objects, we have:

$${}^{t+k}\mathbf{a}^* = m {}^{t+k}\mathbf{W} + (1-m) {}^{t+k}\mathbf{a} \quad (17)$$

where ${}^{t+k}\mathbf{W}$ is the *true* crisp label vector, ${}^{t+k}\mathbf{a}$ is the fuzzy label vector from the monotemporal classifier, and m is a *mixture factor* that takes values in the interval [0,1]. For $m = 0$, the simulated monotemporal classifier is identical to the monotemporal classifier described in the previous section; for $m = 1$, it is equal to the *ideal* classifier.

The monotemporal classifiers, ${}^{t+k}\mathbf{C}$, are replaced in our experiments by the simulated monotemporal classifier, ${}^{t+k}\mathbf{C}^*$, and a continuous variation of m permits to observe how the relative performance of the monotemporal classifiers affects the accuracy of the multitemporal model. It is worth anticipating at this point the low performance of the real monotemporal classifier described in Section 4.2 in comparison to state of the art classification approaches (see experiment results in the next section). This is convenient in view of the objective of the analysis since it permits to assess the multitemporal models for a wide range of monotemporal classification performances.

4.5 Results

The benchmark for the analysis reported in the subsequent sections is the outcome of the monotemporal classifiers that take part of the multitemporal scheme. As the object of comparison is the crisp classification of the later image segments, a defuzzification step was performed over the output of the fuzzy monotemporal classifier, simply assigning to each

segment the class for which it obtained the highest membership value.

In a sequence of experiments using the average class accuracy to estimate transition possibilities, the training set was built in the following way. The image objects were first separated in groups according to the class transition they undergone in two consecutive dates. To estimate the parameters of the monotemporal classifiers as well as the transition possibilities as described in previous sections, approximately 25% of the objects in each group are randomly selected to form the training set. The remaining 25% of the objects were used to evaluate the method in terms of average class accuracy at the later date.

Figure 2 shows the performance achieved by both the monotemporal and multitemporal. The points in the graph represent averages values computed over 30 executions of the same experiment, each time with a distinct random selection of training and testing objects. Each point is associated to a specific mixture factor m .

As it was expected, the average outcome of the monotemporal classifier for 2008 in the various experiments remain almost constant, varying from 75% to 76% (Figure 3). It is also noticeable that the classification performance of the monotemporal classifier for 2008 is considerably better than that

of the monotemporal classifier for 2009, even when the mixture factor is equal to zero, even though the design of the earlier and later monotemporal classifiers are the same. That may be credited to the fact that there are a considerable amount of shadows in the 2009 image, basically due to the different solar elevation angles in the two images. Although the completely shaded areas (segments) were not considered in the experiments, the effect of the shadows on the segments that were not discarded may have influenced the capacity of the classifier to discriminate among the classes of interest. The human interpreted can, however, easily adapt to those conditions.

Anyhow, it is interesting to observe that the multitemporal classification method could benefit from the better monotemporal classification from 2009 (even when the mixture factor m is equal to zero) and improve the classification accuracy by approximately 6.6% (Figure 4) – from 76% to 81% (Figure 3).

As the performance of the earlier monotemporal classifier improves (for 2008), influenced by the increasing mixture factor, so does the performance of the multitemporal classifier for 2009, reaching an average class accuracy of over 89% – an improvement of approximately 16.9% (Figure 4).

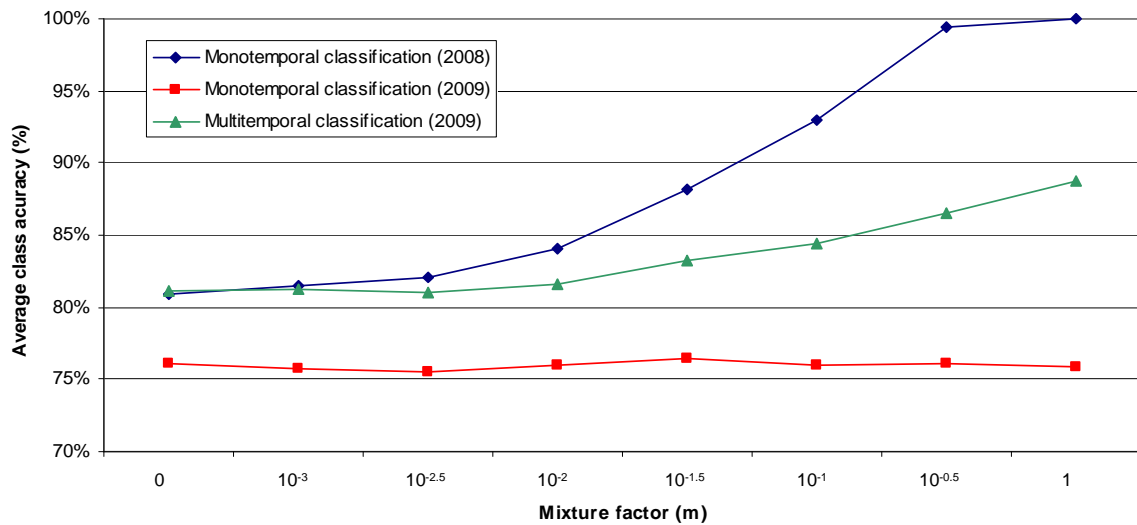


Figure 3. Performance of the monotemporal and multitemporal classifiers.

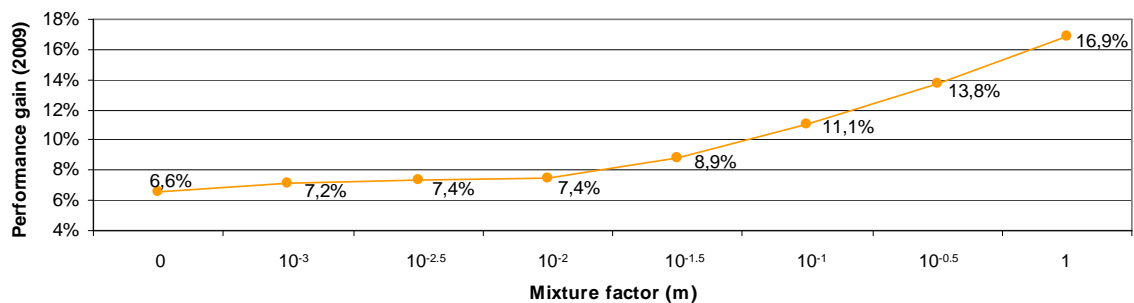


Figure 4. Performance gain in the classification of the 2009 image brought by the multitemporal classification.

5. CONCLUSION

In this paper, we applied the model proposed in (Feitosa et al., 2009) on a set of very high resolution IKONOS II images of urban areas within the city of Rio de Janeiro, Brazil.

The results are consistent with the ones presented in (Feitosa et al., 2009), where series of Landsat images over an agricultural area were subjected to multitemporal interpretation.

The experiments results presented here and in (Feitosa et al., 2009) indicate that the multitemporal classification design based on fuzzy Markov chains generally brings an accuracy gain in relation to the monotemporal approach. Furthermore, it has been shown that the more accurate the information coming from the earlier date, the higher is its contribution to the multitemporal classification performance. In fact, the fuzzy Markov chain method seem to be particularly beneficial whenever there is information regarding the earlier date (t) that is significantly more accurate than the available information about the later date ($t+1$).

We should recall that the assumption underlying the proposed multitemporal classification model is the existence of a significant temporal correlation between the data sets. If an application does not meet this condition, the method is not expected to work properly at all.

Future research should tackle a number of other important issues. Experiments should be performed with more time points. In this case, conditions on the length of the Markov chain could also be investigated. Broader series of experiments with other geographic regions and types of images should also be carried out.

It would be also interesting to investigate other optimization algorithms, since genetic algorithms spend too much processing time and do not guarantee that the global optimum solution is found. A possible candidate for this optimization task could be some sort of least squares-based algorithm.

REFERENCES

- Avranchenkov, K. E., Sanchez, E., 2002. Fuzzy Markov chains and decision-making. *Fuzzy Optimization and Decision Making* 1 (2), 143-159.
- Baatz, M., Schäpe, A. 2000. Multiresolution segmentation – an optimization approach for high quality multi-scale image segmentation. In: Strobl, J., Blaschke, T. *Angewandte Geographische Informationsverarbeitung XII. Beiträge zum AGIT Symposium Salzburg 2000*, Herbert Wichmann Verlag, Karlsruhe.
- Feitosa, R. Q., Costa, G. A. O. P., Mota, G. L. A., Feijó, B., 2009. Cascade classification of Multitemporal. *ISPRS International Journal on Photogrammetry and Remote Sensing* 64 (2), 159-170.
- Mota, G. L. A., Feitosa, R. Q., Coutinho, H. L. C., Liedtke, C. E., Müller, S., Pakzad, K., Meirelles, M. S. P., 2007. Multitemporal fuzzy classification model based on class transition possibilities. *ISPRS International Journal of Photogrammetry and Remote Sensing* 62, 186-200.
- PIMAR, 2010. Projeto PIMAR (Programa Integrado de Monitoria Remota de Fragmentos Florestais e de Crescimento Urbano no Rio de Janeiro). http://www.nima.puc-rio.br/sobre_nima/projetos/pimar (accessed 15 May 2010)
- Schmiedle, F., Drechsler, N., Grosse, D., Drechsler, R., 2002. Heuristic learning based on genetic programming. *Genetic Programming and Evolvable Machines* 3 (4), 363-388.
- Swain, P. H. 1978. Bayesian classification in a time-varying environment. *IEEE Trans. Sys. Man. and Cybern.* 12, 879-883.
- Weismiller, R. A., Kristoof, S. J., Scholz, D. K., Anuta, P. E., Momen, S. A., 1977. Change detection in coastal zone environments. *Photogrammetric Engineering and Remote Sensing* 43, 1533-1539.

ACKNOWLEDGEMENTS

This work was supported by CNPq (Brazilian National Counsel of Technological and Scientific Development), FINEP (Brazilian Innovation Agency) and FAPERJ (Carlos Chagas Filho Research Support Agency of the State of Rio de Janeiro). We would also like to thank the Government of the State of Rio de Janeiro, Secretaria de Estado do Ambiente (SEA) for funding the PIMAR project.

PERSISTENT SCATTERER INTERFEROMETRY BASED ON TERRASAR-X IMAGERY: THE BARCELONA TEST AREA

M. Crosetto^{a,*}, O. Monserrat^a, M. Cuevas^a, B. Crippa^b

^a Institute of Geomatics, Av. del Canal Olímpic, s/n, Castelldefels, E-08860, Spain

michele.crosetto@ideg.es, oriol.monserrat@ideg.es, maria.cuevas@ideg.es

^b Department of Earth Sciences, University of Milan, Via Cicognara 7, 20129 Milan, Italy - bruno.crippa@unimi.it

Commission VII, WG VII/2

KEY WORDS: Remote Sensing, Satellite, Detection, Deformation, Geocoding.

ABSTRACT:

The aim of this paper is deformation monitoring over urban areas using Persistent Scatterer Interferometry (PSI) and Very High Resolution (VHR) X-band SAR imagery. Since the launch of TerraSAR-X and the first COSMO-SkyMed satellite (both were launched in June 2007), the VHR X-band data has grown in importance as source of PSI. This is due to the remarkable increase of the data acquisition capability (for instance, the COSMO-SkyMed constellation consists of three SAR satellites in mid 2010), the progressive loss of key sources of SAR images, as ASAR-Envisat and ERS-2, and the promising technical characteristics of the X-band. This paper illustrates some of the main results of the PSI analysis derived from VHR X-band data. The analysis was carried out over a stack of SAR images captured by the TerraSAR-X sensor and covering the metropolitan area of Barcelona (Spain). This work is the first experience of the authors with PSI analysis of the X-band, which is based on a rich set of 28 StripMap images. These images were processed and analysed using the PSI in-house experimental software chain of the Institute of Geomatics. A description of the Barcelona dataset and the main outcomes of the PSI analysis is given. These outcomes reflect a preliminary assessment of the improvement which can be achieved by VHR X-band PSI, mainly in terms of deformation monitoring capability.

1. INTRODUCTION

This paper describes a technique for deformation monitoring over urban areas based on Persistent Scatterer Interferometry (PSI) and very high resolution (VHR) X-band Synthetic Aperture Radar (SAR) images, captured by the TerraSAR-X sensor. In particular, it summarizes the experience of the authors in the analysis of a test area: the metropolitan area of Barcelona (Spain).

PSI is a radar-based remote-sensing technique to measure and monitor land deformation (see Rosen et al., 2000; Crosetto et al., 2005). PSI represents the most advanced category of DInSAR techniques. Different PSI approaches have been proposed in the last decade (see Ferretti et al., 2001; Berardino et al., 2002; Colesanti et al., 2003; Mora et al., 2003; Lanari et al., 2004; Hooper et al., 2004; Kampes and Hanssen, 2004; Crosetto et al., 2005; Pepe et al., 2005; Crosetto et al., 2008).

The availability of SAR data acquired by space-borne sensors represents a key issue for the successful use of PSI. In particular, image acquisition continuity over large periods of time plays a fundamental role in PSI. Note that the data must be acquired by the same sensor or compatible sensors, as in the case of ERS-1 and ERS-2. The first satellite that allowed demonstrating the potentialities of the PS technique was ERS-1. This satellite has been operative for 10 years and, more importantly, together with its almost exact replica ERS-2, has provided a valuable historical archive of interferometric SAR data. ERS satellites have provided global spatial coverage over a time period of 19 years, with the first images dating back to summer 1991. There are hundreds of high level scientific

publications that demonstrate the success of the ERS mission. Radarsat-1 and ASAR-Envisat have also been particularly important PSI data sources. The latest Differential Interferometric SAR (DInSAR) results based on data acquired by the ERS and Envisat satellites can be found at <http://eopi.esa.int/>

A new generation of sensors has been launched in the last few years, including the C-band Radarsat-2 (launched in December 2007 by the Canadian Space Agency), the X-band TerraSAR-X (launched in June 2007 by a joint venture carried out under a public-private-partnership between the German Aerospace Centre, DLR, and EADS Astrium GmbH; the exclusive commercial exploitation rights are held by Infoterra GmbH), and the X-band COSMO-SkyMed (COntellation of small Satellites for the Mediterranean basin Observation, conducted by the Italian Space Agency, ASI; the current constellation includes three satellites).

The last two systems, TerraSAR-X and COSMO-SkyMed are particularly promising due to their very high spatial resolution imaging capabilities and the use of the X-band. One of the key tasks of the PSI research teams spread all over the world is to study the performance of these two very promising types of SAR data. The goal of this paper is to describe the first experience of the authors in the PSI analysis based on a rich set of TerraSAR-X images. These images were processed using the PSI in-house experimental software chain of the Institute of Geomatics. This paper describes a dataset covering the metropolitan area of Barcelona and the main outcomes of the preliminary PSI analysis.

* Corresponding author.



Figure 1. Metropolitan area of Barcelona: SAR amplitude superimposed over Google Earth. The area covers 45 by 45 km approx.

2. THE BARCELONA DATASET

The VHR X-band SAR dataset analysed in this paper is composed of 28 StripMap images acquired by the sensor onboard the satellite TerraSAR-X. This dataset is an interferometric stack of images covering the same area, i.e. they are suitable to perform a PSI analysis. The spatial coverage of the images is shown in Figure 1, while their temporal distribution, which starts in December 2007 and ends in November 2009, can be found in Table 1. Six of the 28 images were acquired for the Project N°. LAN0634, “Evaluation of DEM derived from TerraSAR-X data”, of the TerraSAR-X Science Service Program. Some preliminary results of a subset of 13 SAR images are described in Crosetto et al. (2010). The images used in this work cover approximately 30 by 50 km, with a pixel footprint of about 1.9 by 1.6 m. The images were acquired with an off-nadir angle of 35.5°. The perpendicular baselines of the interferograms based on these images (i.e. the component of the vector that connects the two satellite positions during image acquisition, measured in the direction perpendicular to the SAR line-of-sight) are approximately in the range of -275 m to 500 m.

In the next sections, the following aspects are analysed: (i) the spatial sampling, (ii) the so-called residual topographic error and the PSI geocoding and (iii) the average displacement rates and the deformation time series.

Acquisition dates	
20071230	20080908
20080110	20081102
20080121	20081216
20080212	20090118
20080223	20090129
20080305	20090220
20080316	20090314
20080429	20090416
20080521	20090530
20080612	20090713
20080623	20090815
20080704	20090917
20080715	20091020
20080817	20091122

Table 1. Temporal distribution of the 28 images considered in this study. The temporal coverage is approximately two years: from December 2007 to November 2009.



Figure 2. Example of the sampling capability of TerraSAR-X StripMap imagery. A photo of the Agbar tower, an emblematic 144 m height skyscraper of Barcelona, is shown in the left image. The mean SAR amplitude image over the same tower is shown in the right image. In this case, the mean amplitude image was obtained using 20 co-registered images. One sample every 0.75 m along the vertical direction can be obtained thanks to the resolution in range of these images (0.9094 m).

3. SPATIAL SAMPLING

As mentioned above, the major advantage of the X-band imagery captured by the sensors onboard the TerraSAR-X and COSMO-SkyMed satellites is its high spatial resolution (see Adam et al., 2008). Figure 1 shows an illustrative example of a skyscraper: a very dense sampling of vertical facades is provided by TerraSAR-X. However, it is worth emphasising that the actual PSI spatial sampling capability, and hence the PSI deformation measurement capability, is usually much lower than the resolution of the original SAR imagery. In fact, PSI deformation measurements can only be achieved for the points where PSI phases maintain good quality over time. An example of PSI sampling density is shown in Figure 3. It is evident that many of the original SAR pixels cannot be exploited to estimate deformation in this case (e.g. see the central part of the image where no measurements were obtained). However, a very dense set of deformation measurement points can be obtained where the PSI phase maintains good quality.

4. PSI GEOCODING

An interesting aspect of the analysis of the TerraSAR-X data described in this work is the accurate PSI geocoding capability, which is a fundamental step to correctly interpret and exploit the PSI results. A key step to achieve this geocoding is the estimation, for each PSI measured point, of the so-called residual topographic error (see Crosetto et al., 2010), which is one of the main PSI products.

An example of PSI geocoding is shown in Figure 4, which shows the residual topographic error estimated over the Camp

Nou stadium. Note that the optical image used as background (to show the geocoding quality) shows the typical geometric distortions of the standard ortho-images (i.e. it is not a so-called true ortho-image). Another interesting example of PSI geocoding is shown in Figure 5.

5. DEFORMATION ANALYSIS

The estimation of the deformation of the area at hand and during the observed period is the main outcome of the PSI analysis. It usually yields two main products: (i) the average displacement rates over the observed period, and (ii) the time series of the deformation. In this paper we only consider the first product. An example of average displacement rates is shown in Figure 3. The most important characteristic of this example is the high density of measurements achieved through PSI analysis. This example is complemented by another deformation measurement result, shown in Figure 6, not obtained by means of a PSI analysis. With a simple standard interferometric analysis based on two images, interesting deformation phenomena may be found. This result, achieved with just two images, is important, especially considering the high commercial price of the TerraSAR-X images.

Even though the results shown in this paper are rather preliminary, they are very promising. Additional work is needed to make a comprehensive assessment of PSI TerraSAR-X: defining the key achievements in terms of new applications, their advantages and limitations, their monitoring performances with respect to costs, etc.

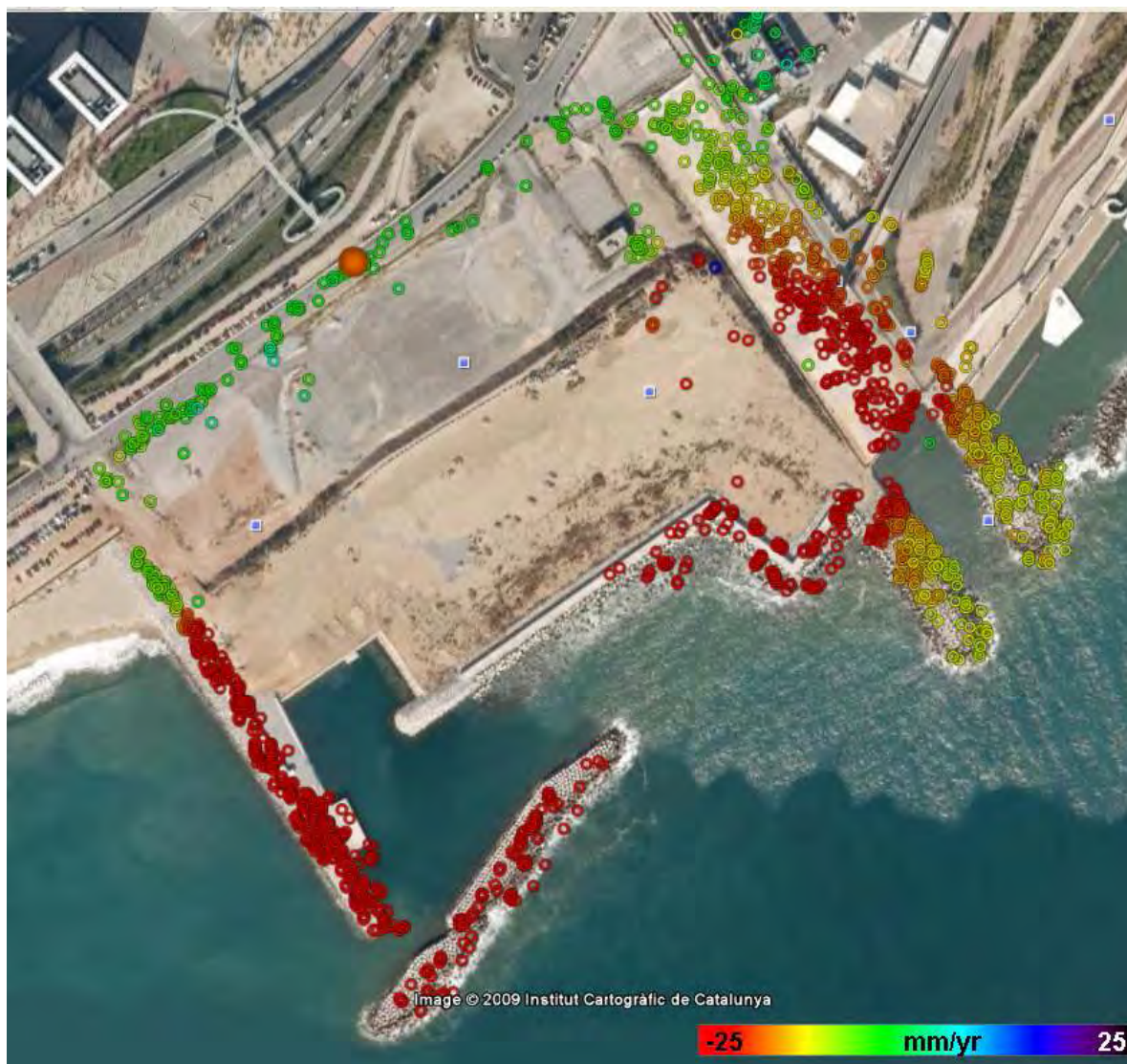


Figure 3. Geocoded deformation velocity map superimposed over a Google Earth image. The red colours represent subsidence areas. The map covers the construction area of the zoo of Barcelona. Significant portions of this area suffer subsidence up to -25 mm/yr. The high sampling density achieved over some of the infrastructures can be observed.

ACKNOWLEDGEMENTS

This work has been mainly funded by the Spanish Ministry of Science and Innovation through the project LIRA (ref. LIRA_MEP_2009_1-0). Six of the 28 images come from the Project N°. LAN0634, “Evaluation of DEM derived from TerraSAR-X data”, of the TerraSAR-X Science Service Program.

REFERENCES

- Adam, N., Eineder, M., Yague-Martinez, N., Bamler, R., 2008. High Resolution Interferometric Stacking with TerraSAR-X. In: *Proceedings of IGARSS 2008*, Boston, USA.
- Berardino, P., Fornaro, G., Lanari, R., Sansosti, E., 2002. A new algorithm for surface deformation monitoring based on small baseline differential SAR interferograms. *IEEE Transactions on Geoscience and Remote Sensing*, 40(11), pp. 2375-2383.
- Colesanti, C., Ferretti, A., Novali, F., Prati, C., Rocca, F., 2003a. SAR monitoring of progressive and seasonal ground deformation using the Permanent Scatterers Technique. *IEEE Transactions on Geoscience and Remote Sensing*, 41(7), pp. 1685-1701.
- Crosetto, M., Crippa, B., Biescas, E., Monserrat, O., Agudo, M., Fernández, P., 2005. Land deformation monitoring using SAR interferometry: state-of-the-art. *Photogrammetr. Fernerkundung Geoinformation*, 6, pp. 497-510.
- Crosetto, M., Biescas, E., Duro, J., Closa, J., Arnaud, A., 2008. Quality assessment of advanced interferometric products based on time series of ERS and Envisat SAR data. *Photogrammetric Engineering and Remote Sensing*, 74(4).
- Crosetto, M., Monserrat, O., Iglesias, R., Crippa, B., 2010. Persistent Scatterer Interferometry: potential, limits and initial C- and X-band comparison. *Photogrammetric Engineering and Remote Sensing*, Special Issue (in press).

(the reference list continues in the last page of the paper)

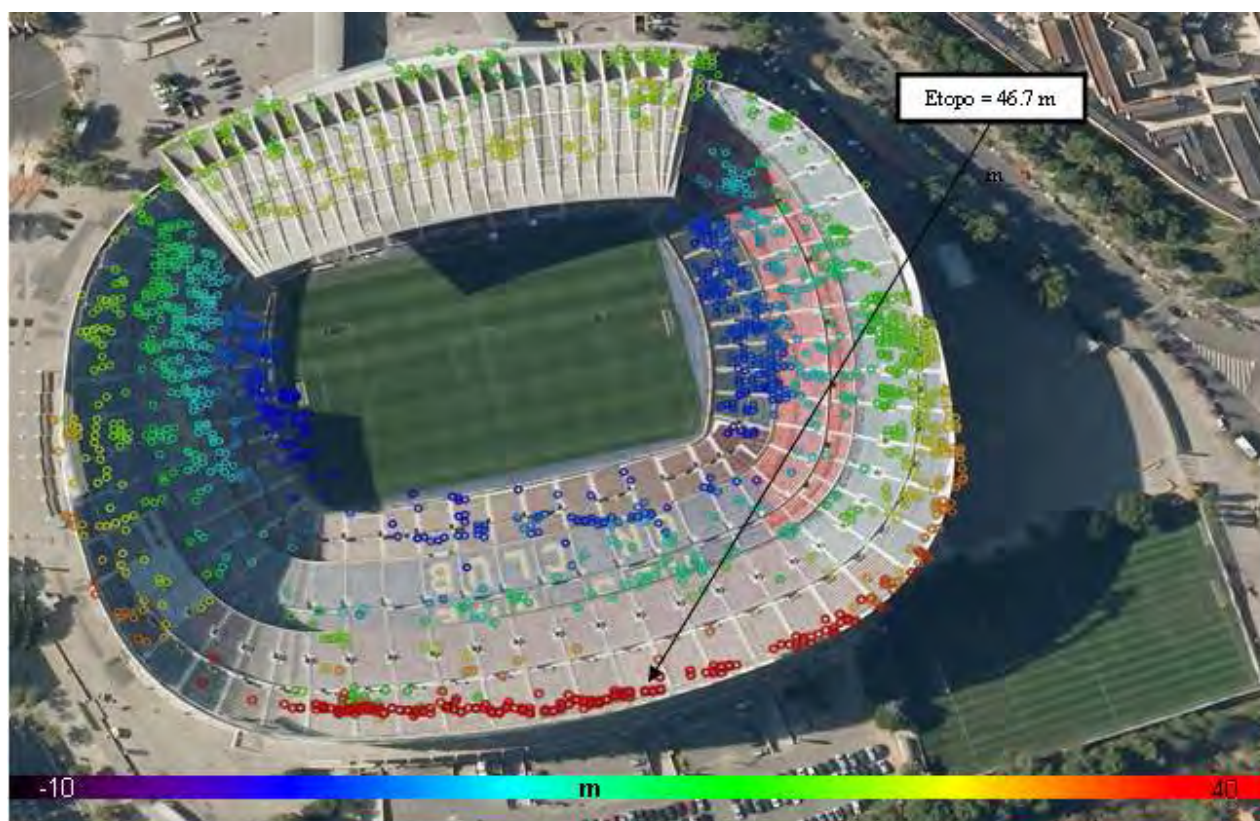


Figure 4. Example of PSI geocoding over the Camp Nou stadium. This is a geocoded map of the residual topographic error estimated for each PSI-measured point, which is superimposed over a Google Earth optical image. The different colours represent residual topographic error, which roughly corresponds to the elevation with respect to a digital terrain model of the area from the Cartographic Institute of Catalonia.

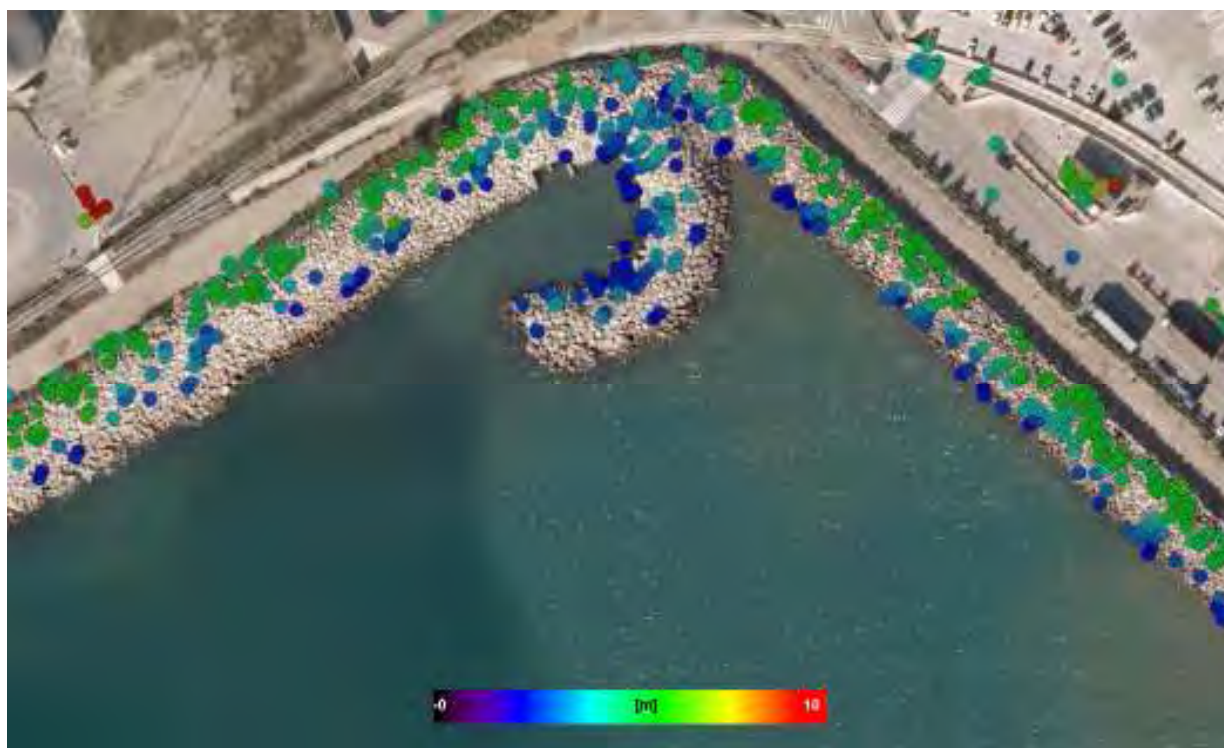


Figure 5. Example of PSI geocoding over a portion of the Port of Barcelona. In this case, the good geocoding accuracy of the PSI results can be observed. The colour of the measured points represents the residual topographic error, which roughly corresponds to the elevation with respect to a digital terrain model of the area from the Cartographic Institute of Catalonia, as in Figure 4.



Figure 6. Example of deformation measurement based on a single interferogram. The image is a wrapped interferogram with a temporal baseline of 11 days, which is superimposed over a SAR amplitude image. Google Earth images are used as background. The red circle shows an ellipse that includes two phase fringes. The maximum deformation is approximately 3 cm. It is therefore a relatively fast deformation of 3 cm in 11 days. This result, achieved with just two images, is important especially if the high commercial price of the TerraSAR-X images is considered.

Ferretti, A., Prati, C., Rocca, F., 2001. Permanent scatterers in SAR interferometry. *IEEE Transactions on Geoscience and Remote Sensing*, 39(1), pp. 8-20.

Hooper, A., Zebker, H., Segall, P., Kampes, B., 2004. A new method for measuring deformation on volcanoes and other natural terrains using InSAR Persistent Scatterers. *Geophysical Research Letters*, 31, L23611, doi: 10.1029/2004GL021737.

Kampes, B.M., Hanssen, R.F., 2004. Ambiguity Resolution for Permanent Scatterer Interferometry. *IEEE Transactions on Geoscience and Remote Sensing*, 42(11), pp. 2446-2453.

Lanari, R., Mora, O., Manunta, M., Mallorquí, J.J., Berardino, P., Sansosti, E., 2004. A small-baseline approach for investigating deformations on full-resolution differential SAR

interferograms. *IEEE Transactions on Geosciences and Remote Sensing*, 42(7), pp. 1377-1386.

Mora O, Mallorquí JJ, Broquetas A (2003) Linear and nonlinear terrain deformation maps from a reduced set of interferometric SAR images. *IEEE Transactions on Geoscience and Remote Sensing* 41(10), pp. 2243-2253.

Pepe A, Sansosti E, Berardino P, Lanari R (2005) On the Generation of ERS/ENVISAT DInSAR Time-Series via the SBAS technique. *IEEE Transactions on Geoscience and Remote Sensing Letters*, 2, pp. 265–269.

Rosen PA, Hensley S, Joughin (2000) Synthetic Aperture Radar Interferometry. *Proc. of the IEEE*, 88 (3), pp. 333-382.

THE LIGHT FANTASTIC: USING AIRBORNE LIDAR IN ARCHAEOLOGICAL SURVEY

S. Crutchley

Aerial Survey & Investigation, Research Department, Conservation and Protection, English Heritage, Kemble Drive, Swindon, Wilts SN2 2GZ UK - simon.crutchley@english-heritage.org.uk

KEY WORDS: LIDAR, Archaeology, Cultural Heritage, LIDAR, Mapping, Analysis, Landscape, Understanding

ABSTRACT:

English Heritage is the national body with the responsibility for the survey and management of archaeological and historic remains in England. The Aerial Survey & Investigation team within the Research Department deals with the recording and interpretation of sites and landscapes visible on aerial imagery. In England aerial photography has been examined in this way for over 40 years, but it is only in the last decade that the potential of using lidar for archaeological survey has become apparent. As greater interest has developed in the technique and its use has become more widespread, it became clear that there was a need to produce guidance to help those intending to use the data for archaeological survey. Lidar data can be immensely useful and has unrivalled capabilities for mapping in certain environments, such as within particular types of woodland. There are, however, still lots of uncertainties within the broader archaeological community about just what it can and cannot do. There are also many aspects of the data collection that need to be clearly understood and correctly specified if the data provided is to be as useful as possible. To this end English Heritage has produced a set of guidelines to help those intending to use lidar for archaeological survey. These cover the major aspects of data collection (i.e. issues of resolution and data formats), as well as issues related to using the data in day-to-day survey ranging from producing viable hard copy printouts for use in the field, to mapping with fully interactive raster surfaces in CAD and GIS.

1. INTRODUCTION

England has a very long history in the use of aerial remote sensing in its broadest sense, for research into aspects of the cultural heritage. It is also recognised as one of the pioneering nations in this field and has developed techniques and systems that are used by many other countries. The earliest aerial photograph of an archaeological site in England was taken of Stonehenge over 100 years ago from a tethered balloon; the earliest mapping from archaeological aerial photographs was carried out less than 30 years later (Crawford & Keiller 1928) and it was only ten years later that entire landscapes were being mapped (Crawford 1934-38). Extensive landscapes in this country have been mapped from aerial photographs for over 50 years with a national programme of mapping dating from the late 1980s. By contrast airborne lidar has only been recognised as a potential new tool since the turn of the century and as such is still very much in its infancy. Interest in the technique, however, is growing at an increasing rate and its use is becoming more widespread within the archaeological world. The experience of English Heritage, working through a number of projects with various partner organisations, has shown that there is a need for guidance to help those intending to use the data for archaeological survey. To this end English Heritage has recently produced a set of guidelines, aimed at end users of lidar data (Crutchley & Crow 2009). It is not the aim of this paper to reproduce the guidance in full, but rather to highlight how the guidance came about and how lidar has been developed to work as a practical day to day mapping tool, together with noting some of the key issues raised.

2. HISTORY

There is no doubt that lidar is an extremely useful tool in the analysis of certain landscapes, such as deciduous woodland. There are, however, still many questions within the broader

archaeological community about how to get the best use out of the lidar data. For example, for the most part airborne lidar is well suited to large area survey such as is categorised as English Heritage Level 2 survey. *Details of the different levels of survey defined by English Heritage are given in the guidance document on understanding the archaeology of landscapes* (English Heritage 2007). Where more detailed survey is required (and ground survey is not thought to be appropriate) it may be more fitting to use photogrammetry, including digital photogrammetry, that has the benefit of allowing both stereo viewing of colour imagery and the creation of DTMs (Stone & Clowes 2004). English Heritage has experienced many of the issues surrounding the use of lidar during the last ten years whilst the application of lidar for archaeological survey in this country was at the developmental stage (Holden et al 2002). After a series of projects beginning with Stonehenge World Heritage Site (Bewley et al 2005) working through the Forest of Dean (Devereux et al 2005; Hoyle 2007), Witham Valley (Crutchley 2006), the Mendip Hills (Truscoe 2006 & 2008) and Savernake Forest (Crutchley 2008; Crutchley et al 2010) we have now reached a stage where we are confident that the lidar data, in various forms, can be effectively utilised for archaeological research and can be integrated into the practical day to day mapping and interpretation carried out by the Aerial Survey & Investigation team.

3. USING THE DATA

The experience of using lidar data has shown that whilst it can be applied to any type of landscape it is particularly useful in two areas, woodland and upland areas that have not seen intensive modern ploughing.

3.1 Woodland

Because of its ability to penetrate certain types of woodland canopy and reveal the archaeological remains below, lidar is

particularly useful in areas with a large percentage of mixed or deciduous woodland; it is less effective in dense conifer plantations and indeed is only really successful if flown at the correct time of year when there is minimal vegetation cover. When used in the right conditions, however, the results can be dramatic. Savernake Forest is an area of ancient woodland that had been established as a royal hunting forest by the time of the Domesday survey in 1068. It is now an area of largely deciduous woodland managed by the Forestry Commission covering an area of some 40 sq kms that is used both as a timber resource and as an area for recreation. As part of a new management plan the Forestry Commission decided to commission a lidar survey to record the area and English Heritage worked in partnership with them to map the area as part of the National Mapping Programme (NMP) (Bewley 2001 & 2003). Using a combination of lidar data and traditional aerial photographs, including historic imagery dating back to the 1930s, over 300 new sites were recorded, doubling the number of known features in the survey area. Some of the most important sites recorded were a potential early roman temple complex and several new prehistoric settlement enclosures (Fig 1). As well as these entirely new features the survey also added considerable detail to the Roman roads that run through the survey area (Crutchley et al 2010).



Figure 1 – A late Iron Age enclosure in Savernake Forest seen in first return (left) and last return (right) lidar data. (lidar © Forestry Commission; source, Cambridge University ULM (May 2006)).

3.2 Uplands

The other sphere where lidar has proven to be particularly useful is in areas of extensive upland archaeology. This is rather different from woodland survey where lidar allows the recording of features that would otherwise be extremely difficult even to see, let alone record; in upland areas the features are generally visible on the ground and could be recorded using traditional techniques, but the use of lidar makes surveying much quicker and more efficient. An area of the North Pennines is being mapped as part of a multi-disciplinary project entitled “Miner–Farmer landscapes of the North Pennines Area of Outstanding Natural Beauty (AONB)” that evolved from the management plan for the AONB. The landscape is sparsely settled with considerable height variation between the valleys and the unenclosed moorland. The area is

being surveyed using a combination of lidar and other remote sensing techniques and then mapped as part of NMP using a combination of this data and what traditional aerial photography of the area exists. Detailed analytical fieldwork is then being undertaken for the core project area, taking printouts of the lidar data and desk based interpretations into the field for further analysis as well as identifying features not seen on the lidar data. Apart from revealing features that are difficult to identify on much of the traditional aerial photography, the lidar data is also proving useful as it provides an extremely accurate base map against which other sources can be registered and mapped (Fig 2).

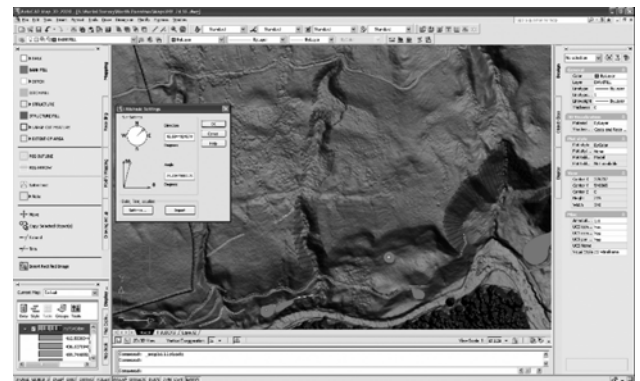


Figure 2 – Using lidar as control

Lidar also allows the accurate mapping of extensive features such as the remains of the mining industry that would otherwise take a long time to survey on the ground and therefore enables field survey time to be concentrated on those areas identified as most important or too confusing from the lidar data alone.

3.3 Environment Agency standard image tiles

Whilst English Heritage has mainly been working with the lidar data specifically captured with archaeological use in mind, we have also been examining the use that can be made of the readily available data that has been collected by other agencies for non-archaeological use. The largest example of this in the UK is the Environment Agency, the body with the role “to protect and improve the environment, and to promote sustainable development”. One of their key areas of interest relates to flood management and to this end they have been carrying out lidar surveys around the UK for over ten years; they have concentrated mainly on the coast and major river valleys to record the topography and how this relates to possible flooding. They have established a reference archive of lidar derived imagery as a series of georeferenced image tiles covering on average 1 – 4 sq km. These tiles are created as hillshaded images and are colour coded according to a consistent set of height gradients. On first viewing, often these do not reveal very much archaeological information, but with a little simple manipulation within Adobe or another standard image processing program it is possible to bring out features of archaeological interest not necessarily visible on standard aerial photographs. Although this is not as effective a method as full manipulation of the source lidar data, it does provide a quick and easy way into the data that is useful for preliminary archaeological survey.

4. ISSUES

The experience of using lidar data through these projects has also revealed a number of issues relating to the data that need to be understood by anyone intending to use lidar for archaeological survey. These include the question of resolution and data formats, as well as issues related to using the data in day-to-day survey, ranging from producing viable hard copy printouts for use in the field, to mapping with fully interactive raster surfaces in CAD and GIS.

4.1 Data capture

One of the key elements that needs to be understood when using lidar data is the question of resolution. This is a twofold issue; it relates not only to the actual final resolution at which the data is displayed, something that limits the size of the features that can be seen and recorded, much in the same way as for other image-based data, such as satellite or standard aerial photography. It also relates to the original resolution of the data defined by the number of hits within a square metre and the footprint of the laser beam when it strikes a surface. A combination of these two elements can mean that although an average of one point per metre is nominally collected, it is possible for small features to be entirely missed by the survey and not recorded. A good example of this, illustrated in the guidance note, is shown by the bluestones at Stonehenge in that the lidar data captured at one hit per square metre does not appear to show several of the bluestones (Crutchley & Crow 2009, p16).

Whilst it is unnecessary for the user to understand everything about the techniques used during data capture and initial processing, it is important to be aware of the stages of processing the data have been put through, as these can result in data artefacts that can be misleading. These issues are discussed in further detail in the guidance note.

4.2 Interpretation

Lidar data is primarily a record of x,y,z coordinates that provide a view of the land surface. In order to differentiate between archaeological features created by human interaction with the landscape centuries or millennia ago and the remains of modern agricultural or other practices this data requires interpretation. There are various aids to viewing the data to aid the interpretation process.

The main product of lidar data tends to be imagery viewed as hill-shaded images. These appear similar to vertical photographs of earthworks lit by low sunlight, so the analysis of lidar for the identification and characterisation of archaeological sites requires similar skills as those applied to air photo interpretation, for example the ability to recognise slight earthwork banks or ditches based on their appearance with reference to shadows and highlights, while filtering out features due to modern agricultural practices, geology and data processing artefacts.

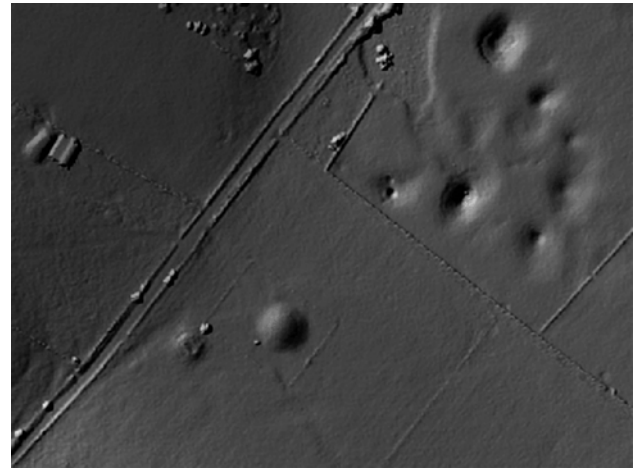


Figure 3 - Feature misinterpretation – lidar derived image (lidar © Mendip Hills AONB; source, Cambridge University ULM (April 2006)).

This can be demonstrated by an example from the guidance note that shows the potential confusion between features of archaeological interest and those of modern origin. The feature seen in the bottom centre-left of figure 3 gives every appearance of being a burial mound, being of a similar size and shape to other known barrows in the vicinity here on the Mendip Hills. Using not only all available mapping data, but also analysing all readily available aerial photographs, both traditional and digital, simultaneously with the lidar data, will help to ensure correct interpretation, as in this case where the evidence from aerial photographs and mapping (Fig 4) reveals that the feature is in fact the site of a covered reservoir.

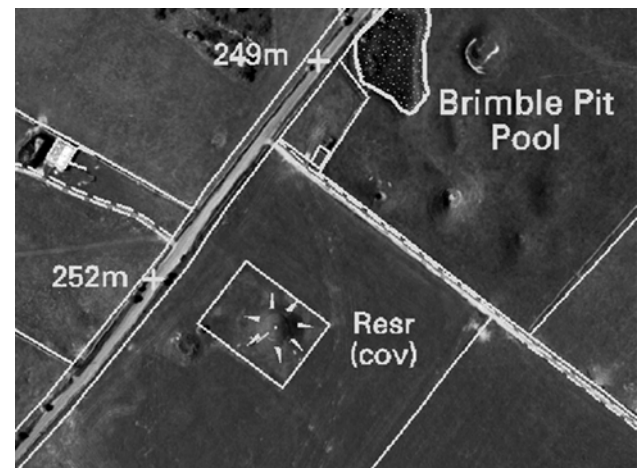


Figure 4 - Feature misinterpretation – aerial photograph showing the true nature of the feature (photo PGA_ST5050_2006-04-30_part. Licensed to English Heritage for PGA, through Next Perspectives™; OS background map © Crown Copyright. All rights reserved. English Heritage 100019088. 2009).

4.3 Usage

Whilst lidar data is remarkably useful and has generated great interest in archaeological circles, it is not necessarily inherently user friendly and many organisations who might wish to make

use of it may not have access to the hardware, software and expertise required to manipulate the data to best effect. The new English Heritage Guidance paper aims to advise people as to how they can get the most out of lidar data in a normal working environment using everyday technology. The most obvious example of this is simply using paper print outs in the field, an application that can be used either by professional analytical field surveyors looking for additional data sources, or by amateur archaeologists undertaking local research or walk through surveys. As noted above, one of the most common ways in which lidar data is used is as a hillshaded image and this is the simplest way to work with a printed image. The advantage that lidar has over a conventional aerial photograph is that it is possible to control the direction of the lighting and thereby light from angles impossible in the natural world so as to reveal otherwise hidden features. Unfortunately the simplest hillshaded image to produce, that lit from a single direction, has the possibility of missing any features that are aligned on the direction of the light source as shown in figs 5 -6.

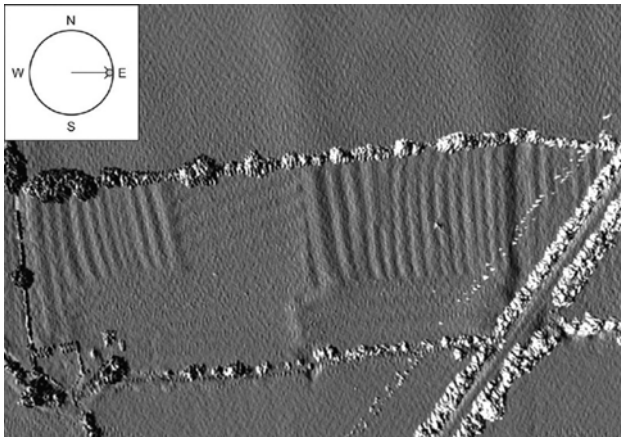


Figure 5 - Ridge and furrow near Alchester illuminated E–W (lidar © Cambridge University ULM (Dec 2005)).

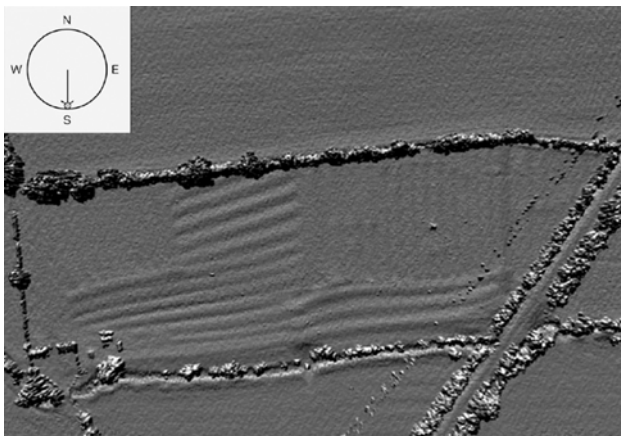


Figure 6 - Ridge and furrow near Alchester illuminated N–S (lidar © Cambridge University ULM (Dec 2005)).

In order to get around this for hardcopy imagery it is necessary to produce composite images. This can be done by creating composite images using the transparency tools within image editing or GIS packages, but a more effective process is now seen in the use of principal component analysis (PCA) a

statistical method to examine multiple hill-shaded images and compile a composite image that shows the main features from each image (Devereux et al 2008). One negative element of this, however, is that the false colours and the multiple combined lighting angles mean it can be difficult to differentiate between cut and built features as shadow and highlights can be present for both.

4.4 Interactive mapping

Whilst high quality “flat” images using hill-shading or PCA techniques can provide a relatively user friendly way of working with lidar, they do not fully capitalize on the interpretative potential of the lidar data. For the professional user there are great benefits from working with lidar data interactively, by manipulating the data as part of the interpretative process, so as to highlight specific features and understand as much as possible about their form and extent. Key to the necessary workflow is the ability to view and manipulate the data in 3D (although currently this is strictly only 2½D within affordable software) something has been made possible by combining viewing and mapping software. English Heritage has developed over time working practices for archaeological interpretation and mapping from aerial photographs, and these have now been greatly enhanced by the integration of the use of lidar data.

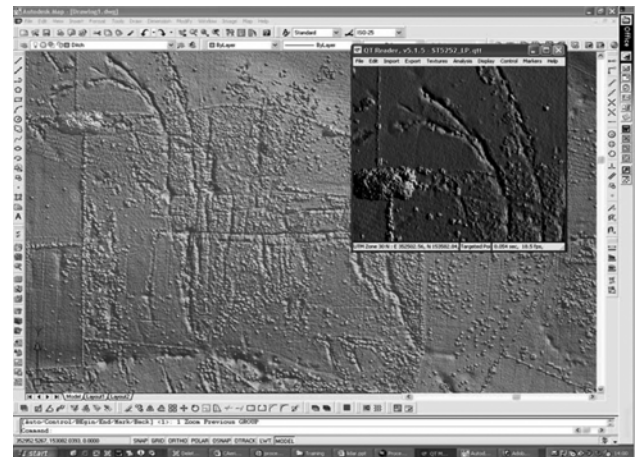


Figure 7 – Interactive use of lidar data in viewing and mapping software

5. CONCLUSION

Lidar data can be an immensely useful tool for archaeologists and has unrivalled capabilities for mapping in certain environments, such as within particular types of woodland. There are, however, still lots of uncertainties within the broader archaeological community about just what it can and cannot do. There are also many aspects of the data collection that need to be clearly understood and correctly specified if the data provided is to be as useful as possible. To this end the English Heritage guidelines will hopefully help those intending to use lidar for archaeological survey to avoid some of the pitfalls and maximize the value for money of this new technique. The guidelines are available as a downloadable PDF through the English Heritage website <http://www.english-heritage.org.uk/publications/light-fantastic/> and there is further information available on the Aerial Survey & Investigation web pages <http://www.english-heritage.org.uk/aerialsurvey>.

6. REFERENCES AND/OR SELECTED BIBLIOGRAPHY

- Bewley, B., 2001. Understanding England's Historic Landscapes: An Aerial Perspective. *Landscapes*, 1, pp. 74-84.
- Bewley, R.H., 2003. Aerial survey for archaeology. *The Photogrammetric Record*, 18 (104), pp. 273-292.
- Bewley, R.H., Crutchley, S.P., and Shell, C., 2005. New light on an ancient landscape: lidar survey in the Stonehenge World Heritage Site'. *Antiquity*, 79, pp. 636-647.
- Crawford, O.G.S., and Keiller, A., 1928. *Wessex from the Air*. Oxford: Clarendon Press.
- Crawford, O.G.S., 1934-38. Annotated Salisbury Plain Maps. Held at N.M.R.C. Swindon.
- Crutchley, S.P., 2006. Lidar in the Witham Valley, Lincolnshire: an assessment of new remote sensing techniques. *Archaeological Prospection* 13, pp. 251-257.
- Crutchley, S., 2008. Ancient and modern: combining different remote sensing techniques to interpret historic landscapes. In: R Lasaponara, R., and Masini, N., (Eds) *Remote Sensing for Archaeology and Cultural Heritage Management; Proceedings of the 1st International EARSeL Workshop on 'Remote Sensing for Archaeology and Cultural Heritage Management'*. Rome: ARACNE, pp. 103-106.
- Crutchley, S., Small, F., and Bowden, M., 2010. *Savernake Forest: Report for the National Mapping Programme*. English Heritage Research Department Report Series No. 29-2009 ISSN 1749-8775.
- Crutchley, S., and Crow, P., 2009. *The Light Fantastic: Using airborne lidar in archaeological survey*. Swindon: English Heritage.
- Devereux, B.J., Amable, G.S., Crow, P., and Cliff, A.D., 2005. The potential of airborne lidar for the detection of archaeological features under woodland canopies. *Antiquity* 79, pp. 648-660.
- Devereux, B.J., Amable, G.S., and Crow, P., 2008. Visualisation of lidar terrain models for archaeological feature detection. *Antiquity* 82, pp. 470-479.
- English Heritage 2007. *Understanding the Archaeology of Landscapes: a guide to good recording practice*. Swindon: English Heritage
- Holden, N., Home, P., & Bewley, R.H., 2002. High-resolution digital airborne mapping and Archaeology. In: Bewley, R., & Raczkowski, W., (Eds.) *Aerial Archaeology - Developing Future Practice: NATO Advanced Research Workshop, Leszno, Poland, 15th-17th November 2000*. NATO Science Series, Series I: Life and Behavioural Sciences, Amsterdam: IOS Press, pp. 173-180.
- Hoyle, J.P., 2007. *The Forest of Dean, Gloucestershire, Lidar survey of selected areas of woodland and the Aggregates Resource Area. The Forest of Dean Archaeological Survey Stage 3A*. Unpublished draft report for English Heritage.
- Stone, J.L., and Clowes, M., 2004. Photogrammetric recording of the Roman earthworks "Cawthorn camps", North Yorkshire. *The Photogrammetric Record* 19, pp. 94-110
- Truscoe, K., 2006. *Interim report for aerial survey component Eastern Mendip Block 1: ST 66 41 to ST 71 46. The Aggregate landscape of Somerset: predicting the archaeological resource*. Aggregates Levy Sustainability Fund project 3994, unpublished report: Somerset County Council/English Heritage.
- Truscoe, K., 2008. *Archaeological aerial survey in the Central Mendip Hills. The Aggregate landscape of Somerset: predicting the archaeological resource*. Aggregates Levy Sustainability Fund project 3994, unpublished report: Somerset County Council/English Heritage.

HYDROLOGICAL SIMULATION OF MAHANADI RIVER BASIN AND IMPACT OF LAND USE / LAND COVER CHANGE ON SURFACE RUNOFF USING A MACRO SCALE HYDROLOGICAL MODEL

V.K. Dadhwal^a, S.P. Aggarwal^{b,*} and Nidhi Mishra^b

^a National Remote Sensing Centre, Balanagar, Hyderabad – 500 625, India

^b Indian Institute of Remote Sensing (NRSC), 4, Kalidas Road, Dehradun – 248 001, India

KEY WORDS: Hydrological Modelling, Landuse Landcover Change, Variable Infiltration Capacity Model, Remote Sensing

ABSTRACT:

In the present study, Variable Infiltration Capacity (VIC) a macro-scale hydrological model was used to simulate the hydrology of Mahanadi river basin of India. The analysis was carried out for the impact of land use/ land cover (LULC) changes on stream flow pattern. Surface runoff was simulated for the year 1972, 1985 and 2003 to quantify the changes that have taken place due to change in LULC. An increase by 4.53% ($3514.2 \times 10^6 \text{ m}^3$) in the annual streamflow was estimated at Mundali outlet of the Mahanadi basin from 1972 to 2003. This may attributed due to decrease in forest cover by 5.71%. The validation of VIC model showed a close agreement between the observed and simulated runoff values with the Nash-Sutcliffe coefficient of 0.821 and relative error of 0.085.

1. INTRODUCTION

Water resources management requires a systems approach that includes not only all of the hydrological components, but also the links, relations, consequences and interactions amongst all the components. Human modifications of the environment, including land cover change, irrigation, and flow regulation, now occur on scales that significantly affect seasonal and yearly hydrologic variations. It thus becomes necessary to understand and quantify various hydrological components of the catchment for efficient water resource management. Runoff representing the response of a catchment to precipitation, reflects the integrated effects of a wide range of landcover, soil, topography, climate and precipitation characteristics of the area. Hence, if one has to study the impact of changes in climate and landcover on basin hydrology, altering streamflow pattern is an important component to investigate.

Quantification of runoff and other hydrological components can be done in many ways; Hydrological modeling is one efficient way for consistent long term behavioral studies. Hydrological modelling is a mathematical representation of natural processes that influence primarily the energy and water balances of a watershed. The fundamental objective of hydrological modeling is to gain an understanding of the hydrological system in order to provide reliable information for managing water resources in a sustained manner. Powerful spatially-distributed models are based on physical principles governing the movement of water within a catchment area, but they need detailed high-quality data to be used effectively. AVSWAT (ArcView Soil and Water Assessment Tool), MIKE-SHE, Variable infiltration Capacity (VIC) model, HEC-HMS (Hydrologic Engineering Centre-Hydrologic Modelling System) are some of the physically based distributed hydrologic models.

In the present study, VIC land surface hydrologic model has been used for modeling the river flow regime. It is a physically based, macroscale hydrological model which represents the partitioning of incoming (solar and long wave) radiation at the land surface into latent and sensible heat, and the partitioning of precipitation (or snowmelt) into direct runoff and infiltration. VIC explicitly represents vegetation, and simultaneously solves the surface energy and water balances. A river routing model when coupled with VIC permits comparisons between the model-derived discharge and observations at gauging stations. Further details of the VIC model can be found in Liang (1994); Liang et. al, (1994); Liang et al. (1996); Lettenmaier (2001). An attempt has been made to model and evaluate the changes in streamflows attributable to changes in landcover throughout the Mahanadi basin. For an understanding of the distribution of the physical characteristics of such large catchments with little available data, a better insight can be provided by remote sensing techniques. The remote sensing data and GIS have already been used by hydrologists to deal with large scale, complex and spatially distributed hydrological processes. Remote sensing has held a great deal of promise for hydrology, mainly because of the potential to observe areas and entire river basins rather than merely points.

2. STUDY AREA

The river basin at the appropriate scale is generally the most logical geographical unit of streamflow analysis and water resources management. In the present study, Mahanadi River basin has been selected as study area. The Mahanadi basin encompassed within geographical co-ordinates of $80^{\circ}30'$ to $86^{\circ}50'$ East longitudes and $19^{\circ}20'$ to $23^{\circ}35'$ North latitudes as shown in Fig. 1. The total catchment area of the basin is $1,41,600 \text{ km}^2$. The average elevation of the drainage basin is 426 m with a maximum of 877 m and a minimum of 193 m.

The river Mahanadi is one of the major inter-state east flowing rivers in peninsular India. It originates at an elevation of about 442 m. above Mean Sea Level near Pharsiya village in Raipur district of Chattisgarh. During the course of its traverse, it drains fairly large areas of Chhatisgarh and Orissa and comparatively small area in the state of Jharkhand and Maharashtra. The total length of the river from its origin to confluence of the Bay of Bengal is about 851 km., of which, 357 km. is in Chattisgarh and the balance 494 km. in Orissa. During its traverse, a number of tributaries join the river on both the banks. There are 14 major tributaries of which 12 are joining upstream of Hirakud reservoir and 2 downstream of it. Approximately 65% of the basin is upstream from the dam. The average annual discharge is 1,895 m³/s, with a maximum of 6,352 m³/s during the summer monsoon. Minimum discharge is 759 m³/s and occurs during the months October through June.

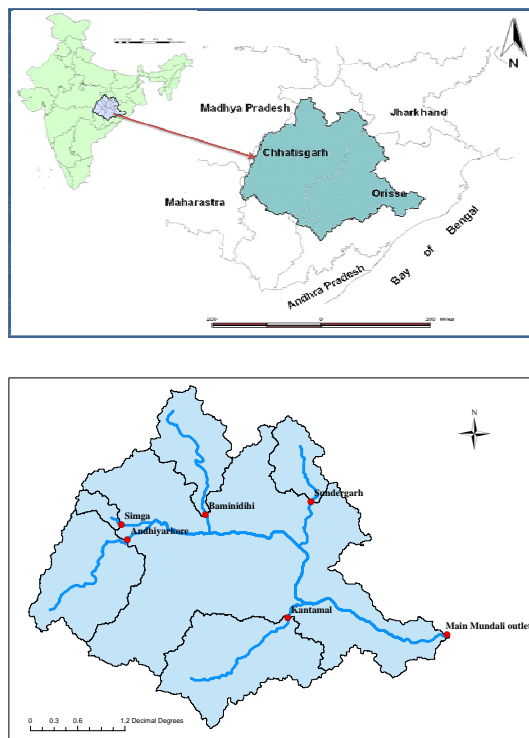


Fig. 1. Location of Study Area (Mahanadi river basin)

Mahanadi basin enjoys a tropical monsoon type of climate like most other parts of the country. The maximum precipitation is usually observed in the month of July, August and first half of September. Normal annual rainfall of the basin is 1360 mm (16% CV) of which about 86% i.e. 1170 mm occurs during the monsoon season (15% CV) from June to September (Rao, 1993). The river passes through tropical zone and is subjected to cyclonic storms and seasonal rainfall. In the winter the mean daily minimum temperature varies from 4°C to 12°C. The month of May is the hottest month, in which the mean daily maximum temperature varies from 42°C to 45.5°C.

3. METHODOLOGY

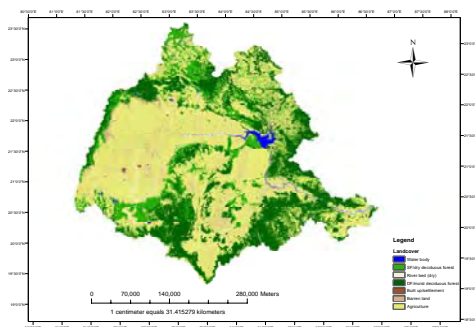
Basin boundary and drainage characteristics of the watershed were derived in HEC -GeoHMS module in ArcView 3.2a

software using 1 km resolution GTopo30 USGS Digital elevation model (DEM) as major input. A fill grid map was generated after correcting the DEM for sinks. Flow direction map was derived from this fill sink map and subsequently a flow accumulation map was derived from it. Stream definition was derived from this flow accumulation by specifying the maximum threshold area for delineating drainages. A sub-basin for each delineated stream is then extracted. To extract the basin boundary, an outlet at Mundali station in the Mahanadi river basin was defined. Finally, a basin for the defined outlet was delineated along with the river network. It was further subdivided into desired number of sub-basins by specifying various outlets where the gauging station exists along the extracted drainage. A square grid of area 25 x 25 km² was generated over the study region. There were in all 267 such grids falling in the basin. This extracted grid network for the basin was used to overlay with the other thematic layers and hence define the distribution of various parameters and properties in the basin. VIC model requires the definition of input parameters for each grid distributed uniformly over the area.

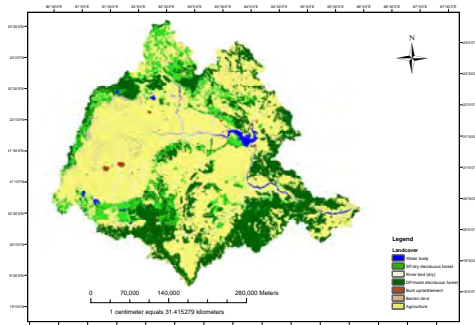
Remote sensing based satellite images being most reliable and offering synoptic views of large areas were the viable option to study landcover dynamics on a regional scale. LANDSAT MSS images of 1972-73 were downloaded, preprocessed and mosaiced to create a seamless image of the whole basin. Since the individual images were of different dates, classifying the mosaic into landcover types was not feasible. So, the individual images were classified using unsupervised classification (Isodata clustering) technique into several classes (200) and they were merged based on their spectral signatures into 7 landcover types namely Water body, DF/moist deciduous forest, SF/dry deciduous forest, Agriculture, Built up/settlement, Barren land and River bed (dry). The preliminary classified layer was then improved using visual interpretation approach. Thus, an integrated digital and visual classification was attempted to map landcover since a single technique would not have been feasible for regional mapping. The individual classified images were then mosaiced and clipped by the basin boundary. Landcover mapping for 1985 was done using NOAA AVHRR images (1 km resolution) whereas AWiFs (56 m resolution) was used to prepare for the year 2003. The same approach of unsupervised classification and visual interpretation technique was followed to perform the task. The landuse/landcover maps of Mahanadi basin for 1972, 1985 and 2003 are shown in Fig. 2. GCP's (ground control points) were used to improve and validate classification scheme. Classification accuracy of more than 70% was achieved using this approach.

Four major input files are required to make the VIC model input database. They are Vegetation parameter file, Vegetation Library file, Soil parameter file and Forcing files. The data in these files were stored in the ASCII format. A soil parameter file describes the characteristics of each soil layer for each grid cell. This is also where other basic grid cell information is defined like grid cell no., lat-long of the grids (which serves as a link to other parameter files), mean elevation etc. Mean elevation values for each grid were derived from Digital elevation model. The primary data source to prepare this input was digital soil texture map prepared from NBSS & LUP (National Bureau of Soil Survey and Landuse Planning, Nagpur) soil maps (scale-1:50,000). Soil texture map was rasterised and overlaid with the grid map to extract dominant soil type in each grid. The second soil layer was taken as FAO global soil map of the world. All other parameters except c, elev, depth, off_gmt, rough, and annual prec are a function of

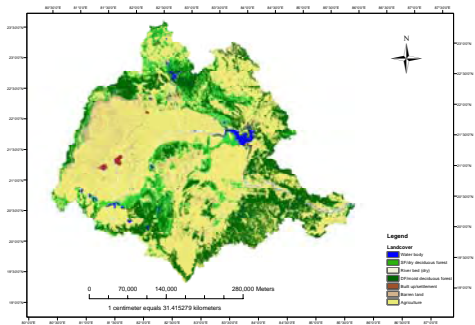
soil texture and were derived using soil hydraulic properties index defined in VIC model documentation.



a. Landuse/Landcover Map of 1972



b. Landuse/Landcover Map of 1985



c. Landuse/Landcover Map of 2003

Fig. 2 Landuse/landuse Map of 1972, 1985 & 2003

Table 1.LULC statistics of 1972,1985 & 2003

	Water body (%)	DF/Moist Decid (%)	SF/Dry decid (%)	Agriculture (%)	Built up (%)	Barren land (%)	River bed (%)
1972	1.16	27.23	11.96	54.08	0.08	4.15	1.34
1985	1.19	26.64	10.92	56.41	0.22	3.83	1.35
2003	1.62	23.52	9.96	59.63	0.31	3.51	1.46

The vegetation parameter file describes the vegetative composition of each grid cell, and uses the same grid cell numbering as the soil file (latitudes and longitudes are not included in the file). This file cross-indexes each vegetation class (from any land-cover classification scheme) to the classes listed in the vegetation library. To prepare this file, landuse map

was overlaid on the grid map and the no. of vegetation classes as well as fraction of grid covered by those classes was extracted. A small code in C language was used to read this information from crossed map and arrange it in the format specified by the model. Root depths for landcover types were accepted as recommended by Canadell et. al. (1996). It was assumed that the specified root zone contains all of the roots of a landcover type. For the selected land cover classification of the study area, a vegetation library file was set up. This describes the static (varying by month, but the same values year-to-year) parameters associated with each land cover class.

LAI defines an important structural property of a plant canopy as the one sided leaf area per unit ground area. For derivation of LAI, MODIS LAI maps (MOD 15A02 product) were downloaded from NASA’s GSFC website (www.modis-land.gsfc.nasa.gov). For each landuse class, sufficient number of cloud free points were chosen and their LAI profile on the stacked image was drawn. An average monthly value of those points was taken as the LAI value in each month for that landuse class. Albedo was also derived from MODIS BRDF/Albedo product in the same way. Other variables like roughness length, displacement height, overstory, architectural resistance, minimum stomatal resistance were derived from LDAS 8th database (http://ldas.gsfc.nasa.gov/LDAS8th/MAPPED.VEG/web_veg_monthly.table.html) and MM5 terrain dataset.

The Meteorological forcing file contains meteorological variables required to force the VIC model like daily precipitation, daily maximum and minimum air temperature. Forcing data files play big role in the model input to produce all the outputs in both water balance and full energy balance modes of the model. Accurate streamflow simulation requires forcing input of high accuracy as it is the most influential variable generating runoff and driving hydrological cycle. Precipitation input was prepared using India Meteorological Department’s 1°X1° gridded rainfall dataset. Daily rainfall values for each 1 degree grid falling in the basin were extracted for 365 days in the year 2003. Rainfall grids were then overlaid with the basin grids to extract precipitation in each basin grid. VIC model requires one forcing file for each grid having 365 rows and 3 columns in ASCII format. Temperature data from NCDC (National Climatic Data Centre, NOAA) is available for some selected stations in the study area. This point temperature data was used to derive maximum and minimum temperature of each basin grid using nearest neighbour and lapse rate method since it is assumed that temperature varies with the altitude. The following relation was applied in MS Excel spreadsheet:

$$T_{grid} = T_{nearest\ point} + 5.5/1000 * (elevation_{nearest\ point} - grid\ elevation) \quad (1)$$

A Global control file where the necessary information to specify various user preferences and parameters was prepared. It contains information like N-layers, Time step, start time, end time, Wind_H, snow temp, rain temp., Location of the input output files, modes which are to be activated etc. The VIC 4.0.5 was compiled using gcc compiler on Linux operating system. The code was compiled using the make file included in the archive, by typing 'make'. The compiled code creates an executable entitled 'vicNI'. To begin running the model, 'vicNI -g (global control file name)' was written at the command prompt. Global control parameters were modified according to the input characteristics and to activate the ware balance. In addition to that input and output path were specified. VIC source code was executed in the LINUX environment to generate the flux files for each basin grid. These flux files

contain fluxes of surface runoff, evapotranspiration, baseflow, soil moisture etc. produced at that location. In order to simulate streamflow at an outlet, routing of runoff component was done using a routing model developed by Lohmann et. al (1998). Routing was done for 6 sub-basins namely Mundali (main outlet), Kantamal, Andhiyarkore, Simga, Baminidihi and Sundergarh. Daily and monthly streamflows in Cusec and mm for each outlet location was obtained as the output.

Calibration of a hydrological model is an iterative process which involves changing the values of sensitive model parameters to obtain best possible match between the observed and simulated values. In general, before conducting numerical simulations, six model parameters of the VIC-2L model need to be calibrated because they cannot be determined well based on the available soil information (Yuan, 2004). These six model parameters are the depths of the upper and lower soil layers (d_i , $i = 2, 3$); the exponent (B) of the VIC-2L soil moisture capacity curve, which describes the spatial variability of the soil moisture capacity; and the three subsurface flow parameters (i.e., D_m , D_s , and W_s , where D_m is the maximum velocity of base flow, D_s is the fraction of D_m , and W_s is the fraction of maximum soil moisture). Three criteria were selected for model calibration: (i) Relative error (Er in percent), (ii) The Nash–Sutcliffe coefficient (C_e) (Nash and Sutcliffe, 1970), and (iii) Coefficient of Determination, (R^2).

4. RESULTS AND DISCUSSION

This study attempts to model the hydrology of Mahanadi river basin and assess landcover change impacts on streamflows at various locations along the river in the basin. For this purpose, mapping of landuse/ landcover was carried out in detail to represent the present and historical landcover conditions and changes that have taken place over whole of the basin in a span of three decades. Analysing landuse changes from 1972 to 2003, it may be concluded that the total forest cover has declined by 5.71% of the total area of the basin. A reduction in barren land (0.64%) is followed by increase in areas of surface water bodies (0.47%), built up land (0.22%), river bed (0.11%) and most prominently agriculture (5.55%). This implies that the total forest cover and barren land has declined at the expense of increase in water body, river bed, agriculture and built up land in a span of 30 years. The simulation results obtained while calibrating and validating the VIC land surface hydrologic model were analysed and simulated streamflows were compared with the observed discharge at outlet station to look for the model efficiency in representing hydrological conditions accurately.

4.1 Hydrological Modelling using VIC land surface model

4.1.1 Pre-calibration simulation: The vegetation, soil, and forcing (meteorological) data as described were applied to the VIC-2L model to simulate evapotranspiration, runoff, and soil moisture at each grid over the Mahanadi River basin for year 2003. To compare the VIC-2L model simulated runoff with the observed streamflow, the simulated runoff is routed through the river network using a simple routing model at the outlet Mundali as suggested by Lohmann et al. (1998). The routed daily and monthly runoff at these stations was compared with the daily and monthly observed streamflows, respectively as shown in Fig. 3. The R^2 showing agreement between the trends of simulated and observed streamflow records were found to be as 0.747, prior to calibration.

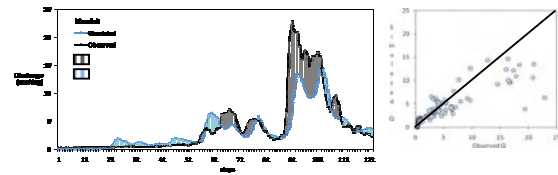


Fig 3. Pre-calibration Comparison b/w Observed & Simulated daily discharges

4.1.2 Model Calibration and validation:

Since streamflow can be measured with relatively high accuracy compared with other water fluxes in the watershed it is mostly used to calibrate model parameters. In general, before conducting numerical simulations, the six model parameters of the VIC-2L model were calibrated and assigned values as: $B = 2.0$, $D_m = 15.0$, $D_s = 0.02$, $W_s = 0.8$ and $d_i = 0.5$ and 2.0 m for $i = 2$ and 3 . The velocity parameter was also adjusted (increased to 2.3 m/s) since the simulated runoff was coming delayed. The stream discharge at Mundali outlet for a period of 6 months was considered as the reference for calibration.

Post calibration comparison of observed and simulated hydrograph at Mundali is shown in Fig 4. A good agreement between the observed and simulated values was found with an R^2 value of 0.836, C_e of 0.821 and Er of -8.49%. It can be seen that low flow simulations were overestimated and an underestimation was found during high flows.

VIC is a model primarily designed to assess and evaluate long term climate and landcover changes on basin hydrology. It therefore essentially ignores the effect due to human induced activities. VIC simulates naturalized flows without considering any effect of reservoirs, dams or any other structural intervention. The Mahanadi basin contains several storage reservoirs and diversion structures and the observed streamflows are thus bias and are not really appropriate for the purpose of calibration. This may be a reason of disagreement between observed and simulated discharge. During low flows, reservoirs come into play and store most of the river waters whereas during high flows a reservoir has to throw out all waters coming into it once filled. This may be the possible reason of overestimation during low flows and underestimation during high flows.

Better simulation results were obtained for monthly time-step when compared with daily and good agreement at Mundali was found. Comparisons of observed versus simulated hydrographs during model validation (daily) are shown in Fig. 4. Monthly comparisons were found good (Fig. 5) with an R^2 value of 0.920, C_e of 0.890 and Er of -8.70%. The VIC model simulated runoff compares well with the daily observed streamflow in general, but significant overestimations of the streamflows are evident. This may be because of erratic spatial distribution of precipitation. Streamflows are most sensitive to vegetation and forcing input, thus near perfect simulations require accurate estimation of these parameters. In the present simulation, precipitation information has spatial resolution of 1 degree which is coarser, high resolution is therefore expected to improve simulation.

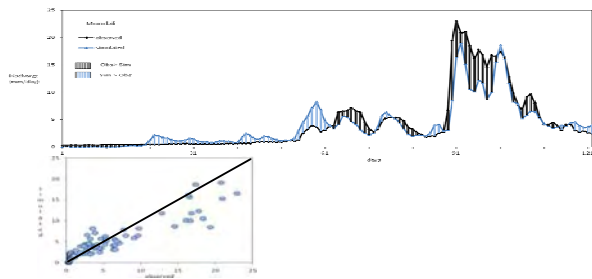


Fig. 4. Comparison of Hydrograph at main outlet (Mundali): Calibration period

Though the agreement between observed and simulated discharges is good, under-estimations and over-estimations are inherent in the simulation. This is because of the fact that VIC simulates naturalized flows and the observed discharge used for validation is biased and affected by human interventions. Model performance showed good agreement at Mundali in spite of a large reservoir since calibration was performed at this outlet. It may be seen from the simulation results that model has generally overestimated (S>O) during months of June, July and under-estimated during August and September. The possible reason may be initial reservoir storage in June-July due to which observed flows are less as compared to simulated whereas observed flow exceeds once the reservoir capacity is filled (in Aug, Sept.). It may be concluded that the agreement between observed and simulated hydrological components is largely dependent on the hydrological and landcover conditions in the basin and model assumptions. The synoptic view and landuse/landcover conditions of various sub-basins are shown in the Figure 2. The landcover classes are same as shown for whole of the Mahanadi basin (Fig. 1) with Mundali as an outlet.

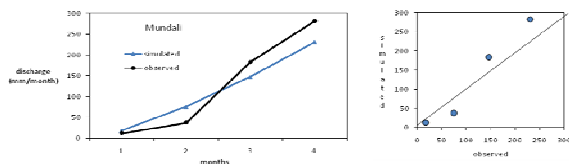


Fig. 5. Simulated and observed monthly hydrographs at outlet

4.2 Effect of landcover changes on streamflows

4.2.1 Historical and current hydrological simulation using VIC model: Simulation was done for year 1972 and 1985 after calibration and validation of the VIC model for 2003. Only the vegetation cover and related parameters were changed in the simulations; the model meteorological forcings and soil parameters were kept same for both the current and historical scenarios. In this way, the effects of vegetation change on basin hydrology were isolated from the effects of climate variability.

4.2.2 Trend of changes in streamflows: Streamflows for year 1972, 1985 and 2003 were compared to look for the changes that have taken place due to change in landcover in the Mahanadi river basin. Monthly discharges were found to be varying significantly as compared to daily flows. Fig 6 shows a scatter plot of monthly flows (mm) for 2003 and 1972, events above the slope line indicates an increase in river flow. A rise of 24.44 mm in the annual discharge is predicted at Mundali outlet of the Mahanadi basin from 1972 to 2003 (16.97 mm being in

the period of 1972-85 and 7.47 mm in 1985-03) which is 4.53% of the flow in 1972. It may be concluded that a decrease in forest cover by 5.71% in the Mahanadi river basin has caused the river flow to increase by 4.53%. This is quite a significant amount in terms of volumetric rise (3514242122 m^3). Table 2 summarizes the predicted incremental changes in runoff (mm) at outlet by season (e.g. JFM refers to cumulative rise for January, February and March). In figure 7, monthly hydrographs for 1972 and 2003 are presented to see the changes that have taken place. A plot of relative percentage difference in runoff (from 1972 to 2003) over 1972 is also shown in the same figure. The rise in percent runoff was prominent during May, June, Oct and November months. The decrease in runoff from 1972 to 2003 may be due to reverse trend in landcover conversions and/or human activities.

In summary, a decrease in natural cover of forest over time has caused a significant rise in streamflows and particularly surface runoff. Removal of forest cover is known to increase streamflow as a result of reduced evapotranspiration. Base-flow is expected to decrease while surface runoff increases owing to the decrease in infiltration and hence groundwater recharge processes. Urban expansion and intensive cultivation will loosen the soil leading to soil loss (soil erosion) due to high flows. Urbanization also tends to decrease infiltration rates and increase extents of impervious surfaces, although the area over which such changes have occurred is a small fraction of the total basin area. The VIC model, being physically based, distributed, macroscale model is particularly suitable for studying climate and landcover change scenarios and their implications on hydrological processes at regional and global scale over long time frames.

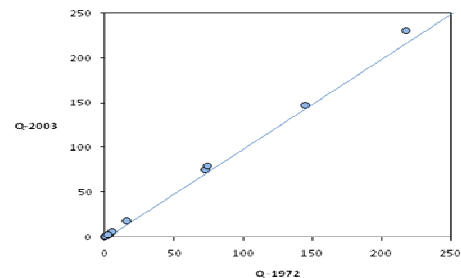


Fig.6. Comparison of streamflows for 1972-2003 at Mundali

Table 2. Changes in runoff by sub-basin and season (in mm)

Stations	JFM	AMJ	JAS	OND	Annual	% increase	Vol. Increase (m^3)
Mundali	0.027	1.79	16.97	5.64	24.44	4.53	3.51×10^6

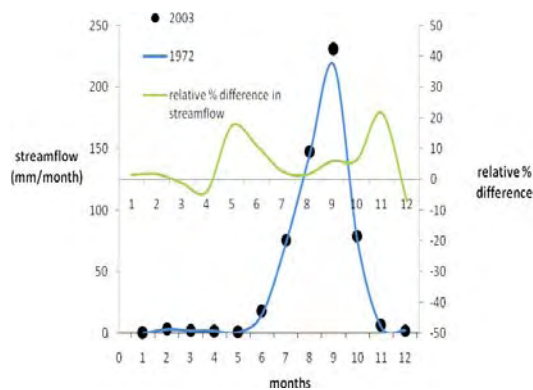


Fig. 7. Monthly hydrographs of historic (1972) and current (2003) naturalized Streamflow stations, and relative percentage difference of runoff

5. SUMMARY AND CONCLUSIONS

Land use and vegetative cover play an important role in watershed runoff and streamflow discharge patterns over time, including peak flows. Increased human interventions have caused rapid transitions in landcover, adversely affecting the watershed processes and hydrological cycle in the long run. Distributed hydrological modelling offers an efficient solution to evaluate the long term hydrological changes by allowing quantification of changes in streamflow patterns. The Mahanadi river basin covering major portions of Chattisgarh and Orissa (India) has been repetitively facing the adverse hydro-meteorological conditions such as floods, droughts and cyclones etc. in the recent times. Frequent occurrence of these events indicates a shift in the hydrological response of the basin attributed to landcover changes. This study attempts to model the hydrology of Mahanadi river basin using physically based, distributed VIC hydrological model and assess landcover change impacts on streamflows at various locations along the river.

A detailed remote sensing based landcover mapping of the basin for years 1972, 1985 and 2003 reveals following changes:

- Total forest cover area has been reduced by 5.71% of the total area of the basin from 1972 to 2003. A reduction in barren land (0.64%) is followed by an increase in areas of surface water bodies (0.47%), built up land (0.22%), river bed (0.11%) and most prominently agriculture (5.55%). This implies that the total forest cover and barren land has reduced at the expense of increase in water body, river bed, agriculture and built up land in a span of 30 years.
- Taking the internal conversion of various landcover classes into account, an overall trend from 1972 to 2003 was a change from forest and barren land to agriculture, built up and water bodies.

Performance of the VIC macroscale hydrological model to simulate streamflows during calibration and validation can be summarized as follows:

- Pre-calibration simulation and comparison of observed and simulated streamflow was done for year 2003. The

coefficient of determination before calibration was found to be as 0.747, for Mundali.

- The calibration of the model at Mundali outlet was performed for year 2003. Streamflow was found sensitive to variables like upper and lower soil layer depth, velocity of flow and vegetation parameters. R^2 of 0.836, Ce of 0.821 and Er of 0.085 was obtained during daily simulation. The model performance was found better for monthly simulations with Ns of 0.89.

Streamflows were simulated using VIC model for the year 1972, 1985 and 2003. Following conclusions can be drawn from the analysis carried for predicting changes over years:

- An increase by 4.53% (24.44 mm) in the annual streamflow is predicted at Mundali outlet of the Mahanadi basin from 1972 to 2003. It may be concluded that a decrease in forest cover by 5.71% in the Mahanadi river basin has caused the river flow to increase by 4.53%. This is quite a significant amount in terms of volumetric rise (3514242122 m³).
- The relative percentage increase in streamflow was found high in the months of May and November in all sub-basins. It may be concluded that the impact of landcover changes are most pronounced during low flows and that during high flows, role of landcover becomes comparatively less.

REFERENCES

- Canadell, J., Jackson, R.B., Ehleringer, J.B. and Moorey, H.A., 1996. Maximum rooting depth of vegetation types at the global scale. *Oecologia*, 108(4), pp. 1432-1939.
- Lettenmaier, D.P., 2001. Present and Future of Modeling Global Environmental Change: Toward Integrated Modeling,. In: T.M. Eds. and H. Kida (Editors), *Macroscale Hydrology: Challenges and Opportunities*, pp. 111-136.
- Liang, X., 1994. A Two-Layer Variable Infiltration Capacity Land Surface Representation for General Circulation Models. *Water Resour. Series TR140*, Univ. of Washington, Seattle.
- Liang, X., Lettenmaier, D.P., Wood, E.F. and Burgess, S.J., 1994. A simple hydrologically based model of land surface, water, and energy flux for general circulation models. *Journal of Geophysical Research*, 99(D7), pp. 14,415-14,428.
- Liang, X., Lettenmaier, D.P. and Wood, E.F., 1996. One-dimensional Statistical Dynamic Representation of Subgrid Spatial Variability of Precipitation in the Two-Layer Variable Infiltration Capacity Model. *J. Geophys. Res.*, 101(D16), pp. 21,403-21,422.
- Lohmann, D.E., Raschke, Nijssen, B. and Lettenmaier, D.P., 1998. Regional scale hydrology:II. Application of the VIC-2L model to the Weser river, Germany. *Hydrological Sciences*, 43(1), pp. 143-158.
- Rao, P.G., 1993. Climatic changes and trends over a major river basin in India. *Climate Research*, 2, pp. 215-223.

RETRIEVAL OF VEGETATION BIOCHEMICALS USING A RADIATIVE TRANSFER MODEL AND HYPERSPECTRAL DATA

R. Darvishzadeh ^{a,*}, Clement Atzberger ^b, Andrew Skidmore ^c, Martin Schlerf ^c

^a RS & GIS Department, Faculty of Earth Sciences, Shahid Beheshti University, Tehran, Iran- (r_darvish@sbu.ac.ir)

^b Joint Research Centre of the European Commission, TP 266, Via Enrico Fermi 1, 21027 Ispra (VA), Italy- (clement.atzberger@jrc.it)

^c NRS Department, ITC Faculty, University of Twente, Enschede, The Netherlands – (skidmore@itc.nl;schlerf@itc.nl)

Commission VII

KEY WORDS: Hyper spectral, Vegetation, Estimation, Model, Spectral

ABSTRACT:

Accurate quantitative estimation of vegetation biochemical characteristics is necessary for a large variety of agricultural and ecological applications. The advent of hyperspectral remote sensing has offered possibilities for measuring specific vegetation variables that were difficult to measure using conventional multi-spectral sensors. In this study, the potential of biophysical modelling to predict leaf and canopy chlorophyll contents in a heterogeneous grassland is investigated. The well-known PROSAIL model was inverted with HyMap measurements by means of a look-up table (LUT). HyMap images along with simultaneous in situ measurements of chlorophyll content were acquired over a National Park. We tested the impact of using multiple solutions and spectral sub-setting on parameter retrieval. To assess the performance of the model inversion, the RMSE and R^2 between independent in situ measurements and estimated parameters were used. The results of the study demonstrated that inversion of the PROSAIL model yield higher accuracies for Canopy chlorophyll content, in comparison to Leaf chlorophyll content ($R^2=0.84$, RMSE=0.24). Further a careful selection of spectral subset, which comprised the development of a new method to subset the spectral data, proved to contain sufficient information for a successful model inversion. Consequently, it increased the estimation accuracy of investigated parameters ($R^2=0.87$, RMSE=0.22). Our results confirm the potential of model inversion for estimating vegetation biochemical parameters using hyperspectral measurements.

1. INTRODUCTION

The spatial and temporal distribution of vegetation biochemical and biophysical variables are important inputs into models quantifying the exchange of energy and matter between the land surface and the atmosphere. Among the many vegetation characteristics, leaf chlorophyll content (LCC) and canopy chlorophyll content (CCC) are of prime importance. Leaf chlorophyll content and canopy chlorophyll content (the latter defined here as the product of LAI and leaf chlorophyll content) contribute to verifying vegetation physiological status and health, and have been found useful for detecting vegetation stress, photosynthetic capacity, and productivity (Boegh et al., 2002; Carter, 1994).

The physical approach for estimating vegetation parameters from remotely sensed data, involves using radiative transfer models. This approach assumes that the radiative transfer model accurately describes the spectral variation of canopy reflectance, as a function of canopy, leaf and soil background characteristics, using physical laws (Goel, 1989; Meroni et al., 2004). As radiative transfer models are able to explain the transfer and interaction of radiation inside the canopy based on physical laws, they offer an explicit connection between the vegetation biophysical and biochemical variables and the canopy reflectance (Houborg et al., 2007). To actually use physically based models for retrieving vegetation characteristics

from observed reflectance data, they must be inverted (Kimes et al., 1998). A drawback in using physically based models is the ill-posed nature of model inversion (Atzberger, 2004; Combal et al., 2002), meaning that the inverse solution is not always unique as various combinations of canopy parameters may yield almost similar spectra (Weiss and Baret, 1999). To overcome this problem, some restriction of the inverse problem may be required to constrain the inversion process. This involves the use of prior knowledge about model parameters (Combal et al., 2002; Lavergne et al., 2007).

Significant efforts to estimate and quantify vegetation properties using radiative transfer models have been carried out in the last two decades. Despite these efforts, literature reveals that studies on heterogeneous grasslands with combinations of different grass species and the use of hyperspectral measurements are rare. The main objective of this paper is to estimate and predict canopy and leaf chlorophyll content by inverting the canopy radiative transfer model PROSAIL (Jacquemoud and Baret, 1990; Verhoef, 1984; Verhoef, 1985). The aptness of the methods is analyzed in terms of prediction accuracy for estimating leaf and canopy chlorophyll content.

* Corresponding Author

2. MATERIALS

2.1 Study area and sampling

The study site is located in a National Park in Italy (latitude 41°52' to 42°14'N, longitude 13°50' to 13°14'E). The park covers an area of 74.095 ha and extends into the southern part of Abruzzo, at a distance of 40 km from the Adriatic Sea. The region is situated in the massifs of the Apennines. The flora of the park includes more than 1800 plant species, which approximately constitute one third of the entire flora in Italy. A total of 45 plots (30 m by 30 m) were selected. For each plot, the relevant biophysical and biochemical parameters were measured within few randomly selected subplots. In each plot the species varied in terms of leaf shape, size and the amount of leaves.

2.2 Vegetation parameter measurements

A SPAD-502 Leaf Chlorophyll Meter was used to assess leaf chlorophyll content. A total of 150 leaves were randomly selected in each plot representing the dominant species and their SPAD readings were recorded. From the 150 individual SPAD measurements, the average was calculated. These averaged SPAD readings were converted into leaf chlorophyll contents [$\mu\text{g cm}^{-2}$] by means of an empirical calibration function provided by (Markwell et al. 1995). The total canopy chlorophyll content (CCC) [g m^{-2}] for each plot then have been obtained by multiplying the leaf chlorophyll content with the corresponding leaf area index

In each plot, leaf area index was measured using the Plant Canopy Analyzer LAI-2000 (LICOR Inc., Lincoln, NE, USA). To prevent direct sunlight on the sensor, samples of below- and above-canopy radiation were made with the sun behind the operator and using a view restrictor of 45°. Table 1 reports summary statistics for some of the measured variables of the plots.

Measured variables	STDV	Min	Mean	Max
SPAD (unit-less)	3.7	24.2	32.7	41.0
Leaf chlorophyll ($\mu\text{g cm}^{-2}$)	4.7	18.9	28.7	40.9
Canopy chlorophyll (g m^{-2})	0.56	0.21	0.86	2.3
LAI ($\text{m}^2 \text{m}^{-2}$)	1.59	0.72	2.87	7.54

Table 1. Summary statistics for some measured variables of sample plots.

2.3 Hyperspectral images

HyMap images of the study area were acquired by DLR, Germany's Aerospace Research Centre and Space Agency. The sensor contained 126 wavelengths, operating over the spectral range of 436 nm to 2485 nm. The spatial resolution of the data was 4 m. The data were collected in four image strips, each covering an area of about 40 km by 2.3 km. The image acquisition was close to solar noon. The image strips were atmospherically and geometrically corrected by DLR. A 7 by 7 pixel window centred around the central position of a plot was used for collection of grass spectra from each sample plot and its average spectrum was calculated.

3. METHODS

3.1 PROSAIL & Inversion

The commonly used PROSAIL radiative transfer model which is a combination of the SAILH canopy reflectance model (Verhoef, 1984; Verhoef, 1985) and the PROSPECT leaf optical properties model (Fourty et al., 1996; Jacquemoud and Baret, 1990; Jacquemoud et al., 1996) was selected for canopy parameter retrieval. The PROSPECT model calculates the leaf hemispherical transmittance and reflectance as a function of four input parameters: the leaf structural parameter N (unitless); the leaf chlorophyll a + b concentration LCC ($\mu\text{g cm}^{-2}$); the dry matter content Cm (g cm^{-2}); and the equivalent water thickness Cw (g cm^{-2}). The SAILH model, apart from the leaf reflectance and transmittance, requires eight input parameters to simulate the top-of-canopy bidirectional reflectance. These are sun zenith angle, t_s (deg); sensor viewing angle, t_o (deg); relative azimuth angle between sensor and sun, ϕ (deg); fraction of diffuse incoming solar radiation, $skyl$; background reflectance (soil reflectance) for each wavelength, rsl ; LAI ($\text{m}^2 \text{m}^{-2}$); average leaf inclination angle, ALA (deg); and the hot spot size parameter, hot (m m^{-1}). To account for the changes induced by moisture and roughness in soil brightness, we used a soil brightness parameter, $scale$ (Atzberger et al., 2003). Sensor viewing angle, azimuth angle, sun zenith angle and fraction of diffuse incoming solar radiation were fixed.

The inversion of PROSAIL radiative transfer model was considered by using a look-up table (LUT). To build the LUT, 100,000 parameter combinations were randomly generated and used in the forward calculation of the PROSAIL model. The ranges (minimum and maximum) for each of the eight "free" model parameters are reported in Table 2. The maximum and minimum values of LAI, LCC and ALA were fixed based on prior knowledge from the field data collection (Combal et al., 2003; Darvishzadeh et al., 2008). To find the solution to the inverse problem for a given canopy spectra, for each modelled reflectance spectra of the LUT the root mean square error between measured and modelled spectra (RMSEr) was calculated.

Parameter	Min	Max
Leaf area index	0	8
Mean leaf inclination angle	40	70
Leaf chlorophyll content	15	45
Leaf structural parameter	1.5	1.9
Dry matter content	0.005	0.010
Equivalent water thickness	0.01	0.02
Hot spot size	0.05	0.10
Soil brightness	0.5	1.5

Table 2. Specific ranges for eight input parameters used for generating the LUT.

4. RESULTS

To find the solution to the inverse problem, the LUT is sorted according to the cost function and the set of variables providing the minimum RMSE is considered as the solution. Figure 1 illustrates measured and simulated canopy reflectance spectra found in this way for two plots with contrasting LAI values.

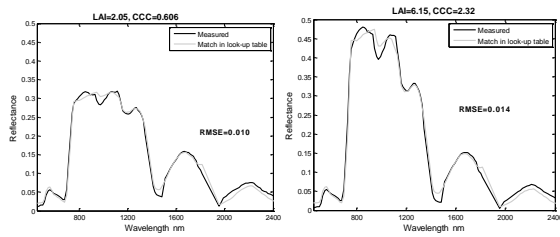


Figure 1. Measured and simulated canopy reflectance spectra of two sample plots.

Generally the simulated reflectances were in relatively good agreement with the measured reflectances for canopies with different LAI values. A more concise analysis reveals that most spectral bands were modelled with average absolute error (AAE) lower than 0.02 reflectance units. As Figure 2 shows the AAE in some regions is relatively high (greater than 0.02), especially close to the water vapour absorption regions (1135 nm to 1400 nm, and 1820 nm to 1940 nm). We considered the bands with an AAE greater or equal to 0.02 as wavelengths being either poorly modelled or poorly measured (Darvishzadeh et al., 2008).

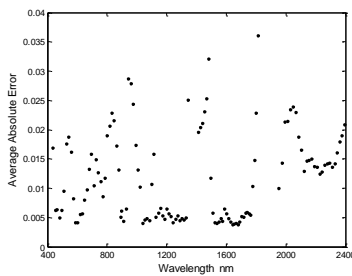


Figure 2. The average absolute error between best-fit and the measured HyMap reflectance.

The relation between the measured and estimated grass canopy chlorophyll content based on the smallest RMSE criterion is demonstrated in Figure 3.

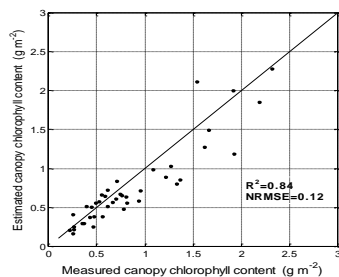


Figure 3. Estimated versus measured canopy chlorophyll using the PROSAIL model and the minimum RMSE criterion in the LUT search.

We also evaluated the retrieval accuracy if multiple solutions are used. Table 3 compares the “multiple solutions” with the “best-fit” LUT solutions. This demonstrates how different solutions affect the accuracy of the estimated variables.

No. of Solu.	Stat. Param	LCC ($\mu\text{g cm}^{-2}$)			CCC (g m^{-2})		
		R^2	RMSE	nRMS	R^2	RMSE	nRMS
Best spectra	/	0.35	3.8	0.17	0.84	0.24	0.12
First 10	Median	0.36	3.8	0.17	0.84	0.24	0.12
	Mean	0.36	3.7	0.17	0.85	0.23	0.11
First 100	Median	0.39	3.1	0.14	0.81	0.25	0.12
	Mean	0.40	3.1	0.14	0.82	0.24	0.11

Table 3. R^2 , RMSE and normalized RMSE between measured and estimated leaf and canopy chlorophyll content from PROSAIL inversion.

An appropriate band selection is known to improve radiative transfer model inversion and prevents bias in the estimation of the variables of interest (Schlerf and Atzberger, 2006). Therefore, to account for band selection the inversion of the model was also tested with wavelengths that had an AAE smaller than 0.02. We considered bands with an AAE greater or equal to 0.02 as wavelengths with high errors (Figure 2). These bands were systematically excluded in the inversion process, and each time the AAE between the measured and best-fit reflectance spectra was re-calculated until all remaining wavelengths had an AAE smaller than 0.02. The elimination of wavelengths stopped after 19 iterations. The remaining wavebands ($n=107$) are called subset II and was used in the inversion procedure.

The assignment of the spectral subset II in the estimation of grass chlorophyll was again evaluated on the basis of the R^2 and the normalized RMSE between the measured and estimated variables. The results showed that, after removing the wavelengths with high AAE ($\text{AAE} \geq 0.02$), the relationships between measured and estimated leaf and canopy chlorophyll content were considerably improved (Table 4).

Spectral sampling set	Stat. Param	LCC ($\mu\text{g cm}^{-2}$)			CCC (g m^{-2})		
		R^2	RMSE	nRMS	R^2	RMSE	nRMS
Using all bands ($n=126$)	Best fit	0.35	3.8	0.17	0.84	0.24	0.12
	median	0.36	3.8	0.17	0.84	0.24	0.12
	mean	0.36	3.7	0.17	0.85	0.23	0.11
Subset II ($n=107$)	Best fit	0.37	3.7	0.17	0.84	0.25	0.12
	median	0.38	3.4	0.15	0.87	0.23	0.11
	mean	0.39	3.2	0.14	0.87	0.22	0.10

Table 4. R^2 , RMSE and normalized RMSE between measured and estimated leaf and canopy chlorophyll content from PROSAIL inversion using subset II.

Overall, the estimation accuracies between measured and estimated leaf and canopy chlorophyll content improved using the spectral subset (Table 4). This reflects the danger with

existing bands that may contain (excessively) high noise levels and/or are poorly modelled by PROSAIL.

5. CONCLUSION & DISCUSSION

The results of the study demonstrated that inversion of the PROSAIL model yield higher accuracies for Canopy chlorophyll content, in comparison to Leaf chlorophyll content. The inclusion of canopy chlorophyll content allows us to assess whether canopy reflectance is a better predictor of leaf or canopy chlorophyll content. The relationships between measured and estimated leaf chlorophyll content were poor in all inversion processes which confirms other studies revealing similar difficulties in estimating leaf chlorophyll (Baret and Jacquemoud, 1994). This is also in line with previous studies that have demonstrated poor signal propagation from leaf to canopy scale. A careful selection of spectral subset, which comprised the development of a new method to subset the spectral data, proved to contain sufficient information for a successful model inversion. By eliminating wavelength having a high AAE (subset II), we eliminated noisy/badly modelled wavelengths. Consequently, it increased the estimation accuracy of investigated parameters ($R^2=0.87$, $RMSE=0.22$). Although our results confirm the potential of model inversion for estimating vegetation biochemical parameters using hyperspectral measurements, its applicability to heterogeneous grasslands requires further experiments and validation work using different hyperspectral data sets.

Acknowledgements

The corresponding Author would like to acknowledge the assistance of Shahid Beheshti University (SBU), and in particular RS & GIS centre at SBU for their support.

References:

Atzberger, C., 2004. Object-based retrieval of biophysical canopy variables using artificial neural nets and radiative transfer models. *Remote Sensing of Environment*, 93(1-2): 53-67.

Atzberger, C., Jarmer, T., Schlerf, M., Kötz, B. and Werner, W., 2003. Retrieval of wheat bio-physical attributes from hyperspectral data and SAILH + PROSPECT radiative transfer model. In: M. Habermeyer, A. Müller and S. Holzwarth (Eds.), *3rd EARSeL Workshop on Imaging Spectroscopy*. Herrsching, Germany, 13-16 May 2003, pp. 473-482.

Baret, F. and Jacquemoud, S., 1994. Modeling canopy spectral properties to retrieve biophysical and biochemical characteristics. In: J. Hill and J. Me'gier (Editors), *Imaging Spectrometry: A Tool for Environmental Observations*. Luxemburg. ECSC, EEC, EAEC, Brussels and Luxemburg, pp. 145-167.

Boegh, E., Soegaard, H., Broge, N., Hasager, C.B., Jensen, N.O., Schelde, K. and Thomsen, A., 2002. Airborne multispectral data for quantifying leaf area index, nitrogen concentration, and photosynthetic efficiency in agriculture. *Remote Sensing of Environment*, 81(2-3): 179-193.

Carter, G.A., 1994. Ratios of leaf reflectances in narrow wavebands as indicators of plant stress. *International Journal of Remote Sensing*, 15(3): 697-703.

Combal, B., Baret, F. and Weiss, M., 2002. Improving canopy variables estimation from remote sensing data by exploiting ancillary information, Case study on sugar beet canopies. *Agronomie*, 22(2): 205-215.

Combal, B., Baret, F., Weiss, M., Trubuil, A., Mace, D., Pragnere, A., Myneni, R., Knyazikhin, Y. and Wang, L., 2003. Retrieval of canopy biophysical variables from bidirectional reflectance: using prior information to solve the ill-posed inverse problem. *Remote Sensing of Environment*, 84(1): 1-15.

Darvishzadeh, R., Skidmore, A.K., Schlerf, M. and Atzberger, C., 2008. Inversion of a radiative transfer model for estimating vegetation LAI and chlorophyll in a heterogeneous grassland. *Remote Sensing of Environment*, 112(5): 2592-2604.

Fourty, T., Baret, F., Jacquemoud, S., Schmuck, G. and Verdebout, J., 1996. Leaf optical properties with explicit description of its biochemical composition: direct and inverse problems. *Remote Sensing of Environment*, 56(2): 104-117.

Goel, N.S., 1989. Inversion of canopy reflectance models for estimation of biophysical parameters from reflectance data. In: G. Asrar (Editor), *Theory and Applications of Optical Remote Sensing*. Wiley & Sons, New York etc., pp. 205-251.

Houborg, R., Soegaard, H. and Boegh, E., 2007. Combining vegetation index and model inversion methods for the extraction of key vegetation biophysical parameters using Terra and Aqua MODIS reflectance data. *Remote Sensing of Environment*, 106(1): 39-58.

Jacquemoud, S. and Baret, F., 1990. PROSPECT: a model of leaf optical properties spectra. *Remote Sensing of Environment*, 34(2): 75-91.

Jacquemoud, S., Ustin, S.L., Verdebout, J., Schmuck, G., Andreoli, G. and Hosgood, B., 1996. Estimating leaf biochemistry using the PROSPECT leaf optical properties model. *Remote Sensing of Environment*, 56(3): 194-202.

Kimes, D.S., Nelson, R.F., Manry, M.T. and Fung, A.K., 1998. Attributes of neural networks for extracting continuous vegetation variables from optical and radar measurements. *International Journal of Remote Sensing*, 19(14): 2639-2662.

Lavergne, T., Kaminski, T., Pinty, B., Taberner, M., Gobron, N., Verstraete, M.M., Vossbeck, M., Widlowski, J.-L. and Giering, R., 2007. Application to MISR land products of an RPV model inversion package using adjoint and Hessian codes. *Remote Sensing of Environment*, 107(1-2): 362-375.

LI-COR, 1992. LAI-2000 Plant Canopy Analyzer Instruction Manual. LICOR Inc., Lincoln, NE, USA.

Markwell, J., Osterman, J.C. and Mitchell, J.L., 1995. Calibration of Minolta SPAD-502 leaf chlorophyll meter. *Photosynthetic Research*, 46(3): 467-472.

Meroni, M., Colombo, R. and Panigada, C., 2004. Inversion of a radiative transfer model with hyperspectral observations for LAI mapping in poplar plantations. *Remote Sensing of Environment*, 92(2): 195-206.

Schlerf, M. and Atzberger, C., 2006. Inversion of a forest reflectance model to estimate structural canopy variables from

hyperspectral remote sensing data. *Remote Sensing of Environment*, 100(3): 281-294.

Verhoef, W., 1984. Light scattering by leaf layers with application to canopy reflectance modeling: the SAIL model. *Remote Sensing of Environment*, 16(2): 125-141.

Verhoef, W., 1985. Earth observation modeling based on layer scattering matrices. *Remote Sensing of Environment*, 17(2): 165-178.

Weiss, M. and Baret, F., 1999. Evaluation of canopy biophysical variable retrieval performances from the accumulation of large swath satellite data. *Remote Sensing of Environment*, 70(3): 293-306.

ASSESSMENT OF THE IMPACT OF UNCERTAINTY ON MODELED SOIL SURFACE ROUGHNESS ON SAR-RETRIEVED SOIL MOISTURE UNCERTAINTY

E. De Keyser ^{a*}, H. Lievens ^b, H. Vernieuwe ^a, J. Álvarez-Mozos ^c, B. De Baets ^a, N.E.C. Verhoest ^b

^a Department of Applied Mathematics, Biometrics and Process Control, Ghent University, Coupure links 653, B-9000 Gent, Belgium

^b Laboratory of Hydrology and Water Management, Ghent University, Coupure links 653, B-9000 Gent, Belgium

^c Department of Projects and Rural Engineering, Public University of Navarre, Spain

* Eva.DeKeyser@UGent.be

KEY WORDS: Soil moisture retrieval, SAR, Uncertainty assessment, Linear regression, Soil surface roughness

ABSTRACT:

Soil moisture retrieval from SAR images using semi-empirical or physically-based backscatter models requires surface roughness parameters, generally obtained by means of *in situ* measurements. However, measured roughness parameters often result in inaccurate soil moisture contents. Furthermore, when these retrieved soil moisture contents need to be used in data assimilation schemes, it is important to also assess the retrieval uncertainty. In this paper, a regression-based method is developed that allows for the parameterization of roughness by means of a probability distribution. This distribution is further propagated through an inverse backscatter model in order to obtain probability distributions of soil moisture content. About 70% of the obtained distributions are skewed and non-normal and it is furthermore shown that their interquartile range differs with respect to soil moisture conditions. Comparison of soil moisture measurements with the retrieved median values results in a root mean square error of approximately 3.5 vol%.

1 INTRODUCTION

Soil moisture is a key variable in various earth science disciplines such as hydrology, meteorology and agriculture. The models that are mostly used in these disciplines generally require spatially distributed soil moisture as an input. As the microwave backscattered signal from a bare soil surface is partly influenced by the soil moisture content, radar remote sensing can be used to meet these high spatial resolution requirements. Currently, only active microwave sensors, of which the Synthetic Aperture Radar (SAR) is the most common imaging configuration, are able to capture small-scale soil moisture patterns.

Several backscatter models exist that calculate the backscattered signal, given soil moisture, soil surface roughness and incidence angle, polarization and wavelength of the radar signal. Soil surface roughness refers to the unevenness of the earth's surface due to natural processes or human activities, and is generally statistically described by the root mean square (rms) height, the correlation length and an autocorrelation function (Ulaby et al., 1982a). Unfortunately, soil surface roughness parameters are difficult to measure as several experiments have shown that roughness parameterization depends on profile length (Callens et al., 2006; Davidson et al., 2000; Ogilvy, 1988; Oh and Kay, 1998) and the measurement technique (Mattia et al., 2003a), meaning that different roughness parameter values can be obtained for the same surface. These problems occur because natural surfaces behave as a self-affine fractal surface (Shephard and Campbell, 1999; Dierking, 1999; Shepard et al., 2001), while most of the backscatter models assume a stationary random surface.

Amongst the various methods that exist to overcome this parameterization problem, Su et al. (1997) suggested the use of an effective roughness parameter, which is estimated by means of remotely sensed data in combination with soil moisture measurements. This parameter then replaces the *in situ* roughness measurements for soil moisture retrieval from successive SAR acquisitions. This concept is applied successfully in different studies (Verhoest et al., 2000; Baghdadi et al., 2002, 2004, 2006; Rahman

et al., 2007; Álvarez-Mozos et al., 2008) and will also be used in this study.

SAR retrieved soil moisture maps are often used in hydrological models or in data assimilation schemes. For the latter applications, the Ensemble Kalman filter (Evensen, 2006) is frequently used to assimilate remotely sensed hydrologic information (Reichle, 2008). This method relies on the value of the observed variable and assumes a normal distribution, for which the mean value and the variance of the observed variable are required. Therefore, retrieval algorithms should provide not only soil moisture content, but also a quantification of its uncertainty.

The research questions to be answered in this study are:

1. How can the uncertainty on effective soil surface roughness be quantified?
2. How does this uncertainty influence the uncertainty on retrieved soil moisture?

For this purpose, all other sources of uncertainty were ignored, such as uncertainty on the backscattered signal, uncertainty induced by vegetation cover or by the backscatter model.

2 METHODOLOGY

The methodology used in this study is based on a relationship that was found between effective roughness parameters and backscatter coefficients. A linear regression model was used to model this relationship (Lievens et al., 2010) and can furthermore be used to quantify the uncertainty on the modeled soil roughness as a probability distribution. Using a Monte Carlo method to propagate this probability distribution through an inverse backscatter model, a probability distribution for soil moisture content is obtained.

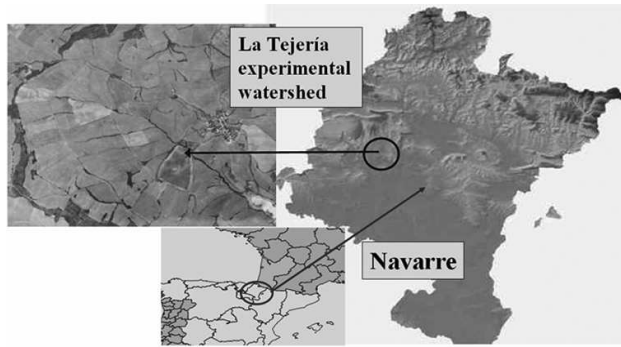
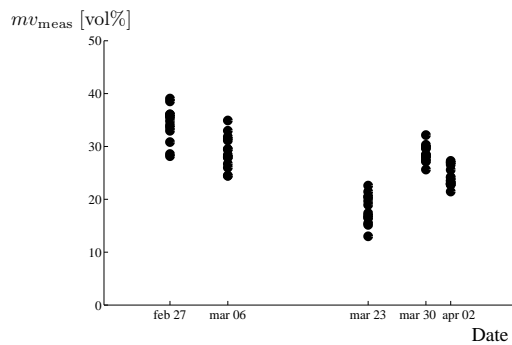


Figure 1: Location of La Tejería experimental watershed

Figure 2: Soil moisture contents (mv_{meas}) measured at different acquisition dates in 2003

2.1 Study site and data

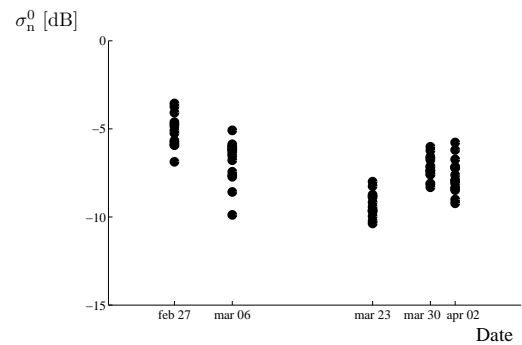
The studied watershed, La Tejería, is situated in the north of Spain (Figure 1), has a humid, submediterranean climate and consists of clayey and silty clay loam textures. It is almost completely cultivated, with an emerging cereal crop covering most of the fields during the experimental period (February - April 2003). A more detailed description of the study site is given by Álvarez-Mozos et al. (2006).

For each acquisition day, field average soil moisture contents were calculated for fifteen seedbed fields based on measurements with a Time Domain Reflectometry (TDR) instrument with 11 cm probes (Figure 2). For a detailed description of the sampling method we refer to Álvarez-Mozos et al. (2006).

Next, five C-band, HH polarized RADARSAT-1 SGF scenes were acquired over the experimental region during spring 2003, at low incidence angles (13° - 29°). This configuration has proved to be particularly well suited for soil moisture research over cereal canopies (Ulaby et al., 1982b; Biftu and Gan, 1999; Mattia et al., 2003b). The images have a range resolution of 20 m or 24 m and an azimuth resolution of 27 m, from which field average backscatter coefficients were calculated. Furthermore, in order to reduce the effect of the local incidence angle on the backscatter coefficients, these coefficients were normalized correspondent to a reference incidence angle, according to Lambert's law for optics (Ulaby et al., 1982b; Van Der Velde and Su, 2009):

$$\sigma_{1,n}^0 = \sigma_1^0 \frac{\cos^2 \theta_{\text{ref}}}{\cos^2 \theta}, \quad (1)$$

where $\sigma_{1,n}^0$ is the linear normalized backscatter coefficient [-], σ_1^0 is the linear measured backscatter coefficient [-], θ_{ref} is the refer-

Figure 3: Normalized backscatter coefficients (σ_n^0) obtained at different acquisition dates in 2003

ence incidence angle [$^\circ$], in this case chosen to be 23° and θ is the local incidence angle [$^\circ$]. The resulting field average backscatter values are shown for every acquisition date in Figure 3.

2.2 Integral Equation model

The single scattering approximation of the Integral Equation Model (IEM) (Fung et al., 1992; Fung, 1994) is the most widely used scattering model for bare soil surfaces (Moran et al., 2004). It allows for the calculation of backscatter coefficients based on bare soil surface roughness parameters, soil dielectric constant, local incidence angle, wave polarisation and frequency. The IEM describes surface roughness by three complementary parameters: rms height (s), correlation length (l), and an autocorrelation function. Davidson et al. (2000) and Callens et al. (2006) demonstrated that for smooth to medium rough agricultural bare fields this autocorrelation function is best represented by an exponential function.

The conversion of the dielectric constant to the corresponding soil moisture content is performed by means of the four-component dielectric mixing model of Dobson et al. (1985), for which the residual and saturated soil moisture content used throughout this study are set to 3 vol% and 45 vol% respectively.

It is expected that the emerging crops on the fields influence the results of the inversion of the IEM, since this was developed for bare soil conditions. However, the canopies were only weakly developed and the incidence angles were low, which are reasons to believe that the effect of the vegetation is minimal (Ulaby et al., 1982b; Mattia et al., 2003b). Furthermore, simulations by Lievens et al. (2010) using a water cloud model (Attema and Ulaby, 1978; Prévot et al., 1993) indicated that the attenuation of the backscatter by the cereal canopy was to a large extent compensated by a direct canopy contribution. This led to insignificant vegetation corrections within the relative radiometric accuracy of the RADARSAT observations, *i.e.* ± 1 dB (Srivastava et al., 1999). Therefore this study will not take into account a possible influence of the crop cover on the backscattered signal.

2.3 Effective roughness

The idea of using effective roughness parameters was first introduced by Su et al. (1997). The effective roughness parameters are estimated using backscatter and soil moisture observations. They replace *in situ* measurements of soil surface roughness for the retrieval of soil moisture content from successive SAR images.

In case of the IEM, two effective roughness parameters need to be defined: rms height (s) and correlation length (l). Lievens

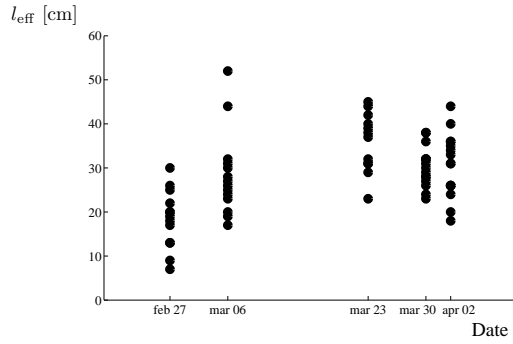


Figure 4: Effective correlation lengths (l_{eff}) obtained with the IEM for the different acquisition dates in 2003

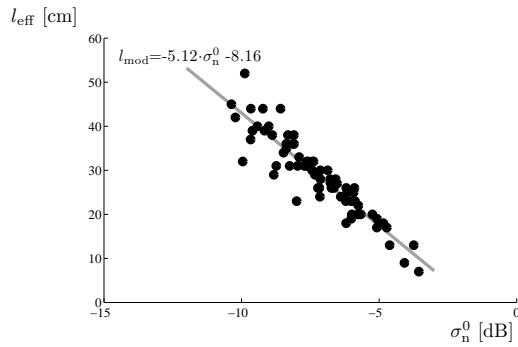


Figure 5: Dependence of the effective correlation length (l_{eff}) on the normalized backscatter coefficient (σ_n^0)

et al. (2010) observed that for a large number of different (s, l)-combinations a very small soil moisture retrieval error is obtained. They furthermore concluded that a fixed value for s is best used on which basis the corresponding value for l_{eff} is determined. Therefore s is fixed at 1.0 cm and l ranges from 1.0 cm to 120 cm in the inversion of the IEM. The value resulting in the lowest observation error, l_{eff} , is retained. Figure 4 shows the effective correlation lengths corresponding to the observed normalized backscatter coefficients on every acquisition date.

A comparison of Figures 3 and 4 shows that the behaviour of the field average effective correlation lengths is strongly related to the normalized backscatter coefficients. A plot of the values of l_{eff} versus σ_n^0 , as presented in Figure 5, reveals this relationship can be modeled by a linear regression model:

$$l_{\text{mod}} = a \cdot \sigma_n^0 + b + \epsilon, \quad (2)$$

with l_{mod} the modeled correlation length, a and b regression parameters and ϵ a random error term, usually considered to be normally distributed. The values of parameters a and b are also shown in Figure 5. Lievens et al. (2010) performed an extensive cross-validation, indicating the robustness of this regression model, however, latter exercise will not be discussed in this work.

The linear regression model can then be further used to estimate the uncertainty around the predicted value. This uncertainty is described by a t-distribution with variance σ^2 , calculated as follows (Neter et al., 1996):

$$\sigma^2 = \frac{\sum_{i=1}^n e_i^2}{n-2} \left[1 + \frac{1}{n} + \frac{(\sigma_{n,h}^0 - \bar{\sigma}_n^0)^2}{\sum_{i=1}^n (\sigma_{n,i}^0 - \bar{\sigma}_n^0)^2} \right], \quad (3)$$

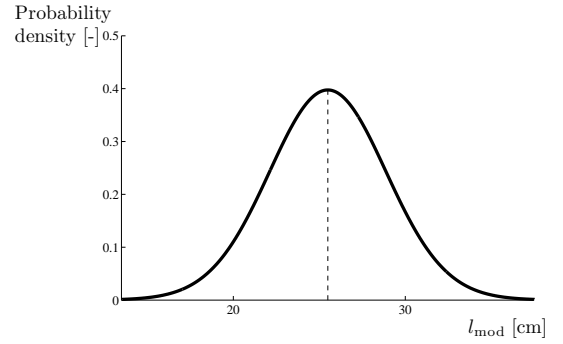


Figure 6: Example of a probability distribution for modeled correlation length (l_{mod})

with n the number of observations, e_i the difference between the i th observed and modeled values of l_{eff} , $\sigma_{n,h}^0$ the normalized backscatter coefficient for which the regression model is applied, $\sigma_{n,i}^0$ the i th observed normalized backscatter coefficient and $\bar{\sigma}_n^0$ the mean of all observed normalized backscatter coefficients. As an example, Figure 6 shows the t-distribution for an arbitrary value of σ_n^0 , from which it can be seen that this distribution is symmetric around the mean value. The obtained distribution for l_{mod} is propagated through the inversion of the IEM by means of a Monte Carlo method. To this end, 1000 values of l_{mod} are randomly sampled from the distribution and further used as input to the IEM. This results in 1000 corresponding soil moisture contents, representing the histogram of soil moisture.

3 RESULTS AND DISCUSSION

3.1 Soil moisture histogram

Figure 7 shows the histogram of the obtained soil moisture values for the arbitrary example. The histograms are cut off at a minimum soil moisture content of 3 vol% (residual soil moisture content) and a maximum of 45 vol% (saturated soil moisture content), which can influence the mean value. Furthermore, it should be noticed that this example histogram is asymmetric, skewed towards higher soil moisture values and therefore not normal. This was confirmed using a Lilliefors normality test (Lilliefors, 1967) for about 70% of the obtained histograms. The remaining histograms were found to be normal, which mostly occurred at low soil moisture values (< 25 vol%). Consequently, using the mean and standard deviation in further applications as representatives for the obtained non-normal soil moisture histograms, may lead to a distorted view of the underlying distributions. Furthermore, the mean value and standard deviation of the normal histograms may be influenced by the fact that the histograms are cut off at the residual and saturated soil moisture content. Therefore it is recommended to use the median value and the interquartile range divided by 1.35 (converted IQR), which are insensitive to the values of residual and saturated soil moisture content.

3.2 Retrieved median soil moisture content

Figure 8 shows a scatterplot of the retrieved versus the observed soil moisture values, where the error bars represent the converted IQR of the resulting histograms. It can be seen that low soil moisture contents (< 20 vol%) are slightly overestimated. Overall, a root mean square error (RMSE) of 3.51 vol% is obtained between the measured soil moisture content and the median of the

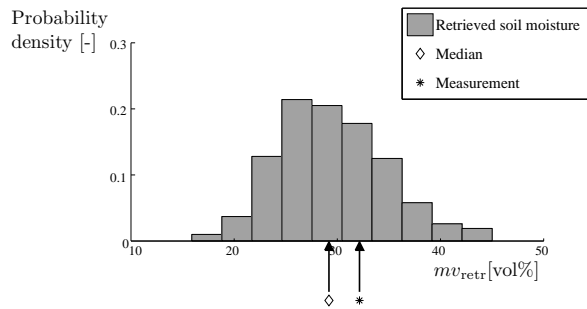


Figure 7: Example of a histogram of retrieved soil moisture content (mv_{retr})

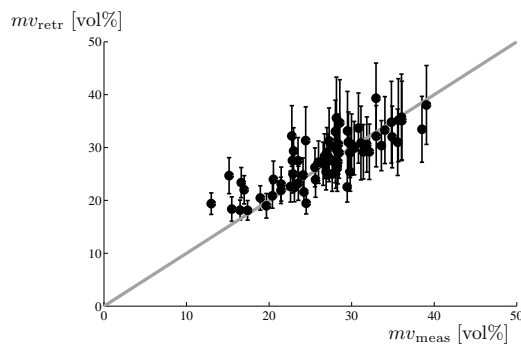


Figure 8: Retrieved (mv_{retr}) versus measured soil moisture (mv_{meas}), the error bars represent $IQR/1.35$

retrieved histograms. Furthermore a Nash-Sutcliffe model efficiency (Nash and Sutcliffe, 1970) of 0.63 was found, indicating the model predicts much better than the mean value of the observations. It is furthermore observed that the uncertainty on the retrieved soil moisture contents increases with the soil moisture content, which is in accordance with the observations of Verhoest et al. (2007).

4 CONCLUSIONS

This study presents a methodology that allows for the retrieval of soil moisture content and its uncertainty based on modeled roughness. Soil surface roughness, in terms of effective correlation length (l_{eff}) is modeled based on its relationship with normalized backscatter coefficients (σ_n^0). The uncertainty on the modeled correlation length l_{mod} is described by a t-distribution, which is then sampled following a Monte Carlo method. The randomly drawn values are propagated through the inversion of the IEM and a corresponding histogram of soil moisture contents is obtained.

Results show that most of these histograms are skewed and non-normal and that a representation of these histograms by means of the mean value and the standard deviation may lead to a distorted view of the underlying distribution. This is particularly important when retrieved soil moisture content and corresponding uncertainty (represented by the mean and standard deviation) are to be used in data assimilation schemes, such as the Ensemble Kalman filter, which rely on normality assumptions of the variables of interest. It would be better to apply the median value and

converted IQR in the data assimilation framework. It is furthermore observed that the interquartile range changes with varying soil moisture conditions, larger interquartile ranges are obtained for higher soil moisture contents.

Future research is required to test whether soil moisture content with a variable uncertainty has a large impact when used in a data assimilation framework.

ACKNOWLEDGEMENTS

This work has been performed in the framework of the STEREO II project SR/00/100 “Hydrasens”, financed by the Belgian Science Policy. RADARSAT-1 data was provided by the Canadian Space Agency (CSA) project DRU-10-02. Spanish Government’s project CGL2007-63453/HID is also acknowledged.

References

- Álvarez-Mozos, J., Casali, J., González-Audícana, M. and Verhoest, N. E. C., 2006. Assessment of the operational applicability of RADARSAT-1 data for surface soil moisture estimation. *IEEE Transactions on Geoscience and Remote Sensing* 44, pp. 913–924.
- Álvarez-Mozos, J., González-Audícana, M., Casali, J. and Larrañaga, A., 2008. Effective versus measured correlation length for radar-based surface soil moisture retrieval. *International Journal of Remote Sensing* 29, pp. 5397–5408.
- Attema, E. P. W. and Ulaby, F. T., 1978. Vegetation modeled as a water cloud. *Radio Science* 13, pp. 357–364.
- Baghdadi, N., Gherboudj, I., Zribi, M., Sahebi, M., King, C. and Bonn, F., 2004. Semi-empirical calibration of the IEM backscattering model using radar images and moisture and roughness field measurements. *International Journal of Remote Sensing* 25, pp. 3593–3623.
- Baghdadi, N., Holah, N. and Zribi, M., 2006. Calibration of the Integral Equation Model for SAR data in C-band and HH and VV polarizations. *International Journal of Remote Sensing* 27, pp. 805–816.
- Baghdadi, N., King, C., Chanzy, A. and Wigneron, J. P., 2002. An empirical calibration of the Integral Equation Model based on SAR data, soil moisture and surface roughness measurement over bare soils. *International Journal of Remote Sensing* 23, pp. 4325–4340.
- Biftu, G. F. and Gan, T. Y., 1999. Retrieving soil moisture from Radarsat SAR data. *Water Resources Research* 35, pp. 1569–1579.
- Callens, M., Verhoest, N. E. C. and Davidson, M. W. J., 2006. Parameterization of tillage-induced single-scale soil roughness from 4-m profiles. *IEEE Transactions on Geoscience and Remote Sensing* 44, pp. 878–888.
- Davidson, M. W. J., Le Toan, T., Mattia, F., Satalino, G., Manninen, T. and Borgeaud, M., 2000. On the characterization of agricultural soil roughness for radar remote sensing studies. *IEEE Transactions on Geoscience and Remote Sensing* 38, pp. 630–640.
- Dierking, W., 1999. Quantitative roughness characterization of geological surfaces and implications for radar signature analysis. *IEEE Transactions on Geoscience and Remote Sensing* 37, pp. 2397–2412.

- Dobson, M. C., Ulaby, F. T., Hallikainen, M. T. and El-Rayes, M. A., 1985. Microwave dielectric behavior of wet soil. Part II: Dielectric mixing models. *IEEE Transactions on Geoscience and Remote Sensing* 23, pp. 35–46.
- Evensen, G., 2006. *Data Assimilation: the Ensemble Kalman Filter*. Springer-Verlag, New York.
- Fung, A. K., 1994. *Microwave Scattering and Emission Models and their Applications*. Artech House, Norwood, MA.
- Fung, A. K., Li, Z. Q. and Chen, K. S., 1992. Backscattering from a randomly rough dielectric surface. *IEEE Transactions on Geoscience and Remote Sensing* 30, pp. 356–369.
- Lievens, H., Verhoest, N. E. C., De Keyser, E., Vernieuwe, H., Matgen, P., Álvarez-Mozos, J. and De Baets, B., 2010. Effective roughness modelling as a tool for soil moisture retrieval from C- and L-band SAR. *Hydrology and Earth System Sciences*. Submitted 06/10.
- Lilliefors, H. W., 1967. On the Kolmogorov-Smirnov test for normality with mean and variance unknown. *Journal of the American Statistical Association* 62, pp. 399–402.
- Mattia, F., Davidson, M. W. J., Le Toan, T., D'Haese, C. M. F., Verhoest, N. E. C., Gatti, A. M. and Borgeaud, M., 2003a. A comparison between soil roughness statistics used in surface scattering models derived from mechanical and laser profilers. *IEEE Transactions on Geoscience and Remote Sensing* 41, pp. 1659–1671.
- Mattia, F., Le Toan, T., Picard, G., Posa, F. I., D'Álessio, A., Notarnicola, C., Gatti, A. M., Rinaldi, M., Satalino, G. and Pasquariello, G., 2003b. Multitemporal C-band radar measurements on wheat fields. *IEEE Transactions on Geoscience and Remote Sensing* 41, pp. 1551–1558.
- Moran, M. S., Peters-Lidard, C. D., Watts, J. M. and McElroy, S., 2004. Estimating soil moisture at the watershed scale with satellite-based radar and land surface models. *Canadian Journal of Remote Sensing* 30, pp. 805–826.
- Nash, J. E. and Sutcliffe, J. V., 1970. River flow forecasting through conceptual models part I - A discussion of principles. *Journal of Hydrology* 10, pp. 282–290.
- Neter, J., Kutner, M. H., Wasserman, W. and Nachtsheim, C. J., 1996. *Applied Linear Statistical Models*. Fourth edn, McGraw-Hill/Irwin, Boston.
- Ogilvy, J. A., 1988. Computer simulation of acoustic wave scattering from rough surfaces. *Journal of Physics D-Applied Physics* 21, pp. 260–277.
- Oh, Y. and Kay, Y. C., 1998. Condition for precise measurement of soil surface roughness. *IEEE Transactions on Geoscience and Remote Sensing* 36, pp. 691–695.
- Prévoit, L., Champion, I. and Guyot, G., 1993. Estimation surface soil moisture and leaf area index of a wheat canopy using a dual-frequency (C and X bands) scatterometer. *Remote Sensing of Environment* 46, pp. 331–339.
- Rahman, M. M., Moran, M. S., Thoma, D. P., Bryant, R., Sano, E. E., Holifield Collins, C. D., Skirvin, S., Kershner, C. and Orr, B. J., 2007. A derivation of roughness correlation length for parameterizing radar backscatter models. *International Journal of Remote Sensing* 28, pp. 3995–4012.
- Reichle, R. H., 2008. Data assimilation methods in the earth sciences. *Advances in Water Resources* 31, pp. 1411–1418.
- Shepard, M. K., Campbell, B. A., Bulmer, M. H., Farr, T. G., Gaddis, L. R. and Plaut, J. J., 2001. The roughness of natural terrain: a planetary and remote sensing perspective. *Journal of Geophysical Research - Planets* 106, pp. 32777–32795.
- Shepard, M. K. and Campbell, B. A., 1999. Radar scattering from a self-affine fractal surface: near-nadir regime. *Icarus* 141, pp. 156–171.
- Srivastava, S. K., Hawkins, R. K., Lubowski, T. I., Banik, B. T., Adamovic, M. and Jefferies, W. C., 1999. RADARSAT image quality and calibration - Update. *Advances in Space Research* 23, pp. 1487–1496.
- Su, Z., Troch, P. A. and De Troch, F. P., 1997. Remote sensing of soil moisture using EMAC/ESAR data. *International Journal of Remote Sensing* 18, pp. 2105–2124.
- Ulaby, F. T., Aslam, A. and Dobson, M. C., 1982a. Effects of vegetation cover on the radar sensitivity to soil moisture. *IEEE Transactions on Geoscience and Remote Sensing* 20, pp. 476–481.
- Ulaby, F. T., Moore, R. K. and Fung, A. K., 1982b. *Microwave Remote Sensing: Active and Passive*. Vol. II, Artech House, Boston, MA.
- Van Der Velde, R. and Su, Z., 2009. Dynamics in land-surface conditions on the Tibetan Plateau observed by Advanced Synthetic Aperture Radar (ASAR). *Hydrological Sciences Journal* 54, pp. 1079–1093.
- Verhoest, N. E. C., De Baets, B., Mattia, F., Satalino, G., Lucau, C. and Defourny, P., 2007. A possibilistic approach to soil moisture retrieval from ERS synthetic aperture radar backscattering under soil roughness uncertainty. *Water Resources Research*. W07435, doi:10.1029/2006WR005295.
- Verhoest, N. E. C., Hoeben, R., De Troch, F. P. and Troch, P. A., 2000. Soil moisture inversion from ERS and SIR-C imagery at the Zwalm catchment, Belgium. In: *Proceedings of the International Geoscience and Remote Sensing Symposium (IGARSS'00)*, Honolulu, Hawaii, pp. 2041–2043.

SUB-PIXEL PRECISION IMAGE MATCHING FOR DISPLACEMENT MEASUREMENT OF MASS MOVEMENTS USING NORMALISED CROSS-CORRELATION

Misganu Debella-Gilo¹ and Andreas Käab²

^{1,2}Institute of Geosciences, University of Oslo, P. O. Box 1047, Oslo, Norway

¹m.d.gilo@geo.uio.no (corresponding author), ²kaab@geo.uio.no,

KEY WORDS: Normalised cross-correlation, Sub-pixel, Image matching, Displacement measurement, Rockglacier, Glacier, Rock slide

ABSTRACT:

This study evaluates the performance of two fundamentally different approaches to achieve sub-pixel precision of normalised cross-correlation when measuring surface displacements on mass movements from repeat optical images. In the first approach, image intensities are interpolated to a desired sub-pixel resolution using a bi-cubic interpolation scheme prior to the actual displacement matching. In the second approach, the image pairs are correlated at the original image resolution and the peaks of the correlation coefficient surface is then located at the desired sub-pixel resolution using three techniques, namely bi-cubic interpolation, parabola fitting and Gaussian fitting. Both principal approaches are applied to three typical mass movement types: rockglacier creep, glacier flow and rock sliding. Their performance is evaluated in terms of matching accuracy and in reference to the images of the resolution they are expected to substitute. Our results show that intensity interpolation using bi-cubic interpolation (first approach) performs best followed by bi-cubic interpolation of the correlation surface (second approach). Both Gaussian and parabolic peak locating perform weaker. By increasing the spatial resolution of the matched images by intensity interpolation using factors of 2 to 16, 40% to 80% reduction in mean error could be achieved in reference to the same resolution original image.

1. INTRODUCTION

Present climatic change shifts geomorphodynamic equilibriums and intensifies related mass movement processes such as landslides and permafrost creep (Haerberli and Beniston 1998; Rebetz et al. 1997). Extension and intensification of human activities in areas affected by such mass movements increase the probability of connected adverse impacts like natural hazards or building stability problems. The consequently growing needs for monitoring mass movements are complemented by growing remote sensing opportunities for doing so. The increasing number of available stacks of multi-temporal space-borne, air-borne and terrestrial images, and the improvements in remote sensing and image processing in general significantly enhance the potential for applying matching techniques to detect and quantify earth surface mass movements from repeat remotely sensed data. All the above needs and developments call for continued efforts to improve terrain displacement matching methods based on repeat images.

Image matching is a group of techniques of finding corresponding features or image patches in two or more images taken of the same scene from different viewing positions, at different times and/or using different sensors (Zitová and Flusser 2003). Image matching is among others used for a large variety of applications such as image (co-) registration, stereo parallax matching for generation of digital elevation models, particle image velocimetry (PIV), or displacement measurements.

The group of area-based matching techniques is the most widely used method due to its relative simplicity (Zitová and Flusser 2003). A number of similarity criteria can be used for the

matching process. Cross-correlation, in particular its normalised form which accounts for intensity variations in image sequences, is the most widely used due to its reliability and simplicity (Lewis 1995). The normalised cross-correlation (NCC) algorithm has been used to investigate earth surface mass movements such as glacier flow, rockglacier creep and land sliding in many empirical studies (Haug et al. 2010; Käab and Vollmer 2000; Scambos et al. 1992).

Although NCC has been documented to be simple and reliable, a number of drawbacks have been reported as well: Firstly, its precision is, in principle, limited to one pixel, and thus varying with the pixel size of the image data used. Secondly, NCC is sensitive to noise in the images. Such noise may result in wrong correlation maxima leading to mismatches. This problem is often partly addressed through image transformation (e.g. Fourier) in case of images with low signal-to-noise ratio (Lewis 1995). Thirdly, NCC is sensitive to significant scale, rotation or shearing differences between the images to be correlated (Zhao et al. 2006). Due to this limitation, NCC is recommended in cases where the movement is mainly due to translation with limited rotation, scaling or shearing. A way to partly overcome this limitation of NCC is to orthorectify the images used before the matching (Käab and Vollmer 2000). Fourthly, for the measurement to be reliable the displacement has to be greater than the mean error of the image (co-)registration. Improving NCC precision improves displacement accuracy twofold: firstly, it reduces image registration error; secondly, it improves the matching accuracy directly.

To achieve sub-pixel precision in NCC, three approaches can be used. One is to improve the imaging system towards a higher spatial resolution. This approach is complicated by a number of

financial and technological limitations. The second option is to resample the image intensity to a higher spatial resolution through interpolation. The third option is to interpolate the cross-correlation surface after the matching process to a higher spatial resolution in order to locate the correlation peak with sub-pixel precision. Since the intensity interpolation approach and the correlation interpolation approach are both generic, and independent of image resolution, they are subject to this study. A number of investigations have explored these two approaches applied to medicine (Althof et al. 1997), mechanics (Westerweel 1993; Willert and Gharib 1991; Zhou and Goodson 2001), and stereo matching and motion tracking (Karybali et al. 2008; Yamaguchi et al. 2003). However, there is no study available that compares the relative performance of the two approaches when measuring the displacement of earth surface mass movements from repeat images.

Many earth surface mass movements such as landslides, glacier flow, and rockglacier creep are characterized by displacement rates of the order of magnitude of cm a^{-1} or m a^{-1} which is often less than the spatial resolution of the space-borne or air-borne imagery typically available for their measurement. Sub-pixel accuracy of image matching algorithms, here NCC, has therefore a large potential to improve the signal-to-noise ratio of the measurements. Using NCC as an example, this study compares the performance of two fundamentally different approaches to reaching sub-pixel precision in mass movement detection and measurement from repeat remotely sensed images.

In the method section of this contribution we describe the dataset used, ways of reaching sub-pixel precision, quantification of matching accuracy, and our experimental set-up. In further sections the matching results and their accuracy are presented and discussed. Short conclusions terminate our contribution.

2. METHODS

2.1 Image data and pyramid

For this study, three different types of mass movements were selected: land sliding, glacier flow, and rockglacier creep. The selection of these mass movement types was made based on their frequency in high mountain areas. Three temporal pairs of images each covering one of these types of earth surface mass movements were used (Table 1). These images were accurately orthorectified prior to displacement matching. Additionally, one image pair was created from one of the original glacier images after artificially inducing a two-dimensional translation of 15 pixels (9 pixels in the X direction and 12 pixels in the Y direction). Since this pair was made from just one original image and the movement applied was only translation the pair serves as a control data set as it is free of noise from temporal surface changes, changes in imaging condition, registration errors and geometric distortions.

Better understanding the influence of spatial resolution on the accuracy of image matching requires images of the same area taken at the same time, under the same flight and ground conditions, but using sensors with different spatial resolutions. Such conditions are not easily met. Instead, resampling of the original images was used here. In our study, different optical satellites were simulated by down-sampling the original high-resolution aerial ortho-images to five levels lowering the resolution by factors of 2, 4, 8, 16 and 32. One image pyramid

with six levels each was finally obtained for each of the image pairs. The down-sampling was performed using the MATLAB module 'imresize' with the relatively most efficient and reliable algorithm for this purpose, bi-cubic convolution. The algorithm assigns the weighted average of pixel values in the nearest 4 by 4 neighbourhood (Keys 1981). Although this resampling process is slightly different from the pure signal averaging happening in the instantaneous field of view of a sensors detector cell, we decided to choose bi-cubic convolution because most images used for matching will in practice have undergone such interpolation during image correction and pre-processing steps, such as orthorectification (Toutin 2004).

Type	Location	Pixel size	Older	Recent
Rockglacier	Muragl (Swiss)	0.2m	1981	1994
Glacier	Ghiacciaio del Belvedere (Italian)	0.5m	Sep. 2006	Oct. 2006
Rock slide	Aletsch (Swiss)	0.2m	1976	2006
Control (Glacier)	Manually translated motion	0.2m		

Table 1. Brief description of the image data used

2.2 Matching and displacement measurement at different pixel sizes

First, the original high-resolution aerial images were matched using the pixel-precision NCC algorithm to determine the matching positions and compute the horizontal displacement magnitude and direction. These results were considered as reference for the accuracy assessment. Mismatches that were characterized by low peak correlation coefficients, very large displacements in relation to their neighbouring templates, or displacements showing distinct upslope movement were removed manually. Additionally, displacements less than the mean orthorectification error were removed as they are not reliably distinct from the error. The orthorectification error (offset between the images) was computed by matching stable grounds. The computation revealed that a maximum of 1 pixel offset exists in each dimension. The positions of the templates with valid matches in the original resolution were then used in the matching of the coarser resolution images.

Matching and displacement measurement were in a next step performed on all resolution levels of the image pyramid pairs for all those locations saved from the reference matching. The absolute sizes and positions of the reference templates and the search windows were kept constant metrically throughout the image pyramid by adjusting the number of pixels according to the resolution. In other words, the ground area covered by the templates remained the same, the respective image resolution changed. This was done in order to avoid variations in signal content as a result of inclusion or exclusion of ground features. The area covered by the images range from 0.25km^2 to just over 3km^2 . The size of the template was kept at around 26m and 65m for the originally 0.2m and 0.5m resolution images, respectively. The size of the search window was kept at around 102m and 265m for the originally 0.2m and 0.5m resolution images, respectively, so that it certainly included the expected maximum surface displacement.

2.3 The sub-pixel precision approaches

2.3.1 Intensity interpolation

The coarse resolution images within the above-computed resolution pyramids were back-interpolated to different finer resolutions using the MATLAB-based ‘*imresize*’ module. Again the bi-cubic interpolation was used for the same reason. After such back-interpolation, the NCC algorithm was applied using the same templates and search windows as used in the original reference image pairs. The interpolation is done on the fly for each reference template and search window, and not for the entire image before the matching process. This was done due to memory restriction by MATLAB.

2.3.2 Similarity interpolation

Bi-cubic interpolation. To find the sub-pixel position, one can interpolate the cross-correlation surface to higher resolution using two dimensional bi-cubic interpolation algorithms. The algorithm uses a two-dimensional cubic convolution of the correlation coefficients to the resampled grid. The peak is then relocated.

Curve fitting. As an alternative to peak interpolation, one can also create a continuous function that optimally fits the correlation coefficient data and compute the precise location of the peak from the maximum of the function. The challenge is that no single function can usually perfectly describe the cross-correlation surface. However, the fact that the correlation surface around its peak often approaches a bell shape can be exploited. Therefore, two dimensional polynomial functions can approximate the surface. A number of interpolation models have been tested in empirical and theoretical researches, particularly in particle image velocimetry (PIV), though with varying successes (Nobach and Honkanen 2005; Westerweel 1993; Willert and Gharib 1991). Some of the well performing ones will be tested here for mass movement analysis. These are parabola fitting and Gaussian fitting, as these have shown successes especially in PIV.

In parabola fitting, the shape of the correlation surface is assumed to fit two separable orthogonal parabolic curves. The location of the ‘actual’ peak is computed by independently fitting one dimensional quadratic function and computing the location of the peak (Nobach and Honkanen 2005; Westerweel 1993).

In Gaussian fitting, the bell shape of the correlation surface is assumed to fit a 2D Gaussian function (Nobach and Honkanen 2005; Westerweel 1993; Willert and Gharib 1991). It is assumed that the two dimensions are separable and orthogonal. Thus, the sub-pixel peak location is calculated separately for the two directions by fitting a second-order polynomial to the logarithm of the maximum sample and the direct neighbours.

2.4 Evaluation of different levels of sub-pixel detail

Section 2.3 evaluates which sub-pixel approach performs best in improving the precision and accuracy of NCC-based image matching. It is also important to know how far sub-pixel interpolation of coarse resolution image intensities or the correlation surface is able to substitute pixel-level matching of images of the corresponding but original resolution. In other words, what is the sub-pixel detail at which the interpolation to achieve sub-pixel precision can no longer sufficiently substitute

image of that resolution. The approach used here to resolve this issue is to compute the sub-pixel precision matching at different levels of the image pyramid and evaluate its performance in reference to the pixel-level matching of images with the same but original resolution. This issue becomes clearer with an example. Suppose we want to know the performance of sub-pixel precision matching at the level of half a pixel. This can be achieved by taking an image of, for instance, 8m resolution, compute the sub-pixel precision matching to 4m and compare the latter sub-pixel performance to the performance of pixel-level matching of an image with 4m original resolution. Or else, take a 4m resolution image, compute its sub-pixel resolution matching to 2m and compare the performance of the latter in relation to a 2m resolution original image, and so forth including the entire pre-processed image pyramid and all resolution steps included in it.

2.5 Performance evaluation

As indicator of accuracy, we used the shift in matching position instead of the often-used difference in displacement magnitude. The matching positions obtained during the correlation of the original images were considered as references. All the matching positions at the different coarser or back-interpolated resolutions were compared to these reference positions. The magnitude of this offset (deviation) is here used as measure for the accuracy of the image and algorithm used. The deviation between the matching position of the interpolated image and that of the same resolution original image is used to assess the relative performance of the sub-pixel approaches.

3. RESULTS

3.1 Displacements of the different mass movement types

Table 2 summarises displacement statistics for the three mass movements investigated. The results are produced from the analyses of the original ortho-images after filtering all the mismatches. One can well see that the glacier moves very fast as compared to the rockglacier and the even slower moving rockslide. Figure 1 and Figure 2 present the displacement vectors of the three mass movements. Image matching showed that all the areas in the scene show non-zero displacements due to the presence of systematic image (co-)registration error. However, after filtering of the vectors based on the estimated overall image (co-)registration error of one pixel, thresholding of the correlation coefficients and excluding upslope movements, only the remaining vectors presented in the figures are considered to be valid and useful as reference.

3.2 Accuracy of the sub-pixel algorithms

Figure 3 and Figure 4 depict the mean deviation of the matching positions against the sub-pixel precisions of each of the sub-pixel approaches for the control set and the three mass movements respectively. The magnitudes of Figure 4 are created by averaging the values obtained for the three mass movement types as the trend is very similar for all the three. Both figures show that interpolation of the image intensity before matching results in the best matching accuracy. If one looks at the interpolation of the correlation surface, the bi-cubic approach follows the intensity interpolation. The curve fitting using parabola and Gaussian models perform only better than bi-cubic interpolations to one half of the original pixel size.

For the real mass movements, there is very little accuracy gain by interpolating to lower than 0.1 pixels. As the result of the control shows, when the movement is only translation, the magnitude of the deviation is very low. Besides, it seems that, for the control set, interpolation to more detail level improves the accuracy further.

Mass movement	Mean displacement (m)	Maximum displacement (m)	Standard deviation of displacement (m)	Maximum velocity (ma ⁻¹)
Aletsch Rock slide	1.5	4.2	0.45	0.14
Muragl Rockglacier	2.4	5.8	1.20	0.45
Ghiacciaio del Belvedere Glacier	12.22	18.83	5.0	226
Control	7.50	7.50	0	7.50

Table 2. Summary statistics for the displacement magnitudes and average velocity of the mass movements and the translation-only control image as estimated from the matching of the high-resolution original ortho-images

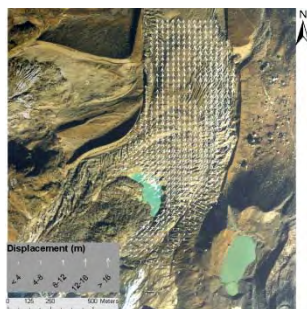


Figure 1. Displacement vectors on the Ghiacciaio del Belvedere (Sept – Oct 2001)

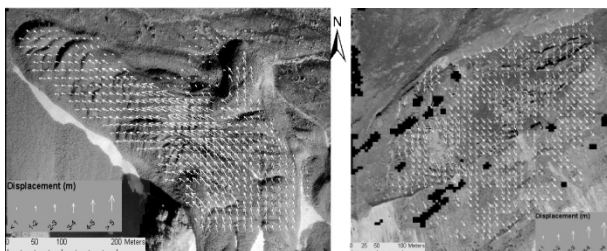


Figure 2. Displacement vectors on the Muragl rockglacier (1981-1994) and Aletsch rockslides (1976 – 2006) from left to right respectively.

3.3 Relative performance of the sub-pixel precisions

Figure 5 shows the mean deviation between the matching position of the interpolated image pairs and that of the same resolution (but original) reference image pairs plotted against sub-pixel precision for the control set. When the difference between the images is only the here-applied translation, sub-pixel interpolation of the image intensities up to 1/8th of the original pixel size prior to matching can perfectly substitute images of comparable original resolution. This perfect substitution can be achieved by using bi-cubic interpolation of the correlation surface only up to 1/4th of the original pixel size.

For example, a 16m resolution image interpolated to 2m using bi-cubic interpolation before matching performs exactly as a 2m resolution image pair as long as there is no other source of difference between the image pairs than rigid translation. But when the level of detail goes beyond 1/8th, there appears deviation between the two. The magnitude of these numbers depends, of course, on the translation magnitude applied in the control set. However, the test shows the better performance of bi-cubic intensity interpolation over the other sub-pixel algorithms tested.

For all the real mass movement types (Figure 6), as the difference in pixel size between the coarse resolution and the reference resolution increases, the deviation of the sub-pixel matching position from the matching position of the same (but original) image resolution increases regardless of the algorithm. This means, not surprisingly, that the sub-pixel algorithm resembles images of comparable resolution less and less as the sub-pixel detail increases. At every resolution, the mean deviation is the lowest when intensity interpolation is used before matching followed by the bi-cubic interpolation of the correlation surface. The parabola- and Gaussian-based peak localisations perform poorer and alike. This confirms the above results.

Remarkably, at a certain level of sub-pixel detail (about 1/16th), the deviation between the sub-pixel algorithm and same resolution original image gets so high that interpolating beyond that level has no meaningful advantage although the control set gives less deviation even at greater level of detail.

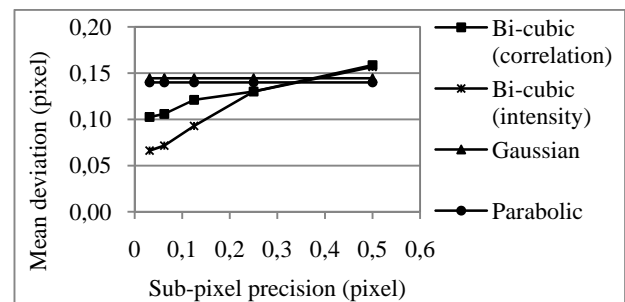


Figure 3 Accuracy of the different sub-pixel precision approaches for the control set expressed as the mean deviation of the matching positions from that of the reference high-resolution original ortho-images

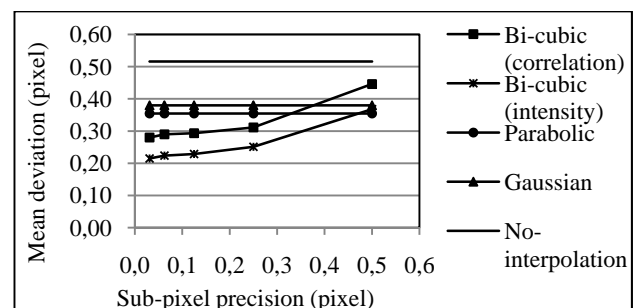


Figure 4 Accuracy of the different sub-pixel precision approaches expressed as the mean deviation of the matching positions from that of the reference high-resolution original ortho-images (averaged for the three mass movement types)

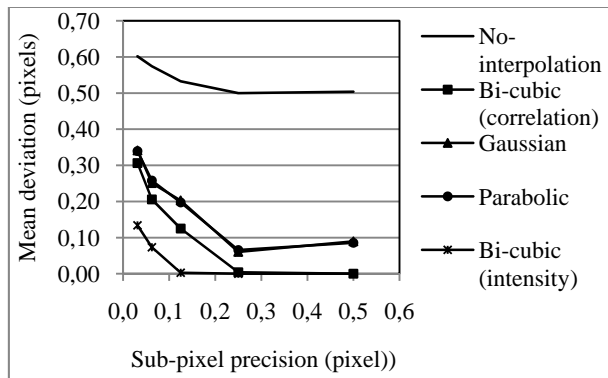


Figure 5 Relative performance of the different sub-pixel approaches for the control set expressed as the mean deviation of the matching positions from that of the same resolution original image

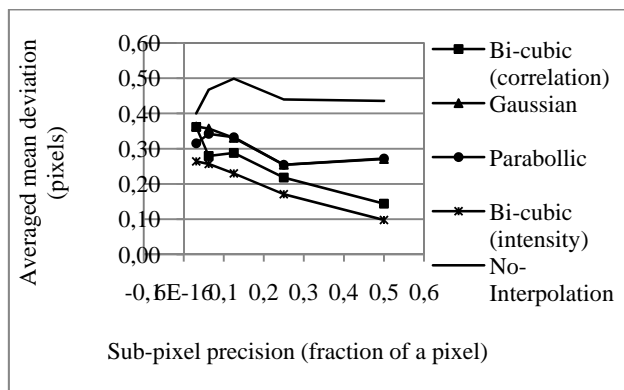


Figure 6 Relative performance of the different sub-pixel approaches expressed as the mean deviation of the matching positions from that of the same resolution original image (averaged from the three mass movement types investigated)

4. DISCUSSION

The results show that intensity interpolation outperforms all the other algorithms of similarity interpolation. There can be two explanations to this. Firstly, in correlation interpolation the positions of the correlation values on which the interpolation is based, and which are computed based on coarse resolution images, influence the position of the recomputed correlation peak. Secondly, the number of pixels in an entity is higher when intensity interpolation is applied leading to the suppression of noise. Fewer numbers of pixels in an entity makes the entity more susceptible to chance-based, i.e. erroneous matching results. This explains the increased difference between intensity interpolation and similarity interpolation at very detailed levels of sub-pixel precision.

The bi-cubic interpolation scheme that was used for the intensity interpolation is known to replicate the reference data better than most interpolation schemes (Keys 1981), and it is known to approximate the sinc interpolation that is ideal in image interpolation (Dodgson 1992). This has led to the fact that the images re-interpolated from coarser resolutions were found to have high correlation with the aerial images of corresponding original resolution. For example, when the down-sampled rockglacier image of resolutions 0.4m, 0.8m, 1.6m, 3.2m and 6.4m were re-interpolated to a resolution of 0.2m (1/2

to 1/32 of a pixel respectively) their global correlation coefficients with the reference image of 0.2m resolution were 0.98, 0.96, 0.93, 0.90 and 0.86 respectively. Although the images deteriorate due to resampling noise, they still remain well-correlated with the reference image due to the good performance of the interpolation algorithm. Correlation is, in fact, one of the quality measures of image interpolation (Lehmann et al. 1999).

The same interpolation algorithm, bi-cubic, performed best in the similarity interpolation approach although not as good as in the intensity interpolation. The better performance in comparison to the Gaussian and parabola fitting is partially ascribed to the reasons explained above. In addition to that, parabola fitting is reported in many occasions to have a systematic bias known as “pixel locking”, which forces the estimated sub-pixel locations to approach integer values (Nobach and Honkanen 2005; Prasad et al. 1992). The presence of a systematic bias is testified by the fact that both parabola and Gaussian fitting could not fully substitute the same resolution original images in the case of the control set unlike the other two algorithms (Figure 5). Although reports from PIV state that Gaussian peak finding does not have that kind of bias and performs better (Westerweel 1993; Willert and Gharib 1991), it performed no better than parabola fitting in the present study. We believe the underlying reason is the fact that the cross-correlation surfaces of the mass movements cannot be perfectly modelled by either parabolic or Gaussian functions. The image resolutions used in the present study are not so high to be compared to that of particle images used in mechanics which is high enough to be approximated by, for example, Gaussian. Besides, noise that is present in the images due to temporal surface changes and other sources contribute to the deviation of the correlation shape from both Gaussian and parabolic.

Finally, two important points regarding the size of the matching entities: Firstly, in this study the absolute metric size of the matching entities was kept constant across image resolutions. This means that the number of pixels in each entity varies with the pixel resolution, leading to a variable signal-to-noise ratio. This was done for the sake of comparison. In reality, the size of matching entities will vary with the resolution of the image pair to keep a good signal-to-noise ratio. Secondly, the size of the matching entities was kept the same for the entire scene. In reality matching entities vary in size.

5. CONCLUSIONS

This study has clarified a number of questions around the relation between accuracy and pixel or sub-pixel resolution when matching terrain displacements such as glacier flow, land sliding or permafrost creep from repeat optical images by using pixel-precision correlation measures, here namely the normalized cross correlation (NCC). That way the study contributes, on the one hand, to better exploiting the unexploited archives of repeat remotely sensed images that exist over actual or potential earth surface mass movements, and on the other hand, to better meeting the increasing needs to quantify and monitor mass movements, in particular when they are accompanied by adverse effects.

This study has in particular evaluated the performance of two different approaches to sub-pixel precision in NCC for displacement measurement based on repeat images. When sub-pixel accuracy is aimed for, interpolating image intensities to a

higher resolution using bi-cubic interpolation prior to the actual image correlation performs better than both interpolation of the correlation surface using the same algorithm and peak localisation using curve fitting. Correlation peak localisation using Gaussian and polynomial algorithms are inferior in such applications.

Therefore, we conclude that more precise and accurate displacement measurements are obtained by interpolating the available images to a higher resolution using bi-cubic interpolation prior to matching. In such approaches, one can gain over 40% reduction in mean error by interpolating the images to up to $1/16^{\text{th}}$ of a pixel. Interpolating to a more detailed sub-pixel resolution than $1/16^{\text{th}}$ of a pixel does not add much. Or in other words, when matching low-resolution images using normalized cross-correlation with intensity-interpolation based sub-pixel precision, 40% or better accuracy increment can be achieved compared to pixel-precision matching of images in reference to the same original resolution as the interpolated one. When real low-resolution images are used together with varying sizes of the matching entities, as opposed to the approach used in this study, even better precision and accuracy might be obtained as the noise due to resampling will not be present, and template and search window sizes will be adjusted with the pixel size.

It should also be noted that although the relative performances of the algorithms is expected to be valid at least for other spatial domain matching approaches and for other applications, the magnitudes given here are strictly only valid for the similarity measure and test sites used in this paper. Further research is needed for their validity outside the conditions described in this study.

REFERENCES

- Althof, R.J., Wind, M.G.J., & Dobbins, J.T., III (1997). A rapid and automatic image registration algorithm with subpixel accuracy. *IEEE Transactions on Medical Imaging*, 16, 308-316
- Dodgson, N.A. (1992). *Image resampling*. London: University of Cambridge Computer Laboratory
- Haerberli, W., & Beniston, M. (1998). Climate change and its impacts on glaciers and permafrost in the Alps. *Ambio*, 27, 7
- Haug, T., Kääb, A., & Skvarca, P. (2010). Monitoring ice shelf velocities from repeat MODIS and Landsat data – a method study on the Larsen C ice shelf, antarctic Peninsula, and 10 other ice shelves around Antarctica. *The Cryosphere Discussions (in review)*, 4, 35-75
- Karybali, I.G., Psarakis, E.Z., Berberidis, K., & Evangelidis, G.D. (2008). An efficient spatial domain technique for subpixel image registration. *Signal Processing: Image Communication*, 23, 711-724
- Keys, R.G. (1981). Cubic convolution interpolation for digital Image processing. *IEEE transactions on acoustics, speech and signal processing*, 29, 1153-1160
- Kääb, A., & Vollmer, M. (2000). Surface geometry, thickness changes and flow fields on creeping mountain permafrost: automatic extraction by digital image analysis. *Permafrost and Periglacial Processes*, 11, 315-326

Lehmann, T.M., Gonner, C., & Spitzer, K. (1999). Survey: interpolation methods in medical image processing. *IEEE Transactions on Medical Imaging*, 18, 1049-1075

Lewis, J.P. (1995). Fast Normalized Cross-Correlation. *Vision Interface*, 120-123

Nobach, H., & Honkanen, M. (2005). Two-dimensional Gaussian regression for sub-pixel displacement estimation in particle image velocimetry or particle position estimation in particle tracking velocimetry. *Experiments in Fluids*, 38, 511-515

Prasad, A., Adrian, R., Landreth, C., & Offutt, P. (1992). Effect of resolution on the speed and accuracy of particle image velocimetry interrogation. *Experiments in Fluids*, 13, 105-116

Rebetez, M., Lugon, R., & Baeriswyl, P.-A. (1997). Climatic change and debris flows in high mountain regions: the case study of the Ritigraben Torrent (Swiss Alps). *Climatic Change*, 36, 371-389

Scambos, T.A., Dutkiewicz, M.J., Wilson, J.C., & Bindschadler, R.A. (1992). Application of image cross-correlation to the measurement of glacier velocity using satellite image data. *Remote Sensing of Environment*, 42, 177-186

Toutin, T. (2004). Review article: Geometric processing of remote sensing images: models, algorithms and methods. *International Journal of Remote Sensing*, 25, 1893 - 1924

Westerweel, J. (1993). *Digital particle image velocimetry: theory and application*. Delft: Delft University Press

Willert, C.E., & Gharib, M. (1991). Digital particle image velocimetry. *Experiments in Fluids*, 10, 181-193

Yamaguchi, Y., Tanaka, S., Odajima, T., Kamai, T., & Tsuchida, S. (2003). Detection of a landslide movement as geometric misregistration in image matching of SPOT HRV data of two different dates. *International Journal of Remote Sensing*, 24, 3523 - 3534

Zhao, F., Huang, Q.M., & Gao, W. (2006). Image matching by normalized cross-correlation. In, *31st IEEE International Conference on Acoustics, Speech and Signal Processing* (pp. 1977-1980). Toulouse, FRANCE

Zhou, P., & Goodson, K.E. (2001). Subpixel displacement and deformation gradient measurement using digital image/speckle correlation (DISC). *Optical Engineering*, 40, 1613-1620

Zitová, B., & Flusser, J. (2003). Image registration methods: a survey. *Image and Vision Computing*, 21, 977-1000

ACKNOWLEDGEMENTS

The research was conducted at the Geosciences department of the University of Oslo and financially supported by the Norwegian Research Council (CORRIA project). The authors are very grateful to both institutions.

WIRELESS SENSOR NETWORKS FOR IN-SITU IMAGE VALIDATION FOR WATER AND NUTRIENT MANAGEMENT

R. Devadas^{a,*}, S.D. Jones^a, G. J. Fitzgerald^b, I. McCauley^c, B.A. Matthews^d, E.M. Perry^b, M. Watt^c, J.G. Ferwerda^e, A.Z. Kouzani^f

^a School of Mathematical and Geospatial Sciences, Royal Melbourne Institute of Technology University, Melbourne, VIC 3001-(rakesh.devadas, simon.jones)^a@rmit.edu.au

^b Grains Innovation Park, DPI Victoria, Horsham, VIC 3401, Australia-(Glenn.Fitzgerald, eileen.perry)^b@dpi.vic.gov.au

^c Future Farming Systems Research, DPI Victoria, Attwood 3049, Australia. (Ian.McCauley, Michelle.Watt)^c@dpi.vic.gov.au

^d Knowledge Information and Technology Branch, DPI Victoria, Queenscliff, Victoria 3225, Australia-Brett.Matthews^d@dpi.vic.gov.au

^e Faculty of Engineering Technology, the University of Twente, Netherlands- J.G.Ferwerda^e@ctw.utwente.nl

^f School of Engineering, Deakin University, Geelong, Victoria 3217, Australia- abbas.kouzani^f@deakin.edu.au

Commission VII

KEY WORDS: Remote sensing, wireless sensor network, precision agriculture, nitrogen, hyperspectral, validation

ABSTRACT:

Water and Nitrogen (N) are critical inputs for crop production. Remote sensing data collected from multiple scales, including ground-based, aerial, and satellite, can be used for the formulation of an efficient and cost effective algorithm for the detection of N and water stress. Formulation and validation of such techniques require continuous acquisition of ground based spectral data over the canopy enabling field measurements to coincide exactly with aerial and satellite observations. In this context, a wireless sensor *in situ* network was developed and this paper describes the results of the first phase of the experiment along with the details of sensor development and instrumentation set up. The sensor network was established based on different spatial sampling strategies and each sensor collected spectral data in seven narrow wavebands (470, 550, 670, 700, 720, 750, 790 nm) critical for monitoring crop growth. Spectral measurements recorded at required intervals (up to 30 seconds) were relayed through a multi-hop wireless network to a base computer at the field site. These data were then accessed by the remote sensing centre computing system through broad band internet. Comparison of the data from the WSN and an industry standard ground based hyperspectral radiometer indicated that there were no significant differences in the spectral measurements for all the wavebands except for 790nm. Combining sensor and wireless technologies provides a robust means of aerial and satellite data calibration and an enhanced understanding of issues of variations in the scale for the effective water and nutrient management in wheat.

1. INTRODUCTION

Water and Nitrogen (N) are critical inputs for wheat production. Judicial application of these inputs is essential for environmentally sustainable and profitable agricultural production. Standard practice is to apply N fertilizers at a uniform rate based on the field level average available soil N or target grain yield (Zillmann et al. 2006). Optimizing the N availability is crucial as N is a vital component for vegetative growth, chlorophyll formation (Gooding and Davies 1997) and grain development in wheat (Wright Jr. 2003). On the other hand, excessive availability of N can heighten the risks of frost damage, foliar disease (Olesen et al. 2003) and can also delay crop maturation (Gooding and Davies 1997). If excessive rates of N are applied, which are not balanced by stored soil water and/or in-crop rainfall, then this can result in moisture stress which in turn results in premature ripening of the crop; referred to as 'haying-off' (Herwaarden et al. 1998). Surplus N application also leads to potential off-farm movement of nitrogen into surface and ground water and can have strong effects on the structure and function of both terrestrial and marine ecosystems like eutrophication (Smith et al. 1999). Application of the optimal rates of N based on spatial variability of soil conditions at high spatial resolutions could lead to cost effective and environmentally sustainable crop production (LaRuffa et al. 2001). Remote sensing techniques are powerful

tools for monitoring spatial variations in crop growth characteristics non-destructively. These techniques are based on the spectral reflectance characteristics of the plant canopy which in turn is dependent on the spatial distribution/orientation of plant leaves and supporting structures, the nature of pigments contained within the individual leaves and internal leaf structure (eg mesophyll arrangements) (Chappelle et al. 1992; Myers 1983).

Nutrient status detection using remote sensing is a relatively new concept, made possible by the development of high spatial and spectral resolution sensors. Over the past few years a number of studies have shown the potential to use remote sensing for the detection of nitrogen status of grains (Haboudane et al. 2002a; Lilienthal et al. 2000; Strachan et al. 2002). These studies have however been unable to resolve the problem of the interacting causes of plant-growth limitation, such as water-shortage and nutrient limitation. A few studies have shown that combining optical narrow band imaging with thermal imaging may provide a solution to this problem (Fitzgerald et al. 2006b; Tilling et al. 2007). These studies demonstrated the utility of hyperspectral and narrow-band multispectral remote sensing techniques, utilizing the canopy reflectance characteristics in wavebands 445, 670, 705, 720, 750 and 790 nm, for the detection of spatial variation in the N status of the crop. Indices such as the Canopy Chlorophyll Content Index (CCCI) (Barnes et al. 2000; Rodriguez et al.

* Corresponding author.

2006) were proposed as an effective tool for the detection of canopy level N status because it also accounts for changes in canopy N concentration during the season.

There are various methods of acquiring remote sensing data, all of which can be useful to farmers, depending on how the methods fit into their management operations. For example, it is possible to use satellite imagery or mount equipment on a light aircraft, to acquire imagery on-demand, but other means of data acquisition include tractor-mounted sensors for on-the-go sensing that can be used to control variable-rate equipment for precision nutrient inputs. All these approaches require the development of robust algorithms that are applicable across different scales/platforms so as to detect canopy nutrients independent of ground cover, water stress and other factors, such as solar zenith angle. Simultaneous and real-time ground based observations are highly beneficial for formulation and validation of such algorithms incorporating airborne or satellite remote sensing data for application from paddock to regional scale.

Acquiring real-time ground based remote sensing data over a continuous period will enable ground observations to coincide exactly with other scales (airborne and satellite) of data acquisition. Deployment and maintenance of multiple ground based sensors at isolated field sites is a labour-intensive exercise. Development of a wireless sensor network (WSN) is considered as a reliable, efficient and cost effective solution to this problem.

A WSN consists of sensor nodes distributed across a geographic area and each sensor node has wireless communication capability and some level of intelligence for signal-processing and networking of data (Li 2008). A WSN system is comprised of radio frequency (RF) transceivers, sensors, microcontrollers and power sources (Wang et al. 2006). WSN has diverse applications and allows Micro-Electro-Mechanical-System (MEMS) sensors to be integrated with signal-conditioning and radio units to form “motes”. A mote is a node in a WSN and normally consists of a processor, radio module and one or more sensors connected to it. This enables motes to acquire data from the sensors, process and communicate with other motes in the network. Motes promote large scale deployment owing their low cost, small size and low power requirement (Akyildiz et al. 2002; Crossbow Technology Inc. 2007; López Riquelme et al. 2009; Wang et al. 2006)

Wireless communication provides enormous flexibility in locating sensor installations, allowing deployment where wired connections are impractical or impossible. The ease with which widely spread sensors can be arranged results in significant reduction in the cost of data acquisition by avoiding installation and maintenance of costly transmission lines. This has led to a myriad of uses of this technology in diverse fields. WSNs have the potential for widespread application in precision agriculture, particularly in the areas of crop and irrigation management, variable rate chemical input application and modeling crop performance (López Riquelme et al. 2009).

A mobile field data acquisition system was developed (Gomide et al. (2001) in Wang et al. 2006) to collect data for crop management and spatial-variability studies. A ZigBee™ / Institute of Electrical and Electronics Engineers, IEEE 802.15.4 (Baronti et al. 2007; IEEE 2003) wireless acquisition device network was established (Morais et al. 2008) for monitoring air and soil temperature, solar radiation and relative humidity for precision viticulture applications. Radio modules IEEE 802.15.4 (IEEE 2006) were used in motes in the formation of wireless network for monitoring soil moisture, water quality and environmental conditions. Vellidis et al. (2008) developed and

evaluated a real time, smart sensor array using Radio Frequency IDentification (RFID) tag for irrigation scheduling.

Studies involving integration of hyperspectral or narrow band multispectral sensors into WSNs for real time monitoring of crop spectral characteristics are very limited. These data sets have been shown to be highly successful in monitoring chlorophyll content (Gitelson and Merzlyak 1994; Haboudane et al. 2002b; Penuelas et al. 1994), light use efficiency (Trotter et al. 2002), N status (Filella 1995; Fitzgerald et al. 2006a; Tarpley et al. 2000; Tilling et al. 2007) and disease conditions (Bravo et al. 2003; Devadas et al. 2009; Moshou et al. 2005). In this context, an experiment was carried out to establish a WSN, integrating seven narrow band sensors (470, 550, 670, 700, 720, 750, 790 nm), critical for real time monitoring of N and water stress in crops (Fitzgerald et al. 2006a; Tilling et al. 2007). By establishing this WSN, the project aims to record *in-situ* ground based remote sensing data concurrently with aerial and satellite image acquisition. Airborne imagery at various spatial scales will form the bridge between ground and satellite remote sensing data. Through these simultaneously acquired remote sensing data from different spatial scales within a sampling framework, this project will attempt to quantify issues of scaling up-linked to the mapping of N and water stress in wheat. This paper illustrates the outcome of the first phase of the experiment involving instrumentation set up and analysis of spectral data recorded by the WSNs.

2. MAIN BODY

INSTRUMENTATION

Instrumentation set up involved three main steps: 1) sensor development, 2) sensor integration with motes and, 3) establishment of the wireless network.

2.1 Development of Sensor System

The primary component of the sensor system was a combined silicon photo detector and optical interference filter (T-5) (Intor, Inc., NM, USA). The filters were 8.4mm in diameter by 7.07mm high. The seven specific filters had central wavelengths of 470, 550, 670, 700, 720, 750 and 790 nm with 10 nm bandwidths.

These optical filters were assembled into a custom designed light sensor multiplexer and amplifier board (Figure 1).

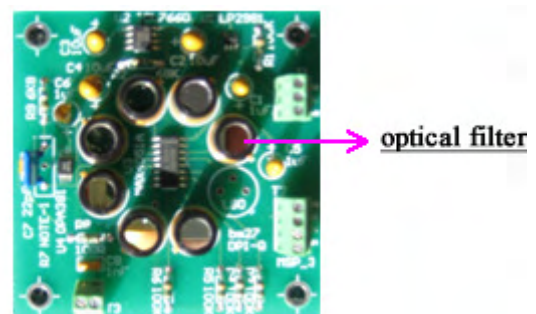


Figure 1. Fully assembled sensor board. One of the seven optical filters is indicated in the figure.

2.2 Housing of Sensor Boards and Calibration Set up

To derive reflectance measurements directly, two sensor boards were designed for each node. One was directed upward, to

measure incoming radiation and the other one looked downward, to measure reflected radiation. This design enabled direct estimation of reflectance values for the specified bands as ratio of reflected to incoming radiation.

Both sensor boards were bolted to poly vinyl chloride (PVC) endcaps. For the downward looking sensors, a PVC pipe of 0.23m long with 0.10m diameter was attached to the endcaps, creating a 26° field of view (Figure 2). For the upward looking sensor boards, a PVC pipe of 0.04m was fitted to generate a field of view of 100°. The open or sensing ends of both the pipes were closed and sealed with 4mm thick flat Delrin (Polyoxymethylene), a polyplastic engineered to facilitate the diffusion of electromagnetic radiation and minimization of angular reflection effects.

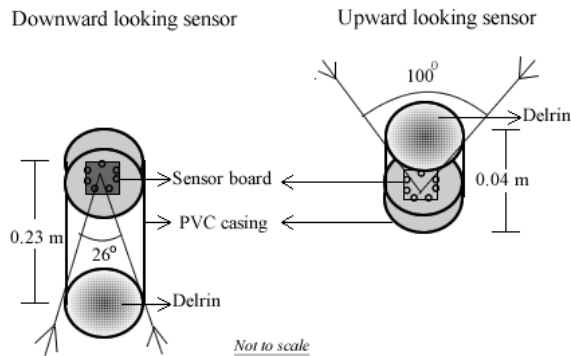


Figure 2. Structure of sensor board mounting with PVC tubes for downward and upward looking sensors.

Each sensor pair was calibrated using 99% reflectance Spectralon (Labsphere, NH, USA) reference panels measured with an Analytical Spectral Devices (ASD) FieldSpec® spectroradiometer (ASD, Inc., CO, USA).

2.3 Sensor Integration with Mote

Data collection, conversion and transmission were achieved using MICA2 wireless motes (Crossbow Technology), operating at an RF frequency of 433 MHz, interfaced to an MDA 300 analogue to digital converter board (Crossbow Technology). The motes were programmed with a version of Xmesh (Crossbow Technology Inc. 2007; Tiny 2009) software (Crossbow Technology) specific for the MDA300 A/D board. The standard Xmesh software was modified and customized (Dragonnorth Pty Ltd, Needham, MA, USA) to provide control of the sensor board used to coordinate the acquisition of readings from the seven sensors on two heads through two data acquisition channels. A 6V sealed lead acid battery provided power for both the sensor boards and the mote.

The network was routed through a gateway consisting of a MICA2 mote connected to a MIB510 serial interface board in turn connected to a laptop computer running the Xserve data acquisition software (Crossbow Technology). The stored data was accessed and the network was managed using the MoteView (Crossbow Technology) as the client.

Broadband connection of the local server to the Internet was provided using a CDM882-SEU wireless router (Call Direct, Sydney, AU) using the Next G network (Telstra, Melbourne, AU).

2.4 Establishment of Wireless Network

Establishment of the wireless network and real-time data acquisition involved 3 software tiers: 1) *Mote layer*- sensor

nodes were connected to form a multi-hopping mesh network and a gateway node forwards data messages into and out of the mesh, 2. *Server layer*- facilitated translation and buffering of data from the wireless mesh network and forms the bridge between the wireless motes and the internet clients, and 3. *Client layer*- provided the user visualization software and graphical interface at PC terminal for managing the network.

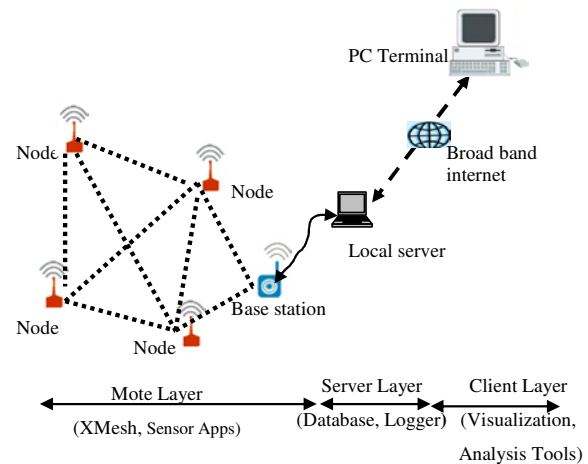


Figure 3. Software and hardware framework for establishment of wireless network.

2.5 Field Installation

For field (ground) installation, sensors were attached to square (width: 3.5mm) base steel poles, such that the sensors were positioned circa 2m above the soil surface (Figure 4). This configuration created a 0.9m diameter footprint, for the downward looking sensor with the 26° field of view (FOV), allowing 4-5 rows of crop to be sensed.

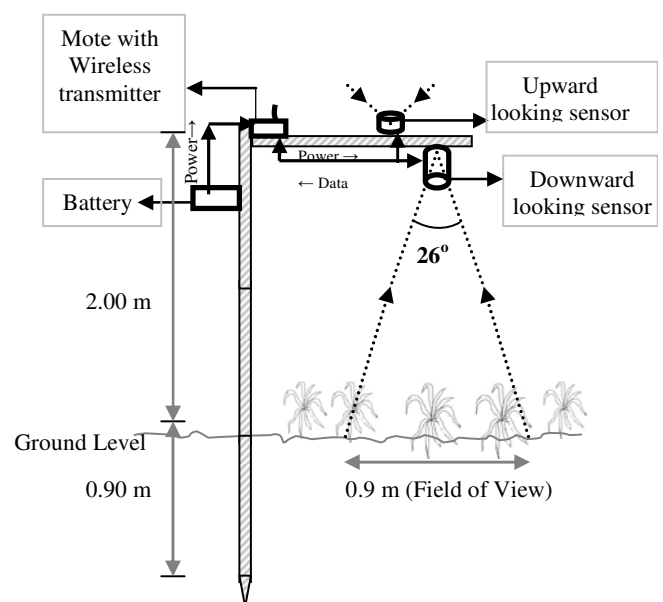


Figure 4. Design of wireless sensor field unit. A voltage regulator in the battery case provides 3V input power to a mote box and 6V power to two sensor boards through a terminal board in the mote box.

The metal frames for attaching the sensors were comprised of three parts, one was inserted into the soil and the other two parts were erected above ground, one fitting inside the other to reach the 2m height. This enabled the above ground sections with sensors to be detached from the lower frame for relocation to other sample locations leaving the base poles in the ground throughout the crop season, out of the way of agricultural field equipment, such as tractors. This design provided the capability to deploy a large number of base poles inserted in the sample locations defined based on four different sampling strategies (Figure 5). This provided the flexibility to change sensor unit locations to accommodate the various sampling strategies without the need to install mounting points when sensors were moved.

The cost of each sensor unit was estimated to be A\$1687 (in 2009 dollars).

Ninety sample positions were identified that encompassed the four sampling strategies in a wheat paddock in Inverleigh, Victoria, Australia (144° 2' 30" E and 38° 8' 10" S, Figure 5). Rapid static and Real Time Kinematic Global Positioning System (RTK GPS) surveys were undertaken to establish the position of the sample points to a x-y accuracy of +/-2cm. Positions were in GDA94/MGA94. The four sampling strategies were devised to facilitate the deployment and operation of 20-25 sensor units at a time. Base poles were inserted in these ninety locations.

In the first phase of the experiment in 2009, 14 sensor units were operational and data were recorded from *systematic pattern* locations, during the winter crop season from July to December.

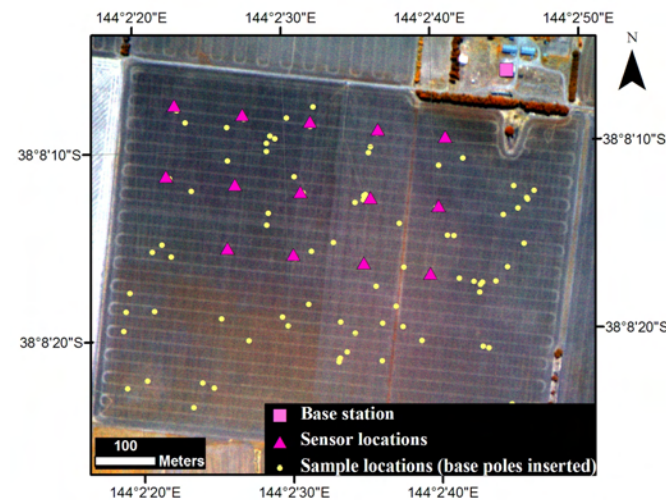


Figure 5. Aerial image of the study site showing the sensor locations.

Yellow dots indicate the 90 sample locations with base poles inserted. These locations were determined based on 4 sampling strategies. The triangles indicate the locations of the 14 functioning sensor units in 2009, which followed a systematic sampling pattern. Square symbols indicate the locations of the base station to which all the motes sent data messages. The aerial image shown here consists of three narrow bands, 790, 720 and 670 nm which are projected as red, green and blue, respectively.

DATA COLLECTION AND ANALYSIS

Wireless remote sensing data collection was observed and monitored through *MoteView* Graphical User Interface (GUI). Sensor nodes were tested for running in two different power modes for understanding the data relay efficiency and battery consumption in these configurations.

In this first phase of the experiment, 14 wireless sensors were introduced during different periods of the crop season, once they were assembled and tested. During this stage, priority was given to calibration of the sensors and analysis of the data quality in comparison with other hyperspectral sensors.

Ground-based hyperspectral data was collected using ASD FieldSpec® spectroradiometer (ASD, Inc., CO, USA) from the same locations as those of the wireless sensor units. The ASD data was integrated based on the bandwidth and central wavelength corresponding to that of WSN and two data sets were compared (Figure 6).

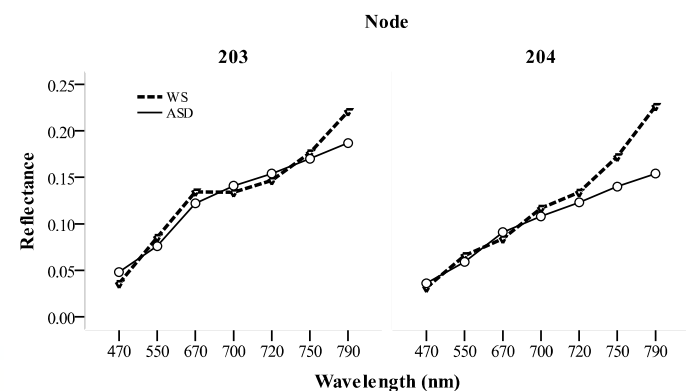


Figure 6. Comparison of the WSN and ASD data at 4 different locations. Sensor locations are represented here as node numbers, which were assigned during the mote board programming.

Comparison of data from WSN and ASD clearly indicated that both sensors followed similar trends in monitoring crop characteristics (Figure 7).

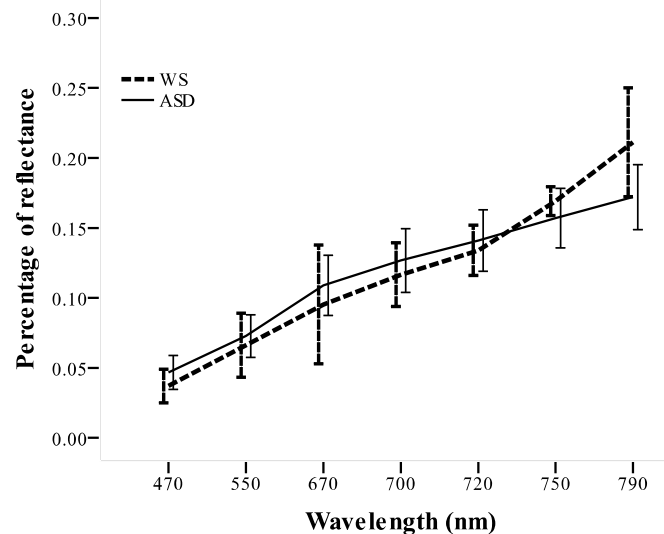


Figure 7. Comparison of mean percentage of reflectance for different wavelengths for the hyperspectral data recorded using WSN and ASD.

Error bars indicate 95% confidence interval.

Further, Analysis of Variance (ANOVA) between spectral data from WSN and ASD for all the seven wavelengths were carried out. Analysis showed that there were no significant differences in the spectral measurements for all the wavebands except for 790nm. At the 790nm wavelength, the WSN data were significantly higher ($p < 0.05$) compared to the ASD data. Estimated standard error value for the wavelength 790nm was 0.101 where for the rest of the wavebands it varied from 0.0033 to 0.0075 (Table 13).

Wavelength (nm)	Standard Error
470	.0033
550	.0046
670	.0075
700	.0047
720	.0045
750	.0044
790	.0101

Table 1. Standard error in percentage of reflectance between WSN and ASD for different wavelengths.

Analysis of the data obtained from the WSN clearly indicated the possibility of employing such sensor network for observing crop spectral characteristics, concurrent with airborne and satellite data acquisitions.

3. CONCLUSIONS

This paper has presented the first of phase of the experiment aimed at the development of a WSN for real time acquisition of spectral data for *in-situ* calibration and validation of aerial and satellite images. Comparisons were made with standard *in situ* field-based verification technology (ASD FieldSpec® spectroradiometer) and WSN. Data analysis showed that the WSN can record spectral data with reliable quality continuously for a reasonably long period of time. WSN is unique with its ability to control the acquisition of a real-time spatially distributed field data set from an office computing system. The capability of the WSN to operate with minimum disturbance to its surroundings (i.e. with high finesse, minimizing perturbation of the variable of interest) brings enormous flexibility of deployment. The technology is cost effective as it reduces the need for logistically expensive field visits.

In the next phase of the project, spectral data from different platforms/scales and crop biophysical data could be utilized for the formulation of robust algorithms for effective and real-time monitoring of N and water stress in crops. The study will also attempt to compare different sampling strategies for optimization of mapping of crop spectral characteristics at paddock level. This experiment is a part of larger Australian calibration and validation processes of satellite data products, under the Terrestrial Environmental Research Network AusCover (Jones et al. 2010).

Acknowledgment

This project was supported by Australian Research Council linkage grant (LP0776656) and was implemented in collaboration with the Department of Primary Industries (DPI), Vitoria, Australia.

Authors express their profound gratitude to Mr. Robin Bendle and Mr. Josh Walter of Murnong Farming at Inverleigh, VIC, 3321 and Andrew Whitlock (www.precisionagriculture.com.au) for providing the logistics for the deployment of WSN.

References

- Akyildiz, I. F., W. Su, Y. Sankarasubramaniam, and E. Cayirci 2002. Wireless sensor networks: a survey. *Computer Networks*, 38(4), pp. 393-422.
- Barnes, E. M., T. R. Clarke, and S. E. Richards 2000. Coincident detection of crop water stress, nitrogen status and canopy density using ground based multispectral data. In *The 5th International Conference on Precision Agriculture*. Bloomington, MN, USA.
- Baronti, P., P. Pillai, V. W. C. Chook, S. Chessa, A. Gotta, and Y. F. Hu 2007. Wireless sensor networks: A survey on the state of the art and the 802.15.4 and ZigBee standards. *Computer Communications*, 30(7), pp. 1655-1695.
- Bravo, C., D. Moshou, J. West, A. McCartney, and H. Ramon 2003. Early Disease Detection in Wheat Fields using Spectral Reflectance. *Biosystems Engineering*, 84(2), pp. 137-145.
- Chappelle, E. W., M. S. Kim, and J. E. McMurtrey 1992. Ratio analysis of reflectance spectra (RARS) - An algorithm for the remote estimation of the concentrations of chlorophyll-a, chlorophyll-b, and carotenoids in soybean leaves. *Remote Sensing of Environment*, 39(3), pp. 239-247.
- Crossbow Technology Inc. 2007. MoteView Users Manual
- Devadas, R., D. W. Lamb, S. Simpfendorfer, and D. Backhouse 2009. Evaluating ten spectral vegetation indices for identifying rust infection in individual wheat leaves *Precision Agriculture*, 10, pp. 459-470.
- Filella, I., Serrano, L., Serra, J., and Penuelas, J. 1995. Evaluating wheat nitrogen status with canopy reflectance indices and discriminant analysis. *Crop Science*, 35, pp. 1400-1405.
- Fitzgerald, G. J., D. Rodriguez, L. K. Christensen, R. Belford, V. O. Sadras, and T. R. Clarke 2006a. Spectral and thermal sensing for nitrogen and water status in rainfed and irrigated wheat environments *Precision Agriculture*, 7(4), pp. 233-248.
- Fitzgerald, G. J., D. Rodriguez, L. K. Christensen, R. Belford, V. O. Sadras, and T. R. Clarke 2006b. Spectral and thermal sensing for nitrogen and water status in rainfed and irrigated wheat environments. *Precision Agriculture*, V7(4), pp. 233-248.
- Gitelson, A., and M. N. Merzlyak 1994. Quantitative estimation of chlorophyll-a using reflectance spectra: Experiments with autumn chestnut and maple leaves. *Journal of Photochemistry and Photobiology B: Biology*, 22(3), pp. 247-252.
- Gooding, M. J., and W. P. Davies 1997. *Wheat production and utilization - systems, quality and the environment*: CAB International, New York, USA.
- Haboudane, D., J. R. Miller, N. Tremblay, P. J. Zarco-Tejada, and L. Dextraze 2002a. Integrated narrow-band vegetation indices for prediction of crop chlorophyll content for application to precision agriculture. *Remote Sensing of Environment*, 81, pp. 416-426.
- Haboudane, D., J. R. Miller, N. Tremblay, P. J. Zarco-Tejada, and L. Dextraze 2002b. Integrated narrow-band vegetation indices for prediction of crop chlorophyll content for application to precision agriculture. *Remote Sensing of Environment*, 81(2-3), pp. 416-426.
- Herwaarden, A. F. v., G. D. Farquhar, J. F. Angus, R. A. Richards, and G. N. Howe 1998. 'Haying-off', the negative grain yield response of dryland wheat to nitrogen fertiliser. I. Biomass, grain yield, and water use. *Australian Journal of Agricultural Research*, 49(7), pp. 1067-1082.
- IEEE 2003. *Wireless Medium Access Control (MAC) and Physical Layer (PHY) Specifications for Low-Rate Wireless Personal Area Networks (LR-WPANs)*. *IEEE Standard*

- 802.15.4. . New York, USA The Institute of Electrical and Electronics Engineers Inc.
- IEEE 2006. *IEEE Standard for Information technology-Telecommunications and information exchange between systems - Local and metropolitan area networks - Specific requirements Part 15.4: Wireless Medium Access Control (MAC) and Physical Layer (PHY) Specifications for Low-Rate Wireless Personal Area Networks (WPANs). IEEE Standard 802.15.4-2006*. New York: Institute of Electrical and Electronics Engineers.
- Jones, S., T. Malthus, A. Held, K. Reinke, E. Farmer, and R. Devadas 2010. AUSCOVER CALVAL: coordinating australian activities in calibration and validation,. In *2010 IEEE Geoscience and Remote Sensing Symposium (IGARSS)*. Honolulu, Hawaii, USA.
- LaRuffa, J. M., W. R. Raun, S. B. Phillips, J. B. Solie, M. L. Stone, and G. V. Johnson 2001. Optimum field element size for maximum yields in winter wheat, using variable nitrogen rates. *Journal of Plant Nutrition*, 24(2), pp. 313 - 325.
- Li, X.-Y. 2008. *Wireless Ad Hoc and Sensor Networks: Theory and Applications*: Cambridge University Press.
- Lilienthal, H., S. Haneklaus, E. Schnug, and E. Haveresch 2000. Utilistation of hyperspectral data for the evaluation of the spatial variability of the nitrogen status of wheat. *Aspects of Applied Biology*, 60, pp. 189 - 194.
- López Riquelme, J. A., F. Soto, J. Suardíaz, P. Sánchez, A. Iborra, and J. A. Vera 2009. Wireless Sensor Networks for precision horticulture in Southern Spain. *Computers and Electronics in Agriculture*, 68(1), pp. 25-35.
- Morais, R., M. A. Fernandes, S. G. Matos, C. Seródio, P. J. S. G. Ferreira, and M. J. C. S. Reis 2008. A ZigBee multi-powered wireless acquisition device for remote sensing applications in precision viticulture. *Computers and Electronics in Agriculture*, 62(2), pp. 94-106.
- Moshou, D., C. Bravo, R. Oberti, J. West, L. Bodria, A. McCartney, and H. Ramon 2005. Plant disease detection based on data fusion of hyper-spectral and multi-spectral fluorescence imaging using Kohonen maps. *Real-Time Imaging*, 11(2), pp. 75-83.
- Myers, V. I. 1983. Remote sensing applications in agriculture. In *Manual of remote sensing- second edition: volume II-interpretation and applications*, edited by N. R. Colwell, Estes,J.E., and Thorley.G.A., 2111-2228: American Society of Photogrammetry, Virginia, USA.
- Olesen, J. E., I. N. Jorgensen, J. Petersen, and J. V. Mortensen 2003. Effects of rate and timing of nitrogen fertilizer on disease control by fungicides in winter wheat.1. Grain yield and foliar disease control. *Journal of Agricultural Science* 140, pp. 1–13.
- Penuelas, J., J. A. Gamon, A. L. Fredeen, J. Merino, and C. B. Field 1994. Reflectance indices associated with physiological changes in nitrogen- and water-limited sunflower leaves. *Remote Sensing of Environment*, 48(2), pp. 135-146.
- Rodriguez, D., G. J. FitzgeraldB, R. BelfordC, and L. K. ChristensenD 2006. Detection of nitrogen deficiency in wheat from spectral reflectance indices and basic crop eco-physiological concepts. *Australian Journal of Agricultural Research*, 57, pp. 781-789.
- Smith, V. H., G. D. Tilman, and J. C. Nekola 1999. Eutrophication: impacts of excess nutrient inputs on freshwater, marine, and terrestrial ecosystems. *Environmental Pollution*, 100(1-3), pp. 179-196.
- Strachan, I. B., E. Pattey, and J. B. Boisvert 2002. Impact of nitrogen and environmental conditions on corn as detected by hyperspectral reflectance. *Remote Sensing of Environment*, 80, pp. 213-224.
- Tarpley, L., K. Reddy, and F. Sassenrath-Cole 2000. Reflectance indices with precision and accuracy in predicting cotton leaf nitrogen concentration. *Crop Science*, 40, pp. 1814-1819.
- Tilling, A. K., G. J. O'Leary, J. G. Ferwerda, S. D. Jones, G. J. Fitzgerald, D. Rodriguez, and R. Belford 2007. Remote sensing of nitrogen and water stress in wheat. *Field Crops Research*, 104(1-3), pp. 77-85.
- Tiny 2009. Tiny-OS 2.0 Home Page.
- Trotter, G. M., D. Whitehead, and E. J. Pinkney 2002. The photochemical reflectance index as a measure of photosynthetic light use efficiency for plants of varying foliar nitrogen contents. *International Journal of Remote Sensing*, 23(6), pp. 1207-1212.
- Vellidis, G., M. Tucker, C. Perry, C. Kvien, and C. Bednarz 2008. A real-time wireless smart sensor array for scheduling irrigation. *Computers and Electronics in Agriculture*, 61(1), pp. 44-50.
- Wang, N., N. Zhang, and M. Wang 2006. Wireless sensors in agriculture and food industry--Recent development and future perspective. *Computers and Electronics in Agriculture*, 50(1), pp. 1-14.
- Wright Jr., D. L. 2003. Using Remote Sensing to Manage Wheat Grain Protein. NASA Earth Science Enterprise Earth Science Applications Directorate, Utah State University Affiliated Research Center, USA, URL: http://www.gis.usu.edu/ArcWebpage/inside_table/2003Presentations/NASAREports/Wheat02b.pdf Accessed on 23-4-2006.
- Zillmann, E., S. Graeff, J. Link, W. D. Batchelor, and W. Claupein 2006. Assessment of Cereal Nitrogen Requirements Derived by Optical On-the-Go Sensors on Heterogeneous Soils. *Agron J*, 98(3), pp. 682-690.

ANALYSIS OF FULL-WAVEFORM ALS DATA BY SIMULTANEOUSLY ACQUIRED TLS DATA: TOWARDS AN ADVANCED DTM GENERATION IN WOODED AREAS

M. Doneus^{a,b,*}, C. Briese^{a,c}, N. Studnicka^d

^a Ludwig Boltzmann Institute for Archaeological Prospection and Virtual Archaeology, Vienna, Austria - Michael.Doneus@archpro.lbg.ac.at, Christian.Briese@archpro.lbg.ac.at

^b Department for Prehistoric and Medieval Archaeology, University of Vienna, Austria

^c Christian Doppler Laboratory for Spatial Data from Laser Scanning and Remote Sensing, Institute of Photogrammetry and Remote Sensing of the Vienna University of Technology, Austria

^d RIEGL Laser Measurement Systems GmbH, Austria - nstudnicka@riegl.co.at

Commission VII

KEY WORDS: Laser scanning, LIDAR, full-waveform, Aerial, Terrestrial, Combination, Analysis, Archaeology

ABSTRACT:

Airborne laser scanning (ALS, also referred to as airborne LIDAR) is a widely used data acquisition method for topographic modelling. In archaeology, it has revolutionised prospection of forested areas. Here, especially full-waveform (FWF) ALS systems show considerable advantages for the generation of digital terrain models (DTM) in vegetated areas, as the FWF-information (e.g. echo width) can improve classification of ALS data into terrain and off-terrain points, resulting in greater DTM quality and higher potential for the subsequent archaeological interpretation. FWF-ALS displays a high potential, but is still in its infancy (in contrast to conventional ALS sensors FWF-ALS is just available since a few years). One key topic to be investigated is the complex interaction of the laser beam with different types of vegetation cover. An in-depth understanding of the FWF-information is essential to enhance the quality of the DTM and to allow a reliable automated interpretation of the acquired data. To study the interaction of ALS and the resulting FWF-information with a vegetation complex, part of a forest was scanned by airborne and terrestrial laser scanning (Riegl LMS-Q680 and Riegl VZ-400). The combined data acquisition took place simultaneously on a calm day. Using tachymetry, the data sets were geo-referenced and the differences between the ALS and TLS data sets were minimized by an adjustment using planar control and tie patches. Based on the TLS dataset, the position of the derived ALS echoes are studied and the additionally derived FWF-parameters are investigated. This analysis allows increasing the knowledge about the interaction of the laser beam with different surface elements and allows to estimate the potential for methods for advanced DTM generation. Based on this knowledge a high quality DTM can be determined which allows an advanced interpretation of archaeological structures which are present on the terrain surface.

1. INTRODUCTION

In the last years, airborne laser scanning (ALS, also referred to as airborne LIDAR (light detection and ranging)) became a widely used data acquisition method for sampling of the topography. The resulting 3D data provides a good basis for modelling the ground surface with or without objects (houses, trees) and is utilized in several different application areas, e.g. hydrology (Mandlbürger et al., 2009), city modelling (Rottensteiner and Briese, 2002) and forest mapping (Naesset, 2007). ALS especially excels in forested areas due to the fact that an active direct 3D sensing principle is utilized (for the estimation of one point on the illuminated surface only one line of sight is necessary). Small footprint ALS systems can penetrate the vegetation layer through small gaps in the canopy and therefore may allow receiving an echo from the terrain surface even in densely vegetated areas.

This advantage of ALS in vegetated areas and furthermore the increasing capabilities of ALS sensor systems (increasing point density with more than 1 point/m²) has also revolutionized archaeological prospection of forests. Due to the availability of

country wide ALS data the study of extended archaeological landscapes becomes possible. However, to successfully apply ALS for archaeological prospection, special demands have to be met during data analysis (Doneus and Briese, 2010).

After geo-referencing of the acquired observations, the result of an ALS data acquisition campaign is a (strip wise) unstructured and unclassified 3D point cloud (often enriched by additional attributes like echo ID, echo intensity or amplitude, GPS time, etc.). This point cloud can be utilized for visualisation purposes, but for an advanced use of the data there is usually the need for further analysis and classification. All of the application areas mentioned have typically in common that a classification of the ALS data into terrain and off-terrain points is essential.

For archaeological prospection, the terrain points and the resulting digital terrain model (DTM) are of vital importance. Here, the separation into surface and object points has to be of high quality, because errors can easily lead to misleading interpretations. Other applications, like city modelling, biology or forestry are especially interested in the identification of

* Corresponding author.

objects (e.g. cars, buildings, individual trees, or brushwood) within the point-cloud.

In any case, sophisticated classification is necessary. For the extraction of a DTM, various algorithms were developed (cf. Briese, 2010). All of them have in common that they study the local geometric properties of the acquired ALS points. Other information, which could help to improve classification, is rarely utilized.

With the advent of full-waveform (FWF)-ALS systems (Hug et al. 2004, Wagner et al., 2004) additional interesting observables for an advanced classification of the FWF-ALS data have become available. Doneus and Briese (2006) demonstrate the advanced capabilities of FWF-ALS data for the generation of digital terrain models (DTM) in vegetated areas. The echo width determined from the FWF information was used to support the classification of the ALS data into terrain and off-terrain points in the presence of low vegetation. Mücke (2009) extended the utilisation of the echo width by introducing a weighting scheme that depends next to the increase of the echo width on the echo amplitude. In both examples, utilizing information from FWF-ALS could improve the quality of the estimated DTM.

FWF-ALS therefore seems to be a very promising approach to enhance the quality of both DTMs and digital object models (DOM). However, it is still in its infancy. In contrast to conventional ALS sensors FWF-ALS is just available since a few years and extended processing chains still have to be developed. Especially the complex interaction of the laser beam with different types of vegetation cover has to be better understood. Enhanced knowledge in this field, i.e. an in-depth understanding of the FWF-information will improve both quality and reliability of DTMs. This is especially desirable in areas with low vegetation. Furthermore, the investigations should lead to advanced geometric models that allow a more reliable automated analysis, which is desirable for different applications (hydrology, etc. as well as archaeology).

This paper can be seen as a first step towards a detailed study of the interaction between FWF-laser beams and various objects within a vegetation complex. For the analysis a vegetated area was simultaneously scanned by airborne and terrestrial (TLS) laser scanning on a calm day. After presenting the study area, we will focus on the process of co-geo-referencing the ALS and TLS data sets. In section 4 and 5, some preliminary results of the analysis of the FWF-ALS data set are presented and discussed.

2. STUDY SITE AND DATA ACQUISITION

For the study of the FWF-ALS data, a small area (approx. 2.25km², cf. Figure 1) was selected in the Leithagebirge, approx. 30km south of Vienna. This area is already well known by the authors due to a small FWF-ALS mission in 2006 (Doneus and Briese, 2006) and a large archaeological FWF ALS data acquisition campaign carried out in 2007 (cf. Doneus et al, 2008). It contains a large building complex of a former monastery (“St. Anna in der Wüste”) in the central northern part. The buildings are encircled by an open meadow which is enclosed by a forest with understory of varying density.



Figure 1. Study Site “St. Anna in der Wüste” in the area of the Leithagebirge (30km in the south of Vienna) with the planned flight lines (approx. length: 1.5km) for the ALS data acquisition. © Google 2010

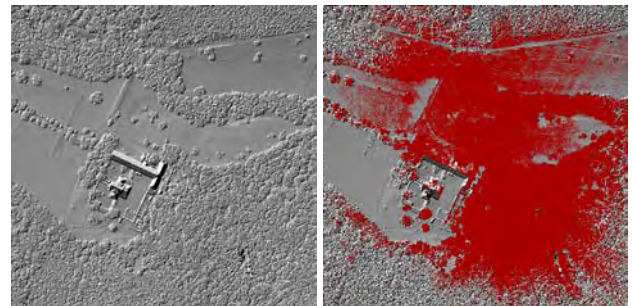


Figure 2. Left: Shading of a digital surface model (DSM, 0.25m raster) of the main area of interest (370m by 370m) derived from the ALS data; Right: DSM shading and TLS data (red).

The data acquisition of the site took place on the 10th of December 2009 in leaf off condition. It was a day with no wind. This was important to exclude the effect of wind on the vegetation canopy and facilitate the co-registration of the simultaneously performed TLS and ALS scans. The FWF-ALS data set was acquired during a test flight of the company RIEGL Laser Measurement Systems GmbH with the novel FWF-ALS sensor RIEGL LMS-Q680 (Riegl, 2010). The area was covered by six strips (both three strips in perpendicular directions) with a flying height of approx. 500m above ground. This resulted in an ALS point density of approx. 20 last echo points/m². A shading of the resulting digital surface model is displayed in the left part of Figure 2.

The TLS data acquisition took place simultaneously to the ALS flight. The TLS data was acquired by a Riegl VZ-400 instrument with online waveform processing capability (cf. Riegl, 2010; Pfennigbauer and Ullrich, 2010). Additionally to the TLS data, images were acquired by an attached digital camera (Nikon D300). Altogether, data from 16 stations were acquired near the north eastern part of the monastery (cf. right part of Figure 2). For an advanced geo-referencing of the ALS and TLS data (see section 3), some of the stations covered the monasteries’ inclined planar roof areas with different exposition. Furthermore, reflector targets were used in order to perform a relative orientation/registration of the individual stations.

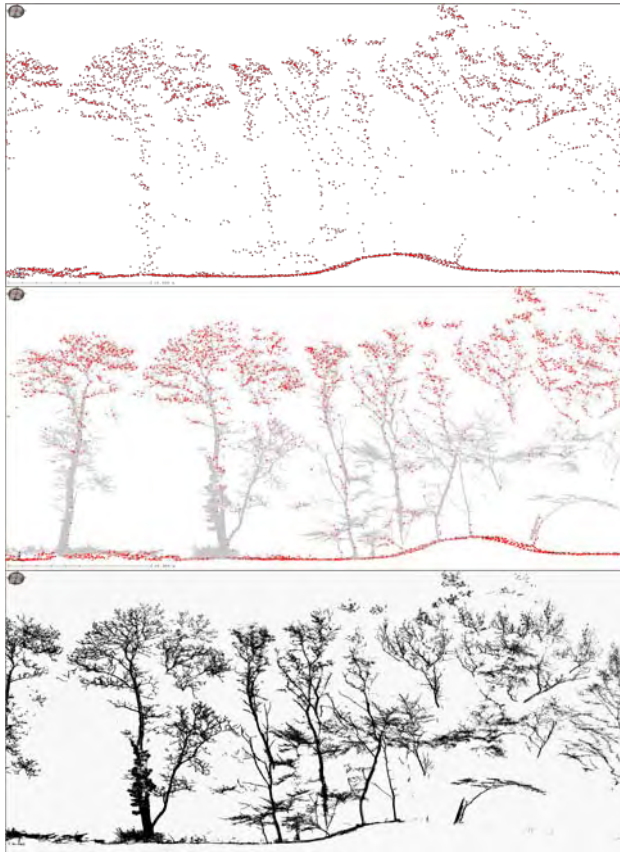


Figure 3. Visualisation of the geo-referenced ALS and TLS point cloud; Upper part: ALS points (red); Middle part: ALS (red) and TLS (grey) points; Lower part: TLS points (black).

For the absolute georeferencing of the ALS and TLS data, 28 of the reflector targets were observed by a total station (Leica TPS 1200). Additionally, the total station was used to measure points within the scanned roof areas in order to determine pass patches for the absolute position and orientation of the scan data. All in all, points on six different roof faces (visible in the ALS and TLS data) were observed.

3. GEOREFERENCING OF ALS, TLS AND TACHEOMETRY DATA

For the study of the simultaneously acquired ALS and TLS data, an adequate geo-referencing of the data sets is essential. For all of the following steps the commercially available Riegl software package (RiANALYZE, RiPROCESS and RiWORLD) was used (Riegl, 2010).

As a first step, a decomposition of the acquired FWF-ALS data set was performed. This includes the detection of all echoes per emitted laser pulse and for each echo the determination of a model in order to derive further echo parameters (amplitude and echo width). For geo-referencing, the trajectory of the airplane has to be determined using the observations from the global navigation satellite system (GNSS) and the inertial measurement unit (IMU). Based on the trajectory in the global co-ordinate system, the detected echoes in the scanner co-ordinate system (SOCS), and the mounting information, the co-ordinates of all echoes can be derived by direct geo-referencing. However, due to the requirements of the study, an advanced geo-referencing of the ALS data was essential. Therefore, based on the absolutely determined roof faces and additional planar tie elements, a strip adjustment of the ALS data was performed (Kager, 2004, Riegl, 2010). Within this adjustment, the differences to both the planar pass and tie patches were minimized

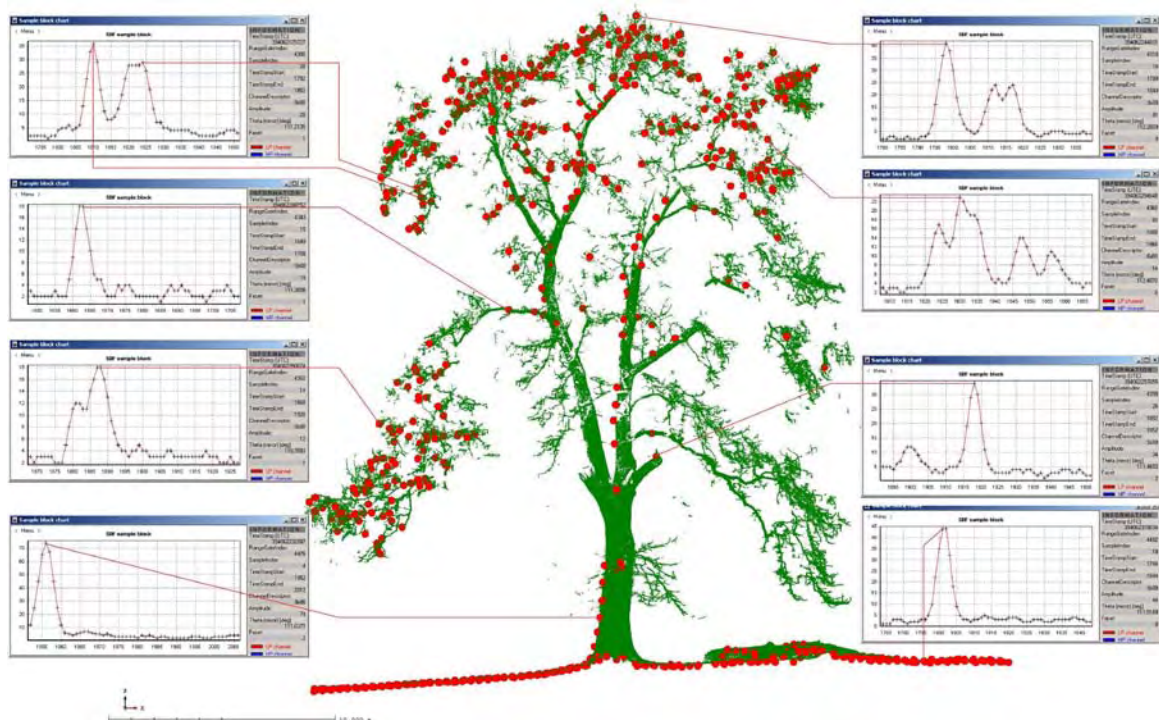


Figure 4. Inspection of the FWF-ALS data (red points) and recorded waveforms by the TLS point cloud (green).

The data of the 16 TLS stations was automatically co-registered using asymmetrically distributed reflectors. The total TLS point-cloud was geo-referenced using 28 absolutely determined reflectors within the Riegl software RiScanPro (Riegl, 2010).

As a result both data sets were finally geo-referenced in the Austrian co-ordinate system GK-M34. This process of geo-referencing could be checked by the comparison of identical surfaces that were observed by ALS and TLS (e.g. some roof faces). Additionally, any possible presence of errors can be inspected by a 3D visualisation of both ALS and TLS point clouds. This is, however, impractical: due to the high point density, individual ALS and TLS points can hardly be recognized. Only profile views with clipped point clouds were suitable to visually inspect the resulting merged point cloud. As displayed in Figure 3, the ALS and TLS data set fit well together (the tree trunks and branches are located at the same position in both data sets). No discrepancies could be detected visually. However, a quantitative study of the accuracy has to be done as a future step in the project.

4. ANALYSIS OF THE FWF-ALS DATA

Based on both geo-referenced data sets, the position of each individual FWF-echo together with the derived FWF-parameters can be studied. This analysis should allow to increase the knowledge of the interaction of the laser beam with the different surface elements. Based on these studies, we see further potential for advanced classification for DTM generation and object separation.

In the first step of the analysis, individual ALS points can be viewed together with the recorded respectively digitised waveform, while the context of the object is provided from the TLS data (see Figure 4). In Figure 4, the ALS-derived terrain points below the tree follow the terrain points of the TLS data set and have a very narrow echo width. The same is true for those ALS points, which have been reflected from the lower stem. ALS points, which are visible on the main branches, coincide perfectly with the TLS points. This emphasizes the high quality geo-referencing of both data sets. When looking on the respective waveforms one can typically find one strong echo resulting from the extended target at the tree surface. When looking at the echo width a slightly broadened echo (caused by the locally sloped surface) can be found.

On the smaller braches on top of the tree typically more than one echo (up to five) can be seen in the waveform display. Some of the echoes are very close or even overlaid. Some of the echo widths are broadened, especially in areas with very dense and thin branches. Concerning the vertical ALS point distribution one can see that the top canopy layers are very densely covered and that many of the ALS echoes are located on thin but dense branches.

All in all the (big) tree is represented well in the ALS point cloud, just small branches below the very dense canopy layer are not covered by ALS points. Holes in the TLS data are caused by shadow or by the profile selection.

In order to study the sequence of echoes that are the result of a single emitted laser pulse, 3D visualisations with connecting lines were generated (Figure 5). In the upper part of Figure 5 ALS echoes that result from the same line of sight are connected by a grey line. In the middle part of the figure the

FWF information (in this case split into two graphs) of the selected line of sight can be inspected. It can be seen that the echo amplitude of the tree echoes caused by the tree top differs significantly. While the second echo is quite weak (just a little bit above the detection threshold) the third echo is even stronger than the first. This might be explained by the vegetation density. It seems that the third echo results from a thicker branch than the first echo, while the second echo must be caused from a very small branch. In the second graph of the FWF information one can see that the first local maximum that is visible in the FWF signal was not accepted in the echo detection step due to its low amplitude. The amplitude of the detected fourth echo is also very low (even lower than the second echo). The last echo of this line of sight has the highest amplitude and my result from an extended target (compare lower part of Figure 5).

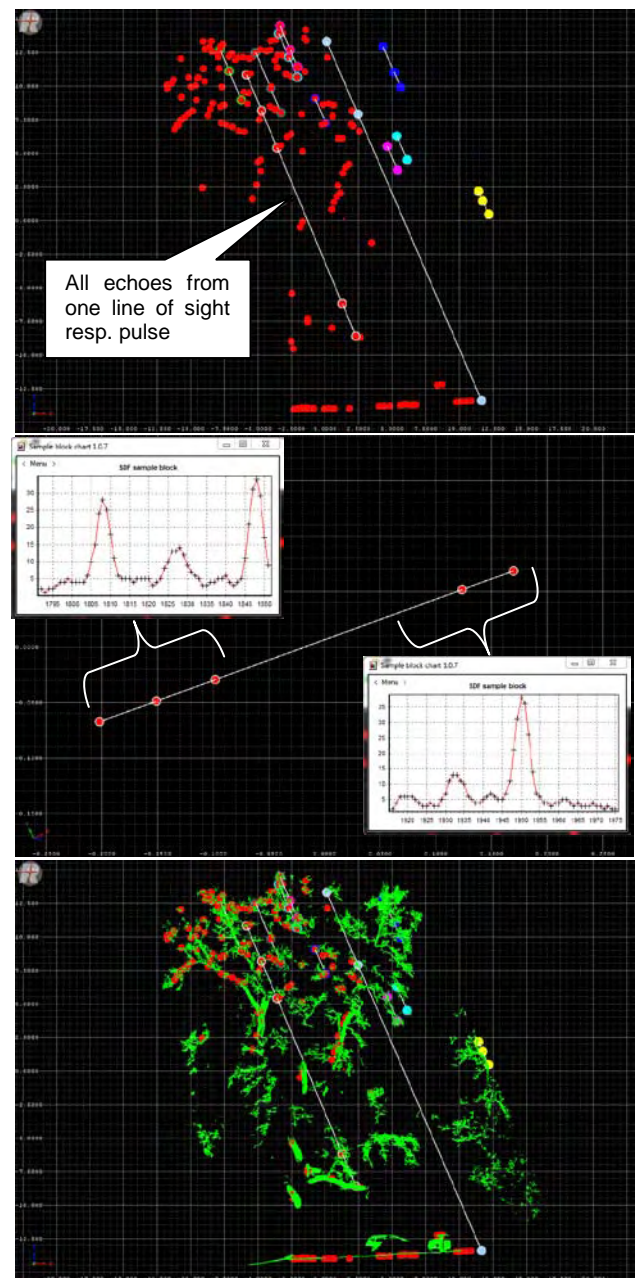


Figure 5. Inspection of all FWF-ALS echoes from one line of sight (red points) and TLS point cloud (green).

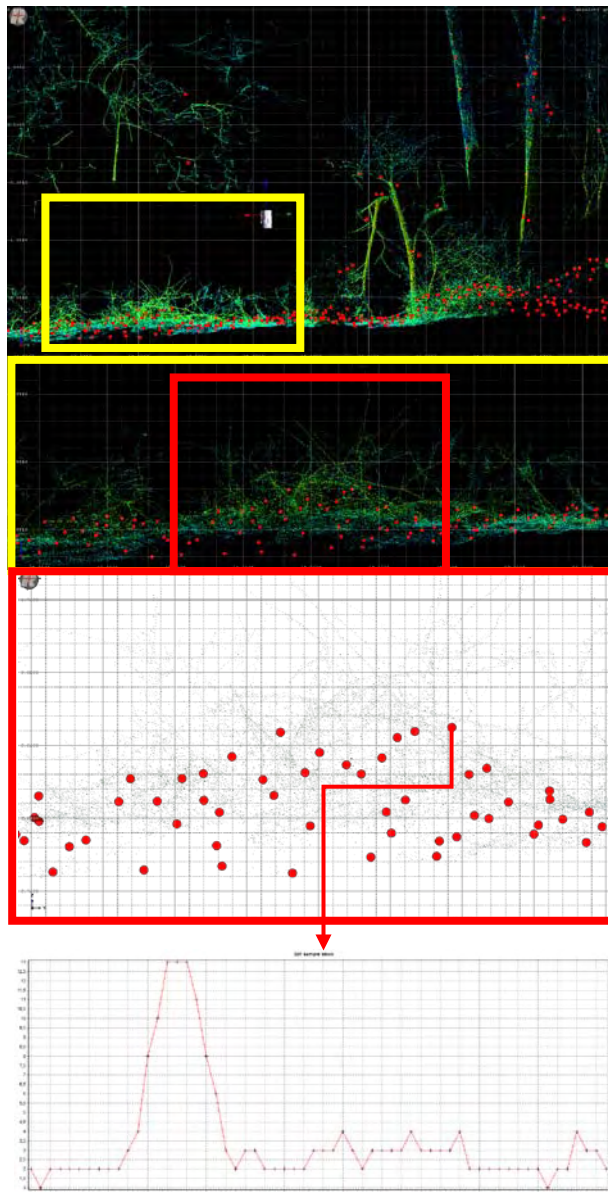


Figure 6. Inspection of FWF-ALS echoes in vegetated areas with dense understory (red points) and TLS point cloud (green).

Next to the examination of the echoes that belong to one line of sight, the influence of low vegetation on the FWF information is analysed. One example for this study is displayed in Figure 6. In the upper part of the figure dense brushwood can be found below a tree (marked by a yellow rectangle). In the middle of the figure a more detailed view of the understory area with the red ALS points attached on the TLS observations can be found. In the lower part of the figure the digitised FWF information for one representative ALS point is displayed in a graph. Compared to other echoes from planar extended targets (compare for example the echoes of the tree trunk in Figure 4) it can clearly be seen that the understory leads to an enlarged echo width. This increase of the echo width is caused by the reflection of a sequence of small reflecting surface elements at different heights and provides therefore a good basis for the automated detection of influence of these low vegetation cover on the resulting ALS points. In these areas, points that are affected by understory will typically lie slightly above the terrain. Without the additional knowledge from FWF-ALS these points are very

difficult to classify as off-terrain echo points and might therefore often influence the run of the terrain surface in a negative way. FWF-ALS with its ability to determine the echo width has a high potential to perform an improved classification of the ALS data in these areas with dense understory and offers the potential to derive an advanced DTM.

5. CONCLUSION AND FUTURE WORK

As ALS constantly finds new fields of application, special demands are increasingly made on the results. Archaeology for example needs a high quality separation of terrain and off-terrain points to derive detailed DTMs displaying micro-topographic variation even under forest canopies. Biology and forestry are interested to extract individual trees from the point-clouds. During the last years, FWF-ALS turned out to have a high potential to meet many of these requirements. However, an in-depth understanding of the FWF-information is essential to enhance the quality of the DTM and to allow a reliable automated interpretation of the acquired data.

This paper aimed to start the investigation of the complex interaction of the laser beam with different types of vegetation cover. Part of a forest was scanned by airborne and terrestrial laser scanning (Riegl LMS-Q680 and Riegl VZ-400). The combined data acquisition took place simultaneously on a calm day. Using tachymetry, the data sets were geo-referenced and the differences between the ALS and TLS data sets were minimized by an adjustment using planar control and tie patches.

The investigation of each individual FWF echo together with the derived FWF parameters and the digitised waveform could be done within the context of the object that is provided from the TLS data. In that way, we could gain interesting results especially from densely vegetated areas, which will help to improve algorithms for the advanced usage of FWF information.

In the future we want to quantify the accuracy of the geo-referencing of the ALS and TLS data in more detail. Furthermore, we aim to study the interaction of the laser beam with the terrain and the attached objects by further advanced visualisations (e.g. by the direct visualisation of the FWF signal and the FWF parameters in the 3D view).

REFERENCES

- Briese, C., 2010. Extraction of Digital Terrain Models. In: Airborne and Terrestrial Laser Scanning, Whittles Publishing, ISBN: 978-1904445876, pp. 135-167.
- Doneus, M. und Briese, C., 2006. Digital terrain modelling for archaeological interpretation within forested areas using full-waveform laserscanning. In: M. Ioannides, D. Arnold, F. Niccolucci und K. Mania (Editors), The 7th International Symposium on Virtual Reality, Archaeology and Cultural Heritage VAST, pp. 155-162.
- Doneus, M., Briese, C., Fera, M. und Janner, M., 2008. Archaeological prospection of forested areas using full-waveform airborne laser scanning. Journal of Archaeological Science, 35, pp. 882-893.

Doneus, M., Briese, C., 2010. Airborne Laser Scanning in Forested Areas - Potential and Limitations of an Archaeological Prospection Technique, in press.

Doneus, M., Briese, C., Fera, M. and Janner, M., 2008. Archaeological prospection of forested areas using full-waveform airborne laser scanning. *Journal of Archaeological Science* 35(4), pp. 882-893.

Hug, C., Ullrich, A. und Grimm, A., 2004. Litemapper-5600 – A Waveform-Digitizing LIDAR Terrain and Vegetation Mapping System. In: *Laser-Scanners for Forest and Landscape Assessment. Proceedings of Natscan, Laser-Scanners for Forest and Landscape Assessment - Instruments, Processing Methods and Applications. International Archives of Photogrammetry and Remote Sensing, Volume XXXVI, Part 8/W2, 24-29.*

Kager, H., 2004. Discrepancies Between Overlapping Laser Scanning Strips- Simultaneous Fitting of Aerial Laser Scanner Strips, In: *International Archives of Photogrammetry, Remote Sensing and Spatial Information Sciences, XXXV Part B1, ISSN: 1682-1750, pp. 555-560.*

Mandlburger, G., Hauer, C., Höfle, B., Habersack, H. and Pfeifer, N., 2009. Optimisation of lidar derived terrain models for river flow modelling. *Hydrology and Earth System Sciences* 13(8), pp. 1453-1466.

Mücke, W., 2008. Analysis of full-waveform airborne laser scanning data for the improvement of DTM generation. Diploma thesis, Institute of Photogrammetry and RemoteSensing, Vienna University of Technology.

Naesset, E., 2007. Airborne laser scanning as a method in operational forest inventory: Status of accuracy assessments accomplished in Scandinavia. *Scandinavian Journal of Forest Research* 22(5), pp. 433-442.

Pfennigbauer, M., Ullrich, A., 2010. Improving quality of laser scanning data acquisition through calibrated amplitude and pulse deviation measurement. In *Proc.: SPIE 7684, 76841F.*

Riegl, 2010. www.riegl.com. Homepage of the company RIEGL Laser Measurement Systems GmbH, accessed: June 2010.

Rottensteiner F., Briese C., 2002. A New Method for Building Extraction in Urban Areas From High-Resolution Lidar Data. *International Archives of Photogrammetry And Remote Sensing, Volume XXXIV / 3A, pp. 295-301.*

Wagner W., Ullrich A., Melzer T., Briese C., Kraus K., 2004. From Single-Pulse to Full-Waveform Airborne Laser Scanners: Potential And Practical Challenges, In: *International Archives of Photogrammetry, Remote Sensing and Spatial Information Sciences, XXXV Part B3, ISSN: 1682-1750, pp. 201 - 206.*

REMOTE SENSING FOR DROUGHT ASSESSMENT IN ARID REGIONS (A CASE STUDY OF CENTRAL PART OF IRAN, "SHIRKOOH-YAZD")

M. Ebrahimi^a, A. A. Matkan^a, R. Darvishzadeh^a

^a RS & GIS Department, Faculty of Earth Sciences, Shahid Beheshti University (SBU), Tehran, Iran-
(mohsen_ebrahimi@hotmail.com; a-matkan@sbu.ac.ir; r_darvish@sbu.ac.ir)

Commission VII

KEY WORDS: Vegetation, Application, Monitoring, Precipitation, LANDSAT, Spectral

ABSTRACT:

Rainfall, soil moisture, increasing temperature and changes in vegetation cover are the most important parameters effecting drought. Therefore, analysis of vegetation fraction and soil spectral signature, especially in red and infra red bands, are essential in drought estimation using remote sensing. In this study, Modified Perpendicular Drought Index (MPDI), which uses Vegetation Fraction (VF) and Perpendicular Drought Index (PDI) (computed based on the amount of rainfall and the soil moisture) has been used for monitoring and drought assessment in arid regions in central part of Iran during a time interval of three years (1999-2002). To do so, ETM+ images of LANDSAT 7 for the years 1999 and 2002 and the rainfall statistics of 23 years have been used. Analysis of vegetation cover using NDVI, RVI, SAVI, MSAVI, SAVI2 and PVI indices demonstrated that in arid regions changes in vegetation cover were best mapped using SAVI2 index. Also, in comparison with PDI and VSWI indices, drought severeness was best demonstrated by MPDI index. Further, the results were analyzed and evaluated using Run-test model and metrological data of the existing stations in the region. The results of the study indicated that in the year 2002 although in comparison to year 1999, the amount of rainfall has been increased, vegetation fraction has been decreased and consequently, drought has been increased in the rangelands of the study area. This is due to the existence of a severe drought and decrease in seeding of rangeland vegetations in previous years (2000, and 2001).

1. INTRODUCTION

Drought is a severe dilemma which influences different aspects of mankind's life. It can cause many economic and eco-environmental problems especially in the agriculture sector (Goddard 2003). In the last three decades, remote sensing has provided a useful tool for drought monitoring and a variety of remotely sensed drought indices based on vegetation indices, land surface temperature (LST), albedo, etc have been developed. Several drought indices have been proposed based on normalised different vegetation index (NDVI, Rouse et al., 1974) to monitor drought severity such as Anomaly Vegetation Index (AVI) and Vegetation Condition Index (VCI) (Chen 1994; Kogan 1995a), Vegetation Condition Albedo Drought Index (VCADI) (Ghulam et al., 2006), Temperature Drought Vegetation Index (TDVI) and Vegetation Temperature Condition index (VTCI) (Wang 2001; Sandholt 2002).

Since there is a lag-time between the drought occurrence and the change of NDVI, the indices which are based on NDVI may not be appropriate for the real time drought monitoring.

In addition, retrieval of the surface albedo and the LST contains uncertainties rooted in the atmospheric correction of satellite data, decomposition of mixed pixel information, BRDF modeling and the spectral remedy by a narrowband to broadband conversion (Zhao 2000; Pokrovsky 2002; Liang 2003). As a consequence, the final error associated with the extraction and quantification of drought information would be magnified.

In 2007 Ghulam et al., presented the Modified Perpendicular Drought Index (MPDI) as a real time index for drought monitoring based on vegetation fraction (estimated using NDVI) and Perpendicular Drought Index (PDI).

In arid areas, background soil has a considerable effect on the recorded reflectance by the sensor. Therefore, the indices, which consider background soil reflectance, may signify vegetation characteristics more accurately than the indices such as NDVI (Kallel 2007; Darvishzadeh 2008). In Iran, many studies have been conducted for monitoring drought disaster, in which, mostly AVHRR images and NDVI have been used (Serajian 2000; Baaqide 2007). As AVHRR images have a 1 km resolution it can give a poor estimation for arid areas.

The main objective of this study was to assess the drought severity in central arid areas of Iran by using MPDI as a real time index and ETM+ images which have a higher spatial resolution comparable to the AVHRR images. We examined the substitution of NDVI with another vegetation index (SAVI2, MSAVI, SAVI, PVI and RVI) for accurate estimation of the vegetation fraction which is used for MPDI calculation. Since in this study, the aim is to calculate the drought severity based on single image, three drought indices which needs only one image were selected (Vegetation Supply Water Index(VSWI), MPDI and PDI).

2. MATERIALS

2.1 Study Area

Shirkooch basin is located in the central part of Iran and expands from longitude of 54° 3' to 54° 18' in East and latitude of 31° 27' to 31° 43' in north. It covers a total area of 525 km². The altitude varies between 1600 and 4055 meters. The basin is

located in arid areas of Iran. Average annual rainfall in the study area is 325.38 mm. The significant amount of rainfall happens during the winter in which agriculture fields and rangeland vegetation depends. Drought which usually occurs in this area causes many problems for its ecosystem.

2.2 Image and Metrological Data

The satellite data used in this research consist of ETM+ images belonging to 19th August 1999 and 10th July 2002. The meteorological data (monthly rainfall) were collected from 18 rain-gauge stations which have 21 years common statistical basis. Table 1 present the annual rainfall of the study area for the considered years. As can be observed from the table, the rainfall increased considerably in 2002 compared to previous years.

Year	Annual (mm)
1999	405.5
2000	134
2001	242
2002	458.97

Table 1. The annual rainfall of the study area.

3. METHODOLOGY

3.1 Image Pre-processing

Since the selected images had different acquisition date, sun angle correction was applied to remove the differences caused by sun. Atmospheric correction was then performed using FLASH algorithm in order to obtain the correct reflectance. After the radiometric pre-processing, the images were geo-referenced using topographical maps in scale of 1/50000 with RMSEs equal to 0.47 and 0.2, respectively.

Since the main objective of this study was to assess drought using different indices, digital numbers recorded by the sensor were converted to the spectral radiance and reflectance using gain and offset parameters provided in the header file of the images.

3.2 Drought Severity by Meteorological Data

Several drought indices based on meteorological data have been introduced by researchers. This includes Palmer Drought Severity Index (PDSI), Standardized Precipitation Index (SPI), Crop Moisture Index (CMI), Reclamation Drought Index (RDI) and etc. each having advantages and disadvantages. In the present research, Run-Test method was used because of its simplicity and also because it only requires annual rainfall. It can be expressed by the equation (1):

$$X_0 = 0.8\bar{P} \Rightarrow \begin{cases} X - X_0 < 0 \Rightarrow \text{Dry} \\ X - X_0 > 0 \Rightarrow \text{Wet} \end{cases} \quad (1)$$

Where X = annual rainfall
 \bar{P} = average of annual rainfalls

The following parameters can be calculating using this method:

1. Drought duration: the number of consecutive years which drought occurs.

2. Drought magnitude: the total of $X - X_0$ amounts in each period.

3. Drought intensity: the average of $X - X_0$ amounts in each period.

4. Drought severity: the maximum amount of $X - X_0$ in each period.

3.3 PDI and MPDI Indices

Ghulam et al, in 2006, offered a new index based on spectral characteristics of surface in red and near infrared spectral space. As it can be seen from Figure 1, the AD line represents the changes in surface vegetation from full cover (A) to partial cover (E) to bare soil (D), while BC refers to an area with a soil moisture status described as wet (B), drier (D) and extremely dry (C) (Ghulam, 2006).

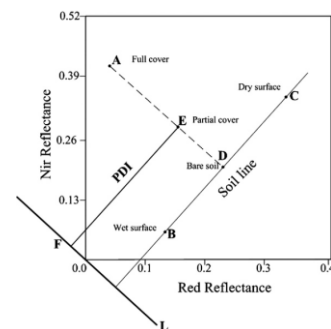


Figure 1. NIR-Red space and PDI (Ghulam, 2006)

The soil line is a linear relationship between NIR and Red reflectance of bare soil (Richardson, 1977). In this paper, in order to obtain the soil line parameters (slope and intercept), about 500 pixels of different types of the bare soils were extracted and were plotted in the feature space of Red-NIR. Here are the soil line parameters for each image:

$$R_{NIR} = 1.19 R_{Red} + 0.001 \quad (1999 \text{ image})$$

$$R_{NIR} = 1.19 R_{Red} + 0.003 \quad (2002 \text{ image})$$

PDI can be calculating using the following equation:

$$PDI = \frac{1}{\sqrt{\alpha^2 + 1}} (R_{Red} + \alpha R_{NIR}) \quad (2)$$

where α = slope of soil line

R_{Red} and R_{NIR} refer to the atmospherically corrected reflectance of the Red and NIR bands, respectively (Ghulam, 2006).

Crop growth is directly related to the soil moisture. Where soil moisture is below a certain level, crops cannot absorb enough water from the soil and are exposed to drought. Consequently, the soil moisture is the main factor in remote monitoring of drought. Soil spectral reflectance decreases with increasing soil moisture, Therefore, the severity of a drought can be estimated by the close relationship between soil moisture and soil spectral reflectance. However, the spectrum received by the sensor is a mixture reflected or emitted information from different surface targets. Therefore, both the soil moisture status and the vegetation status are very important in drought monitoring.

Ghulam et al, in 2007, suggested a robust drought index which takes into account both, the vegetation status and the soil moisture condition. Therefore, they represented a new index called MPDI which can be expressed as follows:

$$\begin{aligned} MPDI &= \frac{R_{Red} + \alpha R_{NIR} - F_V (R_{V,Red} + \alpha R_{V,NIR})}{(1 - F_V) \sqrt{\alpha^2 + 1}} \\ &= \frac{PDI - F_V PDI_V}{(1 - F_V)} \end{aligned} \quad (3)$$

Where, $R_{V,Red}$ and $R_{V,NIR}$ are vegetation reflectances in the red and near infrared bands which in this study was considered 0.05 and 0.5 respectively (Ghulam, 2007). F_V is the percentage of vegetation cover which can be estimated using different methods such as neural networks (Carpenter 1999), linear spectral unmixing (Elmore 2000; Conghe 2005) and vegetation indices (Baret 1995). In the present research, a semi-empirical method presented by Baret in 1995, has been used which expressed as (Baret 1995):

$$F_V = 1 - \left(\frac{VI - VI_{Max}}{VI_{Min} - VI_{Max}} \right)^K \quad (4)$$

Where, VI_{max} and VI_{min} are vegetation index for a surface with 100% vegetation ($F_V=1$) and bare soils ($F_V=0$), respectively. The factor K is a constant value minimizing the estimation of RMSE which was considered 0.6175 in this study (Ghulam, 2007). The amount of vegetation index was calculated in this study based on the most commonly used indices; they are presented in Table 2.

Vegetation Index	Reference
$RVI = \frac{R_{NIR}}{R_R}$	Pearson & Miller. (1972)
$NDVI = \frac{R_{NIR} - R_{RED}}{R_{NIR} + R_{RED}}$	Rouse et al. (1974)
$PVI = \frac{R_{NIR} - \alpha R_{RED} - \alpha}{\sqrt{1 + \alpha^2}}$	Richardson & Wiegand, (1977)
$SAVI = \frac{R_{NIR} - R_{RED}}{R_{NIR} + R_{RED} + L} (1 + L)$	Huete et al. (1988)
$TSAVI = \frac{\alpha(R_{NIR} - \alpha R_{RED} - \beta)}{R_{RED} + \alpha(R_{NIR} - \beta)}$	Baret et al. (1989)
$MSAVI = \frac{2R_{NIR} + 1 - \sqrt{(2R_{NIR} + 1)^2 - 8(R_{NIR} - R_{RED})}}{2}$	Qi et al. (1994)
$SAVI2 = \frac{R_{NIR}}{R_{RED} + (\alpha/\beta)}$	Major et al. (1990)
R_{RED}, R_{NIR} denotes reflectance in NIR and RED wavelengths α and β are the soil line coefficients	

Table 2. Vegetation indices Used in the study

4. RESULTS AND CONCLUSIONS

The results of run-test method indicated that a severe drought with the magnitude of -134.36, the intensity of -67.17, the severity of -121.98 and for the period of 2 years had occurred in 2000 and 2001 (Table. 3). On the other hand, meteorological data showed that in April and May when the crops in the study area are at the peak of the growing season and need enough water, monthly rain fall had decreased considerably. Water shortage causes a decrease in the vegetation cover as well as in the seeding of crops. Consequently, the seed bank of the rangeland would be decreased which will result in diminishing of the F_V in the following year (Jangjoo, 2001). Although in 2002, compared to previous years, the rainfall increased considerably (Table 1) it did not affect the percentage of vegetation cover due to the seed shortage in the rangeland.

Year	Annual rainfall	X-X ₀	Drought status
1999	405.5	145.1956	Wet
2000	134	-126.304	Dry
2001	242	-18.3044	Dry
2002	458.97	198.6656	Wet

Table 3. Drought status in the studying years

Changes in the vegetation cover (F_V) of the study area during the time period of 1999 to 2002 has been evaluated using the commonly used vegetation indices (Table. 2) and the equation 4. Among the indices used, only SAVI2 showed the F_V had decreased except in high-land areas where vegetation had no visible changes (Figure 2). In the high-land areas, there is a certain supply of snow until the end of the vegetation growing season and it provides enough water for the vegetation. Consequently, F_V did not change in these areas.

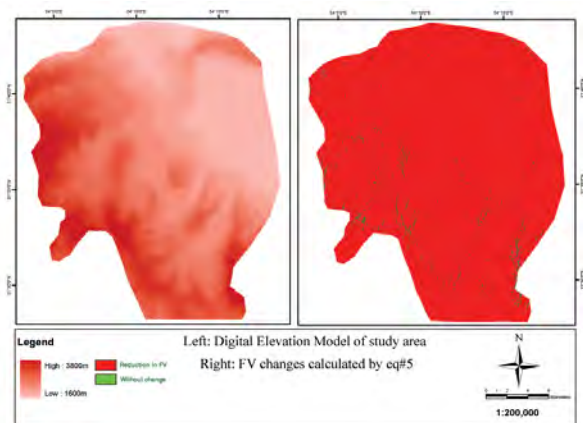


Figure 2. Fraction of vegetation changes (Using SAVI2 and Equation 4)

The study area, since is located in the arid areas of Iran, has sparse vegetation cover and the soil background has a noticeable effect on the recorded reflectance by the sensor. Therefore, RVI and NDVI which are only based on the Red and NIR reflectance are not appropriate indices for assessing vegetation in the arid areas. The results of using these two indices in the current study confirmed this fact and presented vegetation changes as mixed pixels (Figure 3).

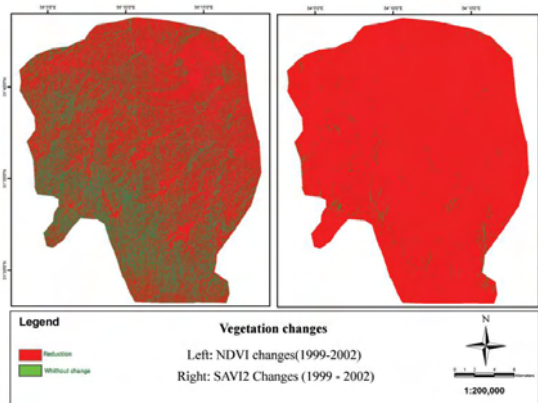


Figure 3. Vegetation changes detected by SAVI2 and NDVI

Among all other indices, only SAVI2 showed a reduction in the fraction of vegetation. The rest of the indices were also returned mixed pixels.

Next, the drought assessment was examined using three indices: VSWI, PDI and MPDI. As table 1 reveals in 2002, annual rainfall increased sharply. The results of PDI approved that the drought severity decreased. Since the PDI is based on soil moisture and the reflectance of the targets in the Red and NIR bands, it is suitable for meteorological drought monitoring.

On the other hand, the results of VSWI, also, showed mixed pixels. This is due to the fact that this index is based on the NDVI (Carlson 1994) and as mentioned before, NDVI is not appropriate for arid areas.

Ghulam et al, in 2007 used the NDVI to assess drought using MPDI, but as the result showed, this index is not very appropriate for arid areas. Consequently, we examined its substitution with another index. Among all studied indices only SAVI2 had well presented the vegetation fraction (F_v). Therefore, the fraction of vegetation has been estimated using the following index.

$$F_v = 1 - \left(\frac{SAVI2 - SAVI2_{Max}}{SAVI2_{Min} - SAVI2_{Max}} \right)^{0.6175} \quad (5)$$

The results of the revised MPDI indicated that the area with higher drought severity (more than 0.4) has largely increased (Figure 4). The regions with moderate drought severity were located in the northern and eastern hillside. These regions, keeps the moisture for a longer time. Therefore, the intensity of drought is lower than the other hillsides especially in comparison with the southern hillsides. The lowest values for the revised MPDI appeared in the high-land regions. In the high-land regions, there is snow until the end of the growing season and provide a supply of water for the vegetation growth.

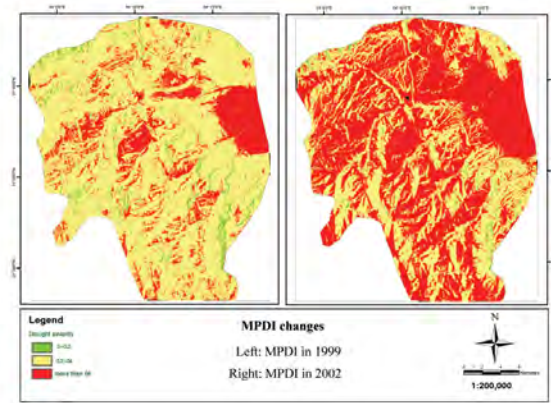


Figure 4. MPDI changes (1999-2002)

Studying the meteorological data reveals that drought did not occurred in 2002 and the results of PDI confirmed that as well. However, the results of the revised MPDI showed that the drought severity has increased. Therefore, it can be concluded that both meteorological data and the indices based on the satellite images, are essential for an accurate assessment of drought disaster.

In summary, this study had the following conclusions:

1. NDVI is not an appropriate index for vegetation assessment in the arid areas.
2. Vegetation indices which consider soil background reflectance such as SAVI2 can be more useful for vegetation assessment.
3. The PDI is suitable for meteorological drought monitoring.
4. Meteorological data and Remote sensing data are both essential for an accurate assessment of drought.

References:

- Baaqide, M. (2007). "Drought monitoring using multi temporal NOAA, NDVI and GIS in Isfahan province." P.H.D thesis, Tarbiat moallem university, Tehran.
- Baret, F., Clevers, J., Steven, M.D. (1995). "The robustness of canopy gap fraction estimations from red and near-infrared reflectances." *Remote Sensing of Environment* 54(3): 14–151.
- Baret, F., Guyot, G. and Major, D.J., 1989. TSAVI: A vegetation index which minimizes soil brightness effects on LAI and APAR estimation, *Geoscience and Remote Sensing Symposium, IGARSS'89*. 12th Canadian Symposium on Remote Sensing. pp. 1355-1358.
- Carlson, T. N., Gillies, R. ., Perry, E.M. (1994). "A method to make use of thermal infrared temperature and NDVI measurement to infer surface soil water content and fractional vegetation cover." *Remote Sensing Environment* 9: 161-173.
- Carpenter, G., Gopal, S ., Macomber, S .,Martens, S ., Woodcock, C ., Franklin J. (1999). "A Neural Network Method for Efficient Vegetation Mapping." *Remote Sensing of Environment* 70: 326–338.
- Chen, W., Xiao, Q ., Sheng, Y. (1994). "Application of the anomaly vegetation index to monitoring heavy drought in 1992." *Remote Sensing of Environment* 9(2): 106-112.

- Conghe, S. (2005). "Spectral mixture analysis for subpixel vegetation fractions in the urban environment: How to incorporate endmember variability?" *Remote Sensing of Environment* 95: 248–263.
- Darvishzadeh, R., Skidmore, Andrew, Atzberger, Clement, Wieren, Sip van. (2008). "Estimation of vegetation LAI from hyperspectral reflectance data: Effects of soil type and plant architecture." *International Journal of Applied Earth Observation and Geoinformation* 10: 358–373.
- Elmore, A. J., Mustard, J. F., Manning, S. J., Lobell, D. B. (2000). "Quantifying vegetation change in semiarid environments: Precision and accuracy of spectral mixture analysis and the normalized difference vegetation index." *Remote Sensing of Environment* 73: 87–102.
- Ghulam, A., Qin, Q. and Zhan, Z. (2006) Designing of the perpendicular drought index. *Environmental Geology*.
- Ghulam, A., Qiming, Q., Tashpolat T., Zhao-Liang L. (2007). "Modified perpendicular drought index (MPDI): a real-time drought monitoring method." *ISPRS Journal of Photogrammetry & Remote Sensing* 62: 150–164.
- Goddard, S., Harms, S., Reichenbach, S., Tadesse, T., Waltman, W.J. (2003). "Geospatial decision support for drought risk management." *Communication of the ACM* 46 1: 35–37.
- Kallel, A., Sylvie, Le., Catherine, O., Laurence, H. (2007). "Determination of vegetation cover fraction by inversion of a four-parameter model based on isoline parametrization." *Remote Sensing of Environment* 111: 553–566.
- Kogan, F. N. (1995a). "Droughts of the late 1980s in the United States as derived from NOAA polar-orbiting satellite data." *Bulletin of the American Meteorological Society* 76(5): 655–668.
- Liang, S. (2003). "A direct algorithm for estimating land surface broadband albedos from MODIS imagery." *IEEE Trans Geosci Remote Sensing of Environment* 41(1): 136–145.
- Major, D.J., Baret, F. and Guyot, G., 1990. A ratio vegetation index adjusted for soil brightness. *International Journal of Remote Sensing*, 11(5): 727–740.
- Pearson, R.L. and Miller, L.D., 1972. Remote mapping of standing crop biomass for estimation of the productivity of the short-grass prairie, Pawnee National Grassland, Colorado. 8th *International Symposium on Remote Sensing of Environment*, ERIMA, Ann Arbor, MI, pp. 1357–1381.
- Pokrovsky, O., Roujean, J-L. (2002). "Land surface albedo retrieval via kernel-based BRDF modeling : 1. Statistical inversion method and model comparison Auditori de Torrent, Spain." *Remote Sensing of Environment* 84: 100–119.
- Richardson, A. J., Wiegand, C.L. (1977). "Distinguishing vegetation from soil background information." *Photogrammetric Engineering and Remote Sensing* 43: 1541–1552.
- Rouse, J.W., Haas, R.H., Schell, J.A., Deering, D.W. and Harlan, J.C., 1974. Monitoring the Vernal Advancement of Retrogradation of Natural Vegetation. NASA/GSFC, Type III, Final Report, Greenbelt, MD.
- Sandholt, I., Rasmussen, K., Andersen, J. (2002). "A simple interpretation of the surface temperature/vegetation index space for assessment of surface moisture status." *Remote Sensing of Environment* 79: 213–224.
- Serajian, M., Tavakoli, A. (2000). "Investigating drought condition using NOAA images in Iran." Usage of GIS and remote sensing in arid area, Tehran university, Tehran.
- Wang, P., Li, X., Gong, J., Song, C. (2001). "Vegetation temperature condition index and its application for drought monitoring." *International Geoscience and Remote Sensing Symposium*, Sydney, Australia, 9–14 July: 141–143.
- Zhao, W., Tamura, M., Takahashi, H. (2000). "Atmospheric and spectral corrections for estimating surface albedo from satellite data using 6S code." *Remote Sensing of Environment* 76: 202–212.

QUALITY ASSESSMENT OF IMAGE FUSION TECHNIQUES FOR MULTISENSOR HIGH RESOLUTION SATELLITE IMAGES (CASE STUDY: IRS-P5 AND IRS-P6 SATELLITE IMAGES)

M. Fallah Yakhdani , A. Azizi

Centre of Excellence for Natural Disaster Management, Department of Geomatics Engineering, College of Engineering, University of Tehran, Iran - (mfallah84@gmail.com, aazizi@ut.ac.ir)

Commission VII, WG VII/6

KEY WORDS: Fusion, IRS, Multisensor, Spatial, Spectral, Evaluation

ABSTRACT:

This paper is concentrated on the evaluation of the image fusion techniques applied on the IRS P5 and P6 satellite images. The study area is chosen to cover different terrain morphologies. A good fusion scheme should preserve the spectral characteristics of the source multi-spectral image as well as the high spatial resolution characteristics of the source panchromatic image. In order to find out the fusion algorithm which is best suited for the P5 and P6 images, five fusion algorithms, such as Standard IHS, Modified IHS, PCA, Brovey and wavelet algorithms have been employed and analyzed. In this paper, eight evaluation criteria are also used for quantitative assessment of the fusion performance. The spectral quality of fused images is evaluated by the Spectral discrepancy, Correlation Coefficient (CC), RMSE and Mean Per Pixel Deviation (MPPD). For the spatial quality assessment, the Entropy, Edge detection, High pass filtering and Average Gradient (AG) are applied and the results are analyzed. The analysis indicates that the Modified IHS fusion scheme has the best definition as well as spectral fidelity, and has better performance with regard to the high textural information absorption. Therefore, as the study area is concerned, it is most suited for the IRS-P5 and P6 image fusion.

1. INTRODUCTION

Due to physical constraint, there is a trade off between spatial resolution and spectral resolution of a high resolution satellite sensor (Aiazzi et al., 2002), i.e., the panchromatic image has a high spatial resolution at the cost of low spectral resolution, and the multispectral image has high spectral resolution with a low spatial resolution (IKONOS: panchromatic image, 1m, multispectral image 4m; QuickBird: panchromatic image, 0.62m, multispectral image, 2.48m). To resolve this dilemma, the fusion of multispectral and panchromatic images, with complementary spectral and spatial characteristics, is becoming a promising technique to obtain images with high spatial and spectral resolution simultaneously (Gonzalez-Audicana et al., 2004). Image fusion is widely used to integrate these types of data for full exploitation of these data, because fused images may provide increased interpretation capabilities and more reliable results since data with different characteristics are combined. The images varying in spectral, spatial and temporal resolution may give a more comprehensive view of the observed objects (Pohl and Genderen, 1998).

2. IMAGE FUSION ALGORITHMS

Many methods have been developed in the last few years producing good quality merged images. The existing image fusion techniques can be grouped into four classes: (1) color related techniques such as intensity–hue–saturation (IHS) ; (2) statistical/numerical methods such as principal components analysis (PCA), high pass filtering (HPF), Brovey transform (BT), regression variable substitution (RVS) methods; (3) Pyramid based Methods such as Laplacian Pyramid, Contrast Pyramid, Gradient Pyramid, Morphological Pyramid and Wavelet Methods and (4) hybrid methods that use combined

methods from more than one group such as IHS and wavelet integrated method. This study analyzes five current image fusion techniques to assess their performance. The five image fusion methods used include Standard IHS, Modified IHS, PCA, Brovey and wavelet algorithms.

IHS (Intensity-Hue-Saturation) is the most common image fusion technique for remote sensing applications and is used in commercial pan-sharpening software. This technique converts a color image from RGB space to the IHS color space. Here the I (intensity) band is replaced by the panchromatic image. Before fusing the images, the multispectral and the panchromatic image are histogram matched.

Ideally the fused image would have a higher resolution and sharper edges than the original color image without additional changes to the spectral data. However, because the panchromatic image was not created from the same wavelengths of light as the RGB image, this technique produces a fused image with some color distortion from the original multispectral (Choi et al., 2008). There have been various modifications to the IHS method in an attempt to fix this problem (Choi et al., 2008; Strait et al., 2008; Tu et al., 2004; Siddiqui, 2003). In this research is used modification method suggested by Siddiqui (2003).

The Principal Component Analysis (PCA) is a statistical technique that transforms a multivariate dataset of correlated variables into a dataset of new uncorrelated linear combinations of the original variables (Pohl and Genderen, 1998). It is assumed that the first PC image with the highest variance contains the most amount of information from the original image and will be the ideal choice to replace the high spatial resolution panchromatic image. All the other multispectral bands are unaltered. An inverse PCA transform is performed on the modified panchromatic and multispectral images to obtain a high-resolution pan-sharpened image.

Brovey Transform uses addition, division and multiplication for the fusion of three multispectral bands (ERDAS, 1999). Its basic processing steps are: (1) add three multispectral bands together for a sum image, (2) divide each multispectral band by the sum image, (3) multiply each quotient by a high resolution pan.

In wavelet fusion method First, three new panchromatic images are produced according to the histogram of R, G, B bands of multispectral image respectively. Then each of the new high-resolution panchromatic images is decomposed into a low-resolution approximation image and three wavelet coefficients, also called detail images, which contain information of local spatial details. The decomposed low-resolution panchromatic images are then replaced by the real low-resolution multispectral image bands (B,G,R), respectively. In the last step, a reverse wavelet transform is applied to each of the sets containing the local spatial details and one of the multispectral bands (B,G,R). After three times of reverse wavelet transforms, the high-resolution spatial details from the panchromatic image are injected into the low-resolution multispectral bands resulting in fused high-resolution multispectral bands (Zhang, 2005).

3. QUALITY ASSESSMENT CRITERIA

Quality refers to both the spatial and spectral quality of images (Wald, 1997). Image fusion methods aim at increasing the spatial resolution of the MS images while preserving their original spectral content. The evaluation of the fusion results is based on the quantitative criteria including spectral and spatial properties and definition of images (Xu, 2004). In this paper, eight evaluation criteria are used for quantitative assessment of the fusion performance. The spectral quality of fused images is evaluated by the Spectral discrepancy, Correlation Coefficient (CC), RMSE and Mean Per Pixel Deviation (MPPD). For the spatial quality assessment, the Entropy, Edge detection, High pass filtering and Average Gradient (AG) are applied and the results are analyzed.

3.1 Spectral Quality Assessment

The basic principle of spectral fidelity is that the low spatial frequency information in the high-resolution image should not be absorbed to the fusion image, so as to preserve the spectral content of original MS image. The indexes which can inflect the spectral fidelity of fusion image include:

3.1.1 Correlation Coefficient: CC measures the correlation between the original and the fused images. The higher the correlation between the fused and the original images, the better the estimation of the spectral values (Han et al.,2008). The ideal value of correlation coefficient is 1.

$$CC(A, B) = \frac{\sum_{mn} (A_{mn} - \bar{A})(B_{mn} - \bar{B})}{\sqrt{(\sum_{mn} (A_{mn} - \bar{A})^2)(\sum_{mn} (B_{mn} - \bar{B})^2)}} \quad (1)$$

where \bar{A} and \bar{B} stand for the mean values of the corresponding data set, and CC is calculated globally for the entire image.

3.1.2 RMSE: RMS error as proposed by Wald (2002), which is computed as the difference of the standard deviation and the mean of the fused and the original image. The formula for RMSE is:

$$RMSE = \sqrt{bias^2 + \sigma^2}$$

$$\sigma = \sigma_{org} + \sigma_{fused} \quad (2)$$

$$bias = \bar{x}_{org} - \bar{x}_{fused}$$

In this formula s is standard deviation, x is Mean, org is Original image and $fused$ is Fused image.

3.1.3 Mean Per Pixel Deviation: For this method it is necessary to degrade the fused image to the spatial resolution of the original image. This image is then subtracted from the original image on a per pixel basis. As final step, we calculated the average deviation per pixel measured as digital number which is based on an 8-bit or 16-bit range, depending on the radiometric resolution of the employed images (Wald, 2002; Ehlers et al., 2008).

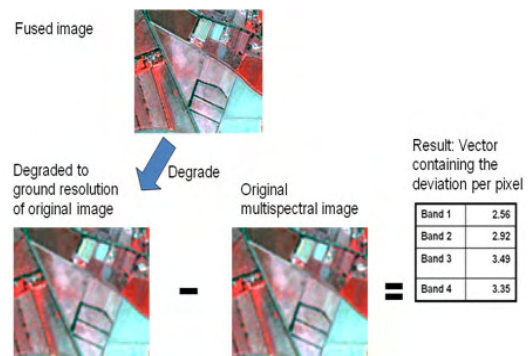


Figure 1. Calculation of Mean Per Pixel Deviation

3.1.4 Spectral discrepancy: The spectral quality of a $P \times Q$ fused image can be measured by the discrepancy D_k at each band (Li et al., 2005):

$$D_k = \frac{1}{P \cdot Q} \sum_{x=1}^P \sum_{y=1}^Q |F_k(x, y) - L_k(x, y)|, k = R, G, B \quad (3)$$

where $F_k(x, y)$ and $L_k(x, y)$ are the pixel values of the fused and original multispectral images at position (x, y) , respectively.

3.2 Spatial Quality Assessment

The basic principle of spatial fidelity is that The high spatial frequency information absorption is that the enhancement of resolution and increasing of information of the fused image relative to the original MS image. The indexes which can inflect the spatial fidelity of fusion image include:

3.2.1 High Pass Filtering: For the spatial quality, we compare the high frequency data from the panchromatic image to the high frequency data from each band of the fused image using a method proposed by Zhou in 2004. To extract the high frequency data we apply the following convolution mask to the images:

$$mask = \begin{bmatrix} -1 & -1 & -1 \\ -1 & 8 & -1 \\ -1 & -1 & -1 \end{bmatrix} \quad (4)$$

The correlation coefficients between the high-pass filtered fusion results and the high-pass filtered panchromatic image is used as an index of the spatial quality (Hong, 2007). The principle is that the spatial information unique in panchromatic image is mostly concentrated in the high frequency domain. The higher correlation between the high frequency components of fusion result and the high frequency component of panchromatic image indicates that more spatial information from panchromatic image has been injected into the fusion result.

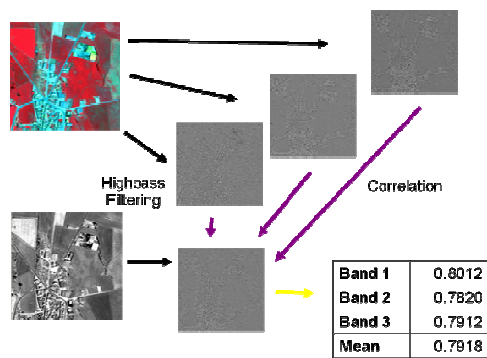


Figure 2. Spatial quality assessment by high pass filtering

3.2.2 Edge detection: In this method first detect the edges of panchromatic and fused image by canny operator. the more closely the edge data of the fused image matches the edge data of the panchromatic, indicating better spatial quality.

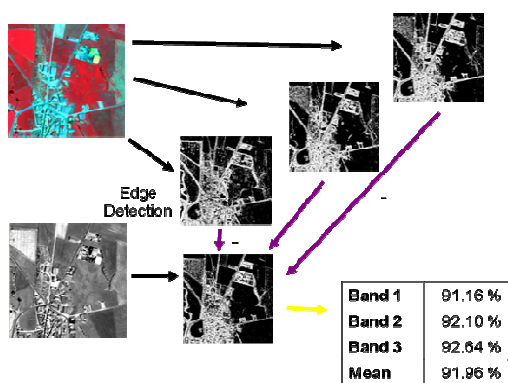


Figure 3. Spatial quality assessment by edge detection

3.2.3 Average gradient: For the spatial quality, we use the average gradient to evaluate the performance of the fused image F. That is

$$ag_k = \frac{1}{(P-1)(Q-1)} \times \sum_{x=1}^{P-1} \sum_{y=1}^{Q-1} \sqrt{\frac{(\frac{\partial F_k(x,y)}{\partial x})^2 + (\frac{\partial F_k(x,y)}{\partial y})^2}{2}}$$

$$k = R, G, B \quad (5)$$

where $F_k(x,y)$ is the pixel value of the fused image at position (x,y) . The average gradient reflects the clarity of the fused image. It can be used to measure the spatial resolution of the fused image, i.e., a larger average gradient means a higher spatial resolution (Li et al., 2005).

3.2.4 Entropy: Entropy as a measure to directly conclude the performance of image fusion. The Entropy can show the average information included in the image and reflect the detail information of the fused image (Han et al.,2008). Commonly, the greater the Entropy of the fused image is, the more abundant information included in it, and the greater the quality of the fusion is. According to the information theory of Shannon, The Entropy of image is:

$$E = - \sum_{i=0}^{255} P_i \log_2 P_i \quad (6)$$

Where E is the Entropy of image, and P_i is the probability of i in the image.

4. EXPERIMENT DATA AND ANALYSIS OF FUSION RESULTS

4.1 Experiment Data

The image fusion techniques applied on the IRS P5 and P6 satellite images. IRS-P6 multispectral image has three 5.8-m resolution spectral bands (Green,Red,NIR) and resolution of IRS-P5 panchromatic image is 2.5-m. The study area is chosen to cover different terrain morphologies. Figure 4 shows an example of the fused IRS-P6 MS and IRS-P5 pan images using five fusion algorithms, such as Standard IHS, Modified IHS, PCA, Brovey and wavelet algorithms.

4.2 Analysis of Fusion Results

Initial qualitative visual inspections reveal that all the fused images have better qualifications than original non-fused images. The sharpness of the fused images has been significantly enhanced. The further quantitative evaluation can be done with above criteria.

4.2.1 Spatial Quality Assessment: Figure 5 shows the correlation coefficients between high pass filtered results and high pass filtered panchromatic image, PC is the highest, Standard IHS is the second and wavelet is the lowest. That means the PC and Standard IHS fusion results are injected into the most spatial information, while the wavelet fusion result is injected into the least spatial information.

The average gradients of the images obtained by different fusion algorithms are shown in figure 6. The ag of Standard IHS is the highest in the five algorithms, and ag of PC and Modified IHS is the further maximum. therefore, the Standard IHS-fused image has absorbed the high spatial frequency information most and thus shows sharper than the others.

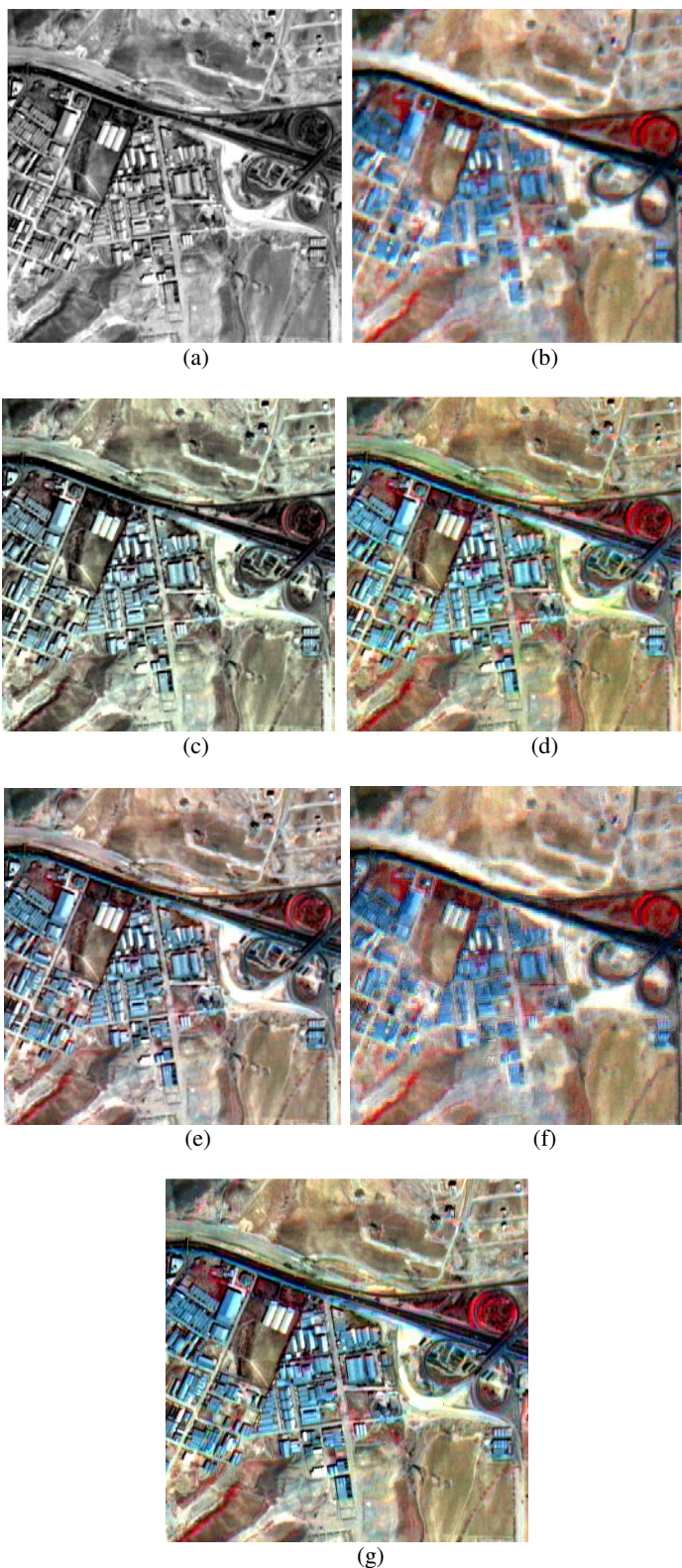


Figure 4. (a) original Pan image. (b) original MS image. (c) Standard IHS fused image. (d) modified IHS fused image. (e) PC fused image. (f) Wavelet fused image. (g) Brovey fused image.

Figure 7 shows the Entropy of each band MS and fused images. The Entropy of Standard IHS is the highest in the five algorithms. The Entropy can reflect the average information included in the fused image, therefore, the Standard IHS-fused image has absorbed the high spatial frequency information most and thus shows crisper than the others. Entropy of PC is the further maximum and Entropy of Brovey is minimum. Figure 8 shows the wavelet fusion result has the lowest of edge accordance with panchromatic image in the five algorithms, that indicating worse spatial quality.

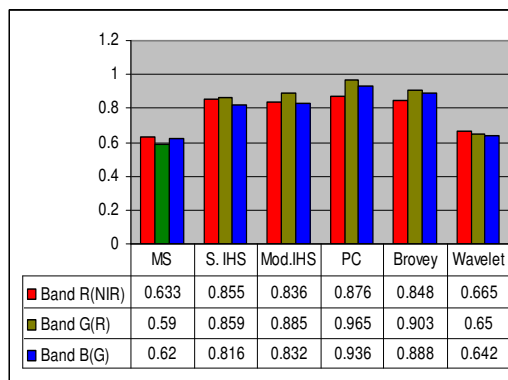


Figure 5. Correlation coefficients between the high pass filtered panchromatic image and high pass filtered fusion results.

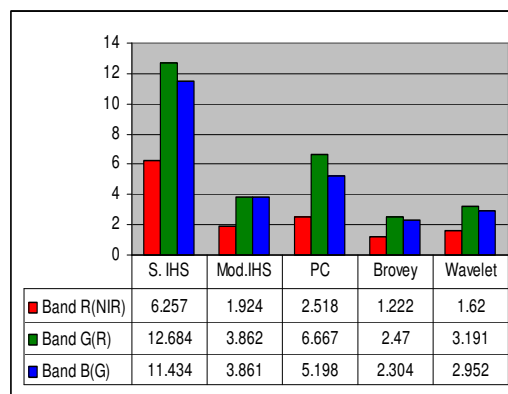


Figure 6. Average gradients of the fused images.

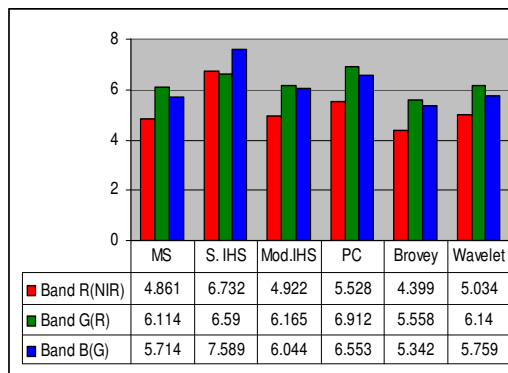


Figure 7. Entropy of the MS and fused images.

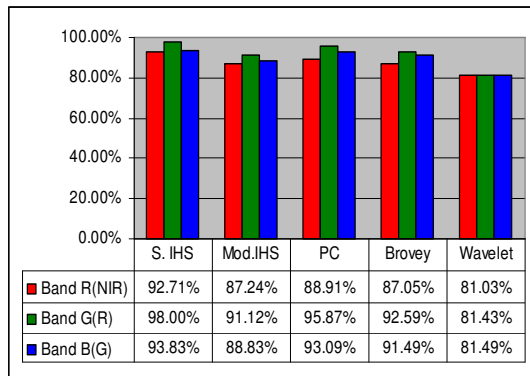


Figure 8. edge accordance of fused images with panchromatic image

4.2.2 Spectral Quality Assessment: In Figure 9, the original panchromatic image has a low correlation with the original multispectral image. The correlation between the fusion result and multispectral image are much greater than the correlation between the panchromatic image and multispectral image. The highest correlation coefficient is wavelet, therefore According to this quantitative analysis, wavelet is the best that means preserve the spectral characteristics of the source multi-spectral image.

Figure 10 shows the spectral discrepancies between the images obtained by different fusion algorithms and the source multispectral image. It clearly indicates that the discrepancy of wavelet is the minimum, and discrepancies of Modified IHS is the further minimum. So wavelet is the best method in retaining spectral property of the original image among the five used methods and Modified IHS takes second place.

Figure 11 shows the RMSE of MS and fused images. It clearly indicates that the RMSE of wavelet is the minimum, and RMSE of Modified IHS is the second minimum.

Figure 12 shows that The MPPD of PC-fused image is the highest in the five algorithms. wavelet is the minimum.

According to the RMSE and MPPD, we can see that the wavelet-fused image has the maximal relativity with MS image. So wavelet is the best method in retaining spectral property of the original image among the five used methods, and Modified IHS takes second place.

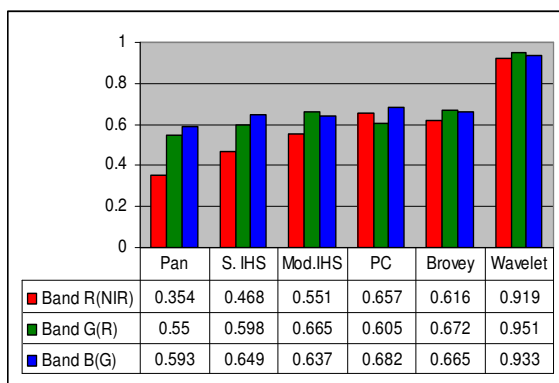


Figure 9. Correlation coefficient between the original multispectral image and fusion results

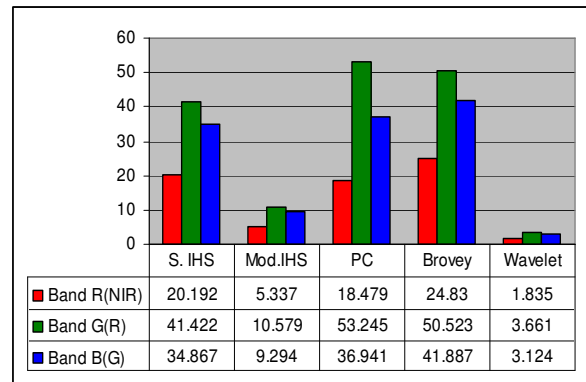


Figure 10. Spectral discrepancies between the the original multispectral image and fusion results

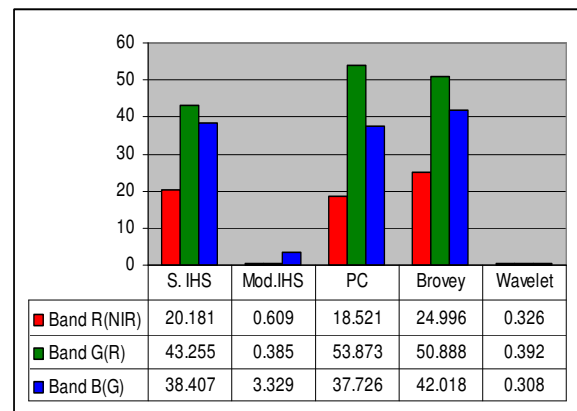


Figure 11. RMSE between the the original multispectral image and fusion results

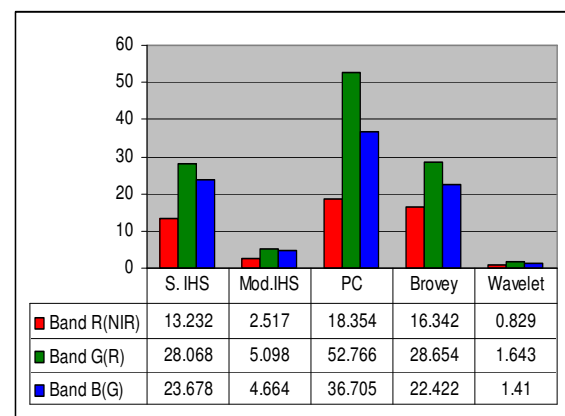


Figure 12. MPPD of the fused images.

5. CONCLUSIONS

Finally, from the above analysis and comparison, we can conclude that Modified IHS algorithm can preserve the spectral characteristics of the source multispectral image as well as the high spatial resolution characteristics of the source panchromatic image and suited for fusion of IRS P5 and P6 images.

In PC and Standard IHS image fusion, dominant spatial information and weak colour information is an often problem, Therefore are suited for visual interpretation, image mapping, and photogrammetric purposes.

wavelet is the best method in retaining spectral property of the original image among the five used methods at the cost of low spatial information, Therefore are suited for digital classification purposes.

References

Aiazzi, B., L. Alparone, S. Baronti, and A. Garzelli, 2002. Context driven fusion of high spatial and spectral resolution images based on oversampled multiresolution analysis. *IEEE Transactions on Geoscience and Remote Sensing*, Vol. 40, No. 10, pp.2300-2312.

Choi, M.-J, H.-C. Kim, N.I. Cho, and H.O. Kim., 2008. An Improved Intensity-Hue-Saturation Method for IKONOS Image Fusion. *International Journal of Remote Sensing*.

ERDAS, 1999. On-Line Manuals version 8.4, Atlanta, Georgia.

Ehlers, M., Klonus, S., Åstrand, P.J., 2008. Quality assessment for multi-sensor multi-date image fusion. *The International Archives of the Photogrammetry, Remote Sensing and Spatial Information Sciences*. Vol. XXXVII. Part B4.

Gonzalez-Audicana, M., J.L. Saleta, and R.G. Catalan, 2004. Fusion of multispectral and panchromatic images using improved IHS and PCA mergers based on wavelet decomposition. *IEEE Transactions on Geoscience and Remote Sensing*, Vol. 42, No. 6, pp. 1204–1211.

Han, S.S., Li, H.T., Gu, H.Y., 2008. The study on image fusion for high spatial resolution remote sensing images. *The International Archives of the Photogrammetry, Remote Sensing and Spatial Information Sciences*. Vol. XXXVII. Part B7.

Li, Z., Jing, Z., Yang, X., Sun, S., 2005. Color transfer based remote sensing image fusion using non-separable wavelet frame transform. *Pattern Recognition Lett.* 26 (13) (2005) 2006–2014.

Pohl, C., and J.L. Van Genderen, 1998. Multisensor image fusion in remote sensing: concepts, methods, and applications. *International Journal of Remote Sensing*, Vol. 19, pp 823-854.

Siddiqui, Y., 2003. The Modified IHS Method for Fusing Satellite Imagery. In: *ASPRS 2003 Annual Conference Proceedings*.

Strait, M., Rahmani, S., Markurjev, D., 2008. Evaluation of Pan-Sharpning Methods, Research Experiences for Undergraduates (REU2008).

Tu, T.M., P.S. Huang, C.L. Hung, and C.P. Chang, 2004. A Fast Intensity-Hue Saturation Fusion Technique with Spectral Adjustment for IKONOS Imagery. *IEEE Geoscience and Remote Sensing Letters* 1, pp. 309-312.

Wald, L., Ranchin, Th., Mangolini, M.,1997. Fusion of satellite images of different spatial resolutions: Assessing the quality of resulting images. *Photogrammetric Engineering and Remote Sensing*, 63(6), pp. 691-699.

Wald, L., 2002. Data fusion - Definitions and architectures - Fusion of images of different spatial resolutions. *École de Mines de Paris*.

Xu, H.Q.,2004. Assessment of The SFIM Algorithm. *Chinese Geographical Science*, 14(1): pp. 48-56.

Zhang, Y., Hong, G., 2005. An IHS and wavelet integrated approach to improve pan-sharpening visual quality of natural colour Ikonos and QuickBird images. *Information Fusion* 6 (3), 225–234.

STUDY ON USER REQUIREMENTS FOR REMOTE SENSING APPLICATIONS IN FORESTRY

B. Felbermeier, A. Hahn, T. Schneider

Technische Universität München, Institute of Forest Management, Hans-Carl-v.-Carlowitz-Platz 2, 85354, Freising, Germany

KEY WORDS: Forestry, User requirements

ABSTRACT:

State forest administrations in Central Europe have to adapt to future climatic and socioeconomic conditions. This results in new demands for actual and precise forest information - especially in regard to increasing forest damages by natural hazards. Therefore the data requirements of professional foresters were investigated to derive development goals for remote sensing applications in forestry. A questionnaire was sent to 655 professionals in Southern Germany and answered by 347 of them. Two third describe deficiencies in their forest information and 90 % of them expect improvements by the application of remote sensing techniques. The majority of the professionals want to be supported by a forest information system integrating existing data bases and remote sensing derived information. More than 200 examples were defined for the potential use of remote sensing applications. The majority of the examples are related to the management of natural hazards and the consulting of private land owners. Improvements of the present situation are expected especially by annual updates of the forest data bases at stand level resolution.

1. INTRODUCTION

Remote sensing is expected to become more important for sustainable forestry in Central Europe. The main reasons are a growing number of geospatial applications, the reorganisation of the forestry sector, and the need to improve forest management especially in regard to forest damages caused by increasing natural hazard frequencies. The study therefore arises from the expected problems of information availability for sustainable forest management and addresses the information needs of forest professionals for remotely sensed forest information in Bavaria/Southern Germany.

2. INFORMATION NEEDS

An inventory of existing literature detected several user need assessments in forest remote sensing from regional to global scales (International Institute for Aerospace Survey and Earth Sciences, 1999; Beule et al., 2004; Institute of Digital Image Processing, Graz et al., 2000; Schneider et al., 1998; Blaschke, 2002). In a globally comprehensive study the user requirements for remote sensing based spatial information in sustainable management of forests were collected from all countries (International Institute for Aerospace Survey and Earth Sciences, 1998) and can be used as a reference:

- The most spatial information is needed in regard to planning/implementation, monitoring/assessment, area demarcation/mapping and policy development/advising.
- The highest demand for remote sensing data exist in the fields of determination of forest area and its change, thematic mapping including past decades, monitoring of species and biodiversity, land use and forest land classification, forest production, and site classification.
- New remote sensing data should be distributed annually or at least every 5 years.

2.1 Demand on regional level

In a workshop user requirements for remote sensing applications were collected from 21 experts of the Bavarian State Forest Administration using business process analysis techniques (Rosenkranz, 2006). As a result the following regional processes and demands for remote sensing were documented:

2.1.1 Surveillance of sustainable forest management: The national forest inventory is not sufficient for the purpose of the state forest administration. Therefore a method is required to conduct a low cost regional forest inventory to quantify the forest area, forest age classes, tree species composition, vertical and horizontal diversity, forest stand height and density, growing stock and increment, and areas of damaged forest. The data are required on forest stand level and should be collected at least every 5 years. The regional inventory would improve the surveillance of a sustainable forest management of all forest owners - especially in regard to the detection of cleared areas and losses of growing stock. It could be used by further processes described below.

2.1.2 Forest protection: The terrestrial detection of insect pests is time consuming and therefore always fragmentary. Hence remote sensing technologies are needed to improve the early localisation of the origin of pests, the prognosis of the propagation, and the development of treatment plans. The information is needed every week during the critical development phases of insects and has to focus on the detection of single tree species, dead wood, and defoliation on stand level. In the case of large scale abiotic and biotic calamities ad hoc data of damaged areas, damage intensities, affected tree species, volumes of damaged timber and reforestation areas are needed on stand level.

Large-scale monitoring of the forest condition is presently based on the annual terrestrial surveys. In order to reduce monitoring costs remote sensing can be used to determine tree species, tree age, defoliation, discolouration and other visible

damages on tree level at the inventory points. The new procedure must coincide with the monitoring standards of the last years to continue the present time series.

2.1.3 Nature conservation: The management of nature conservation areas (e.g. Natura 2000) should be supported by remote sensing. Besides the information of a new regional forest inventory, specific parameters have to be collected in the protected areas e.g. dead wood volumes on stand level, single biotope trees and specific topographical/hydrological features. The linkage of protection areas to biotope networks needs remote sensed data of linear biotope structures in open areas (i.e. hedges) and of the fragmentation effects by infrastructure.

2.1.4 Forest Planning: Planning tasks generally can be improved by the results of a new remote sensed based regional forest inventory. Within the mapping of forest functions specific tasks are the distinction of forest and open areas and the classification of stand structures in regard to habitat, landscape and recreational functions. In the case of the management of mountain protection major inaccuracies can be eliminated by a detailed detection of open forest areas, bare land and avalanche zones. For the rehabilitation of mountain protection forests 5-year information on tree species composition, vitality, regeneration, ground vegetation, forest gaps, snow height and snow dynamics should be supplied on stand and tree level respectively.

2.1.5 Advice and financial support: The technical advice of forest owners shall be improved especially in regard to the expected climate change aspects. Therefore an integrated information system is requested, which combines the results of the regional forest inventory with data about forest owners as address, forest ownership and financial aids. For the control of granted subsidies very detailed information on project areas ($\pm 10\text{m}^2$), species composition ($\pm 5\%$), individual trees (i.e. biotope trees) and unstocked areas ($\pm 10\text{m}^2$) are needed.

2.1.6 Public awareness: Forest management relies on the support by the public. Forest development and human intervention must be understood by the people (e.g. the adaptation of the present forest to climate change conditions). Therefore the results of the remote sensing applications play an important role for the information of the public with quantitative data and visual media.

2.2 Demand on local level

A census of the forestry professional staff at the local forest offices in Bavaria was conducted to derive the information requirements on local level. The postal questionnaire (Atteslander et al., 2008) consists of three parts: (a) Questions on existing information gaps and presently applied remote sensing techniques (4 multiple choice questions and 1 open question). (b) Questions on potential fields of application for remote sensing and on requirements for the determination of forest parameters (12 multiple choice and 4 open questions). (c) Voluntary personal information to build up a user panel. The questionnaire was distributed to 655 individuals anonymously. The evaluation of the questionnaire took place by classification procedures for open questions and descriptive statistics. 347 persons (52 %) responded to the questionnaire. The results of the questionnaire were used to answer the following research questions:

2.2.1 Can any benefits be expected from remote sensing applications for forestry practice? Two-third of the respondents indicated, that they can not sufficiently fulfil all duties, because the required information is not available. 90% of them expect that the information gap can be closed by remote sensing.

2.2.2 Which remote sensing techniques are applied at present? One-half of the respondents interpret visually official aerial photos and satellite images from the internet. Frequently agricultural information systems, which contain remote sensing applications, are applied for forestry tasks.

2.2.3 What are the priorities for a better application of the present remote sensing techniques? Two-third of the respondents awaits a major improvement by more actual remote sensing products - especially aerial photographs. One half expects more information by a better quality of remote sensing data. One fifth of the respondents claimed a higher repetition frequency by high resolution remote sensing techniques.

2.2.4 What are the future potential fields of application for remote sensing in forestry? 217 potential applications for remote sensing were proposed. The main application fields are the management of forest damages caused by natural hazards and the consulting of private forest land owners.

2.2.5 Which forest parameters have to be addressed by remote sensing applications? Out of 63 forest parameters the determination of tree species composition, forest areas, forest boundaries and forest stand heights are the most relevant (Table 1). This information should be available on an annual base and at least updated every 5 years. In most cases there exist no constraints concerning the recording period during the year. The spatial resolution of the delivered information should be at least on forest stand level.

Parameter	Relative frequency
Tree species	12%
Area of forest, forest stands or damages	11%
Boundary of forest, stands or damages	9%
Stand height	9%
Growing stock	5%
Forest stand age	4%
Forest stand density	4%
Location of logging roads	4%
Broadleaved/conifer stands	3%
Succession type	3%
Vitality	2%
Insect pests	2%
Forest gaps	2%
Forest regeneration	2%
Tree species mixture	2%

Table 1 Ranking of the 15 mostly mentioned parameters to be collected by remote sensing

2.2.6 How should forest professionals be supplied with remote sensing products? Two-third of respondents prefers to work with standardized remote sensing products available through a spatial forest information system. One tenth of the staff would use remote sensing data directly or have a demand for case specific data analysis by experts.

3. CONCLUSIONS

The survey showed a high demand for additional forest information concerning most duties of a state forest administration. A comparison of user requirements with available remote sensing technology shows, that the most parameters can be determined by remote sensing methods (Falkowski et al., 2009) or in combination with existing geospatial forest information (Förster, 2008). Therefore it can be foreseen that the integral development of remote sensing based geospatial forest information systems may remove most of the existing information gaps.

The results of this study are generally in line with the findings of other studies from local to global level. Even though there exist differences in the spatial resolution and ecological conditions there appear to be strong similarities in the requirements profile for remote sensing applications in forestry and forest administrations. Therefore new remote sensing products for forestry can be developed according to the demands of the global market.

REFERENCES

- Atteslander, P., Cromm, J. 2008. *Methoden der empirischen Sozialforschung*. Schmidt, Berlin, pp. 359.
- Beule, B., Backhaus, R. 2004. Anforderungsanalyse der Nutzung von satellitenbasierten Erdbeobachtungssystemen für die Umweltpolitik (SATUM). Umweltbundesamt (UBA) Texte 32-04, pp. 120.
- Blaschke, R. 2002. Inventur und Beobachtung der Schutzwälder in alpinen Regionen - Nutzungsmöglichkeiten hochauflösender Satellitendaten Inventur und Beobachtung. Final Report Project V43, pp. 342.
- Falkowski, M.J., Wulder, M.A., White, J.C., Gillis, M.D. 2009. Supporting large-area, sample-based forest inventories with very high spatial resolution satellite imagery. *Progress in Physical Geography*, 33, pp. 403–423.
- Förster, M. 2008. Integration of Geo-Information in Classification Processes of Satellite Imagery for NATURA 2000 Monitoring. PhD Thesis, Berlin, pp. 139.
- Institute of Digital Image Processing/Graz, Department of Remote Sensing and Land Information Systems/Freiburg, Institute for Landuse Planning and Nature Conservation/Freising, Austrian Research Centre/Seibersdorf, Swiss Federal Institute for Forest, Snow and Landscape Research/Birmensdorf, Sachverständigenbüro für Luftbildauswertung und Umweltfragen/Gräfelfing. 2000. ALPMON: Inventory of alpine-relevant parameters for an alpine monitoring system using remote sensing data. Contract ENV4-CT96-0359, Final Report, pp. 123.
- International Institute for Aerospace Survey and Earth Sciences 1998. User requirements study for remote sensing based spatial information for the sustainable management of forests. User needs assessment for spatial forest information: Results and analysis. Workpackage Report. pp. 47.
- International Institute for Aerospace Survey and Earth Sciences 1999. User requirements study for remote sensing based spatial information for the sustainable management of forests: Design of the user needs assessment study. Workpackage Report. pp. 46.

Rosenkranz F. 2006. *Geschäftsprozesse: Modell- und Computergestützte Planung*, Springer, Berlin. pp. 356.

Schneider, T., Ammer, U. 1998. Concept and first results of a remote sensing based monitoring system for the Bavarian Alps. Workshop proceedings, 11-13 October, 1998, Bled, Slovenia, International workshop series on sustainable regional development.

ACKNOWLEDGEMENTS

This study was supported by the Bayerische Staatsministerium für Ernährung, Landwirtschaft und Forsten under project number ST 237.

TARGETED CHANGE DETECTION: A NOVEL SENSOR-INDEPENDENT PARTIALLY-SUPERVISED APPROACH

D. Fernández-Prieto^a, M. Marconcini^{a,*}

^a Dept. of Earth Observation Science, Applications and Future Technologies, European Space Agency, ESA-ESRIN, Via Galileo Galilei, 00044, Frascati, Rome, Italy - (diego.fernandez, mattia.marconcini)@esa.int

KEY WORDS: Change Detection, Land Cover, Satellite, Multitemporal, Multispectral, Hyperspectral

ABSTRACT:

In several real-world applications (e.g., forestry, agriculture), the objective of change detection is actually limited to one (or few) specific “targeted” land-cover transition(s) affecting a certain area in a given time period. In such cases, ground-truth information is generally available for the only land-cover classes of interest at the two dates, which limits (or hinders) the possibility of successfully employing standard supervised approaches. Moreover, even unsupervised change-detection methods cannot be effectively used, as they allow identifying all the areas experiencing any type of change, but not discriminating where specific land-cover transitions of interest occur. In this paper, we present a novel technique capable of addressing this challenging issue (formulated in terms of a compound decision problem) by exploiting the only ground truth available for the targeted land-cover classes at the two dates. In particular, the proposed method relies on a partially-supervised approach and jointly exploits the Expectation-Maximization (EM) algorithm and an iterative labelling strategy based on Markov random fields (MRF) accounting for spatial and temporal correlation between the two images. Moreover, it also allows handling images acquired by different sensors at the two investigated times. Experimental results on different multi-temporal and multi-sensor data sets confirmed the effectiveness and the reliability of the proposed technique, which provided change-detection accuracies comparable with those obtained by fully-supervised methods.

1. INTRODUCTION

Detecting changes occurring on the Earth’s surface represents one of the main applications of satellite remote sensing. Indeed, in a variety of different fields and applications (e.g., urban planning, forestry, agriculture, disaster management, etc.) the employment of multi-temporal satellite data has become essential for identifying where and (when possible) which types of transitions have occurred between two given dates (Jensen, 2009).

Generally, change-detection methods are categorized as either supervised or unsupervised, depending on the availability of suitable prior information (Coppin *et al.*, 2004; Duda *et al.*, 2000; Lu *et al.*, 2004; Radke *et al.*, 2005; Singh, 1989).

When an exhaustive multi-temporal ground truth characterizing all the land-cover classes over the area of interest at both times is available, then, supervised approaches can be applied. These types of techniques are generally robust and effective, and allow identifying all the land-cover transitions occurred between the two considered dates. In this framework, three main approaches are generally employed: post-classification comparison (PCC), supervised direct multi-data classification (DMC) and compound classification (Duda *et al.*, 2000; Lu *et al.*, 2004; Singh, 1989).

When no ground truth is available, instead, unsupervised techniques must be used, which allow detecting areas experiencing changes (being even capable of separating land-cover transitions of different nature and characterizing their distribution), but are unable to provide information on the specific type of changes occurred. Several unsupervised change-detection techniques have been presented so far in the literature. Most of them are based on image differencing, image ratioing, image regression, change vector analysis (CVA) and principal component analysis (PCA), which all require the selection of proper thresholds for determining changed regions (Coppin *et al.*, 2004; Lu *et al.*, 2004; Radke *et al.*, 2005).

It is worth noting that, in the above described framework, su-

pervised methods represent an ideal approach to change-detection analysis, since they permit both to identify areas experiencing changes, as well as to reliably determine the associated land-cover transitions. Nevertheless, their range of applicability is significantly limited by the difficulties in gathering exhaustive and accurate ground-truth information for all the land-cover classes characterizing each date under analysis. Indeed, such a requirement is costly, time consuming and not always possible or feasible to satisfy.

However, in several operational change-detection problems the main objective is not to characterize all the land-cover transitions occurred in the investigated area, but rather to identify a single (or few) targeted land-cover transition(s) of interest. This is typical for instance in agriculture, urban planning, or forestry applications. In such circumstances, when only one (or few) specific land-cover transitions need to be identified, it is reasonable to assume that the collection of ground-truth information associated with the only (or few) land-cover class(es) of interest at the two considered dates is highly simplified. However, under this assumption, neither supervised nor unsupervised change-detection techniques can be effectively employed. Let us consider for instance the case of two images acquired over the same area at different times t_1 and t_2 , where the objective is to identify all the patterns experiencing the targeted land-cover transitions from class “A” (e.g., forest) to “B” (e.g., urban area) under the hypothesis that a ground truth for class “A” at t_1 and for class “B” at t_2 is available (or can be easily retrieved by an operator), respectively. In this context, on the one hand, supervised techniques cannot be used, since the lack of an exhaustive ground truth characterizing all the land-cover classes at the two dates under consideration will not allow a successful training of the classifiers. On the other hand, unsupervised techniques may allow identifying all the areas experiencing any type of change, but not discriminating where specific targeted land-cover transitions of interest occur. In this latter case, a comparison (e.g., through a significance-testing approach (Jeon and Landgrebe, 1999)) of the labelled samples available for the

classes of interest at the two dates against all those identified as changed pixels may provide some degree of information on the type of land-cover transition, but not with the accuracy and reliability provided by fully-supervised approaches).

In this paper, we formulate this complex issue in terms of a compound decision problem (Duda *et al.*, 2000) and propose a novel partially-supervised change-detection (PSCD) technique capable of exploiting the only prior knowledge available for the specific land-cover classes of interest at the two times (thus avoiding the need to rely on exhaustive ground-truth information for all the classes), while providing accuracies comparable with those of fully-supervised methods. Moreover, it has the great advantage of being sensor-independent, which allows selecting at each date the set of sensors and features most suitable for characterizing the targeted class(es) of interest.

The proposed method aims at estimating at each date the probability density function (PDF) and the prior of both the class(es) of interest and the remaining unknown land-cover classes (for which no ground truth is available) represented as a single unknown information class. In particular, PDFs are approximated by a mixture of suitable basis functions whose free parameters are determined employing the iterative Expectation-Maximization (EM) algorithm (Dempster *et al.*, 1977). Changed pixels are then identified using an iterative labelling strategy based on Markov random fields (MRF) (Solberg *et al.*, 1996) which allows taking into account both spatial and temporal correlation between the two images, as well as properly constraining the probability estimates.

For demonstrating the capabilities of the proposed method, extensive experimental trials have been carried out with different combinations of multispectral, hyperspectral and SAR data. Obtained results confirmed the effectiveness and the reliability of the proposed technique, which provided very promising results. In particular, accuracies are comparable to those achieved with the PCC method in the presence of an exhaustive ground truth for each image both considering the maximum likelihood (ML) classifier (Richards and Jia, 2006), as well as support vector machines (SVM) (Cristianini and Shawe-Taylor, 2000).

2. PROBLEM FORMULATION AND ASSUMPTIONS

For the sake of simplicity we will describe the problem and the proposed method under the assumption of a single targeted land-cover transition of interest. The extension to the case of multiple transitions is straightforward.

Let us consider two $I \times J$ co-registered remote-sensing images $\mathcal{X}^1 = \{\mathbf{x}_{ij}^1\}_{i,j=1}^{I,J}$, $\mathbf{x}_{ij}^1 \in \mathbb{R}^{D_1}$, and $\mathcal{X}^2 = \{\mathbf{x}_{ij}^2\}_{i,j=1}^{I,J}$, $\mathbf{x}_{ij}^2 \in \mathbb{R}^{D_2}$, referring the same geographical area at times t_1 and t_2 , respectively, where \mathbf{x}_{ij}^1 , \mathbf{x}_{ij}^2 represent corresponding feature vectors (even derived from different sets of sensors at each date, respectively, and merged using a stacked vector approach (Richards and Jia, 2006)) associated with the pixel at position (i, j) , and D_1 , D_2 define respective dimensionalities.

Let $\Omega^1 = \{\omega^1, \dots, \omega_{N_1}^1\}$ and $\Omega^2 = \{\omega^2, \dots, \omega_{N_2}^2\}$ be the set of land-cover classes characterizing \mathcal{X}^1 and \mathcal{X}^2 , respectively. In the following, we will denote as $\omega_{m_1}^1 \in \Omega^1$ and $\omega_{m_2}^2 \in \Omega^2$ the information classes of interest at t_1 and t_2 , for which N_1 and N_2 labelled training patterns are available, respectively. Hence, $\omega_{m_1}^1 = \{\Omega^1 - \omega_{m_1}^1\}$ and $\omega_{m_2}^2 = \{\Omega^2 - \omega_{m_2}^2\}$ will represent corresponding unknown classes (each consisting of the merger of remaining classes, for which no ground truth is available).

Let $\mathcal{C}^1 = \{C_{ij}^1\}_{i,j=1}^{I,J}$ and $\mathcal{C}^2 = \{C_{ij}^2\}_{i,j=1}^{I,J}$ denote two sets of labels for \mathcal{X}^1 and \mathcal{X}^2 , respectively, where $C_{ij}^1 \in \{\omega_{m_1}^1, \omega_{m_1}^1\}$ and $C_{ij}^2 \in \{\omega_{m_2}^2, \omega_{m_2}^2\}$ are associated with the pixel at position (i, j) . In this framework, our aim is to identify the two sets $\tilde{\mathcal{C}}^1$, $\tilde{\mathcal{C}}^2$

maximizing the posterior probability given the two images \mathcal{X}^1 , \mathcal{X}^2 and, finally, to draw pixels experiencing the targeted land-cover transition from $\omega_{m_1}^1$ to $\omega_{m_2}^2$. This can be formalized as a compound decision problem (Duda *et al.*, 2000):

$$\{\tilde{\mathcal{C}}^1, \tilde{\mathcal{C}}^2\} = \underset{\mathcal{C}^1, \mathcal{C}^2}{\operatorname{argmax}} \{P(\mathcal{C}^1, \mathcal{C}^2 | \mathcal{X}^1, \mathcal{X}^2)\} \quad (1)$$

According with the Bayes theory, finding a solution to (1) is equal to determine the sets of labels maximizing the likelihood $\mathcal{L}(\mathcal{X}^1, \mathcal{X}^2 | \mathcal{C}^1, \mathcal{C}^2) = P(\mathcal{C}^1, \mathcal{C}^2) \cdot p(\mathcal{X}^1, \mathcal{X}^2 | \mathcal{C}^1, \mathcal{C}^2)$.

In the reasonable hypothesis of time-conditional independence, the problem can be written as:

$$\{\tilde{\mathcal{C}}^1, \tilde{\mathcal{C}}^2\} = \underset{\mathcal{C}^1, \mathcal{C}^2}{\operatorname{argmax}} \{\mathcal{L}(\mathcal{X}^1, \mathcal{X}^2 | \mathcal{C}^1, \mathcal{C}^2) = P(\mathcal{C}^1, \mathcal{C}^2) \cdot p(\mathcal{X}^1 | \mathcal{C}^1) \cdot p(\mathcal{X}^2 | \mathcal{C}^2)\} \quad (2)$$

where $p(\mathcal{X}^1 | \mathcal{C}^1)$ and $p(\mathcal{X}^2 | \mathcal{C}^2)$ represent the conditional PDFs at t_1 and t_2 respectively.

3. PROPOSED PARTIALLY-SUPERVISED CHANGE-DETECTION TECHNIQUE

For addressing the complex task described in Section 2, we propose a novel partially-supervised technique aimed at approximating the class-conditional densities $p(\mathcal{X}^1 | \mathcal{C}^1)$, $p(\mathcal{X}^2 | \mathcal{C}^2)$ as mixtures of suitable basis kernel functions and estimating the joint prior probability $P(\mathcal{C}^1, \mathcal{C}^2)$ properly taking into consideration the spatio-temporal context.

The rationale is based on the observation that the PDF of an image can be always approximated by a mixture of suitable kernels (i.e., Parzen density estimation (Duda *et al.*, 2000)). Accordingly, similarly to what is commonly done in the context of Radial Basis Function Neural Networks (RBF-NN) (Bruzzone and Fernández-Prieto, 1999), we model for each pixel of both images the PDFs $p(\mathbf{x}_{ij}^1)$, $p(\mathbf{x}_{ij}^2)$ as a mixture of K circularly symmetric multivariate Gaussian functions. Kernel parameters (i.e., centres and variances) are initialized using the k -mean clustering algorithm (Bruzzone and Fernández-Prieto, 1999), whereas final estimates are obtained by using the EM algorithm (Dempster *et al.*, 1977). Then, class-conditional densities of the interest class $p(\mathbf{x}_{ij}^1 | \omega_{m_1}^1)$, $p(\mathbf{x}_{ij}^2 | \omega_{m_2}^2)$ are modelled by properly weighting the resulting set of kernels using again the EM algorithm over the training samples available for $\omega_{m_1}^1$ and $\omega_{m_2}^2$. This is somewhat analogous to the training phase of RBF-NN which is generally carried out in two steps: i) selection of centres and variances of the kernel functions associated with hidden units on the basis of clustering techniques; and ii) computation of weights associated with the connections between the hidden and output layers on the basis of available training patterns.

The PDF of the entire image is itself a mixture of the interest and unknown class-conditional densities, weighted by corresponding prior probabilities. Accordingly, we obtain a first rough approximation for $p(\mathbf{x}_{ij}^1 | \omega_{m_1}^1)$, $p(\mathbf{x}_{ij}^2 | \omega_{m_2}^2)$ initializing priors to 0.5. Afterwards, estimates are refined using a novel MRF-based iterative labelling strategy accounting for spatio-temporal correlation, which permits to model $P(\mathcal{C}_{ij}^1, \mathcal{C}_{ij}^2)$ mutually considering the local neighbourhood of each pixel in the two images. Finally, changed pixels are identified and associated with the targeted land-cover transition by minimizing a

proper energy function. In the following, we will first introduce the method adopted for modelling both the class-conditional densities and the joint prior probability; then, we will present the iterative strategy for identifying the sets of labels \tilde{C}^1, \tilde{C}^2 maximizing the likelihood $\mathcal{L}(\mathcal{X}^1, \mathcal{X}^2 | \mathcal{C}^1, \mathcal{C}^2)$.

3.1 Conditional Density Modelling

Computing $p(\mathcal{X}^t | \mathcal{C}^t)$, $t=1,2$, requires at the two considered dates the estimation of the class-conditional densities $p(\mathbf{x}_{ij}^t | \omega_{int}^t)$ and $p(\mathbf{x}_{ij}^t | \omega_{unk}^t)$, $\forall \mathbf{x}_{ij}^t \in \mathcal{X}^t$. The proposed approach is based on the observation that the PDF of each pixel can be modelled as a mixture of the conditional PDFs of both the interest and unknown classes:

$$p(\mathbf{x}_{ij}^t) = P(\omega_{int}^t) \cdot p(\mathbf{x}_{ij}^t | \omega_{int}^t) + P(\omega_{unk}^t) \cdot p(\mathbf{x}_{ij}^t | \omega_{unk}^t) \quad (3)$$

According with Parzen density estimation (Duda *et al.*, 2000), we aim at obtaining a reliable nonparametric estimate for $p(\mathbf{x}_{ij}^t)$ as a mixture of a suitable set of kernel functions $\Phi^t = \{\phi^k(\cdot)\}_{k=1}^K$:

$$\hat{p}(\mathbf{x}_{ij}^t) = \sum_{k=1}^K w_k^t \cdot \phi^k(\mathbf{x}_{ij}^t) \quad (4)$$

where K denotes the number of kernels (a free parameter to be set by the user), and $\mathcal{W}^t = \{w_k^t\}_{k=1}^K$ represent the weights regulating the contribution of each kernel.

However, since the density $p(\mathbf{x}_{ij}^t)$ is given by a linear combination of $p(\mathbf{x}_{ij}^t | \omega_{int}^t)$ and $p(\mathbf{x}_{ij}^t | \omega_{unk}^t)$, it is worth noting that, if the set of kernels Φ^t allows obtaining a reliable estimate $\hat{p}(\mathbf{x}_{ij}^t)$, then also both the class-conditional densities can be reliably approximated as a linear combination of Φ^t . Hence, they can be estimated as:

$$\hat{p}(\mathbf{x}_{ij}^t | \omega_{int}^t) = \sum_{k=1}^K w_{int\ k}^t \cdot \phi^k(\mathbf{x}_{ij}^t) \quad (5)$$

$$\hat{p}(\mathbf{x}_{ij}^t | \omega_{unk}^t) = \sum_{k=1}^K w_{unk\ k}^t \cdot \phi^k(\mathbf{x}_{ij}^t) \quad (6)$$

where $\mathcal{W}_{int}^t = \{w_{int\ k}^t\}_{k=1}^K$, $\mathcal{W}_{unk}^t = \{w_{unk\ k}^t\}_{k=1}^K$ are the weights regulating the contribution of each kernel for the interest and unknown classes, respectively.

As commonly done in the literature we consider normalized isotropic Gaussian kernels, i.e.

$$\phi^k(\mathbf{x}_{ij}^t) = \frac{1}{(\sqrt{2\pi\sigma_k^{2t}})^{D_t}} \exp\left[-\frac{\|\mathbf{x}_{ij}^t - \boldsymbol{\mu}_k^t\|^2}{2\sigma_k^{2t}}\right] \quad (7)$$

where $\boldsymbol{\mu}_k^t$ is the centre and σ_k^{2t} is the variance (which tunes the smoothness of the estimate).

In the following, we describe into details the procedures adopted for estimating $\hat{p}(\mathbf{x}_{ij}^t)$, $\hat{p}(\mathbf{x}_{ij}^t | \omega_{int}^t)$ and $\hat{p}(\mathbf{x}_{ij}^t | \omega_{unk}^t)$, respectively.

3.1.1 Estimation of $\hat{p}(\mathbf{x}_{ij}^t)$

For computing both the centres $M^t = \{\boldsymbol{\mu}_k^t\}_{k=1}^K$ and variances $\Sigma^t = \{\sigma_k^{2t}\}_{k=1}^K$ of all the kernels, as well as the set of weights \mathcal{W}^t defining $\hat{p}(\mathbf{x}_{ij}^t)$, we employ the EM algorithm over all the pixels of \mathcal{X}^t . EM allows determining the maximum likelihood (ML) estimator of the parameters characterizing a certain distribution in the presence of incomplete observations (Dempster *et al.*, 1977). Indeed, our objective is to identify the ML estimate for the set of parameters $\theta^t = \{M^t, \Sigma^t, \mathcal{W}^t\} = \{\boldsymbol{\mu}_k^t, \sigma_k^{2t}, w_k^t\}_{k=1}^K$ that allows maximizing the log-likelihood of \mathcal{X}^t , i.e.

$$\ln \mathcal{L}(\theta^t) = \ln [p(\mathcal{X}^t | \theta^t)] = \sum_{i,j=1}^{I,J} \ln [\hat{p}(\mathbf{x}_{ij}^t)] \quad (8)$$

At each iteration l , the set of estimated parameters $[\theta^t]^{(l)}$ provides an increase in the log-likelihood until a local maximum is reached, i.e. $\ln \mathcal{L}([\theta^t]^{(l)}) \geq \ln \mathcal{L}([\theta^t]^{(l-1)})$.

For simplicity, weights are initially set to $1/K$, whereas kernel parameters are initialized using the k -means clustering algorithm (Bruzzone and Fernández-Prieto, 1999) fixing the number of clusters equal to K . In particular, centres and variances of the Gaussians are initialized to the centres and variances of the resulting clusters. Then, according with Dempster *et al.*, 1977, the updated estimates for the unknown parameters are given by:

$$[w_k^t]^{(l)} = \frac{\sum_{i,j=1}^{I,J} [w_k^t]^{(l-1)} \cdot [\phi^k(\mathbf{x}_{ij}^t)]^{(l-1)}}{[\hat{p}(\mathbf{x}_{ij}^t)]^{(l-1)} \cdot I \cdot J} \quad (9)$$

$$[\boldsymbol{\mu}_k^t]^{(l)} = \frac{\sum_{i,j=1}^{I,J} [w_k^t]^{(l-1)} \cdot [\phi^k(\mathbf{x}_{ij}^t)]^{(l-1)} \cdot \mathbf{x}_{ij}^t}{\sum_{i,j=1}^{I,J} [w_k^t]^{(l-1)} \cdot [\phi^k(\mathbf{x}_{ij}^t)]^{(l-1)}} \quad (10)$$

$$[\sigma_k^{2t}]^{(l)} = \frac{\sum_{i,j=1}^{I,J} [w_k^t]^{(l-1)} \cdot [\phi^k(\mathbf{x}_{ij}^t)]^{(l-1)} \cdot \|\mathbf{x}_{ij}^t - [\boldsymbol{\mu}_k^t]^{(l)}\|^2}{D_t \cdot \sum_{i,j=1}^{I,J} [w_k^t]^{(l-1)} \cdot [\phi^k(\mathbf{x}_{ij}^t)]^{(l-1)}} \quad (11)$$

Reasonably, we assume that convergence is reached when the relative increase in the log-likelihood is lower than a prefixed threshold ε .

3.1.2 Estimation of $\hat{p}(\mathbf{x}_{ij}^t | \omega_{int}^t)$

Once M^t and Σ^t have been determined (and hence the set of kernels Φ^t properly defined), we exploit the available ground truth for the class of interest ω_{int}^t at each date for deriving the estimate of the corresponding conditional density $\hat{p}(\mathbf{x}_{ij}^t | \omega_{int}^t)$. In particular, the set of weights \mathcal{W}_{int}^t associated with ω_{int}^t is determined using again the EM algorithm, but solely on the available training samples $\mathcal{T}^t = \{\mathbf{x}_{ij}^t \in \mathcal{X}^t | y_{ij} = \omega_{int}^t\}$, $|\mathcal{T}^t| = N^t$, where y_{ij} denotes the true label for pixel at position (i, j) .

Weights are initialized to $1/K$, and then updated (according with Dempster *et al.*, 1977) using the following equation:

$$[W_{\text{int } k}^t]^{(l)} = \frac{\sum_{i,j=1}^{I,J} \alpha_{ij} \cdot \frac{[W_{\text{int } k}^t]^{(l-1)} \cdot \phi_k^t(\mathbf{x}_{ij}^t)}{[\hat{p}(\mathbf{x}_{ij}^t | \omega_{\text{int}}^t)]^{(l-1)}}}{N_t}, \quad \alpha_{ij} = \begin{cases} 1 & \text{if } \mathbf{x}_{ij}^t \in \mathcal{T}' \\ 0 & \text{if } \mathbf{x}_{ij}^t \notin \mathcal{T}' \end{cases} \quad (12)$$

The corresponding log-likelihood is given by:

$$\ln \mathcal{L}(\theta' \equiv \mathcal{W}_{\text{int}}^t) = \sum_{i,j=1}^{I,J} \alpha_{ij} \cdot \ln[\hat{p}(\mathbf{x}_{ij}^t | \omega_{\text{int}}^t)] \quad (13)$$

Even in this case we assume that convergence is reached if the relative increase in the log-likelihood is lower than ε .

3.1.3 Estimation of $\hat{p}(\mathbf{x}_{ij}^t | \omega_{\text{int}}^t)$

It is worth noting that Eq. (3) can be re-written as:

$$P(\omega_{\text{int}}^t) \cdot \sum_{k=1}^K W_{\text{int } k}^t \cdot \phi_k^t(\mathbf{x}_{ij}^t) = \sum_{k=1}^K w_k^t \cdot \phi_k^t(\mathbf{x}_{ij}^t) - P(\omega_{\text{int}}^t) \cdot \sum_{k=1}^K W_{\text{int } k}^t \cdot \phi_k^t(\mathbf{x}_{ij}^t) \quad (14)$$

Hence, $\forall k=1, \dots, K$ it holds $P(\omega_{\text{int}}^t) \cdot W_{\text{int } k}^t = w_k^t - P(\omega_{\text{int}}^t) \cdot W_{\text{int } k}^t$. Since $P(\omega_{\text{int}}^t) + P(\omega_{\text{int}}^t) = 1$, we have:

$$W_{\text{int } k}^t = \frac{w_k^t - P(\omega_{\text{int}}^t) \cdot W_{\text{int } k}^t}{P(\omega_{\text{int}}^t)} = \frac{w_k^t - P(\omega_{\text{int}}^t) \cdot W_{\text{int } k}^t}{1 - P(\omega_{\text{int}}^t)} \quad (15)$$

Then, as M^t , Σ^t , \mathcal{W}^t and $\mathcal{W}_{\text{int}}^t$ have been determined, we can compute $\hat{p}(\mathbf{x}_{ij}^t | \omega_{\text{int}}^t)$ substituting (15) into (6), upon it is possible to obtain a reliable estimate $\hat{P}(\omega_{\text{int}}^t)$ for the prior probability of the class of interest. This can be properly accomplished throughout the iterative labelling phase presented below.

3.2 Joint Prior Modelling

For modelling the joint prior $P(\mathcal{C}^1, \mathcal{C}^2)$, we propose an approach based on MRF (Solberg *et al.*, 1996). In particular, we assume that the couple of labels C_{ij}^1 , C_{ij}^2 associated with pixel at position (i, j) at times t_1 and t_2 depends on the couples of labels associated with pixels belonging to the spatial neighbourhood \mathcal{G}_{ij} of (i, j) at the two dates (we always considered first order neighbourhoods).

In other words, the higher the number of its spatial neighbours experiencing a certain land-cover transition is, the higher the probability for a given pixel of experiencing the same transition is. In this hypothesis, according with the MRF theory, it holds the equivalence:

$$P(C_{ij}^1, C_{ij}^2 | C_{gh}^1, C_{gh}^2; (g, h) \in \mathcal{G}_{ij}) = Z^{-1} \cdot \exp[-U_{\text{context}}(C_{ij}^1, C_{ij}^2)] \quad (16)$$

where $Z = Z(\mathcal{G}_{ij})$ is a normalizing constant called *partition function*, while U_{context} is a Gibbs *energy function* (accounting for the spatio-temporal context) of the form:

$$U_{\text{context}}(C_{ij}^1, C_{ij}^2) = - \sum_{(g, h) \in \mathcal{G}_{ij}} \beta \cdot \delta[(C_{ij}^1, C_{ij}^2), (C_{gh}^1, C_{gh}^2)] \quad (17)$$

where $\beta > 0$ tunes the influence of the context and δ is the Kronecker delta function defined as:

$$\delta[(C_{ij}^1, C_{ij}^2), (C_{gh}^1, C_{gh}^2)] = \begin{cases} 1 & \text{if } (C_{ij}^1, C_{ij}^2) = (C_{gh}^1, C_{gh}^2) \\ 0 & \text{if } (C_{ij}^1, C_{ij}^2) \neq (C_{gh}^1, C_{gh}^2) \end{cases} \quad (18)$$

3.3 Iterative Labelling

Solving Eq. (2) is equivalent to maximize the log-likelihood $\ln \mathcal{L}(\mathcal{X}^1, \mathcal{X}^2 | \mathcal{C}^1, \mathcal{C}^2)$, which can be written as:

$$\ln \mathcal{L}(\mathcal{X}^1, \mathcal{X}^2 | \mathcal{C}^1, \mathcal{C}^2) = - \sum_{t=1}^2 U_{\text{data}}^t(\mathcal{X}^t, \mathcal{C}^t) - U_{\text{context}}(\mathcal{C}^1, \mathcal{C}^2) - \ln(Z) \quad (19)$$

where $U_{\text{data}}^t(\mathcal{X}^t, \mathcal{C}^t) = -\ln[p(\mathcal{X}^t | \mathcal{C}^t)]$, represents the class-conditional energy function at date $t=1, 2$, while U_{context} is given by (17). Since Z solely depends on the selected type of neighbourhood, the final problem becomes solving:

$$\{\tilde{\mathcal{C}}^1, \tilde{\mathcal{C}}^2\} = \underset{\mathcal{C}^1, \mathcal{C}^2}{\text{argmin}} \{U_{\text{context}}(\mathcal{C}^1, \mathcal{C}^2) + U_{\text{data}}^1(\mathcal{X}^1, \mathcal{C}^1) + U_{\text{data}}^2(\mathcal{X}^2, \mathcal{C}^2)\} \quad (20)$$

To this aim, we propose a strategy based on the Iterated Conditional Modes (ICM) algorithm (Besag, 1996) which allows maximizing local conditional probabilities sequentially. In particular, at each iteration l we update the estimated prior probabilities for the class of interest at each date $\hat{P}(\omega_{\text{int}}^t)$ and, accordingly, also the class-conditional densities of the unknown classes $\hat{p}(\mathbf{x}_{ij}^t | \omega_{\text{int}}^t)$. The algorithm works as follows:

- Step 1.* After estimating $\hat{p}(\mathbf{x}_{ij}^t | \omega_{\text{int}}^t)$, $\forall \mathbf{x}_{ij}^t \in \mathcal{X}^t$, $t=1, 2$ following the approach described in the previous paragraphs, set $\hat{P}(\omega_{\text{int}}^t) = 0.5$ (no prior knowledge is assumed to be available about the true prior $P(\omega_{\text{int}}^t)$) and compute the conditional density of the unknown classes $\hat{p}(\mathbf{x}_{ij}^t | \omega_{\text{int}}^t)$ accordingly;
- Step 2.* Derive the initial sets of labels $\tilde{\mathcal{C}}^1$, $\tilde{\mathcal{C}}^2$ by solely minimizing the non-contextual terms of Eq. (20), i.e. $\{\tilde{\mathcal{C}}^1, \tilde{\mathcal{C}}^2\} = \underset{\mathcal{C}^1, \mathcal{C}^2}{\text{argmin}} \{U_{\text{data}}^1(\mathcal{X}^1, \mathcal{C}^1) + U_{\text{data}}^2(\mathcal{X}^2, \mathcal{C}^2)\}$;
- Step 3.* On the basis of current $\tilde{\mathcal{C}}^1$ and $\tilde{\mathcal{C}}^2$, compute the new estimated prior probabilities ratioing the number of pixels associated with the class of interest over the whole number of pixels, i.e. $\hat{P}(\omega_{\text{int}}^t) = |\tilde{\mathcal{C}}_{\text{int}}^t| / (I \cdot J)$, $\tilde{\mathcal{C}}_{\text{int}}^t = \{C_{ij}^t | C_{ij}^t \in \tilde{\mathcal{C}}^t, C_{ij}^t = \omega_{\text{int}}^t\}_{i,j=1}^{I,J}$; then, update the class-conditional densities for the unknown classes $\hat{p}(\mathbf{x}_{ij}^t | \omega_{\text{int}}^t)$ accordingly;
- Step 4.* Update $\tilde{\mathcal{C}}^1$ and $\tilde{\mathcal{C}}^2$ according with Eq. (20);
- Step 5.* Repeat Step 3 and Step 4 until no changes occur between successive iterations.

At the end of the process, the final targeted change-detection map \mathcal{C}^* is defined as:

$$\mathcal{C}^* = \{C_{ij}^* \}_{i,j=1}^{I,J}, \quad C_{ij}^* = \begin{cases} 1 & \text{if } C_{ij}^1 = \omega_{\text{int}}^1 \text{ and } C_{ij}^2 = \omega_{\text{int}}^2 \\ 0 & \text{otherwise} \end{cases} \quad (21)$$

4. EXPERIMENTAL RESULTS

In order to assess the effectiveness of the proposed technique, we carried out several experiments with different combinations

of multispectral, hyperspectral and SAR data. Nevertheless, due to space constraints, we will focus the attention solely on a representative change-detection problem referring to an intense farming area experiencing several land-cover transitions located in Barrax, a village close to Albacete (Castilla-La Mancha, Spain). In particular, available data consist in: two Landsat-5 Thematic Mapper (TM) images acquired on 15th July 2003 and 17th July 2004, respectively (as generally done in the literature among the 7 spectral bands we did not consider the low-resolution band associated with the thermal infrared channel); one PROBA CHRIS image (composed by 63 spectral bands with centre wavelengths from 400 to 1050 nm) acquired on 16th July 2004; and one Envisat ASAR alternate polarization (VV, HH) image (despeckled using a 3×3 Gamma filter) acquired on 18th July 2004. All of them have been properly co-registered to a common spatial geometry of 30 meters and a study area of 512 × 512 pixels has been selected. July 2003 will be referred to as t_1 , whereas July 2004 will be referred to as t_2 (no significant changes indeed occurred between 16th and 18th July 2004). From the original available images we derived the following three datasets (using the stacked vector approach for multi-source data fusion (Richards and Jia, 2006)) composed by: i) the 6 Landsat TM bands at both t_1 and t_2 (i.e., $D_1=D_2=6$) [Dataset I]; ii) the 6 Landsat TM bands at t_1 and the merger of the 2 Envisat ASAR backscattering intensity images with the 6 Landsat TM bands at t_2 (i.e., $D_1=6$ and $D_2=8$) [Dataset II]; and iii) the 6 Landsat TM bands at t_1 and the 63 PROBA CHRIS bands at t_2 (i.e., $D_1=6$ and $D_2=63$) [Dataset III]. However, it is worth noting that our objective is not to seek for a set of features at both dates which could be more effective for solving the investigated problem, but rather to demonstrate that the presented method is even capable of effectively handling different types of data at the two times.

As described in Section 3, the user is required to set the number of Gaussian kernels K to be employed for approximating the PDFs. Hence, in order to understand how significant the selection of this free parameter is, we performed a series of experiments varying K from 20 to 120 with steps of 10.

According with a variety of experiments on toy and real datasets we fixed $\varepsilon=10^{-4}$ and $\beta=10^2$.

In all the trials we employed the k -means clustering for initializing both centres and variances of kernel functions. Nevertheless, the very high complexity of the algorithm (i.e., approximately $O(N^{D(K+1)} \log N)$, where N and D represent the number of samples to be clustered and their dimensionality, respectively (Inaba *et al.*, 1994)), prevented us from using all the patterns of each investigated image at a time, as this would have required a very high computational burden. In order to overcome this limitation, for each image we ran the k -means algorithm on a random subset containing one third of the total amount of samples. However, as this might affect the final change-detection accuracies of the proposed technique, for each number of considered kernels K , we performed 10 different trials running each time the k -means clustering on a different random subset. Moreover, we finally also combined the 10 resulting change-detection maps through a majority voting ensemble.

For validating the potentialities of the presented method, we compared the results with those obtained by supervised PCC. In particular, we considered ML and SVM fully-supervised classifiers trained by exploiting a complete ground truth for all the land-cover classes characterizing each considered date. ML is a simple yet generally rather effective statistical classifier, which does not require the user to set any free parameter (Richards and Jia, 2006). SVM are advanced state-of-art classifiers, which proved capable of outperforming other traditional approaches

(Cristianini and Shawe-Taylor, 2000). For the selection of the two free parameters (i.e., a penalization parameter and the variance of considered Gaussian kernels) we employed a 10-fold cross-validation strategy (Duda *et al.*, 2000).

Available prior knowledge has been used for defining regions of interest composed on the whole by 21941 pixels whose ground truth was known at the two times, respectively. 10 land-cover classes have been considered at t_1 , whereas 9 have been taken into consideration at t_2 . At both dates, from all the available labeled samples we defined two spatially-disjoint training sets (see Table 1). This means that there is no overlapping between training samples at t_1 and t_2 . All of them have been used for training both the ML and SVM supervised classifiers at each time.

Land-cover class	t_1 (July 2003)	t_2 (July 2004)
alfalfa	2031	634
bare soil	2585	–
corn	1737	2664
garlic	101	302
grasslands	–	42
onions	213	220
poppy	336	–
potatoes	208	283
spring crops	–	3318
stubble	2416	2247
sugar beet	365	–
sunflower	–	449
wheat	369	–
total	10361	10159

Table 1. Number of spatially-disjoint training samples considered at the two dates.

Change-detection results have been evaluated (over those samples whose land-cover class is known at both dates) in terms of: percentage overall accuracy $OA\%$ (i.e., the percentage of samples correctly identified as both changed or unchanged over the whole number of samples), and kappa coefficient of accuracy (which also takes into consideration errors and their type) (Richards and Jia, 2006).

Among the different land-cover transitions occurred between the two dates, here we take into consideration (one at a time) two of them, namely “bare soil to spring crops” and “alfalfa to corn” (experienced by 4583 and 1035 pixels, respectively, over the whole available 21941 whose ground truth was known at both times).

In our trials, we empirically experienced that a common range for K resulting in average high detection accuracies spans from 60 to 80. When instead nearing the lower or the upper bound of the considered interval, performances tend to vary depending on the specific land-cover transition of interest. Accordingly, in Table 2 and Table 3 we show the results obtained with the proposed technique for $K=40, 60, 80, 100$. In particular, we report the median over the 10 realizations with different k -means clustering initialization. Moreover, also accuracies finally obtained with the majority voting ensemble (denoted as $PSCD_{MV}$), as well as those obtained by supervised PCC using ML and SVM (denoted as PCC_{ML} and PCC_{SVM} , respectively) are presented.

While investigating the “bare soil to spring crops” transition with the proposed PSCD technique, from all the training pixels reported in Table 1, we considered the only 2585 available for bare soil at t_1 and the only 3318 spatially-disjoint available for

spring crops at t_2 . Obtained results are very satisfactory, as confirmed by both the high kappa and $OA\%$ values reported in Table 2 (always higher than 0.79 and 92, respectively). Moreover, by employing the majority voting ensemble it is possible to further improve the performances and obtaining for both indexes accuracies even closer to those obtained by PCC_{ML} and PCC_{SVM} with a fully-supervised training at both dates.

K	Dataset I		Dataset II		Dataset III	
	kappa	$OA\%$	kappa	$OA\%$	kappa	$OA\%$
40	0.8925	96.59	0.8403	95.09	0.7955	92.61
60	0.8903	96.53	0.8458	95.21	0.8488	94.97
80	0.8822	96.25	0.8412	95.11	0.8441	94.80
100	0.8878	96.47	0.8470	95.31	0.8502	94.93
$PSCD_{MV}$	0.9076	97.08	0.8649	95.82	0.8622	95.32
PCC_{ML}	0.9339	97.88	0.9323	97.83	0.9330	97.86
PCC_{SVM}	0.9501	98.36	0.9359	97.90	0.9703	99.02

Table 2. kappa coefficient of accuracy and $OA\%$ obtained for the “bare soil to spring crops” land-cover transition.

While addressing the “alfalfa to corn” transition with the proposed PSCD technique, from all the training pixels reported in Table 1, we considered the only 2031 available for alfalfa at t_1 and the only 2664 spatially-disjoint available for corn at t_2 . Such a transition is rather difficult to characterize, as only experienced by few fields in the considered area. Indeed, according with the results in Table 3, this is confirmed by the very low accuracies obtained by PCC_{ML} despite fully-supervised training. Instead, in the light of the high complexity of the problem, performances exhibited by the proposed method are very promising, especially for Dataset II and Dataset III. Moreover, with the majority voting ensemble the gap with respect to PCC_{SVM} becomes very small (Dataset II) or it is even possible to outperform results obtained with SVMs (Dataset III).

K	Dataset I		Dataset II		Dataset III	
	kappa	$OA\%$	kappa	$OA\%$	kappa	$OA\%$
40	0.6725	97.36	0.8549	98.79	0.8117	98.40
60	0.7110	97.79	0.8190	98.49	0.8343	98.60
80	0.6530	97.25	0.8172	98.45	0.8206	98.45
100	0.6553	97.32	0.7233	97.92	0.8367	98.62
$PSCD_{MV}$	0.7524	98.16	0.8896	99.06	0.9079	99.22
PCC_{ML}	0.5163	96.87	0.5134	96.86	0.5353	97.05
PCC_{SVM}	0.9003	99.08	0.9244	99.32	0.8969	99.04

Table 3. kappa coefficient of accuracy and $OA\%$ obtained for the “alfalfa to corn” land-cover transition.

5. CONCLUSIONS

In this paper we presented a novel partially-supervised change-detection (PSCD) technique capable of addressing targeted change-detection problems where the objective is to identify one (or few) targeted land-cover transitions, under the assumption that ground-truth information is available for the only (few) class(es) of interests at the two investigated dates.

In this context, either supervised or unsupervised standard approaches cannot be effectively employed. The proposed method, instead, allows exploiting the only prior knowledge available for the specific land-cover classes of interest at the

two times, while providing accuracies comparable with those of fully-supervised methods. In particular, the PSCD technique relies on a partially-supervised approach and jointly exploits the Expectation-Maximization (EM) algorithm and an iterative labelling strategy based on Markov random fields (MRF) accounting for spatial and temporal correlation between the two images. Moreover, it also allows handling images acquired by different sensors at the two considered times. Experimental results on multi-sensor datasets derived from multispectral, hyperspectral and SAR data confirmed the effectiveness and the reliability of the proposed technique

REFERENCES

- Besag, J., 1986. On the statistical analysis of dirty pictures. *Journal of the Royal Statistical Society, Series B*, 48, pp. 259-302.
- Bruzzone, L., and Fernández-Prieto, D., 1999. A Technique for the Selection of Kernel-Function Parameters in RBF Neural Networks for Classification of Remote-Sensing Images. *IEEE Trans. Geosci. Remote Sens.*, 37(2), pp. 1179-1184.
- Coppin, P., Jonckheere, I., Nackaerts, K., and Muys, B., 2004. Digital change detection methods in ecosystem monitoring: a review. *Int. J. Remote Sens.*, 25(9), pp. 1565-1596.
- Cristianini N., and Shawe-Taylor, J., 2000. *An Introduction to Support Vector Machines*. Cambridge University Press.
- Dempster, A., Laird, N., and Rubin, D., 1977. Maximum Likelihood from Incomplete Data Via the EM Algorithm. *The Royal Statistical Society, Series B*, 39(1), pp. 1-38.
- Duda, R. O., Hart, P. E., and Stork, D. G., 2000. *Pattern Classification*. Wiley, New York.
- Inaba, M., Katoh, N., and Imai, H., 1994. Applications of weighted voronoi diagrams and randomization to variance-based k-clustering. *Proceedings of the 10th Annual Symposium on Computational Geometry*, pp. 332-339.
- Jensen, J. R., 2009. *Remote Sensing Of The Environment*. Pearson, Upper Saddle River.
- Jeon, B., and Landgrebe, D. A., 1999. Partially supervised classification using weighted unsupervised clustering. *IEEE Trans. Geosci. Remote Sens.*, 37(3), pp. 1073-1079.
- Lu, D., Mausel, P., Brondizio, E., and Moran, E., 2004. Change detection techniques. *Int. J. Remote Sens.*, 25(12), pp. 2365-2407.
- Radke, R. J., Andra, S., Al-Kofahi, O., and Roysam, B., 2005. Image Change Detection Algorithms: A systematic Survey. *IEEE Trans. Geosci. Remote Sens.*, 14(3), pp. 294-307, 2005.
- Richards, J. A., and Jia, X., 2006. *Remote Sensing Digital Image Analysis. An Introduction*. Springer, Berlin.
- Singh, A., 1989. Digital change detection techniques using remotely-sensed data. *Int. J. Remote Sens.*, 10(6), pp. 989-1003.
- Solberg, A. H. S., Taxt, T., and Jain, A. K., 1996. A Markov Random Field Model for Classification of Multisource Satellite Imagery. *IEEE Trans. Geosci. Remote Sens.*, 34(1), pp. 100-113.

NDVI (MODIS SENSOR) RESPONSE TO INTERANNUAL VARIABILITY OF RAINFALL AND EVAPOTRANSPIRATION IN A SOYBEAN PRODUCING REGION, SOUTHERN BRAZIL

A. Giarolla ^a, W. E. Baethgen; ^b, P. Ceccato ^b

^a Instituto Nacional de Pesquisas Espaciais, Centro de Ciências do Sistema Terrestre (CCST/INPE), Av. dos Astronautas, 1758, São José dos Campos-SP, 12227-010, email: *angelica.giarolla@cptec.inpe.br*.

^b International Research Institute for Climate and Society (IRI), The Earth Institute, Columbia University, Lamont Campus, Palisades, New York, USA, email: *baethgen@iri.columbia.edu; pceccato@iri.columbia.edu*

KEY WORDS: soybean (*Glycine Max, L. Merr*), NDVI, remote sensing, water balance, GIS.

ABSTRACT:

This study aimed at evaluating the response of the *Normalized Difference Vegetation Index* - NDVI (MODIS sensor, TERRA satellite) of soybean to interannual variability of rainfall and evapotranspiration in Campos Gerais, a region of the state of Parana in southern Brazil. Landsat TM 5 and 7 images were selected for analyzing the spatial soybean field distribution for the region from 2000/01 to 2006/07 and to identify soybean fields. We then identified 175 pixels (250 x 250m) that contained only soybean fields ("pure-pixels") based on the soybean maps obtained with the Landsat TM images. The next step was to extract the NDVI values for these soybean pure-pixels and to analyze the NDVI spectral curves considering the soybean phenology. Data from nearby meteorological stations were obtained and used to calculate the soil water balance for soybean fields in 5 locations distributed in the Campos Gerais region. To obtain actual evapotranspiration values, the water balance was calculated for each year, and for the same period covering the entire soybean growing season. Anomaly values were calculated for each year to verify the interannual rainfall variability. Linear regression models were adjusted between NDVI and i) rainfall and ii) actual evapotranspiration for all time series. Analysis of the evolution of NDVI values allowed identifying the soybean growing season (November to March) and also the dry season for this region according to rainfall anomaly values. Statistical analyses showed that actual evapotranspiration presented best agreement with soybean NDVI in relation to rainfall, probably due to the fact that this variable integrates information of rainfall, temperature and soil water holding capacity for the entire study period.

1 INTRODUCTION

Crops can suffer damage from excess or lack rainfall and investigate this variability in its frequency of occurrence over a crop season becomes essential for agricultural planning systems. Several studies have been made about early warning systems, based on seasonal and interannual climate forecasts (Guillevic, *et al.*, 2002; Nobre *et al.*, 2006; Meinke and Stone, 2005; Ogallo *et al.*, 2008). An objective evaluation system of weather variability as well as the improvement of crop monitoring capabilities for yield prediction can provide knowledge to mitigate weather impacts. Climatic variability plays a major role in promoting meteorological conditions that deviate substantially from mean conditions, including weather extreme events (Seiler *et al.*, 2007). Crop growth, development and yield are affected by climatic variability via linear and nonlinear responses to weather variables (Semenov and Porter, 1995). According to Baethgen (1997) agricultural systems which are currently subject to extreme climatic interannual variability (drought, flood, storms, etc.) are likely to become even more vulnerable under the most commonly expected scenarios of climate change (i.e. increased temperatures, increased rainfall variability). Evapotranspiration (ET) is an essential component of the energy and water budgets in grassland and agricultural ecosystems (Allen *et al.*, 1998) and understanding the processes that affect ET at different temporal scales and under a variety of environmental conditions is important in crop modeling production. In general, remote sensing techniques can not measure evaporation or evapotranspiration directly. However, Engman (1995) mentions that remote sensing does have two potentially very important roles in

estimating evapotranspiration: *i*) to try establish a empirical relationships between remote sensing data and ET to larger areas, including those areas where measured meteorological data may be sparse; and *ii*) remotely sensed measurements may be used to measure variables in the energy and moisture balance models of ET (Bastiaanssen, 2000). Tucker *et al.*, (2001) report that the use of decadal NDVI time series has improved the study of interannual variation in vegetation. Currently, Suzuki *et al.* (2007) examined interannual NDVI data and its relation to ET in northern Asia and significant positive correlations were found between NDVI and ET anomaly interannual variation over vegetated areas. The objective of this study was to evaluate NDVI response to interannual variability of rainfall and evapotranspiration during the entire soybean season for the period 2000-2007 in Campos Gerais region, Southern Brazil.

2. STUDY AREA AND DATA

2.1 Study area

Campos Gerais is a region located in southern Brazil, limited geographically by the coordinates 23°45'00''; 25°50'00''South and 49°10'00''; 51°25'00''West. Agriculture is the principal land use in the region and the three main crops are soybean, maize and dry bean. The highest yields for a short duration soybean cultivar are obtained when planted in October and November and in the southern part of this region, many farmers usually start planting in mid-October (Heinemann *et al.* 2002). Soybean cycle lasts 110 days in average and the harvest occurs

between March and April in the following year. According to IAPAR (2000) the climate in this region is subtropical humid meso-thermic, with warm summers (Dec–Mar).

2.2 Meteorological data

Meteorological data between 2000 and 2007 were collected from the Parana Meteorological System (SIMEPAR). Mean air temperature (°C) and rainfall (mm) data on a daily scale from five meteorological stations were used in this study: *i) Candido de Abreu* (-24.63; -51.25; 645m); *ii) Cerro Azul* (-24.81; -49.25; 66m); *iii) Jaguariava* (-24.22; -49.67; 900m); *iv) Ponta Grossa* (-25.21; -50.01; 885m); *v) Telemaco Borba* (-24.33; -50.62; 768m).

2.3 Remote Sensing information

2.3.1. Landsat TM images

Twelve images from Landsat 5 and 7, Thematic Mapper –TM sensor were used to identify soybean fields during the time period 2000 to 2007. Landsat scenes were provided by INPE (*National Institute for Space Research – Brazil*) covering the Campos Gerais region. Two phenological stages are important to identify soybean crops in the Campos Gerais region: *i) November* and *ii) February*. In November, during sowing and seedling emergence, there is a strong spectral response from the soil, while in January/February (around grain maturation) the main response is from the crop chlorophyll activity (Rizzi and Rudorff, 2005; Wagner *et al.*, 2007). These authors emphasize that during January to March, the soybean crop is at full growth and covers the soil. In these conditions, soybean crops are well characterized in the images, standing out from other land uses such as bare soil or vegetation having different phenology.

2.3.2 MODIS 250m NDVI composites

This study used multi-temporal values of the Normalized Difference Vegetation Index (NDVI) obtained from the MODIS-TERRA sensor (MOD13Q1 product version 5, 16-day image composite). NDVI values for different samples in Campos Gerais representing “pure-pixels” of soybean, i.e., pixels with soybean crops only (identified using Landsat images as described above) were extracted using the IRI Data Library (<http://portal.iri.columbia.edu/portal/server.pt>), for the period 2000 - 2007.

3. METHODOLOGY

3.1 Soybean field mapping

The mapping of soybean areas was performed by analyzing the 12 Landsat images using the following steps. First, ENVI 4.2 software was used to geo-reference the images presented based on RGB color composites (using channels 4, 5 and 3 respectively). Then, a mixture model described by Shimabukuro and Smith, (1991) was used to represent sample targets of green vegetation (soybeans in this case), soil, and shade. This analysis was conducted using SPRING, a Geographical Information System developed by INPE which operates using Microsoft Office Access data base. The method is based on the constrained least squares method and spectral signatures collected directly from Landsat TM images. This procedure was performed interactively until verifying that the component signatures were adequate representations of mixture components for the analyzed area

Fifty-pixel samples were chosen for the test, as described in the procedure described by Rizzi and Rudorff (2005). The next step consisted of using a segmentation approach of growing “regions”, where a “region” is a set of homogeneous pixels grouped according to their spectral and spatial properties. An unsupervised classification based on a ‘clustering’ algorithm, named ISOSEG (Bins *et al.* 1996), was applied to the segmented image. An acceptance threshold was defined (using maximum Mahalanobis distance method) to classify digital numbers of regions based on their closeness to the mean of the class (in this case, soybean gray levels). It differs from Euclidean distance in that it takes into account the correlations of the data set and it doesn’t depend on the scale of measurements. A thematic map containing ‘soybean’ and ‘non-soybean’ areas resulted from this step. In order to correct errors resulting from the digital classification described above, a thorough visual classification was performed in all images. Google Earth images at high spatial resolution were used as ancillary information to check the soybean fields. The Kappa index was computed to check map accuracy. At the end of all of these steps, one soybean field map was generated for each one of the seven years (2000-2007). A methodology was applied in order to construct a sampling frame and to allocate regular pixels to the soybean fields. A direct expansion estimator and a semi-automated procedure as suggested by Adami *et al.* (2007) were used to generate a grid with regular pixels of 250m by 250m. Each pixel was assigned an identification number. This grid spatial resolution was adopted to match soybean pure-pixels with the NDVI-MODIS pixel size.

3.2 Soybean pure-pixel coordinates collection

From each soybean field map and for each year, the coordinates of several soybean pure-pixels were extracted. In addition, the soybean pure-pixels closest to the 5 meteorological stations were selected for further analysis. This process was needed to perform the water balance from the meteorological data and compare it with the NDVI. Five pure-pixels on the soybean field maps were chosen for each location and for each year, totaling 175 pure-pixel samples.

3.3 NDVI data acquisition and processing

NDVI values were extracted for the same 175 pure-pixels collected in the step described above. Then, NDVI means were calculated for each location and for each year.

3.4 Rainfall anomalies and Linear Regressions analyses

In order to verify the rainfall interannual variation during soybean growing season, anomaly values were calculated for each year separately, from 2000 to 2007. In addition, NDVI curves and amount of rainfall (mm) were plotted together to verify the correspondent variations. However, to investigate the relationship between NDVI, rainfall and actual evapotranspiration for the entire study period (2000-2007), regression analyses for each location were made.

3.5 Water Balance Methodology

The water balance model applied in this study was based on the methodology presented by Thornthwaite and Mather (1955). Thornthwaite (1948) developed a method to estimate Potential Evapotranspiration (PE or ETo), using air temperature as the main parameter which was also used in this study. A crop coefficient (Kc) was used to transform

grass ETo into crop potential evapotranspiration (ETc), which is a function of phenological phases, crop species and variety, plant architecture and leaf area. In our research we used the soybean Kc values proposed by Allen *et al.* (1998). The main soil types for these locations are: *Alfisol* (Candido de Abreu and Cerro Azul) and *Oxisol* (Ponta Grossa, Jaguariaíva and Telemaco Borba). Soybean water balance was performed at daily time steps for each location and each year (2000-2007). The water balance was also adjusted according to soybean phenology. November 15th was adopted as the main sowing date in this region (Geosafra, 2007). Outputs of potential evapotranspiration (PE), actual evapotranspiration (AE), soil moisture storage (SME), water deficit (DEF) and water excess (EXC) were thus obtained on a daily time step. However, in this study, only actual evapotranspiration was considered and it was necessary to aggregate the above outputs to 16-day means in order to compare them with the MODIS NDVI data.

4. RESULTS

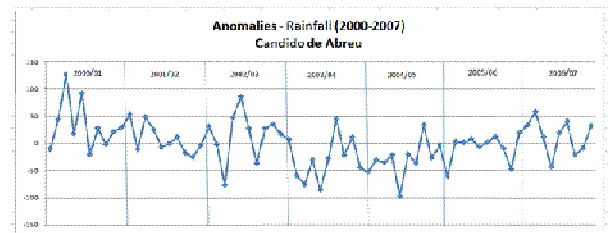
4.1 Rainfall anomalies

Figure 1 contains rainfall anomalies for each location and year from 2000 to 2007. Although state of Parana generally has a seasonal pattern of precipitation, such as, rainy summer and dry winter, it is important to point out the significant rainfall variation for all time series and for each year separately. Due to its location in Southern Brazil, this state is influenced by several macro-climatic factors, such as, migration of air equatorial and tropical masses from Atlantic in summer months; cold air masses (polar front) that come from the South of the continent, (Wrege *et al.*, 1999), and dry air masses from Midwest Brazil, which can bring warm and relative dry weather. So, all this condition leads to high rainfall variability, in terms of amount of rainfall (millimeters) and number of rainy days (frequency). This weather variability influences the agriculture in this region, thus affecting crop productivity. Rainfall anomalies revealed occurrence of drought episodes from 2000 to 2007, but more significantly during 2004/05 year in Candido de Abreu, Cerro Azul and Ponta Grossa locations. This situation was reported by CONAB (2005) which mention a 7.1% yield loss in relation to the previous year yields, in the state of Parana.

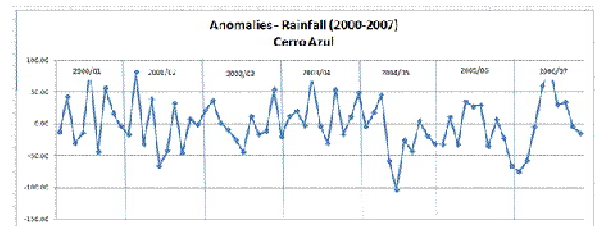
4.2 NDVI temporal analysis

The different phenological stages of soybeans were identified with the NDVI temporal series from 2000 to 2007 for each location (Figure 2). Growth starts around mid November when soybean is planted and the cycle ends in March when the soybean is harvested. A similar pattern was observed for all years and locations indicating that the pixels selected for the analysis were indeed soybean pure-pixels. In 2004/2005 a drop in NDVI values was observed in three locations, according to rainfall anomaly values for Candido de Abreu, Cerro Azul and Ponta Grossa (Figure 1). Rainfall occurrence was low in January and mid February, which coincides with the peak of the reproductive stage of soybean in the study region. Actual evapotranspiration curves presented high values in December, January and mid-February, specially during soybean flowering and grain formation phases and it seems that NDVI response tends to follow this more realistic situation, in terms of biophysical condition, than rainfall occurrence.

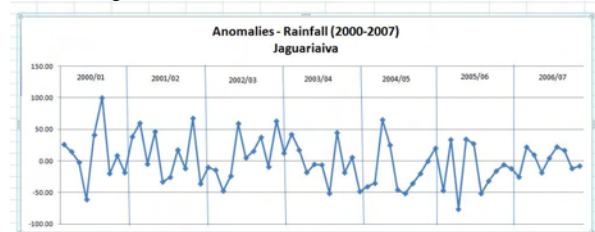
i) Candido de Abreu



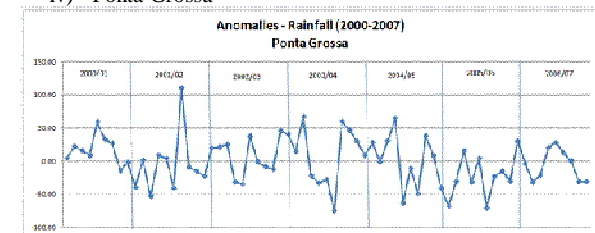
ii) Cerro Azul



iii) Jaguariaíva



iv) Ponta Grossa



v) Telemaco Borba

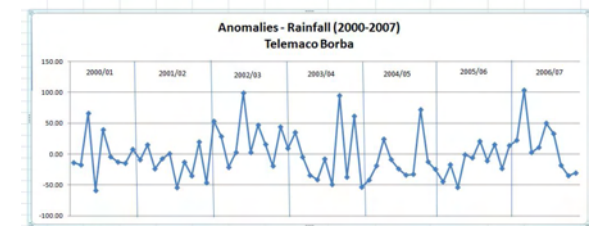
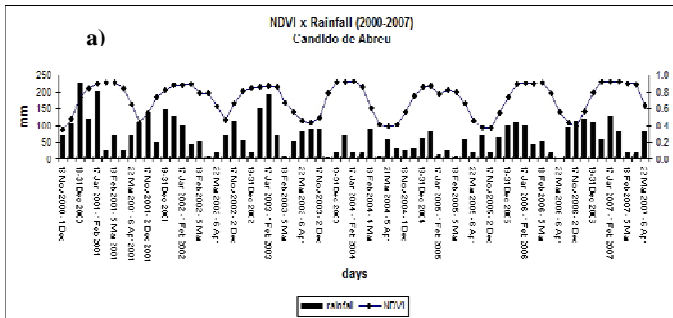


Figure 1. Rainfall anomalies for each year (2000-2007), during soybean growing season and for locations: *i)* Candido de Abreu; *ii)* Cerro Azul; *iii)* Jaguariaíva; *iv)* Ponta Grossa; *v)* Telemaco Borba.

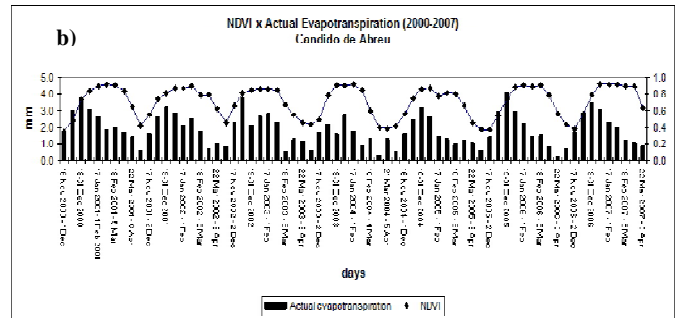
4.3 Linear regression analyses for all time series

Analyses indicated that the simple regression of NDVI with Actual Evapotranspiration (AE) showed much higher R² values than the regressions of NDVI in relation to rainfall (Figure 3). Despite this observed decrease in NDVI values during the Jan-Feb 2005 rainfall deficit period, we found better agreement between NDVI and AE. May be due to the

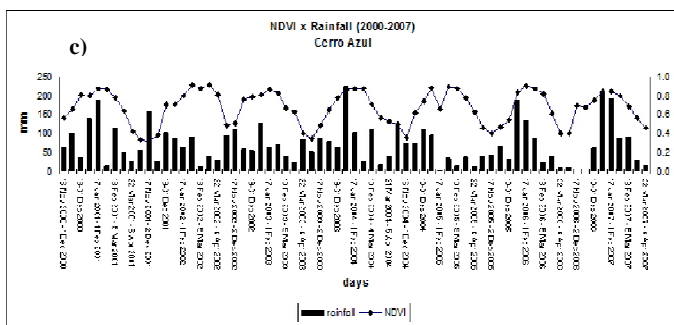
a) Rainfall and NDVI (Candido de Abreu- location 1)



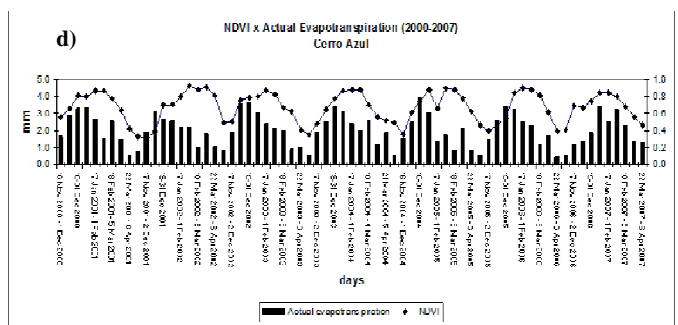
b) Actual Evapotranspiration and NDVI (Candido de Abreu- location 1)



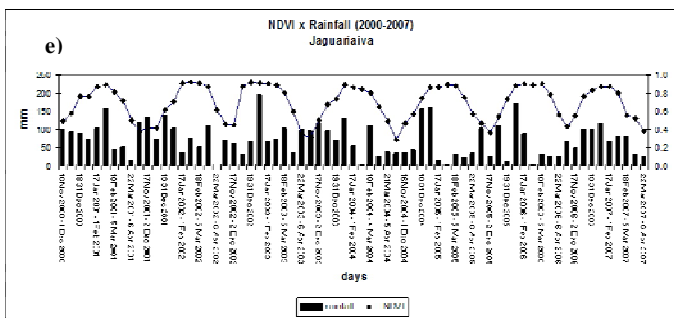
c) Rainfall and NDVI (Cerro Azul – location 2)



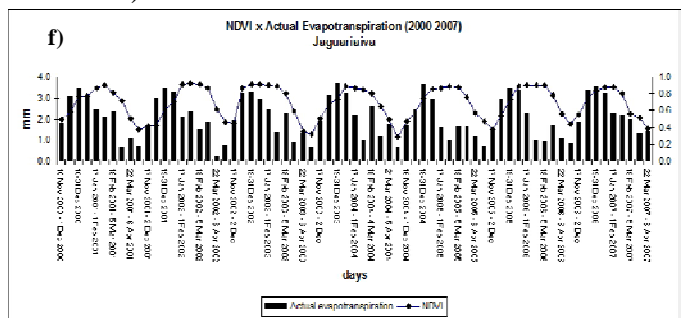
d) Actual Evapotranspiration and NDVI (Cerro Azul – location 2)



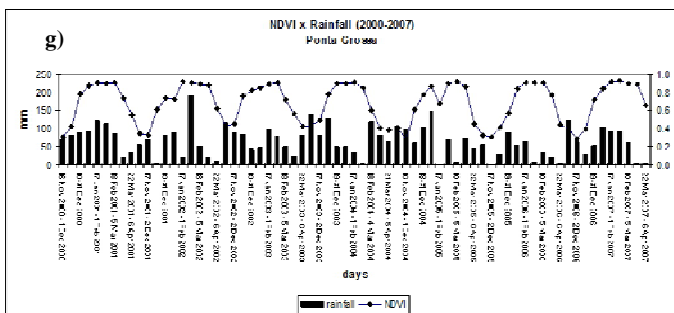
e) Rainfall and NDVI (Jaguariava – location 3)



f) Actual Evapotranspiration and NDVI (Jaguariava – location 3)



g) Rainfall and NDVI (Ponta Grossa – location 4)



h) Actual Evapotranspiration and NDVI (Ponta Grossa – location 4)

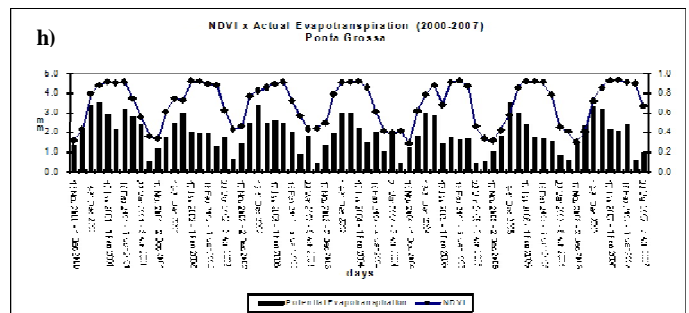
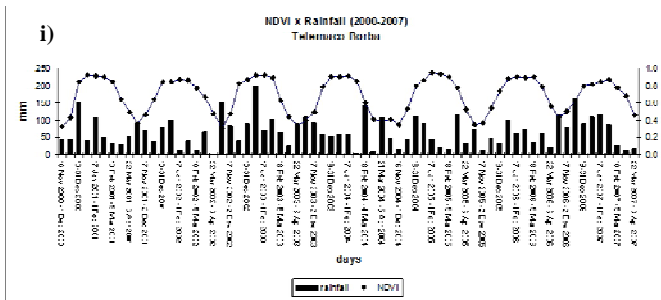


Figure 1 - Continued

i) Rainfall and NDVI (Telemaco Borba – location 5)



j) Actual Evapotranspiration and NDVI (Telemaco Borba – location 5)

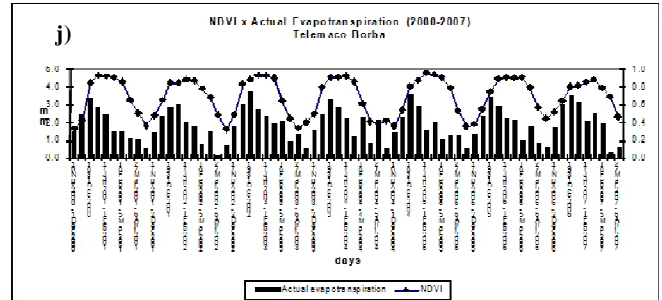


Figure 2. Interannual variation (2000-2007) for NDVI and Rainfall: *a), c), e), g), i)* and for NDVI and Actual Evapotranspiration: *b), d), f), h) and j).*

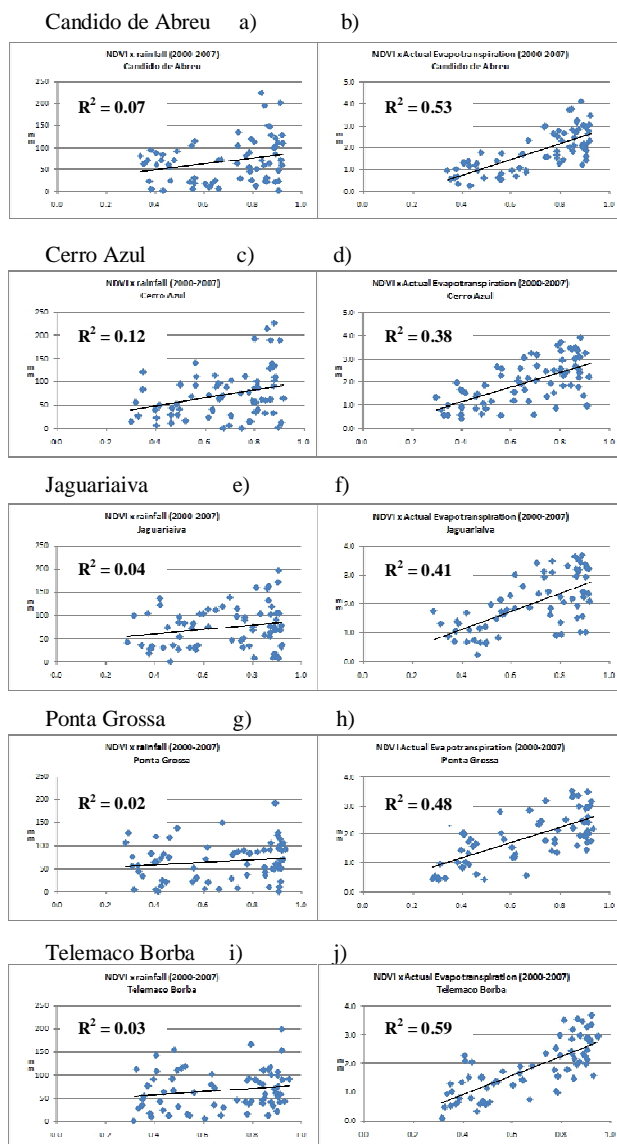


Figure 3. Linear regressions for all time series (2000-2007) between NDVI and rainfall: *a), c), e), g), i)* and for NDVI and Actual Evapotranspiration: *b), d), f), h), and j).*

fact that when the rainfall reaches the land surface, part of the water is diverted as runoff, and part infiltrates and is retained in the upper layers of the soil which is thereafter used for vegetation growth. The vegetation then absorbs the soil water and uses it through the process of evapotranspiration (Sarma and Lakshmi, 2006). Cihlar *et al* (1991) found similar results for the relation between NDVI values from NOAA/AVHRR and Evapotranspiration for different ecosystems. They reported that there was a highly significant association between NDVI and Actual Evapotranspiration values ($r=0.77$) or between NDVI and potential evapotranspiration ($r=0.86$). High correlation was also found between cumulative NDVI and cumulative Actual Evapotranspiration over the entire growing season ($r=0.96$).

5 CONCLUSIONS

Results from the analysis showed that the seasonal and interannual variability of the vegetation index (NDVI) serves as a good indicator for identifying variations, mainly impacts of climate anomalies on vegetation and, consequently, on crops production (in this case, soybean crop). NDVI curves were able to differentiate vegetation responses associated with above and below precipitation during soybean growing season. Actual Evapotranspiration (AE) showed best agreement with soybean NDVI in relation to rainfall, probably due to the fact that this variable integrates information of rainfall, temperature and soil water holding capacity.

6 REFERENCES

Adami, M., Moreira, M. A.; Rudorff, B. F. T.; Corina Da Costa Freitas, C. C. F.; Faria, R. T. F.; and Deppe, F., 2007. Painei amostral para estimativa de áreas agrícolas. Pesquisa Agropecuária Brasileira, v.42, n.1, p.81-88.

Allen, R. G.; Pereira, L. S.; Raes, D; and Smith, M., 1998. Crop evapotranspiration: guidelines for computing crop water requirements. Rome: Food and Agriculture Organization of the United Nations, 300p. (Irrigation and Drainage, Paper 56).

Baethgen, W. E. 1997. Vulnerability of the agricultural sector of Latin America to climate change. Climate Research, 9: 1-7.

- Bastiaanssen, W. G. M. 2000. SEBAL – Based Sensible and Latent Heat Fluxes in the Irrigated Gediz Basin. Turkey. *Journal of Hydrology*, v. 229, p.87-100.
- Bins, L. S.; Fonseca, L. G.; Erthal, G. , 1996. Satellite imagery segmentation: a region growing approach. In: VIII Simpósio Brasileiro de Sensoriamento Remoto, 1996. Anais. São José dos Campos: INPE.
- Burba, G. G.; and Verma, S. B. Seasonal and interannual variability in evapotranspiration of native tallgrass prairie and cultivated wheat ecosystems. 2005. *Agricultural and Forest Meteorology* 135, p. 190–201.
- Cihlar, J. S.; St-Laurent, and L.; Dyer, J. A., 1991. Relation Between the Normalized Difference Vegetation Index and Ecological Variables, *Remote Sensing and the Environment*. v. 35, p.279-298.
- CONAB: Companhia Nacional de Abastecimento. Superintendência Regional do Paraná. Área e produção das safras paranaense e brasileira 2004/05 e 2005/06. 2005. Acesso em 21/08/2009. Disponível em: http://www.conab.gov.br/conabweb/download/sureg/pr/soja/soja_novembro_2005.pdf
- Engman, E. T. 1995. Recent advances in remote sensing in hydrology. *Reviews of Geophysics*, v. 33, p. 967-975.
- GEOSAFRAS: PREVSAFRAS, 2007. Boletim de acompanhamento da safra de soja. Safra 2006/07- Paraná. CONAB. IAPAR. SIMEPAR. Edição: 15 de fevereiro de 2007. (Parcial), 20 p.
- Guillevic, P.; Koster, R. D.; Suarez, M. J.; Bounoua, L.; Collatz, G. J.; Los, S. O.; and Mahanama, S. P. P., 2002. Influence of the interannual variability of vegetation on the surface energy balance - A global sensitivity study. *J. Hydrometeor.*, **3**, 617–629.
- Heinemann, A.B.; Hoogenboom, G.; Faria, R.T.; 2002. Determination of spatial water requirements at county and regional levels using crop models and GIS. An example for the State of Parana, Brazil. *Agricultural Water Management*, 52, 177-196.
- IAPAR, Cartas Climáticas do Paraná. Instituto Agrônomo do Paraná. Londrina-PR, 2000.
- Jensen, M. E.; and Haise, H. R., 1963. Estimating evapotranspiration from solar radiation. *Proc. American Society of Civil Engineering, J. Irrigation and Drainage Division*. 89:15-41.
- Meinke, H.; and Stone, R. C. 2005. Seasonal and inter-annual climate forecasting: the new tool for increasing preparedness to climate variability and change in agricultural planning and operations. *Climatic Change*, v.70, p.221-253.
- Nobre, P.; Marengo, J.A.; Cavalcanti, I.F.A.; Obregon, G.; Barros, V.; Camilloni, I.; Campos, N.; and Ferreira, A.G., 2006. Seasonal-to-Decadal Predictability and Prediction of South American Climate. *J. Climate*, 19, 5988–6004.
- Ogallo, L.; Bessemoulin, P.; Ceron, J.-P.; Mason, S.; and Connor, S. J., 2008: Adapting to climate variability and change: the Climate Outlook Forum process. *BAMS*, 57, 93-102.
- Rizzi, R.; Rudorff, B. F. T., 2005. Estimativa da área de soja no Rio Grande do Sul por meio de imagens Landsat. *Revista Brasileira de Cartografia*, n. 57, v. 3, p. 226-234.
- Sarma, A.A.L.N.; and Lakshmi K. T.V., 2006. Studies on crop growing period and NDVI in relation to water balance components. *Indian Journal of Radio & Space Physics*, n. 35, p 424-434.
- Seiler, R.A.; Kogan, F.; Guo, W.; and Vinocur, M., 2007. Seasonal and interannual responses of the vegetation and production of crops in Cordoba – Argentina assessed by AVHRR derived vegetation indices. *Advances in Space Research*, 39 (1) 00. 88-94.
- Semenov, M.A.; and Porter, J.R., 1995. Climatic variability and the modelling of crop yields. *Agricultural and Forest Meteorology*, v.73, p. 265-283.
- Shimabukuro, Y.E.; and Smith, J.A., 1991. The least-squares mixing models to generate fraction images derived from remote sensing multispectral data, *IEEE Transactions on Geoscience and Remote Sensing*, v. 29, n 1, p. 16-20.
- Suzuki, R.; Masuda, K.; and Dennis, D.G., 2007. Interannual covariability between actual evapotranspiration and PAL and GIMMS NDVIs of northern Asia. *Remote Sensing of Environment*, v.106, p. 387–398.
- Thorntwaite, C.W., 1948. An approach towards a rational classification of climate. *Geographical Review*, London, v.38, p.55-94.
- Thorntwaite, C. W.; and Mather, J. R., 1955. The water balance. Centerton: Drexel Institute of Technology. 104 p. (Publications in Climatology. v. 8, n. 1).
- Tucker, C. J.; Slayback, D. A.; Pinzon, J. E.; Los, S. O.; Myneni, R. B.; and Taylor, M. G., 2001. Higher northern latitude normalized difference vegetation index and growing season trends from 1982 to 1999. *International Journal of Biometeorology*, 45, 184–190.
- Wagner, A.P L.; Weber, E.; Fontana, D.C.; Ducati, J.R.; and Klering, E., 2007. Estimativa de Área de Soja no Rio Grande do Sul Utilizando Imagens NDVI/MODIS. Anais, XIII Simpósio Brasileiro de Sensoriamento Remoto, INPE, Florianópolis, p.457-464.
- Wrege, M. S.; Gonçalves, S. L.; Caramori, P. H.; Vasconcellos, M. E. C.; Oliveira, D.; Abuscarub Neto, M.; Borrozzino, E.; and Caviglione, J. H., 1999. Risco de deficiência hídrica na cultura do milho no estado do Paraná. *Pesquisa Agropecuária Brasileira*, Brasília, v. 34, n.7.

THE USE OF AEROSPACE PHOTOGRAPHIES AND REMOTE SENSING DATA IN CARTOGRAPHY

M.H. Gojamanov

Baku State University, Faculty of Geography, Dept. of Geodesy and Cartography
23, Z.Khalilov Str., Baku, Azerbaijan, AZ-1148

KEY WORDS: Photography, Satellite, Image, Resolution, Ikonos, Orthophototransformation, Update map, QuickBird

ABSTRACT:

This article dedicated to the features of the use of space imagery and remote sensing data for the various tasks of cartography. Maps produced by satellite imagery are more modern and accurate outlines of mapped objects that best represent the phenomena are interrelated and that in the absence of such images in general could not be mapped. There was considered two new directions of space cartography. The first simulates the cosmic view of the Earth on the maps, which led to the creation of so-called "orbital" maps. Combination of traditional cartographic map image with aerospace is the essence of the second direction. Remote Sensing, carried out in a wide range of scales, to update maps of small and medium-size directly from the photographs, not seeking renewal of large-scale maps. The Technical characteristics of modern space images are suitable for mapping scale of 1:5000 and smaller. Cosmic digital images opens up new possibilities: reduction of the cost of repeated surveys, the increase in area coverage areas, reducing the distortions associated with the relief. Therefore, surveying from space can become the main method of updating topographic maps.

1. INTRODUCTION

Cosmonautics and remote sensing images have made in mapping the Earth is truly revolutionary transformation. The main sources of information in remote satellite surveys are satellite imagery - images of objects obtained as a result of registration with the great distance of their own or reflected radiation.

For mapping use are important the properties of these satellite images, as their huge territorial scope and completeness of mapping territory. To this have to add simultaneity fulfill mapping, a sharp reduction of time collecting information and ensuring a high consistency of created on its base the series of thematic maps.

The development of radio electronics led to a flight of aerospace systems for imaging areas, different from traditional photography, such as television, scanner, radar and thermal surveys.

The introduction of aerospace methods of creating maps and the development of automated compilation sheet systems - two major problems of modern theoretical and practical cartography generated by scientific and technological revolution.

2. MAIN BODY OF TEXT

Development of space surveys gave new impetus to the remote methods of mapping. They expanded their capabilities - the global reach of information, including the previously inaccessible area of the Earth and the surface of other planets, regular speed and repeatability of receipt and processing of information, imaging on the satellite pictures of phenomena that otherwise could not fix.

Maps produced by satellite imagery, are more modern and accurate outlines of mapped objects that best represent the phenomena are interrelated and that in the absence of such images in general could not be mapped (eg, deep faults on geological maps).

Using space images allows for control and revision of maps in part: a) the correctness of the boundaries outlines of areals and geographical distribution of mapping objects and phenomena; b) overlay compilation of cartographic representation and the relative position of objects; c) the reliability of the content of individual units and maps in general.

In connection with the aerospace mapping there were developed two new directions. The first simulates the cosmic view of the Earth on the maps, which led to the creation of so-called "orbital" maps. Combination of traditional cartographic map image with aerospace - the essence of the second direction. It led to the creation photomaps. Photomap - this printing impression of photomaps, at which the photo image of the area obtained by mounting transformed aerospace photography (Gruenberg, Lapkina, 1991). These photographs, thanks to the generalization of the optical image passing nature of the Earth in "natural" form and saving the nuances and details, highlight the most significant.

In the U.S. there photomap this state, assembled from 569 images obtained by satellite "Landsat". It is reproduced on the scale of 1: 250000 to 1: 5 000 000 for the different seasons in different spectral regions. Similar photomaps compiled for the territory of other countries (Canada, France, Britain, Japan, etc.).

Modern surveying space materials in the quality and level of resolution can compete with the aerial photographs as a basis for large-scale topographic maps, and the problem of updating topographic maps are generally very successfully solved with satellite imagery. Remote Sensing, carried out in a wide range of scales, to update maps of small and medium-size directly from the photographs, not seeking renewal of large-scale maps. This gives a great gain in time, in the fullness and present information, as well as the rapid cartographic provision of major socio-economic projects.

The modern world is very variable: growing cities, new settlements, built roads, communication networks, engineering structures, and new areas of mining, cut down forests.

Therefore, there is always the task of creating and updating topographic maps.

At the moment on the world map are practically no white spots - topographic maps covering almost the entire surface of the planet's land, although not all are equally detailed. The territory of the Azerbaijan Republic is fully covered with maps in scale 1:25000, and about two-thirds of the country - in scale 1: 10000. Therefore, development of topographic maps is still required less often - only in case of radical changes.

As the primary material for topographic maps have traditionally been used aerial photographs. With the advent of satellite remote sensing of Earth equipped with optical electronic sensors by high-resolution the satellite imagery could compete with aerial photographs as source material for large-scale mapping. The performance characteristics of modern space images suitable for mapping scale of 1:5000 and smaller (Savinykh, Tsvetkov, 2001); despite the relatively high cost of these photographs, they may be cheaper than aerial photography for mapping small areas. Space survey is also preferable in cases where aerial photography is difficult in organization, for example, for mapping of major cities and in the boundary areas; in addition, it more operational.

Over the past few years received a considerable amount of data space imaging, performed with the spacecraft QuickBird and WorldView - 1 with a resolution of 50-70 centimeter (Elerdova, 2009). In the present time space images from these spacecrafts completely cover the Earth globe. This allows the company DigitalGlobe (USA) to develop and offer various categories of users worldwide, including the CIS (Commonwealth of Independent States) countries, projects of direct access to archived data. One of these services are ImageConnect and ImageBuild, providing users with direct access to high-precision data from the satellite QuickBird and WorldView-1. The main advantage ImageBuild is the ability to integrate satellite imagery with vector data user.

Cosmic digital images opens up new possibilities: reduction of the cost of repeated surveys, the increase in area coverage areas, reducing the distortions associated with the relief. In addition, it simplifies the generalization of the image on the small-scale maps: instead of consuming simplify large-scale maps can be immediately used medium-resolution satellite imagery. Therefore, surveying from space can become the main

method of updating topographic maps. When to select images for mapping to have to account the graphical accuracy of maps (0.1 mm). For example, the images should have a spatial resolution better than 10 m for maps of scale 1:100000. Accordingly, the images Ikonos (USA) with a pixel size of 1 m can be many elements of the content maps of scale 1:10000 and smaller ([http:// www / sovzond.ru /](http://www/sovzond.ru/)). However, some elements of topographical maps, such as free-standing trees, the width of the rivers in the map scale, etc., require more detailed imaging.

When you update maps applied only change the contours of the elements, and the mapping to determine the exact position of these elements. Therefore, for the preparation of topographic maps required space images of higher resolution than to update them.

Work on updating topographic plans carried out in several stages: an initial set of data by vectorization the source material, binding and orthophototransformation space image, image decoding and updating of data, field update.

3. CONCLUSIONS

Through remote sensing market expansion, new products, especially in the category of products of high industrial expansion, the use of space imagery in the works on cartography and land is becoming more affordable and widespread. Reducing the cost of remote sensing data has led to the fact that for the production of quality outputs a high degree of accuracy is not required enormous time and material costs.

REFERENCES

Elerdova, M., 2009. Using remote sensing data from space in geoportals and LBS-services. Moscow, *Geoprofi*, 2, pp.20-23.

Gruenberg, G., Lapkina, N., and others, 1991. *Cartography with the basics of Topography*. Education, Moscow, 368 p.

Savinykh, V., Tsvetkov, V., 2001. *GIS analysis of remote sensing data*. Kartgeotsentr-Geodezizdat, Moscow, 228 p.

[http:// www / sovzond.ru /](http://www/sovzond.ru/)

MONITORING OF BEACHES AND SAND DUNES USING DIGITAL AERIAL PHOTOGRAPHY WITH DIRECT GEOREFERENCING

J. A. Gonçalves^{a,b,*}, L. Bastos^{a,b}, Perez, B.^a, Magalhães, A.^a

^a University of Porto - Science Faculty, Rua Campo Alegre, 4169-007, Porto, Portugal

^b CIIMAR - Centre for Marine and Environmental Research, Rua dos Bragas, 4050-123, Porto, Portugal
jagoncal@fc.up.pt

Commission VII

KEY WORDS: Photogrammetry, Change Detection, Matching, DEM/DTM, Georeferencing, Direct

ABSTRACT:

This paper presents an efficient methodology for coastal monitoring based on digital aerial photography acquired periodically, using a Zeiss-Intergraph DMC camera, with a spatial resolution of 10 cm. Images are delivered with exterior orientation given by the direct georeferencing system used by the company providing the images. An assessment of those exterior orientation parameters was done using field check points. It could be concluded that the positional accuracy of 3D coordinates determined by photogrammetric means using the exterior orientation elements has root mean square errors better than 30 cm, which can be accepted for the purposes of this type of work. This level of accuracy was achieved for four different flights. It was decided not to do an aerial triangulation. DSMs were obtained by stereo-matching (least-squares with region growing) using program DPCOR of the software package BLUH. Sand areas are normally very bright and difficult for the matching. Since images were acquired with relatively small sun elevation the automatic extraction of a DSM was very successful. Using check points the vertical accuracy of the DSMs was found to be 30 cm or better. Orthoimages were created using the extracted DSM. The resulting datasets for the four different dates were integrated in a GIS and the method proved to be a very useful tool for the detection of areas where significant volumetric changes occurs and for the quantification of those beach changes.

1. INTRODUCTION

The western part of the Portuguese coast is subject to significant degradation due to the action of the ocean (Ferreira, et al., 1995). Coastal areas are also under a strong anthropic pressure, which have as consequence the destruction of dunes and other natural protections. Significant morphodynamic changes occur in short periods of time which need to be monitored. In order to detect and quantify those changes and foresee the near term evolution of the coastal areas, both for safety and economic reasons, very frequent surveys, are required.

Field survey monitoring programmes are carried, using GPS, in sensible coastal areas in Portugal, in order to detect and quantify changes (Baptista et al., 2008, Gonçalves et al., 2009). However, they are still time consuming and usually applied in small areas if surface models are to be obtained.

Airborne surveying techniques are more cost effective and can achieve a positional accuracy appropriate for coastal evolution assessment. Elevation changes in beach landforms, due to natural or antropic origin, can be of several meters, even in short periods. Elevation errors of a few decimetres in digital surface models (DSMs) are therefore still acceptable for the detection of essential relief changes in coastal areas.

Laser scanning is nowadays a commonly used technique for coastal monitoring. It has an important advantage in that the final DSM/DTM is obtained essentially in an automatic manner (Baltsavias, 1999). However, besides being still quite

expensive, laser scanning alone does not provide the image component, which is also very important for the interpretation and detection of the morphodynamic changes.

Aerial photography, especially with the recent digital aerial cameras, can provide important information to the assessment of changes while allowing a high degree of automation. That is the case if direct georeferencing (DG) can be accurate enough to avoid aerial triangulation and if the DSM generation can be fully automated by stereo matching.

Images of sandy areas may be difficult to treat in terms of standard photogrammetric procedures. For example, for the purpose of aerial triangulation, in the absence of man made features, well defined ground control points (GCPs) may be difficult to obtain, especially in the case of high resolution images. When large parts of the images are occupied by water also tie points cannot be obtained. These are additional reasons to use the exterior orientation data given by DG, if it is accurate enough.

This paper describes the exploitation of aerial photography acquired in the scope of a coastal monitoring program in the Portuguese northwest coast through the referred methodology. Part of the area does not have man made features to be used as GCPs. There is usually a need for fast data production immediately after image acquisition, so there is a strong interest in relying on DG. One of the objectives of this study is to determine the best accuracy achievable using image data provided by a private company.

In this work some basic photogrammetric processing tools, such as the stereo matching, 3D coordinate determination, interpolation algorithms to generate a regular grid DSM, orthorectification and image mosaicking were used. Complementary, some tools of the BLUH software package, created at the Institute for Photogrammetry and Geoinformation, University of Hannover (Jacobsen, 2000), and other programmed by the authors were applied to optimise the procedure efficiency. DSM and orthoimage data integration and analysis were carried using a commercial GIS software.

2. APPLICATION AREA AND DATA ACQUISITION

The application area has an extension of 15 km to the south of the city of Porto, which includes in the north part the estuary of the river Douro (Figure 1). The area is subject to strong effects of the sea (Intensive action from the ocean), which produces significant changes, especially during winter.



Figure 1. Map of the area with the flight plan (created with Google Earth)

In the scope of the monitoring program, it was decided to acquire aerial digital photography twice a year, before and after winter. In this way it is possible to assess the effect of winter storms over the beaches. It was also decided to acquire photographs in very low tide condition in order to map as much as possible the intertidal area.



Figure 2. Example of part of the study area, in the estuary of river Douro, near the city of Porto

The data was acquired with a digital camera Zeiss-Intergraph DMC which allows to obtain images with a ground sampling distance (GSD) of 0.1 meters. The 15 km of the study area were covered by a total of 100 photos in two strips, with a 60%

forward overlap and 30% side lap. Figure 1 shows the centre lines of the two strips.

The pan-chromatic images, used in the process of digital surface model (DSM) generation, have a dimension of 7680 by 13824 pixels, with a pixel size 12 μm . According to the camera specifications the focal length is 120.000 mm, the principal point is at the image centre and images are virtually distortion free.

The base-height ratio in digital cameras is smaller than in conventional analogical cameras. In the present photos a parallax of 1 pixel (10 cm on the ground) corresponds to a height difference of 34 cm, on average.

Images were acquired by a private company, using GPS/INS direct georeferencing equipment (IGI Aerocontrol) and standard processing techniques as for any other large scale topographic mapping work. According to the information provided (Municipia, 2009), a boresight calibration was performed after the camera was mounted and all the relative positions of GPS, IMU and camera were measured with total stations. GPS positioning of the flights was done relative to the Portuguese network of GPS permanent stations (IGP, 2009). The reference system used was ETRS89. The data processing software was IGI Aero-office. According to the processing reports provided, exterior orientation parameters are given in UTM coordinate system with appropriate corrections of scale factor and meridian convergence.

During the monitoring periods four flights were done. Table 1 contains information about date and start time of the image acquisition. A full flight is carried in less than 10 minutes.

Flight no.	Date	Start time (UTC)
1	14-Nov-2008	09:25
2	23-Apr-2009	08:06
3	18-Nov-2009	10:42
4	5-May-2010	14:11

Table 1. Date and start time of the four flights

Some of the times were early in the morning, which would be inconvenient for normal photogrammetric purposes. In the present case, since the area of interest is essentially sand, that can be an advantage because some shadow effects occur in the sand that facilitate the stereomatching.

3. ANALYSIS OF THE EXTERIOR ORIENTATION

One of the objectives of this work is to assess if the results provided through the adopted methodology were appropriate for the main objectives of large scale mapping of coastal areas without field work requirements. Several assessments were done, some without and some with check points.

An algorithm of space intersection incorporated in the BLUH software package was used. It gives the point of shortest distance between the straight lines defined by the co-linearity equations, together with the corresponding y-parallax.

3.1 Relative orientation

The first verification done was to see if the exterior orientation parameters of consecutive photos provide an accurate relative orientation. That is essential if stereoscopic viewing is required as well as if calculation of 3D coordinates.

For selected stereopairs a total of 15 homologous points per pair were manually measured and the corresponding y-parallaxes

were calculated. Table 2 shows the root mean square of the y-parallaxes for a pair of each flight. In general y-parallaxes were not larger than 1 pixel and showed a systematic trend within each stereopair.

Flight number	RMS y-parallax (pixels)
1	0.7
2	1.0
3	1.1
4	0.6

Table 2. RMS of y-parallaxes (1 pair per flight)

3.2 Repetition of 3D coordinates

The second test consisted in analysing the repeatability of 3D coordinates determined from stereopairs, in different flights and different strips. Six points were chosen, distributed along the study area and were measured 8 times: twice in each flight, in pairs of different strips. These were well defined points in man made features, mainly road paintings, that did not change between flights. The standard deviations were calculated for all sets of 8 measurements and are listed in table 3.

Point #	σ_x (m)	σ_y (m)	σ_z (m)
1	0.25	0.28	0.31
2	0.27	0.28	0.22
3	0.29	0.29	0.13
4	0.30	0.27	0.20
5	0.28	0.31	0.13
6	0.29	0.31	0.20

Table 3. Standard deviations of coordinates measured in different stereopairs, of different flights

3.3 Accuracy assessment with check points

The third test consisted in comparing 3D coordinates of well defined check points surveyed on the field using dual frequency GPS receivers, with centimetric accuracy.

Table 4 shows the statistics (mean and standard deviation) of the errors found. The mean values of a few decimetres in X and Y (2-3 pixels) indicate the systematic effects introduced by errors in the exterior orientation. Standard deviations are smaller, closer to 1 pixel, which indicate the obvious conclusion that if an aerial triangulation was performed errors would become of the order of the image resolution. Height errors show also systematic trends but larger standard deviations because attitude errors produce variable height errors along the images.

Pair	No. pts	X Mean \pm Std (m)	Y Mean \pm Std (m)	Mean \pm Std (m)
1	6	0.24 \pm 0.08	-0.09 \pm 0.16	0.24 \pm 0.11
2	4	-0.05 \pm 0.06	0.23 \pm 0.02	0.39 \pm 0.06
3	5	0.18 \pm 0.10	0.43 \pm 0.22	-0.29 \pm 0.25
4	4	0.16 \pm 0.14	0.48 \pm 0.07	-0.10 \pm 0.27
5	6	-0.30 \pm 0.16	-0.14 \pm 0.17	-0.03 \pm 0.25
6	3	-0.39 \pm 0.18	-0.06 \pm 0.05	-0.24 \pm 0.32
7	6	0.26 \pm 0.10	-0.23 \pm 0.08	-0.10 \pm 0.07
8	4	-0.34 \pm 0.11	0.21 \pm 0.01	0.09 \pm 0.35

Table 4. Statistics of errors found in check points

Results obtained with the check points agree with the results of repeated coordinate measurements presented in table 3.

In general it can be concluded that planimetric and altimetric accuracy are of the order of 0.3 metres

This planimetric uncertainty is acceptable for orthoimage production in relatively large map scales, such as 1:2000 or even 1:1000. Height uncertainty is of the same order and is suitable for a quick assessment of the degree of erosion or accretion and quantification of volumetric changes in sandy beaches and dunes.

4. DSM AND ORTHOIMAGE GENERATION

4.1 Stereo matching and DSM generation

For the DSM generation conjugate points were obtained using program DPCOR, of the BLUH software packages (Jacobsen, 2000, Rieke-Zapp and Nearing, 2005). It implements the least squares matching with region growing (Gruen, 1985, Otto and Chau 2000). This algorithm works in image space and doesn't require image orientation or epipolar geometry and only needs a seed point per stereopair. It produced very successful results over the sand and rocks near the sea.

From the homologous points 3D coordinates were calculated by the intersection algorithm. Points were accepted with the following criteria:

- 1 – only accept correlation above 0.8.
- 2 – only accept y-parallax smaller than 2 pixels (large values probably correspond to wrong matches)
- 3 – only accept heights within an interval of expected values: greater than -2 m (the minimum in the lowest tides) and smaller than 10 m. Other heights are either wrong matches or are outside of the interest area.

Points were extracted with 3 pixel spacing in rows and columns. A final single grid was obtained by averaging heights of all points in 1m by 1m cells. Figure 3 shows an extract of one of the DSMs created in this way.

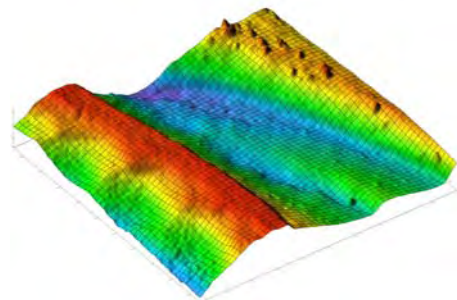


Figure 3. Portion of one of the DSMs generated

A mask was created to limit the areas of beach and dunes. This mask was applied to the 4 grids created from the different flights.

Good detail was extracted, as is the case of small shrubs in dunes and marks of tyres in the sand. The success of the matching was also very good in most of the cases. Usually sand is difficult for stereo matching but as in this case most of the images were taken early in the morning, and some in November, illumination conditions provided shadows in the sand that helped in the matching. Figure 4 shows shaded relief images of two portions of DSMs: (a) obtained in the first flight (November, 9:25 am, local time) and (b) the fourth (May, 3:11 pm). Success was not so good in the second case (black dots indicate no matching). Since these areas of empty pixels were

never very large they were filled by interpolation and in general no significant relief detail was lost.

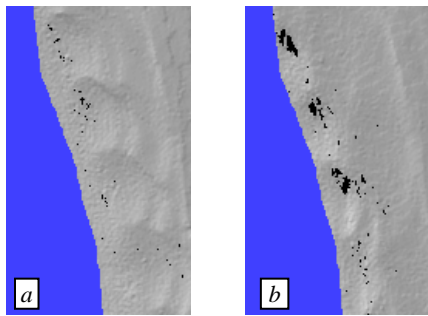


Figure 4. Sample images of different matching success due to different illumination: (a) November, 9:25 am (b) May, 3:11 pm

Finally it was possible to do an error assessment of the extracted DSM. Within the monitoring programme, GPS field data is collected (dual frequency kinematic) along lines over the dunes. For one of the DSMs the data was collected with only a difference of a few days. Figure 5 shows the points over the shaded relief image of the DSM.

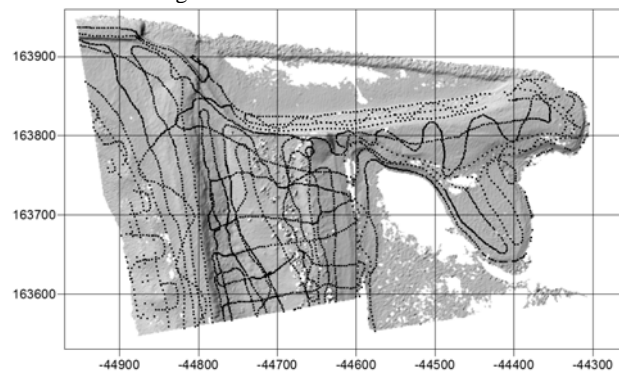


Figure 5. DSM and GPS points used to assess the accuracy

For a total of 3700 points a RMSE of 0.17 meters was found. This result is slightly better than what was found in other images with check points. In general, without aerial triangulation, the 30 cm is a more secure assumption of the accuracy of the DSMs.

4.2 Orthoimage generation

Images were ortho-rectified individually with the DSM extracted, restricted to the mask of beaches and sand. In order to have a complete view of the surrounding areas, outside the DSM area a DTM derived from large topographic map data of scale 1:2,000 was used. Since this DTM does not correspond to the present form of the terrain surface, the quality of the orthos in these areas is not good. They should be seen as research grade products, worth for the analysis of change detection in the interest areas, which are the sandy beaches and the dunes.

Cut lines were defined for all ortho images, choosing the most central parts in order to minimise residual relief distortions. Mosaics of 1 km by 1 km were created.

The following figures show some examples of significant changes detected on the orthoimages, as well as on the DSMs. Figure 6 shows an example of a significant change in a sand bank that got separated in the estuary of the river Douro: image 6a is from November 2008 and image 6b from May 2010. Images 6c and 6d show the effect on the DSMs.

Figure 7 shows the retreat of the shore line in a small area. The four image samples are from the 4 dates. The most significant change occurred on the winter of 2010 (3rd to the 4th image). Figure 8 shows a cross section from the two extreme dates (November 2008 and May 2010). Images and DSM allow for a very detailed assessment of changes.

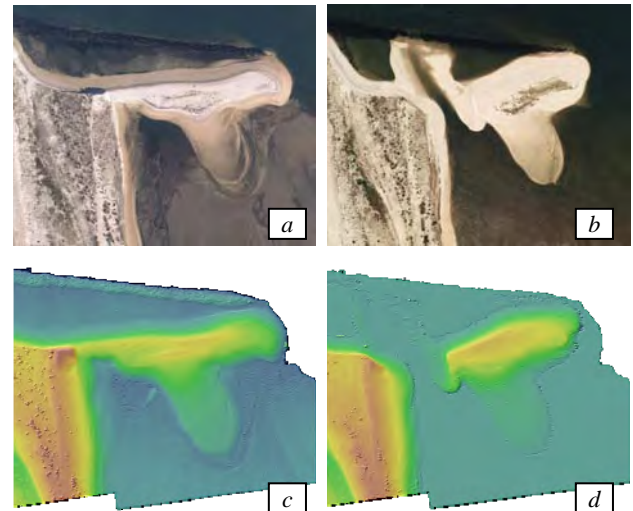


Figure 6. Example of a change detected between Nov-2008 and May-2010: on orthoimages (a and b) and on DSMs (c and d)



Figure 7. Example of retreat of the coast line along the 4 dates. The most significant change occurred from image c to d.

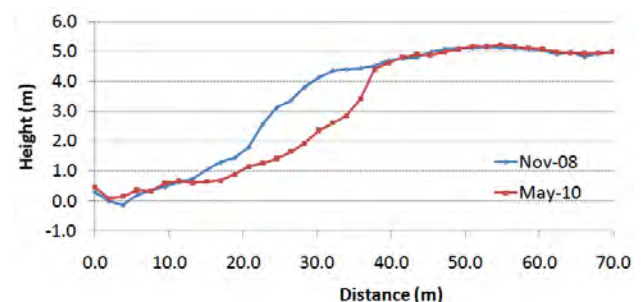


Figure 8. Example of a cross section corresponding to images 7a (Nov 2008) and 7d (May 2010).

5. DISCUSSION AND CONCLUSIONS

The positional accuracy, both planimetric and altimetric, just using the DG information, was estimated as 30 cm, far from what would be achievable by aerotriangulation. Nevertheless, it is compatible with large topographic map scales, such as

1:1000, according, for example, to the USGS standards (USGS, 1999), considering a contour spacing of 1 meter.

The existing changes in dynamic areas, such as this one, are very significant and become clearly detectable. Results presented in the previous section show the usefulness of both orthoimages and DSMs in detecting and quantifying these changes.

The fact that no GCP collection was required for an aerial triangulation is an important advantage. On one hand it allows for a very fast response in deriving DSM and orthoimages after the data acquisition. On the other hand it allows for reasonably accurate mapping in locations where only natural features exist, such as in beaches, dunes and river estuaries.

This methodology has proven to be useful for researchers interested in coastal dynamic studies and also for decision-makers with responsibilities in the management of the coastal zone.

USGS, 1999. Map Accuracy Standards, Fact Sheet FS-171-99 (November 1999). Available online: <http://egsc.usgs.gov/isb/pubs/factsheets/fs17199.html>, (last accessed October, 2009)

Acknowledgements

This project was supported by Parque Biológico de Gaia, EEM. The BLUH Software was provided by the Institute for Photogrammetry and Geoinformation of the University of Hannover.

References from Journals:

Baltsavias, E., 1999. A comparison between photogrammetry and laser scanning. *ISPRS Journal of Photogrammetry & Remote Sensing*. Issue 54, 83–94.

Baptista, P., Bastos, L., Bernardes, C., Cunha, T. & Dias, J.A., 2008. Monitoring Sandy Shores Morphologies by DGPS – A Practical Tool to Generate Digital Elevation Models. *Journal of Coastal Research*. Issue no. 24, 1516–1528.

Otto, G. P. and Chau, T. K. W., 1989. ‘‘Region-growing’’ algorithm for matching of terrain images. *Image and Vision Computing*, 7(2): 83–94.

Gruen, A., 1985. Adaptive least squares correlation: a powerful image matching technique. *South African Journal of Photogrammetry, Remote Sensing and Cartography*, 14(3): 175–187.

Rieke-Zapp, D.H., Nearing, M. A., 2005. Digital Close Range Photogrammetry for Measurement of Soil Erosion. *The Photogrammetric Record* 20(109): 69–87 (March 2005)

References from Other Literature:

Ferreira, O., Dias, J., Gama, C., Taborde, R., 1995. Quantification of Beach Erosion Caused by Storms on the Portuguese Coast. *Directions in European Coastal Management*. Healy and Doody (eds.), 1995, Samara Publishing Limited, Cardigan.

Gonçalves, J.A., Madeira, S., Bastos, L., 2009. Application of a Low Cost Mobile Mapping System to Coastal Monitoring. *The 6th International Symposium on Mobile Mapping Technology - MMT09*, Presidente Prudente, Brasil.

Jacobsen, K., 2000. Program System BLUH user’s manual. Institute of Photogrammetry and Engineering Surveys, University of Hanover, Hanover. 444 pages.

References from websites:

IGP, 2010. <http://www.igeo.pt/produtos/geodesia/vg/renep/renep.asp> (last assessed on April 2010)

Municipia, 2009. <http://www.municipia.pt> (last assessed on April 2010)

THE USE OF SIMILARITY IMAGES ON MULTI-SENSOR AUTOMATIC IMAGE REGISTRATION

H. Gonçalves^{a,b,*}, J. A. Gonçalves^a, L. Corte-Real^{c,d}

^a Departamento de Geociências, Ambiente e Ordenamento do Território, Faculdade de Ciências, Universidade do Porto, Rua do Campo Alegre s/n 4169-007 Porto, Portugal - (hernani.goncalves,jagoncal)@fc.up.pt

^b Centro de Investigação em Ciências Geo-Espaciais, Universidade do Porto, Rua do Campo Alegre, s/n 4169-007 Porto, Portugal

^c Departamento de Engenharia Electrotécnica e de Computadores, Faculdade de Engenharia, Universidade do Porto, Rua Dr Roberto Frias s/n 4200-465 Porto, Portugal

^d INESC Porto, Rua Dr Roberto Frias s/n 4200-465 Porto, Portugal – lreal@inescporto.pt

Commission VII

KEY WORDS: Automation, Correction, Correlation, Georeferencing, Image, Matching, Mathematics

ABSTRACT:

Automatic image registration (AIR) is still a present challenge regarding remote sensing applications. Although several methods have been proposed in the last few years, geometric correction is often a time and effort consuming manual task. The only AIR method which is commonly used is the correlation-based template matching method. It usually consists on considering a window from one image and passing it throughout the other, looking for a maximum of correlation, which may be associated to the displacement between the two images. This approach leads sometimes (for example with multi-sensor image registration) to low correlation coefficient values, which do not give sufficient confidence to associate the peak of correlation to the correct displacement between the images. Furthermore, the peak of correlation is several times too flat or ambiguous, since more than one local peak may occur. Recently, we have tested a new approach, which shortly consists on the identification of a brighter diagonal on a “similarity image”. The displacement of this brighter diagonal to the main diagonal corresponds to the displacement in each axis. In this work, we explored the potential of using the “similarity images” instead of the classical “similarity surface”, considering both correlation coefficient and mutual information measures. Our experiments were performed on some multi-sensor pairs of images with medium (Landsat and ASTER) and high (IKONOS, ALOS-PRISM and orthophotos) spatial resolution, where a subpixel accuracy was mostly obtained. It was also shown that the application of a low-pass filtering prior to the similarity measures computation, allows for a significant increase of the similarity measures, reinforcing the strength of this methodology in multi-spectral, multi-sensor and multi-temporal situations.

1. INTRODUCTION

Multi-sensor automatic image registration (AIR) is a present challenge, with emphasis on remote sensing applications. Direct georeferencing techniques, based on navigation instruments on board the satellites allow for the determination of pixel geolocation. Bringing images to a well defined cartographic reference system allows for an approximate image registration with any other precisely georeferenced imagery. Since ideally image registration should be done at least at the pixel accuracy, improvement is needed for most satellite images.

A wide variety of AIR methods may be found in the literature (Brown, 1992; Fonseca, 1996; Zitová, 2003). However, there are several particularities on the registration of remote sensing images which justifies continuous research in this field. These particularities include differences in the radiometric content (motivated by different spectral bands and/or different sensors), the slope variation of the terrain covered by the image, differences in the image acquisition geometry, among other difficulties. A system which should automatically analyse all these aspects and select the most appropriate method or a combination of methods seems to be the most reasonable solution for the complex problem of multi-sensor AIR.

The most popular methods for AIR are those based on similarity measures, where the correlation coefficient plays an important role (Inglada and Giros, 2004). This class of methods mainly consists on taking a template from an image and pass it throughout the other image, producing a similarity surface. The shift between the images is expected to be associated to a well defined peak on the similarity surface. However, in several times, the surface peak may be associated to a low correlation value, present a smooth peak leading to a less accurate location, or even erroneous peaks may be found.

For the above mentioned facts, (Gonçalves et al., 2008) proposed an automatic image registration method based on correlation and Hough transform, which allows for reducing these weaknesses associated to the traditional approach of correlation-based methods. In this work, this approach was further explored by also considering the mutual information, as well as an analysis regarding the computational time, evaluated for different pairs of images. The proposed methodology is described in section 2, and some examples of its application are provided in section 3. The discussion and conclusions correspond to sections 4 and 5, respectively.

* Corresponding author.

2. METHODOLOGY

A new approach for the use of the correlation coefficient in automatic image registration was recently explored (Gonçalves et al., 2008). In this paper, we generalized this approach, which will be described in the following. In order to simplify the provided analysis, we will focus on the problem of finding a translation in both horizontal and vertical directions, assuming that the considered region is approximately “flat”. Considering (P_{REF}, L_{REF}) and (P_{NEW}, L_{NEW}) as the (Pixel, Line) coordinates of the reference and new (to be registered) images, respectively, their relation may be expressed as

$$P_{NEW} = P_{REF} + \delta_x \quad (1)$$

$$L_{NEW} = L_{REF} + \delta_y \quad (2)$$

where δ_x and δ_y are the displacements (in pixel units) on the horizontal and vertical directions, respectively, between the reference and the new image. The registration of a full scene or images with more complex deformations may be performed according to the description in (Gonçalves et al., 2008), and further evaluated through a proper set of measures (Gonçalves et al., 2009). The several steps of the proposed methodology will be described in the following.

2.1 Division of the image into tiles

As previously mentioned, in this work the focus relies on approximately “flat” regions. Depending on the terrain slope variation and on the image acquisition geometry, it may become difficult to avoid slight differences on the shifts throughout the images. Therefore, the division of the image into tiles is also considered in this work, to evaluate whether it may allow for reducing some of these remaining effects. The tiles must be sufficiently higher than the shift known or estimated a priori, for which a minimum size of 64x64 pixels up to the full image size (a single tile) may be generally applicable. The following steps are applied to each tile.

2.2 Similarity image

Instead of the traditional similarity surface, two similarity images are proposed, each one corresponding to the horizontal and vertical directions. The similarity image is produced by computing a similarity measure along one dimension at a time. Considering a tile with m -by- n pixels, then the similarity image for the horizontal and vertical directions will have n -by- n and m -by- m pixels, respectively. This procedure is schematically represented in Figure 1. The correct shift between the tiles is expected to produce a brighter diagonal strip on the similarity image, corresponding to the higher values of the similarity measure. An example of a similarity image is provided in Figure 2c.

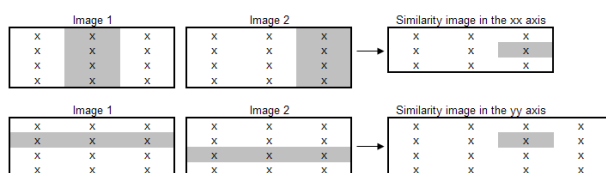


Figure 1. Illustration of the similarity image computation in both xx and yy axis.

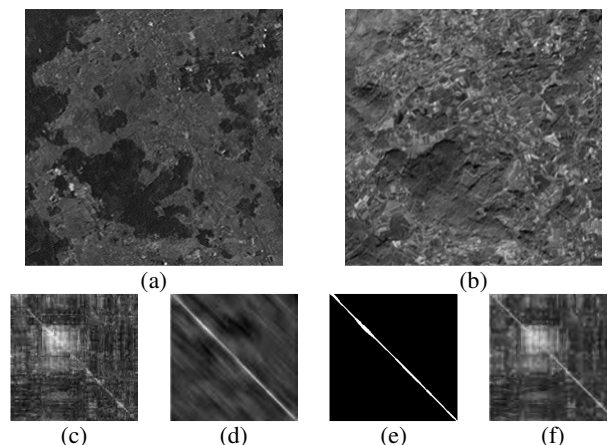


Figure 2. Illustration of the main steps of the proposed methodology (further details in section 2): (a) A segment with 256x256 pixels from a Landsat image; (b) a segment with 256x256 pixels from an ASTER image; (c) similarity image (using the correlation coefficient); (d) filtered similarity image; (e) image in (d) converted to binary; (f) -45° line detected by the Hough transform, superimposed on the similarity image.

2.3 Similarity image filtering

In order to enhance the visibility of the similarity image brighter diagonal strip, the similarity image is filtered using a -45° oriented line. The length of this line is defined to be 15% of the image dimension norm, which may be broadly applied to any sensor (Gonçalves et al., 2008). The filter window is composed by positive values along the diagonal and zeros outside. Its effect is illustrated in Figure 2d.

2.4 Conversion from gray level to binary

Prior to the Hough transform computation, there is the need to convert the filtered similarity image to a binary format. A threshold equal to the percentile $(1-3/n) \times 100$ (rounded to the smaller integer) is considered, where n is the number of lines (or columns) of the similarity image (which is squared). The binary image of the example is provided in Figure 2e.

2.5 Hough transform

At the Hough transform step (Hough, 1962), the θ and ρ resolution is defined as 0.5. The Hough transform is computed for the similarity images in both xx and yy axis. For each of them, more than one line may be identified, associated to the most prominent peaks.

2.6 Main diagonal identification and displacement computation

The slope of the detected line(s) in the previous step is computed, being considered only those with slope between -0.95 and -1.05 . In case of more than one line is detected with a slope of exactly -1.00 , the line with highest height is selected. The displacement on each axis is finally obtained by computing the distance from the selected line to the main diagonal (-45° line starting at row 1 column 1). This step is illustrated in Figure 2f.

2.7 Estimation of δ_x and δ_y

In the case that the image is not divided into tiles (the image being itself a single tile), then the estimates for δ_x and δ_y are

merely the displacements obtained at the previous described step. When more than one tile is considered, then a set of candidates for δ_x and δ_y are obtained, which inevitably may contain some misleading values. Therefore, an outlier removal stage is required, in order to consider only those correct shifts and achieve acceptable (subpixel) accuracy. The estimation of δ_x and δ_y consisted on a statistical procedure based on the 3D histogram obtained from δ_x and δ_y .

3. RESULTS

3.1 Dataset

The proposed methodology was applied to three pairs of images, comprising medium and high (urban and urban/rural context) spatial resolution images (Figure 3). The digital elevation model (DEM) of the considered regions obtained from the shuttle radar topography mission (SRTM) (Farr, 2004) is presented in Figure 4.

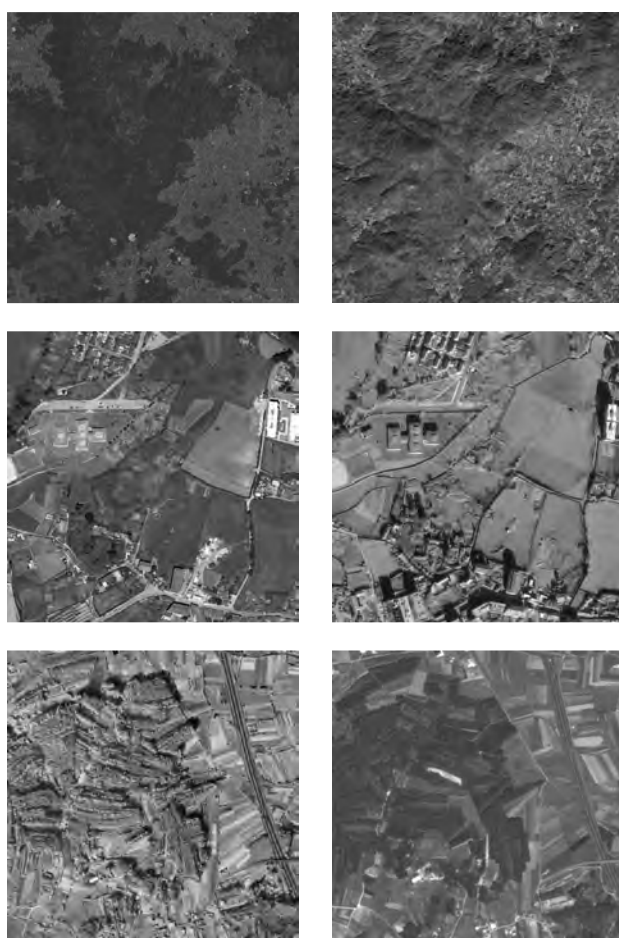


Figure 3. Reference images (left) and new images to be registered (right), regarding a medium spatial resolution pair (first row, Landsat/ASTER), a high spatial resolution pair with urban/rural context (second row, Orthophoto/IKONOS) and a high spatial resolution pair with rural context (third row, Orthophoto/ALOS). Further details in subsection 3.1.

3.1.1 Medium spatial resolution

The first pair of images consists in two segments with 512x512 pixels: one obtained from an orthorectified panchromatic Landsat image; and the other from an ASTER image (NIR

band) with an approximate geometric correction. Both of these images are from the northwest of Portugal. Both images have a pixel size of 14.25m and present a temporal difference of 1.5 years. The two segments are represented in Figure 3 (first row).

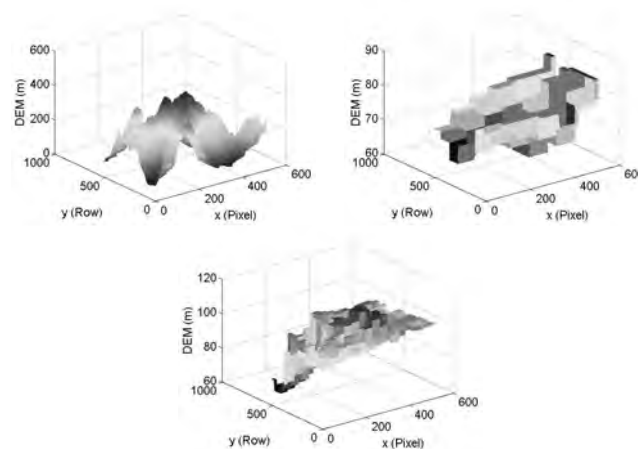


Figure 4. DEM (based on the SRTM) associated to the Landsat/ASTER pair (upper left), orthophoto/IKONOS pair (upper right) and Orthophoto/ALOS pair (bottom). Further details in subsection 3.1.

As can be observed in Figure 4, the considered region for this pair of images presents a considerable terrain height variation, ranging from 29m to 487m (according to the SRTM DEM). However, the transformation function defined in (1) and (2) may be considered adequate due to the ASTER acquisition geometry. The reference shifts were manually obtained through the identification of 4 conjugate points, associated to an average \pm standard-deviation of 2.1 ± 0.1 and 1.4 ± 1.3 pixels, for the horizontal and vertical directions, respectively. The low standard-deviation of the manually identified conjugate points support the adequacy of the transformation function.

3.1.2 High spatial resolution (IKONOS): urban/rural context

The second pair of images is composed by two segments with 512x512 pixels: one corresponding to the green band of an orthophoto; and the other corresponding to a panchromatic IKONOS image with an approximate geometric correction. These images cover a small part of the city of Porto (Portugal) with a mixture of urban with rural context, have a pixel size of 1m and present a temporal difference of around 1 year. The two segments are represented in Figure 3 (second row).

As can be observed in Figure 4, the considered region for this pair of images presents a smooth terrain elevation, ranging from 67m to 87m (according to the SRTM DEM). The reference shifts were manually obtained through the identification of 4 conjugate points, associated to an average \pm standard-deviation of 15.9 ± 1.8 and 5.7 ± 0.2 pixels, for the horizontal and vertical directions, respectively.

3.1.3 High spatial resolution (ALOS): rural context

The third pair of images comprises two segments with 512x512 pixels: one corresponding to the NIR band of an orthophoto; and the other corresponding to a panchromatic ALOS-PRISM image with an approximate geometric correction. These images are from the centre of Portugal (rural context), have a pixel size

of 2.5m and present a temporal difference of around 2 years. The two segments are represented in Figure 3 (third row).

As can be observed in Figure 4, the considered region for this pair of images presents a smooth terrain elevation, ranging from 68m to 114m (according to the SRTM DEM). The reference shifts were manually obtained through the identification of 5 conjugate points, associated to an average \pm standard-deviation of -4.6 ± 0.9 and 0.1 ± 0.8 pixels, for the horizontal and vertical directions, respectively.

3.2 The traditional approach

The traditional approach of AIR based on similarity measures mainly consists on taking a window (template) from one image and pass it throughout the other, aiming to find a peak on the similarity surface. This peak is expected to correspond to the correct shift (in both horizontal and vertical directions) between the images. The location of the template, the size of the template, and the associated computational cost may lead to a wide variety of template selections. The results presented in Figure 5 illustrate the effect of considering different sizes of the template (for the three pairs of images in Figure 3) - defined as a squared region with its centre corresponding to the center of the reference image - considering the correlation coefficient as the similarity measure. Although the computational time increases with the increase in the template size, it still presents a relatively fast performance (Figure 6). The ambiguous aspect associated to the template selection may lead to misleading solutions, as the results presented in Figure 5 clearly illustrate, in particular for the medium spatial resolution images. Furthermore, for the high resolution images, the traditional approach is not able to accurately register them.

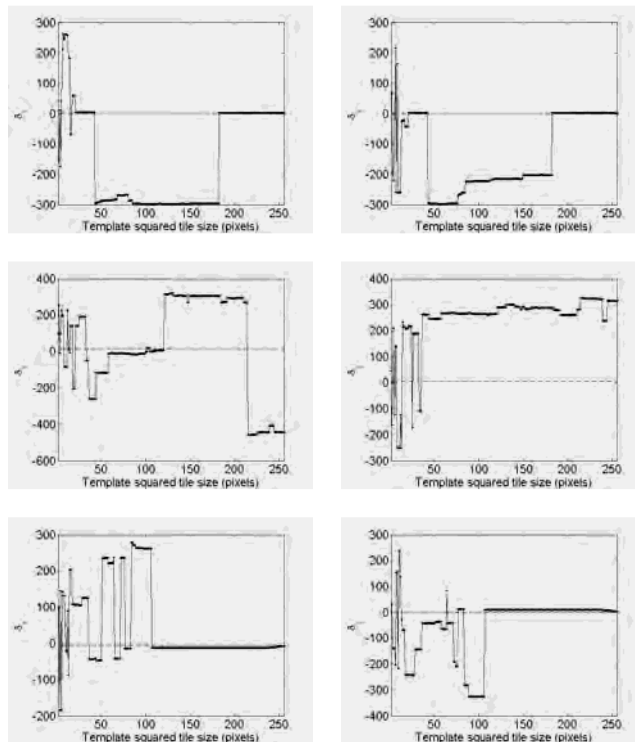


Figure 5. Obtained shifts for horizontal (δ_x) and vertical (δ_y) directions on the first and second columns, respectively, using the traditional approach described in subsection 3.2, applied to the three pairs of images presented in Figure 3 (in the same order from top to bottom). Dashed lines are the reference shifts.

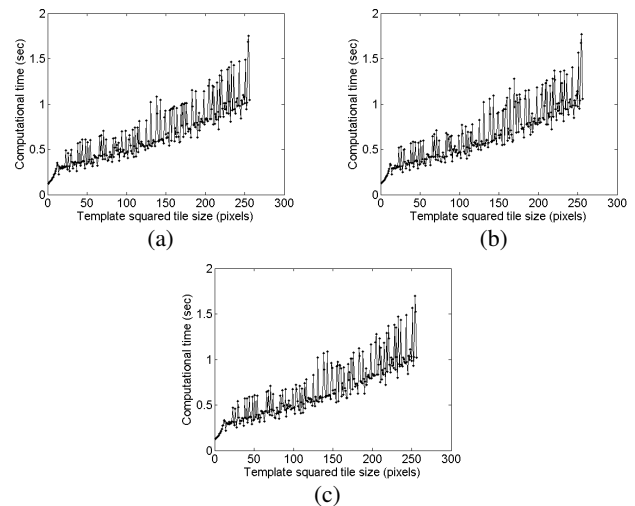


Figure 6. Computational time (in seconds) associated to the traditional approach as described in subsection 3.2, applied to the three pairs of images presented in Figure 3: (a) Landsat/ASTER; (b) orthophoto/IKONOS; (c) orthophoto/ALOS.

3.3 Application of the proposed methodology

There is a wide variety of similarity measures which may be applied in the proposed methodology (Inglada and Giros, 2004). The correlation coefficient (CC) is one of the most used similarity measures regarding image registration applications, and its definition is widely known (Brown, 1992; Inglada and Giros, 2004; Zitová and Flusser, 2003). The mutual information (MI) of two random variables A and B can be obtained as (Cover, 1991)

$$MI(A,B) = H(A) + H(B) - H(A,B) \quad (3)$$

where $H(A)$ and $H(B)$ are the entropies of A and B, and $H(A,B)$ is their joint entropy. The MI-based registration criterion states that the images shall be registered when $MI(A,B)$ is maximal. The remaining definitions of the entropies and corresponding probabilities can be found in (Chen, 2003).

The CC and MI measures were applied to the pair of images represented in Figure 2, considering each image as a single tile. The obtained similarity images for both horizontal and vertical directions are provided in Figure 7. It can be observed that the CC is clearly more adequate than MI. One of the reasons behind this may be the fact that we have applied cross-correlation to all possible lags, and used the maximum among these. This procedure allows for minimizing the misalignment which is present when computing 1D correlation. For instance, when computing the correlation on the horizontal direction, the DN values of each column from the reference image will present some misalignment on the corresponding column of the image to be registered, due to the shift on the vertical direction. Additionally, the CC presents a significant faster performance than MI.

Based on the above mentioned experiments, in this work the application of the proposed methodology will rely on the CC as the similarity measure. The obtained results for both horizontal (δ_x) and vertical (δ_y) directions, with respect to the three pairs of images in Figure 3 are provided in Figure 8 (considering tiles of size 64×64 , 128×128 , 256×256 and 512×512 pixels).

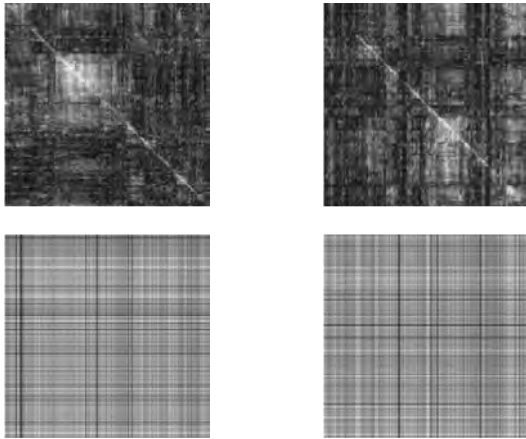


Figure 7. Similarity images (horizontal and vertical directions on the first and second column, respectively), regarding the registration of the pair of images represented in Figure 2, considering as similarity measure the CC (first row) and the MI (second row).

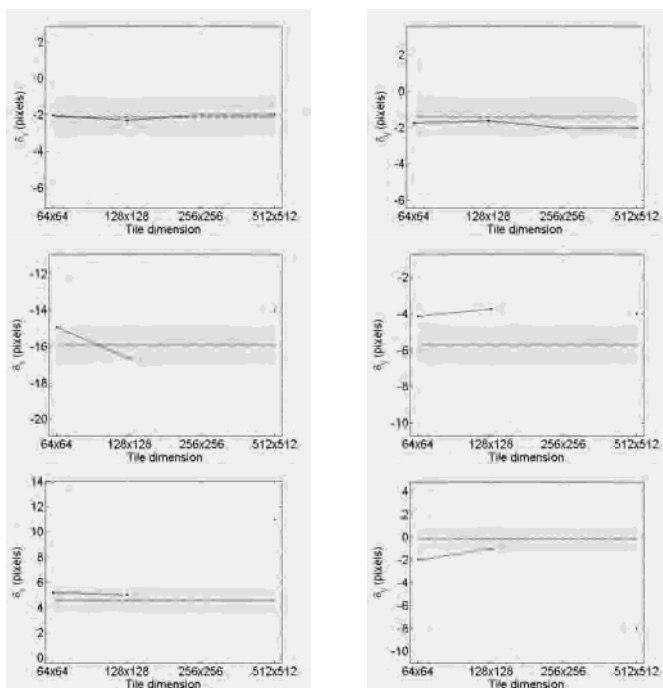


Figure 8. Accuracy in the horizontal (δ_x , left plots) and vertical (δ_y , right plots) directions regarding the registration of the three pairs of images represented in Figure 3 (a single tile), using the CC as the similarity measure: Landsat/ASTER (first row); Orthophoto/IKONOS (second row); Orthophoto/ALOS (third row).

Regarding the medium spatial resolution pair of images, the proposed methodology was able to achieve a subpixel accuracy for all considered tile sizes (Figure 8). The traditional approach was able to achieve a similar accuracy for templates higher than 190x190 pixels, leading to misleading results for smaller templates (Figure 5). Therefore, the proposed methodology presents clear advantages with respect to the traditional approach.

With respect to the high spatial resolution pair of images with urban/rural context (orthophoto/IKONOS), a subpixel accuracy was obtained for tiles with size 64x64 and 128x128 pixels in the horizontal axis, and an error less than 2 pixels in the vertical

axis. Despite the error above the pixel in the vertical direction, it is quite obvious the advantage when compared to the traditional approach, which was quite far from the correct solution for all possible template sizes. For tiles with size 256x256 pixels, the proposed methodology did not provide any solution, which is better than indicating a wrong solution. Even considering the whole images as a single tile, the obtained shifts were quite near the reference values. Moreover, even the manual identification of conjugate points was associated to a standard deviation of 1.8 pixels on the horizontal direction, supporting the difficulty of accurately registering this pair of images.

For the third pair of images, composed by two high spatial resolution segments with rural context (orthophoto/ALOS-PRISM), a subpixel accuracy was also obtained for tiles with size 64x64 and 128x128 pixels. Once again, for tiles with size 256x256 pixels no solution was obtained, which is better than a wrong solution. Considering a single tile (512x512 pixels), an error of around 6 pixels was obtained for both directions. This result indicates that a single tile should be avoided, since when using smaller tiles the statistical based procedure of outliers removal provides generally an accurate registration. Nevertheless, although the traditional approach tends to achieve an accurate solution for templates with size near the whole image, a closer look at the plots in Figure 5 allows for observing that the best obtained results are 4 pixels far from the correct solution. Therefore, the proposed methodology is once again generally better than the traditional approach.

With respect to the computational efficiency (Figure 9), it can be observed that beyond the smaller tiles provide more accurate results, they are also associated to lower computational times, reinforcing their advantage. Although the presented computational times are considerably higher than the traditional approach (Figure 6), it is worth to mention that it was not under the scope of this work the computational time optimization. However, it can be largely improved, since several graphical outputs which are produced and stored are unnecessary to provide the final estimates of δ_x and δ_y .

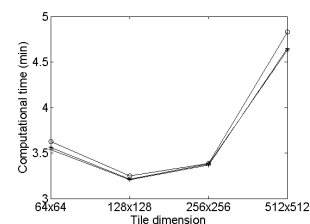


Figure 9. Computational time associated to the results obtained in the registration of the three pairs of images represented in Figure 3 (for different tiles dimension), using the CC as the similarity measure: Landsat/ASTER (+); orthophoto/IKONOS (*); orthophoto/ALOS (o).

3.4 Future improvements

The proposed approach revealed to outperform the traditional approach of image registration using similarity measures, in particular for images with clearly different radiometric content. Nevertheless, some preliminary tests have been performed which may allow for further improvements in the future. A visual inspection from the upper plots in Figure 10 suggest that a low-pass filtering may allow for extracting a profile with less detail, ignoring higher variability related to the spectral characteristics. Therefore, a 2nd-order low-pass Butterworth filter, with a normalized cutoff frequency at 0.1 was applied to

the original profiles, which result is provided in the lower plots of Figure 10. It can be observed that a noticeable improvement on the similarity between the profiles from the Landsat and ASTER images was obtained, supported by a considerable increase of both similarity measures. The potential of this filtering stage deserves further research, in particular with respect to the increase in the computational complexity and subsequent processing time.

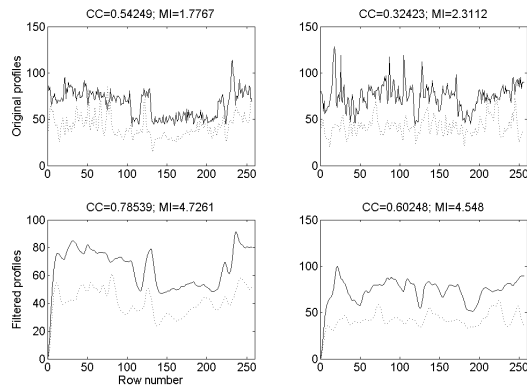


Figure 10. Two different profiles (left and right plots) obtained from the images in Figure 2: solid lines are columns 100 and 250 from the Landsat image; dotted lines are columns 101 and 251 from the ASTER image. The plots from the first row correspond to the original profiles, whereas the lower plots are the same profiles after low-pass filtering. The CC and MI similarity measures are provided above each plot. Further details in subsection 3.4.

4. DISCUSSION

The proposed methodology starts with the division of an image into tiles. With respect to the tiles dimension, it was observed that the smaller tiles led in general to more accurate results. This is related to the fact that when using smaller tiles, a larger set of shifts are obtained. Although a higher number of misleading shifts may be obtained, the statistical based procedure of outliers removal allow for focusing on a “cloud” of correct shifts.

It was shown that the proposed methodology clearly outperforms the traditional approach of using similarity measures on image registration. It should be noticed that through the division of the image into tiles, it was possible to achieve a subpixel accuracy, without requiring the use of fractional shifts.

Although accurate results were obtained using the CC, other similarity measures than the CC and MI could have been used and will deserve further research. In particular, the cross- ApEn (Pincus and Singer, 1996) which is an entropy-based measure will be explored in the future.

The proposed methodology comprises some image processing steps, which are necessarily associated to higher computational costs. However, the presented computational times are far from being optimized, since a large number of graphical outputs which are produced and stored for quality assessment are totally unnecessary for what really cares, which is merely the estimation of δ_x and δ_y . Therefore, further work on this topic will allow for a drastic reduction of the presented computational times.

The selection of the dataset segments was based on considering regions with slight terrain slope variations. However, there were still some significant slopes, which may lead to less accurate results. In the case that smaller tiles are used, the set of obtained shifts may be weighted by a cost function associated to the terrain height variation in each tile. This is an idea which deserves further research.

5. CONCLUSIONS

A new approach for the use of similarity measures was explored, which allows for an accurate registration of multi-sensor, multi-spectral and multi-temporal pairs of remote sensing images. It allows for reducing the ambiguity associated to the traditional approach, providing robust estimations of both horizontal and vertical shifts. A set of local shifts may be used for the registration of full scenes with more complex distortions.

ACKNOWLEDGEMENTS

The first author acknowledges Fundação para a Ciência e a Tecnologia, Portugal, for the financial support.

REFERENCES

- Brown, L.G., 1992. A survey of image registration techniques. *Computing surveys* 24(4), pp. 325–376.
- Chen, H., Varshney, P.K., Arora M.K., 2003 Performance of mutual information similarity measure for registration of multitemporal remote sensing images. *IEEE Transactions on Geoscience and Remote Sensing* 41(11), pp. 2445–2454.
- Cover, T.M., Thomas, J.A., 1991. *Elements of Information Theory*. New York: Wiley.
- Farr, T.G., et al., 1992. The shuttle radar topography mission. *Reviews of Geophysics* 45, pp. RG2004.
- Fonseca, L.M.G., Manjunath, B.S., 1996. Registration techniques for multisensor remotely sensed imagery. *Photogrammetric Engineering & Remote Sensing* 62(9), pp. 1049–1056.
- Gonçalves, H., Gonçalves, J.A., Corte-Real, L., 2008. Automatic image registration based on correlation and Hough transform. In: *Image and Signal Processing for Remote Sensing XIV*, Cardiff, Wales, Vol. 7109. pp. 71090J.
- Gonçalves, H., Gonçalves, J.A., Corte-Real, L., 2009. Measures for an objective evaluation of the geometric correction process quality. *IEEE Geoscience and Remote Sensing Letters*, 6(2), pp. 292–296.
- Hough, P.V.C., 1962. Methods and means for recognizing complex patterns. U.S. Patent 3.069.654, 1962.
- Inglada, J., Giros, A., 2004. On the possibility of automatic multisensor image registration. *IEEE Transactions on Geoscience and Remote Sensing*, 42(10), pp. 2104–2120.
- Pincus, S., Singer, B.H., 1996. Randomness and degrees of irregularity. *Proc. Natl. Acad. Sci. USA*, 93(3), pp. 2083–2088.
- Zitová, B., Flusser, J., 2003. Image registration methods: a survey. *Image and Vision Computing*, 21(11), pp. 977–1000.

A METHOD FOR ROBUST EXTRACTION OF CONTROL POINTS ON HIGH-RESOLUTION SATELLITE IMAGES

J. González^a, V. Arévalo^{*a}, C. Galindo^a

^aDept. of System Engineering and Automation, University of Málaga,
Campus Teatinos, 29071 Málaga, Spain - (jgonzalez,varevalo,cipriano)@ctima.uma.es

Commission VII/7

KEY WORDS: Geometry, Extraction, Registration, DEM/DTM, Imagery

ABSTRACT:

This paper presents a procedure to robustly distribute control point (CP) pairs in high-resolution satellite images as a preliminary step for accurate image registration. The proper distribution of the CPs is achieved by means of a quadtree decomposition of a coarse digital terrain model (DTM) of the sensed region. This technique parcels up the image according to its relief variance yielding almost planar pieces of land. A corner detector is then employed to identify key points in the *reference* image and an affinity-based feature tracker that searches for their corresponding corner in the *target* one. This search is executed in every parcel, selecting (at-least) one CP, ensuring thus denser distributions in rugged regions than in flat ones. Additionally, robustness to mismatches is attained by exploiting the intrinsic affine epipolar geometry of the two images. The proposed method has been successfully tested with a broad variety of panchromatic high-resolution images of the city of the Rincón de la Victoria (Málaga, Spain).

1. INTRODUCTION

Image registration is the process of spatially fitting two images of the same scene acquired on different dates, from different view-points, and/or using different sensors. Image registration is required in a variety of applications, like, image fusion, 3D scene reconstruction, and multi-temporal analysis (i. e. natural disaster monitoring, urban change detection, etc.). See (Schowengerdt, 2007) for a comprehensive survey.

Image registration is typically accomplished by (automatically or manually) identifying common features, called control points (CP) pairs, in the involved images. Through such CPs it is possible to estimate the underlying geometrical transformation between the considered images, which is used to spatially transform (register) the *target* image. The accuracy of this process is, then, strongly tied to:

1. the type of geometrical transformation considered for the registration (affine, projective, piecewise linear, thin-plate-spline, etc.), which should account for the relative geometric differences between the images, and
2. the distribution of CPs over the images, which should take into account the nature of their differences.

A correct combination of both aspects is crucial to guarantee the accuracy of the registration: while only two pairs of CPs suffice to perfectly overlap images of a flat terrain (since they may only differ in shift, scale and rotation), a large number of them will be necessary to capture the geometric difference between images of high-relief surfaces acquired from different viewing angles, requiring, also, complex (so-called elastic) transformations. While elastic transformations have been broadly studied in the remote sensing field (see (Arévalo and Gonzalez, 2008), for example), the proper distribution of the CP pairs has not been addressed indeed. This paper focuses on this issue.

In the absence of information about the relief of the imaged surface, the more effective (but surely not more efficient, see (Fonseca and Kenney, 1999) for an interesting control-point assessment for image registration) approach is the straightforward solution of distributing regularly as many CPs as possible all over the images (Arévalo and Gonzalez, 2008). However, when some information about the terrain profile is available, a more elaborated algorithm can help us to decide their appropriate distribution on the images.

This paper presents an automatic method to distribute CPs for the accurate registration of high-resolution satellite images. Exploiting the terrain profile information provided by a coarse digital terrain model (DTM) of the imaged scene, our approach generates a minimal distribution of CPs, achieving significant speedup in the CPs extraction, without jeopardizing accuracy in the registration.

Our method is intended to be applied to *basic* high-resolution satellite imagery, that is, products that are only featured with corrections for radiometric distortions and adjustments for internal sensor geometry, optical and sensor distortions. As the effect of the terrain is not compensated, two images of a rugged region acquired from different viewpoints may present severe local geometric differences. Main providers, as it is the case of GeoEye (<http://www.geoeye.com>, accessed 1 Jun. 2010) or DigitalGlobe (<http://www.digitalglobe.com>, accessed 1 Jun. 2010), distribute several of these products, as the Ikonos Ortho Kit, QuickBird Orthoready, etc., which are significantly cheaper than geometrically corrected ones.

The rest of this paper is organized as follows. In section 2, we describe in detail the proposed method. In section 3, some experimental results are presented. Finally, some conclusions and future work are outlined.

2. DESCRIPTION OF THE PROPOSED METHOD

The proposed method combines techniques adapted from the computer vision field to divide the images according to their estimated

*Corresponding author.

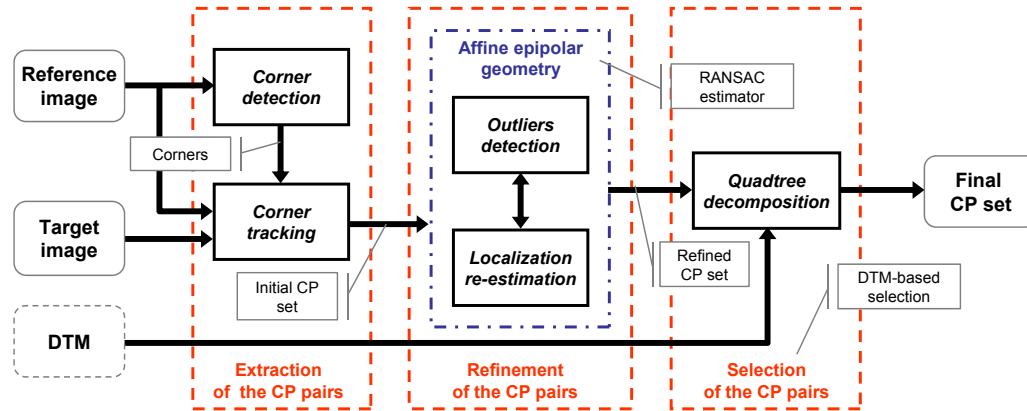


Figure 1: Scheme of the proposed method. Please refer to the section 2 for a detailed description.

relative distortions and to robustly distribute CPs pairs following the obtained partitioning. Figure 1 schematically shows an overview of our approach.

In a nutshell, the proposed method consists of three steps: 1) the extraction of the CP candidates, 2) the detection of mismatches (we take advantage of the affine epipolar geometry of the images to robustly deal with this stage), and finally 3) the selection of the CPs according to the distribution obtained from the DTM.

2.1 Extraction and Matching of the CPs

This stage is accomplished in two steps: first, a corner detector (Harris and Stephens, 1988) is applied to identify distinctive points in the reference image and then, a feature tracker searches for their correspondences in the target image, assuming local affinity deformations (Lucas and Kanade, 1981). Our implementation of the feature tracker relies on a variant of the sum of square differences (SSD) which provides robustness to image brightness differences through a local linear radiometric correction (Fonseca and Kenney, 1999).

We also achieve image scale invariance by means of a Gaussian pyramid decomposition (Burt and Adelson, 1983) of the image pair. This technique, broadly used in image processing, consists of creating a series of images down-scaled by convolving the image with a Gaussian kernel (a low-pass filtering). Thus, a stack of successively smaller images is created, where each pixel contains the local gaussian-weighted average that corresponds to a pixel neighbourhood on a higher level of the pyramid.

More formally, let the 2D original image be denoted by $I(x, y)$. The Gaussian pyramid decomposition of $I(x, y)$ can be recursively defined as follow

$$G_l(x, y) = \begin{cases} I(x, y) & l = 0 \\ \sum_{m=-2}^2 \sum_{n=-2}^2 w(m, n) G_{l-1}(2x + m, 2y + n) & l > 0 \end{cases} \quad (1)$$

where $w(m, n)$ is the gaussian kernel (identical at all levels).

This technique allows the feature tracker to cope with large displacements between corresponding corners.

2.2 Detecting Mismatches and Refining the Coordinates of the CPs

The intrinsic affine epipolar geometry of two views is exploited for attaining robustness to mismatches (the so-called *outliers*) and, collaterally, refining the coordinates of the extracted CPs

(Torr, 2002). To this aim we employ the RANdom SAMple Consensus algorithm (Fischler and Bolles, 1981), a robust estimator which exploits the redundancy of samples to provide a robust estimate of the parameters of a model which fits to the majority of them.

The final step of the RANSAC consists of re-estimating the model but only considering the *inliers*. In our case, this step is accomplished by minimizing the symmetric epipolar error from which we derive the Maximum Likelihood (ML) estimate of the affine epipolar matrix, F_A , and refine the coordinates of the CPs. In this process, we assume that the image point localizations are affected by Gaussian noise.

The ML estimate is obtained by minimizing the following cost function based on geometric image distances:

$$\min_{\{F_A, \hat{x}_i, \hat{x}'_i\}} \sum_{i=1}^n d(x_i, \hat{x}'_i)^2 + d(x_i, \hat{x}_i)^2 \quad (2)$$

where as usual $x_i \longleftrightarrow x'_i$ are the measured correspondences, and \hat{x}_i and \hat{x}'_i are the estimated “true” correspondences that satisfy $\hat{x}_i^T F_A \hat{x}'_i = 0$ exactly for the estimated affine epipolar matrix.

Notice that minimizing expression (2) is equivalent to fitting the hyperplane f to the set of points $X_i = (x_i, y_i, x'_i, y'_i)^T$ in \mathbb{R}^4 . The refined points $\hat{X}_i = (\hat{x}_i, \hat{y}_i, \hat{x}'_i, \hat{y}'_i)^T$ satisfy the equation $\hat{x}_i^T F_A \hat{x}'_i = 0$ which may be expressed as $(\hat{X}_i^T, 1)f = 0$ (i.e. the equation of a point in \mathbb{R}^4 on the plane f) where $f = (a, b, c, d, e)^T$ (Hartley and Zisserman, 2004).

2.3 Distribution of the CPs According to the Image Distortions

The proper distribution of the CPs is regulated by means of a quadtree decomposition of a medium-resolution DTM of the sensed scene. This decomposition uses the relief variance to parcels up the image in almost planar plots of land. The algorithm 1 depicts this process.

An illustrative example of a coastal city surrounded by mountains is shown in figure 2. Upon a DTM of 20 m. of spatial resolution of this region provided by the “Consejería de Medio Ambiente” of the “Junta de Andalucía” (Spain) (figure 2-b), our method generates a quadtree decomposition according to the relief of the different parts: a region is divided in 4 equal pieces, when elevation differences are above 10 m. (i.e. $t = 10$). By doing so, high-relief areas, which provoke large image distortions, will be more intensively decomposed (figure 2-c). If a subdivision operation gives rise to four regions whose size is less than a square of

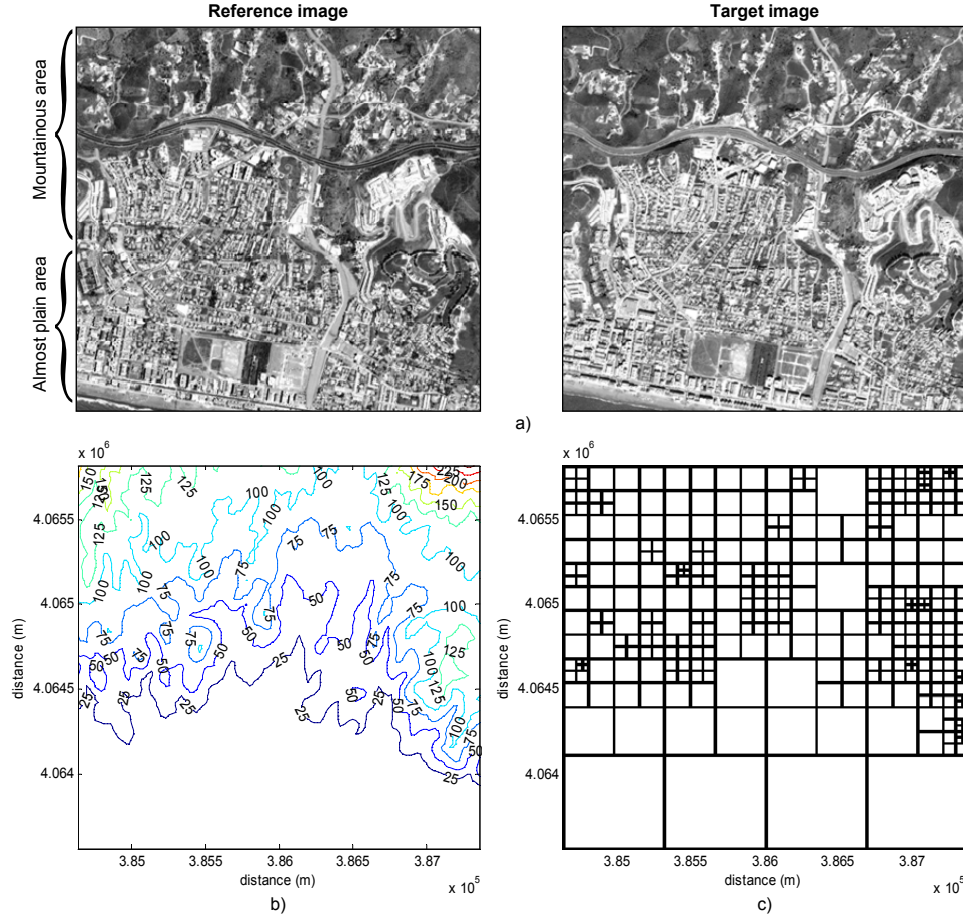


Figure 2: a) Two images of the coastal city of the Rincón de la Victoria (Málaga-Spain). b) Digital terrain model (DTM) of the region of interest. c) Quadtree decomposition of the DTM. Each parcel will contain a CP for posterior image registration.

25 pixels of side (i. e. $s = 25$), it is rejected. This means that the smallest cell size, for this example, will be bigger than 25 pixels and smaller than 50.

Algorithm 1 Quadtree decomposition of the DTM.

```

1: //  $R_0$  contains the coordinates of the regions to be analyzed
2:  $R_0 \leftarrow \{\text{coord}(\text{DTM})\}$  //  $R_0$  is initialized with the
3: // coordinates of the DTM
4: //  $R$  will contain the coordinates of the final regions
5:  $R \leftarrow \emptyset$ 
6: for all  $r \in R_0$  do
7:    $v \leftarrow \text{DTM}(r)$  //  $r = \{x, y, \text{width}, \text{height}\}$ 
8:   if  $\text{size}(r) > s$  and  $(\max(v) - \min(v)) > t$  then
9:     // quad divides  $r$  into 4 equal pieces and returns
10:    // their coordinates
11:     $R_0 \leftarrow \{R_0 \cup \text{quad}(r)\}$ 
12:   else
13:     //  $r$  is not divided and it is stored in  $R$ 
14:      $R \leftarrow \{R \cup r\}$ 
15:   end if
16: //  $r$  is removed from  $R_0$ 
17:  $R_0 \leftarrow \{R_0 - r\}$ 
18: end for

```

Finally, the selection of the final CP set is accomplished as follows: for each parcel of the decomposition, we check the number of detected CP pairs and, if this number is greater than one, we select the CP pair that exhibits the best score in the matching process, that is, the CP pair with the minor SSD value.

3. EXPERIMENTAL RESULTS

The benefits of the proposed method has been successfully verified by elastically registering a number of panchromatic (Orthoready) QuickBird image pairs (0.6 m./pixel), as the one shown in figure 2-a. The multitemporal series considered in our tests present significant relative geometric distortions induced by the off-nadir observation of no-planar regions as well as radiometric changes. The reader can find more details on satellite positioning data and the acquisition dates in (Arévalo and Gonzalez, 2008).

The registration process is accomplished by means of radial basis functions (RBF). Radial basis functions are scattered data interpolation methods where the spatial transformation is a linear combination of radially symmetric basis functions (second term of (3)), each of them centered on a particular CP, typically combined with a global affine transformation (first term of (3)). Mathematically

$$\begin{aligned}
 x &= \sum_{j=0}^m \sum_{k=0}^j a_{jk} (x')^{j-k} (y')^k + \sum_{j=1}^n A_j g(r_j) \\
 y &= \sum_{j=0}^m \sum_{k=0}^j b_{jk} (x')^{j-k} (y')^k + \sum_{j=1}^n B_j g(r_j)
 \end{aligned} \tag{3}$$

where

$$r_j = \|(x', y') - (\hat{x}'_j, \hat{y}'_j)\| \tag{4}$$

being $\hat{x}_j \longleftrightarrow \hat{x}'_j$ the refined CPs.

The type of basis function, g , determines the influence of each CP on the RBF, that is, the CP scope. So, the accuracy of the registration depends extremely on the distribution of CPs on the image. In this work we employ the thin plate spline (TPS) function $g(r_j) = r_j^2 \log r_j^2$ (Bookstein, 1989), which is perhaps the RBF most widely employed for elastic registration.

To evaluate the method performance, we have compared the registration accuracy obtained using the resultant CP set with respect to uniform and random CP distributions. The uniform distribution is obtained by selecting CPs according to a regular grid of squared cells of 50 pixels of side, while the random distribution is obtained by arbitrarily selecting the same number of CPs than the uniform one.

The results of the comparison, displayed in figure 3, show how the proposed method yields better results in terms of accuracy. The accuracy of the registration process has been assessed comparing the geometric errors (RMSE and CE90%) of a set of independent control points (ICPs) manually identified, achieving on average RMS errors under 1.4 m. with CPs distributed according to the DTM information.

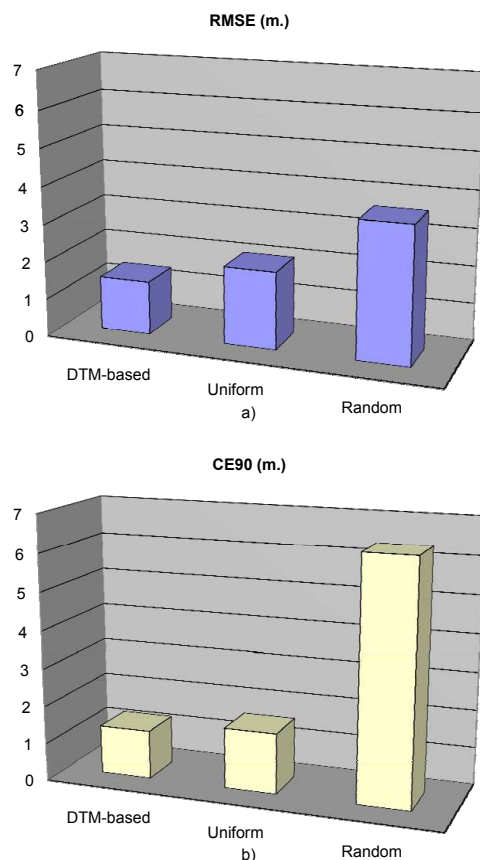


Figure 3: Accuracy of the proposed method compared to uniform and random distribution of CP considering a) RMSE and b) CE90%.

Observe that the results of the uniform distribution and our approach are similar, since the smallest squared cell generated by our approach has the same size that the one considered in the uniform distribution. The number of CP required in our approach, however, is, on average, around 37% lower. The benefits of our approach are clear, specially, when the CP extraction must be manually performed.

4. CONCLUSIONS

This paper presents a technique to distribute the CP pairs according the relative image distortions, more severe in rugged terrains, and proposes an automatic procedure to robustly extract CPs in two images by applying computer vision techniques. The experimental results reveal the advantage of employing our method, in comparison with other two strategies (uniform and random distributions) implemented in most of popular commercial packages of remote sensing like ERDAS, ENVI and PCI.

REFERENCES

- Arévalo, V. and Gonzalez, J., 2008. An Experimental Evaluation of Non-Rigid Registration Techniques on QuickBird Satellite Imagery. *International Journal of Remote Sensing* 29(2), pp. 513–527.
- Bookstein, F., 1989. Principal Warps: Thin-Plate-Splines and the Decomposition of Deformations. *IEEE Transactions on Pattern Analysis and Machine Intelligence* 11(6), pp. 567–585.
- Burt, P. and Adelson, E., 1983. The Laplacian Pyramid as a Compact Image Code. *Communications, IEEE Transactions on [legacy, pre-1988]* 31(4), pp. 532–540.
- Fischler, M. and Bolles, R., 1981. Random Sample Consensus: A Paradigm for Model Fitting with Application to Image Analysis and Automated Cartography. *Communications of the ACM* 24, pp. 381–395.
- Fonseca, L. M. G. and Kenney, C. S., 1999. Control Point Assessment for Image Registration. In: *Proc. XII Brazilian Symposium on Computer Graphics and Image Processing*, pp. 125–132.
- Harris, C. and Stephens, M., 1988. A Combined Corner and Edge Detector. In: *Alvey Vision Conference*, Vol. 4, Manchester, UK, pp. 147–151.
- Hartley, R. and Zisserman, A., 2004. *Multiple View Geometry in Computer Vision*. Second edn, Cambridge University Press, Cambridge, UK.
- Lucas, B. and Kanade, T., 1981. An Iterative Image Registration Technique with an Application to Stereo Vision. In: *International Joint Conference on Artificial Intelligence*, pp. 674–679.
- Schowengerdt, R., 2007. *Remote sensing: Models and Methods for Image Processing*. Academic Press.
- Torr, P., 2002. *A Structure and Motion Toolkit in Matlab: Interactive Adventures in S and M*. Technical Report MSR-TR-2002-56, Microsoft Research.

ACKNOWLEDGEMENTS

DigitalGlobe QuickBird imagery used in this study is distributed by Eurimage, SpA. (<http://www.eurimage.com>, accessed 1 Jun. 2010) and provided by Decasat Ingeniería S.L., Málaga, Spain.

This work has been partly supported by the Spanish Government under research contract CICYT DPI-2008-03527.

AIRBORNE HYPERSPECTRAL IMAGE GEOREFERENCING AIDED BY HIGH-RESOLUTION SATELLITE IMAGES

C. K. Toth^{a,b,*}, J.H. Oh^b, D. A. Grejner-Brzezinska^b

^a Center for Mapping, The Ohio State University, Columbus, Ohio, USA toth@cfm.ohio-state.edu

^b Satellite Positioning and Inertial Navigation (SPIN) Laboratory, Dept. of Civil and Environmental Engineering and Geodetic Science, The Ohio State University, Columbus, Ohio – (oh.174, dbrzezinska)@osu.edu

Commission VII, WG VII/4

KEY WORDS: Georeferencing, Hyperspectral imagery, High-resolution satellite images, Image matching, Pushbroom camera

ABSTRACT:

Over the past decade, airborne hyperspectral systems have shown remarkable performance in identifying and classifying a variety of ground objects, such as differentiating between minerals, vegetations, artificial materials, water, etc. Though the hyperspectral imaging market is still relatively small, yet it is steadily growing. Currently, most of the high performance systems are of the pushbroom camera type, and consequently, the sensor orientation of these systems heavily relies on the integrated GPS/INS (Global Positioning System/Inertial Navigation System) based direct georeferencing solution. In this study, an indirect georeferencing method is proposed that is based on utilizing robust image matching to high-resolution satellite imagery. This solution can be used in circumstances where GPS/INS-based georeferencing is not available or not feasible due to GPS signal loss and/or the lack of GPS infrastructure. The proposed method is motivated by the attractive properties of state-of-the-art high-resolution satellite imagery, including large swath width, high spatial and temporal resolution, and high positional accuracy. For robust image matching, a combination of SURF (Speeded-Up Robust Features) and RANSAC (RANDOM SAmple Consensus) is utilized, and the trajectory modeling of the airborne hyperspectral pushbroom camera is based on the collinearity equation camera model with the Gauss-Markov stochastic error model. Tests on simulation data showed encouraging performance results for the proposed approach.

1. INTRODUCTION

Over the past decade, airborne hyperspectral imaging (HSI) systems have shown excellent performance in several applications to identify and classify a broad range of ground objects, including minerals, vegetations, artificial materials, and water etc. Airborne HSI sensors measure the light from the earth's surface in high spectral resolution; typically, each pixel of hyperspectral data contains dozens or hundreds of spectral bands. HSI technology has been used in many commercial and defence applications.

Airborne HSI systems are predominantly based on the pushbroom camera model, which heavily relies on direct georeferencing. Typically, the georeferencing solution, including platform position and attitude data, is computed by an Extended Kalman Filter (EKF), where first aircraft GPS data are processed in DGPS (Differential GPS) mode based on a nearby ground GPS base station (or network solution), and the DGPS results are feed back to the EKF to control the INS which provides the final georeferencing solution (Zhang *et al.*, 1994; Grejner-Brzezinska, 1999; Haala *et al.*, 2000; Tuo and Liu, 2005; Grejner-Brzezinska *et al.*, 2005). In addition, sensor alignment information, which is obtained by accurate boresight calibration, is applied to the platform georeferencing data to derive the exterior orientation parameters (EOPs) of the camera.

While GPS is generally available, there are certain rare circumstances that direct georeferencing is not available, such as in GPS denied environment. In fact, GPS signals could be vulnerable to interference, such as jamming, broadcast television, ultrawide-band communications, over-the-horizon radar and

cellular telephones (Carroll, 2001). In addition, there are remote, inaccessible areas that lack a geodetic infrastructure and thus GPS/INS-based georeferencing is not always feasible. In these cases, EOPs have to be estimated through the indirect or image referenced georeferencing technique.

Previously acquired and processed geospatial data are a good source for ground control that can be used not only for airborne image georeferencing (Dowman, 1998; Lin and Medioni, 2007; Cariou and Chehdi, 2008; Oh *et al.*, 2010), but also for aircraft navigation (Oh *et al.*, 2006; Conte and Doherty, 2009). The requirements for such reference data include high positional accuracy, and geometric and radiometric properties similar to target airborne imagery. From the various geospatial images obtained from different sensors, high resolution satellite images have clear advantages due to their uniform global accessibility.

Since high resolutions satellite images meet the main requirements in terms of the spatial and spectral resolution and positioning accuracy, this study proposes their use for georeferencing of airborne pushbroom imagery. Note that the spatial resolution of satellite images is lower than that of airborne imagery, yet the currently allowed 50 cm satellite image resolution has a good potential for image matching.

Figure 1 depicts a GPS denied situation. At the epoch t_0 , direct georeferencing becomes unavailable, as GPS is denied and there is no external information until t_1 . Between t_1 and t_2 , there is reference image data available and using common features, georeferencing is possible. Between the epochs t_2 and t_3 , the image referenced georeferencing may not be feasible when there are not enough image features in the reference data, such as in forested areas (Oh *et al.*, 2010).

* Corresponding author.

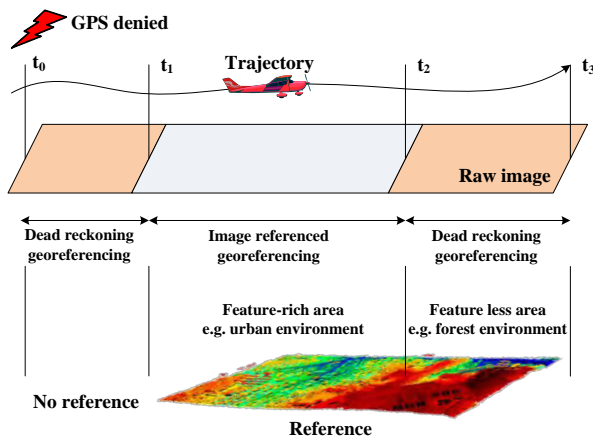


Figure 1. Georeferencing in GPS denied situation

In a recent research for automatic georeferencing of airborne pushbroom scanner by Cariou and Chehdi (2008), the reference data is transformed into the acquired image domain using the initial EOPs from INS, and then mutual information is computed between the transformed reference and acquired image. Through iteration of this computation and image transformation, a pixel-to-pixel correspondence is obtained and used for estimating yaw angle, and small bias in roll, pitch and height constant. This approach requires good initial EOPs from the INS and is computation intensive as a large number of iterative image transformations are needed.

This study proposes the combination of SURF (Speeded-Up Robust Features) (Bay *et al.*, 2008) and RANSAC (Fischler and Bolles, 1981) for robust image matching, and the collinearity equation camera model with the Gauss-Markov stochastic error model for the trajectory modeling of the airborne pushbroom camera. The paper is structured as follows. First, the proposed method is presented, including a brief description on the image matching and platform trajectory modeling. Second, experimental results on simulation data are discussed, followed by a brief conclusion.

2. HIGH RESOLUTION SATELLITE IMAGE AS GROUND CONTROL INFORMATION

Since IKONOS-2 showed its potential in the commercial satellite image market, many high-resolution satellite imaging systems have been launched, see Table 1. The specification of high-resolution satellite images is listed in terms of its spatial, temporal resolution, and swath width. Note that many satellites provide sub-meter resolution with large swath width of more than 10 km. In addition, positioning accuracy has seen a steady increase over the years. For example, GeoEye-1 provides RPC with positional accuracy up to 2 m of circular error at a 90% confidence level (CE90) without GCP in the case of stereo images, and sub-meter accuracy could be achieved using a bias-compensation RFM model with a single GCP (Fraser and Ravanbakhsh, 2009). Moreover, higher performance satellites will be launched in the near future such as CARTOSAT-3, EROS-C, and GeoEye-2. These attractive capabilities motivate the idea of using high resolution satellite images as ground control information for other geospatial images, such as aerial images. In the navigation field, research has started on testing and suggesting the use of satellite imagery to support UAV navigation (Sim *et al.*, 2002; Conte and Doherty, 2008).

Satellite	Resolution [m]	Revisit time [day]	Swath width [km]
IKONOS (1999)	0.82	3~5	11.3
EROS-A (2000)	1.8	3~4	14
Quickbird (2001)	0.61	1~3.5	16.5
SPOT-5 (2002)	2.5	2~3	60
OrbView-3 (2003)	1	~3	8
FORMOSAT-2(2004)	2	1	24
CARTOSAT-1(2005)	2.5	5	30
ALOS PRISM (2006)	2.5	2~46	35
KOMPSAT-2 (2006)	1	4	15
EROS-B (2006)	0.70	3~4	7
WorldView-1 (2007)	0.50	4.6 (60cm)	17.6
CARTOSAT-2(2008)	0.80	4~5	9.6
GeoEye-1 (2008)	0.41	2.8 (50cm)	15.2
WorldView-2 (2009)	0.46	3.7 (52cm)	17.6

Table 1. Current high-resolution satellite imaging systems

3. PROPOSED METHOD

Figure 2 shows the flowchart of the proposed method. As direct georeferencing is unavailable, due to GPS denied condition, and the reference data becomes available, short duration of HSI and INS is processed for georeferencing purposes. Though the INS data is drifting without georeferencing fixes, it can still provide good approximation for georeferencing, and thus reference data is windowed with an error margin, so the image matching with the raw HSI is limited to a smaller reference area (subset). During image matching, SURF is utilized with RANSAC to mitigate the effect of mismatched points. Successful image matching provides ground control information for each extracted raw image point, and thus the trajectory and attitude are estimated based on this information.

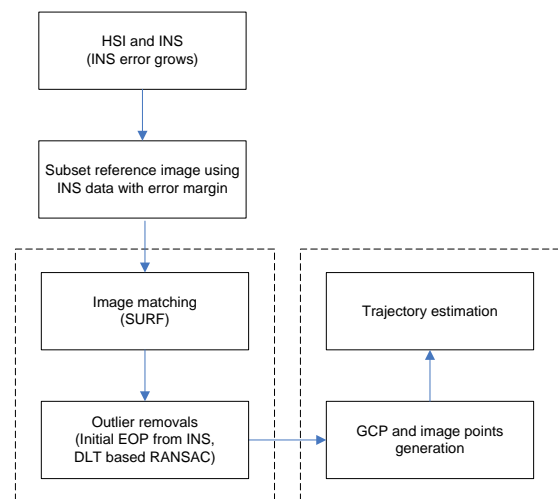


Figure 2. Flowchart of the proposed approach

3.1 Subset ROI reference data

Since images used as reference data tend to be large, it would take too much time and require a lot computer power if the whole reference image is used for image matching. Fortunately, the INS-based estimation of location can provide good approximation to obtain a region of interest (ROI), using the inverse form of collinearity equation. The ground coordinate of ROI can be determined from Equation 1. The ground height information could be selected as a constant value from knowledge about the target area; note that error of the height will be compensated in the error margin terms.

$$X = (Z - Z_L) \frac{U}{W} + X_L + b_x \quad (1)$$

$$Y = (Z - Z_L) \frac{V}{W} + Y_L + b_y$$

$$\begin{bmatrix} U \\ V \\ W \end{bmatrix} = M^T \begin{bmatrix} x \\ y \\ -f \end{bmatrix}$$

where,

- x, y : image coordinate of an object point
 $[X \ Y \ Z]^T$: ground coordinates of an object point
 $[X_L \ Y_L \ Z_L]^T$: the camera perspective center's coordinates
 M : the rotation matrix from ground to camera coordinates frame consisting of roll, pitch, and yaw
 f : camera focal length
 b_x, b_y : error margin which incorporate errors of INS and Z

3.2 Image matching (SURF with RANSAC)

Robust and accurate image matching is difficult due to significant differences between aerial and reference images. Therefore, robust SURF (Bay *et al.*, 2008) is utilized with RANSAC (Fischler and Bolles, 1981) to mitigate the effect of mismatching points.

SURF is a fast, scale and rotation invariant interest point detector and descriptor motivated by SIFT (Scale-Invariant Feature Transform; Lowe, 1999) which is one of the most popular point feature extraction and matching methods since it has been recognized to be very reliable and invariant to changes in imaging conditions. To increase the processing speed, SURF utilizes integral image, Laplacian-based indexing, and wavelets, and SURF is known to execute several times faster than SIFT.

RANSAC is a technique to estimate parameters of a model through iteration from a set of observations containing outliers. Model parameters are estimated from a randomly selected observation set and then every observation is tested if it fits to the model, and is added to the consensus set if it does. In an iterative process, a new consensus set is obtained and a better model is estimated. RANSAC is useful especially when the number of outliers is large. In contrast, other robust techniques, such as the least squares' residual check or Baarda's data snooping (Baarda, 1968) have practical limitations. Note that it is important to select the geometric model to constrain the mismatching in RANSAC. In this study, DLT (Direct Linear Transform) is used because data for small time span is assumed.

3.3 Platform modelling

When point features are used, platform modeling is generally performed using the collinearity equation, see Equation 2. The collinearity equation can be linearized to form a linear observation equation. The EOP parameters can be estimated iteratively using the above linearized observation equation through least square adjustment.

$$F_x = x + f \frac{U}{W} = 0 \quad (2)$$

$$F_y = y + f \frac{V}{W} = 0$$

In the Gauss-Markov (GM) model proposed here, each image line has six unique EOP parameters. However, the EOP parameters in adjacent lines are stochastically constrained, thus the first order Gauss-Markov model can be expressed by Equations 3 and 4.

$$x_k = A_1 x_{k-1} + w \quad (3)$$

where,

$$A_1 = \text{COV}(x_k, x_{k-1}) \text{COV}(x_k, x_{k-1})^{-1} = e^{-\beta_1 \Delta t} \quad (4)$$

w : white noise

Note that the correlation time is $1/\beta_1$. Denoting $\beta_1 \Delta t$ as S , the stochastic constraint equation can be derived.

$$\begin{aligned} F_{G1} &= e^{-s x_L} \Delta X_{L(i-1)} - \Delta X_{L(i)} = 0 \\ F_{G2} &= e^{-s y_L} \Delta Y_{L(i-1)} - \Delta Y_{L(i)} = 0 \\ F_{G3} &= e^{-s z_L} \Delta Z_{L(i-1)} - \Delta Z_{L(i)} = 0 \\ F_{G4} &= e^{-s \omega} \Delta \omega_{(i-1)} - \Delta \omega_{(i)} = 0 \\ F_{G5} &= e^{-s \phi} \Delta \phi_{(i-1)} - \Delta \phi_{(i)} = 0 \\ F_{G6} &= e^{-s \kappa} \Delta \kappa_{(i-1)} - \Delta \kappa_{(i)} = 0 \end{aligned} \quad (5)$$

where,

- i : line number in the image
 s : coefficient for each EOP

Solving the platform modeling with the above stochastic constraint yields a total of $6L$ EOP parameters where L is the total number of lines in the image. Lee (1999) mentioned that the number of unknown EOP parameters could be reduced from $6L$ to 6 through equation reduction. Therefore, three control points could generate a unique solution.

4. SIMULATION TEST

4.1 SURF image matching and outlier removal test

SURF matching with RANSAC outlier removal was tested on simulated images from CASI-1500 hyperspectral imagery (ITRES). The test images were generated by applying image various transformations, such as shear, rotation, intensity and resolution differences to simulate different imaging conditions between the target reference images. After image simulation, SURF matching between original and simulated images was performed and the accuracy was analyzed; the results for shear and resolution differences are presented in Figure 3.

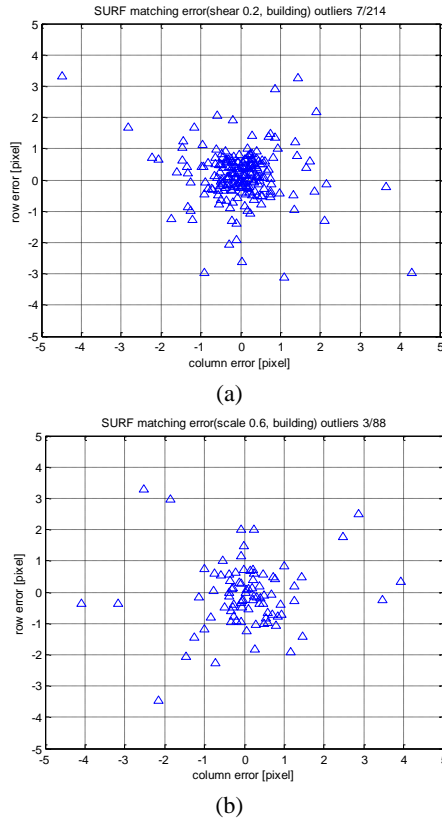


Figure 3. SURF image matching results for (a): 0.2 image shear, and (b): 0.6 times image scale difference

While most matching points are reasonably accurate, several low accuracy points are observed; the number of outliers with accuracy of lower than 5 pixels is shown at the title. Obviously, they should be filtered out to be used as ground control information. Therefore, RANSAC was tested for the same data set and the accuracy is shown in Figure 4. Note that low accuracy points and outliers are successfully removed. Most points show matching accuracy less than one-pixel. These test results show the potential of the method for matching between HSI and satellite images.

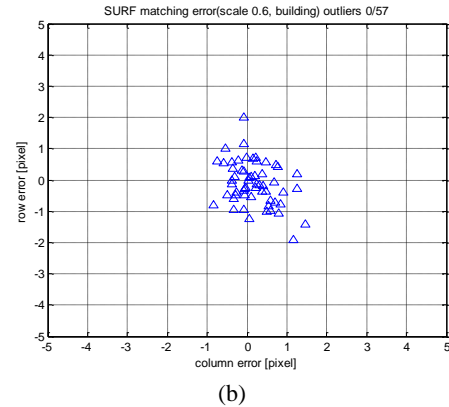
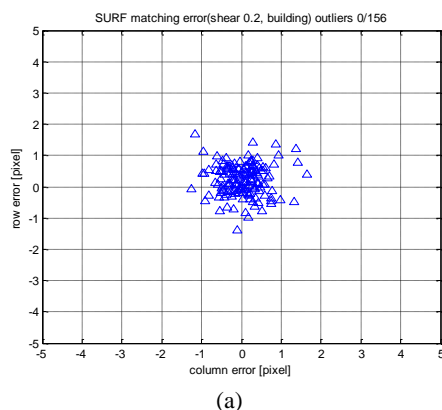


Figure 4. RANSAC tests for (a): 0.2 image shear, and (b): 0.6 times image scale difference

4.2 EOP Simulation

The platform modeling test was performed using simulated data. The camera specification used for simulation is presented in Table 2.

Camera type	Pushbroom
Focal length	79 mm
Pixel size	40 micron
Image size	Row: 1280, Col: 320
Imaging rate	80 lines/sec

Table 2. Camera specification

Given reference EOPs, the INS-only EOPs were simulated assuming drift errors. During 16 sec (1280 lines), the position error was simulated to increase to 8 m and the attitude drifted reached 0.25°. The simulated EOPs are shown in Figure 6.

4.3 Platform modeling test

The ground control points are normally generated by image matching based on SURF with RANSAC between the aerial pushbroom and satellite images. For this study, a total of 186 ground control points were simulated in an irregular distribution, as shown in Figure 5.

The INS-only EOPs are used as initial EOP values for the platform trajectory modeling. The EOPs estimated using the GM model are presented in Figure 6. Perspective center positions follow the initial EOPs values but the attitude accuracy slightly improved. The yaw angle could be estimated well.

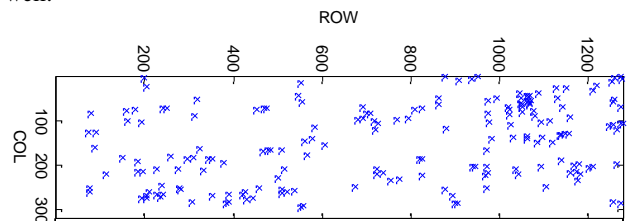
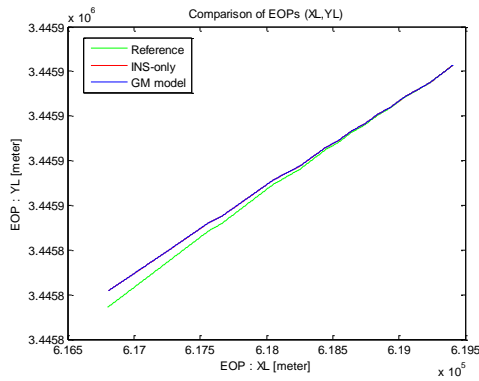
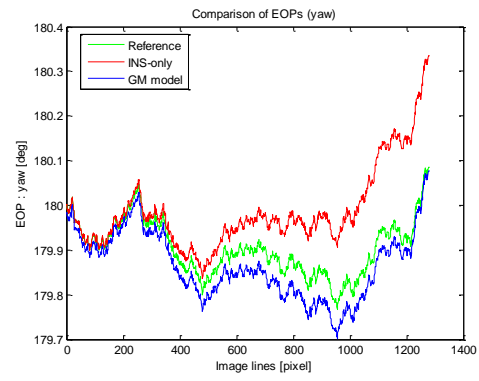


Figure 5. Distribution of simulated ground control points (assumed generated by the image matching)

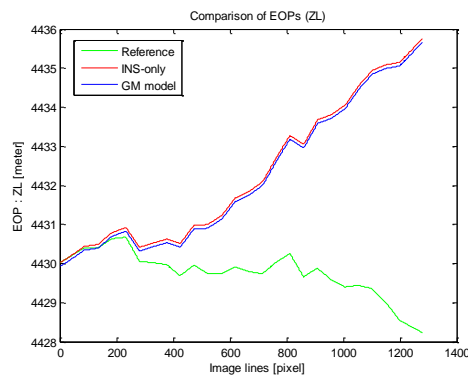


(a)

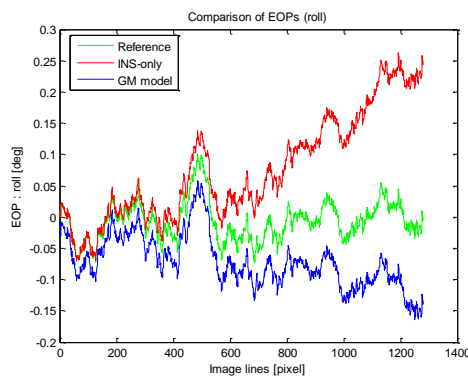


(e)

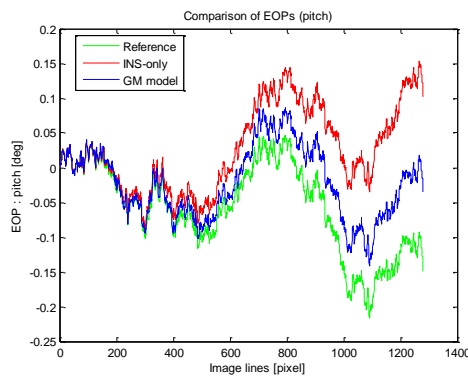
Figure 6. Platform modeling results, (a): X and Y, (b): Z, (c): roll, (d): pitch, and (e) yaw



(b)



(c)



(d)

4.4 Georeferencing accuracy

Since the image is monoscopic, the 3D ground restitution accuracy cannot be analyzed. Therefore, horizontal ground accuracy is analyzed by projecting image points to the ground with given ground height information. Each image point is projected to the ground using the estimated EOPs and the horizontal accuracy was computed. Table 3 shows the RMSE of the computed horizontal accuracy. The georeferencing result was accurate as the RMSE of ground coordinates is less than 1 m, while Gauss-Markov modeling did not accurately estimate the perspective center positions and attitudes due to correlation between EOP parameters.

RMSE	X [m]	Y [m]	# of points
	0.47	0.16	186

Table 3. Ground accuracy of the modeling

5. CONCLUSION

Airborne HSI systems have shown excellent performance in many commercial and defence applications. Most of the state-of-the-art systems are of the pushbroom camera type, and the georeferencing of these systems heavily relies on the GPS/INS based direct georeferencing. Under some rare circumstances, direct georeferencing may not be feasible, such as GPS denied situations. This study addresses these situations and proposes an image referenced georeferencing solution for pushbroom sensors. The approach is based on using high resolution satellite imagery, and the effort was motivated by the attractive properties of high-resolution satellite images, including high geolocation performance and image acquisition capability. The proposed method utilizes robust image matching, using a combination of the SURF and RANSAC techniques, and the platform modeling is based on the Gauss-Markov stochastic model.

The SURF image matching performance with RANSAC was tested using simulated images and showed robustness by successfully mitigating low accuracy matching points. Next, the pushbroom sensor platform modeling was tested using simulated EOPs data and ground controls, which were obtained by simulated image matching. Test results indicated a good performance potential of the approach by showing high ground accuracy while EOPs could be estimated moderately.

6. REFERENCE

References from Journals:

- Bay, H., A. Ess, T. Tuytelaars, L.V. Gool, 2008. SURF: Speeded Up Robust Features, *Computer Vision and Image Understanding (CVIU)*, 110(3): 346-359.
- Cariou, Claude., and K. Chehdi, 2008, Automatic Georeferencing of Airborne Pushbroom Scanner Images With Missing Ancillary Data Using Mutual Information, *IEEE Transactions on Geoscience and Remote Sensing*, 46(5), pp.1290-1300.
- Conte, Gianpaolo., and P. Doherty, 2009, Vision-Based Unmanned Aerial Vehicle Navigation Using Geo-Referenced Information, *Journal on Advances in Signal Processing*, Vol. 2009.
- Dowman, I.J., 1998, Automating Image Registration and Absolute Orientation: Solutions and Problems, *Photogrammetric Record*, 16(91), pp.5–18.
- Fischler, M. A. and R. C. Bolles, 1981. Random Sample Consensus: A Paradigm for Model Fitting with Applications to Image Analysis and Automated Cartography, *Communications of the ACM*. 24: 381–395.
- Fraser, C.S., and H.B. Hanley, 2005. Bias-compensated RPCs for sensor orientation of high-resolution satellite imagery. *Photogrammetric Engineering & Remote Sensing*, 71(8):909-915.
- Grejner-Brzezinska, D. A., 1999. Direct exterior orientation of airborne imagery with GPS/INS system: Performance analysis, *Navigation*, 46(4):261-270.
- Grejner-Brzezinska, D. A., C. Toth, Y.D. Yi, 2005, On improving navigation accuracy of GPS/INS systems, *Photogrammetric Engineering & Remote Sensing*, 71(4), pp.377-389.
- Oh, Y.S., D.G. Sim, R.H. Park, R.C. Kim, S.U. Lee, and I.C. Kim, 2006, Absolute position estimation using IRS satellite images, *ISPRS Journal of Photogrammetry & Remote Sensing*, 60 (2006), pp.256–268.
- Sim, D.G., R.H. Park, R.C. Kim, S.U. Lee, and I.C. Kim, 2002, Integrated Position Estimation Using Aerial Image Sequences, *IEEE Transactions on Pattern Analysis and Machine Intelligence*, 24(1), pp.1-18.
- Tuo, Hongya., Y. Liu, 2005, A new coarse-to-fine rectification algorithm for airborne push-broom hyperspectral images, *Pattern Recognition Letters*, 26(11), pp.1782-1791.

References from Books:

- Baarda, W. 1968. *A testing procedure for use in geodetic networks*, Netherlands Geodetic Commission, Publications on Geodesy, New Series, Vol. 2, No. 5, Delft, 1968.

References from Other Literature:

- Carroll, J., 2001. Vulnerability assessment of the transportation infrastructure relying on the global positioning system, Technical report, Volpe National Transportation Systems Center, August 2001. Report for US Department of Transportation.
- Haala, Norbert., D. Fritsch, D. Stallmann, and M. Cramer, 2000, On the Performance of Digital Airborne Pushbroom Cameras for Photogrammetric Data Processing – A Case Study, *IAPRS*, Vol. XXXIII, Amsterdam.
- Lee, C. N., 1999. Mathematical modeling of airborne pushbroom imagery using point and linear features, Doctoral dissertation, PhD diss, Purdue University.
- Lin, Yuping., and G. Medioni, 2007, Map-Enhanced UAV Image Sequence Registration and Synchronization of Multiple Image Sequences, *IEEE Conference on Computer Vision and Pattern Recognition*, 17-22 June 2007. pp.1-7.
- Lowe, D.G., 1999. Object recognition from local scale-invariant features. In: *Proceedings International Conferences on Computer Vision*, Corfu, Greece, pp.1150-1157.
- Oh, Jaehong., C. K. Toth and D. A. Grejner-Brzezinska, 2010, Automatic Geo-referencing of Aerial images using High-resolution Stereo Satellite Images, *ASPRS 2010 Annual Conference*, San Diego, CA, April 26-30.
- Skaloud, Jan., 1999, Problems in Direct-Georeferencing by INS/DGPS in the Airborne Environment, *ISPRS Workshop on 'Direct versus Indirect Methods of Sensor Orientation' WG III/1*, Barcelona 25-26.
- Zhang, W., J. Albertz, and Z. Li, 1994. Rectification of Airborne Line-Scanner Imagery Utilizing Flight Parameters. In *Proceedings of the First International Airborne Remote Sensing Conference and Exhibition*, Strasbourg, Vol.2, pp. 447–456, ERIM, Ann Arbor.

TREE SPECIES DETECTION USING FULL WAVEFORM LIDAR DATA IN A COMPLEX FOREST

S. Gupta^{a,*}, B. Koch^a, H. Weinacker^a

^a Dept. of Remote Sensing and Landscape Information Systems (FeLis), Faculty of Forestry, Albert-Ludwigs University, Tennenbacher str. 4, 79106 Freiburg, i.Br., Germany - (sandeep.gupta, barbara.koch, holger.weinacker)@felis.uni-freiburg.de

Commission VII, TC VII Symposium

KEY WORDS: LIDAR, Extraction, Reconstruction, Algorithms, Pattern, Three-dimensional

ABSTRACT:

The three-dimensional single tree extraction by applying pattern recognition based modified clustering approach on full waveform normalized raw LIDAR data has been presented in this research work. The LIDAR data of medium density (16 points m⁻²) was collected in August 2007 from the administrative forest district Hardt, Germany. The total study area is 1.75 ha and dominated by various deciduous tree species. The study plots selected contains multi-tier tree species of different age groups. Clusters of single tree extracted after running the algorithm were reconstructed using QHull algorithm. A validation procedure was devised and used for the accuracy assessment of the automatically detected tree species with respect to the forest inventoried data. The average producer's and user's accuracy for the total study area was around 56% and 41%, respectively. The results showed that the modified algorithm worked fairly well in the detection of evergreen conifers (79%) than the deciduous tree species (47%) beside the fact that conifers constitute roughly 18% of the total study area. The result showed that the algorithm for the upper tier trees species which are relatively mature and older worked better as compared to the tree species lying beneath the first-tier. The mixture of multi-storey tree species of varying age and height quintile with dense canopy cover was a limiting factor in the detection of single tree automatically in the presented work and shows the future scope of improvement in the algorithm applied.

1. INTRODUCTION

In a complex forest ecosystem, finding the distribution of different tree species of varying age and height quintile through traditional methods is a very thorny job. In the past one decade, the demand for high quality Light Detection And Ranging (LIDAR) data with more information has tremendously increased for various applications. The increasing demand of individual tree related information, as a basis to improve forest management performance, is the concerned factor for developing various methodologies for single tree extraction and related parameter estimation from airborne laser scanner (ALS) data. Clustering provide a good way of partitioning the whole normalized ALS dataset of the test area into an individual clusters. Because of the high point density full waveform LIDAR data provide a good platform to implement the clustering mechanisms via partitioning the data into individual clusters, each representing single tree. There are different clustering mechanisms, but the most popular *k*-means was chosen which is an iterative hill-climbing method and is a staple of clustering methods (Gupta et al., 2010). These has motivated to test the full waveform ALS data for the extraction of pattern of single tree crowns of different tree species in the selected plots of Hardt administrative forest district of Germany using modified clustering based approach and has been presented in the current work.

2. EXISTING RELATED WORK

Several studies has been carried out in the past on the application of airborne LIDAR data for vegetation related

information retrieval using different methods (Hyyppä and Inkinen, 1999; Hyyppä et al., 2006; Ko et al., 2009; Nilsson, 1996; Persson et al., 2002; Persson et al., 2006; Vauhkonen et al., 2009; Wang et al., 2008). Research work using clustering based approaches for 3-dimensional (3-D) single tree extraction using airborne LIDAR data has been carried out (Cici et al. 2008; Doo-Ahn et al. 2008; Gupta et al., 2010; Morsdorf et al. 2003; Morsdorf et al. 2004; Reitberger et al. 2008). Morsdorf et al. (2003) used first and last pulse data with an overall density of 30 points m⁻² and the *k*-means method to extract single tree in the Swiss National Park. In contrast to the modified algorithm used in the presented work, instead of scaling-down the height values, they scaled-up it by a factor of 3. This has been done to accommodate the aspect ratio of pine tree crowns (ranged from 3 to 6). However, it was concluded on the basis of previous study (Gupta et al., 2010) that by scaling down the height value of the normalized raw LIDAR points and the external seed points (local maxima), squared error function is minimized which is the ultimate objective of the *k*-means method. The closer the points will be, more precise will be the cluster formation with regard to actual tree/tree crown and its shape. The algorithm used in the presented work differs from Morsdorf et al. (2003) in a way that unwanted local maxima points were deleted in the pre-processing step. Riaño et al. (2004) estimated a derivative of foliage biomass, crown bulk density, using lidar metrics with *k*-means clustering at both plot and individual tree scales. However, individual tree level analyses were not completely successful in their work. In a study conducted by Ko et al. (2009) for deciduous-coniferous classification using single leaf-on high density full waveform

* Corresponding author.

LIDAR data, branches of 27 coniferous and 38 deciduous trees were derived by calculating the mean silhouette values repeatedly for different k values using simple k -means approach for improved visualization. The method lacks the efficiency for finding the suitable value of k with respect to different tree types, tree age and forest conditions. In their study the result is not validated using any field data. Ørka et al. (2009) tested the supervised classification strategy using linear discriminant analysis (LDA), random forest (RF) algorithm and support vector machines (SVM) for tree species classification. They also used unsupervised k -means clustering and k -means clustering in combination with the unsupervised random forest algorithm for the same purpose. However, their result showed that accuracies were lower in case of unsupervised one than for supervised methods applied for overall species classification. This shows that supervised methods are more promising which was found true during the investigation after a comparative qualitative analysis of the output by applying different clustering algorithms (Gupta et al., 2010). Vauhkonen et al. (2009) used LDA for the classification of individual trees and alpha shape metrics for tree species classification in Scandinavian test site comprising 92 trees detected and delineated manually from a very dense ALS data. However, the method applied required to be tested for larger dataset with lower or medium point density by automatic detection. Apart from tree detection methods, a method for reconstructing the tree crowns was also provided (Pyysalo and Hyypä, 2002). There are many ways for constructing the shape of extracted points of single tree using different computational geometry concept like convex hull, 3D Delaunay triangulation or can be shown as 3-D surface or mesh.

3. MATERIALS AND METHODOLOGY

3.1 Study Area

Investigations were carried out in the selected plots of administrative forest district Hardt, Baden-Württemberg region in the South-West of Germany. The study area is flat, 1.75 ha in total, comprising 7 rectangular study plots, each of size 0.25 ha.

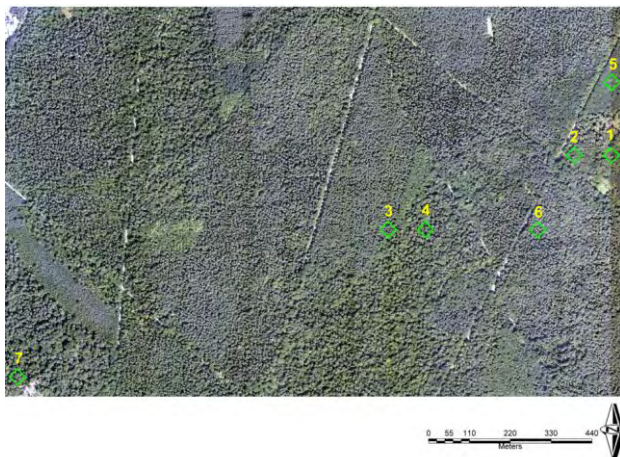


Figure 1. Location of rectangular study plots (green) as seen in the RGB aerial photograph

The study plots in the forest are characterized by a variety of deciduous and coniferous tree species of different ages. The forest is marked with highly interconnected and dense standing deciduous crowns. The overall fraction of deciduous and evergreen coniferous tree species is nearly 82% and 18%, respectively. Except plot 3, rest of the plots are dominated by

deciduous trees species (Table 2). The dominant tree types in the studied field plots are Scots pine (*Pinus sylvestris* – 13.9%), Cherry (*Prunus avium* – 23.7%), Oak (*Quercus petraea* – 24.3%), European Beech (*Fagus sylvatica* – 21.1%), Hornbeam (*Carpinus betulus* – 9.5%) and 7.6% others species (Norway spruce - *Picea abies*, Douglas fir - *Pseudotsuga menziesii* and few other minor species). All the study plots are made up of multi-storey canopy layers. From the field inventory data collected, it was found that the height of different tree species of analyzed study plots varied between 8-35 m and average height ranged between 8-31 m.

Plot Id	Tree type	Tree species	% of tree
1	Deciduous	Hornbeam + Cherry	34.4 + 56.2 = 90.6
	Evergreen conifer	Scots pine	9.4
2	Deciduous	Cherry + Oak	91.8 + 4.1 = 95.9
	Evergreen conifer	Scots pine	4.1
3	Deciduous	Red Oak + European Beech + Black Locust	8.3 + 25.0 + 5.6 = 38.9
	Evergreen conifer	Scots pine + Douglas fir + Norway spruce	44.4 + 13.9 + 2.8 = 61.1
4	Deciduous	Hornbeam + European Beech	68.2 + 9.1 = 77.3
	Evergreen conifer	Scots pine	22.7
5	Deciduous	Oak + European Beech + Linden + Silver Birch	73.2 + 18.8 + 3.0 + 1.0 = 96.0
	Evergreen conifer	Scots pine	4.0
6	Deciduous	European Beech + Sycamore Maple	72.4 + 2.1 = 74.5
	Evergreen conifer	Scots pine	25.5
7	Deciduous	European Beech + Sycamore Maple + Cherry + Hornbeam + Oak	10.0 + 6.7 + 40.0 + 13.3 + 3.3 = 73.3
	Evergreen conifer	Scots pine + Norway spruce	6.7 + 20.0 = 26.7

Table 2. Tree species distribution

The name and distribution of tree species in Table 2 are in the same order.

3.2 Field Data Characteristics

Forest inventory data of the study plots was provided by the Forest Research Institute (FVA) of Baden-Württemberg. All trees in the plot above 7 cm diameter at breast height (DBH) were measured. Two top heights of the main tree and one top height of the dominated tree were measured using a Vertex® instrument. The arithmetic mean of the height measurements was calculated as an average top height for each plot (Straub et al., 2009). Stand height curves with the DBH as input variable were used to estimate the heights of the remaining trees (Korn-Allan et al., 2004). Several height percentiles were calculated

for each inventory plot based on the nDSM and LIDAR points (Straub et al., 2009). Further, field work was conducted for plot establishment and measuring coordinates. Coordinates of center point and four corners of each rectangular plot were measured. Some other parameters like azimuth and distance from the middle point of each sample plot to sampling tree inside the plot were also taken. Tree coordinates were then derived using the azimuth and distance from the center point of each plot using compass and tape.

3.3 LIDAR Data and Pre-processing

Full waveform laser scanner data of density (16 points m^{-2}) was acquired during August 2007 by TopoSys GmbH using the Riegl LMS-Q560 system. Important flight and system parameters are given by Straub et al. (2009). Both the raster terrain and surface models of 50 cm resolution were calculated using the LIDAR raw point clouds. An 'Active Surface Algorithm' implemented in the "TreesVis" - software for LIDAR data visualization and analysis, was used for data filtering and surface interpolation (Weinacker et al., 2004). A normalized digital surface model (nDSM) was derived by subtracting the digital terrain model (DTM) from the digital surface model (DSM) using "TreesVis" software. Raw full waveform LIDAR points were normalized using the DTM to ensure the absolute height of the object and to eliminate the influence of the terrain. Thus, obtained normalized raw data was further used in the main process for clustering.

3.4 Orthophoto Characteristics

RGB/NIR Optical data were collected by TopoSys GmbH in July 2008. Important flight and technical parameters of the RGB/NIR line scanner are given by Straub et al. (2009). The individual flight strips were rectified and georeferenced with the aid of DSM, which was filtered from ALS data (6-7 points m^{-2}) acquired at the same time with the optical data. Orthophotos were computed by the data provider and were delivered at 25 cm spatial resolution.

3.5 Data Processing

3.5.1 Clustering by Modified k -means: The k -means treats each observation in the input data as an object having a location in the space. The objective of k -means algorithm is to minimize the total intra-cluster variance or the squared error function. In the algorithm, the sum of absolute differences between each point and its closest centre in Euclidian 3-D space is minimized. Each centroid is the mean of the points in that cluster. It is also advantageous to implement k -means since it uses the actual observations of the objects (rather than the larger set of dissimilarity measures), and not just their proximities unlike the hierarchical clustering based approaches (Gupta et al., 2010).

The k -means algorithm was supervised to use the local maxima as external seed points to initialize the iteration, instead of selecting it randomly by the user, as in the case of Ko et al. (2009). This was done because finding the pattern of individual tree in natural forest conditions is very difficult by selecting k clusters randomly using the simple k -means algorithm. Another advantage of avoiding trial and error based simple k -means approach is saving of machine memory and total run-time. The performance of the algorithm was improved by reducing the height value of the data points and external seed points by a half. The reason behind the reduction of height value is that it brings the normalized raw points as well as seed points closer in

z -dimension and minimizes the intra-cluster variance. Thus, it fulfils the sole objective of the k -means. The reduction of the height to half was found empirically with trial and error based approach and have been kept constant for all the 7 plots studied.

3.5.1.1 Extraction of external seed points and filtration of unwanted seed points: Local maxima points were extracted as external seed points above 5 m height from the nDSM image having a gray value larger than the gray value of all its 8 neighbors. To avoid the overflow of seed points, the points that were too close to each other were filtered out based on threshold distance. The filtered local maxima as external seed points in the k -means algorithm were finally used. The threshold distance, varied depending on the forest conditions. The plot dominated by mature or old trees requires higher thresholds distance because local maxima from smaller peaks will most likely represent only branches, hence needs to be eliminated. Local maxima from a younger tree's peak will most likely to be a treetop, hence, need smaller threshold distance. The value of threshold distance for younger trees with single and narrow crown at the tree top was found as approximately 2-4 m (plots 2, 5 and 6) without any smoothing. While threshold distance for trees with relatively older ones having wider crown with more intermittent peaks at the tree top was found as 4-6 m (plots 1, 3, 4 and 7) with no smoothing. However, this also varies from dominant tree types.

3.5.1.2 Modified k -means algorithm: The modified k -means algorithm applied to a set of 3-D vectors in the form of pseudo-code is given as follows.

- (i) Select normalized 3-D LIDAR points and external seed points above certain height (for example, above 5 m)
- (ii) For all the external seed points and that of the normalized LIDAR points, $z = z * 0.5$, before initialization of the algorithm
- (iii) Set $i = 1$
- (iv) Select external seed points as a set of k means $C_1(1), C_2(1), \dots, C_k(1)$, where $i = 1$ in this case (mean vector for each cluster centre)
- (v) For each vector x_i , begin computation $D(x_i, C_k(i))$, for each $i = 1, \dots, k$ and assign x_i to the cluster C_j with the nearest Euclidian distance in 3-D space (means)
- (vi) $i = i++$ and update the means (C_j) to get a new set $C_1(i), C_2(i), \dots, C_k(i)$
- (vii) Repeat steps (iii) to (v) until $C_k(i) = C_k(i + 1)$ for all k
- (viii) For all the external seed points and that of the normalized LIDAR points, $z = z/0.5$

3.5.2 3-D Reconstruction of tree clusters: Once the tree clusters are generated, each cluster is reconstructed in 3-D space using the QHull approach (Barber et al., 1996). QHull is a general dimension code for computing convex hulls using Quickhull algorithm (Berg et al., 1997). Each 3-D tree crown cluster is constructed with triangular surface as a 3-D convex polytope. The convex hull of a set of points is the smallest convex set containing those points. For detailed introduction with example codes, see the book by O'Rourke (1994). The main advantages of Quickhull are its output of performance sensitivity (in terms of the number of extreme points), reduced space requirements, and floating-point error handling. Thus, 3-D convex polytope each tree crown is shown as a 3-D object with a triangular surface in the case of 3-D convex polytope. The shape of each polytope is the representation of the respective tree species.

3.6 Validation Method

The automatically extracted tree tops of individual tree in each plot were validated with respect to field measured reference tree tops. A circular buffer of radius 3 m was created around each reference point, in Geographical Information System (GIS) environment. Only those extracted tree tops were considered which were close to a maximum of 5 m in 3-D Euclidean distance (ED) with that of the reference point. The extracted tree tops were intersected with that of the reference points of the identical plot within the buffered area. 3-D ED was calculated for each intersected point. Most suitable validation class as defined below was assigned for each intersected point.

3.7 Validation Classes

Following five validation classes were adopted for classifying the result and accuracy assessment.

- (i) Exact (E) - only one extracted tree top with respect to the nearby reference tree top. 3-D ED between the extracted tree top and reference tree top point is ≤ 3 m.
- (ii) Nearly Exact (NE) - one extracted tree top with respect to a reference tree top nearly at the same height level. 3-D ED between the extracted tree top and reference tree top is 3-5 m.
- (iii) Split - more than one neighbored detected treetops up to the 3-D ED of 5 m from a neighbouring reference tree top.
- (iv) Missing – includes those reference tree top points for which there is no extracted tree top point in the neighbourhood up to the 3-D ED of 5 m. It also includes the reference points for which there is no detected tree tops within the buffer around each reference tree top point.
- (v) Extra - includes those extracted tree top points within the field boundary for which there is no reference tree top point up to the 3-D ED of 5 m. It also includes those extracted points within the field boundary for which there is no reference point within the buffer around each reference tree top point.

4. RESULTS AND DISCUSSION

Before running the modified *k*-means algorithm, normalized raw LIDAR points and local maxima points below 5 m height were filtered. This was done to avoid the effect of low ground vegetation and other smaller objects during the clustering process. After running the algorithm over normalized LIDAR points using local maxima as external seed points, the 3-D cluster points of the corresponding tree were extracted in all the study plots. Accuracy assessment of the five major validation classes of automatically detected tree tops with reference to the field measured tree tops has been presented (Table 3 and 4). Two validation classes, namely, ('Exact' and 'Nearly Exact') played a key role in determining the two kind of accuracy.

Plot ID	E	NE	S	M	Ex	\sum_{EP}	\sum_{ErP}	FD (%)
1	17	4	8	11	15	50	29	58
2	15	10	6	24	24	70	45	64.3
3	17	5	3	14	8	44	22	50
4	11	3	2	8	9	30	16	53.3
5	10	30	7	61	6	97	57	58.8

6	13	21	9	13	12	67	33	49.3
7	2	9	3	19	21	48	37	77.1

Table 3. Distribution of validation classes and other attributes

E = 'Exact' points, NE = 'Nearly Exact' points, S = 'Split' points, M = 'Missing' points, Ex = 'Extra' points, \sum_{EP} = sum of extracted tree top points in the plot, \sum_{ErP} = sum of extracted error tree top points in the plot, FD = False detected points = $\sum_{ErP} * 100 / \sum_{EP}$.

Plot ID	E+NE	\sum_{EP}	RP	P_acy (%)	U_acy (%)
1	21	50	32	65.6	42.0
2	25	70	49	51.0	35.7
3	22	44	36	61.1	50.0
4	14	30	22	63.6	46.7
5	40	97	101	39.6	41.2
6	34	67	47	72.3	50.7
7	11	48	30	36.7	22.9

Table 4. Plot level accuracy

E+NE = sum of exact and nearly exact points in the plot, \sum_{EP} = sum of extracted tree top points in the plot, RP = total reference tree top points in the plot, P_acy (%) = producer's accuracy = $(E+NE) * 100 / RP$ and U_acy (%) = user's accuracy = $(E+NE) * 100 / \sum_{EP}$.

It is visible from Table 4 that the producer's and user's accuracies in the broad-leaved deciduous dominated study plots (all plots except 3) are roughly varying between 37-72% and 23-51%, respectively. In case of plot 3, which is dominated by evergreen coniferous trees, the producer's and user's accuracies are approximately 61% and 50%, respectively. There are highest accuracies obtained in plot 6. The high producer's and user's accuracies in case of plot 6 are detected due to fewer tree species which are present nearly the same height level. Due to this factor closely-matched seed points were generated that resulted in a comparatively more accurately positioned detected tree tops with respect to the referenced tree tops. The false detection is lowest (49%) in plot 6 and highest in plot 7 (Table 3). In case of plots 2 and 7, the false detection is 64% and 77%, respectively, which is relatively higher than the remaining plots. It is noticeable that in both the plots, there are higher proportions of cherry trees. It is assumed that it was found difficult in automatic detection of small crowned and low height cherry trees. The accuracies are comparatively lower in case of study plots 5 and 7. In the former case (plot 5), it is mainly due to the mixed distribution multi-layered Oak and European beech with dense canopy. In the later case (plot 7), it is due to the presence of highly mixed tree species composition of varying age and high canopy density. In case of Oak dominated plot 5, the accuracies are not only lower but more or less in the same range. The average producer's and user's accuracies among all the study plots are 55.7% and 41.3%, respectively.

Table 8 shows the percentage distribution of 'Exact' and 'Nearly Exact' tree tops together and the corresponding reference tree tops for each species in all the 7 study plots.

Tree species	R_Tree %	E_Tree (E+NE) %
Scots pine	13.9	86.4
Norway spruce	2.2	42.9
Douglas fir	1.6	60.0
Hornbeam	9.5	66.7
Cherry	23.7	40.0
Oak	24.3	45.5
Red Oak	0.9	33.3
European Beech	21.1	47.8
Black Locust	0.6	100.0
Linden	0.9	33.3
Silver Birch	0.3	100.0
Sycamore Maple	0.9	33.3

Table 5. % distribution of ‘Exact’ (E) + ‘Nearly Exact’ (NE) tree tops together and corresponding reference tree tops (R_Tree).

The species-wise distribution of the two accuracy determining validation classes (E+NE) gives a meaningful insight while assessing the accuracy. It is evident from Table 5 that the higher fractions of acceptable tree tops were detected for the evergreen Scots pine (86.4%). The detection of ‘Exact’ and ‘Nearly Exact’ tree tops is for few minor deciduous species like Black locust and Silver birch is highest (100%), while that of the other minor deciduous species like Red oak, Linden and Sycamore maple are 33.3% each. Average detection of ‘Exact’ and ‘Nearly Exact’ tree tops were found for the two other minor evergreen species, Norway spruce (42.9%) and Douglas fir (60%). Acceptable tree tops (E+NE) for Oak, Cherry, European beech and Hornbeam, which are the four major deciduous tree species in the study plots, are 45.5%, 40%, 47.8% and 66.7%, respectively. An overall 57.4% of trees were automatically detected together in the ‘Exact’ and ‘Nearly Exact’ validation class among the 7 test plots by applying the modified *k*-means algorithm. It is clear from the Table 5 that modified algorithm yielded higher amount of ‘Exact’ (E) and ‘Nearly Exact’ (NE) tree tops for evergreen coniferous trees despite the fact that it constitutes only 17.7% of total tree cover among all the 7 study plots. The percentage fraction of the sum of the tree top points in ‘Exact’ and ‘Nearly Exact’ validation classes among all the 7 test plots for the evergreen coniferous and deciduous trees are 78.6% and 47.1%, respectively. More than 80% Scots pines were detected in all the study plots by applying the algorithm. This may be due to their dominance in the upper canopy layer.

By applying supervised *k*-means approach, the number of trees to be extracted was decided by the number of external seed points used during the initialization of the *k*-means, which, in turn, is dependent on the distance threshold. During the investigation, it was found that the distance threshold is a forest dependent parameter. For example, the plot dominating with trees of wider canopies requires higher distance threshold because local maxima from smaller peaks will most likely represent only branches, hence needs to be eliminated. Whereas, local maxima from a peak in a plot containing trees with small canopies will most likely to be a treetop, hence requires comparatively smaller distance threshold.

Approximate shape of the individual tree crown was represented in the form of 3-D convex polytope. The convex polytopes were computed from the delineated clusters using QHull approach (Barber et al., 1996). Two examples of European beech and Scots pine from plot 6 containing clusters and the respective 3-D convex polytopes have been represented below in Figure 6 and 7, respectively. The European beech and Scots pine in the given examples are roughly 17 m and 26 m in height. The canopy cover and density played a vital role in computing the geometrical shape of the two tree species.

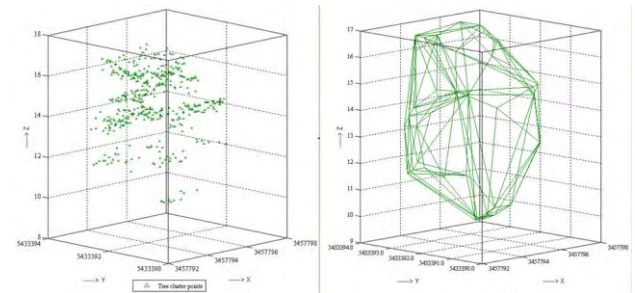


Figure 6. Cluster and convex polytope of a European beech

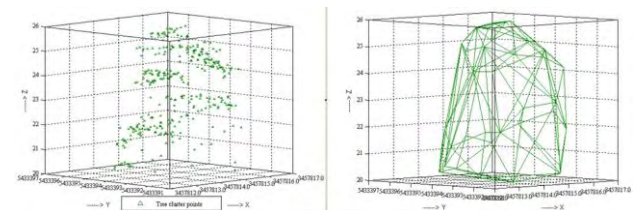


Figure 7. Cluster and convex polytope of a Scots pine

5. CONCLUSIONS

Traditional *k*-means generates arbitrarily bad grouping of objects due to random seed selection procedure and repeated run of the algorithm after cluster analysis to meet the fitness criteria. The algorithm yields comparatively fair results by partitioning the LIDAR data after seeding is done externally and the height value of the LIDAR points are scaled down to half before initialization of the process (Gupta et al., 2010). There is an obvious advantage of the modified approach over the simple *k*-means or hierarchical based clustering (Gupta et al., 2010) or other approaches using *k*-means for single tree extraction by other investigators (Morsdorf et al., 2003; Ørka et al., 2009). The formulation of validation method and classes were crucial in determining the accuracy.

The multi-tier, mixed tree species distribution with varying age groups, low crown diameter and dense canopy closure were big challenge for the algorithmic performance in single tree extraction for different tree species. The average producer’s and user’s accuracies among all the plots are 55.7% and 41.3%, respectively. From Table 4 it is evident that the performance of the algorithm is average in such forest conditions. It was observed that higher accuracies are tending to occur if the trees in plot are at nearly same height and when there are fewer tree species, as in the case of plot 6. The results show that the algorithm for the upper tier trees worked better as compared to the trees lying beneath it. Further algorithmic improvement and more investigation in varying forest conditions will be done to obtain better accuracies in the future.

REFERENCES

- Barber, C.B., Dobkin, D.P., Huhdanpaa, H.T., 1996. The Quickhull algorithm for convex hulls. *ACM Trans. on Mathematical Software*, 22(4), pp. 469-483.
- Berg, M.D., Kreveld, M.V., Overmars, M., Schwarzkopf, O., 1997. *Computational Geometry - Algorithms and Applications*. Springer-Verlag, Heidelberg, pp. 233-244.
- Cici, A., Kevin, T., Nicholas, J. T., Sarah, S., Jörg, K., 2008. Extraction of vegetation for topographic mapping from full-waveform airborne laser scanning data. In: *Proc. of SilviLaser 2008*, 17-19 Sept., Edinburgh, U.K., pp. 343-353.
- Doo-Ahn, K., Woo-Kyun, L., Hyun-Kook, C., 2008. Estimation of effective plant area index using LiDAR data in forest of South Korea. In: *Proc. of SilviLaser 2008*, 17-19 Sept., Edinburgh, U.K., pp. 237-246.
- Gupta, S., Weinacker, H., Koch, B., 2010. Comparative analysis of clustering-based approaches for 3-d single tree detection using airborne fullwave lidar data. *Remote Sensing*, 2(4), pp. 968-989.
- Hyypä, J., Inkinen, M., 1999. Detecting and estimating attributes for single trees using laser scanner. *The Photogrammetric Journal of Finland*, 16, pp. 27-42.
- Hyypä, J., Yu, X., Hyypä, H., Maltamo, M., 2006. Methods of airborne laser scanning for forest information extraction. In: *Proc. of International Workshop on 3D Remote Sensing in Forestry*, 14-15 Feb., Vienna, Austria, pp. 63-78.
- Ko, C., Sohn G., Rimmel, T. K., 2009. Classification for deciduous and coniferous trees using airborne LiDAR and internal structure reconstructions. In: *Proc. of SilviLaser 2009*, 14-16 Oct., Texas, USA, pp. 36-45.
- Korn-Allen, E., V.D. Goltz, H., Blust, M., Nothdurft, A., 2004. *Verfahrenshandbuch betrieb, Sinventur. - version 1.1.*, Landesforstverwaltung Baden-Württemberg, Germany.
- Morsdorf, F., Meier, E., Allgöwer, B., Nüesch, D., 2003. Clustering in airborne laser scanning raw data for segmentation of single trees. In: *The International Archives of the Photogrammetry, Remote Sensing and Spatial Information Sciences*, 8-10 Oct., Dresden, Germany, Vol. XXXIV, part 3/W13, pp. 27-33.
- Morsdorf, F., Meier, E., Kötz, B., Itten, K.I., 2004. Lidar based geometric reconstruction of boreal type forest stands at single tree level for forest and wildland fire management. *Remote Sensing of Environment*, 92(3), pp. 353-362.
- Nilsson, M., 1996. Estimation of tree heights and stand volume using an airborne lidar system. *Remote Sensing of Environment*, 56(1), pp. 1-7.
- Ørka, H. O., Næsset, E., Bollandsås, O. M., 2009. Comparing classification strategies for tree species recognition using airborne laser scanner data. In: *Proc. of SilviLaser 2009*, 14-16 Oct., Texas, USA, pp. 46-53.
- O'Rourke, J., 1994. *Computational Geometry in C*, Cambridge University Press, 2nd edn., New York.
- Persson, Å., Holmgren, J., Söderman, U., 2002. Detecting and measuring individual trees using an airborne laser scanner. *Photogrammetric Engineering & Remote Sensing*, 68, pp. 925-932.
- Persson, Å., Holmgren, J., Söderman, U., 2006. Identification of tree species of individual trees by combining very high resolution laser data with multi-spectral images. In: *Proc. of International Workshop on 3D Remote Sensing in Forestry*, 14-15 February, Vienna, Austria, pp. 91-96.
- Pyysalo, U., Hyypä, H., 2002. Reconstructing tree crowns from laser scanner data for feature extraction. In: *Proc. of the ISPRS Technical Commission III Symposium for Photogrammetric Computer Vision*, 9-13 September, Graz, Austria, Vol. XXXIV, part 3A/B, pp. 293-296.
- Reitberger, J., Krzystek, P., Stilla, U., 2008. Analysis of full waveform LIDAR data for the classification of deciduous and coniferous trees. *International Journal of Remote Sensing*, 29(5), pp. 1407-1431.
- Riaño, D., Chuvieco, E., Condés, S., Gonzáles-Matesanz, J., Ustin, S., 2004. Generation of crown bulk density for *Pinus sylvestris* L. from lidar. *Remote Sensing of Environment*, 92(3), pp. 345-352.
- Straub, C., Deed, M., Weinacker, H., Koch, B., 2009. Using airborne laser scanner data and CIR orthophotos to estimate the stem volume of forest stands. *Photogrammetrie - Fernerkundung - Geoinformation*, Vol. 2009, 3, pp. 277-287.
- Vauhkonen, J., Tokola, T., Packalén, P., Maltamo, M. 2009. Identification of Scandinavian commercial species of individual trees from airborne laser scanning data using alpha shape metrics. *Forest Science*, 55(1), pp. 37-47.
- Wang, Y., Weinacker, H., Koch, B., Sterenczak, K., 2008. Lidar point cloud based fully automatic 3d single tree modelling in forest and evaluations of the procedure. In: *The International Archives of the Photogrammetry, Remote Sensing and Spatial Information Sciences*, 3-11 July Beijing, China, Vol. XXXVII, part B6b, pp. 45-52.
- Weinacker, H., Koch, B., Heyder, U., Weiancker, R., 2004. Development of filtering, segmentation and modelling modules for lidar and multispectral data as a fundament of an automatic forest inventory system. In: *Proc. of ISPRS working group on Laser-Scanners for Forest and Landscape Assessment*, 3-6 Oct., Freiburg, Germany, Vol. XXXVI, part 8/W2.

ACKNOWLEDGEMENTS

Landesgraduiertenförderungsgesetz (LGFG) Commission, Baden-Württemberg, Germany is acknowledged by the author for providing financial support during the research work within the framework of doctoral scholarship program. The authors would like to thank the Forest Research Institute of Baden-Württemberg (FVA) for providing the reference data for the study area. The authors also acknowledges his gratitude to his fellow colleagues Christoph and Johannes who have further conducted the field work for plot establishment in the test sites to get more forest parameters.

SUPER RESOLVED REMOTE SENSING BY FUSION OF MULTI SPECTRAL AND SPATIAL DATA

E. Gur^a, Z. Zalevsky^{b,*} and B. Javid^c

^aFaculty of Engineering, Shenkar College of Eng. & Design, Ramat Gan, 52526, Israel – gur.eran@gmail.com

^bSchool of Engineering, Bar Ilan University, Ramat Gan, 52900, Israel - zalevsz@eng.biu.ac.il

^cUniversity of Connecticut Electrical & Computer Engineering Dept., USA - bahram@enr.uconn.edu

KEY WORDS: Engineering, Processing, Retrieval, Algorithms, Image, Resolution, High resolution, Optical

ABSTRACT:

In this paper the authors present a super resolution approach which is based on iterative data fusion algorithms. The proposed data fusion can be implemented using a plurality of spectral images as well as a plurality of images with varied resolution generated from different regions of the field of view. The data fusion suggested in this paper is gradual, allowing the build up of one single high resolution image from low resolution images and partial high resolution images. The iterative procedure used in this paper is based on iterative ping-pong computation between the spatial domain and its spectral distribution, similar to the Gerchberg-Saxton approach but with dynamic parameters. The iterative approach enables the retrieval of high resolution data from mostly-low resolution data. In both approaches mentioned, one may mix high and low resolution information by the insertion of properly defined constrains, and achieve an enhanced image in terms of clarity, resolution, correlation with true data and contrast.

* Corresponding author.

INTRODUCTION

A well-known phase retrieval algorithm commonly used for optical beam shaping is the Gerchberg and Saxton (Gerchberg and Saxton, 1972) approach in which knowing the magnitude distribution of an image in the spatial and the spectral domain enables the recovery of the phase distributions. Later work by Misell (Misell, 1973a; Misell, 1973b; Misell, 1973c) extended the algorithm for two arbitrary input and output planes along the optical path. These methods are proven to converge to a phase filter with a minimal mean square error (Fienup, 1978; Fienup, 1982).

The concept presented in the Gerchberg-Saxton paper is simple. One starts with an arbitrary phase-only filter in the object domain multiplying the input object (the original image), after a Fourier transform one obtains a Fourier domain image and imposes the required Fourier magnitude, while maintaining the Fourier phase. An inverse Fourier transform brings us back to the object domain. Since we demand a phase-only signal, we impose the intensity of the input object in this plane. Next, one calculates the Fourier transform and returns to the Fourier domain to iterate the process until an acceptable convergence is obtained.

Gerchberg (Gerchberg, 1974) and Papoulis (Papoulis, 1975) suggested the use of this method for super resolution. However, both presented relatively simple test cases and assumed the properties of all iterations to be identical (except when noise reduction was addressed). An improved Gerchberg-Papoulis algorithm was recently suggested by Gur and Zalevsky (Gur and Zalevsky, 2007a; Gur and Zalevsky, 2007b); however, it supplies good result only if the blurred image is actually a lower resolution version of the required image. Similar approaches providing image resolution enhancement by proper digital image processing interpolation and learning-based algorithms can for instance be seen in Refs. (Gevrekci and Gunturk, 2000; Nguyen and Milanfar, 2000; Joshi *et al.*, 2005).

In this paper, the authors propose a modification of the algorithm presented in Ref. (Gur and Zalevsky, 2007a; Gur and Zalevsky, 2007b). In the new algorithm, instead of multiplexing two images, one at high resolution and the other at low resolution, the authors propose a general approach capable of multiplexing a plurality of low and high resolution images. In the proposed approach, the multiplexed images do not have to relate to different regions of the field of view but rather to images that are captured at different spectral wavelengths. In this paper, the authors validate the generalized approach by experiments including both images captured at different spatial resolutions from airborne camera as well as images captured in a multi spectral sensor.

The 2nd section presents the proposed approach. Experimental results are presented in 3rd section. The paper is concluded in the 4th section.

THE PROPOSED ALGORITHM

In this paper the authors address the following situation: We obtain a plurality of low resolution images which can be from different regions in the field of view with lower resolution, or a set of images captured at different wavelengths by a multi-spectral sensor. In addition to the low resolution input images, we obtain a plurality of high resolution images which can be from other regions of the field of view (that may be at different resolution levels) or they may be spectral images captured at shorter wavelengths and thus have higher resolution. Our aim is to reconstruct the higher spatial frequencies by a dynamic iterative procedure.

The flow chart of the proposed algorithm is described in Figure 1. The starting point of the basic algorithm assumes that we possess a plurality of High Resolution (HR) images and a plurality of Low Resolution (LR) images. Each image relates to a different region of the field of view, or we possess several images coming from sensors of different wavelengths while each image contains the full field of view. An overall image is generated from the plurality of given images. The generalized image of the full field of view is either an image combining all of the N regions of the field of view together, or a multiplexing of several spectral images captured at different wavelengths when a different region of the field of view is taken from different wavelengths. In both cases, the first iteration of the newly generated image combines some HR and some LR image regions. Then, a Fourier transform is performed. The Fourier image obtained contains data from all regions of the new image.

Since the lower frequencies are present in the LR image, we impose the lower frequencies constraints from the Fourier transform of the original LR images. Next an inverse Fourier transform is performed. At this stage we replace the various regions of the field of view that were related to HR images by the known a priori HR regions, and we keep the rest of the regions. We again perform a Fourier transform to impose the constraints on lower frequencies and so on. The basic algorithm converges when the difference between images obtained in consecutive iterations is below a certain predefined threshold.

At the final stage, we take the HR reconstructions from regions that were originally imposed by the LR images. The strength of this algorithm with respect to algorithm based directly on Misell's work or Gerchberg and Papoulis' work lies mainly on its dynamic properties. We do not impose all the a priori knowledge at the beginning, but rather start with some of the known constraints and increase the applied constraints according to the improvement in mean-square error results from one iteration to the next.

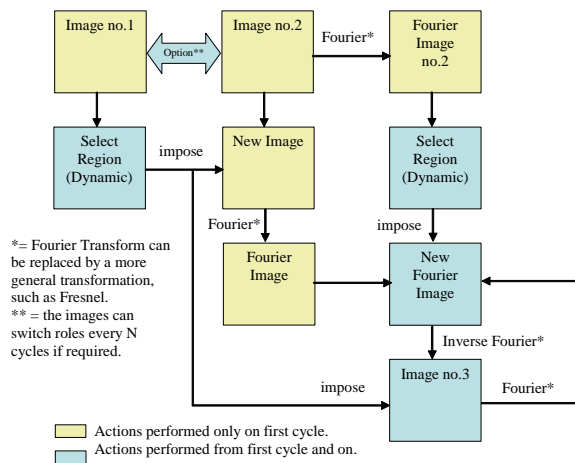
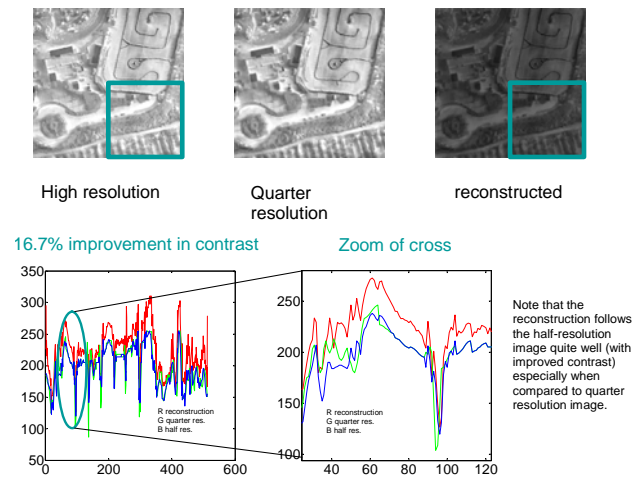


Figure 1. Flow chart of the proposed generalized super resolving approach.

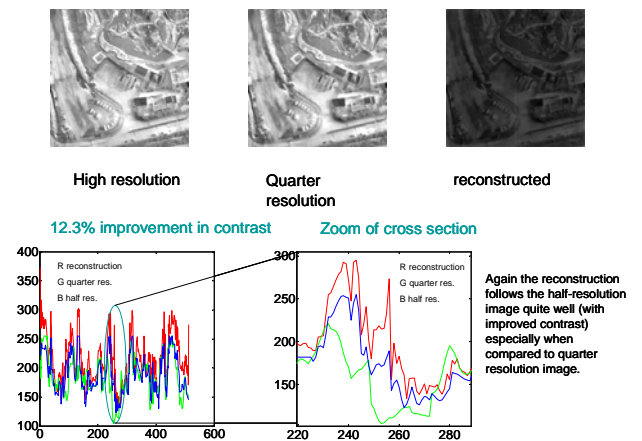
EXPERIMENTAL VERIFICATION

In this section the authors present two types of experimental results, both coming from airborne camera capturing urban area. In Figures 2(a) and 2(b) we present two experimental results. In both, the upper row contains from left to right: a high resolution image, the same image taken at a quarter of the resolution and the obtained reconstruction. The cross section is seen in the lower row. Red corresponds to the reconstruction image, green is the quarter resolution image, and blue is the half resolution image used for comparison. The reconstructed image obtained from the multiplexing of the high resolution image and the quarter resolution image follows the cross section of the half resolution image very well while having an improved contrast by 16.7% in Figure 2(a) and by 12.3% in Figure 2(b). The correlation between the reconstructed image and the HR image is 98.2% and the mean square error is less than 0.8%, for the later test case.

In the second experiment presented in Figure 3, we obtain the photograph of the same scenery using two different wavelengths. We assume that in the shorter wavelength image we succeeded to obtain only the lower right quarter of the image. By the same iterative procedure (but using different parameters) we generate a new image (result) containing high resolution data even outside the imposed data region. In the lower row of Figure 3 one may see the reconstructed result (left) and its cross section (right). An improvement of more than 10% in the contrast is obtained when comparing the reconstruction results (red) and the original image at low resolution (longer wavelength).



(a)



(b)

Figure 2. Experimental results using airborne camera images. (a). Captured image #1. (b). Captured image #2. In both cases, the upper row contains from left to right: a high resolution image, same image at quarter of resolution, and the reconstruction results. The cross section is seen in the lower row. Red is the reconstruction image, green is the quarter resolution image, and blue is the half resolution image used for comparison. The reconstructed image obtained from multiplexing of the high resolution image and quarter resolution image follows the cross section of the half resolution image very well while having an improved contrast (improvement by 16.7% in (a), and 12.3% in (b)).

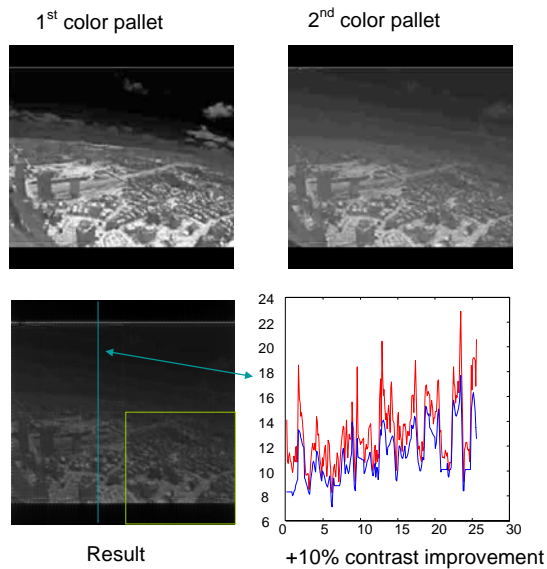


Figure 3. Experimental results taken from airborne multi spectral sensor at mid infra-red of 3.8-4.1 micron (left image of upper row) and at wavelength of and 4.5-4.8 micron (right image of upper row). In the lower row one may see the reconstructed result (left) and the obtained cross section (right). An improvement of more than 10% in the contrast is obtained when comparing the reconstruction (red) and the original image at low resolution (longer wavelength).

CONCLUSIONS

In this paper, the authors have presented a generalized approach for digital super resolution while using a plurality of images with different resolutions corresponding to either different regions of the field of view of the scene or from a multi spectral imager. The proposed algorithm was experimentally tested on images downloaded from an airborne camera capturing an urban scene at different resolutions and different wavelengths. Resolution improvement by a factor of two was observed in the reconstructed image by comparing it with an experimentally captured reference image. In addition, a contrast improvement of more than 10% was observed.

References

- Fienup J. R., 1978. Reconstruction of an object from the modulus of its Fourier transform. *Opt. Lett.* 3, pp. 27-29.
- Fienup J. R., 1982. Phase retrieval algorithms – a comparison. *Applied Optics* 21, pp. 2758-2769.
- Gerchberg R. W. and Saxton W. O., 1972. A practical algorithm for determination of phase from image and diffraction plane picture. *Optik (Stuttgart)* 35, pp. 237-246.
- Gerchberg R. W., 1974. Super-resolution through error energy reduction. *Optica Acta* 21, pp. 709-720.
- Gevrekci M. and Gunturk B.K., 2007. Superresolution under photometric diversity of images. *EURASIP Journal on Applied Signal Processing* 2007, pp. 205-205.

Gur E. and Zalevsky Z., 2007a. Single image digital super resolution: A revised Gerchberg-Papoulis algorithm. *IAENG Int. Journal of Computer Science* 34, pp. 251-255.

Gur E. and Zalevsky Z., 2007b. Iterative single-image digital super-resolution using partial high-resolution data. *Lecture Notes in Engineering and Computer Science, WCE2007*, pp. 630-634.

Joshi M., Chaudhuri S. and Panuganti R., 2005. A learning-based method for image super-resolution from zoomed observations. *IEEE Transactions on Systems, Man, and Cybernetics, Part B* 35, pp. 527-537.

Misell D. L., 1973a. An examination of an iterative method for the solution of the phase problem in optics and electron optics: I. Test calculations. *J. Phys. D: Appl. Phys.* 6, pp. 2200-2216.

Misell D. L., 1973b. A method for the solution of the phase problem in electron microscopy. *J. Phys. D: Appl. Phys.* 6, L6-L9.

Misell D. L., 1973c. An examination of an iterative method for the solution of the phase problem in optics and electron optics: II. Sources of error. *J. Phys. D: Appl. Phys.* 6, pp. 2217-2225.

Nguyen N. and Milanfar P., 2000. A wavelet-based interpolation-restoration method for super resolution. *Journal of Circuit Systems Signal Process* 19, Springer, pp. 321-338.

Papoulis A., 1975. A new algorithm in spectral analysis and band-limited extrapolation. *IEEE Trans. Circuits Syst.* 22, pp. 735-742.

EXTRACTING OLIVINE-RICH PORTIONS OF ULTRAMAFIC ROCKS USING ASTER TIR DATA

O. B. Gurcay

MTA General Directorate, RS&GIS Department, 06520 Cankaya-Ankara, Turkey (gurbora@yahoo.com)

ISPRS Commission VII Symposium

KEY WORDS: Geology, Mapping, Extraction, Satellite, Multispectral, Optical, Thermal

ABSTRACT:

There are several studies for extracting ophiolitic rocks using thermal properties. The algorithms developed to discriminate olivine-rich rocks among ophiolite units, even altered to serpentinite.

Within this study, it was objected to recognize peridotite group rich in olivine minerals among ophiolitic rocks or mélangé, and to map them with distinct boundaries. Besides, these results may point to the chromite occurrences related to dunite rocks as well.

These algorithms were applied to ophiolitic units around Cankiri region. Various rock types exist within the area and were mapped during previous studies. Target ophiolitic rocks have extensive outcrops in Eldivan Mountain. The ophiolitic rocks cover most of ophiolitic sequence around the study area.

The purpose is to discriminate olivine-rich portions of ultramafic lithologies with their thermal infrared properties. Olivine-rich ultramafic rocks have intense reflection near 10.58 and 11.92 micrometers and absorption around 8.86. Those can be identical for extracting dunite or olivine-rich units using ASTER data. Band ratio algorithms were developed by comparing olivine reference spectra with ASTER TIR bands 12, 13, and 14. Consequently, olivine-rich lithologies were clearly identified, and were checked during ground truth in 15 different locations. Petrographical determinations indicate that 13 of 15 samples are mostly serpentinitized but still contain olivine, less orthopyroxene and clinopyroxene as relicts. Additionally, target unit's boundaries were distinctly mapped among ophiolitic mélangé within the area.

1. INTRODUCTION

Ophiolitic units include various types of lithologies such as peridotite, pyroxenite, gabbro, diabase, spilitic basalt, radiolarite, cherty limestone. In some cases, it can be easy to map with their composition and texture in the field. However, altered portions of ultramafic rocks are sometimes rather difficult to distinguish from each other. Various researches and algorithms concerning to the evaluation or identification of ultramafic rocks or related mineralizations have been conducted by using multispectral or hyperspectral satellite data analysis and reflectance or emittance portions of electromagnetic spectrum (Hunt and Wynn, 1979; Ninomiya, 2002, 2003; Chellaiah, 2003; Swayze et al, 2004; Rowan et al, 2004, 2005; Hook et al, 2005).

The aim of this study is to detect olivine-rich bodies of ultramafic rock units belong to ophiolite or mélangé with multispectral thermal infrared portion of ASTER image data.

1.1 Thermal Spectral Properties of Ultramafic Rocks and Minerals

The spectral reflectance, absorption or emittance interactions of surface materials responding to the electromagnetic solar energy have been commonly used in remote sensing studies (Chabrilat et al., 2000; Ninomiya, 2002, 2003; Saldanha, 2004; Swayze et al., 2004; Hook et al., 2005; Rowan et al., 2005)

The reflection and absorption behaviors with respect to VNIR-SWIR and TIR wavelength of electromagnetic energy regions of common minerals constituting ultramafic rocks are given in figure 1A and 1B. The pyroxene group has typical reflection in

0.54 and 2.37 micrometers and has an absorption in 2.32 micrometers according to figure 1A. Mg-rich olivine mineral, forsterite, in VNIR-SWIR region has absorptions in 0.62 and 1.06 micrometers, and reflection in 0.58, 0.67 micrometers and the reflection increases to the longer wavelengths in SWIR region. The alteration product of those minerals, serpentine, has absorptions in 0.72, 1.39 and 2.36 micrometers and the characteristic reflection features in 0.51, 2.20 and 2.37 micrometers.

The electromagnetic energy is absorbed in 8.40, 10.09 and 10.73 micrometers, and reflected in 8.85, 10.41 and 10.89 micrometers when the one of clinopyroxene minerals, like augite, is observed. If the spectral properties of other orthopyroxene group mineral has examined, the hyperstene mineral has absorptions in 8.49, 9.89, 10.37 and 11.03 micrometers, and reflections in 8.22, 9.34, 10.19, 10.45 and 11.34 micrometers. Similarly, besides having unique absorptions in 8.86, 10.05 and 10.39 micrometers, and the olivine mineral has also the reflections in 9.84, 10.19 and 10.49 micrometers, then the reflection is getting decreased to the longer TIR wavelengths.

Reflection and absorption properties of common ultramafic minerals in VNIR, SWIR and TIR regions are given in Figure 1.

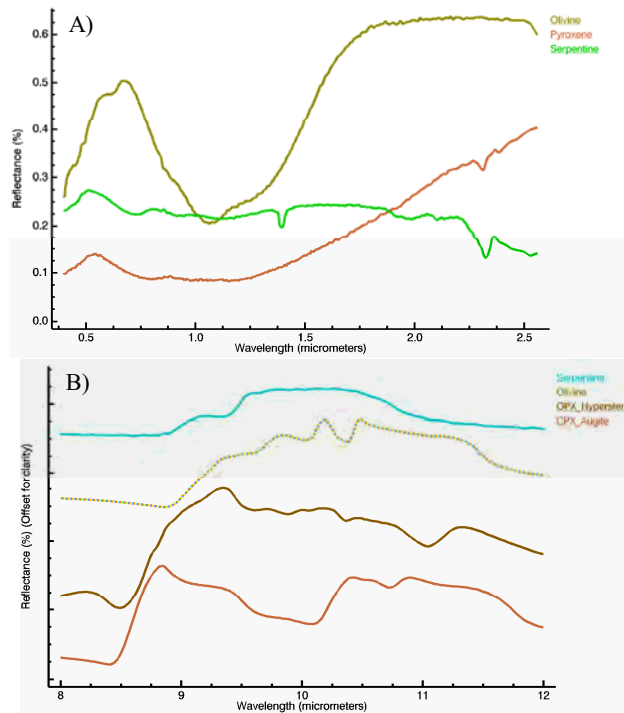


Figure 1. VNIR-SWIR (A) and TIR (B) spectral characteristics of common minerals exist in ultramafic rocks.

The common rock units in ophiolite sequence can be mafic or ultramafic. When the electromagnetic energy interactions with those rock types were compared (figure 2), the absorptions in 8.63, 10.16 and 11.05 for diabase, 9.21 and 10.25 for gabbro, and 8.86, 9.57, 10.33 and 11.81 micrometer wavelengths for olivine-peridotite (dunite) are noticeable. On the contrary, the distinct reflections in wavelengths are 8.56, 9.10, 9.80 and 11.15 for diabase, 8.77, 10.07 and 10.47 for gabbro, and 9.52, 10.17, 10.58 and 11.92 micrometers for olivine-peridotite rocks.

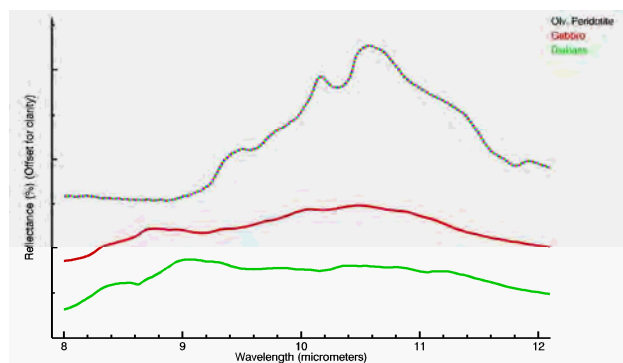


Figure 2. The spectral responses of abundant mafic and ultramafic rock types exist in ophiolite.

1.2 Study Area

Study area is located within the latitudes of 40°20' - 40°45'N and the longitudes of 33°10' - 33°35'E in the northern part of Central Anatolia (Figure 3). There have been conducted various studies covering the area concentrated mainly on regional and local geological features, tectonics and kinematics, paleogeographic evolution etc. (Hakyemez et al, 1986; Türkecan et al, 1991, Koçyiğit et al, 1995; Seyitoğlu et al, 1997; Sümer, 1997; Gökalp, 1999, Kaymakçı et al, 2003a, b).

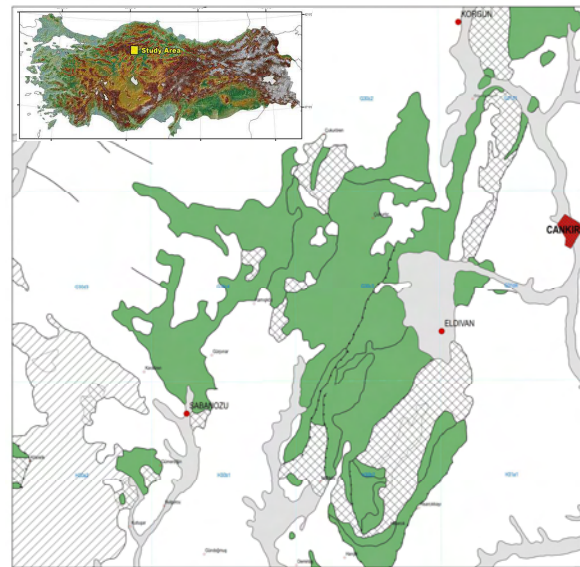


Figure 3. Location and simplified geological map of study area. The green (dark) colour in geological map represents ophiolitic lithologies.

Study area is located at İzmir-Ankara-Erzincan suture zone occurred as a northern branch of Neo-Tethys Ocean and started to activate in Liassic-Late Cretaceous and continued up to Early Lutetian presented by many authors (Akyürek et al, 1979, 1980, 1981; Şengör and Yılmaz, 1981; Görür et al, 1984; Hakyemez et al, 1986). Settlement time of ophiolite, which is a cause of closure of micro-continents (Şengör and Yılmaz, 1981; Görür et al, 1984; Hakyemez et al, 1986; Kaymakçı et al, 2003a, b), is recorded as Cenomanian-Turonian age (Akyürek et al, 1979, 1980, 1981). Tertiary shallow platform sedimentary sequence existed (Sengor and Yılmaz, 1981; Görür et al, 1984; Hakyemez et al, 1986; Seyitoğlu et al, 1997) after Middle Lutetian subsequent to closure of Neo-Tetis Ocean in Early Lutetian (Hakyemez et al, 1986). The geological units and stratigraphy are simplified concerning to the objective lithologies of this study (Figure 3 and Figure 4).

2. IMAGE ANALYSES, RESULTS AND DISCUSSION

Well known ASTER (Advanced Spaceborne Thermal Emission and Reflection Radiometer) level 3A01 ortho image data which was corrected to remove the geographic distortion caused by altitudes is used in order to identify olivine-rich ultramafic rocks. ASTER has spatial resolution of 15 meter for 3 VNIR (Visible-near infrared, 0.556 to 0.807 micrometers) bands, 30 meter for 6 SWIR (Short-wave infrared, 1.656 to 2.400 micrometers) bands and 90 meter for 5 TIR (Thermal infrared, 8.291 to 11.318 micrometers) bands, and radiometric resolution of 8 bit, and 12 bit for VNIR-SWIR and TIR respectively.

AST3A10207260852290603310610, AST3A10507270844 010603311228 and AST3A10404100850300702020025 images were used in the image analyses. The study area was cut after mosaicking those three images. During VNIR-SWIR band ratio image preparation, the masked image was used for better results.

Results obtained from VNIR, SWIR and TIR are frequently efficient to extract information regarding to alteration mineral or lithological mapping from target area (Ninomiya, 2002; Yamaguchi and Naito, 2003; San et al., 2004; Rowan et al.,

2004). Herein this study, thermal reflectance properties of ultramafic rocks rich in olivine minerals will be estimated.

Erathem System	Series	Group	Formation	Member	Lithology	Explanation	
CENOZOIC	Quaternary					Basalt	
						Basalt	
	Tertiary	Pliocene					Basalt
Basalt							
MESOZOIC	Tertiary	Pliocene				Basalt	
						Basalt	
	Cretaceous	UPPER					Sandstone, siltstone, mudstone
							Sandstone, siltstone, mudstone
							Sandstone, siltstone, mudstone
Cretaceous	LOWER					Sandstone, pebbles, mudstone	
						Sandstone, pebbles, mudstone	
Triassic	Upper	Elviran Ophiolite Complex				Sandstone, pebbles, mudstone	
						Sandstone, pebbles, mudstone	
						Sandstone, pebbles, mudstone	
Triassic	Middle	Kecikaya				Sandstone, pebbles, mudstone	
						Sandstone, pebbles, mudstone	
						Sandstone, pebbles, mudstone	
Triassic	Lower	Avkara Group				Sandstone, pebbles, mudstone	
						Sandstone, pebbles, mudstone	
						Sandstone, pebbles, mudstone	

Figure 4. Simplified stratigraphic section of the study area. Lower Cretaceous Eldivan ophiolite, which is given in green (dark) color, overlays Triassic basement units, and overlaid by Tertiary sedimentary sequences.

2.1 VNIR-SWIR Band Ratio

According to the spectral properties of mafic minerals given in figure 1A, characteristic wavelengths can be correlated with ASTER VNIR and SWIR bands.

There are higher reflection responses in ASTER bands 2, 5 and 8, absorption in bands 1, 3 and 6 for olivine mineral while only a broad absorption in band 3 and a reflection in band 1 can be noticeable for pyroxene minerals in the SWIR region of electromagnetic spectrum. Serpentine, the alteration product of those minerals, has also distinguishing absorptions in bands 2, 7 and 8 and reflection in bands 3 and 6. The band ratios, 2/3, 2/3*1/3 for olivine mineral and 6/8 and 6/7 for serpentine mineral were developed.

2.2 TIR Band Algorithms

The pyroxenes exhibit visible reflections in ASTER bands 11 and 12 according to the given figure 1B. Despite, olivine mineral has higher reflection in band 13 and lower in bands 10, 11 and 12. While showing similarities, the olivine mineral is higher in bands 12 and 14 compared to the alteration product of olivine and pyroxenes, serpentine.

As the olivine-peridotite or dunite, composed of mainly olivine and additionally pyroxenes and less silica, is compared with ASTER bands in figure 5, band 13 is highly reflected while the bands 11, 12 has absorption and 14 is relatively low reflected. The absorption properties of ASTER bands 11 and 14 for

olivine display similarities to quartz mineral. However, the difference between those two spectra is noticeable in bands 12 and 13. This difference was also recorded as a result of a change in silicate content within the igneous rocks varies from felsic through mafic to ultramafic by some researchers (Ninomiya and Matsunaga, 1997, 2002, 2003; Hook et al, 2005).

While the higher reflection in band 13 for dunite and neighbouring bands 12 and 14 are taking under consideration in figure 5, the band ratios of 12/13 and 14/13 is achieved. To use opposite band ratios instead of usual ones is the cause of the energy emitted from the surface materials in thermal region. The higher reflection in the spectrum corresponds to the low emissivity. Since above ratios, $(12 \cdot 14) / (13^2)$ is obtained.

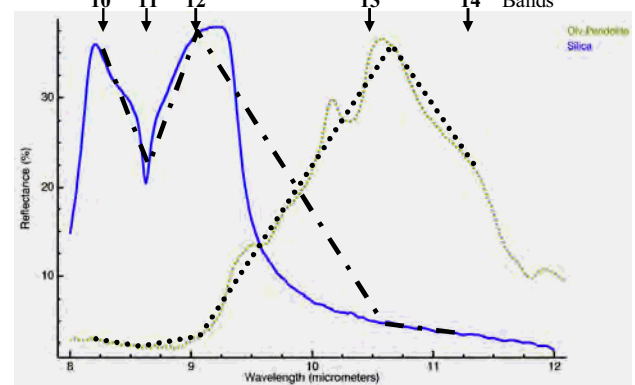


Figure 5. The spectral pattern comparison of olivine-peridotite (dunite) and quartz with corresponding ASTER bands

The formula, $(14/13) / (13/12)^3$, is developed by considering the ratio 14/13 for olivine and pyroxene mineral with comparing to the ratio 13/12 for silicate content. The exponential parameter (herein 3) is a number that is used for decreasing the effect of silica content within the rocks. The number used here, 3, is chosen for giving the best result.

2.3 Results and Discussions

The VNIR-SWIR band ratios developed to extract the ultramafic units have mostly not efficient, except serpentine band ratio 6/8. On the contrary, the better results were attained with thermal infrared (TIR) region for detection of lithology like olivine-peridotite occurrences.

The results of VNIR-SWIR band ratios, 2/3 for olivine and 6/8 for serpentine minerals are given in Figure 6. Besides the matching localities for olivine resultant image, it is also possible to observe the areas unmatched. The serpentine band ratio 6/8 (or even 6/7) can mostly be correlated with the serpentinized ultramafic rock units. Besides the results of the olivine band ratio 2/3 correlating well with the ophiolite formations inside, it has widely wrong results outside the ophiolitic formation boundaries.

The olivine rich ultramafic rock, olivine-peridotite or dunite was noticeably extracted within the ophiolitic melange formation given in simplified geological map (figure 3, 7A, 7B) with distinct boundaries by using the spectral properties of target ultramafic rocks. Additionally, the ground truth studies were conducted to 15 localities of matched or unmatched with either analyses results or geological map units. 13 of 15 collected

samples concerning to TIR image results are mostly serpentinized but still contain olivine, less orthopyroxene and/or clinopyroxene as relicts determined by the petrographical studies. Additionally, target unit's boundaries were distinctly mapped among ophiolitic mélangé within the area.

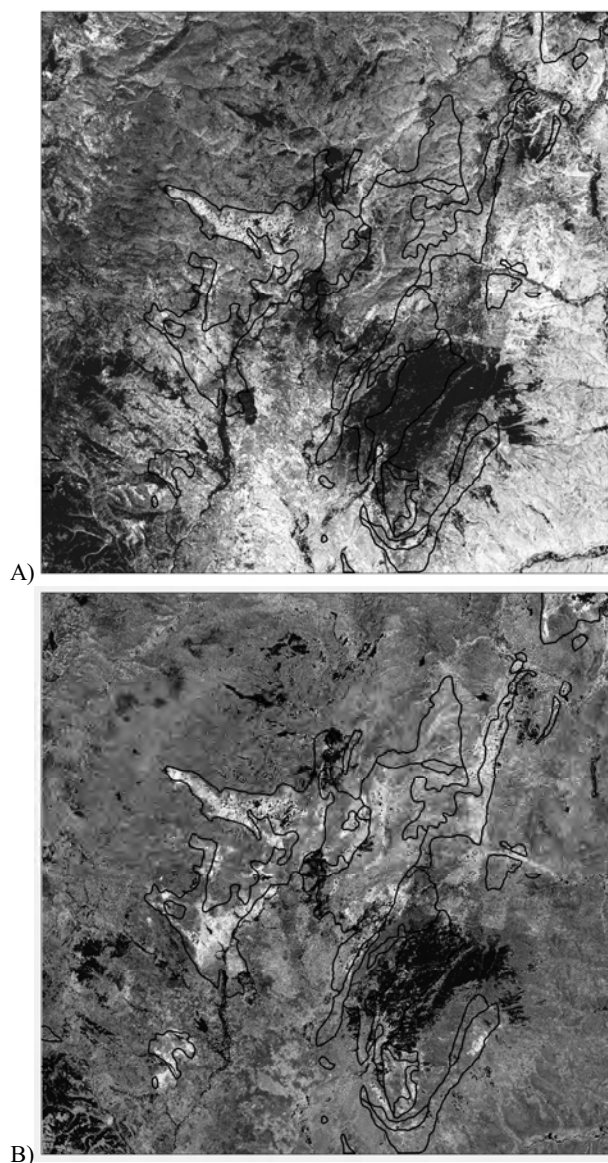


Figure 6. The results of (A) 2/3 and (B) 6/8 band ratio algorithms generated from ASTER SWIR bands.

The both results of TIR band algorithms are similar to each other in terms of lithological boundaries. On the other hand, the topographical effects are mostly observed as removed in the results obtained with the formula $(12 \cdot 14) / (13^2)$, given in figure 7A. Besides, the effect of vegetation on both results is interestingly noticeable. It can be possible to detect olivine rich ultramafic units as well in the central parts of the Eldivan ophiolitic mélangé, at SE of Eldivan Mountain, in the locations of sparse vegetation areas of the pinery. (Figure 3, 7A).

While correlating the simplified geological map of the region with the analyses results, it can be easily recognized that the olivine-peridotite portions of ultramafic units are displayed as bright pixels either inside or outside the boundaries of ophiolitic

melange. Ground truth surveys show that those out-boundary results are also matched with the peridotite units. It is concluded that to improve the geological map details while working with ultramafic lithologies, the band algorithms concerning to the olivine-peridotite (figure 7A, 7B) can be helpful.

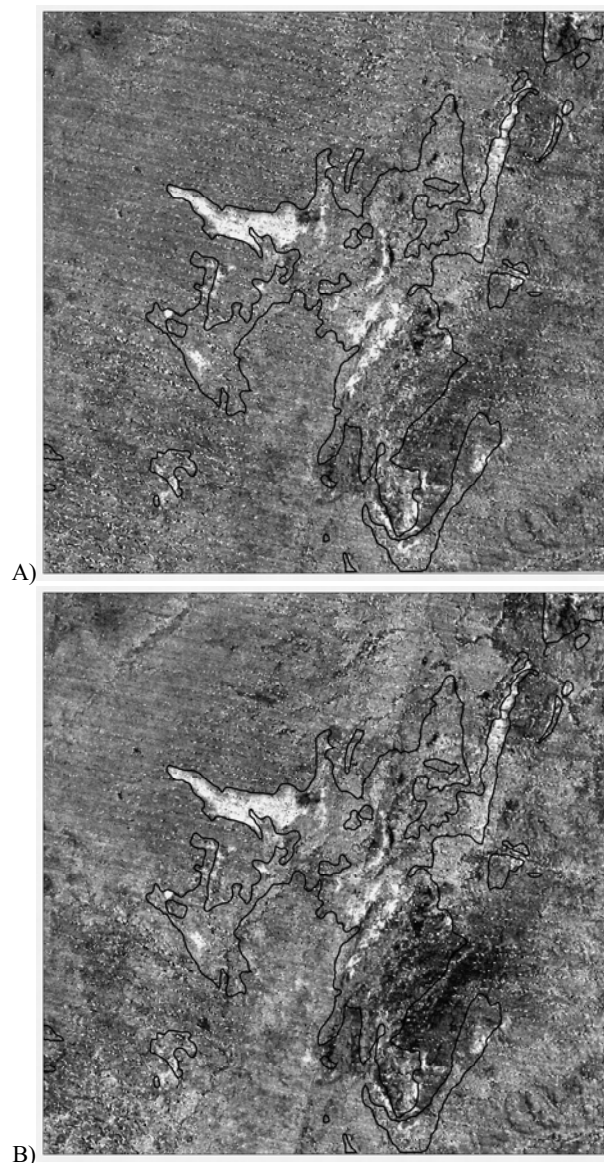


Figure 7. The olivine-peridotite (dunite) band algorithms developed using spectral characteristics of ultramafic rocks. Band algorithm results: (A) $(12 \cdot 14) / (13^2)$ and (B) $(14/13) / (13/12)^3$.

In case of mapping the lithologies related to ultramafic units, the spatial resolution sometimes limits the detail of studies. The band ratio 6/8 could be used in matched areas to correlate boundaries of ultramafic units.

3. SUMMARY AND CONCLUSION

The olivine-rich ultramafic unit, especially olivine-peridotite or dunite and those boundaries was clearly discriminated and mapped within the ophiolitic lithologies.

Among the band ratios introduced by using spectral characteristics of the mafic minerals, olivine, pyroxene, serpentine group, the ratio 6/8 can be used in such cases.

The thermal band algorithms, $(12*14) / (13^2)$ and $(14/13) / (13/12)^3$ were developed by considering the spectral responses of mafic minerals exist in constituting rock units compared with ASTER TIR bands. These algorithms are highly effective to distinguish the olivine-rich ultramafic portions in the region of ophiolitic rocks. It is also capable of mapping those lithologies in a certain boundaries.

4. REFERENCES

- Akyürek, B., 1981. Ankara Melanji'nin kuzey bölümünün temel jeoloji özellikleri. *İç Anadolu'nun Jeolojisi Sempozyumu*, TJK(35), pp. 41-45.
- Akyürek, B., Bilginer, E., Çatal, E., Dağar, Z., Soysal, Y., ve Sunu, O., 1979. Eldivan-Şabanözü (Çankırı) dolayında ofiyolit yerleşmesine ilişkin bulgular. *Jeoloji Mühendisliği*, Eylül, 9, pp. 5-12.
- Akyürek, B., Bilginer, E., Çatal, E., Dağar, Z., Soysal, Y., ve Sunu, O., 1980. Eldivan-Şabanözü (Çankırı) Hasayaz-Çandır (Kalecik-Ankara) dolayının jeolojisi. Report 6741, MTA General Directorate, Ankara, Turkey.
- Chabrilat, S., Pinet, P.C., Ceuleneer, G., Johnson, P.E., Mustard, J.F., 2000. Ronda Peridotite Massif: Methodology for its geological mapping and lithological discrimination from airborne hyperspectral data. *International Journal of Remote Sensing*, 21(12), pp.2363-2383.
- Gökalp, F. G., 1999. Yapraklı (Çankırı)-İskilip (Çorum) Ofiyoliti Eldivan Dağı bölümünün petrolojisi. MSci Thesis, Hacettepe Üniversitesi, Fen Bilimleri Enstitüsü, Jeoloji Müh. Böl., Ankara.
- Görür, N., Oktay, F. Y., Seymen, İ., Şengör, A. M. C., 1984. Paleotectonic evolution of the Tuzgölü Basin Complex, Central Turkey: Sedimentary record of a Neo-Tethyan closure. The Geological Evolution of the Eastern Mediterranean (Ed. by Dixon, J. E. & Robertson, A. H. F.), *Geol. Soc. London Spec. Paper*, 17, 467-482.
- Hakyemez, Y. Barkurt, M.Y., Bilginer, E., Pehlivan, Ş., Can, B., Dağcı, Z., Sözeri, B., 1986. Yapraklı-Ilgaz-Çankırı-Çandır dolayının jeolojisi. Report 7966, MTA General Directorate, Ankara, Turkey.
- Hook, S. J., Dmochowski, J. E., Howard, K.A., Rowan, L. C., Karlstrom, K. E., Stock, J. M., 2005. Mapping variations in weight percent silica measured from multispectral thermal infrared imagery-Examples from the Hiller Mountains, Nevada and Tres Virgenes-La Reforma. Baja California Sur, Mexico. *Remote Sensing of Environment*, Nevada, pp.273-289.
- Hunt, G.R., Wynn, J.C., 1979. Visible and near-infrared spectra of rocks from chromium-rich areas. *Geophysics*, 44(4), pp.820-825.
- Kaymakçı, N., Duermeijer, C. E., Langereis, C, White, S. H., Van Dijk, P. M., 2003a. Palaeomagnetic evolution of the Cankırı Basin (central Anatolia, Turkey): Implications for oroclinal bending due to indentation. *Geological Magazine*, 140 (3), pp. 343–355.
- Kaymakçı, N., De Bruun, H., White, S. H., Van Dijk, P. M., Saraç, G., Ünay, E., 2003b. Tectonic implications of the Neogene stratigraphy of the Cankiri basin with special reference to the Candir locality (North-Central Anatolia, Turkey). *Cour. Forsch.-Inst. Senckenberg*, 240, pp. 9-28.
- Koçyiğit, A., Türkmenoğlu, A., Beyhan, A., Kaymakçı, N., Akyol, E. 1995. Post-collisional tectonics of Eskişehir-Ankara-Çankırı segment of İzmir-Ankara-Erzincan Suture Zone (IAESZ): Ankara orogenic phase. *Turkish Association of Petroleum Geologist Bulletin*, 6(1), pp.69-86.
- Ninomiya, Y. and Matsunaga, T., 1997. Estimation of SiO₂ content using simulated TIR remote sensing data generated from spectra measured on the sawed surfaces of rocks at Cuprite, Nevada. *30th International Geology Congress*, Proceedings, 10, pp.49-62.
- Ninomiya, Y., 2002. Mapping quartz, carbonate minerals and mafic-ultramafic rocks using remotely sensed multispectral thermal infrared ASTER data. *Proceedings of SPIE*, 4710, pp.191-202.
- Ninomiya, Y., 2003. Advanced remote lithologic mapping in ophiolite zone with ASTER multispectral thermal infrared data. *Geoscience and Remote Sensing Symposium*, IEEE International, IGARSS '03. Proceedings, 3, pp.1561- 1563.
- Rowan, L. C., Simpson, C. J., Mars, J. C., 2004. Hyperspectral analysis of the ultramafic complex and adjacent lithologies an Mordor, NT, Australia”, *Remote Sensing of Environment*, 91, pp.419-431.
- Rowan, L. C., Mars, J. C., Simpson, C. J., 2005. Lithologic mapping of the Mordor, NT, Australia Ultramafic Complex by using the Advanced Spaceborne Thermal Emission and Reflection Radiometer (ASTER). *Remote Sensing of Environment*, 99(1-2), pp.105-126.
- Saldanha, D. L., Lime E Cunha, M. C., Haertel, V., 2004. Spectral analysis of soils from mafic/ultramafic rocks of Cerro Mantiqueira, SW of Rio Grande do Sul. *International Journal of Remote Sensing*, 25(20), pp.4381-4393.
- San, B. T., Sümer, E. O., and Gürçay, B., 2004. Comparison of band ratioing and spectral indices methods for detecting alunite and kaolinite minerals using Aster data in Biga Region, Turkey. *International Society for Photogrammetry and Remote Sensing, XXth Congress*, Commission 7, July, Istanbul.
- Şengör, A.M.C. and Yılmaz, Y., 1981. Tethyan evolution of Turkey: A Plate tectonic approach. *Tectonophysics*, 75, pp.181-241.
- Seyitoğlu, G., Kazancı, N., Karakuş, K., Fodor, L., Araz, H., Karadenizli, L., 1997. Does continuous compressive tectonic regime exist during Late Paleogene to Late Neogene in NW Central Anatolia, Turkey preliminary observations. *Turkish Journal of Earth Sciences*, 6, pp.77-83.
- Sümer, M., 1997. Çankırı-Şabanözü çevresinde jeolojik kirlenmeye neden olan minerallerin kökenleri, çevreye etkileri ve riskleri. MSci Thesis, Hacettepe Üniversitesi, Fen Bilimleri Enstitüsü, Jeoloji Müh. Böl., Ankara.

Swayze, G. A., Higgin, C. T., Clinkenbeard, J.p., Kokaly, R. F., Clark, R. N., Meeker, G. P., and Sutley, S. J., 2004. Preliminary report on using imaging spectroscopy to map ultramafic rocks, serpentinites, and tremolite-actinolite-bearing rocks in California. *USGS Open File Report 2004-1304*.

Türkecan, A., Hepşen, N., Papak, İ., Akbaş, B., Dinçel, A., Karataş, S., Özgür, İ. B., Akay, E., Bedi, Y., Sevin, M., Mutlu, G., Sevin, D., Ünay, E. Ve Saraç, G., 1991. Seben-Grede (Bolu)–Güdül-Beypazarı (Ankara) ve Çerkeş-Orta-Kurşunlu (Çankırı) yörelerinin (Köroğlu Dağları) jeolojisi ve volkanik kayaların petrolojisi. Geological Research Library Report 361, MTA General Directorate, Ankara, Turkey.

Yamaguchi, Y. and Naito, C., 2003, Spectral indices for lithologic discrimination and mapping by using ASTER SWIR bands, *International Journal of Remote Sensing*,24(22), pp.4311-4323.

ACTIVE AND PASSIVE MICROWAVE REMOTE SENSING OF SPRINGTIME NEAR-SURFACE SOIL THAW EVENTS AT MIDDLE LATITUDES

L. Han^{*a}, A. Tsunekawa^a, and M. Tsubo^a

^a Arid Land Research Center, Tottori University, 1390 Hamasaka, Tottori 680-0001, Japan
(han, tsunekawa, Tsubo)@alrc.tottori-u.ac.jp

Technical Commission VII Symposium 2010

KEY WORDS: Snow Ice; Soil; Application; Estimation; Algorithms; Radar; Passive

ABSTRACT:

Springtime near-surface soil thaw event is important for understanding the near-surface earth system. Previous researches based on both active and passive microwave remote sensing technologies have paid scant attention, especially at middle latitudes where the near-surface earth system has been changed substantially by climate change and human activities, and are characterized by more complex climate and land surface conditions than the permafrost areas. SSM/I brightness temperature and QuikSCAT Ku-band backscatter were applied in this study at a case study area of northern China and Mongolia in springtime of 2004. The soil freeze–thaw algorithm was employed for SSM/I data, and a random sampling technique was applied to determine the brightness temperature threshold for 37 GHz vertically polarized radiation: 258.2 and 260.1 K for the morning and evening satellite passes, respectively. A multi-step method was proposed for QuikSCAT Ku-band backscatter based on both field observed soil thaw events and the typical signature of radar backscatter time series when soil thaw event occurred. The method is mainly focuses on the estimated boundary of thaw events and detection of primary thaw date. The passive microwave remote sensing (SSM/I) based result had a good relationship with the near-surface soil temperature, while the active microwave remote sensing (QuikSCAT) based result had both relationships with temperature and soil moisture conditions. And also, QuikSCAT result identifies the geographical boundary of water-drove thaw event, which is crucial for understanding the different types of springtime near-surface soil thaw at middle latitudes.

1. INTRODUCTION

Near-surface soil freeze–thaw cycles have an important role in earth systems and directly affect the terrestrial hydrological cycle. Remote sensing provides an effective way for such event detection, especially, the microwave remote sensing (Zhang, et al., 2004). Microwave remote sensing based near-surface soil thaw event detection at mid-latitudes where near-surface changing seriously still rare (Han, et al., 2010). Generally, in active microwave remote sensing, the thaw event was detected based on the radar backscatter change which is responded to the dielectric constant of the surface; and in passive microwave remote sensing, the thaw event was detected based on the brightness temperature's increasing.

Scant attentions have paid in mid-latitude areas, which suggested our objectives as follows: 1) to detect and validate springtime soil thaw event by passive and active microwave remote sensing data; 2) to understand the difference in the results from active and passive microwave remote sensing data.

2. STUDY AREA

Our study area (Figure 1) lies between latitudes 31°N and 55°N and longitudes 71°E and 136°E including different humidity zones from arid to humid.

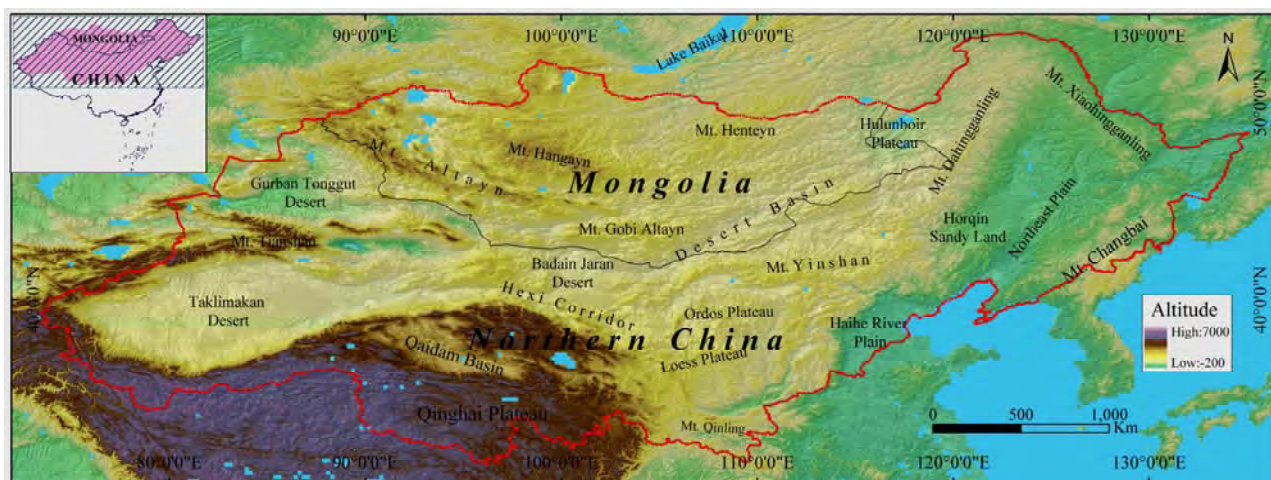


Figure 1. Study area

* Corresponding author

There are strong regional climatic differences within the area and a diverse range of vegetation and land surface including large areas of desert, desert steppe, steppe, forested steppe, and forest. The elevation also has large range from more than 4000m at high mountain areas and Tibetan Plateau to near 0 at the east beach. Vegetation degeneration and extreme environmental events (e.g. sandstorm) are also undergoing or frequently happened (Tsunekawa, et al., 2005; Zhang, et al., 2008). Its various conditions in middle latitude areas make the essential of understanding springtime soil thaw event in this area.

3. MATERIALS AND PREPROCESSING

3.1. Microwave remote sensing records

A practical active microwave remote sensing data, QuikSCAT Ku-band measurement, was acquired from NASA's Jet Propulsion Laboratory as their level 2A product. First, all backscatter measurements at the first 180 days of 2004 were extracted and averaged on a daily basis; second, a grid format time series with 25×25 km spatial resolution was produced by spatially interpolating from the averaged backscatter daily times series. And the out-beam record was adopted in this work because of its wider swath.

Brightness temperature data from Special Sensor Microwave/Imager (SSM/I), provided by National Snow and Ice Data Center, was adopted in this work, as the passive microwave remote sensing data. We used the 19 and 37 GHz vertically polarized brightness temperature ($T_{B,19V}$ and $T_{B,37V}$) data from both ascending and descending tracks at the first 180 days of 2004. This data also have a spatial resolution of 25×25 km. Because daily SSM/I data did not cover the whole study area, we used time series of brightness temperature by 7-day maximum/minimum combined with considering about the revisit period of SSM/I in our study area.

3.2. Soil temperature and moisture data

We obtained soil temperatures and moisture recorded at five reference sites used in the Coordinated Energy and Water Cycle Observation Project from the Centralized Integrated Data Archive (<http://www.ceop.net/>) and selected three of the five stations on the basis of their location and the period covered by their data. Soil temperatures and moistures recorded at Shenmu in northern China and Bayan-Unjuul in Mongolia were also included in our study. We used soil temperatures measured at 5 cm depth because most microwave radiation emitted at the surface emerges from the top layer of soil (Zwally and Gloersen, 1977).

3.3. Meteorological records

The Global Summary of the Day product from the National Climate Data Center of United States was applied in our study. Daily air temperature, precipitation, and snow depth observations were used to support interpretation of springtime thaw events from the QuikSCAT backscatter time series and to estimate the soil moisture by using a water balance based model.

4. METHODOLOGY

4.1. Active microwave remote sensing method

The method in this work is based on our previous approach (Han, et al., 2010b), which studied the typical backscatter signatures when springtime soil thaw occurred and suggested the method for the thaw event deriving from QuikSCAT time series.

Geographical boundary is firstly detected by Equation 1.

$$Slope = \frac{n \times \sum_{i=1}^n i \times \delta_i - \left(\sum_{i=1}^n i \right) \left(\sum_{i=1}^n \delta_i \right)}{n \times \sum_{i=1}^n i^2 - \left(\sum_{i=1}^n i \right)^2} \quad (1)$$

Where *Slope* is the trend of QuikSCAT backscatter with the unit dB serving as the indicator for boundary clarification; *n* represents analyzed range in every 5-day step; *i* is the each 5-day period, *i*=1 for the 5-day period from the 1st day of year (DOY) to the 5th DOY, *i*=2 for the 5-day period from the 6th DOY to the 10th DOY, ...; and δ_i is the average QuikSCAT backscatter of the each 5-day *i*. *Slope* larger than 0 identifies an area of no thaw event, and *Slope* less than 0 identifies an area in which a thaw event occurred.

a primary thaw date, which defines as the middle day of a short period in which backscatter data are most diverse which is deduced as the most significant soil dielectric constant change driving by dominated amount soil water's state changing from ice to liquid water, is estimated by equations as shown below.

$$PI(i) = Stdev(\sigma_{0,i-n} : \sigma_{0,i+n}) \quad (2)$$

$$Ptd = i, \text{ when } PI(i) = \max(PI(i)) \quad (3)$$

Where *PI*(*i*) represents the primary thaw indicator on day *i*, which is a short period's standard deviation of QuikSCAT backscatter ($\sigma_{0,n}$) *n* days (*n* = 4 was set in this research, plus the current day it also means 5-day's step) before and after day *i*; *Ptd* represents the primary thaw date when *PI*(*i*) reaches its maximum. The primary thaw date is only calculated in the areas where soil thaw events happened as estimated in Equation 1.

4.2. Passive microwave remote sensing method

The soil freeze-thaw algorithm was adopted in this research, which requires two parameters: a negative spectral gradient between $T_{B,19V}$ and $T_{B,37V}$, as described by equation (4), and a threshold $T_{B,37V}$ as described by equation (5):

$$\frac{\partial T_B}{\partial f} \leq 0 \quad (4)$$

$$T_{B,37V} \leq T_{37}, \quad (5)$$

Where T_{37} is the threshold derived from the linear relationship between $T_{B,37V}$ and near-surface soil temperature. It is set as 258.2 K and 260.1 K for morning and evening satellite passes based on our previous results (Han, et al., 2010a).

And the pixels from water-covered areas and regions of high elevation (>3000m) were filtered by considering their influences on brightness temperature.

4.3. Soil moisture model

A simplified water balance based model, as shown in Equation 6, is used in this investigation (Yamaguchi and Shinoda, 2002). The top 30 mm soil moisture content at the end of 2003 and the snow water equivalent after consecutive maximum temperature higher than 0°C at the beginning of 2004 were considered in estimating the soil moisture conditions.

$$dW(t)/dt = P(t) - E(t) - R(t) \quad (6)$$

and

$$R(t) = \begin{cases} W(t) - W_{fc}, & W(t) > W_{fc} \\ 0, & W(t) \leq W_{fc} \end{cases}$$

Where W , the soil moisture, is expressed as the equivalent depth of liquid water that exists from the surface to a 30-cm depth, and t is the time in days; P, E, R represent the precipitation, evapotranspiration and runoff, respectively; and W_{fc} represents the field capacity.

5. RESULTS AND DISCUSSION

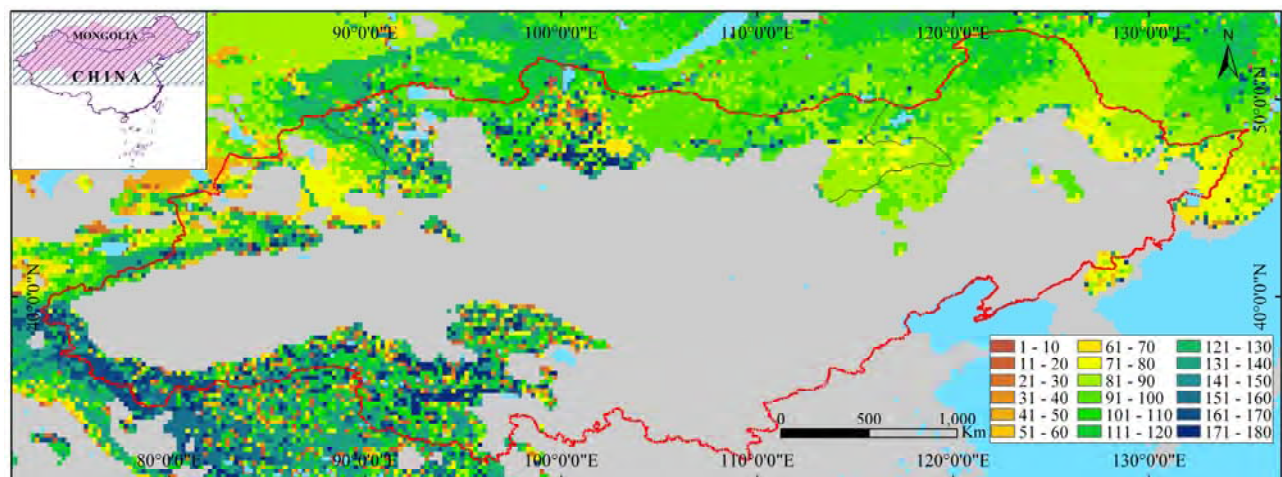


Figure 2. Primary thaw date and geographical boundary of the thaw derived from QuikSCAT data (Julian day). (Gray-colored areas represent regions without water driven soil thaw occurrence.)

5.3. Result from passive microwave remote sensing

Onset and offset of springtime soil thaw event was obtained as shown in figure 3. The onset and offset of near-surface soil thawed in spring begins in the south and southeast of the study area and then progresses northwest and north, but these trends are somewhat disrupted in areas of complex topography.

The main progression of the onset is from Mt. Qinling through the Guanzhong Basin, Loess Plateau, Ordos Plateau, and on

5.1. Validations of the results

Validations have done for both of the results from active and passive microwave remote sensing. For result from active microwave remote sensing, a reliability of $R = 0.8$, $P < 0.05$ was obtained between estimated primary thaw date and the date when consecutive days' average air temperature keeping positive values; and $R = 0.85$, $P < 0.05$ was obtained in result from passive microwave remote sensing with comparison between estimated onset/offset of the thaw and field measured soil thaw event. And the soil moisture model was validated by comparison with the ground truth with root mean square error (RMSE) of 4.10 ± 1.69 mm. Such reliabilities were strongly enhanced our confidence in making the further analysis.

5.2. Result from active microwave remote sensing

Primary thaw date and geographical boundary of the thaw was detected as shown in Figure 2. In the north: the thaw event boundary runs south of the Three River Plain, Mt. Xiaohingganling, and Mt. Dahingganling to the north of the Desert Basin, then to the south of Mt. Henteyn, Mt. Hangayn, and Mt. Altayn. The other area consists of regions of high elevation, such as Mt. Tianshan, Mt. Changbai, and the Tibetan Plateau. No thaw events occurred in the remaining (gray) areas, like the deserts regions and south warmer areas, due to the drier surface conditions or temperatures too high to freeze the surface layer in winter. The primary thaw date follows clear spatial and temporal patterns. In high elevation and high northern areas, thaw events happen later than in lower elevation and southern areas. On the Tibetan Plateau, at Mt. Hangayn, and at Mt. Altayn, the thaw event occurred at the end of the first 180 days. Those three areas are almost entirely covered by permafrost, so only the active layer thaws in the short summer.

toward Mt. Yinshan, the Mongolian Plateau, and finally to the Desert Basin and Hulunboir Plateau. This progression is disrupted by high elevations at Mt. Yinshan and Mt. Henteyn. Another extension of the onset branches northwest from the main northern trend at the Loess Plateau, and extends approximately northwest through the Hexi Corridor and Badain Jaran Desert to Mt. Altayn, where the latest onset of near-surface soil thawed is evident. The third branch of the onset progresses approximately northeast through Haihe River Plain to the Horqin Sandy Land, Northeast Plain, and Songnen Plain,

and then to Mt. Dahingganling, Mt. Xiaohingganling and Three River Plain (also known as the Sanjiang Plain). This progression is disrupted by the high elevation of Mt. Changbai. The onset of near-surface soil frozen begins early in the Gurban Tonggut and Taklimakan deserts, which can perhaps be attributed to these areas being at lower elevations than surrounding areas and having less soil water.

The earliest onset of near-surface soil frozen occurs at Mt. Qinling. It then progresses to the northwest through the Guanzhong Basin, along the west of the Loess Plateau, through the Hexi Corridor and Badain Jaran Desert, and finally to Mt. Altayn and Mt. Hangayn. To the east of the Badain Jaran Desert and Hexi Corridor, the offset of near-surface soil frozen arrives

earlier than in surrounding regions. From Mt. Qinling, the offset progresses north to the Guanzhong Basin, and continues along the area south of Mt. Luliang and Mt. Taihang, then to the Loess and Ordos plateaus and through to Mt. Yinshan, the Mongolian Plateau, and the Desert Basin, until the latest offset of near-surface soil frozen occurs on the Hulunboir Plateau and at Mt. Henteyn. The offset of near-surface soil frozen also progresses northeast from the Haihe River Plain along the coast to the Horqin Sandy Land, and then to the surrounding areas of Mt. Dahingganling, Mt. Xiaohingganling, the Northeast Plain, Mt. Changbai, with the latest offset of near-surface soil frozen occurring to the north of Mt. Dahingganling and the Three River Plain.

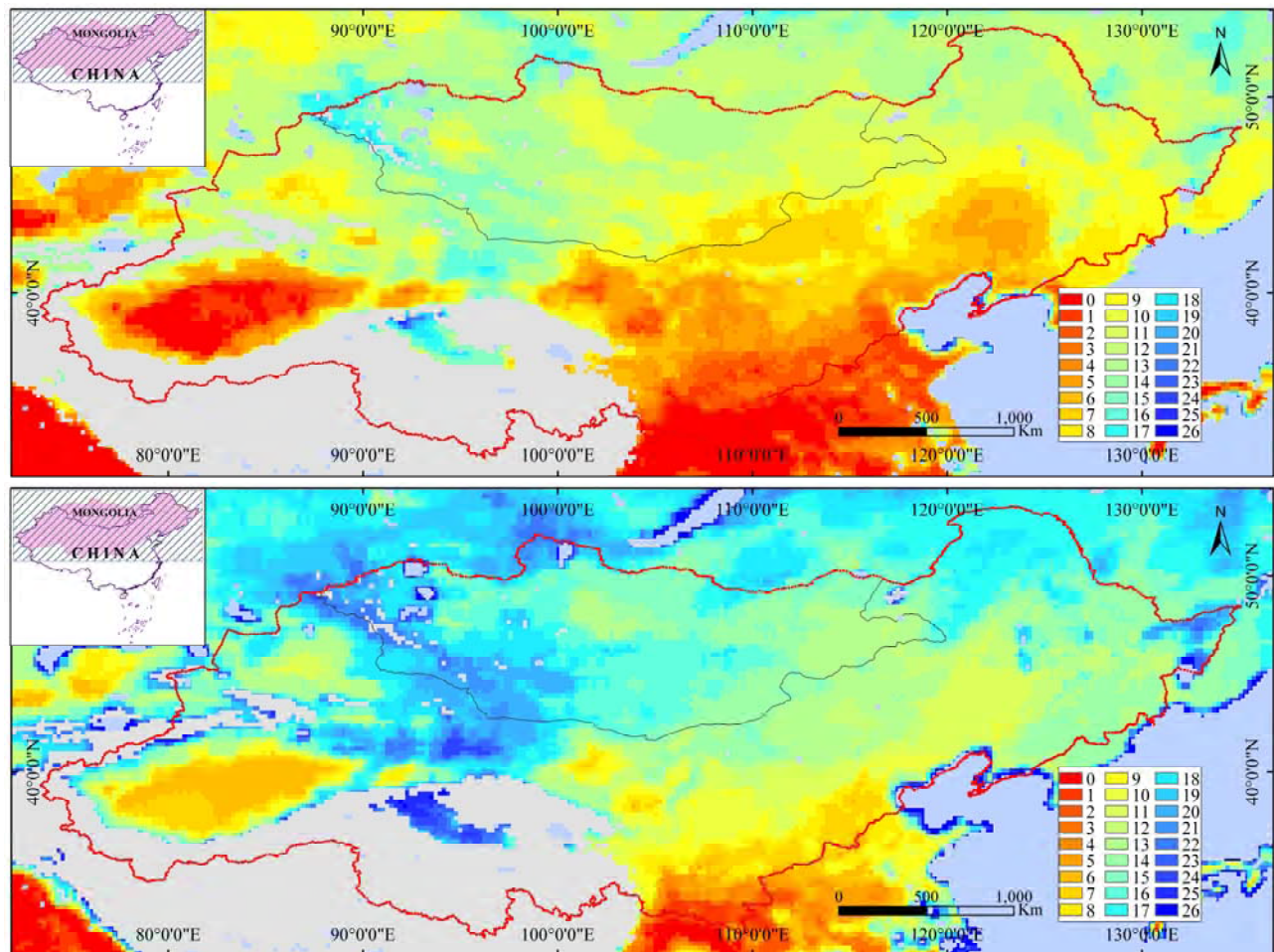


Figure 3. Onset (upper) and offset (nether) of springtime soil thaw derived from SSM/I brightness temperature (Julian week). (Gray-colored areas are the high elevation regions)

5.4. Difference in the results

Result that derived from SSM/I brightness temperature was almost relied on the T_{37} which have significant linear relationship with near-surface soil temperature. From which, we can deduce that the results derived from SSM/I brightness temperature is sensitive to near-surface soil temperature, which is why soil thaw event could be detected in desert regions.

Result that derived from QuikSCAT backscatter time series has regions both soil thaw event occurrence and no soil thaw event occurrence. From the analysis of average air temperature and modeled soil moisture as shown in figure 4, the difference

between samples with/without soil thaw event happened could be clarified: 1) samples with thaw event detected by QuikSCAT backscatter had an average air temperature of -15.29 ± 4.29 °C with soil moisture of 38.27 ± 21.96 mm in the month of thaw event happened; and 2) samples without thaw event detected by QuikSCAT backscatter had an average air temperature of -1.80 ± 6.37 °C with soil moisture of 35.77 ± 24.63 mm in the month when air temperature switch from negative values to positive values. And at the areas where air temperature keeping negative for a long period but no thaw event detected could easily deduce that the region has no enough soil water content to freeze.

The difference of the results derived from active and passive microwave remote sensing time series is essential for understanding the near-surface earth system changes. The SSM/I's result could indicate the soil temperature switch from negative to positive values, while the QuikSCAT's result could deduce the soil water states change from ice to liquid water. Such kind of phenomenon would be related to the climate change and extreme environment (e.g. springtime dust emission) in this area for better understanding the Earth surface interactions.

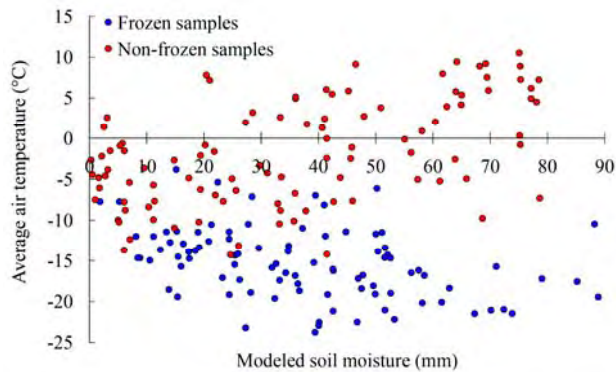


Figure 4. Near-surface air temperature and soil moisture conditions' difference between samples with/without soil thaw events detected by QuikSCAT backscatter.

6. CONCLUSION

SSM/I brightness temperature and QuikSCAT Ku-band backscatter were applied in this study at a case study area of northern China and Mongolia in springtime of 2004. Conclusions could be approached as follows:

1) Both soil freeze-thaw algorithm for SSM/I brightness temperature and multi-step method for QuikSCAT backscatter were effective for springtime near-surface soil thaw events detection. A reliability of $R = 0.8$, $P < 0.05$ was obtained between estimated primary thaw date and the date when consecutive days' average air temperature keeping positive values; and $R = 0.85$, $P < 0.05$ was obtained in result from passive microwave remote sensing with comparison between estimated onset/offset of the thaw and field measured soil thaw event.

2) The passive microwave remote sensing (SSM/I) based result had a good relationship with the near-surface soil temperature, while the active microwave remote sensing (QuikSCAT) based result had both relationships with temperature and soil moisture conditions, especially soil moisture conditions. And also, QuikSCAT result identifies the geographical boundary conditions of the thaw event in springtime of 2004, which is crucial for understanding the different types of springtime near-surface soil thaw at middle latitudes.

Since both SSM/I brightness temperature and QuikSCAT backscatter are available from 1999 to 2009, further analysis is undergoing for understanding the interaction of springtime soil thaw event with other near-surface events.

REFERENCES

- Han, L., Tsunekawa, A., Tsubo, M., 2010a. Monitoring near-surface soil freeze–thaw cycles in northern China and Mongolia from 1998 to 2007. *International Journal of Earth Observation and Geoinformation*, doi: 10.1016/j.jag.2010.04.009.(in press)
- Han, L., Tsunekawa, A., Tsubo, M., 2010b. Radar remote sensing of springtime near-surface soil thaw events at mid-latitudes. Submitted to *International Journal of Remote Sensing*.
- Tsunekawa, A., Ito, T. Y., Shinoda, M., Nemoto, M., Suhama, T., Ju, H., Shimizu, H. 2005. Methodology for assessment of desertification based on vegetation degradation using net primary productivity (NPP) as a key indicator. *Phyton*, 45, 185–192.
- Yamaguchi, Y. and Shinoda, M. (2002). Soil moisture modeling based on multiyear observations in the Sahel. *Journal of Applied Meteorology*, 41, 1140–1146.
- Zhang, B., Tsunekawa, A., Tsubo, M. 2008. Contributions of sandy lands and stony deserts to long-distance dust emission in China and Mongolia during 2000–2006. *Global and Planetary Change*, 60, 487–504.
- Zhang, T., Barry, R. G., Armstrong, R. L., 2004. Application of satellite remote sensing techniques to frozen ground studies. *Polar Geography*, 28, 163–196.
- Zwally, H. J., and Gloersen, P., 1977. Passive microwave images of the Polar Regions and research applications. *Polar Record*, 18, 431–450.

STEREO RADARGRAMMETRY IN SOUTH-EAST ASIA USING TERRASAR-X STRIPMAP DATA

Xueyan He, Timo Balz*, Lu Zhang, Mingsheng Liao

State Key Laboratory of Information Engineering in Surveying, Mapping and Remote Sensing, Wuhan University, China
Luoyu Road 129, 430079 Wuhan
balz@lmars.whu.edu.cn

Commission VII

KEY WORDS: Radar, SAR, Stereo, Radargrammetry, TerraSAR-X

ABSTRACT:

Stereo radargrammetry is a mature technique for deriving height information from SAR image pairs. Because stereo radargrammetry is less sensitive to temporal decorrelation, it can provide better results than interferometric SAR in certain situations. Using TerraSAR-X stripmap stereo pairs, digital surface models (DSM) with good height accuracy can be generated. We use SRTM data as our initial DEM and a pyramid layer based approach for our radargrammetric processing. Our results are relative noisy with a high error standard deviation. Nevertheless, with a mean overall error of less than 3 m in height the final DSM is quite precise.

1. INTRODUCTION

There are various ways for creating digital elevation models (DEM) from synthetic aperture radar (SAR) data. The most common technique is SAR interferometry (InSAR). InSAR uses the phase difference between the backscattered signals received at slightly different positions. From the phase differences the height of the backscattering object can be determined. InSAR is a very precise technique, but especially spaceborne InSAR suffers from errors caused by the atmosphere. The repeat pass interferometry, which is commonly used with today's sensors, as we are waiting for the TanDEM-X data, is very sensitive to temporal decorrelation. In repeat pass InSAR the time between two data acquisitions is rather large, for example 11 days for TerraSAR-X. In this time the situation on the ground can change, especially over vegetated areas, and the data decorrelates.

This massively influences the usability of InSAR over strongly vegetated areas. Our test area around Kuala Kangsar in Malaysia is a strongly vegetated and mountainous area. The nearby mountains reach up to 1500 m, while Kuala Kangsar resides at around 40 m height. Under these conditions, repeat pass InSAR with TerraSAR-X does not provide good results. Most of the scene is strongly decorrelated.

But InSAR is not the only method of creating DEMs from SAR data. Stereo radargrammetry (StereoSAR) is far less affected by the atmosphere and by temporal decorrelation. StereoSAR is therefore, although in general less precise than InSAR, more suitable for this area.

StereoSAR with TerraSAR-X can deliver quite precise results (Raggam *et al.* 2010). In our approach we use the rational polynomial coefficient (RPC) model (Tao & Hu 2001) for the calculation of the 3D geo-coordinates of detected homologous points. In Section 2, the approach for StereoSAR with high-resolution TerraSAR-X data is explained. In Section 3, we describe the usage of the RPC model for stereo radargrammetry. Our experimental results are shown in Section 4 and finally conclusions are drawn.

2. STEREO RADARGRAMMETRY WITH TERRASAR-X

Comparable to InSAR, StereoSAR needs at least two images. But the images need to have a rather large acquisition angle difference. To use StereoSAR with spaceborne systems, the systems must be able to acquire data under different incidence angles. Before the launch of the new generation of high-resolution SAR satellites, Radarsat data was used for StereoSAR (e.g. Toutin 2000). The new satellite generation is also capable of acquiring data to be used for StereoSAR and in our experiments we used a pair of TerraSAR-X stripmap data. StereoSAR can be acquired in a same-side or opposite-side configuration. In the following we always assume a same-side configuration. In a same-side configuration the images are acquired from parallel tracks under different incident angles.

The geometry of a SAR image is different in range and in azimuth direction. In azimuth direction the location of an object in a SAR image depends on the Doppler Effect and is typically precise if the object is not moving. In range direction the location of an object in a SAR image depends on the distance between the object and the sensor. When an object is seen from different angles, this, so called, relief displacements will be different on each SAR image. The resulting difference between the image coordinates of homologous points in a stereo pair is called parallax (Leberl 1990).

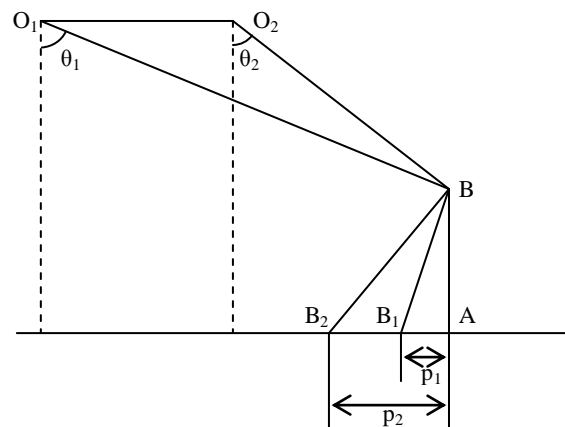


Figure 1. Same-side stereo configuration

* corresponding author

This is schematically shown in Figure 1. Object B is displaced differently depending on the incidence angles θ_1 and θ_2 . By measuring the displacements p_1 and p_2 the relative height h of the object can be calculated with Eq. 1.

$$h = \frac{p_1 - p_2}{\cot \theta_2 \pm \cot \theta_1} \quad (1)$$

The difficult and time consuming part of the StereoSAR method is the search of homologous points in both images. In StereoSAR this is rather difficult because of the speckle noise and the large differences in geometry and radiometry between the two SAR images acquired under different incidence angles.

Our search of homologous points is based on pyramid layers of the images. The search starts at the highest pyramid level, subsequently refining the search using lower pyramid levels. There are many different search criteria suggested for SAR (Tupin and Nicolas 2002), but in our experiments we achieved the best results using the two-dimensional normalized correlation (see also Fayard *et al.* 2007)

$$r = \frac{\sum_i \sum_j (r_{ij} - \bar{r})(m_{ij} - \bar{m})}{(n-1)s_r s_m} \quad (2)$$

where r is the reference image and m is the match image, \bar{r} and \bar{m} are the mean values of the reference and match image values inside the correlation window, s_r and s_m are the standard deviation of the values inside the correlation window and n is the number of pixels in the correlation window. In higher pyramid levels a smaller correlation window is chosen, but in lower pyramid levels the correlation window gets bigger.

One problem of the pyramid level based approach is that small errors on high pyramid levels can propagate and cause large errors and outliers in the final result. In previous experiments we found outliers with height errors of more than 250 m in a rather flat terrain of our test area (Balz *et al.* 2009) caused by this.

The SRTM dataset can be used to improve the accuracy of the process by providing reliable initial values for the iterative search process. Furthermore, the SRTM data can also be used to filter large outliers.

3. USING THE RPC MODEL FOR STEREO RADARGRAMMETRY

A sensor model is established to relate the image coordinates and corresponding object coordinates. Rigorous physical sensor models accurately represent this relationship, but using them is very time-consuming when positioning each pixel by a rigorous sensor model. Moreover, the sensor parameters are needed in rigorous sensor model, which may violate the confidential rules of commercial companies. Although the rigorous sensor models are more accurate, the development of generic sensor models with high fitting accuracy, real-time processing ability and sensor-independent features is very useful.

The rational polynomial coefficients (RPC) model is a typical generic sensor model which describes the relationship between image space and object space by ratios of polynomial functions. It has been successfully applied in geo-coding of high-resolution optical imagery, such as IKONOS, QuickBird, GeoEye-1, etc. (Volpe, 2004; Fraser & Hanley, 2005), and has become a standard component for processing optical data. Our investigation indicates that the RPC model for TerraSAR-X data has an excellent fitting accuracy (Wei *et al.* 2010). The

RPC model uses two main forms for the forward (Eq. 3-4) and two main forms for the inverse transformation (Eq. 5-6).

$$r = \frac{p_1(X, Y, Z)}{p_2(X, Y, Z)} \quad (3)$$

$$c = \frac{p_3(X, Y, Z)}{p_4(X, Y, Z)} \quad (4)$$

$$X = \frac{p1(r, c, Z)}{p2(r, c, Z)} \quad (5)$$

$$Y = \frac{p3(r, c, Z)}{p4(r, c, Z)} \quad (6)$$

r and c are the normalized row and column indices in image space, X , Y and Z are the normalized 3D object coordinates. The purpose of normalization is to improve the numerical stability of the equations. The image coordinates and object coordinates are both normalized to values between -1 and 1 using

$$\left\{ \begin{array}{l} r = \frac{r_{org} - r_{offset}}{r_{scale}} \quad c = \frac{c_{org} - c_{offset}}{c_{scale}} \\ X = \frac{X_{org} - X_{offset}}{X_{scale}} \quad Y = \frac{Y_{org} - Y_{offset}}{Y_{scale}} \quad Z = \frac{Z_{org} - Z_{offset}}{Z_{scale}} \end{array} \right. \quad (7)$$

where the subscript *org* means original coordinates, and *offset* and *scale* are parameters for normalization.

In RPC-based geo-coding, the RPC parameters need to be solved in advance. A virtual regular object grid covering the full extent of the image with several elevation layers is established. Each grid point's corresponding image row and column indices can be calculated using the rigorous physical sensor model and the satellite ephemeris data. After the image coordinates and object coordinates are obtained, the RPC parameters can be estimated using a least-squares solution.

The accuracy of RPC-based geo-location is affected by the computation accuracy of RPC parameters directly. This is the difficult point, because the equations are usually very ill-conditioned. There are two main categories for solving ill-posed equations: biased methods, like ridge trace, GCV, or L-curve, and unbiased methods, like the iteration method by correcting characteristic value (IMCCV). The ridge trace method is quite time-consuming with a low accuracy. The GCV method is sometimes not converging, which is a major drawback. The L-curve method is fast with a high accuracy. But the method is a little less accurate than the IMCCV, while the IMCCV takes a lot of time for the iterative improvement and relies heavily on the initial data. Therefore, we use the L-curve results as the initial data for the IMCCV. This approach can get very accurate results fast.

Given a over-determined linear system

$$AX = L \quad (8)$$

and using the least square solution, the results of X will be

$$X = (A^T P A)^{-1} A^T P L \quad (9).$$

Unfortunately, in this way we usually cannot obtain stable results. To deal with this problem, the ridge estimate is used

$$X(k) = (A^T P A + kE)^{-1} A^T P L \quad (10),$$

where P is the weight matrix and k is the regularization parameter. In order to determine for which k the X -value can get the best result, the L-curve method selects different k -values and calculates the corresponding X . So a group of points are obtained:

$$(\eta(k), \xi(k)) = (\lg \|AX - L\|_k, \lg \|X\|_k) \quad (11).$$

This curve normally is shaped like the letter ‘L’. The optimal value of the regularization parameter k is considered to be the one corresponding to the corner of the ‘L’, i.e. the point with maximum curvature.

The principle of IMCCV method is different from that of the L-curve method. It replaces the ordinary least-square solution with

$$(A^T P A + E)\hat{X} = A^T P L + E \quad (12).$$

Since both sides of the equation have unknowns, we can only solve by using iterative methods.

$$\hat{X}^{(k)} = (B^T P B + E)^{-1} (B^T P L + \hat{X}^{(k-1)}) \quad (13)$$

In our test we use the result of L-curve as the initial value of IMCCV method. The result will be calculated by solving Eq. 13 iteratively until the termination condition is satisfied.

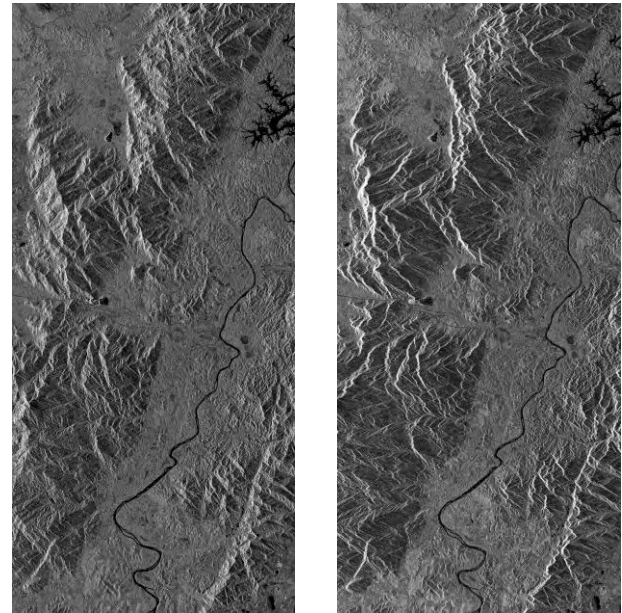
Once the RPC parameters are obtained, we can use them to geocode our data. The forward form of the RPC model is adopted. For each object points with known latitude and longitude and height fetched from our DEM, the corresponding row and column indices can be calculated. After resampling, the height of each point can be acquired.

4. EXPERIMENTAL RESULTS

Our test area is around Kuala Kangsar, Malaysia (N4°29′8″-N5°04′38″, E100°39′33″-E101°3′25″). The area is rather flat along the river, but is flanked by high mountains on both sides. The area is strongly vegetated and the elevation ranges from 40 m up to 1500 m. A TerraSAR-X stripmap image pair acquired on September 13 and September 18, 2008, with incidence angles of 21.4° and 42.7° at the scene centers, is used in our experiments. The amplitude images of the scenes are depicted in Figure 2.

The test data was processed using our own radargrammetric processor. The results are compared to a DSM created by Infoterra’s Pixel Factory™ (Infoterra 2009), to a publically available DEM generated by Infoterra (2010), to GPS ground control points provided by Infoterra, as well as to the SRTM DEM.

Table 1 shows the parameters we used for our experiments. The search for homologous points starts at the pyramid level 5 with 40 meters pixel size, subsequently refining the search using lower pyramid levels until pyramid level 2 with 5 meters pixel size. In higher pyramid levels a smaller correlation window is chosen, but in lower pyramid levels the correlation window gets bigger.



Reference image
Sep. 18, 2009
© DLR/Infoterra

Match image
Sep. 13, 2009
© DLR/Infoterra

Figure 2. TerraSAR-X stereo pair of Kuala Kangsar, Malaysia

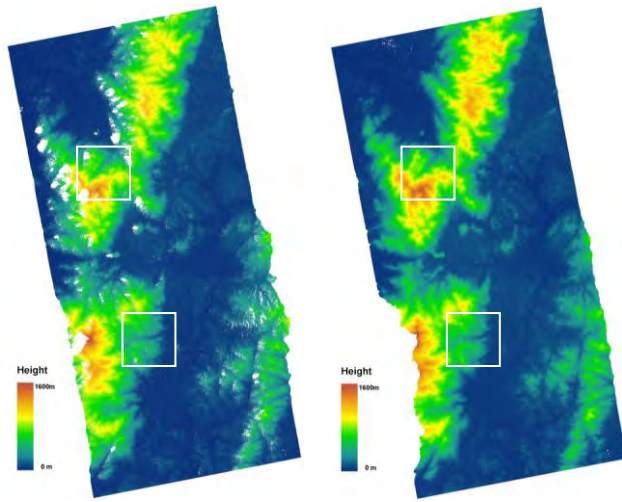
The search size in Y direction is set to be 3 because we found that the azimuth parallaxes are very small. As we can see in Table 1, the mean correlation value is smaller in lower pyramid levels. This is due to the increasing level of noise in the lower pyramid level images. With a mean correlation of only 0.3 in the 2nd pyramid level, we can assume the results to be noisy and less reliable.

Table 1. Correlation Parameters

Level	Pixel size	Corr. Window Size	Search Size in Range	Search Size in Azimuth	Mean Correlation
5	40m	5x5	11	3	0.68
4	20m	7x7	11	3	0.54
3	10m	9x9	17	3	0.41
2	5m	11x11	17	3	0.30

Figure 3 shows the DSM calculated by Infoterra’s Pixel Factory™ and by our radargrammetric processor respectively. As we can see, some pixels with no height information are masked out, appearing white in the Infoterra’s DSM. In our DSM, all pixels are reconstructed except a part in the lower left corner, where no height information can be obtained.

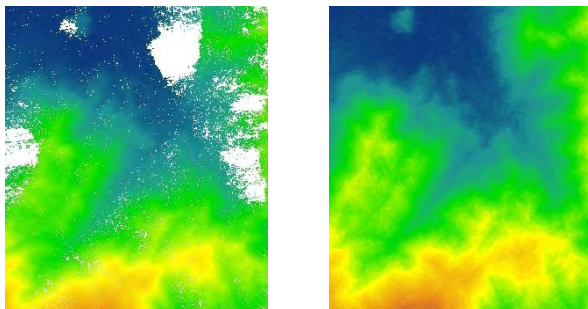
The DSM created using Infoterra’s Pixel Factory™ has a mean absolute height error of about -1.7 m with a standard deviation of 8.4 compared to 26 GPS ground control points. Our DSM was generated fully automatically without using any ground control points. In this way we got a mean error of -44.2 m and standard deviation of 22.88 m. After using one control point, located in the middle of the reference image (100.947 E / 4.79557 N), to correct our results in elevation direction, we got a mean error of 2.79 m. Comparing our DSM with Infoterra’s DSM, the mean error for the full image is 7.07 m and standard deviation is 19.97 m. Compared with the newest DEM available from Infoterra (2010) we have a mean error of -12.64 with a standard deviation of 18.84. We also compared our DSM with the SRTM DSM and got a mean error of 2.8 m with a standard deviation 13.6 m.



DSM calculated by Infoterra's Pixel Factory™ DSM calculated using the procedure explained above

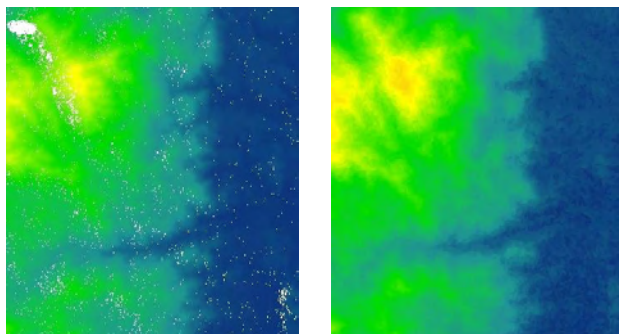
Figure 3. Comparison of the DSMs

The absolute mean error is not very high, but our DSM is quite noisy. The standard deviation of the error is quite high. The GPS control point with the largest absolute error of -68 m is located near the northwestern mountain peak. In Figure 4 and Figure 5 the details of the DSMs marked by white boxes in Figure 3 can be seen.



Subset of the Pixel Factory™ DSM on the mountain ridge Subset of our DSM on the mountain ridge

Figure 4. Detailed DSM comparison



Subset of the Pixel Factory™ DSM on the mountain ridge Subset of our DSM on the mountain ridge

Figure 5. Detailed DSM comparison

The DSM created by Infoterra's Pixel Factory™ includes large areas with no value in Figure 4, whereas our DSM interpolates all areas. Pixel Factory™ is marking the areas where no or no

reliable information is available. This is an important feature of the Pixel Factory™ for mapping applications.

Our DSM is overestimating the heights at the mountain ridges compared to the results from Pixel Factory™. The resulting DSM is noisier, which can be seen very clearly in Figure 5. The mountains are quite comparable to each other, but in the rather flat area on the eastern side of the subset shown in Figure 5 our radargrammetric processor produces very noisy results. This is still the main problem of our approach.

Figure 6 shows the correlation value of the whole scene. The river is very striking with a high correlation value. The lower and flat area near the river also has a high overall correlation, but the results in this area are still noisy. Along the hillside of the mountainous areas the overall correlation is much lower.

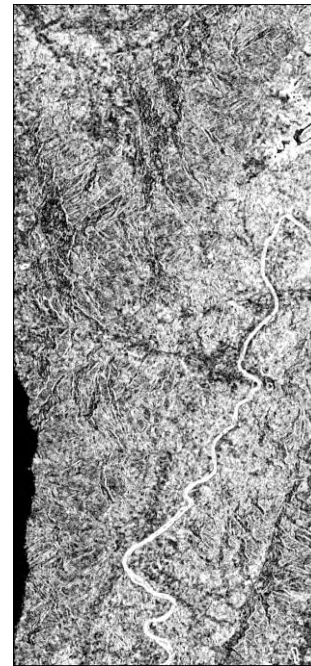


Figure 6. Correlation image

In Figure 7(a) a subset of the correlation image from Figure 6 can be seen. Figure 7(b) shows the amplitude image of the same area. The correlation is high at the mountain ridges and the valleys, but lower at the mountain sides, especially in the layover area. The differences in these areas between the two stereo images are quite high. Interestingly we also find very low coherence in the rather flat areas, where we would assume the image pair to be higher correlated, because these areas are less affected by the strong differences in geometry and backscattering strength caused by the differences in local incidence angles.

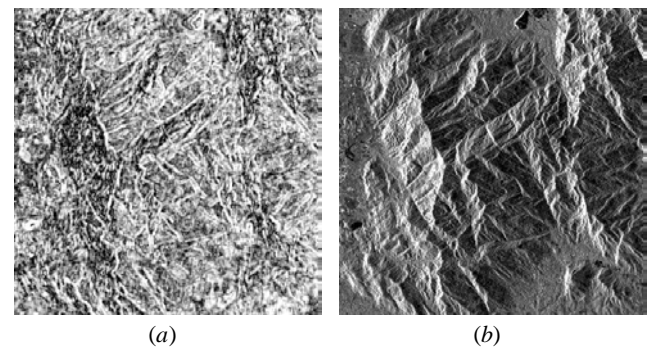


Figure 7. Correlation image (a) and amplitude image (b) subset

But in fact, these flat areas are less correlated, because they are covered by uniform vegetation and not many structural elements can be found.

Figure 8 shows the overlay of the correlation image and the amplitude image at the north-western mountain subset shown in Figure 7. The higher correlation values are painted in darker color, which is opposite to the color code used in Figure 6 and Figure 7, but this allows for a more meaningful visualization. The lakes at the left side and at the top are obviously highly correlated and are shown in a very dark green. The picture also indicates that the mountain sides facing the sensor (towards the left side of the image) have low correlation values due to the layover effect. The mountain sides facing in far-range direction (towards the right side of the image) have higher correlation values. We can see this also when analyzing the no-data-areas of the Pixel Factory™ DSMs in Figure 3 and Figure 4. The large no-data-areas are located in near-range of a mountain.



Figure 8. Overlay of correlation image and amplitude image

5. CONCLUSION

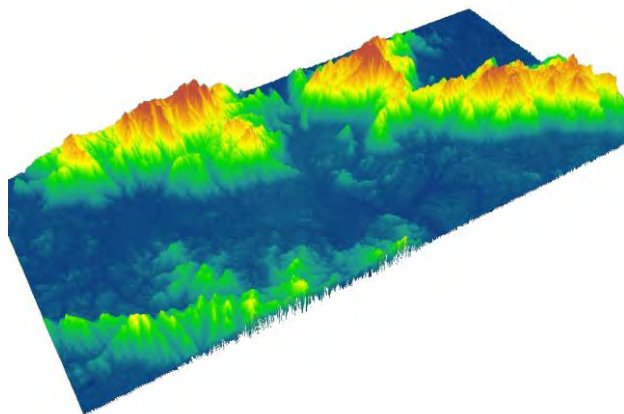


Figure 9. 3D model of the DSM

Stereo radargrammetry with TerraSAR-X can provide precise DSMs even in mountainous and strongly vegetated areas as shown above and in Figure 9. We achieved a low mean error in the DSM, but the standard deviation of the error is comparably high. Compared with our previous work (Balz *et al.* 2009), we improved the accuracy and strongly reduced the number of outliers in the data by using the SRTM data and by improving the processing. We tested different matching criteria but found that

the two-dimensional normalized correlation delivers the best results for our dataset.

The RPC based geo-coding improved our processing speed and the overall geo-accuracy of our DSM. Still, the DSM created by Infoterra's Pixel Factory is more precise and less noisy. There is therefore still a lot of room for improvement.

ACKNOWLEDGEMENT

The authors thank the Infoterra GmbH for providing the test data and the reference data. The work was supported by the Research Fellowship for International Young Scientists of the National Natural Science Foundation of China (Grant No. 60950110351).

REFERENCES

- Balz, T., He, X.Y., Zhang, L., Liao, M.S., 2009. TerraSAR-X stereo radargrammetry for precise DEM generation in South-East Asia. In: *Proc. Asian Conference on Remote Sensing*, Beijing.
- Fayard, F., Méric, S., and Pottier, E., 2007. Matching stereoscopic SAR images for radargrammetric applications. In: *Proc. Geoscience and Remote Sensing Symposium (IGARSS 2007)*, Barcelona, Spain.
- Fraser, C.S. and Hanley, H.B. 2005. Bias-compensated RPCs for Sensor Orientation of High-resolution Satellite Imagery. *Photogrammetric Engineering & Remote Sensing*, 71, pp. 909-915.
- Infoterra, 2009. Pixel Factory™, the Next Generation Solution for Industrial Geo-Production. Available online: http://www.infoterra.fr/Infoterra/Pixel_Factory.php [last accessed on May 26, 2010]
- Infoterra, 2010. Free TerraSAR-X data. Available online: <http://www.infoterra.de/tsx/freedata/start.php> [last accessed on June 3, 2010]
- Leberl, F., 1990. Radargrammetric Image Processing. Artech House, Boston, MA.
- Raggam, H., Gutjahr, K., Perko, R., and Schardt, M., 2010. Assessment of the stereo-radargrammetric mapping potential of TerraSAR-X multibeam spotlight data, *IEEE Transactions on Geoscience and Remote Sensing*, 48, pp. 971-977.
- Tao, C.V. and Hu, Y., 2001. A comprehensive study of the rational function model for photogrammetric processing. *Photogrammetric Engineering & Remote Sensing*, 67, pp. 1347-1357.
- Toutin, T., 2000. Evaluation of radargrammetric DEM from RADARSAT images in high relief areas. *IEEE Transactions on Geoscience and Remote Sensing*, 38, pp. 782-789.
- Tupin, F. and Nicolas, J.M., 2002. Matching criteria for radargrammetry. In: *Proc. IGARSS 2002*, Toronto.
- Volpe, F., 2004. RPC based processing of QuickBird high resolution satellite data. In: *Proc. Polish Remote sensing and GIS Conference 2004*, Bialobrzegi, Poland.
- Wei, X.H., He, X.Y., Zhang, L., Balz, T., Liao, M.S. 2010. RPC modelling for spaceborne SAR and its application in radar image geocoding. In: *Proc. 2010 Dragon-2 Mid Term Results Symposium*, Guilin, China.

AUTOMATIC QUALITY CONTROL OF CROPLAND AND GRASSLAND GIS OBJECTS USING IKONOS SATELLITE IMAGERY

P. Helmholz*, C. Heipke, F. Rottensteiner

IPI - Institute of Photogrammetry and GeoInformation, Leibniz University Hannover, Nienburger Str. 1, 30167 Hannover, Germany - (helmholz, heipke, rottensteiner) @ipi.uni-hannover.de

Commission VII

KEY WORDS: Automation, GIS, Quality Control, Verification, Updating

ABSTRACT:

As a consequence of the wide-spread application of digital geo-data in Geoinformation Systems (GIS), quality control has become increasingly important. A high degree of automation is required in order to make quality control efficient enough for practical application. In order to achieve this goal we have designed and implemented a semi-automatic technique for the verification of cropland and grassland GIS objects using 1 m pan-sharpened multispectral IKONOS imagery. The approach compares the GIS objects and compares them with data derived from high resolution remote sensing imagery using image analysis techniques. Textural, structural, and spectral features are assessed in a classification based on Support Vector Machines (SVM) in order to check whether a cropland or grassland object in the GIS is correct or not. The approach is explained in detail, and an evaluation is presented using reference data. Both the potential and the limitations of the system are discussed.

1. INTRODUCTION

Today, many public and private decisions rely on geospatial information. Geospatial data are stored and managed in Geoinformation Systems (GIS) such as the Authoritative Topographic Cartographic Information System (ATKIS) or the Digital Landscape Model (DLM-DE) in Germany (Arnold, 2009). In order for a GIS to be generally accepted, the underlying data need to be consistent and up-to-date. As a consequence, quality control has become increasingly important. In the European Norm DIN EN ISO 8402 (1995), *quality* is defined as the “Totality of characteristics of an entity that bear on its ability to satisfy stated and implied needs”. In the context of GIS this means that the data model must represent the real world with sufficient detail and without any contradictions (*quality of the model*). Secondly, the data must conform to their specification (*quality of the data*). There are four important measures for quality control of geodata: *consistency*, *completeness*, *correctness*, and *accuracy* (Joos, 2000). Only the consistency can be checked without any comparison of the data to the real world. All the other quality measures can be derived by comparing the GIS data to the real world, as it is represented in aerial or satellite images. In order to reduce the amount of manual work required for quality control, a high degree of automation is required. In this paper, we describe a method for the verification of agricultural objects for quality control that is based on 1 m pan-sharpened multispectral IKONOS images. The focus will be on the separation of grassland and cropland objects for the quality management of ATKIS, because it has been found that these classes are not easily separated, e.g. (Regners & Prinz, 2009). After giving an overview on related work in Section 2, our new approach is described in Section 3. First results are presented in Section 4. The paper concludes with a discussion about the potential and the limitations of this approach.

2. RELATED WORK

Lu and Wenig (2007) gave an overview about the state of the art classification techniques. They emphasise that besides textural and spectral approaches, approaches using context information (such as structures) become more important with increasing resolution of the images. In this section we briefly review approaches for extracting different agricultural object types based on textural, structural and spectral features using high resolution images.

Textural features are related to local spatial patterns of grey levels inside an object. There have been quite a few attempts to use the textural characteristics for the classification of different agricultural object classes. For instance, autocorrelation is used by Warner and Steinmaus (2005) to identify orchards and vineyards in IKONOS panchromatic imagery. After defining a square kernel and after radiometric normalization, the autocorrelation is determined for the cardinal directions and both diagonals, which results in one autocorrelogram per direction. An orchard pixel is detected if an orchard pattern is identified in more than one autocorrelogram centred on that pixel. This method assumes the rows of plants to be equally spaced. Rengers and Prinz (2009) use the neighbourhood grey-tone difference matrix (NGTDM) to classify cropland, forest, water, grassland and urban areas in aerial and IKONOS images. This method is based on the differences of the grey values of two pixels and the differences of the grey values of the local neighbours, from which textural features such as coarseness, complexity and textural strength are derived. The results presented in (Rengers & Prinz, 2009) show that with the exception of grassland and cropland the classes mentioned above can be distinguished well. A similar conclusion is drawn by Busch et al. (2004), who apply a texture-based classification method based on Markov random fields (Gimel'farb, 1996) to aerial and IKONOS satellite images. Their method is well-suited to classify settlement areas, industrial areas, forests, and

* Corresponding author

the combined class cropland/grassland. The results reported in (Rengers & Prinz, 2009) and (Busch et al., 2004) show that a purely textural analysis is not sufficient for separating cropland and grassland. Spectral and / or structural information is required for that purpose.

Haralick et al. (1973) used textural features derived from the grey level co-occurrence matrix such as energy, contrast, correlation and entropy are used along with the mean and standard deviation of the gray values of all four available channels to classify coastline, forest, grassland, urban areas and irrigated and non-irrigated cropland using a linear discriminant function method. By combining a textural analysis with the spectral features the classification accuracy could be improved over a purely radiometric analysis. More recently, Itzerott and Kaden (2007) tried to distinguish various types of farmland using solely the Normalised Difference Vegetation Index (NDVI) that is computed from the near infrared and the red bands of a multispectral image. Analysing typical crops and grassland in Germany, they could show that grassland possesses an NDVI that is significantly larger than zero in all seasons, whereas untilled cropland has a very low NDVI except for a short period. However, they observed strong regional and temporal variations of the NDVI, so that statistical parameters describing the NDVI of the different agricultural classes in one region are hard to transfer to other regions. Training with a multitemporal dataset within a large area would be necessary. Hall et al. (2003) use the NDVI to separate vines and bare soil in aerial images with a spatial resolution of 0.25 m. Afterwards, the orientation of the rows is calculated using a priori knowledge about the distances between the rows and between the individual plants within a row. However, such a priori knowledge is usually not available for cropland objects.

Structural features have been used frequently to distinguish agricultural object classes such as vineyards, orchards, or plantations. The structural characteristics exploited for the extraction of these objects, namely straight parallel lines, also occur in cropland, where they are caused by tilling. However, some assumptions usually made in the extraction of vineyards or orchards cannot usually be made for cropland. For instance, Chanussot et al. (2005) estimate the orientation of vineyard rows automatically from aerial images by using the Fourier spectrum of an image and its Radon transform. Wassenaar et al. (2002) detect orchards and different kinds of vineyards in aerial images using a Fast Fourier Transformation, using specific knowledge about the distances between vine rows to reduce the search space in the frequency domain. Delenne et al. (2008) use a frequency analysis based on Gabor filters to estimate the row width and orientation and to detect the boundaries of vineyards. All these methods assume the rows of vines to be approximately equally spaced or even utilize knowledge about the actual spacing of these rows. Both assumptions cannot be made for cropland. In cropland the distance between furrows can vary from one field to the next depending on the type of crop planted in the field, on the kind of machine used for tilling, and on the visibility of the structures in the image.

Trias-Sanz (2006) uses only structural features to discriminate objects with similar radiometric and textural properties, namely cropland, forest, orchards, and vineyards. These object classes can be distinguished only by orientation characteristics. A small window is extracted randomly inside an object to be classified, and this window (called *texton*) is used to compute a variogram of the image. A histogram of direction angles is derived from the Radon transform of the variogram. The maximum of this histogram corresponds to the primary direction of edges in the

image, and it is used in the classification process. The approach can be used to discriminate a large number of object classes by properly choosing the *texton*, but can give wrong results if the *texton* size is selected inappropriately. Another disadvantage of this approach is that the cultivation structures and field crop have to be homogeneous in appearance. Therefore, LeBris and Boldo (2007) use a segmentation to extract homogenous regions before applying the algorithm of Trias-Sanz (2006).

A differentiation between agricultural classes such as grassland and cropland only on the basis of spectral, structural or textural features in monotemporal imagery seems to be impossible. An approach which combines these features is introduced by Ruiz et al., (2004, 2007) and Recio et al. (2006). Besides spectral (mean and deviation of the red, infrared and NDVI channel) and textural features determined from the grey level co-occurrence matrix (Ruiz et al., 2004), structural features determined from a semi-variogram, Hough- and Fourier transformation (Ruiz et al., 2007) are used to detect olive trees, citrus orchards, forests and shrubs using images of 0.50 m spatial resolution. The final decision is based on a decision tree (Recio et al., 2006). In addition to the features described so far, information about the shape of the object can be used for the classification process. Such information can be derived e.g. from a given GIS. Hermosilla et al. (2010) extend the approach of Ruiz et al. (2007) by using object shape as an additional feature to distinguish the classes building, forest, greenhouse, shrub lands, arable land and vineyard. Whereas this could improve the classification accuracy, it resulted in an increase of the number of undetected errors in a GIS to be verified by that approach.

Our method differs from the cited approaches by the way the textural analysis is carried out and by the definition of the structural, spectral and textural features. Furthermore, we use a different method for classification. The fact that our approach is embedded in a system for the verification of GIS objects has some implications for the strategy used for classification. The parameters of the method have to be tuned according to the quality requirements of the GIS: an undetected false classification in the GIS is penalized higher than a correct classification erroneously highlighted as false.

3. APPROACH

3.1 Overview

The goal of our approach is the separation and verification of cropland and grassland GIS objects using 1 m orthorectified and pan-sharpened multispectral IKONOS images. In this paper we assume that each ATKIS GIS object corresponds to exactly one class. The verification process is carried out separately for each GIS object. The object's boundary polygon given by the GIS is used to limit the analysis to areas inside the object. In a first step we use a supervised classification technique that analyses image texture with the help of Markov Random Fields (Müller, 2007, Busch et al., 2004) to distinguish the combined class 'agriculture', which comprises both cropland and grassland objects, from other classes such as 'settlement', 'industry' or 'forest'. If a cropland or grassland object is classified as belonging to any other class than 'agriculture', it is considered to correspond to an error in the GIS. As the algorithm of Busch et al. (2004) cannot differentiate between grassland and cropland objects, all the other objects (i.e., those passing the first classification stage) are passed on to a second classification process designed to discriminate grassland and cropland. The second classification and the following verification process is the main focus of this paper.

This second classification process is based on Support Vector Machines, which have been applied successfully in the field of remote sensing and pattern recognition, e.g. (Vapnik, 1998; Fujimura et al., 2008). Whereas we only want to distinguish the classes ‘grassland’ and ‘cropland’, it is necessary to split the latter into the two classes ‘tilled cropland’ and ‘untilled cropland’, because they appear differently in the data. Hence, we have to apply multi-class SVM (Vapnik, 1998) to our problem. In the subsequent sections we describe the features used in the SVM classification and the actual classification process, including the training required for the SVM classifier.

3.2 Features

3.2.1 Textural Features: Textural features derived from of the co-occurrence matrix can give important hints to separate different agricultural classes. We use the Haralick features *energy*, *contrast*, *correlation* and *homogeneity* in our classification approach (Haralick et al., 1973). Figure 1 shows a scatter plot of texture homogeneity and contrast for the objects of a reference dataset. There are relatively clear clusters corresponding to grassland and untilled cropland. However, the figure also shows that there is a considerable overlap between the cluster for tilled cropland and the others; hence the need for additional features that support a clear separation of these classes.

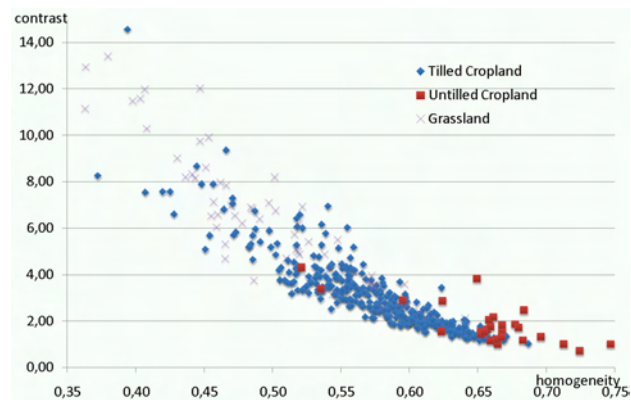


Figure 1. Scatter plot of Haralick features contrast and homogeneity of objects of a reference dataset.

3.2.4 Spectral Features: Information about vegetation is contained in the infrared band of multispectral images and in features derived from it (Ruiz et al., 2004; Hall et al., 2003; Itzerott & Kaden, 2007). Similar to the cited works, we use the *mean and standard deviation of the red, infrared and NDVI* as spectral features. Figure 2 shows a scatter plot of the mean NDVI (scaled from 0 to 255) and the infrared band for the same objects as in Figure 1. The spectral features are well-suited for separating tilled cropland from untilled cropland, but the clusters for grassland and tilled cropland still overlap.

3.2.3 Structural Features: A main difference in the appearance of cropland and grassland objects in satellite images is caused by cultivation, which is conducted more frequently in crop fields than in grassland. The agricultural machines normally cause parallel straight lines which can be observed in the image. The derivation of structural features is limited to the internal area of the object, and starts with the extraction of edge pixels using the Canny operator (Canny, 1986). These edge pixels are transformed into Hough space. In Hough space, parallel lines are mapped into points having the same line orientation ϕ (Figure 3). From the accumulator in Hough space, a histogram

of the line orientations is derived. This histogram is smoothed using a Gaussian kernel. All local minima and maxima in the histogram are detected and sorted (highest maximum/lowest minimum first); if two local maxima are found to be nearly coincident (i.e., if they are separated by an orientation difference smaller than 45°), the stronger maximum is selected, and the smaller one is discarded. The first and second largest surviving maxima (Max_1 and Max_2) and the smallest minimum (Min_1) of the histogram are then used to derive the structural features used in the SVM classification. The first structural features are $s_1 = Min_1$, $s_2 = Max_1$, $s_3 = Max_2$, the *ratio between first minimum and first maximum*: $s_4 = Min_1 / Max_1$, and the *ratio between first minimum and second maximum*: $s_5 = Min_1 / Max_2$. If there is a significant peak in the histogram s_2 will be much higher than s_3 , and s_4 will have a smaller value compared to a histogram without a significant peak (cf. Figure 3). Another structural feature s_5 , also used by Durrieu et al. (2005) is derived from the ratio between Max_1 and Max_2 : $s_5 = 1 - Max_2 / Max_1$. If there is a significant first but no significant second peak, s_5 will be close to 1, whereas in case there are two peaks that are nearly identical, s_5 will be close to 0. The existence of a single significant peak in the histogram indicates tilling, because our model assumes that there is only one significant tilling direction in the GIS object.

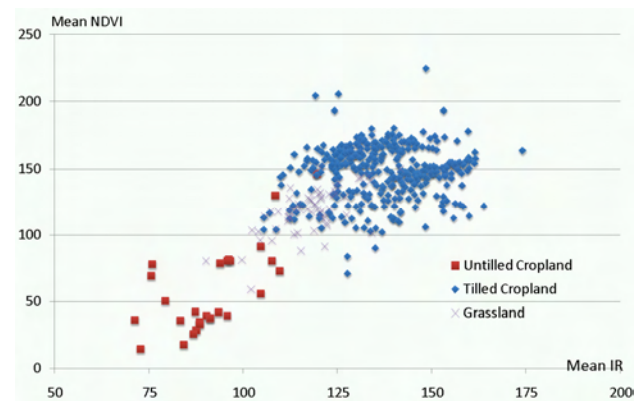


Figure 2. Scatter Plot of mean NDVI and Infrared of the objects of a reference dataset.

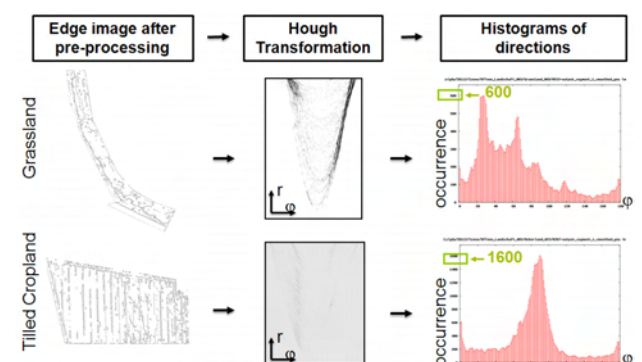


Figure 3. Steps of the structural analysis.

This approach fails if line structures caused by cultivation are not observable (e.g. maize close to harvest, untilled crop fields), if lines in crop fields are not straight respectively parallel to each other (e.g. on hillsides), if grassland possesses parallel lines (e.g. mowed grassland), and at a specific point in time when the crop looks like green grass and structures are not visible. The first three problems may be compensated by spectral features, though the differentiation between cropland and mowed grass may be difficult if the mowed grass (which is

no longer vivid) covers the ground so densely that its spectral signature is close to bare soil. The time when the crop looks like grass (shortly after gestation) has to be avoided by not using images acquired during this time.

3.3 SVM Classification and Verification of GIS Objects

The SVM classifier is a supervised learning method used for classification and regression. Given a set of training examples, each marked as belonging to one of two classes, SVM training builds a model that predicts whether a new example falls into one class or the other. The two classes are separated by a hyperplane in feature space so that the distance of the nearest training sample from the hyperplane is maximised; hence, SVM belong to the class of *max-margin classifiers* (Vapnik, 1998). Since most classes are not linearly separable in feature space, a feature space mapping is applied: the original feature space is mapped into another space of higher dimension so that in the transformed feature space, the classes become linearly separable. Both training and classification basically require the computation of inner products of the form $\Phi(\mathbf{f}_i)^T \cdot \Phi(\mathbf{f}_j)$, where \mathbf{f}_i and \mathbf{f}_j are feature vectors of two samples in the original feature space and $\Phi(\mathbf{f}_i)$ and $\Phi(\mathbf{f}_j)$ are the transformed features. These inner products can be replaced by a Kernel function $K(\mathbf{f}_i, \mathbf{f}_j)$, which means that the actual feature space mapping Φ is never explicitly applied (*Kernel Trick*). In our application we use the Gaussian Kernel $K(\mathbf{f}_i, \mathbf{f}_j) = \exp(-\gamma \|\mathbf{f}_i - \mathbf{f}_j\|^2)$, which implies that the transformed feature space has an infinite dimension. The concept of SVM has been expanded to allow for outliers in the training data to avoid overfitting. This requires a parameter ν that corresponds to the fraction of training points considered to be outliers. Furthermore, classical SVM only can separate two classes, and SVM do not scale well to a multi-class problem. The most common way to tackle this problem is the *one-versus-the rest*-strategy where for each class a two-class SVM separating the training samples of this class from all other training samples is trained, and a test sample is assigned to the class achieving the highest vote from all these two-class classifiers (Vapnik, 1998).

For the classification process in our approach, the SVM algorithm needs to learn the properties of the classes to be classified, namely the classes ‘grassland’, ‘tilled cropland’ and ‘untilled cropland’. The training is done using a set of objects with known class labels. The class labels are assigned to the training objects interactively by a human operator. In a first step a feature vector consisting of the spectral (6), textural (4) and structural (5) features defined in Section 3.2 is determined from the image data for all the training objects. Hence, the overall dimension of the feature vectors is 12. Each feature is normalised so that its value is between 0 and 1 for all training objects. Then, the feature vectors of all segments are used to train the three SVM classifiers required for the one-versus-the rest strategy.

In the classification itself, the feature vector is determined for each test object, and it is normalised using the normalisation parameters determined in training. The object is classified using the previously trained SVM classifiers into one of the classes ‘tilled cropland’, ‘untilled cropland’ or ‘grassland’. However, for the process of GIS verification, the separation between tilled and untilled cropland is meaningless. Hence, for the verification process, a cropland GIS object will be accepted (and classified as ‘correct’) if the object is classified as ‘tilled cropland’ or ‘untilled cropland’. Otherwise it is classified as an error and thus rejected. A grassland object is verified as correct if the

object was classified as ‘grassland’. Otherwise it will be rejected and classified as an error in the data base. The classification and the verification of the test objects are carried out independently from each other.

4. EVALUATION

In this section, we present the evaluation of our approach using a pan-sharpened IKONOS scene in the area of Halberstadt, Germany, acquired on June-18, 2005 and having a ground resolution of 1 m. The reference dataset is based on ATKIS. However, according to the ATKIS specifications, any cropland or grassland object may actually contain areas corresponding to another class as long as certain area limitations are met (AdV, 2010). In this work, we assume each GIS object to correspond to exactly one of the classes. Furthermore, both for training and for the evaluation we have to distinguish untilled cropland from tilled cropland, information that is not contained in ATKIS. The original ATKIS database was thus modified for our tests: each ATKIS cropland or grassland object consisting of units corresponding to different classes was split manually into individual objects corresponding to a single class. All the cropland objects in the resulting GIS data set were classified manually into tilled vs. untilled cropland according to a visual inspection of the images. Finally, GIS objects smaller than 5000 m² were discarded because we cannot assume the structural approach to work with such small objects. Of the remaining GIS objects, less than 50% were used for training, whereas the other objects were used for the evaluation of our method. As the original data base did not contained any errors, we changed the class label of about 10% of the test objects that were chosen randomly. Figure 4 shows the test scene with super-imposed GIS objects. The numbers of objects used for training and evaluation as well as the number of errors added for testing the verification approach are summarised in Table 1.

class	training	test / errors
‘grassland’	32	89 / 8
‘tilled cropland’	165	223 / 23
‘untilled cropland’	11	21 / 2
Σ	208	333 / 33

Table 1. Objects used in the training and test datasets.

In the training phase we fixed the maximum training error ν to $\nu=0.1\%$. The parameter γ of the Gaussian Kernel was fixed at $\gamma=0.01$. The training results were used to classify the test objects. In order to evaluate the classification process, the results of classification were compared to the reference. Table 2 shows the confusion matrix of the classification results, whereas the completeness and the correctness of these classes are presented in

Table 3.

algorithm ref.	‘tilled cropland’	‘untilled cropland’	‘grassland’	Σ
‘tilled c.’	176	0	47	223
‘untilled c.’	1	12	8	21
‘grassland’	3	0	86	89
Σ	180	12	141	333

Table 2. Confusion matrix of the test objects.

The confusion matrix in Table 2 shows that our approach does a good job in separating tilled cropland from untilled cropland, but the separation of both cropland classes from grassland is very uncertain. Since tilled and untilled cropland can be

separated by the textural and the spectral features, the structural features used in the classification are still not efficiency enough, and additional features need to be investigated in the future. The classification errors shown in the confusion matrix also cause some of the completeness and correctness values in Table 3 to be very low.

class	completeness	correctness
tilled cropland	78,9%	97,8%
untilled cropland	57,1%	100%
cropland (untilled + tilled)	77,1%	97,9%
grassland	96,6%	61,0%

Table 3: Completeness and correctness of the classification.

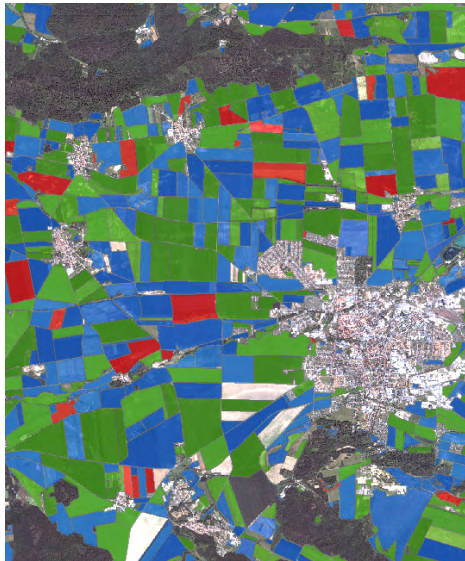


Figure 4. Training and test objects super-imposed to the Ikonos scene. Blue: training objects; green: correct test objects; red: errors.

Figure 5 shows an example for a grassland object misclassified as 'untilled cropland'. The reason for this is the fact that the bare soil is visible in a large part of the object.



Figure 5. Classification errors. 'grassland' object classified as 'untilled cropland'

As mentioned before, the main focus of our approach is the verification of the GIS objects. It is embedded in a semi-automatic system that uses the automatic tool to focus the attention of the human operator to possible errors in the GIS. Thus, work is saved largely due to the fact that the operator needs no longer to check any object that was accepted by the automatic module. Under these circumstances, and given the fact that quality control is essentially carried out to remove errors in the data base, classification errors that cause errors in the GIS to remain undetected, i.e. the erroneous acceptance of a wrong object, are to be avoided by all means. As a consequence, the acceptance of objects has to be very reliable.

On the other hand, the erroneous rejection of a correct GIS object may reduce the economical effectiveness of the system, but it will not result in an error remaining in the data base. The confusion matrices for the verification process carried out on the basis of the classification results described above are presented in

Table 4 and 5 for cropland and grassland objects, respectively. Note that these numbers also contain objects that were rejected based on the texture-based classification described in (Busch et al., 2004).

	automatic	accepted	rejected
reference			
correct		162 (66.4%)	57 (23.4%)
false		1 (0.4%)	7 (2.9%)

Table 4. Confusion matrix for the verification of cropland.

	automatic	accepted	Rejected
reference			
correct		20 (22.5%)	61 (56.6%)
false		0 (0.0%)	25 (28.1%)

Table 5: Confusion matrix for the verification of grassland.

The confusion matrix in Table 4 shows that our approach does a reasonably good job in verifying cropland objects. Only one of eight errors in cropland objects (Table 1) remains undetected, and the number of wrong cropland objects in the GIS is thus reduced by 87.5%. The economical efficiency is at 66.4%, i.e. 66.4% of the cropland objects need not to be inspected by the human operator because these objects were accepted automatically. Of the 23.4% of the objects that are erroneously rejected by the system, 3.3% were rejected by the texture-based classification described in (Busch et al., 2004). Unfortunately, the verification of grassland objects is far less successful. On one hand, all errors contained in the GIS could be detected, but on the other hand, the efficiency of the system is only at 22.5%. Of the objects rejected erroneously by the system, 5.6% can be attributed to texture-based classification. Unlike with cropland, the texture-based classification rejected one object correctly. It is clear that the classification of grassland and cropland objects still needs to be improved. In particular, the structural features used for classification seem to require a revision.

5. CONCLUSION AND OUTLOOK

The method used to separate cropland from grassland objects described in this paper achieved reasonable results when applied to the verification of cropland objects, but the results for grassland objects are still unsatisfactory. In the future we will revise the structural features used for classification, which apparently fail to separate grassland from cropland objects properly in the current version of the approach. For instance, rather than focusing on the orientation of lines alone, we could also consider the distance between lines by designing features that highlight periodical patterns corresponding to parallel lines. Structural features based on other types of analysis, e.g. variograms, could be added to the classification process. In addition, we could try to use training for determining the parameter γ of the Gaussian Kernel in the SVM classification. Finally, we need to analyse which features are the most relevant ones and have the biggest impact on the classification result.

The main goal of our approach is its application for the verification of ATKIS grassland and cropland objects. In ATKIS one agricultural object may consist of different management units. For instance, a cropland object may consist of fields covered by different crops. It has been stated above

that the generalisation of agricultural objects in ATKIS even allows that within such an object there may be small areas having another land use as long as they do not exceed a certain size. This is why segmentation is necessary to subdivide the original GIS objects into radiometrically homogeneous regions (Helmholz & Rottensteiner, 2009). These regions can be classified into ‘grassland’, ‘tilled cropland’ and ‘untilled cropland’ in the way described in this paper. Afterwards, the overall classification of the GIS object is carried out by a combination of the classification results of the individual regions, taking into account the specifications for the generalisation of ATKIS objects. The final decision about acceptance or rejection of an ATKIS object will be based on this combined classification according to the ATKIS object catalogue (AdV, 2010).

We also hope to be able to detect other object classes with similar structural features such as vineyards and plantations. However, in this case, the image resolution would have to be adapted for the structural analysis, because the rows of plants only appear as parallel lines at a coarser resolution than 1 m. This future research would also have to determine the optimal scale for each object class.

ACKNOWLEDGEMENTS

This work was supported by the German Federal Agency for Cartography and Geodesy (BKG).

REFERENCES

- AdV, 2010. ATKIS- Objektartenkatalog Basis-DLM, Version 3.2 (01.07.2003). <http://www.atkis.de/> (accessed 03 June 2010).
- Arnold, S., 2009: Digital landscape model DLM-DE – Deriving land cover information by integration of topographic reference data with remote sensing data. *IntArchPhRS (38)*, Part 1-4-7/WS, Hannover, (on CD-ROM).
- Busch, A., Gerke, M., Grünreich, D., Heipke, C., Liedtke, C. E., Müller, S., 2004. Automated verification of a topographic reference dataset: System design and practical results. *IntArchPhRS XXXV-B2*, pp. 735-740.
- Canny, J.F., 1986. A computational approach to edge detection. *IEEE T-PAMI 8(6)*, pp. 679-698.
- Chanussot, J., Bas, P., Bombrun, L., 2005. Airborne remote sensing of vineyards for the detection of dead vine trees. *Proc. IGARSS*, pp. 3090- 3093.
- Delenne, C., Rabatel, G., Deshayes, M., 2008. An automatized frequency analysis for vine plot detection and delineation in remote sensing. *IEEE Geosc. & Rem.Sen.Letters 5(3)*: 341- 345.
- DIN, EN, ISO (Hrsg.), Qualitätsmanagement. Begriffe. DIN EN ISO 8402: 1995-08. Berlin 1995.
- Durrieu, M., Ruiz, L.A., Balaguer, A., 2005. Analysis of geospatial parameters for texture classification of satellite images. *Proc. of the 25th EARSEL Symposium*, pp. 11-18
- Fujimura, H., Ziems, M., Heipke, C., 2008. De-generalization of Japanese road data using satellite imagery. *PFG 5(2008)*: 363-373.
- Gimel'farb, G.L., 1996. Texture Modelling by Multiple Pairwise Pixel Interactions. *IEEE TPAMI 18*:1110–1114.
- Hall, A., Louis, J., Lamb, D., 2003: Characterising and mapping vineyard canopy using high-spatial-resolution aerial multispectral images. *Computer&Geosciences*, vol. 19, pp. 813-822.
- Haralick, R.M., Shanmugam, K., Dinstein, 1973. Texture features for image classification. *IEEE Trans. systems, man. & cybernetics*, SMC-3, pp. 610-622.
- Helmholz, P., Rottensteiner, F., 2009. Automatic verification of agricultural areas using IKONOS satellite images. *IntArchPhRS XXXVI - 1-4-7* (on CD-ROM).
- Hermosilla, T., Diaz-Manso, J.M., Ruiz, L.A., Recio, J.A., Fernández-Sarrià, A., Ferradans-Nogueira, P., 2010. Parcel-Based image classification as a decision-making supporting tool for the Land Bank of Galicia (Spain). *IntArchPhRS XXXVIII - W9*, pp. 40-45 (on CD-ROM).
- Itzerott, S. and Kaden, K., 2007. Klassifizierung landwirtschaftlicher Fruchtarten. *PFG 2(2007)*: 109- 120.
- Joss, G., 2000: Zur Qualität von objektstrukturierten Geodaten. *Schriftenreihe Studiengang Geodäsie und Geoinformation, Universität d. Bundeswehr München*, Heft 66, Neubiberg, 2000.
- LeBris, A., Boldo, D., 2008. Extraction of landcover themes out of aerial orthoimages in mountainous areas using external information. *The Photogrammetric Record*, vol. 23, part 124, pp. 387- 404.
- Lu, D. und Wenig, Q., 2007. A survey of image classification methods and techniques for improving classification performance. *International Journal of Remote Sensing*, Vol. 28, No. 5, 2007.
- Müller, S., 2007. Extraktion baulich geprägter Flächen aus Fernerkundungsdaten zur Qualitätssicherung flächenhafter Geobasisdaten. *ibidem- Schriftenreihe*, vol. 9, Dissertation
- Recio, J.A., Ruiz, L.A., Fdez-Sarrià, A., Hermosilla, T., 2006. Integration of multiple feature extraction and object oriented classification of aerial images for map updating. *II Recent Advances in Quantitative Remote Sensing*, Torrent (Valencia), pp. 391- 396.
- Rengers, N. and Prinz, T., 2009. JAVA-basierte Texturanalyse mittels Neighborhood Gray-Tone Differenz Matrix (NGTDM) zur Optimierung von Landnutzungsklassifikation in hoch auflösenden Fernerkundungsdaten. *PFG 5(2009)*:455- 467.
- Ruiz, L.A., Fdez-Sarrià, A., Recio, J.A., 2004. Texture feature extraction for classification of remote sensing data using wavelet decomposition: A comparative study. *IntArchPhRS*, vol. XXXV, pp. 1109- 1115.
- Ruiz, L.A., Recio, J.A., Hermosilla, T., 2007. Methods for automatic extraction of regularity patterns and its application to object-oriented image classification. *IntArchPhRS*, vol. 36 - 3/W49A, pp. 117- 121.
- Trias-Sanz, R., 2006. Texture orientation and period estimation for discriminating between forests, orchards, vineyards, and tilled fields. *IEEE TGARS 44(10)*:2755- 2760.
- Vapnik, V.N, 1998. Statistical Learning Theory. Wiley, New York, USA.
- Warner, T.A. and Steinmaus, K., 2005. Spatial Classification of Orchards and Vineyards with High Spatial Resolution Panchromatic Imagery. *PE & RS*, 71(2): 179- 187.
- Wassenaar, T., Robbez-Masson, J.-M., Andrieux, P., 2002. Vineyard identification and description of spatial crop structure by per field frequency analysis. *Int. J. Remote Sensing 23(17)*: 3311- 3325.

URBAN VEGETATION DETECTION USING HIGH DENSITY FULL-WAVEFORM AIRBORNE LIDAR DATA - COMBINATION OF OBJECT-BASED IMAGE AND POINT CLOUD ANALYSIS

B. Höfle^{a,*}, M. Hollaus^b

^a University of Heidelberg, Department of Geography, 69120 Heidelberg, Germany - hoefle@uni-heidelberg.de

^b Vienna University of Technology, Institute of Photogrammetry and Remote Sensing, 1040 Vienna, Austria - mh@ipf.tuwien.ac.at

KEY WORDS: Airborne LiDAR, Vegetation mapping, Open source GIS, Object-Based Image Analysis

ABSTRACT:

In this paper, a new GIS workflow for fully automated urban vegetation and tree parameter extraction from airborne LiDAR data is presented. The strengths of both raster- and point cloud-based methods are combined, in order to derive a vegetation map layer as well as single tree parameters (e.g. tree height and crown width) in an efficient way. The workflow is implemented in GRASS GIS making use of standard GIS functionality and newly developed tools providing access to point cloud analysis. An edge-based segmentation delineates potential tree crowns, which are further aggregated to single trees or group of trees by using local topological information (e.g. percentage of outline touched by neighbors) and constraints on segment geometry (e.g. shape of segments). Furthermore, the classification makes use of segment attributes that have been extracted from the full-waveform point cloud (e.g. percentage of first echoes, echo width and signal amplitude). A representative study area in the City of Vienna is used to demonstrate the applicability of the developed object-based GIS workflow. Buildings and vegetation objects could be separated with high accuracy, where at maximum 14% of classified vegetation segments confuse with buildings (mainly building edges). Concluding, the unique high density (50 pts/m²) full-waveform LiDAR data open a new scale in 3D object extraction but demanding for novel strategies in object-based raster and point cloud analysis.

1. INTRODUCTION

Vegetation monitoring and tree inventory play an important role in modern urban spatial data management, as many benefits and applications inherit from this detailed up-to-date data source such as monitoring of functions (e.g. noise and pollution mitigation) and creation of 3D city models (Vosselman, 2003). Compared to predominant studies on vegetation detection and characterization mainly in purely forested areas (e.g. Hyypä et al., 2001), this study concentrates on urban areas, which have a high structural complexity with a multitude of different objects (e.g. temporary objects, vegetation on top of buildings, road signs, power lines and cables). Previous studies using airborne LiDAR for vegetation and single tree detection, respectively, used image-based methods, e.g. including orthophotos (Hirschmugl et al., 2007; Iovan et al., 2007; Secord and Zakhor, 2007) and derived raster layers e.g. first-last-pulse difference (Liang et al., 2007). Novel approaches include full-waveform (FWF) information (e.g. echo width and amplitude) for urban object detection in the 3D point cloud directly (Mallet et al., 2008; Rutzinger et al., 2007 and 2008) and for 3D segmentation of single trees (Reitberger et al., 2009).

Höfle et al. (2008) showed the suitability of aggregated FWF attributes attached to segments derived from image analysis for tree species discrimination. This paper aims at transferring this combined object-based image (Blaschke, 2010) and point cloud analysis from forested to complex urban areas, in order to

derive a GIS-ready vegetation mask. To date, high point density (~50 echoes/m²) LiDAR data are increasingly available in particular for urban areas. This high point density does not allow to apply computationally intensive 3D point cloud analysis in an operational manner, which is a prerequisite for being used in city map and cadastre generation. Thus, this study presents a novel GIS framework for full-waveform LiDAR data land cover classification, making use of both image and point cloud analysis (cf. Höfle et al., 2009).

2. STUDY AREA AND DATASETS

The study area is located in the city centre of Vienna, Austria, and comprise the three city parks: Rathauspark, Volksgarten and Burggarten (Fig. 1). A great variety of planting and tree species can be found within the test site, e.g. alley of trees, short-cut trees, hedgerows and shrubs. Deciduous trees are predominant, e.g. beech (*Fagus sylvatica*), Norway maple (*Acer platanoides*), plane (*Platanus acerifolia*), linden (*Tilia cordata*, *platyphyllos*) and chestnut (*Aesculus hippocastanum*) and sparsely coniferous species. The area is characterized by large building complexes (e.g. city hall, Burgtheater and parliament). Furthermore, artificial objects such as fences, cars, power lines, park benches as well as a high amount of people are usually present in this central part of the city, and therefore also included in the airborne LiDAR elevation datasets.

* Corresponding author.

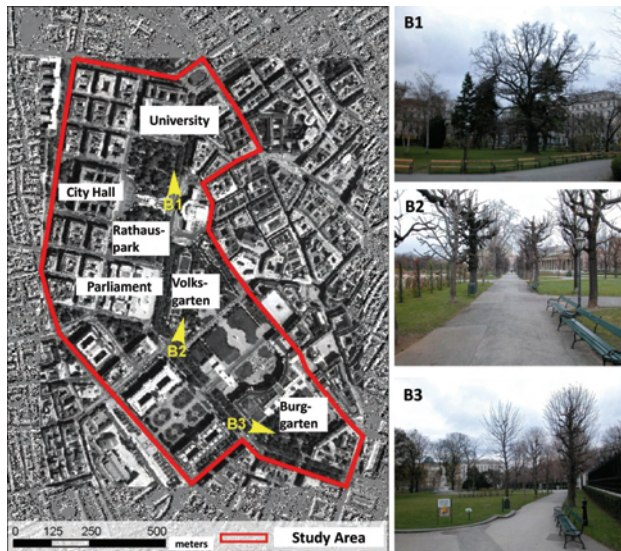


Figure 1. Study area located in the city centre of Vienna, Austria. Diversity in tree species and structure are shown in detailed photographs (B1-B3)

The full-waveform airborne LiDAR data were obtained in the framework of the city-wide laser scanning campaign in the winter season 2006/2007 under leaf-off conditions. Data acquisition was performed with a Riegl LMS-Q560 system, which uses near-infrared (1500 nm) laser pulses with a pulse width of 4 ns. Further settings are a pulse repetition frequency of 200 kHz, scan angle range of $\pm 22.5^\circ$ and a beam divergence of 0.5 mrad. Full-waveform recording can be done with 1 ns temporal resolution. Decomposition of the waveforms was performed by using the Riegl software RiANALYZE. The number of echoes is not limited by the full-waveform recording sensor system, and therefore, the number of detected echoes per laser shot can be higher as with traditional discrete echo recording, particularly in high vegetation. The average echo density of the LiDAR dataset covering the study area is 50 echoes per m^2 with about 6.8% first echoes, 1% intermediate echoes (e.g. 2nd, 3rd echo), 6.8% last and 85.4% single echoes (i.e. only one reflection per shot). A Digital Terrain Model (DTM) with 0.5 m resolution was produced using the software SCOP++ (SCOP++, 2010). For evaluation and comparison a reference dataset including single tree positions of alley trees as well as the official land cover map of Vienna are available: Mehrzweckkarte (MZK), Flächenmehrzweckkarte¹ (FMZK).

3. METHODS

The very high point density of the LiDAR dataset, i.e. about $50 \cdot 10^6$ echoes per km^2 , does not allow a pure point cloud based vegetation detection procedure for large areas (400 km^2 for entire Vienna) in an operational manner. Therefore, a combined object-based image and point cloud approach is introduced, taking advantage of both, fast raster processing and detailed ("interpolation-free") point cloud based information extraction including full-waveform laser point attributes. Furthermore, the high point density of the point cloud allows the derivation of high-resolution derivatives (e.g. DTM with 0.5 m cell size), providing a sufficient planimetric accuracy of the final results.

¹<http://www.wien.gv.at/stadtentwicklung/stadtvermessung/geodaten/fmzk/produkt.html> (last accessed 31.5.2010)

The developed workflow is implemented in the GRASS GIS environment (GRASS Development Team, 2010) and comprises the steps shown in Fig. 2.

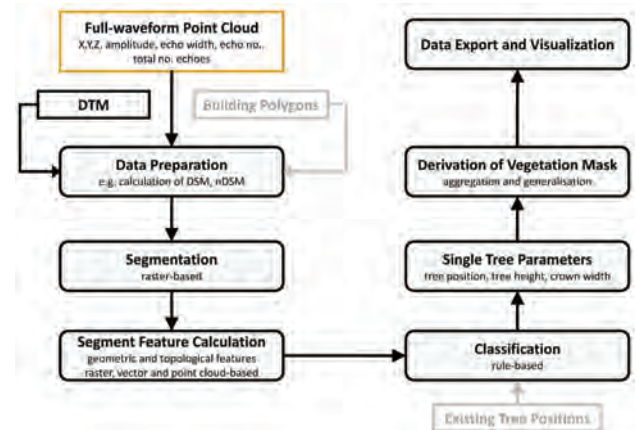


Figure 2. Workflow of urban vegetation detection using raster and full-waveform point cloud input data

3.1 Data preparation

The data preparation of the input point cloud ASCII file includes a classification of the laser points into first, last, single and intermediate echoes. Each laser point has the attributes echo number (EN) and total number (TN) of echoes of the corresponding laser shot, with e.g. single echoes: $EN=TN=1$; first echoes: $EN=1 \ \&\& \ TN>1$; intermediate echoes: $EN>1 \ \&\& \ EN \neq TN$. Using the maximum height per 0.5 m cell a Digital Surface Model (DSM) is derived and finally normalized with the input DTM, in order to get a normalized DSM (nDSM). Empty cells get a normalized height of 0 m. In urban areas generally complete and high quality cadastral data layers are available, which can be used as mask for the subsequent steps. In our study the buildings can be extracted from the official land cover map and could be used optionally to exclude these areas from further investigation. In our study the building polygons are used for evaluation and thus are not considered as input.

3.2 Segmentation

An object-based raster analysis using an edge-based segmentation procedure is applied to the high-resolution nDSM. The procedure has already been tested in densely forested areas where no buildings are present (Höfle et al., 2008) and is transferred to the densely built-up urban area of Vienna in this study. The segmentation aims at delineating convex objects in the nDSM by finding concave edges in between the objects. Additionally, constraints on normalized height ($nDSM > 1.0$ m) and the occurrence of multiple reflections are included. Multiple reflections are parametrized by an echo ratio (ER) defined as (Eq. 1):

$$ER [\%] = (n_{\text{first}} + n_{\text{intermediate}}) / (n_{\text{last}} + n_{\text{single}}) \cdot 100 \quad (1)$$

where n is the respective number of echoes per cell. If no echo is within a cell, ER is set to zero and if no last and single echoes are found within a cell, the echo ratio is set to 100, exhibiting a high vertical extension and transparency of the object. High ER values are assumed to indicate vegetation, which tends to have a high number of first and intermediate echoes compared to other elevated objects in urban areas (e.g. buildings; Fig. 3b).

The edge detector is based on applying a threshold to the minimum curvature in direction perpendicular to the direction of maximum curvature in a certain window (e.g. 7x7 cells), i.e. curvature<0.0 for concave areas (cf. Fig. 3c), and skeletonizing the potential edge areas to reach a final edge map. These edges correspond to the segment boundaries between adjacent objects. By combining the edge map with areas fulfilling height (e.g. >1.0 m; Fig. 3a) and ER threshold (e.g. >5%; Fig. 3b), the final segment raster is derived. In order to derive the segment polygons, a connected component labeling and vectorization of the connected region boundaries are applied (Fig. 3d).

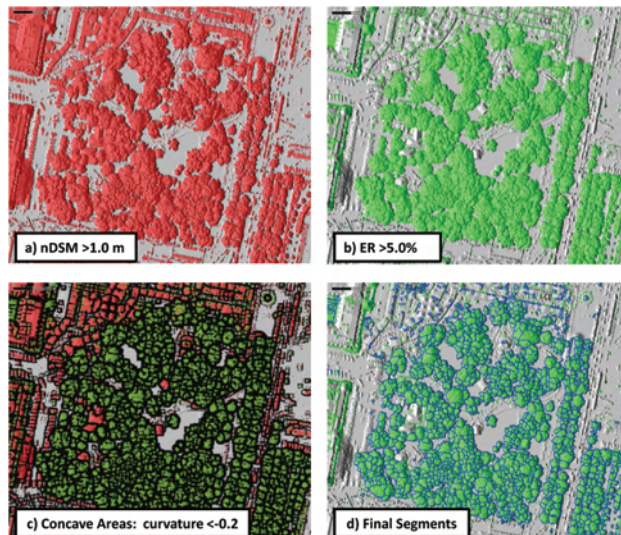


Figure 3. Input layers for segmentation of convex regions in the nDSM having high transparency (i.e. echo ratio)

3.3 Segment feature calculation

For classification of the derived segments the available segment features (i.e. attributes attached to the segment polygons) are essential. In this step an extensive segment feature database is generated, considering segment features based on the point cloud, segment geometry and topology (Fig. 4). The derived features are attached to the attribute table of the GIS polygon layer. By Point-in-Polygon-Test the point attributes (normalized height, amplitude, echo width) stratified by laser echo classes (all, first, multi echoes = first and intermediate, last and single) are aggregated (number of echoes, min., mean, max., standard deviation) per point attribute and segment. In this aggregation step the laser echoes are filtered by the minimum vegetation height value of 1 m above ground, in order to exclude the terrain signature from the segment statistics, except the descriptive statistics for the "all" echo class. Additionally, the number of points falling within a potential height interval for tree stems (i.e. between 1.0 m and 2.5 m) are counted per segment. Furthermore, the ER on segment basis is derived (Eq. 1), and the percentage of points below the minimum vegetation height (i.e. 1.0 m) and above are attached. To include surface information, the statistics of the nDSM cell values are also calculated per segment (e.g. mean nDSM height). Based on segment polygon geometry i) area, ii) perimeter, iii) compactness (perimeter / (2 * sqrt(π * area))) are derived. Due to the topological vector data model in GRASS GIS, topological information can easily be assessed and attached to the segments: i) number of adjacent polygons and ii) percentage of boundary shared with neighbors. All together 66

segment features could be obtained for each segment with 53 point cloud based values.

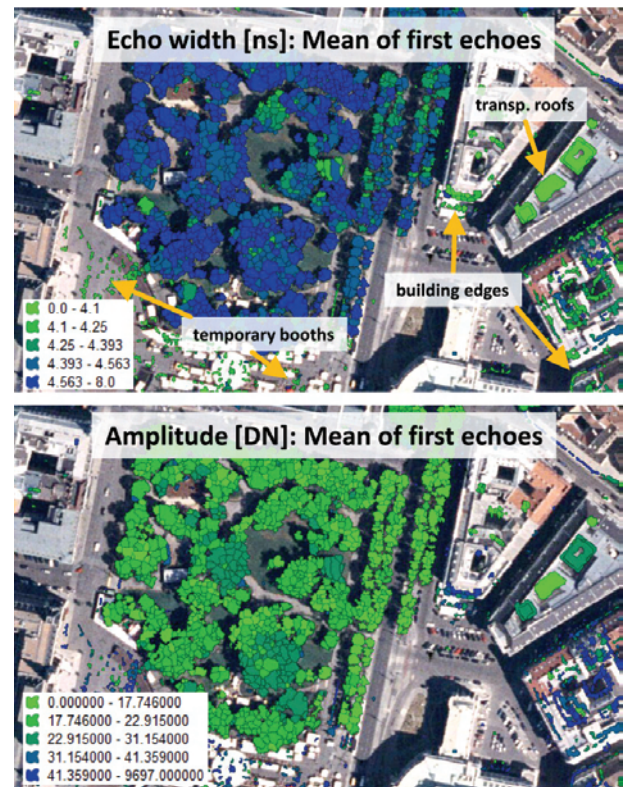


Figure 4. Segments colored by mean echo width (top) and signal amplitude (bottom) of all first echoes within a segment. Non-vegetation segments can clearly be identified by low echo widths and higher amplitudes

3.4 Classification

Exploratory data analysis was performed, in order to set-up a rule-base for supervised classification. A logical rule base for classification was developed, which in a first step aims at separating vegetation from non-vegetation segments. Tree positions from the reference map are included in the classification process. Final classes and classification hierarchy are shown in Fig. 5. The GIS environment easily allows to perform the final classification using SQL statements in the attribute database.

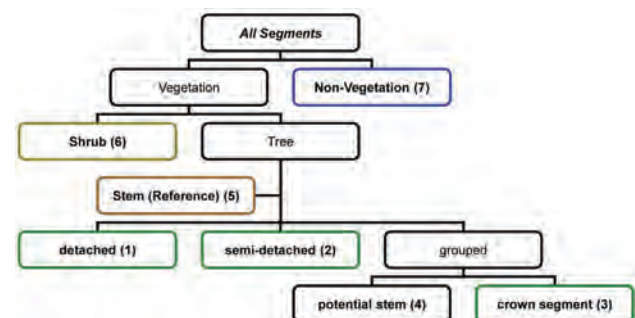


Figure 5. Classification scheme including reference tree positions. Target classes are numbered from 1 to 7.

3.5 Tree segment parameters

The city administration is mainly interested in updating tree parameters for their available tree positions. These parameters serve for the city tree inventory but also for visualization purposes (i.e. virtual reality/city). Tree position, tree height and crown diameter are derived for the classified stem and potential stem segments. Due to the occurrence of power lines, adjacent buildings/roofs a robust calculation of tree height is introduced. The robust tree height is defined as the highest laser point fulfilling the criterion of being within a maximum height above the mean height of the k highest points of a segment (Fig. 6a). Tree crown diameter is approximated by the smallest enclosing circle (SEC) to the segment boundary including calculation of the mean deviation to the maximum diameter, in order to provide a quality measure of the derived diameter value (Fig. 6b). Different methods for tree position estimation are implemented: i) position of robust highest point, ii) circle center of SEC, iii) center of gravity of segment boundary vertices (Fig. 6c). The tree position estimation results in a new point GIS vector layer holding all segment attributes as well as crown diameter and tree height attributes.

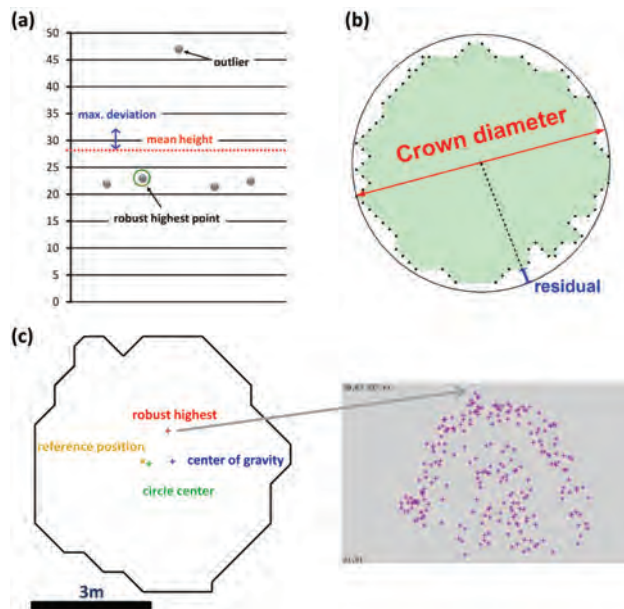


Figure 6. (a) Robust highest point/segment, (b) crown diameter by smallest enclosing circle and (c) different methods of tree position estimation compared with reference position (left) and point cloud cross-section indicating highest point (right)

3.6 Derivation of vegetation mask

Vegetation mask derivation is straightforward, due to the GIS vector topology. Common boundaries between vegetation segments are dissolved, i.e. adjacent polygons are merged. This procedure is followed by a generalization step, where small isolated polygons are removed (e.g. 20 m²) and small holes (i.e. islands; e.g. 20 m²) are closed. Furthermore, the vegetation mask boundary can be generalized by line simplification (e.g. Douglas-Peucker) or smoothing (e.g. Snakes) readily available in the GRASS GIS framework.

4. RESULTS AND DISCUSSION

The defined echo ratio (ER) raster layer based on echo classes (e.g. first, last echo) clearly shows a very good agreement with potential urban vegetation areas (Fig. 3b). Compared to other definitions of echo ratios, such as a purely geometric computation (e.g. Rutzinger et al., 2007; Höfle et al., 2009) where number of neighbors are counted in a defined 2D and 3D neighborhood, the high point density and the increased echo detection sensitivity and echo labeling provided by full-waveform LiDAR allows this faster ER derivation without the need for computationally intensive 3D point cloud neighborhood analysis. Furthermore, the full-waveform based ER is more robust against multi-temporal effects caused by temporary objects (Fig. 7). For example, a truck scanned in one flight strip but not present in a second strip covering the same area will cause an artificial object with a certain height above terrain and a very high transparency but will still have low echo widths and a low number of multiple echoes per shot.

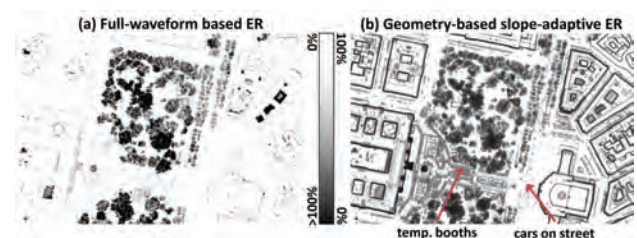


Figure 7. (a) Full-waveform based echo ratio (ER), (b) geometry-based echo ratio (Höfle et al., 2009). Temporary objects can clearly be identified in the geometry-based ER

In order to evaluate the separation capability of vegetation from non-vegetation, the optional building mask was not included for segmentation. Our experiments have shown that optional including of a building mask achieves best results when used as "soft mask", due to the occurrence of buildings below vegetation such as smaller buildings in parks or subway stations below alley trees. A "hard mask" would exclude building areas found in the cadastre from further processing and thus finally classify these areas as non-vegetation. A soft mask means a stricter threshold on ER than for the non-building areas (e.g. ER > 50%), which should exclude most of structures related to free-standing buildings (e.g. walls and antennas) but still enables the detection of vegetation overtopping low buildings. These trees are mainly deciduous species and hence transparent under leaf-off conditions with a high number of laser shots with multiple echoes (i.e. high ER). The choice of window size for curvature calculation controls the degree of detail reflected in over- or under-segmentation (cf. Höfle et al., 2008). The larger the window size, the less segments are found. The threshold on curvature additionally controls the sensitivity for edge detection. The more moderate the threshold is chosen, the more edges can be detected, but also the potential edge zones become wider (Fig. 3c) and thus the location accuracy of the "thinned" edge line gets more uncertain. The location accuracy of the depression line between two objects could be improved by weighted skeletonization (by curvature and height) or drawing profiles for detecting the lowest point or the point with highest concavity in the boundary zone of two segments.

The segmentation step results in 23788 segments (compared to 67 Mio. laser echoes within the study site) with an average size of 10.6 m². A window size of 7x7 pixel (i.e. 0.5 m resolution) for curvature calculation with curvature constraint of lower than -0.2 were chosen. Trees with a compact and convex crown

shape result in one segment, whereas large deciduous trees with multiple tree tops are represented by multiple segments (one per convex tree top). For selected 181 alley trees the average number of segments per tree is 2.6, indicating over-segmentation and trees with multiple tops, respectively. Within the park areas with larger deciduous trees the number of segments per tree lies clearly higher but could not be assessed due to missing reference positions. Over-segmentation can also be reduced by prior filtering (e.g. Gauss filter) of the DSM in order to reduce canopy roughness and suppress small structures (cf. Hirschmugl et al., 2007).

7 - Non-Vegetation	
Perc. of echoes above min. height (2 m) [%]	>99.0
Mean amplitude of first echoes [DN]	>50
Mean amplitude of last echoes [DN]	>100
Mean echo width of first echoes [ns]	< 4.1
Std.dev. of echo width of first echoes [ns]	< 0.35
Std.dev. of heights of first echoes [m]	> 10
Std.dev. of heights of first echoes [m]	< 0.2
ER of segment [%]	< 5
Compactness &&	> 1.7
Mean nDSM height [m] &&	> 3.0
Stddev. of height of first echoes &&	≥ 1.0
Perc. of boundary covered by neighbors	< 60%
6 - Shrubs	
Mean nDSM height [m] &&	< 3.0
Std.dev. of heights of first echoes [m]	< 1.0
5 - Stem (reference)	
Distance to reference tree position [m]	< 1.0
1 - Detached	
No. of adjacent segments	≤ 0
2 - Semi-detached	
Perc. of boundary covered by neighbors	< 20
4 - Potential stem segment	
Number of echoes in height interval 1.0 - 2.5 m	> 10
3 - Crown segment	
All remaining segments	

Table 1. Rules and thresholds on segment attributes for detecting vegetation and further characterization

Although the constraint on ER already excluded the majority of non-vegetation objects, the segments still contain non-vegetation objects such as building walls, roof overhangs, transparent roofs and power lines. Thus, full-waveform point cloud information derived on segment level is valuable for separating vegetation from non-vegetation. Particularly, echo width and signal amplitude show clear signatures for vegetation (refer to Fig. 4). Vertically extended objects with a multitude of small scatterers (e.g. branches) exhibit larger echo widths and lower amplitudes due to the relatively small target areas contributing to each echo (cf. Wagner et al., 2008). The main part is to exclude non-vegetation segments. Through exploratory data analysis and visual inspection suitable attributes and thresholds could be obtained. Table 1 shows the applied rules to the rule base defined in Fig. 5 and Fig. 8 the resulting classified segments. For example, the percentage of echoes above the min. tree height of 1 m indicates a low ground penetration, which mainly occurs at building walls not connected with the ground, transparent roofs, antennas on roofs, and even vegetation on top of buildings, exhibiting an ER above 5%. Building facades can be excluded by high compactness, as they are elongated, and high std.dev. of first echo heights together with low coverage of adjacent segments and relatively high mean nDSM heights. High nDSM heights

for vertical walls are also due to the generation procedure of the DSM, where the maximum height value per cell is taken. Shrubs are distinguished by using mean nDSM height and std.dev. of first echo heights, which is assumed to be lower than for trees.

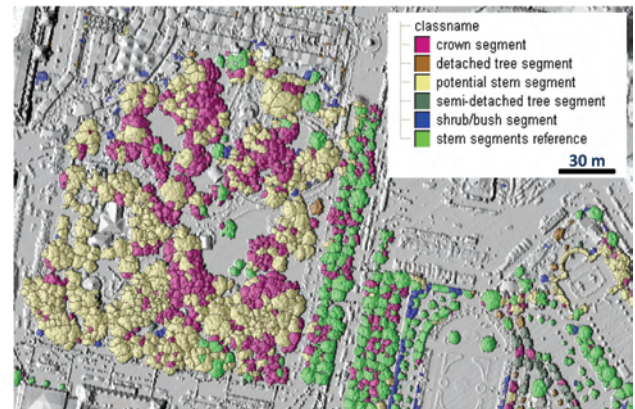


Figure 8. Classified vegetation segments further separated into six sub-classes.

This manual set up and selection of attributes and thresholds will be replaced by automatic classification procedures in future such as statistical classification trees (Rutzinger et al., 2008) or Support Vector Machines (Mallet et al., 2008), which have already been applied to classify single laser points of large point clouds. The segment-based approach may lead to more stable features for classification (e.g. mean echo width per segment; cf. Rutzinger et al., 2008) but is strongly dependent on the quality and delineation accuracy of the segmentation. The current state of segmentation and classification provides the necessary input for vegetation mask generation and derivation of tree segment parameters (e.g. height, diameter, position) for visualization purposes by reconstructing artificial tree objects (cf. Vosselman, 2003). However, for urban tree inventory single tree detection is required and tree positions should be derived from stem detection. The class of potential stem segments could be a starting point for further point cloud based stem extraction. Multi-level/scale segmentation, i.e. further segmentation on the derived segments, could solve the problem of over-segmentation (Blaschke, 2010) and join segments belonging to one tree. Promising studies have already shown the potential of point cloud based single tree detection for airborne (Reitberger et al., 2009) and mobile LiDAR data (Rutzinger et al., 2010). No point cloud segmentation is required for the class of detached tree segments, representing a single tree object. But for trees with multiple tops and no distinct crown shape 3D point cloud segmentation shows great potential, providing the required information inherent in the vertical sampling of the objects by airborne LiDAR. Multi-level LiDAR analysis, such as prior image based detection of candidate regions with following point cloud based object detection increasing delineation and classification accuracy offers the possibility to process large areas even with very high point densities in an operational manner without major loss in classification accuracy, if the pre-selection has high completeness (cf. Höfle et al., 2009).

For evaluation the alley tree inventory (i.e. tree positions) is used. Out of 668 alley trees 639 (95.7%) could be successfully detected and included in the final vegetation mask. The missing trees are mainly young trees with low diameter and crown area,

below the defined minimum segment area of 2 m². Confusion with buildings (mainly the edges) is the major task of separating vegetation in urban areas. Using the cadastral building layer 3.4% of the total vegetation segment area intersects with buildings and 7.7%, if the building polygons are buffered with 2 m, indicating that predominantly building edges are wrongly classified. Note that also buildings overtopped by vegetation are also counted as error. On segment basis 4.8% of segments (402 of 8413) are intersecting with buildings with more than 50% of their area. Looking at the buffered buildings, 14.0% (1182) of the segments confuse with building areas.

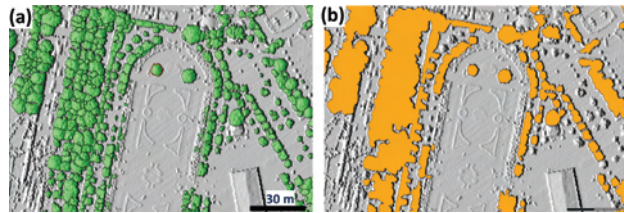


Figure 9. (a) Vegetation segments and (b) derived generalized vegetation GIS layer

The final result is the generalized vegetation mask (Fig. 9), generated by using the segments falling within one of the vegetation classes. Generalization was performed by removing small isolated vegetation areas (<20 m²) and holes within vegetation (<20 m²). Additionally the vegetation layer boundary is smoothed using Snakes ($\alpha=1.0$).

5. CONCLUSIONS

This paper presented a novel workflow of GIS-based urban vegetation mapping using high density full-waveform LiDAR data. The combination of image-based object analysis and point cloud-based segment feature derivation and classification shows promising results for automated, operational applications, such as urban mapping, map updating, 3D visualization and urban tree inventory, when combined with single tree and stem detection algorithms. Future work will concentrate on including radiometric calibration, automated classification (e.g. statistical decision trees) and point cloud based single tree detection.

ACKNOWLEDGMENTS

We would like to thank the MA41-Stadtvermessung, City of Vienna, for their support and providing the airborne LiDAR data and reference datasets.

REFERENCES

Blaschke, T., 2010. Object based image analysis for remote sensing. *ISPRS Journal of Photogrammetry and Remote Sensing*, 65, pp. 2-16.

GRASS Development Team, 2010. Geographic Resources Analysis Support System (GRASS) Software, Version 6.4.0. Open Source Geospatial Foundation. <http://grass.osgeo.org>

Hirschmugl, M., Ofner, M., Raggam, J., Schardt, M., 2007. Single tree detection in very high resolution remote sensing data. *Remote Sensing of Environment*, 110, pp. 533-544.

Höfle, B., Hollaus, M., Lehner, H., Pfeifer, N., Wagner, W., 2008. Area-based parameterization of forest structure using full-waveform airborne laser scanning data. In: *Proc. Silvilaser 2008*, Edinburgh, Scotland, pp. 227-235.

Höfle, B., Mücke, W., Dutter, M., Rutzinger, M., Dorninger, P., 2009. Detection of building regions using airborne LiDAR - A new combination of raster and point cloud based GIS methods. In: *Proc. of the GI_Forum*, Salzburg, pp. 66-75.

Hyypä, J., et al., 2001. HIGH-SCAN: The first European-wide attempt to derive single-tree information from laserscanner data. *The Photogrammetric Journal of Finland*, 17, pp. 58-68.

Iovan, C., Boldo, D., Cord, M., 2007. Automatic extraction of urban vegetation structures from high resolution imagery and digital elevation model. In: *Urban Remote Sensing Joint Event, URBAN 2007 – URS 2007*, Paris, pp. 1-5.

Liang, X., J. Hyypä, J., Matikainen, L., 2007. Deciduous-coniferous tree classification using difference between first and last pulse laser signatures. In: *IAPRS*, Vol. 36, Part 3/W52, pp. 253-257.

Mallet, C., Bretar, F., Soergel, U., 2008. Analysis of Full-waveform LiDAR Data for Classification of Urban Areas. *Photogrammetrie Fernerkundung Geoinformation*, 5, pp. 337-349.

Reitberger, J., Schnörr, C., Krzystek, P., Stilla, U., 2009. 3D segmentation of single trees exploiting full waveform LIDAR data. *ISPRS Journal of Photogrammetry and Remote Sensing*, 64, pp. 561-574.

Rutzinger, M., Höfle, B., Pfeifer, N., 2007. Detection of high urban vegetation with airborne laser scanning data. In: *Proceedings Forestsat 2007*. Montpellier, France, pp. 1-5.

Rutzinger, M., Höfle, B., Hollaus, M., Pfeifer, N., 2008. Object-Based Point Cloud Analysis of Full-Waveform Airborne Laser Scanning Data for Urban Vegetation Classification. *Sensors*, 8(8), pp. 4505-4528.

Rutzinger, M., Pratihast, A.K., Oude Elberink, S., Vosselman, G., 2010. Detection and Modeling of 3D Trees from Mobile Laser Scanning Data. In: *Proc. ISPRS TCV Mid-Term Symposium*, Newcastle upon Tyne, 6p.

Secord, J., Zakhor, A., 2007. Tree Detection in Urban Regions Using Aerial Lidar and Image Data. *IEEE Geoscience and Remote Sensing Letters*, 4(2), pp. 196-200.

SCOP++, 2010. Institute of Photogrammetry and Remote Sensing, www.ipf.tuwien.ac.at/products/products.html, last accessed 31.05.2010.

Vosselman, G., 2003. 3D reconstruction of roads and trees for city modelling. In: *IAPRS*, Vol. 34, Part 3/W13, 6p.

Wagner, W., Hollaus, M., Briese, C., Ducic, V., 2008. 3D vegetation mapping using small-footprint full-waveform airborne laser scanners. *International Journal of Remote Sensing*, 29 (5), pp. 1433-1452.

TERRAIN ROUGHNESS PARAMETERS FROM FULL-WAVEFORM AIRBORNE LIDAR DATA

M. Hollaus^{a,*}, B. Höfle^b

^a Institute of Photogrammetry & Remote Sensing, Vienna University of Technology, Gußhausstr. 27-29, A-1040 Vienna, Austria, mh@ipf.tuwien.ac.at

^b Department of Geography, University of Heidelberg, Berliner Str. 48, D-69120 Heidelberg, Germany, hoefle@uni-heidelberg.de

KEY WORDS: Three-dimensional, LIDAR, Surface, DEM/DTM, Retrieval, Geomorphology, Roughness

ABSTRACT:

As an active remote sensing technique airborne laser scanning (ALS) is able to capture the topography with high precision even for densely forested areas. Due to the high pulse repetition frequency of up to 400 kHz a high sampling rate on the ground can be achieved, which allows the description of the terrain surface in decimeter scale. In this contribution two approaches to characterize terrain roughness are described. In the first approach the standard deviation of detrended terrain points is calculated. To achieve a high spatial resolution of the derived roughness layer a high terrain point density is essential, which requires especially in dense forested areas a very high sampling rate. In addition to the 3D position of backscattering objects, full-waveform ALS systems provide the width of each detectable echo, which provides information on the range distribution of scatterers within the laser footprint that contribute to one echo. It is therefore, an indicator for surface roughness and the slope of the target. In comparison to the roughness layer derived from the first approach using high point densities, the derived echo width image shows similar spatial patterns of terrain roughness even for moderate point densities. The results show that both the echo widths and the vertical distribution of terrain echoes are useful to derive reliable geometric terrain roughness layers of large areas.

1. INTRODUCTION

For the modeling of natural hazards e.g. avalanches (e.g. Margreth and Funk, 1999), rock falls (e.g. Dorren and Heuvelink, 2004) and floods (e.g. Govers et al., 2000), information about the terrain roughness is required. For these different natural processes different levels of detail of the terrain roughness from micro-level (e.g. millimeters to centimeters), to meso-level (e.g. decimeter to meters) to macro-level (e.g. meter to kilometers) are required. For practical applications the terrain roughness is commonly estimated by field investigations, which are typically based on thematic roughness classes as for example described by Markart et al. (2004). Furthermore, the terrain or landscape roughness in the macro-level can be determined from digital terrain model (DTM) analyses as for example shown in Smith et al. (2004). Also for the meso-level investigations exist that use airborne laser scanning (ALS) and spectral remote sensing data for floodplain roughness parameterization (e.g. Straatsma and Baptist, 2008).

Especially for forested areas ALS, also referred to as LiDAR, has been proven as the state of the art technology for the acquisition of topographic information. As an active remote sensing technique ALS is able to capture the topography with high precision even for densely forested areas. The transmitted nanosecond-long (e.g. 4 ns) laser pulses in the near-infrared range of wavelengths (e.g. 1.0 or 1.5 μm) have a typical beam

divergence of 0.5 mrad, resulting in footprint diameters of 0.2 to 0.5 m for typical flying heights above ground of 400 to 1000 m. Due to the high pulse repetition frequency of up to 400 kHz a high sampling rate on the ground can be achieved, which allows the description of the terrain surface in decimeter scale.

In this contribution two approaches to characterize terrain roughness with geometric quantities are described. In the first approach the standard deviation of detrended terrain points is calculated. To achieve a high spatial resolution (e.g. 1.0 x 1.0 m) of the derived roughness layer a high terrain point density is required. Especially in dense forested areas where the laser beam penetration rates can decrease to 10% to 20% (e.g. Hollaus et al., 2006) a very high sampling rate is, therefore, mandatory. In addition to the 3D position of backscattering objects, full-waveform (FWF) ALS systems provide (i) the signal amplitude characterizing the reflectance of the scanned surface and (ii) the width of each detectable echo, which provides information on the range distribution of scatterers within the laser footprint that contribute to one echo (Wagner et al., 2004). Consequently, it is assumed that the echo width is an indicator for roughness and the slope of the target. Thus, in the second approach the potential of the derived echo widths are analysed for terrain roughness characterization. Finally, both derived terrain roughness layers are compared and discussed.

* Corresponding author.

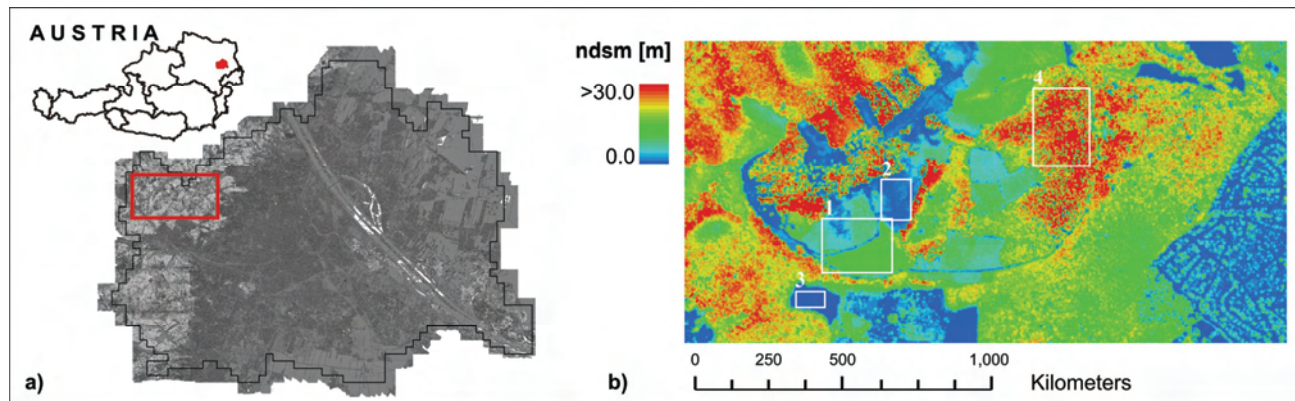


Figure 1. Overview of the study area: a) digital surface model of the city of Vienna, b) normalized digital surface model (nDSM) of the study area in the Vienna Woods. In the subareas 1-4 additional analyses are done (see Sect. 3.3).

2. STUDY AREA AND DATA

The study area is located in the western part of Vienna (Fig. 1), in the so-called Vienna Woods, and covers about 200 hectares forest and a small part of an urban area. The study area is part of the UNESCO biosphere reserve Wienerwald¹, which was installed by the provinces of Lower Austria and Vienna in 2005. Since the 19th century the Wienerwald region has been used as a traditional recreation area for Viennese and inhabitants of Lower Austria, which are living in the immediate vicinity. In general, the landscape of the Vienna wood is characterized by individual deciduous forests, which are closely interlinked with meadows while the forests are dominated by oak and hornbeam, beech at higher altitudes, and ash in the peak region of north-facing slopes. Within the investigated area the dominating tree species are red beech (*Fagus sylvatica*) with ~51%, oaks (*Quercus robur*, *Quercus petraea*) with ~23% and hornbeam (*Carpinus betulus*) with ~16%. The remaining areas are covered with ~6% larch (*Larix decidua*), 2% clearings and other deciduous and coniferous tree species. The forests are characterized by a balanced age class distribution (tree ages vary between 5 and 180 years) and with tree heights varying between 2.0 m and 45.0 m. The clearings are partly covered by very dense brushwood i.e. blackberry. Furthermore, some young forest stands covered with very dense red beech (*Fagus sylvatica*) are available.

For the study area full-waveform airborne laser scanning (FWF-ALS) data was provided by the city of Vienna (MA41 Stadtvermessung) and was acquired in the framework of a commercial terrain mapping project, fully covering the city of Vienna. The FWF-ALS data was acquired with a Riegl LMS-Q560 by the company Diamond Airborne Sensing² in cooperation with AREA Vermessung ZT GmbH³ in January 2007. The average point density is greater than 30 echoes per square meter. The pre-processing of the FWF-ALS data was done from the company AREA Vermessung ZT GmbH using the Riegl software packages⁴. For the current study the georeferenced 3D echo points and the determined attributes for each echo, i.e. the echo width and the amplitude, serve as input for the following analyses.

The digital terrain model (DTM) was calculated using the SCOP++ (2010) software. For the determination of the digital surface model (DSM) the approach described in Hollaus et al. (2010) was applied using the OPALS (2010) software. Finally, the normalized digital surface model (nDSM) was calculated by subtracting the DTM from the DSM (cf. Fig. 1b). The derived topographic models (DTM, DSM, nDSM) have a spatial resolution of 0.5 m. The DTM is used for normalizing the 3D echo points (dz) and therefore, for the selection of terrain and near-terrain echoes (cf. Sect. 3.1 and 3.2). The nDSM is used for visualization purposes only.

3. TERRAIN ROUGHNESS PARAMETERS FROM FWF-ALS DATA

Looking at roughness from the ALS sensing technique point of view (Fig. 2), the spatial scale of observation plays a crucial role. Roughness with a spatial scale of up to a few decimeters cannot be determined directly by using the ALS range measurements (i.e. XYZ of point cloud) because of the range accuracy (Kraus, 2007), which generally lies far above the given laser wavelength of a few micrometers. Hence, micro structures can only be determined indirectly, for example, by using the strength of reflection of a laser echo (i.e. amplitude), which is correlated with target reflectivity but also surface roughness (Wagner et al., 2004).

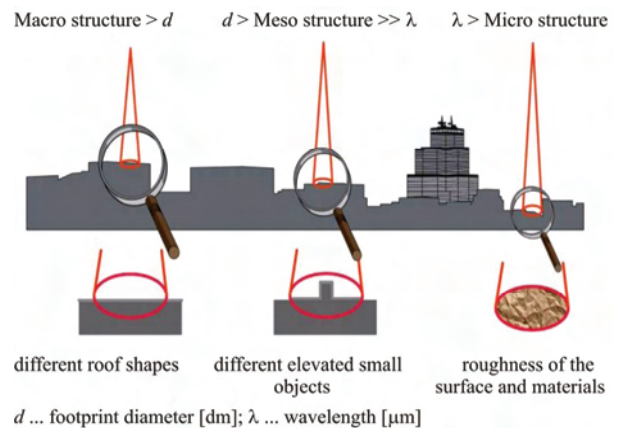


Figure 2. Scales of roughness in terms of the ALS sensing technique (modified from Jutzi and Stilla, 2005).

¹ <http://www.biosphaerenpark-wienerwald.org>

² <http://www.diamond-air.at/airbornesensing.html>

³ <http://www.area-vermessung.at/>

⁴ <http://www.riegl.com/nc/products/airborne-scanning/>

The focus of the current paper is on the terrain roughness parameterization of the meso structure (Fig. 2). For the parameterization of the terrain roughness two approaches are investigated. In the first approach a geometric description by calculating the standard deviation of detrended terrain points is used. In the second approach the potential of the derived echo widths are analyzed for terrain roughness characterization.

3.1 Standard deviation of detrended terrain points

In this first approach the terrain roughness is parameterized by the standard deviation of the detrended z-coordinates of all FWF-ALS echoes within a raster cell or a certain distance of e.g. 1.0 m, which are located below a defined normalized height (dz) threshold (Fig. 3a). For the current study four different height thresholds (0.25 m, 0.5 m, 1.0 m, 2.0 m) are applied. The detrending of the FWF-ALS heights is important for slanted surfaces, where else the computed standard deviation would increase with increasing slope (i.e. height variation), even though the surface is plane. Algorithmically, simply the standard deviation of orthogonal regression plane fitting residuals is chosen. Taking the residuals to a best fit plane can be compared to a prior detrending of the heights. The orthogonal regression plane fitting (Fig. 3b) is favored over vertical fitting because for very steep surfaces the vertical residuals can become very large, even though the plane fits very well to the points. In this sense orthogonal fitting means that the orthogonal distances from plane to points is minimized. In practical, for every laser echo the orthogonal plane fitting is performed in a local neighborhood (i.e. considering all terrain echo neighbors in a certain distance for plane computation; e.g. <1.0 m) and stored as additional attribute to the original laser echo.

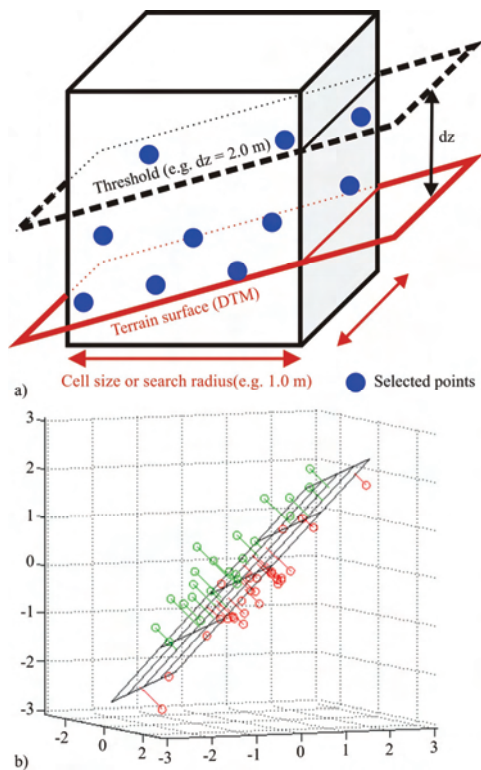


Figure 3. Standard deviation of detrended terrain points: a) Predefined cube or cylinder for selecting echoes used for plane fitting. b) Principle of orthogonal regression plane fitting (modified from www.mathworks.com).

The unit of the so derived terrain roughness parameter is in meters and can be compared between different flight epochs and ALS systems. Finally, the derived standard deviations are averaged per raster cell.

3.2 Echo width of terrain points

The meso structure is defined to be smaller than the footprint diameter (Fig. 2). Such structures can be obtained either directly, if a high point density with overlapping footprints is given or the range resolution of the scanner system allows distinguishing multiple echoes in the magnitude of few decimeters, which is currently not achieved by state-of-the-art scanners. The maximum sampling interval is currently 1.0 ns, which corresponds to approx. 15.0 cm (30.0 cm for both ways) (Wagner et al., 2006). For objects few times larger than the sampling interval, the widening of the echo (i.e. larger echo width) indicates a certain vertical extent of the illuminated object, which can be assigned to roughness in a broader sense. For the used FWF-ALS data the received full-waveforms were digitized with an interval of 1 ns (Fig. 4). A Gaussian decomposition method was applied to estimate in addition to the location the scattering properties of the targets i.e. the amplitude and the echo width (Wagner et al., 2006). Therefore, the derived echo width of each single echo is representative for the roughness within the illuminated footprint (Fig. 4). For deriving the terrain roughness layer laser points within a maximal vertical distance (dz) to the DTM (dz = 0.25 m, 0.5 m, 1.0 m, 2.0 m) are selected. For a laser beam with multiple echoes the illuminated footprint decreases depending on the collision area of the previous reflected echoes. Only single echoes are selected for the terrain roughness parameterization, in order to guarantee that only extended targets with similar footprint sizes are investigated. For this study the influence of varying flying heights and consequently to varying ranges, and the local incidence angle are neglected. Finally the terrain roughness layers are generated by aggregating the selected echo widths per raster cell (e.g. mean value). The unit of the terrain roughness layers is in nanoseconds and could be converted to meters.

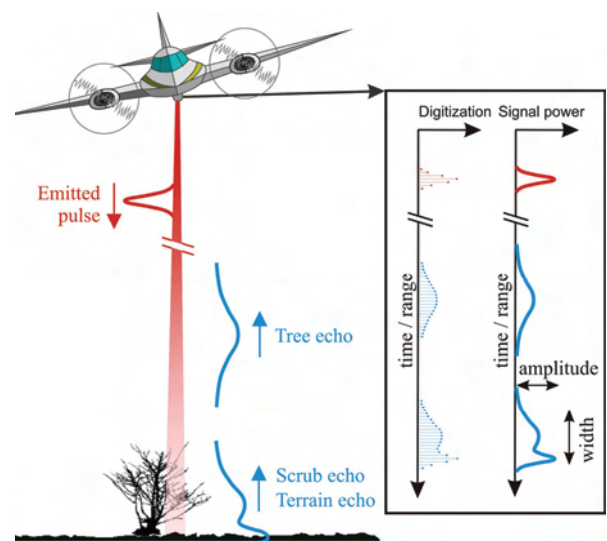


Figure 4. Full-waveform ALS system. A Gaussian decomposition is applied to derive echo widths, which are used for the parameterization of terrain roughness. (adapted from Doneus et al., 2008)

3.3 Validation of the terrain roughness parameters

In a first processing step the derived terrain roughness layers (standard deviation of detrended terrain points, mean echo widths of terrain points) are compared. A linear regression from both roughness images, according to the formula $y = a + b \cdot x$, where x and y represent raster maps was calculated. In addition to the entire image, subareas were selected, each representing an individual land cover type (see subareas in Fig. 1) i.e. grass (3), bushes (2), young (1) and old (4) forest for calculating the linear regression. Finally, a plausibility check was done by field investigations. Furthermore, the effect of varying footprint sizes caused by multiple echoes on the derived echo widths is studied. To ensure, that only echoes with footprint sizes, which are in a similar range, are used, only single echoes (i.e. extended targets) that are below the defined height thresholds were selected. The selected single echoes are used to generate additional roughness layers.

4. RESULTS AND DISCUSSION

Fig. 5 shows the standard deviation of the detrended terrain points as well as mean echo widths of using all echoes. High standard derivations (bright areas) indicate a high terrain roughness. Large echo widths (bright areas) are caused by a certain vertical distribution of scatterers within a laser shot footprint and hence large echo widths indicate high terrain roughness. The visual comparison of the derived roughness layers (Fig. 5) clearly shows similar spatial patterns of areas with high values of terrain roughness. It can also be shown that this similarity is apparent for all applied height thresholds. The highest correlation coefficients ($R=0.62 - 0.63$) are available for the roughness layers derived from echoes with heights (dz) less than 0.25 m and 0.50 m, respectively. The linear regression between the standard deviation of the detrended terrain points and the mean echo widths derived from the extended targets show a slight decrease of the correlation coefficients e.g. for echoes with $dz < 0.5$ m from $R=0.63$ to $R=0.58$.

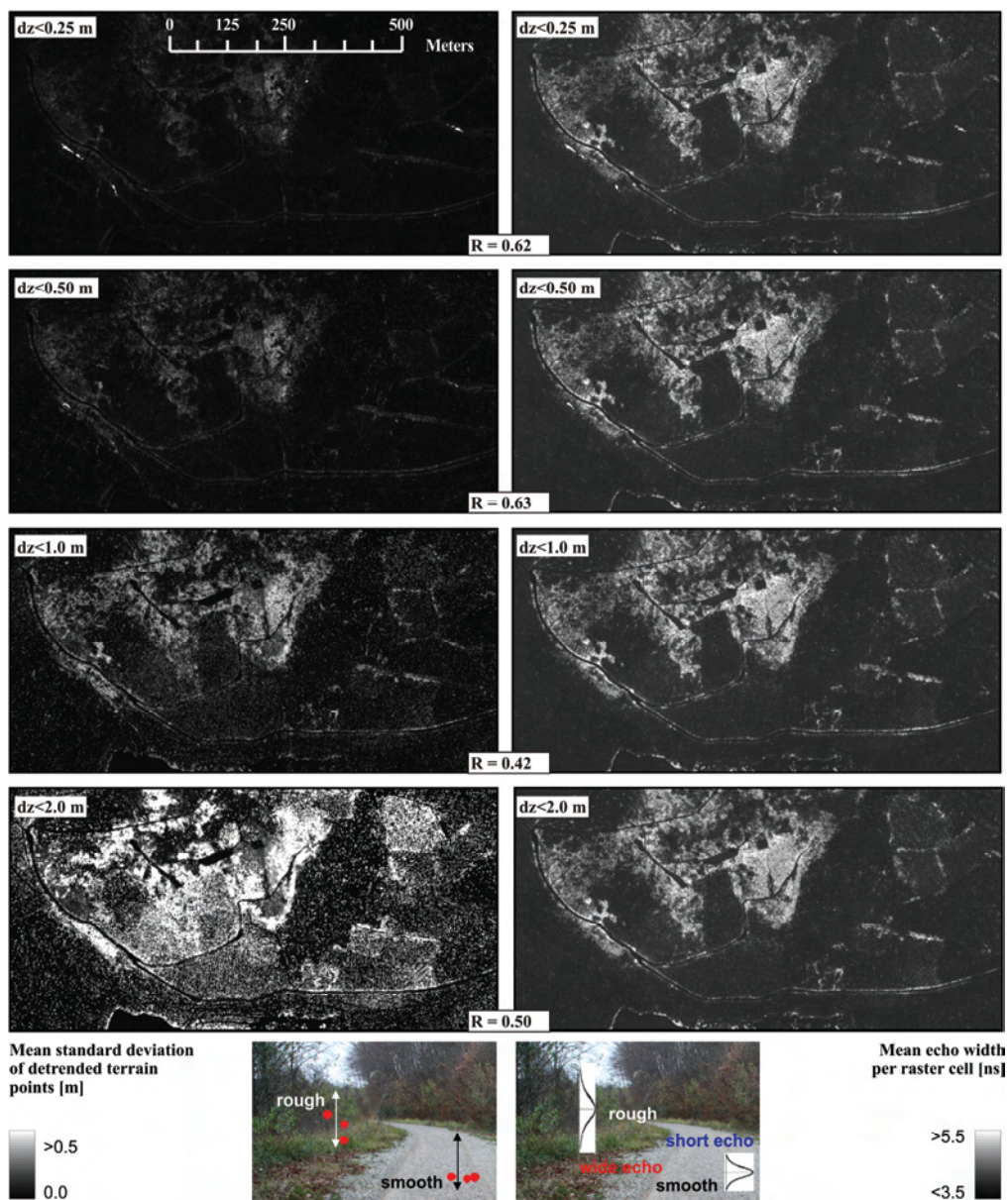


Figure 5. Roughness layers derived from FWF-ALS data. Left: Mean standard deviation per raster cell of detrended terrain points for different height thresholds. Right: Mean echo width per raster cell calculated from terrain and near terrain points respectively.



Figure 6. Shading of the standard deviation of the detrended terrain echoes ($dz < 1.0$ m overlaid with pictures from different features).

This indicates that varying footprint sizes of single and multiple echoes have a negligible influence on the terrain roughness parameterization. For the young forest subarea (see Fig. 1, region 1) the correlation coefficients increases e.g. to 0.68 for echoes with $dz < 0.25$ m. For all other subareas (see Fig. 1, region 2-4) the correlation coefficients decrease. However, as a decrease was not expected further statistics were calculated. For the grassland subarea the standard deviation of the mean echo width is 0.03 ns and for the old forest stand subarea the standard deviation is 0.02 ns. Also the standard deviation of the mean standard deviation per raster cell of detrended terrain points are small and are in the range of 0.4 to 1.9 centimeters. This means that there is only a constant shift between the two roughness layers. Furthermore, this indicates very homogeneous and smooth surfaces, which corresponds to the information derived during the field check. Moreover, this small standard deviations can be interpreted as measurement noise of the used FWF-ALS system. Even in the densely forested areas with FWF-ALS it is possible to acquire a sufficient amount of elevation measurements of the forest terrain surface. As shown in Fig. 6 areas indicated by high roughness values are mainly covered by low vegetation (e.g. bushes) or exhibit a very dense distribution of tree stems, which also account for terrain roughness as defined in this study. High roughness values are also available at the borders of forest roads and tracks where commonly discontinuities (e.g. breaklines) are available. The results let assume that FWF-ALS echo width values are able to identify areas with high terrain roughness without the need of a highly detailed geometrical representation of the ground surface by

acquiring very dense point clouds. However, there are still some uncertainties by using the echo width for terrain roughness parameterization. While pulse width estimates are relatively stable at high amplitudes, there is significant scattering at low amplitudes (Lin and Mills, 2010; Mücke, 2008; Wagner et al., 2006). This needs to be taken into account in future studies. Furthermore, the comparison of the derived roughness layers has shown that small (i.e. in relation to the footprint size) terrain surface discontinuities i.e. breaklines which are not covered with vegetation or stems lying on the terrain are better represented in the geometry-based roughness layer than in the mean echo width (Fig. 7). This can be explained by the small laser footprints, and therefore, by the fact that within the small illuminated area only little vertical variations are available.

5. CONCLUSION AND OUTLOOK

In addition to the 3D-coordinates, FWF-ALS delivers laser point attributes (e.g. signal amplitude, echo width) providing further quantities to characterize Earth surface properties. The presented analyses have shown that the FWF-ALS echo width derived roughness layer indicates areas with high roughness similarly to the geometric definition using very high laser point densities. Concluding the echo width can be used as a terrain roughness parameter even with low terrain point densities compared to the geometry-based computation.

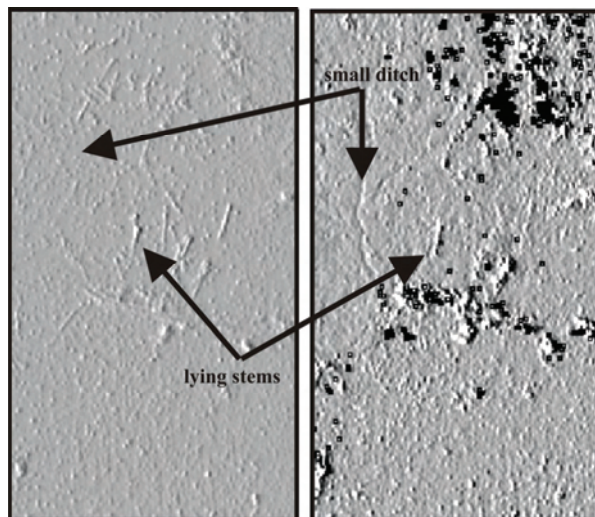


Figure 7. Shading of the geometry-based roughness (left) and of the mean echo widths (right); $dz < 0.5$ m. Black areas are nodata raster cells.

Such roughness layers are valuable input datasets for further analyses as for example shown in Aubrecht et al. (2010) but also directly for a multitude of process models and simulations. In future research the influence of varying flying heights and incidence angles on the echo width is investigated. Furthermore, the increasing uncertainty with weak signals, resulting in low amplitudes, will be studied.

ACKNOWLEDGMENTS

The presented research was funded by the Austrian Research Promotion Agency (FFG) in the frame of the Austrian Space Applications Program (ASAP). The airborne laser scanning data was provided by the MA 41 Stadtvermessung, Wien.

REFERENCES

- Aubrecht, C., Höfle, B., Hollaus, M., Köstl, M., Steinnocher, K., Wagner, W., 2010. Vertical roughness mapping - ALS based classification of the vertical vegetation structure in forested areas. *ISPRS International Archives of the Photogrammetry, Remote Sensing and Spatial Information Sciences*, pp. 6, in press.
- Doneus, M., Briese, C., Fera, M. and Janner, M., 2008. Archaeological prospection of forested areas using full-waveform airborne laser scanning. *Journal of Archaeological Science* 35(4), pp. 882-893.
- Dorren, L.K.A. and Heuvelink, G.B.M., 2004. Effect of support size on the accuracy of a distributed rockfall model. *Int. J. Geographical Information Science* 18(6), pp. 595-609.
- Govers, G., Takken, I. and Helming, K., 2000. Soil roughness and overland flow. *Agronomie* 20, pp. 131-146.
- Hollaus, M., Wagner, W., Eberhöfer, C. and Karel, W., 2006. Accuracy of large-scale canopy heights derived from LiDAR data under operational constraints in a complex alpine environment. *ISPRS Journal of Photogrammetry & Remote Sensing* 60(5), pp. 323-338.
- Hollaus M., Mandlbürger G., Pfeifer N., Mücke W., 2010. Land cover dependent derivation of digital surface models from airborne laser scanning data. *International Archives of Photogrammetry, Remote Sensing and the Spatial Information Sciences. PCV 2010, Paris, France, Vol. 39(3)*. pp. 6.
- Jutzi, B. and Stilla, U., 2005. Waveform processing of laser pulses for reconstruction of surfaces in urban areas. In: M. Moeller and E. Wentz (Eds.): *3th International Symposium: Remote sensing and data fusion on urban areas, URBAN 2005*. *International Archives of Photogrammetry and Remote Sensing*, 36, Part 8 W27, pp. 6.
- Kraus, K., 2007. *Photogrammetry - Geometry from Images and Laser Scans*. Walter de Gruyter, Berlin, pp. 459.
- Lin, Y., Mills, JP., 2010. Factors Influencing Pulse Width of Small Footprint, Full Waveform Airborne Laser Scanning Data. *Photogrammetric Engineering & Remote Sensing* 76(1). pp. 49-59.
- Margreth, S. and Funk, M., 1999. Hazard mapping for ice and combined snow/ice avalanches - two case studies from the Swiss and Italian Alps. *Cold Regions Science and Technology* 30(1-3), pp. 159-173.
- Markart, G., Kohl, B., Sotier, B., Schauer, T., Bunza, G. and Stern, R., 2004. Provisorische Geländeanleitung zur Abschätzung des Oberflächenabflussbeiwertes auf alpinen Boden-/Vegetationseinheiten bei konvektiven Starkregen (Version 1.0). *BFW-Dokumentation 3*, pp. 83.
- Mücke, W., 2008. Analysis of full-waveform airborne laser scanning data for the improvement of DTM generation. Thesis, Institute of Photogrammetry and Remote Sensing, Technical University Vienna, Vienna, pp. 67.
- OPALS, 2010. Orientation and Processing of Airborne Laser Scanning Data, <http://www.ipf.tuwien.ac.at/opals/> (accessed June 2010).
- Scop++, 2010. Programpackage for Digital Terrain Models, <http://www.ipf.tuwien.ac.at/products;> <http://www.inpho.de> (accessed June 2010).
- Smith, M.J., Asal, F.F.F. and Priestnall, G., 2004. The Use of Photogrammetry and LIDAR for Landscape Roughness Estimation in Hydrodynamic Studies. *International Society for Photogrammetry and Remote Sensing XXth Congress, Vol XXXV, WG III/8, Istanbul, Turkey*, pp. 6.
- Straatsma, M.W. and Baptist, M.J., 2008. Floodplain roughness parameterization using airborne laser scanning and spectral remote sensing. *Remote Sensing of Environment* 112(3), pp. 1062-1080.
- Wagner, W., Ullrich, A., Ducic, V., Melzer, T. and Studnicka, N., 2006. Gaussian decomposition and calibration of a novel small-footprint full-waveform digitising airborne laser scanner. *ISPRS Journal of Photogrammetry & Remote Sensing* 60(2), pp. 100-112.
- Wagner, W., Ullrich, A., Melzer, T., Briese, C. and Kraus, K., 2004. From single-pulse to full-waveform airborne laser scanners: Potential and practical challenges. *International Society for Photogrammetry and Remote Sensing XXth Congress, Vol XXXV, Part B/3, Istanbul, Turkey*, pp. 6.

RECOGNITION OF WINDING DISPLACEMENTS FOR STEEL COILS VIA LASER LIGHT SECTION TECHNIQUE

Patrick A. Hölzl, Daniel C. H. Schleicher and Bernhard G. Zagar

Johannes Kepler University
Institute for Measurement Technology
Austria, Linz 4040
patrick.hoelzl@students.jku.at, daniel.schleicher@jku.at, bernhard.zagar@jku.at

KEY WORDS: Laser scanning, Measurement, Three-dimensional, Object, Pattern, Recognition, Segmentation, Industrial

ABSTRACT:

To satisfy the ever increasing quality standards of today's steel industry the basic products, in this case steel coils, must be produced within very small tolerances. To achieve those quality limits, control systems via machine vision are getting more and more popular. For example the quality level of steel coils decreases due to winding displacements based on a non-ideal production process. In this paper a machine vision system for the recognition of winding displacements of steel coils, based on the laser light sectioning technique, will be presented. The introduction of the mathematical model of the laser light sectioning setup allows to compensate some influences of the setups inaccuracies. We show that a reliable recognition of the coil profile with an accuracy below or less than 1mm can be achieved by a rather simple adaptive algorithm. Finally defects can be detected accurately out of the recognized coil profile.

1 INTRODUCTION

Generally metal processing companies, like car manufacturer get their basic material in form of rolled up steel sheets, called coils. These metal processing companies and especially the steel industry are interested in systems to detect defects and to minimize material rejects. One of the major problems which can occur during the coil manufacturing process are displacements of windings, due to a non-conform rolling-up process or a faulty packaging. These winding displacements cause a higher percentage of non usable material and so for quality aspects a preventive detection of these displacements is necessary. Figure 1 shows a model of the coil and winding displacements. The winding displacements $h(r)$ typically are less than 5 mm, larger displacements are problematic and are aimed to be detected by our system. To achieve this requirement for the profil resolution the minimum detectable winding displacement $h_{min}(r)$ is specified to be equal to or less than 1 mm.

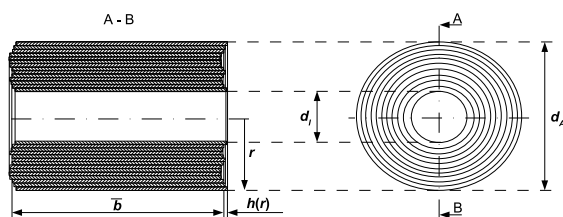


Figure 1: Model of the coil with winding displacements $h(r)$ indicated, d_i and d_o are the inner and outer diameter of the coil respectively and \bar{b} is the mean coil width.

For the above-mentioned model we imply three assumptions which are realistic for further processing:

1. An axial winding displacement $h(r)$ on one side results in an inverse displacement $-h(r)$ on the other side (implying \bar{b} is constant for each winding).
2. The winding displacement $h(r)$ is constant over one winding at radius r .
3. Winding displacements along the radius r occurs only in small steps.

Due to the first assumption we only need to look for defects on one cylinder base. The second assumption limits the ROI to one radial range of zero to $d_A/2$ thus improving resolution. So for the further recognition process the ROI will be limited to the lower half of the coil as indicated in Fig. 2 (red rectangle). The last assumption is necessary for the recognition algorithm presented in Sec. 4 to work correctly. The complete detection should happen during the coils storage process, that means the coil will move during the measurement. Figure 2 shows a typical storing process, with the coil on a transport wagon moving in axial direction with 0.5 m/s. The problem here is that the storage process can not be influenced or changed, so the chosen measurement method must be adapted to these conditions. Therefore an optical 3D measurement method is the best choice with respect to cost and resolution. Due to the varying lighting conditions in the storage facility, which can not be influenced, the realized measurement system and furthermore the machine vision system must be very robust with respect to natural illumination conditions.

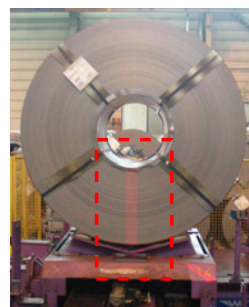


Figure 2: Moving steel coil on transport wagon during the storing process, with a blurred laser line barely visible in the ROI (red rectangle).

Considering the given terms a detection system based on the laser light sectioning technique (Kraus, 1996, Wu et al., 1993) is the preferred choice. Figure 3 shows the principle behind the laser light section technique. The elevation profile of interest is illuminated from an off-center position by a line shaped laser light fan. So the lateral displacement $d(r)$ of the projected line as viewed at from a vantage point orthogonal to the front side of the measure-

ment probe (see Fig. 4) is a scaled replica of the profile height $h(r)$.

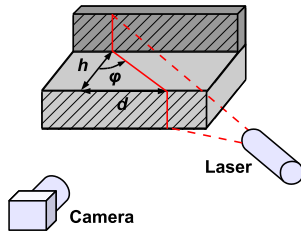


Figure 3: Scheme for the laser light section technique with the geometric triangle drawn in produced by the line shaped light source.

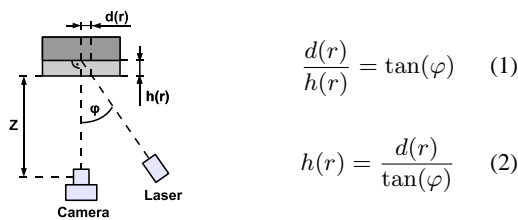


Figure 4: Top view from the laser light section technique scheme.

The smallest clearly recognizable profile height depends on the triangulation angle, φ , which is measured between the incidence direction of the light source and the surveying direction of the camera and the pixel pitch. For optical reasons (reflection properties of the coil) and resolution considerations the triangulation angle φ should be between 30° and 60° (Schäfer and Kirchoff, 2004).

To minimize the influence of the varying lighting conditions a powerful diode laser with 100 mW at 660 nm is used as light source and additionally an optical bandpass filter is used to reduce the ambient lights influence. The optical bandpass (see Fig. 5) consists of two separate filters, a near infrared blocking filter and a red filter. The combination of both filters results in an optical bandpass with a maximum transmission of 94 % at a central wavelength (CWL) of 685 nm and a full width at half maximum (FWHM) bandwidth of 100 nm. Compared to a standard interference filter the assembled optical bandpass has a larger FWHM bandwidth but shows no dependency on the angle of incidence, which is known to cause spectral side effects for interference filters.

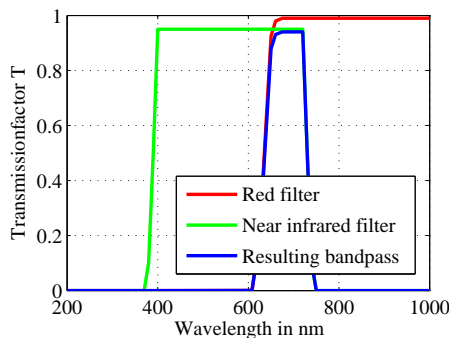


Figure 5: Diagramm of the filter transmittance, the near infrared blocking filter (green), the red filter (red) and the resulting optical bandpass (blue).

The second possibility to minimize the influence of the lighting conditions is to reduce the shutter time. This is also necessary with regard to the movement of the coil during the measurement.

2 EXPERIMENTAL SETUP

Before a recognition system based on the laser light sectioning technique is realized, the camera characteristics and furthermore the depth resolution limits have to be determined. First of all an approximation of the minimum detectable object size is necessary, therefore the specifications of the provided camera and the expected viewing geometry must be known:

- Pixel pitch p : 4.65 μm
- Focal length f : 30 mm (camera constant $c \approx f$)
- Distance between camera and coil Z : 5 m

By using Eqn. 3, which describes the central projection theorem (Luhmann, 2003) (with the object dimensions in real world x and on the CCD chip x'), we obtain a minimum detectable object size x_{\min} of 0.7486 mm.

$$x' = \frac{x}{\frac{Z}{c} + 1} \rightarrow x_{\min} = p \left(\frac{Z}{c} + 1 \right) \quad (3)$$

The minimum detectable object size x_{\min} can now be used to designate the triangulation angle φ (in Eqn. 2). In Fig. 6 the relationship between φ and the minimum detectable winding displacement h_{\min} is plotted.

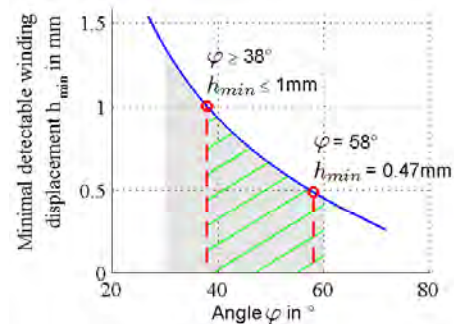


Figure 6: Relationship between φ and the minimum detectable winding displacement h_{\min} . The required and realized operating points for the minimum detectable winding displacement h_{\min} are marked with red dashed lines. The gray colored area indicates the interval of technically relevant triangulation angles φ . The green hatched area labels the interval of valid triangulation angles φ for the realization.

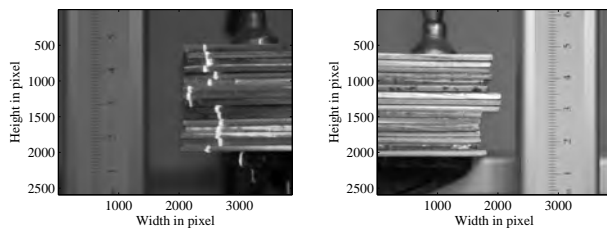
The minimum detectable winding displacement h_{\min} was specified to be equal to or less than 1mm. Therefore the triangulation angle φ is chosen to be 58° , and the resulting minimum detectable winding displacement h_{\min} is 0.47 mm. Due to the measurement error which will be calculated in Sec. 5 a value less than 1mm is advantageous. A major requirement for using the laser light section technique is the presence of a diffusely reflecting object. This can be proved with the Rayleigh criterion (Horbach, 2008) shown in Eqn. 4.

$$R_a < \frac{\lambda}{16 \cos(\varphi)} \quad (4)$$

The Rayleigh criterion is an inequation including the wavelength of light λ , the triangulation angle φ and the mean roughness index R_a . If the mean roughness index R_a of the illuminated object area is less than $\lambda/16 \cos(\varphi)$ no diffuse reflection appears

according to this law. By evaluating the inequation it follows that a diffuse reflection appears if $R_a \geq 77.842 \text{ nm}$. The mean roughness index R_a of the coil front surface is between $6 \mu\text{m}$ and $11 \mu\text{m}$ and therefore it is sufficient to guarantee diffuse reflection.

To proof the assumptions made in this section an experimental setup has been designed. The coil windings are modelled by several steelplates of the same thickness which are stacked upon each other and then deferred fixed. First a frontal photograph of the coil winding model including the laser line was taken to calculate the displacements with the laser light section technique, shown in Fig. 7(a). Because of the good illumination conditions only an optical red filter was used. Additionally a photograph from the side was taken as reference image for the coil winding model, shown in Fig. 7(b).



(a) Frontal photograph of the coil winding model showing the laser line. (b) Lateral photograph of the coil winding model.

Figure 7: Photographs of the coil winding model.

To determine the winding displacement, the first step is to extract the laser line from the acquired image data. Therefore the image is cropped to the probe edges and then the position of maximum intensity in every row is determined. For the experimental setup a commercial photo camera was used, whos images were down-sampled to obtain a comparable resolution to typical video cameras. The reference for the coil winding model is obtained from the lateral image by using a canny edge detection algorithm (Gonzalez and Woods, 2008). In Fig. 8 the results of the previous steps are shown. The laser light section curve is close to the reference curve and also the desired resolution limit is almost reached.

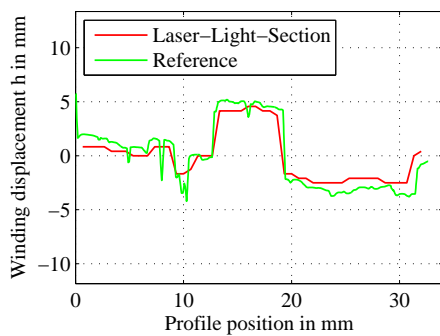


Figure 8: The red colored curve is the result for the displacement recognition by using the laser light section technique and the green colored curve is the reference derived from the frontal probe image (see Fig. 7(a)). A good agreement can be seen.

3 ADVANCED MODELING OF THE SETUP

During the experimental setup the influence of the laser alignment on the result was very low because of the small-sized probe with a height of only 32 mm (a typical coil profile length can be up to 700 mm). Considering a profile length of 700 mm a slight rotation of the laser around its symmetry axis by 0.3° , re-

sults in a maximum error of 6 mm for the displacement determination. Furthermore the coil windings can also be affected by a linear trend due to a non-conform rolling-up process. This linear trend can be used as a quality characteristic too and should therefore also be measured. To estimate the influence of the laser alignment and the linear trend of the coil front on the laser line a model of the setup is introduced in Fig. 9. Here two coordinate systems are considered, a fixed-place coordinate system given by x, y, z and a laser coordinate system given by ξ, η, ζ . The laser coordinate system is rotated by the angles α, β, γ which allow a free rotation of the laser in space with the corresponding rotation matrices (Cook, 2007) shown in Eqns. 5, 6 and 7. For a solvable system of equations it is necessary to pose the following constraint on the coil windings and the laser line. The additional linear trend resulting from the non-conform rolling-up processes is represented by a rotation of the coil front around the y -axis by an angle θ with the corresponding rotation matrix shown in Eqn. 8. That means that when the laser line is projected onto the axis of symmetry in the lower half of the coil only a linear trend is present in the x -direction. This can be achieved by an exact triggering and a limitation on the ROI.

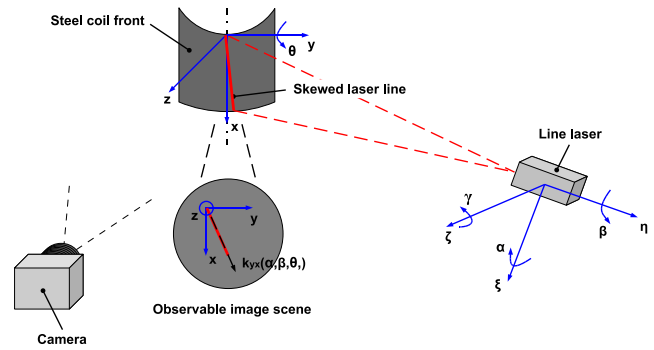


Figure 9: Advanced model of the setup with a fixed-place coordinate system given by x, y, z and a laser coordinate system given by ξ, η, ζ .

The following rotation matrices $R_\gamma, R_\beta, R_\alpha$ and R_θ represent the degrees of freedom in the setup:

- Rotation around ζ , for up or down tilting of the laser.

$$R_\gamma = \begin{pmatrix} \cos(\gamma) & -\sin(\gamma) & 0 \\ \sin(\gamma) & \cos(\gamma) & 0 \\ 0 & 0 & 1 \end{pmatrix} \quad (5)$$

- Rotation around η , for rotation of the laser around its symmetry axis.

$$R_\beta = \begin{pmatrix} \cos(\beta) & 0 & \sin(\beta) \\ 0 & 1 & 0 \\ -\sin(\beta) & 0 & \cos(\beta) \end{pmatrix} \quad (6)$$

- Rotation around ξ , for tangential deviation of the laser due to the laser light section technique in the following form $\alpha = \varphi - \pi/2$.

$$R_\alpha = \begin{pmatrix} 1 & 0 & 0 \\ 0 & \cos(\alpha) & \sin(\alpha) \\ 0 & -\sin(\alpha) & \cos(\alpha) \end{pmatrix} \quad (7)$$

- Rotation around y , for skewness of the coil front.

$$R_\theta = \begin{pmatrix} \cos(\theta) & 0 & \sin(\theta) \\ 0 & 1 & 0 \\ -\sin(\theta) & 0 & \cos(\theta) \end{pmatrix} \quad (8)$$

With the given rotation matrices the normal vector for the coil front \vec{v}_{Cn} and the normal vector for the triangular shaped area spanned by the laser \vec{v}_{Ln} can be calculated in the fixed-place coordinate system, shown in Eqns 9 and 10.

$$\vec{v}_{Ln} = R_\alpha \cdot R_\beta \cdot R_\gamma \cdot \underbrace{\begin{pmatrix} 0 \\ 0 \\ 1 \end{pmatrix}}_{\vec{e}_z} = \begin{pmatrix} \sin(\beta) \\ \sin(\alpha) \cos(\beta) \\ \cos(\alpha) \cos(\beta) \end{pmatrix} \quad (9)$$

$$\vec{v}_{Cn} = R_\theta \cdot \underbrace{\begin{pmatrix} 0 \\ 0 \\ 1 \end{pmatrix}}_{\vec{e}_{CoiL}} = \begin{pmatrix} \sin(\theta) \\ 0 \\ \cos(\theta) \end{pmatrix} \quad (10)$$

Then the direction of the intersection vector \vec{u} between the coil front and the laser can be determined by the cartesian product of the according normal vectors \vec{v}_{Cn} and \vec{v}_{Ln} , shown in Eqn. 11. Now the intersection of the coil front and the triangular shaped area spanned by the laser, results in the visible laser line on the coil with the coordinates (x_L, y_L, z_L) . The intersection vector \vec{u} is a scaled version (by a factor ν) of the laser line with the same orientation, see Eqn. 12. Further the intersection vector \vec{u} is independent of γ so the orientation of the laser line is independent of an up or down tilting of the laser.

$$\vec{u} = \vec{v}_{Ln} \times \vec{v}_{Cn} \quad (11)$$

$$\begin{pmatrix} x_L \\ y_L \\ z_L \end{pmatrix} = \nu \vec{u} \quad (12)$$

To eliminate the influence of the laser alignment and the linear trend of the coil front the remaining angles β and θ must be calculated. Therefore the orientation of the laser line will be separately examined in the y,x -plane and in the y,z -plane. Due to the setup the orientation of the laser line k_{yx} in the y,x -plane is present in the observable image scene in Fig. 9 and can be measured by a trend estimation of the extracted laser line, the associated relation of the laser coordinates y_L and x_L is shown in Eqn. 13.

$$k_{yx} = \frac{y_L}{x_L} = \frac{\cos(\alpha) \cos(\beta) \sin(\theta) - \sin(\beta) \cos(\theta)}{\sin(\alpha) \cos(\beta) \cos(\theta)} \quad (13)$$

The second laser line orientation k_{yz} in the y,z -plane is predetermined by the laser light section technique given by Eqn. 2 and the associated relation of the laser coordinates y_L and z_L is shown in Eqn. 14.

$$k_{yz} = \frac{y_L}{z_L} = \tan(\varphi) = -\frac{\cos(\alpha) \cos(\beta) \sin(\theta) - \sin(\beta) \cos(\theta)}{\sin(\alpha) \cos(\beta) \sin(\theta)} \quad (14)$$

With Eqns 13 and 14 for the orientation of the laser line it is possible to determine the remaining angles β and θ , shown in Eqns 15 and 16.

$$\beta = -\arctan\left(k_{yx} \frac{\cos(\alpha) \tan(\varphi) + \sin(\alpha)}{\tan(\varphi)}\right) \quad (15)$$

$$\theta = -\arctan\left(\frac{k_{yx}}{\tan(\varphi)}\right) \quad (16)$$

Due to Eqn. 13 the gradient of the laser line k_{yx} in the photograph is dependent on the linear trend of the coil windings represented by θ and the laser rotation around the symmetry axis represented by β . Both angles affect the gradient k_{yx} in the same way and so an estimation using the Eqns 15 and 16 will fail because they can not be determined separately by a single measurement. The solution to this problem is to make a reference measurement for the skewness of the laser line related to β by using a plane with a defined angle θ instead of the coil front. A vertical plane as reference ($\theta = 0^\circ$) allows to extract β from Eqn. 13, (see Eqn. 17).

$$\beta = -\arctan(k_{yx}(\theta = 0^\circ) \sin(\alpha)) \quad (17)$$

$$\theta = \arctan\left(k_{yx} \tan(\alpha) + \frac{\tan(\beta)}{\cos(\alpha)}\right) \quad (18)$$

Due the fact that the triangulation angle φ , and so $\alpha (= \varphi - \pi/2)$ is not constant with respect to β , a slight error occurs. Despite the fact that φ is influenced by β , the approximation approach works excellent to determine the laser alignment and the linear trend of the coil front for values of β less than $\pm 15^\circ$. For example a laser rotation by $\beta = -7.5^\circ$ results in an error of θ of less than 0.01° .

4 LASER LINE EXTRACTION ALGORITHM

Before the coil profil can be determined, the laser line must first be extracted out of the image. Figure 10 shows a steel coil and a laser line projected on it. Due to a rotation of the camera of 90° (to obtain the profil length at a higher resolution corresponding to the camera chip with 1392×1040 pixel) the laser line is horizontal in the acquired images. The laser line is clearly visible due to the use of optical filter mentioned in Sec. 1.

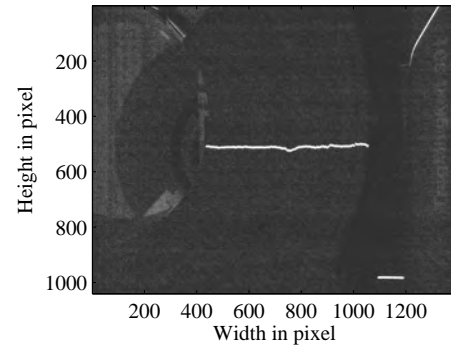


Figure 10: Post-processed image (for better contrast of the laser line) of a steel coil with a laser line.

First of all the algorithm detects if a laser line is present in the image by simply accumulating intensities along rows and searching for a clearly visible maxima. Also a first elimination of packaged coils and a rough estimation of the laser position is done. For coils with packaging material a laser line extraction is meaningless and therefore an early elimination is preferable. After the rough estimation of the laser position, the original image is cropped to a vertical region around the laser. Then a median filter with a rectangular mask (with 15×10 pixel) is applied at the cropped image to reduce noise and to smooth the laser line, the result is shown in Fig. 11.

The detection of the maxima positions is an easy way to extract the whole laser line out of the cropped image. But due to the fact that the horizontal position of the coils in the images can vary in dependence on the coil size, the considered image area extends

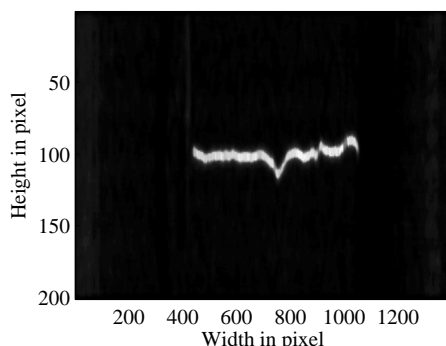


Figure 11: Cropped version of the original image after applying a median filter with differing axes scales.

beyond the coil. So there are also laser lines projected on background geometries present. The background geometries results in sudden steps of the laser line which can lead to a false detections of profile defects. This problem can be reduced by cropping the original image to a vertical region around the estimated laser position. Another problem is the possible presence of edge protection material on the coil that also results in sudden steps of the laser line. Therefore a criterion to only extract reflections of the coil front is needed. The following adaptive algorithm is proposed to extract only valid laser lines:

1. In every row the position of the maximum is detected (under the assumption that only one maximum per column is present, which is referring to the laser) and then saved in the variable $Pos_{Max}(i)$.
2. The maxima positions are normalized to the height of the search region $Pos_{Max}(i) = Pos_{Max}(i) / Height$.
3. Setting of the start point for the adaptive algorithm in the middle of the laser line to become independent of varying coil sizes.
4. Setting of the start values for the adaptive algorithm with $DevAv(1) = Pos_{Max}(StartPoint)$.
5. Run through the maxima positions left and right of the start point and save positions which satisfy the following criterion $|Pos_{Max}(i+1) - DevAv(i)| < \sigma$ for $\sigma \leq 1$.
6. If the next maximum position satisfies the criterion from above a new comparison value is calculated for each position with $DevAv(i+1) = (DevAv(i) + Pos_{Max}(i+1))/2$ otherwise the laser line extraction is finished.

Under the assumption (that the alteration of the winding displacements occurs continuously) made in Sec. 1, a restrictive criterion to exclude invalid steps can be found, see point 5. The local behaviour of the laser line is estimated according to 6 to get an adaptive limitation. The advantages of this algorithm are in its simplicity and speed of operation but still delivers good results. In Fig. 12 the result of the algorithm, the extracted laser line is shown. Alternatively a gray value threshold filter can be used to extract the laser line but this has the disadvantage that unwanted objects are also included. So it is necessary to use post-processing to adapt the laser line by thinning and to exclude background geometries and edge protection material.

After the laser line is extracted, the overlaid linear trend represented by k_{yx} can be determined by approximating a first-order

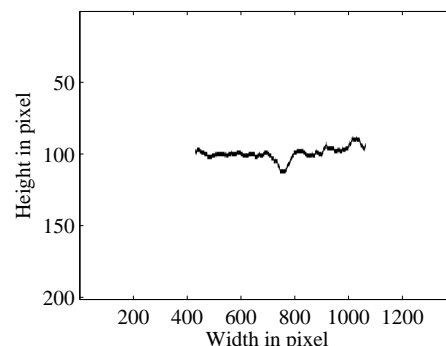
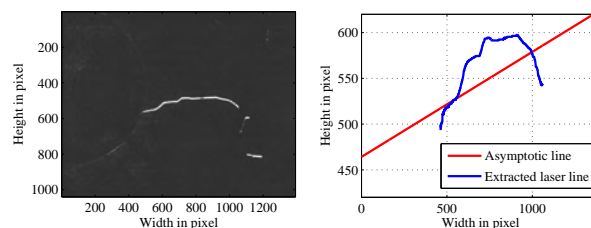


Figure 12: Laser line located on the coil front extracted with an adaptive algorithm out of the cropped image.

polynomial. Subsequently the linear trend of the coil front can be calculated using Eqn. 16. The angle θ is important for quality aspects and also helps to eliminate coils with packaging material, because the packing material results in nontypical values. For example a coil with packaging material is shown in Fig. 13(a) and the extracted laser line with the asymptotic line is shown in Fig. 13(b). In this case θ is 5.7° but it should be less than 1° for unpacked coils.



(a) Post-processed image of a coil with packaging material

(b) Extracted laser line (blue) and the corresponding fitted line (red).

Figure 13: Laser line extraction for a coil with packaging material visible.

By using Eqn. 2 the real coil profile can be calculated out of the extracted laser line. For the detection of defects the first derivative of the coil profile is calculated. Then the profile subsegments with a specified raise related to the deviation and height are marked as critical. Additionally critical subsegments in a close neighbourhood are joined. The coil profile and the result for the detection of defects, that are larger than 2 mm, is shown in Fig. 14.

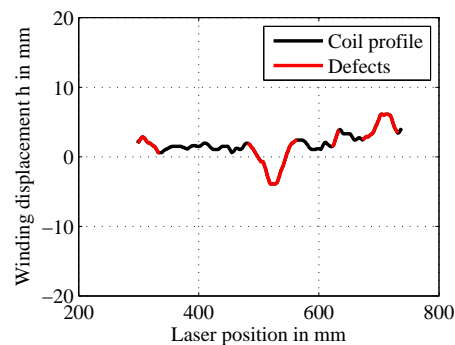


Figure 14: Recognized coil profile (black) and detected defects (red).

5 RESULTS AND DISCUSSION

To evaluate efficiency of the realized measurement system, the maximum systematic error Δh (Schrüfer, 2004) is determined by

Eqn. 19 as a function of the winding displacement h , the triangulation angle φ , the distance Z between camera and coil, and the quantization of the laser position through the camera.

$$\Delta h = \underbrace{\left| \frac{\partial h}{\partial \varphi} \Delta \varphi \right|}_{\text{error due to laser align}} + \underbrace{\left| \frac{\partial h}{\partial Z} \Delta Z \right|}_{\text{error due to camera setup}} + \underbrace{\left| \frac{\partial h}{\partial x} \Delta x \right|}_{\text{error due to quantization}} \quad (19)$$

Before the total systematic error Δh can be calculated by Eqn. 19, the acquisition of the coil profile must be defined. Therefore Eqn. 2 which describes the calculation of the winding displacement due to the laser light section technique and Eqn. 3 for the mapping properties due the central projection theorem are used. So the final function for h is shown in Eqn. 20.

$$h = \underbrace{\frac{1}{\tan(\varphi)}}_{\text{laser light section}} \underbrace{\left(\frac{Z}{c} + 1 \right) x'}_{\text{central projection}} \quad (20)$$

$$\Delta h = \left| -\frac{2}{\sin(2\varphi)} \Delta \varphi \right| \cdot |h| + \left| \frac{1}{Z+c} \Delta Z \right| \cdot |h| + \left| \frac{1}{\tan(\varphi)} \left(\frac{Z}{c} + 1 \right) \Delta x' \right| \quad (21)$$

Equation 21 shows the final result for the systematic error Δh . Considering the specifications for p , c , Z and φ (see Sec. 1) an uncertainly error of $\Delta Z = 100$ mm, $\Delta \varphi = 2^\circ$ and $\Delta x' = p$ results in a maximum systematic error Δh of 1.462 mm for a winding displacement h of 5 mm. The main point is that the terms belonging to the camera setup error and the laser alignment error which are scaled by the winding displacement h are smaller than 10^{-1} and the quantization error is a constant 0.487 mm. The systematic error Δh is increasing with nearly $h/10 + 0.487$ mm. Additionally the first term in Eqn. 21 shows that the error due the laser alignment is minimal for triangulation angles φ between 30° and 60° .

In Fig. 15(a) an example for a unpackaged coil with several defects is shown. The final processed coil profile (black), the detected profile defects (red) and the systematic error (green) is shown in Fig. 15(b). It is observable that the calculated coil profile with an insignificantly small systematic error perfectly corresponds to the laser line in the image and the major defects are detected. Furthermore a second example for an unpackaged coil is shown in Fig. 15(c) and processed results in Fig. 15(d). In the second image additional edge protection material is attached to the coil (visible on the left side) but is excluded from the coil profile by the extraction algorithm, as it was demonstrated before.

6 CONCLUSIONS AND FUTURE WORK

We have shown that a recognition of winding displacements for steel coils using the laser light section technique can be realized with a proposed height resolution of less than 1 mm. Furthermore we introduced a mathematical model to eliminate the dependencies from an inaccurate laser alignment and to determine the linear trend of the coil front as another quality aspect. Finally we also have shown that the designed laser line extraction algorithm extracts reliably with sufficient speed the laser line belonging to the coil front. The next step is to improve the pre-process

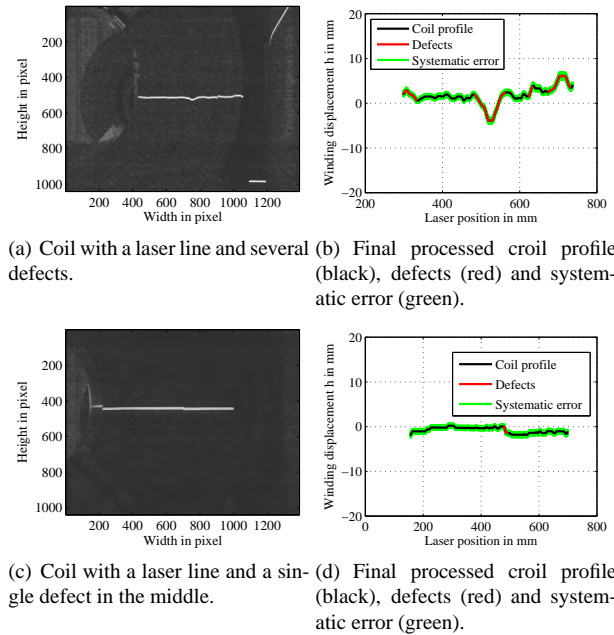


Figure 15: Results of the measurement system for two different steel coils.

elimination of steel coils with packaging material and statistically evaluate the defect detection rate of the realized system.

ACKNOWLEDGEMENTS

The authors gratefully acknowledge the partial financial support for the work presented in this paper by the Austrian Research Promotion Agency under contract grant 814278 and the Austrian COMET program supporting the Austrian Center of Competence in Mechatronics (ACCM). Last but not least the authors thank the company Industrie Logistic Linz (ILL) for its financial and technical support.

REFERENCES

- Cook, M., 2007. Flight Dynamics Principles. Elsevier.
- Gonzalez, R. C. and Woods, R. E., 2008. Digital Image Processing. 3 edn, Pearson Prentice Hall.
- Horbach, J., 2008. Verfahren zur optischen 3D-Vermessung spiegelnder Oberflächen. Universitätsverlag Karlsruhe.
- Kraus, K., 1996. Photogrammetrie - Band2: Verfeinerte Methoden und Anwendungen. Vol. 2, 3 edn, Ferd. Dummlers Verlag Bonn.
- Luhmann, T., 2003. Nahbereichsphotogrammetrie — Grundlagen, Methoden und Anwendungen. 2 edn, Wichmann.
- Schäfter and Kirchhoff, 2004. Laser Light Section, a Key Feature in 3D Laser Measurement Technique. Schäfter and Kirchhoff.
- Schrüfer, E., 2004. Elektrische Messtechnik. 8. edn, Hanser Verlag.
- Wu, P., Yu, F., Li, Z., Yan, Z. and Shun, Y., 1993. Analysis technique for the measurement of a three-dimensional object shape. Appl. Opt. 32(5), pp. 737–742.

AN INVENTED APPROACH IN IMAGE REGISTRATION “NEW ERA IN PHOTOGRAMMETRY”

A. S. Homainejad

Independent Research Group on Geospatial, Tehran, I.R. IRAN - s_homain@yahoo.com

KEY WORDS: Digital Image, Laser Scanning, Transformation, Ortho-image

ABSTRACT:

This paper will discuss an invented approach which focuses on providing an output from registration of an aerial photograph on a 3D model such as DTM, DMS, or 3D model. The approach has been developed in order to omit distortions from output and to increase the reliability. In contrast of other image registration methods which their outputs are an image, this approach provide a 3D model which can be used for mapping, visualising, 3D GIS, ortho rectify image. The approach is able to register a mono image on DEM, DTM, DMS, or 3D model with the minimum requirement to camera calibration parameters. The paper will give a discussion on analysis of registration of an aerial image on laser scanning data and registration of a terrestrial image on a 3D model by using this approach.

1. INTRODUCTION

Photogrammetry since its emergence has had at least two major transitions. The first transition was begun at late 60s or early 70s when analytical stereoplotters were come into the market and edged out analogue stereoplotters. The second transition was started at mid 90s or late 90s when digital photogrammetry was emerged and gradually pushed analytical stereoplotters out. In digital photogrammetry system a simulated stereoplotter digitally created in the computer and all processing have been implemented digitally, but the mathematical concepts are the same. Consequently, all processes in digital photogrammetry were computerised and a supplementary image processing package was integrated to the system. However, before emergence of digital photogrammetry, digital images, digital image processing, and digital image transformation were successfully implemented in remote sensing and in digital close range photogrammetry as well.

For ascertaining a reliable photogrammetric output, enormous studies on photos, cameras, and mathematical modelling have been fulfilled. With a glance research on all studies, it will be recognised that all those studies, despite of in which period they have been fulfilled, have focused on the determination of interior parameters. For example, Hallert (1968) and Hakkarainen and Rosenbruch (1982) measured angles of rays with help of a theodolite and collimator for defining the focal length. Brown (1956) developed analytical camera calibration, and Brown (1966) mathematically modelled the decentring distortion. Kenefick et al (1972) developed an

analytical camera self-calibration with eight physical parameters. Fraser (1997) explained parameters and mathematical model for digital camera self-calibration. Amiri Parian and Gruen (2010) developed a method of self-calibration for panoramic camera.

Photogrammetry has embraced of a number of physics' laws and it needs to fully familiar with them for calibration. Investigation on these physical rules is not the scope of this paper. More details regarding to above issues can be found in photogrammetry and remote sensing textbook, for example Slama (1980) and Lillesand and Kiefer (1987). Photogrammetry during its evolution has tested and implemented different approaches for coping with these issues and producing a reliable and precise output.

This paper will give a report on implementation of the developed approach in two different projects. The first project focused on registering an aerial image on a laser scanning data and the second project registered a terrestrial image on a 3D model.

This paper has been organised as follows. A brief investigation on data fusion and the proposal of data fusion for this project will be given in chapter 2. Chapter 3 will explain the study area. Chapter 4 will describe and evaluate tests and outputs. A conclusion and remarks will be given in chapter 5.

2. DATA FUSION AND ITS APPLICATION IN PHOTOGRAMMETRY

In photogrammetry, data fusion is a technique of image processing for combining two or multi images which were acquired from an object in different times or from different locations for achieving accurate output. Data fusion generally is carried out for change detection, updating existing maps, or ortho image production. There are generally three groups of data fusion: image to map, image to image, and image to database registration. Morgado and Dowman (1997) carried out an image to map registration for automatic absolute orientation. Derenyi (1996) implemented map to image and image to map registration for investigation on change detection and Bouziani et al (2010) carried out image to map registration for change detection. Khoshelham et al (2010) utilised image to image registration for change detection, and Suveg and Vosselman (2004) combined aerial photographs with GIS database for extracting building form aerial images.

Integrating an image with a laser scanning data is another technique in photogrammetry for producing ortho-image or ortho-rectify-image. Laser scanners are able to provide a fair accurate topographic data along intensity values from surface of objects that the data can be used for DTM generation and 3D model. There are various approaches and techniques for integrating images and laser scanning data. For example, Iwashita et al (2007) integrated a grey scale image on a 3D model which was obtained from a laser scanner using fast marching algorithm, or Zhao and Popescu (2009) assessed map leaf area index by investigation the integration of Quickbird image and Lidar data, or Mizowaki et al (2002) registered a CT image on MRS image for developing a method of treatment for prostate cancer. Obviously, there are numerous studies on registration of an image on a scanner data for enhancing the image for extracting an object or producing a map precisely and accurately.

In conventional method of image registration despite of which mathematical model would be utilised, an image which was a two dimensional plane would be finally transferred to another two dimensional plane. The main aspiration of image registration is to convert an image to a map or it is better to say to convert a perspective projection to an orthographic projection. Since the emergence of digital image in photogrammetry, enormous approaches on image transformation have been developed and demand on ortho-image has been significantly raised. The benefit of using digital image over conventional film base photos is the flexibility of

digital image. Digital images can be easily stretched, squeezed, rotated, radiometric and geometric editing, etc. But it has to be always remember that the output of an image processing is a two dimensional image. There are not any defined approaches for omitting or reducing the distortion from final output. The existing approaches transfer whole of an image according to a mathematical modelling which its components are a matrix of rotation (\mathbf{R}), translation vector (\mathbf{V}), and scale factor (\mathbf{s}). It requires at least four control points for obtaining the elements of \mathbf{R} , \mathbf{V} , \mathbf{s} , if \mathbf{R} is a 3x3 matrix and \mathbf{V} has three components.

The proposal for this project is based on developing a novel approach in order to register aerial images on laser scanning data without pre-knowledge about interior parameters and providing a robust and reliable output which is free from any distortion. Then the approach has been extended for registering terrestrial image on a 3D model. The approach can be easily expanded to register any images to any data such as DTM, DMS, Digital Topographic data, and GIS data. According to the proposal, images have been initially divided to sub area according to geometry of object and topography of terrain. Then each sub area will transferred to the host or source data pixel by pixel. During transformation, pixels are converted to points which their elements includes geometric coordinates and intensity values.

Usually a correlation method has been implemented for matching between two or multi images which were acquired by similar sensor from an object. Hence, the camera sensor and laser scanning sensor are different a new approach has been developed for matching between the image and laser scanning data and 3D model. The laser scanners are acquiring data from surface of object and provided those data in point clouds format; however, a digital image is two dimensional format consists of pixels and rasters which included intensity values.

The existing correlation matching for sequence images has been developed based on comparison between the gradients of intensity values of a pixel with its neighbouring pixel on images. Correlation matching has been recognised as template matching, cross-correlation, and convolution. In contrast, scanning matching approaches for matching laser scanning data have been developed based on presentation of location of points in the 2D or 3D space and included point to point matching e.g. Iterative Closest Point (ICP), or feature based matching, or point to feature matching.

In this study the matching between an image and data scanner data has been proposed as following:

1. The image will be initially oriented with the laser scanning data according to provided GCPs. In this step the rotation angle around Z axis “κ” is only rotation angle which is considered for further processing,
2. Equation 1 defining the relationship between the laser scanning data and image according to parameters of orientation will be constructed,
3. The interested features will be extracted from image and will be transformed to laser scanning space according to Equation 1 for matching with their correspondences features.
4. Final transformation

For implementation of above steps correctly, a special filter has been developed that extract the plane from laser scanning data. The filter will remove scattered points that interferes the matching process. For example, each laser scanner pulse signal has three responds from trees and bushes. These additional data affect the process of the matching and transformation and reduce the accuracy of outputs.

$$\begin{bmatrix} x_t \\ y_t \\ z_t \end{bmatrix} = \begin{bmatrix} x_s \\ y_s \\ z_s \end{bmatrix} + sR_{\kappa} \begin{bmatrix} x_i \\ y_i \\ z_i \end{bmatrix} \quad (1)$$

3. STUDY AREA

Test area for registering aerial image on laser scanning data locates in Espoonlahti (approximately 60° 8’N, 24° 38’E) in southern part of Finland. The area can be characterized as low residential urban area having mainly terrace houses and detached houses with a multistorey buildings and apartments in some areas.

Also the most required and applicable data were provided by EuroSDR as well as photographs orientation parameters and GCPs.

GCPs have been measured using real time kinematic (RTK) GPS and some of GCPs represent on cornices of roofs.

Laser Scanning images were acquired with Optech ALTM 3100 and Leica ALS50-II scanners at 2005 and 2007. Technical details of imagery systems and camera are presented below.

Optech ALTM 3100

Scanning angle 24 degrees, 20 degrees is processed ($\pm 10^\circ$)

PRF 100 kHz

Scanning frequency 67 Hz

Flying speed 75 m/s

Leica ALS50-II

Scanning angle 40 degrees ($\pm 20^\circ$)

PRF 148 kHz

Scanning frequency 42.5 Hz

Flying speed 72 m/s

DMC Photogrammetric Images

Pixel depth 16 bit

Size 13824x7680

Ground resolution 5 cm

Forward overlap 60%

Side Overlap 20%

Interior Orientation

Focal length: 120.0000 mm (10000 pixels)

Principle point (differences from the image centre):

Px=0.000 mm

Py=0.000 mm

Pixel size: 0.012 mm

Image size: 13824x7680 pixels (165.888x92.16 mm)

The terrestrial images and 3D data have been acquired from an ancient site in south of IRAN near city of Shiraz. The site’s name is Naqsh-e Rostam which includes a number of rock carvings, Graves, and a building named Ka’ba-ye Zartosht. The images and 3D model were acquired from Ka’ba-ye Zartosht which most of photos were acquired from a non-metric camera.

4. IMPLEMENTATION AND EVALUATION

For implementation and evaluation of the proposed approach, the aerial image and terrestrial images have been split to small area according to geometry of objects. For example all buildings on the aerial image have been extracted and separated from the image. For terrestrial images, all windows and the door have been extracted and separated. Then according to Equation (1), matching between each extracted object and 3D model or laser scanning data has been implemented. Some objects such as multi stories buildings have a significant depth of view and that side wall with windows can be easily recognised.

Topography of area around Ka’ba-ye Zartosht has set a difficulty for stereo image acquiring. The building has been constructed by stones and has 13.5m high and only by a convergence photography can acquire whole of each wall. It was one of the challenging job to compile data of each wall in a map and GIS. At first it was tried by using a **Zeiss** Stereoplotter PLANICOMP **P33** and a digital photogrammetric system to compile data on a map, but both systems failed to provide an accurate map. Then, it was planned to obtain the 3D data by precise engineering surveying approach. A precise 3D model has been provided with less than 1mm STD. This 3D model has provided precise information for analysing the output from registering the image on the 3D model. It needs to mention that the photos were acquired by a non-metric film based camera. Then photos have been scanned by a very basic scanner. The images have a very poor quality and mostly blurred.

Terrestrial images and aerial images have had some distortions as well as relief displacement which can be easily recognised. In aerial images, facets of buildings can be seen, and even details of facets can be recognised.

Both Leica ALS50-II and Optech ALTM 3100 data were individually captured in a CAD system, and 3D model of building has been reconstructed on the CAD system. The area on the image was divided to sub areas according to geometry of object and topography of. Each sub area individually was transferred on the corresponding area on 3D models pixel by pixel. Before transferring sub areas, an initial transformation of whole image has been implemented. The initial transformation was a rotation around principal distance (κ) for a rough orientation of the image with 3D models. For continuing the transformation process of each sub area two points on the image along their corresponding points on 3D models were acquired. Then the program will transferred each individual pixel from the sub area to its corresponding point in the 3D model and the output is a point cloud which has image characteristics. The effect of relief displacement on the image has been removed during transformation. The output shows blank areas which they are scars of relief displacement on the image. Because tall buildings are obstacles the areas behind them, after image rectifying those areas have been remained blank. For filling those blank areas, it is possible to utilise other images has been captured from those areas.

A program has been developed for implementing the process. The program will define a number of windows around the sub areas on the image and their corresponding areas in 3D models. The sizes of windows are varying according to the size of sub area. After matching process has been fulfilled and sub areas on the image and 3D model have been matched according to Equation 1, then pixels of the area on the image will be transferred to 3D models. A note has to be given here that laser scanning data won't precisely locate the corners and edges of building because pulse signals won't precisely hit corners and edges of buildings and each point cloud definitely includes a tolerance errors at X, Y, and Z. And obviously a building will be shrunk in a laser scanning data and its shape will be changed from a rectangle to a non regular four sides shape. For omitting this error, at least three control points on each building are required but it is not feasible because an enormous control points are required a terrain. As small area has been transformed each time, therefore; each area can be corrected individually and also each point can be corrected individually. In image, there is no chance to geometry correct each sub area or a pixel, because all pixels stick

together and any geometry changing on any sub area or any pixel will be distorted other areas and pixels. An important notice has to be given here that points are not geometry connected to each other and they can be corrected individually. Another important notice has to be given here, that each point has an elevation value and the elevation values will help to investigate the accuracy of processing of transformation. For example, a point on a roof of building has a greater elevation value than a point on the ground. Therefore, the elevation values are one of the assessing the process of image transformation.

The STD of outputs from registering the aerial photograph on the laser scanning data consists of two STDs. The first STD is belong to matching laser scanning data with the GCPs which is for X equal 0.453, and for Y equal 0.572, and for Z is 0.3 meter. However the STD of matching each pixel with point clouds is in range of few centimetres, because the program has been developed to match each pixel with its correspondence point on the laser scanner data with accuracy of $\pm 5\text{cm}$ for x, $\pm 1\text{cm}$ for y, and 0cm for z. So it can be realised that the accuracy of registration processing is very much depend to accuracy of master data. The STD for output from terrestrial project is in range of few mm exactly is the similar to accuracy of 3D model.

5. CONCLUSION AND REMARKS

A new approach for data fusion has been created and developed. The approach is able to illuminate image distortions such as lens distortion and relief displacements while image transforming. In this approach the image is split to sub areas and each area will transferred to a 3D model pixel by pixel and the output is a point clouds or a vector image. With compare with the current image registration methods, this approach has a number of advantages. As advantages of this approach, it can be mentioned:

- 1- Unlike an image which its pixels geometrically connected to each other, points of outputs are geometrically independent.
- 2- If any part of the output has been affected by an error, that area can be individually corrected without affecting whole of output.
- 3- Any part ant portion of output can be easily and quickly up-to-dated without affecting all parts of the output.
- 4- The output can be simplified for implementing in other application such as mapping, GIS.

- 5- The output from this approach can be utilised in visualising.
- 6- The approach is able to illuminate camera and image distortion.
- 7- The approach is able to register a mono image on the 3D data and provide an ortho-rectify image.
- 8- The approach is able to combine any images that have been acquired from an object for providing more detail from the object.

Dependency of accuracy of the output to the master data is the main disadvantage of this method.

REFERENCES

- Amiri Parian, J., Gruen, A., (2010), “Sensor modelling, Self-Calibration and Accuracy Testing of Panoramic Cameras and Laser Scanners”, *ISPRS Journal of Photogrammetry and Remote sensing*, Vol. 65, 60-76
- Bouziani, M., Goïta, K., He, D.C., (2010), “Automatic Change Detection of Buildings in Urban Environment from very High Spatial Resolution Images using Existing Geodatabase and Prior Knowledge”, *ISPRS Journal of Photogrammetry and Remote sensing*, Vol. 65, 143-153
- Brown D.C., (1956), “The Simultaneous Determination of the Orientation and Lens Distortion of a Photogrammetric Camera”, *RCA Data Reduction Technical Report No. 33, AFMTC-TN-56-20, ASTIA Document No. 96626*
- Brown D.C. (1966), “Decentring Distortion of Lenses”, *Photogrammetric Engineering*, Vol. 32(3), 444-462
- Derenyi, E.E., (1996), “The Digital Transferscope”, *Photogrammetric Engineering & Remote sensing*, Vol. 62(6), 733-736
- Fraser, C.S. (1997), “Digital Camera Self-Calibration”, *ISPRS Journal of Photogrammetry and Remote sensing*, Vol. 52, 149-159
- Hakkarainen, J., Rosenbruch K.J., (1982), “Image Quality and Lens Aberration of an Aerial Camera” *Photogrammetria*, No. 38, 87-102
- Hallert, B., (1968) “Notes on Calibration Cameras and Photographs in Photogrammetry”, *Photogrammetria*, Vol. 23, 163-178
- Iwashita, Y., Kurazume, R., Konishi, K., Nakamoto, M., Hashisume, M., Hasegawa, T., (2007), “Fast Alignment of 3D Geomatical Models and 2D Greyscale Images using 2D Distance Maps”, *Systems and Computers in Japan*, Vol. 38, No. 14, 52-62
- Kenfick, J.F., Gyer, M.S., Harp, B.F., (1972), “Analytical Self-Calibration”, *Photogrammetric Engineering*, No. 38, 1117-1126
- Khoshelham, K., Nardinocchi, C., Frontoni, E., Mancini, A., Zingaretti, P., (2010), “Performance Evaluation of Automated Approaches to Buildings in Multi-Source Aerial Data”, *ISPRS Journal of Photogrammetry and Remote sensing*, Vol. 65, 123-133
- Lillesand, M.T., Kiefer, R.W., (1987), “Remote Sensing and Image Interpretation”, (Second Edition), John Wiley & Sons. Inc
- Mizowaki, T., Cohen, G.N., Fung, A.Y.C., Zaider, M., (2002), “Towards Integrating Functional Imaging in the Treatment of Prostate Cancer with Radiation: The Registration of MR Spectroscopy Imaging to Ultrasound/CT Images and its Implementation in Treatment Planning”, *Int. J. Radiation Oncology Biol. Phys.*, Vol. 54, No. 5, 1558-1564
- Morgado, A., Dowman, I., (1997), “A Procedure for Automatic Absolute Orientation using Aerial Photographs and a Map”, *ISPRS Journal of Photogrammetry and Remote sensing*, Vol. 52, 169-182
- Slama, C.C., (Editor in Chief), (1980), “Manual of Photogrammetry”, American Society of Photogrammetry
- Suveg, I., Vosselman, G., (2004), “Reconstruction of 3D Building Models from Aerial Images and Maps”, *ISPRS Journal of Photogrammetry and Remote sensing*, Vol. 58, 202-224
- Zhao, K., Popescu, S., (2009), “Lidar Based Mapping of Leaf Area Index and its use for Validating GLOBCARBON Satellite LAI Product in a Temperate Forest of Southern USA” *Remote Sensing and Environment*, 113, 1628-1645

FARMLAND PARCELS EXTRACTION BASED ON HIGH RESOLUTION REMOTE SENSING IMAGES

Tangao Hu ^{a,*}, Wenquan Zhu ^a, Jinshui Zhang

^a State Key Laboratory of Earth Surface Processes and Resource Ecology, Beijing Normal University, Xijiekouwai Street NO. 19, Beijing, China – hutangao@ires.cn

Commission VII, WG VI/4

KEY WORDS: Parcels; Supervised Classification; Watershed segmentation; Image Processing; Regional Merging

ABSTRACT:

Extracting farmland parcels from high resolution remote sensing images is an important issue for land-use dynamic monitoring, precision agriculture and other fields. However, the traditional method, using GIS software and manual digital, has wasted a lot of human and material resources. In addition, the results are impacted by the human factors obviously. Therefore, an automatically extraction method which does not require too much manual intervention is needed urgently. This paper presents a remote sensing images segmentation method based on wavelet transform and watershed segmentation to get the final segmentation results. Firstly, we use the classification results to enhance the contrast of typical features in the original image. Secondly, we use wavelet transform and watershed segmentation to calculate the enhanced image, and then use improved regional merging algorithm to solve the problem of over-segmentation. Finally, we reconstruct the image by inversed wavelet transform with the edge information from Canny operator, and then label the regions to get the final segmentation results. To validate the proposed approach, experiment on Quickbird image is performed, we extract farmland parcels from the image quickly and accurately. It shows that the proposed approach is an effective farmland parcels extraction method based on high resolution remote sensing images.

1. INTRODUCTION

1.1 General Instructions

Parcels as an evaluation unit, has a very important significance in the dynamic monitoring of land use, land cover, precision agriculture, ecological planning, and other fields. Parcels is the smallest unit of land in which it has similar attributes, and it is also the basic spatial units of land assessment and classification. In different scales, parcels have different forms of performance, and its area can be more or less. The parcels have often defined the location and the border clearly, and its spectral characteristics also have a strong similarity in the remote sensing images. At present, the traditional method to extract the parcels information from high-resolution remote sensing images is to use GIS software, and getting the digital images manually. This method requires lots of experienced persons to digit the images, and obviously needs a lot of human and material resources. What's more, the results are also very subjective. Therefore, an automatically extraction method which does not require too much manual intervention is needed urgently. Image Classification and image segmentation are two important methods to get the internal information of the images. Remote sensing images classification is aimed to divide the pixels into different categories according to some rules or algorithms, through their different spectral band brightness and spatial structure characteristics or other information. The main methods of image classification are supervised and unsupervised classification. Image Classification can distinguish the features well, but the results of classification are not in the form of parcels, the same types of regions often mixed other features, for example, large tracts of wheat containing a lot of ridge information; In addition, the

classification results images have no edge information, and is impossible to label region. So it can not be used to extract the parcels automatically. However, some typical features have very obvious characteristics in the original image, such as water body, bared land and others. We can use the method of classification to identify them first, and then use the results to enhance the gray contrast of the typical features, thus contributing to the needs of the target parcels from the border closure and improving the accuracy of image segmentation. Remote sensing images segmentation is the process which will divide a whole image into a number of subsets with certain rules. Nowadays, more and more computer vision image segmentation algorithms are applied to remote sensing images segmentation research, and made a lot of improvement and innovation. These methods can be roughly divided into three groups. The first method is the threshold segmentation. Its threshold was determined according to the distribution of the image's gray values. The second method is the border segmentation. The third method is the region extraction, and the characteristics of this method is based on the different characteristics between the specific region and other background regions. Watershed transform segmentation is a kind of region extraction segmentation method. It has a strong noise suppression capability without setting a prior parameter. It can extract a region border with a single-pixel width. Although the watershed transform segmentation is a more ideal automated parcels extraction method, it is more sensitive to noise, and easily lead to over-segmentation problem. In order to suppress the image noise and reduce the over-segmentation problem, many researchers introduced the wavelet transform method. The low-frequency image decomposed by wavelet transform can suppress the image noise effectively. So it can attenuate the problem of over-segmentation well. In addition,

* Corresponding author.

Canny operator has a good effect on the image edge extraction. However, it can not meet the requirements of parcels extraction because the edges extracted by Canny are not closed. So if we can introduce the marginal information, it must be very helpful to improve the extraction results.

Based on the above considerations, this paper proposed an advanced method which can automatically extract the parcels. Firstly, we enhanced the contrast of the original image's gray value with image classification results. Secondly, the watershed transform method was applied to the enhanced image to segment the low-frequency image. In order to attenuate the problem of over-segmentation, an improved region merging algorithm was used in this paper. Finally, all regions were labeled with the marginal information extracted by Canny.

2. METHOD

The main flow of the proposed segmentation approach can be described as follows: enhancing the gray value contrast of the typical features, wavelet transform and gradient image calculation, watershed segmentation, region merging, image reconstruction, post-processing and so on.

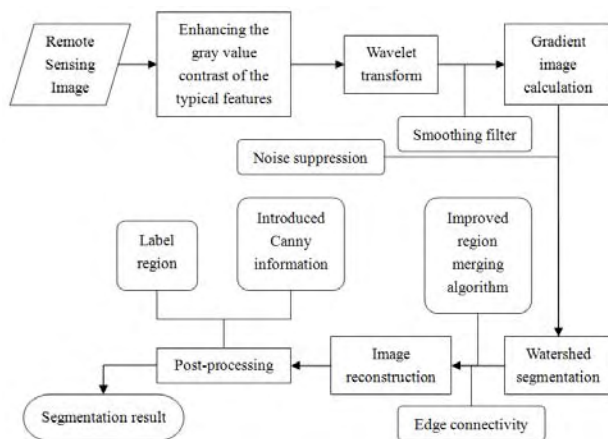


Figure 1. The flow chart of the proposed segmentation approach

2.1 Enhancing the gray contrast of typical features

The space adjacent pixels, although they belong to different features, their gray value are often similar, so using the image segmentation methods directly, is difficult to extract the edge of farmland parcels accurately. Because some typical features can be extracted easily by using conventional image classification methods, and then we can use the results to change their gray value in the original image, then enhance the gray value contrast between typical features and farmland parcels, to avoid the confusion with the edge of farmland parcels. Through this method, we can improve the accuracy of image segmentation.

2.2 Wavelet transform and gradient image calculation

Watershed segmentation has the over-segmentation problem, therefore, at first we should smoothing the image which the gray value contrast of the typical features have already enhanced. A simple low pass filtering method will be loss much image information, so we used wavelet transform method. The wavelet transform is a good mathematical tool for analyzing the multi-resolution image, it can completely represent the image, not only solve the over-segmentation problem partially, but also

suppress the noises effectively. A size of level-1 scale image is only a quarter of the original image, so it can reduce the complexity of the image segmentation and computing time .

Remote sensing images often contain a lot of Gaussian and non-Gaussian noises, in the multi-resolution image, because the low-frequency image losses much of high-frequency information, so in the lower image, the edge will be very rough, in the topography, it is known as the "plateau", which many adjacent pixels have the same gray values. In order to reduce such impact on the watershed segmentation, we can first smooth the results image, and then calculate the gradient, that is smoothing equation,

$$I_{gradsmooth}(x, y, \sigma) = \nabla \|I(x, y) * g_{\sigma}(x, y)\| \quad (1)$$

where $g_{\sigma}(x, y)$ = a Gaussian filter
 σ = standard deviation
 $*$ = convolution

To the image after Gaussian filtering, the paper used Sobel operator to calculate the gradient,

$$h_1 = \begin{bmatrix} -1 & 0 & 1 \\ -2 & 0 & 2 \\ -1 & 0 & 1 \end{bmatrix}, h_2 = \begin{bmatrix} 1 & 2 & 1 \\ 0 & 0 & 0 \\ -1 & -2 & -1 \end{bmatrix} \quad (2)$$

where h_1 = the vertical direction factors
 h_2 = the horizontal direction factors

calculating through them and smoothed image, we can get the vertical and horizontal direction of gradient image I_v and I_h , so gradient image I_g can be expressed as,

$$I_g = \sqrt{I_v^2 + I_h^2} \quad (3)$$

where I_v = gradient image
 I_h = gradient image
 I_g = gradient image

Despite the low-frequency image has been filtered some noises, but not completely, so in the gradient image, there will still exist some false edges generated by the noise. We need to suppress the noise according to Signal Noise Ratio (MSE) and standard deviation (σ).

When the T_g is setting larger than σ , the image can get a greater Signal Noise Ratio. Therefore, we make the following processing,

$$\text{IF } T_g \leq 0.5\sigma, \text{ THEN } T_g = 0 \quad (4)$$

where T_g = the value of gradient image
 σ = standard deviation

2.3 Watershed segmentation

2.3.1 watershed segmentation

The watershed segmentation is a well known image segmentation approach, which is based on the following morphological principles. If we regard a grayscale image as a topographic relief, the gray value at a given location represents the elevation at that point. If this relief is to be flooded, starting at surface global minima, the water would fill up lower elevation points first, and then the water level would increase. At locations where water coming from different minima would meet, a 'dam' is built. Finally, when the whole surface is flooded, each minimum becomes completely surrounded by 'dams' (i.e. the watersheds). These watersheds delimit the segmented regions, which are the minima catchment basins. If this process is applied to a gradient image, where to each pixel corresponds the local gradient modulus, then the watersheds correspond to the gradient image crest lines. In this case, the catchment basins correspond to the segmented image objects. Unfortunately, images are inherently noisy, and contain gray level fluctuations that generate spurious gradients. Such gradients generate spurious watersheds, which are the main cause of over-segmentation, a known limitation of the watershed segmentation approach^[24-25]. Therefore, we need to merge these regions.

2.3.2 Improved regional merging algorithm

The traditional merging methods are based on the adjacent image, each merger will need to update the order of the relevant links in the queue, this approach will consume a lot of times in the sorting, searching, updating and removing links, the efficiency is not high, also needs a great amount of computation. In order to improve the efficiency of the regional merging algorithm^[26], the paper proposes a new method, which using mathematical morphology algorithm to find the adjacent regions, and using the regional merging cost function to set the threshold, then completing the regional merging.

Assuming the watershed segmentation image for I_0 , and was divided into N regions.,

$$R_i(S_i, G_i), i = 1, 2, \dots, N \quad (5)$$

where S_i = the size of the region i
 G_i = average gray value of the region i

To the adjacent regions p and q , merging cost function can be defined like this,

$$MergeCost = \frac{\|S_p\| \times \|S_q\|}{\|S_p\| \times \|S_q\|} \times |G_p - G_q|^2 \quad (6)$$

where S_p = the size of the region p
 S_q = the size of the region q
 G_p = average gray value of the region p
 G_q = average gray value of the region q

The steps of the regional merging algorithm:

Firstly, find the spatial distribution of the gray value of G_1 in the image I_0 , and then record them to a blank image I_1 (I_1 is the same size with I_0), and change these pixels gray value to 1; Secondly use the mathematical morphology (Dilate) algorithm to expand the image I_1 by the structure of 5×5 , and then record these pixels to another blank image I_2 (I_2 is the same size with I_0); Thirdly, get the image I_3 by I_1 subtracts from I_2 , so I_3 recorded the location of the edge information and the adjacent pixels information of G_1 , as shown in Figure 3; Because the watershed segmentation image I_0 's edge pixels value is 0, so if I_3 multiplied by I_0 , the results array can recode all the adjacent pixels gray value of G_1 ; Fourthly, use the regional merging cost function, and calculate the distance between these adjacent pixels and G_1 , if the value is less than the defined threshold value (based on the prior knowledge of the image, users defined), merge two, otherwise not merge. After the merger we can get a new region, the gray value of the new region is the average of two original regions; At last, merge the regions which gray value is $G_{2, \dots, N}$, the process is not end until all the regions are not meet the merging conditions.

2.3.3 Edge connectivity

We found that after the merging process, although the gray value of the adjacent regions which can merged into a new region have been changed, the edge pixels between this two regions still exists, and they have not really connected, so this requires us to remove the redundant edge information.

The steps of the edge connectivity:

Firstly, judging the pixel value whether is equal to 0, if the value is equal to 0, we know that the pixel is the edge of the region; Secondly, judging it's adjacent pixels value whether is equal to 0, if not, then judging it's adjacent pixels value are whether the same, if same, it shows that this edge pixel is redundant, we should amend this pixel vale equal to it's adjacent pixel; The process is not end until all the pixels are not meet the amending conditions.

Through the improved regional merging algorithm, we can suppress the over-segmentation problem well.

2.4 Image reconstruction and post-processing

After watershed segmentation and regional merging, we use inverse wavelet transform to reconstruct the image.

2.4.1 Introduced Canny information

From the edge model and noise model, Canny (1986) put forward the optimal filter of edge detection, and achieved good results, it is an ideal edge detection algorithm. As Canny result is not closed, it is not suitable for extraction enclosed area, but we can introduced the Canny result into reconstructed image, improve the accuracy of image segmentation.

The steps of introducing the Canny information:

Assuming the Canny image for C_0 , first of all, with 1 subtracts from C_0 , we can get the image C_1 which edge gray value is 0 and other pixels gray value is 1, then C_1 multiplied by a large number N (defined by users according to the gray value of the reconstructed image); Secondly, get the image C_2 by C_1 add the reconstruction image; Finally, amending the pixels value in the C_2 which can be seen as the edge pixels to 0, and other pixels value in C_2 subtracts by N , to restore the reconstructed image's original gray value.

2.4.2 Labeling regions

In order to facilitate the distinction between the various regions, we labeled the reconstructed image (label region), and received the ultimate remote sensing images segmentation results.

3. APPLICATIONS

We select Quicbird which is a high-resolution and multi-spectral remote sensing images data as test image, the imaging time is on May 2, 2006, the spatial resolution is 2.4 meters, it covers the Tongzhou District of Beijing, the size is 512*512 (Units: Pixel). From it, we can see the following types of features clearly: water, farmland, bare land and construction sites(buildings). The paper wants to extract the farmland parcels, which is in red. If we extract the parcels by traditional methods, it would be necessary to spend a lot of time, if we use the method proposed by this paper, we can get the results easier. Our method can be achieved by ENVI software and interactive data visualization programming language IDL.

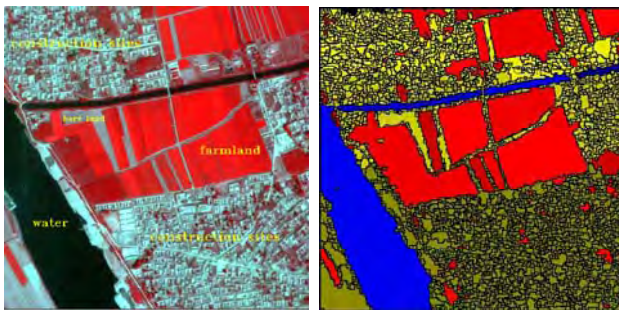


Figure 2. The result of image segmentation

Contrasting experimental results with the original image, we can see that the large area of farmland parcels can extract fast by the proposed method in the paper, but for the smaller parcels, the results of the extraction are also necessary to improve, the main reason is that the gray value contrast of the smaller parcels and the other surrounding parcels are not strong, so it is difficult to extract them from the others. Because the gray value contrast of water and other features is strong, so it is easy to extract. But the construction sites because of its uneven internal conditions, the extraction results are poor. What's more, in the regional merging, the quality of the threshold is very important to the segmentation result.

Obviously, compared to the traditional method, this method has great advantages: (1) Remote sensing images segmentation method based on wavelet transform and watershed is an automatic extraction method, which can save a lot of human and material resources, does not require too much manual intervention, and extracts large area of farmland parcels accurately. (2) Using the image classification results to change the gray value of the typical features in the original image, and then enhance the contrast between typical features and farmland parcels, through this method, we improve the accuracy of image segmentation. (3) Changing the original image into a low-resolution image by wavelet transform, can suppress the noise effectively, and improve the speed of the watershed algorithm, because after wavelet transform, the size of image is only a quarter of the original image. (4) Proposed a simple and effective regional merging algorithm, which reduces the amount of computation, and ensures that little image information is lost.

4. CONCLUSIONS

This paper presents a remote sensing images segmentation method based on wavelet transform and watershed segmentation to get the final segmentation results by the steps of enhancing the gray value contrast of the typical features, wavelet transform, gradient image calculation, watershed segmentation, image reconstruction, post-processing and so on. The experimental results show that it can extract the farmland parcels quickly and accurately.

However, the method proposed in this paper also has some aspects where improvement is needed: (1) Using this method to extract the large area parcels which internal information is homogeneous (such as farmland parcels), we can get the results quickly and accurately, but for those smaller or internal information is uneven parcels, there is still existing some defects; (2) In the regional merging, the threshold is setting manually, it will affect the results of the image segmentation a lot, so to find the threshold automatically is the focus of the study in the future.

5. REFERENCES

- Yang X X, He Z M, Feng X L. , 2006a, Remedying Land Grading Method based on Comparison of the Change of Land Plot and Verification of Land Price. *Resources Science*, 28(6),pp. 80—85.
- Wang S Q, Shu N, Zhou Y., 2007a, Application of Parcels-Oriented MDPA to Classification of Agricultural Land Based on Landsat7. *Geospatial Information*, 5(2),pp.17—19.
- Qin Q M.,2000a, The Problem about Auto-interpretation of Remote Sensing Images and Resolution Ways. *Science of Surveying and Mapping*, 25(2),pp. 21—24.
- Zhao Y , et al., 2003, *Remote Sensing Application Analysis and Theory*. Beijing Science Press, pp. 300-305.
- Zhang Y J.,2000, *Image Segmentation*. Beijing Science Press, pp. 110-115.
- Li S D, Zhang C, Wang Z Z.,2003a, SAR Image Segmentation by Likelihood Criterion. *Journal of Remote Sensing*, 7(2),pp.118-124.
- Liu W P, Chen W J.,1999a, A Segmentation Method for Airport Object in Remote Sensing Images. *J. Infrared Millim. Waves*, 18(1),pp. 73-76.
- Pesaresi M, Benediktsson J A.,2001a, A New Approach for the Morphological Segmentation of High Resolution Satellite Imagery. *IEEE Transactions on Geoscience and Remote Sensing*, 39 (2),pp. 309-320.
- Pekkarinen A.,2002a, A Method for the Segmentation of Very High Spatial Resolution Images of Forested Landscapes. *Int. J. Remote Sensing*, 23 (14),pp. 2817-2836.
- Bosworth J, Koshimizu T, Acton S T.,2003a, Multi resolution Segmentation of Soil Moisture Imagery by Watershed Pyramids with Region Merging. *Int. J. Remote Sensing*, 24(4),pp. 741-760.
- AcharyyaM, De R K, Kundu M K.,2003a, Segmentation of Remotely Sensed Images Using Wavelet Features and Their

Evaluation in Soft Computing Framework. *IEEE Transactions on Geoscience and Remote Sensing*, 41(12),pp. 2900-905.

Provost J N, Collet C, Rostaing P, et al.,2004a, Hierarchical Markovian Segmentation of Multispectral Images for the Reconstruction of Water Depth Maps. *Computer Vision and Image Understanding*, 93(2),pp. 155-174.

Chen Q X, Chen S P, Zhou C H.,2006a, Segmentation Approach for Remote Sensing Images Based on Local Homogeneity Gradient and Its Evaluation. *Journal of Remote Sensing*, 10(3),pp. 357-365.

Zhu H, et al.,2005, *The basis of Digital Image Processing*. Beijing Science Press, pp. 110-115.

Mei T C, Li D R, Qin Q Q.,2004a, Extraction of Linear Feature from Remote Sensing Image Based on Watershed Transform. *Geomatics and Information Science of Wuhan University*, 29(4),pp. 398-341.

Williams H C.,1980a A modification of the RSA public-key encryption procedure. *IEEE transactions on information theory*, VIT-26(6),pp. 726-729.

Wang X, Luo B, Ning C.,2006a, Image Segmentation Method Based on Wavelet and Watersheds Algorithm. *Computer Technology and Development*, 16(1),pp. 17-22.

Huang H, Qi C, Li J.,2001a, Text of Digital Watermarking. *Chinese Information Journal*, 15(5),pp. 52-57.

Chen Z H, Lei Y, Liu H H.,2006a, Image Segmentation Based on Wavelet-Based Watershed. *Journal of South-Central University for Nationalities (Nat. Sci. Edition)*, 25(1),pp. 47-50.

Zha Y F, Niu J L, Bi D Y.,2006a, Algorithm of Watershed Image Segmentation Based on Multi-resolution. *Computer Engineering*, 32(19),pp. 202-204.

Yang S B, Peng F Y, Zhang Z C.,2003a, Research on OmniDirectional Edge Detection Algorithm Based on Morphology in Remote Sensing Image. *Remote Sensing Information*, (1),pp. 2-3.

Liu Y X, Li M C, Mao L.,2006a, An Algorithm of Multi-spectral Remote Sensing Image Segmentation Based on Edge Information. *Journal of Remote Sensing*, 10(3),pp. 350-356.

Ma Z M, Tao C K.,1999a, Regional Fractal And Artificial Object Detection. *Acta Physica Sinica*, 48(12),pp. 2202-2207.

Wang P W, Wu X Q, Zhang M C.,2006a, Watershed Segmentation Based on Multiscale Morphological Fusion. *Journal of Data Acquisition & Processing*, 21(4),pp. 398-402.

Han P Y.,2006, *IDL Visualization Analysis and Application*. Northwestern University Press, pp. 52-55.

Mei Y S, Yang S X, Mo B.,2006a, Improved Edge Detection Algorithm Based on Canny Operator. *Laser & Infrared*, 36(6),pp. 501—503.

J Canny.,1986, A computational approach to edge detection. *IEEE Transactions on Pattern Analysis and Machine Intelligence*, 8(6),pp.679—696.

DETECTION OF FOREST MANAGEMENT OPERATIONS USING BI-TEMPORAL AERIAL PHOTOGRAPHS

P. Hyvönen^{a*}, J. Heinonen^a, A. Haara^b

^a Finnish Forest Research Institute, P.O. Box 68, FI-80101 Joensuu, Finland – (pekka.hyvonen, jaakko.heinonen)@metla.fi

^b Dept. of Forest Science, University of Helsinki, FI00014, Helsinki, Finland – arto.haara@metla.fi

KEY WORDS: Change detection, aerial photograph, segmentation, *k*-NN, rectification

ABSTRACT:

The increased need for timely forest information is leading to the continuous updating of stand databases. In continuous updating, stand attributes are estimated in the field following a forest operation (cutting or silvicultural treatment) and stored in databases. To determine the changes caused by forest operations and forest damage, a semi-automatic method was developed based on bi-temporal aerial photographs.

The field data consisted of 2 362 forest stands, from which the changes between years 2001 and 2004 were collected from different databases. Stands were divided into three classes according to the type of change. The *No-change* class (1 890) included stands with no changes other than growth. The *Moderate-change* class (373) included stands with changes such as thinning, partly operated stand and improvement of young stand. The *Considerable-change* class (99) included stands with major changes such as clear cutting and severe storm damage. The data were randomly divided into training and test data. The aerial photographs were acquired for the years 2001 and 2004 with almost the same image specifications and the photographs were temporally registered. As change detection is sensitive to location errors, locational adjustments were made at the stand and segment levels. Linear stepwise discriminant analysis and the non-linear *k*-nearest neighbour (*k*-NN) method were tested in classification.

The classification results at the stand level were found to be better than at the segment level. Compared to previous studies, the results of this study demonstrate remarkable improvement in the classification accuracy of moderate changes. The results showed that change detection substantially improved when the registration at the stand level was used, especially in the detection of thinned stands.

1. INTRODUCTION

Stand attributes in Finland have been traditionally gathered by periodical field inventories with inventory cycles of 10-15 years. The increased need for timely forest information is leading to the continuous updating of stand databases. In continuous updating, a stand database is kept up-to-date computationally using statistical growth models. After a forest operation (i.e. cutting or silvicultural treatment), stand attributes are estimated in the field.

A forest operation can be reported at the time of the work, but forest damage, for example, must be determined by some other method. There are also errors that should be controlled in the databases. Medium-resolution satellite images (e.g. Landsat TM images) have been successfully used for detecting considerable changes such as clear cuttings, removals of hold-over trees, soil preparations or drastic damage. The detection of moderate changes such as thinnings, preparatory cuttings or slight damage, has been difficult (Holmgren & Thuresson, 1998; Wilson & Sader, 2002; Heikkonen & Varjo, 2004). The reason for this is that typical thinnings, where about 20-40% of the basal area is removed, cause only subtle changes in reflectance (Olsson, 1994).

The reflectance captured by a single pixel in medium-resolution images is the average of the reflectance from an area of more than 100 m² on the ground. However, with high-resolution remote sensing materials, the disappearance of individual trees

can be detected. For example, using data from airborne laser scanning (ALS), Yu et al. (2004) found 61 of 83 harvested trees. However, ALS is very expensive compared to aerial photography.

Operational high-resolution applications for change detection of vegetation cover are based on the visual interpretation of aerial photographs, although more automatic methods have also been proposed. Hudak and Wessman (1998) investigated a transition from grassland to shrubland using historical aerial photographs. The images were classified using variograms that characterised the image texture. Changes were determined by post-classification comparison. Kadmon and Harari-Kremer (1999) also studied vegetation dynamics using pixel-level spectral classification and then averaging the results to larger cells and differencing the cell values. In both studies, good results using automatic change detection were achieved; but compared to the context of the present study, the time-intervals were much wider and the changes more radical. In the study of Saksa et al. (2003), clear cuttings were detected using three approaches: pixel-by-pixel differencing and segmentation, pixel block-level differencing and thresholding, and presegmentation and unsupervised classification. Each method was found to be suitable for operational use. Hyppänen (1999) applied image differencing to bi-temporal aerial photographs. In that study, considerable changes were detected while moderate changes were not. Consequently, the problem of how to detect moderate

changes automatically using aerial photography has remained unsolved.

In automatic change detection, the effect of disturbing factors should be minimised. These factors include differences in atmospheric conditions, sun angle, soil moisture, vegetation phenology and, in the case of aerial photographs, the differences in viewing angles (Singh, 1989). It is important to eliminate factors that might cause differences between similar stands in different parts of the images. By using the present satellite positioning systems, aerial photographs can be taken very close to each other at different times.

The objective of this study was to investigate whether bi-temporal aerial photographs taken with similar image specifications and adjusted at stand and segment levels are useful in change classification, especially in detecting moderate changes such as thinnings.

2. MATERIAL AND METHODS

2.1 Material

The study area is located in Western Finland near the town of Kauhajoki (22°18' E, 62°24' N). The forest holdings are mainly privately owned and are in a so called “stripsharing” configuration so that the holdings are usually long and narrow. The landscape of the area is dominated by flat terrain. The elevation varies between 125 and 185 m above sea level. The main tree species are pine (*Pinus sylvestris* L.) and spruce (*Picea abies* (L.) Karst.). The main broadleaved species are silver birch (*Betula pendula* Roth.) and pubescent birch (*Betula pubescens* Ehrh.). There are also several low-density stands in the study area. The main site types are fresh (26% of the area), dryish (42%) and dry (25%). The site types are according to Kuusela and Salminen (1969) and the fertility of peatlands is determined and classified using the same system as that for mineral soils (Laine & Vasander, 1993).

The field data consists of 2 362 forest stands. The stand attributes were measured during summer 2002 based on a visual stand level inventory system that is used in Finland. In this system, the stands are initially delineated by visual interpretation of aerial photographs. The forest characteristics of the stands are then estimated visually with the aid of some measurements in the field, and the initial delineation is confirmed.

The changes in stands between 2001 and 2004 were determined from different databases of the Regional Forest Centre and all stands were checked visually using bi-temporal aerial photographs. The uncertain cases were checked in the field. Subsequently, all stands were divided into three classes according to the type of change. The *No-change* class consisted of stands with no changes other than growth (1 890 stands). The *Moderate-change* class consisted of stands with moderate changes (373 stands), i.e. thinning, seed tree felling, tending of seedling stand, improvement of young stands, removal of hold-over trees, soil preparation, slight storm damage, partly operated stand and forest road building. Slight storm damage means that storms have felled only few trees in the stand. The *Considerable-change* class consisted of stands with major changes (99 stands), i.e. clear cutting and severe storm damage. Severe storm damage means that storms have felled many trees or groups of trees in the stand.

The image data consisted of two aerial photographs covering the study area. The latter photograph was taken as close to the former one as possible with respect to time, date and location (Table 1). The photographs were acquired using a Leica RC30 camera and an antivignetting and an infrared radiation filter. The nominal scale of the color-infrared photographs was 1:30 000. The photographs were first scanned with a photogrammetric scanner at 14 μ m resolution into RGB-images with no tone adjustment. Secondly, the images were ortho-rectified to a spatial resolution of 0.5 m by using 11 (photo01) and 13 (photo04) control points that were located from digital base maps and a digital elevation model. The digital elevation model had a resolution of 25 m. The root mean square errors (RMSEs) of the rectification were 5.1 m (photo01) and 3.2 m (photo04). These photographs were used as base photographs for the extraction of spectral features.

	Aerial photograph	
	photo01	photo04
Latitude	62.4127	62.4125
Longitude	22.3045	22.3016
Altitude (m)	4,751	4,622
Date	23 June 2001	27 June 2004
Time (UTC)	7:55:58	7:29:06
Course	271	271
Solar azimuth angle (°)	52.8	60.2
Solar azimuth angle (°)	42.8	40.1

Table 1. The metadata of the aerial photographs

2.2 Methods

As change detection is sensitive to location errors, the final adjustment of the aerial photographs taken at two time points was based on statistical correlations that were computed independently for each stand and segment. The geographic location of the new photograph was determined by shifting the location at the photograph to one of the cardinal points one pixel at a time. The search range was ten pixels from the original location and covered 21*21 pixels. At each location a Pearson's correlation coefficient was computed for the digital number values (DNs) of the pixels that referred to a given area after the shift. Pixels on the buffer zone in the new photograph and pixels that were outside the stand (segment) boundaries in the old photograph were not taken into account. The width of the buffer zone was ten pixels from the stand (segment) boundary. The location that resulted in the largest correlation was selected. The process was repeated for each of the channels. A stand might not be the most suitable unit for change detection because some changes may occur in part of the stand only. Change detection was therefore also carried out at the segment (=sub-stand) level and results were adjusted to whole stands. In the segmentation procedure, the most recent aerial photograph was segmented based on the DN values of the three channels and the stand boundaries. With the help of the stand boundary, the segment was attached to the area of one stand. In the other words, the segment boundary did not cross the stand boundary (Figure 1).

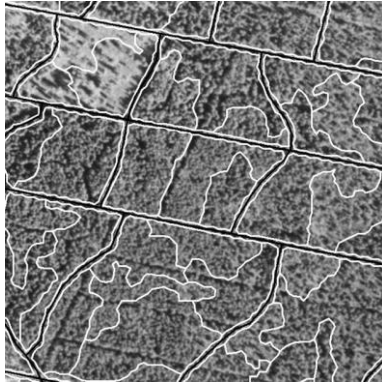


Figure 1. Stand (black) and segment (white) boundaries in aerial photograph (near-infrared channel). Copyright for the aerial photograph owned by Blom Kartta Oy

Altogether, 9 156 segments were used. The segmentation algorithm was same as in the study of Hyvönen et al. (2005).

Altogether, 75 features both at the stand and segment levels were extracted, of which 36 were spectral features extracted from the original photographs and 39 were features from the adjustment of and regression between the photographs. These features were used in the change detection analysis.

Two different methods for change detection were tested; linear stepwise discriminant analysis and the non-linear k -nearest neighbour (k -NN) method. The classification functions of the discriminant analysis and the weights of the variables of the similarity distance functions, as well as the number of the neighbours of k -NN method, were estimated for the three change classes in the training data. The multi-objective optimisation, combined with the k -NN method, was used to choose the weights of the variables of the similarity distance functions, as well as the number of the neighbours of k -NN method (Haara, 2000). The nonlinear programming algorithm presented by Hooke and Jeeves (1961) was used to find the combination of decision variables that minimised the objective function. The optimised objective variable was the sum of the Kappa value and the percentage of correctly classified *moderate-change* stands. Both methods, i.e. the estimated classification functions of the discriminant analysis and k -NN method with the training data as the reference data, were then applied to the test data. The accuracy of the classification was studied at the stand level.

The accuracy of the classification results was evaluated by means of confusion matrices (Campbell, 1987) and the overall (OA), producer's (PA) and user's (UA) accuracies were calculated (Congalton et al., 1983; Story & Congalton, 1986). The OA can give too optimistic results if the proportion of one class is high (Campbell, 1987) and for this reason the κ (kappa) coefficient was calculated (Congalton & Mead, 1983).

3. RESULTS

When stands were used as classification units, the overall accuracy of the discriminant analysis was 91.1%, the Kappa-value 0.74, the omission error 16.1% and the commission error 7.2% (Tables 2 and 6). The main interest concerned thinned stands, of which 90.7% were found. When segments were used as classification units and the results were studied at the stand

level, the overall accuracy of the discriminant analysis was 90.1%, the Kappa-value 0.71, the omission error 13.8% and the commission error 8.8% (Tables 3 and 6). Of the thinned stands 89.7% were found.

When using the k -NN method, the overall accuracy was 91.5% and the Kappa value was 0.72 (Tables 4 and 6). The proportion of correctly classified thinned stands was 82.5%. When the classification was done at the segment level, the stand wise overall accuracy was 86.6% and the Kappa value 0.62 (Tables 5 and 6). In this case, 86.6% of the thinned stands were found.

After rectification (at the image level) 12 stands had been moved more than 5 pixels in every channel in the direction of x and 18 stands in direction of y in the final adjustment between the aerial photographs. Only one stand of these was in the *No-change* class.

Observation	Estimated		
	No-change	Mod.-change	Con.-change
No-change	874	68	0
Mod.-change	35	139	0
Con.-change	0	0	44

Table 2. Classification results of the discriminant analysis at the stand level, stands as a priori classification units.

Observation	Estimated		
	No-change	Mod.-change	Con.-change
No-change	859	83	0
Mod.-change	30	144	0
Con.-change	0	2	42

Table 3. Classification results of the discriminant analysis at the stand level, segments as a priori classification units.

Observation	Estimated		
	No-change	Mod.-change	Con.-change
No-change	900	40	2
Mod.-change	52	121	1
Con.-change	1	3	40

Table 4. Classification results of the k -NN method at the stand level, stands as a priori classification units.

Observation	Estimated		
	No-change	Mod.-change	Con.-change
No-change	834	107	1
Mod.-change	41	130	3
Con.-change	0	3	41

Table 5. Classification results of the k -NN method at the stand level, segments as a priori classification units.

	Kappa	OA%	OM%	CM%
disc., stand	0.74	91.1	16.1	7.2
<i>k</i> -NN, stand	0.72	91.5	24.3	4.5
disc., segment	0.71	90.1	13.8	8.8
<i>k</i> -NN, segment	0.62	86.6	18.8	11.5

Table 6. Classification results of the discriminant analysis (disc.) and the *k*-NN method (*k*-NN) at the stand level. stand: stands as classification units, segment: segments as classification units. OA%: overall accuracy, OM%: omission error, CM%: commission error.

4. DISCUSSION

A semi-automatic method for change detection in boreal forests using bi-temporal aerial photographs was developed. The photographs were taken as close to each other as possible with respect to time, date and location. The change detection was tested at the stand and segment levels.

Considerable changes were classified, at best, without error. The results of moderate changes were also clearly better than achieved by some earlier studies (Saksa et al., 2003; Haapanen & Pekkarinen, 2000). The use of correlation coefficients for image matching at the stand level and in the classification together with other spectral features was considered to be the key element in obtaining the good results.

The use of the *k*-NN method with multi-objective optimisation was also found to be very effective for detecting changes at the stand level. The large number of possible features in the distance function requires an efficient algorithm for determining the optimal formula of the distance function. Furthermore, the definition of the formula of the objective function is crucial for achieving the optimal solution. For example, when the Kappa value was the only objective variable in the optimisation, the Kappa value of the classification of the reference data was same as in the discriminant analysis. However, the classification results of the *Moderate-change* class were then considerably worse.

In practice, obtaining aerial photographs with the same spatial specification is not a problem. Nevertheless, in Finland, weather conditions limit the number of suitable days for aerial photography. Weather conditions may therefore complicate the acquisition of photographs with similar temporal specifications and thus limit the operational use of the method. In this study, photographs with similar specifications were obtained, which enabled an exploration of how reliable change detection is when using the bi-temporal aerial photographs in nearly optimal conditions. Even where bi-temporal aerial photographs are taken at identical locations, the time difference may play an essential role; the shadows of the treetops move several metres in a rather short time. If these shadows are captured in both images, on the ground or some other way, the rectification adjustment based on DN correlations, might move the stands so that the shadows are matched. Thus, the real objects might not be matched in the best possible way and the classification results would then be questionable. The effect of shadow movement was also noticed in the study of Im and Jensen (2005).

There are some issues that require further study. First, one image-pair may not be enough to cover the area of interest. The

mosaicking of images introduces error, which must be quantified in further studies. Secondly, another source of error is the practical training data from operational databases, which, as noted in this study, contain incorrect operations. Thirdly, the method studied should be tested with diverse image material, for example, with images taken with no-optimal image specifications and with images digital by origin. Fourthly, the use of texture features in the classification, together with stand level rectification, should be studied. Tuominen and Pekkarinen (2005) and Hyvönen and Anttila (2006) found that the use of textural features is advantageous in estimation and classification procedures. The effect of different methods of classification on the accuracy of the estimation should be studied. Heikkonen and Varjo (2004) found that nonparametric classification methods worked better than the parametric method tested here. With a maximum likelihood classifier there was a strong tendency to over classify the *Moderate-change* class, as was also the case in this study.

REFERENCES

- Campbell, J.B., 1987. *Introduction to Remote Sensing*. The Guilford Press, New York.
- Congalton, R.G. and Mead, R.A., 1983. A quantitative method to test for consistency and correctness in photo-interpretation. *Photogrammetric Engineering and Remote Sensing*, 49(1), pp. 69-74.
- Congalton, R.G., Oderwald, R.G. and Mead, R.A., 1983. Assessing Landsat classification accuracy using discrete multivariate statistical techniques. *Photogrammetric Engineering and Remote Sensing*, 49(12), pp. 1671-1678.
- Haapanen, R. and Pekkarinen, A., 2000. Utilising satellite imagery and digital detection of clear cuttings for timber supply management. In: *International Archives of Photogrammetry and Remote Sensing*, Vol. XXXIII, Part B7. pp. 481-488.
- Haara, A., 2002. Kasvuennusteiden luotettavuuden selvittäminen knn-menetelmällä ja monitavoiteoptimoinnilla. *Metsätieteen aikakauskirja*, 3/2002, pp. 391-406. (In Finnish).
- Heikkonen, J. and Varjo, J., 2004. Forest change detection applying Landsat thematic mapper difference features: a comparison of different classifiers in boreal forest conditions. *Forest Science*, 50(5), pp. 579-588.
- Holmgren, P. and Thuresson, T., 1998. Satellite remote sensing for forestry planning - a review. *Scandinavian Journal of Forest Research*, 13(1), pp. 90-110.
- Hooke, R. Jeeves, T.A., 1961. 'Direct search' solution of numerical and statistical problems. *Journal of the ACM* 8, pp. 212-229.
- Hudak, A.T. and Wessman, C.A., 1998. Textural Analysis of Historical Aerial Photography to Characterize Woody Plant Encroachment in South African Savanna. *Remote Sensing of Environment*, 66(3), pp. 317-330.
- Hyppänen, H., 1999. Eriaikaiset ilmakuvat metsäkuvioiden muutosten tunnistamisessa. *Metsätieteen aikakauskirja*, 2/1999, pp. 155-166. (In Finnish).

- Hyvönen, P., Pekkarinen, A. and Tuominen, S., 2005. Segment-level stand inventory for forest management. *Scandinavian Journal of Forest Research*, 20(1), pp. 75-84.
- Hyvönen, P. and Anttila, P., 2006. Change detection in boreal forests using bi-temporal aerial photographs. *Silva Fennica*, 40(2), pp. 303-314.
- Im, J. and Jensen, J.R., 2005. A change detection model based on neighbourhood correlation image analysis and decision tree classification. *Remote Sensing of Environment*, 99(3), pp. 326-340.
- Kadmon, R. and Harari-Kremer, R., 1999. Studying Long-Term Vegetation Dynamics Using Digital Processing of Historical Aerial Photographs. *Remote Sensing of Environment*, 68(2), pp. 164-176.
- Kuusela, K. and Salminen, S., 1969. The 5th national forest inventory in Finland. *Communicationes Instituti Forestalis Fenniae*, 69(4).
- Laine, J. and Vasander, H., 1993. *Suotyypit 3rd ed.* Kirjayhtymä, Helsinki. (In Finnish).
- Olsson, H., 1994. Changes in satellite measured reflectances caused by thinning cuttings in boreal forest. *Remote Sensing of Environment*, 50(3), pp. 221-230.
- Saksa, T., Uutera, J., Kolström, T., Lehtikoinen, M., Pekkarinen, A. and Sarvi, V., 2003. Clear-cut detection in boreal forest aided by remote sensing. *Scandinavian Journal of Forest Research*, 18(6), pp. 537–546.
- Singh, A., 1989. Digital change detection techniques using remotely-sensed data. *International Journal of Remote Sensing*, 10(6), pp. 989-1003.
- Stehman, V. and Czaplewski, R., 1998. Design and analysis for thematic map accuracy assessment: fundamental principles. *Remote Sensing of Environment*, 64(3), pp. 331-344.
- Story, M. and Congalton, R.G., 1986. Accuracy assessment: A user's perspective. *Photogrammetric Engineering and Remote Sensing*, 52(3), pp. 397-399.
- Tuominen, S. and Pekkarinen, A., 2005. Performance of different spectral and textural aerial photograph features in multi-source forest inventory. *Remote Sensing of Environment*, 94(2), pp. 256-268.
- Wilson, E. and Sader, S., 2002. Detection of forest harvest type using multiple dates of Landsat TM imagery. *Remote Sensing of Environment*, 80(3), pp. 385-396.
- Yu, X., Hyypä, J., Kaartinen, H. and Maltamo, M., 2004. Automatic detection of harvested trees and determination of forest growth using airborne laser scanning. *Remote Sensing of Environment*, 90(4), pp. 451-462.

FUSION OF PAN AND MULTISPECTRAL IMAGES BASED ON CONTOURLET TRANSFORM¹

Y. Jia^{a,b}, M. Xiao^a

^a School of Remote Sensing and Information Engineering, Wuhan University, 129 Luoyu Road, Wuhan 430079, China - yhjia2000@sina.com

^b State Key Laboratory of Information Engineering in Surveying, Mapping and Remote Sensing, Wuhan University, Wuhan, China - yhjia2000@sina.com

KEY WORDS: Photogrammetry, Fusion, Detection, IKONOS, High resolution, Theory

ABSTRACT:

Contourlet transform can give the asymptotic optimal representation of edges and contours, so it can capture smooth contours and geometric structures in images much more efficiently than the wavelet transform. The nonsampled contourlet transform (NSCT) not only has multiresolution and multidirectional properties but also has shift-invariant property by contrast to the contourlet transform. A new method of fusing panchromatic (Pan) and multispectral (MS) remote sensing images was proposed based on NSCT and IHS transform. IKONOS images were used to verify its validity. The experiment results show that the proposed method has greatly improved spatial resolution and keep the spectral information, and is better than the fusion method based on CT and IHS.

1. INTRODUCTION

In recent years, the fusion algorithm based on multiscale analysis tools is attached a great importance such as ridgelet, wavelet, curvelet and contourlet [Arthur L Da C, Zhou J P, Do M N, 2006]. As a multiscale analysis tool, the contourlet transform (CT) have the characteristics of localization, multi-direction and anisotropy [M. Choi, R.Y. Kim, M.-R. Nam, H.O. Kim, 2005]. The CT can give the asymptotic optimal representation of contours and applied in image fusion effectively. However, the CT is lack of shift-invariance and results in artifacts along the edges in some extend. The nonsampled contourlet transform (NSCT) is in virtue of nonsampled filter banks to meet the shift-invariance [Arthur L Da C, Zhou J P, Do M N, 2006]. Therefore, the NSCT is more suitable for image fusion. So a fusion algorithm based NSCT and HIS (NSCT +HIS) transforms was proposed [YANG X H, Jiao L C. 2008]. They demonstrated that the NSCT+HIS algorithm was better performance compare to PCA, HIS and wavelet transform weighted fusion method. However, the high frequent coefficients of the fused image are the sum of the high frequent coefficients of intensity and the histogram-matched panchromatic image. Different from Yang's method, A new NSCT +HIS fusion method using reasonable fusion rule is proposed in this paper, a lower resolution MS image of IKONOS and its high resolution panchromatic image was fused using the proposed method, and the fusion method based on CT and HIS (CT+HIS), simultaneously. The outputs were evaluated in objective and subjective performances. Compared with the fusion of CT+HIS, the NSCT+HIS fusion technique proved to be a better option.

2. METHODOLOGY

2.1 Nonsampled Contourlet Transform

Do and Vetterli proposed a "true" two-dimensional transform called the contourlet transform, which combined with nonseparable filter banks and provides an efficient directional multiresolution image representation. By virtue of the Laplacian pyramids (LP) and directional filter banks (DFB), the CT provides the multiresolution decomposition and directional decomposition, respectively. The CT can capture the intrinsic geometric structure information of images and achieves better expression than discrete wavelet transform (DWT), especially for edges and contours.

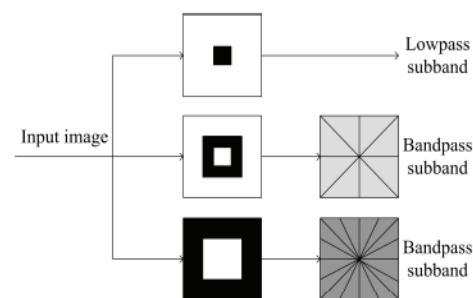


Figure 1(a) NSFB structure

¹ The Project Sponsored by the Scientific Research Foundation for the Returned Overseas Chinese Scholars, State Education Ministry

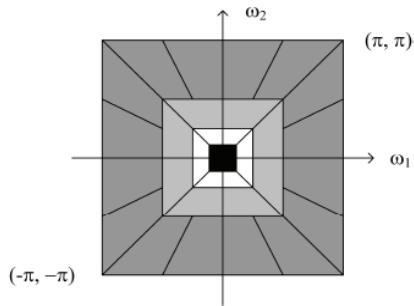


Figure 1(b) Corresponding frequency partition

Figure 1. Two level Nonsubsampled Contourlet transform decomposition

Different to the CT, the multiresolution decomposition step of NSCT is realized by the shift-invariant filter banks satisfied Bezout identical equation (perfect reconstruction) not the LP filter banks. Because of no decimation in the pyramid decomposition, the lowpass subband does not bring frequency aliasing, even the band width of the low-pass filter is larger than $\pi/2$. Hence, the NSCT have better frequency characteristics than CT. The two-level NSCT decomposition is shown in figure 1.

2.2 Fusion Method Based on NSCT combining with HIS (NSCT+HIS)

The core of the NSCT is the nonseparable two-channel nonsubsampled filter banks. It is easier and more flexible to design the needed filter banks that lead to a NSCT with better frequency selectivity and regularity when compared to the CT. Based on mapping approach and ladder structure fast implementation, the NSCT frame elements are regularity, symmetric and the frame is close to a tight frame. The multiresolution decomposition of NSCT can be realized by nonsubsampled pyramid (NSP), which can each the subband decomposition structure similar to LP. A fusion method based on NSCT combining with HIS is proposed. If the multispectral images are registered to the panchromatic image, A general scheme for the NSCT+ HIS fusion methods is shown in Figure 2.

This method can be performed in the following steps:

- Step 1: Perform HIS on the multispectral image and get saturation, hue and intensity components;
- Step 2: Apply histogram matching between the original panchromatic image and intensity to get a histogram-matched panchromatic image.
- Step 3: Employ NSCT on intensity and the histogram-matched panchromatic image, and get low frequent subband and high frequent subbands.
- Step 4: Fuse the intensity and the histogram-matched panchromatic image. The fused low frequent data employ the low frequent coefficient of intensity. The fused high frequent coefficient adopt Ξ Maximum the region-energy for every coefficient of each subband of panchromatic image and intensity get by step 3.
- Step 5: Apply NSCT reconstruction with new coefficient to obtain the new intensity.
- Step 6: Perform the inverse HIS transform to obtain the fused image.

The scheme for the CT +HIS fusion method differ only from NSCT+HIS method in the applied CT .

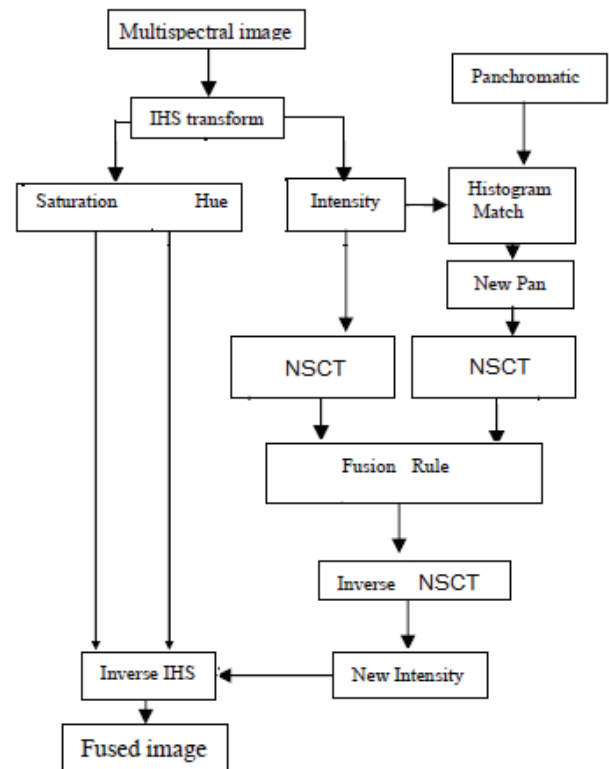


Figure 2. Image fusion flow chart of NSCT+HIS

3. EXPERIMENTS AND FUSION RESULT ANALYSIS

The tested remote sensing images consist of 1m panchromatic and 4m multi-spectral IKONOS images. Figure 3 shows the fusion results of the IKONOS images. The visual inspection shows that the fused images produced by proposed algorithms have more details than that of the algorithm CT+HIS.

Three different measures are used to evaluate the performance of the algorithms under investigation. These measures are: the normalized correlation, the entropy and the average gradient. Detailed equations of these measures can be found in the literature. Table 1 shows the results of the fusion experiment of the fused images where the correlation is measured between the PAN image and the corresponding gray fused image, and correlation between gray MS and gray fused image. The entropy and the standard deviation are measured for the fused images.

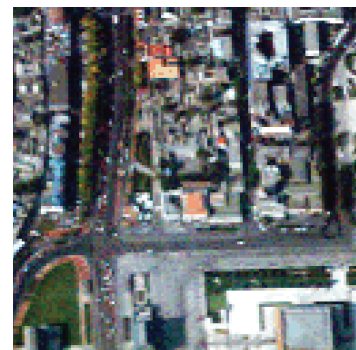


Figure 3(a) Ikonos spectral image



Figure 3 (b) IKONOS Pan image

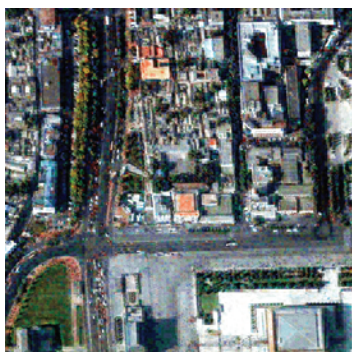


Figure 3 (c) Image fused by CT+HIS

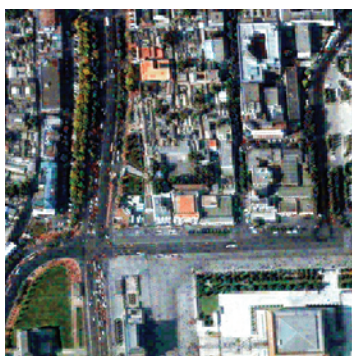


Figure 3 (d) Image by NSCT+HIS

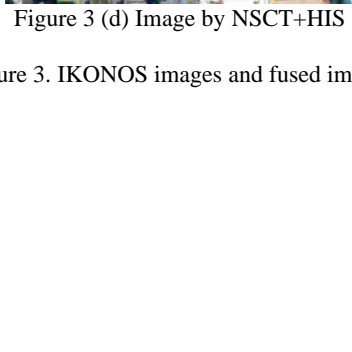


Figure 3. IKONOS images and fused images

	Average correlation of pan to the fused image	Entropy	Average gradient
CT+HIS	0.81	7.84	39.1
NSCT+HIS	0.82	7.86	41.2

Table 1. Performance measures for fused IKONOS images

The results indicated in the Tables 1 and the visual inspection of the images of Figure 3 (c) and Figure 3(d) reveal that, in general, the performances of the proposed algorithms outperform the algorithm CT+HIS.

2. CONCLUSIONS

A panchromatic image and multi-spectral images fusion technique is proposed in this paper, which is based on nonsubsampling contourlet transform combined with HIS transform. NSCT has better frequency characteristics than CT, compared with the CT+HIS method, the proposed fusion technique has better objective and subjective performances.

REFERENCES

- Arthur L Da C, Zhou J P, Do M N. 2006. The nonsubsampling contourlet transform: theory, design and application. *IEEE Trans. on Image Process*, 15(10), pp. 3089–3101.
- Do M N, Vetterli M. 2005. The contourlet transform: An efficient directional multiresolution image representation. *IEEE Trans. on Image Process*, 14(12), pp. 2091–2106.
- M. Choi, R.Y. Kim, M.-R. Nam, H.O. Kim, 2005. Fusion of multispectral and panchromatic satellite images using the curvelet transform. *IEEE Geoscience and Remote Sensing Letters*, vol.2, no.2, pp.136–140.
- M. E. Schetselaar, 2001. On Preserving Spectral Balance in Image Fusion and Its Advantages for Geological Image Interpretation. *Photogrammetric Engineering & Remote Sensing*, vol.67(8), pp.925-934.
- Y. Chibani, A. Houacine, 2002. The joint use of IHS transform and redundant wavelet decomposition for fusing multispectral and panchromatic images. *Int. J. Remote Sens.*, vol. 23, no. 18, pp. 3821–3833.
- YANG X H, Jiao L C. 2008. Fusion Algorithm for Remote Sensing Images Based on Nonsubsampling Contourlet Transform. *Acta Automatica Sinica*, 34(3), pp. 41-45

THE SENSITIVITY OF MULTI-FREQUENCY (X, C AND L-BAND) RADAR BACKSCATTER SIGNATURES TO BIO-PHYSICAL VARIABLES (LAI) OVER CORN AND SOYBEAN FIELDS

Xianfeng Jiao, Heather McNairn, Jiali Shang and Jianguo Liu
Agriculture and Agri-Food Canada, 960 Carling Ave., Ottawa, Ontario K1A 0C6

Key words: Agriculture, Crop, Analysis, SAR, Multifrequency

ABSTRACT:

The objective of this study is to investigate the sensitivity of synthetic aperture radar (SAR) backscatter signatures to crop bio-physical variables. The experimental data were collected over corn and soybean fields in eastern Ontario (Canada) during the 2008 growing season. Remote sensing acquisitions consisted of TerraSAR-X dual-polarized stripmap data (X-band), RADARSAT-2 Fine beam quad-polarized data (C-band) and ALOS PALSAR dual-pol data (L-band), as well as the Compact Airborne Spectrographic Imager (CASI) and SPOT-4 multi-spectral data. Plant variables, such as leaf area index (LAI) and surface volumetric soil moisture were measured to coincide with these acquisitions and key phenological growth stages. Analyses were conducted based on statistical correlation and a simple backscatter process model (the water cloud model). The results of this study show that the lower frequency bands, such as L and C, were closely related with LAI. For both corn and soybean crops, most C-band linear (HH, VV, HV) backscatter coefficients were correlated with LAI; backscatter increased with increasing LAI. L-band backscatter at HH and HV polarizations produced the highest correlations with corn LAI ($r=0.90-0.96$). Conversely, these L-band polarizations were only weakly correlated with soybean LAI. The higher frequency X-band was poorly correlated with both corn and soybean LAI. Based on these findings, the water cloud model was used to express C-band and L-band backscatter for the whole canopy as a function of LAI and surface soil moisture.

1. INTRODUCTION

The monitoring of crop bio-physical variables is a very important task in agricultural management and in yield forecasting. Information from satellites can be exploited to assist in estimating key crop growth indicators including Leaf Area Index (LAI), biomass and crop height. LAI is an important indicator of agricultural productivity and a critical variable in crop growth models. Optical remote sensing data have been used to estimate LAI (Baret and Guyot, 1991; Brown et al., 2000; Chen and Cihlar, 1996). However, operational productivity and yield monitoring activities that rely solely on optical imagery are vulnerable to data gaps during critical crop growth stages as a result of unfavourable atmospheric conditions. Synthetic aperture radars (SARs) are unaffected by atmospheric haze and clouds. In addition to this oft-quoted advantage, SAR data also provide complementary and unique characterizations of vegetation when compared with the information provided by optical imagery.

SAR response is dependent upon the sensor configuration including incidence angle, frequency and polarization. Target characteristics, most notably the soil and crop dielectric and geometric properties, influence scattering behaviour and the magnitude of the radar backscatter. Shorter SAR wavelengths such as X-band (~3 cm) and C-band (~6 cm) interact mainly with the top part of the canopy layers while long wavelengths such as L-band (~20 cm) have a greater penetration depth, interacting with the entire crop canopy and resulting in greater scattering contributions from the soil (Ulaby et al., 1984). Penetration depth depends on whether the bio-physical parameters of the scatters within a vegetation layer (e.g., canopy water content, size and geometry of the canopy components) scatter or attenuate the incident microwaves. Inoue *et al.* (2002) compared backscatter responses from multi-frequency (Ka, Ku, X, C, and L) data in the context of several bio-physical variables of paddy rice. The results showed that

LAI was best correlated with HH- and cross-polarization backscatter at C-band, while fresh biomass was best correlated with HH- and cross-polarizations at L-band. Conversely, the higher frequency bands (Ka, Ku, and X) were poorly correlated with LAI and biomass.

Many experimental studies have linked the bio- and geo-physical characteristics of crops with backscatter recorded by SAR sensors. (Clevers and van Leeuwen, 1996; Ferrazzoli et al., 1999; McNairn, 2002; Taconet et al., 1996). Most of these studies were carried out using C-band SAR due to the availability of this radar frequency on the first generation of satellite SAR sensors (ERS-1/2, RADARSAT-1). The SAR sensors currently operational include TerraSAR-X (X-band), COSMO-SkyMed (X-band), PALSAR/ALOS (L-band), ASAR/ENVISAT (C-band), RADARSAT-1/2 (C-band), and ERS-2 (C-band). With access to such a wealth of SAR satellites, it is now possible to study the sensitivity of multi-frequency and multi-polarization data to LAI through the entire crop growth cycle. Detailed understanding of radar response to crops characteristics as a function of SAR parameters (wavelength, incidence, and polarization) is the first essential step in developing robust methods to retrieve crop bio-physical variables such as LAI.

This study investigates the sensitivity of TerraSAR-X, PALSAR/ALOS, and RADARSAT-2 to crop bio-physical variables. The objective is to assess the radar response of corn and soybean crops with respect to radar wavelength (X, C, and L-bands) and polarization. Leaf area index (LAI) and surface volumetric soil moisture were measured to coincide with remote sensing acquisitions. In this paper, correlation analyses were conducted between radar backscatter and LAI. In addition, a semi-empirical backscatter process model (the water cloud model) was used to develop the relationship between SAR backscatter and target conditions, including LAI and soil moisture.

2. STUDY SITE AND DATA COLLECTION

Two sites were selected near Ottawa, Ontario, Canada for field and satellite data collection, the Canadian Food Inspection Agency (CFIA) research farm and a region of private producers east of Casselman, Ontario. The terrain across these two study sites can be considered level to very gently sloping (<2%) with an average field size of 23 hectares. This region of eastern Canada consists largely of corn and soybean annual crop production.

Ground truth measurements were performed on several selected sites. Within the CFIA site, 13 fields including 16 corn and 21 soybean sample sites were selected. At the Casselman site, 20 fields including 10 corn and 10 soybean sample sites were visited. Total LAI was measured at each sample site using an LAI-2000 (Li-Cor, Inc., Lincoln, NE) plant canopy analyser throughout the growing season. Volumetric surface soil moisture was measured coincident with each SAR acquisition, using Delta-T Theta probes with 6-cm waveguides. At each site, mean soil moisture was calculated from ten replicate moisture measurements.

SAR images were acquired by TerraSAR-X, PALSAR/ALOS, and RADARSAT-2 satellites. During the 2008 growing season, two RADARSAT-2 Fine beam mode quad-pol images (July 6 and 9) and one PALSAR/ALOS (July 2) were acquired over the CFIA site; two RADARSAT-2 Fine beam mode quad-pol images (August 23 and August 26) and one TerraSAR-X stripmap image (August 21) were acquired over the Casselman site. The pixel spacing of TerraSAR-X, PALSAR/ALOS, and RADARSAT-2 is 3 m, 12.5 m and 8 m, respectively. Characteristics of the SAR images used in this study are summarized in table 1.

Date	SAR sensor	mode	pol.	incident angle
07-02-2008	PALSAR	L1.5	HH,HV	34°
05-23-2007	PALSAR	L1.5	HH,HV	21°
07-09-2008	Radarsat-2	FQ20	Quad-pol	40°
07-06-2008	Radarsat-2	FQ6	Quad-pol	26°
08-21-2008	TerraSAR-X	stripmap	HV/VV	44°

Table 1. Main characteristics of SAR images used in this study.

Optical images were acquired by the Compact Airborne Spectrographic Imager (CASI) and SPOT-4 multi-spectral satellite. CASI hyperspectral data were acquired on August 21, 2008 over the Casselman site. SPOT-4 multi-spectral data were acquired on July 6, 2008 over the CFIA site. From the CASI and SPOT-4 data, the Modified Triangular Vegetation Index (MTVI2) (Haboudane et al., 2004) was calculated. A non-linear curve fitting procedure was used to establish an empirical equation for LAI estimation from MTVI2 (Liu et al., 2009):

$$LAI = -6.247 \times \ln(0.946 - 0.643 \times MTVI2)$$

Using this formula, LAI maps for the entire study site were generated from the optical data, with an RMSE of 0.76 and an R^2 of 0.85.

3. METHODOLOGY

3.1 Image processing

Radiometric calibration of TerraSAR-X and PALSAR/ALOS images was carried out using the follow equations. These equations were used to convert the digital number of each pixel DN_i into a backscatter coefficient (σ^0).

For TerraSAR-X,

$$\sigma_i^0 (dB) = 20 \log_{10} DN_i + 10 \log_{10} (CalFact) + 10 \log_{10} (\sin(\theta_i))$$

CalFactor is given in the TerraSAR-X data delivery package annotation file. It is processor and product type dependent.

For PALSAR/ALOS,

$$\sigma_i^0 (dB) = 10 \log_{10} (DN_i^2) + CF$$

The calibration factor (CF) for PALSAR L1.5 products is -83 dB. The ALOS and TerraSAR data products were delivered in ground range. A 3 X 3 Enhance Lee filter was applied to both the ALOS and TerraSAR data to reduce speckle noise. RADARSAT-2 fine quad-pol SLC data were provided as compressed stokes matrix values for each slant range pixel. Prior to extracting the backscatter information, a boxcar filter with a 5 by 5 kernel size was applied to the polarimetric SAR scattering matrix data to suppress SAR speckle. After filtering the covariance matrix was converted to a symmetrized covariance matrix. From the symmetrized 3 by 3 covariance matrix, intensity backscatter (HH/HV/VV) was extracted. All the data were then geometrically corrected and geo-referenced using national road network vector data.

3.2 Water cloud model

The water cloud model was introduced first by Attema and Ulaby (1978). In the general version of the water cloud model, the power backscattered by the whole canopy (σ^0) can be represented as the incoherent sum of contributions of the vegetation, (σ_{veg}^0), and the underlying soil, (σ_{soil}^0). This study selected the model modified by (Prévoit et al., 1993) as it incorporates LAI as a descriptor of vegetation development. In this model, SAR backscatter from a canopy at a given incidence angle can be written as:

$$\sigma^0 = AL^E \cos \theta (1 - \exp(-2BL / \cos \theta)) + \sigma_{soil}^0 \exp(-2BL / \cos \theta)$$

where τ is the two-way attenuation through the canopy layer, L is the LAI, expressed in ($m^2 m^{-2}$), the backscatter coefficients σ^0 , σ_{soil}^0 and σ_{veg}^0 are expressed in power units. A, B, C, D and E are model coefficients to be defined by experimental data. A, B and

E are parameters which depend on canopy type. E is a positive value. Parameters C and D are dependent on soil moisture.

4. RESULTS AND DISCUSSION

Two dates of LAI maps (July 6 and August 21) were near-coincident with SAR acquisitions on July 2 (ALOS), July 6 (RADARSAT-2), July 9 (RADARSAT-2) and August 21 (TerraSAR). With LAI maps derived from optical data, LAI was estimated on a detailed pixel by pixel basis. Definiens software was then used to segment these maps into zones of homogeneous LAI for each corn and soybean field. These homogeneous zones were used as the primary sampling units. The average SAR backscatter and the mean LAI for each sampling unit were extracted for both corn and soybean crops.

4.1 Correlation analysis between SAR data and LAI

To quantify the relationship between SAR backscatter and LAI, and to assess the sensitivity of SAR frequency and polarization to this crop growth parameter, correlation analyses were conducted. Scattering from within the crop canopy and the subsequent scattering back to the radar sensor is related to the physical structure of the scattering elements of the canopy, as well as their dielectric properties. Consequently a strong correlation between plant variables such as LAI and radar return has physical meaning. Table 2 provides the simple correlation analysis results for each SAR data set.

	Corn	Soybean
PALSAR/ALOS		
HH	0.92	0.28
HV	0.96	0.26
RADARSAT-2 FQ20		
HH	0.72	0.60
VV	0.79	0.73
HV	0.79	0.47
RADARSAT-2 FQ6		
HH	0.68	0.80
VV	0.72	0.62
HV	0.90	0.58
TerraSAR-X		
VV	-0.11	-0.20
HV	0.03	-0.65

Table 2. Simple correlation coefficients (r) between SAR data and LAI.

4.1.1 SAR backscatter from corn crops

For corn, a strong correlation was found for both L-band and C-bands. The highest correlation coefficients ($r=0.90$ – 0.96) were reported for L-HH and L-HV backscatter and for C-HV backscatter from the RADARSAT-2 FQ6 mode. Figure 1 plots L-HH, L-HV and C-HV backscatter against corn LAI. Backscatter at these frequencies and polarizations were strongly linearly correlated with LAI. The coefficients of determination (R^2) were 0.92, 0.85 and 0.80 for HV and HH at L-band and HV at C-band, respectively.

Slightly lower correlations ($r=0.68$ – 0.79) were reported for corn for all C-band linear polarizations at the shallower RADARSAT-2 FQ20 mode, as well as for the linear like-polarizations (HH,VV) at the steeper RADARSAT-2 FQ6 mode. Backscatter at X-band was poorly correlated with corn LAI ($r < 0.03$) regardless of polarization.

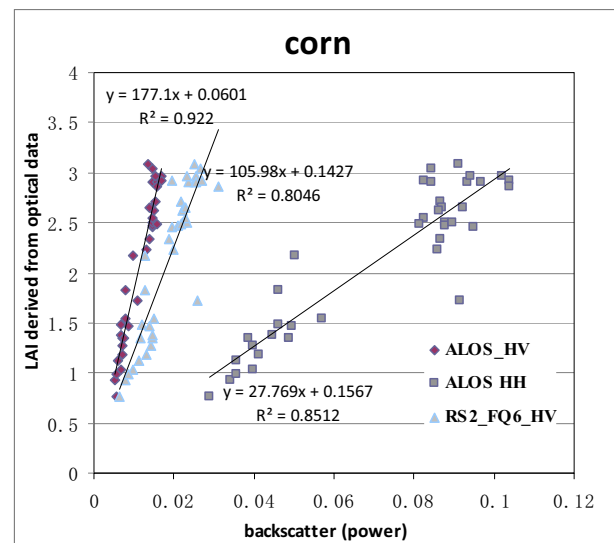


Figure 1 Correlation between L-HH, L-HV and C-HV (FQ6 mode) backscatter and corn LAI.

4.1.2 SAR backscatter from soybean crops

For soybeans, SAR backscatter was only weakly correlated with LAI. The highest correlations were reported for the C-band data ($r=0.58$ – 0.80). Backscatter from L-band and X-band had no significant correlation with LAI. Figure 2 illustrates the linear relationship between HH, VV and HV backscatter at C-band (RADARSAT-2 FQ6 mode) and LAI. The best correlations were observed for C-HH backscatter ($R^2=0.63$).

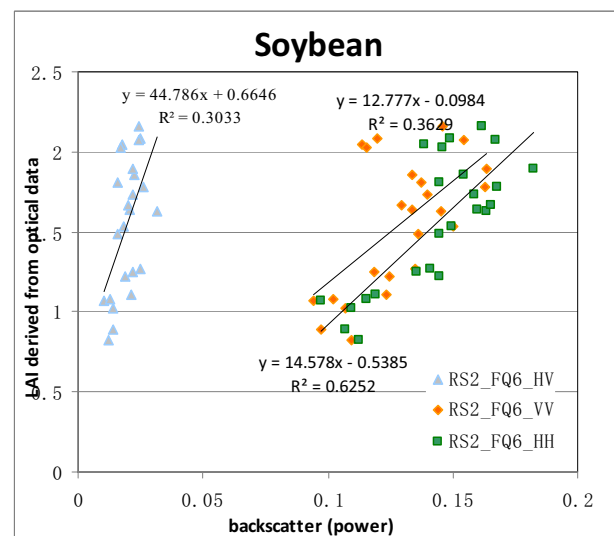


Figure 2 Correlation between C-band HH, VV and HV backscatter (RADARSAT-2 FQ6 mode) and LAI.

In summary, the lower frequencies such as L- and C-band were correlated with LAI, while the higher frequency X-band was poorly correlated. These results may be explained by the wavelength relative to the size of the crop scattering elements, but also by the difference in the canopy penetration. High frequency X-band provides little canopy penetration.

4.2 Water cloud model

The backscatter signal from vegetated surfaces is affected by many factors, including the physical structure of the plants and the canopy (biomass, leaf size, stem density, LAI, etc.) as well as the surface volumetric moisture of the soil below the canopy.

Direct scattering from the canopy and the soil, as well as multiple interactions between the vegetation components and the soil, all contribute to the magnitude and scattering characteristics of the SAR response. Simple linear or non-linear expressions fail to adequately express the interaction of microwaves with a complex vegetation-over-soil target. A physically-based modeling approach is essential for analyzing the interaction of crop biological variables and SAR backscatter over a wide range of crop conditions and sensor configurations.

In this study, L- and C-band backscatter at certain polarizations exhibited a strong correlation with LAI. Some of the unexplained error in these simple correlations may be attributable to contributions from the soil moisture. Therefore, the water cloud model was used to model the effect of LAI and surface soil moisture on SAR backscatter.

Data needed to parameterize soil moisture in the water cloud model were available from the *in situ* measurements taken coincident with the RADARSAT-2 and ALOS overpasses. No *in situ* measurements were available for the August 21 TerraSAR-X acquisition. Thus TerraSAR-X data were not implemented into the water cloud model.

For the corn and soybean crops, the mean backscatter was extracted for a 70 x 70 metre area centred on the soil moisture sampling sites. A similar approach was taken to calculate average LAI for each site, from the LAI maps derived from the optical data.

To overcome instability problems caused by possible correlations between parameters, a two-step procedure was taken. The model parameter D defining the radar sensitivity to soil moisture was first determined using an independent data set. Once parameter D was fixed, the remaining parameters A, B, E, and C were then simultaneously determined. Three of the soybean fields were seeded late because of an unusually rainy spring season, and thus for eleven soybean sites, the soybean crop had not yet emerged at the time of the June 12 FQ6 and June 15 FQ20 RADARSAT-2 acquisitions. For the PALSAR/ALOS acquisition on May 23, 2007, soil moisture measurements were taken during the satellite overpass. At that time, most of fields were bare as crops had not yet emerged. Based on these data, a linear regression model was developed to describe the relationship between SAR backscatter and soil moisture in the absence of vegetation. This process was used to determine and fix the parameter D. Next, the remaining parameters in the model, A, B, E and C, were determined using a non-linear least squares method in the Matlab Curve Fitting Toolbox environment, based on the Levenberg-marquardt algorithm.

The degree of model fit was indicated by the coefficient of determination (R^2) and RMSE, and these statistics are provided in Table 3.

SAR Backscatter	Corn		Soybeans	
	Coefficient of determination (R^2)	RMSE (power)	Coefficient of determination (R^2)	RMSE (power)
PALSAR/ALOS				
HH	0.78	0.013	0.44	0.019
HV	0.81	0.002	0.38	0.005

RADARSAT-2 FQ20				
HH	0.63	0.026	0.10	0.022
HV	0.78	0.004	0.07	0.003
RADARSAT-2 FQ6				
HH	0.26	0.038	0.43	0.019
HV	0.71	0.004	0.38	0.005

Table 3. Statistics describing the fit of the water cloud model to SAR backscatter

A good model fit was achieved for most SAR configurations for corn, with coefficients of determination (R^2) reaching 0.63–0.81. The one exception was the poor correlation for C-HH backscatter (RADARSAT-2 FQ6). For soybeans, the water cloud model provided only weak correlations for all SAR frequencies and polarizations. In figure 3, the fitted models using the L-HV backscatter are plotted against the observed data for corn.

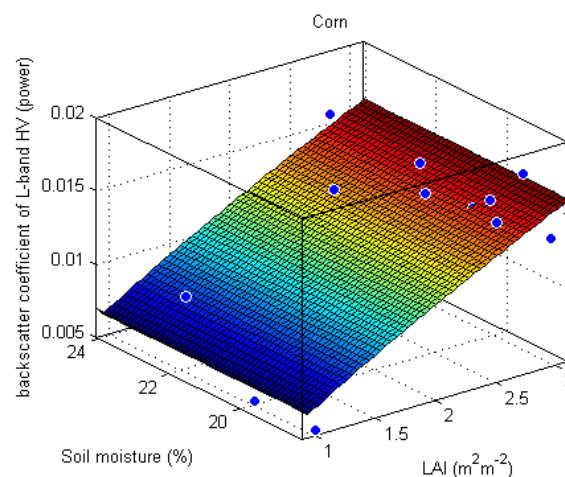


Figure 3. Modeled and observed L-HV backscatter expressed as a function of soil moisture and LAI for corn.

For corn, the highest correlations were again reported for L-band backscatter at HH and HV polarizations. Slightly lower correlations were reported at most C-band polarizations except for C-HH backscatter (RADARSAT-2 FQ6 mode). Backscatter from soybeans, regardless of frequency or polarization, were not significantly correlated with LAI.

5. CONCLUSION

This study investigated the relationship between multi-frequency SAR backscatter and LAI for corn and soybean crops. TerraSAR-X dual-polarized stripmap data (X-band), RADARSAT-2 Fine beam quad-polarized data (C-band) and ALOS PALSAR dual-pol data (L-band), as well as optical data including the Compact Airborne Spectrographic Imager (CASI) and SPOT-4 multi-spectral data were acquired during the 2008 crop growing season. SAR backscatter was extracted from each SAR image. LAI maps were derived from the optical images at a detailed pixel level. Object-based segmentation of the LAI maps defined the basic sampling unit upon which mean LAI and SAR responses were calculated.

A statistical correlation analyses quantified the relationship between the SAR parameters and LAI. High correlation coefficients with corn LAI were found for L-band and C-band. The highest correlation coefficients ($r=0.90$ – 0.96) were reported for L-HH, L-HV and C-HV (RADARSAT-2 FQ6

mode). SAR backscatter was only weakly correlated with soybean LAI. The highest correlations were reported at C-band ($r=0.58-0.80$). X-band backscatter was poorly correlated with both corn and soybean LAI.

The water cloud model was used to parameterize the relationship between LAI and soil moisture, and SAR backscatter at L- and C-band. The correlation between SAR backscatter and LAI didn't show significant improvement following implementation of the model. Further research will couple soil moisture models and/or *in situ* network data with the water cloud model to improve parameterization of the contribution from the underlying soil.

Ulaby, F.T., Allen, C.T., Eger Iii, G. and Kanemasu, E., 1984. Relating the microwave backscattering coefficient to leaf area index. *Remote Sensing of Environment*, 14(1-3): 113-133.

REFERENCE

Baret, F. and Guyot, G., 1991. Potentials and limits of vegetation indices for LAI and APAR assessment. *Remote Sensing of Environment*, 35(2-3): 161-173.

Brown, L., Chen, J.M., Leblanc, S.G. and Cihlar, J., 2000. A Shortwave Infrared Modification to the Simple Ratio for LAI Retrieval in Boreal Forests: An Image and Model Analysis. *Remote Sensing of Environment*, 71(1): 16-25.

Chen, J.M. and Cihlar, J., 1996. Retrieving leaf area index of boreal conifer forests using Landsat TM images. *Remote Sensing of Environment*, 55(2): 153-162.

Clevers, J.G.P.W. and van Leeuwen, H.J.C., 1996. Combined use of optical and microwave remote sensing data for crop growth monitoring. *Remote Sensing of Environment*, 56(1): 42-51.

Ferrazzoli, P., Guerriero, L., Quesney, A., Taconet, O.A.T.O. and Wigneron, J.P.A.W.J.P., 1999. Investigating the capability of C-band radar to monitor wheat characteristics. In: L. Guerriero (Editor), *IGARSS 1999, Processings of the International Geoscience and Remote Sensing Symposium*. IEEE, Hamburg, Germany, pp. 723-725.

Haboudane, D., Miller, J.R., Pattey, E., Zarco-Tejada, P.J. and Strachan, I.B., 2004. Hyperspectral vegetation indices and novel algorithms for predicting green LAI of crop canopies: Modeling and validation in the context of precision agriculture. *Remote Sensing of Environment*, 90(3): 337-352.

Liu, J. et al., 2009. Quantifying Crop Biomass Accumulation Using Multi-temporal Optical Remote Sensing Observations, *Proceedings of the 30th Canada Symposium on Remote Sensing*, Lethbridge, Alberta.

McNairn, H.D., V; Murnaghan, K, 2002. The Sensitivity of C-Band Polarimetric SAR to Crop Condition, *IGARSS 2002, Proceedings of the International Geoscience and Remote Sensing Symposium*. IEEE, Toronto, Canada, pp. 1471-1473.

Prévo, L., Champion, I. and Guyot, G., 1993. Estimating surface soil moisture and leaf area index of a wheat canopy using a dual-frequency (C and X bands) scatterometer. *Remote Sensing of Environment*, 46(3): 331-339.

Taconet, O., Vidal-Madjar, D., Emblanch, C. and Normand, M., 1996. Taking into account vegetation effects to estimate soil moisture from C-band radar measurements. *Remote Sensing of Environment*, 56(1): 52-56.

A DBMS-BASED 3D TOPOLOGY MODEL FOR LASER RADAR SIMULATION

C. Jun^{a,*} G. Kim^a

^aDept. of Geoinformatics, University of Seoul, Seoul, Korea - (cmjun, nani0809)@uos.ac.kr

Commission VII

KEY WORDS: Modelling, Simulation, Data Structures, Database, Laser scanning, Three-dimensional

ABSTRACT:

Developing LADAR(Laser radar) is viewed to be an important technology for next generation guided weapons in many countries. However, experiments using real guided weapons are not practical and we need computing environment that can simulate the 3D detections by LADAR. Such simulations require dealing with large sized data representing buildings and terrain over large area. They also need the information of 3D target objects, for example, material and echo rate of building walls. However, currently used 3D models are mostly focused on visualization maintained as file-based formats and do not contain such semantic information. In this study, as a solution to these problems, a method to use a spatial DBMS and a 3D model suitable for LADAR simulation is suggested. The 3D models found in previous studies are developed to serve different purposes, thus, it is not easy to choose one among them which is optimized for LADAR simulations. In this study, 4 representative 3D models are defined, each of which is tested for different performance scenarios. As a result, one model, “BODY-FACE” structure, is selected as being the most suitable model for the simulation. A process to build a spatial DBMS and to compute and visualize with the proposed model was illustrated using a test area.

1. INTRODUCTION

LADAR(Laser radar), the 3D detection technology is increasingly getting attention as being the next generation guided weapons. Experiments using real guided weapons for the development of the LADAR would require tremendous amount of money. Therefore, we need computing environment that can simulate the 3D detections by LADAR. Such simulations require dealing with large sized data representing buildings and terrain over large area. They also need the information of 3D target objects, for example, material and echo rate of building walls. However, currently used 3D models are mostly focused on visualization and do not contain such semantic information.

Modeling and visualizing terrains in 3D have been well known techniques now and most commercial GIS packages accommodate tools to represent terrain data types (i.e. TINs). However, modeling techniques for buildings in 3D have less been established and are still being studied theoretically without explicit implementations. Current techniques can be categorized into two—CAD and GIS. CAD systems, with diverse data types (e.g. cylinders, cones and freeform shapes), have been extensively used to model complex shapes in architecture or mechanics fields. On the other hand, GIS is mainly designed to represent geographical features and use less number of data primitives than CAD, which are points, lines and polygons. However, 3D representation provided by current commercial GIS packages is limited to 2.5D, which means that one location can have only one z value. Although both approaches have been used for years and suffice visualization purposes at certain application domains, still some issues remain to be resolved.

Neither CAD nor GIS for 3D objects supports topological structure. Topology is the key property implemented in 2D GIS such as adjacency and connectivity that enables diverse analyses.

We need such property in 3D buildings in order to define semantic information in urban models for LADAR simulations. LADAR simulations frequently deal with large areas and, thus, we need to represent a larger number of buildings than a few. Most CAD systems use file-based formats, which are unfavorable for storing and visualizing many building objects due to the computational performances. In contrast, although GIS packages support both file and DBMS formats, they are mostly software-dependent and do not support 3D topology as of now.

A solution to these problems would be using DBMSs, which are widely accepted as reliable method for managing large amount of data. The purpose of this study is to compare DBMS-based 3D models and suggest suitable ones that satisfy spatial operations and visualization for LADAR simulations while minimizing computation time. We first categorized 3D topology data models found in literature including our own model. Then we carried out performance tests for each of the models to test differences in retrieval times for visualization and range queries. The PostgreSQL/PostGIS was used for the tests. We also visualized the queried geometries using VRML and OpenGL.

2. 3D MODELS

2.1 3D models for building details

Architecture may be the field that use 3D models most extensively. CAD-based models have been used widely for detailed 3D building modeling, and there is a growing interest in using IFC(Industry Foundation Classes) format for modeling and developing building information systems. Although these formats offer flexibility in modeling 3D objects with various data primitives, their file-based formats have limitations for

* Corresponding author.

dealing with many objects as in urban scales. On the other hand, CityGML which was adopted as a standard by OGC (Open Geospatial Consortium) is a 3D model that provides different levels of details ranging from region to interior spaces (Stadler *et. al.*, 2007; Ellul *et. al.*, 2008). CityGML is based on XML format for the storage of data and has capability of storing complex semantic information. However, as of writing this paper, it has not provided fully functional database implementation. One of the reasons is attributed to the fact that current commercial DBMSs do not fully support topological structure of 3D objects yet.

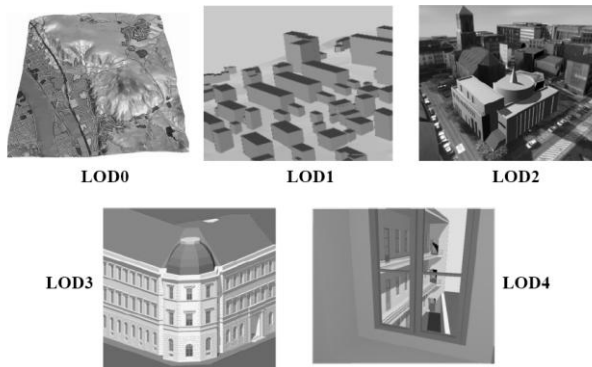


Figure 1. Five. LoDs in CityGML (Kolbe, 2008)

Theoretical 3D models have been studied actively for the last decade, and some researchers have connected their models with

DBMS implementation. Stoter *et. al.* (2003) proposed a 3D data model and applied it to a cadastre problem to solve the property rights in 3D situations. She used a DBMS for storing her model and visualized in VRML. Different model types proposed by others are described in the next section. However, we choose to focus on the cases that use DBMSs rather than purely theoretical models for the purpose of this study.

2.2 3D Topology Models

The possibilities of using DBMS for 3D objects have been recently investigated by many researchers (Ellul, 2008; Stoter, 2002; Stoter *et. al.*, 2003; Zlatanova, 2000). With some variations, they mostly suggested hierarchical relationships between 3D element classes, which are based on SOLID-FACE-EDGE-NODE in order to represent 3D topology. Faces are bounded portions of a solid surface, edges are used to define the face boundary, and nodes constitute the edges. However, as of now, we have not found any literature that shows experiments with large amounts of 3D objects. The major motivation of this paper is testing the applicability of DBMS approaches whether they can accommodate large amount of 3D data while supporting 3D topology. We first categorized 3D topology data models suggested in other literature (Type 1, 2 and 4) including our own model (Type 2) as follows:

- Type 1: SOLID – FACE – EDGE – NODE
- Type 2: SOLID – FACE – EDGE
- Type 3: SOLID – FACE – NODE
- Type 4: SOLID – FACE

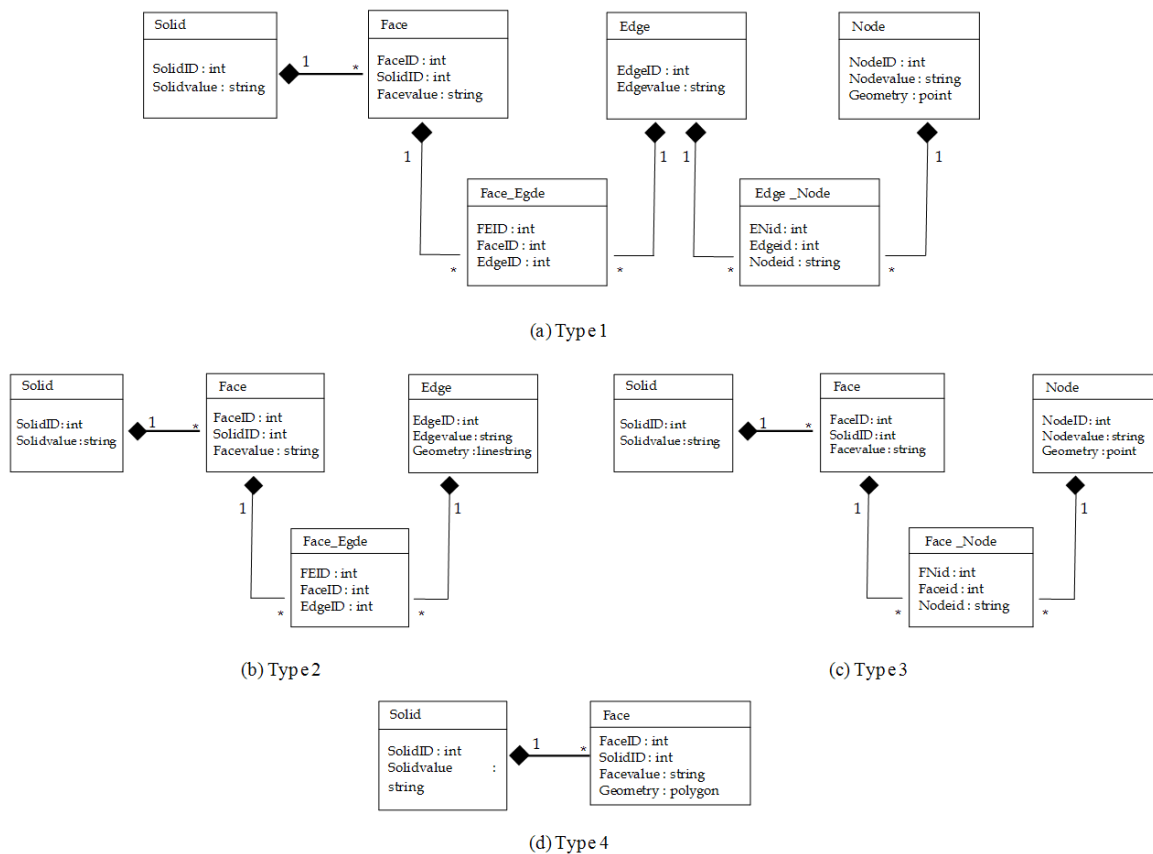


Figure 2. UML class diagrams describing storage of a polyhedron with four types.

In each model here, the last class contains geometries and the rest are non spatial relations. For example, in Type 1, the NODE class stores actual point data and each of SOLID, FACE and EDGE classes corresponds to a non-spatial table.

Figure 2 shows the UML class diagrams that describe storage of a polyhedron using the four types. Type 1 model provides full topology, which enables storing semantic data in each table (Figure 2-(a)). As we mentioned above, actual points are stored in NODE table, and spatial operation query is performed using this geometry. This model has an advantage for storing semantic attribute data in each table. However, many-to-many relationships such as node-edge and edge-face require additional joining of tables leading to inefficiency for computation due to excessive join queries. Also in type 2, only the final class, which is NODE, stores the geometries. Without “EDGE” class, we cannot expect such information as “which edge is this node belonged to?” or “which edge do these two faces share?” In a study (Stoter *et. al.*, 2003), even more reduced form (Type 3) is introduced for storing 3D objects in a DBMS and visualization. While sufficing for the visualization purpose, such “de-normalized” relations as in type 2 or 3 suffer duplicated data storage and less capability of topological information retrieval. As of now, we could not find in the current literature the model having line geometry (Figure 2-(b)). Thus, we included this model (Type 2) and performed comparison tests along with other models in our study.

3. SIMULATION

3.1 Data Construction

Points to be considered in selecting 3D data models in this paper are as follows:

- Easiness of storing 3D objects
- Retrieval time of non-spatial operation query
- Retrieval time of spatial operation query
- Possibility of using spatial operation

Through performance comparison tests for the four models mentioned above, we present 3D data model suitable for 3D visualization and spatial operation. For the tests, we used a number of artificial cube objects and stored them in a spatial database as in figure 3. We used the PostgreSQL/PostGIS for the spatial DBMS.

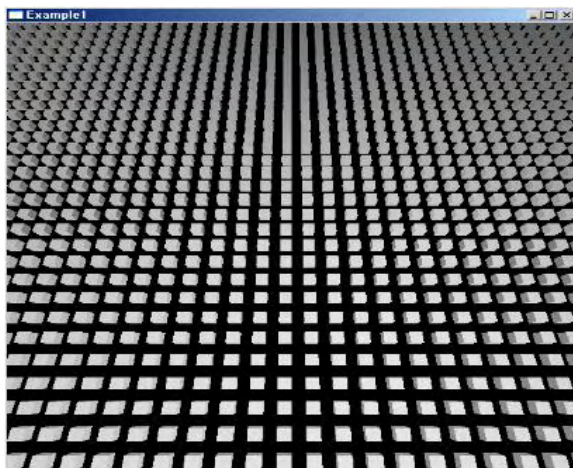


Figure 3. 3D objects used in the tests (100 × 100 size)

The first test measures the performance time for non-spatial operations. For visualizing 3D objects in VRML or OpenGL, coordinate values of polygons constituting a 3D object are needed. Thus, we built a SQL-query to get object ID, spatial feature ID and coordinate values. Table 1 is an example of queries executed for Type 1 and 3.

Another test is to measure the performance time for spatial operations. When range queries are executed, we measured time required to get objects’ IDs and face information consisting the objects. We set up the range of 20×20 unit distance and obtained objects’ values included in this range. Table 3 shows an example of queries for Type 1 and 3. As you can see from Table 1 and 2, spatial queries include spatial functions (i.e. intersect) in the join statements while non-spatial queries do not. We created 500,000 cube objects. And the tests were performed for the sub-ranges of 100, 1,000, 10,000 and 100,000 units. Each test was executed 10 times and the average of them was recorded.

Body-Face-Edge-Node
<pre>SELECT body.bodyid, face.faceid, edge.edgeid, node.nodeid, ST_AseWKT(shape) FROM body INNER JOIN (((face INNER JOIN (((face_edge INNER JOIN ((edge INNER JOIN (edge_node INNER JOIN node ON node.nodeid = edge_node.nodeid) ON edge.edgeid = edge_node.edgeid)) ON face.faceid = face_edge.faceid))) ON body.bodyid = face.bodyid ORDER BY body.bodyid, face.faceid, edge.edgeid, node.nodeid;</pre>
Body-Face-Node
<pre>SELECT body.bodyid, face.faceid, node.nodeid, ST_AseWKT(shape) FROM body INNER JOIN ((face INNER JOIN (face_node INNER JOIN node ON node.nodeid = face_node.nodeid) ON face.faceid = face_node.faceid)) ON body.bodyid = face.bodyid ORDER BY body.bodyid, face.faceid, node.nodeid;</pre>

Table 1. Non-spatial query for Type 1 and Type 3

Body-Face-Edge-Node
<pre>SELECT Distinct body.bodyid, face.faceid FROM body INNER JOIN (((face INNER JOIN (((face_edge INNER JOIN ((edge INNER JOIN (edge_node INNER JOIN node ON node.nodeid = edge_node.nodeid) ON edge.edgeid = edge_node.edgeid)) ON face.faceid = face_edge.faceid))) ON body.bodyid = face.bodyid WHERE ST_Intersects(GeomFromEWKT(node.Shape), GeomFromEWKT('POLYGON((0 0 0,20 0 0,20 20 0,0 20 0,0 0 0)')))=true;</pre>
Body-Face-Node
<pre>SELECT Distinct body.bodyid, face.faceid FROM body INNER JOIN ((face INNER JOIN (face_node INNER JOIN node ON node.nodeid = face_node.nodeid) ON face.faceid = face_node.faceid)) ON body.bodyid = face.bodyid WHERE ST_Intersects(GeomFromEWKT(node.Shape), GeomFromEWKT('POLYGON((0 0 0,20 0 0,20 20 0,0 20 0,0 0 0)')))=true;</pre>

Table 2. Spatial query for Type 1 and Type 3

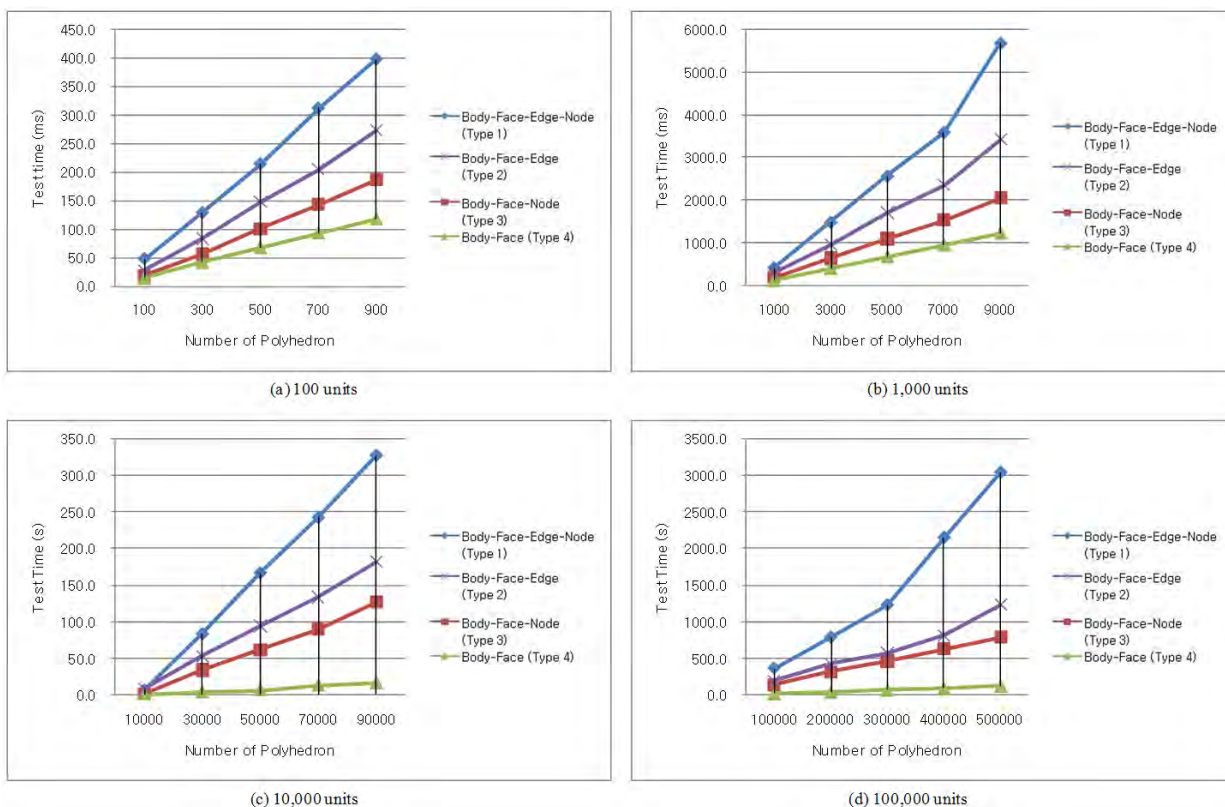


Figure 4. Performance results for non-spatial queries

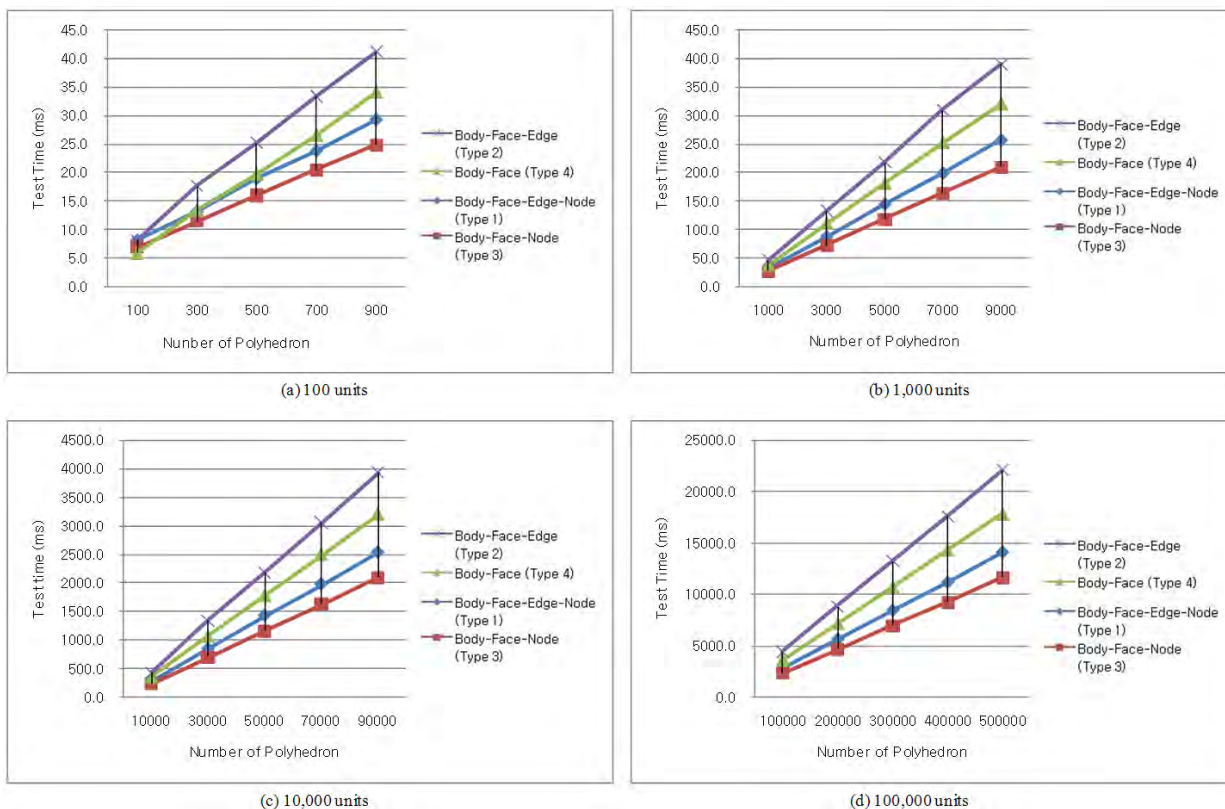


Figure 5. Performance results for spatial queries

3.2 Test Results

Figure 4 and 5 show the results of performance comparisons of the four types. For non-spatial queries, Type 4's retrieval time is fastest in performance followed by 3, 2 and 1 in order. As the number of 3D objects increases, query performance for all four models decreases. While Type 4 shows the smallest increasing rate, Type 1 shows the greatest. As can be seen, with less than 1,000 units, four models show differences up to 6 seconds, implying that all four models are suitable for visualization for the size of urban model including hundreds of building objects. However, with over 1,000 objects, the retrieval performances show significant gaps among the models, implying that Type 4 is the only alternative for visualization.

In the test for the non-spatial queries for 100,000 units in the PostGIS, the retrieval time of each model shows as follows; Type 1 – 369.3 seconds, Type 2 – 202.4 seconds, Type 3 – 143.0 seconds, Type 4 – 19.1 seconds. In the spatial query tests, Type 3's retrieval time is fastest in performance followed by 1, 4 and 2. All four models show steady increase as the number of objects increases. The reason that spatial queries show less time than non-spatial queries is we experimented using a portion (20×20) from entire objects, while non-spatial treats all the objects. The number of objects from the range query was around 10. From the result, we can see that spatial range queries can be applied to all four models for retrieving relatively small number of objects from less than 100,000 units, since the gaps between them area 5 seconds at most.

3.3 Visualization

VRML supports diverse base solid features and allows the combination of multimedia such as animation or sound with applications, which makes visualizing 3D models in VRML relatively easy. Low-level graphic libraries such as OpenGL and Direct X can describe objects more in detail. In the test, we used real 3D building models of around 500 stored in the PostGIS. Although both techniques showed similar quality, VRML showed significant decrease in refreshing speed as the number of objects in the display increases. Thus, it is viewed that OpenGL is more suitable for 3D visualization applications although development with OpenGL requires more time than VRML (Figure 6 and 7).

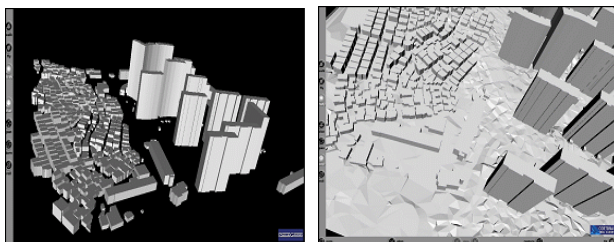


Figure 6. An example of visualization test using VRML

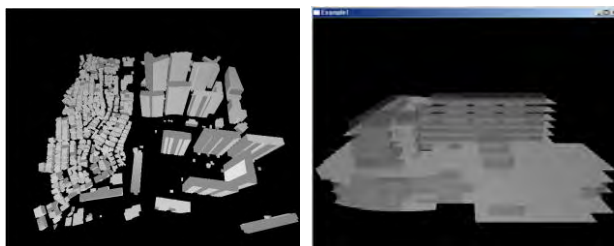


Figure 7. An example of visualization test using OpenGL

4. CONCLUDING REMARKS

Although 3D models are getting used increasingly in many areas including architecture, urban planning and environmental analysis, they mostly have been used as visualization purposes without using topological structure or semantic information. 3D topology models have been studied over the last decade and some of them were connected with DBMS-based implementations. However, we haven't found any attempts for comparing the models in the viewpoint of performances as of now. In this study, we categorized previously proposed 3D models and compared them including our own model using different queries to the SDBMS. We tested the retrieval time by non-spatial and spatial queries and suggested the most computationally favorable models for LADAR simulations. Also, we compared visualization performances between VRML and OpenGL. The results imply that choosing a 3D modeling should be done according to the problem requirement types. Type 1 is shown to be proper for visualization, while type 3 is for spatial queries. However, types of 3D model may additionally be determined by the level of details of the classes where the required semantic information resides. For example, when modeling indoor spaces, we many need a more decomposed model like Type 1 which fully implements the topological relationships between objects.

ACKNOWLEDGEMENTS

This research was supported by the Seoul R&BD Program (10561), Korea.

REFERENCES

- Ellul, C. and Haklay, M., 2008. Using a B-rep structure to query 9-intersection topological relationships in 3D GIS – reviewing the approach and improving performance. In J. Lee and S. Zlatanova, (eds.), *3D Geo-information Sciences*, Springer-Verlag, Berlin, pp. 127 -151.
- Gröger, G., Reuter, M. and Plümer, L., 2004. Representation of a 3-D city model in spatial object-relational databases. In: *The 20th Congress of International Society for Photogrammetry and Remote Sensing*, Istanbul, Turkey.
- Kolbe, T., 2008. Representing and exchanging 3D city models with CityGML. In J. Lee and S. Zlatanova, (eds.), *3D Geo-information Sciences*, Springer-Verlag, Berlin, pp. 15 -31.
- Stadler, A. and Kolbe, T., 2007. Spatio-semantic coherence in the integration of 3D city models. In: *The 5th International ISPRS Symposium on Spatial Data Quality ISSDQ 2007*, in Enschede.
- Stoter, J. and van Oosterom, P., 2002. Incorporating 3D geo-objects into a 2D geo-DBMS. In: *ACSM-ASPRS 2002 Annual Conference*. Washington DC.
- Stoter, J. and Zlatanova, S., 2003. Visualising and editing of 3D objects organised in a DBMS. In: *EUROSDR Workshop : Rendering and Visualisation*, Enschede, The Netherlands, pp. 14-29.
- Zlatanova, S., 2000. 3D GIS for urban development, Ph.D. thesis, Institute for Computer Graphics and Vision, Graz University of Technology, Austria, ITC, the Netherlands.

DATA-DRIVEN ALIGNMENT OF 3D BUILDING MODELS AND DIGITAL AERIAL IMAGES

J. Jung, C. Armenakis*, G.Sohn

Department of Earth and Space Science and Engineering
Geomatics Engineering, GeoICT Lab
York University, Toronto, Canada
{jwjung} {armenc} {gsohn}@yorku.ca

Commission VII, WG VII/6

KEY WORDS: Data fusion, registration, building models, digital image, similarity assessment, updating

ABSTRACT:

Various types of data taken from different sensors or from different viewpoints at different times are used to cover the same area. This abundance of heterogeneous data requires the integration and therefore the co-registration of these data in many applications, such as data fusion and change detection for monitoring of urban infrastructure and land resources. While many data registration methods have been introduced, new automatic methods are still needed due to increasing volumes of data and the introduction of new types of data. In addition, large-scale 3D building models have already been constructed for mapping or for generating 3D city models. These valuable 3D data can also be used as a geometric reference in sensor registration process. This paper addresses data fusion and conflation issues by proposing a data-driven method for the automatic alignment of newly acquired image data with existing large scale 3D building models. The proposed approach is organised in several steps: extraction of primitives in the 3D building model and image domains, correspondence of primitives, matching of primitives, similarity assessment, and adjustment of the exterior orientation parameters of the images. Optimal building primitives are first extracted in the existing 3D building model using a priority function defined by the orientation of building, complexity of building, inner angles of building, and building geometric type. Then the optimally extracted building primitives are projected into image space to be matched with extracted image straight lines data sets followed by a similarity assessment. For the initial localization, the straight lines extracted in the digital image are assessed in the search area based on their location with respect to the corresponding optimal building primitives. The location of the straight line having the highest score is determined. In that designated area location, new straight lines are extracted by weighting straight lines representing each vector of optimal building primitives. The corresponding vertices of the optimal building model are determined in the image by the intersection of straight lines. Finally, the EO parameters of the images are efficiently adjusted based on the existing 3D building model and any new image features can then be integrated in the 3D building model. An evaluation of the proposed method over various data sets is also presented.

1. INTRODUCTION

With the recent advancements in remote sensing technology, various types of data taken from different sensors or from different viewpoints at different times are used to cover the same area. This abundance of heterogeneous data requires the integration and therefore the co-registration of these different data sets in many applications such as detection of changes in the urban infrastructure and mapping of land resources. While many data registration methods have been introduced, new automatic methods are still needed due to the increasing volume of data and the introduction of new types of data. Zitova and Flusser, 2003 presented a comprehensive survey of image registration methods, while Fonseca and Manjunath, 1996 compared registration techniques for multisensory remotely sensed imagery and presented a brief discussion of each of the techniques. Habib et al., 2005 introduced alternative approaches for the registration of data captured by photogrammetric and lidar systems to a common reference frame. However, most studies aim to register images with other sensors data such as lidar and SAR data sets. Although large-scale 3D building

models have been already generated in Google Earth, of Google and Virtual Earth of Microsoft, the application of the building information is limited to a secondary role for text-based data search. However, these valuable 3D data can be also used as a geometric reference in sensor registration process. Therefore, this paper addresses data fusion and conflation issues by proposing a data-driven method for the automatic alignment of newly acquired image data with existing large scale 3D building models. Also, while existing 3D building models have inherent errors, in this study we assume that the existing 3D building models are free of any geometric errors and that the exterior orientation parameters of image are to be adjusted using the 3D building model as reference control data. This paper is organized into four parts. In section 2, we address the proposed new registration method, section 3 deals with the evaluation of the approach, and conclusions are given in section 4.

* Corresponding author.

2. REGISTRATION METHOD

To register the input digital image with existing 3D building models, geometric primitives in both data sets are extracted and their corresponding image coordinates are computed by a similarity assessment. The EO parameters of the images can be efficiently adjusted based on the corresponding image coordinates of primitives. Figure 1 illustrates the outline of our approach.

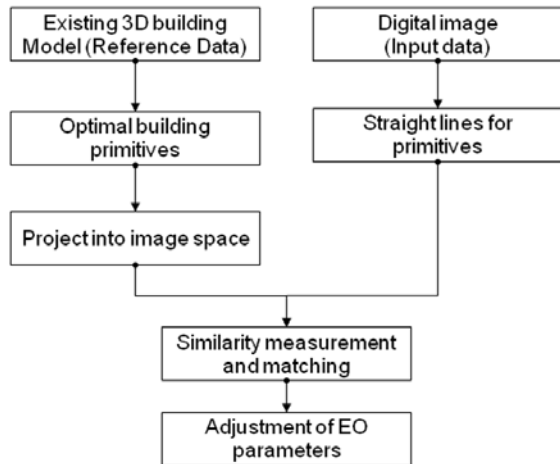


Figure 1. Flowchart of the alignment method

2.1 Feature extraction

2.1.1 Extraction of optimal building primitives

The 3D existing building models derived from various sensors have different accuracy according to generation method. Also, though the 3D building models may have been constructed by same method, all the 3D building models could not be used in the registration process. This is because their accuracy could be different depending on the skill of the operator and because use of the entire 3D building model for registration may be inefficient and time-consuming. We assume that simple buildings which satisfy a defined geometric condition of building are more useful for the registration process. For example, a building polygon which consists of 4 lines with 90 degree inner angles is likely to be a more general and efficient primitive because it is more difficult to describe complex buildings, since there is greater chance that the operator will misrepresent a complex. Therefore, it is important to extract optimal building primitives that satisfy the geometric condition for building and are representative of the existing large scale 3D buildings scene. To extract optimal building primitives, priority function is defined based on the orientation of buildings, number of boundary lines or polygons describing the building, type of buildings, and inner angles between building lines (Equ. 1). The buildings having the minimum value of the priority function are selected to be used in the registering process.

$$M_i = \arg \min_{\forall \{M_i\}_{i=1,2,\dots,N}} S_M [M_i(D, N_L, N_P, P, I_\theta)] \quad (1)$$

where, M_i denotes building model and S_M is the priority function to extract optimal building primitive. D , N_L , N_P , P and I_θ denote orientation of building, number of boundary

lines, number of polygons, building type, and inner angles between building vectors, respectively.

2.1.2 Extraction of image straight lines primitives

Although many line detectors have been introduced, the Burns algorithm (Burns et al., 1986) is selected for our research because the line data extracted by the algorithm include the representative line and its length, contrast, width, location, orientation and straightness. There are three steps to the Burns algorithm in this study. Pixels are grouped into line-support regions based on the similarity of the gradient orientation. This allows for data-derived organization of edge contexts without committing to a particular size. To group the pixels into line-support regions, the connected-components algorithm proposed by Lumia et al., 1983 is used. In the next step the image intensity slope surface is approximated by a planar surface. The planar fit is weighted by the gradient magnitude associated with the pixels so that intensities in the steepest part of the edge will dominate. Finally, straight lines are extracted by computing the intersection between the planar fit and the horizontal surface in each line-support region. As mentioned above, these straight lines have geometric information such as the coordinates of start and end points and attributes of the parameters of lines.

2.2 Domain of comparison

The extracted optimal building models are in the object space while the image straight lines are located in the image space. For comparing both primitives, the optimal building models and the image straight lines should be in the same domain. Therefore, the optimal building models are projected into image space by the collinearity equations using the camera interior orientation parameters and the initial camera exterior orientation parameters obtained by the GPS and IMU sensors. Consequently, the similarity measurement, and thus the matching of primitives, is carried out in the image space.

2.3 Similarity measurement and primitives matching

Due to errors in the initial EO parameter, and geometric errors in the existing 3D building models, the optimal building primitives projected into image space do not correspond with the straight lines extracted in image. In this study, we assume that the existing 3D building models are error-free and the errors are only with the initial EO parameters. Similarity measurement is required for extracting new image coordinates for the optimal building primitives by measuring the relationship between optimal building primitives and image straight lines in the image space. The process of similarity measurement begins by scoring the sum of image line length contained in the buffer zone of the projected vectors comprised of optimal building primitives against the optimal building primitives placed in the designated image area. The image location having the highest score is selected as the image coordinates corresponding to the optimal building primitives. In this location, new image straight lines are extracted by weighing the straight lines representing each vector of optimal building primitives. The intersection points are computed from the new lines and then the points are considered as corresponding image coordinates of the optimal building primitives. Figure 2 shows the proposed method for similarity measurement.

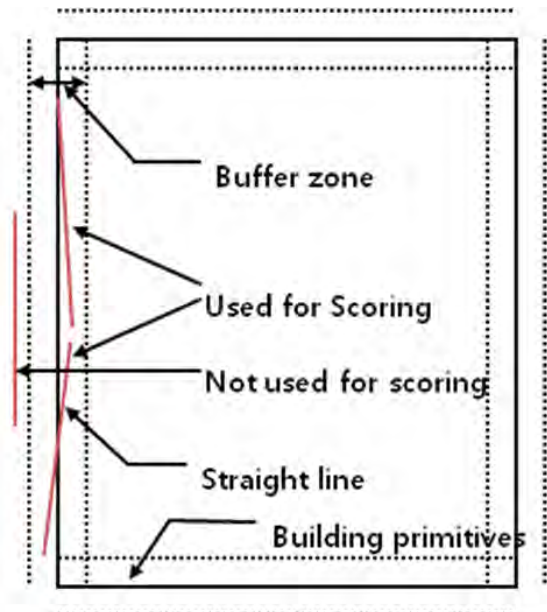


Figure 2. Similarity measurement

2.4 Adjustment of EO parameters

The EO parameters of the image are adjusted through space resection using pairs of the object coordinates (X, Y, Z) of optimal building primitives and their newly derived image coordinates (x, y) derived in the similarity measurement process.

3. RESULTS

3.1 Test data

The testing of the method was carried out in a study area of York University in Toronto. Existing 3D building models and an aerial colour image acquired in 2009 provided by First Base Solution were used in the study. Figure 3 shows the existing 3D building models and aerial image used in this study.



Figure 3. Existing 3D building models and the aerial image

3.2 Feature extraction

A total of 7 optimal building primitives were selected by analysing the orientation of building, complexity of building, inner angles of building, and geometric building type in the study area. Six of the seven optimal building primitives are rectangular and the seventh is hexagon with inner angles of 90 degrees. As well, we can see that the principal axes of the

optimal building primitives point to the same direction. The circles in Figure 3 show shape and distribution of the extracted optimal building primitives. 3 building models indicated by the triangles in Figure 3 are selected as check buildings to evaluate the accuracy of alignment. Straight lines corresponding to the optimal building primitives are extracted in image by the Burns algorithm. Straight lines having a length of less than 3m of the entire extracted straight lines are removed for effective



Figure 4. Extracted straight primitives (building 1)



Figure 5. Extracted straight primitives (building 2)



Figure 6. Extracted straight primitives (building 3)



Figure 7. Extracted straight primitives (building 4)



Figure 8. Extracted straight primitives (building 5)



Figure 9. Extracted straight primitives (building 6)



Figure 10. Extracted straight primitives (building 7)

registration process. Figures 4 to 10 show the results of extracted straight lines primitives for each building in the image.

3.3 Back projection

Optimal building primitives were back projected into image space and figure 11 illustrates the result of each building. Figure 12 shows a closed-up view of the back-projection on the image of building 4. In this figure, the red lines represent the optimal building primitives. Column 2 in Table 1 presents the image coordinates of the optimal building primitives after back projecting them into image space. The back projection results show that there is a small difference in the image coordinates between optimal building primitives projected into image and the building image because of errors contained in the initial EO parameters.



Figure 11. Results of back projecting into image space



Figure 12. Enlarged image of back-projected building 4

3.4 Similarity measurement and matching

Similarity measurement was carried out with a 10 pixel buffer zone in search area. 30 pairs of coordinates corresponding to the vertices of the optimal building primitives are automatically obtained by computing the intersections of the new straight lines after finding new location of optimal building primitives. Table 1, column 3, shows the results of image coordinates corresponding to the extracted optimal building primitives.

Table 1. Quantitative assessment with optimal building primitives

	Optimal building primitives (Object space)			Image coordinates extracted manually(1)		Coordinates of Building primitives projected into image space(2)		Automatically extracted coordinates by similarity measurement(3)	
	X(m)	Y(m)	Z(m)	X(pixel)	Y(pixel)	X(pixel)	Y(pixel)	X(pixel)	Y(pixel)
Building 1	620217.24	4848040.89	167.15	2916	5547	2921.22	5544.96	2915.14	5544.35
	620146.18	4848017.03	167.15	3098	6094	3103.56	6091.23	3098.17	6092.96
	620168.29	4847951.20	167.16	3604	5925	3609.60	5922.73	3607.72	5923.29
	620239.31	4847975.04	167.16	3425	5380	3427.44	5376.69	3424.78	5374.92
Building 2	620285.81	4847945.87	175.68	3635	5032	3640.03	5027.56	3634.55	5031.68
	620297.64	4847909.79	175.74	3915	4939	3919.02	4936.86	3914.40	4940.70
	620350.87	4847927.55	174.70	3778	4526	3783.92	4524.45	3778.02	4524.42
	620338.85	4847963.57	175.75	3498	4619	3503.87	4617.28	3497.11	4617.53
Building 3	620386.56	4847837.71	174.96	4476	4252	4478.37	4250.46	4475.77	4251.39
	620406.61	4847776.84	175.01	4951	4096	4949.13	4096.63	4952.36	4095.65
	620442.84	4847788.77	175.05	4858	3814	4857.49	3816.35	4860.45	3814.55
	620422.79	4847849.64	174.82	4384	3970	4386.87	3970.20	4384.00	3970.30
Building 4	620550.63	4848063.44	169.83	2739	2980	2746.82	2980.75	2738.37	2980.45
	620504.54	4848048.32	169.88	2855	3336	2862.55	3336.07	2854.51	3337.03
	620519.95	4848002.25	169.96	3209	3218	3217.41	3218.14	3208.79	3219.29
	620565.94	4848017.63	169.92	3092	2863	3099.65	2863.53	3090.62	2863.43
Building 5	620753.79	4847797.58	176.63	4795	1406	4793.49	1408.54	4794.11	1407.82
	620675.77	4847771.87	176.59	4992	2008	4991.26	2013.39	4990.29	2007.80
	620705.72	4847682.57	176.74	5682	1777	5683.18	1782.69	5680.77	1777.59
	620783.60	4847708.69	176.61	5482	1178	5482.31	1179.05	5481.51	1178.80
Building 6	620563.73	4847602.66	188.92	6306	2872	6304.02	2876.78	6307.17	2872.21

	620590.78	4847522.45	189.85	6934	2662	6931.69	2666.24	6934.84	2661.68
	620604.89	4847527.20	188.93	6896	2553	6894.12	2556.62	6897.14	2551.67
	620577.84	4847607.41	189.07	6270	2763	6267.26	2766.40	6270.27	2761.45
Building 7	620309.61	4847485.66	177.48	7205	4856	7200.85	4853.73	7205.98	4855.24
	620315.47	4847468.22	177.51	7346	4808	7336.08	4808.71	7342.80	4809.70
	620327.47	4847472.26	177.55	7309	4716	7305.08	4715.75	7307.08	4715.75
	620333.49	4847454.58	177.49	7446	4668	7442.09	4669.44	7444.98	4669.81
	620374.30	4847468.44	177.52	7342	4352	7335.62	4353.18	7338.15	4352.52
	620362.97	4847503.61	177.54	7067	4439	7062.97	4440.27	7067.20	4439.07
Compared to image coordinates extracted manually	Average (pixel)				1.07	0.52	-0.43	-0.23	
	RMSE(pixel)				4.55	2.62	1.62	1.43	

3.5 Adjustment of EO parameters

With the 30 pairs of building model primitives and their image coordinate extracted by similarity measurement, the EO parameters are adjusted in a least squares solutions as shown in table 2.

Table 2. Adjusted EO parameters

	Initial EO parameter	Adjusted EO parameter
X(m)	620455.282	620454.647
Y(m)	4847674.264	4847676.303
Z(m)	1632.24	1629.578
Omega(deg)	0.06556	-0.01266
Phi(deg)	0.14135	0.12273
Kappa(deg)	-89.86594	-89.88080

3.6 Assessment of the proposed method

In order to evaluate the performance of the proposed method, qualitative and quantitative assessments were carried out with both optimal and check building models, respectively. Both optimal and check building models are back-projected into image space using the adjusted EO parameters. Figure 13 shows the results of each optimal building projected into image space after the EO parameters are adjusted, and Figure 14 shows better matching of the building edges using the new EO parameters than the initial EO parameters when compared to Figure 12. Reference coordinates corresponding to optimal and check building models were also manually extracted from the image for quantitative assessments (Table 1, column (1) and Table 2, column (1)). The reference coordinates are compared to coordinates of optimal building automatically extracted in Table 3. While the results with initial EO parameters show that the average difference in X and Y directions are 1.07 and 0.52 pixels

respectively, with RMSE of 4.55 and 2.66 pixels respectively, the results with the new EO parameters show that the average differences in X and Y directions are 0.43 and 0.23 pixels, with RMSE of 1.62 pixel and 1.43 pixels, respectively. The test is also carried out in a similar manner with check building models which were not used in the registration process. The average coordinate differences of check building models with initial EO parameters were 0.42 and 0.13 pixels in X and Y directions, with RMSE of 4.99 and 2.66 pixels, respectively. After adjusting the EO parameters, the result show that the average differences in X and Y direction are 0.45 and 0.59 pixels, with RMSE of 0.66 and 1.49 pixels, respectively.



Figure 13. Back-projection results after adjusting EO parameters



Figure 14. Enlarged image of the back-projected Building 4 using the new EO parameters

Table 3. Quantitative assessment with check buildings

	Check building vectors			Image coordinates of check buildings extracted manually(1)		Image coordinates of check buildings obtained by initial EO parameters		Image coordinates of check buildings obtained by automatically adjusted EO parameters	
	X(m)	Y(m)	Z(m)	X(pixel)	Y(pixel)	X(pixel)	Y(pixel)	X(pixel)	Y(pixel)
Building 8	620426.84	4847296.02	196.82	8717	3951	8712.04	3952.48	8717.21	3950.73
	620434.24	4847273.58	197.00	8894	3894	8888.84	3894.82	8894.19	3892.93

	620462.35	4847283.10	196.90	8820	3673	8814.52	3673.92	8819.71	3671.72
	620454.97	4847305.51	196.97	8644	3731	8638.47	3731.46	8643.48	3729.39
Building 9	620583.17	4848170.14	174.48	1906	2726	1913.42	2725.02	1904.89	2722.50
	620606.54	4848099.71	174.47	2452	2543	2457.80	2545.60	2450.69	2542.62
	620633.01	4848108.29	174.30	2385	2338	2392.24	2340.99	2384.92	2337.57
	620609.43	4848178.84	174.35	1840	2519	1846.87	2522.00	1838.13	2519.04
Building 10	620084.29	4847745.74	178.76	5183	6598	5182.56	6594.73	5182.64	6599.30
	620102.43	4847691.31	178.71	5605	6461	5604.51	6455.31	5605.40	6459.34
	620202.51	4847724.94	178.53	5346	5683	5345.80	5679.46	5345.98	5682.09
	620184.17	4847779.22	178.67	4925	5821	4924.96	5820.60	4924.32	5823.72
Compared to image coordinates extracted manually				Average(pixel)		0.42	-0.13	-0.45	-0.59
				RMSE(pixel)		4.99	2.66	0.66	1.49

4. CONCLUSIONS

In this study, we present a new method for registering existing 3D building models with image data. Optimal building models are extracted with a priority function using information of 3D building model. Straight lines in the image are also extracted by the Burns algorithm. Optimal building primitives are projected into image space to compare both sets of data. Corresponding coordinate pairs are computed by similarity measurement, scoring straight lines contained in the buffer zone of the optimal building model. Finally, computed coordinates pairs are used to adjust the initial EO parameters. The proposed method for registering 3D building models with image data has been tested. The experiment showed that with optimal building models average differences of 0.43 pixel and RMSE of 1.62 pixel in the X direction and of average difference of 0.23 pixel and RMSE of 1.43 pixel in the Y direction were obtained. For the check building models the results were 0.43 pixel with RMSE of 0.66 pixel in the X direction and 0.59 pixel with RMSE of 1.49 pixel in the Y direction. These results indicate that our proposed data-driven method can effectively register and align existing 3D building models with new acquired image data. Further work is needed to improve the proposed method by considering and including the errors of 3D building models and estimate their impact in the registration process.

ACKNOWLEDGEMENT

This research is supported by a grant (07KLSGC03) from the Cutting-edge Urban Development – Korean Land Spatialization Research Project funded by Ministry of Land, transport and Maritime Affairs of Korean government.

REFERENCES

- Burns, J. B., Hanson, A. R. and Riseman, E. M., 1986. Extracting Straight Lines. *IEEE Trans. Pattern Analysis and Machine Intelligence*, Vol. 8, pp. 425-445.
- Fonseca L, M. G. and Manjunath B. S., 1996. Registration Techniques for Multisensor Remotely Sensed Imagery. *Photogrammetric Engineering & Remote Sensing*, Vol. 62, No. 9, pp. 1049-1056.
- Habib, A., Ghanma, G., Morgan, M., and Al-Ruzouq, R., 2005. Photogrammetric and Lidar Data Registration Using Linear Features. *Photogrammetric Engineering & Remote Sensing*, Vol. 71, No. 6, pp. 669-707.
- Lumia, R., Shapiro, L. and Zuniga, O., 1983. A New Connected Components Algorithm for Virtual Memory Computers. *Computer vision, Graphics, and Image Processing*, Vol. 22, pp. 287-300.
- Zitova, B. and Flusser, J., 2003. Image registration method: a survey. *Image and Vision Computing*, Vol. 21, pp. 977-1000.

TERRASAR-X STEREO DIGITAL ELEVATION MODELS FOR COMPLEX TERRAIN CONDITIONS IN ALPINE REGIONS AND ITS SUITABILITY FOR ORTHORECTIFICATION PURPOSES OF OPTICAL AND SAR IMAGERY

N. Kiefl, W. Koppe, S. D. Hennig

Infoterra GmbH, Claude-Dornier-Strasse, 88090, Immenstaad, Germany

KEY WORDS: DEM/DTM, Analysis, SAR, Stereoscopic, Orthorectification

ABSTRACT:

The technology of interferometry is already well established for the generation of digital surface models (DSM). However, the short wavelength of the TerraSAR-X satellite causes temporal incoherence for repeat pass interferometry, thus, the satellite's data is not well suited to derive reliable surface models in many regions of the world using interferometry. However, it is possible to generate reliable surface models with TerraSAR-X data simply by taking advantage of the possibility to acquire data at different incidence angles. The technology used is based on photogrammetry methodologies the so-called radargrammetry. The technology for radargrammetric or stereo DSM processing is already implemented as part of Infoterra GmbH's infrastructure and enables the generation of DSMs with a vertical height accuracy of 5 to 10 meters (LE 90) for slopes smaller than 20° based on StripMap mode data (3 m spatial resolution). In the frame of Infoterra's global DEM verification campaign, a development project focusing on the refinement of the radargrammetric processing methodologies and the verification of results for an area with complex terrain conditions was conducted. The test site is the Juneau Icefield (Alaska, USA), which provides difficult terrain conditions for DEM generation as the area is mainly covered by snow and ice and is characterized by very high slopes. In order to emerge the best acquisition scenarios for DEM generation, several data sets were acquired in different TerraSAR-X modes with varying incidence angle combinations in different seasons. The verification results for the different test cases with respect to height accuracy as well as suitability for orthorectification purposes of SAR and optical (RapidEye) data will be presented. The statistical analysis shows that the vertical accuracies are strongly dependent on the disparity angle of the input scenes. They vary between a vertical error of 16.2 meters (LE90) for small (9°) and 6.5 meters for larger disparity angles (20°) and better.

1. INTRODUCTION

For TerraSAR-X data the usage of repeat pass interferometry for Digital Elevation Model (DEM) processing is limited due to temporal incoherence caused by the short wavelength of the system and a repeat pass of 11 days. In order to overcome this limitation, a technology based on methods from photogrammetry, the so-called radargrammetry, is used. For radargrammetry two SAR images (stereo pair), which cover the same area and are acquired at different incidence angles, are used for DEM processing.

Infoterra GmbH has developed and thoroughly evaluated the capacity of generating digital elevation models from TerraSAR-X data using radargrammetric processing. The development resulted in a product launch of the TerraSAR-X ELEVATION product end of Mai 2010 [1, 5]. During the development of this product, Infoterra performed a global DEM verification campaign for which several test sites with different land cover and relief conditions were selected all over the globe and a detailed statistical and visual inspection on DEM quality was performed. For one of these test sites, a research project with focus on the refinement of the radargrammetric processing methodologies and verification of results for an area with complex terrain conditions was conducted. The test site is the Juneau Icefield (Alaska, USA), which provides difficult terrain conditions for DEM generation. The results of the project are presented in the following.

2. RADARGRAMMETRY FOR COMPLEX TERRAIN CONDITIONS

2.1 Test site: Juneau Icefield, Alaska, USA

The test site covers the main part of the Juneau Icefield which is located northwest of the capital of the state of Alaska: Juneau. The Juneau Icefield covers an area of approx. 8000km², half of the area being covered by a system of glaciers. The area shows quite demanding conditions for DEM processing: The terrain consists of very steep slopes, i.e. the elevation rises from sea level up to 1700 meters within 22 km horizontal distance. Further, nearly the entire area is covered by ice and snow. Ice and snow coverage mostly shows little features in SAR images and is very sensitive to weather changes. Thus, for stereo matching it is a complex case.

In July and August 2009, DGPS measurements were acquired in the area during a field campaign by participants of the Juneau Icefield Research Program. These measurements were made available as reference data.

2.2 Test Scenarios and DEM processing

The test scenarios are mainly based on different acquisition scenarios. The input to radargrammetric processing is at least two stereo pairs. TerraSAR-X data can be acquired with different incidence angles over one area. However, the acquirable incidence angle range is limited to between 20 and 45 degrees for TerraSAR-X StripMap mode. The quality of data acquired with incidence angles in this range, which is called "full performance range", fulfils the specification for TerraSAR-X image products [2]. In order to have more options for the

combination of stereo pairs, data acquired outside the full performance range (15 to 60 degrees) were also used in the project.

The following acquisition scenarios were used for testing:

- Acquisition with StripMap mode, single polarized data (HH)
- Acquisitions in both orbit directions (in order to avoid layover and shadow effects where no stereo matching is possible)
- Acquisition at incidence angles of $\sim 25^\circ$, $\sim 35^\circ$, $\sim 45^\circ$, $\sim 58^\circ$ in ascending orbit direction
- Acquisition at incidence angles of $\sim 29^\circ$, $\sim 45^\circ$, $\sim 56^\circ$ in descending orbit direction
- Two acquisition campaigns: one in July / August 2009 (in parallel to the field campaign), a second one in October 2009

With help of the different acquisition scenarios, stereo pairs with different disparity ranges were composed and used for digital surface model (DSM) calculation by the automated radargrammetry processor integrated into Infoterra's production infrastructure.

2.3 DEM Evaluation

During the development phase of the TerraSAR-X ELEVATION product, Infoterra followed a strict validation approach, which was also applied to the results of this development project.

The evaluation was performed on the results of the different test scenarios:

- Verification based on the raw DSM product for each orbit direction, i.e. DSM product without any filtering, interpolation of smaller gaps or filling of larger gaps with an external DSM source
- Verification of the raw DSM merged from both orbit directions, i.e. no filtering, but gaps are reduced due to availability of height information from the alternate orbit directions.
- Verification of the edited DSM, i.e. TerraSAR-X ELEVATION DSM product, which is produced with the best suited acquisition scenario. It includes outlier removal, filtering, interpolation of smaller gaps, filling of larger gaps with an external DSM source and edited water bodies [1].
- Verification of the edited and calibrated DSM.

2.3.1 Verification methods: The following verification methods are applied to the data:

Visual inspection

Visual inspection is performed on a shaded relief representation of the DSM. This step helps to identify structural irregularities in the data processing, deviations in comparison to other DSM datasets, systematic artifacts, and outliers inside the elevation model.

Additionally a linear profile plot with the available DEM sources is drawn and visually analyzed [3]. A regular shift and irregular undulations in the DEM can easily be identified with this method.

Statistical analysis

In addition to the visual inspection of a DEM, the statistical analysis is the most important step of the validation process. The statistical calculations are based on a 90 % linear error (LE90) for the vertical accuracy [4]. In this project, input to the

statistical calculations was the DGPS measurements acquired during a campaign in July and August 2009. A total of 739 points was available.

For point based data like DGPS measurements a difference between the DSM and the height values from the reference data is calculated. Generally, all reference points are taken into account for statistical analysis independent of slope and sensor dependency. No selection of reference points according to selection criteria was carried out and only data of inconsistency is excluded from the process.

In the standard DEM evaluation procedure a classification of different slope and land cover classes is accomplished if a large number of points with a regular distribution over the entire area are available. In case of the Juneau Icefield, all available reference points were acquired over the glacier, thus falling into the same slope and land cover class. Consequently, no differentiation of classes was possible.

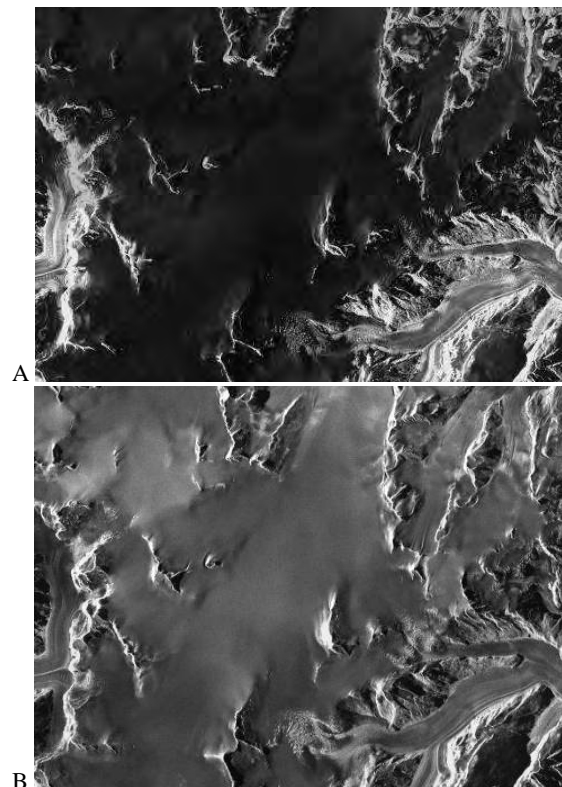


Figure 1. TerraSAR-X StripMap images over the Juneau Icefield: A: Acquired in July 2009, B: Acquired in October 2009

2.3.2 DEM evaluation results: During the visual inspection of the input scenes it was noted that the backscatter of the areas covered by snow and ice was very low for the acquisition performed in the summer season (July / August) due to the warm weather conditions and wet snow and ice (see Figure 1, A). Therefore, it was assumed that the DSM produced with these scenes might have some quality deficiencies in comparison to the DSM calculated on basis on the scenes acquired in autumn (October) (see Figure 1, B). The visual inspection of the DSM confirmed these assumptions. The DSM calculated with the scenes acquired during the summer season show more noise whereas the results received from the autumn scenes looks homogenous (see Figure 2).

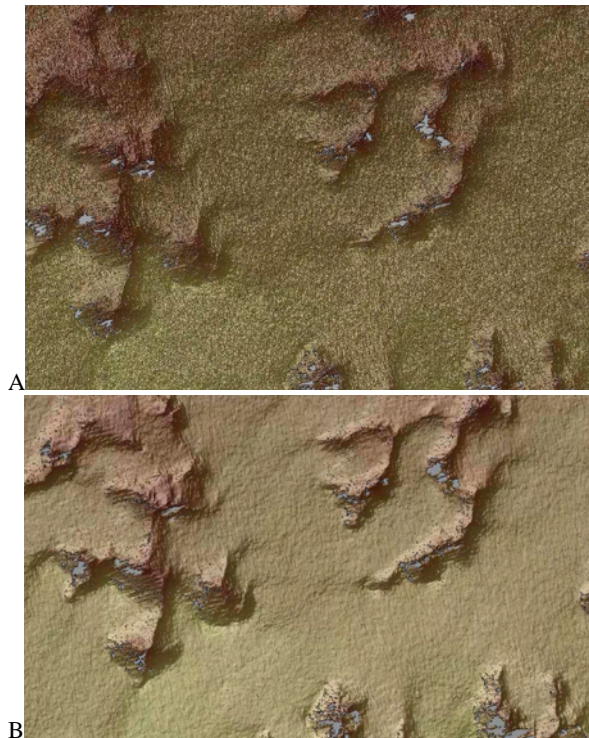


Figure 2. Results of the radargrammetric stereo processing for the summer acquisitions (A) and autumn acquisitions (B)

Furthermore, the acquisitions acquired with an incidence angle of more than 56° were not used for DSM calculation due to strong ambiguities in the images.

The visual inspection of the test results achieved with different disparity angle settings showed the following:

- DSMs calculated with stereo pairs with a small disparity angle (9°) show strong artifacts and noise.
- The artifacts and noise reduces with an increasing disparity angle.
- The results achieved with a disparity angle of $\sim 20^\circ$ showed visually the best results.
- Areas with invalids caused by layover and shadow artifacts (no matching possible) increase with a larger disparity angle.

Scenario	LE 90 [m]	No Points	Mean
Ascending summer (20°), raw	5.8	634	-2.4
Descending summer (20°), raw	6.4	634	-2.0
Descending October (20°), raw	6.7	473	-1.9
Ascending October (9°), raw	16.2	458	-4.2
Ascending October (11°), raw	8.9	453	-2.9
Ascending October (20°), raw	6.5	452	-2.6
Asc / Desc Oct. (20°), raw	5.1	616	-2.2
Asc / Desc Oct. (20°) edited	4.7	616	-2.2
Asc / Desc Oct. (20°) edited (cal.)	3.1	616	-0.2

Table 1. Statistical analysis for test scenarios using different orbit directions and disparity angles (raw = unedited DSM, cal. = calibrated)

In a next step, the statistical analysis was performed. The distribution of the DGPS points in combination with the evaluation result for the DSM calculated for the October scenes (disparity angle $\sim 20^\circ$, combination of ascending and descending

orbit) is depicted in Figure 3. Table 1 shows the statistical analysis for some representative test results.

In contrast to the visual impression, the statistical analysis show better results for the DSM calculated with the summer acquisitions compared to the DSM of the October acquisitions. A reason might be that the reference points were acquired in parallel to the summer acquisitions.

However, the statistics confirm that the quality improves with a larger disparity angle. The accuracy could further be improved by combining of ascending and descending orbit direction, which also reduces the number of invalid pixels. Moreover, the editing (smoothing, outlier removal) improves the visual impression and the statistical result. In a last step, the DSM was calibrated, improving the statistical results even more.

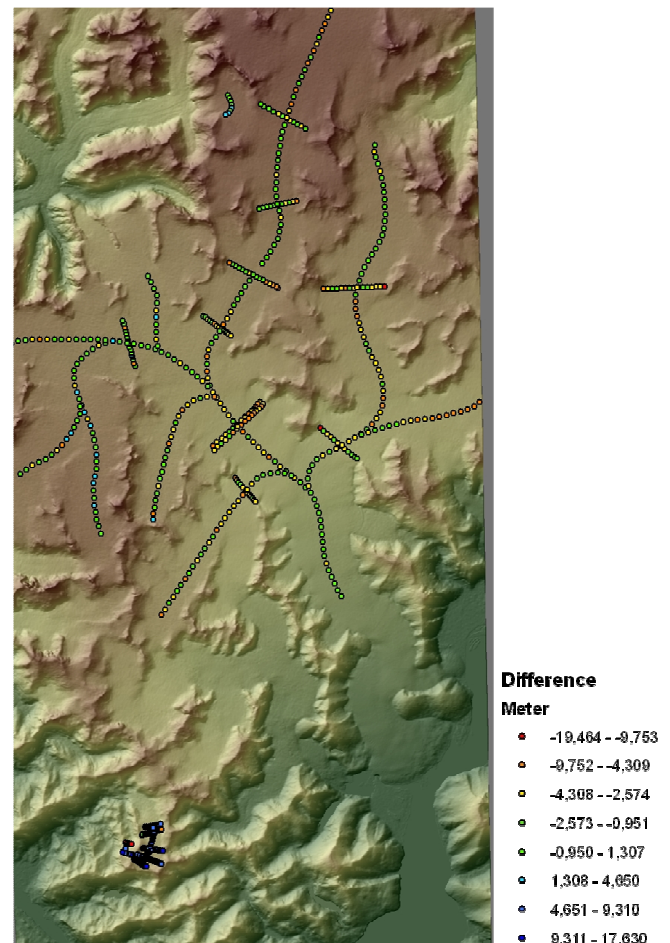


Figure 3. Evaluation result for the DSM (based on October scenes, disparity angle $\sim 20^\circ$, combination of ascending and descending orbit)

2.3.3 Orthorectification: Based on the edited DSM from the October acquisitions, an orthorectification of the TerraSAR-X images was performed with Infoterra's in-house orthorectification processor. For a part of the test site street vector data was available. The overlay of the street vectors and the orthorectified images showed a very good match of 1 to 2 pixels (2.5 meter spacing).

In the frame of the research project, the DSM and the orthorectified TerraSAR-X images were provided to RapidEye AG, where both data sets were used for co-registration and orthorectification of RapidEye data. The achieved geo-location

for the orthorectified RapidEye data was within one pixel (5m spacing) compared to the TerraSAR-X data.

3. CONCLUSION

In the frame of the research project tests considering different acquisition scenarios for radargrammetric processing of TerraSAR-X StripMap data were performed. It was shown that the generation of Digital Surface Models based on TerraSAR-X data using radargrammetry techniques is possible even for very complex terrain conditions. The combination of DSMs derived from ascending and descending orbit helps to minimise significantly void areas from shadow and layover. The results also confirmed theoretical considerations with respect to the acquisition scenarios best suited for radargrammetric processing. All the results were included into the development process of the TerraSAR-X ELEVATION product and processor [1, 5].

Furthermore, it was demonstrated that the resulting TerraSAR-X ELEVATION DSM is very well suited for orthorectification of both optical and SAR satellite data.

ACKNOWLEDGEMENTS

We would like to express our thanks to

- the participants of the Juneau Icefield Research project (Univ. German Forces, TUniv. Munich, TUniv. Darmstadt, ETH Zurich) for providing the reference data.
- DLR for the funding of the development project TERRAPID-3D
- RapidEye AG for the very good cooperation in the frame of the TERRAPID-3D project.

REFERENCES

- [1] Infoterra GmbH: *TerraSAR-X Exploitation - TerraSAR-X Elevation Product Specification, TSXX-ITD-SPE-0014*, 2010.
- [2] DLR (German Aerospace Centre): *TerraSAR-X Basic Product Specification Document*, 2008.
- [3] Hirano, A. et al.: *Mapping from ASTER stereo image data: DEM validation and accuracy assessment*. ISPRS Journal of Photogrammetry & Remote Sensing. 57 (2003), pp. 356-370
- [4] Maune, D. F.: *Digital Elevation Model Technologies and Applications: The DEM User Manual*. 2nd Edition. Bethesda, Maryland: ASPRS, 2007
- [5] Infoterra GmbH: TerraSAR-X Elevation DSM Brochures, Immenstaad, Germany
http://infoterra.de/fileadmin/Verzeichnisdokument/Dokument/e/2_AboutUs/0203_Brochures/e_TSX_ELEVATION_201005_download.pdf (accessed June 2010)

APPLICATION OF MULTISPECTRAL REMOTELY-SENSED IMAGERY IN AGRICULTURE

S. Kokhan

Dept. of Geoinformation Technologies, National University of Life and Environmental Sciences of Ukraine,
17 Vasylykivska St., 03040 Kyiv, Ukraine – GIS_DZZ_chair@nauu.kiev.ua

KEYWORDS: Remote sensing, Image Classification, Agricultural Crops

ABSTRACT:

Most classification projects now make use of digital classification procedures guided by human interpretation. Because of remotely sensed data could be particularly efficient for land use mapping, evaluation of crop status, the objectives of the study are represented by agricultural crops within the crop rotation during the spring-summer period. The use of various classification techniques is shown in the study. The satellite images considered for this paper were IRS-P6/LISS-4 and IRS-1D/LISS-3. The final stage of the classification process involves an accuracy assessment.

Die meisten Klassifikationsprojekte verwenden heutzutage digitale Klassifikationsvorgänge, die durch menschliche Interpretation geleitet werden. Da auf Distanz gewonnene Daten von besonderer Effizienz für Landwidmungen, sowie die Evaluierung von Ernteerträgen sind, werden die Ziele der Studie am Beispiel von landwirtschaftlichen Ernten in der Anbaurotationsfolge während der Frühjahr-/Sommerperiode dargestellt. Die Anwendung verschiedener Klassifikationstechniken wird in der Studie gezeigt. Die Satellitenbilder, die in diesem Paper betrachtet werden, sind IRS-P6/LISS-4 und IRS-1D/LISS-3. Die letzte Stufe des Klassifikationsprozesses schließt eine Genauigkeitsbewertung mit ein.

1. INTRODUCTION

Remotely-sensed data and satellite imagery is an important input to many analyses. It can provide timely as well as historical information that may be impossible to obtain in any other way. The availability of this data provides opportunities for environmental studies particularly in the areas of change detection, land use mapping, land evaluation, land survey that would have been unknown only a few decades ago.

Crop distribution maps are widely used for agricultural management. Remotely-sensed data and satellite imagery in particular have proven their efficiency for crop mapping. A large number of algorithms for image classification have been developed and their application has been shown in the literature (De Wit and Clevers, 2004; Conrad et al., 2010). New image processing techniques have been developed during the last few years. They provided the increase of classification accuracy.

The crop average spectral reflectance per field was used in the study. Validation of classification was performed with field observations for all crop types.

2. MATERIALS AND METHODS

The objectives of the study are represented by crop types within the field boundaries in the crop rotation of Forest-Steppe of Ukraine. The high resolution image IRS-P6 (6.0 m) was used for obtaining field boundaries. Data of medium spatial resolution (IRS-1D, 23 m) was used to classify crop types. Multispectral images were collected for three stages of development for winter cereals and spring crops over the growing season (in May, June and July in 2008). Erdas Imagine software was used to georeference image with ground-control points, for image geometric correction, image enhancement (radiometric enhancement and Ehlers fusion), and image classification. Field boundaries were digitized in

ArcGIS 9.3 from reference IRS-P6 image after Ehlers fusion application.

High pass filter (Laplacian) of the IRS-P6 data was used to delineate boundaries of crops within fields (Kokhan, 2010). Boundaries of fields and crops were evaluated and checked with the plan of the territory organization for Mankivka State Crop Variety Station.

The station is located in the Central part of Ukraine in the Forest-Steppe zone. Soils are mainly represented by chernozem typical. Climate of the region is moderately continental. Winter is mild with frequent thaws. Summer is warm, which is some times hot with precipitation. The annual mean temperature is 7.7°C with minimum in January and maximum in July. The annual rainfall is 517 mm with the maximum amount received in July.

Cereals and pulse crops are grown in 60% of the cultivated areas in the region. Industrial crops (sugar beets, corn) comprise 22% of crops grown in the cultivated area. Crops in the research station are represented by sugar beets, peas (two fields), radish, winter wheat (two fields), winter rape, spring barley (two fields) and sunflower.

3. RESULTS AND DISCUSSION

Land cover and other types of maps may be developed from the classification of remotely-sensed imagery. The majority of image classification is based on the detection of the spectral response patterns of land cover classes. Classification depends on distinctive signatures for the land cover classes in the band set being used, and the ability to reliably distinguish these signatures from other spectral response patterns that may be present (Eastman, 2006).

The classification process can be represented by determining the set to which each pixel belongs. The sets in supervised classification assumed to be known before the process is begun. In the case of supervised classification we delineated fields with different crops based on statistical characterization data drawn from known training sites. Ground truth data was collected nearly

time-synchronous to receiving IRS images. Vegetative period for spring crops usually starts at the end of April - beginning of May. Fields are mainly bare at that time and vegetation has low value of dry matter as well as leaf area index.

Phenological observation of crops during the spring and summer period (Table 1) were used for crop classification

Crops	Field	Vegetation		
		May	June	July
Sugar beets	I			
Peas	II			
Radish	III			
Peas	IV			
Winter rape	V			
Sunflower	VI			
Spring barley	VII			
Winter wheat	VIII			
Spring barley	IX			
Winter wheat	X			

	No vegetation		Medium
	Very low		Medium to dense
	Low		Dense

Table 1. Vegetation development during the spring and summer period.

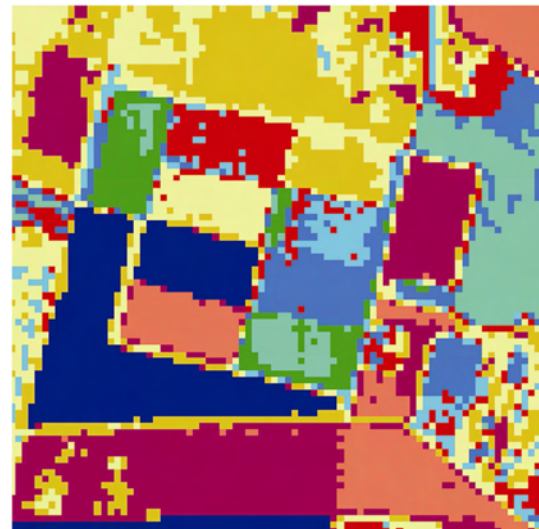
based on IRS-P6 and IRS-1D data. Multispectral data was obtained on May 18, June 16 and July 7. To evaluate the status of vegetation within the period of crop sampling we measured plant height, leaf area index, aboveground biomass and dry matter.

Peculiarities of crop development were used to analyze per field vegetation development. Information on crop cover types and vegetation density (very low, low, medium, medium to dense, dense) based on ground truth data provided information for image classification.

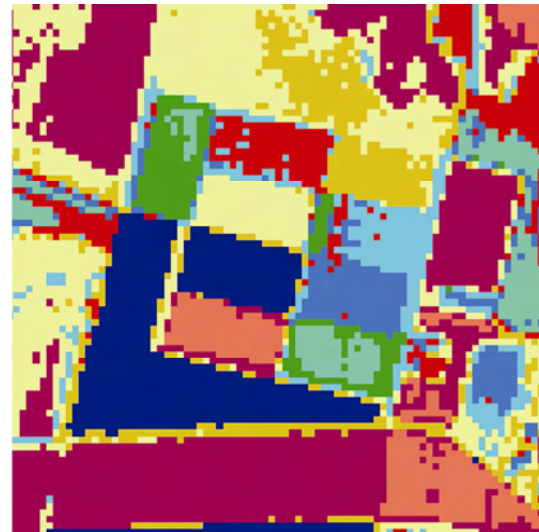
Ten training classes for crop classification were used in spite of that seven crop were cultivated. Peas, winter wheat and spring barley were located within two fields but they differed by the level of fertilization, crop variety and previous crop. It gains to differences in development of aboveground mass and yield components.

After the training sites had been created, the three methods were used to determine if a specific pixel qualifies as a class member. The minimum distance procedure, the minimum distance method with standardized distances and the method of maximum likelihood known to be hard classifiers were applied. They made a definitive decision about the land cover class to which any pixel belongs (Figures 1 to 3).

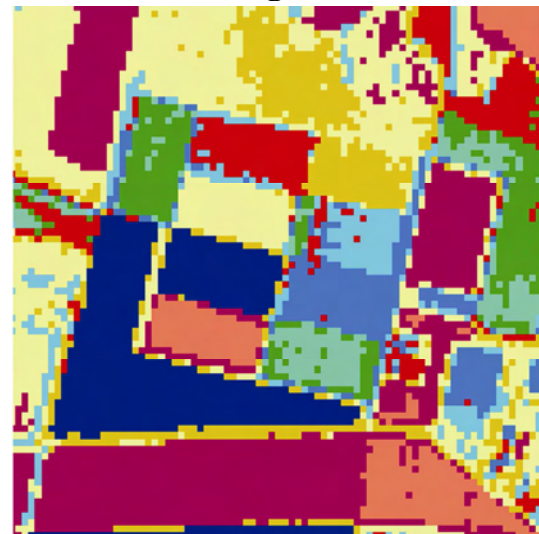
The minimum distance classifier uses the mean vectors of each training site and calculates the Euclidean distance from each unknown pixel to the mean vector for each class. All pixels are classified to the nearest class unless a standard deviation or distance threshold is specified, in which case some pixels may be unclassified if they do not meet the selected criteria. The method made some mistakes in classification results because of standard deviation of pixel spectral characteristics within the polygons.



A

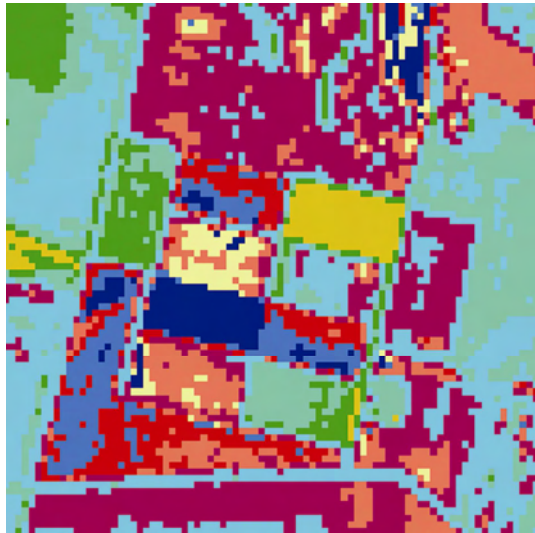


B

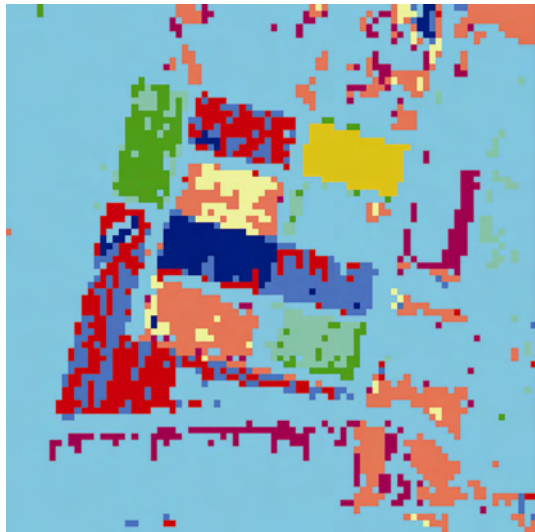


C

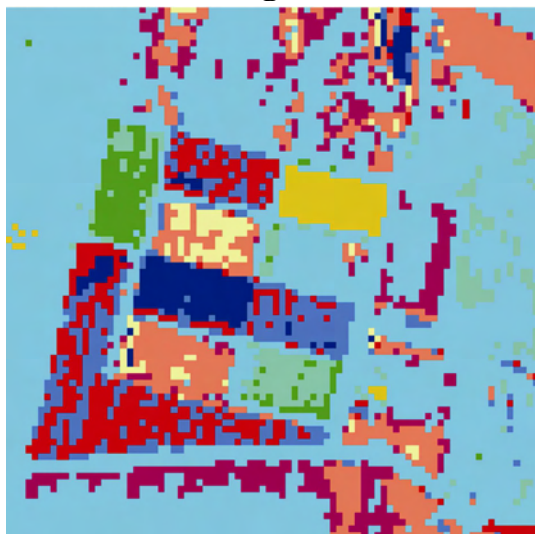
Figure 1. Crop classification maps derived from IRS-1D image (May 18): A - minimum distance procedure; B - minimum distance method with standardized distances; C - maximum likelihood classifier



A

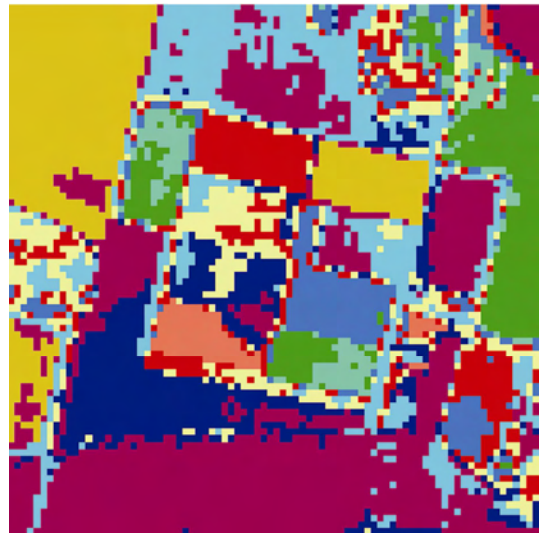


B

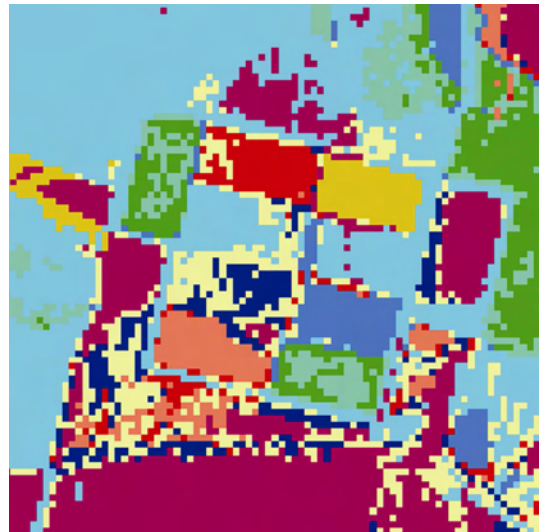


C

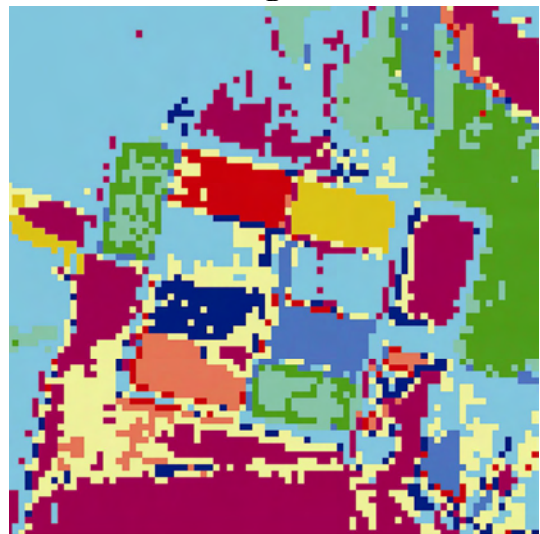
Figure 2. Crop classification maps derived from IRS-1D images (June 16)



A








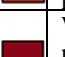
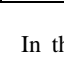
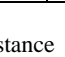


B



C

Figure 3. Crop classification maps derived from IRS-1D images (July 7)

	Sugar beets (I)		Peas (II)
	Radish (III)		Peas (after barley, IV)
	Winter rape (V)		Sunflower (VI)
	Spring barley (after sugar beets, VII)		Winter wheat (after peas, VIII)
	Spring barley (after cereals, IX)		Winter wheat (after radish)

In the case of normalized distance procedure application the classifier calculated standard deviation for reflectance values around the mean value and made contours of standard deviations. The pixel is assigned to the closest category in the form of standard deviations.

The maximum likelihood procedure is one of the most sophisticated, and the most widely used classifier. The classification assumes that the statistics for each class in each band are normally distributed and calculates the probability that a given pixel belongs to a specific class. Each pixel is assigned to the class that has the highest probability.

Multiple schemes of image classification used in environmental and agricultural mapping are either traditionally statistical or heuristic (region growing, fuzzy classification etc.) (Kovalevskaya and Pavlov, 2002).

Agricultural crops within the fields are not homogeneous objects because of the spatial variability of soil quality and soil moisture. In this research project we used the general schemes of supervised image classification. Training sites included only homogeneous areas within fields.

The final stage of the classification process usually involves an accuracy assessment. There are several types of accuracy assessments. Usually it is done by generating a random set of locations in the field conditions to verify the true land cover type. A simple value file is then made to record the true land cover class for each of locations. This values file is then used with the vector file of point locations to create a raster image of the true classes found at the locations examined. This raster image is then compared to the classified map (Eastman, 2006).

The Kappa coefficient is another measure of the accuracy of the classification. The coefficient is calculated by multiplying the total number of pixels in the ground truth classes by the sum of the confusion matrix diagonals, subtracting the sum of the ground truth pixels in a class times the sum of the classified pixels in that class summed over all classes, and dividing by the total number of pixels squared minus the sum of the ground truth pixels in that class times the sum of the classified pixels in that class summed over all classes. We used the Kappa coefficient to estimate the accuracy of the classification and to evaluate the results of applied methods of classification for each crop.

The error matrix produced was used to identify particular crop types for which errors are in excess of that desired. The information in the matrix about which crops are being mistakenly included in a particular class (errors of commission) and those that are being mistakenly excluded (errors of omission) from that class can be used to refine the classification approach.

Results showed that in May winter wheat and winter rape had the highest value of Kappa coefficient compared to another crops in the crop rotation (0.727 and 0.835). For the other crops the very low to low level of aboveground biomass is characterized. Radish can be recognized only during this period because of the early harvesting. The Kappa coefficient is 0.647.

Some fields in May are still bare and some crops have very low aboveground biomass. Therefore, accuracy of the classified fallow land is above 0.760.

Because of the weak biomass development for sugar beet, peas, sunflower and spring barley in the second decade of June the classification results shown that accuracy varied from 0.483 (sugar beet) to 0.614 (sunflower) (Figure 4). Winter rape and winter wheat had the higher value of Kappa coefficient (0.702 to 0.712) compared to the other crops.

Spring barley is one of the main agricultural crops in Ukraine. Results showed that accuracy assessment for this crop in June varied from 0.445 to 0.633. The higher value has been obtained for crop after the previous winter wheat.

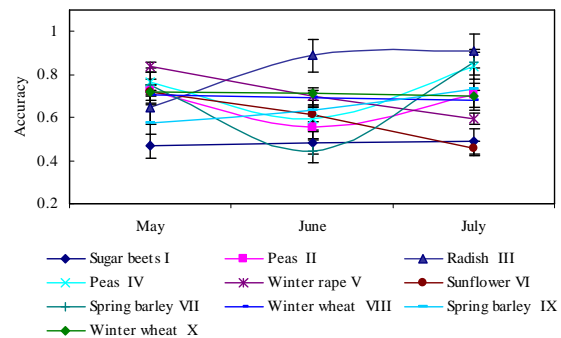


Figure 4. Accuracy assessment of the crop classification

Dense vegetation cover in July was mainly used to classify winter wheat, spring barley and peas with high percentage of identification (from 0.699 for winter wheat to 0.857 for spring barley). Kappa coefficient varied for fields with peas from 0.703 to 0.839. It was related to different nitrogen fertilizer rate applied under crops.

The overall accuracy for cereals and peas was 0.688, for the other crops – 0.608. Low accuracies were obtained for sugar beet, and sunflower. Because of the broad row-spacing and the within-field heterogeneity of crop growth, there was reduced classification accuracy.

4. CONCLUSION

It can be assumed that IRS-1D images acquired in three periods were classified to determine seven different crops. The overall accuracy for cereals and peas was 0.688 and for the other crops was 0.608.

In comparison to the studies (Turker et al., 2005, Conrad et al., 2010) the overall accuracy of classification was lower because of heterogeneity of crops within some fields, differences in agricultural technologies applied to the same group of crops, spatial variability of soil nutrients and moisture.

Additional image acquisition and database development of spectral signatures based on the results received within the experimental stations using sensors with medium resolution can provide images with lower spatial resolution to determine certain crops within the larger territories.

REFERENCES

- Conrad, C., Fritsch, S., Zeidler, J., Rücker, G., Dech, S., 2010. Per-field irrigated crop classification in arid Central Asia using SPOT and ASTER data. *Remote Sens.*, 2, pp.1035-1056.
- De Wit, A.J.W., Clevers, J., 2004. Efficiency and accuracy of per-field classification for operational crop mapping. *Int. J. Remote Sens.*, 25, pp. 4091-4112.
- Eastman, J. R., 2006. *Guide to GIS and image processing*. Clark University: Manual Version 15.00, pp. 188-214.
- Kokhan, S., 2010. Application of spatial enhancement transformations of satellite images for investigation of agricultural resources. *Announcer of Geodesy and Cartography*, 2, (submitted).
- Kovalevskaya, N., Pavlov, V., 2002. Environmental mapping based on spatial variability. *J. Environ. Qual.*, 31, pp. 1462-1470.
- Turker, M., Arıkan, M., 2005. Sequential masking classification of multi-temporal Landsat 7 ETM+ images for field-based crop mapping in Karacabey, Turkey. *Int. J. Remote Sens.*, 26, pp. 3813-3830.

VARIATION AND ANISOTROPY OF REFLECTANCE OF FOREST TREES IN RADIOMETRICALLY CALIBRATED AIRBORNE LINE SENSOR IMAGES – IMPLICATIONS TO SPECIES CLASSIFICATION

I. Korpela*, F. Rohrbach

Faculty of Agriculture and Forestry, University of Helsinki, POB 27, 00014 UH, Finland - (ilkka.korpela@helsinki.fi)

Commission VII

KEY WORDS: Forestry, Radiometry, Modelling, Calibration, Pushbroom, Multispectral, LiDAR,

ABSTRACT:

In Scandinavia, the conventional method of measuring trees is giving way to applications, which combine *in-situ* and airborne optical data, LiDAR in particular. Tree species (sp.) classification is a crucial sub-task and is solved with an insufficient reliability. The continuously varying view-illumination geometry hampers image-based solutions. Line sensors provide a selected subset of the possible view-illumination geometries, but have not been tried for the task in Scandinavia. We examined the variation and anisotropy of reflectance in trees, using radiometrically calibrated multispectral ADS40 data. An experiment in Finland (61°50'N, 24°20'E) that consisted of 121 plots and 15197 pine, spruce, and birch trees was imaged from 1, 2, 3, and 4 km altitudes. Leica XPro was used for producing different image data including the at-sensor radiance (ASR) data, atmospherically (ATM) corrected, and a combined BRDF- and atmospheric correction (FULL). Tree crowns were modelled in LiDAR data, and the resulting envelopes were sampled in the images in 121 points. Using the geometry of the crown envelope and the adjacent LiDAR points to model the geometry of the neighbourhood, camera-visibility and illumination class (Sun-lit, self-shaded, neighbour-shaded) was determined for each point. Using the pixel data of the crown points, different statistical features were derived for each tree. The radiometrically corrected image data did not reduce the intraspecies coefficient of variation, and in sp. classification trials, the ASR data provided equal or better results. The precision of the ATM data was evaluated to be better than 10% with the NIR band being most precise and the BLU band least precise. However, the BLU band was a strong predictor of tree species. Reflectance anisotropy of pine and spruce differed from birch, and it was strongest in the visible bands and varied up to $\pm 40\%$ in nadir lines flown nearly perpendicular to the Sun. Reflectance of crowns in diffuse illumination showed lower anisotropy and features derived in these data were strong predictors of species. We observed notable proximity effects in the NIR band, where the species composition of the adjacent trees affected the observed reflectance of the target tree up to 33%. Intracrown reflectance variation was examined for crown points oriented towards or away from the Sun on different relative heights. Age dependencies were observed in NIR and NDVI, where age explained up to 5% of the reflectance variation, and the dependency was negative. Site fertility was correlated with NIR and NDVI, and the overall stand effect explained 1–19% of the reflectance variation by band and species. This elucidates, why also the tree species classification accuracy varied considerably between stands. Classification accuracy for pine, spruce, and birch was 72–80% in quadratic discriminant analysis, when features of both Sun-lit and diffuse light were used as predictors. Best-case accuracies of 76–80% were achieved using 3 and 4 km monoscopic data, which shows the high potential of the ADS40 line sensor.

1. INTRODUCTION

In Scandinavia, the conventional method of measuring trees is giving way to applications, which combine *in-situ* and RS data. Here, the introduction of airborne LiDAR was a breakthrough. The need for aerial images is a topical question amongst Scandinavian foresters to whom species information is crucial on technical, economic, and ecological grounds. Separation of Scots pine, Norway spruce, and birch is essential for forestry in Finland. Classification accuracies of above 90% are considered adequate for practice. Recently, low-altitude, high-density discrete-return LiDAR data were tested for tree species discrimination with accuracies saturating at the 85–90% level. Owing to the monostatic view-illumination configuration, LiDAR signal is largely free from view-angle effects that have been reported to hamper image-based tree species recognition. In Sweden, an accuracy of 84% was reported in 1 km altitude, digital frame camera data (60 cm GSD DMC) (Holmgren et al 2008).

The validation procedures used for estimating species classification accuracy should provide realistic demonstrations of the performance. The leave-one-out cross-validation is often used.

It results in optimistic evaluation of the performance, omitting the spatial autocorrelation in forests and the similarity of view-illumination effects for neighbouring trees.

A species classification accuracy of 95% would be adequate for foresters in Finland, which is very challenging in airborne optical data, because the observations from the above result in commission and omission errors in tree detection. If a small tree is detected in near-nadir LiDAR, the low solar elevation, $<53^\circ$ in Finland, prevents from observing but the tallest trees in direct light. Species identification in image-based analysis is hampered by the view-illumination geometry (Fig. 1). According to Li and Strahler (1986), the geometric nature of the forest canopy is the major factor explaining the strong anisotropy of directional reflectance. Anisotropy of the reflectance is a fundamental property of most objects, and it means that the observed brightness is dependent on the illumination and observation directions. For point-like illumination and observer, the dependence can be described by the BRDF, depending on two illumination and two observation angles. Illumination conditions in forest canopy range from direct illumination to combinations of diffuse and direct illumination down to the total diffuse illumination,

* Corresponding author

with different levels of adjacent illumination sources. For those conditions various other reflectance quantities are needed (Martonchik et al., 2000).

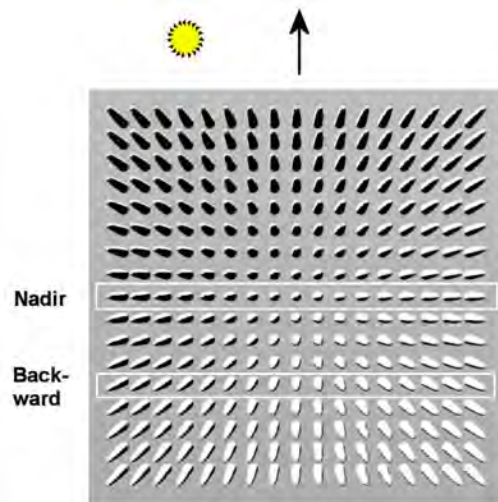


Figure 1. Illustration of the view-illumination geometry of trees in the focal plane of a nadir looking aerial camera. The flying direction is upwards and Sun is 26° left of it. The white rectangles depict the nadir and backward viewing in the ADS40 line sensor, which we used in this study.

Depending on the view and illumination directions, the pixel can view, in the extreme case of hot-spot geometry, shadow-free targets. When a tree crown is back-lit, the pixels sample mostly shadowed targets or forward-scattering canopy elements. The diffuse light incident at a tree consists of the light scattering in the atmosphere, but also of light scattered by the adjacent trees and the background. Taller neighboring trees are both reflectors that contribute to the incident light, but they also attenuate hemispherical diffuse light. Multiple scattering by trees contributes to the total radiance towards the sensor.

The spectra of a tree in an aerial image are measured from a sample of pixels that are geometrically linked to the tree. If the geometry of the canopy is known, it is possible to sample the crown for the Sun-lit and shaded parts (Korpela, 2004; Larsen 2007)..

There are many sources of inter- and intratree reflectance variation. The varying phenological and physiological status affects reflectance. Epiphytic lichens, flowers, and cones constitute sources of variation. The structure of branches, shoots, and needles, and the whole branching pattern and crown shape vary between and inside individuals, and the crown structure changes with age. The functioning, structure, and the environment all interrelate in a tree. Structural differences explain largely the variation in reflectance and anisotropy.

The scale of observation has important implications. In aerial images, a crown can be sampled by hundreds of pixels, while in satellite images several crowns fill a pixel. In sub-meter pixels, the scale is at the level of branches and shoots. Since bidirectional effects have their origin in sub-pixel shadow casting, it is possible to observe branch-level anisotropy. Scale is linked with sensor altitude and the medium. The majority of the atmospheric effects occur below the 3–6 km altitude, which stresses the importance of atmospheric modeling in airborne images if target reflectance data is strived for.

The introduction of digital sensors, direct sensor orientation, and image post processing systems, have all altered photogrammetric practices. In forest applications, this development has been covered by the expansion of LiDAR. Digital sensors are

relatively calibrated to a uniform response or absolutely calibrated to produce at-sensor radiance (ASR) data. Among photogrammetric sensors, absolute calibration exists for the ADS40 line camera. It measures ASR in 4 bands in two directions. A laboratory calibration is applied throughout a radiometry chain that also includes radiometric correction methods, which are implemented in the Leica XPro software (Beisl et al., 2008). The performance of ADS40 in tree species classification in Finland was simulated in Heikkinen et al. (2010). An additional band at 710–725 nm provided the best improvement. With the original 4 bands, the simulated sp. classification accuracy was 75–79%, while it was up to 85–88%, using the fifth band at the red-edge.

The aspects of utilizing reflectance anisotropy or calibrated images in high-resolution RS forest applications are largely unexplored. Studies have indicated that anisotropy might provide additional information for sp. classification (Deering et al., 1999). Line sensors offer fewer viewing directions, but owing to their view-geometry (Fig. 1), they sample the reflectance anisotropy in 1D. This may facilitate the interpretation compared to frame images. Our overall objective was to explore the ADS40 line camera for tree sp. classification of Scandinavian forests, where airborne line sensors or airborne calibrated reflectance data have not been tested thus far. Our three detailed objectives were as follows.

1. Implement an ADS40 sensor model.
2. Develop a method by which Sun-lit, shaded, camera-visible, and occluded parts of crowns can be determined to enable an extraction of image features in different illumination classes (Korpela, 2004; Larsen, 2007).
3. Examine the anisotropy and variation of spectral image features in radiometrically corrected images to study the performance potential of these data for tree species discrimination..

2. MATERIALS AND METHODS

2.1 Study area and reference trees

The experiments were carried out in Hyytiälä, southern Finland ($61^\circ 50'N$, $24^\circ 20'E$). The study area extends 2×6 km and comprises protected and commercial forests. We used reference trees measured in 2005–2009 in 121, 0.04–1.8-ha plots. The age of trees was 15–150 years, and a total of 15687 reference trees were formed by image- or LiDAR-visible trees (visual interpretation). Merely 3.8% of the trees had a relative height of below 0.5. Tree maps were used to derive a proximity class for each tree, which describes the dominant species among the adjacent trees.

2.2 ADS40–SH52 and LiDAR data

The ADS40 flight was carried out on August 23, 2008 at 10–12 local time (7–9 GMT) in 15 strips. Solar elevation was 27° – 37° and there were few clouds during the campaign at 700 m agl. Reflectance targets and *in-situ* radiometric measurements were carried out simultaneously. The strips were flown at 1, 2, 3, and 4 km altitudes and multispectral data was recorded for the nadir (N00A) and backward (B16A) view directions. At 1 and 2 km only N00A or B16A view was active. Strips were flown mostly in S–N direction, but also in E–W. We used discrete-return LiDAR data from 2006–2008 for the tasks of tree crown modelling and occlusion determination (section 2.6).

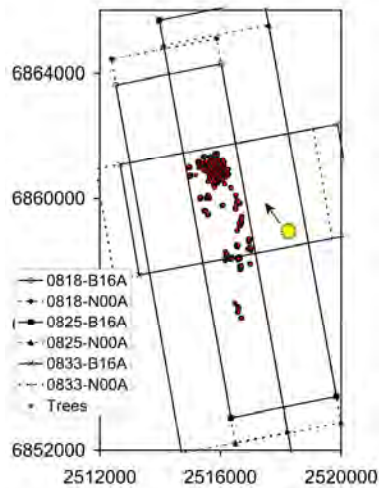


Figure 2. Footprints of 3 km strips 0818, 0825, and 0833.

2.3 Geometric and radiometric post processing of the ADS40 data

Direct georeferencing was used in aerial triangulation with 59 control points and sub-pixel accuracy was reached. Leica XPro (4.2) was used for producing three radiometrically corrected versions of each MS image:

- at-sensor radiance data (“calibrated” option): ASR
- atmospherically corrected target reflectance data (“atmospheric” option): ATM
- atmospherically and BRDF-corrected data (“atmospheric + BRDF” option): FULL

All three were produced for the 2–4 km strips, while ASR and ATM for the 1 km data. The atmospheric correction and reflectance calibration in XPro is based on the radiative transfer equation by Fraser et al. (1992). This atmospheric correction results in images, where the digital numbers are calibrated to ground reflectance. BRDF correction is based on a modified Walthall model. The details of the correction methods are presented in (Beisl et al., 2008). All corrections rely on a priori camera calibration and parameters derived from the image data. We used the default software settings in XPro processing.

2.4 Radiometric *in-situ* measurements and quality assessment of the ADS40 images

Ground measurements of reflectance targets were carried out during the overflight. Targets included reflectance tarps with 5%, 20%, 30%, and 50% nominal reflectance and well-defined surfaces (fine sand, grass, asphalt, gravel, hay). The ATM images were validated by Markelin et al. (2010) for the nadir reflectance. We sampled the targets by 4×4 m rectangles and pixel data were analyzed for precision.

2.5 Photogrammetric operations in the ADS40 data

We implemented an ADS40 sensor model into the digital photogrammetric workstation KUVAMITT, guided by source-code samples from Leica. All analyses were done in epipolar images, where the distortions due to the camera movements are removed. In ADS40, the exterior orientation parameters are needed for each scanline. These were defined in a local XYZ system, which had a 3D offset and rotation with respect to the WGS84. We used accurate transformations to reach the coordinate

system of the trees. Each CCD line had the $xy(z)$ camera coordinates of the 12 000 pixels. The mapping from 3D to image was solved by iteration that limits a range of scanlines for a final sequential search of the pixel position. We used a nearest pixel interpolation.

2.6 Extraction of image features for the reference trees

We collected the image data for a reference tree by first estimating a crown envelope using LiDAR data. The crown was systematically sampled in 121 surface points, which were projected to the images. Parallel to this, each point was determined if it was visible to the camera or occluded by the tree itself or by an adjacent tree (Fig. 3). In addition, an illumination class was determined for each point using the LiDAR data in the vicinity. Accurate crown envelopes were a prerequisite. The model for crown radius was

$$r = a^2 + b \cdot h \cdot \left(\frac{5}{2} x \right)^c, \quad (1)$$

where r is the crown radius at the relative distance $x \in (0, 0.4)$ down from the treetop. The initial values of the unknowns were set using field measurements of tree dimensions and weighted least squares adjustment with additional observation equations for a and c (to constrain their values) was used for the solution. The mean RMSE of r was 0.35 m in 15627 trees. All envelopes were convex with $c \in (0.01, 0.93)$.

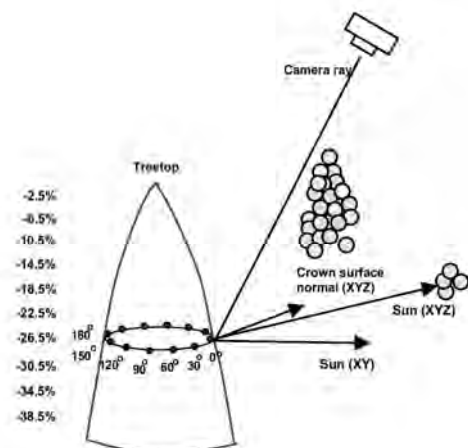


Figure 3. Determination of camera-visibility and illumination class for the 121 crown points. Each tree had 10 layers of points, and the 12 points in each had a 30° azimuth offset between points. The first point was always aligned in the direction of the solar azimuth. Two rays were cast – one towards the camera and another towards the Sun. LiDAR points were treated as 0.7-m-wide spheres (grey circles) and tested for intersection. The vector angles between the crown surface normal and the two rays defined the self-occlusion and self-shading. The example shows a camera-visible, neighbor-shaded point.

The acquisition of pixel data was repeated for the 15627 trees in 54 MS images representing different strips (15), radiometric corrections (2 or 3 per strip), and view configurations (1 or 2). Cloud screening was done in XY polygons of clouds and shadows. Crowns were sampled in 121 crown surface points (Fig. 3) that were at different relative heights symmetrically around

the crown envelope. We did not strive for complete pixel lists or image patches per tree, but samples of them.

A total of 158 features were derived for each tree, using the pixel data of the camera-visible crown points. Crown surface points belonged to an illumination class: Sun-lit (SL), self-shaded (SS), neighbour-shaded (NS), and neighbour-and-self-shaded (BS). Because of the viewing geometry and the peaked shape of the crowns, several points often mapped to the same pixel. Duplicates were filtered. The features for each tree and illumination class and the RED, GRN, BLU, NIR, and NDVI bands were: *min*, *max*, *mean*, *sdev*, and quartiles $q1$ – $q3$. The topmost and lowest SL pixels were stored as separate features and band ratios were also computed.

2.7 Variables describing the view-illumination geometry

To describe the view-illumination geometry we used the *phaseangle*, *azimdiff*, and *offNadir* angles. *Phaseangle*, $[0^\circ, 180^\circ]$ is the vector-angle of the camera and Sun vectors. *Azimdiff*, $[0^\circ, 180^\circ]$ is the azimuth difference of the camera and Sun vectors and it is 0° for perfectly front-lit trees and 180° for back-lit trees. *OffNadir* was the angle between the plumb line and the camera vector. Fig. 4 illustrates the sampling of the view-illumination geometry.

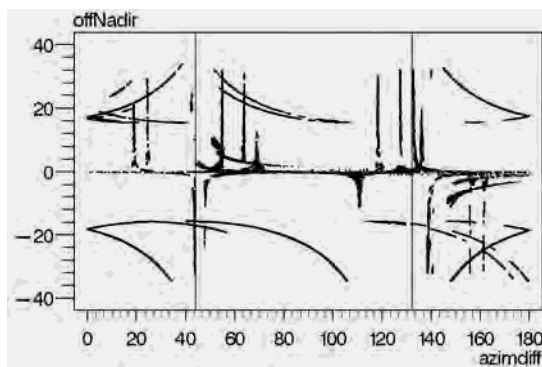


Figure 1. Distribution of $azimdiff \times offNadir$ observations ($N = 202136$) for all trees in all 19 strips/views. Division between front-, side-, and back-lit trees in *azimdiff* is shown by the vertical lines.

2.8 Statistical tools and classification methods

We used analyses of variance and covariance (ANOVA, ANCOVA). Classification trials were done with the quadratic discriminant analysis (QDA) with equal prior probabilities. Overall classification accuracy and the simple Kappa were the performance measures.

3. EXPERIMENTS

3.1 Evaluation of radiometric corrections and reflectance anisotropy in trees

Atmospheric effects, the changing solar elevation and the reflectance anisotropy of trees influence the pixel values in ASR images. Ideally, only the variation due to the reflectance anisotropy remains in the ATM images. In the FULL data, which combines a BRDF-correction with the ATM correction, the reflectances should be corrected also for a general anisotropy.

We first examined the ATM and FULL corrections for the coefficient of variation ($CV = sdev / mean$) of the intraspecies reflectance. The effects of the ATM and FULL corrections in CV were strongest in the BLU band, where the relative CVs ranged from -50% to $+59\%$ (compared to ASR data). In all

bands, the effects were strongest in strips that were flown perpendicular to Sun. The FULL correction did not completely correct for the anisotropy (Fig. 5) although it produced images that are well-suited for seamless mosaicking.

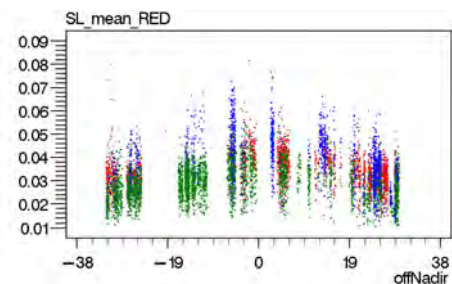


Figure 5. Scatterplot of averaged Sun-lit image data from the RED (strip 0833/N00A) band and the *offNadir* angle. FULL data. Strip 0833 was flown almost perpendicular to the Sun, where the BRDF effects are strong. Red = pine, green = spruce, blue = birch.

We also compared 1–4 km strips from different flying altitudes. The mean SL ATM reflectances per species varied up to 38% and the differences were explained by the changes in the view-illumination geometry between strips. In diffuse light, the relative differences were smaller. In well-defined targets, for the same strips, the differences were less than 10%. In two overlapping 1 km strips having a 22-minute temporal mismatch, the mean reflectances by tree species varied 2–15% depending on the band and species. The well-defined targets in these strips showed reflectance differences of below 2%. In an analysis that combined 15 strip \times view combinations, the well-defined targets showed standard deviations of less than 8% for the relative differences. When restricting to reflectance tarps only, the *sdevs* were less than 6%. The results show that for well-defined targets, the precision in the ATM data was high, while the differences observed in trees were mostly due to strong reflectance anisotropy and to the naturally higher variation.

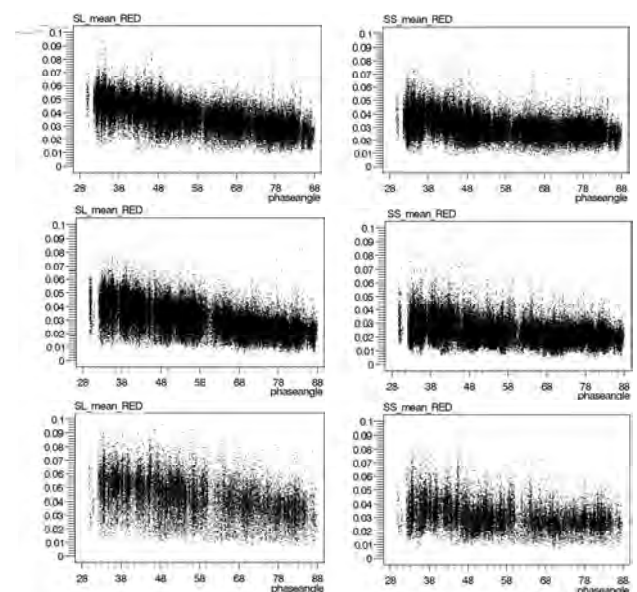


Figure 6. Distribution of RED SL (left) and SS (right) ATM reflectances (0–0.1) and the *phaseangle* (28° – 88°). All 19 strips/views. Pine (top, $N=80073$), spruce (middle, $N=93415$), and birch (bottom, $N=28648$).

For the analysis of anisotropy, we combined the ATM data in the 19 strip/views giving over 200 000 observations. Figure 6 shows the anisotropy in ATM data (RED band) as a function of the *phaseangle*. The high intraspecies variation (CVs 12–38% over all band and species) is also obvious from Figure 6 as well as the small intraspecies differences in the mean reflectance. In diffuse light, there was no trend in high values of *phaseangle* i.e. for the back-lit trees. The anisotropy was stronger in visible bands compared to NIR (with high reflectance). Also, pine and spruce seemed to differ from birch. We tested if strongly back-lit trees would show high maximal reflectances due to forward scattering (of foliage). Such phenomenon was not observed.

3.2 Inter- and intratree reflectance variation

We studied proximity effects i.e. the influence of the immediate neighborhood to the observed reflectance. The effects were considerable in the NIR band, where adjacent birch trees caused an effect up to +33%. In the visible bands the effects were within $\pm 10\%$ being stronger in the diffuse light conditions.

In ANCOVA, reflectance variation was explained by *phaseangle*, *azimdiff*, *phaseangle* \times *azimdiff*, the *strip/view* class (N = 19) variables, and age or siteindex (class). The models were fitted to the combined ATM data of all 19 strips/views. The results showed that 1–4% of the variation was contributed by the age of the trees with strongest effect in NIR and birch. The siteindex explained 1–3% of the NIR and RED band reflectances. When the stand was used as explanatory class variable, 1–19% of the reflectance variation could be contributed to the stand effect, with strongest effects in NIR in all species.

Strip/view	BAND	SL	SS	NS	BS
0825/ B16A, front-lit trees	BLU	1	0.92	0.87	0.84
	GRN	1	0.75	0.67	0.59
	RED	1	0.73	0.66	0.57
	NIR	1	0.70	0.62	0.51
0818/ B16A, back-lit trees	BLU	1	0.96	0.90	0.87
	GRN	1	0.89	0.71	0.63
	RED	1	0.92	0.72	0.64
	NIR	1	0.85	0.63	0.51

Table 1. Relative mean ATM reflectances in illumination classes (all species combined) in 3 km N-S oriented strips 0818 and 0825.

Offset to Sun	Species	BLU	GRN	RED	NIR
0°	pine	1	1	1	1
30°	“	0.99	0.98	0.97	0.97
60°	“	0.97	0.92	0.90	0.91
90°	“	0.94	0.84	0.81	0.83
0°	spruce	1	1	1	1
30°	“	0.98	0.95	0.95	0.96
60°	“	0.95	0.85	0.84	0.84
90°	“	0.91	0.75	0.73	0.73
0°	birch	1	1	1	1
30°	“	0.99	0.96	0.96	0.95
60°	“	0.95	0.87	0.87	0.85
90°	“	0.92	0.77	0.77	0.75

Table 2. Relative mean reflectances of crown points in the SL illumination class with varying solar azimuth offset. Strip 0825/B16A and ATM data with front-lit trees. Values are normalized to the 0° azimuth offset class

Intracrown reflectance variation was examined using the crown point data per tree. Table 1 shows the mean values of ATM reflectances in the for illumination classes for front- and back-lit trees. Table 2 shows the effect due to solar azimuth offset. The determination of the illumination classes succeeded based on data in Table 1, where the order of brightness was SL > SS > NS > BS. The relative difference of SL and SS was not preserved for front- and backlit trees. Table 2 shows how the brightest pixels are found in crown points that are towards the Sun and how the effect is smallest in BLU.

3.3 Feature selection and tree species classification trials

We confined to a suboptimal manual feature selection, which combined ANOVA and correlation analysis. Seven features for the classifications were: *SL_sdev_GRN*, *SL_q3_RED*, *SS_mean_BLU*, *SL_q3_NIR*, *SL_q3_NDVI*, *SL_sdev_NIR*, and *SL_mean_BLU*. The BLU band was a strong predictor, which calls into question the severity of the possible imprecision in the atmospheric correction of the BLU band (Section 3.1). Monoscopic nadir data was used with 3 and 4 km strips. The classification accuracies by strip were 72–80% ($\kappa = 0.56$ –0.67) with ASR (73–80%) and ATM (75–80%) producing higher accuracies than FULL (72–78%). Accuracy varied between strips and was lower in the E–W oriented strips (72–76%) compared to the N–S strips (75–80%). Leave-tree-out and leave-plot-out validation methods produced similar accuracies as well as teaching the QDA-model with randomly selected subsets of 3 \times 300 trees per species, which was 5–10% of the number of trees in the validation data set. Pine was classified most accurately (83–85%) in the N–S strips, with spruce at 73–76% and birch at 76–79%. In a trial, where 182982 observations in the 1–4 km ATM data were combined, the accuracy was only 62% in leave-one-out cross-validation. By restricting to three 3 km N00A views, accuracy was 72%. These results show how the anisotropy hampers classification if the view-illumination geometry is not restricted to the use of single N00A strips. When the N–S oriented strip 0825 was used for teaching and the E–W oriented strips 0843 and 0852 were used for validation, the accuracies were 54% and 68%, which demonstrates the findings of Section 3.1.

4. DISCUSSION

4.1 Confines

The presence of clouds may have affected the results. Also the timing, August 23, was quite late. The number of trees was very high. However, trees younger than 25 years were mostly missing as well as dominated trees, which remain unseen. The number of plots (121) overestimated the number of stands, because of the large size of regeneration areas in Hyytiälä.

4.2 Aim I - Sensor model implementation

We needed to implement the sensor model to do this research. However, this is a technical problem and many modern commercial digital photogrammetric workstations have the ADS40 sensor model implemented allowing standard photogrammetric procedures and workflows.

4.3 Aim II - Crown modelling and determination of illumination classes

We improved an existing method for crown modelling in LiDAR data by imposing constraints on the parameters, which enhanced the solvability of the non-linear regression. We manu-

ally positioned the treetops using photogrammetric techniques (instead of automatic tree detection) and used field measurements (instead of LiDAR measurements) to define the initial approximation of the crown envelope to be fitted in the LiDAR data. The RMSE of 0.35 m for radius suggested that the crown models were rather accurate. However, the XY position of the crown model certainly had small offsets due to measurement errors. Since real crowns are seldom rotationally symmetric, it is evident that the models were imprecise. Thus, when the crown model was sampled in surface points, some points mapped to a pixel belonging to a neighbouring tree or background. These should result in random noise. We cannot, however, exclude possible systematic errors. The ray-tracing based determination of shading and occlusion by neighbours, where LiDAR points were interpreted as opaque spheres, worked satisfactorily based on the analysis of the different illumination classes. Visual examination confirmed that the class was mostly correctly resolved. The division of canopy points between direct and diffuse light is an ill-posed task, since real crowns are semi-transparent, fractal objects.

4.4 Aim III: Evaluation of the ADS40 line sensor data for tree species classification

The ATM and FULL corrections worked well within the limits of the underlying models. The atmospheric correction was validated with well-defined targets that show only small BRDF effects. The results suggest that the precision of the ATM data was better than 10%, with NIR being the most precise and BLU the least precise. The analysis with the ATM data, where nadir views from different flying altitudes were compared, showed that the mean reflectances by species could vary -7% – $+38\%$, depending on the band. The results showed that trees are sensitive to changes in the view-illumination geometry, which resulted in effects larger than the reflectance differences between species. The sp. classification trials demonstrated that the ATM and FULL corrections did not improve the classification performance. One reason is that the standard atmospheric correction theory does not treat shadow pixels correctly. In ANCOVA, 62–79% of the total SL reflectance variation in the BLU band of the ATM data that combined all strips and views was explained by a model that had *azimdiff*, *phaseangle*, *azimdiff* \times *phaseangle*, and the *strip/view* class variables. In NIR, only 15–18% of the variation was explained by the same model, and the R^2 were higher in pine and spruce compared to birch. The results suggest that the anisotropy varies between species, and is strongest in the visible bands. A single BRDF-normalization for pine, spruce, and birch will likely fail. The BLU band features were strong predictors of the species. The proximity effects detected here differ from classical atmospheric scattering induced adjacency effects. To the best of our knowledge, this was the first study to show these effects, which affected the mean reflectance 1–17% in VIS bands and up to 33% in NIR. Effects by tree age and siteindex explained less than 5% of the reflectance variation with the strongest influence in NIR. Plot effect explained 1–19% of the reflectance variation and the effects were again strongest in NIR. The results of intracrown reflectance variation showed that the trends in the mean reflectances of crowns can be traced to intracrown variation, which could be used in improving the feature extraction. The 3 and 4 km nadir data showed best-case classification accuracies of 80%, which are higher than those simulated in Heikkinen et al. (2010). The fact that the reference trees were scattered across a large area and classified as a whole (vs. stand or image frame), resembling to a real forest inventory setup, is very important

practical aspect, and illustrates that ADS40 in general could be very cost-efficient for tree species recognition to complement LiDAR data.

4.5 Suggestions for future research

The results in intracrown variation suggest that a different sampling strategy or weighting of the crown pixels might improve the features. The anisotropy was similar in pine and spruce, suggesting that an anisotropy correction would normalize the reflectances. Otherwise, in noisy data with high intraclass variation and small interspecies differences, the enhanced species recognition algorithm should measure the anisotropy in multiple views and use it to predict the species. This could be possible in frame images having high overlaps. It will be interesting to compare the performance of the ADS40 with other cameras in sp. classification and to complement the image features with LiDAR data to evaluate the combined performance. Also, we did not combine the two CCD views in ADS40. Heikkinen et al. (2010) suggested increasing the number of bands to five and reducing their spectral width in ADS40.

5. REFERENCES

- Beisl, U., Telaar, J., Schönemark, M. V., 2008. Atmospheric correction, reflectance calibration and BRDF correction for ADS40 image data. IAPRS, Beijing, Vol. 37, part B7, pp. 7–12.
- Deering, D.W., Eck, T.F., Banerjee, B., 1999. Characterization of the reflectance anisotropy of three boreal forest canopies in spring-summer. *Rem Sens Env* 67 (2), pp. 205–229.
- Fraser, R. S., Ferrare, R. A., Kaufman, Y. J., Markham, B. L., Mattoo, S., 1992. Algorithm for atmospheric corrections of aircraft and satellite imagery. *Int J Rem Sens* 13 (3), pp. 541–557.
- Holmgren, J., Persson, Å., Söderman, U., 2008. Species identification of individual trees by combining high resolution LiDAR data with multi-spectral images. *Int J Rem Sens* 29 (5), pp. 1537–1552.
- Heikkinen, V., Tokola, T., Parkkinen, J., Korpela, I., Jääskeläinen, T., 2010. Simulated Multispectral Imagery for Tree Species Classification Using Support Vector Machines. *IEEE Transactions Geos Rem Sens* 48 (3), pp. 1355–1364.
- Korpela, I., 2004. Individual tree measurements by means of digital aerial photogrammetry. *Silva Fennica Monographs* 3, pp. 1–93.
- Larsen M., 2007. Single tree species classification with a hypothetical multi-spectral satellite. *Rem Sens Env* 110 (4), pp. 523–532.
- Li, X., Strahler, A. H., 1986. Geometric-optical bi-directional reflectance modeling of a coniferous forest canopy. *IEEE Transactions Geos Rem Sens* 24, pp. 281–293.
- Markelin, L., Honkavaara, E., Beisl, U., Korpela, I., 2010. Validation of the radiometric processing chain of the Leica airborne photogrammetric sensor. ISPRS Vienna 2010.
- Martonchik, J.V., Bruegge, C.J., Strahler, A.H., 2000. A review of reflectance nomenclature used in remote sensing. *Remote Sensing Review* 19, pp. 9–20.

HIGH RESOLUTION IMAGERY RETRIEVAL ON THE BASIS OF SKETCH-MODELLING

N. M. Kovalevskaya^a, K.A.Boenko^a

^a Institute for Water and Environmental Problems SB RAS, Barnaul, 656038, Russia - knm@iwep.asu.ru

KEY WORDS: Environment, Monitoring, Retrieval, Global-Environmental-Databases, Model, Content-based, High resolution

ABSTRACT:

Recent technological advances have made it possible to process and store large amounts of image data. The most impressive example is the accumulation of image data in scientific applications such as satellite imagery. However, in order to realize their full potential, tools for efficient extraction of information and for intelligent search in image data bases need to be developed. The paper describes a new approach to image data retrieval that allows queries to be composed of textured patterns. The textured pattern is converted into a feature representation of reduced dimensionality which can be used for searching similar-looking patterns in the database. This representation is obtained by the texture sketch model based on Gibbs random field approach for high resolution satellite imagery. Experimental results are presented, which illustrate that the proposed representation preserves the perceptual similarities, and provides an effective tool for content-based satellite image retrieval. As well visual and manual image-interpretations produce similar outlines of geographical units.

1. INTRODUCTION

Content-based image retrieval has been a topic for research in the last decades. A number of overviews on image database systems and image retrieval have been published, see e.g. (Veltkamp, 2001; Braveen, 2009). Despite of ongoing research and numerous studies, no effective features have as yet been generally accepted for image retrieval from currently available satellite image data base (SIDB), especially high resolution SIDB (HRSIDB). Quite a few investigations on satellite image retrieval systems are focused on either retrieval by keywords (Smith, 1996) or discerning of very specific features (Kelly, 1995; Wang, 2001). To query an image in accords to user-defined pattern, a pattern's attribute vector that typically relates to 3 descriptive characteristics (i.e. color, shape and texture) is calculated. The next step implies similarity pattern retrieval.

Different Geographical Units to be identified or Mapped (GUMs) differ by their contents in SIDB. Depending upon the specific aim of an interpretation, a GUM may be for example a vegetation patch, a part of the sea surface with a uniform wave pattern, a patch of homogeneous land-use and so on.

Color characteristics (histograms) don't allow for spatial delimitations; therefore, color histogram based image retrieval of (HR)SIDB-images often leads to erroneous query results. One can hardly obtain effective query results by the use of shape characteristics, since shapes of natural GUMs are extremely diverse and complicated. GUMs presented in SIDB by more or less homogeneous patterns in grey level scale, which are decisive for content-based image retrieval. Spatial homogeneity of GUMs in high resolution imagery is directly related to their textural features.

The presented research aims at

1. a formalised description of textural features, and
2. the development of a model presentation that describes homogeneity of textural patterns in terms of probabilistic self-similarity.

The results of content-based image retrieval using the proposed model, are also presented in this paper.

2. SKETCH TEXTURE MODEL

Precise definition of texture doesn't exist yet that is evidence of the term complexity. Texture (from Latin *textura* means "weaving" or "structure") relates to the specific structure of visual or tactile characteristics of individual objects (Gimel'farb, 1999). In a broad sense, texture defines the structure of an object with respect to the pattern along which its components are arranged. For human perception, texture is the specific, spatially repeated (micro- and macro-) structure: the spatial arrangement of major surface components.

For satellite imagery the texture is presented as spatial interactions of raster elements and their spatial arrangement. Visually, such spatial interactions are presented as repeated changes of grey levels in a proximity window. The Gibbs/Markov models of piecewise-constant regions of the Earth surface are an effective representation of textural objects (Kovalevskaya, 2002). In fact, these models are rather flexible; they allow to "seize" essential parts of visual information presented by piecewise-homogeneous images. The key parameters of the Gibbs model for obtaining metadata of visual pattern content are the following:

1. the size of the proximity window of neighbouring pairwise elements,
2. the structure of neighbouring elements representing major visual pattern content,
3. the significance of each element in the structure.

Let us suppose that natural textures in high resolution images possess a spatial self-similarity that can be expressed as the frequency of pairwise elements. Probabilistic self-similarity of a homogeneous texture pattern means that all probable combinations of signals in pairwise cliques are considered as having different likelihood of occurrence on the textural pattern (Gimel'farb, 1999). Then, one can state that *two patterns are*

similar in visual sense – so they represent GUMs of the same class – if they have the same distribution of signal pairs in cliques of the same type.

Let us assume, the more frequent a combination of signals for a pairwise cliques r , the greater distance is observed between the pattern's marginal frequencies and the marginal frequencies of an independent random field (IRF). Therefore, texture sketch corresponding to pattern $S=s$ can be defined as follows:

$$\text{Sketch } (S=s | w) = \{r^* \in R: \text{Dist}(H_{r^*}(d|s), MF(d)) \geq TRESH_{Sketch, r} \mathbf{R}\}, \quad (1)$$

where $R = ((m,n): m=0,\dots,M-1; n=0,\dots,N-1)$ is the finite 2-D lattice of the size $|R|=M*N$,
 $\text{Dist}(\cdot, \cdot)$ is the given type of distance between distributions,
 $H_{r^*}(d|s)$ – grey level difference histogram for clique r^* , $d \in D$,
 $MF(d) = (|Q| - \text{abs}(d)) / |Q|^2$ are marginal frequencies of IRF,
 $Q = \{0, 1, \dots, q_{\max}\}$ is a finite set of grey levels q in lattice sites (m, n) ,
 $D = \{-q_{\max}, \dots, 0, 1, \dots, q_{\max}\}$ – a set of grey level differences,
 w – the given proximity window,
 $TRESH_{Sketch}$ – the threshold for types of the sketch cliques.

The application of the model (1) also means the implicit use of perceptual data. It is evident that the more pronounced is the linearity, regularity, orientation, etc. of textural pattern, the greater will be the visual dissimilarity between the pattern and an IRF.

Experiments with several textures allow to propose the following steps to get texture sketch (Gimel'farb, 1999):

1. Compute grey level difference histograms for all cliques in the proximity window.
2. Compute the distances between the grey level difference histograms and marginal frequencies of IRF.
3. Find the clique family, which differs the least from the IRF (that is, corresponds to the least distance).
4. Compute the distances between the grey level difference histograms and the clique family found in 3.
5. Compute the average distance $AvDist$ and standard deviation STD of the distances in 4.
6. Compute the threshold $TRESH_{Sketch} = AvDist + STD$.
7. Choose the clique families whose distances exceed this threshold to represent the sketch.

Experiments to obtain texture sketch were carried out using two types of model patterns:

1. Dissimilarity patterns allowing instantaneous (not exceeding 200ms at a moment) separation from each other (Marr, 1982).
2. Similarity patterns allowing to make separation only after thorough study.

Table 1 represents sets of patterns according to the expert classification (Ma, 1996) and contains significant structures for diverse proximity; the importance of each element in the

structure is denominated by means of grey level, namely: the darker raster structure element, the higher its significance for visual content representation is. The outcomes of experiments are evidence of strong similarity in sketches of the same class patterns (class 1, Table 1) or even their full similarity (class 2, Table 1), if class patterns are similar in more than one visual criterion.

To the contrary, if class patterns are similar in one visual criterion, significant elements of patterns demonstrate difference in positions of window w (class 3, Table 1).

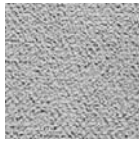
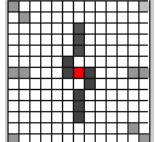
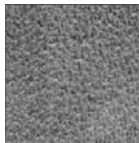
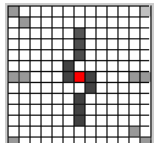
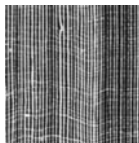
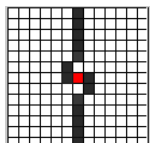
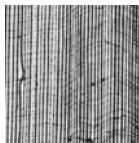
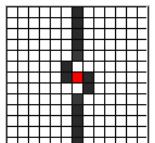
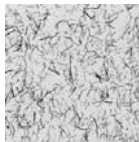
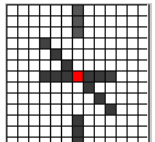
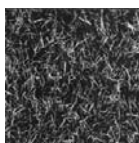
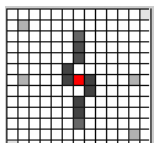
Class #, # in IDB-1	Sketches
 class 1, 57	
 class 1, D92	
 class 2, D106	
 class 2, D105	
 class 3, 107	
 class 3, D108	

Table 1. Classes of similar patterns and corresponding sketches for 13x13 proximity window

The size of a proximity window w depends on the textural pattern. The larger the window, the more accurate estimate of the texture sketch will be, but also the slow will be the search in SIDB. So the choice of the size of a proximity window

should be based upon a reasonable compromise between computational power and representativeness of the sketch.

In particular, for 220x110-patterns a 9x9-window gives already acceptable results. It appeared to be possible to increase the size of the window even to 13x13 (Table 2).

class #, # in IDB-1 (Table 1)	Sketches	
	9x9 window	13x13 window
class 2, D105		
class 3, D107		

Table 2. Sketches for proximity windows of different sizes.

Samples of pine forest	Satellite, resolution, band	Sketches
	Landsat 30 m 0,78-0,90	
	Ikonos 1 m 0,445-0,90	
	QuickBird 0,7 m 0,445-0,90	

Table 3. Pine forest samples and sketches for different resolutions.

It turns out that the property to seize visual information, if patterns are similar in more than one criterion, is sufficient for making comparison of natural objects:

1. Referred to the same class and received with different resolution (Table 3).
2. Referred to different classes and received with the same resolution (Table 4).

In addition, one significant thing was revealed, i.e. spatial position and quantitative composition of raster elements essential for visual representation of a homogeneous region remain the same even at a big change of visual detail (Table 3).

Samples	Sketches	Samples	Sketches
 manufactured forest		 deciduous forest	
 rare forest with sand		 glade with trees	
 resident sites		 dachas	

Table 4. Quickbird-samples and corresponding sketches.

3. CONCEPTUAL QUERY IN IMAGE DATA BASE

The sketch (1) of textural pattern is the characteristic of the pattern that allows us to discern different textures. The measure of visual dissimilarity can be used for the arrangement of all images in image data base (IDB) in order of increasing similarity with the query pattern as follows:

1. Enter the query spatial-homogenous pattern s .
2. Retrieve the pattern sketch in accord with the model (1).
3. Calculate measures of dissimilarity $Dist(s_b, s)$ between the query pattern and images $[s_t: t=1, 2, \dots]$ from IDB.
4. Choose image s_{t^*} with the least value of dissimilarity measure as the first retrieval result:

$$Dist(s_{t^*}, s) = \min_{s_t \in IDB} \{Dist(s_t, s)\}$$

Choose the subsequent retrieval results by ranking the values $Dist(s_b, s)$ in increasing order.

The experiments were carried out with two IDBs:

1. IDB-1 that contains the patterns of Brodatz textures (Brodatz, 1966). The pattern classification for 32 classes was taken as a basis for visual comparison of results of IDB-1 queries (Ma, 1996). The classification of various groups of experts can be different; therefore, the experiment was followed by certain changes in the set of classes as a result of the self-training of retrieval system.
2. IDB-2 that contains 64 patterns of high resolution image (Quickbird, 0.7m) and grouped together into 12 classes of GUMs as follows: bushes, resident sites,

forest, meadow, tilled sites, shrub bogs, abandoned mines, bushes with open forest, mire, river bank, floodplain, saline sites.

All experiments proposed that if the first result of retrieval referred to the same class of GUMs as the query pattern, the result was correct.

In experiments with IDB-1 the fixed number of images for the given patterns was retrieved. As for IDB-2, the retrieval was stopped as soon as all GUMs relating to the same class as the query pattern were received.

Table 5 gives the results of the first queries to IDB-1. Though IDB-1 represents a relatively complex variant for visual retrieval due to ambiguity of objects division into classes, the retrieval results turned out to be rather encouraging. About 90% of queries show the correct result as the first choice of retrieval system. The first two results are correct for more than 65% of queries, and more than 40% of queries showed the first, second and the third retrieval results to be correct.

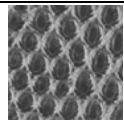
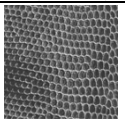
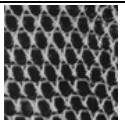
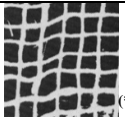
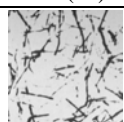

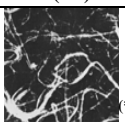
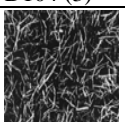
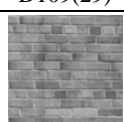
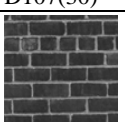
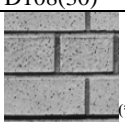
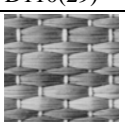
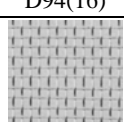
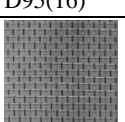
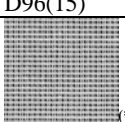
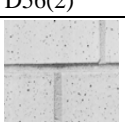
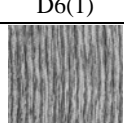
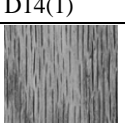
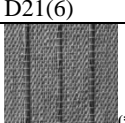
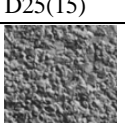
query pattern (class #)	1 st retrieved pattern (class #)	2 nd retrieved pattern (class #)	3 rd retrieved pattern (class #)
 D35(20)	 D3(20)	 D22(20)	 D104(3) (*)
 D109(29)	 D107(30) (*)	 D108(30) (*)	 D110(29)
 D94(16)	 D95(16)	 D96(15) (*)	 D56(2)
 D6(1)	 D14(1)	 D21(6) (*)	 D25(15)
 D76(14)	 D68(14)	 D85(23) (*)	 D4(18)

Table 5. Retrieved patterns for IDB-1.

The retrieval system described was found capable of user training. Though some retrieval results (marked by *) in Table 5) show the incorrect result in accordance with the original classification in (Ma, 1996), *in fact, they are visually similar to the query pattern* by one visual criteria or other. Thus, according to the original classification, the pattern D104(3) refers to the 3rd class, but the retrieval demonstrated the visual resemblance of this pattern to D35(20) from the 20th class. It means that both patterns can be integrated into one class by

certain visual criteria, which was not accounted in the original classification.

In a like manner, the system found new features of visual resemblance for pairs D109 and D107, D109 and D108, D94 and D96, D6 and D21, D76 and D85 that were not included in original classification, but these features are correlated with perception.

The experiments with the patterns taken from high-resolution images and represented in Table 6 turned out to be more optimistic when compared to the results with model patterns from IDB-1. In 50% of cases the system “chose” **all possible** patterns of the corresponding class, namely, bushes, bushes with light forest, resident sites, tilled sites, forest, and meadows as the first retrieval results.

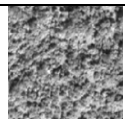
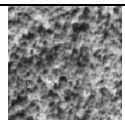
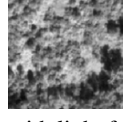
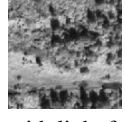
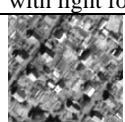

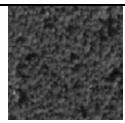
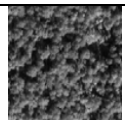

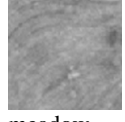
query pattern	1 st retrieved pattern	the next retrieved pattern
 bushes	 bushes	2 nd – 7 th bushes
 bushes with light forest	 bushes with light forest	only 2 patterns in IDB-2
 dachas	 dachas	2 nd – 9 th dachas
 forest	 forest	2 nd – 5 th forest
 meadow	 meadow	2 nd – 6 th meadow

Table 6. Retrieved patterns for IDB-2

4. OUTLINING PIECEWISE-HOMOGENEOUS REGIONS

Experiments were carried out with images received in panchromatic mode from Quickbird (0.7m) and Ikonos (1m) satellites.

The results of the outlining of homogeneous regions according to model (1) as the first step of conceptual retrieval in IDB of high resolution are given in Figure 1, Figure 2. The outlining algorithm was realized by computational comparison of sketches of regions around neighbouring pixels.

5. CONCLUSION

The amount of imagery data increases rapidly, mainly due to the launching of new generation of high resolution satellites (WorldView-1, TerraSAR-X, WorldView-2).

Multiple terabytes of HRSIDB are being collected by many nations across the globe. This raises the question how to retrieve, manage and make best use of the HRSIDB information.

Content-based analysis of all high resolution imagery is a seriously limited by time constraints, and a solution for the content-based image retrieval problem is urgently needed. Also, a new framework is lacking to support content-based search and different levels of analysis and generalization.

Our research proposes a model for homogeneous pattern sketch. The model allows to discern visually meaningful content of a textural pattern. It helps to overcome distinctions between the classes of GUMs in terms of their visual representation.

The experiments show the model parameters' flexibility and the capacity of training and self-training.

Most importantly, this model can be used for automated generation of interpretation results and metadata, and it offers sufficient computational efficiency to support the formalization of ecological expertise and global-environmental-databases.



(a)

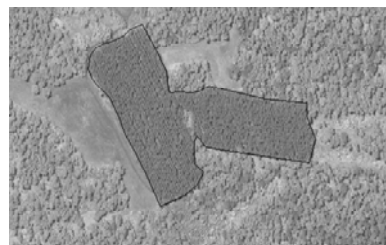


(b)

Figure 1. Outlining homogeneous region of Quickbird-image (0,7m): (a) – according to model (1), (b) - manual..



(a)



(b)

Figure 2. Outlining results of homogeneous region of Ikonos-image (1m): (a) – according to model (1), (b) - manual.

References:

- Braveen, M., 2009. Evaluation of Content Based Image Retrieval Systems Based on Color Feature. *International Journal of Recent Trends in Engineering (IJRTE)*, 1(2), pp.57-62.
- Brodatz, P., 1966. *Texture: a Photographic Album for Artists and Designers*. NY: Dover.
- Gimel'farb, G., 1999. *Image Textures and Gibbs Random Fields*. Kluwer Academic Publishers, 250 p.
- Kelly, P.M., 1995. Query by image example: the CANDID approach. In: *Storage and Retrieval for Image and Video Databases III*, SPIE-2420, Los Alamos National Laboratory Technical Report LA-UR-95-374 T.M., pp 238-248.
- Kovalevskaya, N., 2002. *From Laboratory Spectroscopy to Remotely Sensed Spectra of Terrestrial Ecosystems*. Kluwer Academic Publishers, pp.121-147.
- Ma, W., 1996. Texture Features and Learning Similarity. *Proc. IEEE International Conference on Computer Vision and Pattern Recognition*. San Francisco, 1996. pp. 425-430.
- Manjunath, B.S., 1996. Texture features for browsing and retrieval of image data. *IEEE Transactions on Pattern Analysis and Machine Intelligence*, 18(8), pp. 837-842.
- Marr, D., 1982. *Vision: A Computational Investigation into the Human Representation and Processing of Visual Information*. W.H. Freeman and Company, NY.
- Smith, D., 1996. A Digital library for geographically referenced materials. *IEEE Computer*, pp. 54-60.
- Veltkamp, R.C., 2001. Features in Content-based Image Retrieval Systems: a Survey, State-of-the-Art in Content-Based

Image and Video Retrieval [Dagstuhl Seminar, 5-10 December 1999], pp.97-124.

Wang, J.Z., 2001. SIMPLicity: Semantics-Sensitive Integrated Matching for Picture Libraries. *IEEE Transactions on Pattern Analysis and Machine Intelligence*, 23(9), pp.947-963.

GEOLAND2 - TOWARDS AN OPERATIONAL GMES LAND MONITORING CORE SERVICE; FIRST RESULTS OF THE BIOGEOPHYSICAL PARAMETER CORE MAPPING SERVICE

Roselyne Lacaze^a, Gianpaolo Balsamo^b, Frédéric Baret^c, Andrew Bradley^d, Jean-Christophe Calvet^e, Fernando Camacho^f, Raphaël D'Andrimont^g, Sandra C. Freitas^h, Hassan Makhmaraⁱ, Vahid Naeimi^j, Philippe Pacholczyk^k, Hervé Poilve^l, Bruno Smets^m, Kevin Tansey^d, Isabel F. Trigo^h, Wolfgang Wagner^j, Marie Weiss^c

^a HYGEOS, Cesbio Bpi 2108,18 avenue E. Belin, 31401 Toulouse Cedex 9, France - rl@hygeos.com

^b ECMWF, Shinfield Park, Reading, Berks, United Kingdom – balsamo@ecmwf.int

^c INRA, EMMAH UMR1114, site Agroparc, 84914 Avignon, France – (baret, weiss)@avignon.inra.fr

^d University of Leicester, LE1 7RH, Leicester, United Kingdom – (kevin.tansey, avb4)@le.ac.uk

^e CNRM/Météo-France, 42 avenue G. Coriolis, 31057 Toulouse Cedex, France – calvet@meteo.fr

^f EOLAB, G.V. Marques del Turia, 20-9, 46 005 Valencia, Spain – camacho@eolab.es

^g Université Catholique de Louvain, 2 Croix du sud, B1348 Louvain-la-Neuve, Belgium – dandrimont@uclouvain.be

^h IM Portugal, Rua Cao Aeroporto de Lisboa, 1749-077 Lisboa, Portugal – (sandra.coelho, isabel.trigo)@meteo.pt

ⁱ CNES, 18 av. E. Belin, 31 401 Toulouse Cedex, France- (hassan.makhmara, philippe.pacholczyk)@cnes.fr

^j TU Wien, Gusshausstrass 27-29/122, 1040 Vienna, Austria – (vn, ww)@ipf.tuwien.ac.at

^l Infoterra France, 15 avenue de l'Europe, 31 522 Ramonville Ste-Agne, France – herve.poilve@infoterra.fr

^m VITO, Boeretang 200, 2400 Mol, Belgium – Bruno.smets@vito.be

KEY WORDS: Environment, Monitoring, Land, Parameters, Real-time, Services, Production, Global

ABSTRACT:

The European GMES initiative provides a political framework for future implementations of Services Centres related to environmental applications. The FP7/geoland2 project is the last brick towards the implementation of fully mature GMES Land Services, consisting of Core Mapping Services (CMS) and Core Information Services (CIS). Its goal is to build, validate and demonstrate operational processing lines and products on a user-driven basis. The CMS produce “basic” geo-information on the land state covering a wide variety of thematic content, spatial scales from local to global, and update frequency from sub-daily to several years. Besides being a valuable information source by their own, the “basic” products are input for the Core Information Services focusing on a broad variety of thematic fields, like water quality, forest management, spatial planning, agri-environmental issues, carbon cycle analysis, supporting the European environmental policies and international treaties on climate change, food security, and sustainable development. The Bio-geophysical Parameter (BioPar) CMS aims at setting-up operational infrastructures for providing regional, continental, and global variables describing the vegetation state, the radiation budget at the surface, and the water cycle, both in near real time and off-line mode. The concept, the objectives, and the structure of geoland2, and of the BioPar CMS, in the European GMES context are introduced. The research, development, production, and validation activities of the BioPar CMS are presented with a special focus on the first biophysical products available to the institutional users, and to the scientific community.

1. INTRODUCTION

With the ongoing climate change, the pressure on nature, biodiversity and our own living conditions increases steadily. To mitigate these trends by effective adaptation strategies and counter measures a frequent and area-wide monitoring of the environment is crucial to provide decision makers with accurate, up-to-date and reliable information on the changing conditions of our natural resources.

Within the GMES initiative (Global Monitoring of Environment and Security), led by the European Union (EU) and the European Space Agency (ESA), the Land Services provide cross-border harmonized geo-information at global to local scales in a time- and cost-effective manner. Building upon their results of a series of projects funded by the EU (geoland, Boss4Gmes, Cyclopes, VGT4Africa) and the ESA (GSE Land, GSE Forest Monitoring, DUE Globcarbon, DUE Globcover), geoland2 aims to organise a qualified production network, to build, validate and demonstrate operational processing lines and

to set-up a user driven product quality assurance process, to guarantee that the products meet the actual user requirements.

2. GEOLAND2

Geoland2 is a project of the 7th Framework Program which intends to constitute a major step forward in the implementation of the GMES Land Monitoring Core Service (LMCS). It addresses the three components (local, continental, global) of the LMCS.

The goal of geoland2 is:

- to prepare, validate and demonstrate pre-operational service chains and products that will underpin the LMCS
- to propose and demonstrate a concrete functional organisation of the LMCS

The architecture of geoland2 is made up of two layers (Figure 1): the Core Mapping Services (CMS) provide land cover, land use and land cover change, as well as a range of biogeophysical variables as an input to more elaborated products while the Core Information Services (CIS) offer specific information for European Environmental Policies and international treaties on climate change, food security and the sustainable development of Africa. The CIS are in direct contact with institutional end-users in charge of European policies, and Member State policies which have a generic pan-European character. They serve to estimate the added value of the CMS in comparison to existing approaches and to carry out a utility assessment of selected end-to-end service demonstrations.

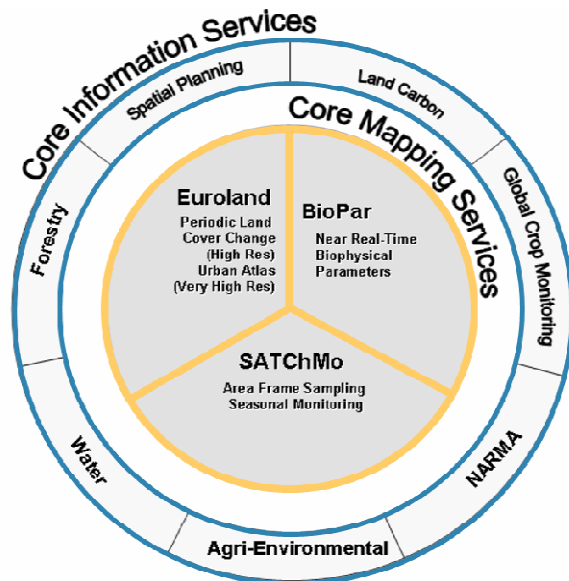


Figure 1. The geoland2 structure

The 3 Core Mapping Service tasks (Table 1) are:

- Land Cover & Land Use (Euroland): at local scale, Euroland produces VHR Urban Atlas inventory and change according to the specifications approved by DG REGIO in November 2007, on several tens of European cities. At continental scale, it produces over Europe and demonstration sites HR Land Cover inventory and change.
- Biogeophysical Parameters (BioPar): it produces in near real time (NRT) and off-line mode a series of biogeophysical variables describing the continental vegetation state, the radiation budget at the surface, and the water cycle. These products are derived mostly with Medium Resolution (MR) and Low Resolution (LR) data, at a global and continental scale, with a time frequency update from 3-hourly to 30 days.
- Seasonal & Annual Change Monitoring (Satchmo): it operates at continental scale over Europe and sub-Saharan Africa. It delivers: (i) a VHR/HR Area Frame Sampling over permanent samples representative for all European and African environmental/ecological conditions for annual statistics of land cover & land cover change; (ii) a complete MR continental coverage of seasonal and annual vegetation parameters to produce land cover change and agricultural land use. The time frequency of the product update is on the order of 3 -12 months.

	Services	Scale	Portfolio Elements / Description	Area covered in geoland2
Core Mapping Services - Baseline	LMCS Infrastructure development and demonstration of production capacity			
	LC /LCC (Euroland)	Local	VHR Urban Atlas Inventory VHR Urban Atlas Change	22 classes, 0.25 ha according to DG Regio definition 8 urban agglomerations 46 urban agglomerations
		Continental	HR Land Cover Inventory HR Land Cover Change	5 HR layers (quantitative layers), pixel-based and validated to 1 ha MMU Europe + demonstration sites
	Seasonal / Annual Land Cover Changes (Satchmo)	Continental	VHR/HR Area Frame Sampling	Permanent Samples representative for all European and African environmental / ecological conditions for annual statistics and calibration & validation of Euroland and BioPar Europe (VHR) & Sub-Saharan Africa (HR) – continental coverage by local representative samples
		MR Seasonal Land Cover Dynamics	Complete continental coverage with medium resolution seasonal and annual vegetation parameters to support Euroland and agricultural monitoring Europe – sub-Saharan Africa	
	Biophysical Parameters (BioPar)	Global	HR / MR / LR Near Real Time and off-line monitoring of biophysical variables Description of the continental vegetation, the radiation budget at the surface, and the water cycle Europe – Africa - Global	

Table 1. The CMS portfolio

	Services	Scale	Portfolio Elements / Description	Area covered in geoland2
Core Information Services – Service Evolution	Verification and Validation of LMCS Core Mapping Services			
	Spatial Planning	Continental / Europe	Land take trends & Indicators, based on Euroland data, supporting spatial planning from regional to European scale	Europe + Demonstration sites
	Agri-Environment	Continental / Europe	AgriEnv indicators based on Euroland and Satchmo for assessing the pressure and impact of agricultural management on the environment	Demonstration sites
	Water	Continental / Europe	Assessing the status of water resources based on Euroland and BioPar by means of baseline & scenario modelling for efficient cross-border water management in support of the WFD	Europe + Demonstration sites
	Forest	Continental / Europe	Forest (environmental) indicators based on Euroland in support of the reporting for MCPE, SEBI2010, UNCBD	Demonstration sites
	Land Carbon	Global	Terrestrial carbon fluxes and the associated soil moisture, vegetation biomass and carbon storage	Globe
	Natural Resources Monitoring	Africa	Contribution to building up the African environmental seasonal / annual change monitoring (“MONDE”) component of the ACP observatory	Africa
	Global Crop Monitoring	Global	Objective, real-time crop assessment and yield forecasts in support of EC policies in field Agriculture and Food Security	Europe + Globe

Table 2. The CIS portfolio

The 7 Core Information Services are being set-up with the following missions (Table 2):

- Spatial Planning: describe, explain and forecast urban land use change in Europe.
- Water: integrate EO derived LC/LU data in water quality models that can contribute to water management in Europe in flexible, sustainable and cost-efficient way.
- Forest: address specific user requirements from the European Environment Agency (EEA), DG JRC, and DG AGRI for improved forest class and biodiversity indicator information required for the LMCS and policy reporting requirements at a Pan-European level.
- Land Carbon: understand and assess the impact of weather and climate variability on terrestrial biospheric carbon fluxes, in the context of international conventions.

- Natural Resource Monitoring in Africa (NARMA): develop an environmental monitoring capacity over African countries for the needs of the EC services and for regional and continental EC partners in African countries.
- Global Crop Monitoring (GCM): provide objective, real-time crop assessment and yield forecasts in support to EC policies in the field “agriculture” (Common Agriculture Policy) and Food Security.

A cross-cutting Spatial Data Infrastructure (SDI) has been set-up with the aim to develop an operational service for the discovery, viewing, access, delivery and support of all products generated in the geoland2 project.

Altogether the geoland2 consortium, led by Astrium GmbH (Germany) and co-led by CNES (France), gathers 50 European partners from 21 European countries, and mixes three categories of private and public organisations: users, service providers and researchers.

3. THE BIOGEOPHYSICAL PARAMETER CORE MAPPING SERVICE (BIOPAR)

3.1 Introduction

The *Biogeophysical Parameter Core Service*, named in short BioPar, is a joint venture of 13 partners: HYGEOS, CNES, Infoterra France, INRA, and Météo-France (France), Université Catholique de Louvain (UCL), and VITO (Belgium), Institute of Meteorology (Portugal), Vienna University of Technology (Austria), EOLAB (Spain), University of Leicester, and ECMWF (United Kingdom), and Igik (Poland).

BioPar aims at setting-up validated operational infrastructure able to provide bio-geophysical variables describing the vegetation state, the radiation budget at the surface, and the water cycle at any scale of interest (regional, continental, and global), both in near real time and off-line mode, and that meets the users’ needs.

3.2 Concept

The BioPar concept relies on research and development activities, shared in 3 topics (vegetation, radiation, water), and on demonstration operations, shared in NRT and off-line processing (Figure 2). In particular, the R&D activities focus on parameters as LAI, FAPAR, albedo, burnt areas or soil moisture, which have been identified by the WMO/GCOS in the context of UNFCCC as Essential Climate Variables (ECV). The research teams define the retrieval algorithms based upon existing and validated methodologies, improve them to match as well as possible the user requirements, and initiate innovative actions to adapt them to the technical specificities of the next generation of sensors in order to ensure the continuity of the service. Effort will be put on the compatibility between historic and current products so that long-time series are available after the reprocessing of available EO archives. Independent teams perform the product validation, following a procedure established in close collaboration with the users and international bodies, relying on comparison with ground measurements collected over site networks, on inter-comparison with existing similar satellite products, and on data assimilation techniques, with the aim to guaranty the scientific relevancy of

the BioPar products. The development teams implement the algorithms in processing lines, and generate test data sets for user evaluation. The pre-operation centers perform the pre-operational production at regional, European and global scales, in NRT and in offline mode. Finally, the resulting biogeophysical parameters are disseminated by the Spatial Data Infrastructure cross-cutting issue, in a format in accordance with the INSPIRE directive.

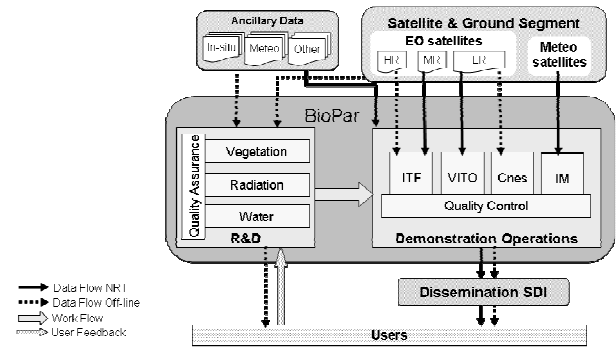


Figure 2. Main building blocks and generic data flow for BioPar processing lines

The BioPar CMS is a strongly user-driven service. The CMS portfolio has been designed from a careful analysis of the needs of CIS and other CMS, considered as good proxys of a large community of users including institutional users, future downstream services and the international science community. The study logic will be such that the products, their timeliness, and the R&D actions have been defined taking into account the users’ needs; the pre-operations, in NRT and in off-line mode, will start only with a user “green light”, given after they have successfully integrated test products into their current practices and working environment.

4. THE BIOPAR PRODUCTS

4.1 Service Portfolio

Product	NRT / Off-line	Spatial Resolution	Spatial coverage	Temporal Resolution	Sensor (Back-up)
Continental Vegetation					
LAI, FCOVER, FAPAR, DMP, NDVI, Phenology	NRT	1 km	Global	10-days	VTG (MODIS)
Times series of vegetation products	Off-line	4 km	Global	10-days	AVHRR + VGT
Burnt areas + seasonality	NRT	1 km	global	Daily	VGT
MERIS FR biophysical variables	NRT	300 m	Europe	10-days	MERIS
HR biophysical products	Off-line	10 m	Pilot Areas	4 times/year	SPOT
Energy Budget					
Downwelling Shortwave Surface Flux	NRT	~5 km	Global	3 hours	ΣGEO + AVHRR
Downwelling Longwave Surface Flux	NRT	~5 km	Global	3 hours, daily	ΣGEO + AVHRR
Land Surface Temperature	NRT	~5 km	Global	10-days	VTG
Surface Albedo	NRT	1 km	Global	10-days	ΣGEO + AVHRR
Surface Albedo	NRT	~5 km	Global	10-days	ΣGEO + AVHRR
Water cycle					
Water bodies + seasonality	NRT	1km, 250m	Africa	10-days	VTG, MODIS
Soil Moisture + Freeze/Thaw	NRT	0.1°	Global	Daily	ASCAT
Time series of soil moisture products	Off-line	25 km	Global	Daily	ERS-1&2 Scatt

Table 3. BioPar CMS Portfolio

The BioPar CMS portfolio includes vegetation (Leaf Area Index (LAI), Fraction of Absorbed PAR, Fraction of green cover, NDVI, Dry Matter Productivity, Phenology), burnt areas, downwelling shortwave and longwave radiation fluxes, land

surface temperature, surface albedo, burnt areas, soil moisture, products, provided at various spatial resolution depending on the sensor data used as input (Table 3).

Most of the products will be delivered in NRT in the sense of few days (less than one week), as requested by the final users who need to know the surface conditions within a few days of delay in order to react appropriately in case of anomaly, and to anticipate and manage the potential resulting problems. Detecting anomalies by comparing the current observation with a reference requires having consistent long time series. BioPar will provide such time series for some Essential Climate Variables (LAI, FAPAR, soil moisture) taking advantage of existing EO data archive, and developing sensor-independent methodologies.

4.2 LAI, FCover, FAPAR, NDVI derived from SPOT/VEGETATION sensor data

The leaf area index (LAI) is defined as half the total foliage area per unit of ground surface. The FCover is the fraction of ground unit covered by green vegetation. The FAPAR is defined as the fraction of photosynthetically active radiation absorbed by green vegetation for photosynthesis activity. The instantaneous FAPAR value at 10:00 solar time is used as a very good approximation to the daily integrated value under clear sky conditions. The Normalized Difference Vegetation Index (NDVI) corresponding to the SPOT-5/VEGETATION-2 sensor characteristics for its Red (B2) and NIR (B3) bands, is also provided.

The algorithm is based on already existing LAI, FAPAR, and FCover products to capitalize on the efforts accomplished and get a larger consensus from the user community. Following the published literature on products validation (Weiss, et al. 2007; Garrigues, et al. 2008), the best performing products were selected and combined to take advantage of their specific performances while limiting the situations where products show deficiencies. The selected products are re-projected onto the VEGETATION plate-carrée 1/112° grid, smoothed through time and interpolated at the 10 days frequency. Then the products are combined, and eventually scaled, to provide the fused product that is expected to give globally the ‘best’ performances. The fused products are generated for few years over the BELMANIP2 set of sites that is supposed to represent the possible range of surface types and conditions over the Earth (Baret, et al. 2006). Neural networks are then calibrated over this set of sites to relate the fused products to the corresponding atmospherically-corrected and directionally-normalized top of canopy SPOT/VEGETATION reflectances (Baret, et al. 2007).

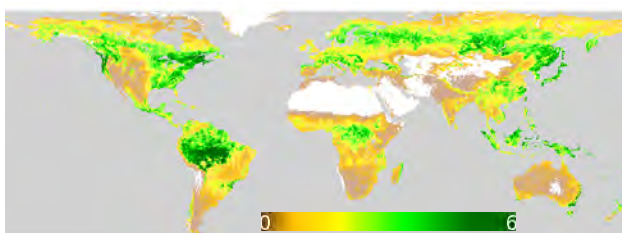


Figure 3: LAI derived from SPOT/VEGETATION, July 2002

Such methodology has been defined by INRA, and the processing line has been adapted by CNES, based upon an existing chain developed previously by Medias-France in the

framework of the FP5/CYCLOPES project. CNES has also generated two years of global, 10-daily products (example on Figure 3). Before the end of the year, the processing line will run in NRT at VITO. These vegetation products are being validated by EOLAB according to the protocol defined by the Land Product Validation (LPV) group of CEOS (Morissette et al., 2006).

The methodology will be adapted to the historical AVHRR surface reflectances made available by the LTDR project. The archive from 1981 will be processed to get a long time series (about 30 years) of vegetation variables fully consistent with the SPOT/VEGETATION products.

4.3 The set of biophysical variables derived from the FR MERIS sensor data.

The MERIS Full Resolution (FR) biophysical products, and the High Resolution (HR) biophysical products, contain a set of variables including estimates of the green, brown & soil cover fractions, the LAI, the FAPAR, the chlorophyll content, a canopy shadow factor, and the water & snow cover fractions.

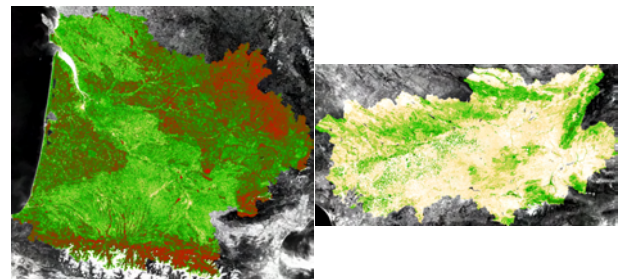


Figure 4. FAPAR over the Adour-Garonne river basin for June 2008 (left), and the Guadalquivir river basin for June 2006 (right) derived from MERIS FR data. The values vary from 0 (white) to 1 (red).

The baseline vegetation model developed for processing the MERIS data uses the SAIL/PROSPECT model as core component (Verhoef, 1984; Jacquemoud et Baret, 1990). This model was upgraded and completed in order to include the contribution of brown vegetation, the modelling of “rough” canopies, the computation of vegetation cover fractions in reference directional conditions, and the computation of FAPAR from the SAIL model. Then, to restore the heterogeneous nature of the MERIS pixels, a further modelling step is applied consisting in having a composite canopy model made of two components: 1) a main canopy component made of predominantly green vegetation, that may have all range of conditions from crops to forest/shrub canopies; 2) a second canopy component made of low brown vegetation, primarily designed to model either senescent crops/grasslands or bare soil conditions. Another important component of the developed model is the soil modelling, the soil reflectance being an input of the SAIL model. In this approach, the variation of soil brightness in relation with soil roughness and humidity is handled by performing an initial learning of the soil mean spectral signature in the MERIS bands at a regional level. Then, this signature is exploited through a physical model of soil variability, accounting for the soil shading and surface humidity effects. This scene model is then coupled with a model of the atmospheric transmission from Earth surface level to the sensor (Verhoef and Bach, 2003). The detection of water and snow covers is done through additional modelling of the

corresponding surfaces which are combined, as linear mixture, with the standard land model.

Infoterra France has elaborated the methodology above, developed the processing line, and ran it in off-line mode. Today, the existing MERIS FR (300m resolution) products covers some river basin across Europe (Rhine, Seine-Normandie, Guadalquivir, Adour-Garonne, Nemunas, Moselle-Sarre, Motala-Ström, Svetojci, Strymonas-Struma) for years of major interest for the final users (Figure 4). The production in NRT covering the whole Europe should start in the next weeks. These products are being validated by EOLAB, jointly with the products derived from SPOT/VEGETATION data (§4.2).

4.4 Soil Water Index (SWI) derived from ASCAT/Metop sensor data

The Soil Water Index is defined as the soil moisture content (in percent) in the soil profile. The retrieval algorithm uses an infiltration model describing the relation between Surface Soil Moisture (SSM) and profile soil moisture as a function of time. The algorithm is based on a two-layer water balance model (Wagner et al., 1999) to estimate profile soil moisture from SSM retrieved from scatterometer data. The remotely sensed topsoil represents the first layer and the second layer extends downwards from the bottom of the surface layer. In this model, the water content of the reservoir, whose depth is related to a characteristic time length (T), is described in terms of an index, which is controlled only by the past soil moisture conditions in the surface layer. A computational adaptation of the original SWI algorithm has been made based on a recursive formulation proposed by Albergel (2008). In this method, a gain factor is introduced that relates the past SWI measurements to the current measurements. The SWI processing algorithm uses ASCAT-25km SSM product as input to generate daily global SWI images, calculated for five different T values (1, 5, 10, 15, 20, 40, 60, 100) together with the respective quality flags.

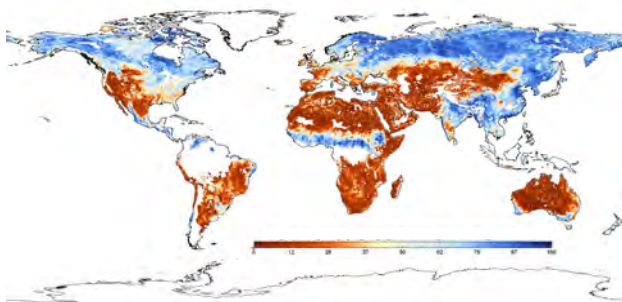


Figure 5. Global SWI derived from ASCAT/Metop data (25km resolution) for T=10 on 20th July 2007.

The retrieval algorithm is defined by Vienna University of Technology, the processing line is developed by CNES which has also generated the SWI products over the period from 1st June 2007 to the present (Figure 5). In few weeks, the processing line will run in near real time at the Institute of Meteorology of Portugal. The SWI products are being validated by Météo-France and ECMWF using in-situ observations, and operational, analyzed products from models running at global and regional scale.

A second version of the product is planned in the project life, including a more accurate detection of the freeze and thaw conditions of the surface. Then, the ERS/Scat data archive will

be re-processed in order to get a long time series of SWI fully consistent with the current ASCAT products.

4.5 The Surface Albedo derived from the SPOT/VEGETATION sensor data

The albedo is the fraction of the incoming solar radiation reflected by the land surface, integrated over the whole viewing directions. The BioPar albedo products include the directional albedo calculated for the local solar noon, and the hemispheric albedo, integrated over the whole illumination directions for 3 broad bands: visible [0.4, 0.7 μ m], near-infrared [0.7, 4 μ m], and the whole solar spectrum [0.3, 4 μ m]. The coefficients resulting from the inversion of a 3-kernels linear bidirectional reflectance model on the atmospherically-corrected SPOT/VEGETATION reflectances (Baret, et al. 2007) acquired during a period of 30 days are then combined with the pre-computed values of the directional kernels integrated over angular domains to estimate albedos. Finally, the broadband albedos are derived by linear relationships of spectral quantities.

This algorithm, and the processing line, have been previously set-up in the framework of the FP5/CYCLOPES project, by CNRM, and Medias-France, respectively. CNES has adapted the existing chain to the geoland2/BioPar specifications, and generated two years of global, 10-days products. Before the end of the year, the processing line will run in NRT at VITO. These SPOT/VEGETATION albedo products are being validated by EOLAB according to the protocol defined by the Land Product Validation (LPV) group of CEOS. An inter-comparison with the other BioPar albedo product (§4.6), derived by merging geostationary and polar sensors data, will be performed.

4.6 Other BioPar products

The radiation variables of the BioPar portfolio (Downwelling Shortwave Surface Flux (DSSF), Downwelling Longwave Surface Flux (DSLFL), Land Surface Temperature (LST), and albedo) will be generated by the fusion of geostationary and polar sensor data. The DSSF represents the short-wave fraction of the solar irradiance (0.3-4 μ m) reaching the soil background. The DSLFL is defined as the irradiance reaching the surface in the thermal infrared part of the spectrum (4-100 μ m). The LST is the radiative skin temperature of land surface. The albedo variables are the same as those retrieved using SPOT/VEGETATION data (§4.5). The Institute of Meteorology of Portugal is in charge of the algorithm definition, the processing lines development, and the production in near real time of the 4 products. These radiation variables correspond to an extension of those currently produced on an operational basis by the Satellite Application Facility on Land Surface Analysis (Trigo et al., 2010). While the latter are restricted to EUMETSAT sensors, Geoland-2 products make use of non-European geostationary satellites to increase area coverage. The demonstration DSLFL, and LST products shall be ready in the coming weeks, and the demonstration DSSF and albedo products shall be available by the end of the year.

The small water bodies product results from the fusion of two existing algorithms: the first one (Gond et al., 2004) was developed in the framework of VGT4AFRICA by the Joint Research Centre and is suited to arid and semi arid condition; the second one was developed for GlobalWatch project and was further developed in the context of Desert Locust prevention FAO product (Pekel, 2009). Both methods rely on different thresholds for the NDVI, the Normalized Difference Water

Index (NDWI), the Hue (from RGB to HSV transformation) and the reflectance in the middle infra-red of SPOT/VEGETATION data. The product includes also information about the seasonality, i.e. the date of filling and the date of drying. The Université Catholique de Louvain (UCL) is in charge of the methodology, whereas the processing line is developed and will run in NRT at VITO. The SPOT/VEGETATION water bodies product should be available before the end of the year. In a second step, the detection algorithm is being adapted to MODIS data (250m resolution) to identify smaller ponds.

The global burnt area product derived from the daily SPOT/VEGETATION data is still in development at the University of Leicester. Seasonality metrics (start, end and timing of maximum burning) are being added to the improved L3JRC algorithm (Tansey et al., 2008). At final, the processing line will be implemented and run at VITO. Further, in the project life, the methodology will be adapted to AATSR sensor data.

5. CONCLUSION

As geoland2 constitutes a major step forward in the implementation of the GMES Land Monitoring Core Service (LMCS), the BioPar CMS intends to bring a main brick to build the Global component of the LMCS. Through a global systematic monitoring service, the Global component of the LMCS aims to provide near real time bio-geophysical parameters at global scale, addressing primarily the 13 terrestrial ECVs, and describing the vegetation state and dynamic. The principal scope of the Global component of the LMCS is to deliver information products and services on the status and evolution of land surfaces in support to specific EU policies at international level and European commitments under international treaties and conventions, such as the three Rio conventions on Climate Change, Desertification and Biodiversity.

6. REFERENCES

- Albergel, C., Rüdiger, C., Pellarin, T., Calvet, J.-C., Fritz, N., Froissard, F., Suquia, D., Petitpa, A., Pignatelli, B., Martin, E., 2008. From near-surface to root-zone soil moisture using an exponential filter: an assessment of the method based on in-situ observations and model simulations. *Hydrol. Earth Syst. Sci.* 12: 1323-1337.
- Baret, F., Morisette, J., Fernandes, R., Champeaux, J.L., Myneni, R., Chen, J., Plummer, S., Weiss, M., Bacour, C., Garrigues, S. et al., 2006. Evaluation of the representativeness of networks of sites for the global validation and inter-comparison of land biophysical products. Proposition of the CEOS-BELMANIP. *IEEE Trans. Geosc. Rem. Sens.*, 44(7): special issue on global land product validation): 1794-1803.
- Baret, F., Hagolle, O. et al., 2007. LAI, fAPAR and fCover CYCLOPES global products derived from VEGETATION. Part 1: Principles of the algorithm. *Rem. Sens. Environ.*, 110: 275-286.
- Garrigues, S., Lacaze, R., Baret, F., Morisette, J., Weiss, M., Nickeson, J., Fernandes, R., Plummer, S., Shabanov, N.V., Myneni, R. et al., 2008. Validation and Intercomparison of Global Leaf Area Index Products Derived From Remote Sensing Data. *J. Geo. Res.*, 113(G02028).
- Gond, V., Bartholomé, E., Ouattara, F., Nonguierma, A., Bado, I., 2004. Surveillance et cartographie des plans d'eau et des zones humides et inondables en régions arides avec l'instrument VEGETATION embarqué sur SPOT-4, *Int. J. Remote Sens.* 25 (5), pp. 987–1004.
- Jacquemoud, S. and Baret, F., 1990. PROSPECT: A model of leaf optical properties spectra, *Rem. Sens. Environ.* 34: 75-91.
- Morisette, J., Baret, F., Privette, J.L., Myneni, R.B., Nickeson, J., Garrigues, S., Shabanov, N., Weiss, M., Fernandes, R., Leblanc, S. et al., 2006. Validation of global moderate resolution LAI Products: a framework proposed within the CEOS Land Product Validation subgroup. *IEEE Trans. Geosc. Rem. Sens.*, 44(7): 1804-1817.
- Pekel, J.-F., Cressman, K., Ceccato, P., Vancutsem, C., Vanbogaert, E., Defourny, P., 2009. Development and application of multi-temporal colorimetric transformation to monitor vegetation in the desert locust habitat. Proceeding MultiTemp 2009 – *The Fifth International Workshop on the Analysis of Multi-temporal Remote Sensing Images - July 28-30, 2009* - Groton, Connecticut
- Tansey, K., Grégoire, J.-M., Defourny, P., Leigh, R., Pekel, J.-F., van Bogaert, E., and Bartholomé, E., 2008. A new, global, multi-annual (2000–2007) burnt area product at 1 km resolution, *Geo. Res. Let.*, 35, L01401, doi:10.1029 / 2007GL031567.
- Trigo, I. F., C. C. DaCamara, P. Viterbo, J.-L. Roujean, F. Olesen, C. Barroso, F. Camacho-de-Coca, D. Carrer, S. C. Freitas, J. García-Haro, B. Geiger, F. Gellens-Meulenberghs, N. Ghilain, J. Meliá, L. Pessanha, N. Siljamo, and A. Arboleda, 2010: The Satellite Application Facility on Land Surface Analysis. *Int. J. Remote Sens.*, in press
- Verhoef, W., 1984. Light scattering by leaf layers with application to canopy reflectance modeling: the SAIL model, *Rem. Sens. Environ.* 16: 125-141.
- Verhoef, W. and Bach, H., 2003., Simulation of hyperspectral and directional radiance images using coupled biophysical and atmospheric radiative transfer models, *Rem. Sens. Environ.* 87: 23–41.
- Wagner, W., Lemoine, G., Rott, H., 1999. A Method for Estimating Soil Moisture from ERS Scatterometer and Soil Data. *Rem. Sens. Environ.* 70: 191-207.
- Weiss, M., Baret, F., Garrigues, S., Lacaze, R. and Bicheron, P., 2007. LAI, fAPAR and fCover CYCLOPES global products derived from VEGETATION. part 2: Validation and comparison with MODIS Collection 4 products. *Rem. Sens. Environ.*, 110: 317-331.

7. ACKNOWLEDGEMENT

The research leading to the results presented in this paper has received funding from the European Community's Seventh Framework Program (FP7/2007-2013) under grant agreement n°218795. All these products are under copyright geoland2.

RADIOMETRIC CALIBRATION OF FULL-WAVEFORM AIRBORNE LASER SCANNING DATA BASED ON NATURAL SURFACES

Hubert Lehner^a and Christian Briese^{a,b}

^aChristian Doppler Laboratory, Institute of Photogrammetry and Remote Sensing,
Vienna University of Technology, Gusshausstrasse 27-19, 1040 Vienna, Austria,
(hl, cb)@ipf.tuwien.ac.at

^bLudwig Boltzmann Institute for Archaeological Prospection and Virtual Archaeology,
Hohe Warte 38, 1190 Vienna, Austria

Commission VII

KEY WORDS: Radiometry, Radiometric Calibration, LIDAR, Laser scanning

ABSTRACT:

Airborne laser scanning (ALS) has become a commercially available and therefore widely used technique for obtaining the geometric structure of the earth's surface. For many ALS applications it is beneficial or even essential to classify the 3D point cloud into different categories (e.g. ground, vegetation, building). So far, most classification techniques use the geometry of the 3D point cloud or parameters which can be gained from analyzing the geometry or the number of echoes per emitted laser shot. Decomposing the echo waveform of full-waveform laser scanners provides in addition to the 3D position of each echo its amplitude and width. These physical observables are influenced by many different factors (e.g. range, angle of incidence, surface characteristics, atmosphere, etc.). Therefore, these attributes can hardly be used without radiometric calibration. In this paper the theory of the radar equation will be used to transform amplitude and echo width into radiometric calibration values, such as backscatter cross section, backscattering coefficients or incidence angle corrected versions of those. For this aim, external reference targets with known backscatter characteristics are necessary for the absolute radiometric calibration. In contrast to other approaches, this paper presents the usage of natural surfaces for this calibration task. These surfaces are observed in order to determine their backscatter characteristics independently from the ALS flight mission by a RIEGL reflectometer. Based on these observations the data of the ALS flight can be calibrated. Calibration results of data acquired by a RIEGL LMS-Q560 sensor are presented and discussed. Next to a strip-wise analysis, the radiometric calibration results of different strips in the overlapping region are studied. In this way, the accuracy of the calibration is analyzed (1) based on a very large area with approximately homogeneous backscatter characteristics, namely a parade yard, and (2) relatively by analyzing these overlapping regions.

1 INTRODUCTION

Airborne laser scanning (ALS, also referred to as airborne LIDAR (light detection and ranging)) is an active sampling method that is widely used for obtaining the geometric structure of the earth's surface. The resulting point cloud is a good basis for the modelling of the landscape for a variety of applications, e.g. hydrology (Mandlbürger et al., 2009), city modelling (Rottensteiner et al., 2007), forest mapping (Naesset, 1997, Hollaus et al., 2007), archaeology (Doneus et al., 2008). For these applications it is typically necessary to classify the ALS data into different classes (e.g. ground, vegetation, buildings). Most of the developed classification methods just rely on the geometric information provided by the acquired point cloud. However, with the introduction of small-footprint full-waveform (FWF) ALS sensors into the commercial market further additional attributes, i.e. the echo width and amplitude, for each echo can be determined. These attributes can be seen as physical observables that allow studying the radiometry of ALS data. However, in order to utilize this information a radiometric calibration of the ALS data is essential (Wagner et al., 2008b).

For the radiometric calibration of ALS data different methods were already published. Next to their mathematical or physical framework the approaches differ in the use of reference data. Some publications do not use reference surfaces at all and only try to compensate for specific influencing factors (Luzum et al., 2004, Donoghue et al., 2007, Höfle et al., 2007). Another group of authors rely on artificial reference targets that were placed within the area of interest during the data acquisition campaign

(Ahokas et al., 2006, Kaasalainen et al., 2007), while the third group of researchers tries to solve the radiometric calibration task with the usage of natural reference targets (Coren and Sterzai, 2006, Wagner et al., 2006, Briese et al., 2008).

Within this paper the practical application and validation of the radiometric calibration of small-footprint FWF-ALS data based on natural surface elements is presented and studied. The calibration procedure relies on the radar equation (Wagner et al., 2006) and on natural reference surfaces. These surfaces are observed in-situ by a RIEGL reflectometer (Briese et al., 2008). Based on these observations, the data of the ALS flight can be calibrated. In order to demonstrate the practical capability and to study the quality of the radiometric calibration this process is applied to an FWF-ALS data set acquired by a RIEGL LMS-Q560 sensor over the city of Vienna, Austria. Next to the practical application of the method the resulting calibrated data set is analysed strip-wise by a visual comparison of the radiometric information in the overlapping area of two strips. Furthermore, a quantitative comparison of the calibrated data sets is performed by an analysis of a difference model in the overlapping zone. Finally, after the discussion of the results, a short summary and an outlook into future research work conclude the paper.

2 RADIOMETRIC CALIBRATION

2.1 Theoretical Background

The basic relation between the transmitted power P_t and the received power P_r of an ALS system can be described by the LIDAR

adapted formulation of the radar equation (see equation 1), which considers all influencing factors: the receiver aperture diameter D_r , the range between sensor and target R , the laser beam divergence β_t and the backscatter cross section, as well as losses occurring due to the atmosphere or in the laser scanner system itself, i.e. a system and atmospheric transmission factor η_{sys} and η_{atm} respectively. The backscatter cross section combines all target parameters such as the size of the area illuminated by the laser beam A_i , the reflectivity ρ and the directionality of the scattering of the surface Ω (Wagner et al., 2006, Briese et al., 2008, Jelalian, 1992):

$$P_r = \frac{P_t D_r^2}{4\pi R^4 \beta_t^2} \cdot \sigma \cdot \eta_{sys} \eta_{atm} \quad \text{with} \quad \sigma = \frac{4\pi}{\Omega} \rho A_i \quad (1)$$

Parameters which are unknown but can be assumed to be constant during one ALS campaign can be combined to one constant, the so-called calibration constant C_{cal} . Due to the fact that, in case of ALS systems with Gaussian system waveform, the received power is proportional to the product of the amplitude \hat{P}_i and the echo width $s_{p,i}$, it can be replaced by the term $\hat{P}_i s_{p,i}$ (Wagner et al., 2006, Höfle et al., 2008). This yields the following form of the calibration equation for calculating the backscatter cross section σ :

$$\sigma = \frac{C_{cal} 4\pi R^4 \hat{P}_i s_{p,i}}{\eta_{atm}} \quad \text{with} \quad C_{cal} = \frac{\beta_t^2}{P_t D_r^2 \eta_{sys}} \quad (2)$$

The range, the amplitude and the echo width in equation 2 are results of the Gaussian decomposition of the full-waveform data, while the atmospheric transmission factor η_{atm} can be determined by meteorological data and radiative transfer models such as MODTRAN (Berk et al., 1998, Briese et al., 2008). In order to estimate the calibration constant in equation 2 only the backscatter cross section of a reference surface is necessary. This can be achieved by the second formula of equation 1, the assumption of a Lambertian scatterer, which means that the scattering solid angle Ω is π steradians, and the knowledge of the reflectivity ρ of the reference surface. For a fast estimation the illuminated area A_i in equation 2 can be replaced by the laser footprint area at the scattering object A_{lf} (see figure 1 and equation 3).

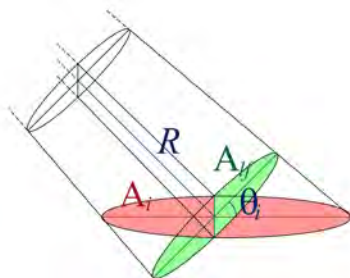


Figure 1: Laser footprint area at the scattering object A_{lf} , i.e. the circular area perpendicular to the laser beam at distance R (green area); area illuminated by the laser beam A_i at distance R and θ_i angle of incidence (red area).

The laser footprint area at the scattering object (see green area in figure 1) can easily be calculated by the range R and the beam divergence β_t , while the area illuminated by the laser beam (see red area in figure 1) can be approximated by an ellipse whose calculation of the area additionally requires an estimation of the

local angle of incidence θ_i (Lutz, 2003):

$$A_{lf} = \frac{\pi R^2 \beta_t^2}{4} \quad \text{resp.} \quad A_i = \frac{R^2 \beta_t^2 \pi}{4 \cos \theta_i} = \frac{A_{lf}}{\cos \theta_i} \quad (3)$$

Once the calibration constant is derived the calibrated backscatter cross sections of the individual echoes for the whole data set can be determined.

Due to different flight heights or beam divergence, the illuminated area A_i and therefore also the backscatter cross section σ can vary a lot. Therefore, Wagner et al. (2008a) introduce area-normalized values, so-called backscattering coefficients, which have the advantage that measurements with different resolution can be compared more easily. The backscatter cross section can be related to the illuminated area A_i , which leads to the cross section per unit-illuminated area σ^0 [$\text{m}^2 \text{m}^{-2}$] (Wagner et al., 2008b):

$$\sigma^0 = \frac{\sigma}{A_i} \quad (4)$$

Since the incidence angles change, it might be more convenient to normalize the backscatter cross section to the illuminated area at zero angle of incidence, i.e. the cross section of the incoming beam, which results in the so-called bistatic scattering coefficient γ [$\text{m}^2 \text{m}^{-2}$] (Wagner et al., 2008b):

$$\gamma = \frac{\sigma}{A_{lf}} \quad (5)$$

The backscatter cross section σ as well as the backscattering coefficients σ^0 and γ are not free from influences caused by the angle of incidence. In case of ideal Lambertian scatterers incidence angle corrected values can be achieved by division with the cosine of the local angle of incidence:

$$\sigma_\theta = \frac{\sigma}{\cos \theta_i} \quad \text{resp.} \quad \gamma_\theta = \frac{\gamma}{\cos \theta_i} \quad (6)$$

Although σ_0 seems to be the most suitable value at first sight, it amplifies the effect of the angle of incidence (for an Lambertian scatterer by the square of the cosine law). The computational advantages of γ are obvious since no time-consuming local plane fits are necessary in order to estimate the local surface normal, which is required for the calculation of the local incidence angle. However, in case homogeneous values are aimed at for a homogeneous surface, incidence angle corrected values such as σ_θ have to be computed. Since the estimation of the local surface normal can be uncertain or even impossible for some echoes, e.g. in vegetated areas, incidence angle corrected values cannot be guaranteed for the whole data set. Therefore, it depends on the subject of interest which calibration value to choose for further processing.

2.2 Practical Method

The practical method for radiometric calibration based on natural surfaces as reference targets is already presented in Briese et al. (2008). Therefore it will be mentioned only briefly. It consists of three parts (see figure 2).

Prior to the ALS flight natural reference targets should be selected in order to be able to measure the reflectivity by using the RIEGL reflectometer and Spectralon[®] diffuse reflectance standards (Labsphere Inc., 2010) at approximately the same time as the ALS data is acquired (see figure 2(a)) (Briese et al., 2008).

Meteorological data such as the visibility at the time of the flight either have to be observed during data acquisition or gained from

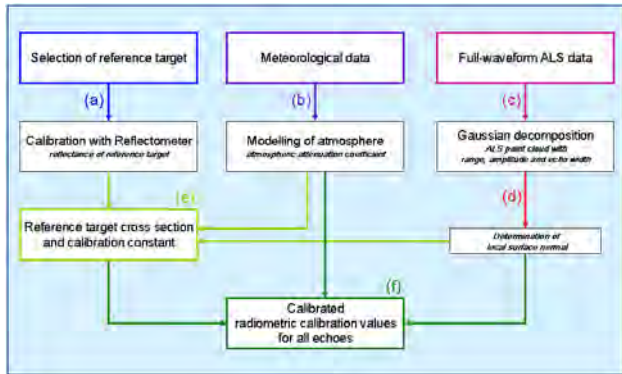


Figure 2: Operational workflow of radiometric calibration of full-waveform ALS data.

observation stations close to the campaign site afterwards. With the help of radiative transfer models an atmospheric attenuation coefficient can be derived (see figure 2(b)).

Decomposing the full-waveform data yields a 3D point cloud with additional information per echo such as range, amplitude and echo width (see figure 2(c)) (Wagner et al., 2006).

From here on the radiometric calibration is further processed by OPALS modules that were developed by the Institute of Photogrammetry and Remote Sensing (IPF) of the Vienna University of Technology (IPF, 2010). The `opalsImport` module is used to load the 3D point data with its attributes and its corresponding trajectory strip-wise into the OPALS data manager system for subsequent use in all OPALS modules dealing with point clouds. During the import process, `opalsImport` reconstructs the beam vector, echo number and number of returns of each echo and stores them as additional attributes in the data manager. Furthermore, the `opalsNormals` module performs a local plane fit for each point based on its neighbouring points in order to derive the local normal vector of each point. However, due to the partly high surface variation, it might not be possible to fit a plane for every echo (only planes with a maximal user specified tolerance value for the adjusted sigma value are accepted), e.g. in case of echoes originating from vegetation. Nevertheless, if the plane is accepted, the normalized normal vector is stored as additional attribute for each point in the data manager (see figure 2(d)).

In order to allow the radiometric calibration of ALS data the OPALS module `opalsRadioCal` was developed to firstly derive a mean calibration constant (see figure 2(e)). Within this step, for every echo within a given reference surface with given reflectivity and atmospheric attenuation coefficient the calibration constant is estimated according to the second formula in equation 1, the first formula in equation 2 and the formula displayed in equation 3. For points within the reference surface the local incidence angle is computed from the local normal vector and the beam vector. These calibration constants for each echo within a reference surface are used to determine a mean calibration constant for the whole ALS campaign. The `opalsRadioCal` module applies this mean calibration constant to secondly calculate the calibrated radiometric values for each echo. This process includes the estimation of the backscatter cross section, backscattering coefficients and incidence angle corrected values as mentioned in section 2.1 (see figure 2(f)).

3 RESULTS AND DISCUSSION

The radiometric calibration procedure was tested on a data subset of the Vienna wide ALS campaign carried out at the end of

2006 and beginning of 2007, namely on the parts of thirteen flight strips covering the area of the Schönbrunn palace, garden, zoo and surrounding living area. This particular full-waveform data set was acquired on the December 27th 2006, by the company Diamond Airborne Sensing GmbH with a RIEGL LMS-Q560, which operates at a wavelength of 1550 nm. The scan frequency was 200 kHz, the aircraft speed above ground 150 km/h, the flying height above ground 500 m and the scan angle $\pm 30^\circ$. These settings resulted in a swath overlap of about 60 %, a mean point density of more than 20 measurements per square meter and a laser footprint size on ground of about 25 cm. The meteorological data for modelling the atmosphere was received from three weather observation stations located within the city of Vienna.

Two smaller asphalt regions, one gravel region, one building roof and the big asphalt regions of the parade yard of the Maria Theresia casern in the south of the Schönbrunn gardens (see figure 3) were chosen as reference surfaces. Reflectances at zero angle of incidence between 15 % for one of the smaller asphalt regions up to 44 % for the gravel region were determined by the RIEGL reflectometer. For the parade yard in the centre of the three big buildings in figure 3 a reflectance of 23.5 % was measured.



Figure 3: RGB-Orthophoto of the Maria Theresia casern in the south of the Schönbrunn gardens (MA41, 2010).

The parade yard of the Maria Theresia casern in the south of the Schönbrunn gardens is by far the largest homogeneous area within the test site. Therefore, it was also used as reference surface during the calibration procedure. Additionally, this area enables to study the different radiometric calibration values, which can be seen in figure 4. The left diagram of figure 4(a) shows the selected echoes for the analysis of two overlapping flight strips, the echoes of the western strip ($> 65\,000$) in green and echoes of the eastern one ($> 113\,000$) in blue. In the eastern strip the parade yard is located close to the centre of the swath, while for the western strip it is located at the swath border. This can also be seen in the right diagram of figure 4(a), which shows range versus angle of incidence. The eastern echoes were acquired at angles of incidence up to 22° and the echoes of the western strip between 18° and 30° . With increasing incidence angles also the ranges increase, approximately up to 70 m. Hence, the effects which can be seen in the diagrams below combine the range and the angle of incidence dependencies. Figure 4(b) shows the original amplitude values versus range and versus angle of incidence. In both cases the decrease with increasing range and angle of in-

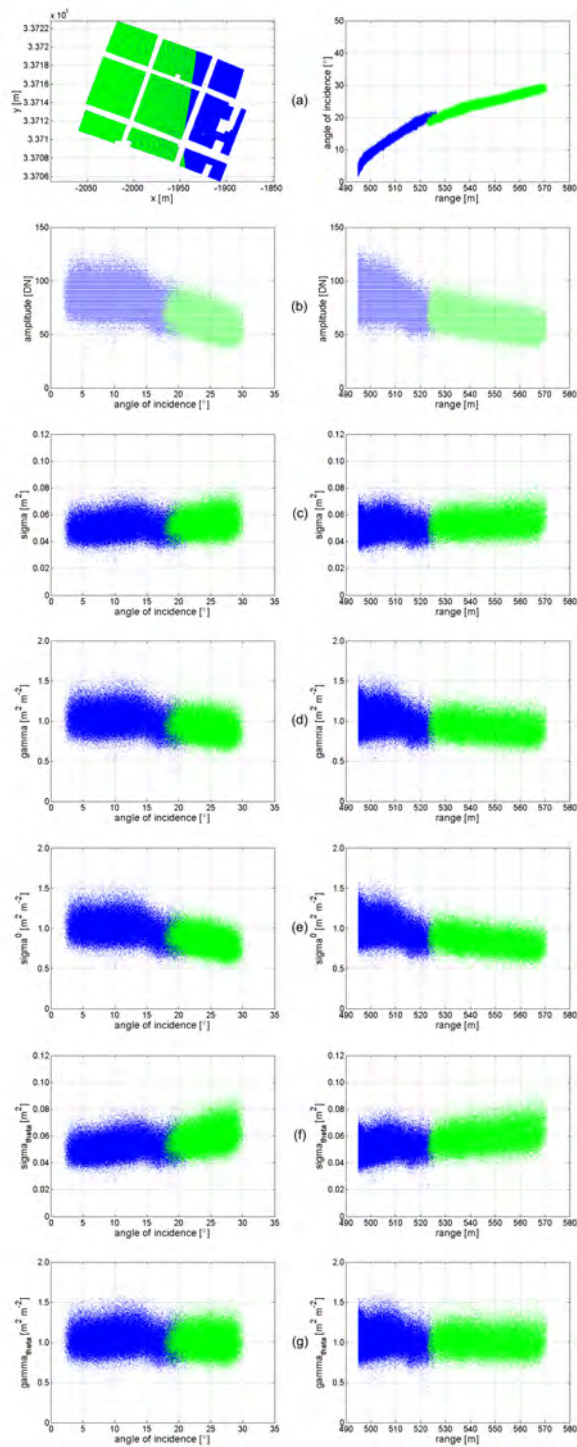


Figure 4: Colour-coded echoes of the parade yard of the Maria Theresia casern: points of western flight strip in green and points of eastern flight strip in blue. (a) coordinates of the echoes next to a diagram of range versus angle of incidence; (b) original amplitude measurements; (c) backscatter cross section σ ; (d) backscattering coefficient γ ; (e) backscattering coefficient σ^0 ; (f) incidence angle corrected cross section σ_θ and (g) incidence angle corrected backscattering coefficient γ_θ . (b) – (g) specific value versus angle of incidence (left) and versus range (right).

idence can clearly be seen. Since the parade yard is a horizontal surface, the backscatter cross section σ (see figure 4(c)) already

shows homogeneous values for increasing range and angle of incidence. The backscattering coefficient γ (see figure 4(d)) shows a slight decrease, while σ^0 (see figure 4(e)) shows a stronger decrease as expected. The incidence angle corrected value σ_θ (see figure 4(f)) seems to overcorrect, while γ_θ (see figure 4(g)) again delivers homogeneous values over the whole observed range and angle of incidence spectrum.

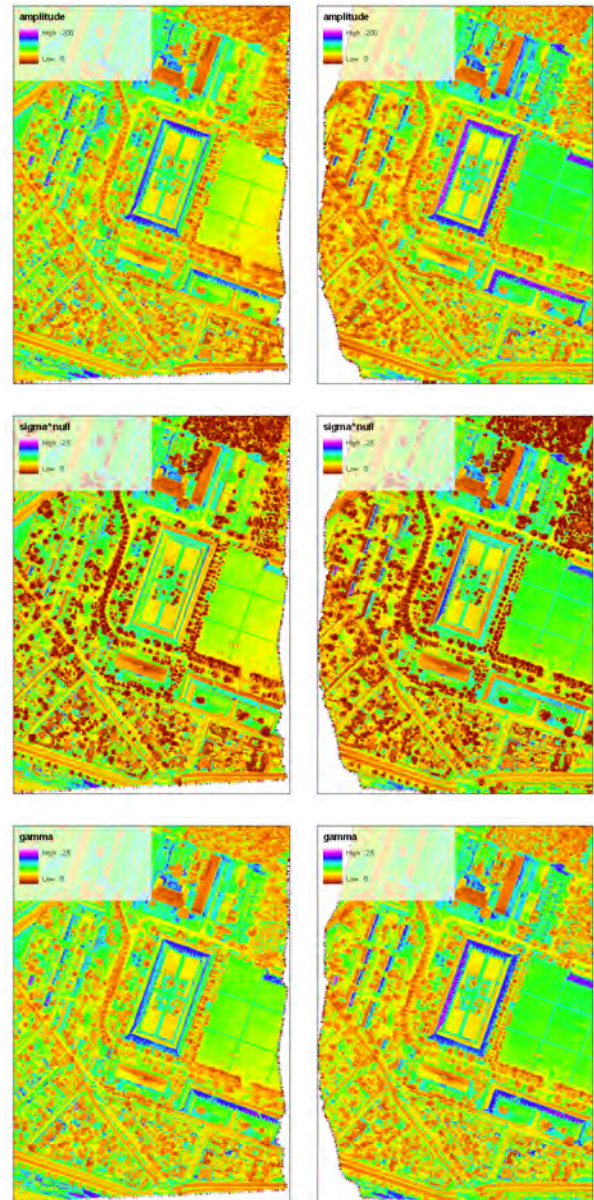


Figure 5: Colour-coded amplitude, σ^0 and γ models of two flight strips for the overlapping region: (left) western flight strip and (right) eastern flight strip.

Figure 5 shows colour-coded amplitude, σ^0 and γ models of two flight strips. Comparing the σ^0 and γ images it can be seen that especially areas where the local normal estimation is critical, e.g. vegetated areas, yield significantly lower values. The roof areas of the big building in the centre of the western strip show unexpected values, which cannot be explained so far. The roof area with surface normals pointing towards the sensor and the area with normals pointing away, both of the eastern section of the building, show similar amplitude values instead of being significantly different. However, in the eastern strip the amplitudes behave like expected.

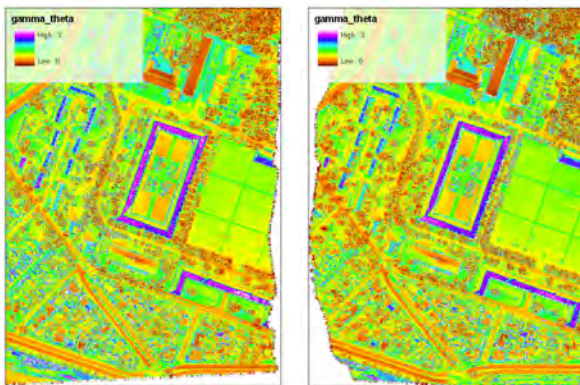


Figure 6: Colour-coded γ_θ models of two flight strips for the overlapping region: (left) western flight strip and (right) eastern flight strip.

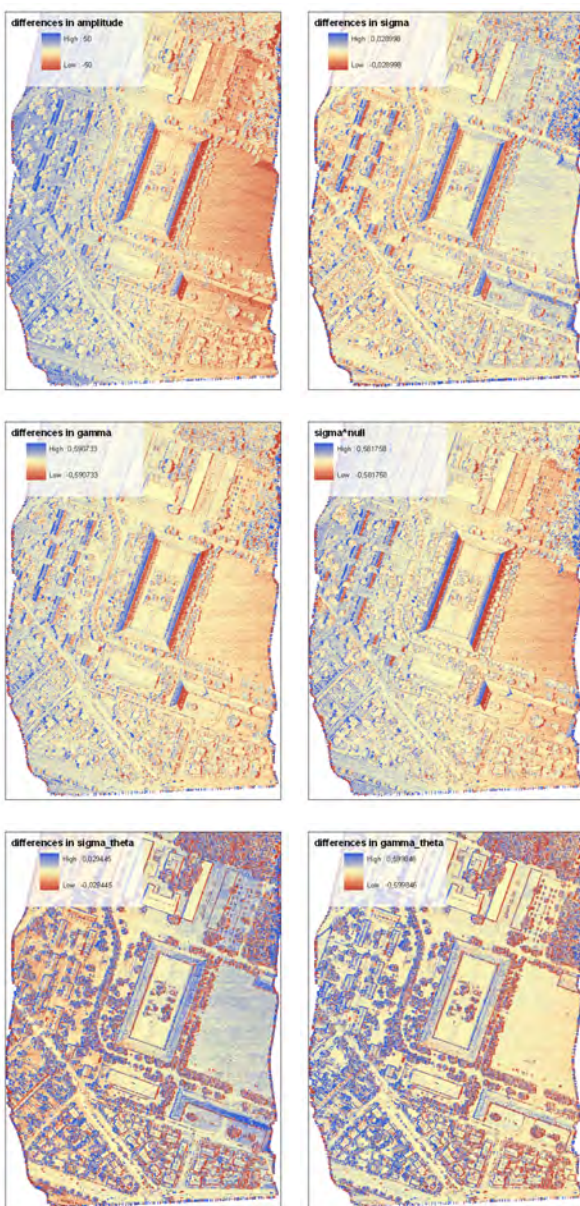


Figure 7: Colour-coded difference models of two overlapping flight strips for the original amplitude measurements and different radiometric calibration values.

The colour-coded incidence angle corrected γ_θ model is displayed in figure 6. It can be seen, that the surfaces of the western and the eastern strip show similar values. However, within one strip roof areas with surface normals pointing towards the sensor and those with surface normals pointing away do not show similar values. This is unexpected but seems to be a result of the unexpected amplitude values as shown in figure 5.

In a next step, difference models of the different radiometric calibration values were calculated for the two overlapping flight strips (see figure 7). The colour-coded difference image of the amplitude values shows the expected increase in difference towards the borders of the overlapping swath. The differences in backscatter cross section σ already indicate similar values in the overlapping flight strips for wide regions, especially for horizontal surfaces. However, inclined roof surfaces still suffer from incidence angle effects. This can particularly be seen at the huge casern building in the centre of the difference image. The difference image of γ shows differences of the same strength as in the difference image of σ . The differences in σ^0 between the overlapping strips on the other hand show again the amplification of the incidence angle dependence at the inclined roof surfaces. The incidence angle corrected values σ_θ and γ_θ strongly minimize the differences for roof areas. Since the incidence angles' estimation in vegetated areas is uncertain and sometimes impossible, this drawback can also be seen in the difference images of σ_θ and γ_θ by strong differences in either one or the other direction.

4 CONCLUSION

This paper presents a comparison of different radiometric calibration values, the assets and drawbacks of each calibration value as well as a quantitative comparison by analyzing difference models of overlapping regions. The backscatter cross section σ delivers usable results especially for horizontal surfaces. However, area-normalized values should be the aim in case measurements with different resolution, e.g. acquired at significantly different flight heights over ground, with significantly different beam divergence and/or by different ALS sensors, shall be compared. Since σ_0 proves to amplify the effect of the angle of incidence, γ turns out to be the preferred quantity of these so-called backscattering coefficients. Due to the fact that all these values still suffer from incidence angle dependencies, only incidence angle corrected values such as σ_θ and γ_θ are able to deliver homogeneous values for a homogeneous surface. Such values can only be derived for echoes, where the estimation of the local surface normal is successful, though. The analysis of the horizontal parade yard shows that σ_θ tends to overcorrect the incidence angle dependence, while γ_θ delivers homogeneous values for the homogeneously reflecting parade yard. Further evaluation has to be done especially concerning multi-temporal data, e.g. acquired by different sensors (e.g. with a different beam divergence, laser wavelength, etc.) and/or from different flight heights. Additionally, the unexpected behavior of the amplitude values that are visible in the upper left part of figure 5 (c.f. section 3) will be studied in the future.

ACKNOWLEDGEMENTS

We would like to thank Stadtvermessung Wien, Magistratsabteilung 41 (MA41, 2010), for providing the full-waveform ALS data, which was used for this study. Furthermore, we would like to thank the company Riegl Laser Measurement Systems GmbH (RIEGL, 2010) for the development of the reflectometer, a tool

which is essential for the proposed calibration method. This paper is a contribution to the EuroSDR project “Radiometric Calibration of ALS Intensity”. EuroSDR is a European spatial data research organisation (EuroSDR, 2010).

REFERENCES

- Ahokas, E., Kaasalainen, S., Hyyp, J. and Suomalainen, J., 2006. Calibration of the Optech ALTM 3100 laser scanner intensity data using brightness targets. ISPRS Commission I Symposium “From Sensors to Imagery”, Paris, France, 2006 XXXVI, Part A1, pp. CD-ROM, T03–11.
- Berk, A., Bernstein, L. S., Anderson, G. P., Acharya, P. K., Robertson, D. C., Chetwynd, J. H. and Adler-Golden, S. M., 1998. Modtran cloud and multiple scattering upgrades with application to aviris. *Remote Sensing of Environment* 65(3), pp. 367–375.
- Briese, C., Höfle, B., Lehner, H., Wagner, W., Pfennigbauer, M. and Ullrich, A., 2008. Calibration of full-waveform airborne laser scanning data for object classification. In: M. D. Turner and G. W. Kamerman (eds), *Laser Radar Technology and Applications XIII, Proceedings of SPIE*, Vol. 6950, SPIE (International Society for Optical Engineering), SPIE Press, pp. 69500H–69500H–8. ISBN: 9780819471413 Defense and Security Symposium (17–20 March 2008, Orlando, Florida, USA).
- Coren, F. and Sterzai, P., 2006. Radiometric correction in laser scanning. *International Journal of Remote Sensing* 27(15), pp. 3097 – 3104.
- Doneus, M., Briese, C., Fera, M. and Janner, M., 2008. Archaeological prospection of forested areas using full-waveform airborne laser scanning. *Journal of Archaeological Science* 35(4), pp. 882–893.
- Donoghue, D., Watt, P., Cox, N. and Wilson, J., 2007. Remote sensing of species mixtures in conifer plantations using lidar height and intensity data. *Remote Sensing of Environment* 110(4), pp. 509–522.
- EuroSDR, 2010. EuroSDR - European Spatial Data Research Network. <http://www.eurohdr.net/>. vistet on 03/06/2010.
- Höfle, B., Geist, T., Rutzinger, M. and Pfeifer, N., 2007. Glacier surface segmentation using airborne laser scanning point cloud and intensity data. ISPRS WG III/3, III/4, V/3 VIII/11 Workshop “Laser Scanning 2007 and SilviLaser 2007”, Espoo, September 12–14, 2007, Finland Volume XXXVI, Part 3 / W52, pp. 195–200.
- Höfle, B., Hollaus, M., Lehner, H., Pfeifer, N. and Wagner, W., 2008. Area-based parameterization of forest structure using full-waveform airborne laser scanning data. In: R. Hill, J. Rosette and J. Surez (eds), *Proceedings of SilviLaser 2008: 8th international conference on LiDAR applications in forest assessment and inventory*, Heriot-Watt University, Edinburgh, UK, pp. 227–235. ISBN 978-0-85538-774-7.
- Hollaus, M., Wagner, W., Maier, B. and Schadauer, K., 2007. Airborne laser scanning of forest stem volume in a mountainous environment. *Sensors* 7(8), pp. 1559–1577.
- IPF, 2010. Institute of Photogrammetry and Remote Sensing (IPF) of the Vienna University of Technology, OPALS - Orientation and Processing of Airborne Laser Scanning data. http://www.ipf.tuwien.ac.at/opals/opals_docu/index.html. vistet on 03/06/2010.
- Jelalian, A. V., 1992. *Laser Radar Systems*. Artech House, Boston London. ISBN: 978-0890065549.
- Kaasalainen, S., Hyyp, J., Litkey, P., Hyyp, H., Ahokas, E., Kukko, A. and Kaartinen, H., 2007. Radiometric calibration of als intensity. ISPRS WG III/3, III/4, V/3 VIII/11 Workshop “Laser Scanning 2007 and SilviLaser 2007”, Espoo, September 12–14, 2007, Finland Volume XXXVI, Part 3 / W52, pp. 201–205.
- Labsphere Inc., 2010. Spectralon - Diffuse Reflectance Standards. http://www.labsphere.com/data/userFiles/DiffuseReflectanceStandardsProductSheet_7.pdf. vistet on 03/06/2010.
- Lutz, E. R., 2003. Investigations of airborne laser scanning signal intensity on glacial surfaces - utilizing comprehensive laser geometry modeling and surface type modeling (a case study: Svar-tisheibreen, norway). Master’s thesis, Institut für Geographie der Leopold-Franzens-Universitt Innsbruck.
- Luzum, B., Starek, M. and Slatton, K. C., 2004. Normalizing alsm intensities. Center Report Rep.2004-07-001, Geosensing Engineering and Mapping (GEM), Civil and Coastal Engineering Department, University of Florida.
- MA41, 2010. Stadtvermessung Wien, Magistratsabteilung 41. <http://www.wien.gv.at/stadtentwicklung/stadtvermessung/index.html>. vistet on 03/06/2010.
- Mandlbürger, G., Hauer, C., Höfle, B., Habersack, H. and Pfeifer, N., 2009. Optimisation of lidar derived terrain models for river flow modelling. *Hydrology and Earth System Sciences* 13, pp. 1453–1466.
- Naesset, E., 1997. Estimating timber volume of forest stands using airborne laser scanner data. *Remote Sensing of Environment* 61(2), pp. 246–253.
- RIEGL, 2010. Riegl Laser Measurement Systems GmbH. <http://www.riegl.com/>. vistet on 03/06/2010.
- Rottensteiner, F., Trinder, J., Clode, S. and Kubik, K., 2007. Building detection by fusion of airborne laser scanner data and multi-spectral images: Performance evaluation and sensitivity analysis. *ISPRS Journal of Photogrammetry and Remote Sensing* 62(2), pp. 135–149.
- Wagner, W., Hollaus, M., Briese, C. and Ducic, V., 2008a. 3d vegetation mapping using small-footprint full-waveform airborne laser scanners. *International Journal of Remote Sensing* 29(5), pp. 1433–1452.
- Wagner, W., Hyyp, J., Ullrich, A., Lehner, H., Briese, C. and Kaasalainen, S., 2008b. Radiometric calibration of full-waveform small-footprint airborne laser scanners. ISPRS XXI ISPRS Congress, Commission I, WG I/2, July 3–11, 2008, Beijing, China XXXVII, Part B1, pp. 163–168. ISSN 1682-1750.
- Wagner, W., Ullrich, A., Ducic, V., Melzer, T. and Studnicka, N., 2006. Gaussian decomposition and calibration of a novel small-footprint full-waveform digitising airborne laser scanner. *ISPRS Journal of Photogrammetry and Remote Sensing* 60(2), pp. 100–112.

URBAN IMPERVIOUS SURFACE EXTRACTION FROM VERY HIGH RESOLUTION IMAGERY BY ONE-CLASS SUPPORT VECTOR MACHINE

P. Li, H. Xu, S. Li

Institute of Remote Sensing and GIS, School of Earth and Space Sciences, Peking University, Beijing 100871, P R China - pjli@pku.edu.cn

KEY WORDS: impervious surface, multi-level segmentation, One-Class SVM, very high resolution imagery, land cover classification

ABSTRACT:

This paper proposes a new method for extracting impervious surface from VHR imagery. Since the impervious surface is the only class of interest (i.e. target class), the One Class Support Vector Machine (OCSVM), a recently developed statistical learning method, was used as the classifier. Rather than use samples from all classes for training in traditional multi-class classification, the method only requires samples of the target class for training. The classification was conducted on object level. The proposed method was evaluated and compared to existing methods using Quickbird image from Beijing urban area. The results showed that the proposed method outperformed the existing method in term of classification accuracy. The method provides an effective way to extract impervious surface from VHR images.

1. INTRODUCTION

Impervious surface is defined as any materials that water cannot infiltrate, and has been recognized as an important indicator in urban environmental assessment and valuable input to planning and management activities (Lu and Weng, 2009; Yuan and Bauer, 2006). The extraction of impervious surface from remote sensing imagery has continued to be an important problem for more than three decades. In recent years, the increasing availability of very high resolution (VHR) imagery, such as IKONOS, Quickbird and GeoEye-1, provides great opportunity for detailed impervious surface mapping in urban areas. Although some methods using VHR images have been developed (Lu and Weng, 2009; Yuan and Bauer, 2006; Goetz et al., 2003; Cablk and Minor, 2003; Zhou and Wang, 2008; Roeck et al., 2009), obtaining highly accurate land cover and impervious surface information from VHR imagery remains challenging, thus new methods and techniques are still required. However, since there is extensive occurrence of shadows in VHR imagery caused by high buildings and trees in dense urban areas, which leads to the reduced or total loss of spectral information in the shaded areas, an important problem to be

addressed is to identify the impervious surfaces in shaded areas (Lu and Weng, 2009). As in general land cover classification of urban areas using VHR images, object based methods are also commonly used to extract impervious surfaces (Cablak and Minor, 2003; Yuan and Bauer, 2006; Zhou and Wang, 2008).

2. METHODS

In this study, we adopted a two-stage object based method to extract impervious surface. At the first stage, shadow areas were identified at object level generated by image segmentation. At the second stage, shadow areas and non-shadow areas were separately classified to extract impervious surface, using one-class Support Vector Machine (One-class SVM or OCSVM).

Prior to these two stages, multilevel hierarchical segmentation using the proposed method was first carried out, different levels of segmentation results were then selected for each stage. For example, since shadow extraction at the first stage and shadow classification at the second stage require different levels of segmentation detail, shadow extraction was conducted at a coarse level of segmentation, whereas the shadow classification

was conducted at a fine level of segmentation. On the other hand, non-shadow areas were classified at an appropriate segmentation level, different from the levels for shadow detection and classification. After all classes were extracted, impervious surfaces in both shadow areas and non-shadow areas were aggregated to a single class, i.e. impervious surface.

2.1 Multi-level segmentation

In this study, an improved watershed transformation method (Li et al., 2010), was adopted for high resolution multispectral image segmentation. However, other image segmentation methods can also be used to produce segmentation results.

In the image segmentation method by Li et al. (2010), multispectral gradient proposed by Li and Xiao (2007) was first used to extend the watershed transformation to multispectral image segmentation, and then the dynamics of watershed contours proposed by Najman and Schmits (1996) was adopted to reduce the oversegmentation in initially segmented image and produce multilevel segmentation results.

After the dynamics of watershed contours (Najman and Schmits, 1996) were obtained, a threshold is applied to the values of the contour dynamics, in order to remove the watershed lines that have less significance and to produce a final segmentation result. The details for algorithm for computation of contour dynamics can be found in (Najman and Schmits 1996, Lemarechal et al. 1998, Schmitt 1998).

2.2 OCSVM

The OCSVM is a recently developed one-class classifier and has been widely used in ecological modeling (Guo et al. 2005), and remote sensing classification (Sanchez-Hernandez et al. 2007) as well as change detection (Li and Xu 2009). In the OCSVM training process, only samples from the target class are used. Thus, it is suitable for the situations where only one class or some classes (but not all classes) are of interest and easy to sample or measure; the other class might be very difficult or expensive to measure. Therefore, the boundary between the two classes has to be estimated from data of the only available target class. The task is to define a boundary around the target class, such that it encircles as many target examples as possible and minimizes the chance of accepting outliers (Tax 2001).

Scholkopf et al. (1999) developed an OCSVM algorithm to deal with the one-class classification problem. The OCSVM may be

viewed as a regular two-class SVM where all the training data lies in the first class, and the origin is taken as the only member of the second class. The OCSVM algorithm first maps input data into a high-dimensional feature space via a kernel function and then iteratively finds the maximal margin hyperplane, which best separates the training data from the origin.

2.3 Impervious surface mapping

After multilevel segmentation was carried out, a hierarchical classification strategy was adopted using the OCSVM and multilevel segmentation results. Since shadows are common in the VHR images, the OCSVM was first used to extract the shadow areas at a coarse level of segmentation. After that the shadow areas and non-shadow areas were separately classified using the OCSVM and different levels of segmentation to extract the impervious surface. Finally, the impervious surface from both shadow areas and non-shadow areas were merged to produce a final impervious surface map. In each step, only samples from the class of interest are used to train the OCSVM. For example, in the stage of shadow extraction, only samples from shadow areas were used in the training process. This is different from traditional classification methods, where samples from all classes are required.

2.4 Result evaluation

In order to validate the proposed impervious surface mapping method, a method based on the use of traditional SVM and multilevel segmentation results was also used to extract the impervious surface. After multilevel segmentation results were obtained, the SVM classifier was first used to classify the image of the study area into several land cover classes, such as grass, tree, soil, impervious surface and shadow. The obtained shadow areas were then further classified using the SVM to several land cover classes, including impervious surface. Finally, the classification result from both shadow and non-shadow areas were merged to an impervious/non-impervious surface map, where the classes, such as tree, grass and soil were merged to a class non-impervious surface.

3. DATA AND STUDY AREA

A Quickbird image of Beijing urban area, acquired in September of 2003 was used in the experiment. The Quickbird imagery contains four multispectral bands with 2.44m

resolution (Blue, Green, Red and NIR) and a panchromatic band with 0.61m resolution. In this study, the multispectral and panchromatic images were fused to produce a four-band pan-sharpened multispectral image with pixel size of 0.61m. The image fusion was carried out using the Gram-Schmidt procedure (Laben and Brower, 2000). A subset of the

pan-sharpened multispectral image with size of 1800×2800 pixels was finally used in the study (Figure 1). The image subset covers a portion of the suburban area. The land cover types in the area include tree, grassland, soil and impervious surface (building, road).



Figure 1 Quickbird image of study area (Bands 3, 4, 2 as R, G, B)

4. RESULTS AND DISCUSSION

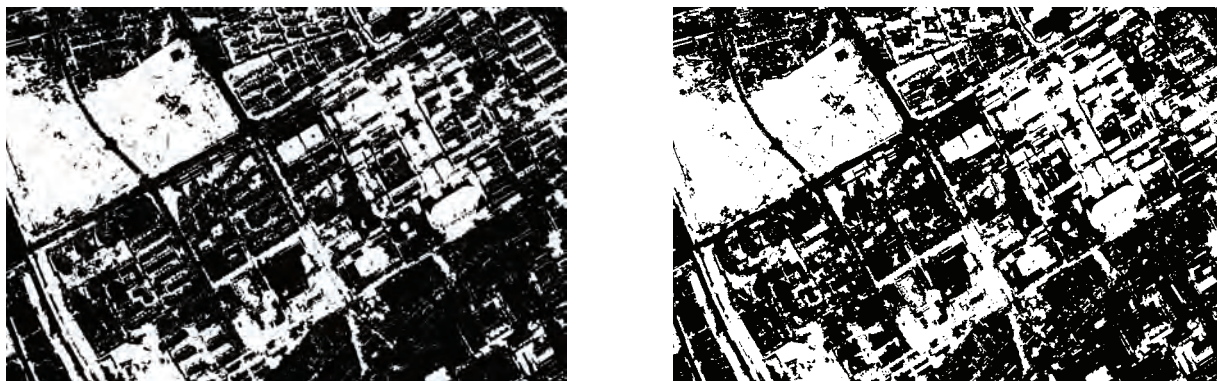
The impervious surface was extracted using the proposed method and the method based on traditional SVM, respectively. Table 1 shows the impervious surface mapping results. From the table, both overall accuracy and Kappa coefficient of the proposed method are higher than those of the method using the SVM. The producer's accuracy and user's accuracy of the

impervious surface are also acceptable. In particular, the higher user's accuracy of the impervious surface indicates that the proposed method produced less commission error than the existing method using the SVM. From Figure 1, although the results from two methods showed very similar appearance, the result from the proposed method are more homogeneous inside the class.

Table 1 Impervious surface mapping results using different methods (all in %)

	OA	Kappa	Accuracies for impervious surface	
			PA	UA
Multi-class				
SVM	83.93	73.20	91.68	79.34
OCSVM	88.56	77.27	81.87	96.51

OA, Overall accuracy; PA, producer's accuracy; UA, user's accuracy.



A

B

Figure 2 Impervious surface mapping results using different methods: A, multi-class SVM; B, One-class SVM.

Black: impervious surface, white: non-impervious surface

5. CONCLUSION

This paper proposed an impervious surface mapping method based on OCSVM and object-based classification method. The results showed that the proposed method outperformed the existing method using traditional SVM. One of the advantage of the proposed OCSVM based method is that it only requires the samples from the target class (or class of interest). Further work will focus on evaluation of the proposed method using more datasets and how to fuse the proposed method and existing method to achieve higher accuracy.

REFERENCES

- B. Scholkopf, Platt, J.C., Shawe-Taylor, J., Smola, A.J. and Williamson, R.C., 1999. Estimating the support of a high dimensional distribution. *Technique report*, Microsoft Research, MSR-TR-99-87.
- Cablk, M.E. and Minor, T.B., 2003. Detecting and discriminating impervious cover with high-resolution IKONOS data using principal component analysis and morphological operators. *International Journal of Remote Sensing*, 24, pp. 4627–4645.
- Goetz, S.J., Wright, R.K., Smith, A.J., Zinecker, E. and Schaub, E., 2003. IKONOS imagery for resource management: Tree cover, impervious surfaces and riparian buffer analyses in the mid-Atlantic region. *Remote Sensing of Environment*, 88, pp. 195–208.
- Laben, A. and Brower, B. V., 2000. Process for enhancing the spatial resolution of multispectral imagery using pan-sharpening, U.S. Patent 6011875. Available online at: <http://www.freepatentsonline.com/6011875.html>.
- Lemarechal, C., Fjortoft, R., Marthon, P. and Cubero-Castan, E., 1998. Comments on “Geodesic saliency of watershed contours and hierarchical segmentation”. *IEEE Transactions on Pattern Analysis and Machine Intelligence*, 20(7), pp.762-766.
- Li, P. and Xiao, X., 2007. Multispectral image segmentation by a multichannel watershed-based approach. *International Journal of Remote Sensing*, 28(19), pp. 4429-4452.
- Li, P. and Xu, H., 2010. Land cover change detection using one-class support vector machines. *Photogrammetric Engineering and Remote Sensing*, 76(3), pp. 255-263.
- Li, P., Guo, J., Song, B. and Xiao, X., 2010. A multilevel hierarchical image segmentation method for urban impervious surface mapping using very high resolution imagery. *IEEE Journal of Selected Topics in Earth Observations and Remote Sensing* (in revision).
- Lu, D. and Weng, Q., 2009, Extraction of urban impervious surfaces from an IKONOS image. *International Journal of Remote Sensing*, 30(5), pp. 1297-1311.
- Munoz-Marí, J., Bruzzone, L. and Camps-Valls, G., 2007. A support vector domain description approach to supervised

classification of remote sensing images. *IEEE Transactions on Geoscience and Remote Sensing*, 45(8), pp. 2683-2792.

Najman, L. and Schmitt, M., 1996. Geodesic saliency of watershed contours and hierarchical segmentation. *IEEE Transactions on Pattern Analysis and Machine Intelligence*, 18(12), pp. 1163-1173.

Roeck, T.D., der Voorde, T. V. and Canters, F., 2009. Full hierarchical versus non-hierarchical classification approaches for mapping sealed surfaces at the rural-urban fringe using high-resolution satellite data. *Sensor*, 9, pp. 22-45.

Sanchez-Hernandez, C., Boyd, D S and Foody, G M., 2007. One-class classification for mapping a specific land-cover class: SVDD classification of Fenland. *IEEE Transactions on Geoscience and Remote Sensing*, 45(4), pp.1061-1073.

Schmitt, M., 1998, Response to the Comment on "Geodesic Saliency of Watershed Contours and Hierarchical Segmentation. *IEEE Transactions on Pattern Analysis and Machine Intelligence*, 20(7), pp. 764-766.

Yuan, F., and Bauer, M. E., 2006. Mapping impervious surface area using high resolution imagery: a comparison of object-oriented classification to per-pixel classification, In *Proceedings of American Society of Photogrammetry and Remote Sensing Annual Conference*, May 1-5, Reno, NV, CD-ROM.

Zhou, Y. and Wang, Y. Q., 2008, Extraction of Impervious Surface Areas from High Spatial Resolution Imagery by Multiple Agent Segmentation and Classification. *Photogrammetric Engineering and Remote Sensing*, 74(7), pp. 857-868.

ACKNOWLEDGEMENTS

This study was financially supported by National High-Tech Program, Ministry of Science and Technology, China (Grant number 2008AA121806).

BUILDING MODEL RECONSTRUCTION WITH LIDAR DATA AND TOPOGRAPHIC MAP BY REGISTRATION OF BUILDING OUTLINES

B. C. Lin^{1*}, R. J. You², M. C. Hsu³

Department of Geomatics, National Cheng Kung University, 1 University Road, Tainan City, Taiwan –

¹p6889102@mail.ncku.edu.tw

²rjyou@mail.ncku.edu.tw

³p66984095@mail.ncku.edu.tw

KEY WORDS: Tensor Voting, Feature Extraction, Registration, Robust Least Squares, Data Fusion

ABSTRACT:

This study integrates LiDAR data and topographic map information for reconstruction of 3D building models. The procedure includes feature extraction, registration and reconstruction. In this study, the tensor voting algorithm and a region-growing method with principal features are adopted to extract building roof planes and structural lines from LiDAR data. A robust least squares method is applied to register boundary points of LiDAR data with building outlines obtained from topographic maps. The registration accuracy is about 11 cm in both x- and y- coordinates. The results of the registration method developed here are satisfactory for the subsequent application. Finally, an actual LiDAR dataset and its corresponding topographic map information demonstrate the procedure for data fusion of automatic 3D building model construction.

1. INTRODUCTION

The needs for building models are growing rapidly in 3D geographic information system (GIS), and hence a large number of accurate building models have become necessary to be reconstructed in a short period of time. Recent developments in airborne LiDAR have made it a new data source for 3D building model reconstruction, since LiDAR can quickly provide a large number of highly qualitative point clouds to represent building surfaces (Maas and Vosselman 1999). However, the LiDAR data has poor texture information so that the accurate building boundary extraction from LiDAR data may be difficult. Therefore, data fusion involving both LiDAR data and the existing topographic maps can improve the 3D building model reconstruction process.

A number of researchers have studied the problem of feature extraction from LiDAR data to reconstruct 3D building models (Vosselman and Dijkman 2001; Filin 2002; Overby *et al.* 2004). In general, building roof patch features are first extracted from LiDAR data. Many methods (Filin, 2002; Maas and Vosselman, 1999; Overby *et al.*, 2004) can be used for the extraction of roof patch features from LiDAR data. Next, building models are reconstructed by combining the building boundaries obtained from ground plans and intersection lines of adjacent planar faces derived from LiDAR data.

These approaches, however, may produce unreliable results in 3D building model reconstruction if the coordinate systems of LiDAR data and the ground plans are not the same. To overcome the problem of coordinate systems of various data sources, data registration is a critical step for fusion of LiDAR data and the topographic map information (Schenk and Csatho 2002; Filin *et al.* 2005; Gruen and Akca 2005; Park *et al.* 2006).

In this study, plane segments in LiDAR data are extracted in the feature space based on the tensor voting computational framework (Medioni *et al.* 2000). The tensor voting algorithm implements features such as faces, lines and points through a symmetric tensor field directly derived from data. All geometric structures (surfaces, lines and points) can therefore be inferred simultaneously. This method also offers extra information about the strength of features which can indicate the main geometric characteristic of a point.

For registration of LiDAR data and topographic maps, a robust least squares method (RLS) is adopted to estimate the transformation parameters in this study. After registration, height information and roof ridges extracted from LiDAR data are introduced to topographic maps and then the spatial positions of building outlines can be reconstructed.

In the following, the tensor voting method and the registration method are first described. Finally, an experimental result based on an actual airborne LiDAR dataset is analyzed.

2. FEATURE EXTRACTION

2.1 Tensor communication

The geometric feature of a point can be described by a second-order symmetric tensor which is expressed as follows:

$$\mathbf{T}^p = \begin{bmatrix} \bar{e}_1 & \bar{e}_2 & \bar{e}_3 \end{bmatrix} \begin{bmatrix} \lambda_1 & 0 & 0 \\ 0 & \lambda_2 & 0 \\ 0 & 0 & \lambda_3 \end{bmatrix} \begin{bmatrix} \bar{e}_1 \\ \bar{e}_2 \\ \bar{e}_3 \end{bmatrix} \quad (1)$$

* Corresponding author.

where \bar{e}_1 , \bar{e}_2 and \bar{e}_3 indicate three independent and orthogonal eigenvectors; λ_1 , λ_2 and λ_3 are eigenvalues with respect to the eigenvectors \bar{e}_1 , \bar{e}_2 and \bar{e}_3 . The eigenvalues are real and $\lambda_1 \geq \lambda_2 \geq \lambda_3$ if \mathbf{T}^p is a positive-semidefinite tensor. Most of LiDAR systems provide only three-dimensional Cartesian coordinates of points, and implied vector information cannot be directly obtained. The tensor voting algorithm presented here can be applied for deriving the vector information. The kernel of the tensor voting is the tensor communication among points. Each point receives vector information from its neighbouring points and stores the vector information by the tensor addition rule. The total tensor can be expressed as follows:

$$\mathbf{T} = \sum_{i=1}^m w_i \mathbf{T}_i^p \quad (2)$$

$$w(s) = \exp(-s^2 / k^2) \quad (3)$$

where w is a Gaussian decay function, s is the distance between the receiving site and the voting site, and k is a scale factor that controls the decay rate of the strength. In our experiments, the scale factor k is equal to 1.2 times the search radius, and the search radius region includes at least 20 points.

2.2 Tensor decomposition

After the tensor voting procedure is completed, the geometric feature information, such as planar, linear and point features, can now be detected according to the capture rules of geometric features mentioned in Medioni et al.(2000). However, the eigenvalues λ_1 , λ_2 and λ_3 are generally smaller in the border region of an object than in the central region of the same object, because the points in the border region collect fewer votes than the points in the central region do. To reduce the effect of the number of votes, the planar feature indicators $\lambda_1 - \lambda_2$ may be normalized as

$$c_1 = \frac{(\lambda_1 - \lambda_2)}{\lambda_1} \quad (4)$$

The normalized value of planar strength are introduced for the planar feature extraction and the region growing in this study, since it is the sensitive indicator for planar features.

2.3 Region growing with principle feature

The region-growing method is adopted to collect the points with similar planar features. The region-growing method used here is based on the homogeneity of the principal features. The principal features of interest are the planar feature strength and the corresponding normal vectors in this study. In region-growing, only the points with the planar feature strength c_1 greater than a threshold can be adopted as seed points. Since the strength of planar features in building areas is often greater than 0.96 in our experiments, the threshold is recommended to be 0.96 or larger. First, the point that has the largest c_1 -value is chosen as the seed point for the planar feature extraction. A point is merged into the region if both the c_1 -value and the

directional difference of the normal vector of that point are less than the corresponding thresholds. Then, the point with the second largest c_1 -value in LiDAR data, excluding all extracted points in the region associated with the first seed point, is adopted as the second seed point for growing the next region. This region-growing procedure proceeds until no more seed points are available. Figure 1 illustrates segmentation result after region growing.

2.4 Ridge lines and boundary points

The method for extracting ridge lines used here is based on the intersection of two adjacent roof faces segmented from LiDAR data, as recommended by Maas and Vosselman (1999). The accuracy of the ridge line is about 0.4° in spatial angle. According to the rule that the triangles on the outer boundary of a triangular irregular network (TIN) mesh have only one or two neighboring triangles(Pu and Vosselman 2007), a TIN structure is adopted to extract boundary points.

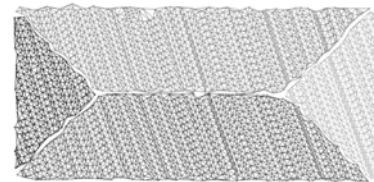


Figure 1. LiDAR points and TIN structure

3. FUSION OF LIDAR AND MAP

3.1 Registration

The first step for fusing LiDAR data and topographic map information is to transform these two datasets to a common coordinate system. The discrepancies between boundary points and building outlines are depicted in Figure 2. To determine the transformation parameters, we use robust least squares matching with the objective function which consists of the sum of squares of the distances from boundary points to building outlines on a local xy-plane.

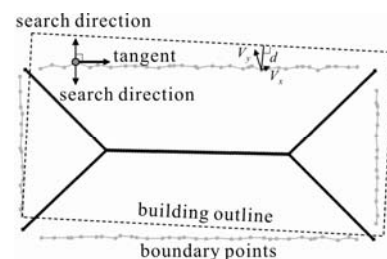


Figure 2. Boundary points and ridge lines

In order to register the boundary LiDAR points of buildings to the corresponding outline segments, a 2D similarity transformation is adopted as a mathematical tool in this study:

$$\begin{bmatrix} x' \\ y' \end{bmatrix} = \begin{bmatrix} w & u \\ -u & w \end{bmatrix} \begin{bmatrix} x \\ y \end{bmatrix} + \begin{bmatrix} r \\ s \end{bmatrix} \quad (5)$$

where (x,y) are the horizontal coordinates of a LiDAR point in a local coordinate system; (x',y') are the new coordinates in the map system after the transformation; and (r,s) are the shifts of the origin. $w = m \cos\alpha$ and $u = m \sin\alpha$, where α is the rotation angle and m is the scale factor.

Assume that boundary points with the new transformed coordinates should fall exactly on an outline segment represented by $L: ax'+by'+c=0$. By inserting Eq.(5) into the line equation L , we have the following relation:

$$(a(x+v_x) + b(y+v_y))w + (-b(x+v_x) + a(y+v_y))u + ar + bs + c = 0 \quad (6)$$

where (a,b,c) can be calculated from the corresponding polygon data of an outline segment, and the residuals v_x and v_y represent two components of the distance vector from a LiDAR point to the corresponding outline segment. The RLS method developed at Stuttgart University is adopted to estimate the transformation parameters (Klein and Foerstner 1984).

The registration process is performed by iterative RLS method. In each iteration of RLS adjustment, the corresponding outline segment for each boundary LiDAR point located now by new transformed coordinates must be re-determined. The procedure proceeds until the estimated standard deviation of the distances is convergent.

3.2 Reconstruction

After registration, an automatic reconstruction of 3D building models is applied. In this procedure, structural lines on roofs and height information of each building outline node are needed. The height of each building node can be determined by the plane equation of a LiDAR surface segment. Structural lines are extracted by the method mentioned in section 2.4. The ridges and the building outlines are automatically connected according to following rules:

1. The structural lines derived from LiDAR data should be first extended to boundary lines on the local xy -plane, when they are shorter than they should be.
2. If the intersection point of a structural line and a boundary line is near a node point within a small region, the structural line is directly connected to the node point (case A in Figure 3).
3. If the height of a structural line at the intersection point is not different from the height of the boundary line, the structural line is directly connected to the boundary line and a new node of the boundary line is added (case B in Figure 3).
4. If the height of a structural line at the intersection point is significantly different from the height of the boundary line, two new additional structural lines may be needed (case C in Figure 3).

Then a 3D building model can be reconstructed.

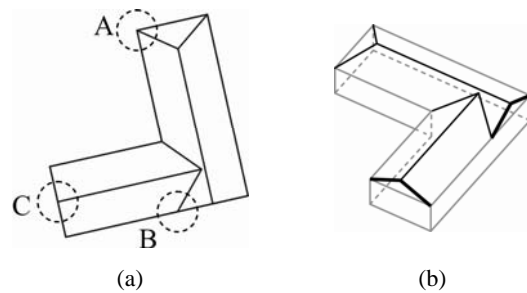


Figure 3. Connection of ridge and eave lines.

3.3 System overview

In summary, the proposed automatic procedure to combine data from LiDAR and topographical maps includes feature extraction, registration and reconstruction. Figure 4 illustrates this procedure. First, boundary points and ridge lines are derived from surface segments extracted from LiDAR data by the tensor voting method, and building outlines are obtained directly from corresponding 2D topographical map data. Since the coordinate systems of these two kinds of data may differ, registration of this data is necessary. Second, since it is insensitive to errors, registration of the boundary LiDAR points and the building outlines using the RLS method is recommended. Third, 3D building outlines are obtained by introducing the heights of 2D building outlines based on the plane equations of the LiDAR surface segments. Finally, the ridge lines are added and combined with the 3D building outlines for constructing building models.

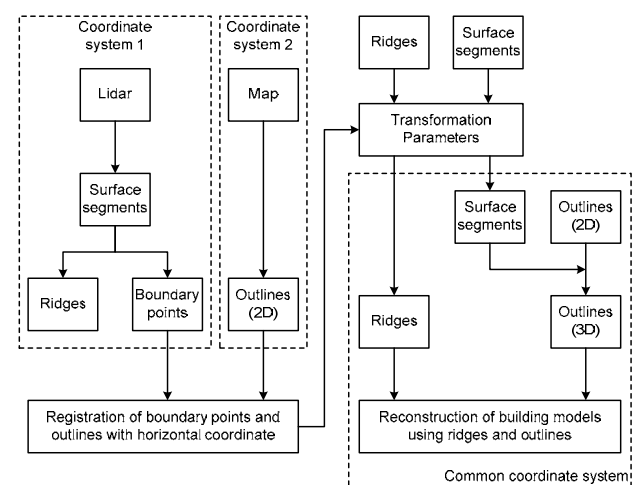


Figure 4. Procedure of automatic building model reconstruction with LiDAR data and topographic map information.

4. EXPERIMENT AND ANALYSIS

An airborne LiDAR dataset (LiDAR97) for an $350 \times 500 \text{ m}^2$ experimental area was acquired by an Optech ALTM 30/70. The flying height for the laser scanning was 500 m AGL. The average LiDAR point density was 6 pts/m^2 . The horizontal and vertical precision was about 25 cm and 15 cm respectively. This dataset was referred to Taiwan geodetic datum 1997.0 (TWD97). The topographic map (Map67) with scale 1:1000 for this area was produced from the aerial images and is based on Taiwan geodetic datum 1967 (TWD67). 45 building corners,

whose coordinates in both TWD67 and TWD97 were known, were selected as check points.

By comparing the registered and the known coordinates of the check points in TWD97 datum, an rms value for the coordinate differences is of about 11 cm in both x- and y- coordinates (Table 1). This indicates that the results of the registration method developed here are satisfactory for the subsequent application.

Difference	$\Delta x(m)$	$\Delta y(m)$
max	0.326	0.309
mean	0.048	-0.030
rms	0.109	0.110

Table 1. Coordinate differences of check points.

The quality of reconstructed building models is evaluated by manual check. In Figure 5, a closed polygon represents a building. Our results have shown that in total 34 of 108 buildings are incorrect building models showed with gray polygons in Figure 5 using our automatic procedure.



Figure 5. Incorrect building models (gray polygons) in the test area.

These incorrect polygons always arise on certain cases. These cases can be divided into two categories: (1) Roof faces are partly or fully covered by neighbouring buildings or trees, as shown in case A in Table 2. (2) Building outlines are not detailed enough, as shown in case B in Table 2. In cases B, small buildings are inside a big building, but the outlines of the small buildings are not drawn in the map. In all these cases, boundary LiDAR points are not sufficient to match with building outlines. This shows that these discrepancies between the boundary points and the outlines of that building influence the results of the reconstruction of building models. All of these incorrect models should be refined manually, by photogrammetry, or even field work, for instance. The complete result of automatic reconstruction of 3D building models is drawn in Figure 6.

	Actual buildings	Map + LiDAR	Reconstructed models
A			
B			

Table 2. Fusion of LiDAR data and topographic map after registration and the results of building model reconstruction.

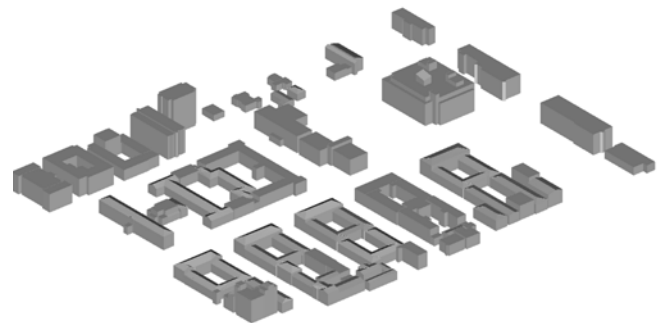


Figure 6. Complete result of automatic reconstructed building models.

5. CONCLUSIONS

This study has presented a novel method to construct building models by fusing LiDAR data and topographic map information. A procedure for registering the boundary points of building roof patches extracted from LiDAR data and outlines of buildings acquired from topographic maps has been proposed by a robust least squares method.

The experiments have shown that the proposed method for the building reconstruction procedure with LiDAR data and topographic map information, including feature extraction, registration and reconstruction, can be processed automatically and yields good results. Although manual editing is needed in order to achieve refined 3D building models, the results have shown that our method takes advantages of both surfaces and boundary information and improves the building reconstruction process.

6. REFERENCES

- Filin, S., 2002. Surface clustering from airborne laser scanning data. *International Archives of Photogrammetry and Remote Sensing*, 34(3A), pp. 119-124.
- Filin, S., Y. Kulakov and Y. Doytsher 2005. Application of Airborne Laser Technology to 3D Cadastre. *FIG Working Week 2005 and GSDI-8*, Cairo, Egypt.
- Gruen, A. and D. Akca, 2005. Least squares 3D surface and curve matching. *ISPRS Journal of Photogrammetry and Remote Sensing*, 59(3), pp. 151-174.

Klein, H. and W. Foerstner, 1984. Realization of automatic error detection in the block adjustment program PAT-M43 using robust estimators. *International Archives of Photogrammetry and Remote Sensing*, 25(A3a), pp. 234-245.

Maas, H. G. and G. Vosselman, 1999. Two algorithms for extracting building models from raw laser altimetry data. *ISPRS Journal of Photogrammetry and Remote Sensing*, 54(2-3), pp. 153-163.

Medioni, G., M. S. Lee and C. K. Tang (2000). *A computational framework for segmentation and grouping*. Elsevier Science, New York.

Overby, J., L. Bodum, E. Kjems and P. M. Ilsoe, 2004. Automatic 3D building reconstruction from airborne laser scanning and cadastral data using Hough transform. *International Archives of Photogrammetry and Remote Sensing*, 35(B3), pp. 296-302.

Park, J., I. Lee, Y. Choi and Y. J. Lee, 2006. Automatic Extraction of Large Complex Buildings Using LiDAR Data and Digital Maps. *International Archives of Photogrammetry and Remote Sensing*, 36(3), pp. 148-154.

Pu, S. and G. Vosselman, 2007. Extracting windows from terrestrial laser scanning. *International Archives of Photogrammetry Remote Sensing and Spatial Information Sciences*, 36(3/W52), pp. 320-325.

Schenk, T. and B. Csatho, 2002. Fusion of LIDAR data and aerial imagery for a more complete surface description. *International Archives of Photogrammetry and Remote Sensing*, 34(3A), pp. 310-317.

Vosselman, G. and S. Dijkman, 2001. 3D building model reconstruction from point clouds and ground plans. *International Archives of Photogrammetry and Remote Sensing*, 34(3/W4), pp. 37-43.

ADVANCES ON REPEATED SPACE-BORNE SAR INTERFEROMETRY AND ITS APPLICATION TO GROUND DEFORMATION MONITORING-A REVIEW

Zhenguo Liu^{a,b,*}, Zhengfu Bian^{a,b}

^a Jiangsu Key Laboratory of Resources and Environmental Information Engineering, Xuzhou, Jiangsu Province 221116, P.R. China

^b School of Environment Science & Spatial Informatics, China University of Mining and Technology, Xuzhou, Jiangsu Province 221116, P.R. China

KEY WORDS: Differential, SAR, Interferometry, Ground Deformation, Permanent Scatterer

ABSTRACT:

Differential synthetic aperture radar interferometry (D-InSAR), is a remote sensing technique that could measure earth surface deformation and has gained extensive use along with its development as a technique and subject, from classical to advanced D-InSAR. The main principles of both were concisely depicted and the differences and relations between highlighted. Then an introductory review concerning applications of InSAR technology in China and obstacles therein to make the technique operational for coal-mining induced deformation was made. The other method developed for a more accurate InSAR application, consisting in GPS assisted and multi-platform SAR interferometry, atmospheric artefact modelling are introduced, and ended up with the conclusion part where the main limitations were put forward.

1. INTRODUCTION

Repeated SAR Interferometry (InSAR) technique, based on the combination of two radar images, has been exposed by Graham (Graham, 1974), allowing not only the retrieval of a Digital Elevation Model (Zebker et al., 1986), but also large-scale surface deformation monitoring (Differential InSAR, D-InSAR). The high density of measurement, with an accuracy of 1cm for single interferogram, allows generation of a map of ground deformation (Gabriel et al., 1989; Massonnet et al., 1993; Massonnet et al., 1995; Carnec et al., 1999).

The principle of D-InSAR(hereafter referred to as Classical D-InSAR, compared with the Advanced D-InSAR techniques to be detailed in Section 2) is to first obtain two interferograms of a study area, called Topo-defo interferogram and Topo respectively, and then make a difference between them to detect the deforming information if any. Just as the name implying, there are topographic and deforming information in the former, while topographic information only in the latter, which can be formed either through synthesizing an existed DEM (2-pass D-InSAR), or two SAR images acquired before the time deformation taking place.

Besides the above mentioned, Classical D-InSAR has gained extensive use elsewhere (Perski, 1998; Strozzi et al., 1999; Ge et al., 2008) and has become one of the efficient tools in surface deformation monitoring, among which there are GPS, VLBI conventional precise levelling and theodolite survey, EDM and remote electronic monitoring, to name a few.

Classical D-InSAR, however, faces several limitations essentially due to temporal and geometric decorrelation, atmospheric inhomogeneity, besides the presence of uncompensated topography due to the limited accuracy of DEM utilized. When random motion takes place within SAR-imaging pixels, such as those caused by crop growth, leaf fluctuation,

interferometric phases will become noisy, thus causing temporal decorrelation, which will certainly prohibit us from accurate low-velocity deformation monitoring, where differential interferograms are forced to have large temporal baseline. Geometric decorrelation happens when there exists the excessive separation between satellites' orbits the perpendicular baseline, B_{\perp} , which will significantly reduce the number of image pairs suitable for interferometric application. (Jarosz et al., 2004). An additional limitation, atmospheric inhomogeneity, common to both large or small baseline interferograms, creates an atmospheric phase screen (APS) superimposed on each SAR image that can sometimes seriously degrade the quality of deformation estimation (Zebker 1997; Goldstein, 1995; Williams, 1998; Hanssen,1998; Carnec C. et al., 1996).

Fortunately, these limitations are well addressed in the advanced D-InSAR techniques, which will be introduced in the following.

2. ADVANCED D-INSAR TECHNIQUES

During several yeas of study, S.Usai et al (Usai et al., 1997; 1998;1999) found that some certain samples, mainly of anthropogenic nature, such as buildings, bridges, railways and roads, highly and reliably coherent in spite of the long-time interval, manifesting themselves as strong, nearly point-like bright dots in an almost completely decorrelated interferograms. The Advanced D-InSAR techniques then hunt for and utilize these pointwise targets to track the temporal evolution of the detected deformation, to which the scientific community has shown great interests.

Based on the coherent-target hunting strategy and the processing method for signal-of-interest isolation, the advanced techniques recently developed are classified as four types, i.e. Least Square approach, Permanent Scatterer SAR

* Corresponding author. Email Address: lzggis@163.com

Interferometry, Small Baseline Subset, Coherent Pixel Technique, which will be introduced chronologically in some detail, together with the differences and relations between each.

2.1 Least Square database approach (LS approach)

After analyzing the phase stability of some man-made features, S.Usai et al (Usai et al., 1997,1999,2000) presented a new approach, known as Least Square approach (LS), for the long-term monitoring of terrain deformations with D-InSAR. This method uses a database of interferograms, and by solving all the deformation velocities as a unique least squares problem provides a chronologically ordered sequence, describing the evolution of the deformation pattern in time (Usai, 2002).

2.1.1 Main principle

The input for the least squares adjustment is a set $y=[I_1, \dots, I_N]$ of N unwrapped interferometric deformation maps (i.e., the unwrapped interferograms are compensated for topographic and flat-earth phases), all coregistered at subpixel level, generated from M SAR images taken at days $x=[d_1, \dots, d_M]$. The day d_1 corresponding to the first image is taken as reference and the deformations at each of the other $(M-1)$ days relative to this day considered as solutions of the problem:

$$y=Ax \quad (1)$$

where in x the element d_1 not been considered.

In the system matrix A , each row corresponds to an interferogram, while the columns correspond to the days. For interferogram $I_k=I_{di}-I_{dj}$, the values on row k are all zero except at columns i and j , being $+1$ and -1 respectively and A an incidence like matrix, directly depending on the set of interferograms generated from the M SAR images.

The unweighted least squares solution x of Eq.1 is straightforward:

$$x=(A^T A)^{-1} A^T y \quad Qx=(A^T A)^{-1} \quad (2)$$

2.1.2 Some notes on LS approach

The LS approach has been applied to measure terrain displacements in the period 1993-1999 at the Phlegrean Fields (Naples, Italy), using a set of 20 ERS-1/2 SAR images, and 43 interferograms generated (Usai, 2002; Usai, 2003). The authors made use of an external DEM to obtain the differential interferograms and found that residual topography had caused systemic effects in the data. In addition, during the processing, a closed-loop method was used to detect and remove image- and interferogram-related biases. In fact, according to Usai, (Usai, 2001) two kinds of biases can be identified: the image-related ones, like for example those caused by atmospheric disturbances; and the interferogram-related ones, i.e. those which have been produced in the interferometric combination of two images, most probably by phase-unwrapping errors.

2.2 Permanent Scatterer (PS)

The Permanent Scatterer technique, developed at the 'Politecnico di Milano' (Milan, Italy) (Ferretti et al., 1999; 2000; 2001), is the first of a family of similar advanced interferometric techniques-Permanent Scatterer Interferometry (PSI).

Given $N+1$ images, a set of N differential interferograms is generated with respect to a single master. High temporal and normal baseline interferograms (affected by a high decorrelation noise) are, thus, part of the dataset. The approach focused on privileged image pixels that, even in these 'extreme conditions',

still exhibit a low noise term, thus the so-called Permanent Scatterers. With PS technique, pixels are selected from the study of its amplitude stability along the whole set of images (typically >30). Therefore, the maximum resolution of the SLC images is preserved (Ferretti et al., 2001)

After PS candidates selection, a linear model is adjusted to the data to estimate the deformation linear velocity and possible DEM errors for each PS Candidate. Then the atmospheric phase screen (APS) for the master image and the nonlinear motion contribution and APS for each image are computed through a spatio-temporal filtering. After estimation and removal of all the APS superimposed on the data, one can identify more PSs and repeating the previous steps allows getting the whole deformation time series and average LOS displacement rate of every single PS, and a refining DEM with sub-metric precision of the exact height of the object corresponding to the PSs.

2.3 Small Baseline Subset (SBAS)

The Small Baseline Subset (SBAS) approach, proposed by Berardino et al. (2001; 2002), extends the Least Squares approach (Usai, 2001; 2002; 2003; Lundgren et al, 2001) to the case of multiple small baseline acquisition subsets. The key point, in addition to the use of multi-look interferograms, is that the data pairs involved in the generation of the interferograms are carefully selected in order to minimize the spatial baseline, thus mitigating the decorrelation phenomenon and topography errors. The Singular Value Decomposition (SVD) method is applied to link otherwise independent SAR datasets separated by large baselines. The SBAS method was originally used to investigate large scale deformations with spatial resolution of about $100m \times 100m$, calculating the time sequence deformation and estimating DEM error and the atmospheric artifact in a similar way as PS. O.Mora et al (O.Mora et al., 2002) promoted a complementary approach, utilizing two different sets of data generated at low (multi-look) and full resolution (single-look) respectively, to monitor localized deformation. The former are used to identify and estimate possible atmospheric phase artifacts and low-wavenumber deformation patterns based on SVD SBAS method or CPT (Mora et al., 2003); the latter to detect, on the high-resolution residual phase components, structures highly coherent over time like buildings, rocks, lava structures, etc.

2.4 Coherent Pixels Technique (CPT)

Developed by O.Mora et al (2003), original CPT gained its first use (Mora et al., 2001) in the long-term subsidence monitoring of an area of small town in Spanish, choosing the temporal-coherence as criterion for permanent scatterers selection only to make flexible the SAR images requirement in PS. The results, utilizing seven SAR images, turned out to be satisfactory and coincided well with the DGPS measurements.

Recently, CPT has been improved (Blanco et al., 2007; Duque et al., 2007) into an operational advanced technique for terrain deformation mapping, in terms of linear and nonlinear deformation extraction, robustness with DEM error, thus allowing DEM refining, and atmospheric phase screen (APS) removal. P.Blanco et al (2008) concluded this approach and detailed the main steps, such as optimal interferogram sets selection, coherent pixels selection, linear and nonlinear blocks for a full deformation extraction. The related algorithms consist of Delaunay triangulation and Minimum Spanning Tree (MST) for best combination of interferograms selection, Conjugate Gradient Method (CGM) for Phase Unwrapping, multi-layer for

liable estimation of linear deformation. What's more, by integrating the amplitude-based criterion for pixels selection, CPT can provide full-resolution deformation. In some sense, we can say CPT is a well-integrated technique of the main PSI techniques.

2.5 Other techniques

Some other multiple-interferogram techniques for deformation monitoring emerge and gained many uses as well, including, Interferometric Points Targets Analysis (IPTA) developed by GAMMA remote sensing research group (Wegmüller et al., 2000; Werner et al., 2003) in Switzerland, Spatio-Temporal Unwrapping Network (STUN) (Kampes et al., 2005) and phase gradient approach to stacking interferograms (Sandwell et al., 1998; Raucoules et al., 2003; Rocca, 2007). Moreover, there is STBAS (Small Temporal BASeline Subset) for monitoring of wetland's water level changes (Hong et al., 2008).

2.6 Remarks on Advanced D-InSAR techniques

Compared with Classical D-InSAR, which employs several SAR images (4 at most for the 4-pass version D-InSAR) to analyze a single deformation episode, Advanced D-InSAR technique fully exploits the SAR archives available, and we may consider it a postprocessing step (Usai, 2003; Berardino et al., 2002) applied to the set of D-InSAR interferograms that may be generated via already available interferometric data processing tools. Based on this, several considerations are in order.

2.6.1 Foundation of Advanced D-InSAR

The input of Advanced D-InSAR is a set of Differential interferograms. Therefore, a careful D-InSAR processing has to be implemented, controlling the quality of all major processing steps (e.g. image co-registration, phase unwrapping, etc.), guaranteeing a high quality set of input data for the Advanced techniques. This is of particular significance for PS method, where no compulsive constraints are enforced on temporal and spatial baseline and any noisy area existed will introduce mis-registration problems. Phase unwrapping, on the other hand, always remaining the most delicate issue, behaves as a sparse and irregularly sampled data unwrapping problem in advanced techniques, and can be performed following a two-step algorithm (Ghiglia et al., 1998)□

1) estimation of the unwrapped phase differences between neighboring pixels; 2) integration of the gradient using one of the known techniques, such as minimum cost flow (Costantini, 1998), weighted least mean squares (Ghiglia et al., 1998; Spagnolini, 1995), and branch and cut (Goldstein et al., 1988).

2.6.2 Data acquisition

Besides the large stack of SAR images required, uniform distribution of temporal and spatial baselines are always preferred in order to acquire more accurate and reliable information about the ongoing deformation. However, global availability of SAR acquisitions is somewhat limited. Many areas have few or no acquisitions unless the area of interest was previously tasked for imaging. For example, there are subsiding areas in Mexico and in the People's Republic of China that have significant aquifer-system compaction problems, however, with limited ERS SAR coverage. For Envisat SAR coverage, the various selectable polarizations of the transmitted electromagnetic SAR signal may limit the availability of SAR-image pairs suitable for InSAR processing (Galloway et al., 2007).

2.7 Difference and similarity among Advanced techniques

Besides several differences among the techniques detailed above, mainly relying in data requirements (minimum number of SAR images, more than thirty needed for PS for a well statistics estimation of phase stability), the limitations on baseline length (SBAS, LS, CPT), the need of multilooking (SBAS, LS, CPT), the multi-pair approach (SBAS, LS, CPT) for interferogram formation, there exist several similarities among them.

2.7.1 Deformation extraction strategy

All the techniques extract deformation through a two-step way, linear and nonlinear. In fact, we'd better regard the introduction of a linear model as a way to clean phase to make easier nonlinear estimation. Such a strategy, dividing and conquering, running through the whole signal isolation process, does help a lot (Blanco et al., 2007).

2.7.2 APS estimation and removal

The output of Advanced D-InSAR includes LOS displacement rate, DEM error, and Atmospheric disturbance, with the latter two byproducts indicating great superiority compared with Classical D-InSAR, and in some way justifying the need of a large number of images (Ferretti et al., 2000).

After the estimation and removal of linear phase (linear deformation and DEM error phases), theoretically, three contributions still remain: APS, nonlinear deformation and noise. In practice, however, the noise contribution was mitigated to the minimum either due to the multilooking process in SBAS and CPT, or due to the neighboring differencing in PS and CPT, thus only APS being the target to be cleaned. Based on the observation that the atmospheric signal phase component is characterized by a high spatial correlation and exhibits a significantly low temporal correlation (random), the desired nonlinear deformation is estimated as the result of the cascade of a spatial low-pass and a temporal high-pass filtering operation, with APS removed (Ferretti et al., 2001; Berardino et al., 2002; Mora et al., 2003).

2.7.3 Multi-plantform interferometry

The frequency difference between ERS and EnviSAT, although a small shift, limits the possibilities of the generation of useful cross-interferograms (Monti et al., 2000). For a flat surface, theoretically, it's possible to compensate for the 31 MHz center frequency difference unless the normal baseline reaches 2100m (Gatelli et al., 1994). Although some researchers found several pairs of images for successful crossing-interferometry by searching, with delicacy, the whole archives (Santoro et al., 2007), we should note that the consequence of such large baselines are, on the one hand, the restrictive elevation of ambiguity with respect to the image, around 4.5m, which makes the interferograms sensitive to topography. On the other hand, interferograms with large baseline are extremely sensitive to volumetric decorrelation, which poses great limitation in urban areas.

Again, Advance DInSAR techniques circumvent the above dilemma elegantly, exploiting pointwise targets, as in the case of the Permanent Scatterer approach (Arrigoni et al., 2003; Ferretti et al., 2004; Wegmüller et al., 2005) that allows investigating the temporal evolution of the detected displacements by analyzing full-resolution (single look) interferograms, or in the SBAS and CPT cases, by considering ERS and EnviSAT as independent subsets, searching for a least

squares solution with a minimum norm deformation velocity vector constraint (Berardino et al., 2004; Pepe et al., 2005; Mallorquí et al., 2005; Blanco et al., 2006)

3. APPLICATION OF INSAR TECHNOLOGY IN CHINA

InSAR technique has penetrated through almost every surface-deformation related monitoring, thanks to the Advanced D-InSAR technique. In general, InSAR has evolved to be able to monitor and track deformation, with great elegance, of different causes including tectonic seismic and volcanic activity, ice and rock glacier motion, slope instability, and subsidence caused by ground water pumping, mining, hydrocarbon extraction, and natural compaction in high precision and reliability.

In the late 1990s, InSAR technology was introduced into China and gained firstly an experimental use and then became operational mainly on the subsidence taking place in urban area due to either water pumping and/or underground construction, besides the active tectonic caused deformation (Zhao et al., 2009; He et al., 2006; Xu et al., 2008) and co-seismic deformation extraction and modeling (Shan et al., 2002; Ji et al., 2009). Recently, Advanced D-InSAR techniques gain their use in long-term series deformation monitoring in urban areas (Fang et al., 2009; Li et al., 2009; Jiang et al., 2009; Huang et al., 2008).

InSAR technique has also been used to monitor mining-induced subsidence, with the main squeeze being coal mining in China (Cao et al., 2008) in a cost-effective way due to the vast area influenced, which could be considered a startup and experimental and there's certainly a long way to go for the operational use. The main reasons may consist in the limited data acquisition and the inherent limitation of InSAR for large-gradient and/or vegetated surface subsidence monitoring.

4. GPS AND D-INSAR INTEGRATION

Due to the unknown phase ambiguity number and the limited knowledge of the satellites's position, measurements from D-InSAR are essentially relative ones. In order to relate these measurements to a reference datum, a priori information is required, such as Ground Control Points, absolute deformations from GPS or other geodetic techniques. What's more, both atmospheric artifacts and orbital fringes feature high spatial correlation, since their correlation typically exceeds 1km. Local spurious components are compensated for by the double difference computation inherent in any Advanced DInSAR analysis, but regional signals affecting hundreds or even thousands of square kilometers can be difficult to discriminate without a priori information, thus justifying the complementarity between GPS and DInSAR data, which can be used in synergy to map surface deformation (Prati et al., 2009).

The idea of InSAR and GPS integration was perhaps first suggested in 1997 (Bock et al., 1997; 1998). Ge et al (1997, 2000) proposed a DIDP approach for this integration. A methodology that uses Markov Random Field (MRF) based regularization and simulating annealing optimization was then proposed by Sverrir Guemundsson (2000) to unwrap InSAR images, obtaining a high-resolution 3-D motion field from combined GPS and interferometric observations. With GPS, MODIS and MORIS data, Li et al (Li, 2005a; Li et al., 2005b)

produced regional water vapor model with a spatial resolution of 1km*1km, which, applied to the ERS-2 repeat-pass data, assisted in discriminating geophysical signals from atmospheric artifacts. Doin et al. (2009) proposed another approach, using global atmospheric models (GAM), to model and remove the stratified tropospheric delay efficiently.

5. DISCUSSIONS AND CONCLUSION

D-InSAR technology has demonstrated unsurpassed capabilities of the technique in terms of deformation monitoring, and has embedded itself one of the most widely used geodesy techniques, combining the characteristics of large-scale imaging and high-accuracy quantitative observations, particularly of dynamic processes. However, there still exist several limitations at present, related as follows:

- A) Excessive subsidence (i.e., big phase gradient) taking place in one repeat cycle of satellite makes impossible deformation measurement without a priori information;
- B) A systematic errors introduced during the D-InSAR process, such as caused by mis-coregistration, orbit perturbation, inaccurate topography model, phase unwrapping, atmospheric artifact, remains unknown, and the precision evaluation of the end-product at present only comparatively known through a so-called Quantitative Analysis step (i.e., making comparisons with respect to traditional implementation geodetic method);
- C) Characteristics of PSs, utilized in PSI techniques, require a thoroughly study, in order to geocode and interpret the studied PS deformation more accurately to the local structure;
- D) In some cases, such as the coal mining influenced area, where typically displacement in all the 3-D takes place, making subsidence not so dominating, chances are unpractical deforming information will be acquired.

With the newly launched satellites and some ongoing research activity, the above-mentioned limitations can be addressed, to a certain extent at least, if not completely. For example, the newly launched four SAR satellites, operating at X-band, feature short repeat cycles: three belong to the dual-use Cosmo-SKymed constellation operated by the Italian Space Agency, with a 4-day cycle, and one is the German TerraSAR-X, with the cycle of 11 days could make less likely excess subsidence. What's more, some ongoing research activity are aiming at the study of the nature of PSs, and striking results have already been reported (Ferretti et al., 2005). With more knowledge of PSs, cross-frequency and/or cross-incidence angle could be possible and extremely promising. We are surely convinced that all these existed and upcoming efforts will lead to an operational and routine use of Spaceborne InSAR technology for ground surface deformation monitoring.

REFERNECES:

- Arrigoni M., Colesanti C., Ferretti A., Perissin D., Prati C., and Rocca F., 2003. Identification of the location phase screen of ERS-ENVISAT permanent scatterers," presented at the Fringe 2003 Conf., Frascati, Italy.
- Berardino P., Fornaro G., Fusco A., Galluzzo D., Lanari R., Sansosti E., Usai S., 2001. A new approach for analyzing the temporal evolution of Earth surface deformations based on the combination of DIFSAR interferograms, IGARSS 2001, Sydney (Australia). July 9-13..

- Berardino P., Fornaro G., Lanari R., Sansosti E., 2002. A new algorithm for surface deformation monitoring based on small baseline differential interferograms,” *IEEE Trans. Geosci. Remote Sensing*, vol. 40, pp. 2375–2383.
- Berardino, P., Casu, F., Lanari, R., 2004. On the exploitation of the SBAS algorithm for the analysis of the deformations detected from the ERS and ENVISAT D-InSAR data[C]. *ERS-ENVISAT Symposium*.
- BLANCO, P., MALLORQUI, J. J., DUQUE S., and NAVARRETE, D., 2006. Advances on DInSAR with ERS and ENVISAT data using the Coherent Pixels Technique (CPT), *Proc. IGARSS 2006, Denver (USA)*.
- Blanco-Sanchez P., Deque S., Mallorquí J.J. and Monells D., 2007. Analysis of highly non-linear deformation due to mining activity with DInSAR: PSIC Test site. *Proc. 'Envisat symposium 2007', Montreux, Switzerland, 23-27 April*.
- Blanco-Sanchez P., Mallorquí J.J., Duque S., and Monells D., 2008. The Coherent Pixels Technique (CPT): An Advanced DInSAR Technique for Nonlinear Deformation Monitoring, *Pure Appl. Geophys.*, No. 165, pp. 1167-1194.
- Bock, Y., and S. Williams (1997), Integrated satellite interferometry in southern California, *Eos Trans. AGU*, 78(29), 293.
- Bock S.Y., Pang P., 1998. Integrated satellite interferometry: Tropospheric noise, GPS estimates and implications for interferometric synthetic aperture radar products, *J. Geophys. Res.*, vol. 103, no. B11, pp. 27 051–27067.
- Cao L., Zhang Y.H., He J.G. et al, 2008. Coal mine land subsidence monitoring by using Spaceborne InSAR data- a case study in Fengfeng, Hebei Province, China, *Remote Sensing and Spatial Information Sciences*, Vol. XXXVII, Part B8, Beijing.
- Carnec C, Massonnet D., King C., 1996. Two Examples of the Use of SAR Interferometry on Displacement Fields of Small Spatial Extent [J] . *Geophysical Research Letters*, 23 (24):3579.
- Carnec, C., Fabriol, H. (1999) Monitoring and modeling land subsidence at the Cerro-Prieto geothermal field, Baja California, Mexico, using interferometry. *Geophysical Research Letters*, 9, 1211-1213.
- Carnec C., Delacourt C., Three Years of Mining Subsidence Monitored by SAR Interferometry, Near Gardanne, France [J]. *Journal of Applied Geophysics*, 2000, 43 (1) :43 - 54.
- Costantini M., 1998. A novel phase unwrapping method based on network programming, *IEEE Trans. Geosci. Remote Sensing*, vol. 36, pp. 813–821.
- Doin, M-P., Lasserre, C., Peltzer, G., Cavalié, O., Doubre, C., 2009. Corrections of stratified tropospheric delays in SAR interferometry: Validation with global atmospheric models. *Journal of Applied Geophysics*, v. 69, iss. 1, p. 35-50.
- Duque S., Mallorquí J.J., Blanco-Sanchez P., Monells D., 2007. Application of the coherent pixels technique (CPT) to urban monitoring, 2007 Urban Remote Sensing Joint Event, vol.2, Paris, France.
- Fang Z.L., Wang H.M., Wu J.Z. et al., 2009. Application research on monitoring land subsidence research in Shanghai using InSAR technology, *Shanghai Geology*, 2(109):22-26
- Ferretti, A., Rocca, F., Prati, C., 1999. Permanent scatterers in SAR interferometry[C]. *Proc. IGARSS'99* :1528–1529.
- Ferretti, A., Prati, C., Rocca, F., 2000. Nonlinear subsidence rate estimation using permanent scatterers in differential SAR interferometry[J] . *IEEE Trans. Geosci. Remote Sensing* , 38 (5) : 2202–2212.
- Ferretti, A., Prati, C., Rocca, F., 2001. Permanent scatterers in SAR interferometry[J]. *IEEE Trans. Geosci. Remote Sensing*, 39 (1) : 8–20.
- Ferretti A., Perissin D., Prati C., and Rocca F., 2004, “ERS–Envisat permanent scatterers,” in *Proc. IGARSS*, vol. 2, pp. 985–988.
- Ferretti A., Perissin D., Prati, C. Rocca F., 2005. On the physical nature of SAR Permanent Scatterers, *Proc. 2005 URSI Commission F Symposium on Microwave Remote Sensing of the Earth, Oceans, Ice, and Atmosphere, Ispra (Italy)*, 20–21 April.
- Galloway, D.L. and Hoffman, L., 2007. The application of satellite differential SAR interferometry-derived ground displacements in hydrogeology. *Hydrogeology Journal*, 15, pp. 133–154.
- Gatelli, F., Guarnieri A. M., Parizzi F., Pasquali P., Prati C., and Rocca F., 1994. The Wavenumber Shift in SAR Interferometry, *IEEE Trans. Geosci. Remote Sensing*, Vol. 32, 855-865.
- Ge, L., Y. Ishikawa, S. Fujiwara, S. Miyazaki, and X. Qiao, 1997. The Integration of InSAR and CGPS: A Solution to Efficient Deformation Monitoring on Current Crustal Movement and Hazard Reduction in East Asia and South-east Asia, Wuhan, P.R. China, 4-7 November.
- Ge L, Han S, Rizos C., 2000. The Double Interpolation and Double Prediction (DIDP) Approach for INSAR and GPS Integration, *IAPRS*, XXXIII.
- Ge, L., Zhang, K., Alex Ng, Dong, Y., Chang, H.-C. and Rizos, C., 2008. Preliminary results of satellite radar differential interferometry for the co-seismic deformation of the 12 May 2008 Ms8.0 Wenchuan earthquake. *Geographic Information Sciences*, 14(1), pp. 12-19.
- Ghiglia D. and Pritt M., 1998. *Two-Dimensional Phase Unwrapping: Theory, Algorithms and Software*. New York: Wiley.
- Graham L.C., Synthetic interferometer radar for topographic mapping, *Proc. IEEE* 62 (1974) 763–768.
- Gabriel A. K., Goldstein R. M., and Zebker H. A., “Mapping small elevation changes over large areas: differential radar interferometry,” *J. Geophys. Res.*, vol. 94, no. B7, pp. 9183–9191, July 1989.
- Goldstein R., Zebker H., and Werner C., 1988. Satellite radar interferometry: Two-dimensional phase unwrapping,” *Radio Sci.*, vol. 23, pp. 713–720.

- Goldstein R., 1995. Atmospheric limitations to repeat-pass interferometry," *Geophys. Res. Lett.*, vol. 22, pp. 2517–2520, Sept.
- Hanssen R., 1998. "Assessment of the role of atmospheric heterogeneities in ERS tandem SAR interferometry," DEOS Report 12 698.1, Delft Univ., Delft, The Netherlands.
- Hanssen R., 2001. *Radar Interferometry. Data Interpretation and Error Analysis*, Kluwer Academic Publishers, Dordrecht, The Netherlands.
- He Q.C., Fang Z.L., Li Z.M., Liu W.B., 2006. Monitoring land subsidence in Cangzhou region using InSAR technology, *Earth Science Frontiers*, 2006, 13(1):179-184.
- Hong S., Wdowinski S., Kim S.W., Amelung F. and Dixon T. H., 2008. Small temporal baseline subset (STBAS): A NEW INSAR TECHNIQUE FOR MULTI-TEMPORAL MONITORING WETLAND'S WATER LEVEL CHANGES. *IGARSS2008*, III, pp. 550-553.
- Huang Q.H., He X.F., 2008. Surface deformation investigated with SBAS-DInSAR approach based on prior knowledge, *Remote Sensing and Spatial Information Sciences*, Vol. XXXVII, Part B1, Beijing.
- Jarosx A., Wanke D., 2004. Use of InSAR for monitoring of mining deformation [EB/OL]. <http://earth.esa.int/workshop/fringes03/day2>.
- Ji L.Y., Liu R.C., Yang C.S., 2009. Engineering of surveying and mapping, Vol. 18, No. 2: 5-8.
- Jiang L.M., Lin H., 2009. Joint analysis of SAR interferometric and geological data for investigating long-term reclamation settlement of Chep Lap Kok Airport, Hong Kong, *Engineering Geology*, doi:10.1016/j.enggeo.2009.11.005.
- Kampes, B., Adam, N., 2005. The STUN Algorithm for Persistent Scatterer Interferometry, *Proceedings of FRINGE 2005 Workshop*.
- Li, Z., 2005a. Correction of atmospheric water vapour effects on repeat pass SAR interferometry using GPS, MODIS and MERIS data, Ph.D. thesis, University College London, London.
- Li, Z., J. Muller, P. Cross, and E. J. Fielding, 2005b. Interferometric synthetic aperture radar (InSAR) atmospheric correction: GPS, Moderate Resolution Imaging Spectroradiometer (MODIS), and InSAR integration, *J. Geophys. Res.*, 110, B03410, doi:10.1029/2004JB003446.
- Lundgren P., Usai S., Sansosti E., Lanari R., Tesauro M., Fornaro G., and Berardino P., 2001. Modeling surface deformation observed with SAR interferometry at Campi Flegrei Caldera, *J. Geophys. Res.*, vol. 106, pp. 19355–19367.
- Massonnet D., Rossi M., Carmona C., et al., 1993. The displacement field of the landers earthquake mapped by radar interferometry, *Nature*, vol. 364, pp. 138–142, July 8.
- Massonnet D., Arnaud A., 1995. Deflation of Mount Etna monitored by space radar interferometry, *Nature*, vol. 375, pp. 567–570.
- Massonnet D., Feigl K.L., 1998. Radar interferometry and its application to changes in the Earth's surface, *Rev. Geophys.* (36)441–500.
- Monti G. A., Prati C., 2000. ERS-ENVISAT Combination for Interferometry and Super-resolution, *ERSENVISAT Symposium*, Gothenburg, Sweden, 16-20.
- Lanari R., Mora O., Manunta M., et al., 2004. A small-baseline approach for investigating deformations on full resolution differential SAR interferograms [J]. *IEEE Trans. Geosci. Remote Sensing*, 42 (7) : 1377-1386.
- Mora O., Mallorqui J. J., Duro J., and Broquetas A., 2001. Long-term subsidence monitoring of urban areas using differential interferometric SAR techniques, in *Proc. IGARSS*, vol. 3, Sydney, Australia, pp. 1104-1106.
- Mora O., Lanari R., Mallorqui J.J., Berardino P., and Sansosti E., 2002. A new algorithm for monitoring localized deformation phenomena based on small baseline differential SAR interferograms. *Proc. IGARSS*, Toronto, ON, Canada, 1237-1239.
- Mora O., Mallorquí J.J., and Broquetas A., 2003. Linear and nonlinear terrain deformation maps from a reduced set of interferometric SAR images, *IEEE Trans. Geosci. Remote Sensing*, vol. 41, pp. 2243-2253.
- Mallorquí J. J., Blanco P., Sanz-Marcos J., Duque S., and Navarrete D., 2005. Application of the coherent pixels technique (CPT) to large ERS and ENVISAT SAR images for deformation series retrieval, in *Proc. FRINGE*, Frascati, Italy, Nov. 28–Dec. 2,
- Pepe, A., Sansosti, E., Berardino, P., 2005. On the generation of ERS/ ENVISAT DInSAR time series via the SBAS technique [J]. *IEEE Geosci. and Remote Sensing Letters*, 2 (3) : 265–269.
- Perski Z., 1998. Applicability of ERS-1 and ERS-2 InSAR for Land Subsidence Monitoring in the Silesian Coal Mining Region, Poland [J]. *International Archives of Photogrammetry and Remote Sensing*, 32 (7) : 555-558.
- Prati, C., Ferretti, A., Perissin, D., 2008. Recent Advances on Surface Ground deformation measurement by means of repeated space-borne SAR observations, *Journal of Geodynamics*, doi:10.1016/j.jog.2009.10.011.
- Raucoules, D., Maisons, C., Carnec, C., Le Mouelic, S., King, C., Hosford, S., 2003. Monitoring of slow ground deformation by ERS radar interferometry on the Vauvert salt mine (France), Comparison with ground-based measurement. *Remote Sensing of Environment* 88, 468–478.
- Rosen P.A., Hensley S., Joughin I.R., Li F.K., Madsen S.N., Rodriguez E., Goldstein R.M., 2000. Synthetic Aperture Radar Interferometry, *Proc. IEEE* 88 (2000) 333–376.
- Rocca F., 2007. Modeling Interferogram Stacks", *IEEE Trans. Geosci. Rem.Sens.*, in Vol. 45, Issue 10, pp. 3289–3299.
- Strozzi T., Tosi L., Carbognin L. et al., 1999. Monitoring Land Subsidence in the Euganean Geothermal Basin with Differential SAR Interferometry [A]. In: *Anon. 2nd ESA International Workshop on ERS SAR Interferometry FRINGE'99* [C].

- Sandwell D. T. and Price E. J., 1998. Phase gradient approach to stacking interferograms, *J. Geophys. Res.*, vol. 103, pp. 30183–30204.
- Santoro, M., Askne, J.I.H., Wegmüller, U., Werner, C.L., 2007. Observations, modeling, and applications of ERS-ENVISAT coherence over land surfaces, *IEEE Transactions on Geoscience and Remote Sensing*, Vol.45, NO.8, pp.2600-2611.
- Shan X.J., Ma J., Song X.Y., Wang C. et al. 2002. Using Deformation Field Obtained by Spaceborne D-INSAR Technique to Research Characteristics of Source Rupture of Zhangbei-Shangyi Earthquake, *Earthquake research in China*, Vol.18, No.2.:119-126.
- Spagnolini U., 1995. 2-D phase unwrapping and instantaneous frequency estimation,” *IEEE Trans. Geosci. Remote Sensing*, vol. 33, pp. 579–589, May 1995.
- Sverrir Guemundsson, 2000. Crustal Deformation Mapped by Combined GPS and INSAR: [M. S.Thesis], Iceland: Technical University.
- Usai S., Hanssen R., Long time scale INSAR by means of high coherence features, Proc.3rd ERS Symposium, Florence, Italy, March 1997, available at <http://florence97.ers-symposium.org:80>.
- Usai S. and Klees R., 1998. On the Feasibility of Long Time Scale INSAR, Proc. of 1998 Int. Geoscience and Remote Sensing Symp. (IGARSS'98), Seattle (WA) 6-10. vol. 5, pp. 2448-2450.
- Usai, S., Delgado C., Borgstrom S., and Achilli V., 1999. Monitoring terrain deformations at Phlegrean Fields with SAR interferometry, 2nd International Workshop on SAR Interferometry (FRINGE99), European Space Agency, Liege, Belgium, unpaginated CDROM.
- Usai S., Klees R., 1999. On the interferometric characteristics of anthropogenic features. Proc.1999 Int. Geoscience and Remote Sensing Symp.(IGARSS'99), vol. 3, Hamburg, June 28-July 2.
- Usai S., Klees R., 2000. An analysis of the interferometric characteristics of anthropogenic features. *IEEE Trans. on geoscience and remote sensing*, vol. 38, NO.3, 1491–1497.
- Usai S., 2001. A new approach for long term monitoring of deformations by differential SAR interferometry, Ph.D. thesis, Delft Univ. of Technol., Delft, The Netherlands. Williams.
- Usai S., 2002. A least-squares approach for long-term monitoring of deformations with differential SAR interferometry, in Proc. IGARSS 2002, vol. 2, Toronto, ON, Canada, pp. 1247–1250.
- Usai, S., 2003. A Least Squares Database Approach for SAR interferometric data, Monitoring terrain deformations at Phlegrean Fields with SAR interferometry, *IEEE Transactions on Geoscience and Remote Sensing*, 41:753–760.
- Wegmüller U., Werner, C., Strozzi T., and Wiesmann A. 2005. ERS-ASAR integration in the interferometric point target analysis, Fringe 2005 workshop, ESA ESRIN, Frascati, Italy, 28, Nov.-2. Dec.
- Wegmüller U., Strozzi T., and Tosi L., 2000. “Differential SAR interferometry for land subsidence monitoring: methodology and examples”, Proceedings of SISOLS 2000, Ravenna, Italy, 25-29.
- Werner, C., Wegmüller U., Strozzi T., and Wiesmann A., 2003. Interferometric point target analysis for deformation mapping, Proc. Int. Geosci. Remote Sens. Symp.
- Xu C.J., Wen Y.M., 2008. Nonhomogeneity of the Crust from Ms 7.9 Manyi(Tibet) Earthquake with InSAR Observation, *Geomatics and Information Science of Wuhan University*, Vol.33, No.8:846-849.
- Zebker H. A. and Goldstein R., “Topographic mapping from SAR observation,” *J. Geophys. Res.*, vol. 91, no. B5, pp. 4993–4999, 1986.
- Zebker H. A. and Rosen P., “Atmospheric artifacts in interferometric SAR surface deformation and topographic maps,” *J. Geophys. Res. Solid Earth*, vol. 102, no. B4, pp. 7547–7563, 1997.
- Zhao C.Y., Zhang Q., Ding X.L., Peng J.B., Yang C.S., 2009. InSAR based evaluation of land subsidence and ground fissure evolution at Xi'an, *17 (3):389-393*.

MULTIRESOLUTION IMAGE FUSION: PHASE CONGRUENCY FOR SPATIAL CONSISTENCY ASSESSMENT

A. Makarau^{a,*}, G. Palubinskas^a, P. Reinartz^a

^a DLR, German Aerospace Center, 82334 Weßling, Germany - (aliaksei.makarau, gintautas.palubinskas, peter.reinartz)@dlr.de

Commission VII, WG VII/6

KEY WORDS: pan-sharpening, multispectral image fusion, spatial consistency assessment, phase congruency

ABSTRACT:

Multiresolution and multispectral image fusion (pan-sharpening) requires proper assessment of spectral consistency but also spatial consistency. Many fusion methods resulting in perfect spectral consistency may leak spatial consistency and vice versa, therefore a proper assessment of both spectral and spatial consistency is required. Up to now, only a few approaches were proposed for spatial consistency assessment using edge map comparison, calculated by gradient-like methods (Sobel or Laplace operators). Since image fusion may change intensity and contrast of the objects in the fused image, gradient methods may give disagreeing edge maps of the fused and reference (panchromatic) image. Unfortunately, this may lead to wrong conclusions on spatial consistency. In this paper we propose to use phase congruency for spatial consistency assessment. This measure is invariant to intensity and contrast change and allows to assess spatial consistency of fused image in multiscale way. Several assessment tests on IKONOS data allowed to compare known assessment measures and the measure based on phase congruency. It is shown that phase congruency measure has common trend with other widely used assessment measures and allows to obtain confident assessment of spatial consistency.

1. INTRODUCTION

Pan-sharpened data have many areas of application and therefore different requirements are posed on the fusion method. The requirements can be on spectral consistency, spatial consistency or on the both together. Spectral consistency assumes that pansharpened data have increased spatial resolution with spectral properties of the original data. Spatial consistency assumes that “A high spatial quality merged image is that which incorporates the spatial detail features present in the panchromatic image and missing in the initial multispectral one” (González-Audícana, 2005). Spectral and spatial consistency together is the ideal case of the fused data and the ideal fusion method is to provide these characteristics. A pan-sharpening method may provide perfect spectral consistency together with poor spatial consistency and vice versa. Therefore, to make proper decision on a fusion method (or to outline the best one), assessment of both spectral and spatial consistency is to be performed.

2. PAN-SHARPENED DATA QUALITY

2.1 Spectral consistency

Spectral consistency assessment usually performed using Wald's protocol in order to make reference multispectral data of high resolution available. There is a variety of developed and well-known similarity measures used for spectral consistency assessment. The most known and popular are: Spectral Angle Mapper, SAM (calculated as the angle between two vectors):

$$\theta(\mathbf{r}, \mathbf{f}) = \cos^{-1} \left(\frac{\sum_{i=1}^K r_i f_i}{\sqrt{\sum_{i=1}^K r_i^2 \sum_{i=1}^K f_i^2}} \right), \quad (1)$$

K is the number of bands, \mathbf{r} and \mathbf{f} are the two vectors created by the values of spectral channels at the same pixel in the reference and fused images A and B ; Structural SIMilarity SSIM (Wang, 2004) or extended SSIM - Q4 (Alparone, 2003), (correlation, contrast, and luminance similarity between two images are used to calculate one similarity value):

$$SSIM(A_i, B_i) = \left(\frac{2\mu_{A_i}\mu_{B_i} + C_1}{\mu_{A_i}^2 + \mu_{B_i}^2} \right) \cdot \left(\frac{2\sigma_{A_i}\sigma_{B_i} + C_2}{\sigma_{A_i}^2 + \sigma_{B_i}^2 + C_2} \right) \cdot \left(\frac{\sigma_{A_i B_i} + C_3}{\sigma_{A_i}\sigma_{B_i} + C_3} \right), \quad (2)$$

where μ_{A_i} and μ_{B_i} are the local sample means of A_i and B_i , respectively, σ_{A_i} and σ_{B_i} are the local sample standard deviations of A_i and B_i , respectively, and $\sigma_{A_i B_i}$ is the sample cross correlation of A_i and B_i after removing their means. The items C_1 , C_2 , and C_3 are small positive constants that stabilize each term; ERGAS (Wald, 1997) (similarity measure for multispectral images, based on MSE estimator):

$$ERGAS(A_i, B_i) = 100 \frac{h}{l} \sqrt{\frac{1}{K} \sum_{i=1}^K \frac{RMSE(A_i, B_i)^2}{\mu_{A_i}^2}}, \quad (3)$$

* Corresponding author. Tel. +49-8153-283672

where A_i and B_i are the compared bands of a multispectral image, RMSE is root mean squared error, μ_{A_i} is the mean value of A_i , K is the number of bands, h/l is high/low resolution images ratio; Zero mean normalised cross-correlation, ZNCC:

$$\begin{aligned} ZNCC(A_i, B_i) &= \\ &= \frac{\sum_{m=1}^M \sum_{n=1}^N (A_i(m, n) - \mu_{A_i})(B_i(m, n) - \mu_{B_i})}{\sqrt{\sum_{m=1}^M \sum_{n=1}^N (A_i(m, n) - \mu_{A_i})^2 \sum_{m=1}^M \sum_{n=1}^N (B_i(m, n) - \mu_{B_i})^2}} \end{aligned} \quad (4)$$

where A_i, B_i are the compared images; μ_{A_i}, μ_{B_i} are the averages of the images A_i, B_i , respectively; M, N is the size of the compared images.

2.2 Spatial consistency

Spatial consistency is another aspect of fused imagery assessment. Up to now not many papers deal with spatial consistency assessment. Almost all the works use single scale edge detector (Gradient, Laplacian, Sobel edge detector) and an evaluation metric to calculate the distance between the edge maps (usually correlation coefficient) (Shi, 2003; Zhou, 1998; Pradhan, 2006). Here the comparison is made between the fused bands and the corresponding panchromatic image. Another approach calculates the percentage of true and false edges introduced into the fused band using Sobel edge detector (Pradhan, 2006). Several works on fusion report use of SSIM and ERGAS measures for spatial consistency assessment (Lillo-Saavedra, 2005) (panchromatic image is used as the reference instead of a spectral band).

In this paper we propose to use an additional measure for spatial consistency assessment. This measure uses phase congruency (PC) (Kovesi, 1999) for feature extraction on an image. Invariance to intensity and contrast change as well as multiscale nature of this measure allows to obtain more confident assessment comparing to single-scale edge detectors.

3. PHASE CONGRUENCY FOR SPATIAL CONSISTENCY ASSESSMENT

3.1 Phase congruency

Phase congruency was proposed as intensity and contrast invariant dimensionless measure of feature significance, and used for signal matching and feature extraction (Kovesi, 1999). Phase congruency at point x may be defined in the following way:

$$PC(x) = \frac{\sum_o \sum_s W_o(x) \left[FA_{so}(x) \Delta \Phi_{so}(x) - T_o \right]}{\sum_o \sum_s FA_{so}(x) + \varepsilon}, \quad (5)$$

where FA_{so} is the amplitude of the component in Fourier series expansion, $\Delta \Phi_{so}$ is the phase deviation function, W_o is the PC weighting function, o is the index over orientation, s is the index over scale, T_o is the noise compensation term, ε is the term added to prevent division by zero, $\lfloor \rfloor$ means that the enclosed quantity is permitted to be non-negative (Kovesi, 1999).

A bank of 2D Log Gabor wavelets is used for feature extraction. Different scale and orientation of the wavelets in the bank allow extracting more information about the structure (detail) of the image under assessment.

Multiscale image analysis instead of single-scale gradient operators allows to extract more information on image structure, features and edges. The result of PC extraction is phase congruency feature map. This map represents the structure of the image and allows to perform feature based image comparison.

3.2 Comparison metric

Zero mean normalized cross correlation was selected as a comparison metric of PC feature maps. Liu et. al. report on successful application of the metric for this task (Liu, 2008). ZNCC produces a real value in the range [-1,1] where 1 indicates full similarity of compared maps and -1 indicates absolute dissimilarity.

Pan-sharpened spectral band and corresponding panchromatic image are used for extraction of PC feature maps, and the maps are compared using ZNCC. The panchromatic image is used as the reference image for spatial consistency assessment (Figure 1).

3.3 Assessment protocol

The benefit of PC application for assessment may be illustrated by comparison with other assessment methods on pan-sharpened dataset, which consists of fused images with known quality. PC is expected to show similar trend with other assessment measures and provide similar assessment results. Well-known fusion methods should be used in order to produce the dataset with expected quality.

Several well-known pan-sharpening methods were selected to produce fused images with expected quality (spatial and spectral consistency): Intensity-Hue-Saturation (IHS) image fusion (Welch, 1987), image fusion using Principal Component Analysis (PCA) (Welch, 1987), wavelet image fusion (Aiuzzi, 2002), and General Image Fusion method (GIF) (Wang, 2005). Generally, well-known methods IHS and PCA produce fusion results with proper spatial consistency; wavelet fusion produces proper spectral consistency; GIF method produces a compromise of acceptable spectral and spatial consistency. Fusion methods can be sorted according to the quality of the produced result: in the sense of spectral or in the sense of spatial consistency. These methods were chosen as reference methods to produce expected results for pan-sharpened dataset used for assessment and comparison.

During the first assessment setup, a set of multispectral images was pan-sharpened by the following methods: IHS, PCA, À trous wavelet image fusion (ATWT, cubic B-spline), and by two modifications of General Image Fusion method (GIF-1 and GIF-2). GIF-1 extracts high-resolution image detail (high frequency component) from panchromatic image and adds to interpolated spectral image. The amount of transferred image detail data is established using regression (Starovoirov, 2007). GIF-2 employs image detail addition to interpolated spectral image (Ehlers, 2004). IHS and PCA image fusion methods were run using ENVI software, while all the other fusion methods were implemented using IDL system.

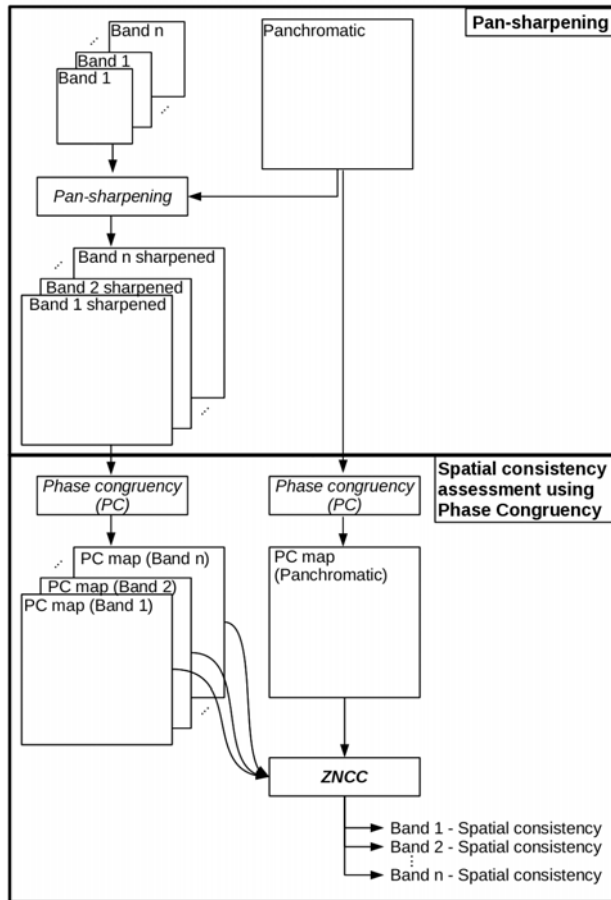


Figure 1. Diagram of spatial consistency assessment using phase congruency

During the second assessment setup, the same images were pansharpened by GIF-2 method with different parameters. GIF-2 has a parameter hf , which varies in the range $[0, 1]$ and controls proportionality (0%-100%) of high-frequency image data to be added to low-resolution spectral image. The high-frequency information is extracted using Butterworth filtering. The higher the value, the wider the Butterworth filter width and the more high frequency data is added. Variation of this parameter allows to create fused images with desired quality: the more high-frequency data is added, the higher spatial and lower spectral consistency, and vice versa. Three different values were taken for the parameter (0.9, 0.75, and 0.5, i.e. 90%, 75%, and 50%, respectively) and three fused images were produced. These created images are used for estimation of the trend between the measures and phase congruency spatial consistency assessment.

High resolution IKONOS multispectral images were used for fusion and assessment. The images were acquired in the areas of Athens (27 July 2004, 08:46 GMT) and Munich (15 July 2005, 10:28 GMT) cities. Full spectral image data (four spectral bands: blue colour range, green colour range, red colour range, NIR range) was used for pan-sharpening and assessment experiments. Sub scenes (panchromatic image size is 4000x4000) were used in the experiments.

In the first and second setups the pan-sharpened images were assessed for spectral and spatial consistency using standard widely used assessment measures. Wald's protocol was used for

spectral consistency assessment (SSIM, ERGAS, and SAM measures). Spatial consistency was assessed using Zero mean normalised cross-correlation coefficient (CORR), High Pass Correlation Coefficient (HPCC) (Zhou, 1998), SSIM, ERGAS, and using Phase Congruency (Zero mean normalized cross-correlation metric) (PC ZNCC). The assessment functions were implemented in IDL, while the original Matlab code was used for calculation of Phase Congruency (www.csse.uwa.edu.au/~pk/Research/MatlabFns/).

One example of quantitative assessment of IKONOS urban subscene (Athens, panchromatic image size is 4000x4000) is presented in Table 1: spectral consistency (SSIM, ERGAS, SAM) and spatial consistency assessment (SSIM PAN, ERGAS PAN, CORR PAN, HPCC, PC ZNCC). The SSIM PAN, ERGAS PAN, CORR PAN are the measures notation for spatial consistency assessment (fused image is compared with corresponding panchromatic image). Mean values of the measures are calculated over the assessed spectral channels.

The results of quantitative assessment during the second assessment setup are presented in Table 2. The dependencies of the measures on the quality of the fused images are presented in Figures 2 and 3. The characteristics of the resulting images are dependent on the GIF-2 hf parameter. Assessment of the pansharpened images with different quality (GIF-2 method, parameter variation) results in different scores and allows to illustrate trends of the measures.

4. RESULTS AND DISCUSSION

One of important questions during this investigation was: does the assessment using PC has the same trend with the other measures? The results produced by assessment measures were analysed for similarity in trend.

The PC ZNCC and SSIM PAN, ERGAS PAN, CORR PAN, HPCC illustrate higher spatial consistency produced by the IHS, PCA, GIF-1 and GIF-2 methods. This agrees with the well-known fact that the IHS, PCA and GIF methods produce the best spatially-consistent results with some loss of spectral consistency. Here the PC ZNCC illustrates similar results comparing with other measures on spatial consistency (Table 1). For the ATWT fusion, the PC ZNCC and SSIM PAN, ERGAS PAN, CORR, HPCC illustrate loss of spatial consistency and the highest spectral consistency (SSIM and ERGAS). PC-based metric resulted in the lowest value on spatial consistency, which correlates with the knowledge about the fusion result. GIF-1 and GIF-2 methods provided a compromise between the spectral (SSIM, SAM) and spatial consistency (PC ZNCC and SSIM PAN, ERGAS PAN, HPCC, together).

Highest score of SAM for GIF-2 method (Table 1) was caused by characteristics of the General Image Fusion (GIF) method, which provides a good compromise between the spatial and spectral consistency. For this particular case, the GIF method resulted in good spectral consistency (according to SAM measure) with acceptable spatial consistency.

Table 1 illustrates better values of ERGAS PAN for ATWT (3.78) than for IHS (11.17). The opposite trend is shown by the PC ZNCC and CORR PAN, HPCC. Such results may originate from instability of the MSE estimator (Wang, 2009) in ERGAS measure. Also SSIM PAN illustrated low spatial consistency of the IHS fusion (SSIM PAN (mean) equals to 0.6314). This

disagreement may be caused by the nature of SSIM measure, which uses comparison of luminance and contrast of the images. For this example, PC ZNCC assessment is not skewed and coincides with results of HPCC and Correlation.

The second assessment setup is expected to illustrate increase of spectral consistency with simultaneous decrease of spatial consistency on the fusion results (GIF-2 method, change of parameter set). Dependency graphs of the assessment measures are presented in Figure 2 (spectral consistency: SSIM mean, ERGAS mean, SAM) and in Figure 3 (spatial consistency: SSIM PAN (mean), ERGAS PAN, CORR PAN (mean), HPCC (mean), PC ZNCC (mean)). Since the ideal values for SSIM, ERGAS, and SAM are (respectively) 1, 0, and 0, the spectral consistency measures are increasing (Figure 2). This corresponds to our assumption and expectation. For the spatial consistency assessment, the ideal values for SSIM PAN, ERGAS PAN, CORR PAN, HPCC, PC ZNCC are (respectively) 1, 0, 1, 1, and 1, the spatial consistency measures are decreasing (Figure 3). This also corresponds to our assumption and expectation for spatial consistency. Figure 3 clearly illustrates similar trend of the PC ZNCC with all the other spatial consistency measures.

Table 2 illustrates common trend on spatial consistency between the results obtained by known measures and the PC-based metric. Spatial consistency assessment using PC illustrates expected decrease of spatial consistency. Also, the PC ZNCC measure is more sensitive to change of spatial consistency, so it is easier to assess and compare the quality of the image.

Visual assessment shows that the best spatial consistency have the IHS, PCA, GIF-1, and GIF-2 methods while ATWT resulted in slightly blurred edges (Figure 4), and coincides with the results of numerical assessment using PC. Figure 5 presents corresponding fragments of panchromatic and fused image (IHS fusion), edge maps (Sobel operator), and maximum moment of PC covariance (indicator of edge strength). It should be noted that PC feature map should not be confused with edge map. Figure 5 illustrates difference of image intensity and contrast (subfigures a, b)). Different edge maps are produced by edge detection operators (subfigures c, d). It is also demonstrated that the PC is more stable to intensity and contrast change (subfigures e, f).

5. CONCLUSIONS

Not many papers report on spatial consistency assessment of pan-sharpened data. Therefore, a need for robust and sufficient measures still exists. Application of phase congruency for spatial consistency assessment is proposed. Multiscale nature of phase congruency as well as invariance to intensity and contrast change allows more thorough analysis of fused data, comparing to single-scale edge detection methods. Identical trend with different assessment measures and with visual assessment showed that phase congruency is relevant for spatial consistency assessment, and the decision on the consistency can be made with higher confidence. Also it was found that ERGAS and SSIM provided less stability for spatial consistency assessment than correlation and edge-based measures. It should be noted that sometimes use of single assessment measure is not sufficient and may give skewed results (not all the characteristics of the fused data are revealed). Therefore use of several assessment measures increases confidence over calculated results.

REFERENCES

- Aiazzi, B., Alparone, L., Baronti, S., and Garzelli, A., 2002. Context-driven fusion of high spatial and spectral resolution images based on oversampled multiresolution analysis, *IEEE TGRS*, 40(10), pp. 2300-2312.
- Alparone L., Baronti S., Garzelli, A., and Nencini, F., 2003. A global quality measurement of pan-sharpened multispectral imagery. *IEEE GRSL*, 1(4), pp. 313-317.
- Ehlers, M., 2004. Spectral characteristics preserving imagefusion based on Fourier domain filtering. In: *Remote Sensing for Environmental Monitoring, GIS Applications, and Geology IV*, Bellingham, USA, pp. 1–13.
- González-Audícana, M., Otazu, X., Fors, O., and Seco, A., 2005. Comparison between Mallat's and the 'à trous' discrete wavelet transform based algorithms for the fusion of multispectral and panchromatic images. *IJRS*, 26(3), pp. 595-614.
- Kovesi, P., 1999. Image features from phase congruency. *Videre: A Journal of Computer Vision Research*, 1(3), pp. 2-26.
- Lillo-Saavedra, M., Gonzalo, C., Arquer, A., and Martinez, E., 2005. Fusion of multispectral and panchromatic satellite sensor imagery based on tailored filtering in the Fourier domain. *IJRS*, 26(6), pp. 1263-1268.
- Liu, Z., Forsyth, D., and Laganière, R., 2008. A feature-based metric for the quantitative evaluation of pixel-level image fusion, *Computer Vision and Image Understanding*, 109(1), pp. 56-68.
- Pradhan, P., King, R., Younan, N., and Holcomb, D., 2006. Estimation of the number of decomposition levels for a wavelet-based multiresolution multisensor image fusion. *IEEE TGRS*, 44(12), pp. 3674-3686.
- Shi, W., Zhu, C., Zhu, C., and Yang, X., 2003. Multi-band wavelet for fusing SPOT panchromatic and multispectral images. *PE & RS*, 69(5), pp. 513-520.
- Starovoitov, V., Makarau, A., Zakharov, I., and Dovnar, D., 2007. Fusion of reconstructed multispectral images. In *IEEE International Geoscience and Remote Sensing Symposium*, Barcelona, Spain, pp. 5146–5149.
- Wald, L., Ranchin, T., and Mangolini, M., 1997. Fusion of satellite images of different spatial resolutions: assessing the quality of resulting images. *PE & RS*, 63(6), pp. 691-699.
- Wang, Z., Bovik, A., Sheikh, H., and Simoncelli, E., 2004. Image quality assessment: From error visibility to structural similarity, *IEEE Transactions on Image Processing*, 13(4), pp. 600-612.
- Wang, Z., Ziou, D., Armenakis, C., Li, D., and Li, Q., 2005. A Comparative Analysis of Image Fusion Methods, *IEEE TGRS*, 43(6), pp. 1391-1402.
- Wang, Z., and Bovik, A., 2009. Mean squared error: love it or leave it? - A new look at signal fidelity measures. *IEEE Signal Processing Magazine*, 26(1), pp. 98-117.
- Welch, R., Ehlers, W., 1987. Merging multiresolution SPOT HRV and Landsat TM data. *PE & RS*, 53(3), pp. 301-303.

Zhang, Y., and Wang, R., 2004. Multi-resolution and multi-spectral image fusion for urban object extraction. In: XXth ISPRS Congress, Commission III, Istanbul, Turkey, pp. 960-966.

Zhou, J., Civco, D., and Silander, J. 1998. A wavelet transform method to merge Landsat TM and SPOT panchromatic data, International Journal of Remote Sensing. 19(4), pp. 743-757.

		Spectral consistency				Spatial consistency								
	Fusion Method	SSIM, ideal=1	SSIM (mean)	ERGAS, ideal=0	SAM, ideal=0	SSIM PAN, ideal=1	SSIM PAN (mean)	ERGAS PAN, ideal=0	CORR PAN, ideal=1	CORR PAN (mean)	HPCC, ideal=1	HPCC (mean)	PC ZNCC, ideal=1	PC ZNCC (mean)
1	ATWT	0.9527 0.8940 0.8604 0.8459	0.8883	1.2804	1.0164	0.6339 0.7474 0.8018 0.8122	0.7488	3.7802	0.7939 0.8467 0.8625 0.8615	0.8412	0.7604 0.7679 0.7685 0.7991	0.77	0.7675 0.7789 0.7738 0.8084	0.7821
2	IHS	0.1737 0.2042 0.2767	0.2182	13.0793	5.2042	0.6184 0.5890 0.6870	0.6314	11.1713	0.9890 0.9930 0.9876	0.9898	0.9864 0.9882 0.9860	0.99	0.9566 0.9630 0.9571	0.9589
3	PCA	0.8036 0.6736 0.6311 0.7103	0.7047	2.4393	1.5413	0.8379 0.9623 0.9879 0.9346	0.9307	3.0968	0.9276 0.9762 0.9825 0.8870	0.9433	0.9914 0.9971 0.9979 0.9912	0.9944	0.9430 0.9630 0.9651 0.9162	0.9468
4	GIF-1	0.7462 0.6079 0.5693 0.6386	0.6405	2.9900	1.1484	0.9040 0.9705 0.9516 0.9567	0.9457	3.0098	0.9349 0.9665 0.9725 0.9443	0.9545	0.9929 0.9941 0.9941 0.9918	0.99	0.9444 0.9507 0.9499 0.9341	0.9447
5	GIF-2 (90%)	0.7057 0.6666 0.7293 0.7288	0.7076	2.3506	0.7142	0.8947 0.9628 0.9551 0.9308	0.9359	3.1691	0.8960 0.9571 0.9520 0.8978	0.9257	0.9846 0.9928 0.9912 0.9854	0.9885	0.9157 0.9494 0.9233 0.8980	0.9216

Table 1. Spectral and spatial consistency assessment of the pan-sharpened image dataset (first assessment setup)

		Spectral consistency				Spatial consistency								
	Fusion Method	SSIM, ideal=1	SSIM (mean)	ERGAS, ideal=0	SAM, ideal=0	SSIM PAN, ideal=1	SSIM PAN (mean)	ERGAS PAN, ideal=0	CORR PAN, ideal=1	CORR PAN (mean)	HPCC, ideal=1	HPCC (mean)	PC ZNCC, ideal=1	PC ZNCC (mean)
1	GIF-2 (90%)	0.7057 0.6666 0.7293 0.7288	0.7076	2.3506	0.7142	0.8947 0.9628 0.9551 0.9308	0.9359	3.1691	0.8960 0.9571 0.9520 0.8978	0.9257	0.9846 0.9928 0.9912 0.9854	0.9885	0.9157 0.9494 0.9233 0.8980	0.9216
2	GIF-2 (75%)	0.7333 0.7011 0.7594 0.7529	0.7366	2.0316	0.7002	0.8591 0.9335 0.9300 0.9139	0.9091	3.2778	0.8827 0.9389 0.9350 0.8980	0.9136	0.9816 0.9874 0.9852 0.9808	0.9837	0.8116 0.8654 0.8097 0.7658	0.8131
3	GIF-2 (50%)	0.8205 0.8053 0.8462 0.8391	0.8277	1.4732	0.6344	0.7706 0.8412 0.8408 0.8302	0.8207	3.5938	0.8521 0.8952 0.8923 0.8638	0.8758	0.9412 0.9464 0.9431 0.9379	0.9421	0.7024 0.6968 0.6368 0.6114	0.6618

Table 2. Spectral and spatial consistency assessment of GIF-2 pan-sharpened image dataset (second assessment setup)

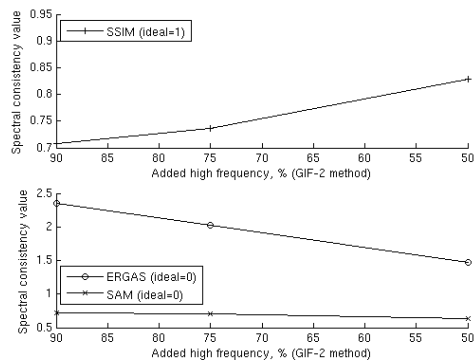


Figure 2. Dependency of spectral consistency measures on added high frequency in GIF-2 method (Table 2)

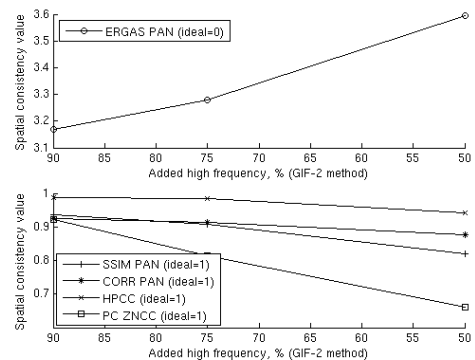


Figure 3. Dependency of spatial consistency measures on added high frequency in GIF-2 method (Table 2)

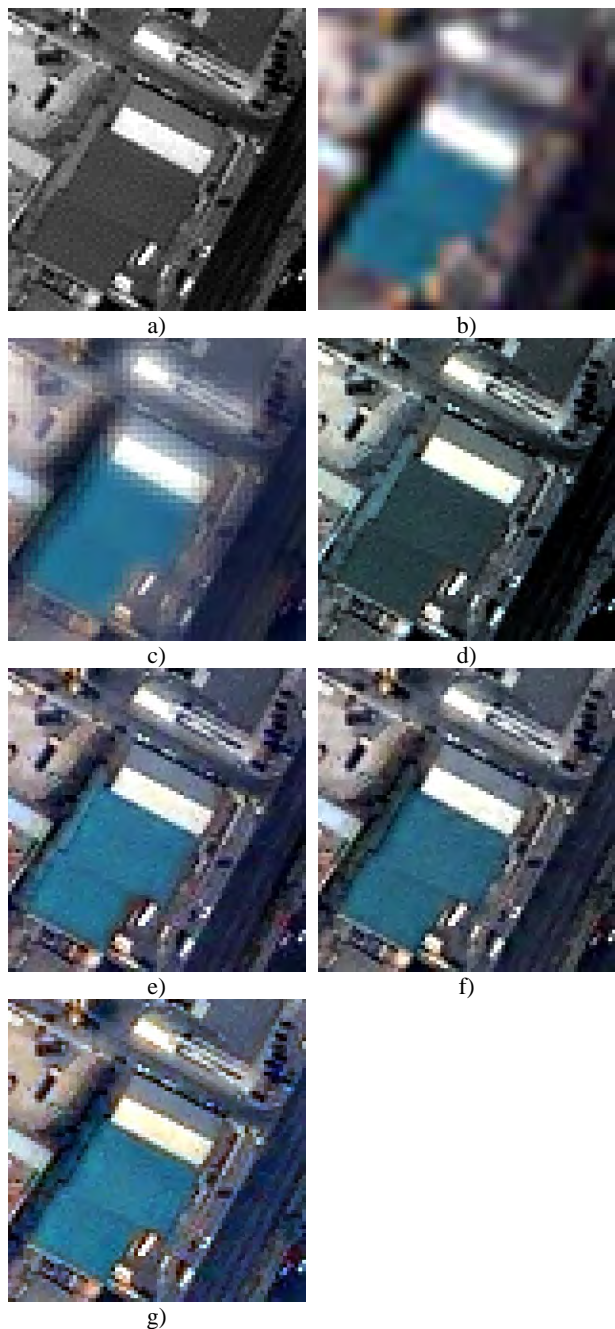


Figure 4. Example of a region taken from a fused urban scene (IKONOS, Athens, region size is 316x316). a) panchromatic image, b) interpolated multispectral (bilinear), c) ATWT, d) IHS, e) PCA, f) GIF-1, g) GIF-2. Fused images are composed of visible range spectral channels. ATWT fusion illustrates some loss of spatial consistency

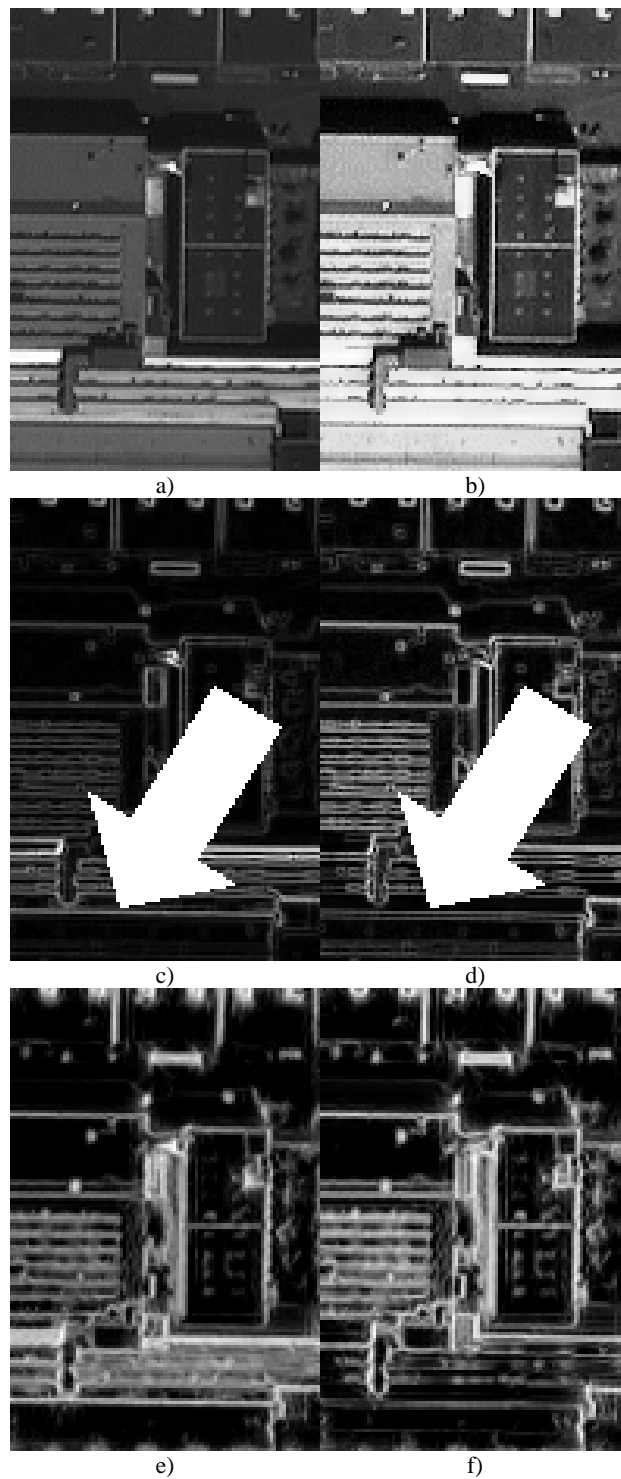


Figure 5. Region of the scene (München), edge and PC feature maps: a) Panchromatic image, b) IHS fusion (Band 3, red colour spectral range), c), d) Sobel edge map on panchromatic image and on IHS fusion, e), f) maximum moment of phase congruency covariance on panchromatic image and on IHS fusion

DETECTING HUMAN-INDUCED SCENE CHANGES USING COHERENT CHANGE DETECTION IN SAR IMAGES

N. Milisavljević^{a,*}, D. Closson^a, I. Bloch^b

^a Royal Military Academy -RMA, Department of Communication and Information Systems & Sensors – CISS,
Rue Hobbema 8, 1000, Brussels, Belgium - (nada, dclosson)@elec.rma.ac.be

^b Télécom Paris Tech, CNRS LTCI, 46 rue Barrault, 75013, Paris, France - isabelle.bloch@telecom-paristech.fr

Technical Commission VII Symposium 2010

KEY WORDS: Land Use, Change Detection, Combination, SAR, Scene, Temporal

ABSTRACT:

The technique of coherent change detection in repeat-pass Synthetic Aperture Radar imagery has the potential to detect very subtle scene changes such as changes in man-made targets or potential human activities. In this paper, we propose a simple method for detecting temporal changes in a scene possibly caused by human activities, such as building up areas of hard surface on a terrain that was previously a part of a desert. This method is based on comparison of coherence change detection results obtained in successive time frames. In order to cover a wide range of applications and situations, the proposed method is intentionally designed so that it does not need any specific knowledge source about the terrain. However, once coherent change detection results are obtained, various knowledge sources can be taken into account in order to improve the final interpretation. These knowledge sources can be related to the sensors, such as their operational principles, or to the situation at hand, referring to the context – terrain type, land-use, historical background etc. A way to include them in the reasoning process is discussed here too. In addition, in order to further improve the quality of the obtained output, usefulness of applying a spatial regularization technique is tested as well. The method is illustrated and validated using ALOS PALSAR multi-temporal data related to a real situation - works performed in building up additional runways of an airport. The results are in concordance with the ground-truth information, showing that the presented method is promising.

RÉSUMÉ:

La technique de détection de changements cohérents en imagerie radar à ouverture synthétique permet de détecter des changements fins dans la scène observée, comme les objets artificiels et les activités humaines, au cours de passages successifs. Dans cet article, nous proposons une méthode simple pour détecter les changements temporels dans une scène qui ont pu être causés par les activités humaines, telles que la construction de zones de surface dure sur un terrain qui était auparavant un désert. Cette méthode repose sur la détection des changements obtenus à partir d'images de cohérence successives. Afin de couvrir un large éventail d'applications et de situations, la méthode proposée est volontairement conçue de sorte qu'elle n'ait besoin d'aucune source de connaissances spécifiques sur le terrain. Cependant, une fois que des résultats de détection des changements cohérents sont obtenus, les sources de connaissances diverses peuvent être prises en compte, si elles sont disponibles, afin d'améliorer l'interprétation finale. Ces sources de connaissances peuvent concerner les capteurs et leurs principes de fonctionnement, ou la situation observée et son contexte - type de terrain, utilisation des terres, contexte historique ... Nous discutons de la manière d'inclure de telles informations dans le processus de raisonnement. Enfin la qualité du résultat peut être encore améliorée par une régularisation spatiale. La méthode est illustrée et validée à l'aide de données multi-temporelles ALOS PALSAR correspondant à une situation réelle - travaux effectués pour la construction de pistes supplémentaires d'un aéroport. Les résultats sont en accord avec la vérité terrain, et montrent que la méthode présentée est prometteuse.

1. INTRODUCTION

Change detection is an application for which Synthetic Aperture Radar (SAR) is particularly well suited as this type of sensors can consistently produce high-quality well-calibrated imagery with good geo-location accuracy (Price and Stacy, 2006). Two forms of change detection in repeat-pass SAR imagery may be considered, namely coherent and incoherent change detection (Price and Stacy, 2006). While incoherent methods compare the backscatter of two images acquired using the same imaging parameters, coherent methods exploit the coherence between

such two images acquired at different times (Scheuchl, Ullmann and Koudogbo, 2009).

Detection of temporal changes in an area of interest using coherent change detection (CCD) in repeat-pass (SAR) imagery (Touzi et al., 1999) is presented in this paper, as a follow-up of the method introduced in (Milisavljević, Closson and Bloch, 2010). The CCD technique has the potential to detect subtle scene changes (Price and Stacy, 2006), e.g. changes in man-made targets (Wright et al., 2005) or potential human activities. Nevertheless, urban areas represent a potential problem (Fanelli et al., 2000; Matikainen, Hyyppä and Engdahl, 2006) for the

* Corresponding author.

interpretation of the decorrelation due to too many possible human activities.

The paper is organized as follows. Firstly, we point out main ideas of the CCD technique. Then we describe our study area together with the data, as well as our method for analysis of CCD results in order to obtain information about potential human-induced scene changes, such as building up areas of hard surface on a terrain that was previously a part of a desert. In order to cover a wide range of applications and situations, the proposed method is intentionally designed so that it does not need any specific knowledge source about the terrain. Still, once CCD results are obtained, various knowledge sources can be taken into account in order to improve the final interpretation. These knowledge sources can be related to the sensors (operational principles and experience) or to the situation at hand (context – terrain type, land-use, historical background etc.). A way to include them in the reasoning process is discussed here too. In addition, in order to further improve the quality of the obtained output, usefulness of applying a spatial regularization technique is tested as well. Finally, we validate the obtained results and propose ways to continue the work.

2. ON COHERENT CHANGE DETECTION

Starting points for CCD processing are the complex images of an interferometric SAR image pair (two images from approximately the same geometry collected at two different times). Namely, CCD uses the correlation between them and provides information on the stability of the target (Matikainen, Hyypä and Engdahl, 2006; Price and Stacy, 2006). For instance, forests have a low coherence value, which means that such a type of target has changed much from one image to another (thus in time corresponding to the collection of these two images), while urban areas typically have high coherence values even between image pairs separated by several years (Luckman and Grey, 2003; Matikainen, Hyypä and Engdahl, 2006).

The coherence can be expressed as the product of five dominant contributions, as shown in (Zebker and Villasenor, 1992; Preiss, Gray and Stacy, 2006):

- 1) the relative backscatter signal to radar receiver noise ratio in the interferometric image pair,
- 2) the volume decorrelation,
- 3) the baseline decorrelation,
- 4) the decorrelation related to mismatch between the coherent acquisition apertures and image-formation processing stages used to produce the primary and repeat-pass imagery, and
- 5) the decorrelation in the scene over the repeat-pass time interval (temporal decorrelation); this type of decorrelation is the one we are interested in, as it is determined by various sources of scene change, such as environmental effects (moisture changes, atmospheric effects) or man-made disturbances.

The value of the product of the first four contributions mentioned above is close to one if the repeat-pass imaging geometry is designed carefully and if interferometric processing steps are performed, such as compensation for aperture and processor mismatch as well as image registration (Preiss, Gray and Stacy, 2006). Therefore, under such conditions, the coherence of the scene image reflects the true scene coherence over the repeat-pass interval. For the data used in this paper, these conditions are fulfilled.

Therefore, a starting point in our analysis is the fact that in this type of scene/terrain, low coherence values can refer to the moving ground (sand), which is perturbed all the time, while high coherence values can be related to a hard surface (e.g., concrete).

3. STUDY AREA AND THE DATA USED

The study area is an airfield that is located in a desert part of Israel. This type of terrain is a good start for analysing the usefulness of the CCD method for detecting potential human activities due to low soil moisture as well as low vegetation.

As far as the data are concerned, four ALOS PALSAR (Phased Array type L-band SAR) images (Rosenqvist, Shimada and Watanabe, 2004) of the scene in the descending mode are processed, corresponding to four different dates of acquisition: 15 November 2007, 15 February 2008, 1 April 2008 and 17 May 2008. Starting from the Single Look Complex data, three CCD results are obtained using the following pairs: 15 November 2007 and 15 February 2008 (period 1), 15 February 2008 and 1 April 2008 (period 2), as well as 1 April 2008 and 17 May 2008 (period 3). As an example of the three obtained CCD results, Fig. 1 contains the CCD result for the images of period 1. The images of the other two periods can be found in (Milisavljević, Closson and Bloch, 2010). The coherence images are generated using the module *Insar* of *Erdas Imagine* 2010 platform.



Figure 1. CCD result for the images acquired on 15 November 2007 and 15 February 2008 (period 1)



Figure 2. Amplitude of the SAR data acquired on 15 November 2007

In order to illustrate the usefulness of the SAR phase information used to obtain the CCD results, Figures 2 and 3

contain amplitude information of the SAR data pair corresponding to the two dates from Figure 1. Visually, there are no significant changes in amplitude values between two images. We have tested two amplitude change detection techniques, i.e., image differencing (Rosin, 1998) and image rationing (Lu et al., 2004), which confirm that no significant change in amplitude occurs between these two time intervals. However, the phase-based change detection result shown in Figure 1 demonstrates that changes occur in that period, which justifies the need for using this part of SAR information in this type of applications.



Figure 3. Amplitude of the SAR data acquired on 15 February 2008

4. OUR METHOD FOR DETECTION OF HUMAN ACTIVITIES

This method is introduced in (Milisavljević, Closson and Bloch, 2010) and we outline it here. Firstly, a noise removal method using median filtering is applied to each of the three CCD results. Then, each of the three CCD results is divided in three classes, based on coherence value:

- if a CCD pixel is dark (low coherence), it is labelled as 1;
- if it has a medium value, it is labelled as 2,
- if it has a high coherence value, it is labelled as 3.

As an illustration, Fig. 4 contains the obtained result in case of the CCD image from Fig. 1. Green colour corresponds to label 1 (so, low coherence), white colour is used for label 2 (medium coherence), and red is used for label 3.

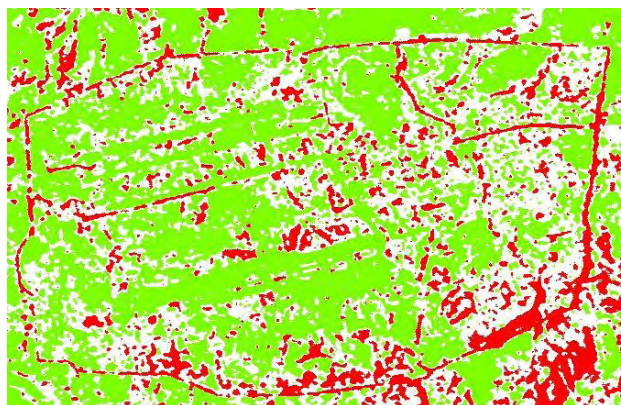


Figure 4. Classification result of Figure 1

In the following, results shown in Fig. 4 are referred to as A, the classification results obtained on the CCD pair from period 2 – B, and those obtained on the CCD pair from period 3 – C.

In a next step, we compare the results A and B, in order to see whether within the first periods of time the coherence values were similar (i.e., there was no change in the soil disturbance from one period to another) or not. The comparison of values A and B (AB) in each pixel can result in one of the following labels: 11 (low coherence in CCD results in period 1 and in period 2), 12 (low coherence in CCD results in period 1 and medium in period 2), 13 (change from low to high coherence, i.e., possible increased human activity), 21, 22, 23, 31, 32, 33.

Since the threshold between low and medium, on the one hand, and medium and high, on the other hand, is crisp and since these changes are not as radical as changes from very low to very high coherence (or the opposite), we regroup these AB values so that

- 11, 12 and 21 are grouped together, labelled as 1,
- 22 is labelled as 2,
- 23, 32 and 33 represent one group, labelled as 3,
- 13 remains 13,
- 31 remains 31.

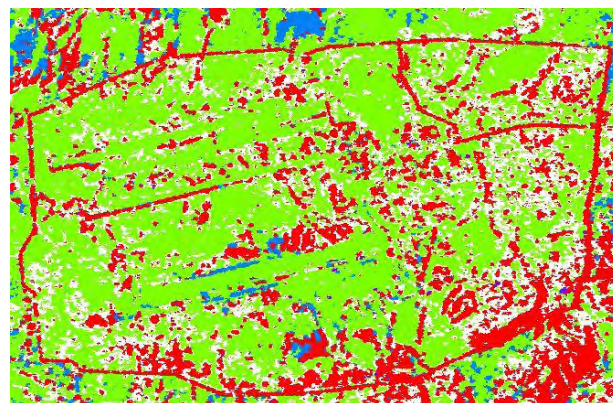


Figure 5. Comparison of values A and B: 1 – green, 2 – white, 3 – red, 13 – blue, 31 – purple

The obtained result is illustrated in Fig. 5. Similar reasoning is applied in comparing the results B and C.



Figure 6. White pixels show where AB is 13 and BC is 3. Region within the blue ellipse is zoomed in Figure 7

Now, if AB value is 13, this means that the coherence was low in period 1 and high in period 2. If BC value is 3 at that same place, meaning that the coherence remained high from period 2 to period 3, this can mean that there were some works in that place (for instance, human activity such as creating built-up areas) which started in the first period ($AB=13$) and have been finished in the following periods ($BC=3$, referring to a built-up area, i.e. hard surface). The pixels where $AB=13$ and $BC=33$ are shown in white in Fig. 6 and zoomed in Fig. 7.



Figure 7. Zoom of the region within the blue ellipse in Fig. 6

5. INCLUSION OF KNOWLEDGE SOURCES

In (Milisavljević, Closson and Bloch, 2010), we mention the possibility of including knowledge sources. We develop this idea here. Namely, once CCD results are obtained, various knowledge sources can be taken into account in order to improve the final interpretation. These knowledge sources can be related to the sensors, such as their operational principles, or to the situation at hand, referring to the context – terrain type, land-use, historical background etc. We illustrate here the inclusion of three knowledge sources:

1. area of interest (airport), extracted manually from a very high resolution image and shown in Fig. 8 - it can be included in the obtained results in a straightforward way, by taking into account only pixels that are within the white region;

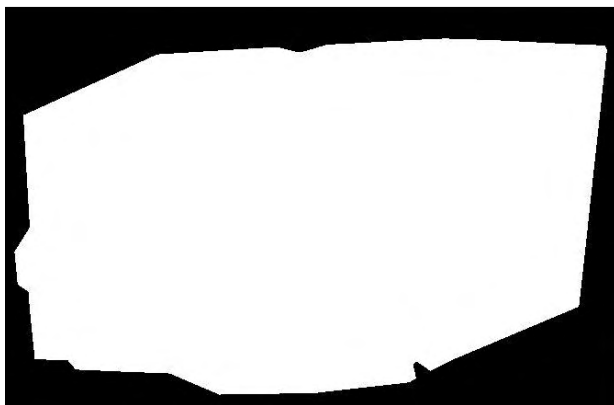


Figure 8. Area of interest (in white)

2. pedologically extracted robustness (i.e., soil hardness), presented in Fig. 9; while dark grey pixels represent areas with low robustness, high (white) values correspond to hard surface; it is difficult to perturb such a soil and detect human activities, so coherence is high in such an area and the reliability to detect human activities is low; therefore, regions with the highest robustness are superimposed to the classification results as areas with surely high coherence (label 3);

3. slope (extracted from the digital elevation model created from contours of topographical maps), presented in Fig. 10, where

the lighter the pixel, the higher the slope, so the lower the possibility to have an airfield; again, regions with the highest slope can be superimposed to the classification results as being of low interest while looking for human activities in an airport (so, labelled as 3).



Figure 9. Pedologically extracted robustness. Black – no data; dark grey – low robustness; light grey – medium robustness; white – highest robustness

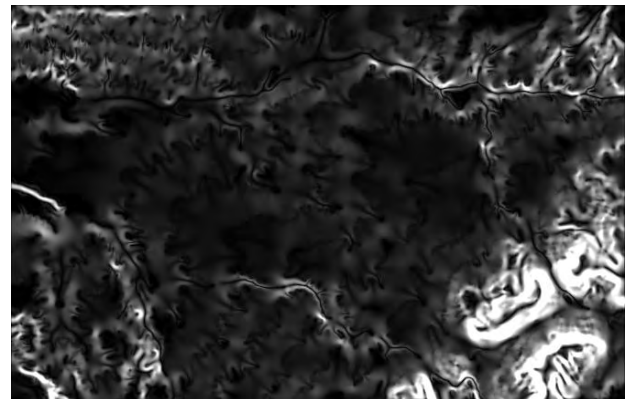


Figure 10. Slope (extracted from the digital elevation model)

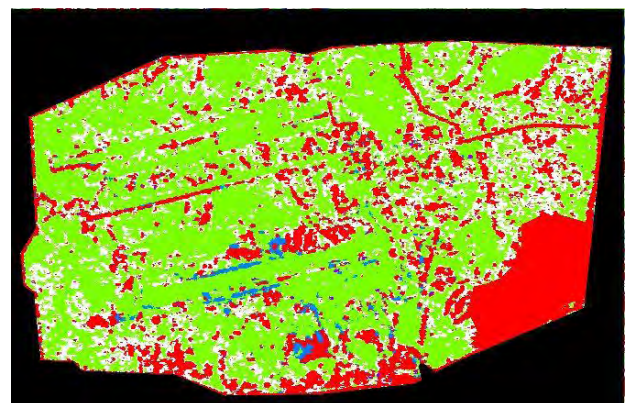


Figure 11. Result of the inclusion of three knowledge sources in results shown in Figure 5

As an illustration, Figure 11 contains the result of the inclusion of the three knowledge sources mentioned above to the result shown in Figure 5.

Based on the way the knowledge sources are included, it is certain that the method itself would not be affected if they were not present. In addition, as these sources, in this particular case, affect only areas that are outside of the region within the blue

ellipse of Figure 6, even the results shown in Figures 6 and 7 would not be affected either.

6. SPATIAL REGULARIZATION

In order to improve the quality of the obtained output, we test here the usefulness of applying a spatial regularization technique as well. Again, in order to test the principle itself, we use a simple spatial regularization method: majority voting within a sliding window. Applying this method to the image shown in Figure 11, we obtain the result presented in Figure 12.

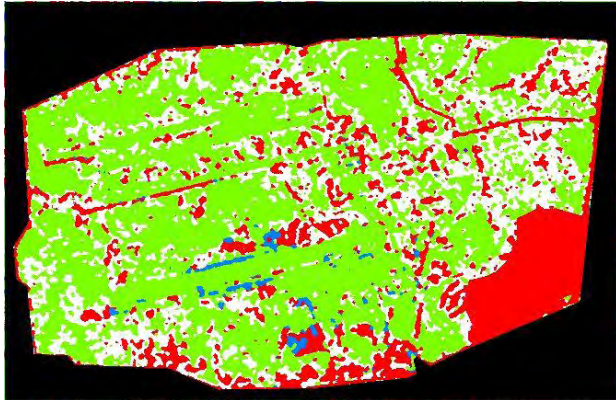


Figure 12. Result of spatial regularization applied to Figure 11

Although spatial regularisation does not affect the method itself either, it improves the quality of the final result by removing isolated points thus clearing the image and emphasizing the detected areas, as can be seen by comparing Figures 6 and 13, i.e., Figures 7 and 14.



Figure 13. Same as Figure 6, but obtained after applying spatial regularization to the starting images. Region within the blue ellipse is zoomed in Figure 14



Figure 14. Zoom of the region within the blue ellipse in Fig. 13

7. VALIDATION

Results presented here indicate that there is a region where human activities might have been performed, with changes in coherence values corresponding to works in building a hard surface on a sand terrain, and that these activities appear mainly in two parallel stripes as well as around them.

A newspaper article from February 2008 (Greenberg, 2008) makes it possible to validate the obtained results. This article speaks about works at this same airfield, mentioning that a new runway is being built, together with other operational buildings around the runway, and that the works are about to be finished. The article also shows aerial photos which correspond to the region extracted by our analysis (Fig. 14). This means that our results are in a complete concordance with the reality, showing that the approach presented in this paper is promising for detecting human activities.

8. CONCLUSION AND FUTURE WORK

A simple method to detect potential human activities using CCD technique in repeat-pass SAR imagery is presented here. The results are validated, showing that the method is promising in extracting zones where a potential temporal change in the human activities occur, such as works in building-up areas of hard surface. As a good study case for a first research step, a desert type of soil is analyzed. Terrains which represent more difficult situations from the point of view of CCD technique will be studied in a next step.

The presented method does not need any specific knowledge sources. Nevertheless, we show in this paper that if knowledge sources exist, it is possible to include them in order to improve final results. These knowledge sources can be related to the sensors, such as their operational principles, or to the situation at hand, referring to the context – terrain type, land-use, historical background etc. Three types of knowledge sources (information on the area of interest, pedologically extracted robustness and slope extracted from the digital elevation model) are included in the obtained results as an illustration. In a next step, possibilities of including some other knowledge sources, such as geological maps or aerial photos will be studied.

In addition, in order to improve the aspect of the final result, the application of a spatial regularization method is tested, showing that it might be useful to further analyze ways to remove artefacts and preserve only the useful information.

Finally, in future work, fusion of the obtained results with data coming from other sensors in order to further improve the quality and the robustness of the results will be investigated.

REFERENCES

- Fanelli, A. et al., 2000. Understanding ERS Coherence over Urban Areas. In: *ESA-SP-461 (Ed.), ERS-Envisat Symposium*, Gothenburg, Sweden.
- Greenberg, H., 2008. "Longest landing field in Middle East to be constructed in Nevatim".
<http://www.ynetnews.com/articles/0,7340,L-3508174,00.html>
 (accessed 30 May 2010)
- Lu, D. et al., 2004. Change detection techniques. *International Journal of Remote Sensing*, 25(12), pp. 2365-2407.

Luckman, A. and Grey, W., 2003. Urban Building Height Variance From Multibaseline ERS Coherence. *IEEE Transactions on Geoscience and Remote sensing*, 41(9), pp. 2022-2025.

Matikainen, L., Hyypä J. and Engdahl, M. E., 2006. Mapping Built-Up Areas from Multitemporal Interferometric SAR Images – A Segment-based Approach. *Photogrammetric Engineering & Remote Sensing*, 72(6), pp. 701-714.

Milisavljević, N., Closson, D. and Bloch, I., 2010. Detecting potential human activities using coherent change detection. In: *International Conference on Image Processing Theory, Tools and Applications (IPTTA10)*, Paris, France.

Preiss, M., Gray, D.A. and Stacy, N.J.S., 2006. Detecting Scene Changes Using Synthetic Aperture Radar Interferometry. *IEEE Transactions on Geoscience and Remote sensing*, 44(8), pp. 2041-2054.

Preiss, M. and Stacy, N.J.S., 2006. Coherent Change Detection: Theoretical Description and Experimental Results. Technical Report, DSTO–TR–1851, Defence Science and Technology Organisation, Edinburgh, Australia.

Rosenqvist, A., Shimada, M. and Watanabe, M., 2004. ALOS PALSAR: Technical outline and mission concepts. In: *4th International Symposium on Retrieval of Bio- and Geophysical Parameters from SAR Data for Land Applications*, Innsbruck, Austria.

Rosin, P.L., 1998. Thresholding for Change Detection. In: *IEEE International Conference on Computer Vision*, Bombay, India, pp. 274-279.

Scheuchl, B., Ullmann, T. and Koudogbo, F., 2009. „Change detection using high resolution Terrasar-X data: preliminary results”, HighRes09, Hannover, Germany. http://www.isprs.org/proceedings/XXXVIII/1_4_7-W5/paper/Scheuchl-185.pdf (accessed 30 May 2010)

Touzi, R. et al., 1999. Coherence Estimation for SAR Imagery. *IEEE Transactions on Geoscience and Remote sensing*, 37(1), pp. 135-149.

Wright, P. et al., 2005. Coherent Change Detection with SAR. In: *European Radar Conference (EURAD 2005)*, Paris, France, pp. 17-20.

Zebker, H.A. and Villasenor, J., 1992. Decorrelation in Interferometric Radar Echoes. *IEEE Transactions on Geoscience and Remote sensing*, 30(5), pp. 950-959.

SELF CALIBRATION OF SMALL AND MEDIUM FORMAT DIGITAL CAMERAS

Donald Moe^a, Aparajithan Sampath^a, Jon Christopherson^a, Mike Benson^b

^aSGT, Inc¹, U.S. Geological Survey (USGS) Earth Resources Observation and Science (EROS) Center, Sioux Falls, SD 57198 USA –(dmoe, asampath, jonchris)@usgs.gov

^bU.S. Geological Survey (USGS) Earth Resources Observation and Science (EROS) Center, Sioux Falls, SD 57198 USA – benson@usgs.gov

KEY WORDS: Photogrammetry, Rectification, Bundle, Camera, Geometric.

ABSTRACT:

The knowledge of a camera's interior orientation parameters are a prerequisite for the camera to be used in any precision photogrammetric project. Historically, the interior orientation parameters have been determined by analyzing the measured ground 3D coordinates of photo-identifiable targets, and their 2D (image) coordinates from multiple images of these targets. Camera self calibration, on the other hand, uses targets on a scene that have not been measured before. In this research, we will briefly discuss existing self calibration techniques, and present two methods for camera self calibration that are being used at the U.S. Geological Survey's Earth Resources Observation and Science (EROS) Data Center. The first method, developed by Pictometry (augmented by Dr C.S. Fraser), uses a series of coded targets on a cage. The coded targets form different patterns that are imaged from nine different locations with differing camera orientations. A free network solution using collinearity equations is used to determine the calibration parameters. The coded targets are placed on the cage in three different planes, which allows for a robust calibration procedure. The USGS/EROS has developed an inexpensive method for calibration, particularly for calibrating short focal length cameras. In this case, the coded targets are pasted on a small prototype box and imaged from different locations and camera orientations. The design of the box is discussed, and the results of the box and the cage calibrations are compared and analyzed.

1. INTRODUCTION

1.1 General

Camera calibration procedure aims to completely characterize the path of a ray of light that enters a camera, at the time of exposure. The parameters that are used for this characterization are termed the interior orientation parameters. The main parameters are the focal length of the lens and the location of the principal point of symmetry. However, for photogrammetric purposes, the knowledge of the deviation of the light ray from a straight line, described by polynomial coefficients, is also important. This deviation is termed lens distortion, and the polynomial coefficients are termed lens distortion parameters. The United States Geological Survey (USGS) has the responsibility for camera calibration in the United States (Lee, 2004). In this research, we shall present two methods used by the USGS to determine these parameters for small and medium format digital cameras. The first method, developed by Pictometry (augmented by Dr C.S. Fraser), uses a series of coded targets on a cage. The coded targets are placed on the cage in three different planes, which allows for a robust calibration procedure. The second method describes the development of a method whereby the coded targets are pasted on a small prototype box. The importance of calibrating a camera used for photogrammetric purposes cannot be overstated. While it is possible to obtain accurate ortho-products without a well calibrated camera, these would require a very dense network of control points. Such a network will make a photogrammetric project prohibitively expensive.

Symbol	Description
f	Gaussian focal length
K_1, K_2, K_3	Parameters for radial distortion
P_1, P_2	Parameters for decentering distortion
B_1, B_2	Differential scale distortion (for digital cameras)
x_p, y_p	Position of the principal point of symmetry with respect to the array pixel frame.

Table 1. List of interior orientation parameters

1.2 Camera calibration methods

There are many approaches to camera calibration. With the increasing popularity of the field of Computer Vision as an area of research, the methods have increased. Camera calibration methods preferred by photogrammetrists can be categorized broadly into three classes.

¹Work performed under U.S. Geological Survey contract 08HQCN0005

1.2.1 In-situ calibration: The in-situ methods of calibration are purported to produce the best camera calibration results. They are mostly used for calibrating large cameras that cannot be easily calibrated in laboratories. The cameras are hence calibrated while they are in operation. In-situ calibration methods require an area (a calibration range) with a very dense distribution of highly accurate control points. While maintaining a high density, the control points in the calibration range should be well distributed in the horizontal, as well as in the vertical direction. A rigorous least squares block adjustment based on the co-linearity equations, augmented by equations modelling radial and decentering distortion (Eq. 5) can generate accurate calibration parameters. The in-situ method requires aerial imagery over a calibration range. Also, careful maintenance of the calibration range is required, over the years. The maintenance may include re-survey of the control points, making sure they are undisturbed etc. All these factors can be expensive and time consuming for the camera operators.

1.2.2 Precision multi-collimator instruments: The USGS operates a multi-collimator calibration instrument located at Reston, Virginia, USA (Light, 1992). The instrument is used to calibrate film based cameras, and while digital cameras are increasingly used, there are a number of photogrammetric companies that still employ film cameras. The aerial camera is placed on top of the collimator bank, aligned and focused at infinity. Images that capture the precision targets located in telescopes lens (of the multi-collimator) are taken. The deviation of the measured image (x,y) coordinates from the known (X,Y) coordinates forms the basis for solving for the calibration parameters (Eq. 5).

1.2.3 Self calibration: Self calibration uses the information present in images taken from an un-calibrated camera to determine its calibration parameters (Fraser, 1997; Fraser 2001; Remondino and Fraser, 2006; Strum, 1998). Methods of self calibration include generating Kruppa equations (Faugeras et al., 1992), enforcing linear constraints on calibration matrix (Hartley, 1994), a method that determines the absolute quadric, which is the image of the cone at a plane at infinity (Triggs). While there are many techniques employed by researchers (Hartley, 1994; Faugeras et al., 1992), most of these do not find solutions for distortion and principal point, as they are not considered critical for Computer Vision. On the other hand, for photogrammetrists, these are critical parameters necessary to produce an accurate product at a reasonable price.

In this study, we will use self calibration techniques to determine camera calibration parameters. Section 2 provides a brief theoretical framework for calibration. It goes on to discuss the design of two methods for self calibration used at the USGS, and describes the experimental set-up. It introduces an inexpensive method for calibrating small and medium format digital cameras, with short focal length. Section 3 analyses the results of calibration, and compares the results obtained from the two methods described in Section 2. Section 4 presents the conclusions and discusses future work.

2. CALIBRATION METHODOLOGY

2.1 Theoretical basis

The self calibration procedure described in this research is based on the least squares solution to the photogrammetric resection problem. The well known projective collinearity equations form the basis for the mathematical model.

$$x - x_p = -f \left[\frac{m_{11}(X - X_c) + m_{12}(Y - Y_c) + m_{13}(Z - Z_c)}{m_{31}(X - X_c) + m_{32}(Y - Y_c) + m_{33}(Z - Z_c)} \right] \quad (1)$$

$$y - y_p = -f \left[\frac{m_{21}(X - X_c) + m_{22}(Y - Y_c) + m_{23}(Z - Z_c)}{m_{31}(X - X_c) + m_{32}(Y - Y_c) + m_{33}(Z - Z_c)} \right]$$

In Eq. 1, (x ,y) are the measured image coordinates of a feature and (x_p, y_p) are the location of the principle point of the lens, in the image coordinate system, f refers to the focal length and

$\begin{pmatrix} m_{11} & m_{12} & m_{13} \\ m_{21} & m_{22} & m_{23} \\ m_{31} & m_{32} & m_{33} \end{pmatrix}$ is the camera orientation matrix. Since the lens

in the camera is a complex system consisting of a series of lenses, the path of light is not always rectilinear. The result is that a straight line in object space is not imaged as one in the image. The effect is termed distortion. Primarily, we are interested in characterizing the radial distortion and de-centring distortion. Radial distortion displaces the image points along the radial direction from the principal point (Mugnier et al., 2004). The distortion is also symmetric around the principal point. The distortion is defined by a polynomial (Brown, 1966; Light, 1992).

$$\begin{aligned} \delta r &= k_1 r^3 + k_2 r^5 + k_3 r^7 + \dots \\ r &= \sqrt{(x - x_p)^2 + (y - y_p)^2} \\ k_i, i &= 1, 2, 3, \dots \text{æ coefficients of the polynomial} \end{aligned} \quad (2)$$

The (x,y) components of the radial distortion are given by:

$$\begin{aligned} \delta x_1 &= x \frac{\delta r}{r} \\ \delta y_1 &= y \frac{\delta r}{r} \end{aligned} \quad (3)$$

The second type of distortion is the decentering distortion. This is due to the displacement of the principle point from the centre of the lens system. The distortion has both radial and tangential components, and is asymmetric with respect to the principal point (Mugnier et al., 2004). The components of de-centering distortion, in the x-y direction are given by

$$\begin{aligned} \delta x_2 &= P_1(r^2 + 2x^2) + 2P_2xy \\ \delta y_2 &= 2P_1xy + P_2(r^2 + 2y^2) \end{aligned} \quad (4)$$

A third distortion element, specific to digital cameras accounting for scale distortion of pixel sizes in the x and y direction is also incorporated

$$\delta x_3 = B_1x + B_2y \quad (5)$$

The final mathematical model is a result of adding Eqs. 3 and 4 and 5 to the right hand side of Eq.

$$\begin{aligned} x - x_p &= -f \left[\frac{m_{11}(X - X_c) + m_{12}(Y - Y_c) + m_{13}(Z - Z_c)}{m_{31}(X - X_c) + m_{32}(Y - Y_c) + m_{33}(Z - Z_c)} \right] + \delta x_1 + \delta x_2 + \delta x_3 \\ y - y_p &= -f \left[\frac{m_{21}(X - X_c) + m_{22}(Y - Y_c) + m_{23}(Z - Z_c)}{m_{31}(X - X_c) + m_{32}(Y - Y_c) + m_{33}(Z - Z_c)} \right] + \delta y_1 + \delta y_2 \end{aligned} \quad (6)$$

2.2 Experimental set-up for cage based self calibration

The camera calibration facility is located at the USGS’s Earth Resources Observation and Science (EROS) Data Center in Sioux Falls, South Dakota. Fig. 1 shows the position of the calibration cage, with respect to the room. Also shown are some of the positions for locating the cameras. The cage consists of three parallel panels. Each panel has a number of circular retro-reflective targets (dots), and a few coded targets (Fig 2a). The coded targets are so referred because the pattern of the placement of the individual circular dots that make up these targets is unique (Fig. 2b). Each coded target has five dots that are positioned in the same relative orientation as the red lines shown in Fig. 2(b). The intersection of the red lines is taken as the centre of the coded target.

For the calibration procedure, the camera lens is always focussed at infinity. The choice of the distance of the camera from the front panel of the cage depends on the focal length of the camera, and the depth of focus that has been selected. Once the camera-cage distance is fixed, three angular positions from the centre of the front panel of the cage are selected. The angular positions are selected keeping in mind the optimal angles for convergent photography, and the limitations imposed by the dimensions of the calibration room. Ideally, the angular positions will be close to what is shown in Fig 1. Once the images are captured, they are processed using software called Australis (Fraser, 2001). Australis uses a free network method of bundle adjustment. It recognizes the patterns in the coded targets and calculates their centre.

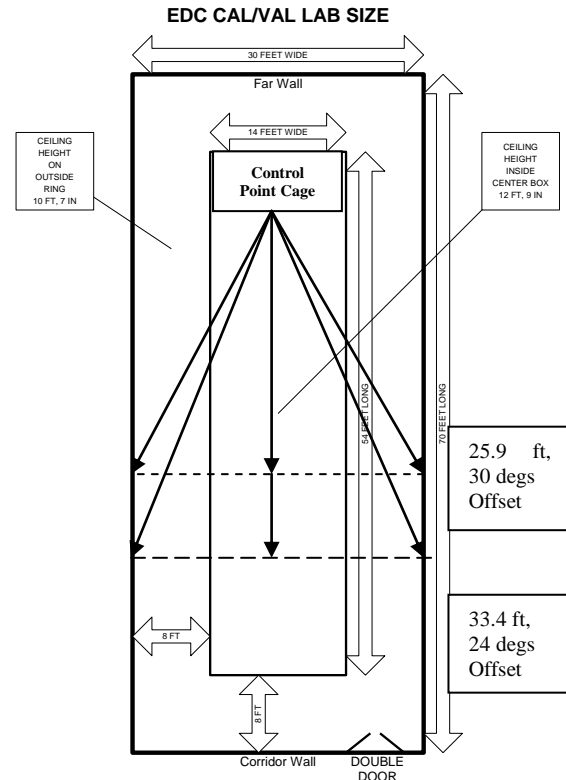
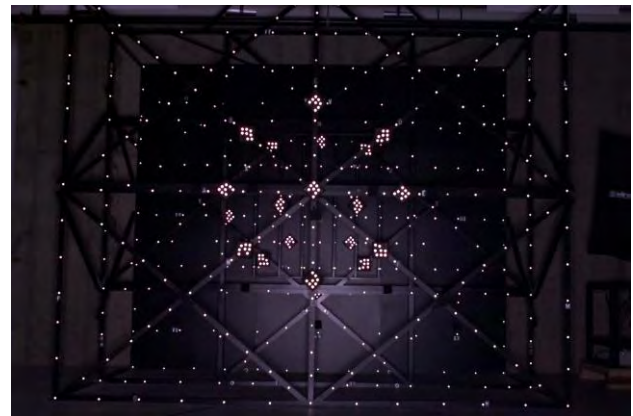
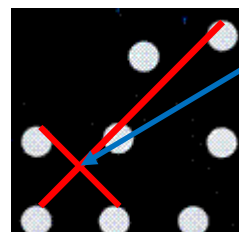


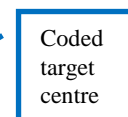
Figure 1. Layout of the calibration lab and the calibration cage



(a) 3D Calibration cage



(b) Coded target



(c) Circular target

Figure 2. (a) Image of the calibration cage, with three panels (b) the pattern in a coded target and (c) the individual circular target

The coded target centre is not the actual centroid of the individual target dots, but determined in a manner shown in Fig. 2(b). The software requires at least four coded targets in each image that are common with other images. It uses the targets to determine the initial relative orientation of the camera at all the exposure stations. It then uses the circular targets to determine a free network least squares bundle adjustment solution of Eq. 5. Since it is a free network solution, the least squares iteration converges easily, and a relative measure of the geometry of the system (the lens, camera, and the targets) is obtained.

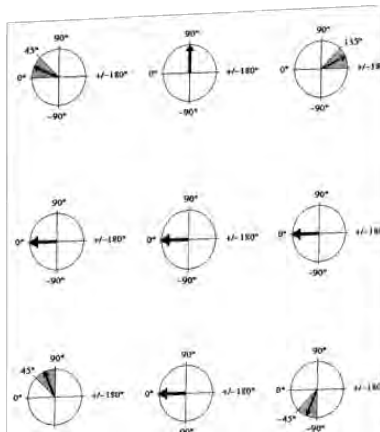


Figure 3. Camera orientations for the nine convergent image exposure stations

2.3 Camera self calibration using a box

With the ever increasing use of digital photography for aerial mapping, the USGS receives many requests to calibrate cameras that are not traditionally used for photogrammetric mapping. Some of these cameras are short focal length small format commercial cameras, (used perhaps from unmanned aerial vehicles, etc.) To handle these requests, the USGS has developed a self calibration procedure that does not require establishing a large calibration cage. Instead, a smaller rigid box that can be easily designed and constructed is used. The current design of the box is as shown in Fig. 4.



Figure 4. A rigid box design for calibration of small format cameras

The box is designed such that its dimensions are approximately 24 inches at the top (outer edge) and 12 inches at the bottom (inner). The inner walls of the box are not vertical, but are sloping at approximately 30 degrees. A scaled down series of coded targets are pasted on all the interior surfaces of the box. The design takes advantage of the simplicity of the free network bundle adjustment solution that requires no outside control structure.

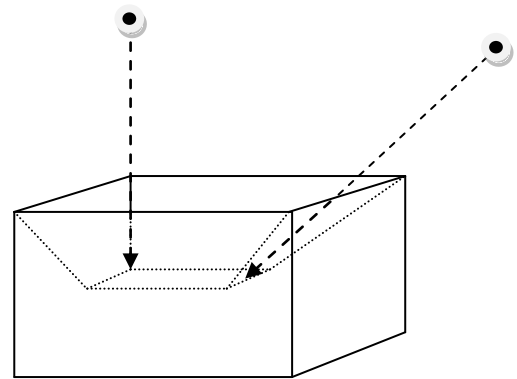


Figure 5. Camera exposure stations for box based calibration

For calibration photography, the optic axis of the camera is usually kept parallel to the inclined interior walls of the box. Three images are obtained from each side, and one image is obtained from each of the four corners, which results in a total of sixteen images. The images are alternatively taken in portrait and landscape modes. For a stable solution, as many targets as possible are obtained from the corners of the camera lens.

3. RESULTS AND ANALYSIS

A Nikon D1x digital single lens reflex (SLR) camera with a 20mm focal length lens (Nikkon AF) was used for this research. F # of 8 was chosen for calibrating with the cage as target, and f # of 22 was chosen for calibrating with the box as the target. The optimal hyperfocal distances for the F# (depth of focus) were calculated using Eq. 6:

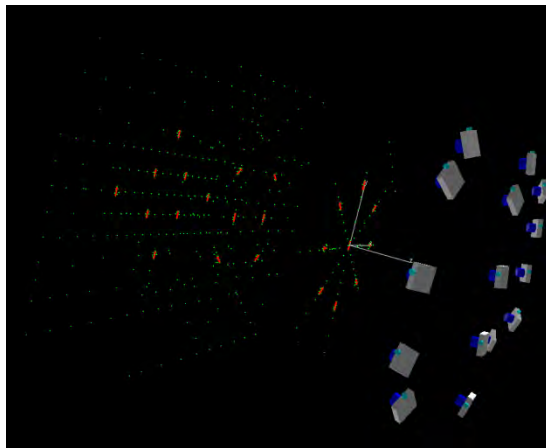
$$H_p = \frac{f^2}{F\# \times c} + f \tag{6}$$

where f is the focal length, and c is the circle of confusion and is approximately 0.072 mm. The hyperfocal distance for the cage was 2.3 ft and for the box was ~ 1ft.

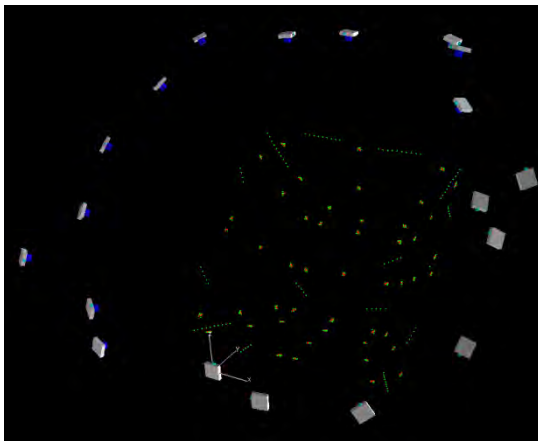
3.1 Results

Since the hyperfocal distance to the front panel of the cage was only 2.4 ft, it was very difficult to cover the entire cage, and the circular and coded targets. To ensure a more complete coverage, it was decided to take more than the standard set of nine images for calibration. A total of 15 images were used in Australis. The free network bundle adjustment solution is graphically displayed in Fig 7 (a). In a similar manner, the hyperfocal distance for the calibration using the box was calculated at 1 ft. A total of 20 images were obtained for the box. The free network solution is graphically shown in Figure 7 (b). The

green dots in Fig. 6 represents a circular target (Fig 2c), while the orange lines represent the coded target patterns (Fig. 2b).



(a)



(b)

Figure 6. Graphical representation of the bundle adjustment solution for (a) Cage and (b) Box based camera calibration

Calibration parameters		Calculated values from cage	Calculated values from box
Focal length		20.601	20.603
Principle point location	x_p	0.056 mm	0.064 mm
	y_p	-0.020 mm	-0.019mm
Radial distortion coefficients	K1	2.781e-004	2.74196e-004
	K2	-4.996e-007	-4.1747e-007
	K3	9.139e-011	-1.5359e-011
De-centring distortion coefficients	P1	-6.173e-007	2.989e-007
	P2	8.341e-006	2.637e-005
Scaling elements	B1	8.1521e-005	1.5082e-005
	B2	-1.0153e-005	9.6088e-006

Table 2 Camera calibration parameters

Table 2 shows the solutions to the bundle adjustment and the calibration parameters obtained from the two experiments. Table 2 lists the calibration parameters that were obtained as a part of the bundle adjustment solution

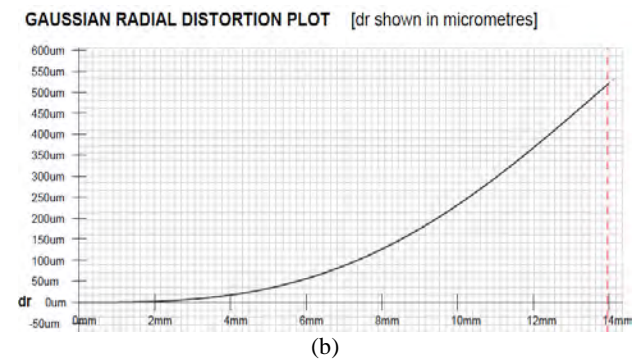
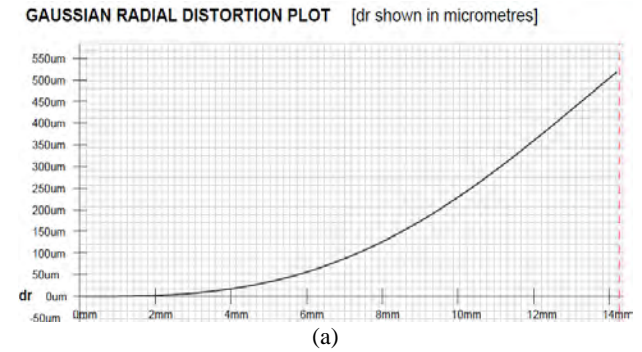


Figure 7. Radial distortion plots showing the distortion (Y-axis, μm) as a function of distance (X-axis, mm) from the principal point for results of camera calibration obtained from (a) Cage and (b) Box. The plots are obtained from Australis software

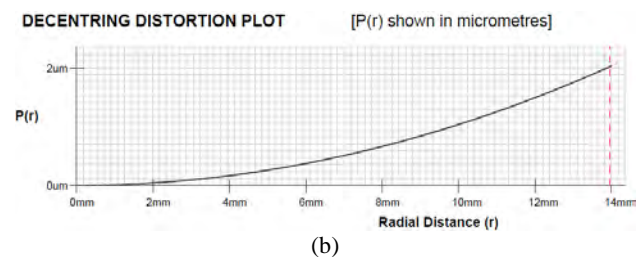
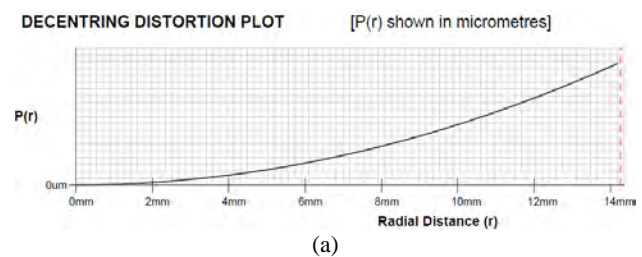


Figure 8. Decentering distortion plots showing distortion (Y-axis, μm), against radial distance (X-axis, mm) for results of camera calibration obtained from (a) Cage and (b) Box. The plots are obtained from Australis software

3.2 Analysis

The results of the two calibration procedures indicate that the parameters are close to being identical (Table 2). The charts in Fig. 7 also show the same phenomena. However, in our experiments, we found that the results start varying if the camera is positioned too close to the targets. This observation seems consistent with previously reported studies on close range photogrammetric camera calibration (Brown, 1971). However, more analysis needs to be done for anything conclusive. Since the Box as a calibration target is meant for small format short focal length cameras, the distance between the targets and the cameras should be close enough so that Australis software is able to recognize the targets. The size of the targets, therefore, needs to be selected accordingly.

4. CONCLUSIONS

In this research, two methods of camera calibration that are used at the USGS EROS at Sioux Falls, South Dakota, USA were presented. The camera calibration lab is housed primarily to calibrate medium format digital cameras, with a focal length range between 20-120mm. The main calibration method uses the principles of self calibration and bundle adjustment on coded targets located on an aluminium cage. A second method to perform calibration was presented. This method used a scaled down version of the coded targets pasted on a small rigid box. Both the methods involve taking images of the targets from different camera locations and orientations. The solution to the bundle adjustment problem is obtained using the software Australis. It was shown that the solutions camera calibration parameters obtained from both the methods are close to each other. The same time the approach using the box yields promising results and can be used for verification of the calibration parameters. Further research on the box by adding more targets may yield results closer to the results obtained from the cage. There has been an increasing interest in calibrating longer focal length cameras (> 150mm) using self calibration methods. The problem becomes non trivial given the limitations of space. Further research is being conducted at the USGS on expanding the range of cameras, with regards to the focal length, that can be calibrated in the lab.

References:

Brown, D.C., 1996. Decentering distortion of lenses. *Photogrammetric Engineering*, 32(3):444– 462.

Brown, D.C., 1996. Close-range camera calibration. *Photogrammetric Engineering*, 37(8):855– 866, August 1971

Faugeras, O., Luong, Q.T. and Maybank, S., 1992. Camera selfcalibration: Theory and experiments. *ECCV'92, Lecture Notes in Computer Science*, Vol. 588, Springer-Verlag, pp. 321-334

Fraser, C.S., 1997. Digital camera self-calibration. *ISPRS Journal of Photogrammetry & Remote Sensing* 52, pp. 149–159, 1997.

Fraser, C.S., 2001. Australis: software for close-range digital photogrammetry users manual.

Hartley, R., 1994: Euclidean reconstruction from uncalibrated

views. In *Applications of Invariance in Computer Vision*, Mundy, Zisserman and Forsyth (eds.), *Lecture Notes in computer Science*, Vol. 825, Springer-Verlag, pp. 237-256

Remondino, F., Fraser, C.S., 2006. Digital camera calibration methods: considerations and comparisons. *IAPRS volume XXXVI, part 5, Dresden 25-27 September 2006*

Lee, G.Y.G. ,2004. Camera calibration program in the United States: past, present and future. In *Post-Launch Calibration of Satellite Sensors*, *ISPRS Book Series*, Vol. 2, A.A. Balkema Publishers, New York.

Light, D.L.,1992. The new camera calibration system at the U.S.Geological Survey. *Photogrammetric Engineering and Remote Sensing*, 58(2):185–188.

Mugnier, C.J., Forstner, W., Wrober, B., Padres, F., Munjy, R., 2004. The mathematics of photogrammetry. In *Manual of Photogrammetry*, Fifth edition. Pp. 181-316.

Strum., P., 1998. A case against Kruppa's equations for camera self-calibration. *IEEE International conference on image processing*, Chicago, Illinois, pp. 172-175.

Triggs, B., 1997. Autocalibration and the absolute quadric, *CVPR*, pages 609–614, Puerto Rico, June 1997.

DISCLAIMER

Any use of trade, product, or firm names is for descriptive purposes only and does not imply endorsement by the U.S. Government.

ACKNOWLEDGEMENTS

Sam Johnson and Alonso Holmes performed most of the camera calibration experiments

THE AERIAL PHOTOS TO DETECT CHANGES IN THE LANDSCAPE AFFECTED BY BLACK COAL DEEP MINING

M. Mulkova, R. Popelková

Department of Physical Geography and Geoecology, Faculty of Science, University of Ostrava,
Chittussiho 10, Ostrava – Slezská Ostrava, Czech Republic – (Monika.Mulkova, Renata.Popelkova)@osu.cz

KEY WORDS: aerial photography, land cover, landscape changes, Ostrava-Karviná Mining District, deep coal mining

ABSTRACT:

Aerial photos are the suitable data source for monitoring landscape changes. The black coal deep mining shows specific way in the landscape. During the coal extraction there is an anthropogenic transformation of surface. The anthropogenic forms of relief rise: waste banks, tailings ponds, handling areas, etc. A large influence on the relief changes has also undermining, which the images show in particular the emergence of the submerged ground subsidences and decrease buildings. As a result, there is a significant change in the land cover of the area.

The study deals with the symptoms of the black coal deep mining on the aerial photos. Changes in the landscape due to underground black coal mining are presented on the example of the central part of the Ostrava-Karviná Mining District (Czech Republic). As the data sources were used archival black and white aerial photos and contemporary color aerial photos from the period from the year 1947 to the year 2003.

1. INTRODUCTION

In the second half of the 19th century the Ostrava and Karviná regions became fast growing industrialized areas for beds of quality hard coal that had been discovered in the territory. One-time agricultural regions gradually change into industrial areas with dominant mining, metallurgic and chemical industries. All these activities, headed by hard coal mining, transform the landscape of the Ostrava and Karviná regions significantly.

The displays of hard coal deep mining in landscape involve the occurrence of anthropogenic landforms directly related to mining activities as well as land cover changes that are related to mining indirectly. A majority of these changes can be interpreted on the basis of aerial photos and their development analysed using multitemporal data.

Central parts of the Ostrava-Karviná Mining District (Karviná-Doly I, Karviná-Doly II and Darkov Allotments) have been chosen for aerial photo presentation of deep mining displays. The Ostrava-Karviná Mining District (OKMD) occupies approximately 50% of the Karviná region situated in the Moravskoslezský Region, in the north-east of the Czech Republic (Figure 1). Northern and eastern border of the Karviná region is the state border with Poland. The OKMD, where coal-bearing layers of the Carboniferous age are found (OKD, 2010), represents the southern part of the Upper Silesian Coal Basin whose major part lies in the territory of the neighbouring Poland (its area is 7000 km², 1500 km² of which in the territory of the Czech Republic). Hard coal deep mining has been taking place in the district since 1850s. The OKMD is divided into 3 parts: Ostrava, Karviná and Southern part. The Karviná District belongs to areas with ongoing hard coal deep mining.

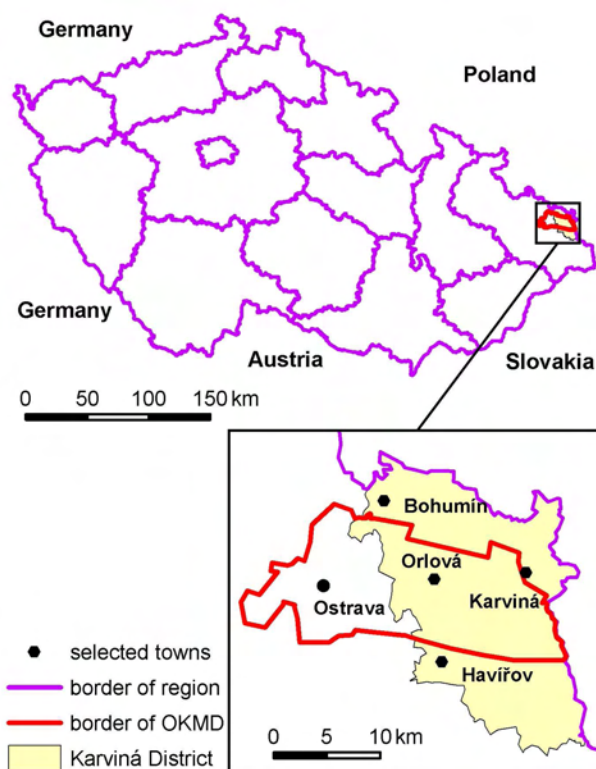


Figure 1. Localization of the Ostrava-Karviná Mining District (OKMD) and the Karviná region within the Czech Republic

Aerial photos represent a significant data source of ongoing landscape transformation with regard to relatively high dynamics of anthropogenically conditioned landscape changes in hard coal deep mining areas. The study of quality photos of mining displays in the landscape is based on the principles of

visual photointerpretation whose aim is to identify individual objects and assess their importance (Philipson, 1997, McGlone, 2004 in Jensen, 2006). Aerial photo interpretation starts from visual perception related to objects of the outer world Ciolkosz, Miszalski, Oledzki, 1999).

The displays of deep coal mining in the landscape were detected using contact copies of archive black-and-white aerial photos from the period of 1947 to 1995 (provided by the Military Geography and Hydrometeorology Office in Dobruška) and a coloured orthophoto from 2003 (map service of the Portal of the Public Administration of the Czech Republic).

The surface consequences of hard coal deep mining are characterized by the occurrence of anthropogenic landforms directly related to mining (waste banks, submerged ground subsidences, tailings ponds, manipulation areas etc.). Secondary subsurface coal mining leads to the process of abandonment (e.g. the transformation of continuous urban fabric into green urban areas), the occurrence of reclamation areas aimed to deal with the consequences of mining activity, or the construction of communications.

2. DISPLAYS OF HARD COAL DEEP MINING

2.1 Primary displays

Hard coal deep mining is primarily manifested by anthropogenic landforms directly related to mining activity. These include post-mining landforms (waste banks, ground subsidences) and industrial landforms (tailings ponds, manipulation areas).

2.1.1 Waste banks: Waste banks represent convex landforms whose area can reach from a few areas to tens of hectares (Havrlant 1980). They originate as a result of the deposition of extracted coal waste. The OKMD area includes the following types of waste banks (Havrlant 1980): cone-shaped waste banks, waste piles, plate-shaped waste banks, terrace-like waste banks, flat waste piles or their combinations. Active waste banks in the photos represent vegetation-free surfaces with clearly visible contours (Figure 2). They are generally found in the proximity of mine buildings.



Figure 2. Waste banks in (a) an aerial photo from 1947 (© MO ČR/GeoSI AČR) and (b) an aerial photo from 2003

Waste banks are reclaimed after waste piling is terminated (Figure 3).



Figure 3. The part of reclaimed waste bank in 2003

2.1.2 Ground subsidences: Ground subsidences originate as a result of the surface subsidence above the mined-out space (Demek, 1988). It concerns flat subsidences whose size depends on geological conditions, tectonics and the area and thickness of coal-seams (Havrlant, 1980). The subsidences can be filled with water. Submerged ground subsidences are displays of unfavourable disturbance of the regime of surface and subsurface waters the level of which has infiltrated above the bottom of subsided terrain (Zapletal, 1969).

The occurrence of ground subsidences is therefore a primary display of mining activity. Aerial photos help to interpret particularly submerged ground subsidences that represent a secondary display of undermining and that, to a large extent, take part in the process of submerging. Unlike other water surfaces they usually have an irregular broken shape (Figure 4). Submerged ground subsidences positively affect ecological value of landscape as they increase species diversity of the territory. Their banks are occupied by wetland plant species, rare invertebrates (e.g. specially protected dragonflies, crayfishes, shells) and other important animal species.





Figure 4. Submerged ground subsidences (a) in an aerial photo from 1947 (© MO ČR/GeoSI AČR) and (b) in an aerial photo from 2003

2.1.3 Tailings ponds: Hard coal deep mining area involves also a few types of ponds: flotation tailing ponds, coal ash ponds, coal sludge ponds and final sedimentation ponds. It particularly concerns water surfaces of a regular, often geometric, shape in the proximity of mine buildings (Figure 5).



Figure 5. Tailings ponds in (a) an aerial photo from 1947 (© MO ČR/GeoSI AČR) and (b) an aerial photo from 2003

Final sedimentation ponds can have a character of natural water surfaces, which makes their interpretation in aerial photos difficult (Figure 6).



Figure 6. Final sedimentation pond in an aerial photo from 2003

2.1.4 Manipulation areas: Manipulation areas are generally found in the proximity of mine buildings, tailings ponds, or waste banks. It concerns bare surfaces, either convex or concave, serving as manipulation areas for e.g. transport (Figure 7).



Figure 7. Manipulation areas (a) in an aerial photo from 1947 (© MO ČR/GeoSI AČR) and (b) in an aerial photo from 2003

2.1.5 Mine buildings: Individual mine buildings including a winding tower and other mining-related buildings can be identified in aerial photographs (Figure 8).



Figure 8. Mine buildings (a) in an aerial photo from 1947 (© MO ČR/GeoSI AČR) and (b) in an aerial photo from 2003

It can include temporary buildings that are renovated after the mining activity termination. For example, the area of the ČSA 3 Mine (Jindřich Pit), which is visible in aerial photos from 1971 in the western part of the Karviná-Doly I Allotment, was

covered with soil and grassed after the demolition of buildings. A contemporary orthophoto shows trees, scrub and herbaceous vegetation associations in this area. What points to one-time mining activities in this area are the foundations of old mining buildings that are visible in the orthophoto from 2003 (Figure 9).



Figure 9. Area of the ČSA (a) in an aerial photo from 1971 (© MO ČR/GeoSI AČR) and (b) in an aerial photo from 2003

2.2 Secondary displays

Hard coal deep mining has also secondary displays in the landscape which are characterized by the occurrence of anthropogenic landforms indirectly related to mining (reclamation areas, dry tailings ponds, communications) or land cover change (vegetation-free surfaces).

2.2.1 Reclamation areas: It concerns temporary convex landforms in a shape of low flat waste banks. These should be aligned with the surrounding landscape after the termination of reclamation works. Reclamation areas are created in order to deal with negative effects of hard coal deep mining. The photos facilitate easy interpretation of new reclamation areas in the form of bare surfaces (Figure 10).

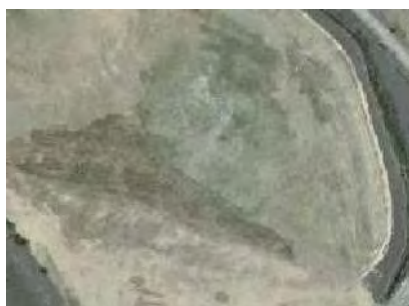


Figure 10. Reclamation areas in an aerial photo from 2003

2.2.2 Dry tailings ponds: These are shallow concave vegetation-free landforms that appear in the landscape after the termination of sludge management activities (Figure 11). Filled tailings ponds dry out and if no reclamation is carried out, they gradually overgrow with self-seeded vegetation.

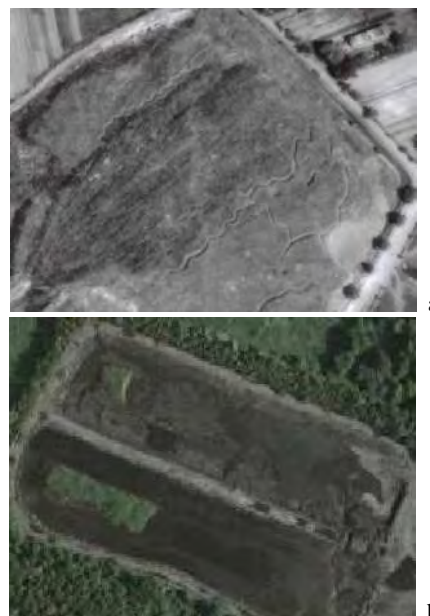


Figure 11. Dry tailings ponds (a) in an aerial photo from 1947 (© MO ČR/GeoSI AČR) and (b) in an aerial photo from 2003

2.2.3 Communication landforms: In the case of undermined area embankments are created to level surface deformations damaging communications. As a result of the modification of communication height embankments reaching up to a few meters are built. The types of embankments, which are characterized by line shapes and therefore easily identifiable in aerial photos, involve railway and road embankments as well as embankments of engineering networks (Figure 12).



Figure 12. Railway embankment in an aerial photo from 2003

2.2.4 Vegetation-free surfaces: Vegetation-free surfaces that represent secondary displays of deep mining are most often related to bare surfaces appearing particularly after building demolition (Figure 13). Their duration is relatively short as they gradually overgrow with self-seeded vegetation.



Figure 13. Vegetation-free surfaces (a) in an aerial photo from 1947 (© MO ČR/GeoSI AČR) and (b) in an aerial photo from 2003

3. PROCESSES RELATED TO DEEP MINING

Time series of aerial photos enable to observe landscape changes on the basis of ongoing processes that can be visually interpreted indirectly from land cover changes. The most frequent mining-related processes involve submergence and abandonment that can consequently lead to the process of forestation.

3.1 Abandonment

As based on multitemporal aerial photos, the process of abandonment can be identified at places where artificial surfaces, agricultural areas, forests or water bodies transform into semi-natural areas of trees, scrub and/or herbaceous vegetation associations (Figure 14).



Figure 14. The process of abandonment in the artificial surfaces (a) an aerial photo from 1947 (© MO ČR/GeoSI AČR) and (b) an aerial photo from 2003

Undermining that causes land surface deformations generally leads to the disturbance of the structural mechanics of buildings and consequently to their demolition. The photos clearly show a visible decrease in the build-up area and its gradual overgrowth by self-seeded vegetation. A typical example is the Church of St. Peter of Alcantara in the northern part of the Karviná-Doly II Allotment (Figure 15). As a result of mining activity the church subsided by 36 m.



Figure 15. Contemporary view of the Church of St. Peter of Alcantara

All buildings in the proximity of the church have been demolished. A submerged ground subsidence is located to the east of the church (Figure 16).

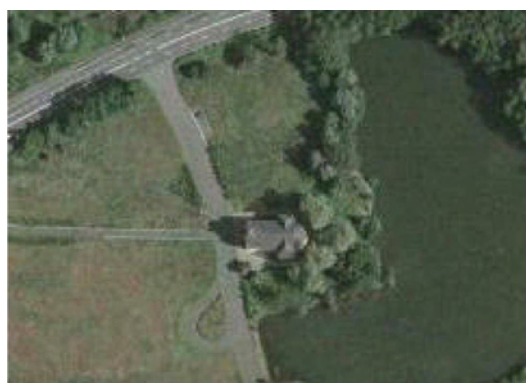


Figure 16. Church of St. Peter of Alcantara and its vicinity in an orthophoto from 2003

Aerial photos also help to identify the process of abandonment in originally agricultural areas which being disused gradually turn into semi-natural areas.

3.2 Forestation

In most cases, the process of abandonment is succeeded by the process of forestation in which abandoned areas overgrow with self-seeded vegetation in the first phase followed by a subsequent gradual transition to forest stands.

3.3 Submersion

Submersion represents a process of the change of artificial surfaces, agricultural areas, forests and semi-natural areas into water bodies. New water surfaces originate primarily as related very closely to mining (tailings ponds) or secondarily as a consequence of undermining (submerged ground subsidences). Aerial photo time series facilitate the identification of the process from both spatial and temporal points of view (Figure 17).



Figure 17. The area before (year 1947, © MO ČR/GeoSI AČR) and after (year 2003) the occurrence of a submerged ground subsidence

4. CONCLUSION

The aerial photo analysis of the effects of mining on landscape showed that both direct and indirect signs must be taken into consideration in visual photointerpretation. In order to identify the primary and secondary displays of mining activities stress is put on direct signs contained in a respective photo: shape, size, tone, colour, texture and structure of an object. However, these signs must be complemented with the interpretation of indirect signs, i.e. logical signs that require deep knowledge on the research phenomena (Ciolkosz, Miszalski, Oledzki, 1999). Indirect signs used in the interpretation of anthropogenic landforms include particularly the location of an object and its relations to other objects in a photo.

Unlike the primary and secondary mining displays, the processes are absent in the photos, however, they can be derived from multitemporal analysis of aerial photos. Such processes are presumed on the basis of indirect signs in combination with supporting information used in order to differentiate between mining-related processes and other processes that take place in the landscape.

Correct interpretation of the displays of deep mining depends on interpreter's direct experience with events taking place in the mining landscape. Subsequently, accurate visual interpretation of the displays of deep mining enables us to quantify the extent of changes, determine their direction and analyse processes in heavily anthropogenically-affected landscape. Aerial photos represent an important source of information in the study of territorial differentiation of changes, their intensity, character and causes. Complex understanding of these processes makes it possible to predict the landscape development and ecological and social consequences in the landscape affected by hard coal deep mining.

5. REFERENCES

- Ciolkosz, A., Miszalski, J., Oledzki, J. R., 1999. *Interpretation of aerial photographs*. PWN, Warszawa, 458 p. (in Polish)
- Havrlant, M., 1980. *Anthropogenic landforms and the environment in Ostrava industrial region*. Pedagogical Faculty, Ostrava, 153 p. (in Czech)
- Jensen, J. R., 2006. *Remote Sensing of the Environment. An Earth Resource Perspective*. Pearson Education, Upper Saddle River, 608 p.
- Mulková, M., Popelka, P., Popelková, R., 2010. *The Impact of Industrialization on the Landscape of the Ostrava-Karviná Mining District*. Landscape Ecology - methods, applications and interdisciplinary approach. (in press)
- OKD, a.s. (*Ostrava-Karviná Mining District*) [online] Available at: <http://www.okd.cz/>
- PVS (*Map service of the Portal of the Public Administration of the Czech Republic*) [online] Available at: <http://geoportal.cenia.cz/>
- Zapletal, L., 1969. *Introduction to anthropogenic geomorphology I*. Palacky University, Olomouc. 280 p. (in Czech)

EFFICIENCY OF TEXTURE MEASUREMENT FROM TWO OPTICAL SENSORS FOR IMPROVED BIOMASS ESTIMATION

J. E. Nichol, M. L. R. Sarker

Department of Land Surveying and Geo-Informatics, The Hong Kong Polytechnic University
Kowloon, Hong Kong - lsjanet@polyu.edu.hk

KEY WORDS: AVNIR-2, SPOT-5, texture measurement, biomass estimation, image processing

ABSTRACT:

No technique has so far been developed to quantify biomass carbon sources and sinks over large areas. Among the remote sensing techniques tested, the use of multisensors, and spatial as well as spectral characteristics of data have demonstrated strong potential for biomass estimation. However, the use of multisensor data accompanied by spatial data processing has not been fully investigated because of the unavailability of appropriate data sets and the complexity of image processing techniques for combining multisensor data with the analysis of spatial characteristics. This research investigates the texture parameters of two high (10m) resolution optical sensors AVNIR-2 and SPOT-5 in different processing combinations for biomass estimation. Multiple regression models are developed between image parameters extracted from the different stages of image processing and the biomass of 50 field plots, which was estimated using a newly developed “Allometric Model” for the study region.

The results demonstrate a clear improvement in biomass estimation using the texture parameters of a single sensor ($r^2=0.854$ and $RMSE=38.54$) compared to the highest accuracy obtained from simple spectral reflectance ($r^2=0.494$) and simple spectral band ratios ($r^2=0.59$). This accuracy was further improved, to obtain a very promising accuracy using texture parameters of both sensors together ($r^2=0.897$ and $RMSE=32.38$), the texture parameters from the PCA of both sensors ($r^2=0.851$ and $RMSE=38.80$) and the texture parameters from the averaging of both sensors ($r^2=0.911$ and $RMSE=30.10$). Improved accuracy was also observed using the simple ratio of texture parameters of AVNIR-2 ($r^2=0.899$ and $RMSE=32.04$) and SPOT-5 ($r^2=0.916$) and finally a surprisingly high accuracy ($r^2=0.939$ and $RMSE=24.77$) was achieved using the ratios of the texture parameter of both sensors together.

1. INTRODUCTION

Remote sensing is the most promising technique to estimate biomass at local, regional and global scales, thereby helping to reduce the uncertainties associated with the role of forests in key environmental issues (Brown et al, 1989; Rosenqvist et al 2003). A number of studies has been carried out using different types of sensors including optical (Mukkönen and Heiskänen, 2005; Fuchs et al 2009; Foody et al, 2003; Dong et al, 2003) SAR (Santos et al, 2003; Kuplich et al, 2005), and Lidar sensors (Zhao et al 2009) for biomass/forest parameter estimation. Apart from the use of a single sensor, combining information from multiple sensors has yielded promising results for the estimation of forest parameters/biomass (Rosenqvist et al, 2003; Hyde et al, 2006; Boyd and Danson, 2005).

Although vegetation indices, have been successfully used in temperate forests (Zheng et al, 2004; Rahman et al, 2005), they have shown less potential in tropical and subtropical regions where biomass levels are high, the forest canopy is closed with multiple layering, and great diversity of species is present (Foody et al, 2001, 2003; Boyd et al, 1996; Lu, 2005). On the other hand, the spatial characteristics of images have such as texture have been found particularly useful in fine spatial resolution imagery (Franklin et al, 2001; Boyd and Danson, 2005), and capable of identifying different aspects of forest stand structure, including age, density and leaf area index (Champion et al, 2008; Wulder et al, 1996). Indeed, texture has shown potential for biomass estimation with both optical (Franklin et al, 2001; Lu, 2005; Fuchs et al, 2009) and SAR data (Santos et al, 2003; Lu, 2005; Kuplich et al, 2005). Moreover, although most previous biomass estimation projects

used Landsat TM data with a 30m spatial resolution (Lu, 2006), texture is expected to be more effective with finer spatial resolution imagery since finer structural details can be distinguished (Kuplich et al, 2005; Boyd and Danson, 2005; Franklin et al, 2001). This research investigates texture processing for biomass estimation using data from two high resolution optical sensors ANVIR-2 and SPOT-5 along with raw spectral processing and some simple band ratios. The overall objective of the study is to explore the potential of texture processing combined with multisensor capability for the improvement of biomass estimation using data from two high resolution optical sensors.

The study area for this research is the Hong Kong Special Administrative Region (Fig. 1) which lies on the southeast coast of China, just south of the Tropic of Cancer. Approximately 40% of Hong Kong is designated as Country Parks which are reserved for forest succession. The native sub-tropical evergreen broad leaf forest has been replaced by a complex patchwork of regenerating secondary forest in various stages of development, and plantations. Forest grades into woodland, shrubland then grassland at higher elevations.



Figure 1. Study area and location of field sampling plots

2. METHODOLOGY

The methodology (Fig. 2) of this study comprises two parts namely allometric model development for field biomass estimation, and processing of AVNIR-2 and SPOT-5 images. Due to the lack of an allometric model for converting the trees measured in the field to actual biomass, it was necessary to harvest, dry and measure a representative sample of trees. Since tree species in Hong Kong are very diverse, the harvesting of a large sample was required. This was done by selecting the dominant tree species comprising a total of 75 trees in 4 DBH classes (less than 10, 10-15, 15-20 and 20 & above cm) and standard procedures were followed for tree harvesting (Ketterings et al, 2001; Overman et al, 1994).

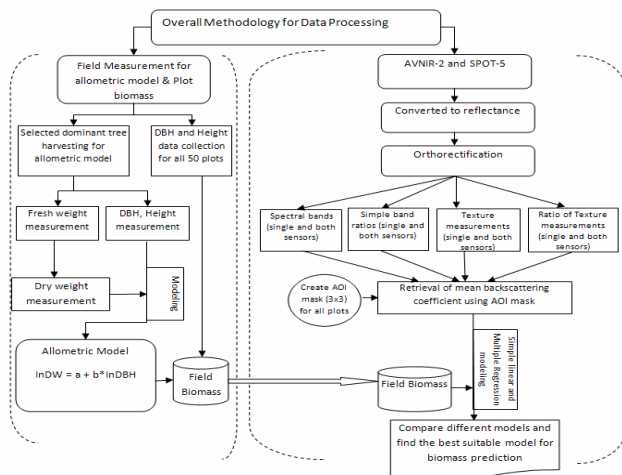


Figure 2. Overall methodology of this research

The harvested trees were separated into fractions including leaves, twigs, small branches, large branches and stem. After measuring the fresh weight, representative samples from every part of the tree were taken for dry weight measurement in an oven at 80°C temperature until a constant dry weight was obtained (Fig 3). The weight of every sample was estimated using the same electric weight balance at 0.002gm precision. The ratio of dry weight (DW) to fresh weight (FW) was calculated for every part of the samples using DW and FW of each part of the tree. Using the ratio, DW was calculated for

every part, and finally the DW of each tree was calculated by summing the DW of all parts.



Figure 3. Preparing the samples for dry weight measurement

Regression models using DW as the dependent variable, and DBH and height as independent variables were tested, and the best fit model (Table 2) was found to be $\ln DW = a + b \cdot \ln DBH$, with the adjusted coefficient of determination (adjusted r^2 0.932) and an RMSE of 13.50. This was deemed highly satisfactory in view of the great variety of tree species, and is similar to the accuracies of several other specialist forest inventories (Brown et al, 1989; 1997; Overman et al, 1994).

To build a relationship between image parameters and field biomass, 50 circular plots with a 15m radius covering a variety of tree stand types were selected using purposive sampling. The DBH of trees was measured at 1.3 m above ground and the heights of small and large trees were measured by Telescopic-5 and DIST pro4 respectively. Using the measured parameter DBH, the biomass of each tree and biomass of all trees in a plot were estimated

3. IMAGE PROCESSING

The DN of the AVNIR-2 and SPOT data were converted to Spectral Radiance, and the images were orthorectified using the Satellite Orbital Math Model to obtain RMS error within 0.5 pixel. All individual spectral bands of AVNIR-2 and SPOT-5 as well as different combinations of band ratios and PCA were tested for biomass estimation. All individual spectral bands of AVNIR-2 and SPOT-5 as well as different combinations of band ratios and PCA were tested for biomass estimation. Additionally, nineteen different types of texture measurements (Table 1) from GLCM based (Haralick, 1973) and SADH based (Unser, 1986) were used to generate texture parameters from 4 spectral bands each of AVNIR-2 and SPOT data using 4 window sizes (3x3 to 9x9). All the generated parameters were tested by comparison with the field biomass using stepwise and multiple regression models of single and dual-sensor data.

Gray level co-occurrence matrix (GLCM) based texture
<p>1. Mean (ME) = $\sum_{i,j=0}^{N-1} i P_{i,j}$</p> <p>2. Homogeneity (HO) = $\sum_{i,j=0}^{N-1} i \frac{P_{i,j}}{1 + (i - j)^2}$</p> <p>3. Contrast (CO) = $\sum_{i,j=0}^{N-1} i P_{i,j} (i - j)^2$</p> <p>4. Standard deviation (Std) = \sqrt{VA} where VA = $\sum_{i,j=0}^{N-1} i P_{i,j} (i - ME)^2$</p> <p>5. Dissimilarity (DI) = $\sum_{i,j=0}^{N-1} i P_{i,j} i - j$</p> <p>6. Entropy (EN) = $\sum_{i,j=0}^{N-1} i P_{i,j} (-\ln P_{i,j})$</p> <p>7. Angular Second Moment (ASM) = $\sum_{i,j=0}^{N-1} i P_{i,j}^2$</p> <p>8. Inverse Differences (ID) = $\sum_{i,j=0}^{N-1} i \frac{P_{i,j}}{ i - j ^2}$</p> <p>9. GLDV Angular Second Moment (GASM) = $\sum_{k=0}^{N-1} V_k^2$</p> <p>10. GLDV Entropy (GEN) = $\sum_{k=0}^{N-1} V_k (-\ln V_k)$</p> <p>P (i, j) is the normalized co-occurrence matrix such that $\sum_{i,j=0}^{N-1} P(i, j) = 1$. V(k) is the normalized grey level difference vector $V(k) = \sum_{i,j=0}^{N-1} P(i, j)$ and $i - j = k$</p>
Sum & difference histogram (SADH) based texture parameter
<p>1. Mean (μ) = $\frac{\sum_{i,j} x_{i,j}}{n}$</p> <p>2. Mean deviation (MD) = $\frac{\sum_{i,j} x_{i,j} - \mu }{n}$</p> <p>3. Mean Euclidean distance (MED) = $\sqrt{\frac{\sum_{i,j} (x_{i,j} - \mu)^2}{n - 1}}$</p> <p>4. Variance ($\sigma^2$) = $\frac{\sum_{i,j} (x_{i,j} - \mu)^2}{n - 1}$</p> <p>5. Normalized Coefficient of Variation (NCV) = $\sqrt{\frac{\sigma^2}{\mu}}$</p> <p>6. Skewness (Sk) = $\frac{\sum_{i,j} (x_{i,j} - \mu)^3}{(n - 1)\sigma^3}$</p> <p>7. Kurtosis (Ku) = $\frac{\sum_{i,j} (x_{i,j} - \mu)^4}{(n - 1)\sigma^4}$</p> <p>8. Energy (E) = $\sum_{i,j} x_{i,j}^2$</p>

<p>9. Entropy (H) = $-\sum_{i,j} p_{i,j} \ln(p_{i,j})$, with $p_{i,j} = \frac{x_{i,j}}{\sum_{i,j} x_{i,j}}$</p> <p>$x_{i,j}$ = pixel value of pixel (i, j) in kernel, N = the number of pixels that is summed, x_c = the kernel's center pixel value, $P_{i,j}$ = the normalized pixel value.</p>

Table 1. Formulae of texture measurements used in this study

4. RESULTS AND ANALYSIS

The field biomass data from the 50 field plots ranged from 52t/ha to 530t/ha. In all modeling processes, the 50 field plots were used as the dependent variable and parameters (AVNIR-2 and/or SPOT-5) derived from different processing steps were used as independent variables.

The best estimates of biomass using simple spectral bands of AVNIR-2 and SPOT-5 as well as different combinations of band ratios and PCA produced only ca. 60% useable accuracy due to (i) the complexity of forest structure and terrain in the study areas, (ii) The very high field biomass in this study area (52t/ha to 530t/ha), and (iii) strong multicollinearity effects among the 8 bands and band ratios from the two sensors used.

A notable improvement was observed for both sensors using texture parameters (Table 2). For single band texture, the highest (AVNIR $r^2 = 0.742$ and SPOT-5 $r^2 = 0.769$) and lowest (AVNIR $r^2 = 0.309$ and SPOT-5 $r^2 = 0.326$) accuracies were obtained from the texture parameters of NIR and Red bands respectively. The pattern of accuracy was similar to that obtained using raw spectral bands although the performance was much higher for texture measurement. Moreover, as with raw data, the second highest accuracies (AVNIR $r^2 = 0.547$ and SPOT-5 $r^2 = 0.615$) were also obtained from green and SWIR bands using AVNIR-2 and SPOT-5 data respectively. These patterns of improvement were consistent for both sensors and very much in agreement with the general behavior of interaction between different wavelengths and vegetation. Thus we found that texture measurement enhanced biomass estimation across all bands but greater improvement was observed from the bands where reflectance from vegetation is higher.

However, unlike raw spectral bands and simple ratios of raw spectral bands, texture parameters from all bands together (either all bands of AVNIR-2 or SPOT-5) were found to be very useful, and obtained accuracies of 0.786 (r^2 for AVNIR-2) (model 1 in Table 2) and 0.854 (r^2 for SPOT-5) (model 2 in Table 2) Apart from the improved accuracies the developed models (using all texture parameters of an individual sensor together) were significant and no multicollinearity effects were evident.

When texture parameters from both sensors were combined together in the model (model 3 in Table 2), as well as all texture parameters of PCA of both sensors together (model 4 in Table 2), and all texture parameters from averaging of both sensors together (model 5 in Table 2), very significant improvements were obtained although PCA was not found to be very effective. The highest ($r^2 = 0.91$) and the second highest ($r^2 = 0.90$) accuracies were obtained from the texture parameters from the averaging of both sensors, and texture parameters of both sensors in the model respectively. These differences were attributed to the fact that averaging is a type of data fusion, and

the synergy between the two sensors probably contributed complementary information in the model.

Model	R ²	RMS error
1. Texture parameters of AVNIR-2 all bands ME_AB4_5, Ku_AB2_9, CO_AB4_9, TEN_AB3_9, Sk_AB2_5, Ske_AB1_9	0.79	46.5
2. Texture parameters of SPOT-5 all bands Sk_SB3_9, ASM_SB1_9, HO_SB4_9, ID_SB3_5, ID_SB2_3, GASM_SB4_5	0.85	38.5
3. Texture parameters of both sensors combined ASM_SB1_9, ASM_AB4_9, HO_AB4_7, Sk_SB3_7, Var_SB3_9, GEN_SB4_7, MDM_AB3_5	0.90	32.4
4. Texture parameters from PCA both sensors ASM_BPC1_9, CO_BPC3_9, Sk_BPC1_7, Var_BPC2_9, Var_BPC1_9, Std_BPC1_5, MED_BPC3_3/4_3	0.85	38.8
5. Texture parameters from Average of both sensors Ku_A4+S4_7, ASM_A2+S1_9, Ku_A2+S1_5, Sk_A4+S3_7, Var_A4+S3_9, ASM_A4+S3_9, HO_A3+S2_3	0.91	30.1
6. Texture parameter ratio of AVNIR-2 GEN_AT1/4_9, ASM_AT2/3_7, GEN_AT2/3_7, DI_AT2/3_9, Std_AT2/4_5, TME_AT2/4_9, ME_AT3/4_9, Ku_ST2/3_5	0.90	32.0
7. Texture parameter ratio of SPOT-5 Sk_ST3/4_9, DI_ST2/4_7, Var_ST3/4_9, ASM_ST1/2_5, MDM_ST3/4_7, CO_ST2/4_9, GEN_ST3/4_9	0.92	29.1
8. Texture parameter ratio of both sensors DI_ST2/4_7, Sk_ST3/4_9, Var_ST3/4_9, ASM_ST1/2_5, MDM_ST3/4_7, CO_ST2/4_9, GEN_ST3/4_9, MDM_aT2/3_5 CO_AT2/3_7	0.94	24.8

Table 2. Results of biomass estimation. For models (ME, Ku, CO etc, see Table 1. AB4_5 means AVNIR Band 4 with kernel 5*5, and SB3_7 means SPOT Band 3 with 7*7 kernel.

Finally, the ratio of texture parameters was found to be more effective for biomass estimation compared to the highest accuracies obtained from all previous steps. The accuracies obtained using all ratios of texture parameters of AVNIR-2 ($r^2=0.899$) (model 6 in Table 2), SPOT-5 ($r^2=0.916$) (model 7 in Table 2) and the texture ratios of both sensors together ($r^2=0.939$) (model 8 in Table 2) were considerably higher than for the simple texture models. Similar to the texture models, no multicollinearity effects were evident.

This great improvement in biomass estimation observed in this study can be explained by the fact that we used three image processing techniques together as follows;

- (i) texture processing which had already shown potential for biomass estimation in many previous studies using optical (Fuchs et al, 2009; Lu, 2005) and SAR data (Santos et al, 2003; Kuplich et al, 2005).

- (ii) datasets from two different sensors were used in this processing. Although both datasets used are from optical sensors (AVNIR-2 and SPOT-5), there are differences in the wavebands, therefore it was anticipated that at least some complementary information could be obtained.
- (iii) finally we tested the ratio of texture parameters. We know from previous research that ratios, whether simple or complex, and whether between different bands, different polarizations, or different frequencies, can improve biomass estimation by minimizing features which are similar in both bands such as topographic and forest structural effects.

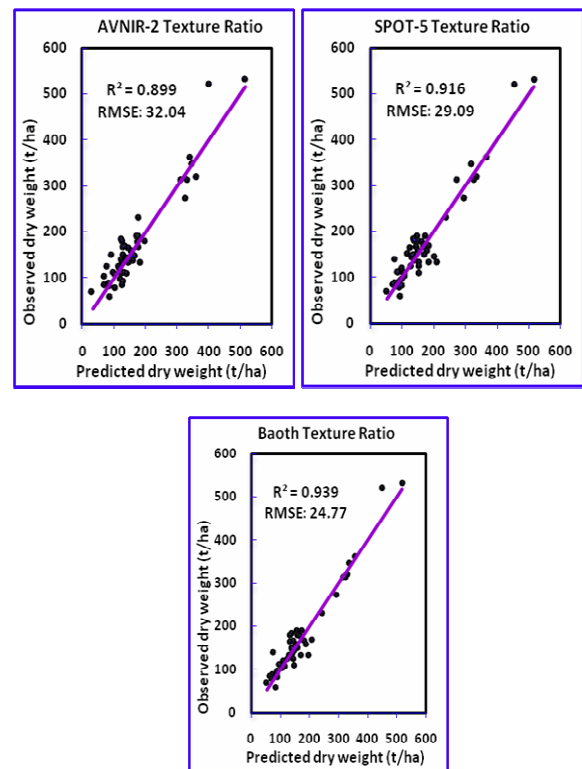


Figure 3. Relationship between field and model biomass

5. CONCLUSION

Data from two high resolution optical sensors were used in this research to establish a relationship between field biomass and remotely sensed observation parameters. The processing of data was conducted for each sensor individually and both sensors together. Spectral reflectance, texture parameters and ratio of texture parameters were evaluated for the improvement of biomass estimation. The results are promising, and except for the simple spectral reflectance, the accuracy (r^2) of biomass varied estimation was higher than 80%, though this varied between the two sensors due to different band availability. The accuracy of SPOT-5 sensor was somewhat higher in all processing steps compared to AVNIR-2 except for the simple spectral reflectance because of the availability of SPOT's SWIR band. However, better results were obtained using data from both sensors because of the complementary information.

In this research we obtained accuracy (r^2) ranging from 0.79 to 0.94 using different processing steps, and the highest accuracy ($r^2=0.94$) was obtained using the texture parameter ratio of both sensors. This accuracy is very promising, and this achievement

can be explained by our step wise processing which included the advantages of texture, ratio and complementary information from different sensors. In addition to the remote sensing data processing, the comprehensive and study area-specific nature of the field biomass data, and demonstrated accuracy of the allometric model (i.e. r^2 of 0.93) devised for this study from the destructive sampling of 75 trees was instrumental in obtaining this high accuracy. This research used numerous processing steps and data combinations, but in other field conditions a similar approach can be adopted to identify the most suitable steps for that particular situation.

ACKNOWLEDGMENTS

The authors would like to acknowledge the Hong Kong Agriculture, Fisheries and Conservation Department (AFCD) for help with tree harvesting in country parks, as well as the Japan Aerospace Exploration Agency (JAXA) for the ALOS images under ALOS agreement no. 376. This project was also sponsored by GRF grant no. PolyU5281/09E.

REFERENCES

- Boyd, D. S. Foody, G. M. Curran, P. J. Lucas R. M., Honzak, M. 1996. An assessment of radiance in Landsat TM middle and thermal infrared wavebands for the detection of tropical forest regeneration, *International Journal of Remote Sensing*, 17, pp.249-261.
- Boyd D. S., Danson, F. M. 2005. Satellite remote sensing of forest resources: Three decades of research development, *Progress in Physical Geography*, 29, pp.1-26.
- Brown, S. A. Gillespie J. R., Lugo, A. E. 1989. Biomass estimation methods for tropical forests with applications to forest inventory data, *Forest Science*, 35, pp.881-902.
- Brown., S. 1997. Estimating biomass and biomass change of tropical forests: A primer. FAO, USA.
- Champion, I. Dubois-Fernandez, P. Guyon D., Cottrel, M. 2008. Radar image texture as a function of forest stand age, *International Journal of Remote Sensing*, 29, pp.1795-1800.
- Dong, J. Kaufmann, R. K. Myneni, R. B. Tucker, C. J. Kauppi, P. E. Liski, J. Buermann, W. Alexeyev V., Hughes, M. K. 2003. Remote sensing estimates of boreal and temperate forest woody biomass: Carbon pools, sources, and sinks, *Remote Sensing of Environment*, 84, pp.393-410.
- Foody, G. M. Cutler, M. E. McMorrow, J. Pelz, D. Tangki, H. Boyd D. S., Douglas, I. 2001. Mapping the biomass of Bornean tropical rain forest from remotely sensed data, *Global Ecology and Biogeography*, 10, pp.379-387.
- Foody, G. M., Boyd D. S., Cutler, M E J, 2003. Predictive relations of tropical forest biomass from Landsat TM and transferability between regions, *Remote Sensing of Environment*, 85, pp.463-474.
- Fuchs, H. Magdon, P. Kleinn C., Flessa, H. 2009. Estimating aboveground carbon in a catchment of the Siberian forest tundra: Combining satellite imagery and field inventory, *Remote Sensing of Environment*, 113, pp.518-531.
- Haralick, R. M. Shanmugam K., Dinstein, I. 1973. Textural features for image classification, *IEEE Transactions on Systems, Man and Cybernetics*, smc 3, 610-621.
- Hyde, P. Dubayah, R. Walker, W. Blair, J. B. Hofton M., Hunsaker, C. 2006. Mapping forest structure for wildlife habitat analysis using multi-sensor (LiDAR, SAR/InSAR, ETM+, Quickbird) synergy, *Remote Sensing of Environment*, 102, pp.63-73.
- Kuplich, T. M. Curran P. J. and Atkinson, P. M. 2005. Relating SAR image texture to the biomass of regenerating tropical forests, *International Journal of Remote Sensing*, 26, pp.4829-4854.
- Lu, D. 2005. Aboveground biomass estimation using Landsat TM data in the Brazilian Amazon, *International Journal of Remote Sensing*, 26, pp.2509-2525.
- Lu, D. 2006. The potential and challenge of remote sensing-based biomass estimation, *Int. J. Remote Sens.*, 27, 1297-1328, Muukkönen P., Heiskänen, J. 2005. Estimating biomass for boreal forests using ASTER satellite data combined with standwise forest inventory data, *Remote Sensing of Environment*, 99, pp.434-447.
- Overman, J. P. M., Witte H. J. L., Saldarriaga, J. G., 1994. Evaluation of regression models for above-ground biomass determination in Amazon rainforest, *Journal of Tropical Ecology*, 10, pp.207-218.
- Rahman, M. M. Csaplovics E. and Koch, B. 2005. An efficient regression strategy for extracting forest biomass information from satellite sensor data, *International Journal of Remote Sensing*, 26, pp.1511-1519.
- Santos, J. R. Freitas, C. C. Araujo, L. S. Dutra, L. V. Mura, J. C. Gama, F. F. Soler L. S., 2003. Airborne P-band SAR applied to the aboveground biomass studies in the Brazilian tropical rainforest, *Remote Sensing of Environment*, 87, pp.482-493.
- Unser, M., 1986. 1986. Sum and difference histograms for texture classification. *IEEE Transactions on Pattern Analysis and Machine Intelligence*, PAMI-8, pp.118-125.
- Wulder, M. A., Franklin S. E., Lavigne, M. B. 1996. High spatial resolution optical image texture for improved estimation of forest stand leaf area index, *Canadian Journal of Remote Sensing*, 22, pp.441-449.
- Zhao, K. Popescu S., Nelson, R. 2009. Lidar remote sensing of forest biomass: A scale-invariant estimation approach using airborne lasers, *Remote Sensing of Environment*, 113, pp.182-196.
- Zheng, D. Rademacher, J. Chen, J. Crow, T. Bresee, M. Le Moine J., Ryu, S. -, 2004. Estimating aboveground biomass using Landsat 7 ETM+ data across a managed landscape in northern Wisconsin, USA, *Remote Sensing of Environment*, 93, pp.402-411,

LAND COVER CLASSIFICATION IN ALBANIA

Pal Nikolli

Tirana University, Faculty of History and Philology, Department of Geography, Tirana, Albania -
palnikolli@yahoo.com

KEY WORDS: land cover, classification, classification system, standardization, harmonization, Albania

ABSTRACT:

Land is one of our most precious assets, and its use is multi-faceted. Land cover and land use are, however, dynamic, and are affected both by natural phenomena, such as climatic events and natural disasters, and by human activities, although the impact of the latter has mainly been felt in the more recent centuries.

The Land Cover Classification System (LCCS) is a comprehensive, standardized a priori classification system, designed to meet specific user requirements, and created for mapping exercises, independent of the scale or means used to map. Any land cover identified anywhere in the world can be readily accommodated.

This article examines the land cover classification in Albania using the FAO/UNEP Land Cover Classification System for codification of classes. For this classification is used satellite remote sensing data. The aim of the land cover classification is to investigate the land cover transformations in the whole territory of Albania.

1. INTRODUCTION

Land cover is a geographical feature which may form a reference base for applications ranging from forest and rangeland monitoring, production of statistics, planning, investment, biodiversity, climate change, to desertification control. Better assessment of the changes of land cover by using digital analysis of remote sensing satellite data can help decision makers to develop effective plans for the management of land (Gordon, 1980; Milington et al., 1986; Franchek and Biggam, 1992).

Land cover classes are defined by a combination of a set of independent diagnostic criteria - the so-called classifiers - that are hierarchically arranged to assure a high degree of geographical accuracy. Because of the heterogeneity of land cover, the same set of classifiers cannot be used to define all land cover types. The hierarchical structure of the classifiers may differ from one land cover type to another.

One of the prime prerequisites for better use of land is information on existing land use patterns and changes in land use through time.

In Albania land cover classification, comprise three levels:

- the first level (five items) indicates the major categories (abstract to a greater or lesser degree) of land cover on the planet;
- the second level (15 items) is for use on scales of 1:500 000 and 1: 1 000 000;
- the third level (44 items) will be used for the project on a scale of 1: 100 000.

Knowledge of the present distribution and area of such agricultural, recreational, and urban lands, as well as information on their changing proportions, is needed by legislators, planners, and State and local governmental officials to determine better land use policy, to project transportation and utility demand, to identify future development pressure points and areas, and to implement effective plans for regional development. As Clawson and Stewart (1965) have stated: In this dynamic situation, accurate, meaningful, current data on land use are essential.

The framework of a national land cover classification system is presented for use with remote sensor data. The classification system has been developed to meet the needs of State agencies for an up-to-date overview of land use and land cover throughout the country on a basis that is uniform in categorization at the more generalized first and second levels and that will be receptive to data from satellite and aircraft remote sensors.

2. GEOGRAPHIC POSITION OF ALBANIA

Republic of Albania is situated on the west of Balkan Peninsula on the eastern littoral coasts of Adriatic and Jonian seas (fig. 1.1).

It is situated in the north geographical latitude 42⁰ 39' (Vermosh), south geographical latitude 39⁰ 38' (Konispol) and eastern geographical longitude 21⁰ 40' (Vernik), west geographical longitude 19⁰ 16' (Sazan). Republic of Albania borders the Montenegro and Kosovo to the north and northeast, the Former Yugoslav Republic of Macedonia to the east, and Greece to the south. Its western coast faces the Adriatic and Ionian Seas. Albania has a total area of 28,748 square kilometres. Its coastline is 362 kilometres long and extends along the Adriatic and Ionian Seas. The lowlands of the west face the Adriatic Sea. The 70% of the country that is mountainous is rugged and often inaccessible from the outside. The length of the border is 1094 km where 657 km are land, 48 km river, 73 km lake and 316 km littoral border. The north - south extension is 340 km, east - west 148 km and over the sea level 2751 m (mountain of Korab).

The relief mainly hilly - mountainous is significant for the various forms, big contrasts. Until 200 m over the sea level lays 23.4 % of the country. The altitudes 200 - 1000 m include 48.1 % and over 1000 m include 28.5 % of the Albanian territory.

Plain field areas suitable for the intensive agricultural development and without erosion problems are few and situated on the west. The rest hilly part which lifts up gradually toward east offers possibility for the

development of the fruit bearing, stock breeding, tourism etc.



Fig. 1.1. Albania on the west of Balkan Peninsula

The climate is Mediterranean on the west. Inside the country are appeared the influences of the continental phenomena in the climate while in height the alpine ones. Summer, in general, is hot and dry, while the winter is wet. The period with equal or higher temperature than 10°C changes from 260 to 300 days in a year. In general there precipitate average 1480 mm in a year. But the average annual quantity of the precipitation changes from 600 mm to 2100 mm. There are met 2000 - 2700 hours with sun radiation. The extraordinary meteorological situations which are accompanied with economical damages happen rather often.

Albania is rich with water richness. It is traversed by a hydrographical network with general length over 49 000 km and mean density 1.7 km/km^2 . The annual volume of the water quantity of the rivers arrives 41.2 km^3 . Main rivers are Buna and Drin with average discharge 680 m³/sec, Vjosa 195 m³/sec, Mati 103 m³/sec, Seman 95 m³/ sec. It has parts of the big tectonic lakes (Shkodra, Ohri and Prespa), glacial lakes (about 30), charstic ones (80), littoral (10) and artificial (700). It is rich with underground water and big karstic springs, mineral springs and thermo mineral ones. Some of the rivers, parts of the littoral and some lakes are polluted by the industrial, agricultural and urban wastes.

Vegetation world is various. There are 3250 kinds of natural plants, which constitute 29 % of the total number grown in Europe and 47 % of the Balkan plants. In Albania are met plants of different regions such as: Mediterranean, north Balkanic, alpine - Carpathian, central of Europe, euroasiatics. etc. 1 % of the Albanian vegetation is endemic

and 5 % is sub endemic. There are four vegetation belts (Mediterranean shrubs, oaks, beeches and conifers, alpine in pastures).

About 35 % of the territory is occupied by the forests, from which to every person belongs 0.3 ha. The high forests occupy about 47 % of the forest area, low forest 29 % and shrubs 24 %. About 10 000 ha forest are proclaimed national parks. The wild world is rich with many kinds of animals, even rare ones (grey dark bear, wild cat and goat, pelican, etc). As we see the country is significant for the biodiversity but is damaged a lot by the man's activity.

3. LAND COVER CLASSIFICATION SYSTEMS

Classification is an abstract representation of the situation in the field using well-defined diagnostic criteria: the classifiers. Sokal (1974) defined it as: "the ordering or arrangement of objects into groups or sets on the basis of their relationships." Classification is one of the most important steps in handling remote sensing imagery and represents important input data for geographic information systems (GIS) (Oštir 2006)

A classification describes the systematic framework with the names of the classes and the criteria used to distinguish them, and the relation between classes. Classification thus necessarily involves definition of class boundaries that should be clear, precise, possibly quantitative, and based upon objective criteria. Land cover classes are defined by a string of classifiers, but due to the heterogeneity of land cover, and with the aim of achieving a logical and functional hierarchical arrangement of the classifiers, certain design criteria have been applied.

A classification should therefore be:

- *Scale independent*, meaning that the classes at all levels of the system should be applicable at any scale or level of detail; and
- *Source independent*, implying that it is independent of the means used to collect information, whether satellite imagery, aerial photography, field survey or some combination of them is used.

Classification systems come in two basic formats, *hierarchical* and *non-hierarchical*. Most systems are hierarchically structured because such a classification offers more consistency owing to its ability to accommodate different levels of information, starting with structured broad-level classes, which allow further systematic subdivision into more detailed sub-classes. The Land Cover Classification System (LCCS) that is used for land cover in Albania is in the format hierarchical.

4. LAND COVER CLASSIFICATION SYSTEM IN ALBANIA

4.1. USING LAND COVER

The words about land/terra/ground that are used until now in Albanian literature, are: "geography", "land/ground", "topographic elements of land/ground", "geographic environment" "geographic landscape",

“geographic surface” etc. The above words are from deferent source and diverse and frequently contradictory.

The Land cover/land use concepts are used in Albania after 1990 year. After this year, land cover/use concepts are analysed and actual land cover/classification in Albania is revised by international standards. Land Cover Classification System (LCCS) is in response to the international need for:

- harmonized/standardized collection of land cover data;
- availability of land cover data for a wide range of applications and users;
- comparison and correlation of land cover classes.

LCCS is a comprehensive methodology for the description, characterization, classification and comparison of most of land cover features identified anywhere in the world, at any scale or level of detail. LCCS is a new language to describe, in a standardized way, the different land cover features. Albania involved with LCCS.

The LCCS is an existing, internationally accepted and widely implemented de facto UN standard, and while it accepts considerable re-organization of its structure as an ISO standard -its existing specifications and LCCS classifiers must be retained within the ISO technical enhancements.

4.2. CLASIFICATION OF LAND COVER.

Today, after international standardisation, land cover classification in Albania, as set out below, comprises three levels:

- the first level (five items) indicates the major categories (abstract to a greater or lesser degree) of land cover on the planet;
- the second level (15 items) is for use on scales of 1:500 000 and 1: 1 000 000;
- the third level (44 items) will be used for the project on a scale of 1: 100 000.

A fourth level could be added for some or all of the items, subject to the following requirements:

- additional items must include all the land covered by the corresponding level-3 item (four-figure codes are used for these items only);
- newly created items must not relate to more than one three-figure item;
- the land cover mapping (three-figure nomenclature) must be completed prior to initiation of level-4 mapping.

At each level the defined classes are mutually exclusive. At the higher levels of the classification system few diagnostic criteria are used, whereas at the lower levels the number of diagnostic criteria increases. Criteria used at one level of the classification should not be repeated at another, i.e., lower, level (tab 3.2.2).

Finally, care must always be taken to see that newly created items are compatible with the scale, the size of the smallest area to be mapped and the basic information, i.e. satellite data.

Tab 3.2.2

Level 1	Level 2	Level 3
1.Artificial	1.1. Urban fabric	1.1.1. Continuous urban fabric surfaces 1.1.2. Discontinuous urban fabric
	1.2. Industrial,	1.2.1. Industrial or commercial units and

	commercial	transport units
		1.2.2. Road and rail networks and associated land
		1.2.3. Port areas
		1.2.4. Airports
	1.3. Mine, dump	1.3.1. Mineral extraction sites and construction sites
		1.3.2. Dump sites
		1.3.3. Construction sites
	1.4. Artificial non-agricultural	1.4.1. Green urban areas vegetated areas
		1.4.2. Sport and leisure facilities
2. Agricultural	2.1.Arable land	2.1.1. Non-irrigated arable land areas
		2.1.2. Permanently irrigated land
		2.1.3. Rice fields
	2.2. Permanent crops	2.2.1. Vineyards
		2.2.2. Fruit trees and berry plantations
		2.2.3. Olive groves
	2.3. Pastures	2.3.1. Pastures
	2.4. Heterogeneous	2.4.1. Annual crops associated with permanent crops agricultural areas
		2.4.2. Complex cultivation
		2.4.3. Land principally occupied by agriculture, with significant areas of natural vegetation
		2.4.4. Agro-forestry areas
3. Forests and semi-natural areas	3.1. Forests	3.1.1. Broad-leaved forest
		3.1.2. Coniferous forest
		3.1.3. Mixed forest
	3.2. Shrub and/or herbaceous	3.2.1. Natural grassland vegetation association
		3.2.2. Moors and heathland
		3.2.3. Sclerophyllous vegetation
		3.2.4. Transitional woodland shrub
	3.3. Open spaces with little	3.3.1. Beaches, dunes, and sand plains or no vegetation
		3.3.2. Bare rock
		3.3.3. Sparsely vegetated areas
		3.3.4. Burnt areas
		3.3.5. Glaciers and perpetual snow
4. Wetlands	4.1. inland wetlands	4.1.1. Inland marshes
		4.1.2. Peatbogs
	4.2. Coastal wetlands	4.2.1. Salt marshes
		4.2.2. Salines
		4.2.3. Intertidal flats
5. Water bodies	5.1. Inland waters	5.1. 1. Water courses
		5.1.2. Water bodies
	5.2. Marine waters	5.2.1. Coastal lagoons

	5.2.2. Estuaries
	5.2.3. Sea and ocean

4.3. LAND COVER CLASSIFICATION USING REMOTE SENSING TECHNIQUES

Everything on earth is changing with time. Land cover map can be a powerful tool to compare the changes of an area over time. It is impossible to cover a large area in short time through manual survey but with remote sensing (land cover map) it is an easier task.

With land cover map it can be revealed how much area of cities of Albania is using for what purpose, what are the pattern of land use change over time etc. which will help the policy makers to take necessary measure to ensure sound physical environment of the city etc.

Land cover maps constitute necessary tools for development planning and management of the territory. Furthermore, land cover maps depicting the current reality are essential in countries where, due to political changes, rapid dynamic phenomena have taken place, resulting in a complete restructuring of the agricultural and other sectors, as in the case of Albania.

For optimal use, land cover maps should be in digital format, which allows easy updating, and associated with a GIS including other information such as soil units, erosion features and provincial/municipal boundaries. The resulting database is an essential tool for decision-making in land management.

But, before the creation of land cover map, it is necessary to have land cover classification (LCCS) (fig. 3.3.1).

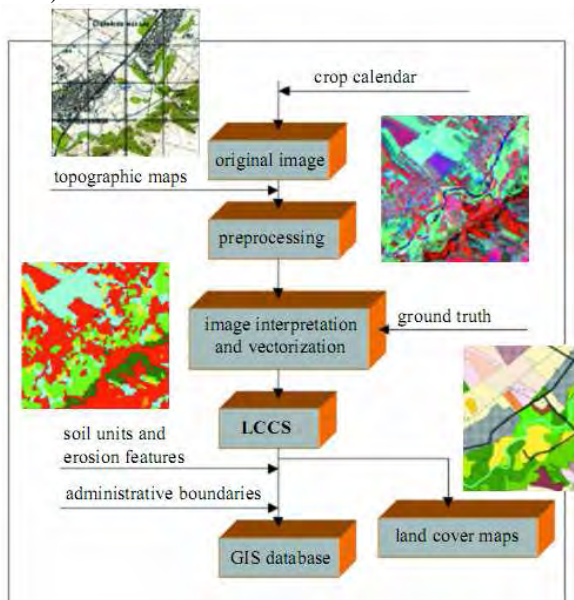


Fig. 3.3.1. The place of LCCS in methodological approach of land cover maps creation

Today, land cover classification based in use of satellite image data. The operational availability of high-resolution satellite imagery, namely Landsat TM, SPOT, Soyouz, ERS-SAR, RADARSAT and others, opens up new possibilities for investigating and monitoring natural resources.

Satellite imagery is recorded in various wavelengths, visible and non-visible, which provide accurate information on ground conditions. Each object has unique and different characteristics of reflection or emission in different environment. An object and its environmental condition can be identified using reflected or emitted electromagnetic radiation from that object.

The use of satellite image is popular world wide but its application is limited in Albania. However a land cover classification in our study is done. The classes were: 1. Vegetation; 2. Built-up Area; 3. River/Deep Water; 4. Shallow Water; 5. Open Ground

LANDSAT TM image was used for this study (table 3.3.1).

Table 3.3.1: Wavelength and application of LANDSAT TM bands

Band	Wavelength (µm)	Application
1	0.45-0.52	Coastal water mapping, soil vegetation differentiation, deciduous, coniferous differentiation
2	0.52- 0.60	Green reflectance by healthy vegetation, excellent for pollution studies.
3	0.63-0.69	Chlorophyll absorption for plant species differentiation identifies contrast between the vegetation classes.
4	0.76-0.90	High reflectance for the vegetation, urban areas less reflective than the vegetation. Soil-crop and land-water contrasts are emphasized.
5	1.55-1.75	Important for the crop identification, crop water content and soil moisture content.
6	10.4-12.5	Hydro thermal mapping
7	2.08-2.35	Plant heat stress

The properties of the image were:

- Image Sensor: LANDSAT TM
- Image Format: BIL
- Number of Lines: 2185
- Number of Pixels per Line: 1441
- Spatial Resolution: Band 1-5, 7 30m x 30m and band 6 120mX120m
- Spectral Resolution: 7 BANDS (1, 2, 3, 4, 5, 6, 7)

Geocoding Wizard of ER Mapper was used for image registration and for registration, rectification and image classification the source image was converted from ERDAS LAN format to ER Mapper ERS format. The parameters of geocoding were:

Geocoding type: Polynomial

Polynomial order: Linear

GCP picking method: A pre registered image of the area.

The procedure of image enhancement makes it easy to identify and select ROIs (Region of Interest). In this study linear stretching and filter operations was performed for image enhancement.

Source image (LANDSAT TM) of this study contained 7 spectral bands. For display purpose 3 bands were selected which helped selection of training areas. For this study R: 7 G: 4 B: 3 were found suitable.

In training stage location, size, shape and orientation of each pixel type for each class was analysed to categories the satellite image accordingly. Some regions have been selected from Mirdita (district of Albania) area for five land cover class through training process.

In classification stage each pixel was categorised into land cover class to which it closely resembles. If the pixel was not similar to the training data, then it was labelled as unknown. Supervised classification of ER Mapper was used for image classification. 'Minimum Distance Classification' was used as it gave best result among all supervised classification available in ER Mapper. The land cover was classified according to the FAO Land Cover Classification System (LCCS) (Di Gregorio, A., & Jansen, L.J.M. 1996, 1997), a comprehensive, standardized *a priori* classification system, created for mapping exercises and independent of the scale or mapping method. The classification uses a set of independent diagnostic criteria that allow correlation with existing classifications and legends. The system could therefore serve as an internationally agreed reference base for land cover. The methodology is applicable at any scale and is comprehensive in the sense that any land cover

identified anywhere in the world can be readily accommodated.

Soil types and erosion features, obtained from traditional sources, will linked to each land cover mapped unit as attributes into a GIS system. This results in a comprehensive database, which provides useful information for agriculture, forestry and urban development planning, for environment protection, and for many other applications. The data collected in the database allow for different kinds of spatial analyses, which are necessary in land management. As the database developed using ArcView, a common GIS software package, it will be easy to combine the database with other data sets, existing or in preparation, for a variety of different applications.

5. CONCLUSIONS

In context of Albania, Remote Sensing technology is an non well unexplored field. By using this rarely used tool a land cover classification of Albania was done. LANDSAT TM image was used for this study. The land cover was classified according to the FAO Land Cover Classification System (LCCS).

REFERENCES

1. Di Gregorio, A., & Jansen, L.J.M. 1996. FAO Land Cover Classification System: A Dichotomous, Modular-Hierarchical Approach. Paper presented at the Federal Geographic Data Committee Meeting - Vegetation Subcommittee and Earth Cover Working Group, Washington, 15-17 October 1996.
2. Di Gregorio, A., & Jansen, L.J.M. 1997. A new concept for a land cover classification system. Proceedings of the Earth Observation and Environmental Information 1997 Conference. Alexandria, Egypt, 13-16 October 1997.
3. FAO. 1995. Planning for sustainable use of land resources. Towards a new approach. *FAO Land and Water Bulletin* No. 2.
4. <http://www.fao.org/docrep/003/x0596e/x0596e00.htm>
5. Meyer, W.B., & Turner II, B.L. 1992. Human Population Growth and Global Land Use/Land Cover Change. pp. 39-61, in: *Ann. Rev. Ecol. Syst.*, No. 23.
6. Mueller-Dombois, D., & Ellenberg, J.H. 1974. *Aims and Methods of Vegetation Ecology*. New York and London: John Wiley.
7. Nasreen, I.K., 1999: Present status of geoinformatics technology in Bangladesh: special Nègre, T. 1995. Report of the Preparatory Mission: Outlines for the Africover Classification System. Draft document. FAO, Rome.
8. Nghia C.X., 1999, Results of afforesting protective forest in the sand areas, *Journal of agriculture and development of rural area*, Vol 9, Ha Noi, 13-14. oi.
9. Olaf B. and Uta S., 2002. Development and perspectives of landscape ecology, Kluwer Academic Publishers, Netherlands. *Operationalization of Remote Sensing, ITC*.
10. Oštir, K., 2006: *Daljinsko zaznavanje*.- Založba ZRC, p. 250, Ljubljana.
11. Reichert, P., & Di Gregorio, A. 1995. Preparation of a forest cover map and reconnaissance forest inventory of Albania. Technical Report of FAO Project GCP/ALB/002/IDA. *Remote Sensing Journal* 2(2), 33-41.
12. Sokal R. 1974. Classification: purposes, principles, progress, prospects. *Science* 185 (4157): 1115-1123.
13. Clawson, Marion, and Stewart, Charles L., 1965, Land use information. A critical survey of U.S. statistics including possibilities for greater uniformity: Baltimore, Md., The Johns Hopkins Press for Resources for the Future, Inc., 402 p.
14. Gordon, S., 1980. Utilizing Landsat imagery to monitor land use change: A case study in Ohio. *Remote Sensing of Environment*, 9, pp. 189-196

LAND COVER REMOTE SENSING IMAGERY WEB RETRIEVAL IN CHINESE SECOND ROUND OF NATIONAL LAND USE INVENTORY PROGRAM

NING Xiaogang^{a,*}, ZHANG Yonghong^a

^a Chinese Academy of Surveying and Mapping, 100830, Beijing, China
 ningxg@casm.ac.cn, yhzhang@casm.ac.cn

KEY WORDS: Image Retrieval, Web Service, Remote Sensing Imagery

ABSTRACT:

To facilitate land cover / land use interpretation of Chinese second round of national land use inventory program, a land cover remote sensing imagery retrieval system was constructed based on multi-source land cover classified remote sensing images, ASP.NET techniques and web service. This paper presents the details of the methodologies of national level land cover remote sensing image classification, the architecture and functions of the system, the methodologies of table construction of the database. The remote sensing images was classified into 8 top-level categories, and further classified into 38 second-level categories according to Chinese land cover standard classes provided by Ministry of Land and Resources P.R.C. The results of this work can be easily browsed, checked, edited by the public or experts.

1. INTRODUCTION

Chinese second round national land use inventory program (from July 1, 2007 to December 31, 2009) is a national conditions and power investigation, which is very significant to economy and social development, the target of which is to make a thorough investigation of land use details, to get exact land use data, to construct a management system based on web services (Leading group office of SRNLUIP, 2008).

To facilitate the process of the land use investigation, and to provide a system to verify the investigation results, a land cover remote sensing imagery web retrieval system is constructed, based on multi-time, multi-sensors, multi-resolutions, multi-terrain conditions land cover classified remote sensing images (Jixian Zhang, 2010). These images belong to 8 top-level or 38 second-level land use categories.

This paper designs and implements the land cover remote sensing imagery retrieval system based on the web service and the ASP.NET technology. The global objective of the system is to offer efficient web query service for the land cover remote sensing sample images based on the 8 top-level and the 38 second-level land categories. The System is used to facilitate the investigation work of the second round of national land use inventory program, especially for the interpretation of the remote sensing image and the verification of the inventory results.

2. THE DESIGN AND IMPLEMENT OF THE SYSTEM

2.1 The architecture and workflow

The system is divided into four subsystems: database constructing subsystem, data importing subsystem, querying subsystem, post-processing subsystem. The workflow chart is shown as Figure 1.

The database constructing subsystem is mainly to construct and organize the database, which will offer strict management of the user power limitation and the regular backup ability to ensure the security of the data. The database is designed according to the principles of relational database system, and Microsoft

Access database platform is chosen according to the size of the database and the capability of the system.

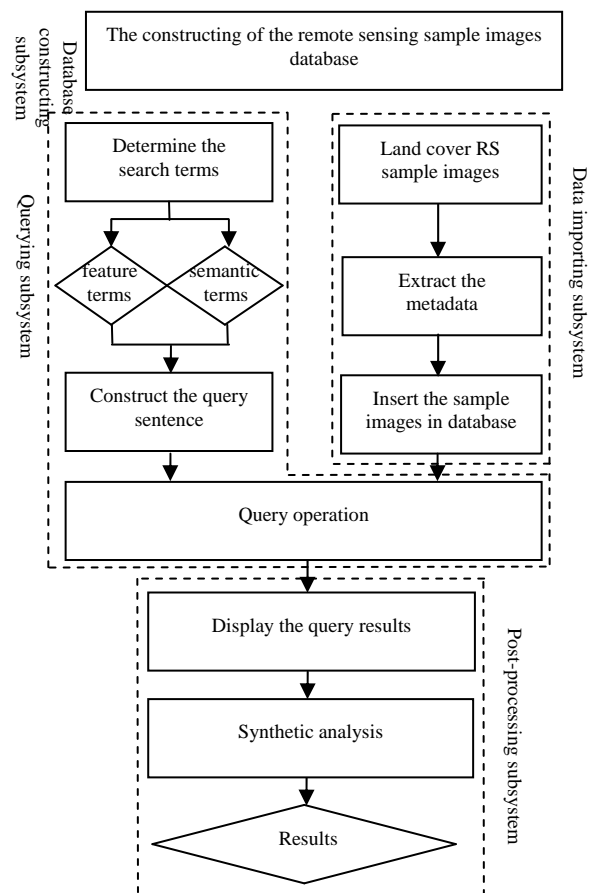


Figure 1. The workflow of the system

The data importing subsystem offers the full and strict function

to insert the sample images and corresponding metadata in the database, auto-check the physical integrity and logical integrity of the import data, ensure the accuracy and completeness of the import data.

Querying subsystem not only supports the single term query but also supports the query based on group of multi condition.

Post-processing subsystem offers friendly user interface, which helps the users make rapid and exact synthetic analysis.

2.2 The organization of the data and the design of the database table

The main data of the system is property data, including the land categories information, the metadata information of the remote sensing image and the information of manual interpretation. The metadata of the remote sensing images include the category of the sensor, the time of imaging, the season of imaging, resolution, the geographic location, and so on. The manual interpretation information is the land category and the terrain of remote sensing sample image. Besides, there are other data in the database, such as the store location, the category code of every land category and the description information of the land category.

Excellent design of the database table could not only simplify the data flow, improve query efficiency, but also benefit the development and maintenance of the system. According to the requirements and functions of the system, three database tables constructed: the province and region table, land category table and sample image table (see Table 1, Table 2, and Table 3).

Field Name	ID	Data Type
Province	A1	Char
Region	A2	Char

Table 1. Province and region database table

Field Name	ID	Data Type
Land Category	B1	Char
Category Code	B2	Integer
Category Description	B3	Char

Table 2. Land category database table

Field Name	ID	Data Type
Ordinal Number	C1	Integer
Province	C2	Char
Land Category	C3	Char
Terrain	C4	Char
Sensor	C5	Char
Imaging Year	C6	Integer
Imagine Season	C7	Char
Resolution	C8	Float
Store Location	C9	Char

Table 3. Sample image database table

The province and region database table records the relationships between all the Chinese provinces and the regions which they belong to, such as North China, Northeast China, East China, Middle China, South China, Southwest China, Northwest China. The land category database table records the names, codes, description information of the 8 top-level land categories, 38 second-level land categories.

The sample image database table is the main table of the database, all the information of the land cover remote sensing sample images stored in this table. The records number in the province and region table and land category table are fixed, but

the records in the sample remote sensing image table could extend or decrease by adding or deleting the sample remote sensing images.

The design of the database table separates the main table and the minor tables, reduces the redundancy of the data. This strategy will benefit database's query and update processing significantly.

2.3 Development

.NET is Microsoft's new generation development platform, which offers the foundation to quickly construct the mutual-communication application system. .NET Framework, as the soul and foundation of the .NET, provides many new features, such as mutual-operation ability, common language runtime, independent language, simple deployment, security, and so on. These features made .Net development widely used now. Any software system based on the powerful .NET Framework can be called .NET application program.

ASP.NET is a web application framework based on the .NET platform, it can be used to establish dynamic web page and offer web application service (John Sharp, 2006; G. Andrew Duthie, 2002)

To satisfy the need of running under the web environment, the system adopts the web service technology. The World Wide Web Consortium identifies the web service as the software system which offers the mutual operation among different machines by the Internet. The system adopts customer/server model to offer the web service, database stores in the server, which can be long-distance browsed and queried by the customers.

The land cover remote sensing imagery retrieval system was constructed based on the ASP.NET and web service technology, adopting the C# language as the development language under Visual Studio .NET 2005 development platform.

2.4 ADO.NET and XML

ADO.NET is a set of computer software components that programmers can use to access data and data services. It is a part of the base class library that is included with the Microsoft .NET Framework. ADO.NET supports the relational database system and the non-relational database system at the same time. Normally, it is considered that the ADO.NET is the upgrade from ADO, but actually the ADO.NET is quite different from ADO. ADO.NET can be considered as a completely new production for mutual data access.

ADO.NET includes two main parts: Data Provider and DataSets. The former can be separated into five parts: Connection, Command, Parameter, DataAdapter and DataReader. This system adopts ADO.NET technology as mutual-access engine for the database of remote sensing sample images. ADO.NET provides stable foundation for realization of the system.

To reduce the pressure of the server, decrease the unnecessary visit to the server, the system caches search result quickly in the customer with the XML technology (Dan Wahlin, 2002). The following is the storing sentences:

```
DataSet dsQuery = db.GetDataset(arraylist, strDbPath);
if (dsQuery == null)
return;
dsQuery.WriteXml(strTempXmlFile);
```

When to load the search results, there is no need to access the server again, with the following sentence to get the search results:

```
dsQuery.ReadXml(strTempXmlFile);
```

3. THE ABILITIES AND FEATURES OF THE SYSTEM

3.1 The management of land cover remote sensing sample imagers

With the expanding of the ability of remote sensing imaging, the size of the land cover remote sensing sample images that can be collected is increased progressively. At the same time, to accomplish the assistant interpretation of the land cover remote sensing images, the remote sensing sample images in different time and space are needed. Therefore, it is more important to manage the data of land cover remote sensing sample images efficiently. This system constructs strict and efficient sample images database in the server, provides the ability of adding record, deleting record, updating record, integrity check, auto-backup, and so on.

3.2 Land cover remote sensing sample image retrieval

To provide powerful and convenient querying functions, the system designs and realizes many query patterns: based on the top-level land category, based on the second-level land category, based on the sensor, based on the season, based on the province or region. Besides, the system supports the query pattern of combination of the above querying conditions. Meanwhile, the system offers two kinds of querying interface: list style and grid style, see Figure 2 and Figure 3. The former mainly shows the feature information of every sample image, and the later mainly shows the sample image. Figure 4 shows the interface of inserting record in the database.



Figure 2. list style interface



Figure 3. grid net interface

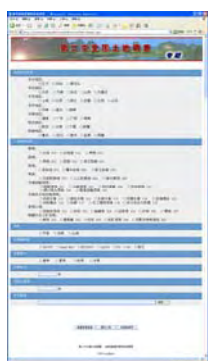


Figure 4 Insert record in the database

3.3 Update of the database

The update of land cover remote sensing sample image database includes modifying, adding and deleting the database records. The database record's modification and deletion must be accomplished by the server, adding records can be operated

either by the server or the customer. If the customer requests to add the sample image records, it is necessary to ensure by the server. Putting the power of updating the database in the server is good to run the system stably and precisely.

3.4 The features of the system

This paper implements the land cover remote sensing sample image web retrieval system based on the Visual Studio .NET platform. This system adopts Visual C# development language and applies the web service, ASP.NET, ADO.NET and XML technology.

The system can be released by the internet, supports the extension of land cover sample image database, which can be based on the internet nodes. It realizes the auto-connection of local picture and the remote sensing sample image, it can accomplish the query work according to the land category, the sensor, the time and other factor, or the random combination of these features. It supports many commercial remote sensing sensors, such as SPOT5, QuickBird, IKONOS, ALOS, IRS-P5/P6, aerial images, and supports different terrain. The system divides the nation into 7 regions: Northeast China, North China, East China, Middle China, South China, Northwest China, Southwest China and 32 provinces.

4. CONCLUSIONS

With the size of the remote sensing image data is progressively growth and the development of the interpretation technology of the remote sensing images, the issue of the remote sensing image retrieval is a research hotspot in the field of the remote sensing images' processing and application. According to the practical situation of the second round of national land use inventory program, this paper focuses on the problem of the land cover remote sensing image web retrieval. It introduces research results in the system's design, workflow, platform, data organization, database table, development skills, provides an effective resolution to remote sensing images retrieval based on web service. The system has been used to the second round of national land use inventory program successfully. It greatly improved the efficiency and accuracy of the remote sensing images' interpretation, promoted the progress of the results' checking work.

References:

- Dan Wahlin., 2002. *XML for ASP.NET Developers*. Sams Publisher.
- G. Andrew Duthie., 2002. *Microsoft ASP.NET step by step*. Microsoft Pres.
- Jixian Zhang, 2010, Multi-source remote sensing data fusion: status and trends. *International Journal of image and data fusion*, 1(1), pp.5-24.
- John Sharp., 2006. *Microsoft Visual C# 2005 step by step*. Microsoft Press .

Leading group office of the Second Round of National Land Use Inventory Program. The total project of the second round of National Land Use Inventory Program.[EB/OL]. <http://www.mlr.gov.cn/pub/mlr/documents/P020070607579882779005.doc> (accessed 28 Sep. 2008)

Production of True Orthophotos in Practice and Various Application Possibilities

Hermann Novak, Martin Ulz, Ludwig Dorfstetter, Jens Schickor

Forest Mapping Management (FMM), 5020 Salzburg, fmm@fmm.at

Commission VII, Symposium “100 Years ISPRS – Advancing Remote Sensing Science”

KEY WORDS: Digital, Environment, Forestry, Mapping, Photogrammetry, Automation, DEM/DTM, Orthoimage

ABSTRACT:

In the last years, the demand for detailed digital surface models in Europe has increased. The sectors of energy providers and mobile network operators need more detailed models for better calculations and more efficient implementation.

Forest Mapping Management GmbH (FMM) located in Salzburg, Austria, has a perennial experience in working with high-resolution digital surface models (DSM) and the following generation of true orthophotos. In the last 3 years, 7500 km² true orthophotos with combined DSM were generated and produced.

The high degree of automation of the process and the reduction of insufficiencies found in normal orthophotos and results needs a newer way of thinking for handling such data, and provides an abundance of new possibilities.

Since 2006, FMM developed and optimised a workflow to generate DSM and True Orthophotos, which allowed the data to be used by many applications, such as calculations of potential of solar collectors, actualisation of land register, documentation of damage caused to the environment or 3D building models and landscape-models.

Especially in the sector of forestry and agriculture, the data has become established and is used by FMM for the development of software applications in the forestry sector.

1. INTRODUCTION

Because of the increasing demand of digital surface models in Europe and the courage for innovative solutions of questions and applications, FMM has begun to work with true orthophotos and high-resolution digital surface models for 3 years. In these 3 years, the company made 7500 km² in Austria, especially in Salzburg, Linz, St. Pölten and the Styrian region.

Hermann Novak is leading the company with 18 employees since 20 years.

Starting as a little cartographical company in the forestry sector, FMM has developed to a modern photogrammetric company with its own aircraft and aerial camera (Vexcel Ultracam). The newest GPS/INS technics and digital workstations let FMM make the basis for working with high-precision data and analyses. More business parts are the software development, including webservices for the forestry sector and vehicle fleet management or the production of base data for municipal and private applications.

The intention of this paper is it to spark interest in the production of true orthophotos and digital surface models and to highlight their various applications.

In the following, the process of planning and production with its high level of automation will be described. We will also demonstrate a tested application from the forestry sector.

Finally we will try to make a look into the future of the production of true orthophotos and make a conclusion of the usage of the data now.

2. WORKFLOW

2.1 Description

Production depends on a really good planning and flight execution like any high-resolution flight. The planning is the base for the flight and should have the flightarea covered completely with an 80/80 overlap.

Often it makes sense to plan rectangular areas, because the overlap and the coverarea will be optimized and the following calculating process of the True Orthophotos will be uninfected by software bugs. The area should be covered in a single flight to avoid crossing shadows which create false interpretations in the automatic matching process. Generally it is recommended to plan a flightarea as compact as possible. Unnecessary images require additional time and delay the processing of the target area. After the flight and the processing of the images, an aerotriangulation (AT) will be calculated. Here it is important to have a good base, especially in the height. Better tiepoint measurements and height precision, allow the software to make better matching points and are the base for a clean and good DSM. To make a clean AT the input data should be correct. That means a high-precision camera calibration and optimal measured ground control points.

A short view of the production is shown in the following figure 1:

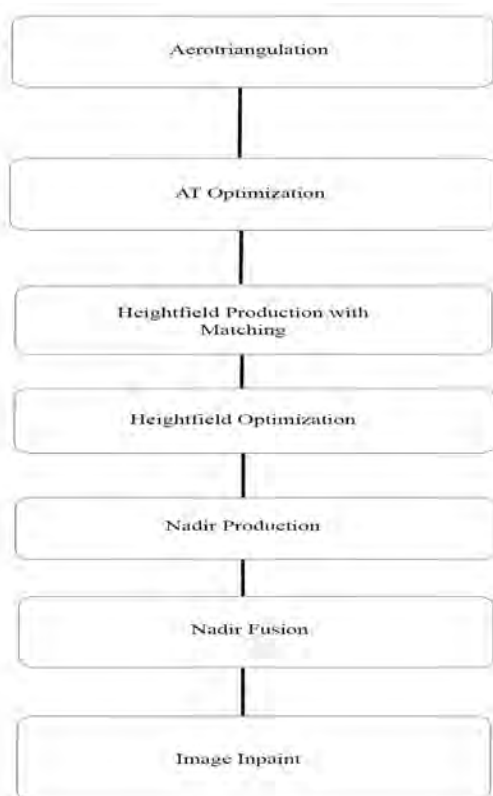


Figure 1. Workflow

In first step, the AT will be optimized. That means insufficient tie points will be eliminated and the data, especially the coordinates and angles of the exterior orientation, will conform to an optimal and readable datastructure for the software.

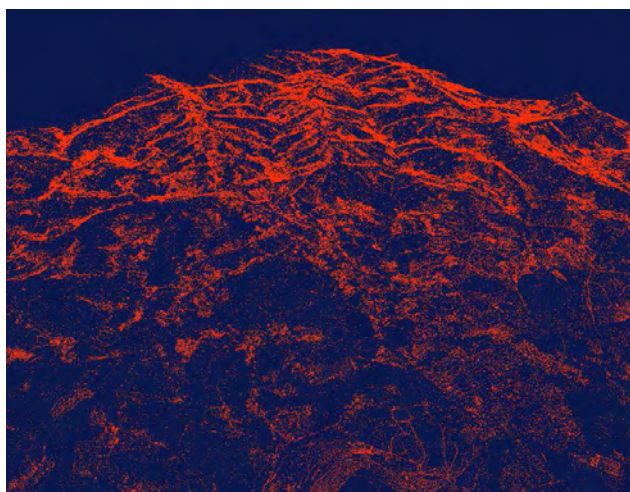


Figure 2. Tiepoints

In the next step the generation of the surface model will be started.

An automatic matching process goes over all images in the project. First it will produce a rough connection and a DSM.

This DSM will be corrected and refined in second part. In the normal way, a minimum of 100 points per square meter can be taken for the calculation of the DSM. That's an enormous pointcloud in comparison to the point density of a laser model. This process will be stated with a precision of ¼ pixel resolution which is specified in the program design. At the end it will be a really accurate digital surface model with a resolution of 12cm, which is the optimal resolution for successive tasks. Assuming like it will be flight in this scale. The resolution can differ, depending on scale. Up to 8cm resolution can be achieved.

This process needs a relatively long calculating time. 2000 images needs circa 10 days for matching.

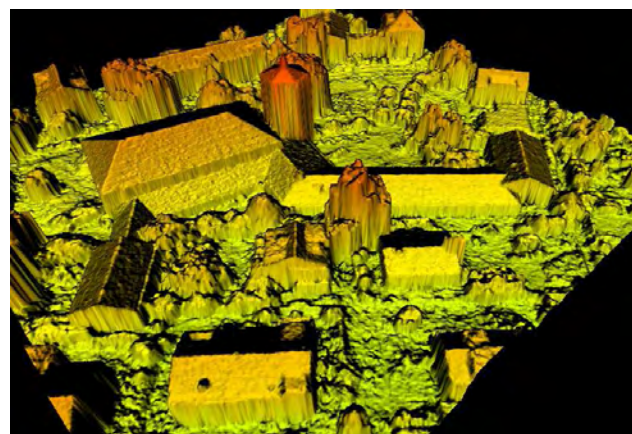


Figure 3. DSM in 3D View

After that the images will be straightened and rectified by the DSM. Nadirs will be produced from individual images, which are the base for the true-orthophoto production.

In connection with this step the nadirs will be connected to orthophotos with a special fading technique to guarantee an areacovered mosaic.

Black areas, which become by the different perspectives and overlapping, will be filled automatically with overlapping images at the end.



Figure 4. Trueorthophoto

2.2 Pros and Cons

The acceptability and utilization of true orthophotos should be compared by the pros and cons of the process and their properties.

The high investment of the flight, the calculating process and the high requirement of the hardware is accompanied by the higher automatism and the endproduct. The output is an orthophoto without any disposal or occlusion in the image, where all visual content will be shown in the correct location.

Furthermore, the long time needed seam line digitalisation of normal orthophotos to correct geometric mistakes is not applicable. Uses, like digitalisation or classification are easier and more detailed. It does not matter if the images are RGB or CIR. In both color spectrums, true orthophotos can be generated.

The nicest secondary effect is that the process of the true orthophoto makes a high resolution surface model as a co-product in the same resolution as the orthophoto. This DSM can be used by other applications and for analysis of questions.

The DSM can be the base for generating a digital elevation model. But it must be said that in large closed areas of vegetation, there are no points on the ground. In this case the generation of the DTM is very difficult and needs other data or more algorithms to calculate and interpolate the ground height.

A semi-automatic process is needed in these cases. With free sight to the ground there will be an accuracy and a level of detail not reached by normal models made by a laserscanner.

Mobile objects, like cars or motor bikes will be displayed diffused, confusing some users.

3. AUTOMATIC TREE EXTRACTION AND CLASSIFICATION IN FORESTRY

Especially in the forestry sector, the working with true orthophotos has proved itself and is the base for the forestry data acquisition in the house of FMM. This includes automatic tree extraction, inventory differentiation and volume calculation.

This information must be updated and renewed permanently, because the forest industry has to react quickly to exterior factors like bug infestations, storm loss and deforestation. A mostly automatic process on the base of true orthophotos is a maintask of the work of FMM.

3.1 Datastructure

For the analysis of forestry information, FMM uses true orthophotos with resolution of 12cm and their digital surface models. With the characteristic of the aerial camera (UltracamX) to make multi spectral images, it is possible to get CIR images in addition to RGB images simultaneously.

The images in the near-infrared range are used for the classification of vegetation data.

This grid data will be split in 500*500m tiles for faster analysis.

Furthermore a DTM from a laserscan flight are used to normalize the surface data. That is affected by the region, where the data will be analysed.

In mountainous regions it is advisable, but in a flat region, a normal interpolation can be used.

3.2 Tree extraction

Generally the tree extraction in the true orthophoto is easier than in normal orthophotos, because the tree have no disposals and are in correct position in picture and DSM.

The combination of DSM and DTM from laserscanning flight provides a quality control between both models and as well as a standardization of forestareas.

With that way it can be taken the relative height of the tree exactly and fast, which is not unimportant for the further development. A DTM is essential, because the consistence of the terrain in big forestareas can be caught in the produced DSM.

Based on an objectoriented algorithm, which registered local maximum in the DSM, will be detect the height and height changes, what from possible treetops can be suggested.

In addition to the position of the tree, information about the characteristics and the species of the trees can be detected. The algorithm was developed by FMM in cooperation with some universities in Austria and optimized for the high requirements of hardware by FMM. High performance the hardware is needed, because of the large amounts of data. With an adequate tile format for the model, the working process can be controlled and accelerated. 380000 trees can be extracted in around 20 hours. That means an area with around 16 square kilometers.

After detection of all heights and topforms of the trees, it is possible to make a segmentation of the species of trees. In the first step it can differ between broadleaf tree and conifer. In a second step with the help of the CIR images, it can be analyzed and filtered for the species of the tree. Every species has its own characteristics.

With example measurements and available data, an accuracy of 90 – 95 % of the extraction in matured timber could be proven.

This statement relates to the mass of the timber in a body and the object extraction as comparably. The last 5 – 10 percent of error is a result of not visible trees in the area of vegetation.

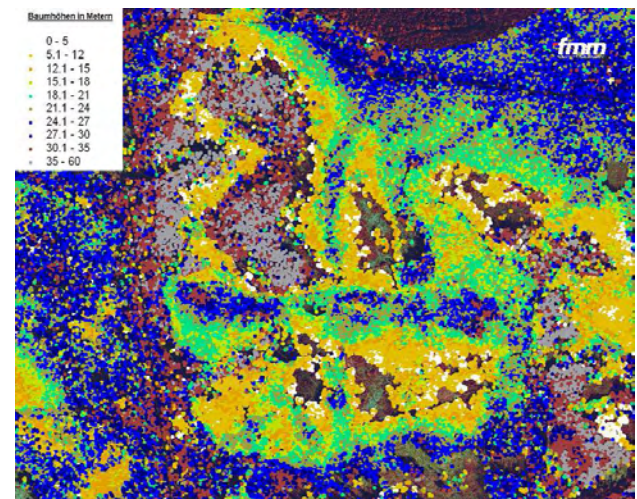


Figure 5. Tree height detection

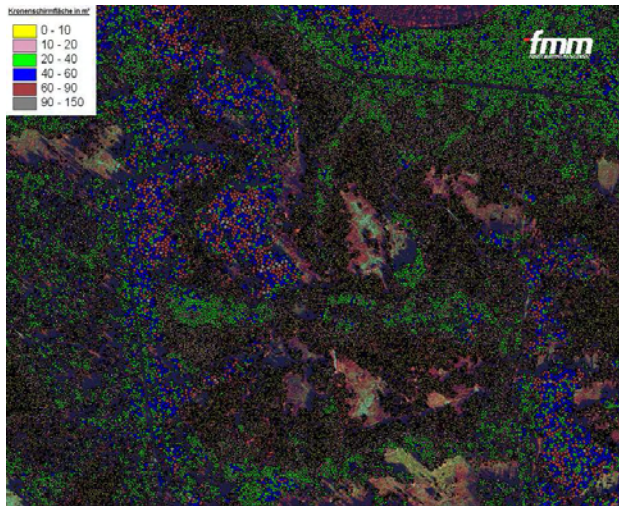


Figure 6. Treetop detection

3.3 Volume calculation and inventory

With the help of the determined tree heights and crown a volume calculation can be made.

In comparison with manual measurements and estimation, for the volume of the tree population a precision of 90% can be achieved.

With classification functions, like maximum – likelihood – classification, the inventory of the tree can be inspected. For this, some sample areas will be digitized and the sample areas will be used to improve the automated classifications.

These function have their fixed position in the way of analysing and in association with true orthophotos these function will reflect a high precision in horizontal and vertical position plus degree of automation.

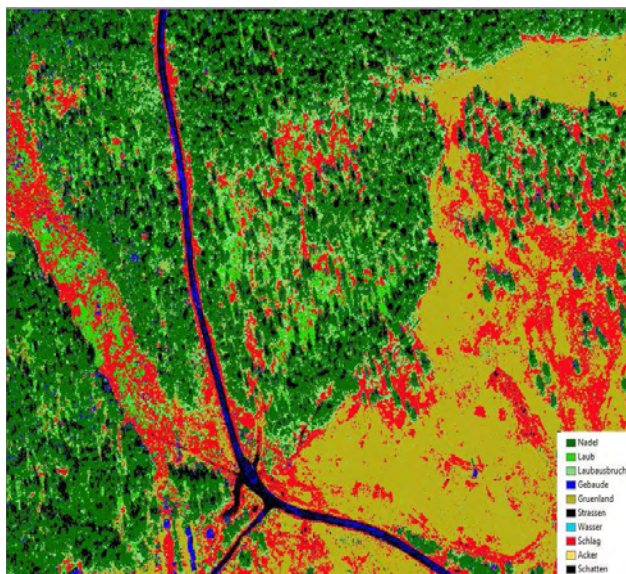


Figure 7. Classification

4. CONCLUSION

For three years, FMM has produced and used true orthophotos. 7500 km², mostly in Austria, are developed and analyzed. This data will be used in forestry reporting and their special applications. The images are to provide a basis for the inventory and correction of forestry information at stationary or mobile devices, on the other hand as illustration in webapplication for the forestry. Exactly in this economical sector these kind of orthophotos with the help of automatic analysis techniques reduces the investment of the data collection and processing at 70%. Inventories after damages are made rapidly and rationally. Total costs for forest enterprise can be reduced, in spite of some minor expenditure in comparison to normal orthophotos.

In webapplication, for planning-, logistics or organisation software, unknown observer getting well with true orthophotos and can to adapt rapidly the displayed landscape. With that fact it is given, that the user, planer or driver can concentrate of the essential of his work.

Other customers, like energy providers uses the true orthophotos and digital surface models. An economization and cost saving can be localized for example by the analysing of cable ducts. Energy providers have a growing interest to work with such data, because it is qualified for a calculation of solarpotential or noise diffusion. FMM is working continuously to develop automatic methods on the base digital surface models and true orthophotos.

Cadastral authorities and municipalities are also customers, which need the data of FMM to standardize and upgrade the actuality and precision of the cadastre.

Generally, true orthophotos und digital surface models are known everywhere but the utilization is just beginning. The potential uses of this data is nearly inexhaustible and will be underrated by many people. There may be questions about the costs and the high hardware profiles, but with optimized operation and automatic techniques this handicap is to overcome. Permanent customers are proof of this.

FMM will continues this way and continues to search for automatic methods to accelerate the production and examination.

4. REFERENCE

Tiede, D., Osberger, A., Novak, H., 2009. *Automatisierte Baumextraktion mit höchstauflösenden Oberflächenmodellen abgeleitet aus UltracamX-Daten*, Extended Abstract, AGIT Band 2009.

Dorfstetter, L. Novak, H., Ulz, M., 2009. *Neue Einblicke von oben*, Arbeit im Wald 2009, pp 14-15.

SPATIO-TEMPORAL CHARACTERIZATION OF AEROSOLS THROUGH ACTIVE USE OF DATA FROM MULTIPLE SENSORS

Z. Obradovic^{a,*}, D. Das^a, V.Radosavljevic^a, K.Ristovski^a, S.Vucetic^a

^a Center for Information Science and Technology, Temple University, Philadelphia, PA, USA

Technical Commission VII Symposium 2010

KEY WORDS: Atmosphere, Environment, Analysis, Data Mining, Retrieval, Algorithms, Spatial, Temporal

ABSTRACT:

One of the main challenges of current climate research is providing Earth-wide characterization of Aerosol Optical Depth (AOD), which indicates the amount of depletion that a beam of radiation undergoes as it passes through the atmosphere. Here, a comprehensive overview will be presented of our ongoing data mining based study aimed at better understanding of spatio-temporal distribution of AOD by taking advantage of measurements collected from multiple ground and satellite-based sensors. In contrast to domain-driven methods for AOD retrieval (prediction from satellite observations), our approach is completely data-driven. This statistical method consists of training a nonlinear regression model to predict AOD using the satellite observations as inputs where the targets are obtained from a network of unevenly distributed ground-based sites over the world. Challenges and our proposed solutions discussed here in context of global scale AOD estimation include (i) AOD regression from mixed-distribution spatio-temporal data; (ii) training such a statistical predictor for robust performance across multiple accuracy measures; (iii) uncertainty analysis of AOD estimation, (iv) active selection of sites for ground based observations, (v) discovery of major sources of correctable errors in deterministic models, and (vi) using conditional random fields to combine nonlinear regression models and a variety of correlated knowledge sources in a unified and more accurate AOD prediction model. The proposed methods is illustrated on experiments conducted using three years of global observations obtained by merging satellite data of high spatial resolution (MODIS Level 2 data from NASA's Terra and Aqua satellites) with ground-based observations of high temporal resolution (a remote-sensing network of radiometers called AERONET network). The experiments revealed that the proposed methods result in more accurate AOD retrieval than the baseline statistical and domain-based predictors.

1. INTRODUCTION

The global impact of environment change to climate is monitored largely by use of remote sensing instruments that measure radiances emitted or reflected from Earth. The observed radiances are used to estimate underlying geophysical characteristics through the predictive process called *retrieval*. The retrieved parameters are then used in various applications ranging from monitoring change of atmospheric temperature, the extent of snow, ice or vegetation cover, cloud and aerosol properties to the development of general circulation models for climate studies. Accurate and timely retrievals of geophysical parameters are therefore critical for the success of many climate change related studies.

In recent years remote sensing instruments of various properties have been employed in an attempt to better characterize important geophysical phenomena. The technology of new generation sensors has improved dramatically, but the collected data still contain large uncertainties due to high noise and a large fraction of missing values. As a consequence, retrieval from such high dimensional spatio-temporal observations is a very challenging problem (Jeong *et al*, 2005).

Aerosols are small particles produced by natural and man-made sources that both reflect and absorb incoming solar radiation.

Aerosol concentration and chemical properties are important parameters in climate change models, in studies of regional radiation balances, and studies of the hydrological cycle (Ramanathan *et al*, 2002). Using radiance observations, it is possible to estimate the attenuation of solar energy as it passes through a column of atmosphere, a quantity commonly known as aerosol optical depth (AOD).

The AOD can be retrieved using ground (Levy *et al*, 2005) or satellite (Remer *et al*, 2006) based observations. Ground-based observations are mostly obtained by the AEROSol robotic NETwork (AERONET) which is the global remote sensing network of about 250 radiometers (spatial distribution shown at Fig. 1) that measure AOD several times an hour at specific locations. AERONET AOD prediction is considered very accurate and is often taken as the ground truth for validation of various satellite-based AOD prediction algorithms aimed at providing global coverage.

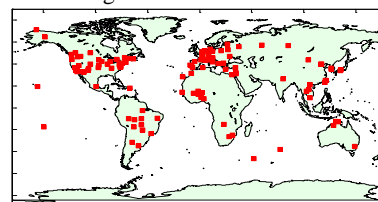


Figure 1: Spatial distribution of AERONET sites.

* Corresponding author (e-mail zoran.obradovic@temple.edu).

The main limitation of ground based observations is their low spatial coverage. Therefore, satellite-based aerosol related observations from several new instruments of high spatial coverage are also considered. The MODerate resolution Imaging Spectrometer (MODIS), aboard NASA's Terra and Aqua satellites launched in 1999 and 2002 with a single camera observes reflected solar radiation from the Earth over a large spectral range in 7 bands. It has a repeating cycle of 16 days and high spatial resolution with almost daily coverage of the entire planet. In comparison, MISR, also aboard Terra satellite, is a nine camera instrument with four bands per camera that provides global coverage every 9 days. MISR collects raw data at 1.1 km resolution, but retrieves aerosol properties at 17.6 km resolution for twenty-four postulated aerosol types. MODIS on the other hand collects data at 1km resolution and its retrievals are provided at 10km resolution.

Designing accurate AOD predictors from satellite observations is a very challenging task due to various problems including reflectance superposition from multiple sources (effects of clouds and surface reflectance are illustrated at Fig. 2). Therefore, satellite based retrievals are less accurate than ground based retrievals. However, they provide high spatial coverage and so are very important for climate studies.

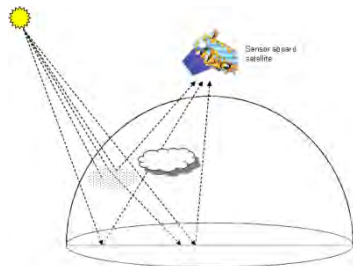


Figure 2: Physics of satellite-based retrieval.

Most operational aerosol retrieval algorithms are constructed as inverse operators of high-dimensional non-linear functions derived from forward-simulation models according to the domain knowledge of aerosol physical properties [35,36,67,68]. For example, MISR uses 24 compositional aerosol models in the Aerosol Climatology Product. These aerosol models, such as mineral dust, biomass burning particles and urban soot, are considered to be representative of the types found over the globe. They are mixtures of individual component aerosols, where each component is defined by a size distribution, particle shape, spectral index of refraction and vertical distribution within the atmosphere. Up to three components can comprise an aerosol mixture, and the fractional optical depths of the components making up a given mixture are pre-specified. For each component aerosol, the corresponding radiative properties are computed using wavelength, illumination, and view geometry information. The results are recorded in a look-up table. By using a modified linear mixing theory, the radiative properties of a mixture are calculated during the retrieval process. These simulated data are then compared to actual observations for the appropriate scene type (land or ocean). According to a set of goodness-of-fit criteria based on the domain knowledge, the matched aerosol model in the look-up table is used for AOD computation.

Drawbacks of deterministic retrieval methods include (1) high computational cost due to inversion of nonlinear forward models; (2) slow development due to manual construction of the postulated physical models; (3) suboptimality due to

difficulties in capturing complex radiance-aerosol relationships in all realistic scenarios; and (4) significant retrieval inaccuracies that are due both to the instrument limitations and imperfections in the retrieval algorithms.

Our team has demonstrated that more accurate retrieval is achievable by a completely data-driven approach using spatio-temporally collocated satellite and ground based observations as shown at Fig 3 (Han *et al.*, 2005a; 2005b; 2006a; 2006b; Das *et al.*, 2008; Obradovic *et al.*, 2006; Xu *et al.*, 2005; Zhuang *et al.* 2008). This statistical method consists of training a nonlinear regression model using the satellite observations as inputs and ground based AOD measurements as target. Some of our recent related activities and findings are discussed in this article (Das *et al.*, 2009; Radosavljevic *et al.* 2008; 2009; 2010a; 2010b; Ristovski *et al.*, 2009; Vucetic *et al.*, 2008).

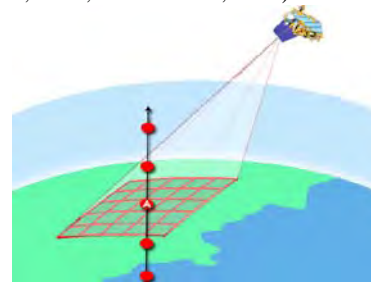


Figure 3: Spatio-temporal collocation of MODIS and AERONET data. A is an AERONET site with AOD retrieved within a short time before and after the satellite overpass (circle dots). The square regions are MODIS observations in a proximity of AERONET site A at the satellite overpass time.

2. METHODOLOGY

The overall objective of our study is to facilitate aerosol retrieval algorithms development, application and modification by developing data mining methodology that utilizes satellite data together with ground-based measurements. Our specific aims are to determine if data mining can

- provide accurate statistical AOD retrievals;
- help discovering the major sources of correctable retrieval errors of deterministic retrievals;
- improve understanding spatio-temporal properties of deterministic retrievals.

An overview of our recently proposed approaches towards achieving these aims is provided in this section.

2.1 Spatio-Temporal Data Partitioning for AOD Retrieval

In principle, AOD retrievals of high spatial resolution can be obtained from satellite observations by training a regression model on a dataset that consists of the satellite observations as inputs and more accurate ground based AOD measurements as output. However, challenges of such supervised learning on aerosol data collected over space and time include existence of different relationships among observations and AOD over various spatio-temporal regions. In such situations an appropriate spatial-temporal data partitioning followed by building specialized predictors could often achieve higher overall prediction accuracy than when learning a single predictor on all the data. In practice, such partitions are typically decided based on prior knowledge.

As an alternative to the domain-based partitioning, we have proposed a method that automatically discovers a soft spatio-

temporal partitioning of Earth AOD through the competition of gating regression models (Radosavljevic *et al.*, 2008). To address the spatio-temporal dependence the algorithm takes information about location and time of data points as inputs for gating function and performs competition among specialized predictors for each point in the dataset. It starts by randomly dividing the dataset into two disjoint subsets. A specialized predictor is then trained on each subset. Iteratively data are reassigned with some weight to each predictor. Weight is determined based on gating output and accuracy of regression models. Predictors and gating network are then retrained taking into account new assignment.

2.2 AOD Retrieval across Multiple Accuracy Measures

Well known accuracy measures such as Mean Squared Error (MSE) are often not informative enough because (1) retrieval error increases with AOD, (2) distribution of AOD is skewed towards small values, and (3) there are many outliers. Instead, domain scientists use an array of accuracy measures to gain better insight into the retrieval accuracy. For example, the Mean Squared Relative Error (MSRE) makes larger absolute errors more tolerable when predicting large AOD than when predicting small AOD. Ideally, one would like to have a retrieval algorithm that provides good accuracy with respect to these alternative accuracy measures.

To address this issue we considered training of neural networks that minimize MSRE instead of MSE. In order to construct a predictor that is also accurate with respect to MSE and several other accuracy measures, we proposed an approach that builds an ensemble of neural networks, each trained with slightly different MSRE measure (Radosavljevic *et al.*, 2010a). The outputs of the ensemble are then used as inputs to a meta-level neural network that produces the actual AOD predictions.

2.3 Uncertainty Analysis of AOD Retrieval

In this task our objective was to explore if neural networks can provide estimates about retrieval uncertainty in addition to providing accurate retrievals. Uncertainty estimation for the confidence of retrieval requires modeling of the whole conditional distribution of the target variable. A standard approaches for neural network uncertainty estimation assume constant noise variance. However, this assumption is not valid for AOD retrieval where noise is heteroscedastic (variance of noise is input-dependent). This is why we explored the Bayesian approach for uncertainty estimation, based on the previous work by Bishop and Quazaz. We also considered alternatives based on the bootstrap technique that are more tractable for large data sets.

A neural network-based regression assumes that target y is related to input vector x by stochastic and deterministic components. The stochastic component is a random variation of target values around its mean caused by heteroscedastic noise with zero-mean Gaussian distribution and input-dependent variance. The deterministic component determines a functional relationship between attributes and prediction. Our goal was to estimate both the stochastic and deterministic component as good as possible.

In (Ristovski *et al.*, 2009) we have evaluated three approaches for estimating the stochastic component. The first was based on training a neural network to predict squared error from

attributes. We used a standard Mean Squared Error (MSE) criterion to train this network. The second approach assumed heteroscedastic noise and defined the conditional target distribution. The uncertainty estimation neural network is obtained by maximizing the corresponding log-likelihood. The second method assumes that the conditional mean is exactly estimated by the bootstrap committee. Since this is only an estimate, in the third approach we also considered the model uncertainty. In this approach error occurs due to both uncertainty in the model and noise in target.

2.4 Selection of Sites for Ground Based Observations

Ground based AOD stations are often located without a rigorous statistical design. Decisions are typically based on practical circumstances (e.g. overrepresentation in urban regions and industrialized nations) and according to domain experts' assumptions about the importance of specific sites. Given these circumstances, our aim was to evaluate performance of the current design of AERONET sensor network and to apply data mining techniques to assist in future modifications of the sensor network.

In (Radosavljevic *et al.*, 2009) we assumed that there is a pending budget cut for maintenance of the existing AERONET sites. The objective was to remove a fraction of the AERONET sites while making sure that the utility of the remaining sites is as high as possible. We made a simplifying assumption that operational costs for each AERONET site around the globe are equal. Common to most selection techniques originating from the spatial statistics is a tendency to overlook the time dimension of data collected by the sensor network. Therefore, we considered series of observations and proposed to optimize AERONET sensor selection based on the concept of retrieval accuracy. Each AERONET site provides a time series which we used for training a regression model to retrieve future AOD. Sites that can be removed are those whose observations are best predicted by the model built on data from the remaining sites.

In (Das *et al.*, 2009) our objective was to determine appropriate locations for the next set of ground-based data collection sites as to maximize accuracy of AOD prediction. Ideally, a new site should capture the most significant unseen aerosol patterns and should be least correlated with the previously observed patterns. We proposed achieving this aim by selecting the locations on which the existing prediction model is most uncertain. Several criteria were considered for site selection, including uncertainty, spatial diversity, temporal similarity, and their combination.

Spatial diversity selects sites that are farthest away from the existing sites. The traditional approach in active learning is to label the most uncertain data points. In our application, instead of selecting an individual data point, we select a site. To address this, we defined uncertainty of a site as the average uncertainty over all its observations. For this purpose, we trained a number of neural networks on data obtained from the existing AERONET sites using the bootstrap method. Then we used these neural networks to predict the value of AOD at all satellite observations over potential AERONET sites. We measured the variance among the network predictions and considered this variance as the uncertainty of prediction at the individual data-points. The selected sites are those with the highest measured uncertainty. One drawback of the site uncertainty selection is that a global measure like average uncertainty might fail to compare the similarity in temporal variation of the uncertainty among sites. Each of the potential sites can be regarded as a

time-series of uncertainty values over a year. It has been observed that the shapes of uncertainty time-series closely match with that of AOD time-series because the uncertainty values are highly correlated with AOD. So, we used uncertainty estimates as a proxy for the actual AOD labels that cannot be observed over candidate sites. A potential drawback of the previous three site selection algorithms is that selection by one metric is not guaranteed to be the same as that selected by another metric. Therefore, we modified these algorithms to combine uncertainty, spatial and temporal correlation criteria in a single measure. Our objective was to evaluate which approach is the most appropriate for AERONET site selection

2.5 Discovering Correctable AOD Retrieval Error

We analyzed performance of the operational MODIS aerosol retrieval algorithm. Overall, the main sources of MODIS aerosol retrieval errors are the separation of surface and atmospheric components of the observed radiances, the inaccuracies in the forward-simulation model, and inversion errors. Some sources of retrieval uncertainties, such as bright surfaces or cloud-contaminated scenes, are due to the limitations of the MODIS instrument and cannot be corrected, while others, such as imperfections in the retrieval algorithm, are correctable. Aerosol scientists' major goal is to understand the primary sources of correctable retrieval errors and to use such knowledge to improve the retrieval algorithms. The goal of this study was to explore if data mining could facilitate this process.

Our approach consisted of the three main components: 1) use collocated AERONET and MODIS data to train neural networks for the retrieval of AOD; 2) compare the accuracy of neural networks and the MODIS operational algorithm, and 3) understand the present conditions in instances when the neural network is more accurate than MODIS retrievals. A neural network trained in the first step is a completely data-driven retrieval algorithm, distinct from the model-driven MODIS operational algorithm. The drawback of neural network retrieval is that its high accuracy is not guaranteed for the conditions unlike those at the AERONET sites. As such, neural networks are not a completely viable alternative to model-driven retrieval algorithms. However, if neural networks can achieve higher retrieval accuracy over the AERONET locations, then it is clear that the accuracy of a model-driven algorithm can be further improved.

2.6 Unifying Multiple Retrievals by Structural Regression

The aerosol data are characterized by strong spatial and temporal dependencies. To exploit these dependencies we have recently developed Continuous Conditional Random Fields (CRF) for AOD retrieval that are able to exploit by defining interactions among outputs using feature functions (Radosavljevic *et al.*, 2010b). The use of features to define the CRF models allowed us also to include arbitrary properties of input-output pairs into the compatibility measure. Our CRF probabilistic model for structured regression uses multiple non-structured predictors as its features. Features were constructed as squared prediction errors of deterministic and statistical models and we showed that this results in multivariate Gaussian conditional $P(\mathbf{y}|\mathbf{x})$ distribution. Consequently, in the proposed approach learning is a convex optimization problem with a global solution for a set of parameters and inference is conveniently conducted through matrix computation.

3. RESULTS

3.1 Spatio-Temporal Data Partitioning for AOD Retrieval

Following methodology summarize in Section 2.1 we performed large scale experiment using 2 years of data from more than 200 ground based AERONET sites located at six continents spatio-temporally collected with data from MODIS instrument aboard NASA's Earth observing Terra and Aqua satellites. The obtained soft partitioning results (illustrated at Fig. 4) were compared to the data partitioning used in the MODIS operational algorithm that divides the world into three spatial-temporal regions based on domain knowledge. The experiments showed that the new soft partitioning of Earth results in significant AOD retrieval accuracy improvements (Radosavljevic *et al.*, 2008).

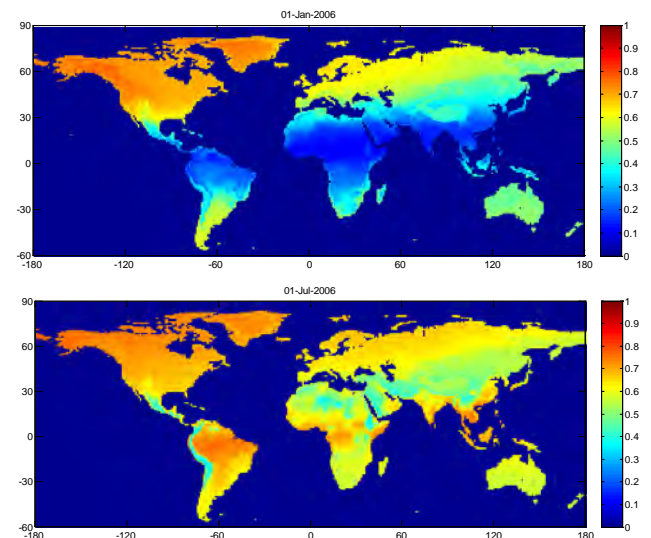


Figure 4: Spatio-temporal partitioning of Earth discovered by competition of two AOD prediction models. Pixel color corresponds to weight w assigned to one AOD predictor in a mixture. The other predictor has weight $1-w$. Top panel: winter partitions, Bottom panel: summer partitions.

3.2 AOD Retrieval across Multiple Accuracy Measures

Neural networks from the ensemble described in Section 2.2 were trained using collocated data points whose attributes were derived from MODIS instrument satellite observations and whose target AOD variable was obtained from the ground-based AERONET instruments. Instead of relying on MSE minimization criterion for neural network training, we used the relative error REL, which can be considered as generalization of MSE.

We observed that REL criterion allowed us to achieve increased accuracy over certain ranges of AOD values. To provide a predictor that is accurate over the whole range of AOD values for each of the 5 commonly used accuracy measures, we developed an ensemble of neural networks with adaptive cost functions. Some networks in the ensemble were specialized in predicting small AOD while others were specialized in predicting large AOD. The experiments showed that the proposed ensemble outperformed an ensemble that used standard MSE optimization; it managed to achieve as high MSE, R^2 and CORR accuracies while it significantly improved MSRE and FRAC accuracies. In addition, AOD prediction accuracy of the proposed ensemble was compared to the

recently developed operational MODIS Collection 005 retrieval algorithm. Results obtained over the entire globe during the first six months of year 2005 showed that the proposed ensemble of neural networks was significantly more accurate for all the considered accuracy measures (Radosavljevic *et al.*, 2010a).

3.3 Uncertainty Analysis of AOD Retrieval

Three years of MODIS data collocated with 201 AERONET sites over whole the globe have been used for uncertainty analysis of AOD retrieval. The average negative log-predictive density (NLPD) of the true targets was used as a measure of the quality of uncertainty estimation. Committees of 30 neural networks were trained on the subset of sites which have data in both training and testing years. The obtained results allowed analysis of uncertainty of AOD retrieval at a given site over time and also uncertainty comparison at multiple sites. As an example, we compared uncertainty of AOD retrieval at Beijing site in China vs. Muana Loa site in Hawaii to conclude that properties of aerosols are much more stable at Muana Loa than in Beijing. By further investigation we found that this discovery is consistent with domain experts' expectations as this site serves for calibration statistics of AERONET instruments.

Our analysis of seasonal uncertainty levels over three years also revealed existence of different interesting patterns. For example, we compared sites with the highest and the lowest average uncertainty over the seasons. The highest uncertainty levels occur in Asia over all seasons, in Africa during the winter and fall, and in the central part of South America during the summer. These levels reach extreme values in summer while for other seasons are almost equal. On the other hand, the lowest levels of uncertainty appear in North America and Europe during winter, summer, and fall, and in South America during the spring (Ristovski *et al.*, 2009).

3.4 Selection of Sites for Ground Based Observations

Data used in sites reduction experiments were distributed over entire globe at 217 AERONET sites during years 2005 and 2006. We performed training on 2005 data and used 2006 data for testing. We considered a scenario when current operational AERONET sites have to be reduced by 33% or 66%. In all experiments, we started from a set of 30 AERONET sites and applied the proposed method and the two alternatives to identify a subset of 20 or 10 AERONET sites to be retained. The two alternatives included a random selection of sites as well as an approach based on spatial distance among the sites was also considered. Sites were selected such that their spatial coverage was maximized. In our experiments, the proposed accuracy-based selection achieved consistently better results than the alternatives. Also, accuracy of the proposed site reduction method did not change much even after removing 20 of the 30 AERONET sites. Interestingly, on average, the spatial selection strategy performed slightly worse than the random selection strategy. According to presented results we concluded that the proposed accuracy-based sites reduction method is superior to spatially-based and random selection alternatives (Radosavljevic *et al.*, 2009).

Our extensive experiments on globally distributed data over 90 AERONET sites from the years 2005 and 2006 provide strong evidence that sites selected using the algorithm proposed in Section 2.5 improve the overall AOD prediction accuracy at a faster rate than those selected randomly or based on spatial diversity among sites (Das *et al.*, 2009). The evaluation data

spanned the entire world, ranging from January of 2005 to December of 2006. A committee of 20 neural networks was used to estimate the model uncertainty, each having 10 hidden nodes. Initial training set was created with 700 training points from 10 randomly selected AERONET sites. We assumed that the AOD values corresponding to the remaining training points are unknown. Then we proceeded to select $t = \{1, 2, \dots, 20\}$ sites in twenty independent experiments using the proposed site selection algorithms. The R-squared accuracy was computed on the test data before and after the selection of prospective sites. Our results show that uncertainty-based site selection gives significantly higher accuracy over random and spatial distance-based selection (especially when only a few sites are to be selected) and marginally higher accuracy than temporal distance-based method. Performance improves further if correlation among the sites is taken into consideration. A comparison between accuracies uncertainty-based and all three other methods which selects site based on combination of uncertainty, spatial and temporal distance shows that there is some improvement in performance due to inclusion of spatial and temporal correlation metrics over purely uncertainty-based selection. Although the improvement in accuracy is small, it is not negligible, keeping in mind the huge variability of AOD over the entire earth.

At the continent scale, we observed that different continents favor different selection algorithms. For Europe, random selection works quite well because a large number of unlabeled sites are from Europe and therefore random selection favors sites from Europe. In North America, despite the large number of candidate sites, the random selection was not very successful. The accuracies for North America generally followed the accuracies obtained on overall test set. In South America and Africa, spatial selection performed better than other methods. Especially in South America, it was able to attain a significantly higher accuracy (Das *et al.*, 2009).

3.5 Discovering Correctable AOD Retrieval Error

Our approach described in Section 2.5 was applied on 3,646 collocated MODIS and AERONET observations within the continental United States. The results showed that neural networks are more accurate than the operational MODIS algorithm over the observed locations. A study of differences between neural networks and the MODIS algorithm revealed interesting findings. For example, NN are more accurate than MODIS when the retrieval is contaminated by clouds, snow, or water (i.e. NDVI ≤ 0). These and other discoveries have been found to be mostly consistent with expert knowledge and revealed some new insights into the MODIS algorithm performance (Vucetic *et al.*, 2008).

3.6 Unifying Multiple Retrievals by Structural Regression

Experiments were conducted on MODIS data at 50x50 km² resolution collocated with observations at 217 AERONET sites during years 2005 and 2006. In nested spatio-temporal 5-cross-validation experiments we determined parameters corresponding to the operational C005 and neural network (NN) retrievals over five continents (Asia and Australia were treated as a single region). In our experiments CRF achieved significantly better accuracy than either NN or C005 alone.

In follow-up experiments when using indicator functions for 5 continents (Asia and Australia were treated as one continent) CRF achieved better accuracy than either NN or C005 alone

over almost all continents. Values of obtained parameters suggest that we should trust *NN* more in the Eastern US, an area well covered by AERONET sites where SR is expected to work well, while in Africa, an area poorly covered by AERONET, we should trust *C005* more (Radosavljevic *et al.*, 2010b).

4. CONCLUSION

The reported results provide strong evidence that accurate statistical AOD retrieval is possible by problem partitioning through competition of local spatio-temporal models (Radosavljevic *et al.*, 2008) and developing an ensemble statistical model with components specialized for small and for large AOD prediction (Radosavljevic *et al.*, 2010a). It was also found in our study how to analyze uncertainly of statistical AOD retrievals (Ristovski *et al.*, 2009) and how to use this tool for optimized placement of ground-based observation sensors (Das *et al.*, 2009). A data mining analysis can also reveal the conditions when deterministic AOD retrievals can be significantly enhanced (Vucetic *et al.*, 2008). Our work in progress on structural regression by continuous conditional random fields suggests that further major improvements of retrieval accuracy can be achieved by unifying multi-source retrievals (Radosavljevic *et al.*, 2010b).

References

- Das, D., Obradovic, Z., Vucetic, S. 2009. Active Selection of Sensor Sites in Remote Sensing Applications, *Proc. IEEE Int'l Conf. Data Mining*, December, Miami, FL.
- Das, D., Radosavljevic, V., Vucetic, S., Obradovic, Z. 2008. Reducing Need for Collocated Ground and Satellite based Observations in Statistical Aerosol Optical Depth Estimation, *IEEE Int'l Geoscience and Remote Sensing Symposium*, Boston, MA.
- Han, B., Vucetic, S., Braverman, A., Obradovic, Z. 2006a. A Statistical Complement to Deterministic Algorithms for Retrieving Aerosol Optical Thickness from Radiance Data, *Engineering Applications of Artificial Intelligence*, vol. 19, no. 7, pp. 787-795.
- Han, B., Obradovic, Z., Li, Z., Vucetic, S., 2006b. Data Mining Support for Improvement of MODIS Aerosol Retrievals, *Proc. IEEE Int'l Geoscience and Remote Sensing Symp.*, Denver, CO.
- Han, B., Vucetic, S., Braverman, A., Obradovic, Z. 2005a. Integration of Deterministic and Statistical Algorithms for Aerosol Retrieval, *Proc. Int'l Conf. Novel Applications of Neural Networks in Engineering*, Lillie, France, pp. 85-92.
- Han, B., Vucetic, S., Braverman, A., Obradovic, Z. 2005b. Construction of an Accurate Geospatial Predictor by Fusion of Global and Local Models, *Proc. IEEE 8th Int'l Conf. Information Fusion*, B.11.2 pp. 1-8, Philadelphia, PA.
- Jeong, M.-J., Li, Z., Chu, D. A., Tsay, S.-C. 2005. Quality and Compatibility Analyses of Global Aerosol Products Derived from the Advanced Very High Resolution Radiometer and Moderate Resolution Imaging Spectroradiometer, *J. Geophys. Res.*, 110, D10S09.
- Levy, R. C., Remer, L. A., Martins, L.V., Kaufman, Y.J., Planafattori A., Redemann, J., Wenny, B. 2005. Evaluation of the MODIS Aerosol Retrievals over Ocean and Land during CLAMS, *J. Atmos. Sci.*, vol. 62(4), pp. 974-992.
- Obradovic, Z., Han, B., Xu, Q., Li, Y., Braverman, A., Li, Z., Vucetic, S. 2006. Data Mining Support for Aerosol Retrieval and Analysis – Project Summary, *NASA Data Mining Workshop*, Pasadena, CA.
- Radosavljevic, V., Vucetic, S., Obradovic, Z. 2010a. A Data Mining Technique for Aerosol Retrieval Across Multiple Accuracy Measures, *IEEE Geoscience and Remote Sensing Letters*, vol. 7, no.2, pp. 411-415.
- Radosavljevic, V., Obradovic, Z., Vucetic, S. 2010b. Continuous Conditional Random Fields for Regression in Remote Sensing, *Proc. 19th European Conf. on Artificial Intelligence*, Lisbon, Portugal.
- Radosavljevic, V., Vucetic, S., Obradovic, Z. 2009. Reduction of Ground-Based Sensor Sites for Spatio-Temporal Analysis of Aerosols, *Proc. 3rd International Workshop on Knowledge Discovery from Sensor Data at the 15th ACM SIGKDD Conf. Knowledge Discovery and Data Mining*, Paris, France.
- Radosavljevic, V., Vucetic, S., Obradovic, Z. 2008. Spatio-Temporal Partitioning for Improving Aerosol Prediction Accuracy, *Proc. Eight SIAM Int'l Conf. Data Mining*, Atlanta, GA.
- Ramanathan, V., Crutzen, P.J., Kiehl, J.T., Rosenfeld, D. 2002. Atmosphere - Aerosols, climate, and the hydrological cycle, *Science*, vol. 294, pp. 2119-2124.
- Remer, L. A., Tanré, D., Kaufman, Y. J., 2006. Algorithm for Remote Sensing of Tropospheric Aerosol from MODIS for Collection 005, <http://modis-atmos.gsfc.nasa.gov/atbd02.pdf>.
- Ristovski, K., Vucetic, S., Obradovic, Z. 2009. Evaluation of a Neural Networks based Approach for Aerosol Optical Depth Retrieval and Uncertainty Estimation, *Proc. Int'l Conf. on Space Technology*, Thessaloniki, Greece.
- Vucetic, S., Han, B., Mi, W., Li, Z., Obradovic, Z. 2008. A Data Mining Approach for the Validation of Aerosol Retrievals, *IEEE Geoscience and Remote Sensing Letters*, vol. 5, no. 1, pp. 113-117.
- Xu, Q., Han, B., Li, Y., Braverman, A., Obradovic, Z., Vucetic, S. 2005. Improving Aerosol Retrieval Performance by Integrating AERONET, MISR, and MODIS Data Products, *Proc. IEEE 8th Int'l Conf. Information Fusion*, B.11.3 pp. 1-8, Philadelphia, PA.
- Zhuang, W., Radosavljevic, Han, B., Obradovic, Z., Vucetic, S. 2008. Aerosol Optical Depth Prediction from Satellite Observations by Multiple Instance Regression, *Proc. Eight SIAM Int'l Conf. Data Mining*, Atlanta, GA.

Acknowledgement

This work was supported in part by the National Science Foundation under Grant IIS-0612149.

AN ASSESSMENT OF THE EFFICIENCY OF LANDSAT, NIGERIASAT-1 AND SPOT IMAGES FOR LANDUSE/LANDCOVER ANALYSES IN EKITI WEST AREA OF NIGERIA

Ojo A G^a, Adesina F A^b

^aAfrican Regional Centre for Space Science and Technology Education, PMB 019 OAU Campus, Ile-Ife.

ojobayous@yahoo.com[±]

^b Department of Geography Obafemi Awolowo University, Ile-Ife, Osun State, Nigeria

faadesin@oauife.edu.ng^b

KEYWORDS: Land-use, Accuracy Assessment, Landsat TM, SPOT XS, NigeriaSat-1, Classification

ABSTRACT:

Several remote sensing data types are now available for environmental studies. The variety has increased as many nations including some African countries invest in satellite remote sensing. However, each data type has its own peculiar features that may limit or enhance its relevance to capture data for specific range of information. This study used geo-information techniques based on multi-source imageries to enhance the utilization of images with coarser resolutions in landuse analysis in Ekiti west area of south western Nigeria. The objective of the study is to evaluate the variations in landuse characterization with multi-source satellite data sets. The remotely sensed data sets used included Landsat TM 1986, SPOT XS 1995 and NigeriaSat-1 2007 satellite images. To make the images comparable, they were georeferenced, re-sampled and enhanced for visualization in a GIS environment. The tonal values recorded in the images with the features on the ground were validated by ground truthing. The data from ground truthing were combined with visual image interpretation for “supervised” classification. The classes defined and analyzed included “built-up area”, “bare rock”, “farmland”, secondary forest regrowth” and “water body”. The results show that each image has certain relative advantage over the other. For instance, while NigeriaSat-1 image was efficient in the analysis of information within the visible portion of the electromagnetic spectrum, SPOT image was better in the Near Infrared. Information from Landsat image was rather weak at both portions (Visible and NIR) of the Electromagnetic Spectrum. The study also shows that SPOT image has the lowest level of data redundancy of the three image providers. The study confirms the relevance of the growing interest in the use of geo-information techniques for landuse analysis.

1. INTRODUCTION

Remotely sensed imageries are one of the most important sources of spatial data for environmental studies. They are data obtained via remotely placed sensors which may be located at heights sometime several hundred of kilometres in space to make it possible for the sensor to “see” a large portion of the earth’s surface at the same time. Such images can also be obtained from low flying aircrafts equipped with suitable cameras to track earth-based features. These data sets allow earth-based phenomena such as landuse and landcover characteristics to be rapidly mapped, if needed repetitively and at relatively low costs. With increasing capacity to rapidly generate maps of large areas, planners in the rural and urban areas are getting more empowered to address issues associated with landuse analysis such land misuse and various forms of incursion into properties and trespassing.

Some of the most commonly used remote sensing data sets for mapping landuse and landcover are those from Landsat, SPOT (Système Probatoire d’Observation de la Terre), IRS (Indian Remote Sensing), ASTER (Advanced Spaceborne Thermal Emission and Reflection Radiometer), MODIS (Moderate Resolution Imaging Spectrometer), JERS-1 (Japanese Earth Resources Satellite), and recently, NigeriaSat-1 satellites. The Landsat data have greater spectral resolution (Gastellu-Etchegorry, 1990) and a longer time series, while SPOT provides better spatial resolution but with shorter historical records. Newer satellite imaging systems are

commonly equipped with enhanced instruments to generate additional data that permit more accurate mapping and analysis. Landuse/landcover analyses usually proceed from classification of the area of study. The classified units can be further analysed in terms of their characteristics particularly size.

Factors that may influence classification accuracy include a sensor’s spatial, radiometry and spectral resolutions. Spatial resolution describes the size each pixel represents in the real world (Cushnie, 1987). For example, a satellite with 30 metre resolution produces pixels that measure a 30x30 metre area on the ground. Radiometric resolution, on the other hand, is the smallest difference in brightness that a sensor can detect. A sensor with high radiometric resolution would therefore have very low “noise”. The “noise” is described as any unwanted or contaminating signal competing with the desired signal. Spectral resolution is the number of different wavelengths that a sensor can detect. A sensor that produces a panchromatic image alone has a very low spectral resolution, while one that can distinguish many shades of each colour has a high spectral resolution (Jensen, 2007).

Generally, spatial resolution is the most important factor of the three for landuse and landcover definition. For example Gastellu-Etchegorry (1990), in Indonesia studied landuse with SPOT and Landsat images. He showed that SPOT Multispectral (XS) images are better than Landsat Multispectral Scanner (MSS) images for mapping of heterogeneous near-urban landcover because of SPOT’s superior spatial resolution. The link between spatial resolution and classification accuracy,

however, is sometimes weak (Jensen, 2005). In heterogeneous areas, such as residential areas, it has been shown that classification accuracies may improve even as spatial resolution decreases (Cushnie, 1987). This occurs due to the potentials of urban features to blend together to form composite distinctive “urban signals” that can be distinguished from other landcovers.

In this study, the capabilities of three satellite imageries including Landsat, NigeriaSat-1 and SPOT-XS for landuse studies are evaluated with a view to amplifying the understanding of their specific potentials, advantages and limitations for environmental studies. This is borne out of the growing recognition of the need to develop “appropriate technology” for developing countries to enable researchers based in these countries to accomplish desirable level of sophistication in earth’s resources analyses even with their limited access to spatial data.

2. THE STUDY AREA/ LOCATION EXTENT

The study area is made up of Ekiti west, Ado-Ekiti, Irepodun/ Ifelodun and Ekiti south-west. Local government areas in Ekiti State of western Nigeria (Figure1). The State lies within Longitudes $4^{\circ} 5'$ and $5^{\circ} 45'$ East of the Greenwich Meridian and Latitudes $7^{\circ} 15'$ and $8^{\circ} 5'$ North of the Equator. It is about 6,353 square kilometers in size. It is bounded in the north by Kwara and Kogi States, in the West by Osun State and Ondo State in the East and in the South. The State has 16 Local Government Areas. By 1991 Census, its population was 1,647,822. The estimated population upon its creation on October 1st 1996 was 1,750,000 with the capital located at Ado-Ekiti (Ekiti Investors Handbook, 2002). The current estimated population based on 2006 census, was 2384212 million people (NPC, 2006).

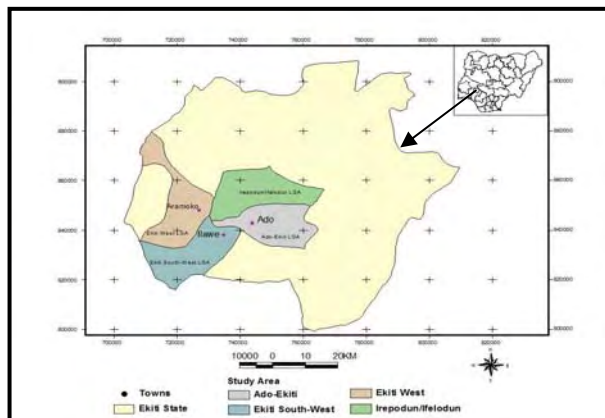


Figure 1: Map of Ekiti State and the LGAs used for the study

The State is mainly an upland area, rising generally around 250 meters above the sea level (Ekiti Investors Handbook, 2002). The landscape consists of ancient plains broken by steep-sided outcropping dome rocks. These rocks occur singly or in groups or ridges and the most notable of these are to be found in Efon-Alaaye, Ikere-Ekiti and Okemesi-Ekiti (EKSG, 1997). The area is underlain by metamorphic rock of the basement complex. The State is dotted with hills of varying heights. The notable ones among them are Ikere-Ekiti Hills in the southern, Efon-Alaaye Hills in the western and Ado-Ekiti Hills in the central parts.

The State enjoys the tropical climate with two distinct seasons. These are the rainy (April-October) and the dry

(November-March) seasons with an annual rainfall of around 1150mm. Temperatures range between 21° and 28°C with high humidity. The South-Westerly wind and the North-Easterly Trade winds blow in the rainy and dry (harmattan) season respectively. The tropical forest originally covered this part of Nigeria. However, as a result of exploitation for many centuries of exploitation, the original vegetation has been removed and now replaced with anthropic covers. Forest is now confined largely in the south, while savanna dominates the natural landscape in the north (Kayode, 1999 and EKSG, 1997).

3. METHODOLOGY

3.1 Data Acquisition and Image Preprocessing

Relevant data were collected on the physical attributes of the five landuse types, i.e. farmland, built-up areas, forest regrowth, bare lands and water bodies, which were the dominant landuse in the area. Sample sites for data collection were determined from the remotely sensed imageries. For each landuse, five sample sites measuring $100 \times 100\text{m}$ were selected and were fully described during field observations, variables examined for site characterization included dominant, concrete among others and drainage characteristics of the site. The coordinates of the sample sites were tracked with Global Positioning System (GPS) receiver. Secondary data used were Landsat TM, SPOT- XS NigeriaSat-1 covering the study area. Table1 shows key parameters of the data used for the study. Images were obtained from the National Centre for Remote Sensing Jos, Forest Monitoring, Evaluation and Coordinating Unit (FORMECU) Abuja and Global Land Cover Facility (GLCF) an Earth Science Data Interface. The topographic map covering the study area was collected from the Ministry of Land and Surveys, Lagos.

The satellite data were extracted one after the other as sub-scenes from the original datasets. For the purpose of landuse/cover assessment, a common window covering the same geographical coordinates of the study area was extracted from the scene of the images obtained. This made the band Red, Blue, Green (RGB-123) colour combination. For SPOT XS data, Channel 3 was assigned red plane, Channel 2 to green and channel 1 to blue plane. The band combination then consisted of Blue, Green and Red (BGR-321) colour combination. For NigeriaSat_1 data set, colour combination, channel 1 was assigned to red plane, channel 2 to green plane and 3 to blue plane. This puts the band combination as Red, Green and Blue (RGB-123).

The geometric errors were corrected using ground control points (GCP). The process of georeferencing in this study started with the identification of features on the image data, which can be clearly recognized on the topographical map of the study area and whose geographical locations were clearly defined. Stream intersections and the intersection of the highways were used as ground control points (GCP). The latitude and longitude of the GCPs of clearly seen features obtained in the base map were used to register the coordinates of the image data used for the study. All the images were georeferenced to Universal Transverse Mercator projection of WGS84 coordinate system, zone 31N with Clarke 1866 Spheroid. Nearest-neighbor re-sampling method was used to correct the data geometrically.

Table 1 Attributes of the images used for the Study

Image Name	Source	Sensor	Acquisition Date	Resolution	Resolution	Spectral Range (um)	Area (km ²)
Topographic Map	MLSL Lagos	-	1966	-	-	-	-
Landuse Map	NCRS, Jos	-	1995	-	-	-	-
Land sat TM	GLCF	TM	1986	1-7	30m	0.45-0.90	185 x 185
SPOT	FORM ECU, Abuja	MS S	1995	1-3	10m	0.45-0.69	60x 80
NigeriaSat-1	NCRS, Jos	Imager	2007	1-3	32m	0.52-0.90	600x 580

3.2 Landuse Classes

Based on the knowledge of the study area, reconnaissance survey and additional information from previous studies in area, a classification scheme was developed after Anderson *et al.*, (1976). The scheme gives a broad classification where each of the land use/ land cover was identified by a class (Table 2). These classes are apriori well defined on the three images used for the study.

Table 2 Landuse classification scheme (after Anderson *et al* 1976)

LANDUSE/LANDCOVER CATEGORIES	DESCRIPTION OF THE LANDUSE/LANDCOVER
Built-up Area	Roads, buildings, open spaces
Bare Rock	Bare soil, bare land
Farm Land	Shrubs, fallow, cropped land.
Secondary forest	Agro forest, riparian forest, advanced bush re-growth
Water Body	Dam, rivers streams.

3.3 LandCover/ Landuse Analysis

For Landuse/Landcover analyses, the satellite images were classified using the supervised classification method. The combined processes of visual image interpretation of tones/colours, patterns, shape, size, and texture of the imageries and digital image processing were used to identify homogeneous groups of pixels, which represent various land use classes already defined. This process is commonly referred to as “training” sites because the spectral characteristics of those known areas are used to “train” the classification algorithm for eventual land use/ cover mapping of the remaining parts of the images.

A Map of the study area was produced and was used to locate and identify features both on ground and on the image data. The geographical locations of the identified features on the ground were clearly defined. These were used as training samples for supervised classification of the remotely sensed images. The five categories of land uses/ land covers were clearly identified during ground truthing. Locations were tracked with the GPS to facilitate transference of the field information onto the images.

3.4 Classification

In this study, the satellite images were classified using supervised classification method. The combined process of visual image interpretation of tones/colours, patterns, shape, size, and texture of the imageries and digital image processing were used to identify homogeneous groups of pixels, which

represent various land use classes of interest. The study engaged in ground truthing to the four Local Government Area of the study area. These are Ekiti west, Ado-Ekiti, Irepodun/Ifelodun and Ekiti south-west Local government areas in Ekiti State (Figure1). Before the ground truthing, map of the study area was printed and was used as guide to locate and identify features both on ground and on the image data. The geographical locations of the identified features on the ground were clearly defined. These were used as training samples for supervised classification of the remotely sensed images. Five categories of land uses and land covers were clearly identified during ground truthing. These are secondary re-growth forest, water body, bare rocks, built-up areas and farm land. The processed images were subject to band correlation analysis to assess the nature and strength of the relationship among the bands in the imageries.

4 RESULTS

4.1 Comparison of Basic Features among the Three Sensor Data

Table 3 summarizes the correlation analysis of bands with each other within each of the three sensors. In the NigeriaSat-1 image, the Near-Infrared (NIR) band was negatively correlated with the visible bands (Green and Red) ($-0.16 \leq r \leq -0.04$; $p < 0.05$). In the Landsat TM image, the NIR band positively correlated with visible bands ($0.02 \leq r \leq 0.22$; $p < 0.05$). For the SPOT image, the NIR band also positively correlated with the visible bands ($0.53 \leq r \leq 0.63$; $p < 0.05$). The relationship between the visible bands were strongest in SPOT ($r = 0.98$), relatively strong in NigeriaSat-1 images ($r = 0.53$) and relatively low in Landsat TM ($r = 0.22$).

Table 3 Correlation matrix analysis results for the three sensors

Sensor	Bands	Green	Red	NIR
Landsat	Green	1.00	0.22	0.02
	Red	0.22	1.00	0.93
	NIR	0.02	0.22	1.00
NigeriaSat-1	Green	1.00	0.95	-0.04
	Red	0.95	1.00	-0.16
	NIR	-0.04	-0.16	1.00
SPOT	Green	1.00	0.98	0.63
	Red	0.53	1.00	0.98
	NIR	0.63	0.53	1.00

Level of significance (p) < 0.05

The results imply that the SPOT image is likely preferable to either of the other image types for the study of earth base features at the Visible and Near Infrared portions of the Electromagnetic Spectrum. On the other hand, NigeriaSat-1 imageries could give better information at the visible portion while Landsat imageries could be better in the Visible and Near Infrared portions of the spectrum. The results indicate that the strength of the correlation among the bands increases with increase in the spectral resolution of the imageries. This corresponds with what many authors have observed. For example, Kuplich *et al.* (2000) have suggested based on their studies, that high correlation between spectral bands is indicative of high degree of information. Spectrally adjacent bands in a multispectral remotely sensed image are often highly correlated. Multiband visible/near-infrared images of landuse areas will show negative correlations between the near-infrared

and visible red bands and positive correlations among the visible bands because the spectral characteristics of land use are such that as the vigour or tone of the feature increases, the red reflectance diminishes and the near-infrared reflectance increases.

4.2 Landuse Classes

Table 4, 5, and 6 contain summaries of the results accuracy assessment generated from the three images on the five land use. The overall, user as well as producer accuracies of individual classes were consistently high for the three imageries. The accuracies for Landsat, NigeriaSat-1 and SPOT were 66.5%, 81.2% and 82.8% respectively. The Kappa statistics were 0.87, 0.97 and 0.89 respectively. The user and producer accuracies of individual classes in Landsat ranged from 51.9% to 87.3%, whereas in NigeriaSat-1, they varied from 60% to 97.3% and in SPOT from 74.7% to 89%. On Landsat image for the ‘built-up area’ category of land use, the producer accuracy is 82.8% and the user is 87.3%. This means that more than 80% of the built-up area in the image was correctly defined and mapped. The other four land use classes i.e. bare rocks, farm land; secondary forest regrowth forest and water body had relatively low producer and user accuracies. For instance secondary forest regrowth has a producer accuracy of 66.5% and user accuracy of 51.9%. The four categories are thus not as well defined as the built-up areas. The ‘built-up area’ of NigeriaSat-1 had the highest accuracy on producer accuracy (97.3%), it also had user accuracy of 96.9%. On the SPOT image, the statistics on built-up area category are 81.98% for producer accuracy and 91.58% for user accuracy.

It appears that Landsat has lower value for accuracies than either SPOT or NigeriaSat-1. Different reasons may be responsible for this outcome. One reason may have to do with the intrinsic characteristics of the images. For instance Landsat has a spatial resolution of 30metres, NigeriaSat-1 32 metres and the SPOT 10metres. Chen, et al., (2004) has shown that these can variously have effect on the levels of accuracies obtained from the images. Another reason could be that, spectral characteristics among the different land cover types (e.g. built-up, bare rock) are similar, while spectral variation within the same land cover type or even within the same image might be high (Cushine, 1987).

TABLE. 4 ACCURACY ASSESSMENT OF LANDSAT TM IMAGERY

Satellite Image	Classified Data	Reference Data					Ref. Totals	Class Totals	Number Correct %	PA %	UA % Kappa	
		Built-up Area %	Bare Rock %	Farm land %	Sec. Forest %	Waterbody %						
Landsat	Built-up Area	82.79	5.60	4.67	1.15	0.67	100	94.88	82.79	82.79	87.26	1.00
	Bare rock	8.26	58.84	12.13	8.21	4.52	100	91.96	58.84	58.84	63.98	1.00
	Farm land	7.02	19.14	52.15	12.29	0.90	100	91.50	52.15	52.15	56.99	1.00
	Sec. forest regrowth	1.79	9.41	29.21	66.49	21.14	100	128.04	66.49	66.49	51.93	0.8601
	Water body	0.15	8.02	1.84	11.87	72.76	100	94.64	72.76	72.76	76.89	1.00
Overall Landsat Classification Accuracy = 66.47% (i.e. $82.79+58.84+52.15+66.49+72.76$), Overall Kappa Statistics = 0.8714												
501.02												

TABLE. 5 ACCURACY ASSESSMENT OF NIGERIA SAT-1 IMAGERY

Satellite Image	Classified Data	Reference Data					Ref. Totals	Class Totals	Number Correct %	PA %	UA %	Kappa
		Built-up Area %	Bare Rock %	Farm land %	Sec. Forest %	Waterbody %						
NigeriaSat-1	Built-up Area	97.32	3.03	0.02	0.05	1.16	100	100.42	97.32	97.32	96.91	1.0000
	Bare rock	1.89	77.27	0.22	3.09	3.57	100	117.55	77.27	77.27	65.73	1.0000
	Farm land	0.02	0.39	88.07	12.07	0.00	100	100.60	88.07	88.07	87.55	1.0000
	Sec. forest regrowth	0.04	7.64	1.37	82.38	3.77	100	105.20	82.38	82.38	78.31	0.9230
	Water body	0.73	11.67	0.33	2.37	6.00	100	75.08	60.00	60.00	79.92	1.0000
Overall NigeriaSat-1 Classification Accuracy = 81.20% (i.e. $97.32+77.27+88.07+82.38+60.00$), Overall Kappa Statistics = 0.9712												
498.85												

TABLE. 6 ACCURACY ASSESSMENT OF SPOT IMAGERY

Satellite Image	Classified Data	Reference Data					Ref. Totals	Class Totals	Number Correct %	PA %	UA %	Kappa
		Built-up Area %	Bare Rock %	Farm land %	Sec. Forest %	Waterbody %						
SPOT	Built-up Area	81.98	4.65	2.86	0.03	0.00	100	89.52	81.98	81.98	91.58	1.0000
	Bare rock	11.15	88.99	2.17	4.26	3.91	100	110.48	88.99	88.99	80.55	1.0000
	Farm land	5.72	2.10	83.40	4.98	3.91	100	100.11	83.40	83.40	83.31	0.8681
	Sec. forest regrowth	1.05	3.27	11.19	78.11	10.94	100	104.56	78.11	78.11	74.70	0.8714
	Water body	0.10	0.98	0.37	12.62	81.25	100	95.32	81.50	81.50	85.50	0.9781
Overall Spot Classification Accuracy = 82.75% (i.e. $81.98+88.99+83.40+78.11+81.25$), Overall Kappa Statistics = 0.8718												
499.99												

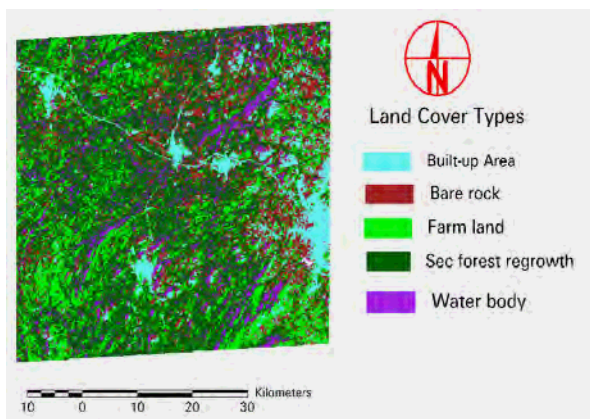


Fig2: Classified print of the Landsat TM image

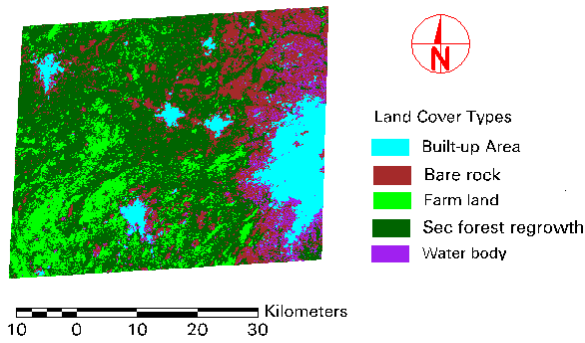


Fig3: Classified print of the NigeriaSat-1 image

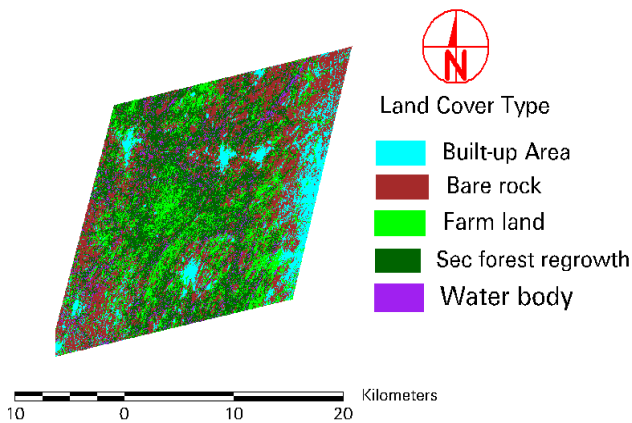


Fig4: Classified print of the SPOT image

The SPOT image had been rectified but was resampled to 32m in order to have the three imageries in the same spatial resolution.

4.3 Land use characterization of the study

Table 4.3 Shows the area covered in hectares, by the five landuse classes' namely built-up areas, bare rocks, farmland and secondary forest regrowth and water body. On the Landsat image, "built-up area" covered 4,388.15 hectares which represented 9.6% of the total area of land under study. "Bare rock" covered 8,925.8 hectares (19.4%); "farmland" 9,461.96 hectares (20.6%); "secondary forest regrowth" 19,881.9 hectares (43.3%) and water body 3,241.56 hectares (7.1%). On NigeriaSat-1, "built-up area" covered an area of 4,547.69 hectares which represented 10% of the total land area under study. "Bare rock" was 8,016.2 hectares (18%) "farmland" 6,682.6 hectares (15%); "secondary forest regrowth" 23,266.60 hectares (52%) and "water body" 2,326.32 hectares (5%).

With respect to SPOT image, "built-up area" covered 4,891.85 hectares which was 12% of the total land area under study. "Bare rock" was 12,887.70 hectares (30%); "farmland" 7,565.11 hectares (18%), "secondary forest regrowth" 14,665.7 hectares (34%) and "water body" covered 2,642.84 hectares (6%). In general, the land cover characterizations of the three imageries are over comparable area cover, despite the differences in the spatial resolutions of the images. "Secondary forest regrowth" is the largest in the three images and farmlands are comparable in size. The main difference is with respect to bare rock which was shown to cover a larger area in SPOT. The difference may be related to the time of imaging. Images taken in dry seasons would reveal more bare surfaces than those taken in the wet season.

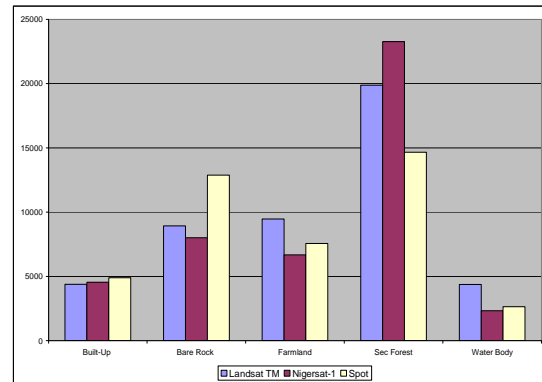


Figure . 5 Histogram showing the three imageries with their respective landuses types.

4.4. Discussion: Variation in land use characterization and Accuracy

The most basic output in remote sensing applications to landuse/landcover studies is land use characterization. This is information about the sizes of various landuse. When such information is available over a long period of time, it allows an assessment of landuse dynamics. Such characterizations are invaluable for the monitoring and managing of land resources and are increasingly vital for natural and regional development in Africa.

Landuse characterization has been most used particularly in the developing countries, (Adesina and Amamoo 1994; Oyinloye and Adesina 2006). Differences in the spatial and spectral characteristics of features make a differentiation of landuse/landcover types possible.

As a result of fundamental differences in the characteristics of the images used for this research, the study has proceeded with the assumptions that land use characterization will some how be different from one image to the other. Thus, SPOT, because of its higher resolution, would be more able to capture information than the two others. Also, Landsat would generate more details than NigeriaSat-1.

In general, the point raised above was demonstrated in this study. For example SPOT image had higher correlation of important wave bands with each other than both Landsat and NigeriaSat-1. This implies that, SPOT captures more information than either of Landsat and NigeriaSat-1. Also with respect to landuse recognition, built-up areas were more efficiently identified and defined on the SPOT image than on the two others. However, the three satellite images were relatively inefficient in defining the other land use categories. It appears from the results that the superiority of enhanced spatial resolution declines with the size of the land use category to be defined.

Table. 7 Areas of Landuse categories on the image

LANUSE/LAND COVER CATEGORIES	LANDSAT		NIGERIASAT-1		SPOT	
	AREA (Ha)	AREA %	AREA (Ha)	AREA %	AREA (Ha)	AREA %
BUILT-UP AREA	4388.15	9.56	4547.69	10.14	4891.85	11.47
BARE ROCK	8925.80	19.44	8016.18	17.88	12887.70	30.22
FARM LAND	9461.96	20.62	6682.62	14.90	7565.11	17.74
SEC. FOREST REGROWTH	19881.90	43.31	23266.60	51.89	14665.70	34.38
WATER BODY	3241.56	7.07	2326.32	5.19	2642.84	6.20
TOTAL	45899.37	100	44839.41	100	42653.20	100

Different reasons may be responsible for the differences in accuracies. One reason may have to do with accurate spatial registration of the intrinsic characteristics of the images. For instance Landsat has a spatial resolution of 30metres, NigeriaSat-1 32 metres and the SPOT 10metres. Chen, et al., (2002) has shown that these can variously have effect on the levels of accuracies obtained from the images. Another reason could be that, spectral characteristics among the different land cover types (e.g. built-up, bare rock) are similar, while spectral variation within the same land cover type or even within the same image might be high (Cushine, 1987).

5. CONCLUSION

This study was conducted with the intention of evaluating the difference in landuse characterization, relative accuracy of feature definitions and the usage of spatial data with Landsat, NigeriaSat -1 and SPOT images. The result of the study supports the knowledge that each image has certain relative advantage over the other. For stance, while NigeriaSat-1 images are shown to be very efficient in the analysis of information within the visible portion of the electromagnetic spectrum, SPOT images are better in the Near Infrared. Information from Landsat images was rather weak at both portions (Visible and NIR) of the Electromagnetic Spectrum. The study also showed that SPOT images have the lowest level of data redundancy of the three image providers. This observation is similar to that of Kuplich, et al (2000), which concluded that SPOT has relatively smaller data redundancy than ‘some’ other image producers. This is because high correlation between spectral bands is indicative of high degree of information. Spectrally adjacent bands in a multispectral remotely sensed image are often highly correlated. Multiband visible/near-infrared images of landuse areas will show negative correlations between the near-infrared and visible red bands and positive correlations among the visible bands because the spectral characteristics of land use are such that as the vigour or tone of the feature increases, the red reflectance diminishes and the near-infrared reflectance increases.

The study also showed that SPOT images have higher level of accuracy (> 97%) than Landsat and NigeriaSat-1. The reasons for this may be the intrinsic characteristics of the images. Another reason of course, is that spectral characteristics among the different land cover types (e.g. built-up, bare rock) could be similar.

In addition, it was also revealed that the distinguishing spectral characteristics between “farmland” and “rock surfaces” and “farmland” and “secondary forest” in the Landsat images were relatively poor. However, seamed data sets of NigeriaSat-1 and Landsat images on the one hand, and NigeriaSat-1 and SPOT on the other produce landuse classifications of better accuracies (>80%) than the individual images i.e. SPOT, NigeriaSat-1 or Landsat especially when representing land uses such as built-up area, bare rock, water body and farmland.

Finally, the images differ in their ability to reveal landuse characteristics and differences in spatial resolution may not be a challenge to accuracy and details of reporting depending on the subject of interest.

ACKNOWLEDGEMENT

We are grateful to the National Centre for Remote Sensing and FORMECU for releasing of the satellite images. The authors wish also to thank the department of geography of Obafemi Awolowo University for intellectual support during this research work. Also

an appreciation to African Regional Centre for Space Science and Technology Education for their supportive ways to see to the completion of this research work. The authors and the researchers of the literatures we referred to should also get our appreciations. We extend our sincere appreciation to the editor and anonymous reviewers, whose comments are valuable in improving the quality of the article.

REFERENCES:

- Adesina, F. A. and Amamoo O. E., (1994): “Land Cover Characterization with SPOT Satellite imagery in the forest areas of Nigeria. *The Nigeria Geographical Journal, New series*, 1, 70- 90.
- Anderson, J.R., Hardy, E.T., Roach, J.T. and Witmer, R.E., (1976): A land use and land cover classification system for use with remote sensing data, Professional Paper 964, U.S. Geological Survey, and Washington D.C. Appraising the anatomy and spatial growth of the Bangkok Metropolitan area
- Chen, D., Stow, D., (2002): The effect of training strategies on supervised classification at different spatial resolutions. *Photogrammetric Engineering and Remote Sensing* 68, 1155–116
- Cushnie, J.L. (1987): "The Interactive Effect of Spatial Resolution and Degree of Internal Variability within Land-Cover Types on Classification Accuracies." *Photogrammetric Engineer. Remote Sensing* 8, 1 (1987): 15-29.
- Ekiti Investors Handbook, 2002
- EKSG (Ekiti State Government) (1997): First Anniversary Celebrations of Ekiti State Government. Government Press, Ado-Ekiti. 22pp.
- Gastellu-Etchegorry, J.P., (1990): "An Assessment of SPOT XS and Landsat MSS Data for Digital Classification of Near-Urban Land Cover." *International Journal of Remote Sensing* 11, 2 (1990): 225-235.
- Jensen, J.R. (2005): *Digital Image Processing: a Remote Sensing Perspective*, 3rd ed., Prentice Hall.
- Jensen, J.R. (2007): *Remote sensing of the environment: an Earth resource perspective*, 2nd ed., Prentice Hall.
- Kayode, J. (1999): Phytosociological investigation of composite weeds in abandoned farmlands in Ekiti State, Nigeria. *Composite Newsletter* 34, 62 – 68
- Kuplich, T. M., (2000): Estudo da complementaridade de imagens óticas (Landsat/ TM) e de radar (ERS-1/SAR) na discriminação temática de uso da terra. INPE-5608-TDI/554, MSc dissertation, INPE, São José dos Campos, Brazil
- NPC, (2006): Population census and post enumeration survey chart National Population Commission (NPC), Abuja, Nigeria.
- Oyinloye, R.O and Adesina F. A., (2006): “Some Aspects of the Growth of Ibadan and Their Implications for Socio-economic Development” *Ife Social Sciences Review* Vol 20, No. 1, pp. 113-120

Studying Bio-Environmental Potentials of Kusalan Area, Based on IUCN criterions, using RS and GIS technologies

Oladi Djafar^a, Ahsany Nabi^b

^a = PhD. Faculty of Natural Resources, University of Mazandaran, Sari, Iran,
Oladi123@yahoo.com

^b =MSc. Faculty of Natural Resources, University of Mazandaran, Sari, Iran

Key Words: Kusalan, Remote Sensing, Bioenvironmental Potentials, Protected Area, GIS and Zoning

Abstract

Kusalan habitat is located on a northwest-southeast mountain with an intensive topography near the Sarvabad town in the west of Kurdistan. This habitat encompasses a set of unique bioenvironmental phenomenon (such as *Quercus* forests and dense ranges) as well as three permanent rivers and numerous springs. So far, there was no study on the bioenvironmental habitat potentials. This persuaded us to conduct a research on the bioenvironmental potentials of the region, to protect the area, according to IUCN criterions. Field surveys, remote sensing and geographic Information System (GIS) were used to identify and analyze the ecological, social and economical resources of the study area. Hybrid method was also employed using digital classification of 10m SPOT5 image of 2005 and field data as visual interpretation. Applying this method, the potential resources were identified. Then the maps of land forms, Hydrology, soil, vegetation, wildlife habitat, ecological potentials, current applications and the conventional boundaries were provided. In the next stage, bioenvironmental units were determined through applying GIS analysis along with gathering the maps and overlaying them. Zoning of the bioenvironmental resources was performed on the basis of IUCN definitions. The results of this study demonstrated that the study area involves 224 of flora species and 195 of fauna species as well as 5 main zones including: 29% secure zone, 40.75% protection zone, 13.7% alternative recreation zone, 3.21% mass recreation zone and 0.14% cultural and historical zone and 13.2% reconstructing zone along with the many scientific and training values and a unique wild natural landscape. Thus, Kusalan habitat is worth to be introduced as a national park (II) and to be considered as one of the four national protected areas in Iran. According to the results of this research, the GIS and RS can be used for identifying inaccessible bioenvironmental resources with an intensive topography and providing their maps with the aim of protecting the area, based on IUCN criterions.

1- Introduction

Establishing protected areas is considered as a conscious attempt to support the last remainders of a biodiversity which preserved their natural properties in the current instable developing process. Applying scientific principles to study the bioenvironmental potentials and evaluating the ecological potentials determines the land use type and the natural potential (ecological potential) (Makhdom, 1999). These studies has been already conducted in traditional ways by using the ground data collection, however, this method was an expensive, time consuming method and in some cases difficult to access. To address this problem, remote sensed images are used to study the natural resources, forests, ranges, wild life, erosion and other bioenvironmental factors (Chaderi 1996). Consequently, studying the ecological potentials of western habitats of Mazandaran, involving forests, ranges, apparent animal types such as some kinds of Mammals, birds, reptilian, etc. seems very necessary.

2- Materials and Methods

Ecological resources include biological and physical sources, each of them involving different parameters. In general, 3 methods of identifying ecological sources include:

- 1- Inventory and sampling
- 2-Automatic visual interpretation of aerial photographs, remotely sensed images and topographic maps

3- Geographic information system (Makhdom, 1999).

At first, a supervised digital classification method was applied using a maximum likelihood classifier. To do this, seven groups of training samples were selected as a model of spectral reflectance for different phenomena in the study area (including water, Gardens, planted crops, unplanted crops, forests, pastures, rocky lands and manufactured areas) based on the ground survey data.

The resulted map has a total accuracy of 57.4% and a kappa coefficient of 72.3%. Then, a visual classification method was applied. To do this classification, the raster map was transferred to a vector one. In the next step, the obtained map was laid on SPOT 5 panchromatic image. Then, it was interpreted, reviewed and edited using ground data in an Arc view 3.2 environment. The resulted map had a total accuracy of 65.15% and a kappa coefficient of 78.65%. This matter indicates the high capability of spot5 data associated with using a hybrid classification method to provide maps of the mountainous and non accessible areas. Ecological resources include:

2-1 Physical sources: Due to lack of a meteorological station in the study area, we used Synoptic station of Marivan and Paveh which are located near Kusalan. Rivers and Brooklets were extracted from topographic maps and remote sensed images. Then, they were digitized. The registered points were transferred to GIS in order to identify the existing springs. Ground samples and geographic characteristics of springs obtained by GPS system were used. In the next stage, hydrographic maps of the Kusalan area were also provided.

2-2 Land Shape maps: To assess the parameters forming the land shape (height classes, slope classes and five main geographic directions) and to prepare the necessary maps, four sheets of topographic maps at the scale of 1:50000 of year 1997 were used. Finally, the land shape maps were obtained by overlaying the map layers of height, slope and geographic direction.

2-3 Biological Resources

2-3-1 Plants: The extinction rates of plants in the study area were measured after careful frequent ground checking at different phenological stages of plant growth by collecting vegetation samples.

2-3-2 Animals: The information about the animals in the study area was collected by the wildlife habitat experts. To prepare the wildlife scattering map, the animal species index was determined. Then, habitat location was registered by GPS device and spatial data was transferred to GIS environment. The vector map of wildlife habitat was obtained through the hybrid interpretation of remotely sensed images.

2-3-3 Land shape: Since the land shape is a qualitative factor, remotely sensed images and a topographic map of 1:50000 associated with the field data were used to identify the scenery of Kusalan area.

2-4 Socio-economical studies

Conventional boundary map was prepared via hybrid interpretation of SPOT5 images and ground surveys with local people.

2-4-1 Evaluating the Bioenvironmental Potentials: The following processes are used in all methods of evaluating the bioenvironmental potentials:

- 1- Ecologic resources identification
- 2- Socio-economic data collection
- 3- Ecologic data collection and analysis
- 4- Evaluating the ecological potential for each unit, then comparing them with the ecological properties of each unit in the model
- 5- Zoning
- 6- Providing the land use potentials in terms of the global criteria

3- Results

The results of bioenvironmental resource identification (ecologic and socio-economic resources) are as follows:

3-1 Ecologic resource

3-1-1 Physical resources: Results of studying the physical resources show:

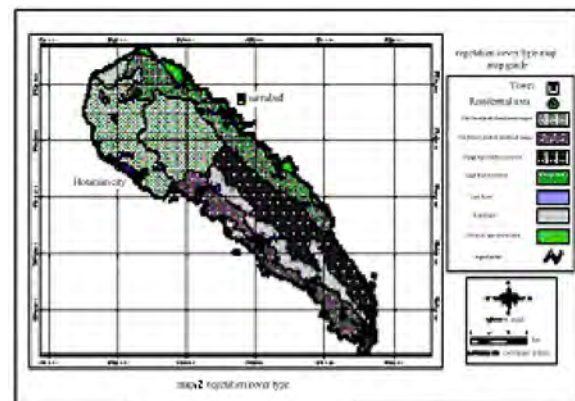
3-1-2 Climate: The Combination of climatic conditions in Marivan and Paveh stations, and the average of climatic parameters show the cold wet climate of Kusalan area.

3-1-3 Hydrology: There are abundant steep slope brooklets and springs in Kusalan habitat which all of them ends to Sirvan River. The main springs of Kusalan include: Hooseian, Lar, Odele, Hevar, Hevar Heye Shour.

3-1-4 Land shape: According the obtained results, there are many mountains and elevations with crest or round tops in the cornice or precipices shapes. The walls of valleys often have a steep or moderate slope, ending to bottom-line of brooklets. Direction of brooklets is mainly observed in linear form having a low width and a V shape profile view. The studies on topographic factors demonstrated the mountainous high altitude topography of Kusalan. Based on table 1 and map2, height variation range is 1800m and the main height classes are 1200-1800m in 40% of the study area. 27% of the area is covered with 2000-2500m classes which are suitable for protection according to evaluation models. Table 1 shows the percentage and area of each slope class. Distribution of classes is heterogeneous and the permanent predominant slope class is 30-60%. The slope above 60% covers 1/3 of the study area. Based on the results of this study, the area for the classes is north orientation (28/8%), west orientation (25/6%), east orientation (25/1%), and south orientation (20/2%). Due to the uniformity of area distribution of the main orientations, the summer and winter time is proper for wildlife, so, animals won't migrate to the neighbor habitats. Land shape was determined by resultant of 3 physiographic factors of slope, height, orientation. As the result, 509 small ecosystems are obtained from Kusalan big ecosystem.

Table 1 : height classes

Area (%)	Area (ha)	Height from sea level(m)	Height class
17.4	4474.98	800-1200	1
40.6	10457.55	1200-1800	2
14	3652.2	1800-2000	3
26.9	6927.93	2000-2500	4
1	251.73	Over 2500	5



3-2 Biological resources

3-2-1 Plants: 224 plant species were identified using field data and through a process of plant collection and identification in

Kusalan. These identified species include: 78% forbs, 13% grasses, 8% trees and bushes and 1 % brushes. Figures 3-5 demonstrates the natural resource preservation value in Kusalan area. 30 species among these 224 species are exposed to extinction threats.

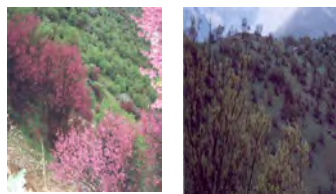


Figure 3: oak forests

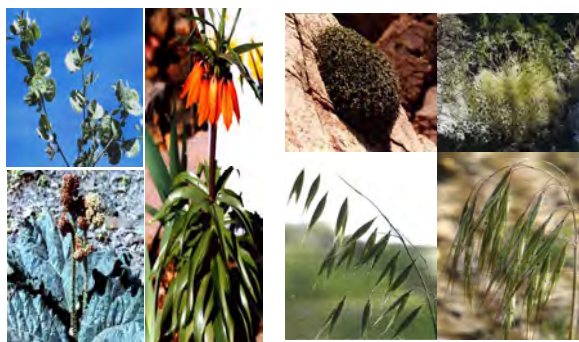


Figure3: image1) *Medicago radiate*, 2) *Rheum Ribes*, 3) Down Tullip

Figure4:images1: *Alkana sp.2: prangos sp.3: Avena Sativa*, 4: *Bromus tectorum*

3-2-2 Animals: According to the studies, there are 23 species of mammals in Kusalan habitat. The most outstanding of them are: *Canis lupus*, *canis aureus*, *vulpes*, *Ursus*, *Mustela nivalis*, *Meles*, *Vormela peregusna*, *Lutra*, *Felis catus*, *Lynx*, *Felidae*, all of them belongs to *Carnivora* family. Five families and subfamilies of *Rodents* observed in this habitat, including: *Sciuridae*, *Criceinae*, *Gerbilinae*, *Muridae*, *Hystriidae*.

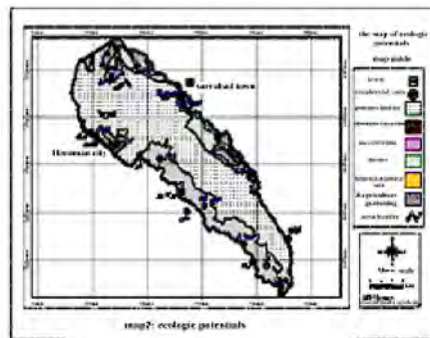


Figure 6: *Capra aegagrus*

3-3 evaluating the ecological potentials

This area was prepared for evaluation via ecologic resource identification, data collection and analysis. The evaluation was

in terms of the ecologic resources (land shape, soil, vegetation cover, wildlife scattering, and other physical resources) playing a role in ecologic models and it was conducted through a multi-factor method according to an ecologic model. Six types of land use were determined for the study area involving preservation, mass recreation, alternative recreation, forestry, gardening and agriculture (map7).



3-4 Historical and cultural events

a) Horaman ancient village: Horaman ancient village located at the study area has a unique view. This village has a pyramidal shape with echelon construction and an ancient castle is located at top of this village.

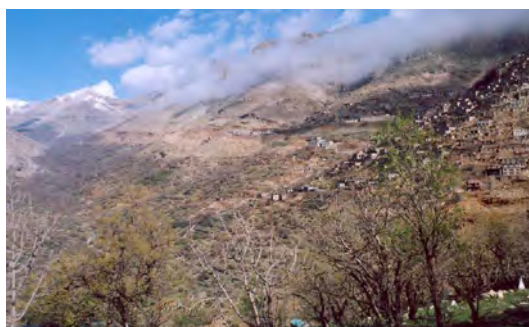


Figure 8: Horaman valley

b) Pirshalizar ceremony

This ceremony is annually held at the wedding anniversary of Pirshalizar. He was the most well-known philosopher of that area. This ceremony is held in eight days and people spend a great time together.



Figure9: Pirshalizar Ceremony

3-5 Zoning

Zoning was based on the ecological and socio-economical factors. The results obtained by combining and overlaying the maps of ecological potentials and conventional boundary, reveal 12978 biological units in Kusalan area. Combining the uniform units, we obtained 6 main zones: 1- safe zone, 2-protected zone, 3- mass recreation, 4- alternative recreation, and 5- cultural and historical zone, 6- reconstruction zone.

Area of each zone and its ratio to the total area were measured. Zone 1(safe zone) covering 29% of the study area is extended over the eastern and western ranges of Doab River. Some parts of this zone are observed in southern range with a slope over 60%. The vegetation cover has a low density in this zone. Rocks are the main coverage of the area.

Some other factors such as some threatened species of goat (main habitat) and Ursus have also affected on the selection of this zone. Zone 2 (preservation zone) with an area of 40/7% surrounds zone 1. This zone involves some parts of forests in the north and north-east ranges. Lynx habitat can be observed in this zone. 13/7% of the study area pertains to alternative recreation (zone 3), mainly observed in south ranges of Sirvan Permanent River and north ranges of Shahoo Mountain. Zone 4 (mass recreation) is located at north ranges with an area of about 3/21%. This zone was chosen because of the asphalt road of Marivan-Sanandaj and also the gravel rural road of Bahramabad –Bandol. Historical town of Horaman with special customs for holding Pirshalizar ceremony is selected as zone 5 (cultural and historical zone). The reconstructive zone is 13/2%. Totally, 70/7% of the study area has the potentiality to be preserved. In continue, the final zoning was done with regard to their natural condition, wetland shape and their combination with the conventional boundary map. According to the results of zoning, 29% of the study area pertains to zone 1 and 40/7% is considered as zone 2. In total, 70% of the study area has the potentiality to be preserved. About 17% of the study area (zones 3&4) has recreative potentiality. 14% of zone 5 and the rest 13/2% are considered as zone 6 or the reconstructive area.

4- Conclusion

Results of this study indicate the high potentiality of study area (Kusalan) to be a national park and receive the IUCN criteria. In this study, it is also verified that the biological potentials of an area or a natural habitat can be studied using data extracted from SPOT5 remotely sensed images (panchromatic 10 m images) via optical interpretation and supervised digital classification (hybrid method) and based on the global criteria (IUCN) to establish protected areas. It is also emphasized on using GIS to save and analyze the special data and also on providing proper outputs (maps, tables, etc.) as a significant and applicable method.

References

1. Ahsani, Nabi. 2004, practical strategies for natural resource conservation. *Moje Sabz Journal*. No 3. P 47.
2. Colwell, R. N. (1968) *Aerial and space photographs as aide to land evaluation*. In *Lland Evaluation*; Macmilan of Aust. Melbourne: 324-341.
3. Dahdouh-Guebas, F. (2002) *The use of remote sensing and GIS in the sustainable management of tropical coastal ecosystems*, *Environment, Development and Sustainability*, 4:93-112.
4. Eskandar Firuz. 1974. *Bioenvironment in Iran*. National committee of natural resource conservation. P 105.
5. FAO (1976) *Nitional park planning with annotated examples*. Forestry Paper NO. 6, FAO, Rom. 173 pp.
6. Faust, N. I. (1991) *Geographical information system and remote sensing future computing environment*, *Photogrammetric Engineering & Remote Sensing*. 57(8): 655-668.
7. Francoismass, J. & I. ramierZ. (1996) *Comparsion of landuse classification obtained by visual Interpretation and digital processing*, *ITC Journal*, 3(4): 278-282.
8. Ghaderi Morteza. 1996. *Remote Sensing*. Translated. Second edition. Tehran University publication center. P 257.
9. Ghasriani Farhang and Hossein Marufi. 1999. *Identifying ecologic areas in Iran (vegetation cover in Kurdistan province)*, published by forests and rangelands research Institution. P 78.
10. Howard, J, A, and Mitchell, C, W. (1985) *Photo geomomophology*, John Wiley and Sons. Newyork. 222pp.
11. IUCN (1994) *Guidelines for protected areas management categories*. IUCN, Cambridge, UK and Gland, Switzerland. 261pp.
12. IUCN (2006) *Red list catagories*. 341pp.
13. IUCN (1992) *Park for life- report of ivth world congress national parks and protecte areas*. IUCN, Cambridge, UK and Gland, Switzerland. 152pp.

14. IUCN/US.NPS. (1972) the second world conference on national park international biological programme (IBP). 83pp.
15. Jalili, A. Jamzad, Z. (1999) Red data book of Iran, a preliminary survey of endemic, rare & endangered plant species in Iran. Research Institute of Forests & Rangelands. Publication No: 1999-215. 742pp.
16. Karami, Prviz. 2003. Studying the Kusalan habitat. Bioenvironmental conservation Administration in Kurdistan. P 90.
17. Kenchington, R & Kelleher, G. (1995) Making a management plan. Chapman & Hall. 212pp.
18. Kiestler, P. (1996) First example of GAP analysis for an entire state (Idaho), Part of USGS Nationalwide Gap Analysis, Idaho. 112pp.
19. McNab, W. H. et al. (1999) An unconventional approach to ecosystem unit classification in western north Carolina. USA. Forest Ecology and Management, 4(2):102-112.
20. Mcneely, A. J. (1994) Protected areas in the modern world. Protecting Nature, Regional Reviews of Protected Areas. 210pp
21. Mcneely, Jeffrey, ed (1993). Parks for life: report of the 10th world congress on national parks and protected areas. IUCN/Gland, 51: 109-126
22. Mottaghi Mohammad, 2000. The use of TM digital image in studying the vegetation cover of rangelands (case study: Jahan Nama protected area), MSc. Thesis. Gorgan University of Agricultural science and natural resources. Rangeland and Watershed College. P 98.
23. Majnounian Henric, 2000. The protected areas in Iran. Parks and natural area conservation basics and strategies. Published by bioenvironment conservation organization. P 742.
24. Mjnounian Henric, 1997. Designing national parks. . Published by bioenvironment conservation organization. P459.
25. Mjnounian Henric, 1998. Guidelines for preparing national parks and protected areas for tourism. (From bioenvironmental plan of United Nations). Published by bioenvironment conservation organization. P200.
26. Makhdom Majid, 1995. Living in Environment, translated. Tehran University publication. P322.
27. Makhdom Majid. Land Preparations basics. Second edition. Tehran University publication. P289.
28. Mozafarian Valiollah, 1998. A dictionary of Iranian flowers. Farhang Moaser Publications, Tehran. P594.
29. Moghaddam Mohammadreza. 1998. Rangelands and rangeland management. Tehran University publication. P470.
30. PCI Geomatica 8.2 user's guide (2002). Ontario, Canada.
31. Pedly, M. I. & P. J. Curran (1991). Per-field classification: an example using SOPT HRV imagery. Int. J. Remote Sensing, 12(11): 2181-2192.
32. Rafieyan Omid, 2003. Studying the changes in northern forests of Iran between 1994-2001 using ETM+ images. MSc thesis. Tehran University of Natural Sciences. P 122.
33. Scott (1995) Conservation of biological diversity: perspectives and the future for the wildlife protection, Wildlife Society Bulletin, 23 (4): 657-661.
34. Tabatabaei Mohammad and Ghasriani Farhang 1992. Natural resources of Kurdistan (forests and rangelands), University Jihad, Tehran, p 650.
35. Twumasi, Y. A (2004). Development of a protected area management scheme using GIS and multi-temporal satellite imagery: The Case of the Dygira National Park Reserve in Ghana. PhD Dissertation, Alabama A&M University, 247 pp.
36. Yachkachi Ali (1974). Stand und Entwicklung der Nah- und Ferienerhelungsgebiete in Iran University of Goetting. 112pp.

PROVIDING PROCESSING LINES AND TEST DATA FOR THE GMES LAND MONITORING CORE SERVICE

P. Pacholczyk^{a,*}, H. Makhmara^a, R. Lacaze^b

^a Centre National d'Etudes Spatiales, DCT/ME/OT, 18 Avenue Ed. Belin, 31401 Toulouse Cedex 9, France – (philippe.pacholczyk, hassan.makhmara)^a@cnes.fr

^b HYGEOS, CESBIO, 18 Avenue Ed. Belin, 31401 Toulouse Cedex 9, France – rl@hygeos.com

Technical Commission VII Symposium 2010

KEY WORDS: Environment, Land, Soil, Vegetation, Monitoring, Processing, Multisensor, Multispectral

ABSTRACT:

Geoland2 project is part of the GMES EU-lead initiative and intend to prepare, validate and demonstrate pre-operational service chains and products of the Land Monitoring Core Service (LMCS), and to propose its specific functional organization. The architecture of geoland2 is made of 3 Core Mapping Services (CMS) providing “basic” land products, and 7 Core Information Services (CIS) which are thematic elements using the CMS products to generate more “elaborated” information addressing specific European policies. One CMS, called BioPar, is dedicated to the production in near real-time and off-line mode of biophysical variables describing the continental vegetation state, the radiation budget at the surface, and the water cycle.

We focus here on the following product lines: the Leaf Area Index, the Fraction of green Vegetation Cover, the Fraction of PAR absorbed by the vegetation, the NDVI, the surface albedo, and the Soil Water Index. Until 2012, the objective is to define, develop, validate, and run 2 versions of the processing lines. For each version, test data sets are generated: they are dedicated to the scientific validation performed by independent team, and to the product utility assessment carried out by the CIS users.

The talk will describe the organization setup to build the system, including the interfaces upstream with the team in charge of the algorithm definition, and downstream with the production centre which will perform the operation and dissemination. The emphasis will be put on the qualification procedure applied at each step of the development process. The test data sets, available during the

second quarter of 2010, will be presented. Furthermore, we will show the main results of the validation procedure which relies on comparison with ground measurements, and on inter-comparison with similar EO-based products, and the first feedback about the utility of these products for the users’ applications.

1. THE GEOLAND2 PROJECT

1.1 Structure

The FP7 GEOLAND2 project is part of the GMES EU-lead initiative and intend to prepare, validate and demonstrate pre-operational service chains and products of the Land Monitoring Core Service (LMCS), and to propose its specific functional organization. The GEOLAND2 consortium includes 50 European partners : private companies, public institutions, service providers, research laboratories, etc .

GEOLAND2 is made of 3 Core Mapping Services (CMS) providing “basic” land products, and 7 Core Information Services (CIS) which are thematic elements using the CMS products to generate more “elaborated” information addressing specific European policies (Figure 1). The 3 CMS deliver global or local maps at various temporal scales in the following areas of interest :

- Euroland : Periodic land cover change and urban atlas
- BioPar : near real-time and off-line biophysical parameters
- SATChMo : Area frame sampling for seasonal monitoring and global land cover change

The 7 Core Information Services (CIS) use the CMS products to provide high level analysis maps on the following topics :

- Land Carbon

- Global Crop Monitoring
- Natural Resource Monitoring in Africa (NARMA)
- Agricultural Environment
- Forest
- Water
- Spatial Planning.

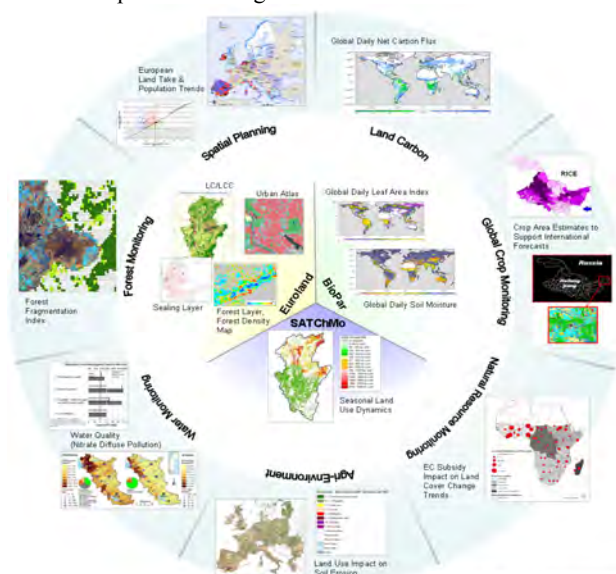


Figure 1 : GEOLAND2 project organization

Products and services provided by the GEOLAND2 project will be available to users to the Spatial Data Infrastructure (SDI) portal.

1.2 The BioPar Core Mapping Service

The goal of the Biogeophysical Parameters Core Mapping Service (BioPar CMS) is to set up pre-operational infrastructures for providing an extensive range of biogeophysical parameters on regional, European, and global scale, both in near-real-time (NRT) and off-line mode. The biogeophysical variables of the BioPar portfolio (see table 1) describe the vegetation state, the energy budget at the surface level, and the water cycle [1].

Product	NRT Off-line	Spatial Resolution	Spatial coverage	Temporal Resolution	Sensor (Back-up)
Continental Vegetation					
LAI, fCover, fAPAR, DMP, NDVI, Phenology	NRT	1 km	Global	10-days	VGT (MODIS)
Climatology : LAI, fAPAR, fCover	Off-line	1 km	Global	Yearly	VGT
Times series of vegetation products	Off-line	4 km	Global	10-days	AVHRR + VGT
Burnt areas + seasonality	NRT	1 km	Global	Daily	VGT
MERIS FR biophysical variables	NRT	300 m	Europe	10-days	MERIS
HR biophysical products	Off-line	10 m	Pilot Areas	4 times/year	SPOT
Energy Budget					
Downwelling Shortwave Surface Flux Downwelling Longwave Surface Flux	NRT	~5 km	Global	3 hours	SEGO + AVHRR
Land Surface Temperature	NRT	~5 km	Global	3 hours, daily, 10-days	SEGO + AVHRR
Surface Albedo	NRT	1 km	Global	10-days	VGT
Surface Albedo	NRT	~5 km	Global	10-days	SEGO + AVHRR
Water cycle					
Water bodies + seasonality	NRT	1km 250m	Africa	10-days	VGT, MODIS
Soil Moisture + Freeze/Thaw	NRT	0.1°	Global	Daily	ASCAT
Time series of soil moisture products	Off-line	25 km	Global	Daily	ERS-1&2 Scatt

Table 1 : BioPar products characteristics

CNES is involved in the development of the following products (see table 1) :

- Leaf Area Index (LAI), fraction of vegetation Cover (fCover), fraction of Absorbed Photosynthetically Active Radiation (fAPAR), Normalized Density Vegetation Index (NDVI) derived from SPOT/VGT data in NRT
- The long time series of these vegetation variables derived from AVHRR and SPOT/VGT archives
- The climatology of LAI, fAPAR and fCover variables
- Soil Water Index (SWI) and Freeze / Thaw index derived from Metop/ASCAT data in NRT and from the ERS scatterometer archive
- Surface albedo derived from SPOT/VGT data in NRT

2. DEVELOPMENT OF PROCESSING LINES

2.1 Organization

The development concept relies on user product assessment and feedback : the development team implement algorithms specified by the definition team and generate test data sets for validation and user utility assessment. The user feedback is taken into account for the development of the second version.

The research teams define the retrieval algorithms based upon existing and validated methodologies, improve them to match as well as possible the user requirements, and initiate innovative actions to adapt them to the technical specificities of the next generation of sensors in order to ensure the continuity of the service. Effort will be put on the compatibility between historic and current products so that long-time series are available after the reprocessing of existing EO archives.

Independent teams perform the product validation, following a procedure established in close collaboration with the users, relying on comparison with ground measurements collected over site networks, on inter-comparison with existing similar satellite products, and on data assimilation techniques, with the aim to guaranty the scientific relevancy of the BioPar products. For such activity, we will test the usefulness of an innovative network of automatic sensors to monitor the vegetation variables on a long term basis.

The development teams implement the algorithms in processing lines, and generate test data sets for user evaluation. The pre-operation centres perform the pre-operational production at regional, European and global scales, in NRT and in offline mode, with the periodicity required by the users. Finally, the resulting biogeophysical parameters will be disseminated by the Spatial Data Infrastructure cross-cutting issue, in a format in accordance with the INSPIRE directive.

Table 2 shows the sharing of activities among the BioPar partner for the providing of vegetation and humidity products where CNES is involved. Definition, development, validation and production are shared between several European institutions from Austria, Belgium, France, Spain, Poland and Portugal.

INRA (F), HYGEOS (F) & TU Wien (A) define the product content and produce the specification set (documentation, prototype, reference products).

CNES (F) develop the processing lines and produces the test data set.

EOLAB (Sp), INRA (F), IGiK (Pl), Meteo-France & ECMWF validate the test data set and asses the scientific content of the product.

VITO (Be), CNES (F) & IM (P) perform the operational production disseminated through the SDI portal.

Product	Type	Definition	Development & test data	Product validation	Production
Vegetation variables : LAI, fCover, fAPAR, NDVI	NRT	INRA (F) HYGEOS (F)	CNES (F)	EOLAB (Sp) INRA (F), IGiK (Pl)	VITO (Be)
Climatology : LAI, fAPAR, fCover, NDVI	Off-line	INRA (F)	CNES (F)	EOLAB (Sp)	CNES (F)
Time series of vegetation products	Off-line	INRA (F)	CNES (F)	EOLAB (Sp)	VITO (Be)
Soil moisture & Freeze / Thaw	NRT	TU Wien (A)	CNES (F)	Meteo-France, ECMWF	IM (Pl)
Time series of soil moisture & Freeze / Thaw	Off-line	TU Wien (A)	CNES (F)	Meteo-France, ECMWF	CNES (F)

Table 2 : Activities sharing for vegetation and humidity product

2.2 Inputs

There are several inputs needed by CNES for the development phase and test data production.

First the definition team provided Algorithm Theoretical Based Documents (ATBD) which describe in detail the algorithm to be implemented : methodology, formulas, input data description, processing steps, flowcharts, ...

For the vegetation products INRA provided the vegetation variable ATBDs and HYGEOS provided the albedo and filtering/gap filling ATBDs. For the soil moisture product TU Wien provided the SWI ATBD.

Secondly, the operational centres expressed their interfaces requirements.

VITO provided the coding specification document, which explains the software convention that shall be used (general coding rules, computer platform issues, filename and directory structure conventions) and the Product Output Format document, which specifies the format used at VITO and gives a detailed description of files contents and name conventions.

IM provided the Algorithm Plugging Interface Document (APID), which includes their software conventions, and their Product Output Format document.

Thirdly, TU Wien delivered to CNES an IDL prototype used for the development of the SWI V1 product line. This prototype has been used as an example of algorithm implementation and for the technical qualification of the product by cross-checking of prototype output and test data, before delivery of them to the validation team.

Fourthly, the vegetation products derive from an existing processing line named Cyclopes, developed and used by the former land surface thematic centre POSTEL [2 & 3]. This processing line has been used until 2009 to produce vegetation variable products from VGT instrument data until year 2007 (see figure 2). This issue of vegetation variables is named version 0 (V0).

CNES has taken over the former activities around Cyclopes and the version V0 is used as the baseline from the development of new vegetation variable processing lines.

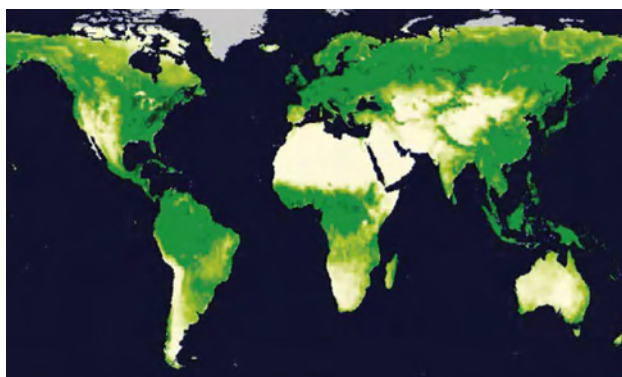


Figure 2 : FCover map (0 = white = bare soil, 1 = dark green = fully vegetated) from Cyclopes V0, © POSTEL/INRA

INRA delivered to CNES a Matlab prototype of the Neural Network used at the last stage of the processing line, in order to verify the implementation of the new structure and weights.

2.3 Development process

During the design phase, CNES gathered requirement set (ATBD, operational interface, output format, ...) and made a call for proposal for the development and test data phase. Vega Technologies company, based in Toulouse (Fr), has been selected in June 2009 and has developed the first versions of processing lines.

The development is performed in an industrial environment for two reasons.

The re-use of Cyclopes V0 needs a detailed and accurate knowledge of the existing processing line, in order to modify efficiently the six processing steps providing the albedo product (Level 3A) and the four vegetation products (Level 3B) from the VGT level 1 data.

More important, the industrial context includes a better quality frame by the use of external reviews at different steps of the development process. CNES has performed three reviews with its subcontractor, where experts from the BioPar partners were present.

The System Requirement Review took place in July 2009 and demonstrated how far:

- the Service Specification answers to the User Requirements Document (URD)
- the processing line design answers to the Service Specification requirements
- the external interfaces and operation requirements are taken into account during the development
- the Service Validation Plan (SVP) implements the necessary verification steps to validate the requirements of the URD and the commitments of the Service Specification.

VEGA Technologies has shown his deep knowledge of the existing processing line of the vegetation variables and was able to propose discerning changes to match the specifications and the requirements of the production centres, and also a rigorous methodology of validation based upon unit & integration tests, and upon scientific analysis of the output using tools including visual control, and statistic data analysis

Due to the huge reuse of Cyclopes processing line, the Preliminary and Critical Design reviews have been merged in one review which took place in October 2009. The purpose of the Preliminary Design Review is to assess and approve the preliminary design and assess the readiness to start the implementation phase. The purpose of the Critical Design Review is to assess and approve the detailed design of the processing lines and the detailed definition of the interfaces.

The P-CDR review raised 50 questions & answers from the review group, which have been analyzed and discussed. The P-CDR concludes that all the objectives are fulfilled, excepted for BUFR interfaces of the SWI product (lack of detailed format).

The Industrial Acceptance Review address the result of the acceptance test (installation from scratch and testing of the processing line) performed at the sub-contractor premise and at CNES. The IAR has been performed and accepted for the vegetation variables and is currently performed for the SWI product.

After this milestone, CNES delivers the processing lines to VITO and IM, with a support of the subcontractor if needed. Then VITO and IM will organize the Validation Readiness Review (VARR) and the Operational Readiness Review (ORR) of their processing line. CNES will participate in these reviews.

2.4 Outputs

2.4.1 Processing lines

The version 1 of vegetation variable processing line has been delivered to VITO in June 2010. After integration in the operational environment, expected before the end of the year, VITO will produce in NRT the vegetation variable and albedo product, and reprocess off-line the VGT archive to produce the time series of vegetation products.

CNES is currently developing the climatology processing line which will process this archive to provide, in 2011, the yearly climatology products (see tables 1 & 2).

The SWI processing line has been delivered to the Institute of Meteorology (IM) from Portugal in June 2010. After integration in the operational environment, expected before the end of the year, IM will produce in NRT the soil moisture product.

2.4.2 Demonstration products

Together with the processing lines, CNES delivers to the validation team and end users a test data set corresponding to the products that will be delivered by the operational processing line. All these data sets are available on the SDI web portal, with a Product User Manual document (PUM) describing their technical characteristics.

In 2009 CNES has generated 4 years of Cyclopes V0 vegetation products (2004 to 2007) which have been used by INRA to calculate the best neural network weights for the V1 vegetation processing line. These products are available on the Postel web server.

The vegetation variables test data set includes 10-day LAI, fAPAR, fCover & NDVI products from February 2003 to January 2005, issued from VGT2-P data provided by VITO.

The first test data sets have been delivered mid-April 2010 and analysed by INRA (Fr), who detected a large difference with former products (V0 Cyclopes, MERIS products). This difference came from the fact that the neural network had been calibrated on Cyclopes V0 L3A data, while these new neural network weight were applied on V1 L3A data.

During May 2010 the neural network has been calibrated on V1 L3A data and L3B test data have been re-produced with the new neural network weights.

The new vegetation test data sets have been delivered to the users beginning of June 2010.

The albedo test data set includes 10-day albedo products from February 2003 to January 2005, issued from VGT2-P data provided by VITO.

The first delivery of SWI test data sets to TU Wien and Meteo-France took place end of March 2010, with a time length value of $T = 10, 20, 40, 60$ & 100 . The analysis shown that above $T = 20$ the SWI values were the same, and a code mistake has been corrected.

More, after analysis, it has been decided to extend the product range to lower values of $T = 1, 5$ & 15 , in order to have a better analysis depth by avoiding the figure stagnation due to the T exponential integration (see §3.3 SWI product characteristics).

The second version of test data sets have been delivered end of April 2010 and validated mid-May 2010. In order to have a

service continuity with the end users until the product availability at IM (Pt), CNES produces monthly the SWI products and keep available the current archive, from June 2007 up to the present.

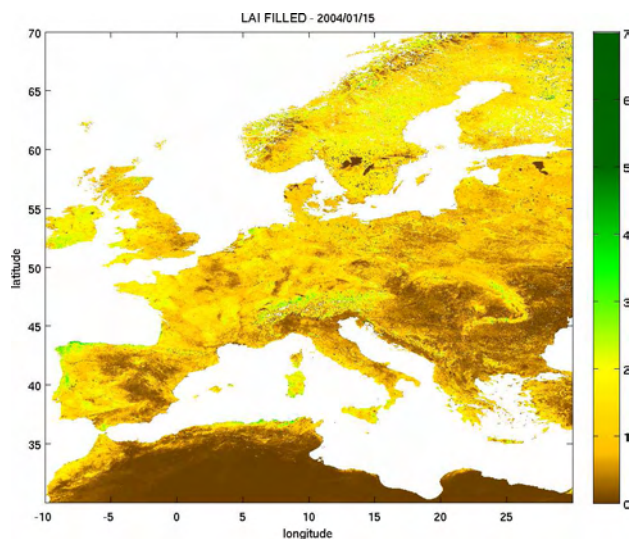
3. THE DEMONSTRATION PRODUCTS

3.1 LAI/fAPAR/FCover/NDVI from SPOT/VGT

The leaf area index (LAI) is defined as half the total foliage area per unit of ground surface. The FCover is the fraction of ground unit covered by green vegetation. The fAPAR is defined as the fraction of photosynthetically active radiation absorbed by green vegetation for photosynthesis activity. The instantaneous fAPAR value at 10:00 solar time is used as a very good approximation to the daily integrated value under clear sky conditions. The Normalized Difference Vegetation Index (NDVI) corresponding to the SPOT-5/VEGETATION-2 sensor characteristics for its Red (B2) and NIR (B3) bands, is also provided.

The algorithm is based on already existing LAI, fAPAR, and FCover products to capitalize on the efforts accomplished and get a larger consensus from the user community. Following the published literature on products validation (See [3]), the best performing products were selected and combined to take advantage of their specific performances while limiting the situations where products show deficiencies. The selected products are re-projected onto the VEGETATION plate-carrée $1/112^\circ$ grid, smoothed through time and interpolated at the 10 days frequency. Then the products are combined, and eventually scaled, to provide the fused product that is expected to give globally the 'best' performances. The fused products are generated for few years over the BELMANIP2 set of sites that is supposed to represent the possible range of surface types and conditions over the Earth. Neural networks are then calibrated over this set of sites to relate the fused products to the corresponding atmospherically-corrected and directionally-normalized top of canopy SPOT/VEGETATION reflectances.

The product has the following characteristics (see the PUM document on SDI for more details) : variables values with error and quality flags, spatial resolution 1 km, temporal resolution 10 days, geometric accuracy < 300 m, thematic target accuracy 5% to 15%, global coverage by square tiles of 10° .



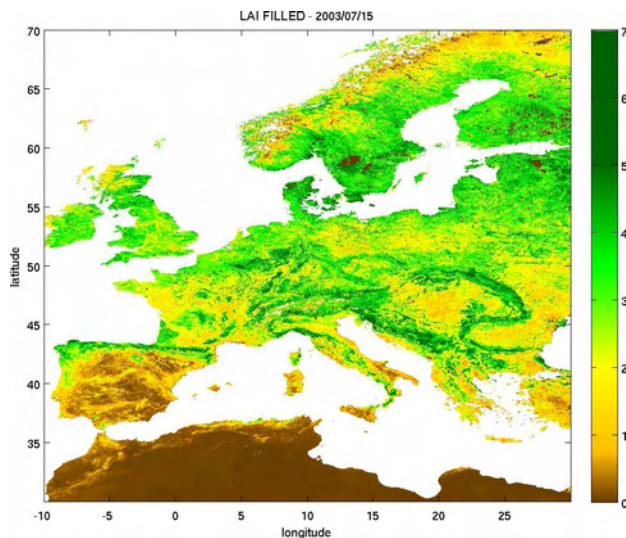


Figure 3 : LAI data sets, © CNES/INRA/HYGEOS/VITO.

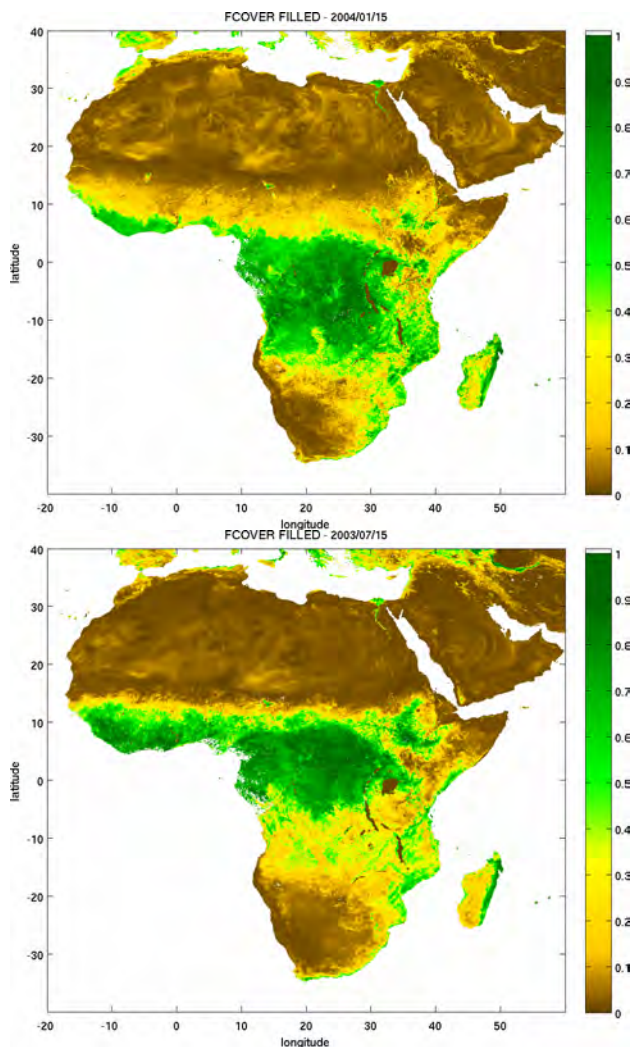
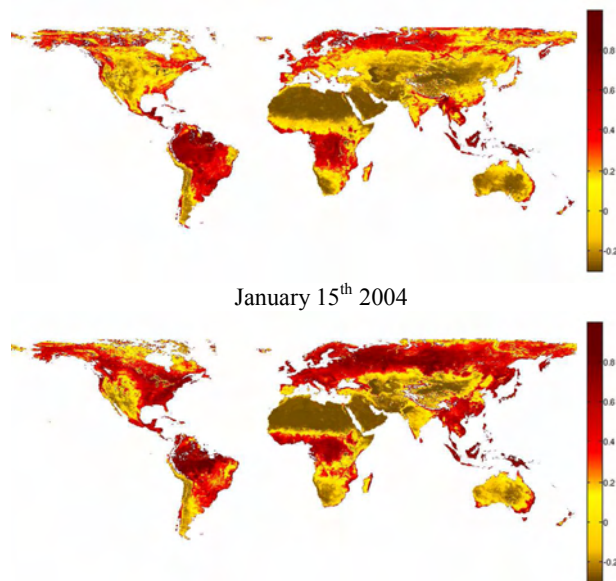


Figure 4 : fCover data sets, ©CNES/INRA/HYGEOS/VITO.



July 15th 2003

Figure 5 : fAPAR data sets, © CNES/INRA/HYGEOS/VITO.

3.2 Albedo from SPOT/VGT

The albedo is the fraction of the incoming solar radiation reflected by the land surface, integrated over the whole viewing directions. The BioPar albedo products include the directional albedo calculated for the local solar noon (also called “black-sky albedo), and the hemispheric albedo, integrated over the whole illumination directions (also called “white-sky albedo”) for 3 broad bands: visible [0.4, 0.7 μ m], near-infrared [0.7, 4 μ m], and the whole solar spectrum [0.3, 4 μ m]. The coefficients resulting from the inversion of a 3-kernels linear bidirectional reflectance model on the atmospherically-corrected SPOT/VEGETATION reflectances (Baret, et al. 2007) acquired during a period of 30 days are then combined with the pre-computed values of the directional kernels integrated over angular domains to estimate albedos. Finally, the broadband albedos are derived by linear relationships of spectral quantities.

The product has the following characteristics (see the PUM document on SDI for more details) : reflectance values with error and quality flags, spatial resolution 1 km, temporal resolution 10 days, geometric accuracy 10%, thematic target accuracy 10%, global coverage by square tiles of 10°.

3.3 Soil Water Index (SWI)

The Soil Water Index is defined as the soil moisture content (in percent) in the soil profile. The retrieval algorithm uses an infiltration model describing the relation between surface soil moisture and profile soil moisture as a function of time. The algorithm is based on a two-layer water balance model proposed by Wagner et al. (1999) to estimate profile soil moisture from SSM retrieved from scatterometer data. The remotely sensed topsoil represents the first layer and the second layer extends downwards from the bottom of the surface layer. In this model, the water content of the reservoir, whose depth is related to a characteristic time length (T), is described in terms of an index, which is controlled only by the past soil moisture conditions in the surface layer. A

computational adaptation of the original SWI algorithm has been made based on a recursive formulation proposed by Albergel (2008). In this method, a gain factor is introduced that relates the past SWI measurements to the current measurements. The SWI processing algorithm uses ASCAT-25km Level 2 Soil Surface Moisture product as input to generate daily global SWI images, calculated for 8 different T values (1, 5, 10, 15, 20, 40, 60, 100) together with the respective quality flags.

The product has the following characteristics (see the PUM document on SDI for more details) : index values quality flags, spatial resolution 25 km, temporal resolution 1 day, geometric accuracy 4 km, thematic target accuracy 10%, global coverage.

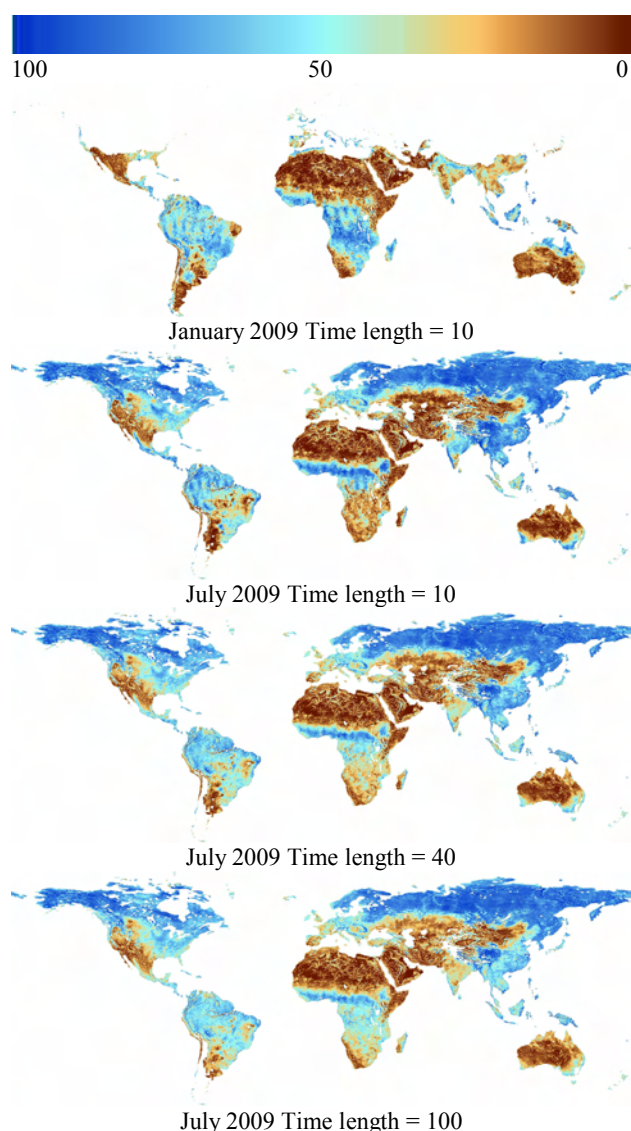


Figure 6 : Soil Water Index data sets, © CNES/TU Wien.

4. CONCLUSION

These first deliveries of BioPar test data show that vegetation and humidity variables products are now qualified and available for end users analysis. The product lines shall be operational for NRT processing in the production centres (VITO & IM) before the end of the year. All the products are available on the SDI web portal.

Development will continue on the same scheme and new versions are foreseen :

- Version 2 of vegetation variable processing line will improve the overall performance of the product line by applying directly the neural network to the VGT-P top of atmosphere reflectance. Products shall be available end of 2011.
- SWI & F/T Version 2 will improve the detection of freeze/thaw surface conditions and shall be available beginning of 2012.

CNES participate also to the SATChMo Core Monitoring Service (see figure 1) and will deliver end of 2011 a medium resolution land cover change map from MODIS data, on Europe and Africa. The development activities, shared with Université Catholique de Louvain in Belgium and the Institute of Geodesy and Cartography in Poland, will follow the same engineering cycle that BioPar.

5. REFERENCES

- [1] Lacaze R. & al., Geoland2 - Towards an operational GMES Land Monitoring Core Service; First Results of the Biogeophysical Parameter Core Mapping Service, ISPRS 2010
- [2] Baret, F., Hagolle, O. et al., 2007. LAI, fAPAR and fCover CYCLOPES global products derived from VEGETATION. Part 1: Principles of the algorithm. *Rem. Sens. Environ.*, 110: 275-286.
- [3] Weiss, M., Baret, F., Garrigues, S., Lacaze, R. and Bicheron, P., 2007. LAI, fAPAR and fCover CYCLOPES global products derived from VEGETATION. part 2: Validation and comparison with MODIS Collection 4 products. *Rem. Sens. Environ.*, 110: 317-331.
- [4] Albergel, C., Rüdiger, C., Pellarin, T., Calvet, J.-C., Fritz, N., Froissard, F., Suquia, D., Petitpa, A., Pignatelli, B., Martin, E., 2008. From near-surface to root-zone soil moisture using an exponential filter: an assessment of the method based on in-situ observations and model simulations. *Hydrol. Earth Syst. Sci.* 12: 1323-1337.
- [5] Wagner, W., Lemoine, G., Rott, H., 1999. A Method for Estimating Soil Moisture from ERS Scatterometer and Soil Data. *Rem. Sens. Environ.* 70: 191-207.

6. WEB SITES

Geoland 2 : <http://www.land.eu>
 SDI portal : <http://www.geoland2.eu/>
 POSTEL : Land surface thematic centre,
<http://postel.mediasfrance.org/>
 CNES : <http://www.cnes.fr>
 VEGA Technologies : <http://www.vegatechnologies.fr>

A COMPARISON OF TOTAL SHORTWAVE SURFACE ALBEDO RETRIEVALS FROM MODIS AND TM DATA

M. Pape^a, M. Vohland^{b,*}

^a formerly Faculty of Geography/Geosciences, University of Trier, D-54286 Trier, Germany

^b Remote Sensing Department, Faculty of Geography/Geosciences, University of Trier, D-54286 Trier, Germany - vohland@uni-trier.de

KEY WORDS: MODIS, Landsat TM, broadband albedo, sensor simulation

ABSTRACT:

Total shortwave albedo is one key variable controlling the radiation energy budget of the land surface. Thus, the monitoring of its spatial and temporal variations is one important issue e.g. for the application of climate models. Routine albedo products are available from the Moderate Resolution Imaging Spectroradiometer (MODIS), e.g. MODIS MCD43A3 as 16-day 500m combined product generated from data of Terra and Aqua MODIS. Furthermore, surface spectral reflectances from monotemporal multispectral sensor data may be used to estimate broadband albedos; for this purpose, conversion formulae have been developed for a number of sensors. Mismatches between different albedo products may arise e.g. from the atmospheric correction process, different scan view geometries, BRDF adjustments, the range of wavelengths used or the particular narrowband to broadband conversion formulae. In this study, albedo retrievals from Thematic Mapper (TM) data and MODIS data/products were analysed for their consistency. In detail, the following MODIS products were considered: MOD09 - daily bidirectional surface reflectance, and 16 days albedo-product MCD43A3. To allow a comprehensible comparison between TM and MODIS, TM data have been aggregated to 500m MODIS resolution using the Point Spread Function (PSF) of MODIS. The analysis was performed for different acquisition periods, which resulted in different levels of consistency and thus uncertainties associated with the particular products.

1. INTRODUCTION

Currently a number of satellite sensors are used to receive information about the reflectance of the earth's surface. As a key parameter controlling the radiation budget and thus the energy budget of the surface, the hemispherical reflectance called albedo is required by climate models as input parameter. With the appearance of routine albedo products derived from data of satellite sensors like MODIS (Gao et al., 2005; Lucht et al., 2000; Schaaf et al., 2002) and the Multi-angle Imaging SpectroRadiometer (MISR) (Martonchik et al. 1998), albedo data sets with different spatial and temporal resolutions have become available. In addition to automatically generated albedo composites, a derivation of daily albedo from provided surface reflectances is also possible. Effects by scan view geometry, atmospheric correction or spectral interpolation remain to distort the signal and cause uncertainties and variabilities between the data derived from different sensor types.

Therefore the main issue of this paper was the use of MODIS (500m) and TM (30m) data to derive and compare data fields of shortwave broadband albedo. As method for converting reflectance values to albedo, the conversion formulae of Liang (2000) were applied to atmospherically corrected MODIS and TM data. A validation of the calculated albedo was achieved by the MODIS albedo product MCD43A3 ("black-sky" albedo under clear-sky conditions, 0.25-5 μ m). This product is derived by means of a semi-empirical BRDF model using 16-day observations (Liu et al., 2009).

The bidirectional spectral reflectance received bandwise from satellite observations equals surface spectral albedo under the assumption of Lambertian surfaces. To retrieve the broadband albedo from narrowband sensors, Liang (2000) developed formulae based on radiative transfer simulations that incorporated many different atmospheric conditions and surface

reflectance spectra (taken from spectral libraries and AVIRIS-Airborne Visible/Infrared Imaging Spectrometer data). In our study, the formulae for MODIS and TM broadband albedo were verified using ideal (simulated) data prior their application to real sensor data.

2. SATELLITE DATA AND STUDY SITE

MODIS is an instrument onboard the Earth Observing System (EOS)-AM1 (Terra) and EOS-PM1 (Aqua). Designed as an opto-mechanical cross-track scanner, MODIS is observing nearly the entire earth every two days. The scanner receives radiances in 36 spectral bands with 250m, 500m and 1km geometric instantaneous-fields-of-view (GIFOV's) at nadir. The bands numbered 1-2 with 250m GIFOV and the bands 3-7 with 500m GIFOV are responsible for observing land cover features as well as cloud and aerosol properties (Barnes et al., 1998). The spectral coverage of the bands is very similar to Landsat TM bands (Figure 5), only for MODIS band 5 there is no correspondent.

In this study, the MODIS products MOD09GA and MCD43A3 were used. The bidirectional reflectance product MOD09GA contains an estimate of the surface spectral reflectance without atmospheric influences like scattering or absorption. The used bands cover the spectral range from 0.459 to 2.155 μ m. The albedo product MCD43A3 covers 16 days of observation and provides both directional hemispherical reflectance (black-sky albedo) and bihemispherical reflectance (white-sky albedo). Both data products (surface reflectance and albedo) are available as a gridded data set in sinusoidal projection with a geometric resolution of 500m and were received for this study through the NASA "Warehouse Inventory Search Tool" (WIST).

* Corresponding author.

The multispectral sensor TM captures high spatial resolution scenes onboard the Landsat-5 platform. The instrument has the capability to observe earth's surface via a set of six reflective bands with wavelengths ranging from 0.45 to 2.35 μm (Figure 5) and a geometric resolution of 30m at nadir. With a revisit cycle of 16 days, one of the sensor's major applications is the monitoring of land cover and land cover changes, although the operational use of the data is often limited by a restricted availability of cloud-free observations.

For our analysis, the following acquisition dates have been selected (by reason of clear-sky conditions and availability of both Terra MODIS and TM data): 19 July 2003, 4 August 2003 and 28 May 2005. Changes of atmospheric and surface conditions due to different overpass times of Terra MODIS and Landsat-5 TM were assumed to be negligible. At all dates, data were taken from the same satellite paths.

The study site was located in western Rhineland-Palatinate (Germany) close-by Luxembourg and had a size of approximately 2000 km² (Figure 1). The heterogeneous land cover included different types of forests, grassland, cropland and some urban settlements.



Figure 1. Subset of the MODIS data set (19 July 2003) with the TM scene near the edge of the scan swath. The red line illustrates the MODIS nadir line

To test the performance of broadband albedo conversion formulae, ideal MODIS and TM data have been simulated using a HyMap dataset (cf. chapter 3.1). The airborne hyperspectral scanner HyMapTM operates over a wavelength range from 0.44 to 2.5 μm . With a narrow bandwidth of 10-20nm the sensor is used as a nearly continuous spectrometer for tasks like environmental pollution monitoring, agriculture and forestry as well as soil and natural vegetation mapping (Cocks et al., 1998). The HyMap data (126 spectral bands, acquisition date 28 May 2005) covered an area that is 2.8km wide, 13km long and extends from the city of Trier (Rhineland-Palatinate, Germany) northwestbound. After an across-track illumination correction, the atmospheric correction was performed with the FLAASH (Fast Line of-sight Atmospheric Analysis of Spectral Hypercubes) module of ENVITM. The geometric correction was accomplished with the PARGETM software (see Vohland et al., 2010).

The implemented radiometric correction of the Landsat-5 TM data comprised sensor calibration and full radiative transfer modelling; earth's surface was assumed to be a Lambertian. Pre-processing of the TM data from 28 May 2005 was validated with the HyMap dataset; the radiometric consistency of all three TM scenes was validated using a set of pseudo-invariant objects.

3. METHODOLOGY

Different terminologies of albedo exist why a systematic definition is necessary. "Inherent albedo" can be distinguished from "apparent albedo". Inherent albedo at a given solar zenith angle and wavelength solely depends on surface properties and thus is independent from the current atmospheric conditions.

Apparent albedo is defined as the ratio of upwelling irradiance to downward irradiance in dependency of solar zenith angle and wavelength. By the influence of the total downward radiance (direct and diffuse), apparent albedo is obviously a function of atmospheric conditions (Liang et al., 1999). This implies that apparent albedo received via remote sensing systems under specific conditions of the atmosphere may not be suitable for an application to other atmospheric conditions. The distribution of the downward flux after passing through the atmosphere is the weighting function for converting spectral albedo to broadband albedo. Apparent albedo is equivalent to the measurands registered by albedometers or pyranometers in the field (Liang, 2000). In absence of an atmosphere inherent albedo would be equivalent to apparent albedo.

To retrieve the broadband albedo from narrowband sensors a method based on radiative transfer simulations has been developed by Liang (2000). The formulae of Liang (2000), presented by Eq. (1) and (2), are used to compute MODIS and TM total shortwave broadband albedo (0.25-2.5 μm) from its spectral albedos. Assuming Lambertian surfaces, surface inherent narrowband albedos are equal to bidirectional spectral surface reflectances received from atmospherically corrected satellite observations.

MODIS:

$$\alpha_{\text{short}} = 0.16\alpha_1 + 0.291\alpha_2 + 0.243\alpha_3 + 0.166\alpha_4 + 0.122\alpha_5 + 0.081\alpha_7 - 0.0015 \quad (1)$$

TM:

$$\alpha_{\text{short}} = 0.356\alpha_1 + 0.13\alpha_3 + 0.373\alpha_4 + 0.085\alpha_5 + 0.072\alpha_7 - 0.0018$$

where α_{short} = total shortwave albedo (0.25-2.25 μm)
 α_i = spectral albedo from spectral band i

Simulated Data

To avoid effects caused by sensor-specific scan geometries, "ideal" data have been simulated from the HyMap dataset. Due to the nearly continuously spectral coverage of the complete VIS/NIR/SWIR-region with narrow bands, the hyperspectral dataset is appropriate to generate both synthetic MODIS and TM data as a weighted combination of HyMap bands. This was achieved by integrating the relevant HyMap bands according to the spectral response function of each MODIS and TM band (Figure 5). Finally, each channel of MODIS and TM was represented as a linear combination of specifically weighted HyMap bands (Figure 2).

Besides the simulation of the spectral characteristics, an additional processing step was necessary to account for the spatial characteristics of both instruments. For this purpose, the Point Spread Function (PSF) of the scanning system was applied. Every image collected by an instrument onboard a satellite or aircraft platform is affected by current atmospheric conditions, blurring caused by the instrument's optics, detectors and electronics and platform motion. These influences lead to an image with low contrasts and loss of details (Kavzoglu, 2004). This degradation can be described by the PSF, which has the approximate shape of a Gaussian function in both scan- and track-direction (Huang et al., 2002; Townshend et al., 2000). To fulfill a realistic spatial simulation of the MODIS and TM data based on HyMap, each band was convolved with the according sensor PSF and afterwards aggregated to the pixel size of MODIS (463m) and TM (30m), respectively. This step was

followed by the calculation of the broadband shortwave albedos from the generated reflectance data. In order to avoid confusion the terms $MODIS_{sim}$ and TM_{sim} will be used in the following to define the data that resulted from the spectral and spatial processing described above.

Real Data

From the MODIS scenes, subsets were defined to cover the relatively small study area. The “MODIS reprojection tool” (MRT) was used to trim the data to the desirable extent and to adapt the geodetic projection systems.

To allow a quantitative comparison of the albedo values received from MODIS and TM, a systematic degradation of the TM data was performed (Justice et al., 1989; Kavzoglu, 2004) using the PSF of MODIS (derived from a series of prelaunch measurements at system level; Barnes et al., 1998).

The normalized PSF of each MODIS band was applied to the corresponding TM band. As a final degradation step, TM data were aggregated to a pixel size of 463m, which corresponds to the MOD09 product. In the following, broadband albedos calculated from MOD09 and the aggregated TM data (TM_{agg}) were compared for all acquisition dates.

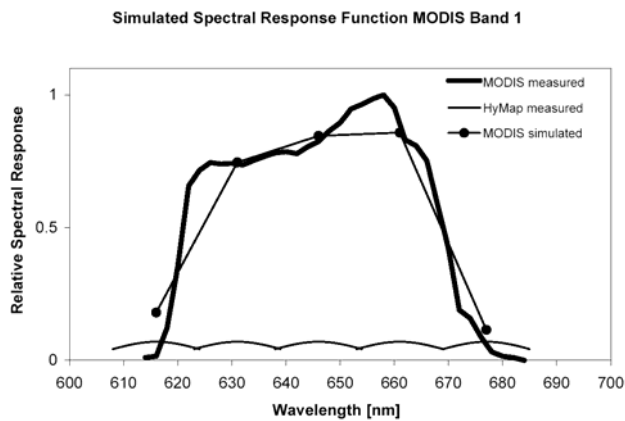


Figure 2. Example of using HyMap data to generate ideal MODIS data: HyMap channels 13 - 17 (Gaussian response functions) were weighted according to the MODIS spectral response function to generate MODIS band 1

4. RESULTS & DISCUSSION

Simulated Data

The comparison of albedos derived from $MODIS_{sim}$ and TM_{sim} showed an almost perfect linear relationship (Figure 3). Values scattered marginally around the 1:1-line at the highest range of values, but in total, deviations from the 1:1-line were negligible. Pearson's r was 0.996, and the root mean squared deviation (RMSD) equalled 0.006 (Figure 3). The conversion formulae have been provided by Liang (2000) to cover a wide range of natural surface types. The almost perfect match between both datasets found here verified these formulae that obviously can be applied consistently for surface characteristics found in the central European study region with a heterogeneous mixture of different cover types in one pixel. This again suggests that a linear mixing principle is valid for heterogeneous (mixed) surface types (Liang et al., 2002). As the results of the applied processing scheme to degrade TM data to broad MODIS-like pixels were consistent, this approach was applied without modification to the real TM data.

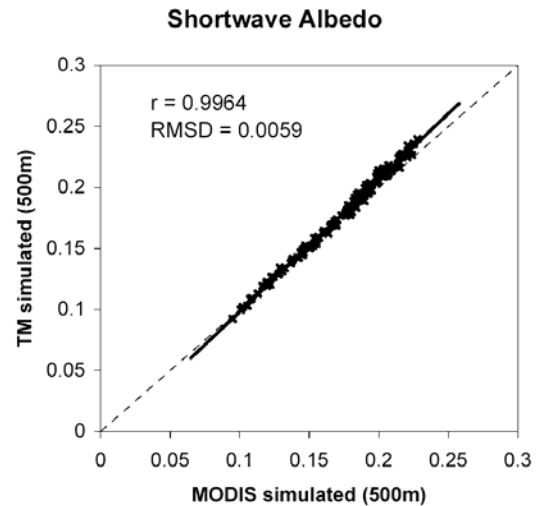


Figure 3. Comparison of shortwave albedo derived from $MODIS_{sim}$ and from TM_{sim} after aggregation

Real Data

For the real data acquired at 28 May 2005, the albedos retrieved from the degraded and aggregated TM data correlated highly with those from the MOD09 product (Pearson's $r = 0.88$) and grouped around the 1:1-line (Figure 4), although viewing geometries differed significantly between both sensors (see Figure 1 for MODIS, TM with near-nadir viewing geometry). Daily albedos (MOD09) were also highly correlated with the 16-day composite, but with an offset of about 0.03 ($MOD09 > MCD43A3$). Different from MOD09 and TM data, MCD43A3 reproduces the 16-day average condition. It also encloses a correction of the surface BRDF effects.

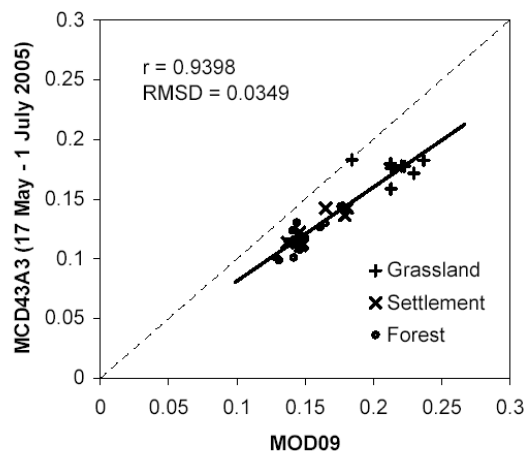
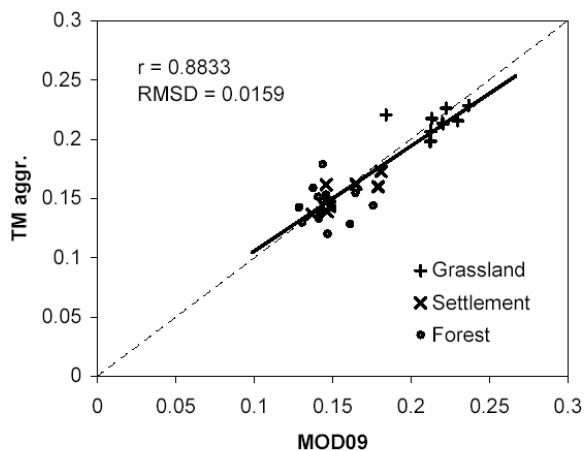
Results were different for 19 July and 4 August 2003. Again, linear relations between albedos from MOD09 and TM_{agg} were found, r equalled 0.94 and 0.86, respectively, but at both dates albedos from TM_{agg} had a clear offset towards MOD09 results ($TM_{agg} > MOD09$). One explanation for these results differing from 2005 might be, that effects from BRDF changed distinctly from July/August to May (mainly due to phenology). As for example coniferous forests with relatively small phenological variations were also included in the analysis, this yields not a full explanation. MOD09 and MCD43A3 showed a very good match at both dates in 2003 with low deviations around the 1:1-line (19 July 2003: $r = 0.9751$; 4 August 2003: $r = 0.9121$). The mismatch between TM albedos and MCD43A3 is not in line with the findings of Liang et al. (2002), who stated a very good agreement of total shortwave albedos retrieved from these data. Nevertheless, Fang et al. (2004) also found some moderate mismatches between albedos obtained from MODIS and Landsat ETM+. For these deviations, uncertainties associated with the atmospheric corrections (water vapor content and aerosol corrections) may provide some explanation (Liang et al., 2002).

5. CONCLUSIONS

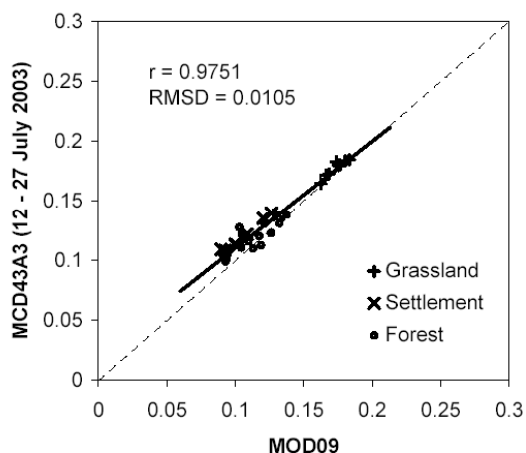
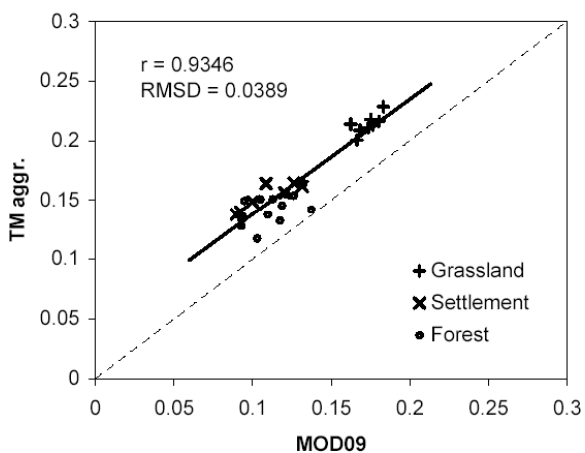
From our findings, the following main two conclusions may be drawn:

- The formulae of Liang (2000) to calculate land surface broadband albedos from TM and MODIS data were successfully applied to specifically degraded HyMap data. Conversion formulae were suitable for mixed surfaces of different land cover types.

Shortwave Albedo 28 May 2005



Shortwave Albedo 19 July 2003



Shortwave Albedo 4 August 2003

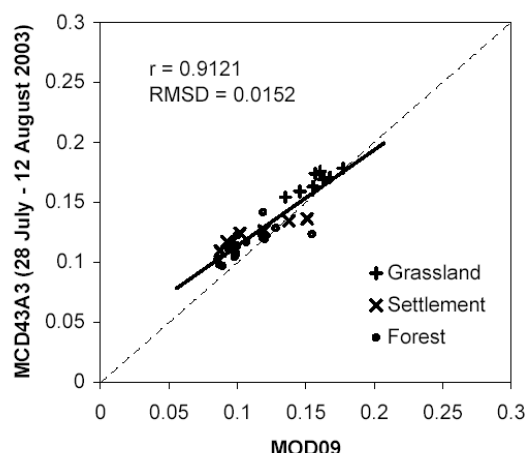
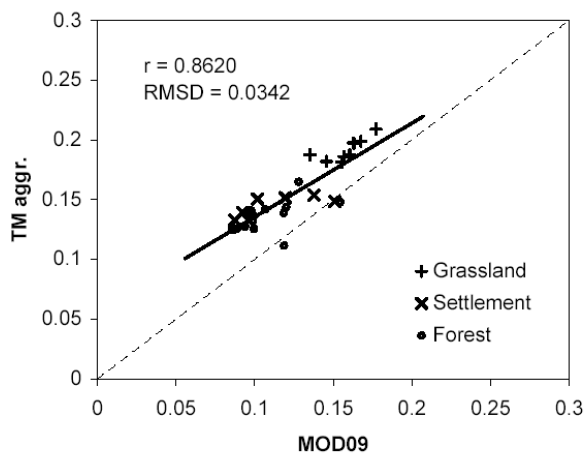


Figure 4 Comparison of albedos calculated from MOD09 with retrievals from smeared and aggregated TM data (left column) and albedos from the MODIS albedo product MCD43A3 (right column)

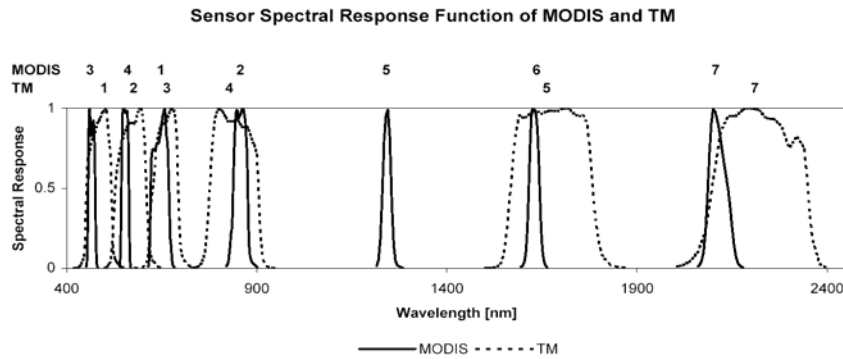


Figure 5. Relative spectral response functions of MODIS and TM

– Albedo retrievals from the different data and products were highly correlated ($0.98 \geq r \geq 0.86$). The reason why data showed (moderate) offsets was not fully understood from the processing schemes associated with the different datasets.

ACKNOWLEDGEMENTS

The authors would like to thank Tim Sanders and Thomas Wagner for their support in HyMap data processing.

REFERENCES

- Barnes, W.L., Pagano, T.S., Salomonson, V.V., 1998. Pre-launch characteristics of the Moderate Resolution Imaging Spectroradiometer (MODIS) on EOS-AM1. *IEEE Transactions on Geoscience and Remote Sensing*, 36(4), pp. 1088-1100.
- Cocks, T., Janssen, R., Stewart, A., Wilson, I. & Shields, T., 1998. The HyMap™ Airborne Hyperspectral Sensor: The System, Calibration and Performance. *1st EARSEL Workshop on Imaging Spectroscopy*, Zurich, pp.37-42.
- Fang, H., Liang, S., Chen, M., Walthall, C., Daughtry, C., 2004. Statistical comparison of MISR, ETM+ and MODIS land surface reflectance and albedo products of the BARC land validation core site, USA. *International Journal of Remote Sensing*, 25(2), 409-422.
- Gao, F., Schaaf, C.B., Strahler, A.H., Roesch, A., Lucht, W., Dickinson, R., 2005. Variability of MODIS Albedo for Major Global Vegetation Types. *Journal of Geophysical Research*, 110(D01104), doi:10.1029/.
- Huang, C., Townshend, J.R.G., Liang, S., Kalluri, S.N.V., DeFries, R.S., 2002. Impact of sensor's point spread function on land cover characterization: assessment and deconvolution. *Remote Sensing of Environment*, 80(2), pp. 203-212
- Justice, C.O., Markham, B.L., Townshend, J.R.G., Kennard, R.L., 1989. Spatial degradation of satellite data. *International Journal of Remote Sensing*, 10(9), pp. 1539-1561.
- Kavzoglu, T., 2004. Simulating Landsat ETM+ imagery using DAIS 7915 hyperspectral scanner data. *International Journal of Remote Sensing*, 25(22), pp. 5049-5067.
- Liang, S., 2000. Narrowband to broadband conversions of land surface albedo – I Algorithms. *Remote Sensing of Environment*, 76(2), pp. 213-238.
- Liang, S., Strahler, A. H., Walthall, C., 1999. Retrieval of Land Surface Albedo from Satellite Observations: A Simulation Study. *Journal of Applied Meteorology*, 38, pp. 712-725.
- Liang, S., Fang, H., Chen, M., Shuey, C. J., Walthall, C., Daughtry C., Morisette, J., Schaaf, C., Strahler, A., 2002. Validating MODIS land surface reflectance and albedo products: methods and preliminary results. *Remote Sensing of Environment*, 83(1-2), pp. 149-162.
- Liu, J., Schaaf, C., Strahler, A., Jiao, Z., Shuai, Y., Zhang, Q., Roman, M., Augustine, J.A., Dutton, E.G., 2009. Validation of Moderate Resolution Imaging Spectroradiometer (MODIS) Albedo retrieval algorithm: Dependence of Albedo on solar zenith angle. *Journal of Geophysical Research - Atmospheres*, 114, D01106.
- Lucht, W., Schaaf, C.B., Strahler, A.H., 2000. An Algorithm for the Retrieval of Albedo from Space using Semiempirical BRDF Models. *IEEE Transactions on Geoscience and Remote Sensing*, 38(2), pp. 977-998.
- Martonchik, J.V., Diner, D.J., Pinty, B., Verstraete, M.M., Myneni, R.B., Knyazikhin, Y., Gordon, H.R., 1998. Determination of land and ocean reflective, radiative, and biophysical properties using multiangle imaging. *IEEE Transactions on Geoscience and Remote Sensing*, 36(4), pp. 1266-1281.
- Schaaf, C.B., Gao, F., Strahler, A.H., Lucht, W., Li, X., Tsang, T., Strugnell, N.C., Zhang, X., Jin, Y., Muller, J.-P., Lewis, P., Barnsley, M., Hobson, P., Disney, M., Roberts, G., Dunderdale, M., Doll, C., d'Entremont, R.P., Hu, B., Liang, S., Privette, J. L., Roy, D., 2002. First operational BRDF, albedo nadir reflectance products from MODIS. *Remote Sensing of Environment*, 83(1-2), pp. 135-148.
- Townshend, J.R.G., Huang, C., Kalluri, S.N.V., Defries, R.S., Liang, S., 2000. Beware of per-pixel characterization of land cover. *International Journal of Remote Sensing*, 21(4), pp. 893-843.
- Vohland, M., Mader, S., Dorigo, W., 2010. Retrieving stand variables of summer barley with PROSPECT + SAIL and different model inversion techniques. *International Journal of Applied Earth Observation and Geoinformation*, 12(2), pp. 71-80.

THE CAPABILITIES OF TERRASAR-X IMAGERY FOR RETRIEVAL OF FOREST PARAMETERS

Roland Perko, Hannes Raggam, Karlheinz Gutjahr and Mathias Schardt

Institute of Digital Image Processing, Joanneum Research, Graz, Austria
{roland.perko,hannes.raggam,karlheinz.gutjahr,mathias.schardt}@joanneum.at

Technical Commission VII Symposium 2010

KEY WORDS: Forestry, Mapping, Photogrammetry, Classification, DEM/DTM, SAR, High resolution.

ABSTRACT:

The TerraSAR-X mission was launched in June 2007 operating a very high resolution X-band SAR sensor. In Spotlight mode images are collected with 0.75m GSD and also at various look angles. The presented paper reports methodologies, algorithms and results emerged from the Austrian research project “Advanced Tools for TerraSAR-X Applications in GMES” with emphasis on retrieval of forest parameters. For deriving forest features like crown closure, vertical stand structure or stand height a digital forest canopy model serves as an important source of information. The procedures to be applied cover advanced stereo-radargrammetric and interferometric data processing, as well as image segmentation and image classification. A core development is the multi-image matching concept for digital surface modelling based on geometrically constrained matching, extending the standard stereo-radargrammetric approach. Validation of surface models generated in this way is made through comparison with LiDAR data, resulting in a standard deviation height error of less than 2 meters over forest. Image classification of forest regions is then based on TerraSAR-X backscatter information (intensity and texture), a 3D canopy height model and interferometric coherence information yielding a classification accuracy above 90%. Such information is then directly utilized to extract forest border lines. Overall, the TerraSAR-X sensor delivers imagery that can be used to automatically retrieve forest parameters on a large scale, being independent of weather conditions which often cause problems for optical sensors due to cloud coverage.

1 INTRODUCTION

TerraSAR-X is the first German satellite out of a public private partnership (PPP) between German Aerospace Center (DLR) and Astrium GmbH and was launched in June 2007. The novel X-band SAR sensor can acquire image products in Spotlight, Stripmap and ScanSAR mode at very high resolutions down to 0.75m (Eineder et al., 2008). One main aspect of the Austrian research project “Advanced Tools for TerraSAR-X Applications in GMES” (AT-X) dealt with the derivation of forest related parameters using TerraSAR-X imagery. The first part consists of precise image matching of such imagery for fully automatic derivation of digital surface models (DSM) which are subsequently used to derive a canopy height models (CHM). The second part concerns image classification with the focus on distinguishing forest from non-forest regions.

2 OUR METHODS

The big picture of our workflow is sketched in Figure 1. As seen, a DSM is extracted using multi-image radargrammetry. This DSM is utilized together with InSAR products and backscatter information to derive a forest classification. Finally, this segmentation helps to correct the height of canopy regions resulting in the final corrected DSM.

2.1 Multi-Image DSM Generation

The accurate 3D reconstruction of timbered regions using TerraSAR-X imagery alone is very challenging due to two reasons. First, the traditional InSAR-based processing does not yield appropriate results over forest as the InSAR phase decorrelates within the 11 days TerraSAR-X repeat cycle (Bamler et al., 2008). Second, even in cases of temporal phase correlation the resulting canopy height is systematically

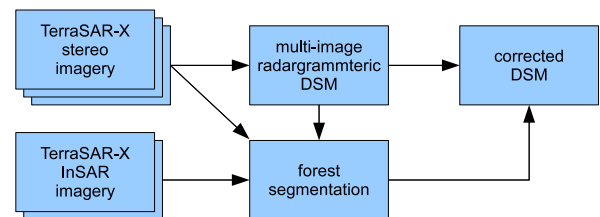


Figure 1: Proposed workflow for deriving forest parameters using TerraSAR-X data.

underestimated. The reason for that is the fact, that the SAR signal in X-band penetrates into the forest canopy changing the InSAR phase center and therefore the reconstructed height. This aspect has been observed on InSAR-based processing of airborne X-band data (Izzawati et al., 2006, Tighe et al., 2009). To tackle all these difficulties we first derive digital surface models using a multi-image stereo-radargrammetric approach. Then, the resulting DSMs are corrected (undoing the canopy height underestimation) by applying an empirically learned correction model on regions of forest.

The radargrammetric processing is described in detail in (Raggam et al., 2010a) and can be applied successfully due to the very exact pointing accuracy of the TerraSAR-X sensor (Bresnahan, 2009, Raggam et al., 2010b). The main steps in the DSM extraction are pairwise stereo matching followed by a joint point intersection procedure. To get robust matching results image triplets are used, i.e. three TerraSAR-X images acquired under different look angles. The main point is, that adjacent images (similar look angles) provide good matching, however unfavorably geometric properties. Therefore, for triplets image 1 can be matched to image 2 and image 2 to image 3. Thus, points from image 1 are transferred to image 3 yielding a large intersection angle and therefore a more robust result. In addition image 1 and image 3 are directly matched resulting in

over-determination in the spatial point intersection.

Stereo matching of a TerraSAR-X image pair is improved by including geometric constraints. First, one image is pseudo epipolar registered based on an affine polynomial transformation using both sensor models. Second, in image matching a starting location for each pixel is predicted, again using sensor models and a coarse DSM (SRTM or ASTER model).

The presented approach yields an areal digital surface model. When subtracting a reference digital terrain model (DTM), e.g. available from airborne laser scanning, a canopy height model (CHM) can be extracted (cf. Figure 2 and Eq. (1)). Such CHMs serve as an important information for the retrieval of forest parameters. As mentioned before, the canopy height underestimation can be quantified using laser scanner ground truth data. Such comparison enables to determine the underestimation factor τ in percent. In regions of forest the TerraSAR-X DSM is then corrected by multiplication with the factor $1/(1 - \tau/100)$. The forest segmentation presented in the next section is then used to correct the canopy height bias (see Figure 1). It should be noted that this problem is not straight forward, as such underlying image segmentation often is just not available.

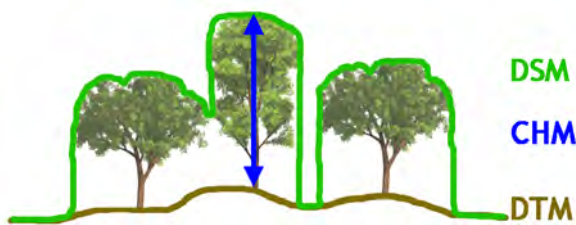


Figure 2: Explanation of relation between digital surface model (DSM), digital terrain model (DTM) and canopy height model (CHM).

$$\text{CHM} = \text{DSM} - \text{DTM} \quad (1)$$

2.2 Forest Segmentation

The proposed forest segmentation should allow separating regions of forest from non-forest areas. Recently, first results on this topic were published in (Breidenbach et al., 2009). They perform the classification on TerraSAR-X backscatter mean and standard deviation statistics alone. We extend their method by including backscatter intensity and texture information, a 3D canopy height model and interferometric coherence information. For classification a supervised approach is chosen by selecting multiple regions together with their ground truth class labels (forest / non-forest) and training a maximum likelihood classifier. This classifier is then applied to the whole spatial extent of given images. The resulting classification is constructed with a GSD of 5 meters. Next, very small areas are rejected based on a region labeling approach.

Texture Description. As observed in (Breidenbach et al., 2009) regions of vegetation are less textured, i.e. more homogenous, than regions of settlements or agricultural areas. (Haaek et al., 2000) suggest to describe this texture information by a variance filter. However, our tests showed that such simple parameter is not working satisfactorily on TerraSAR-X data. Therefore, we choose the Texture-transform (Tavakoli Targhi et al., 2006) which is invariant to illumination, computationally simple and easy to parameterize so that it also performs reasonably on high resolution radar data. This transform can be seen as a spatial frequency analysis, where the key idea is to investigate the singular values of

matrices formed directly from gray values of local image patches (the backscatter information in our case). More specifically, the gray values of a square patch around a pixel are put into a matrix of the same size as the original patch. The texture descriptor is computed as the sum of some singular values of this matrix. The largest singular value encodes the average brightness of the patch and is thus not useful as a texture description. However, the smaller singular values encode high frequency variations characteristics of visual texture. Therefore, the singular values of this matrix are sorted in decreasing order. Then the Texture-transform at each pixel is defined as the sum of the smallest singular values. For the tests several window sizes and singular values ranges were chosen, where a window of size 33×33 and a range of 20 to 33 smallest singular values performed best.

Canopy Height Model. Obviously, vegetation heights are a useful information to segment regions of forest. The canopy height model is extracted employing the methodology described in Section 2.1.

InSAR Coherence. For forest segmentation the interferometric coherence, which is a measure of the interferogram's quality, can be of great value since regions of vegetation suffer from temporal decorrelation (see also the detailed study on interferometric decorrelation (Zebker and Villasenor, 1992)). The standard coherence estimation is based on a local complex cross-correlation and is known to over-estimate the real coherence value. In general, a larger window within cross-correlation provides a better coherence estimate. At the time of radar sensors like ERS the standard procedure was to estimate the coherence over the same window used for multi looking. As the multi looking sizes become smaller for TerraSAR-X imagery the coherence was highly over-estimated resulting in a noisy coherence image. Therefore, a decoupling of the window size of multi looking and cross-correlation is introduced. The resulting coherence estimate uses a correlation window of 10×10 pixel and a multi looking window of 2×3 pixel (azimuth \times range). Regions of very low coherence correspond mainly to vegetation (forests and agricultural areas). Thus, such coherence information is used in the classification process as one feature.

3 TEST DATA

Within the AT-X project the proposed algorithms have been applied to several test sites. For the presented study only a single test site called "Burgau" is chosen to keep the results clearly arranged. The test site of interest spans an area of $12 \times 12 \text{ km}^2$ in Austria. This rural test area covers agricultural as well as forest areas and shows flat to slightly hilly terrain, the ellipsoidal heights ranging from 270 to 445 meters above sea level (cf. Figure 3). The forested regions in the area mainly consists of dense stands of deciduous trees.

Multi-Image DSM Generation. For multi-image DSM derivation the test data consist of multiple TerraSAR-X multi-look ground range detected (MGD) Spotlight products from ascending, respectively descending, orbit. All images were ordered as single-polarization products (HH) with science orbit accuracy and were acquired in the period of July and August 2009. Table 1 reports the major parameters of the "Burgau" test site. It should be noted that the images acquired at steep look angles (i.e. MGD_asc1 and MGD_desc1) have a lower GSD than all other products.



Figure 3: Overview of the test site “Burgau”. This topographic map shows regions of forest in green color.

Name	Look angle	GSD	Date
MGD_asc1	22.3°	1.25m	2009-07-28
MGD_asc2	37.2°	0.75m	2009-08-02
MGD_asc3	48.5°	0.75m	2009-08-07
MGD_dsc1	21.3°	1.25m	2009-07-30
MGD_dsc2	36.5°	0.75m	2009-08-05
MGD_dsc3	48.0°	0.75m	2009-07-31

Table 1: Detailed parameters for the Spotlight images.

Forest Segmentation. The InSAR coherence used in the segmentation process is derived from a TerraSAR-X single look complex (SSC) InSAR pair (see Table 2). These images were ordered as dual-polarization products (HH,VV) with science orbit accuracy and were acquired in March 2008.

Name	Look angle	Date
SSC_dsc1	36.0°	2008-03-17
SSC_dsc2	36.0°	2008-03-28

Table 2: Detailed parameters for the Spotlight InSAR pair.

Reference Data. To enable quantitative evaluations LiDAR data is used as ground truth information. The LiDAR reference data covers four measurements per square meter, which are processed to highly accurate DSMs and DTMs. While the DSMs are automatically extracted, the DTMs are semi-automatically generated by classifying regions of vegetation, building, bridges and other man-made structures.

To evaluate the DSMs derived using TerraSAR-X multi-image radargrammetry, 30 regions on bare ground and 70 regions in forest are selected. The average residual height error over such regions describes the DSM quality. Over forest, the average canopy height underestimation τ is extracted and used to correct the canopy height.

To evaluate the image segmentation quality a ground truth reference mask is derived using LiDAR data. The 1m GSD LiDAR CHM is filtered with an order-statistic filter of size 7×7 and order 37, i.e. the 75th percentile. The CHM is then down sampled to a GSD of 5m using a 5×5 average resampling. Next, pixels with a height larger than 8 meters are considered as forest regions and small regions are filled to eliminate noise.

4 RESULTS AND DISCUSSION

Multi-Image DSM Generation. For visual interpretation some detailed results are shown in Figure 4. All results are given with a GSD of 2 meters in UTM33 projection. Figure 4(a) shows the TerraSAR-X DSM, (b) the LiDAR reference DTM, (c) the TerraSAR-X and LiDAR based CHM, (d) the pure LiDAR CHM, (e) the TerraSAR-X based height error (i.e. the ground truth LiDAR DSM subtracted from the TerraSAR-X derived DSM) and (f) a topographic map. The TerraSAR-X CHM corresponds visually very well to the LiDAR CHM and to the topographic map, however the TerraSAR-X DSM is too low over forest, as seen in Figure 4(e). Regions of bluish color indicate height underestimations and such regions are placed in forests or on forest borders. The quantitative accuracy analysis is listed in Table 3. Heights over bare ground are reconstructed with very high accuracy (mean value below 20 cm and standard deviation of about 2 meters). The canopy height however is systematically underestimated by approximately 27.5% for this test site. In our previous work we estimated an average underestimation using Spotlight and Stripmap imagery and multiple scenes which was $26.6\% \pm 1.4\%$ (Perko et al., 2010). When correcting the height bias with this learned value the reconstruction over forest becomes a lot better. In particular it decreases to a residual height error of 20 cm, like on bare ground (see Table 3 bottom). Figure 5 and Figure 6 show detailed analyses of the canopy height underestimation w.r.t. the canopy height before and after the discussed correction, clarifying that the underestimation over forest can be corrected for this test site.

	bare ground		forest			
	μ [m]	σ [m]	μ [m]	σ [m]	τ [%]	
asc	0.07	2.04	-5.81	1.87	28.5	
dsc	0.18	1.90	-5.45	1.83	26.4	
			forest after height correction			
			asc	0.22	1.87	-1.16
			dsc	0.08	1.83	-0.42

Table 3: Detailed 3D height analysis of the TerraSAR-X derived DSMs.

Forest Segmentation. The features used for forest segmentation are shown in Figure 7. Obviously, the most important information for the segmentation are the InSAR coherence and the canopy height model. The confusion matrix in Table 4 reveals that 90% of pixels (here one pixel has a GSD of 5 meters) are correctly classified. About 8% of non-forest regions are classified incorrectly as forest. This especially happens in small forest clearances which are not seen due to the slant range SAR geometry or which result from image matching failures. The 2% of pixels classified wrongly as non-forest are mainly small forest stands where image matching is unsuccessful and thus such regions get interpolated. In addition it should be noted that this evaluation is relative to the LiDAR ground truth segmentation. Therefore, the achieved accuracy is most likely above the 90% since some artifacts exist in the LiDAR model. For instance some power supply lines are classified as forest. In comparison to the state-of-the-art classification of TerraSAR-X data in (Breidenbach et al., 2009) the proposed method performs very well. On first glance their method also reaches a classification accuracy of 90%. However, the evaluation is based on image blocks with $20 \times 20 m^2$. When reducing the GSD to 5 meters, like in our study, the classification accuracy of (Breidenbach et al., 2009) drops to 72.5%. Obviously, our method performs better as a diversity of information like canopy height model, coherence or texture descriptors is incorporated into the classification process.

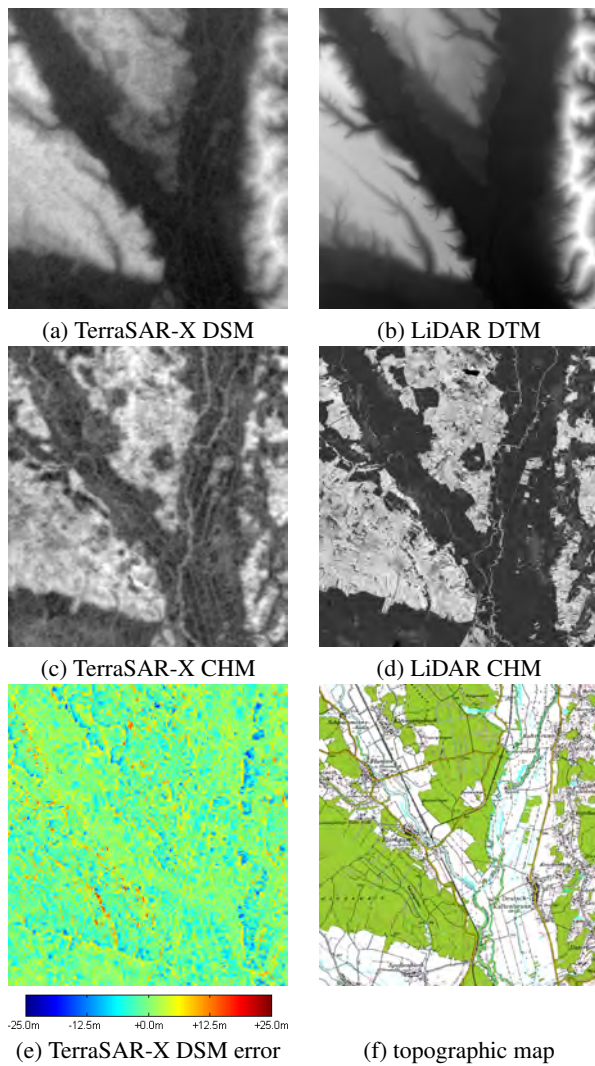


Figure 4: Exemplary results of DSM and CHM extraction. The TerraSAR-X DSM (a), LiDAR reference DTM (b), TerraSAR-X CHM (c), LiDAR CHM (d), color coded TerraSAR-X height error (e), and a topographic map for visual comparison (f). A subset of $7.1 \times 7.6 \text{ km}^2$ is shown.

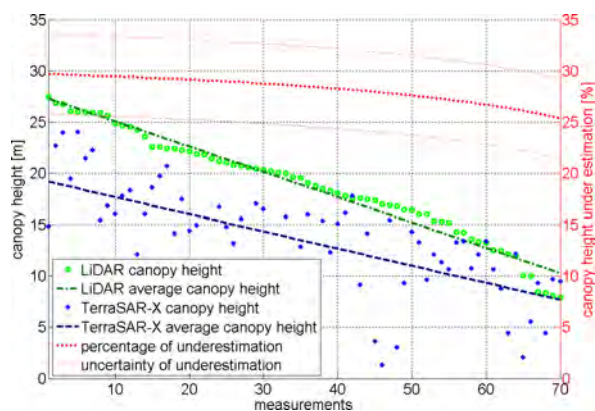


Figure 5: Canopy height underestimation for the ascending triplet before the proposed height correction.

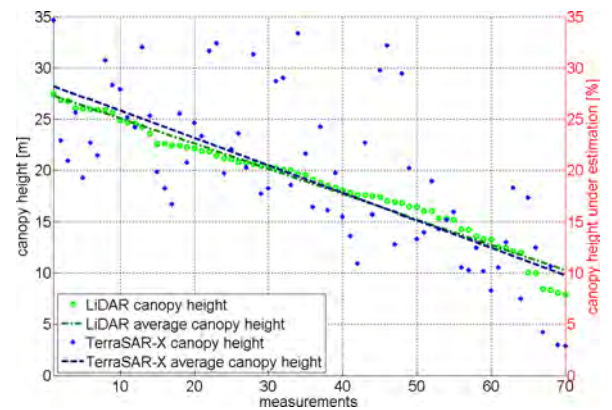


Figure 6: Canopy height underestimation for the ascending triplet after the proposed height correction.

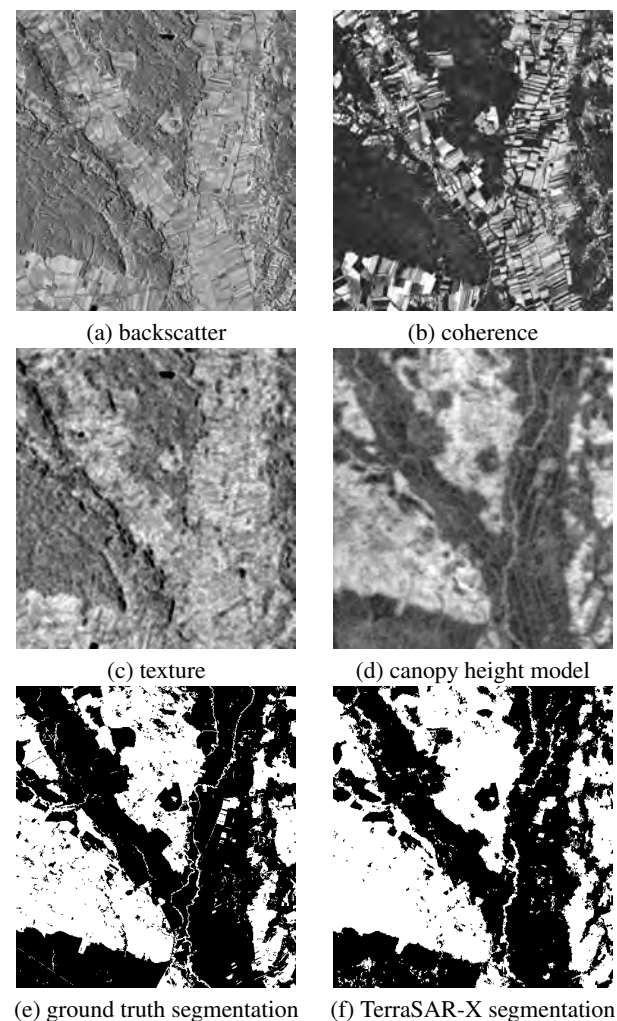


Figure 7: Exemplary input data used for image segmentation (a-d), ground truth segmentation based on laser scanner vegetation height model (e) and TerraSAR-X based segmentation (f).

correct: 90.37%		ground truth	
		forest	non-forest
estimation	forest	40.01%	7.68%
	non-forest	1.96%	50.36%

Table 4: Confusion matrix of forest segmentation.

Forest Border Lines. Finally, forest border lines can directly be extracted from the segmentation result via edge detection. Figure 8 shows some examples. Overall, the quality of extracted forest border lines is higher for huge dense forests than for small isolated stands (this aspect was also observed in (Breidenbach et al., 2009)), where small stands are often not detected at all. Nevertheless, forest border lines are in general very well extracted and their accuracy is directly dependent on the forest segmentation.

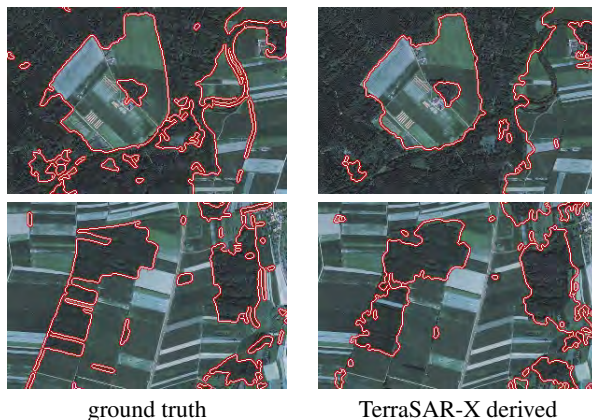


Figure 8: Detailed views on forest border line extraction for two subsets. On the left ground truth border lines are given and on the right the automatically extracted borders using TerraSAR-X alone.

5 CONCLUSIONS AND FUTURE WORK

TerraSAR-X imagery enables the retrieval of certain forest parameters. In particular, multiple TerraSAR-X images representing the same area on ground under different look angles can be used to fully automatically derive accurate DSMs. In case when reference DTMs are available the canopy height model can be extracted. Such forest canopy height is an important parameter as it is strongly correlated with forest parameters, such as forest biomass, timber volume or carbon stocks. Furthermore, it serves as an important cue for classification of forest types and condition, forest morphology, crown closure, vertical structure and stands height (Hyypä et al., 2000). The presented study revealed that the height of the canopy is systematically underestimated as the SAR signal in X-band penetrates into the canopy. Therefore, a forest segmentation is proposed yielding an accuracy of 90%. This segmentation result is subsequently applied to correct the canopy height bias in regions of forest. Incorporating this approach, the TerraSAR-X DSMs have an average height accuracy of 20 cm and a standard deviation of about 2 meters on bare ground and over forest.

However, the canopy underestimation depends on various aspects, including tree species, forest stand density, tree height and look angles. The forest used in the presented study consists more or less exclusively of dense stands of deciduous trees. It is therefore expected that the canopy underestimation

will be larger for coniferous trees and for clearer stands.

Future work should focus on a comparison to TanDEM-X DSMs comprising multiple InSAR pairs with different look angles to further understand the penetration into the canopy of X-band signals.

REFERENCES

- Bamler, R., Adam, N., Hinz, S. and Eineder, M., 2008. SAR-Interferometrie für geodätische Anwendungen. *Allgemeine Vermessungs-Nachrichten* pp. 243–252.
- Breidenbach, J., Oritz, S. and Reich, M., 2009. Forest monitoring with TerraSAR-X: first results. *European Journal of Forest Research*.
- Bresnahan, P. C., 2009. Absolute geolocation accuracy evaluation of TerraSAR-X-1 spotlight and stripmap imagery - study results. In: *Civil Commercial Imagery Evaluation Workshop*.
- Eineder, M., Fritz, T., Mittermayer, J., Roth, A., Boerner, E. and Breit, H., 2008. TerraSAR ground segment - basic product specification document, doc. tx-gs-dd-3302, issue 1.5, 103 pages. Technical report, DLR, Cluster Applied Remote Sensing.
- Haack, B., Herold, N. and Bechdol, M., 2000. Radar and optical data integration for land-use/land-cover mapping. *Photogrammetric Engineering and Remote Sensing* 66(6), pp. 709–716.
- Hyypä, J., Hyypä, H., Inkinen, M., Engdahl, M., Linko, S. and Zhu, Y.-H., 2000. Accuracy comparison of various remote sensing data sources in the retrieval of forest stand attributes. *Forest Ecology and Management* 128(1), pp. 109–120.
- Izzawati, Wallington, E. and Woodhouse, I., 2006. Forest height retrieval from commercial X-band SAR products. *IEEE Transactions on Geoscience and Remote Sensing* 44(4), pp. 863–870.
- Perko, R., Raggam, H., Gutjahr, K. and Schardt, M., 2010. Analysis of 3D forest canopy height models resulting from stereo-radargrammetric processing of TerraSAR-X images. In: *EARSeL Symposium, Paris, France*.
- Raggam, H., Gutjahr, K., Perko, R. and Schardt, M., 2010a. Assessment of the stereo-radargrammetric mapping potential of TerraSAR-X multibeam spotlight data. *IEEE Transactions on Geoscience and Remote Sensing* 48(2), pp. 971–977.
- Raggam, H., Perko, R., Gutjahr, K., Kiefl, N., Koppe, W. and Hennig, S., 2010b. Accuracy assessment of 3D point retrieval from TerraSAR-X data sets. In: *European Conference on Synthetic Aperture Radar, Aachen, Germany*.
- Tavakoli Targhi, A., Björkman, M., Hayman, E. and Eklundh, J.-O., 2006. Real-time texture detection using the LU-transform. In: *Workshop on Computation Intensive Methods for Computer Vision, in conjunction with ECCV*.
- Tighe, M., Balzter, H. and McNairn, H., 2009. Comparison of X/C-HH InSAR and L-PolInSAR for canopy height estimation in a lodgepole pine forest. In: *Proceedings of 4th International Workshop on Science and Applications of SAR Polarimetry and Polarimetric Interferometry*.
- Zebker, H. A. and Villasenor, J., 1992. Decorrelation in interferometric radar echoes. *IEEE Transactions on Geoscience and Remote Sensing* 30(5), pp. 950–959.

ROAD EXTRACTION FROM ALOS IMAGES USING MATHEMATICAL MORPHOLOGY

F. S. P. de Castro ^{a, b *}, J. A. S. Centeno ^b

^a IBGE, Brazilian Institute of Geography and Statistics, Porto Alegre R.G. do Sul, Brazil, - fabiana.piresc@gmail.com

^b UFPR, Department of Geomatic, Curitiba Paraná, Brazil - (centeno)@ufpr.br

Commission VII

KEY WORDS: Extraction, Identification, Programming, Image, Satellite, Mathematics, Method

ABSTRACT:

Over the past few years have seen the need to use remote sensing data to accomplish the complex task of automatic extraction of features. Among the sensor systems currently used for mapping can be highlighted the recent launches of new orbital satellites, for example, the Advanced Land Observing Satellite (ALOS). The problems currently involved in the extraction of features like road presents the following issues: The roads may be partially hidden and stretches of road may not be recorded due to limitations of the sensors. Given the need for analysis of the potential of ALOS images, development of methodologies for roads extraction, and the study of problems involved in the process, the aim of this paper is the roads extraction with ALOS images through the use of mathematical morphology. At first step, an initial selection of stretches of road is done using algorithms of mathematical morphology and segmentation. At this stage, most of other classes, such as vegetation were eliminated. However, at this moment the road had not complete obtained, performing inconsistently. This happens due to the spectral similarity between some sections of the road and vegetation present in the scene. Thus, to segment the image in order to eliminate the vegetation, parts of the road were also eliminated. In a second step, within the MATLAB environment, were developed a routine to complement the road obtained after the application of morphological operators. This routine used other techniques of mathematical morphology, and the Euclidean distance for complementation. At the end of the process, the road was complete, resulting in a road consistently. Further tests must still be performed, since the methods and techniques used to extract features modify by the area of study and the type of image being used.

1. INTRODUCTION

Given the continental dimensions of Brazil, a trend to research for a solution to the problem of outdated mapping in the country is the use of remote sensing data to accomplish the task of automatic extraction of features. According to Dal Poz et al. (2007), the problem of features extraction have been of fundamental importance for more than two decades at the automation of processes that extract cartographic features such as buildings, rivers, roads, etc. However, the developed solutions always depend on the type of sensor used to generate the images.

New images are being made available with the recent launches of new orbital satellites, such as the Advanced Land Observing Satellite (ALOS). According to the Brazilian Institute of Geography and Statistics (IBGE, 2007), the ALOS images are intended mainly to serve the scientific community and the non-commercial User, thus practicing a policy of cost where the images will have an affordable price. This cost policy is to make possible the mapping of a large country like Brazil.

The roads are features on maps which can be highlighted for its dynamism due to changes in their shape or texture, type - pavement or not pavement - and / or inclusion of new roads or road sections in the system. These changes are constant due the result of transformation resulting from the socio-economic growth. Soon, the roads are cartographic features that require constant updating.

The problems currently involved in the features extraction like road presents the following issues: first, the roads may be partially hidden; second, some stretches of road may not be registered due to limitations of the orbital images and third, the radiometric resolution of the selected road. The first issue is due to clouds that may be present in the images and shadows of structures such as buildings, bridges and cars as well as vegetation can hide parts of the road feature. The second question is a function of spatial resolution of the orbital images used for extraction. The third question refers to the radiometric similarity between different features, for example roads without pavement may present a feature similar to exposed soil. According Cleynebreugel et al. (1990), one of the problems of roads extraction from satellite images is the spatial resolution of the image. This may involve many details of the roads were not visible in the images, so cannot be used for extraction.

Solutions to the problem of roads extraction have been studying in different ways. The way to approach the issue has been modifying according to new sensors developing. Nowadays high spatial resolution images and laser scanner data are used. The difference between the proposals for roads extraction due to the strategy used, for example: type and resolution of the images are being used, configuration of the experiments, methods of preparation and general assumptions (Wang et al., 2005).

Some solutions for roads extraction are described in the literature, as in Baumgartner et al. (1999) that used the same aerial image with different resolutions for an automatic road extraction based on multi-scale, grouping, and context. Wiedemann and Wessel (2003) extract roads from synthetic

* Corresponding author. This is useful to know for communication with the appropriate person in cases with more than one author.

aperture radar (SAR) imagery. Clode et al. (2004), who used data only laser scanner for automated extraction of roads. Maillard and Cavaye (1989) developed methodologies for the extraction of roads using only the multispectral images. Zhang and Murai (1999); Mohammadzadeh et. al. (2004) introduces an extraction based on mathematical morphology. Among the existing solutions can highlight the use of Mathematical Morphology, which includes the study of topological and structural properties of objects from their images. (Gonzales; Woods, 2000).

Given the need for an analysis of the potential of ALOS images, development of methodologies for the roads extraction and the study of problems involved in the process, this paper present a method to road extraction with ALOS images through the use of mathematical morphology. The paper have the following specific objectives: Analyze the potential of use ALOS images for the roads extraction and evaluate the use of mathematical morphology in this case.

2. THE ALOS SATELLITE

The ALOS is a Japanese satellite that was launched by the Japanese Space Agency (JAXA) on January 24, 2006, becoming operational on October 20, 2006. This was launched by the rocket H-IIA from Tanegashima Space Center, Japan. His original name in Japanese language is "DAICHI.

The ALOS satellite carries onboard 3 sensors:

AVNIR-2: Advanced Visible and Near Infrared Radiometer - type 2;

PRISM: Panchromatic Remote-sensing Instrument for Stereo Mapping;

PALSAR: Phased Array L-band Synthetic Aperture Radar.

In this work it is worth highlighting the AVNIR-2 and PRISM. The AVNIR-2 is an optical sensor with 4 spectral bands, 3 bands of the visible and 1 near infrared band with a spatial resolution of 10 meters. The PRISM sensor operates in the visible light, with a panchromatic band and spatial resolution of 2.5 m. This is a set of 3 independent imaging telescopes that allow scenes nadir, leaning forward and leaning back. This system makes possible the acquisition of stereoscopic images along the path.

3. MATHEMATICAL MORPHOLOGY

The mathematical morphology has been widely used in digital image processing and focuses on the area that studies the geometric properties of objects in the images. This allows the extraction of image components that are useful in the representation and description of the shape of a region, such as borders and skeletons (Gonzales; Woods, 2000). The extraction of elements present in an image is accomplished with the help of a suitable structural element. The structural elements are matrices responsible for the removal or addition of labeled pixels in the image, which depend on their size and shape, usually defined by the User, according to the area to be applied.

In this paper the mathematical morphology adopted is binary, thus only binary morphological operators were used. The basic operations of morphology are erosion and dilation, at the first the pixels that do not conform to a given pattern are deleted

from the image and at the second a small area related to a pixel is changed to a given pattern. These operations are the basis for most of the operations used in mathematical morphology, in other words, they are combinations of these such as opening, closing, skeletonization, among others.

The dilation is a morphological operation that combines two sets using the vector addition of elements of sets. Its symbol is \oplus , the result as the name suggests is a dilated image, like this the effect of the dilation on an image is the growth or expansion of the object. These objects refer to the pixels whose gray level is greater than zero in relation with the background. The dilation can also be understood as the union of translations of A by elements of B. The Dilation of a set A by B denoted by $A \oplus B$, is given as:

$$A \oplus B = \{x \mid (B) x \cap A \neq \emptyset\} \quad (1)$$

where A represents the image being operated on and B is called structuring element and its composition defines the dilation, so the dilation expands an image.

Therefore, the dilation of A by B is the set of all x displacements such that \hat{B} and A overlap in at least one nonzero element.

Unlike the dilation, the erosion reduces the object present in the image against the background. It is a morphological operation that combines two sets using vector subtraction of elements of sets, its symbol is \ominus . The erosion of A by the structuring element B, denoted by $A \ominus B$, is given as

$$A \ominus B = \{x \mid (B) x \subseteq A\} \quad (2)$$

The erosion of A by B is the set of all points x such that B, when translated by x, be contained in A.

The result of successive erosions and dilations allow the elimination of specific details of the image, smaller than the structuring element without distortion of the features not deleted. The effect of re-application is no longer to modify the previously transformed result.

The opening operator is used to remove parts of objects or even objects smaller than the structuring element. Thus, the opening operator can eliminate noise due to the erosion operator that is applied initially. The opening of a set A by B, denoted by $A \circ B$ is given by equation 3.

$$A \circ B = (A \ominus B) \oplus B \quad (3)$$

where A represents the image being operated on and B is called structuring element.

The closing operator tends to join "islands" which the distance between them is less than the structuring element and closing holes smaller than this element. Being the same set A and a structuring element B, the closing of A by B, denoted by $A \bullet B$, is given by equation 4.

$$A \bullet B = (A \oplus B) \ominus B \quad (4)$$

Soon, these operated jointly applied enable the formation of the most compact and at the same time, eliminate regions very small or thin.

4. DEVELOPMENT

Inputs such as images, digital topographic mapping and software are needed to perform the work. The materials used and the methodology are presented as follows.

4.1 Materials

The ALOS images and the topographical mapping comprising the study area are shown in Figure 01. This area lies at Paraná (Brazil) state, specifically in the municipality district of Guaraqueçaba, Brazil, near the coastline.

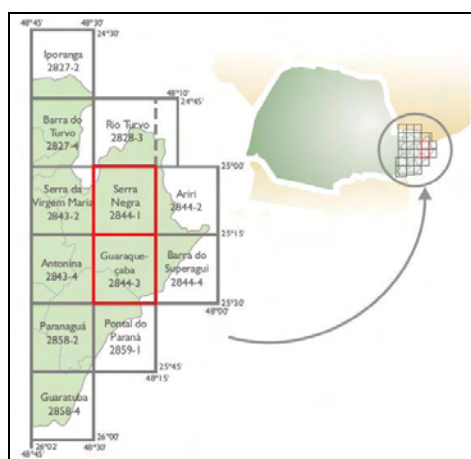


Figure 01: Area of study

The area is bounded between the coordinates UTM:

- Upper left:
Latitude $-25^{\circ} 11' 25.95''$
Longitude $-48^{\circ} 22' 00.20''$
- Bottom right:
Latitude: $-25^{\circ} 17' 05.17''$
Longitude $-48^{\circ} 14' 37.92''$

The ALOS images were acquired through the research program of the Brazilian Institute of Geography and Statistics (IBGE), which is responsible for distributing the ALOS images for federal government agencies, research institutions and other non-commercial users in Brazil. The software used is the ENVI 4.5 and MATLAB R2007b. The ENVI 4.5 allows the manipulation of ALOS images as well as the topographic mapping; the MATLAB is used for the development of routines that take the mathematical morphology.

4.2 Methodology

The roads extracted were not pavement and belonging to PR – 405. To obtain the field reality, topographic maps at 1:25.000 scales were used to identify the roads on the scene. From the step 01 to step 03, the processing was performed in the software ENVI 4.5.

STEP 01 - REGISTRATION: The registration is required for the integration of images acquired by different sensors, for example the AVNIR-2 and PRISM, integration of images

obtained at different times, among other applications. For its implementation is necessary to choose control points. After collection of control points, which must be distributed across the entire image, is needed to define the interpolation process. In this work the bilinear interpolation method was chosen.

STEP 02 - FUSION: The images available are of different sensors, in this case AVNIR-2 and PRISM and with different spatial resolution, 10 meters and 2.5 meters respectively. Thus, for the analysis of mixed spatial databases, which may consist of images from different sensors with different spatial resolutions, it is necessary to perform the fusion process. Fusion was performed by principal components. After obtaining the principal components, the first component is removed and placed in the panchromatic image, in this case the PRISM image. After PRISM assume to be the first principal component is necessary to reverse transformation to return the multispectral bands.

STEP 03 - CLASSIFICATION: This step is performed the classification of the image obtained in the fusion process. The method used was the supervised classification, where the classes of information are pre-defined, and from its definition are acquired samples of each class. To perform the classification, classifiers are needed. The classifier used was the statistical Maximum Likelihood - ML. The classified image is used for verification of stretches of roads which are not possible to identify with the PRISM image.

From the step 04, all processes have been developed in MATLAB.

STEP 04 - EXTRACTION: An initial selection of stretches of road is done using algorithms of mathematical morphology and segmentation. For this process has generated a routine for the PRISM image binarization. Armed with binary image the morphological operators were applied to it. Operators of closing, erosion were applied. Several tests using different structuring elements were performed to find the best solution for the image used. At this stage, most other classes, such as vegetation, are eliminated. To eliminate other unwanted traces of features the connected components of the image were calculated and the smallest areas excluded. The product of this post-processing was a cleaner image of traces of unwanted features. However, at this moment the road obtained has not complete linear features, performing inconsistently.

STEP 05 - FILLING: Was developed a routine to complement the road obtained in extraction (step 04). This routine used other techniques of mathematical morphology and an algorithm for calculating the Euclidean distance. From a User-defined threshold, based on the calculated Euclidean distance, the road extracted was completed. At the end the images (PRISM binary code, classified, filled) were overlaid to verify the areas filled by the algorithm.

5. RESULTS

The methodology has been applied and the results were as follows. Initially the PRISM image panchromatic was binary code in MATLAB and the road cut into two parts. For this result was used a threshold equal to 90. This threshold is defined as object to be extracted in the image. After the application of morphological operators like dilation, was not

possible to recover parts of roads that have been eliminated. The results are shown in figures 02 and 03.

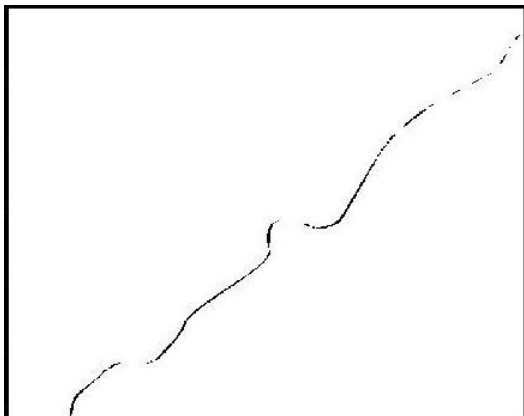


Figure 02: Road segmented – stretch 01

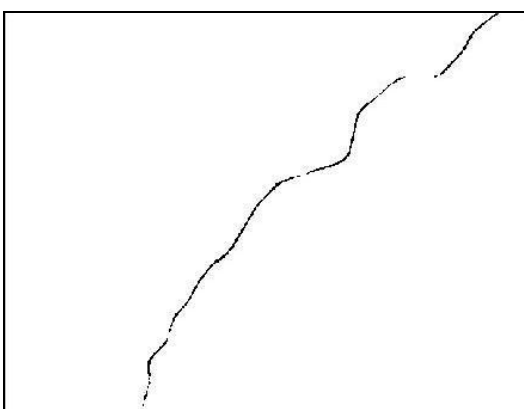


Figure 03: Road segmented – stretch 02

This is due to the spectral similarity between some parts of the road and vegetation present in the scene. Thus, to segment the image in order to eliminate the vegetation, parts of the road were also eliminated.

Thus, the road must be completed. The process of filling by calculating the Euclidean distance can be seen in Figure 04 e 05. It is observed that the areas highlighted in both figures have not been the appropriate completion.

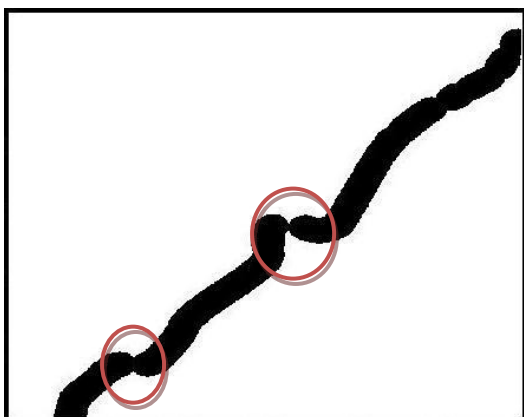


Figure 04: Euclidian distance – stretch 01

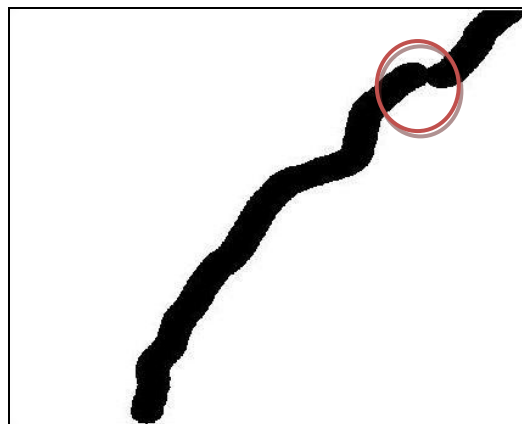


Figure 05: Euclidian distance – stretch 02

This fact is due both to the curvature of the road, and the amount of road lost in the segmentation process. The morphological closing operator was applied to correct such failures. The Figure 06 and 07 present the results. The same areas were highlighted in both figures to verify the result.

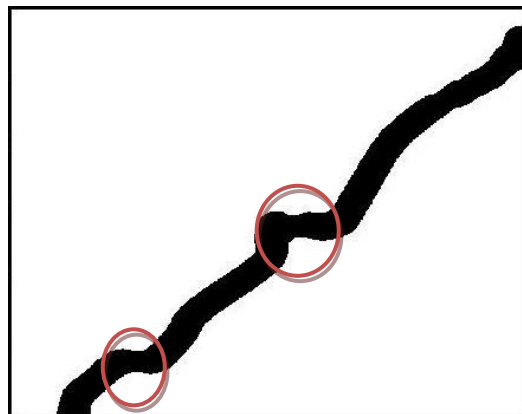


Figure 06: Closing – stretch 01

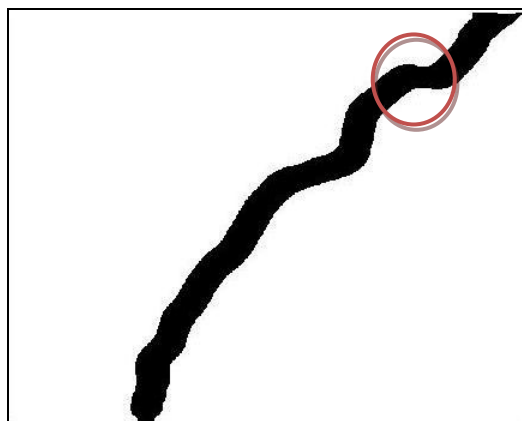


Figure 07: Closing – stretch 02

After applying the closing operator, was possible to define the linear feature complete, in this case the complete road. However, the road was still showing a dilated form, requiring the operator's application of erosion operator to obtain a road consistently. The result can be seen in Figures 08 and 09.

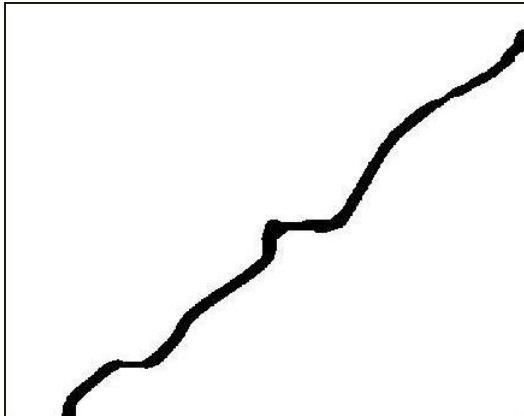


Figure 08: Erosion – stretch 01

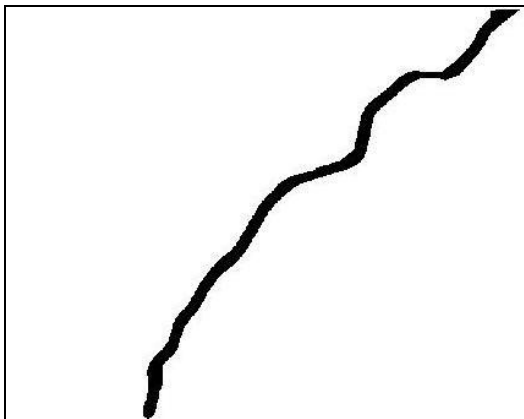


Figure 09: Erosion - stretch 02

At the end of the process the roads were overlaid with the classified image in order to check the area filled by the algorithm.



Figure 10: Overlay – stretch 01

6. CONCLUSIONS

The roads extracted still need to be refinement, because the edges have not yet obtained homogeneity along the stretch. Further tests must still be performed, since the methods and techniques used to extract features vary by area of study and type of image being used. The results are satisfactory as it was possible to fill the roads with the use of mathematical

morphology and the result is close to the classification made. The extraction using mathematical morphology showed good performance, and only need the panchromatic band for its realization.

6.1 References

Baumgartner, A., Steger, C., Mayer, H., Eckstein, W. and Ebner, H., 1999. *Automatic Road Extraction Based on Multi-Scale, Grouping, and Context*. Photogrammetric Engineering and Remote Sensing, v. 65(7), p. 777–785.

Cleynenbreugel, J. et. al. *Delineating Road Structures on Satellite Imagery by a GIS-Guided Technique*. IAPRS - International Archives of Photogrammetry and Remote Sensing, v. 56(6), p. 893 – 898. 1990.

Clode, S.; Kootsookos, P; Rottensteiner, F. *The automatic extraction of roads from LIDAR data*. IAPRS - International Archives of the Photogrammetry, Remote Sensing and Spatial Information Sciences, Istanbul, v. 35, p. 231 – 237. 2004.

Dal Poz, et. al. *Extração automática de feições rodoviárias em imagens digitais*. Revista Controle e Automação. v. 18, n. 01, jan./fev./mar. 2007.

Gonzales, R. C., Woods, R. E. *Processamento de imagens digitais*. Traduzido. Editora Edgard Blücher Ltda. 2000. 509p.

Instituto Brasileiro de Geografia e Estatística (IBGE). *IBGE como sub-nó de distribuição de imagens do satélite ALOS*. Rio de Janeiro, 2007. No prelo.

Maillard, P.; Cavayas, F. *Automatic map-guided extraction of roads from SPOT imagery for cartographic database updating*. IAPRS - International Archives of Photogrammetry and Remote Sensing, v. 10, p. 1775-1787. 1989.

Mohammadzadeh, A.; Tavakoli, A.; Zoj, M. *Automatic linear feature extraction of Iranian roads from high resolution multi-spectral satellite imagery*. IAPRS - International Archives of the Photogrammetry, Remote Sensing and Spatial Information Sciences, v. 35, p. 764- 767. 2004.

Wang, L.; Qin, Q.; Du, S.; Chen, D.; Tao, J. *Road Extraction from Remote Sensing Image Based on Multi-resolution Analysis*. In: International Symposium on Remote Sensing of Environment (ISRSE) – Global Monitoring for Sustainability and Security, 31st, 2005, Saint Petersburg. Proceedings... Saint Petersburg: ISRSE, 2005.

Wessel, B.; Wiedemann, C. *Analysis of automatic road extraction results from airborne SAR imagery*. IAPRS - International Archives of Photogrammetry and Remote Sensing, Munich, v. 34(3), 2003.

Zhang C.; Murai, S.; Baltasvias, E. *Road Network Detection by Mathematical Morphology*. IAPRS - International Archives of Photogrammetry and Remote Sensing, Paris, p. 185-200, 1999.

6.2 Acknowledgements

The digital topographic maps used for the rectification of ALOS images and reality in the field, were kindly provided by the Management of the Army Geographic Service (DSG), with 1^o Survey Division responsible for the region covering the study area.

INFERRING FLUCTUATIONS OF THE AQUIFER BY MONITORING THE AREA OF SMALL LAKES IN A BRAZILIAN SAVANNA REGION USING A TEMPORAL SEQUENCE OF 50 LANDSAT IMAGES

Carlos H. Pires-Luiz and Philippe Maillard

IGC, Department of Geography
Universidade Federal de Minas Gerais
31270-901, Belo Horizonte, Brazil
carloshpl@ig.com.br, philippe@cart.igc.ufmg.br

KEY WORDS: Multi-temporal, Water index, Water level monitoring, Interpolation, Hydrologic Budget

ABSTRACT:

Water availability is subjected to a complex dynamic involving fluctuation of the aquifer level, itself subject to climatic and edaphic factors as well as land use and land cover. Human pressure can have a drastic effect on the aquifer level, the effect of which are often only noticeable after years of continuous usage. In this article we are using a temporal sequence of 50 Landsat images to study a complex of small lakes in Northern Minas Gerais. Our objective is to quantify the fluctuations of the aquifer for the 1984-2009 period by monitoring the area of these lakes bi-yearly and compare it with the hydric balance to understand its evolution. Having no measurements of the aquifer, we developed a methodology entirely based on remote sensing and meteorological data. Because these lakes are very small, the 30 m resolution of the Landsat data rendered very poor results. Based on the postulate that the water pixels behave like a smooth continuous surface, we increased the resolution to 5 m using minimum curvature interpolation. Two methods were tested for extracting the lake surface pixels: supervised classification and thresholding of the normalized difference water index. The results show that the interpolated Landsat data compared well with a high resolution Ikonos image of the same date and can improved the contouring of water bodies. For extracting the water pixel the classification approach performed better by about 15%. Statistical tests showed that the lakes have been systematically decreasing but that these changes cannot be attributed to climatic factors.

RÉSUMÉ:

La disponibilité en eau est soumise à une dynamique complexe impliquant la fluctuation du niveau de l'aquifère, elle-même soumise à des facteurs climatiques et édaphiques, ainsi qu'au couvert et à l'utilisation du sol. La pression humaine peut avoir un effet drastique sur le niveau des aquifères, dont l'effet n'est souvent perceptible qu'après des années d'utilisation continue. Dans cet article, nous utilisons une séquence temporelle de 50 images Landsat pour l'étude d'un complexe de petits lacs dans le nord du Minas Gerais. Notre objectif est de quantifier les fluctuations de l'aquifère pour la période 1984-2009 par le suivi bi-annuelle de l'aire de ces lacs et de les comparer au bilan hydrique afin de comprendre leur évolution. N'ayant aucune mesure du niveau de l'aquifère, nous avons développé une méthodologie basée entièrement sur la télédétection et les données météorologiques. Comme ces lacs sont très petits, la résolution de 30 m des données Landsat donnait de piètres résultats. En se basant sur le postulat que les pixels d'eau se comportent comme une surface lisse et continue, nous avons augmenté la résolution à 5 m par interpolation de courbure minimale. Deux méthodes ont été testées pour l'extraction des pixels surface du lac: la classification supervisée et l'application d'un seuil sur l'indice différentiel normalisé de l'eau. Les résultats montrent que les données interpolées Landsat se comparent bien avec une image Ikonos de haute résolution de la même date et permettent d'améliorer l'extraction du contour des plans d'eau. Pour extraire les pixels d'eau, la classification supervisée a fourni des résultats à peu près 15% supérieurs. Des tests statistiques ont montré que les lacs ont systématiquement diminué, mais que ces changements ne peuvent être attribués à des facteurs climatiques.

1 INTRODUCTION

The watershed of the Peruaçu River hosts two important protected areas totaling over 80,000 ha yet it suffers from strong human pressure for water which is the most sought resource in this semiarid zone. In particular, the Veredas do Peruaçu State Park is apparently suffering from continuous lowering of its aquifer which is observable from the few small lakes inside the park and one larger lake outside. Although the phenomenon is quite obvious to the local population, it still needed to be demonstrated in a scientific non-refutable manner. One such argument is that the lowering could be caused by local changes in the precipitation and water balance (AW). Since no records of the level of the aquifer or the lakes are available for the past, we had to develop a methodology entirely based on historical remote sensing and meteorological data to unambiguously demonstrate and quantify the phenomenon.

Although human occupation can be considered sparse, but since the Peruaçu watershed is relatively small (1450km^2) and the region receives almost no precipitation during seven months of the year, we argue that the pressure of the irrigation for agriculture, eucalyptus plantations and the numerous wells that have been dug in the past 30 years is too great for the capacity of the watershed.

A remote sensing multi-temporal approach was chosen to create a time sequence of images to monitor the size of the Peruaçu lakes and Landsat images stood as the most logical choice for analyzing the dynamics of these lakes for being the largest record of systematical remote sensing data available for civil use. Passive optical infrared images are also considered the most effective type of data for delineating water bodies since they absorb almost totally the incoming radiation and produce a sharp contrast with the surrounding vegetation and soil (Bonn and Rochon, 1992; Jensen, 2005).

Because the lakes under investigation are relatively small, the resolution of Landsat images is somewhat marginally acceptable when considering the mixed pixel problem. The fact that these water bodies are smooth continuous surfaces let us postulate that mixed border pixels have a predictable behavior and could be sub-sampled using some interpolation technique.

The objective of this article is to infer the dynamics of the fluctuations of the water level of the aquifer through the past monitoring of the successive receding and inflating of the open water surface of six lakes found in the *Veredas do Peruaçu State Park* and surroundings. To achieve this goal it was necessary to:

1. create a valid methodology for the extraction of the open water surfaces of these lakes from the historical series of past Landsat images knowing that there would not be any validation data for the past records;
2. establishing the relationship, if any, with the AW computed from meteorological data.

2 MATERIAL AND METHODS

Because our objectives have a twofold aspect, our methodology was also split. On one hand we needed to define a reliable approach to extract systematically the contours of the lakes in the long series of Landsat images given that we would only be able to validate the data for two of these images (using one high resolution image of 2006 and one geodetic survey of 2010). On the other hand we want to use the data extracted from these lake contours to cross with AW data to verify our hypotheses that the lakes surfaces are receding at an alarming rate.

2.1 Study Area

The study area (Figure 1) is located in Northern Minas Gerais - Brazil, a savannah region that can be marginally classified as semiarid with less than 900 mm of rain per year. The lakes under study are all inside or within the vicinities of the *Veredas do Peruaçu State Park*. The hydrographic network is part of the Peruaçu River Basin being a left tributary of the San Francisco River. Rainfall is unevenly distributed during the year and is mostly concentrated between November and March. The whole region is mostly flat with deep soils composed mostly of sand and less than 15% of clay that have a low capacity of water retention.

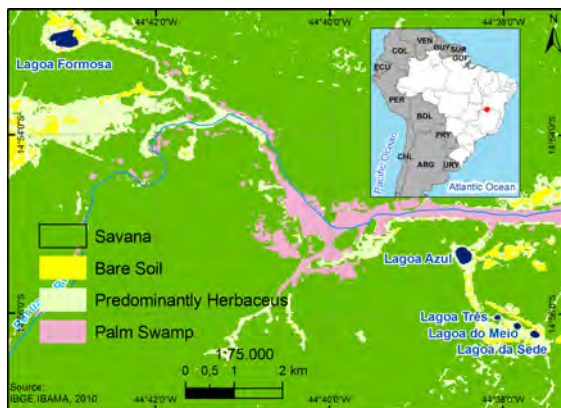


Figure 1: Location of the study area in Northern Minas Gerais.

The lakes themselves are small with the largest having an average area of around ten hectares. Six lakes are analyzed in this

article; they are from the largest to the smallest: *Lagoa Formosa*, *Lagoa Azul*, *Lagoa da Sede*, *Lagoa do Meio*, *Lagoa Três* e *Lagoa da Pista* (now dry) (Figure 1). Although there has been a few hypothesis to explain the genesis of these lakes and their relative alignment, no conclusive results were ever presented. The last of these lake (*Lagoa da Pista*) had open water until 2000 but has dried up and is now but an intermittently saturated herbaceous round field. Unofficial reports by the local population all outline the gradual decrease of the open water surface of most of these lakes but no actual study was ever undertaken.

Until the 1970s the region was occupied by small family groups descended from the Indian tribe *Xacriabá*. In the middle of that decade the Brazilian government offered subsidies and incentives to companies that were willing to invest in eucalyptus plantations for wood supply. This was also the beginning of a much denser occupation of the area by workers and farmers. The impacts of the plantations were reflected in the decrease of biodiversity, both in terms of fauna and flora, and also by an increased pressure on water resources. Plantings occurred until the early 1990's, then the companies abandoned the planting of eucalyptus in the region due to the low productivity of the plantation that was not well adapted to the natural conditions. The region was recognized as having unique biological characteristics and the Brazilian authorities created a national park (*Cavernas do Peruaçu*) and a state park (*Veredas do Peruaçu*) to protect the natural beauties and the archeological heritage (rock paintings) of the Peruaçu watershed (Maillard et al., 2009). Although the area is now protected by law, the effect of the previous uses can still be observed and the area surrounding the parks still suffer from human pressure, especially on water.

2.2 Data and data pre-processing

Landsat images. Images from Landsat-5 TM were chosen for the obvious reason that they constitute the largest multi-temporal image bank existing today. Landsat-5 has been continuously collecting image data for the past 26 years. The period considered by this research starts in 1984 and ends in 2009. In all, 53 images were acquired from Landsat-5 TM and two from Landsat-7 ETM+, all for the orbit/scene 219/70 (World Reference System). Table 1 shows the exact dates for the images. The dates of the image correspond ideally to the end of the wet season (first image) and the end of the dry season (second image) but had to be slightly shifted in cases where images were either of low quality (clouds) or unavailable.

Year	1 st image	2 nd image	Year	1 st image	2 nd image
1984	13/jun	13/oct	1998	20/jun	26/oct
1985	31/may	06/oct	1999	19/mar	11/sep
1986	15/mar	09/oct	2000	24/apr	15/oct
1987	02/mar	12/oct	2001	24/mar	01/oct
1988	21/apr	30/oct	2002	20/apr*	13/oct*
1989	Excluded	Excluded	2003	20/jul	08/oct
1990	10/mar	20/oct	2004	01/apr	24/sep
1991	30/apr	07/oct	2005	04/apr	13/oct
1992	18/may	23/sep	2006	20/jun	30/sep
1993	18/mar	12/oct	2007	Excluded	03/oct
1994	22/apr	12/aug	2008	24/feb	05/oct
1995	24/apr	02/oct	2009	14/mar	06/sep
1996	26/mar	20/oct	2010	4/may**	
1997	09/feb	07/oct			

Table 1: List of Landsat images (* indicates Landsat-7, the rest are Landsat-5; ** the 2010 image was only used to validate the lake contour extraction method).

The images had to be geometrically and radiometrically corrected and an atmospheric compensation also had to be applied. The

geometrical correction was done with an “image-to-image” approach using a one-meter Ikonos image as basis (which was geometrically adjusted using control points from a geodetic GPS survey). The atmospheric and radiometric correction were applied using an in-house program build for that purpose: *Corat_Landsat*. The program takes as input a table containing 1) the name of the image file, 2) the DN value for the dark object subtraction (Chavez Jr., 1988) for bands 1, 2, 3, 4, 5 and 7, 3) the sun elevation angle and 4) the sun-earth distance in astronomical units. The output is a 16 bit reflectance image (reflectance values were redistributed between 0 and 10 000).

Meteorological data - Water balance. The calculation of the AW was first proposed by Thornthwaite in 1948 and improved in 1955 (Thornthwaite and Mather, 1955). The main objective of the methodology is to determine the hydraulic characteristics of a given region without direct measurements on the ground (Pereira, 2005). The water balance is the simple budget between input and output of water within a watershed:

$$\Delta S = \left(\underbrace{P + G_{in}}_{Inflow} \right) - \left(\underbrace{Q + ET + G_{out}}_{Outflow} \right) \quad (1)$$

where P is the precipitation, G_{in} and G_{out} represents the ground water flow, Q is the runoff water and ET is the evapotranspiration.

The Thornthwaite procedure simplifies the AW calculation by estimating all its components from only two input parameters: average daily temperature and precipitation:

$$AW_t = AW_{t-1} \exp \left(- \frac{PET_t}{AWC} \right) \quad (2)$$

where AW_t is the available water at time t , AW_{t-1} is the available water at time $t - 1$ (in our case we set t to be every ten days), PET_t is the potential evapotranspiration at time t and AWC is the soil’s water holding capacity. The water balance can be summarized in three situations.

- $\Delta P < 0$; net precipitation (precipitation - potential evapotranspiration) is less than zero: the soil is drying.
- $\Delta P > 0$ but $\Delta P + AW_{t-1} \leq AWC$; net precipitation is more than zero but net precipitation plus the available water from time $t - 1$ is less or equal than the soil’s water holding capacity: soil is wetting.
- $\Delta P > 0$ but $\Delta P + AW_{t-1} > AWC$; net precipitation is more than zero and net precipitation plus the available water from time $t - 1$ is more than the soil’s water holding capacity: soil is wetting above capacity and water goes to runoff.

2.3 Extraction of lake contours

Water in liquid form is usually well contrasted from its surrounding dry(er) land unless it is overshadowed by vegetation cover like mangroves, flooded forests or aquatic plants (Caloz and Puech, 1996). In many cases, a simple threshold in an infrared image histogram can reliably separate water from the other land covers with a relatively good rate of success and investigators have developed simple techniques for doing so in a systematical manner (Bryant and Rainey, 2002; Jain et al., 2005). Histograms of near

infrared images containing a fair amount of open water surfaces are usually bimodal with the first peak directly related to water. Yet, when one looks closer, the water-land limit is often blurred by a varying width occupied by aquatic plants that can fluctuate over various time scales (yearly or seasonally). Using a sequence of historical Landsat images for which we had no validation data, we needed to have a very strict definition of the water-land interface. We defined the lake “water-margin” as the point at which water overwhelmingly dominates the surface and estimated that point to correspond to 70-80%.

2.3.1 Resampling through interpolation: Another source of error comes from the mere sampling resolution of 30 meters used by the TM and ETM sensors. Although not considered an issue when measuring an ocean or a large lake, it rapidly becomes a problem when studying very small lakes such as the ones found in the VPSP that range from just over ten hectares to just under one hectare. In these small lakes, the number of mixed pixels can represent a large proportion of the total lake pixels (up to about 35% in the case of the smallest lake). A half pixel shift in image registration could signify an important difference in water pixel count.

Scale (or spatial resolution) can have various effects on image classification accuracy. A finer resolution can usually decrease the proportion of pixels falling on the border of objects (hence less mixed pixels) which can result in less classification confusion. Conversely, a finer resolution will generally increase the spectral variation of objects that can, in turn increase classification confusion (Markham and Townshend, 1981). Fortunately, water (especially clear and deep) is spectrally a relatively smooth surface for which a finer resolution will bring more benefit (less border pixels) than disadvantage (spectral variation). Based on the fact that water is spectrally smooth and that it strongly contrasts with dry land, we argue that artificially increasing the resolution of an image containing water surfaces can generate a better definition of the water-land limit. To do so, a number of tests were prepared to define an appropriate interpolation method to resample the images.

Amongst the various interpolation methods we opted for the minimum curvature interpolation (a variation of bi-cubic spline) with tension as described in Smith and Wessel (1990). This interpolation method has the advantage of being able to generate a smooth surface without generating undesirable fluctuations (artifact peaks or dips) by using a tension parameter. This interpolation proved better than “inverse distance weighted” that tends to produce artifact dips between sampling points (Maune et al., 2001). The minimum curvature worked well and fast and generated smooth ramps while keeping a sharp water-land edge. Figure 2 illustrates the effect of interpolating the Landsat data to 5 m on the lake extraction processing.

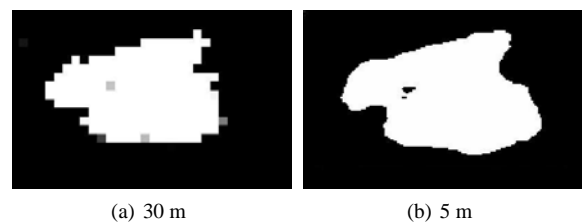


Figure 2: Comparison of the lake extraction methods using the original 30 m Landsat data (a) and the 5 m interpolated data (b).

2.3.2 Classification: Because of the nature of our study, unsupervised and automatic segmentation methods were discarded. These approaches are most suited with single date image applications when terrain validation is possible. Two supervised methods

were then chosen: 1) enhanced image classification and 2) thresholding the normalized difference water index (NDWI; McFeeters, 1996; Ji et al., 2009).

Image Classification. Traditional image classification is carried out on a pixel-by-pixel basis. Although an increasing number of studies show that region-based or object-based classification tends to improve results significantly, it was not judged necessary in this particular case for two main reasons. First because of the spectral nature of water being a smooth surface with small variations (at least in the optical infrared) and secondly because these methods usually offer little control over what is defined as an object. Conversely, classification approaches such as Maximum likelihood can produce posterior probability maps that can be thereafter thresholded (hardened). The latter approach had the advantage to require training data only for the object of interest whereas classical classification procedures require all classes to have been defined using training data. In this case we opted for the posterior probability which can be simplified as the Gaussian probability density of the "water class". In simple nominal classification, a pixel can be classified as pertaining to a particular class even if its probability is low, as long as it is higher than for all the other classes. By using a high threshold value (i.e. > 90%) to attribute a water label to a pixel, we are able to use but a single class and avoid having to gather training data for other objects or surfaces.

NDWI threshold. Using the same logic as the normalized difference vegetation index (NDVI) the normalized difference water index (NDWI) was proposed by McFeeters (1996) as a means to separate water from other surfaces (Eq. 3).

$$NDWI = \frac{\rho_{green} - \rho_{NIR}}{\rho_{green} + \rho_{NIR}} \quad (3)$$

where ρ_{green} is the green reflectance (Landsat TM band 2: 0,52–0,60 μm) and ρ_{NIR} is the near infrared reflectance (Landsat TM band 4: 0,77–0,90 μm). The NDWI varies between -1 and 1 and uses zero as the threshold between land (≤ 0) and water (> 0). A number of variations were later proposed for NDWI. In their article, Ji et al. (2009) compared a number of these variations applied to Landsat, ASTER, SPOT and MODIS images. They found that the modified NDWI (MNDWI) proposed by Xu (2006) performed better (Eq. 4).

$$MNDWI = \frac{\rho_{green} - \rho_{SWIR}}{\rho_{green} + \rho_{SWIR}} \quad (4)$$

where ρ_{SWIR} is the reflectance in short wave infrared (Landsat TM band 5: 1,55–1,75 μm).

2.4 Validation and Statistical Testing

Two validation data sets were used for testing the performance of the extraction of the lake contours from the interpolated Landsat data which also involved our definition of the "water-land" edge. First, the contours from the dry season image of 2006 were compared against the contours extracted from a fusionned Ikonos image (1 m) five days apart from the Landsat image. Secondly, the four lakes of the VPS (data from the larger lake outside the park could not be acquired) were surveyed using a geodetic GPS in kinetic mode to be compared with the contour from the Landsat image (with a five days difference). Coordinates of the lake contour were acquired at an interval of 15 meters with an approximate precision of 10 cm.

The validation was done by two complementary methods: 1) by expressing the difference between the areas as a proportion of the validated area ($\frac{A_{real} - A_{observed}}{A_{real}} \times 100$); and 2) by overlapping the two contours (interpolated Landsat and validation data) and dividing the overlap area (intersection) by the merged areas (union) of both contours as illustrated in Figure 3.

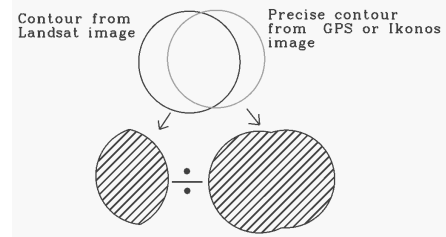


Figure 3: Validation method for testing the accuracy of the lake contours extracted from the interpolated Landsat images.

The statistical testing consists in establishing the strength of the relationship between the areas of all six lakes and the AW of the same period as the images. Although the response of the water level is not spontaneous, the trend should still be statistically perceptible. Because the areas of the lakes are not normally distributed, a regression was not recommended. Spearman's correlation does not assume a normal distribution of the dependant variable and was chosen instead. The correlation was also computed between the area of the lakes themselves as a mean to infer a generalized trend.

3 RESULTS AND DISCUSSION

3.1 water balance

The AW was calculated for the period 1983 - 2009 using the Thornthwaite method trimonthly (the year 1983 was added in order to feed the Available Water for the beginning of the 1984 budget). Figure 2 shows the annual budget averaged every five years for the period along with the average budget for the whole period (white line). Apart from the two first periods (1984-1989 and 1990-1994) which appear as exceptionally high and exceptionally low respectively, the other periods do not show any trend towards an increase or a decrease.

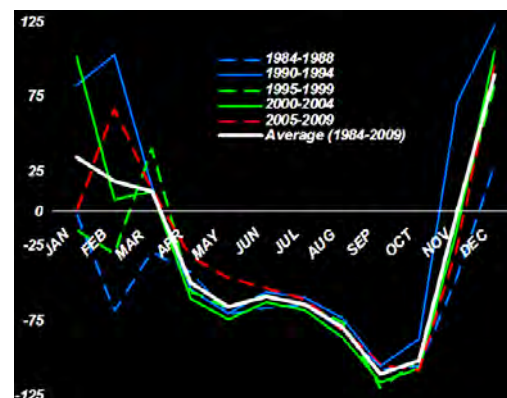


Figure 4: water balance averaged for every five years between 1984 and 2009 and overall average (white line).

3.2 Lake Contours Extraction and validation

The 50 selected Landsat images were geometrically corrected, registered to a UTM grid, corrected for atmospheric interferences

(using Chavez’s DOS method) and transformed in reflectance values. The images were also interpolated to a 5 m resolution using the minimum curvature algorithm. It is visually striking to see that, apart from a few exceptions, the multi-temporal dataset shows an almost constant shrinking of the lake surfaces and even the disappearance of one small water body. Figure 5 illustrates the difference in lake surfaces for the whole period. The triangular area at the bottom of the 1984 image, was part of the eucalyptus plantation and is now regenerating.

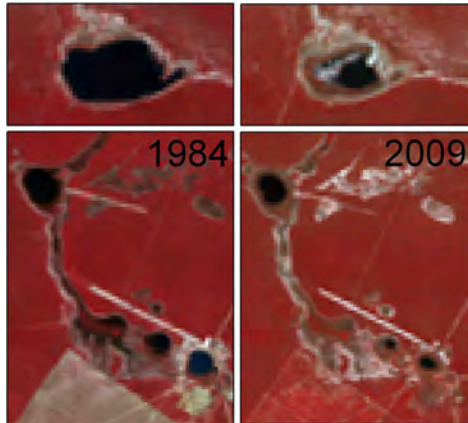
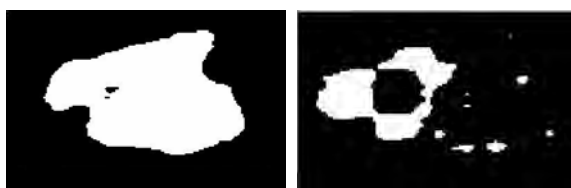


Figure 5: Comparison of the lakes for the same time of the year in 1984 (left) and 2009 (right).

Two lake extraction methods were used: 1) threshold of the posterior probability of the maximum likelihood classification and 2) threshold of the modified normalized difference water index (MNDWI). The former approach yielded far superior results in almost all images. We attribute this result to the presence of aquatic vegetation and turbidity (for the Formosa lake) mixed with the water which tends to increase reflectance in the near and mid-infrared. Figure 6 shows the extreme example of the Formosa lake which is outside the State Park and suffers from eutrophication and aquatic vegetation bloom. Figure 6 should also be compared with the false color image at the top right of Figure 5.



(a) Classification - 5 m (b) NDWI threshold - 5 m

Figure 6: Comparison of the contour extraction methods using classification (a) and MNDWI threshold (b).

By using the posterior probability of a single water class, we found that there was always an easily identifiable break between the water and non-water classes that made the selection of a threshold very easy. The threshold was applied to all 50 images and the area of all six lakes computed for every date. The graph in Figure 7 shows how these areas have changes between 1984 and 2009. Table 2 gives an over view of the shrinking of the six lakes. The lake areas of 1990 are also indicated for being the record size for all lakes. While lake “Pista” has completely disappeared since 2000, four other lakes have lost between 59 and 80% of their area. The lake “Azul” has somewhat retained much more of its original area (loss of 29%) and it is also the only lake surrounded by hydromorphic gley soil with a higher clay content.

Since we did not have reliable elevation data at the time of writing, the areas water surfaces could not be associated with precise

Areas <i>km</i> ²	Lakes					
	Pista	Três	Meio	Sede	Azul	Formosa
1990	4962	28778	37413	56402	105389	296237
1984	375	14795	32471	39030	92670	291502
2009	0	2928	7228	12243	65829	170409
% loss	100%	80,2%	77,7%	68,6%	29,0%	58,5%

Table 2: Comparison of the areas of all six lakes between 1984 and 2009 with the shrinking expressed in percentage (1990 was the record year for all lakes).

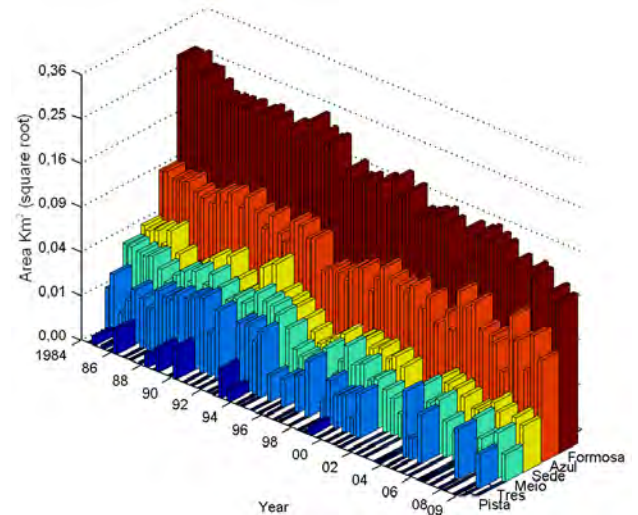


Figure 7: Graph showing the evolution of the area of all six lakes for the period 1984-2009.

altimetric level measurements. These data will be available at the third quarter of 2010. Using the digital elevation model (DEM) from the ASTER sensor, and overlaying the contours over it we were able to estimate the lowering of the water level for the 1984-2009 period to about 1 meter for the lake “Azul” and to slightly over 2 meters for the lakes “Sede”, “Meio”, “Três” and “Formosa”, being outside the State Park. Figure 8 shows the 1984 and 2009 levels on the ASTER DEM profile.

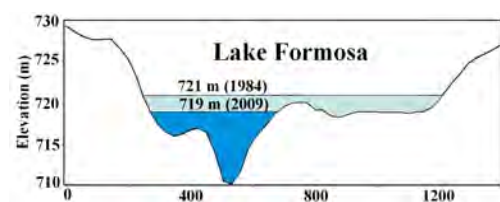


Figure 8: Water level differences between 1984 and 2009 on an ASTER DEM profile for lake “Formosa”.

The validation of the data was done using the approach described in section 2.4. Table 3 shows the validation obtained with both control datasets (GPS and Ikonos image) and with the two methods of comparison (simple comparison of areas and “intersection ÷ union” approach). As expected, the accuracies with the latter method are slightly lower but since all accuracies but two are well above 80%, we conclude that both our extraction method and our geometric correction are within very acceptable boundaries. Figure 9 shows the contours extracted from the Landsat image of 2010 and the GPS survey contours for three of the lakes.

3.3 Statistical Testing

Spearman’s correlation test was applied to the area series of all lakes along with the AW data for the same period. The results

Lakes	Area Comparison		Intersection/Union × 100	
	GPS	Ikonos	GPS	Ikonos
Três	94,54%	n/a	81,05%	n/a
Meio	93,34%	86,01%	91,53%	71,04%
Sede	89,50%	94,41%	89,16%	83,85%
Azul	94,18%	96,36%	92,13%	93,20%
Formosa	n/a	95,08%	n/a	92,66%

Table 3: Validation of the lake contour extraction using the GPS survey and the Ikonos scene. Column 2 and 3 show the results for the area comparison; column 4 and 5 show the accuracy obtained with the $\frac{\text{intersection}}{\text{union}} \times 100$ approach.

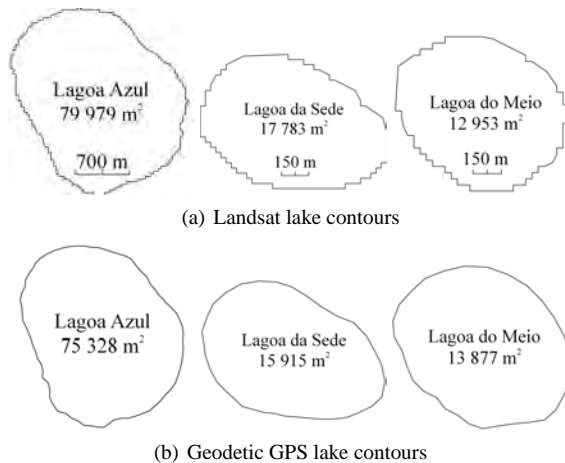


Figure 9: Comparison of the contours of three of the six lakes using the interpolated Landsat data (left) and the geodetic GPS survey data (right).

are presented in Table 4. The only correlation between the areas of the lakes and the AW is with the “Pista” lake which has dried up since 2000 and the level of significance is $p=0,05$. Conversely, all the lakes are strongly related among themselves with a significance of 0,01. This confirms that the trend is statistically significant and that we can infer that the lakes are rapidly shrinking. Even lake “Azul” which has kept a much more constant surface area is strongly correlated with all the other lakes (0,601 to 0,871). Since the AW cannot be said to be correlated with the shrinking of the lakes, the meteorological explanation becomes much less plausible and the human pressure on the watershed can more easily be pinpointed as responsible.

Table 4: Results of the Spearman’s correlation tests.

	AW	Lakes					
		Pista	Três	Meio	Sede	Azul	
Pista	Corr.	*0,329					
Três	Corr.	0,209	**0,455				
Meio	Corr.	0,209	**0,611	**0,834			
Sede	Corr.	0,075	**0,566	**0,735	**0,957		
Azul	Corr.	0,259	**0,601	**0,871	**0,866	**0,789	
Formosa	Corr.	0,068	**0,524	**0,674	**0,899	**0,897	**0,730

* Significant at 0,05

** Significant at 0,01

4 CONCLUSIONS

Multi-temporal remote sensing offers countless opportunities for monitoring past and present changes in land cover and land use. By monitoring the size and shape of water bodies, we can infer on human pressure and climate change. In this article we proposed an innovative approach for monitoring small lakes using medium resolution Landsat data. The approach uses minimum curvature

interpolation to artificially improve the resolution of the image data and produce a much cleaner lake contour that matches the actual measured contour with a high success rate (15 validation out of 16 with better than 80% and 10 better than 90%). Using posterior probability of a maximum likelihood classifier, we were able to systematically extract contours from six lakes for 50 different dates with ease and good matching of control data. The Modified Normalized Difference Water Index (MNDWI) did not perform well for these small shallow lakes with the presence of aquatic vegetation. The water balance using the Thornthwaite approach is well suited for area with limited climatological information and provides valuable insight on the climatological condition ruling water availability. In this study, the water balance could not be statistically correlated (Spearman’s correlation) to the shrinking of six small lakes in Northern Minas Gerais, Brazil.

ACKNOWLEDGEMENTS

The authors are thankful to the Forestry Institute of Minas Gerais for providing the Ikonos data and field support. We are most thankful to Thiago Alencar Silva and Thaís Amaral for their help and support.

REFERENCES

- Bonn, F. and Rochon, G., 1992. Précis de Télédétection: Principes et Méthodes. Vol. 1, Presses de l’Université du Québec. 485 p.
- Bryant, R. G. and Rainey, M., 2002. Investigation of flood inundation on playas within the zone of chotts, using a time-series of AVHRR. Remote Sensing of Environment (3), pp. 360–375.
- Caloz, R. and Puech, C., 1996. Précis de Télédétection: Applications Thématiques. Vol. 2, Presses de l’Université du Québec. 633 p., chapter Hydrologie et imagerie satellitaire, pp. 159–196.
- Chavez Jr., P. S., 1988. An improved dark-object subtraction technique for atmospheric scattering correction of multispectral data. Remote Sensing of Environment 24(2), pp. 459–479.
- Jain, S. K., Singh, R. D., Jain, M. K. and Lohani, A. K., 2005. Delineation of flood-prone areas using remote sensing technique. Water Resources Management 19(4), pp. 337–347.
- Jensen, J. R., 2005. Introductory Digital Image Processing. 3rd edn, Pearson Prentice Hall, New Jersey. 526 p.
- Ji, L., Zhang, L. and Wylie, B., 2009. Analysis of dynamic thresholds for the normalized difference water index. Photogrammetric Engineering and Remote Sensing 75(11), pp. 1307–1317.
- Maillard, P., Augustin, C. H. R. R. and Fernandes, G. W., 2009. Arid Environments and Wind Erosion. Novascience Publisher, chapter Brazil’s Semiarid Cerrado: A Remote Sensing Perspective.
- Markham, B. L. and Townshend, J. R. G., 1981. Land cover classification accuracy as a function of sensor spatial resolution. In: Proceedings of the 15th Int. Symp. on Remote Sensing of the Environment, Ann Arbor, MI, pp. 1075–1090.
- Maune, D., Kopp, S., C.A., Crawford and Zerdas, C., 2001. Digital Elevation Model Technologies and Applications. 1 edn, American Society for Photogrammetry and Remote Sensing, Bethesda, MD, chapter Introduction, pp. 1–34.
- McFeeters, S., 1996. The use of normalized difference water index (NDWI) in the delineation of open water features. International Journal of Remote Sensing 17(7), pp. 1425–1432.
- Smith, W. H. F. and Wessel, P., 1990. Gridding with a continuous curvature surface in tension. Geophysics 55, pp. 293–305.
- Thornthwaite, C. W. and Mather, J. R., 1955. The water balance. Publications in Climatology, Drexel Institute of Technology, New Jersey.
- Xu, H., 2006. Modification of normalised difference water index (NDWI) to enhance open water features in remotely sensed imagery. International Journal of Remote Sensing.

REAL-TIME IMAGE PROCESSING FOR ROAD TRAFFIC DATA EXTRACTION FROM AERIAL IMAGES

D. Rosenbaum, J. Leitloff, F. Kurz, O. Meynberg, and T. Reize

DLR - German Aerospace Center, Remote Sensing Technology Institute,
Münchner Str. 20, 82234, Weßling, Germany

Commission VII Symposium 2010

KEY WORDS: Monitoring, Recognition, Orthorectification, Georeferencing, Image, Pattern, Sequences, Tracking

ABSTRACT:

A world with growing individual traffic requires sufficient solutions for traffic monitoring and guidance. The actual ground based approaches for traffic data collection may be barely sufficient for everyday life, but they will fail in case of disasters and mass events. Therefore, a road traffic monitoring solution based on an airborne wide area camera system has been currently developed by DLR. Here, we present a new image processing chain for real-time traffic data extraction from high resolution aerial image sequences with automatic methods. This processing chain is applied in a computer network as part of an operational sensor system for traffic monitoring onboard a DLR aircraft. It is capable of processing aerial images obtained with a frame rate of up to 3 Hz. The footprint area of the three viewing directions of an image exposure with three cameras is 4 x 1 km at a resolution of 20 cm (recorded at a flight height of 1500 m). The processing chain consists of a module for data readout from the cameras and for the synchronization of the images with the GPS/IMU navigation data (used for direct georeferencing) and a module for orthorectification of the images. Traffic data is extracted by a further module based on a priori knowledge from a road database of the approximate location of road axes in the georeferenced and orthorectified images. Vehicle detection is performed by a combination of Adaboost using Haar-like features for pixel wise classification and subsequent clustering by Support Vector Machine based on a set of statistical features of the classified pixel. In order to obtain velocities, vehicle tracking is applied to consecutive images after performing vehicle detection on the first image of the burst. This is done by template matching along a search space aligned to road axes based on normalized cross correlation in RGB color space. With this processing chain we are able to obtain accurate traffic data with completeness and correctness both higher than 80 % at high actuality for varying and complex image scenes. The proposed processing chain is evaluated on a huge number of images including inner city scenes of Cologne and Munich, demonstrating the robustness of our work in operational use.

1 INTRODUCTION

Mass events with a large attendance hold in big cities overload road infrastructure at regular intervals, since metropolis roads are used to full capacity in normal course of life. In case of disaster, maybe with parts of the road network being impassable, total collapse of road traffics menaces. Both cases require sufficient methods of traffic monitoring and guidance. Common infrastructure for traffic monitoring like induction loops and video cameras is ground based and mainly distributed on main roads. New monitoring approaches collect data by means of mobile measurement units which flow with the traffic as test particles for local traffic situations and travel times. The so called floating car data (FCD, e.g. Schaefer et al., 2002; Busch et al., 2004) obtained from taxicabs can deliver useful traffic information within cities, but they are only available in few big cities today.

These methods and sensors are suited for everyday life, but traffic monitoring and guidance based on these sensors may fail in case of mass events or disaster. In those cases a coverage as complete as possible of road level of service is mandatory. Such a complete coverage could not be provided by common sensor networks with their low spacial resolution data obtained by punctual traffic registration limited to main roads as provided by ground based sensor networks. In case of disaster, sensor networks based on ground infrastructure may fail completely. Not only publicity but especially security authorities and organizations which have to coordinate and route action and relief forces into and within affected areas require precise traffic information. Furthermore, a spacial complete area wide traffic surveillance at high actuality provides the possibility to generate precise predictions of traffic situation in near future by simulations (e.g. Behrisch et al., 2008).

For these purposes airborne and satellite based solutions for wide area traffic monitoring have been produced or are currently under development at DLR. In Reinartz et al. (2006) the general suitability of image time series from airborne cameras for traffic monitoring was shown. Tests with several camera systems and various airborne platforms, as well as the development of an airborne traffic monitoring system and thematic image processing software for traffic parameters were performed within the projects "LUMOS" and "Eye in the Sky" (Ernst et al., 2003; Börner et al., 2004). The actual project for airborne traffic monitoring and simulation is called "VABENE" (German: *Verkehrsmanagement bei Großereignissen und Katastrophen*, that means: traffic management under mass event and disaster conditions). Aim of the project among others is to develop operational airborne optical and radar systems for automatic traffic data extraction in real time. First results on traffic monitoring based on remote sensing synthetic aperture radar (SAR) systems were already shown in e.g. Bethke et al. (2007) or Suchandt et al. (2006). On the optical regime, a first proposal for a prototype processing chain capable of traffic data extraction from sequences of optical aerial images in near real time was shown in Rosenbaum et al. (2008). There, algorithms and methods for edge and line based roadside extraction, vehicle detection based on edge detection and geometry validation, and vehicle tracking by template matching using a normalized cross correlation operator were presented. That template matching for car tracking works sufficiently had already been proven in Lenhart et al. (2008). There, a similar algorithm using a shape based matching operator was introduced. Furthermore, different methods for validation of potential vehicle tracks and vehicle detections for outlier elimination were presented. Some of them are used in the present processing chain.

The present publication shows a vehicle detection approach based on the Viola-Jones detector (Viola and Jones, 2004) trained by Gentle AdaBoost (Friedman et al., 2000). Vehicle detectors based on Boosting had already been applied to aerial images successfully in literature (e.g. Nguyen et al., 2007; Grabner et al., 2008).

In the optical system for online traffic monitoring the DLR in-house developed sensor called 3 K camera (e.g. Kurz et al., 2007) is included, which is capable of direct orthorectification / georeferencing in conjunction with a IGI IId Aerocontrol RT IMU/GPS navigation system and several PCs for image processing. Furthermore, the sensor provides a high image repetition rate of up to 3 Hz which offers a high overlap of sequential images and makes vehicle tracking possible. With a big footprint of 4 km across track at a typical flight level of 1500 m over ground and a high native resolution of 20 cm GSD (Nadir) it is well suited for recording road traffic data. After several years of development our system has reached an operational state and is ready for application in disasters and mass events.

The paper is structured as follows. Second section presents the system for airborne traffic monitoring and the data sets obtained. Then, the processing chain for automatic road traffic data extraction from aerial images is introduced in section 3. Section 4 deals with the validation of the processing chain, and the last section gives conclusions and presents the plans for future work.

2 SYSTEM AND DATA SETS

The real-time road traffic monitoring system consists of two parts. One part is installed onboard the aircraft, consisting of the 3 K camera system, a real-time GPS/IMU unit, one PC for each single camera processing image data, one PC for traffic monitoring tasks, a downlink-antenna with a band width of 5 Mbit/s (actual, upgradeable to a bandwidth of about 20 Mbit/s) automatically tracking the ground station, and a PC for steering the antenna and feeding the downlink with data. The ground station mainly consists of a parabolic receiving antenna, which is automatically aligned with the antenna at the aircraft, and a PC system for visualization of the downlinked images and traffic data. Given an internet access at the place of the ground station, the obtained traffic data will be directly transferred to an internet traffic portal.

2.1 Onboard System

The system for traffic monitoring aboard the airplane uses aerial image sequences obtained with the so called 3 K camera system. All results shown in this publication are based on this sensor. In near future this optical sensor will be replaced by the successor, the 3 K+ camera system. Both wide area digital frame camera systems offer similar properties (Tab. 1). Each consists of three non-metric Canon EOS 1Ds cameras mounted on a ZEISS aerial platform. One look in nadir direction and two looks in oblique sideward direction result in an increased FOV of up to 104 degree or 31 degree in side resp. flight direction based on a focal length of 50 mm. The cameras acquire images with a frame rate of up to 5 Hz; here the absolute number of images is limited due to an overflow of the internal memory. Based on the image size of up to 21 MPix and a colour depth of 24 bits the overall output data rate of the three camera system lay between 6 and 10 MByte/s for jpeg compressed images. The data rates at the cameras depend also on the flight and image acquisition mode, e.g. the overlap and the flight height. The image acquisition geometry of the DLR 3 K and 3 K+ camera system are similar except the smaller GSD of the 3 K+ system. Typical flight heights of the camera systems are between 500 m and 3000 m above ground.

	3K camera system	3K+ camera system
Cameras	3 × EOS 1Ds Mark II	3 × EOS 1Ds Mark III
Image size	4992 × 3328 (16.7MPix)	5616 × 3744 (21.0 MPix)
Max. frame rate	3 Hz (~50 images ¹)	5Hz (63images ¹)
File size	20MByte (RAW) 5.5MByte (JPEG level 8)	25MByte (RAW) 6.5 MByte (JPEG level 8)
ISO	100 - 1600	100 - 3200
Aperture	1.4 - 22	1.4 - 22
Lenses	Canon EF 1.4 50mm	Zeiss Makro-Planar 2/50mm
Tilt angle of sideward cameras	Max 32° /variable	Max 32° / variable
Data rates (3 cameras, JPEG): 60% overlap, 1000m a.g., 2s 3xbursts (2Hz), 1000m a.g., 6s pause (traffic modus)	8.3MByte/s 6.6MByte/s	9.8MByte/s 7.8MByte/s
Interface	Firewire IEEE 1394a	USB 2.0
Image sensor	full frame CMOS sensor	full frame CMOS sensor
Pixel size	7.21µm	6.41µm
Footprint / GSD, 1000m a.g.	2560m × 480m / 15cm nadir	2560m × 480m / 13cm nadir
Footprint / GSD, 3000m a.g.	7680m × 1440m / 45cm nadir	7680m × 1440m / 39cm nadir
FOV (side resp. in flight)	104°/31°	104°/31°
Calibration (interior orientation)	5 parameters: focal length, focal point, radial distortion A ₁ and A ₂	Not calibrated yet.
GPS/IMU accuracies postproc. (rp/yaw/xy/z) real time (rp/yaw/xy/z)	IGI IId 0.003°/0.007°/0.08m/0.05m 0.01°/0.05°/0.1m/0.1m	IGI IId 0.003°/0.007°/0.08m/0.05m 0.01°/0.05°/0.1m/0.1m
Georeferencing accuracies Direct georeferencing plus bundle adjustment	2-4m <1m	Not tested yet.

¹Depending on the motif and other configuration parameters

Table 1: Overview about 3K and 3K+ camera system.

The high input data rate on the one hand and the processing intensive modules on the other hand put high demands on the on-board image processing hardware, which consequently leads to a multi-host solution with five PCs in total (Fig. 1). All of them run 32bit-Windows XP due to the fact that some of the third-party software we use in our processing system only supports Windows. Each camera is connected via Firewire IEEE 1394a to a dedicated host. It streams the images directly without memory-card buffering to the camera PCs (PC1 - PC3). The EOS Digital Camera Software Development Kit (EDSDK) is installed on each of these hosts and provides a C language interface for the control of the cameras and the download of images to the host PC. Supported operating systems are Microsoft Windows 2000 or higher and Mac OS X since version 10.4. Since the orthorectification and georeferencing process needs the exact position and orientation of the airplane, the IGI IId GPS/IMU system is connected via Ethernet to the onboard system. The fibre-optic gyro based Inertial Measurement Unit with its integrated 12-channel L1/L2 GPS receiver are triggered by the cameras external flash signal. Every time a flash signal is received, the IGI IId sends coordinates and orientation via a TCP connection to one of the camera PCs. A module runs a TCP client and matches the received geo-data with the image received from the camera. The image is written to disk where it can be read by the orthorectification module. The geo data is sent to this module via message passing. After the orthorectification process (Müller et al., 2002) has completed, the orthorectified image is written to disk, copied to PC 4 and could be processed for automatic traffic data extraction or sent down to ground station.

The onboard system was ready to fly in mid 2009. Unfortunately the assignation of the permit to fly certificate of this system onboard the DLR aircraft Cessna 208 B was delayed. We got the certificate in April 2010 and we are currently carrying out series of test flights. During first flights, several problems have been exposed and fixed as well as an optimal start-up procedure for hardware and software of this complex system had to be found. Meanwhile the sensor and system components for orthorectification and automatic traffic data extraction are running properly during test flights and we recorded road traffic data aboard the aircraft during flights successfully. Due to a hardware defect of the S-band downlink, we have not yet transmitted traffic data to the ground, but we are sure to catch up on this very soon. Although the onboard traffic data processing is already working, re-

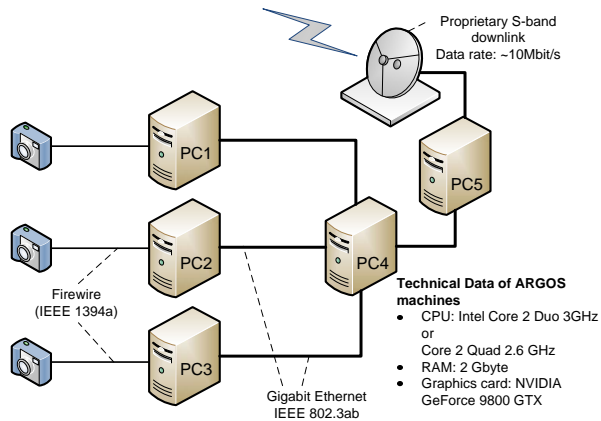


Figure 1: Topology of the onboard network. Each camera is directly connected to PC1,2,3 which perform georeferencing and orthorectification. Vehicle detection and tracking takes place on PC4. PC5 sends the results via a proprietary S-band transmitter to the ground.

sults presented in this publication are based on data processed offline after flight at the ground for evaluating the processing chain.

2.2 Test Sites and Imagery

In the previous and current project the metropolitan areas Munich and Cologne have been selected for system flight tests and to demonstrate the airborne traffic monitoring system to the stakeholders. Therefore the NAVTEQ road database installed on the system is limited to these regions. Hence, all data and results presented here are obtained during four campaigns in Munich and Cologne.

First campaign was performed in Munich on 30.4.2007 with two flight strips across the city core and the main city ring road at sunny weather conditions and a flight height of 1000 m. Second campaign was flown in Cologne on 2.06.2009 at a flight height of 1500 m. Third and fourth campaign were performed in Munich on 22.04.2010 and 24.04.2010 during BAUMA exhibition, both during fair to nice weather conditions at a flight height of 1000 m above ground.

All images were resampled to a resolution of 20 cm GSD independent from flight height, since vehicle detection is trained to that resolution. For evaluation in section 4 traffic data of the campaign three and four were analysed. Due to the huge amount of images, not every flight strip of the campaigns was probed for manual reference. However, the analyzed flight strips give a good mix of scenarios ranging from downtown over suburban to rural areas including road categories from lowest category back road over inner city main road to interstate motorway. Results from the first and fourth campaign are shown in Figures 3, 4, and 6.

During all campaigns images were taken in burst mode with 3 images per burst and a repetition rate of 2 Hz. During flight strips the bursts were activated every 7 seconds. Image recording in burst mode makes vehicle tracking and measuring vehicle speed possible within burst image pairs but reduces amount of data produced significantly in comparison to a continuous mode with a high frame rate. Images were resampled to a resolution of 20 cm GSD

3 PROCESSING CHAIN

Automatic traffic data extraction works on the georeferenced images produced by the orthorectification process in the step before.



Figure 2: Upper: Horizontal aligned original image. Lower: Confidence image with zero crossing.

Preprocessing consists of a first module reading images from the camera ring buffer and receiving the corresponding exterior orientation from the GPS/IMU navigation system in real time. Second preprocessing module performs direct georeferencing / orthorectification (section 2.1). Each image burst is processed separately. Processing for traffic data extraction starts with vehicle detection on the first image of each image sequence (burst) followed by a vehicle tracking based on template matching between the image pair consisting of the first and second image of the sequence.

With this strategy the traffic parameters flux and density can be derived from image sequences. Vehicle detection performed on the first georeferenced image of the sequence gives the vehicle density whereas vehicle tracking applied on all consecutive (georeferenced) image pairs gives the velocity of the vehicles so that the flux of the traffic can be calculated.

3.1 Vehicle Detection

Prior to vehicle detection, image buffers along road axes obtained from NAVTEQ road database are cut out of the georeferenced images. This reduces the search space for vehicles in the images. Then all roads are straightened along road axes, so that vehicles travelling along each road in the image are aligned in the same direction. This reduces calculation time, since the classifiers of vehicle detection do not have to be rotated.

In this work the vehicle detection is performed in three stages. The first step is based on the Gentle AdaBoost algorithm as introduced in Friedman et al. (2000). Compared to other boosting variants, e.g. Real AdaBoost (Schapire and Singer, 1999) or Discrete AdaBoost (Freund and Schapire, 1997), Gentle AdaBoost is less sensitive to errors in the training set as reported by Friedman et al. (2000) and Lienhart et al. (2003). Furthermore, AdaBoost is the only classification algorithm with can handle the huge amount of features used in this work. Our training database contains 4662 sample of vehicles under different lightning condition and with various appearance. Furthermore, 15,000 negative samples are generated from designated areas. The complete set of standard and rotated Haar-like features as presented in Lienhart et al. (2003) are calculated for each sample in a 30 by 30 search window. The total number of 657,510 features for the horizontal aligned gray value image of each training sample is reduced to the 200 most significant features during the training. Only these few features are used for later classification, which can be fast calculated by use of integral images as shown in Viola and Jones (2004). The application of the learned classifier results in confidence rated image reflecting the probability of each pixel belonging to a vehicle or the background respectively. Afterwards the confidence image is clustered by means of zero crossings as



Figure 3: Upper: Confidence image with detected blobs (red circles) and final SVM detection (green crosses). Lower: Original image with final detection.

shown in Fig. 2. Since the confidence image is normalized, grey values range from -1 to 1 with zero crossings typically closing regions of pixels potentially belonging to vehicles.

As it can be seen in the confidence image, vehicle areas exhibit a blob-like structure. Thus, in the second processing stage an interest point operator for blobs was implemented based on the work of Lepetit and Fua (2006). The parameters of the algorithm have been tuned for the used image resolution of 20 cm by 5-fold cross validation. These parameters mostly reflect geometrical properties of the vehicle clusters. Thus 80 % the non-vehicle areas can be rejected from further processing. Nearly all remaining wrong hypotheses are classified in the last processing stage. Therefore, a number of statistical values are calculated from geometric and radiometric properties of the remaining clusters in the confidence image and in all channels of the RGB image. Due to the partially high correlation between those channels the total number of more 100 statistical features is reduced by principal component analysis (PCA) transformation to the first 40 components which contain 99 % of the descriptive information. This reduced feature set is used to train a Support Vector Machine (SVM). The slack variables and kernel type of the SVM are also optimized for the specific resolution by cross validation leading to an average False-Positive-Rate of approximately 12 %. As it will be shown 4 section, this accuracy is reflected in the correctness of the numerical evaluation. Figure 3 shows the results of the interest point operator (marked by circles) and the final vehicle detection (marked by crosses).

3.2 Vehicle Tracking

Vehicle tracking between two consecutive images of the burst is done by template matching based on normalized cross correlation. At each position of a detected vehicle in the first image of the image sequence a template image is created. Then, in the second image of the sequence a search space for this vehicle is generated. Its size and position depends on the position of the vehicle in the first image, driving direction obtained from NAVTEQ road database, and the expected maximum speed for the road plus a certain tolerance. Within that search space, the template is correlated and the maximum correlation score is stored in connection with the template position within the maximum appeared. This normally represents the found match of each vehicle in generally. The correlation is done in RGB-color space. Fig 4 shows a typical result of the tracking algorithm obtained on the motorway A96 near Munich. Left image was taken 0.5 s before right image. The dashed lines show corresponding matching pairs from normalized cross correlation. Since all images are stored with their recording time, vehicle speed can directly be calculated from both the



Figure 4: Tracking of a group of cars on motorway A96 near Munich. Corresponding matches are marked by dashed lines. Mind, that the motorbike was not tracked, because it was not detected (the classifier of detection was not trained to two-wheeled vehicles).

position of the vehicle detected in the first image and the position of the corresponding match in the second image. Then, vehicle tracking is applied to the following image pair of the sequence. Several measures to chase mismatches are implemented mainly based on plausibility of velocity and driving direction, constance of velocity and driving direction within a burst, and plausibility of individual speed and direction with respect to local average values. Several potential mismatches as well as matches based on false positive vehicle detection can be eliminated that way.

After traffic data extraction the results are immediately copied to PC 5 (Fig. 1) and directly sent to the ground via S-band downlink. There, data can be used in a traffic internet portal for road level of service visualization and for traffic simulation.

3.3 Performance

Actuality of road traffic data is a general concern. For the use of aerial recorded data in the traffic simulation an actuality of less than five minutes is required. This means between exposure and receiving traffic data on the ground a maximum delay of five minutes is permitted. Hence, the processing chain must be optimized for processing speed. If traffic data extraction is limited to main roads, the bottle neck of the chain is produced by the orthorectification process that takes 10 to 12 s for each nadir image. The actuality criterion is fulfilled for the first bursts of each flight strip easily, but a stack of unprocessed images is built up that leads to a critical length of the flight path. If the critical length is exceeded, the actuality criterion of the simulation will be overrun. This critical length of the flight path can be estimated. Taking into account a typical flight speed of 70 m/s, 3 images recorded per burst, a break of 7 s between each burst, the critical length is around 5 km. In case of full traffic data extraction in urban cores the bottle neck moves to the traffic processor that slightly cannot keep orthorectification performance (Fig. 5). Nevertheless, for road level of service visualization, the performance of the present processing chain is sufficient, since the hard actuality criterion of the simulation does not apply in that case. However, the present processing chain holds potential for improvement of calculation time, even in the orthorectification process (section 5).

Scene	Suburban & Motorways	Urban Core	Total
Images evaluated	73	6	79
True Positives	5545	2911	8456
False Positives	613	429	1042
False Negatives	424	317	741
Correctness	90 %	87 %	89 %
Completeness	93 %	90 %	92 %
Quality	84 %	80 %	83 %

Table 2: Evaluation of vehicle detection quality.

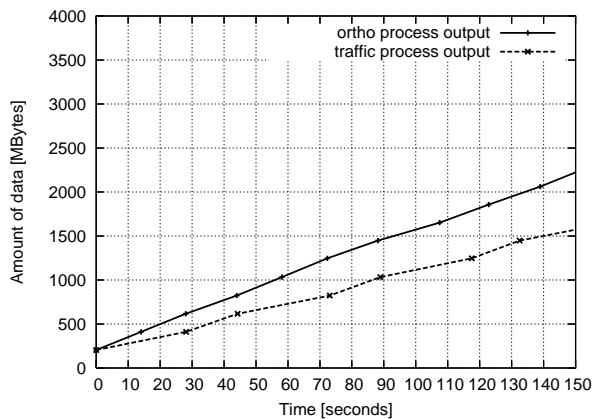


Figure 5: The diagram shows the amount of data which is processed by the Ortho Module but not by the Traffic Processor in case of full traffic data extraction including all road categories and urban core scenarios.

Campaign	BAUMA 1	BAUMA 2	Total
Bursts evaluated	29	19	48
True Positives	1002	724	1726
False Positives	75	47	122
False Negatives	36	23	59
Correctness	93 %	94 %	93 %
Completeness	97 %	97 %	97 %
Quality	90%	91%	91 %

Table 3: Evaluation of vehicle tracking quality.

4 RESULTS AND ACCURACY

Quality of traffic data obtained from the processing chain was evaluated on image sequences obtained on Cologne and "BAUMA" Munich campaigns. The Cologne image data were used for validating detection accuracy, whereas Munich data were used for evaluating tracking. The data represent a mix of scenarios ranging from urban core and suburban roads to motorways. Due to the higher complexity of the scenes, the quality of traffic data extracted in metropolitan cores is somewhat lower than on motorways and suburban areas. This deposits in vehicle detection notably. Therefore, the quality of vehicle detection is examined while distinguishing between these different scenes. However, each campaign contains a mix of both scenes, since German city cores are typically limited to a diameter of a few kilometers, even in German major cities. Therefore, a total quality containing both scene types is listed as well, giving the typical quality of the detection to be expected in operational use. The evaluation of tracking distinguishes between the two Munich "BAUMA" campaigns, since the weather and illumination conditions were better at the flight on 22.04. The definitions for completeness, correctness and quality are:

$$\begin{aligned} \text{Correctness} &= \frac{\text{true positives}}{\text{true positives} + \text{false positives}} \\ \text{Completeness} &= \frac{\text{true positives}}{\text{true positives} + \text{false negatives}} \\ \text{Quality} &= \frac{\text{true pos}}{\text{true pos} + \text{false pos} + \text{false neg}} \end{aligned}$$

with *true positives* being the number of vehicles detected, *false positives* the number of non-vehicle detections, and *false negatives* the number of vehicles missed. In tracking evaluation *true positives* is the number of vehicles tracked correctly, *false positives* the number of mistracked vehicles, and *false negatives* the number of vehicles detected, but not tracked (vehicles that are ob-

scured during image bursts and cannot be tracked are not counted as *false positives*).

Table 2 shows the results of detection algorithm. With a value of around 90 % correctness of vehicle detection is at high level in total and in suburban and motorway situations. In urban cores the correctness drops slightly to 87 %. The completeness with 93 % in suburban and motorway scenes and 92 % in total is at high level again providing precise estimates of local traffic density for traffic simulations or road level of service visualization. In urban core regions it drops a little to a value of 90 %. This all results in a total quality of 83 %. Table 3 presents the results of evaluating vehicle tracking algorithm. The underlying image database represents a mix of urban core and suburban/motorway scenes. Tracking performs well with a correctness of about 93 % and a completeness of 97 %. There is nearly no difference between the results obtained from two flights at different dates indicating that tracking algorithm might be robust against slight changes in weather and illumination conditions.

The system accuracy is the product of detection and tracking quality. In the present case it is about 75 %. This makes the system accuracy competitive to that of ground based sensor networks. The quality of a typical induction loop is better than 90 % (e.g. Leonhardt, 2004) at time of production. During years of continuous operation it decreases slowly. In a complete sensor network of a metropolitan area there is a mix of new and older sensors, and some of them have even failed completely. This drops down the average quality or system accuracy of the sensor network. In Munich, the system accuracy of the complete ground based sensor network for traffic data acquisition is at a value of 80 %, as stated by Munich integrated traffic management center. The quality of traffic data obtained by the presented remote sensing system being competitive to that of road sensor networks in connection with the good spacial resolution (including minor roads) and the reliability in case of ground damage makes the system well suited for its operation during mass events and disasters.

5 CONCLUSIONS AND FUTURE WORK

The quality of traffic data obtained by the presented remote sensing system being competitive to that of road sensor networks in connection with the good spacial resolution (including minor roads) and the reliability in case of ground damage makes the system well suited for its operation during mass events and disasters. In the evaluated case with a mixture of urban core, suburban roads, and (local) motorways, the overall system accuracy is approximately 75 %. This accuracy value is comparable to that of typical metropolis ground based sensor networks with the advantage of the remote sensing system, that traffic data on all road categories (including smallest minor roads) can be recorded. E.g. in case of traffic congestion on main roads and motorways not only the traffic density of the main road but also densities on alternative routes (that are not covered by induction loops or stationary traffic cameras) can be determined. However, the operating costs of this prototype system are quite high which limits its application to temporally limited scenarios like mass events or disasters. With the ongoing development of UAV or HALE unmanned aircrafts, further applicability of the system may occur in future.

The system is sufficient for real-time traffic data extraction from aerial image time series on main roads, even in metropolitan core scenarios. In case of full traffic data extraction including all roads in urban core scenes with several thousands of vehicles per scene, a slight lack of performance in the traffic data algorithms is present. In order to close this gap, two measures are taken. Firstly, Adaboost classifier will be cascaded. Secondly,

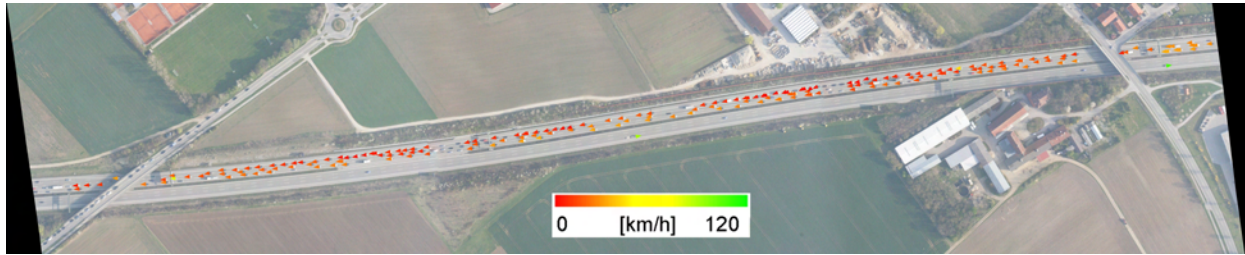


Figure 6: Traffic data extracted automatically by the processing chain on BAUMA campaign 2010 near exit "Munich exhibition center" of motorway A 94. Quality of traffic data is 80 % in case of that campaign. Periodic gaps in traffic data are due to missing overlap between image bursts (which can be corrected easily by flight planning in future campaigns).

car tracking algorithm by template matching will be implemented as extreme parallelization on actual high-performance graphics adapters. In spite of scope for increasing performance we can conclude that our system has reached an operational state and is ready for application in crisis and events.

References

- Behrisch, M., Bonert, M., Brockfeld, E., Krajzewicz, D. and Wagner, P., 2008. Event traffic forecast for metropolitan areas based on microscopic simulation. In: Third International Symposium of Transport Simulation 2008 (ISTS08), Queensland, Australia.
- Bethke, K.-H., Baumgartner, S. and Gabele, M., 2007. Airborne road traffic monitoring with radar. In: World Congress on Intelligent Transport Systems (ITS), Beijing, China, pp 16.
- Börner, A., Ernst, I., Ruhe, M., Sujew, S. and Hetscher, M., 2004. Airborne camera experiments for traffic monitoring. In: XXth ISPRS Congress, 1223 July 2004, Vol. XXXV, Part B, 6 p.
- Busch, F., Glas, F. and Bermann, E., 2004. Dispositionssysteme als fcdquellen fr eine verbesserte verkehrs-lagerekonstruktion in stden-eine erblick. Straen-verkehrstechnik.
- Ernst, I., Sujew, S., Thiessenhusen, K.-U., Hetscher, M., Rassmann, S. and Ruhe, M., 2003. Lumos - airborne traffic monitoring system. In: Proc. IEEE Intelligent Transportation Systems, Vol. 1, pp. 753–759.
- Freund, Y. and Schapire, R. E., 1997. A decision-theoretic generalization of on-line learning and an application to boosting. Journal of Computer and System Sciences 55(1), pp. 119–139.
- Friedman, J., Hastie, T. and Tibshirani, R., 2000. Additive logistic regression: a statistical view of boosting. Annals of Statistics 28(28), pp. 337–407.
- Grabner, H., Nguyen, T., Gruber, B. and Bischof, H., 2008. On-line boosting-based car detection from aerial images. 63(3), pp. 382–396.
- Kurz, F., Müller, R., Stephani, M., Reinartz, P. and Schroeder, M., 2007. Calibration of a wide-angle digital camera system for near real time scenarios. In: ISPRS Hannover Workshop 2007, High Resolution Earth Imaging for Geospatial Information, Hannover, 2007-05-29-2007-06-01, ISSN 1682-1777.
- Lenhart, D., Hinz, S., Leitloff, J. and Stilla, U., 2008. Automatic traffic monitoring based on aerial image sequences. Pattern Recognition and Image Analysis 18(3), pp. 400–405.
- Leonhardt, A., 2004. Detektortest siemens ld4. Technical report, TU München <http://www.siemens.nl/ITS/getfile.asp?id=52>.
- Lepetit, V. and Fua, P., 2006. Keypoint recognition using randomized trees. Pattern Analysis and Machine Intelligence, IEEE Transactions on 28(9), pp. 1465–1479.
- Lienhart, R., Kuranov, A. and Pisarevsky, V., 2003. Empirical analysis of detection cascades of boosted classifiers for rapid object detection. Pattern Recognition 2781, pp. 297–304.
- Müller, R., Lehner, M., Müller, R., Reinartz, P., Schroeder, M. and Vollmer, B., 2002. A program for direct georeferencing of airborne and spaceborne line scanner images.
- Nguyen, T. T., Grabner, H., Bischof, H. and Gruber, B., 2007. On-line boosting for car detection from aerial images. In: Proc. IEEE Int Research, Innovation and Vision for the Future Conf, pp. 87–95.
- Reinartz, P., Lachaise, M., Schmeer, E., Krauss, T. and Runge, H., 2006. Traffic monitoring with serial images from airborne cameras. 61(3-4), pp. 149–158.
- Rosenbaum, D., Charmette, B., Kurz, F., Suri, S., Thomas, U. and Reinartz, P., 2008. Automatic traffic monitoring from an airborne wide angle camera system. In: ISPRS08, p. B3b: 557 ff.
- Schaefer, R.-P., Thiessenhusen, K.-U. and Wagner, P., 2002. A traffic information system by means of real-time floating-car data. In: Proceedings of ITS World Congress, October 2002, Chicago, USA.
- Schapire, R. E. and Singer, Y., 1999. Improved boosting algorithms using confidence-rated predictions. Machine Learning 37(3), pp. 297–336.
- Suchandt, S., Eineder, M., Breit, H. and Runge, H., 2006. Analysis of ground moving objects using srtm/x-sar data. 61(3-4), pp. 209–224.
- Viola, P. and Jones, M., 2004. Robust real-time face detection. International Journal of Computer Vision 57, pp. 137–154.

CHANGE DETECTION OF BUILDING FOOTPRINTS FROM AIRBORNE LASER SCANNING ACQUIRED IN SHORT TIME INTERVALS

M. Rutzinger^{a,*}, B. Rűf^{b,c}, B. Höfle^d, M. Vetter^e

^a ITC - Faculty of Geo-Information Science and Earth Observation of the University of Twente, 7500 AA Enschede, The Netherlands - rutzinger@itc.nl

^b alpS-Centre for Natural Hazard Management, 6020 Innsbruck, Austria

^c University of Innsbruck, Department of Geography, 6020 Innsbruck, Austria - benno.ruef@uibk.ac.at

^d University of Heidelberg, Department of Geography, 69120 Heidelberg, Germany - hoefle@uni-heidelberg.de

^e Vienna University of Technology, Institute of Photogrammetry and Remote Sensing, 1040 Vienna, Austria - mv@ipf.tuwien.ac.at

Commission VII

KEY WORDS: Airborne laser scanning, building segments, classification, object-based change detection, urban areas

ABSTRACT:

Several recent studies have shown that airborne laser scanning (ALS) of urban areas delivers valuable information for 3D city modelling and map updating. Building footprint detection from multi-temporal ALS lacks in comparability because of changing ALS flight parameters, flying season, interpolation settings if digital elevation models are used, and the ability of the used building detection method to deal with these influences. So far, less attention has been paid to change detection of buildings within a short time span (approx. three months), where major problems are the high variability of vegetation over time and to distinguish temporary objects from small changes of buildings, which are currently under construction and demolition, respectively. We introduce an object-based workflow to investigate how unchanged objects can be defined, which variability in the object appearance is allowed to define an object as unchanged, and at which threshold a change can be indicated. The test site is situated in the city of Innsbruck (Austria) where ALS data is available from summer and autumn in 2005. In an initial step building footprints are derived by an object-based image analysis (OBIA) detection method for each flight independently. The parameters for building detection are derived for a training site in order to automatically derive the rules of the classification tree. Then the object features of buildings derived from the different flights are compared to each other and separated into the classes unchanged building, new building, demolished building, new building part, and demolished building part. The results are verified by a reference, which was created manually by visual inspection of the elevation difference image of both epochs. For new buildings and building parts 90% and for demolished buildings and building parts 32% were detected correctly. The detection of demolished buildings is strongly influenced by the appearance of high vegetation, which is caused by the decreasing heights of trees by comparing summer (leaf-on) and autumn (leaf-off) ALS data.

1. INTRODUCTION

Urban areas are highly dynamic landscapes where changes occur in different rates and frequencies. Nowadays airborne laser scanning (ALS) data is available for several urban areas in Europe. The purpose of acquiring multi-temporal ALS data is on the one hand to have the most recent surface representation of a certain area and on the other hand to be able to perform change detection analysis for monitoring purposes. Change detection plays a key role in urban planning i.e. monitoring of urban sprawl and its dynamics (e.g. Durieux et al., 2008; Maktav et al., 2005) and to detect changes after natural hazards such as earthquakes (e.g. Vu et al., 2004; Rehor et al., 2008).

The objective of this paper is to show how changes appear in ALS data, caused by either seasonal differences or by urban dynamics i.e. construction activities. It is interesting to see how these changes are captured in data, which was flown within only three months, which is a very short time period for urban multi-temporal ALS data sets. The aim is to explore the

performance of multi-temporal building detection by applying the method of Rutzinger et al. (2006).

2. RELATED WORK

Champion et al. (2009) test four different building detection approaches (Champion, 2007; Matikainen et al., 2007; Olsen and Kudsen, 2005; and Rottensteiner, 2008). The input data were infrared orthophotos and digital surface models (DSMs) from image matching and for one test site from ALS. A comprehensive comparison was undertaken in order to investigate the impact of input data types, resolution, scene complexity and methods. The authors state that high quality DSMs are important for reliable building and change detection. However, the ALS data available in this study was first echo data, which made it difficult to differentiate buildings from vegetation. The detection of changing buildings in ALS DSMs was already early investigated by Murakami et al. (1999) by subtracting two DSMs and filtering the difference image in

* Corresponding author.

order to remove elevation differences along edges of unchanged buildings. A building change detection method using exclusively ALS data in an object-based approach was presented by Vögtle and Steinle (2004). Vosselman et al. (2004) developed a method for updating cadastral maps by detecting buildings from ALS data and comparing them to an existing building footprint database. Further work on building footprint extraction and changed detection such as combining aerial images with ALS DTMs or using more recent remote sensing data for updating of existing cadastral maps is not reviewed here since the work presented focuses on the usage of ALS data only. However, for a comprehensive overview of related work on building footprint detection methods and building change detection the reader is referred to the recently published article by Matikainen et al. (2010).

3. TEST SITE AND DATA SETS

3.1 Test site

The test site covers the major part of the city centre of Innsbruck (Austria). It comprises a densely built-up area with varying building types (multi-story block buildings, single family houses with gardens, large industrial buildings), agricultural land, and forested areas. The data sets also contain temporary objects such as cars, trains, market booths, etc. which appear as changes in the data (Fig. 2).

3.2 Data sets

The ALS data were acquired as pilot surveys for the laser scanning project Tyrol, Austria (Anegg, 2007). The two data sets overlap the major part of the city of Innsbruck, the city centre and parts to the west including the airport (Fig. 1). The overlapping area represents the border of two larger ALS campaigns in the north (summer scan) and south (autumn scan). Both flights were acquired with an Optech ALTM 2050. The average point density of both flights is around 4 pts/sqm. The test site covers an area of 10 km² and contains 2441 building footprints in the summer data set.

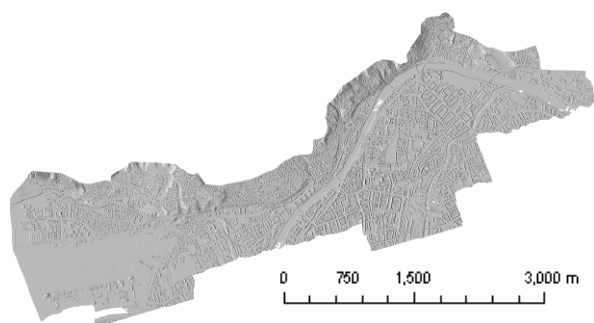


Fig. 1. Shaded relief map of the last echo DSM of the autumn flight showing the test site of Innsbruck (Austria) where multi-temporal airborne laser scanning data is available

3.3 Change detection

As a manual reference a difference raster (diffDSM) of both DSMs was calculated, which visualizes all differences in

elevation, which might disturb the building change detection procedure. Figure 2 shows in green areas, where the elevation decreased and in red, where the elevation increased.

First of all, building edges show increases and decreases, indicating here a shift to north west, which can be caused by (i) insufficient registration of the data, (ii) difference of scan angle in both scans and therefore different amount of echoes on building walls, and (iii) different echo distribution and local point density which effects the aggregation of points to raster cells when calculating the DSM. Further decreases are reasoned by parking cars, umbrellas in front of restaurants in the inner city, which were removed in the autumn scan (Fig. 2, lower arrow), maize fields, which were harvested, and deciduous trees, which lost their leaves. While in the summer scan the laser beam was reflected on the tree canopy, in the autumn scan the laser beam was reflected on the branches or even on the ground, which leads to negative heights in the diffDSM. An increase of elevation can be found in the city centre where the Christmas tree for the Christmas market was already installed (Fig. 2, upper arrow).

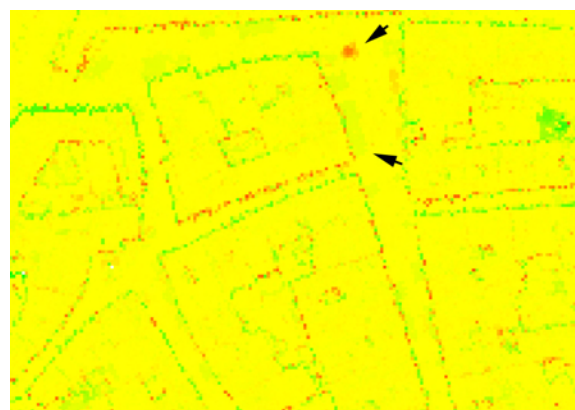


Fig. 2. Different aspects on elevation changes in the difference digital surface model from the city centre

4. METHOD

The workflow of the proposed building change detection comprises two major steps, which are firstly the object-based building footprint detection (Sect. 4.1), which is applied for each laser scan independently and secondly the change detection procedure (Sect. 4.2).

4.1 Extraction of building footprints

In a first step a first-last-echo difference model (FLDM) is calculated, by subtracting the last reflection (lowest elevation) from the first reflection with the highest elevation in order to derive a vegetation mask. Elevation differences of reflections within a single laser beam mainly occur at the canopy of high vegetation and building edges. Hence, the difference model is further enhanced by applying a filter for removing long thin structures representing building edges and small areas (Fig. 3). The areas covered by the vegetation mask are set to “no data” and are not considered any more in the building detection process.

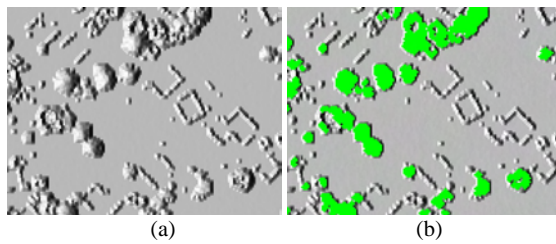


Fig. 3. (a) First-last-echo difference model and (b) the derived enhanced vegetation mask

Next, building regions are segmented by inverting the DSM and applying a fill sinks procedure (Arge et al., 2001; GRASS Development Team, 2010). All high objects are considered as sinks and filled up to the minimum elevation in the individual region in order to guarantee a hydrologically consistent elevation model. This model is subtracted from the original DSM and thresholded at a certain minimum height in order to remove artefacts, i.e. overestimation of building outlines or the influence of low vegetation (Fig. 4).

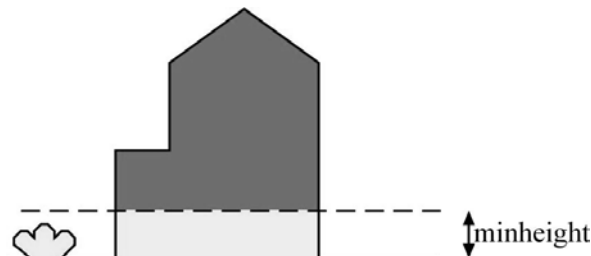


Fig. 4. Outline detection of building footprints by fill sinks and height constraint

The remaining building segments are enhanced by applying a morphological opening, which further smoothes and removes remaining overestimation of the building outlines (Fig. 5).

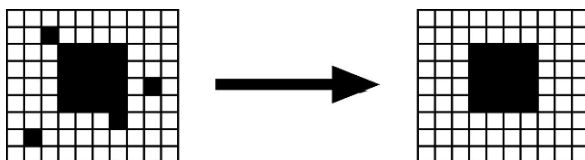


Fig. 5. Outline enhancement by morphological opening.

The segments are classified into buildings and non-buildings using a classification tree (Breiman et al., 1993; Maindonald and Braun, 2007) derived from a training area. As training segments building footprints and non-building segments are selected from the derived segments. For those, several statistical features such as first order statistic on elevation, object heights, first-last-echo difference, standard deviation of slope and aspect derived from the DSM, and geometrical object properties such as area and shape indices. Table 1 lists all the input features which were calculated to build up the classification tree.

By applying the classification tree (Therneau and Atkinson, 1997) the sample set is divided into subsets which are tested and compared in order to define the optimal splitting rule between both classes. In fact, the developed rule base is a box-classifier in feature space, which has crisp thresholds at each node (rule). The features can occur in multiple hierarchies of

the classification tree. The levels, i.e. the complexity of the classification tree, can be regulated by defining a complexity parameter, which is also known as pruning. In general, the complexity of a classification tree should be kept minimal in order to avoid modelling the data itself instead of describing the class specific characteristics.

Object Feature	DSM	FLDM	Segments
Stdev object height	X		
Mean object height	X		
Max object height	X		
Min object height	X		
Mean FLDM		X	
Area			X
Shape (perimeter/area)		X	X
Shape (circumscribing circle)		X	X
Stdev slope	X		
Stdev curvature	X		

Table 1. Object features calculated as classification input

4.2 Change detection

The building change detection procedure is based on the automatically extracted building footprints and their attributes exclusively. The procedure distinguishes the following cases:

- unchanged building or building part
- new building
- demolished building
- new building part
- demolished building part

The change detection compares spatially related building footprints and their attributes derived from each epoch individually. In order to be able to detect also gradual changes at buildings such as the construction of a new story, not only the appearance of another object polygon is checked but also the mean difference of the elevation in the segment part. There are several methods how to measure detection success of building footprint extraction (Rutzinger et al., 2009) In the following the change detection results are evaluated by calculating the overall accuracy as

$$\text{overall accuracy} = \text{TP} / (\text{TP} + \text{FP} + \text{FN}) \quad (1)$$

with true positives (TP), which are segment parts classified as change which are also changes in the reference and the false positives (FP), which are segment parts classified as change where no changes occur in the reference. False negatives (FN) are changes which are in the reference but are not detected by the method.

5. RESULTS

5.1 Building detection

The vegetation mask is derived for both input data sets and then merged in order to get maximum vegetated area. The building segments from both epochs are derived by the fill sinks approach (Sect. 4.1) and were further selected by a minimum height of 2.5 m and minimum area of 10 sqm. The shape of the

building segments is enhanced using morphological opening of 3 m and 4 m kernel size, respectively. For a training area containing 103 buildings two classification trees were derived independently. The features automatically selected for classification were area, shape index, and first-last-echo difference. The complexity of the derived trees is very low. The trees consist of one and two splitting nodes, respectively. Figure 6 shows a subsection of the classified building footprints from the autumn data set.

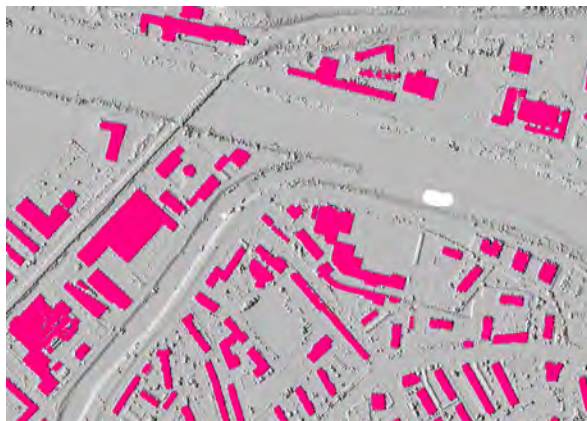


Fig. 6. Classified building footprints from the autumn data set

5.2 Change detection

The comparison of the building footprints from the two epochs is done by a simple overlay of the segments. This leads to an extreme overestimation of changes since also small differences, which occurred from slightly different building outlines in both data sets (i.e. due to differing sensor position in each epoch, registration and rasterization) and uncertainty in the building detection method.

These wrongly detected changes are apparent as long and thin segment parts, which can be identified by calculating the shape index. Furthermore, the mean elevation within a segment part must not differ more than 3 m, which ensures that detected changes are equal or larger than the approximate floor height of a building. The overestimation of changes can be enhanced by selecting and relabeling segments parts based on their shape index, height difference between both DSMs, and area.



Fig. 7. Automatically detected locations of changed buildings with two zoomed-in examples from the city centre

The final result of the automatic building footprint change detection is shown in Figure 7. The overall accuracy of detected changes reaches 54%. This comes from a remaining overestimation of detected changes at demolished buildings. The plot in Figure 8 shows all the detected changes labelled by the actual changes derived from the reference. The changes are plotted by their area and height difference. It can be seen that the new and partly new buildings are detected very well reaching an overall accuracy of 90%. The problem arises for demolished and partly demolished buildings where the overall accuracy drops to 32%. This is mainly caused by trees and tree parts wrongly classified as buildings. Further changes not relating to buildings occur at the terrain such as road construction or come from extensive registration errors, which were apparent at the boundary of the test site.

Figure 9 shows the overall accuracy plotted as solid black line for areas from 0 to larger than 500 sqm with a bin size of 50 sqm. The strong influence of changes caused by vegetation for segments smaller than 150 sqm is clearly indicated. If the vegetation removal could be improved, the overall accuracy for the 100 and 150 bin would increase to 100% and 75%, respectively as indicated by the dashed grey line.

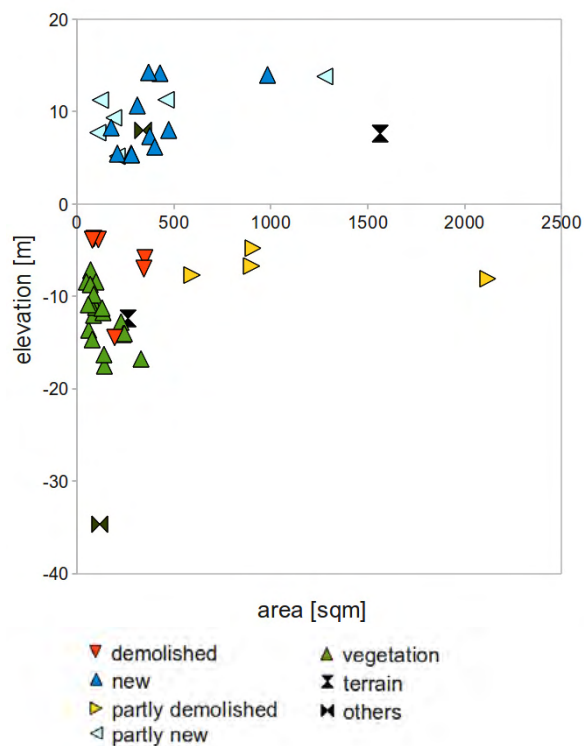


Fig. 8. Detected changes labelled by reference and clustered by elevation change and area

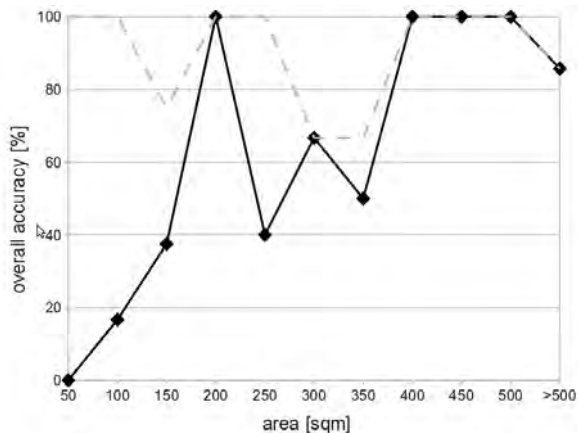


Fig. 9. Overall accuracy of detected building changes as a function of changed area. The solid line shows the actual accuracy distribution, while the dashed line shows the theoretical accuracy distribution, if vegetation would be classified correctly.

6. CONCLUSION AND OUTLOOK

The presented study shows that urban areas are highly dynamic environments where major changes on buildings occur also in rather short time intervals (three months). Changes in ALS data appear from several sources such as anthropogenic objects, temporary objects, vegetation, and changes due to data capture conditions and data quality. The assessment of the change detection results shows that the appearance and phenological

changes of high vegetation influence the detection success most. If the building detection method tends to misclassify vegetation, care has to be taken to the phenological behaviour of the vegetation between the data acquisition times. One would expect similar good detection results for demolished buildings if a winter and spring data set is compared. Misclassification due to planting of new trees did not occur in the data set. The results show the importance of a reliable vegetation detection procedure in order to be able to monitor changes in urban areas. A more advanced vegetation detection working in the point cloud and making use of full-waveform information might improve the results significantly (e.g. Rutzinger et al., 2008). Future work should focus on the detection and differentiation of building footprints with an area below 100 sqm and height changes below 3 m in order to be able to detect changes on small buildings and to distinguish them from temporary objects. In order to be able to analyse objects in this scale an algorithm working in the point cloud directly might be needed.

REFERENCES

- Anegg, J., 2007. *Laserscanning Tirol – Bayern*. Presentation, Federal State of Tyrol, Geoinformation. <http://www.interreg-bayaut.net> (accessed 2.6.2010)
- Arge, L., Chase, J., S., Halpin, P., N., Toma, L., Vitter, J., S., Urban, D., Wickremesinghe, R., 2001. Flow computation on massive grids. In: *Proceedings of the Ninth ACM International Symposium on Advances in Geographic Information Systems*, pp. 82-87.
- Breiman, L., Friedman, J., H., Olsen, R., A., Stone, C., J., 1993. *Classification and Regression Trees*. Chapman & Hall, CRC, New York, p. 358
- Champion, N., 2007. 2D building change detection from high resolution aerial images and correlation Digital Surface Models. In: *International Archives of the Photogrammetry, Remote Sensing and Spatial Information Sciences*, Vol. XXXVI-3/W49A, pp. 197-202.
- Champion, N., Rottensteiner, F., Matikainen, L., Liang, X., Hyypä, J., Olsen, B., P., 2009. A test of automatic building change detection approaches. In: *International Archives of Photogrammetry, Remote Sensing and Spatial Information Sciences*, Vol. XXXVIII, Part 3/W4, pp. 145-150.
- Durieux, L., Lagabrielle, E., Nelson, A., 2008. A method for monitoring building construction in urban sprawl areas using object-based analysis of Spot 5 images and existing GIS data. *ISPRS Journal of Photogrammetry & Remote Sensing* 63, pp. 399-408
- GRASS Development Team, 2010. *GRASS 6.4 Users Manual*. ITC-irst, Trento, Italy. http://grass.itc.it/grass64/manuals/html64_user/ (accessed 2.6.2010)
- Maindonald, J., Braun, J., 2007. *Data analysis and graphics using R - An Example-based approach*, second edition. Cambridge Series in Statistical and Probabilistic Mathematics. Cambridge University Press. p. 509.

Maktav, D., Erbek, F., S., Juergens, C., 2005. Remote sensing of urban areas. *International Journal of Remote Sensing*, 26(4), pp. 655-659.

Matikainen, L., Hyyppä, J., Ahokas, E., Markelin, L., Kaartinen, H., 2010. Automatic Detection of Buildings and Changes in Buildings for Updating of Maps. *Remote Sensing*, 2(5), pp. 1217-1248.

Matikainen, L., Kaartinen, K., Hyyppä, J., 2007. Classification tree based building detection from laser scanner and aerial image data. In: *International Archives of the Photogrammetry, Remote Sensing and Spatial Information Sciences*, Vol. XXXVI, pp. 280-287.

Murakami, H., Nakagawa, K., Hasegawa, H., Shibata, T., Iwanami, E., 1999. Change detection of buildings using an airborne laser scanner. *ISPRS Journal of Photogrammetry & Remote Sensing*, 54, pp. 148-152.

Olsen, B., Knudsen, T., 2006. Building change detection: a case study comparing results from analog and digital imagery. Technical report, KMS (National Survey and Cadastre) and Danish National Space Centre.

Rehor, M., Baehr, H.-P., Tasha-Kurdi, F., Landes, T., Grussenmayer, P., 2008. Contribution of two plane detection algorithms to recognition of intact and damaged buildings in lidar data. *The Photogrammetric Record*, 23(124), pp. 441-456.

Rottensteiner, F., 2008. Automated updating of building data bases from digital surface models and multi-spectral images: Potential and limitations. In: *International Archives of Photogrammetry, Remote Sensing and Spatial Information Sciences*, Beijing, China, Vol. XXXVII, Part B3A, pp. 265-270.

Rutzinger, M., Höfle, B., Geist, T., Stötter, J., 2006. Object-based building detection based on airborne laser scanning data within GRASS GIS environment. In: *Proceedings UDMS 2006: Urban Data Management Symposium*, Aalborg, Denmark., digital media.

Rutzinger, M., Höfle, B., Hollaus, M., Pfeifer, N., 2008. Object-Based Point Cloud Analysis of Full-Waveform Airborne Laser Scanning Data for Urban Vegetation Classification. *Sensors*, 8(8), pp. 4505-4528.

Rutzinger, M., Rottensteiner, F., Pfeifer, N. 2009. A comparison of evaluation techniques for building extraction from airborne laser scanning. *IEEE Journal Selected Topics in Applied Earth Observation and Remote Sensing*, 2(1), pp. 11-20.

Therneau, T., M., Atkinson, E., J., 1997. *An introduction to recursive partitioning using the rpart routines*. Department of Health Science Research, Mayo Clinic, Rochester, MN., technical report 61 edition. <http://www.mayo.edu/hsr/techrpt/61.pdf> (accessed 2.6.2010)

Vögtle, T., Steinle, E., 2004. Detection and recognition of changes in building geometry derived from multitemporal laserscanning data. In: *International Archives of Photogrammetry, Remote Sensing and Spatial Information Sciences*, Istanbul, Turkey, Vol. XXXV, Part B2, pp. 428-433.

Vosselman, G., Gorte, B.G.H., Sithole, G., 2004. Change detection for updating medium scale maps using laser altimetry. In: *International Archives of Photogrammetry, Remote Sensing and Spatial Information Sciences*, Istanbul, Turkey, Vol. XXXV, Part B3, pp. 207-212.

Vu, T., T., Matsuoka, M., Yamazaki, F., 2004. LIDAR-based change detection of buildings in dense urban areas. In: *Proceedings of IGARSS'04*, Anchorage, AK, USA, Vol. 5, pp. 3413-3416.

ACKNOWLEDGEMENTS

The authors want to thank the company TopScan GmbH for acquiring the data within the alpS project A1.5. LISA (LiDAR Surface Analysis).

LAND COVER AND LAND USE RESEARCH FOR A CREATION OF A NATIONAL MAPPING AGENCY FRAMEWORK

C Sanchez Hernandez ^a, G. Hart

^a Ordnance Survey, Research, Romsey Road, Southampton, SO16 4GU, UK

KEY WORDS: Land Cover, Land Use, Ontology, Framework, Classification

ABSTRACT:

Historically Ordnance Survey has collected information on land cover and land use but as this for primarily cartographic purposes it has not been done in a methodical and comprehensive way. As a result the land cover and land use information currently captured by Ordnance Survey fits more into historic cartographic categories than a classification system designed to be used for computational purposes..

In future, the challenge for a National Mapping Agency is that designing a classification system that can respond to the needs of a variety of users, and where all possible end uses cannot be known *a priori*. However, there is no one ideal or universal classification of land use and land cover. A review of different land cover and land use classifications within the UK shows that a classification is usually designed for a particular purpose, a particular geographical area or a particular user. An attempt to create a national categorisation of land use and land cover was the NLUD (National Land Use Database) classification. However, this has gained little traction within government agencies and it lacks the degree of flexibility that a national classification should allow for.

Our research has concentrated on two different levels: (i) the design of a flexible framework that would allow for the integration and relation of different classification systems and taxonomies and (ii) the design of an ontology and a high level classification system for use with data collected from different sources including remote sensing and GIS and fit for the purposes of a National Mapping framework.

A test performed in the urban area of Bournemouth has showed promising results. This test has helped to identify what research needs to be done next in terms of methods and data.

1. INTRODUCTION

Land Cover and Land Use Information are widely used by different governmental and commercial organisations in a variety of ways and it is collected and classified differently for every single purpose. However it is currently not possible to link all these data in order to have an integrated set of information at national, regional or even local level.

As a National Mapping Agency we could potentially provide a land cover and land use framework that could respond to the needs of a high variety of users. Although Ordnance Survey currently collects land cover and land use information this is not done in a comprehensive way and it is not delivered to our users in a clear manner. If we were to provide a framework we would have to design a structured data capture, a system for the integration of current classifications and a high degree of flexibility so that users can customise this information for their own purposes. In this paper we will (i) describe the partitioned land cover and land use information scene in the United Kingdom, and (ii) describe the structure for an ontological framework that could help to ultimately incorporate all this information and (iii) describe a trial in an urban area south of the United Kingdom (Bournemouth) that was performed in order to identify further research.

1.1 Current Land Cover and Land Use classifications in the UK

It is well known that land cover and land use information has become increasingly important in order to make many types of national, regional and local decisions. Problems such as natural hazards, uncontrolled development and deteriorating environmental quality need quality and up to date information on land cover and land use.

However, there has been an uncoordinated attempt to categorise and classify different land cover and land use classes by different organisations. All these classifications are some how subjective and there is not a single way of describing the reality that surround us (Lofvenhaft et al. (2002). A look at different land cover and land use classifications within the UK shows that a classification is usually designed for a particular purpose, a particular geographical area or a particular user. According to the Joint Nature Conservation Committee (JNCC) the more widespread classifications used within the UK are:

1.1.1 Biodiversity Action Plan Priority Habitats: These priority habitats cover a wide range of semi-natural habitat types that are judged to be particularly important for biodiversity conservation. The list of priority habitats comprises 65 habitats.

1.1.2 Biodiversity Action Plan Broad Habitats: This classification was developed as part of the UK Biodiversity Action Plan. The Broad Habitats are the framework through which the Government is committed to meet its obligations for monitoring in the wider countryside. The list of Broad Habitats consists of a list of 27 Broad Habitats.

1.1.3 Marine Habitat Classification: The Marine Habitat classification for Britain and Ireland provides a tool to aid the management and conservation of marine habitats. The classification is presented in hierarchical format, and through a series of habitat matrices. It comprises 5 Broad Habitat types, 24 Habitat complexes, 75 Biotope complexes, and 370 Biotopes and Sub-Biotopes.

1.1.4 National Vegetation Classification (NVC): The NVC aims to describe the whole range of British vegetation as a series of plant communities. The NVC comprises 286 community types subdivided amongst 12 major types of vegetation. Many, but not all, of the NVC communities are broken down further into sub-communities, which total 578 in all. A very small number of especially bulky and complex communities have a third level of sub-division, into variants.

1.1.5 Phase 1 Habitat Classification: The Phase 1 Habitat Classification and associated field survey technique provide a standardised system to record semi-natural vegetation and other wildlife habitats. The Phase 1 classification comprises ten broad high level categories. Amongst these, 155 specific habitat types are recognised, each having its own name, alpha-numeric code, description and mapping colour.

1.1.6 Vegetation communities of British lakes: The first comprehensive classification scheme for standing waters in Britain (Palmer 1992; Palmer et al. 1992) was based on macrophyte surveys carried out by the Nature Conservancy Council (NCC) from 1124 standing waters throughout England, Scotland and Wales between 1975 and 1988. This dataset became an important source of information used for a variety of purposes including conservation site selection and the identification of aquatic communities in the National Vegetation Classification (NVC). It shows separate ecological descriptions of 11 distinct lake groups.

1.1.7 BTO Bird Habitat Coding Scheme: The list of species officially recorded in Great Britain is maintained by the British Ornithologists' Union. Information on habitats occupied is derived from the BTO's Breeding Bird Survey. There are four different levels within the classification. There are 10 habitats in the first level and 60 in the second level, 70 in the third level and 88 in the fourth level.

1.1.8 Peterken Woodland Stand Types: The Stand Type system (Peterken 1981) divides woodland into twelve Stand Groups and 39 Stand Types largely on the basis of the trees and shrubs, but also using some soil characters. It was the main woodland classification system used by the conservation 7 agencies from 1977 to 1986, after which it was largely replaced by the NVC. Although there is a broad correlation between these two classifications, there is not a one-to-one relationship (Cooke & Kirby 1994).

1.1.9 Shimwell Urban Habitats: The need for more detailed information on practically all wildlife habitat sites in urban areas results in the need for Phase 2 survey to cover virtually the full extent of the Phase 1 survey, in terms of both the number of sites and the range of habitats.. Urban Phase 2 survey is therefore usually a relatively comprehensive multi-habitat survey and may be carried out either concurrently with the Phase 1 survey or as a follow-up after completion of Phase 1. Up to the present, most urban Phase 2 surveys have been based on a Conspectus of urban vegetation types devised by Shimwell (1983). This describes and classifies some 160 different plant communities of urban habitats, but some users have found it necessary to add to this list.

1.1.10 Vegetation communities of British Rivers: The Vegetation Communities of British Rivers is a revised classification based upon the composition of aquatic plant communities in rivers. It comprises three different levels of classification: (i) River Groups. This highest level consists of four distinct broad groups (ii) River Community Types. This second tier of division comprises ten River Community Types and (iii) Sub-types. This final sub-division includes 38 river sub-types.

1.1.11 UK Land Cover Map: Land Cover Map 2000 records terrestrial and inshore examples of widespread 'Broad Habitats'. The Habitats are elements in a classification designed for monitoring and maintaining biodiversity under the UK Biodiversity Action Plan. In practice, LCM2000 identified 16 Target classes (Level-1); it subdivided these into 27 Subclasses (Level-2). The subclasses included a variety of cover components (Level-3).

1.1.12 The Use Classes Order (UCO): The *Use Classes Order (UCO)* is used to classify use of buildings or other land for the purposes of section 22(2)(f) of the Town and Country Planning Act 1971 which specifies operations or uses and changes of use which are not regarded as involving development and therefore do not require planning permission.

1.1.13 National Land Use Database (NLUD): The *National Land Use Classification (NLUC)* was developed during the early 1970's by a team drawn from central and local government with the aim to devise a standard land use classification for new style development plans introduced by the Town and County Planning Act 1968. Legislative substance was provided by Department of Environment (DOE) Circular 71/74 which requested annual returns on land use change from local authorities classified into the 15 major orders of the NLUC. However the slow and incomplete response led to this exercise being abandoned in the late 1970s.

A modified version of the NLUC formed the basis of the *Land Use Change Statistics (LUCS)* classification developed by DOE in the early 1980s. The classification was designed for recording land use change by Ordnance Survey (OS) field surveyors during the course of map revision. It is a hybrid classification that comprises land use and land cover categories. Since 1985 the LUCS classification has provided the basis for recording land use and land cover change derived from OS mapping and is used in the preparation of annual statistics by ODPM.

A final modification of the NLUD was finalised in 2005 The resulting nomenclatures for use and cover have been

specifically designed to provide a system for classification and reporting that is appropriate to the national level.

1.2 Land Cover and Land Use European classifications

1.2.1 EUNIS Classification: The EUNIS classification is a comprehensive pan-European system to facilitate the harmonised description and collection of data across Europe through the use of criteria for habitat identification; it covers all types of habitats from natural to artificial, from terrestrial to freshwater and marine. EUNIS data are collected and maintained to be used as a reference tool or dataset: for assistance to the NATURA 2000 process (EU Birds and Habitats Directives) and coordinated with the related EMERALD Network of the Bern Convention, for the development of indicators (EEA Core Set, Bio-IMPS, IRENA) for environmental reporting connected to EEA reporting activities

1.2.2 CORINE Biotopes Project Habitats: The CORINE Land Cover Map for 2000 (CLC2000) is produced jointly by the European Commission and the Member States and is an update of a similar map produced for 1990. CLC2000 is designed to be used at a scale of 1:100,000 and has a minimum mappable unit of 25 ha. It records 44 land cover and land use classes which represent the major surface types across Europe.

1.2.3 EU Habitats Directive Annex I : The main aim of the EC Habitats Directive is to promote the maintenance of biodiversity by requiring Member States to take measures to maintain or restore natural habitats and wild species at a favourable conservation status, introducing robust protection for those habitats and species of European importance. The 189 habitats listed in Annex I of the Directive and the 788 species listed in Annex II, are to be protected by means of a network of sites.

1.2.4 Geoland classification : Geoland is a multi-purpose Land Cover data and is the basis for a multitude of applications in environmental management and spatial planning. Hence, the Geoland Core Service Land Cover (CSL) serves the Geoland regional Observatories and a number of national level user organisations with harmonized, topical and geometric correct basic information on Land Cover. The CSL Land Cover database has been designed to easily plug in additional objects (thematic classes) and/or increase the minimum mapping unit, as needed.

1.2.5 LUCAS classification: The LUCAS classification system was established by applying best practise for the construction of land cover and use classifications, as recommended in Eurostat "Manual of Concepts on land use/cover" (Eurostat 2000). The land cover classification is defined in 3 hierarchical levels of detail with 57 classes at the 3rd level, and the land use nomenclature is distinguished in 14 classes at the 3rd level.

Most of the European classification systems are an attempt to standardize land cover and land use nomenclatures across countries for the compilation of an European inventory of land covers and land uses. However, at practical level this has created a two tier classification system in most countries where the different classification systems are still in place and further

classifications are created or compiled from existing ones to report to European institutions or programs.

2. LAND COVER AND LAND USE NATIONAL FRAMEWORK

As the previous section illustrates, the provision of land cover and land use information is varied, partitioned and most of the time focused on specific purposes. In Land Cover a big proportion of the existing classifications are vegetation classifications, broad land cover classifications, or systems related to the description of a specific feature. Thus, they are limited in their capacity to define the whole range of possible land cover classes (di Gregorio, A. and Jansen L., 2000). Land Use classifications seem to be less common or less published but equally customised to user requirements.

From the point of view of National Mapping Agency, instead of creating yet again a new classification that claims to be the best suited to the majority of users maybe the question is how to create a framework that can incorporate all the classifications that already exist so that the user can choose, analyse and visualise the information as it is most suited for their purposes. This is of course very difficult to achieve. Ultimately all classification systems are applied to phenomena that they define in the real world, and where these phenomena differ it may be impossible to always incorporate different systems. Different ways of classifying vegetation may for example result in the emergence of areas that overlap. However, when considering classification systems the tendency is to think in terms of simple hierarchies, but an ontological approach enables classifications to be built in more complex ways than simple subsumption hierarchies. We argue, that whilst such an approach still cannot achieve total resolution, it offers a much better and more flexible approach that should be capable of dealing with the majority of cases and allowing users to adapt the system to their own needs.

One way of creating this framework is to define geographic space as geographical objects, their attributes and relationships (Nunes, 1991). This is an object oriented approach that very much suits the structure of Ordnance Survey data. Each Feature in OS MasterMap® has a primary topographical classification into a descriptive group. The feature is assigned to one or more of 21 groups most of which are categories of real world topographic objects such as Path, Building or Natural Environment. A Descriptive Term gives further classification information about the feature. For example an area feature can have a descriptive group with value Natural Environment that can have one or more descriptive terms specifying the natural land cover types present in the area (OS MasterMap user guide v2.0). Apart from this attribution, MasterMap offers an Address layer and Integrated Transport Network layer (ITN) that provide more attribution related to the use of those geographical features. There is also imagery that forms an Imagery layer that could aid land cover information (although this imagery would have to be processed in a different way that is currently is to take advantage of infrared data).

However there is no relationship established between these attributes or between different layers. Descriptive groups encompass feature classes as well as feature geographic shapes and the group of descriptive terms is also a mixture of attributes that are not grouped in a consistent manner. A descriptive term could include anything from a rock or a top of a cliff to an

electoral or district division. At the moment there is no automatic conversion of addresses or ITN features into land uses or integration of derived information from remote sensing sources. There is a need for content specification of the data in terms of land cover and land use that is currently not in place.

In order to have a clear internal structure of land cover and land use information there was therefore a need to develop an ontology that could establish links and associations. This ontology was developed in the Protégé environment. In the ontology a high level set of classes were created for both land cover and land use and relationships established with each other. It was important to clearly define the different nature of land use and land cover classes as they are normally mixed up in many of the existing classifications. For example, the NLUD land cover classification included classes such as agricultural land or features such as roads and pavements and the land use includes water and open land. Also CORINE land cover classification includes industrial, commercial and transport units as well as mine, dump and construction sites. So a clear definition of terms and relations is obviously needed.

The integration of this ontology within the framework follows the suggestion of Fonseca et al (2000). They suggested an inheritance structure by which we define general classes that contain the structure of a generic type of object and then specialise these classes into subclasses. The subclasses would inherit all the properties of the super-class and add some more of its own. In this way the combined use of objects and ontologies could provide a rich model to represent geographic entities. It also allows us to provide a sensible relationship between land cover and land use in order to help define topographic objects. For example by knowing that the land cover for a “field” is “trees” and also knowing that the land use is “fruit production” then we can deduce that a more specific classification for the area of land is “orchard”. Similarly if we know that an object is classified as an orchard that it must have land cover of trees and its land use is “fruit production”. Also different users have different views on classes. With this framework they could use the main class as a common starting point and add their own subclasses that would inherit all the main properties of that class and serve their particular purpose. Figure 1 reflects this principle.

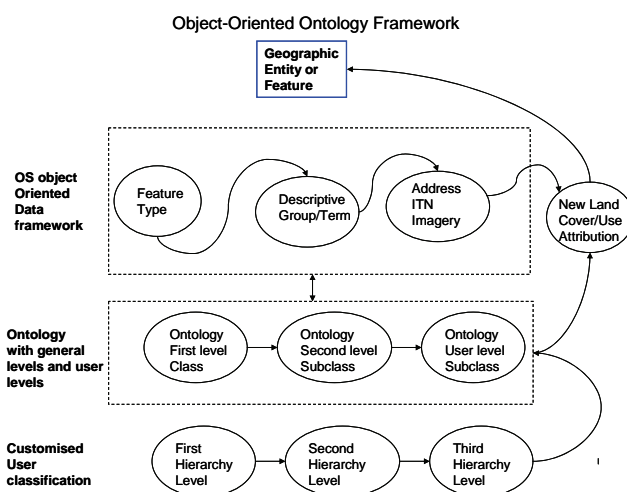


Figure 1: Object-Oriented Ontology Framework

The link between the object oriented structure of Ordnance Survey data and a user classification is done through the intermediate ontology that can translate or incorporate new attributes or subclasses that then can be added to the existing features. Ultimately this framework would allow having automatic customised legends for bespoke maps.

3. BOURNEMOUTH CASE STUDY

3.1 Data and methods

A preliminary trial was focused on the centre of the urban area of Bournemouth (south of England). The framework was used as guidance as there was still not an automatic transformation devised for the trial. The data used for both land cover and land use comprised:

- MasterMap Topography layer
- MasterMap Address Layer 2
- Mastermap Integrated Transport Network (ITN) layer
- Aerial imagery acquired in June 2006, 4 band spectral resolution and spatial resolution of 60 cm.

The customised user classification included in this trial was the NLUD classification.

3.1.1 Land Cover: For the Land Cover classification we used a combination of the layers described above. The ITN layer was used to identify artificial non-build up surfaces whereas the Topography layer did so for artificial build-up areas. For the classification of natural surfaces there was some information available on the Topography layer but the attribution was not rich enough to create a complete classification. So it was a classification from aerial photography that provided the most useful information. The classification consisted of a combination of texture, NDVI and height data that helped to identify high vegetation (trees) from low vegetation (shrubs and grass) and bare surfaces using a Maximum Likelihood classifier in Erdas Imagine.

3.1.2 Land Use: For the Land Use classification Address layer 2 provided basic information about uses in different addresses. ITN layer provided information about transport uses. Topography layer and aerial photography were used to assess whether there were any morphological or visual signs that could help distinguish different areas within the urban space (residential, services, industrial, green open space, etc)

3.2 Results

The Bournemouth trial highlighted different issues for Land Cover and Land Use.

A Land Cover classification that uses the general classes defined in the ontology could be quite straight forward using the data sources available. However this information could be insufficient depending on the level of granularity of other classifications. Also it has to be taken into account that the land cover classification of an urban environment is less complicated than that of a rural environment. The link between the ontology general classes and the NLUD classes worked well. However,

the ontology classes allowed for more flexibility than some of the very specific NLUD classes.

Land Use was a much more complicated subject. The link between the NLUD classification and the classes in the ontology did not present major problems. However, when it came to the actual classification using the data available there were a high number of polygons with unknown land use. Also, the diverse nature of land use meant that some polygons had several potential numbers of uses which could complicate the management and display of information for those using a detailed classification. Granularity is therefore an issue.

There was a clear aid from aerial photography to distinguish residential areas from other that could be categorised as commercial or industrial buildings. It also helped to identify uses such as hospitals or schools and verify some land covers such as sand or scrub. However this assessment was done manually. More research is needed to investigate the possibility of an automatic way of identifying these areas.

3.3 Discussion and further work

The results from the trial in Bournemouth highlighted the following issues:

- Need to assess other data sources. There are a few sources of ancillary data that could help complement the information that OS already hold. Some of them could come from directories such as Thomson, Yell, Experian and Valuation Office. One of the problems with these directories is that their information is generally not georeferenced. A test matching some of these directories to references on the ground achieved a 60% success. However it proved to be very time consuming.

- Need to assess other methods of data capture. (i) Web harvesting. We performed a trial on web harvesting to complement and validate the information held by Ordnance Survey. The first obstacle are legal constraints on use of the data which meant 80% of all sites could not be harvested. Furthermore, it is usually difficult to find the currency of data provided in the web. The conclusion from this study was that automatic web harvesting is not suitable for land cover and land use information. (ii) Other sources of data capture to consider are surveyors and video surveying. Surveyors are used daily by Ordnance Survey to record changes in OS Mastermap layers. We have to explore the way of taking advantage of this resource so that they record land cover and land use information at the same time. A video capture trial is planned for this summer (iii) Automatic capture of land uses using aerial photography. The main objective of this assessment would be to determine what can be classified and in which way this information could complement that collected through other sources.

- Need for user feedback. We need to know whether this approach answers any of the current or future land cover and land use user's needs and could be a way of integrating different datasets.

In conclusion, the design of an object-oriented ontology framework for land use and land cover that provides a high level classification seems like the right approach in order to provide a starting point and place of agreement for different users. However, there is still a lot of work to do in terms of data

capture, data storage and maintenance, linkage with other widely used classifications and the understanding of user needs.

References

Fonseca, F., Egenhofer, M., Davis Jr. C.A., Borges, K.A.V. 2000, Ontologies and Knowledge Sharing in Urban GIS, Computer, *Environment and Urban Systems*, 24, 251-271

Di Gregorio, A. and Jansen, L.J.M, 2000, Land Cover Classification System (LCCS): Classification Concepts and user manual, FAO

Eurostat (2000): *Manual of Concepts on Land Cover and land Use Information Systems*. Theme 5: Agriculture and Fisheries: Methods and Nomenclatures. Office for official Publications of the European Communities, Luxembourg, 2000, 110 pp

Löfvenhaft, K., Bjorn, C. and Ihse, M., 2002. Biotope patterns in urban areas: a conceptual model integrating biodiversity issues in spatial planning. *Landscape and Urban Planning*, 58 (2/4), 223-240.

MasterMap user manual v.2, 2006, Ordnance Survey

Nunes, J., 1991, Geographic Space as a Set of Concrete Geographical Entities, in : Mark, D. and Frank, A., (eds), *Cognitive and Linguistic Aspects of Geographic Space*, pp. 9-33, Luwer, Dordrecht, The Netherlands

Peterken, G.F. 1981 *Woodland conservation and management*. London: Chapman & Hall.

Shimwell, D. 1983. A conspectus of urban vegetation types. University of Manchester. Unpublished report to Nature Conservancy Council.

References from websites:

FAO www.fao.org, (accessed 5th May 2010)
JNCC www.jncc.org (accessed 20th April 2010)

ACKNOWLEDGEMENTS

I would like to thank Marion Seitz for her excellent work on web harvesting during her time at Ordnance Survey.

OBJECT-ORIENTED METHODS FOR LANDSLIDES DETECTION USING HIGH RESOLUTION IMAGERY, MORPHOMETRIC PROPERTIES AND METEOROLOGICAL DATA

I. Sandric^{a,b,*}, B. Mihai^a, Z. Chitu^a, A. Gutu^b, I. Savulescu^a

^a University of Bucharest, Faculty of Geography, Bdul. Nicolae Balcescu, No.1, Sect. 1., 010041, Bucharest, Romania – sandricionut@yahoo.com

^b ESRI Romania SRL, Roma Street, No 8, Sect. 1, 011774, Bucharest, Romania

Commission VI, WG VI/4

KEY WORDS: Landslides, Identification, Modelling, Recognition, Object, Pattern, Segmentation

ABSTRACT:

Mapping landslides and building landslides inventory have received a special attention from a wide range of specialist. In building a landslide inventory an important step is the spatial delineation of the landslides body, followed by the landslides classification according with an international used classification system and the identification of other landslides characteristics. The main methods for landslides mapping are based on field observation, image interpretation and stereo-restitution. Our paper discusses a semi-automated process based on objected-oriented analysis for landslides bodies' delineation. Several recent papers Moine et al. 2009, Tapas et al. 2010 had similar approaches for landslides bodies' delineation and classification using objected-oriented analysis combined with spectral and morphometric properties of the landslides. Our approach is similar with Tapas et al. 2010, but we take into account, besides the morphometric properties, the meteorological data for the periods when the landslides have occurred. The algorithm is using high resolution aerial images with a spatial resolution 0.5 meters, a DEM with a spatial resolution of 2.5 meters and daily meteorological data for the year 2005. The meteorological data was spatial interpolated and the images were used in the objected oriented analysis and this has led to a significant increase in the number of corrected indentified landslides. The algorithm was tested in the administrative area of Breaza Town from Romanian Curvature Sub- Carpathians, for which a detailed landslides inventory was available

1. INTRODUCTION

1.1 Aim of the paper

Landslides are frequent phenomenon for the Subcarpathians regions of Romania. Lithological features based mainly on clay and marl combined with permeable rocks, the torrential rainfall regime as well as a strong human impact has a key role for the landslide related hazards (Balteanu, 1986, 1997; Ielenicz et al., 1999, 2002).

The landslide-related hazards are a real environmental problem within the local and regional development of Subcarpathian areas, because the phenomenon occurs on almost all hill slopes, including the afforested ones. Superficial and shallow landslides superposes on large, old and deep landslide bodies (Ielenicz et.al., 1999; Armas et. al. 2004).

Landslide spatial occurrence in Romania was the subject of some recent papers. Most of the authors focuses on landslide susceptibility issues (Armas et al, 2004; Chitu et al., 2009; Mihai et al., 2010 etc.) and some of them focused also on hazard analysis (Sandric, 2008 unpublished) at different scale approaches, from local and regional analysis and to the whole Romanian territory (Balteanu et. al., 2010 in press). The GIS modeling (deterministic and probabilistic approaches) and mapping techniques are largely used within these papers

The aim of the paper is to develop a semi-automated algorithm for landslide body's identification and classification. The

algorithm is based on object based image analysis (segmentation and classification) applied on high resolution air-photos in combination with lithology, morphometrical features and meteorological data

For the areas with complex morphodynamic features like the Subcarpathians, the image visual interpretation and field surveys are usually a time consuming step (Sandric, 2009, Moine, 2009, Tapas, 2010). It is usually very difficult to extract all the landslide bodies even on smaller areas (a catchment or a small administrative unit like a town or a community), because they have a complex typology (landslides, earthflows etc), they occurs on the whole slope area, the landslide bodies of different generation are superposed

1.2 Main contributions in the international literature

International contributions on landform automatic classification are quite recent approaches (Dragut, Blaschke, 2006). Landslide analysis on satellite imagery is an older research field (Mantovani et al., 1996, McDermid, Franklin, 1994, Brardinoni et al., 2003; van Westen, 2003; etc.). Since 2006, there is an increasing interest in developing algorithms for landslide classification, based on spectral data (Borghuis et al., 2007) as well as on digital elevation data (van van Asselen, Seijmonsbergen, 2006). Landslide mapping based on remote sensing imagery object based image analysis and classification (Nichol et al., 2005; Moine et al., 2009), remote sensing

* Corresponding author. This is useful to know for communication with the appropriate person in cases with more than one author.

imagery in combination with morphometrical features (Tapas et al., 2010) were developed and tested within different areas with encouraging results

These latest studies focuses on the integration of data with different spatial resolutions together with data derived from elevation models, as well as other segmentation rules within landslide algorithms. These are relevant contributions but they are limited in terms of the data variety. Our study considers that besides the favorable factors for landslides landslide, the triggering factors like the amount of precipitation that reaches the terrain surface can complete the segmentation rules for landslide bodies. Testing the proposed algorithm on a representative case study from the Prahova Valley in the Subcarpathians can help the improvement of the existing methods for landslide mapping and classification

1.3 Study area

The study area we focuses our analysis is the Breaza town administrative area, which is situated along the Prahova River Valley within the Prahova Subcarpathians (SE Romania, Curvature Subcarpathians). This area has an interesting situation because of the great density of landslide bodies (156 bodies were mapped by Sandric, 2008, on a surface of about 70km²). They are covering almost all the slopes in a complex lithological and structural-tectonic background. Breaza town is located along the main transcarpathian railroad and European road between Bucharest and Brasov.

From the geological point of view, the study area superposes on a nappe system, thrusting each other from the North to the South. These nappes belong to the Cretaceous and the Palaeogene flysch areas, as well as to the Upper Cretaceous and Lower Miocene posttectonic sedimentary covers. The folds configuration, as an effect of the tectonical transformations, shows a system of parallel synclines and anticlines, oriented from the East to the West.

The most affected lithostratigraphic units are: Gura Beliei marls (Upper Cretaceous posttectonic sedimentary covers) which produce rotational and translational slides, earthflow; molasse deposits of Doftana (marls, clays, sandstones of Lower Miocene posttectonic sedimentary cover) affected by rotational and translational slides, Pucioasa Strata (marls, clays of Paleogene Flysch) affected by earthflow, rotational and translational slides.

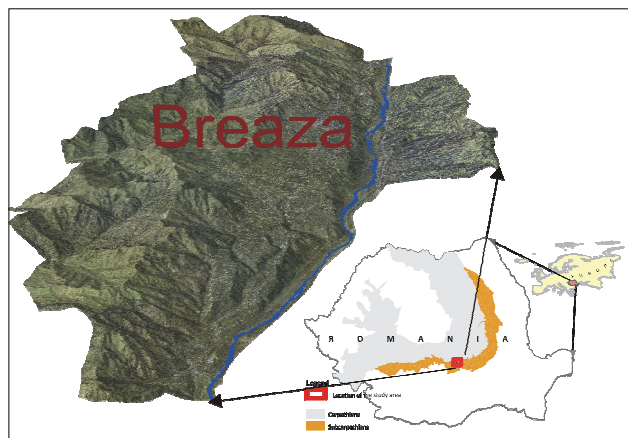


Figure 1. Location of the study area

The area is characterized by high slopes gradients with values between 15-30°, specific to most of the hillslopes within the area, medium drainage density, with values between 0.3-1 km/km²

The natural vegetation of the area was replaced during the last two centuries by the secondary vegetation, with a high deforestation degree (50-60%) The human activity has relevant impact for this area, with a population density of about 50-75 inhabitants/km² (higher values in the Breaza town built-up area). There are 10 built-up areas, mostly rural areas attached since 1968 to the Breaza town (mainly scattered farms). The local economy is dominated by agricultural activities, based mainly on grazing and orchards. These are favorable conditions for landslides

2. MATERIALS AND METHODS

2.1 Materials

The analysis is based on image segmentation techniques for an object-oriented classification. These datasets were integrated in digital format in order to define the landslide body's configuration according to their spectral and morphometric features (McDermid, Franklin, 1994, Tapas et al., 2010). Our main interest was to extend the analysis with other relevant datasets like lithology and the amount of precipitation that reaches the terrain surface

The high resolution imagery consists in digital orthophotos acquired from the National Agency for Cadastre and Real Estate Advertisement (ANCPI Bucuresti). The acquisition date of the air-photos is July 2005. Images are in natural colors and have a spatial resolution 0.5 m. They are co-registered with 1:5000 scale topographic maps. These images were integrated within a digital mosaic covering the whole administrative area of Breaza town. Some problems are featuring these images: the orthorectification errors (limited) and their temporal resolution. They are summertime imagery limiting the identification of a lot of the slope morphodynamics features (including landslide bodies). Forests and meadow vegetation occurs in green signatures while eroded areas are in shades of light brown.

Visual interpretation opportunities of this imagery were limited by the uncertainty of the limits of the superficial and shallow landslide bodies. Field mapping and observation was usually applied for the validation of the landslide inventory based on aerial imagery.

Since the year 2008, new imagery was obtained for the Subcarpathian sector of the Prahova Valley by Ionut Sandric, in order to validate and to improve the landslide inventory for the Breaza town administrative area. The high resolution digital imagery obtained with a Canon 400D camera from a Cessna aircraft is frequently oblique which are usually better for landslide bodies' interpretation. Some of the nearly vertical images were geometrically corrected and used for landslide body extraction in digital format The DEM was obtained using the ANUDEM interpolation method implemented in ArcGIS Desktop 9.3.1 – ArcINFO version. The layers used in the ANUDEM method are: contours with intervals from 5 to 5 meters, point elevation and rivers, all collected from the topographical maps at a scale of 1:5000. The spatial resolution of the DEM was 2.5 meters and it was calculate by dividing the contour intervals by 2. The accuracy of the DEM was tested by comparing random selected point elevation with the values of the generated surface. The standard deviation was 3.6 meters (Sandric, 2008). From the DEM we derived the slope gradient, plan curvature and profile curvature, which we assumed that

plays an important role in landslide body delineation. These morphometrical parameters were used also by Tapas et al., 2010 to create rules for objects classification

Weather data and mainly the rainfall data is a feature we proposed for this analysis. As landslidings depends on the rainfall thresholds we used the opportunity to collect data with the help of an automatic weather station. This was installed eastern from Breaza town, in Cornu village since 2007 in a characteristic position in order to obtain reliable data for rainfall every 15 minutes. From the total amount of data we selected only the records corresponding to the most relevant landslidings episodes around the area of the station. They feature mainly the torrential rainfall periods during the months of June and July.

Another data set was that from Cimpina weather station data, which is situated southernwards from Breaza town. This rainfall data (since 2005) was selected according to the above mentioned principle (for the torrential rainfall episodes with landslidings re-activation). This digital data was the subject of interpolation in order to generate a special layer for image segmentation. The main target is to extend the analysis to other spatial data in order to improve the landslide inventory.

Other data is represented by geological features in digital format. This layer was derived from 1:50000 scale geological maps on paper (edited by the Geological Institute). The role of this data within the analysis is quite limited because landslide inventory made between 2004-2009 in the Breaza town administrative area showed that landslide bodies occurs on almost every geological formations. Even sandstones and conglomerates alternating with clay and marls are featured by landslides in combinations with rockfalls. The lithological data was used only as ancillary data in the image segmentation and classification steps

Materials	Spatial resolution/Acquisition time	
Orthophotos	0.5m	2005
Oblique air-photos	0.1m	2008
DEM	2.5m	1980
Lithology	30m	1980
Precipitation	10m	2000-2009

Table 1. Materials

2.2 Methods

For OBIA analysis we used ENVI EX product, developed by ITT (ENVI EX). The steps necessary to complete the feature extraction module from ENVI EX are: choosing the scale parameter; merging the object primitives; refine the objects using a threshold value for just one band of the image and it is an optional step; extraction of the attributes; object classification based on rules or examples. The segmentation algorithm used by ENVI EX is developed by ITT and is a patented product (Xiaoying, 2009). Choosing the right scale for the segmentation process is an important step in the OBIA analysis, which can lead to important errors in the final result. The scale parameter is related with the size of the objects that have to be identified and in ENVI EX the scale can take values from 0 to 100. Choosing a low scale value leads to small size objects and sometimes to over-segmentation on the other hand, choosing high scale can lead to under segmentation and large objects. It is always recommended that the scale parameter should be choosing after several trials should be combined with the merge objects step from the segmentation process. In ENVI

EX the merge option presented in the second step is developed based on Robison et al 2002

For the morphometrical analysis it was used ArcGIS Desktop 9.3.1 – ArcINFO version with Spatial Analyst extension. The spatial analyst extension provides advanced tools for generation of DEM (the ANUDEM, Hutchinson, 1989) and for terrain analysis. From the DEM the slope, plan curvature and profile curvature were generated. An image with the amount of precipitation fallen in one week was generated for the entire area. The image was generated based on the measurements from the automatic meteo stations located in Cornu and on a linear relation between altitude and the amount of precipitation. This linear relation allowed us to spatialize the precipitation, even though the area has only ~350m difference in altitude

In order to use the orthophotos and the morphometrical parameters for the segmentation and classification process, it is first required that all the data should be fusion. The fusion process was carried out in the ENVI 4.7 image analysis software and the file was saved and ENVI standard format. The schema of the analysis is presented in figure 2.

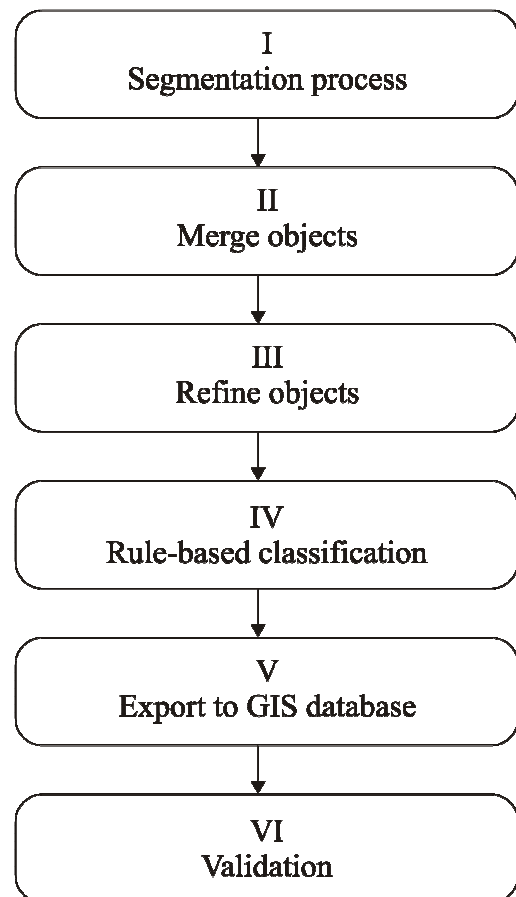


Figure 2. Schematic representation of the analysis process

3. RESULTS AND DISCUSSION

The first step of the process was to choose the appropriate scale for the segmentation process. Several trials were performed with different scale values ranging from 20 to 65 and the best segmentation was obtained with a scale value of 35

The second step was the objects merge and like for the first step, several trials were made. The best merge values for a scale parameter of 35 for our study area was 95

The third step of the segmentation process is the option of refining the objects based on an interval values for just one band. For the Breaza area it wasn't necessary to refine the objects and no thresholding was applied for either band (Table 2)

Scale	Merge	Refine
35	95	-

Table 2. Segmentation parameters

In the classification process the aim was to identify only the deep seated rotational slides according with the Cruden and Varnes 1996, landslide classification system. The deep seated rotational slides are characterized by a longitudinal profile in which the convex and concave curvature is alternating due to the landslide morphological features created by the curved sliding surface. Because we decided to identify the deep seated slides the land-use and land-cover doesn't play a very important role and this was the reason for which it hasn't been used an ancillary data in the segmentation process. The amount of precipitation that it should be considered in order for a deep seated landslide to occur is approximate 100mm (Sandric, 2008). The slope gradient usually is ranging from 5 degree in the accumulation zone up to 35 degree on the landslide scarp. Taken into consideration all this we have developed the following classification rules presented in the table below (Table 3)

Band	Value
Slope gradient	4 - 40
Plan curvature	< 0
Profile curvature	-5 – 5
Elongation	< 5
Area	1500 - 4000
Effective precipitation	80mm

Table 3. Classification rules

The slope gradient interval was choose between 4 degrees in order to indentify the accumulation zone, where the values are lower and the value of 40 degree was chosen in order to identify the landslide scarp. The values were extended over the natural limits observed during the field works due to the uncertainties presented in the DEM and also propagated from the slope algorithm.

The size of the landslides in the Breaza administrative unit is ranging from 1500 sqm up to 3500 sqm. There are some exceptions where the size of the mapped landslides is bigger than 3500sqm. This situation is presented only in areas where due to the complexity of the spatial relations between landslides it wasn't possible to delineate them and they were mapped as areal landslides.

An important parameter in the classification rules was considered the elongation of the objects. Usually the shape of a landslide is elongated along the slope and the relation between length and width is more or less from 3 to 5 sizes bigger the length than the width. Taken into consideration this relation length to width for this area we established that a value of 5 for the elongation, from the shape attributes, would be suitable to separate objects that are not landslides from objects that are landslides

The longitudinal profile of a rotational landslide has zone with convex curvature in alternation width zone with concave curvature. Because of this morphological feature, the profile curvature of the slopes was taken into consideration for the classification rules. The profile curvature derived from the DEM had values from -12 to +10. By overlapping the field mapped landslides onto the profile curvature we managed to identify the average interval specific to rotational slides, being between -5 to +5 and it was introduced as rule in the classification process

The plan curvature plays an important role in the identification of the landslide boundaries, because the landslides occur mainly on areas with concave plan curvature. This is an important aspect and it was used as a rule in the classification process. For the plan curvature the concave curvature was considered as favorable for landslides appearances

The precipitation data was introduced also as a classification rule, by the amount of water that arrives at the terrain surface. The map algebra method was used to calculate the amount of water intercepted by the vegetation and then to eliminate it from the total amount of precipitation. The effective precipitations higher than 80mm were retained as a rule in the classification process. This rule also helped to take into account the role of the forest in the landsliding process

For the area of Breaza a detailed landslide inventory was created, based on field surveys and image interpretation. The landslides inventory includes 177 landslides, mostly deep-seated rotational slides (ca. 92%) and several translational slides (3%), complex landslides (3%) and earth flows (2%).

The rotational slides are spread over the entire area with no particular pattern. The slope gradient intervals are between 5 and 25 with a maximum of 40 on the landslide scarps of the hillslopes of the Provita River in the area of the Irimesti village and on the terrace scarp over Breaza town. Over 70% of the rotational slides are present on marls, marls with clay and marls with sandstone and over 85% are present in areas with grass and low density tree cover, the remainder being old landslides, present in areas with deciduous forest and in a dormant state of activity.

The lithological units affected by the translational slides are almost entirely marls with sandstone (over 95% from the translational slides). The complex landslides are present on marls with clay and marls (over 85%) and the earth-flows on clay and marls (over 95%).

The most affected land-use/land-cover classes are the areas with grass and low density tree cover, where during the heavy rain from spring and autumn the shallow and deep landslides are reactivated (Sandric, I., Chitu, Z., 2008).

The OBIA has identified 615 features as being rotation slides. From the 615 features a number of 259 (approximate 42%) are located inside the mapped landslides or are intersecting the existing landslides. In terms of spatial location the feature are well distributed and are covering areas where it could be landslides or in areas that are landslides, but they have not been mapped due to errors or misinterpretation. The size of the classified features is from 1400sqm up to 65000sqm, but most of the features are from 1400sqm up to 10000sqm. None of the features identified as rotational slide is fully overlapping a mapped landslide. Most of the features are outside of the mapped landslide in areas where there is a potential for sliding, but so far there hasn't been seen any landslides. The best overlap between the features identified as slides and the actual slides is presented in figure 3 and is located on the terrace scarp from the eastern part of Breaza de Jos town.

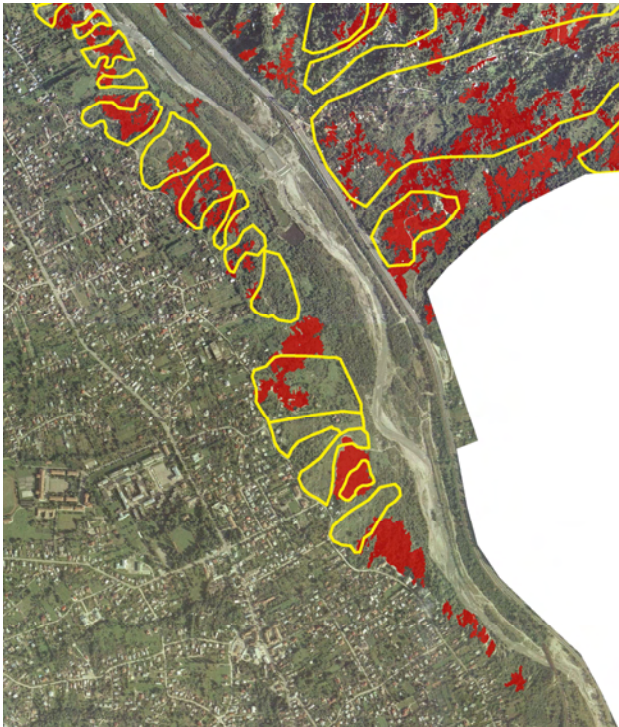


Figure 3. Identified features versus mapped landslides (in red classified objects and in yellow mapped landslides); terrace scarp from eastern part of Breaza de Jos town

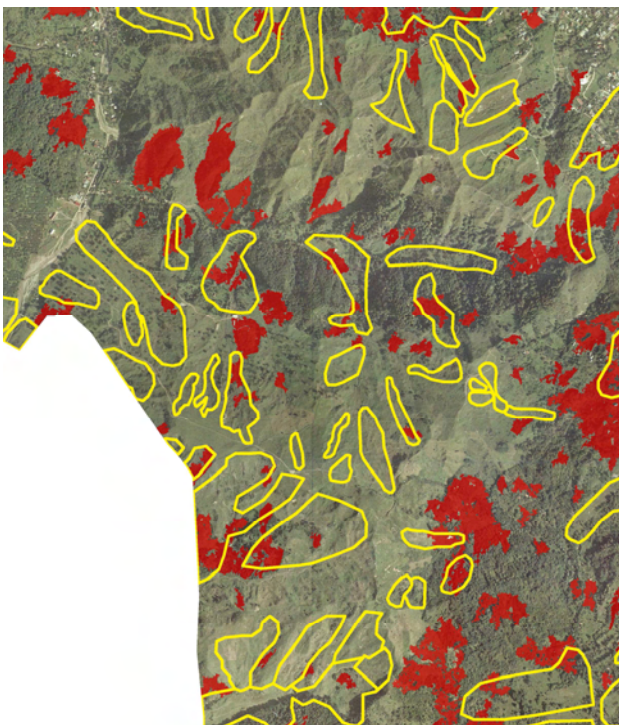


Figure 4. Identified features versus mapped landslides (in red classified objects and in yellow mapped landslides); hillslopes from the south-western part of the study area

In the center of the image (Figure 3) can be seen the almost full overlap between the classified objects and the mapped

landslides, although the classified objects is extending outside of the mapped landslides. The outside part is corresponding to a particular lithology in that area, that couldn't be taken into account in the classification process. On the other sites of the image it can be seen the overlapping areas between the mapped landslides and the classified objects and the degree in which they are overlapping. On the right side of the image, they are big rotational slide which cover the entire slope and the identification of these big landslides were only partially. There is because of the slope gradient values, that here were below the minimum threshold value. The slope gradient is the effect of the uncertainties propagated from the DEM resolution and the slope algorithm.

Figure 4 presents the south-eastern part of the study area, where the overlap between the classified objects as being landslide and the mapped landslides is almost inexistent. Most the features classified as being landslides are presented on the upper part of the hillslopes where the slope gradient and the profile curvature have met the criteria, but not on the grass lands with high texture ranges from the center of the image

4. CONCLUSION

The use of OBIA for landslides identification and classification has been proven as a promising method, but the results obtained are still far from obtaining a good and scientifically reliable landslide inventory. More attention should be given to the classification rules and to the data in the analysis. The lack of the DEM with a spatial resolution equal with the orthophotos and the lack of a more detailed lithological and pedological map have brought to many uncertainties in the classification process. Future approaches should take into consideration the quality of the data, but also the possibility of using more parameters in the segmentation process

4.1 Acknowledgements and Appendix (optional)

This study was partial financed from the following research projects:

TD 221, 2006-2007, financed by the National Research Council, coordinated by Dr Ionut Sandric;

AT147, 2006-2007, financed by the National Research Council, coordinated by Dr Mihai Bogdan;

IDEI 2007-2009 financed by the University of Bucharest, coordinated by Dr Comanescu Laura

Special thanks to ESRI Romania

5. REFERENCES

Ahearn, S., 2008. Object orientation, In: K.Kemp (ed.) *Encyclopaedia of Geographic Information Science*, SAGE Publications, Los Angeles, pp. 323-326.

Armas I., Damian, R., Sandric I., Osaci- Costache, G., 2003. *Vulnerabilitatea versantilor la alunecari de teren in sectorul subcarpatic al vaili Prahova*, Editura Fundatiei Romania de Maine, Bucuresti, pp. 10-21.

Balceanu, D., 1986. The importance of mass movements in the Romanian Subcarpathians. *Zeitschrift fur Geomorphologie*, Suppl. Band 58, pp. 173-190.

- Balteanu, D., 1997. Romania. In: C. Embleton & C. Embleton-Hamann (eds.), *Geomorphological hazards of Europe*, Elsevier, Amsterdam, pp. 409-427.
- Balteanu, D., Chendes, V., Sima, M., Enciu, P., 2010. A country level spatial assessment of landslide susceptibility in Romania, *Geomorphology* (in press) http://www.sciencedirect.com/science?_ob=ArticleURL&_udi=B6V93-4YK7HW8-1&_user (accessed, 22 may 2010).
- Borghuis, A.M., Chang, K., Lee H.Y., 2007. Comparison between automated and manual mapping of typhoon-triggered landslides from SPOT- 5 I imagery, *International Journal of Remote Sensing*, 28, pp.1843-1856.
- Brardinoni, F., Slaymaker, O., Hassan, M., 2003. Landslide inventory in a rugged forested watershed: a comparison between air-photo and field survey data, *Geomorphology*, 54, pp. 179-196.
- Chitu, Z., Sandric, I., Mihai B., Savulescu, I., 2009. Evaluate Landslide Susceptibility using Statistical Multivariate Methods: A case-study in the Prahova Subcarpathians, Romania, In: Malet, J.-P., Remaitre, A., Borggaard, T. (Eds.), *Landslide Processes:From Geological Mapping to Dynamic Modelling*, Editions du CERG, Strasbourg, pp. 265-270
- Cruden, D. and Varnes, D. (1996) Landslide types and processes, *Transportation Research Board*, Washington, 36-75 pp.
- Dragut, L., Blascke, T. , 2006. Automated classification of landform elements using object-based image analysis, *Geomorphology* 81, pp. 330-344
ENVI EX, <http://www.ittvis.com/ProductServices/ENVI/ENVIEX.aspx> (accessed, 1 July 2010)
- Hutchinson, M.F. 1989. A new procedure for gridding elevation and stream line data with automatic removal of spurious pits. *Journal of Hydrology* 106: 211-232
- Ielenicz, M., Patru, I. G., Mihai, B., 1999. Some geomorphic types of landslides in Romania, *Transactions. Japanese Geomorphological Union.*, 20(3), pp. 287-296.
- Ielenicz, M., Ghincea-Clius, M., Patru, I.G., 2005. *Subcarpatii Romaniei*. Editura Universitara, Bucuresti, pp. 3-10
- Mantovani, F., Soeters, R., van Westen, C.J., 1996. Remote sensing techniques for landslide studies and hazard zonation in Europe, *Geomorphology*, 15, pp. 213-225.
- Mc.Dermid, G.J., Franklin, S.E., 1994. Spectral, spatial and geomorphometric variables for the remote sensing of slope processes, *Remote sensing of environment*, 49, pp. 57-71.
- Mihai, B., Sandric, I., Savulescu, I., Chitu, Z., 2010. Detailed Mapping of Landslide Susceptibility for Urban Planning Purposes in Carpathian and Subcarpathian Towns of Romania, In: *Lecture Notes on Geoinformatics and Cartography*, Springer Verlag, Berlin-Heidelberg, pp. 417-427.
- Moine, M., Puissant, A., Malet, J-P., 2009. Detection of landslides from aerial and satellite images with a semi-automatic method. Application to Barcelonnette basin (Alpes-de-Haute-Provence, France). In: Malet, J.-P., Remaitre, A., Borggaard, T. (Eds.), *Landslide Processes:From Geological Mapping to Dynamic Modelling*, Editions du CERG, Strasbourg, pp. 63-68.
- Nichol, J., Wong, M.S., 2005. Satellite remote sensing for detailed landslide inventories using change detection and image fusion, *International Journal of Remote Sensing*, 26, pp. 1913-1926.
- Radoane, M., Radoane, N., 2007. *Geomorfologie aplicata*, Editura Universitatii din Suceava, pp.210-220
- Robinson, D. J., Redding, N. J., and Crisp, D. J. (2002). *Implementation of a fast algorithm for segmenting SAR imagery*, Scientific and Technical Report, 01 January 2002. Australia: Defense Science and Technology Organization
- Sandric, I., 2008. *Sistem informational geografic temporal pentru analiza hazardelor naturale. O abordare Bayesiană cu propagare a erorilor*, Unpublished PhD thesis, Bucharest, Romania
- Sandric, I. and Chitu, Z., 2009. Landslide inventory for the administrative area of Breaza, Curvature Subcarpathians, Romania, *Journal of Maps*, v 2009, pp. 75-86 <http://www.journalofmaps.com/crossrefMap.php?mid=1051> (accessed, 22 May 2010).
- Surdeanu, V. , 1998. *Geografia terenurilor degradate. I. Alunecari de teren*, Editura Presa Universitara Clujeana, pp.1-274.
- Tapas, R. M., Kerle, N., Jetten, V., van Westen, C.J., Vinod-Kumar, K., 2010. Characterising spectral, spatial and morphometric properties of landslides for semi-automatic detection using object-oriented methods, *Geomorphology*, 116, pp. 24-36.
- van Asselen, C.J., Seijmonsbergen, A. C., 2006. Expert-driven semi-automated geomorphological mapping for a mountainous area using a laser DTM, *Geomorphology*, 78, pp. 309-320.
- van Westen, C.J. Lulie Getahun, F., 2003. Analyzing the evolution of the Tessina landslide using aerial photographs and digital elevation models, *Geomorphology*, 54, pp. 77-89
- Xiaoying, 2009. *Segmentation-based image processing system*, US Patent 20,090,123,070, filed Nov. 14, 2007 and issued May 14, 2009, <http://www.faqs.org/patents/app/20090123070> (accessed, 1 July 2010)

ASSESSMENT OF VERY HIGH RESOLUTION SATELLITE DATA FUSION TECHNIQUES FOR LANDSLIDE RECOGNITION

L. Santurri^a, R. Carlà^{a,*}, F. Fiorucci^b, B. Aiazzi^a, S. Baronti^a, M. Cardinali^b, A. Mondini^b

^a IFAC-CNR, Institute of Applied Physics – Italian National Research Council, Via Madonna del Piano 10, I-50019, Sesto Fiorentino, Firenze, Italy (r.carla, b.aiazzi, s.baronti, l.santurri)@ifac.cnr.it

^b Istituto di Ricerca per la Protezione Idrogeologica, Via Madonna Alta n. 126, I-06128, Perugia, Italy (f.fiorucci, m.cardinali, a.mondini)@irpi.cnr.it

KEY WORDS: Data Fusion, Ikonos, Landslide, Multispectral Images, Pan-sharpening, Quality Assessment

ABSTRACT:

Pan-sharpening is gaining an increasing attention in the remote sensing community, and its usefulness have been demonstrated in several environmental applications. A variety of pan-sharpening techniques, aiming at improving the quality of the fused image have been proposed in literature, but the ranking of their efficiency is a difficult task since the quality of the pan-sharpened image depends on the considered applications. In the literature the IHS-based technique has been proposed as the most effective for landslide detection, but in a more generic framework, other methods such as the Gram-Schmidt Adaptive (GSA) and the General Laplacian Pyramid (GLP) have been found as most performing than the IHS, together with their improved Context Adaptive versions, the GSA-CA and GLP-CA, that relies on local statistics. In the context of the MORFEO project, funded by the Italian Spatial Agency (ASI), this work aims at verifying these conclusions by comparing the performances of IHS, GSG and GSA-CA methods together with those of the Principal Component (PC) and the widely used Gram Schmidt (GS) methods. The comparison have been performed on IKONOS multispectral data, by evaluating the results both in a quantitative and qualitative way. The qualitative assessment has been performed by means of a visual assessment in terms of landslide detection by photointerpretative techniques. Possible correlation and or differences found among the quantitative and the visual assessment have been analyzed.

1. INTRODUCTION

Data fusion techniques are widely applied in the scientific community to exploit the potentiality of complementary data (Pohl and Gendren, 1998), and in particular the Pan-sharpening that is a branch of data fusion devoted to the improvement of multispectral data quality by merging Multispectral (MS) and Pancromatic (Pan) data characterized by complementary spatial and spectral resolution (Chavez, 1991; Wang, 2005). This is due to the increasing quantity of multispectral data acquired by the new spaceborne sensors (SPOT, IKONOS QuickBird). The usefulness of pan-sharpened data have been demonstrated in several environmental applications, (Couloigner, et al., 1998; Fanelli et al., 2001; González and Seco, 2002; Yang et al., 2000) and a variety of pan-sharpening techniques have been proposed in literature (Wang et al. 2005; Chavez et al. 1991; Zhang, 2002), aiming at improving the quality (from the qualitative and/or quantitative point of view) of the fused images. As a matter of fact, the resulting quality of a fused image is related to many factors, such as spatial, spectral, radiometric accuracy and feature distortion, and therefore different pan-sharpening methods have been developed aiming at different goals.

An important family of pan-sharpening techniques is that of the component substitution (CS) methods, such as those based on IHS (Carper et al., 1990; Edwards et al. 1994; Liu, 2000; Tu et al. 2001), on the Brovey transform (Gillespie, 1987) and on the Principal Component (PC) Analysis (Chavez and Kwarteng, 1989). These methods are fast, have good spatial performances and are useful for many visual interpretation tasks (Wang et al. 2005), but PC and IHS methods are highly sensitive to bands

misalignment, as it happens for some VHR (Very High Resolution) imager such as IKONOS (Zhang, 2004); therefore the Gram-Schmidt (GS) technique has been developed to improve CS methods accuracy in such context. Concerning the spectral quality, these methods generally provide pan-sharpening images with a high visual quality, but having often a noticeable spectral distortion (colour changes) and differences in mean (Alparone, 2007); to partially overcome these drawbacks, a generalization of the CS methods has been proposed by considering a synthetic intensity generation that takes into account the different spectral responses of the multispectral bands and the Pan image.

In fact, a high spectral quality of the pan-sharpened images is important for some remote sensing application such as soil and vegetation analysis (Liu, 2000, Garguet-Duport et al. , 1996). Therefore other methods different from the CS one, such as the HPF filter (Chavez et al. 1991; de Béthune et al. 1998) and the SFIM (Liu, 2000) have been developed aiming at a better performance in terms of spectral fidelity. A statistic based fusion method named Pansharpen has been also presented by Zhang (Zhang, 2002) to mitigate colour distortion and the dependency of the data fusion performances on operator skill and dataset characteristics. Finally, Multi-Resolution Analysis techniques (MRA) have been extensively studied, based on performing tools such as the à trous wavelet transform (AWT), and Laplacian Pyramids (AWLP) (Aiazzi, et al., 2002; Ranchin et al., 2003). These methods show a potentiality in tuning the trade-off among spatial and spectral quality (Zhou et al., 1998), at the cost of a most time-consuming process, and critical requirement for co-registration accuracy (Liu, 2000). To overcome these drawbacks, Aiazzi et al (Aiazzi et al, 2002)

* Corresponding author. This is useful to know for communication with the appropriate person in cases with more than one author.

proposed a context-based injection model that operates at a local level (GLP-CBD).

In a comparison work (Alparone et al. 2007) the GLP-CBD and the AWLP methods result as the most performing among a set of data fusion techniques such as FSRRF, G-IHS-GA, GIHS-TP, GLP-CBD, UNB Pansharpen, WiSpeR, WSiS; in particular the conclusion is that the MRA-based algorithms generally perform better than the CS based ones, even if MRA method may originate ringing and aliasing effect in the fused images, emphasized if a misregistration among MS and Pan images is present. Because of this drawback, the CS techniques are still investigated by the scientific community, and especially the method based on the Gram-Schmidt (GS) spectral sharpening, patented by Eastman Kodak (Laben and Braver, 2000) and implemented in the Environment for Visualizing Image (ENVI) program package. The GS method and some of its improved versions has been considered in a recent work of Aiazzi et al. (Aiazzi et al. 2009). In this paper, two GS based methods, namely the Gram-Schmidt Global Adaptive (GSG) (Aiazzi et al. 2007) and the Gram-Schmidt Adaptive – Context Adaptive (GSA-CA) have been considered in comparison with the Generalized IHS method (GIHS), which is an improved version of the IHS algorithm, and reaches performances next to those of the most performing techniques of the MRA family, the Generalized Laplacian Pyramids (Aiazzi et al., 1999) and the Generalized Laplacian Pyramid (GLP) – Context Adaptive (GLP-CA). The PC method and the widely used GS method has been also taken into account.

As previously mentioned, because of the different quality characteristics required by the different utilization of the pan-sharpened images (Wald, 1999), an original gold reference is not available to globally evaluate the quality of the fused image, and the efficacy of the pan-sharpening techniques (Alparone et al., 2007); nevertheless some general score indexes have been developed, by considering some average metrics such as the Q4 (Alparone et al., 2004) that is an MS extension of the Q index (Wang and Bovik, 2002), the Spectral Angle Mapper (SAM) (Alparone et al., 2008), the Erreur Relative Globale Adimensionnelle de Synthèse (ERGAS) (Ranchin and Wald, 2000) and the Quality with No Reference (QNR), that is computed at full scale even if the reference is not available (Alparone et al., 2008).

Some works based on the aforementioned indexes and on statistical and visual considerations have been presented in literature to compare the performances of pan-sharpening techniques (Wang et al. 2005, Alparone et al., 2007, Nikolakopoulos, 2008). Te Ming To (Te-Ming To, 2004) showed that the IHS fusion technique is fast and computationally light, but may introduce spectral distortion in presence of spectral mismatch between Pan and MS bands, and Chavez (Chavez et al, 1991) established that PC techniques performances are better than those of the IHS; moreover Zhang (Zhang, 2004) found that if Panchromatic and Multispectral bands are not perfectly overlapped, as it happens in some advanced sensors such as IKONOS and QuickBird, the IHS- and PC- based methods may yield poor performances in terms of spectral accuracy.

Notwithstanding the great effort in assessing the performances of the various pan-sharpening techniques, the resulting ranking could not be suitable in certain contexts with particular quality requirements. In this case a devoted quality assessment could be necessary, such as in the landslide detection field.

As a matter of fact, in the context of landslide detection from remote sensing data, the work of Marcelino (Marcelino et al, 2009) compares six image fusion techniques (Brovey, HSV, PC, IHS, WTVE and WTYO) to select the most performing in

landslide visualization on pan-sharpened image. The result was that the IHS method appears to be the best available technique for preserving and enhancing the spatial and spectral information useful to identify landslides. On the opposite side, Nichol (Nichol et al., 2005) found that Pan-sharp methods perform better than IHS, Brovey, SFIM for landslide detection. A first conclusion is that at the present the performances of some of the most performing methods have not yet clearly assessed in the landslide detection task.

This work has been carried out in the framework of MORFEO project, an ASI funded study devoted to the evaluation of the potentiality of EO optical data acquired by satellite platform in landslide detection. It aims at comparing the performances of the GSG and GSA methods together with those of the G-IHS, the PC, the GS fusion methods in the specific context of the landslide detection by considering an IKONOS data set. The quality of the resulting pan-sharpened MS images are then compared in a quantitative and qualitative way. From the quantitative point of view, some quality score indexes related to the characteristics useful in landslide detection have been selected and evaluated, whereas the qualitative assessment has been performed by considering a visual inspection of skilled photointerpretes.

2. STUDY AREA

This study has been performed on a test site located in the Umbria region (Italy); the test area has an extension of about 80 Km² and corresponds to a part of the catchment basin on the left of Tevere river. Elevation range from 145 to 634 m without high slope gradients. The soil is characterized by sedimentary rocks, such as limestone, sandstone and unconsolidated sediment, and the vegetation coverage is varied and mainly consists in agricultural area and woodlands. The climate is of Mediterranean type; the annual precipitation average is lower than 900 mm and the rain is usually concentrated in the period from September to December. Because of its geological nature, this area is affected each year by a high number of landslides, the most part of which are soil slides of small to medium dimensions, caused mainly by rainfall or in some cases by the snow melting.

3. DATA SET

The assessment of data fusion techniques have been performed on IKONOS data, composed by a Panchromatic (PAN) band with a nominal Ground Sampling Distance (GSD) of 1m, and by four multispectral (XS) bands (near-infrared, red, green, blue) with a nominal GSD of 4m. The PAN and the XS bands are simultaneously acquired during the summer season and image the same area with a radiometric resolution of 11 bits. Table 1 reports the main characteristics of the IKONOS data set.

IKONOS		
Date of acquisition	Summer 2005	
Spectral band	PAN	R, G, B, NIR
Spatial Resolution	1 m	4 m
Radiometric resolution	11 bit	

Table 1. Main characteristics of the IKONOS image.

To evaluate the potentiality of the IKONOS pan-sharpened images in terms of the landslide study, an inventory of the landslide to be considered as “ground truth” was needed. To this purpose, a thematic map reporting soil slide phenomena occurred on the test area during autumn-winter 2004-2005 has been produced by IRPI-CNR with the usual “state of art” stereoscopic photointerpretation techniques.

4. METHODOLOGY

The IKONOS multispectral images have been aligned with the related panchromatic image by a suitable pre-processing. Then the multispectral bands have been pan-sharpened with the panchromatic image by means of the fusion techniques under analysis, that is the GIHS, the PC, the GS, the GSG and the GSA-CA. The PC and the GS pan-sharpening have been performed by means of the related tools of ENVI, whereas the GIHS, the GSG and the GSA-CA fusion techniques have been carried out with a devoted software developed by IFAC-CNR. The radiometric correction, usually performed before the fusion procedure to achieve a conformity with a mean and variance equalization of the bands (Gauguet-Duport et al., 1996, Schowengerdt, 1997; Mather, 1999) have not been performed in our study because not necessary, since a physical significance of the pixel value is not required in the proposed procedure of quality evaluation. As a matter of fact, the study is based on a qualitative visual inspection and on a quantitative evaluation of suitable score indexes: the visual inspection is focused only on the analysis of the features of the images, and since no threshold with physical given value is applied, it is not a-priori necessary to have pixel value with a physical significance. The quantitative assessment is made by performing a comparison with the original images by considering the Wald’s protocol, and can be carried out in terms of the digital number all the same. Moreover, the GSG and GSA-CA methods perform an injection of details that is weighted by some statistical functions of the images, and the generation of the synthetic intensity band from the multispectral bands is carried out in order to obtain the desired conformity with the original Panchromatic image. In the application of the GIHS-based pan-sharpening method, an histogram matching is instead necessary. The pan-sharpened data are then orthonormalized with the related tools of ENVI by considering a DEM at 10m of spatial resolution and the Rational Polynomial Coefficient (RPC) provided together with the IKONOS data, and finally the quality assessment is performed.

5. QUALITY EVALUATION

Quality evaluation of the pan-sharpened images can be performed, as a general rule, in two ways, that based on quantitative assessment, spatial and/or spectral, and that based on a qualitative visual inspection. It is important to point out that either the quantitative and the qualitative assessment can be performed globally or by considering local characteristics of the images. This procedure is of particular interest in some given task, such as the landslide detection considered in this paper. Therefore, the quality ranking produced with a general visual inspection could differ from the quality ranking obtained when the specific task of landslide detection is considered; similarly, the quantitative result obtained with a general-purpose score index could be not suitable to assess the quality of the fused products for this particular task. The correlation among the

quality measured by some quantitative score indexes proposed in literature and the quality in term of landslide detection assessed with a visual inspection is therefore an interesting question to be analysed.

5.1 Quantitative evaluation

The quality assessment has been performed by evaluating the *synthesis property* proposed by Wald (Wald et al. 1997). As depicted in Figure 1, the original Panchromatic (Pan) and Multispectral (MS) images are spatially reduced by the same factor, so that the new spatial resolution of the Pan image is equal to the original resolution of the MS images.

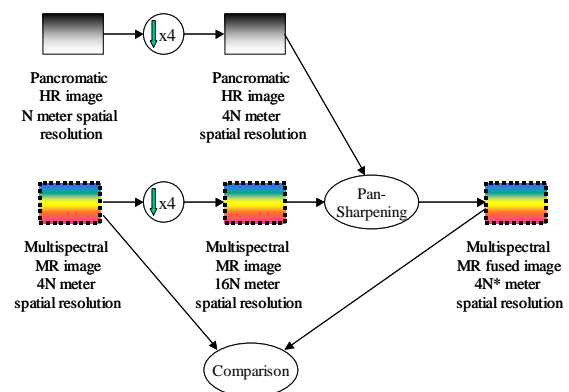


Figure 1. The adopted quality assessment procedure.

The degraded MS image is then pan-sharpened with the degraded Pan image, thus originating a fused MS image at the same spatial resolution of the original MS image; in such a way the original MS image can be adopted as reference. Trivially, the fused image has to be as similar as possible to the reference, to fulfill the so-called *synthesis property*. The synthesis properties have been evaluated by means of some quality indexes. The definition of quality index suitable for such task is still an open question (Li, 2000; Thomas and Wald, 2005), and the fidelity comparison is often performed by more than one index, each of them defined to take into account different characteristic of the image, such as spectral or spatial matching. In this work, five score indexes have been considered. The overall assessment on the entire data set has been performed by considering the ERGAS (relative dimensionless global error in synthesis) index, defined as:

$$\text{ERGAS} \triangleq 100 \frac{h}{l} \sqrt{\frac{1}{K} \sum_{k=1}^K \left(\frac{\text{RMSE}(k)}{\mu(k)} \right)^2} \quad (1)$$

where h/l is the ratio between the pixel size of PAN and MS image respectively, K is the number of bands labelled with the k index and $\mu(k)$ is the mean of the k -th band. The fidelity from spectral point of view has been assessed by using the Spectral Angle Mapper (SAM) index, a point-wise score defined for each pixel (i,j) as:

$$SAM(v, \hat{v}) = \cos^{-1} \left(\frac{\langle v, \hat{v} \rangle}{\|v\|_2 \|\hat{v}\|_2} \right) \quad (2)$$

where v is the n -dimensional vector for each pixel position (i, j) composed by the multispectral values of the n pan-sharpened bands, while \hat{v} is the correspondent one for the reference bands. High values of SAM are related to high spectral distortion, but the radiometric distortion is not taken into account by the SAM index. A global evaluation of the image can be obtained by averaging the SAM values of all the pixels. Together with the ERGAS and SAM indexes, the usual RMSE, PSNR and Correlation score indexes have been also evaluated. The overall quality of a pan-sharpened image can be assessed by using a quality budget composed by a combination of more indexes, such as that proposed by Thomas and Wald (Thomas and Wald, 2007), but in the context of this paper the score indexes have been considered separately, in order to analyse the possible correspondence between the related ranking and the visual evaluation.

5.2 Qualitative evaluation

The qualitative evaluation has been performed on the full resolution pan-sharpened images by means of a visual inspection carried out by skilled photointerpreters, relying on a landslide inventory obtained by usual photointerpretation techniques on aereophotos of the study area. A suitable subset of the landslides present in the landslide inventory has been chosen, in order to consider the most significant ones. The analysis has been performed by considering the characteristics that allow the photointerpreter to map the landslide, such as quality of the linear features and textures, contrast and colour; the evaluation results have been averaged on the adopted subset and a related global quality evaluation has been finally produced.

6. RESULTS

The quantitative assessment of the GSA_CA, the GSG, the GS, the GIHS, and the PC fusion techniques have been performed by evaluating the ERGAS, the PSNR, the SAM, the RMSE and the Correlation Coefficient (CC) score indexes between the fused images and the reference ones. The adopted study area has not a rectangular shape, but the evaluation of the aforementioned quality indexes has been performed on a square subimage, in which the pixels outside the study area have been masked and set to the zero value. As a consequence, the high number of corresponding zero values between fused and reference image introduce a bias in the score indexes. In order to overcome this drawback and to obtain values that are easily comparable among the different fusion methods, the resulting score indexes have been normalized in percentage of the best achieved value. A value of 100 is therefore assigned to the better method among the tested ones, and consequently the higher is the number the worst is the performance for the ERGAS, the SAM, and the RMSE, whereas for the PSNR and the Correlation value the worst methods are characterized by the lower values. The normalized score indexes achieved by the tested fusion methods are listed in Table 2, together with the

performance achieved by the “expanded” image, that is a simply resampled image obtained by interpolating the MS bands to be used as a reference to evaluate the improvement introduced by the pan-sharpening procedures.

	ERGAS %	SAM %	RMSE %	PSNR %	CORR %
GSA-CA	100.0000	104.1346	100.0000	100.0000	100.0000
GSG	104.0293	115.8417	195.1536	98.6895	99.9305
GS	112.2316	121.4751	114.3788	96.9539	99.7860
IHS	135.1306	130.9472	138.5633	92.4371	99.3656
PC	124.1912	128.3047	125.1895	94.9071	99.5846
EXP	134.9381	100.000	139.3647	91.8082	99.3706

Table 2. Results of the quantitative evaluation.

As expected, the GSA-CA and the GSG achieve the best performances for the most part of the adopted score indexes, even if GSG shows some problems in terms of RMSE, whereas the GS is found to be the best among the fusion methods implemented by ENVI.

From the visual point of view, the results have been summarized in the table 3, in which for each studied fusion technique the resulting quality in terms of the characteristics used by the photointerpreter to map the landslide are assessed together with a global judgment of the fused image; the evaluation is provided by means of a detectability rating scale, based on a five levels ranking, namely: 5 (insufficient), 4 (poor), 3 (medium), 2 (good), 1 (excellent).

	Features	Texture	Contrast	Colour	Overall
GSA	2	3	2	2	2
GSG	1	1	2	2	2
GS	1	1	2	2	1
IHS	3	3	2	3	3
PC	1	1	1	2	1

Table 3. Qualitative evaluation

By considering the scores of Table 3, the PC and the GS pan-sharpening techniques result as the best in the context of landslide detection among the tested ones. Also the GSG does not change linear features and texture, but is less satisfactory in term of colour quality, whereas GSA slightly suffers for some changes in linear features and texture useful in landslide detection.

7. CONCLUSIONS

Five pan-sharpening techniques, the Gram-Schmidt Global Adaptive (GSG), the Gram-Schmidt Adaptive – Context Adaptive GSA-CA, the Gram-Schmidt method (GS), the Principal Component method (PC) and the generalized-IHS (GIHS) method have been tested on a IKONOS multispectral data set acquired over Umbria region in Italy, and the quality of the resulting pan-sharpened images have been compared quantitatively and qualitatively in the specific context of landslide detection task. From the quantitative point of view, the synthesis property introduced by Wald et al. (Wald et al.

1997) have been evaluated by using five score indexes, namely the ERGAS, the SAM, the RMSE, the PSNR and the correlation value, usually adopted for such task, whereas the qualitative assessment have been performed by a visual inspection of skilled photointerpreters. This analysis has been focused on the characteristics of the image useful for landslide detection, such as linear features, textures, contrast and colour. Quantitative assessment confirms the result of some previous comparative works: the GSG and GSA-CA pan-sharpening techniques have been found as the most performing, and the performances of the GS method is however higher than those of the PC and the GHS ones, because of a residual misalignment among panchromatic and multispectral IKONOS bands. On the opposite side, the visual analysis does not agree with the quantitative conclusions; as a matter of fact the GS method has been found as the most performing for the landslide detection tasks together with the PC. The GSG shows a similar high quality but presents some problems concerning the quality of the colour useful for landslide recognition, whereas the GSA-CA slightly suffers for some changes in linear features and textures useful in landslide detection task. As a consequence of the comparison among the quantitative and the qualitative assessment, it has been found that the procedures and the score indexes often proposed for the assessment of pan-sharpened images quality are not fully suitable for the ranking of the fusion techniques when landslide detection with photointerpretative techniques task is considered.

8. REFERENCES

- Aiazzi B., Alparone L., Argenti F., and Baronti S., 1999. Wavelet and pyramid techniques for multisensor data fusion: A performance comparison varying with scale ratios, *Proc. SPIE, EUROPTO Series Image Signal Process. Remote Sensing V*, S. B. Serpico, Ed., vol. 3871, pp. 251–262.
- Aiazzi B., Alparone L., Baronti S., and Garzelli A., 2002. Context-driven fusion of high spatial and spectral resolution images based on oversampled multiresolution analysis, *IEEE Trans. Geosci. Remote Sensing*, vol. 40 (10), pp. 2300–2312.
- Aiazzi B., Alparone L., Baronti S., Garzelli A., and Selva M., 2006. MTF-tailored multiscale fusion of high-resolution MS and Pan imagery, *Photogramm. Eng. Remote Sens.*, vol. 72 (5), pp. 591–596.
- Aiazzi B., Baronti S., and Selva M., 2007. Improving component substitution Pan-sharpening through multivariate regression of MS+pan data, *IEEE Trans. Geosci. Remote Sens.*, vol. 45 (10), Oct., pp. 3230–3239.
- Aiazzi B., Baronti S., Lotti F., and Selva M., 2009. A Comparison Between Global and Context-Adaptive Pan-sharpening of Multispectral Images, *IEEE Geoscience And Remote Sensing Letters*, Vol. 6 (2), 302–306.
- Alparone L., Baronti S., Garzelli A., and Nencini F., 2004. A global quality measurement of pan-sharpened multispectral imagery, *IEEE Geosci. Remote Sens. Lett.*, vol. 1 (4), pp. 313–317.
- Alparone L., Wald L., Chanussot J., Thomas C., Gamba P., and Mann Bruce L., 2007. Comparison of Pan-sharpening Algorithms: Outcome of the 2006 GRS-S Data-Fusion Contest, *IEEE Transactions On Geoscience And Remote Sensing*, Vol. 45 (10), pp. 3012–3021.
- Alparone L., Aiazzi B., Baronti S., Garzelli A., Nencini F., and Selva M., 2008. Multispectral and panchromatic data fusion assessment without reference, *Photogramm. Eng. Remote Sens.*, vol. 74 (2), pp. 193–200.
- Carper W. J., Lillesand T. M., and Kiefer R. W., 1990. The use of intensity- hue-saturation transformations for merging SPOT panchromatic and multispectral image data, *Photogramm. Eng. Remote Sens.*, vol. 56, pp. 459–467.
- Chavez P. S. and Kwarteng A. Y., 1989. Extracting spectral contrast in Landsat Thematic Mapper image data using selective principle component analysis, *Photogramm. Eng. Remote Sens.*, vol. 55 (3), pp. 339–348.
- Chavez, Jr. P. S., Sides S. C. and Anderson J. A., 1991. Comparison of three different methods to merge multiresolution and multispectral data: Landsat TM and SPOT panchromatic, *Photogramm. Eng. Remote Sens.*, vol. 57 (3), pp. 295–303.
- Couloigner I., Ranchin T., Valtonen V. P., and Wald L., 1998. Benefit of the future SPOT-5 and of data fusion to urban road mapping, *Int. J. Remote Sens.*, vol. 19 (8), pp. 1519–1532.
- de Béthune S., Muller F., and Donnay J. P., 1998. Fusion of multi-spectral and panchromatic images by local mean and variance matching filtering techniques, *Fusion of Earth Data*, Jan. 28–30.
- Edwards K. and Davis P. A., 1994. The use of Intensity-Hue-Saturation transformation for producing color shaded-relief images, *Photogramm. Eng. Remote Sens.*, vol. 60 (11), pp. 1369–1374.
- Fanelli A., Leo A., and Ferri M., 2001. Remote sensing images data fusion: A wavelet transform approach for urban analysis, in *Proc. Joint IEEE/ISPRS Workshop Remote Sens. Data Fusion Over Urban Areas*, pp. 112–116.
- Garguet-Duport B., Girel J., Chassery J.-M., and Pautou G., 1996. The use of multi-resolution analysis and wavelets transform for merging SPOT panchromatic and multi-spectral image data, *Photogramm. Eng. Remote Sens.*, vol. 62 (9), pp. 1057–1066.
- Gillespie A. R., Kahle A. B., and Walker R. E., 1987. Color enhancement of highly correlated images—II. Channel ratio and ‘chromaticity’ transformation techniques, *Remote Sens. Environ.*, vol. 22, pp. 343–365.
- González Audicana M. and Seco A., 2003. Fusion of multispectral and panchromatic images using wavelet transform. Evaluation of crop classification accuracy, in *Proc. 22nd EARSeL Annu. Symp. Geoinformation Eur.-Wide Integr.*, Prague, Czech Republic, 4–6 June 2002, T. Benes, Ed., 2003, pp. 265–272.
- Laben C. A. and Brower B. V., 2000. Process for enhancing the spatial resolution of multispectral imagery using Pan-sharpening, U.S. Patent 6 011 875, Jan. 4, 2000. Tech. Rep., Eastman Kodak Company.

- Li J., Spatial quality evaluation of fusion of different resolution images, 2000. *ISPRS Int. Arch. Photogramm. Remote Sens.*, vol. 33, no. B2-2, pp. 339–346.
- Liu, J. G., 2000. Smoothing filter-based intensity modulation: A spectral preserve image fusion technique for improving spatial details, *Int. J. Remote Sens.*, vol. 21 (18), pp. 3461–3472.
- Marcelino E.V., Formaggio A. R., Maeda E. E., 2009. Landslide inventory using image fusion techniques in Brazil, *International Journal of Applied Earth Observation and Geoinformation* 11, pp. 181–191.
- Mather, P.M., 1999. *Computer Processing of Remotely-Sensed Images: An Introduction*. John Wiley & Sons, Chichester, 292 pp.
- Nichol J., and Wong M.S., 2005. Satellite remote sensing for detailed landslide inventories using change detection and image fusion, *Int. Journal of Remote Sensing*, Vol. 26 (9), 1913-1926.
- Nikolakopoulos K. G., 2008. Comparison of nine fusion techniques for very high resolution data, *Photogrammetric Engineering & Remote Sensing*, Vol. 74 (5), pp. 647-659.
- Nunez J., Otazu X., Fors O., Prades A., Pala V., and Arbiol R., 1999. Multiresolution- based imaged fusion with additive wavelet decomposition, *IEEE Trans. Geosci. Remote Sensing*, vol. 37, pp. 1204–1211.
- Pohl, C., Van Genderen, J.L., 1998. Multisensor image fusion in remote sensing: concepts, methods and applications. *International Journal of Remote Sensing* 19, pp. 823–854.
- Ranchin T. and Wald L., 2000. Fusion of high spatial and spectral resolution images: The ARSIS concept and its implementation, *Photogramm. Eng. Remote Sens.*, vol. 66 (1), pp. 49–61.
- Ranchin T., Aiazzi B., Alparone L., Baronti S., and Wald L., 2003. Image fusion—The ARSIS concept and some successful implementation schemes, *ISPRS J. Photogramm. Remote Sens.*, vol. 58 (1/2), pp. 4–18.
- Schowengerdt, R.A., 1997. Remote Sensing, Models and Methods for Image Processing. *Academic Press, San Diego*, 522 pp.
- Tu Te-Ming, Huang Ping S., Hung Chung-Ling, and Chang Chien-Ping, 2004. A Fast Intensity–Hue–Saturation Fusion Technique with Spectral Adjustment for IKONOS Imagery, *IEEE Geoscience And Remote Sensing Letters*, Vol. 1 (4), pp. 309-312.
- Thomas C. and Wald L., 2005. Assessment of the quality of fused products, in *Proc. 24th EARSeL Annu. Symp. New Strategies Eur. Remote Sens.*, Dubrovnik, Croatia, May 25–27, 2004. M. Oluic, Ed., Rotterdam, The Netherlands: Balkema, pp. 317–325.
- Thomas C. and Wald L., 2007. Comparing distances for quality assessment of fused products, in *Proc. 26th EARSeL Annu. Symp. New Develop. Challenges Remote Sens.*, Warsaw, Poland, Z. Bochenek, Ed., Rotterdam, The Netherlands: Balkema, pp. 101–111.
- Tu T.-M., Su S.-C., Shyu H.-C., and Huang P. S., 2001. A new look at IHS-like image fusion methods, *Inform. Fusion*, vol. 2, pp. 177–186.
- Wald L., Ranchin T., and Mangolini M., 1997. Fusion of satellite images of different spatial resolutions: Assessing the quality of resulting images, *Photogramm. Eng. Remote Sens.*, vol. 63 (6), pp. 691–699.
- Wald L., 1999. Some terms of reference in data fusion, *IEEE Trans. Geosci Remote Sens.*, vol. 37 (3), pp. 1190–1193.
- Wald L. and Baleynaud J.-M., 1999. Observing air quality over the city of Nantes by means of Landsat thermal infrared data, *Int. J. Remote Sens.*, vol. 20 (35), pp. 947–959.
- Wang Z. and Bovik A. C., 2002. A universal image quality index, *IEEE Signal Process. Lett.*, vol. 9, no. 3, pp. 81–84.
- Wang Z., Ziou D., Armenakis C., Li D., and Li Q., 2005. A comparative analysis of image fusion methods, *IEEE Trans. Geosci. Remote Sens.*, vol. 43 (6), pp. 1391–1402.
- Yang W., Cauneau F., Paris J.-P., and Ranchin T., 2000. Influence of landscape changes on the results of the fusion of P and XS images by different methods, in *Proc. 3rd Conf. Fusion of Earth Data: Merging Point Measurements, Raster Maps Remotely Sensed Images*, T. Ranchin and L. Wald, Eds. pp. 47–56.
- Zhang Y., 2002. Problems in the fusion of commercial high-resolution satellite images as well as Landsat 7 images and initial solutions, in *Geospatial Theory, Processing and Applications: Proc. ISPRS Commission IV Symp.*, Ottawa, ON, Canada.
- Zhang Y., 2004. Understanding image fusion, *Photogramm. Eng. Remote Sens.*, vol. 70, no. 6, pp. 657–661.
- Zhou J., Civco D. L., and Silander J. A., 1998. A wavelet transform method to merge Landsat TM and SPOT panchromatic data, *Int. J. Remote Sens.*, vol. 19 (4), pp. 743–757.

SIMULATION ASSISTED HIGH-RESOLUTION PSI ANALYSIS

A. Schunert^{a,*}, T. Balz^b, K. Liu^b, M.S. Liao^b, U. Soergel^a, JD Wegner^a

^a Institute of Photogrammetry and GeoInformation, Leibniz Universität Hannover, Hannover, Germany

^b State Key Laboratory of Information Engineering in Surveying, Mapping and Remote Sensing, Wuhan University, Wuhan, China

Commission VII

KEY WORDS: SAR, Radar, PSI, Simulation, TerraSAR-X

ABSTRACT:

Since the first demonstration of the potential of the differential SAR interferometry in the early 1990s a lot of effort has been made to accurately estimate ground deformation with imaging radar sensors. This led to the invention of the Persistent Scatterer Interferometry (PSI) in the late 1990s. PSI enables the estimation of ground deformation for a set of temporally stable radar reflectors, the so called PS, with millimeter accuracy. The main advantage compared to methods commonly used for ground deformation monitoring like GPS is the possibility to cover large areas very economically. One of the main drawbacks is the opportunistic sampling of the target area, which is mainly governed by the distribution of stable radar reflectors within the scene. Besides problems caused by undersampling the main issue is due to the fact, that the real world feature related to a PS is usually not known. This makes the interpretation of the results particularly difficult. While the assignment of these real world features is very difficult in the case of ERS like sensors, modern high resolution SAR sensors like TerraSAR-X (TSX) render this task possible. We investigate the use of SAR simulation to match real world features with PS extracted from a TSX stack acquired over the city of Berlin Germany. The simulation is based on a 3D city model of the area around the Potsdamer Platz, Berlin.

1. INTRODUCTION

With the help of the Persistent Scatterer Interferometry (PSI) surface deformation can be estimated with millimetre accuracy. The sampling of the phenomenon under investigation is thereby determined by the backscattering behaviour of the scene at hand since only temporally stable radar targets can be used.

Despite the high accuracy of the PS results, their interpretation is quite difficult due to the fact that it is unknown a priori which real world feature appertains to a given PS. If the aim of a PS analysis is, for instance, the determination of ground deformation, building movements due to thermal dilation or settling may be confused with the signal of interest. This is especially a problem in case of ERS-like sensors, where a mapping of PS to single buildings is almost impossible. Against this the modern high resolution SAR sensors like TerraSAR-X (TSX) provide a resolution, which is sufficient to recognize even small features of buildings. We investigate the joint use of PSI and SAR simulation for determining the physical cause of PS. Therefore, a stack of 20 TSX high resolution spotlight images, acquired over the city of Berlin is used for the PSI analysis. The images exhibit a ground range resolution of 1.2 meter.

For the simulation a 3D city model was used, which was derived from airborne laserscanning data.

2. PERSISTENT SCATTERER INTERFEROMETRY

The PSI technique is an extension of the classical SAR interferometry, to mitigate the problems due to temporal

decorrelation and atmospheric disturbances. Temporal decorrelation arises through changes in the backscattering behaviour of a resolution cell over time, which can be alleviated by restricting the analysis to a set of temporally stable radar targets, referred to as Persistent Scatterers (PS).

Tropospheric water vapour influences the refraction coefficient and therefore the velocity of light. Hence, different atmospheric conditions at the times of master and the slave image acquisitions may result in an undesired term of the interferometric phase caused different path delay. This term has to be removed to estimate topography or deformation with reasonable accuracy. Within the framework of PSI this is usually done with the help of a stack of interferograms.

The first step of a PSI analysis is to extract a set of PS candidates. This can be achieved in several ways. We used the amplitude dispersion index introduced by Ferretti *et al.* (2001) for that purpose, which is computed for every image pixel as follows:

$$D_A = \frac{\sigma_A}{m_A} \quad (1)$$

The variables σ_A and m_A denote the standard deviation and the mean of the amplitude of every pixel estimated over time, respectively. As shown in Ferretti *et al.* (2001) the amplitude

*corresponding author

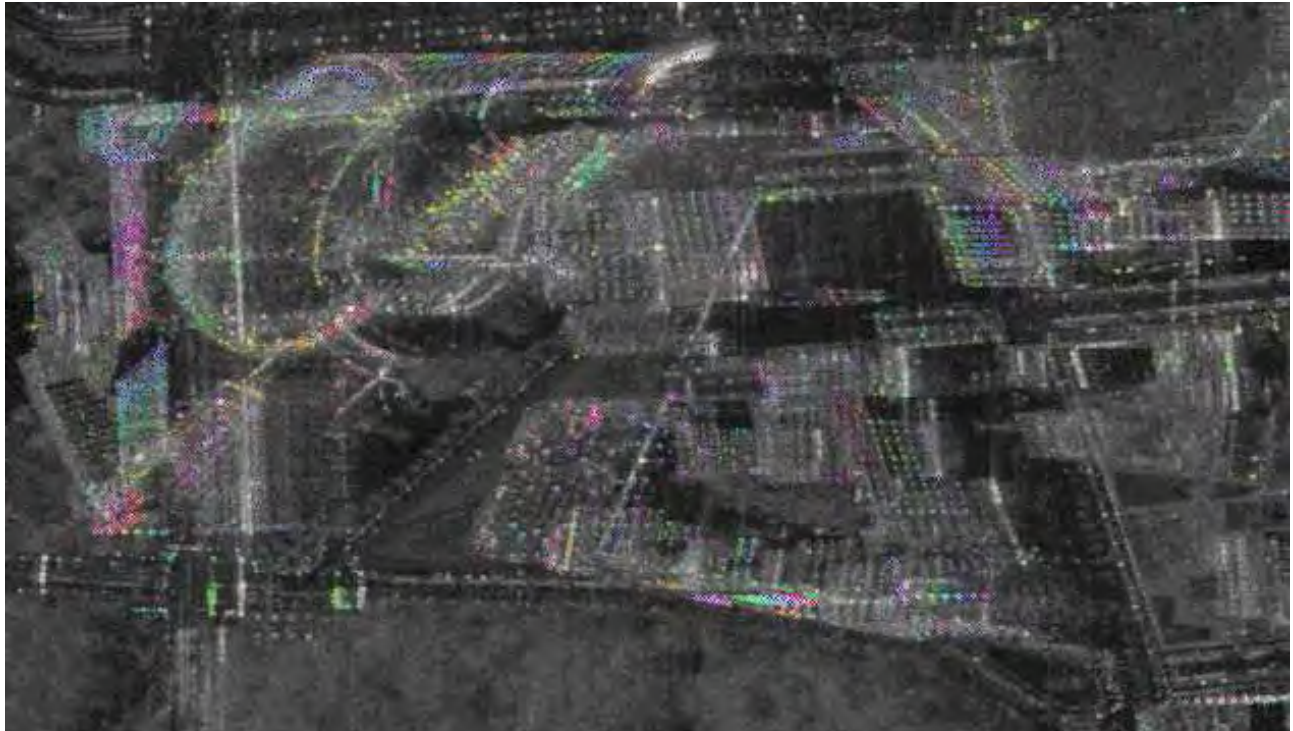


Figure 1. Phase of one interferogram of the stack overlaid on the mean amplitude image.

dispersion is a good estimate of a scatterer's phase stability if the scatterer's signal exhibits a high signal to noise ratio. However, the quality of resolution cells with low signal to noise ratio is overestimated, leading to the necessity to set a quite strict threshold in the beginning to avoid false positives. We choose the amplitude dispersion threshold to be 0.2, to have a negligible number of those. Additionally, groups of adjacent PS are thinned out by just considering the best PS in a 4 connectivity neighbourhood. The distribution of the PS is illustrated in Figure 1 overlaid on the mean amplitude image of the TSX data stack. The colours represent phase values of one interferogram.

The PS density is about 20 000 PS per km², which is quite low compared to PS densities found by Bamler *et al.* (2009), which can be explained by the quite strict selection criteria. It can be seen, that many PS reside at building façades. We expect those to be generated by structures such as windows or balconies. For some PS it is not clear if they are caused by scattering at the façade or the roof of a building since both target areas may be mapped to the same image position.

After the initial selection signal processing is carried out for the candidate set, in order to discriminate between the respective contributions forming the interferometric phase, which can be modelled according to Hooper *et al.* (2007) as

$$\psi_{\text{int},x,i} = W \left\{ \varphi_{\text{def},x,i} + \varphi_{\text{atm},x,i} + \Delta\varphi_{\text{orb},x,i} + \Delta\varphi_{\theta,x,i} + \varphi_{n,x,i} \right\} \quad (2)$$

where

- $\varphi_{\text{def},x,i}$ contains the phase due to the surface movement projected to the sensors line of sight;
- $\varphi_{\text{atm},x,i}$ is the phase due to different atmospheric states during master and slave acquisitions;

- $\Delta\varphi_{\text{orb},x,i}$ denotes the phase emerging from errors in the satellites orbit determination;
- $\Delta\varphi_{\theta,x,i}$ is called look angle error and is caused by two effects. These are contributions due to residual topographic phase components and deviation of the pixels phase centre from its geometric centre in range direction. The latter effect is considered to be negligible because of the high resolution of the data. The residual topography terms the vertical distance between the reference surface and the PS. In this case the WGS 84 ellipsoid is used as a reference surface.
- $\varphi_{n,x,i}$ is the phase noise which is largely caused by changes of the pixels reflectivity with time and look angle;

In this paper we are just interested in estimating the residual topography to get information about a scatterers 3D position. We use a standard PS approach following the ideas of Ferretti *et al.* (2000) and Liu *et al.* (2009) here. The phase due to deformation is modelled as a linear function of time. Atmosphere and effects related to orbit errors are assumed to be low pass components in space. Finally residual topographic phase is a linear function of the effective spatial baseline separating every interferometric image pair.

In a first step phase differences between neighbouring PS are calculated, which mainly cancels out the phase caused by atmosphere and orbit errors. Thereby the neighbourhood is given by a Delaunay triangulation. For every phase difference between two PS at positions x and y velocity and height increments denoted by v_{xy} and H_{xy} respectively are calculated using a coherence maximisation approach (see for instance Liu *et al.* (2009)), which can be stated as

$$\gamma_{xy} = \max_{v_{xy}, H_{xy}} \left| \frac{1}{N} \sum_{i=1}^N e^{j \left(\psi_{\text{int}, x, i} - \frac{4\pi}{\lambda} \frac{B_i^\perp}{R \sin \theta} H_{xy} - \frac{4\pi}{\lambda} T_i v_{xy} \right)} \right| \quad (3)$$

where

- B_i^\perp is the spatial baseline,
- T_i is the temporal baseline,
- λ is the wavelength of the sensor,
- R is the distance from sensor to target,
- θ is the off nadir angle of the radar.

The term γ_{xy} denotes the so called temporal coherence factor and serves as quality measure to evaluate how good the observations fit the assumed model. Results having a value below 0.7 are removed before the next step.

In order to calculate the PS height from the height increment a overdetermined system of linear equation has to be solved, which is done by means of an iteratively reweighted least squares approach. Within the inversion of this system remaining gross errors are removed from the data (see Liu *et al.* (2009) for reference).

The result is a height and a velocity estimate for every PS relative to a reference PS in the scene. While the height can be estimated with submeter accuracy, accuracies of the subsidence rate are in the order of few millimetres per year. The geocoded PS overlaid to the 3D model used for simulation are shown in Figure 2.

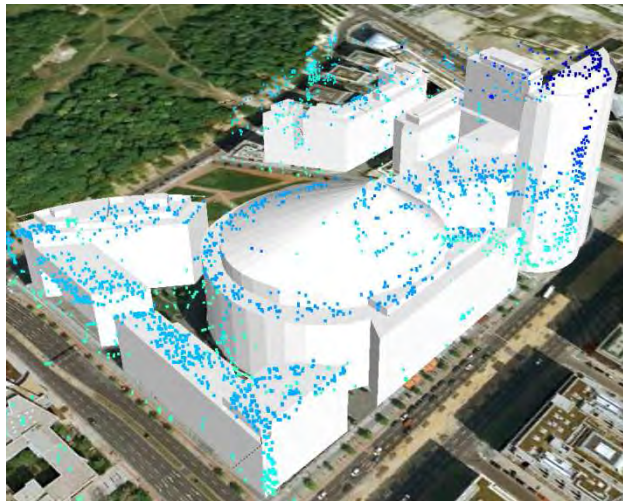


Figure 2. 3D model of the Sony-Center overlaid with PS

3. SAR SIMULATION

3.1 3D city model

The 3D city model, which is the basis for simulation was derived from airborne laser scanning data. We used the free software tool sketchup to reconstruct surfaces from the point cloud. The whole procedure was conducted manually, i.e., no meshing algorithms were used. The result is displayed in Figure 2 together with the geocoded PS.

3.2 Fast ray-tracing SAR simulation approach

SAR simulations aiming at precise prediction of PS positions require high geometrical correctness, whilst radiometric features are less important. According to the classification of Franceschetti *et al.* (1995) SAR simulation systems can be differentiated into raw data and image simulation systems. For our application SAR image simulation systems are feasible, because the focus is on the geometry. To ensure geometrical correctness together with computational efficiency, we use ray-tracing for our SAR simulation. Ray-tracing based SAR simulations can simulate the SAR geometry precisely, while keeping the amount of new software to be coded small by reusing and editing ray tracing tools developed for computer graphics applications (see e.g. Auer *et al.* 2010).

In our experiments we use a SAR simulator prototype based on the GPU ray-tracing library Optix™ from NVIDIA (2009). Optix™ traces the rays by using the tremendous calculation speed of modern graphics processing units (GPU), allowing for real-time or near real-time ray tracing. By adjusting the library, a real-time SAR simulator can be developed.

In this way, a fast, widely used, and extensively tested ray tracing library can be applied, which speeds up the developing process.

The simulation system we used was tailored for airborne SAR systems. Simulating TerraSAR-X data required some adjustments. The distance between the sensor and the objects on the ground are much larger in the spaceborne case, which caused troubles due to the limits of the 32-bit floating point values used in data processing. The real distances were just too large to be simulated. By setting the simulated sensor distance to around 200 km, we believe we found an acceptable compromise. The differences in the simulated geometry due are rather small, especially compared to the errors in the simulated building models.

The radiometric simulation is based on the model of Zribi *et al.* (2006) model, which does not exactly fit for urban environments. Because for our application the simulated radiometry does not need to be very accurate, we believe this is an acceptable simplification.



Figure 3. Mean amplitude image of the data stack



Figure 4. Simulated image containing single and double bounce contributions

3.3 SAR simulation for PSI analysis

In order to compare the PS extracted from the data stack with the results of the simulation, the simulated image is warped to the geometry of the data stack. This is necessary due to different coordinate systems of the simulated scene and the real scene, and because of small geometrical errors caused by the simulation of an airborne sensor system.

We applied an affine transformation for the warping procedure. The coefficients of this model were estimated using a number of six tie points distributed over the whole simulated scene. The result is displayed in Figure 3 and Figure 4. The mean amplitude image of the stack is displayed in Figure 3, while the simulated scene containing single and double bounce contributions is shown in Figure 4. It can be clearly seen, that the main structures of the buildings are reproduced by the simulation.



Figure 5. Simulated image overlaid with PS

Within the simulation we can distinguish between single- and double-bounce reflections. Locations of double-bounce between the dihedral corner reflector spanned by building walls and the ground in front are clearly visible in the real and the simulated SAR image.

However, the details of the façades are not visible, even facade structures which cause very strong reflections are often too small to be represented in the 3D model.

The PS set superimposed on the simulated image is shown in Figure 5. It is clearly visible, that besides some geometrical inconsistencies (see skyscraper at the top of the image) the PS set matches fairly well with the simulated image. On the other hand the main problem of the whole approach shows up. Since most of the PS are generated by small scale building features (like the above mentioned balconies and windows), which are not modelled in the simulation, detailed analysis of the physical nature of the PS is virtually impossible.

The whole situation can be best illustrated by considering the part of Figure 5 marked by the red rectangle. In this area lots of PS appear, but the simulation just indicates a homogeneous area. These PS reside mainly on the roof of the round shaped building in the centre of the building block, as can be seen from the height data in

Figure 2. An oblique view aerial image shown in Figure 6 reveals the structures leading to this group of PS. First of all, a lot of hardware, which may be used for ventilation purposes, is visible. Additionally, a metallic frame surrounds the dome-like part of the roof in Figure 6. Both types of structures are likely to produce PS, but are not contained in the 3D model used for simulation. Therefore an assignment of the respective PS to these building features using the shown simulation results is hardly possible.

For simulating these structures we would need a 3D building model reconstructed from terrestrial laser scanning or close-range photogrammetry. Less accurate, but for some applications still acceptable, would be models reconstructed using façade grammars describing the façade (Becker 2009). In this way, models of simple standardized buildings can be generated without using high-resolution laser scanning data or close-range photogrammetry.

The Sony-Center and the surrounding buildings used in our experiments are not standardized buildings easily representable in a façade grammar. We also do not have high resolution façade data. Therefore, we couldn't reconstruct a 3D building model in the required quality.

However, the simulation is useful to retrieve information about the PS within the green box. We know that virtually all scattering within this area is due to the roof of the building, which encompasses the round shaped one.



Figure 6. Oblique view aerial image

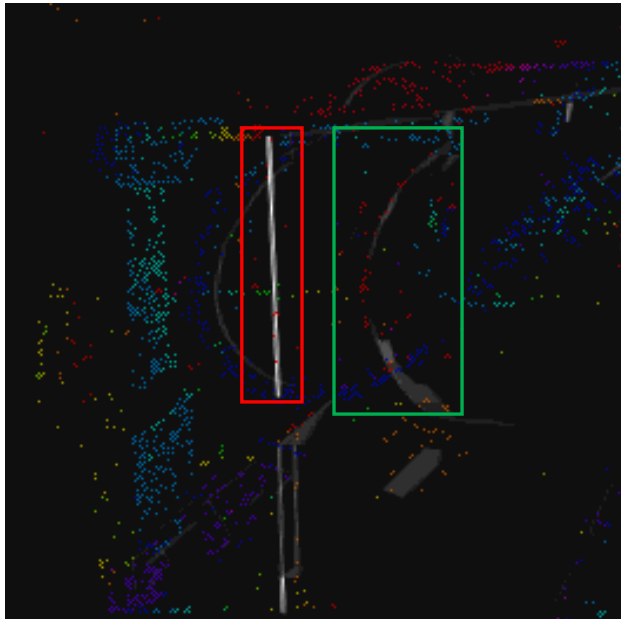


Figure 7. Simulated double bounce reflections overlaid with PS

Therefore, it is reasonable to assume that the PS are caused by structures on this roof and not by scatterers located at the upper part of the facade. This assumption is verified by the estimated height of the PS (see Figure 2).

It is furthermore possible to assess PS located on double bounce lines induced by large scale building features (e.g. curb-to-wall scattering). These are displayed in Figure 7. The PS heights arranged in five meter classes are overlaid to simplify the discrimination of PS on and off the double bounce lines. It is apparent, that the PS densities on the double bounce lines are not always as high as one may expect due to the strong backscattering. An example is marked by the red box in Figure 7, where there are hardly any PS resident (PS coloured in light red). In contrast to that, there are lots of PS on the double bounce feature marked by the green box. The reason for that is to be investigated.



Figure 8. Oblique view aerial image of the DB-Tower

As can be seen from the oblique view aerial image in Figure 6 the virtue of the respective façades differ in terms of material and geometry.

Finally it is remarkable, that there are almost no PS at the façades visible in Figure 6, which is apparent from Figure 2 and Figure 5. This is surprising, since there are usually plenty of PS at building fronts oriented towards the sensor. It is conceivable, that this is due to the texture of the façades. However, there are at least some PS located on the skyscraper at the top of the SAR image (see Figure 1 and Figure 2), whose façade looks quite similar as can be seen from the oblique view aerial image displayed in Figure 8.

4. CONCLUSIONS

In theory a SAR simulator can assist the PSI analysis by helping to determine the exact location of the PS. This is true, if very precise and detailed 3D building models are available. Although 3D building models are available for many urban areas, they seldom contain the geometry of the façades. The façade is mostly represented with an image texture, which is feasible for visualization purposes, but not for SAR simulation. To simulate the façade reflection, a 3D model containing the façade geometry is necessary.

However, the simulation still proved to be useful. We could demonstrate that the double bouncing between building and ground does not cause many PS. Most PS in our test scene are caused by scatterers located on the building roofs.

Without highly detailed building models, SAR simulation can only provide very rudimentary assistance for the PSI analysis. In future work we will augment the 3D model by close range Photogrammetry in order to represent also pillars, doors, windows and balconies. In a next step we want to group PS and match those against facade structures.

ACKNOWLEDGEMENTS

Part of the work was supported by the Research Fellowship for International Young Scientists of the National Natural Science Foundation of China (Grant No. 60950110351).

REFERENCES

- Auer, S., Hinz, S., and Bamler, R., 2010. Ray-tracing simulation techniques for understanding high-resolution SAR images. *IEEE Transactions on Geoscience and Remote Sensing* 48(3), pp. 1445-1456.
- Bamler, R., Eineder, M., Adam, N., Zhu, X., Gernhardt, S., 2009. Interferometric Potential of High Resolution Spaceborne SAR. *Photogrammetrie - Fernerkundung - Geoinformation* 5, pp. 407-419.
- Becker, S., 2009. Generation and application of rules for quality dependent facade reconstruction. *ISPRS Journal of Photogrammetry and Remote Sensing* 64, pp. 640-653.
- Ferretti, A., Prati, C., Rocca, F., 2000. Nonlinear subsidence rate estimation using permanent scatterers in differential SAR interferometry. *IEEE Transactions on Geoscience and Remote Sensing* 38(5), pp. 2202-2212.

Ferretti, A., Prati, C., Rocca, F., 2001. Permanent scatterers in SAR interferometry. *IEEE Transactions on Geoscience and Remote Sensing* 39(1), pp. 8-20.

Franceschetti, G., Migliaccio, M., and Riccio, D., 1995. The SAR simulation: an overview. In: *Proc. IGARSS 1995*, Florence, 1995.

Hooper, A., Segall, P., Zebker, H., 2007. Persistent scatterer InSAR for crustal deformation analysis, with application to Volcán Alcedo, Galápagos. *Journal of Geophysical Research* 112.

Liu, G., Buckley, S., Ding, X., Chen, Q., Luo, X., 2009. Estimating Spatiotemporal Ground Deformation With Improved Permanent-Scatterer Interferometry. *IEEE Transactions on Geoscience and Remote Sensing* 47(8), pp. 2762-2772.

NVIDIA, 2009. NVIDIA OptiX Ray Tracing Engine. Programming Guide. Available online: <http://developer.nvidia.com/object/optix-home.html>. [last accessed on June 4, 2010]

Zribi, M., Baghdadi, N., and Guérin, C., 2006. A new semi-empirical model for the analysis of surface roughness heterogeneity. In: *Proc. IGARSS 2006*, Denver, Colorado, 2006.

TOPOGRAPHIC ESTIMATION BY TERRASAR-X

U. G. Sefercik^{a,*}, U. Soergel^b

^a Zonguldak Karaelmas University, Engineering Faculty, Department of Geodesy and Photogrammetry Engineering, 67100 Zonguldak, Turkey - ugsefercik@hotmail.com

^b Leibniz University Hannover, Institute of Photogrammetry and Geoinformation, 30167, Hannover, Germany - soergel@ipi.uni-hannover.de

Commission VII, WG VII/2

KEY WORDS: SAR, Estimation, DEM, Generation, Comparison, Accuracy, Visualization, Analysis

ABSTRACT:

SAR Interferometry (InSAR) is a technique to derive Digital Elevation Model (DEM) from at least two complex SAR images. The data are either taken simultaneously (single-pass mode) or sequentially (repeat-pass mode) by airborne or space-borne sensors (carriers: plane, satellite, shuttle etc.). To date, one of the most important single-pass interferometry measurement campaigns is the Shuttle Radar Topography Mission (SRTM) completing its mission successfully after 11 days of operation between 11th and 22nd of February 2000. On the other hand, repeat-pass InSAR has been used by several satellite systems: ENVISAT, ERS 1-2, RADARSAT 1-2, ALOS, JERS-1 etc. One of the most advanced systems is the German TerraSAR-X (TSX) satellite launched on June 15th, 2007. TSX offers high resolution (~1m by Spotlight mode) imagery which could not be achieved from radar technologies up to this time similar to high resolution optical imagery. In contrast to optical sensors, TSX can be operated under all weather conditions without being influenced by clouds. The data sets provided by TSX newly obtained by scientific community and evaluations are currently being performed. As mentioned above, utilizing the advantages of SAR technology, indeed the planimetric locations of target ground objects, elevations of them can be determined using interferometry. Through the interferometric data, interferograms (fringe maps) can be generated and applying interferometric processing steps height models can be created for large coverage interest areas. The main targets of this investigation can be summarized as; generation of height models derived from TSX InSAR image-pairs and evaluation by comparison with more accurate reference height models as well as height models based on high resolution optical satellite images. Absolute and relative accuracy, stability, homogeneity and dependency upon various parameters are determined. The approach will be demonstrated using TSX data covering Istanbul area, Turkey.

1. INTRODUCTION

As it is known, Radar remote sensing has a significant role in remote sensing technologies and develops rapidly. Once in a few years new SAR (synthetic aperture radar) satellites are launched to space including various types of operation modes which offer different resolutions and advantages to each other. The most actual SAR satellite is German TerraSAR-X was launched to its orbit on 15th June 2007. This satellite is a revolution for the SAR technologies at the resolution side and offers 1m high resolution in Spotlight mode. To assess the quality of DSM which is derived from this high resolution data of this current satellite a comparison has been made between the DSM of one of the most advanced optical systems IKONOS. For this aim, the DSMs have been generated using both satellites' data in Istanbul, Turkey and compared with a more accurate DEM of same area, produced by photogrammetry.

2. TEST FIELD AND DATA SETS

2.1 Test Field

Istanbul is located in north-west area of Turkey. The Greater Municipality Area has a coast line to the Black Sea and the Marmara Sea connected by the Bosphorus. Istanbul is one of the biggest cities in the world. About 14 million people live in the city and most of settlements are at the surrounding of Bosphorus

and coast line of Marmara Sea. The city is a suitable test area for the accuracy analysis because its topography contains various characteristics and this enables to understand the quality of evaluated DEMs in different types of terrain formations. In patches, terrain is open-flat, hilly-steep and woody. The test area is a part of Istanbul and covers 10km×8km. It includes the historical peninsula and near surroundings. Historical Peninsula (Old City) is one of the most important regions in Istanbul, located on the European side, neighbored to the Bosphorus and Marmara Sea. This part named as Historical Peninsula because of its historic heritage. Figure 1 shows the high resolution satellite image of the test field with the frequency distribution of terrain inclination. This area has smoother topography in relation to the rest of Istanbul. The elevation reaches from sea level up to 130m.

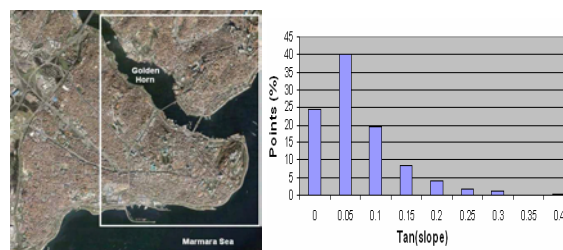


Figure 1. Test area and slope distribution of terrain inclination

* Umut Günes Sefercik, ugsefercik@hotmail.com

2.2 Data Sets

In these days, TSX is one of the most modern SAR satellites and its data will be evaluated in this study. The satellite has been launched on June 15th 2007 from oldest Russia’s space launch facility, Baikonur Cosmodrome in Kazakhstan. It is built in German; the lifetime will be at least 5 years on the space. The mission is a joint project in a public private partnership (PPP) between the German Ministry of Education and Science (BMBF), the German Aerospace Center (DLR) and the Astrium GmbH. Under DLR contract Astrium constructed and built the satellite while DLR is responsible for the development of the ground segment, instrument calibration and scientific use of satellite at its lifetime (URL 1).

TSX is one of the most advanced SAR satellites using interferometry until this day and offers the highest quality spatial data that were not available from space before using high frequency X-band SAR sensor which can be operated in different imaging and polarization modes. Figure 2 and Table 1 present the system components of the satellite.

As it can be seen from Table 1, TSX uses 3 different operation modes as Stripmap, Spotlight, and ScanSAR. These modes provide high resolution images for detailed analysis as well as width swath data whenever a larger coverage is required and imaging can be possible in single, dual and quad-polarization. Besides, TSX data can be used for interferometry by this way the DSM generation is possible.

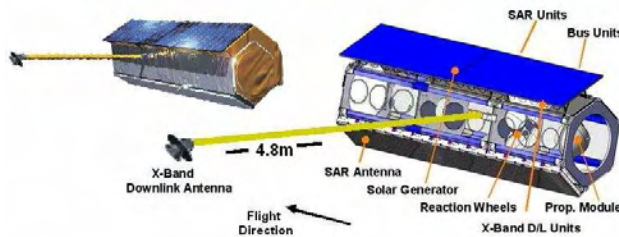


Figure 2. System components of TSX

Launch date, Life	15 June 2007, at least 5 years
Launch site	Baikonur, Kazakhstan (Russia)
Carrier	Dnepr-1
Satellite mass	1230 kilogram
Satellite size	5 m height x 2,4 m diameter
Orbit characteristics	514 km altitude, 11 days repetition, 97.44° inclination
Antenna	4.8 m active array, multi-pol, steerable in elevation and azimuth
Radar frequency	9.65 GHz
Power consumption	800 W in average
Data reception, Mission operation	DLR, Neustrelitz, Oberpfaffenhofen, Weilheim
Bandwidth	150 MHz (300 MHz experimental)
Memory	256 Gbit (end of life)
Downlink	300 Mbit/s
Imaging modes	Stripmap (3m), Spotlight (1-2m), and ScanSAR (16m)

Table 1. System components of TSX (URL 1)

TSX is capable to operate two types of Spotlight modes. The first type purely named as Spotlight mode the scenes of interest area can be obtained for an area of 10kmx10km (length and width) and recorded with 2m resolution. At the second type, the lengths of the scenes are shorter by 5kmx10km but offer higher resolution. This type is named as high resolution Spotlight mode and the scenes have 1m azimuth resolution. Between these two types of Spotlight mode just the geometric azimuth resolution is different in order to increase the azimuth scene coverage of Spotlight mode. During the observation of a particular ground scene the radar beam is steered like a spotlight so that the area of interest is illuminated longer and hence the synthetic aperture becomes larger. The Maximum azimuth steering angle range is $\pm 0.75^\circ$ (Roth, 2003).

At the investigation, for the generation of a DSM, two HRS mode TSX SAR images were used which have 1m resolution and five months time interval. Figure 2 shows these images and the following Table 2 presents the characteristics of them.

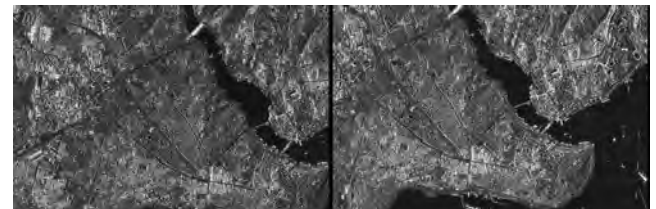


Figure 3. HRS TSX SAR images

Characteristics	HRS TSX Image 1	HRS TSX Image 2
Sensor Id	SAR	SAR
Sensor mode	High resolution Spotlight	High resolution Spotlight
Start date	2008-05-05T15:57:33,98	2008-10-06T15:57:42,52
End date	2008-05-05T15:57:34,73	2008-10-06T15:57:43,26
Polarization mode	Single polarization	Single polarization
Polarization channel	HH	HH
Looking direction	Right looking	Right looking
Pass direction	Ascending pass	Ascending pass
Centre incidence angle	40.9752891207	41.0898290780
Length and width of scene	5km×10km	5km×10km

Table 2. Characteristics of high resolution TSX SL images

For the generation of TSX DSM, interferometric processing steps of Sarscape module of program ENVI Version 4.6 have been used. Interferometric processing steps of DSM generation are not as simple as DSM generation with optical imagery. The operator has to apply several complex steps and assign threshold application values depending up on quality and characteristics of the SAR images which are used for DSM generation (e.g. co-registration settings, best choice of azimuth and range looks etc.). At the interferometric processing, after the registration of images, baseline estimation, interferogram generation along with co-registered single look complex (SLC)

generation, flattening, filtering and coherence generation, phase unwrapping, orbital refinement, phase to height conversion and geocoding steps have been performed step by step and DSM of TSX HRS mode SAR image-pairs has been obtained (Figure 4).

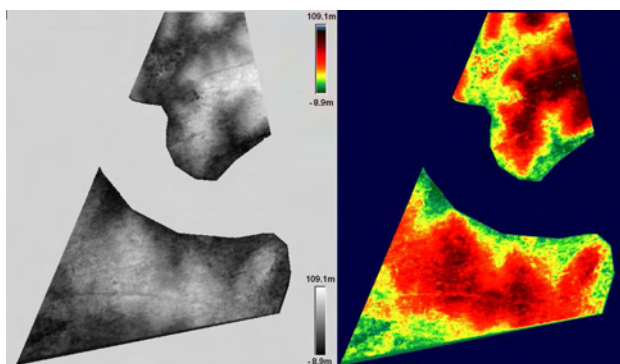


Figure 4. TSX SL DSM, grey value and color coded presentation

The world's first commercial very high resolution optical satellite IKONOS (means image in Greek) was launched to space in 1999 by Geoeye, USA. It has panchromatic and multispectral sensors and is able to take images with a ground resolution of 0.82m (PAN) and 4m (MS) with 11.3km swath width from 681km orbital altitude. By the combination of both sensor products 1m pan-sharpened color images can be created. The more than 300 million square kilometers of imagery that IKONOS has been collected over every continent; they are used for national security, military mapping, air and marine transportation, by regional and local governments and others (URL 2).

In this study, in Istanbul test field, PAN IKONOS GEO stereo model with a ground sampling distance (GSD) of 1m was available. The height-to-base (h/b) ratio value was 1.6 (angle of convergence 35°) and the sun elevation angle is 65.5° (Alobeid et. al., 2009). Using this stereo model DSM have been generated in 3m grid spacing overlapping with test field and with the refinement processes (shifting, blunder filtering etc.) regulated for the evaluation analysis. Figure 5 shows the IKONOS stereo-images and figure 6 illustrates the generated DSM along with its color coded version after the refinement process.



Figure 5. High resolution IKONOS PAN images

Against optical images, SAR images have some speckle effects which can be reduced by filtering but this causes also a loss of information. On the other hand some special objects like railroads with the metallic rails can be seen clearer like in optical images. The information contents of SAR images can be improved by multi polarization like shown in Figure 7. By the

combination of HH and VV polarization the image interpretation is improved (Jacobsen, 2008).

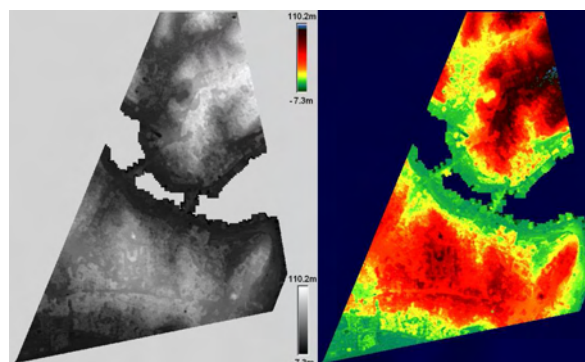


Figure 6. IKONOS DSM, grey value and color coded



Figure 7. Multi-polarization (HH/VV) TSX SL image from the city of Dresden

The reference DEM was derived from 1:1000 scale digital aerial photogrammetric maps, a project of Greater Istanbul Municipality and involves the large part of Historical Peninsula and near surroundings. This DEM was generated between 2007 and 2009. The original grid spacing of the DEM is 5m but it has been resampled into 1m according to the needs of the project. Figure 8 illustrates this reference DEM along with colored version to visualize the elevation levels easier.

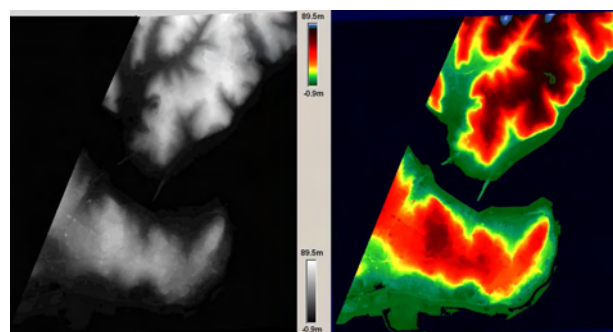


Figure 8. High resolution IKONOS PAN images

This DEM overlaps with the test field, approximately 5km×5km and covers more than 95% built-up areas that's why accuracy analysis were not performed for open and forest areas separately. It has 10cm up to 1m accuracy and the elevations are in between sea level and 90m. This reference DEM is named as 'REFDEM' in the study.

3. DEM EVALUATION STRATEGY

In the project, initially, the common coordinate system was defined as UTM (universal transverse Mercator) for the whole of data sets and references. That's why before the evaluation processes, the transformation of the coordinate systems of all of data sets into UTM suitable zone have been performed using program BLTRA. This program is a member of system BLUH (Bundle Block Adjustment Leibniz University Hannover), developed by Dr. Karsten Jacobsen, Institute of Photogrammetry and Geoinformation (IPI), Leibniz University of Hannover, Germany.

After the transformation of all models into UTM suitable zone, for the evaluation analysis, a number of investigations have been performed using several modules of the software package BLUH. Table 3 shows these evaluation programs and their functions.

Program	Function
RASCOR	Filtering, analysis, correction and plot of a DEM
DEMSHIFT	Shifting of a DEM to another in X, Y, Z and scaling in Z
DEMANAL	Accuracy Analysis of DEM against a reference DEM
MANI	Manipulation of object coordinates, image orientations, IMU-data and pixel addresses, numbering the points
BLCON	Conversion of ground coordinates window function, reduction to equal distributed points, change of spacing
DEMINT	Computation of Z-value for points with given X and Y by interpolation of a raster-digital elevation model
ZANAL	Analysis of a DEM
ZPROF	Plot profiles
UNDUL	Calculation of Geoid Undulation
HPSHOW	Creation of aspects

Table 3. Evaluation programs and their functions

Besides, for the visualization, interpolation (by triangulation, moving surfaces etc.) and regular gridding of DSMs and DEMs, program LISA has been used. This program has been generated at the Institute of Photogrammetry and Geoinformation, Leibniz University of Hannover, Germany by Dr. Wilfred Linder. In program LISA, a height model and its height levels can be seen in a color scale accompanied minimum up to maximum heights at the same screen and different color palettes can be created and used for visualization. Using the optimum palette in every process, the details can be established clearly. All color coded versions of the height models have been created by this program.

4. RESULTS AND DISCUSSION

4.1 Shift of DSMs and Preparations

In order to perform the correct accuracy analysis, the DSM which will be evaluated must have the same location as the reference DEM. For this the determination of shifts to the reference height model has to be determined. Initially, using program DEMSHIFT shifts against the reference DEMs are determined. In this operation, maximum accepted ΔZ is selected

as 50m and based on the handling the number of iterations are preferred as 11.

As the result of this first determination, the large shift values which cause large incorrect RMSZ values up to 14m have been seen and the radius of convergence for the shift adjustment was exceeded. Accordingly, for the elimination of large shifts the DEMs were pre-corrected by manual shift via point matching using program MANI. The points of corresponding location and their planimetric coordinates (X and Y) were selected from evaluated DSMs and reference DEMs. The coordinate differences were calculated and used for the rough shifts. Figure 9 shows the selected points at the corresponding locations for the pre-correction of the evaluated DSMs and reference DEMs in the test field.

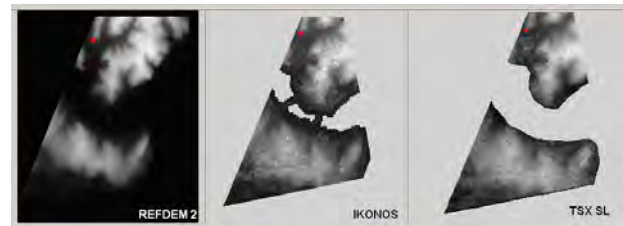


Figure 9. High resolution IKONOS PAN images

The Table 4 shows the RMSZ values before and after the pre-correction of the shifts, adjusted shift values by DEMSHIFT and the final RMSZ values.

DEM	Original RMSZ (m)	RMSZ After Manual Shift(m)	Shift by DEMSHIFT (m)		Final RMSZ (m)
			ΔX	ΔY	
IKONOS	13.67	7.44	-11.38	+8.03	7.32
TSX SL	13.78	8.44	-7.93	+21.4	8.25

Table 4. Adjusted shifts after pre-correction by MANI

4.2 Accuracy Analysis of DSMs

After shifting of DEMs, the accuracies of them have been analyzed in relation to the reference DEMs using program DEMANAL. For the analysis by DEMANAL, the maximal accepted DZ was limited as 50m and the maximal accepted tangent of terrain inclination was selected as 1.00. In the second iteration, shift and vertical scale were respected. These settings were made depending upon the characteristic of the test fields.

Following Tables and Figures show the results of accuracy analysis for IKONOS and TSX SL DSMs against REFDEM. Nearly full area of test field is built-up area and the forest coverage is so less that's why the accuracy analysis were performed just for the general area not separate for open and forest layers.

DSM	General	
	SZ [m]	NAP[%]
IKONOS (3m)	$7.04+1.03 \times \tan(\alpha)$	0.00
TSX SL (3m)	$7.09+11.22 \times \tan(\alpha)$	0.00

Table 5. Adjusted shifts after pre-correction by MANI

The frequency distribution of DZ values between evaluated models and reference models is shown in Figure 5.23. The components of this graphic are achieved from the list file of program DEMANAL after the analysis and generated by Microsoft Excel. The height differences and the corresponding number of points can be seen in this graphic presentation. The main point which should be analyzed in this graphic is the symmetric distribution. If the frequency distribution is symmetric, no influence of the buildings and vegetation exist. In this project, these graphic visualizations have been prepared between all evaluated models and reference models to form an opinion about the frequency distribution of DZ values. Figure 10 shows the frequency distribution of DZ values between IKONOS and TSX SL DSMs and REFDEM.

As mentioned before, at the accuracy analysis of heights, for the elimination of blunders, the maximal accepted DZ value is selected to 50m in program DEMANAL and the points which exceed this threshold value are automatically excluded by the program. If the image of this exception process is generated, the parts which are constituted by eliminated points can be seen clearly. By this way, these parts which have problems can be excluded when the models will be used for the precise applications. Using program DEMANAL, images have been created containing the excluded points. Figure 11 illustrates the image which contains the excluded points for IKONOS and TSX SL DSMs against REFDEM. The excluded points are represented by the dark spots.

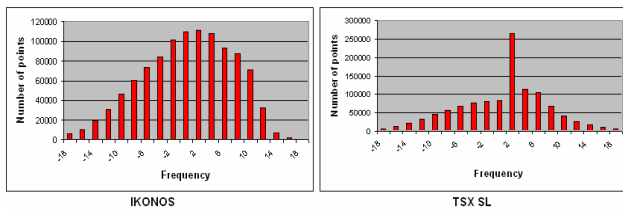


Figure 10. Height differences distribution of DZ between IKONOS and TSX SL DSMs and REFDEM

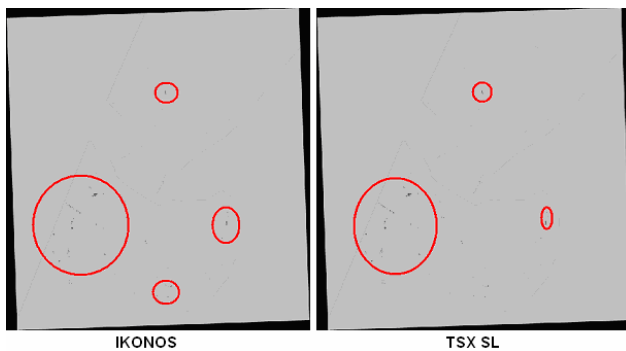
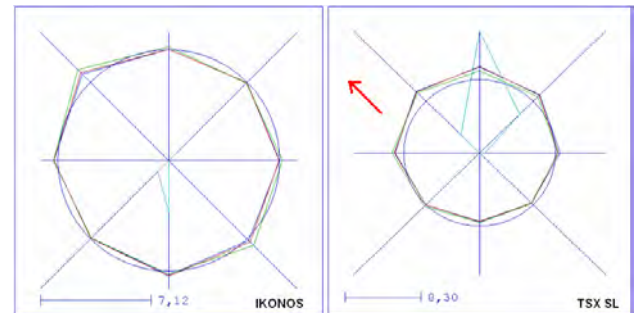


Figure 11. Excluded points of IKONOS and TSX SL

Besides these information's, RMSE of evaluated models against reference models as a function of the terrain inclination direction (aspects) can be visualized using program HPSHOW. Especially, in SAR imagery the accuracy shows dependency upon the aspects. As mentioned above aspects are the functions of the terrain inclination direction and present information about the mean value, the situation for zero inclination, factor for multiplication 'tan(slope)' and for average inclination. Considering aspects, the most effective contents on the accuracy results can be appeared easily. Figure 12 shows the aspects of

the accuracy analysis between IKONOS and TSX SL models and REFDEM.

As expected, the IKONOS DSM shows no dependency upon the aspects but TSX SL DSM has a clear dependency up on the red arrow's direction and differences from mean value are obvious.



MEAN VALUE FACTOR FOR MULTIPLICATION BY TAN(SLOPE) FOR INCLINATION = 0 FOR AVERAGE INCLINATION

Figure 12. Excluded points of IKONOS and TSX SL

Besides the absolute accuracy assessments the relative accuracies (relative standard deviations) of evaluated DEMs have been identified in the study. As distinct from absolute accuracies, relative accuracies indicate the interior accuracy of a model that means a point in relation to the neighbored points.

$$RSX = \sqrt{\frac{\sum (Dxi - Dxj)^2}{2 \cdot nx}}$$

RSX = relative standard deviation, d = distance between points
 $dl < d < du$ dl = lower distance limit du = upper distance limit of the distance

The relative accuracy is important especially for the morphologic details. The morphologic details for example, are not influenced by an error of phase unwrapping, leading to a local absolute error of the DSM, but not to a relative error of closely neighbored points. In this study, for the evaluation of relative accuracy, the accuracy from each point to the neighbored points was calculated for each evaluated DSM. For example, for a DSM has 3m grid spacing the relative accuracies were calculated between 3m and 30m at the 3m distance interval. The relative accuracies of the evaluated DSMs can be seen on the Table 6. Depending upon the reference model's grid spacing, the relative accuracies have been calculated from 1m to 10m.

Distance [m]	IKONOS	TSX SL
1	.98	.69
2	1.63	.98
3	2.14	1.31
4	2.57	1.57
5	2.92	1.82
6	3.23	2.04
7	3.48	2.21
8	3.70	2.37
9	3.89	2.52
10	4.05	2.65

Table 6. Relative accuracies of IKONOS and TSX SL DSMs

It can be seen in Table 6 TSX SL DSM has a better relative accuracy than IKONOS DSM. That means the interior integrity of TSX model is powerful, limitations may be caused by phase unwrapping.

4.3 Differential DEMs

Here differences between height models (DIFFDEMs) have been created for visualization. During the generation of three dimensional DIFFDEMs with program LISA, a view direction of 160° (0= North, 90= East) and an inclination angle of 35° was chosen for all DIFFDEMs. An exaggeration factor of 5 was used to provide an optimal visibility of the differences. Figure 13 shows the DIFFDEMs between IKONOS and TSX SL DSMs.

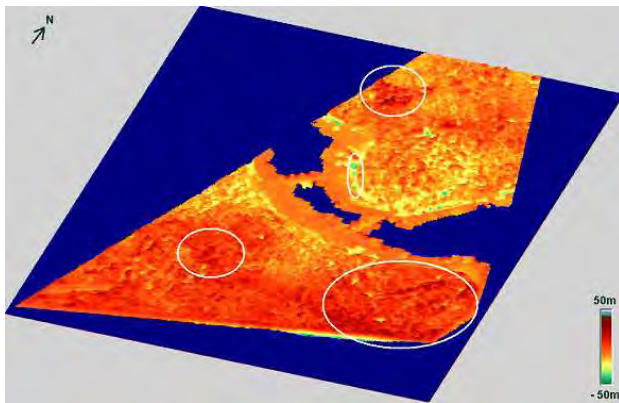


Figure 13. DIFFDEM between IKONOS and TSX SL

Height differences are obvious in patches especially in woody areas (black parts). Except woody regions TSX SL and IKONOS DSMs are coherent and the height differences are in between 0-5m

4.4 Shading

The shading is one of the best possibilities of visualizing a DSM. All buildings, vegetation and forest coverage in a DSM can be seen clearly. By this method, the shadings of IKONOS and TSX SL DSMs which have the same grid spacing (3m) have been generated and compared. Figure 14 and 15 illustrate the results of shadings.

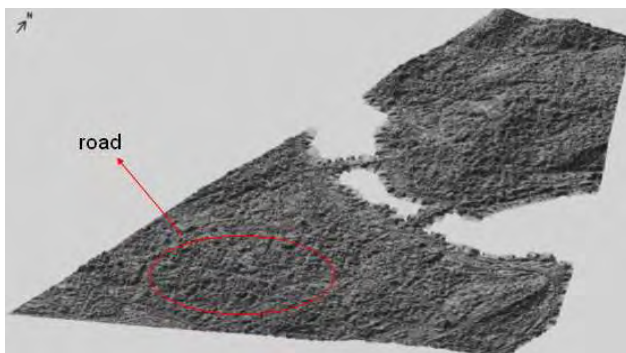


Figure 14. Shading (IKONOS)

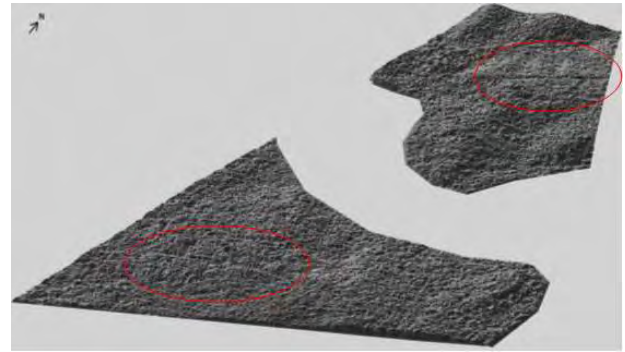


Figure 15. Shading (TSX SL)

Looking at the results, it can be mentioned that the visualizations of both DSMs are pretty good. They illustrate the ground objects like roads (in red circles), buildings, vegetation and forest.

5. CONCLUSION AND FUTURE TARGETS

In this study, DSMs which have 3m grid spacing have been generated from TSX SL and IKONOS Pan image-pairs. And these models have been compared in Istanbul test field, Turkey using a reference digital elevation model, derived from 1:1000 scale aerial photos and has 10cm up to 1m accuracy.

In the densely build up area of Istanbul DSMs are strongly influenced by buildings, partly also by trees and forest. The influence of the buildings and the vegetation can not be filtered totally because of missing satisfying number of points on the ground.

InSAR height models have a clear dependency upon the aspects. TSX SL DSM have a better relative accuracy as absolute accuracy, which may be explained by the influence of phase unwrapping, but also the case that DSMs are compared with reference elevation model containing the height of the bare ground.

It can be mentioned that TSX SL image-pair which has suitable baseline length (135m) presents an absolute accuracy competitive to the height model based on the very high resolution optical images. A dominating effect of the accuracy is still the vegetation and buildings.

Future investigations and development will be DSM fusion with optical DEMs based on space and/or aerial images and support high resolution optical images for generation of maps 1/5000 scale and below.

ACKNOWLEDGEMENTS

Thanks are going to TUBITAK, Turkey and DLR, Germany for their supports to this research. And to Dipl. -Ing. Abdalla Alobeid for supporting the generation of IKONOS DSM.

REFERENCES

Alobeid, A., Jacobsen, K., Heipke, C., 2009. *Building Height Estimation in Urban Areas from Very High Resolution Satellite Stereo Images*, ISPRS Hannover Workshop, 2-5 June, Hannover, Germany

Jacobsen, K., 2008. 3D-Remote Sensing, *Status Report 2008*, 28th EARSeL Symposium: Remote Sensing for a Changing Europe, 2-5 June, Istanbul, Turkey

Roth, A., 2003. *TerraSAR-X: A new perspective for scientific use of high resolution spaceborne SAR data*, 2nd GRSS/ISPRS Joint Workshop on "Data Fusion and Remote Sensing over Urban Areas, 22-23 May, Berlin, Germany

URL 1, 2008: <http://www.dlr.de/>, German Aerospace Center (DLR), November

URL 2, 2009: <http://www.geoeye.com/CorpSite/>, GeoEye, United States, 15th September

CHARACTERISATION OF LONG-TERM VEGETATION DYNAMICS FOR A SEMI-ARID WETLAND USING NDVI TIME SERIES FROM NOAA-AVHRR

R. Seiler^a

^a TU Dresden, Dept. Geosciences, Helmholtzstrasse 10-12, 01062, Dresden, Germany – rseiler@rcs.urz.tu-dresden.de

KEY WORDS: Land Cover, Statistics, Change Detection, Modelling, Multitemporal

ABSTRACT:

The Niger Inland Delta represents a flat area of around 40.000 km², which is annually inundated by the Niger River system. As the flood is driven by the rainfall in the catchment areas, it is not linked to the low precipitation of the Sahelian region. Thus, local rainy season and inundation show a temporal delay of 3 months and the Niger Inland Delta's ecology can be described as a mosaic of permanent, periodical and non-periodically flooded areas. AVHRR GIMMS Data provide NDVI values over 25 years with 2 data / month on a 8 x 8 km grid. Dynamics in vegetation density were modelled from the temporal variability of the NDVI. Therefore each time series was detrended and transformed into the frequency domain. The power spectra then were decomposed into a long-term cyclic component by applying a FIR with a cut-off frequency slightly lower 1 cycle / year, a seasonal (annual) and an irregular component. For modelling the seasonal component of a time series, an algorithm is proposed that reduces the no. of frequencies by referring to the most significant ones, but at the same time keeps different time series comparable, as all frequencies are retained that were needed to preserve an a-priori defined level of information for any of the time series.

1. INTRODUCTION

To investigate the state and/or the amount of vegetation is one of the main objective in the field of land surface related remote sensing applications. A prerequisite for successful monitoring of vegetation cover is the availability of frequent data that are internally consistent over a sufficient period and that provide information on the spatial complexity as well as on the temporal dynamics of vegetation. Many methods and in particular various vegetation indexes have been introduced, to quantify certain vegetation parameters. All of them take into account that vivid green vegetation shows a specific reflection signal in the red and near infrared part of the electromagnetic spectrum. The normalised difference vegetation index (NDVI) has become a commonly used index that is routinely derived from NOAA AVHRR images since mid 1981. To reduce atmospheric effects and noise, present in the direct reflectance measurements of an individual image, considerable effort has gone into the generation of multi-day composites. Such vegetation index composites proved to be very sensitive to a wide range of biophysical parameters, among them photosynthetically active biomass (Goetz et. al., 1999) or the presence of green vegetation (Myeni et al., 1995).

Numerous studies have been conducted that use AVHRR NDVI data to analyse vegetation parameters on a regional to global scale, among them the estimation of terrestrial net primary production (npp) (Ruimy et. al., 1994) or the analysis of changes in vegetation phenology (Heumann et. al., 2007). The long term NDVI time series from AVHRR were related to climate variables such as air temperature or rainfall data with the objective of revealing geo-biophysical linkages for observed changes in vegetation parameters (greenness or npp) (Herrmann et. al., 2005, Xiao & Moody, 2005).

The regional focus of this paper is the Niger Inland Delta, situated in the western Sahel region in Africa (see. Figure 1. for details). Whereas precipitation is the main constraint for vegetation growth in the semi arid Sahel, the Inland Delta's

biosphere relies on water that flows in the region during the annual flooding period. This paper aims to analyse the long-term dynamics of vegetation cover in the Niger Floodplain over a 25 year period, based on 15day-composites of NDVI values from NOAA-AVHRR. To detect influences on vegetation cover for different time scales each time series was decomposed into 3 components according to the conventional component model. For this unbundling each time series was transferred into the frequency domain by a Discrete Fourier Transformation (DFT), making use of the advantages of the globally addressed (in terms of “the entire time series”) operators of the frequency domain.

2. GEOGRAPHIC PARAMETERS FOR THE NIGER INLAND DELTA

The geographic term „Niger Inland Delta“ stands for a vast, extremely flat area of some 10.000 km² extend, which is annually inundated by the water of the Niger - Bani river system during September to December. The ecology of the delta can be described as a mosaic of permanently, periodically and episodically flooded pat-tern, which contrasts sharply to the semi-arid environment of the Sahel. Spatial and temporal extent of the flood patterns vary due to fluctuating water supply by the river system caused by irregular rainfall in the catchment areas. Thanks to a comparatively good availability of (surface) water, the Niger Inland Ecosystem serves as stop-over for many migrating birds and other wildlife species as well as economic base for farmer and pastoral people. To foster the sustainable usage of its natural resources and to protect this natural heritage, the entire Niger Inland Delta became RAMSAR site in 2004 (RAMSAR 2008). (see Fig. 1 for an overview of the area)

In contrast to its semi-arid environment, the Niger Inland Delta's ecology can be described by a mosaic of permanently, periodically and episodically flooded areas. Their extent varies both in scale and in time due to irregularities of amount

and seasonal distribution of annual rainfall in the catchment areas and the resulting water supply contributed by the Niger-Bani system. As it takes some time for the water to run off from the catchment areas in the Fouta Julon Mountains (Guinea) towards the Niger Inland Delta, the inundation occurs with a temporal delay of some months, compared with the rainy season. Flooding starts in mid October at the southern entry of the Delta and lasts until end of December / mid January.

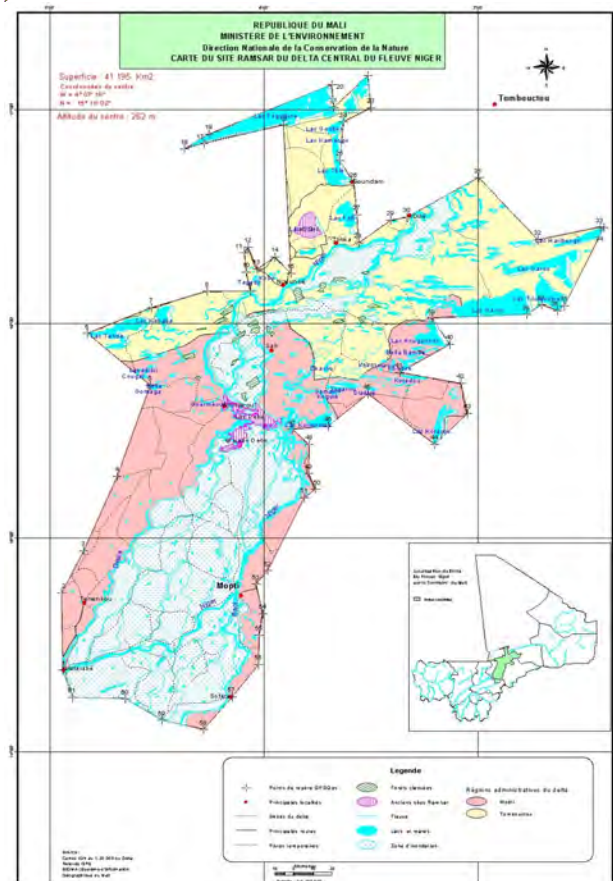


Figure 1. Niger Inland Delta (RAMSAR site) scale 1:200,000 http://www.wetlands.org/Reports/Country_maps/Mali/IML001/IML001map.jpg

From this relation result 2 seasonal variations, a rainy ↔ dry phase and a flooding ↔ drainage phase, as illustrated in Fig. 2. They appear with a temporal delay of about 3 to 4 months and are superimposed by a 3rd undulation that counts for several years (period between dry years and years with sufficient precipitation). This latter variation is dominantly affected by the 2 seasonal ones, but high spatial variability of precipitation does not permit a causal linkage. In particular, low amount of rainfall in the delta may profit from extended rainfall in the head-waters, thus inducing reasonable extent of flooding.

The availability of water represents the main restricting factor for vegetation growth in the Sahel. Vegetation follows the above described water cycles with a temporal delay, which varies from few days (germination of grasses) up to several months (death of trees caused by lack of water). A

development of (annual) grasslands with sparsely distributed patches of shrubby vegetation (dominantly composed of Combretaceae sp.) is characteristic for the Sahelian landscape (Breman and DeRidder 1991). According to (LeHouérou 1989), these vegetation pattern can be categorised into the following 3 layers (see Fig. 2 for a scheme):

- grass layer with annual grasses and herbs (height 40 cm – 80 cm)
- shrub layer (height 50 cm – 300 cm)
- tree layer, sparsely distributed single trees (height 3 m to 6 m)

Ligneous layers of shrubs and trees cover only small parts (up to 25 %) of the surface, while the grass layer extend over up to 80 %, (Kußerow 1995). Annual grasses are withering during dry season, thus grassy layers are affected and/or destructed by bush fires and strong winds. Pat-terns of bare soil appear as a result, that extend during the mid- and late dry season. The generally low vegetation cover therefore disappears periodically completely.

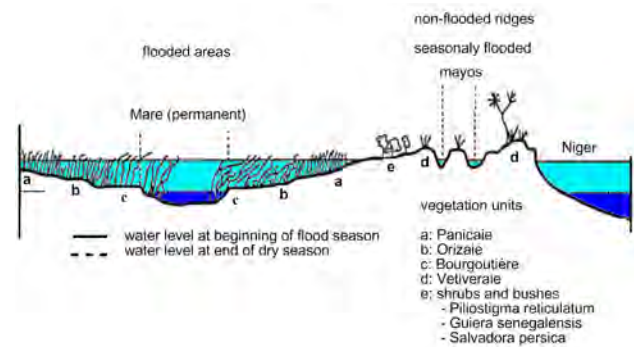


Figure 2. Subsection of the Niger Inland Delta - landscape profile and vegetation pattern, adapted from (Diallo 2000)

3. DATA AND METHODS

3.1 GIMMS 15-day NDVI composite data

The GIMMS (Global Inventory Monitoring and Modelling Study) NDVI data record combine measurements from several satellite sensors. To ensure consistency between the multi-temporal data, several corrections for a wide range of factors that affect the calculation of NDVI values have to be applied. According to (Pinzon et al., 2005) GIMMS data are corrected for sensor degradation and intercalibration differences, global cloud cover contamination, viewing angle effects due to satellite drift, volcanic aerosols, and low signal-to-noise ratios due to sub-pixel cloud contamination and water vapour. A well known fact are the shortcomings of the AVHRR sensor design for a vegetation monitoring, as for instance the AVHRR channel 2 (nIR) overlaps a wavelength interval in which considerable absorption by atmospheric water vapour occurs (Steven et al., 2003, Cihlar et al., 2001).

This global dataset, known as the GIMMS NDVIg, is the only publicly available AVHRR dataset to extend from 1981 to 2006 (Tucker et al., 2005). Due to the correction scheme it is a dynamic data set, that must be recalculated every time a new period of data is added. The Niger Inland Delta and a small

buffer of surrounding area is covered by 1298 AVHRR pixel on a 8 km spatial resolution and each of these GIMMS time series consist of 612 data points, covering 25 ½ years from July 1981 until December 2006 with a scan frequency of 2 data / month. This work was done with the updated GIMMS data that were release in 2007.

3.2 Decomposition of NDVI time series

Provided that the NDVI value represents the photosynthetic active vegetation amount, the dynamics of vegetation cover can be characterised by the temporal behaviour of the NDVI value. Thus, NDVI values for a specific pixel over the period from July 1981 to December 2006 will be considered as a time series.

For an analysis of the statistical characteristics - mean, variance and auto-correlation function (acf) - a given time series needs to be stationary. The GIMMS NDVI doesn't fulfill this constraint, as they contain significant cyclic (seasonal and/or multi-annual) components. To derive stationary time series, each NDVI series x_t is decomposed into the following components:

- (a) long-term mean \bar{x}_t
- (b) Cyclical Component c_t
- (c) Seasonal Component s_t
- (d) Irregular Component i_t

Where the cyclical component consists of a (linear) trend m_t and long term (multi-annual) anomalies a_t . The latter model variations that last over more than 1 year, or that are even not periodically. Variations with periodicities shorter than 1 year are modelled within the seasonal component. The last component i_t describes short term anomalies and allows therefore an interpretation of alterations of the variance of the NDVI signal. It is supposed in the context of this work that all components superimpose, so as to the time series can be written as:

$$x_t = m_t + a_t + s_t + i_t \quad (1)$$

This decomposition of a NDVI time series aims the differentiation of long-term and seasonal dynamics as well as an interpretation of alterations from these periodical behaviour.

3.3 Determination of the Cyclical Component c_t

As c_t models long-term components of the NDVI signal, it can be separated by filtering the time series with a low-pass filter. To design an appropriate filter and to apply filtering efficiently, the time series was transformed into the frequency domain with a Discrete Fourier Transformation (DFT). According to (Meier and Keller 1990) describes

$$X_T(f) = \int_{-\infty}^{\infty} X(\hat{f}) W(f - \hat{f}) d\hat{f} \quad (2)$$

where $X(\hat{f})$ = Fourier transform

$W(f - \hat{f})$ = weighting function for the observed time series

the filtered estimation of the spectral density $X_T(f)$ for a time series with finite length. The Fourier transform $Y(f)$ of a filtered signal then results from

$$Y(f) = |H(f)|^2 \cdot X(f) \quad (3)$$

where $H(f)$ = filter transfer function

A moving average (MA), with window size 24, could serve as a simple realisation of such a low-pass filter. As MA-filter show significant side lobes in their step response, these kind of filter produce a leakage for the filtered time series. Furthermore, the negative values around the odd side lobes result in a phase shift of 180° for the filtered signal in these parts. Both disadvantages can be avoided by using a Raised Cosine filter as FIR.

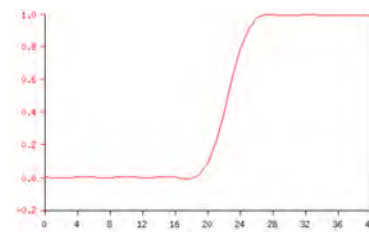


Figure 3. normalised step response of the used FIR filter, due to a sampling rate of 2 / month the value 24 represents a frequency of 1 year⁻¹

3.4 Determination of the Seasonal Component s_t , extracting significant frequencies

Seasonal variations in the NDVI signal can be modelled with the phase mean or stack method in the time domain. This algorithm estimates the seasonal component by calculating mean values for each observation date of a year as given in (4)

$$\hat{s}_t = \sum_{r=1}^{24} \left(\left(\frac{1}{25} \sum_{n=1}^{25} [x_r(n) - c_r(n)] \right) \cdot s_r(t) \right) \quad (4)$$

where r = date of observation within the year ($r = 1, \dots, 24$)
 n = year of observation ($n = 1, \dots, 25 - [1981 - 2006]$)
 $[x_r(n) - c_r(n)]$ = time series adjusted for c_t
 $s_r(t) = \begin{cases} 1, & \text{if } t \text{ belongs to } r \\ 0, & \text{else} \end{cases}$

While this approach gives direct access to time related information such as the date of the annual max./min NDVI value or the temporal run of the NDVI curve, an analysis in the frequency domain provides information about the frequencies / periodicities of NDVI dynamics. But due to the great number of data points also the no. of frequencies goes usually beyond the scope of interpretation for longer time series. Reducing the number of frequencies should preserve the information (Σ of power for all frequencies) of a time series as much as possible.

A formal selection of a set of frequencies would only be suitable, if one could a-priori specify the range of relevant periodicities within the time series and adjust the band of preserved frequencies according to this knowledge. Otherwise information about the time series would randomly discarded. If one retains for instance the first few frequencies, one preserves a rather rough approximation of the time series, as these frequencies correspond to the low frequent parts of the signal. Using the largest few frequencies would preserve the individual time series much better, but makes them no longer comparable, as different parts of the signals would be kept. (Möhrchen, 2006) proposes the use of one subset of frequencies for all time series, thus achieving, that all series have the same dimensionality (In the context of a feature space point of view on the time series, frequencies represent the components of the feature vector that characterises an individual time series.) and keeping them comparable. A frequency belongs to the subset, if it is necessary to preserve an a-priori defined level of information for any of the time series. Where all frequencies of a given time series are sorted according to their magnitude. And the information level is calculated cumulative, starting with the largest frequency, for each time series individually.

3.5 Analysis of the Irregular Component i_t

After subtraction of the long-term mean, the Cyclical and Seasonal Components from the original time series remains the Irregular Component. This part represents a time series that is stationary in wide-sense, as the variance is not independent from time. The annual aggregated variance differs between years, especially for pixel at the edges of the Inland Delta that are not flooded regularly. Provided that the variance is constant over the period of 1 year, the quotient of the Irregular Component and the variance results in a time series that is nearly stationary.

4. DISCUSSION OF RESULTS

The individual components of the time series provide specific information about the character of the underlying vegetation dynamics. The long term mean (calculated for the entire period of 25 ½ years) varies a lot between pixel that cover areas in the central Inland Delta and those that cover the edges of the Floodplain next to the semi arid environment. The NDVI values variability of a specific time series is significantly positive correlated with the long term mean. Thus, areas with overall high NDVI values show higher variability too.

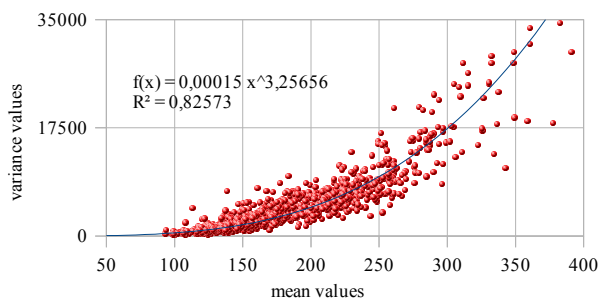


Figure 4.: relation between long-term mean and variance of the NDVI values

The following conclusions for the Cyclical and Seasonal Component will be illustrated, using pixel listed in Table 5 that represent the main ecological categories of the Niger Inland Delta. The more an area is located towards the edges of the delta, the higher its variability in dynamics with low frequencies.

pixel ID	description	
	located	ecological category
13 31	western edge, close to delta mort	periodically flooded, semi-arid surrounding
15 45	central delta, southern part	flooded
15 48	central delta, southern part	flooded
18 26	northwestern edge	episodically flooded
17 29	Lake district	regularly flooded
20 26	North of Lake Debo	regularly flooded, semi-arid surrounding
16 49	central delta, southern part	flooded
19 43	central delta, southern part	flooded

Table 5. Reference pixel for Cyclical and Seasonal Component

The Cyclical Component unfolds dynamics that last for more than one year. It describes therefore relations between wet and dry years. Clearly visible in Figure 6 is the drop in vegetation cover during the dry years 1984 / 85 and the strong recovery followed 1986 / 87. The 2nd half of the 1980 years and the beginning 90-ies had vegetation cover below the long-term mean, while the mid 90-ies showed a at least for parts of the Inland Delta a recovering of vegetation above the long-term mean.

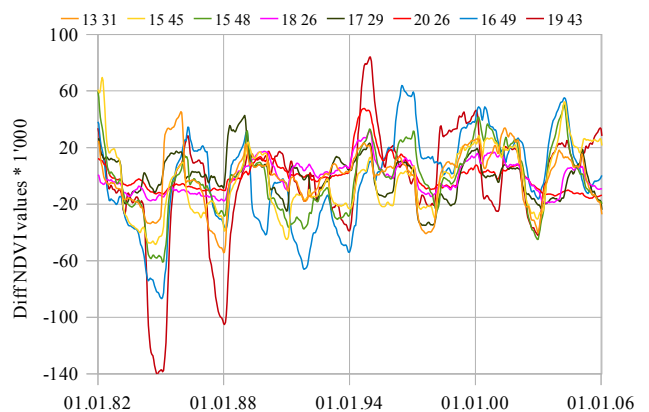


Figure 6.: Cyclical Component (lag 24) represent dynamics with periodicities greater 12 month

A discrimination of pixel according to their month of highest vegetation density can be done with the Seasonal Component (Figure 7). While all pixel show the vegetation drop during the late dry season (May / June), the different causes for vegetation growth result in specific dates of maximum vegetation cover. Areas that are mainly influenced by the semi

arid rainfall and not flooded, have their maximum vegetation during end of August or early September. Contrary to this, flooded areas show maximum vegetation during October / November and these extrema show significantly higher values see pixel 19 43 as an example for this ecological category.

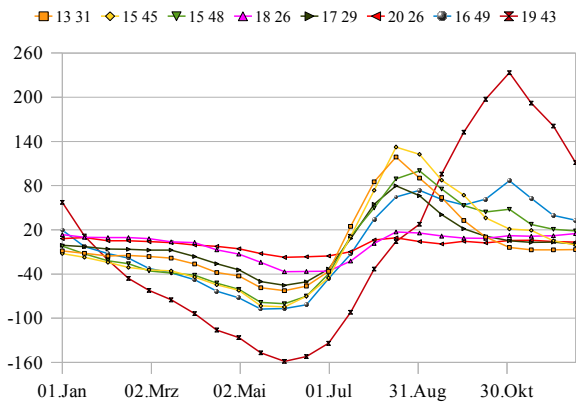


Figure 7.: Seasonal Figure derived with phase mean algorithm

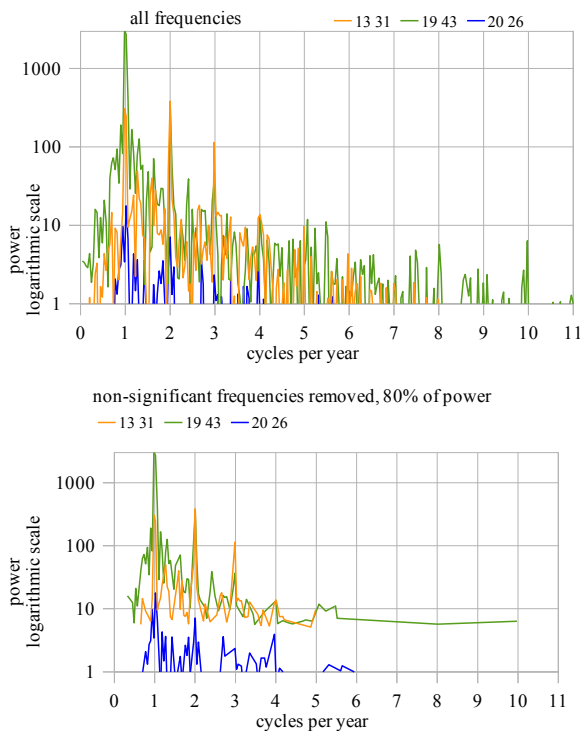


Figure 8.: power spectra for low-pass filtered time series; top – a) all 294 frequencies, bottom – b) only frequencies that preserve min. 80% of total power for each of the time series

The Analysis of seasonal features in the frequency domain can be reduced to the question, which frequencies shall be considered as significant for the seasonal figure. As explained in Section 3.3 of this paper, it is mandatory to retain the same set of frequencies throughout all time series to ensure the

comparability between different series. The effect of reducing the no. of frequencies is shown in Figure 8b, where the lower graph shows a reduced spectrum to 80% level of power. This preserved information level is achieved with only 25% of the original 294 frequencies. Even a nearly complete preservation of the information of the time series (99% level of power) yields to a reduction in frequencies to approx. 75% of the original frequencies (223 out of the 294).

After normalisation with the annual variance, the irregular component should form a stationary time series. If so, no specific feature should be detectable within the series. This is true for some time series but as can be seen in Figure 9 it is not for all the case. While the series from pixel 19 43 can be treated as stationary for most of the time, the series from pixel 13 31 shows significant extrema. This gives evidence that the seasonal figure is imperfectly modelled with the approaches suggested in this paper (and therefore seasonal features fall partially by mistake into the irregular component) and / or the vegetation dynamics contain significantly non-periodic elements. Therefore a non-stationary time series for an irregular component points out a not periodically growth of vegetation due to an episodically flooded area.

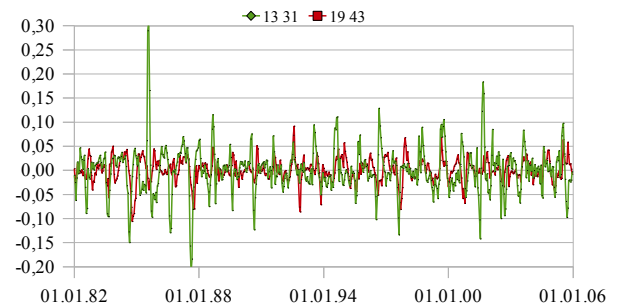


Figure 9.: examples for the Irregular Component, the one for pixel 13 31 shows strong extrema

5. SUMMARY AND CONCLUSIONS

Long-term dynamics are clearly detectable within the NDVI GIMMS time series. These features can be extracted by filtering the time series with an appropriate FIR. Modelling the seasonal dynamics is somewhat more ambiguous. The phase mean algorithm treats all values of a certain acquisition date as source for a mean value that is representative for the period of the entire time series. Every difference between a value of the time series and the corresponding modelled phase mean is treated as part of the Irregular Component. If the seasonal figure is modelled from the power spectra of the Fourier Transform, the shape of the figure depends on the no. of frequencies that is used. The Irregular Component of the time series contains information about non-periodic dynamics of the vegetation cover. These are significantly present in the time series as the extent of flooding varies widely between the years.

REFERENCES

Breman H. and DeRidder, N., 1991. *Manuel sur les pâturages des pays sahéliens*. Karthala, Paris.

- Cihlar, J., Tcherednichenko, I., Latifovic, R., Li, Z. and Chen, J., 2001. Impact of variable atmospheric water vapor content on AVHRR data corrections over land. *IEEE Transactions Geoscience and Remote Sensing*, Vol. 39(1), pp. 173-180.
- Diallo, O. A., *Contribution à l'étude de la dynamique des écosystèmes des mares dans le Delta Central du Niger, au Mali*. Thèse, Université Paris I, 2000.
- Goetz, S. J., Prince, S. D., Goward, S. N., Thawley, M. M., Small, J. and Johnson, A., 1999. Mapping net primary production and related biophysical variables with remote sensing: Application to the BOREAS region. *Journal of Geophysical Research Atmospheres*, 104(D22), pp. 27719 - 27734.
- Herrmann, S. M., Anyamba, A. and Tucker, C. J., 2005. Exploring relationship between rainfall and vegetation dynamics in the Sahel using coarse resolution satellite data. www.isprs.org/publications/related/ISRSE/html/papers/293.pdf
- Heumann, B., Seaquist, J. W., Eklindh, L. and Jonsson, P., 2007. AVHRR derived phenological change in the Sahel and Soudan, Africa, 1982-2005. *Remote Sensing of Environment*, Vol. 108(4(29)), pp. 385-392.
- Kußerow, H., 1995. *Einsatz von Fernerkundungsdaten zur Vegetationsklassifizierung im Südsahel Malis*. Verlag Dr. Köster, Berlin.
- LeHouérou, H. N., 1989. *The grazing land ecosystem of the African Sahel*. Springer, Berlin New York.
- Meier, S. and Keller, W., 1990. *Geostatistik*. Springer, Vienna.
- Mörchen, F., 2006. *Time Series Knowledge Mining*. PhD. Thesis, Dept. of Mathematics and Computer Science, University of Marburg.
- Myeni, R. B., Hall, F. G., Sellers, P. J., and Marshak, A. L., 1995. The interpretation of spectral vegetation indexes. *IEEE Transactions Geosciences and Remote Sensing*, Vol. 33(2), pp. 481 - 486
- Pinzon, J., Brown, M. E. and Tucker, C. J., 2005. Satellite time series correction of orbital drift artifacts using empirical mode decomposition. in Huang, N. (Ed.) *Hilbert - Huang Transform: Introduction and Applications*. pp. 167 – 186.
- RAMSAR convention,
http://www.ramsar.org/wwd/4/wwd2004_rpt_mali1.htm
(accessed 15. Sep. 2008)
- Ruimy, A., Saugier, B. and Dedier, G., 1994. Methodology for the estimation of terrestrial net primary production from remotely sensed data. *Journal of Geophysical Research*, Vol. 99(3), pp. 5263-5283.
- Steven, M. D., Malthus, T. J., Baret, F., Xu, H. and Chopping, M. J. 2003. Intercalibration of vegetation indices from different sensor systems. *Remote Sensing of Environment*, Vol. 88(4), pp. 412-422.
- Tucker, C. J., Pinzon, J. E., Brown, M. E., Slayback, D., Pak, E. W., Mahoney, R., Vermote, E. and El Saleous, N., 2005. An Extended AVHRR 8-km NDVI Data Set Compatible with MODIS and SPOT Vegetation NDVI Data. *Int. Journal of Remote Sensing*, Vol. 26(20), pp. 4485-5598.
- Xiao, J. and Moody, A., 2005. Geographic distribution of global greening trends and their climatic correlates: 1982 to 1998. *Int. Journal of Remote Sensing*, Vol. 26(11), pp. 2371-2390.

SEMI – AUTOMATIC ASSESSMENT OF NORWAY SPRUCE (*PICEA ABIES*) IN MODERN DIGITAL AERIAL PHOTOGRAPHS

R. Seitz^a, A. Troycke^a, P. Rebhan^b, B. Grubert^b

^a Bavarian State Institute of Forestry, Hans-Carl-von-Carlowitz Platz 1,85354 Freising Germany - (rudolf.seitz, armin.troycke)@lwf.bayern.de

^b GeoCreativ, Steigerwaldstraße 30, 97483 Eltmann Germany – (rebhan, grubert)@geo-creativ.de

KEY WORDS: Forestry, Land Cover, Development, Extraction, Classification, Segmentation, Infrared, Spectral

ABSTRACT:

In present times, forest conversion due to climate change confronts forest owners and forest administrations with great challenges if vast areas of forested surfaces are concerned by the effects of temperature rise and drought. In Bavaria, especially Norway Spruce (*Picea abies*) will lose terrain in favor of other tree species by decreasing vitality and the proliferation of bark beetle damage. The Bavarian Forest Service is confronted with the problem, that there is only little information available about the approximately 1.6 Mio ha of nongovernmental forest property in Bavaria to fulfill its advisory tasks, because of data privacy convention. For this reason, the Bavarian State Institute of Forestry conducted a research project focusing on possible semi-automatic approaches of anonymous information extraction from digital aerial photographs. This method mainly comprises the segmentation and object-based classification of 4-channel 16 bit aerial photographs in combination with a preceding image homogenization process. The project showed a classification accuracy of 80% (young stands) up to more than 90% (old stands). A reliable classification (up to 80% accuracy) has even been achieved for Norway Spruce stands younger than 30 years, that cannot be interpreted by visual stereoscopic interpretation. The new methodology enables the Bavarian State Institute of Forestry to gain an identification of Norway Spruce for vast non-governmental forest areas. In a subsequent investigation, the method has to prove its cost efficiency and is to be transferred on larger areas and to other tree species of interest in the debate of environmental change.

KURZFASSUNG:

Zurzeit stellt der Waldumbau in Folge des Klimawandels die Waldbesitzer und Forstverwaltungen vor großen Herausforderungen, sobald in bedeutendem Umfang Waldflächen von den Auswirkungen des Temperaturanstiegs und zunehmender Trockenheit betroffen werden. In Bayern wird in diesem Zusammenhang vor allem die Fichte (*Picea abies*) durch verminderte Vitalität und vermehrte Borkenkäferkalamitäten Areal zu Gunsten anderer Baumarten verlieren. Aus Gründen des Datenschutzes verfügt die Bayerische Forstverwaltung über nur wenige Informationen bezüglich der ca. 1.6 Mio. ha nicht-staatlicher Wälder Bayerns, um ihre Beratungsaufgaben vor diesem Hintergrund erfüllen zu können. Aus diesem Grund führte die Bayerische Landesanstalt für Wald und Forstwirtschaft ein Forschungsprojekt mit dem Fokus auf halb-automatische Verfahren zur anonymen Informationsextraktion aus digitalen Luftbildern durch. Die dabei entwickelte Methodik umfasst in erster Linie die Segmentierung und objektbasierte Klassifizierung von 4-Kanal-Luftbildern mit einer Farbtiefe von 16 bit in Verbindung mit einem vorgeschalteten Bildhomogenisierungsprozess. Die Projektergebnisse weisen eine Klassifikationsgenauigkeit von 80 % (Jungbestände) bis über 90 % (Altbestände) auf. Eine verlässliche Klassifizierung (bis zu 80 % Trefferquote) wurde sogar für Fichtenbestände unter 30 Jahren erreicht, die nicht im Rahmen einer visuellen stereoskopischen Interpretation erfasst werden können. Die neue Methodik ermöglicht der Bayerischen Forstverwaltung somit die Identifikation von Fichtenbeständen auf den nicht-staatlichen Waldflächen Bayerns. Im Rahmen eines Folgeprojektes wird die Methodik auf ihre Kosteneffizienz hin untersucht und sowohl auf größere Flächen als auch auf weitere Baumarten ausgedehnt, die im Rahmen der Diskussion über die Umweltveränderungen von besonderem Interesse sind.

1. INTRODUCTION

1.1 Background

Climate change with all its implications is already in progress. Norway Spruce (*Picea abies*) is expected to be the tree species that will suffer most severely from it. The necessary forest conversion of Spruce-dominated forest areas means an outstanding challenge in relatively dry, warm regions of Bavaria (Bernhart 2007). Approximately 260.000 ha of Spruce stands are threatened momentarily in Bavarian private and communal forests (StMELF 2008), where the Bavarian Forest Administration disposes only little information. At the moment, the assessment of Spruce distribution within forest stands of severe conversion urgency bases commonly on the results of the second German Forest Inventory (Bundeswaldinventur (BWI) 2, Kölling et al. 2008). Because of the tenuous BWI inventory

grid of 4x4 km however, the assessed data are insufficient for the deduction of detailed results. In order to face these challenges, remote sensing approaches seem to offer appropriate methods.

The applicability of the spectral reflection characteristics of forest trees for their assessment and identification has been investigated and described many times (for ex. in Akça et al. 1984, Koch 1988).

Until several years ago, optical data that can be ideally classified (this means in digital form with separated bands) have only been available from space borne sensors in a resolution inferior to that of aerial imagery.

The recent technical progress in the development of digital aerial cameras laid the foundation for approaches to distinguish tree species out of digital aerial image data. *Neubert* (2006) and *Tiede et al.* (2009) for ex. describe first approaches for the assessment of tree species composition by the use of digital aerial photographs. The Bavarian Office for Surveying and Geographic Information (Landesamt für Vermessung und Geoinformation (LVG)) conducts flight campaigns since 2008 on the basis of the latest digital camera systems. Thus, every year about one third of Bavaria's surface is covered by high resolution aerial photographs.

Against this background, the Bavarian Ministry of Food, Agriculture and Forestry financed a project of the Bavarian Institute of Forestry in cooperation with the enterprise GeoCreativ in order to investigate the potential of the actual digital aerial images for the semi-automatic assessment of Spruce. The project areas Eltmann and Gerolzhofen share more or less the same climatic conditions like the regions of western Middle Franconia and Lower Franconia that were struck by wide-spread losses of Spruce in 2005/2006. Even in this time, the observed phenomenon have been supposed to be the precursors of a development that would consider vast areas, caused by climate change (*Ammer et al. 2006*).

1.2 Objectives

Because of climate change, within short time an overview of Spruce stands that are in need of urgent conversion has to be achieved. Therefore, reliable, actual information about the dispersion of Spruce stands has to be created, using aerial photographs furnished by the LVG. In this project, by the help of modern software for image analysis and object-based classification, vast areas were supposed to be semi-automatically analyzed efficiently and in due time. At the end, a GIS-layer locating "Spruce" and "other coniferous trees" was planned to be available for the project regions.

2. BASIC INFORMATIONS

The project regions comprised of two separate areas in the „Steigerwald“ (Bavarian forest growth area 5.2 Steigerwald). One area contained the communal forest of Eltmann (ca. 2.500 ha), the second area is located within the „Bürgerwald“ Gerolzhofen (ca. 300 ha). Within the project areas grow intensively mixed deciduous and coniferous forests on vividly undulated terrain of a great variety of expositions. The Bavarian Office for Surveying and Geographic Information furnished 4-channel aerial photographs (color depth 16 bit, tiff-files; original data sets as well as ortho-rectified images). The images have been taken by the matrix camera Vexcel Ultracam-X. Ground sample distance (GSD) for the research area was 20 cm. The spectral bands green, blue, red and near infra-red are available in separated form. The flight campaign took place in August 31st, 2008.

3. METHODOLOGY

3.1 Pre-processing of image data

The original image tiles show great differences within their spectral bands, with the infra-red band possessing the least differences between the images. The transfer of classification criteria from one original image to another seemed thus to be impossible. Furthermore, the individual images partially show a distinct color drop especially at forest edges.

For the preparation of the supplied picture material, it was therefore necessary to develop a method for adjusting the four spectral channels between the individual images, to extend their histograms and to calculate new channels. For this purpose ERDAS Imagine 9.3 was used. The different algorithms have been combined with the help of the "Spatial Modeler" to an overall model. Thus, the enhancement of the individual images in each case was feasible in one single step.

The following processes have been conducted:

Step 1: Compensation of chromatic heterogeneity between images and within individual image tiles.

The color heterogeneity between the individual images could be largely offset by adjusting the individual color channels.

Exposure differences within the image tiles, particularly at the edges of forest areas however, could be corrected only to a limited extent.

Step 2: Enhancement of spectral differences between individual trees.

With the exception of forest edges with strong illumination decline, a very significant increase in visual recognition of the individual conifer species was achieved on the basis of their different colors when displayed on the screen.

The advantage of this method of image processing is a significant time reduction of the effort for the determination of training trees.

3.2 Segmentation / Classification

To classify coniferous forests covering a great area as training samples, Spruce trees and other coniferous trees were used. In this operation a probability filter has been applied, that separates coniferous and deciduous trees.

By the use of AOI's (Area of Interest) for Spruce and other coniferous tree species, 8 to 14 training trees in the best possible allocation within the individual image tile were assigned. With increasing heterogeneity of the picture, a larger amount of training trees per target class was required.

The basic settings were chosen in a way that as large as possible crown areas were recorded for each segment. The collection of several small-crown trees of the same species in a segment was deliberately taken into account, in order to improve the formation of the segment averages of the spectral bands as far as possible. The resulting polygons were attributed by their mean values and probabilities with which each segment of a species has been classified. Using a probability filter, a pre-selection of segments for all aspired classes was then conducted.

3.3 Post-processing and visualization in a GIS

Fine adjustment, post-processing and visualization of the classification results have been accomplished by ArcGIS 9.3 by ESRI. For this reason, the generated shapefiles of the segments were imported into ArcGIS. A pre-selection was achieved by the use of mean values of the reflectance (exclusion of shadows, etc.). In a next step, the generated probability limits were adjusted to enlarge the target class, while limiting misclassifications to a modest range. In this process, the necessary border values of the probabilities determined by ERDAS Imagine Objective varied considerably.

For typical training trees, a probability of 60% already proved to be sufficient for a reliable classification. For training trees with atypical radiation spectrum (e.g. along forest edges, damaged trees) a probability threshold of 90% has to be chosen

in order to avoid misclassifications. In spectrally heterogeneous to very heterogeneous images, the classification had to be restricted to sufficiently homogeneous areas, since the segmentation of training trees led only in those areas to a reliable classification. As a result, in heterogeneous images, an increased number of training trees was necessary for a reliable classification, causing a much bigger effort.

4. RESULTS

4.1 Image data homogenization

As mentioned above, the heterogeneity of the image data within their spectral bands caused a major problem, with the infra-red band showing the least differences between the images. This means, that even within one flight strip adjacent images showed decisive spectral differences (figures 1 and 2).



Figure 1: Example for the spectral heterogeneity of the used image data: Adjacent ortho-rectified images within one flight strip of the research area (illustration in true color without histogram stretch).

The quality control of the original image data histograms proved, that the reflection values for all spectral bands only covered about 1/3 of the possible histogram width. For this comparison, the histogram of digital image data from a flight campaign in 2006, equally using a matrix camera system, has been selected. The histograms of these images showed an almost ideal distribution over the whole possible reflection spectrum (figure 3). The shortening of the pixel-value area within the LVG image data from 2008 complicated the spectral delimitation and visual perceptibility of a tree species decisively.

As another severe quality limitation of the image data in use, spectral differences between each single spectral band of the Vexcel images have been identified. The reflection values within the spectral bands red, green and blue varied up to 15 % in one flight strip. This strong spectral differentiation between the spectral bands originally averted the transfer of the classification algorithms from one image to its neighbors. These effects necessitated a homogenization and a histogram stretching of each spectral band as an essential prerequisite to the subsequent classification. Figure 2, 4 and 5 illustrate the extent of the spectral differences between the single images and the various spectral bands within the single image as well as the efficiency of the developed methodology for the image data improvement.

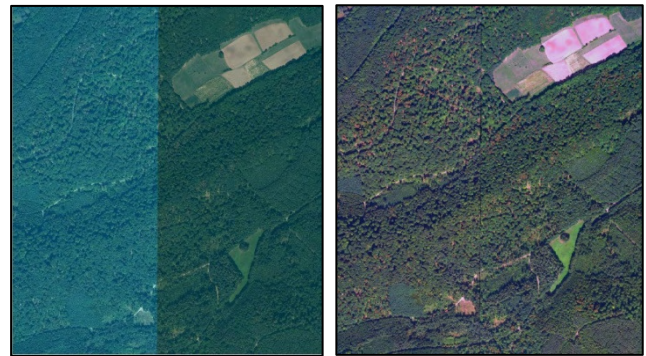


Figure 2: Detail of two adjacent images (true color illustration) within one flight strip (cf. to figure 1): left side: original image prior to pre-processing; right side: enhanced and homogenized image data.

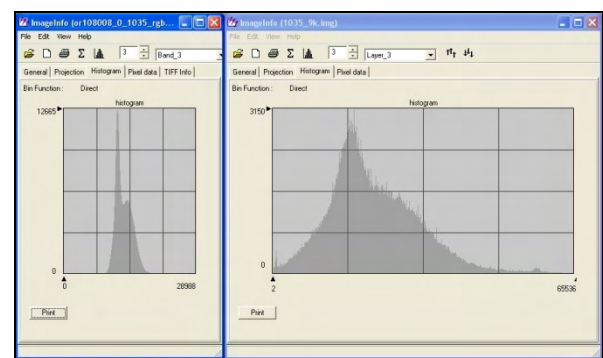


Figure 3: Histogram comparison of blue band. Left original, right after enhancement

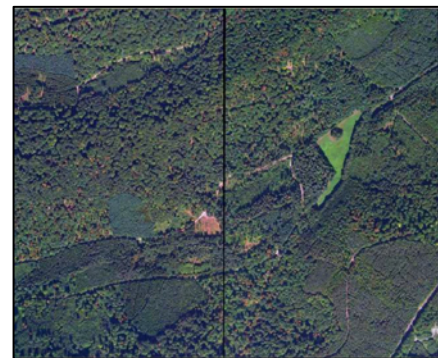


Figure 4: Two adjacent images after the pre-processing (True color illustration after pre-processing with broadened value range)

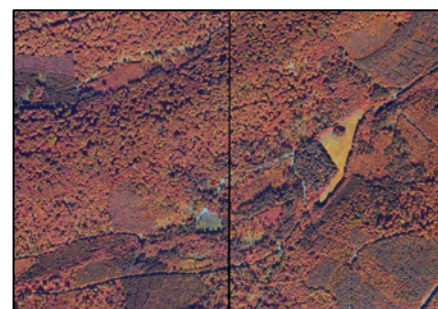


Figure 5: Two adjacent images after the pre-processing (infra-red illustration)

Only with radiometrically aligned images, a spectral respectively visual recognition of tree species is possible. Image homogenization is thus fundamental for a Spruce stands classification over large areas.

It can thus be stated conclusively, that the available Vexcel UltraCam X data required an intensive spectral enhancement and homogenization in order to prepare them for the following classification. The developed procedure for this process proved its effectiveness and reliability.

4.2 Classification of Norway Spruce

The spectral reflection of vegetation varies decisively according to the camera angle relative to the object. Within an aerial photograph, the northern part of the image represents mainly the southern, well illuminated part of the tree canopy; the southern part of the image represents the northern, shadowy parts of the canopy. This phenomenon, besides others like varying vitality status within a tree species, results in the necessity to create several classes for each tree species. For this project the following classes have been distinguished accordingly:

- Old Spruce (older than 50 years)
- Middle Old Spruce (age 30 – 50 years)
- Young Spruce (younger than 30 years)
- Spruce forest edge (up to 200 m from open country)
- Inner area of Spruce stand
- Other coniferous stands (*Larix* spec., *Pseudotsuga* spec., *Pinus* spec., *Abies* spec.)

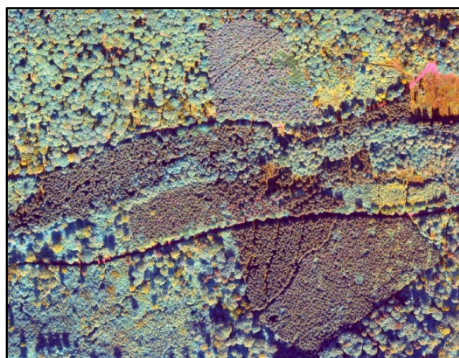


Figure 6: Processed image; scale 1:5000 with coniferous stands intensified. Grey – blue: deciduous trees blurred out.



Figure 7: Classified image, scale 1:5000 with segments of coniferous classification. Grey – blue: deciduous trees blurred out.

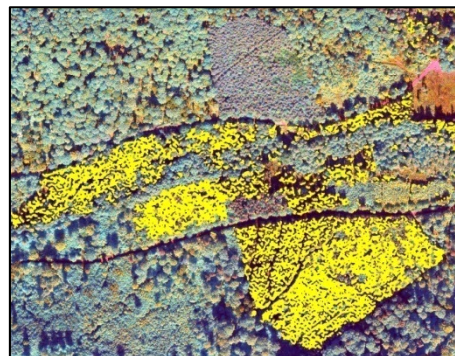


Figure 8: Classified image, scale 1:5000 with segments of Norway Spruce classification. Grey – blue: deciduous trees blurred out.

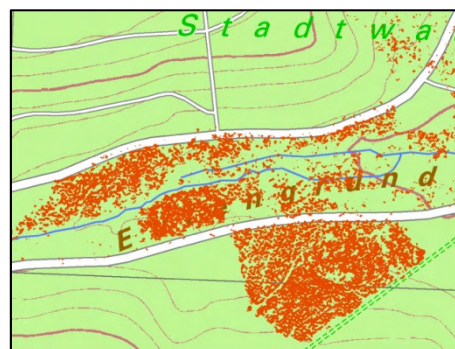


Figure 9: A topographic map, scale 1:5.000, superimposed by polygons of the Spruce classification

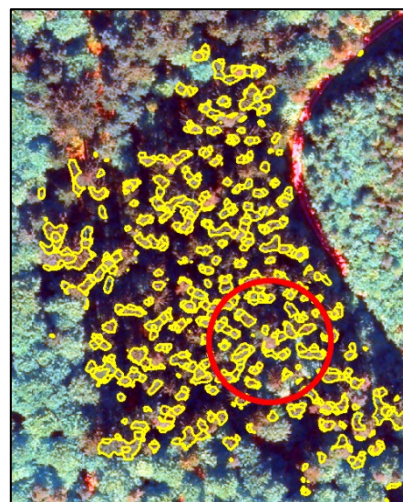


Figure 10: Classified Spruce in detail with sample plot (diameter 20m); scale 1:1000. Grey – blue: deciduous trees blurred out.

A total of 8 to 14 classes had to be distinguished according to the different research areas and the illumination decline at the forest edges.

As mentioned above, within the furnished Vexcel UltraCam X data, an illumination decline from forest areas towards open country areas had to be stated. The effect resulted in a decisively higher amount of work during the classification and in poorer classification accuracy for the concerned forest edges (cf. to chapter 3.1 and 3.3)

The decisive criteria for the classification step however is not the absolute likelihood value of the investigated tree species, but first of all their relative distance towards spectrally adjacent coniferous tree species.

Because of this reason, a previous classification of the totality of all coniferous trees is obligatory in order to distinguish the transitions between the single classes. Out of the initial overall classification of all coniferous trees (cf. to figures 6 and 7), division criteria for each Spruce class has been developed by the use of probabilities and mean segmentation values. Figures 6, 7, 8, 9 and 10 demonstrate the results of the various classification steps

Finally, an average hit rate of 86 % has been achieved for the classification of Spruce (cf. to chart 1).

The results in detail show a classification accuracy of more than 90% for old Spruce stands and more than 80% in middle-old stands. The classification accuracy of Spruce in mixed young stands is about 80%. In this age class especially the difficult segmentation of the individual crowns caused a higher error ratio.

4.3 Verification of results

In order to verify results, 500 randomly distributed grid-points have been created with a minimum distance of 50 m by the use of the ArcInfo tool „Create Random Points“. From these 500 points, a selection of points that were situated inside Spruce stands or inside forest stands with Spruce trees has been extracted for an accuracy validation. The selected grid points have been buffered then to sample plots between 15 and 25 m radius, according to their age and tree species composition. Inside the sample plots, the quantity of trees for each tree species has been assessed as well in the field as in an ortho-rectified aerial image. In the next step, the tree species percentage for every sample plot has been compared with the according classification results. The hit rate had to be referred exclusively to the crowns in the upper storage of the Spruce stands because of the shadow effects inside the gaps between the tree crowns (cf. to chart 1).

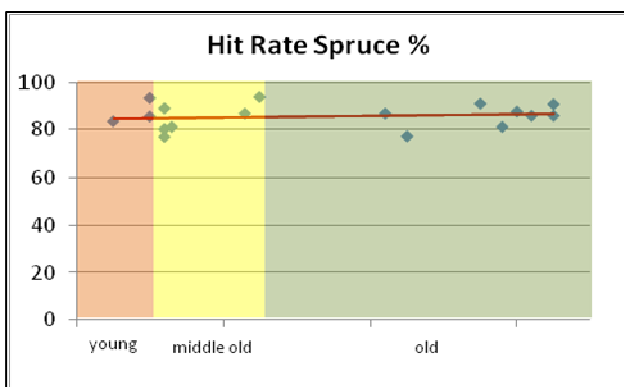


Chart 1: Hit rates for the classification of the classes young, middle old, old Spruce

5. SUMMARY AND CONCLUSION

The spectral characteristics of digital aerial image data depends decisively on the factors

- time and date of image acquisition,
- camera system,

- pre- resp. post-processing of the image data.

The image data used in the project described above was characterized by strong spectral differences between the single images within the flight strips as well as within the spectral bands within the single images. In detail, shortened histogram widths, illumination declines from forest stands towards non-forested areas and spectral heterogeneities between the several spectral bands had to be stated.

Despite the heterogeneity of the image data, the objective of the project to produce a GIS-layer locating “Spruce” and “other coniferous trees” for two test areas out of actual digital image data has been achieved. In detail, the following results have been achieved:

- The preparation of heterogeneous image data for use within the research approach
- The assessment of Spruce within the accuracy as described above
- A clear separation of deciduous from coniferous trees
- The successful transfer of the methodology on digital aerial image data of a second test region in the same flight campaign
- The semi-automatic assessment of Spruce even in young growth stands within the accuracy limitation as described above

These results outline the possibility to develop a practicable methodology for the further use of aerial imagery to gain information about the tree species composition of forested areas.

6. FUTURE PROSPECTS

6.1 Image data quality

Within the future flight campaigns of the Bavarian LVG, different camera systems are supposed to be in use. Because of the lack of standards for the image acquisition and processing of aerial imagery in common, the problematic effects as stated above are expected to turn up again in future image acquisition campaigns. This would cause negative impacts on the cost-efficiency of the methodology and thus its transferability into practice. Therefore common standards should be developed accordingly. Moreover, the stated illumination decline from forest towards open areas requires further research activities in the field of image analysis and optimization.

6.2 Segmentation/ Classification

The preparation of the image data prior to the segmentation and classification in this project as described above allowed the successful segmentation of most Spruce classes with a high accuracy. First hints lead to the conclusion that the developed methodology enables the semi-automatic assessment of even more tree species.

Further research efforts in the field of the semi-automatic tree species assessment from digital aerial imagery should therefore be conducted. The approaches should thereby concentrate on the transfer of the described results on other camera systems as well as different acquisition conditions (with concern to acquisition time, topography, illumination). Finally a focus has to be laid on the cost-efficiency of the methodology when transferred into practice on vast areas.

7. REFERENCES

7.1 References from Books:

Akça, A., Huss, J., 1984: *Luftbildmessung und Fernerkundung in der Forstwirtschaft*. Wichmann, Karlsruhe, ISBN 3-87907-131-4

Brosinger, F., 2004: *Integriertes Schutzwaldmanagement im Bayerischen Alpenraum; Konzept und Umsetzung*. INTERPRAEVENT 2004, Band 1, Thema 3, S. III/23 – 33. Riva del Garda, Trient

Koch, B., 1988: *Untersuchungen zur Reflexion von Waldbäumen mit unterschiedlichen Schadsymptomen auf der Grundlage von Labor- und Geländemessungen*; Dissertation, Ludwig-Maximilians-Universität München

Neubert, M., 2006: *Bewertung, Verarbeitung und segmentbasierte Auswertung sehr hoch auflösender Satellitenbilddaten*; Dissertation, Fakultät Forst-, Geo- und Hydrowissenschaften der Technischen Universität Dresden; Rhombos-Verlag, Berlin.

Tiede, D., Osberger, A., Novak, H., 2009: *Automatisierte Baumextraktion mit höchstauflösenden Oberflächenmodellen abgeleitet aus UltracamX-Daten*; in: Strobl, Blaschke, Griesebner (Hrsg.): *Angewandte Geoinformatik 2009 – Contributions to the 21st. AGIT-Symposium Salzburg*; Wichmann Verlag, Heidelberg

7.2 References from Other Literature:

Ammer, C., Dully, I., Faißt, G., Immler, T., Kölling, C., Marx, N., Holland-Moritz, H., Seidl, G., Seitz, R., Triebenbacher, C., Wolf, M., Wolferstetter, T., 2006: *Hinweise zur waldbaulichen Behandlung von Borkenkäferkalamitätsflächen in Mittelfranken*; LWF Wissen Nr. 54; Lerchl-Druck, Freising

Bernhart, K., 2007: *Finanzielle Förderung des Waldumbaus*; LWF Aktuell Nr. 60; Lerchl-Druck, Freising

Kölling, C., Bachmann, M., Falk, W., Grünert, S., Wilhelm, G., 2008: *Soforthilfe Baumarteneignung-Anbaurisiko-Klimawandel*, Technical Report; unpublished, Freising

StMELF (Bavarian Ministry of Food, Agriculture and Forestry), 2008: *Waldumbau – Stabile Wälder für kommende Generationen*; Brochure; Appl-Sellier Druck, Freising

USING REMOTE SENSING PRODUCTS FOR ENVIRONMENTAL ANALYSIS IN SOUTH AMERICA

Y. E. Shimabukuro^{a,*}, G. Pereira^a, G. B. S. Silva^a, F. B. Silva^a, F. S. Cardozo^a, E. C. Moraes^a

^a INPE, Instituto Nacional de Pesquisas Espaciais, Brazil (yosio, gabriel, bayma, fabricio, cardozo, bete)@dsr.inpe.br

KEY WORDS: Land use, land cover, GLOBCOVER, vegetation cover fraction, fire radiative power, biomass burning.

ABSTRACT: Land cover plays a major role in many biogeochemical models that represent processes and connections with terrestrial systems; hence, it is a key component for public decisions in ecosystems management. The advance of remote sensing technology, combined with the emergence of new operational products, offers alternatives to improve the accuracy of environmental monitoring and analysis. This work uses four remotely sensed databases: the GLOBCOVER, the Vegetation Continuous Field (VCF), MODIS Fire Radiative Power (FRP) and the Tropical Rainfall Measuring Mission (TRMM). The objective of this study is to analyze the environmental characteristics in South America from 2000 to 2005 using these four remotely sensed databases. Initially, GLOBCOVER was assessed based on VCF product, and was afterwards analyzed for its quantitative and spatial distribution of the fires with the FRP database. The results show that GLOBCOVER has a tendency to overestimate forest classes and to underestimate urban and mangroves areas. The fire quantification on GLOBCOVER product shows that the highest incidence of fires can be observed in the deforestation arc, located in the Amazon forest border, with vegetation cover composed mainly of broadleaved evergreen or semi-deciduous forest. A time series analysis of FRP database indicates that biomass burning spreads to areas of broadleaved evergreen or semi-deciduous forest and savannah regions, even with rainfall anomalies observed with TRMM database. We suggest to improve the map of vegetation and urban areas and to use other products derived from satellites, such as the images of City Lights, created out of data from the Defence Meteorological Satellite Program (DMSP).

1. INTRODUCTION

Land cover plays a major role in many environmental models that represent processes and connections between surface and atmospheric processes, which modify the energy balance (Kaufman et al., 1998; Christopher et al., 1998; Tarasova et al., 1999; Tarasova et al., 2000; Tarasova & Eck, 2000; Christopher et al., 2000; Li et al., 2000; Wagner et al., 2001), atmospheric chemistry (Crutzen & Andreae, 1990; Fishman et al., 1996; Reid et al., 1996, 1999), evapotranspiration and precipitation reduction (Nobre et al., 1991, 1998). Hence, land cover is a key component for public decisions on ecosystems management and in the assessment of the impacts of anthropogenic actions on the equilibrium of ecosystems.

Overtime, biomass burning consumes vast areas of grassland and forests around the globe, releasing large and unknown quantities of aerosols and trace gases into the atmosphere (Crutzen & Andreae, 1990). In South America, land use and land cover (LULC) maps show temporal and spatial variability in anthropogenic biomass burning, which are directly associated with agricultural land clearing, grassland management and with the deforestation of Amazon tropical rainforest, the highest incidences of fires are located in the arc of deforestation, located in Amazon forest border (Kaufman et al., 1990, 1992).

The GLOBCOVER project is an initiative of European Space Agency (ESA) in cooperation with international institutions; it is useful in monitoring the dynamics of land cover and forests (Arino et al., 2005). The EOS (Earth Observing System) initiative of NASA (National Aeronautics and Space Administration) is another program that provides important data for environmental monitoring of land, ocean and atmospheric ecosystems.

Among the many products provided by the EOS, the VCF (Vegetation Continuous Field) and the MODIS (Moderate Imaging Spectroradiometer) provide phenological studies in annual time series (Hansen et al., 2003).

Despite the efforts of each program in implementing environmental, hardware, software and data distribution, these aforementioned products have their respective limitations and are creating confusion in distinguishing the different classes of land cover (Herold et al., 2008).

Integration of different data sources from different sensors can improve the accuracy of environmental monitoring. Thus, the objective of this study is to verify GLOBCOVER LULC product assessment with VCF tree cover data. Furthermore, using MODIS data, the patterns of fire radiative power over LULC and VCF values are compared by analysing the annual biomass burning distribution in South America from 2000 to 2005.

2. DATA AND METHODOLOGY

2.1 GLOBCOVER

Figure 1 shows South America GLOBCOVER product. South America has a distinct and important biodiversity in the world, spatially distributed in its many natural ecosystems. However, this complex system is constantly exposed to anthropogenic activities such as deforestation, agriculture expansion and burning.

The objective of the ESA-GLOBCOVER project is the production of a land cover map of the world using an automated processing chain on 300m MERIS time series. The GLOBCOVER Land Cover map for the period of December

* Corresponding author.

2004 to June 2006 is derived by an automatic and regionally-tuned classification of a MERIS full resolution (FR) time series. Its 22 land cover classes are defined with the UN Land Cover Classification System (LCCS).

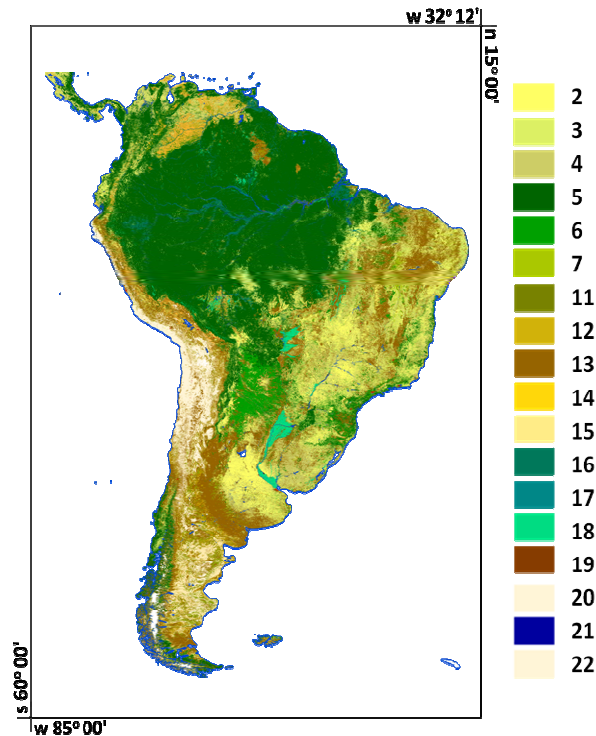


Figure 1. GLOBCOVER product of South America.

In South America (Figure 1) the following classes are found: 2 - Rainfed croplands; 3 - Mosaic cropland (50-70%) / vegetation (grassland/shrubland/forest) (20-50%); 4 - Mosaic vegetation (grassland/shrubland/forest) (50-70%) / cropland (20-50%); 5 - Closed to open (>15%) broadleaved evergreen or semi-deciduous forest (>5m); 6 - Closed (>40%) broadleaved deciduous forest (>5m); 7 - Open (15-40%) broadleaved deciduous forest/woodland (>5m); 8 - Closed (>40%) needleleaved evergreen forest (>5m); 9 - Open (15-40%) needleleaved deciduous or evergreen forest (>5m); 10 - Closed to open (>15%) mixed broadleaved and needleleaved forest (>5m); 11 - Mosaic forest or shrubland (50-70%) / grassland (20-50%); 12 - Mosaic grassland (50-70%) / forest or shrubland (20-50%); 13 - Closed to open (>15%) (broadleaved or needleleaved, evergreen or deciduous) shrubland (<5m); 14 - Closed to open (>15%) herbaceous vegetation (grassland, savannas or lichens/mosses); 15 - Sparse (<15%) vegetation; 16 - Closed to open (>15%) broadleaved forest regularly flooded (semi-permanently or temporarily) - Fresh or brackish water; 17 - Closed (>40%) broadleaved forest or shrubland permanently flooded - Saline or brackish water; 18 - Closed to open (>15%) grassland or woody vegetation on regularly flooded or waterlogged soil - Fresh, brackish or saline water; 19 - Artificial surfaces and associated areas (Urban areas >50%); 20 - Bare areas; 21 - Water bodies; 22 - Permanent snow and ice; and 23 - No data (burnt areas, clouds,...) (Bicheron et al., 2009).

2.2 Vegetation Continuous Fields (VCF)

The Vegetation Continuous Fields (VCF) (Figure 2) is a global percent tree cover map based on 500 meter MODIS data, and represents the finest scale global forest information to date. In this study, the MODIS composited data are transformed into

annual metrics which capture the salient points in the forest phenologic cycle. The VCF algorithm is an automated procedure which employs a regression tree algorithm. Percent canopy here refers to the amount of skylight obstructed by tree canopies which are equal to or greater than 5 meters in height (Hansen et al., 2003).

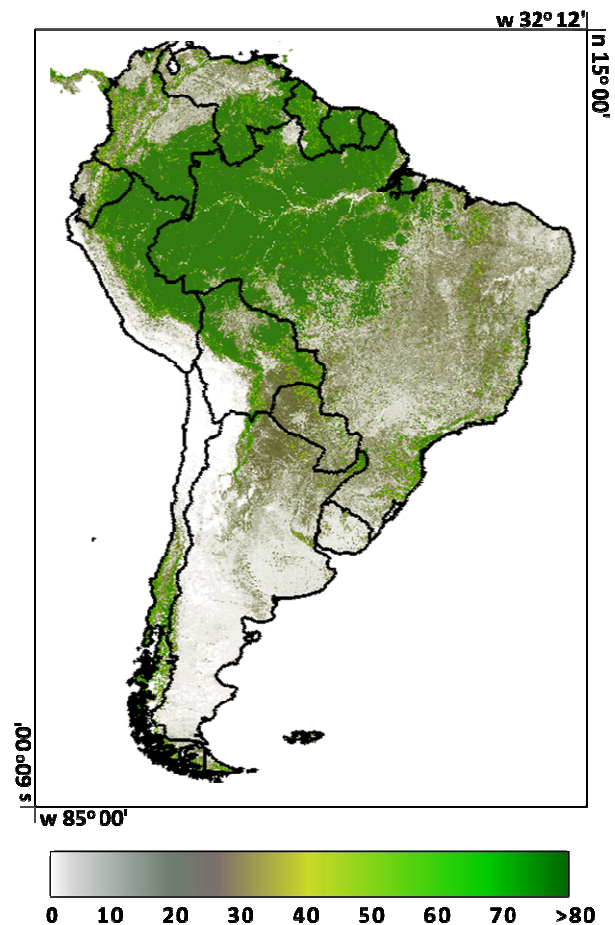


Figure 2. 2005 South America Vegetation Continuous Fields product.

2.3 Tropical Rainfall Measuring Mission (TRMM)

The TRMM satellite data are used in this study to characterize the seasonal pattern of precipitation. The TRMM satellite is a partnership between the National Aeronautics and Space Administration (NASA) and the Japan Aerospace Exploration Agency (JAXA). Since 1997, these agencies have collected precipitation data encompassing more than two thirds of global precipitation. These data are generated by an algorithm that estimates the combined global precipitation estimations from multiple orbital sensors (Huffman et al., 2007). The data used in this work are related to the 3B42 product with 3 hours of temporal resolution; geographic covering: latitude from 50° S to 50° N and longitude from 180°W to 180°E; and horizontal resolution of 0.25° x 0.25° (available in: <<http://mirador.gsfc.nasa.gov/>>).

2.4 MODIS Fire Radiative Power (FRP)

The fraction of chemical energy emitted in biomass burning as electromagnetic radiation can be defined as Fire Radiative Power (FRP). Temporal integration of FRP gives the Fire Radiative Energy (FRE). Moreover, the FRE indicates the

amount of particulate matter and trace gases emitted into the atmosphere over a region (Pereira et al., 2009). Initial studies with FRP were performed with MODIS Airborne Simulator (MAS) in the SCAR-C and SCAR-B (Smoke, Cloud and Radiation - California / Brazil) experiments are available on MODIS fire products, also called MOD14 (Terra) and MYD14 (Aqua); these products utilize a contextual algorithm applied to brightness temperatures in 4 μm and 11 μm mid-infrared radiation channels (Kaufman et al., 1998a, 1998b; Chu et al., 1998; Justice et al., 2002; Giglio, 2005) and for each fire detection FRP is calculated through the method proposed by Kaufman et al. (1996, 1998a, 1998b):

$$FRP_{MODIS} = 4.3 \times 10^{-19} \cdot (T_{f\ 4\mu m}^8 - T_{b\ 4\mu m}^8) \cdot A_{s\text{ampl}} \quad (1)$$

where $T_{f\ 4\mu m}$ and $T_{b\ 4\mu m}$ are, respectively, the MODIS brightness temperatures of the fire and the non-fire background in Kelvin (K), $A_{s\text{ampl}}$ is the real area of the pixel (m) and FRP is the Fire Radiative Power in Megawatts (MW) as shown for the 2005 fire data (Figure 3).

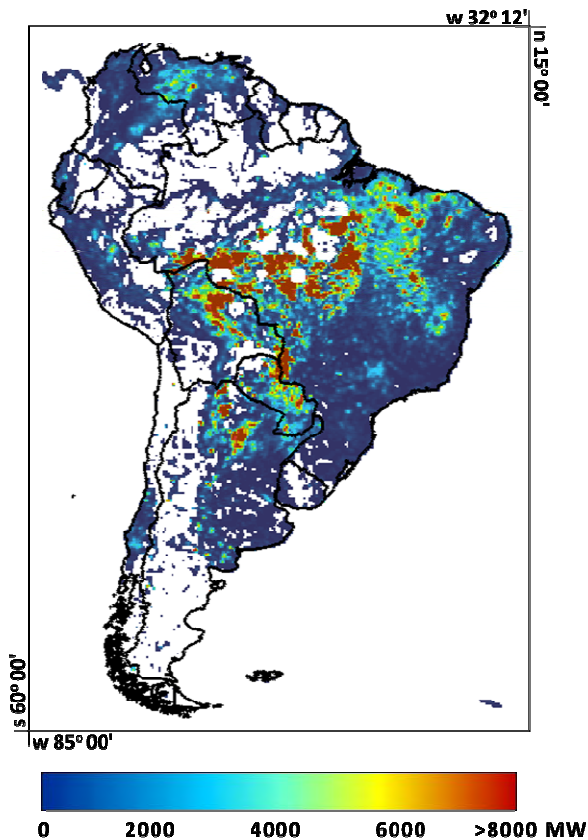


Figure 3. 2005 South America MODIS FRP product.

2.5 Data processing

All data used in this work are inserted in SPRING, a free GIS application developed by the National Institute for Space Research (INPE) of the Brazilian Ministry of Science and Technology (MCT). Part of the data processing stage (transformation and compilation of different data, random sampling, assignment of thematic classes and cross tabulation analysis) was made in LEGAL Language implemented in the SPRING (SPRING, 2005). LEGAL is a command language used to geographic analysis that is not implemented on graphic interface of SPRING. This command language, proposed by

Câmara Neto (1995), has as objective to support a command line tool to perform spatial queries operations and numerical and statistical analysis.

Figure 4 shows the flowchart of the adopted methodology. The first step (I) consists in acquire remote sensing derived products; follow by data processing and SPRING data base inclusion (II). After this step, derived data was compared in pairs (III) and the results analyzed (IV).

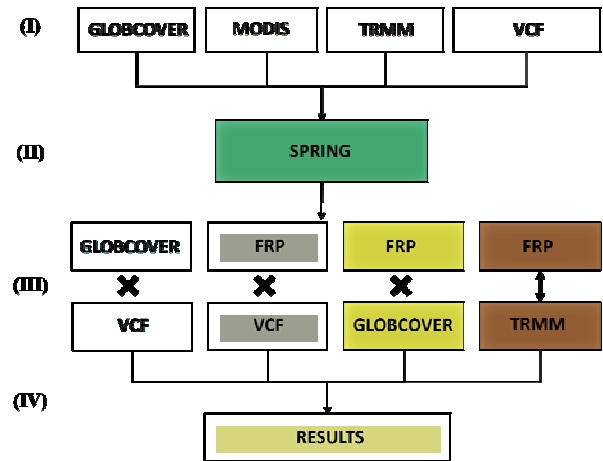


Figure 4. Flowchart of methodology.

3. RESULTS

3.1 GLOBCOVER assessment with VCF

GLOBCOVER product characterizes South America LULC in 19 classes, which represents approximately 40% broadleaved evergreen or semi-deciduous forest such as Amazon forest and Atlantic Forest (tropical and subtropical moist forest), 17% are a merger of vegetation and cropland, 16% represents closed to open broad-leaved or needle-leaved, evergreen or deciduous shrubland and 6% is rainfed croplands. Also, there are minority class areas such as bare areas (3%), Sparse Vegetation (3%) and Grassland/Shrubland Forest (9%).

Operational landscape characterization methodologies could introduce systematic errors due to surface elements with spectral signature similarities (Wang & Howarth, 1993). Consequently, remote sensing derived products such as VCF could be used to assess LULC maps. Figure 5 shows the cross tabulation between the mainly LULC South America GLOBCOVER classes and 2005 VCF tree cover product. Broad-leaved evergreen or semi-deciduous forest land cover, mainly represented by Amazon Rainforest, are expected to have a high value of VCF tree cover due to the large area of vast forests that perform homogeneous tree cover. However, the results showed that only approximately 72% of the total LULC area is composed of VCF values greater than 70. The same occurs with Closed broadleaved deciduous forest, located essentially in Paraguay and North of Argentina, where approximately 40% of this class area are composed of VCF tree cover lower than 40.

This discrepancy could be originated by the heterogeneity of vegetation on pixel formation. In this area, we can find mixed areas of short grass, tall grass, Evergreen broadleaf trees and

Forest-Field Mosaic that introduces errors in classification process.

However, LULC classes dominated mainly by agricultural and grassland fields show good conformity with VCF values, with low percentage (less than 5%) of VFC values greater than 70.

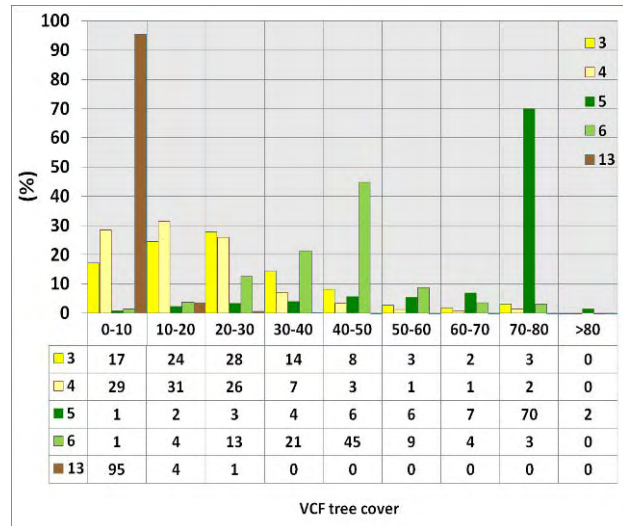


Figure 5. Graphic of cross tabulation between GLOBCOVER and VCF products, showing the percentage of vegetation continuous field tree cover present in selected land use and land cover map.

GLOBCOVER product exhibits a tendency to overestimate forest classes mainly by clustering surrounding lower biomass density LULC areas such as shrubland and grassland. Also, we can notice that it underestimates urban areas and mangroves biome. These errors, associated with the algorithm classifier, could be introduced in the pre-processing of MERIS imagery, in the radiometric rectification and in cloud-free processing algorithm. Figure 6 shows a sample area with broad-leaved evergreen forest LULC GLOBCOVER (in dark green) with the respective VCF tree cover product and MODIS True color composition (3B4G1R) cloud-free mosaic sections, (a), (b) and (c), respectively. This figure is an example of the overestimation that occurs in LULC product.

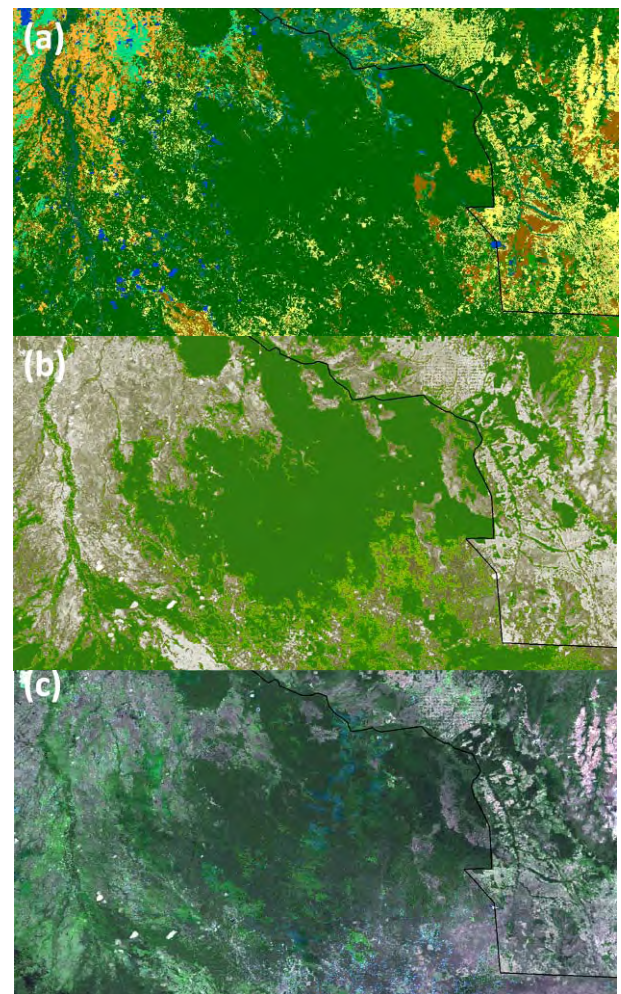


Figure 6. (a) Example of Closed to open (>15%) broadleaved evergreen or semi-deciduous forest (>5m) overestimation (in dark green); (b) VCF tree cover; and (c) MODIS surface reflectance composition (3B4G1R).

3.2 2000 to 2005 South America Biomass Burning

In South America, biomass burning presents spatial and temporal variability, associated directly with LULC management. The highest incidences of fires are located in the arc of deforestation, located in the Amazon forest borders. Therefore, the greatest number of fires can be found in areas of vegetation composed by broad-leaved evergreen or semi-deciduous forest; this is followed by herbaceous vegetation (grassland, savannas or lichens/mosses); mosaic vegetation (grassland /shrubland/forest) / cropland; mosaic cropland / vegetation (grassland/shrubland/forest) and rainfed croplands. Table 1 shows the LULC for South America and its percentage of 2005 fires presented in each class.

GLOBCOVER LULC	(%)
2	6.4
3	7.8
4	9.3
5	38.9
6	3.8
7	0.5
11	3.2
12	1.5
13	16.6
14	2.0
15	3.3
16	1.6
17	0.1
18	1.4
19	0.1
20	3.1
22	0.4

Table 1. GLOBCOVER LULC and the percentage of 2005 fires presented in each class.

Figure 7 shows the annual (2000 to 2005) accumulative fire pixels that occur in each VCF tree cover classes (y-axis in logarithm of base 10). We can notice that most of South America’s biomass burning is located in VCF tree cover classes of, 0-10, 20-30 and 70-80. Also, this figure shows a propensity to increasing the number of fire focus in all VCF classes, mainly in VCF values greater than 70, that represents biomes with a high quantity of biomass. When comparing 2005 to 2000, notice that biomass burning spread to areas of Broad-leaved evergreen or semi-deciduous forest and savannah regions. These areas are composed mainly of Amazon Forest biome and Brazilian Cerrado (savannah biome). Also, the highest increase occurs in vegetation whit continuous field tree cover greater than 79% due the deforestation expansion.

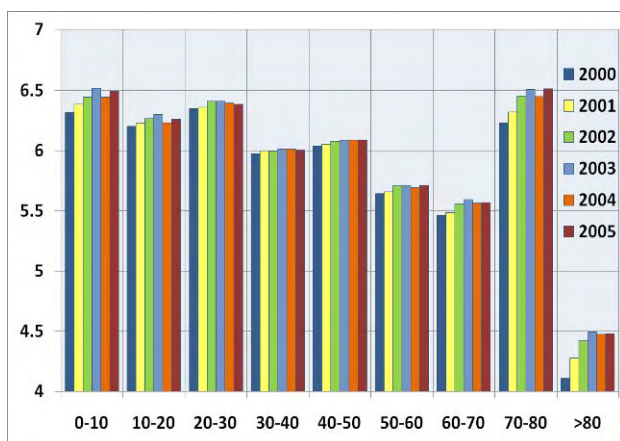


Figure 7. Graphic of annual fire pixel inserted in each VCF tree cover class (values are in logarithm base 10).

Figure 8 shows the annual fire radiative power released per pixel as retrieved from MODIS. This product gives information of active fires 4 to 5 times per day for the same area. The FRP

values are clustered in 10km grid, where the pixel value is the sum of all-year FRP values. The highest annual occurrence are detected between 0-1000 MW, in this class we notice a low variation of FRP among the yearly measurements. In the other classes the number of FRP pixels increased significantly especially in values greater than 6000 MW.

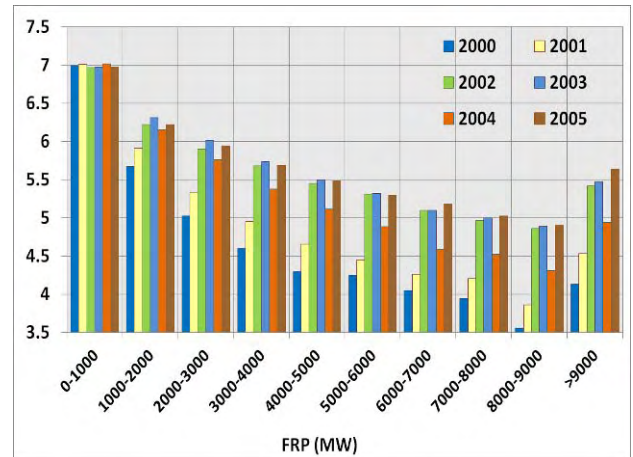


Figure 8. Graphic of annual fire radiative power (in Megawatts) with y-axis in logarithm base 10.

Some variations in FRP clusters can be attributed to the rainfall anomalies, such as in 2004, when South America had a positive rainfall anomaly analysed by TRMM data. During the studied period (2000 to 2005), Amazon region had negative rainfall anomalies in 2002, 2003 and 2005 and positive rainfall anomalies in 2000, 2001 and 2004. Moreover, the increase in energy released by South American fires could be related to increasing of biomass burning in areas with large amounts of biomass exposed annually to anthropogenic burning located in the arc of deforestation (as shown in Figure 3). Figure 9 shows the rainfall anomaly for 2004 derived from TRMM rainfall data.

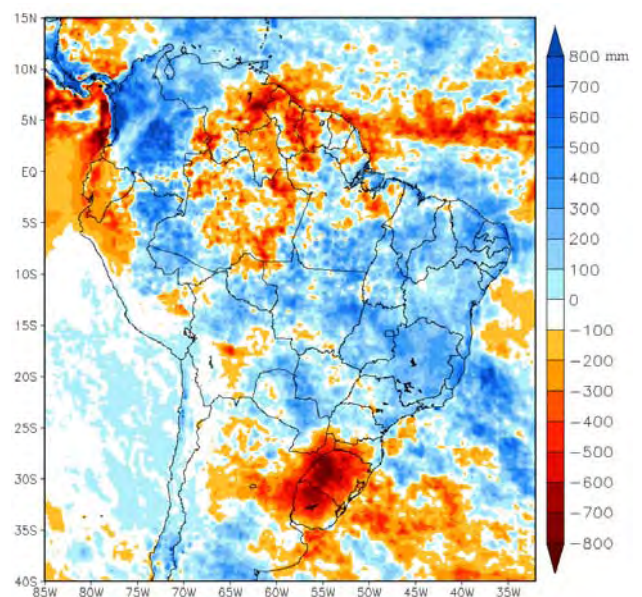


Figure 9. 2004 Rainfall Anomaly, blue represents positive values of rainfall and red represents negative rainfall values.

4. CONCLUSIONS

Although GLOBCOVER is a global product, it proved effective in representing the land use and land cover (LULC) of the region. However, like all products derived from automatic classification, some errors present in the results, such as the overestimation of broad-leaved evergreen or semi-deciduous forest and the under-estimation of urban areas and vegetation composed by mangroves. Therefore, to improve the map of vegetation areas and urban areas, we suggest verification using other products derived from satellites, such as the images of City Lights, created with the data from the Defence Meteorological Satellite Program (DMSP).

Concerning the burned areas, it is noticeable that classes with the largest number of fires are related to the Amazon Forest and Cerrado (savannah) biomes and there was a significant increase in the number of fires in areas with a large amount of biomass, resulting therefore in a larger number of emissions of aerosols and trace gases into the atmosphere.

5. REFERENCES

- Arino, O. et al., 2005. The GLOBCOVER Initiative, ESA ESRIN, Via Galileo Galilei, Frascati, Italy.
- Bicheron, P., Defourny, P., Brockmann, C., Schouten, L., Vancutsem, C., Huc, M., Bontemps, S., Leroy, M., Achard, F., Herold, M., Ranera, F., Arino, O., 2009. GLOBCOVER-Products Description and Validation Report. 47p. Available at: <ftp://guestglobcover:Pir8Eefo@usextnas.eo.esa.int/global/GL_OBCOVER.Products_Description_Validation_Report_I2.1.pdf >. Accessed on: 18 Nov 2009.
- Câmara Neto, G., 1995. Modelos, linguagens e arquiteturas para banco de dados geográficos. [Tese de Doutorado]. Instituto Nacional de Pesquisas Espaciais.
- Christopher, S. A.; Wang, M.; Berendes, T. A.; Welch, R. M., 1998. The 1985 biomass burning season in South America: Satellite Remote Sensing of fires, smoke and regional radiative energy budget. *J. Appl. Meteorol.*, 37, 661-678.
- Christopher, S. A.; Li, X.; Welch, R. M.; Reid, J. S.; Hobbs, P. V.; Eck, T. F.; Holben, B., 2000. Estimation of downward and top-of-atmosphere Shortwave Irradiances in Biomass Burning Regions during SCAR-B. *Journal of Applied Meteorology*, v. 39, n.10, p.1742-1753, Out.
- Chu, D. A., Kaufman, Y. J., Remer, L. A., Holben, B. N., 1998. Remote sensing of smoke from MODIS airborne simulator during the SCAR-B experiment. *J. Geophys. Res.*, 103, 31, 979-31, 987.
- Crutzen, P. J.; Andreae, M. O., 1990. Biomass Burning in the Tropics: Impact on Atmospheric Chemistry and Biogeochemical Cycles. *Science* 250 (4988): 1669-1678.
- Fishman, J.; Hoell, J. M.; Bendura, J. R.; Meneal, R. J.; Kirchhoff, V. W. J. H., 1996. NASA GTE TRACE-A experiment (September-October, 1992). Overview. *Journal of Geophysical Research – Atmospheres*, v.101, n. D19, p. 23865-23880.
- Giglio, L., 2005. MODIS Collection 4 Active Fire Product User's Guide. Available on the Internet: http://maps.geog.umd.edu/products/MODIS_Fire_Users_Guide_2.1.pdf.
- Hansen, M. C.; Defries, R. S.; Townshend, J. R. G.; Carroll, M.; Dimiceli, C.; Sohlberg, R. A., 2003. Global Percent Tree Cover at a Spatial Resolution of 500 Meters: First Results of the MODIS Vegetation Continuous Fields Algorithm. *Earth Interactions*, v. 7, n. 10, p. 1-15.
- Herold, M., Mayaux, P., Woodcock, C. E., Baccini, A., Schmullius, C., 2008. Challenges in global land cover mapping: an assessment of agreement and accuracy in existing 1km datasets, *Remote Sensing of Environment* 112: 2538-2556.
- Huffman, G. J., Adler, R. F., Bolvin, D. T., Gu, G., Nelkin, E. J., Bowman, K. P., Hong, Y., Stocker, E. F., Wolff, D. B., 2007. The TRMM Multi-satellite Precipitation Analysis (TMPA): Quasi-Global, Multiyear, Combined-Sensor Precipitation Estimates at Fine Scale. *Journal of Hydrometeorology*, v. 8, p. 38-55, Feb.
- Justice, C. O., Giglio, B., Korontzi, S., Owens, J., Morisette, J. T., Roy, D. P., Descloitres, J., Alleaume, S., Petitcolin, F., Kaufman, Y., 2002. The MODIS fire products. *Remote Sensing of Environment*, 83, 244-262.
- Kaufman, Y. J., Tucker, C. J., Fung, I., 1990. Remote Sensing of Biomass Burning in the Tropics. *Journal of Geophysical Research*, v. 95, n. D7, 9927-9939.
- Kaufman, Y. J.; Setzer, A. W.; Ward, D.; Tanré, D.; Holben, B. N.; Menzel, P.; Pereira, M. C.; Rasmussen, R., 1992. Biomass Burning and Spaceborne Experiment in the Amazonas (BASE-A). *Journal of Geophysical Research*, 97, D13, 14581-14599.
- Kaufman, Y. J., Remer, L. A., Ward, D. E., Kleidman, R., Flynn, L., Shelton, G., Ottmar, R. D., Li, R. -R., Fraser, R. S., McDougal, D., 1996. Relationship between remotely sensed fire intensity and rate of emission of smoke: SCAR-C Experiment. In J. S. Levine (Ed.), *Global biomass burning: Atmospheric, climatic and biospheric implications* (pp. 685-696). Cambridge: MIT Press.
- Kaufman, Y. J., Justice, C. O., Flynn, L., Kendall, J. D., Prins, E. M., Giglio, L., Ward, D. E., Menzel, W. P., Setzer, A. W., 1998a. Potential global fire monitoring from EOS-MODIS. *Journal of Geophysical Research*, 103, 32, 215-32, 238.
- Kaufman, Y. J., Kleidman, R. G., King, M. D., 1998b. SCAR-B fires in the tropics: properties and remote sensing from EOS-MODIS, *Journal of Geophysical Research*, 103, 31, 955-31, 968.
- Li, X.; Christopher, S. A.; Chou, J.; Welch, R. M., 2000. Estimation of shortwave direct radiative forcing of biomass burning aerosols using angular dependence models. *Journal of Applied Meteorology*, v. 39, n. 12, p. 2278-2291.
- Nobre, C. A.; Sellers, P. J.; Shukla, J., 1991. Amazonian deforestation and regional climate change. *J. Clim.*, 4, 957-988.

Nobre, C. A.; Mattos, L. F.; Dereczynski, C. P.; Tarasova, T. A.; Trosnikov, I. V., 1998. Overview of atmospheric conditions during the smoke, clouds and Radiation-Brazil (SCAR-B) field experiment. *Journal of Geophysical Research*, v. 103, n. D31, p. 809-820.

Pereira, G.; Freitas, S. R.; Moraes, E. C.; Ferreira, N. J.; Shimabukuro, Y. E.; Rao, V. B.; Longo, K.M., 2009. Estimating trace gas and aerosol emissions over South America: Relationship between fire radiative energy released and aerosol optical depth observations, *Atmospheric Environment*, v. 43, p. 6388-6397.

Reid, J. S.; Hobbs, P. V.; Ferek, R. J., 1996. Physical and chemical characteristics of biomass burning aerosol in Brasil. In: SCAR-B Proceedings. São José dos Campos, Transtec editorial: 1996. p.165-169.

Reid, J. S.; Eck, T. F.; Christopher, S. A.; Hobbs, P.; Holben, B., 1999. Use of the Angstrom Exponent to Estimate the Variability of Optical and Physical Properties of Aging Smoke Particles in Brazil. *Journal of Geophysical Research-Atmospheres*, v.104, n. D22, p. 27473-27490.

SPRING. 2005. Sistema de Processamento de Informações Georreferenciadas. Versão 4.3. Instituto Nacional de Pesquisas Espaciais (INPE).

Tarasova, T. A.; Nobre, C. A.; Holben, B. N.; Eck, T. F.; Setzer, A., 1999. Assessment of smoke aerosol impact on surface solar irradiance measured in the Rondonia region of Brazil during smoke, cloud and radiation – Brazil. *Journal of Geophysical Research*, v. 104, D19, p. 161-170.

Tarasova, T. A.; Nobre, C. A.; Holben, B. N.; Eck, T. F.; Setzer, A., 2000. Modeling of gaseous, aerosol and cloudiness effects on surface solar irradiance measured in Brazil's Amazonia 1992 - 1995. *Journal of Geophysical Research*, v. 105, D26, p. 961-969.

Tarasova, T. A.; Eck, T. F., 2000. Improvements in the broadband radiative transfer code aimed to achieve better agreement between modeled and measures solar irradiances on the ground. *Proceedings of IRS' 2000*. St. Petersburg, Russia,

Wagner, F.; Müller, D.; Ansmann, A., 2001. Comparison of the radiative impact of aerosols derived from vertically resolved (lidar) and vertically integrated (Sun photometer) measurements: Example of an Indian aerosol plume. *Journal of Geophysical Research-Atmospheres*, v. 106, n. D19, p. 22861-22870.

Wang, M., Howarth, P. J., 1993. Modeling errors in remote sensing image classification. *Remote Sensing of Environment*, v. 45, Issue 3, p. 261-271.

DETECTION OF HIGHWAYS IN HIGH RESOLUTION IMAGES USING MATHEMATICAL MORPHOLOGY TECHNIQUES

A. S. Ishikawa^a, E.A. Silva^b

^{a,b} UNESP - São Paulo State University, 305 Roberto Simonsen St., Brazil, 19060-900

^a aline.ishikawa@gmail.com

^b erivaldo@fct.unesp.br

KEYWORDS: mathematical morphology, cartographic feature, updating, digital image processing, remote sensing, high resolution images

ABSTRACT:

This paper seeks to apply routine for highways detection through the mathematical morphology tools in high resolution image. The Mathematical Morphology theory consists of describing structures geometric presents quantitatively in the image (objectives or features). This explains the use of the Mathematical Morphology in this work. As high resolution images will be used, the largest difficulty in the highways detection process is the presence of trees and automobiles in the borders tracks. Like this, for the obtaining of good results through the use of morphologic tools was necessary to choose the structuring element appropriately to be used in the functions. Through the appropriate choice of the morphologic operators and structuring elements it was possible to detect the highways tracks. The linear feature detection using mathematical morphology techniques, can contribute in cartographic applications, as cartographic products updating.

1. INTRODUCTION

Cartographic documents in different scales are fundamental tools to know the environment in way local, regional and global, and to help in the socket of necessary decisions for the planning and administration of resources. The current situation of the world cartography indicates that, for many areas of the planet, don't exist cartographic documents that they supply information with appropriate quality, being this a so much common problem for developed nations as for developing countries (Estes; Mooneyhan, 1994).

The Brazilian Cartography presents great deficiency in cartographic products updating. This happens due to the existent emptiness, incorrect scales, products that aren't adapted to the established quality pattern or for lack of an effective politics gone back to the territory mapping. Aiming at to reduce that mapping lack in great scales, the cartographic community is addressing efforts in the search of alternative methodologies so that the cartographic products can be updated with larger speed, efficiency and smaller cost. This process is of great importance for the obtaining of reliable and economically viable cartographic bases, without the need to accomplish conventional procedures, that you are costly and slow.

A fundamental factor in the process of cartographic updating is the changes detection, which according to Colwell (1974) it consists of the modifications recognition happened in the terrestrial surface through the time. Among the techniques of changes detection, it was chosen for this paper the integrated use of Remote Sensing products and Digital Image Processing (DPI) techniques. Among the several tools of DPI, it was chosen the Mathematical Morphology (MM) for the interest features detection in orbital images. The MM is a technique very used and researched in Universities and Research Centers of everyone, tends as base to study the sign geometry, being a powerful tool for images analysis, mainly where geometric aspects are relevant.

Considering the country wide national cartography deficiency, this work seeks to contribute for the automation of the Cartography field through the integrated utilization of Remote Sensing data and Digital Image Processing techniques. The main objective of this work was to apply a routine for highways detection in high resolution images (QuickBird) through the Mathematical Morphology tools, with views to the cartographic updating.

2. MAIN BODY

2.1 Mathematical Morphology

The Mathematical Morphology (MM) was originally developed by Matheron and Serra at the École des Mines in Paris. It is a set-theoretic method of image analysis providing a quantitative description of geometrical structures.

According to Soille (1999), MM can be defined as theory for the analysis of spatial structures. It is called of morphology, because it consists at analysing the shape and form of objects. It is mathematical because the analysis bases on set theory, integral geometry, and lattice algebra. Goutsias and Heijmans (2000) mention that, the main idea of the MM is to analyze the shape of objects in an image by probing the image with a small geometric template (e.g., line segment, disc and square) known as the structuring element.

2.1.1 Structuring Element

Facon (1996) defines the structuring element as a completely defined and known set (form and size). The basic principle of the mathematical morphology lives in the operation of sets among the image tests and the structuring element known, obtaining the relative information to the geometry and the topology of that set.

For the obtaining of good results through the use of morphologic tools is necessary to choose the structuring element appropriately to be used in the functions. The element estruturante is the key for the success of the operations, since it is chosen in an appropriate way.

The choice of the element estruturante depends on the geometric form object to be extracted in the image. For instance, linear structuring elements are appropriate for the linear objects extraction. It can also be considered several rotations of the structuring element to extract the wanted forms from the objects contained in the image. For instance, it is wanted to extract the highways, the ideal would be to use a structuring element with mask in form of line segment, however this element should be rotated in several directions to answer the multiple orientations of the highways. The size of the structuring element depends on the characteristics that you want to extract in the image. Structuring elements larger preserve larger characteristics while smaller elements preserve smaller details in the image. Some examples of structuring elements are shown in the Figure 1.

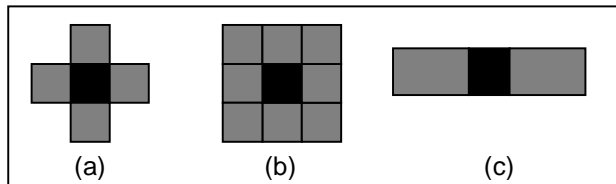


Figure 1. Structuring elements: (a) cross, (b) square and (c) line.

The type and nature of detected information depend of the structuring element and studied image choice. The shape and size of the structuring element must be adapted to the geometric properties of the image objects to be processed.

The Mathematical Morphology presents as principle two basic operations: Erosion and Dilation, from which all other morphological operations are derived.

- a) Erosion:** According to Soille (1999), the erosion of a set X by a structuring element B is denoted by $\varepsilon_B(X)$ and is defined as the locus of points, x , such that B is included in X when its origin is placed at x :

$$\varepsilon_B(X) = \{x \mid B_x \subseteq X\} \quad (1)$$

This definition indicates that the structuring element B slides on the image and it compares the neighborhood of each pixel with the neighborhood of the central point (that most of the time will correspond to the physical center of the structuring element) preserving the pixels where the neighborhoods coincide. In general, the erosion presents the following effects in their results: decrease of particles, elimination of the inferior size grains than of the structuring element, increase of the holes and it allows the separation of close grains.

- b) Dilation:** According to Soille (1999), the dilation of a set X by a structuring element B is denoted by $\delta_B(X)$ and is defined as the locus of points x such that B hits X when its origin coincides with x :

$$\delta_B(X) = \{x \mid B_x \cap X \neq \emptyset\} \quad (2)$$

For this definition, when the structuring element is verifying the image, the neighborhood of the central point should have a intersection with the relevant points of the image, capturing more pixels. The application of this operator produces the following effects: increases the objects in the image, fills out small holes and connects close objects.

Erosion and dilation can be used in a variety of ways, in parallel and series, to give other transformations including thickening, thinning, pruning and many others.

- c) Thinning:** According to Soille (1999), the thinning of a set X by a composite structuring element B is denoted by $X \circ B$ and defined as the set difference between X and the hit-or-miss transform of X by B ($HMT_B(X)$):

$$X \circ B = X \setminus HMT_B(X) \quad (3)$$

The hit-or-miss transformation of a set X by a composite structuring element $B=(B_1, B_2)$, is the set of points, x , such that when the origin of B coincides with x , B_1 fits X and B_2 fits X^c .

$$HMT_B(X) = \varepsilon_{B_1}(X) \cap \varepsilon_{B_2}(X^c) \quad (4)$$

- d) Pruning:** According to Soille (1999), the pruning transformation is implemented through the detection of final points and their removal up to the idempotency, in other words:

$$PRUNE(X) = (X \text{ AFIs } E)^{(\infty)} \quad (5)$$

Where E is related to the structuring element used to detect final points and ∞ indicates that the sequential thinning is iterated up to stability.

When the pruning is taken into stability, the only parts of the skeleton not suppressed are the closed arcs or "ties" of the skeleton.

2.2. Data Used

The test image chosen corresponds is a panchromatic image of the high resolution satellite QuickBird, with spatial resolution of 61 cm. This contains as main feature a part of the Raposo Tavares highway, located in the area of Presidente Prudente city (SP), Brazil. The Figure 2 presents the original image.



Figure 2. Original Image.

2.3 Method

This paper consisted of using morphologic operators with the objective of to detect highways in high resolution images. For this, the Mathematical Morphology toolbox developed by SDC Information Systems, coupled to the software Matlab 7.0 was used in this experiment.

Initially, with base in the type of present structure in the image, the morphologic operators and structuring elements more appropriate were selected to process the image with intention of to detect highways in other words, to detect elongated image structures. The flowchart of the Figure 3 illustrates the stages accomplished for the highways detection.

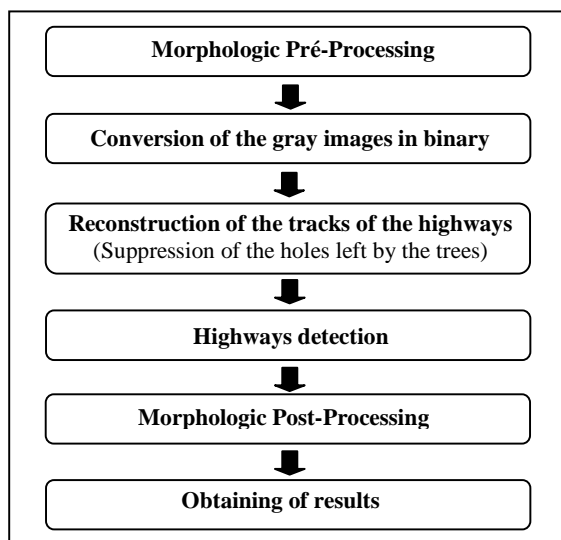


Figure 3. Flowchart of the developed routine.

Firstly, the developed routine consisted in accomplishing a stage of Morphologic Pre-processing where the brightness and contrast values were altered, enhancing the interest features. This stage is of great importance, because it allows the elimination of many noises that aren't part of the interest feature, making possible the detection process. The next step was to convert the gray image in binary. In the sequence, due to the presence of trees in the borders tracks, these were rebuilt with the intention of obtaining its

original plan. Being the tracks without the presence of the "holes" left by the trees, the next step was to accomplish its detection. For this, the tracks were thinning and afterwards they went by the pruning process, where the resulting segments of the thinning stage were eliminated. Finally, with the intention of obtaining the best result to be represented in the Cartography, a stage of Morphologic Powder-processing was accomplished, which consisted in dilatation the highway tracks seeking to obtain them with its original thickness. For proof ends, the image containing the highway detected was put upon on its original image, verifying if there was some position displacement of the feature detected.

2.4. Presentation and Analysis Results

Initially, a stage of Morphologic Pre-processing was accomplished with the objective of increasing contrast of the highway tracks, contributing for the features detection process to be successfully performed. For this, the first operator used was the opening for reconstruction. This operator accomplishes the reconstruction of an image starting from the eroded original image that works as markers. The structuring element used was the *mmsebox* (square mask). In the sequence, with the intention of enhancing the features tracks, the addition operator was applied with the value 120 by the whole scene. The result obtained is illustrated in Figure 4.



Figure 4. Image with the enhanced tracks.

The next step was to convert the gray image in a binary image. The image was binarized with a threshold 90, transforming all of the pixels that have digital number below this threshold for the value "0" (black) and the ones that were above in "1" (white). The choice of this threshold was made in agreement with tests accomplished through of the image histogram analysis. In the sequence, seeking to eliminate the noises that aren't part of the interest feature, the erosion operator was applied on the image through structuring element *mmse* (mask line) with the intention of disconnecting the noises close to the highway tracks. The disconnected noises were eliminated through the operator opening, which removed components with inferior size to 500 pixels. The obtained result is display in Figure 5.



Figure 5. Elimination of the noises around the feature.

By analyzing the result showed in Figure 4 it can be noticed that the highway present continuity loss. This happened due to the presence of trees in the borders tracks in the scene acquisition instant, hiding information regarding the plan of the same ones. This way, it was necessary to accomplish a reconstruction of the tracks in order to obtain them with its real plan. Then, the morphologic opening operator was applied through the structuring element *mmsepline* (line mask). For the use of this structuring element was necessary to define two parameters, the line thickness and orientation, like this, with base in the accomplished tests, it was defined the values 40 and 125 respectively. The obtained result is exhibited in Figure 6.

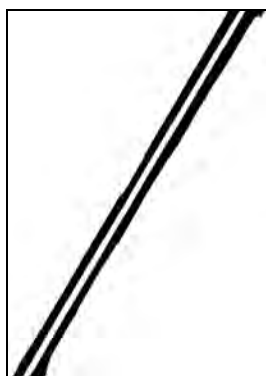


Figure 6. Reconstruction of the tracks

For the highway tracks detection, the image was thinning and the result submitted to the pruning operation. The pruning consisted of removing the segmentation left by the thinning process. The result is shown in Figure 7.



Figure 7. Result of the pruning process.

The next step was to apply a dilation on the image through the structuring element *mmsebox* (square mask), seeking to obtain the tracks with its original thickness. The Figure 8 presents the obtained result.



Figure 8. Image dilated

Analysing the Figure 8, it is verified that the employed morphologic processing was adapted for the highway detection in high resolution image. The quality of the obtained registration proves the efficiency of the Mathematical Morphology technique in the area of Cartography seeking to the future cartographic products updating. With regard to the application of morphological operators, the work could be considered as concluded, presenting as the best result, as already explained, the result obtained in Figure 8.

3. CONCLUSIONS

The experiences accomplished with the tools of the Mathematical Morphology, with intention of reaffirming its use potential in the area of Cartography, they were well happened. It is observed that the obtained final product assisted to the objective proposed in to demonstrate the viability of the morphologic tools in the process of features detection in high resolution images, with view the cartographic products updating.

The key for the obtaining of good results lives in the appropriate choices of the structuring elements and thresholds values for the several stages of the detection process. For so much, it is

necessary that the user has minimum notions of mathematical morphology for the choice of the best structuring elements to be adopted and also, have knowledge on digital image processing so that it can choose the thresholds values appropriately to be used by the morphologic operators employees in the processing.

In the Cartography the obtained results are of extreme importance once, they were resulting of the application of alternative methodology for the features detection in digital images. The detected features can be used in conventional processes of cartographic products updating.

REFERENCES

- J. Facon, *Morfologia Matemática: teoria e aplicações*, Universitária Champagnat da Pontífica Universidade Católica do Paraná, Curitiba, 1996.
- J. E. Colwell, *Vegetation canopy reflectance*, Remote Sensing of Environment. V. 3, n. 3, p. 175-183, Mar. 1974.
- J. Goutsias; H.J.A.M. Heijmans, *Mathematical morphology*, Amsterdam, 2000.
- P. Soille, *Morphological Image Analysis: Principles and applications*, Springer-Verlag, Berlin, 1999.

CANASAT PROJECT: MONITORING OF THE SUGARCANE CULTIVATION AREA IN SOUTH CENTRAL BRAZIL

Wagner Fernando da Silva¹, Daniel Alves de Aguiar¹, Bernardo Friedrich Theodor Rudorff¹, Luciana Miura Sugawara¹

¹ National Institute for Space Research (INPE), Remote Sensing Division (DSR),
São José dos Campos, 12227-010, São Paulo State, Brazil.
{wagner, daniel, bernardo, lmiura}@dsr.inpe.br

KEYWORDS: expansion of sugarcane, satellite monitoring, TM/Landsat, CCD/CBERS, mapping.

ABSTRACT

Brazil is the world's largest producer of sugarcane and ethanol derived from this crop, which is grown in several Brazilian states. The Canasat project monitors the area under sugarcane cultivation using remote sensing satellite images. The project has collected data since 2003 for the state of São Paulo, which is the largest producer in the country, and since 2005 for five other states that altogether are responsible for 87% of the Brazilian sugarcane production. The data are available on the Canasat project website and are used by several public and private institutions connected to the sugar, ethanol and environmental sectors. The objective of this paper is to present the methodology of the Canasat project and to analyze the changes in the areas of sugarcane cultivation in south central Brazil from the 2005/06 crop year to the 2009/10 crop year. The total area available for harvest grew by 76.2% between 2005/06 and 2009/10, reaching 7.43 million ha in the most recent season. All six states showed growth in the area available for harvest each season. The state of Goiás had the highest total growth rate, while the state of Mato Grosso do Sul was the only state where the annual growth rate increased each season. The state of Mato Grosso possesses the smallest area available for annual harvest. The state of São Paulo showed the largest expansion in sugarcane cultivation area; the western portion of the state was responsible for 47% of this expansion.

1. INTRODUCTION

The production of ethanol from sugarcane in Brazil began in the 1970s with the National Ethanol Program, Proalcool. In the mid-1990s, production declined because of the low prices paid to producers and the international decline in the price of oil (Nass et al., 2007). Since 2003, however, the growing production of flex-fuel vehicles and the need to reduce production of greenhouse gases has rapidly promoted ethanol production. Currently, Brazil is the largest producer and exporter of sugarcane derivatives (Smeets et al., 2008).

Information on the production cycle of sugarcane is important for the construction of processing facilities and for the development of market strategies. Agricultural statistics are generally based on data obtained from direct interviews with the producers and technicians involved and on credit and financing information received from banks, among other sources. This process expends considerable time and money. On the other hand, time series images acquired through satellite-based remote sensing provide information that enables the operational monitoring of the production chains of diverse agricultural crops, including sugarcane, which has large areas of cultivation and an extended cultivation period (Abdell-Rahman and Ahmed, 2008).

Since 2003, the National Institute for Space Research (*Instituto Nacional de Pesquisas Espaciais* - INPE), the Industry Sugarcane Association (UNICA), the Center for Advanced Studies on Applied Economics (CEPEA) of the Luiz de Queiróz Agricultural School (Esalq/USP) and the Center for Sugarcane Technology (CTC), has maintained the Canasat project, which monitors areas under sugarcane cultivation using remote sensing satellite images and geospatial processing techniques. Initially, the state of São Paulo was mapped. In 2005, mapping was extended to five other sugarcane-producing states.

The data generated by the project are made available on the website <www.dsr.inpe.br/canasat/eng/> and have been used by private and governmental institutions to meet the demands of the sugar, ethanol and environmental sectors. Mapping of sugarcane producing areas serves as a basis for predicting and planning annual harvests and for indentifying environmental incompatibilities pertaining to the planting of sugarcane, e.g., crops located in permanent preservation areas as defined by the Forest Code.

The maps generated by the Canasat project are also used in other activities, such as monitoring harvest methods (with or without the burning of straw) and determining land use and occupation prior to sugarcane cultivation (Nassar et al., 2008; Rudorff et al., 2009). Availability of the maps at the beginning of the season enables users to plan activities related to the sector in advance. Images, maps of sugarcane production according to various classes and seasons, and locations of facilities are shown on the project website. Reports, tables and graphs can be obtained or searches performed by town, by state or by season.

The objective of this paper is to present the methodology used by the Canasat project and to analyze the changes in the areas of sugarcane cultivation in south central Brazil between 2005/06 and 2009/10. Analysis of changes in sugarcane cultivation during this period enabled the establishment of the spatial pattern of occupation and provided input data for dynamic spatial models and for the generation of future scenarios for the production of sugar and ethanol.

2. METHODOLOGY

The study area includes the states in south central Brazil monitored by the Canasat project: São Paulo, Goiás, Mato Grosso, Mato Grosso do Sul, Minas Gerais and Paraná. Although south central Brazil includes ten states, the South-Central region referred to in this article includes only the six states of major sugarcane production that have an area of 2.63 million km², approximately 31% of the Brazilian territory. These states are responsible for more than 87% of sugarcane production in the country (UNICA, 2009). Figure 1 illustrates the location of the Brazilian states covered by the Canasat project.

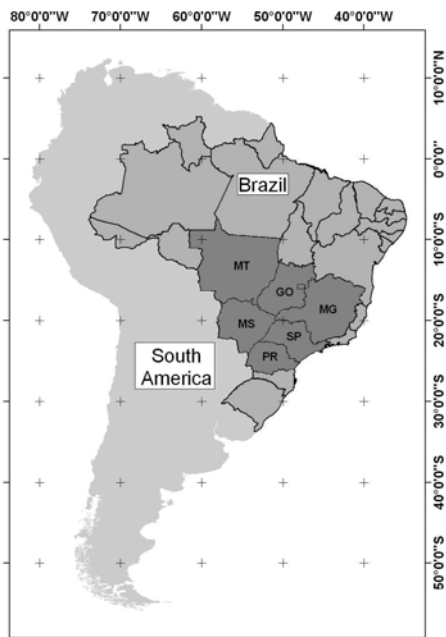


Figure 1. States monitored by the Canasat project: São Paulo - SP, Goiás - GO, Mato Grosso - MT, Mato Grosso do Sul - MS, Minas Gerais - MG and Paraná - PR.

Areas of sugarcane cultivation were identified in images from the TM/Landsat-5 sensor. As an alternative to the TM images that were obscured by cloud cover, images from the CCD (Charge Couple Device) sensor on board of the CBERS-2 and CBERS-2B satellites were used (Ephânio et al., 2007). For each orbit/point of the TM/Landsat sensor, a database of images obtained by the two sensors on the dates of interest was created. All images were registered using first-order polynomials and nearest-neighbor interpolations based on orthorectified mosaics of TM/Landsat-7 images obtained from NASA (NASA,2007).

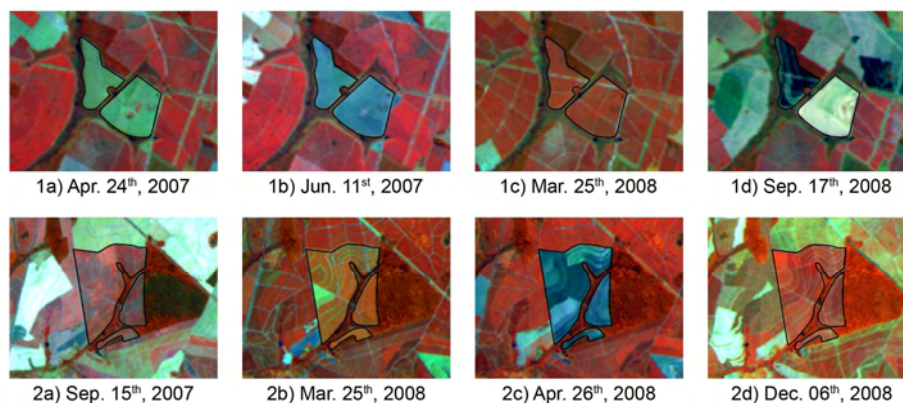


Figure 2. Temporal sequence of TM/Landsat-5 images [color composition 4(R)5(G)3(B)] illustrating the identification of areas of expansion (2.1) and under renovation (2.2).

From the first maps generated by the Canasat project (Rudorff et al., 2005), which were produced by means of digital and visual classification of the satellite images, annual updates were made through visual interpretation of a temporal sequence of images for each crop year. In developing the map for the current season, the map from the last season was used as a basis. Two steps were followed: visual interpretation of the images and reclassification of isolated pixels. Although digital classification was used only in the first mapping, it is less relevant in updating maps for the current season because this procedure tends to commit many errors of omission and inclusion, making visual classification and editing necessary to obtain a satisfactory thematic map.

In the visual interpretation step, the matrix edit function within the SPRING program was used (Câmara et al., 1996). This function permits modification or correction of the classification results and definition of new class polygons. In this procedure, the interpreter used images from several dates contained in the database to confirm the appropriate class for each sugarcane stage. To homogenize the results, the resulting map from each database was revised by a more experienced interpreter and subsequently subjected to reclassification of isolated pixels. This technique enables the controlled and automatic correction of isolated pixels or groups of pixels that were incorrectly classified or unintentionally inserted by the interpreter.

To distinguish sugarcane from other targets, images from specific periods of the plant development were used, that is, images from dates when the sugarcane crop was well developed (January to March). Therefore, the mapping of areas to be harvested in the current season is based on images acquired prior to the beginning of the harvest season in April. However, it is more likely to acquire cloud free images from April on and, therefore, whenever necessary images from April and May were also used in the mapping procedure, especially during the revision part.

Mapping and estimation of sugarcane cultivated area available for harvest incorporated three distinct classes:

Sugarcane available for harvest – This class included areas of sugarcane that could be harvested in the current season. This class included three groups:

a) *Ratoon Cane* – This term refers to areas of sugarcane available for harvest from sprouting after first or more cuts;

b) *Renovated* – This term refers to areas of sugarcane that have undergone renovation during the previous crop year. In these areas, the less productive ratoons were replaced by sugarcane plants grown during a year-and-half and will be available for harvest in the current season;

c) *Expansion* – This term refers to areas that were under other land use and are now being cultivated with sugarcane and will be available for harvest for the first time.

Sugarcane under renovation – This class included areas that were cultivated with sugarcane during the previous crop season but no longer present a sugarcane patterns indicating that the area is being renewed or replaced by another land use. If this area returns to sugarcane then it belongs to the renovation class; otherwise, it will be excluded. This class includes only sugarcane plants renewed with the year-and-half plant.

Total cultivated – This class encompassed the total area occupied by sugarcane, that is, the sum of the area of sugarcane available for harvest and the area of sugarcane under renovation.

Figure 2 illustrates a temporal sequence of TM images used in mapping of sugarcane cultivation in the various classes for the 2008/09 season. Figure 2.1 illustrates the identification procedure for areas of expansion. The region around the highlighted area was already cultivated and monitored by the project. Therefore, for this class, the map for the previous season was used as a mask, so that the interpreters analyzed only the region outside the mask. Based on the composition of the image (i.e., texture, tonality and shape), the area highlighted in Figure 2.1a shows a pattern characteristic of pasture, indicating that at the beginning of the 2007/08 season (April 2007) the area was not cultivated with sugarcane. In Figure 2.1b (June 2007), the same area shows a pattern characteristic of bare soil, indicating that it may be converted to sugarcane, available for harvest in the 2008/09 season. Figure 2.1c (March 2008) illustrates well-developed patterns characteristic of sugarcane, with tonality, texture and presence of access routes typical of this crop. In September 2008 (Figure 2.1d), the area was harvested, confirming that sugarcane was planted in 2007 and harvested in the 2008/09 season. After this area was identified as sugarcane, it was monitored in subsequent seasons, being denominated as ratoon after the first cut.

Figure 2.2 illustrates a temporal sequence of images in which the highlighted area was renovated during the 2008/09 season. In Figure 2.2a (September 2007), the area shows a pattern characteristic of sugarcane cultivation. However, it shows planting flaws and a pattern of plants with low productivity, which indicates that the sugarcane field should be renewed. In Figure 2.2b, an image from March 2008, this area shows a pattern characteristic of soybean cultivation and in Figure 2.2c (April 2008) it shows a pattern of bare soil. With the image from December 2008 (Figure 2.2d) it can be confirmed that the field is again cultivated with sugarcane; however, it will be available for harvest only for the 2009/10 season.

After estimating the sugarcane area in each class, the changes in the area of cultivated sugarcane between the 2005/06 and 2009/10 seasons were analyzed for the states in the South-Central region.

3. RESULTS AND DISCUSSION

The total area of sugarcane cultivation in the South-Central Region during the most recent season analyzed (2009/10) was 7.91 million hectares (ha), of which 7.43 million ha (94%) were available for harvest. The remainder was in the process of renovation. Figure 3 illustrates the map visualization page of the Canasat website, which shows the spatial distribution of the various classes of sugarcane cultivation in the states included in the project. On this page, searches and visualizations of sugarcane area and density can be performed by municipality or by season. The boundaries of municipalities and remote sensing satellite image mosaics can also be viewed, and measurements of area and length can be performed. Figure 3 indicates a much greater concentration of sugarcane cultivation in the state of São Paulo when compared to the other states.

Figure 4a shows the change over time in the area of sugarcane available for harvest and the annual growth rate between the 2005/06 and 2009/10 seasons for the South-Central region and for each state. Between the 2005/06 and 2009/10 seasons, the area available for harvest in the South-Central region grew by 3.21 million ha, an increase of 76.2%.

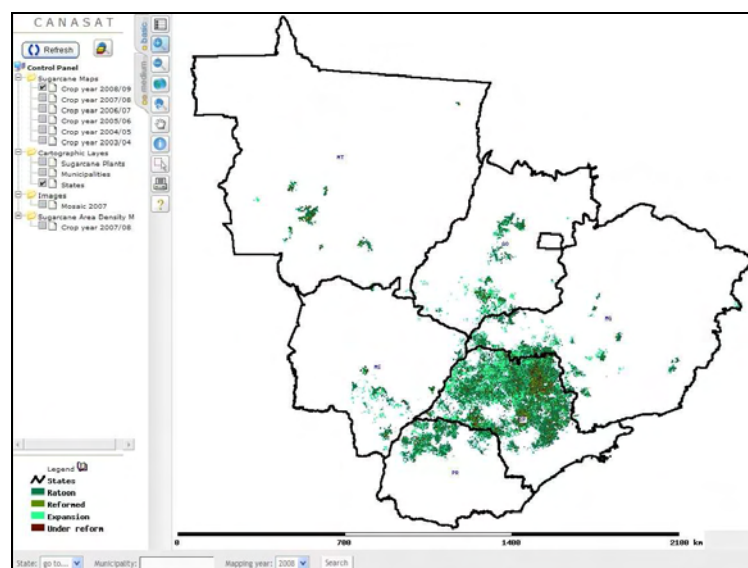


Figure 3. A sample map visualization page from the Canasat website.

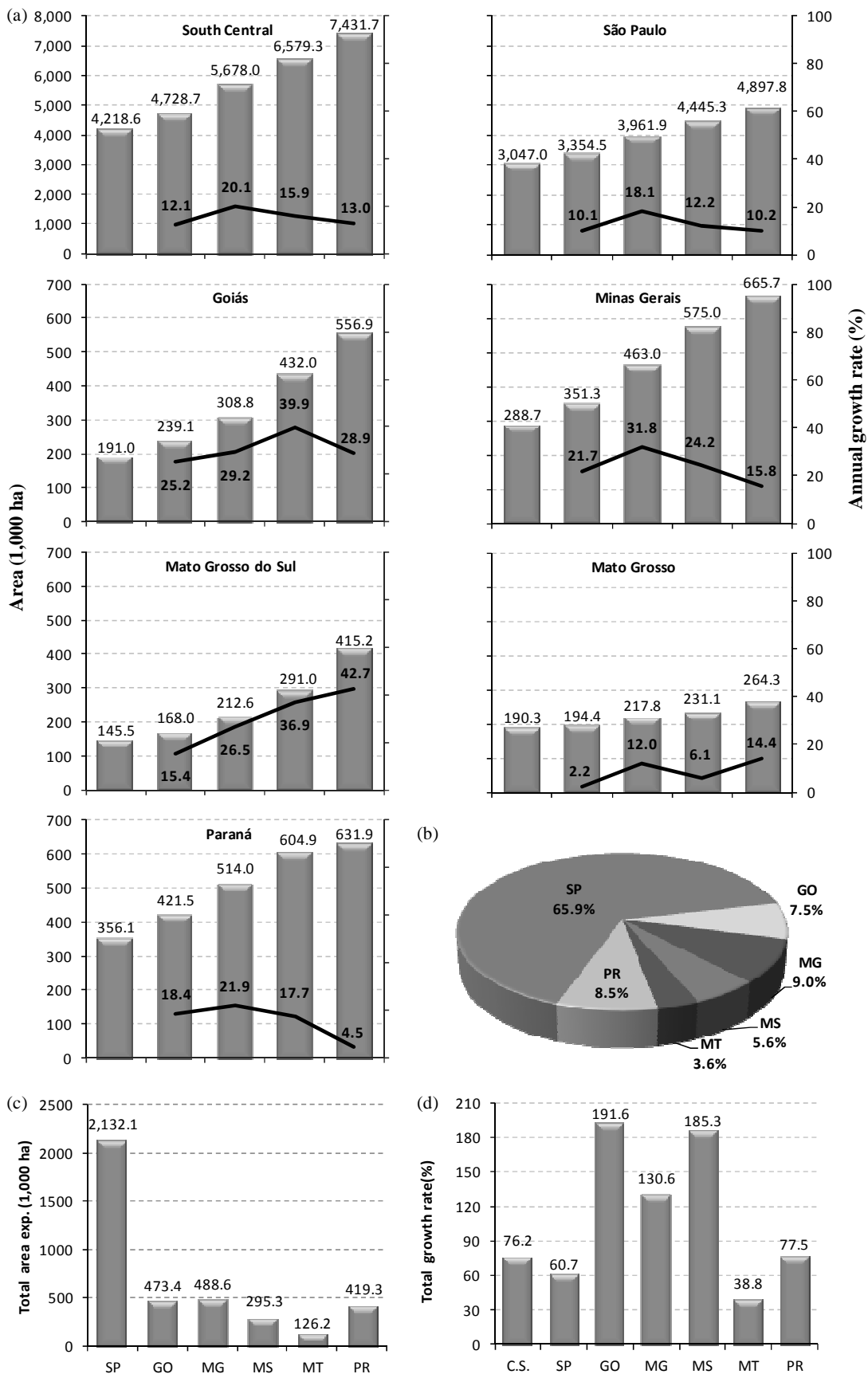


Figure 4. (a) Change over time in the area available for harvest between the 2005/06 and 2009/10 seasons for the South-Central region and for the states monitored by the Canasat project. (b) Percentage of the total area available for harvest in the South-Central region found within each state during the 2009/10 season. (c) Total area of expansion from the 2005/06 season to the 2009/10 season. (d) Total growth rate from the 2005/06 season to the 2009/10 season. S.C. = South-Central region; SP = São Paulo; GO = Goiás; MG = Minas Gerais; MS = Mato Grosso do Sul; MT = Mato Grosso; PR = Paraná.

In all states, the area of sugarcane cultivation increased in every season. São Paulo was the state with the largest area, which reached approximately 4.9 million ha during the most recent season, representing 65.9% of the total area of sugarcane cultivation in the South-Central region (Figures 4a and 4b).

The state of Mato Grosso had the smallest cultivated area and, consequently, the smallest area available for harvest, which reached 264.3 thousand ha during the most recent season, representing 3.6% of the available area in the South-Central region. Compared with the 2008/09 season, the annual growth rate declined in the 2009/10 season in all states except Mato Grosso and Mato Grosso do Sul. The latter was the only state where the annual growth rate increased in every season. Furthermore, it was the state with the greatest growth rate in the most recent season (42.7%).

The state of Goiás had the greatest total growth rate (191.6%) between the 2005/06 and 2009/10 seasons (Figure 4d), followed by the states of Mato Grosso do Sul (185.3%) and Minas Gerais (130.6%). This fact can be explained by Goiás having shown the highest growth rates in every season except the most recent, in which it had the second highest rate. The primary reason for the strong growth of the area of sugarcane cultivation in these three states was the construction of new processing facilities in these locations.

The lowest growth rate in the 2009/10 season was obtained for the state of Paraná (4.5%). This state was the second largest producer of sugarcane in the country until the 2008/09 season (Figure 4a and UNICA, 2009). However, after the 2009/10 season, Paraná lost its position to Minas Gerais, which showed a higher growth rate (15.8%). The state of Paraná is the second largest producer of soybeans in Brazil, and this crop competes with the expansion of sugarcane in the state. When the area of soybean cultivation in Paraná declined during the 2005/06 and 2007/08 seasons (CONAB, 2009), the area of sugarcane cultivation showed greater growth rates (Figure 4a). When the area of soybean cultivation increased again during the 2008/09 and 2009/10 seasons, the expansion rate of the area of sugarcane cultivation declined again. In the 2009/10 season, the area of soybean cultivation in Paraná showed its highest growth rate among recent seasons (6.0%; CONAB, 2009). This may be one of the reasons why this state showed the lowest growth rate for sugarcane cultivation in the 2009/10 season.

Although the state of São Paulo showed only the fifth highest total growth rate between the 2005/06 and 2009/10 seasons (60.7%; Figure 4d), the total area of expansion in that state was 2.13 million ha. This area is 4.4 times greater than that of the state with the second greatest expansion, Minas Gerais, where sugarcane cultivation expanded by 488.6 thousand ha. São Paulo has a much larger total cultivated area than the other states; therefore, even a low growth rate will result in a large area of expansion. Notably, the total area of expansion is the sum of the new areas of sugarcane cultivation between the 2005/06 and 2009/10 seasons. This area differs from the increase in the area available for harvest between the two seasons because it considers the variation in the areas under renovation, renovated areas, and areas that were no longer planted with sugarcane during each season.

Figure 5 illustrates the total area of expansion between the 2005/06 and 2009/10 seasons and the concentration of sugarcane in each Administrative Region (AR) of the state of São Paulo. The RAs were created by the Geographic and

Cartographic Institute (IGC) of the state of São Paulo for governmental planning purposes. Each RA is made up of several municipalities within a given geographical area with economic and social similarities (<http://www.igc.sp.gov.br/mapasRas.htm>).

The four RAs located in the southeastern part of the state (São José dos Campos - SC, São Paulo - SP, Baixada Santista - BS and Registro- RE) do not cultivate sugarcane for agro-industrial purposes because they possess less extensive cultivated areas. These RAs present less favorable environmental conditions for the cultivation of this crop, such as high rainfall and rugged terrain (Alfonsi et al., 1987). Therefore, these RAs are not monitored by the project.

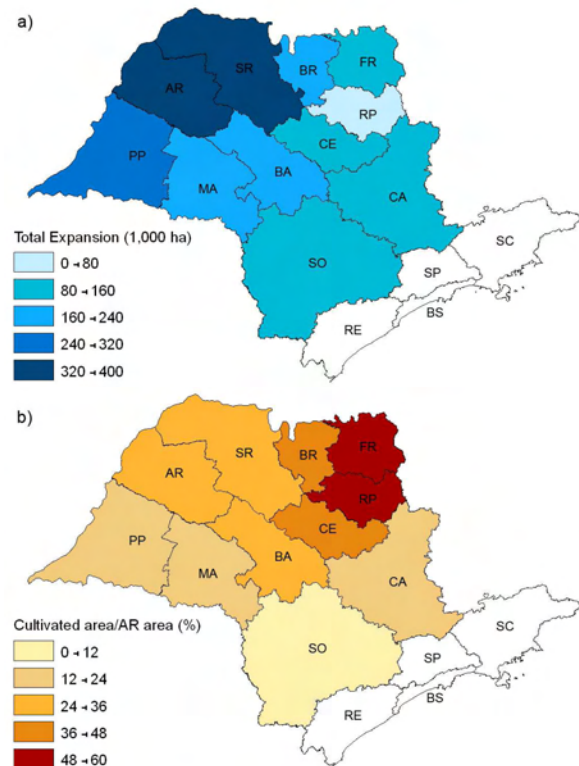


Figure 5. Total area of expansion between the 2005/06 and 2009/10 seasons (a); concentration of sugarcane (total cultivated area/RA area) for the 2009/10 season (b) in the Administrative Regions of Araçatuba (AR), Baixada Santista (BS), Barretos (BR), Bauru (BA), Campinas (CA), Central (CE), Franca (FR), Marília (MA), Presidente Prudente (PP), Registro (RE), Ribeirão Preto (RP), São José do Rio Preto (SR), São José dos Campos (SC), São Paulo (SP) and Sorocaba (SO).

The greatest expansions occurred in RAs located in the western part of the state (Figure 5a). The RA of São José do Rio Preto (SR) showed the greatest expansion (398 thousand ha) between the 2005/06 and 2009/10 seasons, followed by the RAs of Araçatuba (AR) and Presidente Prudente (PP), which showed expansions of 326 thousand ha and 282 thousand ha, respectively. These RAs were responsible for 47.2% of the expansion in the state during the analyzed period. According to Canasat data, SR and AR have been the RAs with the largest areas of sugarcane cultivation in the state since the 2008/09 season. However, the concentration of sugarcane in these RAs is not high, remaining between 24% and 36% (Figure 5b). Thus, these RAs have potential for further expansion of sugarcane cultivation. Furthermore, Western São Paulo state has a

tradition of extensive cattle farming, but many cattle farmers have been changing their production and management strategies, restoring degraded pastures and adopting confinement systems. These changes make new areas available for the cultivation of sugarcane (Torres et al., 2009). Nassar et al. (2008) have also demonstrated that in the state of São Paulo, new areas of sugarcane cultivation mostly occupy areas that were previously occupied by pastures.

The north central part of the state has a stronger tradition of sugarcane cultivation and ARs of small territorial extent. For this reason, concentrations of sugarcane are high, especially in the ARs of Ribeirão Preto (RP) and Franca (FR) (Figure 5b). This explains the low expansion observed in these ARs. For example, RP provided only 2.7% of the total area of expansion for the state during the analyzed period.

The AR of Sorocaba has the lowest concentration of sugarcane cultivation because, in addition to being the AR with the largest territorial extent, it has the smallest cultivated sugarcane area.

4. FINAL CONSIDERATIONS

The methodology used by the Canasat project allowed to monitoring the cultivated sugarcane area in south central Brazil, making it possible to determine, by means of remote sensing satellite images, newly cultivated areas, areas under renovation and areas available for harvest during each season. The south center region represents almost one third of the Brazilian territory and has by far the greatest potential for sugarcane cultivation expansion and the use of remote sensing techniques to monitor this expansion and the land use cover change is very relevant for a sustainable ethanol production as an alternative to reduce green house gas emissions.

A total of 7.91 million hectares are currently under sugarcane cultivation in the South-Central region, of which 7.49 million hectares are available for harvest during the 2009/10 season. Between the 2005/06 and 2009/10 seasons, the area of sugarcane cultivation increased in all states monitored by the project. The state of Mato Grosso do Sul showed an increase in annual growth rate in every season analyzed and the highest rate in the most recent season. However, the state of Goiás had the highest total growth rate.

The state of São Paulo showed the largest area of expansion in across the seasons analyzed, with the western part of the state being responsible for most of this expansion. The north central part of the state, with a longer tradition of sugarcane cultivation, had the highest concentrations of this crop and the smallest areas of expansion.

Data generated by the Canasat project are available on its website and are relevant to several sectors that require specialized information about the area of sugarcane cultivation according to the various classes.

5. REFERENCES

Abdell-Rahman, E. M.; Ahmed, F. B., 2008. The application of remote sensing techniques to sugarcane (*Saccharum* spp. hybrid) production: a review of the literature. *International Journal of Remote Sensing*, 29 (13), pp. 3753-3767.

Alfonsi, R. R.; Pedro Júnior, M. J.; Brunini, O.; Barbieri, V. Condições climáticas para a cana-de-açúcar. In: Paranhos, S. B.

(coord.), 1987. *Cana-de-açúcar: cultivo e utilização*. Campinas: Fundação Cargill, pp. 42-55.

Câmara, G.; Souza, R. C. M.; Freitas, U. M.; Garrido, J.; Ii, F. M., 1996. SPRING: Integrating remote sensing and GIS by object oriented data modeling. *Computers and Graphics*, 15 (6), pp.13-22.

CONAB – Companhia Nacional de Abastecimento, 2009. *Safras – Grão*. <http://www.conab.gov.br/conabweb/index.php?PAG=131> (accessed on Nov. 5th 2009).

Epiphânio, J. C. N.; Soares, J. V.; Ferreira, H. S.; Câmara, G. CBERS: the Chinese-Brazilian Earth Resources Satellite programme. In: *The Full Picture*. GEO - Group on Earth Observations, 2007. Geneva, Switzerland: Tudor Rose, v. 1, pp. 116-117. http://www.earthobservations.org/documents/the_full_picture.pdf (accessed on 04 Nov. 2009).

NASA. Orthorectified Landsat Enhanced Thematic Mapper (ETM+) Compressed Mosaics. Washington, DC, 2004. Available at: <https://zulu.ssc.nasa.gov/mrsid/>. Access on: mar. 13rd 2007.

Nass, L. L.; Pereira, P. A. A.; Ellis, D., 2007. Biofuels in Brazil: an overview. *Crop Science*, 47, pp. 2228-2237.

Nassar, A. M.; Rudorff, B. F. T.; Antoniazzi, L. B.; Aguiar, D. A.; Bacchi, M. R. P.; Adami, M. Prospects of the sugarcane expansion in Brazil: impacts on direct and indirect land use changes. In: Zuurbier, P. and van de Vooren, J., 2008. *Sugarcane ethanol: Contributions to climate change mitigation and the environment*. Wageningen, Netherlands: Wageningen Academic Publishers, pp. 63-93.

Rudorff, B. F. T.; Adami, M.; Aguiar, D. A.; Gusso, A.; Silva, W. F.; Freitas, R. M., 2009. Temporal series of EVI/MODIS to identify land converted to sugarcane. In: 2009 *IEEE International Geoscience and Remote Sensing Symposium*. Cape Town, South Africa, pp. ?.

Rudorff, B. F. T.; Berka, L. M. S.; Moreira, M. A.; Duarte, V.; Xavier, A. C.; Rosa, V. G. C.; Shimabukuro, Y. E., 2005. Imagens de satélite no mapeamento e estimativa de área de cana-de-açúcar em São Paulo: ano-safra 2003/04. *Agricultura em São Paulo*, 52 (1), pp. 21-39.

Smeets, E.; Junginger, M.; Faaij, A.; Walter, A.; Dolzan, P.; Turkenburg, W., 2008. The sustainability of Brazilian ethanol - an assessment of the possibilities of certified production. *Biomass and Bioenergy*, 32, pp. 781-813.

Torres, A. J.; Pino, F. A.; Francisco, V. F. S.; Ângelo, J. A.; Maciel, E. L. F.; Drugowich, M. I.; Interliche, P. H.; Piedade, J. A.; Sousa, A. C.; Lorena Neto, B.; Caser, D. V., 2009. *Projeto LUPA 2007/08: censo agropecuário do Estado de São Paulo*. São Paulo; IEA, CATI, SAA, 381p.

Unica - Sugarcane Industry Association, 2009. *Quotes & Stats*. <http://english.unica.com.br/dadosCotacao/estatistica> (accessed on: Nov. 5th 2009).

6. ACKNOWLEDGEMENTS

We thank team of Laboratory of remote sensing in Agriculture and Forest (LAF) for mapping work and contributions.

ENHANCING URBAN DIGITAL ELEVATION MODELS USING AUTOMATED COMPUTER VISION TECHNIQUES

B. Sirmacek, P. d'Angelo, T. Krauss, P. Reinartz

German Aerospace Center (DLR), Remote Sensing Technology Institute
PO Box 1116, 82230, Wessling, Germany
(Beril.Sirmacek, Pablo.Angelo, Thomas.Krauss, Peter.Reinartz)@dlr.de

Commission VII

KEY WORDS: Urban, Modelling, Detection, DEM/DTM, Cartosat-1

ABSTRACT:

In recent years Digital Elevation Models (DEM) gained much interest because of their high capability to give information about urban regions. DEM can be used for detailed urban monitoring, change and damage detection purposes. However, initially a DEM with very sharp details should be constructed. The DEM can be derived from very high resolution stereo satellite images, but for most of the cases just one stereo pair is available. Unfortunately after this process, regions which are occluded in one of the stereo images have no height value in the DEM data. This is a major problem especially in urban DEM, since many regions are occluded by buildings. However these occluded regions can be filled using interpolation techniques, which lead to lose sharpness in building edges. Besides due to low resolution of input stereo images, the generated DEM resolution can be too low to represent buildings.

In order to increase details, herein we propose a special automated urban DEM enhancement technique. To do so, first we detect possible building locations using height information of the DEM. Then using corresponding panchromatic image, we detect building shapes with an automatic shape approximation approach. Using detected building shapes, we refine buildings in the DEM. Finally, for a better representation we locate constructed three-dimensional building models on Digital Terrain Model (DTM) of the corresponding region. We believe that the implemented enhancement will not only provide better three-dimensional urban region representation, but also will lead to more detailed change and damage investigation in future studies.

1 INTRODUCTION

An important research field in remote sensing is three-dimensional analysis and reconstruction of urban objects. Especially urban monitoring, damage assessment, and disaster monitoring fields need to achieve realistic three-dimensional urban models. A rather new technology in this context is the Digital Elevation Model (DEM) generation based on stereo image matching principle using satellite data. Unfortunately, there are several problems in generated DEM. First, regions which are occluded in one of the stereo images have no height value in DEM data. Interpolation techniques, which are used to fill these non-value regions, lead to lose sharpness in building edges. Generated DEM have limited resolution and raw DEM data may not represent buildings correctly. In addition to that, DEM does not provide intensity and color information. Therefore, some advanced processes are required to enhance the DEM.

In literature, many researchers developed techniques for DEM enhancement. A considerable amount of these studies has been published on reducing errors in DEM which generally belong to rural regions (Skarlatos and Georgopoulos, 2004, Ostrowski and He, 1989). In recent years, three-dimensional modeling of urban regions gained great interest. Thus, some of the researchers focused on enhancing urban DEM data for better urban region representation. Haala et al. (Haala et al., 1998) proposed a method to reconstruct building rooftops using surface normals extracted from DEM data. They assumed that building boundaries are detected previously. In a following study (Haala and Brenner, 1999), they detected building boundaries automatically by classification DEM and corresponding color image before applying their automatic rooftop reconstruction method. Brunn and Weidner (Brunn and Weidner, 1997) used surface normals on DEM to discriminate buildings and vegetation. After extracting buildings, they measured geometry of rooftops using surface normals and

they interpolated polyhedral building descriptions to these structures. Fradkin et al. (Fradkin et al., 1999) proposed segmentation based method to reconstruct three-dimensional models of dense urban areas. To this end, they used very high resolution color aerial images and DEM data. Canu et al. (Canu et al., 1996) used high resolution DEM to reconstruct three-dimensional buildings. First, they segmented DEM into homogeneous regions. Then, they interpolated flat surfaces on these regions. Ortner et al. (Ortner et al., 2002) used point process to model urban areas. They represented urban areas as interacting particles where each particle stands for an urban object. Preknowledge about building shapes is used to model these particles. Arefi et al. (Arefi et al., 2008) extracted above-ground objects from LIDAR data. Then, three-dimensional buildings are reconstructed by hierarchical fitting of minimum boundary rectangles (MBR) and RANSAC based straight line fitting algorithm. In these studies, good results are achieved generally using very high resolution (more than 1 m. spatial resolution) DEMs which are generated from airborne data sets. However, enhancement of buildings in very low resolution urban DEM data which is generated from satellite images is still an open research problem. As a different approach, Elaksher (Elaksher, 2008) proposed a multi-photo least squares matching based DEM enhancement method. They detected discontinuities in a least squares matching model. Using multiple photos of a region, they applied a least squares matching process recursively until the refinement is sufficient. However, the proposed method can smooth noises and enhance details in very coarse DEM data, it needs multiple photos of the same region taken from different looking angles which is generally difficult to obtain, especially from satellites.

In another study, Vinson et al. (Vinson et al., 2001, Cohen and Vinson, 2002) developed an approach for detecting rectangular buildings in DEM. For this purpose, they segmented above ground objects in the DEM. Then, they tried to model each above ground

segment by a rectangle. They used estimated rectangular shapes to enhance building representation in DEM. Herein, we provide a fast and fully automatic approach to enhance DEM data based on building shape approximation. For this purpose, first we extract above ground objects in DEM. Since our DEM data are in very low resolution (in 5 m. spatial resolution), it is not convenient to extract building shapes. Therefore different from Vinson et al., we detect building shapes from panchromatic image of region. To detect building shapes, we benefit from automatic rectangular shape approximation approach (Box-Fitting) (Sirmacek and Unsalan, 2008). Finally, using detected building shapes we refine the DEM data. For a better representation, we also reconstruct building shapes on interpolated and smoothed Digital Terrain Model (DTM) of the corresponding region. The resulting enhanced three-dimensional data will not only provide better visual result, but also will provide a basis for detailed three-dimensional modeling and change detection analysis.

2 DETECTING BUILDING LOCATIONS USING DEM AND DISTANCE TRANSFORM

In a previous study, d'Angelo et al. proposed a fully automated method to generate DEM (d'Angelo et al., 2009). For this purpose, they applied hierarchical intensity based matching, and then dense epipolar matching to stereo images with 2.5 m. ground sampling distance (GSD) taken from the Cartosat-1 satellite. Looking angle differences of two satellite images are about 31° , which is too much higher than normally wanted to reconstruct buildings. Normally, 10° angle difference between stereo image pairs is wanted to reconstruct buildings. Unfortunately, it is very difficult to obtain stereo image couples with this small looking angle from satellite images. In another study, Arefi and Hahn (Arefi and Hahn, 2005) proposed a DTM generation method from LIDAR based on geodesic dilation. Then, Arefi et al. (Arefi et al., 2009) developed the algorithm for DTM generation from DEM. Herein, we use DEM and DTM data which are generated using methods of d'Angelo et al. and Arefi et al. which are reported in (d'Angelo et al., 2009) and (Arefi et al., 2009) respectively.

The difference between DEM and DTM is known as normalized Digital Elevation Model (nDEM). In the normalized DEM ground height is referenced to zero, therefore it provides information about approximate building heights independent from the terrain. To estimate urban areas, we first generate nDEM ($N(x, y)$) by taking difference of DEM ($E(x, y)$) and DTM ($T(x, y)$) image matrices which belong to the same region. Then, we apply Otsu's automatic thresholding method to detect urban area in $N(x, y)$ (Otsu, 1979). After applying thresholding, we assume output $M(x, y)$ binary image as urban area mask which holds K number of binary subregions. In order to eliminate effect of trees, we analyze each $M_k(x, y)$ $k \in [1, 2, \dots, K]$ subregion in $M(x, y)$ urban area mask. If $\max(N(x, y) \times M_k(x, y))$ is smaller than 2 meters, we eliminate $M_k(x, y)$ subregion since it is not high enough to represent a building. In Fig. 1(a), we represent *Jedda*₁ test image from our data set, and in Fig. 1(b) we show detected urban area boundaries.

After finding the urban area from the DEM, we label buildings in order to model each of them with a rectangular shape. Unfortunately, due to very low resolution of this DEM and high complexity of the region, it is not possible to always distinguish adjacent buildings from DEM data. Therefore we pick panchromatic image of region ($I(x, y)$) for further analysis. First, we apply a preprocess to $I(x, y)$ image using bilateral filter which performs a non-linear smoothing with preserving edge information (Tomasi and Manduci, 1998). In this way, we eliminate noise and redun-

dant details in image. Sirmacek and Unsalan provides an extensive explanation about usage of bilateral filter in panchromatic satellite images (Sirmacek and Unsalan, 2009). To find buildings, we benefit from Canny edges (Canny, 1986). We extract Canny edges of $I(x, y)$ test image, then we use $M(x, y)$ urban area mask to obtain only building edges. For our *Jedda*₁ sample test image, detected building edges can be seen in Fig. 1(c). Then, we use distance transform to find a location inside of each closed building edge shape. For binary images (like our building edges in Fig. 1(c)), distance transform calculates the distance between each pixel that is set to zero and the nearest nonzero pixel. In our study, we use *Euclidean Distance* as distance metric. After applying distance transform to our building edges, centers of building shapes get highest values. Consequently, we pick local maximum values in distance transform, and assume their locations (x_b, y_b) as possible building centers. In Fig. 1(d) we represent detected building locations for our *Jedda*₁ test image. As can be seen in this figure, most of the buildings are labeled correctly. Next, we describe the proposed automatic building shape approximation method.

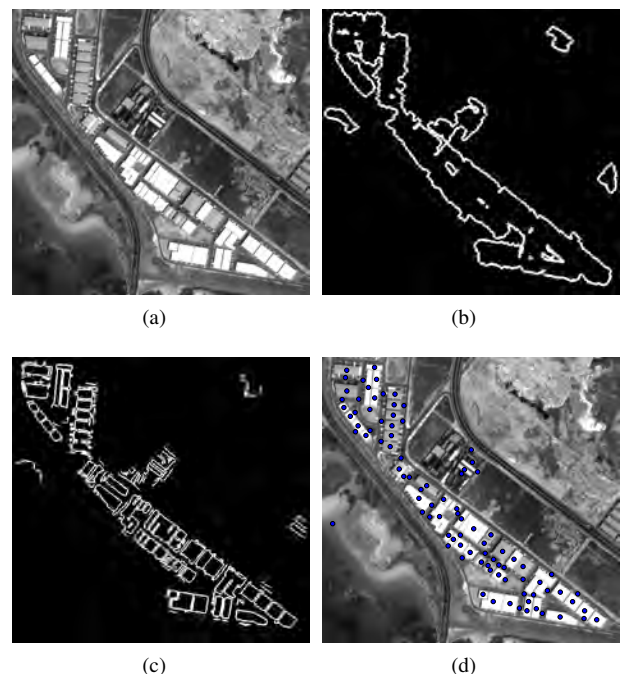


Figure 1: (a) *Jedda*₁ test image. (b) Detected urban area boundaries. (c) Canny edges detected in urban area. (d) Possible building centers (x_b, y_b) .

3 EXTRACTING BUILDING SHAPES (BOX-FITTING)

In complex urban areas which contain adjacent buildings, very low resolution DEM data can not be used for detecting shapes of buildings. Therefore, we use Canny edges which are extracted from panchromatic image to estimate building shapes. In a previous study Sirmacek and Unsalan (Sirmacek and Unsalan, 2008) proposed an automatic shape approximation approach (called Box-Fitting) after a seed-point is detected on the building rooftop. In this study, we benefit from this Box-Fitting approach to detect approximate building shapes. We assume (x_b, y_b) possible building centers as seed-points to run Box-Fitting algorithm.

To estimate building shapes for each (x_b, y_b) location, we locate a $[w \times w]$ size window on this building center. Considering resolution and approximate building sizes in our test images, we assume w as equal to 60 pixel. Box-Fitting method discards edges

out of this window to deal only with candidate building edges and to decrease the number of unnecessary edges. From these edges, the rectangle that represents the building is reconstructed. For each possible building location, we put an initial virtual box on (x_b, y_b) coordinate with $\theta = 0$ angle. Here, θ is the slope of the rectangle. Then, the edges belonging to the virtual box are swept outwards, until they hit to building edges. After our virtual box stops growing, we calculate the energy E_θ . The energy of the detected box shape is defined as the sum of minimum distance between virtual building edge pixels and real building edge pixels in perpendicular direction as given below;

$$E_\theta = \sum_{i=1}^n \min(\text{sqrt}((x_v(i) - x_e(j))^2 - (y_v(i) - y_e(j))^2)) \quad (1)$$

Here, E_θ is the calculated energy in θ direction. $(x_v(i), y_v(i))$ represent coordinates for i th pixel on the edges of the virtual box shape. $(x_e(j), y_e(j))$ represents the j th pixel on the real building edges. For same seed-point, we put an initial virtual box and start growing again for all $\theta \in [0, \pi/6, \pi/3, \pi/2, 2\pi/3, \dots, 2\pi]$ angles. As we increase step sizes here, we can obtain more accurate approximations, however we need more computation time. After calculating E_θ for $\theta \in [0, \pi/6, \pi/3, \pi/2, 2\pi/3, \dots, 2\pi]$ angles, we pick the estimated box which has smallest E_θ energy as detected building shape. Since buildings are generally in rectangular shapes, it makes sense to extract rectangular shapes on buildings. Main advantage of using Box-Fitting approach is that approximate building shape still can be found even the building edges are not well-determined, or even if there is not a closed shape. However, other region growing algorithms fail to extract an object shape in these cases.

In Fig. 2, we represent our original *Jedda*₁ sample image, and $B(x, y)$ binary image which holds detected approximate building shapes. As one outcome of using the Box-Fitting approach, we can reject some false seed-points if the virtual box can not converge to a shape in this region. We also reject the detected box-shape if its area is very small (less than 100 pixels), or if its area is very large (more than 5000 pixels) since it can not represent a real building considering image resolutions. As a result, we also verify building appearance using Box-Fitting algorithm. In the next part, we use detected approximate building shapes to refine the DEM.

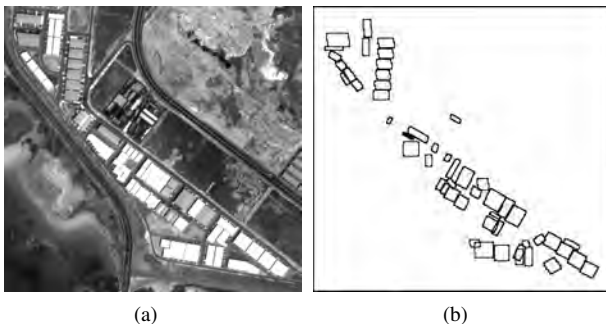


Figure 2: (a) Original *Jedda*₁ test image. (b) Detected approximate shapes using box-fitting approach ($B(x, y)$ binary image).

4 ENHANCING BUILDING SHAPES IN DEM

After finding approximate building shapes from the panchromatic satellite image, we try to enhance DEM data using this information. For this purpose, we first calculate gradient magnitudes in

DEM to investigate discontinuities. To find gradient magnitudes, we use smoothed gradient filters in x and y directions as below,

$$g_x(x, y) = \frac{-x}{2\pi} \exp\left(-\frac{x^2 + y^2}{2\sigma^2}\right) \quad (2)$$

$$g_y(x, y) = \frac{-y}{2\pi} \exp\left(-\frac{x^2 + y^2}{2\sigma^2}\right) \quad (3)$$

where σ is the smoothing parameter and equal to 0.5. Although our method is fairly robust to this parameter, one may need to adjust it according to the resolution of DEM. We calculate the smoothed gradients for the DEM data $E(x, y)$ as,

$$E_x(x, y) = g_x(x, y) * E(x, y) \quad (4)$$

$$E_y(x, y) = g_y(x, y) * E(x, y) \quad (5)$$

where $*$ stands for a two-dimensional convolution operation. We calculate gradient magnitudes of image as,

$$G(x, y) = \sqrt{E_x(x, y)^2 + E_y(x, y)^2} \quad (6)$$

If a pixel in $G(x, y)$ has a higher value than t_d , we assume there is a significant discontinuity. Here, t_d threshold value is obtained by Otsu's automatic thresholding approach (Otsu, 1979). After detecting significant discontinuities in the DEM, we pick each rectangle and investigate the corresponding region. If there are discontinuities in the DEM pixels where rectangle have edges, we assume the inside of this rectangle as a building rooftop. In order to eliminate noise that appears on building rooftops, we calculate only one height for each rectangular building. To calculate an approximate building heights, we pick DEM values which are inside of the detected rectangular region and calculate their mean value. Then we set each pixel, which exists inside of the rectangular region, to the calculated mean value. As a result, we have only one height value for each detected building. In the Experimental Results section, we analyze effects of choosing mean and median of DEM values as a building height.

We assume that there may be buildings in the DEM which are missed in previous building detection and shape approximation steps. Therefore, after removing reconstructed building pixels from DEM we make a post-analysis on it. If there are regions with high values for a large area, we assume that they can be missed buildings and insert them to our final result after smoothing their DEM values with a $[9 \times 9]$ size median filter to remove the noise on DEM. We picked this median filter window size after extensive tests on our test image dataset. If window size is chosen larger, this post-processed buildings will have smoother edges. On the other hand, if window size is chosen smaller, median filtering process can not be adequate to remove noise within DEM. In this post-analysis, if a region has very high value (more than 40 meters) we remove this region from DEM since it can not represent a building. In this way, we also eliminate errors in the DEM which occur because of stereo image matching errors in the DEM generation process.

5 EXPERIMENTAL RESULTS

To test the performance of our proposed method, we use a test image data set of Jedda city. We use DEM which is generated from

stereo Cartosat-1 images using the DEM generation method of d'Angelo et al. (d'Angelo et al., 2009). We also use orthorectified panchromatic Cartosat-1 image of the corresponding region. For better representation, we locate reconstructed buildings on a smoothed DTM of the region which is generated using method of Arefi and Hahn (Arefi and Hahn, 2005). Our panchromatic Cartosat-1 test images have 2.5 m. spatial resolution, however DEM and DTM have 5 m. spatial resolution.

In the first row of Fig. 3, we represent the orthorectified panchromatic Cartosat-1 image, the original DEM, and the enhanced DEM for our *Jedda₁* sample test image respectively. For a better visual representation we covered the DEM with the panchromatic image of the region. In the second row of Fig. 3, we represent another example from our test image dataset. In this row, we represent the orthorectified panchromatic Cartosat-1 image, the original DEM, and the enhanced DEM for our *Jedda₃* test image. As can be seen in these examples, the enhanced DEM data reflects building reconstruction in urban area more clearly. Besides, DEM errors which come from automatic the DEM generation method are also corrected in the enhanced DEM. However, we could not detect exact shapes of complex buildings and we can not discriminate some of the adjacent buildings, the final improvement in DEM data is informative. We will analyze detection of complex building shapes in our future studies. Next, we analyze performance of our proposed method on a sample test image to give a sight to possible readers.

5.1 Performance Analysis on Sample Image

We pick *Jedda₁* test image to evaluate the performance of our method. To analyze performance we consider two measures; shape accuracy (p_1) and height accuracy (p_2). First, we start with measuring shape accuracy of the shape approximation (Box-Fitting) approach. We use the method used by Ruether et al. (Ruether et al., 2002) to measure the shape accuracy. For a $[m \times n]$ size test image shape accuracy performance (p_1) is calculated as follows,

$$p_1 = \left(\frac{\sum_{x=1}^m \sum_{y=1}^n |B_f(x, y) - B_{gth}(x, y)|}{\sum_{x=1}^m \sum_{y=1}^n B_{gth}(x, y)} \right) \times 100 \quad (7)$$

in this equation $B_f(x, y)$ is the binary image which is obtained by filling holes as '1' in $B(x, y)$ binary image. B_{gth} is the binary groundtruth shape mask that we labeled buildings as '1' and other regions as '0' manually. We calculate p_1 value as 78,02% for *Jedda₁* test image. Unfortunately, 53 of 66 buildings are detected in the region. Therefore, our groundtruth masks includes some buildings which are not detected in building shape detection method, so those buildings are not labeled after our shape approximation method. Therefore, we obtain slightly low shape accuracy performance. If shape accuracy is calculated for each building one by one, we can observe higher shape accuracy performance for each building.

In order to calculate height accuracy, we first calculate each building height in *Jedda₁* test image using panchromatic stereo CartoSat-1 images. Using triangulation techniques, we measure each building height manually and list obtained height values as vector data. We also list building heights in the same order measuring the heights in the final enhanced DEM data. We generated enhanced DEM both using mean and median values of building rooftop values. As a result, two enhanced DEM building height value vectors are used in performance calculation. By subtracting groundtruth building height vector from these vectors, the differences can be

obtained. In the ideal case, we expect to obtain zero values as difference. In order to measure height accuracy (p_2), we used RMS values of these difference vectors. For the vector generated by using the mean of DEM values, RMS of difference vector is calculated as 1.80. For the vector generated by using the median of DEM values, RMS of difference vector is calculated as 2.63. We pick the method which generates p_2 value closer to zero. Therefore, using mean value of DEM when calculating building heights gives more accurate results.

5.2 Computation Times

We finally analyze computation time needed for our method. The computation time of the proposed DEM enhancement method is also very impressive. For our sample *Jedda₁* test image which is in $[566 \times 590]$ pixel sizes, we tabulate timing requirements of all modules in the DEM enhancement method in Table 1. We obtain these timings using an Intel Core2Quad 2.66GHz PC and Matlab coding environment. As can be seen in this table, segmenting urban area from DEM data requires only 0.28 seconds. We detect possible building locations in 1.74 seconds. The longest computation time is needed for shape approximation (Box-Fitting) step. For *Jedda₁* test image which includes 76 buildings, shape approximation step requires 65.14 seconds. In this step, timing directly depends on the test image. As the number of buildings increases in given test image, the shape approximation module needs more computation time. However, this module can run faster if it is coded in C. Finally, enhancing building shapes in DEM requires 0.82 seconds. Consequently, running our proposed DEM enhancement method on *Jedda₁* test image requires 67.98 seconds. This short computation time may lead for the proposed method to be used in fast damage and change detection applications.

Unfortunately, our method is not able to detect exact shapes of very complex buildings. Therefore, edges of these buildings are not sharpened in DEM data. We will handle detection of complex building shapes in our future studies.

Module	Time (in Sec.)
Urban area segmentation	0.28
Detecting buildings	1.74
Shape approximation (Box-Fitting)	65.14
Enhancing building shapes	0.82
TOTAL	67.98

Table 1: CPU Times (In Seconds) for DEM Enhancement on *Jedda₁* test image

6 CONCLUSIONS

In this paper, we proposed a new method for automatic DEM enhancement based on building shape approximation. First, we detected the urban area using DEM. Then, we used panchromatic image of corresponding region to detect possible building centers. For this purpose, we extracted Canny edges of buildings in the previously detected urban area. After that, we applied distance transform to these edges to detect building centers. We used detected edges and building centers to run the shape approximation algorithm. Extracted approximate shapes helped us to sharpen building edges, and to smooth rooftops in the DEM. We also corrected errors in DEM, which appear due to stereo image matching errors in DEM generation.

After extensive tests on very low resolution and noisy DEMs, we obtained encouraging results with our method. Comparing with

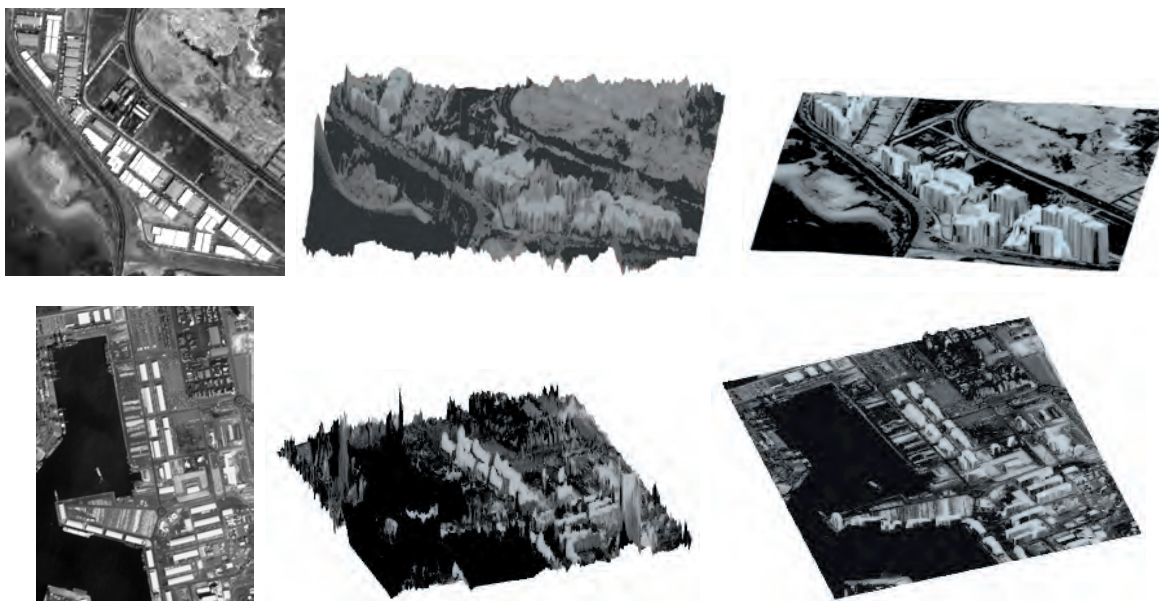


Figure 3: Orthorectified pancromatic Cartosat-1 images, original DEM, and enhanced DEM are given in each row for *Jeddah*₁, and *Jeddah*₃ test regions respectively.

studies presented in the literature, we can conclude that our proposed urban DEM enhancement method is fast and reliable even in complex urban regions. The proposed automatic method will decrease operator work-loads in three-dimensional reconstruction of urban areas. In addition to that, we believe that proposed method will be of use for detailed urban monitoring, damage and change detection systems. The next step of this study will be the detection of more complex building shapes and textured rooftops.

REFERENCES

- Arefi, H. and Hahn, M., 2005. A morphological reconstruction algorithm for separating off-terrain point. In Proceedings of the International Archives of Photogrammetry, Remote Sensing, and Spatial Information Sciences 46, pp. 1–6.
- Arefi, H., d'Angelo, P., Mayer, H. and Reinartz, P., 2009. Automatic generation of digital terrain models from cartosat-1 stereo images. In Proceedings of the International Archives of the Photogrammetry, Remote Sensing and Spatial Information Sciences.
- Arefi, H., Engels, J., Hahn, M. and Mayer, H., 2008. Levels of detail in 3d building reconstruction from lidar data. In Proceedings of the International Archives of the Photogrammetry, Remote Sensing, and Spatial Information Sciences 37, pp. 485–490.
- Brunn, A. and Weidner, U., 1997. Extracting buildings from digital surface models. In Proceedings of International Archives of Photogrammetry, Remote Sensing, and Spatial Information Sciences.
- Canny, J., 1986. A computational approach to edge detection. IEEE Transactions on Pattern Analysis and Machine Intelligence 8 (6), pp. 679–698.
- Canu, D., Gambotto, J. and Sirat, J., 1996. Reconstruction of building from multiple high resolution images. In Proceedings of International Conference on Image Processing.
- Cohen, L. and Vinson, S., 2002. Segmentation of complex buildings from aerial images and 3d surface reconstruction. In Proceedings of 6th IEEE Workshop on Applications of Computer Vision (WACV) 1, pp. 215–219.
- d'Angelo, P., Schwind, P., Krauss, T., Barner, F. and Reinartz, P., 2009. Automated dsm based georeferencing of cartosat-1 stereo scenes. In Proceedings of International Archives of Photogrammetry, Remote Sensing, and Spatial Information Sciences.
- Elaksher, A., 2008. A multi-photo least squares matching algorithm for urban area dem refinement using breaklines. In Proceedings of International Archives of Photogrammetry, Remote Sensing, and Spatial Information Sciences 37, Part B3A, pp. 33–38.
- Fradkin, M., Roux, M., Maitre, H. and Leloglu, U., 1999. Surface reconstruction from multiple aerial images in dense urban areas. In Proceedings of IEEE Computer Vision and Pattern Recognition 2, pp. 262–267.
- Haala, N. and Brenner, C., 1999. Extraction of buildings and trees in urban environments. ISPRS Journal of Photogrammetry and Remote Sensing 54, pp. 130–137.
- Haala, N., Brenner, C. and Anders, K., 1998. 3d urban gis from laser altimeter and 2d map data. In Proceedings of International Archives of Photogrammetry, Remote Sensing, and Spatial Information Sciences 32, pp. 339–346.
- Ortner, M., Descombes, X. and Zerubia, J., 2002. Building extraction from digital elevation models. INRIA Research Report.
- Ostrowski, J. and He, D., 1989. Error correction of digital elevation models produced by automatic matching of digital stereo images. In Proceedings of International Geoscience and Remote Sensing Symposium (IGARSS) 2, pp. 446–449.
- Otsu, N., 1979. A threshold selection method from gray-level histograms. IEEE Transactions on Systems, Man, and Cybernetics 9 (1), pp. 62–66.
- Ruether, H., Martine, H. M. and Mtaló, E., 2002. Application of snakes and dynamic programming optimisation technique in modelling of buildings in informal settlement areas. ISPRS Journal of Photogrammetry and Remote Sensing 56 (4), pp. 269–282.
- Sirmacek, B. and Unsalan, C., 2008. Building detection from aerial imagery using invariant color features and shadow information. In Proceedings of International Symposium on Computer and Information Sciences (ISCIS) 1, pp. 1–5.

Sirmacek, B. and Unsalan, C., 2009. Urban-area and building detection using sift keypoints and graph theory. *IEEE Transactions on Geoscience and Remote Sensing* 47 (4), pp. 1156–1167.

Skarlatos, D. and Georgopoulos, A., 2004. Automating the checking and correcting of dems without reference data. In *Proceedings of International Archives of Photogrammetry, Remote Sensing, and Spatial Information Sciences* 35, Part B2, pp. 553–558.

Tomasi, C. and Manduci, R., 1998. Bilateral filtering for gray and color images. In *Proceedings of International Conference on Computer Vision* 1, pp. 839–846.

Vinson, S., Cohen, L. and Perlant, F., 2001. Extraction of rectangular buildings in aerial images. In *Proceedings of Scandinavian Conference on Image Analysis (SCIA'01)*.

AN ADABOOST-BASED ITERATED MRF MODEL WITH LINEAR TARGET PRIOR FOR SYNTHETIC APERTURE RADAR IMAGE CLASSIFICATION

Xin SU^a, Chu HE^{a,*}, Xiping DENG^a, Wen YANG^a, Hong SUN^a

^a School of Electronic Information, Wuhan University, Wuhan, 430079, Chian

Commission III/3

KEY WORDS: SAR, image classification, Linear Targets Prior, Ratio Response, MRF, AdaBoost

ABSTRACT:

A supervised classification method based on AdaBoost posterior probability and Markov Random Fields (MRF) model with Linear Targets Prior (LTP) is proposed in this paper. Firstly in contrast with most existing regions (*superpixels*) based models, this approach captures contiguous image regions called *superpixels* from ratio response maps of original images. Secondly, Adaboost classifier is employed to get likelihood probability for Markov Random Filed (MRF). Meanwhile, linear targets prior information (LTP) is introduced into MRF model combining with Potts prior model to engage better edges in classification results. Finally, iterative strategy in MRF model improves the performance of classification. Compared with traditional MRF model, the proposed approach has effective improvement in SAR images classification in the experiments of this paper.

1. INTRODUCTION

Since they can operate days and nights and under any weather conditions, Synthetic Aperture Radar (SAR) has been widely used in many fields. Furthermore, the resolution of SAR images has become higher and higher, which makes automatic analysis of SAR images rivet more people's attention. Nevertheless, strong speckle noise existing in SAR images leads to difficult image processing. And, many articles are still published on this issue, such as segmentation presented in F. Galland, 2003 and R.F.Rocha, 2008, classification in C. Tison, 2004. Segmentation, classification and annotation are the fundamental tasks of images automatic analysis, which are called as image parsing (Zhouwen Tu, 2005). Recently, popular approaches for image parsing can be considered as a combination of three strategies, Pre-Segmentation, Features Extraction and Model. See fig.1.

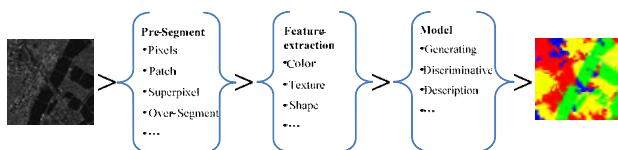


Fig 1. Framework of popular approaches for images parsing

Recent publications present many pre-segmentation methods. Such as 20×20 patches are extracted in a pLSA based MRF classification method (Verbeek, 2007). Superpixel over-segmentation is used in Regional Label Features based CRF method (Stephen, 2008). Meanshift over-segmentation method (Dorin, 2002) has been widely used in some classification articles. Multiscale segmentation based on geodesic morphology is used to get local regions for spatial reasoning (Jordi Inglada, 2009). However, there are some approaches

using pixels directly without pre-segmentation. In general, a pixel can be seen as a specific style of pre-segmentation.

After pre-segmentation, features descriptors calculate the features of local regions. General features are color, texture and shape, such as SIFT-color (Joost van de Weijer, 2006) Gabor (B.S.Manjunath, 1996), LBP (T. Ojala, 2002), HOG (N. Dalal, 2005) and so on. Because of imaging principle, SAR images get specific features. Only one kind of general features can't describe SAR image sufficiently. Gray histogram and SoftLBP (Ahonen T, 2007) are used in this paper.

The most popular image models can be seen as one of the three basic models, or combination of two or three of them. The three basic models are (F. Han, 2008): generating model, description model and discriminant model. Generating model is a model which infers prediction from samples such as pLSA (Verbeek, 2007) and LDA (David M. Blei, 2003). Description model describes the relations of samples such as MRF (Verbeek, 2007). Discriminant model has discriminative functions which can get results from samples directly such as Adaboost (Robert E. Schapire, 2003). Meanwhile, there are some models combining two of the basic models. Specially, CRF is a unified model which combines discriminant model with description model (S.C. Zhu, 2006), and it can integrate different kinds of features and sorts of prior in a unified model more easily, and get better results by optimization.

In common sense, land surface on one side of a certain length of road always belongs to the same category, and rivers, railways and other liner targets have similar situation. The idea in this paper is to introduce this linear targets prior into MRF description model. This paper focuses on improving the edges of regions in SAR images classification results. There are three contributions of this paper: 1) Linear targets priors are introduced into MRF model. The Potts model prior can infer

* Corresponding author. Phone: +86-27-87548181; Fax: +86-27-87548181; E-mail: chuhe@whu.edu.cn

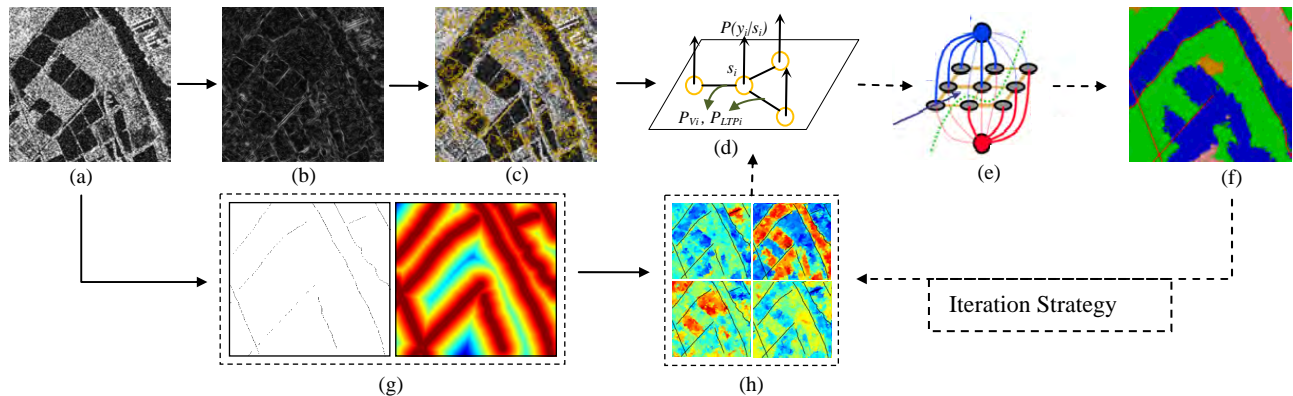


Fig. 2. Flowchart of the proposed model. (a) original image; (b) edges probability map (Ratio response map); (c) over-segmentation results (superpixels); (d) graph structure for GraphCut segmentation; (e) GraphCut segmentation; (f) segmentation results; (g) map of linear target and distance map from pre-pixels to linear targets; (h) linear target prior maps. The iteration strategy is marked with dotted lines.

consistency among homogenous regions, but can hardly consider the consistency along the linear targets like roads and rivers. 2) Superpixels of Pre-segmentation are captured on edges probability maps instead of original images. Since shapes of linear targets are always the boundaries of superpixels. In this case, more information of edges can be used for classification process. 3) Iterative MRF description model is more likely to remove noise in classification map compared with standard MRF model.

2. RELATED WORK

2.1 Edge detection

Ratio line detector D1 (F.Tupin, 1996) is derived from a coupling of two ratio edge detectors on both sides of a region (as shown in fig.3.a). Due to multiple responses to a structure, detector D1 is not accurate enough to locate the edges. Cross-correlation line detector D2 (F.Tupin, 1996) utilizes variances of regions to improve locating accuracy but with higher missing alarm ratio. Tupin (F.Tupin, 1996) merged the information from both D1 and D2 in 8 orientations.

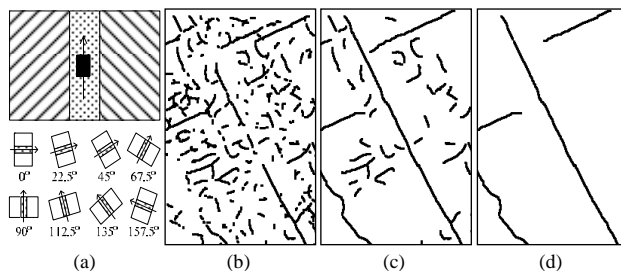


Fig.3. (a) Template and 8 orientations of template used in ratio edge detection. (b) Results of ratio edge detection. (c) Grouping results. (d) Linear targets detection results

Once again, the main motivation of this paper is improving region edges in classification results. So, the traditional edge detection can get wealth and accurate edge information from SAR images which is useful for classification. And, the proposed approach in this paper gets use of this information in over-segmentation, see details in section 3.

2.2 AdaBoost based MRF Model

MRF is a type of classical discriminative model. Given an image $I = \{s_1, s_2 \dots s_{N_I}\}$ with N_I pixels or superpixels s_i and a label set $Y = \{y_1, y_2 \dots y_{N_I}\}$ with N_C labels, MRF model constructs a posteriori probability of s_i , as shown in Eq.1. Where, $\lambda > 0$ is a constant coefficient. P_{V_i} is prior probability and $V_{ij}(y_i, y_j) = 1$ when $y_i = y_j$, $V_{ij}(y_i, y_j) = 0$ when $y_i \neq y_j$. P_{L_i} is always captured by feature-based discriminant model like AdaBoost classifier and P_{L_i} tends to be $P_{L_i}(y_i | f(s_i))$ where $f(s_i)$ is the features of s_i . For the whole image, the posterior probability is $P(Y|I, \Theta)$ where Θ is the parameter of model. Some optimization algorithms, such as GraphCut and Simulated Annealing Algorithm (SAA), can be utilized to get maximums of $P(Y|I, \Theta)$.

$$\begin{aligned}
 P(y_i | s_i) &\propto P_{L_i}(y_i | s_i) P_{V_i}(y_i | y_{v_i}) \\
 P_{V_i}(y_i | y_{v_i}) &= \exp\left(\lambda \sum_{y_j \in v_i} V_{ij}(y_i, y_j)\right) \\
 P(Y | I, \Theta) &= \prod_{i=1}^{N_I} P(y_i | s_i) \\
 \bar{Y} &= \underset{Y}{\operatorname{argmax}} \{P(Y | I, \Theta)\}
 \end{aligned} \tag{1}$$

As one of the most popular description model, MRF model can balance the likelihood and prior probability in the whole image and get global optimal solution with optimization algorithms like algorithm presented in (Boykov Y, 2001). So, a linear target prior can be introduced into MRF model in this paper simply and obviously, see details in section 3.

3. METHODOLOGY

3.1 Pre-segmentations and Features Extraction

The proposed approach in this paper begins with pre-segmentation strategy using over-segmentation method to get *superpixels*. Firstly, we utilize ratio edge detector to get edges probability map of each input image (as shown in fig. 4.b).

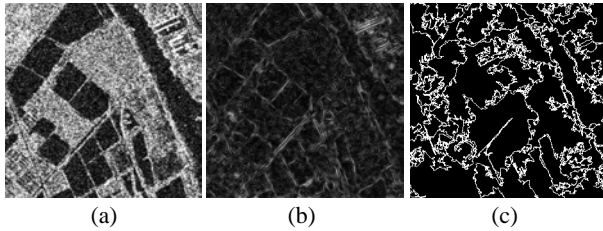


Fig. 4. (a) Original image; (b) Ratio response map (edges probability map); (c) Over-segmentation results

And then, Meanshift (Dorin Comaniciu, 2002) based over-segmentation algorithm is employed on the edges probability map to divide original images into superpixels (as shown in fig. 4.c).

A superpixel captured from pre-segmentation is the smallest unit in an image and can be assigned only a class label. Each superpixel in images is extracted a set of features consisted of gray histogram, SoftLBP (Ahonen T, 2007).

3.2 Linear Target Prior

Linear Target Priors (LTP) utilizes the shape of linear target to improve the edges of classification results. This prior information comes from the relative location between linear targets and image pixels (or superpixels) around them. For example, we wish to make use of the fact that all pixels adjoining river banks are *water* or *farmland* (in a certain length). Thus, the first is detecting the linear targets in SAR images. In this paper, the fusion operates of D1 and D2 operates is employed to detect linear targets (edges). And then, the LTP is captured in the following ways.

3.2.1 Distance Map: The distances from points (pixels) to lines (linear targets) are calculated as the method presented in (Kumar M.P., 2005). Given lines Ω , the distance $d = \text{dist}(p, \Omega)$ between point p and Ω is the distance between point p and point p' which is the nearest point in lines Ω to point p (as shown in fig.5.a). The distance map is shown in fig.5.c.

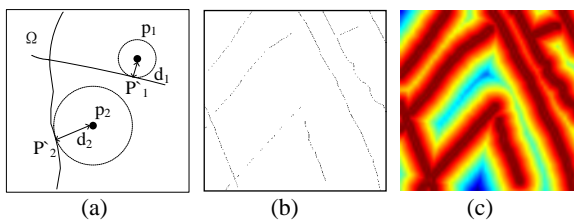


Fig. 5. (a) sketch of distance from pixels to lines; (b) linear target map; (c) distance map from pre-pixels to linear targets.

3.2.2 LTP Map: LTP is learned from the labelled image data (classification results of previous iteration in practice), so it changes from iteration to next iteration. Firstly, the linear target Ω are divided into sub-lines with a certain length, $\Omega = \{\Omega_1, \dots, \Omega_{N\Omega}\}$. And a sub-line Ω_j divides its adjacent area into K regions, we address them sub-line regions $R = \{R(\Omega_j)\}^k$. Then, the LTP of a pixel p_i for class c is shown by Eq.2:

$$P_{LTP_i}(c | p_i, \Omega, Y^{(t)}) = \exp\left(\sum_{j=1}^{N\Omega} \left[\mu \text{dist}(p_i, \Omega_j) \sum_{k=1}^K \text{cont}(c, p_i, R_{\Omega_j}^k) \right]\right) \quad (2)$$

$$\text{cont}(c, p_i, R_{\Omega_j}^k) = \begin{cases} 1, & \text{if } p_i \in R_{\Omega_j}^k \text{ and } c = \text{maxlabel}(Y^{(t)}, R_{\Omega_j}^k) \\ 0, & \text{other} \end{cases}$$

Where, μ is LTP weight and $\text{maxlabel}(Y^{(t)}, R_{\Omega_j}^k)$ is the maximum class of pixels in region $R = \{R_{\Omega_j}^k\}$ of previous iteration classification results $Y^{(t)}$. Fig.6 shows an example of LTP map for class *building*, *water*, *farmland* and *woodland* in SAR image. These LTP probability values map to the full range of values in the cool-hot colormap.

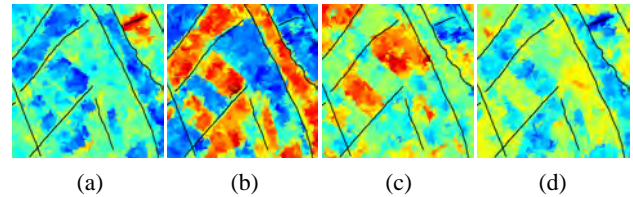


Fig. 6. (a) linear target prior map for building; (b) linear target prior map for water; (c) linear target prior map for farmland; (d) linear target prior map for woodland.

3.3 Iterative MRF Model with LTP

The posteriori probability of the proposed model is added LTP based on Eq.1 as shown in Eq.3:

$$P(y_i | s_i, \Omega, Y^{(t)}) \propto P_{Li}(y_i | s_i) P_{Vi}(y_i | y_{Vi}) P_{LTP_i}(y_i | s_i, \Omega, Y^{(t)}) \quad (3)$$

$$P_{LTP_i}(y_i | s_i, \Omega, Y^{(t)}) = \sum_{p_i \in s_i} P_{LTP_i}(y_i | p_i, \Omega, Y^{(t)})$$

Where, s_i is i -th superpixels in image and p_i is a pixel in s_i , P_{LTP_i} is linear targets prior of s_i . The overall image posteriori probability is:

$$P(Y | I, \Omega, Y^{(t)}, \Theta) = \prod_{i=1}^{N_i} P(y_i | s_i, \Omega, Y^{(t)}) \quad (4)$$

$$\bar{Y}^{(t+1)} = \underset{Y^{(t+1)}}{\text{argmax}} \{P(Y^{(t+1)} | I, \Omega, Y^{(t)}, \Theta)\}$$

A GraphCut-based optimization algorithm presented in Boykov Y, 2001 has been used to effectively capture the global optimal resolution of Eq.4. The training steps of the proposed Iterative MRF model with LTP have been listed in the following:

- 1) Utilize edge detection template in fig.3.a to get edges probability map of input images;
- 2) Over-segment the edges probability map to get superpixels;
- 3) Extract features in each superpixel;
- 4) Training AdaBoost classifier with labeled groundtruth data;

The testing steps of Iterative MRF model with LTP are shown in the following:

- 1) The same as steps 1~3 in training;
- 2) Detect linear targets with fusion operate of D1 and D2 in testing images;
- 3) Utilize AdaBoost classifier in training stagey to get P_{LTP_i} ;
- 4) Construct MRF model as Eq.1 and get optimal solution $Y(0)$;
- 5) Get P_{LTP_i} with l -th iterative solution $Y^{(l)}$;
- 6) Construct MRF model as Eq.4 and get optimal solution $Y^{(t+1)}$;
- 7) Repeat steps 4 and 5 until little changes existing in $Y^{(t+1)}$.

4. EXPERIMENTS

4.1 Experiments setup

Experiments are done on SAR image datasets. The datasets and parameters are illustrated as following.

4.1.1 Data: The SAR datasets contains a 1500×1200 pixels image that are selected from VV polarization SAR images of Guangdong Provinces of China in May 2008 of TerraSAR satellite. The spatial resolution is $1.25m \times 1.25m$. Each image of the SAR datasets has a ground truth getting from manual labeling under ArcGIS software. Our experiments consist of 4

classified: *farmland, woodland, building, water*. Half of this image is used for training, the remaining for testing.

4.1.2 Parameters: In linear target detection, the template is selected with 15 pixels high, 13 pixels width and 3 pixels centre region. The threshold of D1, D2 and fusion operate are 0.35, 0.45 and 0.35 individually. The minimum region area of superpixels in Meanshift based over-segmentation is 400 pixels, with spatial bandwidth and range bandwidth are both 3 pixels. Features used here are gray histogram and SoftLBP 0. The length of sub-lines is 50 pixels and the width of sub-line regions is 20 pixels.

4.2 Classification Performance

The classification results of the proposed approach in this paper are shown in fig.7. Fig.7.c is the beginning of iteration result where $P_{LTP_i} = 0$, that is without LTP. And there are some isolated points in the classification map. Moreover, there are many indented edges along the linear targets. In the fig.7.d, e and f, isolated points and indented edges decrease gradually since the addition of LTP.

Compared with groundtruth data labeled artificially, classification accuracies are listed in table.1. It shows that the average accuracy has been improved only a little from iteration-0 to iteration-3, but the overall classification performance has large improvement.

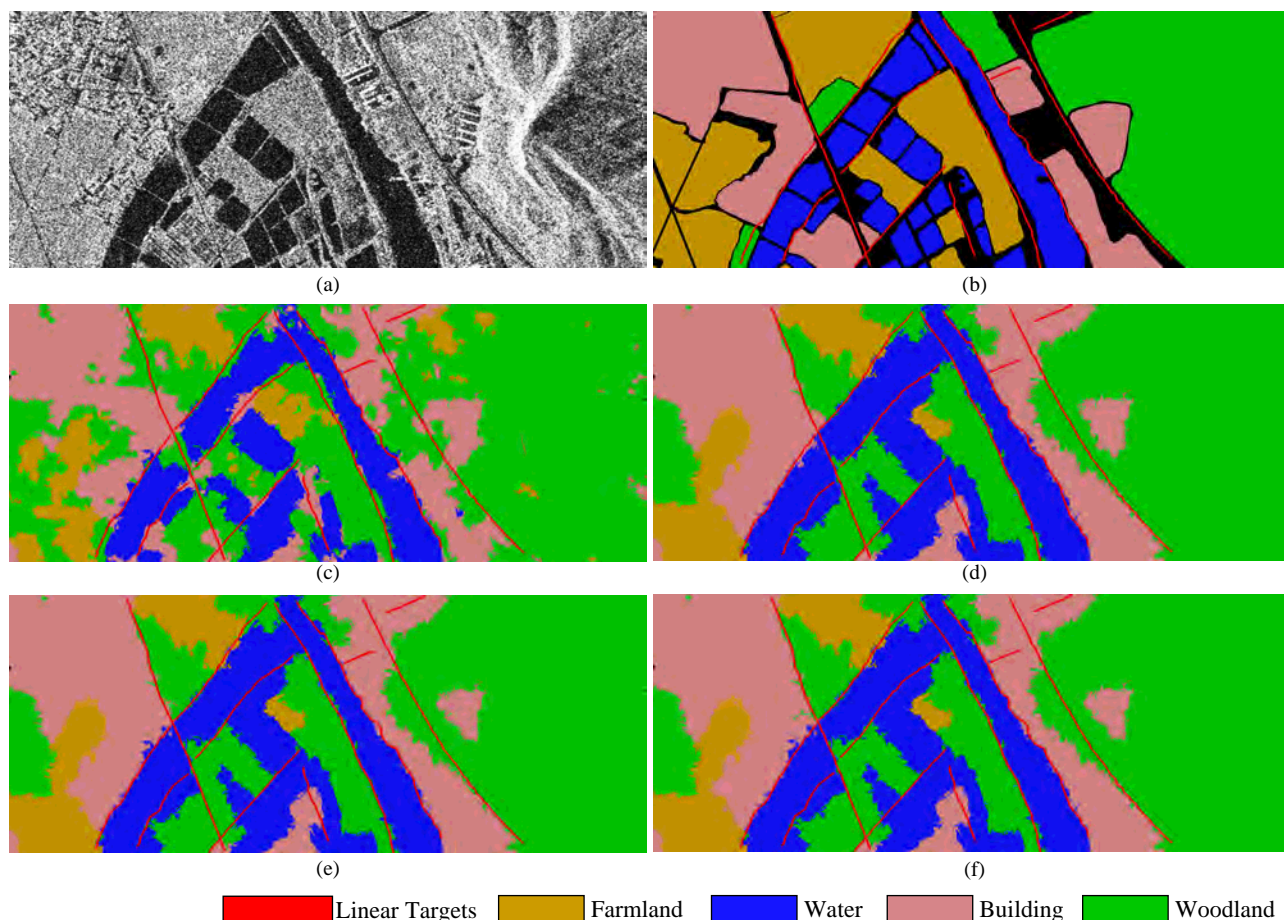


Fig. 7. Experimental Results, (a) original image; (b) groundtruth data with linear targets detected with fusion operate of D1 and D2 operates; (c) classification results in iteration 0 (without LTP); (d) classification results in iteration 1 (with LTP); (e) classification results in iteration 1 (with LTP); (f) classification results in iteration 1 (with LTP);

Category (%)	Accuracy			
	Iteration 0	Iteration 1	Iteration 2	Iteration 3
Building	80.75%	88.28%	88.92%	89.46%
Water	92.12%	92.93%	90.26%	90.14%
Farmland	39.96%	36.86%	34.11%	34.11%
Woodland	92.03%	95.28%	93.97%	93.84%
Average	77.89%	80.27%	78.84%	78.89%

Tabel 1. Segmentation accuracy

5. CONCLUSIONS

In this paper, an AdaBoost-based iterative Markov Random Fields (MRF) with Linear Target Prior (LTP) has been proposed. Applied to Synthetic Aperture Radar (SAR) images classification, three strategies have been provided in this model to improve regions edges and isolated points in classification results and effective performance has been obtained. Firstly, due to superpixels captured from ratio response map of SAR images instead of original SAR images, edge information has been utilized more effectively. In this case, classification experiment results show distinct edges of regions. Secondly, linear target prior introduces consistency information along the linear targets into Markov model. Combined with traditional neighbourhood prior information, more reasonable classification results have been gotten in the experiment. Thirdly, the employment of iterative strategy makes the proposed approach have self-perfection in a stated degree. And the experiments have a certain improvement with the increase of iteration times.

Nevertheless, lots of information extracted from polarimetric SAR data, interferometric SAR data and polarimetric SAR interferometry data can be used for SAR image analysis.

6. REFERENCES

F. Galland, N. Bertaux, and P. Réfrégier, Minimum description length synthetic aperture radar image segmentation. *IEEE Transactions Image Processing*, vol. 12, no. 9, pp. 995–1006, Sep. 2003.

C. Tison, J.-M. Nicolas, F. Tupin, and H. Maître, A new statistical model for Markovian classification of urban areas in high-resolution SAR images. *IEEE Transactions on Geoscience and Remote Sensing*, vol. 42, no. 10, pp. 2046–2057, Oct. 2004.

R.F.Rocha. Use of Statistical Distribution for Segmentation of SAR Images of Oceanic Areas. *International Society for Photogrammetry and Remote Sensing*. Vol XXXVIII, 4/C1, 2008

Zhouwen Tu, X.R. Chen, A.L. Yuille, and S.C. Zhu. unifying segmentation, detection and recognition. *International Journal of Computer Vision*, 63(2), 113-140, 2005.

Verbeek. J., Triggs. B; Region Classification with Markov Field Aspect Models. *IEEE Conference on Computer Vision and Pattern Recognition*: 1-8, 2007.

Stephen Gould, Jim Rodgers, David Cohen, Gal Elidan, Daphne Koller. Multi-Class Segmentation with Relative Location Prior. *International Journal of Computer Vision*. 1-16,

2008.

Dorin Comaniciu, Peter Meer, Senior Member. Mean Shift: A Robust Approach Toward Feature Space Analysis. *IEEE Transactions on Pattern Analysis and Machine Intelligence*, Vol 24, No.5: 603-613, 2002.

Jordi Inglada, Julien Michel. Qualitative Spatial Reasoning for High-Resolution Remote Sensing Image Analysis. *IEEE Transactions on Geoscience and Remote Sensing*, VOL. 47, NO. 2: 599-612, FEBRUARY 2009.

Joost van de Weijer, Cordelia Schmid. Coloring local feature extraction. *Proceedings of the European Conference on Computer Vision*, pages 334–348, 2006.

B.S.Manjunath, W.Y.Ma, Texture Features for Browsing and Retrieval of Image Data, *IEEE Transactions on Pattern Analysis and Machine Intelligence*, vol. 18, no. 8, pp. 837-842, Aug. 1996.

T. Ojala, M. Pietikäinen, T. Mäenpää, Multiresolution gray-scale and rotation invariant texture classification with local binary patterns, *IEEE Transactions on Pattern Analysis and Machine Intelligence*, vol. 24, no. 7, pp. 971-987, Jul. 2002.

N. Dalal, B. Triggs. Histograms of oriented gradients for human detection. *IEEE Conference on Computer Vision and Pattern Recognition 2005*, volume 1, pages 886–893, 2005.

Ahonen T, Pietikäinen M. Soft histograms for local binary patterns. Finnish Signal Processing Symposium, Oulu, Finland. 2007.

S.C. Zhu and D. Mumford, A Stochastic Grammar of Images, *Foundations and Trends in Computer Graphics and Vision*, Vol.2, No.4, pp 259-362, 2006.

David M. Blei, Andrew Y. Ng, Michael I. Jordan. Latent Dirichlet Allocation. *Journal of Machine Learning Research* 2003 3: 993–1022. 2003.

Robert E. Schapire. The boosting approach to machine learning: An overview. *Nonlinear Estimation and Classification*. Springer, 2003.

Boykov Y, Veksler O, Zabih R. Fast Approximate Energy Minimization via Graph Cuts. *IEEE Transactions on Pattern Analysis and Machine Intelligence*, 2:1 222-1 239. 2001.

F.Tupin, H.Maitre, J.F.Margin, etc. Detection of linear features in SAR images: application to road network extraction. *IEEE Transactions on Geoscience and Remote Sensing*, 36:434-453, 1998.

Kumar M.P., Torr P.H.S., Zisserman A. OBJ CUT. *Computer Vision and Pattern Recognition*, 20-25 June 2005, Volume 1, Page(s):18 – 25, 2005.

7. ACKNOWLEDGMENTS

The work was supported by the NSFC grant (No. 60702041, 60872131, 40801183) and Hi-Tech research and development program of China (863) (No. 2007AA12Z155, 2007AA12Z180). The authors would like to thank the SPOT IMAGE Corporation for providing the TerraSAR image.

DERIVING WATER FRACTION AND FLOOD MAP WITH THE EOS/MODIS DATA USING REGRESSION TREE APPROACH

D. L. Sun^a, Y. Y. Yu^b

^aDepartment of Geography and Geoinformation Sciences, George Mason University
Fairfax, VA 22030, USA (dsun@gmu.edu)

^bNOAA/NESDIS, Center for Satellite Applications and Research, Camp Spring, MD 20746, USA -
yunyue.yu@noaa.gov

KEY WORDS: Regression Tree, Flood, MODIS, Water fraction

ABSTRACT:

This study investigates how to derive water fraction and flood map from the Moderate-Resolution Imaging Spectroradiometer (MODIS) onboard the Earth Observing System (EOS) using a Regression Tree (RT) approach. The RT approach can integrate all the possible candidate predictors, such as the MODIS channel 2 reflectance (CH2), reflectance ratio (CH2/CH1), reflectance difference (CH2-CH1) between MODIS channels 2 and 1, vegetation and water indices. Meanwhile, it provides accuracy estimates of the derivation. The recent floods in New Orleans area in August 2005 were selected for the study. MODIS surface reflectance with the matched surface water fraction data were used for the RT training. From the training set, 60% were used for training, and the remaining 40% for test. Rules and regression models from the RT training were applied for real applications to New Orleans flooding in 2005 to calculate water fraction values. Flood distributions in both space and time domains were generated using the differences in water fraction values after and before the flooding. The derived water fraction maps were evaluated using higher resolution Thematic Mapper (TM) data from the Landsat observations. It shows that correlation between the water fractions derived from the MODIS and TM data is 0.97, with difference or “bias” of 2.16%, standard deviation of 3.89%, and root mean square error (rmse) of 4.45%. The results show that the RT approach in dynamic monitoring of floods is promising.

1. INTRODUCTION

Satellite-derived flood maps in near-real time are vital to stakeholders and policy makers for disaster monitoring and relief efforts. Precise mapping of floods and standing water is also required for detecting deficiencies in existing flood control and for damage claims.

Satellite sensors used in river and flood studies may be classified into two types: (1) passive, in which the sensor receives energy naturally reflected by or/and emitted from the earth's surface; and (2) active, in which the sensor provides illumination and records the amount of incident energy returned from the sensed surface (Smith, 1997). Sample passive sensors in visible and infrared spectrums are the Thematic Mapper (TM) and Multi-Spectral Scanner (MSS) onboard the Landsat satellites, the Advanced Very High Resolution Radiometer (AVHRR) onboard NOAA polar-orbiting meteorological satellites, Visible High Resolution (HRV) sensor onboard the Satellite Pour l'Observation de la Terre (SPOT), the Advanced Spaceborne Thermal Emission and Reflection Radiometer (ASTER) and the Moderate-Resolution Imaging Spectroradiometer (MODIS) onboard the Earth Observation System (EOS) satellites. Passive microwave radiometers, such as the Special Sensor Microwave/Imager (SSM/I) on board the defense meteorological satellites, can transpire clouds and measure the microwave energy naturally emitted from the Earth's surface. The coarse spatial resolution of these microwave sensors (ca. 27 km at 37 GHz) has been mitigated through the combined use with the visible and infrared sensors for the flood detection (Hallberg et al., 1973; Sipple et al., 1992; Toyra et al., 2001; 2002).

Much of the pioneering work on the remote sensing of floods was accomplished using the MSS sensor on the First Earth Resources Technology Satellite, later renamed Landsat-1.

With a spatial resolution of about 80 m, MSS data was used to mapping the extent of flooding in Iowa (Hallberg et al., 1973; Rango and Salomonson, 1974), Arizona (Morrison and Cooley, 1973), Virginia (Rango and Salomonson, 1974) and along the Mississippi River (Deutsch et al., 1973; Deutsch, and Ruggles, 1974; Rango and Anderson, 1974; McGinnis and Rango, 1975; Deutsch, 1976; Morrison and White, 1976). All of these studies show that MSS band 7 (0.8-1.1 μm) was the most useful for separating water from dry soil or vegetated surfaces due to the strong absorption of water in the near-infrared range. This feature was further confirmed by analyzing MSS band 5 (0.6-0.7 μm), band 7 and field spectral radiometer data along shoreline water-wet soil-dry soil transitions by Gupta and Banerji (Gupta and Banerji 1985). Flooded areas were delineated based on the sharp contrast between water spread and adjacent areas. The standing water areas appeared as dark blue to light blue depending upon the depth of water, while the receded water and wet areas appeared as dark to light gray.

Other studies have continued the methodology developed with the MSS, using Landsat TM and SPOT data (France and Hedges, 1986; Jensen et al., 1986; Watson, 1991; Blasco et al., 1992; Pope et al., 1992; da Silva, 1992). The coarser spatial resolution (ca. 1 km) sensors, such as the AVHRR, have been successfully used for studying large river floods (Ali et al., 1989; Gale and Bainbridge, 1990; Rasid and Pramanik, 1993).

Sheng et al. (2001) summarized the spectral characteristics of the main features (i.e. water, vegetation, soil, and clouds) during floods at the observation scale of NOAA satellites. Although AVHRR data can be displayed in 3-channel color

composites for visual analysis (flood and standing water absorbs infrared wavelengths of energy and appears as blue/black in the RGB composite imagery), water body identification in AVHRR imagery evolved from qualitative visual interpretation to automatic quantitative extraction. The reflectance of AVHRR channel 2 (0.73-1.1 μ m, similar to MSS band 7), the reflectance difference (CH2-CH1) and ratio (CH2/CH1) between channel 2 and 1 (0.58-0.68 μ m, similar to MSS band 5) are used to discriminate water from land if these parameters are less than the threshold values.

Domenikiotis *et al.* (2003) tried to use surface temperature to discriminate water from land surfaces. However, the temperature model may not work well with the flood caused by heavy rainfall during rainy seasons in the summer when there is relatively low or no temperature difference between land and water. Domenikiotis *et al.* (2003) also used Normalized Difference Vegetation Index (NDVI) to identify water from land considering that water covered surfaces usually have very small or even negative NDVI values. It can be seen from its mathematical definition that the NDVI of an area containing a dense vegetation canopy will tend to have positive values (say 0.3 to 0.8), while standing water (e.g., oceans, seas, lakes and rivers), which have a rather low reflectance in both visible (VIS: from 0.4 to 0.7 μ m) and near-infrared (NIR: from 0.7 to 1.1 μ m) spectral bands, result in very low positive or even slightly negative NDVI values.

Regression trees have been used with remote sensing observations (DeFries *et al.*, 1997; Mchaelson, Schimel, Friedl, Davis and Dubayah, 1994; Prince and Steninger, 1999; Hansen *et al.*, 2002, Solomatine and Xue, 2004). They provide a robust tool to handle nonlinear relationship within large data sets.

As described above, in previous studies, several parameters, including the reflectance of near infrared (NIR) channel, the reflectance ratio and difference between NIR and visible (VIS) channels, NDVI, brightness temperature at 11 or 12 μ m, and surface temperature, might be used to identify water from land. Linear mixture model has been used by Sheng *et al.* (2001) to derive water fraction. However, it has not yet been shown which parameter or combination of several parameters is the most effective?

This paper explores how to derive water fraction and flood map from the MODIS data using regression tree (RT) method. Section 2 introduces the dataset used. The physics of the problem and decision algorithms are described in Section 3. Section 4 presents the results and Section 5 gives a summary and discussion.

2. DATA USED

- Surface water percentage data derived from derived from the 1km land/water map supplied by the [USGS Global Land Cover Characterization Project](#). The percentage water was created by simply determining the percentage of 1km pixels designated as water in each 10' region. This data can be obtained from the Surface and Atmospheric Radiation Budget (SARB) working group, part of NASA Langley Research Center's Clouds and the Earth's Radiant Energy System (CERES) mission
- MODIS L3 8-day composite surface reflectance product (MYD09A1) that is computed from the MODIS Level 1B land bands 1, 2, 3, 4, 5, 6, 7, which are centered at 0.648 μ m, 0.858 μ m, 0.470 μ m, 0.555 μ m, 1.24 μ m, 1.64 μ m, and 2.13 μ m, respectively. The product is an estimate of the surface reflectance for each band as it would have been measured at

ground level after removing the atmospheric scattering and absorption.

- MODIS L1B calibrated reflectance at the Top of Atmosphere (TOA) with 1 km resolution (MOD021KM).
- MODIS geolocation fields (MOD03).
- MODIS cloud mask (MOD35) data.
- TM (Thematic Mapper) data from the Landsat observations at 30-meter spatial resolution is used to evaluate water fraction derived from MODIS.

3. METHODOLOGY

The RT, such as the M5P, is a powerful tool for generating rule-based models that balance the need for accurate prediction against the requirements of intelligibility. RT models generally give better results than those produced by simple techniques such as multivariate linear regression, while also being easier to understand than neural networks. Unlike neural networks, the RT program generates a model with rules that describe the relationships between the independent and dependent parameters in the data set. Instead of simple regression analysis techniques, RT uses a piecewise regression technique. The piecewise regression analysis (classifying the data into different subsets) will yield different regression fits for different meteorological conditions, unlike a simple regression analysis. The RT program constructs an unconventional type of tree structure, with the leaves containing linear models instead of discrete classes by DT. A decision tree would categorize the predictions into discrete classes, but the regression tree predicts actual continuous values.

Since RT integrates DT with traditional regression analysis. Like DT algorithm, RT algorithm can integrate all the possible candidate predictors, such as the MODIS channel 2 reflectance (CH2) and channel 1 reflectance CH1, the reflectance ratio (CH2/CH1) and difference (CH2-CH1) between MODIS channel 2 and channel 1, NDVI, Normalized Water Difference Index (NDWI), etc., meanwhile it can determine continuous values, in this case water fraction, and giving accuracy estimates. The NDWI [45], a satellite-derived index from the Near-Infrared (NIR) and Short Wave Infrared (SWIR) channels, is also included as one input attribute. According to Gao [45], NDWI is a good indicator for vegetation liquid water content and is less sensitive to atmospheric scattering effects than NDVI. The MODIS 8-day composite data at 500-m resolution is aggregated to the same 1/6 degree resolution of the surface water percentage map.

In this study, the M5P (Wang and Witten, 1997), a reconstruction of Quinlan's M5 algorithm (Quinlan, 1992) for inducing trees of regression models, is used to derive water fraction from MODIS observations. The M5P combines a conventional decision tree with the possibility of linear regression functions at the nodes. Techniques devised by Breiman *et al.* (1984) for their CART (Classification and Regression Trees) system are adapted in order to deal with enumerated attributes and missing values. Uses features from the well-known CART system and reimplements Quinlan's well-known M5 algorithm with modifications and seems to outperform it. M5P can deal effectively with enumerated attributes and missing values.

4. RESULTS

4.1 Results from the RT training

Training set is critical to RT. MODIS 8-day composite surface reflectance and Surface water percentage data derived from derived from the 1km USGS land/water map, as shown in Figure 1, are used as the training datasets.

Figure 2 shows an example of the output regression tree structure with the M5P algorithm. The tree employs a case's attribute values to map it to a leaf designating one of the regression models (Figure 3). The first number in brackets following each leaf is the number of training instances falling into this leaf and the second number is the root mean squared error of the linear model on these training examples divided by the global absolute deviation.

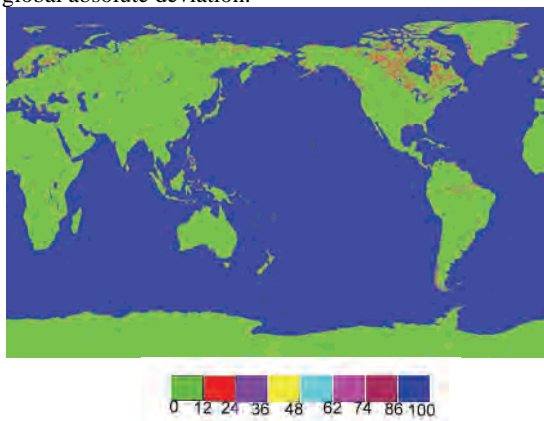


Figure 1. Water percentage map derived from the 1km USGS land/water map.

Regression models generated from the M5P regression tree algorithm are shown in the following:



Figure 2. An example of regression tree structure derived from the M5P algorithm.

LM1: $WF = -162.6945*CH1 - 0.583*CH2 - 320.8135*(CH2-CH1) + 0.3253*CH2/CH1 + 39.981*NDWI + 39.7147$
LM2: $WF = -0.0152*CH1 - 0.583*CH2 - 11.6055*(CH2-CH1) + 0.1568*CH2/CH1 + 0.9568*NDWI + 3.9752$
LM3: $WF = -0.0152*CH1 - 0.336*CH2 - 71.4079*(CH2-CH1) - 0.7859*CH2/CH1 + 19.7358*NDWI + 8.5573$
LM4: $WF = 0.2117*CH1 - 9.0327*CH2 - 0.9369*(CH2-CH1) - 33.0853*CH2/CH1 - 7.0218*NDWI + 43.6346$

LM5: $WF = -2.223*CH1 + 0.5925*CH2 - 5.2925*(CH2-CH1) + 0.0591*CH2/CH1 + 0.4396*NDWI + 2.2389$
LM6: $WF = -4.0638*CH1 + 0.5925*CH2 - 8.7526*(CH2-CH1) + 0.0591*CH2/CH1 + 20.3801*NDWI - 0.7155$
LM7: $WF = -1.7928*CH1 + 0.9452*CH2 - 4.5942*(CH2-CH1) + 0.0591*CH2/CH1 + 0.2035*NDWI + 1.2859$
LM8: $WF = -0.0818*CH1 - 0.0378*CH2 - 1.0327*(CH2-CH1) + 0.0524*CH2/CH1 - 1.7571*NDWI + 1.0939$
LM9: $WF = -0.6528*CH1 + 0.0744*CH2 - 1.2964*(CH2-CH1) - 0.0338*CH2/CH1 + 0.064*NDWI + 0.4347$
LM10: $WF = -0.2448*CH1 - 4.3881*CH2 - 0.9276*(CH2-CH1) - 0.5367*CH2/CH1 + 0.009*NDWI + 2.8895$

Each regression model consists of:

- A linear model (LM) number -- this serves to identify the regression model.
- Every enumerated model is composed of a regression equation.

Figure 2 just shows an example of the output regression tree structure. The actual tree structure is too complicated to be shown in a figure.

4.2 Results from the tests with real applications

Since we wish to get the geolocation information, instead of using surface reflectance data (MOD09), we chose to use the MODIS L1B calibrated TOA reflectance data (MOD021KM) in conjunction with the MODIS geolocation fields (MOD03). An accurate cloud filter for the Imager data is critical for reliable results. Since our method uses satellite visible and infrared observations, the water detection will be limited to clear conditions. MODIS cloud mask (MOD35) data is used to filter the cloudy conditions. The rules and threshold values obtained from the training with surface reflectance data are applied to “re-predict” the New Orleans flooding at the end of August in 2005 due to the landfall of Hurricane Katrina, which caused over 1500 deaths and total damage costs exceeding \$50 billion. Figure 3 shows the water fraction map on these three days, calculated by using the CH2 reflectance and (CH2-CH1) predictors. From these images, we can clearly detect flooded areas by comparing water fraction maps after flooding with those before flooding. Figure 4 presents the flood maps on August 31 and 30 as the difference in water fraction values after flooding with those before flooding on August 27. The flooded regions are identified in red, the original water bodies are shown in blue, while clouds are marked in grey. We can see clearly that New Orleans and its surrounded areas were inundated on August 30 and 31, 2005 after Hurricane Katrina made landfall on August 29, 2005.

4.3 Evaluations

Since there are no direct ground measurements of water fraction as the truth data, quantitative evaluations of water fraction derived from satellite observations are challenging. The use of higher resolution satellite data is a feasible way to solve this problem. In this study, TM data with 30-m spatial resolution are used to evaluate water fraction estimates from MODIS observations.

The Landsat TM pixels can be assumed to be a pure pixel composed of land or water. Using a decision tree method to perform classification to TM data, the fraction of water in a MODIS grid (1 km×1 km) can be calculated. The water fractions at the MODIS resolution aggregated from the TM

observations are then used to evaluate water fractions derived from MODIS observations. The scatter plot is shown in Figure 5, the evaluation results show correlation between MODIS and TM water fractions is 0.966 with bias of 2.16%, standard deviation of 3.89%, and rms of 4.45%, for total sample number of 50423.

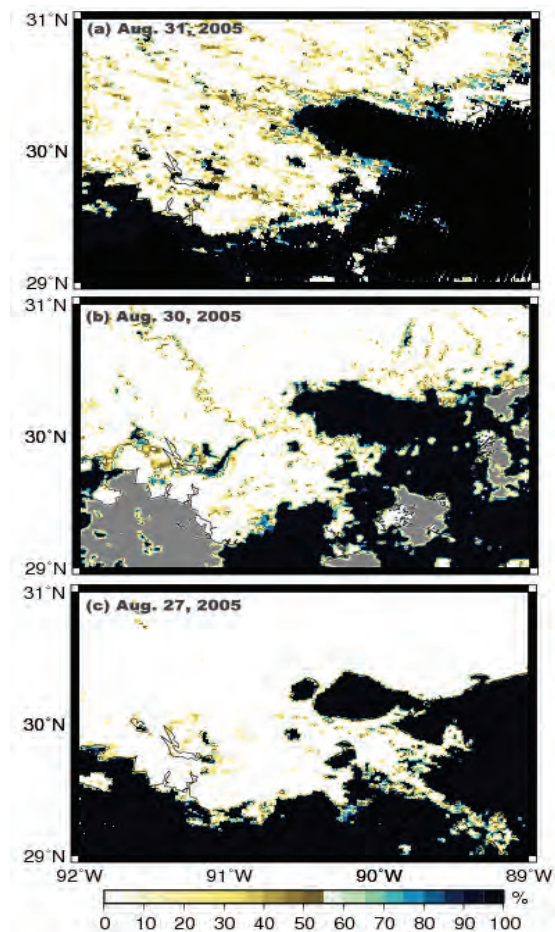


Figure 3. Water fraction map on August 31 (a), 30 (b), and 27 (c), 2008. Figure 3. Water fraction map on August 31 (a), 30 (b), and 27 (c), 2008.

5. SUMMARY

In this study, the Regression Tree technique is applied to water body and flood identification with the EOS MODIS data. MODIS data has the advantage of global coverage, and so can be available worldwide. MODIS surface reflectance with the matched surface percent water data before flooding are used for training with the RT method. MODIS surface reflectance data at 500m resolution are aggregated to the same 1/6 degree resolution as the percent water data. When we test the rules and regression models obtained from the training to “predict” or model future flood, in order to get the geolocation information, we use the Level 1B swath 1km calibrated reflectances at the TOA with the matched geolocation fields.

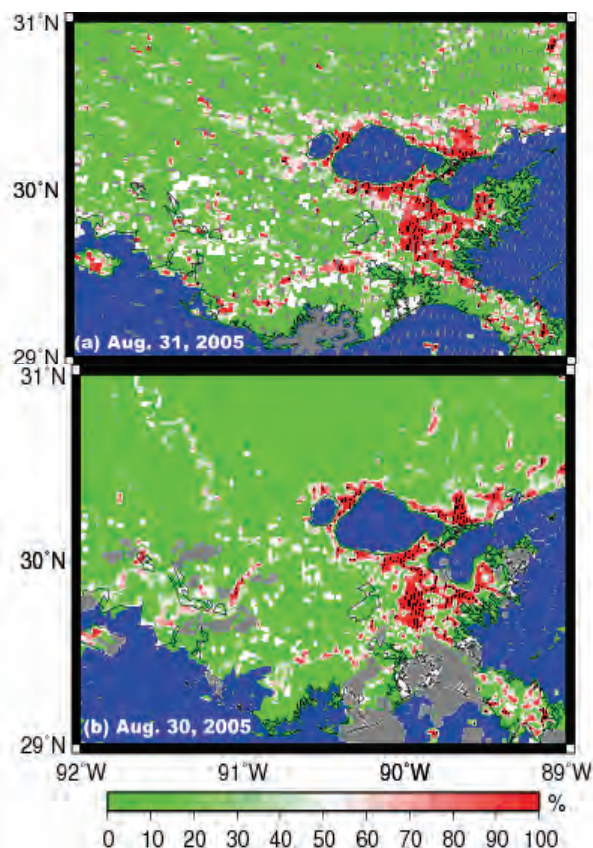


Figure 4. Flood map on August 31 (a) and 30 (b), 2005 shown as the water fraction difference after and before flooding (August 27).

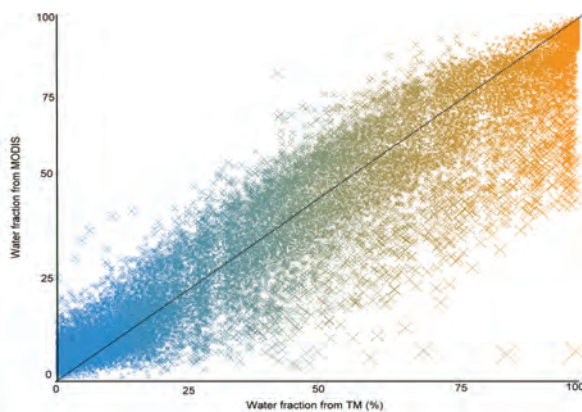


Figure 5. Scatter plot of water fractions of MODIS and TM on 08/27/2005 using regression-tree algorithm.

The time series of water fraction maps are generated, monitoring area changes of inundation. The flood maps are derived by calculating the difference in water fraction before and after flooding, and show promising results. The successful applications of MODIS observations to water body and flood identification demonstrate the effectiveness of the RT approach.

REFERENCES

Ali, A., D. A. Quadir, O. K. Huh, 1989. Study of river flood hydrology in Bangladesh with AVHRR data. *International Journal of Remote Sensing*, 10 (12), pp.1873-1891.

- Blasco, F., M. F. Bellan, and M. U. Chaudhury, 1992. Estimating the extent of floods in Bangladesh using SPOT data. *Remote Sensing Environment*, 39, pp.167-178.
- Breiman, L., 2004. Random Forests. *Machine Learning*, 45 (1), pp. 5-32.
- Breiman, L., J. H. Friedman, R. A. Olshen, C. J. Stone, 1984. Classification and Regression Trees. Wadsworth & Brooks/Cole Advanced Books & Software, Pacific Grove, CA, 1984.
- Deutsch, M., F. Ruggles, 1974. Optical data processing and projected applications of the ERTS-1 imagery covering the 1973 Mississippi River Valley floods. *Water Resource Bulletin*, 10 (5), pp. 1023-1039.
- Domenikiotis, C., A. Loukas, N. R. Dalezios, 2003. The use of NOAA/AVHRR satellite data for monitoring and assessment of forest fires and floods. *Natural Hazards Earth System Science*, 3, pp. 115-128.
- France, M. J., P. D. Hedges, 1986. A hydrological comparison of Landsat TM, Landsat MSS, and black and white aerial photography in Damen. Smit, and Verstappen (Eds),” Proceedings 7th International Symposium, ISPRS (International Society Photogrammetry and Remote Sensing) Commission VII, Enschede, pp. 717-720.
- Gale, S. J., S. Bainbridge, 1990: The floods in eastern Australia. *Nature*, 345, pp. 767.
- Gao, B.-C., 1996. NDWI - A normalized difference water index for remote sensing of vegetation liquid water from space. *Remote Sensing of Environment*, 58, pp. 257-266.
- Gupta R. P., S. Banerji, 1985. Monitoring of reservoir volume using Landsat data. *Journal of Hydrology*, 77, pp. 159-170.
- Hallberg, G. R., B. E. Hoyer, A. Rango, 1973. Application of ERTS-1 imagery to flood inundation mapping. NASA Special Pub. No. 327, Symposium on significant results obtained from the Earth Resources Satellite-1, Vol. 1, Technical presentations, section A, 745-753.
- Hansen, M.C., R.S. DeFries, J.R.G. Townshend, R. Sohlberg, C. Dimiceli, M. Carroll, 2002. Towards an operational MODIS continuous field of percent tree cover algorithm: examples using AVHRR and MODIS data. *Remote Sensing of Environment* 83, 303–319.
- Han, J.W., Kamber, M., 2001. Data Mining: Concept and Techniques. Morgan Kaufmann Publishers, San Francisco, CA, 550pp.
- Kohavi, R., 1996. Scaling Up the Accuracy of Naive-Bayes Classifiers: a Decision-Tree Hybrid. Proceedings of the Second International Conference on Knowledge Discovery and Data Mining, 1996.
- Jensen, J. R., M. E. Hodgson, E. Christensen, H. E., Jr. Mackey, L. R. Tinney, R. Sharitz, 1986. Remote sensing inland wetlands: a multispectral approach, *Photogrammetric Engineering Remote Sensing*, 52, pp. 87-100.
- McGinnis, D. F. and A. Rango, 1975. Earth Resources Satellite systems for flood monitoring. *Geophysical Research Letters*, 2 (4), pp. 132-135.
- Morrison, R. B., P. G. White, 1976. Monitoring flood inundation. U.S. Geol. Surv. Prof. Pap. 929, ERTS-1, A New Window on Our Planet, pp. 196-208.
- Pope, K. O., E. J. Sheffner, K. J. Linthicum, C. L. Bailey, T. M. Logan, E. S. Kasichke, K. Birney, A. R. Njogu, C. R. Roberts, 1992. Identification of Central Kenyan Rift Valley Fever virus vector habitats with Landsat TM and evaluation of their flooding status with airborne imaging radar. *Remote Sensing of Environment*, 40, 185-196.
- Quinlan, R. J., 1992. Learning with Continuous Classes. In: 5th Australian Joint Conference on Artificial Intelligence, Singapore, pp. 343-348.
- Quinlan, J.R., 1993. C4.5: Programs for Machine Learning. Morgan Kaufmann Publishers, San Francisco, CA, 316pp.
- Rasid, H., M. A. H. Pramanik, 1993. Areal extent of the 1988 flood in Bangladesh: how much did the satellite imagery show? *Natural Hazards*, 8, pp. 189-200.
- Running, S., T. R. Loveland, L. Pierce, 1995. A Remote Sensing Based Vegetation Classification Logic for Global Land Cover Analysis. *Remote Sensing Environment*, 51, pp. 39-48.
- Sheng, Y., P. Gong, Q. Xiao, 2001. Quantitative dynamic flood monitoring with NOAA AVHRR. *International Journal of remote sensing*, 22 (9), pp. 1709–1724.
- Smith, L. C., 1997. [Satellite remote sensing of river inundation area, stage, and discharge: A review](#). *Hydrological Processes*, 11 (10), pp. 1427-1439.
- Toyra, J., A. Pietroniro, L. W. Martz LW, et al., 2002. [A multi-sensor approach to wetland flood monitoring](#). *Hydrological Processes*, 16 (8), pp. 1569-1581.
- Toyra, J., A. Pietroniro, L. W. Martz, 2001. [Multisensor hydrologic assessment of a freshwater wetland](#). *Remote Sensing of Environment*, 75 (2), pp. 162-173.
- Vila da Silva, J. S., H. J. H. Kux, 1992. Thematic mapper and GIS data integration to evaluate the flooding dynamics within the Panatal, Mato Grosso do Sul State, Brazil, Proceedings, 1992. *Int. Geosci. Remote Sens. Symp.* (IGARSS '92), pp. 1478-1480.
- Wang, Y., Witten, I. H., 1997. Induction of model trees for predicting continuous classes. Poster papers of the 9th European Conference on Machine Learning, 1997.
- Watson, J. P., 1991. A visual interpretation of a Landsat mosaic of the Okavango Delta and surrounding area. *Remote Sensing of Environment* 35, 1-9.

ACKNOWLEDGEMENTS

This study was supported by the GOES-R program through the GOES-R Algorithm Working Group. The manuscript contents are solely the opinions of the authors and do not constitute a statement of policy, decision, or position on behalf of NOAA or the U. S. Government.

ENVIRONMENTAL IMPACT ASSESSMENT USING NEURAL NETWORK MODEL: A CASE STUDY OF THE JAHANI, KONARSIAH AND KOHE GACH SALT PLUGS, SE SHIRAZ, IRAN

M. H. Tayebi^{a,*}, M. H. Tangestani^a, H. Roosta^b

^a Dept. of Earth sciences, Faculty of sciences, Shiraz University, 71454, Shiraz, Iran- Mhtayebi@shirazu.ac.ir- Tangestani@susc.ac.ir

^b Dept. of Civil Engineering, Marvdasht Branch, Islamic Azad University, Marvdasht, Iran – Hasan.Roosta@gmail.com

KEY WORDS: Salt plug, Environmental impact, MLP neural network, ASTER

ABSTRACT:

This study employs Multi-Layer Perceptron (MLP) to estimate environmental impact of salt plugs using Advanced Spaceborne Thermal Emission and Reflection Radiometer (ASTER). VNIR and SWIR datasets of ASTER were assessed in mapping and detecting Jahani, Konarsiah, and Kohe Gach salt plugs and the affected areas located at SE Shiraz, Iran. PC color composite and geological map of the region were used to select training areas. Three datasets including, IARR, PCA and MNF were used as input to the MLP. The results of each input were compared with the ground truth and the geological map to determine the accuracy and therefore to select the more appropriate dataset to be input to MLP approach input. The results demonstrated a number of the polluted sites and the main polluted tributaries that convey the water as well as the salt plug materials into the Firouzabad River. It is also indicated that the MNF input (with 85% overall accuracy) can obtain a slightly more accurate estimation than the IARR (79%) and PCA inputs (82%). It is concluded that the result of MNF input to MLP is more applicable to effective environmental impact assessment and sustainable water resources management at salt plug-affected areas.

1. INTRODUCTION

Salinity caused by natural processes is a major environmental hazard and can have hazardous effects on agricultural production, water quality, ecological health, soil erosion, flood risk, infrastructure and the society. The effects and damages of salinity are not stronger than earthquake or landslide (Metternicht and Zink, 2003), but it is a major threat in semi-arid and arid regions such as Iran. The most important impact of salinity is salinization of fresh rivers, which affects the quality of water for drinking and irrigation.

More than 150 known salt plugs (Kent, 1970) are exposed at the south eastern Zagros Folded Belt, southern Iran. These saline formations are important because: (1) they can potentially trap the hydrocarbons, (2) for their potential in ore deposition, and (3) they can provide harmful environmental impacts. Three of these salt plugs, namely Konarsiah, Jahani and Kohe Gach are exposed at the SE Shiraz, southern Firouzabad (Fig. 1). These salt plugs increase the salinity of groundwater, surface water (especially Firouzabad River), and the adjacent soils by direct dissolution and transport of soluble salt plug minerals, which directly influence the economy and ecosystem of the area.

Information on the extent of the salt plug-affected areas is required for effective environmental planning and sustainable water resources management. Assessing the spread of salinity by salt plugs has traditionally been implemented by geochemical, hydrologic, and geophysical (Zadneek, 2008; Ghanbarian, 2007; Dehghan, 2008) methods requiring the collection of numerous samples followed by laboratory measurements. However, remote sensing can act as an effective

means of detecting environmental pollution and is a useful tool for acquiring basic information particularly on a regional scale (Sabins, 1997). The task of identifying salinity largely depends on the peculiar way salts distribute at the soil surface and within the soil mantle, and on the capability of the remote sensing tools to identify salts (Zinck, 2001). Many remote sensing techniques and datasets have already been used to map salt-affected areas (Hunt and Salisbury, 1976; Hick and Russell, 1990; Mougnot *et al.*, 1993; Ben-Dor *et al.*, 2002; Metternicht and Zink, 2003; Farifteh *et al.*, 2006), but there is lack of a publication focusing on the application of remote sensing in mapping and detecting the salt plug environmental impact. An unpublished work of Tavakkoli (2008), however, used the ASTER data for enhancing the lithological units of the same salt plugs.

Artificial neural network (ANN) is an interconnected group of nodes using mathematical methods to process information. It is a self adaptive system, which can change its structure based on the internal or external information (Hu and Weng, 2009). Among all the techniques, artificial neural networks (ANN) have been widely used (Ji, 2000; Zhai *et al.*, 2006) due to its advantages over statistical methods (Bischof *et al.*, 1992) such as no assumption about the probabilistic models of data, robust in noisy environments, and the ability to learn complex patterns (Ji, 2000). Neural networks have been applied in the large number and wide variety of applications (Liu *et al.*, 2001; Kavzoglu & Mather, 2003; Verbeke *et al.*, 2004; Chormanski *et al.*, 2008; Hu and Weng, 2009). The primary aim of this study was identifying and mapping the salt plugs as well as the salt plug-affected areas. The second aim is to evaluating the use of

* Corresponding author. Dept. of Earth Sciences, Faculty of Sciences, Shiraz University, 71454 Shiraz, Iran. Tel: +9809177173319 ; fax: +982284572. Mhtayebi@shirazu.ac.ir.

different input datasets (IARR, PCA and MNF) in identifying the environmental impact of the salt plugs. Bands 1-9 of ASTER in combination with Principal Component Analysis (PCA), Minimum Noise Fraction (MNF) transformation and Multi-Layer Perceptron (MLP) were used in this study.

2. STUDY AREA

The study area ($28^{\circ} 31' - 28^{\circ} 53' N$; $52^{\circ} 16' - 52^{\circ} 33' E$) is situated in the Zagros fold-and-thrust belt, western the Iranian province of Fars, southeastern Shiraz, and about 25Km south west of Firouzabad (Fig. 1). The Zagros mountain range is divided into three tectonic zones from the NE to the SW: the High Zagros, the Zagros Simply Folded Belt, and the Zagros Foredeep Zone (Stöcklin 1968; Falcon, 1974). The study area is located in the Simply Folded Belt (SFB) which has particularly been studied owing to the salt plugs and its structure. The geology consists of Infracambrian diapirs (salt plugs) surrounded by the Cretaceous to recent formations.

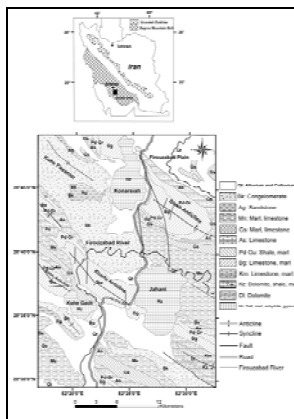


Figure 1. Geological map of the study area, Southern Firouzabad, SE Shiraz, Iran

3. METHODS

VNIR+SWIR dataset of ASTER were used to detect and map salt plugs-affected areas by the MLP neural network. ASTER instrument measures reflected radiation in three bands between 0.52 and 0.86 μm (VNIR) and six bands from 1.6 to 2.43 μm (SWIR), with 15- and 30-m resolution, respectively (Fujisada, 1995). The ASTER Level 1B data used in this study were acquired on March 24, 2001. The following steps constitute the data processing and analysis of the ASTER bands: (1) spatial registration of the 30-m SWIR data to the 15-m VNIR data; (2) the data were geometrically corrected using 1:25000 topographic maps; (3) Internal Average Relative Reflectance (IARR) calibration was then carried out on the data to normalizing images to a scene average spectrum. This method is particularly effective in areas where no ground measurements exist and little is known about the scene (Kruse, 1988); (4) A spectral reduction and data compression was performed using the principal components analysis; (5) To train and validate the use of MLP networks, training areas of each lithological unit were selected using knowledge of the PCA and the geological map. To do this, several ROIs were measured and extracted from ASTER image.

3.1 Principal Components Analysis (PCA)

Principal components analysis (Richards, 1984; Eklundh and Singh, 1993) has become a standard statistical approach in image processing for two main reasons: (1) to reduce the number of correlated image bands to form a small number of independent principal components to represent most of the variability carried by the multiple image bands, and (2) to increase the interpretability of the components as combinations of multiple bands (Jing and Panahi, 2006). PCA output results were used to create RGB color composite images to discriminating various lithological units and reducing the information included in the raw data into two or three bands without losing significant information (Monger, 2002).

Component	Eigenvalue	Variance (%)	Total (%)
PC1	0.2735	87.989	87.99
PC2	0.0238	7.661	95.65
PC3	0.0094	3.044	98.70
PC4	0.0016	0.520	99.22
PC5	0.0012	0.388	99.60
PC6	0.0005	0.173	99.78
PC7	0.0003	0.108	99.89
PC8	0.0001	0.060	99.95
PC9	0.0001	0.052	100.00

Table 1. PCA statistics of VNIR-SWIR ASTER bands on study area

PCA statistics were accounted to selecting components with the highest information to be used in selecting training areas. Table1 shows the eigenvalues, variances and total cumulative variances for the nine PC image of ASTER data. The PC1 image shows 87.99 percent of variances. The PC2 and PC3 images show 7.66 and 3.04 percent of variance respectively. Therefore the first three components represent 98.7% variances of the image data. On the other hand components 4-9 only contain 1.3% of the information.

In order to mapping lithology and environmental impact assessment of the salt plugs components 1-3 were used to generate colour composite image and to select training areas.

3.2 Minimum Noise Fraction (MNF)

The MNF transformation is a linear transformation related to principal components that orders the data according to signal-to-noise-ratio (Green *et al.*, 1988). It can be used to determine the inherent dimensionality of the data, to segregate noise in the data, and to reduce the computational requirements for subsequent processing (Green *et al.*, 1988; Boardman and Kruse, 1994). The MNF was applied to the ASTER to enhance lithological units and salt plugs-affected areas.

3.3 Multi-layer perceptron (MLP)

The multilayer perceptron (Rumelhart, and MacClelland, 1986) is by far the most well known and most popular neural network among all the existing neural network paradigms. (Hu and Neng Hwang, 2002; Carvalho, 2001). It is a mathematical approach (Hu and Weng, 2009), with some advantages and disadvantages as compared with other existing neural networks. For example, nonparametric statistical methods may be more useful for

describing the relationship between remotely sensed imagery and environmental variables since these tests make no a priori assumptions about the data. An artificial neural network (ANN) offers a powerful method for analyzing complex relationships among variables without making assumptions about the data. ANNs are capable of handling non-normality, nonlinearity and collinearity in a system (Haykin, 1994). There are many examples of successful MLP applications (Heermann, and Khazenie, 1992; Kanellopoulos, and Wilkinson, 1997; Verbeke, *et al.*, 2004; Roosta *et al.*, 2007; Hu and Weng, 2009). However, it is widely recognized that MLPs are sensitive to many operational factors including the size and quality of the training dataset, network architecture, training parameters, and over-fitting problems. (Yuan *et al.*, 2009; Kavzoglu and Mather, 2003). The parameters have to be set up properly to find the global minimum of error function instead of a local minimum (Hu and Weng, 2009).

A MLP neural network model used in the back-propagation (BP) learning algorithm has a nonlinear activation function (sigmoid function) contains several neurons (nodes), each having several inputs. These neurons are organized in layers, labeled as the hidden layer 1, hidden layer 2, and the output layer. Specifically to image classification, the input layer represents the original image, and each input layer node represents one image band. The hidden layer is used for image classification and passing the results to the output layer. The output layer outputs classified images (Hu and Weng, 2009). The name hidden layer refers to the fact that the output of these neurons will be fed into upper layer neurons and, therefore, is hidden from the user who only observes the output of neurons at the output layer (Yu and Neng Hwang, 2002). Figure 2 illustrates a configuration of MLP.

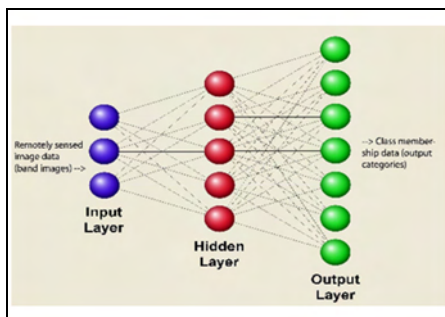


Figure 2. The structure of three-layer MLP neural network

The MLP approach consists of the following steps: (1) entering ASTER dataset as input (9 bands); (2) entering the training sites; (3) entering the number of training and testing sample pixels per category (The training pixels will be used in the analysis and will be a subset of the total pixels found in the training site). The testing pixels will be used to validate the results. The number of training samples will affect the accuracy of the training result. Too few samples may not represent the population for each category, while too many samples may cause samples to overlap, leading to a possible over training of the network. Additionally, too much iteration can also cause over training; (4) specifying the network topology (the number of hidden layers, the number of the input layer nodes, the number of the output layer nodes). The number of the hidden layer nodes is estimated by the following equation:

$$N_h = INT(\sqrt{N_i + N_o}) \quad (1)$$

Where N_h , N_i and N_o are the number of the hidden, input and output layer nodes respectively; (5) specifying the number of training parameters (the learning rate- the momentum factor- the stopping criteria- the number of iterations- set an accuracy rate); (6) training the network which is required to be implemented before classifying the image. Training a neural network is a key step in classification processes, the forward and backward passes continue until the network has "learned" the characteristics of all the classes and the neural network modified its internal representation by changing the values of its weights to improve the mapping of input to output relationships (Ziaai *et al.*, 2009). During training, each sample (for example, a feature vector associated with a single pixel) is fed into the input layer and the receiving node sums the weighted signals from all nodes to which it is connected in the preceding layer. Formally, the input that a single node receives is weighted according to:

$$net_j = \sum_{i=1}^m w_{ij} o_i \quad (2)$$

Where w_{ij} represents the weight between node i and j , and o_i is output from node i . The output from given node j is then computed from:

$$o_j = f(net_j) \quad (3)$$

The function f is usually a non-linear sigmoidal function that is applied to the weighted sum of inputs before the signal passes to the next layer.

Once the forward pass is finished, the activities of the output nodes are compared with their expected activities. Each node in the output layer is associated with a class. When a pattern is presented to the network, each output node will generate a value that indicates the similarity between the input pattern and the corresponding class. Except in very unusual circumstances, the actual output will differ from the desired outcome; the difference is associated with error in the network. This error is then propagated backward with weights for relevant connections corrected via a relation known as the delta rule:

$$\Delta w_{ij(t+1)} = \eta \delta_j o_i + \alpha \Delta w_{ij(t)} \quad (4)$$

Where η is the learning rate, α is the momentum factor, and δ_j is the computed error. The forward and backward passes continue until the network has "learned" the characteristics of all the classes. The purpose of training the network is to get the proper weights both for the connection between the input and hidden layer, and between the hidden and the output layer for the classification of the unknown pixels. The input pattern is classified into the class that is associated with the node with the highest activation level; (7) classifying image (hard classification image), and (8) accuracy assessment.

IARR, PCA and MNF datasets of ASTER were used as a first layer (the input layer) that is composed of nine neurons. Based on PC1, PC2 and PC3 color composite and exiting geological map, 7 training sites including salt plug (salt, gypsum, anhydrite), Bg (limestone, marl), Pd-Gu (shale, marl), As (limestone), Mn (marl, limestone), Bk (conglomerate) and Farmland were selected for defining the categories that should be classified. 100 pixels were used as training pixels and 100 pixels as testing pixels for validating the results. By using equation (1), 8 neurons were calculated to use in the hidden

layer and the 7 output layer nodes were defined based on the number of training site categories. For balance between training time and overall error reduction, learning rates between 0.01 - 0.2 were used, and to reduce the oscillatory problems, momentum factor between 0.5 and 0.6 were applied. To terminate the training process, the accuracy rate was set to 90% and 10000 iteration were chosen.

The more appropriate network parameters considered in this study were shown in table 2. For comparing the MLP results of IARR, PCA and MNF inputs this structure was used separately for each input. Three Hard classification images based on different input were produced by MLP approach to showing the lithological units and distribution of salt plug-affected areas (Fig 3).

Parameter	Value
Hidden layers	8
Learning rate	0.10
Momentum factor	0.5
Sigmoid constant a	1.0
Accurate rate %	90%

Table 2. The more appropriate network parameters that were used in this study.

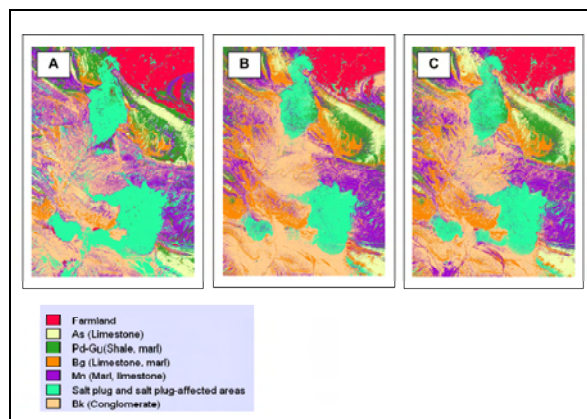


Figure 3. MLP mapping results, (A) result of IARR input to MLP, (B) result of PCA input to MLP, (C) result of MNF input to MLP.

4. ACCURACY ASSESSMENT OF INPUT DATASETS

To evaluate the results of MLP classification maps obtain from three input datasets (IARR, PCA and MNF), the accuracy of salt-affected areas and lithological units were assessed using ground reference information by determining the overall accuracy and Kappa coefficient.

The accuracy results are summarized in table 3. Comparison of the results of different input datasets shows higher capability of the MNF input to detect salt-affected areas. The accuracy results indicated that operating MLP with MNF input has higher accuracy (85%) than the IARR input with 79% accuracy and PCA inputs with 82% accuracy, so the hard classification image produced by MNF input was used to assessment of the salt plug-affected areas.

Input to MLP	Overall accuracy	Kappa coefficient
IARR	79%	0.64
PCA	82%	0.77
MNF	85%	0.79

Table 3. Accuracy assessment of hard classification maps

5. RESULT AND DISCUSSION

This study investigated the utility of the MLP network with different input (IARR, PCA and MNF) for detecting salt plug-affected areas southeastern Shiraz, Iran.

The ability to map salt plugs, and extent of the salt plug's materials are essential to understand and minimize salt plug's environmental impact and provides practical solutions to more advantageous water resources management.

At first, ASTER datasets of the area were analyzed by using the PCA method. By this method, the ASTER data were limited to 3 bands. Table 1 shows PCA eigen analysis of ASTER image. These components were used to find suitable training areas for the classification, as well as gathering sufficient number of training samples for each lithological unit with the aim of existing geological map. The training areas were used to training the MLP neural network and detecting salt plug-affected areas. Hard classification image of MNF input to MLP provide the opportunity to map salt plugs and salt plug-affected areas, as well as to estimate extent of salt plug materials. This may be important to identify impacts of salt plug on the adjacent areas, especially on the Firouzabad River (Fig 4).

The Jahani (central part of the scene), Konarsiah (upper part of the scene) and Kohe Gach (western part of the scene) were identified from this neural network method. The Hard classification image of the southern Firouzabad show Konarsiah salt plug in elliptical shape. This salt plug is located at the top of the image, surrounded by salt plug-affected areas along the slopes and margins of the salt plug (Fig 4). Yellow boxes in figure 4 indicate polluted areas surrounding the Konarsiah. The spatial distribution of salt plug-affected areas observed in the hard classification image revealed three main spatial trends. Relatively, high distribution of salt plug materials is seen in the northern, southern and western parts of the Konarsiah. It seems that morphology of the salt plug plays a major role on the shaping of the salt plug-affected areas, because it controls the flow of surface runoff and hence the distribution of salt plugs materials. The main tributaries that convey water as well as Konarsiah salt plug materials are shown in figure 4, drainages 1, 2 and 3, including branches that convey the Konarsiah materials into the Firouzabad River. The branch 1, located at the northern Konarsiah salt plug, drains its materials toward the east, but branches 2 and 3 are situated in the eastern and western sides of this salt plug respectively, draining their materials toward the south.

The Jahani salt plug is located at the center of the hard classification image (Fig 4). High distributions of salt plug materials occur in the eastern, western and south western parts of the Jahani. This image shows that the salt plug materials are extending down to the Firouzabad River. The amounts of materials decrease from the salt plug to the Firouzabad River. The results show a good differentiation between salt plugs materials and other lithological units however, some misclassifications occur in south east Jahani salt plug due to the spectral similarities. The main tributaries that convey the water as well as the Jahani salt plug materials are shown in figure 4.

Drainages 4, 5, and 6, located at the western side, drain the salt materials toward the west.

The distribution patterns of salt plug materials show a similarity to the spatial pattern of the Firouzabad river tributaries (Fig 4). The most important part of Firouzabad River that was polluted directly by the salt plug is situated at the northern part of the Jahani. This contact was clearly detected by the image processing (Fig 4).

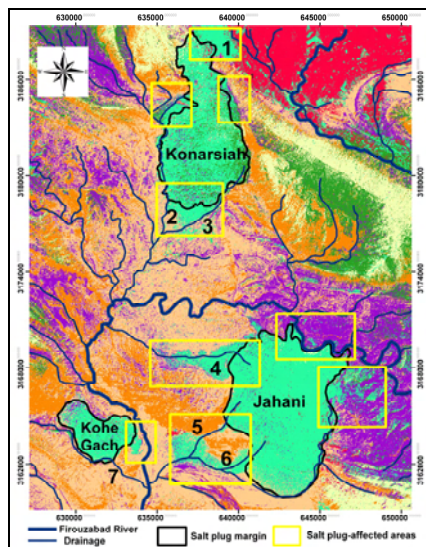


Figure 4. MLP mapping result, GIS layer of Firouzabad River and its tributaries are overlaid the image. Yellow boxes indicate the locations of polluted areas surroundings the Konarsiah, Jahani and kohe Gach. The labels 1, 2, 3, 4, 5, 6, and 7 illustrate the main polluted drainages.

Kohe Gach is a small salt plug and is located at the western part of the scene. The materials of this salt plug are identified as having the same composition as the Konarsiah and Jahani (Fig 4). Relatively high distribution of salt plug materials is seen in the eastern part of the Kohe Gach. This salt plug is another potential source of pollution, although the affected areas are relatively low. The main tributary that is polluted by this salt plug is branch number 7 (southern the salt plug), draining salt materials toward the east (Fig 4).

6. CONCLUSION

Results of MLP neural network at the south Firouzabad plain, SE Shiraz, demonstrated a number of the polluted sites and the main polluted tributaries that convey water as well as salt plug materials into the Firouzabad River. It is evident from the results that as water flows over and through the salt plugs, it picks up and carries contaminants towards the outlet of the basin. Surface water also carries pollutants into the underground water. Soil and the Firouzabad River, nearby the salt plugs, are polluted due to the erosion of these salt plugs. Therefore, it is necessary to plan to reduce their impacts on the water quality. Four affected areas around the Konarsiah salt plug, four affected areas surrounding the Jahani and one affected area adjacent to the Kohe Gach were identified and mapped using MLP approach.

Comparison of using different input to MLP approach showed that MNF input provides more accurate result than the IARR and PCA inputs. Results also demonstrated the viability of VNIR+SWIR dataset of ASTER in combination to the MLP approach for mapping the salt plugs and identifying their environmental impacts.

7. ACKNOWLEDGEMENT

The authors would like to thank the Research Vice Chancellor of Shiraz University, Iran. The ASTER data were provided by the Land Processes Distributed Active Center (LP DAAC), located at the U.S. Geological Survey (USGS) Earth Resources Observation and Science (EROS) Center.

8. REFERENCE

- Ben-Dor, E., 2002. Quantitative remote sensing of soil properties. *Advanced in Agronomy*, 75, pp. 173-243.
- Bischof, H; Schneider, W; Pinz, A.J., 1992. Multispectral classification of landsat images using neural networks. *IEEE Trans. Geosci. Remote Sens.* 30, pp. 482-490.
- Boardman J. W., and Kruse, F. A., 1994, Automated spectral analysis: A geologic example using AVIRIS data, north Grapevine Mountains, Nevada: in Proceedings, *Tenth Thematic Conference on Geologic Remote Sensing*, Environmental Research Institute of Michigan, Ann Arbor, MI, pp. I-407 - I-418.
- Carvalho, L. M. T., 2001. Mapping and monitoring forest remnants: A multiscale analysis of spatio-temporal data. Doctoral thesis. Wageningen University, Wageningen, The Netherlands.
- Chormanski, J., Voorde, T. V. D., Roeck, T. D., Batelaan, O., & Canters, F., 2008. Improving distributed runoff prediction in urbanized catchments with remote sensing based estimates of impervious surface cover. *Sensors*, 8, pp. 910-932.
- Dehghan Ghasr Ahmadi, M., 2008. Geological investigation of Sarvestan Salt dome and its influence on the Groundwater; MSc thesis, Dept. Of Earth Sciences, Shiraz University, Iran, pp. 119.
- Eklundh, L. and Singh, A., 1993. A comparative analysis of standardized and unstandardized principal components analysis in remote sensing. *International Journal of Remote Sensing*, 14, pp. 1359-1370.
- Falcon, N.L., 1974. Southern Iran: Zagros Mountains, in Mesozoic-Cenozoic Orogenic Belts, Data for Orogenic Studies, ed. Spencer, A.M., *Geol. Soc. Spec. Publ. London*, 4, pp. 199-211.
- Farifteh, j., Farshad, A. and George, R.J., 2006. Assessing salt-affected soils using remote sensing, solute modelling and geophysics, *Geoderma*, 130, pp. 191-206.
- Fujisada, H., 1995. Design and performance of ASTER instrument. *Proceedings SPIE* (International Society for Optical Engineering), Fujisada, H., Sweeting, M. N., eds, pp. 2583, 16-25.

- Ghanbarian, M. A., 2007. Tectonic and Geoelectrical studies of Salt domes in Southern fars with emphasis on Groundwater quality; MSc thesis, Dept. Of Earth Sciences, Shiraz University, Iran, pp. 230.
- Green, A. A., Berman, M., Switzer, B., and Craig, M. D., 1988. A transformation for ordering multispectral data in terms of image quality with implications for noise removal: *IEEE Transactions on Geoscience and Remote Sensing*, v. 26, no. 1, pp. 65 - 74.
- Haykin, S., 1994. Neural networks: A comprehensive foundation. Upper Saddle River, NJ7 Prentice Hall.
- Heermann, P.D., and Khazenie, N., 1992. Classification of multispectral remote sensing data using a backpropagation neural network. *IEEE Trans. Geosci. Remote Sens.*, 30, pp. 81–88.
- Hick, P.T., Russell, W.G.R., 1990. Some spectral considerations for remote sensing of soil salinity. *Aus. J. Soil Res.*, 28, pp. 417-431.
- Hunt, G., Salisbury J.W., 1976. Visible and near infrared spectra of minerals and rocks: XII. Metamorphic rocks. *Modern Geology*, 5, pp. 219-228.
- Hen Hu, Y and Neng Hwang, J., 2002. Hand book of neural network signal processing. CRC Press, pp. 1-1-1-30.
- Hu, X., and Weng, Q., 2009. Estimating impervious surfaces from medium spatial resolution imagery using the self-organizing map and multi-layer perceptron neural networks. *Remote Sensing of Environment*, 113, pp. 2089–2102.
- Ji, C. Y. (2000). Land-use classification of remotely sensed data using Kohonen selforganizing feature map neural networks. *Photogrammetric Engineering & Remote Sensing*, 66, pp. 1451–1460.
- Kanellopoulos, I., and Wilkinson, G.G. 1997. Strategies and best practice for neural network image classification. *Int. J. Remote Sens.*, 18, pp. 711–725.
- Kavzoglu, T., and Mather, P. M. 2003. The uses of backpropagating artificial neural networks in land cover classification. *International Journal of Remote Sensing*, 24(23), pp. 4907–4938.
- Kent, P.E., 1979. The emergent Hormuz salt diapirs of southern Iran, *J. Petrol. Geol.*, 2, pp. 117-144.
- Kruse, F.A., 1988. Use of airborne imaging spectrometer data to map minerals associated with hydrothermally altered rocks in the Northern Grapevine Mountains, Nevada, and California. *Remote Sens. Environ.* 24, pp. 31–51.
- Liu, J., Goering, C.E., Tian, L., 2001. A neural network for setting target corn yields. *Trans. ASAE* 44 (3), pp. 705–713.
- Metternicht, G.I., Zink, J.A., 2003. Remote sensing of soil salinity: potential and constraints. *Remote sensing of Environment*, 85, pp. 1-20.
- Monger, M., 2002. Soil classification in arid lands with Thematic Mapper data. *Terra*, 20(2), pp. 89-100.
- Mougenot, B., Pouget, M., Epema, G.F., 1993. Remote sensing of salt-affected soils. *Remote Sensing reviews*, 7, pp. 241-259.
- Jing, Q. C. L and Panahi, A., 2006. Principal component analysis with optimum order sample correlation coefficient for image enhancement. *International Journal of Remote Sensing*, 27(16), pp. 3387 - 3401.
- Richards, J.A., 1984. Thematic mapping from multitemporal image data using principal components transformation. *Remote Sensing of Environment*, 16, pp. 35-46.
- Roosta, H., Farhudi, R., Afifi M., 2007. Comparison between Sub-pixel Classifications of MODIS images: Linear Mixture Model and Neural Network Model, *WSEAS Transactions on Environment and Development*,
- Rumelhart, D.E, and MacClelland, J.L., 1986. Parallel Distributed Processing. *Explorations in the Microstructure of Cognition*, vol. I, MIT Press, Cambridge, MA.
- Sabins, F.F., 1997. Remote Sensing, Principles and Interpretation, third ed, Freeman, New York, pp. 494.
- Stöcklin, J., 1974. Possible ancient continental margin in Iran, In: Burk, C.A., Drake, C.L. (Eds.), *The Geology of Continental Margins*. Springer, Berlin, pp. 873–887.
- Tavakkoli, H., 2008. Comparison of TM and ASTER datasets for enhancement of lithological units of salt domes, a case study from Firouzabad area; MSc thesis, Dept. Of Earth Sciences, Shiraz University, Iran, pp.152.
- Verbeke, L.P.C., Vancoillie, F.M.B., De Wulf, R.R., 2004. Reusing back-propagation artificial neural networks for land cover classification in tropical savannahs. *Int. J. Remote Sens.*, 25, pp. 2747–2771.
- Yuan, H., Van Der Wiele, C. F., Khorram, S., 2009. An Automated Artificial Neural Network System for Land Use/Land Cover Classification from Landsat TM Imagery. *Remote Sens. I*, pp. 243-265.
- Zadnec, T., 2008. Environmental effects of Konarsiah Salt dome on pollution of water resource of Firouzabad area; MSc thesis, Dept. Of Earth Sciences, Shiraz University, Iran, pp.120.
- Zhai, Y., Thomasson, J.A., Boggess III, J.E., Sui, R., 2006. Soil texture classification with artificial neural networks operating on remote sensing data. *Computers and Electronics in Agriculture* 54 (2), pp. 53–68.
- Ziaii, M., a., Pouyan, A.A., Ziaei, M., 2009. Neuro-fuzzy modelling in mining geochemistry: Identification of geochemical anomalies. *Journal of Geochemical Exploration*. 100, pp. 25-36.
- Zinck, J. A., 2001. Monitoring salinity from remote sensing data. In R. Goossens, & B. M. De Vlieghe (Eds.), Proceedings of the 1st Workshop of the EARSeL Special Interest Group on Remote Sensing for Developing Countries (Belgium: Ghent University), pp. 359-368.

HYPERSPETRAL EVALUATION OF THE PEAR TREES ON THE BASIS OF THE GENETIC COLLECTION OF THE DIFFERENT SPECIES

J. Tamas ^a, Z. Szabó^b

^a University of Debrecen, Water and Environmental Management, Boszormenyi 138., 4032, Debrecen, Hungary -
tamas@gissserver1.date.hu

^b University of Debrecen, Department of Horticulture, Boszormenyi 138., 4032, Debrecen, Hungary-
zszabo@agr.unideb.hu

KEY WORDS: Hyper spectral, Agriculture, Precision, Sustainable, Vegetation, Land Use, GIS, High resolution

ABSTRACT:

The principle task of the sustainable development is the preservation of the genetic variety, which is similar challenge in the horticulture regarding the sublimation of fruit species. The breeders of the traditional fruit strains give stock to the sustenance diversity of the agri-environment on the species and landscape level. In 2009, hyperspectral images have been taken by AISA Dual sensors from the pear gene pool in Újfehértó, Hungary. The hyperspectral data cube (in the wavelength range of 400-2500 nm, with 1.5 m ground resolution) ensured possibility to make the spectral library of pear species. In the course of the simultaneously field work the spatial position and individual extent of all pear trees was defined to set up a detailed GIS data base. The water stress sensitivity of single species and the descriptive spectral curves were determined with common evaluation of the spectral and spatial data. Based on the unique methodology processing and the hyperspectral data base suitable strains can be chosen for agri-environment and let take adaptive stocks regarding climate change into the genetic grafting work. Furthermore we could determine and map the sparsely species in the region with the help of the hyperspectral data.

1. INTRODUCTION

On the basis of the United Nations Earth Summit in Rio de Janeiro in 1992 the biodiversity conversation is the important task for every country. Even so numerous species is disappearing off the earth decreasing Earth's biodiversity. Plant and animal species collected by human genetic breeding works and selected over more hundred years are less emphasized contrary to wild species.

Our experimental respects the pear species (*Pyrus communis* L.). The pear is the second more important fruit in temperate zone following apple worldwide. It produces 4-4.5 million tonnes per year in Europe especially in Italy, France and Spain, while the pear is the fourth important fruit in Hungary with the amount of 40000-80000 tonnes.

There are numerous species of these, which can only be found in a certain landscape. These species mean irreparable genetic sources same as wild and rare species. There are innumerable genetically encoded qualities – eg. resistivity against the diseases and frost, drought tolerance, unique colour and taste, and storage tolerance, which lack partly or in gross from the commercial species. Because of the continually changing consumer demand, and environmental and landscape aspect the preservation of every pear species having special or useful quality is necessary.

The countries maintain this particular genetic property in the special plantations – gene pool. In Hungary these examination plantation can be found in 4 different production site - Cegléd, Érd, Fertőd, Újfehértó, where 7833 trees are cultivated with professional technology and high cost. The items of the genetic collections are fully documented and the data are registered by international norm. The recorded data ensure the identification, central registration, suitable access to provide using for the national or international researchers, breeders and teachers.

The greater part of data was in analogous form and the smaller part of it was in digital form until 2008. The most important cause of the establishment of the geoinformatical system was the dismembered database and the difficult management or actualizing.

The aim was to create a new GIS – Remote Sensing data system, which can be the basis of the later agri-ecological decision support system.

2. MATERIAL AND METHODS

The Fruit growing Research and Consultant non-profit company created the genetic collection of pomum fruits (apple, pear, quince, naseberry) at Újfehértó (47° 49' 30" N; 21° 40' 27" E) in 1980, which recorded 1876 trees in 2009. The area of the research company is situated in north direction from the town of Újfehértó, in Nyírség landscape NE Hungary. It consists of fixed sand dunes accordingly the relief is heterogeneous. The total cultivated area (fruit plantations and arable land) of the research company is approximately 3 km².

In the 5 ha plantation of genetic collection it can be found 673 apple, 480 pear, 57 quince and 28 naseberry species, variety and hybrid at present. The pear plantation is situated in the east part of the gene pool covered by 28000 m², where the planting started in 1982. According to the traditional cultivation methods the row pace is 8 m and the space between the trees is 2 m.

In course of the establishment of the GIS logical model we determined the types of the accessible data and the forms of utilization in the geoinformatics system. The fruit tree was the smallest unique entity, which has individually pollable attributes (name of species, planting date, height, condition etc.) It was also important to ensure the uploading of the phenological data such us blossoming, ripening time, and

yields. To grant the agricultural subsidy it had to record the cultivation data of the area too. On the basis of field works new digital soil and nutrient supply maps were created to evaluate agri-ecological environment. Digital elevation model with 1 m vertical and 0.2 m horizontal RMS was produced.

In the course of the field works every stock place in the pear genetic collection were measured by DGPS methods, where the survey accuracy was $RMS < 0.2$ m after the TRIMBLE PATHFINDER compensating calculation in Geostation environment. The height and width of trees were defined with the help of Leica Distro 8 laser distance meter. To prepare the hyperspectral flight we used a digital orthophoto, which was taken in 2007 with a ground resolution of 0.5×0.5 m.

The spatial data were completed by airborne hyperspectral data, which in general makes possible to perform botanical and special soil investigations (Nagy et al, 2006).

Since the applied joint camera is less known in Europe and it can also be reached as an investigation delivery, the details of the measurement are described below.

In 2007, the first high-tech AISA DUAL airborne hyperspectral image spectroscopy system (AIS) was installed and operated in cooperation the University of Debrecen, AMTC, Department of Water and Environmental Management with the Hungarian Institute of Agricultural Engineering in Gödöllő-Hungary funded by NKTH. The most important parts of the hyperspectral sensors are the spectrograph, which dissolve the electric waves arrived through the optical rift with the help of prisms and optical screen. The two hyperspectral sensors are mounted and synchronized in a common house; therefore it is known ASIA DUAL system (Milics et al. 2010).

The two cams can perceive in the visible wavelength, near infrared range and short wave infrared range. Technical information of applied ASIA DUAL hyperspectral system as follows: Push-broom hyperspectral imagery sensor with the fibre optic radiation meters (FODIS); Miniature integrated GPS/INS sensor, which serves the position, height and momentary situation (pitch, roll, yaw) of plane, Compact PC-based data collector and mobile receiver unit; CaliGeo software runs as a separate software package under the ITT ENVI software package to do the spectral and geometrical corrections. The parameters of the hyperspectral image: Wavelength: 400-2450 nm (EAGLE: 400-970 nm and HAWK: 970-2450 nm); Spectral sample taking: 1,2-10 nm; Ground resolution: 0,4-3 m (with plane flight altitude), The photogrammetric and spectral accuracies were evaluated by different GPS/Inertia systems in different flight conditions in Europe (Germany, Finland, Switzerland and Hungary) in 2008-2009.

OxTS – RT 3003 was showed pixel sized accuracy of 1m without external DGPS data while the C-MIGITS III provided about 6m RMS position error, when the average flight altitude was 800-1000 m and the average speed was 200-250 km/h, with minimum swath width of 500m. Studying the navigation data it can be determinable that the angle deflection of the flight remains within 10 degree in case of taking image in general climatic conditions (Table 1.). However in special meteorological condition we also measured larger deflections rates, which was rarely exceeded 15 %.

Angle deflecti on	Roll		Pitch		Yaw	
	(%)	sum (%)	(%)	sum (%)	(%)	sum (%)

0-2	31.2	31.2	31.5	31.5	35.8	35.8
2-4	39.6	70.8	54.0	85.6	18.6	54.4
4-6	17.1	87.9	9.3	94.9	28.3	82.7
6-8	8.1	96.0	1.9	96.8	15.6	98.4
8-10	3.9	100	3.18	100	1.58	100

Table 1. Flight parameters

The hyperspectral DUAL sensor is fixed without gyrostabilizer in the airplane, so the deflection originating from the motion of the airplane is corrected by CALIGEO program with the navigation data of GPS/INS system in the course of the geometric correction. Before the flight boresight type calibration was carried out (Holzwarth et al., 2005).

The images of the flight campaign using in this paper were taken in the early afternoon in cloudless condition in June 2009, where the mean angle deflection was lower than 4%.

Before mosaicing of the images parametrical correction and radiometrical normalization between the bands were applied (Burai and Tamás, 2004) (Figure 1.).

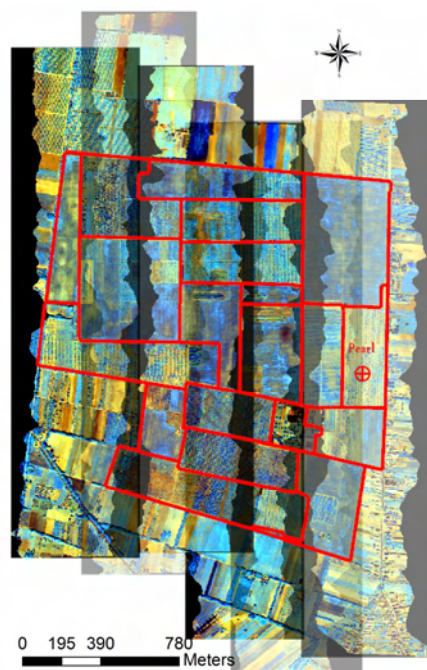


Figure 1. Georectified flight strips of the hyperspectral images and the Újfehértó Research Station (red border lines)

The accurate geometrical correction of the hyperspectral image taken by AISA DUAL push-broom sensor with high spatial resolution (< 1.5 m) could be achieved by OxTS RT 3003 positioning system working with two antenna. The atmospherical correction was done on the basis of the direct radiation measured by FODIS sensor detecting the changing of the radiation above the sensor. We modified the effects from the movements of the airplane with the navigation values, which is necessary to define the FODIS ratio. The high angle deflection values were separated from the FODIS data, which was replaced by data generated linear interpolation.

3. RESULTS

In our investigations, the airborne imaging system was used in fruit researches to develop a new GIS based recording system of

fruit plantations and study the relationships between remotely-sensed indices and ground control measures of fruit trees. Based on field work unique data of all pear trees, registered in the genetic collection, were collected to one ESRI ARCGIS data base. Height measurements and digital photos of the trees were also carried out during the survey. Digital photos were taken of the fruits as well, although earlier taken photos of genetically typical, ripe fruits were set to the database. The pictures were geotagged to air photo based on coordinates.

The n-dimensional hyperspectral image contained 359 channels. The bad bands, having bad signal/noise rate were excluded from further assessments (Tamás et. al 2005).

The characteristics of the reflectance curves of each pear tree species result from the large amount of absorption of chlorophyll content at 450 – 670nm wavelength intervals. On the other hand, reaching the near infra-red (NIR) interval, the reflectance of the healthy fruit tree leaves are raising markedly at 700nm (Tamás, 2010). Besides, the reflectance value of the vegetation without any stress is high at NIR intervals, but low at red wavelength interval. The chlorophyll content is one of the indicators of the state of health before ripening phenological phase (Burai et al. 2009). The leaf samples taken with R-Row/T-Tree positions in the study area were collected and analyzed on the basis of the field measured spectral curves (Table 2).

Pearl Species	R/T	NDVI	SRI	REP	chlorophyll µg/g
Napoca	19/ 103	0.62	4.96	718.4	883.52
Márianosztrai	19/ 113	0.41	4.95	720.7	509.12
Republica	19/ 83	0.58	3.39	712.1	982.72
Ananász (Ananas)	19/ 79	0.69	5.26	710.9	4522.88
Nyári esperes (summer dean)	19/ 70	0.67	4.84	712.9	3960
Kiev	19/ 109	0.489	2.79	721.7	407.36

Table 2. Example for chlorophyll content and spectral indices

The Pearson correlation between chlorophyll and Normalized Vegetation Index (NDVI) was 0.8, between chlorophyll and Simple Ratio Index (SRI) was 0.54, between chlorophyll and Red Edge Position (REP) was -0.76.

During the survey NDVI index was calculated from the hyperspectral image. The segmentation of the NDVI image was based on the GIS database of field measurements. After vectorising the obtained segments, those pear species having different biomass weight were selected. Pixels covered by canopies of these trees, could be spectrally clear and unmixed. Although the results show, that real endmember pixels can only be found at trees having several canopy level and at least 1 m canopy diameter. Because of the replacement of necrotized trees the spectral properties of grass zone between rows can provide spectrally mixed values (as a 2nd type errors of commission) due to the possible underdevelopment of trees. On the other hand, the spectral properties of neighboring trees can be mixed due to the overdeveloped tree canopy having more than 4 m diameter, which larger than the spacing in the row. Generally these errors of omission (1st type) had minor role. The resulted, classified spectral data could be applied as a spectral library, which are

suitable for the detailed examination of plant physiology and spectral data. The optimal climatic conditions for pear are generally cooler and humid, with at least 65% of relative air humidity. There is a lack of these conditions in Újfehértó at the 30-40% in a year. At the examined site, pear species with large biomass concerned as those species which had major tolerance against drier and unfavourable environmental conditions. These genetic properties could be very important in the frame of the potential climate change. Stress, caused by the relative water lack, evolves in a short term physiological process. The first symptoms of water stress are often not visually observed, although those have negative effect on the yield quantity and quality. The conventional invasive measurements can hardly be reproduced, because of the sampling (cut) of the vegetation tissue (i.g. leaf, shoot) or only few cm² of leaf area is measured, which limits the representative sampling. The airborne hyperspectral remote sensing data eliminate these disadvantages, since it can provide detailed spectral data from the whole canopy.

In Figure 2 the continuum removed spectra of Bajai, KörteB/3, Szentendrei császár, Vérteskozmai pear species are shown descending order of biomass. Continuum Removal is to normalize reflectance spectra to compare individual absorption features from a common baseline. The continuum is a convex hull fit over the top of a spectrum using straight-line segments that connect local spectra maxima. The first and last spectral data values are on the hull; therefore, the first and last bands in the output continuum-removed data file are equal to 1.0. The resulting image spectra are equal to 1.0 where the continuum and the spectra match, and less than 1.0 where absorption features occur.

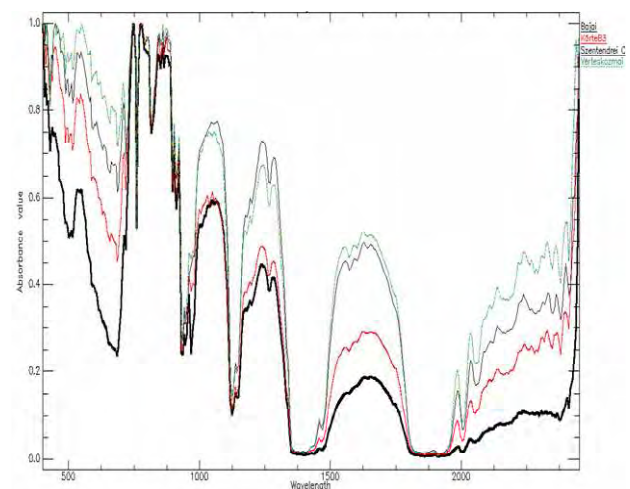


Figure 2. The pear species have species specific spectral properties

Based on the horticultural data, the four biomass segments showed strong correlation with the water stress tolerance. The pear tree species were grafted to the same wild pear rootstock, thus there were no differences in the water consumption root zone. In accordance with the spectral data, the “Bajai” species produced large canopy with 5.7 m height and large yield quantity (Figure 3).



Figure 3. The water stress tolerable „Bajai” species

The “Szentendrei császár” species grown on the same soil type, just some meters away from the presented “Bajai”, has just 2m height canopy and its yield is the one quarter of the “Bajai” one (Figure 4).



Figure 4. The water stress sensitive “Szentendrei Császár” species

The Water Band Index (WBI) is a reflectance measurement that is sensitive to changes in canopy water status. As the water content of vegetation canopies increase, the strength of the absorption around 970 nm increases relative to that of 900 nm. WBI is defined by the following: $WBI = \delta_{900} / \delta_{970}$ (Champagne et al. 2001). According to our examinations as well, channel with 900nm is found to be a sensitive water stress indicator, although the minimum value of the first derivative of the reflectance curve was at 930-940 nm wavelength interval. The 970 nm channel provided less usable values as a denominator for WBI (Figure 5).

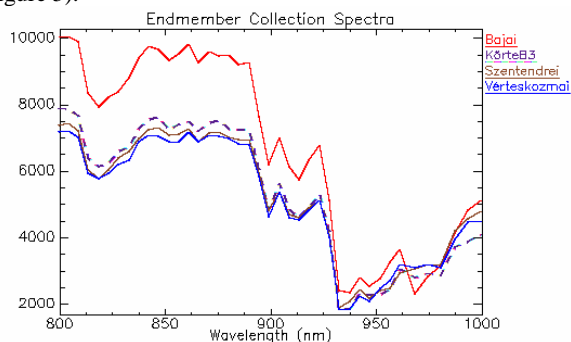


Figure 5. Spectral interval regarding water stress in the case of 4 pear species.

Based on the abovementioned results, the reflectances of 886 and 937 nm can result more accurate WBI ($WBI = \delta_{886} / \delta_{937}$) in the case of pear trees. The spectral data also confirmed that the “Bajai” pear species can tolerate more the dry conditions of Újfehértó than the “Szentendrei császár” or the “Vértesszomszmai” pear species.

4. CONCLUSIONS

Based on the results, the airborne hyperspectral remote sensing is a very effective method for surveying the vegetation. The environmental a climatic stress has an effect on vegetation, as well as other living creature. Species, grown in the concerned landscape had enhanced tolerance for harmful effects and water stress, thus it is especially important to prevent these genetic properties for further generations. The spectral library of the pear genetic collection in Újfehértó and the integrated GIS research database provide new opportunity to researchers and breeders in vegetation analysis. Due to this complex database and spectral library the effectiveness of understanding spectral anomalies and changing detection can be significantly increased.

REFERENCES

- Burai, P., Tamás, J. 2004. Hyper- and multispectral remote sensing technologies in precision agricultural water management. III. Alps-Adria Scientific Workshop. Dubrovnik. Croatia. pp.54-57.
- Burai, P., Kovács, E., Lénárt, Cs., Nagy, A., Nagy, I. 2009. Quantification of vegetation stress based on hyperspectral image processing. *Cereal Research Communications*. Akadémiai Kiadó. Budapest. 37. pp. 581-584.
- Champagne, C. A., Pattey, E., Bannari, A., Strachan, I.B. 2001. Mapping Crop Water Status: Issues of Scale in the Detection of Crop Water Stress Using Hyperspectral Indices. In: Proceedings of the 8th International Symposium on Physical Measurements and Signatures in Remote Sensing. Aussois. France. pp.79-84.
- Holzwarth, S., Müller, R., Simon, C., 2005. Determination and monitoring of boresight misalignment angles during the hymar campaigns HYEUROPE 2003 and HYEUROPE 2004. In: Zagajewski, B. - Sobczak, M. - Wrzesień, M. (eds.): Proceedings of 4th EARSeL Workshop on Imaging Spectroscopy. New quality in environmental studies.. EARSeL and Warsaw University. Warsaw 119-128
- Nagy, A., Burai, P., Tamas, J. 2006. Evaluation of heavy metal distribution by using hyperspectral data analysis and field portable XRF technology. [In: Maghiar, T.T., Nagy, J., Bara, V., Kátai, J., Csép, N.I., Jávör, A., Tamás, J. Natural Resources and sustainable development]. University of Oradea Publishing House. Oradea. 795-801.
- Milics, G., Virág, I., Farouk, M., Burai, P., Lénárt, Cs. 2010. Airborne hyperspectral imaging for data collection for resilient agro-ecosystems. *Novenyterm*.59.Suppl. 6. pp. 593-597.
- Tamás, J., Kardeván, P., Kovács, E., Kovács, E., Takács, P. 2005. Evaluation of environmental risks of nonpoint source heavy metal contamination using DAIS sensor. In: Zagajewski, B., Sobczak, M., Wrzesień, M. (eds.): Proceedings of 4th EARSeL Workshop on Imaging Spectroscopy. New quality in

environmental studies. EARSeL and Warsaw University. Warsaw. 415-423.

Tamás, J. 2010. New evaluation method to detect physiological stress in fruit trees by airborne hyperspectral image spectroscopy. *International Journal of Horticultural Science*. Agroinform Publishing House. Budapest. Hungary. 16(1). pp. 37-40.

ANALYSIS OF RAPIDEYE IMAGERY FOR ANNUAL LANDCOVER MAPPING AS AN AID TO EUROPEAN UNION (EU) COMMON AGRICULTURAL POLICY

Brooke Tapsall, Pavel Milenov and Kadim Taşdemir*

Monitoring Agricultural Resources Unit, Institute for the Protection and Security of the Citizen,
European Commission Joint Research Centre
Via E. Fermi 2749, 21027, Ispra (VA), Italy
{brooke.tapsall, pavel.milenov, kadim.tasdemir}@jrc.ec.europa.eu
<http://mars.jrc.ec.europa.eu/>

KEY WORDS: Agriculture, GIS, Land Cover, Change Detection, Classification, Farming, Modelling, Monitoring

ABSTRACT:

The Common Agricultural Policy (CAP) of the European Union (EU) was established to maintain balance between farming industries and the environment as well as to provide economic sustainability in rural areas. EU Regulations for agricultural and rural development, adopted by countries upon their admission to the EU, allow payments to farmers for each eligible hectare of agricultural land (CAP reform), under different payment schemes. Remote sensing data is currently used as an efficient tool in determining areas potentially eligible for payments, through land cover identification and mapping. Launched in August 2008, RapidEye consists of five constellation multispectral sensors with a ground sampling distance (GSD) of 6.5m and a daily overpass. The satellite has a predicted lifespan of 7 years and with the target application of the sensor being agriculture; contains a high potential for the application of agricultural monitoring, necessary to some new Member States, such as Bulgaria and Romania. Analysis of RapidEye imagery, combined with local ancillary data over pre-selected test zones lead to determination and classification of land cover features which have potential or no potential to be eligible under the Single Area Payment Scheme (SAPS). This classification was completed using object oriented analysis and was run concurrently alongside a pixel based (self-organizing maps) analysis for comparison.

1 INTRODUCTION

The European Union (EU) established the Common Agricultural Policy (CAP) to support the agricultural sector in Europe, assess its impact to the environment and ensure economic sustainability in rural areas. One of the principal payment schemes under the CAP is the Single Area Payment Scheme (SAPS) which regulates payment of uniform amounts per eligible hectare of agricultural land. For most EU member states applying SAPS, the agricultural area eligible for payments is the utilised agricultural area, maintained in good agricultural condition (GAC) at a given reference date. As a consequence, the land which can be declared by the farmers and is the subject of the administrative and control processes that manage the CAP payments is limited to the historical extent, fixed at the reference date. Two exceptions are Bulgaria and Romania where the requirement for the reference year was omitted in their accession treaties. As a result, for these countries any utilised agricultural area, maintained in good agricultural condition at the time of the farmer declaration, regardless of its past status, can be considered eligible for payment. This creates a particular challenge for land management in the years following the EU accession, as agricultural land eligible for payment should be assessed on annual basis.

The objective of this study is to investigate and develop an operationally efficient methodology for annual monitoring and assessment of land eligible for subsidy payments under SAPS in Bulgaria. In order to ensure a correct assessment of the agricultural land suitable for SAPS payments, a necessary preliminary step

is to clarify the concept of what is ‘good agricultural condition’ (GAC) in the national context, as there is no common legal definition of GAC at EU level. The proposed methodology envisages remotely sensed imagery, as an efficient source of up-to-date information, to detect and quantify (for the entire country) the agriculture land, that may represent eligible area, through monitoring of land cover dynamics. The recently launched constellation of RapidEye satellites was considered particularly suitable for this study, as the satellites were designed to be used mainly for monitoring of agricultural and natural resources at relatively large cartographic scale. The methodology was based on multi-temporal analysis of RapidEye time-series.

In order to detect eligible agricultural land and estimate their impact at reference parcel level, two different approaches were considered: *i*) object oriented classification techniques (Gamanya et al., 2007, Mathieul and Aryal, 2005) based on red edge normalized difference vegetation index (Wu et al., 2009, Gitelson et al., 1996) and *ii*) automated clustering of self-organizing maps (Taşdemir and Milenov, 2010). The proposed methodology was tested using zones selected according to the variability of land cover features across the country, which potentially represent eligible land (Milenova et al., 2001).

The outline of the paper is as follows: Section 2 introduces the concept of Good Agricultural Condition (GAC) elaborating on a proposal for its legal definition; Sections 3 and 4 briefly overview the test areas of the study and RapidEye sensor specifications; Section 5 describes proposed methodology for detection and quantification of the GAC/non-GAC land cover types and features, using object oriented approach; Section 6 briefly presents the first results of the study and the ongoing validation, Section 7 provides results from a concurrent testing using Self-Organizing Maps, as an alternative of the object oriented approach; Section 8 concludes the paper.

*This study is a joint research between the GeoCAP Action of the Monitoring Agricultural Resources (MARS) Unit at the Institute for the Protection and Security of the Citizen in Joint Research Centre of European Commission, the Bulgarian Ministry of Agriculture and Food, ASDE/RESAC, Bulgaria and RapidEye AG, Germany. Figures in this paper are in color. Request color reprint from the authors.

2 GOOD AGRICULTURAL CONDITION

In order to suggest a robust and plausible concept of GAC, current legal definitions within regulations were consulted. The driver behind the need for a GAC concept in Bulgaria is Council Regulation 73/2009, Article 124 paragraph 1, which states:

“For Bulgaria and Romania, the agricultural area under the single area payment scheme shall be the part of its utilised agricultural area which is maintained in good agricultural condition, whether or not in production, where appropriate adjusted in accordance with the objective and non-discriminatory criteria to be set by Bulgaria or Romania after approval by the Commission.”

According to this statement, ‘utilised agricultural area’ subject to the Single Area Payments Scheme (SAPS) must be maintained in ‘good agricultural condition’, even if the land is not in production. The *utilised agricultural area* is defined as ‘the total area taken up by arable land, permanent grassland, permanent crops and kitchen gardens ...’ in Regulation 73/2009 Art 124 with definitions of other terms in current EU regulations: arable land [380/2009 Art 1 s2(a)], permanent grassland [380/2009 Art 1 s2(b)], permanent crops [370/2009 Art 1 (b)] and kitchen gardens [1444/2002 Annex 1]. This definition is important to the foundation of GAC concept as it lists the main land cover types, which can represent eligible land, but also can be easily detected (monitored) on the ground or through remote sensing data. By integrating the definitions from regulations, GAC (for Bulgaria) can be defined as follows:

Definition: *Good Agricultural Condition shall apply to accessible land which is maintained as active, or has the potential to become active, agricultural area or agricultural activity within a reference parcel.*

Definitions for agricultural area and agricultural activity are defined in Regulation 73/2009 Art 2 while the reference parcel is defined in Regulation 796/2004 Art 2 (26). The two key elements in the proposed GAC definition are:

- *the potential of the land to become agricultural:* the land shall have the potential to produce biomass either due to its natural properties or due to the implementations of certain standard agriculture activities, a general European farmer can implement.
- *the accessibility of the land:* there are no obstacles, neither natural nor man-made, preventing the access and use of the land for agriculture activities.

For a consistent technical framework, which will allow a proper classification of the agricultural land in GAC, the proposed definition lays a good foundation to build methodology. However, another challenge for GAC analysis in Bulgaria (as well as Romania) is the significant decline of the Utilised Agricultural Area (UAA) in Bulgaria (as well as Romania) in the last few decades mainly due to farmland abandonment and soil sealing. There are two types of “abandoned” land in Bulgaria: (1) land, not-cultivated for a maximum of 3 years, which could be easily recovered with the minimum agronomic measures applied; and (2) “deserted” land, not-cultivated for more than 3 years, and is more difficult to be recovered. The first case could be definitely considered as long fallow and part of arable land (according to EU definition), while the second case is considered really “abandoned”.

Since Bulgaria became an EU member, the interest to the “abandoned” land increased, due to the possibilities given by EU Common Agriculture Policy to receive subsidies for its utilization. In this respect, a certain portion of this “abandoned” land, even if

currently not utilised, can be brought back into use by the farmers, at any given moment, and thus should be considered potentially part of the “SAPS envelope”. From a physiognomic-structural (biotic or abiotic) aspect, land not cultivated for several years, may acquire certain land cover properties, common to natural vegetation. This means that an estimation of the land in GAC, based on detection of the land currently under cultivation (using remote sensing), will not be correct, as it will omit the former agricultural areas (presently appearing as naturally vegetated), which can be brought back into use through the application of common agriculture practices. Supplementary information from the LPIS or other sources such as NATURA 2000¹ may be needed to support the interpretation. To incorporate and manage correctly all possible cases of land cover, the features captured during the classification, will be grouped in three distinctive categories according to the physiognomic-structural point of view and to the LPIS information:

- *GAC* includes land cover features which can be classified as agricultural land being in GAC,
- *Potential non-GAC* includes land cover features which are unlikely to represent agricultural land in GAC; however, a cross-check using up-to-date VHR data or a rapid field visit is necessary to finalise conclusions,
- *Non-GAC* includes land cover features which cannot be, and have no potential to be, agricultural land in GAC.

3 STUDY AREA

After joining to the EU in 2007, Bulgaria adopted the legislation of the European Community for management and monitoring of their agricultural land and benefit payments. Bulgaria is approximately 111.000 km² in size, extending from the western boundaries of the Black Sea to Serbia and FYROM on the East. The country borders Romania on the North and Turkey and Greece on the South. The northern boundary follows closely the Danube River. To capture the diversity of landscape within the country, the study area has been divided (stratified) into three testing zones: Zone 1–Kardzhali (KARD); Zone 2–Plovdiv (PLOV) and Zone 3–Varna (VARN). Two additional ‘back-up’ zones, were also selected in the event suitable RapidEye imagery over the main zones could not be obtained. This paper presents the analysis and results obtained for the KARD zone.



Figure 1: Map of Bulgaria and Test zones.

The KARD zone is located in a highly segmented part of Strumni Ridge, situated in the area of Eastern Rhodope, Bulgaria. The landscape is hilly to mountainous, with an average altitude of 444 meters. The climate is mild to Mediterranean with an average annual temperature about 11°C, and an average annual rainfall between 650-700mm. Droughts are common during the summer. The soil, having limited mineral chemical elements, makes

¹<http://ec.europa.eu/environment/nature/index-en.htm>

the area suitable for the cultivation of vines, tobacco (main cultivation in the region), fruits and grains. Slopes are deforested and eroded; with areas prone to landslides. Most of the hills are covered by low-productivity grassland used for grazing. There are alluvial and deluvial-meadow soils along the major rivers in the region, where vegetables and hemp can be grown, due to the larger quantity of moisture, they receive from the soil layers.

4 REMOTE SENSING IMAGERY

A constellation of 5 multispectral satellite sensors were launched by RapidEye in August 2008 with a primary focus on agricultural applications. These satellites have a lifespan of seven years; a ground sampling distance of 6.5m resampled to 5m; and a daily overpass. A new feature in RapidEye sensor is the Red Edge band (690-730nm), which could allow better estimation of the ground cover and chlorophyll content of the vegetation (Haboudane et al., 2002, Vinal and Gitelson, 2005). All 5 satellites have the same calibration coefficients. The radiometric scale factor converting the image DN values into reflectance is 0.01.

Imagery was obtained from RapidEye AG at standard processing level 3A² (orthorectified) for the dates indicated in Table 1. Pre-processing of imagery was carried out in ERDAS Imagine and ESRI ArcGIS software. This entailed further geo-referencing of the satellite imagery to the national orthoimagery provided by the Bulgarian government, thus ensuring data consistency between the RapidEye imagery and the LPIS datasets. Nearest neighbour approach was used for the resampling. In addition to the RapidEye imagery, VHR data from IKONOS has been acquired in the frame of the annual CwRS campaign and was also provided for the study. The availability of this imagery was an important source of ground truth. An orthorectification of this VHR data was carried out using the reference national orthophoto, additional ground control points and the SRTM DEM provided freely.

Zone	Acquisition dates in 2009				
	April	May	June	July	September
KARD	12.04	20.05	10.06	15.07	10.09
				23.07	16.09
				24.07	

Table 1: Acquisition dates of all RapidEye images over KARD

5 METHODOLOGY

The proposed methodology is based on the key elements derived from the GAC definition in Section 2. From the adopted GAC definition, we can conclude that, a land could be considered in GAC, if at least the following two criteria are met: *i*) vegetation is growing or can be grown on that land; *ii*) the land is accessible for agriculture activities (cropping, grazing, etc.). Both criteria can be evaluated by monitoring the development of the vegetation during the year (phenological cycle), together with the analysis of the texture properties of the land cover and the relevant spatial context. Thus, the methodological approach was based on a multi-temporal analysis of RapidEye time-series, using object oriented classification techniques in order to detect and qualify the land cover features in respect to their potential to represent agriculture area in GAC. Considering that the proposed definition of GAC is quite broad, it was agreed that the first estimation of the land potentially useful for agriculture (and being in GAC) can be done through detection and quantification of the non-GAC (and potential non-GAC) features. From land cover (physiognomic-structural) point of view, land which is not in GAC is constantly

²<http://www.rapideye.de/home/products/standard-image-products/standard-image-products.html>

bare or non-vegetated during the (cultivation) year (for example sealed surfaces; natural bare areas) and contains features preventing the agricultural activity even though it is vegetated (for example closed forest, woodland, wetland, etc.)

An overview of the proposed methodology used for decision-making and analysis can be seen in Figure 2. The selection, acquisition and pre-processing of imagery was important to provide a solid foundation for future analysis. The acquisition windows were carefully defined on the base of crop calendars, provided by ReSAC. Imagery from April, May, June, July and September were acquired over the test zones to reflect the phenological cycles of the vegetation (see Table 1).

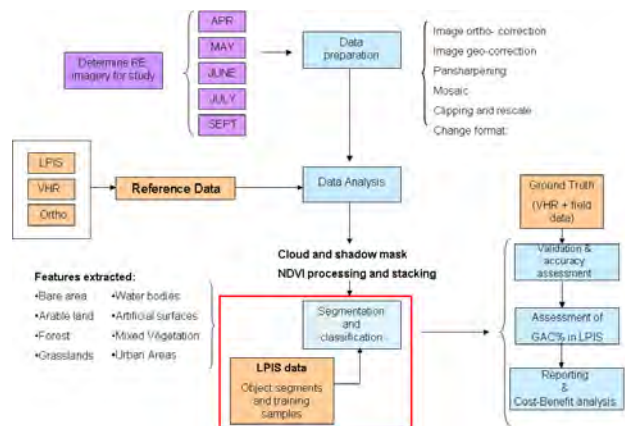


Figure 2: Proposed methodology

Data analysis: Capture and qualification of the permanently non-vegetated areas and the areas not accessible for agriculture were the primary targets. Most of the non-vegetated area with artificial anthropogenic origin, as urban structures, roads, hardpans, etc. can be efficiently extracted from a single RapidEye image, if acquired in the correct period of the year. The same is also valid for the naturally vegetated areas, not suitable for agriculture activities (such as forested areas, wetlands), or water bodies. However, for most of the natural bare areas, unsuitable for agriculture (such as eroded surfaces, degraded soils), the analysis has to be based on several time series, in order to filter out temporary bare areas, for example, harvested agricultural fields. Another important land cover, requiring multi-temporal approach, is low-productivity grassland, quite common in the area of KARD. This type of mountain grassland, used for grazing, appears vegetated (on the satellite imagery) only during particular periods of the year (early spring); usually its spectral signature is similar to bare surface, especially during the summer when it becomes dry. The only option to efficiently capture those areas is through the use of multi-temporal imagery covering the entire active agriculture period so that various aspects of the vegetation growth and climatic conditions can be considered.

It was assumed that permanent bare areas should have low NDVI values in all time series. For that purpose Red Edge Normalized Difference Vegetation Index (NDVI) (equation 1) (Wu et al., 2009) was calculated for all images.

$$NDVI_{Red\ Edge} = \frac{NIR - Red\ Edge}{NIR + Red\ Edge} \quad (1)$$

The choice of the Red Edge channel, instead of the Red channel for the NDVI calculation, was mainly driven by lesser saturation of the Red Edge NDVI comparing to the traditional NDVI over highly vegetated (forested) regions, as reported in the literature (Haboudane et al., 2002, Vinal and Gitelson, 2005). Figure 4.b

shows stacked imagery composed by the NDVI images calculated for four consecutive months from April to July. Analysis of the stacked NDVI imagery clearly highlights permanent bare areas (low NDVI values) as dark features, contrary to the forested or vegetated agricultural areas (high NDVI values), which appear in brighter shades of blue and yellow. After obtaining the Red Edge NDVI images, a 5-band image containing the stacked NDVI images for the months of April, May, June, July and September were created in ERDAS Imagine. It was finally rescaled to the dynamic range of the RapidEye imagery, which is 12 bit.

Segmentation and Classification: The 5-band stacked NDVI image was segmented in Definiens eCognition, using the spatial data of the LPIS as an input thematic layer. The aim was to aggregate into single objects, the image pixels with similar temporal behaviour in respect to the vegetation cover. The segmentation was performed at high detail to preserve features up to 0.1 ha within the imagery; as a consequence the land cover features larger than the minimum mapping unit, were over-segmented (Figure 3).

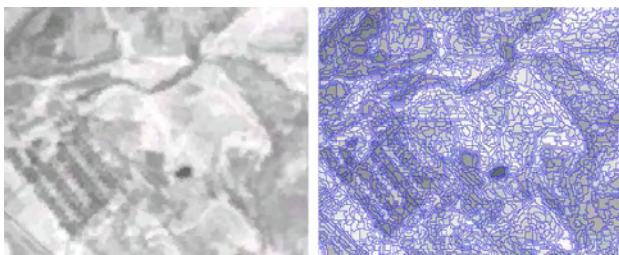


Figure 3: An extracted part from the original stacked NDVI imagery and its segmentation by Definiens eCognition.

The spatial and alphanumeric data from the LPIS plays an integral role in the segmentation and classification of the RapidEye imagery. As a consequence, the resulting land cover segments were coherent with the spatial extent and design of the reference parcels of the LPIS. In addition, valuable information regarding the type of the land use and the farmer restrictions at reference parcel level (stored in the LPIS attribute data), was used in the subsequent classification and aggregation of the image segments into meaningful land cover features at a higher object level.

The resulting segments were further classified in eCognition, to extract various land cover features. Different variables, such as Brightness, Mean value of Red, Relative Border to, Border Index and Thematic Attribute, have been used. The exhaustive toolbox of eCognition, together with the extensive use of abundant RapidEye and LPIS data, gave the possibility to define and extract more land cover types thus, enrich the initial simple binary classification of vegetated and non-vegetated areas. The land cover types were further grouped in GAC, Potential non-GAC and Non GAC categories, based of the pre-defined rules.

6 PRELIMINARY RESULTS

The first results obtained for the test area of KARD (Figures 4.c and 4.d) indicate that non-GAC features can be detected with high success rate. The overall thematic accuracy of the land cover classification is about 81% (See Table 2). The major confusion, which was between natural bare areas and urban areas, was not considered critical as both classes, eventually, are classified into the same (non-GAC) group. For KARD zone 55.1% (10118.8 ha out of 18361.3 ha) is in GAC, 8.8% (1614.2 ha) is in potential non-GAC and 36.1% (6628.2 ha) is in non-GAC group.

Some mixed land cover of bare areas and natural vegetation were incorrectly validated as agricultural areas because of the vagueness associated with ground truth samples. Unfortunately, due

	Urban Areas	Agriculture	Forest	Bare area (natural)	Water
Urban areas	44	0	0	9	0
Agriculture	0	141	0	0	0
Forest	0	0	58	0	0
Bare area	0	7	0	27	5
Water	0	0	0	0	26
Other	0	37	0	10	0
Producer acc.	1.0	0.76	1.0	0.59	0.84
User acc.	0.83	1.0	1.0	0.69	1.0
Overall acc.	0.81				

Table 2: Producer and user accuracies for the clusters extracted by object oriented analysis

to the limited ground truth taken directly in the field, the validation of the classification was done solely on the base of information obtained from the VHR imagery. Even though having sufficient spatial, spectral and radiometric resolution, the IKONOS imagery represents only a single snapshot of the ground, a limitation, which cannot always ensure that the information available on the VHR image will be sufficient for a proper interpretation of the ground truth. A further validation of the results is planned with more reliable ground truth data, available from the annual field inspection done by the National Administration on selected agriculture parcels from the test zones.

7 CONCURRENT TESTING

In addition to the object oriented analysis of stacked red edge NDVI images, a pixel based method using automated clustering of the Self-Organizing Maps (SOMs) (Taşdemir and Milenov, 2010) has also been utilised. This SOM based analysis has exploited information in all bands, i.e., each pixel has a 20-band (5 RapidEye bands for 4 consecutive months from April to July).

SOMs are unsupervised artificial neural networks that use a self-organizing learning algorithm inspired from the neural maps on the cerebral cortex (Kohonen, 1997). They are successfully used in remote sensing applications due to their two main properties: *i*) providing an adaptive vector quantization of the data samples to approximate the unknown density distribution of the data; *ii*) distribution of these quantization prototypes on a rigid lattice by preserving neighborhood relations in the data space so that high-dimensional data spaces can be visualized in lower dimensions (preferably 2D or 3D). Comprehensive knowledge learned by SOMs can be used for cluster extraction and knowledge discovery from large data sets using interactive or automated methods (Taşdemir and Merényi, 2009, Taşdemir and Milenov, 2010).

An automated hierarchical clustering of SOMs based on detailed local density distribution, proposed in (Taşdemir and Milenov, 2010), was used for GAC detection and extraction from the 20-band stacked RapidEye imagery. A 50×50 SOM was trained by Matlab SOMtoolbox and a cluster map, focusing on the land cover types of permanent bare areas, water, forest and vegetated areas, was extracted. Figure 5 shows the resulting cluster map and compares it to the map extracted by the object oriented analysis. SOM based approach is unable to capture spatial context such as inland grass (for example vegetation within forest) whereas object oriented approach is unable to correctly capture small fields due to its averaging property. Despite these minor details, the resulting cluster maps are quite similar in terms of GAC detection. The SOM based clustering is advantageous because it is a faster, semi-automated method which requires much less user interaction than the object oriented segmentation.

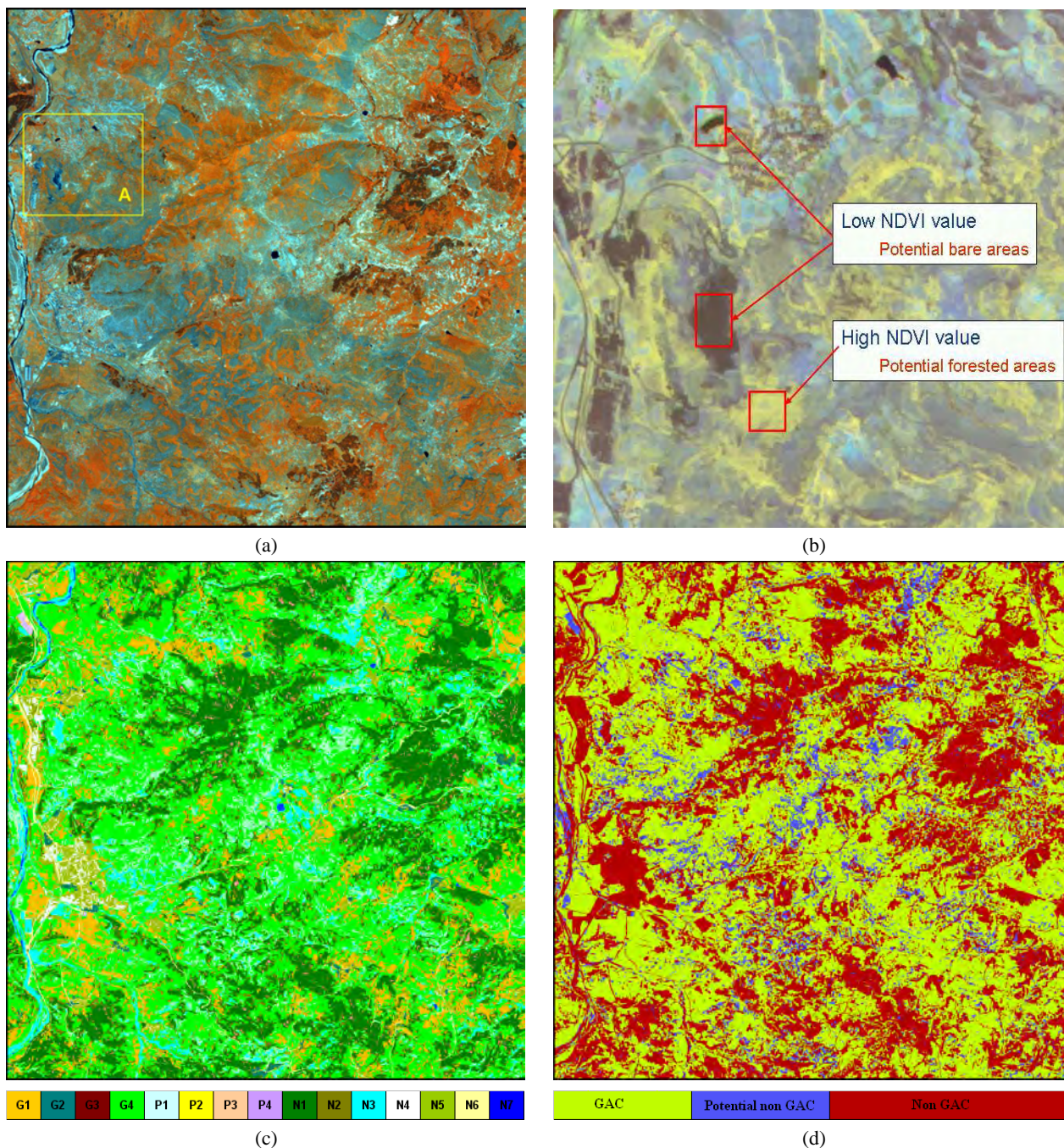


Figure 4: (a) Colour composite (NIR, Red Edge, and Red) image of KARD zone. (b) Colour composite image of the NDVIs from 4 consecutive month (April to July) for a subset (A, outlined on the left) of KARD zone. Dark regions (low NDVI for 4 months) indicate potential bare areas whereas light regions (high NDVI for 4 months) indicate potential forested areas. (c) Preliminary results for the land cover map of KARD. GAC is represented by cultivated land (G1, arable and grassland), family gardens (G2), permanent crops (cultivated) (G3), and mixed pattern of cultivated land, mountain grassland and natural vegetation (G4). Potential non GAC includes mixed pattern of bare area and natural vegetation (P1), fallow land (P2), inland vegetation or grassland (P3), permanent crops (not cultivated) (P4). Non GAC consists of closed (N1) or open (N2) forests, permanent natural bare areas (N3), urban areas (N4), vegetation in urban (N5), other sealed surfaces such as roads (N6), and water bodies (N7). (d) Resulting GAC, Potential non GAC and non GAC mask for KARD zone.

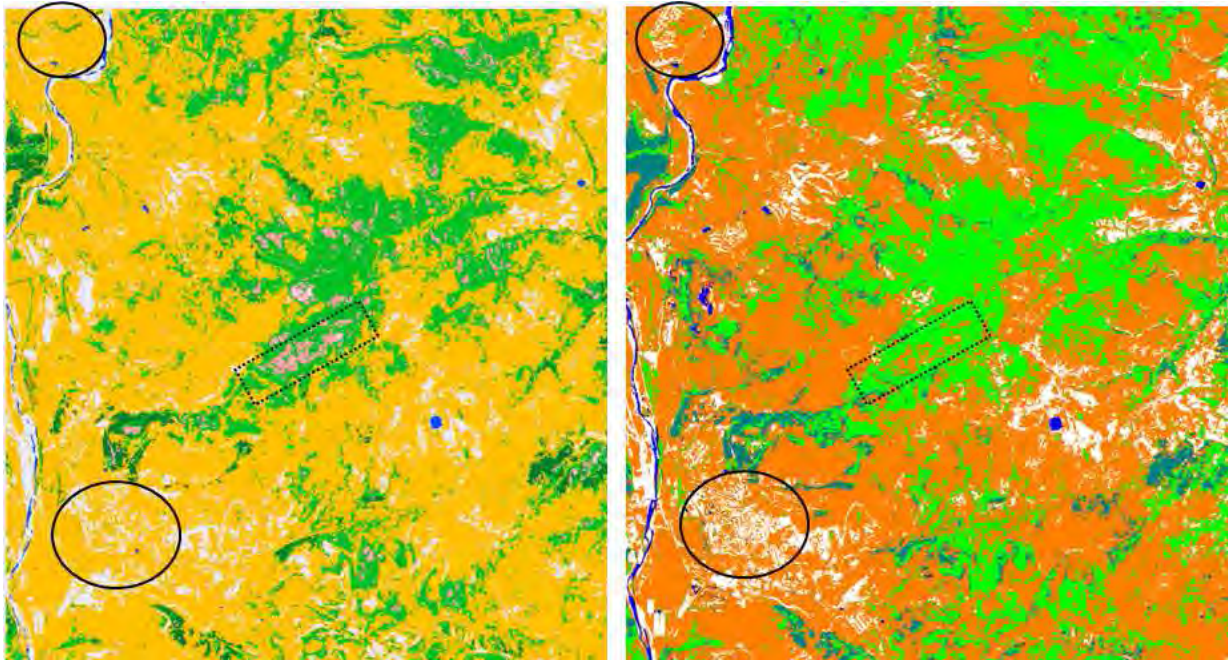


Figure 5: Comparison of cluster maps extracted using object oriented analysis (left) and self-organizing maps (right) for GAC detection. GAC regions are orange, urban areas are white, deciduous forests are light green whereas coniferous forests are dark green, and water bodies are blue. There is high degree of similarity between these cluster maps. SOM correctly extracts urban areas (white regions within ellipses on the right) whereas they are captured as GAC by object oriented analysis (orange within ellipse on the left). However, inland grass, pink regions within the rectangle on the left, cannot be extracted by the SOM (orange on the right) due to the necessity of spatial context whereas SOM clustering is pixel based.

8 CONCLUSIONS

The paper proposed a methodology for annual inventory and monitoring of the land which may be ‘eligible’ under SAPS in Bulgaria, using RapidEye imagery. A legal definition of “Good Agricultural Condition (GAC)” was introduced as a starting point for assessment of eligible area. An object oriented classification of multi-temporal RapidEye data was performed in order to quantify agricultural area in GAC on annual basis. In addition to the object oriented analysis, an alternative method based on self-organizing maps has also been used. Preliminary results are encouraging and they clearly indicate that multi-temporal remote sensing data can effectively contribute to differentiate currently active and potential agriculture land, and land which cannot be considered suitable for agriculture in the context of SAPS. However further validation of the methodology for the other test zones is necessary. It is envisaged to follow-up discussions of results with the Bulgarian Administration.

RapidEye imagery (in terms of information content) seems to be particularly suitable for feature detection and land cover mapping of agriculture landscapes. As the spatial resolution doesn’t correspond to 1:10 000 scale, the imagery cannot be used directly for LPIS update; however it can provide essential information on the overall accuracy of the LPIS in relatively short time frame, provided that the acquisition approach is adapted to the user expectations. The proposed methodology may also help Bulgaria (and Romania) to further develop their concept in respect to the eligibility conditions currently applied under SAPS.

REFERENCES

Gamanya, R., Maeyera, P. D. and Dappera, M. D., 2007. An automated satellite image classification design using object-oriented segmentation

algorithms: A move towards standardization. *Expert Systems with Applications* 32(2), pp. 616–662.

Gitelson, A. A., Merzyak, M. N. and Lichtenthaler, H., 1996. Detection of red edge position and chlorophyll content by reflectance measurements near 700 nm. *Journal of Plant Physiology*.

Haboudane, D., Miller, J. R., Tremblay, N., Zarco-Tejada, P. J. and Dextraze, L., 2002. Integrated narrow-band vegetation indices for prediction of crop chlorophyll content for application to precision agriculture. *Remote Sensing of Environment* 81(2), pp. 416–426.

Kohonen, T., 1997. *Self-Organizing Maps*. 2nd edn, Springer-Verlag Berlin Heidelberg.

Mathieul, R. and Aryal, J., 2005. Object-oriented classification and ikonos multispectral imagery for mapping vegetation communities in urban areas. In: *The 17th Annual Colloquium of the Spatial Information Research Centre (SIRC-2005)*, University of Otago, Dunedin, New Zealand, November.

Milenova, L., Nedkov, R., Vassilev, V., Milenov, P., Radkov, R. and Pironkova, Z., 2001. Preparation of land cover database of Bulgaria through remote sensing and GIS, Carlo Travaglia FAO. Technical report, Environment and Natural Resources Service, Sustainable Development Department Food and Agriculture Organization of the United Nations.

Taşdemir, K. and Merényi, E., 2009. Exploiting data topology in visualization and clustering of Self-Organizing Maps. *IEEE Transactions on Neural Networks* 20(4), pp. 549–562.

Taşdemir, K. and Milenov, P., 2010. An automated SOM clustering based on data topology. In: *Proc. 18th European Symposium on Artificial Neural Networks (ESANN’10)*, Bruges, Belgium, D-Facto, April 28–30, pp. 375–380.

Vinal, A. and Gitelson, A. A., 2005. New developments in the remote estimation of the fraction of absorbed photosynthetically active radiation in crops. *Geophysical Research Letters*.

Wu, C., Niu, Z., Tang, Q., Huang, W., Rivard, B. and Feng, J., 2009. Remote estimation of gross primary production in wheat using chlorophyll-related vegetation indices. *Agricultural and Forest Meteorology* 149(6–7), pp. 1015 – 1021.

IDENTIFICATION OF BEACH FEATURES/PATTERNS THROUGH ARTIFICIAL NEURAL NETWORKS TECHNIQUES USING IKONOS DATA

A. C. Teodoro ^{a,*}, H. Gonçalves ^a, J. Pais-Barbosa ^a, F. Veloso-Gomes ^b, F. Taveira-Pinto ^b

^a CICGE, Faculty of Sciences, University of Porto, Rua do Campo Alegre, 687, Porto, Portugal - (amteodor, hernani.goncalves, jpbarbosa)@fc.up.pt

^b Faculty of Engineering, University of Porto, Rua Roberto Frias, Porto, Portugal – (vgomes, fpinto)@fe.up.pt

Commission VI, WG VI/4

KEY WORDS: Coast, Neural, Recognition, Identification, Geomorphology, IKONOS

ABSTRACT:

Evaluation of beach hydromorphological behavior and classification of beach hydroforms and hydromorphologies is a complex issue. The main objective of this study is to explore pattern recognition methods to identify coastal features/patterns. One of the best known approaches for pattern recognition is artificial neural networks (ANNs). In this study an ANN was applied to an IKONOS image in order to classify the beach features/patterns. Based on the knowledge of the coastal features, five classes were defined. The most common type of ANN used in remote sensing is the multi-layer perceptron (MLP) which was also chosen for this study. The number of nodes in the input layer was determined by the number of input bands – the four IKONOS bands (reflectance values): blue, green, red and NIR. The output layer consisted of five binary nodes, one for each class: Sea, Suspended-Sediments, Breaking-Zone, Beachface and Beach. The ANNs consisted of one hidden layer, with 10 hidden nodes. The dataset was composed by 13775 pixels unequally comprising the five previously mentioned classes. The dataset was randomly divided into training (70% of each class) and validation subsets (30% of each class). Weights connecting the nodes between each layer are initially randomly assigned and adjusted during the learning process in order to minimize the global error. The maximum number of allowed iterations was 300. The ANN that had been trained with the training data was applied to the validation data. The ANN presented a very good performance, demonstrated by the results of the individual class accuracy and overall accuracy (98.6%). The ANN applied in this work have been shown to be useful in the recognition of beach features/patterns.

1. INTRODUCTION

Beach morphological classification was mainly established for Australian and American microtidal sandy environments. Different beach morphologic and classification models were presented by several authors (Wright and Short, 1984; Sunamura, 1988; Lippmann and Holman, 1990; Short and Aagaard, 1993; Masselink and Short, 1993; Masselink and Hegge, 1995; Short 1991, 1999 and 2006) based on wave, tidal and sediment parameters.

Parameters related to wave, tidal and sediments diameter are usually unavailable or nonexistent for the Portuguese coastal zone (Pais-Barbosa, 2007 and Pais-Barbosa *et al.*, 2007). Therefore, without these parameters, the morphologic analysis of high resolution satellite images seems to be a good approach to identify and to classify beach morphologies along the Portuguese coast. Based on this concept, two different approaches were already established in order to identify, measure and classify hydroforms and hydromorphologies.

The first attempt was developed by Pais-Barbosa *et al.* (2007 and 2009). This methodology consisted on the visual analysis of vertical aerial photographs datasets in a Geographical Information System (GIS) environment. However, there are some disadvantages associated to this methodology, such as the time consumption, the subjectivity introduced by the operator, and the impossibility of evaluating the accuracy of this visual analysis.

Teodoro *et al.* (2009) presented a new approach where a pixel-based classification (supervised or unsupervised) and region-based approaches (object-oriented classification) were employed. These results were compared with the visual

identification performed by Pais-Barbosa *et al.* (2007 and 2009), showing a good agreement between the visual identification and the “automatic” classification (Teodoro *et al.*, 2009), as illustrated in Figure 1.

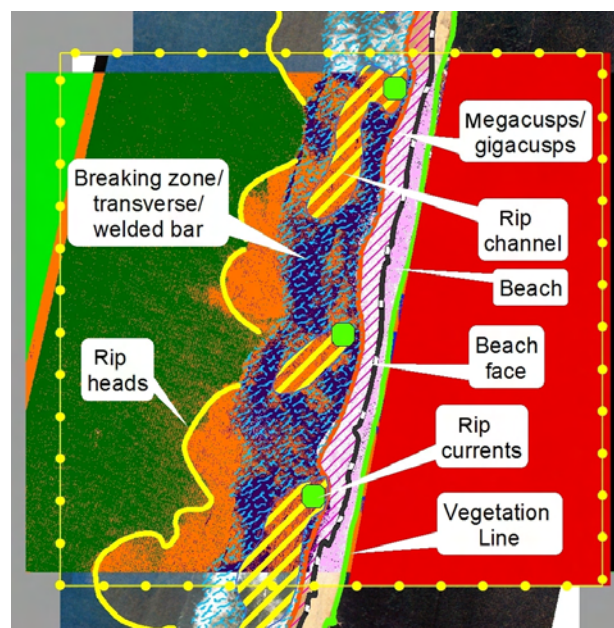


Figure 1. Visual and supervised classifications (parallelepiped classifier) overlapping (Teodoro *et al.*, 2009)

* Corresponding author.

Satellite remote sensing has revolutionized modern oceanography and coastal applications, providing frequent synoptic-scale information that can be used to deduce ocean/coastal processes. However, it is often difficult to extract interpretable patterns from satellite images, as data sets are large and often non-linear.

A technique that has been applied with success to extract interpretable patterns from different types of data sets is the artificial neural network (ANN). The ANNs have a number of advantages over traditional statistical methods (Wassermann, 1989). Firstly, they can solve non-linear problems of almost infinite complexity (Dayhoff, 1990). Secondly, they are more robust in handling noisy and missing data than traditional methods. This is especially desirable for satellite data from visible and infrared sensors that often have a considerable portion of the image not visible because of clouds. Finally, they do not require prior knowledge and assumptions about the data, such as normality or equality of variances (Chen and Ware, 1999).

There are many examples of the use of ANNs in remote sensing, including many studies that illustrate the ability of ANNs to generalize (Lippmann, 1987; Atkinson and Tatnall, 1997; Wilkinson, 1997). The use of ANNs to classify remotely sensed data has often resulted in a higher or equal mapping accuracy than that achieved with traditional classification methodologies or mixture modeling (Benediktsson *et al.*, 1990; Atkinson *et al.*, 1997; Teodoro *et al.*, 2007). There is considerable interest in the development of a classifier that can be applied to images of coastal areas not only for quantifying water quality parameters (Teodoro *et al.*, 2007) or monitoring protected coastal environments (Palandro *et al.*, 2008), but in many other applications as beach features/patterns classification.

This study focuses on the application of one ANN to an IKONOS image in order to classify the beach features/patterns, in a stretch of the northwest coast of Portugal.

2. METHODOLOGY

The methodology adopted in this work consists in the application of an ANN to an IKONOS image in order to classify the beach features/patterns.

Pais-Barbosa *et al.*, (2007 and 2009) and Teodoro *et al.*, (2009) developed methodologies to identify, to measure and to classify hydroforms and hydromorphologies, based on the visual analysis of vertical aerial photographs datasets in a GIS environment and in image classification techniques, respectively. The hydroforms were identified based on several criteria (location, spectral differences between morphological elements, shape and tide) presented in APPENDIX A. Based on the knowledge of the coastal features, five classes were defined: Sea (S), Suspended-Sediments (SS), Breaking-Zone (BZ), Beachface (BF) and Beach (B).

2.1 Study area

A stretch of the northwest coast of Portugal was chosen as the study area (Figure 2), limited to the north by the Douro River mouth (Vila Nova de Gaia city) and to the south by a small fisherman village (Aguda), with an extension of approximately 9.5 km. This coastal stretch represents a dynamic environment, which is constantly changing in response to natural processes and human activities.

Over the last few years, some coastal erosion in this particular area had been reported (e.g. Southern of Aguda breakwater). The main causes of this serious environmental problem have

been identified as a coastal response to the construction of Aguda breakwater, weakening of the river basin sediment sources and river-sediment transport (Teodoro *et al.*, 2007).

The study area is a rocky coast, with highly dynamic beaches presenting coastal patterns/forms that change continuously. It is composed by very dynamic beach systems, adjusting to wave climate and tide range. The tide regime is semidiurnal (period or cycle of approximately one-half of a tidal day), reaching up to 4.0 m for spring tides (mesotidal coast). The littoral drift has a dominant north–south direction.



Figure 2. Study area (Google Earth®)

2.2 IKONOS data

The IKONOS image (2005/09/18) was acquired under the scope of an ESA funded research project. The IKONOS image was already geometrically corrected. The image bands were calibrated for radiance values (L_λ), through equation (1),

$$L_\lambda = \frac{10^4 * DN_\lambda}{CalCoef_\lambda * Bandwidth_\lambda} \quad (1)$$

where DN_λ is the digital value for spectral band λ , L_λ is the radiance for spectral band λ at the sensor's aperture ($W/m^2/\mu m/sr$), $CalCoef_\lambda$ is the radiometric calibration coefficient [$DN/(mW/cm^2-sr)$] and $Bandwidth_\lambda$ is the band width of spectral band λ (nm).

The surface reflectance (R_λ) was obtained through equation (2),

$$R_\lambda = \frac{\pi * L_\lambda * d^2}{ESUN_\lambda * \cos \theta_\theta} \quad (2)$$

where $ESUN_\lambda$ is the mean solar exoatmospheric irradiances for the spectral band λ , d is the Earth-Sun distance (astronomical units) and θ is the solar zenith angle (degrees). The computed calibration coefficients are listed in Table 1.

Parameter	Spectral band			
	Blue	Green	Red	NIR
Calibration coefficient	728	727	949	843
Band width	71.3	88.6	65.8	95.4
ESUN	1930.9	1854.8	1556.5	1156.9

Table 1. Calibration coefficients for visible and NIR bands of IKONOS image (Thenkabail *et al.*, 2000)

2.3 Training and validation data

As previously mentioned, five classes were defined based on the knowledge of the coastal features: Sea (S), Suspended-Sediments (SS), Breaking-Zone (BZ), Beachface (BF) and Beach (B). The signature separability function must be used to examine the quality of training site and class signature, before performing the classification. The signature separability contains all the available information about signature and information for each class.

Analyzing the transformed divergence values presented in Table 2, only the separability between “Suspended-Sediments” and “Sea” classes is not very good (<1.9).

Class	S	SS	BZ	BF
SS	1.834241			
BZ	2.000000	2.000000		
BF	2.000000	2.000000	2.000000	
B	2.000000	2.000000	2.000000	1.999229

Table 2: Signature separability values (transformed divergence) for the IKONOS image.

The dataset was composed by 13775 pixels unequally comprising the five classes, as presented in Table 3. The dataset was randomly divided into training (70% of each class) and validation subsets (30% of each class).

Class	Training	Validation	Total
S	4133	1771	5904
SS	4091	1754	5845
BZ	329	141	470
BF	88	38	126
B	1001	429	1430
Σ	9642	4133	13775

Table 3. Distribution of the data set into training and validation pixels (number of pixels)

2.4 Artificial Neural Network (ANN)

An ANN is a parallel-distributed processor that resembles the human brain by acquiring knowledge through a learning process, and then stores the knowledge in the connection strength between computational units called neurons. Figure 3 shows a nonlinear model of a neuron. The x_1, \dots, x_m are the input signals, w_{k1}, \dots, w_{km} are the synaptic weights of neuron k , b_k is the bias, v_k is the activation potential of neuron k , $\phi(\cdot)$ is the activation function and y_k is the output signal (Haykin, 1999). An ANN comprises several layers: an input layer, an

output layer and one or more hidden layers between them (Figure 4).

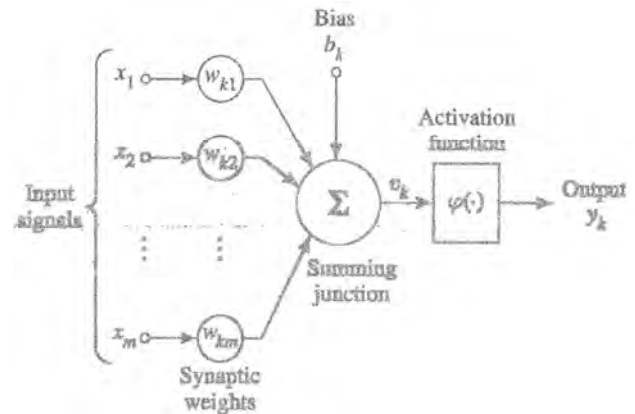


Figure 3. Nonlinear model of a neuron (Haykin, 1999)

The number of nodes in the input layer is determined by the number of input bands, which in this case consisted of four input nodes – the four IKONOS bands: blue, green, red and NIR.

The number of output nodes is dependent upon the number of classes in the classification scheme. In this study, the output layer consisted of five nodes, one for each class: Sea, Suspended-Sediments, Breaking-Zone, Beachface and Beach, as explained in section 2.3.

The hidden layer allows the network to form its own internal representation of the data. If too few nodes are selected, the ANN may not contain sufficient degrees of freedom to form a representation. The ANN implemented consisted of one hidden layer. Networks consisting of more than one hidden layer have not shown significant increases in accuracy compared with those containing just one. Several rules and recommendations exist concerning the calculation of the optimal number of hidden nodes. In this study, the number of hidden nodes was calculated as the number of pairwise separating hyperplanes over the number of classes, according to Dunne and Campbell (1994).

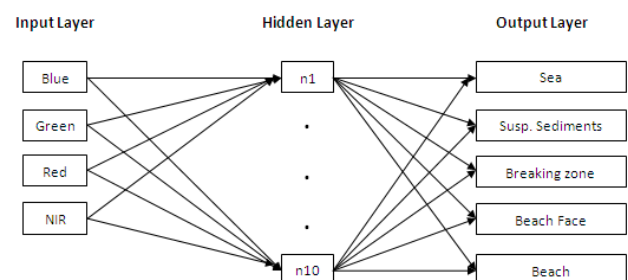


Figure 4. Illustration of the ANN used in this study, consisting of four input nodes, ten hidden nodes (one hidden layer) and five output nodes.

The network performance depends upon the choice of initial weights. Weights connecting the nodes between each layer are initially assigned randomly and adjusted during the learning process to minimize the global error. The weights of the ANN were estimated, using a statistical software (R), based on the Back-Propagation Algorithm (Haykin, 1999). The training process can be stopped according to one of the following user-defined options (Bishop, 1995): after a fixed number of epochs;

after a certain CPU time; when a minimum error function is reached; after minimum gradient is reached and learning per epoch is only marginal; when the error value of validation datasets starts to increase (cross-validation). The highest classification accuracy for the validation data was found when the networks were trained with early stopping (Mehner et al., 2003). The stopping criterion was defined to be the maximum number of allowed iterations, which was defined as 300.

3. RESULTS AND DISCUSSION

In Figure 5, the beach features/patterns map obtained through the application of the developed ANN to the IKONOS image is given, with the discrimination of each identified class.

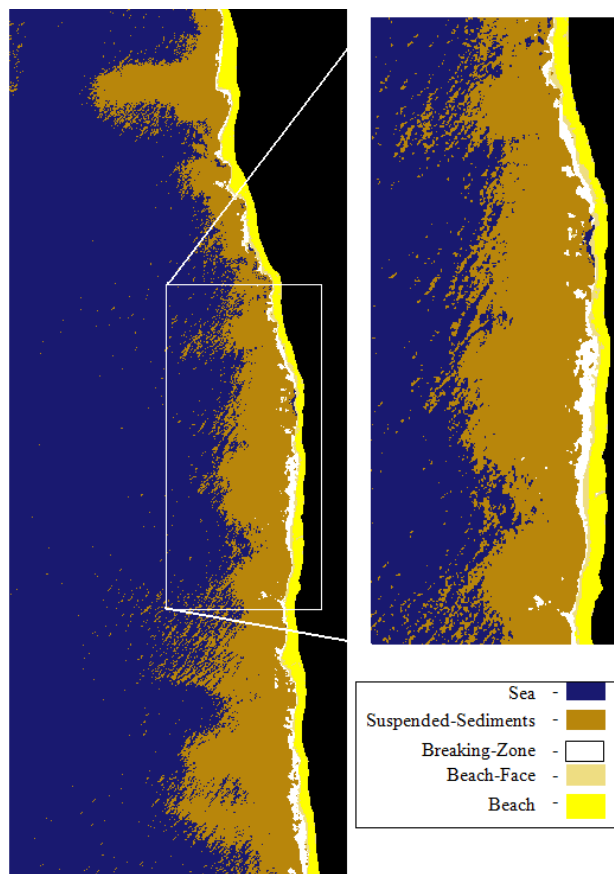


Figure 5. Beach features/patterns map for the IKONOS image, obtained through the implemented ANN.

The network performance was assessed by estimating the accuracy with which the validation data were classified. The ANN presented a very good performance, demonstrated by the results of the individual class accuracy (Table 4) and overall accuracy (98.6%).

Class	S	SS	BZ	BF	B	Accuracy (%)
S	1748	23	0	0	0	98.7
SS	27	1727	0	0	0	98.5
BZ	0	2	139	0	0	98.6
BF	0	1	0	35	2	92.1
B	0	0	0	2	427	99.5

Table 4. Individual class accuracy

This approach conducted to better results than the traditional classification methodologies. For instance, for the same dataset, the best result for the supervised classifications was achieved with the parallelepiped classifier, with a value of 97.5% for overall accuracy. The better result using an objected-oriented approach was found for the pan-sharpened true color imagery with an overall accuracy of 65.8%.

4. CONCLUSIONS

The ANN presented a very good performance, demonstrated by the results of the individual class accuracy and overall accuracy (98.6%). The ANN applied in this work have been shown to be useful in the recognition of beach features/patterns. Given the results obtained, some conclusions can be drawn:

1. The spatial resolution of the IKONOS image suggests that it is adequate for the identification of the considered beach features/patterns, through ANN techniques.
2. The use of ANNs for beach classification from remotely sensed data resulted in an increased classification accuracy when compared with traditional classification methods.
3. When applied to the validation dataset, ANNs performed successfully, with high classification accuracies observed. This fact justifies the future application of this methodology for others locations.

In the future, we are interested in the recent developments in classifier design with the introduction of the support vector machine classifier.

In conclusion, the ANN's have been shown to be useful in the recognition of beach features/patterns.

REFERENCES

- Atkinson, P.M. and Tatnall, A.R.L., 1997. Neural networks in remote sensing. *International Journal of Remote Sensing*, 18, pp. 699-709.
- Atkinson, P.M., Cutler, M.E.J. and Lewis, H.G., 1997. Mapping sub-pixel proportional land cover with AVHRR imagery. *International Journal of Remote Sensing*, 18, pp. 917-935.
- Benediktsson, J.A., Swain, P.H. and Ersoy, O.K., 1990. Neural network approaches versus statistical methods in classification of multisource remote sensing data. *IEEE Transactions on Geosciences and Remote Sensing*, 28, pp. 540-551.
- Bishop, C.M., 1995. *Neural Networks for Pattern Recognition*, 1st edn. Oxford: Clarendon Press.
- Chen, D. G., and Ware, D. M., 1999. A neural network model for forecasting fish stock recruitment. *Canadian Journal of Fisheries and Aquatic Sciences*, 56, pp. 2385-2396.
- Dayhoff, J. E., 1990. *Neural network architectures - An introduction*. New York: Van Nostrand Reinhold.
- Dunne, R.A. and Campbell, N.A., 1994. Some practical aspects of pruning multi-layer perceptron models applied to remotely sensed data. Technical Report 94/06, Murdoch University.
- Haykin, S., 1999. *Neural Networks: a comprehensive foundation*, 2nd edition. Prentice Hall, pp. 117-173.
- Lippmann, R.P., 1987. An introduction to computing with neural nets. *IEEE ASSP Magazine*, April, pp. 4-22.

- Lippmann, T. C. and Holman, R. A., 1990. The spatial and temporal variability of sand bar morphology. *Journal of Geophysical Research*, 95, pp. 11575-11590.
- Masselink, G. and Short, A. D., 1993. The effect of tide range on beach morphodynamics and morphology: A conceptual beach model. *Journal of Coastal Research*, 9, pp. 785-800.
- Masselink, G. and Hegge, B., 1995. Morphodynamics of meso and macrotidal beaches: Examples from central Queensland, Australia. *Marine Geology*, 129, pp. 1-23.
- Mehner, H., Cutler, M.E.J. and Fairbairn, D., 2003. Issues concerning the transferability of artificial neural networks. In: *Scales and Dynamics in Observing the Environment. Annual Conference of the Remote Sensing and Photogrammetry Society*, Nottingham, UK.
- Pais-Barbosa, J., 2007. Hidroformas e Hidromorfologias costeiras locais (in Portuguese). Faculty of Engineering of Porto University (Ed.), PhD Thesis, 2 Vol.
- Pais-Barbosa, J., Veloso-Gomes, F., and Taveira-Pinto, F., 2007. Coastal features in the energetic and mesotidal west coast of Portugal. *Journal of Coastal Research*, SI 50, pp. 459-463.
- Pais-Barbosa, J., Veloso-Gomes, F., and Taveira-Pinto, F., 2009. Portuguese northwest beach classification using aerial photographs and GIS tools. *Journal of Coastal Research*, SI 56, pp. 1552-1556.
- Palandro, D.A., Andréfouët, S., Hu, C., Hallock, P., Muller-Karger, F.E., Dustan, P., Callahan, M.K., Kranenburg C., and Beaver, C.R., 2008. Quantification of two decades of shallow-water coral reef habitat decline in the Florida Keys National Marine Sanctuary using Landsat data (1984–2002), *Remote Sensing of Environment* 112, pp. 3388–3399.
- Short, A. D. and Aagaard, T., 1993. Single and multi-bar beach change models. *Journal of Coastal Research*, SI 15, pp. 141-157.
- Short, A. D., 1991. Macro-meso tidal beach morphodynamics - An overview. *Journal of Coastal Research*, 7(2), pp. 417-436.
- Short, A. D., 1999. *Beach and Shoreface Morphodynamics*. Chichester, United Kingdom: John Wiley and Sons (ed.).
- Short, A. D., 2006. Australian beach systems – nature and distribution. *Journal of Coastal Research*, 22(1), pp. 11-27.
- Sunamura, T., 1988, Beach morphologies and their change. In: *Horikawa, K. (Ed.), Nearshore Dynamics and Coastal Processes*, University of Tokyo Press, pp. 136-166.
- Teodoro, A. C., Veloso-Gomes, F., and Gonçalves, H., 2007. Retrieving TSM concentration from multispectral satellite data by multiple regression and artificial neural networks. *IEEE Transactions on Geoscience and Remote Sensing*, 45(5), pp. 1342-1350.
- Teodoro, A. C., Pais-Barbosa, J., Veloso-Gomes, F., and Taveira-Pinto, F., 2009. Evolution of beach hydromorphological behaviour and classification using image classification techniques. *Journal of Coastal Research*, SI 56, pp. 1607-1611.
- Thenkabail, P. S., Enclona, E. A., Ashton, M. S., Legg, C., and De Dieu, M. J., 2000. Hyperion, IKONOS, ALI, and ETM+ sensors in the study of African rainforests. *Remote Sensing of Environment*, 90, pp. 23-43.
- Wassermann, P. D., 1989. *Neural computing theory and practice*. New York: Von Nostrand Reinhold.
- Wilkinson, G.G., 1997. Open question in neurocomputing for earth observation. In: *Neurocomputation in Remote Sensing*, I.
- Wright, L.D. and Short, A.D., 1984, Morphodynamic variability of surf zones and beaches: a synthesis. *Marine Geology*, 56, pp. 93-118.

ACKNOWLEDGEMENTS

The authors would like to thank to the European Space Agency (ESA) for providing the IKONOS image (Earth Observation Program, Category 1, ID- 6495).
J. Pais-Barbosa thanks Fundação para a Ciência e a Tecnologia, Portugal, for the financial support (SFRH/BPD/44929/2008).

APPENDIX A**BEACH FEATURES/PATTERNS IDENTIFICATION CRITERIA**

(Adapted from Pais-Barbosa (2007))

Hydroform	Identification criteria			
	Location	Spectral differences between morphological elements	Shape	Tide
Beach	Between dune feet and beachface	Vegetation, dry sand and wet sand	Homogenous land stripe parallel to the coastline	- -
Beachface	Between beach and breaking zone	Dry sand, wet sand and breaking zone	Homogenous land stripe parallel to the coastline	High tide – neap tide
Breaking Zone	Between beachface and sea and/or Suspended Sediments zone	Breaking zone (white), suspended sediments (light brown) and sea (deep-blue); Breaking zone (white) and transverse or alongshore channel (blue);	Alongshore, Crescentic, Transverse welded to land	High tide – neap tide
Suspended Sediments	Between breaking zone and sea	Breaking zone (white), suspended sediments (light brown) and sea (deep-blue);	Irregular alongshore stripe	High tide – neap tide
Sea	Offshore	Deep blue	Homogenous	

REMOTELY SENSED DATA & GIS IN LAND RESOURCES MANAGEMENT FOR REGIONAL PLANNING OVER SEMI-ARID PARTS OF NE BRAZIL

Harendra S.Teotia, Klaus A Ulbricht, Guttemberg da Silva Silvino

Laboratory of Remote Sensing and GIS, DSER/CCA/UFPB, Areia-PB, Brazil - teotia@terra.com.br

KEY WORDS: Semi-Arid, Land Resources Management, SPOT Imagery, ERDAS, Image Processing, Regional Planning, Remote Sensing, Geographical Information system

ABSTRACT:

The present study was carried out by digital interpretation (**Supervised Classification-MAXCLAS**), which is based on the methodology utilized by **Kennard et al** (The research work of our project was carried out through the **1988**). The Satellite Data were received from the **Aero Space Research Establishment of Germany (DLR-Oberpfaffenhofen)**. The LANDSAT and SPOT data were processed with ERDAS Software, operating on a high performance micro-computer. The digital interpretation was applied to one million pixels in each area of each State (**Paraíba, Ceará and Piauí**) to derive land use/land cover and major soil associations information. In the digital image classification, based on the field observations and using interactive capabilities of ERDAS, total 120 observations (40 observation in each area), were selected for land use/land cover classes. The digital interpretation was modified and corrected in accordance with the conditions of the area. By using RECODE program of ERDAS Software for land use/land cover classes, two maps, such as, land use/land cover map at the Level-II and major soil associations map for each area were generated. The comparison of digital interpretation with reference information indicated that the digital interpretation is closely resembled field observation and the overall classification accuracy was observed more than 85% in all the three areas of three States. The results of our study were found very beneficial for land development, natural resources management, land evaluation, soil conservation and land reforms programs of the Federal Government in the semi-arid region of northeastern Brazil.

1. INTRODUCTION

The northeast part of Brazil comprises of nine states and covered by various physiological relief features and morphological forms. The area generally has leveled to slightly undulating and mountainous topography. At some locations the area is also covered by natural pastures and waste lands, forest patches, and a network of rivers, many of which run only during the rainy seasons. The approach for natural resources development and management varies from one type of environment to another. The soil and land management in semi-arid region is totally different from the soil and land management in humid areas. Nowadays, there is a tremendous pressure on the availability of soil and land resources due to increasing population and grow consumption of land for constructing houses and buildings in major cities. In such a situation we must make an optimum planning and management of our land through remote sensing and GIS technology. These two technologies are the major tools for solving of our complex natural resources planning problems.

The purpose of our research using remote sensing and GIS technologies and ERDAS Software is to apply image processing and pattern recognition techniques to Satellite Data, such as LANDSAT-TM and SPOT HRV to drive various earth resources information for the land development and management of the region. Also, provide information about the land use/land cover classification, Soil classification, land capability classification, soil slope and relief features, which are used for the resources management and regional planning of semi-arid regions of northeastern Brazil. The aim of this research was to know the realistic assessment of the extent to which SPOT and LANDSAT data can be used for the survey of the study area, and to provide basic information on the nature of the digital remote sensing data and how they can be used for different applications.

2. BACKGROUND DISCUSSIONS:

Various types of remote sensing data, such as, **SAR, MSS, TM, ETM, MOMS, AVHRR** and **SPOT** etc. have been used for earth resources management and development of semi-arid regions by various governmental agencies, institutions, and universities of the world. For example: **Kennard et al. (1988)** have worked on a GIS system for land use planning and management of semi-arid regions of northeastern Brazil, using digital image processing on Landsat-TM and SPOT data. **LaBash et al (1989)** conducted a digital image analysis of Landsat-TM data in eastern Connecticut for regional land use and land cover classification. The results were found most satisfactory for regional planning in the state of Connecticut. **Ulbricht et al. (1992)** used the supervised classification for the soil and land use studies for a part of semi-arid regions of Brazil. **Teotia et al. (1996)** did a very comprehensive work for land use planning in semi-arid regions of NE Brazil, using SPOT HRV data. According to **Silva Junior (2003)** the remote sensing and GIS are economic and adequate for the land survey and land use classification of semi-arid regions of Paraíba state of Brazil. **Ribeiro G. do N (2006)** studied some remotely sensed data and found that the ERDAS Imagine Software and SPOT data is a good combination for land use and land cover mapping in order to develop the Agreste region of the Paraíba state of Brazil.

STUDY AREA: (Figures-1 and 2); (Photos 1, 2, 3 & 4) :

The study area falls in the states of Paraíba, Ceará, and Piauí, which is mainly semi-arid. The area has various types of dry lands and altitudes varying from 200 to 900 meters. Various types of physiological relief features and geomorphologic forms are encountered in the study area. Hydrologically, the area is covered by a network of rivers, many of which are intermittent. Soils derived from recent streams sediments are rich, whereas others are poor to moderate in fertility. The major soil groups of the area

are: Entisols, Alfisols, Inceptisols, Ultisols, and Lithic Sub-Groups of various orders and rock outcrops. The study area also has extensive areas of various drought-resistant trees and shrubs; mainly Caatinga Hipoxerofila, Caatinga Hiperxerofila and Xerophytic Forests. The Climate of the region is semi-arid and has a rainfall of 300 to 700 mm per annum and temperatures from 30 to 40 °C in the summer.



Figure-1: Composition of northeastern part from 9 States of Brazil



Figure-2: Study Area in three northeastern States of Brazil (Paraiba, Piaui and Ceara)



Photo 1 (Part of Semi-Arid Region of Paraiba State)



Photo 2 (Part of Semi-Arid Region of Paraiba State)



Photo 3 (Part of Semi-Arid Region of Ceara State)



Photo 4 (Part of Semi-Arid Region of Piauí State)

Geographic Information Required

Data about various components required for this research have been gathered from various, Federal, State, and Municipality Agencies, such as, Land Use, Soil, Soil Conservation, Slope and Elevation, Drought and Flood, Climate (Precipitation, Temperature and Humidity), Geology and Hydrology, Vegetation and Forest, Irrigation and Drainage, Socio-Economic, Municipality and State boundaries etc.

Programs of ERDAS used for study

Following programs of ERDAS Software in systematic sequence were used for unsupervised, supervised classification & accuracy assessment.

For Unsupervised Classification:

READ-CLUSTR-DISPLAY-COLORMOD-CLASNAM-RECODE-COLORMOD-CLASNAM-ANNOTAT-CLASOVR-BSTATS-LISTIT

For Supervised Classification:

READ-SEED-SIGDIST-SIGMAN-ELLIPSE-CLASNAM-MAXCLAS-DISPLAY-COLORMOD-CLASNAM-ANNOTAT-CLASOVR-RECODE-INDEX-RECODE-INDEX-COLORMOD-CLASNAM-ANNOTAT-SCAN-BSTATS-LISTIT.

For Accuracy Assessment:

READ-DISPOL-DIGSCRN-GRDPOL-CLASOVR-CLASNAM-SUMMARY.

Criteria used for land use classification

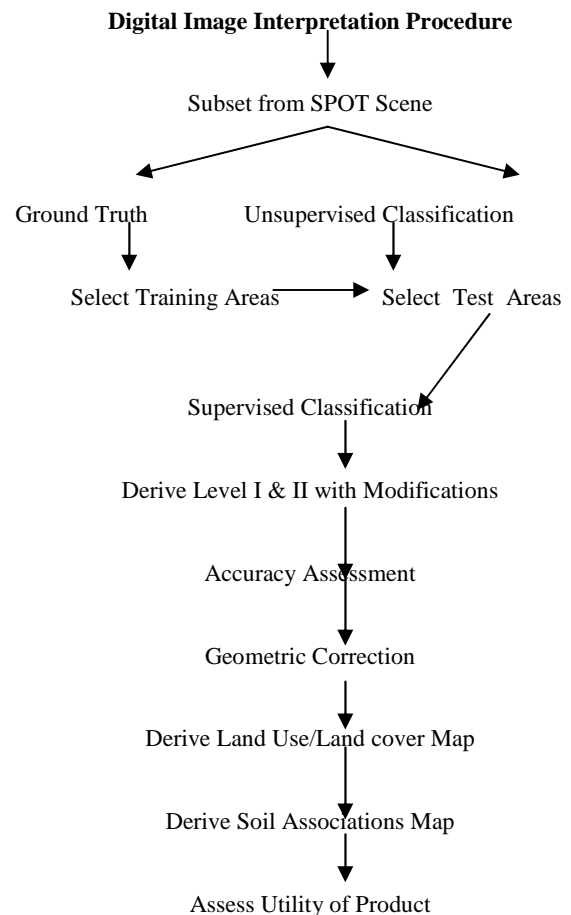
For our study of semi-arid regions of NE Brazil, the land use and cover classification system (Anderson et al., 1976) is modified in accordance with the local climate, local needs and existing conditions. During the conduct of our project, we used the following important criteria:

1. The interpretation accuracies in the identification of land use and land cover categories from remote sensor data should be 85% or greater.
2. The multiple use of land should be recognized where possible.

3. Individual land use and cover classifications should be customized to facilitate interpretations of digital images with different resolutions.
- 4.

Image Processing

A 1000 by 1000 pixel sub-scene of LANDSAT-TM and SPOT multi-spectral data (band 3,4, 5 & 1,2,3) were used for image analysis. More than 40 sites were visited in the study area, and reference data, such as soil, vegetation, geology, topography, climate and others are made to assist in supervised classification (Maximum Likelihood Classification-MAXCLAS). Various field trips served as a basis for accuracy assessment to derive various earth resources information. The digital interpretation was checked by three field trips. The relevant statistics, such as mean, mode, median, standard deviation, variance and co-variance matrices were applied for our study. After inspection of the digital classification combined with the field work, finally resulted into 15, 17 and 12 categories of land use/land cover classification in Paraíba, Piauí and Ceará states at the Level II. (Anderson et al., 1976). The accuracy assessments of the transformed and no-transformed LANDSAT-TM and SPOT image were concluded to compare the best areas of known reference data with the same areas on Level II land use and land cover classification on a pixel by pixel base produced by supervised classification. The overall accuracy was found more than 85% in all the three areas. By using RECODE program of ERDAS Software on land use/land cover information resulted into 11, 11 and 6 categories of soil associations in each area. Re-coding was possible because of the high degree of correlation of land use and land cover with the features of other maps. Field observations conducted at the sites confirmed this relationship.



Results and Discussions (Tables-1 to 6 and Images 1 to 6)

The tables 1, 3 and 5 present a summary for the maximum likelihood classification results of the three regions of northeastern Brazil. The overall classification accuracy for all the areas was found always more than 85%, which is good with respect to the classification categories used for this study. The classification shows that the percentage accuracy decreases as the level of detailed is increased. The more spectrally heterogenous areas also reduce the accuracy percentage of the classifications. The results of computer classification (Supervised Classification) of LANDSAT-TM and SPOT-2 Satellite data gained through various programs of ERDAS software into 15,17 and 12 mapping units.

Table 1: Paraiba Land Use/Land Cover

V1 Deep to very deep water
V2 Moderately deep to deep water
V3 Very shallow to shallow water
U1 Dense Urban area
U2 Sparse Urban and barren rocky land
CF1 Cotton cultivated and fallow land
MF1 Mixed cultivated and fallow land
CP1 Mixed cultivated and Pasture
A1 Alluvial land with dense shrubs/trees
A2 Alluvial cultivated and eroded land
F1 Sparse Caatinga forest and rocky land
F2 Sparse to moderate Caatinga forest and rocky land
F3 Moderate to dense Caatinga forest
F4 Dense Caatinga forest on undulating land
F5 Dense Caatinga forest on hills

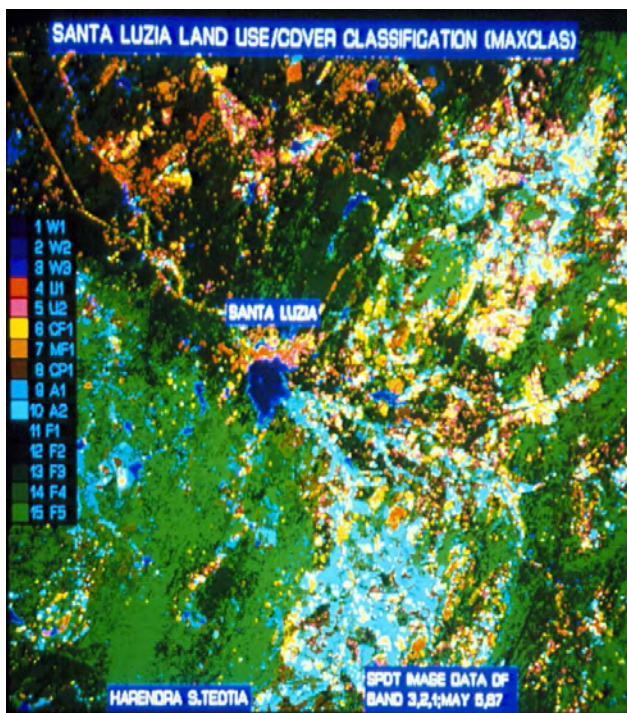


Figure 3 Paraiba Land Use/Land Cover Map

Table-2: Piaui Land Use/Land Cover

V0: Deep clean water
V1: Moderately deep water
V2: Shallow silted water
V3: Very shallow water or moist area
FA: Swampy flooded area
UO: Urban area with barren rocky land
EFA: Eroded flooded area
DC: Poor drained cultivated with eroded land
DC1: Poor drained cultivated
IC: Alluvial mixed cultivated
CB: Cultivated river bed
CB: Cultivated river bed with dense shrubs/vege.
CD: Saline cultivated depression
VERM: Weathered eroded rocky and moist land
DCF: Dense Caatinga Forest
MDCF: Mode. Caatinga forest on undulating relief
PC: Sparse Caatinga forest on undulating relief

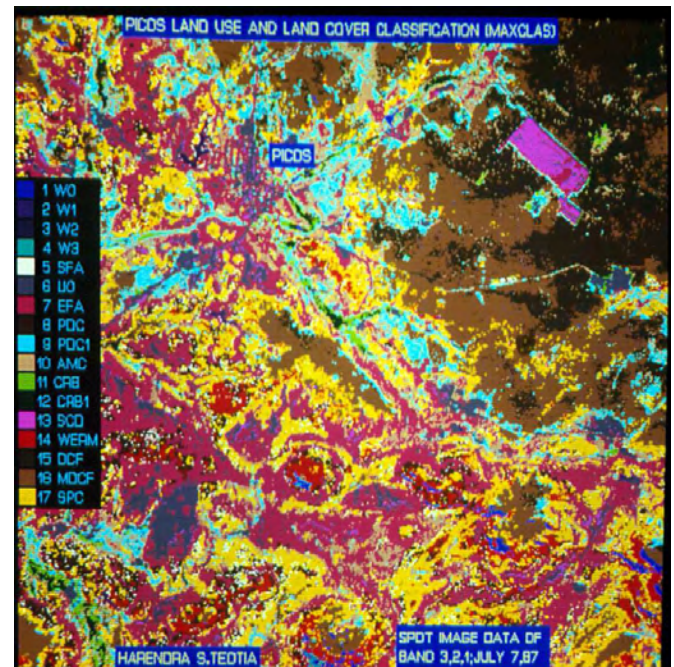


Figure 4 Piaui Land Use/Land Cover Map

Table-3: Ceara Land Use/Land Cover

W1 Deep to very deep water
W2 Moderately deep to deep water
W3 Shallow silted water
W4 Shallow and polluted water
U1 Urban area with rock outcrops
C1 Cultivated nearly leveled land
C2 Sparse to moderately cultivated undu. land
A1 Alluvial moderately to dense cultivated land
A2 Alluvial mode. culti.& eroded undu. land
F1 Dense Caatinga forest on hills
F2 Mode.denseCaatinga forest on undu. relief
F3 Sparse Caatinga forest on eroded undulating

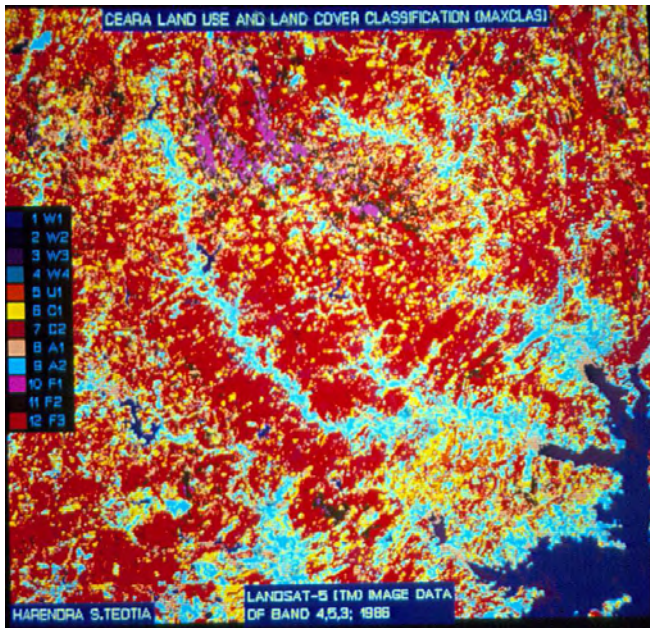


Figure 5 Ceara Land Use /Land Cover Map

Table-4: Paraíba Soil Associations

Water
. Urban
. LS-RO : Lithic Subgroup-rock outcrops
.UP-UO-UC: Ustipsa.-Ustorthents-Ustochrepts
.UO-HU-LS: Ustorthents-Haplustalfs-LithicSubgr
.UF-UP-UC: Ustifluents-Ustipsa.- Ustochrepts.
.UF-UP-UO: Ustiflu.-Ustipsaments-Ustorthents
.LS-RO-UO: Lithic SubGr, Rock outcrops –Ustorthents
.LS-HU-UO:: Lithicsubgr-Haplustalfs-Ustorthents
0.LS-HU-RO: LithicSubgr-Haplustalfs-Rock Outc
1.S-RO-HU: Lithic Subgroup-Rock Outcrops- Haplustalfs

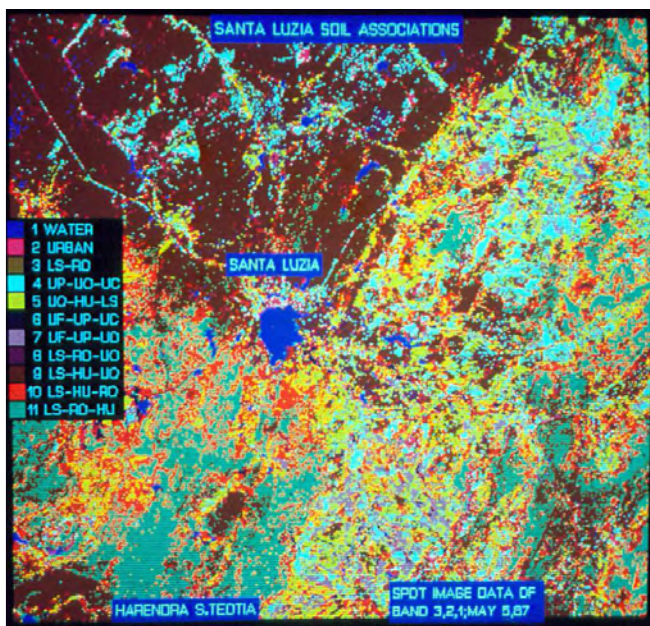


Figure 6 Paraíba Soil Associations Map

Table-5: Piauí Soil Associations

.Water
.E-L-R: Entisols-Lithic Subgr.-Rock outcrops
.E-I: Entisols-Inceptisols
.E-I-L: Entisols-Inceptisols-Lithic Subgroup
.I-E: Inceptisols-Entisols
.I-E-A: Inceptisols-Entisols-Alfisols
.I-E-L: Inceptisols-Entisols-Lithic subgroups
.I-A: Inceptisols-Alfisols
. L-R-E: Lithic subgr.-Rock Outcrops-entisols
0. L-A: Lithic Subgr.-alfisols
1. L-R-A: Lithic Subgr.Rock Outcrops-Alfisols

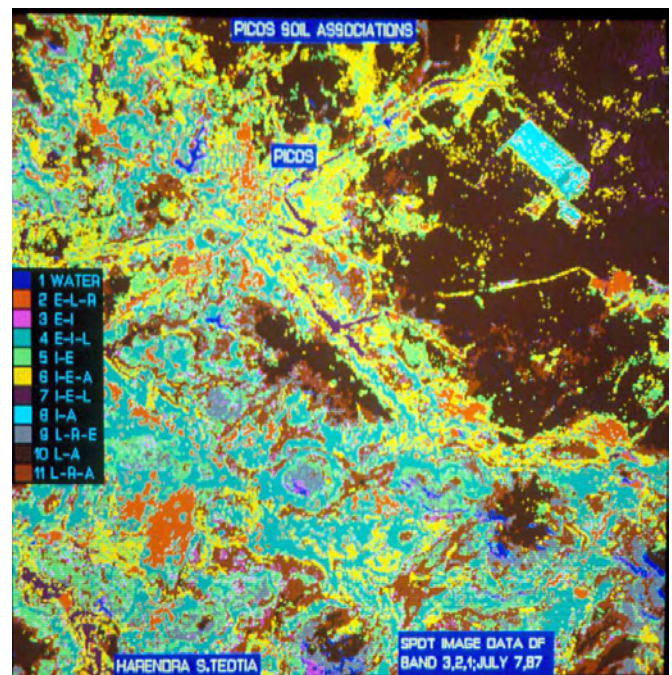


Figure 7 Piauí Soil Associations Map

Table-6: Ceara Soil Associations

Water
Urban/Barren
V(HU)FA-CU:Vertisols-Haplustalfs-Ustochrepts-Ustorthents
UF-UP-UO: Ustifluents-Ustipsaments-Ustorthents
.LSGR-RO-UO: Lithic Sub Groups-Rock-Outcrops-Ustorthents
.LSGR-HU(V)-RO: Lithic Sub-groups-Haplustalfs-Vertisols-Rock-Outcrops

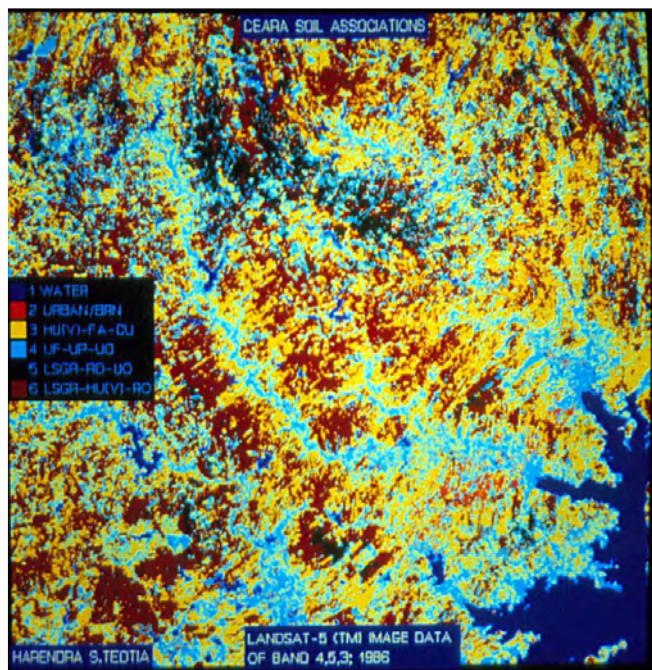


Figure 8 Ceara Soil Associations Map

3. GENERAL RECOMMENDATION

1) The LANDSAT-TM and SPOT imagery are found more reliable for land use/land cover and major soil associations mapping and could be used effectively for any part of semi-arid regions of Brazil in order to submit the natural, ecological and environmental resources information for the development and management of the study area.

2) The orbital images proved to be an extremely useful source of data for the purpose of detailed regional, local and rural planning and management and development of our natural resources.

3) The supervised classification of SPOT and LANDSAT-TM data for Land Use/Land Cover mapping and accuracy assessment provided satisfactory results. In terms of operational reliability, the per pixel maximum likelihood classification of SPOT and LANDSAT-TM images offered the most satisfactory results in comparison to other classification systems.

4) Accuracy assessment of the digital classification showed that some categories such as water, forest and alluvial land were identified more accurately than other categories. The more accurately identified categories may be used as framework for the addition of residual classes through a more conventional approach, such as aerial photo-interpretation. The comparison of digital interpretation with reference information indicated that digital interpretation, closely resembled to

field observation and the overall classification accuracy was observed always more than 85% except the urban and rock outcrops mapping units..

5) Maps of soil associations prepared using the RECODE program and other information may be used for detailed planning and development and management of semi-arid regions of northeastern Brazil.

ACKNOWLEDGEMENT

The authors wish to thank the Federal University of Paraiba (UFPB, Brazil and the DLR, Oberpfaffenhofen of Germany to supply all the Remotely sensed data (Landsat-TM and SPOT) and other necessary material in order to conclude this project.

REFERENCES

Anderson, J.R., E.E. Hardy, J.T. Roach, and R.E. Witmer (1976): A Land Use and Land Cover Classification system for Use with Remote Sensing Sensor Data: U.S. Geological survey Professional Paper 964, pp.28

Civco, D.L. 1987, Knowledgebased classification of Landsat-Thematic Mapper digital imagery, Ph.D dissertation, The University of Connecticut, Storrs, CT (USA), pp.214. ERDAS 7.5 (1991) Field Guide

Harendra S.Teotia, Seemant Teotia, K.A. Ulbricht, P. Reinartz (1996). Relevance of MOMS-02 in developing Countries's future programs of natural resources, cultural resources and environmental resources information management. In ECO-INFORMA, 1996. Lake Buena Vista, Florida (USA).

Kennard, W.C., Teotia, H.S. and Civco, D.L. (1988). The Role of an automated GIS in the development and management of renewable natural resources of northeastern Brazil. In XVI ISPRS Congress, Kyoto, Japan International Archives of Photogrammetry and Remote Sensing, 27 (89), pp. 220-231

LaBash, C.L. D.L.Civco and W.C. Kennard, 1989. the use of linearly transformed Landsat Thematic Mapper Data in land use and cover classification. Technical Papes, 1989. ASPRS/ACMS Annual Convention, Baltimore, Maryland (USA), pp. 2:53-66

Ribeiro, G.do N. (2006), Mapeamento do Uso da Terra e Cobertura Vegetal em Área do Agreste Paraibano, utilizando Técnicas de Sensoriamento Remoto e Geoprocessamento, Areia: UFPB, pp 93 (Dissertação de Mestrado).

Silva Junior, E.B. (2000), Avaliação multitemporal da atividade antrópica na região de Santa Luzia-PB com o uso de Geoprocessamento, Areia: UFPB, pp 66 (M.S.thesis)

Teotia, H.S. and Ulbricht, K.A. (1992), The Integration of Remote Sensing and GIS Technologies for Land Development and Irrigation Potential in the State of Ceara, NE Brazil. In: ISPRS-General Convention, Washington, D.C. August 2-14 Intl. Arch. Photogrammetry and Remote Sensing xxIX, Comm. VII, pp. 466-472

AUTOMATIC 3D CHANGE DETECTION BASED ON OPTICAL SATELLITE STEREO IMAGERY

J. Tian, H. Chaabouni-Chouayakh, P. Reinartz, T. Krauß, P. d'Angelo

German Aerospace Center (DLR), Remote Sensing Technology Institute, 82234 Wessling, Germany –
(Jiaojiao.Tian, Houda.Chaabouni, Peter.Reinartz, Thomas.Krauss, Pablo.Angelo)@dlr.de

KEY WORDS: Optical Stereo Data, DSM, Change Detection, Building, 3D-Analysis

ABSTRACT:

When monitoring urban areas from space, change detection based on satellite images is one of the most heavily investigated topics. In the case of monitoring change in 2D, one major shortcoming consists in the lack of height change detection. Thereby only changes related to reflectance values or local textures changes can be detected. However, changes in the vertical direction are completely ignored. In this paper we present a new 3D change detection approach. We focus our work on the detection of changes using Digital Surface Models (DSMs) which are generated from stereo imagery acquired at two different epochs. The so called “difference image” method is adopted in this framework where the final DSM is subtracted from the initial one to get the height difference. Our approach is a two-step approach. While in the first step, reduction of the noise effects (coming from registration noise, matching artifacts caused by the DEM generation procedures, etc), the second one exploits the rectangular property of the building shape in order to provide an accurate urban area monitoring change map. The method is tested, evaluated and compared with manually extraction results over the city centre of Munich in Germany

1. INTRODUCTION

Change detection using automated image processing methods is a very important topic in satellite image processing. Numerous detection methods using various image types have been developed to satisfy a wide range of applications and user requirements (e.g. Singh 1989, Bruzzone 1997, Lu 2004). One major problem often met when restricting the change detection to the 2D information extracted from satellite images, is the lack of monitoring height changes, the 3D component of the surface to be analyzed. Thereby only changes related to the reflectance values and/or local textural changes are detected. However, changes in the vertical direction, such as building height changes are completely ignored. Such information could play an important role in different applications such as disaster assessment and urban area construction and/or destruction monitoring. Moreover, with the increasing availability of high resolution stereo imagery acquisition as well as the steady development of automatic DSM generation techniques (Zhang, 2005; Krauß, 2007; Akca, 2007; d'Angelo, 2008), comparison of the higher resolution DSMs acquired at different epochs on a same urban area should provide valuable information about the potential changes that have occurred at higher levels (e.g. building construction/destruction).

In the literature, several studies have been dedicated to the detection of changes using DSMs generated from stereo imagery. They can mainly be divided into two categories. The first change detection method is based on the joint-use of stereo and multi-spectral images (when they are available) and the generated DSMs are used in order to detect the changes that occur in the 2D space (spatial changes) as well as in the 3D space (height changes). In fact, the DSMs do not include spectral or textural information which could be of

great help when the task is to perform an accurate change monitoring. For example, Sasagawa (Sasagawa, 2008) integrated the DSM-difference map with the multispectral satellite images as an input to manual interpretation. Krauß (2007) applied a vegetation mask derived from multispectral data to the DSMs in order to concentrate only on urban structure changes. The second change detection method is based on DSM difference (when stereo or multispectral data is not available like in the case of Laser DSMs). The changed areas are detected through a simple subtraction of one DSM from another. This approach has been used in several researches (Zhang, 2005; Reinartz, 2006; Akca, 2007) for DSM precision assessment tasks. However, in this category of 3D change detection, the quality of the generated DSMs is quite determining regarding the accuracy of the final change maps. In fact, miss-coreregistrations and significant height differences that may arise between DSMs generated from different sources often results in the detection of virtual or irrelevant changes. In the work of Chaabouni-Chouayakh (2010) for example, post-processing steps such as morphological operations and contextual knowledge introduction have been proposed to remove virtual changes and to keep only the real ones.

In this paper, we focus on the detection of urban area changes (building construction/destruction). Our work includes vertical change as well as horizontal change. In this paper, the vertical change means the changes in height direction, while horizontal changes mentions the changes in planimetric direction, especially to detect the changing size of the subject in x and y . For the vertical changes, we compute the so-called “difference image” (Singh, 1989; Fung, 1990, Bruzzone, 2000) between two DSMs acquired over the city centre of Munich between 2003 and 2005. We adopt the robust image differencing method to eliminate the noise edges. After that,

different approaches have been adopted to highlight the real horizontal and vertical changes. For the horizontal changes, we apply an edge detection approach followed by a box-fitting method in order to extract the real changes relative to the constructed/destroyed building borders and remove the virtual ones coming from the different nature of the used DSMs. In the case of the vertical changes, we extract the height values of the changed objects based on a statistical method. Finally, the detection results are compared with the manual extraction records.

2. APPROACH TO THE 3D CHANGE DETECTION

2.1 Workflow of the proposed 3D change detection

We aim at extracting height information from the stereo imagery, then generating a change-detection map that represents 3D changes between the two datasets. We focus our research on noise reduction and change detection areas extraction.

The overall workflow of the proposed 3D change detection method is shown in Figure 1. The first step consists in generating DSMs from two pairs of registered optical stereo imagery acquired over the same area (here the city centre of Munich) at two different epochs t_1 and t_2 . In this paper, the DSMs are computed using the Semi-Global Matching (SGM) method (Hirschmüller 2008, d’Angelo 2008). A further co-registration between the two resulting DSMs has been necessary to remove any shift in three dimensions that might exist between the two DSMs. After that, the “difference image” is produced where real changes are highlighted and the influence of the noise (or virtual changes) is reduced (sub-section 2.2). Then, this difference image is analyzed by means of building edge detection in order to retrieve the borders of the different constructed/destroyed buildings. Both of the positive change (new constructed buildings) and negative changes (destroyed places) in vertical and horizontal direction are extracted.

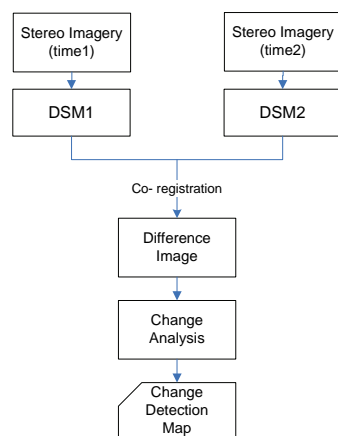


Figure 1. 3D Change detection process proposed in this paper.

2.2 Noise reduction

A major problem to cope with during change detection is the reduction of different kinds of noise. In our research, the noise is defined caused from: 1) Mis-coregistration. In practice, when two images are co-registered at sub-pixel accuracy, the true location of a pixel’s central point may be

anywhere within the pixels surrounding the point (Goodchild et al., 1994, Guillermo et al., 2009). It is unlikely that the footprints of two coincident pixels of the DSMs correspond to the same area (Bruzzone et al., 2003). 2) Quality of the DSM. Due to the erratic variations of the stereo images acquisition conditions, the DSM that generated from stereo imagery has some missing information (called holes in the DSM) caused by the unsuccessful stereo image matching of corresponding pixels. If we analyse the DEM from the pixel level in the change detection procedure, the “holes” will be detected and displayed as noise in the difference image. Many noise reduction methods have been developed in the literature (e.g. Gong et al., 1992; Bruzzone et al., 2003; Im et al., 2005 and Guillermo et al., 2009). In this research, we assume that each pixel in the first DSM shows the least difference with its true corresponding pixel in the second DSM. Therefore, we have chosen the “robust image differencing” method proposed in the work of Guillermo (2009). The robust difference between the initial DSM x_1 and the final DSM x_2 for the pixel (i, j) , is defined as the minimum of differences computed between the pixel $x_2(i, j)$ in the final DSM and a certain neighbourhood (with size $2*w+1$) of the pixel $x_1(i, j)$ in the second DSM x_1 . In mathematical words, the robust positive and negative differences $X_{Pdif}(i, j)$ and $X_{Ndif}(i, j)$ relative to the pixel (i, j) are defined as written in equations (1) and (2), respectively:

$$X_{Pdif}(i, j) = \min_{(p \in [i-w, i+w], q \in [j-w, j+w])} \{x_2(i, j) - x_1(p, q) > 0\} \quad (1)$$

$$X_{Ndif}(i, j) = \max_{(p \in [i-w, i+w], q \in [j-w, j+w])} \{x_2(i, j) - x_1(p, q) < 0\} \quad (2)$$

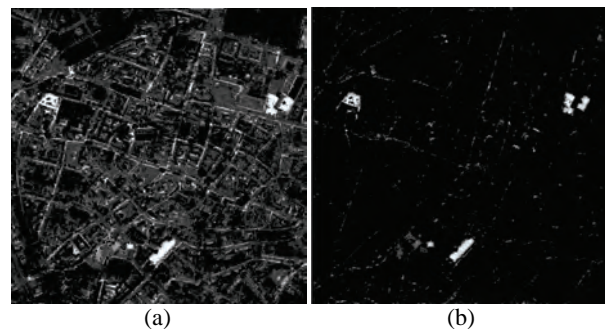


Figure 2. Noise reducing procedure: (a) Original image difference result; (b) Robust image difference result.

Figure 2 shows a comparison between a simple pixel-to-pixel difference between the DEMs and a robust DEM difference. In Figure 2 (a), although the changed areas are highlighted to some extent, the background is very noisy, which will be a problem in the change information extraction procedure. In contrast, after executing the robust image difference in Figure 2 (b), the noise in the background is successfully reduced, while the white areas, which are more likely to be real changed areas, are not influenced significantly.

2.3 Change areas extraction

In binary change detections, one of the most important final steps consists in highlighting real positive and negative changes. For spectral images, a simple thresholding of the histogram has been widely used to stress real changes and remove the virtual ones (Bazi, 2005; Bovolo, 2006; Sen and Pal, 2009). While for the 3D change detection, in the DSM generation procedure, much information is already missing. Simple thresholding on the “difference image” will destroy the more original information. Therefore, automatic building extraction approach is adopted in our research. It can be divided into 3 steps,

- 1) Edges extraction: In this step, the Canny edge (Canny, 1986) extraction method has been adopted. As our focus in this work consists in the detection of the urban changed man-made structures (building construction/destruction), small edges will not be considered in our research.
- 2) Mask generation: Since most of the Canny edges are open, and could not be filled automatically, we choose to close all of the edges with morphological algorithms. We fill each closed edge to single mask, which presents the changed area.
- 3) Box-fitting based building shape refinement: In general, according to the quality of the original DSM data and also the edge detection and mask filling result, most of the edges are highly curved and much information is missed. Therefore, the building edges need to be refined so that they regain their sharp shapes. In this work, we used the box-fitting method proposed by (Sirmacek and Unsalan, 2008). For this method, we need seed points, which show the location of the changed building; the edges which control the size of the box for the changed building; and also the automatic box growing direction and stop condition. In our research, we locate the seed points in the centre of each mask that is generated in step 2. Only the original edges around each buffered mask area are considered to be the edge of this building.

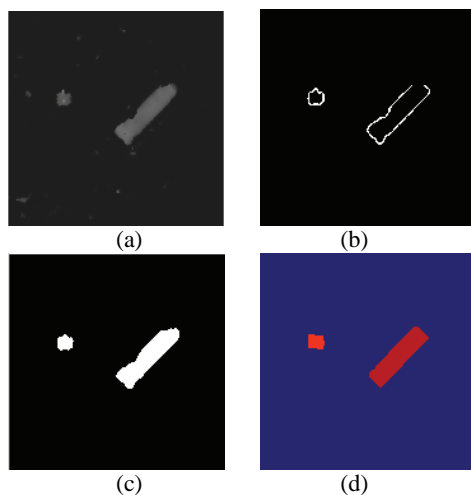


Figure 3. Change areas extraction: (a) Robust difference image; (b) Edges extraction; (c) Changed building masks generation; (d) Box-fitting-based shape refinement of the changed areas.

Figure 3 summarizes the results of the already described steps when applying our changed areas extraction on a subset from

the original difference image of Figure 2 (b) that is depicted in Figure 3 (a). Figure 3 (b) shows the edges extraction results where only important edges are kept (small edges are removed). The mask generation output is displayed in Figure 3(c). The result of the box-fitting method is depicted in Figure 3 (d) where a more refined version of the changed objects is obtained.

In the change value extraction procedure, the horizontal change can be easily calculated according to the pixel numbers of the mask area and the DSM resolution. In order to get only one vertical change value C_i for each constructed/destroyed building defined by $Mask_i$ or box-fitting result. We average the pixels values in the “difference image” belonging to the same changed object, and define this value as the vertical change of each building. In the following, we exclude all pixels, which have ‘0’ value (no height in the changed area), very low values or very high values and could therefore be artifact change, so that these pixels will not be involved in the mean value calculation procedure. As displayed in Figure 4, only the middle part (gray colour filled) of the height difference values are used.

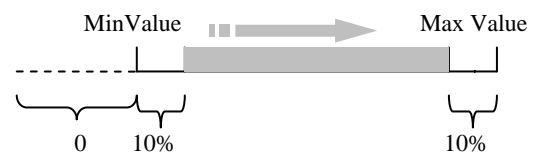


Figure 4. Vertical change value extraction strategy.

3. EXPERIMENTAL RESULTS

3.1 Description of the data

In order to evaluate the performance of our approach, we have chosen the city centre of Munich in Germany as study site. Two DSMs from two different epochs have been used to detect the potential changes. The first DSM (called in the following as IKONOS-DSM) is computed from IKONOS in-orbit stereo imagery (level 1A, viewing angles $+9.25^\circ$ and -4.45°) with one meter spatial resolution, acquired in July 2005. It has been generated using the Semi Global Matching (SGM) algorithm implemented at DLR (d’Angelo, 2009). Due to the lack of another stereo pair, the second one we use instead a DSM which is generated from a LiDAR point cloud data acquired in February 2003 (called in the following as LiDAR-DSM).

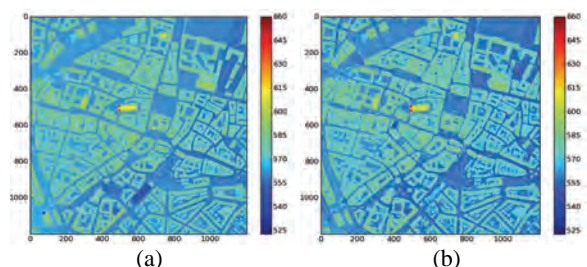


Figure 5. DSMs of the city centre of Munich: (a) LiDAR-DSM (2003); (b) IKONOS-DSM (2005), vegetation cover removed.

Since the LiDAR data used in this work is generated from the last return pulses, which represent the bare earth terrain, the vegetation cover information is almost fully removed.

Therefore, changes at the vegetation level could not be detected. In order to focus on the urban changes, a vegetation mask, computed from the IKONOS multispectral data, has been used. This mask has been generated using the Normalized Differenced Vegetation Index (NDVI). Figure 5 displays the two DSMs used in this article after removing of the vegetation area applying the vegetation mask.

3.2 Generation of the difference image.

Following the procedure described in subsection 2.2, after the co-registration of the two DSMs depicted in Figure 5, we apply the “robust difference” approach to calculate the difference images, where noise has been reduced and changes can be better analyzed. As we can see from Figure 5, in the LiDAR-DSM, the building edges are sharper than in the IKONOS-DSM. Therefore, we choose a 7×7 window ($w=3$ in equations (1) and (2)) in the noise reduction procedure for this evaluation.

Both the positive (which highlights the new constructed areas) and negative difference image (which highlights the destroyed areas) were generated in this step. Figure 6(a) displays the positive robust image difference obtained when applying a 7×7 window in the noise reduction step. The dark blue colour means no change, and the light blue colour corresponds to height changes of about 20 meters.

3.3 3D change detection maps

The different steps of the proposed 3D change detection method applied to the city centre of Munich are displayed in Figure 6. Figures 6 (a-c) present the positive change results. The positive difference image is displayed in Figure 6 (a). The corresponding change mask is shown in figure 6 (b). Figure 6 (c) depicts the final change detection map, under the assumption that each building has only one height value. As can be seen from the change detection results, 6 new buildings are detected. The buildings No.4 and 5 are detected as one building in the mask map (showed in figure 6(b)), due to errors in the DSM generation procedure. To separate the two buildings, in the box-fitting procedure, we extract two seed points in this area based on image eroding result. And we use the original edges in the box growing procedure, so the image eroding will not influence the accuracy of the result.

The same steps have been adopted to detect the negative changes (presented in figures 6 (d-f)). According to the negative change detection results, four building masks are detected. But three of them are in strange shape, with relative low height values. Also, the box-fitting procedure fails in

fitting these buildings to regular rectangular shape. This suggests them to be false alarms (as shown in Table 1). Therefore, only one building is remaining in the negative change map.

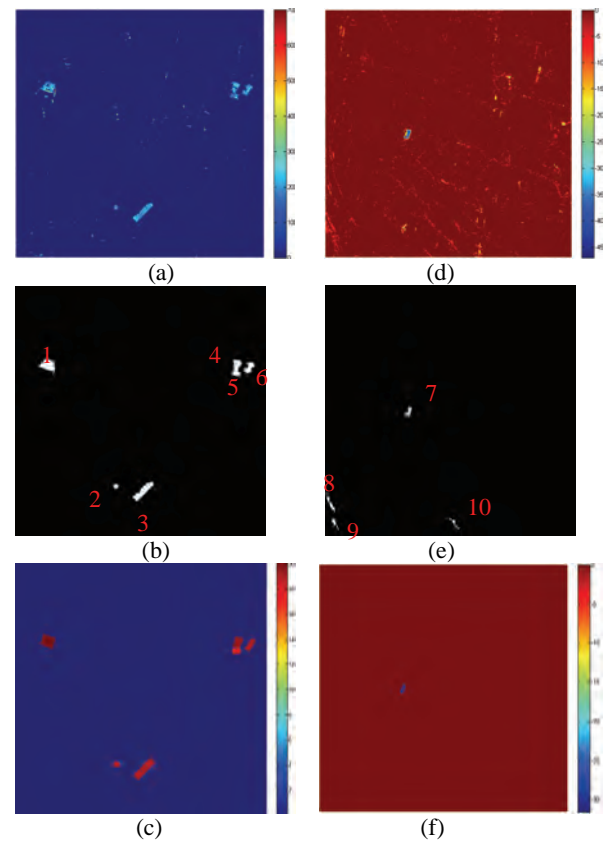


Figure 6. Change detection results: (a) Positive difference map; (b) Positive change mask; (c) positive change map; (d) Negative difference map; (e) Negative change mask; (f) Negative change map

4. RESULTS AND DISCUSSION

In order to allow a quantitative evaluation of the effectiveness of the presented methods, and also to study the influence of the building shapes on the change extraction procedure, we compare the mask-based change maps to the box-fitting based ones. A manually annotated change map has also been included in the evaluation scheme:

Table 1. Change Detection Result Comparison

No.	Change Type	Mask-Based		Box-fitting Based				Manual Extraction			
		Height [m]	Area [m ²]	Height [m]	Area [m ²]		Height [m]	Area [m ²]			
1	Positive change	19.58	3247	19.80	3077		22.0	2788			
2	Positive change	19.10	491	16.46	576		17.00	465			
3	Positive change	18.97	3344	19.10	3748		18.8	3694			
4	Positive change	18.78	2553	19.55	18.26	1818	2911	19.2	17.90	1377	2289
5	Positive change			16.97		1093		16.6		912	
6	Positive change	18.64	1683	18.69	1409		20.2	945			
7	Negative change	-33.72	762	-32.42	800		-36.0	1007			
8	Negative change	-6.2	1044	----	----		----	----			
9	Negative change	-6.43	578	----	----		----	----			
10	Negative change	-6.30	565	----	----		----	----			

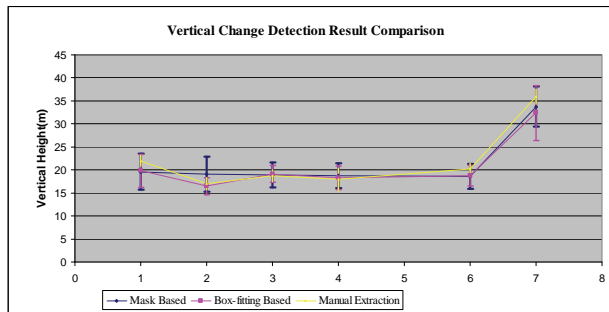


Figure 7. Vertical Change Detection Result Comparison

- For the annotation of the horizontal changes (areas of the changed objects), the areas of the positive (resp. negative) changed objects have been manually extracted using the original IKONOS panchromatic channel (resp. using the LIDAR DSM data).
- For the annotation of the vertical changes (height of the changed objects), we extract the height value in the changed area from each DSM manually, and calculate the difference.

The final change detection results are summarized in Table 1. To compare the two automatic detection result and manual extraction result, we show the vertical and horizontal change extraction result separately in Figures 7 and 8 (For the negative changes, we use the absolute values in Figure 7). As the 4th and 5th changes could not be separated in the detected mask, we consider them as one changed object in the comparison procedure. Also false alarms are omitted in our comparison scheme. According to the error bars (get from the standard deviation of the height value distribution in the mask area), the detected vertical changes fit well with the manual extraction result. For the 1st building, the manual extraction result shows relatively larger difference with both the mask based and box-fitting based automatic extraction result. In order to explain such behaviour, we compare the generated DSMs to the IKONOS panchromatic image. As showed in Figure 9, the IKONOS-DSM in this area has poor quality, resulting in 3 big holes in the middle of the building, and the building shape is strongly transformed. This explains well the large height difference found between our change maps and the manual extraction one.

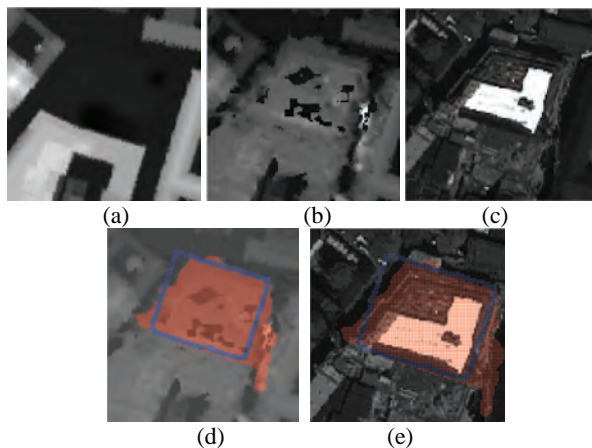
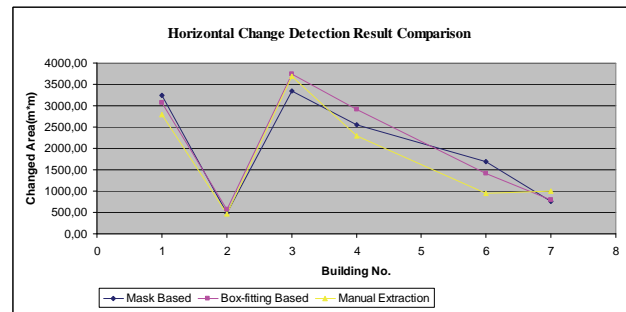
Figure 9. 1st changed building analysis: (a) LiDAR-DSM; (b) IKONOS-DSM; (c) IKONOS-PAN-2005; (d) Mask with IKONOS-DSM; (e) Masks with the IKONOS-PAN-2005

Figure 8. Horizontal Change Detection Result Comparison

In the Figure 9 (d-e), the red mask represents the masked shape, while the blue rectangle is the extracted change building shape after box-fitting. We can see that the mask fits well with the building area in IKONOS-DSM, but has quite large difference with IKONOS-PAN-2005, after the box-fitting, the right parts of the outliers are successfully recovered. But the result is limited by the rectangular shape assumed in the box-fitting procedure, which displayed by the false alarm pixels in the left upper part inside the blue colour rectangle. Those situations conduct the relative lower vertical changes, while higher horizontal changes in the extraction results.

5. CONCLUSION

In this paper, a 3D change detection approach based on DSMs is proposed and evaluated to detect changes that have occurred in the city centre of Munich between 2003 and 2005.

The whole procedure is divided into 3 steps. First, we generate and co-register DSMs acquired at two different epochs. Then, we compute the “robust difference images” in order to reduce the noise coming from the different nature of the DSMs used. In fact, the random variations of the stereo images acquisition conditions as well as the blunders caused during the automatic matching and DEM generation process makes urban structures look different from one DSM to another, especially for building walls and edges. As our focus in this paper is the monitoring of urban changes, noise reduction is essential. After that, we generate the change map with both vertical and horizontal change information. To overcome the poor quality of the DSM, we refine the changed buildings to rectangular shape. To confirm the validity of our approach, we compare our results with manual extracted ground truth figures.

It has been shown that DSMs generated from optical stereo imagery could be reliable sources for efficient 3D change detection. The extracted change maps demonstrate the ground surface changes in most parts of the test areas. But when the DSM does not meet the required quality and can not show the real situation, the result will be influenced. In addition, only rectangular building shapes have been considered in our refinement procedure, the change results will certainly improve when more building shapes are included.

ACKNOWLEDGEMENTS

The authors wish to thank Beril Sirmacek for contributing her box-fitting algorithm, and Hossein Arefi for his advice in the pre-processing of the DSM.

REFERENCES

- Akca, D., 2007. Least Squares 3D surface matching. Ph.D. thesis, *Institute of Geodesy and Photogrammetry*, ETH Zurich, Switzerland
- Bazi, Y., Bruzzone, L., and Melgani, F., 2005. An Unsupervised Approach Based on the Generalized Gaussian Model to Automatic Change Detection in Multitemporal SAR Images, *IEEE Transactions on Geoscience and Remote Sensing*, Vol. 35, No. 4, July 1997
- Bovolo, F., 2006. Advance Methods for Automatic Change Detection in Multitemporal Remote Sensing Images Acquired by SAR and Multispectral Sensors, *PhD Dissertation*, University of Trento. December 2006
- Bruzzone, L., and Serpico, S.B., 1997. An Iterative Technique for the Detection of Land-Cover Transitions in Multitemporal Remote-Sensing Images, *IEEE Transactions on Geoscience and Remote Sensing*, Vol. 35, No. 4, July 1997
- Bruzzone, L., and Prieto, D.F., 2000. Automatic Analysis of the Difference Image for Unsupervised Change Detection. *IEEE Transactions on Geoscience and Remote Sensing*, Vol. 38, No. 3, May 2000
- Bruzzone, L., and Cossu, R., 2003, An Adaptive Approach to Reducing Registration Noise Effects in Unsupervised Change Detection. *IEEE Transactions on Geoscience and Remote Sensing*, Vol. 41, No. 11, November 2003
- Canny, J., 1986. A computational approach to edge detection. *IEEE Transactions on Pattern Analysis and Machine Intelligence*, 8 (6), pp. 679-698
- Castilla, G., Guthrie, R. ., and Hay, G.J., 2009. The Land-cover Change Mapper(LCM) and its Application to Timber Harvest Monitoring in Western Canada, *Photogrammetric Engineering & Remote Sensing, Special Issue on Change Analysis*, Vol. 75, No. 8, August 2009
- Chaabouni-Chouayakh, H., Krauss, T., d'Angelo, P., and Reinartz, P., 2010. 3D Change Detection inside Urban Areas using different Digital Surface Models, *ISPRS International Archives of the Photogrammetry, Remote Sensing and Spatial Information Sciences*, Vol. 39 (3), Accepted
- Choi, K., Lee, I., and Kim, S., 2009. A feature based approach to automatic change detection from lidar data in urban areas, *ISPRS Workshop Laserscanning 2009*, Paris, France
- d'Angelo, P., Lehner, M., and Krauss, T., 2008. Towards Automated DEM Generation from High Resolution Stereo Satellite Images, *International Society for Photogrammetry and Remote Sensing*, pp. 1137-1342
- Fung, T., An Assessment of TM Imagery for Land-cover Change Detection, *IEEE Transactions on Geoscience and Remote Sensing*, Vol. 28, No. 12, 1990
- Goodchild, M.F., 1994. Integrating GIS and Remote Sensing for Vegetation Analysis and Modelling: Methodological Issues. *Journal of Vegetation Science*, 13 (4), pp 773-779
- Hirschmüller, H., 2008. Stereo processing by semiglobal matching and mutual information. *IEEE Transactions on Pattern Analysis and Machine Intelligence*, 30 (2), Feb. 2008.
- Krauß, T., Reinartz, P., and Stilla, U., 2007, Extracting Orthogonal Building Objects in Urban Areas From High Resolution Stereo Satellite Image Pairs, *International Archives of Photogrammetry, Remote Sensing and Spatial Information Sciences*, 36(3/W49B)
- Murakami, H., 1999, Change Detection of Buildings Using an Airborne Laser Scanner, *ISPRS Journal of Photogrammetry & Remote Sensing*, Vol. 54, pp.148-152.
- Lu, D., Mausel, P., Brondizio, E. & Moran, E., 2004, Change Detection Techniques. *International Journal of Remote Sensing*, 25 (12), pp 2365-2407.
- Reinartz, P., Müller, R., Lehner, M., and Schroeder, M., 2006. Accuracy Analysis for DSM and Orthoimage Derived from SPOT HRS Stereo Data Using Direct Georeferencing. *ISPRS Journal of Photogrammetry and Remote Sensing*, Vol. 60, No. 3, pp 160-169
- Singh, A., 1989, Digital change detection techniques using remotely-sensed data. *International Journal of Remote Sensing*, 10 (6), pp 989-1003
- Sirmacek, B., and Unsalan, C., 2008, Building Detection From Aerial Imagery using Invariant Color Features and Shadow Information. *In Proceeding of International Symposium on Computer and Information Science (ISCIS)*, 1, pp 1-5
- Zhang, L., 2005, Automatic Digital Surface Model (DSM) Generation from Linear Array Images. Ph.D. Thesis, *Institute of Geodesy and Photogrammetry*, ETH Zurich, Switzerland

PROSPECTIVE SPACE MISSIONS WITH L-BAND MICROWAVE RADIOMETRIC SYSTEMS

Yu. Tishchenko^a, V. Savorskiy^a, M. Smirnov^a, V. Abyazov^b, A. Khaldin^b

^aFryazino Department, Kotelnikov Institute of Radioengineering and Electronics, RAS, Vvedenskogo sq., 1, Fryazino, Moscow region, 141190, Russia - (savor, tishchen)@ire.rssi.ru

^bSpecial Design Bureau of the Institute of Radioengineering and Electronics RAS, Vvedenskogo sq., 1, Fryazino, Moscow region, 141190, Russia - ahaldin@sdb.ire.rssi.ru

Commission VII, Working Group VII/5

KEY WORDS: microwave radiometric systems, scientific programs, remote sensing, decimeter waves, small satellite, Russian segment of International Space Station.

ABSTRACT:

Prospective Russian space missions include aims directed in developing and enhancing Earth remote sensing techniques by means of microwave radiometry. New L-band (wavelength about 21 cm) microwave radiometric systems for space applications are constructed in the Special Design Bureau of the Institute of Radioengineering and Electronics RAS. Scientific programs of experiments with these instruments, which incorporate numerous proposals of Russian scientific organizations, are prepared in the Institute of Radioengineering and Electronics RAS. The main goals of scientific programs are: development of radio physical Earth remote sensing methods from space in L-band for investigation of physical events and processes in earth surface-atmosphere system; investigation of external factors (galaxy emission, ionosphere, etc.) impact into measured parameters of investigated objects; analysis of radio interference problems; development of new techniques for processing of data with different space resolution.

1. INTRODUCTION

Theoretical and experimental investigations show that L-band radiometry is very prospective (optimal) for soil moisture and sea surface salinity investigations. These measurements practically not influenced by weather conditions in the atmosphere. Now one of the most important problems for L-band radiometry is the problem of radio interference (RFI). RFI may be not so important in open ocean region, but are very strong in urban areas. The second important problem consists in necessity to make relatively large antenna for reasonable spatial resolution of the instrument.

Despite this difficulties interest to investigations with use of microwave radiometers in this band is very high. One of the most powerful L-band instruments launched several months ago is European project SMOS [1]. It contains very sophisticated interferometric imaging radiometer MIRAS with synthetic aperture antenna. In USA under developments is a project SMAP with combination of microwave radiometer and scatterometer [2]. In Russia under development are simpler microwave radiometers for small satellite and for Russian segment of International Space Station (ISS) [3]. Time of SMOS and our instruments operation may overlap and it should provide the possibility to compare some results.

2. SPACE L-BAND MICROWAVE RADIOMETRIC SYSTEMS

Leading scientific organization for creation of payload for two space projects with use of L-band radiometers is Kotelnikov Institute of Radioengineering and Electronics of RAS (IRE

RAS). Head design organization of these radiometric systems is Special Design Bureau of IRE RAS (SDB IRE RAS).

The first creating radiometric system PN1 consists of L-band microwave radiometer with 2 beams antenna. It is compact module and will be attached to the outer side of the small satellite (planned launching – 2010). General specification of the instrument is presented in the middle column of Table 1.

	PN1	ALRS
Main frequency, MHz	1410	1410
Bandwidth, MHz	20	20
Radiometric sensitivity, K	0,2-0,3	0,2-0,3
Polarization	linear	linear
Number of beams	2	8
FOW, km	350	50
Swath width (at orbit height 350 km), km	700	400
Power consumption, VA	≤ 60	120
Weight, kg	≤ 13	35
Size, mm		
radiometer	400x300x50	
antenna	800x510	1200x1920

Table 1. General specification of the satellite radiometric systems

Observation geometry of the small satellite system is presented in Fig. 1. Antenna of the radiometric system will be oriented for observation in nadir direction and provide spatial resolution about 350 km and swath width 700 km. In the main operational mode two beams of the system oriented across the flight direction in order to have wider swath width. In addition to this mode it may be possible to rotate the satellite so that two beams will be in a flight plane. This mode may be useful for calibration purposes and development of RFI suppression algorithms.

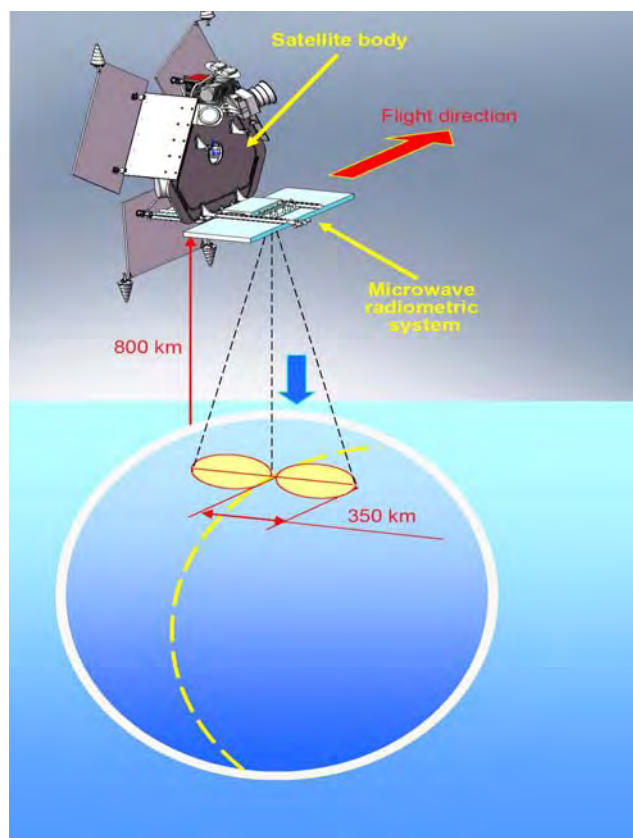


Fig.1. Observation geometry of the small satellite microwave system

Advanced L-band radiometric system (ALRS) will be installed on the module of Russian segment of International Space Station (RS ISS) (planned installation - 2010). General specification of the instrument is presented in the last column of Table 1. It is a set of radiometers with pushbroom 8 beams antenna. Each beam will have spatial resolution about 50 km. Observation geometry of the advanced microwave system is presented in Fig. 2.

Due to relatively large size of the ALRS antenna and requirements to deliver instrument in compact state through the manhole it has folding elements and will be deployed manually. General view of L-band radiometric system in compact (transport) state is shown in Fig. 3.

Now both radiometric systems are made in technological versions and are in the procedure of laboratory testing. Results of testing are in a good agreement with technical requirements.

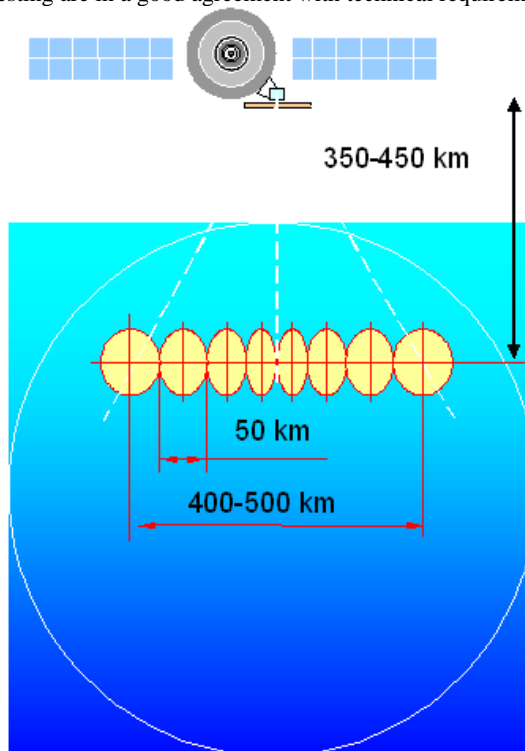


Fig.2. Observation geometry of the advanced microwave system

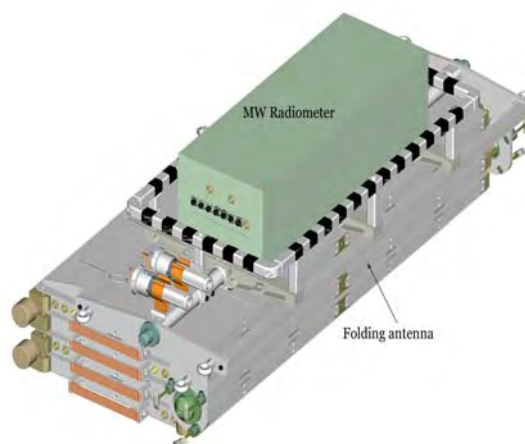


Fig.3. L-band radiometric system ALRS in compact (transport) state.

3. SCIENTIFIC OBJECTIVES AND GENERAL FEATURES OF THE EXPERIMENTS

Microwave radiometers despite their low spatial resolution are widely used in space remote sensing of environment. It is due to ability of microwave radiometry to get data which are impossible or at least very difficult to get by any other means. Such data are data on averaged by surface and/or depth thermodynamic temperature of physical objects, their integral

dissipative features, and information on complex dielectric permittivity (see, for example, [4-6]). Moreover these data could be received at any day time and do not depend on weather conditions.

Merits of microwave radiometers promote them to be used as one of the first instruments installed on satellites for Earth exploration. The main observed objects were both land covers with vegetation canopy and those without canopy featured with different soil moisture, ground water level, vegetation type, temperature, and soil density, as well water basins with different salinity, mineralization, and temperature. Nowadays microwave radiometers are used in synchronous measurements with optical and IR sensors. As a result the relation between microwave radiation intensity and soil water level down to 1.5-2 m depth in overmoistured and down to 3-5 m in dry regions are retrieved [5]. As well it is revealed that agriculture vegetation canopy with biomass up to 2-3 Kg/m² is semi-transparent media for decimeter wave range. So, it is possible to get estimations of soil moisture and biomass (for above part of water plants) for those levels of biomass [4,6].

Scientific programs for PN1 and ALRS radiometric systems were prepared IRE RAS on the base of proposals from Russian institutions. This work explores IRE RAS experience on developing scientific programs for such space projects as PRIRODA, OCEAN-O No.1.

The main contribution to working out of key proposals in the Scientific programs (priority directions of researches, objects of researches) have submitted the following organizations:

- Kotelnikov Institute of Radioengineering and Electronics of the Russian Academy of Sciences,
- Institute of Space Researches of the Russian Academy of Sciences,
- Shirshov Institute of Oceanology of the Russian Academy of Sciences.

The Programs are directed on the decision of problems on working out of radio physical methods of remote sensing of the Earth from space in a perspective decimeter range of electromagnetic waves for studying of the physical phenomena and processes in atmosphere-surface system; on research of influence of external factors (a galactic background, an ionosphere, etc.) on measured characteristics of investigated objects; on studying of radio interference at carrying out of researches; on development of methods of joint data processing with the different spatial resolution.

In 70 and 80th years in the IRE RAS and other organizations in the USSR and the abroad the large-scale theoretical researches of microwave radiometry possibilities of soils, vegetation and water investigations in a range of wavelengths to 30 cm, and also experimental researches from airplanes carried out. Researches have shown the possibility of estimation, in particular, of soil humidity and vegetation biomass, and also salinity of water areas by radiometric method [5-7]. At the same time, the experimental data of using of decimeter waves for working out of practical methods of estimation of soil moisture and vegetation biomass, sea salinity from space it is not enough to make conclusion about possibility of radiometric space operative observations application of soils, vegetation, water areas state in regional and global scales.

Realization of Programs will allow estimate the efficiency of microwave radiometric method for definition of soil moisture and vegetation biomass, sea salinity from space (accuracy of estimation, spatial and time variations). Necessary models and algorithms will be developed. The technique of carrying out of

corresponding space measurements, calibration and validation of experimental data is fulfilled. Data for the decision of various scientific and practical problems will be obtained:

- mapping of soil moisture (including under the forest canopy) within the regional and global scales,
- research of temperature and moisture conditions of forest-swamp systems,
- studying of vegetation biometric characteristics,
- study of water areas salinity,
- study of glacial and permafrost zones,
- study of the ocean-land-atmosphere exchange energy (in conjunction with data from other sensors),
- research of geothermal activity, estimation of border of zones and temperature regime,
- development of methods for joint processing of data with different spatial resolution.

Results can be used in areas such as agriculture, forestry, hydrology, climatology, ecology.

Programs consist of five sections and attachments. Sections of Programs cover the following objects of researches:

- research on land,
- research of ocean,
- study of the atmosphere,
- conducting of calibration measurements,
- information support of scientific programs.

Experiments on remote sensing of land, ocean and atmosphere are systematized in the first three sections. The basic directions of researches are presented.

Experiments on remote sensing of a land are systematized in the first section. The following main research directions are planned:

- study of vegetation,
- study of the hydrological situation of individual regions the Earth surface,
- study of forest-swamp systems state,
- study of seismic zones, zones of geothermal and volcanic activity,
- study of glacial and permafrost zones.

Experiments on remote sensing of ocean are systematized in the second section. The following main research directions are planned:

- development of techniques of remote definition of ocean surface layer salinity,
- research of thermal and dynamic interaction of ocean and atmosphere,
- research of ocean hydrophysical fields,
- study of ice conditions.

Experiments on remote sensing of atmosphere are systematized in the third section. The following main research directions are planned:

- influence of external factors (galactic background, ionosphere, etc.) impact into measured parameters of investigated objects,
- study of radio interference problems.

The experiments concerning to calibration measurements and Scientific programs information support are placed in separate section since these experiments provide basis for all research experiments. They are connected with development of methods and technologies of measuring equipment calibration and data validations; of methods and technologies of using of active archive of experimental researches data; of means and techniques of data processing, storage and distribution. Effective data exchange allows to expand the possibilities of researches, for example, by use of the various information from various sources.

In many cases it can be a basic condition for successful realization of planned researches at carrying out of complex space experiments.

During the programs realization it must be solved a wide range of scientific problems, part of which is an associated sub-satellite (calibration) measurements. Such measurements are needed for

- calibration of remote sensing devices, control of their working capacity in functioning, experimental data informativeness in remote control tasks,
- working out of new, improvement and check of existing geophysical parameters restoring techniques;
- development of techniques of joint interpretation of the space data received in various spectral bands and results synchronous sub-satellite measurements,
- validation of space data,
- complex studying of natural objects by use of the information received from various levels and with the different spatial resolution.

For calibration uniform sites of terrestrial and water surfaces with known radiating and geophysical parameters are selected. The sizes of these sites are defined by resolution of measuring devices. For the radio spectrum - from a few kilometers to tens and hundreds kilometers depending on the wavelength. Test sites (on which subsatellite measurements are carried out synchronously or quasisynchronously with satellite observations) are chosen in different regions of the Earth for wider coverage of studied objects types. List of measured on test sites parameters, content of measurements are determined with concrete purpose of test site and experiment tasks.

In Attachments to Programs are presented:

- structure and characteristics of scientific equipment;
- levels of the space data presentation (processing),
- proposals on development of Scientific programs.

It is worthwhile to coordinate the developed Scientific programs with similar researches of existing and planned to realization in near future of russian and foreign space projects.

At the first stage of our space experiments the main goals are to develop and test new space microwave radiometric instrument in new band of electromagnetic spectrum in order to solve the following technical objectives:

- investigation of RFI situation in L-band all over the globe,
- development of in-flight calibration techniques,
- development of subpixel data processing algorithms for information simultaneously obtained from different satellites with different spatial resolutions.

During this stage we expect to select main regions with low level of RFI and made adjustments of preliminary prepared data calibration techniques.

Relatively low space resolution of the L-band radiometric systems restricts us in the list of possible applications. In the large field of view of the radiometer may be objects with quite different characteristics of emission. In this case high importance has development of algorithms for subpixel microwave data processing. During the data processing will be used simultaneous data from all available satellites with microwave and optical instruments having different space resolution.

At the second stage it is expected to concentrate more on the scientific objectives and environment investigations. Main directions are:

- soil moisture retrieval over the territories in regional and global scales,
- sea salinity estimation in open ocean,
- study of the geothermal activity regions,
- investigation of energy-exchange in the ocean-land-atmosphere system (in combination with the data of other sensors).

4. CONCLUSIONS

Experiments with space L-band microwave radiometers will provide new information on key characteristics of the oceans and land surface, mostly sea salinity and soil moisture. To achieve this goal it will be required to solve several technical problems concerning calibration, removing RFI effects and etc.

Scientific program of the experiments should be coordinated with similar programs of European and USA projects.

5. REFERENCES

1. Hubert M. J. P. Barré, Duesmann , and Yann H. Kerr "SMOS: The Mission and the System," IEEE Transactions on Geoscience and Remote Sensing, 2008, Vol. 46, n.3, pp. 587-593.
2. <http://smmap.jpl.nasa.gov> (accessed at 27 May 2010).
3. Armand N.A., Smirnov M.T., Tishchenko Yu.G. "Hardware for scientific and applied studies in Earth resource remote sensing and in environment monitoring from the International Space Station Russian segment", Cosmonautics and rocket engineering, No 4 (49), 2007, pp. 91-94 (in Russian)
4. Basharinov A.E., Shutko A.M. Measurements of moisture of land cover by microwave radiometry methods. – Meteorology and hydrology, 1971, №9, c. 17-20(in Russian).
5. Shutko A.M. Microwave radiometry of water surface and soils. – M.: Nauka, 1986 (in Russian).
6. Jackson, T.J., A.Y. Hsu, A. Shutko, Yu. Tishchenko, B. Petrenko, B. Kutuza, and N. Armand. Priroda microwave radiometer observations in the Southern Great Plains 1997 Hydrology experiment. Int. J. Remote Sensing, 23 (2), 2002, p. 231-248.
7. Tishchenko Yu.G., Shutko A.M., Savorskiy V.P., Smirnov M.T., Krapivin V.F., Petkov D., Kancheva R., Nikolov H., Borisova D. Regional Monitoring of the Earth Surface in Black Sea Basin in Interests of Natural Disasters Mitigation // Proceedings of RAST 2007. Istanbul. 2007. P.540-542.

6. ACKNOWLEDGEMENTS

This work was supported in part by grants RFBR 08-05-00890-a, 09-02-00780-a.

VALIDATION OF A SEMI-AUTOMATED CLASSIFICATION APPROACH FOR URBAN GREEN STRUCTURE

Øivind Due Trier^{a,*} and Einar Lieng^b

^a Norwegian Computing Center, Gaustadalléen 23, P.O. Box 114 Blindern, NO-0314 Oslo, Norway – trier@nr.no

^b Asplan Viak AS, P.O. Box 701, NO-4808 Arendal, Norway – einar.lieng@asplanviak.no

KEY WORDS: Segmentation, classification, multispectral Quickbird imagery, urban vegetation

ABSTRACT:

Municipalities in Norway need to develop an urban green structure plan. Traditional mapping has its limitation, since the land use is in focus and not the actual land cover. This study evaluated the appropriateness of using multispectral Quickbird images for the semi-automated mapping of green structures in urban and suburban areas. A Quickbird image of Oslo from 2 June 2008 was used. A classification algorithm was implemented in Definiens Developer. The algorithm was applied to the whole image, and tested on six randomly selected subsets. The validation was performed by manual editing of the classification result. The main focus of the editing process was to detect misclassifications between grey areas (such as roads and buildings) and green areas (trees, grass, and sparse vegetation). The most striking problem with the automated method was that the object borders were very rugged. However, these segmentation problems were to some extent ignored in the evaluation process, concentrating on correcting major parts of objects being misclassified rather than correcting all minor segmentation inaccuracies. The classification step had approximately 9% misclassification rate in the two-class problem grey area versus green area. This is a very good basis for further improvement. The obvious segmentation problems are clearly the first things to address when further improving the method. Another problem is to what extent the automated method can be used on other images with different light conditions, e.g., with the presence of clouds or light haze and another solar elevation. Will a simple retraining of the classification rules be sufficient, or will the rules have to be redesigned? It could even happen that redesigning the rules is not sufficient, so that other methods have to be developed.

1. INTRODUCTION

This work was initiated to meet the need of municipalities in Norway to develop a green structure plan. Traditional mapping has its limitation, since the land use is in focus and not the actual land cover. Therefore, other sources of information about urban and suburban green structure are being sought. A municipality is interested in a green structure plan for several reasons:

1. To map current status of green areas and their changes over time. For example, what happens with the vegetation in public parks over time, even if the mapped land use does not change?
2. To maintain biological diversity. Different species or groups of species use different varieties of green structure as corridors. For example, small birds would avoid open areas, and need a corridor of trees to move safely. In open areas, they would expose themselves to predators.
3. Green structures are being used for recreation.
4. Vegetation converts carbon dioxide to oxygen, reduces noise, and has aesthetical value. Vegetation also binds water, reducing the prospect of floods after heavy rainfall.
5. If accurate, the green structure map can be used in overlays

The green structure includes private gardens. Although not accessible to the public, private gardens containing trees contributes to items 2 and 4 above.

Forest and farmland are not in the focus of this study, since they are well mapped, and the land cover aligns well with the land use classification of traditional mapping.

The purpose of this study was to evaluate the appropriateness of using Quickbird 0.6 m – 2.4 m resolution satellite images for the automatic mapping of green structures in urban and suburban areas. The rest of the report is organized as follows: Section 2 presents the available Quickbird image data, followed by a description of the segmentation, training, classification and postprocessing steps of the automatic algorithm in Section 3. In section 4, the validation methodology is described. The validation results are presented in Section 5 and discussed in Section 6. This paper is a condensed version of a project report (Trier, 2009), available at <http://publ.nr.no>.

2. DATA

The project has acquired parts of a cloud-free Quickbird scene of parts of Oslo and surrounding area, acquired on 2 June 2008. The image has a 0.6 m ground resolution panchromatic band, and four 2.4 m resolution multispectral bands (blue, green, red and near infrared).

3. CLASSIFICATION PROCEDURE

Definiens Developer (Definiens, 2007) was used to segment the image, based on pixel colors and parameters describing the segment shapes. Then the user defined a set of rules to classify the segments based on texture, neighborhood, color and other attributes. The final classification result consists of five classes: (1) grey areas, (2) grass, (3) trees, (4) little vegetation, and (5) water and missing data.

* Corresponding author.

3.1 Segmentation

The segmentation was done in two levels in a bottom-up fashion.

The segmentation has to be a compromise between conflicting needs. On one hand, one would like to obtain large building blocks. At the same time, one would like to keep narrow corridors of green structure. Multiresolution segmentation was used, with two levels. The level 1 segmentation was based on the panchromatic image alone, whereas the level 2 segmentation also used the multispectral image bands (Table 1). The level 2 segmentation is based on the level 1 segmentation, which means it is locked to the segment boundaries that were created in level 1. The level 2 segmentation essentially aggregates segments from level 1.

Table 1. Segmentation parameters in Definiens Developer.

Level settings	level name	
	level1	level2
Level Usage		Create above
Image layer weights		
QB_PAN	1	1
QB_NIR	0	1
QB_Red	0	1
QB_Green	0	1
QB_Blue	0	1
Thematic layer usage	(not used)	(not used)
Scale parameter	20	50
Composition of homogeneity criterion		
Shape	0.1	0.1
Compactness	0.5	0.5



Figure 1. Homogeneity criteria in Definiens Developer. The figure is from (Definiens 2007), page 160.

On each level, the segmentation process iterates several times. In the first iteration in level one, all segments are one pixel each. The mutually best pairs according to a homogeneity criterion are found, and each identified segment pair is merged into a new segment. This continues as long as segments can be merged without breaking the scale parameter constraint. The scale parameter is a threshold on the homogeneity value of a segment, and the homogeneity value is computed as the standard deviation from the ideal situation. The following criteria can be used, in combination

- Color: homogeneity is computed as standard deviation of the spectral colors.
- Shape: divided into smoothness and compactness
 - Compactness: homogeneity is computed as the deviation from a compact object
 - Smoothness: homogeneity is computed as the deviation from a smooth object boundary.

The color and shape weights sum to 1. Within the shape criterion, the compactness and smoothness weights sum to 1

(Figure 1). So, the shape value of 0.1 in Table 1 denotes that the shape criterion has weight 10% and the color criterion 90%. By increasing the shape weight, the segmentation will be more eager to find objects which are compact and/or smooth, and less eager to find objects with low color variation.

If, for a segment, the color homogeneity is, say, 12, the smoothness homogeneity is 48 and the compactness homogeneity is 60 then the weighted homogeneity (Table 1) is

$$0.9 \times 12 + 0.1 \times 0.5 \times 48 + 0.1 \times 0.5 \times 60 = 9.2 + 2.4 + 3.0 = 14.6,$$

which is below the scale threshold for level 1, so this segment is accepted. However, if the shape homogeneity had been set to 0.5, then the weighted homogeneity had been

$$0.5 \times 12 + 0.5 \times 0.5 \times 48 + 0.5 \times 0.5 \times 60 = 6 + 12 + 15 = 33,$$

which is above the scale threshold for level 1.

In level 2, equal weight is placed on the four multispectral bands (blue, green, red and near infrared (NIR)) (Table 1). One could place a higher weight on NIR for vegetation mapping, and also reduce the weight of blue if there is haze in the image.

The scale parameter indicates how large objects one is interested in. To find individual trees, a low value should be used. To segment parts of a forest, a large value is used. We are interested in private gardens, where trees are present but the pattern is less homogeneous than in a forest. So we are interested in single trees and groups of trees, and a value of 50 seemed to work well.

3.2 Classification

The classification was done in a hierarchical fashion. At each level, there are competing rules, and the rule that gives the highest score is selected. (In the documentation, the rules are called membership functions (Definiens, 2007).) There is also a threshold for setting an object to be unclassified. This was set to 0.1. One can set this to, say, 0.9 during training.

The rules used on the 2008 Quickbird image are outlined in Figure 2, and the actual values for the thresholds should be adjusted for a new image. However, one may also want to use different rules for another image, due to different colors, phenological cycle, date, haze, etc.

Both the panchromatic 0.6 m resolution and the four bands multispectral 2.4 m resolution information was used in the classification procedure.

The classification rules are organized in a hierarchical fashion (Figure 2). Note that so-called soft thresholds are being used. This means that instead of using a simple if-test on a threshold value, essentially producing a sharp transition from 0 to 1, there is a smooth transition zone where the response goes gradually from 0 to 1. Then the rule with the highest score wins. The actual threshold values are given in (Trier, 2009).

When working with the rules, one might add new rules or tune the thresholds. At the end, one has a handful of misclassified and unclassified objects. One may then add "cleanup rules". Six cleanup rules were used, see (Trier, 2009) for details.

3.3 Comments

The segmentation and classification modules in Definiens Developer provided a means to quickly obtain a fairly good

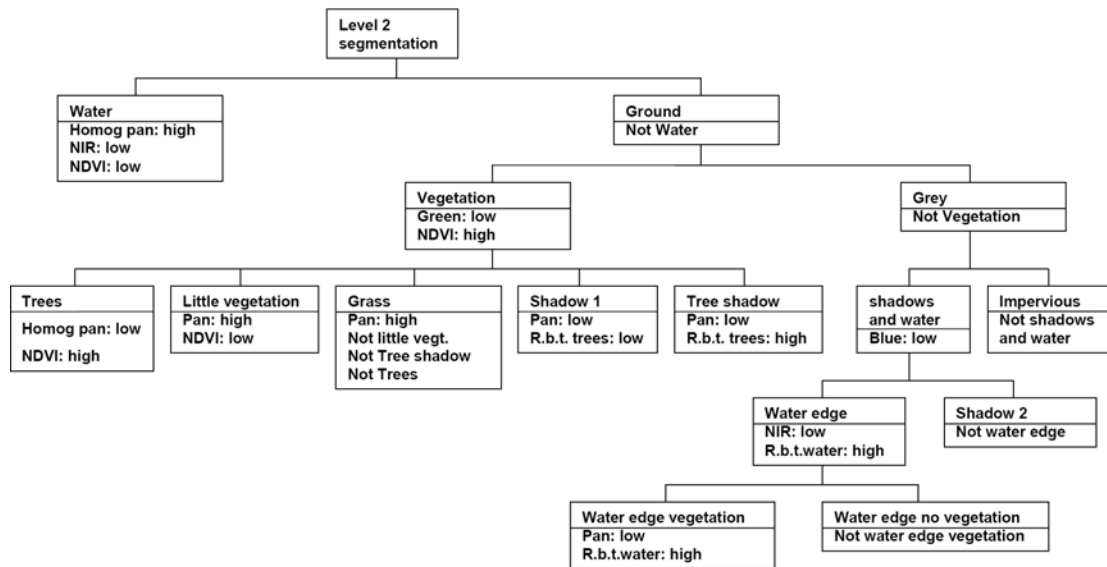


Figure 2. Hierarchy of classification rules.

classification result. Some time was spent on optimizing the parameters, but it was felt that it was not a good idea to spend too much time on this, as this would have to be repeated for a new model.

Agricultural land, rivers and lakes are not considered important in this project, as they are well mapped, and can be obtained from GIS. However, the positional accuracy is often lower than for buildings and roads.

The result of the classification procedure was a 0.6 m resolution image with the following classes:

1. Open grass land and lawns.
2. Bushes, trees, forest. (Parts of) private gardens are expected to fall into this class.
3. Little vegetation: Paths, grass areas with substantial wear and tear.
4. “Grey” areas, that is, covered by buildings, roads, parking lots, etc; thus with no vegetation.
5. Not classified or missing data, also used for water.

The three first classes are regarded as “green” areas, and can be seen as subclasses of green areas.

3.4 Postprocessing of classification result

The classified image can be combined with GIS data of buildings and roads. Trees overlapping buildings and roads are kept, based on the NDVI value, but other parts of the buildings and roads are subtracted from the vegetation classes.

Enhanced versions of the Oppegård and Lørenskog areas were created by using GIS data for buildings and roads. The houses and roads were subtracted from the green areas if the NDVI was low. In cases where the NDVI was high, for example, caused by a tree overlapping a house or a road, the tree was kept.

4. VALIDATION METHODOLOGY

The classification may be validated manually or automatically. In order to perform an automatic validation, a ground truth must be established. For Oppegård and Lørenskog municipalities, we

have obtained digital maps, free of charge, of roads and buildings, for use within the project. These maps can be used to validate grey versus green area classification, but can not be used to validate which of the three green area classes that has been assigned.

One major shortcoming of the digital map we had access to is that not all grey areas are included. Large parking lots are missing, as well as private driveways. So, the digital map could be used to find houses and public roads that were partially or fully missing in the automatic classification. However, areas that had been misclassified as grey areas could not be flagged, since many grey areas are missing in the digital map.

Thus, manual validation of the automatic classification was needed. The intention was also that the manual classification be used to validate the subclasses of green areas. However, this turned out to be too difficult to do in a quantitative manner. Only some general observations could be made. Where available, the digital map was used to guide the manual validation

4.1 Manual validation method

4.1.1 Selection of validation area

Given the size of the image, and the available resources for the project, a complete inspection of the classification result of the entire image was considered infeasible. Instead, a selection had to be made. Manual selection of areas that could be considered “representative” would lead to a biased result. On the other hand, some of the selected areas should cover the areas of which we had map coverage. These considerations led to the following selection procedure of validation areas.

1. Set the image counters $N_{Oppegård}$, $N_{Lørenskog}$ and N_{Oslo} all to zero.
2. Pick an x,y coordinate within the image at random. The range of possible values are $1 \dots x_{max}-x_{size}$ for the x coordinate, and $1 \dots y_{max}-y_{size}$ for the y coordinate, with x_{max} , y_{max} being the Quickbird image size and x_{size} , y_{size} being the validation area size.

3. If the validation area only contains missing or no data, discard the area and jump back to step 2 above.
4. If the new validation area partially overlaps an existing validation area, then replace the overlap with missing data in the new validation area
5. Compute the fraction of the area within the Oppegård map coverage ($f_{Oppegård}$), within the Lørenskog map coverage ($f_{Lørenskog}$), outside map coverage (f_{Oslo}), and with no or missing data (f_{Nodata}). These four fractions should sum to 1.
6. Add the map fractions to the counters, for example, $N_{Oppegård}(i+1) = N_{Oppegård}(i) + f_{Oppegård}(i+1)$, where i and $i+1$ denote iterations i and $i+1$, respectively.
7. Continue, by jumping back to step 2 above, until all three counters are above predefined thresholds $M_{Oppegård}$, $M_{Lørenskog}$ and M_{Oslo} .

The Quickbird image size, $(x_{max}, y_{max}) = (28090, 36602)$, and the validation area size $(x_{size}, y_{size}) = (1000, 1000)$. The validation thresholds are $M_{Oslo} = M_{Oppegård} = M_{Lørenskog} = 2$. Initially, we intended to have M_{Oslo} much higher, but the manual editing was so time-consuming that we ended up with $M_{Oslo} = 2$.

4.1.2 Validation of automatic classification

For each validation area, make a copy which is then edited, as described below. The difference between the validation area and the edited version is then used to compute a confusion matrix, counting the number and type of misclassification. Although the editing is object-based, see below, the counts in the confusion matrix are pixel-based.

For each validation area, the classified image is compared with the original image and an aerial orthophoto with 0.5 m resolution or 0.1 m resolution (Oppegård, Figure 4). All obvious misclassifications are corrected. The editing is mainly object-based, that is, individual pixels are not edited. The classified image has quite rugged object boundaries, many which could have been cleaned by using road and building outlines as a guide in the segmentation process. Noting this, we have, to some extent, avoided editing these rugged boundaries.

On some occasions, however, what should have been two or more objects have by mistake been segmented into one object only. In such cases, the object has been split and parts of it reclassified in the editing process.

On some occasions, parts of water bodies have been mistaken as grey areas, probably due to wind patterns. Since water bodies can be easily removed by using GIS data, we have not counted these as misclassifications, but regarded them as missing/no data.

Although originally intended, a validation of the three subclasses of green areas is not performed. Only a few occasional substitutions of one subclass of green with another are done.

During the manual verification, the need for a gravel subclass emerged. This class has been used in some instances to denote grey areas that are not sealed, and thus may be recovered as green areas. This is indeed the case for construction sites. Typically, when a new house is being built, the entire garden looks like a grey area in the Quickbird image, but is planted shortly after. In practice it is difficult to see the difference

between gravel, asphalt and concrete, so the gravel class is only used in very obvious occasions. It is in practice a subclass of grey areas.

5. VALIDATION RESULTS

The manual validation procedure, as described in section 4, was applied, resulting in 6 validation areas. Of these, two were from Oppegård, two from Lørenskog, and two from Oslo. The overall classification performance is about 89% correct classification rate (Table 2). This figure hides the fact that the object boundaries from the segmentation step are far from ideal. Further, in the manual validation procedure, almost no objects from one of the three green structure classes were reclassified as another green structure class. In this respect, it is more meaningful to look at the two-class problem: green versus grey areas. In this case, the recognition performance was slightly better, about 91% (Table 3)

Table 2. Classification performance when using six classes.

correct classification	89.13%
misclassification	10.87%
total	100.00%

Table 3. Classification performance when using two classes.

correct classification	91.38%
misclassification	8.62%
total	100.00%

Table 4. Combined confusion matrix for all six verification areas, in number of pixels.

Area 1-6		Edited						Sum classified
		Grass	Forest	Little vege.	Grey area	Gravel	No data	
Classified	Grass	535353	0	1	4479	110	1	539944
	Forest	931	2737263	4568	110921	2013	8650	2855696
	Little vege.	59	3164	499868	135870	3387	432	642348
	Grey area	3029	65620	178704	1575587	126162	3256	1949102
	Gravel	0	0	0	0	0	0	0
	No data	0	558	0	13	0	1	571
Sum edited		539372	2806605	683141	1826870	131672	12340	6000000

Table 5. Combined confusion matrix, in percentages.

Area 1-6		Edited					
		Grass	Forest	Little vege.	Grey area	Gravel	No data
Classified	Grass	99.25%	0.00%	0.00%	0.25%	0.08%	0.01%
	Forest	0.17%	97.53%	0.67%	6.07%	1.53%	70.10%
	Little vege.	0.01%	0.11%	73.17%	7.44%	2.57%	3.50%
	Grey area	0.56%	2.34%	26.16%	86.25%	95.82%	26.39%
	Gravel	0.00%	0.00%	0.00%	0.00%	0.00%	0.00%
	No data	0.00%	0.02%	0.00%	0.00%	0.00%	0.01%
Sum edited		100.00%	100.00%	100.00%	100.00%	100.00%	100.00%

The most common misclassification is to confuse little vegetation and grey areas. This resulted in about 300,000 pixels being reclassified (Table 4). This is about 5% of the 6,000,000 image pixels. Of the 683.141 pixels that were regarded as little vegetation after the manual validation step, 178,704, or 26%, were originally classified as grey area (Table 4 – Table 5).

6. DISCUSSION

The classification results show that the classification part of the automatic algorithm is able to classify between green and grey areas, with approximately 10% misclassification. This is clearly a good starting point for improvements. However, the

ruggedness of objects suggests that the segmentation step of the automatic algorithm has a great potential for improvement.

Another issue is to what extent the automatic algorithm can be used on another Quickbird image or not. The classification rules in the automatic classification method have been trained on a subset of the image, and then evaluated on random portions of 1000 by 1000 pixels. The illumination conditions were very close to ideal and uniform over the entire scene, whereas many other Quickbird images of Oslo have clouds. It is possible that the classification rules will have to be adjusted for every image to be processed. Also, it is not known what problems the presence of clouds will result in. All in all, it could happen that redesigning the rules is not sufficient, so that other methods have to be developed.

One minor issue was dealt with wrongly in the manual evaluation procedure. Whenever a house or road was partly obscured by a tree, the tree was ignored and the house or road was edited to show its extent. However, in the context of green structure, one is more interested in the trees than in the houses and roads. So, some correct classifications have been marked as misclassifications. However, the total number of pixels that have wrongly been edited in this manner, is small, so the main findings of the evaluation are still valid.

The smallest mapped area is approximately 100 m². If for example there is a piece of grass land in a private garden of 10 by 10 meters, then it will be mapped. However, if a medium to large tree appears in the middle, then the homogeneity criterion may flag the entire area as forest.

Private gardens appear as a mixture of the three green structure classes in addition to the houses and driveways. Gardens also contain a mix of different materials in addition to vegetation, including furniture, trampolines, etc. In the classification rules, there are additional classes. Many of these are merged into the grey area class. In addition, there are two shadow classes, one for tree shadows, which are regarded as part of green vegetation, and one for other shadows.

The manual editing resulted in an additional class: gravel, which is considered as grey area. This class was added mainly to meet a potential need to indicate temporary grey areas, and was used on construction sites. Gravel also indicates an area that is not sealed, permitting water drainage. However, gravel and sand is difficult to discriminate spectrally from concrete.

6.1 Segmentation

The results of the segmentation step are not directly available to us in the classified image, since neighboring segments in many cases have been assigned the same class in the classification step. From the classification result, it is obvious that the object boundaries of classified grey areas deviate substantially from the true outlines of houses and roads. This is especially true in suburban areas (Figure 3), where there are a lot of small roads and buildings. However, the segmentation results can be examined in Definience. This was done for a few selected areas. Level 1 segmentation often creates border segments one pixel wide and very long. These pixels are often a spectral mixing of the two neighboring regions, for example, building and vegetation, or at the edge of shadows. Many roads are also segmented into many parallel narrow and long segments. In other instances, the gradual transitions between different objects allowed segments to be merged across the true object boundaries.

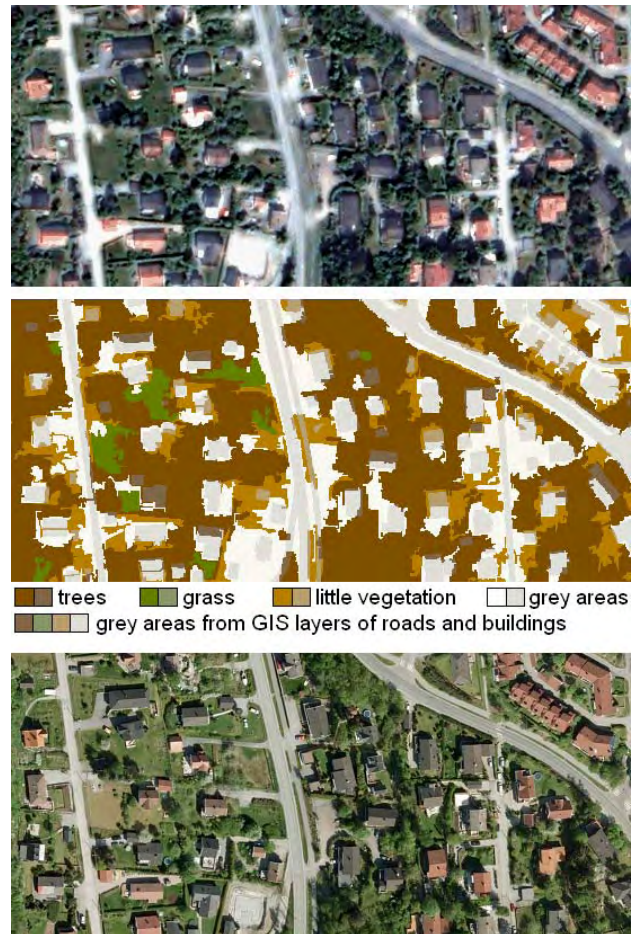


Figure 3. Segmentation problems in suburban areas in Oppegård municipality. Top: a 330 m x 250 m part inside validation area 1 of the Pan-sharpened Quickbird image. Middle: the automatic classification result for this subimage, with houses and roads from a digital map superimposed in grey. Bottom: Aerial orthophoto of the same area, captured with 10 cm ground resolution.



Figure 4. Close-up of the upper left corner of the part of the aerial image of Oppegård in Figure 3.

Many of the segmentation problems are due to shadows from buildings (Figure 5) and trees (Figure 6). Building shadows are often classified as grey areas. It could be possible to predict these shadows from the building height and the sun's position. The building height might be available from a digital map, and the sun's position can be computed from the acquisition time and date for the satellite image.

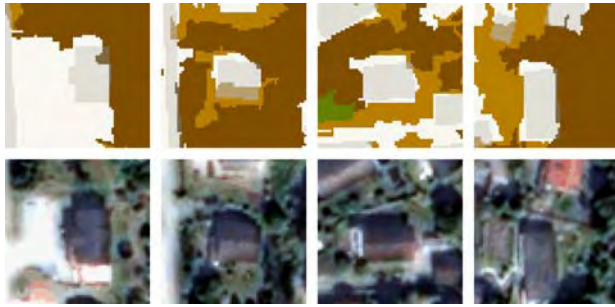


Figure 5. House shadows are sometimes misclassified as grey areas.

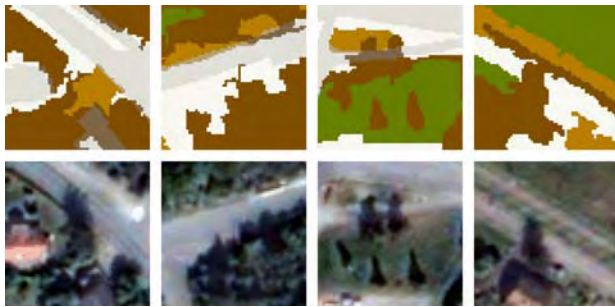


Figure 6. Tree shadows are sometimes mistaken as grey areas (far and middle left), and other times they block grey areas (far and middle right).

Tree shadows are sometimes classified as grey areas, other times they block grey areas (Figure 6). In both cases, the shadows need to be detected and removed. The tree height is not readily available, but one can make a few guesses and see if one of the heights matches the shadow length fairly well.

For both tree shadows and building shadows, the shadow outline must be extracted, and the intensity values inside the shadow increased to the level outside the shadow.

Shadows aside, there are many more segmentation issues to solve. The most important shortcoming of the current segmentation approach is that no prior information is used. By including outlines of buildings, roads, rivers and lakes from a digital map, the outlines could be used to guide the segmentation step so that the outlines from the map were preferred to some extent. In some cases, there might be coregistration errors in the order of 1–2 m between the GIS and the Quickbird image. Ideally, the segmentation algorithm should be aware of this uncertainty and allow that a, say, house be moved 1–3 pixels.

6.2 Time series of chlorophyll or NDVI

An entirely different approach than the current could be to use time series of medium or low resolution satellite images to directly measure the variation from year to year in chlorophyll, which is often estimated from the so-called *normalized difference vegetation index*, NDVI. The NDVI for a pixel (x, y) is computed from the *near infrared* (NIR) spectral band and the red (R) spectral band as

$$NDVI(x, y) = \frac{NIR(x, y) - R(x, y)}{NIR(x, y) + R(x, y)}$$

By using 250 meter resolution images from MODIS, or even 1 km resolution images from AVHRR, one obtains average values, in which a decrease in chlorophyll in one small area

may be cancelled by an increase in another small area within the same pixel. However, the general trend can be monitored, since these images are captured daily.

The Norwegian Computing Center has developed time series analysis algorithms for vegetation monitoring in other projects (Salberg, 2010; Aurdal et al., 2005). These algorithms could be modified for use on monitoring of green structure in urban and suburban areas. The time series analysis algorithm models change on three scales:

1. Daily variations due to imaging conditions
2. Phenological variation during one year
3. Changes from year to year.

During one year, the green vegetation goes through one cycle, which has nearly the same shape from one year to another, but with variations in the start and end dates of the summer season, as well as the strength of the peak of the cycle (Huseby et al., 2005). By eliminating the modeled changes on the daily, seasonal and yearly scale, one can detect statistically significant changes in individual pixels, and detect areas in which the green structure has been reduced or improved.

7. CONCLUSION

In the present work, Definiens Developer was used for segmentation and classification of a Quickbird scene from 2008. The result is validated in the present paper, and the conclusion is that this is a good starting point for further improvements of the method. The most striking problems are related to the segmentation. Object contours are often ragged, and do not follow the true boundaries of houses and roads very well. Another difficulty is shadows from buildings and trees, resulting in frequent misclassifications of whatever happens to be in the shadow areas.

REFERENCES

- Aurdal, L., Huseby, R. B., Eikvil, L., Solberg, R., Vikhamar, D., Solberg, A. H. S., 2005. Use of hidden markov models and phenology for multitemporal satellite image classification – applications to mountain vegetation classification. In *Proc. Int. Workshop Analysis Multi-Temporal Remote Sensing Images*, Biloxi, Mississippi, USA, May 16–18, 2005, pp. 220–224.
- Definiens Developer 7, User Guide, 2007. Definiens AG, Munich, Germany.
- Huseby, R. B., Aurdal, L., Eikvil, L., Solberg, R., Vikhamar, D., Solberg, A. H. S., 2005. Alignment of growth seasons from satellite data. In *Proc. Int. Workshop Analysis Multi-Temporal Remote Sensing Images*, Biloxi, Mississippi, USA, May 16–18, 2005, pp. 213–216.
- Salberg, A. B., 2010. Land cover classification of cloud-contaminated multi-temporal high-resolution images. Revised version submitted to *IEEE Transactions on Geoscience and Remote Sensing*.
- Trier, Ø. D., 2009. *Urban green structure – validation of automatic classification*. Norwegian Computing Center, Note No. SAMBA/39/09, 52 pp., <http://publ.nr.no/5159>.

COMPARISON OF GRID-BASED AND SEGMENT-BASED ESTIMATION OF FOREST ATTRIBUTES USING AIRBORNE LASER SCANNING AND DIGITAL AERIAL IMAGERY

S. Tuominen ^{a,*}, R. Haapanen ^b

^a Finnish Forest Research Institute, Metsätutkimuslaitos, PL 18, 01301 Vantaa, Finland - sakari.tuominen@metla.fi

^b Haapanen Forest Consulting, Kärjenkoskentie 38, 64810 Vanhakylä, Finland - reija.haapanen@haapanenforestconsulting.fi

KEY WORDS: Forestry, LIDAR, Inventory, Photography, Segmentation

ABSTRACT:

Forest management planning in Finland is currently adopting a new-generation forest inventory method, which is based on interpretation of airborne laser scanning data and digital aerial images. The inventory method is based on systematic grid, where the grid elements serve as inventory units, for which the laser and aerial image data are extracted and, for which the forest variables are estimated. As an alternative or a complement to the grid elements, image segments can be used as inventory units. The image segments are particularly useful as the basis for generating the silvicultural treatment and cutting units, since their borderlines should follow the actual stand borders, whereas the grid elements typically cover parts of several forest stands. In this study we carried out an automatic segmentation of two study areas on the basis of laser and aerial image data with a view to delineating ecologically homogeneous micro-stands. Further, we extracted laser and aerial image features both for systematic grid elements and segments. For both units, the set of features used for estimating the forest attributes were selected using a genetic algorithm, which aims at minimizing the estimation error of the forest variables. The estimation accuracy produced by both approaches was assessed by comparing their estimation results. The preliminary results indicate that despite of the theoretical advantages of the image segments, the laser and aerial features extracted from grid elements seem to work better than features extracted from image segments in estimating forest attributes.

1. INTRODUCTION

In Finland, the forest inventory for the forest management planning has traditionally been based on visual inventory by stands. In this method, the forest stands that are delineated on the basis of aerial photographs and their growing stock and site-related characteristics are measured or estimated in field. The method is considered too labour-intensive, and it requires large amount of the fieldwork. Thus, the visual inventory method will be replaced by a new-generation forest inventory method, which is now at the pilot phase and which employs more remote sensing data and less fieldwork.

The new generation forest inventory method will be based on interpretation of airborne laser scanning (ALS) data and digital aerial imagery using field sample plots as a reference data. Statistically the new generation forest inventory method is based on two-phase sampling with stratification, where inventory database is based on systematic grid of sample units (i.e. grid elements as sample units), and the size of grid elements should correspond to the size of field plots. Field measurements are allocated into strata that are derived on the basis of earlier stand inventory data. The typical remote sensing data sources that are used in the new generation forest inventory system are low density ALS-data (typically 1–2 laser pulses/m²) and color-infrared (CIR) digital aerial imagery with spatial resolution of approx. 0.5 m.

The inventory units in the new generation forest inventory method are typically defined by a systematic grid of sample units. The forest variables are estimated for each grid element that covers a square shaped area. As an alternative to the grid based approach, the use of automatic stand delineation has been studied for defining the inventory units. Automatically delineated stands (i.e. image segments) have an advantage compared to grid elements (e.g. Pekkarinen & Tuominen, 2003; Hyvönen et al., 2005). They can be delineated in such a way that they follow exactly the actual stand borders, whereas the grid elements are spatially "sparse" in relation to the actual borders of stands and other ecological units in forest, so they do not follow the borderlines accurately and they usually cover trees from more than one stand (e.g. Pekkarinen & Tuominen, 2003). On the other hand, grid elements are unambiguously defined by their coordinates and, thus, the same units can be used in consecutive inventories.

In delineating forest stands the primary input variables are the height of the trees and tree species composition (or dominance). Stand density usually is a secondary parameter for stand delineation. The height of the trees can be derived on the basis the ALS-data but, on the other hand, ALS data with the applied pulse density does not serve well the purpose of the recognition of tree species. Thus, optical aerial imagery is needed for the estimation of the tree species composition.

The objective of this study was to find a suitable combination of laser and aerial data for automatic stand delineation and to test

* Corresponding author.

the laser and aerial image features extracted from grid elements and automatically delineated stand polygons in order to find out which unit serves better the purpose of extracting image features for estimating forest attributes.

2. MATERIAL AND METHODS

2.1 Study areas

The laser scanning and aerial image based estimation was tested in two study areas. Study area 1 was located in the municipality of Lammi in southern Finland and its field data consisted of 282 fixed-radius (9.77 m) circular field sample plots that were measured in 2007. Study area 2 was located in eastern Finland and 546 fixed radius (9 m) sample plots measured in 2009 were available as field reference data here. For the field sampling both study areas were stratified on the basis of earlier stand inventory data and the field sample plots were allocated to these strata in order to cover all types of forest in the study areas.

There was some variation between the forest characteristics of the two study areas. In study area I the total growing stock was more evenly distributed between tree species groups pine, spruce and deciduous trees, whereas the study area 2 was clearly dominated by spruce. Furthermore, the study area 2 had somewhat higher average stand volume, as well as larger distribution of sample plot volumes. The statistics of the study areas based on the sample plots are presented in table 1.

	Study area 1		Study area 2	
	Average	Max	Average	Max
Total volume, m ³ /ha	178.7	575.4	205.5	798.5
Volume of pine, m ³ /ha	69.8	560.6	52.7	561.8
Volume of spruce, m ³ /ha	63.7	575.4	109.3	739.2
Volume of deciduous, m ³ /ha	45.2	312.0	43.5	400.4
Height, m	17.0	30.5	17.3	35.2
Diameter, cm	21.1	50.2	21.9	60.3

Table 1. Forest statistics of the study areas (average and maximum values of sample plots)

2.2 Remote sensing data

In study area 1 the remote sensing data consisted of color-infrared digital aerial imagery (containing near-infrared, red and green bands) and ALS data acquired from a flying altitude of 1900 m with the density of 1.8 returned pulses per square meter. In study area 2 the remote sensing data consisted of color-infrared (containing near-infrared, red and green bands) and natural color (red, green and blue bands) digital aerial imagery and ALS data acquired from a flying altitude of 2000 m with the density of 0.6 returned pulses per square meter. Here the aerial image data was combined to a 4-band composite image containing blue, green, red and near-infrared bands.

The aerial images were ortho-rectified and resampled to a spatial resolution of 0.5 m. The ALS point data was also

interpolated to a raster image format (height and intensity images) using second degree polynomial model. The output laser images had similar spatial resolution as the aerial images.

2.3 Automatic image segmentation

Automatic stand delineation was carried out in the study areas by automatic segmentation of aerial images and ALS data interpolated to raster format. The segmentation was carried out in two phases. In the first phase initial segmentation was done using a modified implementation of Narendra & Goldberg (1980) algorithm, which employs local edge gradient. This method typically produces a large number of small polygons, and the objective is to find all potential segment borders at this phase. In the second phase the initial segments were processed using a region merging algorithm that was guided by parameters such as desired minimum size of final segments and the similarity/dissimilarity of the segments to be merged (t-ratio threshold).

In this study, the initial segmentation was based entirely on laser height corresponding mainly to the stand height (Mustonen et al., 2008). The merging of initial segments into larger spatial units (i.e. final segments) was carried out on the basis of laser and aerial image data, taking into account also the tree species structure of the initial segments. Two automatic segmentations with minimum segment sizes of 350 m² and 0.1 ha were carried out in both study areas.

2.4 Extraction of laser and aerial image features

Three remote sensing feature data sets were extracted from each of the study areas. In these sets the remote sensing features were allocated to each sample plot from a square window or a segment in which the sample plot was located. The feature set Grid was extracted from a 20 x 20 meter square window centered around each sample plot. The feature set Seg350 was extracted from image segments, whose minimum size was set as 350 m². The feature set Seg1000 was extracted from image segments, whose minimum size was set as 0.1 ha.

The following statistical and textural features were extracted from the remotely sensed material for each feature data set:

- Means, standard deviations and Haralick textural features (Haralick et al. 1973, Haralick 1979) of spectral values of aerial photographs, ALS height and intensity (first pulse only)
- Height statistics for the first and last pulses of the points inside the field plot area or the segment area (Suvanto et al., 2005). These included mean, standard deviation (std), maximum, coefficient of variation, heights where certain percentages of points had accumulated and percentages of points accumulated at certain relative heights. Only points over 2 m in height were considered and the percentage of points over 2 m in height was included as a variable.
- A number of std's extracted from a 32 x 32 pixel window using block sizes from 1 to 8 pixels.

All features were standardized to a mean of 0 and std of 1.

2.5 Selection of features for the estimation of forest attributes

The k -nearest neighbor (k -nn) method was used to estimate forest variables (e.g. Kilkki & Päivinen, 1987; Tokola et al., 1996). The value of k was set to 5, euclidean distances were used to measure closeness in the feature space and the nearest neighbors were weighted with the squared inverse distances.

The accuracy of the estimates produced by the k -nn estimator was tested via leave-one-out cross-validation on the field plots by comparing the estimates of each field plot to the measured value (ground truth) of the plot. The accuracy of the estimates was measured by the relative root mean square error RMSE (Equation 1).

$$RMSE\% = 100 * \frac{RMSE}{\bar{y}} \quad (1)$$

where:

$$RMSE = \sqrt{\frac{\sum_{i=1}^n (\hat{y}_i - y_i)^2}{n-1}}$$

y_i = measured value of variable y on plot i

\hat{y}_i = estimated value of variable y on plot i

\bar{y} = mean of the observed values

n = number of plots

Automatic feature selection was carried out using a simple genetic algorithm presented by Goldberg (1989), and implemented in the GALib C++ library (Wall 1996). The GA process starts by generating an initial population of strings (chromosomes or genomes), which consist of separate features (genes). The strings evolve during a user-defined number of iterations (generations). The evolution includes the following operations: selecting strings for mating using a user-defined objective criterion (the better the more copies in the mating pool), letting the strings in the mating pool to swap parts (crossing over), causing random noise (mutations) in the offspring (children), and passing the resulting strings into the next generation.

In the present study, the starting population consisted of 300 random feature combinations (genomes). The length of the genomes corresponded to the total number of features in each step, and the genomes contained a 0 or 1 at position i , denoting the absence or presence of image feature i . The number of generations was 30. The objective variable to be minimized during the process was a weighted combination of relative RMSEs of k -nn estimates for mean total volume, mean volumes of Scots pine, Norway spruce and deciduous species, mean diameter and mean height, with total volume having a weight of 50%, and the remaining variables 10% each. Genomes that were selected for mating swapped parts with each other with a probability of 80%, producing children. Occasional mutations (flipping 0 to 1 or vice versa) were added to the children (probability 1%). The strings were then passed to the next generation. The overall best genome of the current iteration was always passed to the next generation, as well. Four successive steps (all including 30 generations) were taken to reduce the

number of features to a reasonable minimum. Only features belonging to the best genome in each step were included in the next step. Feature selection was run separately for both areas and each feature extraction unit (field plot, small segments, large segments).

There were 14 (study area 1) or 19 (study area 2) features selected into the final Grid sets, 17 or 19 into the Seg350 sets and 12 or 17 into the Seg1000 sets. Of the selected features, majority (63–79%) were based on the ALS data.

3. RESULTS AND DISCUSSION

In both study areas the features extracted from square grid elements worked better in estimating the forest attributes than the features extracted from image segments. Furthermore, features from image segments derived using minimum size of 350 m² performed better in the estimation than features extracted from larger segments (minimum size 0.1 ha).

Study area 2 had generally better estimation accuracy compared to data sets of study area 1. The main reason for this is probably the higher number of sample plots in study area 2, which gives higher number of potential nearest neighbors for each sample plot in the k -nn estimation. The estimation accuracy results for the forest attributes used in this study are presented in tables 2 and 3.

	GRID	SEG350	SEG1000
Height	18.5	22.4	25.5
Diameter	25.5	27.7	32.0
Total volume	27.8	34.0	36.6
Volume of pine	74.2	77.1	99.9
Volume of spruce	83.9	87.5	103.3
Volume of deciduous sp.	85.3	88.7	93.9

Table 2. Estimation results for the feature sets (relative RMSE, %) of study area 1

	GRID	SEG350	SEG1000
Height	12.5	13.9	16.5
Diameter	19.8	23.1	25.2
Total volume	29.6	32.9	36.6
Volume of pine	125.2	138.5	137.0
Volume of spruce	59.0	61.5	63.8
Volume of deciduous sp.	99.2	113.4	111.3

Table 3. Estimation results for the feature sets (relative RMSE, %) of study area 2

There were large differences between the study areas in the estimation accuracy of the volumes per tree species groups. Apparently, the differences were caused by the different tree species structure of the two study areas. Typically, the dominant tree species had the highest estimation accuracy, and the less dominant lowest. On the other hand, the volume of deciduous trees had better estimation accuracy compared to the minority

coniferous tree species group since the presence of the deciduous trees is more easily recognizable in the aerial images.

Despite the theoretical advantages of the segment-based approach, the features extracted for segments did not perform well in the estimation procedure. There are some possible reasons for this. First, the field data was measured per sample plots and not per segments. Because of this the areas of the field measurement and the extracted remote sensing features correspond to each other best in the feature set Grid. Furthermore, the automatic segmentation often produces segments that are irregularly shaped, i.e. not compact, and in forest stands with large trees the segment borders are typically located in gaps between trees, in which case the variation within the segments may be more significant than the variation between segments. On the other hand, using geographically larger segments in extracting the features typically resulted in lower estimation accuracy compared to other feature sets, which indicates that the larger the units are the more internal variation they have.

Based on the results of this study the most feasible inventory procedure utilizing ALS and aerial image data seems to be the following: 1) estimation based on ALS data and aerial imagery for the systematic grid elements, 2) automatic segmentation utilizing ALS height, ALS intensity and aerial imagery, 3) deriving the estimates for image segments on the basis of the estimates of grid elements and 4) manual combination of image segments for deriving spatial units for forest management purposes.

4. REFERENCES

Haralick, R., 1979. Statistical and structural approaches to texture. *Proceedings-IEEE*, 67(5), 786–804.

Haralick, R. M., Shanmugan, K. and Dinstein, I., 1973. Textural features for image classification. *IEEE Transactions on Systems, Man and Cybernetics*, SMC-3(6), 610–621.

Hyvönen, P., Pekkarinen, A. and Tuominen, S., 2005. Segment-level stand inventory for forest management. *Scandinavian Journal of Forest Research* 20(1), 75–84

Kilkki, P. and Päivinen, R., 1987. Reference sample plots to combine field measurements and satellite data in forest inventory, *Department of Forest Mensuration and Management, University of Helsinki, Research Notes*, 19:210–215.

Mustonen, J., Packalén, P. and Kangas, A., 2008. Automatic segmentation of forest stands using a canopy height model and aerial photography. *Scandinavian Journal of Forest Research* 23(6): 534–545.

Narendra, P. and Goldberg, M., 1980. Image segmentation with directed trees. *IEEE Transactions on Pattern Analysis and Machine Intelligence*. Pami-2: 185–191.

Pekkarinen, A. and Tuominen, S., 2003. Stratification of a forest area for multisource forest inventory by means of aerial photographs and image segmentation. In P. Corona, M. Köhl, & M. Marchetti (Eds.), *Advances in forest inventory for sustainable forest management and biodiversity monitoring*.

Forestry Sciences, vol. 76. (pp. 111–123). Kluwer Academic Publishers.

Suvanto, A., Maltamo, M., Packalén, P. and Kangas, J., 2005. Kuviokohtaisten puustotunnusten ennustaminen laserkeilauksella. *Metsätieteen aikakauskirja*, 4/2005, 413–428.

Tokola, T., Pitkänen, J., Partinen, S. and Muinonen, E., 1996. Point accuracy of a non-parametric method in estimation of forest characteristics with different satellite materials. *International Journal of Remote Sensing*, Vol. 17, No. 12, pp. 2333–2351.

ACKNOWLEDGEMENTS

The authors wish to thank M.Sc. Risto Viitala at the HAMK University of Applied Sciences and Lic.Sc. Juho Heikkilä at Forestry Development Centre Tapio for providing the field and remote sensing materials for this study.

ALTM ORION: BRIDGING CONVENTIONAL LIDAR AND FULL WAVEFORM DIGITIZER TECHNOLOGY

Valerie Ussyshkin ^a, Livia Theriault ^a

^a Optech Incorporated, 300 Interchange Way, Vaughan, Ontario, Canada L4K 5Z8

valerieu@optech.ca, liviati@optech.ca

KEY WORDS: Data, Digitisation, Forestry, Fusion, LIDAR, Measurement, Modelling, Urban

ABSTRACT:

Over the past decade airborne lidar technology has seen the development of new systems capable of digitising and recording the entire waveform of each emitted laser pulse through waveform digitisers (WFD). WFD technology holds enormous potential for forestry and urban mapping, but the high cost and complexity of data handling and analysis has confined it mainly to research institutions. Alternatively, conventional lidar systems used in the commercial lidar sector for high-quality mapping of complex targets such as power lines and vegetation have been limited in their ability to collect and record data of sufficient quality for sophisticated data analysis, including waveform interpretation.

This paper focuses on technical characteristics of the ALTM Orion, a new airborne lidar mapper manufactured by Optech Incorporated, and in particular, its ability to discriminate consecutive multiple laser returns. Unlike a conventional lidar, the ALTM Orion offers fundamentally improved specifications for multiple return data. High-density, multiple return ALTM Orion data with unique pulse separation characteristics and exceptional precision might be viewed as a new cost-effective alternative to WFD for applications requiring complex target analysis and partial waveform modelling, such as forest research and urban mapping. The new technology bears the potential to create an application niche where top-quality dense point clouds, enhanced by fully recorded intensity for each return, may provide sufficient information for modelling the received waveforms. Recognizing the importance of further development in existing WFD technology, the paper also discusses the possibility of data fusion interpretation and analysis tools for both technologies.

1.0 INTRODUCTION

Airborne lidar technology has been widely accepted by the surveying and mapping community as an efficient way of generating high-accuracy spatial data for a variety of applications (Renslow, 2005). Unlike two-dimensional aerial imagery, the elevation component of airborne lidar data provides the inherent ability of this technology to represent complex vertical structures and ground surfaces with very high precision, which is a prerequisite to most lidar applications, many of which focus exclusively on analysis of the elevated features (Hudak et al., 2009).

The capability of an airborne lidar to map complex vertical structures and generate high-quality complex target data is solely determined by system hardware design. A vast majority of airborne lidar sensors currently used in the lidar industry can be categorized into two types: discrete return, and waveform. Optech has worked extensively with full waveform digitization for several decades, and continues with leading-edge algorithm development in its current waveform digitizers for ALTM. This expertise has been refined within the ALTM Orion, which incorporates an onboard real-time waveform analyzer as part of its iFLEX™ technology base for rapid, precise and accurate XYZ data output.

The most common type of commercial lidar sensors (Optech's ALTM and Leica's ALS series) are small-footprint discrete return systems that record two to four returns for each emitted laser pulse. Waveform sensors, which can be large- or small-footprint systems, digitize the full profile of a return signal in fixed time (i.e., distance) intervals, providing a quasi-continuous distribution of the reflected energy for each emitted laser pulse. Some lidar system manufacturers (Optech Incorporated) offer airborne sensors capable of both operational

modes, where conventional discrete-return operation is provided by the main sensor, while full waveform data collection is supported by an optional unit, which may or may not be used during data collection missions (Optech, 2010).

Each data collection mode, whether full waveform or discrete return, has distinct advantages and disadvantages that determine the potential applications. Most conventional discrete return systems can provide extremely high ground point density. This enables the high-resolution representation of complex targets in the horizontal plane with a somewhat coarsely resolved elevation structure, which makes the discrete return system a perfect choice for mapping. The additional information about 3D elevation structure provided by multiple-return point clouds can be used for a variety of mapping applications including flood modeling (Bates et al., 1999), urban and vegetation analysis (Evans et al., 2009), and power line mapping (Ussyshkin and Sitar, 2009). In particular, airborne lidar with multiple-return capability has proved to be the most efficient among different remote sensing techniques to characterize both forest structure and ground topography (Chauve et al., 2007). However, the coarse vertical resolution, which is typically a few meters for many commercial airborne lidar systems, and a lack of detailed 3D spatial information, limit the user's ability to apply more sophisticated analysis such as vegetation composition and change detection in land surface if the scale at which processes occur is less than a few meters (Wu et al., 2009).

On the other hand, commercially available full waveform airborne lidar systems (Riegl, Optech, 2010) capture full profiles of the laser backscattered energy for each emitted laser pulse as a function of time (distance) with a typical sampling rate of 1 ns, which is equivalent to a one-way distance of 30 cm. They can provide much more detailed information about the vertical elevation structure, which could potentially be used

as the most valuable input for sophisticated scientific analysis including deriving target physical properties (Chauve et al., 2009a). It has been demonstrated that full waveform data provide a significantly more complete and accurate assessment of the surface, the canopy and potential obstruction detection than the discrete return system (Magruder et al., 2010). Moreover, full waveform lidar data capture gives the user much more flexibility and control in data processing and interpretation steps (Chauve et al., 2009b). However, dealing with full waveform datasets takes lidar data management to a drastically higher level of complexity compared to conventional 3D point cloud data. First, the volume of full waveform data is overwhelming: about 140 GB for 1.6 hours of data acquisition time at a 50-kHz pulse repetition frequency (Chauve et al., 2009b). This can be compared to 12 GB of discrete-return data with four full records (four ranges, four intensities) for the same acquisition time and pulse frequency (Optech). Moreover, there are neither commercial nor open-source toolkits to handle full-waveform lidar data, but only custom-made solutions typically designed for specific sensors (Bretar et al., 2008). Therefore, managing full-waveform lidar data is a very challenging and expensive task. This limits the commercial use of full waveform lidar data, confining it mainly to research institutions.

This paper presents a revolutionary change in the discrete return airborne lidar technology. It will show that the new, most advanced airborne lidar system—ALTM Orion—manufactured by Optech Incorporated, is capable of mapping targets with complex vertical structure with much higher resolution than has ever been available before in any discrete return airborne lidar. A simplified waveform analysis of high-resolution discrete return data collected over low and medium canopy vegetation will be presented and discussed in the context of methodology typically used for full waveform data analysis. It will show that the new-generation discrete return airborne lidar technology can provide quality data and some characteristics approaching that of full waveform data.

2. EVOLUTION OF DISCRETE RETURN AIRBORNE LIDAR TECHNOLOGY

Initial commercial airborne lidar systems, such as Optech's ALTM 1020, 1210 and 1225 models manufactured between 1993 and 1998, had the ability to capture only two returns (first and last) for each emitted laser pulse. This feature, though seemingly modest compared to the capabilities of contemporary advanced airborne lidar systems, already provided enriched information for sophisticated analysis of both returns for potential applications such as feature extraction in forest (Hopkinson et al., 2004; Roberts et al., 2005) or urban areas (Alharthy and Bethel, 2002). With further evolution of lidar technology, more advanced ALTM models capable of capturing four range and four intensity returns became commercially available, and for the last decade the maximum number of multiple returns per emitted laser pulse has been stabilized at this limit.

However, as mentioned, not only the number of multiple returns is important for the proper mapping of targets with a complex vertical structure, but also the minimal discrimination distance between two consecutive returns. The vertical discrimination distance, that is, minimum distance (time) separation between consecutive pulse returns, is solely determined by the lidar system hardware design, and along with range precision it would determine the type, quality and

accuracy of the consequent data analysis based on discrete return data. In most commercial discrete return lidar systems the minimal pulse discrimination distance is close to 2–3.5 m (Optech ALTM 3100 and Gemini, Leica's ALS series). This means that targets separated by any distance less than this minimum cannot be resolved by consecutive multiple returns.

Until recently the numbers characterizing minimal target separation distances had not been typically specified in the brief data sheets of most commercial lidar systems, but could be found in more detailed specification documents, or provided to users upon request. This situation created some misunderstanding in the lidar community as users expect to detect four discrete returns from objects a few meters high without considering the minimum vertical discrimination distance. The lack of knowledge of this parameter may also lead to misinterpretation of multiple return data and even gross systematic errors due to wrong interpolation. Since the minimum target separation distance seems to be one of the best performance parameters to characterize the ability of an airborne lidar system to map complex vertical targets, it is very important for users to have this knowledge.

Figures 1–2 present typical examples of multiple return data for the ALTM 3100 and Gemini systems. In both cases the laser beam penetrated through 16–20 m of vegetation, and the last return with strong intensity clearly indicates the signal reflected from the ground.

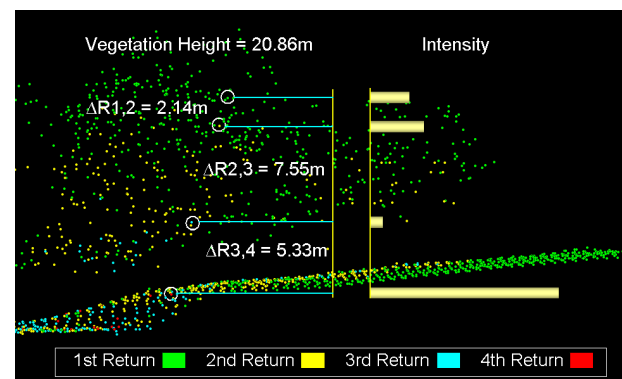


Figure 1. ALTM 3100: An example of a four-return record for one emitted laser pulse with a minimum pulse separation distance of 2.14 m.

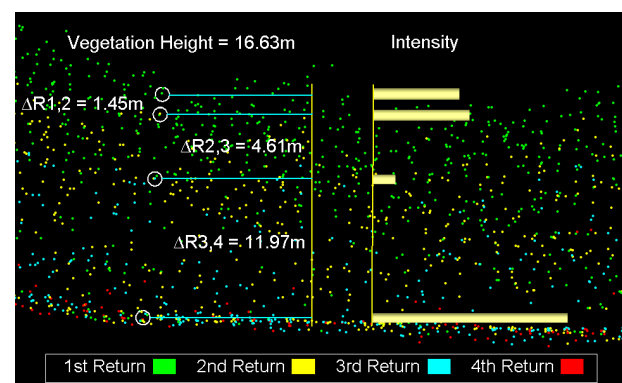


Figure 2. ALTM Gemini: An example of a four-return record for one emitted laser pulse with a minimum pulse separation distance of 1.45 m.

Although these two examples represent leading-edge discrete return airborne lidar technology, it is clear that full waveform

technology with a 1-ns sampling rate would provide much more detailed information about the complex vertical structure of vegetation. It is for this reason that, in the last decade, full waveform technology has been the only choice for lidar applications requiring analysis of complex vertical targets with fine structure. However, the introduction of the ALTM Orion, representing a new breakthrough in discrete return lidar technology, has changed this situation.

3. ALTM ORION: NEW-GENERATION AIRBORNE LIDAR

The ALTM Orion system represents a radical departure from previous generations of airborne lidar instruments. First, the physical form factor—size, weight and displacement—has been reduced by a whole order, making the Orion the first ultra-compact complete lidar solution, with the volume reduced by factor of 7 compared to the previous ALTM 3100 and Gemini models (Hussein et al., 2009). Second, the lidar data produced by the Orion has established a new benchmark in the industry for data quality, accuracy and precision (Ussyshkin and Theriault, 2010). It was shown that the outstanding performance characteristics of both ALTM Orion models, Orion-M and Orion-C, include a highly efficient system design that provides the best combination of maximum area coverage rate, exceptional ground data accuracy and precision, and the sub-centimeter precision of data comprising small-size complex targets such as the thinnest wires in power line corridors.

The third radical advantage provided by both ALTM Orion models is the revolutionary small minimal pulse discrimination distance, which is of particular importance in complex target mapping applications such as urban and low-canopy vegetation mapping. Figure 3 shows an example of ALTM Orion-M data collected over 6-m high vegetation, with four returns for one emitted laser shot with a minimum pulse separation of 73 cm. Such a small sub-meter pulse separation has never been achieved before by any discrete return airborne lidar, and in combination with the excellent ability of the system to detect weak partial signal returns from low-canopy layers of vegetation, it provides unprecedented data quality with exceptionally rich content.

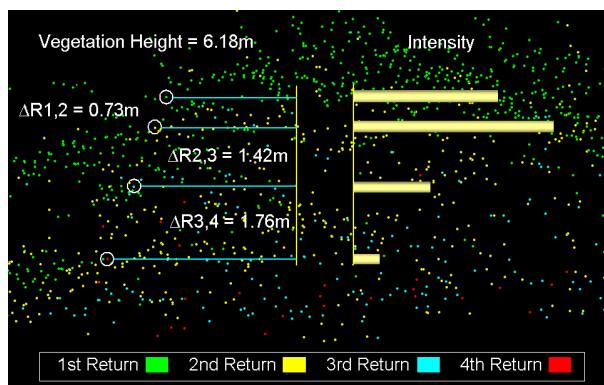


Figure 3. ALTM Orion-M: An example of a four-return record for one emitted laser pulse with a minimum pulse separation distance of 0.73 m.

Figure 4 shows another advantage of the exceptionally small pulse separation distance of the ALTM Orion. The data presented in this example was collected over a dense cornfield 2.2 m in height, and yet the lidar system was still capable of detecting three consecutive pulse returns, with the last showing strong intensity representing the ground return. The unique

capability of the ALTM Orion to generate data so rich in content with fine sub-meter elevation resolution from dense cornfields enables the user to take data analysis to a different level with highly accurate biomass calculations. This was not previously possible with discrete return lidar data without using full waveform technology.

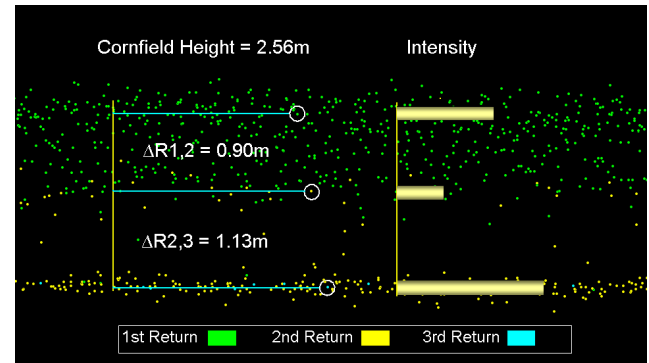


Figure 4. ALTM Orion-M: Three consecutive pulse returns with a minimal sub-meter pulse separation are detected over dense cornfield, while the last return represents the signal penetrated from the ground.

Figure 5 illustrates the even more impressive pulse separation capabilities of the ALTM Orion-C with a minimal pulse separation distance of 68 cm. As one can see, these sub-meter vertical target discrimination characteristics would provide the quality of mapping of complex vegetation structures similar to that usually expected only for full waveform digitizer data.

Thus, looking at the evolution of the discrete return airborne lidar technology presented in Figure 5, one can see a clear trend towards the sub-meter scale of vertical discrimination distance, which bridges the capabilities of advanced discrete return lidar and full waveform technology to map complex 3D targets. Moreover, it will be shown in the next section that, by combining range and intensity data information from an advanced multiple return lidar, a simplified waveform analysis can potentially be applied to discrete return data in a way that is similar to that done for full waveform data.

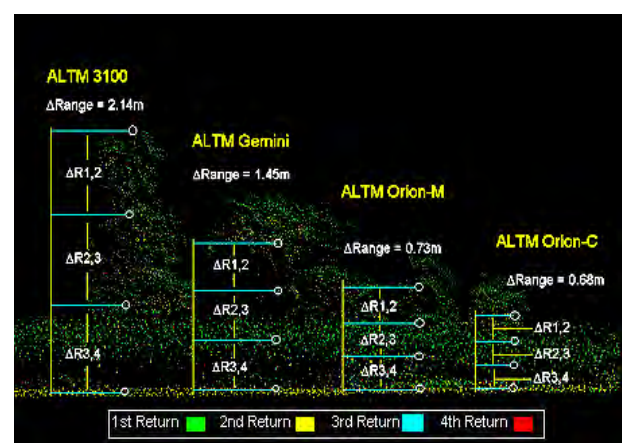


Figure 5. Evolution of minimal pulse separation for discrete return airborne lidar systems.

4. DISCRETE RETURN ANALYSIS

The simplified analysis of discrete multiple returns presented in this section is based on the approach used for full waveform data analysis described by Chauve and co-authors (Chauve et

al., 2007). It was a parametric approach using either simple (three parameters) or generalized Gaussian (four parameters) or a Lognormal function to model extracted relevant peaks as echoes. Since the discrete return data used in our analysis represent the peaks of partial signal returns, we assumed that the entire reflected laser pulse energy could be decomposed into a sum of components while each one would be represented by a single discrete return:

$$f(x) = \sum_{i=1}^n f_i(x) \quad (1)$$

Here $n = 4$ for four returns or 3 for three returns. For modeling of each function f_i in our analysis we used only a simple three-parametric Gaussian:

$$f_i = a_i \exp\left(-\frac{(x - \mu_i)^2}{2\sigma_i^2}\right) \quad (2)$$

Figure 6 gives a graphic representation of our approach, where the peak of each discrete return is modeled by a simple Gaussian (2) while a , μ , and σ were used as fitting parameters so that the amplitude of each peak would be proportional to the recorded intensity value. Furthermore, we assumed that the superposition (1) of all four simple Gaussian functions representing the waveforms of the discrete partial returns would represent the total optical receiver power P_r , which can be modeled through the lidar equation (Measures, 1984). Considering partial signal returns P_i , the intensity of each one was modeled using the lidar equation in the form derived by Jelalian (1992):

$$P_i = \frac{P_t D_r^2 Q}{4\pi \mathcal{G}^2 T_{atm}} \frac{\sigma_i}{R_i^4} \quad (3)$$

Here:

- P_i is the received signal power for i -return
- P_t is the transmitted laser pulse power
- D_r is the diameter of the lidar receiver aperture
- Q is the optical efficiency of the lidar system
- \mathcal{G} is the laser beam divergence
- T_{atm} is the atmospheric transmittance factor
- R_i is the range from the sensor to i -target
- σ_i is the effective backscattering cross section of i -target

Here the reflective properties of each target for each partial return P_i are described by the backscattering cross-section σ_i , which is proportional to the target reflectance ρ_i and the i -fraction of the total received power P_r in each return:

$$\sigma_i = k_i \rho_i A_i \quad (4)$$

Here A_i is the area of the target illuminated by the i -fraction of the laser footprint, which created the discrete return f_i . and k_i is the fitting parameter, characterizing scattering properties of i -target, which could be calibrated using redundant measurements.

A similar approach, based on waveform generalization of the lidar equation (Jutzi and Stilla, 2006) and Gaussian

decomposition, was applied to the analysis of full waveform data by Wagner and co-authors (Wagner et al., 2006; Wagner et al., 2008).

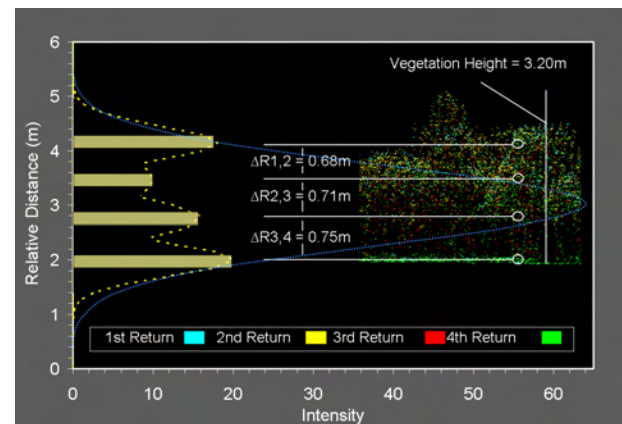


Figure 6. Graphic representation of the modeling approach for ALTM Orion data.

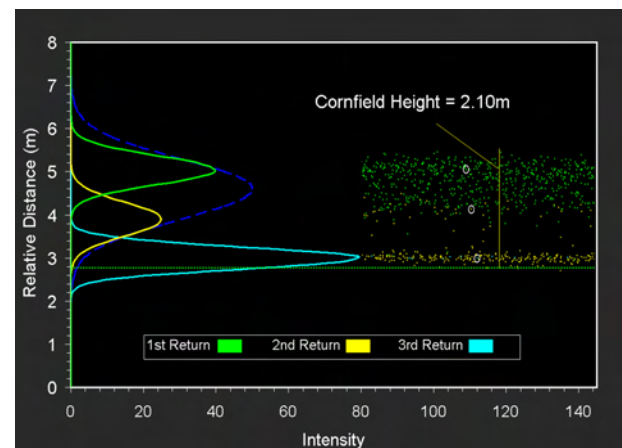


Figure 7. Illustration of the modeling for cornfield data collected by ALTM Orion-M (Figure 4).

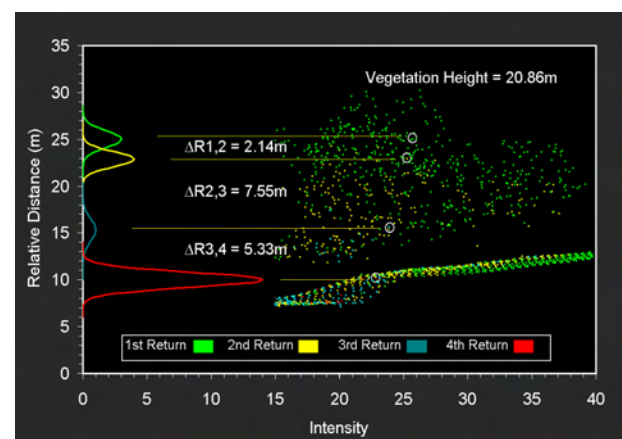


Figure 8. Illustration of the modeling for high-canopy vegetation data collected by ALTM 3100 (Figure 1).

Based on the approach described by equations (1-4) and using the known characteristics of the emitted laser pulse and lidar system hardware, it was possible to model waveform of each discrete return (Figure 7-8) and estimate the effective reflectivity of complex vegetation targets like cornfields and coniferous trees. This work is still in progress and requires

more detailed analysis, but the preliminary results partly presented here demonstrate the huge potential of discrete return technology, the evolution of which has achieved a level approaching in some aspects that of full waveform technology. The discrete return data analysis described above has much similarity with the procedures applied to full waveform data analysis, and might potentially be used in applications similar to those which to date have been considered as solely belonging to full waveform technology.

The modeling of the discrete signal profiles for vegetation data presented above could be compared with the analysis of the full waveform data collected over similar vegetation targets (Wagner et al., 2004). An example of a coniferous tree profile with a total length of 35 ns recorded with a 1-ns sampling rate showed three Gaussian-shaped peaks with a target separation distance of 1.5 m. Comparing these numbers with the ALTM Orion data presented in Figure 3, one can conclude that the discrete return lidar data of enhanced quality can provide equivalent or in some aspects better representation of vegetation structure than the full waveform data. Another example (Wagner et al., 2004) of the full waveform data collected over a wheat field of 2.5 m height can be compared with the cornfield data collected by ALTM Orion (Figures 4 and 7), where three discrete return data with excellent target separation characteristics provide equivalent or even better input for Gaussian modeling of the crop and ground signals.

This may be considered an indication of a potential fusion of two types of airborne lidar data on the application side when similar approaches and tools can be used for the analysis of both data types. However, it is clear that the full waveform technology will continue to be essential and irreplaceable for applications requiring the analysis of very complex vertical targets including consideration of pulse-broadening effects associated with laser beam-target interaction and interception geometry (Schaer et al., 2007). In these cases, modeling and deriving physical parameters should be more reliable if based on full waveform technology.

5. CONCLUSION

The analysis presented above indicates that the evolution of discrete return airborne lidar technology has achieved a new level, with capabilities that can be considered equivalent to those of full waveform technology for many applications. The trade-off between the high complexity and cost associated with the handling of WFD data on the one hand, and the conventional discrete return data of enhanced quality on the other hand, has the potential to create a new application niche in the lidar industry. In this niche, top-quality dense point clouds, with fully recorded intensity information for each of multiple returns, may provide sufficient information for modeling the received waveforms.

The fine pulse separation characteristics and vegetation penetration capabilities demonstrated by the ALTM Orion, the new advanced discrete return airborne lidar, is based on Optech's long experience with full waveform digitization and its recent leading-edge algorithm development. This real-time waveform analyzer enables users to consider new applications for discrete return data of sub-meter vertical resolution and sub-centimeter precision. It has been demonstrated that discrete multiple return data with enhanced characteristics can provide information sufficiently rich in content for a waveform type of data analysis, applying similar methodology but without the

high complexity and cost associated with the handling of full waveform data.

Acknowledgements

The authors are very thankful to Brent Smith, Eric Yang, Mike Sitar and Helen Guy-Bray for fruitful discussions.

References

- Alharthy, A., Bethel, J., 2002. Heuristic filtering and 3D feature extraction from lidar data. Proceedings of the *International Archives of Photogrammetry, Remote Sensing and Spatial Information Sciences*, 34 (Part 3), Graz, Austria.
- Bates, P.D., Pappenberger, F., Romanowicz, R., 1999. Uncertainty and risk in flood inundation modeling. In: K. Beven and J. Hall (Editors), *Flood Forecasting*. Wiley & Co, New York.
- Bretar, F., Chauve, A., Mallet, C., Jutzi, B., 2008. Managing full waveform lidar data: a challenging task for the forthcoming years. *The International Archives of the Photogrammetry, Remote Sensing and Spatial Information Sciences*, 37 (Part B1), pp. 415-420.
- Chauve, A., Mallet, C., Bretar, F., Durrieu, S., Pierrot-Deseilligny, M., Puech, W., 2007. Processing full-waveform lidar data: modelling raw signals. In: *The International Archives of Photogrammetry, Remote Sensing and Spatial Information Sciences*, Espoo, Finland, Vol. 36, Part 3/W52, pp. 102–107.
- Chauve, A., Vega, C., Bretar, F., Durrieu, S., Allouis, T., Pierrot-Deseilligny, M., Puech, W., 2009. Processing full-waveform lidar data in an alpine coniferous forest: assessing terrain and tree height quality. *International Journal of Remote Sensing*, 30 (19), pp. 5211-5228.
- Chauve, A., Bretar, F., Pierrot-Deseilligny, M., Puech, W., 2009. Full Analyze: A research tool for handling, processing and analyzing full-waveform lidar data, Proceedings of the *IEEE International Geoscience and Remote Sensing Symposium (IGARSS)*, Cape Town, South Africa.
- Evans, J.S., Hudak, A.T., Faux, R., Smith, A.M.S., 2009. Discrete return lidar in natural resources: Recommendations for project planning, data processing, and deliverables, *Remote Sens.*, 1, pp. 776-794.
- Hopkinson, C., Sitar, M., Chasmer, L., Treitz, P., 2004. Mapping snowpack depth beneath forest canopies using airborne lidar. *Photogrammetric Engineering & Remote Sensing*, 70(3), pp. 323-330.
- Hudak, A.T., Evans, J.S., Smith, A.M.S., 2009. Review: LiDAR Utility for Natural Resource Managers. *Remote Sens.*, 1, pp. 934-951.
- Hussein, M., Tripp, J., Hill, B., 2009. An ultra compact laser terrain mapper for deployment onboard unmanned aerial vehicles, Proc. SPIE, Vol. 7307, 73070B.
- Jelalian, A.V., 1992. *Laser Radar Systems*. Artech House, Boston, Massachusetts.

- Jutzi, B., Stilla, U., 2006. Range determination with waveform recording laser systems using a Wiener Filter. *ISPRS Journal of Photogrammetry and Remote Sensing*, 61, pp. 95-107.
- Magruder, L.A., Neuenschwander, A.L., Marmillion, S.P., Tweddale, S.A., 2010. Obstruction detection comparison of small-footprint full-waveform and discrete return lidar, Proc. SPIE, Vol. 7684, 768410.
- Measures, R.M., 1984. *Laser Remote Sensing, Fundamentals and Applications*. Wiley Interscience, New York.
- Optech Incorporated, <http://www.optech.ca/gemini.htm> (accessed 25 May 1999)
- Optech Incorporated. Internal communication, 2010.
- Renslow, M., 2005. The Status of LiDAR Today and Future Directions, 3D Mapping from InSAR and LiDAR, ISPRS WG I/2 Workshop, Banff, Canada, June 7-10
- Riegl USA. <http://www.rieglusa.com/products/airborne/lms-q680/index.shtml>; and Optech Incorporated. <http://www.optech.ca/pdf/ALTMWaveformDigitizerPC.pdf> (accessed 25 May 2010)
- Roberts, S.D., Dean, T.J., Evans, D.L., McCombs, J.W., Harrington, R.L., Glass, P.A., 2005. Estimating individual tree leaf area in loblolly pine plantations using LiDAR-derived measurements of height and crown dimensions, *Forest Ecology and Management*, 213(1-3), pp. 54-70.
- Schaer, P., Skaloud, J., Landtwin, S., Legat, K., 2007. Accuracy estimation for laser point cloud including scanning geometry. ISPRS - The 5th International Symposium on Mobile Mapping Technology, Padua, Italy, May 29-31.
- Ussyshkin, V., Sitar, M., 2009. Applications and Benefits of Airborne Lidar Technology for Transmission Line Asset Management, *CIGRE Canada Conference on Power Systems*, Toronto, Ontario, October 4-6 (on CDROM).
- Ussyshkin, V., Theriault, L., 2010. Precise mapping: ALTM Orion establishes a new standard in airborne lidar performance, *ASPRS Annual Conference*, San-Diego, California, April 26-30 (on CDROM).
- Wagner, W., Ullrich, A., Melzer, T., Briese, C., Kraus, K., 2004. From single-pulse to full-waveform airborne laser scanners: Potential and practical challenges. Proceedings of the *International Society for Photogrammetry and Remote Sensing 20th Congress*, 35(Part B/3) 6-12, Commission 3, Istanbul, Turkey, July 12-23.
- Wagner, W., Ullrich, A., Ducic, V., Melzer, T., Studnicka, N., 2006. Gaussian decomposition and calibration of a novel small-footprint full-waveform digitising airborne laser scanner. *ISPRS Journal of Photogrammetry and Remote Sensing*, 60(2), pp. 100-112
- Wagner, W., Hollaus, M., Briese, C., Ducic, V., 2008. 3D vegetation mapping using small-footprint full-waveform airborne laser scanners, *International Journal of Remote Sensing archive*, 29(5), 3D Remote Sensing in Forestry, pp. 1433-1452.
- Wu, J., van Aardt, J., Asner, G.P., Mathieu, R., Kennedy-Bowdoin, T., Knapp, D., Wessels, K., Erasmus, B.F., Smit, I., 2009. Connecting the dots between laser waveforms and herbaceous biomass for assessment of land degradation using small-footprint waveform lidar data. Proceedings of the *International Geoscience and Remote Sensing Symposium (IGARSS-2009)*, Cape Town, South Africa.

SURFACE TEMPERATURE ESTIMATION USING ARTIFICIAL NEURAL NETWORK

M. R. Veronez^a, G. Wittmann^a, A. O. Reinhardt^b, R. M. Da Silva^a

^a Graduate Program in Geology, Remote Sensing and Digital Cartography Laboratory, Vale do Rio dos Sinos University (UNISINOS), Av. Unisinos, 950, CEP 93022-000, São Leopoldo, RS, Brazil veronez@unisinos.br

KEY WORDS: Artificial Neural Networks; image from NOAA satellite; surface temperature, split window

ABSTRACT:

This research presents an alternative method to extrapolation land Surface Temperature (ST) through artificial neural network, using positional variables (UTM coordinates and altitude), temperature and air relative humidity. The study region was the Rio dos Sinos Hydrographic Basin (BHRS), in Rio Grande do Sul state, Brazil. For training the neural network was used a thermal image from NOAA satellite, with pixel size of 1X1 km, with known ST information referring to 12/06/2003. After training many network sets were done and one of them with the best performance and composed by a single intermediate layer (with 4 neurons and logistic sigmoid activation function) was selected. The training network was tested inside the BHRS where were collected 60 points of ST values supported by a portable laser sensor on date 3/18/2008. The average error provided by this model for ST measurement was 2.2°C and through executed statistical tests was possible to verify that not exist variation between average ST values accepted as true and the values provided by the neural model with a significance level of 5%.

1. INTRODUCTION

Artificial Neural Networks (ANN) are organized and interconnected collections of processing units (neurons or nodes), whose operation is analogue to a neural structure of intelligence organisms (Müller and Fill, 2003). ANN extract its computational power from its solid parallel distribution structure and ability to learn/generalize, allowing the resolution of complex propositions in many knowledge areas (Haykin, 2001).

ANN execution is inspired on human brain (Haykin, 2001) and has been used in many applications with success. In agreement with Galvão et al. (1999), by the reason of its nonlinear structure the ANN can acquire more complex data characteristics, which are not always possible using traditional statistical techniques.

According to Müller and Fill (2003), conventional methods don't have the necessity to know the problem intrinsic theory and also don't need to analyze relations that aren't totally known between involved variables in modeling, so ANNs have a greater advantage over them.

Surface Temperature (ST) is established by a fenologic parameter that is significantly influenced by climate variations and is an indicator of plants hydrous state. Therefore its estimation has a large utility to surveys that need to assure the observation of hydrous culture demand, contributing in a significative way the irrigation programs (Silva, 2007).

Currently a mostly used method to ST estimation is through the use of thermal satellite images. Rivas (2004) recommends the use of NOAAVHRR (National Oceanic Atmospheric Administration/Advanced Very High Resolution Radiometer) images adapted to split windows equation to estimate ST values. Such modeling connects emissivity variables and atmospheric data. Is a complex method because beyond it processes not simple statistical models, it has the necessity to work with digital images in the emissivity determination process.

So is much important to have methods of ST estimation in a more convenient way as, for example, the combination of temperature, air relative humidity and geographical data position (Veronez et al., 2006).

Some authors realized researches using ANNs with the finality of ST estimation based on climate elements (Yang et al., 1997; Atluri et al., 1999; George, 2001; Veronez et al., 2006; Mao & Shi, 2008), where all of them have found satisfactory results.

Yang (1997) describe the importance to develop a model capable to assist agricultural processes, once that ST estimation in distinct depths is complex due its large number of involved variables. The author have used as ANN input the following variables: daily precipitation, evapotranspiration, air maximum and minimum temperature and days of year, been all these information easy to obtain on meteorological station.

Atluri (1999) has modeled through ANNs the humidity and soil ST with the Levenberg-Marquardt algorithm and after many tests he obtained an accuracy estimation of 98.7% with these variables. The same author describes the importance to establish an efficient system to extrapolate such information, once that these variables are required by distinct geosciences areas.

George (2003) describes the importance of usage ANNs to estimate soil surface temperature using easy access data. Thinking on it Veronez et al. (2006) proposed the ANN usage to model such variable using only positional information (East and North UTM coordinates), altitude and air average temperature. The network was established through a supervised training, where ST information was extracted from NOAA satellite images.

The results found by Veronez et al. (2006) show that is possible to extrapolate ST values on distinct periods from NOAA image processing date using as ANN input a variable that changes with the time. For the specific case of this research the used variable was air average temperature. The ST processing was based on NOAA satellite image with a surface coverage from 6/12/2003. ST values were extrapolated on 10/8/2005 and the model validation was accomplished in a municipality urban area located on Rio dos Sinos Hydrographic Basin (BHRS). The authors collected ST information with a laser thermometer and compared them with values provided by ANN, having an average error less than 2.3°C.

Although some researches aim to simplify the input data on ST estimation process, is understood that exist another options to be learned using climate data associated with thermal images. So the purpose of this research was propose an ANN aiming to

extrapolate values of ST during a period of time taking as modeling variables only altitude, position and air average temperature. For ANN supervised training was used ST information from processing NOAA thermal image with a surface coverage from 6/12/2003. The research was developed on BHRS and its validation was executed inside the Vale do Rio dos Sinos University campus where was collected ST information with a laser thermometer on 3/18/2008.

2. MATERIALS AND METHODS

2.1 Study area

This research was based on Rio dos Sinos Hydrographic Basin located on Rio Grande do Sul state as illustrated on Figure 1. In this same figure the Vale do Rio dos Sinos University campus located in São Leopoldo city is emphasized because sample points for model validation process were taken from this location.

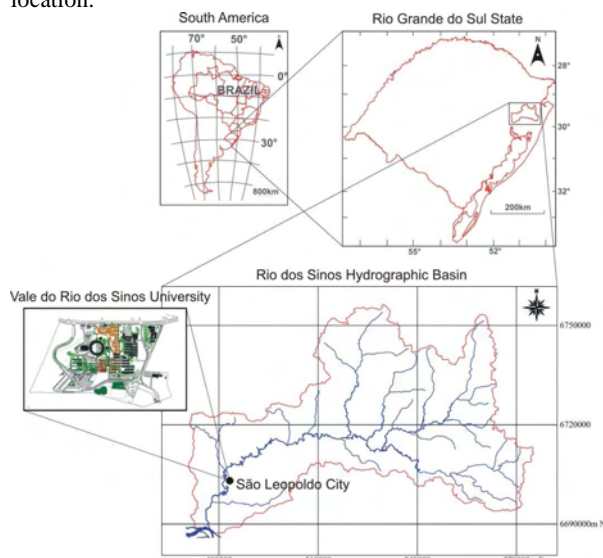


Figure 1. Study area location

2.2 ST obtainment for neural network training

As first stage the NOAA/AVHRR image with a surface coverage from 6/12/2003 and pixel size of 1X1 km was radiometrically and geometrically corrected. The radiometric correction was obtained through radiancebased procedure developed by NOAA (Kidwell, 1998). So the digital number values (DN) were converted in radiance and after in reflectance for channels 1 (0.58-0.68 μm) and 2 (0.725-1.10 μm) and in brightness temperatures for thermal channels 4 (10.3-11.3 μm) and 5 (11.5-12.5 μm).

The equation that transformed the digital number registered by sensor in radiance – for a given channel j centered in a determinate number of wave v – is given by equation 1:

$$B_{j(v)} = S_{j(v)} \cdot \text{DN} + I_{j(v)} \quad (1)$$

where:

- $B_{j(v)}$ correspond to radiance ($\text{mW}/\text{sr m}^2 \text{ cm}^{-1}$);
- $S_{j(v)}$ correspond to angular coefficient from calibration equation for channel j ($\text{mW}/\text{m}^2 \text{ sr cm}^{-1}$);
- DN correspond to digital number from image;
- $I_{j(v)}$ correspond to linear coefficient from calibration equation for channel j ($\text{mW}/\text{m}^2 \text{ sr cm}^{-1}$).

The coefficients from calibration equation have information relative to sensor answer function in a determinate channel. More details about these coefficients can be found on user guide on polar orbit data from NOAA (Kidwell, 1998).

Due the linearity deficiency from AVHRR sensor answer, became necessary to execute radiance corrections obtained by equation 2, in the following way:

$$B_{j(v)\text{corr}} = A_j \cdot B_{j(v)} + B_j \cdot B_{j(v)}^2 + D_j \quad (2)$$

where: $B_{j(v)\text{corr}}$ correspond to corrected radiance ($\text{mW}/\text{sr m}^2 \text{ cm}^{-1}$);

- A_j , B_j and D_j correspond to correction coefficients for a determinate channel j , due the linearity deficiency from AVHRR sensor.

The coefficients A_j , B_j and D_j , in the case of NOAA-14 satellite, assume values equal to 0.92378; 0.0003822 and 3.72, respectively, for channel 4 from AVHRR.

For channel 5 these values are equal to 0.96194; 0.0001742 and 2.00, respectively. The radiance conversion from brightness temperature to a given temperature strip (265 to 320K) is given by equation 3:

$$T_{bj} = \frac{1,438833 \cdot v_j}{\ln \left(\frac{1 + 1,1910659 \times 10^{-5} \cdot v_j^3}{B_{j(v)\text{corr}}} \right)} \quad (3)$$

where: T_{bj} correspond to brightness temperature on channel j ;

- v_j correspond to wave number on channel j ;
- $B_{j(v)\text{corr}}$ correspond to corrected radiance according to equation 2.

The channels 4 and 5 were used to calculate the surface temperature applying the split-window algorithm approached by Czajkowski et al. (1998). Many split-window algorithms were developed to estimate surface temperature by authors that use information from AVHRR sensor (Dash et al., 2002): AVHRR on NOAA-7 (Preço, 1984), AVHRR on NOAA-9 (Becker and Li, 1990), AVHRR on NOAA-11 (Sobrino et al., 1991), etc. The filter functions for channels 4 and 5 from AVHRR lightly differ from each sensor of NOAA satellite series, been necessary different coefficients to the split-window model. This fact can conduct to a considerable error of surface temperature estimation with approximately 2.3 K (Czajkowski et al., 1998). An incorrect calibration can generate an error of 0.3 K on surface temperature determination (Cooper and Asrar, 1989) and the variation on surface emissivity (approximately 0.2%) can provide and error of 1 K (Ottle and Vidal-Madjar, 1992). Using the algorithm proposed by Czajkowski et al. (1998) with coefficients from split-window model for NOAA-14/AVHRR satellite, the ST was determined in the following way:

$$T_s = 5,54 + T_4 + 2,08 \cdot (T_4 - T_5) \quad (4)$$

where: T_s correspond to surface temperature;

- T_4 and T_5 correspond to brightness temperature of channels 4 and 5 from AVHRR, both in degrees Kelvin.

Following the NOAA/AVHRR satellite image was georeferenced on UTM projection system (Universal Transverse Mercator) using 15 control points on terrain and rectified with an average quadratic error of approximately 1 pixel. The

processing image from study area wasn't polluted by clouds. Figure 2 illustrates the processing image with ST values.

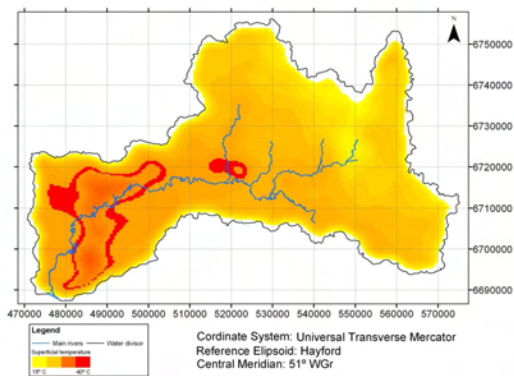


Figure 2. NOAA image processed with ST information from 6/12/2003 on Rio dos Sinos Hydrographic Basin

With the processing and georeferencing image was possible to put over it a digital elevation model obtained from isolines at vertical equidistant of 20m and georeferenced on Torres vertical datum. Next, for each pixel centroid was obtained the following information: east and north UTM coordinates, altitude and ST.

2.3 Proposed neural network structure

The ANN was structured on multilayer perceptron (MLP), whose algorithm principle is based on error correction learning. When a pattern is presented to the network for the first time, it produces a random output. The difference between this output and the intended compose the error, that is calculated by the self algorithm. The backpropagation algorithm makes that the weights from output layer been the first to be adjusted and after the weights from residual layers, correcting them from back to front, with the objective of reduce the error. This process is repeated during the learning until the error become acceptable (Silva et al., 2004).

The neurons utilized in the ANN were set based on the model proposed by Haykin (2001), as show the Figure 3. In the synaptic weights (W_{kj}) the k index refer to the neuron in question while the j index report to the synapse input signal which weight has relation. The function of the weight is multiply the synapse input signal connected to the neuron. ANNs can also present additional weights, called "bias", that have the role in preventing error generation when all input data are null, because so the matrix of weights don't suffer modifications in the training. Activation function is a function of internal order, been a decision made by self neuron over what do with the resultant value from the sum of pondered inputs. Transference function is a function of output or logic threshold. It controls the activation intensity to obtain the wanted performance from network.

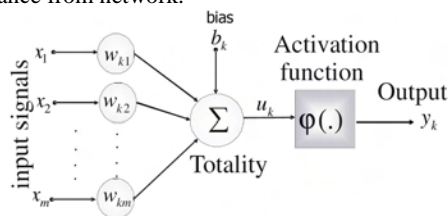


Figure 3. Artificial neuron structure utilized on ANN. Adapted from Haykin (2001)

Mathematically, Figure 3 can be expressed in equations 5, 6 and 7.

$$u_k = \sum_{j=1}^n (w_{k,j} \cdot x_j) \quad (5)$$

$$v_k = u_k + b_k \quad (6)$$

$$y_k = \varphi(v_k) \quad (7)$$

where: u_k is the output from linear combinator (additive junction);

- $w_{k,j}$ are the synaptic weights;
- X_j are the input variables;
- φ is the activation potential;
- b it the bias;
- y_k is the output signal of k neuron;
- φ is the activation function.

For the network was used a supervised training through the Levenberg-Maquardt algorithm, which used the Newton method that applies the minimum approximation for error function (Haykin, 2001). In this case, ANN was trained through pairs of input and output presentations, in others words, for each input provided for network exist an expected output that is also provided for the training. The network produces an output answer where it self is compared with the expected output (that was provided). The difference between network answer and expected answer (known), generate a residue (error). This obtained error is used to calculate the necessary adjust for synaptic weights from network, that will be corrected until the network answer coincide with expected output. Such is the minimization error process (Haykin, 2001).

Continue talking about this learning type (Haykin, 2001), the necessary calculations to minimize the error are important and related to utilized algorithm, like on backpropagation, for example, where the consider parameters as interactions number by input pattern are used to get the minimum error value on training (network capability to escape from local minimums). Equation 8 shows the error function (MSE – Mean Squared Error) that will be minimized on training step:

$$MSE = \frac{\sum_{j=1}^n (d_j - y_j)^2}{n} \quad (8)$$

- where:• d_j is the expected output value from ANN;
- y_j is the obtained output value;

With the objective to select an ANN that could supply a better performance, were realized many tests, modifying the number of intermediate layers, the number of neurons per layer and the activation function, enable the selection of the best ANN for ST estimation.

The ANN variables from input and output layers were normalized inside the interval [0-1].

2.4 Results analysis

ANN was trained by information extracted from processing NOAA thermal satellite image with a surface coverage from 6/12/2003. Its pixel size of 1X1 Km provided a quantity of 3737 points for the training process. The existing meteorological stations on BHRS enabled the temperature and averages of air relative humidity obtainment from satellite image period.

To test the proposed model were collected in field ST information with a laser thermometer on 3/18/2008. With the assistance of a GPS receiver model Trimble Pocket were obtained the UTM coordinates (SIRGAS) for ST sample points. Temperature and averages of air relative humidity were taken

from a meteorological station located inside the test area. The test was made inside Vale do Rio dos Sinos (UNISINOS) campus situated on São Leopoldo/RS city. The sample points for test were located on places with vegetation, concrete and asphalt paving.

Each collected point had the necessary information to be inserted in the trained neural model (UTM coordinates, altitude, temperature and averages of air relative humidity). The model supplied for each point a ST value that was compared with the value obtained in field by laser thermometer.

The statistical analysis used on research results presentation were based on a comparison between ST values modeled through ANN and ST values considered true by obtainment by a laser thermometer. Were used the statistical t-student test and coefficient of determination (R^2) analysis with linear regression. Being x the size of certain elements attribute from an A population (ST modeled by ANN);

Being y the size of the same elements attribute from a B population (ST obtained by laser thermometer);

Being x and y ordinarily distributed with unknown variances;

Being the hypothesis: $\mu_x = \mu_y$ which $\mu_x =$ average of x and $\mu_y =$ average of y.

For testing the hypothesis of averages equality from the two populations was utilized the t test, but for that was necessary to initially test if the two populations presented equal variances using the F test from Fischer:

$$F = \frac{SQD_x}{SQD_y} \quad (09)$$

$$s_x^2 = \frac{SQD_x}{(n_x - 1)} \quad (10)$$

$$s_y^2 = \frac{SQD_y}{(n_y - 1)} \quad (11)$$

$$F_{calculated} = \frac{s_x^2}{s_y^2} \quad (12)$$

where: SQDx and SQDy correspond, respectively, to the sums of square deviations from x and y;

and correspond, respectively, to sample variances from x and y;

n_x and n_y correspond, respectively, to the number of variables from x and y.

The tested hypothesis (H_0) was that the population variance from x is equal to the population variance from y. If $Prob > F$ is less than 5% then H_0 is accepted. If $Prob > F$ is bigger than 5% then H_0 is refused. If the population variances were statistically equals, then a common variance is calculated ():

$$s_c^2 = \frac{(SQD_x + SQD_y)}{[(n_x - 1) + (n_y - 1)]} \quad (13)$$

$$s_c^2 = \frac{[(s_x^2 \cdot (n_x - 1)) + (s_y^2 \cdot (n_y - 1))]}{[(n_x - 1) + (n_y - 1)]} \quad (14)$$

Afterward was tested the H_0 for population average equality using the t random variable, defined by:

$$t = \frac{\mu_x - \mu_y}{\sqrt{v \cdot (\mu_x - \mu_y)}} \quad (15)$$

Being:

$$v \cdot (\mu_x - \mu_y) = v(\mu_x) + v(\mu_y) = \frac{s_x^2}{n_x} + \frac{s_y^2}{n_y} \quad (16)$$

where: v correspond to the average variance.

Accepting $s_x^2 = s_y^2 = s_c^2$ there are:

$$v \cdot (\mu_x - \mu_y) = \frac{s_c^2}{n_x} + \frac{s_c^2}{n_y} = s_c^2 \cdot \left(\frac{1}{n_x} + \frac{1}{n_y} \right) \quad (17)$$

$$t = \frac{\mu_x - \mu_y}{\sqrt{s_c^2 \cdot \left(\frac{1}{n_x} + \frac{1}{n_y} \right)}} \quad (18)$$

$$\text{In degrees of freedom } (n) = (n_x + n_y - 2) \quad (19)$$

In case of different variances there are:

$$t = \frac{\mu_x - \mu_y}{\sqrt{\frac{s_x^2}{n_x} + \frac{s_y^2}{n_y}}} \quad (20)$$

The degree of freedom is calculated with the following equation:

$$n = \frac{\left(\frac{s_x^2}{n_x} + \frac{s_y^2}{n_y} \right)^2}{\frac{\left(\frac{s_x^2}{n_x} \right)^2}{n_x - 1} + \frac{\left(\frac{s_y^2}{n_y} \right)^2}{n_y - 1}} \quad (21)$$

3. RESULTS AND DISCUSSIONS

The ANN that presented the best performance was composed with an input layer (5 variables), an intermediate layer (with 4 neurons) and an output layer (with one neuron), as show on Figure 4. The fact that the selected network, with the best performance, has only one intermediate layer, is in accord with the results found by Kumar et al. (2002) and Zanetti et al. (2008), because these authors have modeled the evapotranspiration and concluded that an ANN with only one intermediate layer was sufficient to represent a nonlinear relation between the climatic elements and the modeled variable.

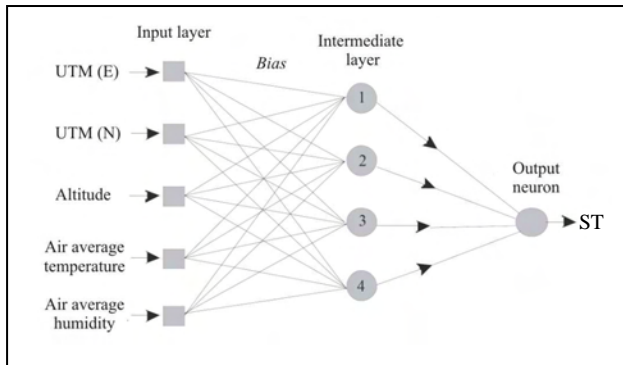


Figure 4. Neural network structure used on ST modeling

The activation function utilized was the logistic sigmoid and the number of training cycles was 600.

On Figure 5 is presented the modeled ST values (maximum of 54 °C, minimum of 19.1 °C and average of 39.18 °C) and the known ones (maximum of 54 °C, minimum of 25 °C and average of 37.39 °C) where is possible to verify a similar behavior between the two curves. In terms of discrepancy between the modules of ST values the model afforded an average value of 2.2 °C with a standard deviation around 1.4 °C. If we analyze the obtainment of ST values through processing thermal images associated with the Split Window algorithm, which its average error is 1.5 °C (Coll and Caselles, 1997), and if we compare with the results found on this research, is possible to ascertain that the method can be an efficient way to obtain the ST. A great advantage of this method is its capability to generate ST values based only on climatic and positional variables that have easy access.

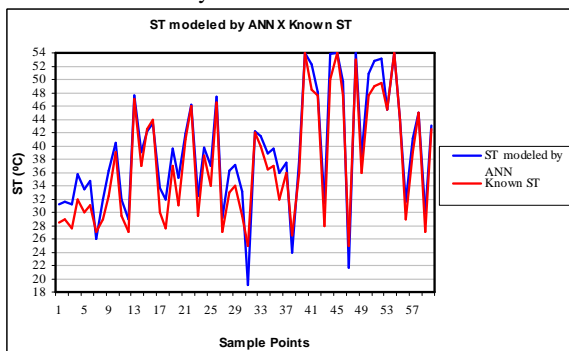


Figure 5. Graph of comparison between ST modeled by ANN and Known ST.

On regression analysis (Figure 6) was verified a strong correlation between modeled and known ST values ($R^2 = 0.948$) given efficiency evidences of ST extrapolation process on proposed ANN.

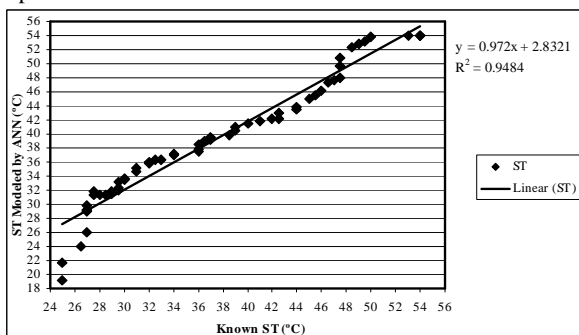


Figure 6. Linear regression between ST values modeled by ANN and Known

Beyond the regression analysis was implemented a test of hypothesis to verify if the proposed model is statistically equal to the one taken as real.

For a significance level of 5%, through the t-student test was evaluated the equality from the two averages ($M1 \neq M2$). The tested hypothesis was $H_0: M1 = M2$ e $H_1: M1 \neq M2$. In this case, if $Prob > t$ was less than 0.05 the hypothesis would be rejected and then $M1$ would be different from $M2$. Table 1 shows the results from accomplished statistical test.

Table 1. Statistic indexes between ST values obtained by ANN and taken as real ($M1$ = real values and $M2$ = simulated values)

M	N	Average	Standard deviation	Variance	t	Degree of freedom	Prob >(t)
1	60	37.39	8.68	Unequal	-1.1276	118.0	0.2618
2	60	39.18	8.66	Equal	-1.1276	118.0	0.2618

For H_0 : variances are equals, $F= 1.00$

Prob > F= 0.9898

Level of significance = 5%

$H_0: M1 = M2$ $H_1: M1 \neq M2$

Analyzing Table 1 and comparing the values of real and modeled temperature with application of t test for independent samples was found that the averages are statistically equals. Therefore the modeling by ANN was capable to calculate ST values that driven to an average value equal to the mean of values measured in field with a level of significance of 5%.

4. CONCLUSIONS

This research proposed a method to extrapolate ST values for the Rio dos Sinos Hydrographic Basin/RS, based on an ANN that was trained in a supervised way through a NOAA thermal satellite image from 6/12/2003, using on it the split window algorithm. The involved variables were positional (UTM coordinates and altitude) and climatic information (temperature and air relative humidity). The model was tested through an experiment realized on 3/18/2008 inside the Vale do Rio dos Sinos University campus. Seeing the average error (2.2 °C) and the maximum error (5.9 °C), the conclusion that the ANN is suitable for simulation will depend on the application of itself. If the associated errors for each observation didn't were relevant for practice finalities, then could be concluded that network rightly simulates the temperature values.

New experiments have been realized in direction of better evaluations for ANN efficiency on the process to determinate ST values based on variables of easy obtainment.

REFERENCES

Atluri, V., Hung, C., Coleman, T. 1999. Artificial Neural Network for Classifying and Predicting Soil Moisture and Temperature Using Levenberg-Marquardt Algorithm, Alabama, pp. 10-13.

Becker, F., Li, Z. 1990. Temperature independent spectral indices in thermal infrared bands, *Remote Sensing of Environment*, v. 32, n. 1, pp. 17–33.

Coll, C., Caselles, V. 1997. A split window algorithm for land surface temperature from advanced very high resolution radiometer data: Validation and algorithm comparison, *Journal of Geophysical Research*, v. 102, n. 14, pp. 16697-16713.

Cooper, D., Asrar, G. 1989. Evaluating atmospheric correction models for retrieving surface temperatures from the AVHRR

- over a tallgrass prairie*1, *Remote Sensing of Environment*, v. 27, n. 1, pp. 93–102.
- Czajkowski, K., Goward, S., Ouaidrari, H. 1998. Impact of AVHRR filter functions on surface temperature estimation from the split window approach, *International Journal of Remote Sensing*, v. 19, n. 10, pp. 2007–2012.
- Dash, P., Gottsche, F., Olesen, F., Fischer, H. 2002. Land surface temperature and emissivity estimation from passive sensor data: theory and practice current trends, *International Journal of Remote Sensing*, v. 23, n. 13, pp. 2563–2594.
- Galvão, C., Valença, M., Vieira, V., Diniz, L., Lacerda, E., Carvalho, A., Ludermit, T. 1999. Sistemas inteligentes: Aplicações a recursos hídricos e ciências ambientais, Porto Alegre, UFRGS/ABRH, 246 pgs.
- George, R. 2001. Prediction of soil temperature by using artificial neural networks algorithms, *Nonlinear Analysis*, v. 47, n. 3, pp. 1737–1748.
- Haykin, S. 2001. Redes Neurais: princípios e prática. Porto Alegre: Editora Bookman, 900 pgs.
- Kidwell, K. 1998. NOAA Polar Orbiter Data Users Guide. NOAA, US Department of commerce, Washington DC.
- Kumar, M., Raghuwanshi, N., Singh, R., Wallender, W., Pruitt, W. 2002. Estimating evapotranspiration using artificial neural network, *Journal of Irrigation and Drainage Engineering*, v. 128, n. 4, pp.224–233.
- Mao, K., Shi, J. 2008. A Neural Network Technique for Separating Land Surface Emissivity and Temperature From ASTER Imagery, *IEEE Transactions on Geoscience and Remote Sensing*, v. 46, n. 1, pp. 200–208.
- Muller, M., Fill, H. 2003. Redes Neurais aplicadas na propagação de vazões, in: Simpósio Brasileiro de Recursos Hídricos, 2003, Curitiba, Brazil, unpaginated CD-Rom Proceedings.
- Ottle, C., Vidal-Madjar, D. 1992. Estimation of land surface temperature with NOAA 9 data, *Remote Sensing of the Environment*, v. 40, n. 1, pp. 27–41.
- Price, J. 1984. Land surface temperature measurements from the split window channels of the NOAA 7 advanced very high resolution radiometer, *Journal of Geophysical Research*, v. 89, n. 5, pp. 7231–7237.
- Rivas, R. 2003. Propuesta de un modelo operativo para la estimación de la evapotranspiración, Tesis Doctoral, Universitat de València, Valencia, Spain, 140 pgs.
- Silva, J. 2007. Estimativa da temperatura da superfície do solo de uma região semiárida a partir do IRMSS (banda 4) do CBERS-2, in: Simpósio Brasileiro de Sensoriamento Remoto (SBSR), 2007, Florianópolis, Brazil, unpaginated CD-Rom Proceedings.
- Silva, A., Ramos, R., Souza, L., Rodrigues, D., Mendes, J. 2004. SIG – Uma plataforma para introdução de técnicas emergentes no planejamento urbano regional e de transportes, São Carlos, Editora da EESC/USP, 221 pgs.
- Sobrino, J., Coll, C., Caselles, V. 1991. Atmospheric correction for land surface temperature using NOAA-11 AVHRR channels 4 and 5, *Remote Sensing of Environment*, v. 38, n. 1, pp. 19–34.
- Veronez, M., Thum, A., Luz, A., Da Silva, D. 2006. Artificial Neural Network applied in the determination of Soil Surface Temperature-SST, in: International Symposium of Accuracy Assessment in Natural Resources and Environmental Sciences, (Accuracy 2006), Lisboa, Portugal, pp. 889–898.
- Yang, C., Prassher S., Mehuys G., Patni, N. 1997. Application of artificial neural networks for simulation of soil temperature, *Transactions of the ASAE*, v. 40, n. 3, pp. 649–656.
- Zanetti, S., Sousa, E., De Carvalho, D., Bernardo, S. 2008. Estimação da evapotranspiração de referência no Estado do Rio de Janeiro usando redes neurais artificiais, *Revista Brasileira de Engenharia Agrícola e Ambiental*, v. 12, n.2, pp. 174–180.

ANALYSING THE FACIAL MORPHOLOGY WITH A THREE-DIMENSIONAL GEOMETRICAL FEATURES APPROACH

F. Calignano^a, S. Moos^a, E. Vezzetti^{a*}

^a Politecnico di Torino, Dipartimento di Sistemi di Produzione ed Economia dell’Azienda, 10129 Torino, Italy - (flaviana.calignano, sandro.moos, enrico.vezzetti)@polito.it

KEY WORDS: 3D scanner, Shape analysis, Facial morphology, Soft tissue shifts

ABSTRACT:

To obtain the best surgical results in orthognathic surgery, treatment planning and the evaluation of results should be performed. In these operations it is necessary to provide to the physicians powerful tools able to underline the behaviour of soft tissue. For this reason, considering the improvements provided by the use of 3D scanners, as photogrammetry, in the medical diagnosis this paper proposes a methodology for analysing the facial morphology working with geometrical features. The methodology has been tested over patients affected by malocclusion, in order to analyse the reliability and efficiency of the provided diagnostic results.

1. INTRODUCTION

The assessment of the dimensions and arrangement of facial soft tissues is important for medical evaluations. Orthodontists and orthognathic maxillofacial and plastic surgeons often require quantitative data about the association between soft and hard tissues (Ferrario 1999, Sforza 2005). For many years, this information has been obtained from two-dimensional (2D) radiographs and photos, even if these have been consistently limited (Chew 2005, Koh 2004). Significant improvements have been obtained with the use of computer vision algorithms, even if the use of 2D supports to analyze 3D objects seems to be quite inadequate. For this reason, many research efforts over the last 10 years have been directed toward developing computer vision tools that with the use of 3D scanner devices are able to provide reliable and more complete data. These systems use different technologies such as active or passive light reflection analysis and are able to describe 3D real shapes with a point cloud, analyzable with 3D software. However, while image-processing methodologies are well known in the medical context, the situation for 3D scanners is still quite marginal and fragmented. Some studies have proposed structured procedures that could be used for guiding physicians in the use of 3D scanners in medical diagnosis (Hoffman 2005, Katsumata 2005), but at present no one has succeeded in developing a standardized and accepted strategy.

Actually, it is possible to move from morphometric tools that implement statistical shape analysis, such as Generalised Procrustes Superimposition (GPS) and Principal Component Analysis (PCA). The first iterative method (GPS) applies geometrical transformations (scales, translations, rotations, and reflections) in order to compare reference points (landmarks) (Mori 2005, Sforza 2004) taken from different point clouds of the patient’s face. The PCA method evaluates the tendency of the landmark distributions along the x and y axes, locating a new working frame centered on the average shape center. The method creates new variables named principal components (PCs) that describe how much the landmark configuration of each sample is different from the average shape.

Moving to the 2D radiographs, Thin-Plate Spline analysis (TPS) is used on a point set of anatomical landmarks over the pre- and post-surgery radiograph. Then the postsurgery radiograph is considered as an infinitely thin metal plate that must be bent in a direction orthogonal to the plane in order to match its landmarks to those of the presurgery radiograph while the bending energy is minimized (Hajeer 2004). If the two shapes are identical, the bending energy is zero and the plate is flat.

To provide information regarding face morphology in the regions around the landmarks, the Multisectional Spline method uses section planes passing through a set of specific reference points of a point cloud (landmarks) in order to obtain specific section spline. The shifts of the facial morphology between the pre- and post-surgery point clouds can be analyzed by comparing the two section profiles passing through homologous landmarks and section planes (Soncul 2004).

Working with the entire point cloud instead of only some portions, with the Clearance Vector Mapping method (CVM) the pre- and post-surgery point clouds are first aligned (iterated closest point (ICP), CSM) (McIntyre 2003) and then the magnitude of the 3D shape displacement can be computed by working on triangulated meshes, following different approaches (radial, normal) (Harmon 1981). The displacement is shown by color mapping.

At present, even if the most used methodology for maxillofacial diagnosis remains the Conventional Cephalometric Analysis (CCA) (Bookstein 1991), the Multisectional Splines method seems to be the most reliable and complete methodology because it is able to provide reliable information about the tissue shifts, as does the CCA approach, but it is also able to provide additional global information, e.g., some pathologies such as lateral asymmetry.

Some significant points need work for development of a diagnostic procedure that could be accepted by the entire medical context. It is necessary to define a method that extracts shape morphology measures, starting from the landmarks as reference points, to guarantee consistent morphological comparison, but that also takes into consideration the entire facial shape (point cloud) in order to consider all useful

* E. Vezzetti, Dipartimento di Sistemi di Produzione ed Economia dell’Azienda, Politecnico di Torino, Corso Duca degli Abruzzi 24, 10129 Torino, Italy, email: enrico.vezzetti@polito.it

information. For this reason some studies (Swiderski 1993) have tried to exploit the 3D information from non invasive 3D scanners, such as laser scanners, to extract area and volume measurements. One of the most significant studies (Richtsmeier 1992) has worked on soft tissue landmarks, creating a geometrical model that approximates the facial features with flat

triangles in which vertexes have been represented by the facial landmarks. This approach has provided a simple and direct methodology for supporting the evaluation of facial areas and volumes. However, while the morphological behaviour of the face is characterized by smooth surfaces, this methodology of working with flat triangles is able to provide only a first approximation of the face behavior and neglects a series of features. Considering that 3D scanners provide accurate point clouds, it would be more useful to use methodologies that can exploit the entire point cloud morphology.

Therefore, starting with this concept, we propose a methodology that employs geometrical features for approximating the facial shape, but instead of using only a tetrahedron for describing the face morphology, this methodology employs different 3D geometries that can better fit the face morphology.

2. THE PROPOSED METHODOLOGY: GEOMETRICAL FEATURES BASED APPROACH

To identify the geometries required to develop a geometrical features-based model, it was necessary to define how to decompose the facial morphology. Starting from the head-modelling guidelines (Coombes 1991) and from the coordinates of the facial soft tissue landmarks (Table 1), the face has been divided into four different regions (Fig.1), sectioning the model with a series of planes passing through the vertex, the upper and lower part of the nose, and the chin.

Name	Abbreviation
Nasion	N
Pronalase	Prn
Subnasale	Sn
Labiale superius	Ls
Stomion	Sto
Labiale inferius	Li
Sublabiale	Sls
Pogonion	Pog
Tragion	$t_{right} - t_{left}$
Nasal alar crest	$al_{right} - al_{left}$
Chelion	$ch_{right} - ch_{left}$
Gonion	$go_{right} - go_{left}$
Vertex	V

Table 1. List of soft tissue morphological reference points

Once the four regions are defined, it is necessary to determine which geometry would be the most suitable fit for the different possible shapes in each zone. Starting with the number of landmarks that characterize every identified region, the available 3D geometries, and all the different possible facial morphologies, and working with hypothesis developed from the correlations between the cranial shapes and polygons (Raby 1997), it has been possible to identify the best fitting geometries (Hyun 1998):

Zone 1 (upper face portion): This region could be described by an ellipsoid (Fig.2).

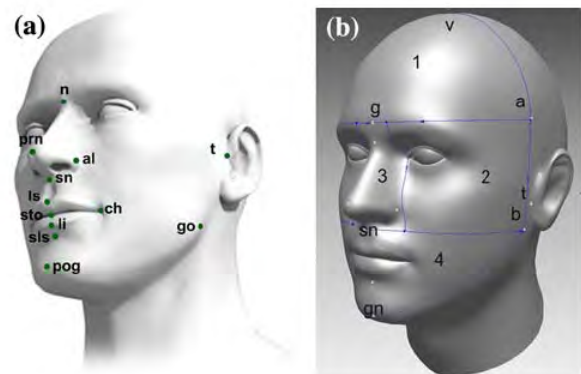


Figure 1. Soft tissue landmarks and face decomposition

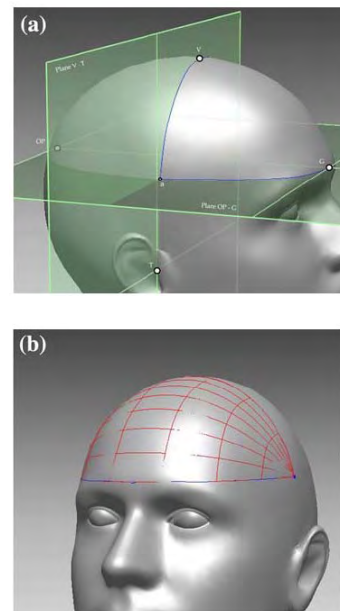


Figure 2. Upper face portion geometrical feature: a) landmarks, b) ellipsoid

Zone 2 (middle face portion): This region could be described by a cylinder with an elliptical shape (Fig.3).

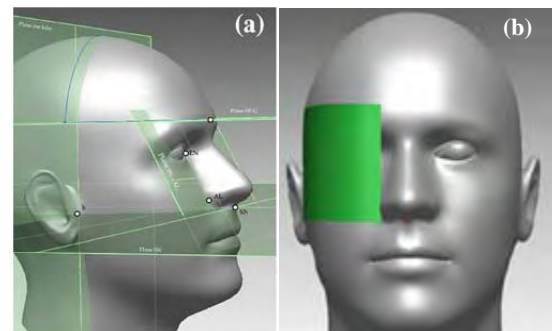


Figure 3. middle face portion geometrical feature: a) landmarks, b) cylinder

Zone 3 (nose): The nose could be described by a conical frustum with an elliptical base (Fig.4).

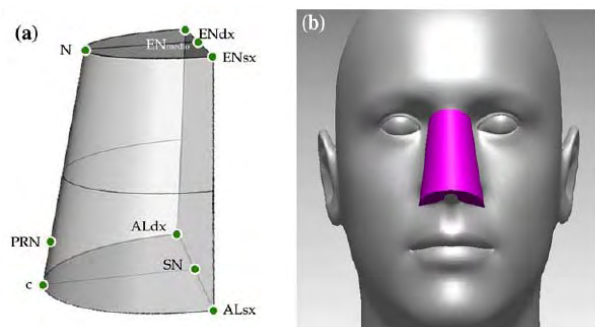


Figure 4. Lower-face portion geometrical feature: a) landmarks, b) conical frustum

Zone 4 (lower-face portion): This region could be described by an ellipsoid (Fig.5).

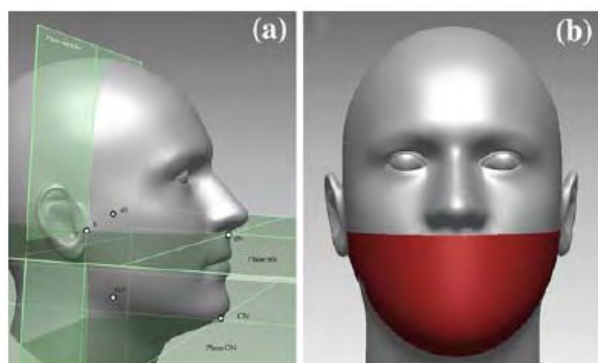


Figure 5. Lower-face portion geometrical feature: a) landmarks, b) ellipsoid

3. EXPERIMENTAL VALIDATION

To evaluate the performance of the proposed methodology in the area evaluation, the geometrical features-based approach was compared with the tetrahedron method (Sforza 2005). First the facial areas of five patients were estimated using the point cloud meshes and adding the area of every single triangle covering the different specific regions. The results from this evaluation were considered reference values because the mesh approximation is very precise and depends only on the 3D scanner device employed for data acquisition. However, using the mesh approximation, it is possible to obtain reliable information about the soft tissue area modifications, but it is impossible to understand, comparing pre and post-surgery point clouds, where the face was modified (shift, scaling, rotation). With the use of specific geometries, such as those used in the proposed method, it is possible to extract spatial information together with reliable data about area and volume. From the results of the different comparisons, the geometrical features-based approach yields data closer to reality than the tetrahedrons methodology.

Looking at the graphical comparison (Fig. 6), it is possible to see that for the nose, while the geometrical features-based approach gives a good fit, the tetrahedron approach does not match the real nose shape. This is verified by the fact that the tetrahedral structure is composed of five vertices: nasion, nose

tip, left and right nose lobes, and nose base. For example, looking at the nose top, while the real shape shows one unique arc profile connecting the eyebrows, the tetrahedron solution employs only one point.

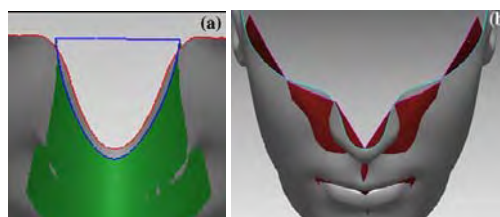


Figure 6. Feature Based Method applied to the nose: a) Feature Based Method, b) Tetrahedron method

This morphological mismatching between the real nose shape and the tetrahedron shape confirms the experimental data that show a more reliable area evaluation using with the conical frustum instead of the tetrahedron.

4. CONCLUSIONS

Face decomposition using solid geometries provides reliable information about the soft tissue shift comparable to that from traditional cephalometric data, but it also provides a more complete set of three-dimensional information, such as facial area modification, that is not attainable with traditional methodology. The presence of elementary geometries that synthesize the real shape is able to support the use of 3D scanners for diagnostic purposes instead of point clouds that contain a huge quantity of morphological data but are very difficult to employ and that sometimes, using inappropriate measurements solutions, provide false information.

Although the method proposed is to study the quantification of postoperative changes, it could also be a starting point for other applications in medical diagnosis thanks to the ability to synthesize facial morphometric data using simple geometrical elements, which is more reliable than the simple tetrahedron.

5. REFERENCES

- Bookstein FL (1991) Morphometrics tools for landmark data. Cambridge University Press, Cambridge
- Coombes AM, Moss JP, Linney AD, Richards R, James DR (1991) A mathematical method for comparison of three dimensional changes in the facial surface. *Eur J Orthod* 13:95–110
- Ferrario VF, Sforza C, Schmitz JH, Santoro F (1999) Threedimensional facial morphometric assessment of soft-tissue changes after orthognathic surgery. *Oral Surg Oral Med Oral Pathol Oral Radiol Endod* 88(5):549–556
- Hajeer MY, Ayoub AF, Millett DT (2004) Three-dimensional assessment of facial soft-tissue asymmetry before and after orthognathic surgery. *Br J Oral Maxillofac Surg* 42:396–404
- Harmon LD, Khan MK, Lashc R, Ramig PF (1981) Machine identification of human faces. *Pattern Recognit* 13(2):97–110
- Hoffmann J, Westendorff C, Leitner C, Bartz D, Reinert S (2005) Validation of 3D-laser surface registration for image-guided craniomaxillofacial surgery. *J Craniomaxillofac Surg* 33(1):13–18

Hyun CD, Dong YI, Uk LS (1998) Registration of multiple-range views using the reverse-calibration technique. *Pattern Recogn* 31(4):457–464

Katsumata A, Fujishita M, Maeda M, Ariji Y, Ariji E, Langlais RP (2005) 3D-CT evaluation of facial asymmetry. *Oral Surg Oral Med Oral Pathol Oral Radiol Endod* 99(2):212–220

Koh CH, Chew MT (2004) Predictability of soft tissue profile changes following bimaxillary surgery in skeletal class III Chinese patients. *J Oral Maxillofac Surg* 62:1505–1509

Manual XLSTAT. Available at <http://www.xlstat.com/en/support/tutorials/gpa.htm> [accessed April 21, 2008]

McIntyre GT, Mossey PA (2003) Size and shape measurement in contemporary cephalometrics. *Eur J Orthod* 25:231–242

Mori A, Nakajima T, Kaneko T, Sakuma H, Aoki Y (2005) Analysis of 109 Japanese children's lip and nose shapes using 3-dimensional digitizer. *Br J Plast Surg* 58(3):318–329

Richtsmeier JT, Cheverud JM, Lele S (1992) Advances in anthropological morphometrics. *Ann Rev Anthropol* 21:283–305

Raby GP (1977) Current principles of morphoanalysis and their implementations in oral surgical practice. *Br J Oral Surg* 15:97–109

Sforza C, Dellavia C, Tartaglia GM, Ferrario VF (2005) Morphometry of the ear in Down's syndrome subjects. A three-dimensional computerized assessment. *Int J Oral Maxillofac Surg* 34:480–486

Chew MT (2005) Soft and hard tissue changes after bimaxillary surgery in Chinese class III patients. *Angle Orthod* 75:959–963

Sforza C, Dellavia C, Colombo A, Serrao G, Ferrario VF (2004) Nasal dimensions in normal subjects. Conventional anthropometry versus computerized anthropometry. *Am J Med Genet* 130A:228–233

Soncul M, Bamber MA (2004) Evaluation of facial soft tissue changes with optical surface scan after surgical correction of Class III deformities. *J Oral Maxillofac Surg* 62(11):1331–1340

Swiderski DL (1993) Morphological evolution of the scapula in three squirrels, chipmunks, and ground squirrels (Sciuridae): an analysis using thin-plate splines. *Evolution* 47:1854–1873

QUANTITATIVE PROGNOSIS OF OIL AND NATURAL GAS FIELDS

V.I. Lyalko^a, A.J. Hodorovsky^a, A.A. Apostolov^a, A.B.Vostokov^{b*}

^a Scientific Centre for Aerospace Research of the Earth(CASRE), National Academy of Sciences of Ukraine, 55-B, Oles Gonchar street, Kiev, 01601, Ukraine – (casre, artur, alex)@casre.kiev.ua

^b The companies “Tvis Ltd”, office 171 build. 123, Kievskaya str., Obykhov town, Ukraine - ab@tvis.com.ua

KEYWORDS: Remotely Sensed data, Geology, Resources, Mapping, Data mining, Landsat, Cost.

ABSTRACT:

Technology of practical use of remotely-sensed data is shown. A developed method is allowing perform computations for quantitative estimate the potential of petroleum, natural gas and minerals on the different territories. The scale of works is 1:10,000 to 1:200,000. Prognosis estimation of the territory potential is based on the relationship between the features of oil-and-gas content and discontinuous structures with diverse scale level. The forecast of pools location is carried out on the basis of the complex attributes. As a result of study we have quantitative estimating the probability for determining forecasted objects in each point of the research area. The research point responds to the minimal area, which is identified in satellite digital imagery (5x5M, 15x15M, 30x30M etc.). The results of the successful use of the method in different territories are documentary proof.

Die Technologie und der praktische Einsatz von auf Distanz gewonnenen Daten wird in der Studie gezeigt. Eine entwickelte Methode ist zur quantitative Einschätzung von Territorien in Bezug auf Öl, Gas und Mineralien gedacht. Der Maßstab der Arbeiten ist 1:10,000 bis 1:200,000. Die Prognosenschätzung der Wahrscheinlichkeit eines Territoriums basiert auf der Verwendung der Verwandtschaft der Eigenschaften von Öl-und-Gas Inhalten und explosiven Strukturen auf einer anderen Maßstabsebene. Die Voraussage von Lagerstätten wird auf der Basis der komplexen Attribute vorgenommen. Als Ergebnis der Studie wurde eine quantitative Einschätzung der Wahrscheinlichkeit, die Objekte der Voraussage zu finden, für jeden Punkt des Forschungsgebietes erhalten. Die Forschungsarbeit beantwortet das kleinste Gebiet, das in digitaler Satellitenabbildung dargestellt wird (5x5M, 15x15M, 30x30M etc.). Die Ergebnisse der erfolgreichen Anwendung der Methode in verschiedenen Territorien werden betrachtet.

1. INTRODUCTION

Different countries are constantly increasing expenditures to search for pools. Increased expenditures on augmenting the depths of the drilling wells and costs of basic methods of exploration are defined.

The decrease of expenditures and increase of efficiency of search works are possible in two ways:

- 1) Complex use of comparatively inexpensive methods for exploration on the remotely- sensed data are based.
- 2) Preliminary results of prognosis are used for all studied territory.

Efficiency increases due to abbreviated exploration on non-perspective territories. Even the insignificant increase of exploration efficiency provides income. It is incomparable with expenditures on implementation of traditional exploration.

Tradition approach using the remotely-sensed data for the study the faults-mosaic and folds structure. The research results are represented as maps. It hampers using these maps for prognosis of territories in a complex with data of other exploration methods.

We developed the method of using remotely-sensed data for complex exploration of oil-and gas content. These results can be used together with the results from other types of research for complex prognosis of perspective territories. This method was patented (# 32050, 2008).

This method was used to explore oil-and-gas content for different provinces of Dneprovo-Donetsk depression, West-Siberia, Timano-Pechora and Sakhalin Island. These provinces are located in a variety of geological landscapes. In most cases, the prognosis results are confirmed by the data from the exploration wells.

A.B. Vostokov

2. BASIC STATUTES OF METHODS OF RESEARCH

2.1. Sequence of implementation of works

The offered method contains some basic stages of research. In each stage are used the special methods of analysis. On the first stage the collection and systematization of all material about the geological formation of the territory, the data of the oil-and gas content, results of geophysical survey and landscape terms are conducted. All remotely-sensed data are collected and analyzed. Special attention is devoted to reception and checking of data of geographical co-ordinates of the wells and results of the drilling.

By results of researches the representations about geology, tectonics, structure and oil-and-gas content of area of works, factors of the control of pools, landscape conditions and other are formed. Results are prepared in the GIS environment. The choice of research methods will be based on these data.

The second stage contains structural interpretation of the remotely-sensed data. The faults, breakings and circular structures are selecting. The faults-mosaic and scheme of morphological structures are constructed. Special attention is devoted to the permeability of rocks.

The third stage contains several types of methods for calculating the potential of research territory. In the beginning perspective meanings are defining for separate search features. Then spatial-probabilistic estimation is used to analyze the values for all the search features. The method of spatial-probabilistic estimation is used (Nagorskiy and other, 1970, 1971, 2004).

The fourth stage is analysis the received results, estimates authenticity and recommends further research. Two groups of principal and different methods of research the during works are used. The first groups of methods are used for interpretation of remote-sensing materials and construction of morphometry. As a

result, we have the initial quantitative information for search features, which the possible, can be controlling of the pools. Another group of methods is allowing the assessing of connection of the searches of features, which was selected, with the objects of prognosis for the complex estimate of prognosis of territory.

These exploration methods include the traditional methods and methods developed by authors or with their participation. Methods, which were developed by authors in this article, are submitted.

2.2. Methods of structural of research

For the study of anticline structures of sedimentary cover is used the method of selection of anomalous values of the height field of modern relief. Relief is created from the Shuttle satellite data. For most regions the anticlines in modern relief are revealed as raising. Authenticity of the selected anticline fields are estimating by comparing seismic research data and materials of structural interpretation.

We use the structural interpretation results of multispectral space images as the initial information for studying breaks, knots of cross breakings and circular structures. We used the structural interpretation results of multispectral space images as the initial information for studying breaks, knots of cross breakings and circular structures. The structural interpretation of multispectral images is conducted by sight by known methods of interpretations (Kats and et. 1988, Aerospace research, 1988, Barret, Kurtis, 1979, Kravtsova and Dr., 1985, Kronberg, 1988, Multispectral remote sensing, 2006, et.). Parallel comparative analysis of interpretation of multispectral images and topographical maps is performed for control and delete the man-made lineaments. It is very important to fulfill the works for territory that have the high loading man-made. If the multispectral images did not show of the lineaments or they are expressed badly, interpretation is conducted on the topographical maps. The 3D relief model will be interpreted.

As a result of interpretation, the maps are created for breaks, circular and plicate structures and scheme of breakings and blocks structures for the studied territory. All information is present in a vector form. It allows the constructed maps to be juxtaposed with other different geologic-geophysical data and prepared in GIS. It is very important for further use.

2.3. Method of study of crack permeability of rocks

The special attention is given to studying breaks of rock permeability. It is one of important search features. Traditional methods studies of permeability of breaks are use of study for rock exposure, in the production excavation and of core drilling. These methods are expensive and labor intensive and limited the opportunities of study of breaks permeability of rocks.

We developed method of rock permeability study for poorly naked territory and large areas. Method is based on lineaments study. Lineaments are characterized by different sizes of break in the earth's surface such as large faults, raised strips, fracture zones, fold structures and etc. Lineaments are characterized by different sizes of break in the earth's surface such as large faults, raised strips, fracture zones, fold structures and etc.

Due to inherent evolution of rock structure, a new relief is reorganized and the ancient relief is saved. Naturally, lineaments can give generalize and integrate schemes of breaks of the earth's crust. As a result of joint action of several exogenous processes, the numerous lineaments for any territory may be detailed. Lineaments have diversity of orientation and extent. In the process of structural interpretation of

multispectral images for the study of crack permeability of rocks all lineaments are selecting. Their quantity does not depend on size, orientation or landscape of indicators. Our method differs from the structural interpretation method with the purpose of studying faults and folds. The number of selected lineaments are considerably more that the quantity of faults and breaks, which are selected by other methods of research (Mesheryakov, 1965, Golbrayh and et., 1968, Chebanenko, 1977, Tyapkin, 1998, Palienko and et. 2005, Multispectral remote sensing, 2006, and other).

Furthermore we must to know such the parameter of permeability of zone of exploration as fissure opening. It is impossible to do on the remotely-sensed data. We assume that within the limits of every lineament system all fissures are characterized by nearest values of opening. The common quantity of fissures of every system can be evaluate for cracked rock permeability (i.e., rock crack permeability can be quantitative value estimated in every point of territory as the quantity or total length of lineaments of every system, attributed to unit of area).

The results of studying rock break permeability are represented in a quantitative form. It is very important and allows mathematical methods to be used for processing and analysis. The results of special research showed that the accumulation of hydrocarbons did not have maximal or minimal permeability values. These values are conformed to intermediate (optimum) of permeability. The quantitative analysis methods determine optimum interval values for these features. They can be incorporated with other search features, and first of all, with the geophysical research data. It is necessary and important for reliable evaluate of potential of territory.

For the decision of tasks of prognosis to present the lineament maps in a quantitative form are necessary. The methods of lineament analysis include:

- 1). Analysis of orientation regularity and selection of borders of the lineaments.
- 2). Select of indexes for quantitative description of the lineaments field.
- 3) Analysis and interpretation of geological maps for graph tightness and total length of lineaments for every system.

The characteristic features of this analysis method are:

- 1) The attention is focused for localization of the borders of the lineament systems. The modal values of every system are second-rate. This analysis provides of the orienting the maximums and minimums on the graphs of azimuth distribution of extending lineaments.
- 2) For the selection of the systems of lineaments are using the graphs of dispensation of their distribution azimuths. The graphs are constructed with differing sites of initial points.
- 3) The interval width is specially selected for lineament groupings. This value is used to construct and analyze graphs of azimuth distribution of extended lineaments. Easily is showed that the quantity of the lineament systems, which is possible select on the analyzed graphs, relies on the interval width of grouping which is used to construct these graphs.

The analyses of regularity of orientation of lineaments are conducted in two stages. The first stage is calculated azimuth trends of all selected lineaments within the limits of separate blocks or local areas with the relatively homogeneous measured geological structure. The significant distribution values for azimuths of extended lineaments from normal distribution are determined. Meaningful distinctions testify to existence of the separate lineaments systems. For reliability, the nonparametric statistical criteria of Pirson (χ^2) are used to estimate separate maximums and minimums.

The second stage is selecting of the general lineaments systems for explored territory only. The data are used on separate blocks to construct azimuth distribution of modal values of local maximums

and minimums. Authenticity of their selection has been verified for clearness of border definition of the separate lineament systems and their general modal of values for all research territory. The effectiveness of further of research is depended on authenticity of selection of the lineaments systems.

Then the estimation of conformity of the allocated systems of lineaments to systems of cracks and breaks of research region established by other authors must be carried out.

The same analysis method uses orientation of linear anomalies of the physical fields and geophysical data on the studied territory. Two indexes for quantitative description of the lineament fields are used: the quantity (density) and summary of total length of lineaments. These indexes for unit of territory are counted. These two indexes are associated, but they do not duplicate and each complements the other.

For each of the systems are calculated the quantity and total length of lineaments. Limits of the extended sliding window are used for this calculation. Windows are oriented in accordance with azimuths of extended modal (most often met) lineaments of every system. The sizes of the sliding window depend on the value of pool depth and quantity of selected lineaments.

Data of special research are ascertained functionally interdependence of the extent and value of depth of breaks (Nechaev and other, 1991, Petrov, 1974, Rugich, 1977, Rugich, Sherman, 1978, Sankov, 1989, Chernishev, 1983, Sherman, 1984, and other). The account of this dependence is used at a choice of the size of a window of averaging. For this purpose the analysis of distribution of potential of objects in researched area on occurrence depth will be carried out. The maps of density and total length of lineaments are defined with the help of sliding windows of averaging; the sizes of windows are defined proceeding from occurrence depths of the basic horizons of accumulation for prognosis pools.

At a choice of the sizes of sliding window the quantity of lineaments in window is accountable factor. The calculating the quantity of lineaments occurring in a sliding window is necessary for determination of quantity of windows with the zero values. The quantity of the sliding windows with the zero values of graph tightness or total length of lineaments must not exceed 10% from a common quantity. It is defined experimentally. Otherwise maps of potential are impossible for interpretation and have small information for the prognosis research.

In the process of prognosis researches and for geological interpretation of maps of closeness and total length of lineaments the method of spatial correlation of values of these maps with the pools (deposits) and structures selected by the geologic and geophysical data is used.

For realization of methods and algorithms of analysis of lineaments fields are written the author's complex programs in Delphi. We developed programs for the decision of tasks which had not been included in well-known software's. The programs are used to analyze lineaments orientation, excretions of the systems of lineaments, creation of maps of graph tightness and total length of lineaments, creation of maps of knots of crossing of lineaments and transformations of data. The data formats of our programs are compatible with well-known software. Calculation control and verification of the results are tested in GIS, ERDAS Imagine or MapInfo Professional.

The following sequence of operations was set in the total:

- 1) Visual decoding of space images with use of the program of ERDAS Imagine.
- 2) Translation of data vector for the format accepted in the developed program.
- 3) Data analysis and receipt of results with use of the developed program.

- 4) Construction of maps in an isolines form by the Surfer program.
 - 5) Translation of the file of raster format got by Surfer program.
- For the control of calculations and verification of results the data in GIS-program are visualization.

2.4. Basic prognosis method of oil-and-gas content for territory with remotely-sensed data

The method of spatial-probabilistic prognostication is used for oil-and-gas content estimate of the territory. The program, based on this method, creates maps in the quantitative form for studied territory. This maps are used for predict potential oil and gas content of territory. The program uses any quantity of search features. The minimum area of prognosis potential are corresponded to pixel size of satellite image used for created of the prognosis maps.

The complex informative features are formed in the beginning. For this purpose is used the program of spatial-probabilistic prognostication for calculating the probabilities of interconnection of informative features with the objects of prognosis. Self-descriptiveness of attributes is established by comparison of distributions of meanings of analyzed attributes within the limits of known objects of the forecast with distribution of their meanings which were defined for a uniform network in the most investigated territory. For comparison of distributions the Pearson criterion is used. In a case wide disagreement the functions of the relation of plausibility are used. On them the interval of meanings of an attribute is defined, to which the objects of the forecast are connected and the probability of interconnectivity of objects with the values of every search feature are calculated. Then the multidimensional functions of likelihood for complex analysis of all search features are used. The results of complex analysis prognosis of territory are maps of potential of oil-and-gas content in isolines.

The next stage is containing the analyses of maps of prognosis of potential oil-and-gas content in isolines. Local perspective areas are selected with the use of expert appraised results. All information, which for diverse reasons was not used in the process of prediction, is used. As result we have the calculated potential values for selected areas. Then for calculated of the values are realizing ranking and are prepared the recommendations for conducting research on perspective areas.

Characteristics of the spatial-probabilistic prognostication method are: realization of semantic control of the results on the all stages of works; possibility of removal of spurious of features and inexplicable results.

The potential maps are created on the results of remotely-sensed data or in a complex with different geological explorations (if they are available).

The important question is the authenticity of the prognosis results. Undoubtedly, only drilling can verify the reliability of the prognosis. It is rarely on the practice. If in the region are known pool areas, part of them are not used to estimate potential of territory. They are used as control points to verify the authenticity of search features in every case. The control points are determined in every case.

2.5. Results of prognosis research

These research methods were used to creation prognosis maps for oil and gas pools of the following provinces: West Siberian (Latitudinal Priobie and Yamalo-Nenetskiy autonomous region), Sakhalin (North-Sakhalin and West-Sakhalin pools), Timano-Pechora and Dneprovo-Donetsk.

The explorations were conducted the south-east of the Dneprovo - Donetsk Province on a territory of about 1000 sq. km. Relief of research territory is hilly with by the many ravines. Small

rivers present a hydrographical network. A greater part of district area consists of field crops.

Three oil and three gas pools in the terrigenous-carbonate sediments of lower - middle carbon are present in the research territory. Three oil and three pools in the lower - middle carbon also are located in the research area. The pools are small areas of no more than 5 sq. km. They are inherent to local dome sedimentary cover. Twenty local structures are selected based on seismic works data. Most structures are not studied by drilling. The territory and adjoining area are studied by seismic exploration and prospecting wells.

The initial information for prognosis research are maps of lineaments and circular structures; they were created on the results of the structural interpretation of the multispectral images of satellite Landsat and the 3-D digital model of relief from the Shuttle satellite data. Data of 15 wells were selected. They had results of testing for oil or gas.

For the creating of maps of the forecast oil-and-gas content the connection of objects of the forecast with numerical meanings of the following attributes were analyzed:

- 1) Density and total length lineaments for each of 8 systems lineaments.
- 2) Density of units of crossing lineaments of all systems.
- 3) Marks of high of a modern relief established on digital model of a relief.
- 4) Character of moving of territory on the neotectonic of stage of evolution. Were estimated a direction (relative rise or lowering) and amplitude of moving (in numbers).

As a result of calculation is determined, that the all mentioned features maybe use for quest of oil and gas as they are interrelated with the prognosis objects. This connection has the complicated character. This connection has the complicated character; the objects of prognosis avoid both maximum and minimum values. They are conformed to the intermediate values of features. These compares are very well with data of previous researchers (Nevskiy, 1955, Pospelov, 1963 and others).

The pools are located outside the limits of anticline dome practically for all potential areas. They are disposed on anticline limbs or between local domes. Results of drilling are confirming these inferences on separate structures within the limits of the studied area and in other regions.

For all areas of exploration the maps of potential oil-and-gas content are constructed in the scales of 1:50000 and 1:25000. On the maps the many relatively small areas with the highest potential for pool discovery are selected.

The smaller area has the higher potential value. Areas with high potential inside areas with more low perspective practically always are disposed. Most potential areas have complex form and are characterized by elongated orientation.

As a rule, the potential areas which were selected on the maps of scale 1:25000 and 1:50000 are coincided from 60 to 80 percent. In other words, results of regional explorations the results of the detailed research are confirmed. Exploration reliability on coinciding data is validated

The potential areas are located in the form of strips on the created maps and are composed in the three bands of N-W - sub-latitude; are crossing all studied area. The selected strips have sub-parallel direction for the border of the Dneprovo-Donetsk depression. For pools of the Dnepr-Donetsk Region this type of strips distribution is inherent.

Results of exploration: area having no potential is 66%; area with low potential is 28 %; area with middle potential is 5% and area with high potential is 1% of all studied territory. There are 131 local potential areas with sizes from 0.5-1.0 to 2-4 sq. km. The 25 potential areas are recommended as primary objects for detailed exploration; their territory is 75 sq. km. (Fig.1).

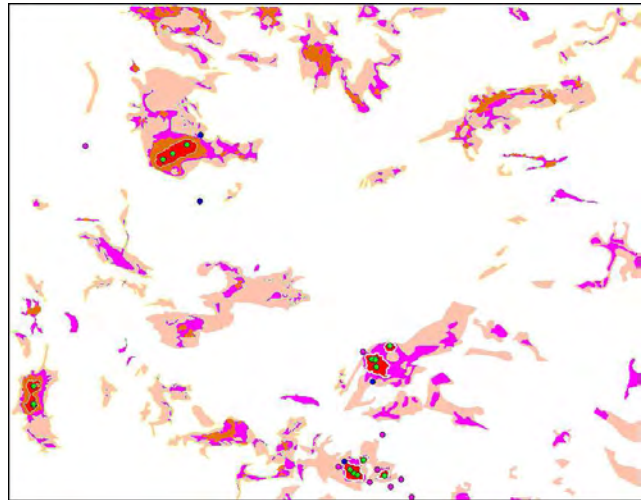


Figure1. Map of potential of oil-and-gas content of the S-E of path of Dneprovo-Donetsk depression, the scale 1:50000.

Legend:

	Areas are maximum potential		Non potential area
	Areas are high potential	●	Productive wells
	Areas are middle potential	●	Well are brine water and oil film
	Areas are low potential	●	Well are brine water

At first, authenticity of results of the conducted prognosis research was confirmed by indirect data. Three known pools with maximum values of potential were characterized. They are located outside the studied territory but in proximity of its border. Information for these pools was not used in the research process. After completion of prognosis researches on the remotely sensing data, on the flanks of two industrial of pools of territory, the works for the search of new accumulation of hydrocarbons were conducted by the method of vertical seismic prospective (VSP). VSP data confirmed the results of our prognosis data.

One of prospective areas, selected on the prognosis map was tested using a prospecting borehole. The potential production of oil is obtained. In addition, on the seismic exploration data was selected the point for prospecting boreholes within the limits of the local structure. Our data identified this local structure as non potential. An exploration well was drilled on this local structure. The drilling data was confirmed that this local structure has no potential.

In the Sakhalin Province the researches for oil-and-gas content were conducted within the limits of the North- Sakhalin area. Greater part of exploration area is occupied by grassy-shrub vegetation with tailings of larch forests and the medley of birch trees. A hydrographical network is weak; permanent rivers and brooks are absent. The area is described as wavy relief. The west part is transformed to off-shore lowland.

Within the limits of the exploration area, on the test boreholes data were uncovered the multimass of the sandstones, aleurolites, argillites and clays. It is data from the Pliocene Age to the Upper Cretaceous Period. Location of the territory of the mega-anticline of sub-meridional direction is related by the numerous broken breakings. Forming of structures of area with phase of tectogenesis of Sakhalin is related (Late Pleistocene). The large breaks of the sub-meridional direction influenced on the organization of the sedimentary framework. The multihorizon oil-and gas field is located within the limits of the work area.

Natural gas forms an independent pool. Gas cap is higher than the petroleum field and gas was found in the dissolved condition in the petroleum. The pool is characterized by the single hydrodynamic system characterized.

Sixteen pools are located here. Occurrence depths are from 1160m to 2710m. All pools are relating to a type of the mass-pool roof and tectonic of shielded. Productive layers are sand and sandstone. They are characterized by the lithological of changeability. The sizes of oil and gas fields are small. They occupy the limited areas in the pool in pool roof of the isolated blocks of each bed.

The studied pool is multihorizon. The difference of depth layer of pools exceeds 1.5 km. Prognoses of oil-and-gas content were calculated separately for the layers that are located at the different depths. Source of the initial information for potential of researches are the maps of lineaments and ring structures; they are constructed on the results of structural interpretation of multispectral images Landsat satellite and digital model of relief on the data of the Shuttle satellite. The processing of results interpretation was carried out according to the stated above technique of works. The studied pool is multihorizon. The difference in depth of layers of pools exceeds 1.5 km. Prognoses of oil-and-gas content were calculated separately for the layers that are located at the different depths. Maps of graph tightness and total length of lineaments were created for this. These maps were created with use of the sliding windows; the sizes of windows were determined from the requirements of known dependence between the sizes of a window of average value and occurrence depth of the investigated object.

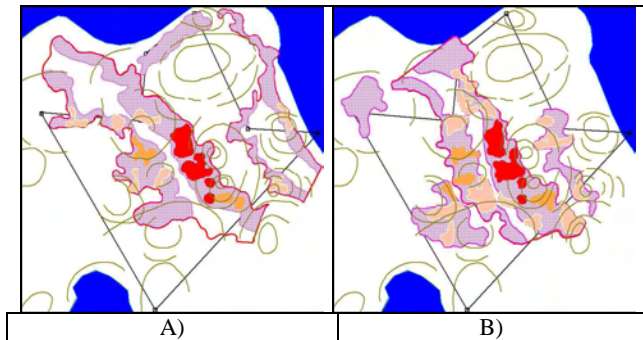
On the drilling data, disposition frequencies of pools non-uniformly are located; they are grouped in two horizons. The pools of overhead horizon are located at depths from 1160 m to 1950 m. The maximal quantities of pools are located on depths about 1750 m. The gas fields for this horizon prevail. The pools of lower horizon are located at depths from 2080 m to 2710 m. The maximal quantities of pools are found on the depth about 2400 m. The petroleum layers are prevailing. Separate maps of pool prognosis were created for different upper and bottom horizons. The sizes of sliding windows were chosen taking into account the depth values of maximal quantity of pools. Data of 23 prospecting holes were used for exploration as objects of teaching.

For creating of maps of the potential of oil-and-gas content the connection of objects of the forecast with meanings of the following features was analyzed:

- 1) Tightness of graph and total length of lineaments for each of 8 lineament systems.
- 2) Remoteness from the axis of maximum of graph tightness and total length of lineaments for all systems.
- 3) Tightness of graph of knots of crossing of lineaments for all systems.
- 4) By the marks of hypsometry of relief; they on the digital model of relief are determined; model is created on the remotely sensed data.

On the result of research were determined all search features which had influence on the location of known pools. All analyzed features not depended from the occurrences depth. They can be used as of the searches features. The prognosis objects avoid both maximal and minimum values. They conform to the intermediate values of features.

Further the probability of connection of objects of the forecast with all complexes of attributes separately for objects of the top and bottom horizons was appreciated and the maps of the forecast of pools for each of horizons are constructed (Fig. 2).



A) Map of potential for horizon 1750 m

B) Map of potential for horizon 2400 m

Figure 2. Potential map of oil-and-gas content for license site in limits of the North-Sakhalin Basin, the scale 1:50000.

Legend:

	Contour of license site		Areas are low potential
	Border of potential areas		Faults are interpretation on the remotely sensed data
	Potential regions		Water surface
	High potential areas		Land surface
	Potential areas		

On the map of potential of pools are 38 percent non-potential areas of upper horizon and 52% of the bottom horizon. The areas, which have not received potential values, occupy 45 % and 34% of the work area. The potential areas occupied 14 % and 11 % for all work areas. Only 3 % of the territory has high potential for both of maps.

The comparative analysis created of map potential showed they have as many distinctions as they have in common. On both maps the areas with increased meanings potential are three strips in direction N-NW. The greatest area of maximum potential value is located in the central part of the exploration territory. It is well visible on maps of potential for lower and upper horizons. Productive wells are located in the limits of this strip. The other two strips occupy fewer areas and are characterized by lower potential values.

Their spatial location well is coordinating with prospective on geologic-geophysical data of pools localization, but that requires check by test drilling.

The 21 local potential areas with the high potential values are located on maps of potential pools within the limits of the selected strips. Potential areas are small; their sizes are from 0.145 to 1.0 sq. km. In most cases, the planned location of the potential areas on the prognosis maps spatially coincides with the upper and bottom horizons.

As a result exploration is recommended to conduct detailed seismic survey and semi-wild-cat well for two potential local areas. Conducting complex of detailed geophysical researches is recommended for the other three areas. The results of this exploration will be determining the potential requirements for drilling a prospecting hole or exploratory well.

For areas with lower potential, the explorations are executed only after results are verified for the best potential areas.

The results of exploration allow asserting that the investigated site is perspective as on detection of new pools within of the known area of research and on discovery of new pools to

west and to east from the researches territory. Drilling confirms the reliability of prognosis research results.

Results of our exploration on the north of Western Siberia and the Yamalo-Nenetskiy Region were tested by drilling. Two prospecting wells were recommended within the limits of two potential areas. Both prospecting wells are producing an efficient oil production rate.

The above mentioned results of works for forecasting pools on the remotely sensed data and estimations of reliability of the received results by test drilling in areas with completely different physics-geographical conditions, geological structures and type of deposits, on our opinion, convincingly testify to an opportunity, reliability and expediency of realization of such researches with use of the offered technique of works.

3. CONCLUSION

Analysis of results of works by the quantitative prognosis estimation of oil-and-gas content, were fulfilled with the use of the developed technology, on territory about 18.000 sq. km. Their result allows doing the following conclusions:

- 1). The offered technology of works allows executing quantitative prognosis estimation of potential of pools for territories with different natural-climatic conditions, geological structure and character of structures. Authenticity of results of prognosis in most cases is confirmed by data of the boring drilling.
- 2). The results of prognosis estimation of oil-and-gas content of territory are appeared in a quantitative form. It allows executing the complex analysis of its data with materials of geologic-geophysical researches and is increasing probability of reliability and efficiency of results of prognosis.
- 3). Prognosis researches are conducted operatively for different territories, regardless of time of year, in the different natural-climatic conditions and in the required scales. Result is shorted time for acceptance of decisions on conducting of the detailed explorations.
- 4). Concentration of works on the most perspective sites, were selecting on the results of quantitative prognosis estimation of oil-and-gas content of territory, allows to shorten financial expenditures and period of conducting of the exploration. For example, prognosis works for license site about 1000 sq. km. on territory of Russia was executed for 7 months, and was shorted the financial expenditures on 2.500.000 USD. Detailed survey for oil-and-gas accumulation for territory about 12.000 sq. km on the Arabian peninsula for 7 months was executed.
- 5) The offered technology of works can be used and for prognosis estimation of potential of territory on the discovery of ore mineral resources.

REFERENCES

- V.I. Lyalko, M.A. Popov. 2006. Multispectral remote sensing in nature management. "Scientific book project". Kiev. p. 360.
- D.M.Trofimov, L.P.Polkanova. 1988 Aerospace of research are fulfill for regional stage of geological survey on an oil and gas. Nedra. Moscow. 160 p. (in Russian).
- E. Barret, L. Kurtis. 1979. Introduction in space physical geography. M. Progress. (in Russian).
- Y.G. Kats, A.V. Tevelev, A.I. Poletaev. Bases of space geology. Nedra. Moscow. 988- 235 p. (in Russian).
- V. I. Kravtsova, E.K. Kozlova, Y.I. Fivenskiy. 1985. Space images (methodical guidance). MGU. Moscow.. (in Russian).

P. Kronberg. 1988. Remote study of Earth. Bases and methods of the remote researches in geology. Mir. Moscow. p. 349. (in Russian).

V.A. Nagorskiy. 1970. Evaluation of sequences of geological objects and features are used how the basis of quantitative prognostication. Edition "Questions of geochemistry, mineralogy, petrology and ore-bearing rock". Naykova dymka. Kiev. p.163-169. (in Russian).

V.A. Nagorskiy, A.V. Netreba, V.S. Tepikin. 2004. The «Kiev-Geoprognoz system» how a new level of spatial-stochastic geologic-geophysical, geochemical and aerospace information for the use for effective prognostication of minerals. Edition "The theoretical and applied aspects of geoinformation" V.1. Kiev. p. 81-89 (in Russian).

V.A Nagorskiy, L.A Prikazchikov, V.V Skvortsov, A.Y. Hodorovsky. 1971. Spatial-probabilistic prognostication. Bases of scientific prognosis of deposits of ore and non-metallic minerals. VSEGEI. Leningrad.. p. 68-69. (in Russian).

V.A. Nevskiy. About some regularity placing of hydrothermal of mineralization in the large breaking and more shallow faults. IGN AS USSR. V.162. 120-129 p. (in Russian).

U.V.Nechaev, E.A. Rogogin. 1991. Analysis of the tectonic fragmentation of seat region of the Spitak`s earthquake.. Report AS USSR. v.320 №6. p. 1441-1445 (in Russian).

Patent 32050 Ukraine. MPK (2006) G01V 9/00, G01V 11/00. The method of prognostication of deposits of minerals. V.I. Lyalko, V.A. Nagorskiy, A.J.Hodorovsky, A.A.Apostolov, A.B.Vostokov. 04. 25. 2008. Bulletin #8 (in Ukrainian).

DEM GENERATION FROM AIRBORNE LIDAR DATA BY AN ADAPTIVE DUAL-DIRECTIONAL SLOPE FILTER

C. K. Wang^a, Y. H. Tseng^{a,*}

^a Dept. of Geomatics, National Cheng Kung University, No. 1, University Road, Tainan, 701, Taiwan - (p6896102, tseng@mail.ncku.edu.tw)

KEY WORDS: LIDAR, DEM, Generation, Classification, Aerial

ABSTRACT:

An airborne LiDAR system is capable of collecting three-dimensional information over a large area effectively. Because of the rapid data collection, DEM generation using airborne LiDAR data has become a standard process since last decade. Filtering out non-ground points from point clouds to obtain terrain relief is the key process for DEM generation from airborne LiDAR data. Many filtering methods have been proposed for this process. Basically they can be categorized into three main approaches: linear regression methods, slope-based methods, and morphology-based methods. Filters apply a certain assumption of smooth terrain, which cause an over-filtering problem in some terracing fields and cliff areas. This paper proposes an adaptive dual-directional filter based on a slope filter to deal with this problem. While the original slope filter is performed according to its whole adjacent covered window, the dual-directional adaptive filter is designed along an alternative direction in one dimension. The main difference between them is the designed filter shapes. The adaptive filters of different directions are complementary to each other, so that over-filtering situation can be avoided. Comparing with original slope-based filter and the commercial software TerraScan, our method shows better results in handling data of abrupt surfaces. The data used for comparison is the ISPRS test data. The variance, omission errors and commission errors are shown for the comparison. Our method has better performance in avoiding over-filtering situation and can keep a good accuracy as the compared methods.

1. INTRODUCTION

The rapid development of Airborne LiDAR system makes the acquisition of three-dimensional surface information more conveniently and directly. Comparing with photogrammetry, LiDAR system has two advantages which are more cost-effective to obtain the vertical information over a large area and fewer pre-processing of data (Meng et al., 2009). Besides, the less limitation of weather and time of a day to enable a LiDAR measurement assignment also makes LiDAR more and more popular in obtaining 3D information (Shan and Sampath, 2005). Many applications have been applied so far, e.g. mapping of corridors, mapping of transmission lines, measurement of coastal areas, rapid mapping and damage assessment after natural disasters, ground surface modelling, object classification (Axelsson, 1999; Wehr and Lohr, 1999) and so on. Among them, DEM generation is the most important application and has become a standard process.

Since the raw data of LiDAR encodes the 3D coordinates already, DEM generation using Airborne LiDAR data can be simplified only by filtering non-ground points out from point clouds. Many methods about filtering have been proposed. Sithole and Vosselman (2004) and Zhang and Whitman (2005) have compared some of these methods. Generally, these methods can be categorized into three main approaches: linear regression methods, slope-based methods, and morphology-based methods (Silván-Cárdenas and Wang, 2006). For linear regression, Kraus and Pfeifer (2001) present two models which are the stochastic model and the functional model to estimate the ground surface. The stochastic model defines a weight

function and the functional model determines the interpolated ground surface. In their research, an approximate ground surface would be estimated and then the residuals between point clouds and the estimated surface can be calculated. The residual of a point would give the point a new weight through stochastic model and then a new approximated surface would be estimated again until a regression stop condition is satisfied. For example, the difference between later and previous estimated ground surface is slight. For slope-based filter, Shan and Sampath (2005) use slope and elevation conditions to determine a point is a ground point or non-ground point. Since the slope value usually would be significantly large between non-ground areas and ground areas, and the elevation of ground surface usually higher than non-ground surface, using the above two conditions, they design a mathematical model to describe the ground surface. For morphology-based filter, it is known that the opening operation would smooth tall objects. For filtering out non-ground objects which are taller than grounds, opening operation is therefore suitable as a DEM filter. However one major problem in using morphology-based filter is the window size of the filter. If a large size of window is chosen, the non-ground objects can be smoothed effectively but an over-smoothed situation will occur in the abrupt surface. For this reason, this paper develops a dual-directional filter to overcome this problem.

* Corresponding author.

2. DUAL DIRECTIONAL SLOPE-BASED FILTER

2.1 Slope-Based Filter

The slope-based filter was firstly proposed by Vosselman (2000). This filter is designed by a kernel function which is composed of two parameters, slope and searching scope (d), expressed in eq. (1).

$$k(\Delta x, \Delta y) = -\Delta h_{\max}(d) = slope \times d \quad (1)$$

Figure 1 shows the diagram of the kernel function and indicates the principle of filtering. The cone-like searching window is determined by the kernel function. To decide a measured point is a ground point or not, the algorithm checks any other points locate under the cone window. If yes, the point will be labelled as a non-ground point, or it is labelled as a ground point.

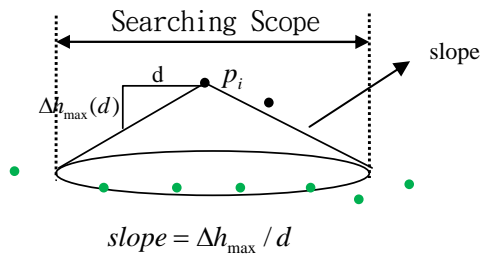


Figure 1. Diagram of a kernel function

It is obvious that the slope threshold should be properly determined based on the terrain type. An adaptive slope-based filter(ASF)(Sithole, 2001; Tseng et al., 2004) is therefore designed to determine the slope threshold before running the slope-based filter.

The adaptive slope-based filter work well either for a flat surface or an oblique surface. However, areas near terracing fields and cliff areas may result in unreliable estimation of slope. Classification errors would occur in this kind of areas. Figure 2 indicates an unwanted filtering situation. Figure 2(a) shows the filtering processing using an adaptive slope-based filter and some points near the break line would be eliminated. This situation is called over-filtering and the missing points will result in a smoother DEM than the true DEM(Figure 2(c)).

2.2 Dual Directional Slope-Based Filter

To overcome over-filtering, a dual-directional adaptive slope-based filter(DDASF) is presented in this paper. The basic idea is to divide original filter into two filters(see Figure 3). If we reconsider the over-filtering problem and perform the two filters, the missing points will be retained in the filtering result by alternative one of the two filters (see Figure 4(b)). The final filtering result can be the union of the two results. In other words, any point which as long as passes one of the two filters will be labelled as a ground point. Since the shape of ASF is symmetric, ASF is non-directional. The filtering results will be the same if we rotate ASF. However DDASF is designed to deal

with along forward and backward, it is called dual-directional in this paper.

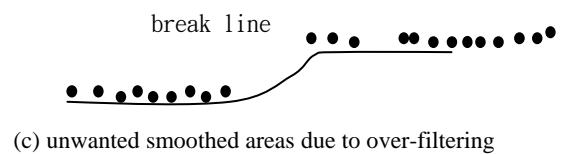
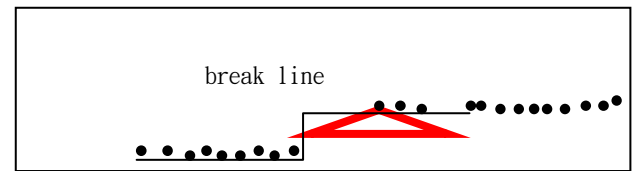
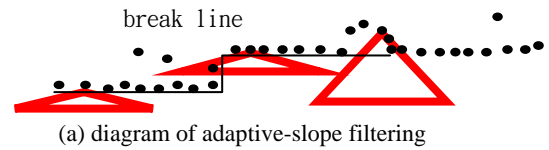


Figure 2. Diagram of over-filtering

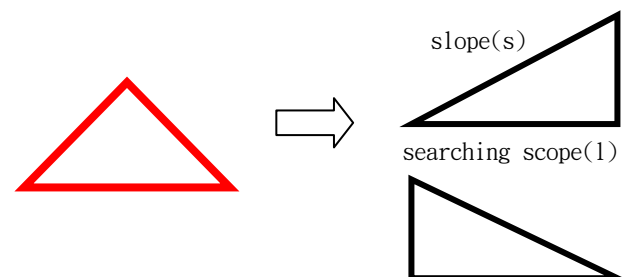


Figure 3. Diagram of dual-directional slope-based filter

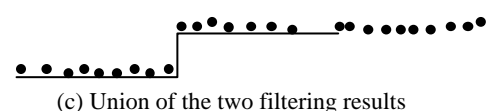
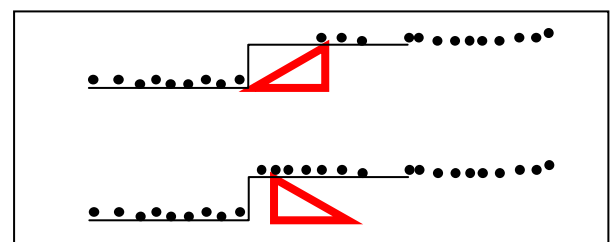
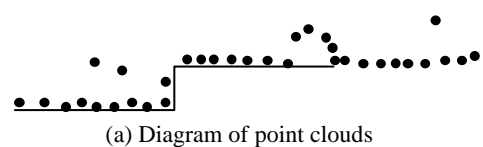


Figure 4. Diagram of DDASF filtering

The shape of DDASF is determined by the two parameters, slope(s) and searching scope(l). The slope can be estimated by adjacent points and the searching scope can be determined by the biggest size of objects in the landscape. If l is not big enough, a tall and big object may remain some non-ground points near the break line which is shown as Figure 5.

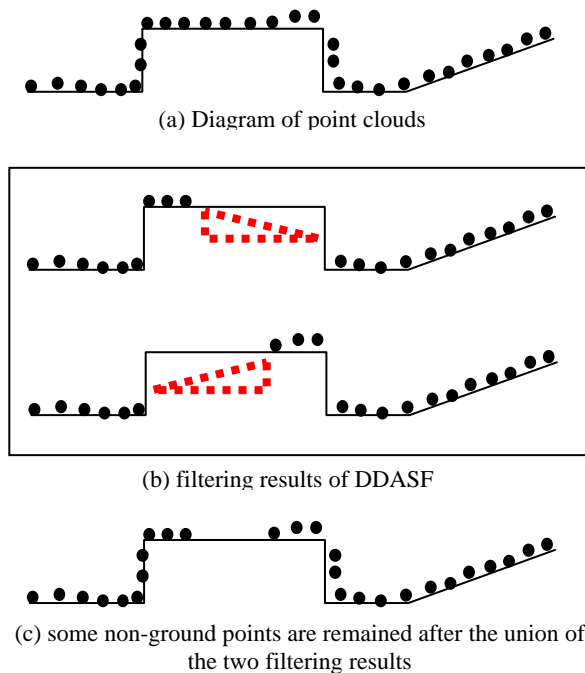


Figure 5. Filtering errors resulted from insufficient searching scope

2.3 Procedure of DEM generation by DDASF

The flow chart of DDASF is shown in Figure 6. Firstly the outliers of LiDAR point cloud are removed. Normally they are extremely higher or lower than adjacent points and isolated from other points. The outliers can be removed from raw LiDAR data using the above conditions, the remaining points are then structured for constructing a spatial relationship between points. Triangle irregular network and regular voxels are both common methods to structure scattered points. In this paper, the regular voxel is used. The complete scattered spatial is divided into voxels of the same size. DX, DZ denote the length and height of a voxel respectively. Since the ground points are normally located on lower voxels, the lowest voxels which contain at least one point are searched. The initial ground surface can be therefore obtained by those points contained in the lowest voxels. Once the initial ground surface is determined, the local plane of a voxel is calculated with its adjacent voxels. The rough filter refers to remove the points which exceed a threshold from the local plane to its position. The remaining points are again filtered by DDASF. And then the procedure iterates until a condition is satisfied. The final output is therefore used to generate DEM.

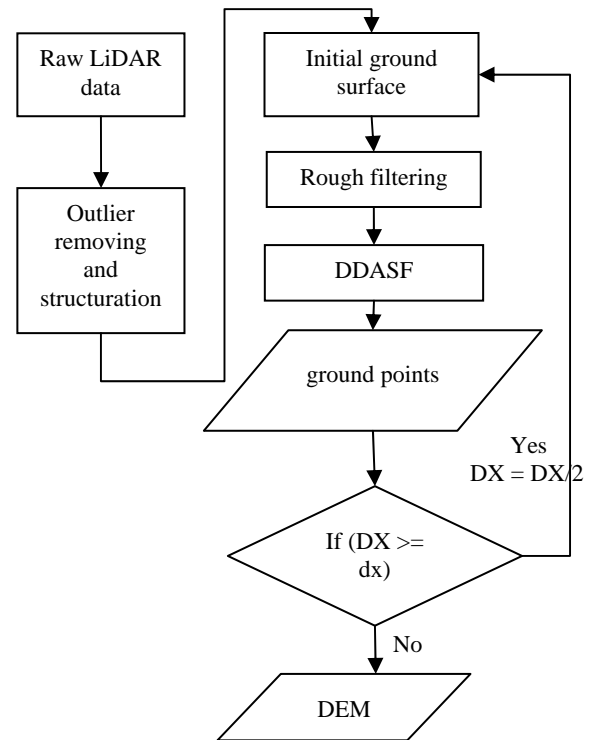


Figure 6. Flow chart of DEM generation by DDASF

3. EXPERIMENTS AND ANALYSES

Three DEM generation methods were compared. One is the adaptive slope-based filter (ASF) developed by Tseng, et al. (2004). The second one is using the commercial software, TerraScan. The last is our developed method. The LiDAR data used in this experiment is provided by ISPRS Commission III (<http://www.itc.nl/isprswgIII-3/filtertest/index.html>). Fifteen samples chosen as reference data are generated by manual filtering. To test the effectiveness of filtering in terracing fields and cliff areas by DDASF, Sample 23 and Sample 53 are chosen because disconnected terrain exists in both data.

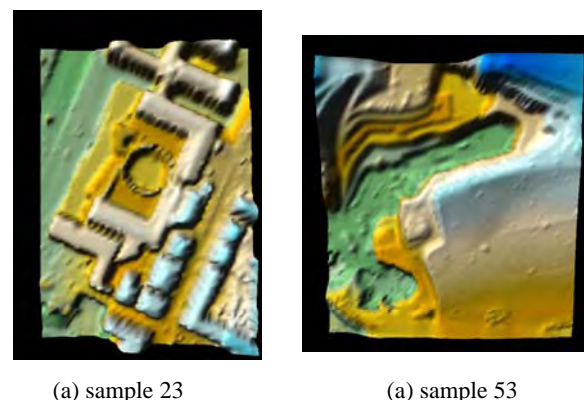


Figure 7. Test data

3.1 Filtering results of Sample 23

Sample 23 is located at urban areas. The buildings are complex, large and some of them are even connected. The lower left of

the landscape shows a disconnected area. Figure 8 (a)~(d) show the reference DEM and the filtered DEM by three filters respectively. We can see that the erosions and smoothness were produced at the disconnected areas which generated by TerraScan and ASF. The disconnected area generated by DDASF is closer to reference DEM.

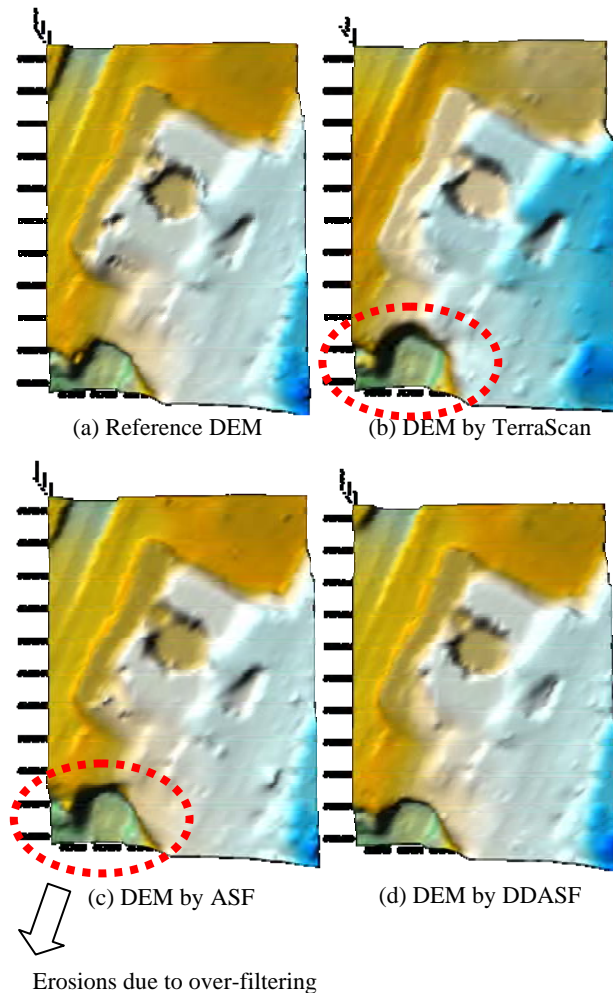


Figure 8. Filtering results of Sample 23 by three different filtering methods.

3.2 Filtering results of Sample 53

Sample 53 is located at suburb areas and contains many features of discontinuity preservation. There are cliffs with large elevation-difference over the lower-right landscape and terraced filed over the upper-left landscape. Figure 9 (a)~(d) show the reference DEM and the filtered DEM by three filters respectively. We can see that there is less difference between the DEMs produced by TerraScan and DDASF while DEM generated by ASF reveals a quite difference at the discontinued areas. This is due to the over-filtering situation. Figure 10 represents the differences between reference DEM and DEMs which generated by the different filtering methods. From Figure 10(b) and (c), DDASF shows an improved result when a directional window is implemented. Generally DDASF can generate the closest DEM over the discontinued areas in this case, since the black (represents larger difference) areas in Figure 10(c) are thinner than others.

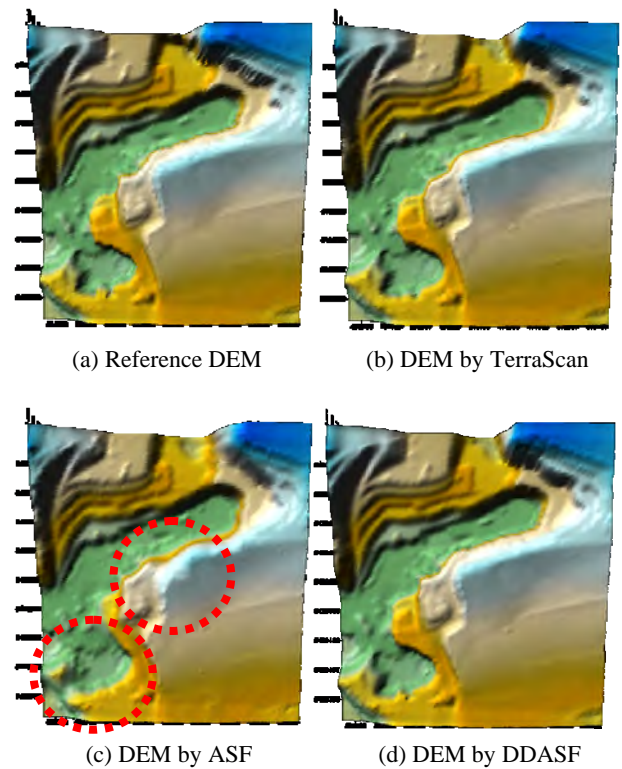


Figure 9. Filtering results of Sample 53 by three different filtering methods.

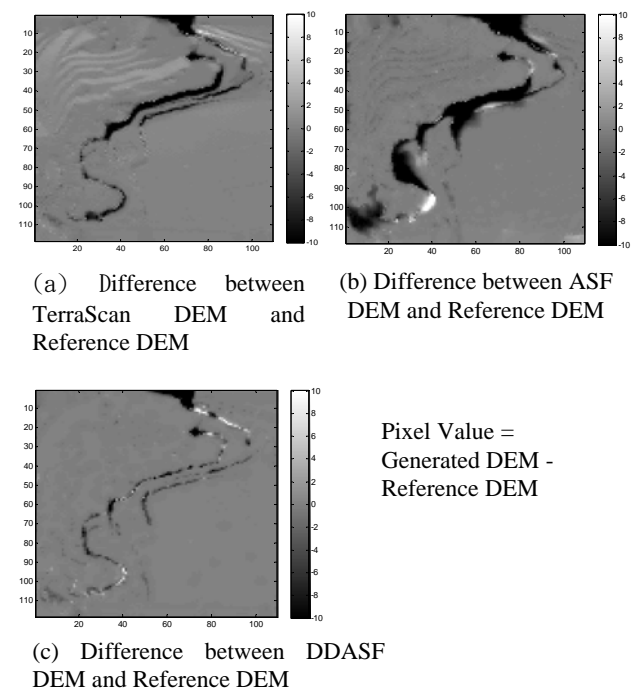
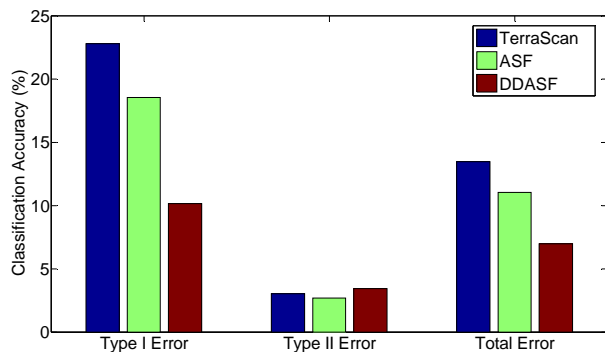


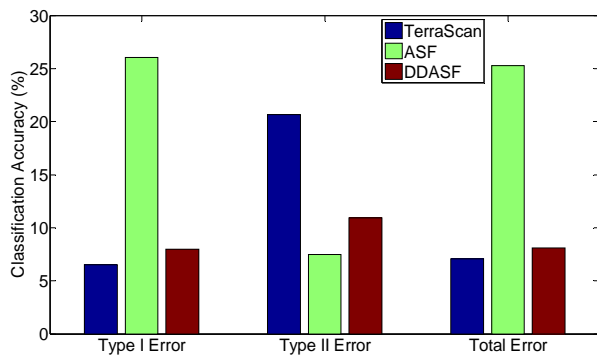
Figure 10. Difference between reference DEM and generated DEM

Besides, the classification accuracy and RMSE are also calculated to evaluate the three methods. It is noticed that a good classification accuracy on a sample does not stand for a well RESM on the corresponding sample, too. For example the total error of Sample 53 produced by TerraScan is minimum

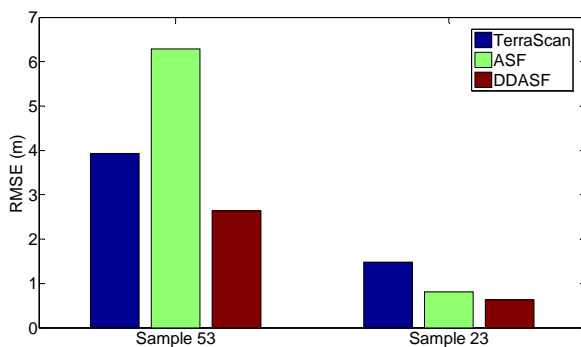
while the RMSE of Sample 53 is worse than DDASF. Generally speaking, DDASF is much stable than the other two methods based on the results of classification accuracy and RMSE.



(a) classification accuracy on Sample 23



(b) classification accuracy on Sample 53



(c) RMSE on Sample 23 and Sample 53

Figure 11. Classification accuracy and RMSE on both data

4. CONCLUSION AND SUGGESTION

This paper proposes a modified slope-based filter, DDASF, with an additional consideration of filter directions. The experimental results show that DDASF can improve the over-filtering situation over the discontinued areas and improve DEM quality over other areas compared with the other two filters. For classification accuracy, DDASF behaves more stably. Since the points near the cliff areas can be retained, both of classification errors and RMSE values decrease. For future

works, a variety of terrain features need to be tested to ensure the reliability of DDASF.

References:

- Axelsson, P., 1999. Processing of laser scanner data--algorithms and applications." *ISPRS Journal of Photogrammetry and Remote Sensing* **54**(2-3), pp. 138-147.
- Kraus, K. and N. Pfeifer, 2001. ADVANCED DTM GENERATION FROM LIDAR DATA. *International Archives of Photogrammetry and Remote Sensing Volume XXXIV-3/W4 Annapolis, MD, 22-24 Oct. 2001*.
- Meng, X., L. Wang, J. L. Silván-Cárdenas and N. Currit, 2009. A multi-directional ground filtering algorithm for airborne LIDAR. *ISPRS Journal of Photogrammetry and Remote Sensing* **64**(1), pp. 117-124.
- Shan, J. and A. Sampath, 2005. Urban DEM Generation from Raw Lidar Data: A Labeling Algorithm and its Performance. *International Journal of Remote Sensing* **71**, pp. 217-222.
- Silván-Cárdenas, J. L. and L. Wang, 2006. A multi-resolution approach for filtering LiDAR altimetry data. *ISPRS Journal of Photogrammetry and Remote Sensing* **61**(1), pp. 11-22.
- Sithole, G., 2001. Filtering of laser altimetry data using a slope adaptive filter. *International Archives of the Photogrammetry, Remote Sensing and Spatial Information Sciences XXXIV - 3/W4*, pp. 203-210.
- Sithole, G. and G. Vosselman, 2004. Experimental comparison of filter algorithms for bare-Earth extraction from airborne laser scanning point clouds. *ISPRS Journal of Photogrammetry and Remote Sensing* **59**(1-2), pp. 85-101.
- Tseng, Y. H., M. Wang and F. C. Chou, 2004. DEM Generation Using 3D Rasterized Airborne LIDAR Data. *Proceedings of ISPRS 20th Congress (Commission III), Istanbul*.
- Vosselman, G., 2000. Slope Based Filtering of Laser Altimetry Data. *International Archives of Photogrammetry and Remote Sensing, Amsterdam*.
- Wehr, A. and U. Lohr, 1999. Airborne laser scanning--an introduction and overview. *ISPRS Journal of Photogrammetry and Remote Sensing* **54**(2-3), pp. 68-82.
- Zhang, K. and D. Whitman, 2005. Comparison of three algorithms for filtering airborne lidar data. *Photogrammetric Engineering and Remote Sensing* **71**(3) pp. 313-324.

SEMI-AUTOMATIC CLASSIFICATION OF TREE SPECIES BY MEANS OF MULTI-TEMPORAL AIRBORNE DIGITAL SENSOR DATA ADS40

L. T. Waser^{a,*}, E. Baltsavias^b, C. Ginzler^a, M. Küchler^a

^a WSL, Landscape Inventories, Swiss Federal Research Institute WSL, 8903 Birmensdorf, Switzerland - (waser, ginzler, kuechler)@wsl.ch

^b Institute of Geodesy and Photogrammetry, ETH Zurich, 8093 Zurich, Switzerland - manos@geod.baug.ethz.ch

Commission VII

KEY WORDS: Forestry, Ecosystem, Classification, Modelling, Aerial, High resolution, Multi-temporal

ABSTRACT:

Temporally frequent, cost-efficient and precise forest information requirements for national forest inventories, monitoring or protection tasks have grown over time and will continue to do so in the future. New perspectives are given by the airborne digital sensor ADS40, which provides entire image strips with high geometric, radiometric and temporal resolution (every three years for entire Switzerland). This study presents an approach for semi-automated tree species classification in different types of forests using multi-temporal ADS40-SH40 and ADS40-SH52 images from May and July 2007 and August 2008 to support tasks of the Swiss National Forest Inventory.

Based on image segments seven different tree species were classified by combined logistic regression models using spectral variables derived from each of the three different ADS40 images. Additional classification was established combining the May and July 2007 imagery. Explanatory variables were derived from each image data set using a step-wise variable selection.

Classifications were five-fold cross-validated for 230 trees that had been visited in field surveys and detected in the ADS40 images. The 7 tree species were therefore classified up to four times providing its spectral variability during the vegetation period. The overall accuracies vary between 0.67 and 0.8 and Cohen's kappa values between 0.6 and 0.69 whereas the classification based on the May 2007 images performed best. Independent from the sensors and acquisition date of the images lowest accuracies were obtained for *Acer sp.* This study reveals the potential and limits of the ADS40 data to classify tree species and underscores the advantage of a multi-temporal classification of deciduous tree species with spectral similarities.

1. INTRODUCTION

1.1 General Instructions

New methods for the extraction of forest attributes from airborne remote sensing data have grown over time and will continue to do so in the future since exact information on forest composition is needed for many environmental, monitoring or protection tasks. The present study focuses on the classification of tree species using multi-temporal ADS40 imagery and was carried out in the framework of the Swiss National Forest Inventory (NFI) (Brassel and Lischke, 2001; Brändli, 2010). Tree species classification is highly correlated to a large number of other forestry attributes (e.g. composition, biomass, volume, tree damage etc.) and is an essential index in forest studies, inventories, management and other forest applications. Several studies have integrated multisensoral data to perform tree species classification which lead to better accuracies than using only a single data input (St-Onge et al., 2004; Hirschmugl et al., 2007; Waser et al., 2008b, Waser et al., 2010) or LiDAR (Heinzel et al., 2008; Holmgren et al., 2008; Chubey et al., 2009). A few studies have incorporated multi-temporal data (Key et al. 2001)

According to Guisan et al. (2004) modern regression approaches such as generalized linear models (GLMs) have proven particularly useful for modelling the spatial distribution of plant species and communities. Küchler et al. (2004) show that spatially explicit predictive modelling of vegetation using remotely sensed data can be used to construct current

vegetation cover using information on the relations between current vegetation structure and various environmental attributes. Thus, logistic regression models seem also promising for modelling tree species when analyzing the relationship between categorical dependent variables (e.g. tree species) and explanatory variables derived from remotely sensed data (Waser et al., 2008a and 2008b).

The objective of this study was to classify semi-automatically three deciduous and four coniferous tree species. The contribution of three multi-temporal ADS40 images was tested and best image combination for tree species classification was assessed. Preliminary results are very promising for future monitoring, updating and management tasks of a continuous Swiss National Forest Inventory (NFI).

2. MATERIAL

2.1 Study area

The study area is characterized by open and closed mixed forests and is located in the Swiss central Plateau (approx. 47°22' N / 8°28' E) and has an extent of approx. 7.5 km². The altitude ranges from 450 m to 850 m a.s.l. The forest area covers approx. 5.1 km², and is mostly characterized by mixed forest. The dominating deciduous tree species are *Fagus sylvatica* and *Fraxinus excelsior* and less frequently *Acer sp.* The main coniferous trees are *Abies alba*, *Larix decidua*, *Picea abies* and *Pinus sylvestris*.

* Corresponding author

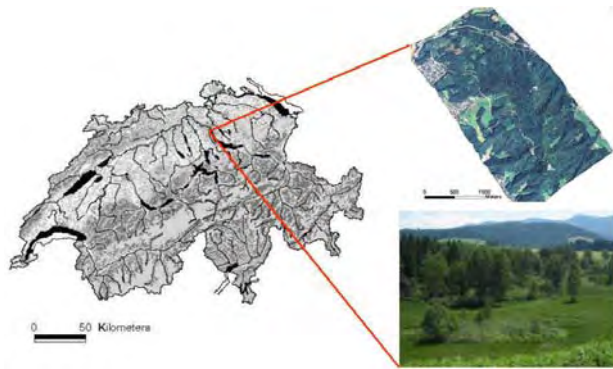


Figure 1. Study area. © SWISSTOPO.

2.2 Ground truth

The ground truth data to validate the tree species classifications was collected in the natural environment to be representative. Two ground surveys were carried out in summer 2008 and 2009 focusing on the most frequent tree species (at least 10% coverage in Switzerland) which were also visible in the aerial images. For a total of 230 sampled trees we recorded the species (table 1) and delineated in the field the crowns of all visited trees on the corresponding aerial images. This information was used as reference to digitize the corresponding tree crowns on the ADS40 RGB images.

Scientific tree species name (common tree species name)	Num. of samples	Species prop.
<i>Acer sp.</i> (maple)	28	< 10%
<i>Fagus sylvatica</i> (beech)	42	20%
<i>Fraxinus excelsior</i> (ash)	32	15%
<i>Abies alba</i> (white fir)	28	15%
<i>Larix decidua</i> (larch)	20	<10%
<i>Picea abies</i> (Norway spruce)	56	25%
<i>Pinus sylvestris</i> (Scots pine)	24	<10%

Table 1. Tree species sampled with number of samples. Species proportion is based on estimates by an expert during the field surveys

2.3 Remotely sensed data

2.3.1 Airborne Digital Sensor Data (ADS40): First generation ADS40-SH40 and second generation ADS40-SH52 images Level 1 (Leica Geosystems AG, Switzerland) were used in this study (for further details on the sensor see e.g. Reulke et al. (2006). The main drawback of the first-generation ADS40-SH40 is that the NIR line CCD is placed 18° forward from the nadir RGB CCDs which makes it difficult to combine all four lines. The second generation ADS40-SH52 provides the NIR band in the same nadir position as the RGB bands. Three Digital Surface Models (DSMs) were generated automatically from the above images with a spatial resolution of 0.5 m using modified strategies of NGATE of SOCET SET 5.4.1 (BAE Systems). Prior to the DSM generation, a Wallis filter was applied to enhance contrast, especially in shadow regions, and to equalize radiometrically the images for matching.

Sensor	ADS40-SH40	ADS40-SH52
Acquisition date	24/05/2007 &	18/08/2008

	13/07/2007	
Focal length	62.8 mm	62.8 mm
Spectral resolution (nm)	Red: 610-660 Green: 535-585 Blue: 430-490	Red: 608-662 Green: 533-587 Blue: 428-492 NIR: 833-887
Ground pixel size	~25 cm	~25 cm
Orthoimage resolution	25 cm	25 cm
Radiometric resolution	11 bit	11 bit

Table 2. Summary of characteristics of the image data used

2.3.2 LiDAR: National LiDAR digital terrain data (DTM) produced by the Swiss Federal Office of Topography (SWISSTOPO) for the study area (acquisition date: March 2002, reflight March 2003 leaves-off) were used. The data were acquired by Swissphoto AG / TerraPoint using a TerraPoint ALTMS 2536 system with an average flying height above ground of 1200 m. The DTM has an average point density of 0.8 points / m² height accuracy (1 sigma) of 0.5 m (Artuso et al., 2003) and was interpolated to a regular grid with 0.25 m.

3. METHODS

3.1 Variables derived from ADS40 imagery

To extract tree area and classify tree species, several variables (geometric and spectral signatures) were derived from the remote sensing data using standard digital image processing methods as described in e.g. Gonzales and Woods (2002). Details about extraction of geometric and spectral explanatory variables derived from airborne remote sensing data are described in Waser et al. (2007, 2008a and 2008b). A good fit to the given (training) data is not a sufficient condition for good predictive models. To obtain good predictions, a small set of powerful variables has to be selected.

Therefore stepwise variable selection (AIC, both directions, Akaike, 1973) was applied using the defaults of R version 2.9.1. A separate stepwise selection was performed for each tree species. The variables were ranked according to their contribution to the model.

The input variables used in this study consist of four commonly used geometric parameters derived from the CHMs (slope, curvature, and two local neighborhood functions). For further details, see Burrough (1986) and Moore et al. (1991). Spectral variables were derived from each of the three images. This includes for each set of variables the mean and standard deviations of: 3 x 3 original bands of ADS40-SH40 RGB and ADS40-SH52 RGB and CIR images and the colour transformation from RGB and CIR (only from the 2008 images) to IHS into the 3 channels intensity (I), hue (H), and saturation (S).

3.2 Image segmentation

Homogenous image segments of individual tree crowns or tree-clusters are needed to classify tree species (see below). Both the ADS40-SH40 and /ADS40-SH52 orthoimages were therefore subdivided into patches by a multi-resolution segmentation using the Definiens 7.0 software (Baatz & Schäpe, 2000). Segmentation was iteratively optimized using several levels of detail and adapted to shape and compactness parameters. The final segmentation provided groups of trees and individual trees

with similar shapes and spectral properties. Finally, the means and standard deviations of the geometric and spectral variables were calculated for each segment.

3.3 Tree cover

The extraction of the area covered by trees is required for the area-wide mapping of the classified tree species. Tree cover and non-tree area masks were generated as described in detail in Waser et al. (2008). Briefly summarized: First, digital canopy height models (CHM) were produced subtracting the LiDAR DTM from the three DSMs. In a second step, pixels with CHM values ≥ 3 m were used to extract potential tree areas according to the definition in the Swiss NFI (Brassel and Lischke, 2001). In a third step, non-tree objects, e.g. buildings, rocks, and artifacts were removed using spectral information from the ADS40-SH40 and ADS40-SH52 RGB images (low IHS pixel values) as well as information (curvature) about the image segments (e.g. segments on buildings have lower curvature values and ranges than trees or large shrubs). These four steps resulted in three canopy covers providing sunlit tree area for each study area.

3.4 Classification of tree species

3.4.1 Evaluation of modelling procedures: Image segments representing single trees were to be assigned to classes (species) by predictive modelling. The classes were given by a field sample from the 7 dominant tree species of the study area as described in section 2.2. As the response variable has more than two possible states, a multinomial model had to be applied. The logistic regression model is a special case of the generalized linear model (GLM) and described in e.g. McCullagh and Nelder (1983). Combination of logistic models was implemented by fitting a binomial logistic regression model to each class (species) separately and assigning the respective segment to the species with the highest probability. For details on the logistic regression function with quadratic terms see e.g. Hosmer and Lemeshow (2000). The explanatory variables as given in section 3.1 were used.

In a first run, a single classification was performed using each set of variables separately. Then the explanatory variables from both the 2007 May and July images were tested together within a logistic regression model since the same flight path was used and the shadows were quite similar. Due to large differences in the flight paths and shadows between 2007 and 2008 the 2008 data had to be used separately in a separate logistic regression model (see Fig. 2). In total, tree species were classified four times using different logistic regression models and input imagery (see also table 3).

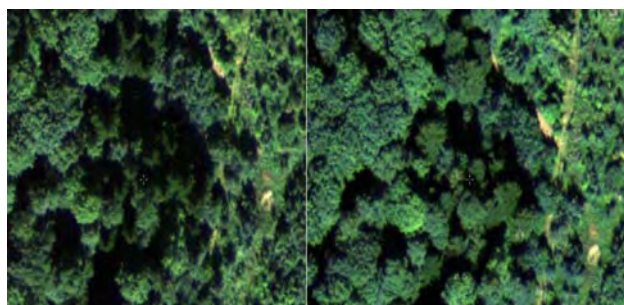


Figure 2. Example of the same area of trees acquired by different flight paths between 2008 August (left) and 2007 July (right) images.

3.4.2 Validation: In order to validate the predictions of tree species, the digitized reference tree data (see section 2.2) had to be assigned to the corresponding image segments. Since the delineations of the field samples were not always congruent with the automatically generated image segments each of the 230 digitized reference trees was assigned to an image segment using the following rule: If one segment contained more than one digitized field sample, the segment was assigned to the field sample covering the greater part of the segment. If less than 10% of the image segment was covered by the sample polygon, the segment was not assigned at all. The predictive power of the models was verified by a 5-fold cross-validation. The statistical measures used to validate the results were: producer's (PA)- and user's accuracy (UA), correct classification rate (CCR), and kappa coefficient (K).

4. RESULTS

4.1 Confusion matrices

The classification of the seven tree species was achieved semi-automatically and, depending on the image data used, quite high accuracies were obtained. The overall accuracies for tree species classification obtained by the different input imagery are summarized in table 3. The confusion matrices of the May, July and August classifications with best CCR and K are summarized in Tables 4 - 6. The classified main tree species are: *Abies alba* (Aa), *Picea abies* (Pa), *Pinus sylvestris* (Ps), *Larix decidua* (La), *Acer sp.* (Ac), *Fagus sylvatica* (Fs), and *Fraxinus excelsior* (Fe).

Input data sets	CCR	K
05-2007	0.798	0.691
07-2007	0.668	0.598
05 and 07-2007 combined	0.691	0.632
08-2008	0.757	0.667

Table 3. Overall accuracies for four different tree species classifications.

Table 4 shows that five of seven tree species are classified with accuracies $> 73\%$ when using the May 2007 images. Best agreements are obtained for *Picea abies* (92%) and *Fagus sylvatica* (86%). The most frequent failures happen in classifying the non-dominant tree species *Acer sp.* (43%), and *Larix decidua* (56%) which are often misclassified either as *Fagus sylvatica* or *Picea abies*.

May 2007 Field	Classified as							PA
	Aa	Pa	Ps	La	Ac	Fs	Fe	
Aa	29	2	--	--	--	--	4	0.83
Pa	--	77	--	2	2	2	1	0.92
Ps	--	--	14	--	--	--	--	0.76
La	--	12	1	10	--	--	--	0.43
Ac	1	2	--	--	19	9	3	0.56
Fs	1	3	--	--	3	55	2	0.86
Fe	3	4	--	--	2	2	54	0.83
UA	0.85	0.76	0.93	0.67	0.73	0.81	0.84	

Table 4. Confusion matrix for tree species classification using the explanatory variables from May 2007 ADS40-SH40

imagery with the producer's- and user's accuracy of the classified tree species.

Table 5 shows that best agreements for the classification based on the summer 2007 images are obtained for *Picea abies* (89%) and *Larix decidua* (78%). The confusion matrix clearly reveals that especially deciduous trees are misclassified. But also *Pinus sylvestris* is confused with *Picea abies*. *Acer sp.* and *Fraxinus excelsior* are generally overestimated.

July 2007		Classified as						
Field								
	Aa	Pa	Ps	La	Ac	Fs	Fe	PA
Aa	28	5	0	0	1	6	4	0.64
Pa	2	68	2	3	1	0	0	0.89
Ps	0	5	12	1	2	1	0	0.57
La	0	4	0	14	0	0	0	0.78
Ac	1	0	0	0	19	10	12	0.45
Fs	6	4	0	1	11	54	15	0.59
Fe	4	1	0	0	5	8	38	0.67
UA	0.68	0.78	0.86	0.74	0.49	0.68	0.54	

Table 5. Confusion matrix for tree species classification using the explanatory variables from July 2007 ADS40-SH40 imagery with the producer's- and user's accuracy of the classified tree species.

Table 6 shows that five of seven tree species are classified with accuracies > 74% when using the Summer 2008 images including the NIR band.

The obtained accuracy for *Acer sp.* remains very low because it is often misclassified as *Fagus sylvatica* and *Fraxinus excelsior*.

August 2008		Classified as						
Field								
	Aa	Pa	Ps	La	Ac	Fs	Fe	PA
Aa	29	3	1	0	0	1	2	0.81
Pa	2	78	2	5	0	2	2	0.86
Ps	0	7	16	0	0	1	0	0.67
La	0	4	0	23	0	0	2	0.79
Ac	0	1	0	0	12	14	8	0.34
Fs	2	1	0	1	7	64	11	0.74
Fe	3	0	0	0	8	8	84	0.82
UA	0.81	0.83	0.84	0.79	0.44	0.71	0.77	

Table 6. Confusion matrix for tree species classification using the explanatory variables from August 2008 ADS40-SH52 images with the producer's- and user's accuracy of the classified tree species.

4.2 Predictive mapping

The tree species which have been modelled with > 90 % probability in the 2007 and 2008 images are depicted in Fig. 3. At first glance, a visual image analysis suggests that the agreements in most parts of the site are good. However, a more detailed image inspection confirms the results of tables 4-6 and indicates that *Acer sp.* is often misclassified as *Fagus sylvatica* or *Fraxinus excelsior* - independently from the acquisition date of the images. Fig. 3 also shows that the predictions of the tree species slightly vary in each of the maps. The underestimation of *Larix decidua* is clearly visible in the May images whereas the overestimations of *Fraxinus excelsior* and *Fagus sylvatica* are clearly visible in the July 2007 images.

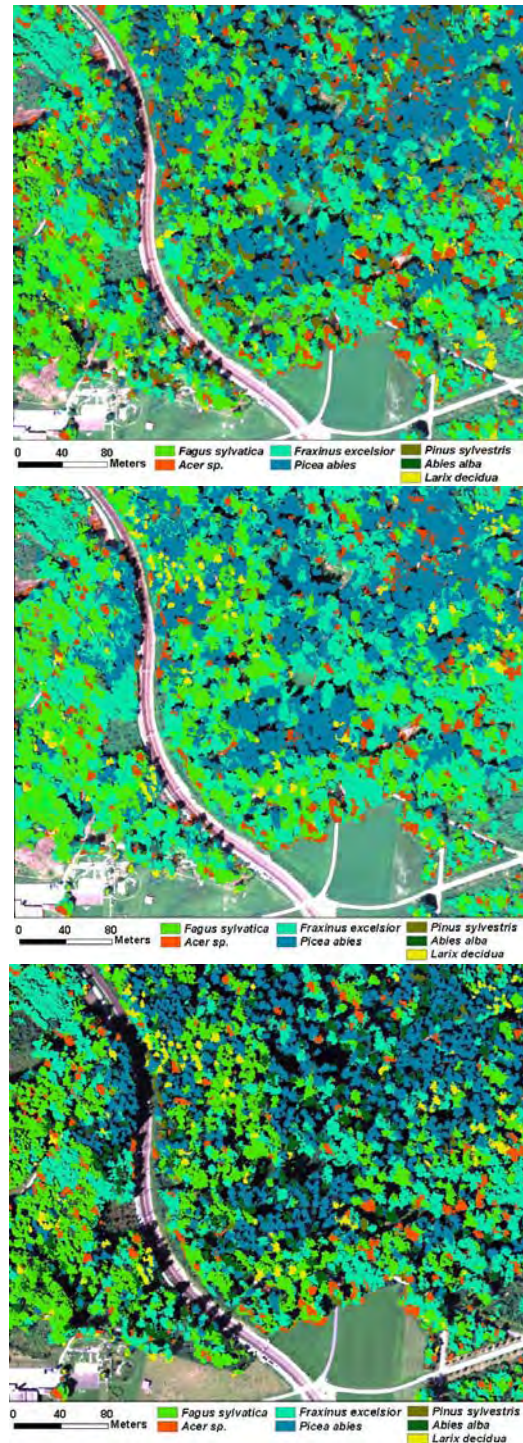


Figure 3. Tree species classification maps based on imagery from May 2007 (top), July 2007 (middle) and August 2008 (bottom) with the largest shadows.

5. DISCUSSION

The potential and the limits of classifying seven tree species has been tested using multi-temporal multispectral ADS40 imagery. The most significant achievement is the demonstration that spring ADS40 imagery as input for the classification of tree species is superior to the summer imagery – even without the additional information of the NIR band. Summer imagery from

the second generation ADS40-SH52 (including the NIR band) is superior to the summer RGB images of the first generation ADS40-SH40.

The study shows that logistic regression models proved to have a high potential to produce meaningful tree species classifications with a minimum amount of effort involved in image acquisition, data pre-processing, derivation of explanatory variables and field work. Some limitations of this approach are briefly discussed below.

5.1 Ground truth

The tree samples were delineated in the field on aerial images, which means that well visible trees may have been preferred, or only the lighted parts of trees have been delineated. Additionally, trees may be shaded or partly hidden by others so that one image segment could contain more than one species. However, when comparing correct classification rates or kappa values to other studies, we emphasize that this is a qualitative approach. For the same reasons the model results were checked for plausibility by visual examination of the aerial photographs. These uncertainties render the statistical evaluations relative.

5.2 Comparison with other studies

Overall, the species accuracies obtained in this study are in the line or higher with those in similar studies.

Our best result (spring 2007 data) with an overall accuracy of nearly 80% for seven tree species is higher to those obtained in other studies. Overall accuracies between 75% (based on CIR aerial images, Brandtberg, 2002) and 89% (based on DMC camera, Olofsson et al., 2006) are obtained in most studies to classify Norway spruce, Scots pine, birch or aspen

Obviously, classification accuracies are lower the more tree species there are and if non-dominant tree species are included as well. Chubey et al. (2009) classified 4-6 coniferous and 4-6 deciduous species in Canadian forests with an overall accuracy around 70%.

5.3 Multispectral versus multi-temporal

Although we found that our approach produces in general good results and is suitable a more detailed analysis of the misclassifications is needed. The full potential of a multi-temporal approach could not be realized in this study. Due to differences in the flight paths and different acquisition daytimes (different shadows) between the 2007 and 2008 images a classification based on all three datasets could not be established. The 2008 data was therefore used separately.

Although multi-temporal multispectral data is known as valuable (e.g. Key et al., 2001), in the present study combinations of the two images of May and July 2007 tended to give lower accuracies. For the classification of *Larix decidua* and *Picea abies*, the single usage of multispectral information obtained by the August 2008 imagery was more valuable than multi-temporal information of the May and July 2007 imagery. The reason for this might be the additional usage of the NIR information provided by the ADS40-SH52 2008 images.

Problems for classifying deciduous tree species are increasing when using summer imagery. Visual analysis of the spectral ranges of each species moreover revealed very similar spectral properties between the summer 2007 and 2008 images for *Fagus sylvatica* and *Fraxinus excelsior*. Even within species, spectral variability can be large because of illumination and

view-angle conditions, openness of trees, natural variability, age of the trees, shadowing effects and differences in crown health. Fig. 4 illustrates this situation.

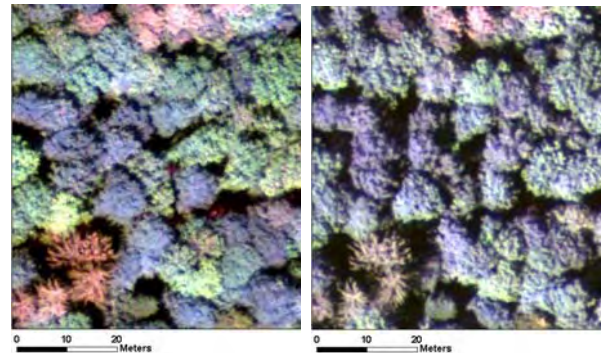


Figure 4. Examples of the deciduous tree species *Fagus sylvatica* (blue-grey), *Fraxinus excelsior* (light green) and *Acer sp.* (green-blue) as they appear in the May 2007 images (left) and July 2007 images (right).

5.4 Non-dominant tree species

Generally, a relatively small sample size of non-dominant tree species - compared to the other species in a study area - leads to underestimation of these species. Tables 4 - 6 clearly reveal that most frequent failures happen in classifying the non-dominant tree species *Acer sp.* Visual image inspection showed that *Acer sp.* are often short and therefore partly obscured by nearby large and dominant trees, or by the merging of close crowns. The two other non-dominant (coniferous) tree species *Larix decidua* and *Pinus sylvestris* in this study are classified with higher accuracies.

6. OUTLOOK

The promising results and experiences made in this study are of great practical interest for the Swiss National Forest Inventory. Actual and accurate maps of tree species and composition are needed by environmental agencies and land surveying offices to assess possible changes in species distribution or condition of other habitat.

The most obvious opportunities for follow up are: The usage of NFI field sample plots as training data to reduce field work. Further development is needed for testing larger areas, which may consist of several image strips. BRDF-related problems or influences of the BRDF in terms of classification accuracy should also be investigated.

7. REFERENCES

- Akaike, H., 1973. Information theory as an extension of the maximum likelihood principle. In: Petrov, B.N., Csaki, F. (eds.), *Second International Symposium on Information Theory*. Akademiai Kiado, Budapest, Hungary, pp. 267-281.
- Artuso, R., Bovet, S., and Streilein, A., 2003. Practical Methods for the Verification of countrywide Terrain and Surface Models, In: *International Archives of Photogrammetry and Remote Sensing*, vol. XXXIV-3/W13

- Baatz, M., and Schäpe, A., 2000. Multiresolution Segmentation – an optimization approach for high quality multi-scale image segmentation. In J. Strobl, T. Blaschke and G. Griesebner (eds.), *Angewandte Geographische Informationsverarbeitung Vol. XII* (pp. 12-23). Heidelberg, Germany: Wichmann
- Burrough, P.A., 1986. *Principles of Geographical Information Systems for Land Resources Assessment*. New York: Oxford University Press, 50 p.
- Brändli, U.-B., 2010. Schweizerisches Landesforstinventar. Ergebnisse der dritten Erhebung 2004-2006. Birmensdorf, Eidgenössische Forschungsanstalt für Wald, Schnee und Landschaft WSL, Bern, Bundesamt für Umwelt, BAFU. 312 p.
- Brandtberg, T., 2002. Individual tree-based species classification in high spatial resolution aerial images of forests using fuzzy sets. *Fuzzy Sets and Systems*, 132, pp. 371-387.
- Brassel, P. and Lischke, H., 2001. *Swiss National Forest Inventory: methods and models of the second assessment*. Birmensdorf, Swiss Federal Research Institute WSL, 336 p.
- Chubey, M., Stehle, K., Albricht, R., Gougeon, F., Leckie, D., Gray, S., Woods, M., and Courville, P., 2009). Semi-Automated Species Classification in Ontario Great Lakes - St. Lawrence Forest Conditions. Final Report: Great Lakes - St. Lawrence ITC Project (2005/2008). Ontario Ministry of Natural Resources. January 2009. 71 p.
- Gonzales, R.C., & Woods, R.E., 2002. *Digital image processing*. Second edition. New Jersey: Upper Saddle River.
- Guisan, A., Weiss, S.B., and Weiss, A.D., 2004). GLM versus CCA spatial modeling of plant species distribution. *Plant Ecology* 143(1), pp. 107-122.
- Heinzel, J.N., Weinacker, H., and Koch, B., 2008. Full automatic detection of tree species based on delineated single tree crowns – a data fusion approach for airborne laser scanning data and aerial photographs, *Proceedings of the SilviLaser 8th international conference on LiDAR applications in forest assessment and inventory*, (pp. 76-85), September 18-19, 2008, Edinburgh, UK.
- Hirschmugl, M., Ofner, M., Raggam, J., and Schardt, M., 2007. Single tree detection in very high-resolution remote sensing data. *Remote Sensing of Environment*, 110, pp. 533-544.
- Holmgren, J., Persson, Å., and Söderman, U., 2008. Species identification of individual trees by combining high resolution LiDAR data with multi-spectral images. *International Journal of Remote Sensing*, 29, pp. 1537-1552.
- Hosmer, D.W., and Lemeshow, S., 2000. *Applied logistic regression, 2nd edition*, New York: Wiley, 373 p.
- Key, T., McGra, J.B., and Fajvan, M.A., 2001. A comparison of multispectral and multitemporal information in high spatial resolution imagery for classification of individual tree species in a temperate hardwood forest. *Remote Sensing of Environment*, 75, pp. 100-112.
- Küchler, M., Ecker, K., Feldmeyer-Christe, E., Graf, U., Küchler, H., & Waser, L.T., 2004. Combining remotely sensed spectral data and digital surface models for fine-scale modelling of mire ecosystems. *Community Ecology*, 5(1), pp. 55-68.
- McCullagh, P., and Nelder, J.A., 1983. *Generalized linear models*. London: Chapman and Hall, 511 p.
- Moore, I. D., Grayson, R. B., and Landson, A. R., 1991. Digital Terrain Modelling: a Review of Hydrological, Geomorphological, and Biological Applications. *Hydrological Processes*. Vol. 5, pp. 3-30.
- Olofsson, K., Wallermann, J., Holmgren, J., and Olsson, H., 2006. Tree species discrimination using Z/I DMC imagery and template matching of single trees. *Scandinavian Journal of Forest Research*, 21, pp. 106-110.
- Reulke, R., Becker, S., Haala, N., and Tempelmann, U., 2006. Determination and improvement of spatial resolution of the CCD-line-scanner system ADS40. *ISPRS Journal of Photogrammetry & Remote Sensing*, 60, pp. 81-90.
- Scott, J.M., Heglund, P.J., Samson, F., Haufler, J., Morrison, M., and Wall, B., 2002. *Predicted species occurrences: issues of accuracy and scale*, Island Press, Covelo, California, 868 p.
- St-Onge, B., Jumelet, J., Cobello, M., and Vega, C., 2004. Measuring individual tree height using a combination of stereophotogrammetry and lidar. *Canadian Journal of Forest Research*, 34(10), pp. 2122-2130.
- Waser, L.T., Küchler, M., Ecker, K., Schwarz, M., Ivits, E., Stofer, S., and Scheidegger, C. (2007). Prediction of Lichen Diversity in an Unesco Biosphere Reserve - Correlation of high Resolution Remote Sensing Data with Field Samples. *Environmental Modeling & Assessment*, 12(4), pp. 315-328
- Waser, L.T., Baltasvias, E., Ecker, K., Eisenbeiss, H., Ginzler, C., Küchler, M., Thee, P., and Zhang, L. (2008a). High-resolution digital surface models (DSM) for modelling fractional shrub/tree cover in a mire environment. *International Journal of Remote Sensing*, 29(5), pp. 1261 – 1276
- Waser, L.T., Ginzler, C., Kuechler, M., and Baltasvias, E. (2008b). Potential and limits of extraction of forest attributes by fusion of medium point density LiDAR data with ADS40 and RC30 images. *Proceedings of the SilviLaser 8th international conference on LiDAR applications in forest assessment and inventory*, September 18-19, 2008, Edinburgh, U, pp. 625-634.
- Waser, L.T., Klonus, S., Ehlers, M., Küchler, M., and Jung, A., 2010. Potential of Digital Sensors for Land Cover and Tree Species Classifications - A Case Study in the Framework of the DGPF-Project. *Photogrammetrie, Fernerkundung und Geo-information*, Vol. 10 (2), pp. 132- 141.

8. ACKNOWLEDGEMENTS

The study was carried out within the framework of the Swiss National Forest Inventory (NFI) and funded by the Swiss Federal Office for the Environment (FOEN) and WSL. We are grateful to Patrick Thee for his valuable help in the field surveys.

FUSION OF ALS POINT CLOUD DATA WITH HIGH PRECISION SURVEYING DATA

A. Wehr^{a,*}, H. Duzelovic^b, Ch. Punz^b

^a Institute of Navigation, University of Stuttgart, Breitscheidstr. 2, 70174 Stuttgart, Germany –
wehr@nav.uni-stuttgart.de

^b rmDATA, Datenverarbeitungs GmbH, Prinz Eugen-Straße 12, A-7400 Oberwart, Austria –
(duzelovic, punz)@rmdata.at

KEY WORDS: LIDAR, Fusion, Modelling, Algorithms, DEM/DTM, Multisensor

ABSTRACT:

In today airborne laser scanning (ALS) extended areas are surveyed with a high point density and with decimetre elevation accuracy in a very short time. However, due to the finite sampling process the correct modelling of the surveyed earth surface is difficult, if break lines and special topographic features like railway tracks and highways are to be modelled. To improve the ALS derived models more and more additional surveying data are used which are measured by e.g. GNSS or tacheometers. These measurements have higher accuracy and are sampled in a way that they describe best the features to be modelled. For example break lines are described by splines derived from a tacheometric survey. As these supplement data are provided from independent sensors in their own coordinate system, all data sets to be fused have to be transformed so that the most accurate model can be computed. This means the algorithms must regard data property of the different data sets. In addition the most accurate and precise data set has to be used as reference. In this paper algorithms for the fusion of ALS data and additional surveying data obtained from tacheometric and DGNSS measurements are presented and discussed based on results of empirical computations on different data sets. The additional surveying data consists either of single point measurements or profiles. The presented algorithms are developed under the objective to use primarily existing functionalities of a commercial program

1. INTRODUCTION

Today airborne laser scanning (ALS) makes possible surveying the topography of extended areas with high point density and with decimetre elevation accuracy in a very short time. For example the ALTM Gemini of the Optech company achieves a swath width of 1865 m flying at an altitude of 2000 m and sampling data with a point density of about 1.5 m realizing the mentioned accuracy. Although this advanced technology revolutionized the surveying with regard to the amount of data and elevation accuracy, there is still a deficiency in precise modelling special topographical features, e.g. break lines, highways, railway tracks etc. due to the sampling process. However, very often these special topographical elements are surveyed by distinct surveying means like GNSS and tacheometric measurements, which reach accuracy down to millimetres. Therefore, it is obvious to combine these complementary measurements for an advanced modelling. In addition, it must be regarded that more and more the modelling process using ALS data is supported by using information of geoinformation systems (GIS). Following the trends in generating precise Digital Terrain Models (DTMs) out of ALS data makes clear that all available additional information is integrated into the modelling process to speed up, to improve the robustness of calculations and to increase the precision. This paper deals only with the integration of supporting surveying measurements obtained by conventional means e.g. GNSS real time kinematic and tacheometric measurements. These measurements exhibit in general a much lower point density but offer a point accuracy which is an order of magnitude better compared to ALS data.

Working with commercial software which derives a DTM out off ALS point clouds one very often faces the problem that certain structures e.g. break lines or sharp corners etc. are not correctly modelled. This problem becomes very obvious, if the surveyed surface is modelled by a Triangulated Irregular Network (TIN) and the TIN is not modelled accurately to shape of the surface. This is especially the case if an unsupervised Delauney Triangulation is applied. A typical example concerning this case is shown in Figure 1.

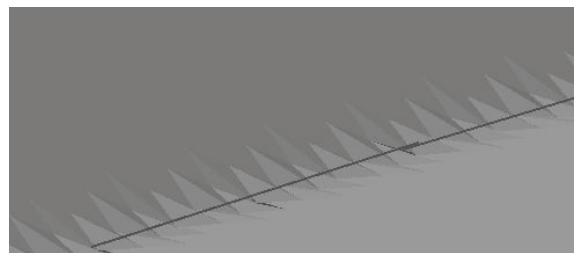


Figure 1. Modelling bad in form to the surface

(Wehr et al., 2009) showed that the triangulation model can be improved, if break line points are regarded in the triangulation process (s. Figure 2). In (Wehr et al., 2009) the break line is determined out of the point cloud data by a special algorithm. However, very often this additional information is already available for section of interest from other surveying sensors. Fusing data of different sensors the problem arises, that the independent data sets are not exactly registered. Therefore, supplementary processing steps are required for coregistering. The algorithms presented in the following are developed with

* Corresponding author.

the objective to improve the TIN-models and to use the information about the order of the points of the point cloud available in the TIN-model. In this paper an algorithm is presented which covers the following tasks:

- a) Fusing GPS-RTK points with ALS-TIN-Model
- b) Fusing profiles with ALS-TIN-Model
- c) Fusing two models with different accuracy

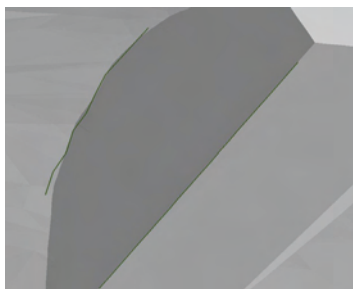


Figure 2. Model using profile line information

2. FUSION ALGORITHM

In this chapter the basic algorithm is presented which is applied in the three tasks mentioned in the introduction. A basic algorithm can be defined as the three tasks have in common, fusing 3D surveying points of an independent sensor with ALS-points (s. Figure 3) which corresponds directly with case a).

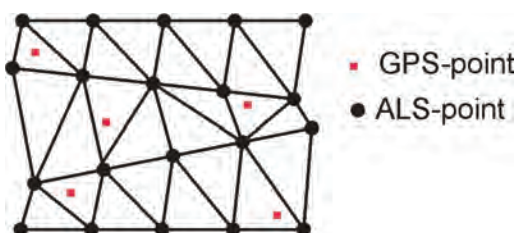


Figure 3. Setup fusing GPS-points and ALS-TIN-model

The algorithm is founded on the moving plane algorithm of (Kraus, 2000) and the least square matching (LSM) based analysis presented in (Ressl a.l., 2008). In the following it is assumed that both data sets are well registered, so that only shifts in x, y and z direction remain. As all data are already modelled it is assumed furthermore that all data are available in a plane projection e.g. UTM-coordinates, so that the z-component corresponds to the elevation.

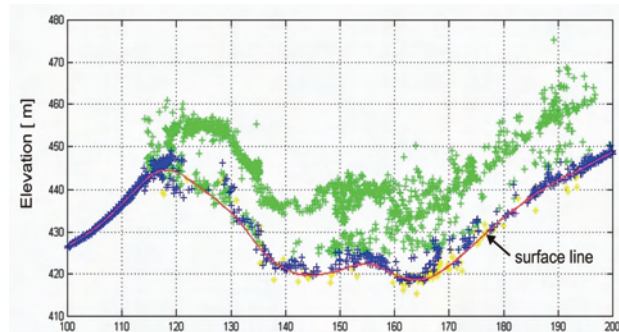


Figure 4. With polynomial approximated surface

The moving plane algorithm is extended to a polynomial approach, because (Thiel and Wehr, 2001) showed that DTMs can be modelled from ALS-data by using third order polynomials (s. Figure 4).

2.1 Fusion Process

The procedure explained in the following was developed regarding Figure 3. If \vec{r}_{ALS_i} is the vector to the i^{th} ALS point and \vec{l}_{GPS_j} the vector to the j^{th} surveyed GPS point, then look for each GPS point with $j \in \{\text{GPS points}\}$ all ALS points $i \in \{\text{ALS points}\}$ which satisfy the following condition:

$$|\vec{r}_{ALS_i} - \vec{l}_{GPS_j}| \leq \epsilon \quad (1)$$

The bound ϵ should be larger than the expected shifts. If the number of identified ALS points for each GPS point satisfies the number of required points for a polynomial approximation the polynomial parameters are approximated by least square matching LSM. Accordingly to the empirical modelling in (Thiel and Wehr, 2001) and to Figure 4 seven parameters have to be computed so that more than 7 ALS points have to be identified for each GPS point. This leads to j surface patches each described by a polynomial:

$$\underline{S} = \begin{pmatrix} a_{01} & a_{11} & a_{21} & a_{31} & a_{41} & a_{51} & a_{61} \\ a_{02} & a_{12} & a_{22} & a_{32} & a_{42} & a_{52} & a_{62} \\ a_{03} & a_{13} & a_{23} & a_{33} & a_{43} & a_{53} & a_{63} \\ \vdots & \vdots & \vdots & \vdots & \vdots & \vdots & \vdots \\ a_{0j} & a_{1j} & a_{2j} & a_{3j} & a_{4j} & a_{5j} & a_{6j} \end{pmatrix} \cdot \begin{pmatrix} 1 \\ x \\ x^2 \\ x^3 \\ y \\ y^2 \\ y^3 \end{pmatrix} \quad (2)$$

\underline{S} represents the elevations $z_j(x,y)$. The three dimensional shifts Δx , Δy and Δz between the ALS-points and the j^{th} GPS-point can be described by

$$S_j(x + \Delta x, y + \Delta y) = z_{GPS}(x_j, y_j) + \Delta z \quad (3)$$

The shifts can be determined by linear LSM. The corresponding observation equation derived from (3) is given by

$$h_j = \frac{\partial S_j(x_j + \Delta x^*, y_j + \Delta y^*)}{\partial x} \cdot dx + \frac{\partial S_j(x_j + \Delta x^*, y_j + \Delta y^*)}{\partial y} \cdot dy + dz - (S_j(x_j + \Delta x^*, y_j + \Delta y^*) - z_{GPS}(x_j, y_j) - \Delta z^*) \quad (4)$$

where Δx^* , Δy^* and Δz^* are the initial estimates for the shifts and h_j are the elevation residuals. The derivatives of S_j are

$$\begin{aligned} \frac{\partial S_j}{\partial x} &= a_{1j} + 2a_{2j} \cdot x_j + 3a_{3j} \cdot x_j^2 \\ \frac{\partial S_j}{\partial y} &= a_{4j} + 2a_{5j} \cdot y_j + 3a_{6j} \cdot y_j^2 \end{aligned} \quad (5)$$

The Gauss-Markov LSM formula is then

$$\underline{\xi} = (\underline{A}^T \cdot \underline{A})^{-1} \underline{A}^T \underline{\Phi} \quad (6)$$

with

$$\underline{\mathbf{A}} = \begin{pmatrix} a_{11} + 2a_{21} \cdot x_1 + 3a_{31} \cdot x_1^2 & a_{41} + 2a_{51} \cdot x_1 + 3a_{61} \cdot y_1^2 & 1 \\ \vdots & \vdots & \vdots \\ a_{1n} + 2a_{2n} \cdot x_n + 3a_{3n} \cdot x_n^2 & a_{4n} + 2a_{5n} \cdot x_n + 3a_{6n} \cdot y_n^2 & 1 \end{pmatrix} \quad (7),$$

$$\underline{\Phi} = \begin{pmatrix} S_1(x_1 + \Delta x^*, y_1 + \Delta y^*) - z_{GPS}(x_1, y_1) - \Delta z^* \\ \vdots \\ S_n(x_n + \Delta x^*, y_n + \Delta y^*) - z_{GPS}(x_n, y_n) - \Delta z^* \end{pmatrix} \quad (8)$$

and n the number of GPS points used for the fusion process. The vector $\underline{\xi}$ contains the adjustments

$$\underline{\xi} = \begin{pmatrix} dx \\ dy \\ dz \end{pmatrix} \quad (9).$$

In Figure 5 the functioning of the algorithm is demonstrated.

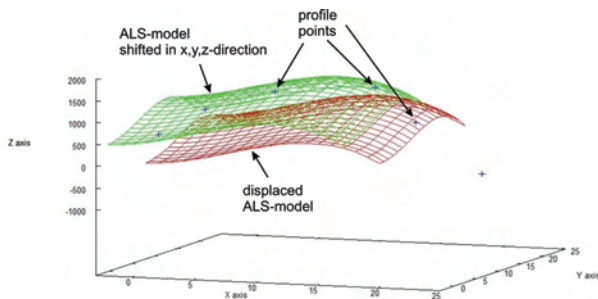


Figure 5. Functioning of fusion algorithm

3. APPLYING THE ALGORITHM FOR THE THREE TASKS

The algorithm described in the preceding section is implemented in the software which carries out the fusing tasks defined in the introduction.

3.1 Fusing GPS-RTK points with ALS-TIN-Model

This case is graphically shown in Figure 3 and the algorithm can be used directly. The key preparing task is here to find the closest ALS points for each given GPS point in order to model the surface in the vicinity of the GPS points. Due to the triangulation process, which was carried out before, this information can be easily drawn out of the TIN model internally stored during the runtime.

3.2 Fusing profiles with ALS-TIN-Model

In this case profile lines are available which are surveyed either by RTK-GPS or tacheometric measurements. These profile models are composed of a number of lines. These lines are defined by precise measurement points which are linked together by straight lines. As shown in Figure 6, the points along the lines exhibit a much lower density than the ALS points. In a first step the shift parameters Δx , Δy and Δz can be determined only on the basis of the measured profile points. In order to put more weight into the profile model it is advisable to interpolate additional profile points along the profile lines and use those for fusing. Here a linear interpolation is sufficient.

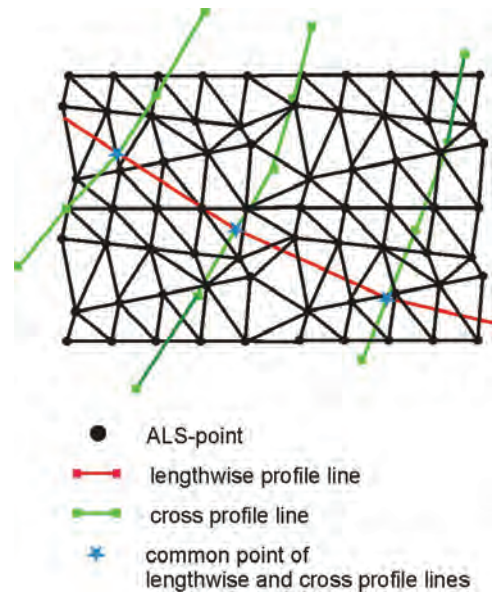


Figure 6. Profiles and ALS-model

3.3 Fusing two models with different accuracy and different horizontal resolution

It is supposed that one model is derived from an ALS point cloud and the other is derived from very precise surveying measurements e.g. DGPS-RTK. The second model exhibits a much higher accuracy and describes well the shape of the surface. It covers only a small area of the first model (s. Figure 7).

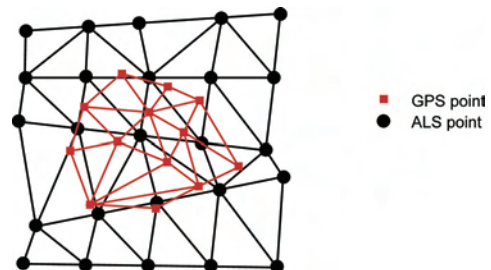


Figure 7. Two models with different accuracy

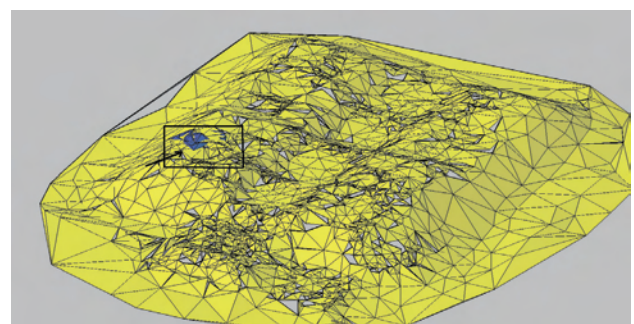


Figure 8. DGPS-RTK model in ALS-model

Figure 8 shows a typical configuration with real data. The small blue shaded area consists of GNSS- and ALS-data. A zoomed image (s. Figure 9) depicts that discontinuities are observed at the transition of both models, although the described fusing algorithm was applied. Here a sophisticated smoothing filter is required to realize a perfect matching.

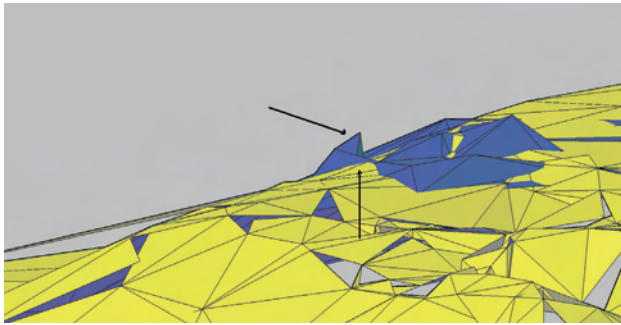


Figure 9. Discontinuities in overlapping area of both models

The developed filter is based on the “Multiquadratic Method” explained in (Kraus, 2000). Before the filter is processed the user has to determine which model has the highest accuracy. As in general the user has a priori information about the data sets to be fused, this step is done best manually. The most accurate model is named M1, the other one M2. As shown in Figure 8, M1 is a subset of M2. In a follow on step a border line in the xy-plane between M1 and M2 is calculated (s. Figure 10) and for all points defined by the intersections of the border line with the models an elevation difference Δh_i between both models can be computed:

$$\Delta h_i = P_{Z(M1)_i} - P_{Z(M2)_i} \quad (10)$$

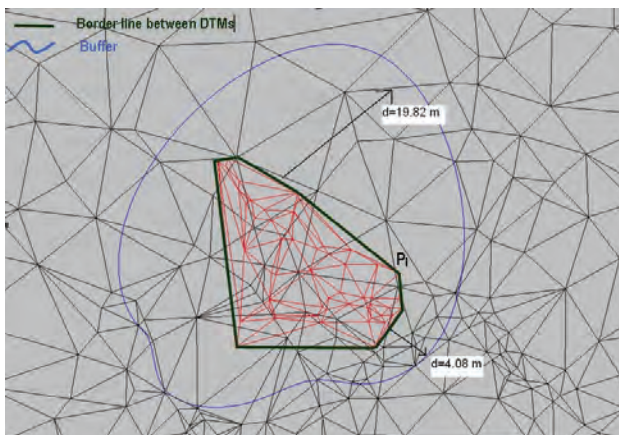


Figure 10. Definition border line and buffer are

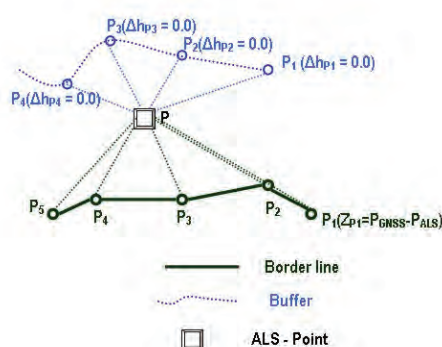


Figure 11. Interpolation setup

In a next step a so called buffer area is setup about M1 in the xy-plane (s. Figure 10). The outer boundary of the buffer is displayed by a blue line in Figure 10. The elevation differences are set to zero on this line. This means, the elevation differences have their maximum (Δh_i) at the inner line of the buffer (border

line) and zero at the outer line. This makes clear that transition between M1 and M2 is done within the buffer. The smoothed elevation difference will be some what in between. The buffer size has to be selected very carefully, because the number of points, which should be used for the calculation, is strongly dependent on the buffer size (s. Figure 10).

The interpolation of the elevation differences within the buffer is carried out by the “Multiquadratic Method”. Looking at Figure 11), which shows an arbitrary point P within the buffer and P_i intersecting points, the distance $\overline{PP_i}$ in the xy-plane between P and P_i is given by

$$k(P, P_i) = \sqrt{(X - X_i)^2 + (Y - Y_i)^2} \quad (11),$$

if X,Y are the coordinates of P and X_i, Y_i the coordinates of P_i . $k(P, P_i)$ is also called the core function. The elevation difference Δh for point P can be interpolated by

$$\Delta h = \Delta h(X, Y) = \sqrt{(X - X_1)^2 + (Y - Y_1)^2} * m_1 + \dots + \sqrt{(X - X_n)^2 + (Y - Y_n)^2} * m_n \quad (12)$$

Here is m_i a scale factor for distance from point P to the i^{th} tie point and n is the number of tie points. In matrix notation one can write:

$$\Delta h = \underline{\mathbf{k}}^T \cdot \underline{\mathbf{m}} \quad (13),$$

with

$$\underline{\mathbf{k}}^T = (k_1, k_2, k_3, \dots, k_n) \text{ and } \underline{\mathbf{m}}^T = (m_1, m_2, m_3, \dots, m_n).$$

For n elevation differences Δh_i a linear equation system can be setup with Equation (13):

$$\begin{pmatrix} k(0) & k(P_1 P_2) & \dots & k(P_1 P_n) \\ & k(0) & \dots & k(P_2 P_n) \\ & & \vdots & \vdots \\ \text{symm.} & & & k(0) \end{pmatrix} \begin{pmatrix} m_1 \\ m_2 \\ \vdots \\ m_n \end{pmatrix} = \begin{pmatrix} \Delta h_1 \\ \Delta h_2 \\ \vdots \\ \Delta h_n \end{pmatrix} \quad (14)$$

which corresponds to

$$\underline{\mathbf{K}} \cdot \underline{\mathbf{m}} = \underline{\mathbf{d}} \quad (15)$$

Now, the actual elevation difference for $\Delta h(X, Y)$ can be easily computed by

$$\Delta h = \underline{\mathbf{k}}^T \cdot \underline{\mathbf{K}}^{-1} \cdot \underline{\mathbf{d}} \quad (16)$$

Figure 12 proves the smoothing effect of this filter for the transition area between M1 and M2. Here the ALS- and GNSS-DTMs already presented in Figure 8 are matched and smoothed around the GNSS-DTM.

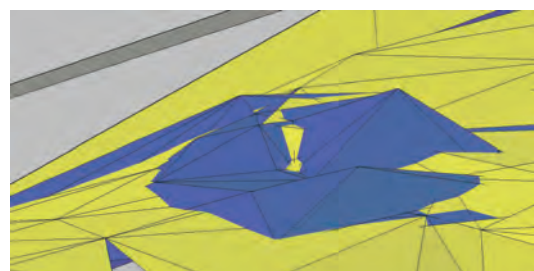


Figure 12. TIN-model after smoothing

4. CONCLUSIONS AND IMPROVEMENTS

The empirical test runs of the fusion algorithm show that good fusing results can be obtained. However, it performs best, if the models exhibit high elevation dynamic. In case of a plane the algorithm fails, because shifts in the horizontal are arbitrary. In this case the vertical shift can be determined by a special algorithm which first models the two planes and then determines the vertical shift between them.

Operational test runs on real data show that if profile lines are regarded in ALS data modelling an improvement in the determination of excavated material in e.g. open mining is in the order of 0.1 m³/(m² surveyed area).

In a further development step the algorithm will be extended so that also the three Euler orientations between the different data sets are determined.

The smoothing algorithm proves its performance. All presented algorithms will be implemented in a commercial program.

5. REFERENCES

Kraus, K., 2000. *Photogrammetrie, Band 3: Topographische Informationssysteme*. 1. Aufl., Dümmler, Köln, pp. 137-145.

Ressl, C., Kager, H., Mandlbürger, G., 2008. Quality checking of ALS projects using statistics of strip differences. In: *The International Archives of the Photogrammetry, Remote Sensing and Spatial Information Sciences*, Beijing, China, Vol. XXXVII, Part B3b, pp. 253-260.

Thiel, K.-H., Wehr, A., 2001. Operational production of DTMs using ScaLARS. In: *Proceedings of OEEPE workshop on Airborne Laserscanning and Interferometric SAR for Detailed Digital Elevation Models*, Stockholm, Sweden, paper 9.

Wehr, A., Petrescu, E., Duzelovic, H., Punz, Chr., 2009. Automatic break line detection out of high resolution airborne laser scanner data. In: *Optical 3-D Measurement Techniques IX*, Vienna, Austria, Vol. II, pp. 72-78.

CHANGE ANALYSIS WITH TERRASAR-X DATA

D. Weihing^{a,*}, F. von Poncet^a, M. Schlund^b, O. Lang^a

^a Infoterra GmbH, Claude-Dornier-Strasse, 88090 Immenstaad, Germany - (Diana.Weihing, Felicitas.Poncet, Oliver.Lang)^a@infoterra-global.com

^b Department of Geography, University of Jena, Germany - Michael.Schlund@uni-jena.de

Commission VII

KEY WORDS: Analysis, Change Detection, Monitoring, Change, SAR

ABSTRACT:

Change analyses play an important role for different applications, ranging from small- to large-scale monitoring. To identify changes from SAR images of repeat pass acquisitions different methods are commonly applied, which differ with respect to the parameter as an indicator of changes. The backscatter intensity is analysed in incoherent change detection methods, whereas in the coherent change detection the complex correlation coefficient is analysed as a change indicator. These methods provide complementary characterisations, since they are sensitive to different measures of a SAR scene.

However, often not only the detection of changes, but also the assessment of the detected changes is of interest, which automated is a challenging task.

In this paper a combination of detection and assessment of changes is shown. Additional information is integrated into the proposed scheme to separate relevant changes from less relevant ones in order to decrease unrequested changes and evaluate the type of change. Texture measures provide information on the spatial variation of the backscatter and thus information of the local surface characteristics within the scene. This information is used to restrict the search for areas and changes of interest as well as for the assessment of changes.

The goal of our analysis is to support the implementation of an operational change detection process and to define a suitable assessment of changes from TerraSAR-X data regarding different customers' requirements.

1. INTRODUCTION

In many different geoinformation applications, the detection and assessment of changes is of much interest. These applications can vary from specific site monitoring to large-scale assessment after certain events and for updating existing geoinformation databases.

Satellite SAR missions like TerraSAR-X entail potential for such applications, not only because of the large coverage in combination with high resolution, but also due to the independence regarding daytime and weather conditions.

The identification of changes implies a comparison of datasets or knowledge about a scene of different dates, like e.g. updating of existing geoinformation with recent remote sensing data. Different approaches for change detection have been studied depending on the sensor and available data.

In this paper the focus is set on the image-to-image change detection with TerraSAR-X data, and in particular on repeat-pass images with the same acquisition parameters, which allow a direct comparison. Therefore, acquisitions of pre- and post events are required.

Detecting changes means that every variation causing a different echo signal/backscatter is detected. However, often customers are only interested in relevant changes concerning their applications. To be able to offer the user-specific change information, an assessment of the detections is required. The

preferably automatic detection and assessment is a goal for a worldwide operational process and service. The integration of additional information, like e.g. GIS data, in such a process can be helpful for this purpose. However, in many regions often this required a-priori information is missing or not available in the time frame for rapid assessment. Therefore, the used pre- and post-event imagery for change detection as a single source has to be exploited also to assess the changes. Hence, different measures have to be deduced from the images to derive more information about the scene.

2. CHANGE DETECTION

Change detection based on SAR images has been subject in different publications. To identify changes from SAR images of repeat pass acquisitions different methods are commonly applied. These methods differ with respect to the parameter which is used to indicate changes and the method to reduce the noise. Since SAR data contains amplitude and phase information, both parameters can be used as change indicators.

A common method is the analysis of the radar backscatter intensity in time to identify changes between different acquisitions, also called incoherent change detection (Preiss et al., 2003). This power change estimate is affected by the speckle noise component, whose reduction is discussed in several publications, e.g. in (Schmitt et al., 2009).

* Corresponding author.

In SAR data, additionally the interferometric phase information is sensitive to surface changes and ground motion. The coherence, which expresses the complex correlation of two SAR scenes, can be used as an indicator of changes (Scheuchl et al., 2009; Wright et al., 2005). However, since the phase is sensitive to sub-wavelength changes, the information is related to very subtle changes, especially for X-Band. Therefore, change detection based on the interferometric coherence is susceptible to high false alarm rates, since several impacts, like e.g. weather and surface properties, can cause decorrelation.

Incoherent and coherent change detections provide complementary characterisations, since they are sensitive to the different measures of a SAR scene: backscatter intensity and phase. Therefore, the joined use of both statistics often provides a better description of surface changes. Preiss et al., 2006 showed a statistical test for change detection combining incoherent and coherent change statistics.

To respond to certain customer-specific applications, the detected changes have to be assessed in a fast and efficient way. However, the automatic assessment of changes is a challenging task. Classification of the scene gives information about surface characteristics (Wegmüller et al., 2003), which can be used to restrict the search areas and reduce unrequested changes. Additionally, this information gives an indication about the type of change.

3. CHANGE ANALYSIS – DETECTION AND ASSESSMENT

To detect changes, the different parameters of a complex SAR signal can be exploited, see Sec. 2. In the suggested process further information is integrated to decide whether the change is of interest or not for the customer-specific case. The following sketch shows a brief processing overview for the automatic detection and assessment of changes.

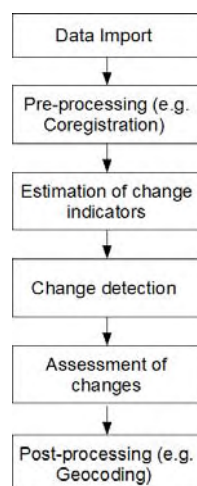


Figure 1: Processing scheme – change detection and assessment

3.1 Change Detection

In our work we use both, the intensity ratio and the coherence as change indicators. We assume certain distributions of those

features to estimate the thresholds to distinguish changes. The known distribution functions of the intensity ratio (Touzi et al., 1988) and of the coherence (Hanssen, 2001) are used to separate changed from non-changed pixels, assuming a certain false alarm rate.

The intensity ratio contains, not only the information that a change happened, but also if the backscatter increased or reduced between the acquisition dates. This information will be kept and can also be used in the following assessment step.

3.2 Assessment of changes using additional information

Into the proposed scheme further information for the assessment is integrated resulting in a context based change detection approach. Broad land cover classification of the pre-event scene is used as context information.

Since there is not a unique descriptor applicable to various surfaces, different textures and statistics are estimated to improve land cover discrimination. Texture measures provide information on spatial variation of the backscatter and thus information of the local surface characteristics within the scene. This information together with coherence and backscatter statistics is used in a classification approach to restrict the search for areas and changes of interest and for the evaluation of changes.

In a first attempt a straight forward pixel-wise classification based on coherence and backscatter intensity has been tested and achieved in general reasonable results concerning broad land cover classes such as urban, forest, open land, water and coastal areas. However, combining the classification result with the change indicator showed that the pixel-wise classification approach is too noisy to reduce unrequested changes.

Therefore, object based classification methods have to be applied in order to first divide the image into homogeneous regions (segmentation) and second, derive image characteristics such as co-occurrence texture measures, coefficient of variation, and class related features from resulting image objects. Based on these features a simple decision tree can be set up to classify the pre-event scene.

This kind of information gives a hint about the type of change. Additionally the change direction of the backscatter can be used to evaluate if an object disappeared or showed up. Hence it supports the classification of the type of change.

4. APPLICATION TO DATA

The combined detection and assessment of changes has been applied to TerraSAR-X StripMap acquisitions to demonstrate the approach.

4.1 Available Data and Scenery

Two TerraSAR-X StripMap (3m resolution) acquisitions are available. The images are repeat-pass acquisitions with the following acquisition parameters: HH polarisation, ascending orbit, incidence angle: 36-38,6 °.

The scene is located in Panama close to the capital and the southern entrance to the Panama Canal. The following Figure 2 and Figure 3 show only a detail of the StripMap scenes with an airport in the south western part, the entrance to the Panama

canal at the right top of the image and a wetland in between them. Most of the rest of the scene is covered by forest.

4.2 Results

The high degree of vegetation cover and the time difference of three month between the acquisitions result in an overall low coherence due to temporal decorrelation which is typical for temperate and tropical regions. Following, the emphasis for the change indicator was put on the intensity ratio. The detection mask overlaid on the first image is shown in Figure 4. The red pixels signify areas where the backscatter reduced and the blue ones stand for an increased backscatter.

Different kinds of changes are detected within this scene. For example on the left bottom of the subset a clearing of the forest was conducted, which is clearly visible in the changing backscatter of the two images. Also new constructions are detected in the north of the buildings belonging to the airport. Regions where varying soil moisture in the wetland caused a different backscatter, as well as temporarily present objects, like e.g. wagons on the runway and ships on the sea appear also in

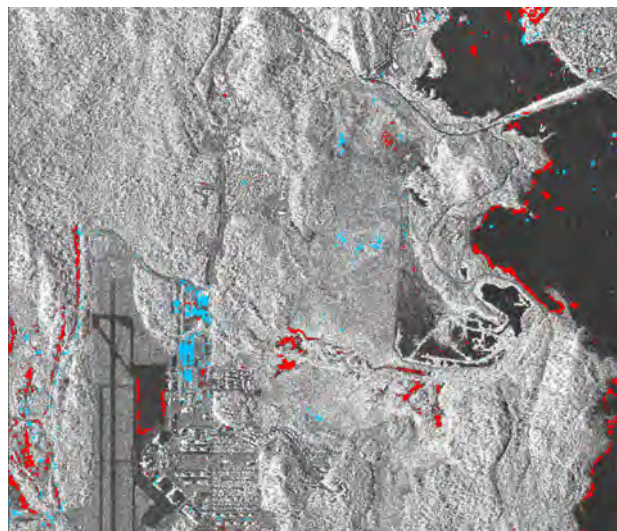


Figure 4: Change detection mask; red: backscatter reduced, blue: backscatter increased.

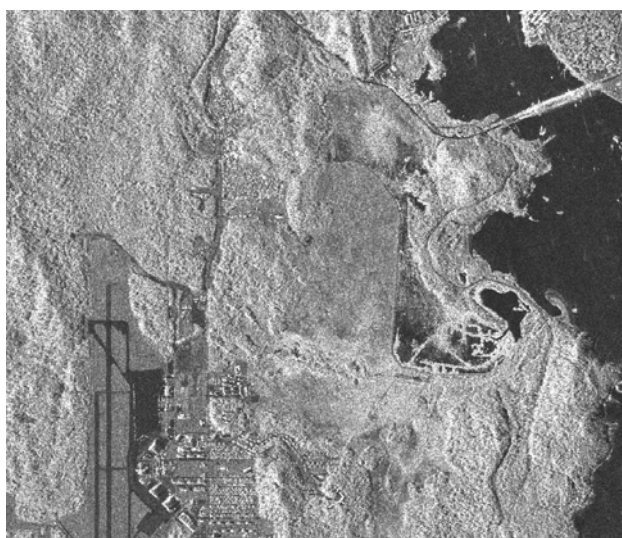


Figure 2: TerraSAR-X acquisition of 25.01.2009.

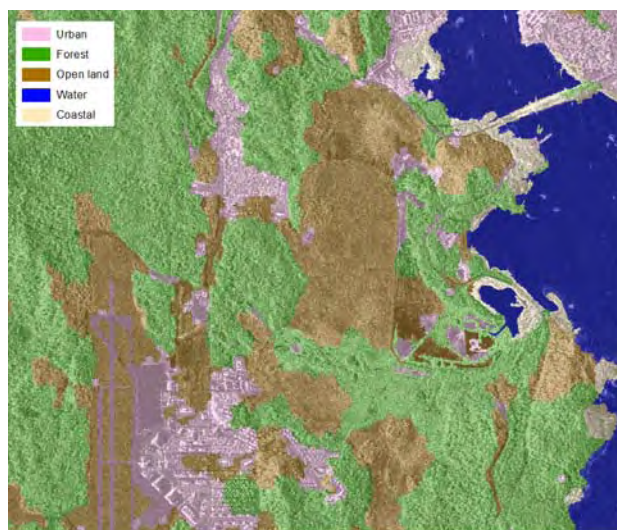


Figure 5: Land cover classification of TerraSAR-X derived features (25.01.2009).

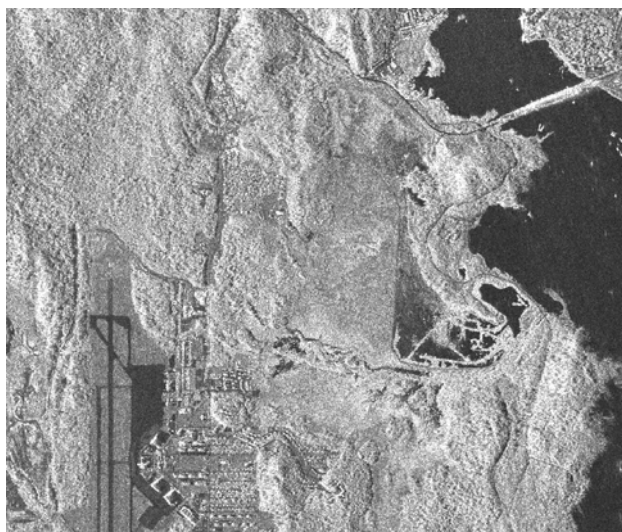


Figure 3: TerraSAR-X acquisition of 12.04.2009.

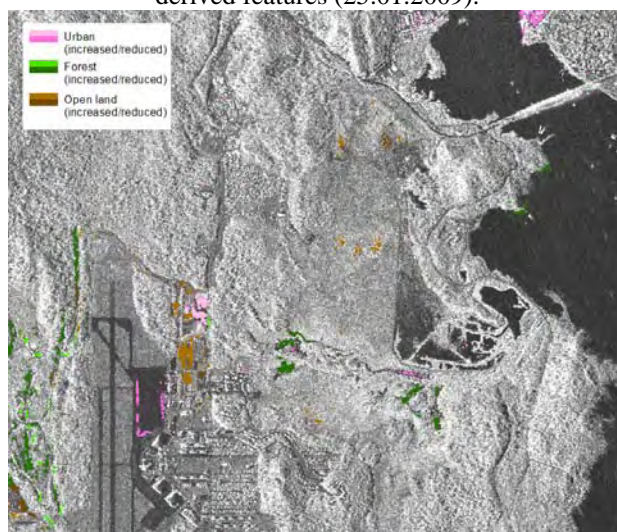


Figure 6: Detected and assessed changes.

the detection mask. Varying water level can result in detected changes at the coast.

Obviously, every object or parameter which caused a significant backscatter change will result in a detection. However, customers may only be interested in specific changes, like e.g. in new constructions.

To analyse the scenery to gain additional knowledge for the qualification of detected changes, different measures have been used for segmentation and classification: Coefficient of variation, Coherence and statistics of the intensity.

Five broad classes have been evaluated: water, forest, open land, urban and coastal areas. The result of this classification is shown in Figure 5.

Assuming a certain application and that a user is only interested in changes on land and not in variations on the sea e.g. due to waves, varying water level and ships, the following reduction has been applied. Changes on water and coastal areas have been eliminated as unrequested changes.

The information about the change direction of the backscatter (reduced or increased) has been combined with the classification results of Figure 5. The result is shown in Figure 6 and a detail of it in Figure 7.

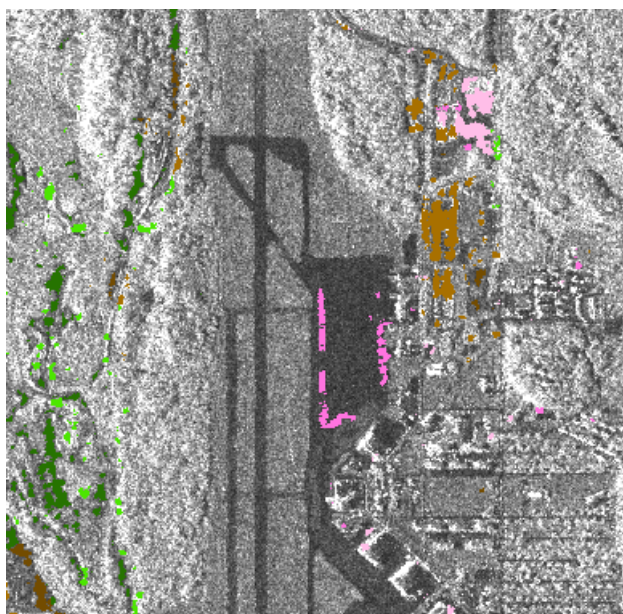


Figure 7: Detail of detected and assessed changes.

The clearing on the left hand side has been classified as a change type in forest areas with a decreased backscatter, which is typically the case for clearings. At the new forest edges an increased backscatter is caused by layover.

The new construction at the area around the airport were classified as open land, which is true since in the first acquisition there was bare soil and the increased backscatter gives the indication of a new object. The temporarily parked wagons at the runway are classified as a change in urban areas, where usually many changes are occurring independent on the change direction. Domain specific interpretation knowledge is needed to verify the plausibility of such changes and qualify it as temporary change.

The detected and assessed changes are plausible. However, the assessment depends on the quality of the classification. Even

though no apriori information and only a small amount of SAR data sets have been available the customer can be provided with, a rough idea about the type of occurring changes.

5. CONCLUSION

In this paper an approach for a combined detection and qualification of changes has been presented. The integration of additional information derived directly from the images is helpful to restrict search areas and to give more information to judge the plausibility of changes, if other a-priori information is not available.

The assessment depends on the accuracy of the classification of the imagery. However, an indication about the change direction can be given and can be helpful for further interpretation.

In future tasks, the improvement of the assessment can be conducted by using e.g. dual-polarised data and a comparison of classifications of pre and post event images.

REFERENCES

- Hanssen, R. F., 2001. *Radar Interferometry, Data Interpretation and error analysis*. Kluwer Academic Publishers, Dordrecht.
- Preiss M., Gray D., Stacy N., 2003. A change detection technique for repeat pass interferometric SAR. *IEEE International Geoscience and Remote Sensing Symposium (IGARSS)*, Vol. 2, pp. 938-940.
- Preiss M., and Stacy N.J.S., 2006. Coherent Change Detection: Theoretical Description and Experimental Results. *STO-TR-1851*
- Scheuchl B., Ullmann T., Koudogbo F., 2009. Change Detection using high resolution TerraSAR-X data preliminary results. *The International Archives of the Photogrammetry, Remote Sensing and Spatial Information Sciences*. XXXVIII-1-4-7/W5.
- Schmitt A., Wessel B., Roth A., 2009. Curvelet approach for SAR Image denoising structure enhancement and change detection. *City Models, Roads and Traffic (CMRT)*, 03.-04.09.2009, Paris (France).
- Touzi, R. Lopes, A. Bousquet, P., 1988. *A statistical and geometrical edge detector for SAR images*. *IEEE Transactions on Geoscience and Remote Sensing*, Vol 26 (6), pp. 764-773.
- Wegmüller, U., Strozzi, T., Wiesmann, A., Werner, C., 2003. *ENVISAT ASAR for land cover information*. In *Proceedings of IGARSS'03*, Toulouse.
- Wright P., Macklin T., Willis C., Rye T., 2005. Coherent Change Detection with SAR. *2nd EMRS DTC Technical Conference*, Edinburgh

AN OVERVIEW OF TWO DECADES OF SYSTEMATIC EVALUATIONS OF CANOPY RADIATIVE TRANSFER MODELS

J-L. Widlowski

Global Environment Monitoring Unit, Institute for Environment and Sustainability, DG Joint Research Centre of the European Commission, Via E. Fermi 1, Ispra 21020 (VA), Italy - Jean-Luc.Widlowski@jrc.ec.europa.eu

KEY WORDS: Model Intercomparison, Canopy Radiative Transfer, Quality Assurance, Optical Remote Sensing

ABSTRACT:

Space borne observations constitute a highly appropriate source of information to quantify and monitor Earth surface processes. The reliability that may be associated with the outcome of interpretation and assimilation efforts of these data, however, relies heavily on the actual performance of the available modeling tools. Scientists, space agencies and policy makers that want to make use or support the derivation of quantitative information from space observations must therefore have access to indicators describing the quality of the models and algorithms that are used in retrievals. As a formalization of earlier model verification efforts the RADIATION transfer Model Intercomparison (RAMI) initiative was launched in 1999 in an attempt to shed light on the reliability and accuracy of physically-based canopy radiative transfer models simulating the interactions between sunlight and vegetation. This contribution documents the evolution and achievements of RAMI and provides an outlook of challenges and opportunities that still lie ahead.

1. INTRODUCTION

1.1 Purpose of Canopy Radiative Transfer Models

The exploitation of global Earth Observation data hinges more and more on physically-based radiative transfer (RT) models. These models simulate the interactions of solar radiation within a given medium (*e.g.*, clouds, plant canopies) and are used to generate look-up-tables, to train neural networks or to develop parametric formulations that are then embedded in quantitative retrieval algorithms such as those delivering the operational surface products for MODIS, MISR and MERIS, for example. Assessing the quality of RT models is thus essential if accurate and reliable information is to be derived from them. Biases and errors in RT models may also affect the outcome of new mission concept studies, as well as our capacity to quantify Earth surface processes and the reliability of downstream applications that assimilate such remotely sensed data streams. The focus of this contribution lies with the quality of physically-based models that deal with the representation of radiative processes in vegetated environments within the optical domain of the solar spectrum.

Most land surfaces are strongly anisotropic reflectors when observed from optical to thermal-infrared wavelengths. The angular dependence of their reflectance function (termed the bidirectional reflectance distribution function or BRDF) results from 1) the three-dimensional (3-D) nature of terrestrial targets, *i.e.*, the size, shape and spacings of trees in a forest or crops in a field, which produces distinct patterns of shadows that change with the direction of view (and illumination), and 2) the scattering behaviour of individual foliage, wood and soil elements together with their density and orientation with respect to the illumination and viewing directions (Ross, 1981). Physically-based canopy RT models, when used in *forward mode*, are capable to predict the BRDF of a vegetation target on the basis of architectural, spectral and illumination related descriptions. Conversely, when used in *inverse mode*, physically-based canopy RT models may, in principle, retrieve the structural and spectral canopy properties that gave rise to the

directionally (and spectrally) varying reflectance observations. Knowledge of the BRDF of terrestrial surfaces is necessary for 1) the accurate retrieval of surface albedo (via a hemispherical integral of the BRDF), 2) the specification of the lower boundary condition in atmospheric corrections and for the estimation of cloud and aerosol properties (*e.g.*, Hu et al., 1999), and 3) the retrieval of sub-pixel surface characteristics (*e.g.*, Widlowski et al, 2004).

1.2 Types of Canopy RT Models

A large variety of physically-based canopy RT models have been developed over the past five decades or so. According to Qin and Liang (2000) the purpose of modelling the radiation distribution in the 1960s was primarily to estimate the canopy photosynthetic rate; in the 1970s the focus was on the calculation of surface albedo and net radiation for energy-balance and micro-meteorological research; in the 1980s and 90s canopy RT modelling was driven by the need to accurately describe the angular distribution of the reflected radiation. In the last decade or so the emphasis was placed on efficient representations of radiative processes in increasingly complex 3-D canopy architectures and the retrieval of sub-pixel surface structure information. In a landmark paper, Goel (1987) grouped canopy RT models into 4 different categories:

1. *Geometrical models*, that assume the canopy to be made up of a ground surface (of known reflective properties) with geometrical objects of prescribed shapes and dimensions (*e.g.*, spheres, ellipsoids, cones) and optical properties (reflectance, transmittance and absorption) placed on it in a defined manner (random or clustered) to represent the spatial distribution of tree crowns. The canopy reflectance is the weighted sum of four components: sunlit and shaded crown, and sunlit and shaded background. These models are best suited for small view and sun zenith angles and for sparse canopies with high leaf densities, where the effects of mutual

- shading and multiple scattering are minimal (for a recent review see Chen et al., 2000),
2. *Turbid medium models* assume the canopy to be horizontally uniform and to be composed of plane parallel layers that are filled with dimensionless scatterers randomly distributed throughout the available volume and oriented in accordance with a given leaf normal distribution function. These models are best used for dense canopies with small vegetation elements (e.g., mature agricultural crops) and relatively inappropriate for open forest canopies (for a recent review see Qin and Liang, 2000),
 3. *Hybrid models* represent vegetation canopies using both of the above approaches. Typically they assume that the interior of geometric objects (representing tree crowns) are uniformly filled with a ‘gas’ of point-like oriented scatterers of specified orientations and spectral properties. These models can be used to represent both sparse and dense canopies. However, multiple scattering is not rigorously treated and the models are often limited by one single type of crown geometries (Goel and Thompson, 2000),
 4. *Computer simulation models* can represent arbitrarily complex canopy architectures using constructive solid geometry or similar computer graphics techniques. All facets of a geometric object (needle, trunk, leaf, twig, etc.) can be tagged with spectral and directional scattering properties. In ray-tracing models a Monte Carlo procedure is then used to determine the location and direction of incident light beams; the type of interaction, i.e., reflection, absorption or transmission, that such rays undergo when intersecting with an object, and in the case of a scattering event also the direction of further propagation. To compute the BRDF of a plant canopy one keeps shooting rays into the scene, follows them through their various interactions until they exit the scene and end up in certain small solid angles around predefined viewing directions. Due to the large number of photons needed for reliable statistics this type of RT model tends to be relative computer intensive (Disney et al., 2000).
2. *In-situ or laboratory measurements*, that were acquired with sensors – typically supported by a tram system or goniometer structure – looking down at the canopy target, are used as a means to evaluate the quality of RT model simulations based on the spectral, structural and illumination characteristics of the canopy target (ideally acquired at the same time as the BRDF measurements), e.g., Franklin and Duncan (1992), Strahler and Liang (1994),
 3. *Canopy RT model simulations*, that were (ideally) generated by sophisticated Monte Carlo RT models on the basis of detailed 3-D description of the canopy architecture, are used to assess the output of simpler canopy RT models making use of the same canopy-target characteristics (albeit adapted to their need for input parameter specifications), e.g., Goel and Kuusk, (1992), Liang and Strahler (1992).

In some cases the quality of canopy RT models is also addressed in inverse mode, that is, by looking at how well a model allows to retrieve certain biophysical parameters on the basis of measured BRDF data. Such an approach is, however, more suited to comment on the numerical inversion procedure than the physical correctness of the canopy RT model. Pinty and Verstraete (1992) advocated the use of both forward and inverse modes. Their idea was to acquire detailed descriptions of the structural and spectral properties of a canopy target and to feed these into an RT model to simulate BRDF patterns of the target under a specific set of illumination and observation conditions. These forward simulations can then be compared to actual observations previously acquired over the target in question at the same viewing and illumination geometries. The RT model can then be inverted against the measured and/or simulated data sets and the output of this operation compared to the canopy characteristics that had been measured initially and used as input to the forward simulations.

Unfortunately, the verification of canopy RT models on the basis of actual measurements has always been hampered by the lack of accurate, comprehensive and self-consistent field data sets, e.g., Strahler, (1997). This situation has not changed much since the 1990s and even the use of artificial targets in laboratory environments suffer from the same difficulties, that is, instruments and methods that allow for a highly precise characterisation of 1) the light environment surrounding the target, 2) the position, orientation, size and shape of all the physical components making up the target, 3) the magnitude, directionality and spatial variation of scattering properties of all canopy and background elements, and 4) the detector location, foreoptics (if present) and spectral response functions. None of these issues are present, however, when canopy RT models are compared using virtual plant environments.

1.3 Early Canopy RT Model Validation Efforts

With the availability of a large set of canopy RT models in the 1980s the question arose as to how one could assess their quality and reliability. Of primary interest here was the validation of ‘simple’ canopy RT models that – because of fast execution times and small numbers of parameters – were likely to play a role in the operational retrieval of quantitative surface information from optical remote sensing data. So far the verification of canopy RT models in forward mode has always relied on comparison strategies with respect to one or more of the following types of reference data:

1. *Air or space borne observations*, that were acquired over specific test sites and subsequently corrected on the basis of concurrently measured atmospheric properties, are used as a means to evaluate the simulations of canopy RT models based on structural, spectral and illumination related information pertaining to the same canopy target and (ideally also) the same time of acquisition as the space or air-borne observations, e.g., Schaaf et al., (1994), Soffer et al., (1995),

2. SYSTEMATIC RT MODEL EVALUATION

2.1 Strategy

The RAdiative transfer Model Intercomparison (RAMI) initiative was launched in the late 1990s to provide a platform for the systematic evaluation of physically-based canopy RT models (Pinty et al., 2001). Of primary relevance was the need to eliminate sources of uncertainty that affect the outcome of verification efforts but that do not pertain to the quality of the canopy RT models themselves. At the time, this strategy precluded the evaluation of RT model simulations on the basis

of laboratory, in-situ, air and space-borne measurements. This was primarily due to difficulties associated with the acquisition of accurate and spatially detailed descriptions of 1) plant architectural properties, like foliage orientation and density, wood distribution and branching patterns, *etc.*, 2) directional scattering characteristics of plant and background constituents suitable for inclusion into canopy RT models, and 3) directionally resolved solar radiation fields, that are all needed to guarantee a faithful reproduction of the actual 3D target (at the time of observation) within the RT models. The evaluation of models through comparison with observation requires also access to information regarding the angular and spectral resolution of the measuring devices, as well as, the uncertainties associated with eventual up-scaling and correction techniques (*e.g.*, atmosphere, adjacency effect, point spread function).

To avoid these issues RAMI evaluates models under perfectly controlled experimental conditions, *i.e.*, all structural, spectral, illumination and observation related characteristics are known without ambiguity. Deviations between RT simulations can thus only be due to – explicit or implicit – assumptions and shortcuts entering model-specific implementations of the radiative transfer equation. This mathematical foundation of physically-based canopy RT models allows furthermore to verify model predictions of arbitrary sub-components of the total (absorbed, transmitted and reflected) radiation, *i.e.*, quantities that could not be measured in reality, and to check that the model simulations remain consistent with physical reasoning even if the environmental conditions deviate from those encountered in nature. The latter two aspects are crucial since they allow – in a few select cases – to assess RT model performance in absolute terms, *i.e.*, against analytical solutions of directionally-varying or hemispherically-integrated radiative quantities and to increase the confidence in model simulations relating to new species/biomes and phenological conditions, respectively.

As a general rule, RT model comparison activities have to deal with the fact that the true solution is not known. RAMI deals with this issue through a three-pronged evaluation approach based on:

1. *model consistency tests*: that verify the internal consistency of RT models, for example, with respect to energy conservation, or, when radiative quantities are modelled that vary in a pre-determined manner across spectral bands, with background brightness, or, with changing illumination conditions,
2. *absolute performance tests*: that compare the magnitude of model simulated radiative quantities against those predicted by analytical solutions (which can be derived for some types of canopy targets having certain well defined characteristics),
3. *relative performance tests*: that compare simulations of different models in the light of knowledge obtained from 1) the above model consistency and absolute performance tests, and 2) an analysis of the shortcuts and assumptions contained in their respective implementations/formulations of the RT equation.

In order to obtain viable assessments of the trends, patterns and perhaps also biases in the performance of canopy RT models it is imperative to compare model simulations over an as large as possible set of structural, spectral and illumination related conditions. Such an approach is also conform with the paradigm stating that computer simulation models can never be completely validated and that efforts should focus instead on

the *invalidation* of such tools (Oreskes, 1994). In other words, a model may yield the correct solution but for the wrong reasons, and therefore nothing can be said with absolute certainty about the reliability/accuracy of its predictions when applied to cases that were not actually tested beforehand.

2.2 Outcome

As an open-access and community-driven activity RAMI operates in successive phases each one aiming at re-assessing the capability, performance and agreement of the latest generation of RT models (<http://rami-benchmark.ec.europa.eu/>). RAMI-1 involved a small yet somewhat abstract set of canopy scenarios specifically designed to suit both 1-D and 3-D canopy RT models. The results of RAMI-1 underlined the need for model verification since many of the submitted simulations differed quite substantially between the 8 participating models (Pinty et al., 2001). In some cases, the cause of these discrepancies may have been due to operator errors or software bugs (some of which were identified during the data analysis stage). RAMI-2, therefore proposed a rerun of all earlier experiments together with two new test cases addressing issues of topography and spatial resolution. This time 13 canopy RT models participated and their agreement was much better especially for the homogeneous canopies (Pinty et al., 2004a). Expanding the set of experiments yet again, RAMI-3 concluded with an unprecedented level of agreement amid its 18 participating RT models and this for both the homogeneous and heterogeneous vegetation canopies (Widlowski et al., 2007).

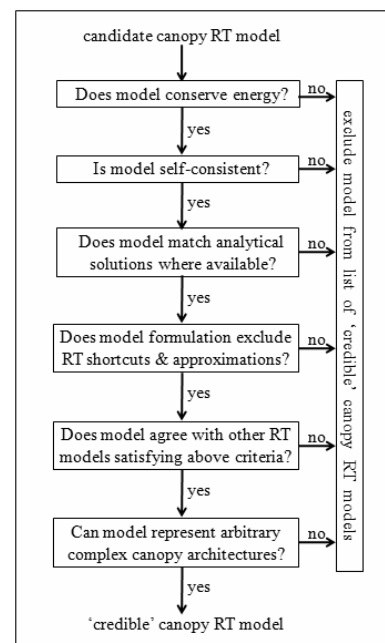


Figure 1. The selection process of 'credible' canopy RT models.

Using the process outlined in Figure 1 it was possible to identify six 3-D Monte Carlo models from among the RAMI-3 participants that differed by ~1% over several thousands of BRF and flux simulations. A 'surrogate truth' reference data set was then generated on the basis of the simulations of these 'credible' canopy RT models (Widlowski et al, 2008). This, in turn, led to the development of the RAMI Online Model Checker (ROMC), a web-based benchmarking facility providing quasi-real time statistics of the differences existing between the simulations of a user's canopy RT model and the RAMI-3 "surrogate truth" data set (<http://romc.jrc.ec.europa.eu/>).

Currently, over 30 models have been registered in the ROMC and several scientific publications use ROMC-generated graphs to provide independent and traceable proof of the quality of a canopy RT model. Of particular interest here is the fact that the ROMC provides an indication of model skill, defined as:

$$Skill = 100 \cdot \frac{(1 + R)^4}{\left(\frac{\bar{x}_{mod} + \bar{x}_{ref}}{\bar{x}_{ref} + \bar{x}_{mod}} \right)^2 \left(\frac{\sigma_{mod} + \sigma_{ref}}{\sigma_{ref} + \sigma_{mod}} \right)^2}$$

where R is the correlation coefficient, \bar{x} is the mean value, and σ is the standard deviation of N simulations provided by the candidate model (_{mod}) and ROMC reference data set (_{ref}), respectively. The skill metric depends on N and reaches 100 for a perfect match with the ROMC reference data.

With the availability of the ROMC it became feasible for RAMI to address new issues. As such, RAMI proposed to utilize ‘credible’ 3D Monte Carlo models to provide benchmark solutions against which the shortwave radiative flux formulations in the land surface schemes of SVATs and GCMs could be evaluated. This proposal was endorsed during the first Pan-GEWEX meeting in late 2006 and led to the launch of the RAMI4PILPS suite of experiments in 2008 (where 10 modelling groups from around the world participated). In parallel, the fourth phase of RAMI was launched in 2009 with a completely new set of test cases, some of which, were based on detailed field inventories and exhaustive in-situ and laboratory measurements of actual forest stands. In addition, RAMI-IV expanded also the range of model simulations beyond that of passive optical space sensors to include also waveform LiDAR instruments and devices typically used during *in-situ* validation campaigns of remotely sensed products. Figure 2 provides an overview of the evolution of the RAMI activity with depictions of the canopy architecture of various test cases.

The strategy of RAMI benefited 1) model developers, who were able to debug their software codes and receive indications as to where future development efforts were most needed, 2) users of canopy RT models, who can now make better choices regarding the selection of canopy RT models, and 3) the RT modelling

By its very nature, RAMI and the I3RC (its sister activity dealing with clouds: <http://i3rc.gsfc.nasa.gov/>), are both dynamic and evolving activities. As a result, the benchmarks, reference data sets and evaluations issued by the RAMI process must be considered snapshots describing the state of the art at the time of the exercise, and not as a final, absolute and definitive judgment on the worthiness and performance of any particular model. In fact, it is through its systematic approach to RT model verification that RAMI contributes to the quality assurance of space derived information.

3. OPPORTUNITIES AND CHALLENGES

3.1 Expanding the scope of RAMI

Through its systematic benchmarking efforts the various phases of RAMI have allowed to 1) identify ‘credible’ canopy RT models, 2) generated ‘surrogate truth’ reference data sets, 3) automate the model verification process via quasi-real time web-based benchmarking facilities, and 4) gradually increased the complexity and realism of the simulated plant environments. This allows RAMI to envisage the expansion into new thematic areas (soils, coastal zones, urban areas), spectral regions (thermal, SAR), and specific instruments (both space and in-situ based). Similarly, the benchmarking of RT model simulations under truly ‘controlled experimental conditions’ – such as are nowadays achievable in reference laboratory facilities – should be addressed in the future. This would both strengthen the credibility of the 3-D Monte Carlo models that were used to generate the ROMC reference dataset, and also enable the set-up of a traceable quality assurance system to relate the performance of simpler canopy RT models – via the above 3-D Monte Carlo models – to a series of absolute reference standards of the real (as opposed to virtual) world.

Ultimately, however, it is the accuracy of the retrieved state variable values that counts in many RT model applications. During RAMI-1 it had already been proposed to address the inversion of RT models against predefined sets of spectral and angular observations, similar to those provided by the current fleet of space borne sensors. In this way, it was hoped, that in this manner the impact of the various structural and radiative canopy model assumptions could be thoroughly assessed since

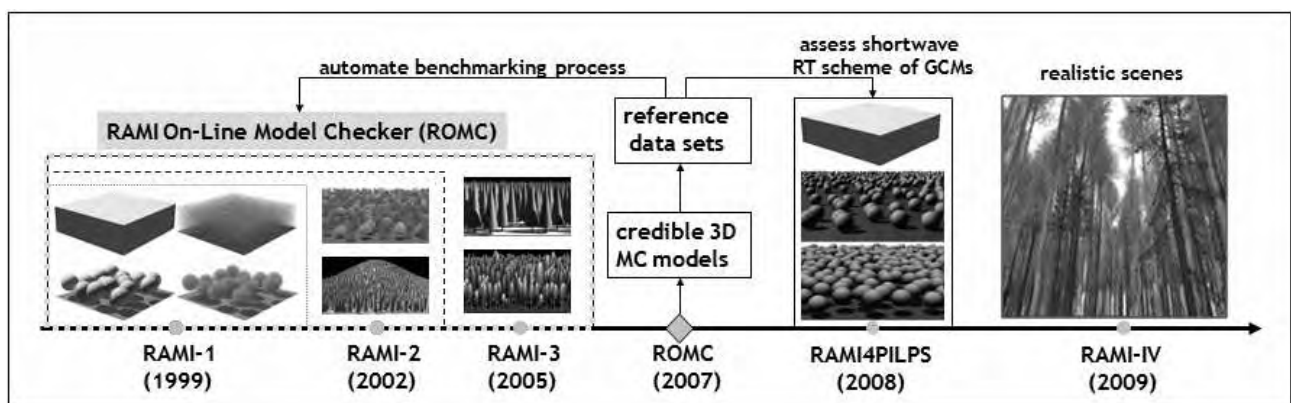


Figure 2. Evolution of the RAMI initiative.

community which, through its continuing support and active encouragement of RAMI, was able to increase its visibility and maturity. About 60–65% of all currently existing canopy RT models have voluntarily participated in the RAMI initiative.

the uncertainties of the available surface BRFs were known *a priori*. This approach had to be abandoned though due to a severe lack of participants. Now, with the identification of ‘credible’ canopy RT models new sensor-specific (top-of-

canopy or top-of-atmosphere) data sets could be generated to revisit the model inversion issue once again.

3.2 Revisiting model evaluations with measurements

RAMI was conceived as an open-access community exercise and will continue to pursue that direction. As such its goal is to move forward in a manner that addresses the needs of the majority of RT model developers and users. With every model having its own implementation of ‘reality’ it has become necessary to provide as detailed descriptions as possible of increasingly realistic canopy architectures. During the fourth phase of RAMI explicit 3-D tree generations (accounting for the position and orientation of every single leaf, twig and branch) were generated on the basis of detailed forest inventory data and L-system based or interactive tree generation software tools, e.g., Streit (1992) and Lintermann and Deussen (1999). Such tree representations, although realistic looking by design, are not exact copies of the trees actually present at the test sites. At best the RAMI-IV canopies agree in terms of the location of the overstorey trees and their outer dimensions and leaf content with what was present at the actual stands. Foliage orientation, distribution and colour, as well as, the branching patterns and densities in trees, however, are in all likelihood different. The same is also true for the directionality of scattering interactions between the sunlight and foliage, branch or background components, or, the directionality of the incident radiation. The apparent realism of some of the RAMI-IV test cases is thus at best an example of the capabilities of some of the 3-D canopy RT models but not proof of our abilities to generate structurally and radiatively accurate replicas of existing forest stands (that are suitable for the validation of canopy RT models).

The fourth phase of RAMI has shown that 3-D canopy RT models are capable of representing forest stands over 1 hectare or more where every single leaf/needle is accounted for. The time thus may have come to revisit our capabilities in building spectrally and architecturally accurate replicas of actual forest sites. Earlier efforts in this direction, like the work of Martens et al. (1991) and those associated with large field campaigns like BOREAS (Sellers et al., 1997) and/or the Kalahari transect (Scholes et al., 2004), were not providing sufficient structural and spectral details to allow for an unambiguous verification of RT model simulations against remotely sensed observations over actual test sites. Structural clumping – occurring at various scales within the canopy – may have a significant impact on the BRDF of a vegetation target and thus a very fine description of plant architectures are needed for model verification purposes. Recently, Coté et al. (2009) showed that terrestrial laser scans could be used to generate faithful reconstructions of individual trees that – when ingested into state-of-the-art 3-D Monte Carlo ray-tracing models – yielded accurate simulation results whether for *in-situ* observations, like those acquired by hemispherical photography, or for medium spatial resolution optical space-borne sensors. In addition, upward pointing field goniometers now exist that can be deployed to provide multi-spectral characterizations of the incident radiation field at a given test site at the time of satellite overpass. What is still needed perhaps are suitable protocols (and instruments) allowing to characterize the scattering directionality of foliage, wood and background material (as well as their spatial variability) in a manner that is both efficient and independent of the illumination conditions at the target site.

One way to evaluate the fidelity of such ‘virtual validation sites’ would be to use credible canopy RT models (having known uncertainties) to simulate atmospherically-corrected air

or space borne observations acquired over the same canopy targets under the *proviso* that both the characteristics of the remote sensor(s) and the directionality of the incident solar radiation at the time of overpass were accurately known. In this way canopy RT models could actively contribute toward the systematic validation of remote sensing data, products, and field protocols as promoted by the Committee on Earth Observation Satellites (CEOS).

4. CONCLUSION

Through a decade of systematic benchmarking efforts RAMI allowed to 1) identify a series of ‘credible’ canopy RT models, 2) generate ‘community’ reference data sets, 3) establish web-based benchmarking facilities, and 4) increase the realism of the simulated plant environments. A variety of thematic domains, spectral regions and individual sensors could all benefit from being included in future RAMI activities. Due to rapid improvements in space sensors and physically-based retrieval algorithms systematic RT model validation activities are essential to document whether the quality of space derived information is improving. Here, a more proactive support from space agencies, scientific bodies and policy makers may help, for example, by making the provision of funding conditional on quality certificates that testify as to the aptitude of models and/or algorithms contained in a given proposal. Automated web-based benchmarking facilities, like the ROMC, can already now deliver such quality assurance support.

REFERENCES

- Chen, J. M., Nilson, T. and Strahler, A., 2000, Recent Advances in Geometrical Optical Modelling and its Application, *Remote Sensing Reviews*, 18, 227-262.
- Coté, J-F., Widlowski, J-L., Fournier, R. A., Verstraete, M. M., 2009, The structural and radiative consistency of three-dimensional tree reconstructions from terrestrial Lidar, *Remote Sensing of Environment*, 113, pp. 1067-1081.
- Disney, M. I., Lewis, P. E., North, P. R. J., 2000, Monte Carlo Ray Tracing in Optical Canopy Reflectance Modelling, *Remote Sensing Reviews*, 18, 163-196.
- Franklin, J., and Duncan, J., 1992, Testing the Li-Strahler Four-component Canopy Reflectance Model in the Hapex-Sahel Shrub Savanna Sites Using Ground Reflectance Data, In: *Proceedings of the IEEE International Geosciences and Remote Sensing Symposium*, pp. 200-202.
- Goel, N., 1988, Models of Vegetation Canopy Reflectance and their use in Estimation of biophysical parameters from reflectance data, *Remote Sensing Reviews*, 4(1), 1-222.
- Goel, N., and Kuusk, A., 1992, Evaluation of One Dimensional Analytical Models For Vegetation Canopies, In: *Proceedings of the IEEE International Geosciences and Remote Sensing Symposium*, pp. 505 - 505.
- Goel, N., and Thompson, R., 2000, A snapshot of canopy reflectance models and a universal model for the radiation regime, *Remote Sensing Reviews*, 18, 197-225.
- Hu, B. X., Lucht, W. and Strahler, A. H., 1999, The interrelationship of atmospheric correction of reflectances and

- surface BRDF retrieval: A sensitivity study, *IEEE Transactions on Geoscience and Remote Sensing*, 36, 724-738.
- Liang, S., and Strahler, A., 1992, An Explicit Canopy BRDF Model and Inversion, In: *Proceedings of the IEEE International Geosciences and Remote Sensing Symposium*, Vol. 2, pp. 1487 - 1489.
- Lintermann, B. and Deussen, O., 1999, Interactive Modelling of Plants, *IEEE Computer Graphics and Applications*, 19(1), pp. 2-11.
- Martens, S. N., Ustin, S. L., Norman, J. M., 1991, Measurements of tree canopy architectures, *International Journal of Remote Sensing*, 12(7), pp. 1525-1545.
- Oreskes, N. K., 1994, Verification, validation and confirmation of numerical models in the earth sciences. *Science*, 263, 641-646.
- Pinty, B., and Verstraete, M. M., 1992, On the Design and Validation of Surface Bidirectional Reflectance and Albedo Models, *Remote Sensing of Environment*, 41, pp. 155-167.
- Pinty, B., Gobron, N., Widlowski, J. -L., Gerstl, S. A. W., Verstraete, M. M., Antunes, M., Bacour, C., Gascon, F., Gastellu, J-P., Goel, N., Jacquemoud, S., North, P. R. J., Qin, W., Thompson, R., 2001, Radiation Transfer Model Intercomparison (RAMI) exercise. *Journal of Geophysical Research*, 106, pp. 11,937–11,956.
- Pinty, B., Widlowski, J.-L., Taberner, M., Gobron, N., Verstraete, M. M., Disney, M., Gascon, F., Gastellu, J.-P., Jiang, L., Kuusk, A., Lewis, P., Li, X., Ni-Meister, W., Nilson, T., North, P., Qin, W., Su, L., Tang, S., Thompson, R., Verhoef, W., Wang, H., Wang, J., Yan, G., and Zang, H., 2004a. Radiation Transfer Model Intercomparison (RAMI) Exercise: Results from the Second Phase. *Journal of Geophysical Research*, 109, D06210.1-D06210.19, doi:10.1029/2003JD004252.
- Pinty, B., N. Gobron, J.-L. Widlowski, T. Lavergne, and M. M. Verstraete, 2004b, Synergy between 1-D and 3-D radiation transfer models to retrieve vegetation canopy properties from remote sensing data, *Journal of Geophysical Research*, 109, D21205, doi:10.1029/2004JD005214.
- Qin, W. and Liang, S., 2000, Plane-parallel Canopy Radiation Transfer Modeling: Recent Advances and Future Directions, *Remote Sensing Review*, 18, 281-305.
- Ross, J., 1981, *The Radiation Regime and Architecture of Plant Stands*. Kluwer Academic Publishers, Boston, pp. 391.
- Schaaf, C., Li, X., and Strahler, A., 1994, Validation of Canopy Bidirectional Reflectance Models with Asas Imagery of a Spruce Forest in Maine, In: *Proceedings of the IEEE International Geosciences and Remote Sensing Symposium: Surface and Atmospheric Remote Sensing: Technologies, Data Analysis and Interpretation*, Vol. 3, pp. 1832-1834, doi:10.1109/IGARSS.1994.399581.
- Scholes, R. J., Frost, P. G. H., and Tian, Y., 2004, Canopy structure in Savannas along a moisture gradient on Kalahari sands, *Global Change Biology*, 10, 292–302.
- Sellers, P. J., et al., 1997, BOREAS in 1997: Experiment overview, scientific results and future directions, *Journal of Geophysical Research*, 102, 28,731– 28,770.
- Soffer, R. J., Miller, J. R., Wanner, W., and Strahler, A., 1995, Winter boreal forest canopy BRDF results: comparison between airborne data, laboratory simulations and geometric-optical model data, In: *Proceedings of the IEEE International Geosciences and Remote Sensing Symposium: Quantitative Remote Sensing for Science and Applications*, Vol. 1, pp. 800 - 802, doi:10.1109/IGARSS.1995.520589.
- Strahler, A. and Liang, S., 1994. Comparison of Radiative Transfer Models of Vegetation Canopies with Laboratory Measurements, In: *Proceedings of the IEEE International Geosciences and Remote Sensing Symposium: Surface and Atmospheric Remote Sensing: Technologies, Data Analysis and Interpretation*, Vol. 4, doi:10.1109/IGARSS.1994.399733, pp. 2345-2347,.
- Strahler, A., 1997, Vegetation canopy reflectance modeling – recent developments and remote sensing perspectives. *Remote Sensing Reviews*, 15:1, 179-194.
- Streit, C., 1992, *Graptal user manual*. Berne, Switzerland: University of Berne, SIG Computer Graphics.
- Widlowski, J.-L., Pinty B., Gobron, N., Verstraete, M. M., Diner, D. J., Davis, A. B., (2004), Canopy Structure parameters derived from multi-angular remote sensing data for terrestrial carbon studies, *Climatic Change*, 67, 403-415.
- Widlowski J.-L., Taberner M., Pinty B., Bruniquel-Pinel, V., Disney, M., Fernandes, R., Gastellu-Etchegorry, J-P., Gobron, N., Kuusk, A., Lavergne, T., Leblanc, S., Lewis, P. E., Martin, E., Mottuse, M., North, P. R. J., Qin, W., Robustelli, M., Rochdi, N., Ruiloba, R., Soler, C., Thompson, R., Verhoef, W., Verstraete, M. M., Xie, D., 2007. The Third Radiation Transfer Model Intercomparison (RAMI) Exercise: Documenting Progress in Canopy Reflectance Modelling. *Journal of Geophysical Research*, 112, doi:10.1029/2006JD007821.
- Widlowski J.-L., Robustelli, M., Disney, M., Gastellu-Etchegorry, J-P., Lavergne, T., Lewis, P., North, P. R. J., Pinty, B., Thompson, R., and Verstraete, M. M., 2008. The RAMI On-line Model Checker (ROMC): A web-based benchmarking facility for canopy reflectance models. *Remote Sensing of Environment*, 112, doi:10.1016/j.rse.2007.07.016, pp. 1144-1150.

ACKNOWLEDGEMENTS

I would like to acknowledge the support of the various RAMI participants who through their efforts and contributions managed to advance not only the quality of canopy RT models but also keep RAMI alive and developing. Similarly, I want to acknowledge the support of Dr. Alan Belward and my colleagues in the SOLO action of the Global Environment Monitoring unit of the Institute for Environment and Sustainability of the Joint Research Centre of the European Commission in Ispra, Italy for their continuing support for the RAMI project.

TROPICAL BIODIVERSITY MAPPING FROM HYPERION IMAGE IN BOGOR INDONESIA

A. Wijanarto^{*a}, F. Amhar^a

^aGeomatics Research Division, National Coordinating Agency for Surveys and Mapping, Jl. Jakarta Bogor km 46 Cibinong Bogor, 16911, Cibinong, Indonesia
wijanarto_ab@yahoo.com.au, famhar@yahoo.com

Technical Commission VII Symposium 2010

KEY WORDS: Hyper spectral, Land Cover, Mapping, Soil, Vegetation

ABSTRACT:

Hyperspectral remote sensing is increasingly used for many applications, and one of them is biodiversity mapping. Commonly used data are MODIS and other low resolution satellite images, which have been freely accessed and obtained, while the use of medium resolution hyperspectral images was rare, until mid 2009 when EO-1 Hyperion was declared free. This has motivated some studies to make first step of ambitious project: tropical biodiversity mapping. As tropical country with rich biota, biodiversity mapping is very important in Indonesia. A terrestrial spectrometry completed the data for deeper analysis. A biodiversity map will be derived from EO-1 Hyperion data over Bogor Botanical Garden. The area covers about one kilometer square. The study shows that there is a need for building better tropical spectral library.

1. INTRODUCTION

Biodiversity map is an important issue for today's global earth condition. It is not just an interest for biologists and environmentalists, but now it deals with the global issue of climate change, where biodiversity richness in every part of the earth is under threat for extinction. Biodiversity (richness) occurs at many scales and includes genetic diversity, species diversity (species richness), functional diversity, and ecosystem diversity (Gamon, 2008). Tropical ecosystems are among the world's hotspots of species richness and endemism. Many of the forested ecosystems are disappearing or being degraded at rapid rates. In the past, remote assessment of biodiversity has been largely indirect because satellite sensors have generally lacked the spectral and spatial resolution needed to capture patterns of species richness directly. Additionally, optical remote sensing of biodiversity is generally limited to what can be detected from above and is heavily weighted by the signal returning from top surface layer – for example, the upper canopy layers of a forest.

With the advent of new imaging spectrometers, we now have several more direct pathways for linking remote sensing to some measure of biodiversity. Some of these alternate measures of diversity may be more accessible from remote sensing than species richness. When combined with spatial detail (small pixel sizes) and temporal resolution (multitemporal imagery), hyperspectral sensors provide a rich array of tools for direct assessment of vegetation functional and structural diversity from remote sensing.

The use of remote sensing to detect biodiversity depends on the biodiversity level being measured and this relates to either spatial or spectral resolution. If there is high correlation between remote sensing and biodiversity then there will be a

strong correlation between the optical diversity with the surface canopy or other measures of biodiversity detectable.

Hyperspectral data are narrow band information of the reflectance of objects on the earth surface. The data are usually acquired from satellite, aircraft, or from a spectroradiometer. This kind of technology provides advantages in analysing the spectral object information in detail. One of the spectral data that are still under research stage is the Hyperion, carried by the EO-1 satellite (Nemani *et al.* 2003). Hyperion data contain 242 spectral bands that can be classified into AVNIR spectral range (bands 1-70) to SWIR spectral range (bands 71-242). There are 220 unique spectral bands or channels in Hyperion images, with a complete spectrum covering from 357 to 2567 nm. From the 242 bands contained in Hyperion data only 198 bands were calibrated, and the uncalibrated channels were due to the detectors' low responsivity. These are the level 1 Radiometric product. There is an overlap between the VNIR and SWIR so that only 196 bands are unique. The calibrated channels are band 8 to 57 for the VNIR and 77-224 for the SWIR (University of Cincinnati, 2003).

In general, the capability of hyperspectral sensor to detect many narrow spectral bands can be applied to detect chemical and anatomic characteristics from many plant reproductivity. Some studies have shown the advantages of using narrow bands (hyperspectral data) using certain spectrum in comparison to wide spectral band (multi-spectral data) for example, to obtain quantitative and qualitative information of the most sensitive part in vegetation or crop plants (Elvidge, 1990; Adams *et al.*, 1995; Gao, 1996; Ceccato *et al.*, 2001).

Because of different spectral width used by hyperspectral data, this requires different approaches in its processing procedures. For mapping purposes, the commonly applied project is the

* Corresponding author.

land cover classification. The capability of narrow bands in the hyperion data will be assessed to map the land cover in general and the biodiversity of tropical plants in particular.

2. MATERIALS

2.1 Study Area

The study area for this research is in Bogor Botanical Garden area and surrounding, Indonesia (Figure 1). Bogor Botanical Garden is managed by the Ministry of Forestry in Indonesia and contains more than one thousand plant species. The area covers about 1.2 X 1.2 kilometer squares, and this is equivalent to about 1600 pixels in the Hyperion image. From Figure 1 it can be seen that the only homogenous type of vegetation covering at least one pixel in Hyperion is the grass. Therefore, in this exercise biodiversity will focus on extracting limited vegetation cover, but will be extended to cover more land cover such as manmade (asphalt), residential/roof, water (freshwater), etc.

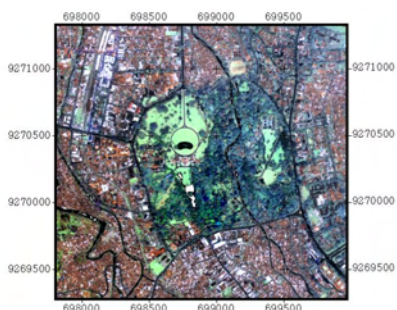


Figure 1. Bogor Botanical Garden, viewed from IKONOS image, West Java, Indonesia (UTM Zone 48S).

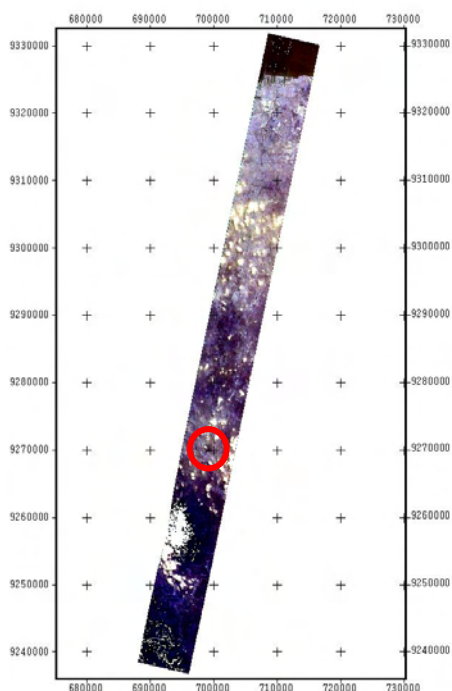


Figure 2. Whole scene of Hyperion Image of Bogor, Jakarta and surrounding areas using RGB combination of bands 24, 12 and 8 (Botanical Garden in red circle) Image was obtained from <http://eo1.usgs.gov>.

2.2 Hyperion Data

The hyperion data were acquired on 13 September 2002 with less than 10% of cloud cover. Unfortunately, some cloud covers some little parts of the botanical garden. The image can be seen in Figure 2. The zoomed image display in RGB for VNIR and SWIR bands can be seen in Figure 3 and 4.



Figure 3. Zoomed Hyperion Image of Bogor Botanical Garden and surrounding areas using RGB bands 29, 23 and 16 (VNIR).

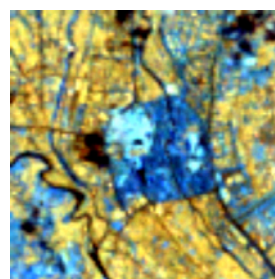


Figure 4. Zoomed Hyperion Image of Bogor Botanical Garden and surrounding areas using RGB bands 204, 150 and 93 (SWIR).

3. METHODS

The general procedures for classifying the Hyperion data can be seen in Figure 5. The procedures mainly consist of data preprocessing that include conversion of data into absolute radiance, atmospheric correction to get reflectance value and classification using the spectral angle mapper method.

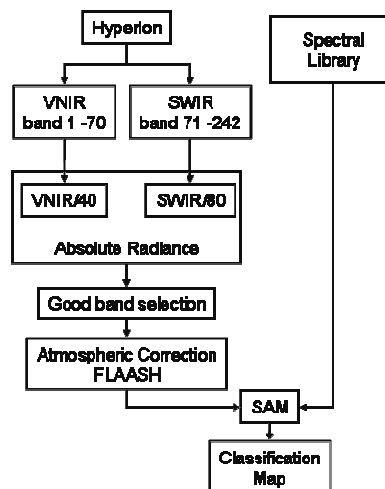


Figure 5. Classification procedures using spectral angle mapper from Hyperion satellite data.

3.1 Hyperion Data Preprocessing

The first step of the preprocessing of Hyperion data is the geometric correction. It aimed at validating the coordinate system to the local coordinate system so that it can be compared to the existing local map and the GPS data. The second step of the preprocessing is the atmospheric correction following the extraction of the absolute radiance.

Atmospheric correction is one of the key step to obtain the surface reflectance of remote sensing optical satellite data operating in visible and near infra-red spectrum. In this preprocessing, spectral (excluding uncalibrated and overlapping bands) and spatial subsets were generated within the scene. The image was masked to exclude water bodies and to minimize under- or over-correction in subsequent processing steps. Calibrated radiance data were converted to surface reflectance using Fast Line-of-sight Atmospheric Analysis of Spectral Hypercubes (FLAASH). For the FLAASH input data, the Hyperion data were scaled down by the factor of 400 for the AVNIR and 800 for the SWIR. For this exercise, only AVNIR data were used for the classification.

3.2 Classification of Hyperion Data

The classification applied for vegetation mapping here uses the Spectral Angle Mapper method. The Spectral Angle Mapper matches the hyperspectral pixels to the known or reference spectra. The algorithm determine the spectra similarity by calculating the angle between the spectra, where the smaller angle represents better correlation than the wider angle. In the spectral angle mapper technique for identifying pixel spectra only the angular information is used (Richards and Jia, 2006).

The classification of hyperspectral using spectral end members derived from the spectral library is aimed at producing a map of surface composition where the interpreter does not have any prior knowledge to the surface condition. Here, there is no ground truth data is used for the supervised classification. The available spectral libraries are mainly written using reflectance information as a function wavelength.

4. RESULTS AND DISCUSSION

4.1 Spectral Library

Some of the spectral references for certain objects are available in ENVI (Figure 6). From Figure 4 it can be said that for the classification process, the image must be converted to reflectance, instead of just the radiance.

4.2 Absolute Radiance Images

The absolute radiance images displayed in Figure 7 are the results following the down scaling of the digital number by 40 and 80 for the VNIR and SWIR images, respectively. The unit for the image is $\mu\text{W}/\text{cm}^2.\text{nm}.\text{sr}$. Following the FLAASH computation, the profile of the reflectance of the point sampled in Figure 7 can be seen in Figure 8. The graph produced is slightly different from the reflectance of the distilled water from the spectral libraries (Figure 6). This may be due to the material contained by the river water.

4.3 Selecting Good Bands

Not all of the spectral band in the Hyperion data are used.

Several good bands include bands 9-52, 77-120, 130-167, and 180-222.

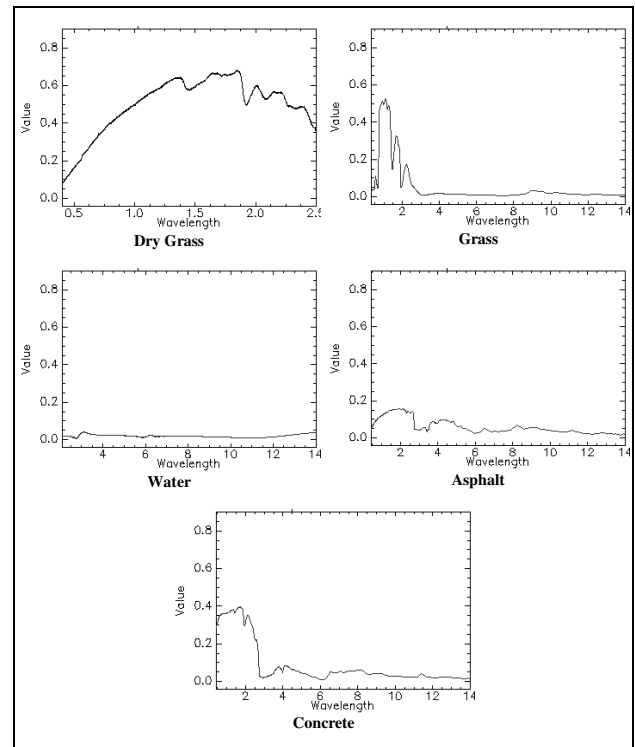


Figure 6. Selection of spectral references for land cover and biodiversity mapping. The y axis indicates the values of object reflectance.

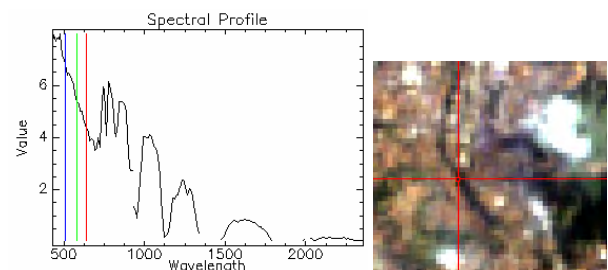


Figure 7. The profile of the radiance Image of Figure 5 (River water).

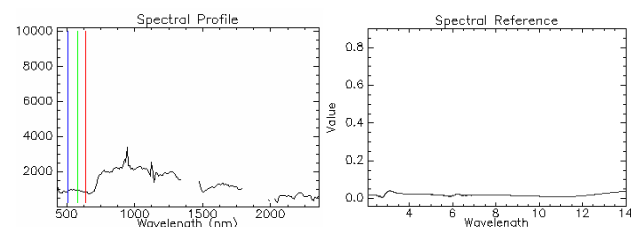


Figure 8. The profile of the reflectance Image (left) of the point in Figure 7 (River water) compared to distilled water from the spectral library (right).

4.4 Classification Results

The classification scheme used maximum angle of 0.1 radians with good VNIR bands only (bands 9-52). The results of the classification can be seen in Figure 9 and Table 10.

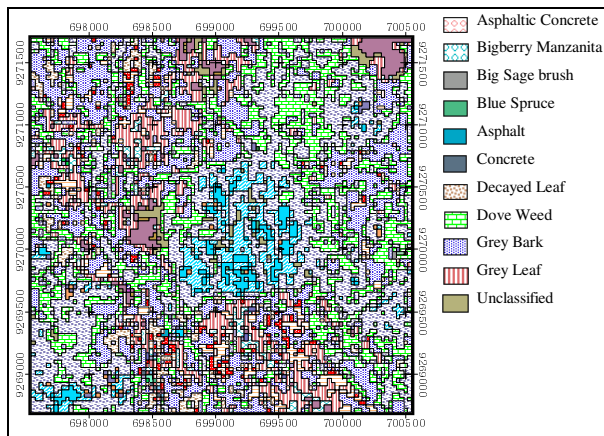


Figure 9. Classification results using SAM with maximum angle of 0.1 applied to all good VNIR bands.

Class	Points	%	Area (m ²)
Asphaltic Concrete	2	0.020%	1,800
Bigberry Manzanita	549	5.490%	494,100
Big Sage brush	2,192	21.920%	1,972,800
Blue Spruce	4	0.040%	3,600
Asphalt	17	0.170%	11,700
Concrete	13	0.130%	2,700
Decayed Leaf	265	2.650%	238,500
Dove Weed	2,300	23.000%	2,070,000
Grey Bark	2,317	23.170%	2,085,300
Grey Leaf	982	9.820%	876,600
Unclassified	151	1.510%	135,900

Table 10. Class Statistics.

5. CONCLUSION

From the results above it can be concluded that the spectral data of VNIR bands work better than the SWIR, at least for mapping land cover of the study area. This means that bands selection is very important for matching different objects. Secondly, the spectral libraries obtained from the ENVI match with some objects in the study area, therefore, there is a need for building own spectral library of tropical features. The spectral angle can then be tightened for more confident results.

REFERENCES

- Adams, J.B., Sabol, D.E., Kapos, V., Filho, R.A., Roberts, D.A., Smith, M.O., Gillespie, A., 1995. Classification of multispectral images based on fractions of endmembers; application to land-cover change in the Brazilian Amazon, *Remote Sensing of Environment*, 52(2), pp. 137-154.
- Ceccato, P., Flasse, S., Tarantola, S., Jacquemoud, S., Grégoire, J.-M., 2001. Detecting vegetation leaf water content using reflectance in the optical domain, *Remote Sensing of Environment*, 77(1), pp. 22-33.
- Elvidge, C.D., 1990. Visible and near-infrared reflectance characteristics of dry plant materials, *International Journal of Remote Sensing*, 11(10), pp. 1775-1795.
- Gamon, J.A., 2008. Tropical Remote Sensing-Opportunities and

Challenges. In *Hyperspectral Remote Sensing Of Tropical And Subtropical Forests*: Edited by Margaret Kalacska and G. Arturo Sanchez Azofofeifa. CRC Press, Taylor & Francis Group, pp. 297-304.

Gao, B., 1996. NDWI– a normalized difference water index for remote sensing of vegetation liquid water from space. *Remote Sensing of Environment*, 58 (3), 257-266.

Nemani, R. R., Keeling, C. D., Hashimoto, H., Jolly, W. M., Piper, S. C., Tucker, C. J., et al. (2003, June 6). Climate-driven increases in global terrestrial net primary production from 1982 to 1999, *Science*, 300, pp. 1560– 1563.

Richards JA and Xiuping Jia., 2006. *Remote Sensing Digital Analysis, An Introduction*. 4th Edition. Springer Berlin Heidelberg New York, pp. 368-373.

University of Cincinnati, 2003. EO-1 User Guide v. 2.3. Obtained from the website: <http://eo1.usgs.gov> & <http://eo1.gsfc.nasa.gov> (accessed 20 Dec 2009).

A NEW STRATEGY FOR DSM GENERATION FROM HIGH RESOLUTION STEREO SATELLITE IMAGES BASED ON CONTROL NETWORK INTEREST POINT MATCHING

Z. Xiong^a, Y. Zhang^a

^a Department of Geodesy & Geomatics Engineering, University of New Brunswick,
15 Dineen Drive, PO Box 4400, Fredericton, NB, Canada E3B 5A3- zxiong@unb.ca, yunzhang@unb.ca

Commission VII

Key Words: Control Network, Interest Point Matching, High Resolution Satellite Image, Digital Surface Model

ABSTRACT:

Image matching is the key for automatic DSM generation. Currently two kinds of image matching method represent two different trends: area-based method and feature-based method. However, both of them seriously rely on the gray distribution of the image. Therefore, they share a common drawback: ambiguity in homogeneous areas, such as grass land, heavily forested area, highway, and building roofs etc. To solve this problem, a popular way is to apply different conditions to image matching to limit the search window, so that reduce the ambiguity in the homogeneous area. In the photogrammetric community, eppipolar condition is widely used in image matching to reduce the search window from two dimensions to one dimension. Unfortunately, in many cases, the eppipolar condition is not applicable. In order to solve this problem, the control network interest point matching algorithm was recently developed. This method constructs a control network based on the prominent feature points and the spatial information is provided to the image matching to limit the search window. In this paper, we proposed a new strategy based on the control network interest point matching to generate digital surface model from high resolution satellite stereo images. We commence our paper with a brief review of current research on image matching. We then introduce the proposed algorithm in detail and describe experiments with high resolution satellite images. Through experiment, the digital surface model was successfully created from the stereo images. The experiment results show that the proposed algorithm can successfully process local distortion in high resolution satellite images and can avoid ambiguity in the homogeneous areas.

1. INTRODUCTION

Image matching is the key technique for image processing. It is commonly used for DSM generation, 3D shape reconstruction, change detection, medical diagnosis, computer vision and pattern recognition. Currently numerous algorithms have been developed for different applications, and these algorithms can be grouped into two categories: area-based and feature-based. Both kinds of algorithms have their own particular advantages in specific circumstances. However they all seriously depend on the gray distribution of image and face the common problem: ambiguity in homogeneous areas, such as grass land, highway surfaces, building roofs, etc. In order to solve this problem, the eppipolar condition is usually applied to limit the search window from two dimensions to one dimension so as to reduce the ambiguity in the homogeneous area. Unfortunately, in many real-time image matching cases, the eppipolar condition is not applicable. The recent developed control network interest point matching algorithm successfully solved this problem. This algorithm constructs a control network based on the prominent feature points and then the control network provides spatial information for those interest points in the homogeneous area so as to reduce the ambiguity.

In this research, we tried to apply the control network interest point matching algorithm to generate the digital surface model from the stereo satellite images. Without the eppipolar condition, the control network is used to provide the constraint to limit the search window. Because of the large ground relief variation, an image pyramid is generated first. Then the grid point image matching is conducted based on the control network.

In the following sections of the paper, we introduce the proposed algorithm first. Then present the experiment with a stereo satellite images. Finally we give the conclusions.

2. PROPOSED ALGORITHM

The control network is generated from the prominent feature points. So the interest point is extracted first. Many interest point extraction algorithms are available. The Harris detector was used in this research. Later on a threshold is applied to those extracted interest points to extract the prominent feature points. These prominent feature points are also named super points. A super point matching is executed and a control network is formed.

This control network is used to provide spatial information to the grid points. So the grid point matching is constrained by this spatial information. The correspondence is searched in a small search window so as to reduce the ambiguity and avoid local minimum problem. However, due to the large variation of the ground relief, the control network cannot provide support to limit the search window in a small enough area to completely avoid ambiguity. So a pyramid structure is applied in this algorithm. In this way, the correspondence is found gradually so as to avoid large relief variation. The cross correlation is also used to determine the correspondence in the search window.

Finally, the conjugate points are used to determine the 3D points by using space intersection. The breakline can be added into it before the TIN is generated. The DSM is created based on TIN. Figure 1 shows the flowchart of this algorithm.

3. EXPERIMENT

A stereo pair of IKONOS images, acquired in February of 2003 in Hobart, Tasmania, Australia was used for this experiment (**Figure 2**). The incidence angles are forward 75° and backward 69° respectively (Fraser and Hanley, 2005). **Table 1** lists the main characteristics of images in Hobart test field.

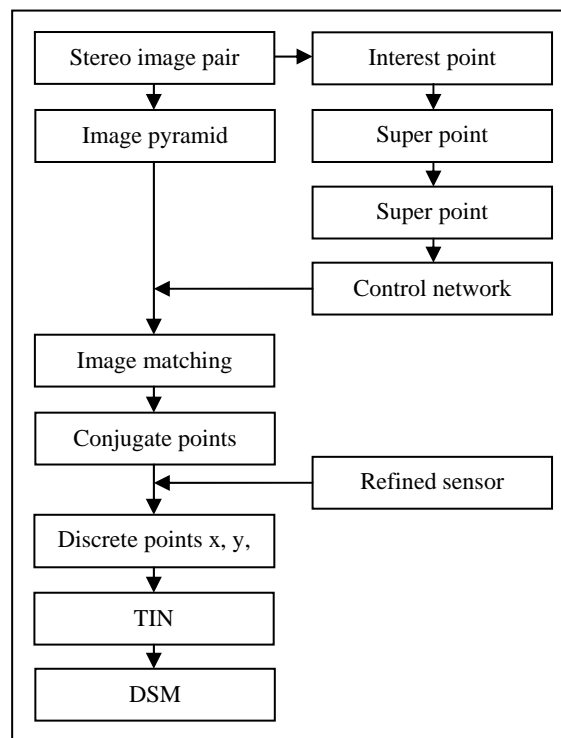


Figure 1. Flowchart of the image matching strategy for DSM extraction from stereo satellite image pair.



Figure 2. Stereo pair of IKONOS images in Hobart (courtesy of the University of Melbourne)

Table 1. Characteristics of the IKONOS Imagery in Hobart Test Field (Fraser and Hanley, 2005)

	IKONOS, Hobart
Area	120 km ² (11×11 km)
Elevation Range	Sea level to 1280 m
Image Coverage (elevation angles)	Stereo triplet (69°, 75°, 69°)
Number of GCPs	113
Notable Features	Full scene; mountainous terrain
Base-to-height ratio	0.8
Date of acquirement	February, 2003
GCP measurement on image	Sub-pixel accuracy for roundabout features; pixel accuracy for other features.
Scan model	Reverse model for 69° images; Forward model for 75° image

The test area includes urban area and mountain area. The elevation ranges from zero to one thousand meters. Because of its large relief variation, this is an ideal area to test the DSM generation algorithm. We have one hundred and thirteen ground control points normally distributed in the

test area and collected with geodetic GPS receiver. The satellite sensor model was refined to sub-pixel accuracy (in image space) and sub-meter accuracy (in object space). Figure 3 demonstrate the original image of test area (left) and the generated DSM with the proposed algorithm.

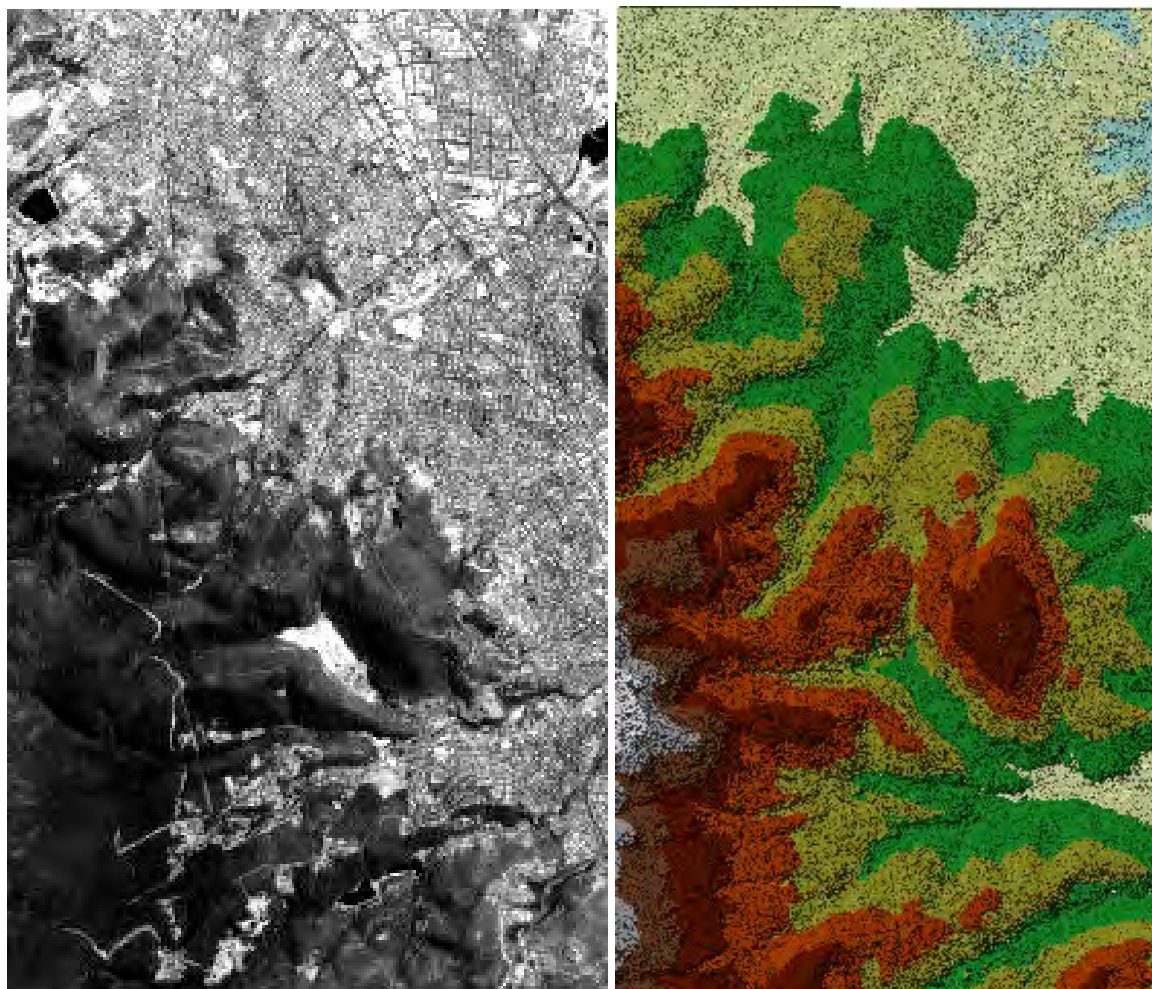


Figure 3. Original satellite image of the test area (left) and the DSM (right) generated with the proposed algorithm.

In order to observe more detail of the DSM, we cut the image and the DSM into two parts and zoom in it (**Figure 4**

and 5). Figure 4 shows the upper part of Figure 3 and Figure 5 demonstrate the lower part of Figure 3.

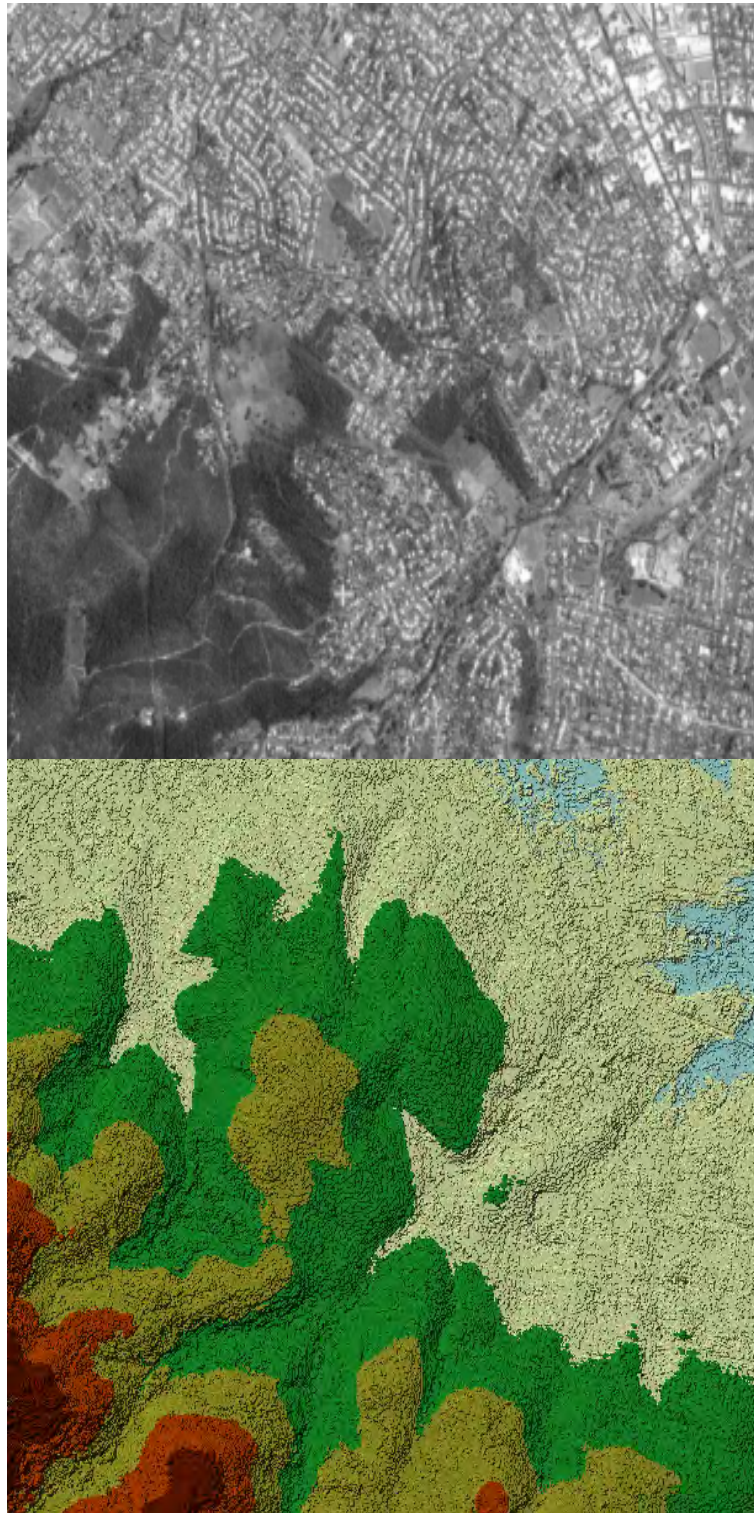


Figure 4. The original image (upper) and DSM (lower) (corresponds to the upper part of Figure 3).

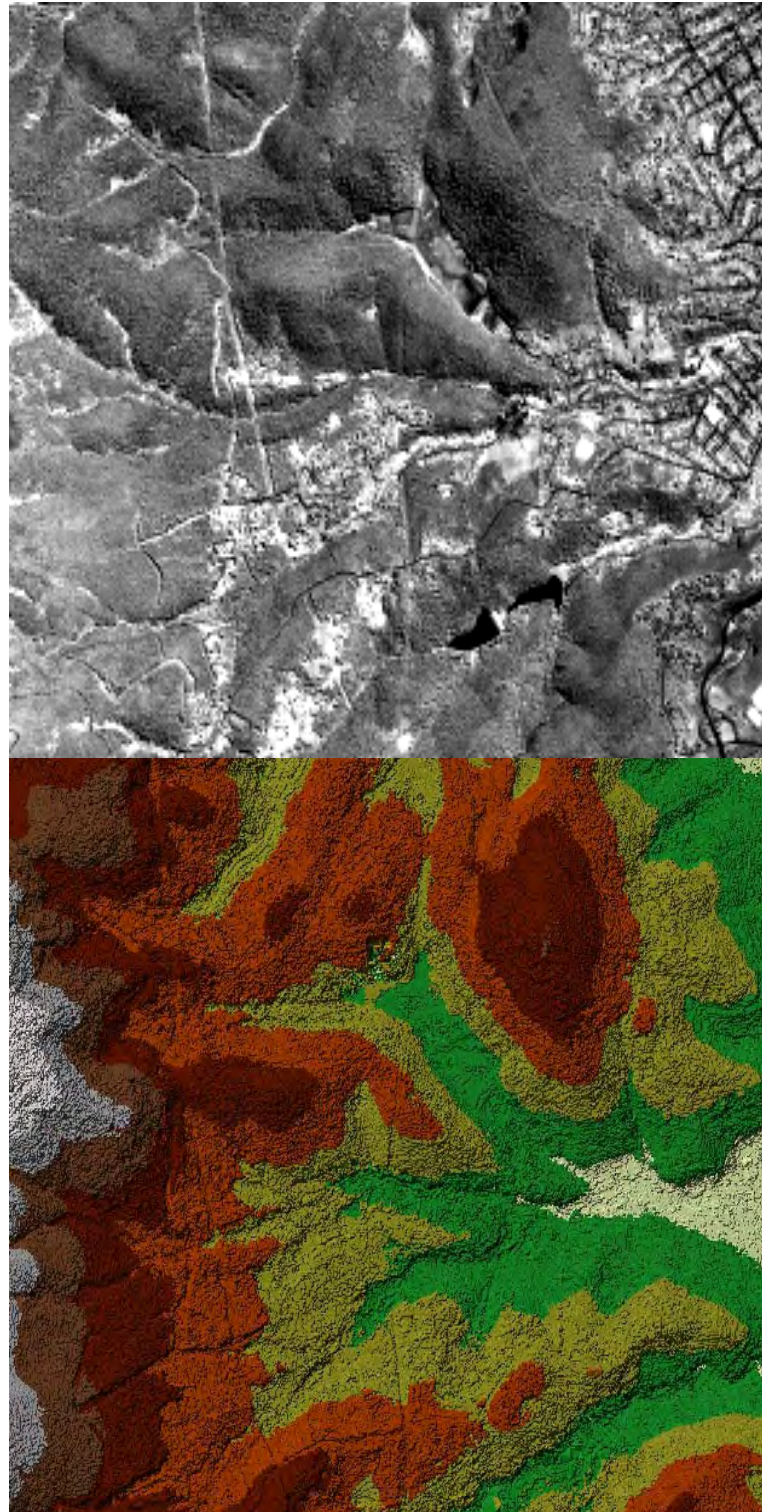


Figure 5. The original image (upper) and DSM (lower) (corresponds to the lower part of Figure 3).

In order to check the accuracy of the generated DSM, we randomly selected twenty five correspondences. We manually measured the image coordinates of the correspondences and then compared it with the image

coordinates of the correspondences which are automated generated by the program. We applied space intersection to these correspondences to determine their coordinates and check their difference in the object space. Table 2

demonstrates the detail of the accuracy assessment. From this table, we can find that only one of twenty five points has deviation from the manually measured correspondences

and resulted in 3.30 meters, -1.78 meters, and -3.60 meters deviation in x, y, and z dimension.

Table 2. Accuracy evaluation of DSM

No	Tie points Extracted by algorithm				Tie points extracted manually				Deviation		
	Column	Row	Column	Row	Column	Row	Column	Row	$\Delta x(m)$	$\Delta y(m)$	$\Delta z(m)$
1	2594	551	2654	546	2594	551	2654	546	0	0	0
2	4664	480	4701	571	4664	480	4701	571	0	0	0
3	7904	690	7940	791	7904	690	7940	791	0	0	0
4	1381	1938	1450	1903	1381	1938	1447	1903	0	0	0
5	4478	1565	4518	1648	4478	1565	4518	1648	0	0	0
6	6842	1549	6880	1645	6842	1549	6880	1645	0	0	0
7	1245	2376	1309	2347	1245	2376	1309	2347	0	0	0
8	3064	2927	3109	2988	3064	2927	3109	2988	0	0	0
9	6196	2412	6237	2488	6196	2412	6237	2488	0	0	0
10	177	3521	246	3479	177	3521	246	3479	0	0	0
11	3083	3310	3127	3371	3083	3310	3127	3371	0	0	0
12	5837	3903	5881	3964	5837	3903	5881	3964	0	0	0
13	929	4879	995	4839	929	4879	995	4839	0	0	0
14	2532	4965	2597	4941	2532	4965	2597	4941	0	0	0
15	5321	4839	5369	4885	5321	4839	5369	4885	0	0	0
16	7850	4150	7891	4232	7850	4150	7891	4232	0	0	0
17	2153	5575	2225	5515	2153	5575	2225	5515	0	0	0
18	4826	5352	4877	5380	4826	5352	4877	5380	0	0	0
19	7815	5005	7859	5062	7815	5005	7859	5062	0	0	0
20	5114	298	5151	393	5114	298	5150	395	0	0	0
21	2982	1621	3036	1640	2982	1621	3036	1640	3.30	-1.78	-3.6
22	6944	1740	6990	1838	6944	1740	6982	1833	0	0	0
23	5070	2186	5111	2265	5070	2186	5111	2265	0	0	0
24	2246	3935	2296	3974	2246	3935	2296	3974	0	0	0
25	4368	4772	4426	4776	4368	4772	4426	4776	0	0	0

4. CONCLUSIONS

Based on the experiment and accuracy evaluation, we draw following conclusions.

Without the help of epipolar condition, the proposed algorithm can process homogeneous area with the assistant of control network and.

With the help of control network and the pyramid structure, the proposed algorithm can process the large relief variation of the satellite images.

The proposed algorithm can successfully generate DSM from the complicated area which includes both urban area and high mountain area. And the accuracy of the DSM is encouraging.

Therefore, we believe this technology has the potential to be used for 3D reconstruction in case of no camera geometry can be used to constrain the image matching to deal with the ambiguity in the homogeneous area.

This is an initial attempt of this technology. We plan to conduct extensive test to this algorithm in the near future.

ACKNOWLEDGMENTS

This research is sponsored by the Natural Sciences and Engineering Research Council of Canada through the Discovery Grant (NSERC Discovery Grant) awarded to Dr. Yun Zhang, the second author of the paper. We would like to acknowledge that Professor Clive Fraser, Department of Geomatics Engineering, University of Melbourne, Australia, provided us with satellite images and ground control points for the tests.

REFERENCES:

Omitted.

SAR STEREO-MAPPING BASED ON DEM

Shucheng Yang^{a, b}, Guoman Huang^b, Zheng Zhao^b

^a School of Geodesy and Geomatics, Wuhan University, Wuhan, Hubei, P.R.China - yangshucheng20032001@yahoo.com.cn

^b Chinese Academic of Surveying and Mapping, No.16 Beitaiping Road, Haidian District, 100039, Beijing, P.R.China - huang.guoman@163.com; zhengzhaochina@163.com

KEY WORDS: SAR image, stereo-mapping, parallax, DEM, stereoscopic image pair, topographic map;

ABSTRACT:

In the western region of China, Synthetic Aperture Radar images have been used in extraction of topographic maps. Stereo mapping with stereoscopic image pair is very useful for extraction of feature elements (roads, buildings and other surface features) from SAR image. The basis of stereo-mapping is stereoscopic image pair, of which the vertical parallax must be removed, and the horizontal parallax reserved. This paper presents a method of generating SAR stereoscopic image pair based on Digital Elevation Model, which is used in stereo-mapping. First of all, orientation of SAR image must be completed; then according to DEM, stereoscopic image can be generated through image re-sampling along the range direction from original image. The vertical parallax will be removed, when re-sampling, and the horizontal parallax will be reconstructed with central projection or slant-range projection. There are two ways to generate stereoscopic images from single original image or two different original images. The two images generated from single original image are called mono-source pair. The two images generated from the two different images are called dual-source pair. Experiment is done in this paper with high-resolution space-borne SAR images. Mono-source and dual-source stereoscopic image pairs are generated with central and slant-range projection, and feature elements of topographic map are extracted with the image pairs in the experiment. It proves that the method above is feasible.

1. INTRODUCTION

SAR is an active microwave imaging system with high resolution. Compared with optical sensors, it has series of advantages, such as all-day, all-weather and penetrating through cloud, mist and a certain depth of ground, and so has been used in many fields. As the development of SAR technology, its applications are expanding continuously. The technologies, generating ortho-image with SAR image, extracting three-dimensional topographic information with InSAR and deformation monitoring with D-InSAR (M.Gelautz, 2004), have been relatively mature, but research on SAR analytical stereo-mapping is still limited. The key technique of stereo-mapping is generation of ideal stereoscopic image pair, of which the vertical parallax must be eliminated, and the horizontal parallax reserved (Franz.W.Leberl, 1985). Because of existence of epipolar line, ideal stereoscopic image pair can be made with optical stereo image pair re-sampling along the epipolar line and eliminating the vertical parallax between the left and right images (Z.X. Zhang, 1997). The method of this paper is re-sampling along the same geographic direction with SAR images to eliminate the vertical parallax and reconstruct the horizontal parallax according to DEM. The mono-source stereoscopic image pair has well stereoscopic vision, and can be used to assistant image interpretation. The dual-source stereoscopic image pair has more detailed topographic information, and can be used to map and edit contours. The principle and method of mono-source and dual-source will be introduced, and the experiment with SAR image will be done.

2. GENERATION OF IMAGE PAIR

In the method of this paper, the two images of stereoscopic image pair can be re-sampled from single SAR image, and also can be from two different SAR images with overlapping regions.

The specific approach is extracting the relatively independent stereoscopic image firstly, and then making up a stereoscopic image pair with two stereoscopic images.

The procedure of extracting stereoscopic image is actually a process of image simulation. Establish the map between the simulated image and the original SAR image with simulated imaging orbit and imaging parameters (resolution), and then resample to get stereoscopic image. The image re-sampling depends on DEM in the same direction, so two maps should be established. One is the map between original image coordinates and geographic coordinates, the other is between geographic coordinates and simulated image coordinates. In this way, the vertical parallax will be eliminated, and the map between the original image coordinates and simulated image coordinates is established indirectly.

2.1 SAR Image Geometry

Establishing the map original image coordinates and geographic coordinates is geo-location of SAR image, the key is the establishment of SAR Geo-location model. SAR Geo-location model is the basis of SAR image geometric process, several models have been raised at home and abroad at present. Among them, the Range and Duppler (R-D) model follows SAR imaging geometry strictly, so it can be used for the basic model of SAR image geometric process (E.X.Chen, 2004). With an SAR image, the formulation of R-D model is as follows:

$$\begin{cases} R = |R_{sc} - R_{tc}| \\ f_d = -\frac{2}{\lambda} \frac{(R_{sc} - R_{tc})V_{sc}}{|R_{sc} - R_{tc}|} \end{cases} \quad (1)$$

Where R = the slant range from objective to sensor

R_{sc} = the position of sensor

R_{tc} = the position of objective

V_{sc} = the velocity of sensor

f_d = the central duppler frequency

λ = the wavelength

The first equation is the range equation, the other is duppler equation. Model parameters can be extracted original image parameter file, in the solution process of the model calculation need to know the sensor orbit information. Along with the development of inertial navigation technology, currently a number of SAR satellites have been able to provide very. When there is no accurate sensor orbit, the sensor orbit can be inversed with a certain amount of image control points.

2.2 Image Simulation Parameter

Simulation parameters mainly contain simulated imaging orbit parameters and simulated image parameters. Orbit parameters are mainly orbital altitude, orbital direction, image parameters are mainly imaging resolution.

Generally, the simulated orbital altitude is approximately equal to the original SAR image orbital altitude. The re-sampling direction is the same as the range direction of original image normally, and perpendicular to the orbital direction. For example, the orbital direction for Spaceborne SAR is roughly north-south direction, simulated imaging orbit can be true north-south direction and re-sampling direction is west-east direction. Simulated image resolution depends on mapping resolution or mapping scale. The following briefly on what set the principle of simulated orbital parameters.

Imaging region can be determined by the coordinate of four corners of the original image. The simulated orbit direction is set to be Y direction. Then in the Fig.1 is a re-sampling scan line. The bound coordinate X_b is from imaging region, orbital altitude is set to be H . R_0 is equal to the nearest slant range of original image. So the orbital X -axes coordinate is X_s :

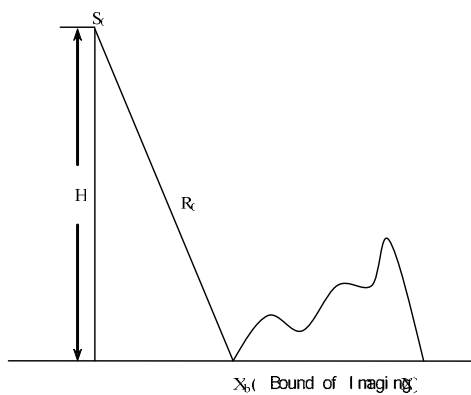


Figure 1. Simulation Parameter

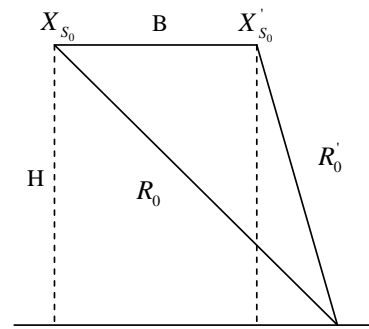


Figure 2. Baseline

In order to obtain well imaging results, the base-height ratio should be designed before simulation. The designed base-height ratio can be obtained with moving simulated imaging orbital position. As the Fig.2, the orbit is moved, and then the orbital

X -axes coordinate after moving is X'_s .

2.3 Simulated Image Geo-location

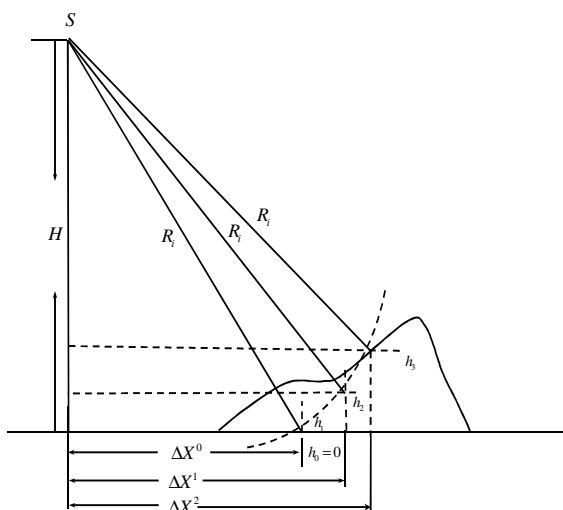
It is necessary to establish the map between simulated image coordinates and geographic coordinates. The geographic coordinate Y of corresponding point on simulated image can be obtained from the orbital position, while X needs to be solved with DEM and simulation imaging model (central projection imaging model or slant-range projection imaging model). The coordinate X and the elevation is obtain through iterative solution, the principle is:

- 1). set initial value of elevation h_0 ;
- 2). solve X_0 with the initialization;
- 3).interpolate h_1 from DEM with X_0 and Y ;
- 4).solve X_1 with h_1 ;
- 5).circling iteratively until $|X_{i+1} - X_i| < \epsilon$, the geographic coordinate is (X_i, Y, h_i) ;

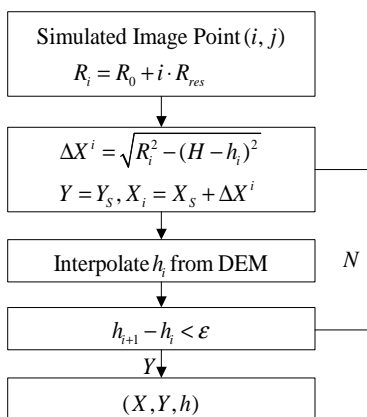
For the slant-range projection imaging model, the iterative solution depends on the slant-range equation:

$$R_i = \sqrt{(\Delta X^i)^2 + (H - h_i)^2} \quad (2)$$

Get elevation information from DEM and solve the geographic coordinates. The Fig.3 is sketch map and procedure of iterative solution.



(a) Sketch map



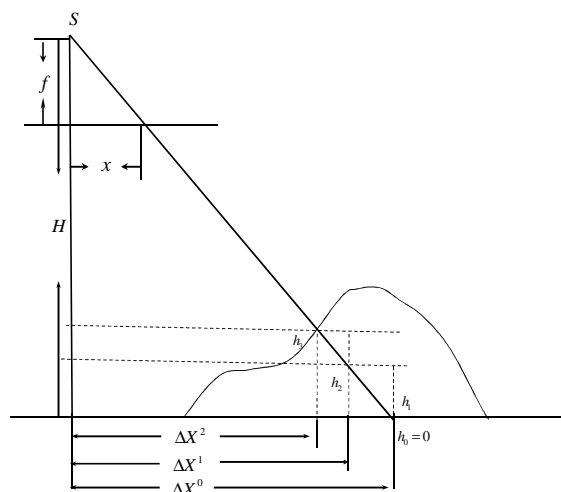
(b) Procedure

Figure 3. Geo-location of slant-range projection

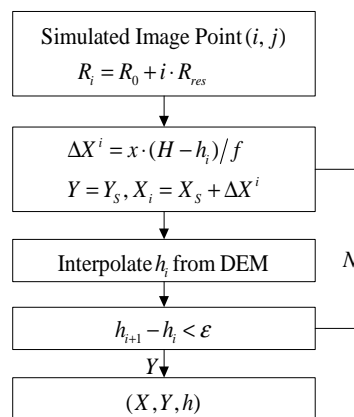
For the central projection imaging model, the iterative solution depends on the collinear equation:

$$\frac{f}{H - h_i} = \frac{x}{\Delta X^i} \quad (3)$$

The Fig.4 is sketch map and procedure of iterative solution.



(a) Sketch map



(b) Procedure

Figure 4. Geo-location of slant-range projection

2.4 Re-sampling

Choose indirect sampling as re-sampling style, start with image point on target stereoscopic image, get pixel gray value from the corresponding image point on original SAR image. The procedure is as follows:

- 1). Get imaging bounds with geo-location of original image, calculate the size of simulated image according to simulated imaging resolution;
- 2). Solve corresponding geographic coordinates from simulated image point;
- 3). Calculate the original image coordinates with geographic coordinates
- 4). Set gray value of the simulated image point to be the original image gray value.

The procedure is as the Fig.5:

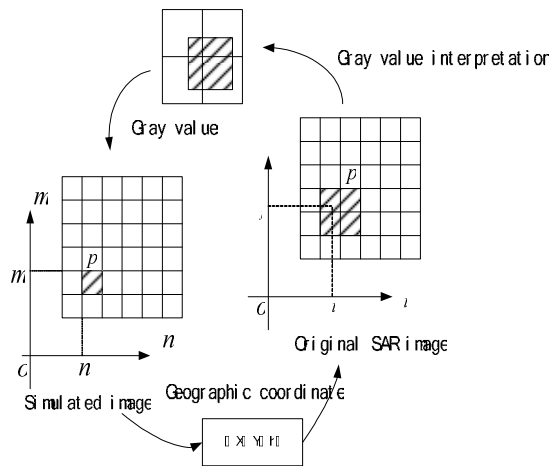


Figure 5. Process of re-sampling

2.5 Stereo Measurement Model

Two stereoscopic images with parallel simulated imaging orbit can make up of a stereoscopic image pair. A stereo measurement model must be established when stereo-mapping with the image pair. Select a different simulated projection imaging model, build a model not the same.

For the slant-range projection model, stereo geometrical model in Fig.6, according to the model:

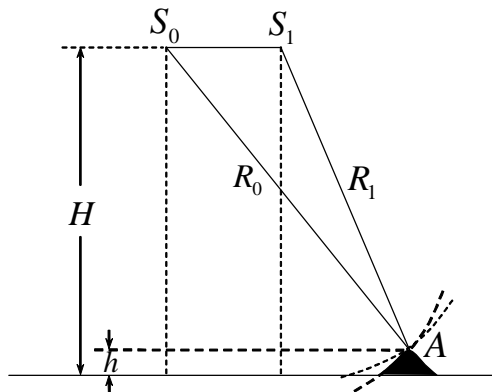


Figure 6. Slant-range projection mode

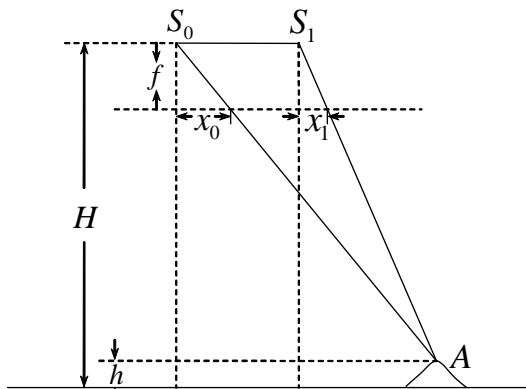


Figure 7. Central projection model

$$\left. \begin{aligned} R_{A0}^2 &= (X_A - X_{S_0})^2 + (H - h)^2 \\ R_{A1}^2 &= (X_A - X_{S_1})^2 + (H - h)^2 \end{aligned} \right\} \quad (4)$$

To be stereo measurement equation:

$$\left. \begin{aligned} X_A &= \frac{(R_{A0}^2 - R_{A1}^2) - (X_{S_0}^2 - X_{S_1}^2)}{2(X_{S_1} - X_{S_0})} \\ Y_A &= Y_{S_0} \\ h &= H - \sqrt{R_{A0}^2 - (X_A - X_{S_0})^2} \end{aligned} \right\} \quad (5)$$

For the central projection model, stereo geometrical model in Fig.7, according to the model:

$$\left. \begin{aligned} \frac{x_0}{X_A - X_{S_0}} &= \frac{f}{H - h} \\ \frac{x_1}{X_A - X_{S_1}} &= \frac{f}{H - h} \end{aligned} \right\} \quad (6)$$

To be stereo measurement equation:

$$\left. \begin{aligned} X_A &\approx \frac{x_1 X_{S_0} - x_0 X_{S_1}}{x_1 - x_0} \\ Y_A &= Y_{S_0} \\ h &= H - (X_A - X_0) \frac{f}{x_0} \end{aligned} \right\} \quad (7)$$

An ideal stereoscopic image pair from single SAR image is called Mono-source Ideal Image Pair. An ideal stereoscopic image pair from two different SAR images is called Dual-source Ideal Image Pair.

3. EXPERIMENT

In this paper, experiment is done with a TerraSAR-X stereo image pair which locate at west of China. The resolution of the two images, S_1 and S_2 , is 3m. Their polarizations are all HH. The incidence angle of S_1 is 46° , and that of S_2 is 29° . In Fig.8 is single-model stereoscopic image pair generated from S_1 . In Fig.9 is dual-model stereoscopic image pair generated from S_1 and S_2 .

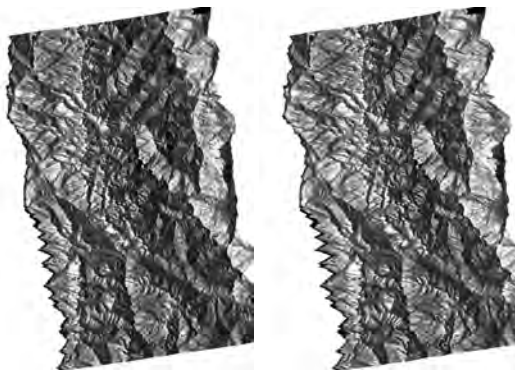


Figure 8. Mono-source image pair

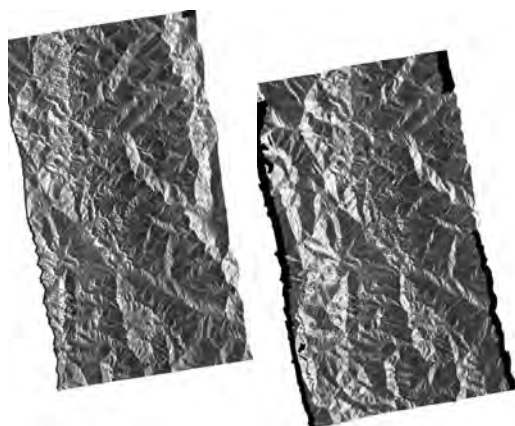


Figure 9. Dual-source image pair

Well stereoviewability can be get with the image pairs under stereo observation condition. The vertical parallax was eliminated effectively. Contour lines of some parts in this region were mapped with the dual-model image pair. The precision of contour lines was checked using DEM, and the result confirmed that the contour lines could be used in making topographic maps. In Fig.10 are the contour lines.



Figure 10. Contour lines

4. CONCLUSION

Mono-source and dual-source method for generation of ideal stereoscopic image pair based on DEM are raised in this paper for stereo-mapping of SAR images. Image pairs were generated

in the experiment with high-resolution spaceborne SAR images. We achieved well stereoscopic vision, and well elimination of vertical parallax. The contour lines mapping with the image pairs can meet the needs of producing topographic maps. Experiment confirmed that the method proposed in this paper is feasible.

There are still many problems to be resolved in SAR analytical stereo-mapping. For example, shadow and layover are significant features of SAR image because of side-looking imaging method, and cause lack of information in these areas. The problem cannot be avoided in SAR analytical stereo-mapping. Extracting information from SAR images obtained from different side-looking direction in the same area is an effective solution of this problem.

REFERENCES

- E.X. Chen, 2004. "Study on Ortho-rectification Methodology of Space-borne Synthetic Aperture Radar Imagery", *Chinese Academy of Forestry*, China, pp. 47-81.
- Franz. W. Leberl, Johannes Raggam, and Michael Kobrick, 1985. "On Stereo Viewing of SAR Images", *IEEE Transactions On Geoscience and Remote Sensing*, pp. 110-117.
- Franz. W. Leberl, Johannes Raggam, and Michael Kobrick, 1986. "Radar Stereomapping Techniques and Application to SIR-B Images of Mt. Shasta", *IEEE Transactions On Geoscience and Remote Sensing*, July, 473-480.
- M. Gelautz et.al, 2004. "A Comparative Study of Radar Stereo and Interferometry for Dem Generation", *Proceedings of ESA FRINGE 2003 workshop*, ESA SP-550,
- Thieny Toutin, 1995. "Airborne SAR Stereo Restitution in a Mountainous Area of Costa Rica: First Results", *IEEE Transactions On Geoscience and Remote Sensing*, pp. 500-504
- Z.X. Zhang, J.Q. Zhang, 1997. *Digital Photogrammetry*, Wuhan University Publisher, Wuhan, pp. 128-195,

WEAKLY SUPERVISED POLARIMETRIC SAR IMAGE CLASSIFICATION WITH MULTI-MODAL MARKOV ASPECT MODEL

Wen Yang, Dengxin Dai, Jun Wu, Chu He

School of Electronic Information, Wuhan University
LuoJia Hill, Wuhan 430072, China
yangwen@whu.edu.cn
http://dsp.whu.edu.cn

Commission VII

KEY WORDS: Land Cover, Classification, Polarization, SAR, RADARSAT, Imagery

ABSTRACT:

In this paper, we present a weakly supervised classification method for a large polarimetric SAR (PolSAR) imagery using multi-modal markov aspect model (MMAM). Given a training set of subimages with the corresponding semantic concepts defined by the user, learning is based on markov aspect model which captures spatial coherence and thematic coherence. Classification experiments on RadarSat-2 PolSAR data of Flevoland in Netherlands show that this approach improves region discrimination and produces satisfactory results. Furthermore, multiple diverse features can be efficiently combined with multi-modal aspect model to further improve the classification accuracy.

1 INTRODUCTION

During the last decade, several space-borne sensors with polarimetric SAR (PolSAR) imaging have been launched and produce terrabytes of PolSAR images. PolSAR remote sensing offers an efficient and reliable means of collecting information required to extract geophysical and biophysical parameters from Earth's surface, which shows potential for improved results in many successful applications. As it becomes increasingly viable to acquire, store, order and share large amounts of polarimetric SAR data, accurate and ease-to-use supervised classification method is crucial to extracting information from these datasets.

Earlier supervised classification methods for polarimetric SAR data are mainly pixel-based schemes. The widely used methods are the maximum likelihood classification based on the complex Wishart distribution (Lee et al., 1994) and its variations (Lee et al., 2001) (Beaulieu and Touzi, 2004). The classification performances of these methods are affected by speckle seriously since they are unable to capture and utilize the spatial information in the scene. To overcome this problem, region-based methods have been employed, which use a over-segmentation step (or grid partition step) and form groups of pixels that represent homogeneous regions. In (Wu et al., 2008), Wu et al. proposed a region-based classification method for polarimetric SAR images with a Wishart Markov Random Field model, which can efficiently use the statistical properties of the data and the spatial relation of neighboring pixels. Ersahin et al. (Ersahin et al., 2010) proposed to use spectral graph partitioning approach for segmentation and classification of POLSAR data, and achieved promising classification accuracy superior to the Wishart classifier. Recently, classifiers originated from machine learning and pattern recognition domain have attracted more attention, such as neural networks (Shimoni et al., 2009), support vector machine (SVM) (Lardeux et al., 2009), and Random Forests (Zou et al., 2010). These methods are also usually implemented on region level, and they can easily handle many sophisticated image features and get remarkable performance. However, existing supervised classification methods most require the labor-intensive and time-consuming works to label every pixel in the training samples. Furthermore, as to general user, it is very difficult to

make ground truth for pixel-level labeled training samples in SAR image, sometimes only experts of SAR image interpretation are qualified for this job. In this work, we are interested in weakly supervised classification of PolSAR images, which is aimed at partitioning a PolSAR scene into their constituent semantic-level regions with only keywords labeled training data.

In this study, we present a solution using a multi-modal markov aspect model proposed by Verbeek and Triggs (Verbeek and Triggs, 2007), which can be learned from image-level keywords without detailed pixel-level labeling. The whole classification process consists of four cascaded stages. In the first stage, we partition the whole PolSAR scene into hundreds of subimages. From each subimage we extract overlapping patches on a grid, representing them by polarimetry, intensity and texture descriptors. We assume that each subimage patch belongs either to one of the label classes or to a vague background class "void". Then, we model each subimage as a mixture of latent aspects with a multi-modal markov aspect model which can be learnt from image-level keywords. Next, we use an efficient expect maximization (EM) algorithm to learn the model and apply loopy belief propagation (LBP) (Yedidia et al., 2005) inferring algorithm to label every patch in the test subimages with the trained model. Finally, we apply a over-segmentation based soft mapping to propagate patch-level labeling to pixel-level classification, and group the large PolSAR scene classification result from the labeled subimages.

The rest of the paper is organized as follows. Section 2 briefly introduces the three type features we used for classifying PolSAR images. Section 3 describes the baseline classifier-Wishart maximum likelihood classifier. The multi-modal markov aspect model is reviewed in Section 4. Section 5 gives comparative experimental results and quantitative evaluation, and section 6 concludes the paper.

2 FEATURE DESCRIPTORS FOR POLSAR IMAGES

Classification problem is challenging because the instances in SAR images belonging to the same class usually have very high

intra-class variability. To overcome this problem, one strategy is to design feature descriptors which are highly invariant to the variations present within the classes, however none of the feature descriptors will have the same discriminative power for all classes. The other widely accepted strategy is that, instead of using a single feature type for all classes, it is better to combine multiple diverse and complementary features based on different aspects. Therefore, we extract multiple polarimetric and low-level image features for describing the small patches in each PolSAR subimage. A more detailed description of these feature parameters is given below:

2.1 Polarimetry

PolSAR is sensitive to the orientation and characters of target and thus yields many new polarimetric signatures which produce a more informative description of the scattering behavior of the imaging area. There are many polarimetric descriptors summarized in (Shimoni et al., 2009). For simplicity, we just use the nine parameters obtained by Huynen decomposition (Huynen, 1990).

Given a scattering matrix measured in the orthogonal linear (h, v) basis, the classical 2×2 Sinclair scattering matrix S can be obtained through the construction of system vectors.

$$S = \begin{pmatrix} S_{HH} & S_{HV} \\ S_{VH} & S_{VV} \end{pmatrix} \quad (1)$$

The coherency matrix is constructed from a scattering vector in the base of Pauli basis. In the monostatic backscattering case, for a reciprocal target matrix, the reciprocity constrains the Sinclair scattering matrix to be symmetrical, that is, $S_{HV} = S_{VH}$. Thus, the target vectors k_p can be constructed based on the Pauli basis sets, respectively. With this vectorization we can then generate the coherency matrix T as follows,

$$k_p = \frac{1}{\sqrt{2}} \begin{bmatrix} S_{HH} + S_{VV} \\ S_{HH} - S_{VV} \\ 2S_{HV} \end{bmatrix}, [T] = \langle k_p \cdot k_p^{*T} \rangle, \quad (2)$$

The Huynen decomposition (Huynen, 1990) is the first attempt to use decomposition theorems for analyzing distributed scatterers. In the case of coherence matrix, this parametrization is

$$[T] = \begin{bmatrix} 2A_0 & C - jD & H + jG \\ C + jD & B_0 + B & E + jF \\ H - jG & E - jF & B_0 - B \end{bmatrix} \quad (3)$$

The set of nine independent parameters of this parametrization allows a physical interpretation of the target: $A_0, B_0 + B, B_0 - B, C, D, E, F, G, H$. The nine Huynen parameters are useful for general target analysis without reference to any model, and each of them contains real physical target information.

2.2 Texture

The Gray Level Co-occurrence Matrix (GLCM), Gabor filters, Gaussian Markov random fields (GMRF) Texture are three widely used features for SAR image texture segmentation. Former experiments show that GMRF yields the best performance in terms of classification accuracy, although it has high computational complexity in high order case (Clausi, 2001). The Gaussian Markov Random Field models characterize the statistical dependency between a pixel and its neighbors by representing the gray level intensity at site s , as a linear combination of gray levels in a neighborhood set $N(s)$ around s , and Gaussian zero mean stationary noise. The specific definition of neighbours and their influence on other points give GMRF the freedom to model many types of

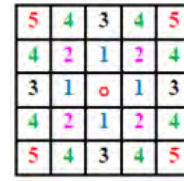


Figure 1: The first to fifth-order MRF neighborhood system

textures. GMRF model is fitted on the patches, and the model parameters are used to form a multi-dimensional feature space. Figure 1 illustrates the different orders of MRF, which is related to the location of neighbors. To balance the computation complexity and classification accuracy, we use a four-order GMRF, which can be expressed as follows:

$$f(m, n) = \sum_{(t,s) \in N} \theta(t, s) f(m-t, n-s) + e(m, n) \quad (4)$$

where N represents the 20 neighborhoods, and $e(m, n) \sim N(0, \sigma^2)$ with zero mean and variance σ^2 . For each pixel, we train the mean μ, σ , and due to the symmetry of correlation function, only the 10 parameters, $\theta(t, s), (t, s) \in N$, over a window W centered on this, by Least Square Estimation (LSE). The feature space is formed as 12 dimensions vector $\mu, \sigma, \theta(t, s), (t, s) \in N$.

2.3 Intensity

In our previous work, we learn that histogram is a simple but informative descriptor for single polarimetric SAR imagery classification. For full polarimetric SAR images, unlike the SPAN histogram used in (He et al., 2008), we propose to use the multi-channel histogram which is a cumulative enumeration of its underlying HH, HV and VV channels.

3 BASELINE CLASSIFIER-SUPERVISED ML CLASSIFICATION OF [T] MATRIX DATA

According to Bayes optimal decision rule, a pixel is assigned to the most probable class conditionally to the observation over the pixel under consideration. If the prior probabilities are supposed to be equal, the optimal decision rule reduce to the maximum likelihood supervised segmentation.

It has been shown that a n -look coherence matrix follows a complex Wishart distribution with n degrees of freedom, $W_c(n, [\Sigma])$, given by

$$P([T]) = \frac{n^{qn} |[T]|^{n-q} \exp(-tr(n[\Sigma]^{-1}[T]))}{K(n, q) |[\Sigma]|^n} \quad (5)$$

with $K(n, q) = \pi^{q(q-1)/2} \prod_{i=1}^q \Gamma(n-i+1)$

where q stands for the number of elements of target vector, equal to 3 in the monostatic case, $|\cdot|$ represents the determinant, tr represents the trace of a matrix and $\Gamma(\cdot)$ denotes the Gamma function. A pixel p can be assigned to a class $\{\Theta_i, \dots, \Theta_M\}$ in maximum likelihood way, according to the following steps,

- Initialize pixel distribution over M classes from training samples;
- For each class, $[\hat{\Sigma}_i = \frac{1}{N_i} \sum [T] \in \Theta_i]$, where $[\Sigma_i]$ is the coherence matrix of class Θ_i computed during the training phase;

- For each pixel, $[T] \in \Theta_i$ if $d([T], \Theta_i) < d([T]/\Theta_j), j = 1, \dots, M, j \neq i$

In the following experiments, we will employ the pixel-based and patch-based wishart ML classifier as the baselines.

4 WEAKLY SUPERVISED CLASSIFIER-MARKOV ASPECT MODEL

Recently, many research works on labeling natural images focus on the utilization of high-level semantic representation with topic models, such as the Probabilistic Latent Semantic Analysis (PLSA) (Hofmann, 2001) or its bayesian form, the Latent Dirichlet Allocation (LDA) (Blei et al., 2003). They consider visual words as generated from latent aspects (or topics) and express image as combination of specific distributions of topics, which can solve some cases of visual “polysemy” by capturing thematic coherence (image-wide correlations). Verbeek and Triggs (Verbeek and Triggs, 2007) proposed to use markov aspect model that captures both spatial coherence (local correlations between labels) and thematic coherence (image-wide correlations), and further employed a multi-modal aspect model to combine multiple cues for improving classification accuracies. Experimental results on the Microsoft Research Cambridge data sets show their model significantly improves the region-level classification accuracy. Li et al. (Li and Perona, 2005) proposed two variations of LDA to generate the intermediate theme representation to learn and recognize natural scene categories, and reported satisfactory categorization performances on a large set of complex scenes.

In remote sensing domain, Liéno et al. (Liéno et al., 2010) proposed to exploit the LDA model to semantically annotate panchromatic QuickBird images with 60-cm resolution, and demonstrated that using simple features such as mean and standard deviation for the LDA-image representation can lead to satisfying labeling results. However, PLSA is computationally more efficient than LDA and it has comparable accuracy in practice (Verbeek and Triggs, 2007). In this work, we use multi-modal PLSA-MRF framework (Verbeek and Triggs, 2007) for polarimetric SAR image classification, which naturally introduces the spatial information by combining Markov Random Fields with Probabilistic Latent Topic Models. PLSA-MRF basically just adds pairwise MRF couplings to the PLSA label inference process, we use LBP for MRF inference and EM algorithm for maximum likelihood estimation of the model as done in (Verbeek and Triggs, 2007). Unlike multi-modal LDA (Li and Perona, 2005), multi-modal PLSA-MRF (i.e. multi-modal markov aspect model) assumes that the different types of features are independent given the topic.

$$P(w|d) = \sum_{t=1}^T P(w^{huy}|t)P(w^{hist}|t)P(w^{gmrf}|t)P(t|d) \quad (6)$$

$$P(t|w, d) = \frac{P(w^{huy}|t)P(w^{hist}|t)P(w^{gmrf}|t)P(t|d)}{P(w|d)} \quad (7)$$

5 RESULTS AND DISCUSSION

We validate the above-mentioned multi-modal markov aspect model on the semantic annotation of a large scene Radarsat-2 Polarimetric SAR image. In this Section, we present our experimental setup, show a detailed performance evaluation illustrated with the classification results, and we finally discuss the limits of the labeling algorithm.

5.1 Data Description and Experimental Setup

The experiments are performed on RadarSat-2 fully polarimetric SAR images of Flevoland in Netherlands, with $12m \times 8m$ resolution at fine quad-pol mode. The PolSAR scene to be labeled is of size 4000×2400 pixels, which mainly contains four classes: woodland(Wo), cropland(Cr), water(Wa), building area(Bu). We divide the PolSAR scene into 240 subimages, each subimage is 200×200 pixels. Fig.2 shows 8 examples of keywords labeled training subimages, and we use 40 subimages with such keywords annotation as the training set.

5.2 Post-processing with over-segmentation mapping

In our labeling algorithms, learning and inference take place at the patch level, but the results are propagated to pixel level for visualization and performance quantification. We apply a mean-shift based over-segmentation mapping to map the patch-level labelings to pixel-level classification. It combines the nearest mapping result (we compute the class label at the pixel level as the nearest patch label) with a low level over-segmentation since segment boundaries can be expected to coincide with the image edges, which can reduce the block effect of the nearest mapping and also can improve the accuracy slightly. Here we compute the over-segmentation with the Edge Detection and Image Segmentation (EDISON) System of Mean Shift (Comaniciu and Meer, 2002) implementation. The parameters of the segmentation are chosen to mostly over-segment the subimages.

5.3 Classification results and quantitative evaluation

For quantitative evaluation of the classification accuracy with different features and classifiers, we select a region from the original test site of size 1400×1200 with corresponding elaborately labeled ground truth. Pixels are assigned to four semantic classes or void. The four classes are building area, woodland, water and cropland. The void pixels either do not belong to one of the four classes or lie near boundaries between classes and were labeled as void to simplify the task of manual segmentation. About 6% of the pixels are unlabeled (“void”) in the evaluation data. Table 1 gives the performance of different classifiers and features. We can find that multi-modal markov aspect model using image-level labeled training data outperforms traditional Wishart ML methods with detailed pixel-level labeled training data by %3.8. In fact, even when using only one feature-GMRF or Hist, they provide pixel-level classification accuracies outperform those of Wishart ML classifier trained using detailed pixel-level labelings by 0.5% or 2.1%, respectively. The classification results of the original test site (4000×2400) using multi-modal markov aspect model and Wishart ML (pixel-based and patch based) are presented in Fig.4.

Est. \ True	Wo	Wa	Bu	Cr	ave.acc.
ML-pixel	86.2	90.5	34.1	76.3	71.3
ML-patch	91.5	73.8	44.3	78.1	72.8
MMAM-Huy	75.1	70.0	80.0	57.6	69.4
MMAM-GMRF	89.3	64.3	86.6	52.4	71.8
MMAM-Hist	78.1	81.3	94.0	51.9	73.4
MMAM-All	81.8	77.0	90.0	59.1	75.1

Table 1: Comparison of classification accuracies with different classifiers(%)

6 CONCLUSIONS AND FUTURE WORK

This paper presents the utilization of multi-modal markov aspect model for weakly supervised PolSAR image classification.

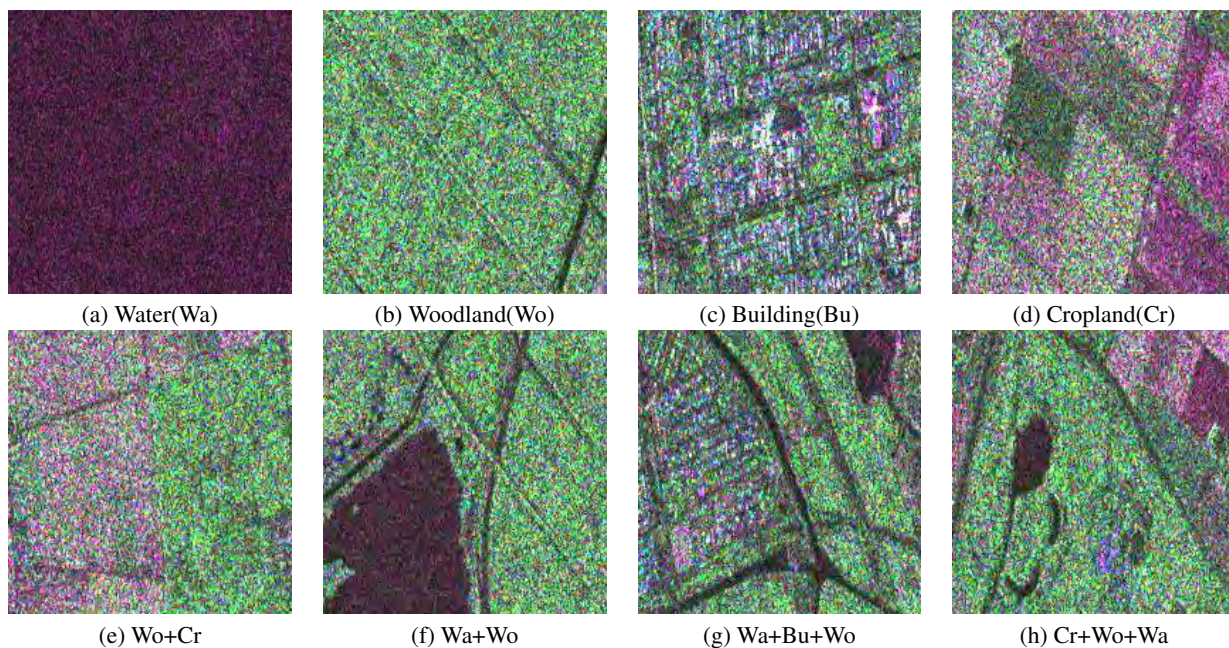


Figure 2: Some training samples annotated with keywords.

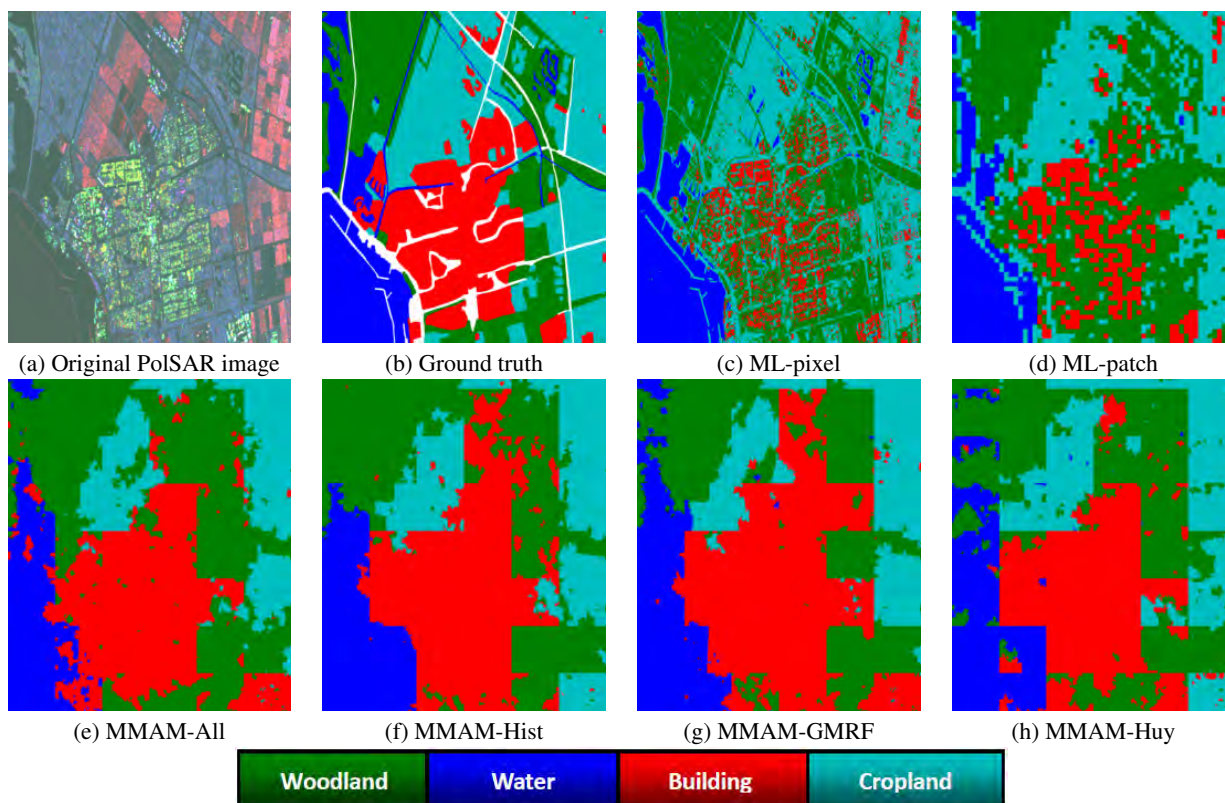


Figure 3: (a) Quantitative evaluation area of 1400×1200 pixels; (b) The corresponding hand-labeled ground truth; (c) Classification result using pixel-based Wishart ML; (d) Classification result using patch-based Wishart ML (patch size: 20×20); (e) Classification result using MMAM with all features; (f) Classification result using MMAM with histogram features ;(g) Classification result using MMAM with GMRF features ;(h) Classification result using MMAM with Huynen decomposition features.

It has been tested and validated on a large RadarSat-2 PolSAR scene image classification task, and produces satisfactory classification results, it outperforms traditional Wishart ML methods with detailed pixel-level labeled training data, even when using only one feature-multichannel histogram. Moreover, we use the over-segmentation based soft assignment techniques (Patch to Pixel labels mapping) to reduce the block effect in each subimage

and improve the visual effects. While the results presented here are encouraging, there is still a need for further improvements. Future extensions would be the introduction of other sources of contextual information like scale information and the combination with more informative feature descriptors.

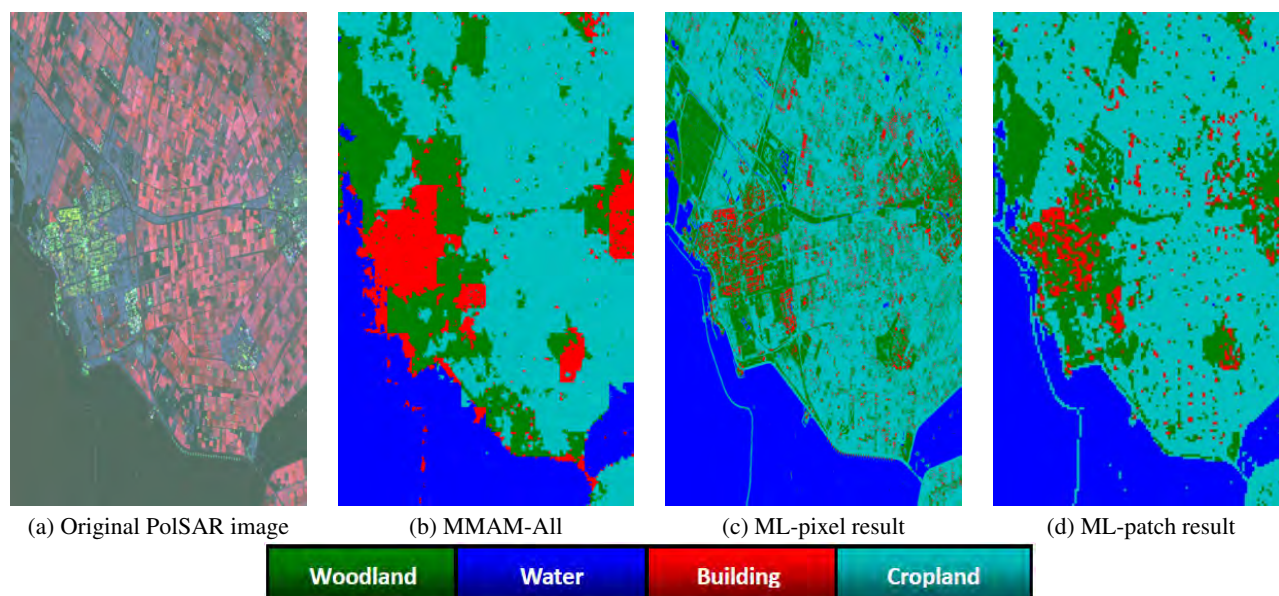


Figure 4: Results of the classification of a large PolSAR image (RadarSat-2 polarimetric SAR data of Flevoland in Netherlands, with size of 4000×2400 pixels) into the four semantic classes: woodland, cropland, water, building.

REFERENCES

- Beaulieu, J. M. and Touzi, R., 2004. Segmentation of textured polarimetric sar scenes by likelihood approximation. *IEEE Transactions on Geoscience and Remote Sensing*, 42(10), pp. 2063–2072.
- Blei, D., Ng, A. and Jordan, M., 2003. Latent dirichlet allocation. *Journal of Machine Learning Research* 3(3), pp. 993–1022.
- Clausi, D. A., 2001. Comparison and fusion of co-occurrence, gabor, and mrf texture features for classification of sar sea ice imagery. *Atmosphere & Oceans*, 39(4), pp. 183–194.
- Comaniciu, D. and Meer, P., 2002. Mean shift: A robust approach toward feature space analysis. *IEEE Transactions on Pattern Analysis and Machine Intelligence*, 24(5), pp. 603–619.
- Ersahin, K., Cumming, I. G. and Ward, R. K., 2010. Segmentation and classification of polarimetric sar data using spectral graph partitioning. *IEEE Transactions on Geoscience and Remote Sensing*, 48(1), pp. 164–174.
- He, W. J., Jager, M., Reigber, A. and Hellwich, O., 2008. Building extraction from polarimetric sar data using mean shift and conditional random fields. *The 7th European Conference on Synthetic Aperture Radar (EuSAR), III*, pp. 439–442.
- Hofmann, T., 2001. Unsupervised learning by probabilistic latent semantic analysis. *Machine Learning* 42(1-2), pp. 177–196.
- Huynen, J. R., 1990. The stokes matrix parameters and their interpretation in terms of physical target properties. *Journé es Internationales de la Polarimétrie Radar*, pp. 524–531.
- Lardeux, C., Frison, P.-L., Tison, C., Souyris, J.-C., Stoll, B., Fruneau, B. and Rudant, J.-P., 2009. Support vector machine for multifrequency sar polarimetric data classification. *IEEE Transactions on Geoscience and Remote Sensing*, 47(12), pp. 4143–4152.
- Lee, J. S., Grunes, M. R. and Kwok, R., 1994. Classification of multi-look polarimetric sar imagery-based on complex wishart distribution. *International Journal of Remote Sensing*, 15(11), pp. 2299–2311.
- Lee, J. S., Grunes, M. R. and Pottier, E., 2001. Quantitative comparison of classification capability: Fully polarimetric versus dual and single-polarization sar. *IEEE Transactions on Geoscience and Remote Sensing* 39(11), pp. 2343–2351.
- Li, F.-F. and Perona, P., 2005. A bayesian hierarchical model for learning natural scene categories. *Proc. of IEEE Computer Society Conference on Computer Vision and Pattern Recognition*, pp. 524–531.
- Liéno, M., Maître, H. and Datcu, M., 2010. Semantic annotation of satellite images using latent dirichlet allocation. *IEEE Geoscience and Remote Sensing Letters*, 7(1), pp. 28–32.
- Shimoni, M., Borghys, D., Heremans, R., Perneel, C. and Acheroy, M., 2009. Fusion of polsar and polinsar data for land cover classification. *International Journal of Applied Earth Observation and Geoinformation*, 11(3), pp. 169–180.
- Verbeek, J. and Triggs, B., 2007. Region classification with markov field aspect models. *Proc. of IEEE Computer Society Conference on Computer Vision and Pattern Recognition*.
- Wu, Y. H., Ji, K. F., Yu, W. X. and Su, Y., 2008. Region-based classification of polarimetric sar images using wishart mrf. *IEEE Geoscience and Remote Sensing Letters*, 5(4), pp. 668–672.
- Yedidia, J., Freeman, W. and Weiss, Y., 2005. Constructing free-energy approximations and generalized belief propagation algorithms. *IEEE Transactions on Information Theory*, 51(7), pp. 2282–2312.
- Zou, T. Y., Yang, W., Dai, D. X. and Sun, H., 2010. Polarimetric sar image classification using multi-features combination and extremely randomized clustering forests. *EURASIP Journal on Advances in Signal Processing*, 2010, pp. 1–9.

ACKNOWLEDGEMENTS

This work was supported in part by the National Natural Science Foundation of China (No.40801183, 60890074), the National High Technology Research and Development Program of China (No.2007AA12Z180, 155) and LIESMARS Special Research Funding.

LUNAR GEOMORPHY 3D VISUALIZATION METHOD

Z. Yang, X. Qing, Z. BaoMing, L. JianSheng, L. ChaoZhen

Institute of Surveying and Mapping, ZhengZhou 450052, China – Zhouyang3d@163.com

KEY WORDS: Lunar exploration, Moon Image, Moon DEM, Level of Detail, Visualization

ABSTRACT:

Based on research of large-scale terrain visualization methods, we improve the planar Geometry Clipmaps method by making use of GPU Vertex Processor to projection transform planar terrain into spherical terrain, spherical view culling and spherical viewpoint controlling. We collected and deal with the lunar image and DEM to render the lunar 3D map. The results show that the rendering algorithm' efficiency is independent on datum but there is distort problem in Lunar Pole.

1 INTRODUCTION

Back to Moon, building Lunar base and exploration Lunar resources have been the trend and hot dot of international spaceflight. Lunar exploitation is the first step of Chinese deep space exploration missions. The successful launch of ChangE No.1 satellite indicated that china have the ability to explore the deep space. Obtain lunar remote image and 3D physiognomy data in satellite remote and surveying technology and rendering the 3D map in 3D visualization technology is the one of main tasks of ChangE No.1 satellite. In this paper, based on the research of large range terrain visualization algorithm, we improved the Geometry Clipmaps algorithm and the planar terrain be transformed to the spherical terrain with GPU shaders. We collect the lunar image and DEM and rendered the lunar 3D map by use of the spherical view culling technique and spherical viewpoint control technique to assist human to know well the moon.

2 PREVIOUS WORK

2.1 The terrain render algorithm

A primary difficulty in terrain rendering is displaying realistic terrains to the user at real-time frame rates. Several terrain-rendering techniques have been proposed that use Level of Detail (LOD) to generate a simplified representation of a terrain.

Previous publications and applications can be divided into two parts: Those with static level of detail (S-LOD) and continuous level of detail technique (C-LOD).

(1) S-LOD technique

Here the terrain is divided into tiles each of which is represented by a set of TINs with varying resolutions. Depending on the distance to the viewer for each tile a TIN with appropriate projective triangle size is chosen from the set. If regularly coarsened meshes are used instead of TINs the method is called geo-mipmapping [1].

(2) C-LOD Algorithms

The most elaborate terrain rendering technique known today is the continuous level of detail technique

(C-LOD). It improves the sub-optimal approximation quality of the S-LOD algorithms in a sense that the triangulation is altered on a per triangle and not on a per tile basis. This allows much better approximations which adapt optimally both to the viewing distance and to surface roughness.

Several main C-LOD algorithms include Lindstrom [2], Duchaineau [3], Roettger [4], and Losasso [5].

The geometry clipmap is a recently proposed approach that utilizing the potential of modern graphics hardware. The Algorithm caches the terrain in a set of nested regular grids centered about the viewer (fig 1). The grids are stored as vertex buffers in fast video memory, and are incrementally refilled as the viewpoint moves. This simple framework provides visual continuity, uniform frame rate, complexity throttling, and graceful degradation [6].

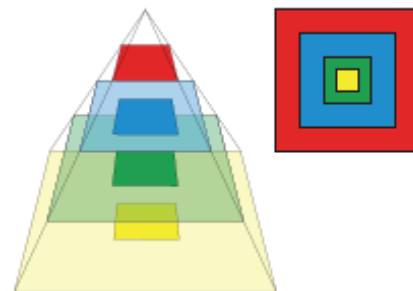


Figure 1: The clipmap contains a fixed-size segment of each mipmap level around an arbitrary focus point. [6]

Those algorithms mentioned in previous section deal with planar terrain. Clasen describe a terrain rendering algorithm for spherical terrains based on clipmaps [7]. The algorithm replaces the underlying geometry with one that maps better to the sphere. No matter how far away the viewer is relative to the planet, he cannot see more of it than one hemisphere. So the algorithm uses concentric rings instead of rectangles. The resulting spherical Geometry Clipmap is displayed in fig. 2.

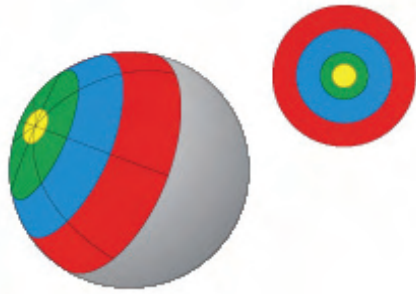


Figure 2: We use circular instead of rectangular rings to cover the hemisphere.^[7]

Spherical clipmaps avoid the terrain distortion in high latitude region and the different levels of detail can be blended smoothly even when they are more than one level apart. But the transformation of the world space (x, y, z) that provides an absolute orientation of the spherical terrain to the view space (x', y', z') that locates the viewer at the lunar pole must be implemented in real time and the concentric rings are transformed into plane irregularly (Fig 3). So reading and updating data is complex and the algorithm is implemented difficultly and inefficiently.

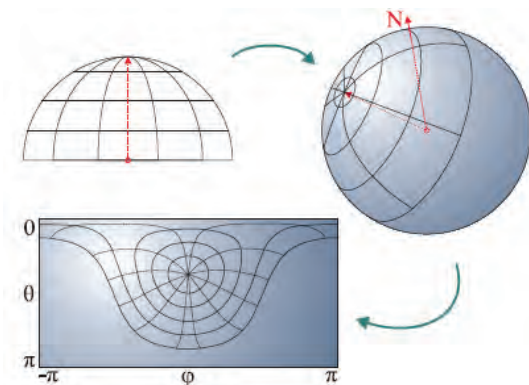


Figure 3: Points on the view hemisphere are transformed into world space to sample the rectangular height map.^[7]

2.2 Earth visualization system

With being short of data, terrain rendering focused on earth mainly and the research of visualization in lunar terrain and space environment is absent. At present, the system of 3D digital earth applied successfully include: Google Earth, World Wind, ArcGlobe, and so on. Those systems focus on earth mainly and the digital moon visualization system aren't enough mature and perfect. Google bring forth the Google-Moon in internet^[8]. But There are only "Clementine" and "Appolo" remote image and not include DEM data, so there have no the function of 3D visualization. Figure 4 shows the Google-Moon. The NASA brings forth the lunar visualization system- WorldWind-Moon. But the resolution of image and DEM is low and is not meet to the request of application.

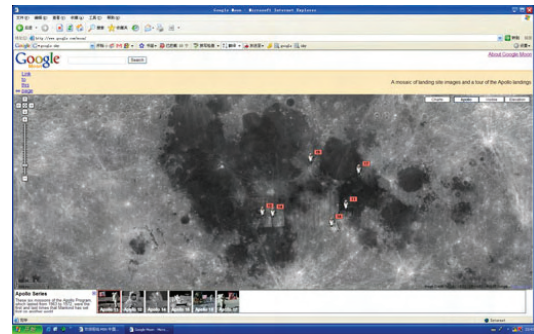


Figure 4: Google-Moon

3 ALGORITHM OVERVIEW AND IMPLEMENTATION

3.1 Geometry Clipmaps

A geometry clipmap renders a set of nested regular grids centred around the viewpoint, with small grids of high detail and large grids of low detail(Fig5). Each grid contains $n \times n$ values and is called a clipmap level. The levels are numbered starting from $l = 0$ for the coarsest level. The distance between values at level l is the grid spacing, denoted g^l . The vertices in a clipmap level are stored in a vertex buffer on the graphics card. The rectangular rings are divided into 12 parts, for more efficient rendering and view range culling. As the viewpoint moves, the clipmap data is updated so the grids remain centred around the viewer.

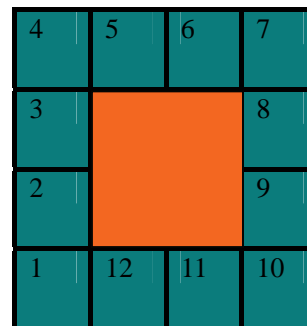


Figure 5: Geometry Clipmaps nested regular grids

The vertices are stored as a toroidal array to enable incremental updates, where only vertices from newly visible areas are added, replacing areas that are no longer visible. Figure 6 shows how toroidal arrays make incremental updates possible. The heightmap and viewer position are shown, as well as the actual clipmap level data. Suppose the viewer is positioned as in Figure 6(a). If we move to the southeast, as shown in Figure 6(b), only the newly visible areas along the bottom and right edges of the heightmap need to be put in the array, and they are put in the top and left edges of the clipmap, respectively, overwriting the data that is no longer needed.

With the use of ring array and mod operation, after the transformation, the vertex's position is no change in array. For example, if $n = 129$, the vertex's number a is $0 \rightarrow 128$. When viewpoint is move and the

number is changed to $1 \rightarrow 129$, the $\text{mod}(129,129)=0$.

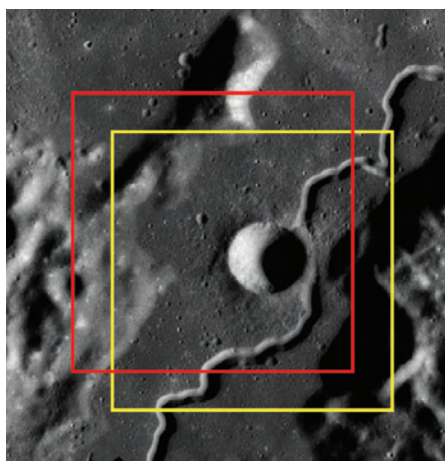


Figure 6 (a): Before a change in viewpoint

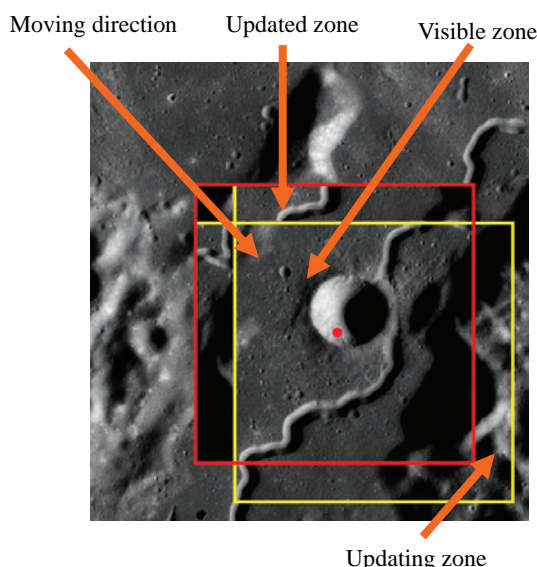


Figure 6 (b): After a change in viewpoint to the southeast

Figure 6: An example of the data in the heightmap (top) and toroidal array (bottom).before and after a change in viewpoint. The position of the viewer in the heightmap is shown by the red dot.

3.2 Transformation of planar terrain to spherical terrain

The test data is Lunar DEM and image in WGS84 coordinate system. If the coordinate of a grid point is (B, L, H) , where B is longitude, L is latitude, and H is elevation. We must transform the WGS84 coordinate system to OpenGL world space coordinate system for spherical terrain rendering.

According to Eq.(3), we can transform the WGS84 coordinate system to OpenGL world space coordinate system.

$$\begin{cases} X = (N + H) \cos B \cos L & (1) \\ Y = [N(1 - e^2) + H] \sin B \\ Z = (N + H) \cos B \sin L \end{cases}$$

where ,
$$\begin{cases} N = \frac{a}{\sqrt{1 - e^2 \sin^2 B}} \\ e^2 = \frac{a^2 - b^2}{a^2} \end{cases}$$

$a = 1738000\text{m}$, $b = 1737400\text{m}$, a is lunar long radius, and b is short radius. For reducing the CPU' burden and optimizing efficiency, we can implement the equation by GPU.

3.3 Spherical view range culling

As shown in Figure 7, for optimizing efficiency, we use view range culling and back face culling algorithm to eliminate invalid data.

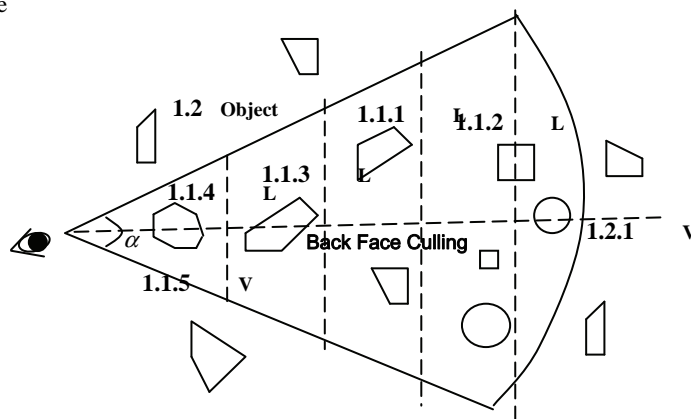


Figure 7: Data culling based on viewpoint and visible face

As shown in Figure 8, the spherical terrain can be divided into two parts. One part is face to viewpoint and one part is back to viewpoint. The $a'b'$ in back to viewpoint part is in view cone, but it is invisible to viewer. So we must eliminate it with spherical view range culling algorithm:

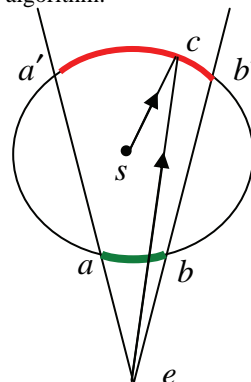


Figure 8: spherical view range culling

$$\begin{cases} \vec{sc} \cdot \vec{ec} > 0, \text{ invisible} \\ \vec{sc} \cdot \vec{ec} \leq 0, \text{ visible} \end{cases} \quad (2)$$

Where, S is the center point of earth, e is viewpoint, and C is a point on spherical surface in view range. If the angle α from vector sc to vector $ec \leq 90^\circ$, point S is invisible. Whereas point S is visible.

As shown in Figure 9, We implement Geometry Clipmaps algorithm with spherical culling, the efficiency be shown by blue dashed. The red dashed show the efficiency of Geometry Clipmaps algorithm without spherical culling. The x-coordinate is the deferent viewpoint and the y-coordinate is render fps. Compared the result, we can find the Geometry Clipmaps algorithm with spherical culling is more efficient than Geometry Clipmaps algorithm without spherical culling. The average frame of Geometry Clipmaps algorithm with spherical culling is 23 fps and the average frame of Geometry Clipmaps algorithm without spherical culling is 9 fps.

Analyzing the test result, the render efficiency of Geometry Clipmaps is steady. Using Geometry Clipmaps algorithm with spherical culling, because we must read different data file in hard disk, when viewpoint ramble to boundary of data block, the rendering efficiency is low. For example, a point in Figure 9. Because the efficiency of Geometry Clipmaps algorithm without spherical culling is low, so the data file's searching and reading don't influence the rendering efficiency.

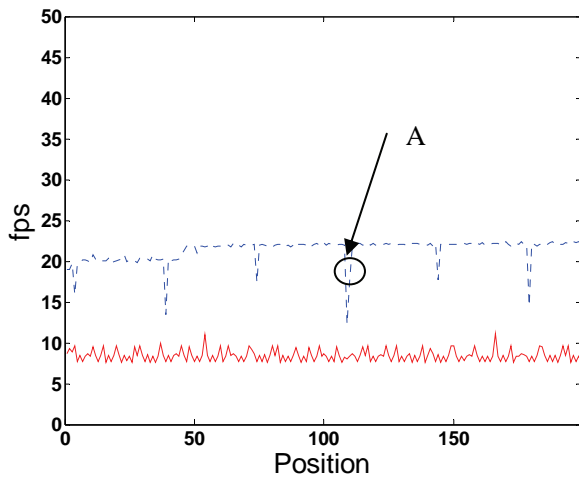


Figure 9: Comparing the rendering frame of view range culling

3.4 Viewpoint control

Rambling in spherical surface, the controlling of view point is more complex than ramble in plane. As shown in Figure 10, if we rotate the line of sight n in viewpoint P , we can rotate the line of sight n about vector OP . Defining the great circle from

point P_1 to P_2 is AP_1P_2A' . Translating P_1 to P_2 , we can rotate vector OP_1 about great circle's normal OY . As shown in Figure 10, A θ rotation of vector V about vector n should produce the vector V' . The Equation is^[12]

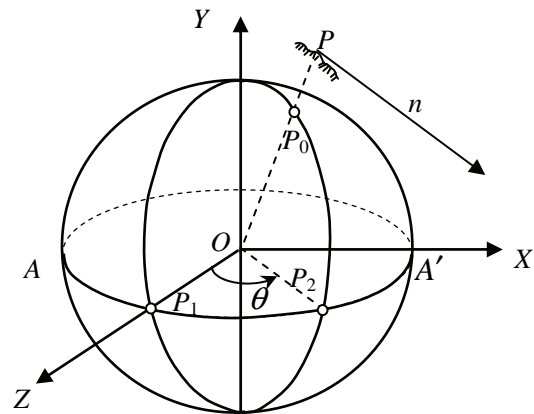
$$\vec{V}' = \vec{V} \cdot \cos\theta + \vec{V} \cdot \vec{n} \cdot (1 - \cos\theta) + (\vec{V} \times \vec{n}) \cdot \sin\theta \quad (3)$$


Figure 10: Transformation of spherical view point

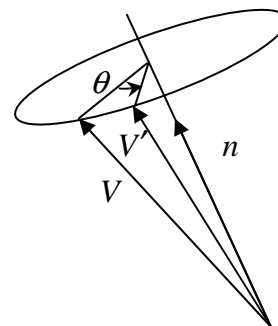


Figure 11: Rotating vector about pointed axis

4 RESULTS AND DISCUSSION

4.1 Test Data and Results

The test data was from USGS's web. The global lunar digital elevation models (DEMs) is at a resolution of 16 pixels/degree (e.g. about 1.895 km resolution). As shown in Figure 12, the size of DEM grid is 5760x2880, created from a triangle irregular network (TIN) of the original points-Unified Lunar Control Network (ULCN2005). See Tables 1 for statistics on this and the other networks.

The global lunar image data is Clementine UVVIS(5 bands, 100m/pixel). The size of data is 163840x81920. In addition, there are high resolution Appolo15 image and DEM in the zone of Appolo15 land in moon. The resolution of Appolo15 image is 1.5m/pixel, the size of data is 3319x3226 and grid cell size is 50m.

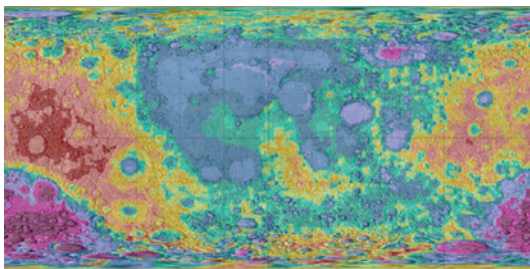


Figure 12: Lunar DEM

The spherical Geometry Clipmaps request the DEM size equal to image half size in same LOD layer. For example, if image size is 1024×1024, then the DEM size must be 512×512. So we must resample the low resolution DEM data with bi-linear interpolation method.

Finally, we built the pyramid of DEM and image. The amounts of pyramid layer are nine. The test results are shown in Figure 13 to Figure 17.



Figure 13: Lunar front face 3D map



Figure 14: Lunar back face 3D map

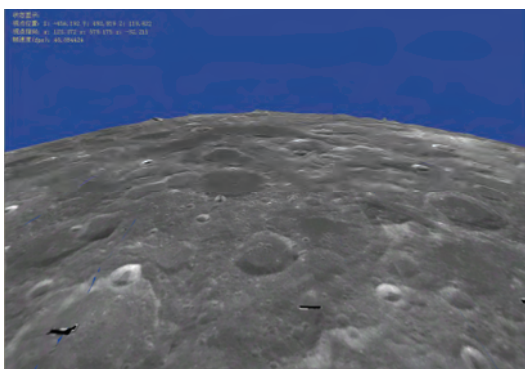


Figure 15: Lunar local zone 3D map

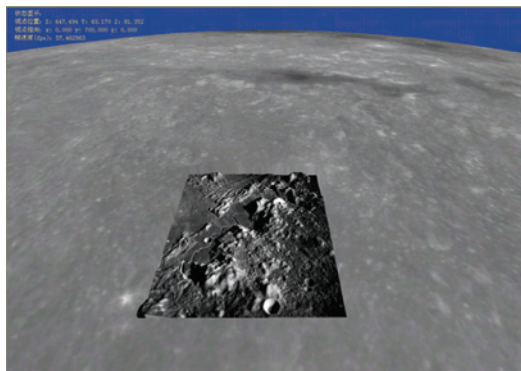


Figure 16: Different resolution mosaic 3D map

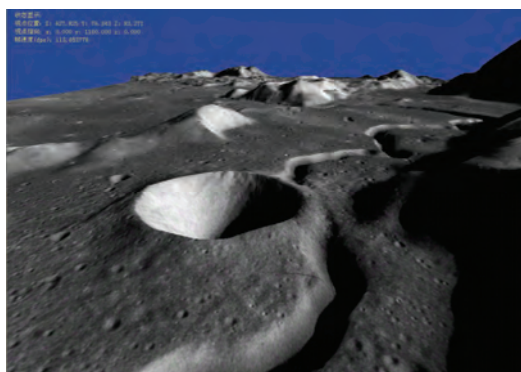


Figure 17: The high resolution 3D map in Apollo15 zone

4.2 Conclusion and Future Work

We collected Lunar DEM and remote image, eliminated data's gross error, resampled the data, built the data pyramid, and rendered the global lunar 3D map real time. The frame of rendering is independent on size of data. The future works include:

(1) The solution of distortion in lunar pole. Using the Eq.(1) performing in GPU, We can transform the planar terrain to spherical terrain. But the problem of projection distortion in lunar pole will worsen the rendering effect. The projection result be shown in Figure 18. Because there are best zone to human explore moon and build lunar base, so we must optimize the LOD and projection algorithm to improve the rendering result.

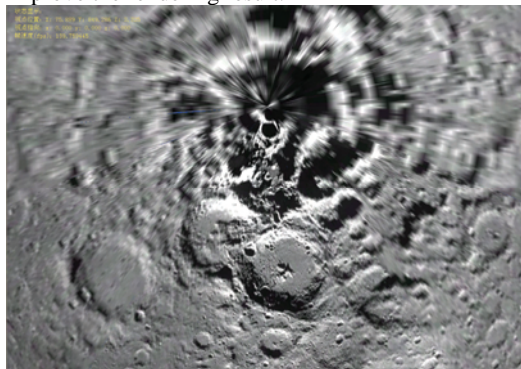


Figure 18: projection distortion in lunar pole

(2) Higher precision lunar terrain rendering. With the restriction of data gained means, the lunar

terrain and image's resolution is low. So the rendering result is not satisfied. New means of data gained must be developed.

(3) The parallel visualization of multi-planet

The rendering algorithm presented in this paper focused on single planet. Building 3D virtual space environment, we must realize the parallel visualization and seamless rambling on earth, moon, mars, and so on. So we must study on space-time reference frame, coordinate system transformation, data structure, view range culling, data storage and searches.

GPU-Based Geometry Clipmaps, ACM Transactions on Graphics (2004).

- [7] MALTE, C. HANS-CHRISTIAN, H. Terrain Rendering using Spherical Clipmaps, Eurographics/ IEEE-VGTC Symposium on Visualization (2006)

- [8] <http://www.google.com/moon/>

ACKNOWLEDGEMENTS

We would like to thank Kan Ning, Zhang Yong, Cheng Jinwei and Yao ZhiQiang for the work of dealing with data and testing algorithm. We also appreciate the publication of the Lunar DEM and image data by NSGS

(<http://pubs.usgs.gov/of/2006/1367/dems/>).

REFERENCES

- [1] DE BOER, W. H. Fast Terrain Rendering Using Geometrical Mipmapping. E-mersion Project (2000).
- [2] LINDSTROM, P., KOLLER, D., RIBARSKY, W., HODGES, L. F., FAUST, N., AND TURNER, G. Real-Time, Continuous Level of Detail Rendering of Height Fields. In Proc. SIGGRAPH '96 (1996), ACM, pp. 109–118.
- [3] DUCHAINEAU, M., WOLINSKY, M., SIGETI, D. E., MILLER, M. C., ALDRICH, C., AND MINEEV-WEINSTEIN, M. B. ROAMing Terrain: Real-Time Optimally Adapting Meshes. In Proc. Visualization '97 (1997), IEEE, pp. 81–88.
- [4] ROETTGER, S., HEIDRICH, W., SLUSALLEK, P., AND SEIDEL, H.-P. Real-Time Generation of Continuous Levels of Detail for Height Fields. In Proc. WSCG '98 (1998), EG/IFIP, pp. 315–322.
- [5] LOSASSO, F., AND HOPPE, H. Geometry clipmaps: terrain rendering using nested regular grids. ACM Transactions on Graphics (2004), 769–776.
- [6] HOPPE, H. Terrain Rendering Using

PIXEL LEVEL FUSION METHODS FOR REMOTE SENSING IMAGES: A CURRENT REVIEW

Yang Jinghui*, Zhang Jixian, Li Haitao, Sun Yushan, Pu Pengxian

Chinese Academy of Surveying and Mapping, Lianhuachi Xi Road 28, Beijing 100830, P. R. China

*: Corresponding author. Email: jhyang@casm.ac.cn. Tel: +86-10-63880532. Fax: +86-10-63880535.

KEYWORDS: Image Fusion, Pansharpening, Pixel Level, Remote Sensing

ABSTRACT:

Image fusion is capable of integrating different imagery to produce more information than can be derived from a single sensor. So far, many pixel level fusion methods for remote sensing images have been presented, in which the lower resolution multispectral image's structural and textural details are enhanced by adopting the higher resolution panchromatic image corresponding to the multispectral image. For this reason, it is also called pansharpening. In this paper we will list current situation of pixel level image fusion by dividing those methods into three categories, i.e., component substitution technique, modulation based technique and multi-resolution analysis based technique according to fusion mechanism. Also, the properties of the three categories for applications are discussed.

1. INTRODUCTION

Data fusion is capable of integrating different imagery data to produce more information than can that be derived from a single sensor. There are at least two limitations accounting for demanding pixel level image fusion technology. One is that the received energy of multispectral sensor for each band is limited because of the narrow wavelength range of the multispectral band. In general, the values of Ground projected Instantaneous Field Of View (GIFOV) (Schowengerdt, 1997) of multispectral bands are larger than those of the panchromatic bands. In order to obtain smaller GIFOV value in relatively narrow wavelength range, image fusion technology is demanded to enhance structural and spatial details. The other is that the capability transmitting the acquired data to the ground is restricted. However, at present the transmission equipments of remote sensing system can not address the requirements. Henceforth, after ground stations receives multispectral images containing relatively less data, the combination of multispectral bands with the higher resolution panchromatic band can resolve the problem to some extent. So far, many pixel-level fusion methods for remote sensing image have been presented where the multispectral image's structural and textural details are enhanced by adopting the higher resolution.

In the recent literature, IEEE Transaction on Geoscience and Remote Sensing had published a special issue on data fusion in May 2008, which includes several new developments for current situation of image fusion (Gamba and Chanussot, 2008). In January 2006, the Data Fusion Committee of the IEEE Geoscience and Remote Sensing Society launched a public contest for pansharpening algorithms (Alparone, et al., 2007), which aimed to identify the ones that perform best. The fusion results of eight algorithms (GLP-CBD, AWLP, GIHS-GA, WiSpeR, FSRE, UNB-Pansharpen, WSIS, GIHS-TP) from worldwide participants were assessed both visually and quantitatively. These published literatures show that data fusion for remote sensing as an active research field has attractive interests. This paper will review the current situation for pixel-level image fusion technology.

Typically, the algorithms for remote sensing image pixel level fusion can be divided into three general categories shown in Fig. 1 (Yang, et al, 2009): component substitution (CS) fusion technique (Pellemans et al, 1993; Shettigara, 1992; Chavez, 1991; Aiazzi, 2007), modulation-based fusion technique (Liu, 2000; Zhang, 1999; Gangkofner, et al., 2008) and multi-resolution analysis (MRA) based fusion technique (Aiazzi, 2002; Amolins, et al., 2007). In addition, some fusion techniques integrating component substitution with multi-resolution analysis were developed, such as the

algorithms combining wavelet transform and IHS transform or PCA transform. Recently, some authors introduce sensors' spectral response and ground spectral features into fusion technology on the basis of previous three categories, and other authors utilize the regularization method to optimize the last fusion results so as to satisfy the higher resolution multispectral image model.

2. COMPONENT SUBSTITUTION FUSION TECHNIQUE

In general, the Component Substitution fusion Technique consists of three steps: Step 1, Forward transform is applied to the multispectral bands after they have been registered to the panchromatic band; Step 2, A component of the new data space similar to the panchromatic band is replaced with the higher resolution band; Step 3, The fused results are finally obtained via inverse transform to the original space.

The typical algorithms of component substitution fusion technique are IHS transform fusion algorithm (Carper, 1990, Shettigara, 1992, Chavez, 1991). This algorithm is suitable when exactly three multispectral (MS) bands are concerned since the IHS transform is defined for three components only. Usually, Panchromatic band (PAN) is histogram-matched, i.e., radiometrically transformed by a constant gain and bias in such a way that it exhibits mean and variance that are the same as Intensity, before substitution is carried out. When more than three bands are available, Tu et al (Tu, et al, 2004) present a generalized IHS (GIHS) transform by including the response of the near-infrared (NIR) band into the intensity component. The GIHS-GA (Garzelli and Nencini, 2006) is based on CS strategy and genetic algorithm. The weights of the MS bands in synthesizing the intensity component and the injection gains are achieved by minimizing a global distortion metrics (Q_4 , in this case) by means of a GA. The GIHS-TP (Choi, 2006) is a CS-based method that trades off the performances of GIHS in terms of spectral distortion and spatial enhancement. Aiazzi et al (Aiazzi, et al, 2007) introduce multivariate regression to improve spectral quality. In the method based on IHS, a generalized intensity component is defined as the weighted average of the MS bands. The weights are obtained as regression coefficients between the MS bands and the spatially degraded PAN image with the aim of capturing the spectral responses of the

sensors. González Audícana and Otazu (González Audícana and Otazu, et al, 2006) present a low computational-cost method to fuse IKONOS images using the spectral response function of its sensors. Andreja and Krisťof (Andreja and O. Krisťof, 2006) found that for preserving spectral characteristics, high level of similarity between the panchromatic image and the respective multispectral intensity is needed. In order to preserve spectral and spatial resolution, spectral sensitivity of multispectral and panchromatic data was performed, and digital values in individual bands have been modified before fusion. Malpica (Malpica, 2007) present a technique which consists of a hue spectral adjustment scheme integrated with an intensity–hue–saturation transformation for vegetation enhancement. Ling and Ehlers, et al (Ling, Ehlers, et al, 2007) present a method which combines a standard IHS transform with FFT filtering of both the panchromatic image and the intensity component of the original multispectral image.

Other common used CS-based method, PCA transform, (Shettigara, 1992, Chavez, 1991) make an assumption that the first principal component (PC) of high variance is an ideal choice for replacing or injecting it with high spatial details from the high-resolution histogram-matched PAN image. Shah, et al (Shah, Younan, and King, 2008) use the adaptive PCA to reduce the spectral distortion in the fusion scheme combining adaptive PCA approach and contourlets. Another CS technique reported in the literature is Gram–Schmidt (GS) spectral sharpening (Laben and Brower, 2000), which is widely used since it has been implemented in the Environment for Visualizing Images (ENVI) program package. Aiazzi et al (Aiazzi, et al, 2007) adopts multivariate regression to create the synthetic low-resolution-intensity images which is used in the Gram-Schmidt transform. The proposed enhanced strategy is effective in improving the quality of the images than ordinary GS technique. UNB-pansharp (Zhang, 2002) algorithm developed at the UNB, Canada, is based on CS. The least squares technique is utilized to reduce color distortion, by identifying the best fit between gray values of individual image bands and adjusting the contribution of the individual bands to the fusion result.

3. MODULATION-BASED FUSION

TECHNIQUE

The modulation-based fusion technique utilizes the concept that the spatial details are modulated into the multispectral images by multiplying the multispectral images by the ratio of the panchromatic image to the synthetic image, which is a lower resolution version of the panchromatic image generally. The fusion results are expressed as (1).

$$xS_{(k,i,j)}^H = \frac{pan_{(i,j)}}{syn_{(i,j)}} xS_{(k,i,j)}^L \quad (1)$$

$syn_{(i,j)}$ is the value of the (i,j) pixel of the synthetic band.

According to the method calculating the synthetic image, the typical modulation based fusion algorithms include:

1) Brovey: $syn_{(i,j)} = \frac{1}{3} (R_{(i,j)} + B_{(i,j)} + G_{(i,j)}) \quad (2);$

2) SFIM: $syn_{(i,j)} = \frac{1}{n} \sum_1^n pan_{(i,j)} \quad (3)$

, n is the number of $k \times k$ neighbors;

3) HPF: $syn_{(i,j)} = LPH(pan)_{(i,j)} \quad (4)$

, LPH: low-pass filter;

4) SVR: $syn_{(i,j)} = \sum \varphi_k xS_{(k,i,j)}^L \quad (5)$

, $pan = \sum \varphi_k xS_{(k,i,j)}^L + \varepsilon \quad (6)$

, linear regression.

For Brovey transform fusion algorithm (Vrabel, 2000), the synthetic image is the average band of Blue, Green, Red bands, which can be expressed as (2). For Smoothing Filter Based Intensity Modulation (SFIM) fusion algorithm, Liu (Liu, 2000) point out that by using a ratio between a higher resolution image and its low pass filtered (with a smoothing filter) image, spatial details can be modulated to a co-registered lower resolution multispectral image without altering its spectral properties and contrast. The technique can be applied to improve spatial resolution for either colour composites or individual bands. The synthetic image is the local mean of the panchromatic image pixels with 3×3 , 5×5 , or 7×7 size smoothing filter kernel, which can be expressed as (3). For high-pass filter (HPF) method (Chavez, 1991) the higher spatial resolution data have a small high-pass spatial filter applied. The results of the small high-pass filter contain the high-frequency component that is related mostly to spatial information. The HPF results are

added, pixel by pixel, to the lower spatial resolution, but higher spectral resolution data set. This process can be transformed into the form of (1), whose synthetic image can be expressed as (4). Gangkofner et al (Gangkofner, et al, 2008) optimizes the high pass filter addition technique whose improvements are the standardization of the HPF parameters over a wide range of image resolution ratios and the controlled trade-off between resulting image sharpness and spectral properties. Zhang (Zhang, 1999) presents Synthetic Variable Ratio (SVR) merging method which is calculated through the equation (1). The synthetic image is the grey value of the high-resolution synthetic panchromatic image formulated by (5). Zhang had developed a new method that can directly derive parameters φ_i through (6).

These parameters φ_i are calculated directly through multiple regression analysis of the original panchromatic image and the original multispectral bands.

4. MULTI-RESOLUTION ANALYSIS FUSION TECHNIQUE

MRA-based fusion techniques (Amolins, et al. 2007) adopt multi-scale decomposition methods such as multi-scale wavelet (Núñez et al. 1999) and Laplacian pyramid (Aiazzi 2002) to decompose multi-spectral and panchromatic images with different levels, and then derive spatial details that are imported into finer scales of the multi-spectral images in the light of the relationship between the panchromatic and multi-spectral images in coarser scales, resulting in enhancement of spatial details. MRA-based fusion techniques consist of three main steps: 1) MRA: Wavelet multi-resolution decomposition; 2) Fusion: Replacement of approximation coefficients of PAN by those of multispectral band; and 3) IMRA: Inverse multi-resolution transform.

It has been found that the earlier studies (Garguet-Duport et al., 1996; Yocky, 1996) adopting discrete wavelet transform (DWT) more preserves the spectral characteristics of the MS imagery than CS fusion schemes (e.g. IHS, PCA), but there are some negative aspects, such as the introduction of artifacts in the fused image. Núñez, et al (Núñez, et al, 1999) present the additive wavelet fusion algorithm (AWL) by using the “à trous” algorithm which allows to use a dyadic wavelet to merge nondyadic data in a simple and efficient

scheme. To improve the spectral quality, the high-pass details are injected proportionally to the low-pass MS components in such a way that the fused MS pixel vector is always proportional to that before fusion. Aiazzi et al present the GLP-CBD fusion algorithm (Aiazzi, et al 2002), which exploits MRA, achieved through GLP, with the spatial frequency response of the analysis filters matching a model of the modulation transfer function (MTF) of the MS instrument. The injection model employs a decision based on locally thresholding the correlation coefficient (CC) between the resampled MS band and the low pass approximation of the Pan. Ranchin et al. (Ranchin et al, 2003) present the “Amélioration de la Résolution Spatiale par Injection de Structures” (ARSIS, Improving Spatial Resolution by Structure Injection) concept based on the assumption that the missing information is linked to the high frequencies of the datasets to be fused. Some fusion techniques jointly using component substitution with multi-scale analysis were developed, such as the algorithms combing wavelet transform and IHS transform (González-Audícana, et al, 2004, Chibani and Houacine, 2002, Zhang and Hong, 2005) or PCA transform (González-Audícana, et al, 2004, Shah, Younan, and King, 2008). These hybrid schemes use wavelets to extract the detail information from one image and standard image transformations to inject it into another image, or propose improvements in the method of injecting information (e.g. Garzelli and Nencini, 2005; Otazu et al., 2005). Otazu et al introduce sensors’ spectral response and ground spectral features into fusion technology on the basis of MRA (Otazu, et al, 2005).

Other authors utilize the regularization method to optimize

the fusion results so as to satisfy the higher resolution multispectral image model (Aanaes, et al. 2008). Yang, et al. (2009) generalized this idea and proposed a new model quantifying the mathematical relationship between the fused higher multispectral images and the original multispectral image, the spatial details being extracted from the high-resolution panchromatic image, and the adopted fusion strategies.

5. DISCUSSIONS AND CONCLUSIONS

Currently, the pixel-level image fusion algorithms are divided into three categories, i.e., CS technique, modulation based technique and MRA based technique according to fusion mechanism. With these three categories, similarity and difference between fusion techniques can be derived, which is important for applications. We discuss two typical classes of fusion application, i.e., automatic classification and visual interpretation. Automatic classification relies on the spectral feature than spatial details, while visual interpretation is opposite. Thus, if the fused images are used for automatic classification, modulation based technique and MRA technique with a lower number of decomposition levels are preferable, which better preserve the spectral characteristics of multispectral bands. For visual interpretation, which benefits from spatial and textural details, CS technique and MRA technique with a higher number of decomposition levels are appropriate.

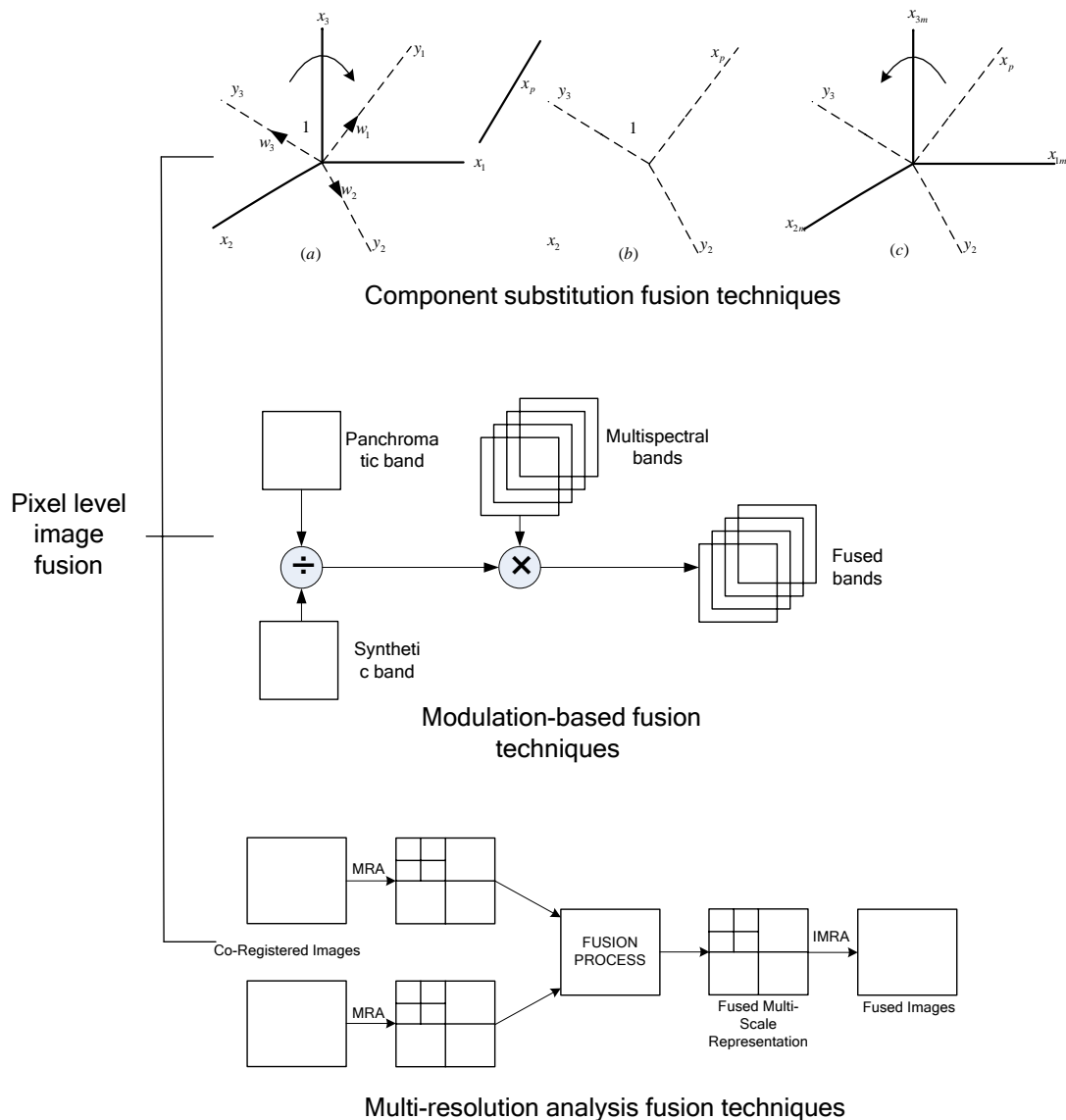


Fig. 1 Three categories of pixel level image fusion

References

- A. H. J. M. Pellemans, R.W.L. Jordans, and R. Allevijn, 1993. Merge Multispectral and Panchromatic SPOT Images with respect to the Radiometric Properties of Sensor. *Photogramm. Eng. Remote Sens.*, vol. 59, No.1 pp. 81 – 87.
- A. Garzelli, F. Nencini, 2005. Interband structure modeling for Pan-sharpening of very high-resolution multispectral images. *Information Fusion*, vol.6, pp.213 ~ 224.
- A. Garzelli and F. Nencini, 2006. Fusion of panchromatic and multispectral images by genetic algorithms. in *Proc. IEEE Int. Geosci. Remote Sens. Symp.* pp. 3810–3813.
- B. Aiazzi, L. Alparone, S. Baronti, A. Garzelli, 2002. Context-driven fusion of high spatial and spectral resolution images based on oversampled multiresolution analysis. *IEEE Transactions on Geoscience and Remote Sensing*, vol.40, pp. 2300 ~ 2312.
- B. Aiazzi, S. Baronti, M. Selva, 2007. Improving Component Substitution Pansharpening Through Multivariate Regression of MS +Pan Data. *IEEE Transactions on Geoscience and Remote Sensing*, vol. 45, no. 10, pp. 3230 – 3239.
- B. Garguet-Duport, J. Girel, J. M. Chasseny, and G. Pautou, 1996. The use of multiresolution analysis and wavelet transform for merging SPOT panchromatic and multispectral image data. *Photogramm. Eng. Remote Sens.*, vol. 62, pp.

1057–1066.

C. A. Laben and B. V. Brower, 2000. Process for enhancing the spatial resolution of multispectral imagery using Pan-sharpening. U.S. Patent 6 011 875, Tech. Rep., Eastman Kodak Company.

C. A. Yocky, 1996. Multiresolution wavelet decomposition image merger of Landsat Thematic Mapper and SPOT Panchromatic data. *Photogramm. Eng. Remote Sens.*, vol. 62, pp. 1067–1074.

H. Aanæs, J. R. Sveinsson, A. A. Nielsen, T. Bøvith, and J. A. Benediktsson, 2008. Model-Based Satellite Image Fusion, *IEEE Transactions on Geoscience and Remote Sensing*, vol. 46, no. 5, pp.1336-1346.

J. Vrabel, 2000. Multispectral imagery advanced band sharpening study. *Photogramm. Eng. Remote Sens.*, vol.66, pp. 73 ~ 79.

J. N´uñez, X. Otazu, O. Fors, A. Prades, V. c Pal`a, and R.Arbiol, 1999. Multiresolution-Based Image Fusion with Additive Wavelet Decomposition. *IEEE Transactions on Geoscience and Remote Sensing*, vol.37, pp.1204 ~ 1211.

J. W. Carper, T. M. Lillesand, and R. W. Kiefer, 1990. The use of intensity–hue–saturation transformations for merging SPOT panchromatic and multispectral image data. *Photogramm. Eng. Remote Sens.*, vol.56, pp. 459–467.

J. G. Liu, 2000. Smoothing Filter-based Intensity Modulation: a spectral preserve image fusion technique for improving spatial details. *International Journal of Remote Sensing*, vol.21, pp.3461 ~ 3472.

J. A. Malpica, 2007. Hue adjustment to IHS Pan-sharpened Ikonos imagery for vegetation enhancement. *IEEE Geosci. Remote Sens. Lett.*, vol. 4, no. 1, pp. 27–31.

J. X. Zhang, J. H. Yang, Z. Zhao, 2006. Block-regression based Fusion of Optical and SAR Imagery for Feature Enhancement. *ISPRS Mid-term Symposium Remote Sensing: From Pixels to Processes*. ITC, the Netherlands.

J. H. Yang, J. X. Zhang, and H. T. Li, 2009. Generalized Model for Remotely Sensed Data Pixel-Level Fusion and Its implementation technology. *Journal of Image and Graphics (Chinese)*, vol. 14, no. 4, pp. 604 – 614.

K. Amolins, Y. Zhang, P. Dare, 2007. Wavelet based image fusion techniques — An introduction, review and comparison. *ISPRS Journal of Photogrammetry & Remote Sensing*, vol.62, pp. 249–263.

L. Alparone, L. Wald, J. Chanussot, C. Thomas, P. Gamba, and L. M. Bruce, 2007. Comparison of Pansharpening Algorithms: Outcome of the 2006 GRS-S Data-Fusion Contest. *IEEE Transactions on Geoscience and Remote Sensing*, vol. 45, no. 10, pp. 3012-3021.

M. González-Audícana, J. L. Saleta, R. G. Catalán, et al, 2004. Fusion of Multispectral and Panchromatic Images Using Improved IHS and PCA Mergers Based on Wavelet Decomposition. *IEEE Transactions on Geoscience and Remote Sensing*, vol. 42, no. 6, pp. 1291~1299.

M. Choi, 2006. A New Intensity-Hue-Saturation Fusion Approach to Image Fusion With a Tradeoff Parameter. *IEEE Transactions on Geoscience and Remote Sensing*, vol. 44, no.6, pp. 1672~1682.

M. Gonzáles Audícana, X. Otazu, O. Fors, and J. A. Alvarez-Mozos, 2006. A low computational-cost method to fuse IKONOS images using the spectral response function of its sensors. *IEEE Trans. Geosci. Remote Sens.*, vol. 44, no. 6, pp. 1683–1691.

P. Gamba, J. Chanussot, 2008. Guest Editorial Foreword to the Special Issue on Data Fusion. *IEEE Transactions On Geoscience And Remote Sensing*, vol. 46, no. 5, pp.1283-1288.

R. A. Schowengerdt, 1997. *Remote Sensing: Models and Methods for Image Processing*, 2nd ed. Orlando, FL: Academic.

S. Chavez, C. Sides, and A. Anderson, 1991. Comparison of three different methods to merge multiresolution and multispectral data: Landsat TM and SPOT panchromatic.

- Photogramm. Eng. Remote Sens., vol.57, pp. 295 ~ 303.
- S. Andreja and O. Krisťtof, 2006. High-resolution Image Fusion: Methods to Preserve Spectral and Spatial Resolution. *Photogramm. Eng. Remote Sens.*, vol. 72, no. 5, pp. 565-572.
- T.-M. Tu, P. S. Huang, C.-L. Hung, and C.-P. Chang, 2004. A fast intensityhue-saturation fusion technique with spectral adjustment for IKONOS imagery. *IEEE Geosci. Remote Sens. Lett.*, vol. 1, no. 4, pp. 309–312.
- T. Ranchin, B. Aiazzi, L. Alparone, S. Baronti, and L.Wald, 2003. Image fusion—the ARSIS concept and some successful implementation schemes. *ISPRS Journal of Photogrammetry and Remote Sensing*, vol.58, pp.4-18.
- U. G. Gangkofner, P. S. Pradhan, D. W. Holcomb, 2008. Optimizing the High-pass filter addition technique for image fusion. *Photogrammetric Engineering and Remote Sensing*, vol. 74, no.9, pp.1107-1118.
- V. K. Shettigara, 1992. A generalized component substitution technique for spatial enhancement of multispectral images using a higher resolution data set. *Photogramm. Eng. Remote Sens.*, vol. 58, pp. 561–567.
- V. P. Shah, N. H. Younan, and R. L. King, 2008. An efficient pan-sharpening method via a combined adaptive PCA approach and contourlets. *IEEE Trans. Geosci. Remote Sens.*, vol. 46, no. 5, pp. 1323–1335.
- X. Otazu, M. González-Audfca, O. Fors, et al, 2005. Introduction of Sensor Spectral Response Into Image Fusion Methods: Application to Wavelet-Based Methods. *IEEE Transactions on Geoscience and Remote Sensing*, vol. 43, no. 10, pp. 2376~2385.
- Y. Chibani, and A. Houacine, 2002. The joint use of IHS transform and redundant wavelet decomposition for fusing multispectral and panchromatic images. *International Journal of Remote Sensing*, vol. 23, no. 18, pp. 3821~3833.
- Y. Zhang, G. Hong, 2005. An IHS and wavelet integrated approach to improve pan-sharpening visual quality of natural colour IKONOS and QuickBird images. *Information Fusion*, vol. 6, no. 3, pp. 225~234.
- Y. Zhang, 2002. A new automatic approach for effectively fusing Landsat-7 as well as IKONOS images. in *Proc. IEEE Int. Geosci. Remote Sens. Symp.*, 2002, pp. 2429–2431.
- Y. Zhang, 1999. A new merging method and its spectral and spatial effects. *International Journal of Remote Sensing*, vol. 20, no. 10, pp. 2003~2014.
- Y. R. Ling, M. Ehlers, E. L. Usery, and M. Madden, 2007. FFT-enhanced IHS transform method for fusing high-resolution satellite images. *ISPRS J. Photogramm. Remote Sens.*, vol. 61, pp. 381–392.

Acknowledgements: This work was supported by National Natural Science Foundation of China under Grant No. 40901229 and National Institutes Fund for Basic Scientific Research.

IDENTIFICATION OF HISTORICAL LAND USE BY THE HELP OF AERIAL PHOTOGRAPHY.

V. Zdimal*^a

^aMendel University in Brno, Department of Applied and
Landscape Ecology, Zemedelska 1, 61300, Brno, Czech Republic

Technical Commission VII Symposium 2010

KEY WORDS: Agriculture, History, Human Settlement, Land Cover, Land Use

ABSTRACT:

Southern Moravia region (Czech Republic) belongs to old development areas settled by a man from of old. A man had influenced it since primeval ages and up to the present days we have been finding here survivals from his activity both out of this time. To recognize a certain place thoroughly, it is necessary to use all accessible resources and to synthesize them in a suitable way. One of the information sources about a local countryside are aerial photographs. Human intervention into the landscape in the past led to overlay of mould and to the change of soil rates of a particular place and thus to a change of the soil plants surroundings. This is one of the reasons why the land cover on this place is different from the one in the surroundings. And just for this diversity, monitoring the aerial photography in spectral channels NIR and RED is very suitable, just for differential reflectivity of green matter in these channels. For information highlighting we can use so called vegetation indexes that declare the relation between reflectivity of NIR and RED channels. Land use in the past was watched on the fields of University agriculture enterprise in Zabcice near the village Prisnotice (ninety kilometres to the north of Vienna). In the monitored area, which is presently agriculturally exploited, five hundred-hectare plot, there was identified and by other surveys designated the region settlement in the past and its destruction, the gas conduit location and the place after sand mining.

1. INTRODUCTION

Southern Moravia in the Czech Republic has been the site of settlements stretching back to the dawn of man. The landscape has been under human influence since people first arrived on the scene, with individual eras leaving their mark in the form of layers which may be read almost like a palimpsest. A single location may show evidence of human activity from the eneolithic period, the age of the Romans, the medieval era and contemporary times. Human activity during these periods has been of varied intensity, with the greatest influence on the structure of the landscape being attributable to agriculture. Deforestation took place initially, followed soon after by use of the land for farming. Every intrusion on the land in times past, whether it involve relocation, the addition of new layers, excavation or topsoil, has changed its structure to varying degrees, with results still visible today. All of these intrusions on the soil have left their mark on the vegetation. These allow past human activities to be observed. They are easily seen from above and therefore amenable to monitoring by aerial photography using various spectral bands. The use of remote sensing has been described by various authors.

Spectral characteristics of plants are influenced by the size of leaf surface per unit of area (leaf area index LAI). The difference in the amount of chlorophyll in leaves has a great influence on the determination of LAI. An influence of the amount of chlorophyll on the LAI determination was studied by Haboudane et al. (2004). Convenience of used spectral bands is often discussed question. Primary, standard red (RED, 630-690 nm) and near infrared (NIR, 750-900 nm) bands are used. Zhang

et al. (2006) used these spectral bands and NDVI, respectively, for the determination of the amount of nitrogen in rice and Reyniers et al. (2006) observed dependence between the amount of nitrogen and NDVI in plants. Additionally, studies that evaluate convenience of various spectral bands in different plant growth phases or conditions are also made. Ferwerda, Skidmore a Mutanga (2005) observed that the most convenient spectral region for the monitoring of the nitrogen amount lies between 1770 and 693 nm. Lee et al. was then comparing hyperspectral and multispectral data.

Large-scale aerial photography in the infrared band has been taking place in the Czech Republic since last year. (Figure 1.)



Figure 1. Aerial photography in the infrared band (© GEODIS)

2. METHODS

2.1 Study site

Past land use was monitored on parcels belonging to the Zabcice UAE at Prisnotice, 90 km from Vienna. (Figure 2.) The project took place in the same location as that used for a precision agriculture project. The project was solved on the land of University agriculture enterprise (Mendel University in Brno), placed in Žabčice, which is working mainly in the maize area. Field production is focused on the production of cereals and fodder crops and livestock production is focused on beef and pig-rising. Additional activities are focused first of all on the practical aspects of the student education. ŠZP Žabčice controls 1602 ha of the farmland (1353 ha of arable land). The chosen locality has an area of 61 ha (Czech Republic, 48°59'11" N 16°37'40" E, 175 m above sea-level).

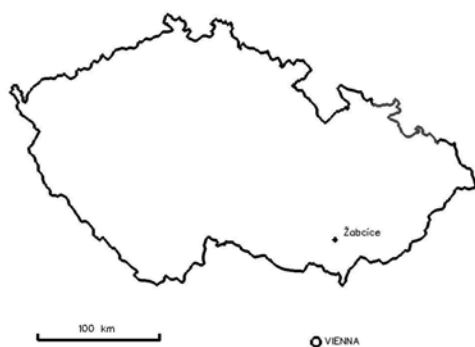


Figure 2. Study site

2.2 Digital aerial imagery

The first step was aerial photo. Based on our experience, and for the reason of data comparison with other research studies in the area, the monitoring was done in two spectral bands (RED, 630-690 nm and NIR, 750-900 nm). Aerial images was done by GEODIS BRNO Ltd. using Z-37A Čmelák airplane equipped with digital medium-format camera Hasselblad H1 with lens of 50.4 mm focal length and Phaseone P25 digital back. Hasselblad H1 is a medium format SLR camera with a number of unique features that support digital backs and provides a similar handling and functionality as an integrated digital camera. The image format is 6 x 4,5 cm (actual size 56 x 41.5 mm). A Phaseone P25 digital back incorporates a 22 megapixel CCD chip with a size of 48.9 x 36.7 mm, 9 x 9 μm pixel pitch, ratio 4:3 ratio and 16 bits per pixel ADC. The images were sensed using custom-made optical filters to obtain two bands (RED and NIR) with spectral properties similar to Landsat TM bands. Each single exposition was directed using GPS according to in advance planed snapshot program using the pin-point method (according to pre-determined centers of projection). For the precise determination of the corrected center of projection and of tilt-angle against normal line to index display plane, the camera was connected with Aparature POS AV 310 (GPS/INS) from Applanix Ltd. The resulting orthophotomaps of the corresponding spectral bands are prepared by orthogonalization of the aerial digital images to the pre-prepared digital model of the corresponding landscape. The interpretation bases are then

obtained by the correct synthesis of the resulting orthophotomaps. The accuracy of position of the orthophotomap corresponds approximately to 2.5 times the size of the ground element. For the standard aerial monitoring, where the size of the ground element is 25 cm, the resulting possible root-mean-square error of position in the orthophotomap generated according to the above given procedure is approx. 65 cm.

2.3 Data processing

The history of the landscape is specific to particular locations. Thorough knowledge requires that all available resources be used and an appropriate synthesis made. Aerial photography provides one source of information about the local landscape, which may be integrated using a geographic information system. Interpretive signs were used for manmade shapes. Regular lines and shapes were sought for structures which had been built and disappeared in past times, along with evidence of the former course of waterways which have currently been regulated and the appearance of crops which do not correspond to the presumed condition of soils which differ from their surroundings. Observed differences were supplemented by land surveys and the study of archival materials, primarily maps, and with the collection of information from witnesses.

3. RESULTS AND DISCUSSION

Changes in the spectrum characteristic of agricultural fields with past human activity were identified in a 500 ha area at this location, arranged in chronological order by era of origin.

An archaeological site (Gojda, 2000) includes remains from the eneolithic era – circular trenches with a burial pit at center – as well as traces of Roman earth dwellings and the outlines of a medieval village. This 50 ha area is part of the cultural heritage and may be used for agricultural purposes but other uses are limited. (Figure 3.)



Figure 3. Archaeological site

At the start of the 1970s, wells for potable water were constructed at the location of interest. The fence around them increased from 50 ha in 1976 to 100 ha in 2000. The Level 1 Hygienic Protection Zone encompasses 50 fenced hectares and the entire area is included in a Level 2 Hygienic Protection Zone. Two gas pipelines were run through the area in 1974 and 1984 which are still visible on aerial images. Including a 50-meter protected zone, they occupy 50 ha. (Figure 4.)

Specific to the area are locations at which sand has been excavated. Sand was first removed from the location, where farming had earlier taken place, and subsequently the remaining pit was filled with sludge from the nearby sugar refinery in Zidlochovice, with the land then forested via volunteer seeding. When the area of arable land was increased in the 1970s, this land came under cultivation and was not reclaimed. Although it is used for agricultural purposes today, under adverse moisture conditions cultivation is not possible. Any other use is therefore practically impossible. The entire process has taken place without clear ownership relations. The area at which sand was excavated is not large – it consumes 10 ha – but its history is most interesting. (Figure 5.)

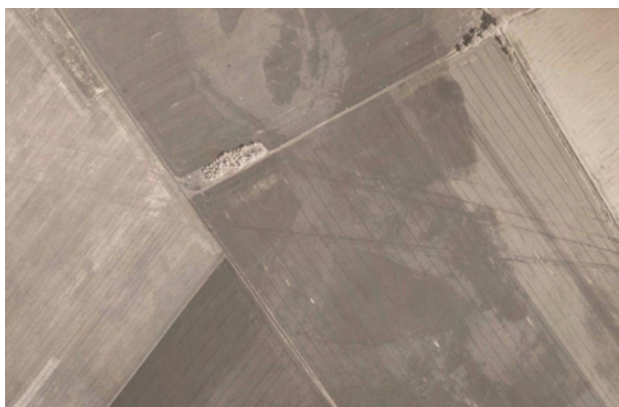


Figure 4. Two gas pipelines



Figure 5. Sand excavation

4. CONCLUSIONS

Human intrusions on the landscape during the past have resulted in new layers of soil and changes in soil conditions at particular locations, thereby modifying the soil environment for plants. This is one reason why vegetation at this location differs from its surroundings. Aerial photography using the NIR and RED bands is thus particularly well-suited to observing these differences because of the varied reflectivity of green materials in these bands. This method allows the use of remote sensing in archaeology. Archaeological sites may be identified in this way, along with pipelines, water wells and the traces of sand excavation. This type of management is limited of past activities and must be taken into account for the future.

REFERENCES

- Ferwerda, J. G., Skidmore, A. K. & Mutanga, O., 2005. Nitrogen detection with hyperspectral normalized ratio indices across multiple plant species. *International Journal of Remote Sensing*, 26 (18), p. 4083-4095.
- Gojda, M., 2000 *Archeologie krajiny*. Academia, Praha, 240 p.
- Haboudane, D., Miller, J. R., Patey, E., Zarco-Tejada, P. J. & Strachan, I. B., 2004. Hypespaktral vegetation indices and novel algorithms for predicting green LAI of crop canopies: Modeling and validation in the context of precision agriculture. *Remote Sensing of Environment*, 90, p. 337 – 352.
- Reyniers, M., Vrindts, E. & DE Baerdemaeker, J., 2006. Comparison of an aerial-based system and an on the ground continuous measuring device to predict yield of winter wheat. *European Journal of Agronomy*, vol. 24, no. 2, p. 87-94.
- Zhang, P., Anderson, B., Tan, B., Huang, D. & Myneni, R., 2005. Potential monitoring of crop production using a satellite-based Climate-Variability Impact Index. *Agricultural and Forest Meteorology*, vol. 132, no. 3-4, p. 344-358.

DEVELOPMENT OF A SUPERVISED SOFTWARE TOOL FOR AUTOMATED DETERMINATION OF OPTIMAL SEGMENTATION PARAMETERS FOR ECOGNITION

Y. Zhang^{*a}, T. Maxwell, H. Tong, V. Dey

^aUniversity of New Brunswick, Geodesy & Geomatics Eng., 15 Dineen Dr., E3B 5A3, Fredericton, Canada

Technical Commission VII Symposium 2010

KEY WORDS: Land Cover, Classification, Abstraction, Image, Software, High resolution, Advancement

ABSTRACT:

Image segmentation is one of the most important steps in object-based classification. The commercial software eCognition has been proven to be the most advanced software tool for object-based classification of high resolution remote sensing imagery. However, its segmentation process still relies on trial and error to find proper segmentation parameters. The segmentation process is very time consuming and the segmentation quality directly depends on the experience of the operator. To overcome this problem, a supervised software tool—Fuzzy-based Segmentation Parameter optimizer (FbSP optimizer)—was developed to determine the optimal segmentation parameters through a training process and a fuzzy logic analysis. The optimal segmentation parameters are then used in eCognition to segment the entire image, achieving an optimal segmentation result. The FbSP optimizer can radically increase the efficiency of segmentation parameter selection, and achieve improved segmentation results. It also reduces the influence of the operator's experience on the quality of segmentation results.

1. INTRODUCTION

Since the successful launch of the very high resolution (VHR) Ikonos satellite in 1999, object-based classification has quickly become the mainstream technology for land cover classification of VHR remote sensing images, such as Ikonos, QuickBird, GeoEye-1, WorldView-2 and airborne digital imagery (Smith and Morton, 2010; Blaschke, 2010). In object-based classification, image segmentation is a crucial process which directly influences the efficiency of the classification process and quality of the classification result. To date, eCognition software developed by Definiens has proven to be the most effective technique for object-based classification among a variety of object-based classification techniques (Lavigne et al., 2006).

However, trial and error is still a standard approach of eCognition to finding proper segmentation parameters for achieving a proper segmentation of objects of interest. In the segmentation, operator's knowledge of the image and experience of the segmentation process play an important role for the success of the segmentation. In addition, the segmentation process is time consuming. These drawbacks have significantly limited the potential of eCognition for a broad range of practical applications.

To overcome the limitation of eCognition in finding proper segmentation parameters for image segmentation, a software tool has been developed in the CRC-AGIP Lab (Canada Research Chair Laboratory in Advanced Geomatics Image Processing) at the University of New Brunswick, based on previous work done in the lab (Maxwell, 2005; Zhang and Maxwell, 2006). The software tool, named Fuzzy-based Segmentation Parameter optimizer (FbSP optimizer), can automatically determine optimal segmentation parameters for eCognition through a supervised training process and fuzzy logic analysis. Using the FbSP optimizer in combination with eCognition, the segmentation of an object of interest can be achieved within minutes, instead of hours by solely using eCognition. In addition, the segmentation result can be significantly improved.

This paper will first introduce the general concept of image segmentation used in eCognition and the role of segmentation parameters. It will then introduce the concept and process of the developed of the FbSP optimizer for identifying optimal segmentation parameters for eCognition. The experiment results and the comparison between the segmentation qualities and time used in the segmentation processes will also be given to allow readers to judge the improvement made by the supervised software tool—FbSP optimizer.

2. SEGMENTATION TECHNIQUE OF ECOGNITION

2.1. Region Merging

To find the boundary of an image object or segment an object, eCognition implemented a region merging approach to segmentation called "Fractal Net Evolution" approach (Batz and Schape, 1999). This technique starts with individual adjacent pixels as initial objects, and then measures (1) the spectral heterogeneity change, $h_{spectral}$, and (2) the shape heterogeneity change, h_{shape} , between the two neighbor pixels (objects) to determine whether they need to be merged together, or not. Once the two pixels are merged into one object, the region of the object grows one step. This measurement and merging process continues iteratively until a user defined threshold is reached. Then, the region of the object stops growing; resulting in one image segment. The region merging and region growing process was designed with the view to meeting six aims including the (Batz and Schape, 2000):

- Production of homogeneous image object-primitives;
- Adaptability to different scales;
- Production of similar segment sizes for a chosen scale;
- Applicability to a variety of data sets;
- Reproducibility of segmentation results; and
- Requirement for reasonably fast performance.

2.2. Role of Segmentation Parameters

Figure 1 illustrates the relationship between spectral heterogeneity change, $h_{spectral}$, the shape heterogeneity change, h_{shape} , and the corresponding segmentation parameters. Where

- $h_{spectral}^c$ is spectral heterogeneity change of individual

spectral bands,

- $h_{compact}$ is compactness heterogeneity change,
- h_{smooth} is smoothness heterogeneity change,
- w_c are the weights associated with each layer,
- $w_{compact}$ is compactness weight (parameter),
- $1-w_{compact}$ is smoothness weight (parameter),
- w is weight (parameter) for overall spectral heterogeneity change, and
- $1-w$ is weight (parameter) for shape heterogeneity

change.

The $h_{spectral}^c$, $h_{compact}$, and h_{smooth} are calculated according to the image grey values within the two neighbor objects in each spectral bands, whereas the weights (parameters) w_c , $w_{compact}$ (or $1-w_{compact}$), and w (or $1-w$) must be given by the user. The user must also give a scale value (s) as a threshold to stop the merging. Figure 2 shows the interface of eCognition to allow users to input the parameters to guide and control the segmentation process.

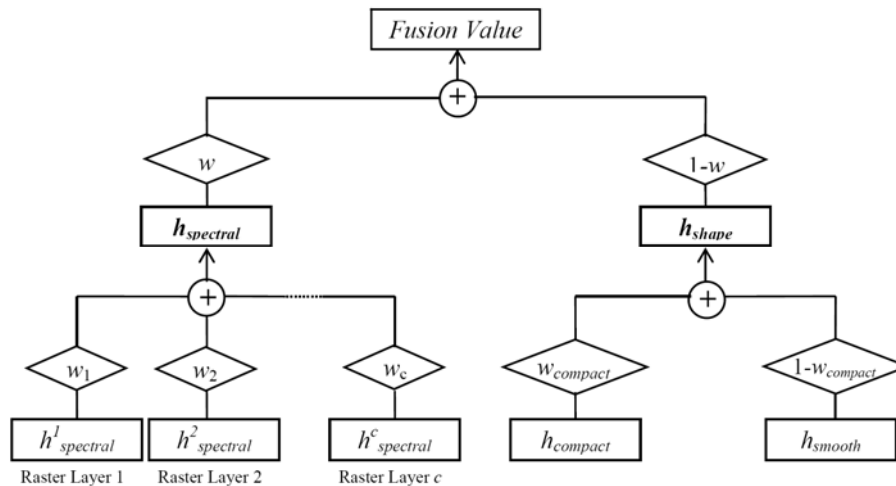


Figure 1. Relationship between the segmentation parameters (user determined weights) in eCognition. Usually, the weights for individual spectral layers (bands) (w_1, w_2, \dots, w_c) are set to 1. Users need to give the value for Smoothness weight ($1-w_{compact}$) (or Compactness weight ($w_{compact}$)) and Shape weight ($1-w$). The weights ($1-w_{compact}$) and ($1-w$) are used to calculate the Fusion Value (f). The value f is then compared with a user specified Scale value (s) to estimate whether the two adjacent objects need to be merged, or not (if $f < s^2$, merge the two objects; if $f \geq s^2$, stop the merging).

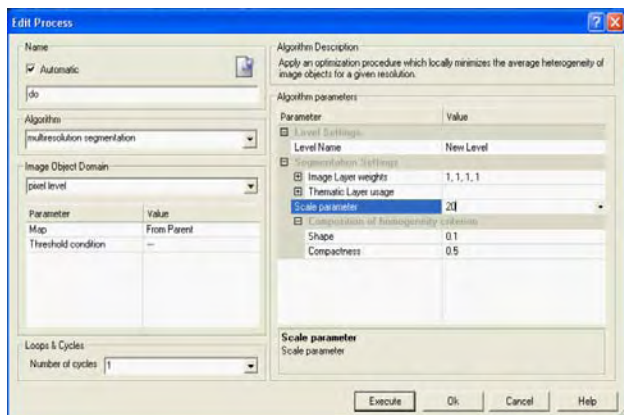


Figure 2. Interface of eCognition to allow users to input user defined segmentation parameters (Image Layer weights (w_1, w_2, \dots, w_c), Scale parameter (s), Shape ($1-w$), and Compactness ($w_{compact}$))

The purposes of the segmentation parameters are (Hofmann, 2001):

- (1) Scale parameter: influence the average object size. It determines the maximal allowed heterogeneity of the objects. The larger the scale parameter, the larger the objects become.
- (2) Shape/Color: adjust the influence of shape vs. color homogeneity on the object generation. The higher the shape value, the less spectral homogeneity influences the object generation.
- (3) Smoothness/Compactness: determine the compactness or smoothness of the resulting object. With a selected

shape value, the user can influence the compactness or smoothness of the final object.

- (4) Image Layer weights: determine the weight of each spectral band in the segmentation. It is used to control the influence of each band on the object generation.
- (5) Level settings: determine whether a newly generated image level will either overwrite a current level or whether the generated objects shall contain sub- or super-objects of a existing level. The order of the level generation affects the objects' shape (top-down vs. bottom-up segmentation).

2.3. Difficulty of Segmentation Parameter Selection

The segmentation parameters to be selected by the user are interrelated to each other. It is impossible to directly find a set of proper segmentation parameters at one time. Users have to repeatedly select a set of segmentation parameters and test them through a trial-and-error process, until a reasonable segmentation result is achieved or the user does not want to continue the trial and error any more. The change of any of the parameters affects the influences of other parameters on the segmentation, so that it is a tedious and time-consuming process. The segmentation results directly depend on the knowledge and experience of the user. The segmentation process is considered by users as a "black art" (Smith and Morton, 2010). Normally, only those users who are familiar with the spectral characteristics of the land-cover objects of interest and understand the segmentation procedure can select proper segmentation parameters in a relatively efficient way. But, this is not always available in practice (Flanders et al.,

2003; Hay et al., 2003; Maxwell, 2005; Li et al., 2009; Smith and Morton, 2010).

3. SUPERVISED DETERMINATION OF SEGMENTATION PARAMETERS

3.1. Design of the Segmentation Tool

To address the issues existing in the trial-and-error selection of segmentation parameters, a tool for supervised segmentation parameter determination should meet the following requirements (Maxwell, 2005):

- a. Each execution of the tool is aimed at extracting one land cover type and results in one level of the object hierarchy;
- b. Segmentation must be controlled and refined in an iterative manner based on an object model;
- c. The tool must rely on an initial segmentation as a start state;
- d. Scale, shape, and smoothness parameters must be determined;
- e. Parameter selection must be reproducible; and
- f. The tool must demonstrate reasonably fast and efficient performance.

The segmentation of an input image is performed on a number of different levels to permit objects of different scales to be

extracted on their own level. By using this approach, objects can be classified on the level where the segments are the most meaningful and best represent the object of interest. This infers that the user must have a specific land cover class in mind when segmenting the image so that the parameters can be best estimated and then refined through iteration. As a result, the tool must aim to extract one particular land cover type each time it is executed. By running the tool a number of times, a hierarchy of object levels can then be developed.

3.2. Workflow of FbSP Optimizer

To meet the design requirements of the software tool, the workflow for the supervised fuzzy-based determination of segmentation parameters, i.e. the FbSP optimizer, was developed as shown in Figure 3. To train the FbSP optimizer, the input image needs to be initially segmented achieving an over segmentation, i.e. the segments are smaller than the objects of interest (see Figure 5.a). The small segments, also called sub objects, can be selected to form a meaningful target segment/object. The information of the target object and its sub objects is then used to train the FbSP optimizer to determine the optimal segmentation parameters for the target object (Figure 4).

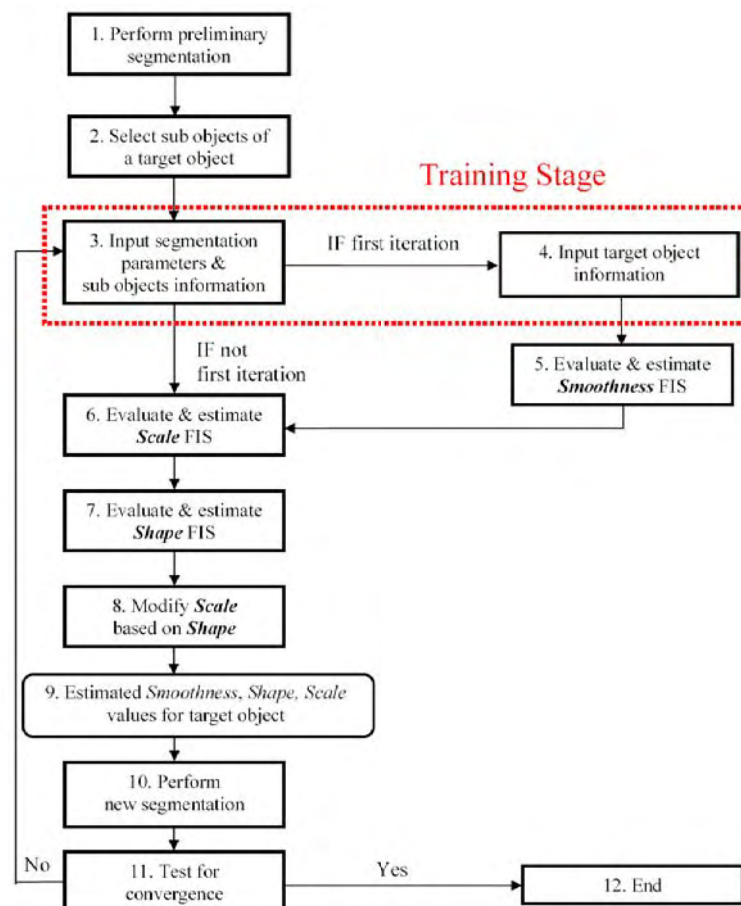


Figure 3. Workflow of the proposed FbSP optimizer. The values of the current Segmentation Parameters (*Smoothness* ($1-w_{compact}$), *Shape* ($1-w$) and *Scale* (s)), Sub objects information (*Texture*, *Stability*, *Brightness*, and *Area*) and Target Object information (*Texture*, *Stability*, *Brightness*, *Area*, *Rectangular Fit*, and *Compactness*) are inputted into FbSP optimizer to train the FISs (Fuzzy Inference Systems) to estimate the optimal Segmentation Parameters ($1-w_{compact}$, $1-w$, and s) for the Target Object in an iterative process.

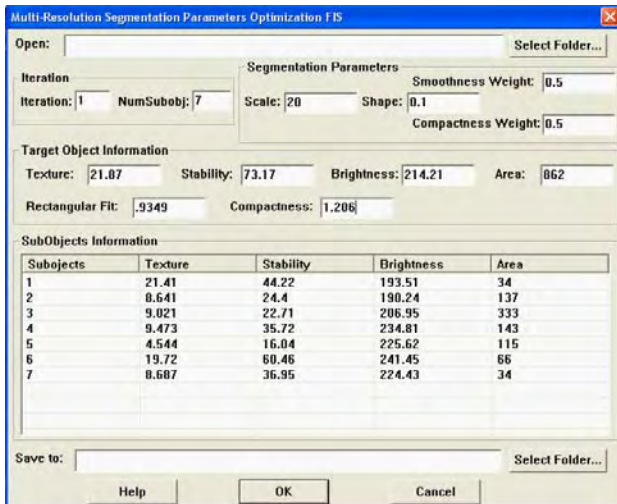


Figure 4. Interface of FbSP optimizer. The Segmentation Parameters, Target Object Information and Sub Object Information are inputted into the system to train FbSP optimizer to estimate the optimal Segmentation Parameters for the Target Object through fuzzy logic analyses.

In Figure 4, the Segmentation Parameters (Scale, Shape, and Smoothness weight) for performing a preliminary over segmentation are initially selected and inputted by user. They are then updated by the FbSP optimizer in the next iteration according to the information of the target object and its sub objects. The Texture, Stability, Brightness and Area for the target object and sub objects are calculated according to the pixel grey values within the target object and individual sub objects, respectively. The Compactness and Rectangular Fit are calculated according to the shape of the target object.

4. EXPERIMENT AND RESULTS COMPARISON

4.1. Data Sets

Pan-sharpened QuickBird MS image and pan-sharpened Ikonos MS image over Fredericton, Canada, and pan-sharpened QuickBird MS image of Oromocto, Canada, were used to test the FbSP optimizer. The UNB-Pansharpen was used to fuse the Pan and MS images. The four pan-sharpened multispectral bands were used as input bands.

4.2. Segmentation Process and Results

For small objects, the FbSP optimizer can find optimal segmentation parameters through one or two iteration(s) of segmentation parameter estimation (Figure 3 and Figure 5). For example, for small buildings shown in Figure 5, the FbSP optimizer used just one iteration to find the optimal segmentation parameters for the object of interest—small buildings. If the initial parameter selection by the user for the initial over segmentation is counted as one iteration, two iterations of parameter selection in total were needed, one by the user and one by the FbSP optimizer (Figure 5.a and 5.c, and Table 1).

Table 1 shows the segmentation parameters selected by the user for initial over segmentation (Iteration 1), and the parameters estimated by the FbSP optimizer in the first loop (Iteration 2). Table 2 shows the feature information of the sub objects (Figure 5.a, red) selected to form a target object. Table 3 lists the feature information of the target object (Figure 5.b, red).



Figure 5. Segmentation process and final segmentation result using the FbSP optimizer for small buildings (pan-sharpened QuickBird MS, Oromocto). (a) Initial over segmentation using user selected initial segmentation parameters (first iteration) and the sub objects (red) selected to form a target object, (b) Target object formed by the sub objects for training the FbSP optimizer, (c) Segmentation result achieved using the parameters estimated by FbSP optimizer in the first loop (second iteration in total), (d) Final segmentation result using the parameters estimated in (c).

According to the feature information in Table 2 and Table 3, the FbSP optimizer estimated the optimal segmentation parameters (Table 1, Iteration 2) for the target object. Using the parameters in Iteration 2 of Table 1 to segment the input image, the segmentation result shown in Figure 5.c was achieved. The feature information (Table 4) of the resulting segment (Figure 5.c, red) is almost identical to that of the target object (Table 3 and Figure 5.b, red), i.e. the resulting segment converges with the target object (Figure 3, step 11), so that the segmentation parameters estimated by FbSP optimizer in the first loop (Iteration 2 of Table 1) was accepted as the optimal segmentation parameters for small buildings.

For large objects, more sub objects need to be selected to form a target object, so that more iterations are usually needed to reach the convergence between the target object and the resulting segment. For example, four iterations were needed to reach the convergence for large buildings shown in Figure 6.

4.3. Result Evaluation

Figure 7 shows the segmentation result of large buildings using trial-and-error approach for segmentation parameter selection. The result was achieved by a very experienced operator through approximately two hours of parameter selection and test. Comparing the result from FbSP optimizer (Figure 6) and that from trial and error (Figure 7), we can see that the FbSP

optimizer achieved better segmentation result, especially for complex buildings (compare the circled buildings in Figure 6 and 7).

In terms of time used for the segmentation, the FbSP optimizer presented a much more significant improvement. To achieve the segmentation shown in Figure 6, only 30 minutes were needed under the current software implementation condition, i.e. the operator needs to generate feature information for sub objects and target object and then input and output between eCognition and FbSP optimizer manually and iteratively. The manual, iterative input and output between the two systems occupied more than 90% of the time in the parameter determination process of FbSP optimizer. If the FbSP optimizer can be integrated into eCognition through a API (Application Programming Interface), the 90% of time can be saved. Then, the FdSP optimizer just needs a few minutes to obtain the optimal segmentation parameters for the building segmentation in Figure 6, demonstrating a radical improvement in terms of speed.

Table 1. Segmentation parameters for small buildings

Parameter	Iteration	
	1	2
Scale	20	35.1809
Shape	0.1	0.551
Smoothness	0.5	0.5

Table 2. Feature information of the sub objects (Figure 5.a, red) forming a target object

Sub object	Texture	Stability	Brightness	Area
1	25.35	55.51	189.56	60
2	14.21	51.6	179.3	123
3	15.63	25.9	194.59	44
4	24.64	50.91	164.07	44
5	16.06	72.52	151.61	15

Table 3. Feature information of the target object (Figure 5.b, red) formed by the sub objects (Figure 5.a, red)

Texture	Stability	Brightness	Area	Rectangle Fit	Compactness
35.81	143.8	183.92	299	0.9792	4.048

Table 4. Feature information of the sub object (Figure 5.c, red) obtained using the parameters estimated by FbSP optimizer (Table 1, Iteration 2)

Sub object	Texture	Stability	Brightness	Area
1	35.81	142.34	183.92	299



Figure 6. Segmentation result of large buildings obtained using the segmentation parameters of FbSP optimizer, operating time: 30 minutes (90% of the time was used for manual and iterative input and output of the object feature information between eCognition and FbSP optimizer, which can be reduced once the two systems are integrated) (pan-sharpened QuichBird MS, Fredericton)



Figure 7. Segmentation result of large buildings obtained through trial-and-error parameter selection, operating time: 2 hours (pan-sharpened QuickBird MS, Fredericton)

Segmentation of other objects was also tested. The trial-and-error approach needs 2 to 6 hours to reach acceptable segmentation results, whereas FdSP optimizer just needs 30 to 60 minutes. If the 90% of the time for manual input and output is reduced through software integration, FdSP optimizer will just need less than 10 minutes to select optimal segmentation parameters for large complex objects.

5. CONCLUSIONS

A Fuzzy-based Segmentation Parameter (FbSP) optimizer was developed to improve the efficiency of segmentation parameter selection and accuracy of object segmentation for eCognition. The FbSP optimizer can be trained using initially segmented sub segments and the corresponding targeted object of interest. The FbSP optimizer can then find the optimal segmentation parameters for the target object, through fuzzy logical analyses of the target object and its sub objects.

Experiments with QuickBird and Ikonos pan-sharpened MS images demonstrated that the FbSP optimizer can effectively find optimal segmentation parameters for objects of interest within 30 to 60 minutes under the current software implementation condition. If the current manual and iterative input and output of feature information between FbSP optimizer and eCognition is reduced through software integration, FbSP optimizer will just need a few minutes to find optimal segmentation parameters for an object of interest. In contrary, 2 to 6 hours are usually needed for an experienced

operator to find proper segmentation parameters through trial and error. The proposed supervised approach to automated determination of optimal segmentation parameters has demonstrated its superior advantage in speeding up the segmentation parameter selection and improving the segmentation quality. It exhibits the potential to boost segmentation techniques from current trial-and-error stage into the next stage—semi-automated or automated process.

Further tests with other remote sensing images will be conducted. The FbSP optimizer will be further improved.

6. ACKNOWLEDGMENTS

This research was supported by the Discovery Research Grants Program of NSERC (Natural Science and Engineering Research Council of Canada), Canada Research Chairs Program, and the Department of National Defence (Canada). The original QuickBird and Ikonos satellite images were provided by CFB Gagetown and the City of Fredericton, NB, Canada.

7. REFERENCES

- Baatz, M. and A. Schäpe, 2000, Multiresolution Segmentation - An Optimization Approach for High Quality Multi-Scale Image Segmentation. *Angewandte Geographische Informationsverarbeitung XII*, Ed. J. Strobl et al. AGIT Symposium, Salzburg, Germany, 2000. pp. 12-23.

- Baatz, M., Schäpe, A., 1999. Object-Oriented and Multi-Scale Image Analysis in Semantic Networks. In: Proc. of the 2nd International Symposium on Operationalization of Remote Sensing, August 16-20, 1999. Enschede. ITC.
- Blaschke, T., 2010. Object based image analysis for remote sensing, *ISPRS Journal of Photogrammetry and Remote Sensing*, Vol. 65(1), pp. 2-16..
- Flanders, D., M.Hall-Beyer, and J. Pereverzoff, 2003. Preliminary Evaluation of eCognition Object-Based software for Cut Block Delineation and Feature Extraction. *Canadian Journal of Remote Sensing*, Vol. 29, No. 4, pp. 441-452.
- Hay, G., T. Blaschke, D. Marceau, and A. Bouchard, 2003. A Comparison of Three Image-Object Methods for the Multiscale
- Hofmann, P , 2001. Detecting Urban Features from IKONOS Data using an Object-Oriented Approach. *Proceedings of the First Annual Conference of the Remote Sensing & Photogrammetry Society*. RSPS, Munich, Germany, 12-14 September 2001, pp. 79-91.
- Lavigne, D.A., G. Hong and Y. Zhang, 2006. Performance Assessment of Automatic Feature Extraction Tools on High Resolution Imagery, *MAPP/ASPRS 2006 Fall Conference*, November 6-10, 2006, San Antonio, Texas.
- Li, H., Gu, H., Han, Y. and Yang, J., 2009. An efficient multiscale SRMMHR (Statistical Region Merging and Minimum Heterogeneity Rule) segmentation method for high-resolution remote sensing imagery. *IEEE Journal of Selected Topics in Applied Earth Observations and Remote Sensing*, 2(2), pp. 67-73.
- Maxwell, T., 2005. Object-Oriented Classification: Classification of Pan-Sharpned QuickBird Imagery and a Fuzzy Approach to Improving Image Segmentation Efficiency. M.Sc.E. thesis, Department of Geodesy and Geomatics Engineering Technical report No. 233, University of New Brunswick, Fredericton, New Brunswick, 157 pp.
- Smith, G.M., and R.D. Morton, 2010. Real World Objects in GEOBIA through the Exploitation of Existing Digital Cartography and Image Segmentation, *Photogrammetric Engineering & Remote Sensing*, Vol. 76, No. 2, , pp. 163–171.
- Zhang, Y., and T. Maxwell, 2006. A trained segmentation technique for optimization of object-oriented classification, *ISPRS Commission VII Mid-term Symposium “Remote Sensing: From Pixels to Processes*, Enschede, the Netherlands, 8-11 May 2006.

Research on Change Detection in Remote Sensing Images by using 2D-Fisher Criterion Function Method

Baoming Zhang, Ke Chen, Yang Zhou, Mingxia Xie, Hongwei Zhang

Remote Sensing Information Engineering Department, Zhen Zhou Institute of Surveying and Mapping, Zhen Zhou, China,
 E-mail: zbm2002@vip.371.net, ck1702@163.com, zhouyang3d@163.com, xmx0424@yahoo.cn, hongwei0691@163.com

KEY WORDS: change detection, Fisher criterion function, Image Threshold, two-dimension histogram, remote sensing image

ABSTRACT:

In this paper, 2D-Fisher criterion function was introduced to change detection in remote sensing images based on classic one dimension fisher criterion function, and this expanded the space of grey value from one-dimension to two-dimension and greatly improved the image noise-sensitivity. Meanwhile, in order to enhance the computing speed, we refined the solution method of 2D threshold in 2D-Fisher criterion function through transforming computing method from two-dimension threshold to two one-dimension thresholds and greatly reduced the detection time. Refined 2D-Fisher criterion function method was suitable not only for the change detection in remote sensing images, but also for other aspects in data processing.

1. INTRODUCTION

The auto extraction of change area is the key of the change detection of multi-temporal remote sensing image. It's easy to compute and has a fast computation speed. So how to find a threshold finding method with wide range of applications, good results of extraction and good performance of anti-noise becomes one of the main content of the research on remote sensing image change detection. Until now, domestic and foreign scholars have carried out extensive research on this problem and proposed kinds of methods to select threshold, for example, maximum variance between-class, maximum entropy method and so on. However, whether the maximum variance between-class or the maximum entropy method, its rule function only considers maximizing the variance between-class, in other words to maximize the degree of separation but without considering the discrete level in class within. And the two methods are only suitable when pixel number of change class and no change class are not different a lot. While the number of the two kinds of pixels is significantly different, neither one method is applicable.

A good remote sensing image change detection method should not only maximize the separation degree between change class and no change class, but also make the change class and no change class's dispersion degree minimum, that is, similarity of pixel in every class should be maximal. As we all know, in the pattern recognition theory, the Fisher criterion function can be used to get the best projection direction of feature vector. In this projection direction we can get the greatest distance between classes and the smallest distance in class. At this time, value of Fisher criterion function reached the maximum. Thus, Fisher criterion function is a good criterion to analyze the degree of class separation.

The classical Fisher criterion function method is introduced into remote sensing image change detection and extended its original one-dimensional space of gray value to the two-dimensional space, such as the gray value – mean neighborhood gray (G-Mean), gray value - the Medium value of neighborhood gray (G-Medium) and so on. 2D-Fisher criterion function method is bring forward to apply to the remote sensing image change detection. Because 2D-Fisher criterion function method for solving adaptive threshold is complex to compute, we try to improve remote sensing image change detection 2D-Fisher criterion function method proposed in this paper. So it can

effectively de-noising, and achieve rapid change detection.

2. FISHER CRITERION FUNCTION METHOD

The essence of solving Fisher criterion function is to solve optimization problems, that means using a few linear combination (called the discriminant or canonical variate)

$y_1 = a_1'x, y_2 = a_2'x, \dots, y_r = a_r'x$ in p-dimensional vector $x = (x_1, x_2, \dots, x_p)'$ (usually r is significantly less than p) to replace the original p variables x_1, x_2, \dots, x_p , in order to achieve the reduced-dimensional purpose, and in the new projection space $y = a'x$, making the largest distance between the various classes and the smallest in one class. As is shown in Figure 1, for the two categories ω_n and ω_c , assuming that all classes are characterized by two-dimensional distribution (A, B part in Figure 1) and project them in straight line Y_1 and Y_2 , you can clearly see that the separation between classes are particularly good at the direction of straight line Y_2 .

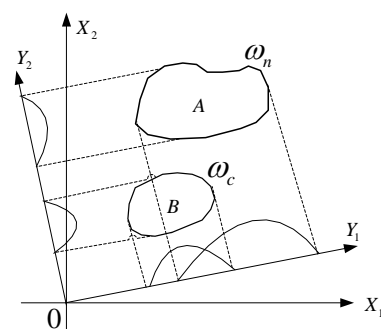


Figure 1. Projection of two-dimensional feature vector in a straight line

The bi-objective problem, namely class space will be the largest and the smallest category from, is transformed into single-objective optimization problem, that makes the formula 1 get a maximum.

$$\Delta(a) = \frac{SSTR}{SSE} = \frac{a'Ba}{a'Ea} \quad (1)$$

Where, $SSTR$ is the sum of squares between groups of y_{ij} , SSE is the sum of squares in the group y_{ij} , B is sum of squares between groups and sum of cross-product, E is sum of squares in group and sum of cross-product. This paper applies it to remote sensing image change detection process, so that pixels of change class and no change classes have the minimum dispersion in class and the maximum distance between classes (distance between the center of every class represent distance between classes), in change detection, we must consider the priori probability of change pixels and no change pixels, $P(\omega_c)$ and

$P(\omega_n) = 1 - P(\omega_c)$, therefore, taking into account of the priori probability circumstance, the definition of Fisher criterion function is:

$$J(t) = \frac{|P(\omega_c)\mu_c - P(\omega_n)\mu_n|}{P(\omega_c)\sigma_c^2 + P(\omega_n)\sigma_n^2} \quad (2)$$

When t is the best threshold value, $J(t)$ gets maximum value, selection criteria of Fisher threshold is:

$$t^* = \text{Arg max}_{0 \leq t \leq L-1} [J(t)] \quad (3)$$

3. 2D-FISHER CRITERION FUNCTION IN CHANGE DETECTION OF REMOTE SENSING IMAGES

As the classical Fisher criterion function method merely reflects the distribution of pixel's gray value, when SNR (signal to noise of the remote sensing image) is small, the one-dimensional grey level histogram of the difference images will have no noticeable wave crest and trough, so the threshold is difficult to select. Then if only according to one-dimensional grey histogram, the change detection, according to Fisher criterion function, will make a serious mistake. In view of this situation, in this chapter the classical Fisher criterion function will be introduced into the process of change detection, while the one-dimensional gray-scale space will be expanded. Taking full advantage of the neighborhood pixel spatial information, we put forward remote sensing image change detection 2D-Fisher criterion function method.

3.1 The basic principle of the 2D-Fisher criterion function method

Suppose two-dimensional space is a G-Mean space, $f(x, y)$ is the gray value at (x, y) point of different images, $g(x, y)$ is the average gray value in $k \times k$ adjacent area, (x, y) is the center, and

$$g(x, y) = \frac{1}{k^2} \sum_{m=-k/2}^{k/2} \sum_{n=-k/2}^{k/2} f(x+m, y+n) \quad (4)$$

$1 \leq x \leq m$, $1 \leq y \leq n$, m and n are the width and height of the changed image respectively, and k generally takes 3. The value of the two-dimensional histogram of changed image is expressed as the pixel gray value. The pixel number of the Neighborhood average gray value $g(x, y) = j$ is $(i, j = 0, 1, \dots, L-1)$. Three-dimensional description is shown in Figure 2 and its projection to the plane is shown in Figure 3

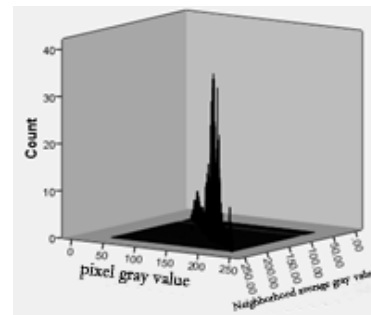


Figure 2. Three-dimensional description

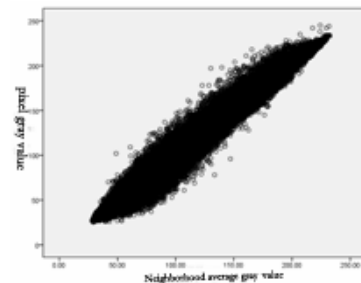


Figure 3. two-dimensional histogram display on plane

Difference image is divided into two parts, pixels changed and no changed. And their pixel gray value and the neighborhood average gray value is almost equal, so it is mainly distributed in the vicinity of the diagonal and the clustering phenomenon is apparent. Similarly, for noise in the difference image, the difference between pixel gray value and the average gray value in pixel's neighborhood area is large, so mainly in the non-diagonal part. In the difference image, the roughly distribution of changed pixels, no changed pixels and noise area in two-dimensional histogram is shown in Figure 4. It can be seen, regardless of high and low SNR of the difference image, selecting an appropriate threshold values to separate change class and no change classes, we can get a better test results. So it fully embodies the anti-noise performance after extending the original one-dimensional gray-value space to two-dimensional space.

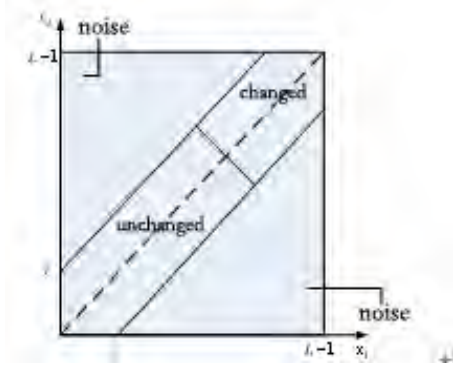


Figure 4. distribution of changed and no changed pixels and noise area Difference image.

The two-dimensional joint probability density of Pixel gray value and its neighbourhood average gray-scale is as follows:

$$p_{ij} = \frac{N(i, j)}{N}, \quad p_{ij} \geq 0, \quad \sum_{i=0}^{L-1} \sum_{j=0}^{L-1} p_{ij} = 1 \quad (5)$$

Given any two-dimensional threshold value, the corresponding changed class and no changed class are ω_c and ω_n . Their gray and average neighborhood gray are:

$$P(\omega_{ni}) = \sum_{j=0}^{s-1} p_{ij}, \quad j = 0, 1, \dots, L-1 \quad (6)$$

$$P(\omega_{nj}) = \sum_{i=0}^{t-1} p_{ij}, \quad i = 0, 1, \dots, L-1 \quad (7)$$

$$P(\omega_{ci}) = \sum_{j=s}^{L-1} p_{ij}, \quad j = 0, 1, \dots, L-1 \quad (8)$$

$$P(\omega_{cj}) = \sum_{i=t}^{L-1} p_{ij}, \quad i = 0, 1, \dots, L-1 \quad (9)$$

The corresponding mean and variance vectors:

$$\mu_c = (\mu_{ci}, \mu_{cj})^T, \quad \mu_n = (\mu_{ni}, \mu_{nj})^T \quad (10)$$

$$\sigma_c^2 = (\sigma_{ci}^2, \sigma_{cj}^2)^T, \quad \sigma_n^2 = (\sigma_{ni}^2, \sigma_{nj}^2)^T \quad (11)$$

And

$$\mu_{ni} = \frac{\sum_{i=0}^{s-1} iP(\omega_{ni})}{\sum_{i=0}^{s-1} P(\omega_{ni})}, \quad \mu_{nj} = \frac{\sum_{j=0}^{t-1} jP(\omega_{nj})}{\sum_{j=0}^{t-1} P(\omega_{nj})} \quad (12)$$

$$\mu_{ci} = \frac{\sum_{i=s}^{L-1} iP(\omega_{ni})}{\sum_{i=s}^{L-1} P(\omega_{ni})}, \quad \mu_{cj} = \frac{\sum_{j=t}^{L-1} jP(\omega_{nj})}{\sum_{j=t}^{L-1} P(\omega_{nj})} \quad (13)$$

$$\sigma_{ni}^2 = \frac{\sum_{i=0}^{s-1} (i - \mu_{ni})^2 P(\omega_{ni})}{\sum_{i=0}^{s-1} P(\omega_{ni})}, \quad \sigma_{nj}^2 = \frac{\sum_{j=0}^{t-1} (j - \mu_{nj})^2 P(\omega_{nj})}{\sum_{j=0}^{t-1} P(\omega_{nj})} \quad (14)$$

$$\sigma_{ci}^2 = \frac{\sum_{i=s}^{L-1} (i - \mu_{ci})^2 P(\omega_{ci})}{\sum_{i=s}^{L-1} P(\omega_{ci})}, \quad \sigma_{cj}^2 = \frac{\sum_{j=t}^{L-1} (j - \mu_{cj})^2 P(\omega_{cj})}{\sum_{j=t}^{L-1} P(\omega_{cj})} \quad (15)$$

According to Equation 2, we can derive that 2D-Fisher criterion function is:

$$J(s, t) = \frac{\sqrt{(P(\omega_{ci})\mu_{ci} - P(\omega_{ni})\mu_{ni})^2 + (P(\omega_{ci})\mu_{cj} - P(\omega_{ni})\mu_{nj})^2}}{P(\omega_{ci})\sigma_{ci}^2 + P(\omega_{cj})\sigma_{cj}^2 + P(\omega_{ni})\sigma_{ni}^2 + P(\omega_{nj})\sigma_{nj}^2} \quad (16)$$

When $J(s, t)$ reaches the maximum the corresponding Split point should be the best change detection threshold, then the 2D-Fisher threshold selection rule is:

$$(s^*, t^*) = \text{Arg max}_{\substack{0 \leq s \leq L-1 \\ 0 \leq t \leq L-1}} [J(s, t)] \quad (17)$$

3.2 The improvement of 2D-Fisher criterion function

2D-Fisher criterion function can make use of the gray information of a single pixel and related information of pixel's neighborhood space. The considering scope is extended from a single point gray value into the point and its neighborhood gray-spatial information. Relative to the classical one-dimensional Fisher criterion function, anti-noise performance has been greatly improved in the process of image change detection. According to the basic principles and formulas of 2D-Fisher criterion function, it can be known that along with the increasing of solution space dimension, the entire solution space need to traverse when to find the optimal threshold is $[0, L-1] \times [0, L-1]$. At this time, computing

time is too long, and real-time is bad. To some extent, it limits the 2D-Fisher criterion function method in the practical application of remote sensing image change detection. Therefore, the following content will consider how to improve the timeliness of 2D-Fisher criterion function method.

In order to improve the speed of remote sensing image change detection of 2D-Fisher criterion function, it can be considered from two aspects to improve the proposed 2D-Fisher criterion function: for one thing, narrow the solution space of 2D-Fisher criterion function; for another, transform the two-dimensional threshold into two one-dimensional thresholds. The following will discuss these two mentioned-above aspects.

1) Narrow the scope of the original solution space, so as to achieve the purpose of improving the speed of detection. Since the extraction of the change area is similar to the two types of clustering problem, to maximize the distance between classes, the initial cluster centers generally select the point where the rule function value is the largest. Because it is two types of clustering, the initial cluster centers always select the two points where the function gets two largest values. In specific clustering process, the optimal threshold value will fall

between two points. According to this theory, the specific solving steps are as follows:

Step 1: To obtain two-dimensional histogram of difference image;

Step 2: According to two-dimensional histogram to Select k extreme points from the difference image, as is shown in Figure 5 (usually make $k = 6$);

Step 3: Obtain the corresponding values of each extreme point in the 2D-Fisher criterion function.

Step 4: Select the two extreme points (s_1, t_1) and (s_2, t_2) corresponding to the largest two function value, (s_1, t_1) as the center and (s_2, t_2) as the vertex to make a rectangle. As shown in Figure 6, namely, the area of red rectangle

$$\left[s_1 - |s_1 - s_2|, s_1 + |s_1 - s_2| \right] \times \left[t_1 - |t_1 - t_2|, t_1 + |t_1 - t_2| \right]$$

is the improved scope of the solution space.

From the above analysis we can get that the improved solution space is the original solution space.

$$\frac{\left[s_1 - |s_1 - s_2|, s_1 + |s_1 - s_2| \right] \times \left[t_1 - |t_1 - t_2|, t_1 + |t_1 - t_2| \right]}{[0, L-1] \times [0, L-1]}$$

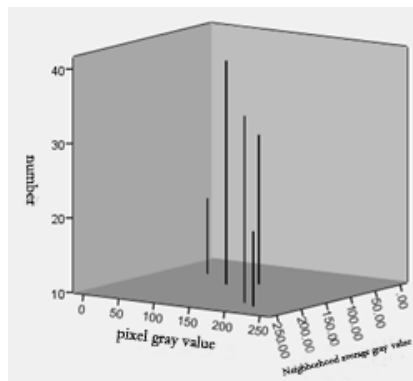


Figure 5. The selection of maximum in two-dimensional histogram

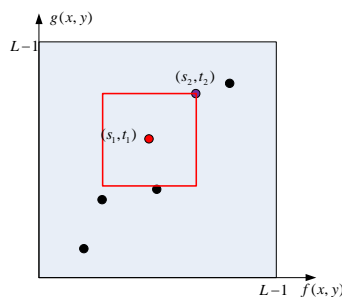


Figure 6. Improvement of solution space

2) Transform two-dimensional threshold into two one-dimensional thresholds, so as to achieve the purpose of improving the speed of detection

Respectively make use of each pixel gray value and neighbourhood spatial information, according to the classical Fisher criterion function method, to solve the optimal gray

threshold value s^* and the best neighborhood threshold t^* , both of which constitute the two-dimensional threshold (s^*, t^*) of remote sensing image change detection. Then

according to the two-dimensional threshold (s^*, t^*) , do change detection of the difference images.

In method 1), the improvement of solution space of 2D-Fisher criterion function is the original solution space $\frac{\left[s_1 - |s_1 - s_2|, s_1 + |s_1 - s_2| \right] \times \left[t_1 - |t_1 - t_2|, t_1 + |t_1 - t_2| \right]}{[0, L-1] \times [0, L-1]}$.

However, we need to traverse the entire image to obtain the two-dimensional joint probability density of pixel gray value and its neighborhood spatial information according to the two-dimensional histogram. After that, it has nothing to do with the image size itself. The number of run times (one run means the process of calculating all kinds of probability, the mean and variance each time) of the original solution space for solving is $(1 + 2 + \dots + 256) \times (1 + 2 + \dots + 256)$ (Assuming gray-scale of the image is 256). After improved, the number

is $4|s_2 - s_1||t_2 - t_1|$. In the Intel Pentium Dual 2.0 CPU, 2G memory environment, the time one run required is probably $0.0384s$. Since the two extreme values fall mostly on both sides of the middle-class gray, suppose that $(120, 120)$ is the maximum point, and $(129, 129)$ is the second, the time is $12.4416s$ the best two-dimensional threshold required. It can be known that no matter how narrow the solution space is, the solution time can not satisfy the needs of practical applications. Therefore, we chose method 2).

3.3 The specific process to improve 2D-Fisher criterion function method.

The specific process of remote sensing image change detection makes use of the improved 2D-Fisher criterion function method (taking two-dimensional space of choosing G-Mean for example):

Step 1: According to the pixel gray values and formula 4, obtain the grey level histogram of the difference image and the histogram of the mean value of gray scale in 3×3 neighbourhood area.

Step 2: On the histogram, as well as neighborhood average gray histogram, take advantages of classical Fisher criterion function method to get the one-dimensional optimal threshold s^* and t^* and the two-dimensional threshold (s^*, t^*) respectively.

Step 3: According to two-dimensional threshold, analyze the various elements to generate the results of image change detection.

For (x, y)

$$\text{If } ((f(x, y) \geq s^*) \&\& (g(x, y) \geq t^*))$$

$$\text{Then } (x, y) \subset \omega_c$$

Else

$$(x, y) \subset \omega_n$$

(s^*, t^*) is the optimal threshold of image change detection.

4. EXPERIMENT AND ANALYSIS

In the above sections, through the Fisher criterion function in the pattern recognition theory, we propose the remote sensing

image change detection method: 2D-Fisher criterion function. Then, we will use the simulation data and real data experiments to validate the effectiveness of the change detection algorithm proposed in this chapter.

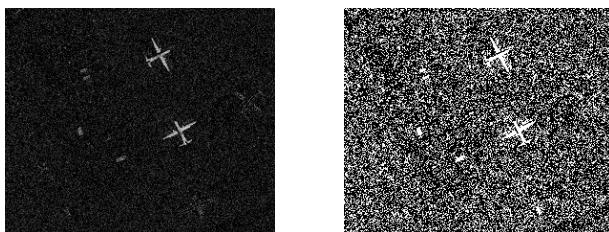
The experimental environment is Intel Pentium Dual 2.0 CPU, 2G memory. First is the simulation experiment. The remote sensing simulation images of multi-phase are constituted by an airport image and the corresponding changed image, as shown in Figure 7. Make linear transformation on the original image to simulate another phase of the remote sensing data, and then add two aircraft on the simulation image to make the changed area.



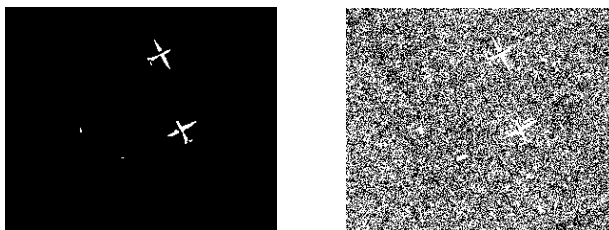
(a) Phase 1 Original simulation image (b) Phase 2 Original simulation image

Figure 7. the simulation image at different time but in the same area

The following plus noise (Gaussian noise) in the difference image of the original simulation image, let SNR=10, according to One-dimensional Otsu, One-dimensional Fisher, two-dimensional Otsu, and two-dimensional Fisher, do change detection test on the image with noise. The comparison is shown in Figure 8.



(a) Difference image with noise (SNR=10) (b) Result of One-dimensional Otsu ($s^* = 28$)



(c) Result of two-dimensional Otsu ($s^*, t^* = (28, 105)$) (d) Result of One-dimensional Fisher



(e) Result of 2-D Fisher (before improvement) ($s^*, t^* = (19, 73)$) (f) Result of 2-D Fisher (after improvement) ($s^*, t^* = (18, 67)$)

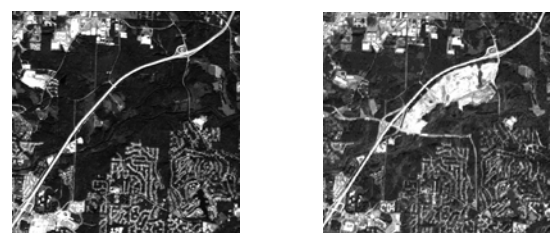
Fig.8 results compare of change detection with noise

From fig.8 we can see that improved 2D-Fisher change detection algorithm can effectively detect the changed area in the difference image with noise. Its anti-noise is superior to the classical one-dimensional Otsu, one-dimensional Fisher, and has the pretty same performance as pre-2D-Fisher criterion function method and two-dimensional Otsu method, namely, neighbourhood information are obvious for Removal of Gaussian noise. From the result of two-dimensional Otsu method we can see that this method is not very complete for the extraction of the aircraft, namely, existing problems of missing detection. The time occupied by two-dimensional change detection method is shown in Table 1.

Algorithm	2D-Otsu	2D-Fisher (before improvement)	2D-Fisher (after improvement)
Time of detection	57.19 s	74.51 s	0.68 s

Table 1 The Time of every two-dimensional change detection methods

In order to further verify the effectiveness of the proposed method in this chapter, the actual remote sensing images in an area of two-phase is chosen to do the experiment. The experimental data is SPOT panchromatic image with registration and relative radiometric correction, and is a region in 1987 and 1992 provided by ERDAS. The spatial resolution is 10m, region size 512×512 pixels and 256 gray levels. Experiments are carried out using the above method, in which select (gray value, neighborhood gray-scale median) space as two-dimensional space of 2D-Fisher criterion function method. The result is shown in Figure 9



(a) Remote Sensing Image in 1987 (b) Remote Sensing Image in 1992

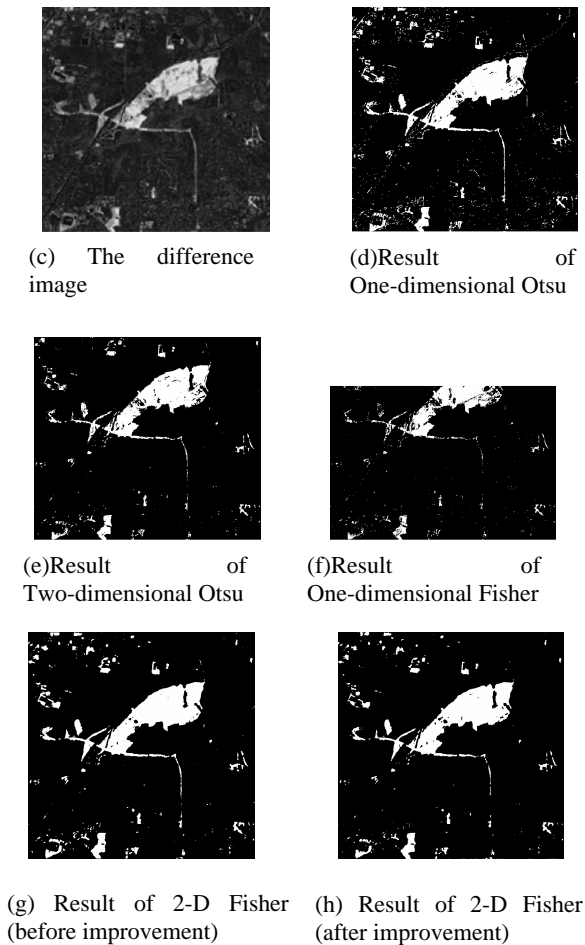


Fig.9 the results of real image change detection

The time occupied by two-dimensional change detection method in the image change detection process is shown in Table 2.

Algorithm	2D-Otsu	2D-Fisher (before improvement)	2D-Fisher (after improvement)
Time of detection	14.46 min	75.24 s	0.79 s

Table 2 the time occupied by two-dimensional change detection method in the image change detection process

Experimental results show the excellent of the change detection method based on the improved 2D-Fisher criterion function, whose superior anti-noise, and speed could have been fully embodied, whether in the simulation experiment or on the actual image. And, it's able to meet the needs of practical application of remote sensing image change detection in effect of real-time and change detection.

5. SUMMARY

The classical Fisher criterion function is introduced into the remote sensing image change detection. The approach based on

2D-Fisher criterion function method is proposed. Remote sensing image change detection 2D-Fisher criterion function method extended the one-dimensional gray value space of the classical Fisher criterion function to two-dimensional space, such as (G-Mean), (G-Medium), etc. Among them, the choice of two-dimensional space is based on the specific circumstances of the actual images. For example, G-Mean has a good effect of removing Gaussian noise, while G-Medium are obvious for the salt and pepper noise. In the process of the solution, the two-dimensional threshold, we split it into two one-dimensional thresholds, and the detection speed is greatly improved.

The 2D-Fisher criterion function method takes into account of the anti-noise and detection speed of the change detection process, making the method much more suitable for practical application needs of remote sensing image change detection. Experiments show that the improved 2D-Fisher criterion function method of remote-sensing image change detection is superior to the classical one-dimensional Otsu method, one-dimensional Fisher criterion function method in the anti-noise, and is far superior to the Two-dimensional Otsu in the speed of change detection.

6. REFERENCE

- [1] Richard O.Duda, Peter E.Hart, David G.Stork.,2003.*Pattern classification*, translate by Li Hong-dong, Yao Tian0xiang, Beijing: *China Machine Press*(Chinese).
- [2] Zhao Feng, Fan jiu-lun, 2007. One Image Segmentation Method Combining 2D Otsu's Method and Fuzzy Entropy. *Application Research of Computers* (Chinese), 24(6), 189-191.
- [3] Tong Ying, Qiu Xiao-hui,2004. A new algorithm of image segmentation using two-dimensional histogram based on Fisher criterion function. *Telecommunications for Electric Power System* (Chinese), 25(9), 36-39, 47.
- [4] Yu Jin-hua, Wang Yuan-yuan, Shi Xin-ling, 2007. Image segmentation with two-dimension fuzzy cluster method based on spatial information. *Opto-electronic Engineering* (Chinese), 34(4), 114-119
- [5] Chen Guo, 2003. The Fisher criterion function method of Image Thresholding. *Chinese Journal of Scientific Instrument*, 24(6), 564-567,576.
- [6] Xie Mingxia, Chen Ke, Guo Jianzhong, 2008. Research of FCM for image segmentation based on graph theory. *Journal of Computer Applications* (Chinese), 28(11), 2912-2914.
- [7] Zhong Jia-qiang,Wang Run-sheng, 2005. Multitemporal Remote Sensing Image Change Detection Based on Adaptive Parameter Estimation. *Acta Geodaetica et Cartographica Sinica* (Chinese), 34(4), 331-336.

EVALUATION OF TIME-SERIES OF MODIS DATA FOR TRANSITIONAL LAND MAPPING IN SUPPORT OF BIOENERGY POLICY DEVELOPMENT

F. Zhou, A. Zhang, H. Wang, G. Hong

Canada Centre for Remote Sensing, Booth Street, Ottawa, Ontario, K1A 0Y7 Canada -
(Fuqun.Zhou, Aining.Zhang, Huili.Wang, Gang.Hong)@nrcan.gc.ca

KEYWORDS: Land cover, Vegetation, Change Detection, Data mining, Research, Decision Support

ABSTRACT:

Demanding for information on spatial distribution of biomass as feedstock supply and on land resources that could potentially be used for renewable bioenergy production is rising as a result of increasing government investment for bioenergy and bioeconomy development, and as a way of adaptation to climate warming. Lands transitioned over the past between the types of forest, grassland, forage land, and cropland are considered as the most promising for the production of dedicated bioenergy crops as a primary source of biomass feedstock for the development of the second generation biofuels, without compromising regular agriculture production.

Aimed at the transitional land mapping at a region scale, Earth Observation data with medium spatial resolution are considered as one of the most effective data sources. Time series of 10 days cloud-free composite MODIS images and its derivation, NDVI and vegetation phenology in the vegetation-growing season, are then used to derive the required information. With these datasets, three groups of data combinations are explored for the identification of the best combinations for land cover identification, then for transitional land mapping, using a data mining tool.

Results showed that longer time series of Earth Observation data could lead to more accurate land cover identification than that of shorter time series of data; Bands (1-7) only and NDVI or phenology with other bands (3-7) could yield almost the same highest accurate information. Results also showed that land cover identification accuracy depends on the degree of homogeneity of the landscape of the region under the study.

1. INTRODUCTION

Demanding for information on spatial distribution of biomass as feedstock supply is rising as a result of increasing government investment for bioenergy and bioeconomy development, and as a way of adaptation to climate warming. The recent global food crisis has raised an important question of how to develop a sustainable bioenergy and bioeconomy without compromising the food production for a growing world population. A response to this challenge involves information on land cover, both for lands currently used in crop production and for transitional lands that could be used for growth of dedicated energy crops. Such information will have to be available over large areas, usually at regional, even at national scale (Zhou et al., 2009; Gang et al., 2010).

Transitional lands refer to the lands transitioned over the past between types such as forest, grassland, forage land, and cropland due to factors such as climate or market fluctuations or other reasons. This category of lands is considered most promising for the production of dedicated bioenergy crops as a primary source of biomass feedstock for the development of the second generation biofuels, without compromising regular agriculture production. Identification of these lands for biomass growth potential is a gap in the Canadian national biomass inventory, which has been undertaken by Canadian Forest Service and Agriculture and Agri-food Canada, with funding from the federal, interdepartmental Program for Energy Research and Development (PERD) operated by Natural

Resources Canada. The purpose of the transitional land mapping is to enable the application of earth observation data to fill this gap and to provide science-based information in support of bioenergy policy development.

Aimed at the task at a regional scale, Earth Observation data with medium spatial resolution are considered as the most effective data sources. Time series of the Moderate Resolution Imaging Spectroradiometer (MODIS) images and its derived information, such as Normalized Difference Vegetation Index (NDVI) and vegetation phenology, are then used to derive the required information. Time series of data have many advantages compared to a single time image as the former captures dynamic spectral information at various vegetation growth stages. However, it also poses challenge of such as how to efficiently use the 'high-dimensional' and a large volume of data and extract needed information for the issues at hand (Zhou et al., 2009). In this regard, a data mining tool is applied to explore and identify the optimal data combinations from all the data available in the vegetation growing season for land cover identification, and then for transitional land mapping. Results showed that, in general, longer time series of data set would yield higher accurate land cover classification than that of a shorter time series of data, and due to the medium spatial resolution of MODIS data, land cover identification accuracy also depends on the degree of homogeneity of the landscape setting of the region under study. The following sections will describe in some details about the data used, the methodology

developed, and the results produced, as well as give a brief discussion.

2. DATA AND METHOD

MODIS sensors aboard the Terra and Aqua satellites have a revisiting frequency of 1 to 2 days, acquiring data in 7 spectral bands for land surface applications, with a spatial resolution ranging from 250 – 500 metres. It is one of the most advanced sensors available for large-scale terrestrial applications (Salomonson et al., 1989). To facilitate use of the datasets, Canada Centre for Remote Sensing has developed a new technology to produce 10 days cloud-free composites of MODIS 7 land bands covering Canada and North America. Additional to other characteristics of this product, bands 3-7 are downscaled from the original spatial resolution of 500 meters to 250 meters (Luo et al., 2008). Therefore all the 7 bands of the cloud-free composites have the same spatial resolution and dimension.

For the study, only the data in the vegetation growing season (April to October) of the time series of MODIS 10 days cloud-free composites are analyzed. For the selected datasets there are 3 composites every month, and in total 21 composites are available from the beginning of the vegetation growing season to the end of the growing season. Considering all the 7 bands for each composite, there is a total of 147 ‘bands’ at various periods of the vegetation growing season.

Two additional datasets, NDVI and phenology in the vegetation-growing season, are derived from the time series of MODIS bands. NDVI, representing ‘greenness’ of vegetation, has been widely used for vegetation mapping. In total, same as the number of the MODIS bands, there are also a time series of 147 NDVI values in the vegetation growing season as they are derived from MODIS band 1 and band 2.

Another derived dataset from the MODIS data is vegetation phenology parameters. Phenology represents vegetation periodic biological phenomenon, which can be derived from NDVI time series by function fitting. There are total 11 vegetation phenology parameters including starting and ending of growing season, seasonal amplitude, seasonally integrated NDVI, rate of increase at the beginning of the season, rate of decrease at the end of the season, etc. Vegetation phenology is derived from the MODIS data by the aid of TIMESAT (Jonsson and Eklundh, 2003) software.

The rationale of using NDVI and vegetation phenology to aid land cover information extraction is that different vegetation types at different growing stages may have distinctive NDVI and phenology phenomenon.

With all the information available (MODIS 10 days cloud-free composite bands, NDVI, and phenology parameters), all possible data combinations for maximizing the overall land cover identification accuracy for targeted land cover types are sought and assessed by using See5/C5.0 data mining tool which has been used or discussed by various studies (Keane et al., 2004; Pal and Mather 2003).

Year 2000 is the first year when MODIS was operational; also there is a good reference of Circa 2000 land cover map (Figure 1a shows the reference land cover map of Saskatchewan, the case study province of the activity) which was generated from Landsat TM images. Therefore year 2000 is set as the starting point for transitional land assessment.

10 major land cover types of Circa 2000 land cover map (Agriculture and Agri-Food Canada, 2008) were mapped in the study. They are Annual Cropland, Water bodies, Developed land, Native Grassland, Shrubland, Perennial (crop and pasture), Wetland, Deciduous, Coniferous and Mixed Forest.

From bioenergy land cover mapping point of view, it is not critical to separate Deciduous, Coniferous, and Mixed Forest land cover. They are grouped into Forest land cover type in the study. Wetland is conservative land, so it was masked out before the mapping. All the analysis and results described below are based on the redefined types for the land cover mapping.

It is found that point samples like ground reference collected from field survey using GPS are not the best representations for model training and for verification of results derived from MODIS images due to the relative coarse spatial resolution of the data. Instead, area sample method was used in the study. Area sampling means that ground reference is established not by a point data, but by an area which has a homogenous land cover.

A homogeneous pixel (area) means that the ground represented by the pixel on the image is covered by only one land type. Truly, land cover is not always homogeneous, and heterogeneity is universal. However, homogeneity and heterogeneity are relative terms. When they are applied to EO-based applications, they are determined by spatial resolution of images in relation to the size of features on the ground. A piece of land is heterogeneous for a coarse resolution image, but may be homogeneous for all its sub-areas with a finer spatial resolution imagery (also depends on object size). Homogeneity and heterogeneity are also affected by the level of a land cover classification system.

For the study, three types of landscape settings are considered within the dimension of a MODIS pixel: they are homogenous, dominant and heterogeneous. As described above, a homogeneous pixel implies that the ground represented by the pixel on the image is covered by only one land type; a dominant pixel means that over a half of the ground area is occupied by one land cover with other land covers mixed; and the rest are heterogeneous cases.

To identify and evaluate the distribution of these types within the study area, the reference Circa 2000 land cover map is geometrically matched to and superimposed on the MODIS images. A MODIS pixel then corresponds to 25 pixels of circa 2000 land cover map (which was rescaled from 30 m to 50m). A MODIS pixel is classified as homogeneous if and only if all the corresponding 25 sub-pixels on the Circa land cover map have the same land cover, or dominant if a land cover type (the dominant one) has more than 13 or more sub-pixels, or heterogeneous (other land cover combinations).

The total number of the MODIS pixels of the study area is 6,355,364, among which, the number of homogeneous pixels is 3,101,288, and the number of the pixels with a dominant land cover type is 2,954,431. The proportion of the two types of MODIS pixels is 48.80%, and 46.49%, respectively. In total, they occupy more than 95% of the study area. Less than 5% of the area is occupied by multiple land cover types without a dominant land cover defined above. Therefore the analysis for the homogeneous and dominant pixels represents over 95% of the landscape of the study region.

3. RESULT ANALYSIS

Using the method developed based on data mining technology for land cover information extraction, we evaluated three groups of variable combinations, 1) band combinations only, 2) band and NDVI combinations, and 3) band and phenology combinations. In the last two cases, in order to avoid redundancy, band 1 and 2 are excluded as they are used to derive NDVI and phenology parameters. In all the three groups of variable combinations, time parameter is factored in, which means that data at various time periods (of the 10 days composites) are combined for optimal classification results.

Sampling data both for training and verification are selected from the reference map: 4500 (500 for each land cover type) samples for training and 4500 (also 500 for each land cover type) samples for verification. Deciduous, Coniferous, and Mixed Forest are sampled and classified separately, and their results are aggregated as Forestland. Therefore, as a group, Forest has 1500 samples in total. In the selection process, it is ensured that the samples were selected independently and randomly over the study region. These samples are considered as area ones.

For accuracy evaluations, two cases are explored: 1) training and verification samples are all homogeneous pixels, and 2) training samples are homogeneous pixels and verification samples are dominant pixels. The former represents around 49% of the situations of the study region while the later represents more than 95% of the situations, so it is more realistic.

3.1 Results and analysis of homogeneous pixels for training and verification

Table 1 lists the lowest and highest Kappa values of the three groups of variable combinations (over 20,000 combinations in total) for land cover identification using homogeneous pixels for both training and verification processes. The highest Kappa values of the three groups of data combinations are almost the same, but the lowest has remarkable variations. For the low end of Kappa, the single band of a single time stamp yields the lowest Kappa (0.24), while the combination of band and vegetation phenology yields the highest Kappa (0.70). An analysis of the Kappa values of different variable combinations reveals that, in general, the longer the length of the timer series of data used, the higher the Kappa value, then the higher identification accuracy. This observation thus suggests that time series data are better than a single snapshot for pattern extraction of land cover. Usually, the longer the time series is, the better. For example, the lowest Kappa for phenology/band

combination has much bigger value than that of other two combinations as phenology parameters are derived from all the season data.

Data combination	Kappa	
	Lowest	Highest
Bands in different time period	0.24	0.84
NDVI + Bands in different time period	0.51	0.85
Vegetation phenology + Bands in different time period	0.70	0.85

Table 1. Kappa for land cover classification

Land cover type	Cropland	Forest	Grassland	Shrubland	Perennial	Developed	Water	%
Cropland	463		8	3	18	8		92.60
Forest Land	1	1447	1	41	7		3	96.47
Grassland	10	2	412	3	62	11		82.40
Shrubland	4	68	10	388	27	1	2	77.60
Perennial	34	4	79	12	359	12		71.80
Developed	9	1	1	3	13	473		94.60
Water	3					5	492	98.40
Average								87.70

Table 2. Accuracy matrix of a phenology/band combination for land cover information extraction (one of the best combinations)

Table 2 shows the result of one of the NDVI/band combinations with the highest Kappa value against the reference data. The numbers in bold in the diagonal of the matrix represent the number of pixels that are correctly classified. The numbers suggest that the developed method with the data combination can discriminate most of the land cover types with an averaged accuracy percent about 88%. Among the 7 land covers, 4 of them have accuracy over 90%, and two of them are lower than 80% -- they are Perennial (~72%) and Shrubland (~78%) land cover types. Among the targeted land covers, native Grassland is mostly mixed with Perennial land cover (62 out of 500 samples). This is explainable as Perennial land includes tamed Grassland which is similar to native Grassland. Perennial land is also mostly mixed with native Grassland (79 out of 500 samples). This can also be explained with the same reason that native Grassland is mixed with Perennial land in a certain degree in real situations. If the native Grassland and Perennial land cover types were combined (both land types could be potentially used for bioenergy crop growth), the classification accuracy would become higher. Shrubland and Forest land are mostly mixed as thick Shrubland may have the similar spectral signatures as Forest land.

For transitional land mapping, the transitions among Cropland, Forest land, Perennial and Grassland are of the most interest. From Table 2, it can be seen that, Cropland is not confused with Forest land, and only has 1.6% and 3.6% misclassified as Grassland and Perennial land, respectively. It means that if a

piece of Cropland is changed to forest land from one year to another, we have a chance of 92.6% that the change is true, and if Cropland is changed to Grassland or Perennial land, the rate of the mistakes made for detecting the change is also very small.

Similarly, Forest land (Coniferous, Deciduous, and Mixed Forest) is almost not confused with Cropland (only 1 out of 1500 forest land samples was classified as cropland). This fact implies that if Forest land cover is changed to Cropland, we have a confidence that the change is true. Table 2 also indicates that Forest land is not mixed much with Perennial and Native Grassland, with only 1 and 7 out of 1500 were classified as Grassland, and Perennial land, respectively. Hence, if a piece of Forest land cover is detected a change to Grassland or Perennial land, the change is likely true.

Although Grassland and Perennial land are mixed by each other, they are separable with Forest land, and only 2 and 4 out of 500 samples of Grassland and Perennial land are classified as Forest land cover, respectively. This means that if a change is detected from Grassland or Perennial land to Forest land, the change is highly likely. The same conclusion can be made for a change from Grassland or Perennial land to Cropland, although the confidence is slightly lower as there are 10 out of 500, and 34 out of 500 samples of native Grassland and Perennial land are classified as Cropland, respectively.

Figure 1 shows the comparison of the reference map and the classified land cover map using the method discussed above with the time-series of 10 days cloud-free MODIS composite data. Figure 1a is Saskatchewan portion of Circa 2000 land cover map. The reference map was generated by Agriculture and Agri-food Canada using 30m Landsat TM data, while Figure 1b is generated by using 250m MODIS data (NDVI + bands) and the developed method. Although Figure 1b is not as rich in term of spatial details, it is evident that the identified land cover types are generally agreeable to the Circa 2000 land cover map.

3.2 Results of homogeneous pixels for training and dominant pixels for verification

The above assessment and analysis are based on the results generated using homogeneous samples for training and verification, which can be applied to the landscape with homogeneous land cover.

For the evaluation, we used the same homogeneous sample pixels for model training, but randomly and independently selected dominant land cover pixels (which could enclose some homogenous pixels) for verification. Statistically, the verification samples represent more than 95% situations of the MODIS pixels of the study region. The same three groups of variable combinations described above were evaluated for the process. Table 3 lists the highest accuracy from the three variable combinations above, respectively.

In comparison with the results of using homogeneous pixels for training and verification, the three variable combinations using homogeneous pixels for training and dominant pixels for verification yield similar but lower accuracy. However, the

overall accuracy of the land cover identification reaches about ~80%. Considering the spatial resolution of MODIS, the results are encouraging.

Land Cover Type	Accuracy (%)		
	Bands	NDVI + bands	Phenology + bands
Cropland	89.20	90.40	88.80
Forest land	87.13	87.73	88.40
Grassland	70.40	70.80	70.80
Shrubland	68.60	70.40	70.00
Perennial	70.00	71.80	73.00
Developed	78.00	77.80	76.40
Water	87.40	89.00	88.60
Average	78.68	79.70	79.43

Table 3. Accurate percent of land cover identification using dominant pixels for verification

It can be seen from Table 3 and Table 2, Cropland cover type has similar accuracies from the two methods. This is because Cropland in Saskatchewan has large parcels. Once Cropland cover becomes dominant, it is likely that all the 25 sub-pixels of a MODIS pixel are Cropland cover. Other land covers yield a lower accuracy (~2%~8% lower) except Perennial land cover. The results are explainable because the land covers other than the dominant one within a MODIS pixel would contribute to the spectral information, and then somewhat confuse the tool for accurately identifying the dominant land cover. The degree of the confusion may depend on the number and the types of land covers within the pixel of the dominant land cover.

An exception is that Perennial land cover which has an equal or a slightly higher accuracy for NDVI and phenology with bands combinations. The reason for the higher accuracy needs further investigation.

4. CONCLUSION AND DISCUSSION

Land cover mapping and its subsequent transitional land assessment at a regional and national level require large coverage and adequate spatial and temporal resolutions of EO data. MODIS data is a reasonable choice. Although promising, however, based on our evaluations, its usefulness depends on two critical variables: 1) landscape and 2) spectral characteristics of targeted objects. Once the targets are determined, the major factors of affecting land cover identification are the spatial distribution patterns of land covers. The degree of landscape heterogeneity under the study area determines the degree of mixed information within a pixel, and then plays a major role in affecting the accuracy of land cover identification.

Our study shows that, in the study region of Saskatchewan, about 49% of landscape is homogeneous with only one land cover, and 46% of the land is dominated by one land cover based on the size of a MODIS pixel and Circa 2000 land cover map. The accuracies of the land cover identification for the homogeneous and dominant landscape (includes homogeneous landscape) are about 88% and 80%, respectively. These suggest that MODIS may provide valuable information for the transitional land mapping for Saskatchewan region although further evaluation is needed such as improving the quality of the time-series of MODIS data and the method developed. For

other regions of Canada, the similar analysis needs to be conducted in order to determine if medium spatial resolution of EO data is efficient for transitional land mapping.

The current step is to identify land cover (biomass) classes and to map its spatial distribution as a potential feedstock for bioenergy production. The next step is, through analyzing multi-year time-series of MODIS, to identify the transitional lands that are potentially most sensitive to climate and market conditions, and therefore most likely to become available for bioenergy cropping when these environments change which is underway now.

REFERENCES

Agriculture and Agri-Food Canada, 2008. Land Cover. <http://www4.agr.gc.ca/AAFC-AAC/display-afficher.do?id=1227635802316&lang=eng>

Hong G., A. Zhang, F. Zhou, L. Townley-Smith, B. Brisco, I. Olthof. 2010. Biomass type identification potential of Radarsat-2 and MODIS images for the Canadian prairies. Submitted to Canadian Journal of Remote Sensing. 2010.

Jönsson, P. and Eklundh, L. 2003. Seasonality extraction from satellite sensor data. In *Frontiers of Remote Sensing Information Processing*, edited by Chen, C.H. World Scientific Publishing. pp 487-500.

Luo, Y, A. P. Trishchenko, K. V. Khlopenkov, 2008. Developing clear-sky, cloud and cloud shadow mask for producing clear-sky composites at 250-meter spatial resolution for the seven MODIS land bands over Canada and North America. *Remote Sensing of Environment, Volume 112, Issue 12, 15 December 2008*, pp 4167-4185.

Keane R. E., G. J. Cary, I. D. Davies, M. D. Flannigan, R. H. Gardner, S. Lavorel, J. M. Lenihan, C. Li, T. S. Rupp. 2004. A classification of landscape fire succession models: spatial simulations of fire and vegetation dynamics. *Ecological Modelling*, 179 (2004) pp.3-27.

Pal, M. and Mather, P.M. 2003. An assessment of the effectiveness of decision tree methods for land cover classification. *Remote Sens. of Env.*, 86:554-565.

Salomonson V.V., W.L. Barnes, P.W. Maymon, H.E. Montgomery and H. Ostrow, 1989. MODIS: Advanced facility instrument for studies of the earth as a system, *IEEE Transactions on Geoscience Remote Sensing* 27 (2) (1989), pp. 145–153.

Zhou, F., A. Zhang, G. Hong, L. Sun, 2009. NDVI derived vegetation phenology for land use change investigation. *Oral presentation at The Second Conference on Earth Observation for Global Changes (EOGC2009)* in Chengdu, China, 25-29 May 2009.

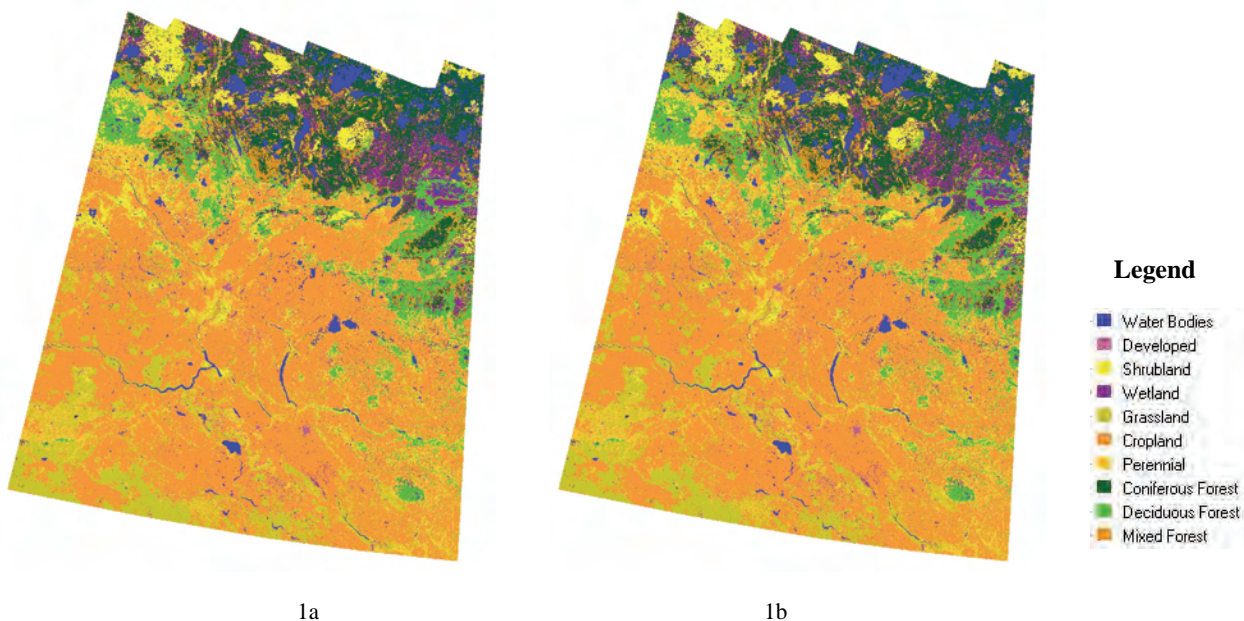


Figure 1. Land cover maps of Saskatchewan in 2000
 1a) Land cover circa 2000 (30m spatial resolution)
 1b) Land cover map generated by using MODIS data (250m spatial resolution)

Author Index

A

Abbasi, Mozghan **1**
 Abdelfattah, Riadh **6**
 Ablyazov, Vladimir **592**
 Adami, Marcos **10**
 Adesina, Francis Abiodun **430**
 Adiguel, Muzaffer **80**
 Aggarwal, SP **165**
 Aguiar, Daniel Alves de .. **10, 535**
 Ahmadi Foroushani, Mansour . **16**
 Ahn, Jae Hyun **132**
 Ahsani, Nabi **436**
 Aiazzi, Bruno **492**
 Aigner, Bernhard **23**
 Alencar-Silva, Thiago **26**
 Alvarez-Mozos, J. **176**
 Amhar, Fahmi **654**
 Andrew, Bradley **354**
 Apostolov, Aleksander **622**
 Armenakis, Costas **327**
 Arévalo, Vicente **239**
 Asmat, Ali **32**
 Atzberger, Clement **171**
 Aubrecht, Christoph **35, 41**
 Azari, Hamid **47**
 Azizi, Ali **204**

B

Baillarin, Simon **51**
 Balick, Lee **56**
 Balsamo, Gianpaolo **354**
 Baltsavias, Emmanuel **633**
 Balz, Timo **270, 498**
 BaoMing, Zhang **674**
 Barbosa, Ivan **62**
 Baret, Frédéric **354**
 Bargiel, Damian **68**
 Baronti, Stefano **492**
 Bastos, Luisa **228**
 Beccati, Alan **74**
 Beisl, Ulrich **80**
 Belhadj, Z. **6**
 Ben-Dor, Eyal **98, 103**
 Benson, Mike **395**
 Bevilacqua, Vitantonio **86**
 Bignalet-Cazalet, François ... **51**
 Bitenc, Maja **92**
 Bloch, Isabelle **389**
 Boenko, K.A. **348**
 Briese, Christian **193, 360**
 Brook, Anna **98, 103**

C

Cabral, Ana **107**

Calignano, Flaviana **618**
 Calvet, Jean-Christophe **354**
 Camacho, Fernando **354**
 Caprioli, Mauro **86**
 Cardinali, Mauro **492**
 Cardozo, F.S. **523**
 Carlà, Roberto **492**
 Ceccato, Pietro **219**
 Chaabouni-Chouayakh, Houda
 586
 Chang, Eunmi **113**
 Chang, Wen-Chi **117**
 ChaoZhen, Lan **674**
 Chen, Ke **697**
 Chen, Liang-Chien **117, 121**
 Chen, Yen Hung **137**
 Chen, Ying Chih **137**
 Cheng, Chunquan **127**
 Cheng, Hong-Kuei **121**
 Chitu, Zenaïda **486**
 Choi, Minha **132**
 Choi, Y.S. **113**
 Chou, Tien-Yin **137**
 Christopherson, Jon **395**
 Clevers, Jan **143**
 Closson, Damien **389**
 Corte-Real, Luís **233**
 Cortellino, Marco **86**
 Costa, Gilson A O P. **148**
 Crippa, Bruho **154**
 Crosetto, Michele **154**
 Crutchley, Simon **160**
 Cuevas, Maria **154**

D

D'Andrimont, Raphaël **354**
 d'Angelo, Pablo **541, 586**
 D'Elia, Sergio **74**
 da Silva Silvino, Guttemberg . **580**
 Da Silva, R.M. **612**
 Dadhwal, VK **165**
 Dai, Dengxin **669**
 Damadi, S. **16**
 Danilina, Iryna **56**
 Darvishsefat, Ali A. **1**
 Darvishzadeh, Roshanak **171, 199**
 Das, Debashish **424**
 De Baets, Bernard **176**
 De Keyser, Eva **176**
 Debella-Gilo, Misganu **181**
 Deng, Kazhong **127**
 Deng, Xinping **547**
 Devadas, Rakhesh **187**

Dey, Vivek **690**
 Doneus, Michael **193**
 Dorfstetter, Ludwig **420**
 Duzelovic, Hamid **639**

E

E. Baethgen, Walter **219**
 Ebrahimi, Mohsen **199**
 Elmzoughi, A. **6**
 Elvidge, Chris **41**

F

Fabrizi, Roberto **74**
 Fallah Yakhdani, Mohammad **204**
 Feitosa, Raul Q **148**
 Felbermeier, Bernhard **210**
 Fernández-Prieto, Diego **213**
 Ferwerda, Jelle **187**
 Fiorucci, Federica **492**
 Fitzgerald, Glenn **187**
 Folegani, Marco **74**
 Freitas, Sandra **354**

G

Galindo, C. **239**
 Giannini, Marco **86**
 Giarolla, Angelica **219**
 Gil, Artur **41**
 Gillespie, Alan **56**
 Ginzler, Christian **633**
 Gojamanov, Magsad **225**
 González, J. **239**
 Gonçalves, Hernâni **233, 574**
 Gonçalves, Jose **228**
 Gonçalves, José A. **233**
 Grejner-Brzezinska, Dorota .. **243**
 Grubert, Bernd **517**
 Gupta, Sandeep **249**
 Gur, Eran **255**
 Gutjahr, Karlheinz **452**
 Gutu, Andreea **486**
 Gürçay, O. Bora **259**

H

Haapanen, Reija **602**
 Haara, Arto **309**
 Hahn, Andreas **210**
 Han, Lijian **265**
 Hart, Glen **481**
 Hashemi Tangestani, Majid .. **557**
 He, Chu **547, 669**
 He, Xueyan **270**
 Heinonen, Jaakko **309**
 Heipke, Christian **275**

Helmholz, Petra 275
 Hennig, Simon D. 333
 Herrmann, Sylvia 68
 Hodorovsky, Arthur 622
 Hollaus, Markus 35, 281, 287
 Homainejad, Amir Saeed 299
 Hong, Gang 703
 Hsu, Man-Chia 371
 Hu, Tangao 304
 Huang, Guoman 664
 Hur, Y-M. 132
 Hyvönen, Pekka 309
 Höfle, Bernhard 35, 281, 287, 475
 Hölzl, Patrick 293

J

Javidi, Bahram 255
 Jia, Yonghong 314
 JianSheng, Li 674
 Jiao, Xianfeng 317
 Jolin, John 56
 Jones, Simon 187
 Jun, Chulmin 322
 Jung, Jaewook 327

K

Khaldin, Alexander 592
 Khoshelham, Kourosh 92
 Kiefl, Nadine 333
 Kim, G.S. 113
 Kim, G. 322
 Kim, Hyun Woo 132
 Kim, JR. 113
 Kim, Tae Woong 132
 Koch, Barbara 249
 Kokhan, Svitlana 337
 Koppe, Wolfgang 333
 Korpela, Ilkka 342
 Kouzani, Abbas 187
 Kovalevskaya, Nelley M. 348
 Krauss, Thomas 541
 Krauß, Thomas 586
 Kurz, Franz 469
 Kääb, Andreas 181
 Köstl, Mario 35
 Küchler, Meinrad 633

L

Lacaze, Roselyne 354, 441
 Lang, Oliver 644
 Lebegue, Laurent 51
 Lee, I.H. 113
 Lee, Shin-Hui 121
 Lehner, Hubert 360
 Leitloff, Jens 469
 Li, Haitao 680
 Li, Peijun 366
 Li, Shukun 366
 Liao, Mingsheng 270, 498

Lieng, Einar 596
 Lievens, Hans 176
 Lin, Bo-Cheng 371
 Lin, Li-Jer 121
 Lindenbergh, Roderik 92
 Liu, Kang 498
 Liu, Zhenguo 376
 Lohmann, P. 68
 Lyalko, Vadim 622

M

Magalhaes, A. 228
 Maillard, Philippe 26, 463
 Makarau, Aliaksei 383
 Makhmara, Hassan 354, 441
 Marconcini, Mattia 213
 Marie, Weiss 354
 Mastronardi, Giuseppe 86
 Matkan, A.A. 47
 Matkan, Ali Akbar 199
 Matthews, Brett 187
 Maxwell, Travis 690
 Mayer, Walter 23
 McCauley, Ian 187
 McNairn, Heather 317
 Meynberg, Oliver 469
 Mihai, Bogdan 486
 Milenov, Pavel 568
 Milisavljevic, Nada 389
 Mishra, Nidhi 165
 Moe, Donald 395
 Mondini, Alessandro 492
 Monserrat, Oriol 154
 Moos, Sandro 618
 Moraes, E.C. 523
 Mulkova, Monika 401
 Mushkin, A. 56

N

Naeimi, Vahid 354
 Natali, Stefano 74
 Nichol, Janet 407
 Nikolli, Pal 412
 Ning, Xiaogang 417
 Novack, Tessio 148
 Novak, Herman 420

O

Obradovic, Zoran 424
 Oh, Jaehong 243
 Ojo, Adebayo Gbenga 430
 Oladi, DJafar 436
 Oom, Duarte 107

P

Pacholczyk, Philippe 441
 Pais-Barbosa, Joaquim 574
 Palubinskas, Gintautas 383
 Panem, Chantal 51

Pape, Marlon 447
 Pattey, Elizabeth 317
 Pereira, G. 523
 Perez, B. 228
 Perko, Roland 452
 Perry, Eileen 187
 Philippe, Pacholczyk 354
 Pires de Castro, Fabiana Silva 457
 Pires-Luiz, Carlos Henrique .. 463
 Poilvé, Hervé 354
 Popelkova, Renata 401
 Pourali, H. 47
 Pu, Pengxian 680
 Punz, Christian 639

Q

Qing, Xu 674

R

Radosavljevic, Vladan 424
 Raggam, Hannes 452
 Rebhan, Peter 517
 Rego, Luiz F G 148
 Reinartz, Peter 383, 541, 586
 Reinhardt, A. O. 612
 Reize, Tanja 469
 Ristovski, Kosta 424
 Rodrigues, Pedro 41
 Rohrbach, Felix 342
 Roosta, Hasan 557
 Rosenbaum, Dominik 469
 Rottensteiner, Franz 275
 Rudorff, Bernardo Friedrich Theodor
 10, 535
 Rutzinger, Martin 475
 Rüf, Benno 475

S

Sampath, Aparajithan 395
 Sanchez Hernandez, Carolina 481
 Sandric, Ionut 486
 Santarcangelo, Vito 86
 Santurri, Leonardo 492
 Sarker, Muhammad Latifur Rahman
 407
 Savorskiy, Victor 592
 Savulescu, Ionut 486
 Schaeppman, Michael E. 1
 Schardt, Mathias 452
 Schickor, Jens 420
 Schleicher, Daniel C. H. 293
 Schlerf, Martin 171
 Schlund, Michael 644
 Schneider, Tomi 210
 Schunert, Alexander 498
 Sefercik, Umut Gunes 504
 Seiler, Ralf 511
 Seitz, Rudolf 517
 Shakiba, Alireza 47

Shang, Jiali 317
Shimabukuro, Yosio Edemir .. **523**
Silva Centeno, Jorge Antonio .457
Silva, Erivaldo **530**
Silva, F.B. 523
Silva, G.B.S.....523
Silva, Wagner Fernando da ... 10,
535

Sirmacek, Beril **541**
Skidmore, Andrew 171
Smets, Bruno 354
Smirnov, Mikhail 592
Sohn, Gunho 327
Steinnocher, Klaus 35
Studnicka, Nikolaus 193
Su, Xin **547**
Sugawara, Luciana Miura ... 535
Sun, Donglian Lillian..... **552**
Sun, Hong 547
Sun, Yushan 680
Szabó, Zoltán 563
Sörgel, Uwe 68, 498, **504**

T

Tamas, Janos **563**
Tansey, Kevin 354
Tapsall, Brooke 568
Tasdemir, Kadim **568**
Taveira-Pinto, Francisco 574
Tayebi, Mohammad Hasan ... **557**
Teo, Tee-Ann 117
Teodoro, Ana **574**
Teotia, Harendra S. **580**
Theriault, Livia 606
Tian, Jiaojiao **586**
Tishchenko, Yuriy **592**
Tong, Hengjian 690
Toth, Charles 243

Trier, Øivind Due **596**
Trigo, Isabel 354
Troycke, Armin 517
Tseng, Yi-Hsing 628
Tsubo, Mitsuru 265
Tsunekawa, Atsushi 265
Tuominen, Sakari **602**

U

Ulbricht, Klaus A..... 580
Ulz, Martin 420
Ussyshkin, Valerie **606**

V

van Waarden, Pieter 92
Vasconcelos, Maria 107
Veloso-Gomes, Fernando ... 574
Verhoest, Niko 176
Vernieuwe, Hilde 176
Veronez, Maurício Roberto ... **612**
Vetter, Michael **475**
Vezzetti, Enrico **618**
Vittuari, Luca 74
Vohland, Michael **447**
von Poncét, Felicitas 644
Vostokov, Anatoliy **622**
Vucetic, Slobodan 424

W

Wagner, Wolfgang 35, 354
Wang, Cheng-Kai **628**
Wang, Huili 703
Waser, Lars **633**
Watt, Michelle 187
Wegner, Jan Dirk 498
Wehr, Aloysius **639**
Weihing, Diana **644**
Weinacker, Holger 249

Widlowski, Jean-Luc **648**
Wijanarto, Antonius **654**
Wittmann, G. 612
Wu, Jun 669

X

Xiao, Moyan 314
Xie, Mingxia 697
Xiong, Zhen 658
Xu, Haiqing 366

Y

Yang, Jinghui **680**
Yang, Shucheng **664**
Yang, Wen 547, **669**
Yang, Zhou **674**
Yeh, Mei-Ling 137
You, Rey-Jer 371
Yu, Yunyue 552

Z

Zagar, Bernhard G. 293
Zalevsky, Zeev 255
Zdimal, Vaclav **687**
Zhang, Aining 703
Zhang, Baoming **697**
Zhang, Hongwei 697
Zhang, Jinshui 304
Zhang, Jixian 127, 680
Zhang, Li 127
Zhang, Lu 270
Zhang, Yonghong 417
Zhang, Yun **658, 690**
Zhao, Zheng 664
Zhou, Fuqun **703**
Zhou, Yang 697
Zhu, Wenquan 304
Ziskin, Daniel 41

Keyword Index

Symbols

3D Analysis 586
3D Geometric Modelling 86
3D Scanner 618

A

Abstraction 690
Accuracy 504
Accuracy Assessment 430
AdaBoost 547
Adjustment 117
Advancement 690
Aerial 121, 193, 628, 633
aerial photograph 309
aerial photography 401
Agricultural Crops 337
Agriculture 23, 317, 563, 568, 687
Airborne laser scanning 475
Airborne LIDAR 281
Albania 412
Algorithms 26, 143, 249, 255, 265,
424, 639
AMSR-E 132
Analysis . 160, 193, 317, 333, 424,
504, 644
Anomaly Detection 103
Application 199, 265
Archaeology 160, 193
Artificial Neural Networks ... 612
ASTER 557
Atmosphere 80, 424
Atmospheric Effects 6
Automatic registration 98
Automation 233, 275, 420
AVNIR-2 407

B

Bi-spectral 47
Bioenvironmental Potentials .. 436
biomass burning 523
Biomass Estimation 407
Bore Sight 103
Brightness Temperature 47
Broadband albedo 447
Building 121
Building models 327
building segments 475
Buildings 586
Bundle 395
burnt sugarcane 10

C

CAD 86
Calibration 80, 342, 360

Camera 80, 395
Canopy Radiative Transfer ... 648
Carbon emission 113
cartographic feature 530
Cartography 23
Cartosat-1 541
CCD/CBERS 535
Change 644
Change Detection . 121, 137, 213,
228, 389, 511, 568, 586,
644, 703
Change detection 98
change detection 309, 697
Classification 35, 62, 68, 107, 113,
412, 430, 452, 481, 517,
568, 596, 628, 633, 669,
690
classification 475
Classification System 412
Cloud Classification 47
Coast 92, 574
Combination 193, 389
Comparison 504
Content-based 348
Control Network 658
Correction 80, 117, 233
Correlation 233
Corridor Based Data 16
Cost 622
Crop 317
Cultural Heritage 160

D

Data 606
Data Acquisition 32
Data Fusion 371, 492
Data fusion 327
Data Mining 424, 622
Data mining 703
Data Structures 322
Database 322
Decimeter waves 592
Decision Support 703
deep coal mining 401
Deformation 154
DEM 504, 664
DEM/DTM ... 92, 228, 239, 287,
333, 420, 452, 541, 628,
639
Detecting Moving object 16
Detection 154, 314, 541
Development 23, 517
Differential 376

Digital 420
Digital Image 299
Digital image 327
digital image processing 530
Digital Surface Model 658
Digitisation 606
Direct 228
Displacement measurement .. 181
DSM 586
Dual pushbroom line-based hyper-
spectral sensors 103

E

Ecology 143
Ecosystem 41, 68, 633
Engineering 255
Environment . 348, 354, 420, 424,
441
environmental 10
Environmental impact 557
ERDAS 580
Estimation 171, 265, 504
Evaluation 204
expansion of sugarcane 535
Extraction 239, 249, 259, 457, 517

F

Facial morphology 618
Farming 568
Feature Extraction 371
fire radiative power 523
First derivative 1
Fisher criterion function 697
Flood 552
Forestry .. 35, 210, 342, 420, 452,
517, 602, 606, 633
Framework Data 481
Full-waveform 193
Fusion 204, 314, 606, 639
Fuzzy Logic 148

G

Generation 504, 628
Geocoding 127, 154
Geographical Information system
580
Geography 23
Geology 259, 622
Geometric 395
Geometry 239
Geomorphology 287, 574
Georeferencing ... 117, 228, 233,
243, 469
GIS 23, 219, 275, 563, 568

GIS and Zoning	436	Interpolation	463	Model Intercomparison	648
Glacier	181	Intpretation	148	Modelling 74, 117, 143, 322, 342,	
Global	74, 354	invasion of the pipelines corridor		486, 511, 541, 568, 606,	
Global-Environmental-Databases		16		633, 639	
348		Inventory	602	MODIS	132, 447, 552
GLOBCOVER	523	IRS	204	Monitoring 41, 137, 199, 348, 354,	
GPS/INS	23			441, 469, 568, 644	
Grand based Remote sensing ..	16	K		Moon DEM	674
Ground Deformation	376	k-NN	309	Moon Image	674
Guinea-Bissau	107	Knowledge Base	26	Mosaic	51
		Kompsat II images	113	MRF	547
H		Korea	132	Multi-level segmentation	366
Harmonization	412	Kusalan	436	Multi-sensors airborne and space-	
Hazards	35, 92, 137			borne fusion	98
High Resolution	51, 148, 633	L		Multifrequency	317
High resolution . 26, 62, 107, 255,		Land	354, 441	Multiresolution	74
314, 348, 452, 563, 690		Land Cover 62, 74, 107, 148, 213,		Multisensor	204, 441, 639
High Resolution Satellite Image		401, 412, 481, 511, 517,		Multispectral ... 56, 80, 213, 259,	
658		568, 654, 669, 687, 690,		342, 441	
High-resolution images	530	703		multispectral image fusion ...	383
High-resolution satellite images		land cover	523	Multispectral Images	492
243		Land cover classification	366	Multispectral Quickbird imagery,	
High-yielding variety	1	Land Resources Management	580	596	
History	687	Land Use .. 68, 74, 148, 389, 430,		Multitemporal .. 68, 74, 148, 213,	
Huambo	107	481, 563, 687		463, 511, 633	
Human Settlement	687	Land use	523	multitemporal analysis	10
Hydrologic budget	463	Landsat	199, 622		
Hydrological Modelling	165	Landsat TM	430, 447	N	
Hyper spectral . 56, 143, 171, 213,		Landscape	160	NDVI	132, 219
563, 654		landscape changes	401	Neural	574
hyperspectral	187	Landslide	492	NigeriaSat-1	430
Hyperspectral imagery	243	Landslides	137, 486	nitrogen	187
		Landuse Landcover Change ..	165	Normalised cross-correlation .	181
I		Laser Scanning	299		
Identification	457, 486, 574	Laser scanning .. 35, 92, 193, 293,		O	
IKONOS	62, 314, 574	322, 360		Object	293, 486
Ikonos	225, 492	Level of Detail	674	Object Orient	47
Image ... 121, 225, 233, 255, 457,		LIDAR .. 121, 160, 193, 249, 287,		object-based change detection	475
469, 690		342, 360, 602, 606, 628,		Object-Based Image Analysis	281
Image Classification	337	639		One-Class SVM	366
image classification	547	Linear regression	176	online monitoring	16
image from NOAA satellite ..	612	Linear Targets Prior	547	Ontology	481
Image Fusion	680	Lunar exploration	674	Open Source GIS	281
Image matching	181, 243			Optical	51, 255, 259
Image Positioning	127	M		Optical Remote Sensing	648
Image Processing .. 304, 407, 580		Mapping ... 35, 92, 160, 259, 420,		Optical Stereo Data	586
Image processing	86	452, 622, 654		Ortho-Image	299
Image Retrieval	417	mapping	535	Orthoimage	23, 51, 420
Image Threshold	697	Marine	41	Orthophototransformation	225
Imagery	239, 669	Matching	228, 233	Orthorectification	333, 469
Imaging Equation	127	mathematical morphology	530	Ostrava-Karviná Mining District,	
Impact Analysis	41	Mathematics	233, 457	401	
Impervious surface	366	Measurement	56, 293, 606		
Industrial	293	Method	457	P	
Infrared	56, 517	Microwave radiometric systems		Pakistan	32
InSAR	6	592		Pan-sharpening	492
Interest Point Matching	658	MLP neural network	557	pan-sharpening	383
Interferograms	6	Mobile	92	Pansharpening	680
Interferometry	376	Model	171, 348	parallax	664

Parameters	354
Parcels	304
Passive	265
Passive Microwave Sensors ..	132
Pattern	47, 249, 293, 469, 486
Permanent Scatterer	376
phase congruency	383
Photogrammetry ..	127, 137, 228, 314, 395, 420, 452
Photography	225, 602
Pixel Level	680
Polarization	669
Precipitation	199
Precision	563
precision agriculture	187
Processing	255, 441
Production	354
Programming	457
Protected Area	436
PSI	498
Pushbroom	342
Pushbroom camera	243
Q	
Quality	92
Quality Assessment	492
Quality Assurance	648
Quality Control	275
QuickBird	225
R	
Radar	68, 265, 270, 498
Radargrammetry	270
RADARSAT	669
Radiometric	80, 360
Radiometry	56, 342, 360
Ratio Response	547
Real-Time	354
Recognition ...	293, 469, 486, 574
Reconstruction	249
Recording	160
Rectification	395
rectification	309
Red edge position	1
Regional Merging	304
Regional Planning	580
Registration	239, 327, 371
Regression	552
Remote Sensing	32, 154, 165, 219, 337, 436, 580, 592, 680
Remote sensing	187
remote sensing	530
remote sensing image	697
Remote Sensing Imagery	417
Remotely Sensed Data	622
Research	703
Resolution	225, 255
Resources	622
Retrieval.	255, 287, 348, 424
Rice	1
Robust Least Squares	371
Rockglacier	181
Rockslide	181
Roughness	287
Russian segment of International Space Station	592
S	
Salt plug	557
SAR	127, 176, 270, 317, 333, 376, 389, 452, 498, 504, 547, 644, 669
SAR image	664
Satellite ..	41, 117, 154, 213, 225, 259, 457
satellite monitoring	10, 535
Scaling and image rotation ...	98
Scene	389
Scientific programs	592
Segmentation ...	26, 47, 293, 309, 486, 517, 596, 602
Semi-Arid	580
Sensor	51
Sensor Model	127
sensor simulation	447
Sequences	469
Services	354
Shadow Map	103
Shape analysis	618
Side-Looking Radar	127
Signal delay	6
Similarity assessment	327
Simulation	322, 498
Small satellite	592
Snow Ice	265
Soft tissue shifts	618
Software	690
Soil	265, 441, 654
Soil Moisture	132
Soil moisture retrieval	176
Soil surface roughness	176
Soybean (Glycine Max, L. Merr) 219	
Spatial	26, 204, 424
spatial consistency assessment	383
Spectral	171, 199, 204, 517
Spectral reflectance	1
split window	612
SPOT Imagery	580
SPOT XS	430
SPOT-5	407
Standardization	412
Statistics	511
Stereo	270
Stereo 3-D Map	103
stereo-mapping	664
Stereoscopic	333
stereoscopic image pair	664
Sub-pixel	181
Supervised Classification ...	304
Surface	56, 287
surface temperature	612
Surveying and Mapping	32
Sustainable	563
System	74
T	
Temporal	389, 424
Tensor Voting	371
TerraSAR-X	270, 498
Terrestrial	193
Terrorism	32
Texture	26, 47, 62
Texture measurement	407
Theory	314
Thermal	56, 259
Three-dimensional	249, 287, 293, 322
TM/Landsat	535
topographic map	664
Tracking	469
Transformation	299
Tree	552
two-dimension histogram ...	697
U	
unburnt sugarcane	10
Uncertainty assessment	176
Understanding	160
Update map	225
Updating	275, 327
updating	530
Urban	148, 541, 606
urban areas	475
urban vegetation	596
User Requirements	210
V	
validation	187
Variable Infiltration Capacity Model	165
Vegetation ..	26, 35, 62, 143, 171, 199, 441, 563, 654, 703
vegetation cover fraction	523
Vegetation Mapping	281
Verification	275
Very high resolution imagery	366
Visualization	137, 504, 674
W	
Water Balance	219
Water fraction	552
Water index	463
Water level monitoring	463
Watershed segmentation	304
Web based	74
Web Service	417
Weight-based topological map- matching algorithm (tMM)	98
Wetlands	62
wireless sensor network	187